ISBN 978-4-909106124 C3051

GEOMATE Proceedings

THE 15th INTERNATIONAL CONFERENCE ON

Geotechnique, Construction Materials & Environment

11-13 November 2025, Kyoto Research Park

Kyoto, Japan

Edited By

Prof. Zakaria Hossain

Conference Chairman

PROCEEDINGS OF THE FIFTEENTH INTERNATIONAL CONFERENCE – GEOMATE 2025
GEOTECHNIQUE, CONSTRUCTION MATERIALS AND ENVIRONMENT, KYOTO, JAPAN
11-13 NOVEMBER, 2025

Geotechnique, Construction Materials and Environment

Edited by

Prof. Zakaria Hossain
Department of Environmental Science and Technology
Graduate School of Bioresources
Mie University, Japan

THE GEOMATE INTERNATIONAL SOCIETY

Copyright @ 2025 by The GEOMATE International Society

All rights reserved. In principle, no part of this publication or the information contained herein may be reproduced in any form or by any means, translated in any language, stored in any database or retrieval system, or transmitted in any form or by any means without prior permission in writing from the publisher.

Disclaimer: The editors and the publisher have tried their best effort to ensure the integrity and the quality of this publication and information herein. However, they give no warranty of any kind, expressed or implied with regard to the material contained in this book, and will not be liable in any event for the consequences of its use.

Published by:
The GEOMATE International Society
Tsu city, Mie, Japan
E-mail: society@geomate.org
http://www.geomate.org/

ISBN Number: 978-4-909106124 C3051

Table of Contents

	Preface	iv
	Organization	xix
ID	***Keynote Papers***	**1**
g15k1	BRITTLE BEHAVIOR IN SOIL, TAILINGS AND ROCK MASS: AN OVERVIEW John Victor Smith	**2**
g15k2	ADVANCED TECHNOLOGIES FOR EXISTING PILE EXTRACTION AND ASSOCIATED BOREHOLE BACKFILLING Shinya Inazumi	**10**
	Technical Papers	**17**
ID	***Geotechnique***	**18**
g15103	GEOTECHNICAL AND MICROSTRUCTURAL ASSESSMENT OF RIVER SLUDGE STABILIZED WITH SUSTAINABLE ADDITIVE SYNERGY Md Yachin Islam and Zakaria Hossain	**19**
g15111	RELIABILITY ANALYSIS OF DAMPALIT MEGA DIKE USING MONTE CARLO SIMULATION AGAINST SLIDING FAILURE Isaiah Sam Bartolome and Albert Griño Jr	**26**
g15122	DEBRIS FLOW CAUSED BY HEAVY RAINFALL IN NAGISO-TOWN IN NAGANO PREFECTURE IN JULY 2014 Naomasa Honda	**32**
g15127	EFFECT OF RICE HUSK ASH AS A PARTIAL CEMENT REPLACEMENT ON STRENGTH OF SUBBASE Chotikan Ratchakrom, Pisut Rodvinij, Sattaya Chaiwithee and Pitiwat Wattanachai	**38**
g15129	INVESTIGATING THE SOIL ARCHING PHENOMENON IN MICROPILES USING NUMERICAL ANALYSIS Muhammad Adeel Mazhar, Adnan Anwar Malik, Hung Manh Ho and Umair Ali	**44**
g15130	APPLICATION OF MULTI-CHANNEL ANALYSIS OF SURFACE WAVES IN PROBABILISTIC SEISMIC HAZARD ASSESSMENT: A CASE STUDY IN ISLAMABAD, NORTHERN PAKISTAN Muhammad Qasim Mirza, Ghulam Mohyuddin Sohail, Adnan Anwar Malik, Talha Qadri, Faiqa Shahid, Fatima Ijaz and Aneeza Munir	**49**
g15136	EVALUATION OF FLASH FLOOD SUSCEPTIBILITY IN RELATION TO LAND USE CHANGES IN CHIANG RAI, THAILAND Zhaolong Gu, Daisuke Komori and Thapthai Chaithong	**55**

g15138	THE STUDY OF HELICAL PILE BEHAVIOR UNDER COMPRESSION FORCE IN KHON KAEN LOESS Natchaphon Noiphang, Ratamanee Nuntasarn and Jitrakon Prasomsri	61
g15140	EFFECTS OF FREEZE-THAW HISTORY ON PILE PULL-OUT RESISTANCE Yusaku Fujita, Dai Nakamura, Kenta Nakai, Takanori Kadota and Yuki Minabe	67
g15143	SLOPE STABILITY OF SOIL-ROCK MIXTURE: A CASE STUDY ON LIMESTONE FORMATION AND HIGH RAINFALL AREA Arief Rachmansyah, Adefi Abioga Tiswa and Fajar Rahmanto	73
g15145	BACK-CALCULATED PARAMETERS AND THEIR ATTENUATION COEFFICIENTS FOR PILE DESIGN IN SEDIMENTARY ROCK Ketkaewngoen Mahakhotchasenichai, Kuo Chieh Chao and Shinya Inazumi	81
g15147	INTEGRATION OF SOIL RESISTIVITY AND BOREHOLE DATA TO EVALUATE GEOMATERIALS AND N_{60}-VALUE USING CLUSTERING ANALYSIS Ratchadakorn Chumkhiao, Sukit Yindeesuk, Kuo Chieh Chao and Shinya Inazumi	86
g15148	EVALUATION OF CHEMICAL GROUTING IN HETEROGENEOUS SOILS BY INTEGRATING FEM ANALYSIS AND AI MODELS Khin Nyein Chan Kyaw, Toshiyuki Motohashi, Shigeo Sasahara and Shinya Inazumi	92
g15150	MOVING PARTICLE SIMULATION VALIDATION AND APPLICATION TO CONCRETE FLOW IN CAST-IN-PLACE PILES Ayumi Morota and Shinya Inazumi	98
g15151	COMPARATIVE ANALYSIS OF SOIL RESISTIVITY PREDICTION USING REGRESSION MODELS AND POLYNOMIAL NEURAL NETWORK Kornkanok Sangprasat, Avirut Puttiwongrak and Shinya Inazumi	102
g15153	THE BEACHROCK DISTRIBUTION, CHARACTERISTICS AND FORMATION MECHANISMS IN TROPICAL ASIA: A SYSTEMATIC REVIEW Rahubadda Kankanamge Hiroshima Surangani, Anjula Buddhika Nayomi Dassanayake, Chulantha Lakmal Jayawardena, Niki Evelpidou and Satoru Kawasaki	108
g15154	BACTERIAL DYNAMICS BY MICROBIALLY INDUCED CALCIUM CARBONATE PRECIPITATION (MICP) UNDER MICROGRAVITY CONDITION FOR EXTRATERRESTRIAL BIOCEMENTATION ENGINEERING Yuru Chen, Tomoya Hamada, Chikara Takano, Kazunori Nakashima, Satoru Kawasaki	114
g15155	EVALUATION OF SHEAR PROPERTIES AT CONSTRUCTION BOUNDARIES FOR LATTICE-SHAPED GROUND IMPROVEMENT Miu Kanagawa, Kouta Kanno, Kenji Niwa and Shinya Inazumi	120
g15157	UNRAVELING THE MECHANISMS OF LIQUEFACTION-INDUCED SOIL EJECTA: A RULE-BASED APPROACH Emerzon S. Torres and Jonathan R. Dungca	126
g15159	SOME FEATURES OF EARTHQUAKES DISTRIBUTION IN TURKMENISTAN Valeriy Burmin and Goharik Petrosyan	132
g15163	CORRELATION BETWEEN STANDARD PENETRATION TEST AND CONE PENETRATION TEST FOR LIQUEFACTION ASSESSMENT Nami Nitta, Misko Cubrinovski and Shinya Inazumi	138
g15165	STRENGTH OF BAGASSE ASH GEOPOLYMER-STABILIZED RECYCLED MATERIALS FOR PAVEMENTS BASE: MLR AND PATH ANALYSIS Sattawat Chatchawan, Ratamanee Nuntasarn and Supakorn Tirapat	144
g15167	EFFECT OF SOIL CLODS INCLUSION ON THE END BEARING CAPACITY OF A PILE WITH AN ENLARGED BASE Asuka Takahashi, Naoaki Suemasa, Yoshiaki Tsukada, Tadashi Maejima and Jemy Chua	150
g15174	STUDY ON IMPACT FORCE OF GRANULAR FLOW ACTING ON RETAINING WALL Makoto Kobayashi, Akinobu Ogasawara, Naoto Naito and Tatsuya Matsuda	156

g15178	EXPERIMENTAL STUDY ON SWELLING CHARACTERISTICS OF BENTONITE BUFFER MATERIAL CONSIDERING VARIOUS INITIAL CONDITIONS Kira Iida, Shin-ichi Kanazawa, Masanori Kohno, Zihao Liu and Osamu Yoshino	161
g15181	EFFECT OF LONG-TIME SEEPAGE ON MULTI-LAYERED GROUND Yixuan Li, Yamato Kadoi and Mari Sato	167
g15182	POROSITY ASSESSMENT IN ONE-DIMENSIONAL PERMEATION GROUTING USING SUSPENSION-TYPE GROUT SOLUTION Jemy C. Chua, Naoaki Suemasa, Takamitsu Sasaki and Koichi Nagao	172
g15184	NUMERICAL SIMULATION OF SCOURING AROUND CYLINDRICAL BRIDGE PIERS UNDER STEADY FLOW USING REEF3D Shu Tsuyumine, Tatsuya Matsuda and Naoto Naito	178
g15185	PRECISION-CONTROLLED BACKFILLING METHODOLOGY FOR ENHANCING POSITIONAL ACCURACY IN FOUNDATION ELEMENT REPLACEMENT Haruka Kiyotomo, Yuji Taya, Masahiro Ueda, Tomio Tsuchiya and Shinya Inazumi	183
g15187	A STUDY ON THE EFFECT OF INJECTION FLOW RATE ON GELATION TIME IN CHEMICAL GROUTING METHOD Midori Suzuki, Jemy C. Chua, Naoaki Suemasa and Takamitsu Sasaki	187
g15188	INFLUENCE OF SEEPAGE AND SEISMIC DISASTERS ON THE FAILURE BEHAVIOR OF LARGE-SCALE EMBANKMENTS Satoko Io, Kazuya Itoh and Naoaki Suemasa	193
g15189	VISUALIZATION OF PORE WATER FLOW IN GRANULAR MEDIA USING CYLINDRICAL TRANSPARENT PARTICLES Shingo Hamano, Tatsuya Matsuda and Naoto Naito	199
g15190	GROUND IMPROVEMENT OPTIMIZATION USING DYNAMIC NUMERICAL ANALYSIS IN THE DEVELOPMENT OF THE BANYUWANGI AIRPORT IN INDONESIA Christopher Tanjung, Andhika Sahadewa, Pebri Herry, Reza Ismaniar and Aris Wibowo	204
g15195	EVALUATING THE VALIDITY OF MULTI-STAGE DIRECT SHEAR TESTING ACROSS DENSITY AND FINE CONTENT VARIATIONS IN SAND–CLAY MIXTURES María José Toledo Arcic and Jens Engel	210
g15200	UNCONFINED COMPRESSIVE STRENGTH OF RIVER-DREDGED SOIL STABILIZED WITH ZEOLITE-BASED GEOPOLYMER Jonathan R. Dungca, Roberto Gabriel A. Bas, Chris Anthony C. Elhig and Dana Isabelle P. Villano	216
g15203	A STUDY ON THE METHOD OF ESTIMATING THE BEARING CAPACITY OF TAPERED PILES Takaki Asano, Naoaki Suemasa, Tsuyoshi Tanaka, Satoshi Shingai and Yasutaka Sakamoto	222
g15205	STUDY ON INTERACTION OF PULL-OUT TESTING BETWEEN TIN TAILING AND REINFORCEMENT FOR GEOSYNTHETIC REINFORCED SOIL ABUTMENT Wijit Itthiwongkul, Peet Homchuen, Suphamat Chaichana, Tanapon Khunin and Zhen Zhang	228
g15209	SEISMIC BEHAVIOR OF STEEL STRIP REINFORCED SOIL WALLS WITH HIGH GROUNDWATER LEVEL Akinobu Ogasawara, Makoto Kobayashi and Kento Mori	234
g15210	THREE-DIMENSIONAL SIMULATION ANALYSIS OF OPEN-ENDED STEEL PIPE PILE BY USING FINITE ELEMENT METHOD Kiyoka Kono, Koji Watanabe, Shihchun Lin and Shuichi Kamei	239
g15212	DYNAMIC RESPONSE OF UNDISTURBED SOFT CLAY SOIL WITH SOIL DISTURBANCE EFFECT UNDER CYCLIC LOADING Angelo B. Edora, Taiju Ichizono and Kentaro Nakai	244
g15213	ALTERNATIVE APPROACH FOR SOIL IMPROVEMENT USING HYDRAULIC CEMENT COMBINATION WITH STEEL SLAG AND BIOCHAR Nattapas Khumsuprom, Supakij Nontananandh, Apiniti Jotisankasa, Susit Chaiprakaikeow and Shinya Inazumi	250

g15214	INVESTIGATION ON DISPERSIVE CHARACTERISTICS OF SOILS EXCAVATED FROM FLOOD RETENTION POND Supakij Nontananandh, Kittipong Tongphet, Susit Chaiprakaikeow, Patipan Thaimthong, Yuki Fuka and Shinya Inazumi	256
g15235	RESISTIVITY PATTERNS IN LOOSE BEDROCK USING DRONE-BASED ELECTROMAGNETIC EXPLORATION METHOD Hiroaki Hoshino, Atsuko Nonomura, Haruki Ojyuku, Shuichi Hasegawa and Akira Jomori	262
g15236	IMAGE-BASED ESTIMATION OF SOIL PARTICLE SIZE AS A SUPPLEMENT TO SIEVE ANALYSIS Jose Manuel U. Subido, Erica Elice S. Uy and Joenel G. Galupino	268
g15239	GEOTECHNICAL INVESTIGATION OF COMPACTION EFFORT, MOISTURE CONTENT, AND SOIL TYPE ON MAXIMUM DRY DENSITY IN PATHUM THANI, THAILAND Pattaraporn Nueasri and Rattanachot Thongpong	274
g15240	CENTRIFUGE MODEL TEST AND NUMERICAL ANALYSIS ON EVALUATION OF VERTICAL BEARING CHARACTERISTICS FOR SOIL-CEMENT COMPOSITE PILE Shohei Koga, Koji Watanabe and Nobuaki Tsuchiya	280
g15250	BEARING CAPACITY AND BEHAVIOUR OF SHALLOW FOUNDATIONS SUBJECTED TO CYCLIC LOADINGS: A STUDY IN 1G Fabien Szymkiewicz, Lamis Makki, Philippe Reiffsteck, Taisuke Sanagawa and Hidetoshi Nishioka	286
g15252	LANDFILL MINING IN BRAZIL: SOME CHALLENGING ASPECTS FOR APPLICATION Thiago Villas Bôas Zanon and Maria Eugênia Gimenez Boscov	292
g15256	IMPROVING THE PROPERTIES OF MATERIAL USED IN BUILDING CLAY HOUSES WITH CEMENT Nathiya Jaokaenkaew and Pongsakorn Punrattanasin	298
g15259	EFFECT OF ANTECEDENT RAINFALL ON POER WATER PRESSURE DISTRIBUTION CHARACTERISTICS IN RESIDUAL SOIL UNDER TROPICAL RAINFALL Mohamed Elbyhagi Elfadil	304
g15266	GEOTECHNICAL PROPERTIES OF RECYCLED GLASS STABILIZED WITH CEMENT Sereyroath Chea, Arul Arulrajah, Annan Zhou, Suksun Horpibulsuk and Kanagesperan Verumandy	312
g15270	PRACTICAL APPLICATION OF GEOLOGICAL STRENGTH INDEX FOR EXCAVATABILITY ASSESSMENT John Victor Smith	317
g15274	A CASE STUDY OF SLOPE FAILURE POTENTIAL MAPPING BASED ON WATERSHED UNIT IN THE NOTO PENINSULA DISTRICT Suguru Kaneko and Masanori Kohno	323
g15275	SSESSING LIQUEFACTION RISK AT LHOKSEUMAWE BEACH: IMPACT OF THE 2004 ANDAMAN AND 2016 PIDIE JAYA EARTHQUAKES Abdul Jalil, Lindung Zalbuin Mase and Yovi Chandra	329
g15286	NONLINEAR INERTIAL EFFECTS IN CAISSON FOUNDATIONS WITH SUPERSTRUCTURES: AN EXPERIMENTAL STUDY UNDER VARIABLE-AMPLITUDE SEISMIC LOADING Zain Bin Mazhar, Faruk Md Omar and Masato Saitoh	334
g15287	AN APPLICATION OF ELECTRICAL RESISTIVITY CONFIGURATION AS ELECTRO-OSMOSIS FOR PREFABRICATED VERTICAL DRAINAGE (PVD) ENHANCEMENT USING SANDBOX EXPERIMENT Khin Phyu Sin, Thanapong Lamphoei and Avirut Puttiwongrak	341
g15293	EVALUATION OF VISCOSITY REDUCTION USING ADVANCED AGENT IN HIGH-PRESSURED GROUT INJECTION FOR BANGKOK SOILS Sai Wunna Kyaw Khaung, Morris I-Min Wang, Ricky K. N. Wong, Yasuharu Nakanishi, Koike Shoko and Matsuda Takato	349
g15300	EXCAVATION TESTS ON ALUMINUM ROD MODEL GROUND TO SIMULATE GROUND HEAVE Moe Yagawa, Hidetoshi Nishioka, Shinji Konishi and Satoshi Sakata	357

g15302	TWO-DIMENSIONAL MODEL EXPERIMENTS ON THE SEISMIC BEHAVIOUR OF THE HEAD-FIXED DOUBLE SHEET PILE TEMPORARY EARTH RETAINING WALL METHOD Akihiro Kikuchi, Hidetoshi Nishioka, Ayaka Nasu, Michitaka Okamoto and Hideki Nagatani	363
g15305	TWO-DIMENSIONAL MODEL EXPERIMENTS ON SEISMIC RESISTANCE OF SPREAD FOUNDATION DAMAGED BY LOCAL SCOURING Yuki Yamakuri, Tomohito Ishii and Hidetoshi Nishioka	369
g15313	EROSION CONTROL EFFECT OF VEGETATION WORKS BY PHALARIS ARUNDINACEA L. AGAINST SURFACE RUNOFF Enkhzaya Batbayar, Dai Nakamura, Keishin Tsutsumi, Yuichiro Murakami, Eiji Tateyama, Yuki Minabe and Takayuki Kawaguchi	375
g15317	ENHANCING MITIGATION STRATEGIES FOR RAINFALL INDUCED ROADSIDE LANDSLIDES IN NEW ZEALAND Roohollah Kalatehjari, Lokesh Vemuri and Rajitha Sachinthaka	380
g15326	RELATIONSHIP BETWEEN PUBLIC SPACE AND PEDESTRIAN BRIDGES IN SUBURBAN RESIDENTIAL AREAS Ryunosuke Komatsu and Kazunari Tanaka	386
g15327	METHOD ON THE PREDICTION ABOUT FLOW LINES IN WALKING SPACES Ryuga Toda and Kazunari Tanaka	390
g15346	ARTIFICIAL INTELLIGENCE-BASED EARLY WARNING SYSTEMS FOR RIVERBANK EROSION IN THE MEKONG DELTA REGION Thang Ngoc Nguyen, Phong Vu Phuong Le and Tru Thi Tu	394
g15350	ECOFRIENDLY SLOPE STABILIZATION: FIELD APPLICATION OF BIOCEMENTATION WITH NATIVE BACTERIA AND LOW‐COST MATERIALS Azizul Moqsud	399
g15354	FINITE ELEMENT ANALYSES OF MEASURES TO MITIGATE ROCK SPALLING HAZARDS BY ASSESSING TUNNEL FACE DISPLACEMENT Rintarou Doi, Naotaka Kikkawa and Kazuya Itoh	404
g15358	THE DEVELOPMENT OF SUBSURFACE UTILITY ENGINEERING PRACTICES IN THAILAND Sitthiphat Eua-apiwatch, Rungroj Arjwech, Kanisorn Klamsuk, Anirut Nitas and Sirichai Pethrung	410
g15365	ANOMALY DETECTION FOR SLOPE EXCAVATION WORK USING BACKGROUND SUBTRACTION AND OPTICAL FLOW Masoho Ide, Nobutaka Hiraoka and Kazuya Itoh	418
g15369	SLOPE STABILITY STUDIES BASED ON DIFFERENT MATERIALS AND CONSTRUCTION METHODS Satoe Suzuki and Shin-ichi Kanazawa	424
g15371	EFFECT OF DEM PARAMETERS ON DEFORMATION BEHAVIOR OF ROCKFALL PROTECTION WALLS SUBJECTED TO ROCK SLOPE FAILURE Ayumu Takehara, Naoto Naito, Tatsuya Matsuda, Katsuhito Agui, Yuji Ushiwatari, Kazumichi Shimakura and Akinori Nakao	430
g15392	LABORATORY INVESTIGATION OF THE IMPACT OF RISING SOIL WATER CONTENT ON LIQUIDITY INDEX AND SLOPE INSTABILITY Nofrizal, Fauzan, Abdul Hakam, Bambang Istijono and Andriani	436
g15407	DESIGN AND CONSTRUCTION OF PRECAST BOX CULVERTS (DRAINAGE CHANNEL) IN AN URBAN ENVIRONMENT: A CASE STUDY OF KANIE TOWN IN JAPAN Md. Aminul Islam and Zakaria Hossain	442
ID	***Construction Materials***	456

g15101	GREENER OPPORTUNITIES: AN EXPERIMENTAL INVESTIGATION INTO TRANSFORMING BUILDING MATERIALS THROUGH WASTE-BASED TECHNOLOGIES Muhammad Ali Fardoush Siddquy and Zakaria Hossain	457
g15102	APPLICATION OF SEASHELL POWDER ISOLATELY AND COMBINED WITH RICE HUSK ASH IN CONCRETE AS CEMENT REPLACEMENT MATERIALS Md Soybur Rahman and Zakaria Hossain	463
g15104	SYNERGISTIC EFFECTS OF AMORPHOUS SILICA ON ADMIXTURE DEMAND, STRENGTH DEVELOPMENT, AND CO2 MITIGATION IN MODIFIED LOW-CARBON CONCRETE Alex Otieno Owino, Noma Tamaki and Zakaria Hossain	469
g15106	WATER ABSORPTION CHARACTERISTICS OF EPS-BASED LIGHTWEIGHT CONCRETE: EFFECTS OF FLY ASH COATING AND CEMENT REPLACEMENT Andi Prasetiyo Wibowo	481
g15114	USING NICKEL SLAG AND GOLD TAILINGS AS PARTIAL SUBSTITUTES IN CONCRETE FOR SUSTAINABLE CONSTRUCTION Lisa Oksri-Nelfia, Julien Meret, Ouali Amiri and Yohans Sunarno	487
g15215	HYDROGEOLOGICAL INTERPRETATION USING GEOELECTRICAL AND HYDROCHEMICAL DATA IN CIMANIS WATERSHED, KUNINGAN, WEST JAVA, INDONESIA Boy Yoseph CSS Syah Alam, Hadi Hidayat and Deden Zaenudin	494
g15131	WATER HYACINTH FIBER FOR LIMITED-LIFE GEOSYNTHETIC GEONET AS SUBGRADE REINFORCEMENT OF RURAL ROADS Mary Ann Adajar, Patricia Gwenn Ang, Judith Dungca, Julia Dominic Espinola and Nicole Gabrielle Tan	503
g15149	DEVELOPMENT OF SOLIDIFIED CULTIVATING SOIL BLENDED WITH WASTE WOODY BIOMASS PREPARED BY THE EICP METHOD Daiki Kawamura and Satoru Kawasaki	509
g15152	ANALYTICAL STUDY ON THE CONCRETE BREAKOUT STRENGTH OF HEADED REINFORCEMENT BAR EMBEDDED IN ROOF EXTERIOR BEAM-COLUMN JOINT Zev Al Jauhari and Tomoya Matsui	515
g15172	RECYCLING COAL BOTTOM ASH IN THE PRODUCTION OF FIRED CLAY BRICKS Nonthaphong Phonphuak, Anuwat Srisuwan, Anujit Phumiphan, Sarawut Dakaew and Siwat Lawanwadeekul	522
g15199	EXPERIMENTAL INVESTIGATION ON APPLICATION OF ALKALI-ACTIVATED MATERIAL WITH HIGH VISCOSITY TO HIGH FLUIDITY CONCRETE Kosuke Matsuoka, Yoichi Mimura and Itaru Horiguchi	528
g15245	INFLUENCE OF BIOCHAR WATER HYACINTH ON THE SHEAR STRENGTH OF ULTISOLS Erica Elice S. Uy, Jeann Patrick B. Barcelona, Juan Angelo V. Malaca, Lance Matthew R. Santiago, Jose Gabriel R. Zamora and Angelo B. Edora	534
g15260	SUSTAINABILITY ANALYSIS OF OPTIMIZED CONCRETE MIXES (PSC, PPC, HVFA) AGAINST STANDARD OPC MIXES FOR GRADES M15 TO M30 Pallavi Badry, Saikrishna Bondugula, Ravi Shankar Badry, N.Sudharsan, Srihari Saduwale and Ivaturi Sarma	541
g15279	INFLUENCE OF PRINTING ORIENTATION ON MECHANICAL BEHAVIOR OF MULTILAYER 3D-PRINTED CEMENT MORTAR Piti Sukontasukkul, Satharat Pianfuengfoo, Manote Sappakittipakorn, Sittisak Jamnam and Worathep Sae-Long	547
g15295	INVESTIGATION OF THE SHEAR STRENGTH OF STEEL BOLTED BAMBUSA BLUMEANA T-CONNECTION Bernardo A. Lejano, Richard Steven Lee and Carlo Cacanando	553
g15307	CORRELATION BETWEEN INFILL DENSITY AND MECHANICAL PROPERTIES IN 3D PRINTING Boonthum Wongchai	559
g15315	TWO-AXIS VIBRATION RESPONSE ATTENUATION OF BUILDING STRUCTURE USING ROLLING CYLINDER DYNAMIC VIBRATION ABSORBER Lovely Son, Mulyadi Bur, Bima Anugrah Saputra and Zeki Midi	565

g15319	CRITICAL ANALYSIS OF OLIVINE PERFORMANCE AND POTENTIAL FOR CARBON SEQUESTRATION IN SUSTAINABLE CONSTRUCTION Roohollah Kalatehjari, Sara Bayandor and Yousef Adeeb Chamachaei	572
g15329	A STUDY ON THE CORRELATION BETWEEN THE COEFFICIENT OF AIR PERMEABILITY AND AIR INFLOW AS AN INDEX OF PCM MATERIAL PERMEABILITY Arisa Nakamura, Barchinoyhon Sayfullaeva, Yuki Sakoda and Shushi Sato	578
g15337	EFFECT OF FLY ASH AND SILICA FUME AS PARTIAL REPLACEMENTS OF CEMENT ON THE MECHANICAL PROPERTIES OF SELF‐COMPACTING CONCRETE Fauzan, Suci Andini, Suci Meilita and Muhammad Johafis	583
g15338	ANALYTICAL STUDY ON THE SEISMIC BEHAVIOR OF NON‐STANDARD REINFORCED MASONRY HOUSES RETROFITTED WITH CROSSED FERROCEMENT LAYERS Fauzan, Abdul Hakam, Febrin Anas Ismail, Rio Yulanda and Muhammad Zulfian Saputra	589
g15339	SEISMIC ASSESSMENT AND RETROFITTING OF THE WEST SUMATRA BPBD OFFICE BUILDING USING SHEAR WALLS Fauzan, Abdul Hakam, Muhammad Ridho Zainadi, Arifin Shaleh and Muhamad Rezki	595
g15340	RETROFITTING OF ULAK KARANG SHELTER BUILDING IN PADANG CITY, INDONESIA, USING CONCRETE JACKETING Fauzan, Febrin Anas Ismail, Annisa El Husna, Muhammad Zulfian Saputra and Yozi Yuliardi	600
g15362	NUMERICAL ANALYSIS OF SMALL-SCALE EARTH RETAINING STRUCTURES DURING LIQUEFACTION Kakuta Fujiwara and Yan Boyu	606
g15368	DEVELOPMENT AND PERFORMANCE EVALUATION OF A UPV-BASED MODEL FOR EARLY FROST DAMAGE Sohee Moon, Youngwoong Jung, Seongpyo Kim, Jayeon Yun and Hyeonggil Choi	612
g15374	STUDY ON THE BEHAVIOR OF RECYCLED AGGREGATE CONCRETE UNDER HIGH TEMPERATURE EXPOSURE AND RECOVERY THROUGH RE-CURING Husnah, Herlien Dwiarti Setio, Ivan Sandi Darma and Patria Kusumaningrum	618
g15376	A NEW APPROACH TO PRELOAD CONTROL: DEVELOPMENT OF A FRACTURE-BASED HIGH-STRENGTH NUT FOR STEEL JOINTS Min-woo Choi and Yeol Choi	624
g15383	RSM OPTIMIZATION OF MECHANICAL AND DURABILITY PROPERTIES OF SELF-COMPACTING CONCRETE INCORPORATING ZINC ASH AND BLASTING GRIT NANOPARTICLES Rabeea W. Bazuhair, Ehab A. Mlybari and Wasayo Sanam Sahito	628
g15385	FOAM CONCRETE WITH UNIFORMLY GRADED AGGREGATES AND TAILINGS: STRENGTH AND MICROSTRUCTURE Kevin Chandra Nurwadji, Herlien Dwiarti Soemari and Ivan Sandi Darma	640
g15388	THE BEHAVIOR OF AN EXPERIMENTAL HOUSE IN RESPONSE TO SHRINKAGE Lamis Makki, Fabien Szymkiewicz, Céline Chesnais and Ning Sun	645
g15394	IMPROVING RUTTING RESISTANCE IN STONE MASTIC ASPHALT PAVEMENT USING FINE SEIZED WASTE TIRE RUBBER Enohmbey Chubisong Moses and Yoshitaka Kajita	651
g15400	PHYSICAL AND MECHANICAL PROPERTIES OF FLY ASH-BASED CELLULAR LIGHTWEIGHT CONCRETE Reni Suryanita, Yohannes Firzal, Harnedi Maizir and Raihan Arditama	657
g15401	EXPERIMENTAL INVESTIGATIONS ON SUSTAINABLE GROUND IMPROVEMENT USING SEASHELL POWDER AND RICE HUSK ASH Rufayda Jannat and Zakaria Hossain	663
g15404	INFLUENCES OF BASALT GEOSYNTHETICS ON SOIL SHEAR STRENGTH Mohamed Eltaher and Zakaria Hossain	669

g15405	CHARACTERIZATION OF SOIL-RICE HUSK ASH-CEMENT MIXTURES FOR SUSTAINABLE GROUND IMPROVEMENT: MECHANICAL AND MICROSTRUCTURAL INSIGHTS Abdelmageed Atef and Zakaria Hossain	678
g15408	ENVIRONMENTAL AND MECHANICAL PROPERTIES OF CONCRETE PAVEMENTS INCORPORATING REFUSE-DERIVED FUEL FLY ASH Menglim Hoy, Suksun Horpibulsuk and Chutichai Tonueng	685
g15412	EFFECT OF SUPERPLASTICIZER ON WORKABILITY OF RICE HUSK ASH AND SEASHELL POWDER BLENDED CONCRETE Md Soybur Rahman and Zakaria Hossain	689
g15118	EFFECT OF CEMENTITIOUS MORTAR FOR REPAIRING REINFORCED CONCRETE (RC) BEAMS Leandro Madeira Branco, Abel Fernandes, Isamu Yoshitake	694
g15402	SUSTAINABLE SOIL IMPROVEMENT: THE SYNERGISTIC EFFECTS OF BASALT FIBER AND RICE HUSK ASH ON THE ONE-DIMENSIONAL CONSOLIDATION Nguyen Thi Hong Nhung* and Zakaria Hossain	703
ID	***Environment***	712
g15113	DATA-DRIVEN APPROACH TO GREENHOUSE GAS MITIGATION: SEM ANALYSIS OF SUCCESS FACTORS AMONG LOCAL GOVERNMENTS IN KHON KAEN, THAILAND Narongdet Mahasirikul, Narongwit Mahasirikul and Sirawit Rattasia	713
g15116	A STUDY OF TEMPERATURE REDUCTION METHODOLOGY IN URBAN HEAT ISLAND USING MICROCLIMATE TECHNIQUE Ekarin Sangthammarat and Chokchai Chutakositkanon	721
g15120	OPERATION PRINCIPLE OF ACTUATOR SYSTEM THAT COMBINES PHASE-CONTROLLED ACTUATOR WITH DIFFERENT DRIVE FREQUENCIES Hiroyuki Yaguchi and Sota Abe	726
g15144	A LIDAR-BASED DEEP LEARNING FRAMEWORK FOR DRIFTWOOD RECOGNITION AND QUANTIFICATION Shanpeng Liu, Koichi Isobe, Toshiki Iwasaki, Kensuke Shioda and Diyuan Li	735
g15146	APPLICATION OF LONG SHORT-TERM MEMORY MACHINE LEARNING NETWORKS FOR TEMPERATURE VARIATIONS PREDICTION OF ENERGY PILES Thiti Chanchayanon, Apiniti Jotisankasa, Susit Chaiprakaikeow and Shinya Inazumi	743
g15161	A PERFORMANCE STUDY OF DEHUMIDIFICATION IN AN EVAPORATIVE COOLING SYSTEM USING THERMOSYPHON HEAT PIPES Niran Watchrodom, Jeerattikul Kaharn, Aekchai Rattanabanlue, Luedate Phatedoung and Thana Ananacha	749
g15164	A STUDY ON FLOOD INUNDATION ANALYSES AND HAZARD MAPPING APPROACHES FOR SMALL-SIZED RIVERS Shengping Zhnag and Jie Qi	755
g15166	ENHANCING FLOOD RESILIENCE THROUGH UPDATED IDF CURVES: LESSONS LEARNED FROM RECENT EXTREME RAINFALL EVENTS IN THE UAE Khalid B. Almheiri and Rabee Rustum	761
g15169	HEAVY METAL CONCENTRATIONS OF CICADA SHELL AND CICADA ADULT IN JAPAN Hiroyuki Ii	770
g15170	STABILIZATION OF KHON KAEN LOESS FOR THE PAVEMENT STRUCTURE USING RICE HUSK ASH AND KAOLIN CLAY. Stanley Emeka Ovuta and Ratamanee Nuntasarn	776
g15173	OPTIMIZATION OF MICROORGANISM-ENRICHED BIO-COATED CLAY GRANULES FOR SUSTAINABLE PLANT GROWTH USING RESPONSE SURFACE METHODOLOGY Piyawadee Saraphirom, Orn-Anong Chaiyachet, Piyarat Namsena, Chakkrit Sreela-or, Nonthaphong Phonphuak and Mullika Teerakun	782

g15177	DEVELOPMENT OF NEW BASE MATERIALS FOR SEAWEED BEDS USING PROBLEMATIC SOILS, RECYCLED MATERIALS AND RICE BRAN AND ITS VERIFICATION MONITORING IN THE SEA Kentaro Yamamoto, Kazumasa Fukuda, Takehito Negami, Mizuki Hira and Yoshihisa Tsurunari	788
g15191	VIBRATION ANALYSIS OF AN AC MOTOR FOR PREDICTIVE MAINTENANCE AND ENVIRONMENTAL IMPACT ASSESSMENT Suphattharachai Chomphan	794
g15196	AI-BASED GEOTECHNICAL INFORMATION PREDICTION AND LIQUEFACTION HAZARD MAPPING FOR THE TOKYO METROPOLITAN AREA Arisa Katsuumi, Koutaro Takasuna and Shinya Inazumi	800
g15197	APPLICATION OF SROI FRAMEWORK IN COST-EFFECTIVENESS ANALYSIS FOR THE ENVIRONMENTAL PROTECTION INVESTMENTS OF QUARRY MINES. Ngwu Tochukwu, Somprasong Komsoon and Chanapol Charoentanaworakun	805
g15198	PERFORMANCE OF ENVIRONMENTALLY FRIENDLY SOLIDIFIERS UTILIZING WASTE GLASS AND BLAST FURNACE SLAG FOR LIQUEFIED STABILIZED SOIL Koki Shinohara, Kohei Maru and Shinya Inazumi	811
g15201	TROPICAL SOIL BEYOND THE TROPICS: THE INFLUENCE OF PALEOENVIRONMENTS ON ENGINEERING PROPERTIES John Victor Smith	817
g15202	WATER QUALITY CHARACTERISTICS OF THE TRADITIONAL WATER MANAGEMENT FACILITY "MANBO" IN HOKUSEI CHUO PARK, MIE PREFECTURE Maki Oyagi, Rion Ito and Toyokazu Hirozumi	823
g15208	EXTRACTION OF SLOPE VARIATION EXTENT USING OPTICAL SENSORS AND SAR FOR THE MANASLU CIRCUIT TRAIL, NEPAL Hijiri Shimojima	829
g15217	HEAVY METAL CONCENTRATIONS OF PLANTS GROWING AROUND MINES IN VICTORIA, AUSTRALIA Daiki Yamamoto	837
g15223	DEVELOPMENT OF A HAZARD ASSESSMENT APPROACH BASED ON AN INTEGRATED MODEL FOR LARGE WOODY DEBRIS DISCHARGE IN DAM WATERSHEDS Yunhao Liu, Daisuke Komori, Sartsin Phakdimek and Yuta Abe	842
g15225	ECOSYSTEM-LEVEL ASSESSMENT OF THE ADSORPTION AND REMOVAL CAPACITY OF CALCIA-IMPROVED SOILS USING MICROCOSM-WET TEST Sosuke Sato and Kazuhito Murakami	848
g15227	LABORATORY EXPERIMENTS OF ARSENIC ADSORPTION CHARACTERISTICS FOR LATERITE GRAINS BY USING FIXED-BED COLUMN STUDY Nayaka Bandaralage Indraji Madhushan Nayaka Bandara, Kengo Nakamura, Akihiro Matsuno and Ken Kawamoto	856
g15230	DEVELOPMENT OF ROOFTOP AREAS WITH THERMAL PERFORMANCE FOR REDUCING HEAT ACCUMULATION IN CONDOMINIUMS Anon Anan-archa and Thana Ananacha	863
g15234	THE ROLE OF ENVIRONMENTAL IMPACT ASSESSMENT AS AN EFFECTIVE TOOL FOR SUSTAINABLE DEVELOPMENT IN THAILAND Chutarat Chompumth	869
g15265	EFFECT EVALUATION OF TAILING SAND SOLIDIFICATION BY MICROBIALLY INDUCED CARBONATE PRECIPITATION Lai Yongming, Satoru Kawasaki and Liu Qian	875
g15269	DEVELOPMENT AND OPTIMIZATION OF MICROBIAL COMPOST POWDER FOR CLAY PELLETS: TOWARD A FUNCTIONAL AND MARKETABLE GROWING MEDIA Songklot Phonphuak, Wimolkarn Nithisiriwaritkun, Nonthaphong Phonphuak, Piyarat Namsena and Piyawadee Saraphirom	881
g15277	PLANT COLONIZATION AND WILDLIFE UTILIZATION ON A DISUSED ROAD IN WESTERN JAPAN Taizo Uchida, Takeya Matsumoto, Teruo Arase, Masaaki Furuno and Daisuke Hayasaka	887

g15278	RECHARGE ESTIMATION AND SITE IDENTIFICATION FOR MANAGED AQUIFER RECHARGE IN SUPHANBURI, THAILAND USING GIS AND MODFLOW Pinit Tanachaichoksirikun, Uba Sirikaew, Uma Seeboonruang and Jutamas Srisuk	897
g15280	ANALYSIS OF SPATIAL PLANNING OF WATERSHED AREAS IN DESIGNING URBAN DRAINAGE SYSTEM Ade Tricia Miranda, Dinar Dwi Anugerah Putranto, Rosidawani, Agus Lestari Yuono and Riani Muharohmah	904
g15283	REPRODUCING REGION-BY-REGION WATER QUALITY CHANGES IN THE SETO INLAND SEA FROM 1990S TO 2010S BY USING MONTE CARLO BASED FOOD CHAIN MODEL Yutaro Koga, Yuichi Sato, Tomohito Matsuo and Hikari Shimadera	911
g15285	EXPECTED GROUNDWATER DEVELOPMENT AND WATER SECURITY IN DEFICIT SMALL TOURISM ISLAND Jutamas Srisuk, Pinit Tanachaichoksirikun, Uba Sirikaew and Uma Seeboonruang	918
g15291	INCREASING AGRICULTURAL LAND PRODUCTIVITY USING A COMBINATION OF RAINFALL SYSTEMS AND CANAL BLOCKING Robi Sahbar, Dinar Dwi Anugerah Putranto, Rosidawani, Agus Lestari Yuono and Riani Muharohmah	926
g15298	A SOURCE-DECOUPLED LIGHTGBM FOR BIAS CORRECTION IN CMAQ-SIMULATED PM2.5 CONCENTRATIONS OVER THAILAND Supitcha Sukprasert, Pongpisit Thanasutives, Shin Araki, Katsushige Uranishi, Tomohito Matsuo and Hikari Shimadera	934
g15303	EVALUATION OF SEASONAL IMPACTS OF RIVER INFLOW ON PHYSICAL FIELDS IN HARIMA NADA BY USING OCEAN MODEL Nar Wuriga, Valentina Pintos Andreoli, Yutaro Koga, Tomohito Matsuo and Hikari Shimadera	940
g15306	ELECTRIC VEHICLE SERVICE CENTRE (EVSC) FACILITIES OPTIMIZATION IN JAKARTA USING GEOGRAPHIC INFORMATION SYSTEMS (GIS) Jiang Liangliang, Lita Sari Barus, Irene Sondang Fitrinitia, Fidan Safira and Luzern Yuven Luis	946
g15309	THE IMPACT OF URBAN VILLAGE DEVELOPMENT ON FEMINIZATION OF INDONESIAN MIGRANT WORKERS (PMI) IN WEST JAVA: A SPATIO-TEMPORAL ANALYSIS FROM 2018, 2021, AND 2024 VILLAGE POTENTIAL (PODES) MICRO DATA Chotib, Mohamad Axel Putra Hadiningrat, Beti Nurbaiti and Adzkia Nabila Zahrani	953
g15310	AN EVALUATION OF THE AIRPORT NOISE AROUND AIRPORT OF THAILAND USING AVIATION ENVIRONMENTAL DESIGN TOOL Patcharida Sungtrisearn, Chaiwat Sangsrichan and Preda Pichayapan	959
g15325	STUDY OF DRIFTWOOD ACCUMULATION CONDITIONS IN MOUNTAIN RIVERS THROUGH FIELD SURVEYS AND HYDRAULIC EXPERIMENTS Yuriko Matsubayashi, Sae Nagahata and Motoki Makino	965
g15331	DEEP LEARNING-AUGMENTED LAKE ECOSYSTEM MODELING FOR IMPROVED FORECASTING OF ALGAL BLOOMS AND HYPOXIA IN ENCLOSED AREA Jinichi Koue, Sota Yoshikawa and Katsutoshi Hirayama	970
g15334	FLOATING OFFSHORE AIRPORTS: PLANNING, ENGINEERING FEASIBILITY, AND ENVIRONMENTAL IMPACT ASSESSMENT—A CASE STUDY OF TAIWAN'S COASTAL DEVELOPMENT AND GLOBAL IMPLEMENTATIONS Lin Jen-Liann, Lin Yuan-Ho and Lin Yong-Zhi	977
g15355	THE ECONOMIC RESILIENCE MODELING OF STREET VENDORS HOUSEHOLDS WITH SOCIAL CAPITAL AS AN INTERVENING VARIABLE: A CASE STUDY OF STREET VENDORS IN EAST JAKARTA Beti Nurbaiti, Mohamad Axel Putra Hadiningrat and Chotib Hasan	983
g15367	SOLIDIFICATION CHARACTERISTICS OF SOIL CONTAINNING COAL WASTE (PART II) Shoji Kamao, Rin Itagaki, Satoshi Shigemura and Yuta Murakami	989
g15373	CHARACTERISTICS OF FATAL WATER ACCIDENTS IN JAPAN AND THE IMPACT OF CHANGES IN THE AGE COMPOSITION OF THE POPULATION Masaaki Kondo, Yusaku Mizoguchi and Kaede Yoshida	995
g15377	WHY IS SEEDLING'S REGENERATION OF RHODODENDRON QUINQUEFOLIUM POPULATION ON MT. RYUGATAKE NOT GOING WELL? Mei Takeoka, Masaharu Sakakibara and Michiko Masuda	1002

g15378	ESTIMATING THE DISTRIBUTION OF WATER CHESTNUT LEAVES ON THE WATER SURFACE OF IRRIGATION PONDS USING THRESHOLD PROCESSING Yusaku Mizoguchi and Masaaki Kondo	1008
g15387	CESIUM LEACHING UNDER SEVERE CONDITIONS FOR CEMENT /GEOPOLYMER SOLIDIFIED BODY OF CESIUM ADSORBED MORDENITE Takahito Yasukochi, Yasumasa Tojo, Kanako Toda, Kazuo Yamada and Kazuto Endo	1013
g15393	DECOLORIZATION OF REACTIVE DYE SOLUTIONS USING CONTINUOUS FLOW ELECTROCOAGULATION SYSTEMS Jareeya Yimrattanabovorn, Nattapat Chanlert, Chutidet Chosongnoen and Ammarin Reabroy	1019
g15395	ANALYSIS OF INFRASTRUCTURE RESILIENCE AND WATER QUALITY OF THE ANDALAS UNIVERSITY CAMPUS, INDONESIA, IN THE UPSTREAM OF BATANG KURANJI WATERSHED FOR SEDIMENT AND RAW WATER CONTROL Nofra Masdaf, Fauzan, Bambang Istijono and Revalin Herdianto	1024
g15403	ADVANCING SUSTAINABLE COMPOSITES: A STUDY ON BIO-EPOXY RESIN WITH RECYCLED CORE LAYERS Kitsana Khodcharad, Kreetiwat Chaiyasin, Wipada Boransan, Watcharapong Patangtalo and Veena Phunpeng	1030
g15356	EVALUATION OF THE FUNCTIONALITY OF ALGAL BED CREATION STRUCTURES UTILIZING POROUS MATERIALS Masashi Miyagawa and Yoshihiro Suenaga	1036
g15107	SOLVING OPTIMAL RESERVOIR OPERATIONS PROBLEMS WITH A GENETIC ALGORITHM AND KEPLER OPTIMIZATION ALGORITHM Teerapat Moonlaong, Rittayut Gonthong, Nonthaphong Phonphuak, Anongrit Kangrang and Anujit Phumiphan	1042
g15135	APPLYING SELENA FOR STRATEGIC POST-EARTHQUAKE SHELTER PLACEMENT: A CASE STUDY FROM NEPAL Khadiga Al-Nagar, Kevin Karanja Kuria, Dr. Md Faiz Shah and Dr. Orsolya Kegyes-Brassai	1048
g15176	RECOVERY OF METALLIC IRON FROM ILMENITE BY THE PROCESS OF MECHANOCHEMICAL TREATMENT, ACID LEACHING AND ELECTRODEPOSION Takaaki Wajima	1056
g15180	SEMANTIC SEGMENTATION AND AUTOMATIC DETECTION TECHNOLOGY OF BALLAST RAILWAY BY INTEGRATING MULTI-SCALE GEOMETRIC FEATURES AND DEEP LEARNING OF POINT CLOUD Diyuan Li, Shanpeng Liu, Koichi Isobe and Junling Si	1062
g15183	CONVERSION OF WASTE GLASS FIBER REINFORCED PLASTICS USING MOLTEN ALKALI HYDROXIDES Nobuyuki Kawagoe and Takaaki Wajima	1071
g15206	POLICY IMPACT EVALUATION ON LAND PRICE: A CASE STUDY OF THE LOCATION OPTIMIZATION PLAN IN HACHIOJI USING PROPENSITY SCORE MATCHING Kaichen He, Toru Nagahara and Shinya Inazumi	1078
g15207	RADIAL JOINT PERFORMANCE IN SHIELD TUNNELS UNDER LARGE DEFORMATION: A COMPARATIVE STUDY USING EXPERIMENTAL AND NUMERICAL APPROACHES Quoc Viet Tran, Kosuke Kawata and Nobuharu Isago	1084
g15233	EFFECTIVE CUTTING TO CONTROL THE REGROWTH OF BAMBOO GRASS FOR THE CONSERVATION OF MOUNTAIN TRAILS Teruo Arase, Ren Yokota, Masamichi Yoshizawa, Taizo Kato, Taizo Uchida and Masaaki Furuno	1090
g15238	EFFECT OF DIFFERENT GRAYSCALE CONVERSION METHODS ON ROUGHNESS MEASUREMENT USING BINARIZATION Nozomu Urahata, Kenji Okajima and Seiya Nagaoka	1097
g15290	ANALYSIS AND INTERVENTION DESIGN FOR HIGH-RISK ROAD SEGMENTS IN BUENG KAN PROVINCE, THAILAND Pattarawadee Prasomsab, Jintapha Besun, Chamroeun Se, Thanapong Champahom, Sajjakaj Jomnonkwao and Vatanavongs Ratanavaraha	1103
g15328	INFLUENCE OF PORE SPATIAL DISTRIBUTION ON THE RELATIONSHIP BETWEEN MINOR LOSS AND FORCHHEIMER COEFFICIENTS Junichiro Takeuchi and Masayuki Fujihara	1110

g15353	URBAN PUBLIC SPACE DESIGN AND UTILIZATION AS WELL AS THE DKI JAKARTA CITY GOVERNMENT'S EFFORTS TO EMPOWER STREET VENDORS Elisabeth Ratu Rante Allo, Ruslan Prijadi and Chotib	**1116**
g15359	MODELING WELFARE-DRIVEN COMMUNITY TRANSFORMATION: AN INVESTIGATION IN REMOTE AREA, LABUAN BAJO, EAST NUSA TENGGARA, INDONESIA Mohamad Axel Putra Hadiningrat, Beti Nurbaiti and Chotib Hasan	**1123**
g15397	A PILE DOWNDRAG STUDY FOR LNG PROJECTS Anil Bhandari and Jianchun Cao	**1129**
g15193	DESERTIFICATION IN SAUDI ARABIA: IMPACTS OF EXCESSIVE IRRIGATION AND CLIMATE CHANGE ON VEGETATION LOSS THROUGH MATHEMATICAL MODELING Dalal Adnan Maturi	**1137**
g15375	AUTOMATION AND INNOVATION IN PRECAST CONCRETE MANUFACTURING: A STRATEGIC APPROACH Amalia Rizka Sugiarto and Yusuf Latief	**1143**
g15226	CHARACTERIZING pH DEPENDENCE OF ARSENIC ADSORPTION AND DESORPTION FOR LATERITE GRAINS IN VIETNAM Akihiro Matsuno, Tessin Fujisaki, Kengo Nakamura2and Ken Kawamoto	**1149**

Preface

On behalf of the GEOMATE 2025 Organizing Committee, we would like to welcome you to attend the Fifteenth International Conference on Geotechnique, Construction Materials and Environment held at Kyoto Research Park (KRP), Kyoto, Japan, in conjunction with The GEOMATE International Society, Mie University Research Center for Environmental Load Reduction, Glorious International, Japan.

On Friday, 11 March 2011, at 14:46 Japan Standard Time, the northeast of Japan was struck and severely damaged by a series of powerful earthquakes, which also caused a major tsunami. This conference was first dedicated to the tragic victims of the Tohoku-Kanto earthquake and tsunami disasters. The Geomate 2025 conference covers three major themes with 17 specific themes including:

- Advances in Composite Materials
- Computational Mechanics
- Foundation and Retaining Walls
- Slope Stability
- Soil Dynamics
- Soil-Structure Interaction
- Pavement Technology
- Tunnels and Anchors
- Site Investigation and Rehabilitation
- Ecology and Land Development
- Water Resources Planning
- Environmental Management
- Public Health and Rehabilitation
- Earthquake and Tsunami Issues
- Safety and Reliability
- Geo-Hazard Mitigation
- Case History and Practical Experience

This year, we have received many submissions from different countries. The participating countries are Australia, Azerbaijan, Bangladesh, Brazil, China, Czech Republic, Egypt, France, Ghana, India, Indonesia, Iraq, Japan, Malaysia, Morocco, New Zealand, Nigeria, Pakistan, Philippines, Poland, Saudi Arabia, Taiwan, Thailand, United Arab Emirates, United Kingdom and Vietnam. The technical papers were selected from the vast number of contributions submitted after a review of the abstracts. The final papers in the proceedings have been peer-reviewed rigorously and revised as necessary by the authors. It relies on the solid cooperation of numerous people to organize a conference of this size. Hence, we appreciate everyone who supports as well as participates in this joint conference.

Last but not least, we would like to express our gratitude to all the authors, session chairs, reviewers, participants, institutions, and companies for their contribution to GEOMATE 2025. We hope you enjoy the conference and find this experience inspiring and helpful in your professional field. We look forward to seeing you at our upcoming conference next year.

Best regards,

Prof. Zakaria Hossain,
Mie University, Japan,
Chairman (General)

Organization

Conference Honorary Chairmen:

Emeritus Professor Dr. Sohji Inoue, Mie University, Japan
Emeritus Professor Dr. Teruo Nakai, Nagoya Institute of Technology, Japan
Emeritus Professor Dr. Fusao Oka, Kyoto University, Japan
Prof. Dr. Bajang B.K. Huat, UPM, Malaysia

Scientific Committees:

Conference Chairmen:
Prof. Dr. Zakaria Hossain, Mie University, Japan

Conference Organizing Committee:

Prof. Dr. Zakaria Hossain, Prof. Mie University, Japan (Chair)
Prof. Dr. Satoshi Kaneco, Prof., Mie University, Japan (Co-Chair)
Prof. Dr. Sohji Inoue, E/Prof. Mie University, Japan (Co-Chair)
Prof. Dr. Toshinori Sakai, Prof. Mie University, Japan (Co-Chair)
Prof. Dr. Takamitsu Kajisa, E/Prof. Mie University, Japan (Co-Chair)
Prof. Dr. Kenji Okajima, Prof. Mie University, Japan (Co-Chair)
Prof. Dr. Masaaki Kondo, A/Prof. Mie University, Japan (Co-Chair)

National & International Advisory Committee:

Prof. Dr. Fumio Tatsuoka, E/Prof., Tokyo University of Science, Japan
Prof. Dr. Junichiro Takeuchi, Prof., Kyoto University, Japan
Prof. Dr. Kingshuk Roy, Prof., Nihon University, Japan
Prof. Dr. Sai Vanapalli, Prof., University of Ottawa, Canada
Prof. Dr. Musharraf Zaman, Prof. Univ. of Oklahama, USA
Prof. Dr. Rafiqul Tarefder, Prof. University of New Mexico, USA
Prof. Dr. M. Bouassida, Prof., National Sch. of Engg. of Tunis
Prof. Dr. L.R. Austriaco, E/Prof., Angles Univ. Found., Philippines
Prof. Dr. M. Ibn Ibrahimy, Prof., Int. Islamic Univ., Malaysia
Prof. Dr. Bujang B.K. Huat, Prof., Univ. Putra Malaysia
Prof. Dr. Nemy Banthia, Prof., UBC, Canada
Prof. Dr. Ian Jefferson, Prof., Univ. of Birmingham, UK
Prof. Dr. John Bolander, Prof., Univ. of California, USA
Prof. Dr. Shamsul Chowdhury, Prof., Roosevelt Univ., USA
Prof. Dr. Isabel Pinto, Prof., University of Coimbra, Portugal
Prof. Dr. Mark Jaksa, E/Prof., University of Adelaide, Australia
Prof. Dr. Hj. Ramli Bin Hj. Nazir, A/Prof., UTM, Malaysia
Prof. Dr. M.S. Hossain, International Islamic Univ. Bangladesh
Prof. Dr. Suksun Horpibulsuk, Suranaree Uni of Tech, Thailand
Prof. Dr. Muzamir Hasan, Director, CERRM, Univ. Malaysia Pahang
Prof. Dr. Afshin Asadi, S/Lecturer, Int. College of Auckland, New Zealand

International Technical Program Committee:

Prof. Adolf Heinrich Horn, Geological Institute - Federa University of Minas Gerais, Brazil
Prof. Bang-Fuh Chen, National Sun Yat-sen University, Taiwan
Prof. Bindeshwar Singh, Kamla Nehru Institute of Technology, India
Prof. Catherine Mulligan, Concordia Institute of Water, Energy and Sustainable Systems, Canada
Prof. Chi-Min Liu Chienkuo Technology University, Taiwan
Prof. Daffalla Rabih, Kenana Sugar Company, Sudan
Prof. Essaid Bilal, Ecole Nationale Superieure Des Mines De Saint Etienne, France
Prof. Hakan Caliskan, Usak University, Faculty of Engineering, Turkey
Prof. Ibrahim Maiyza, National Institute of Oceanography & Fisheries, Egypt
Prof. Loc Nguyen, Sunflower Soft Company, Vietnam
Prof. Marilia Hagen, Indiana University, United States
Prof. Md Najib bin Ibrahim, Universiti Teknologi MARA, Malaysia
Prof. Md. Abdul Baset Mia, BSMR Agri. Univ., Bangladesh
Prof. Mihaela Popescu, University of Craiova, Romania
Prof. Mohamed Abdou, Faculty of Education Department of Mathematics, Egypt
Prof. Mohamed Tahiri, Présidnce de l'Université Hassan II de Casablanca, Morocco
Prof. Nazar Oukaili, University of Baghdad, Iraq
Prof. Radim Cajka, Technical University Ostrava, Faculty of Civil Engineering, Czech Republic
Prof. Rajaraman Jambunathan, AMET University, India
Prof. Saad Farhan Ibrahim Alabdullah, University of Almustansiriyah, Iraq
Prof. Salem Alsanusi, Benghazi, Libya
Prof. Sudhir Kumar Das, Retired Senior Project Manager of Indian Railways, India
Prof. Zachary Senwo, Alabama A&M University, United States
Prof. Imed Jabri, University of Tunis, Tunisia
A/Prof. Bindeshwar Singh Kamla Nehru Institute of Technology, India
A/Prof. Hasi Rani Barai, Yeungnam University, South Korea
A/Prof. Jamaluddin Mahmud, Universiti Teknologi MARA, Malaysia
A/Prof. Mohamed Ramadan, University of Hail, Saudi Arabia
A/Prof. Najam Hasan, Dhofar University, Oman
A/Prof. Nosina Krishna Chaitanya, Jawaharlal Nehru Technological University, India
A/Prof. Nurbek Saparkhojayev, Almaty Management University, Kazakhstan
A/Prof. Pandian Vasant, Universiti Teknologi Petronas, Malaysia
A/Prof. Teodor Lucian Grigorie, University of Craiova, Romania
A/Prof. Zawawi Daud, Universiti Tun Hussein Onn Malaysia
A/Prof. Abdull Halim Abdul, OIl and Gas department, Malaysia
A/Prof. Baoping Cai, China University of Petroleum, China
A/Prof. Dariusz Jakóbczak, Koszalin University of Technology, Poland
A/Prof. Edgar Allan Mendoza, University of the Philippines
A/Prof. Lakhveer Singh, Universiti Malaysia Pahang (UMP) Malaysia, Malaysia
A/Prof. Lidia Sas Paszt, Research Institute of Pomology, Poland
A/Prof. Mahmood Barbooti, University of Yechnology, Iraq
A/Prof. Majid Mirzaei, Universiti Tunku Abdul Rahman, Malaysia
A/Prof. Najeh Lakhoua, University of Carthage, Tunisia
A/Prof. Ryan Joseph Calinao, Lyceum of the Philippines University-Laguna
A/Prof. Sarawut Thepanondh, Mahidol University, Thailand
A/Prof. Yasir Al Hussein, Jerash University, Faculty of Engineering, Jordan
A/Prof. Grigorie Teodor Lucian, University of Craiova, Romania
A/Prof. Hêriş Golpîra, Islamic Azad University, Sanandaj, Iran
A/Prof. Muhammad Aslam, King Abdulaziz University, Saudi Arabia
A/Prof. Tomasz Plech, Medical University of Lublin, Poland
A/Prof. Fellah Mamoun, Abbes laghrour University, Algeria
A/Prof. R. S. Ajin, GeoVin Solutions Pvt. Ltd., India
A/Prof. Roman Szewczyk, Industrial Research Institute for Automation and Measurements, Poland
Dr. Abolghasem Akbari, University Malaysia Pahang, Malaysia
Dr. Ahmad Safuan A Rashid, Universiti Teknologi Malaysia, Malaysia
Dr. Akinola Johnson Olarewaju, Federal Polytechnic Ilaro, Ogun State, Nigeria

Dr. Alexandre Costa, Federal University of the valleys of Jequitinhonha and Mucuri, Brazil
Dr. Angelo Gallone, Scotland’s Rural College (SRUC), United Kingdom
Dr. Azizul Azhar Ramli, Universiti Tun Hussein Onn Malaysia
Dr. Bashir Dar, University of Kashmir Delina Baramulla J&K India, India
Dr. Bassam Abdellatif, National Authority for Remote Sensing and Space Sciences, Egypt
Dr. Binh Phu Nguyen, National University of Singapore, Singapore
Dr. Cazacu Gabriela, S.C. Geotech Dobrogea, Romania
Dr. Chengen Yang, Intel Corporation, United States
Dr. Dayang Norulfairuz Abang Zaidel, Universiti Teknologi Malaysia
Dr. Evgeni Starikov, KIT, Karlsruhe, Germany; Chalmers, Gothenburg Sweden, Germany
Dr. Fatma Khanchel, University of Tunis El Manar, Tunisia
Dr. Hamidreza Khataee, Griffith University, Australia
Dr. Hêriş Golpîra, Islamic Azad University, Iran
Dr. Iskhaq Iskandar, Dept. Physics, University of Sriwijaya, Indonesia
Dr. Jingwei Zhao, University of Wollongong, Australia
Dr. Jitendra Agrawal, Rajiv Gandhi Proudyogiki Vishwavidyalaya, India
Dr. Liza Patacsil, Malayan Colleges Laguna, Philippines
Dr. Mohamed Amine, Ferrag Guelma University, Algeria
Dr. Mohd Afendi Rojan, Universiti Malaysia Perlis, Malaysia
Dr. Mohd Altaf, University of Kashmir Delina Baramulla J&K India, India
Dr. Mohd Hairy Ibrahim, Sultan Idris Education University, Malaysia
Dr. Mostafa Khater, Egypt - El Sharqia - Zagazig, Egypt Dr. Najam Hasan, Dhofar University, Oman
Dr. Namir Alkawaaz, University of Almustansiriyah, Iraq
Dr. Nashrul Fazli Mohd Nasir, Universiti Malaysia Perlis, Malaysia
Dr. NaufaL Mansor Kampus Uniciti Alam, Universiti Malaysia Perlis (UniMAP), Malaysia
Dr. Obed Majeed Ali, Northern Technical University, Iraq
Dr. Piyapong Janmaimool, King Mongkhut' University of Technology, Thailand
Dr. Po-Sheng Chiu, National Cheng Kung University, Taiwan
Dr. Prabu Mohandas, Adhiyamaan College of Engineering, India
Dr. Raman Kumar, D A V Institute of Engineering and Technology, India
Dr. Riccardo Colella, University of Salento, Italy
Dr. Rolando Javellonar, Romblon State University, Philippines
Dr. Shikha Agrawal, Rajeev Gandhi Technical University, India
Dr. Stefania Tomasiello CORISA, University of Salerno, Italy
Dr. Sumiyyah Sabar, Universiti Sains Malaysia, Malaysia
Dr. Suphaphat Kwonpongsagoon, Mahidol University, Thailand
Dr. Wei Hong Tan, Universiti Malaysia Perlis, Malaysia
Dr. Yoshiro Fujii, Shin Kobe Dental Clinic, Japan
Dr. Yuk Feng Huang, Universiti Tunku Abdul Rahman (UTAR), Malaysia
Dr. Zongyan Zhou, Monsh University, Australia
Dr. Purnanand Savoikar, Goa Engineering College, India
Dr. Ahmed Toaha Mobashsher, University of Queensland, Australia
Dr. Chupong Pakpum, Maejo University
Dr. Emanuele Quaranta, Politecnico di Torino, Italy
Dr. Jiangling Yin, Apple Inc., Cupertino, CA, United States
Dr. Khor Shing Fhan, Universiti Malaysia Perlis, Malaysia
Dr. Mario Chauca, Ricardo Palma University, Peru
Dr. Santosh Gaikwad, Model College, Ghansawangi, India
Dr. Tse Guan Tan, Universiti Malaysia Kelantan
Dr. Vikas Panthi, National Institute of Technology, India
Dr. Watoo Phrompittayarat, Naresuan University, Thailand
Dr. Hamidreza Namazi, Nanyang Technological University, Singapore
Dr. Parichat Phumkhachorn, Ubon Ratchathani University, Thailand
Dr. Subhasis Roy, University of Calcutta, India

Conference Correspondence:

Prof. Dr. Zakaria Hossain, Conference Chairman,
Dept. of Env. Sci. & Tech., Mie University, Japan,
E-mail: conference@geomate.org
Tel & Fax: +81-59-231-9578

Editorial Committee and Executive Committee:

Prof. Zakaria Hossain
Dr. Abd Elmageed Atef
Eng. Md. Yachin Islam
Eng. Md. Soybur Rahman

Keynote Papers

15th Int. Conf. on Geotechnique, Construction Materials & Environment, Kyoto, Japan, 11-13 November 2025, ISBN 978-4-909106124 C3051

BRITTLE BEHAVIOR IN SOIL, TAILINGS AND ROCK MASS: AN OVERVIEW

John Victor Smith[1,2]

[1]School of Engineering, RMIT University, Australia; [2]CMW Geosciences, Australia

ABSTRACT

The understanding of the mechanisms of loss of strength responsible for many significant slope failures has developed over recent years. Unforeseen slope failures, including tailings dam collapses, have been one of the main catalysts for the improvements to geotechnical understanding. For example, in the case of earthquake design, international protocols no longer rely on pseudo-static seismic analysis where the focus is to emphasize the role of the transient change in loading. Rather the focus is on the loss of strength expected due to seismicity which can be assessed in order to establish adequate factors of safety. One driver for this has been an awareness that sudden loss of strength or brittleness can occur even without a trigger such as earthquake shaking. The extreme case of these processes is liquefaction which can cause very sudden loss of strength. The mechanism is typically understood to involve the rapid transition from drained to undrained behavior. Other slope failure mechanisms, including those that occur in rock masses, can be considered as examples of strength loss. One such mechanism is toppling. In toppling the layers or columnar blocks are initially in contact with each other and are in a configuration allowing down-slope rotation. The rate of movement is moderated by the frictional strength of the rock interfaces. Face-to-face contact between layers is lost as space opens up during rotation. This stage of failure can occur rapidly as the assemblage of layers loses its frictional strength and is effectively in a free-fall condition. The layers retain frictional strength once they have rotated into a condition of symmetry that restores the contact of rock interfaces. The new orientation of the toppled layers does not have the potential energy of the pre-toppling condition and the slope is locally self-stabilized.

Keywords: Brittleness, Strength loss, Soil, Tailings, Rock, Toppling

INTRODUCTION

It is understood that strength and strain are intimately related in geotechnics [1]. In particular, the strength of a material can change during strain. The reduction in strength, 'strength loss', being the most problematic for engineering purposes [1]. Loss of strength as a result of shearing has been described as brittleness since 1940s [1]. The strength of soil at large strain conditions can be referred to as the residual strength [2]. The brittleness index, a ratio of peak minus residual strength divided by peak strength has been attributed to Bishop in the 1960s [2]. The brittleness index defined this way only measures the magnitude of the strength loss but the rate of reduction should also be considered part of the concept [2]. Brittleness is sometimes considered to apply to the drained condition of soil and has been distinguished from 'sensitivity' which occurs in the undrained condition [2]. According to [2], brittleness is a function of fabric change during shear whereas sensitivity is a result of pore pressure increase. In this paper the term brittleness will be used broadly to refer to a wide range of strength loss conditions.

The history of the development of geotechnical knowledge has largely occurred when the strength of materials has been overestimated or the mechanisms of strength loss have not been fully appreciated and a catastrophic failure has unexpectedly occurred [3].

Some selected examples of 'unexpected' slope failures were presented in a previous GEOMATE conference and journal article [4]. Slope failures can be considered 'unexpected' if the strength has been under-estimated due to either inadequate investigation or incorrect assessment of material properties. The three examples cited in [4] were the Vajont dam in Italy, Guinsaugon landslide, Philippines and Yallourn coal mine, Australia.

The Vajont landslide occurred in 1963 during reservoir filling. The effect of reservoir filling on the groundwater and stress conditions in the surrounding hillside had not been adequately assessed and a large landslide occurred as a result and triggered failure of the dam due to the displaced water. Strength loss occurred due to hydrogeological processes which in hindsight could have been anticipated with a more comprehensive assessment of the risks.

The Guinsaugon landslide occurred in 2006. A later review [5] assessed that the natural slope's underlying rock mass had undergone strength deterioration. The transition from peak to residual strength during failure added to the large run-out of the failure debris. Earthquakes and rainfall were associated but the review [5] questioned the role of these as a trigger due to uncertain timing.

The Yallourn landslide, Victoria, Australia

occurred in 2007. This open cast coal mine is located near a river. As mining approached the river the buffer to encroaching groundwater was reduced. Relaxation of the rock mass during mining was inferred to have led to activating the inter-seam clay layers with low residual strength leading to slope failure [4].

These three examples show that rock mass, like soil, can undergo strength loss in an unexpected manner [4].

In the case of the Ontake landslide in Japan in 1984 an earthquake triggered a rock slide of over 30 million cubic meters with a run-out distance of over 5 km. The event was inferred to have been influenced by the preceding rainfall and movement focused on a weak pumice layer [6]. Studies of landslide prone areas after earthquakes show that landslides can continue to occur at an elevated rate for years after a major seismic event which is inferred to be a result of the progressive change from peak to residual strength [7].

Fig.1 Ontake landslide scarp (photograph by the author 1992)

RESEARCH SIGNIFICANCE

Brittleness, meaning rapid, significant strength loss can be considered a key concept across a wide range of geotechnical issues. Mechanisms of brittle strength loss are well known in soils and fine mine waste known as tailings. Understanding of brittle strength loss can be extended to rock mass conditions also. All these materials can have multiple strength conditions. If the conditions rapidly change from a stronger to a significantly weaker one then brittle strength loss has occurred. If an engineering design is based on a higher strength condition without regard to the potential transition to lower strength then serious consequences can occur. The overview of these concepts here is intended to draw attention to a range of brittle strength loss behaviors that can occur. All geotechnical engineers should consider whether the materials they are constructing on or with could undergo a rapid and significant reduction in strength and ensure that this risk is adequately covered in the design process.

CONCEPTS

The examples covered in this paper have been selected for illustration of general concepts. The overarching aim is to use ‘brittleness’ or ‘brittle strength loss’ as a conceptual lens to view a wide range of processes related to geomechanics. The aim is not to imply that all these processes are fundamentally related in terms of physics and mechanics. Rather, the aim is to make conceptual linkages that assist practitioners and researchers to work across areas of geotechnical application.

This way of thinking has developed from a career spanning multiple fields from structural geology, tectonics, volcanology, engineering geology and geotechnical engineering. In working across these fields the conventional boundaries of soil, rock and industrial materials such as tailings and also the boundary between natural processes of slope stability including volcanic activity versus engineered conditions are somewhat dissolved.

Two main areas emphasized are firstly the importance of the potential for brittle strength loss in assessing the safety of tailings dams. Assessing strength loss is seen by many as more significant than determining the likelihood of a triggering event such as an earthquake and assessing the pseudo-static force of the earthquake as will be outlined with relevant references below. Secondly, toppling kinematics in rock slopes is addressed to illustrate brittle strength loss in a rock mass.

In this broad coverage the references cited are inevitably highly selective and many important sources and authors have not been included. Citing a particular author in relation to a topic is only intended to indicate a source where a concept is well explained rather than to imply that the author cited is necessarily the originator of a concept.

General

The stability of a slope is typically described in terms of factor of safety or probability of failure [8]. In order to calculate such numbers the strength of the material must be understood in terms of its range of properties. Soil properties can be understood as drained versus undrained and as peak, fully softened and residual [8]. The terminology residual strength of soil needs to be differentiated from residual soil meaning a soil which has formed directly from the underlying rock without significant transportation [9]. These residual soils are typically quite dense as they are undisturbed by transportation [9]. Their behavior is typically comparable to over consolidated soils [9]. Experimental laboratory studies can be conducted to assess the peak and residual shear strength of various material compositions and moisture conditions [10].

The strength of cohesive and granular soils typically increases with depth [11]. Specifically, the strength of soils is influenced directly by the confinement condition [11]. Various studies have explored the relationships of plasticity via the 'velocity field' or kinematics of the deforming system in relation to the stress distribution. These models can be applied to common problems such as loading of soft soils by embankments or other earthworks [11].

Strain softening behavior of soil and rock can be observed in laboratory experiments and applied in geotechnical analysis [12]. It has been observed that at low confinement the rate and magnitude of the reduction in strength can be most pronounced [12]. A plastic shear strain threshold was applied to define the transition from a linearly decreasing strength with strain from a constant strength (residual) condition at greater strain [12]. The extent of strength loss has been described as the brittleness of the material [12].

Brittleness

The concept of brittleness and the brittleness index can express the sudden loss of strength of soils and other granular materials and has been used since the 1980s and earlier [13]. The original definition of brittleness was based solely on the magnitude of the strength reduction. However, the normal meaning of brittle includes a sense of rapid loss of strength. One approach to quantifying degrees of brittleness and the relationship to strain has been developed for tailings [14]. In this scheme, non-brittle or moderately brittle materials do not undergo any reduction in shear strength until 3% axial strain is developed (Fig.2).

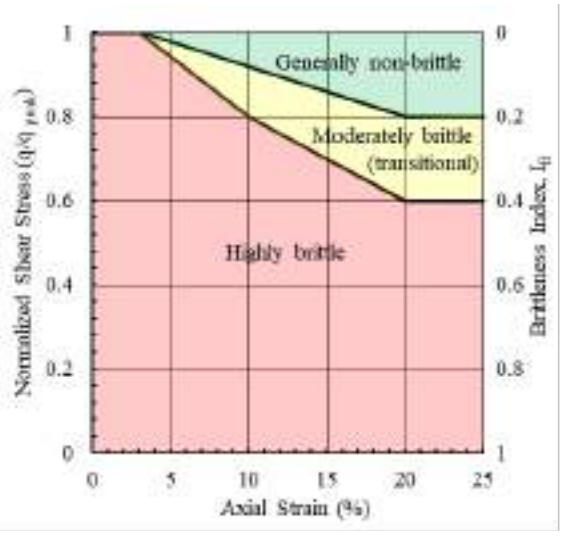

Fig.2 Definition of brittleness developed for tailings materials [14]

Non-brittle and moderately brittle materials can undergo 20% and 40% strength reduction, respectively. However, if these strength reductions occur prior to development of 20% axial strain then the materials may qualify for a higher degree of brittleness in this scheme (Fig.2).

Seismicity

Earthquakes stand out as a natural phenomenon that have the ability to cause destruction and damage through their effects on structures. A seminal work by the US Corps of Engineers (1980's) [15] outlined the pseudo-static method by stating "the seismic stability of embankment dams may be evaluated by a relatively simple method … in cases where there is no threat of liquefaction or severe loss of shear strength under seismic shaking.". That study emphasized that the pseudo-static approach to earthquake impact on dams is a 'screening tool' meaning it is not a sufficient check on stability itself but can be used to classify levels of concern that lead to applying appropriate acceptance criteria [15]. That work emphasized that dams with embankments or foundations that are susceptible to liquefaction or significant softening by cyclic loading require more specific stability assessments than can be achieved by pseudo-static approaches [15]. That work also refers to the "dynamic yield strength" of many earth materials being approximately 80% (i.e. 20% strength reduction) of the pre-seismic condition and that such strength reduction in analysis can be an appropriate way to assess seismic/cyclic conditions [15].

Further developments in seismic responses of dams in the 1990's [16] considered the strength of liquefied materials and noted they have a 'steady-state' or 'residual' (interchangeable terms) strength in the liquefied condition. Those studies found that triggering of failure in laboratory testing occurred at "the point at which control of the test is lost: if one were to stop the test in a load-controlled fashion after sufficient strain (with the stresses still applied) the sample would creep and ultimately flow in the steady-state mode" [16]. The residual strength of liquefied material is typically given as a strength to stress (i.e. depth) ratio [16].

Dilation and Contraction

The behavior of granular material is dependent on its density which is commonly measured as void ratio [16]. During shearing, granular materials will contract if they are loose or dilate if they are dense relative to a critical void ratio that represents a condition of shearing with constant volume. The critical void ratio varies with the degree of confining stress [16].

A mechanism called 'void redistribution' has been proposed as an explanation for the time delay that has been observed between possible triggers and actual slope failure [16-18]. The typical void redistribution scenario can occur where granular

material is below an impermeable layer. The trigger event causes some contraction of the granular material which expels excess water upward. However, the upward progress of water is prevented by the presence of the impermeable layer above [17,18]. In an extreme case, a film of water forms at the base of the impermeable layer with detrimental effects on stability of sloping ground. This mechanism is postulated in some rapid and significant loss of strength events [17]. It is understood that the void redistribution process takes time, leading to a delay between trigger and failure [17]. The process of void redistribution has been verified by centrifuge tests by various authors as reviewed by [17].

Strain Compatibility

Strain compatibility refers to the general concept that where different materials are in contact they may undergo different strains or strain rates in response to the stress conditions. Consequently, local stress variation or disturbances to the velocity field can cause strain incompatibility and can lead to discontinuity formation. Strain compatibility is also related to strain localization during shearing as the emerging shear zone must be oriented in a direction of zero longitudinal strain to maintain strain compatibility between the sheared and unsheared material [19]. These lines of no longitudinal strain are also known as the characteristic lines and are at less than 90^{o} to each other in conditions of dilatancy [19].

SOIL AND LANDSLIDES

Soils are typically derived from natural rock weathering either as a residuum or transported. Soil behavior is strongly influenced by the interaction of clay and water [8]. The ‘fully softened’ condition indicates that the shear strength of clay-dominated materials moves toward a low strength condition through the absorption of water over time, especially concurrent with strain [8].

The ability of pore water to migrate through a soil under stress defines the undrained and drained strength conditions. Undrained strength can exceed drained strength over parts of the confining stress range, particularly in over-consolidated conditions [20]. Pressure changes in the water within the pores of soils are intimately related to strain and control the drained strength via the effective stress principle. Negative pore pressures can develop in unsaturated soils and when lost by saturation can result in rapid loss of strength [8].

Non-Newtonian or thixotropic behavior can affect the stress-strain relationships as can creep in a wide range of materials [21-25]. Other processes that can influence soil behavior include progressive changes to grain-size through particle crushing and the discontinuous deformation of fissured clays [3].

Analysis of a faulted coarse gravel deposit in New Zealand showed a reduction from 78% clasts to 33% clasts. The process of faulting in this gravel deposit occurred by dilation of the clast-supported fabric to facilitate movement and concurrently for clay matrix material to migrate to the fault zone. This process is representative of inter-particle dilation to a critical state as is required for shearing of particulate systems generally. Due to the coarse grain-size of the gravel the changes caused by dilation can be observed directly in the field [25] (Fig.3).

Fig.3 Dilatation of a fault zone in a gravel deposit observed by reduced clast concentration [25]

TAILINGS

Tailings are the end product of rock and mineral grinding in mineral processing. Many mines place these tailings in impoundments by hydraulic methods [26]. A number of high profile tailings impoundment failures have occurred causing significant loss of life and environmental impact [27]. The comments made here are general in nature and original sources and guidelines should be referred to for all tailings impoundment works. Selected significant failure events are only briefly described here and readers should address the extensive literature for additional data and interpretation.

Various events and their analysis have been used in developing international [14] and National guidelines [28]. Limit-equilibrium analysis remains the main tool for assessment. Factor of safety of 1.5 has been used for static conditions and 1.1 or 1.0 for seismic conditions [28]. The seismic assessment must be based on cyclic and post-liquefaction parameter reduction rather than pseudo-static analysis [14, 28].

One of the well studied events was the of failure of the Mount Polley tailings storage facility in British Columbia, Canada in 2014. The failure mechanism was found to be complex and involved strain weakening in the foundation and its strain incompatibility relative to the rockfill embankment [29].

A significant development has been the recognition that critical state soil mechanics is fundamental to tailings behavior [30,31]. The

materials of the foundation, embankment and tailings can be defined relative to the critical state line in void ratio terms. This value is the state parameter and is positive for materials loose of critical state and negative for materials dense of the critical state [30,31]. The precision of void ratio measurement is approximately 0.05 due to variations in sample preparation [16]. The relationship between strength and confinement is related to important concepts of dilation and contraction [32]. The value used for boundary between dilative (non-liquefiable) and contractive (liquefiable) is -0.05 [33]. This value recognizes that materials just dense of the critical state can undergo liquefaction-like flow [33].

While limit-equilibrium is currently the prime method of analysis it has been recognized that limit-analysis applied in a finite element formulation can overcome some limitations of limit-equilibrium in the area of slip surface identification [32]. In limit-analysis the lower bound is based on an admissible stress field and the upper bound is based on a kinematically admissible velocity (plastic strain rate) field [32]. Limit-analysis and finite element analysis generally can also complement limit-equilibrium by responding to latent instability to undrained failure and stress rotation causing undrained failure [32]. A limit-analysis model of the 2015 Fundao tailings impoundment failure in Brazil was presented at a previous GEOMATE conference [34].

Another aspect of tailings impoundment failure that is not covered here is dam breach. Tailings dam breach outflow is a highly complex process and is critical to assessing potential impacts [35]. In dam breach events water ponded on the tailings surface erodes tailings and re-hydrates it to a more flowable form even beyond the effects of tailings liquefaction.

ROCK

Volcanic Processes

Many volcanic processes are driven by gravity and can provide insight into the behaviour of natural materials. For example, Bromhead [1] gives an example of his observation of a lava flow base directly over a mangrove swamp mud providing insight into the geomechanical processes in the location [1]. The flow of lavas and other volcanic products can inform understanding of viscous-granular flow, especially non-Newtonian effects [36,37].

Rock Mass

Rock material is typically brittle in nature and at high deviatoric stress can undergo microscopic damage (starting at about 40% of uniaxial compressive strength [38]. Rock mass refers to the rock material and the naturally occurring fractures that are typically present. These systems of fractures are the main control on how the rock mass behaves [38]. In order for a rock mass to deform, the confinement is typically low such that the blocks of rock can move relative to each other. The extreme example of low confinement is where fractures daylight in a face making the sliding or rotating motions of blocks feasible [38].

Toppling

Where rock mass deforms mainly by the rotation of elongate blocks, toppling is the failure mechanism [39]. Free fall toppling where columns or layers of rock at a face rotate under the influence of gravity is a very recognized type of toppling. Toppling also occurs where the adjacent blocks form a confining condition which can influence the rotation [40]. This type of toppling is similar to the processes observed in hillside creep of layered bedrock [40].

Toppling of columns or layers within a slope has a dilative and contractive phase (Fig.4). The dilative phase develops until the layers are perpendicular to the basal surface of rotation. The contractive phase then continues until the layers reach a mirror image configuration compared to their starting postion. At this point the toppling can self-stabilize. During the dilative phase the frictional contact between adjacent blocks decreases and the rock mass strength decreases.

Therefore, the toppling mechanism can be considered brittle in the sense that strength decreases as strain is accumulated in the early phase of deformation. Examples of toppled slopes in layered rocks are shown in Figure 5 and 6. The layers have buckled (Fig. 5B, Bk) where the layers have rotated to be perpendicular to the basal surface. Separation of layers in this zone also shows the occurrence of local dilation (Fig. 5B, D). Layers of different thickness can respond differently by having different angles of rotation compensated for by shearing in the same sense as the downslope movement (Fig. 5B, location 1 and 2 and shear arrows).

Figure 6 shows a location where layers have reached the self-stabilized configuration. The slip between layers with the opposite sense of movement to the downslope shearing is anotated by shear arrows with ‘s’. Local block rotation and other shears on joints with an opposite sense to the downslope shearing are also anotated on Fig.6. These mechanisms have been shown to be relevant to deep-seated (>100 m deep) toppling rock slides [41-43].

CONCLUSIONS

Geotechnical engineering for foundations, excavations and earthworks is fundamentally based on determining the strength of earth materials. These materials include soils and rock and also industrial waste products such as the finely ground rock residue

known as tailings. The strength of these materials can be determined by field and laboratory tests. However, the strength can change under a wide range of conditions including saturation by water, loading and strain. When strength changes to a lower value this can be considered to be a strength loss. If the strength loss is unexpected then failure may be the result.

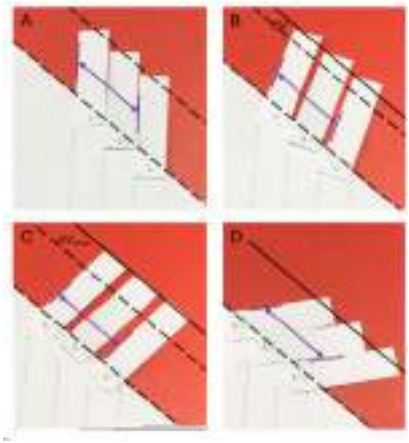

Fig.4 Toppling dilatancy in a paper model. A) Initial configuration. B) Opening phase. C) Maximum separation of blocks. D) Closure (self-stabilization)

The strength of geological materials including soils, tailings and rock masses is intimately associated with the amount, rate and type of strain that occurs. In particular 'loss of strength' that is sudden or unexpected reduction in strength of these materials should be considered along with the strain occurring.

The case of rock toppling can be included in brittle behavior in that the gravitational force induces shear strain in a downslope direction. If this shear strain induces rotation of elongate blocks of rock the kinematics of this proces can cause expansion of the deforming zone occuring in concert with separation of the side faces of the elongate blocks. If this toppling occurs within a confined condition such as hillslope creep or deep-seated toppling then complex internal kinematics can be observed or anticipated within the toppling rock mass. For example, 1) shear displacement of block faces with a sense of shear opposite (antithetic) to the overall downslope shear strain, 2) shearing of block faces sub-parallel to the overall shear strain with the same sense of shear (synthetic), 3) delamination of layers, 4) buckling of layers and 5) local deformation of weak layers. These processes introduce mechanisms of deformation which would not occur without the dilation of the rock mass driven by the rotation of elongate blocks. Therefore, this pattern of strain (kinematics) leads to a reduction in strength. The rotation of the elongate blocks eventually leads to a more stable configuration as the blocks attain an orientation equal and opposite to the original configuartion relative to the basal plane of the toppling. This stabilising configuration has been referred to as the mirror image configuration that leads to self-stabilization of toppling.

Fig.5 Constrained toppling showing the complex shearing and rotation accommodated in the dilating zone (Melbourne Formation, Plenty Gorge, Victoria Australia). A) Large arrows show the gravity-driven shear sense. B) Detail with features described in the text

This overview encourages geotechnical engineers and related professionals to ensure that foundations, excavations and earthworks are designed with a full understanding of the potential of the materials to reduce in strength under a range of conditions. Importantly, a safe design is one which can maintain stability even when the strength of the material decreases to a lower level – especially if the change in strength is rapid.

Fig.6 Toppled strata showing the complex shearing and rotation accommodated in the dilating zone (Maitai Valley, New Zealand) [40]

ACKNOWLEDGMENTS

Colleagues at CMW Geosciences and RMIT University have provided insights and examples.

REFERENCES

[1] Bromhead E. N., Reflections on Slope Stability Engineering. CRC Press, 2024, pp.1-182.

[2] Bromhead E.N., Reflections on the Residual Strength of Clay Soils, With Special Reference to Bedding-Controlled Landslides. Quarterly Journal of Engineering Geology and Hydrogeology, Vol. 46, Issue 2, 2013, pp.132-155.

[3] Duncan J. M., Wright S. G., and Brandon, T. L., Soil Strength and Slope Stability, John Wiley and Sons., 2014, pp.1-333.

[4] Sonnekus M., and Smith J. V., A Review of Selected Unexpected Large Slope Failures. International Journal of GEOMATE, Vol. 15, Issue 48, 2018, pp.66-73.

[5] Guthrie R. H., Evans S. G., Catane S. G., Zarco M. A., and Saturay R. M., The 17 February 2006 Rock Slide-Debris Avalanche at Guinsaugon Philippines: a Synthesis. Bulletin of Engineering Geology and the Environment, Vol. 68, 2009, pp.201-213.

[6] Voight B. and Sousa J., Lessons from Ontake-san: a Comparative Analysis of Debris Avalanche Dynamics. Engineering Geology, Vol. 38, Issue 3, 1994, pp.261-297.

[7] Kincey M. E., Rosser N. J., Robinson T. R., Densmore A. L., Shrestha R., Pujara D. S., and Swirad Z. M., Evolution of Coseismic and Post‐Seismic Landsliding After the 2015 Mw 7.8 Gorkha Earthquake, Nepal. Journal of Geophysical Research: Earth Surface, Vol. 126, Issue 3, 2021, pp.1-27.

[8] Idries A., and Stark T. D., Uncertainty in Drained Fully Softened and Residual Strength Correlations. Journal of Geotechnical and Geoenvironmental Engineering, Vol. 150, Issue 1, 2024, pp.6023010.

[9] Wesley L. D., Geotechnical Engineering in Residual Soils. Proceedings of the 18th International Conference on Soil Mechanics and Geotechnical Engineering, Paris, John Wiley and Sons. 2010, pp.3479-3482.

[10] Rusdiansyah A. and Barkiah I. (2021). The Behavior of Residual Shear Strength of Laterite Soil Due to the Addition of Coarse Sand and Low Plasticity Clay Fractions. International Journal of GEOMATE, Vol. 21, Issue 86, 2021, pp.100-107.

[11] Davis E. H., and Booker J. R. (1973). The Effect of Increasing Strength with Depth on the Bearing Capacity of Clays, Geotechnique, Vol. 23, Issue 4, 1973, pp.551-563.

[12] Renani H. R., and Martin C. D., Factor of Safety of Strain-Softening Slopes, Journal of Rock Mechanics and Geotechnical Engineering, Vol. 12, Issue 3, 2020, pp.473-483.

[13] Highter W.H. and Tobin R.F., Flow Slides and the Undrained Brittleness Index of Some Mine Tailings, Engineering Geology, Vol. 16, Issue 1, 1980, pp.71-82.

[14] International Commission on Large Dams (ICOLD). Tailings Dam Safety Bulletin N° 194, Version 1.0, Paris, Tailings Dams and Waste Lagoons 2022, pp.1-308.

[15] Hynes M. E., and Franklin A. G., Rationalizing the Seismic Coefficient Method, USCE, GL-84-13, 1984, pp 1-21.

[16] Marcuson III W. F., Hynes M. E., and Franklin A. G., Evaluation and Use of Residual Strength in Seismic Safety Analysis of Embankments, Earthquake Spectra, Vol. 6, Issue 3, 1990, pp.529-572.

[17] Kulasingam R., Malvick E. J., Boulanger R. W., and Kutter B. L., Strength Loss and Localization at Silt Interlayers in Slopes of Liquefied Sand, Journal of Geotechnical and Geoenvironmental Engineering, Vol. 130, Issue 11, 2004, pp.1192-1202.

[18] Kokusho T., and Kabasawa K., Effect of Void Redistribution or Water Films on Shear Strength of Liquefied Deposits, In, Geomechanics: Testing, Modeling, and Simulation, American Society of Civil Engineers (ASCE) 2005, pp. 475-503.

[19] Smith J. V., and Durney D. W., Experimental Formation of Brittle Structural Assemblages in

Oblique Divergence, Tectonophysics, Vol. 216, Issue 3, 1992, pp.235-253.
[20] Shewbridge S., Undrained Strengths and Long-Term Stability of Slopes, Journal of Geotechnical and Geoenvironmental Engineering, Vol. 145, Issue 11, 2019, pp. 2519002.
[21] Haghighat E., Rassouli F. S., Zoback M. D., and Juanes R. A Viscoplastic Model of Creep in Shale, Geophysics, Vol. 85, Issue 3, 2020, MR155-MR166.
[22] Jiang H., and Jiang A., Numerical Analysis and Application of Nishihara Creep Nonlinear Damage Model Considering Ubiquitous Joints, Tunnelling and Underground Space Technology, Vol. 157, 2025, pp.106335.
[23] Bougouin A., Metzger B., Forterre Y., Boustingorry P., and Lhuissier H., A Frictional Soliton Controls the Resistance Law of Shear-Thickening Suspensions in Pipes. Proceedings of the National Academy of Sciences, Vol. 121, Issue 17, 2024, pp. 2321581121.
[24] Smith J. V., Shear Thickening Dilatancy in Crystal-Rich Flows, Journal of Volcanology and Geothermal Research, Vol. 79, Issue 1, 1997, pp. 1-8.
[25] Smith J. V., Dilatancy Fabrics in Conglomerates in the Awatere Fault Zone, New Zealand, Journal of Structural Geology, Vol. 20, Issue 11, 1998, pp.1449-1454.
[26] Blight G. E., Geotechnical Engineering for Mine Waste Storage Facilities. CRC Press, 2009, pp.1-634.
[27] Blight G. E., and Fourie A. B., Catastrophe Revisited–Disastrous Flow Failures of Mine and Municipal Solid Waste, Geotechnical and Geological Engineering, Vol. 23, 2005, pp.219-248.
[28] Australian National Committee on Large Dams (ANCOLD), Guidelines on Tailings Dams: Planning, Design, Construction, Operation and Closure, 2019, pp.1-79.
[29] Zabolotnii E., Morgenstern N. R., and Wilson G. W., Mechanism of Failure of the Mount Polley Tailings Storage Facility. Canadian Geotechnical Journal, Vol. 59, Issue 8, 2022, pp.1503-1518.
[30] Been K., Characterizing Mine Tailings for Geotechnical Design, Australian Geomechanics Journal, Vol. 50, Issue 4, 2016, pp. 59-78.
[31] Jefferies M., On the Fundamental Nature of the State Parameter, Géotechnique, Vol. 72, Issue 12, 2022, pp.1082-1091.
[32] Whittle A. J., El-Naggar H. M., Akl S. A., and Galaa A. M., Stability Analysis of Upstream Tailings Dam Using Numerical Limit Analyses, Journal of Geotechnical and Geoenvironmental Engineering, Vol. 148, Issue 6, 2022, pp.4022035.
[33] Reid D., Fanni R., and Fourie A. B., Assessing the Brittleness of Tailings–Some Common Pitfalls and Uncertainties. Dams for People, Water and Environment and Development - 92nd ICOLD Annual Meeting New Delhi , India, 2024.
[34] Hernandez Espinoza J., Smith J. V. and Nazem M., Limit Analysis of the Fundao Tailings Dam Slope Failure in Brazil 2015, 10th Int. Conf. on Geotechnique, Construction Materials and Environment (GEOMATE), Melbourne, Australia, 2020, pp 164-169.
[35] Sreekumar U., Gildeh H. K., Mohammadian A., Rennie C., and Nistor I., Tailings Dam Breach Outflow Modelling: A Review. Mine Water and the Environment, 2024, pp.1-25.
[36] Bougouin A., Lhuissier H., Forterre Y., and Metzger, B., Dam-Break of Shear-Thickening Suspensions: A New Perspective for Crystal-Rich Lava Flows and Lahars, EGU24, 2024, pp. 14-19.
[37] Smith J. V., Ductile-Brittle Transition Structures in the Basal Shear Zone of a Rhyolite Lava Flow, Eastern Australia. Journal of Volcanology and Geothermal Research, Vol. 72, Issue 3, 1996, pp. 217-223.
[38] Hoek E. and Brown E. T. (1997) Practical Estimates of Rock Mass Strength, International Journal of Rock Mechanics and Mining Sciences, Vol. 34, Issue 8, 1997, 1165–1186.
[39] Martin C. D., Alzo'ubi A. K., and Cruden D., Progressive Failure Mechanisms in a Slope Prone to Toppling, In Proc. International Symposium on Rock Slope Stability in Open Pit Mining and Civil Engineering, Vancouver, Canada, Vol. 1, 2011, pp. 1-12.
[40] Smith J. V., Self-Stabilization of Toppling and Hillside Creep in Layered Rocks. Engineering Geology, Vol. 196, 2015, pp.139-149.
[41] Ning Y., Tang H., Zhang G., Smith J. V., Zhang B., Shen P., & Chen H., A Complex Rockslide Developed from a Deep-Seated Toppling Failure in the Upper Lancang River, Southwest China, Engineering Geology, Vol. 293, 2021, pp.106329.
[42] Ning Y., Tang H., Peng J., Shen Y., Smith J. V., and Zhang B., A Stability Evaluation Method for Deep-Seated Toppling in the Upper Lancang River, Southwestern China, Journal of Rock Mechanics and Geotechnical Engineering, Vol. 16, Issue 7, 2024, pp.2388-2410.
[43] Zhang L., Zhang R., Dou J., Hou S., Xiang Z., Wang H., Yang P., and Liu X. (2025). Advancing Reservoir Landslide Stability Assessment Via TS-InSAR and Airborne LiDAR Observations in the Daping Landslide Group, Three Gorges Reservoir Area, China, Landslides, Vol. 22, Issue 1, 2025, pp. 169-188.

Copyright © Int. J. of GEOMATE All rights reserved, including making copies, unless permission is obtained from the copyright proprietors.

15th Int. Conf. on Geotechnique, Construction Materials & Environment,
Kyoto, Japan, 11-13 November 2025, ISBN 978-4-909106124 C3051

ADVANCED TECHNOLOGIES FOR EXISTING PILE EXTRACTION AND ASSOCIATED BOREHOLE BACKFILLING

Shinya Inazumi

College of Engineering, Shibaura Institute of Technology, Japan

ABSTRACT

This keynote addresses the critical challenges facing modern urban redevelopment through innovative approaches to existing pile extraction and borehole backfilling. As aging infrastructure worldwide requires comprehensive renewal, the development of safe and efficient methodologies for existing pile removal has become paramount for sustainable land use and environmental stewardship. This presentation introduces groundbreaking technologies developed within Japan's unique geological and urban context, including the pile tip gripping and lifting method and advanced cement-based backfill materials enhanced with sodium carbonate and thickening agents. These innovations demonstrate significant improvements in safety, operational efficiency, and environmental sustainability compared to conventional extraction methodologies.

Keywords: Pile extraction, Borehole backfilling, Infrastructure aging, Urban redevelopment

INTRODUCTION

The Global Infrastructure Aging Crisis

The rapid economic growth experienced globally during the post-war period has resulted in extensive infrastructure networks that are now approaching end-of-life conditions, necessitating comprehensive renewal strategies [1,2]. Japan exemplifies this challenge with iconic structures constructed around the 1964 Tokyo Olympics, including Tokyo International Airport, the Metropolitan Expressway, and the Tokaido Shinkansen bullet train line, all of which now require systematic renewal and reconstruction [3]. This infrastructure aging phenomenon extends beyond Japan, creating urgent global needs for innovative demolition and reconstruction methodologies that prioritize safety, efficiency, and environmental sustainability.

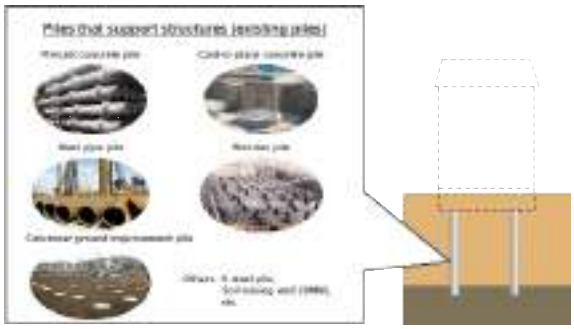

Fig. 1 Overview of various types of pile foundations

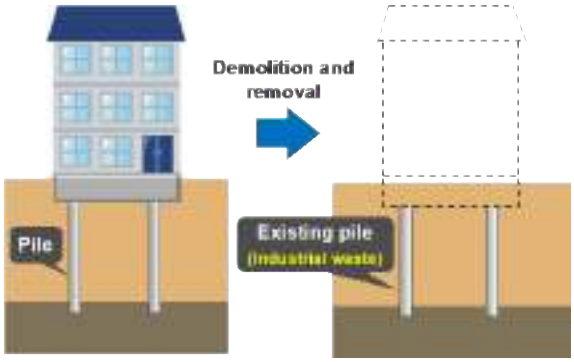

Fig. 2 Definition of piles and existing piles designated as industrial waste

The demographic shifts associated with declining birth rates and aging populations have fundamentally altered infrastructure utilization patterns, leading to decreased demand for certain public facilities while simultaneously increasing the need for disaster-resilient reconstruction following major seismic events such as the 1995 Kobe Earthquake, 2011 Great East Japan Earthquake, and 2016 Kumamoto Earthquakes [4,5]. These natural disasters have heightened awareness of disaster prevention requirements, driving comprehensive infrastructure renewal initiatives that extend far beyond simple replacement strategies [6,7].

The widespread utilization of pile foundations in urban environments, particularly in soft soil conditions prevalent in many global cities, presents unique challenges following structural demolition. As demonstrated in Fig. 1, various pile foundation types support existing infrastructure systems, including precast concrete piles, cast-in-place concrete piles, steel pipe piles, wooden piles, and specialized ground improvement systems. Upon demolition, these foundations become "existing piles in the ground," as illustrated in Fig. 2, often classified as industrial waste requiring specialized removal techniques [8,9].

Consequences Of Inadequate Pile Management

The improper management of existing piles

following structural demolition creates substantial geotechnical and environmental challenges that extend beyond immediate construction sites. Fig. 3 demonstrates the local subsidence caused by incomplete backfilling of boreholes with sand, illustrating the critical importance of proper soil stabilization following pile extraction. Such differential settlement can lead to significant land degradation, affecting not only the immediate construction site but also adjacent structures and infrastructure systems [10,11].

The presence of remnant piles in the ground creates complications in land transaction processes, as these underground obstructions are often perceived as defects that can significantly impact property values and future development potential [12]. Fig. 4 illustrates the common problems associated with partial pile remnants remaining in the ground and poor backfilling practices following pile removal, highlighting the dual challenges that must be addressed through integrated technical solutions.

Current practices in Japan for pile removal remain outdated and rely heavily on empirical field experience without comprehensive standardized guidelines, leading to persistent unresolved issues in process improvement and quality assurance [13,14]. This lack of systematic approaches has resulted in various technical uncertainties and safety concerns that require immediate attention through innovative technological development and implementation.

CRITICAL ANALYSIS OF CONVENTIONAL WIRE ROPE METHODS

The wire rope method, illustrated in Figs. 5 and 6, represents the conventional technique widely employed in the construction industry for existing pile extraction and removal [15,16]. This method involves a sequential process beginning with borehole drilling around the pile circumference using protective casing to maintain structural integrity and minimize ground disturbance. Following casing installation, wire rope attachment to the existing pile enables upward force application through heavy equipment for pile extraction.

The wire rope extraction process presents significant technical challenges and safety risks that have persisted throughout decades of implementation. Fig. 7 demonstrates the critical accidents encountered with wire rope methods, including wire rope breakage due to underestimated loads and pile structural failure during extraction processes. These failures often result from increased frictional forces around pile circumferences caused by borehole wall collapse and soil backfill into extraction cavities [17,18].

The mechanical failure modes associated with wire rope methods create substantial safety hazards in dense urban environments. Wire rope breakage, as shown in Fig. 7a, frequently occurs at the initiation of

Fig. 3 Example of local subsidence due to poor backfilling of boreholes with sand

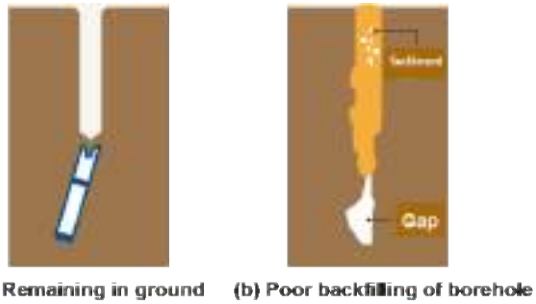

Fig. 4 Image of partial pile remaining in ground and poor backfilling of borehole after removal of existing pile

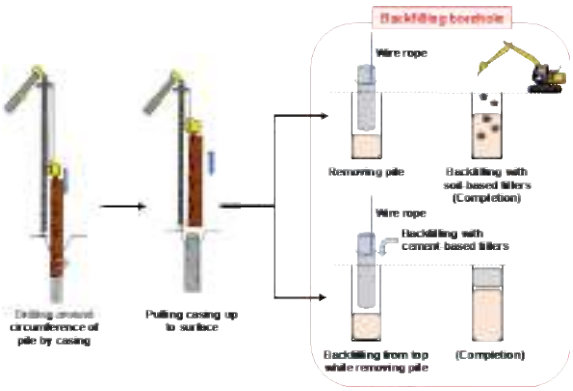

Fig. 5 Methods of borehole backfilling that can be employed in wire rope method

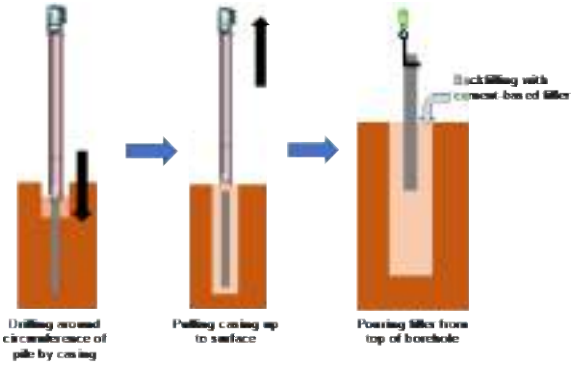

Fig. 6 Schematic of wire rope method (conventional technique)

extraction operations due to inadequate load estimation during design and operational phases. Additionally, pile breakage during extraction,

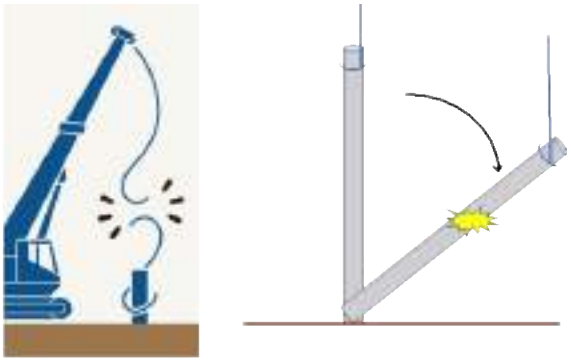

(a) Breaking of wire rope (b) Breaking of pile

Fig. 7 Accidents encountered with wire rope method

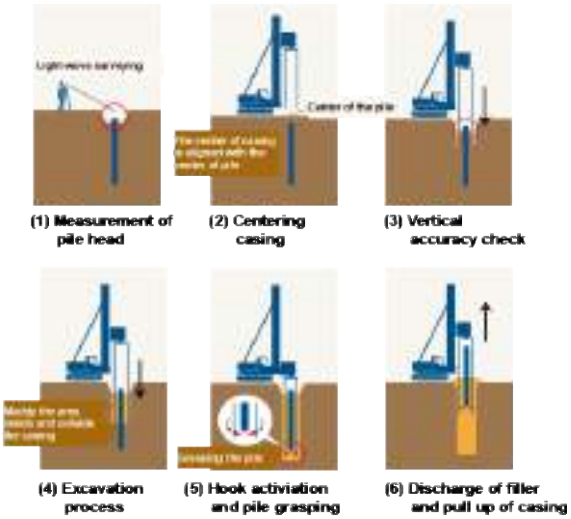

Fig. 8 Schematic of pile tip gripping and lifting method (commonly referred to as PG method)

illustrated in Fig. 7b, can lead to severe secondary disasters, particularly when extracted pile segments fall unexpectedly or when sudden tension release causes equipment instability [19].

The incomplete removal of existing piles through conventional methods creates long-term geotechnical challenges that affect subsequent construction activities. Remnant pile segments buried in the ground can impede new foundation installation, causing alignment problems and compromising the structural integrity of newly constructed foundations. Even when remnant piles do not directly interfere with new pile installation, their presence affects foundation design and performance evaluation, particularly under seismic loading conditions [20].

INNOVATIVE PILE TIP GRIPPING AND LIFTING TECHNOLOGY

The development of the pile tip gripping and lifting method, commonly referred to as the PG method, represents a significant advancement in pile extraction technology specifically designed to address the quality and safety limitations of conventional extraction techniques [15,19,21,22]. This innovative approach fundamentally differs from traditional wire rope methods through its unique pile gripping mechanism and integrated backfilling capabilities.

Fig. 8 illustrates the comprehensive operational sequence of the PG method, demonstrating the systematic approach to pile extraction that ensures precision and safety throughout the process. The method employs specialized hooks located at the casing tip to securely grasp existing piles while simultaneously discharging filler material to backfill the extraction cavity. This integrated approach not only streamlines the extraction process but also enhances safety by eliminating wire rope failure risks and providing immediate ground stabilization.

The operational sequence begins with precise pile head measurement to ensure accurate extraction planning, followed by careful casing alignment with the existing pile centerline to minimize potential ground disturbance and structural damage. Vertical accuracy verification ensures proper casing orientation before commencing excavation activities. During the excavation process, water or cement slurry discharge from the casing tip creates muddy conditions that reduce ground resistance while preventing borehole wall collapse and existing pile damage from soil movement.

The hook activation and pile grasping phase represents the critical technical innovation of the PG method. Once casing excavation reaches completion, specialized hooks engage to securely grip the existing pile structure. The subsequent filler discharge and casing extraction phase enables simultaneous pile removal and backfill placement while maintaining continuous monitoring of injected filler volumes through precision flow measurement systems.

The PG method offers substantial advantages over conventional extraction techniques through elimination of wire rope failure risks, reduced frictional resistance around pile circumferences, and integrated backfilling capabilities that ensure immediate ground stabilization [27]. Additionally, the method addresses pile damage concerns by safely containing damaged pile segments within the protective casing throughout the extraction process.

ADVANCED BACKFILL TREATMENT TECHNOLOGIES

The critical importance of backfill treatment in pile extraction processes cannot be understated, as proper soil stabilization directly affects long-term site performance and construction quality. Fig. 9 demonstrates the adverse effects of poor backfilling practices on surrounding soil conditions, illustrating various failure modes including subsidence occurrence, structural tilting and collapse, retaining wall deformation, heavy machinery instability, new

pile installation complications, and negative impacts on cast-in-place concrete pile construction.

Conventional backfilling methods present significant technical limitations that compromise treatment effectiveness. Fig. 10 illustrates the traditional top-pouring approach employed in wire rope methods, highlighting the formation of stratified structures within boreholes due to sediment attached to existing piles and drilling mud accumulation based on specific gravity differences [15,21]. This stratification creates uneven filler distribution throughout borehole depths, leading to weak zones and potential long-term stability problems.

The performance requirements for effective backfill materials encompass multiple technical specifications that must be simultaneously satisfied to ensure adequate ground stabilization. Fillers must provide uniform strength characteristics regardless of depth, prevent material segregation during placement and curing, develop adequate strength rapidly to accommodate construction scheduling requirements, and resist groundwater infiltration effects that can compromise material properties [23-26].

Soil-based fillers such as sand and gravel offer economic advantages but present significant challenges in achieving uniform fill characteristics and stable strength development throughout borehole volumes. Cases have been documented where loose soil-based backfilling resulted in settlement of backfilled areas compared to original soil conditions, particularly during the first month following installation or during heavy rainfall events [11,12,17].

Fig. 9 Example of adverse effects of poor backfilling of borehole on surrounding soil

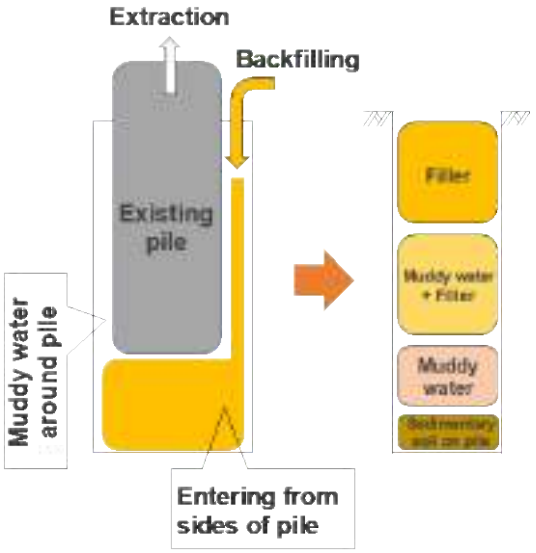

Fig. 10 Backfilling from top of borehole in wire rope method and inadequate backfilling conditions

CEMENT-BASED FILLER DEVELOPMENT AND ENHANCEMENT

The development of advanced cement-based fillers represents a critical advancement in borehole backfilling technology, addressing the fundamental limitations of conventional soil-based approaches. Cement slurry formulations consisting of water, cement, and bentonite provide high fluidity characteristics and self-setting properties that enable effective filling of irregular cavities where mechanical compaction is not feasible [23,26].

However, traditional cement slurries face significant technical challenges including material segregation due to constituent density differences and susceptibility to groundwater infiltration effects that can compromise design strength achievement. The incorporation of sodium carbonate (Na_2CO_3) into cement slurry formulations addresses these limitations through multiple enhancement mechanisms [27,28].

Fig. 11 illustrates the comprehensive mechanism of property enhancement achieved through sodium carbonate addition to cement slurries. The process involves ion exchange reactions that promote bentonite swelling characteristics while accelerating

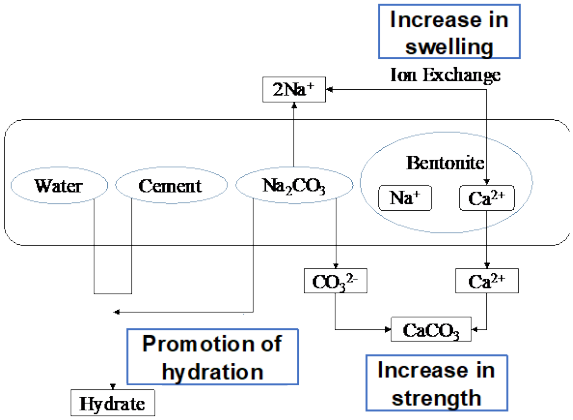

Fig. 11 Mechanism of various properties in cement slurry mixed with sodium carbonate

cement hydration processes. The formation of calcium carbonate ($CaCO_3$) as a reaction product contributes to long-term strength development and improved material durability.

Extensive laboratory investigations have demonstrated that sodium carbonate addition

significantly reduces cement slurry bleeding to less than 1% within one hour of mixing, compared to substantially higher bleeding rates in conventional formulations [28,29]. This bleeding reduction ensures improved material homogeneity and prevents strength reduction associated with water segregation and surface concentration.

The strength development characteristics of sodium carbonate-enhanced cement slurries demonstrate accelerated early strength gain compared to conventional formulations. Fig. 12 illustrates the enhanced bentonite swelling mechanism achieved through sodium carbonate treatment, showing the transformation from calcium-type bentonite with limited swelling capacity to sodium-type bentonite with significantly improved swelling characteristics that enhance void-filling capabilities and reduce material segregation potential.

THICKENER TECHNOLOGY INTEGRATION

The integration of thickening agents into cement slurry formulations provides additional performance enhancements that address specific challenges associated with borehole backfilling applications. Thickeners modify rheological properties including flowability and viscosity characteristics, enabling improved material placement control while maintaining workability for extended periods [30-32].

Fig. 13 demonstrates the comparative material segregation characteristics between standard cement slurry and thickener-enhanced formulations when exposed to aqueous environments. The thickener-enhanced cement slurry maintains structural integrity and prevents constituent separation, ensuring uniform material properties throughout the backfilled volume.

Research investigations have demonstrated that thickener incorporation enables effective blowout prevention even in dilute cement slurries with water-cement ratios exceeding 400%, while maintaining rheological properties for up to two hours following mixing [30-32]. The prevention of cement slurry dissolution in drilling mud represents a critical advantage for borehole operations, contributing to more reliable and consistent construction practices.

COMPREHENSIVE SOLUTION INTEGRATION AND QUALITY ASSURANCE

The integration of PG method extraction technology with advanced cement-based backfill materials creates a comprehensive solution that addresses the full spectrum of technical challenges associated with existing pile removal and site stabilization. This integrated approach provides complete pile extraction assurance while ensuring immediate ground stabilization through high-performance backfill material placement.

The quality assurance framework for integrated

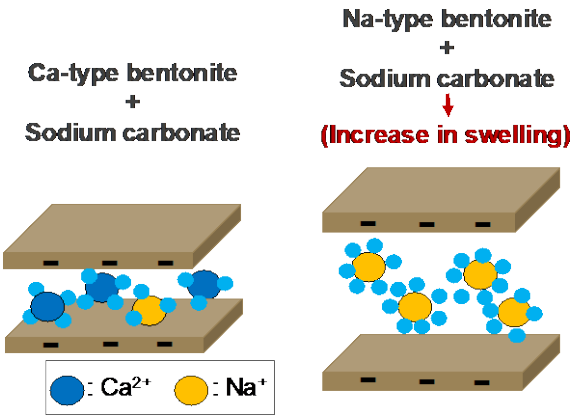

Fig. 12 Effect of mixing sodium carbonate on swelling of bentonite

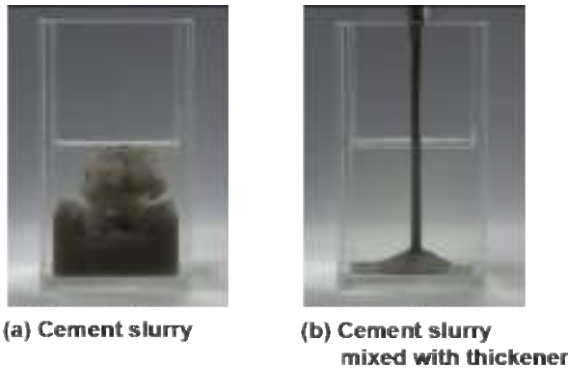

Fig. 13 Comparison of material segregation characteristics in water for cement slurry alone and cement slurry mixed with thickener

pile extraction and backfilling operations requires comprehensive monitoring protocols including boring tests, standard penetration testing, and screw weight sounding assessments to verify treatment effectiveness [17,18]. Continuous quality control throughout extraction and backfilling processes ensures that performance specifications are consistently achieved across project sites.

The sustainability considerations associated with integrated pile extraction and backfilling technologies extend beyond immediate construction benefits to encompass long-term environmental stewardship and resource efficiency optimization. The enhanced land reuse potential achieved through complete pile removal and proper ground stabilization contributes to more sustainable urban development practices while minimizing environmental disruption during construction activities.

CONCLUSIONS AND FUTURE DIRECTIONS

The innovative technologies presented in this keynote demonstrate transformative approaches to existing pile extraction and borehole backfilling that address critical challenges in modern urban redevelopment. The pile tip gripping and lifting

method represents a paradigm shift in extraction technology that enhances safety through elimination of wire rope failure risks while improving operational efficiency through integrated backfilling capabilities.

The development of advanced cement-based backfill materials enhanced with sodium carbonate and thickening agents provides superior performance characteristics compared to conventional soil-based approaches, ensuring long-term ground stability and construction quality. These material innovations demonstrate the potential for chemical enhancement strategies to address fundamental limitations in geotechnical applications.

The integration of extraction and backfilling technologies creates comprehensive solutions that support sustainable urban redevelopment through improved safety, enhanced efficiency, and environmental stewardship. The continued development of these technologies, coupled with comprehensive guideline establishment and international technology transfer initiatives, will be essential for addressing the worldwide infrastructure renewal challenge while maintaining public safety and environmental protection standards.

Future research directions should focus on advanced material formulation optimization, automated system development, real-time monitoring technology integration, and sustainable material sourcing strategies that support global implementation across diverse geological and urban contexts. The establishment of standardized testing protocols and performance evaluation criteria will facilitate international adoption of these innovative technologies for sustainable infrastructure renewal worldwide.

REFERENCES

[1] Wuyts W., Miatto A., Sedlitzky R., and Tanikawa H., Extending or ending the life of residential buildings in Japan: A social circular economy approach to the problem of short-lived constructions. Journal of Cleaner Production, Vol. 231, 2019, pp. 660-670.

[2] Fujita M., Hamaguchi N., and Kameyama Y., Spatial Economics for Building Back Better. Springer Singapore, 2021, pp. 1-200.

[3] Duan H., Miller T.R., Liu G., and Tam V.W.Y., Construction debris becomes growing concern of growing cities. Waste Management, Vol. 83, 2019, pp. 1-5.

[4] Goto K., Ishizawa T., Ebina Y., Imamura F., Sato S., and Udo K., Ten years after the 2011 Tohoku-oki earthquake and tsunami: Geological and environmental effects and implications for disaster policy changes. Earth-Science Reviews, Vol. 212, 2021, pp. 103417.

[5] Daimon H., Miyamae R., and Wang W., A critical review of cognitive and environmental factors of disaster preparedness: research issues and implications from the usage of "awareness (ishiki)" in Japan. Natural Hazards, Vol. 117, Issue 2, 2023, pp. 1213-1243.

[6] Bertino G., Kisser J., Zeilinger J., Langergraber G., Fischer T., and Osterreich D., Fundamentals of building deconstruction as a circular economy strategy for the reuse of construction materials. Applied Sciences, Vol. 11, Issue 3, 2021, pp. 939.

[7] Hjort J., Streletskiy D., Doré G., Wu Q., Bjella K., and Luoto M., Impacts of permafrost degradation on infrastructure. Nature Reviews Earth & Environment, Vol. 3, Issue 1, 2022, pp. 24-38.

[8] Inazumi S., Intui S., Jotisankasa A., Chaiprakaikeow S., and Shinsaka T., Applicability of mixed solidification material based on inorganic waste as soil stabilizer. Case Studies in Construction Materials, Vol. 12, 2020, pp. e00305.

[9] Konda T., Reclaiming the underground space of large cities in Japan (Saveur ed.). Reclaiming Underground Space, Vol. 1, 2022, pp. 13-23.

[10] Inazumi S., Shiina M., and Nakao K., Aeration curing for recycling construction-generated sludge and its effect of immobilizing carbon dioxide. Case Studies in Construction Materials, Vol. 20, 2024, pp. e02704.

[11] Kuwahara S. and Inazumi S., Settlement of surrounding grounds due to existence of pile pulling-out holes. International Journal of GEOMATE: Geotechnique, Construction Materials and Environment, Vol. 16, Issue 54, 2019, pp. 81-85.

[12] Kuwahara S., Inazumi S., Jotisankasa A., and Chaiprakaikeow S., Influence of the condition of pullout holes on the surrounding ground. International Journal of Geo-Engineering, Vol. 11, Issue 1, 2020, pp. 10.

[13] Inazumi S., Kuwahara S., Jotisankasa A., and Chaiprakaikeow S., MPS-CAE simulation on dynamic interaction between steel casing and existing pile when pulling out existing piles. International Journal of GEOMATE: Geotechnique, Construction Materials and Environment, Vol. 18, Issue 70, 2020, pp. 68-73.

[14] Inazumi S., Tanaka S., Komaki T., and Kuwahara S., Evaluation of effect of insertion of casing by rotation on existing piles. Geotechnical Research, Vol. 8, Issue 1, 2021, pp. 25-37.

[15] Kuwahara S., Hamaguchi S., Shimada Y., and Inazumi S., Construction theories and examples for method of powerfully chucking the tip of existing pile at removal of existing piles (in Japanese). Japanese Geotechnical Journal, Vol. 14, No. 1, 2019, pp. 69-76.

[16] Inazumi S., Kuwahara S., and Shishido K., MPS-CAE analysis of developed spiral agitation method for backfilling of pullout holes of existing piles (in Japanese). Japanese Journal of JSCE, Vol. 76, No. 4, 2020, pp. 441-452.

[17] Inazumi S., Kuwahara S., Nontananandh S., Jotisankasa A., and Chaiprakaikeow S., Numerical analysis for ground subsidence caused by extraction holes of removed piles. Applied Sciences, Vol. 12, Issue 11, 2022, pp. 5481.

[18] Shakya S., Nakao K., Kuwahara S., and Inazumi S., Impact of the boreholes on the surrounding ground. Water, Vol. 15, Issue 1, 2023, pp. 188.

[19] Inazumi S., Kuwahara S., Nakao K., and Sakaida A., Reliability evaluation of filling material injection after pulling-out existing piles by pile-tip chucking system (PG method) (in Japanese). Journal of the Society of Materials Science Japan, Vol. 69, No. 3, 2020, pp. 204-209.

[20] Randolph M.F., Carter J.P., and Wroth C.P., Driven piles in clay—the effects of installation and subsequent consolidation. Géotechnique, Vol. 29, Issue 4, 1979, pp. 361-393.

[21] Inazumi S., Kuwahara S., Jotisankasa A., and Chaiprakaikeow S., Construction method for pulling out existing piles and influence of pulling-out holes on the surrounding ground. Geotechnical and Geological Engineering, Vol. 38, Issue 1, 2020, pp. 6107-6123.

[22] Inazumi S., Kuwahara S., Ogura T., Hamada S., and Nakao K., Visualization and performance evaluation of existing pile pulling method with pile tip chucking by MPS-CAE (in Japanese). Japanese Geotechnical Journal, Vol. 15, No. 2, 2020, pp. 383-393.

[23] Javadi H., Ajarostaghi M.S.S., Rosen M.A., and Pourfallah M., A comprehensive review of backfill materials and their effects on ground heat exchanger performance. Sustainability, Vol. 10, Issue 12, 2018, pp. 4486.

[24] Inazumi S., Shigematsu Y., and Nakao K., Flowability evaluation of higher fluidization treated soils by granules analysis with distinct element method (in Japanese). Journal of the Society of Materials Science Japan, Vol. 69, No. 2, 2020, pp. 165-172.

[25] Kowsura S., Chaiprakaikeow S., Jotisankasa A., Malaikrisanachalee S., Nontananandh S., Nusit K., Sawangsuriya A., and Inazumi S., Properties and performances of soil cement modified with concentrated para-rubber. International Journal of GEOMATE: Geotechnique, Construction Materials and Environment, Vol. 24, No. 102, 2023, pp. 42-49.

[26] Shigematsu Y., Inazumi S., Chaiprakaikeow S., and Nontananandh S., Properties of high-flowability liquefied stabilized soil made of recycled construction sludge. Recycling, Vol. 8, Issue 5, 2023, pp. 67.

[27] Inazumi S., Kuwahara S., and Hashimoto K., Cement-bentonite fillings mixing sodium carbonate for holes formed by pulling-out piles (in Japanese). Journal of the Society of Materials Science Japan, Vol. 68, No. 7, 2019, pp. 572-577.

[28] Inazumi S., Kuwahara S., Jotisankasa A., and Chaiprakaikeow S., Improvement mechanism of sodium carbonate on traditional composite filler. Proceedings of the Institution of Civil Engineers - Ground Improvement, Vol. 174, Issue 2, 2021, pp. 132-139.

[29] Bernal S.A., Nicolas R.S., van Deventer J.S., and Provis J.L., Alkali-activated slag cements produced with a blended sodium carbonate/sodium silicate activator. Advances in Cement Research, Vol. 28, Issue 4, 2016, pp. 262-273.

[30] Saida K., Uehara T., and Inazumi S., Physical properties of cement milk of a high water-cement ratio with surfactant-type liquid thickener (in Japanese). Journal of the Society of Materials Science Japan, Vol. 71, No. 5, 2022, pp. 475-480.

[31] Shigematsu Y., Inazumi S., Hashimoto R., and Yamauchi H., Experimental study on properties of liquefied stabilized soil produced with different types of solidifiers and thickeners. Case Studies in Construction Materials, Vol. 19, 2023, pp. e02407.

[32] Chen X., Wang C., Xue Y., Chen Z., Jin J., and Wang R., A novel thermo-thickening viscosity modifying admixture to improve settlement stability of cement slurry under high temperatures. Construction and Building Materials, Vol. 295, 2021, pp. 123606.

Copyright © Int. J. of GEOMATE All rights reserved, including making copies, unless permission is obtained from the copyright proprietors.

Technical Papers

Geotechnique

15th Int. Conf. on Geotechnique, Construction Materials & Environment,
Kyoto, Japan, 11-13 November 2025, ISBN 978-4-909106124 C3051

GEOTECHNICAL AND MICROSTRUCTURAL ASSESSMENT OF RIVER SLUDGE STABILIZED WITH SUSTAINABLE ADDITIVE SYNERGY

Md Yachin Islam[1] and Zakaria Hossain[1]

[1]Graduate School of Bioresources, Mie University, Japan

ABSTRACT

The utilization of river sludge (RS) in geotechnical engineering offers an environmentally sustainable solution; however, its practical application is hindered by high compressibility and low strength, primarily due to its organic content. This study explores the potential of enhancing RS through stabilization using rice husk ash (RHA) and cement, with a focus on sustainable additive synergy. A series of oedometer tests were conducted on RS blends incorporating varying proportions of RHA and cement to assess key consolidation characteristics-the coefficient of consolidation (cv), coefficient of volume change (mv), and permeability (k). Microstructural analyses using scanning electron microscopy (SEM) and energy-dispersive X-ray spectroscopy (EDS) were conducted to investigate changes in the internal structure and to identify pozzolanic interactions. Among the tested mixtures, the combination of 10% RHA and 6% cement demonstrated optimal performance, significantly reducing compressibility and permeability. These results highlight the effectiveness of RHA in combination with minimal cement content in improving the geotechnical behavior of river sludge. The study contributes to the development of sustainable soil stabilization techniques, offering practical applications in embankment construction, subgrades, and other foundational works.

Keywords: River sludge, Rice husk ash, Geotechnical properties, Pre and post consolidation, Microstructural analysis

INTRODUCTION

Construction on problematic soils often faces challenges such as differential settlement, which can lead to costly structural damage [1]. To address these issues, soil stabilization using cementitious materials is a common and practical approach. River sludge, a typical soft soil, is known for its low strength, high compressibility, and elevated water content, making stabilization essential to achieve acceptable engineering properties [2].

Traditional binders, such as cement and lime, have been widely used to enhance soil strength and reduce compressibility and porosity. Among them, Ordinary Portland Cement (OPC) is the most prevalent stabilizer [3,4]. However, OPC production is highly energy-intensive and contributes significantly to global CO_2 emissions, with approximately 0.95 tons of CO_2 emitted per ton of cement produced. This environmental impact drives the need for more sustainable and energy-efficient alternatives that still provide effective soil improvement [5].

Rice husk ash (RHA), a by-product of agricultural waste combustion, has attracted attention as a sustainable stabilizer due to its high silica content and pozzolanic properties [6-8]. Its unique microporous structure and large specific surface area help reduce moisture in river sludge, improving compaction and stability. RHA's chemical composition primarily consists of amorphous silica (SiO_2), along with various oxides depending on combustion conditions. When produced at optimal temperatures (600-700°C), RHA exhibits high pozzolanic activity, reacting with calcium compounds to form cementitious phases such as calcium silicate hydrates, thereby enhancing the strength and durability of stabilized soils [9].

Recent research has increasingly focused on stabilizing river sludge using various innovative additives [10-12]. For example, Jaditager and Sivakugan [13] examined sedimentation improvements in dredged mud slurry from Townsville, Australia, using a fly ash-based geopolymer binder. Their settling tests showed enhanced sedimentation with higher geopolymer content, despite limited chemical interaction between the binder and soil particles [13]. Similarly, Peng, L. & Chen, B [14] evaluated the influence of polyacrylamide (PAM) on the compressibility of river sludge from Tianjin, China. They found that the coefficient of consolidation (cv) generally increased with PAM concentration in normally consolidated samples, while over-consolidated samples showed more complex behavior depending on PAM dosage [14]. Further, Jaditager and Sivakugan [13] reported that increasing fly ash-based geopolymer content effectively reduced the coefficient of volume compressibility (mv) in dredged soils. These studies demonstrate diverse methods of enhancing river sludge properties through novel stabilization

techniques [15].

Addressing gaps in sustainable stabilizer combinations, this study investigates river sludge stabilization with varying proportions of rice husk ash (RHA) at 5%, 10%, and 15%, alongside cement at 2%, 4%, and 6%. The key objectives include:

- Determining optimal RHA-cement ratios to improve compressibility and consolidation behavior of river sludge composites.
- Evaluating the effects of these additives on consolidation parameters such as coefficient of consolidation (cv), coefficient of volume change (mv), and permeability (k) under different conditions.
- Characterizing microstructural changes in stabilized samples through advanced techniques including scanning electron microscopy (SEM), energy-dispersive X-ray spectroscopy (EDS), and X-ray diffraction (XRD).

RESEARCH SIGNIFICANCE

This study provides a systematic evaluation of the compressibility and consolidation behavior of river sludge stabilized with rice husk ash (RHA) and cement, focusing on critical geotechnical parameters such as the coefficient of consolidation, coefficient of volume change, and permeability through oedometer testing. By integrating advanced microstructural and chemical analyses, including energy-dispersive X-ray spectroscopy (EDS) and X-ray diffraction (XRD), the research offers valuable insights into the interaction mechanisms between RHA and cement within the composite material. Although RHA has demonstrated potential in enhancing soil properties, the combined effects of varying RHA proportions with cement on consolidation characteristics remain underexplored. This investigation addresses this gap, contributing to the advancement of sustainable, low-carbon soil stabilization methods suitable for geotechnical applications, thereby promoting eco-friendly construction practices.

MATERIALS AND METHODOLOGY

Materials

River sludge

The river sludge samples were sourced from Saga Prefecture, Japan. After collection, the sludge was air-dried for three weeks and passed through a 200 µm sieve to prepare it for laboratory testing. Soil classification was performed using sieve and hydrometer analyses, along with liquid and plastic limit tests. The sludge exhibited liquid and plastic limits of 62.31% and 52.27%, respectively. According to the AASHTO classification system, the material was classified as A-2-5(0), indicating a silty and clayey gravelly sand. All procedures adhered to the Japan Industrial Standards (JIS), specifically JIS A 1204 for particle size distribution and JIS A 1205 for Atterberg limits [16].

Binder materials

Two additives-rice husk ash (RHA) and ordinary Portland cement (OPC)-were employed to stabilize the river sludge. The RHA, containing 93.30% silica, was sourced from Make Integrated Technology Co., Ltd., Osaka, Japan. It was produced by incinerating rice husks for 27 hours in a computer-controlled furnace at temperatures ranging from 650 to 700°C, resulting in a high silica content. The RHA particle sizes ranged from 0.07 to 0.3 mm.

OPC was added in small amounts to act as a supplementary binder by providing calcium oxide ions that promote pozzolanic reactions. Its physical and chemical properties are also detailed in Table 1. The combined use of these additives was intended to improve both the geotechnical performance and microstructural integrity of the stabilized river sludge composites.

Methodology

Consolidation behavior testing

River sludge (200 g) was mixed with rice husk ash (5%, 10%, 15%) and cement (2%, 4%, 6%) by dry weight. Water content was adjusted to just below the liquid limit (50.5%–58%) to optimize handling and mimic natural conditions. The mixtures were blended, shaped into 30 mm thick cylinders, and equilibrated for 24 hours before trimming to 60 mm diameter and 20 mm height.

Figure 1 illustrates a step-by-step outline of specimen preparation for all 16 combinations, following the Japan Industrial Standards (JIS). Filter papers were placed to prevent clogging during consolidation testing. Samples underwent incremental loading from 9.8 to 1256 kPa and stepwise unloading, each stage lasting 24 hours to ensure complete consolidation. Settlement was monitored continuously using an LVDT system over 16 days. After testing, specimens were dried for final moisture content, and samples were taken for SEM analysis.

Microstructural analysis

A detailed microstructural and mineralogical investigation of the RS-RHA-C composites was performed using Scanning Electron Microscopy (SEM), Energy-Dispersive X-ray Spectroscopy (EDS), and X-ray Diffraction (XRD). SEM provided high-resolution images of particle arrangement, pore structure, and cementitious bonding by examining polished, gold-coated specimens. EDS analysis identified elemental compositions, revealing the

formation of key hydration products like calcium silicate hydrate (C-S-H) and calcium aluminosilicate hydrate (C-A-S-H), which enhance soil stabilization. XRD was used to detect mineralogical changes and crystalline phases induced by the additives. Together, these techniques offered comprehensive insights into the microstructural evolution and chemical interactions within the composites, supporting improved consolidation and durability in geotechnical applications.

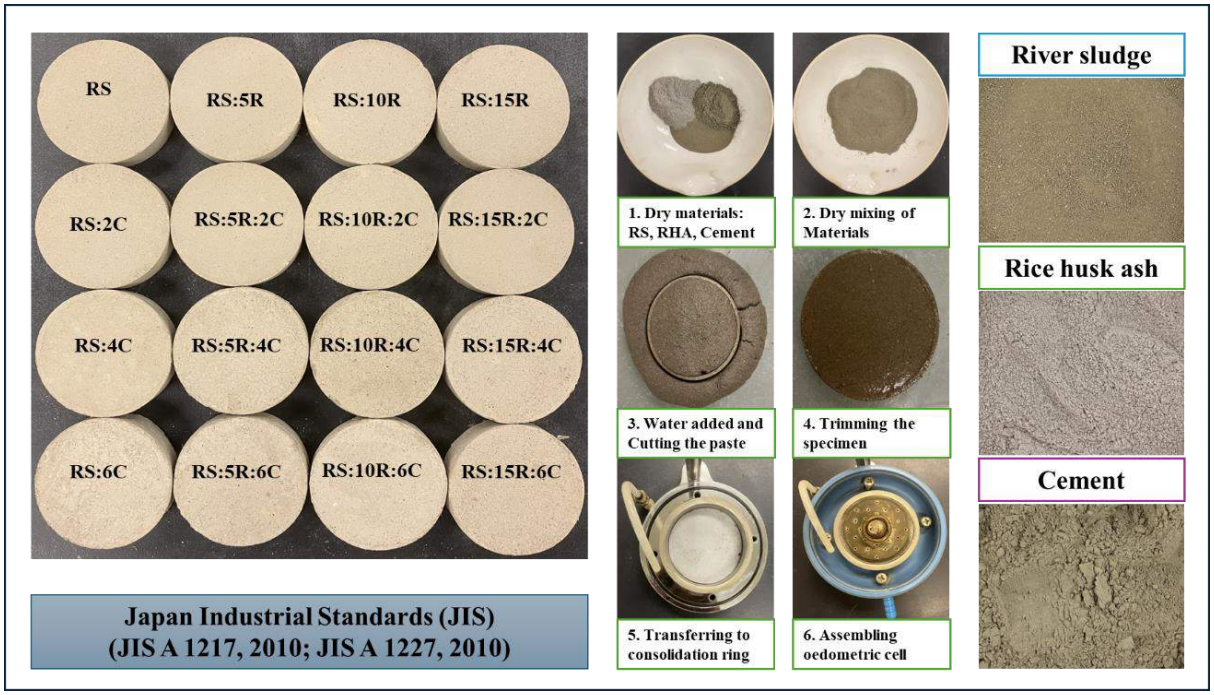

Fig.1 Comprehensive specimen preparation procedure with constituent materials and oedometer cell configuration

RESULTS AND DISCUSSIONS

Geotechnical Analysis

The conditions of the specimens before and after consolidation are presented in Table 1, along with their corresponding statistical descriptions.

The stabilized specimens showed an average saturation of 94.54%, with mean void ratio and wet density values of 1.21 and 1.51 g/cm³, respectively. Low standard deviations confirmed uniform specimen preparation and test consistency. Interestingly, saturation exceeded 100% in some mixes (RS:4C, RS:5R:2C, RS:10R:2C), likely due to the influence of RHA and cement on pore structure and water retention. This behavior may enhance microstructural bonding but also suggests the need to consider specific gravity changes, hydration effects, and possible air entrapment when interpreting consolidation results.

In one-dimensional consolidation, soil undergoes time-dependent deformation under an applied load, leading to the gradual dissipation of excess pore water pressure. According to consolidation theory, key assumptions include soil linear elasticity, incompressibility of soil grains and water, vertical loading, one-dimensional drainage, and constant consolidation parameters.

The time-displacement trends revealed that at low pressures, the transition between primary and secondary consolidation was subtle, but became more distinct as pressure increased. Using the log-time method [17], T50 − the time for 50% primary consolidation- was determined. An increase in RHA content from 5% to 15% resulted in a noticeable reduction in T50, indicating faster consolidation under constant stress, consistent with previous studies. Additionally, RHA-cement-stabilized specimens showed shorter T50 durations at higher pressures, reflecting improved consolidation behavior and reduced settlement delays. These results highlight the effectiveness of RHA and cement in accelerating the consolidation process and enhancing soil stability.

The permeability coefficient (k) of the stabilized specimens ranged between 10^{-10} and 10^{-9} m/s and was strongly influenced by consolidation pressure. An initial rise in k was observed during the pre-yield stage, followed by a marked reduction in the post-yield phase across all samples. Permeability tended to increase with higher RHA content, likely due to the porous nature of RHA introducing more voids into the soil structure. In contrast, specimens with moderate RHA and cement content showed lower permeability, as pozzolanic reactions promoted

effective bonding and reduced pore spaces. The 10% RHA with 6% cement mix demonstrated particularly efficient permeability control, aligning with trends reported in earlier studies.

With increased consolidation pressure, the permeability coefficient gradually decreased and stabilized around 10^{-10} m/s for all specimens. This reduction reflects the densification of the soil-RHA-cement matrix due to void elimination and improved particle arrangement. The strong correlation between void ratio and permeability confirms that voids are the primary factor influencing water flow, consistent with previous findings by Cheng, X., Huang, H., Li, R., Pu, X., Huang, W., & Yuan, X. [18]. Additionally, the influence of RHA content on permeability diminished beyond a certain threshold, indicating that high RHA percentages may stabilize the permeability response under varying pressures. This understanding is useful for predicting field performance of stabilized soils.

Table 1 Statistical summary of the specimen conditions during consolidation

Description (Unit)	Specimen number	Mean	Standard deviation	Coefficient of variation	Mean absolute deviation	Maximum	Minimum
Initial moisture content (%)	16	53.18	3.87	0.07287	3.24578	59.84	48.67
Final moisture content (%)	16	51.84	4.01	0.0775	3.42818	58.01	45.83
Void ratio	16	1.21	0.12	0.10295	0.09535	1.43	0.97
Wet density (g/cm^3)	16	1.51	0.06	0.03996	0.04462	1.64	1.40
Saturation (%)	16	94.54	6.19	0.06551	5.17194	105.82	84.91

Microstructural Analysis

Figure 2 presents SEM images showing significant microstructural improvements in the stabilized specimens. The RS:10RHA:6C composite exhibited a dense, well-bonded matrix with reduced pore spaces and strong interparticle bonding, suggesting active pozzolanic reactions. In contrast, other combinations exhibited a more porous structure due to the presence of unreacted RHA, resulting in weaker bonding and higher compressibility. EDS analysis confirmed the presence of key elements such as Ca, Si, and Al, indicating the formation of cementitious compounds like C-S-H and C-A-S-H.

XRD results (Figure 3) further supported these findings, identifying mineral phases associated with hydration, including portlandite and other reaction products. These results align with the consolidation behavior observed, confirming that moderate RHA-cement ratios enhance structural integrity, while excessive RHA reduces pozzolanic efficiency.

CONCLUSIONS

This study investigated the consolidation behavior of river sludge stabilized with varying ratios of rice husk ash (RHA) and cement through oedometer testing and microstructural analysis. The results showed that the inclusion of RHA and cement significantly influenced consolidation parameters, with the RS:10RHA:6C mix offering the most favorable performance. This composition exhibited the lowest coefficient of consolidation and permeability due to the formation of a dense, well-bonded matrix, attributed to pozzolanic reactions between RHA and cement.

While the coefficient of volume change was more dependent on applied pressure than composition, stabilized specimens consistently demonstrated reduced compressibility compared to untreated sludge. SEM, EDS, and XRD analyses supported these findings by revealing the development of compact cementitious networks in optimized mixes, while excess RHA led to unreacted particles and increased porosity. Empirical equations were developed to predict key consolidation parameters, offering a useful reference for similar stabilization efforts, though further validation is needed.

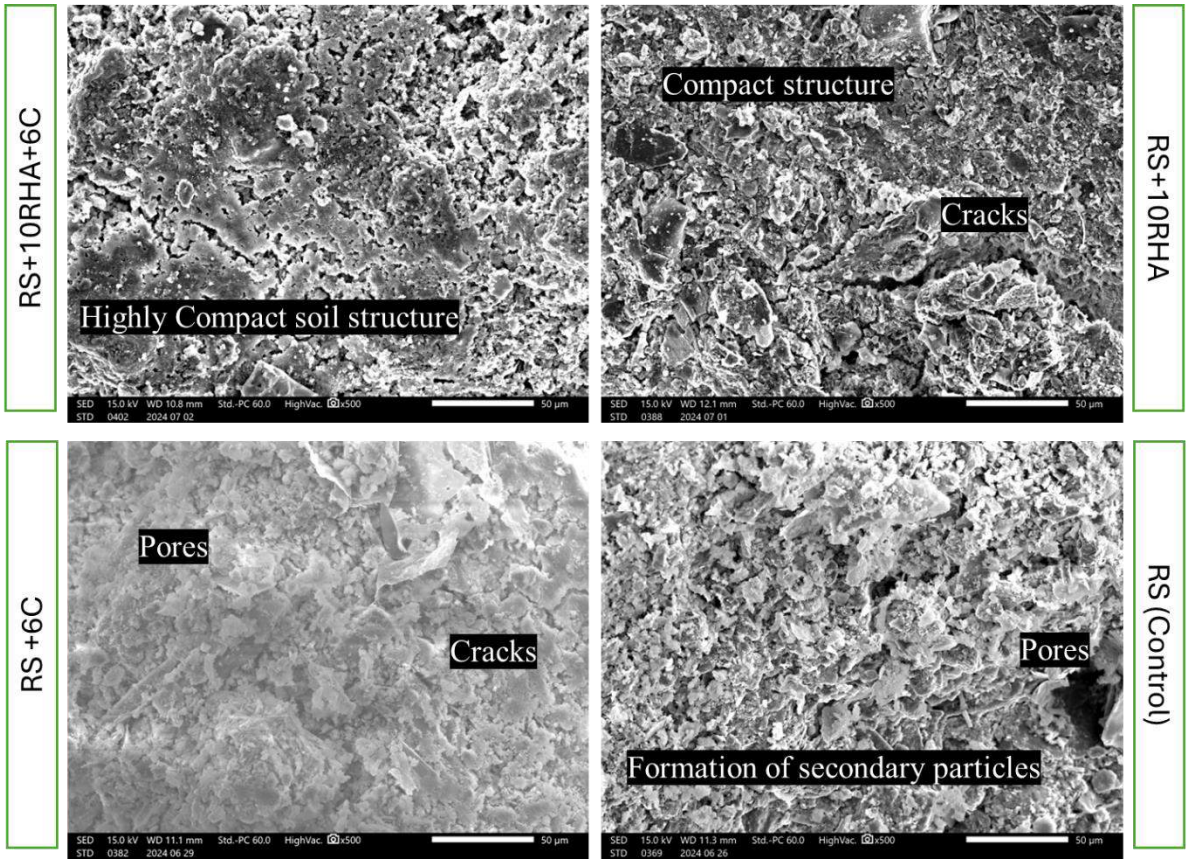

Fig.2 SEM images of RS and stabilized composites with varying RHA and cement content

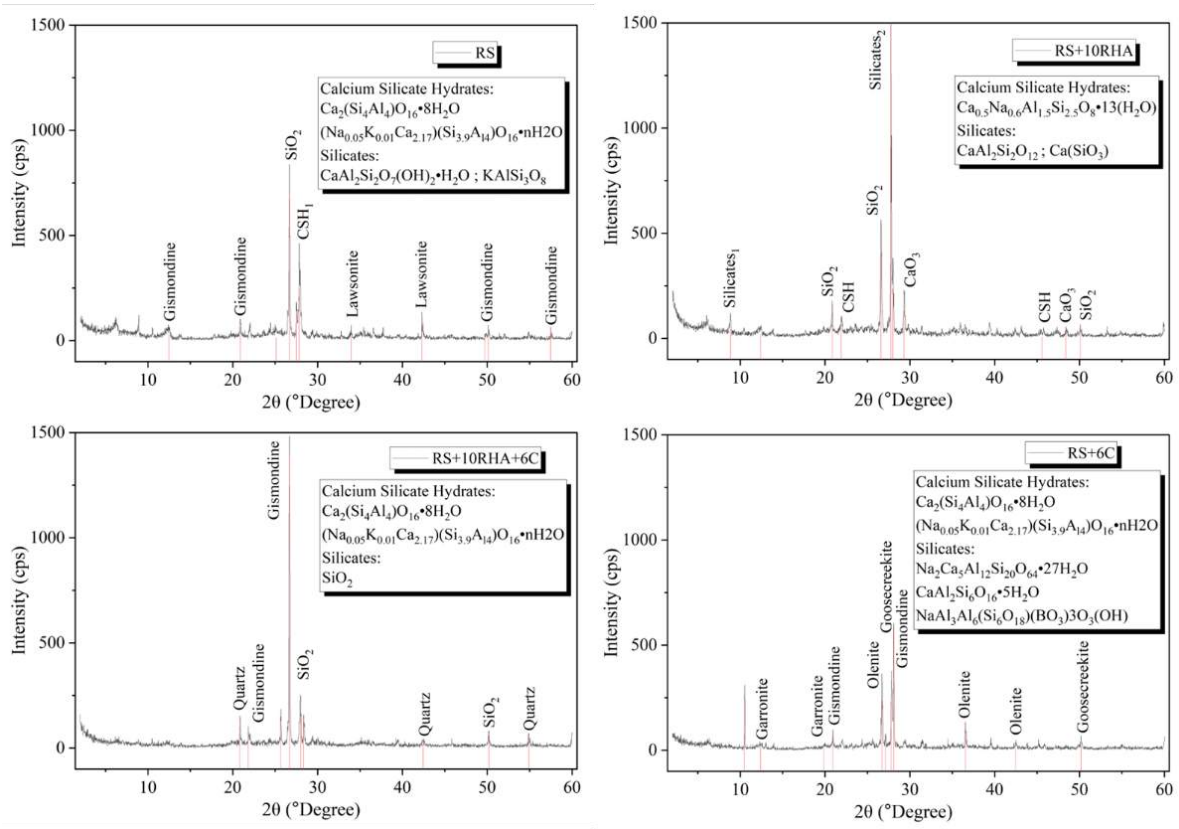

Fig.3 XRD patterns of RS and stabilized composites with varying RHA and cement content

Although commercial RHA was used in this study, the findings underscore the potential of using natural RHA as a low-carbon stabilizer, promoting sustainable practices in geotechnical engineering. Further research is encouraged to evaluate long-term durability, field-scale application, and the efficiency of natural RHA in diverse soil conditions.

ACKNOWLEDGMENTS

The authors extend their sincere appreciation to the Japan Ministry of Education, Culture, Sports, Science, and Technology (MEXT) for awarding the MEXT scholarship, which facilitated the completion of this research at Mie University.

REFERENCES

[1] Islam, M. Y., & Hossain, Z. (2025). Investigating the one-dimensional consolidation properties of river sludge enhanced by sustainable additive synergy for eco-friendly stabilization. Journal of Building Engineering, 101, 111851. https://doi.org/10.1016/j.jobe.2025.111851

[2] Otieno Owino, A., Nahar, N., Hossain, Z., & Tamaki, N. (2022). Dimensional influence of basalt fiber reinforcements on the consolidation behaviour of rice husk ash stabilized soils. Construction and Building Materials, 339, 127686. https://doi.org/10.1016/j.conbuildmat.2022.127686

[3] Xia, Y., Liu, M., Zhao, Y., Guo, J., Chi, X., Du, J., & Du, D. (2023). Sewage sludge and rice husk co-combustion ash: Combustion behavior and cementitious property. Journal of Building Engineering, 71, 106497. https://doi.org/10.1016/j.jobe.2023.106497

[4] Adrian Oshioname, E., Paul, Y., Mustapha, A., & Abdullahi, A.-A. (2022). Consolidation characteristics of lateritic soil treated with rice husk ash. Malaysian Journal of Civil Engineering, 34(1), 19–28. https://doi.org/10.11113/mjce.v34.17663

[5] Zidan, A. F. (2020). Strength and Consolidation Characteristics for Cement Stabilized Cohesive Soil Considering Consistency Index. Geotechnical and Geological Engineering, 38(5), 5341–5353. https://doi.org/10.1007/s10706-020-01367-6

[6] Nakayenga, J., Omaki, N., Kim, D., & Hata, T. (2025). Influence of diatom-amorphous silica on strength and durability of steel slag and cement-treated clays. Soils and Foundations, 65(3), 101613. https://doi.org/10.1016/j.sandf.2025.101613

[7] Yan, K., Lan, H., Li, Q., Ge, D., & Li, Y. (2022). Optimum utilization of recycled aggregate and rice husk ash stabilized base material. Construction and Building Materials, 348, 128627. https://doi.org/10.1016/j.conbuildmat.2022.128627

[8] Ngo, D. H., Horpibulsuk, S., Suddeepong, A., Hoy, M., Udomchai, A., Doncommul, P., Rachan, R., & Arulrajah, A. (2020). Consolidation behavior of dredged ultra-soft soil improved with prefabricated vertical drain at the Mae Moh mine, Thailand. Geotextiles and Geomembranes, 48(4), 561–571. https://doi.org/10.1016/j.geotexmem.2020.03.002

[9] Islam, M. Y., Owino, A. O., Atef, A. E., & Hossain, Z. (2024). The Effects of RHA Dosage on Compressibility and Microstructural Development of Stabilized Calcite-Rich River Sludge. Proceedings of the 5th International Conference on Geotechnics for Sustainable Infrastructure Development, Vol. 395, pp. 1375–1391. Springer Nature Singapore. https://doi.org/10.1007/978-981-99-9722-0_92

[10] Islam, M. Y., Atef, A., Owino, A. O., Islam, A., Rahman, S., & Hossain, Z. (2023). Critical Review on Utilization of River Sludge, Rice Husk Ash, and Cement: Sustainability and Implications. 13th Int. Conf. on Geotechnique, Construction Materials & Environment, pp. 471-475.

[11] Islam, M. Y., & Hossain, Z. (2024). Enhancing The Strength of River Sludge Through The Utilization of Rice Husk Ash: A CBR Approach.14th Int. Conf. on Geotechnique, Construction Materials & Environment, pp. 50-55.

[12] Develioglu, I., & Pulat, H. F. (2019). Compressibility behaviour of natural and stabilized dredged soils in different organic matter contents. Construction and Building Materials, 228, 116787. https://doi.org/10.1016/j.conbuildmat.2019.116787

[13] Jaditager Mohamed & Sivakugan Nagaratnam. (2017). Influence of Fly Ash–Based Geopolymer Binder on the Sedimentation Behavior of Dredged Mud. Journal of Waterway, Port, Coastal, and Ocean Engineering, 143(5), 04017012. https://doi.org/10.1061/(ASCE)WW.1943-5460.0000390

[14] Peng, L., & Chen, B. (2021). Mechanical behavior, durability, thermal performances and microstructure of GGBFS – Modified MPC solidified dredged sludge. Construction and Building Materials, 303, 124557. https://doi.org/10.1016/j.conbuildmat.2021.124557

[15] Li, J., Shan, Y., Ni, P., Li, Y., Cui, J., & Zhou, J. (2023). Multiscale experimental analysis of marine clay stabilized with coal gangue–calcium carbide residue geopolymer. Acta Geotechnica, 18(11), 5921–5939. https://doi.org/10.1007/s11440-023-02055-4

[16] JIS A 1217, Test method for soil consolidation

test. Japanese Industrial Standard, Guidance and Basic - Soil Test, The Jpn. Geotech. Soc. (in Japanese) (2010) 215-227.

[17] Casagrande, A., Fadum, R.E., 1940. Notes on soil testing for engineering purposes. Harvard University Graduate School Engineering Publication, No. 8

[18] Xiaolong Cheng, Yanan Huang, Ran Li, Xunchi Pu, Wendian Huang, Xianfan Yuan, Impacts of water temperature on phosphorus release of sediments under flowing overlying water, Journal of Contaminant Hydrology, Volume 235, 2020, 103717, ISSN 0169-7722, https://doi.org/10.1016/j.jconhyd.2020.103717.

Copyright © Int. J. of GEOMATE All rights reserved, including making copies, unless permission is obtained from the copyright proprietors.

15th Int. Conf. on Geotechnique, Construction Materials & Environment,
Kyoto, Japan, 11-13 November 2025, ISBN 978-4-909106124 C3051

RELIABILITY ANALYSIS OF DAMPALIT MEGA DIKE USING MONTE CARLO SIMULATION AGAINST SLIDING FAILURE

Isaiah Sam Bartolome[1] and Albert Griño, Jr [1]

[1]Faculty, Adamson University, Philippines

ABSTRACT

The main purpose of coastal defenses is to mitigate the effects of an increased rise in sea levels and the abrupt changes in storm surges brought about by various uncertainties. Evaluation of the Dampalit Mega Dike's resistance against sliding failure using Reliability Analysis provides an avenue for considering these uncertainties that would affect the structural safety of the dike. In this study, random variables, including the angle of friction, water level, and wind speed, were considered as the parameters in determining the dikes' probability of failure. Wave action and storm surges were considered, which were vital since these would greatly affect the resistance of the dike. A deterministic approach was initially performed using PLAXIS 2D to compare the conventional design and analysis with a probabilistic approach. For the probabilistic method, both serviceability (SLS) and ultimate limit states (ULS) were evaluated with 100,000 iterations using Monte Carlo Simulation, wherein results show a probability of failure of 0.54 for SLS and 0.86 for ULS. The significant deviation from the acceptable value of x 10^{-3} to the computed values highlights a potentially critical issue in the structural system or the underlying assumptions used in the analysis. A high risk of failure in terms of sliding was concluded; however, biases were observed in the data since no correlations were found between the variables. Moreover, to increase the soil stability of the dike, an additional embankment on the seaward side was recommended to improve the resistance against sliding failure of the dike.

Keywords: Reliability analysis, Storm Surge, Monte Carlo Simulation, Probability of failure, Dike

INTRODUCTION

The rise of sea levels contributes to the increase in flooding, especially in Asian deltaic cities, which include Ho Chih Minh City, Jakarta, Tokyo, and Manila. Exposure to tropical cyclones, excessive groundwater extraction, and rapid urbanization leads to elevated flood levels, affecting the city's socioeconomic development. By 2100, the global mean sea level will rise to 2.92 m. This will affect about 150 – 250 million people, especially those living near coastal areas and low-elevation areas [1]. According to the National Integrated Climate Change Database and Information Exchange System, or NCCDIES (2024), the Philippines is experiencing an exceptionally high rate of sea level rise of 60 centimeters, which is roughly three times faster than the global average of 19 centimeters, which puts 13.6 million Filipinos at risk. Climate models provide a range of predictions for future sea level rise, reflecting different greenhouse gas emission trajectories.

The city of Manila in the Philippines is considered one of the most vulnerable megacities in Southeast Asia in terms of the rapid rise in sea levels. The Dampalit Mega Dike, which is located in Barangay Dampalit, Malabon City, is an 8.6-kilometer mega dike that was constructed for the protection against flooding of the surrounding areas [2]. The Dampalit Mega Dike is important for Malabon's safety and economy. Failure could lead to widespread flooding, endangering lives and disrupting the economy.

Uncertainties are dominantly present in every structure constructed, and these affect its overall function. In the Philippines, the design of numerous structures, including flood defenses, was mainly based on a deterministic approach, which only considers normal ranges based on structural codes. The problem with a purely deterministic designed structure is that the data is gathered under various environmental and material conditions, including imposed loads and material properties. The utilization of statistics and probability in the design of the structure is beneficial in considering the uncertainties that are present in the location [3].

RESEARCH SIGNIFICANCE

The relevant information of this study would help benefit local government authorities and community stakeholders as they contribute to informed decision-making, policy formulation, and the overall resilience of Manila Bay Coastal Defenses. The present study's outcomes would assist LGUs in identifying gaps and challenges inherent in their existing risk management practices. It provides insights into how risk management strategies in Manila City and neighboring areas can be effective. This study can serve as a valuable reference for establishing performance functions that address serviceability and ultimate limit states for sliding of sea dikes.

LITERATURE REVIEW

Probabilistic structural analysis is defined as the art of formulating mathematical models wherein one can acquire results concerning the probability of a structure behaving in a definite manner through calculations. It involves analyzing the behavior of a structure using random material properties and the effect of an external factor on the stability of a structure with random or incomplete known properties [4]. Reliability analysis provides an advanced and more accurate calculation of structures since safety factors from the deterministic method more often than not offer a safety margin that is relatively not 100% safe due to the effects of uncertainties [5].

Random Variables

The presence of uncertainties in various parameters used in the conventional design and analysis contributes to the difficulty in providing a safe and resilient structure through a deterministic approach [6]. This is why establishing a reasonable basis is beneficial, as it provides a means of assessment that can be fulfilled through the evaluation of its reliability and probability of failure. Failure does not always mean losing the function of a structure; rather, it signifies that the structure does not meet the expectations based on its design.

For this study, the random variables considered were based on the primary phenomenon of sliding failure and the effects of storm surges on the dike. The random variables chosen for this study include the sea level h, angle of friction ϕ, and wind speed V_s. These random variables were evaluated since these are where uncertainties can be readily observed, and abrupt changes in these factors can contribute to the overall safety of the dike [7]. Furthermore, since the location of the structure under consideration is near a flood-risk area, the sudden changes in sea levels will affect its stability to some extent. Since the main concern of this study is the strength, it is best to provide an assessment of the present situation of the Dampalit Mega Dike using reliability analysis.

Loads and Forces

According to the National Structural Code of the Philippines (2015), the dead load includes the permanent self-weight of a structure and its installed utilities, such as in the case of a mega dike, while live loads account for temporary loads like human occupancy and vehicles. Dikes are subject to various lateral and vertical forces such as earth pressure—governed by Rankine's and Coulomb's theories—hydrostatic pressure, wave forces [9,10], and storm surge [11,12] loads, all of which require careful consideration in structural design. These forces, which include dynamic factors like wave impact and storm surge elevation, must be properly accounted for to ensure the stability and effectiveness of the dike structure.

Performance Function

The performance function or limit state function $g(X)$ is an expression used to identify the safe and unsafe zones for R (resistance of the structure) and S (load on the structure). Structural conditions are set to provide a depth analysis of the performance function based on the established random variables. Two structural conditions will be considered for this study, namely the Serviceability Limit State (SLS) and the Ultimate Limit State (ULS). SLS describes that the failure of the structure is based on the serviceability loss, which doesn't imply a valuable impact on the overall safety of the structure. On the other hand, the ULS dwells more on the structural integrity and safety of the structure, which may eventually lead to complete failure [13].

Monte Carlo Simulation

Simulations governing both systems of physical and mathematical relations are the main objective of Monte Carlo Simulation. The Monte Carlo Simulation or Monte Carlo Method involves the generation of random events through a computer model wherein the procedure is done multiple times. The occurrence number for a specific condition set by the researcher is then counted and recorded.

The probability of failure of the system can be calculated through the integration of the random variables in a performance function. In some instances, it would be hard to determine the probability of failure through analytical methods since some boundaries of the integral are not known. The use of reliability methods, specifically Monte Carlo Simulation, is more applicable for data sets that are relatively small [14].

The Monte Carlo Simulation is a highly regarded statistical technique that assists organizations in effectively managing risk and making informed decisions when faced with uncertain situations. This powerful tool can be utilized in disaster risk management by simulating a significant number of random variables to analyze the potential outcomes of a complex system. By generating a comprehensive set of individual realizations of sea level time series, decision-makers can leverage descriptive statistics to understand the probability and consequences of disasters. As a result, they can implement more effective risk management strategies [15].

METHODOLOGY

This study utilizes various uncertainties that can

affect the structural integrity of the dike. This includes the effects of storm surges, which are not common in the design of the dike. The occurrence of uncertainties, which are determined through various historical data and reports, is used to determine the probability of failure due to sliding phenomena through the evaluation of the limit state equations using Monte Carlo Simulation.

Moreover, the evaluation of the Dampalit Mega Dike considers the effect of storm surge as the ultimate load that would affect the structure. The random variables that were considered are the angle of friction, sea level, and wind speed, and these are incorporated in the resistance and loads of each limit state equation. The values for these parameters were set based on the simulations performed on the data collected, and the results are used to calculate the probability of failure of the dike.

Data Gathering

The main sources of data for this study came from the geotechnical investigation report which was obtained from the Department of Public Works and Highways (DPWH), the sea level data which was requested from the local government of Dampalit, and the wind speed data were obtained from Philippine Atmospheric, Geophysical and Astronomical Services Administration (PAG-ASA).

Deterministic Method

In the Philippine setting, the common method used in the design of most buildings and infrastructures is governed by the use of a deterministic approach. This is through the use of various codes for design and analysis, which includes the NSCP and other codes vital in providing a safe and resilient structure. These codes were mostly based on theoretical analysis and experimental models in which several assumptions are made [16]. According to Skrzypezak, Slowik, and Buda-Ozog (2017), a purely deterministic approach cannot completely define the reliability and safety of a structure since it is mostly based on a single globally used factor and does not take into consideration the effects of uncertainties with regards to the load and strength assessments provided by the structure.

This study employed deterministic and probabilistic approaches to accurately represent the failure due to the sliding of the Dampalit Mega Dike. The study utilized PLAXIS 2D software for the structural analysis of the dike.

Probabilistic Method

Several parameters were not considered in the deterministic method; thus, it was difficult to provide an overall assessment of the safety of the dike. Therefore, reliability analysis must be done to assess the structure thoroughly. Random variables were viewed as the governing parameters in quantifying uncertainties and risks that a system would experience. The first step in determining the structure's probability of failure and reliability index was to identify the possible variables that would affect the overall safety [17].

In this study, pre-existing mathematical models were considered for the selected random variables wherein the angle of internal friction followed a log-normal distribution while both sea level and wind speed followed a Weibull distribution as presented in Table 1. The mean and coefficient of variation were derived from the data acquired, which were then used to determine the distributions by performing simulations using MATLAB.

Table 1 Distribution of random variables

Random Variable	Distribution	Mean, μ	Coefficient of Variation, *COV*
Angle of internal friction, ϕ	Log-normal	27.19°	0.001°
Sea level, h	Weibull	10.07 m	0.002 m
Wind speed, V_s	Weibull	2.87 m/s	0.198 m/s

Calculation of the probability of failure

This study considers the sliding failure mechanism's effect on the dike's safety with the impending rise of sea levels. The SLS and ULS equations for the sliding failure mechanism is defined in Eq. (8) and Eq. (9), respectively.

$$g(X) = F_k - (P_h + W_A + P) \quad (8)$$

$$g(x) = F_k - (P_h + W_A + P + S_L) \quad (9)$$

Where F_k is the sliding force or Law of Kinetic Friction derived from Amonton's and Coulomb's Law of Friction. The sliding force acted as the resistance of the dike; it was used for both the serviceability and ultimate limit state equations. The load for SLS was based on the summation of the applied loads on the structure which includes lateral earth pressure P_h, wave action W_A, and hydrostatic force P while for that of the ULS.

In relation to the factor of safety, the probability of failure can be defined as the probability where the factor of safety falls below 1.0 if there are adverse effects of certain variables present in the calculations [18] which is shown in Eq. (10).

$$Pf = P(S > R) \quad (10)$$

This study utilized 100,000 simulations for both the random variables and performance functions to be able to generate several data points. This would provide a good balance between obtaining increased

accuracy and calculation duration for the equations. Moreover, it has been a common practice to use 100,000 simulations in performing the Monte Carlo Simulation wherein larger numbers lean to a more statistically reliable result [19].

The results for both the deterministic and probabilistic methods would provide reliable results that would support the occurrence of failure on the dike. Determining the failure points of the dike using PLAXIS would provide the necessary results to attest to the decrease in safety in terms of sliding. Moreover, probabilistic methods using reliability analysis would present the probability of failure due to the presence of uncertainties in the environment.

RESULTS AND DISCUSSION

The initial results of the deterministic method using PLAXIS 2D, as seen in Fig. 1, show a significant displacement, mostly due to hydrostatic forces and lateral earth pressure applied on the dike. The red regions represent the failure points where increased values of hydrostatic forces can cause the displacement of the soil beneath the dike, leading to failure.

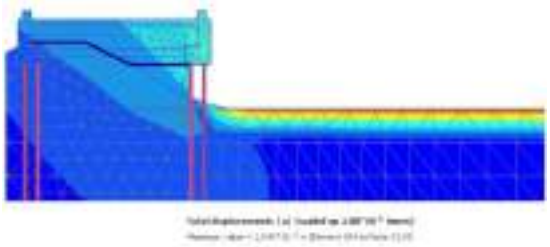

Fig. 1 Result of PLAXIS 2D analysis (total displacement of Dampalit Mega Dike)

Based on the results, there is an evident failure on the seaside of the dike where possible sliding is due to increased pressure brought by both hydrostatic and lateral earth forces on the structure. Lack of sufficient support or increased soil stability caused the structure to fail at that specific point, especially with the effects of storm surges, which can cause higher wave impact, which weakens the soil [20].

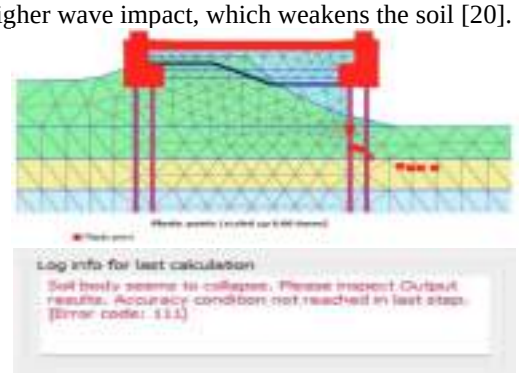

Fig. 2 Results of PLAXIS 2D (failure points)

Based on the results of PLAXIS 2D, the software indicates that the dike would slide by about 0.002045 meters or 2.045 mm. towards the seaside. PLAXIS 2D also indicated that the “soil body seems to collapse” as presented in Figure 10 which is due to the uplift pressure caused by the sea water causing instability in the bottom-right part of the dike. The steepness of the topography of the soil where station C0+040.00 is situated, the soil could not handle the weight and forces applied on the dike, which resulted in its sliding.

The gathered data for the angle of friction, wind speed, and water level were simulated 100,000 times to properly provide a reliable distribution which was utilized for the calculation of the probability of failure. It was important to identify the distribution of these random variables through their mean and coefficient of variance to be able to appropriately apply the right method of estimate for the performance functions.

The statistical parameters derived from the analysis were implemented in MATLAB, where custom-developed code facilitated simulations and probabilistic assessments. The methodology relied on the Monte Carlo Simulations, enabling a comprehensive evaluation of system performance by quantifying the effects of variability and uncertainty in the input parameters. This approach allowed for robust predictions of system behavior under diverse conditions and informed decision-making regarding soil-structure interaction and environmental considerations.

The probability of failure was calculated for each limit state equation and its corresponding resistance and loads. To provide an accurate result of the probability of failure in multiple occurrences presented by each simulated value of the random variables, 100,000 simulations were also done using Monte Carlo Simulation for both SLS and ULS. It must also be taken into account that the computation of the load combinations followed a modified loading combination since the National Structural Code of the Philippines does not have a specific section for dike structures.

Based on the results, it is evident that there is no direct correlation between resistance and the load. However, the probability of failure for both performance functions shows a significant value. Moreover, a change in the load would not affect the resistance of the dike since both acts independently of each other.

The probability of failure of the dike against sliding failure was calculated using 100,000 simulations with the equation $Pf = P(S > R)$ which is determined by a normal cumulative distribution that resulted in $Pf = 0.54$ for SLS and $Pf = 0.86$ for ULS. Based on the graph, the failure point for the resistance is determined to be at around 3.1 x

10^{-3} for both SLS and ULS, while that of the load is estimated to be around 1,300 kN of force.

Based on the results of both deterministic and probabilistic methods, it is evident that the water level, wind speed, and angle of friction would affect the dike's sliding resistance. These uncertainties would affect the overall stability of the Dampalit Mega Dike, especially with the capacity of the soil to prevent the sliding of the dike. Varying degrees of pressure brought by the hydrostatic force on the dike induce displacement of the soil where the dike is constructed.

According to Zhang, et al (2017), a great factor that affects the destabilization of a dike is the combined effects of normal hydrostatic force exerted by seawater and the increased shearing effect from overtopping flows. The abrupt increase and decrease in wave pressure affect the resistance of the dike, resulting in sliding and eventually failure. Coastal dikes are most vulnerable to drastic changes in hydrostatic and hydrodynamic loads.

The knowledge and understanding of wave loads and storm surges are typically not common [21]. Furthermore, overtopping waves in dikes are considered a detrimental threat to both properties and lives in coastal areas. The inclusion of a probabilistic method in the analysis of structures, especially with dikes, can provide a more conservative and resilient design.

The results for the probability of failure for SLS shows a value of 0.54 while that of the ULS shows a value of 0.86. Such a result suggests that the structure under consideration is highly unreliable and fails to meet the minimum safety requirements. Moreover, a result that shows an almost 100% failure is very unlikely, and certain parameters must be checked to ensure the viability of the results

According to Li and Yang (2023), the significant deviation from the acceptable value of $x10^{-3}$ to the computed value of 1.000000 highlights a potentially critical issue in the structural system or the underlying assumptions used in the analysis. This discrepancy may arise from inadequacies in design parameters, improper material properties, or unforeseen environmental loads. It underscores the necessity for an immediate reassessment of the design, including a comprehensive review of the input parameters, modeling assumptions, and boundary conditions.

These findings emphasize the critical importance of accurate reliability analysis in engineering design. The ability to detect such high probabilities of failure ensures that corrective measures can be implemented to prevent catastrophic outcomes. Future work should focus on refining the computational framework, validating input data, and exploring alternative design solutions to align with acceptable safety margins.

CONCLUSIONS

Based on the analysis conducted on the Dampalit Mega Dike, this study assessed the likelihood of failure due to sliding using both deterministic and probabilistic methods. The deterministic analysis carried out using PLAXIS 2D revealed that the dike would experience sliding with a minimal displacement of 0.002 meters under current conditions. The displacement was so minimal that it was nearly unnoticeable, suggesting that the structure remains functional under serviceability loads.

This indicates that, based on static loading conditions, the dike is still operational and capable of performing its intended function. However, the results of the probabilistic analysis, which included random variables such as angle of friction, water level, and wind speed, showed that the dike falls into a "failure zone" due to the combined effects of these uncertainties. Specifically, the probabilistic approach highlighted that the variability in environmental forces (wind speed and wave action) and soil properties can lead to an increased likelihood of failure.

In line with the study, the geotechnical report clearly shows pre-determined values and lacks actual results since there are few boreholes used for the geotechnical analysis of the soil where the dike was constructed. Although evidence of failure is prominent in the results of the study, further investigations should be made, especially with the soil parameters concerning the stability of the dike. Issues regarding the actual reports must be investigated to prevent loss of structural integrity on the part of the construction of dikes near bodies of water, since an increase in water pore pressure due to elevated water levels can affect the sliding failure, which in turn affects the dike [22].

ACKNOWLEDGMENTS

The authors would like to express their sincere appreciation to the Center of Research and Development (CRD) at Adamson University, for it was with their generous support that this study was made possible.

REFERENCES

[1] Cao A., Esteban M., Valenzuela V., Onuki M., Takagi H., Thao N., and Tsuchiya N., Future of Asian Deltaic Megacities under sea level rise and land subsidence: current adaptation pathways for Tokyo, Jakarta, Manila, and Ho Chi Minh City, Current Opinion in Environmental Sustainability, pp. 87 – 97.

[2] Dioquino A.H., Probabilistic Characterization of Soil Properties Based on the Maximum Entropy Method from Fractional Moments: Model Development, Case Study, and Application, Reliability Engineering and System Safety, pp. 1-15

[3] Holickey M., Reliability Analysis for Structural Design, SUN MeDIA Stellenbosch, 2009, pp. 5 – 15.

[4] Skrzypezak I., Slowik M., and Buda-Ozog L., The Application of Reliability Analysis in Engineering Practice – Reinforced Concrete Foundation, International Conference on Analytical Models and New Concepts in Concrete and Masonry Structures, pp. 145-147.

[5] Li C.Q. and Yang W., Assessment of Safety and Reliability, Time-Dependent Reliability Theory and its Application, Woodhead Publishing, 2023, pp. 1-50.

[6] Li W., Hong C., Qiao L., Ma J., Peng Z., and Wang Z., Reliability Analysis of Underground Water-sealed Storage Caverns Stability: Method and Application, Tunnelling and Underground Space Technology Incorporating Trenches Technology Research, pp. 1-11.

[7] Jörges C., Berkenbrink C., Gottschalk H., and Stumpe B., Spatial Ocean Wave Height Prediction with CNN Mixed-Data Depp Neural Networks Using Random Field Simulated Bathymetry, Ocean Engineering, Vol. 271, 2023, pp. 1-16.

[8] Abram N., Gattuso J.-P., Prakash A., Cheng L., Chidichimo M.P., Crate S., Enomoto H., Garschagen M., Gruber N., Harper S., Holland E., Kudela R.M., Rice J., Steffen K., and von Schuckmann K., 2019: Framing and Context of the Report. In: IPCC Special Report on the Ocean and Cryosphere in a Changing Climate, Cambridge University Press, Cambridge, UK and New York, NY, USA, pp. 73–129.

[9] Chen Z., Jiao J., Chen Y., Jiang C., and Chen S., Influence of Wave Directional Spreading of Short-Crested Irregular Waves on Ship Motion and Irregular Loads., Marine Structures, Vol. 103, 2025, pp. 1-25.

[10] Liu J., He J., Hong Y., and Gong Z., Experimental and Numerical Study on Impact Loads During Wedge Water-Entry Under Wave Conditions, Ocean Engineering, Vol. 330, 2025, pp. 1-2.

[11] Haddow G.D., Bullock J.A., and Coppola D.P., Natural and Technological Hazards and Risk Assessment, 6th Ed., Introduction to Emergency Management, Elsevier Inc., 2017, pp. 33-77.

[12] Griño Jr. A., Prediction of Storm Surge Level Using Artificial Neural Network: A Case Study of Typhoon Haiyan, International Journal of GEOMATE, Vol. 28, Issue 126, 2025, pp. 8-15.

[13] Nwofor T.C., Worlu B., and Ezegbirika M.C., Reliability Analysis of a Semi-gravity Retaining Wall Designed to Eurocode 7, Journal of Industrial Safety Engineering, Vol. 10, No. 3, 2023, pp. 35-47.

[14] Betz W., Papaioannou I., and Straub D., Bayesian post-processing of Monte Carlo Simulation in Reliability Analysis, Reliability Engineering and Safety, Vol. 227, 2022, pp. 1-13.

[15] Weiss R., Dura T., and Irish J.L, Modeling Coastal Environmental Change and Tsunami Hazard, Global Change and the Future Ocean, Vol. 9, 2022, pp. 1-12.

[16] Grocel J., Comparison of Deterministic and Stochastic Method in Operational Modal Analysis in Application for Civil Engineering Structures, Procedia Engineering, Vol. 91, 2014, pp. 130-135.

[17] Bastidas-Arteaga E., and Soubra A.-H., Reliability Analysis Methods, Stochastic Analysis and Inverse Modeling, 2014, pp. 53-77.

[18] Ching J., and Phoon K., Risk and Reliability in Geotechnical Engineering, 1st Ed., CRC Press, Boca Raton, pp. 1-624.

[19] Rahman Md.S., Selim Reza A.H.M., Sattar G.S., Siddique Md.A.B., Akbor Md.A., Moniruzzaman Md., Uddin Md.R., and Shafiuzzaman S.M., Mobilization Mechanisms and Spatial Distribution of Arsenic in Groundwater of Western Bangladesh: Evaluating Water Quality and Health Risk using EWQI and Monte Carlo Simulation, Chemosphere, Vol. 366, 2024, pp. 1-14.

[20] Peng M., Zhang J., Zhu Y., Gao L., Li S., and Pan X., Experimental Study on Wave Attenuation and Stability of Ecological Dike System Composed of Submerged Breakwater, Mangrove, and Dike Under Storm Surge, Applied Ocean Research, Vol. 151, 2024, pp. 1-16.

[21] Chen X., Hofland B., Altomare C., Suzuki T., and Uijttewaal W., Forces on Vertical Wall on a Dike Crest due to Overtopping Flow, Coastal Engineering, Vol. 95, 2015, pp. 94-104.

[22] Merckelbach L., Kranenburg C., and Winterwerp J., Strength Modeling of Consolidating Mud Beds, Proceedings in Marine Science, Vol. 5, 2022, pp. 359-373.

Copyright © Int. J. of GEOMATE All rights reserved, including making copies, unless permission is obtained from the copyright proprietors.

15th Int. Conf. on Geotechnique, Construction Materials & Environment,
Kyoto, Japan, 11-13 November 2025, ISBN 978-4-909106124 C3051

DEBRIS FLOW CAUSED BY HEAVY RAINFALL IN NAGISO-TOWN IN NAGANO PREFECTURE IN JULY 2014

Naomasa Honda[1]

[1] Faculty of Regional Environment Science, Tokyo University of Agriculture, Japan

ABSTRACT

In 2014 in the Nashizawa basin in Nagiso-Town in Nagano Prefecture, a huge, devasting debris flow was caused by a heavy rainfall due to typhoon No.8. Based on effective rainfalls and rainfall index *R'*, we discuss the relationship between the rainfall characteristics and the debris flow occurrence. Judging from the results, the rain's influence before the debris flow occurrence remained as *R'* = around 50mm until just before the occurrence. A heavy amount of rain fell (70mm/h) and a debris flow occurred. Based on our debris flow runoff analysis, two check dams provided a debris flow control function. The debris flow might continue at slightly less than 20% of the sediment flux concentration at the valley's exit with earth flow characteristics. The flow directly continued in the curved section of the channel works and arrived at the Kizu River junction.

Keywords: Previous Prolonged Rainfall, Last Short Strong Rainfall, Effective Rainfall, Rainfall Index R', Debris Flow Runoff Analysis

INTRODUCTION

In Nagiso-Town in Nagano Prefecture, typhoon No. 8 caused heavy rainfall in July 2014, followed by a huge debris flow through the Nashizawa Valley. Concerning the characteristics of this debris flow occurrence, the hourly precipitation just before was smaller than the past maximum amount. On the other hand, the previous prolonged rainfall, which continued for 72hours before the event occurrence, was considerably large.

Generally, debris flow occurrences are affected by both the previous prolonged rainfalls and the most recent brief, strong one [1][2]. Clarifying such relations is critical for practically predicting debris flow occurrences and examining the timing of evaluation warnings and announcements by local governments.

For the debris flow generated in Nagiso-Town, in this paper, we discussed the relationship between the rainfall characteristics and debris flow occurrences, based on effective rainfalls and rainfall index *R'*. We also analyzed the debris flow runoff to specify such debris flow characteristics as flow depth, flow velocity, sediment flux concentration, and flow discharge along the river's path.

METHOD AND PROCEDURE FOR STUDY

Outline of debris flow disaster

In the Nashizawa Valley in Nagiso-Town (Fig. 1), a huge debris flow occurred at about 17:40 on July 9, 2014 due to heavy rainfall from typhoon No. 8 (Fig. 2(a)). During this debris flow, one person died, and many houses, buildings, and roads were damaged or destroyed. Railroad tracks also deluged [3].

Fig.1 Location of Nagano Prefecture and Nagiso-Town

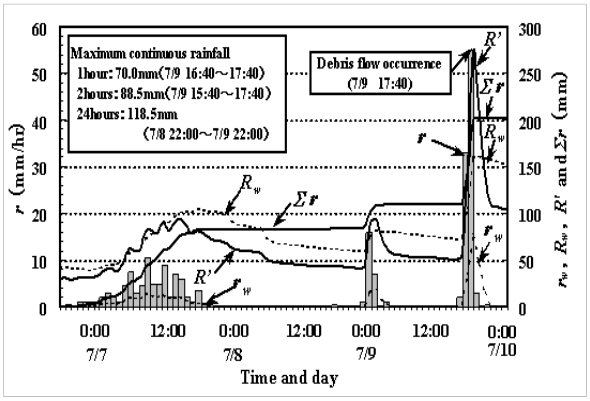

(a) Rainfall data: Nagiso rainfall gauging station

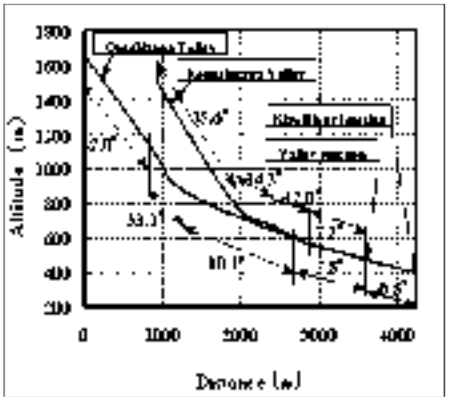

(b) Bed profile: Nashizawa Valley [3]

Fig.2 Rainfall data and bed profile: Nashizawa basin in July 2014

Figure 2(a) shows the observed rainfall data and the debris flow occurrence times at the nearest rainfall gauging station. Fig. 2(b) shows the river-bed profile in the Nashizawa Valley.

As shown in Fig.2(a), the hourly precipitation just before the debris flow occurrence was 70mm. A localized, heavy amount rain fell near Mt. Nagiso, but it didn't exceed 89mm/h, which was the previous maximum amount recorded at the Nagiso rainfall gauging station.

On the other hand, 111.5mm of precipitation continued for 72hours before the event occurrence. This amount is considerably larger than any previous prolonged rainfall; since the mountain slope held too much water, it was susceptible to a sediment-related disaster. The debris flow occurred approximately two hours after the strong rainfall's start (88.5mm per 2 hours, Fig. 2(a)).

As shown in Fig. 2(b), the Nashizawa basin, which is on the side of the Kiso River basin, is comprised of the Ohnashizawa and Konashizawa Valleys that merge downstream and join the Kiso River. In the upper basin, which is the debris flow occurrence zone, the river-bed slope exceeds 30 degrees, and the surface geology is weak granite [4]. We assume unstable sediment deposits on the river-bed. In the Nashizawa basin, debris flows often occurred in the past and formed an alluvial fan downstream. The houses and buildings that were destroyed by this debris flow were also built on this alluvial fan.

The above inherent factors are characterized by the unstable bed sediment on the river-bed runoff with excessive water from the heavy rainfall and formed a debris flow. It flowed down while entraining the bed sediment in a flow process, and its size greatly increased. The debris flow traveled on the curved section of the channel works downstream and overflowed onto residential areas. The incline of the channel works downstream from the flooding's start spot ranged from about 7 to 8 degrees, and the flood area's gradient ranged from about 5 to 6 degrees. Since both values are relatively large, the debris flow arrived at the Kizu River which was approximately more than 300m downstream from the spot of the flooding's start.

Effective rainfall

Effective rainfall R_t is a standard value of debris flow occurrences that investigates the influence of previous rainfall. It is calculated by Eqs. (1) and (2) [1]:

$$R_t = r_t + \sum a_n r_{t-n} = r_t + a_1 r_{t-1} + \cdots + a_n r_{t-n} \quad (1)$$

$$a_n = 0.5^{n/T} \quad (2)$$

where t is time, r_t is its precipitation, a_n is the decrease coefficient, and T is the half-life. In this study, short-term effective rainfall is denoted by r_w, and long-term effective rainfall is denoted by R_w.

Rainfall index *R'*

Rainfall index R' is calculated by Eqs. (3) and (4) [5]:

$$R_{fw} = \sqrt{(R_1 - R_w)^2 + a^2 (r_1 - r_w)^2} \quad (3)$$

$$R' = R_{fw0} - R_{fw} \quad (4)$$

where R_{fw} is the long diameter of the oval, R_1 and r_1 are its central coordinates ($R_1 = ar_1$), R_{fw0} is a value for $R_w = r_w = 0$, and a is a coefficient that replaces an oval with a circle (Fig. 3).

r_w and R_w are calculated based on the observed rainfall data (Fig. 2). For T, 1.5 hours are generally applied for short-term effective rainfall, and 72 hours are applied for long-term effective rainfall. Therefore, we used them.

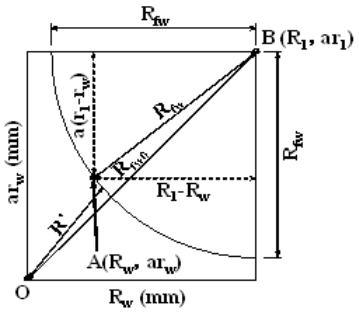

Fig.3 Diagram of rainfall index *R'*

R_1, r_1, and a (R_1=ar_1) are required for calculating *R'*. R_1 is given by the value of R_w (graph's cross axis) that can clearly express all the calculation results by a quadrant, and a is decided by the test calculations that produced R_1 and assumed a. In this study, R_1 is given by 600mm, and a is assumed to be 3, 4, and 5. Since a=3 most closely matches all the examples, we adopted the following values: a=3, R_1=600mm, and r_1=200mm.

Debris flow runoff analysis

Governing equations for debris flow

The following are the mass conservation equations for the flow mixture and for sediment alone:

$$\frac{\partial h}{\partial t}+\frac{1}{B}\frac{\partial Bvh}{\partial x}=\frac{E}{c_*} \tag{5}$$

$$\frac{\partial \varepsilon ch}{\partial t}+\frac{1}{B}\frac{\partial \varepsilon cBvh}{\partial x}=E \tag{6}$$

where t is the time, x is the coordinate axis along the flow, h is the flow depth, B is the flow width, v is the flow velocity, E is the erosion velocity (its negative value designates the deposition), c is the sediment concentration by volume, ε is the correction factor (see Egashira et al. [6], where $\varepsilon c = c_t$, c_t is the sediment flux concentration), and c_* is the sediment concentration of the river-bed layer.

The following is the momentum conservation equation:

$$\frac{\partial v}{\partial t}+v\frac{\partial v}{\partial x}=g\sin\theta-\frac{1}{\rho_m h}\frac{\partial P}{\partial x}-\frac{vE}{c_* h}-\frac{\tau_b}{\rho_m h} \tag{7}$$

$$\rho_m=(\sigma-\rho)c+\rho \tag{8}$$

The second term on the right-hand side in Eq. (7) is the pressure gradient and the third term is the resistance due to the sediment erosion. g is the gravity acceleration, θ is the river-bed slope, P is the pressure, τ_b is the river-bed shear stress, ρ_m is the mass density of the flow mixture defined by Eq. (4), σ is the mass density of the gravel, and ρ is the mass density of the water.

The following is the mass conservation equation of the river-bed sediment:

$$\frac{\partial Z_b}{\partial t}=-\frac{E}{c_*\cos\theta} \tag{9}$$

$$\theta=\sin^{-1}\left(-\frac{\partial Z_b}{\partial x}\right) \tag{10}$$

where Z_b is the river-bed elevation, and θ is expressed by Eq. (10).

Even though E and τ_b play critical roles in the above governing equations, no general formulas have been developed for them. We used the formulas for E and τ_b developed by Egashira [7], [8]. The following is erosion velocity E:

$$\frac{E}{v}=c_*\tan(\theta-\theta_e) \tag{11}$$

$$\theta_e=\tan^{-1}\left\{\frac{(\sigma/\rho-1)c}{(\sigma/\rho-1)c+1}\tan\phi_s\right\} \tag{12}$$

where θ_e is the equilibrium river-bed slope corresponding to the sediment concentration defined by Eq. (12) and ϕ_s is the internal friction angle of the sediment.

The following is the formula for τ_b, developed by Egashira et al. [9]:

$$\tau_b=\tau_y+\rho f v^2 \tag{13}$$

$$\tau_y=\left(\frac{c}{c_*}\right)^{1/5}\rho(\sigma/\rho-1)cgh\cos\theta\tan\phi_s \tag{14}$$

$$f=\frac{25}{4}\left\{k_f\frac{(1-c)^{5/3}}{c^{2/3}}+k_g\frac{\sigma}{\rho}(1-e^2)c^{2/3}\right\}\left(\frac{h}{d}\right)^{-2} \tag{15}$$

In Eq. (13), τ_y is the yield stress caused by the particle-to-particle contacts defined by Eq. (14), and f is the friction factor defined by Eq. (15), where e is the restitution coefficient, d is the reference grain size, and k_f and k_g are the following coefficients: k_f =0.16, k_g =0.0828.

River conditions

We analyzed the 4,240m long river reach of the Ohnashizawa Valley that ranges from 400 to 1660m above sea level (from its upper spot to the Kizu River junction, Fig. 2(b)). The river-bed and river-width profiles are shown in Fig. 4. In this reach, two check dams are located downstream [3].

Based on the analytical result of the vibration wave pattern of the debris flow provided by a seismic observation meter installed at the Kizu River junction, we assumed that the peak flow discharge occurrence time of the Konashizawa Valley was different from that of the Ohnashizawa Valley [3]. Therefore, in this paper, we ignored the inflow of the debris flow from the Konashizawa Valley to the Ohnashizawa Valley.

Bed material entrainment conditions

We have no hillside landslide data at the upstream reach or any river-bed erosion data throughout it. So we assume that the sediment is mainly supplied by river-bed erosion and estimate that the critical erosion depth of the bed material equaled 2.0m based on the previous field survey results [3].

Water supply conditions

We also have no runoff data upstream. But if a little water is supplied and the bed sediment (which is basically in saturated soil state) begins to move, it is sufficient for a numerical simulation. We constantly supplied 0.10m^3/sec as the inflow water discharge at the upstream boundary and assumed for convenience that sediment concentration c_{in} is 5 % by volume.

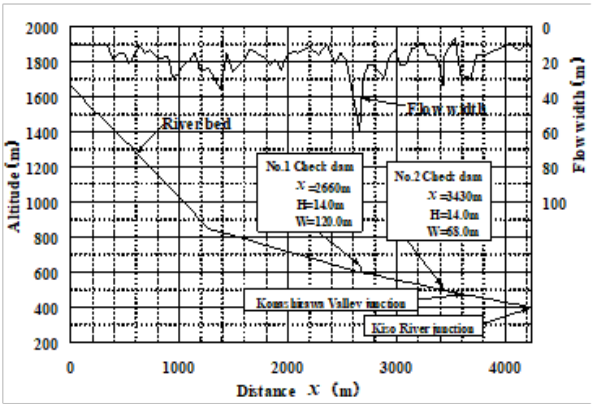

Fig.4 Bed profile and flow width of Onashizawa Valley

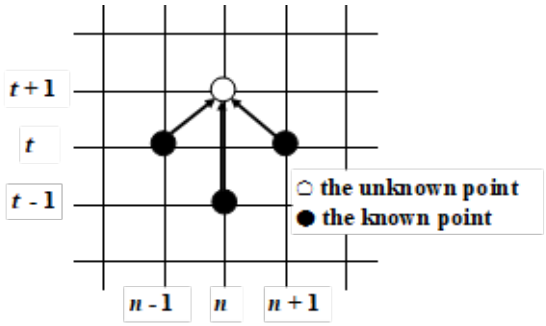

Fig. 5 Schematic diagram of leap-frog scheme

Physical conditions of sediment

The following parameters are required for computation: σ= 2.70g/cm^3, ϕ_s = 39.0degrees, d= 5.0cm, and c_*= 0.50.

Relationship between water density and fine sand concentration in water

The fine sand concentration in water, c_s, is closely related to a rise in the water's density (muddy water). Because such a rise increases buoyancy, our analysis cannot ignore its influence [10]. When we assume that c_s equals 10%, ρ is calculated by Eq. (8) as follows: ρ =1.17g/cm^3 (c_s = 10%)

Numerical analytical conditions

We used the finite difference method (leap-frog scheme in Fig. 5). The time and distance are discriminated as Δt=0.025 seconds and Δx=5.0m, respectively.

RESULTS AND DISCUSSIONS

Relationship between rainfall characteristics and debris flow occurrence

Figure 2(a) shows the calculation results of R_w, r_w, and R' that were determined by precipitation per hour r. The precipitation, which was the previous continued rainfall, began to fall at 18:00 on July 6 and stopped at 20:00 on the next day. A rainless state continued for 26 hours until 22:00 on July 8, though a mere 0.5mm did fall at 18:00.

When we focused on R_w in Fig. 2(a), we confirmed that the influence of the previous prolonged rainfall remained as of 22:00 on July 8. When we looked at R', which included the influences of r_w and R_w, we also confirmed that it equaled around 40mm. It began to rain again at 22:00 on July 8 and stopped at 3:00 on the next morning; a rainless state continued for 12 hours until 15:00 on July 9.

But as shown by R' in Fig. 2(a), the influence of the previous prolonged rainfall remained as R' = around 50mm as of 15:00 on July 9, which was 69hours after the rainfall began at 18:00 on July 6 and just before the debris flow occurrence at 17:40 on July 9. Consequently, the huge debris flow occurred approximately two hours after the final, short strong rainfall's start, which was 88.5mm per 2hours, and although it was smaller than the previous maximum rate.

Debris flow runoff characteristics

Figure 6 shows the temporal changes of the bed elevation near two check dams after 600 seconds with

the water supply. Two check dams deposited sediment at their storage areas, softened the river-bed slopes, and controlled the debris flow's power. The river-bed erosion immediately downstream of the check dam was caused by overflow from the dam.

Figures 7(a), (b), (c), and (d) show the temporal changes of such debris flow characteristics as flow, depth, flow velocity, sediment flux concentration by volume, and flow discharge.

As shown in Figs. 7(a) and (d), the debris flow traveled down and increased its scale with entrainment of the river-bed material, and the flow depth and discharge became maximum near x=2,000m. In addition, the flow discharge decreased downstream of the dams (x= 2,700m and 3,500m) and we confirmed that the check dams controlled the debris flow's power.

As shown in Fig. 7(c), the sediment flux concentration was high from around 20 to nearly 50 % upstream and midstream from x= 1,000 to 2,000m. But it fell as the incline softened downstream.

The sediment flux concentration was around 14% at the Konashigawa Valley junction (x= 3,600m), and the sediment transport mode changed from a debris flow to an earth flow.

The x= 3,900m spot was equivalent to the curved section of the channel works (the flooding's start spot). As shown in Fig. 7(c), its sediment flux concentration was maintained by around 13% after 600 seconds with water supply.

At the x= 3,900m in Figs. 7(a), (b), and (d), the maximum flow depth was 3.3m, the maximum flow velocity was 4.5m/sec, and the maximum flow discharge was 176m^3/sec. Based on previous field survey results [3], the mean flow depth was 3.4m, the mean flow velocity was 6.5m/sec, and the mean flow discharge was 196m^3/sec. Thus, a comparison of our numerical results with field survey results showed relatively good agreement.

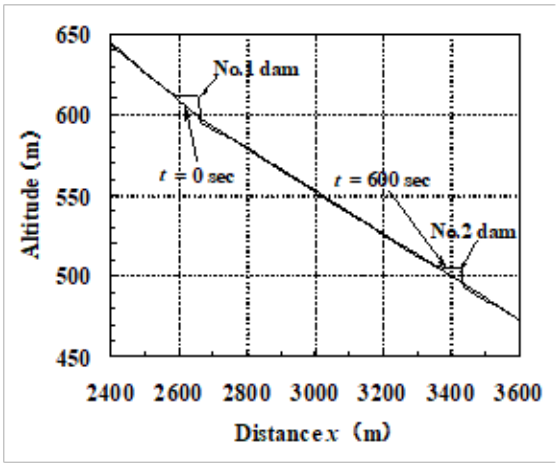

Fig.6 Temporal changes of bed elevation: Onashizawa Valley

CONCLUSION

We discussed the relationship between the rainfall characteristics and a debris flow occurrence, based on effective rainfalls and the rainfall index R'. In addition,

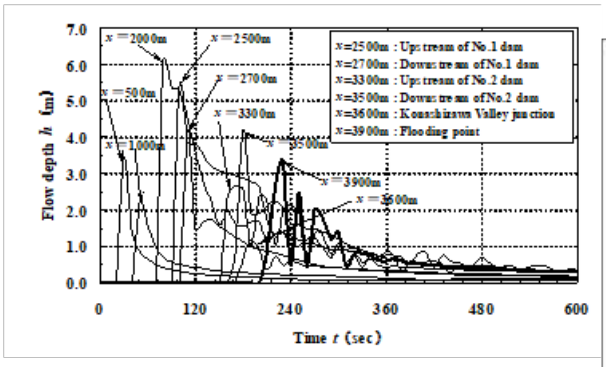

(a) Flow depth

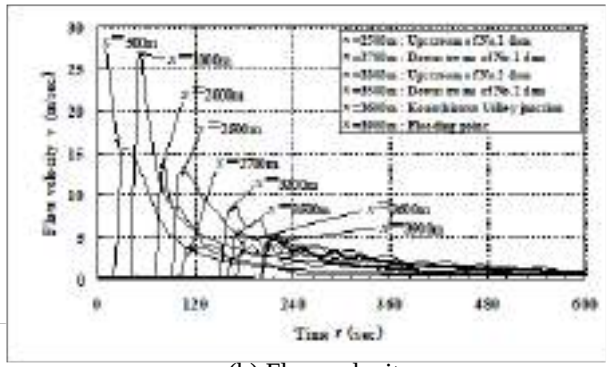

(b) Flow velocity

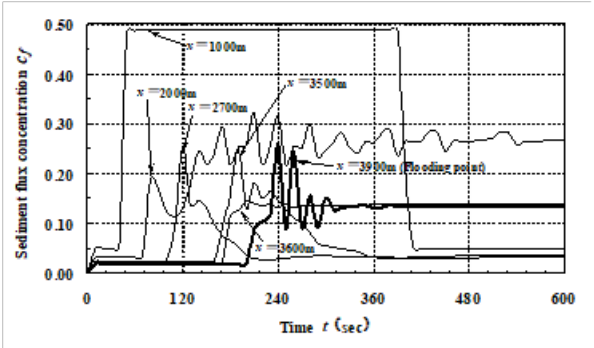

(c) Sediment flux concentration

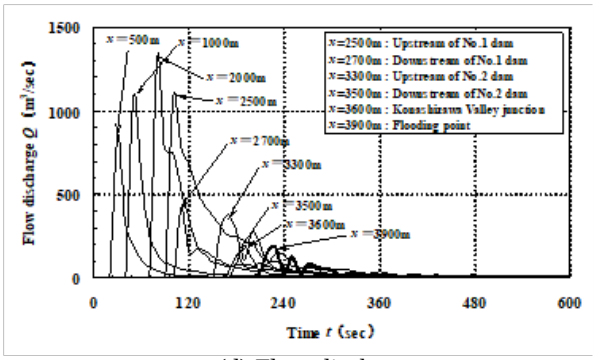

(d) Flow discharge

Fig. 7 Temporal changes of debris flow characteristics value: Onashizawa Valley

we analyzed a debris flow runoff to identify the debris flow characteristics along the river's path and obtained the following interesting results.

(1) The influence of the previous prolonged rainfall remained as *R'* = around 50mm just before the debris flow occurrence. Consequently, a huge debris flow occurred approximately two hours after a final, short strong rainfall's start, although it was smaller than the previous maximum scale.

(2) Two check dams deposited sediment in their storage areas and softened the river-bed slopes. The flow discharge decreased downstream of the dams, and we confirmed that the check dams controlled the debris flow's power.

(3) The sediment flux concentration was high from around 20 to nearly 50% upstream and midstream, but it fell downstream as the incline became softer. The sediment flux concentration was around 14% at the Konashigawa Valley junction, and the sediment transport mode changed from a debris flow to an earth flow.

(4) Rainfall index *R'* is very useful for judging the risk of debris flow occurrences and examining the timing of such emergency warnings as evaluation announcements from local governments.

(5) Our proposed numerical simulation of debris flow can reproduce the actual sediment runoff processes in a mountain torrent where such sabo facilities as check dams and channel works are constructed. Predicting sediment runoff characteristics yields valuable results for the evaluation of debris flow control with sabo facilities.

ACKNOWLEDGEMENTS

Part of this study was supported by the Strategic Research Project from Tokyo University of Agriculture.

REFERENCES

[1] Yano K., Study of the Method for Setting Standard Rainfall of Debris Flow by the Reform of Antecedent Rain. Journal of the Japan Society of Erosion Control Engineering, Vol. 43, Issue 4, 1990, pp. 3-13 (in Japanese with English abstract).

[2] Ushiyama, M., Ohido, S. and Takara, K., The Critical Line for Sediment Disaster Warning Based on Precipitation Data in Hiroshima Prefecture in June 1999. Advances in River Engineering, Japan Society of Civil Engineering, Vol.7, 2001, pp.167-170 (in Japanese with English abstract).

[3] Hiramatsu, S., Fukuyama, T., Yamada, T., Ohsaka, O., Nakatani, K., Matsumoto, N., Fujimura, N., Kato, N., Shimada, T., Kubo, T., Matsuo, S., Nishio, Y. and Yoshino, K., Disaster Report on the Debris Flow occurred on 9 July 2014 in Nagiso, Nagano prefecture. Journal of the Japan Society of Erosion Control Engineering, Vol. 67, Issue 4, 2014, pp.38-48 (in Japanese with English abstract).

[4] Wakatsuki, T., Yamada, R., Sakai, M. and Takeda H., Sediment-related Disasters in Nagiso on July 9, Iwakuni on August 6 and Fukuchiyama and Tanba on August 17. News of the Geological Society of Japan, Vol. 17, Issue 11, 2014, pp.45-46 (in Japanese).

[5] Nakai, S., Kaibori, M., Sasaki, Y. and Moriwaki, T., Applicability of a New Rainfall Index R' for Recent Cases and Proposal of the Method for Warning against Sediment-related Disaster. Journal of the Japan Society of Erosion Control Engineering, Vol. 60, Issue 1, 2007, pp. 37-42 (in Japanese with English abstract).

[6] Egashira, S., Itoh T., Miyamato K. and Honda N., Importance of Correction Factor Associated with Sediment Concentration Profile in Debris Flow Simulation, The 2nd International Symposium on Flood Defence 2002, Vol.2, 2002, pp.1658-1666.

[7] Egashira, S., Mechanism of Sediment Deposition from Debris Flow (Part 2), Journal of the Japan Society of Erosion Control Engineering, Vol. 46(1), May 1993, pp. 45-49 (in Japanese).

[8] Egashira, S., Prospects of Debris Flow Studies from Constitutive Relations to Governing Equations, Journal of Disaster Research, Vol. 6(3), June 2011, pp. 313-320.

[9] Egashira, S., Miyamoto K. and Itoh T., Constitutive Equations of Debris Flow and Their Applicability, 1st International Conference on Debris Flow Hazards Mitigation, American Society of Civil Engineering, 1997, pp. 340-349.

[10] Egashira, S., Honda N. and Miyamoto K., Numerical Simulation of Debris Flow at the Gamaharazawa in the Hime River Basin, Annuals of Hydraulic Engineers, Japan Society of Civil Engineering, Vol.42, 1998, pp. 919-924(in Japanese with English abstract).

Copyright © Int. J. of GEOMATE All rights reserved, including making copies, unless permission is obtained from the copyright proprietors.

15th Int. Conf. on Geotechnique, Construction Materials & Environment,
Kyoto, Japan, 11-13 November 2025, ISBN 978-4-909106124 C3051

EFFECT OF RICE HUSK ASH AS A PARTIAL CEMENT REPLACEMENT ON STRENGTH OF SUBBASE

Chotikan Ratchakrom[1], Pisut Rodvinij[1], Sattaya Chaiwithee[2] and Pitiwat Wattanachai[2]

[1]Faculty of Engineering, Rajamangala University of Technology Lanna, Thailand; [2]Faculty of Engineering, Chiang Mai University, Thailand

ABSTRACT

Lateritic soil is used as a construction material for road subbase in Thailand. However, lateritic soil obtained from some areas still does not meet the required standards. Therefore, soil stabilization techniques are considered suitable for being economical and sustainable. This study focused on the utilization of rice husk ash (RHA) to improve the strength of subbase. Rice husk is one of the most abundant agricultural wastes and a major cause of air pollution problems in northern Thailand. Therefore, the utilization of rice husk ash can relieve waste management and air pollution. Rice husk ash in this study was burned in an oven at 600 °C for 3 hours and then mashed by ball mill grinding machine. Soil samples were mixed with cement at 3% by weight, and then RHA was used to replace cement in the mixture at 10%, 30%, 50% and 70% by weight. The samples were conducted on unconfined compressive strength tests and capillary rise tests to investigate the strength and water absorption of the improved soil. The results demonstrated that replacing cement with 10% RHA can enhance the strength of soil more than using cement alone at 28, and 56 days. However, when RHA was used to replace more than 10% of cement, the results showed that the strength tended to decrease as the proportion of RHA in the mixture increased. Moreover, soil mixed with 10% RHA as a replacement for cement showed a water absorption similar to soil mixed with 3% cement.

Keywords: Rice husk ash, Unconfined compressive strength, Cement replacement, Soil improvement, Subbase

INTRODUCTION

In Thailand, lateritic soil is widely used for building subbase in road construction. This is due to lateritic soil is abundant in Thailand and the price is low. However, it has become a realized problem because of poor-quality lateritic soil which has low compressive strength and durability. Lateritic soil obtained from some areas still does not meet the required standards. Moreover, rain infiltration or the water inundates of the subbase can cause road damage [1,2]. Therefore, soil stabilization techniques are considered suitable due to their economic and sustainable benefits. Soil stabilization refers to the treatment of soils to improve their strength and durability [3]. The most commonly used additive for soil stabilization is ordinary Portland cement. However, soil stabilization by using cement alone resulted in high construction costs. Therefore, the use of cement with by-product materials from industry or agriculture can be an alternative for soil stabilization at present. Therefore, replacing cement with high volumes of pozzolanic materials can improve the cost efficiency of subbase construction. Additionally, Portland cement's production is inherently carbon-intensive, generating substantial CO_2 per ton manufactured. Thus, replacing portions of the Portland cement with secondary cementitious materials in soil stabilization can reduce the overall environmental impact of the stabilization process [3]. This established method confirms that pozzolanic materials can effectively improve soil bearing capacity through stabilization [1,2,4]. However, the engineering properties of subbases improved with pozzolanic materials should be evaluated according to the requirements of Thailand's Department of Highways.

This study focused on replacing cement with rice husk ash to improve the strength of subbase materials. Rice husk is one of the most abundant agricultural wastes in Thailand [5], where approximately 21-26 million tons of rice are produced annually. Most rice husks are burned in the open air unless utilized otherwise. Such wasteful practice provides no benefits and instead causes significant environmental problems [6]. This contributes to increased PM2.5 levels, which is a major air pollution issue in northern of Thailand. However, utilizing biomass for power generation presents a viable solution. Using rice husks for power generation is a sensible strategy to reduce environmental damage and air pollution caused by open burning. Additionally, rice husk ash is produced as a by-product and can be repurposed for various applications. Due to its high silica content, rice husk ash can be used as an ingredient in industrial materials such as cement, and more [6].

When rice husk is properly burned at a temperature below 800 °C, rice husk ash (RHA) with a cellular microstructure and a high percentage of amorphous SiO_2 is produced [5]. The resulting RHA

is highly suitable for use as a pozzolanic material to enhance the compressive strength and durability of cement-based materials [7]. RHA can act as a source of excess SiO_2 to chemically reacting with $Ca(OH)_2$ to form additional calcium silicate hydrate (C-S-H), the primary strength-contributing compound in cement-based materials [5]. Additionally, a literature review demonstrated the potential of RHA as soil stabilization materials. The optimal amount of RHA in soil can enhance long-term strength [3]. The increase in the RHA content at specified cement content also improved UCS values with curing age [8]. Therefore, this study focused on replacing cement with RHA to improve subbase strength.

RESEARCH SIGNIFICANCE

This study examines the utilization of rice husk ash (RHA) to enhance soil strength for subbase construction while reducing the cement content. This approach leads to reduce environmental impact from the stabilization process. The research investigates the effects replacing 10-70% of cement with RHA on soil strength and water absorption properties. Rice husk ash in this study was burned in an oven at 600 °C. The strength of soil mixed with RHA was evaluated using unconfined compressive strength tests, while water absorption was measured through capillary rise tests. The finding demonstrated the optimal RHA replacement ratio for cement and RHA's effectiveness in developing soil strength.

MATERIALS AND METHODOLOGY

Lateritic Soil

The soil used in this study is lateritic soil from local areas in Chiang Mai, Thailand. The properties of the soil samples, including a particle size distribution, specific gravity, liquid limit, plastic limit, optimum moisture content and maximum dry density were investigated. The engineering properties of the soils were measured in accordance with the standard set by the Department of Highway (DOH), Thailand, for use as soil-cement subbase material [9].

The specific gravity of the soil samples was determined in accordance with ASTM D854 [10]. To analyze the particle size distribution, wet sieving tests and hydrometer tests were conducted following ASTM D422 [11]. Liquid limit and plastic limit tests were performed on soil samples passing through a 0.425 mm sieve, following ASTM D4318-00 [12]. Additionally, the optimum moisture content and maximum dry density of the soil were determined using modified Proctor compaction tests in accordance with ASTM 1557 [13].

Rice Husk Ash

The rice husk used in this study was collected from the Lanna Rice Research Center at Chiang Mai University. The rice husk was golden to light brown, with a curved and rigid shape and a rough surface. Its bulk density ranged between 100-150 kg/m^3. In this study, RHA was used as cement replacement material. A commercial type of Portland Cement (Type 1) was used as the base material.

To prepare the rice husk ash (RHA), rice husk was burned in an oven at 600 °c for 3 hours. Color of burning RHA illustrated blackish grey and whitish grey. The whitish grey color shows higher content of silica. However, blackish grey color shows high content of unburnt carbon. Subsequently, the RHA was mashed using a ball mill grinding machine for 90 minutes to achieve a particle size finer than 0.075 mm, as shown in Fig.1.

Fig.1 Burning rice husk ash and rice husk ash mashed ball mill grinding machine

Sample Preparation and Testing

Unconfined compressive strength (UCS) testing

The UCS tests were conducted in accordance with ASTM D1633 (Method A) [14] using cylindrical specimens measuring 101.6 mm in diameter and 116.4 mm in height. The soil samples were mixed with a binder at 3% by weight of soil in different ratio, as shown in Table 1. Ordinary Portland cement was partially replaced with RHA at 10%, 30%, 50%, and 70% by weight. The water content for each mixture was set at the soil's optimum moisture content.

The samples were compacted in five layers, with each layer compacted 25 blows from a 10 lb hammer to achieve modified compaction energy. After compaction, each sample was extruded from the mold and cured in a seal plastic bag to prevent moisture loss during the curing period of 7, 28 and 56 days. Prior to testing, the cured samples were soaked in the water for 2 hours and air-dried for 15 minutes. The samples were then subjected to compression testing to evaluate the strength improvement of the soil. The compressive strength values for each mixture represent the average of three specimens. The results demonstrate the potential of using agricultural wastes materials (RHA) as a partial cement replacement to enhance the strength of subbase materials.

Table 1 Mixture proportion of soil-cement-RHA

Mixture	Cement replacement by RHA (%)	Raw materials (g)		
		Soil	Cement	RHA
C3%	0	2700	81	0
RHA10	10	2700	72.9	8.1
RHA30	30	2700	56.7	24.3
RHA50	50	2700	40.5	40.5
RHA70	70	2700	24.3	56.7

Capillary Rise Testing

Capillary rise tests were conducted on the stabilized specimens to evaluate water absorption in the improved soil. The tests followed the Australian Standard AS1141.53 [15]. The specimen dimensions were identical to those used in the UCS tests.

The specimens were prepared using the modified compaction method and cured in seal plastic bag for 7 days, following the same procedure as the UCS sample preparation. Prior to testing, the specimens were oven- dried at 60 °C for 72 hours and air-cooled for 2 hours. Subsequently, the samples were partially submerged in a water container, maintaining a 10 mm water height for 72 hours. The capillary rise (increase in water height) was measured as shown in Figure 2. The reported water height for each mixture represents the average of three specimens. Height (h) of water rise from base of specimen was measured using a ruler and was recorded at various times. The capillary rise (CR) as a percentage of the specimen height (H) were determined as follows Eq. (1). The complete testing scheme for this study is presented in Table 2.

Fig.2 Capillary rise test conducted on specimens

$$CR = \frac{h \times 100}{H} \quad (1)$$

Table 2 Testing scheme

Properties	Tests	Moisture	Curing Time (days)
Compressive Strength	Unconfined compressive strength	OMC of soil	7, 28 and 56
Water absorption	Capillary rise test		7

RESULTS AND DISCUSSION

Engineering Properties of Lateritic Soil

Soil samples were tested for Atterberg limits test (liquid limit and plastic limit), particle size distribution (sieve analysis and hydrometer tests), and compaction characteristics (modified compaction test) to determine their engineering properties. The test results showed liquid limit, plastic limit, and plastic index values of 20%, 17%, and 3%, respectively. The particle size distribution of the soil samples is presented in Fig 3.

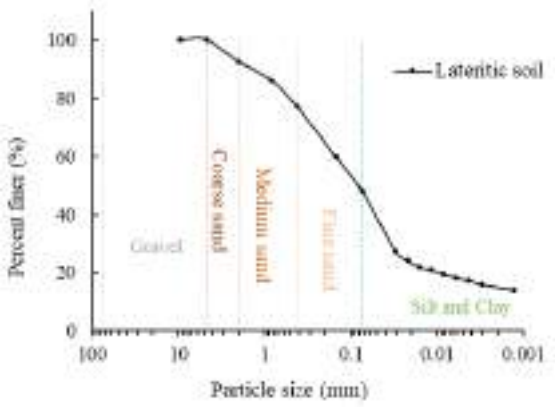

Fig.3 The particle size distribution of soil sample

The results indicated that 48% of the soil particles were finer than 0.075 mm. Based on these characteristics, the soil was classified as silty sand (SM) according to the Unified Soil Classification System (USCS). All tests were conducted in accordance with the standards specified by the Department of Highways (DOH), Thailand, for soil-cement subbase materials [9]. The complete test results are summarized in Table 3.

Table 3 The engineering properties of lateritic soils

Properties	Lateritic Soils	DOH Standard (Subbase Materials)
Specific gravity, G_s	2.65	Not specified
Liquid Limit, LL (%)	20	≤35
Plastic Limit, PL (%)	17	Not specified
Plastic Index, PI (%)	3	≤11
Passing No. 200 (%)	48	≤40

The results of modified compaction tests are shown in Fig 4. The compaction curve represents the relationship between dry density and moisture

contents of the soil samples in this study. The results demonstrated maximum dry density and optimum moisture content (OMC) of soil samples was 2,035 kg/m^3 and 10.2%, respectively. Consequently, the optimum moisture content of 10.2% was used for sample preparation in both unconfined compressive strength tests and capillary rise tests.

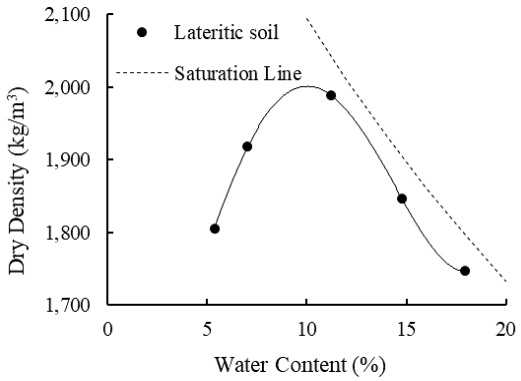

Fig.4 Compaction test results of soil sample

Unconfined Compressive Strength of Stabilized Soil

The UCS test results for stabilized soil are summarized in Table 4 and illustrated in Fig 5. The unconfined compressive strength of untreated soil was 427 kPa. The results demonstrated the soil strength increase with binder addition. Specimens with 10% RHA replacement demonstrated the highest strength at 28 days and 56 days curing periods, while 3% cement mixtures showed the highest strength at 7 days. According to DOH standards [9], the minimum required 7 days UCS for subbase applications is 689 kPa. The tested mixtures (C3%, RHA10, RHA30, and RHA50) all exceeded this requirement, with C3% showing particular effectiveness for early strength development.

The effect of RHA as a partial cement replacement on the strength development of the stabilized soil was considered, as shown in Fig. 6. The results demonstrated that the strength of the samples tended to decrease as the proportion of RHA in the mixture increased after 7 days of curing. This is due to the early strength of the soil mixed with cement results from the formation of primary cementitious compounds, such as C-S-H, which are generated by the hydration reaction between cement and water [16].

Additionally, Fig. 6 shows that replacing cement with 10% RHA can enhance long-term strength more effectively than using cement alone, as observed after 28, and 56 days of curing. The strength of the RHA10 mixture was approximately 19-22% higher than that of the C3% mixture. When RHA is incorporated into the mix, a pozzolanic reaction occurs, producing calcium silicate hydrates (CSH) and calcium aluminate hydrates (CAH), which results in increased soil strength [17]. However, when RHA was used to replace more than 10% of cement, the strength tended to decrease as the RHA proportion increased.

Table 4 Results of unconfined compressive strength test

Specimen symbol	Cement replacement by RHA (%)	UCS (kPa)			
		0 day	7 days	28 days	56 days
Soil	-	427	-	-	-
C3%	0		1,484	1,698	1,874
RHA10	10		1,398	2,078	2,238
RHA30	30	-	1,097	1,276	1,621
RHA50	50		1,033	1,212	1,446
RHA70	70		613	736	882

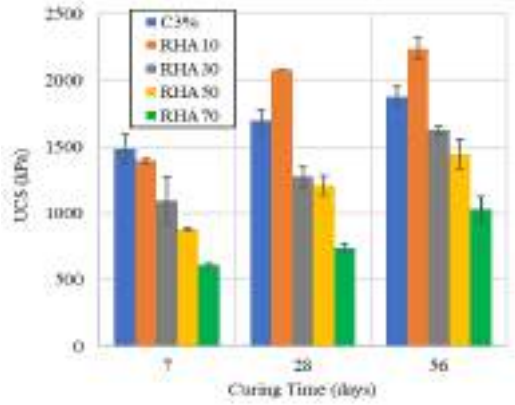

Fig.5 Unconfined compressive strength of stabilized soil

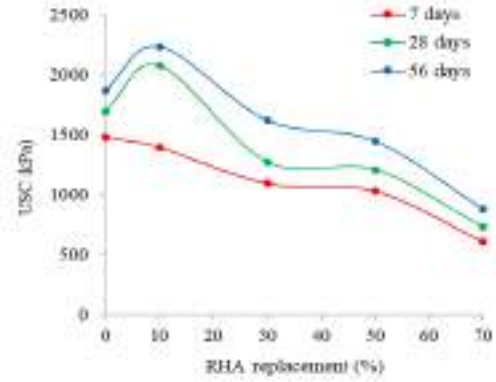

Fig.6 Effect of RHA as a partial cement replacement on unconfined compressive strength

Fig. 7 shows the strength increase rate of all the samples. The results demonstrated that RHA10 was the most effective in developing strength between 7 and 28 days, with an increase of approximately 49%. The strength increase rate of RHA10 was about 35%

higher than that of C3%. Thus, the results indicate that RHA is effective in enhancing the strength of stabilized soil after 7 days.

When considering the strength increase rate between 28 and 56 days, the results showed that replacing cement with 30% RHA (RHA30) was the most effective, achieving a strength increase of approximately 27%. Moreover, cement replacement with 30-70% RHA was more effective in developing long-term strength compared to RHA10. This suggests that RHA in the mixture triggers a pozzolanic reaction, leading to an increased long-term strength gain.

Overall, replacing cement with 10% RHA (RHA10) was the most effective for strength development, as evidenced by 60% strength increase rate observed over 7-56 days. In contrast, C3% showed only a 26% increase. Additionally, RHA30, RHA50, and RHA70 exhibited higher strength increase rates than C3%, further confirming the effectiveness of RHA in improving the long-term strength of stabilized soil.

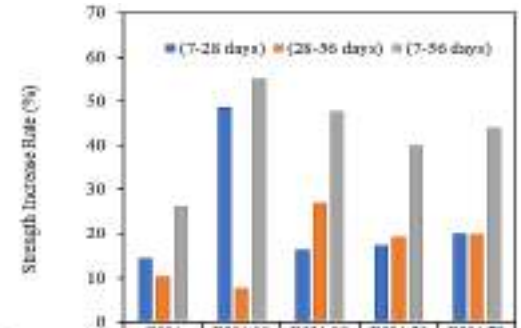

	C3%	RHA10	RHA30	RHA50	RHA70
(7-28 days)	14	49	16	17	20
(28-56 days)	10	8	27	19	20
(7-56 days)	26	60	48	40	44

Fig.7 Strength increase rate of stabilized soil

Capillary Rise of Stabilized Soil

Fig. 8 shows the capillary rise of the sample after 7 days of curing. The results are presented in terms of the capillary rise as a percentage versus time. The capillary rise percentages of soil, RHA50, and RHA70 were similar, all reaching 100% capillary rise at 480 minutes. In contrast, RHA30 and RHA10 showed lower capillary rise percentages at the same time: 86% and 71%, respectively.

The results indicate that capillary rise tends to increase with higher proportions of RHA in the mixture. Additionally, the data clearly demonstrate that RHA10 had a lower capillary rise than C3% by approximately 5-10% after being submerged in water for 60 minutes.

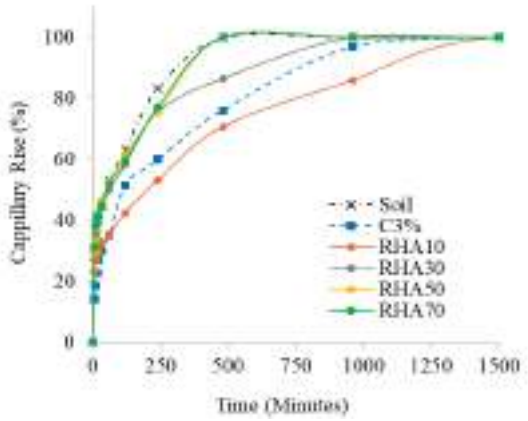

Fig.8 Capillary rise percentage versus time of stabilized soil after 7 days of curing

CONCLUSION

Based on the investigation into the use of rice husk ash (RHA) as a partial cement replacement to enhance the strength of lateritic soil for subbase construction, the key finding of this study are summarized as follows:

1. Soil mixed with 3% cement or soil mixed with RHA replacing 10-50% of cement achieved strength values exceeding the Department of Highway (Thailand) requirement of 689 kPa after 7 days of curing.

2. Replacing 10% of cement with RHA enhanced soil strength more than using cement alone at 28, and 56 days. Specially, 10% RHA replacement increased strength by approximately 19-22% compared to soil stabilized with 3% ordinary Portland cement (OPC). However, at 7 days of curing, the strength of stabilized soil decreased as the RHA proportion increased.

3. RHA demonstrated long-term strength development in stabilized soil. A 10% RHA replacement was the most effective for strength gain between 7-28 days, showing 35% higher strength increase rate than cement alone. However, higher RHA replacements (30-70%) resulted in greater strength development at 28-56 days.

4. A 10% replacement of cement with rice husk ash (RHA) represents the optimal ratio for balancing cement reduction and RHA's effectiveness in enhancing soil strength. However, RHA replacements of up to 50% still maintain compressive strength exceeding the Department of Highways' requirements.

5. Replacing 10% of cement with RHA reduces water absorption in stabilized soil to levels comparable to soil mixed with cement alone. However, higher replacement ratios (50-70%) exhibit

water absorption similar to non-stabilized soil.

6. The use of RHA increases subbase soil strength while decreasing cement usage, consequently reducing the environmental impact associated with soil stabilization.

REFERENCES

[1] Rodvinij, P., and Ratchakrom, C., Effect of Cement Replacement by Fly ash FGD Gypsum on Strength of Subbase, International Journal of GEOMATE, Vol. 20, Issue 80, 2021, pp. 9-16.

[2] Ratchakrom, C., The Effect of Bottom Ash and Kaolin on The Strength of Poor Subbase, International Journal of GEOMATE, Vol. 16, Issue 57, 2019, pp. 76-81.

[3] Fattah, M. Y., Rahil, F. H., and Al-Soudany, K. Y. H., Improvement of Clayey Soil Characteristics Using Rice Husk Ash, Journal of Civil Engineering and Urbanism, Vol. 3, Issue 1, 2013, pp. 12-18.

[4] Wibowo, D. E., Ramadhan, D. A., Endaryanta, and Prayuda, H., Soil stabilization using rice husk ash and cement for pavement subgrade materials, Revista de la Construccion Journal of Construction, Vol. 22(1), 2023, pp. 192-202.

[5] Prasanphan, S., Sanguanpak, S., Wansom, S., and Panyathanmaporn, T., Effect of Ash Content and Curing Time on Compressive Strength of Cement Paste with Rice Husk Ash, Vol. 17(3), 2010, pp. 1-10.

[6] Ueda, T., Kunimitsu, Y., and Shinogi, Y., Potential conflicts for the reuse of rice husk in Thailand, Paddy and Water Environment, Vol. 5, Issue 2, 2007, pp. 123-129

[7] Zhang, M. H., Lastra, R., and Malhotra, V. M., Rice-husk ash paste and concrete: Some aspects of hydration and the microstructure of the interfacial zone between the aggregate and paste, Cement and Concrete Research, Vol. 26, Issue 6, 1996, pp. 963-977.

[8] Alhassan, M., and Mustapha, A. M., Effect of Rice Husk Ash on Cement Stabilized Laterite, Leonardo Electronic Journal of Practices and Technologies, Issue11, 2007, pp. 47-58.

[9] Department of Highway, Soil Cement Subbase, DH-S 206/1989, Bangkok, Thailand, 1989, pp. 1-13.

[10] ASTM International, ASTM D854, Standard Test for Specific Gravity of Soil Solids by Water Pycnometer, Annual Book of ASTM Standards, Vol. 04.08, West Conshohocken, PA, 2002, pp. 1-7.

[11] ASTM International, ASTM D422, Standard Test Method for Particle Size Analysis of Soils, Annual Book of ASTM Standards, Vol. 04.08, West Conshohocken, PA, 2002, pp. 1-8.

[12] ASTM International, ASTM D4318, Standard Test Method for Liquid Limit, Plastic Limit, and Plastic Index of Soils, Annual Book of ASTM Standards, Vol. 04.08, West Conshohocken, PA, 2000, pp. 1-16.

[13] ASTM International, ASTM D1557, Standard Test Method for Laboratory Compaction Characteristics of Soil Using Modified Effort (56,000 ft-lbf/ft3 (2,700 kN-m/m3)), Annual Book of ASTM Standards, Vol. 04.08, West Conshohocken, PA, 2002, pp. 1-10.

[14] ASTM International, ASTM D1633, Standard Test Methods for Compressive Strength of Molded Soil-cement Cylinders, Annual Book of ASTM Standards, Vol. 04.08, West Conshohocken, PA, 2000, pp. 1-4.

[15] Austroads, AS1141.53, Method for Sampling and Testing Aggregates Absorption Swell and Capillary rise of Compacted Materials, Standards Australia, 1996, pp. 1-7.

[16] Maichin, P., Jitsangiam, P., Nongnuang, T., Boonserm, K., Nusit, K., Pra-ai, S., Binaree, T., and Aryupong, C., Stabilized High Clay Content Lateritic Soil Using Cement-FGD Gypsum Mixtures for Road Subbase Applications, Materials, Vol. 14, Issue 8, 2021, pp. 1-20.

[17] Teshnizi, E. S., Mirzababaei, M., Karimiazar, J., Arjmandzadeh, R., and Mahmoudpardabad, K., Gypsum and rice husk ash for sustainable stabilization of forest road subgrade, Vol. 57, 2023, pp. 1-15.

Copyright © Int. J. of GEOMATE All rights reserved, including making copies, unless permission is obtained from the copyright proprietors.

15th Int. Conf. on Geotechnique, Construction Materials & Environment,
Kyoto, Japan, 11-13 November 2025, ISBN 978-4-909106124 C3051

INVESTIGATING THE SOIL ARCHING PHENOMENON IN MICROPILES USING NUMERICAL ANALYSIS

Muhammad Adeel Mazhar[1], Adnan Anwar Malik[2], Hung Manh Ho[3] and Umair Ali[4]

[1]Equipment Consulting Service Department (ECSD), Saudi Aramco, Dhahran, Saudi Arabia; [2]School of Engineering, The University of Newcastle Australia; [3]Bentley Systems, Singapore; [4]Department of Civil and Environmental Engineering, King Fahd University of Petroleum and Minerals, Dhahran, Saudi Arabia

ABSTRACT

The application of micropiles is increasing as more and more research outcomes highlight their advantages in various ground conditions. Additionally, its sustainability aspects, including minimal site impact, adaptability, and efficient material use, further enhance its applicability. These piles can be used under embankments to reduce stress on weaker soils, resulting in reduced localized and differential settlements. Under embankments, the number of piles is high; therefore, the group effect of piles has a more significant influence on the overall performance of the pile-supported improvement system. Soil arching is a critical factor in group piles that needs to be precisely investigated for an economical design that increases the service life of the structure. To further explore this, experimental trapdoor experiments were conducted to establish the arching effect in the sand, which was subsequently simulated using the hardening soil model with small-strain stiffness with PLAXIS 2D (FEM code). A parametric study was conducted to investigate the effect of the arching phenomenon on stress concentration and load in micro piles with varying interface conditions that reflect the roughness of the pile associated with micro pile shaft threading. Results showed that due to the arching phenomenon, stresses were transferred to the pile, and this transfer of stresses increases with the increase in interface stiffness in the axial direction.

Keywords: Soil arching, Micro piles, Sand, Shaft roughness effect, Numerical analysis

INTRODUCTION

Soil arching is defined as the increase or decrease of vertical stress on the buried structure due to the relative movement of the soil [1]. Stress reduction occurred in the yielding zone due to the redistribution of stress resulting from soil arching [2]. The soil arching mechanism can be studied for various geotechnical applications, such as underground cavities, tunnels, pile embankments, underground pipelines, culverts, retaining structures, and excavation support structures [2-9]. George and Dasaka [2] proved numerically that the equilibrium of stress transfer exists in the trapdoor experiment, i.e., an increase or decrease in pressure at the trapdoor is similar to the increase or decrease at the rigid portion. A very small movement in the trapdoor setup can generate load transfer due to soil arching [10]. Iglesia [11] stated that during the initial movement of the trapdoor, the load decreased considerably to reach its minimum value, indicating a fully developed arch. However, further movement gradually increases the load on the trapdoor. Another study indicated that an increase in soil density has no considerable effect on soil arching [12].

According to Ali [3], the height of the model and the particle shape affect the arching behaviour. Moreover, arching development is related to the height-to-width ratio of the buried structure. Many studies have been conducted to develop an expression to estimate the pressure reduction on the trapdoor. According to George and Dasaka [2], the cubic polynomial profile represents soil arching over the trapdoor in the yielding area.

Pile embankments are used in highway and railway construction as a ground improvement technique in areas with problematic soils [13]. Zhuang [14] stated that in areas of soft soils, embankments on floating piles are a cost-effective choice. In addition, the study indicated that soil arching began to develop when the embankment height to clear spacing ratio is greater than or equal to 1.6. The study also highlighted that the internal friction angle and cohesion of embankment fill improve the soil arching phenomenon. The use of micro piles has seen a notable rise in recent years across different geotechnical applications. Their performance mainly relies on skin friction, which is the friction developed at the contact surface between the surrounding soil and the micro-pile or grout. Despite their growing use, limited research has been conducted on how the arching phenomenon affects micro piles. This study aims to address this gap by employing numerical analysis to investigate how arching affects stress concentration and load transfer in micro piles, with special emphasis on the role of the soil–pile interface.

RESEARCH OBJECTIVE AND METHODOLOGY

The objective of this study is to investigate the arching phenomenon in terms of stress concentration and load on the pile in micro piles with varying interface conditions that reflect the roughness of the pile associated with micro pile shaft threading. To achieve the set objectives, the following methodology is adopted.

- Trapdoor experimental results are modelled in the PLAXIS 2D software using the Hardening Soil Model with Small Strain Stiffness (HSS).
- Validating the stress concentration ratio between the experimental and numerical analysis at the height of the soil (H) to fixed section (B) ratios (H/B) of 4.0 and 4.5.
- Including micro pile(s) in the model using embedded beam elements.
- Parametric study by increasing the interface stiffness in the axial direction (R_s) to reflect the increase in roughness between the soil and the pile section of micro piles.

EXPERIMENTAL AND NUMERICAL MODEL

Experimental Model

The experimental model consisted of a rectangular container whose floor was divided into seven sections (100 mm each), which could move upward and downward at a selected movement rate [3, 15]. The container was 700 mm long, 555 mm high, and 294 mm deep, as shown in Fig.1. Load cells that can measure both vertical and horizontal loads were mounted on all seven plates. Toyoura sand was used to prepare the model ground at a relative density of approximately 95 %. The dry pluviation method was used to achieve the desired relative density. The used sand material properties are D_{50} = 0.203 mm, C_u = 1.61, G_s = 2.64, e_{min} = 0.637, and e_{max} = 0.946. Ali's [3] paper contains more details on the experimental model.

Numerical Model

The numerical model was created in PLAXIS 2D, a FEM code, [16] with plane strain conditions. The model's width was 300 mm, representing three floor sections (each 100 mm) as shown in Fig.1. The middle section had fixed boundary conditions, whereas the other two sections were movable through a prescribed downward displacement of 0.25 mm (similar to the experiment), as shown in Fig.2. The soil is modelled as a Hardening Soil (HS) Model [17] with small-strain stiffness [18]. The material properties of Toyoura sand with a relative density of 95 % are shown in Table 1.

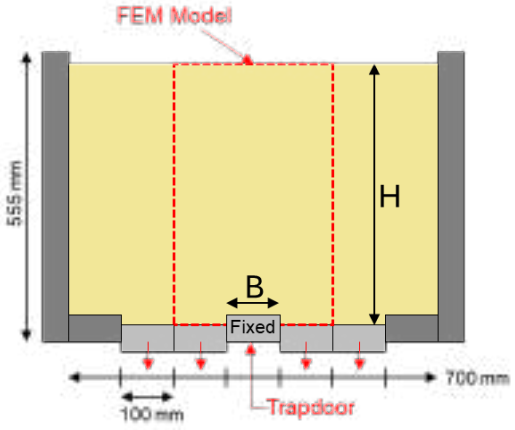

Fig.1 Schematic illustration of the trapdoor experiment setup

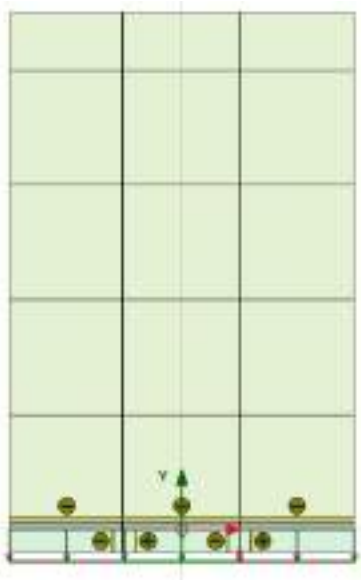

Fig.2 PLAXIS 2D FEM model to represent trapdoor experimental model

Table 1: Toyoura sand properties with relative density of 95 % considered in the numerical model

Description	Values
E_{50} in kPa	29,000
E_{oed} in kPa	30,000
E_{ur} in kPa	85,000
ν_{ur}	0.2
G_0^{ref} in kPa	300,000
c´ in kPa	1
ϕ´ in degrees	41
Ψ in degrees	16

After validating the arching phenomenon using experimental data, a parametric study was conducted, where micro piles were modeled as embedded beam elements with single and two-pile arrangements in the

PLAXIS model, as shown in Fig. 3. The considered length of the micro pile was 195 mm, and its diameter was 75 mm. The spacing between the piles was considered to be 150 mm. The distance of the pile head from the ground surface was considered to be 105 mm. In the parametric study, the interface axial stiffness (R_s), which reflects soil-pile interaction, varied from 2 to 4 times its default value to investigate its effect on the stress concentration and load on the pile due to the arching phenomenon. A prescribed displacement of 0.25 mm (reflecting ground settlement due to embankment load) was applied at the ground surface to see the stress concentration and load on the pile. The bottom of the model was kept in a fixed boundary condition.

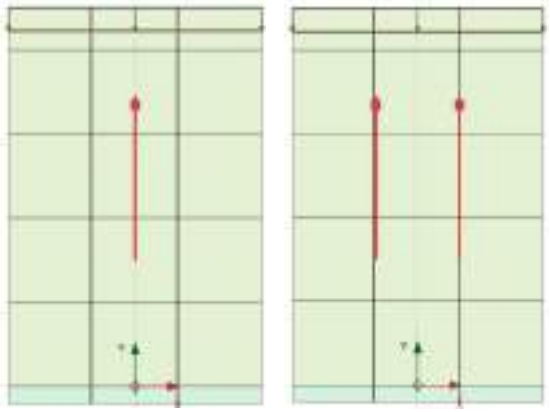

(a) (b)

Fig.3 PLAXIS 2D FEM models including micro piles as embedded beam element (a) 1-pile (b) 2-piles

The parametric study details are shown in Table 2. According to PLAXIS 2D 2024.3 reference manual [16], the default value of ISF is calculated as,

$$ISF_{RS,\ RN,\ KF} = 2.5\left(\frac{Lspacing}{D}\right)^{-0.75} \quad (1)$$

The interface stiffness in PLAXIS is calculated as follows [16].

$$R_S = ISF_{RS}\frac{G_{Soil}}{L_{spacing}} \quad (2)$$

$$R_N = ISF_N\frac{G_{Soil}}{L_{spacing}} \quad (3)$$

$$K_F = ISF_{KF}\frac{G_{Soil}R_{eq}}{L_{spacing}} \quad (4)$$

$$R_{eq} = \frac{D_{eq}}{2} = \sqrt{\frac{12EI}{EA}} \quad (5)$$

Where ISF stands for Interface Stiffness Factor, R_N stands for stiffness in lateral direction, Rs stands for stiffness in axial direction, K_F stands for base stiffness, $L_{spacing}$ represents spacing between the piles, G_{soil} represents surrounding soil shear stiffness, and R_{eq} represents equivalent radius.

Table 2 Parametric study details

Case No.	Interface Axial Stiffness Factors (ISF_{RS})	Increase in RS
1	1.844	-
2	3.68	2 x Case 1
3	7.37	4 x Case 1

RESULTS AND DISCUSSIONS

Validation of the Arching Phenomenon

The trapdoor experiment was conducted with soil heights (H) of 400 mm and 450 mm, with the central section (B) having a width of 100 mm of the container floor (trapdoor) fixed. The H/B ratios were 4.0 and 4.5. The floor sections around the central fixed section were lowered at a constant rate of 0.0012 mm/sec until the downward displacement reached 10 mm. Figure 4(a) shows the arch formation in the experiment. In the case of the PLAXIS 2D model, the movable sections surrounding the central fixed section were displaced downward by 0.25 mm to achieve the arching effect in the model, as shown in Fig.4(b). Ali's [3] paper contains more details on the experimental model.

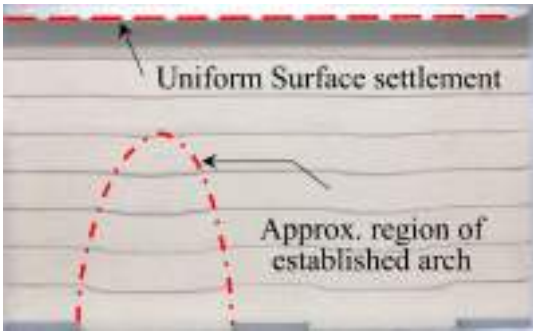

(a)

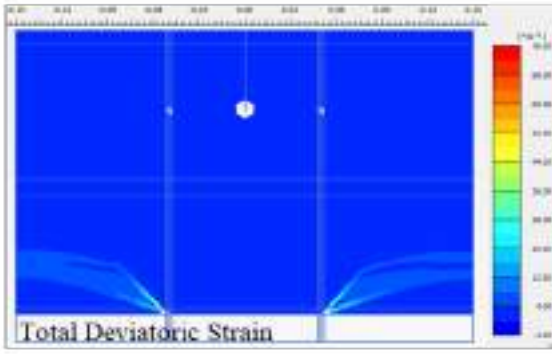

(b)

Fig.4 Arch formation for H/B = 4.0 (a) Experiment [3] (b) PLAXIS 2D model using HSS

The normalized stress concentration, measured using load cells mounted on the floor during the experiment, is compared with the stress concentration extracted from the PLAXIS model, as shown in Fig.5, and shows good agreement, reflecting the validity of the created 2D FEM model.

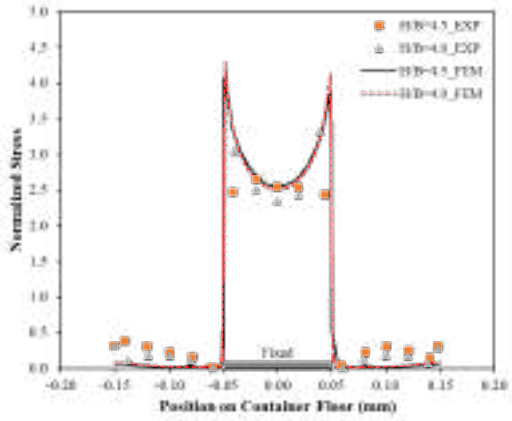

Fig.5 Comparison of normalized stress concentration on the floor between experimental and FEM model for H/B = 4.0 and H/B = 4.5

Effect of Arching on Micro Piles

To investigate the effect of arching on micro piles, a parametric study was conducted using the validated FEM model in PLAXIS 2D. As micro piles contain threading along their shafts, frictional resistance depends on the spacing and depth of the threading. In this parametric study, the interface stiffness in axial direction (R_s), which reflects soil-pile interaction, varied from 2 to 4 times its initial value to investigate its effect on stress concentration and load on the pile due to the arching phenomenon. Figure 6 illustrates the arching phenomenon observed between the two piles when a prescribed displacement of 0.25 mm is applied to the model ground surface, reflecting ground settlement due to the embankment load.

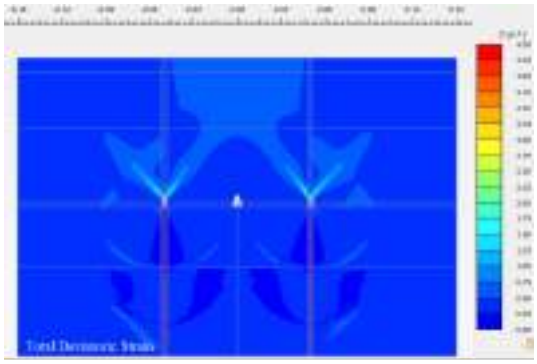

Fig.6 Development of arching in micro piles, 2-pile case

After observing the arching phenomenon in micro piles, the interface stiffness in axial direction (R_s) is increased by 2 to 4 times the initial value (using Eq. 2) in PLAXIS FEM model and its effect on the increase in load and stress concentration on the pile is recorded under prescribed downward displacement of 0.25 mm (represents ground settlements due to embankment load). The results showed that with an increase in R_s, the load on the pile also increases, as shown in Fig.7. Stress concentration on the pile (stress on pile/stress on soil) also increases with the increase in R_s, but in a non-linear way, as shown in Fig.8. These results indicate that due to arching the stresses are transferred to the pile and this transfer of stresses increases with the increase in the pile soil interface axial stiffness (R_s).

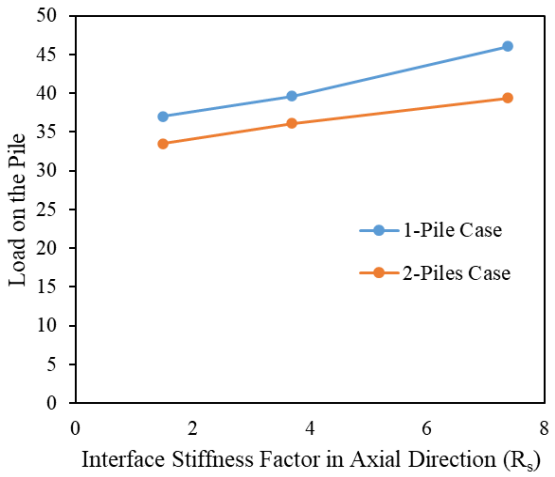

Fig.7 Relationship between interface stiffness factor in axial direction and load on the pile due to arching

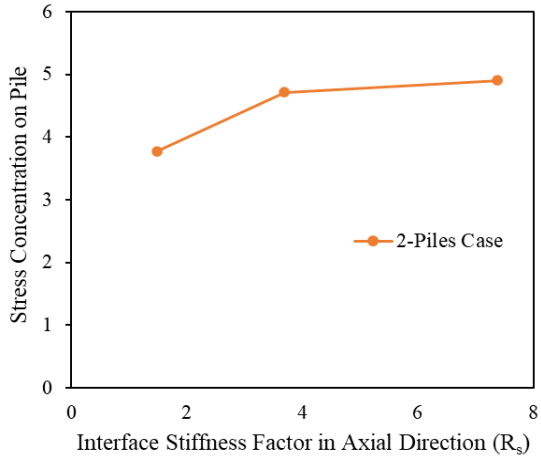

Fig. 8 Relationship between interface stiffness factor in axial direction and stress concentration on the pile due to arching

CONCLUSIONS

This paper investigated the effect of the arching phenomenon in terms of stress concentration and load on the micro piles with varying interface conditions, which reflect the roughness of the pile associated with micro pile shaft threading. The trapdoor experiment is modelled in PLAXIS 2D, and the arching phenomenon is validated. After validation, a parametric study was conducted, in which interface stiffness in the axial direction was increased from 2 to 4 times the initial value to examine the increase in stress concentration and load on the pile due to the arching phenomenon produced by ground settlement. The following are the primary outcomes of this study.

- The Hardening Soil Model with Small-Strain Stiffness can accurately reflect arching in soils, yielding a good agreement with the normalized stress concentration from the trapdoor experiment.
- Transfer of load on the pile due to arching increased linearly with the increase in interface axial stiffness.
- Transfer of stress concentration on the pile due to arching increased non-linearly with the increase in axial stiffness.
- These results indicate that due to arching, the stresses are transferred to the pile, and this transfer of stresses increases with the increase in the pile soil interface axial stiffness (R_s).

REFERENCES

[1] Terzaghi K., Arching in Ideal Soils. Theoretical Soil Mechanics. John Wiley & Sons Ltd, 1943, pp. 66-76.

[2] George T.I., and Dasaka S.M., Mechanics of Arch Action in Soil Arching. Acta Geotechnica, Vol. 18, 2023, pp. 1991-2009.

[3] Ali U., Otsubo M., Ebizuka H., and Kuwano, R., Particle-scale Insight into Soil Arching under Trapdoor Condition. Soils and Foundations, Vol. 60, Issue 5, 2020, pp. 1171-1188.

[4] Lai H., Zheng J.J., Zhang J., Zhang R.J., and Cui L., DEM Analysis of "Soil"-Arching within Geogrid-Reinforced and Unreinforced Pile-Supported Embankments. Computers and Geotechnics, Vol. 61, 2014, pp. 13-23,

[5] Wang Z.Q., Zhang Y.X., Wang C.J., and Chen Z.M., Mechanical Analysis of Soil Arch and Suitable Spacing between Cantilever Piles. Electronic Journal of Geotechnical Engineering, Vol. 18, 2013, pp. 6163-6172.

[6] Britton E., and Naughton P., An Experimental Investigation of Arching in Piled Embankments. In the proceedings of the 4th European Geosynthetics Conference, 2008.

[7] Pham V.H., Vu M.N., and Dang Q.H., Analysis of Stress Transfer and Distribution of an Embankment on Unreinforced and Stone Column Reinforced Soft Soils. International Journal of GEOMATE, Vol. 26. Issue 117, 2024, pp. 19-26.

[8] Tran D.Q., Nishimura S., Senge M., and Nishiyama T., Research on Cause of Dam Failure from Viewpoint of Hydraulic Fracturing – Case Study of Dam Failure in Vietnam. International Journal of GEOMATE, Vol. 14, Issue 41, 2018, pp. 86-94.

[9] Le P.H., Nishimura S., Nishiyama T., Fang C., and Nguyen T.C., Evaluation of Stress of Box Culvert for Agricultural Dam. International Journal of GEOMATE, Vol. 20, Issue 77, 2021, pp. 132-140.

[10] Chevalier B., and Otani J., Arching Observation in Three-dimensional Trapdoor Problem with X-ray CT and Discrete Element Method. Soils and Foundations, Vol. 51, Issue 3, 2011, pp. 459-469.

[11] Iglesai G.R., Einstein H.H., and Whitman R.N., Investigation of Soil Arching with Centrifuge Tests. Journal of Geotechnical and Geoenvironmental Engineering, Vol. 140, Issue 2, 2013.

[12] Dewoolkar M.M., Santichaianant K., and Ko H.Y., Centrifuge Modeling of Granular Soil Response over Active Circular Trapdoors. Soils and Foundations, Vol. 47, Issue 5, pp. 931-945.

[13] Dolati S.S.K., and Mehrabi A., Review of Available Systems and Materials for Splicing Prestressed-Precast Concrete Piles. Structures, Vol. 30, 2021, pp. 850-865.

[14] Zhuang Y., Hu S.H., and Fan Hu., Bearing Capacity of Foundation and Soil Arching in Rigid Floating Piled Embankments: Numerical Study, Applied Sciences, Vol. 13, 2023, 10296.

[15] Otsubo M., Kuwano R., Ali U., Ebizuka H. Trapdoor model test and DEM simulation associated with arching. Proceedings of the 9th International Conference on Physical Modelling in Geotechnics, City University of London. 233-238. July 2018.

[16] Bentley Systems, Plaxis 2D 2024.3 Reference Manual. 2024.

[17] Schanz T., Vermeer P.A., and Bonnier P.G., The Hardening Soil Model: Formulation and Verification. Beyond 2000 Comput. Geotech. Ten Years Int. Proc. Int. Symp. Amsterdam, 199, pp. 281-296.

[18] Benz T., Small-Strain Stiffness of Sils and Its Numerical Consequences. PhD thesis, University of Stuttgart, 2007.

Copyright © Int. J. of GEOMATE All rights reserved, including making copies, unless permission is obtained from the copyright proprietors.

15th Int. Conf. on Geotechnique, Construction Materials & Environment,
Kyoto, Japan, 11-13 November 2025, ISBN 978-4-909106124 C3051

APPLICATION OF MULTI-CHANNEL ANALYSIS OF SURFACE WAVES IN PROBABILISTIC SEISMIC HAZARD ASSESSMENT: A CASE STUDY IN ISLAMABAD, NORTHERN PAKISTAN

Muhammad Qasim Mirza[1], Ghulam Mohyuddin Sohail[2], Adnan Anwar Malik[3], Talha Qadri[4], Faiqa Shahid[2]
Fatima Ijaz[2] and Aneeza Munir[2]

[1]National Engineering Services Pakistan (NESPAK), Pakistan
[2]Geological Engineering Department, UET Lahore, Pakistan
[3]School of Engineering, The University of Newcastle Australia
[4]Energy Geosciences, Government of Northwest Territories, Canada

ABSTRACT

The Multi-channel Analysis of Surface Waves (MASW) technique is a modern geophysical method for measuring shear wave velocity (Vs_{30}), a critical parameter in Seismic Hazard Assessment (SHA) for determining seismic design parameters. While MASW is widely used globally, its application in Pakistan remains very limited and in the initial phase, where traditional methods like downhole or cross-hole surveys, often impractical due to cost, time, and accessibility constraints, are still dominant. As a result, researchers and engineers frequently rely on generalized literature-based Vs_{30} values, which may not accurately represent site-specific conditions. To address this, greater adoption of MASW in Pakistan is essential, particularly for preliminary infrastructure design and research, as it offers a faster and more cost-effective solution. This paper presents novel research on MASW adoption in SHA for Islamabad to evaluate seismic design parameters, aiming to encourage its broader use in Pakistan for more accurate and efficient hazard assessments.

Keywords: Multichannel Analysis of Surface Waves, Seismic Hazard Assessment, Probabilistic Seismic Hazard Analysis, Shear Wave Velocity, Vs30, Peak Ground Acceleration, Non-Destructive Testing

INTRODUCTION

Non-destructive geophysical methods, especially when combined with artificial intelligence (AI) and machine learning, have become highly useful in engineering and environmental studies due to their cost and time efficiency. One such technique, Multi-channel Analysis of Surface Waves (MASW), measures shear wave velocity (Vs_{30}), the average speed of seismic waves down to 30 meters, which is crucial for assessing soil types, earthquake risks, liquefaction potential, and foundation strength. While MASW is gaining global popularity, its use in Pakistan remains limited, despite its potential to improve geotechnical and seismic studies.

The estimation of seismic parameters is critical not only for ensuring stable and safe design but also for achieving an economically sound design of civil infrastructures. The financial constraint is one of the hurdles in attaining accurate parameters as it requires extracting high-quality, undisturbed samples and conducting direct laboratory tests that reflect site conditions in terms of stress path or loading sequence, in-situ stress state, drainage, and other relevant factors at the site [1]. Non-destructive testing (NDT) is one of the ways to overcome this constraint, as it does not disturb the in-situ conditions [2]. Additionally, non-destructive testing (NDT) is a safe, environmentally friendly, and cost-effective method when compared to other options [3,4]. According to Park [5], the estimation of soil stiffness from shear wave velocity obtained from Multichannel Analysis of Surface Waves (MASW) has increased worldwide. The soil stiffness parameter is critical in evaluating site stability.

The purpose of this study is to showcase the application of Multichannel Analysis of Surface Waves and its benefits in achieving safe and economical design. This study represents a significant step forward in utilizing MASW for earthquake risk assessment. This method is executed in Islamabad's northern region, and its results are analyzed to determine key earthquake safety factors. The findings of this study help demonstrate how MASW can be effectively applied in earthquake engineering across Pakistan.

RESEARCH SIGNIFICANCE

This research offers a crucial first application of the Multichannel Analysis of Surface Waves (MASW) method for site-specific seismic hazard assessment in Pakistan. It directly addresses a significant gap in local practice, where reliance on imprecise literature-based values or costly traditional methods continues. By demonstrating MASW's efficiency and cost-effectiveness, this study creates a practical framework for obtaining accurate shear wave velocity (Vs_{30}) profiles. The results provide a reproducible model for improving seismic safety in

infrastructure design, promising more economical and reliable hazard assessments across Pakistan and other developing regions with similar geological conditions and constraints.

APPLICATION OF MASW IN SEISMIC HAZARD

The Multichannel Analysis of Surface Waves (MASW) is a common geophysical method that measures shear-wave velocity (V_s) to study the properties of soil and rock [6,7]

MASW is useful for seismic hazard studies, as shear-wave velocity helps assess ground shaking risks [6,8]. It calculates Vs_{30} (average V_s in the top 30 meters), which is vital for seismic site classification (NEHRP, Eurocode 8). MASW also detects liquefaction risks and soft soils that worsen earthquakes [9,10]. It identifies faults, supports seismic zoning, and enhances earthquake predictions with detailed V_s data [11,12]. In the Pakistani context, this study will provide a guide in using MASW for seismic hazard studies.

DATA COLLECTION AND RESEARCH PROGRAM

Given MASW's growing role in earthquake risk studies and geotechnical engineering, a well-planned research effort is needed to enhance its application, especially in high-risk areas such as Pakistan, where these methods are still relatively new. This study will focus on determining local shear-wave velocity (Vs_{30}), a key factor in seismic analysis. Working with geotechnical, geophysical, and earthquake experts will help apply MASW in real projects. The goal is to make MASW a standard, affordable tool for seismic safety, supporting safer urban development in earthquake-prone areas. Unlike costly methods like Downhole or Crosshole tests (which require drilling and additional steps), MASW is faster and more cost-effective, making it ideal for feasibility studies, design, and research.

The MASW method measures subsurface shear-wave velocity (Vs) by analyzing surface waves. It starts with field tests using geophones placed in a line and a seismic source (like a hammer strike), as shown in Fig.1. The geophones record surface waves (mainly Rayleigh waves), which are then processed to study how wave speeds change with frequency (dispersion curve). This data is converted into a velocity profile using computer models, sometimes with the aid of known geology. The final Vs profile reveals soil stiffness, layers, and earthquake response, making MASW useful for geotechnical and seismic safety studies.

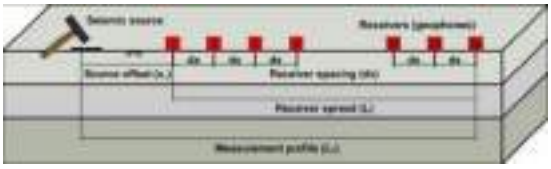

Fig.1 Field setting of MASW survey

To measure shear-wave velocity down to 30 meters (Vs_{30}), MASW surveys were conducted in Islamabad and nearby areas in northern Pakistan. The study examined the surface geology that consists of silty clay, clayey silt, gravel, boulders, loose soil, and soft to moderately weak rock beneath the sites. The region has sedimentary rock layers. The MASW surveys adhered to the [13], utilizing various tools, hammers, ropes, and operating methods.

CALCULATION OF SHEAR WAVE VELOCITY (V_S AND V_{S30})

MASW data processed using Seismic Pro 9.3, a specialized software from Geogiga Technology Inc. First, we examined the color-coded images showing how wave speeds change with frequency for each test location. We focused on the clearest wave patterns (fundamental mode) for our analysis. The software calculated wave speeds multiple times using different settings until we got the cleanest results (highest signal-to-noise ratio). For each test site, we converted these wave speed measurements into a depth-based velocity profile. The software automatically compared calculated and measured wave patterns, selecting the most accurate match (lowest RMSE error) to create the final Vs_{30} profile. The average Vs_{30} of six profiles is interpreted as 745 meters/second. The inverted S-wave Velocity Models of MASW are shown in Figures 2 and 3.

USE OF V_{S30} IN SEISMIC DESIGN PARAMETERS

The study area is in the close vicinity of the tectonic boundary between the Indian and Eurasian tectonic plates, thus lying within a seismically active zone. Several moderate to large earthquakes have been recorded in northern Pakistan over the last 100 years. The study area lies in a region dominated by thrust-type faults, which also exhibit some strike-slip components in certain places. These faults are considered active due to the association of observed seismicity with them. As per available published literature/geological maps of regional extent, the Main Boundary Thrust (MBT) is the major Fault of the study region/surrounding, as shown in Fig.4.

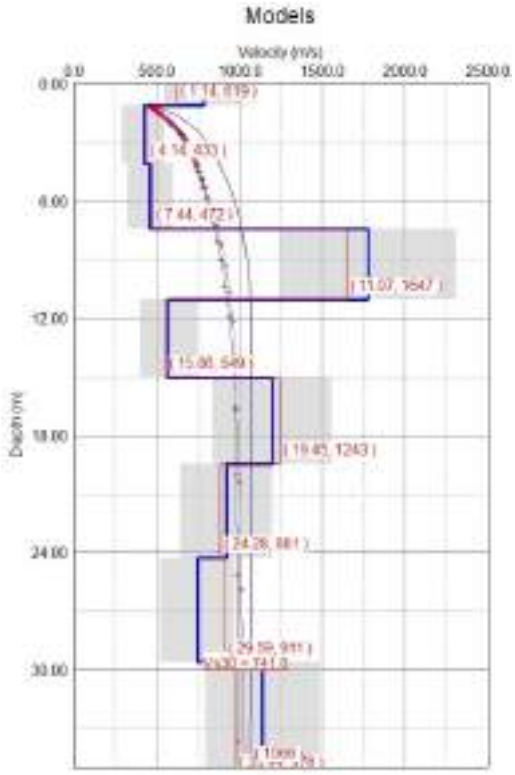

(a)

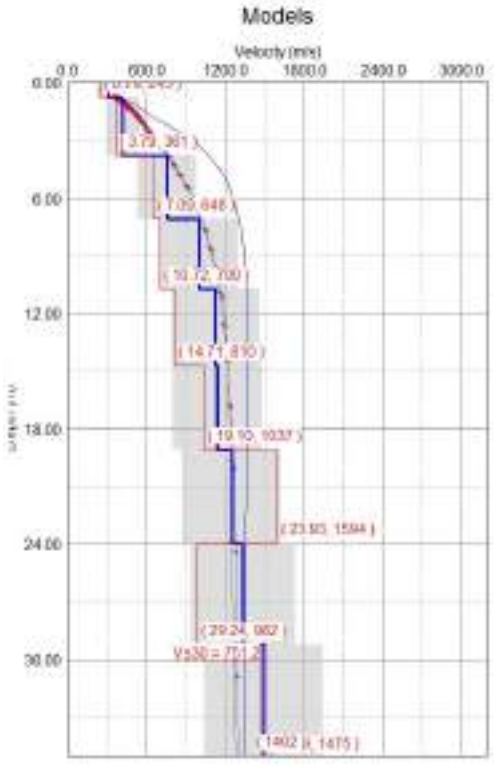

(a)

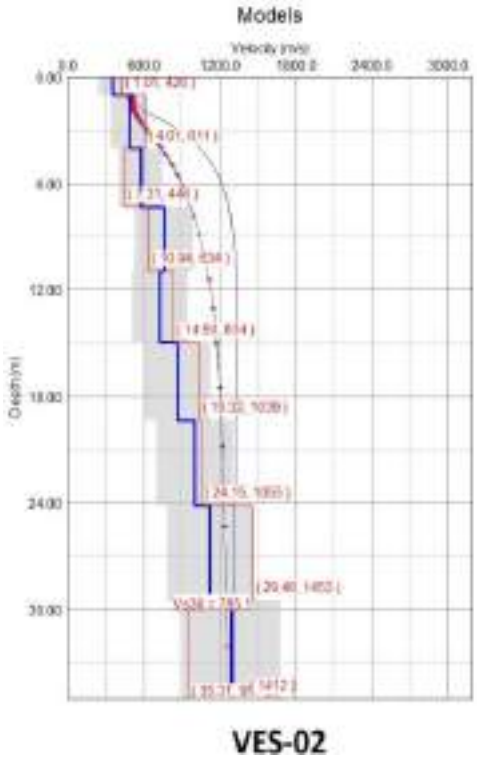

(b)

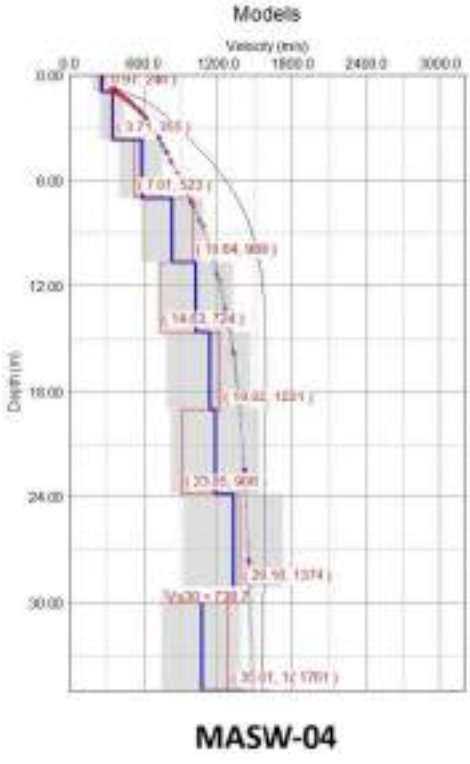

(b)

Fig.2 Inversion models of MASW survey

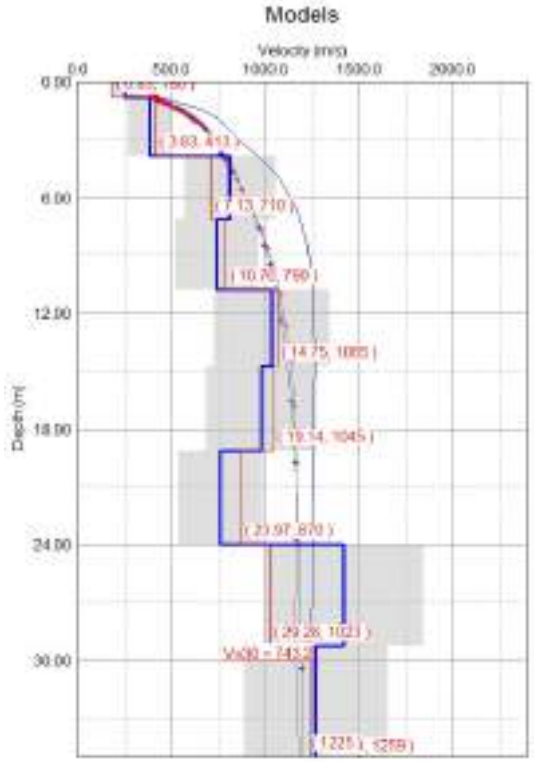

(c)

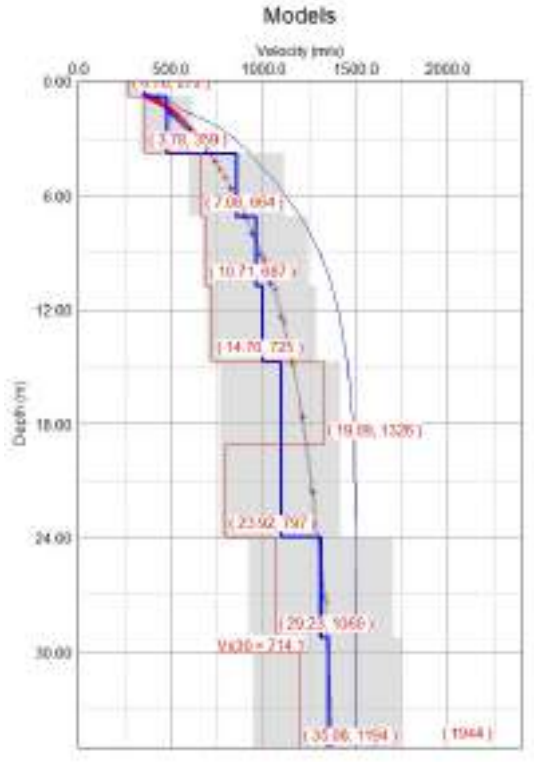

(d)

Fig.3 Inversion 1D and 3D models of MASW survey

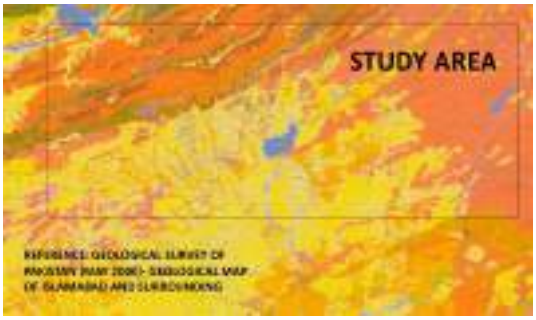

Fig.4 Geological map of the study region (Modified after Geological Survey of Pakistan-GSP, 2000)

The Probabilistic Seismic Hazard Analysis (PSHA) for the current study is conducted using the methodology developed by [14]**.** For PSHA, the Next Generation Attenuation (NGA) West2 equations developed under Pacific Earthquake Engineering Research (PEER) Centre by [15-17] were used as these equations are valid for tectonically active regions of shallow crustal faulting worldwide. The site foundation condition with Vs_{30}=745 m/sec (adopted on the basis of results of site-specific determination of shear wave velocity- Vs_{30} by Multichannel Analysis of Surface Waves. The probabilistic hazard analysis was carried out by using EZ-FRISK software developed by FUGRO Consultants, USA. The results of the probabilistic seismic hazard analysis are presented in Fig. 5 for a very dense soil/soft rock site foundation condition with Vs_{30} =745 m/sec, showing the annual frequency of exceedance of horizontal peak ground acceleration (PGA) at the study area. Peak Ground Acceleration (PGA) value against very dense soil/soft rock foundation conditions with V_{s30} = 745 m/sec. (Soil Profile Type SC) has been calculated as 0.24g for 10% probability of exceedance in 50 years, i.e. 475 return period (Fig. 5).

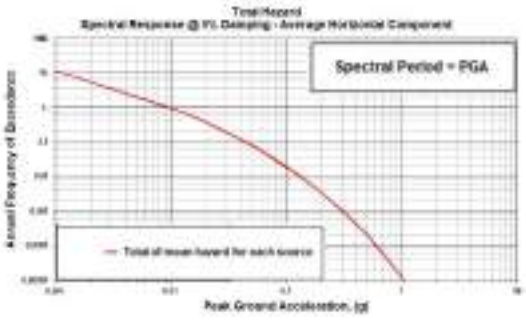

Fig.5 Total hazard curve for site foundation condition with V_{s30} = 745 m/sec

The uniform hazard response spectra obtained by probabilistic seismic hazard analysis are shown in Fig. 6.

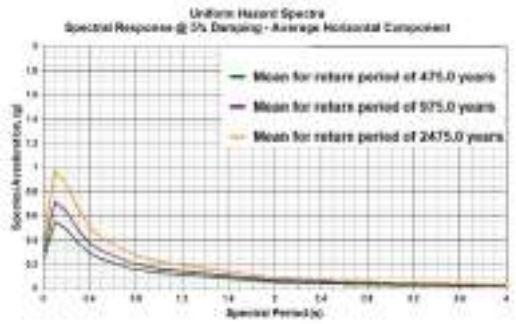

Fig.6 Uniform hazard spectra for site foundation condition with V_{s30} = 745 m/sec

RESULTS/CONCLUSIONS

The current local practice in Pakistan for obtaining Vs_{30}, a critical seismic design parameter, is hampered by significant limitations. Engineers often have to rely on generalized values from literature that may not reflect site-specific conditions or on traditional methods like Downhole or Crosshole tests, which are prohibitively expensive, time-consuming, and often impractical for preliminary studies. This paper demonstrates how applying the MASW method directly addresses these constraints by offering a standardized, non-destructive, and highly efficient alternative. By providing accurate, measured Vs_{30} profiles cost-effectively, this study establishes a reproducible framework that enhances local seismic hazard assessment practices, leading to safer and more economically optimized infrastructure design in Pakistan and similar settings.

The Multi-channel Analysis of Surface Waves (MASW) is a modern method for measuring shear wave speed (Vs_{30}, the average speed down to a 30m depth). It is becoming increasingly crucial in earthquake and soil engineering to study ground layers, calculate earthquake risks, assess liquefaction danger, and evaluate soil strength. While MASW is growing globally, Pakistan is just starting to use it.

This paper shows how MASW can improve earthquake safety practices in Pakistan. It is expected that this study will start a new approach by combining MASW results with earthquake risk studies. As Pakistan's major MASW research for seismic hazard assessment, it aims to guide future earthquake safety planning using this advanced technique.

The key conclusions and recommendations of this current research are as follows.

- Peak Ground Acceleration (PGA) value against very dense soil/soft rock foundation conditions with Vs_{30} = 745 m/sec. (Soil Profile Type S_C), has been calculated as 0.24g for 10% probability of exceedance in 50 years, i.e. 475 return period.
- Pakistan urgently needs to use MASW more for Vs_{30} measurements. This faster, cheaper method is especially useful for early-stage projects and research work.

REFERENCES

[1] Phoon K.K., and Ching J., Better Correlations for Geotechnical Design. International Society for Soil Mechanics and Geotechnical Engineering (ISSMGE), 2024.

[2] Hoła J., and Sadowski, Ł., Non-Destructive Testing in Civil Engineering. Applied Sciences, Vol. 12, Issue 14, 2022, 7187.

[3] Jayale V., Patil A., Gawande S.P., Rajguru V.S., and Adhau, S.P., Non-destructive Test Techniques and Methods in the Assessment of Concrete Structures a Review. AIP Conference Proceedings, Vol. 3188, Issue 1, 2024.

[4] Pana T., Taipodia J., Philley P.D., and Anshu, A. K., Landslide Hazard Vulnerability Assessment using Surface Wave Method Coupled with Slope Stability Analysis: A Case Study, Sadhana, Vol. 49, Issue 3, 2024.

[5] Park C., MASW for Geotechnical Site Investigation. Leading Edge, Vol. 32, Issue 6, 2013, pp. 656–662.

[6] Salas-Romero S., Applications of MASW in Geotechnical and Seismic Hazard Studies. Geophysical Journal International, Vol. 205, Issue 2, 2021, pp. 1120-1135.

[7] Marwan, Asrillah, Yanis M., and Furumoto Y., Lithological Identification of Devastated Area by Pidie Jaya Earthquake Through Poisson's Ratio Analysis. International Journal of GEOMATE, Vol. 17, Issue 63, 2019, pp. 210-216.

[8] Wijayanto W., Mardiatno D., Daryono, Nehren U., Marfai M.A., and Pramono S., Spatial Distribution of VS30 Based on MASW and HVSR Inversion in Gunungkidul, Yogyakarta. International Journal of GEOMATE, Vol. 22, Issue 94, 2022, pp. 29-38.

[9] Park C.B., Miller R.D., and Xia J., Multichannel Analysis of Surface Waves (MASW). Geophysics, Vol. 64, Issue 3, 1999, pp. 800-808.

[10] Bejaj, K., and Anbazhagan P., Seismic Site Classification and Correlation between Vs and SPT-N for Deep Soil Sites in Indo-Gangetic Basin. Journal of Applied Geophysics, Vol. 98, 2013, pp. 70-83.

[11] Hayashi K., Matsuoka, T., and Hatayama, K., Surface-wave Profiling for Seismic Hazard Assessment in Urban Areas. Journal of Environmental & Engineering Geophysics, Vol. 10, Issue 1, 2005, pp. 39-52.

[12] Xia J., Miller R.D., and Park C.B., Estimation of Near-surface Shear-wave Velocity by Inversion of Rayleigh Waves. Geophysics, Vol. 64, Issue 3, 2009, pp. 691-700.

[13] ASTM D 7400-08, Standard Test Methods for Downhole Seismic Testing. American Society for Testing and Materials.
[14] Cornell C.A., Engineering Seismic Risk Analysis. Bulletin of the Seismological Society of America, Vol. 58, Issue 5, 1968, pp. 1583-1606.
[15] Abrahamson N.A., Silva W.J., and Kamai R., Summary of the ASK14 Ground-motion Relation for Active Crustal Regions. Earthquake Spectra, Vol. 30, 2014, pp.1025-1055.
[16] Boore D.M., Stewart J.P., Seyhan E., and Atkinson G.M., NGA-West2 Equations for Predicting PGA, PGV, and 5% Damped PSA for Shallow Crustal Earthquakes. Earthquake Spectra, Vol. 30, 2014, pp. 1057-1085.
[17] Campbell K. W., and Bozorgnia Y., NGA-West2 Ground Motion Model for the Average Horizontal Components of PGA, PGV, and 5%-Damped Linear Acceleration Response Spectra, Earthquake Spectra, Vol. 30, Issue 3, 2014.

Copyright © Int. J. of GEOMATE All rights reserved, including making copies, unless permission is obtained from the copyright proprietors.

15th Int. Conf. on Geotechnique, Construction Materials & Environment,
Kyoto, Japan, 11-13 November 2025, ISBN 978-4-909106124 C3051

EVALUATION OF FLASH FLOOD SUSCEPTIBILITY IN RELATION TO LAND USE CHANGES IN CHIANG RAI, THAILAND

*Zhaolong GU[1], Daisuke Komori[2] and Thapthai Chaithong[3]

[1]Graduate School of Environmental Studies, Tohoku University, Japan;
[2]Green Goals Initiative, Tohoku University, Japan;
[3]Faculty of Social Sciences, Kasetsart University, Thailand

ABSTRACT

Flash floods are among the most destructive hazards, threatening lives and infrastructure in steep, rapidly changing landscapes. This study assessed flash flood susceptibility in Chiang Rai, Thailand, by integrating remote sensing, GIS, and hydrological modeling. Land use maps from 2007, 2012, and 2018—classified as agriculture, grassland, urban, woodland, water, and bare soil—revealed shifting surface characteristics. Terrain slope was extracted from the Copernicus GLO-30 DEM, and soil types were identified using the HYSOGs-250 m dataset, highlighting high-runoff group C and D soils. Curve Number analysis yielded values above 70, indicating elevated runoff risk. A multi-criteria weighted overlay combined slope, land use, soil, and CN to compute the Flash Flood Potential Index (FFPI), which was then divided into five risk classes. Results showed that in Chiang Rai no areas are at Low risk; the regions are ranged from Moderate to High risk. Conversion of woodland to agriculture (2007–2012) and agriculture to urban (2012–2018) notably increased flood vulnerability.

Keywords: Flash Flood, Urbanization, Land Use Change, GIS, Flash Flood Potential Index

INTRODUCTION

Flash floods are sudden inundations triggered by short duration, high intensity rainfall events and, because of their rapid onset and unpredictability, are considered among the most destructive hydrological hazards worldwide [1]. They typically occur within minutes to a few hours after rainfall cessation, inundating normally dry areas and posing severe threats to life and property. In recent years, climate change has intensified both the frequency and magnitude of extreme precipitation, while urbanization and deforestation have diminished natural water-retention capacity and increased surface runoff, further amplifying flash flood risk [2]. Northern Thailand exemplifies these challenges: Chiang Rai Province, situated in the mountainous, monsoonal upper Mekong basin, experiences intense rainfall from May to October that frequently produces riverine flooding and flash floods with very limited warning time [3]. Conventional reliance on river gauges and rain-gauge networks is inadequate in such sparsely instrumented mountainous terrain, often leaving authorities unprepared for upstream flood peaks. To enable spatially explicit flash flood risk assessment, Smith (2003) developed the Flash Flood Potential Index (FFPI), which standardizes and weights physio-graphic factors-slope, soil type, land cover, topographic curvature, and others-within a GIS framework to generate grid-based susceptibility scores [4]. This approach has been widely applied in ungauged catchments to identify potential flash flood source areas. Numerous global and regional studies demonstrate the efficacy of integrating FFPI with remote sensing and GIS data: Lazar (2020) compared FFPI maps for 1989 and 2019 in Romania's Zabala catchment, revealing that deforestation markedly elevated FFPI values [5]; Shehata (2018) evaluated the risk in the Kyushu Island and confirmed that steep, sparsely vegetated subcatchments exhibit high FFPI scores [6]. These studies underscore that multi source data such as DEMs, land-cover maps, and vegetation indices can effectively delineate flash flood hotspots. Globally, as urbanization accelerates and ecosystems fragment, dynamically assessing how specific land use transitions (e.g., forest to agriculture, agriculture to urban) drive flash flood susceptibility has become a critical challenge in hydrology and disaster management. While Lazar (2020) employed bi-temporal FFPI comparisons to highlight the impact of singular land use changes on runoff and flood potential, their work was limited to static two date analyses and did not directly couple multi temporal land-use changes with quantitative FFPI variation [5]. Meanwhile, Chiang Rai Province with its complex terrain, monsoonal rainfall regime, and recurring extreme floods remains without high resolution FFPI based susceptibility mapping. To address these gaps, the present study uses 2007, 2012, and 2018 satellite-derived land use data to construct corresponding FFPI raster models, performs detailed susceptibility analyses in representative Chiang Rai catchments, and introduces a dynamic "risk transition" metric-calculating the proportion of area shifting among FFPI risk categories to quantify the spatiotemporal

evolution of flash flood susceptibility and inform regional flood mitigation planning and land-use management.

STUDY AREA

Chiang Rai province occupies the northernmost tip of Thailand, sharing borders with Myanmar to the north and Laos to the east. Encompassing approximately 11,460 km², the province forms part of the upper Mekong River Basin. Its terrain is dominated by rugged mountain ranges, deeply incised river valleys, and undulating hills, with elevations rising from about 400 m in the lowlands to over 2,000 m in the highest peaks. Two principal river systems-the Nam Kok and Nam Mae-drain much of the province, flowing southeastward toward the Mekong main stem [3]. Annual precipitation in the highlands commonly exceeds 2,000 mm, with individual storms sometimes delivering more than 100 mm of rain within 24 hours. However, the Thai government's current hydrological monitoring framework is confined to lowland flood events and lacks any systematic observation of flash floods in highland regions [7]. Land cover in Chiang Rai is a mosaic of tropical evergreen and deciduous forests in the upper catchments, interspersed with shifting-cultivation zones and terraced agriculture on mid-slope benches. In the lower valleys, paddy fields, small-holder orchards, and expanding peri-urban developments dominate. This heterogeneous landscape, combined with steep slopes and narrow floodplains, creates highly variable surface runoff responses. As agricultural frontiers and urban fringe areas encroach upon formerly forested hill slopes and valley bottoms, the natural infiltration capacity diminishes, exacerbating flood peaks and reducing lead times for warnings [2]. Given this complex physiography, climate regime, and land-use pattern, Chiang Rai provides an ideal setting for applying the Flash Flood Potential Index (FFPI) to identify spatial flash-flood hot spots and to assess how evolving land-use dynamics influence susceptibility across multiple time points.

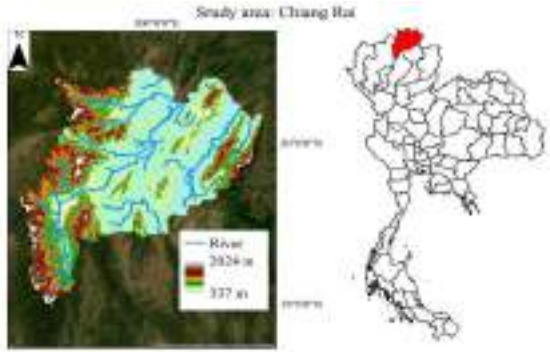

Fig.1 Study area design

METHODOLOGY

This study adopts an integrated geospatial approach to evaluate flash flood susceptibility under changing land use conditions. The overall methodology consists of five main steps described as follow. First, Land use/land cover (LULC) data of 2007, 2012, and 2018 were obtained and classified to map the spatial distribution of land use categories across Chiang Rai. Next, a high-resolution Digital Elevation Model (DEM) was analyzed to extract slope gradients, representing the terrain's influence on runoff generation. Soil data for the region were then processed to determine Hydrologic Soil Groups (HSGs), which indicate the infiltration capacity of different soil types. Using the land cover and HSG information, Curve Number (CN) values were assigned to quantify runoff potential for each land use‐soil combination. Finally, a Flash Flood Potential Index (FFPI) model was implemented by integrating the slope, land use, and soil (CN) datasets to produce a composite flash flood susceptibility map. The following subsections describe each step in detail.

The Land Use Classification

The Land use data for 2007, 2012, and 2018 were obtained from official Thai government sources. The datasets were classified into agriculture, grassland, road, built-up areas, woodland, water, and bare soil. The land use map for 2007, 2012, and 2018 is presented in Figure 2, illustrating the distribution of major land cover types across Chiang Rai. This land use information provides the basis for analyzing how changes in land cover (e.g. deforestation or urban expansion) might affect runoff and flash flood susceptibility.

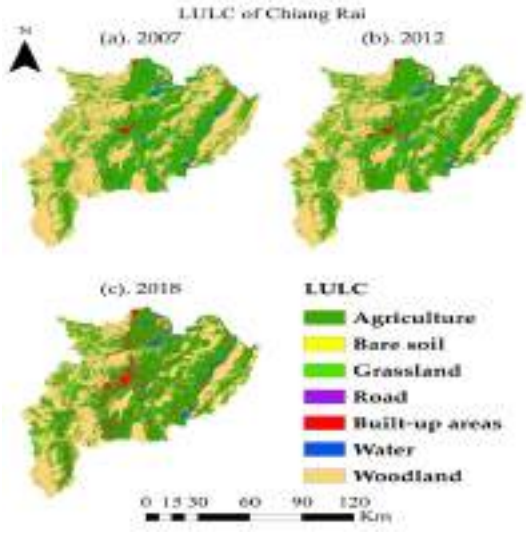

Fig.2 LULC in Chiang Rai (2007, 2012, and 2018)

Slope Extraction

Topographic slope is a critical factor influencing surface runoff velocity and concentration. In this study, slope values were derived from a DEM of the Chiang Rai region [6]. The Copernicus GLO-30 Digital Elevation Model (DEM) was used to extract slope data across Chiang Rai. Slope plays a critical role in determining runoff accumulation, flow velocity, and erosion potential. The DEM data were processed in a GIS environment to generate a slope map, which was later incorporated into the flash flood potential analysis. Fig 3.(a) showed the distribution of slope in Chiang Rai. This categorized slope layer was then prepared for input into the flash flood susceptibility analysis.

Hydrologic Soil Groups Determination

Soil characteristics were incorporated via the Hydrologic Soil Group classification, which distinguishes soils by their infiltration capacity [6]. To determine the hydrologic soil types in Chiang Rai, this study utilized the Global Hydrologic Soil Groups (HYSOGs-250m) for Curve Number-Based Runoff Modeling data set [8]. The dominant soil types in the study area were identified and each was assigned to an HSG category (A, B, C, or D) according to its texture and permeability. In general, Group A soils have high infiltration rates and low runoff potential (e.g., sandy or well-drained loams), whereas Group D soils have very low infiltration (high runoff potential, often clayey or shallow soils). Intermediate groups B and C represent moderate and low infiltration capacities, respectively. Figure 3(b) displays the spatial distribution of these HSGs across the study area. Notably, Chiang Rai's soil (Fig 3.(b)) is consist of soil group C and D, indicating a high runoff potential. This HSG layer serves as a crucial input for assessing runoff generation, as it provides a spatial representation of soil-driven infiltration variability.

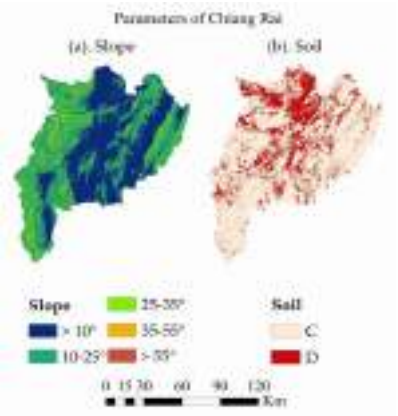

Fig.3 (a).Slope and (b). Hydrologic Soil groups of Chiang Rai

Curve Number (CN) Assignment and Analysis

The NRCS Curve Number method was employed to quantify the runoff generation potential based on combined land use and soil conditions [6]. Using the land use classification (Fig.2) and the HSG map (Fig.3 (a)), a CN value was assigned to each unique land use – soil group combination in the study area. Standard Curve Number lookup tables developed by the USDA Soil Conservation Service for Antecedent Moisture Condition II guided the assignment [9]. For example, forested areas on well-drained Group A soils typically receive a low CN (indicating high infiltration and low runoff potential), whereas urban or paved areas on Group D soils are given a high CN (indicating very high runoff potential). The output of this step was a spatial CN map representing the runoff coefficient across Chiang Rai for 2007, 2012, and 2018, showed in Fig.4. This CN map was examined to understand how land use changes have altered runoff potential over time. Specifically, by comparing CN distributions between the historical and recent land use scenarios, we could identify areas where urban expansion or deforestation has significantly increased runoff susceptibility. The CN analysis thus provides a quantitative link between land cover change and hydrologic response, serving as a foundation for the subsequent flash flood risk modeling.

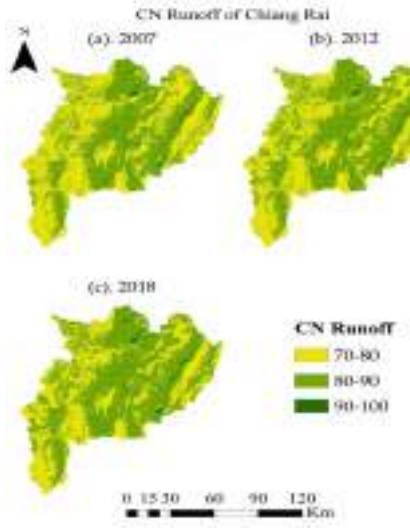

Fig.4 CN runoff in Chiang Rai (2007, 2012, and 2018)

Hydrologic Soil Groups Determination

The final step involved modeling the Flash Flood Potential Index to delineate areas with high Flash flood susceptibility [6]. The FFPI is a dimensionless index that integrates the key contributory factors-topography, land cover, and soil/infiltration

characteristics-into a single susceptibility score for each location. In this study, the FFPI was computed by combining the LULC (Fig.2), slope (Fig.3 (a)), and soil/infiltration information (Fig.3 (b)). Each input parameter was first standardized to an appropriate scale so that higher values correspond to higher flash flood risk. Land use categories were likewise assigned risk scores reflecting their imperviousness or vegetation cover (for instance, urban areas and bare land were given high risk scores, while forested areas were given low scores due to better rainfall absorption). Slope classes and HSGs were converted to rank scores (1 to 10) based on their tendency to generate runoff (with steep slopes and low-infiltration soils receiving higher scores). The CN runoff values were also utilized to inform the weighting of land use and soil contributions, ensuring that areas with high CN (indicative of high runoff potential) are represented as high-risk in the FFPI computation. The integrated FFPI was then calculated on a cell-by-cell basis by combining the factor scores referred to Table 1 [6], effectively averaging or summing the contributions of slope, land cover, and soil.

The final FFPI values were classified into five risk categories:

1.Low (1–3): Low flash flood risk.

2.Moderate (3–5): Potential flash flood risk.

3.Medium (5–6): Increased flash flood likelihood.

4.Elevated (6–8): Significantly prone to flash floods.

5.High (8–10): Frequent flash floods expected.

Table 1. The weighted contribution of each parameters and the ranks of each parameters category [6]

Layer	Weight	Category	Rank
Slope	40	< 10°	1
		10°-25°	3
		25°-35°	5
		35°-55°	8
		> 55°	10
Soil	20	C	7
		D	10
LULC	20	Woodland	5
		Bare soil	3
		Built up	9
		Roads	9
		Agriculture	7
		Grassland	7
		Water	4
CN runoff	20	70-80	8
		80-90	9
		90-100	10

RESULTS

FFPI Distribution in Chiang Rai (2007, 2012, and 2018)

Fig.5 illustrates the spatial distribution of the Flash Flood Potential Index (FFPI) across Chiang Rai for 2007, 2012, and 2018. Notably, no areas in the province fell into the “Low” FFPI category during this period. Instead, the entire landscape was classified within the Moderate, Medium, Elevated, or High risk classes, indicating a generally elevated baseline of flash flood susceptibility throughout Chiang Rai. The Medium FFPI category covered the majority of the area in all three years, followed by the Moderate category, whereas Elevated-risk zones constituted a much smaller fraction of the area, and High-risk zones were extremely limited (consistently <0.1% of the province’s area in each year). This absence of Low-risk areas and dominance of at least Moderate FFPI values suggest that most of Chiang Rai had non-trivial flash flood susceptibility.

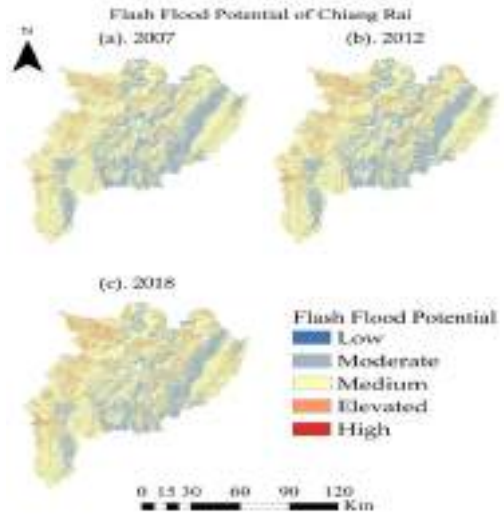

Fig.5 The FFPI results in Chiang Rai (2007, 2012, and 2018)

Relationship between FFPI and flash flood records

To validate the ability of the FFPI distributions to reflect local flash flood conditions in Chiang Rai, recorded flash flood events from 2019 to 2023 were compared with the 2018 FFPI map at the sub-district level. In the absence of detailed inundation extents or depth measurements, the analysis employed the count of severe flash flood occurrences per sub-district. Fig.6 illustrates the spatial correspondence between event frequency and 2018 FFPI values, revealing a concentration of higher flash flood frequency in the regions where elevated and medium FFPI values are more concentrated. The higher number of events within a given period indicates the elevated flood risk [2], this spatial clustering

supports the predictive capability of FFPI. Collectively, this comparison indicated that the FFPI can meaningfully approximate the temporal and spatial patterns of flash floods in Chiang Rai.

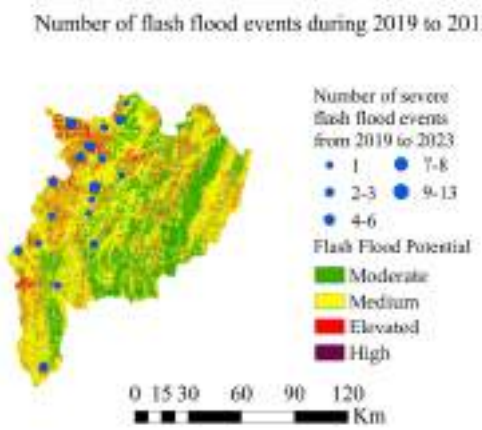

Fig.6 Number of flash flood events during 2019 to 2023 in Chiang Rai

Relationship between FFPI Distribution Changes and Land Use/Land Cover Changes

Overall FFPI trends

The region's FFPI distribution shifted toward higher risk categories over time, as showed in Fig.7. Across the entire province, the area classified as High FFPI increased substantially, while Elevated-risk areas also expanded, especially by 2018. In contrast, Moderate-risk zones shrank continuously, and Medium-risk areas fluctuated (slightly decreasing from 2007 to 2012, then increasing by 2018).

Fig.7 The FFPI distributions in Chiang Rai (2007, 2012, and 2018)

According to Table 2, during the initial 2007-2012 period, changes were modest. For example, the total area under High FFPI rose by only about 55.5% relative to 2007, and Elevated by 28.3%, whereas Medium and Moderate categories saw small declines (around -2.5% each). However, in the subsequent 2012 – 2018 interval a more pronounced escalation in risk occurred: High FFPI area grew by an additional 17.8%, and Elevated by 10.0% (relative to 2012 values), while Medium-risk area rebounded by 3.9% and Moderate continued to decline by -9.3%. The net result by 2018 was a greater proportion of the landscape in the High and Elevated categories than in 2007. These trends underscore an overall increase in flash flood susceptibility in Chiang Rai between 2007 and 2018, pointing to underlying drivers that intensified flood potential over time.

Table 2. Changes in FFPI category coverage across Chiang Rai

FFPI Category	Change in Area (2007–2012)	Change in Area (2012–2018)
High	+55.45%	+17.83%
Elevated	+28.29%	+10.01%
Medium	-2.53%	+3.87%
Moderate	-2.86%	-9.25%

FFPI changes in urban areas

When focusing on urbanized areas (built-up land and roads), the FFPI shifts were even more concentrated and extreme. Table 3 shows that in areas of urban growth, higher-risk FFPI classes expanded dramatically, especially during 2012 – 2018. In that period, the area classified as High FFPI in urban regions increased fivefold (approx. +500%), while Elevated-risk urban areas tripled (+208%), and Medium-risk urban areas nearly quadrupled (+296%). By contrast, from 2007 to 2012 the urban FFPI changes were minimal – High-risk urban area remained effectively unchanged (0% increase), and only modest growth occurred in the Elevated (+26%) and Medium (+21%) categories. The sharp rise in High and Elevated FFPI within urban and peri-urban zones after 2012 indicates that rapid urban expansion considerably intensified local flash flood potential. In other words, new development has been occurring in, or contributing to, areas of higher inherent flood risk, raising concern for those urbanizing locales.

Table 3. Changes in FFPI category coverage in Urban areas of Chiang Rai

FFPI Category	Change in Area (2007–2012)	Change in Area (2012–2018)
High	0.00%	+500.00%
Elevated	+26.23%	+207.82%
Medium	+21.18%	+295.61%

Land use/Land cover (LULC) change linkages

The observed FFPI increases are closely linked to major land use transitions in Chiang Rai over the study period. The extensive LULC changes by area are showed in Fig.8. Between 2007 and 2012, the largest transition was the conversion of

approximately 754.58 km^2 of woodland to agricultural land. Replacing forest cover with agriculture tends to increase runoff and flash flood potential. This woodland-to-agriculture conversion corresponds with the moderate rise in Elevated FFPI areas observed in 2007-2012. In the 2012-2018 period, the dominant change was urban expansion: about 437.87 km^2 of agricultural land was transformed into urban/built-up use (including road networks). This extensive agriculture-to-urban conversion greatly reduced infiltration and further increases runoff, aligning with the marked surge in High and Elevated FFPI areas after 2012. Another major change was an additional 407.01 km^2 of woodlands (intact through 2012) being converted to agriculture by 2018, reinforcing the pattern of deforestation contributing to flood hazard. Overall, these land use changes explain the FFPI distribution shifts: early-stage deforestation for agriculture created conditions for higher runoff (elevating flood risk), and subsequent urbanization of farmland amplified that effect, leading to a notable increase in high flash-flood-susceptibility zones across Chiang Rai by 2018.

Fig.8 Proportions of the major LULC in Chiang Rai (2007, 2012, and 2018)

CONCLUSIONS

The results indicated that sub-districts in western Chiang Rai with steeper slopes exhibit higher FFPI values compared to lower-gradient eastern lowlands, particularly where urban expansion has occurred on steep terrain. This observation suggests that high-slope areas accelerate surface runoff and reduce infiltration time, thereby amplifying the intensity and sudden onset of flash floods. From an exposure standpoint, human activities in these high-slope zones are inherently more susceptible to flash flood impacts than those in gentler areas. Moreover, ongoing urbanization and deforestation further exacerbates the surface runoff formation in rainfall events, increasing community vulnerability. Consequently, land use in high-slope regions must be rigorously regulated, and targeted flood-control infrastructure, such as check dams designed to retard runoff velocity, should be implemented to mitigate flash flood hazards and protect at-risk populations.

REFERENCES

[1] Saharia M., Kirstetter P.-E., Vergara H., Gourley J. J., Hong Y., Giroud M., Mapping Flash Flood Severity in the United States. Journal of Hydrometeorology, Vol. 18, Issue 2, 2017, pp. 397‑411.

[2] Gu Z., Phakdimek S., Nagami K., Komori D. Relationship Between Urbanization–Induced Land Use Changes and Flood Risk: Case Study in Chiang Mai, Thailand. Water, Vol. 17, Issue 3, 2025, pp. 327.

[3] Piman T., Babel M. S., Prediction of Rainfall-Runoff in an Ungauged Basin: A Case Study in the Mountainous Region of Northern Thailand. Journal of Hydrologic Engineering, Vol. 18, Issue 2, 2013, pp. 285‑296.

[4] Smith J. D., Flash Flood Potential Index: Development and Application. Hydrological Sciences Journal, Vol. 30, Issue 4, 1985, pp. 393‑408.

[5] Lazar I., Chitu E., Teodoru C. R., Bi‑temporal Analysis of Flash Flood Potential Index in Response to Land‑use Changes: A Case Study in the Zăbala Catchment, Romania. Natural Hazards, Vol. 102, Issue 3, 2020, pp. 1539‑1551.

[6] Shehata M., Mizunaga H., Flash Flood Risk Assessment for Kyushu Island, Japan. Environmental Earth Sciences, Vol. 77, 2018, Article 76, pp. 1‑20.

[7] Chantip S., Jermsittiparsert K., Nakhapakorn K., Development of a Dynamic Flash Flood Hazard Index (DFFHI) for the Wang River Basin, Northern Thailand. Environmental Hazards, Vol. 19, Issue 1, 2020, pp. 65‑81.

[8] Ross, C.W., L. Prihodko, J.Y. Anchang, S.S. Kumar, W. Ji, and N.P. Hanan. 2018. Global Hydrologic Soil Groups (HYSOGs 250m) for Curve Number-Based Runoff Modeling. ORNL DAAC, Oak Ridge, Tennessee, USA.

[9] Soil Conservation Service (SCS), Urban Hydrology for Small Watersheds: Technical Release 55, 2nd Edition, U.S. Department of Agriculture, Soil Conservation Service, Conservation Engineering Division, Washington, DC, June 1986, Appendix 4B "Curve Number Tables for Antecedent Runoff Condition II", pp. 4B-4‑4B-6.

Copyright © Int. J. of GEOMATE All rights reserved, including making copies, unless permission is obtained from the copyright proprietors.

15th Int. Conf. on Geotechnique, Construction Materials & Environment,
Kyoto, Japan, 11-13 November 2025, ISBN 978-4-909106124 C3051

THE STUDY OF HELICAL PILE BEHAVIOR UNDER COMPRESSION FORCE IN KHON KAEN LOESS

Natchaphon Noiphang, Ratamanee Nuntasarn and Jitrakon Prasomsri

Faculty of Engineering, Khon Kaen University, Thailand

ABSTRACT

Khon Kaen loess soil is classified as collapsible and poses a serious challenge to foundation design, particularly under varying moisture conditions. While it exhibits high strength in dry conditions, moisture infiltration can cause significant settlement and structural damage over time. This study compares the design of a 6.5-meter-long triple helix helical pile with a helix spacing-to-diameter ratio (S/D) = 3 in Khon Kaen loess, using parameters obtained from Consolidated Drained (CD) triaxial tests on undisturbed and unsaturated soil. Theoretical predictions of ultimate bearing capacity were calculated using the individual bearing method. This study focuses on soil strength parameters from the Saturation, Transition and Residual Regime of the Soil-Water Characteristic Curve (SWCC) for the Khon Kaen loess. Results indicate that matric suction significantly affects shear strength parameters, especially cohesion, thereby influencing the bearing capacity of the pile. This research provides valuable insights for improving the accuracy and safety of foundation designs in collapsible soils, offering practical guidelines for engineering applications under seasonally fluctuating moisture conditions.

Keywords: Helical pile, Bearing capacity, Khon Kaen loess, Triaxial test, Consolidated drained

INTRODUCTION

Khon Kaen Loess is a type of collapsible soil [2] that exhibits high strength when dry but experiences rapid settlement upon wetting. The region is generally characterized as arid due to its relatively low average annual rainfall, which ranges from approximately 1,200 to 1,257 mm/year, with most rainfall occurring between May and October. These climatic conditions result in unsaturated soil. Therefore, the increase in soil moisture content during the rainy season can lead to structural damage.

Helical piles are deep foundations that are installed by screwing into the ground, thus avoiding excavation. Additional advantages of helical piles include minimal disturbance to the surrounding environment, suitability for limited-access sites, and the ability to be installed in a wide range of soil conditions and low vibration, quick installation. It provides resistance to both compressive and tensile loads [3]. Their load capacity depends on the surrounding soil properties, especially shear strength.

Designing helical piles for Khon Kaen Loess requires a deep understanding of unsaturated soil behavior, particularly the influence of matric suction on shear strength. This study utilizes results from Consolidated Drained (CD) triaxial tests conducted under varying suction levels (0, 10, 100, and 200 kPa). It focuses on the saturation, transition, and residual regimes in the Soil-Water Characteristic Curve (SWCC) of Khon Kaen Loess to analyze the soil strength parameters. Incorporating these parameters into design calculations improves the accuracy of estimating soil resistance around the pile under different suction conditions, leading to more efficient helical pile designs that align with the complex and seasonally variable behavior of the soil.

The scope of this research is to design helical piles and compare their ultimate bearing capacity based on the results of unsaturated triaxial tests.

Extended Mohr-Coulomb failure envelope

The extended Mohr-Coulomb failure envelope consists of shear stress at failure (τ_f), the net stress ($\sigma - u_a$) and matric suction ($u_a - u_w$). The equation of unsaturated soil was proposed by [1], as shown in Eq. (1) and (Fig. 1).

$$\tau_f = c' + (\sigma - u_a)_f \tan\phi' + (u_a - u_w)_f \tan\phi^b \quad (1)$$

Where;
τ_f = shear stress at failure
c' = effective apparent cohesion
u_w = pore water pressure
u_a = pore air pressure
$(u_a - u_w)_f$ = matric suction at failure
$(\sigma - u_a)_f$ = the net stress at failure
ϕ' = friction angle of effective stress
σ = total normal stress
ϕ^b = angle indicating the rate of increase in shear strength relative to the soil suction at failure plane

$$c = c' + (u_a - u_w) \tan\phi^b \quad (2)$$

Where
c = the cohesion intercepted

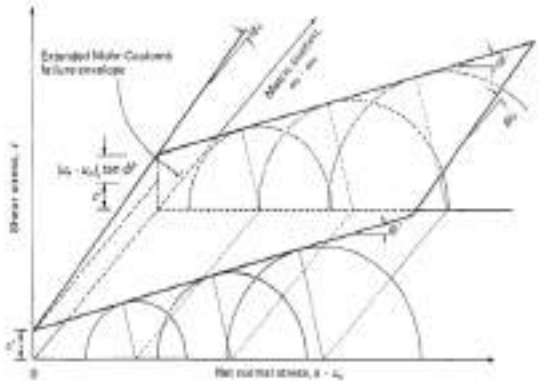

Fig.1 Extended Morh-Coulomb failure envelope for unsaturated soils.[1]

RESEARCH SIGNIFICANCE

Incorporating parameters that vary with matric suction into the design of helical piles can enhance the accuracy of soil resistance analysis and evaluation. This results in pile designs that are better suited to actual environmental conditions and more effectively accommodate the seasonally variable behavior of soils.

METHODOLOGY

Unsaturated CD Triaxial Test

Preparation of Specimens

The Khon Kaen loess soil sample was collected as an undisturbed sample from a depth of 2 m. The basic soil properties are presented in Table 1.

Table 1 Basic properties of soil

Properties	
Liquid limit (LL), %	19
Plastic limit (PL), %	NP
Plasticity index (PI), %	-
Specific gravity	2.65
Dry density (γ_d), t/m^3	1.73
Sand (%)	54.87
Silt (%)	28.09
Clay (%)	17.04
USCS classification	SM

Due to the difficulty in obtaining undisturbed soil samples, a multistage triaxial testing method is used. In this method, each stage applies a different confining pressure to a single soil specimen. According to the study by [4], the results of multistage testing on compacted Khon Kaen loess soil were found to be comparable to those obtained from single stage testing. Therefore, the multistage method is adopted in this research.

Table 2 Program of this study.

Sample No.	stage	σ_{net} (kPa)	u_a (kPa)	u_w (kPa)	ψ (kPa)
1	1	150	0	20	0
	2	300			
	3	450			
	4	600			
2	1	150	30	20	10
	2	300			
	3	450			
	4	600			
3	1	150	120	20	100
	2	300			
	3	450			
	4	600			
4	1	150	220	20	200
	2	300			
	3	450			
	4	600			

The soil specimens used for the consolidated drained triaxial test were 50 mm in diameter and 100 mm in height.

The unsaturated soil shear strength testing using the consolidated drained triaxial test [5] can be divided into the following steps.

Step 1, The soil specimen was placed into the triaxial compression apparatus. Water pressure was applied to the specimen until it became saturated, indicated by a B-value of 95%, as calculated using "Eq. (3)"

$$B = \frac{\Delta u}{\Delta \sigma_3} \quad (3)$$

Where
Δu = pore pressure change in the chamber pressure when drainage valves closed
$\Delta\sigma_3$ = isotropic change in the chamber Pressure

Step 2, The specimen was consolidated by increasing the net confining pressure. Both air and pore water pressures were applied according to Table 2. The drainage valve was opened to allow air and water to escape from the specimen.

Step 3, The specimen was shared at the rate determined in Eq. (4). The shearing process continued until the specimen approached the peak of the stress-strain curve. After reaching near-maximum stress, the axial load was reduced to 0 kPa to complete the test.

Steps 2 and 3 were repeated. After the final stage, which is stage 3 (σ_{net} = 600 kPa), the specimen was sheared to failure.

$$\text{Shear rate} = \frac{4\%}{16t_{90}} \quad (4)$$

Where

t_{90} = square root time derived from x- intercept in the relationship of the graph between total volume change and square root time.

RESUALS

Soil water characteristic curve

The results of the soil-water characteristic curve (SWCC) of compacted Khon Kaen Loess [8], shown in (Fig.2), indicate the first and second air entry values at 3 kPa and 650 kPa, respectively. At the first residual point, the degree of saturation is 42%. In this study, the soil parameters are compared across different suction ranges: Saturation Regime (0 kPa), the 1st Transition Regime (10 kPa), and the 1st Residual Regime (100kPa and 200 kPa).

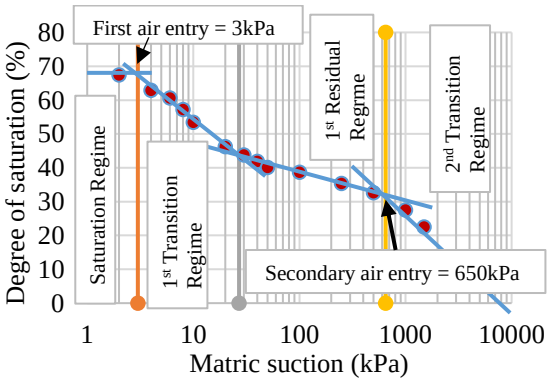

Fig.2 Khon Kean Loess Soil-Water Characteristic Curve.[8]

Consolidated drained triaxial test

The consolidated drained triaxial test was conducted saturated and unsaturated from Khon Kaen Loess using a multistage method. The confining pressures applied were 150, 300, 450, and 600 kPa,

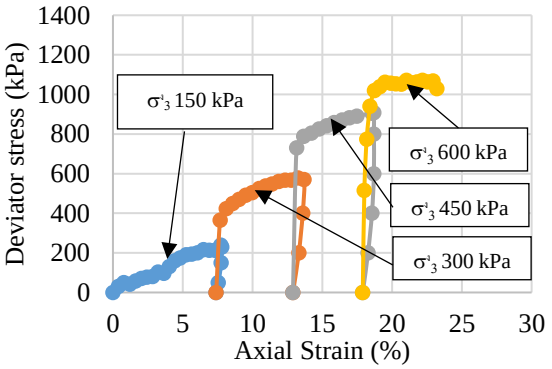

Fig.3 The stress-strain curve form multistage testing at saturated (Matric suction = 0 kPa).

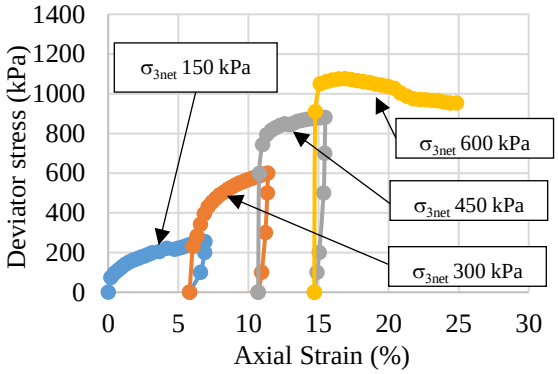

Fig.4 The stress-strain curve form multistage testing at matric suction of 10 kPa.

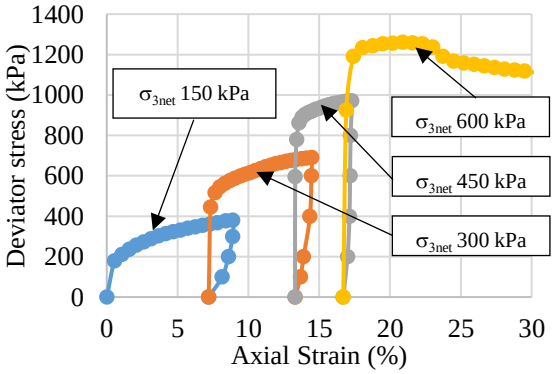

Fig.5 The stress-strain curve form multistage testing at matric suction of 100 kPa.

with a pore water pressure of 20 kPa. The test results, as shown in (Figs.3-6) illustrate the relationship between deviator stress and axial strain. The Mohr-Coulomb failure envelope shown that in (Figs.7-10)

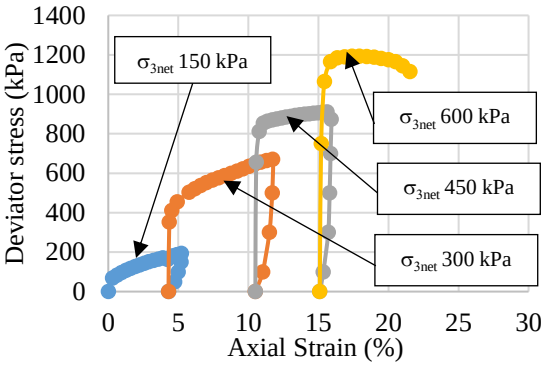

Fig.6 The stress-strain curve form multistage testing at matric suction of 200 kPa.

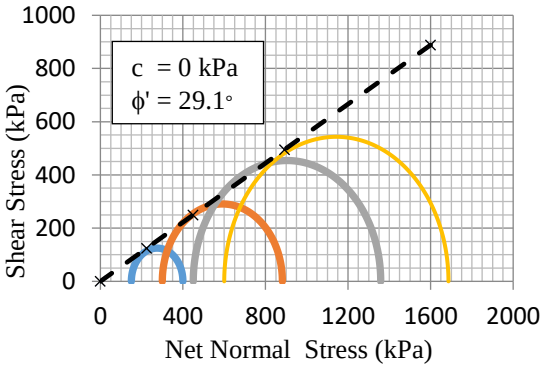

Fig.7 Mohr-Coulomb failure envelope at saturated (Matric suction = 0 kPa)

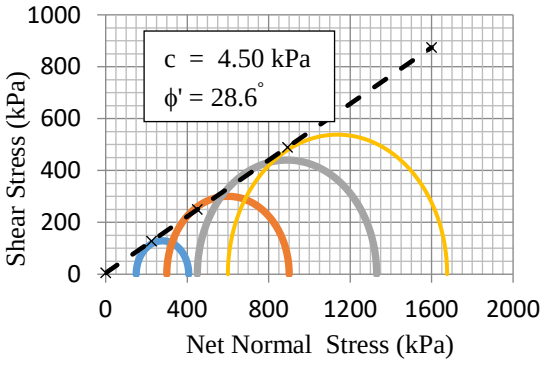

Fig.8 Mohr-Coulomb failure envelope at matric suction of 10 kPa

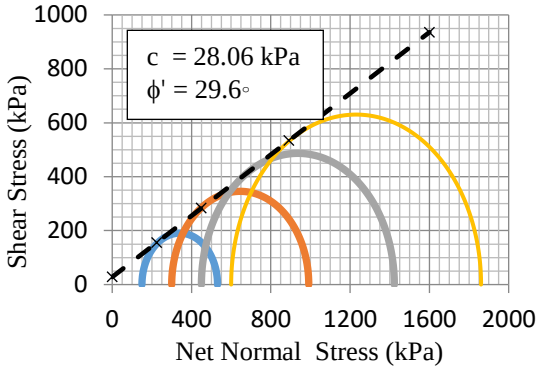

Fig.9 Mohr-Coulomb failure envelope at matric suction of 100 kPa

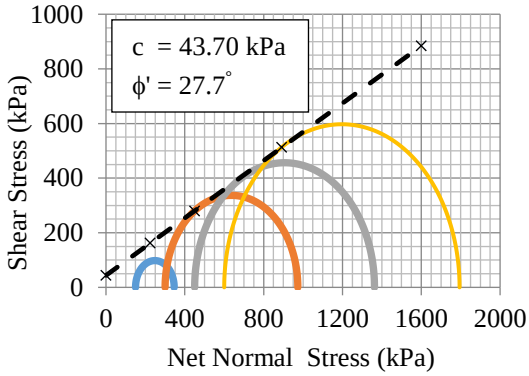

Fig.10 Mohr-Coulomb failure envelope at matric suction of 200 kPa

Table 3 Result of Unsaturated shear strength parameter

Sample No.	Matric suction	Cohesion Intercept (c)	ϕ' (deg)	ϕ^b (deg)
1	0	0	29.1	29.1
2	10	4.5	28.6	24.2
3	100	28.1	29.6	14.7
4	200	43.7	27.7	8.9

The relationship between matric suction shown that in (Fig.11), the value of ϕ^b, and the ϕ'are equal in saturation regime. The value of ϕ'remains relatively constant across the saturation regime, transition regime, and residual regime, whereas the angle ϕ^b decreases, which is consistent with the study of [4].

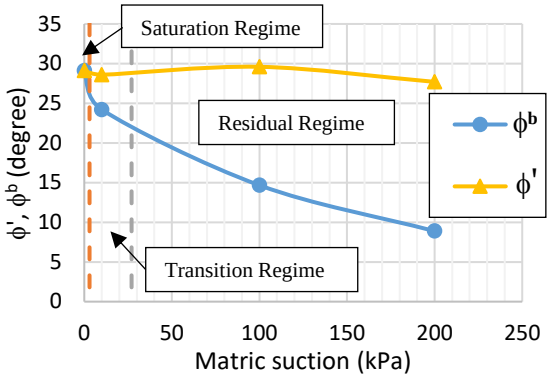

Fig.11 The relationship between matric ϕ^b, ϕ' between matric suction.

The relationship between matric suction and cohesion, as shown in (Fig.12), indicates an increase in cohesion across the saturation regime, transition regime, and residual regime, respectively.

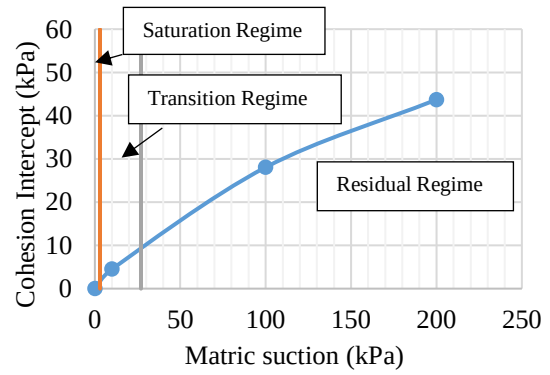

Fig.12 The relationship between matric suction and cohesion intercept.

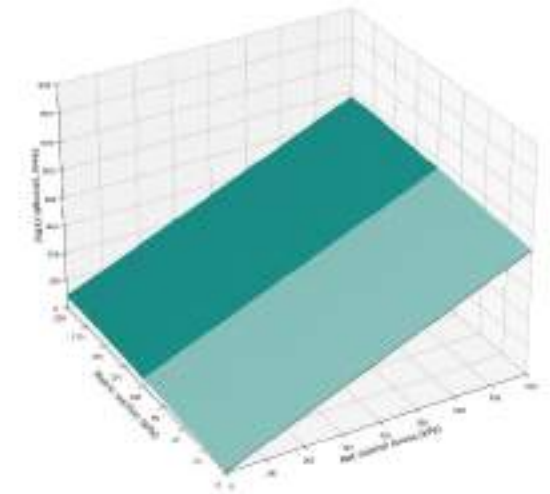

Fig.13 The 3D graph extended Mohr-Coulomb failure envelope.

ANALYSIS AND DISCUSSION

The bearing capacity calculation of helical piles can be performed using two methods: the individual bearing method and the cylindrical shear method, as presented by [3]. The individual bearing method involves summing the bearing capacity at each helix plate along the pile and shaft friction. The cylindrical shear method calculates the bearing capacity at the lowest helix plate, combined with the shear resistance of the soil between the helix plates and the undisturbed soil, as well as shaft friction. According to laboratory experiments by [10], to switch the calculation method from the cylindrical shear method to the individual bearing method, the pile must have a ratio of the spacing between helix plates to the diameter of the helix plate (S/D) greater than 2.1 to 3.4.

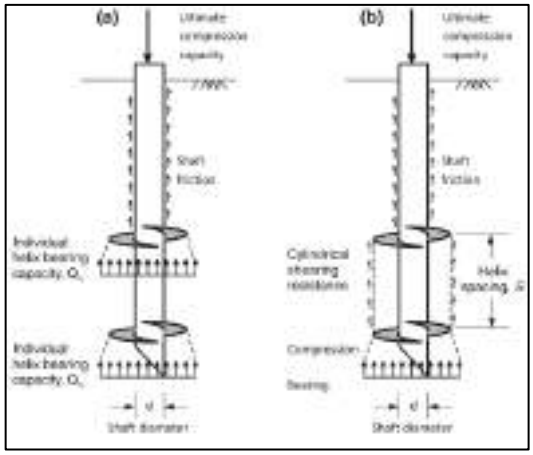

Fig.14 Analytical for estimating helical pile bearing capacity; (a) The individual bearing method, (b) The cylindrical shear method.[7]

This study designed the helical pile with a length of 6.5 m, a pile shaft diameter of 6 inches, a helix diameter of 45 cm, and a helix spacing ratio (S/D) = 3, applying the individual bearing method to calculated ultimate bearing capacity. The result shows that in (Fig.15)

$$Q_u = \sum Q_{helix} + Q_{shaft} \quad (5)$$

$$Q_{helix} = A_n(cN_c + qN_q + 0.5\gamma' BN_\gamma) \quad (6)$$

$$Q_{shaft} = \sum q_{si}\Delta L_i \pi d \quad (7)$$

Where
Q_u = ultimate bearing capacity.
A_n = area of the helical bearing plate.
N_c, N_q, N_γ = the bearing capacity factor [6]
d = diameter of helical pile.

DL_i = the pile segment length in soil layer *i*
q_{si} = the average unit shaft friction of soil layer *i*

The unit shaft friction for the sand layer can be estimated using $q_{si} = \sigma'_v K_0 \tan(\delta)$ where σ'_v is the effective vertical stress at the mid-depth of each soil layer [9], K_0 is the coefficient of lateral earth pressure.

Based on the design results from Eq. (5-7), it was found that the ultimate bearing capacity of the helical pile increases from the saturation regime to the residual regime. However, within the residual regime, the ultimate bearing capacity remains relatively constant. It is also observed that the bearing capacity behavior of helical piles primarily relies on the capacity of the helix plates.

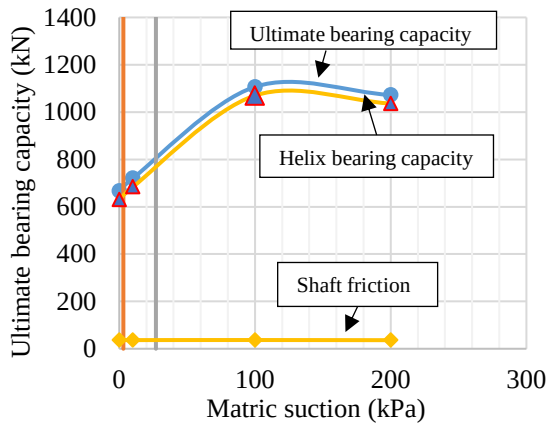

Fig.15 The Ultimate bearing capacity compares with increasing the matric suction.

CONCLUSIONS

This study focused on analyzing the influence of matric suction on the shear strength parameters of unsaturated Khon Kaen Loess and its impact on the design of helical piles. Consolidated Drained (CD) triaxial tests were conducted under various suction levels (0, 10, 100, and 200 kPa), and an extended Mohr-Coulomb failure envelope was developed to reflect the shear strength behavior of unsaturated soil.

The results of the consolidated drained triaxial tests show that increasing matric suction has a significant effect on cohesion, while the effective internal friction angle (ϕ') remains relatively constant across all suction levels, whereas ϕ^b was decreased. Based on the calculation of the ultimate bearing capacity of helical piles using the individual bearing method, it was found that the ultimate bearing capacity of pile increases 7.4% in Transition Regime and 63.3% in Residual Regime, compared to the Saturation Regime.

Due to the nature of Khon Kaen Loess, the soil exhibits high strength in dry conditions but collapses easily upon wetting. Therefore, seasonal moisture variations and the influence of matric suction must be carefully considered to achieve more accurate and stable foundation designs. In the case of helical pile foundations, it is recommended that design parameters be derived from laboratory testing rather than the site investigation data. Applying unsaturated soil mechanics in the design process can significantly improve the efficiency and safety of geotechnical structures in similar soil environments.

ACKNOWLEDGMENTS

Acknowledgement is given to the Faculty of Engineering in Khon Kaen University for the support of this research.

REFERENCES

[1] Fredlund, D.G. & Rahadjo, H., Soil mechanics for unsaturated soils. New York: Wiley., 1993, pp.1-509.

[2] Udomchoke V. (1991). Origin and Engineering Characteristics of the Problem Soil in the Khorat Basin, Northeastern Thailand. Ph.D. dissertation Asian Institute of Technology, Bangkok Thailand.

[3] Perko, H.A., Helical Piles: A Practical Guide to Design and Installation, 1st ed. John Wiley & Sons, Inc, USA.,2009, pp.1-512.

[4] Chatchawan S., Nuntasarn R. "The drained shear strength of compacted Khon Kaen Loess from multistage triaxial test". International Journal of GEOMATE, Nov., 2019 Vol.17, Issue 63, pp.172 - 180

[5] American Society for Testing and Materials. (D7181-11). Standard test method for consolidated drained triaxial compression test for soils.

[6] Terzaghi, K., Peck, R. B., & Mesri, G. Soil mechanics in engineering practice. John Wiley & Sons, 1996, pp.1-512.

[7] Sakr M., (2009). Performance of helical piles in oil sand. Can. Geotech. J. 46: 1046–1061

[8] Nuntasarn R., Wannakul V. "The Relationship between soil suction and the maximum unsaturated undrained shear strengths of compacted Khon Kaen Soil, Int. J. of GEOMATE, March., 2012, Vol. 2, No. 1 (Sl. No. 3), pp.166-170.

[9] Mohajeranin A., Bosnjak D., Bromwich D., "Analysis and design methods of screw piles: A review"., The Japanese Geotechnical Society, Soils and Foundations 56, 2016, pp.115–128

[10] Narasimha Rao S., Prasad, T.V.S.N., Shetty D. "The behaviour of model screw pile on cohesine soils. The Japanese Geotechnical Society, Soils and Foundations Vol.31, No.2, 1991, pp.35-50

Copyright © Int. J. of GEOMATE All rights reserved, including making copies, unless permission is obtained from the copyright proprietors.

15th Int. Conf. on Geotechnique, Construction Materials & Environment,
Kyoto, Japan, 11-13 November 2025, ISBN 978-4-909106124 C3051

EFFECTS OF FREEZE-THAW HISTORY ON PILE PULL-OUT RESISTANCE

Yusaku Fujita[1], Dai Nakamura[2], Kenta Nakai[3], Takanori Kadota[4] and Yuki Minabe[5]

[1]Graduate School of Engineering, Kitami Institute of Technology, Japan
[2, 4, 5]Faculty of Engineering, Kitami Institute of Technology, Japan
[3]Asano Taiseikiso Engineering Co., Ltd, Japan

ABSTRACT

In recent years, the construction of photovoltaic power generation facilities has been actively promoted in mountainous areas and on idle farmland in Hokkaido, a region characterized by snowy and cold climates. However, significant damage due to the frost heave phenomenon—where the foundations and piles are lifted, leading to deformation of the panel mounts and warping of the panels themselves—has been occurring with increasing frequency. Continued deformation may lead to panel tilting, damage, or even collapse. Moreover, Japan has seen an increasing trend in extreme weather events such as heavy rainfall and sudden gusts of wind. If frost heave occurs during the winter and compromises the pile bearing capacity and pull-out resistance, these weakened conditions may lead to severe damage—such as the collapse of solar power facilities—when subjected to heavy rain or strong winds during the summer. This study aimed to clarify the frost heave behavior of spiral piles and straight piles, commonly used in the construction of photovoltaic power generation facilities, under freeze-thaw history. In addition, a series of three pull-out tests were conducted—from immediately after installation through the summer months—to examine the effects of freeze-thaw history on the pull-out resistance of the piles. The results indicated that frost heave displacement was suppressed in spiral piles, whereas residual frost heave displacement remained in straight piles during spring. Furthermore, it was confirmed that the pull-out resistance of both pile types decreased following exposure to freeze-thaw history.

Keywords: Freeze-thaw History, Frost Heave, Pile, Pull-out Resistance

INTRODUCTION

In recent years, decarbonization—aimed at reducing greenhouse gas emissions to zero—has become a global trend, placing pressure on Japan to transition from fossil fuels to renewable energy sources. As a result, photovoltaic power generation facilities are being actively constructed even in mountainous areas and idle farmland in Hokkaido, a region characterized by snowy and cold climates. However, significant damage due to the frost heave phenomenon has been occurring with increasing frequency.

Figure 1 presents examples of frost heave damage to solar panel mounts that have occurred in eastern Hokkaido. When frost heaving occurs in the ground, the foundations and piles supporting the solar panels are lifted, resulting in the deformation of the panel mounts and the warping of the panels themselves. Continued deformation may lead to tilting, damage, or even collapse of the solar panels. Such damage is not limited to Japan; similar cases have been reported in other cold regions, including Canada (e.g., Levasseur et al. [1]) and parts of North America (e.g., Kibriya [2]).

In Japan, a primary cause of frost heave damage to photovoltaic power generation facilities is the lack of established methods for predicting and mitigating

Fig. 1 Examples of frost heave damage to solar panel mounts.

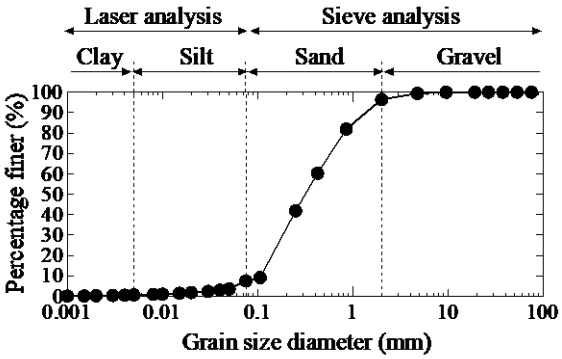

Fig. 2 Grain size accumulation curve.

such occurrences. Accordingly, there is a pressing need for the development of effective countermeasures and corresponding design methodologies.

Moreover, Japan has seen an increasing trend in extreme weather events such as heavy rainfall and sudden gusts of wind. If frost heave occurs during the winter and compromises the pile bearing capacity and pull-out resistance, these weakened conditions may lead to severe damage—such as the collapse of solar power facilities—when subjected to heavy rain or strong winds during the summer.

This study aimed to clarify the frost heave behavior of spiral piles and straight piles, commonly used in the construction of photovoltaic power generation facilities, under freeze-thaw history. In addition, a series of three pull-out tests were conducted—from immediately after installation through the summer months—to examine the effects of freeze-thaw history on the pull-out resistance of the piles.

OVERVIEW OF THE EXPERIMENT

Soil Properties of the Experimental Site

In this study, an embankment was first constructed using locally sourced soil. Then, an excavation was carried out to a depth of 2 meters, after which the excavated area was backfilled with frost-susceptible sandy soil in October 2022. A full-scale pile models of a pile were subsequently installed in the backfilled ground. Various physical properties of the soil at the experimental site were measured through tests conducted in accordance with the Japanese Geotechnical Society Standards.

Figure 2 shows the grain size accumulation curve of a soil sample obtained in accordance with the method stipulated by JIS A 1204 [3]. Based on the coarse-grained and fine-grained contents, the soil sample is classified as sand.

The soil particle density ρ_s is 2.51 g/cm^3, as determined in accordance with the method stipulated by JIS A 1202 [4].

Figure 3 shows the compaction curve of a soil

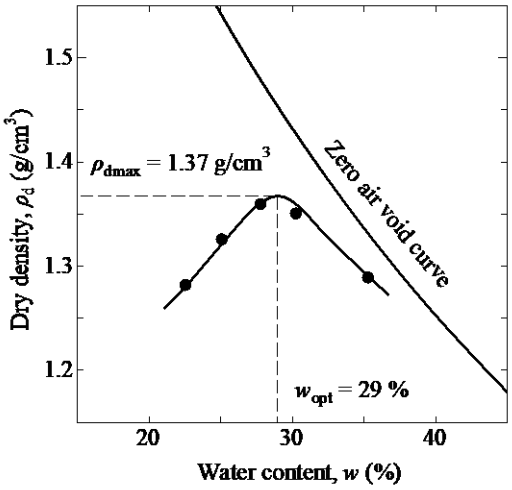

Fig. 3 Compaction curve.

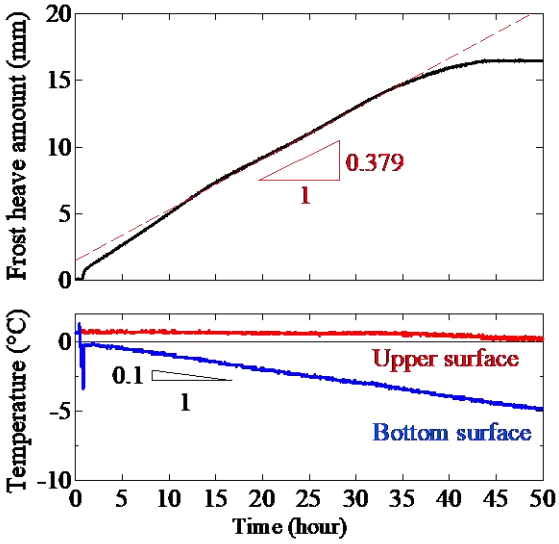

Fig. 4 Frost heave test result.

sample obtained in accordance with the A-a method stipulated by JIS A 1210 [5] (Compaction energy E_c is 550 kJ/m^3 (Standard proctor)). The optimum water content W_{opt} is 29% and the maximum dry density ρ_{dmax} is 1.37 g/cm^3.

The dry density measured at the experimental site using a sampler (100 cm^3 volume) was 1.22 g/cm^3 and the degree of compaction D_c was about 90%.

Figure 4 shows the result of the frost heave test conducted in accordance with the method stipulated by JGS 0172-2020 [6]. The frost heave rate obtained from the temporal change in the frost heave amount is 0.379 mm/hour. This value exceeds 0.3 mm/hour, which is the threshold for high frost susceptibility according to the Japanese Geotechnical Society Standards.

Details of the Installed Piles and the Embedded Sensors

Table 1 Experimental conditions.

Case	Type of pile	Embedment depth (m)	Blade width (mm)	Number of blades (pieces)	Mass (kg)
1	Spiral pile	1.5	0.100	3.5	26
2	Spiral pile	1.5	0.050	6.5	24
3	Straight pile	1.5	0.000	0.0	21
4	Spiral pile	1.5	0.025	9.0	23
5	Spiral pile	1.0	0.100	2.0	19
6	Spiral pile	1.0	0.050	4.0	18
7	Straight pile	1.0	0.000	0.0	16
8	Spiral pile	1.0	0.025	5.5	17

Table 1 summarizes the experimental conditions of this study. In this experiment, the superstructure—including the solar panel and its mounting frame—was not installed. All piles, regardless of type, were made of steel and were installed using the rotary penetration method.

Figure 5 schematically illustrates the installed piles and the arrangement of various measurement instruments. In this study, eight types of piles were used, combining different embedment depths, the presence or absence of blades, and variations in blade width and number. The piles were classified into two categories: spiral piles with blades (Cases 1, 2, 4, 5, 6, and 8) and straight piles without blades (Cases 3 and 7). Two embedment depths were adopted: 1.5 m (Cases 1 to 4) and 1.0 m (Cases 5 to 8). The blade widths for the spiral piles were set to three values: 0.100 m (Cases 1 and 5), 0.050 m (Cases 2 and 6), and 0.025 m (Cases 4 and 8). Notably, the number of blades increases as the blade width decreases.

Temperature measurement rods and soil moisture sensors were embedded as measurement instruments. The temperature measurement rods were installed to monitor the freezing depth of the ground around the piles, while the soil moisture sensors were used to assess the moisture conditions in the surrounding soil. Soil temperature and moisture were automatically measured every hour. The amount of frost heave in each case was observed by conducting leveling surveys periodically (approximately once every one to two weeks). Snow removal was continuously performed around the piles throughout the measurement period.

Pile Pull-Out Test

Figure 6 shows the pull-out test conducted in this study. The test was carried out using a backhoe. First, a tension-type load cell suspended from the arm was connected to a fixture attached to the top of the pile using a wire. Then, a displacement gauge was installed on the top of the pile, and the arm was slowly lifted to pull the pile vertically.

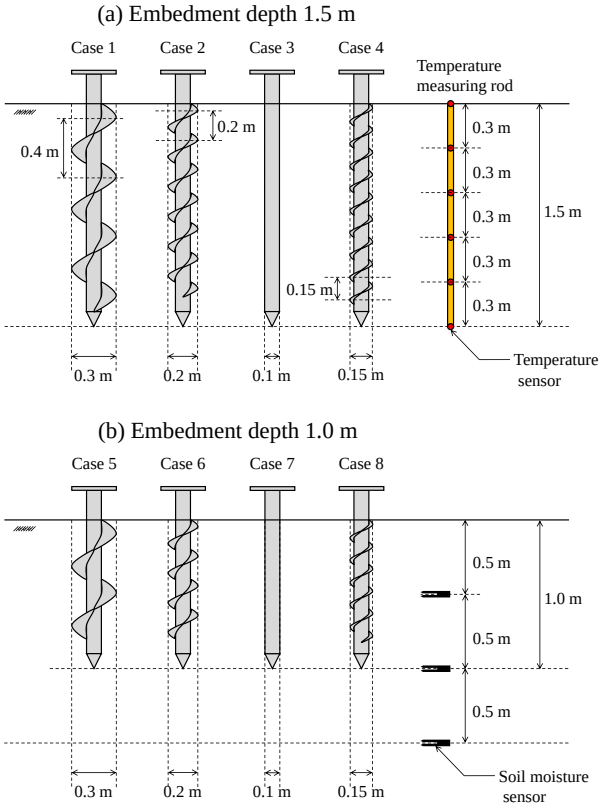

Fig. 5 Schematic diagram of the piles installed in this study.

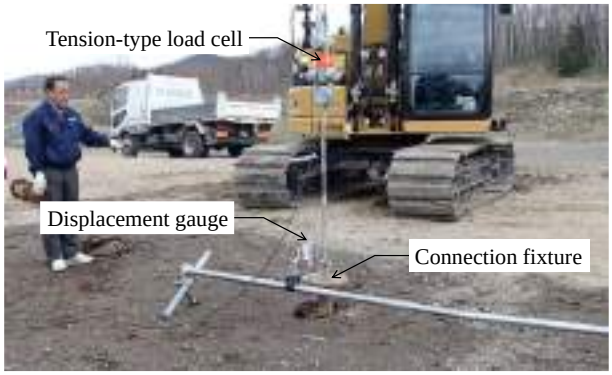

Fig. 6 Pile pull-out test.

The pull-out test was conducted three times: immediately after installation on November 18, 2022; immediately after the freeze-thaw cycle on April 24, 2023; and during summer on September 1, 2023. In addition, to understand the ground conditions before and after each pull-out test, a simplified dynamic cone penetration test and a density test were conducted.

RESULTS AND DISCUSSIONS

Frost Heave and Thaw Behavior of Piles

Figure 7 presents the temporal variations in the freezing depth and volumetric water content of the ground around the pile, and the vertical displacement of the piles.

During the winter of 2022–2023, the maximum frost depth was approximately 0.65 m. However, because the piles were made of steel, the freezing depth in the surrounding ground may have been greater than this value.

Focusing on the vertical displacement during the freezing period, it was observed that piles with greater embedment depths exhibited smaller amounts of frost heave when compared to those with shallower embedment, under the condition of identical blade width. This trend was more pronounced as the blade width increased.

During the thawing period, although most piles generally settled and returned to their original positions, the straight pile without blades and with an embedment depth of 1.5 m (Case 3) did not exhibit any significant settlement. Consequently, the displacement caused by frost heave remained as residual deformation.

These results suggest that in spiral piles with greater embedment depth, the blades are likely to facilitate downward movement during the thawing period by mobilizing earth pressure, thereby contributing to the reduction of residual frost heave deformation.

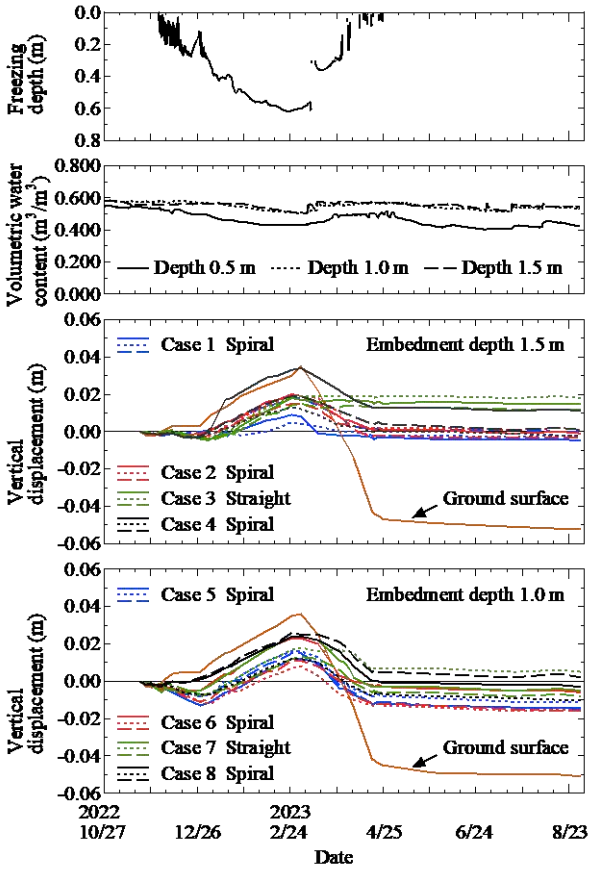

Fig. 7 Temporal variations in the freezing depth and volumetric water content of the ground around the pile, and the vertical displacement of the piles.

Pull-Out Resistance of the Piles

Figure 8 shows the results of the pile pull-out tests conducted before and after the freeze-thaw cycle, and Table 2 presents the average maximum pull-out load of each pile and its relative change.

In the pull-out tests conducted before freezing, all

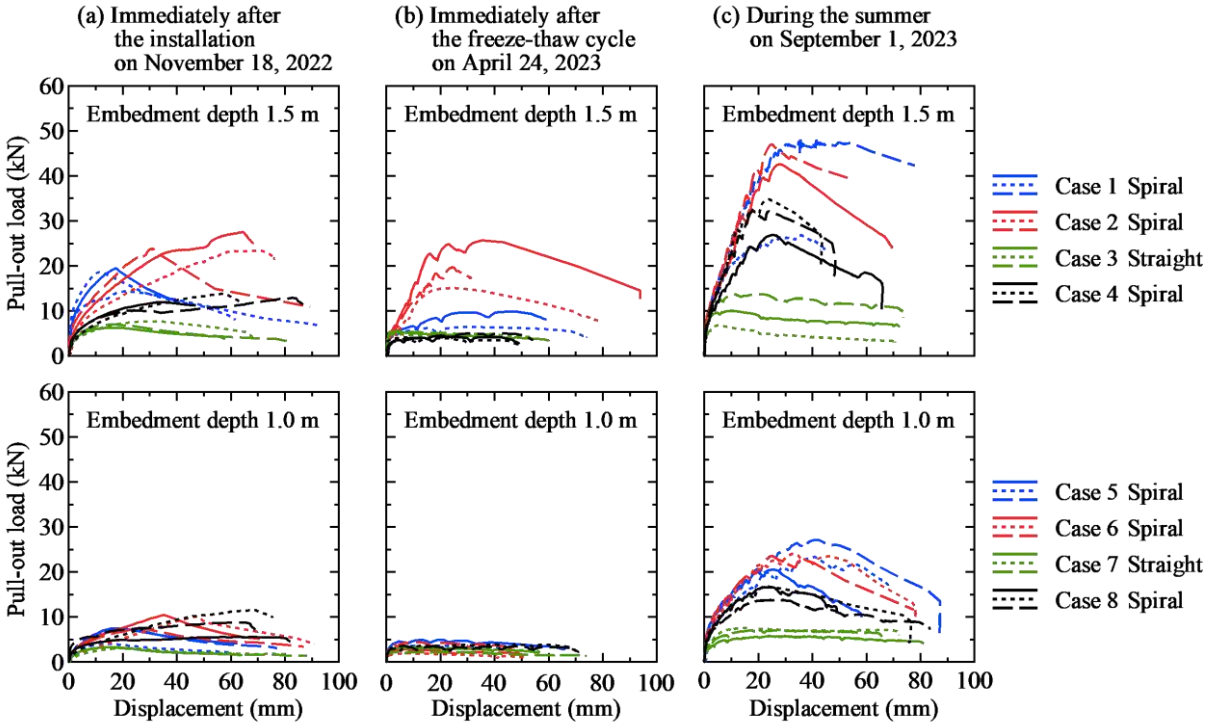

Fig. 8 Results of the pile pull-out tests conducted before and after the freeze-thaw cycle.

Table 2 Average maximum pull-out load of each pile and its relative change.

Case	Type of pile	Embedment depth (m)	Immediately after the installation on November 18, 2022	Immediately after the freeze-thaw cycle on April 24, 2023		During the summer on September 1, 2023	
			Average maximum pullout load (kN)	Average maximum pullout load (kN)	Relative change (%)	Average maximum pullout load (kN)	Relative change (%)
1	Spiral pile	1.5	17.5	8.1	46	37.4	214
2	Spiral pile	1.5	25.0	20.2	81	44.8	180
3	Straight pile	1.5	7.0	5.2	74	10.2	146
4	Spiral pile	1.5	12.9	4.5	35	31.3	243
5	Spiral pile	1.0	6.3	4.3	68	23.7	374
6	Spiral pile	1.0	9.4	3.1	33	23.7	253
7	Straight pile	1.0	3.2	2.9	90	6.8	212
8	Spiral pile	1.0	8.6	3.8	44	15.8	183

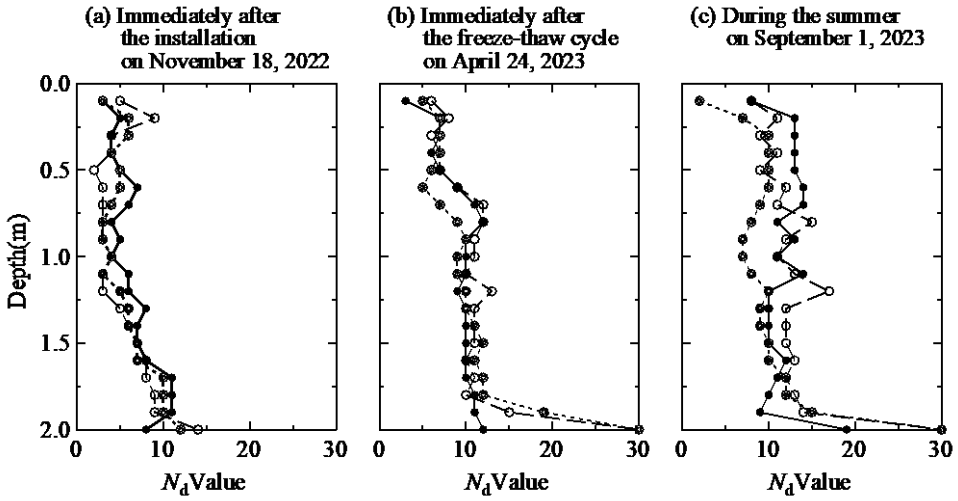

Fig. 9 Results of the simplified dynamic cone penetration tests.

spiral piles were extracted following rotation, which occurred before any soil failure was observed. In contrast, no rotation was observed in any of the piles either immediately after the freeze-thaw cycle or during the summer.

When comparing the results obtained immediately after installation (unfrozen condition) with those obtained immediately after the freeze-thaw cycle, a certain degree of variability was noted in the experimental data. However, the pull-out loads generally decreased after the freeze-thaw cycle, indicating a reduction in pull-out resistance.

In particular, the piles with an embedment depth of 1.0 m appeared to exhibit almost no pull-out resistance after the freeze–thaw cycle.

However, in the case of the spiral pile with a blade width of 0.050 m and an embedment depth of 1.5 m (Case 2), the reduction in pull-out load was relatively small. These results suggest that spiral piles with sufficiently wide blades and a greater number of blades located below the freezing depth are less affected by the freeze-thaw history.

Furthermore, a comparison between the results obtained immediately after the freeze-thaw cycle and those obtained during the summer indicates that the pull-out loads increased in the summer, reflecting an improvement in pull-out resistance.

Investigation of Ground Conditions Using Simplified Dynamic Cone Penetration Test Results

Figure 9 shows the results of the simplified dynamic cone penetration tests, and Table 3 presents the results of the density tests.

Immediately after installation, the N_d values were below 10 down to a depth of approximately 1.5 m, and the degree of compaction D_c was as low as 90%, indicating low ground strength.

Following the freeze-thaw cycle, although the N_d values remained below 10 down to a depth of 0.7 m, they were generally around 10 at greater depths. The depth at which the N_d values fell below 10 roughly corresponded to the maximum freezing depth,

suggesting that the reduction in pull-out resistance observed after the freeze-thaw cycle was due to a weakening of the surface layer of the ground.

During the summer, however, the N_d values exceeded 10 at all depths, and the D_c reached 96%, indicating that the ground had become more compacted after thawing and that its strength had increased.

CONCLUSIONS

In this study, the frost heave behavior of piles used in the construction of photovoltaic power generation facilities was investigated, along with the effects of freeze-thaw history on their pull-out resistance.

Experimental results revealed that the pull-out resistance of piles was low immediately after installation and decreased further in the spring following freeze-thaw cycles. These findings suggest that there may be an increased risk of photovoltaic power generation facilities collapse due to strong winds during the periods immediately after installation and in early spring following freeze-thaw events.

In the future, using the knowledge obtained in this study, we would like to propose a design method for economical and effective frost heave countermeasures for piles.

ACKNOWLEDGMENTS

These findings were obtained as a result of work commissioned by the New Energy and Industrial Technology Development Organization (NEDO), a national research and development agency.

REFERENCES

[1] Levasseur. P., Maher. M. L. J. and Dittrich. J. P. A case study of frost action on lightly loaded piles at Ontario solar farms, in Proc. Int. Conf. GeoQuebec, 2015, pp. 1-7.

Table 3 Results of the density tests.

(a) Before freezing (sample collected on November 8, 2022)

Sampling depth (m)	Wet density ρ_t (g/cm^3)	Dry density ρ_d (g/cm^3)	Water content w (%)	Degree of compaction D_c (%)
0.5	1.67	1.22	37.3	90
1.0	1.67	1.22	37.3	89
1.5	1.69	1.23	37.2	90
Average	1.68	1.22	37.3	90

(b) After freeze-thaw (sample collected on November 6, 2023)

Sampling depth (m)	Wet density ρ_t (g/cm^3)	Dry density ρ_d (g/cm^3)	Water content w (%)	Degree of compaction D_c (%)
0.2	1.74	1.31	32.6	96
0.3	1.72	1.32	30.4	96
Average	1.73	1.32	31.5	96

[2] Kibriya. T. Rehabilitation techniques to address frost effects on pile foundations of solar power generation facilities in north America, International Journal of Applied Engineering Research, Vol. 13, No. 10, 2018, pp. 7333-7339.
[3] Japanese Industrial Standards, JIS 1204:2020, Test method for particle size distribution of soils, 2020.
[4] Japanese Industrial Standards, JIS 1202:2020,
[5] Test method for density of soil particles, 2020.
[6] Japanese Industrial Standards, JIS 1210:2020, Test Method for Soil Compaction Using a Rammer, 2020.
[7] Japanese Geotechnical Society, JGS 0172-2020, Test method for frost susceptibility of soils, 2020.

Copyright © Int. J. of GEOMATE All rights reserved, including making copies, unless permission is obtained from the copyright proprietors.

15th Int. Conf. on Geotechnique, Construction Materials & Environment,
Kyoto, Japan, 11-13 November 2025, ISBN 978-4-909106124 C3051

SLOPE STABILITY OF SOIL-ROCK MIXTURE: A CASE STUDY ON LIMESTONE FORMATION AND HIGH RAINFALL AREA

Arief Rachmansyah[1], Adefi Abioga Tiswa[2], Fajar Rahmanto[2]

[1]Civil Engineering Department, Brawijaya University, Indonesia
[2] Geotechnical Independent Consultant, Malang, Indonesia

ABSTRACT

The weathering process of limestone in areas with high rainfall, such as in Java Island, Indonesia, produces soil and rock masses ranging in size from gravel to boulders. The slope stability analysis of the mixed mass cannot be approached from rockslide or landslides, but requires a different approach. The stratification of the rock and soil in the slide zone is complicated because there are several blocks of rock and fine-grained soil. The thickness of the mixed soil-rock mass layer also needs to be known. Electrical resistivity tomography (ERT) survey and geotechnical drilling were conducted to create a subsurface model of soil–rock mixture stratification. The properties of the soil-rock mixture (SRM) were estimated by rock block proportion on the slope. A transient model of slope stability analysis was created using the SEEP/W program to simulate slope seepage and SLOPE/W to compute slope stability. The elevation of the groundwater level and the pore water pressure on the slope are altered by antecedent rainfall. When examined, these phenomena will have an impact on the slope's safety factor. The slope safety factor (FoS) was reduced by 31.48% from 1.542 to 1.057 in the event of extreme rainfall, which does not satisfy the requirement for a slope safety factor of 1.25.

Keywords: slope stability, soil-rock mixture, limestone formation, high rainfall area.

INTRODUCTION

In 2010, the East Java Provincial Government began construction of the South Coast Road to accelerate economic growth in the south region, which had been left behind compared to the northern part. Most of the route passes through hilly areas composed of limestone or karst areas. One of the problems faced during the construction of the road was mass movement.

Mass movement is a common disaster in areas with high rainfall and seismicity, because both are triggering factors. Many slope failures occur on soil-rock mixture slopes, where the slip plane is the boundary between the fresh or impermeable rock layer and the layer of soil or weathered material above it. To calculate slope stability and plan for mass movement mitigation, it is generally approached from the factor of safety. The initial factor of safety of a slope is primarily controlled by slope geometry, material properties, and the initial depth of the water table. In some cases, the occurrence of mass movement is largely influenced by changes in material properties induced by rainfall [1].

Soil-rock mixtures (SRM) are a combination of soil and rock blocks, and the shear strength of these mixtures depends on the volume of rock that are mixed into the soil. [2,3,4]. The size distribution, rock position, shape and roughness of the rock shape affect the stability of the slope [5,6]. Nevertheless, numerous engineers frequently disregard the impact of rock mixed with soil, presuming that SRM is an authentic form of soil. While simplifying the behavior of slopes with this specific type of SRM to pure soil may enhance slope safety, it is important to note that the behavior and properties of SRM slopes remain uncertain [7].

The effect of the proportion of rock matrix in the soil on the SRM slope was studied using a combination of physical modeling and numerical modeling by the finite difference method approach. The results indicated that an increase in the proportion of rock in the slope resulted in an enhanced safety factor. However, this study employed a statistical approach to determine the position of rocks in the slope [8,9].

The position and size of rocks in the SRM can be determined using electrical resistivity tomography (ERT) investigation [10,11]. The quantity of rock matrix present on the slope can be calculated using the resistivity value obtained through the application of the ERT method [12]. Nevertheless, this approach is limited by its reliance on soil moisture, which can significantly influence the outcome [13] Therefore, verification of ERT results using boring is required.

Several studies have attempted to statistically approximate the critical rainfall conditions that cause slope failure [14.15.16]. In general, it is recognized that heavier rainfall might result in a more substantial rise in the slope's negative pore water pressure and a larger decrease in the groundwater table [17,1]. Under the same rainfall conditions, a higher value of k_{sat} (saturated soil permeability) will result in a higher pore water pressure buildup than the initial condition resulting in a reduced slope safety factor. Soils with lower k_{sat} values will reduce matric suction and a rise in groundwater level [18]. Rainfall duration and intensity, however, are correlated variables. Antecedent rainfall can cause a decrease in the safety

factor of low conductivity soil slopes up to 45% and a decrease in the safety factor of high conductivity soil slopes up to 13% before the occurrence of major rainfall [19].

In the rainfall-induced landslides the soil properties are determined by hydraulic properties including soil water characteristic curve properties (SWCC) and unsaturated soil permeability [20]. A landslide caused by rainwater analysis using SLOPE/W and SEEP/W showed that a severe rainstorm that lasted for 16 hours and with an intensity of 112.5 mm/h was the cause of the landslide [21]. The total amount of precipitation that fell before the landslide was 306.5 mm. Slope instability resulted from the antecedent rainfall's impact on the slope's initial state, which raised the soil pore water pressure. The occurrence of slope failure is significantly influenced by the characteristics of topographic hollows [22].

Experiment modeling slopes subjected to artificial rainfall to determine the effect of slope angle on slope stability that can be validated by numerical show the slope's vulnerability to abrupt collapse during rainstorms rises with slope angle. Failure is caused by the loss of soil suction when the slope angle is 1.2 times more than the soil friction angle, and by positive pore water pressure at the slope's toe when it is smaller or equal to 1.2 times the soil friction angle [23]. These studies demonstrate that slope failure variables rely on slope geometry in addition to soil characteristics and rainfall.

RESEARCH SIGNIFICANCE

The goal of this study is to establish the safety factor of post-failure slopes at the research site by analyzing the slope stability of soil-rock mixture slopes while considering the impact of previous rainfall. Slope stability calculations are generally carried out using only soil or rock approach, however the moving material is composed of a mixture of both, especially in weathered limestone.

This paper discusses the results of landslide research on soil rock mixture materials, and the effect of rainfall on landslide mechanisms. The landslide slip plane, and the percentage of material mixture are determined based on the results of geoelectric investigations combined with drilling data. Combination between Electrical Resistivity Tomography (ERT) and boring investigations are used to proposed model of subsurface material and its stratification. This model will be used for numerical analysis using the SLOPE/W and SEEP/W programs, so the results are like natural condition.

RESEARCH LOCATION

The site of the study is located at coordinates 112.069852° E and 8.294235° S (Figure 1.). Administratively a landslide occurred in Bululawang village, Blitar Region.

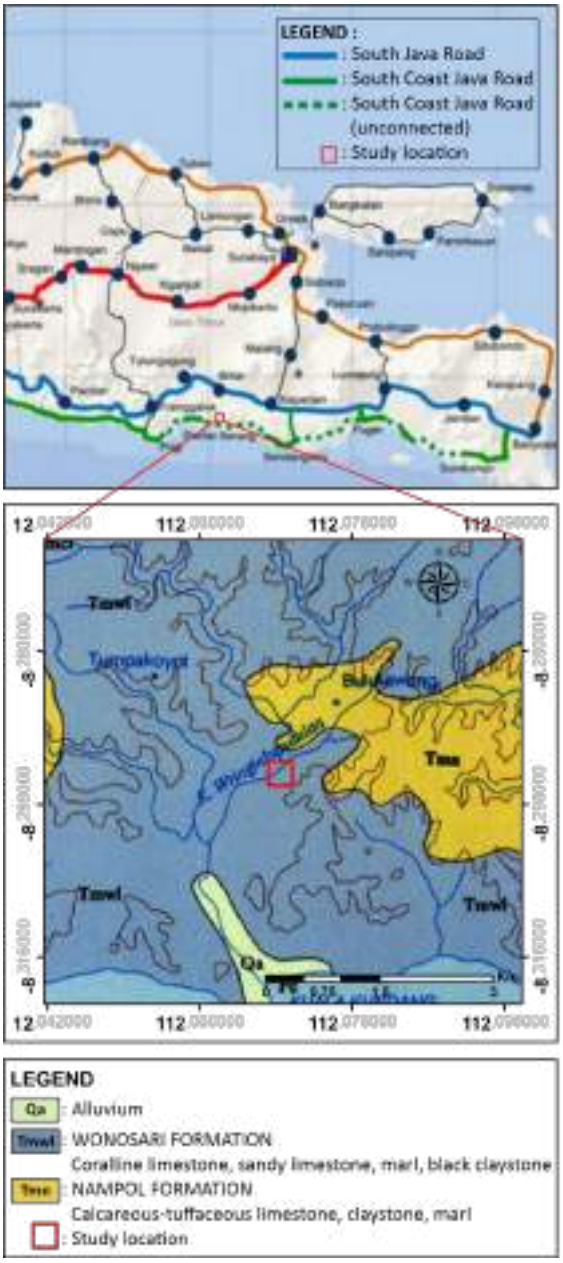

Figure 1. National Road Network on East Java Province Indonesia, and Geological Map of Study Area

According to the geologic map of Blitar sheet [24], this study site is in the Wonosari Formation – (Tmwl). This unit consists of coralline limestone, argillaceous-tuffaceous-sandy limestone, marl, black claystone with peats. A visual of the slope at the study site shows limestone gravel and boulder mixed with soil, limestone blocks are spread over the landslide area. This material is known as soil rock mixture (SRM) or debris (Figure 2).

Figure 2. Soil Rock Mixture (SRM) on Research Location

RESEARCH METHOD

Soil - Rock Properties and Stratification

The slope elevation results are plotted into the CAD Civil 3D program and a closed polygon is created according to the equipment elevation readings to form the slope geometry. Several boring geotechnical and geophysical surveys are required to determine soil stratigraphy. Electrical resistivity tomography (ERT) is one of the most reliable techniques for generating images of the subsurface condition. Soil resistivity can reflect groundwater content, porosity, and clay content. Therefore, the ERT results are integrated with boring can be used as a basis for creating subsurface soil stratification.

Geoelectric data acquisition carried out at the research location consists of 3 lines, with each having a length of 200 meters. The line consisted of 2 lines aligned east-west, BLL-2 and BLL-3, and 1 line (BLL-1) cutting perpendicular to both lines BLL-2 and BLL-3 with a north-south direction. The configuration used for this geoelectric survey is Wenner-alpha. The ERT survey line, boring position and cross section used for this research can be seen in Figure 3.

.

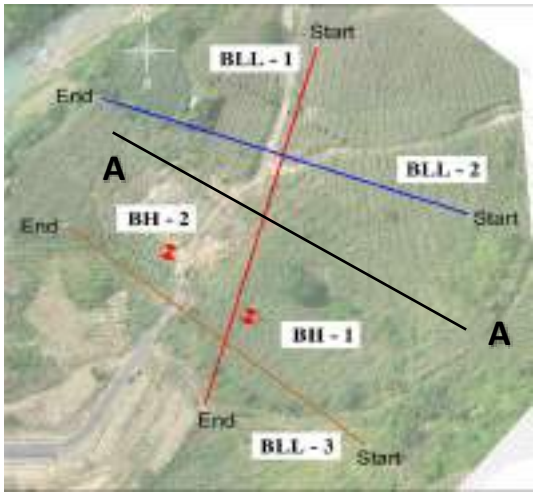

Figure 3. ERT Line and cross section of the slope and location of geotechnical boring

Permeability of the soil at saturated state was determined using the falling head method. Shear strength of silty clay soil are investigated using triaxial unconsolidated undrained method. To determine the shear strength of the debris or SRM, which was predominantly composed of sand, clay, and boulders, an empirical approach proposed by Zhang et al [25] was employed. The shear strength of unsaturated soil is determined by the Vanapalli equation [26] which is a function of volumetric water content, soil shear strength and residual water content.

Rainfall

The lack of a weather station in close approximation to the research location, as well as the absence of rain records with hourly time intervals, directed to the utilization of GPM satellite data. The rainfall data used is from the Giovanni Online Data System website developed by NASA GES DISC. The data is Integrated Multi Satellite Retrieval for Global Precipitation Measurement (GPM-IMERG), which contains rain infiltration data throughout the world. Precipitation data at the research site was collected in hourly time intervals in the time frame of 2014 to 2023 (10 years).

Antecedent rainfall was evaluated because it can alter the pore water pressure profile on the slope [27]. Antecedent rainfall has a duration of 5 days with 3 different rain patterns. The rain patterns are called delayed, normal, and advanced. This antecedent rain pattern uses cumulative maximum rainfall data for 5 days [19].

Numerical Modeling

In this study, permeability, shear strength parameters, and soil water characteristic curve parameter (SWCC) are random variables. Limit equilibrium base analysis will be conducted using the SEEP/W and SLOPE/W programs.

Safety factors of the slope calculated using General Limit Equilibrium (GLE) in unsaturated condition provided by SLOPE/W program. A water flux boundary condition is used above the slope model to simulate rainwater infiltration, a constant head boundary condition is used on the right side, and a no flow boundary condition is used on the left and bottom sides to stop water from flowing in the area. Flowchart for modelling in SLOPE/W and SEEP/W for this study can be seen in Figure 4.

RESULT AND DISCUSSION

Antecedent Rainfall

When satellites conduct observations of precipitation, the data may not reflect the immediate precipitation events, as it takes time for the precipitation to reach the earth's surface [28]. The

satellite data is validated using several statistical techniques, including the linear correlation coefficient (R^2), the observation standard deviation ratio (RSR) and the Nash-Sutcliffe efficiency (NSE). These are used to determine the extent of any discrepancy between the data collected at the rain station and that obtained from the GPM satellite.

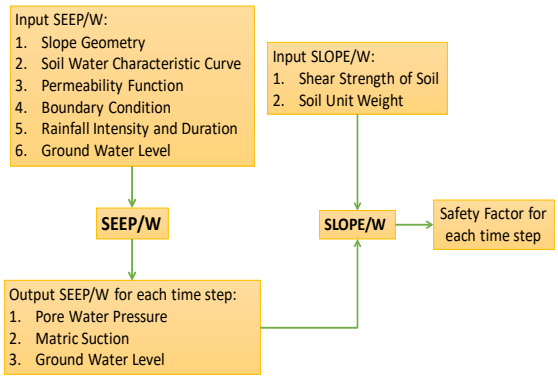

Figure 4. Modeling in SEEP/W and SLOPE/W

Monthly precipitation data from the GPM satellite have been validated with data from a rainfall station, which is 105 km from the research location [29]. The results of the calibration of GPM rain data and rain stations demonstrate a strong correlation, as indicated by the RSR, NSE, and R^2 values of 0.359, 0.917, and 0.964, respectively. Statistical testing on the GPM satellite indicates that the mean accuracy value for GPM data is 0.75 and showed a relatively high degree of correlation [30].

The available data from GPM, the maximum cumulative rainfall for 5 days at the study site was 428.853 mm. Figure shows the antecedent rainfall pattern used in this analysis. The delayed type of rain is low in intensity and increases over time, the advance type is a rain that is high in intensity and then steadily decreases, and the normal pattern is a rain that increases in intensity until a certain time and then decreases in intensity like a normal distribution.

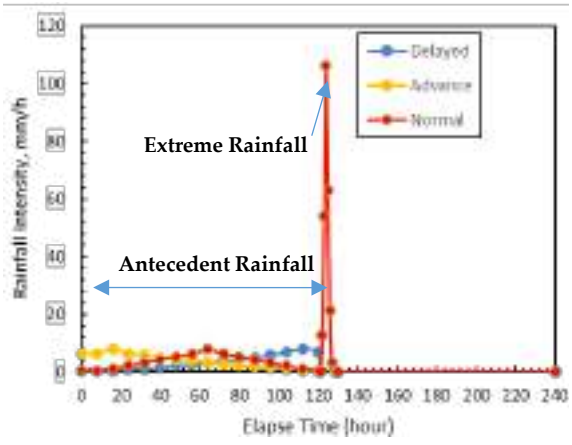

Figure 5. Rainfall pattern on the study area after GPM

The extreme rainfall event has been applied to the slope after the end of the antecedent rainfall event. Extreme rainfall was obtained from the maximum hourly rainfall over a 10-year period. Extreme rainfall was applied for 8 hours with a normal pattern and the maximum rainfall was 106,144 mm/hr (Figure 5).

Subsurface Profile

The ERT measurement results are processed in the Res2div program, and the results can be seen in Figure 6. Soil interpretation was conducted using the ERT profile results combined with borehole BH-1 and BH-2. The boring results can be seen in Figure 7.

The correlation was carried out on BLL-1 with BH-1 at the 160 m position and the BH-2 boring was correlated with BLL-1 at the 105 m position. From the correlation results, the resistivity pattern of the soil conditions from the boring results is obtained. The resistivity value of 1 - 15 ohm is debris dominated by sand and clay, 15 - 20 ohm is Silty clay, 20 - 30 ohm is debris dominated by boulder, and the value above that is limestone block.

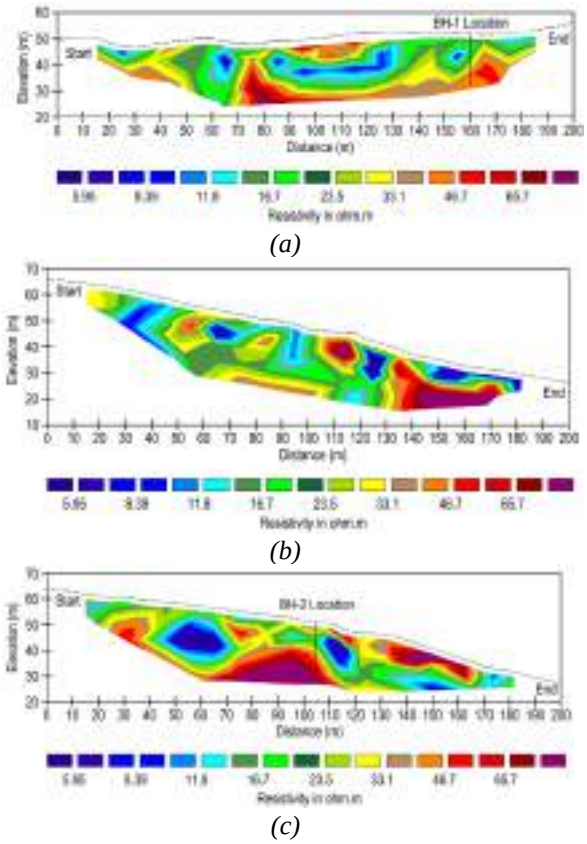

Figure 6. Electrical Resistivity Tomography (a) BLL-1 Cross Section; (b) BLL-2 Cross Section; (c) BLL-3 Cross Section

Soil - Rock Properties and Stratification

The soil at the study location varies, such as silty clay, SRM (debris) dominated by boulder, SRM dominated by sand and clay, and limestone block.

Properties of silty clay were obtained from laboratory tests. The limestone block was modeled as a high strength material with a unit weight of 21.62 kN/m^3. Table 1 is a recapitulation of the soil properties. The results of soil stratification in cross section BLL-1, BLL-2, BLL-3 can be seen in Figure . The results of soil stratification in cross section A-A are obtained from interpolation of the results of soil stratification BLL-1, BLL-2, BLL-3 and boring. The results are presented in Figure 8.

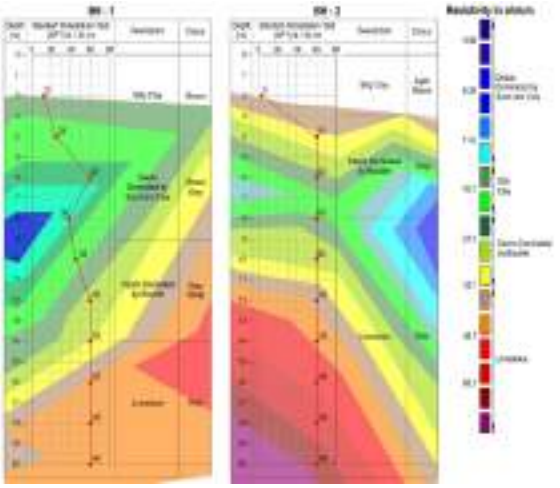

Figure 7. ERT Verification with boring data

Table 1. Soil Properties

Material Description	γ_b (kN/m^3)	Cohesion (kN/m^2)	Internal friction (deg)	Saturated Permeability (cm/s)	Void Ratio	Plasticity Index (%)	Fine Content (%)
Silty Clay Soil	17.464	21	9	4.20E-04	1.11	40.26	68.37
SRM Dominated by Sand and Clay	19.58	15.14	14.69	1.32E-03	0.65	41.11	71.78
SRM Dominated by Boulder	19.24	8.00	20.38	1.39E-02	0.72	38.30	68.90

The shear strength of SRM depends on the rock block proportion (RBP) of the soil and the compressive strength of the SRM. The SRM compressive strength is a function of the strength of the soil-rock contact surface (Parameter A) and the soil compressive strength. Parameter A in the calculation of SRM shear strength can be determined from the approach by Kalender, et al [31] which depends on the roughness of block surface and angle of repose of rock block. The average SPT value of debris dominated by sand and clay had N-SPT value of 35, from Hara, et al [32] the compressive strength of soil can be correlated with SPT after correction and the compressive strength of debris dominated by sand and clay is 386 kPa. Parameter A is set at 0.50 and the RBP value used for this analysis in debris dominated by sand and clay is 30%.

Debris dominated by boulder had average corrected N-SPT value of 49.68 had compressive strength of 494 kPa. Parameter A was determined to be 0.52 with an RBP of 50%.

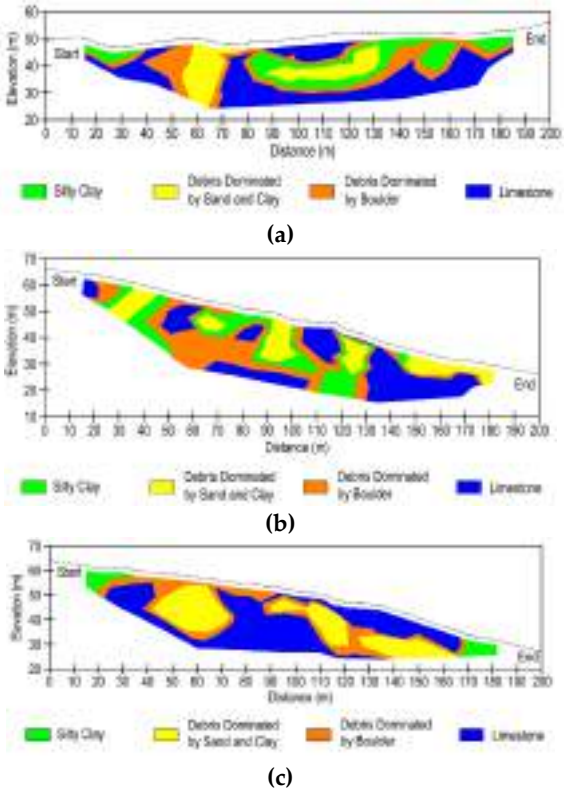

Figure 8. Soil Stratification (a) BLL-1 Cross Section; (b) BLL-2 Cross Section; (c) BLL-3 Cross Section

Rain infiltration's impact on soil saturation level is examined using the soil water characteristic curve (SWCC). The equation to estimate the SWCC is based on the Fredlund, et al method [33]. Because the soil has a high proportion of plastic clay and silt, a plastic soil approach was used to calculate the curve fitting SWCC parameters using the estimation method developed by Zapata et al [34]. The calculation of hydraulic conductivity was used Fredlund grafts. [35]. Permeability and matric suction curves have different slopes depending on the shape of the SWCC curve. Soil permeability with zero matric suction is the permeability when the soil is saturated.

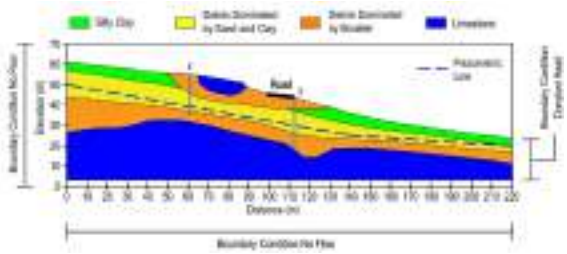

Figure 9. Soil stratification model in section A-A, initial condition, and boundary condition used in model

Depending on the level of soil saturation, the model's soil unit weight will change. The soil's unit weight will rise in proportion to its saturation level. The original unit weight at the time the soil samples were gathered is the γ_b value (Table 1). Initial

moisture content of silty clay is 41.97%, initial moisture content of sand and clay-dominated debris is 24.65%, and initial moisture content of boulder-dominated SRM is 27.14%.

Numerical Modelling

Slopes subjected to antecedent rainfall have a difference in FoS, which is 30.37% for delayed pattern, 30.69% for advance pattern and 31.48% for normal pattern from the initial FoS (t = 0 h). Therefore, the value of the slope safety factor is greatly influenced by the antecedent rainfall factor. The results of the analysis were that slope failure does not occur in extreme rainfall alone, but significant antecedent rainfall can cause slope failure, which is consistent with this study [36].

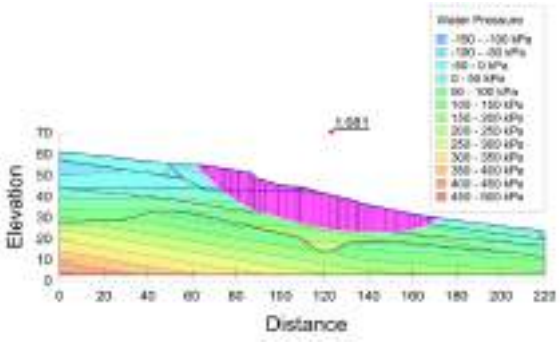

(a)

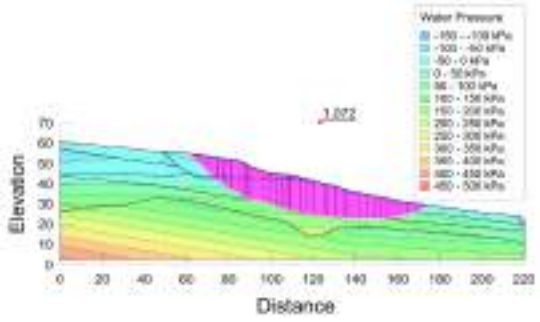

(b)

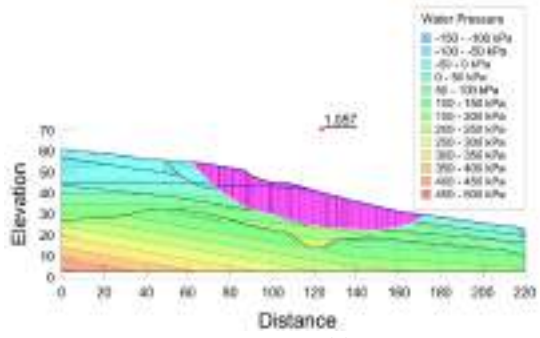

(c)

Figure 20. Shape of the Sliding Plane, t = 130 h (a) Delayed; (b) Advance; (c) Normal

Table 2 illustrates the lowest possible value of Factor of Safety (FoS) in each antecedent rain pattern. The lowest FoS value is observed in the Normal pattern, with a value of 1.057, followed by the Advance pattern (1.072) and the Delayed pattern (1.081). The greatest disparity in FoS values between t = 120 h and 130 h is observed in the Advance pattern, with a difference of 0.196 (15.44%), followed by the Normal pattern with a difference of 0.186 (14.96%) and the Delayed pattern with a difference of 0.149 (12.09%). The maximum discrepancy in FoS values for each rain pattern is 0.024 (2.22%), which is not particularly indicative of a significant difference. This is because there is a correlation between precipitation intensity and saturated soil permeability. The maximum rainfall intensity on the slope is 106.144 mm/hour, which is less than the maximum soil permeability coefficient on the slope, which is 498.60 mm/hour ($1.39x10^{-2}$ cm/sec) with a rainfall intensity of 0.2128 x saturated soil permeability.

Therefore, the infiltration of water into the soil will be absorbed into the soil, resulting in a significant increase in groundwater level and, consequently, slope instability. This result is in accordance with the states that high permeability soil (>10^{-5} m/s) is highly influential in extreme rainfall with short duration and intensity [1]. A rainfall intensity of less than 1 x saturated permeability is sufficient to result in the lowest FoS for the slope.

Figure 20 illustrates the configuration of the sliding plane and the distribution of pore water pressure on the slope in the event of extreme rainfall. In general, regardless of the rainfall pattern, the configuration of the sliding plane remains consistent and the groundwater level (pore water pressure = 0 kPa) contacts the slope surface, thus resulting in a saturated slope.

Table 2. Factor of safety reduction from t = 120 h to t = 130 h

Pattern	Value of FoS t = 120 h	FoS Minimum t = 130 h	FoS Reduction	
Delayed	1.229	1.081	0.149	(12.09%)
Advance	1.268	1.072	0.196	(15.44%)
Normal	1.242	1.057	0.186	(14.96%)

CONCLUSIONS

The combination of electrical resistivity tomography (ERT) and soil boring is an effective method for modeling soil and rock stratification of slope. The use of soil boring data is beneficial for supporting the results of ERT that are highly sensitive to the presence of water.

For analyzing the stability of limestone slopes in areas with high rainfall, where block and gravel-sized rock fragments are common, a soil-rock-mixture (debris) material approach is very logical.

The safety factor of slopes is affected by antecedent rainfall prior to the application than extreme rainfall. It was found that the cumulative infiltrated water in the slope resulted in a reduction of the lowest factor of safety, which was greatest for the normal pattern, followed by the advance and delayed patterns. The location and depth of the sliding plane in this slope stability analysis did not change significantly for each antecedent rainfall pattern.

ACKNOWLEDGMENTS

The authors would like to thank that the completion of this research project would not have been possible without support by Dinas PUPR Kabupaten Blitar and PT. Dhiratama Cipta Persada.

REFERENCES

[1] H. Rahardjo, T. Ong and R. Rezaur, "Factors Controlling Instability of Homogeneous Soil Slopes under Rainfall," Journal of Geotechnical and Geoenvironmental Engineering, pp. 135-143, 2010.

[2] W. Hu, "Experimental study on shear strength of soil-rock-mixture in Xiluodu reservoir," Inst. Rock and Soil Mechanics, Chinese Academy of Sciences, Wuhan, China, 2014.

[3] M. Afifipour and P. Moarefvand, "Mechanical behavior of bimrock having high rock block proportion," Int J Rock Mech Min Sci, vol. 65, p. 40–48, 2014.

[4] W. Hu, H. Min, J. Chen and Q. Sheng, "Study on the effect of gravel on unconfined mechanical properties of soil-rock mixture," J Yangtze River Sci Res, vol. 11, p. 55–61, 2015.

[5] Cao, VH., Go and GH, "A novel approach to stability analysis of random soil-rock mixture slopes using finite element method in ABAQUS," Nat Hazards, 2024.

[6] L. S, W. H and X. W, "Numerical Investigation of the Influence of Rock Characteristics on the Soil-Rock Mixture (SRM) Slopes Stability," KSCE J Civ Eng, vol. 24, p. 3247–3256, 2020.

[7] W. C. Hanerberg, "Simulation of 3D Block Populations to Characterize Outcrop," Geomechanics and Tunneling, vol. 22, no. Felsbau Rock and Soil Engineering, pp. 19-26, 2004.

[8] K. E, A. M, H. MF and M. E, "Evaluating the effect of inclination of rock block on stability of bimrock slopes," Geomechanics and Engineering, vol. 17, no. 3, pp. 281-287, 2019a.

[9] K. E, A. M, H. MF and M. E, "Statistical analysis of bimslope stability using physical and numerical models," Engineering Geology, vol. 10, pp. 465-477, 2019b.

[10] R. Rossi, Amato, Mariana, A. Pollice, G. Bitella, Gomes, João, Bochicchio, Rocco, Baronti and Silvia., "Electrical resistivity tomography to detect the effects of tillage in a soil with a variable rock fragment content," European Journal of Soil Science, vol. 62, pp. 239-248, 2013.

[11] Mita, M. &. Glazer, M. &. Kaczmarzyk, M. &. M. Radosław & Dabrowski and Karolina, "Case study of electrical resistivity tomography measurements used in landslides investigation," Contemporary Trends in Geoscience, vol. 7, p. 10, 2018.

[12] Z. Zhou, H. Yang, Z. H. Wan and B. C. Liu, "Computational Model for Electrical Resistivity of Soil–Rock Mixtures," Journal of Materials in Civil Engineering, vol. 28, no. 8, 2016.

[13] E. A. Suryo, Y. Zaika, C. Gallage and B. Trigunarsyah, "A non-destructive method for investigating soil layers of an individual vulnerable slope," International Journal of GEOMATE, vol. 18, pp. 1-8, 2020.

[14] M. Afifipour and P. Moarefvand, "Mechanical behavior of bimrock having high rock block proportion," Int J Rock Mech Min Sci, vol. 65, p. 40–48, 2014.

[15] W. Hu, H. Min, J. Chen and Q. Sheng, "Study on the effect of gravel on unconfined mechanical properties of soil-rock mixture," J Yangtze River Sci Res, vol. 11, p. 55–61, 2015.

[16] Cao, VH., Go and GH, "A novel approach to stability analysis of random soil-rock mixture slopes using finite element method in ABAQUS," Nat Hazards, 2024.

[17] L. S, W. H and X. W, "Numerical Investigation of the Influence of Rock Characteristics on the Soil-Rock Mixture (SRM) Slopes Stability," KSCE J Civ Eng, vol. 24, p. 3247–3256, 2020.

[18] C. Ng and Q. Shi, "Numerical investigation of the stability of unsaturated soil slopes subjected to transient seepage," Computers and Geotechnics 22(1), pp. 1-28, 1998.

[19] A. Rahimi, H. Rahardjo, E. C. Leong, J., "Effect of antecedent rainfall patterns on rainfall-induced slope failure," Journal of Geotechnical and Geoenvironmental Engineering, pp. 483 - 491, 2011.

[20] L.L.Zhang, L.M.Zhang and W,H,Tang, "Rainfall-induced slope failure considering variability of soil properties," Geotechnique, pp. 183-188, 2004.

[21] S. Jeong, K. Lee, J. Kim and Y. Kim, "Analysis of Rainfall-Induced Landslide on Unsaturated Soil Slopes," Sustainability, pp. 1-20, 2017.

[22] K. P. Acharya, N. P. Bhandary, R. K. Dahal and R. Yatabe, "Seepage and slope stability modelling of rainfall induced slope failures in topographic hollows," Geomatics, Natural Hazards and Risk, 7:2, pp. 721-746, 2016.

[23] C. Gallage, T. Abeykoon and T. Uchimura, "Instrumented model slopes to investigate the effect of slope inclination on rainfall-induced landslide," Soils and Foundation 61, pp. 160-174,

2021.
[24] M. Z. Sjarifudin and S. Hamidi, "Peta geologi lembar Blitar," Badan Geologi Kementrian ESDM, 1992.
[25] Z. Zhang, Q. Sheng, X. Fu and e. al, "An approach to predicting the shear strength of soil-rock block proportion," Bull Eng Geol Environ 79, pp. 2423-2437, 2020.
[26] S. Vanapalli, F. D.G., D. Pufahl and A. Clifton, "Model for the prediction of shear strength with respect to soil suction," Canadian Geotechnical Journal, vol. 33, pp. 379-392, 1996.
[27] H. Rahardjo, E. C. Leong and R. B. and Rezaur, "Effect of antecedent rainfall on pore-water pressure distribution characteristics in residual soil slopes under tropical rainfall," Hydrol. Processes, vol. 22, no. 4, pp. 506-523, 2008.
[28] R. N. &. L. U, "Keandalan Data Curah Hujan TRMM (Tropical Rainfall Measuring Satelit Mission) Terhadap Data Curah Hujan Stasiun Bumi pada Beberapa sub DAS di DAS Brantas," Jurnal Aplikasi Teknik Sipil, vol. 20, no. 2, pp. 207-222, 2022.
[29] S. Marta, E. Suhartanto and J. Sidqi, "Validasi Data Curah Hujan Satelit dengan Data Stasiun Hujan di DAS Ngasinan Hulu, Kabupaten Trenggalek, Jawa Timur," Jurnal Teknologi dan Rekayasa Sumber Daya Air, vol. 3, no. 1, pp. 35-45, 2023.
[30] I. Kurniawan and M. D. Jendra, "Evaluation of GPM-IMERG (Global Precipitaion Measurement Integrated Multi-Satellite Retrieval for GPM) in NTB Province," Megasains, vol. 13, no. 1, pp. 6-13, 2022.
[31] A. Kalender, H. Sonmez, E. Medley, C. Tunusluoglu and K. E. Kasapoglu, "An approach to predicting the overall strengths of unwelded bimrocks and bimsoils," Eng Geol, vol. 183, pp. 16-79, 2014.
[32] A. Hara, T. Ohta, M. Niwa, S. Tanaka and T. Banno, "Shear modulus and shear strength of cohesive soils," Soils and Foundations, vol. 14(3), pp. 1-12., 1974.
[33] D. Fredlund and A. Xing, "Equations for the soil-water characteristic curve," Canadian Geotechnical Journal, 31(4), pp. 521-532, 1994.
[34] C. Zapata, W. H. S. Houston and K. Walsh., "Soil-water characteristic curve variability," ASCE Geotechnical Special Publication 99., vol. 99, pp. 84-124, 2000.
[35] D. Fredlund, A. Xing and S. & Huang, "Predicting the Permeability Function for Unsaturated Soils using the Soil-Water Characteristic Curve," Canadian Geotechnical Journal, 31(3), 521 – 532., vol. 31(3), pp. 521-532, 1994.
[36] A. S. Muntohar, J. Ikhsan, H.-J. Liao, A. Jotisankasa and V. G. Jetten, "Rainfall Infiltration-Induced Slope Instability of the Unsaturated Volcanic Residual Soils During Wet Seasons in Indonesia," Indonesian Journal on Geoscience , vol. 9, no. 1, pp. 71-85, 2022.

Copyright © Int. J. of GEOMATE All rights reserved, including making copies, unless permission is obtained from the copyright proprietors.

15th Int. Conf. on Geotechnique, Construction Materials & Environment,
Kyoto, Japan, 11-13 November 2025, ISBN 978-4-909106124 C3051

BACK-CALCULATED PARAMETERS AND THEIR ATTENUATION COEFFICIENTS FOR PILE DESIGN IN SEDIMENTARY ROCK

Ketkaewngoen Mahakhotchasenichai[1], Kuo Chieh Chao[2] and Shinya Inazumi[3]

[1] Graduate School of Engineering and Science, Shibaura Institute of Technology, Japan;
[2] Geotechnical and Earth Resources Engineering, Asian Institute of Technology, Thailand;
[3] College of Engineering, Shibaura Institute of Technology, Japan

ABSTRACT

This research paper focuses on the load capacity of piles anchored in sedimentary rock, specifically sandstone and siltstone, which often present unique challenges in pile design and construction. The study emphasizes the importance of considering factors such as the degree of weathering when designing pile capacity in rock formations. The authors conducted static load tests on 16 large-diameter bored piles, applying loads of 2.5 times the working load (1,625-2,500 tons). Following these tests, back-analysis calculations were performed to determine critical parameters and equations used in pile capacity design, including adhesion factors. The research also proposes a method for adjusting the rock strength to more accurately reflect its condition based on the degree of weathering. Key findings from the study show that the bearing capacity of sandstone is comparable to that of clay, while siltstone has a bearing capacity approximately 60% higher than clay. This research provides valuable insight into the field of geotechnical engineering, particularly in the design of pile foundations in sedimentary rock formations, by addressing the effects of weathering on pile bearing capacity.

Keywords: Bored piles, Weak rocks, Degree of weathering, Siltstone and sandstone, Pile capacity

INTRODUCTION

The study of pile bearing capacity in soil has been extensively studied. In general, soil layers present greater homogeneity compared to rock layers, resulting in relatively straightforward calculations of pile bearing capacity. In contrast, evaluating the bearing capacity of piles in rock is more complex due to the presence of inhomogeneity. Rock masses often contain imperfections such as fractures and weathering, which pose additional challenges in the design of pile capacity in these materials. In the pile construction industry, piles socketed in rocks are frequently designed with high conservation due to insufficient geotechnical investigation and adequate understanding of pile behavior, leading to uneconomic designs.

This research focuses on the calculation of design parameters for evaluating the bearing capacity of bored pile socketed in weak rock, based on back-calculation from pile test data obtained through static load test method. Skin friction equations of piles socketed in weak rocks are proposed, along with a method for adjusting rock strength by considering the degree of weathering.

RESEARCH SIGNIFICANCE

In this research, an attempt was made to identify appropriate parameters for the design of bored piles constructed in weak sedimentary rocks such as sandstone and siltstone. These rocks are characterized by their high susceptibility, especially when the construction is carried out using the wet-process bored pile system, which causes these rocks to exhibit slaking behavior. Consequently, the pile capacity observed in practical situations often deviate from calculated values. This research therefore attempts to identify pile design parameters that provide engineers with more accurate data, leading to further design developments and reduced material usage.

DATA AND ANALYSIS

Static Pile Load Test Results

The data analyzed for this research were obtained from 16 test piles, all of which were constructed using the wet-process bored pile construction method using polymer mixed with bentonite solution as a borehole stabilization. After drilling was complete, the borehole was left to allow for sedimentation and then cleaned with a cleaning bucket to ensure a stable pile base prior to concrete placement.

Static load tests were conducted on all 16 bored piles subjected to varying applied loads. Each test involved three cycles of loading, corresponding to 1.25, 1.25 and 2.5 times the allowable load, respectively. The test piles had diameters of 1.2 and 1.5 m., with pile lengths ranging from 9.3 m. to 36 m., and socketed lengths in rocks varying between 0.3 m. and 9.8 m. The allowable working load ranged from 650 to 750 tons for piles with a diameter of 1.2 m. and 1,000 tons for piles with a diameter of 1.5 m. General

information of piles is summarized in Table 1.

Table 1 General information of test piles

Pile no.	d (m.)	Pile Length (m.)	Soil or rock at the pile tip	Socket length (m.)	Allowable working load (tons)	Max. applied load (tons)
1	1.2	9.3	Siltstone	0.3	700	1,750
2	1.2	36	Clay	-	700	1,750
3	1.2	14.5	Siltstone	4.0	700	1,750
4	1.2	35.3	Clay	-	700	1,750
5	1.2	19.8	Sandstone	3.3	700	1,750
6	1.2	20.3	Siltstone	8.3	700	1,750
7	1.2	18.6	Siltstone	7.6	700	1,750
8	1.2	15	Siltstone	4.5	700	1,750
9	1.2	15.5	Clay	-	700	1,750
10	1.2	16.5	Sandstone	2.5	700	1,750
11	1.2	15	Sandstone	1.0	700	1,750
12	1.2	18.5	Sand	-	700	1,750
13	1.2	35	Sand	-	700	1,750
14	1.2	22	Clay	-	650	1,625
15	1.2	14	Siltstone	9.5	750	1,875
16	1.5	14.3	Siltstone	9.8	1,000	2,500

The test results of 16 piles illustrate the relationship between the applied load (P) and the pile head settlement (δ_h), as shown in Fig. 1. The data indicate that, for most piles, pile heads settlement increases progressively with applied load up to approximately 2.25 times the allowable load. Beyond this point, a remarkable increase in the pile head settlement is observed, indicating that the load starts to transfer to the pile tip. This indicates that all test piles exhibit generalized load-settlement behavior, where the applied load is resisted through a combination of shaft friction along the pile surface and end bearing resistance at the pile tip.

In addition, most piles exhibit the pile head settlement values ranging from 5 to 11 mm. When considering the influence of ground conditions, it is found that the piles socketed in weak rocks exhibit lower pile head settlement compared to those embedded in soil.

To compare the load-settlement behavior of all piles with varying allowable working loads and pile diameters (d), the maximum settlement under the maximum applied load was normalized by the diameter of each pile, as presented in Table 2. The pile head settlement of the most piles was less than 1% of the pile diameter (except for Pile no.2, which exhibited a soft base due to an improper cleaning of the borehole). According to Eurocode7 [1], a pile under compressive load is considered to have reached a failure state when the pile head settlement equals 10% of the pile diameter. Additionally, Ng et al. (2001a) [2] suggested that a moderately conservative estimate for the pile toe mobilization in large-diameter bored piles has been determined to be 4.5% of the pile diameter. Based on these criteria, the settlement of all piles in this study remained below both thresholds proposed. Nevertheless, in this study, the mobilization between soil-pile and rock-pile interfaces is determined based on strain gauge measurements, which will be discussed in the following chapter.

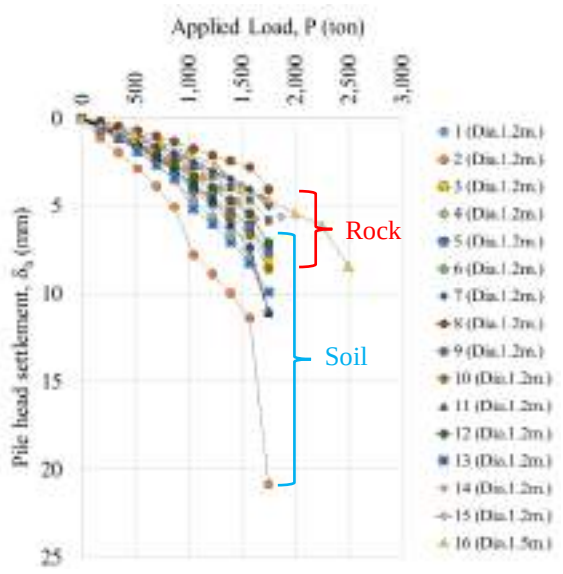

Fig. 1 Applied load vs pile head settlement for 16 test piles

Table 2 Maximum pile head settlement normalized by pile diameter

Pile no.	Maximum pile head settlement (δ_h, mm.)	Pile diameter (d, mm.)	δ_h/d (%)
1	11.09	1200	0.74
2	20.86	1200	1.39
3	8.11	1200	0.54
4	11.02	1200	0.73
5	7.63	1200	0.51
6	7.17	1200	0.48
7	5.04	1200	0.34
8	4.05	1200	0.27
9	5.84	1200	0.39
10	8.59	1200	0.57
11	11.05	1200	0.74
12	7.08	1200	0.47
13	9.94	1200	0.66
14	5.74	1200	0.38
15	5.65	1200	0.38
16	8.44	1500	0.56

Skin Friction (f_s) Discussion

Skin friction (f_s) and displacement were measured using strain gauges on each test pile. The data indicate that most rock layers did not reach full mobilization, with an average maximum displacement of approximately 3 mm. In contrast, all soil layers showed soil-pile displacements in the range of 5–10 mm, indicating full mobilization in those layers. Extrapolation is therefore applied by using a hyperbolic equation to predict the fully mobilized skin friction for rock layers. The skin friction (f_s) at a displacement of 5 mm. was chosen to represent the maximum displacement of the rock layer (Horvath et

al. 1983) [3]. Skin friction values of all soil and rock layers are shown in Table 3 to Table 5. The data in Table 4 and Table 5 are arranged according to skin friction (f_s) and the degree of weathering. From the tables, they are shown that skin friction (f_s) of siltstone and sandstone varies in the range from 22-120 t/m^2. A comparison between the uniaxial compressive strength (σ_i) of intact rocks and the skin friction (f_s) reveals inconsistencies in the data. In certain cases, rock layers exhibiting high uniaxial compressive strength (σ_i) values correspond to relatively low skin friction (f_s) values. However, when considering the degree of weathering as described by BS5930 (1981) [4], a consistent correlation with skin friction (f_s) is observed. Rock layers classified as having a low degree of weathering tend to exhibit high skin friction (f_s) values.

Accordingly, in this research, the strength of intact rock was adjusted by considering the influence of weathering to better reflect practical performance.

Table 3 Ranges of mobilized skin friction for each type of soil and rock

Soil or rock type	Mobilized skin friction (ton/m^2)
Stiff clay	2.5-15.0[(1)]
Hard clay	15.0-84.0[(1)]
Loose sand	6.0-8.0[(1)]
Dense sand	8.0-75.0[(1)]
Rock salt	20.0[(1)]
Siltstone	22.0 – 120.0[(2)]
Sandstone	27.0 – 95.0[(2)]

Note: [(1)]Fully mobilized, [(2)]Extrapolated

Table 4 Mobilized skin friction from strain gauges for siltstone

Pile no.	Depth of layer	σ_i (ton/m^2)	f_s (ton/m^2)	Degree of weathering
1	-8.0 to -9.0	2,920	120.1[(1)]	Fresh
3	-10.5 to -12.0	1,318	107.0[(2)]	Fresh
3	-12.0 to -13.0	1,318	92.0[(2)]	Slightly weathered
15	-10.0 to -13.0	2,114	82.7[(2)]	Moderately weathered
7	-11.0 to -15.0	1,270	81.4[(1)]	Moderately weathered
6	-12.0 to 15.5	1,900	68.2[(2)]	Moderately weathered
6	-15.5 to -19.0	1,900	60.7[(2)]	Moderately weathered
16	-10.0 to -13.0	2,114	55.3[(1)]	Moderately to highly weathered
8	-10.5 to -14.0	746	33.6[(2)]	Moderately weathered
15	-4.5 to -10.0	2,114	23.8[(2)]	Highly weathered

Note: [(1)]Fully mobilized, [(2)]Extrapolated

Table 5 Mobilized skin friction from strain gauges for sandstone

Pile no.	Depth of layer	σ_i (ton/m^2)	f_s (ton/m^2)	Degree of weathering
10	-14.0 to -15.5	3,146	98.7[(2)]	Fresh
5	-16.5 to -18.5	1,898	38.1[(2)]	Slightly to moderately weathered
7	-15.0 to -18.0	1,270	37.4[(2)]	Slightly weathered
13	-16.5 to -22.0	1,663	28.9[(1)]	Slightly weathered
13	-22.0 to -28.0	1,663	26.8[(1)]	Slightly weathered

Note: [(1)]Fully mobilized, [(2)]Extrapolated

The data obtained from the static load tests were back-analyzed to determine critical parameters and equations applied in pile capacity design, including adhesion factors (α) and skin friction (f_s) for weak rock. The details of the results are presented in the following content.

RESULTS

Adhesion Factor (α) for Clay and Weak Rock

The adhesion factor (α) of clay is back-calculated from skin frictions obtained from strain gauges. The corresponding results are presented in Fig. 2, plotted on a logarithm scale on both axes and compared with the empirical relationship proposed by Kulhawy and Phoon (1993) [5]. The undrained shear strength of the clay (S_u) is normalized by atmospheric pressure (p_a). It is important to note that all unit skin friction values for the clay represent fully mobilized conditions. The equation of adhesion factors for clay, derived from this study, is as follows:

$$\alpha = x(S_u/p_a)^{-0.5} \quad (1)$$

Where x is equal to 0.6. To cover 90% of the data points, the upper and lower bounds of the x value would be about 1.2 and 0.3, respectively.

The adhesion factor (α) of weak rocks is back-calculated from the mobilized skin friction obtained from strain gauges, which were extrapolated as previously described. It is acknowledged that the strength of in-situ rock is generally lower than that of intact rock. Therefore, the analysis is adopted by considering a reduction factor based on the degree of weathering of the rock, as proposed by Kulhawy and Prakoso (2007) [6], who indicated that the uniaxial compressive strength of weathered rocks can decrease to about 15 to 20 % of that of unweathered rocks. The resulting values are presented in Fig. 3.

The uniaxial compressive strength of the rock (σ_c) is normalized by atmospheric pressure. The adhesion factor data are plotted from both extrapolated and fully mobilized data in logarithm graph. The regression of adhesion factor for the siltstone is given by the following equation:

$$\alpha = 1.02(\sigma_c/2p_a)^{-0.5} \quad (2)$$

Which can be simplified as follows:

$$\alpha = (\sigma_c/2p_a)^{-0.5} \quad (3)$$

Equation (3) corresponds to Kulhawy and Phoon (1993)'s approach where x is equal to 1 to 3 for weak rocks. For the sandstone, the regression line is:

$$\alpha = 0.50(\sigma_c/2p_a)^{-0.5} \quad (4)$$

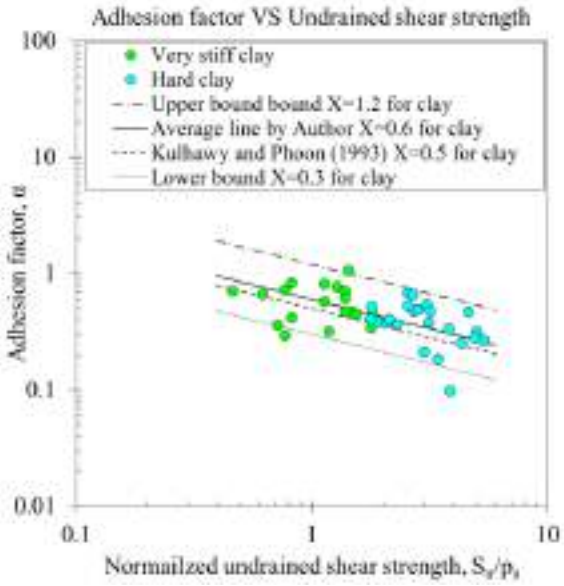

Fig. 2 Adhesion factors for clay (logarithm plotting)

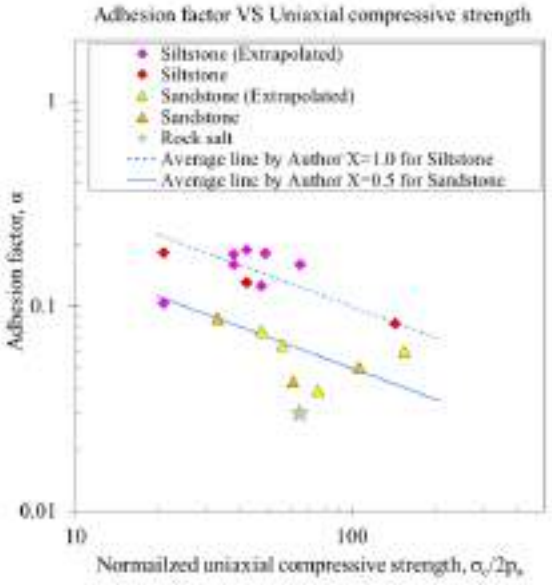

Fig. 3 Adhesion factors for weak rock (logarithm plotting)

Skin Friction (f_s) for Weak Rocks

The skin friction derived from stress gauge measurements and extrapolations can be directly expressed as an equation without the need to determine the adhesion factor. The relationship commonly presented by other researchers is shown in Equation (5), which is in the form of an exponential equation representing the relationship between skin friction (f_s) and uniaxial compressive strength of rock (σ_c).

$$f_s = x\sigma_c^{0.5} \quad (5)$$

Various values of parameter x have been proposed by different researchers. For example, Ng et al. (2001b) [7] studied the skin friction of decomposed granitic rocks in Hong Kong and, based on a displacement of 1% of the pile diameter (approximately 10 mm), proposed a value of x = 0.19. Kulhawy et al. (2005) [8] conducted a comprehensive review of available data and proposed x = 0.31 and x = 0.08 for drilled and grouted piles, corresponding to 70% and 100% data coverage, respectively. Rowe and Armitage (1987b) [9] proposed x values based on roughness classes, with x = 0.45 for regular clean sockets (R1, R2, and R3 classes), and x = 0.6 for clean-rough sockets (R4 class). Zhang and Einstein (1998) [10] reviewed data from several key researchers and recommended x = 0.8 for rough sockets.

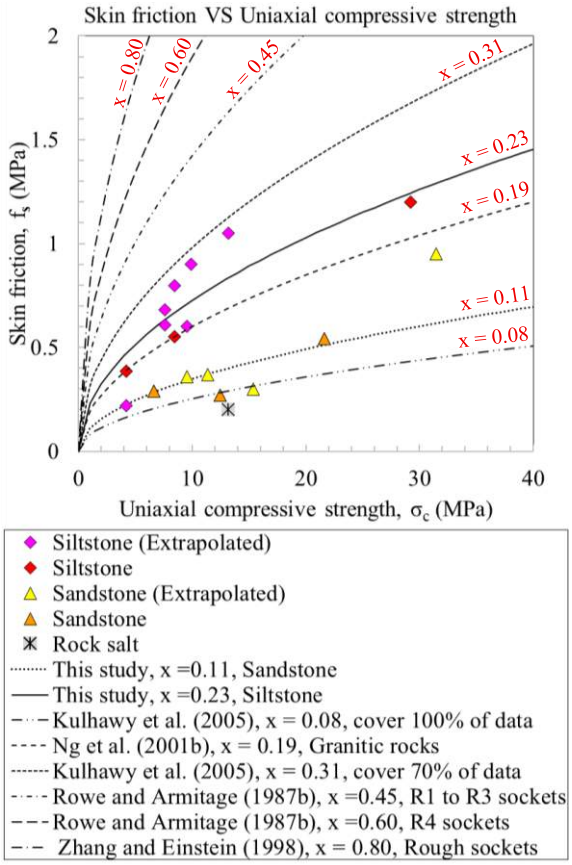

Fig. 4 Side friction resistance for weak rock versus the uniaxial compressive strength of rock (linear fitting)

For this study, the following empirical equation to estimate the skin friction of piles in sandstone is proposed as:

$$f_s = 0.11\sigma_c^{0.5} \quad (6)$$

For piles socketed in siltstone, the skin friction is observed to be higher than that of piles in sandstone.

Based on the analyzed data, the following empirical equation to estimate skin friction is proposed for piles in siltstone:

$$f_s = 0.23\sigma_c^{0.5} \quad (7)$$

The relationship between skin friction (f_s) and uniaxial compressive strength of rock (σ_c) of this study is illustrated in Fig. 4 in comparison with the results reported by the aforementioned researchers. The graph indicates that the skin friction values for siltstone in this study are comparable to those proposed by Ng et al. (2001b) and Kulhawy et al. (2005). Nonetheless, the siltstone in this study is more comparable to the rock group investigated in the research of Kulhawy et al. (2005), which also included sedimentary rocks. For sandstone, the obtained values are relatively low but align with the lower bound of the data presented by Kulhawy et al. (2005), who proposed an x value covering the full range of observed data.

CONCLUSION

This study demonstrates that the bearing capacities of piles in both sandstone and siltstone are relatively comparable when evaluated at equivalent degrees of weathering. When the adhesion factors are calculated back, key findings reveal that the bearing capacity of sandstone shares the same trend as that of clay, whereas siltstone exhibits a bearing capacity approximately 60% higher than that of clay. The corresponding equations for adhesion factors are presented in Table 6.

When skin friction is directly evaluated as a function of the uniaxial compressive strength of rock for both siltstone and sandstone, the results are represented in Table 7. In this context, it is essential to account for the degree of weathering of rock in order to appropriately adjust the strength of intact rock when calculating skin friction values.

Table 6 the adhesion factors of clay, siltstone and sandstone

Clay	Siltstone	Sandstone
$\alpha = 0.60(S_u/p_a)^{-0.5}$	$\alpha = 1.02(\sigma_c/2p_a)^{-0.5}$	$\alpha = 0.50(\sigma_c/2p_a)^{-0.5}$

Table 7 Summary of the results of skin friction for rocks

Method	Siltstone	Sandstone
Exponential fitting	$f_s = 0.23\sigma_c^{0.5}$	$f_s = 0.11\sigma_c^{0.5}$

Note that the load-bearing behavior of rock is typically characterized by a bilinear relationship. The compressive strength of rocks should be limited to not exceed the 28-day compressive strength of concrete.

ACKNOWLEDGMENTS

I would like to thank SEAFCO Public Limited Company, a bored pile construction company, for providing me rock core samples and static load test reports that made this research possible.

REFERENCES

[1] CEN, Eurocode 7 Geotechnical design - Part 1: General rules. Final Draft, EN 1997-1:2004 (E), (F) and (G), November 2004, European Committee for Standardization: Brussels, 2004, pp. 168 pages (E).

[2] Ng, C., Tau, T., Li, J., and Tang, W, New failure criterion for large diameter bored piles in weathered geomaterials. Journal Geotechnical Geoenvironmental Engineering, 127(6), 2001a, pp. 488-498.

[3] Horvath R.G., T.C. Kenney and P. Kozicki, Methods of improving the performance of drilled piers in weak rock. Canadian Geotech. J. 20(4), 1983, pp. 758-772.

[4] BS 5930, Code of Practice for Site Investigations, British Standards Institution (BSI), London, 1981, pp. 147.

[5] Kulhawy, F.H. and Phoon, K.K., Drilled shaft side resistance in clay soil to rock. Proc. on Conf. on design and performance of deep foundation: piles and piers in soil and soft rock. Geotechnical Special Publication No.38, 1993, pp. 172-183.

[6] Kulhawy, F.H. and Prakoso, W.A., Issues in evaluating capacity of rock socket foundations. In: Proceedings of the 16th SE Asian geotechnical conference, Kuala Lumpur, 2007, pp. 51-61.

[7] Ng, C. W. W., Yau, T. L. Y., Li, J. H. M., and Tang, W. H., Side resistance of large diameter bored piles socketed into decomposed rocks. Journal Geotechnical Geoenvironmental Engineering, 127(8), 2001b, pp. 658–669.

[8] Kulhawy, F.H., Prakoso, W.A. & Akbas, S.O., Evaluation of Capacity of Rock Foundation Sockets, Alaska Rocks 2005 (Proc., 40th U.S. Symp. Rock Mech.), Ed. G. Chen, S. Huang, W. Zhou & J. Tinucci, Anchorage, Alaska, 05-767, 2005, 8 pages.

[9] Rowe, R.K., and Armitage. H.H., A design method for drilled piers in soft rock, Canadian Geotechnical Journal, 24, 1987b, pp. 126-142.

[10] Zhang, L., and Einstein, H.H., End bearing resistance of drilled shafts in rock. Journal of Geotechnical and Geoenvironmental Engineering (ASCE) 124 (7), 1998, pp. 574–584.

Copyright © Int. J. of GEOMATE All rights reserved, including making copies, unless permission is obtained from the copyright proprietors.

15th Int. Conf. on Geotechnique, Construction Materials & Environment, Kyoto, Japan, 11-13 November 2025, ISBN 978-4-909106124 C3051

INTEGRATION OF SOIL RESISTIVITY AND BOREHOLE DATA TO EVALUATE GEOMATERIALS AND N_{60}-VALUE USING CLUSTERING ANALYSIS

Ratchadakorn Chumkhiao [1], Sukit Yindeesuk [2], Kuo Chieh Chao [3] and Shinya Inazumi [4]

[1]Graduate School of Engineering and Science, Shibaura Institute of Technology, Japan;
[2]Department of Highways, Thailand;
[3]School of Engineering and Technology, Asian Institute of Technology, Thailand;
[4]College of Engineering, Shibaura Institute of Technology, Japan

ABSTRACT

Geotechnical data is the foundation of geotechnical engineering. Primarily, drilling was the technique for obtaining subsurface data. In recent decades, non-intrusive methods such as electrical resistivity surveys, enhanced by machine learning, have proven to be very useful for in-depth geotechnical site investigations. The goal of this study is to use 2D Electrical Resistivity Imaging (2D ERI) and Standard Penetration Test (SPT) data together to sort geomaterials using K-Means Clustering Analysis (KMCA), which will help us learn more about the properties of the subsurface. We created a power equation by analyzing soil electrical resistivity with N_{60}-value along a designated 2D ERI line, which was verified with borehole data. This power equation was then used to calculate estimated N_{60}-value in slope regions where SPT data was not directly accessible. The KMCA proved to be an adaptable tool, facilitated categorizing geomaterials in the study area into three main clusters aligned with different competency levels based on SPT data. These clusters include low competency materials (loose sand), medium competency materials (medium - stiff clay), and high competency materials (stiff - hard clay). The power equation effectively calculated the N_{60}-value for 2D ERI lines 1 and 2, confirmed by borehole data from BH6 and BH7, respectively, achieving high accuracy with R^2 of 0.8396 and 0.9283, MAE of 4.86 and 6.38, and RMSE of 6.21 and 7.39. This framework demonstrates how combining geophysical surveys with machine learning methods can help to better characterize subsurface geomaterials and make conventional methods more useful.

Keywords: Electrical resistivity imaging (ERI), Estimated SPT N_{60}-values, K-means clustering analysis (KMCA), Unsupervised machine learning, Soil classification

INTRODUCTION

Subsurface properties are essential in engineering projects, including foundation design and slope stability evaluation. Direct data collection through borehole drilling is a fundamental method for acquiring the engineering properties of geomaterials and assessing subsurface conditions at specific locations and depths. The traditional approach is time-consuming and costly, and the data acquired lacks comprehensiveness relative to the broad area, resulting in insufficient data in certain regions and ambiguous subsurface properties. To cope with the constraints of drilling techniques, 2D electrical resistivity imaging (2D ERI) and machine learning (ML) have been utilized.

Ciampi [1] examined subsurface litho-stratigraphy by merging 2D ERI with drilled boreholes through clustering analysis. In a manner, Akingboye [2], they combined seismic wave velocity (v_P) with electrical resistivity and borehole logs to elucidate the surface-subsurface properties of soil and rock, optimizing the analysis using a regression model. Furthermore, Dick [3] employed clustering and regression to characterize the link between resistivity and SPT N-value, subsequently identifying lithologies in the research area. Previous research facilitated the application of combined methodologies in several contexts, including the oil and gas sector, to assess reservoir rocks and slope instabilities. Nonetheless, KMCA has not been extensively utilized alongside drilling and electrical resistivity techniques for geotechnical site investigation procedures.

This study seeks to (1) categorize subsurface geomaterials and (2) estimate the N_{60}-value in an area devoid of SPT data by merging 2D ERI and borehole data analyzed with KMCA. Consequently, a thorough understanding of subsurface conditions can be achieved through integrated methodologies, serving as a framework for geotechnical site investigations to facilitate foundation and slope stability designs, as well as landslide assessments, to implement protective measures and forecast future events.

RESEARCH SIGNIFICANCE

This study aims to bridge the gap between conventional methods that yield discrete data points and continuous data across various dimensions. Furthermore, it classifies geomaterials, estimates N-

values in areas absence of borehole data, and enhances the understanding of subsurface characteristics by integrating 2D ERI with borehole data, refined through KMCA, thereby covering extensive specific areas while minimizing costs and time through strategically placed boreholes.

Moreover, the developed framework can be applied as a realistic guideline for geotechnical site investigations in various regions to gather subsurface data and subsequently analyze subsurface characteristics with precision and reliability.

METHODOLOGY

Borehole Drilling

Six boreholes were drilled at distinct locations along the upside-down slope area, positioned adjacent to 2D ERI lines 1, 2, 3, and 5 (Fig. 1) using the wash boring method. Boreholes KB1 (9.04 m), KB2 (10.78 m), KB3 (12.09 m), and BH10 (60.45 m), near 2D ERI line 5, were used for analysis, while BH6 (7.8 m) and BH7 (9.45 m), aligned with 2D ERI lines 1 and 2, were used for validation. In situ tests, including Standard Penetration Tests (SPT), were conducted to estimate blow counts per 30 cm, following ASTM D1586. However, SPT N-value is influenced by factors such as hammer operation, guide rod verticality, sampler type, and hammer–anvil dimensions. Therefore, the N-value should be standardized to the standard energy ratio into N_{60} - value deriving from equation provided as shown in Eq. (1), without considering the overburden corrections [4].

$$N_{60} = C_{ER} C_B C_S C_R N_f \quad (1)$$

where N_f, C_{ER}, C_B, C_S, and C_R are SPT N-value measured in the field, energy ratio correction factor, borehole diameter correction factor, sampling method correction factor, and rod length correction factor, respectively.

Corrected N-value obtained from field testing in this study represented details in Table 1.

Soil samples at various levels were obtained for laboratory study to evaluate fundamental soil parameters, including soil classification via sieve analysis to examine grain-sized distribution of soils (ASTM D 422), Atterberg Limits to measure the critical water contents of fine-grained soils (ASTM D 4318), and water content to measure the mass of water contained in the pore spaces of soil (ASTM D 2216), as detailed in Table 2.

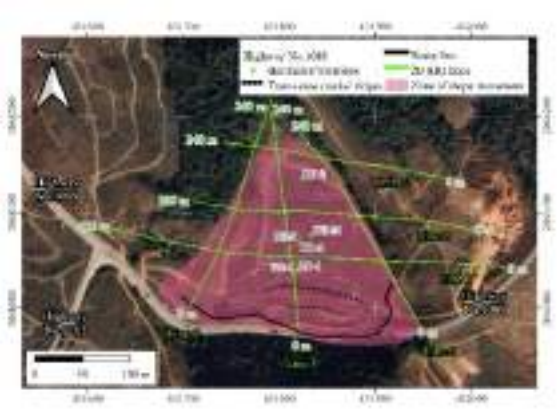

Fig. 1 Geotechnical and geophysical data collecting for the study area, featuring six drill locations and 2D ERI lines 1 through 6

Table 1 Corrected N-value (N_{60}-value) derived from Eq. (1) [4]

Depth (m)		Soil type	N_{60}-value for KMCA (blow counts/ ft)				N_{60}-value for validation	
			KB 1	KB 2	KB 3	BH 10	BH 6	BH 7
0	0.45	SC	5	3	7	n/a	n/a	n/a
0.5	0.95	SC	5	4	13	n/a	n/a	n/a
1	1.45	SC	2	4	11	n/a	n/a	n/a
1.5	1.95	SC	3	4	8	9	1	1
2	2.45	CL	2	5	4	n/a	3	5
2.5	2.95	CL	3	7	5	n/a	4	6
3	3.45	CL	11	9	4	11	6	8
4.5	4.95	CL	23	12	4	31	8	7
6	6.45	CH	33	22	11	11	19	18
7.5	7.95	CH	30	41	23	25	30	31
9	9.45	CL	30	30	35	26	End	31
10.5	10.95	CL	End	30	30	26		End
12	12.45	CL		End	30	30		
13.5	13.95	CL			End	30		
15	15.45	CL				30		
16.5	16.95	CL				30		
.	.	.				.		
.	.	.				.		
58.5	58.95	CL				30		
60	60.45	CL				30		
					End			

Table 2 Basic soil properties obtained from laboratory tests (BH10, KB1, KB2, and KB3)

Depth (m)	US CS	N_{60}-value*	Water Content (%)	PI	Passing #200 (%) **
0-2	SC	2-5	9.5-18.8	-	32-45
	GC	7- 13	5.6-6.1	-	23
2-6	CL	2-23	15.4-27.3	14.5-25.2	50-66
6-60.45	CH	11 to > 30	21-29.6	27.1-32.2	73-99
	CL	11 to > 30	11.1-25.7	10.3-20.5	54-99

*Note: *N_{60}-value (blow counts/ ft), **fine-grained size passing #200.*

2D Electrical Resistivity Imaging

2D ERI studies primarily employ multi-electrode configurations, necessitating extensive data coverage

across a broad area, particularly for assessing the subsurface resistivity distribution in both vertical and lateral continuity. Consequently, the 2D ERI is the most suitable technique for this study in comparison to alternative electrical resistivity methods.

2D ERI was conducted at the slope of Highway No.1088 for six 2D ERI lines to cover the entire slope area (Fig.1). To collect data and comprehend the subsurface conditions, the electrical resistivity meter as ABEM Terrameter LS tool accompanied with multi-electrode for 81 electrodes (and up to 141 electrodes with roll-along cable and electrodes technique) were employed and protocol for multiple-gradient array was conducted via electrode spacing 3 m constantly along 2D ERI lines (Table 3) with a maximum depth of investigation reaching approximately 46 m from the surface. After data acquisition, the data in each profile lines were processed with ABEM Terrameter LS toolbox, then RES2DInv software was used for data inversion based on the least-square method and reveal into two dimensional distribution of apparent resistivity subsurface model called pseudo-section.

Table 3 Arrangements in individual 2D ERI lines.

2D ERI lines/ distance (m)	No. of electrodes	Orientation	RMS error (%)
1 (0 – 420 m)	141	E - W	1.8
2 (0 – 300 m)	101	E - W	1.1
3 (0 – 240 m)	81	E - W	1.6
4 (0 – 240 m)	81	N -S	1.6
5 (0 – 240 m)	81	N -S	1.0
6 (0 – 240 m)	81	N -S	1.2

The reliability of inversion result was proved by absolute error (RMS error, %) comparing between measured and calculated apparent resistivity.

Thereafter, the inverted data was extracted [5] by deriving from Eqs. (2-3).

$$X_{\rho_a} = X_{MN} \quad (2)$$

$$Z_{\rho_a} = min\{(X_{MN} - X_A),\ (X_B - X_{MN})\}/3 \quad (3)$$

where X_{MN}, X_A, X_B, X_{ρ_a}, and Z_{ρ_a} are distance between a pair of potential electrodes (MN), distance of current electrode A from the first electrode, distance of current electrode B from the first electrode, distance of apparent resistivity data points from the first electrode (x-axis), and depth of apparent resistivity data points at X_{ρ_a} (y-axis), respectively.

K-means Clustering Analysis

K-means is a partitioning clustering technique that segments an N-dimensional dataset into k groups based on sample data. Each cluster is associated with a centroid, assuming a spherical or circular distribution of data within each cluster. The method minimizes the sum of squared errors (SSE) between data points and centroids, using Euclidean distance to assess similarity. The variance within clusters is minimized, while the variance between clusters is maximized [6] and their corresponding cluster centroids, as demonstrated in Eq. (4).

$$SSE = \sum_{i=1}^{k} \sum_{x_j \in P_i} \left\| x_j - c_i \right\|_2^2 \quad (4)$$

where x indicates data points inside k number of P clusters; $\|.\|_2$ indicates Euclidean L2 norm; and c corresponds to cluster centroids.

The modeling commences with a specified number of clusters. Subsequently, the Elbow approach and Silhouette analysis were utilized to determine the prospective number of initial clusters. The Elbow technique determines the optimal number of clusters at the elbow where the error stabilizes.

However, if the Elbow technique plot does not exhibit a distinct elbow, it may be beneficial to utilize Silhouette analysis as an alternative or supplementary approach to the elbow method. The Silhouette analysis assesses clustering effectiveness by analyzing intra-cluster similarity and inter-cluster dissimilarity, as illustrated in Eq. (5). In the Eq. (5), the coefficient values (S, Silhouette Score) span from "-1" to "1". A number near “1” signifies that the sample inside one cluster is far from other clusters, but a value near “-1” implies that the sample may have been erroneously allocated to the wrong cluster. If the coefficient is 0, the sample is in close contact with adjacent clusters.

$$S = \frac{(b-a)}{max(a,b)} \quad (5)$$

where a is Mean distance to other points in the same cluster (intra-cluster distance); and b is Mean distance to points in the nearest neighboring cluster (inter-cluster distance).

When applying KMCA, it is essential to use standardized data to avoid distortion from variables with larger variances. Additionally, KMCA does not account for cluster dimensions, which may result in varying cluster sizes **[7]**.

This study employs KMCA using the Python platform. The procedure begins with data pre-processing, which entails preparing and selecting suitable parameter inputs for clustering analysis, as these inputs affect the outcome. This encompasses: (1) data integration and feature selection, (2) data cleansing, (3) statistical imputation for managing missing data, (4) data abstraction to condense the data into a usable format while maintaining its critical attributes for effective processing and cross-platform collaboration, and (5) feature engineering, including feature rescaling. Table 4 presents processed data, consisting of 30 data points, with soil resistivity and N_{60}-value. Fig. 2 shows the complete KMCA process.

Table 4 Data points collected along 2D ERI line 5 and data from KB1, KB2, KB3, and BH10

Data No.	Depth (m)	Resistivity (Ω.m)	N_{60}-value	Soil type, USGS
1	3	114.55	8	Stiff silty clay, CH
2	6	47.72	28	Very stiff silty clay, CH
3	3	73.03	7	Stiff sandy clay, CL
4	5	29.8	14	Stiff sandy clay, CL
5	5	24.15	14	Stiff sandy clay, CL
6	6	28.06	25	Very silty clay, CH
7	6	26.22	25	Very silty clay, CH
8	7	19.32	32	Hard silty clay, CH
9	7	18.22	32	Hard silty clay, CH
10	3	27.55	5	Medium sandy clay, CL
11	6	20.58	13	Stiff silty clay, CH
12	10	26.02	30	Hard silty clay, CH
13	3	87.09	17	Very stiff clay, CL
14	3	65.06	17	Very stiff clay, CL
15	5	22.13	18	Hard clay, CL
16	5	25.84	18	Hard clay, CL
17	7	16.12	20	Very stiff clay, CL
18	7	17.1	20	Very stiff clay, CL
19	9	16.5	25	Hard clay, CL
20	14	22.96	30	Hard clay, CL
21	15	25.44	30	Hard clay, CL
22	21	29.26	30	Hard clay, CL
23	21	30.1	30	Hard clay, CL
24	21	30.02	30	Hard clay, CL
25	27	32.44	30	Hard clay, CL
26	27	34.49	30	Hard clay, CL
27	27	34.28	30	Hard clay, CL
28	27	34.9	30	Hard clay, CL
29	33	37.4	30	Hard clay, CL
30	33	38.52	30	Hard clay, CL

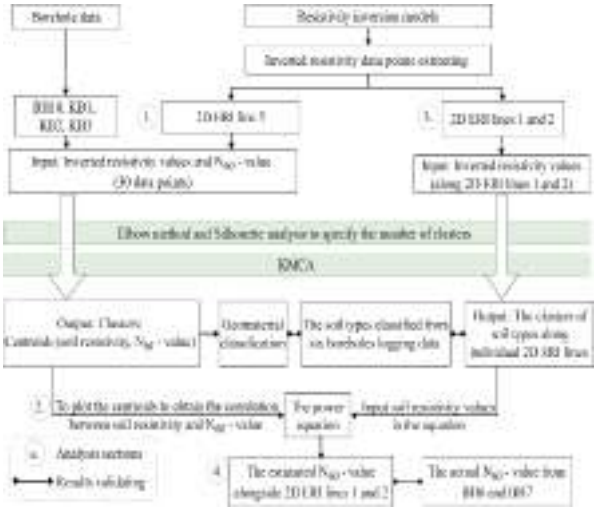

Fig. 2 Methodological flowchart regarding KMCA

RESULTS AND DISCUSSIONS

Borehole Drilling and 2D ERI by KMCA

Six 2D ERI lines and six boreholes were conducted at the slope site to interpret the subsurface conditions. Line 5, located near boreholes BH10, KB1, KB2, and KB3, revealed four main geomaterial groups. (1) Clayey gravelly sand (SC) occurs from the surface to 2 m depth with resistivity of 100-500 Ω.m. (2) Sandy clay and silty clay (CL) are found between 2-6 m and 8-24 m, with resistivity of 50-100 Ω·m and 10-20 Ω·m, respectively. (3) Saturated silty clay (CH) appears at 6-8 m (20-50 Ω.m). (4) Moist fractured rock (>24 m) shows 20-500 Ω.m resistivity. These classifications are summarized in Table 5.

According to 30 data points of soil resistivity and N_{60}-value along 2D ERI line 5, they were clustered with KMCA. The subsurface geomaterials along the 2D ERI line 5 were categorized as follows: Cluster 1, characterized by a centroid at (27.51, 25), was categorized as soft to very stiff clay (CH); Cluster 2, with a centroid at (75.06, 14), was defined as medium to stiff clay (CL); and Cluster 3, identified by a centroid at (114.55, 8), was designated as medium clay (CL). These classifications are based on the combination of resistivity values and corrected N_{60}-value as details shown in Table 6 and Fig. 3.

The classification of geomaterials utilizing 2D ERI and borehole logging at designated depths revealed four principal geomaterial categories. Nonetheless, KMCA findings, linking soil resistivity with N_{60}-value, identified three primary geomaterials. This mismatch may result from dependence solely on the N_{60}-value, which limits the ability to differentiate between very stiff clay and highly weathered rock at higher depths.

Table 5 Data interpretation along 2D ERI line 5 combining with borehole logs

Materials	Depth from surface (m)	Resistivity (Ω.m)
Topsoil, Clayey gravelly sand (SC)	0 - 2	100 – 500
Sandy clay (CL)	2 - 6	50 -100
Silty clay (CH)	6 - 8	20 – 50
Silty clay (CL)	8 - 24	10 – 20
Silty clay (CL) to highly weathered bedrock	24 - 46	20 - 500

Table 6 K-means clustering with soil resistivity and N_{60}-value inputs along 2D ERI line 5

Line 5 Cluster No.	Centroid values		Relative soil stiffness*	Soil type**
	Resistivity, *x* (Ω.m)	N_{60} -value, *y* (blow counts/ ft)		
1	27.51	25	Soft-very stiff clay	CH
2	75.06	14	Medium-stiff clay	CL
3	114.55	8	Medium clay	CL

*Note: *Relative soil stiffness is referred to N_{60}-value, **USCS.*

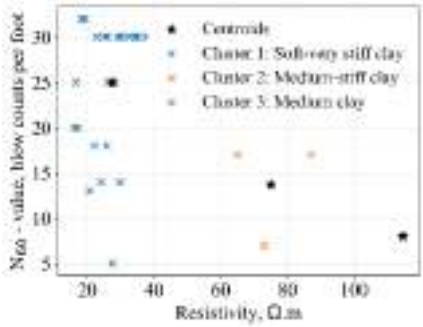

Fig. 3 K-means clustering with resistivity and N_{60}-value inputs along 2D ERI line 5

Relationship between soil resistivity and N_{60}-value could be derived with pairs of centroids plotting, then deriving the power equation Eq. (6) with R^2=0.9774, indicating that N_{60}-value decreases as resistivity increases as shown in Fig. 4.

$$N_{60} = 323.58\rho_a{}^{-0.762} \quad (6)$$

Where N_{60} represents N_{60}-value; and ρ_a is soil resistivity (Ω.m).

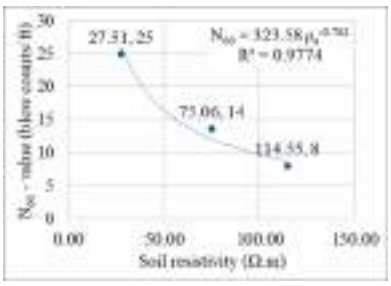

Fig. 4 Correlation between soil resistivity and N_{60}-value

To predict N_{60}-value in the area without SPT N-value data, therefore, 2D ERI lines 1 and 2 were selected. Then soil resistivity values along the two lines were extracted and clustered with KMCA. The result shows that along 2D ERI line 1, geomaterials could be classified into three groups, including loose sand, soft-medium clay, and medium-hard clay as depicted in Fig. 5.

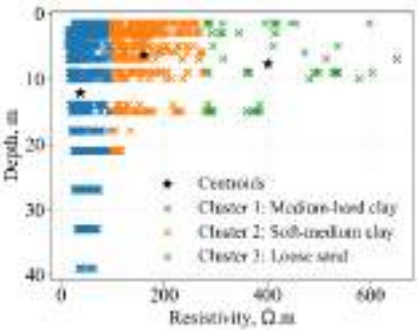

Fig. 5 Clustering results along 2D ERI line 1

While 2D ERI line 2, geomaterials could be classified into four groups, composing loose sand, loose-medium dense sand, soft-medium clay, and medium-hard clay (Fig. 6). The geomaterial categorization along 2D ERI lines 1 and 2 reveals consistent results.

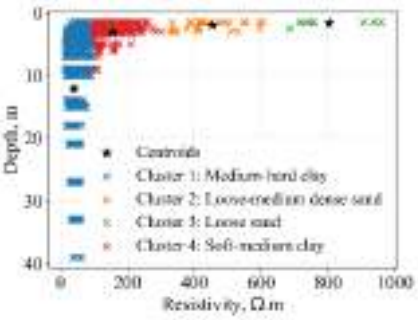

Fig. 6 Clustering results along 2D ERI line 2

After categorizing geomaterials based on soil resistivity at various depths, resistivity values from lines 1 and 2 were applied in Eq. (6) to estimate the N_{60}-value. The estimated N_{60}-value were then compared with the actual N_{60}-value from BH6 and BH7 for validation. As shown in Figs. 7, the trends of actual and estimated N_{60}-value are similar. However, some discrepancies exist in BH6 with R^2= 0.8396, MAE = 4.86, RMSE = 6.21 that could be interpreted as the estimated N_{60}-value will shift from the actual average by 5-7 blow counts/ft. In Fig. 8 shows that BH7 with R^2= 0.9283, MAE = 6.38, RMSE = 7.39 this means the estimated N_{60}-value will shift from the actual value averaged by 6-8 blow counts/ft. The limitation is soil resistivity varies that are influenced by factors such as water content, fine-grained components, and grain size distribution that result in discrepancies of estimated N_{60}-value derived from

Ep. (6) (Table 2). At shallow depths (loose sand to medium clay), both actual and estimated N_{60}-value are closely aligned, registering low values below 10 blow counts/ft. However, at greater depths, as the geomaterials transition to medium-hard clay, a significant gap between the actual and estimated N_{60}-value emerges.

At greater depths, overburden pressure increases soil density, enhancing shear strength and raising the N_{60}-value. Soil resistivity, influenced by factors such as water content, fine-grained content, and grain size distribution, contributes to discrepancies between the red and blue lines at deeper depths. Elevated fine-grained content and moisture lead to lower resistivity, causing the estimated N_{60}-value, derived from Eq. (6), to be lower than the actual value.

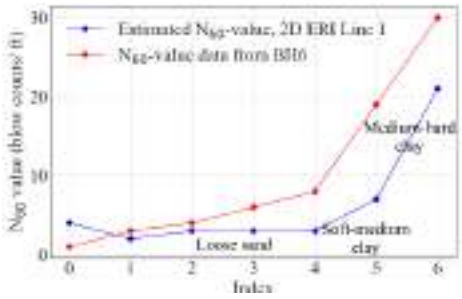

Fig. 7 Comparation between actual and estimated N_{60}-value along 2D ERI line 1, yielding R^2 = 0.8396, MAE = 4.86, and RMSE = 6.21

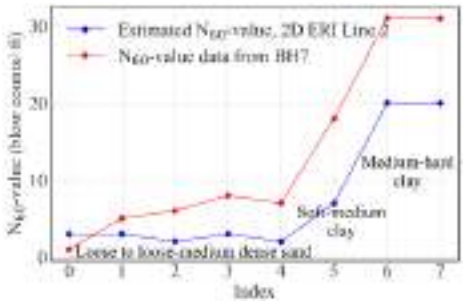

Fig. 8 Comparation between actual and estimated N_{60}-value along 2D ERI line 2, yielding R^2 = 0.9283, MAE = 6.38, and RMSE = 7.39

CONCLUSIONS

This study categorizes the underlying geomaterials in the area into three primary soil types: loose sand, medium-stiff clay, and stiff-hard clay, based on the integration of 2D ERI and borehole data with KMCA. The association between soil resistivity and the N_{60}-value is expressed as a power equation with R^2 = 0.9774 illustrating negative relationship between soil resistivity and N_{60}-value of soil.

Additionally, the N_{60}-value could be inferred in regions devoid of SPT data by utilizing soil resistivity for estimation. The estimated N_{60}-value aligns with the actual N_{60}-value derived from borehole data, evidenced by a high R^2 and moderate loss functions as the following values. BH6 yields R^2= 0.8396, MAE = 4.86, and RMSE = 6.21. While BH7 yields R^2= 0.9283, MAE = 6.38, and RMSE = 7.39.

Consequently, 2D ERI facilitated by KMCA encompasses extensive regions with necessary drilled boreholes, potentially reducing costs and time as being conducted in the real-world project at Highway no.1088 in Chiang Mai, Thailand.

Moreover, the framework derived from this study could be applied as an achievable guideline for geotechnical site investigations in different regions to gather data and enhance understanding of subsurface properties.

REFERENCES

[1] P. Ciampi, L. M. Giannini, G. Cassiani, C.Esposito, and M. P. Papini, Geo-constrained clustering of resistivity datarevealing the heterogeneous lithological architectures and the distinctivegeoelectrical signature of shallow deposits. Eng. Geol., vol. 337, 2015, p.107589.

[2] A. S. Akingboye, A. A. Bery, M. B. Aminu, M. D.Dick, G. A. Bala, and T. O. Ale, Surface–subsurface characterization viainterfaced geophysical–geotechnical and optimized regression modeling. Model.Earth Syst. Environ., vol. 10, no. 4, 2024, pp. 5121–5143.

[3] M. D. Dick, A. A. Bery, A. S. Akingboye, K. R.Ekanem, E. Moses, and S. Purohit, Subsurface Lithological Characterization ViaMachine Learning-assisted Electrical Resistivity and SPT-N Modeling: A CaseStudy from Sabah, Malaysia. Earth Syst. Environ., 2024

[4] J. J. Tan and H. Ramli, EFFECT OF STANDARDPENETRATION TEST CORRECTIONS ON THE ESTIMATION OF UNDRAINED SHEAR STRENGTH. J.Civ. Eng. Manag., vol. 29, no. 6, 2023, pp. 501–515.

[5] M. Loke, Tutorial :2-D and 3-D Electrical Imaging Surveys. Available for Download fromwww.geotomosoft.com, Revision 2020, pp. 1-221.

[6] J. Macqueen, Some methods for classification andanalysis of multivariate observations. Proc. Fifth Berkeley Symp. Math. Stat.Probab., vol. 1, 1967, pp. 281–297.

[7] S. Firdaus and A.Uddin, A Survey on Clustering Algorithms and Complexity Analysis. Int. J.Comput. Sci. Issues, vol. 12, no. 2, 2015, pp. 62–85.

Copyright © Int. J. of GEOMATE All rights reserved, including making copies, unless permission is obtained from the copyright proprietors.

15th Int. Conf. on Geotechnique, Construction Materials & Environment,
Kyoto, Japan, 11-13 November 2025, ISBN 978-4-909106124 C3051

EVALUATION OF CHEMICAL GROUTING IN HETEROGENEOUS SOILS BY INTEGRATING FEM ANALYSIS AND AI MODELS

Khin Nyein Chan Kyaw [1], Toshiyuki Motohashi [2], Shigeo Sasahara [3] and Shinya Inazumi [4]

[1]Graduate School of Engineering and Science, Shibaura Institute of Technology, Japan
[2]Osaka Bousui Construction Co. Ltd., Japan
[3]Fuji Chemical Co. Ltd., Japan
[4]College of Engineering, Shibaura Institute of Technology, Japan

ABSTRACT

This study proposes an integrated framework combining Finite Element Method (FEM)-based permeation analysis and Artificial Intelligence (AI) models to assess chemical grout behavior in heterogeneous sandy soils with low-permeability zones. FEM analysis was performed to investigate grout flow patterns and permeation risks in such soils, revealing that proximity to low-permeability zones significantly affects grout flow velocity and grout distribution. Simplified regression equations were developed to efficiently predict permeation risks. AI models, including neural networks and gradient boosting trees, were trained on FEM datasets and accurately predicted permeation velocities and ranges with high accuracy (R^2 = 0.849). Even with 5.5% low-permeability content, average fill rates reached 94.5% (FEM) and 96% (AI), with worst cases at 81% and 83%, respectively. The results demonstrate that the effectiveness of integrating FEM, regression models, and AI-based modeling to optimize chemical grouting strategies and mitigate permeation risks due to soil heterogeneity. The proposed framework offers an effective approach to improve chemical grouting practices in heterogeneous soil conditions.

Keywords: Chemical grouting, Low permeability zone, Permeation analysis, FEM, AI prediction model

INTRODUCTION

Liquefaction poses a major threat to infrastructure in Japan, as demonstrated by the 2011 Great East Japan Earthquake, highlighting the critical importance of soil improvement techniques to mitigate liquefaction risks [1]. Among various soil improvement techniques, chemical grouting is widely recognized for mitigating liquefaction risks by replacing pore water and solidifying the ground through injection [2]. While homogeneous sandy soils permit uniform grout permeation, the presence of low-permeability zones can disrupt flow paths, leading to uneven treatment and diminished performance [3].

This study aims to understand how soil heterogeneity influences chemical grout permeation and to accurately predict permeation risk and range by integrating FEM-based analysis with AI-based predictive models. To achieve this, an innovative framework is proposed that uses random soil models with low-permeability zones, simplified regression equations for risk prediction, and an integrated approach combining FEM-based permeation analysis with AI-based predictive models for rapid and practical assessment of grout permeation behavior in real-world projects. FEM captures detailed flow behavior in various soil types [4], while AI enhances prediction even when input variables are uncertain or missing [5]. Therefore, this integrated approach combines the precision and reliability of FEM-based permeation analysis with the flexibility and efficiency of AI, improving the predictive accuracy and practical applicability of chemical grouting methods.

RESEARCH SIGNIFICANCE

This study addresses the challenge of predicting chemical grout permeation in heterogeneous soils, where low-permeability zones hinder uniform treatment. By integrating Finite Element Method (FEM) simulations with regression models and AI-based predictive models, the proposed framework offers a novel and practical solution for assessing grout flow behavior in such soil. This research contributes to improving the reliability and efficiency of chemical grouting permeation, especially under complex soil conditions commonly encountered in real-world geotechnical projects.

FEM-BASED PERMEATION ANALYSIS FOR RISK ASSESSMENT

This study presents the assessment of permeation risk using 2D FEM simulations of chemical grouting in heterogeneous soils containing low-permeability zones. Risk, which means inadequate grout flow, was calculated based on permeation velocity and proximity to these zones. The high-risk cases (≥10%) were used as inputs for multiple regression analysis. Key inputs included permeation velocity, distance to low permeability zone, its size, and geometry.

Grout permeation behavior was modeled using VGFlow 2D, a FEM-based program solving

Richards' equation for saturated–unsaturated flow derived from Darcy's Law that describes fluid flow through porous media [6]. A 1.5 m × 0.75 m rectangular, fully saturated, isotropic sandy soil domain with 5.5% (550 cm^2) low-permeability zone was used. All boundaries were modeled as leaky, with a central injection point and a grouting rate of 16 L/min. The low-permeability zone, comprising 100 cells, was positioned as shown in Fig. 1. It used vertical and horizontal permeability coefficients of 5.200×10^{-5} cm/sec and 2.080×10^{-4} cm/sec for sand layer, and 4.525×10^{-7} cm/sec and 1.810×10^{-6} cm/sec for the low-permeability soil zone, respectively.

Three configurations of low-permeability zone were analyzed, each zone sized 0.025 m × 0.025 m. Case 1 (Fig. 2) included one zone; Case 2 (Fig. 3), two horizontally aligned zones; and Case 3 (Fig. 4),

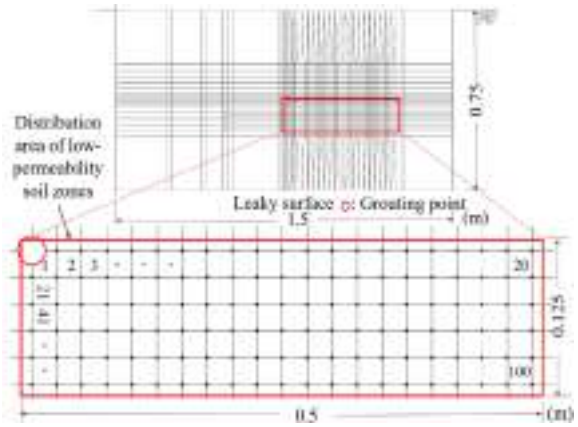

Fig.1 Configuration of the FEM analytical section

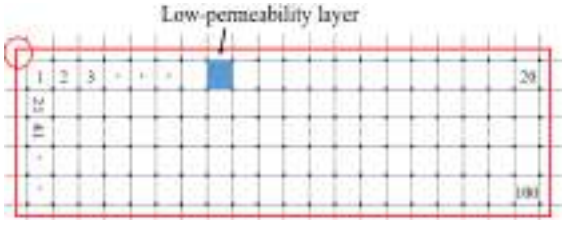

Fig.2 Case 1: Single low-permeability soil zone configuration

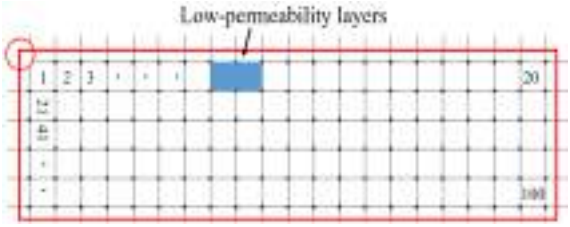

Fig.3 Case 2: Two horizontally aligned low-permeability soil zones

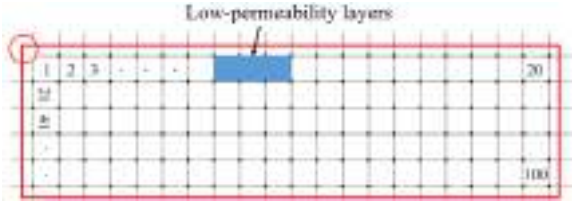

Fig.4 Case 3: Three horizontally aligned low-permeability soil zones

three horizontal zones. The model mesh was subdivided into rectangular sections, each split into four cells, serving as an evaluation rectangular section and then yielding 400 data points per analysis. Permeation velocities were calculated using Eq. (1). The velocity of permeation flow in homogeneous soil without low-permeability soil zone is v_{1i} (m/s), and the velocity of permeation flow in soil with low-permeability soil zone is v_{2i} (m/s). Then, permeation risk in this study were calculated using Eq. (2).

$$\boldsymbol{v}_{\mathrm{i}} = \sqrt{\boldsymbol{v}_{\mathrm{xi}}{}^{2} + \boldsymbol{v}_{\mathrm{yi}}{}^{2}} \tag{1}$$

$$R_{1\mathrm{i}} = 1 - \frac{v_{2\mathrm{i}}}{v_{1\mathrm{i}}} \tag{2}$$

STATISTICAL MODEL FOR PERMEATION RISK PREDICTION

In this study, the predicted risk is calculated by multiple regression analysis as shown in Eq. (3).

$$R_{2\mathrm{i}} = \beta_1 x_{1\mathrm{i}} + \beta_2 x_{2\mathrm{i}} + \beta_3 x_{3\mathrm{i}} + \beta_4 x_{4\mathrm{i}} + \beta_5 x_{5\mathrm{i}} + u_{\mathrm{i}} \tag{3}$$

Where, $x_{1\mathrm{i}}$ is horizontal distance of low-permeability soil zone from grouting point, $x_{2\mathrm{i}}$ is vertical distance from grouting point to the zone, $x_{3\mathrm{i}}$ is horizontal distance from the zone to evaluation section, $x_{4\mathrm{i}}$ is vertical distance from the zone to evaluation section, $x_{5\mathrm{i}}$ is horizontal length of the zone, and u_{i} is the error term. For regression analysis, only data from the right side of the zone were used, assuming sufficient grout permeation on the left. These data were further categorized vertically into upper, middle, and lower sections, and later grouped by horizontal distance: within 0.05 m and beyond 0.05 m, yielding 6 total cases (Fig. 5). Only evaluation sections with risk >10% (from Eq. 2) were included in the regression; risks <10% were treated as zero, indicating minimal influence.

In this study, each node was assigned coordinates, such as grouting point (x_{i}, y_{i}), lower left corner of the low-permeability zone (x_{pl}, y_{pl}), upper right corner (x_{pr}, y_{pr}) and the coordinates of the evaluation section (X,Y). The required distances are calculated by Eqs. (4) to (8).

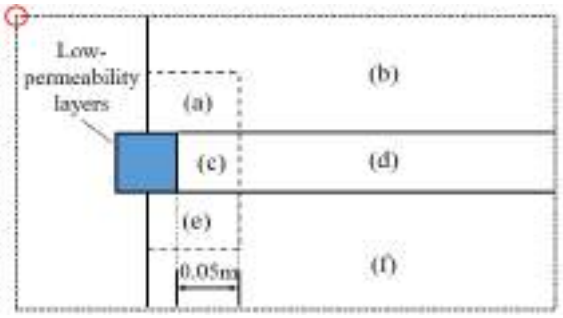

Fig.5 Classification of evaluation sections based on distance from low-permeability soil zones.

$$x_1 = x_{pl} - x_i \tag{4}$$

$$x_2 = \frac{y_{pl}+y_{pr}}{2} - y_i \tag{5}$$

$$x_3 = \begin{cases} X - x_{pr} & (X > x_{pr}) \\ 0 & (x_{pl} < X < x_{pr}) \\ X - x_{pl} & (x_{pl} > X) \end{cases} \tag{6}$$

$$x_4 = \begin{cases} Y - y_{pr} & (Y > y_{pr}) \\ 0 & (y_{pl} < Y < y_{pr}) \\ Y - y_{pl} & (y_{pl} > Y) \end{cases} \tag{7}$$

$$x_5 = x_{pr} - x_{pl} \tag{8}$$

EVALUATION OF PERMEATION RANGE USING FEM-BASED ANALYSIS

This section describes the FEM-based permeation analysis used to develop and validate AI models that evaluate permeation behavior in heterogeneous soil. In this study, FEM analysis captures complex permeation behavior under both homogeneous and heterogeneous conditions. A model spans 120 cm × 120 cm, centering a 100 cm × 100 cm improvement area to account for grout-induced distortions. Due to computational constraints, low-permeability zones were confined to a 70 cm × 70 cm region (Fig. 6).

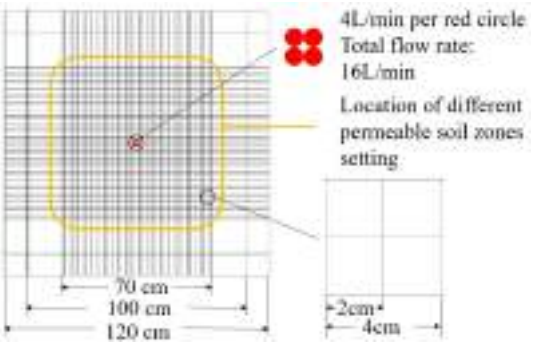

Fig.6 Model geometry and finite element mesh

Grouting points were positioned at central nodes with an injection rate of 16 L/min (4 L/min per node), reflecting the double-pipe strainer method. Leaching boundaries were applied to the model edges. Each element was treated as an evaluation section, generating 3,721 data points per analysis. A total of 88 simulations were conducted to assess the influence of low-permeability zones on permeation behavior. The range of chemical grout permeation is calculated using a geometric formula shown in Eq. (9). Permeation efficiency was evaluated by comparing these permeation areas with a reference permeation area.

$$S = \frac{1}{2}\sum_{l=1}^{n}(x_l - x_{l+1})(y_l + y_{l+1}) \tag{9}$$

AI-BASED PREDICTIVE MODELING FOR PERMEATION BEHAVIOR

Artificial Intelligence (AI) offers powerful capabilities for modeling complex processes and analyzing large, incomplete, or nonlinear datasets [5]. In this study, AI was integrated with FEM-based permeation analysis to predict permeation flow and range in sandy soils with low-permeability zones. The FEM analysis provided element-specific permeation velocities, which served as input for two AI models: a neural network and a gradient boosting decision tree (GBDT). Input features comprised element coordinates, distances from the grouting point, and permeability coefficients.

To assess the effect of input feature, models X-11 and Y-11 used all 11 input features, while X-9 and Y-9 excluded x- and y-coordinates. Adjustments to permeation velocity values (scaled by 1.2 and 1.5) generated refined variants such as X-11-1.2, X-11-1.5, Y-9-1.2, and Y-9-1.5 to correct overestimation. Model performance was evaluated using the coefficient of determination (R^2) and five additional performance metrics which are mean distance (D_m), standard deviation distance (D_{SD}), hausdorff distance (D_H), total distance (D_R) and least squares distance (D_{SLS}). A final performance was calculated by combining these metrics with appropriate weights, as shown in Eq. (10).

$$\text{Score} = D_m + 2D_{SD} + 2D_H + 0.5D_R + D_{SLS} \tag{10}$$

RESULTS AND DISCUSSION

Permeation Behavior Analysis and Risk Mapping

The permeation analysis results flow direction and velocity for each mesh element, enabling visualization through a heat map. Fig.11 illustrates the Case 3 heat map, highlighting how the low-

permeability zones influence flow velocity.

From Fig. 7, flow velocity is most affected at the center of the low-permeability soil zone, with noticeable changes along the line connecting it to the grouting point. However, the figure alone does not quantify this impact. Therefore, multiple regression analysis was conducted to assess this effect quantitatively. Eq. (11) to (16) present the regression results, with coefficient frequencies shown in Table 1, highlighted in red for high risk and blue for low risk. Fig. 8 displays uniform grout distribution in homogeneous soil while Fig. 9 shows flow disruption and uneven permeation caused by low-permeability zones.

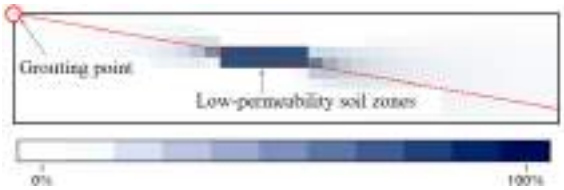

Fig.7 Heatmap visualization of permeation risk based on flow velocity distribution

case (a), $$R_{2i} = -0.09x_{1i} + 0.09x_{2i} + 0.61x_{3i} - 5.48x_{4i} + 0.3x_{5i} - 0.12 \quad (11)$$

case (b), $$R_{2i} = -0.01x_{1i} + 0.44x_{2i} - 11.5x_{3i} + 1.25x_{5i} + 0.55 \quad (12)$$

case (c), $$R_{2i} = -0.64x_{1i} - 0.64x_{2i} - 4.79x_{3i} - 8.92x_{4i} + 2.46x_{5i} + 0.36 \quad (13)$$

case (d), $$R_{2i} = -0.35x_{1i} - 0.03x_{2i} + 0.03x_{3i} - 8.92x_{4i} + 2.46x_{5i} + 0.36 \quad (14)$$

case (e), $$R_{2i} = -0.19x_{1i} + 0.30x_{2i} - 1.12x_{3i} + 0.04x_{5i} + 0.26 \quad (15)$$

case (f), $$R_{2i} = -0.42x_{1i} + 0.60x_{2i} - 0.66x_{3i} - 1.52x_{4i} + 0.66x_{5i} + 0.27 \quad (16)$$

Table 1 Frequency distribution of coefficients in multiple regression analysis equations

	x_{1i}	x_{2i}	x_{3i}	x_{4i}	x_{5i}
(a)	1.4%	1.4%	9.3%	83.4%	4.6%
(b)	0.1%	3.3%	87.1%	0.0%	9.5%
(c)	3.7%	3.7%	27.4%	51.1%	14.1%
(d)	3.0%	0.3%	0.3%	75.7%	20.9%
(e)	11.5%	18.2%	67.9%	0.0%	2.4%
(f)	10.9%	15.5%	17.1%	39.4%	17.1%

Note: High and low influence of regression coefficients are indicated by red and blue colors, respectively.

In case (a), the vertical distance to the evaluation section is the dominant factor, accounting for 83.4% of the influence. Similarly, in the case (d), vertical distance remains critical, though the horizontal length of the zone also plays a notable role (20.9%). According to both cases, the risk decreases as the evaluation rectangular section moves away from the low-permeability soil zone in the vertical direction. In cases (d) and (f), increasing the horizontal length of the zone significantly hinders grout permeation, due to reduced initial inflow caused by pressure differences.

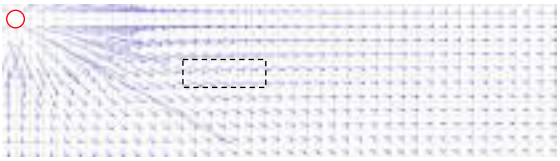

Fig.8 Vector map illustrating grout permeation behavior in homogeneous soil conditions

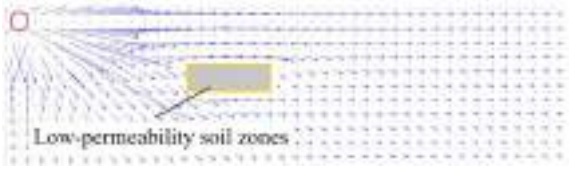

Fig.9 Vector map showing disrupted grout flow due to the presence of low-permeability soil zones

In case (e), horizontal distance contributes to risk reduction, unlike in case (b). The coefficient for vertical distance from the grouting point to the low-permeability zone is consistently negative, indicating that greater separation lowers risk. In cases (c) and (f), other parameters, especially the distances from the grouting point and the size of the low-permeability zone, show stronger influence. As the zone grows larger, it more effectively blocks grout penetration, increasing risk. Overall, the risk predictions maintained an error margin within approximately 10%, indicating reliable model performance.

Performance Comparison of FEM and AI-Based Models

To evaluate the effectiveness of AI-based predictive models, a total of 300 cases were generated. Permeation velocities were predicted using trained AI-based models and compared with FEM-based results. As shown in Table 2, models X-11-1 and Y-9-1.5 are closest to the reference. Model X-11-1 performed best, requiring no correction to the target variable. As shown in Fig.10, AI model predicted a wider permeation range than the FEM-based analysis. Table 3 summarizes the model scores, and Table 4

along with Fig.11 shows the filling rate distribution. Although the AI model slightly overestimated results, the difference was small. Model reliability was validated through FEM comparisons and previous studies, showing high accuracy (R^2 = 0.849). The average fill rate difference is less than 2% (AI: 96%, FEM: 94.5%), with the worst-case values of 83% (AI) and 81% (FEM), confirming the model's effectiveness even in heterogeneous soils.

Table 2 Coefficient of determination (R^2) values for different AI models.

Model	Coefficient of determination
X-11-1	0.849
X-11-1.2	0.828
X-11-1.5	0.819
X-9-1	0.810
X-9-1.2	0.803
X-9-1.5	0.805
Y-11-1	0.836
Y-11-1.2	0.818
Y-11-1.5	0.789
Y-9-1	0.834
Y-9-1.2	0.821
Y-9-1.5	0.814

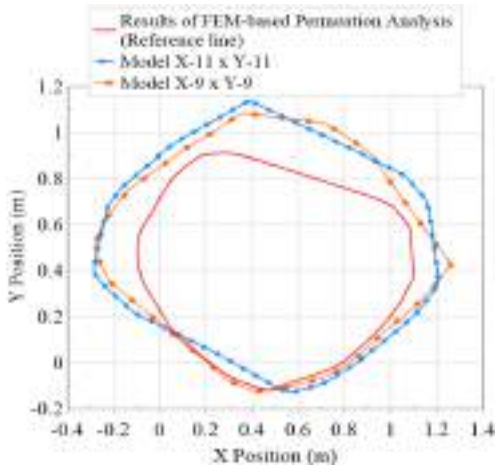

Fig.10 Comparison of permeation ranges predicted by the AI model and FEM-based analysis.

Table 3 Performance evaluation of the most accurate AI-based model

Name	Average result of 88 cases
D_m	0.06
D_{SD}	0.05
D_H	0.31
D_R	1.55
D_{SLS}	0.15
Score	2.58

Even with the same percentage (5.5%) of low-permeability soil, variations in shape and properties caused large fill rate differences. This underlines the need to understand permeation risks in heterogeneous soil. Unlike FEM, which takes 30–40 minutes per case, AI models provide similar accuracy in under 2 seconds, making them practical tools for quick assessment and design support.

Table 4 Distribution of predicted permeation fill rates from the AI-based model

Permeation fill rate (%)	Frequency	Probability (%)
81～85	5	1.7
86～90	5	1.7
91～95	78	26.2
96～100	210	70.5

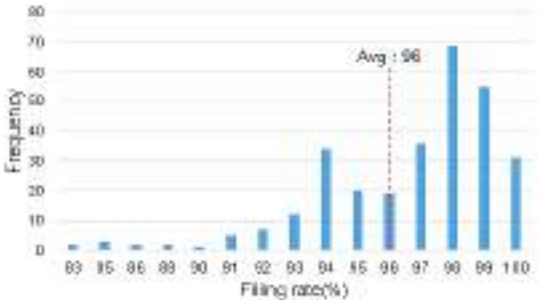

Fig.11 Histogram of fill rates derived from AI-based predictive modeling

Practical Implications for Chemical Grouting Techniques

Fig.12 shows the permeation areas in both homogeneous and heterogeneous soils. In homogeneous conditions, the nearly circular shape

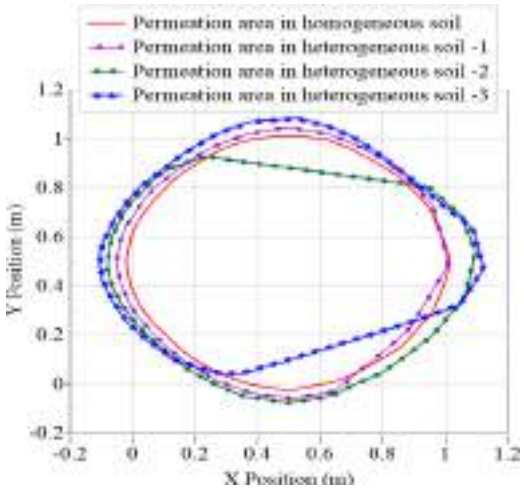

Fig.12 Permeation area comparison between homogeneous and heterogeneous soil conditions

confirms the model accurately reproduces expected permeation behavior under uniform permeability. In heterogeneous soils, however, permeation shapes vary, some remain circular, while others deviate significantly, reflecting the impact of low-permeability zones on flow patterns. Table 5 shows a 54.3% probability of achieving fill rates between 96% and 100%, indicating that design expectations are met in about half the cases. A key concern is the 45.7% probability of "risky events" where fill rates fall between 81% and 95%, indicating that nearly half of the cases may result in sub-optimal fill and pose risks to soil improvement.

Table 5 Distribution of permeation fill rates obtained from FEM-based permeation analysis.

Permeation fill rate (%)	Frequency	Probability (%)
81～85	4	4.3
86～90	12	12.8
91～95	27	28.7
96～100	51	54.3

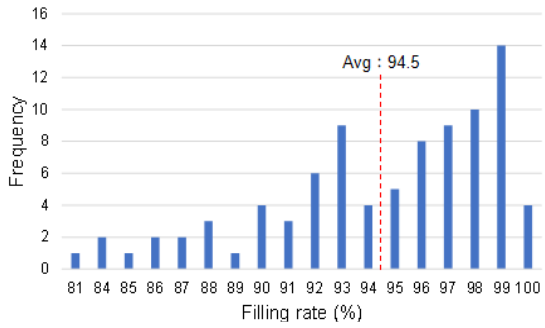

Fig.13 Histogram of fill rates obtained from FEM-based permeation analysis.

CONCLUSIONS

The study developed an integrated approach combining FEM-based permeation analysis and AI-based predictive modeling to evaluate chemical grout permeation behavior in heterogeneous soil. The FEM-based analysis clarified the impact of low-permeability zones on grout flow, while AI-based predictive models provided predictive capabilities for permeation range. A statistical regression model was also introduced to effectively estimate permeation risk. The key findings of this study are as follows:

(1) The FEM analysis revealed that the location of low-permeability zones is the most influential factor in permeation risk, as it disrupts flow velocities and patterns, narrows permeation ranges, and increases permeation risk.

(2) Simplified regression models accurately estimated permeation risk using simple inputs such as soil geometry and proximity to low-permeability zones, reducing the need for computationally intensive FEM simulations.

(3) FEM-based permeation analysis and AI-based predictive models showed consistent results, with a strong R^2 value of 0.849 and prediction fill rates closely matching within 2%, even in soil with 5.5% low-permeability material. However, the AI models showed a tendency to overestimate in some cases, highlighting the need for further refinement.

Future work should include experimental field validation to enhance model reliability. Expanding the diversity of training data and conducting sensitivity analyses can reduce overestimation. Moreover, extending the FEM model to simulate unsaturated soil conditions would significantly enhance the applicability of the framework. Finally, integrating grout rheology, injection parameters, and soil properties into the simulations will provide a more realistic modeling approach.

REFERENCES

[1] Yasuda S., Harada K., Ishikawa K., and Kanemaru Y., Characteristics of liquefaction in Tokyo Bay area by the 2011 Great East Japan Earthquake, Soil Dynamics and Earthquake Engineering, Vol. 47, 2013, pp. 72-82.

[2] Bao X., Jin Z., Cui H., Chen X., and Xie X., Soil liquefaction mitigation in geotechnical engineering: An overview of recently developed methods, Soil Dynamics and Earthquake Engineering, Vol. 120, 2019, pp. 273-291.

[3] Shishido K., Hashida H., Inazumi S., and Soralump S., Penetration behavior of chemical grouting considering soil uncertainty, International Journal of GEOMATE, Vol. 14, Issue 45, 2018, pp. 22-27.

[4] Sazzad M.M., and Islam M.M., A comprehensive study of different types of permeation control measures for earth dam using FEM, Journal of Civil and Construction Engineering, Vol. 5, Issue 1, 2019, pp. 24-37.

[5] Baghbani A., Choudhury T., Costa S., and Reiner J., Application of artificial intelligence in geotechnical engineering: A state-of-the-art review, Earth-Science Reviews, Vol. 228, 2022, Art. no. 103991.

[6] Holtz R.D., Kovacs W.D., and Sheahan T.C., Chapter 7: Fluid flow in soils and rock, In Introduction to Geotechnical Engineering, 2nd ed., Pearson Education, 2011, pp. 282-344.

Copyright © Int. J. of GEOMATE All rights reserved, including making copies, unless permission is obtained from the copyright proprietors.

15th Int. Conf. on Geotechnique, Construction Materials & Environment, Kyoto, Japan, 11-13 November 2025, ISBN 978-4-909106124 C3051

MOVING PARTICLE SIMULATION VALIDATION AND APPLICATION TO CONCRETE FLOW IN CAST-IN-PLACE PILES

Ayumi Morota [1] and Shinya Inazumi [1]

[1] Shibaura Institute of Technology, Japan

ABSTRACT

This study presents a unified framework for evaluating concrete flow behavior in cast-in-place pile construction using the Moving Particle Semi-implicit (MPS) method integrated with Computer-Aided Engineering (CAE) tools. Two core investigations form the basis of this research: a laboratory-based validation of slump behavior through both physical testing and MPS-CAE simulation, and a field-scale simulation of fresh concrete placement in reinforced pile shafts. In the first phase, rheological parameters were determined from B-type viscometer and slump tests, and a bi-viscosity model was used to simulate the viscoplastic behavior of Bingham-type fresh concrete. Simulation results exhibited high fidelity with experimental measurements in terms of slump value, spread, and flow termination. In the second phase, full-scale simulations visualized flow behavior during tremie placement, particularly identifying flow obstructions and segregation zones around rebar cages. Numerical results aligned well with physical element tests, confirming the utility of MPS-CAE as a predictive tool for placement diagnostics. The findings underscore the potential of particle-based modeling for construction planning, quality assurance, and defect mitigation in reinforced concrete applications.

Keywords: MPS-CAE, Bingham fluid, slump simulation, cast-in-place piles, concrete flow

INTRODUCTION

Urban centers in Japan are increasingly situated atop soft or liquefiable soils, making the adoption of reliable foundation techniques essential. Among these, cast-in-place concrete piles are widely employed for their structural adaptability and load-bearing capacity. However, ensuring uniform and complete concrete placement within heavily reinforced shafts presents a persistent engineering challenge. Inadequate filling around reinforcement can lead to structural deficiencies, long-term durability concerns, and costly remediation.

Traditional methods such as full-scale physical testing to evaluate filling performance are laborious and economically restrictive. In contrast, computational techniques—especially those that enable visual and quantitative assessments—offer promising alternatives. Recent advancements in mesh-free numerical methods, particularly the Moving Particle Semi-implicit (MPS) approach, have enabled detailed simulations of complex concrete flow behaviors.

The present study integrates two research components previously reported in Japanese technical literature. The first component involves validating the MPS-CAE approach through slump tests that capture flow dynamics of fresh concrete under standardized conditions. The second component extends the validated model to simulate concrete placement in cast-in-place piles, emphasizing interactions with reinforcement, flow arrest behavior, and the formation of potential defects.

By combining physical testing, rheological modeling, and advanced particle-based simulation, this study aims to contribute to the ongoing development of predictive tools for construction quality management. The outcomes are expected to aid practitioners in optimizing concrete placement techniques and mitigating risks associated with insufficient filling or segregation in reinforced structures.

METHODOLOGY

Theoretical Framework of MPS-CAE

The Moving Particle Semi-implicit (MPS) method is a mesh-free numerical technique suitable for simulating incompressible, free-surface fluid flows [1]. In this approach, the fluid domain is discretized into particles that interact through local kernel functions, enabling direct tracking of deformation, collision, and flow cessation without reliance on fixed computational grids. Each particle carries properties such as velocity, pressure, and density, which evolve according to the incompressible Navier–Stokes equations shown in Eqs. (1) and (2):

$$\frac{\overrightarrow{Du}}{Dt} = -\frac{\nabla P}{\rho} + \nu\nabla^2\vec{u} + \vec{g} \quad (1)$$

$$\frac{D\rho}{Dt} = 0 \quad (2)$$

where u is velocity, ρ is density, P is pressure, ν is kinematic viscosity, and g is gravitational acceleration.

To capture the non-Newtonian characteristics of fresh concrete, a bi-viscosity Bingham model was implemented as shown in Fig. 1. In this model, concrete behaves as a highly viscous material below a yield stress τ_y, transitioning to a lower plastic viscosity η above a critical shear strain rate π_c. The flow stops when 90% of particles experience shear strain rates below π_c, mimicking physical flow arrest.

This assumption allows accurate modeling of viscoplastic behavior, especially for evaluating flow through reinforcement-congested geometries.

Determination of Rheological Properties

The rheological parameters were determined by laboratory tests using B-type rotational viscometers and slump tests based on specimens simulating the poor filling conditions observed in the field. The concrete used had the physical properties shown in Table 1.

Coarse aggregate volume fraction was 35.8%, and solid fraction was 59.6%. The shape coefficient of the aggregate was assumed as 2.4. Using empirical relations derived from previous studies [8], these properties were integrated into the MPS model.

Slump Test and Simulation Setup

To validate the numerical approach, a standard slump test was conducted per JIS A-1101 using a truncated cone mold (height 300 mm, bottom diameter 200 mm, top diameter 100 mm) as shown in Fig. 2. Fresh concrete was poured into the mold and the cone was lifted to initiate free deformation. The slump height, spread diameter, and cessation time were recorded and used as benchmarks for simulation.

The corresponding MPS-CAE model replicated these boundary conditions using a particle spacing of 7.5 mm and a total of 13,182 particles. Flow behavior was observed until flow termination was achieved based on the 90% shear rate criterion. Simulated results were then compared with experimental data for slump height, spread, and time to cessation.

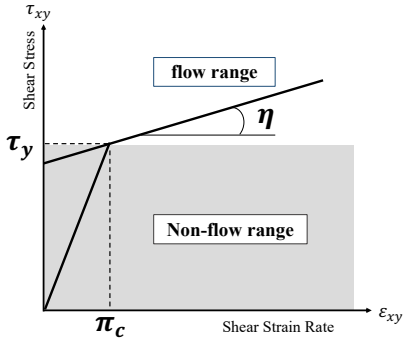

Fig. 1 Bi-viscosity model for simulating Bingham-type fresh concrete behavior

Table 1 Physical properties of fresh concrete used in simulation

Density (kg/m^3)	Yield Stress (N/m^2)	Plastic Viscosity (Pa·s)	Critical Shear Strain Rate (1/s)
2310	1087	19.6	3.84

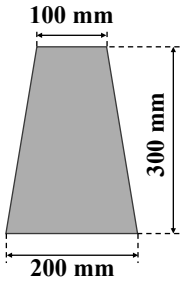

Fig. 2 Slump cone apparatus used for validation tests (JIS A-1101 standard)

VALIDATION OF SLUMP BEHAVIOR

Experimental Observations

The physical slump test produced a final slump height of 19.5 cm and a spread diameter of 29.7 cm. Flow ceased approximately 1.7 seconds after the slump cone was lifted. The flow profile exhibited a smooth radial spread without aggregate segregation, confirming that the tested mix behaved as a homogeneous Bingham fluid. These results served as the reference baseline for evaluating simulation fidelity.

Simulation Results

The MPS-CAE simulation replicated the test under identical rheological and geometric conditions. As shown in Figs. 3 and 4, the particle model achieved a slump height of 9.5 cm and a spread diameter of 30.4 cm. Flow was computationally judged to have ceased at 0.43 seconds, as 90% of the particles registered shear strain rates below the critical threshold.

Snapshots of the slump deformation (see Figs. 3 and 4) illustrate the temporal evolution and shape conformity, consistent with previous simulations of slump flow using MPS methods [1,2]. Despite the shorter flow duration compared to the experiment, the final geometry and radial symmetry were consistent. The timing discrepancy is attributed to idealized frictional and drag assumptions in the model, which slightly accelerate settling. However, the dimensional accuracy supports the reliability of the chosen rheological parameters and flow-termination criteria.

Comparative Analysis

As illustrated in Fig. 5, the simulated and experimental slump behaviors exhibit high correlation in spread magnitude, although slight deviations occur in time-dependent dynamics. This is consistent with prior findings [8] regarding measurement limitations in plastic viscosity

Fig. 3 Reproduction of slump test using particle-based simulation (MPS-CAE method)

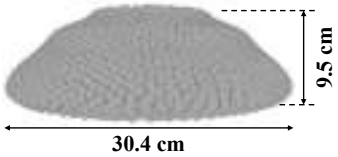

Fig. 4 Flow profile at 043 seconds in MPS-CAE simulation of slump test

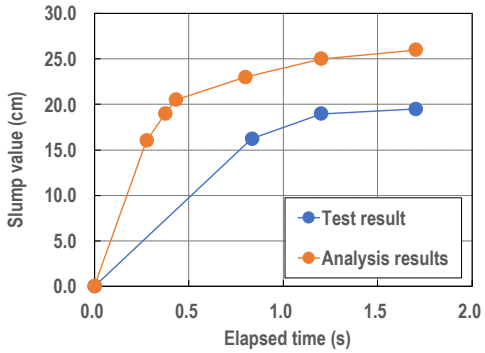

Fig. 5 Comparison between experimental and simulated slump flow behaviors

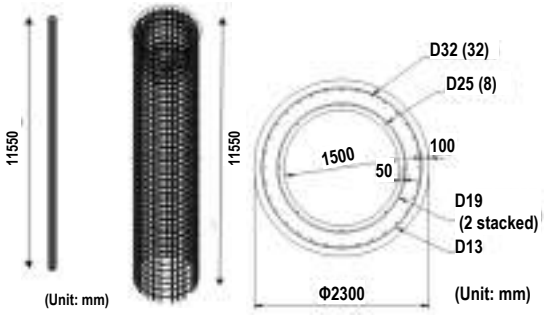

(a) (b)

Fig. 6 3D CAD model of the analysis domain: (a) tremie pipe and reinforcement cage; (b) geometric dimensions

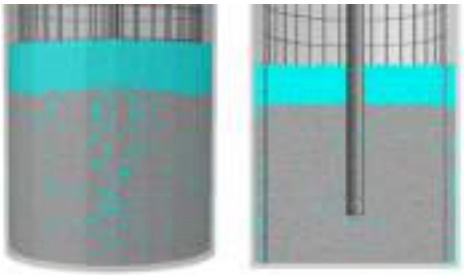

(a) (b)

Fig. 7 Simulation results of concrete flow in the lower segment of the reinforcement cage: (a) lateral view; (b) cross-sectional view

Fig. 8 Simulation results of concrete flow in the upper segment of the reinforcement cage

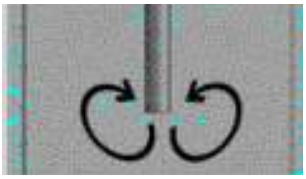

Fig. 9 Flow behavior near the tremie pipe discharge outlet showing turbulence and mixing

determination using rotational viscometers. Nonetheless, the simulation's ability to reproduce deformation geometry and terminal behavior affirms its validity for use in predicting fresh concrete placement performance.

APPLICATION TO CAST-IN-PLACE PILE FOUNDATIONS

Simulation Model Configuration

To extend the MPS-CAE model beyond laboratory conditions, a field-scale simulation was conducted to replicate concrete placement in a cast-in-place pile. The pile shaft was modeled as a vertical cylinder 2300 mm in diameter and 11,500 mm in depth. As illustrated in Fig. 6, the reinforcement cage consisted of a single-layer lower segment and a double-layer upper segment, emulating real-world reinforcement complexity.

Concrete was introduced from the base via a tremie pipe at a velocity of 1.69 m/s. The model adopted particle spacing of 50 mm to balance detail with computational cost [3]. Rheological properties derived from slump tests were used, and additional sensitivity analyses were conducted based on previous studies.

Visualization and Flow Analysis

Simulation results, shown in Figs. 7 and 8, revealed distinct differences in flow behavior between lower and upper regions of the shaft. While concrete filled the lower region uniformly, significant stagnation and incomplete replacement of pore water occurred in the upper segment, especially around the dense rebar network.

As depicted in Fig. 9, turbulence near the tremie discharge induced mixing zones with entrapped water, highlighting potential risks for cold joints and void formation. The observed water retention correlated with flow obstructions caused by reinforcement congestion [4].

Fig. 10 Experimental results showing internal concrete distribution in hardened specimens

Fig. 11 Simulation results of concrete distribution corresponding to experimental observations

Experimental Validation

Comparative element tests were conducted using 3D CAD-modeled formworks and reinforcement cages (see Figs. 10 and 11). Concrete was cast through a tremie at controlled velocities, and the internal distribution was assessed by cutting hardened specimens. The results confirmed the presence of unfilled regions and entrapped water in the upper cage zone [5].

Engineering Implications

These findings demonstrate that MPS-CAE simulation is effective not only for visualizing complex flow patterns but also for proactively identifying risks such as insufficient filling and entrapped fluid. By adjusting boundary conditions or tremie insertion strategies within the model, practitioners can refine placement procedures before field execution. The simulation also provides a valuable communication tool for conveying internal construction behavior to project stakeholders.

CONCLUSIONS

This study developed and validated a computational framework combining the Moving Particle Semi-implicit (MPS) method with Computer-Aided Engineering (CAE) techniques to simulate and assess the flow behavior of fresh concrete in both controlled and field-scale scenarios.

Key conclusions are as follows:

(1) MPS-CAE simulations accurately replicated slump test results, achieving dimensional agreement within 1 cm and capturing radial flow symmetry and final deformation profiles. The bi-viscosity Bingham model and critical shear rate threshold effectively reproduced flow cessation behavior.

(2) The simulation model successfully predicted flow obstructions and segregation zones in large-scale pile placements. Especially in double-reinforced regions, incomplete filling and water entrapment were visualized, aligning with physical test outcomes.

(3) The integrated framework enables predictive evaluation of fresh concrete flow, supporting construction planning and defect mitigation. By simulating different material and operational parameters, engineers can identify high-risk areas and optimize placement strategies.

(4) MPS-CAE offers a practical enhancement to traditional construction workflows, allowing virtual prototyping, real-time visualization, and quality control in complex geometries without full-scale physical mockups.

Future work will focus on extending this simulation framework to include real-time sensor feedback, adaptive meshing for finer resolution around reinforcement, and coupling with multi-physics models to capture thermal and hydration effects during curing. These developments will further increase the relevance of particle-based methods in construction engineering.

REFERENCES

[1] Xu, T., Koshizuka, S., Inaba, Y., & Gakuhari, Y. (2024). An explicit incompressible scheme based on the MPS method to simulate slump flow. Computational Particle Mechanics.

[2] Tamai, T., & Koshizuka, S. (2014). Least squares moving particle semi-implicit method. Computational Particle Mechanics, 1, 277–305.

[3] Kondo, M. (2021). A physically consistent particle method for high-viscous free-surface flows. Computational Particle Mechanics, 8, 69–86.

[4] Inazumi, S., Shigematsu, Y., Nakao, K. & Shishido, K. (2018). 3-D particle flow analysis for fluidization treated soils, American Journal of Civil and Environmental Engineering, 3(3), 59-67.

[5] Morota, A., Nakao, K. & Inazumi, S. (2024). Interaction between stabilizing solution and mortar during installation of cast-in-place concrete piles, Proc. of the 14th Int. Conf. on GEOMATE, 207-212.

Copyright © Int. J. of GEOMATE All rights reserved, including making copies, unless permission is obtained from the copyright proprietors.

15th Int. Conf. on Geotechnique, Construction Materials & Environment,
Kyoto, Japan, 11-13 November 2025, ISBN 978-4-909106124 C3051

COMPARATIVE ANALYSIS OF SOIL RESISTIVITY PREDICTION USING REGRESSION MODELS AND POLYNOMIAL NEURAL NETWORK

Kornkanok Sangprasat [1], Avirut Puttiwongrak [2] and Shinya Inazumi [3]

[1] Graduate School of Engineering and Science, Shibaura Institute of Technology, Japan
[2] School of Engineering and Technology, Asian Institute of Technology, Thailand
[3] College of Engineering, Shibaura Institute of Technology, Japan

ABSTRACT

Soil electrical resistivity is a critical parameter in geotechnical engineering, particularly for assessing subsurface conditions in power substation projects. Understanding how resistivity responds to fundamental soil properties can improve both site evaluation and the design of grounding systems. This study investigates the relationship between resistivity and key geotechnical variables, namely water content, plasticity index, and dry density, using both traditional statistical techniques and a Polynomial Neural Network (PNN) approach. Among the tested variables, water content showed the strongest inverse correlation with resistivity ($r_s = –0.92$), confirming its significant influence on soil conductivity. Plasticity index and dry density had only weak correlations. An exponential regression model captured this nonlinear trend reasonably well ($R^2 = 0.439$), while the PNN, constructed with a single hidden layer and third-degree polynomial terms, achieved comparable performance ($R^2 = 0.433$). The strong inverse correlation between moisture and resistivity observed in this study confirms the critical influence across varied soil types and demonstrates the value of PNNs as an interpretable machine learning tool for modeling nonlinear relationships in geotechnical data.

Keywords: Geotechnical parameters; Soil resistivity; Regression; Polynomial Neural Networks

INTRODUCTION

Soil electrical resistivity plays a key role in geotechnical and environmental engineering, assisting engineers assess subsurface conditions, conducting soil investigations, and designing effective grounding systems. Its ability to indirectly reflect changes in soil composition, water content, and structural integrity makes it a non-destructive and cost-effective tool for field investigations. Previous study has established that geotechnical index properties, particularly water content, plasticity index, and dry density, significantly influence resistivity values [1]. However, due to the inherently nonlinear and multivariate nature of these relationships, traditional regression models often fall short in accurately capturing such complex interactions.

Recent developments in machine learning, especially the use of Polynomial Neural Networks (PNNs), offer a compelling alternative for modeling complex systems. PNNs are designed to model nonlinear systems using higher-order polynomial expressions instead of conventional activation functions, enabling the generation of closed-form equations that enhance model transparency and interpretability. These characteristics make PNNs well-suited for geotechnical applications, where understanding feature interactions is essential.

In this study, we aim to investigate the predictive relationship between soil resistivity and three key geotechnical parameters: water content, plasticity index, and dry density. This study aims to: (1) assess the relationships between soil resistivity and key parameters; (2) develop regression models for both single-variable and multivariable cases; (3) apply and evaluate Polynomial Neural Networks (PNNs) to capture nonlinear interactions; and (4) compare the performance and interpretability of regression and PNN-based approaches. The analysis is based on field-collected soil samples from substations across Thailand. The findings aim to improve the accuracy of resistivity prediction models while providing insights into the relative influence of input variables in geotechnical engineering contexts.

METHODOLOGY

This study set out to examine the relationship between soil geotechnical properties and electrical resistivity through a hands-on experimental approach. The research involved collecting soil samples in the field, conducting detailed laboratory tests, and monitoring changes over time under controlled environmental conditions. As illustrated in Fig. 1, the overall process was divided into six main stages, beginning with field sampling and the laboratory measurement of geotechnical properties and electrical resistivity.

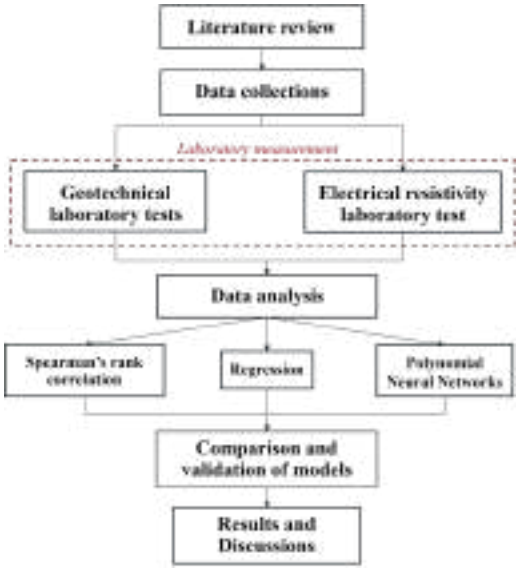

Fig. 1 Workflow diagram of the research methodology.

Data Acquisition

Soil samples were collected from power substations across three different regions of Thailand. These samples were subsequently tested in the laboratory to determine key properties such as moisture content, plasticity index, specific gravity, and compaction behavior. At the same time, electrical resistivity was measured using the Wenner array method, with readings taken at regular intervals to monitor how resistivity responded to changes in moisture content.

In total, 30 samples were collected from shallow backfill layers (approximately 1 meter deep) at the substations. The laboratory tests focused on both geotechnical and electrical properties, including water content, liquid limit, plasticity index, specific gravity, clay content, and compaction characteristics. All tests were conducted in accordance with established ASTM standards.

Electrical resistivity was measured in the laboratory using a one-dimensional, four-electrode Wenner array setup, following ASTM G57 [2] and the method described by Giao [3]. The test employed a cylindrical acrylic mold measuring 6.4 cm in diameter and 12 cm in height. A SYSCAL R2 resistivity meter (IRIS Instruments), powered by a 1.5 V battery, was used to supply current and measure the resulting voltage difference.

In the electrical resistivity laboratory setup, brass discs were positioned at both ends of the soil specimen to serve as current electrodes, while a pair of brass pins, placed 4 cm apart within the sample, acted as potential electrodes. In uniform soil, the electric current spreads evenly in all directions, forming a radial flow pattern.

To ensure consistent results, all soil samples were prepared using the same procedure. Each sample was oven-dried, thoroughly mixed with distilled water, and sealed in a plastic bag for 24 hours to allow the moisture to distribute evenly. The soil was then compacted into the mold to achieve 95% of the maximum dry density and 85% of the optimum moisture content, based on the Standard Proctor Test.

Resistivity readings were taken over a 28-day period at four time points: Days 0, 7, 14, and 28. Before each reading, the samples were weighed, and their moisture content was measured. Throughout the testing period, the laboratory environment was maintained at 25 ± 2 °C with a relative humidity of 50–55% to minimize external influences. These environmental controls were based on previous research indicating that variations in temperature and moisture can significantly affect resistivity values [4].

DATA ANALYSIS

In this study, careful selection of analytical tools allowed us to identify how geotechnical parameters influence soil resistivity. In both scientific and engineering research, selecting the appropriate analytical methods is crucial for helping find trends, understand relationships between variables, and create accurate prediction models. This section introduces three commonly used techniques in quantitative analysis: Spearman's rank correlation, regression analysis, and Polynomial Neural Networks (PNNs), each offering unique strengths for exploring and modeling data in the context of this study.

Spearman's Rank Correlation Coefficient

Spearman's rank correlation coefficient (r_s) is a non-parametric statistical measure used to evaluate the strength and direction of a monotonic relationship between two variables [5].

One of the advantages of Spearman's correlation is that it does not require prior specification of dependent or independent variables, although such designations can still be made when relevant. Instead, it evaluates the degree of agreement between two sets of ranks, reflecting how consistently the values of one variable increase or decrease with those of another. To calculate Spearman's rank correlation coefficient, the following formula is used:

$$r_s = 1 - \frac{6 \sum d_i^2}{n(n^2-1)} \quad (1)$$

where d_i is the rank difference for each pair and n is the number of observations. r_s can be interpreted

as the coefficient ranges from –1 to +1, where values close to +1 indicate a perfect positive correlation, and values near –1 denote a perfect negative correlation. A value of 0 suggests no association between the variables.

Regression

Regression analysis is one of the most commonly applied statistical methods for exploring relationships between variables and determining the extent to which independent variables influence a dependent variable. In its simplest form, linear regression describes the relationship between two variables, typically one predictor and one response, using the following equation:

$$y = \beta_0 + \beta_1 x + \varepsilon \quad (2)$$

In this equation, y is the dependent variable, x is the independent variable, β_0 represents the intercept, β_1 is the slope or regression coefficient, and ε denotes the error term which accounts for variability not explained by the model [6].

Polynomial Neural Network

Polynomial Neural Networks (PNNs) have gained attention as a more interpretable alternative to traditional Artificial Neural Networks (ANNs) for modeling nonlinear systems. Rather than depending on weighted sums and nonlinear activation functions, PNNs incorporate higher-order polynomial expressions within their network layers to approximate complex input–output relationships. This design allows the model to produce closed-form mathematical equations, offering greater transparency and making the model's behavior easier to interpret [7]. One of the most widely used variants of PNNs is the Pi-Sigma Network (PSN). In this architecture, each neuron in the hidden layer calculates the product of several linear combinations of the input features. This structure can be represented mathematically as follows:

$$h_{j,k} = \sum_{i=1}^{I} w_{i,j,k} x_i + b_{j,k}, \;\; u_j = \prod_{k=1}^{K} h_{j,k} \quad (4)$$

where x_i are the input variables, $w_{i,j,k}$ and $b_{j,k}$ denote the weights and biases, respectively, and K is the polynomial degree. The final output of the network is computed through a linear combination of the hidden neuron outputs:

$$y_{PNN} = \sum_{j=1}^{n_H} w_j u_j + b \quad (5)$$

where n_H represents the number of hidden neurons, w_j are the output layer weights, and b is the output bias.

RESULTS AND DISCUSSION

Laboratory test results

The laboratory test results for all collected soil samples revealed key geotechnical characteristics. Based on particle size distribution and Atterberg limits, the samples were primarily classified as either silty clay or clayey silt. Plasticity index (PI) values ranged from 9.8% to 37.2%, with higher plasticity index samples falling above the A-line, indicating clay-type soils, while lower plasticity index values aligned more closely with silt-type classifications [1]. According to the Unified Soil Classification System (USCS), all samples were identified as low-plasticity soils.

Specific gravity measurements ranged from 2.68 to 2.80, while the maximum dry density values were between 1.77 and 1.86 g/cm³. The optimum moisture content varied from 13.2% to 16.4% across all samples. These results reflect a moderate range in physical properties, indicating slight variations in mineral composition and compaction behavior among the tested soils.

The results of the electrical resistivity laboratory tests showed substantial variation in both resistivity and geotechnical properties. Resistivity values ranged from 8.67 to 911.05 Ω·m, with a mean of 148.76 Ω·m and a standard deviation of 189.29 Ω·m, reflecting a strongly right-skewed distribution. Some samples showed unusually high resistivity values, which increased the overall kurtosis and pointed to inconsistent conductivity among the soils. Water content ranged from 0.08% to 16.35%, with an average of 7.24% and a standard deviation of 5.34%.

Soil Resistivity and Water Content

Water content is widely recognized as a key factor influencing soil electrical resistivity. To quantify this relationship, we applied three methods: Spearman's rank correlation, exponential regression, and Polynomial Neural Network (PNN) modeling. As illustrated in Fig. 2 and Table 1, the Spearman's correlation coefficient between water content and resistivity was –0.92, indicating a strong inverse monotonic relationship. This result is consistent with the well-established principle that higher moisture levels increase ionic conductivity, which in turn reduces resistivity. The relationship can be further described using an exponential regression model, expressed as:

$$\rho = 315.50\exp(-0.2037WC) \quad (6)$$

where ρ is the predicted soil resistivity in Ω·m

and WC is water content of the soil.

The exponential model achieved an R^2 of 0.439, with RMSE of 141.00 and MAE of 74.70 (Fig. 3). It successfully captured the nonlinear decrease in resistivity as water content increased and provided a straightforward, easy-to-interpret equation. A more flexible approach using a PNN delivered comparable results, with an R^2 of 0.433, MAE of 86.91 (Fig. 3).

In comparing the three methods, all consistently identified water content as the dominant factor affecting soil resistivity. Spearman's correlation confirmed a strong monotonic relationship, the regression model provided a clear and interpretable mathematical equation, and the PNN demonstrated flexibility and robustness in handling nonlinear patterns. Notably, the similar R^2 values achieved by both the regression and PNN models suggest that exponential regression is a practical and effective method, especially when model simplicity and interpretability are important.

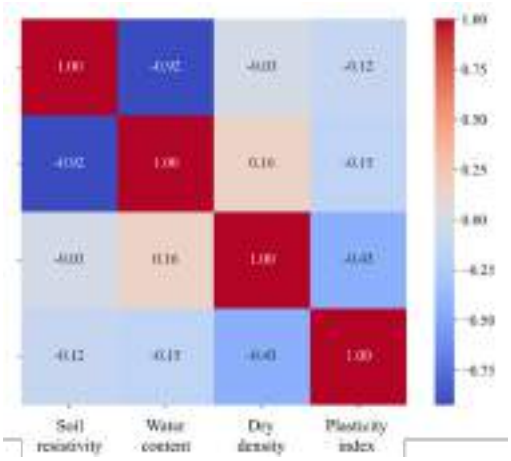

Fig. 2 Heatmap of Spearman's rank correlations among geotechnical variables and soil resistivity.

Soil Resistivity and Plasticity Index

The relationship between plasticity index (PI) and soil resistivity was investigated using Spearman's correlation, simple regression, and a PNN model, as shown in Table 1.

The Spearman's rank correlation coefficient between plasticity index and resistivity was –0.12, indicating a weak negative relationship. This suggests that plasticity index alone has limited influence on resistivity in a monotonic pattern, especially when compared to water content, which exhibited a much stronger correlation.

A simple linear regression was performed using plasticity index as the only input variable, resulting in the following equation:

$$\rho = 189.77 - 1.77PI \quad (7)$$

where ρ is the predicted soil resistivity in Ω·m and PI is plasticity index of the soil.

This model showed very poor predictive performance, with an R^2 of 0.007, an RMSE of 187.60 and an MAE of 138.88. The weak linear trend is consistent with the low correlation observed earlier and confirms that plasticity index alone is not sufficient to explain variations in soil resistivity.

To further investigate possible nonlinear patterns, a PNN model was developed using both the linear and squared terms of plasticity index. However, the model performed poorly, with an average R^2 of –0.099 across five-fold cross-validation. The negative R^2 value indicates that the model did worse than simply predicting the mean of the data.

Overall, all three methods consistently indicate that the plasticity index alone has a weak and unreliable relationship with soil resistivity. While plasticity index is relevant in geotechnical characterization, it is not a dominant predictor of resistivity on its own, though its influence may increase in multivariable models.

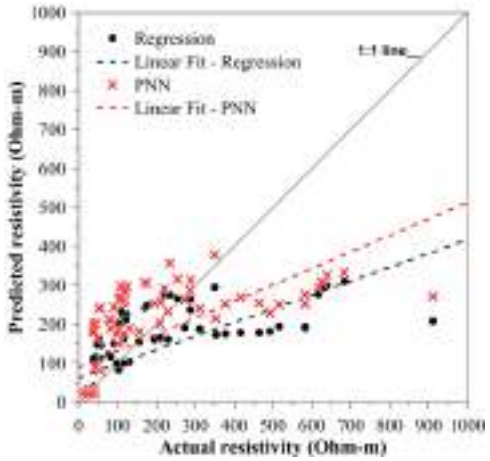

Fig. 3 Comparison of predicted vs. measured soil resistivity with water content is input variable.

Soil Resistivity and Dry Density

The relationship between soil resistivity and dry density was analyzed using Spearman's rank correlation, simple linear regression, and a PNN model, as shown in Table 1.

The Spearman's correlation coefficient between dry density and resistivity was –0.03, indicating a negligible monotonic relationship. This result suggests that variations in dry density alone do not have a consistent effect on soil resistivity.

A simple linear regression using dry density as the only input variable resulted in the following equation:

$$\rho = 460.27 - 190.16\gamma_d \quad (8)$$

where ρ is the predicted soil resistivity in Ω·m

and γ_d is dry density of the soil in g/cm^3.

The model yielded an R^2 of 0.007 and an MAE of 137.99, indicating very poor predictive performance. The near-zero R^2 shows that the model performed worse than simply predicting the average, reinforcing the weak relationship between dry density and resistivity. Overall, these findings suggest that dry density alone does not have a meaningful correlation with soil resistivity, regardless of the modelling method used. However, it may still add value in multivariable models—especially when combined with stronger predictors like water content.

Multiple Variables Analysis Results

Relationship Between Soil Resistivity, Water Content, and Plasticity Index

The combined effects of water content and plasticity index (PI) on soil resistivity were analyzed using both exponential regression and a PNN, as summarized in Table 2. These two approaches provide a comparison between traditional curve-fitting techniques and machine learning-based models for capturing nonlinear relationships.

The exponential regression model produced the following equation:

$$\rho = 578.66\exp[(-0.2082WC) - (0.0247PI)] \quad (9)$$

where ρ is the predicted soil resistivity in Ω·m, WC is water content of the soil and PI is plasticity index of the soil.

This model achieved an R^2 of 0.503, RMSE of 132.75, and MAE of 65.64. The equation reflects that both water content and plasticity index are inversely related to soil resistivity. As illustrated in Fig. 4, the regression residuals do not follow a normal distribution. In particular, the values at the high and low ends stray from the reference line, suggesting the model may have limitations in capturing the full range of variation in the data.

The PNN model, which included both linear and polynomial terms for water content and plasticity index, showed better performance, with an average R^2 of 0.618. As illustrated in Fig. 4, the comparison between the measured soil resistivity and the values predicted by the PNN model aligned more closely with the diagonal line, indicating that the residuals were more normally distributed and the model was better calibrated. Feature importance analysis confirmed that water content remained the most influential factor, while plasticity index played a secondary role—mainly through higher-order and interaction terms.

These results demonstrate that while regression offers a simple and interpretable model, PNN captures more complex patterns and produces residuals that better satisfy model assumptions. Thus, PNN is more suitable when modeling resistivity from multiple interacting soil parameters.

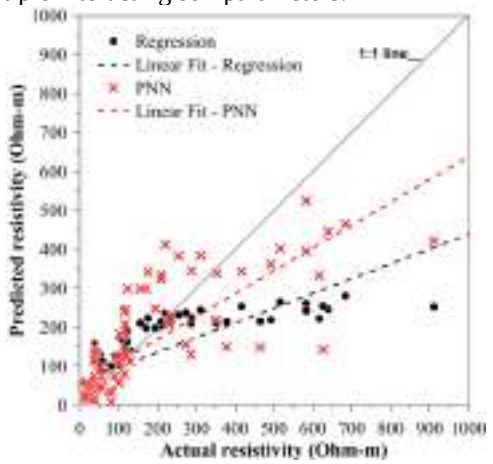

Fig. 4 Comparison of predicted vs. measured soil resistivity with water content and plasticity index are input variables.

Relationship Between Soil Resistivity, Water Content, and Plasticity Index

The combined effects of water content and dry density on soil resistivity were evaluated using both exponential regression and PNN models, as summarized in Table 2.

The exponential regression model produced the following equation:

$$\rho = 128.76\exp[(-0.2044WC) + 0.5499\gamma_d] \quad (10)$$

where ρ is the predicted soil resistivity in Ω·m, WC is water content of the soil and γ_d is dry density of the soil in g/cm^3.

This model achieved an R^2 of 0.439, with RMSE is 142.22 and MAE is 74.57. The results suggest that soil resistivity tends to decrease as water content increases but slightly increases with higher dry density. However, the comparison between the measured and predicted soil resistivity values (Fig. 5) revealed clear deviations from the diagonal line—particularly at the ends—suggesting that the regression model may have difficulty capturing the full complexity of the data.

To better capture nonlinear patterns and interactions, a PNN model was developed using water content, dry density, and their polynomial terms. The model showed improved performance, achieving an R^2 of 0.522, with an MSE of 0.66 and an MAE of 0.67 (based on log-transformed resistivity). As shown by the comparison between the measured and predicted soil resistivity values in Fig. 5, the residuals from the PNN model aligned more closely with the expected normal distribution, indicating better model calibration and a more balanced distribution of prediction errors.

These results show that although dry density on its own does not predict soil resistivity well, combining it with water content improves overall model accuracy. The PNN performed better than the exponential regression model in both overall fit and its ability to handle prediction errors, making it a more suitable choice for modeling soil resistivity in complex, multi-variable situations.

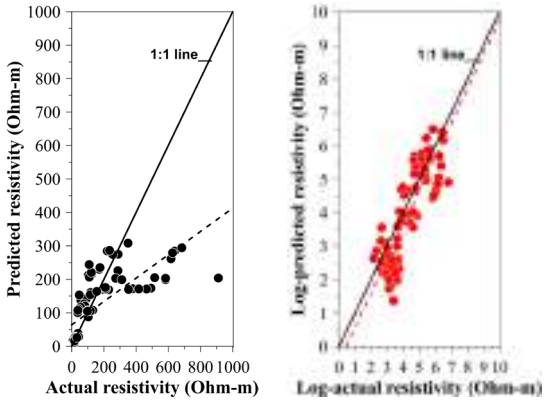

(a) (b)

Fig. 5 Comparison of predicted vs. measured soil resistivity with water content and dry density (γ_d) are input variables: (a) Regression model and (b) PNN.

Table 1 Summary of soil resistivity prediction using single-variable models

Input variable	Spearman's Correlation (r_s)	Regression model	Regression R^2	PNN R^2
WC	-0.92	Exponential	0.439	0.433
PI	-0.12	Linear	0.007	-0.099
γ_d	-0.03	Linear	0.007	-0.057

Table 2 Summary of soil resistivity prediction using two-variable models with output (soil resistivity) and input parameters including water content, plasticity index (PI), and dry density (γ_d)

Input variable		Regression model	Regression R^2	PNN R^2
WC	PI	Exponential	0.503	0.618
WC	γ_d	Exponential	0.429	0.522

CONCLUSIONS

This study evaluated how soil resistivity relates to key geotechnical parameters using both statistical and machine learning approaches. The main findings can be summarized as follows:

Water content was identified as the most influential parameter affecting soil resistivity, exhibiting a strong inverse correlation (r_s = –0.92). In contrast, plasticity index and dry density showed weak individual correlations with resistivity and contributed less significantly to model performance.

Regression models were developed for both single-variable and multivariable cases, with exponential regression performing best in the single-variable context.

The Polynomial Neural Network (PNN) achieved comparable R^2 values (~0.43) to regression models and proved more effective in capturing nonlinear interactions among variables. Although PNNs require greater computational effort, they provide valuable and accuracy in predicting soil resistivity for engineering applications.

The findings, based on soil samples collected from substations across Thailand, offer practical insights into variable influence and support more reliable geotechnical site assessments.

REFERENCES

[1] Sangprasat K., Puttiwongrak A., and Inazumi S., "Comprehensive analysis of correlations between soil electrical resistivity and index geotechnical properties," Results in Engineering, Vol. 23, 2024, Article 102696.

[2] ASTM International, Standard Test Method for Measurement of Soil Resistivity Using the Wenner Four-Electrode Method (ASTM G57-20), ASTM, 2020.

[3] Giao P.H., Chung S.G., Kim D.Y., and Tanaka H., "Electric imaging and laboratory resistivity testing for geotechnical investigation of Pusan clay deposits," Journal of Applied Geophysics, Vol. 52, 2003, pp. 157–175.

[4] Hen-Jones, R.M., Hughes, P.N., Stirling, R.A., Glendinning, S., Chambers, J.E., Gunn, D.A., and Cui, Y.J., "Seasonal effects on geophysical–geotechnical relationships and their implications for electrical resistivity tomography monitoring of slopes," Acta Geotechnica, Vol. 12, 2017, pp. 1159–1173.

[5] Lehmann E.L. and D'Abrera H.J.M., Nonparametrics Statistical Methods Based on Ranks, Springer, New York, US, 2006, pp. 1–426.

[6] Montgomery D.C., Peck E.A., and Vining G.G., Introduction to Linear Regression Analysis, 5th ed., Wiley, Hoboken, NJ, USA, 2012, pp. 1–672.

[7] Chaffart D. and Yuan Y., "Polynomial Neural Networks for improved AI transparency: An analysis of their inherent explainability (operational rationale) capabilities," Digital Chemical Engineering, Vol. 15, 2025, Article

Copyright © Int. J. of GEOMATE All rights reserved, including making copies, unless permission is obtained from the copyright proprietors.

15th Int. Conf. on Geotechnique, Construction Materials & Environment, Kyoto, Japan, 11-13 November 2025, ISBN 978-4-909106124 C3051

THE BEACHROCK DISTRIBUTION, CHARACTERISTICS AND FORMATION MECHANISMS IN TROPICAL ASIA: A SYSTEMATIC REVIEW

Rahubadda Kankanamge Hiroshima Surangani[1], Anjula Buddhika Nayomi Dassanayake[2], Chulantha Lakmal Jayawardena[2], Niki Evelpidou[3] and Satoru Kawasaki[4]

[1]Graduate School of Engineering, Hokkaido University, Japan; [2] Faculty of Engineering, University of Moratuwa, Sri Lanka; [3] Faculty of Geology and Geoenvironment, National and Kapodistrian University of Athens, Greece; [4] Faculty of Engineering, Hokkaido University, Japan

ABSTRACT

Global beachrock distribution, characteristics, and formation mechanisms remain subjects of ongoing debate. A comprehensive database incorporating all published research is essential for a clearer understanding of their formation processes and their distribution. However, compiling such a database requires systematic data collection and analysis on a global scale. This study contributes to this effort by developing a database of beachrock occurrences and characteristics, specifically focusing on the tropical Asian region. A comprehensive literature review was conducted, resulting in the compilation of 122 documented records of beachrock occurrences. The collected records were then analyzed to determine sediment compositions, cement types, and cementation mechanisms. The findings reveal that beachrock formations are mostly concentrated in the East China Sea (Western Japan), while regions such as Bhutan, Brunei, and Indonesia have limited reported occurrences, possibly due to limited research or publications generated. Beachrocks primarily consist of quartz, heavy minerals, carbonate shells, and organic materials, with porosity varying based on cementation progress. Cement analysis records reveal that aragonite and High Magnesium Calcite (HMC) are the dominant types. Cementation occurs through seawater precipitation, microbial activity, and freshwater processes, with seawater precipitation being the most prevalent mechanism. The findings contribute to the development of a global beachrock database and offer insights into formation processes in tropical regions.

Keywords: Asian Tropical Coasts, Calcareous Rocks, Carbonate Cements, Formation Mechanism, Shoreline Stability

INTRODUCTION

Beachrocks are unique, naturally occurring consolidated shoreline sedimentary formations commonly found in tropical and subtropical regions [1], particularly within intertidal and supratidal zones. They typically appear as layered deposits inclined towards the sea. They vary in size from small patches to extensive outcrops that extend several kilometers and range from friable to well-cemented [2,3,4]. Beachrocks consist of beach sediments, including sands and gravels derived from siliciclastic, bioclastic, and/or volcaniclastic sources [2], bound together through rapid cementation. This process is primarily facilitated by the precipitation of carbonate cement, predominantly composed of calcite or aragonite [5,6]. Beachrock formation processes, occurrences, and characteristics vary with regional climate zones such as tropical, subtropical, temperate, and Mediterranean and sea water level conditions. To achieve a clear and comprehensive understanding of global beachrock distribution and their characteristics, region-specific studies are essential.

Numerous global studies on beachrocks indicate that over 90% of beachrock occurrences are concentrated between 40°N and the Tropic of Capricorn (~23°S) [7]. Similarly, Vousdoukas et al. (2007) observed that most documented occurrences lie between 20° and 40° latitude and suggested that the apparent scarcity of beachrock formations in tropical regions may not indicate a true absence but rather reflect a lack of focused scientific investigation in those areas [6].

In addition, numerous global studies have consistently shown that beachrocks predominantly form in tropical and subtropical climates. However, more recent research has identified sporadic occurrences in temperate and colder regions, challenging the traditional assumption that beachrock formation is restricted to tropical and subtropical zones [1,8]. Tropical and subtropical beachrocks typically develop as extensive, shore-parallel ledges with a uniform distribution, facilitated by stable, low-energy beach conditions and high temperatures that promote dynamic cementation. In contrast, temperate beachrocks often occur as isolated concretions embedded deeper within the beach profile, forming under more variable conditions that may include erosion and instability. However, some temperate regions, such as Northern Ireland, exhibit beachrock

formations that developed during prolonged periods of stability, highlighting a key distinction from the more dynamic cementation processes commonly observed in tropical environments. Cementation processes in temperate regions may resemble those occurring in tropical areas [1].

The exact mechanisms behind beachrock formation are still not fully understood. However, past studies have proposed several dominant theories to explain them. These include direct cement precipitation, mixing of marine and freshwater, precipitation triggered by the release of carbon dioxide, and biological contributions [6].

This study aims to collect and analyze the existing records on beachrock occurrences and characteristics in the tropical Asian region. This will provide foundational insights into natural beachrock formation in tropical Asian region.

RESEARCH SIGNIFICANCE

The beachrock distribution, characteristics, and formation mechanisms remain subjects of ongoing debate. A comprehensive database compiling all published research is crucial for better understanding their formation, characteristics and distribution. However, compiling such a database requires systematic data collection and analysis on a global scale. This study contributes to this effort by developing a database, with a focus on the tropical Asian region. The findings contribute to the development of a global beachrock database and offer insights into formation processes in tropical regions.

METHODOLOGY

A systematic literature review was conducted using major scholarly search platforms, including *Web of Science, Scopus, Google Scholar, ScienceDirect, SpringerLink,* and *Wiley Online Library*. The search was guided by specific keywords targeting publications from 1960 to 2025. In the first step, all retrieved publications were screened for relevance to tropical regions of Asia based on geographic descriptions. If a publication did not meet this criterion, it was excluded, and the search was repeated. The inclusion criteria were established to ensure the relevance and scientific quality of the records, focusing on peer-reviewed journal articles. Studies were excluded from unpublished reports, Abstract-only publications, lacked sufficient geospatial information. Geospatial coordinates provided in publications were verified using *Google Earth* and *ArcGIS*. When coordinates were missing, maps and contextual descriptions were used to estimate locations. The collected records from each beachrock site were systematically analyzed to identify sediment compositions, cement types, and cementation mechanisms, and the resulting database was referred to as the tropical Asian region beachrock database (TARBD). In cases of conflicting data, original publications were re-examined, and metadata were annotated for discrepancies. The summary of methodology is illustrated in Fig.1 below.

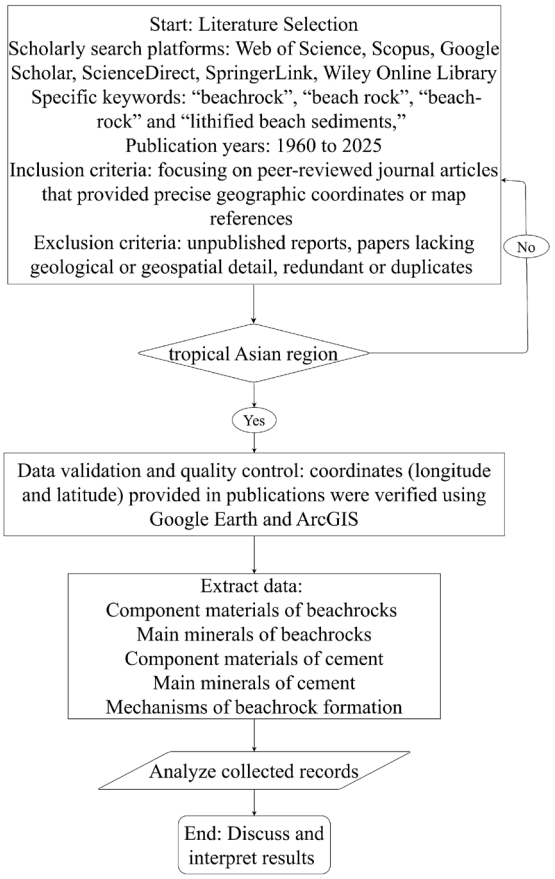

Fig.1 Methodology flowchart

RESULTS AND DISCUSSIONS

Beachrock Occurrences

The TARBD related to this study is openly available in the *Mendeley Data repository* and can be accessed using the *DOI: 10.17632/9ysc29xmx2.1*.

A total of 122 records of beachrock occurrences were compiled from 44 published studies across the tropical Asian region, and their distribution by area or country is presented in Fig. 2. The East China Sea (Western Japan) has the highest number of occurrences, while Bangladesh and the northwestern South China Sea report the fewest. The absence of documented beachrock occurrences along the coasts of Brunei, Cambodia, Myanmar, Papua New Guinea, Indonesia, and Singapore likely reflects limited research attention and insufficient field

investigations, highlighting gaps in the TARBD.

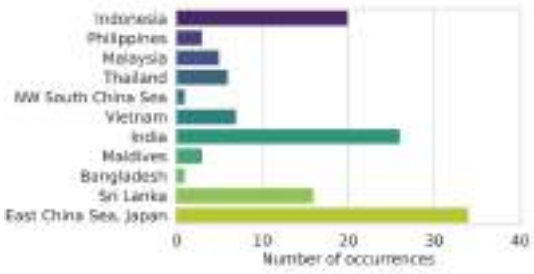

Fig.2 The distribution of beachrock occurrences by area or country

A spatial distribution map of 122 beachrock occurrences was generated using *ArcMap* to validate the geographic coordinates of each record. Fig. 3 presents the spatial distribution of the 122 beachrock occurrence records. Fig. 4 highlights areas of higher occurrence density, primarily concentrated in the East China Sea (Western Japan), as identified through hot spot analysis.

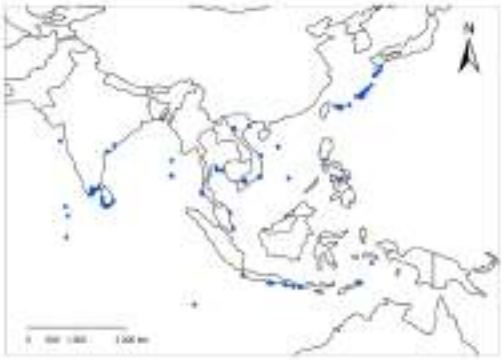

Fig.3 The spatial distribution of the 122 beachrock occurrence records

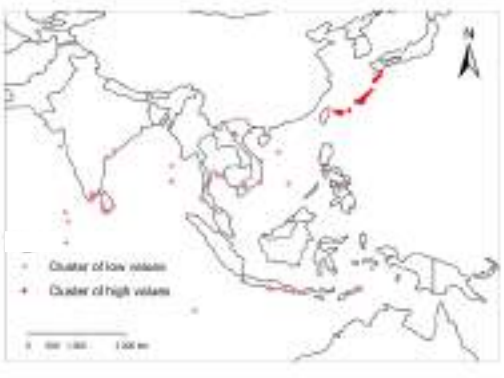

Fig.4 The areas of higher occurrence density, as identified through hot spot analysis

In addition to research limitations, several natural and anthropogenic factors contribute to the lack of recognized beachrock sites. Naturally, rising sea-levels can submerge beachrock formations, making them difficult to access or observe, while wind-driven sediment accumulation may bury them beneath surface layers leading to seasonal exposure. Human activities such as coastal development, dredging, sand mining, and constructions may have disturbed or destroyed beachrocks before they are documented. Furthermore, legal restrictions in protected, historical, or conservation areas may limit scientific access, as regulations often prohibit the extraction of geological materials to preserve cultural and ecological value.

Fig.5 illustrates the increasing number of beachrock-related publications focused on the tropical Asian region from 1960 to 2025. The publication records are grouped into 10-year intervals.

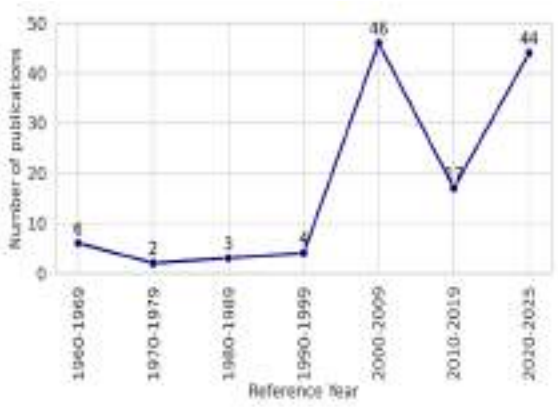

Fig.5 The publication timeline for reported beachrock occurrences

Beachrock-related publications were minimal prior to 1999, reaching their lowest point during 1970–1979. A significant rise occurred between 2000 and 2009, marking the highest number of publications, followed by another notable increase during 2010–2019. These trends suggest that the research gap identified by Vousdoukas et al. (2007), who highlighted the lack of studies in tropical regions [6], is now being progressively addressed.

Fig.6 illustrates the relationship between count of beachrock occurrences and latitudes. The majority of reported beachrock occurrences were associated with coastal regions within latitudes 0–10°N. Based on the TARBD, a notable number of beachrock occurrences were identified within the 20°S to 40°N latitude range. These findings contribute to a slight increase in the percentage previously reported by Danjo and Kawasaki (2014) [7], who observed that over 90% of global beachrock occurrences were concentrated between 40°N and the Tropic of Capricorn (~23°S).

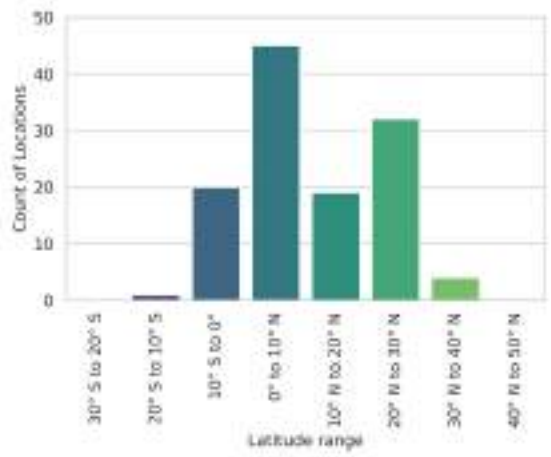

Fig.6 The beachrock occurrence counts across different latitudes

Beachrock Morphology and Coastal Sediments

Based on the extracted records on beachrock morphology from the TARBD, beachrocks typically formed between the high and low tide levels, extending extensively along shorelines and often reaching inland, where they were sometimes buried beneath a thin layer of loose beach sediments. These formations ranged from small, localized patches of cemented sediments to expansive outcrops extending over several kilometers (Fig.7). The thickness of beachrocks varied considerably, from less than 0.5 m to over 2.5 m. Thicker formations were generally located in areas with a significant tidal range, indicating the influence of tidal dynamics on their development [6].

Fig.7 Beachrock outcrops at Uswatakeiyawa beach, Sri Lanka, visibly exposed on land and extending seawards towards the submerged zone

The morphology of beachrocks varied widely due to factors such as sea-level fluctuations, environmental conditions, climatic events, tectonic activity, and coastal morphodynamics [6,9]. Stratified beachrock outcrops (Fig. 8) are common and typically consist of medium-bedded layers with occasional thin layers, often exhibiting graded bedding that may be continuous or discontinuous. These formations occurred along the coast in both underwater and above-water settings, generally extending over a width range of 10 m to 40 m. For example, observations from the Qilian Islets and Cays reveal that beachrock outcrops consisted of multiple beds, typically ranging from 5 to 8 layers. Each bed generally varied in thickness from about ten centimeters to several tens of centimeters, showcasing a complex stratification pattern [9].

Fig.8 Visual representation of stratified beachrock outcrops at Koggala beach, Sri Lanka

Beachrocks buried onshore have smooth surfaces primarily due to their lithification process, protection from erosive forces, limited exposure to weathering, and their similarity in texture to the surrounding sediments [6,9].

The dips of stratified beachrock beds generally align with the coastal slope, exhibiting low inclination angles of 8° to 12° towards the open sea, with their strike oriented parallel to the coastline. These dip angles varied depending on local factors such as beach slope, and sea wave intensity [9].

Coastal hydrodynamic intensity, which refers to the strength and movement of water along the shoreline, plays a critical role in the formation and distribution of beachrocks. It influences their width, the thickness of their layers, and the sedimentary structures and development patterns within the deposition sequence [6,9]. Beachrocks provide valuable insights into past environmental conditions, including sea-level changes, climate variations, and coastal processes. Their sedimentary structures and stratification patterns serve as essential records of historical coastal dynamics [9].

Beachrock beds often display a range of grain textures, including both well-sorted and poorly sorted sediments. This variation in grain textures is largely driven by hydrodynamic conditions. For example, during storms or under strong wave action, large coral and shell fragments are deposited quickly, resulting in poorly sorted and highly porous sediments. In contrast, calmer waves and tides lead to repeated washing of sediments, producing better sorted and

rounded grains, with slower deposition and more uniform porosity [9].

Beachrocks were composed of cemented beach sediments, which include a wide range of particle sizes. The sedimentary particles exhibit significant diversity, reflecting the composition of the surrounding sedimentary environment [1,2,3,6,9]. These particles included quartz, garnet, iron oxides, feldspars, heavy minerals (Fig. 9), recycled clasts, volcanic materials, carbonate ooids, molluscan shells, and skeletal fragments [2,3,5,6]. For example, the beach sediments on the Tiruchendur coast in Tamil Nadu, India primarily consisted of quartz and shells, while the Pag-Asa Reefs feature medium to coarse carbonate sand interspersed with coralline clasts. Additionally, beachrock incorporated organic materials such as wood fragments and coconut shells, as well as man-made objects like bottles and ceramic pieces [6,9]. They contained pore spaces, and their porosity decreased as cementation progressed, with porosity values varying significantly depending on the degree of cementation.

Fig.9 Presence of heavy minerals, primarily ilmenite, observed at Uswetakeiyawa beach, Sri Lanka

Cement and Cementation Mechanism

According to the records analysis of the TARBD, beachrock cement is primarily calcite or aragonite, depending upon factors like temperature, salinity, pH, and abundance of magnesium in the environment. Calcite typically precipitates from freshwater, while aragonite forms from seawater. Calcite occurs in two distinct forms, High Magnesium Calcite (HMC) and Low Magnesium Calcite (LMC), both of which are polymorphs of calcium carbonate ($CaCO_3$). HMC contains more than 1.2 wt.% magnesium carbonate ($MgCO_3$) [6] while LMC contains less than 4 mol% $MgCO_3$. Aragonite is commonly associated with phreatic, shallow-marine, and vadose environments. It typically appears as acicular crystals, fibrous rims, bladed spar rims, and irregular needles, forming isopachous cement rims around grains. It was produced by pelagic organisms like pteropods, corals, algae, and mollusks. Conversely, HMC is formed by benthic organisms like foraminifera and sea urchins, thus it occurs in shallow marine zones and appears in micritic, granular, or bladed crystal forms. LMC was linked to meteoric vadose and phreatic zones, displaying meniscus and spar forms. Environmental changes result in aragonite growing atop existing calcite cements, highlighting dynamic diagenetic processes [6].

Among the 122 beachrock occurrences compiled in the TARBD, 81 records with complete cement mineralogical data were selected for statistical analysis (Fig. 10). The remaining 41 records were excluded due to incomplete or missing mineralogical information. The analysis reveals that aragonite was the most prevalent cement type, followed by HMC. Interestingly, silica was identified as a cement type at only one site. These findings represent the current state of published knowledge, which remains limited and subject to change as more studies are undertaken in this area.

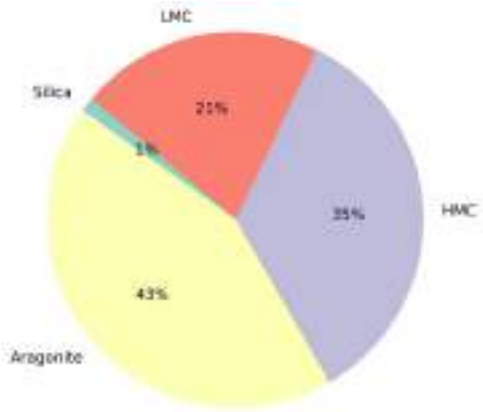

Fig.10 The statistical comparison of cement mineralogy in the tropical Asian region

According to the records analysis of the TARBD, the primary cementation mechanisms in tropical Asian region include precipitation from seawater, precipitation from freshwater, microbial-induced cementation, and cementation from both marine and meteoric water. A total of 60 records with complete cementation mechanism data were selected for statistical analysis (Fig. 11), while the remaining 62 records were excluded due to incomplete or missing information on cementation mechanisms. The analysis indicates that seawater precipitation is the dominant process, followed by the 'various' category, which include sites where multiple mechanisms contribute to beachrock formations.

In contrast, only a limited number of sites exhibit beachrock formation through freshwater precipitation. Lithification driven by biological processes is identified at approximately four sites, while cement precipitation from mixed marine and meteoric waters is observed at nine sites.

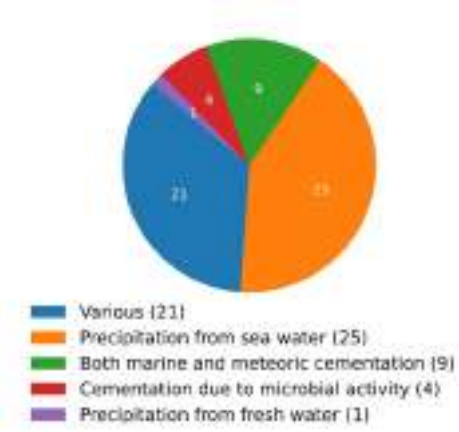

Fig.11 The statistical comparison of cementation mechanisms in the tropical Asian region

CONCLUSIONS

In conclusion, the compiled data of 122 beachrock occurrences from 44 studies highlights significant regional variation across tropical Asia, with the highest concentration in the East China Sea (Western Japan) and the lowest in Bangladesh and the northwestern South China Sea. Several countries lack documented records primarily due to limited research and field access. Beachrock-related publications were limited before 1999, with the lowest record in the 1970s. The notable increase in beachrock-related publications from 2000 onward especially during 2000–2009 and 2010–2019, indicating a progressive response to earlier research gaps in tropical regions. Most beachrock occurrences are concentrated within low latitudes, particularly between 20°S and 40°N, with the highest densities observed around 0–10°N. This supports and slightly expands previous global distribution estimates.

Beachrock formations typically develop between tide levels, varying from small patches to extensive outcrops, often buried under loose sediments. Beachrocks are composed of cemented sediments, including quartz, heavy minerals, shells, organic materials, and even man-made objects, with porosity depending on the degree of cementation.

Beachrock cement is primarily composed of calcite and aragonite, influenced by temperature, salinity, and pH. HMC and aragonite dominate cement composition. The main cementation mechanisms include seawater precipitation, microbial activity, and freshwater precipitation, with seawater precipitation being the most prevalent.

ACKNOWLEDGMENTS

This work was partially supported by the Japan Society for the Promotion of Science (JSPS) KAKENHI Grant Number JP22H01581. The authors gratefully acknowledge the support.

REFERENCES

[1] Kneale D., and Viles H., Beach Cement: Incipient CaCO3 -Cemented Beachrock Development in the Upper Intertidal Zone, North Uist, Scotland, Sedimentary Geology, Vol. 132, No. 3, 2000, pp. 165–170.

[2] Ginsburg R. N., Beachrock in South Florida, Journal of Sedimentary Petrology, vol. 23, 1953, pp. 85–92.

[3] Howie F. M. P., Beachrock Development Along the North Coast of Cornwall, Geosci South-West Engl, Vol. 12, 2009, pp. 85-94.

[4] Nayanthara P. G. N., Dassanayake A. B. N., Nakashima K., and Kawasaki S., Distribution and Cementation Characteristics of Beachrocks Along Southern, Southwestern and Western Coast of Sri Lanka, Journal of Sedimentary Environments, Vol. 6, No. 1, 2021, pp. 93–106.

[5] Scoffin T.P., and Stoddart D.R., Beachrock and Intertidal Sediments, Chemical Sediments and Geomorphology, 1983, pp. 401–425.

[6] Vousdoukas M. I., Velegrakis A. F., and Plomaritis T. A., Beachrock Occurrence, Characteristics, Formation Mechanisms and Impacts, Earth-Science Reviews, vol. 85, 2007, pp. 23–46.

[7] Danjo T., and Kawasaki S., Characteristics of Beachrocks: A Review, Geotechnical and Geological Engineering, vol. 32, 2014, pp. 215–246.

[8] Arrieta N., Goienaga N., Arkarazo I. M., Murelaga X., Baceta J. I., Sarmiento A., and Madariaga J. M., Beachrock Formation in Temperate Coastlines: Examples in Sand-Gravel Beaches Adjacent to the Nerbioi-Ibaizabal Estuary (Bilbao, Bay of Biscay, North of Spain), vol. 80, No. 1, 2011, pp. 55–65.

[9] Shen J. W., Wang Y., Zhao N., Yang H. Q., Fu F., and Jin Y. B., Carbonate Sedimentary Characteristics of the Beach Rocks Around Qilian Islets and Cays, Xisha Islands: Implication for Coral Reef Development and Decline, Palaeogeography, Palaeoclimatology, Palaeoecology, Vol. 474, 2017, pp.264-278.

[10] Dubey A. A., Dhami N. K., Ravi K., and Mukherjee A., Erosion Mitigation with Biocementation: A Review on Applications, Challenges, and Future Perspectives, Reviews in Environmental Science and Biotechnology, 2023.

Copyright © Int. J. of GEOMATE All rights reserved, including making copies, unless permission is obtained from the copyright proprietors.

15th Int. Conf. on Geotechnique, Construction Materials & Environment,
Kyoto, Japan, 11-13 November 2025, ISBN 978-4-909106124 C3051

BACTERIAL DYNAMICS BY MICROBIALLY INDUCED CALCIUM CARBONATE PRECIPITATION (MICP) UNDER MICROGRAVITY CONDITION FOR EXTRATERRESTRIAL BIOCEMENTATION ENGINEERING

Yuru Chen[1], Tomoya Hamada[1], Chikara Takano[2], Kazunori Nakashima[2], Satoru Kawasaki[2]

[1] Graduate School of Engineering, Hokkaido University, Japan
[2] Faculty of Engineering, Hokkaido University, Japan

ABSTRACT

The loose regolith on the lunar surface presents significant challenges for base construction. Microbially induced calcium carbonate precipitation (MICP) has been proposed as a promising method for enhancing lunar regolith strength. However, the microgravity environment may affect microbial growth and mineralization efficiency, potentially influencing the feasibility of MICP-based stabilization. This study investigated the microbial growth behavior, urease activity, and microstructural changes of *Lederbergia lenta* (RII-2) under different culture medium and gravitational conditions. Experiments were conducted using NH4-YE, R2A, and R2A-Urea medium to assess bacterial performance over 168 h. The results indicate that RII-2 exhibited the highest OD_{600} value in R2A-Urea medium, significantly surpassing NH_4-YE and R2A. Urease activity tests revealed that R2A-Urea medium exhibited the highest overall enzymatic activity among the three media. Under microgravity conditions, RII-2 showed a 40% increase in OD_{600} and a 22-28% decline in urease activity compared to normal gravity. These findings suggest that the experimental conditions affect bacterial growth and enzymatic function, which may impact the efficiency of regolith stabilization by MICP in space environments.

Keywords: Lunar regolith stabilization, Microbially induced calcium carbonate precipitation (MICP), Microgravity, Bacteria growth, Urease activity,

INTRODUCTION

The establishment of permanent infrastructure on the Moon is a key objective in advancing extraterrestrial exploration. However, this goal is significantly constrained by the need to transport large quantities of construction materials from Earth, which imposes severe logistical and economic burdens. As a result, attention has shifted toward utilizing in-situ resources, particularly the abundant lunar regolith, as a primary construction material. The lunar surface is covered by a layer of regolith formed through continuous meteoritic bombardment and space weathering [1-3]. This layer is characterized by its fine-grained, angular texture, low density, and lack of cohesion [4], resulting in poor bearing capacity and high susceptibility to dust dispersion and surface instability [5]. These properties not only hinder direct construction but also pose risks to equipment operation and structural safety. Therefore, effective solidification and mechanical reinforcement of the regolith are essential prerequisites for enabling stable and sustainable lunar surface operations.

Among various ground improvement strategies, Microbially Induced Calcium Carbonate Precipitation (MICP) has attracted increasing attention as a biologically mediated method for stabilizing loose granular soils [6, 7]. MICP utilizes the urease activity of specific microorganisms to catalyze urea hydrolysis, leading to the formation of carbonate ions that react with calcium to precipitate calcium carbonate ($CaCO_3$), which serves as a bonding agent between particles [8]. In contrast to conventional solidification methods that often depend on energy-intensive processing and externally supplied materials [9], MICP operates under mild conditions using biologically derived reactions [10]. These features make it a promising approach for in-situ ground stabilization in constrained environments such as the lunar surface. However, as a biologically driven process, its performance may be influenced by external physical conditions, including gravity.

Microgravity is known to influence a wide range of biological processes [11], including bacteria morphology, nutrient transport, metabolic activity, and gene expression [12]. These effects arise from the absence of buoyancy-driven convection, altered fluid dynamics, and the lack of sedimentation under reduced gravitational acceleration. In microbial systems, such changes can affect growth behavior, enzyme production, and the formation of biofilms or precipitates—all of which are critical to the effectiveness of MICP. Although studies have investigated microgravity impacts on higher organisms and mammalian cells, research on how microgravity affects microbial biomineralization processes remains limited. Therefore, clarifying how microgravity affects microbial behavior and carbonate precipitation is an important step toward evaluating the potential use of MICP in low-gravity

environments.

In light of these considerations, the present study explores the potential of MICP under simulated microgravity conditions, focusing on microbial growth behavior and urease activity. By comparing these processes with those observed under normal gravity, the work aims to clarify how microgravity may influence the biological behavior involved in MICP, thereby providing a basis for future application in space-related environments.

MATERIALS AND METHODS

Materials

Bacteria

The ureolytic bacterium *Lederbergia lenta* (RII-2), isolated in previous studies at Hokkaido University, was used in this study. Glycerol stocks were prepared and stored at –80°C, and pre-cultures were initiated in NH_4-YE liquid medium before experimental use.

Culture medium

To accurately evaluate bacterial growth and urease activity under varying conditions, it was first necessary to identify an appropriate culture medium. Since medium composition strongly affects bacterial proliferation and enzyme expression, three media were selected to systematically examine the influence of nutrient availability and urea supplementation on RII-2. The detailed compositions of the three media are listed in Table 1.

Table 1 Composition of three types of culture medium (per 100 mL, solvent: distilled water)

Medium	Component	Amount （g）
NH_4-YE	Yeast Extract	4.00
	Ammonium Sulfate	2.00
	Tris aminomethane	1.58
R2A	R2A Medium	0.32
R2A-Urea	R2A Medium	0.32
	Urea	0.60

(1) NH_4-YE Medium: A nutrient-rich medium used extensively in previous MICP research, known to support rapid cell growth and high biomass. It served as a benchmark for optimal conditions [13].

(2) R2A Medium: A minimal medium typically used for environmental isolates, chosen to simulate low-nutrient environments similar to those encountered in extraterrestrial settings where resource input must be limited [14].

(3) R2A-Urea Medium: A variation of R2A containing urea as a direct substrate for urease activity. This medium was included to assess whether urease induction could be achieved under minimal nutritional conditions without relying on ammonium-based nitrogen.

Methods

Bacteria Cultivation

Pre-cultures of RII-2 were prepared by inoculating 1 mL of glycerol stock into 5 mL of sterilized NH_4-YE medium in test tubes, followed by incubation at 30°C with shaking at 160 rpm for 24 h.

For the main cultivation, 0.4 mL of the pre-cultured suspension was transferred to 25 mL vented-cap flasks (Falcon® 353018) containing 42 mL of one of the three test media (NH_4-YE, R2A, or R2A-Urea). Care was taken to prevent air bubbles during filling. For each condition, six replicate flasks were prepared.

Microgravity and Normal Gravity Experimental Setup

To evaluate the effect of gravitational conditions on bacterial behavior, cultures were incubated under both simulated microgravity and standard gravity. Simulated microgravity was generated using a rotating wall vessel bioreactor (Zeromo CL-1000, Yamato Scientific Co., Ltd.), where the culture flasks were mounted horizontally and rotated continuously during incubation. By maintaining a constant rotational speed that prevents sedimentation, the direction of the gravitational vector is randomized over time. This dynamic state suppresses convective flow and mimics a low-shear, microgravity-like environment suitable for biological studies [15]. In contrast, control cultures were placed statically in an incubator under normal gravity. Both setups were maintained at 30°C, and humidity was kept high by placing water-saturated towels inside the incubators to minimize evaporation. As shown in Fig. 1, sampling was performed at 48, 120, and 168 h for OD_{600} and urease activity measurements.

(a) NH_4-YE (b) R2A (c) R2A-Urea

Fig. 1 After 48,120,168 h of culture medium

Optical Density (OD_{600}) Measurement

To evaluate the growth behavior of RII-2 under different nutrient and gravitational conditions, OD_{600} was measured as an indicator of bacteria concentration over time. Sampling was performed at 48, 120, and 168 h after the start of cultivation. Prior to measurement, each flask was gently agitated to

ensure a homogeneous suspension. A portion of the culture liquid was then transferred to a disposable cuvette, and OD_{600} was measured using a UV-visible spectrophotometer (V-730, JASCO Corporation). Measurements were conducted in triplicate for each condition to ensure reproducibility.

Urease Activity Test

To evaluate the enzymatic activity of RII-2 under varying medium and gravity conditions, urease activity was measured using two methods: the indophenol colorimetric method and the electrical conductivity (EC) method.

The indophenol colorimetric method was employed to quantify urease activity by indirectly measuring the concentration of NH_4^+ produced during urea hydrolysis. In this method, NH_4^+ released from the enzymatic breakdown of urea react with phenol nitroprusside and sodium hypochlorite to form a blue-colored compound, indophenol, whose absorbance at 630 nm is proportional to the amount of ammonium generated. Since the production of NH_4^+ is stoichiometrically linked to urease activity, the rate of absorbance increase over time provides a quantitative indicator of enzymatic performance.

The EC method estimates urease activity by measuring the increase in ionic concentration resulting from urea hydrolysis. As urease catalyzes the breakdown of urea, ions such as NH_4^+ and HCO_3^- are released, increasing the electrical conductivity. For each measurement, 0.5 mL of culture was added to 50 mL of urea solution pre-equilibrated at 30°C. Conductivity was measured every 5 min for 20 min using a portable conductivity meter (LAQUAtwin EC-33, HORIBA).

RESULTS AND DISCUSSIONS

To evaluate the biological feasibility of applying MICP under space-relevant conditions, the performance of RII-2 was assessed across varying culture medium and gravitational environments. The analysis focused on two fundamental biological indicators, that is bacterial growth and urease activity, which directly influence the efficiency of carbonate precipitation in MICP. By examining how these parameters respond to environmental variations, particularly under reduced gravity, insights can be gained into the potential adaptability of ureolytic bacteria for use in extraterrestrial construction.

Bacterial growth

Fig. 2 presents the growth curves of RII-2 cultivated in three different media: NH_4-YE, R2A, and R2A-Urea. At 48 and 120 h, the NH_4-YE medium exhibited the highest OD_{600} values, indicating superior cell proliferation under nutrient-rich conditions. The consistent growth observed in NH_4-YE is attributed to the availability of both organic nitrogen and inorganic nitrogen, which together support rapid microbial metabolism.

In contrast, the R2A medium displayed negligible growth during the initial 120 h, followed by a sharp increase in OD_{600} to approximately 0.45 at 168 h. This pattern suggests an extended lag phase in low-nutrient conditions, potentially due to slower metabolic activation or delayed adaptation. Once the bacteria adapted to the minimal nutrient environment, exponential growth was initiated, resulting in the sudden OD_{600} increase observed at 168 h. This suggests that RII-2 can eventually activate key metabolic pathways even under nutrient-limited conditions, albeit with significant delay. The R2A-Urea medium showed moderate and steady growth throughout the cultivation period, with OD_{600} values increasing gradually from 0.23 to 0.26, indicating that the addition of urea partially improved nitrogen availability but did not fully compensate for the nutrient limitations inherent in the base R2A formulation.

These results demonstrate that NH_4-YE is the most effective medium for promoting early-stage bacterial growth, while R2A supports delayed but significant proliferation. R2A-Urea provides an intermediate growth environment, with modest improvement over R2A alone. The differences in OD_{600} trends underscore the importance of medium composition in regulating bacterial growth dynamics.

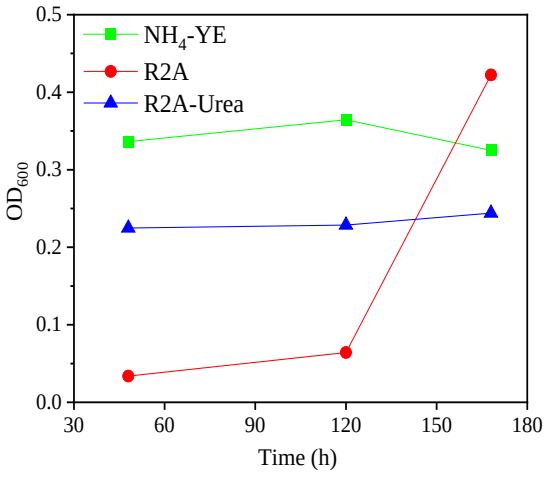

Fig. 2 OD_{600} with different culture medium

Urease activity

Urease activity of RII-2 was examined in three different media using both the indophenol colorimetric method and EC method. As shown in Fig. 3 to 5, the NH_4-YE medium supported vigorous cell growth but yielded lower urease activity values, with negative values observed particularly at 48 h. This

phenomenon may be attributed to the chemical complexity of the medium, which can introduce background signals or interfere with ion-sensitive measurements, especially under conditions where enzymatic activity remains low relative to baseline conductivity or optical density.

In the R2A medium, moderate urease activity was observed, with values generally decreasing over time. This decline may reflect a gradual loss of enzyme functionality under nutrient-limited conditions. Additionally, a wider discrepancy between the two measurement methods was observed, likely due to the limited buffering and ionic capacity of the base medium, which amplifies variability in both optical and conductivity-based assays.

In contrast, the R2A-Urea medium demonstrated stable and reproducible urease activity profiles across all time points, with consistent agreement between the two analytical methods. The inclusion of urea provided a direct and sustained substrate source, while the simpler background composition minimized interference with both optical and electrochemical measurements.

In terms of total urease activity, R2A-Urea medium exhibited the highest values among the three tested media, indicating strong overall enzyme production. However, when normalized by OD_{600} to reflect catalytic efficiency per unit biomass, R2A showed the highest specific activity, reaching approximately 3.22 U/mL, compared to 1.29 U/mL in R2A-Urea and 0.31 U/mL in NH_4-YE. Despite not having the highest unit activity, R2A-Urea was ultimately selected for microgravity experiments due to its stable and reproducible measurements, low bacterial aggregation, and good consistency between the EC and indophenol methods. These characteristics made it the most practical and reliable medium for evaluating MICP performance under space-relevant conditions.

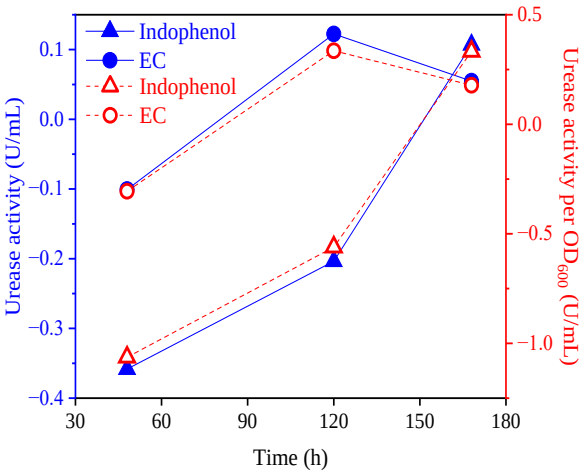

Fig. 3 Urease activity of RII-2 in NH_4-YE medium

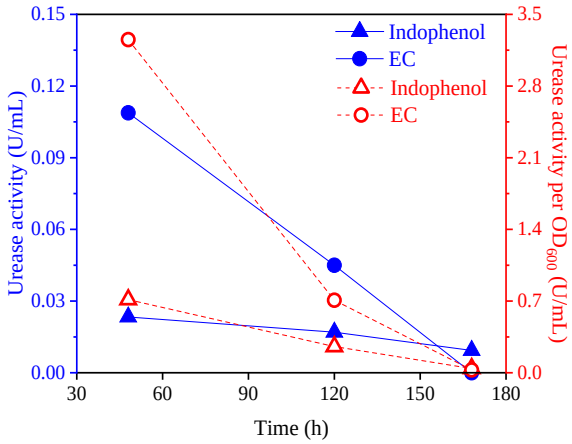

Fig. 4 Urease activity of RII-2 in R2A medium

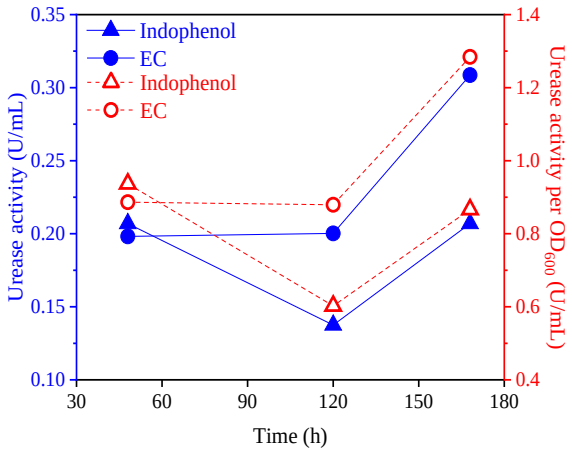

Fig. 5 Urease activity of RII-2 in R2A-Urea medium

Microgravity and normal gravity

To evaluate the effects of gravitational conditions on microbial growth, RII-2 was cultivated in R2A-Urea medium under simulated microgravity and normal gravity. R2A-Urea was selected based on prior evaluation of growth stability and minimal aggregation, making it suitable for use in rotating wall vessel systems. As shown in Fig. 6, cultures under simulated microgravity consistently exhibited higher OD_{600} values than those incubated under normal gravity. After the initial 24 h, OD_{600} values in the microgravity condition stabilized within the range of 0.33 to 0.41, whereas those under normal gravity remained between 0.22 and 0.30. The maximum difference between the two conditions reached approximately 0.12, corresponding to a relative increase of nearly 40% in bacterial suspension density under microgravity.

In the microgravity system, continuous horizontal rotation of the culture vessel disperses the gravitational vector over time, thereby reducing

sedimentation and suppressing shear forces. This creates a low-shear, diffusion-dominated environment in which bacteria remain suspended and experience more uniform access to nutrients. The microgravity environment may also contribute to more stable local environments around bacteria, supporting sustained metabolic activity and biomass accumulation.

These findings suggest that RII-2 is capable of maintaining active proliferation under microgravity, with growth levels exceeding those observed under normal gravity despite the low-nutrient conditions provided by the R2A-Urea medium. This implies that reduced gravitational forces do not impair, and may even enhance, the growth of ureolytic bacteria under appropriately controlled conditions.

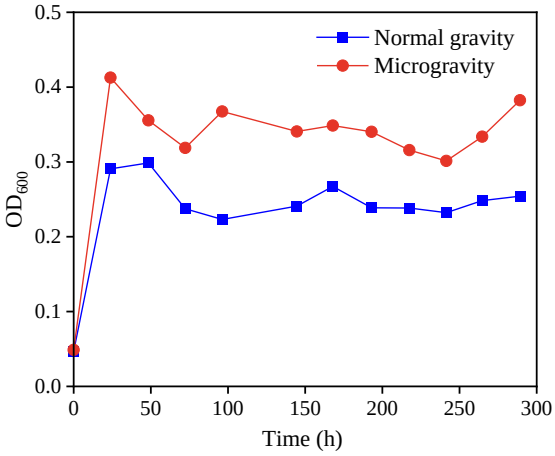

Fig. 6 OD_{600} under different gravity environments

Fig. 7 illustrates the variation in urease activity under microgravity and normal gravity conditions. While both conditions supported sustained enzymatic activity, urease efficiency was consistently lower under microgravity at most time points. The difference was particularly evident after 96 h, where activity values under microgravity generally ranged between 0.5 and 0.7 U/mL, while those under normal gravity were maintained at 0.7 to 0.9 U/mL. On average, urease activity under microgravity was 22–28% lower across the cultivation period.

This trend may reflect disruptions in the regulatory processes governing urease expression in bacteria. As an inducible enzyme, urease production involves multi-level control, including transcriptional activation, cofactor incorporation, and protein maturation. Microgravity may interfere with intracellular organization or spatial gene regulation, impairing the coordinated responses required for efficient enzyme expression. Furthermore, gravitational changes can affect ribosomal function and protein folding kinetics in bacteria, potentially reducing the yield or catalytic integrity of urease even in growing populations.

These results suggest that the reduction in urease activity per OD_{600} under microgravity may compromise the overall efficiency of MICP. Even if sufficient bacteria are present, a slower rate of urea hydrolysis could lead to delayed or insufficient $CaCO_3$ precipitation, especially in time-sensitive or structurally demanding applications. In addition, lower enzymatic output may affect the spatial uniformity of precipitation, potentially resulting in uneven solidification. This limitation should be considered when evaluating the feasibility of MICP-based soil stabilization in extraterrestrial environments, where consistent strength development and process controllability are essential. Moreover, it is important to note that all experiments in this study were conducted under a controlled temperature of 30°C. However, maintaining such a stable thermal environment in outer space is technically challenging. Therefore, the impact of temperature fluctuations on microbial activity and carbonate precipitation should also be investigated in future studies.

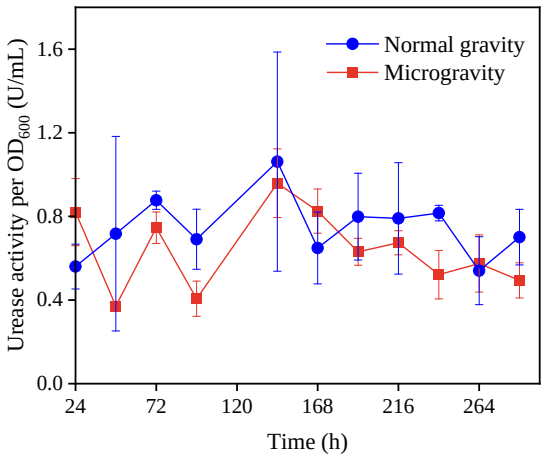

Fig. 7 Urease activity under different gravity environments

CONCLUSIONS

This study systematically evaluated the growth behavior and urease activity of the ureolytic bacterium RII-2 under varying culture media and gravitational conditions, with the aim of assessing the feasibility of MICP in space environments. The conclusions are summarized as follows:

(1) R2A-Urea supported the most robust microbial growth and the highest total urease activity among the three tested media. While NH_4-YE facilitated moderate bacterial proliferation, it showed low and unstable enzymatic output. R2A, despite exhibiting higher specific activity per biomass, was limited by poor growth, resulting in lower overall enzyme production. These characteristics established

R2A-Urea as the most suitable medium for subsequent microgravity experiments.

(2) Bacterial growth, as measured by OD_{600}, was not impaired under simulated microgravity. In fact, proliferation was enhanced compared to static controls, likely due to reduced sedimentation and improved suspension homogeneity.

(3) Despite increased biomass, urease activity per OD_{600} was moderately reduced under microgravity. This indicates that gravitational changes may influence enzyme regulation or cofactor dynamics, which could limit the overall carbonate precipitation rate in MICP processes.

REFERENCES

[1] Dong Z, Fang G, Zhou B, et al. Properties of Lunar Regolith on the Moon's Farside Unveiled by Chang'E‐4 Lunar Penetrating Radar[J]. Journal of Geophysical Research: Planets, 2021, 126(6): e2020JE006564.

[2] Awal ASMA, Hosseini H. and Hossain M.Z., Strength, Modulus of Elasticity and Shrinkage Behaviour of Concrete Containing Waste Carpet Fiber, International Journal of GEOMATE, Vol. 9, Issue 17, 2015, pp. 1441-1446.

[3] Vanga S, Fassett C I, Zanetti M, et al. Rock abundance on the lunar mare on surfaces of different age: Implications for regolith evolution and thickness[J]. Geophysical Research Letters, 2022, 49(4): e2021GL096710.

[4] Osinski G R, Melosh H J, Andrews-Hanna J, et al. Lunar impact features and processes[J]. Reviews in Mineralogy and Geochemistry, 2023, 89(1): 339-371.

[5] Subramanian S, Wilson A, White C, et al. Crater formation and particle ejection induced by supersonic jet impingement in near-vacuum[J]. Acta Astronautica, 2025, 232: 439-452.

[6] Jiang L, Xia H, Wang W, et al. Applications of microbially induced calcium carbonate precipitation in civil engineering practice: A state-of-the-art review[J]. Construction and Building Materials, 2023, 404: 133227.

[7] Fouladi A S, Arulrajah A, Chu J, et al. Application of Microbially Induced Calcite Precipitation (MICP) technology in construction materials: A comprehensive review of waste stream contributions[J]. Construction and Building Materials, 2023, 388: 131546.

[8] Jiang L, Xia H, Wang W, et al. Applications of microbially induced calcium carbonate precipitation in civil engineering practice: A state-of-the-art review[J]. Construction and Building Materials, 2023, 404: 133227.

[9] Xu F, Wang D. Review on soil solidification and heavy metal stabilization by microbial-induced carbonate precipitation (MICP) technology[J]. Geomicrobiology Journal, 2023, 40(6): 503-518.

[10] Fouladi A S, Arulrajah A, Chu J, et al. Application of Microbially Induced Calcite Precipitation (MICP) technology in construction materials: A comprehensive review of waste stream contributions[J]. Construction and Building Materials, 2023, 388: 131546.

[11] Ludtka C, Silberman J, Moore E, et al. Macrophages in microgravity: the impact of space on immune cells[J]. npj Microgravity, 2021, 7(1): 13.

[12] Salavatifar M, Ahmadi S M, Todorov S D, et al. Impact of Microgravity on Virulence, Antibiotic Resistance and Gene Expression in Beneficial and Pathogenic Microorganisms[J]. Mini Reviews in Medicinal Chemistry, 2023, 23(16): 1608-1622.

[13] Liu S, Ding X, Song P, et al. Effects of nitrogen sources on MICP-related metabolic mechanism of Sporosarcina pasteurii and soil reinforcement[J]. Journal of Rock Mechanics and Geotechnical Engineering, 2024, 16(12): 5147-5161.

[14] Fagervold S K, Rohée C, Lebaron P. Microbial consortia degrade several widely used organic UV filters, but a number of hydrophobic filters remain recalcitrant to biodegradation[J]. Environmental Science and Pollution Research, 2023, 30(60): 125931-125946.

[15] Mastroleo F. Molecular characterization of the life support bacterium Rhodospirillum rubrum S1H cultivated under space related environmental conditions. Université de Mons-Hainaut, Mons, Belgium[J]. Mons, Mons-Hainaut (UMH), 2009, 171.

Copyright © Int. J. of GEOMATE All rights reserved, including making copies, unless permission is obtained from the copyright proprietors.

15th Int. Conf. on Geotechnique, Construction Materials & Environment,
Kyoto, Japan, 11-13 November 2025, ISBN 978-4-909106124 C3051

EVALUATION OF SHEAR PROPERTIES AT CONSTRUCTION BOUNDARIES FOR LATTICE-SHAPED GROUND IMPROVEMENT

Miu Kanagawa [1], Kouta Kanno [2], Kenji Niwa [2] and Shinya Inazumi [1]

[1] Shibaura Institute of Technology, Japan
[2]Kato Construction Co., Ltd., Japan

ABSTRACT

Ground improvement using grid-type deep mixing methods is a widely adopted countermeasure against soil liquefaction, particularly in seismic regions where ground deformation poses serious risks to infrastructure. However, practical constraints during construction often necessitate segmented execution, resulting in construction boundaries, discontinuities formed between adjacent improved bodies, that compromise the mechanical continuity and uniformity of the treated ground. This study presents a comprehensive investigation into the shear characteristics of cement-stabilized ground both with and without construction boundaries, through an integrated approach combining systematic laboratory direct shear testing and finite element method (FEM) simulations employing joint elements. Experimental results demonstrate a pronounced reduction in peak shear strength, exceeding 200 kN/m^2, along with a transition from cohesive-frictional to friction-dominated failure characteristics due to the presence of boundaries. Stress–displacement behavior further reveals the loss of ductility and interlocking at boundary planes. Numerical analyses, calibrated using inverse analysis of the experimental data, show that joint elements are effective in replicating boundary mechanics, particularly in capturing residual strength behavior. The modeling framework enables quantitative evaluation of boundary performance and highlights the influence of boundary parameters on global ground behavior. The findings not only clarify the mechanical impact of construction boundaries on the performance of deep mixing ground improvement systems, but also establish a robust foundation for performance-based design and objective quality control. This contributes to enhancing the safety and reliability of ground improvement practices in liquefaction-prone and seismically active areas.

Keywords: Liquefaction, Ground Condition Prediction, Ensemble Learning, Hazard Map, AI

INTRODUCTION

Soil liquefaction, often induced by seismic events, results in a sudden loss of soil strength and stiffness, leading to severe ground deformation and structural damage. To counteract these effects, grid-wall soil improvements, comprising orthogonally arranged soil-cement columns or panels, have been widely employed. This method enhances the shear rigidity of liquefiable layers and mitigates lateral spreading by confining the soil matrix within a reinforced grid structure [1,2].

Despite its effectiveness, the practical implementation of grid-wall soil improvement often involves segmented construction processes due to limitations in equipment reach, scheduling, or site conditions. This segmented execution inevitably produces construction boundaries as shown in Fig. 1, contact surfaces between adjacent improved columns or panels formed at different times. These boundaries, typically resulting from cold joints or differential curing, represent potential planes of weakness due to incomplete bonding and discontinuity in material properties.

The mechanical behavior of such boundaries, particularly their shear strength and failure characteristics, remains insufficiently understood. In design practice, these zones are frequently treated as homogeneous with the surrounding improved soil, potentially overlooking localized reductions in strength and stiffness. Moreover, current quality control practices for boundary integrity largely rely

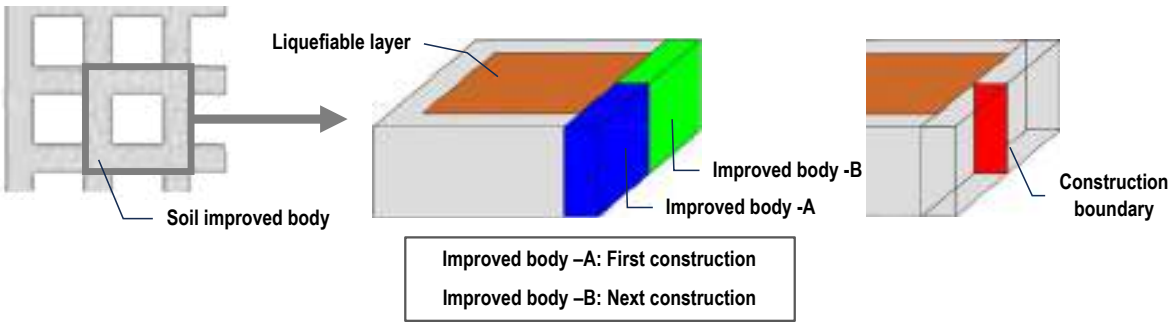

Fig. 1 Schematic illustration of construction boundarys in grid-type deep mixing improvement

on visual inspection, which lacks the objectivity and resolution needed to detect subtle but critical mechanical deficiencies.

Addressing this knowledge gap requires a rigorous, mechanics-based investigation into the influence of construction boundaries on the overall performance of improved ground. In particular, a quantitative understanding of how these boundaries alter stress transfer, shear strength, and failure characteristics is essential for ensuring structural safety, especially under seismic loading conditions where slip or separation at boundaries may trigger progressive failure.

The present study combines laboratory-scale direct shear testing with finite element modeling to comprehensively evaluate the mechanical role of construction boundaries. Two types of specimens, monolithic (without boundaries) and jointed (with construction boundaries), were subjected to controlled shear testing to extract key strength parameters and failure behaviors. Parallel to this, a finite element analysis framework incorporating joint elements was developed and calibrated to simulate boundary mechanics with high fidelity.

Through the integration of empirical and numerical approaches, this research aims to elucidate the fundamental mechanics governing construction boundary behavior and to establish a rational basis for their evaluation in engineering practice. The findings are expected to contribute not only to improved design accuracy but also to the development of objective, performance-based quality control methods in ground improvement engineering.

MATERIALS AND EXPERIMENTAL METHODS

Specimen Preparation

To evaluate the shear behavior of construction boundaries, two types of cylindrical specimens were prepared to simulate conditions representative of grid-type ground improvement using cement-stabilized clay. Each specimen had a diameter of 6 cm and a height of 10 cm, designed to provide sufficient resolution of shear failure while ensuring compatibility with the direct shear apparatus (see Fig. 2).

- Monolithic Specimens (No Boundary): These were prepared in a single pour to represent homogeneously mixed and continuously constructed soil-cement bodies, serving as a control condition with no discontinuity.
- Specimens with boundary (With Construction Boundary): These were fabricated by casting and curing the lower and upper halves of the specimen separately. After a predetermined curing period for the first layer, the second layer was placed on top, simulating the time-lagged construction sequence commonly encountered in segmented deep mixing operations. This process intentionally introduced a horizontal construction boundary at mid-height, representing a cold joint.

Both specimen types were prepared using a consistent clay-cement mixture, formulated to reflect field-representative material conditions. Mixing ratios, moisture content, and curing regimes were carefully controlled to ensure uniformity. The material properties of the untreated clay and the stabilized mixture, along with detailed mixing and curing protocols, are summarized in Table 1.

To minimize variability, the same batch of clay and cement was used throughout specimen preparation, and all specimens were cured under standardized temperature and humidity conditions. This ensured that any observed differences in mechanical behavior could be attributed primarily to the presence or absence of construction boundaries.

Direct Shear Testing

Direct shear testing was employed to quantify the shear strength parameters and failure characteristic of the specimens under controlled normal stress conditions. This method was selected for its ability to provide continuous monitoring of shear stress–displacement responses and to isolate the shear plane, making it particularly suitable for specimens with boundary [1,3,4].

Each specimen was trimmed to a testing height of either 2 cm or 1 cm, depending on the intended shear plane and specimen configuration. The specimens were then placed within a shear box apparatus, where the boundary plane in jointed specimens was aligned with the horizontal shear plane to facilitate targeted evaluation.

Tests were conducted under four distinct normal stress levels: 30, 100, 200, and 300 kN/m^2. These

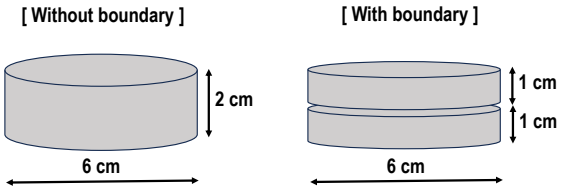

Fig. 2 Dimensions of shear test specimens

Table 1 Physical properties of untreated clay and cement-stabilized specimens

(a) Untreated clay

Soil type	Gairome-clay
Wet density (g/cm^3)	1.535
Natural water content (%)	75.28
Dry density (g/cm^3)	0.876
Particle density (g/cm^3)	2.640

(b) Cement stabilized clay (specimens)

Cement addition (kg/m^3)	250
Curing age (days)	10
Unconfined compressive strength (kN/m^2)	1,000

stress levels were chosen to span a range representative of both shallow and moderately deep subsurface conditions in typical geotechnical applications. For each normal stress level, three replicate tests were performed on both monolithic and specimens with boundary, resulting in a total of 24 tests. Additionally, shear tests were conducted on untreated clay to provide a baseline for assessing the effects of stabilization (see Table 2).

The shear loading was applied at a constant rate to ensure quasi-static conditions. Throughout each test, both shear stress and horizontal displacement were continuously recorded until post-peak behavior was clearly observed, allowing for a detailed evaluation of peak and residual strength parameters.

Data Collection and Analysis

The following data were systematically collected during testing:

- Shear stress–displacement curves for all specimens under each normal stress condition
- Peak and residual shear strengths, extracted from the stress–displacement profiles
- Failure characteristics, determined through visual observation and post-test examination of the shear plane

After each test, the failure planes were inspected to evaluate boundary integrity, evidence of interlocking, surface roughness, and bonding characteristics. Particular attention was given to the contrast between the shear planes of monolithic and specimens with boundary, as these observations provide qualitative insight into the failure characteristics (e.g., brittle slippage, ductile shear, or mechanical interlock).

The collected data formed the basis for subsequent statistical analysis, including regression modeling to fit the Mohr-Coulomb failure envelope and to compare the mechanical responses between specimen types. These results also informed the calibration of material and joint parameters used in the numerical simulations (see Table 3).

EXPERIMENTAL RESULTS AND INTERPRETATION

Shear Strength and Failure Characteristics

The results of the direct shear tests reveal a clear and consistent distinction in mechanical behavior between monolithic specimens and those containing construction boundaries. Under all tested normal stress conditions, monolithic specimens exhibited significantly higher peak shear strengths, approximately 250 kN/m^2 greater on average, compared to specimens with boundary (see Fig. 3). This reduction underscores the critical role that cohesive bonding plays in resisting shear failure

Table 2 Specimen configuration and direct shear test matrix

Normal stress (kN/m^2)		30	100	200	300
Number of tests	Without boundary	3	3	3	3
	With boundary	3	3	3	3

Table 3 Shear strength parameters derived from direct shear tests

Boundary condition	Without boundary	With boundary
Cohesion (kN/m^2)	245.61	3.65
Internal friction angle (°)	28.27	27.07

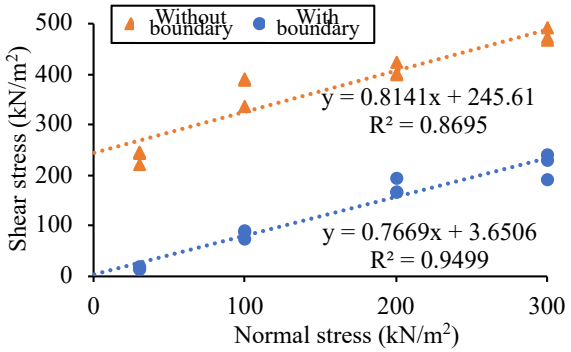

Fig. 3 Peak shear strengths under different normal stress conditions

within stabilized soils.

In monolithic specimens, the shear strength was mobilized through a combination of internal cohesion and friction. These specimens consistently demonstrated failure along well-developed, rough shear planes, indicative of significant material interlocking and bond continuity. The roughness and irregularity of the failure planes suggest substantial energy dissipation through internal cracking and frictional engagement at the microstructural level.

Conversely, specimens with construction boundaries exhibited drastically different behavior. Shear failure predominantly occurred along the planar boundary between the two separately cast segments, where bonding was weak or absent. These failures were characterized by smooth, featureless shear surfaces with minimal evidence of interlocking, leading to markedly lower resistance and stable residual strength. The data indicate that in the presence of boundaries, the shear strength was governed almost entirely by frictional resistance, with cohesion approaching negligible values.

This contrast in failure characteristics is particularly relevant in the context of ground improvement design, where assumptions of monolithic behavior may significantly overestimate actual performance when boundaries are present. The suppression of cohesion and lack of interfacial roughness fundamentally alter the stress transfer capacity of the improved ground under shear loading.

Stress–Displacement Behavior

Analysis of the stress–displacement curves further clarifies the mechanical response differences between specimen types. Specimens with boundary exhibited a rapid rise in shear stress, reaching peak strength within approximately 1 mm of horizontal displacement. This was followed by an immediate and sustained drop to a relatively constant residual strength level. Such behavior is characteristic of brittle boundary failure with minimal energy absorption and post-peak ductility (see Fig. 4).

In contrast, monolithic specimens showed a broader range in peak displacement values and a more gradual decline to residual strength. Notably, several monolithic specimens displayed secondary increases in shear resistance after the initial peak, suggesting the mobilization of additional interlocking or shear surface roughness during deformation. These fluctuations imply a more complex characteristic involving progressive damage and potential dilation along the shear plane (see Figs. 4 and 5).

The differences in stress–displacement responses not only reflect distinct failure processes but also carry implications for deformation behavior under service loading conditions. Specimens with boundary, with their lower ductility and reduced peak strength, may be more susceptible to sudden displacement or progressive failure under seismic or cyclic loading.

Statistical and Reproducibility Analysis

To evaluate the consistency and reliability of the experimental results, regression analysis was conducted using the Mohr-Coulomb failure criterion. The shear strength data for both specimen types were plotted against normal stress, and linear fits yielded

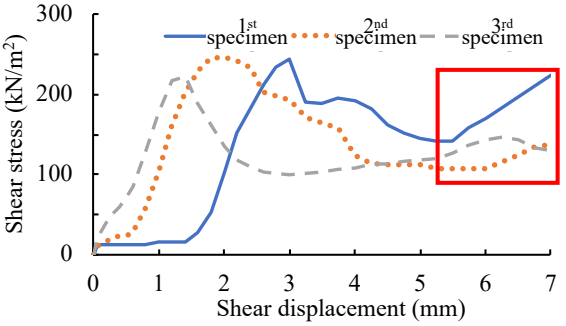

Fig. 4 Shear stress–displacement behavior under 30 kN/m^2 (without boundary)

Fig. 5 Surface roughness of post-failure shear planes (monolithic vs. boundary specimens)

high coefficients of determination ($R^2 \approx 1$), indicating excellent agreement with the theoretical model.

For monolithic specimens, the linear fit confirmed the presence of both cohesive and frictional components in shear resistance. In contrast, the regression line for specimens with boundary passed near the origin, reinforcing the earlier observation that these specimens exhibited negligible cohesion and friction-dominated behavior.

The tight clustering of data points and low variability across repeated tests for each condition further validate the experimental methodology and suggest that the observed differences are systematic and reproducible. This robustness is critical for the subsequent calibration of numerical models and for establishing generalizable conclusions about the role of construction boundaries in ground improvement.

NUMERICAL SIMULATION USING FINITE ELEMENT METHOD

Model Construction

To simulate the shear behavior observed in the direct shear tests, a two-dimensional finite element method (FEM) model was developed, replicating the experimental geometry and boundary conditions with high fidelity. The model geometry represented a simplified cross-section of the shear box, including upper and lower soil-cement blocks in contact at a defined shear boundary.

A key feature of the model was the incorporation of joint elements at the boundary between the upper and lower blocks in the specimens with boundary. These joint elements are specialized numerical constructs that allow discontinuous displacement and independent assignment of mechanical properties, specifically, normal and shear stiffness, friction angle, and cohesion. This formulation enables realistic simulation of boundary slip, separation, and post-peak behavior, which are not adequately captured by standard continuum elements (see Figs. 6 and 7).

The surrounding improved ground was modeled using linear elastic–perfectly plastic material properties, calibrated to match the experimentally observed behavior of monolithic specimens. Mesh resolution was refined near the joint elements to enhance numerical accuracy in regions of expected high stress gradients.

Parameter Calibration

Accurate simulation of boundary behavior critically depends on the selection of appropriate joint element parameters. To this end, an inverse analysis approach was employed, wherein the FEM model output was iteratively compared to experimental shear stress–displacement curves, and the parameters were adjusted to minimize the deviation.

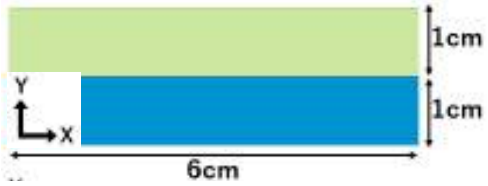

Fig. 6 FEM model configuration for simulating direct shear tests

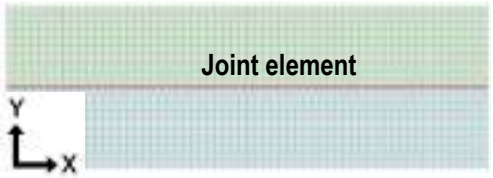

Fig. 7 Assigned position of joint elements in the FEM model

The optimal parameter set for the joint elements was determined as follows:

- Normal stiffness: 1×10^6 kN/m^3
- Shear stiffness: 50 kN/m^3
- Cohesion: 100 kN/m^2
- Friction angle: 15°

These values were selected to reflect the observed frictional nature of the boundary and to reproduce the residual strength levels documented in the specimens with boundary.

The high normal stiffness value ensured realistic constraint against dilation and separation under compressive loading, while the relatively low shear stiffness allowed for slip behavior that matched experimental deformation profiles. The low cohesion and moderate friction angle captured the diminished bonding and interfacial friction characteristic of cold joints (see Fig. 8).

Model Validation

Model validation was performed by comparing the FEM results with the experimentally measured shear stress–displacement curves for both specimen types. For specimens with boundary, the model successfully replicated the initial peak shear strength and subsequent transition to a constant residual strength, with discrepancies limited to within ±10 kN/m^2 across all normal stress conditions.

However, for monolithic specimens, the model underpredicted the observed peak strengths. This discrepancy is attributed to the inability of the current model to capture interlocking effects and surface roughness at the failure plane (see Fig. 9), mechanisms which contribute significantly to peak resistance but are not explicitly modeled in a continuum or joint element framework.

Despite this limitation, the model accurately reflected the residual behavior, confirming its reliability for simulating friction-governed failure characteristics typical of construction boundaries.

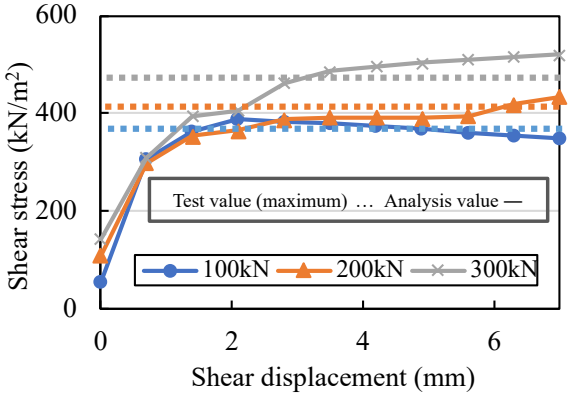

Fig. 8 Comparison between experimental and simulated results using inverse analysis parameters

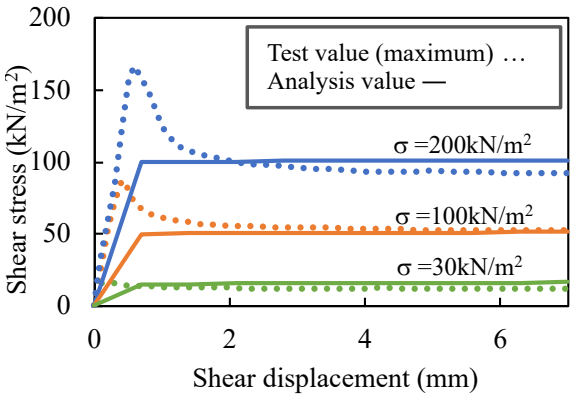

Fig. 9 Comparison of simulated and experimental results for monolithic specimens

The results demonstrate that joint elements are well suited for capturing post-peak behavior, which is particularly important in performance-based design and safety assessments.

DISCUSSION FOR GEOTECHNICAL IMPLICATIONS OF CONSTRUCTION BOUNDARIES

Mechanical Implications of Construction Boundaries

The experimental and numerical findings clearly demonstrate that the presence of construction boundaries substantially alters the shear resistance characteristics of cement-treated ground. The loss of cohesion and reduction in interfacial roughness result in a transition from mixed-mode (cohesive–frictional) failure, as seen in monolithic specimens, to predominantly frictional failure in specimens with boundary. This shift in failure characteristic leads to a decrease in peak shear strength of over 200 kN/m^2, highlighting the critical vulnerability introduced by construction discontinuities [1,2,3,5].

From a geotechnical design perspective, this reduction in shear capacity cannot be neglected. Grid-type deep mixing systems are typically assumed to act

as a continuous shear-resisting skeleton. However, the introduction of construction boundaries compromises this assumption, potentially enabling localized slippage under shear loading. In seismic regions, this becomes especially significant, as the combination of cyclic loading and reduced boundariestrength may accelerate strain accumulation and increase the risk of progressive failure.

Comparison with Previous Studies

The experimental results align well with previous studies on geomaterial boundaries, such as those involving clay–concrete and soil–geosynthetic systems [3-5]. In these studies, reductions in boundaries strength and cohesion were also observed when discontinuities or weak bonding were present. The failure mode transition, from adhesion-dominated to friction-dominated behavior, has been widely reported, reinforcing the generality of the present findings across boundary types and material systems.

Practical Applications and Quality Control

One of the primary contributions of this study is the development of a practical, mechanics-based framework for evaluating construction boundary behavior. The combination of direct shear testing and calibrated FEM simulations provides both quantitative insight and predictive capability. Specifically, the use of joint elements allows designers to account for boundariespecific parameters in numerical models, enabling realistic simulation of field conditions.

This approach offers a pathway toward more objective and performance-driven quality assurance in ground improvement projects. While current field practices rely heavily on visual inspection and indirect indicators of quality, the results presented here support the introduction of mechanical metrics, such as boundarieshear strength and friction angle, as quantifiable indicators of construction integrity.

CONCLUSIONS

This study investigated the shear characteristics of cement-stabilized ground with and without construction boundaries through laboratory direct shear testing and finite element simulations employing joint elements. The key findings are summarized below:

(1) Construction boundaries lead to significant strength reduction, with peak shear strength decreasing by more than 200 kN/m^2 due to the loss of cohesion and interfacial bonding. Friction-dominated failure was observed in specimens with boundary.
(2) Failure characteristics differ between specimen types, with specimens with boundary showing brittle, low-ductility behavior, while monolithic specimens exhibited rough shear planes and interlocking-driven resistance.
(3) FEM modeling with joint elements successfully captured residual shear behavior in specimens with boundary when calibrated with experimental data, demonstrating its applicability for simulating boundary mechanics.
(4) The integrated testing–modeling approach offers a rational framework for assessing construction boundary effects in ground improvement, contributing to more objective and performance-based design and quality control.

These insights lay the groundwork for the rational design, evaluation, and management of construction boundaries in ground improvement engineering, contributing to the safety and reliability of infrastructure in liquefaction-prone regions.

REFERENCES

[1] Rahmani F., Hosseini S.M., Khezri A., and Maleki M., Effect of Grid-Form Deep Soil Mixing on the Liquefaction-Induced Foundation Settlement, Using Numerical Approach, Arab J. Geosci., Vol. 15, 2022, Article ID 1112.
[2] Ishii I., Towhata I., Hiradate R., Tsukuni S., Uchida A., Sawada S.I., and Yamauchi T., Effect of Grid-Form Deep Soil Mixing on the Liquefaction-Induced Foundation Settlement, Using Numerical Approach, Arab J. Geosci., Vol. 15, 2022, Article ID 1112.
[3] Zeng F., Li Y., and Labuz J.F., Paul-Mohr-Coulomb Failure Criterion for Geomaterials, J. of Geotech. and Geoenviron. Eng., Vol. 144, Issue 2, 2018, Article ID 06017018.
[4] Zhu Y., Li G., Mi Z., Wei K., and Chen Z., Experimental Investigation on the Shear Behavior of Boundary Between High Plastic Clay and Concrete, Adv. in Mater. Sci. and Eng., Vol. 2022, Issue 1, 2022, Article ID 9313881.
[5] Zhou J., Ban C., Zhou H., Ren J., and Liu Z., Experimental Study on the Shear Strength and Failure Mechanism of Cemented Soil–Concrete Boundary, Materials, Vol. 16, Issue 12, 2023, Article ID 4222.

Copyright © Int. J. of GEOMATE All rights reserved, including making copies, unless permission is obtained from the copyright proprietors.

15th Int. Conf. on Geotechnique, Construction Materials & Environment, Kyoto, Japan, 11-13 November 2025, ISBN 978-4-909106124 C3051

UNRAVELING THE MECHANISMS OF LIQUEFACTION-INDUCED SOIL EJECTA: A RULE-BASED APPROACH

Emerzon S. Torres[1], and Jonathan R. Dungca[1]

[1]Department of Civil Engineering, De La Salle University, Philippines

ABSTRACT

Soil ejecta, commonly observed as sand boils, is a prominent manifestation of soil liquefaction during earthquakes, often leading to ground settlement, structural damage, and post-earthquake site instability. Despite their impact, traditional liquefaction models largely focus on triggering mechanisms and rarely address the conditions that govern ejecta formation. This study applies Rough Set Machine Learning (RSML), an interpretable rule-based algorithm, to analyze 96 historical case histories of liquefaction, including 85 cases with observed soil ejecta. Six geotechnical and seismic parameters—moment magnitude, peak ground acceleration, groundwater table depth, average critical layer depth, corrected SPT N-value, and fines content—were used as model inputs. IF–THEN rules were induced and evaluated using support, strength, certainty, and coverage metrics. Sensitivity and interaction analyses revealed the critical influence of corrected penetration resistance, groundwater conditions, and fines content on ejecta occurrence. Notably, soil ejecta was found to occur even in moderately dense or fine-grained soils, challenging conventional assumptions. The parameter interaction map further highlighted the combined effects of seismic and subsurface conditions. This interpretable model provides valuable insights into post-liquefaction behavior and supports improved hazard assessment, mitigation planning, and resilience strategies. The findings contribute to the advancement of data-driven approaches in earthquake geotechnical engineering.

Keywords: Sand boils, Interpretable machine learning, Rough set theory, Liquefaction hazard assessment, Artificial intelligence

INTRODUCTION

Soil liquefaction is still considered one of the most important and complex phenomena in soil dynamics [1]. Soil liquefaction's complex relationships refer to the dynamic and nonlinear interactions between multiple factors, including seismic parameters (magnitude, frequency), soil properties (grain size, density), hydraulic conditions (pore water pressure, drainage), and other geotechnical factors (soil stratification, confining pressure) that determine how soil responds to stress.

Sand boils, or soil ejecta, are a prominent manifestation of soil liquefaction during earthquakes, contributing to ground settlement, structural damage, and post-earthquake site instability [2].

The ejection of subsurface material can result in differential settlement, tilting, and structural cracking, while also compromising foundation support and damaging underground utilities. Despite these significant consequences, traditional liquefaction assessment models primarily focus on triggering mechanisms and often overlook the factors governing the formation of soil ejecta. Some studies have calculated liquefaction indices based on SPT and validated by sand boil observations [3]. Others have explored the mechanisms of lateral spreading as a major effect of liquefaction [4]. However, a notable gap remains in the analysis of historical liquefaction databases that explicitly account for the presence and characteristics of soil ejecta.

This study employs Rough Set Machine Learning (RSML), an interpretable machine learning algorithm, to analyze and extract patterns from historical case histories of liquefaction-induced soil ejecta. IF–THEN rules were generated to identify and understand the parameters contributing to the susceptibility of soil ejecta. Further data analyses were also conducted to determine which individual parameters and parameter combinations most significantly influence the occurrence of sand boils.

RESEARCH SIGNIFICANCE

The outputs of this study—decision rules, sensitivity, and parametric analyses—provide valuable insights for researchers and engineers aiming to understand the mechanisms underlying soil ejecta. Furthermore, the results may guide the selection of suitable ground improvement techniques and disaster risk reduction strategies tailored to specific site conditions and project requirements. The unconventional patterns revealed by the induced rules may highlight potential directions for future research.

METHODS

The research flow is illustrated in Fig. 1. From the soil liquefaction database [5-6], a total of 96 case histories involving soil ejecta were utilized in this

study. Minor data cleansing was performed, followed by discretization to prepare the data for machine learning. The Rough Set Exploration System (RSES 2.2) [7], a rough set-based software, was employed to induce decision rules from the constructed decision table. Rule pruning and shortening were applied to eliminate redundant and weak rules. The resulting rule sets were evaluated to identify the most robust and informative set. The optimal rule set was subsequently subjected to sensitivity and parametric analyses to assess the influence of individual parameters and their interactions.

Soil Ejecta Database

From the available global database of liquefied sites, 96 events were selected for this study, as summarized in Table 1. Among these, 85 sites exhibited manifestations of soil ejecta, while 11 showed no such occurrence. Six conditional attributes (input parameters) and one decision attribute (output parameter) were collected and used for the simulation. The field names and definitions, along with the discretization schemes and frequency distributions of the variables, are presented in Table 2. The decision attribute represents the presence or absence of observed soil ejecta.

Rough Set Machine Learning

Rough Set Theory (RST), developed by Pawlak (1982), addresses vagueness and uncertainty in knowledge-based systems [8]. In RST, knowledge is typically represented using a decision table composed of rows and columns, where attributes are categorized into condition and decision attributes. Each row in the decision table represents a rule in the form: IF (conditions) … THEN (decision). An inductive process is applied to extract rules from the data contained in the decision table. RST has been successfully applied in various machine learning tasks, including clustering, feature selection, and rule induction. In this study, rule induction was carried out to generate interpretable IF-THEN statements that define patterns associated with soil ejecta occurrence. The induced rules were evaluated using four key validation statistics: *support*, *strength*, *certainty factor*, and *coverage*. *Support* indicates the number of observations that follow a given rule, while *strength* is the proportion of these supports relative to the total number of observations in the dataset. The *certainty factor* reflects the likelihood that an observation belongs to the decision class when the conditions of a rule are met. Lastly, *coverage* measures the extent to which a particular rule accounts for the instances within the decision class.

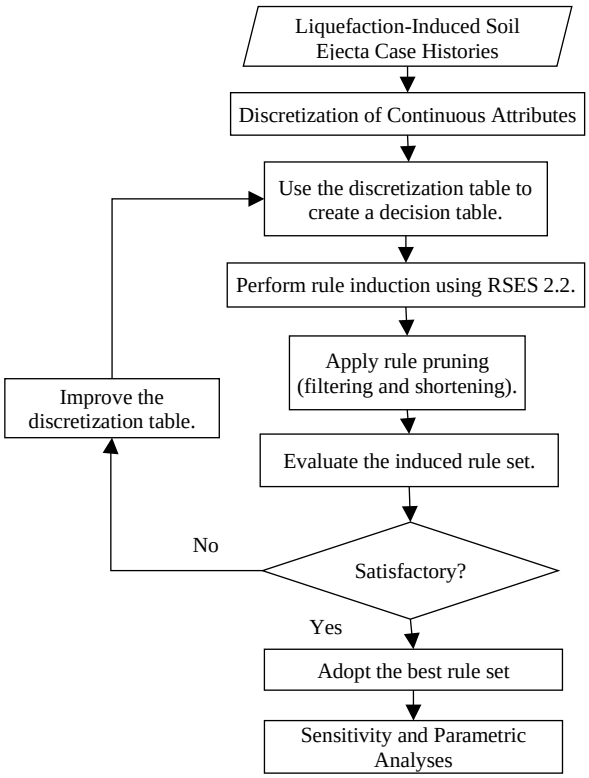

Fig.1 General framework of the study.

Table 1 Soil ejecta database used.

Earthquake Event	No.of Sites	Earthquake Event	No. of Sites
1944 Tohnankai	3	1979 Imperial Valley	4
1948 Fukui	2	1981 WestMorland	3
1964 Niigata	4	1983 Nihonkai-Chubu June 21	1
1968 Tokachi-Oki	3	1983 Nihonkai-Chubu May 26	12
1971 San Fernando	2	1987 Superstition Hills	1
1975 Haicheng	3	1989 Loma Prieta	14
1976 Guatemala	2	1990 Luzon	1
1976 Tangshan	1	1993 Kushiro-Oki	2
1977 Argentina	3	1994 Northridge	3
1978 Miyagiken-Oki Feb 20	1	1995 Hyogoken-Nambu (Kobe)	5
1978 Miyagiken-Oki June 12	14	1999 Kocaeli	12
Total no. of sites		96	

Table 3 presents a sample decision table used in this study, with attributes discretized into two to three bins: very high, high, and low. This table was input into the RSES 2.2 to generate decision rules along with their corresponding validation statistics.

Table 2 Field names, attributes, and discretization of variables.

Attributes	Definition	Low		High		Very High	
		Range	Count	Range	Count	Range	Count
M	Moment Magnitude	[5.9, 7.5)	20	[7.5, 8.3]	76	-	-
a_{max} (g)	Maximum Acceleration	[0.09, 0.28)	51	[0.28, 0.693)	43	[0.693, 0.84]	2
Avg depth (m)	Average Depth	[1.8, 4.9)	47	[4.9, 10. 3)	46	[10.3, 11.5]	3
Depth GWT (m)	Depth of Groundwater Table	[0, 1.7)	47	[1.7, 4.275]	38	[4.275, 7.2]	11
$(N_1)_{60}$	Corrected SPT N Value	[1.7, 10.3)	51	[10.3, 24.1)	44	[24.1, 25.9]	1
FC (%)	Fines Content	[0,8)	42	[8, 60.5)	43	[60.5, 92]	11
Sand boil?	No or Yes	No	11	Yes	85	-	-

Sensitivity and Parametric Analyses

Ablation-based sensitivity analysis was conducted to assess the importance of each input attribute in the rule-based model. By systematically removing one condition attribute at a time and measuring the change in model accuracy through cross-validation (10 and 50 k-folds), the analysis revealed each attribute's contribution to model performance. This method provided valuable insights into the stability and robustness of the model and the interplay between input parameters.

To enhance interpretability, a parametric analysis in the form of a parameter interaction map was developed using insights from sensitivity analysis and rule-based interactions. Ablation analysis measured the impact of removing individual parameters on model accuracy, classifying their importance as high, moderate, or low based on performance delta from 100-fold cross-validation. Additionally, parameter interactions were quantified by the frequency of co-occurrence within the induced rule set, categorized as strong, moderate, or weak. The interaction map visually represents these relationships, offering a clearer understanding of how parameters influence each other and contribute to soil ejecta susceptibility.

RESULTS AND DISCUSSION

This study developed a liquefaction-induced soil ejecta rule-based model using RSML. Its primary objective was to identify and understand the key factors influencing the occurrence of soil ejecta. The model incorporates six conditional attributes and a single decision attribute—the presence or absence of soil ejecta.

To improve model performance, an iterative optimization of the discretization process was conducted until the best rule-based model emerged, yielding the most favorable validation statistics. The model is characterized by a highly imbalanced distribution of decision classes, with 85 events showing the presence and only 11 showing the absence of soil ejecta. This imbalance reflects the frequent occurrence of ejecta in liquefaction events and introduces challenges in rule induction. The selected optimal model was selected, achieving 96.4% accuracy and 87.5% coverage, balancing predictive performance with reliable representation of liquefaction-induced soil ejecta.

Table 3 Sample decision table used in this study.

M	a_{max} (g)	Avg depth (m)	Depth GWT (m)	$(N_1)_{60}$	FC	Sand boil?
H	L	L	H	L	L	No
H	L	H	H	H	H	No
H	L	H	L	L	H	No
H	H	H	H	H	L	No
H	H	L	H	VH	L	No
L	VH	H	VH	H	H	No

Note: H = High, L=Low, VH=Very High

Table 4 presents the optimal rule set for the soil ejecta rule-based model, comprising 24 rules—1 for the absence and 23 for the presence of soil ejecta. This distribution reflects the common occurrence of soil ejecta in liquefaction events. As shown in Fig. 2, several rules (specifically Rules 2–8 and 14) exhibit coverage factors exceeding 20%, indicating strong explanatory power within the dataset.

Notably, soil ejecta was observed even at lower ranges of moment magnitude and peak ground acceleration, suggesting that ejecta can occur under varied seismic conditions once liquefaction is initiated. This observation aligns with recent findings by [9] on the complex nature of liquefaction-induced ground deformation. Furthermore, the presence of ejecta was associated with corrected SPT N-values ranging from 10.3 to 24.1 and high fines content (60.5–92%).

These findings suggest that excess pore pressure generation may occur even in moderately dense or

Table 4 The chosen best rule set for the sand boils rule-based model.

Rules	M (magnitude)	A_{max} (maximum acceleration)	Avg depth (m) Average Depth	Depth GWT (m) Depth of Groundwater Table	$(N_1)_{60}$ Corrected SPT N Value	FC Fines Content	Soil Ejecta?
1	Low			Very High	High		No
2				Low		Low	Yes
3			Low		High		Yes
4			Low			High	Yes
5		Low		Low			Yes
6					Low	High	Yes
7		Low				Low	Yes
8					High	Low	Yes
9	Low				Low		Yes
10	Low		Low				Yes
11	Low			High			Yes
12				Very High	Low		Yes
13	Low	Low					Yes
14			High		Low		Yes
15	High			Very High			Yes
16	Low			Low			Yes
17	Low					Very High	Yes
18		Low				Very High	Yes
19			Very High				Yes
20		Low		Very High			Yes
21	Low					Low	Yes
22			High			Very High	Yes
23				Very High		Low	Yes
24		High			Low	Low	Yes

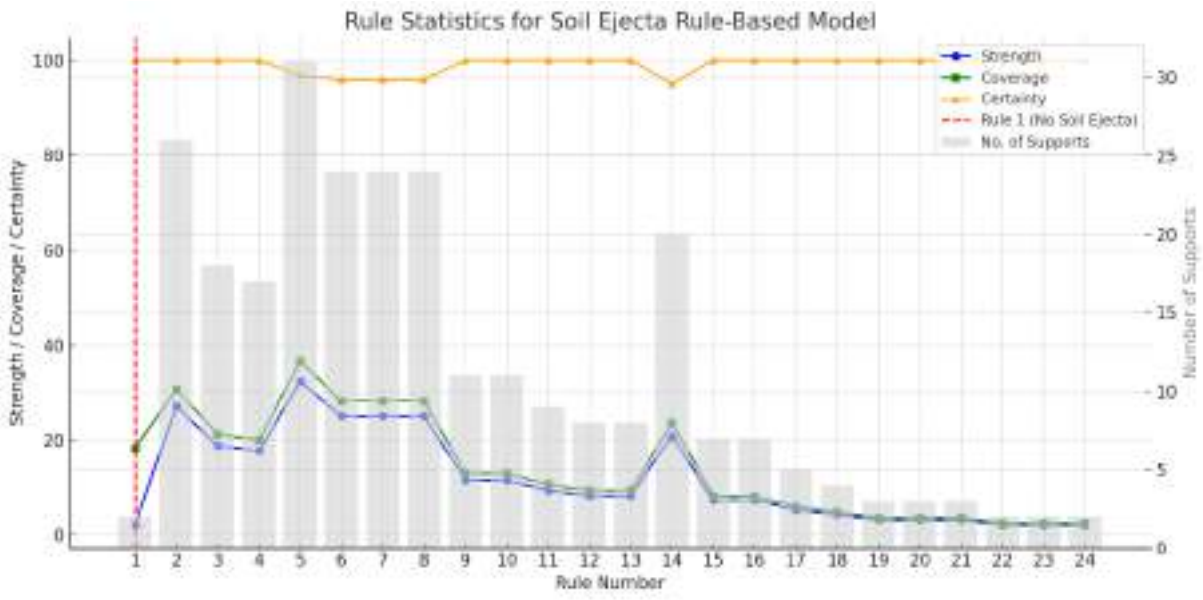

Fig. 2 Validation rule statistics for the generated rules.

fine-grained soils—challenging conventional assumptions. Similar conclusions were drawn by [5,10], who emphasized the nuanced behavior of silty soils under liquefaction conditions. These insights highlight the multifaceted nature of soil ejecta formation and underscore the importance of data-driven approaches in advancing our understanding of liquefaction phenomena.

While the model demonstrates high certainty factors across its 24 rules, the strength and coverage factors—generally below 33%—suggest limited generalizability. This limitation is likely due to the relatively small dataset (96 cases). Despite this, Rule 5 emerged as the most influential, exhibiting the highest coverage. It can be expressed as follows:

"If the maximum acceleration is low and the groundwater table is shallow, then soil ejecta is likely to occur."

This rule indicates that even with peak ground acceleration below 0.28g, the occurrence of soil ejecta remains probable when the groundwater table is shallow (approximately 1.7 meters). This finding highlights the critical role of groundwater conditions in soil ejecta formation, even under moderate seismic loading [2,10].

The sensitivity analysis of the soil ejecta rule-based model demonstrates its strong predictive capability, with baseline accuracies of 77.8% (10-fold cross-validation) and 78.0% (50-fold). These values are within the published efficiency of other state-of-practice liquefaction models [11]. Among the parameters analyzed, corrected penetration resistance emerged as the most critical, as its removal resulted in the largest drop in accuracy (62.2% and 60.0%, respectively), highlighting the importance of soil density and stiffness in resisting liquefaction. Groundwater table depth was the second most influential factor, with its removal decreasing accuracy to 65.6% and 66.0%, affirming that high water tables increase susceptibility to liquefaction by reducing effective stress. The average depth of the critical layer also significantly impacted model performance, aligning with observations that shallow liquefiable layers facilitate the upward movement of fluidized soil. Notably, fines content showed a strong influence, reflecting its role in both liquefaction potential and soil erodibility.

The parameter interaction map highlights interactions spanning various levels of importance and strength. The most significant interaction occurs between moment magnitude and groundwater table depth, emphasizing their joint role in enhancing liquefaction potential and driving soil ejecta formation.

Table 5 Soil ejecta sensitivity analysis.

Attribute Removed	Total Accuracy (k=10 folds)	Total Accuracy (k=50 folds)
No Attribute Removed	77.8	78.0
Moment Magnitude	70.0	70.0
Maximum Acceleration	75.6	76.0
Average Depth of Critical Layer	70.0	72.0
Depth of Groundwater Table	65.6	66.0
Corrected Penetration Resistance	62.2	60.0
Fines Content	64.9	62.0

Prolonged shaking enables pore pressure build-up, while shallow groundwater conditions reduce effective stress, promoting upward movement of liquefied soil. These conditions also contribute to uneven ground settlements and extensive ejecta in stratified subsurface profiles. Moderate interactions—such as those between corrected SPT N-values and fines content, and between maximum acceleration and fines content—underscore the combined influence of soil density, composition, and seismic energy. The model's interaction patterns mirror those of the other published RSML-based models [4,10], indicating that the same parameters influencing liquefaction triggering also govern post-liquefaction surface manifestations. This continuity highlights the importance of interpretable models in uncovering the physical dependencies behind complex geotechnical behavior.

CONCLUSIONS

This study developed and evaluated a rule-based model for liquefaction-induced soil ejecta using RSML, offering an interpretable, data-driven framework for understanding soil behavior under seismic loading. By analyzing 96 case histories and generating IF-THEN rules, the model identified key parameters influencing soil ejecta, including corrected SPT N-value, groundwater table depth, fines content, and an average depth of the liquefiable layer.

Sensitivity and interaction analyses revealed that ejecta occurrence is not solely dependent on strong seismic events but also significantly influenced by shallow groundwater conditions and soil composition—especially in silty soils.

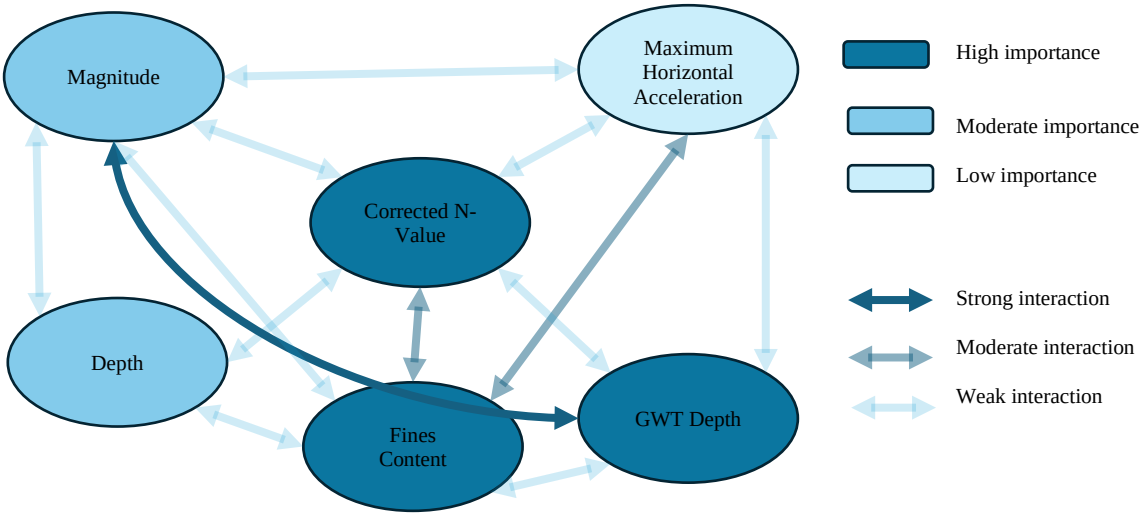

Fig. 3 Parameter interaction map for liquefaction-induced soil ejecta.

The model achieved a high accuracy of 96.4% and a coverage of 87.5%, demonstrating its robustness despite the dataset's class imbalance. Although the generalizability is limited by the small sample size, the model's findings align with field observations and existing literature. The interaction map further highlighted complex interdependencies between parameters, emphasizing the need for multi-parameter analysis in liquefaction studies.

Overall, this study contributes to the current understanding of soil ejecta that can be used for hazard assessment, risk reduction, and resilience planning. Future research should expand the dataset and explore hybrid models to further refine predictive capabilities and support infrastructure safety in earthquake-prone regions.

ACKNOWLEDGMENTS

The authors would like to express their deepest gratitude to DOST-ERDT for funding this research, and to the DLSU Geotechnical Engineering Division Faculty for their support.

REFERENCES

[1] Latifi F.E., and Baba K., Predicting Liquefaction Susceptibility in North-East Morocco: Comparative Analysis of Semi-empirical Methods and UBC3D-PLM Model, Civil Engineering and Architecture, Vol. 12, Issue 3, 2024, pp.1474–1489.

[2] Kramer S.L., Chapter 9, Geotechnical Earthquake Engineering, Prentice Hall, Inc., 1996, pp.348–417.

[3] Kim H.S., Kim M., Baise L.G., and Kim B., Local and Regional Evaluation of Liquefaction Potential Index and Liquefaction Severity Number for Liquefaction-Induced Sand Boils in Pohang, South Korea, Soil Dynamics and Earthquake Engineering, Vol. 141, 2021, pp.1–16.

[4] Torres E.S., and Dungca J.R., An Interpretable Machine Learning Approach in Understanding Lateral Spreading Case Histories, International Journal of GEOMATE, Vol. 26, Issue 116, 2024, pp.110–117.

[5] Boulanger R.W., and Idriss I.M., CPT and SPT Based Liquefaction Triggering Procedures, UCD/CGM-14/01, Center for Geotechnical Modeling, University of California, Davis, 2014, pp.1–134.

[6] Cetin K.O., Seed R.B., Kayen R.E., Moss R.E.S., Bilge H.T., Ilgac M., and Chowdhury K., Dataset on SPT-Based Seismic Soil Liquefaction, Data in Brief, Vol. 20, 2018, pp.544–548.

[7] Bazan J.G., and Szczuka M., The Rough Set Exploration System, in Transactions on Rough Sets III, Peters J. F. and Skowron A. (Eds.), Springer, Berlin, Vol. 3400, 2005, pp.37–56.

[8] Pawlak Z., Rough Sets, International Journal of Computer & Information Sciences, Vol. 11, Issue 5, 1982, pp.341–356.

[9] Ntritsos N., and Cubrinovski M., Ground-Motion Effects on Liquefaction Response, Soil Dynamics and Earthquake Engineering, Vol. 177, 2024, pp.1–15.

[10] Torres E., and Dungca J., Prediction of Soil Liquefaction Triggering Using Rule-Based Interpretable Machine Learning, Geosciences, Vol. 14, Issue 6, 2024, pp.1–23.

[11] Maurer B.W., and Sanger M.D., Why "AI" Models for Predicting Soil Liquefaction Have Been Ignored, Plus Some That Shouldn't Be, Earthquake Spectra, Vol. 39, Issue 3, 2023, pp.1883–1910.

Copyright © Int. J. of GEOMATE All rights reserved, including making copies, unless permission is obtained from the copyright proprietors.

15th Int. Conf. on Geotechnique, Construction Materials & Environment, Kyoto, Japan, 11-13 November 2025, ISBN 978-4-909106124 C3051

SOME FEATURES OF EARTHQUAKE DISTRIBUTION IN TURKMENISTAN

Valeriy Burmin [1], Goharik Petrosyan [2]

[1,2] Institute of Physics of the Earth named after. O.Yu. Schmidt, RAS, Moscow, Russia

ABSTRACT

To date, not many works have been published on the issues of seismicity in the territory of Turkmenistan and the Northeast of Iran. At the same time, some areas of Turkmenistan are characterized by high seismicity, along with the most seismically active zones of the former USSR. It is enough to mention the famous destructive Ashgabat earthquake, which occurred on October 5, 1948.

This article compares the distributions of earthquake hypocenters in Turkmenistan obtained from the ISC catalog data for the period from 1964 to 2021 and the results of the recalculation of hypocenters according to the ISC bulletin for the same period. In total, the ISC catalog for the specified period contains about 6000 events with a magnitude greater than 2.5. The authors recalculated the hypocenters of slightly more than 2100 earthquakes. It is shown that the depths of earthquake sources in the areas under consideration can be located at depths of up to 600 km, while according to the ISC catalog, the maximum depths of earthquake sources do not exceed 100 km. In this work, to determine the coordinates of hypocenters, the method of minimizing the functional of the residuals of theoretical and observed travel times of seismic waves is used, which was first proposed in [1,2].

Keywords: Turkmenistan, ISC Catalog, Times of Arrival Seismic Waves, Determination of Coordinates, Recalculation

INTRODUCTION

The first documented information about earthquakes in Turkmenistan appeared in the catalog of I.V. Mushketov and A.P. Orlov [3]. The study of seismicity in Turkmenistan itself began after a strong earthquake that occurred on May 1, 1929, in the Kopetdag Mountains south of Ashgabat [4].

G.P. Gorshkov, in his work, identified two areas of increased seismicity: in the Krasnovodsk region (now Turkmenbashi) and south of Ashgabat in the Central Kopetdag region [5,6]. The idea that it is necessary to identify two isolated areas with high seismic intensity in Turkmenistan was first expressed in the work [7]. The most complete coverage of modern seismicity in Turkmenistan is given in the periodicals of the Unified Geophysical Service of the Russian Academy of Sciences "Earthquakes of Northern Eurasia" (see, for example, [8]).

Based on geological and seismotectonic characteristics, the territory of Turkmenistan can be divided into three regions: Prikopetdag region (Central Turkmenistan); Krasnovodsk region (Western Turkmenistan); Eastern Turkmenistan [9]. According to the results of earthquake observations, the highest seismic activity is observed in the region of Western Turkmenistan, Ashgabat, and the Shirvan-Kuchan region (Khorasan province) bordering it in the South in Northern Iran [10].

In recent years, events that have occurred have revealed the high seismicity of Turkmenistan. On December 6, 2000, the Balkan earthquake (also known as the Western Turkmen earthquake) became one of the strongest in Turkmenistan in recent decades and one of the strongest in the Balkan region of Turkmenistan in 100 years. The magnitude at the epicenter was 7.3. According to the MSK-64 intensity scale, shaking exceeded 8 points.

The earthquake was accompanied by aftershocks, especially strong on December 7, with a magnitude of more than 3.5. Just a couple of weeks earlier, another strong earthquake occurred in the region, which is associated with the Balkan earthquake due to common causes (Baku, November 25, 2000). The magnitude was 6.2. The epicenter of the earthquake was in the Balkan corridor, on a flat plain between the Big and Small Balkan ridges, east of the city of Nebit-Dag and northwest of the city of Kazandzhik.

Among the large settlements where the intensity was greatest, the city of Kazandzhik (now Bereket) suffered. The shaking reached 7-8 points.

In the regional administrative center of Nebit-Dag (now Balkanabad) they reached 6-7 points. 8-magnitude tremors were recorded at the Pereval railway station.

More than 150 thousand people lived in the zone where the intensity of the shaking exceeded 6 points.

In Turkmenbashi (Krasnovodsk) the intensity was about 5 points, in Kizyl-Arvat 5 points, in Ashgabat 4 points.

Currently, the Seismic Service of Turkmenistan includes 19 stationary and 22 autonomous stations, which are located in all regions of the country. All

stationary seismic stations are equipped with sets of modern GEOSIG equipment, and records of seismic events are processed. Data from all stations is collected and processed in the Service located at the Institute of Seismology and Atmospheric Physics of the Academy of Sciences of Turkmenistan [8].

Over the course of a number of years, an analysis of the seismic study of the region has shown the need to increase the density of the seismological observation network, as well as to equip the Seismic Service of Turkmenistan with modern recording equipment. Today, the registration of seismicity in the Central Kopetdag is controlled by stationary seismic stations located in Ashgabat, the villages of Manish, Yzgant, Germab, Archabil and Suncha.

As part of the implementation of the State Program for the Comprehensive Development of Seismological Science in Turkmenistan for 2022–2028, the Institute is carrying out a lot of work to create a unified nationwide seismic monitoring system for the territory of Turkmenistan. The Institute prepared technical specifications for the tender announced by the Academy of Sciences of Turkmenistan for the purchase of equipment for the construction of fiber-optic communication lines between digital seismic stations located throughout the country, modern seismic geophysical equipment and office equipment.

RESEARCH SIGNIFICANCE

In our previous works and in this work, from the analysis of modern seismicity in Turkmenistan and Northern Iran, it follows that over the past fifty-seven years, the seismic activity of the region has changed from year to year. Moreover, from 1964 to 1984, seismic activity increased noticeably, and from 1985, seismic activity stabilized, until 2000. From 2001 to 2004, there was a sharp decline in seismic activity in Turkmenistan and Northern Iran. From 2005 to 2016 there is a gradual increase in seismic activity in the region, and then again its decline. But since 2019, there has again been a noticeable increase in activity [3,5,7,11-14].

DISTRIBUTION OF EPICENTERS AND HYPOCENTERS OF EARTHQUAKES IN TURKMENISTAN ACCORDING TO THE ISC CATALOG DATA

Fig.1 shows a map of epicenters on the territory of Turkmenistan and Northeast Iran according to the ISC catalogue.

Fig.2 and Fig.3 show the distribution of hypocenters according to the ISC catalog in the latitude and longitudinal planes.

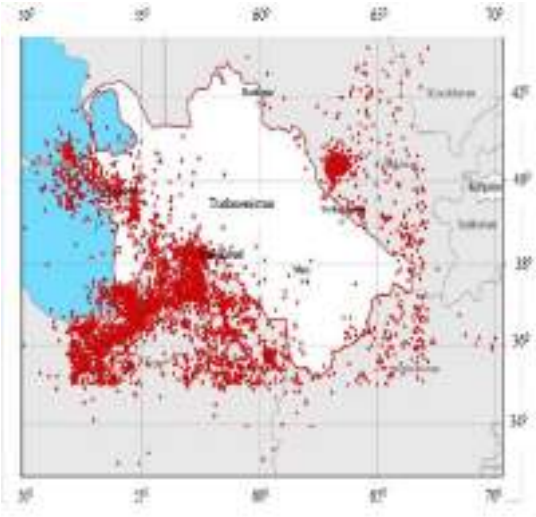

Fig.1 Distribution of epicenters in the territory of Turkmenistan and Northern Iran according to the ISC catalog

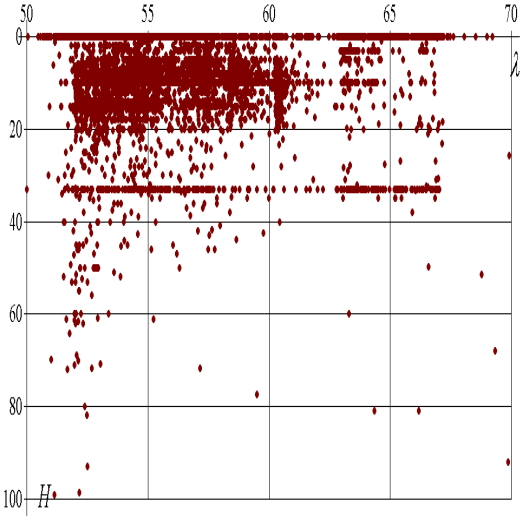

Fig.2 Distribution of hypocenters in the latitudinal plane in the territory of Turkmenistan and Northern Iran according to the ISC catalog

As can be seen from these figures, the bulk of the hypocenters are located in the depth range of 0-20 km. It is worth noting two horizons at depths of 0 and 33 km, where earthquake foci are concentrated. Both of these horizons are most likely determined by the method used to determine earthquake hypocenters. Moreover, the location of the hypocenters at zero depth, in our opinion, is due to the fact that it was not possible to determine the true depth of the foci. The depths of earthquake sources mainly in the Krasnovodsk region reach 100 km.

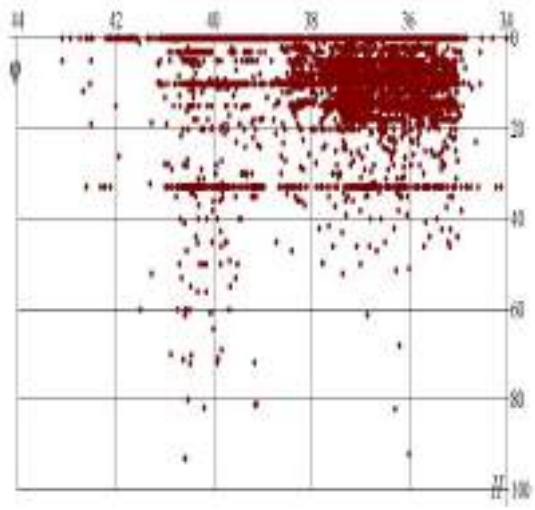

Fig.3 Distribution of hypocenters in the longitudinal plane in the territory of Turkmenistan and Northern Iran according to the ISC catalog

REDEFINITION OF COORDINATES OF EARTHQUAKE FOCI IN TURKMENISTAN

In fact, almost all methods for determining the coordinates of hypocenters come down to minimizing the functional of the residuals of theoretical and observed travel times of seismic waves, which was first proposed in (1), [1,2]:

$$S_t = \sum_{i=1}^{n} (t_i - \tilde{t}_i)^2 \qquad (1)$$

where t_i is the theoretical travel time of seismic waves; $\tilde{t}$ is the travel times of seismic waves obtained from observed data.

However, as shown in [15,16], this approach to determining the coordinates of hypocenters is not optimal. In these works, the problem of determining the coordinates of earthquake hypocenters is posed as a problem of minimizing the functional (2) [15],

$$S = \sum_{i=1}^{n} \rho_i (D_i - d_i)^2 + \mathrm{Y}(H - h)^2 \qquad (2)$$

where D_i and H are determined from the solution of the system of nonlinear equations (3)

$$(X - x_i)^2 + (Y - y_i)^2 + H^2 = v_i^2 (t_i - t_0)^2 \qquad (3)$$

The values of h are specified on a one-dimensional grid Δh in the interval $[0, \mathrm{h_M}]$ and $\mathrm{h_M}$ is calculated from the condition (4):

$$\tau_{\min} = \int_0^{\mathrm{h_M}} \frac{dz}{v(z)} \qquad (4)$$

where $\tau_{\min}$ is the travel time of the seismic wave to the seismic station closest to the source.

For each h, the values of d_i are determined by solving the direct kinematic seismic problems from the condition of proximity of theoretical times t_i the seismic waves travel (determined, for example, from the Wadati plot) with observed times $\tilde{t}_i$.

DISTRIBUTION OF EPICENTERS AND HYPOCENTERS OF EARTHQUAKES IN TURKMENISTAN AFTER RECALCULATION

To clarify the parameters of earthquake hypocenters on the territory of Turkmenistan, we carried out work to redefine the coordinates of earthquake hypocenters using the method mentioned above. The results of the recalculation are presented (Figs.4-6).

Fig.4 shows the distribution of earthquake epicenters after the recalculation. The map shows the epicenters of those earthquakes for which the errors in determining the coordinates are no more than 25 kilometers. The average absolute value of the errors is approximately 8.3 km.

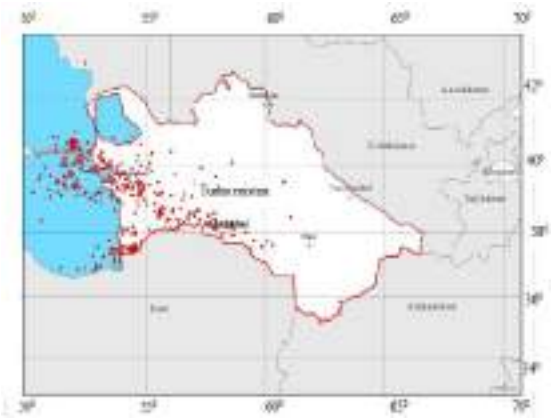

Fig.4 Distribution of epicenters on the territory of Turkmenistan after recalculation

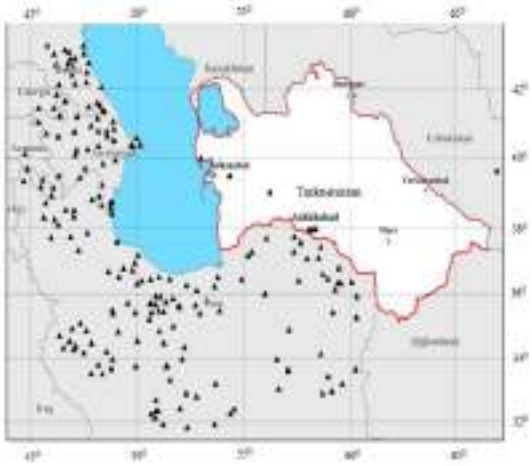

Fig.5 Seismic stations that recorded earthquakes in Fig.4

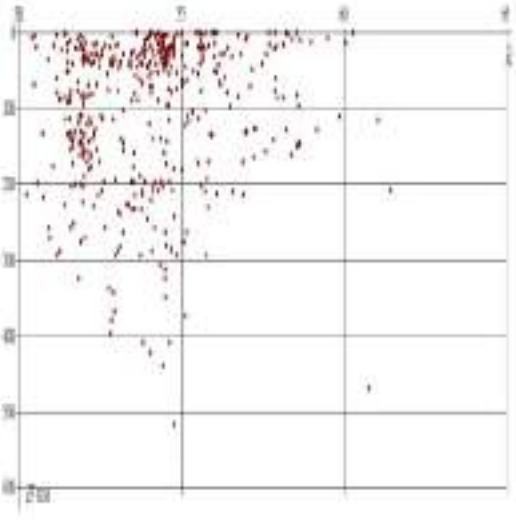

Fig.6 Distribution of hypocenters in the latitudinal plane on the territory of Turkmenistan after recalculation

As can be seen from a comparison of Fig.1 and Fig.4, the distributions differ mainly only in the density with which the epicenters are located.

In Fig.5 shows seismic stations that recorded the earthquakes shown in Fig.4. Each earthquake was recorded by from three to seventy stations.

Fig.6 and Fig.7 show the distributions of earthquake hypocenters after recalculation in the latitude and longitudinal planes. It is clear from the figures that the bulk of the earthquake foci are located in the depth range of 0-40 km. At the same time, a fairly large number of foci are located at depths from 60 to 300 km. At depths from 300 to 500 km there are also a sufficient number of foci. And several foci are located in the range of 500-600 km.

In Figure 8 shows the distribution of earthquake epicenters on the territory of Turkmenistan with foci deeper than 150 km.

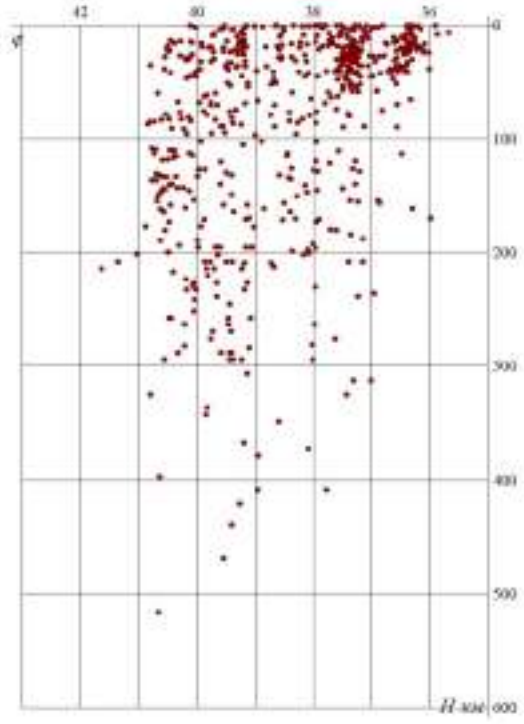

Fig.7 Distribution of hypocenters in the longitudinalplane on the territory of Turkmenistan after recalculation

Fig.8 Distribution of earthquake epicenters on the territory of Turkmenistan with foci deeper than 150 km.

ACKNOWLEDGMENTS

Gratitude to the chief researcher of laboratory 302 of the Schmidt Institute of Physics of the Earth of the Russian Academy of Sciences Valery Yurievich Burmin for his great contribution and for his role as the main author.
The work was carried out within the framework of the state assignment of the Schmidt Institute of Physics of the Earth of the Russian Academy of Sciences No. 0144-2019-0011.

CONCLUSIONS

From the analysis of the ISC catalog data, it follows that the bulk of the hypocenters are located in the depth range of 0-20 km. There are two horizons at depths of 0 and 33 km, where earthquake foci are concentrated. Both of these horizons are most likely determined by the method used to determine earthquake hypocenters. Moreover, the location of the hypocenters at zero depth, in our opinion, is due to the fact that it was not possible to determine the true depth of the foci. The depths of earthquake foci mainly in the Krasnovodsk region reach 100 km.

The recalculation of earthquake hypocenters in Turkmenistan was carried out according to the methodology outlined in [1]. As can be seen from a comparison of the catalog data and the results of recalculation, the distributions of epicenters differ mainly only in the density with which they are located on the surface.

At the same time, the results of the recalculation showed that the bulk of the foci are located in the depth range of 0-300 km. At depths from 300 to 500 km there are also a sufficient number of sources. And several foci are located in the range of 500-600 km.

In conclusion, we can say that the existence of deep earthquakes is not unique. Thus, for the Crimean-Black Sea region, earthquake foci with depths of up to 300 km have been recorded [17], and in the Caucasus to depths of 500 km [18]. On the territory of Turkmenistan, the depths of the foci reach 600 km.

The issues of data reliability are of fundamental importance when constructing certain theories or conclusions. In this case, three factors influence the results of determining the coordinates of earthquake hypocenters in Turkmenistan. The first factor is the accuracy of determining the time of occurrence of the earthquake (time at the source). The second factor is the assignment of the velocity distribution of seismic waves adequate to the true distribution. And the third factor is the choice of the method for determining the coordinates of earthquake hypocenters.

REFERENCES

[1] Sarycheva G.Ch., Petrova N.V., Bezmenova L.V., Seismicity of the Kopetdag Region in 2018-2019, Earthquakes of Northern Eurasia, 2023, Issue 26, pp. 92-101.
[2] Geiger L., Herbsetimmung bei Erdbeben aus den Ankunfzeiten, K. Gessell. Wiss. Goett., 1910, Vol. 4, pp. 331-349.
[3] Odekov O.A., Muradov Ch., Yuvshanov A., Structure of the earth's crust of the main structural elements of Southern Turkmenistan, Izvestiya AN TSSR. Ser. Phys.tech., chem. and geol. Nauk, 1972, Issue 3, pp. 42-51.
[4] Burmin V.Yu., Shemeleva I.B., Avetisyan A.M., Kazaryan K.S., Deep Earthquakes in the Caucasus, Results of Redefinition, Questions of Engineering Seismology, 2019, Vol.46, Issue 2, pp. 25–36. https://doi.org/10.21455/vis2019.2-3
[5] Notes of the Imperial Russian Geographical Society on General Geography. edited by I. Musketov, St. Petersburg, Printing House of the Imperial Academy of Sciences, 1893, Vol. XXVI, Issue 4, pp. 1-582.
[6] https://www.koob.ru/gorshkov_g_p/
[7] Seismicity in Turkmenistan, Answer, Editor Nepesov R.D., Ed. ylym, 1968, pp. 1- 201.
[8] Savarensky E.F., Linden N.A., Masarsky S.I., Earthquakes in Turkmenistan and the Ashgabat Earthquake of 1948, Bulletin of the USSR Academy of Sciences, Geophys. Series., 1953, Issue 1, pp. 3-16.
[9] Rustanovich D.N., Seismicity of the Territory of the Turkmen SSR and the Ashgabat Earthquake of 1948, Questions of Engineering Seismology, 1967, Vol.12, pp. 1- 95.
[10] Rezanov I.A., Tectonics and Seismicity of the Turkmen-Khorasan Mountains, Moscow, Ed. USSR Academy of Sciences, 1959, pp. 1-246.
[11] Geiger L., Probability method for the determination of earthquake epicenters from the arrival time only, Bull., St. Louis Univ., 1912, Vol. 8, pp. 60-71.
[12] Burmin V.Yu., Petrosyan G.R., Some patterns of manifestation of modern seismicity in Turkmenistan and the adjacent territory of Northern Iran, Questions of engineering seismology, 2024, Vol. 51, Issue 1, pp. 18–24. https://doi.org/10.21455/VIS2024.1-2
[13] Kharikov B.A., Dotsuk E.M., Seismic studies along profile № 62001 KMPV - DSS in Western Turkmenistan, Izv. AN

TSSR., Ser. Phys.tech., chem. and geol. Sciences, 1970, Issue 6, pp. 23-27.

[14] Fomenko K.E., Deep seismic sounding in South-Eastern Turkmenistan, Izv. Academy of Sciences of the TSSR, Ser. Phys.tech., chem. and geol. Sciences, 1960, Issue 4, pp. 71-73.

[15] Burmin V.Yu., Petrosyan G.R., Analysis of ISC Earthquake Catalogue Data in Turkmenistan from 1964 to 2021. Tectonophysics and Current Issues of Earth Sciences 2024, Vol.51, Issue 1, pp. 107–113. https://tph.ifz.ru/wp-content/uploads/2025/05/tph_2024.pdf

[16] Burmin V.Yu., A new approach to determining the parameters of hypocenters of nearby earthquakes. Volcanology and Seismology, 1992, Issue 3, pp.73-82.

[17] Burmin V.Yu., Some inverse problems of Seismology, Theory, Experiments, Results, Moscow, Ed. The science, 2019, pp. 1-276.

[18] Burmin V.Yu., Shumlyanskaya L.A., On the issue of deep earthquakes in the Crimean-Black sea region, Questions of Engineering Seismology, 2017, Vol.44, Issue 3, pp. 83–94. doi:10.21455/vis2017.3-5

Copyright © Int. J. of GEOMATE All rights reserved, including making copies, unless permission is obtained from the copyright proprietors.

15th Int. Conf. on Geotechnique, Construction Materials & Environment, Kyoto, Japan, 11-13 November 2025, ISBN 978-4-909106124 C3051

CORRELATION BETWEEN STANDARD PENETRATION TEST AND CONE PENETRATION TEST FOR LIQUEFACTION ASSESSMENT

Nami Nitta [1], Misko Cubrinovski [2] and Shinya Inazumi [1]

[1] Shibaura Institute of Technology, Japan; [2] University of Canterbury, New Zealand

ABSTRACT

Currently, the Standard Penetration Test (SPT) and the Cone Penetration Test (CPT) are widely used for ground investigations. In Japan, SPT is the most commonly adopted method due to its long history of use and has well-established correlations with geotechnical design standards. However, since SPT measurements are taken at 1-meter intervals, it has some limitations, such as missing thin layers and reduced accuracy in identifying loose soils. On the other hand, CPT is widely used in many other countries because it provides continuous data, allowing for a more detailed and accurate assessment of subsurface conditions. When combined with SPT, CPT can improve the reliability and accuracy of ground investigations. However, despite its advantages, it is not widely used in Japan, as the country's geotechnical design standards mainly rely on SPT data. To effectively utilize CPT into ground investigations in Japan, an appropriate conversion framework between SPT and CPT parameters is essential. This research aims to analyze the relationship between SPT and CPT using a liquefaction evaluation method. Specifically, it examines the correlation between the corrected SPT blow count $(N_1)_{60cs}$ and the normalized CPT tip resistance q_{c1Ncs} is examined using the QNR ratio, which is defined as $QNR = q_{c1Ncs}/(N_1)_{60cs}$, to evaluate the accuracy and reliability of conversions between these two parameters. Furthermore, this research discusses the benefits of using both SPT and CPT in combination and evaluates their effectiveness in improving ground investigations, ultimately contributing to the establishment of more reliable ground investigation techniques.

Keywords: Standard penetration test (SPT); Cone penetration test (CPT); Liquefaction assessment; QNR ratio

INTRODUCTION

Soil liquefaction is one of the most critical geotechnical phenomena associated with seismic activity. It occurs when saturated loose soils, typically sands or silty sands, temporarily lose strength and stiffness in response to ground shaking, behaving like a liquid. Liquefaction has caused severe infrastructure damage in numerous earthquakes, highlighting the importance of accurately evaluating its potential, especially in earthquake-prone countries like Japan.

Among various investigation methods, the Standard Penetration Test (SPT) and the Cone Penetration Test (CPT) are the most commonly used for assessing liquefaction potential. The SPT has long been the standard in Japan, valued for its simplicity and the large empirical database developed over decades. However, it provides only discrete data at intervals (typically every 1 m), potentially missing thin weak layers. In contrast, CPT offers continuous, high-resolution data, making it especially suitable for detecting weak layers that are susceptible to liquefaction. Despite its advantages, CPT is not widely adopted in Japan due to design standards and evaluation methods being primarily based on SPT results. Japanese engineers are generally more familiar with SPT-based procedures. Therefore, to promote CPT use, it is essential to develop reliable conversion relationships between CPT and SPT parameters. This would enable engineers to interpret CPT data within the existing SPT based framework, enhancing both the accuracy and efficiency of liquefaction evaluations.

This study aims to address this need by investigating the correlation between SPT and CPT using the liquefaction evaluation procedure developed by Boulanger and Idriss (2014). In particular, it focuses on the relationship between the corrected SPT blow count $(N_1)_{60cs}$ and the normalized CPT tip resistance q_{c1Ncs}, using the QNR ratio defined as $QNR = q_{c1Ncs}/(N_1)_{60cs}$. This research investigates the accuracy and reliability of such conversions and examines the potential advantages of combining SPT and CPT to improve liquefaction assessment and promote more integrated and flexible ground investigation methods.

RESEARCH SIGNIFICANCE

The reliability of liquefaction assessments directly affects the safety, design, and long-term performance of infrastructure in seismic regions. The SPT is widely used due to its long history, extensive empirical database, and high familiarity among engineers, but it has several limitations such as operator dependency, low repeatability, and discontinuous data collection. In contrast, the CPT provides continuous, high-resolution measurements

and more objective, reproducible data. This study aims to systematically compare these two methods and analyze their interrelationships in order to improve the accuracy, reliability, and practicality of liquefaction evaluations.

OVERVIEW OF SPT AND CPT

Standard Penetration Test (SPT)

The Standard Penetration Test (SPT) is a widely used field test for evaluating subsurface conditions in Japan and many other countries. In this test, a 63.5 kg hammer is dropped from a height of 76 cm to drive a sampler into the ground. The number of blows required to drive the sampler 30 cm is recorded as the N-value, which serves as an indicator of soil stiffness and density. The N-value is extensively used for liquefaction assessment and foundation design. SPT can be applied to a wide range of soil types, including sand, clay, and gravel, enabling a comprehensive evaluation of ground conditions. A key benefit is that it allows for the collection of disturbed soil samples, which can be analyzed in the laboratory to determine properties such as grain size distribution and moisture content. However, SPT also has some limitations. Laboratory testing is required to analyze the samples, which increases both time and cost. Additionally, the reproducibility of test results is relatively low, and accuracy may vary depending on field conditions. Since measurements are taken at 1-meter intervals, thin weak layers may be overlooked. In very loose soils where the N-value is 0, the accuracy of strength estimation is reduced.

Cone Penetration Test (CPT)

The Cone Penetration Test (CPT) involves pushing a cone shaped probe into the ground at a constant rate while continuously measuring cone resistance q_c, sleeve friction f_s, and pore pressure u, as shown in Fig. 1. This test provides detailed information about soil stratigraphy, density, and strength characteristics. CPT offers continuous, high-resolution data in real time, allowing for accurate detection of subtle changes in soil composition. Compared to SPT, CPT results are more reproducible and consistent. Furthermore, because it does not require soil sampling or borehole drilling, it minimizes disturbance to the ground and has a lower environmental impact. However, CPT is not suitable for all ground conditions. Penetration can be difficult in very dense soils or gravelly layers, limiting its applicability in such situations. Moreover, unlike SPT, CPT does not provide physical soil samples, so additional sampling is required for laboratory analysis of properties such as particle size distribution or chemical composition.

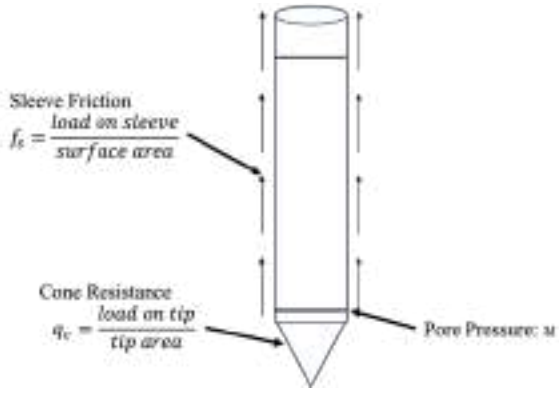

Fig. 1 Overview of the Cone Penetration Test (CPT)

Effectiveness of Combined Use

The SPT and CPT each have their own strengths, so using them together provides a more comprehensive and accurate understanding of ground conditions than relying on just one method. Each test performs better under certain circumstances depending on soil type, site conditions, and the required level of detail. For example, in areas with coarse or gravelly soils, CPT may not perform well or might fail to reach the target depth. In such cases, SPT can still be conducted and provide valuable information about soil strength. On the other hand, CPT offers continuous, high-resolution data at small depth intervals, which helps detect subtle variations in soil layers that SPT might overlook. By combining both methods, the strengths of one can compensate for the limitations of the other. CPT data can fill in the gaps between SPT boreholes, improving the overall understanding of the subsurface conditions. This combined approach enhances the accuracy of ground surveys and supports the development of better liquefaction hazard maps, especially in areas with complex ground conditions. Therefore, using both SPT and CPT together is a highly effective way to assess liquefaction risk and ground stability at specific sites.

RESEARCH METHODOLOGIES

Boulanger & Idriss (2014) Procedure

This study investigates the correlation between the SPT and the CPT using the liquefaction assessment method proposed by Boulanger and Idriss (2014). The cyclic resistance ratio (CRR) under conditions of moment magnitude $M = 7.5$ and effective vertical stress $\sigma_v' = 1atm$ is expressed by

Eq. (1) for SPT and Eq. (2) for CPT. Since liquefaction occurs based on the relative relationship between liquefaction resistance and the applied shear stress, it is common practice to compare the CRR with the cyclic stress ratio (CSR). Based on the derived CRR values, the corresponding CSR values under the same conditions were also computed. Fig. 2 and Fig. 3 illustrate the relationships between CSR and $(N_1)_{60cs}$ as well as $q_{C1N_{CS}}$, respectively. The analysis focuses on clean sand, defined as having a fines content FC of 5% or less.

$$CRR_{M=7.5,\sigma'_v=1atm} = exp\left(\frac{(N_1)_{60_{cs}}}{14.1} + \left(\frac{(N_1)_{60_{cs}}}{126}\right)^2 - \left(\frac{(N_1)_{60_{cs}}}{23.6}\right)^3 + \left(\frac{(N_1)_{60_{cs}}}{25.4}\right)^4 - 2.8\right) \quad (1)$$

$$CRR_{M=7.5,\sigma'_v=1atm} = exp\left(\frac{q_{C1N_{CS}}}{113} + \left(\frac{q_{C1N_{CS}}}{1000}\right)^2 - \left(\frac{q_{C1N_{CS}}}{140}\right)^3 + \left(\frac{q_{C1N_{CS}}}{137}\right)^4 - 2.80\right) \quad (2)$$

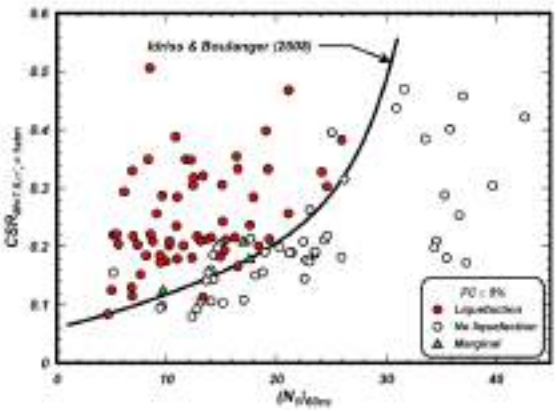

Fig. 2 Curves of $CSR_{M=7.5,\sigma'_v=1atm}$ versus $(N_1)_{60cs}$

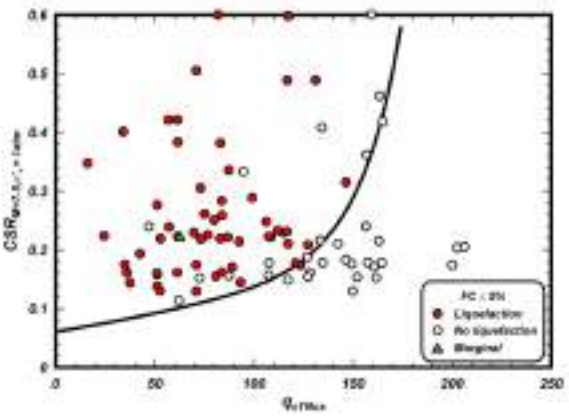

Fig. 3 Curves of $CSR_{M=7.5,\sigma'_v=1atm}$ versus $q_{C1N_{CS}}$

QNR Ratio

To investigate the correlation between SPT and CPT data, this study introduces the QNR ratio, a normalization approach that enables the conversion between normalized cone resistance $q_{C1N_{CS}}$ and corrected SPT blow count $(N_1)_{60cs}$. The QNR ratio is defined as $QNR = q_{c1Ncs}/(N_1)_{60cs}$. This equation provides a common basis for comparing and integrating data obtained from both testing methods. By using QNR, it becomes possible to cross validate results from CPT and SPT, thereby improving the consistency and reliability of subsurface evaluations. This is particularly valuable in multi-method site investigations, where data from different sources need to be interpreted together to develop a coherent and accurate geotechnical model. The introduction of QNR thus enhances data compatibility and supports more robust site characterization, especially in areas with variable soil conditions.

CORRELATION BETWEEN QNR AND $(N_1)_{60cs}$, $q_{C1N_{CS}}$

The correlation between $q_{C1N_{CS}}$ and QNR, derived using the aforementioned method, is shown in Fig. 4. It indicates that QNR remains relatively constant at approximately 8 when $q_{C1N_{CS}}$ is below 100. However, as $q_{C1N_{CS}}$ increases beyond this threshold, the QNR value gradually decreases, eventually reaching around 6 when $q_{C1N_{CS}}$ approaches 150. This observed trend suggests a nonlinear relationship between the two parameters and is consistent with findings from previous research on liquefaction resistance correlations. The noticeable decrease in QNR at higher $q_{C1N_{CS}}$ values may be attributed to a range of geotechnical factors influencing soil behavior. Specifically, soil characteristics such as particle size distribution D_{50} and fines content FC are likely to have a significant impact on cone penetration resistance. These soil properties may affect the measurements obtained by CPT and SPT in different ways, leading to variability in QNR values. This observation highlights the importance of accounting for soil type and composition when applying QNR based conversions in practical site investigations to ensure accurate interpretations.

Furthermore, in order to further investigate the relationship with SPT, which is commonly used in Japan, a correlation between $(N_1)_{60cs}$ and QNR was created and is illustrated in Fig. 5. It shows that QNR remains relatively stable, staying close to approximately 8 when $(N_1)_{60cs}$ is below 10. This indicates a relatively stable relationship in this range. However, as $(N_1)_{60cs}$ increases and approaches around 25, the QNR value gradually declines to about 6. This suggests that the correlation between the two

parameters weakens at higher $(N_1)_{60cs}$. This trend might be reflective of changes in soil behavior or composition as soil resistance increases, emphasizing the need to account for such variations when interpreting test results.

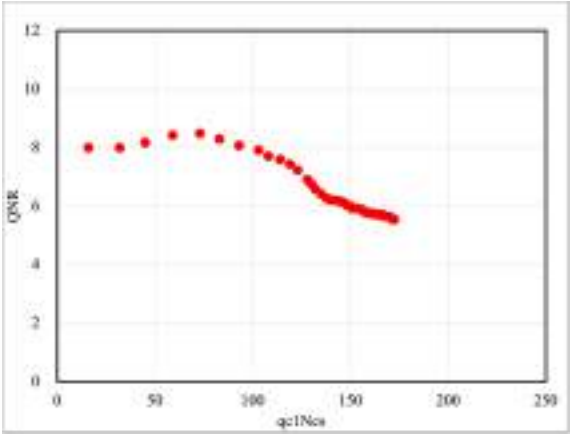

Fig. 4 Correlation between $q_{C1N_{CS}}$ and QNR

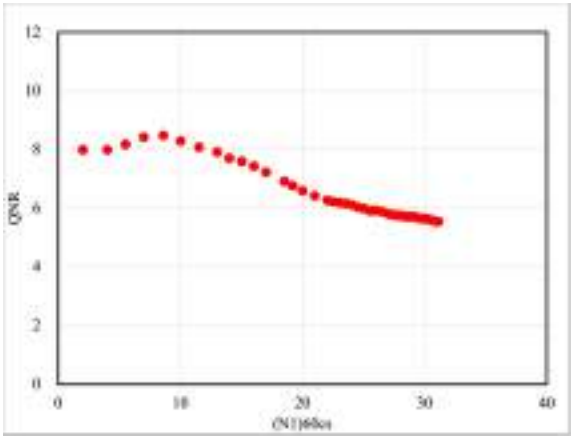

Fig. 5 Correlation between $(N_1)_{60_{cs}}$ and QNR

In addition, to better visualize and understand the correlation between SPT and CPT results, a detailed correlation plot between $(N_1)_{60cs}$ and $q_{C1N_{CS}}$ was created and is shown in Fig. 6. As illustrated in the figure, the data points collectively follow a smooth and continuous curve, which clearly indicates a stable and consistent relationship between these two important geotechnical parameters. Specifically, $q_{C1N_{CS}}$ exhibits a gradual increase as $(N_1)_{60_{cs}}$ rises, reaching values of approximately 100. Beyond this threshold, the rate of increase in $q_{C1N_{CS}}$ becomes noticeably more rapid, implying a change or shift in the underlying correlation pattern between the parameters. This observed nonlinear trend highlights the complex nature of soil behavior captured by these tests. Building upon this established relationship, a set of conversion equations were then derived to enable the mutual transformation between SPT and CPT data, facilitating seamless comparison and integration of results obtained by either method. These conversion equations serve as a practical and valuable tool for geotechnical engineers, providing a reliable means to interpret and correlate data from both testing techniques. The specific formulas for these conversions are presented as Eq. (3) and Eq. (4).

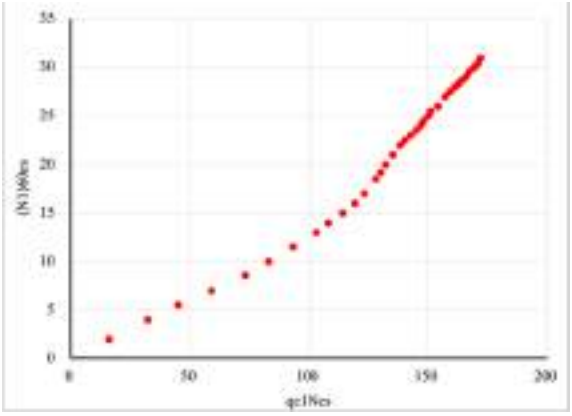

Fig. 6 Correlation between $q_{C1N_{CS}}$ and $(N_1)_{60_{cs}}$

$$(N_1)_{60_{cs}} = 0.12q_{C1N_{CS}} + 0.04 \quad (0 \le q_{C1N_{CS}} \le 100) \tag{3}$$

$$(N_1)_{60_{cs}} = 0.27q_{C1N_{CS}} - 15.48 \quad (q_{C1N_{CS}} > 100) \tag{4}$$

These conversion equations are useful for evaluating SPT and CPT data on a unified basis and enable adjustments between the test methods in liquefaction assessments.

COMPARISON BETWEEN ESTIMATED AND MEASURED N-VALUE

Observed Data Profiles

Fig. 7 presents the cone resistance q_c, sleeve friction f_s, pore pressure u_2, and measured SPT N-values at locations where both SPT and CPT data were obtained. Since the CPT data were recorded at 2 cm intervals, which is much finer than the standard SPT sampling interval, the CPT values were averaged using the mean over the corresponding depth range to enable a meaningful comparison with the SPT results. Using the mean CPT data, N-values were estimated by applying an empirical correlation proposed by Boulanger and Idriss (2014), which is widely used for converting CPT parameters into equivalent SPT N-values. These estimated N-values were then compared with the actual measured N-values obtained from the SPT tests conducted at the same locations.

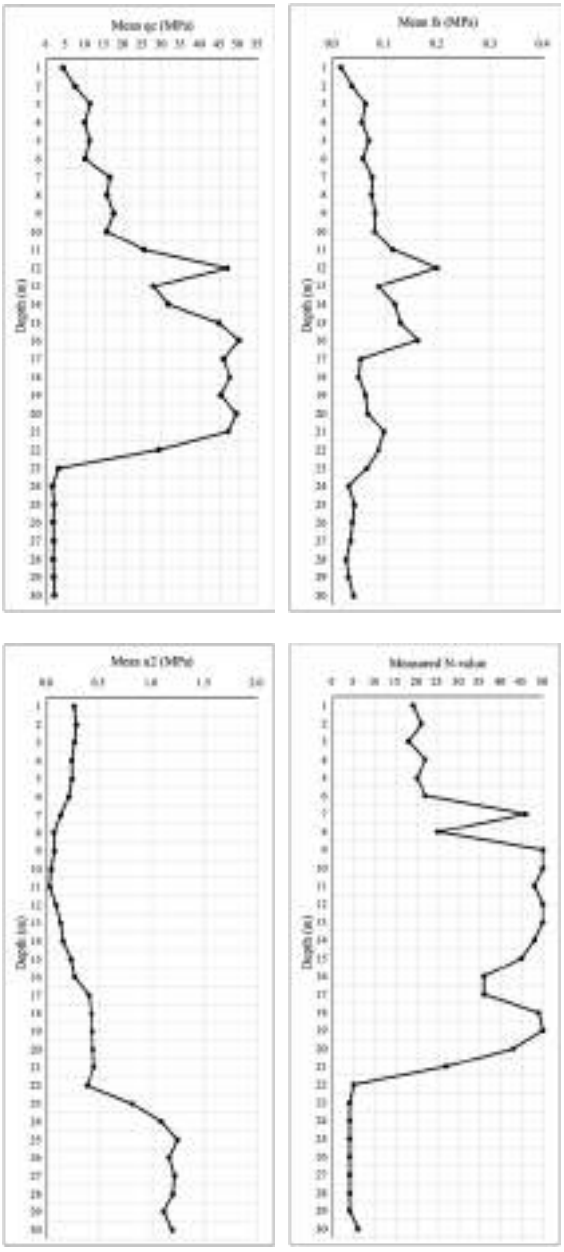

Fig. 7 Measured profiles of q_c, f_s, u_2, and N-value

Results

Using the following equation proposed by Boulanger and Idriss (2014), estimated N-values were calculated from the CPT data. A comparison between the measured and estimated N-values is shown in Fig. 8.

In this study, although the dataset was limited and caution is required when generalizing the results, a moderate correlation was observed between the estimated and measured N-values. The coefficient of determination R^2 was 0.602, indicating a weak but consistent linear relationship between the two. This suggests that the conversion between SPT and CPT penetration resistances may serve as a preliminary reference for liquefaction evaluation, even though it may not yet be considered sufficiently robust for practical application. In addition, the estimated N-values tend to be slightly lower than the measured values overall. This discrepancy may be attributed to the accuracy of the conversion formula and its underlying assumptions, as well as the influence of soil properties critical to liquefaction, such as fines content and particle size distribution. These soil characteristics can affect SPT and CPT measurements differently, potentially impacting the precision of the conversion.

Future research should focus on expanding the dataset to include a wider range of soil conditions and on developing improved estimation formulas that incorporate fines content and particle size. Such efforts will enhance the consistency between SPT and CPT results and improve the reliability of liquefaction assessments in practical geotechnical investigations.

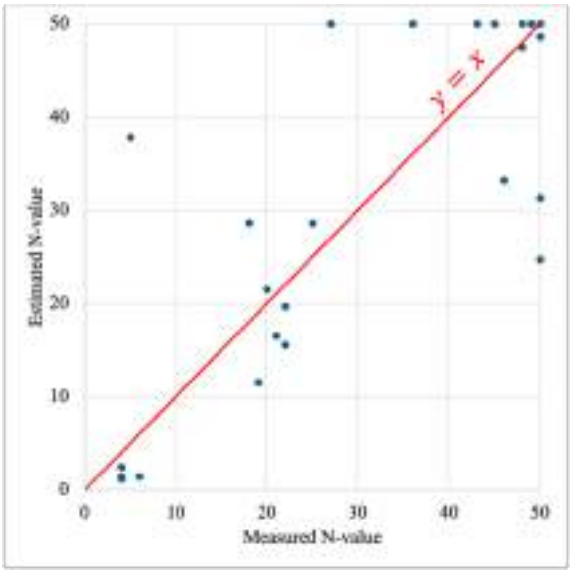

Fig. 8 Comparison between the measured N-value and estimated N-value

CONCLUSIONS

In this study, the relationship between the SPT and CPT was analyzed based on the liquefaction evaluation framework proposed by Boulanger and Idriss (2014). Specifically, the correlation between the corrected SPT blow count $(N_1)_{60cs}$ and the normalized cone resistance $q_{c1N_{CS}}$ was examined using the QNR ratio. This normalization method enabled consistent comparison across datasets obtained from different in-situ testing methods.

Through this analysis, a conversion formula was developed to express the relationship between $(N_1)_{60cs}$ and $q_{c1N_{CS}}$, allowing for more reliable translation of CPT data into equivalent SPT based parameters. This conversion is particularly useful for integrated liquefaction hazard assessments in cases

where both SPT and CPT data are available or when one type needs to be estimated from the other. Practicing engineers can apply the QNR ratio and the developed conversion equations to estimate missing data based on the available in-situ test (SPT or CPT). For example, when only CPT data is available, the conversion formula allows estimation of equivalent SPT blow counts, making it possible to use SPT-based liquefaction evaluation methods. This supports appropriate decision-making even when only one type of data is available. However, it is important to recognize the uncertainties and limitations of such conversions and apply them with caution.

The key findings and conclusions drawn from this study are summarized below.

1) As shown in Fig. 4, QNR is approximately 8 when $q_{C1N_{CS}}$ is below 100 and gradually decreases to around 6 as $q_{C1N_{CS}}$ approaches 150.
2) From the correlation between $(N_1)_{60cs}$ and QNR in Fig. 5, it was observed that QNR is approximately 8 when $(N_1)_{60cs}$ is below 10, and decreases to about 6 when $(N_1)_{60cs}$ reaches 25. This indicates that $(N_1)_{60cs} = 10$ serves as a useful threshold for the conversion between SPT and CPT.
3) The data trend shown in Fig. 6 follows a smooth curve, where $q_{C1N_{CS}}$ increases gradually up to around 100, followed by a sharp rise beyond that point. Based on this relationship, conversion equations between SPT and CPT were derived, as presented in Eq. (3) and Eq. (4).
4) Fig. 8 compares the estimated and measured N-values, showing a coefficient of determination $R^2 = 0.602$, which indicates a weak but consistent linear relationship between the two. In addition, the estimated values tend to be slightly lower than the measured ones, possibly due to assumptions in the conversion formulas and the influence of soil properties such as fines content and particle size distribution.

For future research, developing correction factors for soil particle size and fine content, which influence QNR reduction, is essential for accurate liquefaction assessment. Incorporating these factors into corrections will enhance precision. Additionally, further test data should be collected under different ground conditions to expand the applicability of the derived conversion formula. This will contribute to the development of a more versatile conversion formula that can be applied to a wider range of ground conditions, improving its practical use in engineering applications.

REFERENCES

[1] Boulanger, R. W. & Idriss, I. M., CPT and SPT Based Liquefaction Triggering Procedures, Report No. UCD/CGM-14/01, Center for Geotechnical Modeling, University of California, Davis, April 2014.

[2] Cubrinovski. M., Some important considerations in the engineering assessment of soil liquefaction, NZ Geomechanics News, 97, 6-1. ISSN 011-6851, 2019.

[3] Suzuki Y, Tokimatsu K, and Sanematsu T, Correlations Between CPT Data and Soil Characteristics obtained from SPT, Journal of Structural and Construction Engineering (Transactions of AIJ). 2003, Vol.68, No.566, p.73-80.

[4] H. Zhou, L. M. Wotherspoon & C. Hayden, C. R. McGann & A. Stolte and I. Haycock, Applicability of empirical SPT-CPT correlations for New Zealand soils, 21st NZGS Symposium 2021.

Copyright © Int. J. of GEOMATE All rights reserved, including making copies, unless permission is obtained from the copyright proprietors.

15th Int. Conf. on Geotechnique, Construction Materials & Environment,
Kyoto, Japan, 11-13 November 2025, ISBN 978-4-909106124 C3051

STRENGTH OF BAGASSE ASH GEOPOLYMER-STABILIZED RECYCLED MATERIALS FOR PAVEMENT BASE: MLR AND PATH ANALYSIS

Sattawat Chatchawan [1], Ratamanee Nuntasarn [2], Supakorn Tirapat

[1,2,3] Faculty of Engineering, Khon Kaen University, Thailand

ABSTRACT

Thailand faces an increasing demand for natural aggregates due to road infrastructure expansion and a corresponding rise in demolition waste. Recycling these materials and stabilizing them with bagasse ash (BA), which is a byproduct of biomass power plants, provides an eco-friendly alternative to cement stabilization. This research investigates the stabilization of construction and demolition (C&D) waste, consisting of recycled crushed rock (RCR) and recycled asphalt pavement (RAP), using a BA-derived geopolymer for pavement base applications. The study examines the effects of alkali solution content, NaOH concentration, BA content, and RAP quantity on unconfined compressive strength (UCS) using multiple linear regression (MLR) and path analysis. Results indicate that material density has the strongest positive influence on UCS, while higher NaOH concentration and alkali solution content also improve UCS. However, increased BA content and RAP quantity reduce UCS by lowering material density. Overall, most of these materials met the UCS criteria set by Thailand's Department of Highways (DH.-S. 203/2556) for cement-modified crushed rock for high-traffic pavement base applications. The findings demonstrate that recycling C&D waste stabilized with BA geopolymer can serve as a viable alternative to cement stabilization for pavement base layers.

Keywords: Bagasse Ash Geopolymers, Pavement Base, Recycled Materials, Construction and Demolition Waste

INTRODUCTION

Thailand is currently expanding its road network to accommodate increasing traffic volumes driven by economic growth [1]. Traditional road construction relies heavily on natural aggregates for the base structure of flexible pavements. However, the availability of these aggregates is declining, while construction and demolition (C&D) waste is rising, totaling approximately 6–9 million tons annually [2]. This situation leads to environmental impacts and disposal challenges. Recycling C&D waste to replace natural aggregates can help reduce dependence on new materials and minimize waste.

Recycled asphalt pavement (RAP) and recycled crushed rock (RCR), derived from deteriorated roads, are often used; however, Previous research indicates that recycling these materials without quality enhancement leads to substandard products. For instance, Akinwumi [3] found that mixing RAP with clay reduces both density and strength, consistent with findings from other studies [4-6]. While improving these materials with Portland cement is effective and widely practiced, it also contributes nearly 7% of global GHG emissions annually [7]. Consequently, the sustainable binder known as 'geopolymer' has garnered significant interest.

Geopolymer is a synthetic material derived from precursors containing silica (SiO_2) and alumina (Al_2O_3). When mixed with an alkaline solution, these precursors form a sodium aluminosilicate hydrate (N-A-S-H) compound with binding properties comparable to those of cement [8]. Typical precursors include fly ash and rice husk ash, as well as bagasse ash (BA)—a by-product of biomass energy generation in the sugar industry. Several studies have demonstrated that BA geopolymer can significantly enhance the compressive strength of materials [9–11]. However, its potential in road construction remains underexplored and its usage limited. In Thailand, the use of BA is minimal, leading to waste management challenges associated with landfill disposal.

To address these challenges, this study analyzes the stabilization of RAP and RCR using bagasse ash (BA) as the primary precursor in geopolymer synthesis to develop eco-friendly pavement base materials. The unconfined compressive strength (UCS) is assessed against the standards of the Department of Highways, Thailand. Multiple linear regression and path analysis, conducted using IBM SPSS Statistics and IBM AMOS, are employed to examine the influence of key variables—particularly mix ratios—on UCS, aiming to optimize the performance of BA and other biomass ash-based geopolymers.

RESEARCH SIGNIFICANCE

This study addresses the critical need for sustainable construction practices in Thailand by investigating recycled materials, specifically recycled asphalt pavement (RAP) and recycled crushed rock

(RCR), and improving their strength with bagasse ash geopolymer. Analyzing the influence of the mix ratio on compressive strength properties will reveal potential pathways for improving these alternative materials. The findings are expected to promote the adoption of eco-friendly materials for pavement base applications, influencing industry practices and enhancing environmental conservation and resource management in civil engineering.

MATERIALS AND METHODS

Materials

Recycled aggregates

Recycled asphalt pavement (RAP) and recycled crushed rock (RCR) were obtained from the demolition of roads within the Khon Kaen area, Thailand. The basic properties of both types of aggregates are summarized in Table 1.

Table 1. Basic properties of RAP and RCR aggregates

Properties	Standards	RCR	RAP
Gradation	ASTM C136-06	Well-graded (C_u = 17.43, C_c = 2.27)	Well-graded (C_u = 14.81, C_c = 2.37)
Specific gravity, G_s	ASTM C127-15	2.63	2.29
Water absorption (%)	ASTM C127-15	2.45	0.82
Percentage of wear (%)	ASTM C131/C131M-20	21.07	29.39
Liquid Limit (%)	ASTM D4318-17e1	-	-
Plasticity Index (%)	ASTM D4318-17e1	NP	NP
Unified Classification	ASTM D-2487	SM	SM
AASHTO Classification	AASHTO T-234	A-1-a	A-1-a

Bagasse ash

The bagasse ash (BA) used in this study was a byproduct of biomass power generation at the Nam Phong Sugar Mill in Khon Kaen, Thailand. The average particle size (D_{50}) was 450 microns, and the specific gravity (G_s) was 2.15. The ash exhibited irregular shapes with angular edges and a highly porous structure, as shown in Fig. 1. Results from X-ray fluorescence (XRF) testing indicated that the BA contained 72.75% silica (SiO_2), 2.02% alumina (Al_2O_3), and 1.17% calcium oxide (CaO).

Alkaline solution

The alkaline solution used in this study consists of industrial-grade sodium silicate (Na_2SiO_3) with the following composition: Na_2O = 13.44%, SiO_2 = 32.39%, and H_2O = 54.17%. Additionally, sodium hydroxide (NaOH) solutions at concentrations of 8, 10, and 12 M were used, maintaining a ratio of Na_2SiO_3 to NaOH of 1:1.

Mixing Ratios

In the unconfined compression tests, specimens were compacted using the dry density and alkaline solution content obtained from the modified compaction test (ASTM D1557-12). UCS tests were conducted at three compaction conditions: the optimum alkaline liquid content (OLC), OLC−3%, and OLC+3%, using bagasse ash (BA) contents of 0%, 5%, 10%, and 15% by weight, and NaOH concentrations of 8, 10, and 12 M. Each mix design was tested in triplicate, as summarized in Table 2.

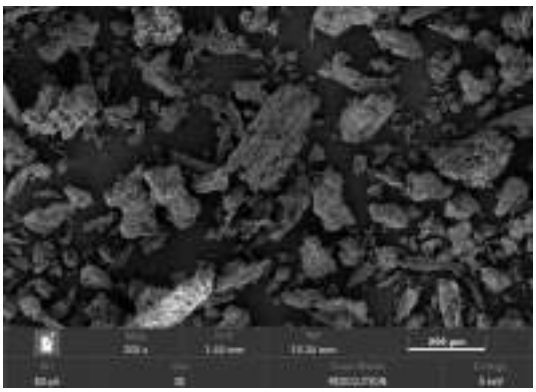

Fig. 1 SEM image of the bagasse ash used in this study

Table 2. Mix details for unconfined compression test.

Recycled material	BA (%)	NaOH Concentration (Molar)	Alkaline solution condition
RCR RCR+RAP RAP	0, 5, 10 and 15	8, 10 and 12	OLC-3% OLC OLC+3%

Laboratory Testing Methods

The strength of the materials was evaluated by determining the unconfined compressive strength (UCS) through unconfined compression tests conducted according to ASTM D2166/D2166M-24. The samples were cylindrical specimens with a diameter of 15 cm and a height of 30 cm. They were cured at ambient temperature for 7 days and submerged in water for 2 hours prior to testing, as specified by the standards for cement-modified crushed rock base materials in Thailand (DH.-S. 203/2556). Subsequently, the samples were applied to compression at a loading rate of 0.5% strain per minute until failure. The UCS results were analyzed to determine the suitability of the material for pavement base applications, following the DH-S. 203/2556 standards, which set a minimum requirement of 2,413 kPa for heavy-traffic roads.

Statistical Analysis

Multiple linear regression

The multiple linear regression (MLR) in this study was conducted using the Enter method with IBM SPSS Statistics 28 software. The analysis set the confidence interval level at 95% ($\alpha = 0.05$) and considered the preliminary assumptions of linear regression to obtain appropriate prediction results [12][13].

The statistical significance of the independent variables on the dependent variable was tested according to the following statistical hypotheses: H_0: The independent variable does not have an effect on the dependent variable; H_1: The independent variable has an effect on the dependent variable. Decision criteria: If sig. < 0.05, reject H_0 and accept H_1; if sig. > 0.05, accept H_0 and reject H_1.

The regression model is expressed as a linear equation: $Y = a + b_1x_1 + b_2x_2 + \ldots + b_nx_n + c$, and the influence of the independent variables is evaluated using standardized regression coefficients (Beta).

Path analysis

Path analysis was conducted to further clarify the influence pathways from independent variables to the dependent variable. The analysis used IBM AMOS V.28 software, under the assumption that the relationships between mixture ratios and UCS may involve both direct and indirect effects. Model evaluation followed the fit criteria recommended in the IBM AMOS Manual [14], including: p-value > 0.05, relative Chi-square (CMIN/DF) < 3, Goodness of Fit Index (GFI) > 0.90, and Root Mean Square Error of Approximation (RMSEA) < 0.08.

Independent variables used

The independent variables (mixture ratios) in this study include RAP aggregate content, alkaline solution content, NaOH concentration, and bagasse ash (BA) content. The symbols and value ranges for these variables used in the statistical analysis are shown in Table 3. The dependent variable is the unconfined compressive strength (UCS), based on data from 81 laboratory test results.

Table 3. Independent variables used

Variable	Symbol	Unit	Range
RAP content	RAP_Content	% w/w	0 to 100
Bagasse ash content	BA_Content	% w/w	5 to 15
Alkali solution content	Alkali_Content	% w/w	*6 to 19.5
NaOH concentration	NaOH_Molar	Molar	8 to 12

*Note: *According to the results of the modified compaction tests.*

RESULTS AND DISCUSSIONS

Unconfined Compressive Strength (UCS)

The unconfined compressive strength (UCS) results of the mixture, as specified in Table 2, indicate that most mixtures met the minimum DH.-S. 203/2556 requirement (UCS > 2,413 kPa), as presented in Fig. 2. These results indicate that stabilizing recycled materials with BA-based geopolymer is a viable alternative to cement stabilization for base layers.

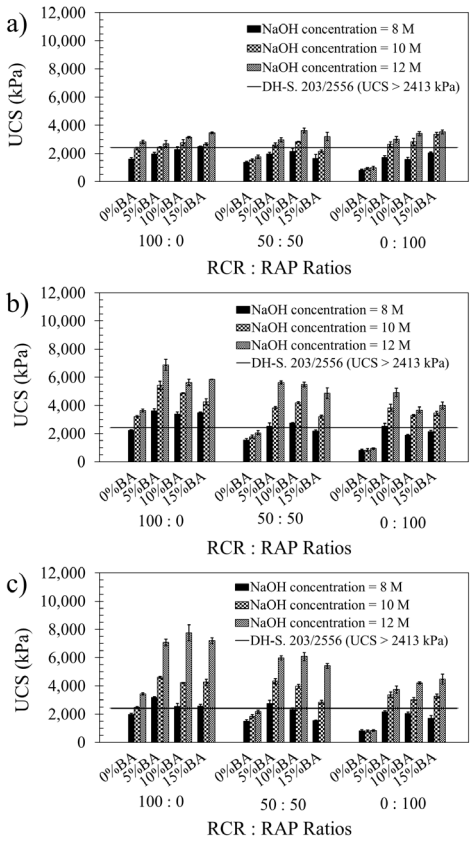

Fig. 2 UCS values of materials at alkaline solution contents of a) OLC-3%, b) OLC, and c) OLC+3%

A preliminary assessment indicates that mixtures failing to meet the DH.-S. 203/2556 standard typically used low NaOH concentrations (8 M) and low alkaline solution content (OLC-3%). The UCS increased with higher NaOH concentrations but decreased with greater RAP proportions in the mix.

The results also showed that mixtures containing BA had significantly higher UCS values than those without, indicating effective geopolymer formation and improved strength. However, increasing BA content from 5% to 10% and 15% did not yield substantial UCS gains, likely due to interactions with other influencing variables. Therefore, multiple linear regression and path analysis were employed to better understand these effects.

Statistical Analysis Using Multiple Linear Regression and Path Analysis Models

Multiple linear regression

The multiple linear regression (MLR) analysis revealed that the independent variables significantly influenced the unconfined compressive strength (UCS) at the 0.001 level (ANOVA; sig. of F < 0.05). The null hypothesis (H_0) was rejected, and the alternative hypothesis (H_1) was accepted, confirming the combined effect of the independent variables on UCS. The model explained 73.3% of the variance (R^2 = 0.733), with a multiple correlation coefficient (R) of 0.856 and a standard error of ±750.871, as shown in Tables 4–5.

The results of the partial t-test for the significance of each independent variable on the UCS of the materials, as shown in Table 6, indicated that all independent variables significantly influenced UCS ($p < 0.05$), including NaOH concentration, BA content, alkaline solution content, and RAP aggregate content. NaOH concentration had the strongest positive effect ($\beta = 0.696$), followed by alkaline solution content ($\beta = 0.507$). In contrast, RAP content ($\beta = -0.454$) and BA content ($\beta = -0.378$) had negative effects, with BA content being the least influential. The predictive MLR equation for UCS is shown in Eq. (1). The comparison between predicted and observed UCS values reveals that most data points lie along the X = Y line within the 95% confidence interval (Fig. 3). Furthermore, the residuals followed a normal distribution, supporting the MLR assumptions.

Table 4: Summary of multiple linear regression model analysis (model summary)

Model Summary[b]				
Model	R	R Square	Adjusted R Square	S.E. of the Estimate
1	0.856[a]	0.733	0.719	750.871

Note: [a]. Predictors: (Constant), NaOH_Molar, AlkaliContent, RAPcontent, BAcontent.
[b]. Dependent Variable: UCS.

Table 5: Results of the simultaneous F-test

ANOVA[a]					
	Sum of Squares	df	Mean Square	F	Sig.
Regression	117685016.92	4	29421254.230	52.183	<.001[b]
Residual	42849358.94	76	563807.355		
Total	160534375.86	80			

Note: [a]. Dependent Variable: UCS.
[b]. Predictors: (Constant), NaOH_Molar, AlkaliContent, RAPcontent, BAcontent.

From the output of this model, the B values in the unstandardized coefficients section, as shown in Table 6, provide the regression equation for predicting the UCS, presented in Eq. (1) as follows:

$$UCS = -15.65(RAP_content) - 130.40(BA_content) + 216.82(Alkaline_content) + 599.86(NaOH_Molar) - 3257.52 \quad (1)$$

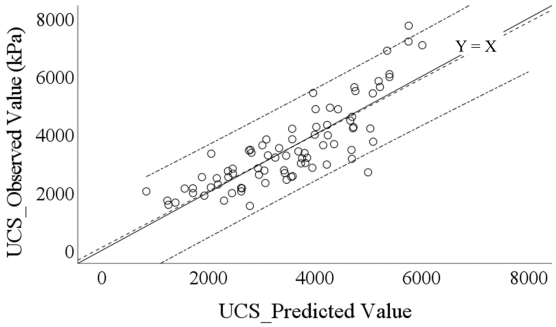

Fig. 3 Comparison of predicted and actual UCS

Path analysis

The prediction of UCS using multiple linear regression (MLR) explained 73.3% of the variance (R^2), but with a relatively high standard error (±750.871), indicating that UCS is influenced by more complex interactions than captured by direct effects alone. Given the importance of compaction in base layer materials, dry density was introduced as a mediator variable to account for indirect effects in a path analysis framework. Initial MLR analysis showed that the alkaline solution content had the lowest tolerance (0.569) and highest VIF (1.757), suggesting a relatively high correlation with other variables. Therefore, a path model was developed using BA content, RAP content, and NaOH concentration as independent variables, and alkaline solution content and dry density as mediators.

Path analysis confirmed that UCS is influenced by both direct and indirect effects of the independent variables through mediator variables. The final model (Fig. 4) best explains the variance in UCS and satisfies the model fit criteria from the IBM Amos Manual [14], with p = 0.427 (p > 0.05), CMIN/DF = 0.962, GFI = 0.985, and RMSEA = 0.000. This model accounts for 79.0% of the variance in UCS (R^2), providing a more accurate explanation than the MLR analysis. Some variables influence UCS directly, while others act through mediators, highlighting complex relationships, as follows:

1) The NaOH concentration (8–12 M) did not significantly affect the dry density (p = 0.443) or the optimum alkaline solution content (p = 0.895), as both p-values exceeded the 0.05 significance level.

2) The mediator variables—dry density and alkaline solution content—were influenced by BA and RAP contents. BA, with a low specific gravity (G_s = 2.15), significantly reduced material density as its content increased, with a regression weight of −0.78, consistent with previous findings [15].

Table 6: Results of partial t-test for the significance of each independent variable on the UCS of the materials

Coefficients [a]							
Independent variable	Unstandardized Coefficients		Standardized Coefficients	t	Sig.	Collinearity Statistics	
	B	Std. Error	Beta			Tolerance	VIF
(Constant)	-3257.517	617.003		-5.280	<0.001		
RAP_content	-15.651	2.182	-0.454	-7.173	<0.001	0.877	1.140
BA_content	-130.398	25.983	-0.378	-5.019	<0.001	0.619	1.617
Alkali_content	216.821	33.585	0.507	6.456	<0.001	0.569	1.757
NaOH_Molar	599.859	51.090	0.696	11.741	<0.001	1.000	1.000

Note: [a] Dependent Variable: UCS.

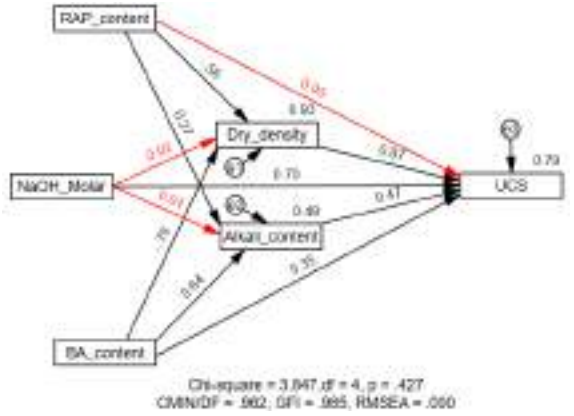

Fig. 4 Path analysis model

RAP, with G_s = 2.45, also reduced material density (regression weight = −0.56) compared to RCR (G_s = 2.63), due to its asphalt coating [16]. Moreover, BA content strongly increased the alkaline solution demand (regression weight = 0.64), attributed to its porous structure, which aligns with results showing increased moisture requirements in BA-soil [17].

3) Dry density had the strongest direct positive influence on UCS (regression weight = 0.87), suggesting that denser mixtures result in greater strength. NaOH concentration followed, with a direct effect of 0.70, due to its role in enhancing silica and alumina dissolution, thereby improving geopolymer gel formation and interparticle bonding [18, 19].

4) The alkaline solution content has a direct positive effect on UCS, with a regression weight of 0.47. This effect may arise from adequate liquid in the system, combined with the increased concentration of NaOH, both of which enhance the material's potential for geopolymerization reactions and effective development of compressive strength.

5) RAP content had no significant direct effect on UCS (p = 0.701). However, it indirectly affected UCS through two pathways: a negative influence via reduced dry density (regression weight = −0.56), resulting in an indirect effect size of −0.487 (−0.56 × 0.87), and a positive influence via increased alkaline solution content (regression weight = 0.27), giving an effect size of 0.127 (0.27 × 0.47). The total effect of RAP content on UCS was −0.360, confirming that higher RAP content tends to decrease compressive strength, as supported by previous studies [4–6, 20].

6) BA content had a direct positive effect on UCS (regression weight = 0.351) and an additional indirect positive effect through alkaline solution content (0.301; 0.64 × 0.47). However, the indirect negative effect through reduced dry density (−0.679; −0.78 × 0.87) slightly outweighed the positive effects. Thus, the net total effect of BA content on UCS was −0.027 (0.351 + 0.301 − 0.679), indicating that while moderate BA content (e.g., 5%) is beneficial, excessive BA reduces UCS due to its impact on compaction quality and density. These findings are consistent with [21], which reported peak strength at 5% BA in expansive soil mixtures.

CONCLUSION

Recycled aggregates from C&D waste (RCR and RAP) were stabilized using bagasse ash (BA)-based geopolymers with 5%, 10%, and 15% BA by weight. A 1:1 alkaline solution of NaOH and Na_2SiO_3 at concentrations of 8, 10, and 12 M was used, with compaction at optimum alkali content and ±3%. Most mixtures achieved UCS values exceeding the DH.-S. 203/2556 standard (UCS > 2,413 kPa), confirming their suitability for flexible road base applications under heavy traffic. This method reduces dependence on natural aggregates and cement stabilization.

MLR and path analysis clarified the influence of mix design variables on UCS, offering valuable guidance for optimizing BA-geopolymer-stabilized recycled aggregates. Key findings are as follows:

1) MLR analysis showed that all independent variables significantly influenced UCS, with NaOH concentration having the strongest positive effect, followed by alkaline solution content. The regression equation is presented in Eq. (1), with an R^2 of 0.733.

2) Path analysis showed that the independent variables affect UCS through both direct and indirect effects, mainly via dry density and alkaline solution content. It explained a greater proportion of variance (R^2 = 0.790) than MLR.

3) NaOH molarity and the alkaline liquid content improve UCS via geopolymerization, but excessive levels are not cost-effective. A 10 M NaOH solution in the NaOH–Na_2SiO_3 activator with compaction at OLC–3% is sufficient.

4) Dry density is a key factor in enhancing biomass ash geopolymer for road construction, with path analysis showing it has a greater impact on UCS than NaOH concentration.

5) Although BA improves compressive strength by contributing to geopolymer formation, excessive amounts reduce dry density and hinder strength. Therefore, 5% BA by weight is optimal.

6) The UCS decreases with higher RAP content; however, a 50:50 RAP:RCR ratio remains viable and supports waste management of both materials.

ACKNOWLEDGMENTS

The authors appreciate the support from NRCT grant No. 174/2563 and Faculty of Engineering at Khon Kaen University.

REFERENCES

[1] Office of transport and traffic policy and planning of Thailand, Transport infrastructure annual report 2022, Ministry of transport, Thailand, 2023, pp. 1-78.

[2] Pollution Control Department (PCD) of Thailand, Thailand's Construction and Demolition Waste Management, Ministry of Natural Resources and Environment, Thailand, 2020, pp. 1-228.

[3] Akinwumi I. I., Plasticity, strength and permeability of reclaimed asphalt pavement and lateritic soil blends, International Journal of Scientific & Engineering Research, Vol. 5, Issue 6, 2014, pp. 631-636.

[4] Ansori M., and Radam I. F., The use of reclaimed asphalt pavement as a foundation for pavements based on the Indonesian national standard, International Journal of Engineering Research and Applications, Vol. 15, Issue 2, 2015, pp. 14-18.

[5] Arulrajah A., Piratheepan J., and Disfani M. M., Reclaimed asphalt pavement and recycled concrete aggregate blends in pavement subbases: laboratory and field evaluation, Journal of Materials in Civil Engineering, Vol. 26, Issue 2, 2013, pp. 349-357.

[6] Suebsuk J., Horpibulsuk S., Suksan A., Suksiripattanapong C., Phoo-ngernkham T., and Arulrajah A., Strength prediction of cement-stabilised reclaimed asphalt pavement and lateritic soil blends, International journal of pavement engineering, Vol. 20, Issue 3, 2019, pp. 332-338.

[7] Miller S. A., Habert G., Myers R. J., and Harvey J. T., Achieving net zero greenhouse gas emissions in the cement industry via value chain mitigation strategies, One Earth, Vol. 4, Issue 10, 2021, pp. 1398-1411.

[8] Davidovits J., Geopolymer chemistry and applications, Geopolymer Institute, 2nd ed, Saint-Quentin, 2008, pp. 1-585.

[9] Saloma, Hanafiah, and Pratiwi K. I., Effect of NaOH Concentration on Bagasse Ash Based Geopolymerization, MATEC Web of Conferences, Vol. 78, 2016, p. 01025.

[10] Magar J. R., and Acharya I. P., Soft Soil Stabilization with Alkali Activated Sugarcane Bagasse Ash, International Journal of Civil and Structural Engineering Research, Vol. 6, Issue 2, 2019, pp. 65-73.

[11] Jongphimai D., Suksiripattanapong C., and Thumrongvut J. (2019, August). Effect of Na_2SiO_3/NaOH ratio on compressive strength of lateritic soil mixed with bagasse ash geopolymer. In IOP Conference Series: Materials Science and Engineering, IOP Publishing, Vol. 600, No. 1, p. 012015.

[12] Phengsawat W., Applied statistics for social science research, Suveriyasan, Bangkok , 2010, pp. 1-412.

[13] Vanichbuncha K., Statistical Analysis: Statistics for decision making, 4th ed, Dhammasarn Co., Ltd, Chula Press, Bangkok, 2001, pp. 1-550.

[14] Arbuckle J. L., IBM SPSS Amos 20 user's guide, Amos Development Corporation, SPSS Inc, Mount Pleasant, 2011, pp. 1-680.

[15] Ochepo J., Stabilization of laterite soil using reclaimed asphalt pavement and sugarcane bagasse ash for pavement construction, Journal of Engineering Research, Vol. 4, Issue 2, 2014, pp. 1-13.

[16] Taha R., Al-Harthy A., Al-Shamsi K., and Al-Zubeidi M., Cement stabilization of reclaimed asphalt pavement aggregate for road bases and subbases, Journal of Materials in Civil Engineering, Vol. 14, Issue 3, 2002, pp. 239-245.

[17] Osinubi K. J., Bafyau V., and Eberemu A. O., Bagasse ash stabilization of lateritic soil, in Appropriate Technologies for Environmental Protection in the Developing World, Dordrecht: Springer, 2009, pp. 271-280.

[18] Rattanasak U., and Chindaprasert P., Influence of NaOH solution on the synthesis of fly ash geopolymer, Minerals Engineering, Vol. 22, Issue 12, 2009, pp. 1073-1078.

[19] Chindaprasirt P., and Chalee W., Effect of sodium hydroxide concentration on chloride penetration and steel corrosion of fly ash-based geopolymer concrete under marine site, Construction and Building Materials, Vol. 63, 2014, pp. 303-310.

[20] Suebsuk J., Suksan A., and Horpibulsuk S., Strength assessment of cement treated soil-reclaimed asphalt pavement (RAP) mixture, GEOMATE Journal, Vol. 6, Issue 12, 2014, pp. 878–884.

[21] Adajar M. A., and Valbuena K., Optimization of the strength properties of expansive soil stabilized with agricultural wastes, GEOMATE Journal, Vol. 21, Issue 88, 2021, pp. 35–41.

Copyright © Int. J. of GEOMATE All rights reserved, including making copies, unless permission is obtained from the copyright proprietors.

15th Int. Conf. on Geotechnique, Construction Materials & Environment,
Kyoto, Japan, 11-13 November 2025, ISBN 978-4-909106124 C3051

EFFECT OF SOIL CLODS INCLUSION ON THE END BEARING CAPACITY OF A PILE WITH AN ENLARGED BASE

Asuka Takahashi[1], Naoaki Suemasa[1], Yoshiaki Tsukada[2], Tadashi Maejima[2] and Jemy Chua[1]

[1]Integrative Science and Engineering, Tokyo City University, Japan
[2]Asahikasei Construction Materials Corporation, Japan

ABSTRACT

In the field of geotechnical engineering, there are various methods in pile construction. One of these is the pre-cast pile method, a type of embedded pile construction technique. This method involves injecting and mixing cement milk—a blend of cement and water—into the excavated gravel bed to form an enlarged grouted base. A pre-cast pile is then installed into this base to achieve proper anchorage. However, during the mixing and stirring processes involved in constructing the base, soil clods, or accumulation of soil particles, may inadvertently become incorporated into the cement milk. The formation of the base under such conditions may lead to a reduction in its strength. To address this concern, this study investigates the failure mechanisms and the degree of strength reduction caused by soil clods inclusion within the enlarged grouted base. Specimens with various rates of soil clods inclusion representing the enlarged grouted base were prepared, and laboratory load tests were conducted. The effects of failure modes and soil clods inclusion on the maximum bearing capacity and the ultimate bearing capacity of the enlarged grouted base were analyzed. The results revealed that tensile and compressive failures occurred at the bottom of the pile, creating a conical wedge within the enlarged grouted base below the pile tip, which subsequently penetrated the concrete. It was also observed that the inclusion of soil clods in the enlarged grouted base adversely affected both the pile's maximum and ultimate bearing capacities.

Keywords: Pre-cast pile method, End bearing capacity of pile, Unconfined compression test, Triaxial compression test, Failure mechanism

INTRODUCTION

In the field of geotechnical engineering, there are various methods in pile construction. One of which is the pre-cast pile method. This is a type of embedded pile construction technique that uses cement milk, a blend of cement and water, which is injected and mixed within the excavated bedrock to create an enlarged grouted base. A prefabricated pile is then installed into this zone to ensure proper anchorage. During the mixing and stirring processes involved in constructing the enlarged grouted base, soil clods may inadvertently become incorporated into the cement milk. These are lumps or accumulation of soil particles. If the enlarged grouted base is formed under such conditions, there is a risk of reduced strength in the enlarged grouted base.

Chen et al. conducted both theoretical and experimental analyses on the bearing capacity of cylindrical and prismatic concrete blocks under rigid punch loading. Applying upper- and lower-bound limit analysis within a perfect-plasticity framework, they demonstrated that the bearing capacity increases with block height and base friction, and that their theoretical predictions closely align with laboratory observations. These findings support the use of rigid-punch mechanics to interpret pile–grouted base interactions, offering a sound theoretical basis for understanding load transfer and failure mechanisms in enlarged grouted bases [1].

Previous studies have reported uniform or localized gravel inclusion in completed piles due to sedimentation effects [2]. Mixing tests show that greater gravel content reduces unconfined compressive strength [3], consistent with concrete studies reporting similar trends with aggregate size or content [4]. In terms of load-bearing characteristics, studies have investigated how the dimensions of the enlarged grouted base and the type and amount of inclusions influence initial stiffness and failure modes [5][6]. Kusakabe [7] reported that increasing the height of the enlarged grouted base improves load-bearing capacity and alters failure modes, based on results from triaxial compression and loading tests. Few studies have quantitatively addressed how clay, crushed stone, or sand inclusion affects bearing characteristics. In a study by Kuze [8], it was shown that the inclusion of clay and clay clods significantly reduces the initial stiffness of the enlarged grouted base.

Despite these findings, systematic investigations focusing specifically on the inclusion of cohesive soil clods remain limited, and a comprehensive understanding of their influence has yet to be established. Since the inclusion of such clods is often unavoidable in actual construction sites, clarifying their impact on the mechanical properties of the enlarged grouted base holds considerable practical significance.

To address this concern, this study investigates the

failure mechanisms and the degree of strength reduction in the enlarged grouted base caused by soil clods. Focusing on embedded piles constructed using the enlarged grouted base method, varying amounts of cohesive soil clods were examined focusing on compressive strength, load-bearing characteristics (including tip resistance and settlement behavior), and failure modes using various experimental procedures like unconfined compression tests, triaxial compression, and loading tests.

UNCONFINED COMPRESSION TEST

Experimental Setup

Fig. 1 provides an overview of the specimen configuration. Cement milk with a water–cement ratio of 0.6 was poured into a φ50 mm × H100 mm mold in four layers, and soil clods were incorporated during the pouring process. The specimens were then cured for one week. The soil clods were designed to simulate clay or mudstone, having a uniaxial compressive strength of 1.00 N/mm². Each clod was prepared with a volume of approximately 1 cm³, using a water–cement ratio of 0.6 and a cement-to-clay ratio of 2:8. These clods were cured for four days prior to incorporation to the specimens. Both the cement milk and soil clods were formulated to have the same specific gravity. Under these conditions, five types of specimens were prepared with soil clod inclusion rates of 0%, 5% (10 clods), 10% (20 clods), 15% (30 clods), and 20% (40 clods). The inclusion rate was calculated as the volume ratio of soil clods to the total volume of the cemented portion.

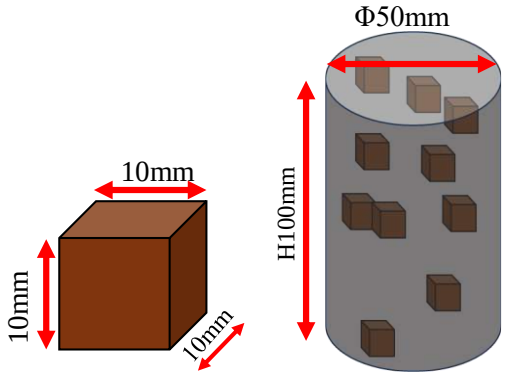

Fig. 1 Overview of a soil clods and specimen

An unconfined compression test was conducted to evaluate the strength of the enlarged grouted base in isolation, without considering earth pressure. An Autograph (Shimadzu corporation) universal testing machine was used with a loading speed of 0.1 mm/s and a maximum load capacity of 30 kN. Given the potential variability in specimen strength due to the positional distribution of the soil clods, six specimens were tested and labeled as Tests 1 to 6.

Experimental Results

After conducting the compression tests, the results obtained were compiled and shown in Fig. 2 This illustrates the relationship between the soil clod inclusion ratio and the maximum compressive stress. Due to variability in the results, the maximum and minimum values (excluding outliers) are shown as error bars, and the average values are plotted. The results indicate that the maximum compressive stress tends to decrease as the inclusion ratio of soil clods increases, suggesting a reduction in strength associated with the presence of clods. The results,

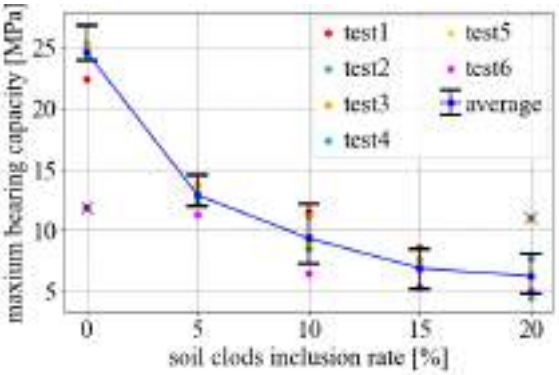

Fig.2 Relationship between maximum bearing capacity and soil clos inclusion rate

however, were associated with the assumption that the clods were uniformly distributed throughout the specimen. But this is not always the case in the real-world setting. Localized placement of soil clods may happen which may incur a different effect to the maximum bearing capacity.

Special Case: Localized Soil Clods Placement

To investigate how the inclusion rate and placement of soil clods affect the bearing capacity of the enlarged grouted base, additional testing was made. The cement and soil clod mix proportions and conditions were kept the same. In addition to the five types of specimens with varying soil clod inclusion rates, three additional patterns were prepared, in which the soil clods were concentrated in the upper, middle, or lower part of the specimen (Fig. 3(a)–(c)).

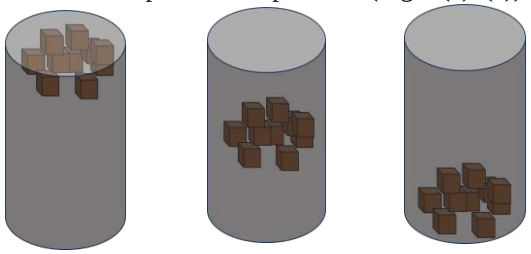

(a)upper part (b)center part (c)lower part

Fig.3 Overview of specimens

This created a localized, or a non-uniform placement of soil clods. Similar uniaxial compression tests were done and the relationship between the location of soil clods, the maximum compressive stress, and the soil clod inclusion ratio, along with the average values from the uniform distribution case, are compiled in Fig. 4 The soil clod inclusion ratio was calculated based on the volume ratio of soil clods to the cement-treated part excluding the pile in the specimen. Similar to the uniform case, the compressive strength tended to decrease with increasing inclusion of soil clods, even when they were unevenly distributed. It was also observed that the maximum compressive stress was lower when the clods were concentrated in the upper part of the specimen compared to the middle and lower parts. The average values for the middle and lower concentration cases fell within the range of the average values for the uniform distribution. Therefore, within the scope of this experiment, it was confirmed that uneven placement of soil clods did not have a significant effect on the maximum compressive stress.

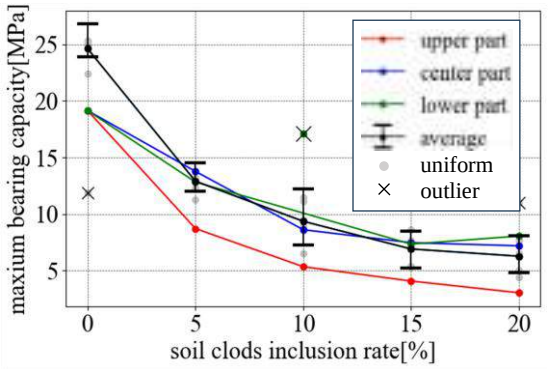

Fig.4 Relationship between soil clod inclusion rate, position and maximum bearing capacity

LOADING TEST OF AN ENLARGED BASE PILE UNDER CONFINING PRESSURE

To investigate the influence of soil clods inclusion under confining stress conditions, triaxial compression tests were performed. Specimens were fabricated by installing steel rods that resembled piles to simulate actual construction conditions. A schematic diagram of the specimen is shown in Fig. 5 The piles were made of S45CD round-cut steel rods with a diameter of 25 mm, which was half the diameter of the enlarged grouted base. The height was made to be 66 mm, equivalent to two-thirds of the root section height, in accordance with the tip-rooted pile method. To simulate the surrounding soil and concentrate surface-applied loads onto the pile, each pile was inserted into a 10 mm-high expanded polystyrene (EPS) mold with an outer diameter of 50 mm and a central hole of 25 mm. The pile was then placed inside a cylindrical mold (φ50 mm × H100 mm), and cement milk with a water–cement ratio of 0.6 was poured in four layers, incorporating soil clods in the process. The mix proportions of the cement milk and soil clods, as well as the specimen preparation procedure, were consistent with those used in the rooting experiment.

Five patterns were prepared with soil clod inclusion rates of 0%, 5% (7 clods), 10% (15 clods), 15% (22 clods), and 20% (30 clods). The inclusion rate was calculated as the volume ratio of soil clods to the cemented portion of the specimen, excluding the steel rod. After curing, the specimens were removed from the molds and positioned with the pile facing upward, as shown in Fig. 6

Triaxial compression tests were conducted on the specimens prepared as described above. These tests were designed to evaluate the strength of the enlarged grouted base embedded in soil, under the assumption that confining pressure from surrounding ground is present. Each specimen was enclosed in a rubber membrane and placed in a triaxial compression apparatus. Confining pressures of 100 kPa and 200 kPa were applied using compressed air. Loading was performed using the universal testing machine testing machine at a loading speed of 0.1 mm/s, with a maximum load capacity of 50 kN.

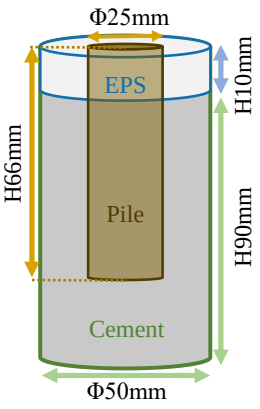

Fig.5 Overview of a specimen
Fig.6 Photo of a specimen

Loading Test Of An Enlarged Base Pile Under Confining Pressure Triaxial Compression Test Results

Fig. 7 shows a cross-section of the model pile after loading. The image reveals that failure occurred near the lower end of the pile. Upon removing the fractured section, a conical failure surface was observed at the bottom cemented part of the model pile, as shown in Fig. 8.

Although the precise sequence of failure is unclear, the lower end of the cemented portion appeared to have undergone punching failure due to concentrated stress. As deformation progressed, a wedge-shaped zone formed at the pile base, leading to horizontal expansion of the transition zone. Longitudinal cracks, transverse cracks caused by

relative displacement between the pile and the rooting section, and cracks due to lateral movement of the transition zone were observed on the side face of the rooting portion.

Fig.7 cross-section of the model pile after loading

Fig.8 the bottom cemented part of the model pile

Fig. 9 presents the relationship between the pile tip bearing capacity and the normalized settlement (St/d), where St is the settlement and d is the pile diameter. The pile tip bearing capacity was calculated by dividing the applied load by the cross-sectional area of the pile. After the onset of failure, stiffness tended to decrease as the maximum compressive stress decreased under each confining pressure. While

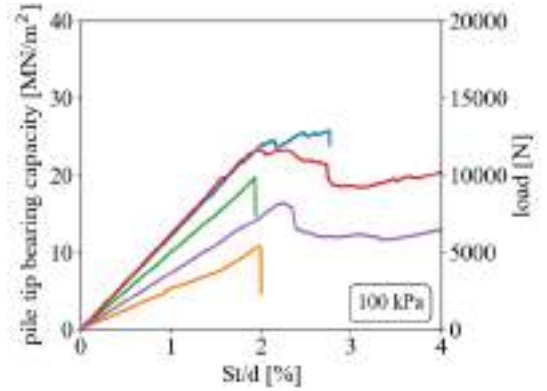

(a)100kPa

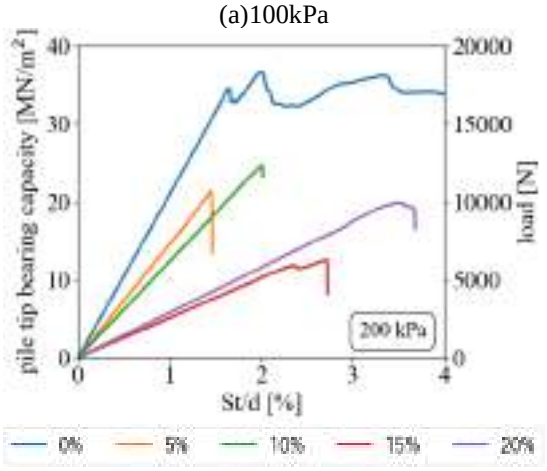

(b)200kPa

Fig.9 Relationship between the pile tip bearing capacity and the normalized settlement (St/d)

some variation was observed due to soil clod inclusion, the maximum compressive stress was highest in the 0% inclusion case, indicating that soil clods reduced the bearing capacity.

Fig. 10 shows the relationship between the maximum compressive stress and confining pressure for various soil clod inclusion rates. Each data point represents a result from a triaxial compression test, with average values indicated by a dotted line. The 0 kPa confining pressure corresponds to the results of the uniaxial compression test. It was observed that, for all levels of confining pressure, the bearing capacity tended to decrease as the soil clod inclusion rate increased. A comparison of the average values at each confining pressure confirmed that the maximum compressive stress was influenced by the confining pressure and increased in the 0% to 10% inclusion range.

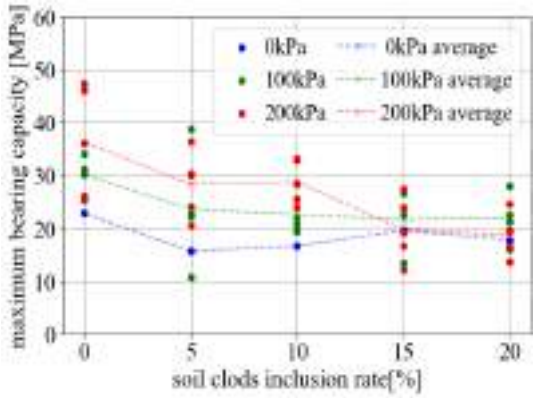

Fig.10 Relationship Between Soil Inclusion Rate, Maximum Bearing Capacity, and Confining Pressure

LOADING TEST OF AN ENLARGED BASE PILE

To investigate the effect of soil clods inclusion in the enlarged grouted base in sandy ground, gravity loading tests were conducted using a cylindrical soil tank. Silica sand No. 6 was used for the soil, with Dr=90% for the bearing layer and Dr=80% for the area above the specimen. After the air-drop method, the soil was compacted by vibration and tamping, and the relative density was controlled by measuring the thickness of the soil layer using a laser instrument. The pile diameter of the specimens was set to 25 mm, half the radius of the rooted portion, as in the tip-rooted pile method. The pile length was 416 mm, and H66 mm, which is two-thirds of the root-cast radius, was built into the cement. Three types of piles, (1) H66mm (used for the rooting portion), (2) H100mm x 2 piles, and (3) H50mm x 3 piles, were connected

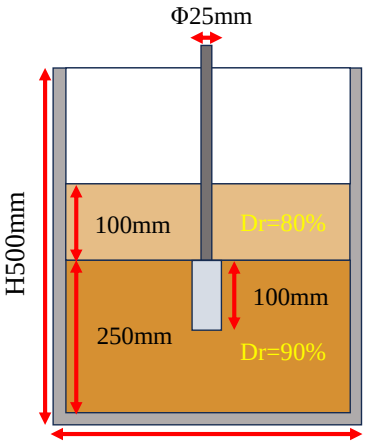

Fig.11 Schematic diagram of the model ground

by screws to achieve the set length. When preparing the specimens, (1) H66 mm piles were fixed to the bottom of a φ50 mm-H100 mm mold using double-sided tape, and then soil clods were mixed into the mold by pouring cement milk with a water-cement ratio of 0.6 into the mold in four separate batches. The conditions for the cement milk and soil mass and the procedure for preparing the specimens were the same as those used in the rooting experiment. The specimens were allowed to cure for one week, and after demolding, the piles (2) and (3) were connected to form the root-consolidation section. Under the conditions described above, three different specimens were prepared: 0%, 10% (15 clods), and 20% (30 clods). To give the specimens roughness and increase their adhesion to the ground, silica sand No. 6 was bonded to the sides of the specimens using epoxy resin. When the specimens were placed in the ground, the center position was set by placing a guard, and the specimens were fixed vertically with a leveler. The finished cross section of the soil model is shown in Fig. 11 The specimens were loaded and quantified using a loading tester (Shimadzu AutoGraph) at 0.09 mm/s.

Gravity Loading Test Results

Different failure mechanisms were observed with the specimens. Fig. 12 shows the specimen with a 0% soil inclusion rate after the loading test. It can be observed that failure occurred around the bottom end of the pile. This kind of failure is attributed to punching failure between the bottom of the pile and the bottom of the root-compacted zone, which caused horizontal tensile cracks on the sides of the root zone due to shear resistance generated by the punching failure. Fig. 13 shows the specimen with a 20% soil inclusion rate after the loading test. Unlike the 0% soil inclusion case, a conical active zone was formed

Fig.12 & 13. Failure mechanism of 0% and 20%

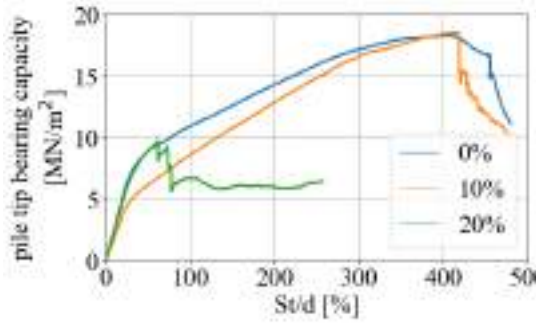

Fig.14 Relationship between pile tip bearing capacity and settlement

at the pile tip and penetrated through the pile. Although punching failure also occurred in this case, the compressive strength was lower than in the 0% soil inclusion case, resulting in a wedge-shaped slip line extending from the bottom end of the pile. The failure shape for the specimen with a 10% soil inclusion rate was similar to that of the 20% inclusion case.

The relationship between pile tip bearing capacity and the normalized settlement (St/d), where St represents the displacement and d is the pile diameter, is illustrated in Fig. 14. When comparing the maximum bearing capacity, the 0% and 10% soil inclusion rates yielded similar values, while the 20% soil inclusion rate produced a value approximately half of 0% and 10% cases. Similarly, the settlement values were comparable between the 0% and 10% inclusion rates. With this, it can be inferred that the increased amount of soil clods can lower the maximum bearing capacity of the pile.

In all cases, following the attainment of the maximum bearing capacity, the stress briefly recovered before failing again, resulting in a sharp decline. Looking at the 20% soil inclusion specimen, the initial drop in stress was attributed to punching failure around the pile, failure shown in Fig. 13. The subsequent drop may be caused by the bottom end of the pile penetrating through the soil. After the second decline, the bearing capacity stabilized, suggesting the formation of residual stress. These residual stresses were found to be approximately 60% of the maximum bearing capacity. Although this was not confirmed in the 0% and 10% soil inclusion cases, it may be possible that residual stress might have been generated with additional settlement. In the 0% and

10% inclusion cases, the maximum bearing capacity was experienced when St/d exceeded 400%. A settlement of four times the pile diameter is impractical in real-world scenarios. Therefore, a settlement ratio (St/d) of 10% is used as the practical reference. The bearing capacity at this 10% St/d ratio is referred to as the ultimate bearing capacity. Fig. 15 shows the range of normalized settlement for inclusion rates between 0% and 20%. Comparing the ultimate bearing capacity of each specimen, approximately 20% reduction in strength was observed between the best and worst performing specimen. Therefore, like the maximum bearing capacity, the presence of soil clods within the enlarged grouted base affects the ultimate bearing capacity.

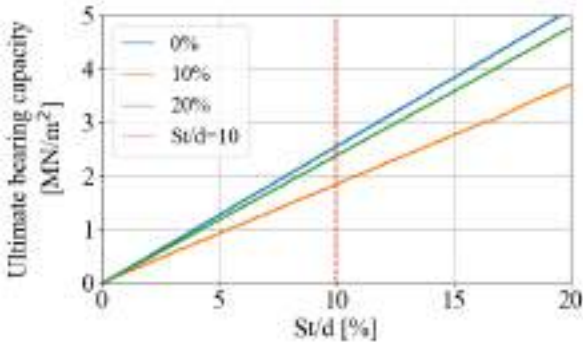

Fig.15 Comparing the ultimate bearing capacity

CONCLUSIONS

Various experimental investigations were conducted to evaluate the effect of the soil clods inclusion rate on the enlarged grouted base in the pre-cast pile method. The following findings were obtained from the results.

- The maximum compressive stress tended to decrease as the soil clods inclusion rate increased across all experiments, with a reduction to less than half observed at a 20% inclusion rate.
- In triaxial compression tests, the maximum compressive stress increased with confining pressure, confirming the influence of lateral constraint. Specifically, it rose by approximately 1.5 to 1.8 times as the confining pressure increased from 0 kPa to 200 kPa, within the inclusion range of 0% to 10%.
- The location of soil clods—whether concentrated or distributed—had little effect when placed in the lower or middle sections, but upper concentration resulted in approximately 1.5 times lower compressive strength.
- Failure typically initiated at the bottom end of the pile, where a conical wedge was formed and propagated upward under continued loading
- On average, the ultimate bearing capacity decreased by approximately 20% when soil clods were included. However, this reduction was relatively minor, suggesting that the effect of soil contamination on the ultimate capacity is limited under the tested conditions.

These results indicate that although the inclusion of soil clods leads to a reduction in compressive strength, its influence on the ultimate bearing capacity is not substantial. Future studies will include loading tests using centrifuge models in soil tanks to further investigate the influence of soil clods in more realistic ground conditions.

REFERENCES

[1] Chen, W. F. and Covarrubias, S., Bearing Capacity of Concrete Blocks, Fritz Laboratory Reports. Lehigh University, 1970.
[2] Kon, H., Yoshida, E., Kawabara, K., Komatsu ,G., Kuwabara, F. and Kimura, M., Investigation of soil cement around nodular piles after pile-toe load test installed by pre-bored piling method, Japanese Geotechnical Journal ,Vol.5, No.4, 2010, pp. 615-623
[3] Kon, H., Yoshida, E., Hosoda, T. and Kimura, M., A study on laboratory mixing test of soil cement by pre-bored piling method, Japanese Geotechnical Journal, Vol.8, No.4, 2013. pp. 567-578
[4] Kawakami, H., Effect of Size and Volumetric Content of Coarse Aggregate on Compressive Strength of Concrete, Journal of Structural and Construction Engineering (Transactions of AIJ), No.20, 1971, pp. 34-40
[5] Kiya, Y., Kato, Y., Tanaka, K. and Kuwabara, F., Model tests on vertical bearing performance of enlarged base bulb of buried piles, J. Struct. Constr. Eng., AIJ, No.615, 2007, pp. 137-143
[6] Ishikawa, K., Ito, A. and Ogura, H., Effect of tip length and strength of enlarged grouted base on bearing capacity of straight pile, J. Struct. Constr. Eng., AIJ, Vol.77 No.676,883-889 2012
[7] Kusakabe, O., Foundation studied with physical modeling, Soil and Foundations Volume 64, Issue 6, 2024
[8] Kuze, N, Inoue, N, Yokoyama, M., Hirayama, Y., Tsukada, Y. and Okada, N., Effect of grouted pile base quality on vertical bearing capacity characteristics of embedded piles, J. Struct. Constr. Eng. AIJ, Vol.89, No825, 2024, pp. 1238-1249

Copyright © Int. J. of GEOMATE All rights reserved, including making copies, unless permission is obtained from the copyright proprietors.

15th Int. Conf. on Geotechnique, Construction Materials & Environment,
Kyoto, Japan, 11-13 November 2025, ISBN 978-4-909106124 C3051

STUDY ON IMPACT FORCE OF GRANULAR FLOW ACTING ON RETAINING WALL

Makoto Kobayashi[1], Akinobu Ogasawara[1] , Naoto Naito[2] and Tatsuya Matsuda[2]

[1]Department of Civil Engineering, National Institute of Technology, Toyota College, Japan, [2]Toyohashi University of Technology, Japan

ABSTRACT

It has been pointed out that retaining walls, which protect against granular flow due to soil slips, are designed to be overly cautious. Centrifuge model tests are often carried out in research on slope failure. This is done by applying centrifugal acceleration to a model ground to match the stress level due to its own weight to that of a full-scale structure. Thus, although centrifugal model tests are useful as a method for observing the development process of large-scale phenomena. In this study, the objectives are to verify the feasibility of conducting highly reproducible granular flow tests under centrifugal conditions, and to perform DEM analysis based on these test results using a model that faithfully replicates the application of centrifugal acceleration, in order to validate its accuracy. In the experiment, alumina balls with particle sizes of 1 mm and 3 mm were used as soil particles, loadcells were installed on the retaining wall, and a soil slip test was carried out in a centrifugal acceleration field of 30G. The behavior of the soil particles during the experiment was photographed with a high-speed camera to verify the reproduction of the flow phenomenon. It was confirmed that the particles flowed at a speed of 4.75 m/s can be said that the soil slip phenomenon was reproduced. Furthermore, DEM analysis, which accounted for the Coriolis force, was able to successfully reproduce the experimental results.

Keywords: Granular Flow, Impact Force, Centrifuge Model Test, Discrete Element Method

INTRODUCTION

The slope failures triggered by heavy rainfall cause the loss of human life and serious threat infrastructure [1]. In addition, the impact forces acting on protective structures due to slope failures caused by earthquake has been studied [2,3].

In Japan, where mountainous regions account for approximately 70% of the national land area, it is crucial to understand the behavior of granular flows associated with slope failures. Research has been conducted on the effects of dry condition of granular flows, used as simplified models of granular flow, on rigid and flexible protective structures [4-7]. However, given that the local climate condition of Japan, it is rare for natural ground surfaces to remain dry. In fact, the mountainous areas are generally in a wet or saturated condition. Although some experiments on wet granular flows have been conducted [8], the number of previous research is relatively small compared to those on dry granular flows, especially in terms of evaluating impact forces. When assessing the impact forces acting on protective structures, it has been pointed out that the flow velocity of granular flows decreases significantly on flat terrain at the base of slopes. Therefore, when there is a clearance between the base of the slope and the protected structures such as roads or buildings, it is desirable to evaluate the impact forces by considering the velocity reduction effect within that clearance [9].

A predictive equation for the impact forces exerted by dry granular flows on rigid walls has been proposed, but the void ratio of the granular materials used in the numerical simulations that form the basis of the model is small [10]. From the standpoint of modeling high void ratio of granular materials flowing down steep slopes, further investigation is needed.

A series of study of centrifuge model tests measuring pressure distribution produced by dry granular flows on rigid walls, along with their Discrete Element Method (DEM), have been carried out [11-13]. These analyses simulated the behavior of individual particles under acceleration equivalent to Coriolis force. While this series of studies has provided significant insights into dry granular flows, it has also been reported that experimental results show considerable variability. On the other hand, in Japan, there are indications that the impact forces acting on retaining walls with a design are often overestimated in current practice [14].

In light of these issues, it is desirable to generalize findings based on systematic results from centrifuge model tests and to visualize the progression of phenomena through validated DEM simulations, with the aim of appropriately evaluating the impact forces acting on retaining walls and rationalizing the design and improving the maintenance of protective structures. Therefore, the present study aims to obtain knowledge useful for designing impact forces acting on retaining walls. This is achieved by reproducing granular flow phenomena using a centrifuge, focusing on highly reproducible experiments with minimized

variability, and confirming the validity of DEM analysis through comparison with experimental results under diverse flow conditions.

CENTRIFUGE MODEL TESTS

Cross section of a series of centrifuge model tests are illustrated in Fig.1. The acrylic board was placed at an angle of 45 degrees as slope which has flow distance of 190 mm in model scale. In order to reproduce the granular flow, alumina balls with a density of 3.26 g/cm^3 were used. To examine the effect of particle size, two particle sizes, diameter 1 mm and 3 mm, were employed. The sample, with a total weight of 242.2 g, was deposited in the same initial shape as shown in Fig.1, above a gate installed perpendicular to the slope. Fig.2 shows the arrangement of the load cells. To measure the impact force of granular flow model, the wall surface at the bottom of the slope model, regard as a retaining wall, was divided into three sections, with two load cells installed on each section in depth direction.

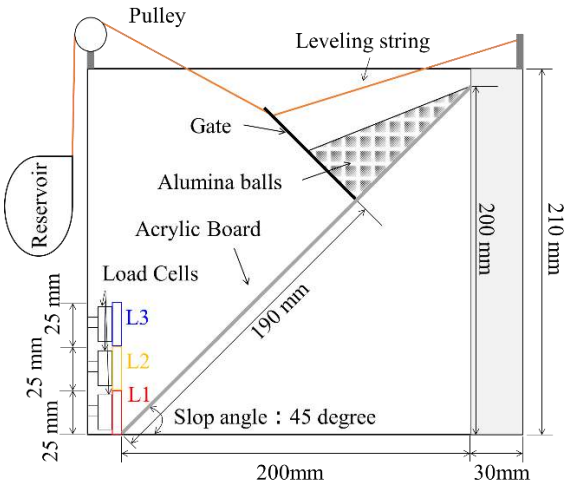

Fig.1 Cross section of the model tests

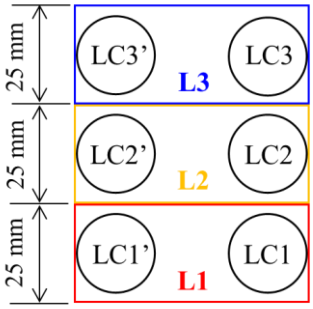

Fig.2 Arrangement of the load cells

After applying a centrifugal acceleration 30 times greater than gravitational acceleration to the model ground, water is supplied to the reservoir from outside the centrifugal apparatus which opens the gate connected to a pulley, allowing the granular flow model to flow down. The granular flow phenomenon is recorded inside the centrifuge apparatus using a high-speed camera. The centrifuge model tests were conducted more than twice to confirm their reproducibility.

THE EFFECT OF PARTICLES SIZE OF GRANULAR FLOW ON IMPACT FORCE

Fig. 3 shows images captured at three time points during the granular flow reproduced using 3 mm alumina balls: immediately after gate release, during flow, and immediately after collision with the retaining wall.

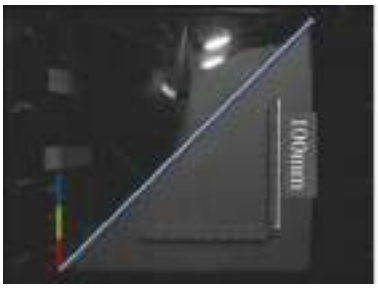

(a) Immediately after gate release

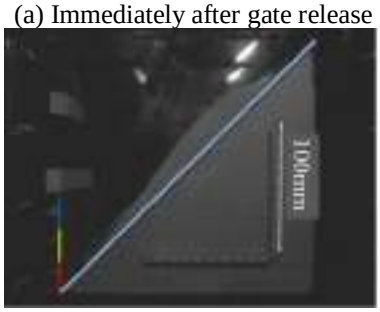

(b) During flow

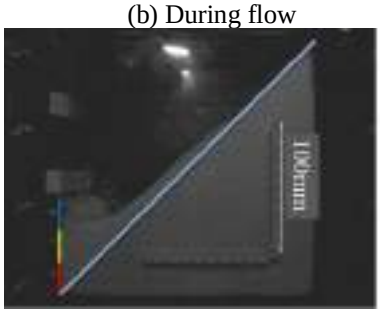

(c) Immediately after collision with the retaining wall

Fig.3 Images captured by high-speed camera during the granular flow (3 mm alumina balls)

In all test cases, the time for the alumina balls front to flow, as observed in the high-speed camera images, is 0.04 seconds, indicating a flow velocity of 4.75 m/s. Since the general velocity range of granular flows is 2–20 m/s, it indicates that the centrifugal model test can be considered an effective means of

observing the development process of granular flow. Moreover, the Fig.3 reveals that the flowing material is not a uniform soil mass of constant thickness but rather consists of individual soil particles flowing independently. This can be regarded as a particularly distinctive result, because conventional designs for collapsing debris have been based on the assumption that the granular flows as a solid mass [14].

Fig.4 shows the temporal changes in the layer thickness of the granular flow at the midpoint of the slope model, located 95 mm from the gate, as determined from the images recorded by the high-speed camera. It is confirmed that the layer thickness increases with larger particle sizes. This is presumed to be because, as the particle size increases, the particles collide and rebound against each other, resulting in an increased apparent layer thickness.

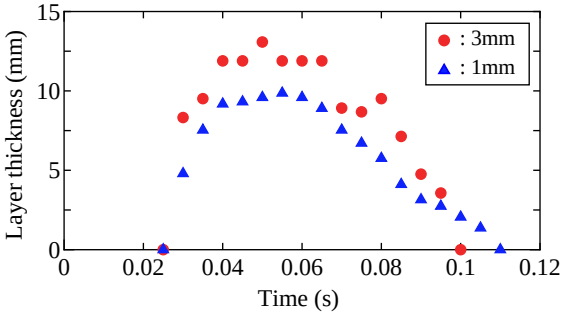

Fig.4 Temporal changes in the layer thickness of the granular flow.

Fig.5 and 6 shows the temporal changes of the impact force acting on the retaining wall. These results indicate that the impact force on the bottommost segment (L1) of the segmented retaining wall is the largest. Furthermore, comparing the two cases, it can be pointed out that the magnitude of the impact force acting on the retaining wall depends more on the weight of the flowing debris than on the particle size, as there is no significant difference in the impact force between the two cases. On the other hand, in the case of 3 mm particles, the peak impact force at the time of collision is slightly higher and exhibits fluctuations, which suggests that larger particles tend to rebound against each other more strongly. Subsequently, in both test cases, the impact force stabilizes at a constant value as the granular flow accumulates.

Based on the formula published by the Ministry of Land, Infrastructure, Transport and Tourism (MLIT) [14], the impact force acting on a retaining wall under the ground conditions used in this study was calculated as Fsm=144.4 kN/m². On the other hand, the maximum total impact force measured in the centrifuge model tests which divided by the area of the retaining wall is 23.5 kN/m². When compared, the experimental result is found to be one-sixth of the impact force obtained through calculation. This difference is considered to be due to the fact that, in the experiment, the collapsing sediment did not behave as a soil mass but rather as individual particles colliding with each other while flowing. In other words, even if the collapsing sediment has the same total weight, factors such as increased void leading to a lower density of the sediment mass, and the reduction in velocity due to particles rebounding off one another, are considered to have influenced the result.

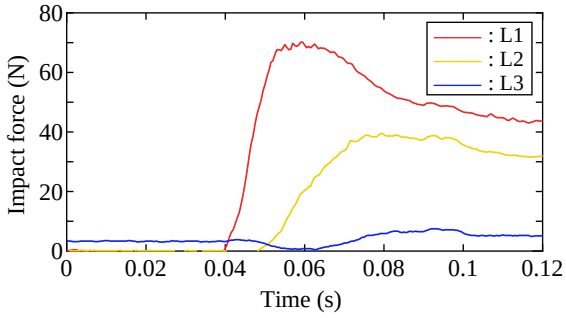

Fig.5 Temporal changes of the impact force in case of 1 mm alumina balls.

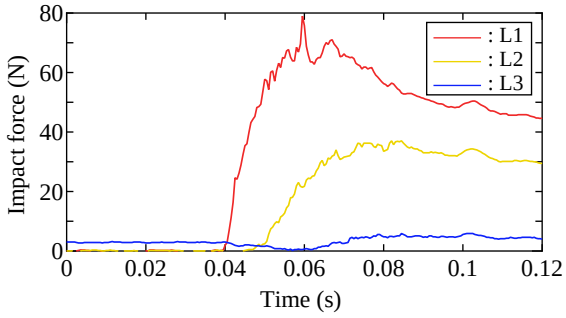

Fig.6 Temporal changes of the impact force in case of 3 mm alumina balls.

DEM ANALYSIS CONDITIONS

In this study, DEM simulations were conducted using LIGGGHTS [15]. Spherical particles were used in the analysis. The contact interactions between particles were modeled using Hertzian contact theory and a rolling resistance model. When the main contact parameters such as Young's modulus, Poisson's ratio, friction coefficient, rolling friction coefficient, and restitution coefficient were defined, the remaining mechanical parameters were calculated based on elasticity theory. Previous studies have shown that Young's modulus has little effect on the flow behavior of granular materials [16]. Therefore, in this study, the friction and viscous parameters were determined based on rebound and dam-break tests,

following the approach of a previous study [17].

The particle size was set equal to 3 mm, which matches the alumina balls used in both the centrifuge and dam-break experiments as a model of soil particles. The Poisson's ratio was set to 0.24, a typical value for alumina, and the Young's modulus was set to 3×10^7 N/m². Based on the rebound test, the restitution coefficient between particles and acrylic was set to 0.7925. To reproduce the flow velocity distribution and final deposition shape observed in the dam-break experiment, the following parameters were used in the simulation: particle friction coefficient was set to 0.2, wall friction coefficient to 0.38, rolling friction coefficient to 0.2, and particle restitution coefficient to 0.4. Using the above simulation parameters, a particle assembly was generated, deposited, and trimmed, as shown in Fig. 7, to reproduce the initial conditions consistent with the experiment.

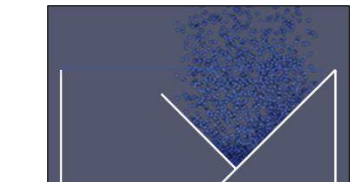

(a) Particle Generation and Free Fall

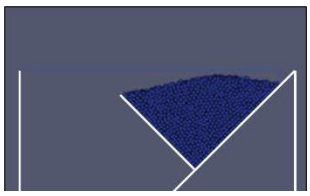

(b) Deposition

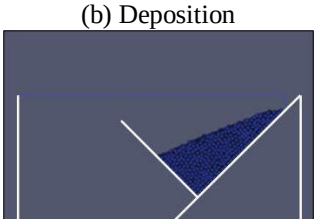

(c) Trimming

Fig. 7 Initial particle configuration for DEM analysis

DEM ANALYSIS RESULTS OF THE CENTRIFUGE MODEL TEST

As the first case (Case01), an acceleration of 30G in the vertical direction and 1G in the longitudinal direction of the container was applied in the DEM analysis to simulate the same acceleration conditions as in the physical experiment. Gate movement was identified from sequential images taken during the experiment, and the simulation was adjusted to reproduce the observed gate behavior. Fig.8 shows the temporal changes in the layer thickness of the granular flow obtained from both the centrifuge model tests and the DEM analysis. In Case01, the simulated flow layer thickness was greater than that measured in the experiment under the same 30G vertical acceleration.

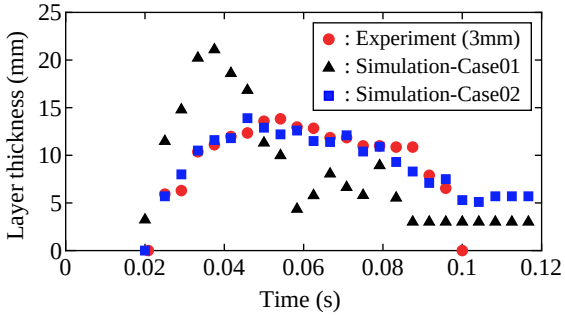

Fig.8 Temporal changes in the layer thickness of the granular flow from centrifuge model test and DEM simulation.

Based on this result, the simulation was further improved by rotating the container, as in the experiment. In Case02, the container was rotated with an effective radius of 0.55 meters at the center of the container, which created a vertical centrifugal acceleration of 30G. Therefore, the simulation conditions in Case02 completely matched those of the experiment. Figure 3 shows that in Case02, where the centrifugal acceleration was applied by rotating the container, the flow layer thickness matched the experimental result. The difference between Case01 and Case02 was the presence or absence of the Coriolis force. As shown in Figure 1, the rotation direction of the container generated a leftward Coriolis force relative to the velocity vector of the particles. This force acted in the slope-normal direction and pressed the particles downward. Therefore, the difference in flow layer thickness between Case01 and Case02 can be explained by the effect of the Coriolis force.

CONCLUSIONS

In this study, the impact force of granular flow acting on retaining walls were reproduced through centrifugal model tests and also verified the reproduction of the experimental results using DEM analysis. Following conclusions were obtained.

1) Centrifuge model tests with extremely simplified particle size, particle shape, and slope roughness were found to be a highly reproducible method for investigating the impact force acting on a retaining wall.

2) Since the impact force of the granular flow is exerted by individual soil particles flowing independently, it was suggested that the actual impact

force may be lower than the value calculated using the design formula.

3) The DEM analysis, which accounted for the Coriolis force, was able to successfully reproduce the experimental results.

ACKNOWLEDGMENTS

This work was gratefully supported by JSPS KAKENHI (Grant Numbers JP23K13402).

REFERENCES

[1] Moriguchi, S., Matsugi, H., Ochiai, T., Yoshikawa, S., Inagaki, H., Ueno, S., Suzuki, M., Tobita, Y., Chida, T., Takahashi, K., Shibayama, A., Hashimoto, M., Kyoya, T., Dolojan, N.L.J., Survey report on damage caused by 2019 Typhoon Hagibis in Marumori Town, Miyagi Prefecture, Soils and Foundations, Vol61, Issue2, 2021, pp.586–599.

[2] Nakajima, S., Abe, K., Shinoda, M., Nakamura, S, Nakamura, H., Experimental study on impact force due to collision of rockfall and sliding soil mass caused by seismic slope failure, Landslides 18, 2021, pp.195–216.

[3] Nakajima S, Abe K, Shinoda M, Nakamura S, Nakamura H, Chigira K., Dynamic centrifuge model tests and material point method analysis of the impact force of a sliding soil mass caused by earthquake-induced slope failure, Soils and Foundations, Vol.59, Issue6, 2019, pp.1813–1829.

[4] Jiang, Y. J. and Towhata, I., Experimental study of dry granular flow and impact behavior against a rigid retaining wall, Rock Mechanics and Rock Engineering, 46, 2013, pp.713–729.

[5] Zhang, B., Huang, Y., Liu, J., Micro-mechanism and efficiency of baffle structure in deceleration of granular flows, Acta Geotechnica, Vo.16, 2021, pp.3667–3688.

[6] Albaba, A., Lambert, S., Kneib, F., Chareyre, B., Nicot, F., DEM Modeling of a Flexible Barrier Impacted by a Dry Granular Flow, Rock Mechanics and Rock Engineering, 50, 2017, pp.3029–3048.

[7] Berger, S.M., Hofmann, R., Preh, A., Impacts on Embankments, Rigid and Flexible Barriers Against Rockslides: Model Experiments vs. DEM Simulations, Rock Mechanics and Rock Engineering, Vol.57, 2024, pp.2793–2808.

[8] Major, J. J., Depositional Processes in Large-Scale Debris-Flow Experiments, The Journal of Geology, Vol.105, No.3, 1997, pp.345-366.

[9] Naito, N., Matsuda, T., Miura, K., Omura, T., Azmi, A. D. B., Effect of rock mass diameter on runout distance and velocity attenuation of dry granular avalanche. International Journal of GEOMATE, Vol.25, Issue 107, 2023, pp.1–8.

[10] Redaelli, I., di Prisco, C., Calvetti, F., Dry granular masses impacting on rigid obstacles: numerical analysis and theoretical modelling, Acta Geotechnica, Vo.16, 2021, pp.3923–3946.

[11] Zhang, B., Huang, Y., Impact behavior of superspeed granular flow: Insights from centrifuge modeling and DEM simulation. Engineering Geology, Vol. 299, 2022, Article 106569.

[12] Zhang, B., Li, W., Pu, J., Bi, Y., Huang, Y., Dilative and compressive coriolis effect on granular impact behavior based on centrifuge modeling and DEM simulation, Engineering Geology, Vol.323, 2023, Article 107232.

[13] Zhang, B., Li, W., Pu, J., Pu, J., Bi, Y., Huang, Y., Centrifuge and DEM investigation of dry granular impacts: Effect of granular volume under high-speed impact conditions, Landslides Vol.21, 2024, pp.1439–1459.

[14] Hasegawa, Y., Yusa, N., Kanazawa, A., Takiguchi, S., Nakaya, H. and Ojima, T., Consideration about setting of the coefficient of fluid resistance used for the design of the retaining wall, The 56th Annual Meeting of the Japan National Conference on Geotechnical Engineering, 2020, 13-10-4-05.(in Japanese)

[15] Kloss C., and Goniva C., LIGGGHTS – a new open source discrete element simulation software, In Proceedings of the 5th International Conference on Discrete Element Methods, 2010, pp. 25-26.

[16] Naito, N., Matsuda, T., Miura, K., Omura, T., Three-dimensional discrete element modelling of granular avalanche under multiple flow conditions. International Journal of GEOMATE. 24(106), 2023, pp.77–84.

[17] Naito, N., Okugawa, Y., Matsuda, T., Miura, K., Slope flow behavior of granular materials with different side constraint conditions. Proc. of 13th Int. Conf. on Geotechnique, Construction Materials & Environment, 2023, pp.239–243.

Copyright © Int. J. of GEOMATE All rights reserved, including making copies, unless permission is obtained from the copyright proprietors.

15th Int. Conf. on Geotechnique, Construction Materials & Environment,
Kyoto, Japan, 11-13 November 2025, ISBN 978-4-909106124 C3051

EXPERIMENTAL STUDY ON SWELLING CHARACTERISTICS OF BENTONITE BUFFER MATERIAL CONSIDERING VARIOUS INITIAL CONDITIONS

*Kira Iida[1], Shin-ichi Kanazawa[2], Masanori Kohno[3], Zihao Liu[1] and Osamu Yoshino[4]

[1]Graduate School of Science and Technology, Niigata University, Japan;
[2]Civil Engineering Program Faculty of Engineering, Niigata University, Japan;
[3]Faculty of Engineering, Tottori University, Japan;
[4]Nishimatsu Construction Co. LTD, Japan

ABSTRACT

Bentonite is considered as a buffer material between vitrified waste and bedrock in the geological disposal of high-level radioactive waste because of its high swelling and low permeability properties. Swelling pressure is one of the most important material properties for evaluating the self-sealing performance of buffer materials and is being investigated through swelling pressure tests. In a geological disposal facility, the bentonite buffer material is subjected to high temperatures due to the decay heat generated from the waste. At the same time, as groundwater infiltrates the buffer, its mechanical properties change due to swelling and deformation, gradually leading to saturation. Therefore, understanding the swelling characteristics of bentonite buffer materials under thermal effects is crucial for designing buffer material specifications. In this study, swelling pressure tests were on Na-bentonite and silica sand mixtures compacted to a dry density of 1.6 Mg/m^3 at different initial water contents and temperature, to establish a database and experimentally investigate how thermal effects influence the time-dependent changes in swelling pressure.

Keywords: Bentonite, Swelling Pressure, Temperature, Initial Water Content

INTRODUCTION

Geological disposal has been considered as a promising disposal method for long-lived radioactive waste, such as the high-level radioactive waste generated from the nuclear fuel cycle in 1950s Japan. To date, scientific and technological studies have investigated the safety and feasibility of geological disposal. The objective of geological disposal is to physically isolate a geological repository from the human environment. This is achieved by constructing a multi-barrier system, in which engineering measures (engineered barriers) are applied to enhance confinement within deep underground rock mass (natural barriers) that exhibit isolation properties [1].

While nuclear power plants are designed to operate for a period of about 40 years, geological disposal is required to ensure long-term safety for tens of thousands of years, considering the half-life of radio nuclides.

In geological disposal, bentonite is used as a buffer between the vitrified waste and the bedrock, because of high swelling and low permeability. The buffer material is expected to self-sealing barriers to water channels by swelling, provide stable support for the overpack, and relieve stress when the rock mass is subjected to creep, thereby ensuring and maintaining performance over the long term. Therefore, attempts have been made to understand various material properties, such as swelling pressure.

Swelling pressure of bentonite has been determined through swelling pressure tests [2-5].

The swelling behavior that occurs during the transition from the unsaturated to the saturated state is a coupled hydraulic and mechanical behavior that is extremely complex. In geological disposal, bentonite buffer material is in an unsaturated state when the engineered barrier is installed and is exposed to a high temperature environment due to radioactive decay heat from the waste body. At the same time, bentonite buffer absorbs water as it is infiltrated by groundwater from the surrounding area and gradually shifts to a saturated state while changing its mechanical properties. In this process, thermal, hydraulic, and mechanical factors interact with each other in the bentonite buffer material, a so-called coupled thermo-hydro-mechanical (THM) process. To evaluate the long-term mechanical performance of buffer materials, it is essential to understand their mechanical behavior, especially at high temperatures. Therefore, when bentonite is used as an engineered barrier, the effect of heat on the material properties must be considered in the evaluation.

In this study, swelling pressure tests were conducted on Na-bentonite and silica sand mixtures compacted to a dry density of 1.6 Mg/m^3 at different initial water contents and temperature. The purpose of this study was to construct a database based on the test results and to experimentally understand the

effects of each initial condition on the change in swelling pressure over time.

RESEARCH SIGNIFICANCE

Long-term evaluations of the mechanical performance of bentonite buffer materials are greatly affected by the mechanical state during transient periods of continuous high-temperature environments. Therefore, it is essential that the characteristics of coupled phenomena, including thermal effects, be properly considered in the design of engineered barriers using bentonite.

The results of this research will contribute to the expansion of the basic database for the specification and design of bentonite buffer materials and can also be used as reliable test data to verify the validity of numerical analysis, contributing to the development of rational performance evaluation methods.

MATERIALS AND METHODS

Materials

This study used KuniGel V-1, a sodium type bentonite from Tsukinuno Mine, Japan. The swelling properties of this bentonite have been widely studied. Table 1 shows the physical properties and chemical composition of KuniGel V-1. It is composed mainly of montmorillonite (about 55%), quartz, feldspar, calcite, and clinoptilolite. The cation exchange capacity is 80.0 (meq/100g), and the major exchange cautions are Na^+ (53.4 mmol/100g), Ca^{2+} (4.7 mmol /100g), Mg^{2+} (0.4 mmol/100g) and K^+ (0.4 mmol/100g). Soil particle density was measured by measuring the volume excluded by gas expansion using a Micromeritics helium pycnometer (Accu Pyc) to obtain the true volume.

The sample used bentonite mixed with Tohoku silica sand No. 8, mined from the Ōishida Mine, Japan. Mixing sand with bentonite enhances both thermal conductivity and compaction properties, making this mixed buffer material an important subject of investigation [1]. The soil particle density of the Tohoku silica sand was 2.702 Mg/m³.

Method for producing test material

All samples used in the swelling pressure tests were bentonite-silica sand mixtures with a bentonite content of 70%. The natural water content of the bentonite mixture was approximately 7%. To compare the change over time in swelling pressure at different initial water contents, this test was conducted twice at higher initial water contents of 12% and 17%. In adjusting the initial water content, water was added by misting ion-exchanged water. of the vessel to prevent water droplets from accumulating, and the water content of the sample gradually increased while alternating between kneading and water addition.

Table 1 Basic properties of KuniGel V-1.

Properties	KuniGel V-1
Cation type	Na
Main minerals	Smectite, Quartz, Calcite, Zeolite, Plagioclase
Soil particle density (Mg/m^3)	2.605
Liquid limit (%)	436.4
Plastic limit (%)	26.4
Montmorillonite content (%)	55
Cation exchange capacity (meq/100g)	80.0
Extracted cation (meq/100g)	Na^+(53.4), Ca^{2+}(9.3), K^+(0.4), Mg^{2+}(0.8)

Table 2 Test Conditions.

Test case	Dry density (Mg/m^3)	Water content (%)	Temperature (°C)
A-1-1	1.6	7.4	30
A-1-2	1.6	6.9	30
A-2-1	1.6	12.3	30
A-2-2	1.6	12.3	30
A-3-1	1.6	17.8	30
A-3-2	1.6	17.2	30
B-1-1	1.6	7.0	60
B-1-2	1.6	7.1	60
B-1-3	1.6	6.8	60
B-2-1	1.6	12.5	60
B-2-2	1.6	12.5	60
B-3-1	1.6	17.5	60
B-3-2	1.6	18.0	60
C-1-1	1.6	7.0	90
C-1-2	1.6	7.1	90
C-1-3	1.6	6.8	90
C-2-1	1.6	12.6	90
C-2-3	1.6	12.9	90
C-3-1	1.6	17.6	90
C-3-2	1.6	17.6	90

Specimen details for the swelling pressure tests are presented in Table 2. The water-adjusted cylindrical specimens used in the swelling pressure tests were prepared by static compaction with a dry density of 1.6 Mg/m^3, a diameter of 28 mm, and a height of 10 mm. To prepare a specimen, the sample was first placed in a metal mold with an inner diameter of 28 mm, and a stick was inserted into the mold. A piston was then lowered into the top of the

rod, and the specimen was compacted with a hydraulic jack so that its height was 10 mm. The compaction pressure was approximately 6 to 8 MPa, depending on the initial water content, and the pressurization holding time was 10 minutes. After unloading, the compaction rod was removed, and the specimens were placed in the mold for testing.

Test method

The main components of the swelling pressure test apparatus are the reaction frame, load cell, compressor, air cylinder, water tank, temperature control device, and thermocouple. Figure 1 shows a schematic diagram of the swelling pressure test apparatus. The load cell is connected to a data logger and PC, and data can be collected every second. The specimen was transferred to the pedestal of the testing machine one mold at a time, and the upper and lower pedestals were fixed with screws. Membrane filters and porous metal were inserted between the specimen and the pedestal as filter materials. To prevent swelling and deformation of the specimen during the test, the piston was lowered onto the top plate of the testing machine and vertical displacement was fixed with a clamp knob. The vertical load at this time was taken as the initial vertical load, which was approximately 0.08 MPa. The swelling pressure was then measured by supplying ion-exchanged water to the tank. Water was supplied only from the underside of the specimen to expel air from inside the specimen. Ion-exchanged water was used as the test water, and the test temperature was set at 30°C,60°C, and 90°C.

The water temperature was controlled to be ±1°C above the target temperature, and the temperature was measured using thermocouples. The water level was maintained at approximately 100 mm from the top of the specimen. The test period was about one week, when the swelling pressure of the bentonite was expected to reach equilibrium.

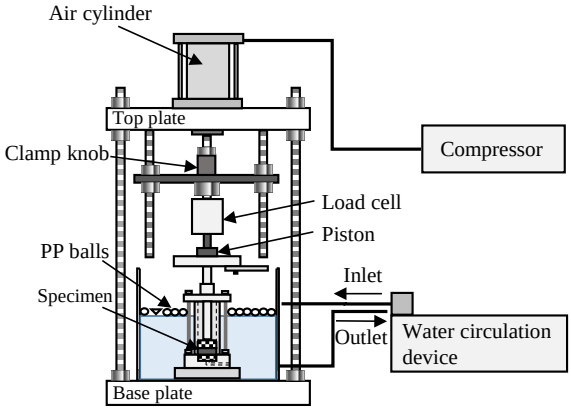

Fig.1 Schematic diagram of the swelling pressure test apparatus.

EXPERIMENTAL RESULTS

Figure 2 to Figure 10 shows the change over time of swelling pressure for each initial water contents and temperature. In this study, swelling pressure tests were conducted multiple times under each condition, which were categorized based on the initial water content as follows: 7% was defined as small, 12% as medium, and 17% as large.

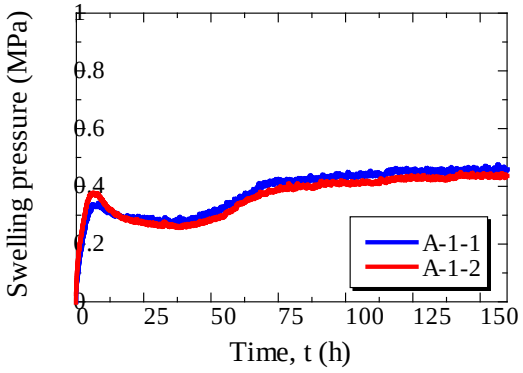

Fig.2 Time history of swelling pressure. (Initial water content: small, Temperature: 30°C)

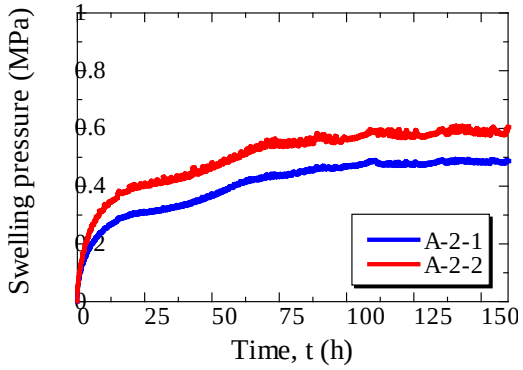

Fig.3 Time history of swelling pressure. (Initial water content: middle, Temperature: 30°C)

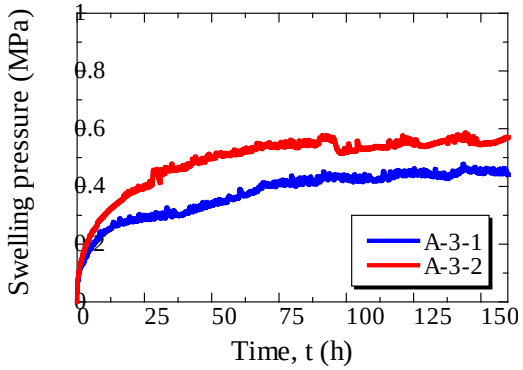

Fig.4 Time history of swelling pressure. (Initial water content: large, Temperature: 30°C)

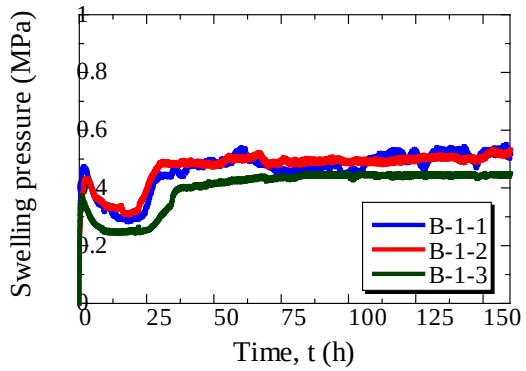

Fig.5 Time history of swelling pressure. (Initial water content: small, Temperature: 60℃)

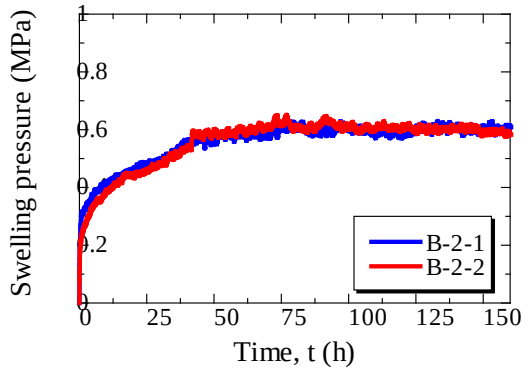

Fig.6 Time history of swelling pressure. (Initial water content: middle, Temperature: 60℃)

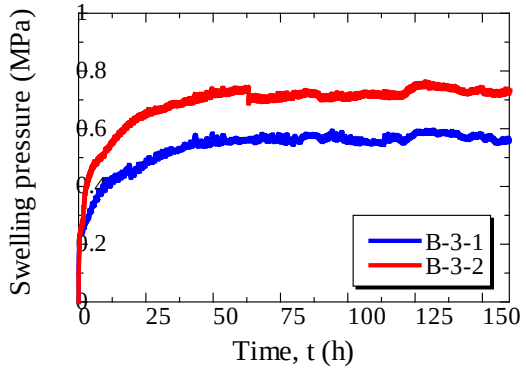

Fig.7 Time history of swelling pressure. (Initial water content: large, Temperature: 60℃)

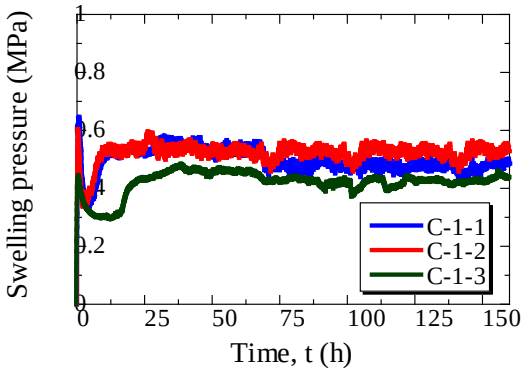

Fig.8 Time history of swelling pressure. (Initial water content: small, Temperature: 90℃)

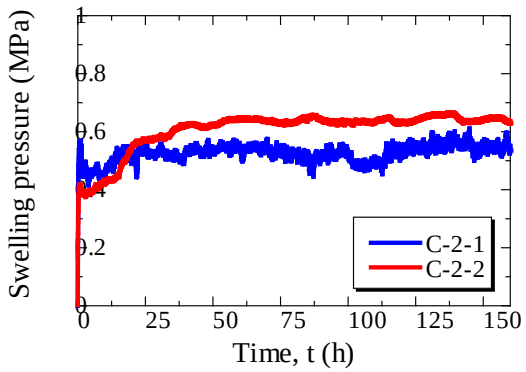

Fig.9 Time history of swelling pressure. (Initial water content: middle, Temperature: 90℃)

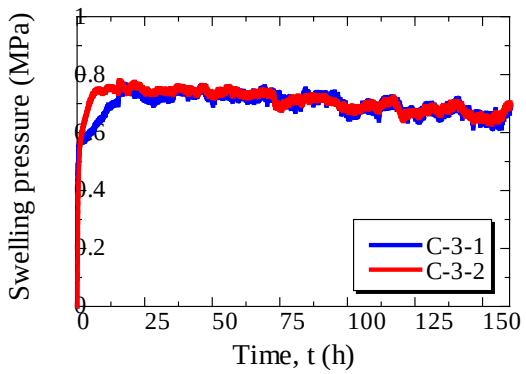

Fig.10 Time history of swelling pressure. (Initial water content: large, Temperature: 90℃)

Effect of initial water content on swelling pressure change over time

Figure 2 to Figure.4 shows the change over time of swelling pressure for each initial water content at 30°C. In the initial water content is relatively small, swelling pressure increased, then temporarily decreased and then increased again. On the other hand, as the initial water content increases, the swelling pressure did not decrease under the condition of low initial moisture content, and it increased relatively slowly. Furthermore, where the initial water content was large, the swelling pressure tended to increase monotonically, and the change over time in the swelling pressure differed depending on the initial water content.

A possible cause of the difference in swelling pressure with time depending on the initial water

content due to the presence or absence and wetting-induced collapse in the unsaturated region and its magnitude, which affected the swelling behavior. Since swelling pressure tests are conducted under volume-constrained conditions, swelling and compaction associated with water absorption are considered to occur continuously within the specimen [6]. Under conditions of initial water content is small, it is assumed that collapses occur due to increased water absorption, and the entire specimen tends to compress, resulting in a temporary decrease in swelling pressure. On the other hand, under the condition of initial water content is high, the effect of collapses is weak due to relatively low water absorption, and the swelling pressure is considered to increase monotonically.

Effect of temperature on swelling pressure change over time

Figure 5 to Figure 10 shows the change over time of swelling pressure for each initial water content at temperatures of 60°C and 90°C. In the initial water content is relatively small, the swelling pressure increased after the start of water supply, reached a peak, temporarily decreased, and then increased again to reach equilibrium for all temperature conditions. In particular, the initial swelling pressure peaked after the start of water supply tended to increase as the temperature increased. In addition, the time required for the swelling pressure to reach the equilibrium state tended to be shortened at higher temperatures. When the test temperature was 30°C, it took about 60 hours for the swelling pressure to increase again after the initial peak, while at 60°C it took about 24 hours and at 90°C it took about 10 hours. These trends were also observed at high initial water contents.

The increase in the initial swelling pressure peak is caused by the increase in osmotic pressure. Kanazawa [7] reported that the increase in maximum swelling pressure in a swelling pressure test that considered temperature history and temperature variation was due to the increase in osmotic pressure and the expansion of the diffusion electric double layer. In the swelling pressure test, ion-exchanged water was used and it is considered that the concentration difference between the montmorillonite interlayer and the external solution caused water to move into the interlayer, and the increase in temperature accelerated this movement, resulting in the increase in the initial peak. In addition, Towhata [8] investigated the effects of elevated temperature on the volume-change behavior of clays. They reported that, in swelling clays with low permeability, thermal expansion of pore water results in an instantaneous increase in sample volume. In this study, specimens with high initial water content exhibited pore spaces saturated with considerable amounts of pore water. As a result, the thermal expansion of pore water with increasing temperature may have contributed to the increase in initial swelling pressure.

On the other hand, the shortening of the time required to reach equilibrium is caused by the increase in hydraulic conductivity due to the rise in temperature. Matsumoto [9] conducted hydraulic permeability tests on bentonite with temperature as a parameter and reported that at 60°C and 90°C, the hydraulic conductivity increased approximately 2 to 3 times compared to that at room temperature, which they attributed to temperature changes in the density and viscosity of water. In this test, the viscosity of the water decreased as the temperature increased, and the permeability of the bentonite increased, which is thought to have shortened the time required to reach equilibrium. In addition, the time required to reach equilibrium was significantly shorter at 90 °C, suggesting that, in addition to the improvement in permeability, the effect of osmotic pressure may have facilitated water movement between the layers.

Effect of temperature on equilibrium swelling pressure

Under all test conditions, the equilibrium swelling pressure tended to increase with increasing temperature. Specifically, it increased by approximately 0.05 to 0.1 MPa as the temperature rose. However, the equilibrium swelling pressures at 60°C and 90°C were nearly the same, suggesting that the effect of temperature on equilibrium swelling pressure is relatively small when the effective clay density is approximately 1.36 Mg/m³.

Previous studies have pointed out the following four main factors in the effect of temperature on equilibrium swelling pressure [10]. 1) change in the state of adsorbed water in the interlayer, 2) expansion of the diffused electric double layer, 3) volume expansion of free water, and 4) thermal expansion of mineral particles.

Montmorillonite, the primary constituent of bentonite, swells by absorbing water into its interlayer spaces upon water infiltration. As the montmorillonite swells, it begins to fill the pore spaces within the material, and under saturated conditions, these pores become almost entirely occupied. Consequently, in the saturated state, the influence of temperature changes on the volume expansion of free water in the pores and on the behavior of interlayer-adsorbed water is minimal. The observed increase in equilibrium swelling pressure with rising temperature can be attributed to the expansion of the diffuse electric double layer and the thermal expansion of the mineral particles.

The surface of clay minerals carries either a positive or negative charge, attracting oppositely charged ions and forming an electric double layer around the particles. The thickness of this electric

double layer increases with rising absolute temperature, and when the double layers of adjacent particles overlap, repulsive forces are generated. In the present study, the electric double layer was observed to expand with increasing temperature, leading to an increase in repulsive forces and, consequently, an increase in the equilibrium swelling pressure. However, the increase in the thickness of the electric double layer at 90°C was only about 1.1 times greater than that at 30°C. Therefore, although the effect of enhanced repulsion was evident, it is presumed to have been limited.

In addition, Shimizu [11] conducted consolidation tests on both swollen and unswollen clays under varying temperature conditions and determined the thermal expansion coefficient of each sample based on the relationship between temperature and soil particle density. The results indicated that the thermal expansion coefficient of montmorillonite, a major component of bentonite, is higher than that of other minerals due to the weak bonding between its crystal particles. During the temporal evolution of swelling pressure, swelling and compression induced by water absorption occur continuously within the specimen. In this process, the thermal expansion of mineral particles caused by the rise in temperature is believed to contribute to compression, thereby resulting in an increase in swelling pressure.

CONCLUSION

In this study, swelling pressure tests were conducted, considering initial water contents and temperature, to experimentally understand the effect of each initial condition on the change in swelling pressure over time. The following is a summary of the findings.

(1) No clear dependence of the temporal evolution of swelling pressure on the initial water content was observed. Although the overall trend of swelling behavior remained largely unaffected by temperature variations, an increase in temperature led to higher permeability and a reduction in the time required to reach equilibrium swelling pressure.

(2) Under conditions of low effective clay density, it was confirmed that changes in temperature have a significant effect on the initial swelling pressure peak. Furthermore, the combined effects of osmotic pressure, increased repulsion due to the expansion of the diffuse electric double layer, and thermal expansion of the mineral affect the change in swelling pressure over time and the equilibrium swelling pressure.

ACKNOWLEDGMENTS

This study was supported by The Obayashi Foundation. We here express our deepest gratitude.

REFERENCES

[1] JNC 1999. Technical reliability of the geological disposal for high-level radioactive waste in Japan - geological disposal research and development Second compiled - General report. Japan Nuclear Cycle Development Institute, JNC TN1400 99-020, pp. 41-62.

[2] Kohno, M., Nishimura, T., 2022. Swelling characteristics and permeability of bentonite-based materials immersed in various solutions. Materials Transactions, Vol. 63, No. 8, pp. 1144-1150.

[3] Komine, H., Ogata, N., 1994. Experimental study on swelling characteristics of compacted bentonite. Canadian Geotechnical Journal 31 (4), pp. 478-490.

[4] Takayama, Y., Kikuchi, H., 2021. Observation of collapse behavior of bentonite during swelling pressure test using X-ray CT measurement. JSCE(c), 77(3), pp. 302-313.

[5] Villar, M.V., Lloret, A., 2008. Influence of dry density and water content on the swelling of a compacted bentonite. Applied Clay Science 39, pp. 38-49.

[6] Takayama, Y., Sato, D., Kikuchi, H., 2022. Effect of collapse behavior on changes in swelling pressure of bentonite during swelling pressure test. Journal of Nuclear Fuel Cycle and Environment, Vol. 29, No. 2, pp. 101-111.

[7] Kanazawa, S., Kobayashi, S., Ichikawa, N., Yanai, M., Ishiyama, K., 2020. The swelling behavior of bentonite buffer material considering the effect of temperature. International Journal of GEOMATE, Vol. 19, Issue 74, pp. 216-221.

[8] Towhata, I., Kuntiwattanakul, P., Seko, I., Ohishi, K., 1993. Volume change of clays induced by heating as observed in consolidation tests. Soils and Foundations, Vol. 33, No. 4, pp. 170-183.

[9] Matsumoto, K., Kannno, T., Fujita, T., Suzuki, H., 1997. Saturated permeability characteristics of buffer material. JAEA-DATA/PNC TN8410 970296, pp. 1-21.

[10] Ruan, K., Wang, H., Komine, H., Ito, D., 2022. Experimental study for temperature effect on swelling pressures during saturation of bentonites. Soils and Foundations, 62, 101245.

[11] Shimizu, M., Onishi, T., 2003. Heating-induced acceleration of secondary compression with account of thermal expansion of soil particles. Proceedings of the 38th Annual Meeting of the Japanese Geotechnical Society, D-08, pp. 197-198.

Copyright © Int. J. of GEOMATE All rights reserved, including making copies, unless permission is obtained from the copyright proprietors.

15th Int. Conf. on Geotechnique, Construction Materials & Environment, Kyoto, Japan, 11-13 November 2025, ISBN 978-4-909106124 C3051

EFFECT OF LONG-TIME SEEPAGE ON MULTI-LAYERED GROUND

Yixuan Li [1], Yamato Kadoi [2] and Mari Sato [3]

[1]Faculty of Life and Environmental Science, Shimane University, Japan; [2] Japan Conservation Engineers & Co., Ltd., Japan; [3] Academic Assembly, Shimane University, Japan

ABSTRACT

We investigated the effects of long-term seepage behavior and internal erosion on the stability of simulated ground comprising multiple soil layers with different hydraulic conductivities, such as a reservoir or river embankment. Special focus was placed on the movement of soil particles due to seepage flow and the resulting changes in the soil interior. A two-layer experimental soil model with high-permeability in the lower part and fine-grained sand in the upper part was constructed. Water was supplied to the lower soil layer from the walls for an extended period and drainage was facilitated through a slit at the center of the bottom surface. During water supply, the upper surface gradually expanded, albeit to a small extent. After the water supply was completed, the ground contracted and grain size tests showed that the specific range of fine grains decreased at the left and right edges near the upper soil layer boundaries, whereas the same range of fine grains increased at the center. These results indicate that long-term infiltration into multiple layers of ground with varying permeabilities may result in the gradual movement of fine-grained sediment within the ground. The small amount of sediment movement in this experiment did not directly affect soil strength. However, the risk of disasters such as boiling may increase owing to the accumulation of sediment that cannot escape from the coarse-grained sediment and the local decrease in permeability. Future studies are required to determine whether similar phenomena can be observed in actual levees.

Keywords: Boiling, Grain size distribution, Internal erosion, Ground deformation

INTRODUCTION

Internal erosion phenomena within the ground can cause various disasters in the earth's structures [1,2].

In river embankments, piping becomes a significant issue when infiltration occurs in the underlying permeable layers at high water levels, particularly in ground conditions where a surface layer of fine-grained soil is present [3].

This study aims to clarify the effects of internal erosion caused by repeated daily infiltrations into the underlying permeable layers prior to any damage. Model experiments were conducted to investigate behavior during infiltration as well as the strength reduction and changes in particle size distribution after infiltration.

Previous research [4] has pointed out the possibility of local changes in fine particle content due to sediment movement within the ground and an increased risk of boiling. However, in this study, the coarse-grained soil layer was replaced with a sample of even larger particles to reproduce the conditions that facilitate sediment movement.

Specifically, during water supply, sensors installed within the ground were used to continuously measure changes in the volumetric water content, surface displacement of the ground, and inflow and outflow volumes. After the water supply ended, changes in the particle size distribution and the presence of density reduction were examined.

This study aimed to elucidate the factors that promote boiling and piping during heavy rainfall events and contribute to the safety management of embankment structures.

RESEARCH SIGNIFICANCE

In this study, a model-scale experiment was conducted. This revealed that the soil particle migration and change in the local grain size distribution by the long-term seepage in the surface layer consisted of fine sand above a highly permeable layer. The influence of soil migration on permeability and ground looseness was estimated. A slight expansion during penetration may facilitate soil transportation. Long-term seepage increases the risk for generation of localized clogging and high-permeability zones near the boundary between the two layers.

EXPERIMENTAL METHOD

For the model ground preparation, a box-shaped acrylic soil chamber with a width of 30 cm, depth of 10 cm, and height of 40 cm (Fig.1) was used. Silica sand No.1 was compacted into the lower layer and silica sand No.7 was compacted into the upper layer, each to a height of 15 cm, resulting in a total ground height of 30 cm. The actual height of each layer was measured after the preparation, as shown in Fig.1.

To observe deformation in the silica sand No.7 layer, the colored sand was thinly layered on the front side of each compaction layer (at approximately 4 cm intervals). The filter rule D_{15}/d_{85} between silica

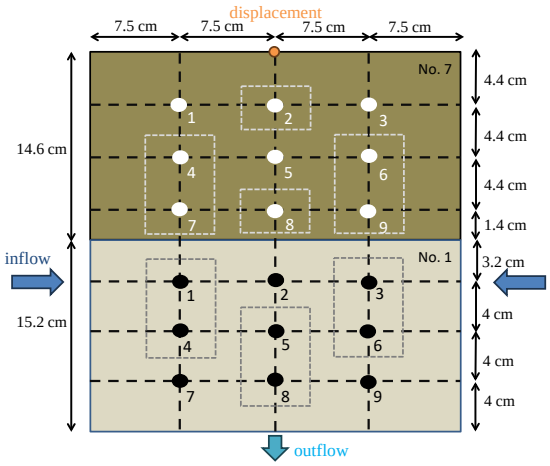

Fig.1 Schematically figure of the model ground

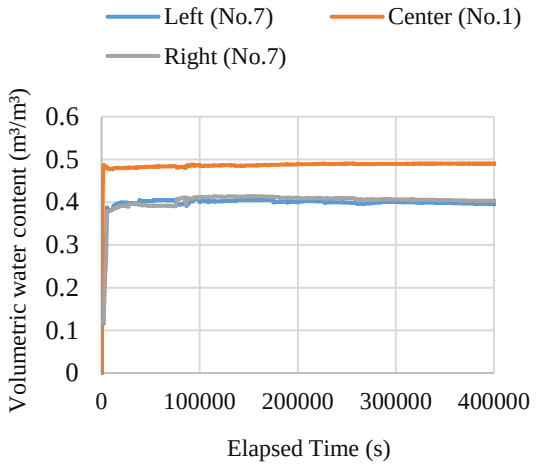

Fig.2 Change in volumetric water content (overall)

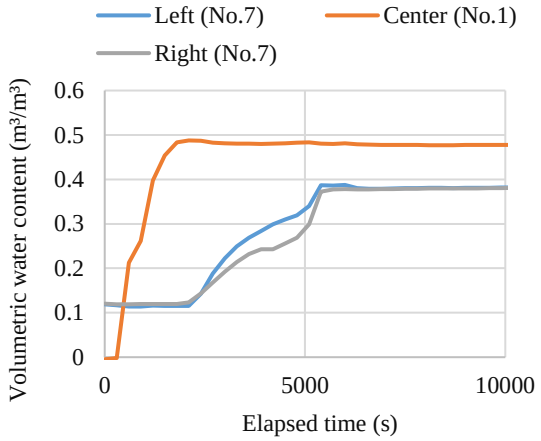

Fig.3 Change in volumetric water content (detailed)

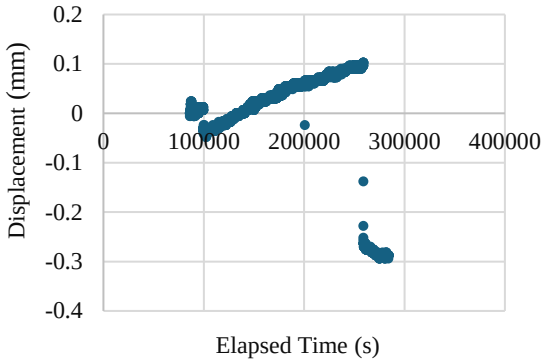

Fig.4 Variation in surface displacement

sand No. 1 and No. 7 was approximately 12.5. The initial water content during compaction was adjusted to 4% for silica sand No.1 and 10% for silica sand No.7. The relative density was set to 40% for silica sand No.1 and 60% for silica sand No.7.

Water was supplied from the same height as the top of the silica sand No.7 layer by overflowing a funnel connected to the tubing. The water entered the upper part of the silica sand No.1 layer through 12 cm-high and 8 mm-diameter holes located on both sidewalls of the soil chamber. Drainage was conducted through a 5 mm-wide slit filled with sponge at the center of the bottom of the tank. The sponge prevents soil particles from escaping and restricts water outflow. Consequently, several hours after the water supply was started, the surface of silica sand No.7 became visibly saturated.

Water supply was continued for 72 h (3 days). During this time, soil moisture sensors were used to measure the volumetric water content inside the model ground. The sensors were installed at three locations: one at a height of 12 cm from the bottom in the center (within the silica sand No.1 layer), and two at a height of 23 cm from the bottom and 7.5 cm from each side edge (within the silica sand No.7 layer). Measurements were taken at 5-minute intervals.

A flow meter was attached near the water inlet of the right-side tube to measure the inflow rate (mL/min) during water supply. A laser displacement meter was installed at the top center of the soil chamber to measure the vertical displacement of the surface layer. These meters were measured at 30-second intervals. In addition, the outflow volume was measured eight times over three days at several-hour intervals, each over a 10-minute period.

After the water supply was completed, the model ground was left undisturbed for several days. The front cover of the soil chamber was then removed, and the chamber was placed face up. Soil hardness was measured at nine points in the silica sand No.1 layer and six points in the silica sand No.7 layer using a Yamanaka-type soil penetrometer. From around one or two of the measurement points, samples were collected for grain size distribution tests: three from silica sand No.1 layer and four from silica sand No.7 layer. Fig.1 shows the measurement and sampling points for the soil hardness and grain size analyses.

EXPERIMENTAL RESULTS

From Water Supply to Pre-Drainage Completion

Observations during water supply are described in terms of the elapsed time since the start of supply and daily progress from day 1 to day 3 of supply.

Approximately two hours after the start of the water supply on day 1, the water level rise was less than expected. An additional sponge was inserted to adjust the drainage conditions. Around this time, both inflow and outflow rates began to decrease and remained nearly constant thereafter, with only minor fluctuations. The initial changes in flow may have been influenced by the added sponge. In particular, for outflow measurements, leakage from the soil chamber was observed. Therefore, quantitative evaluation based on inflow and outflow values remains a topic for future improvement. After the sponge was added, the ground surface became visibly saturated, and silica sand No.7 layer was confirmed to contain water. No distinct deformation of color sand was observed during the water supply.

Fig.2 and Fig.3 show the changes in volumetric water content during water supply. As shown in the graph, the sensor installed in the central part of the silica sand No.1 layer recorded an increase in volumetric water content until approximately 1,800 seconds from the start of the water supply on day 1, after which it remained nearly constant. The sensors installed in the left and right sections of the silica sand No.7 layer showed a continued increase in water content until approximately 5,400 seconds after the end of increase in that in Silica sand No. 1, after which the values stabilized with no significant fluctuations. No noticeable differences were observed between the left and right measurements, indicating that the water level increased uniformly.

During drainage, unlike the findings of a previous study [4], the volumetric water content in silica sand No.1 layer showed only a slight decrease. This may be due to insufficient drainage resulting from the increased amount of sponge. Therefore, the post-infiltration drainage conditions observed in previous experiments could not be reproduced in this study.

Fig.4 shows the results of vertical displacement measurements at the central surface of the model. Owing to the malfunction of the displacement sensor,

Table 1 Soil hardness in No. 7 silica sand layer

Point	Bearing capacity (kg/cm²)
1	-
2	-
3	-
4	0.22
5	0.25
6	0.39
7	0.17
8	0.17
9	0.22

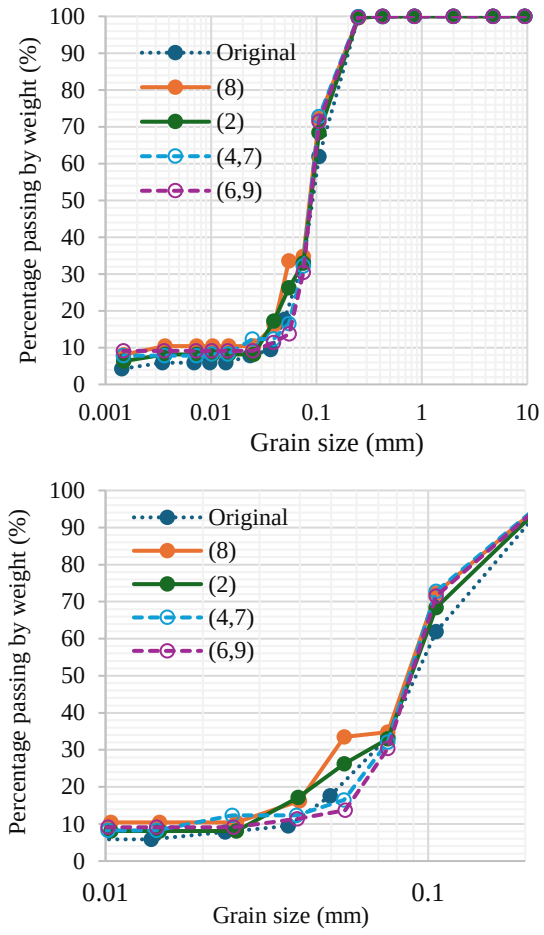

Fig.5 Grain size distribution of silica sand No. 7 (top: overall, bottom: detailed view)

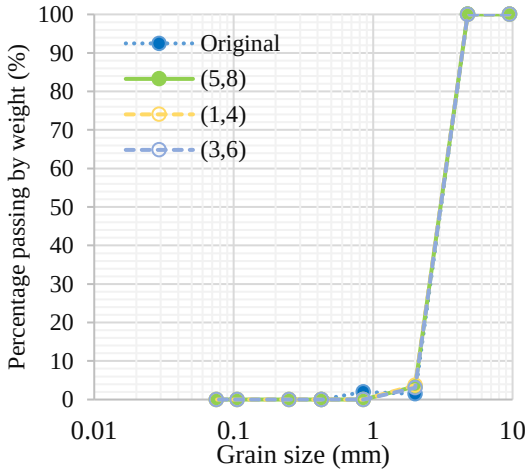

Fig.6 Grain size distribution of silica sand No. 1

Table 2 Summery of grain size distribution of silica sand No.1

Grain size (mm)	Original	(5,8)	(1,4)	(3,6)
9.50	100.00	100.00	100.00	100.00
4.75	100.00	100.00	99.94	99.97
2.00	1.52	3.37	3.69	3.07
0.85	0.02	0.00	0.00	0.00
0.43	0.00	0.00	0.00	0.00

no data were collected for the first 24 hours (from 0 to 86,371 seconds on day 1), and this period was excluded from the analysis. The value was set to zero at the resumption of measurement on day 2. After 100,000 seconds from the start of water supply, the ground gradually exhibited expansion, followed by a sudden contraction of approximately 0.4 mm at approximately 259,231 seconds on day 3, indicating the end of the water supply period. Following the rapid contraction, almost no further volumetric changes were observed.

Post-Drainage Observations

The results of the soil hardness measurements are listed in Table 1. Data from measurement points 1 to 3 in the silica sand No.7 layer were missing because, upon tilting the soil chamber onto its back, the high moisture content caused a collapse due to self-weight before measurements could be conducted. No significant differences in the bearing strength were observed among the various measurement locations. In the silica sand No.1 layer, owing to the large particle size, substantial variation was observed in the measured values, depending on how the penetrometer tip contacted the individual particles. Because the results were not suitable for evaluating looseness, they were omitted from the analysis.

The results of the particle size distribution tests for silica sand No. 7 and silica sand No.1 are shown in Fig.5 and 6, respectively. In the legends, "Original" refers to the original gradation determined separately prior to infiltration. The values in parentheses indicate the sampling locations around the measurement points shown in Fig. 1, following the completion of infiltration. The lower part of Fig.5 shows a magnified view of the portions showing large difference among original and other cases within the overall range depicted in the upper part.

For the central sampling locations (2) and (8) in the silica sand No.7 layer, the mass-passing ratio in the 0.055–0.075 mm particle size range increased compared to the pre-experiment sample. Conversely, the mass-passing ratio decreased at the lateral sampling locations (4, 7) and (6, 9). Around the 0.106 mm particle size, the mass-passing ratio increased at all locations relative to the original gradation. In the silica sand No.1 layer, no significant differences were observed in the mass-passing ratio across all sampling locations before and after infiltration.

DISCUSSION

The slight expansion observed during the water supply phase was most likely due to a decrease in the effective stress caused by the infiltration pressure from the water inflow of silica sand No.1 into silica sand No.7. Therefore, it is presumed that the expansion ceased immediately after the water supply ceased. However, because the extent of expansion from the beginning of the experiment was not measured, the movement of fine particles may have also contributed to this behavior. Although the impact of such an expansion on the ground remains unclear, it may increase the likelihood of fine particle migration during infiltration. As described later, localized changes in permeability due to particle size distribution variations may have occurred within the soil. However, no significant changes were observed in the measured inflow or outflow rates during the infiltration test, suggesting that the overall permeability was not significantly affected.

Regarding localized permeability changes, the permeability of the silica sand No.7 layer was estimated at each sampling location based on the 20% particle diameter using the Creager formula. Compared to the original gradation, the permeability at locations (2) and (8) was estimated to be approximately 0.6 times lower, indicating a localized permeability reduction owing to clogging near the interface, consistent with previous studies [4,5]. Even at location (2), which is closer to the surface than location (8), a decrease in the permeability was observed. In contrast, the permeability at location (4,7) and (6,9) was estimated to be approximately 1.3 and 1.4 times higher, respectively. Migration of soil particles induced both concentration and clogging.

In an infiltration flow analysis study using a similar two-layer soil configuration [5], it was shown that water infiltrated through silica sand No.1 layer into silica sand No.7 layer, and downward infiltration occurred near two-layers' interface above the drainage outlet, allowing infiltration back into silica sand No.1. According to Kenny and Lau [6], in narrowly graded (NG) materials such as silica sand No.7, particles with diameters below 20% are considered fines and are capable of movement within the pores. This aligns with the present experimental results, where particles approximately 0.05 mm, corresponding to 20% of the diameter of the original material, increased at central locations (2) and (8),

while decreasing at lateral positions (4, 7) and (6, 9).

The negligible difference in the particle size distribution below 0.025 mm suggests that the fine particles mobilized by the infiltration flow passed directly through the interface and were discharged into the silica sand No.1 layer. However, particles approximately 0.05 mm may have been unable to pass through the pores of the silica sand No.1, leading to deposition. At location (2), even particles approximately 0.04 mm showed an increased proportion. Because this location is farther from the boundary interface than in (8), it is possible that fewer fines were discharged, and the migrated particles remained within the ground. The mechanism by which the 0.05 mm particles fail to outflow into the silica sand No.1 layer warrants further investigation in conjunction with existing research findings.

CONCLUSIONS

In this study, a model experiment was conducted to investigate the effects of infiltration behavior and erosion phenomena in cases where a highly permeable layer existed beneath a surface layer composed of fine sand. The volumetric water content results confirmed that water infiltrated from the lower soil layer into the upper layer and reached near-surface saturation. In addition, upward infiltration combined with drainage from the slits induced soil particle movement in the upper layer, suggesting that the resultant water pressure during infiltration may have caused ground expansion and potential loosening.

These findings imply that, in long-term scenarios following embankment construction, internal erosion near the highly permeable layer should be considered a possible risk. However, no apparent loosening owing to particle movement was observed in terms of soil hardness. As for the particle size distribution, both similarities and differences were found in comparison with a previous study [4]. An increase in the mass fraction at approximately 0.106 mm particle size was observed, as in the previous study; however, because this size does not correspond to finer components within silica sand No.7, the possibility of erosion at the layer interface cannot be ruled out and warrants further investigation.

Fine-particle migration, which significantly changes the particle diameter by 20 %, is likely to affect permeability. The observed local decrease in permeability owing to clogging is consistent with previous findings and suggests a heightened risk of piping. Furthermore, the range of particle sizes capable of migration is within the ground-matched predictions based on prior knowledge. Among the fine particles that moved with the infiltration flow, the finer fractions likely escaped through the interface between the two layers, whereas slightly larger particles may have accumulated at the interface, leading to clogging.

The above phenomena were confirmed through model experiments. Therefore, in the future, it will be necessary to clarify the conditions under which similar phenomena occur in actual embankments and with real embankment materials, as well as their effects on the embankment, with reference to previous studies [4]. In actual embankments, there are long-term water level fluctuations, and the thickness of each geological layer at the bottom of the embankment may vary locally. Hence, there is a possibility that areas prone to phenomena similar to those observed in the model experiments exist. Furthermore, in real embankments, such phenomena may progress over a longer time scale than in the model experiments, making it necessary to consider cases in which sediment transport advances further than observed in the experiments.

ACKNOWLEDGEMENTS

This study was supported by JSPS KAKENHI (grant number: JP 22K04312). We would like to thank Editage (www.editage.jp) for English language editing.

REFERENCES

[1] Bonelli, S. (ed.), Erosion of Geomaterials, ISTE Ltd and John Wiley & Sons, Inc., pp.1-371, 2012.
[2] Sato, M. and Kuwano, R., Laboratory testing for evaluation of the influence of a small degree of internal erosion on deformation and stiffness, Soils and foundations, Vol. 58, No. 3, 2018, pp. 547-562.
[3] Japanese Geotechnical Society, From Investigation and Study to Maintenance of River Embankments, Maruzen Publishing Co., Ltd., pp. 1-149, 2020.
[4] Sato, M. and Sakamoto, N., Piping Risks because of Internal Erosion to an Embankment Having a Permeable Foundation, Ground Engineering, Vol. 40, No. 1, 2022, pp.89-99.
[5] Sakamoto, N. and Sato, M., Seepage flow analysis considering the effects of internal erosion due to long-term seepage into ground comprising surface impermeable ground, 7th Int. Conf. on Structure, Engineering & Environment (SEE), 2021, pp.98-103.
[6] Kenney, T. C. and Lau, D. Internal stability of granular filters, Canadian Geotechnical Journal, 22(2), 1985, pp.215-225, DOI: 10.1139/t85-029.

Copyright © Int. J. of GEOMATE All rights reserved, including making copies, unless permission is obtained from the copyright proprietors.

15th Int. Conf. on Geotechnique, Construction Materials & Environment,
Kyoto, Japan, 11-13 November 2025, ISBN 978-4-909106124 C3051

POROSITY ASSESSMENT IN ONE-DIMENSIONAL PERMEATION GROUTING USING SUSPENSION-TYPE GROUT SOLUTION

Jemy C. Chua[1], Naoaki Suemasa[2], Takamitsu Sasaki[3] and Koichi Nagao[4]

[1,2]Graduate School of Integrative Science and Engineering, Tokyo City University, Japan
[3]Kyokado Engineering Co., Ltd., Japan; [4]Sato Kogyo Co., Ltd., Japan

ABSTRACT

Soil liquefaction, triggered by seismic activity, destabilizes loose and saturated ground leading to extensive damage. This research explores the application of permeation grouting as a mitigation technique for liquefaction. Grouting is a ground improvement technique that involves injecting grout solutions at low pressures into soil pores to enhance its properties. To promote sustainability, alternative materials to conventional cement-based grouts were proposed and demonstrated to be viable. Suspension-type grouts densify and solidify the ground, offering higher performance compared to solution-type grouts. However, a limitation of suspension-type grouts is the occurrence of clogging. As permeation progresses, porosity of the soil reduces, along with the performance of grouting. To evaluate the flow behavior and interaction of the grout to the soil, one-dimensional permeation tests using varying grout concentrations were conducted. The relationship between permeation pressure, permeation volume, and porosity of the soil were analyzed. Results demonstrated that densification happens as permeation volume and pressure increases. While beneficial for increasing liquefaction resistance, immediate densification impedes further grout permeation, reducing the improvement radius. Therefore, porosity assessment is critical in balancing densification and permeation volume. Numerical estimation using Kozeny-Carman equation was found to be feasible, with porosity estimations approaching the actual experimental results.

Keywords: Soil liquefaction, Permeation grouting, Suspension-type grout, Porosity assessment, Kozeny-Carman equation

INTRODUCTION

Amidst the continuous growth of cities and infrastructures, the field of geotechnical engineering becomes increasingly important as this serves as the foundation of every structure. Despite its apparent stability, the ground is composed of plates that are constantly in motion. When these plates collide, the immense force generated can lead to a sudden release of energy, resulting in an earthquake. The recent 2024 Noto Peninsula earthquake in Japan caused severe casualties and incurred several geotechnical-related disasters like slope failure and soil liquefaction.

Soil strength relies on intergranular contact forces (total stress). However, pore water pressure reduces this strength. Ground movement causes temporary excess pore water pressure, and when this equals or exceeds total stress, the soil liquefies, losing its load-bearing capacity. This liquefaction leads to significant ground consolidation, damaging infrastructure and impacting community safety and economic stability by blocking transportation.

Permeation grouting is one of many ground improvement methods that helps mitigate the risk of liquefaction. Grouting offers several advantages, like its simplicity, compact procedure, and minimal disturbance to the soil during improvement [1]. This makes it suitable for remediating existing foundations or to soil that cannot tolerate disturbance [2][3]. Grouting works by permeating a grout solution into the ground at low pressures. The solution consists of materials designed to improve the physical properties of the soil by means of densification and/or solidification. There are two types of solutions that are commonly used, solution-type and suspension-type. Compared to solution-type which uses liquid chemicals, suspension-type is a type of grout made with fine particles suspended in water. These particles are commonly composed of cement or pozzolans that solidify when activated, improving the properties of the soil its injected into. Suspension-type grouts offer higher versatility and generally develop greater strength due to particle densification, but estimating the quantity and area of improvement can be difficult, and particle clogging is a critical factor affecting performance [4].

Scope and Objective

Grouting is a three-dimensional ground improvement technique. As a first step for analyzing the permeation performance, one-dimensional permeation tests were conducted and analyzed. For the experiments, only one type of soil was used for all samples and were all in fully saturated condition prior to permeation. The study aims to assess the porosity changes of the soil throughout the permeation process using both experimental data and numerical analysis.

RESEARCH SIGNIFICANCE

Permeation grouting using suspension-type grouts has recently gained attention for its versatility and exceptional performance. However, the relationship between the grout material to its performance in grouting is not well backed. This study aims to establish a connection or understanding of the relationship between permeation pressure and changes in soil porosity based on both experimental and numerical modeling results. By doing so, prediction of grout performance concerning other types of material or soil may be plausible.

CLOGGING MECHANISM

Clogging is a major problem concerning the permeation of suspension-type grout. Clogging happens when the particles suspended in the grout accumulates into the voids of the soil to a point where either the void space has been fully filled, or the pore throat becomes obstructed. Figure 1 shows three scenarios dealing with permeation grouting. V_s, V_w, and V_g depict the volume occupied by the solid (soil), water, and grout respectively. Scenario (a) just shows the initial condition of the sample without any permeation. Scenario (b) shows the ideal grouting scenario, wherein the grout particles are evenly distributed throughout the voids of the soil sample. In contrast, scenario (c) shows the most realistic scenario that happens during permeation. The grout particles get trapped, or clogged in the direction of flow, hindering further permeation and resulting in uneven distribution of the grout particles within the voids of the soil. This also increases the flow resistance of the ground, thereby requiring increased permeation pressure to push grout particles deeper into the soil.

Clogging occurs erratically and it is difficult to pinpoint the exact locations. Several factors influence clogging, including soil type, relative density, pore throat size, particle size and shape, and many more. While difficult to pinpoint exactly, predictions can be made using external factors such as pressure and concentration or the amount of material injected into the pore spaces of the soil.

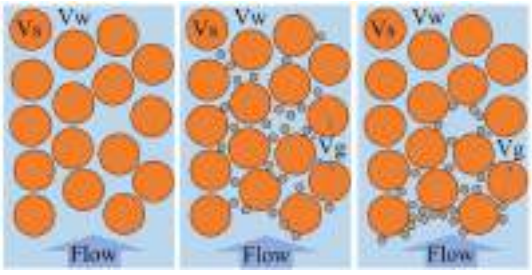

(a) (b) (c)

Fig.1 Grouting illustration. (a): Soil only (b): Ideal scenario; (c): Clogging scenario

EXPERIMENTAL SETUP AND MATERIALS

One-dimensional permeation tests were done to analyze the flow of the grout during permeation. This was achieved using the apparatus shown in Fig. 2. The model soil height was 100 cm with a diameter of 5 cm, divided into 10 segments. Silica sand #6 at a relative density of 60% was used as the soil medium. Several water pressure sensors were installed along the column, at the inlet, 5 cm, 15 cm, 25 cm, 45 cm, and 75 cm away from the inlet. These sensors record the pressure as permeation commenced. Smaller increments were considered near the bottom as a non-linear pressure profile was expected within the soil.

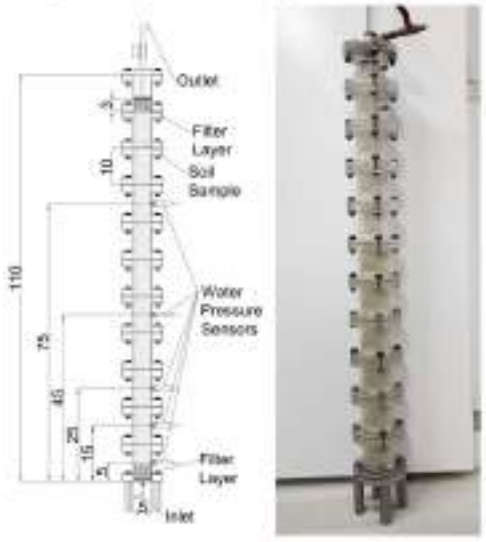

Fig.2 One-dimensional permeation apparatus (in cm)

Grouting is a very complex procedure in which several factors influence performance. The grout material used for the permeation tests were ground-granulated blast furnace slag (BS) and calcium carbonate ($CaCO_3$) in a 1:1 ratio, by weight. Varying concentrations were tested from 3%, 5%, and 7% powder-water ratio, also by weight. Permeation flowrate of 100 mL/min was deemed to be the optimal flow rate considering pressure developed and overall performance [1]. The permeation process was carried out until one of the following conditions was satisfied: (1) the pressure reached 400 kPa in the inlet ;(2) the pressure remained constant or (3) a sharp change in pressure was observed.

EXPERIMENTAL RESULTS

Permeation continued until one of the defined conditions was met. The amount of grout permeated as well as the grout retained within the soil column among the cases are summarized in Table 1. Despite having the most grout mass permeated, 7% concentration had a lower grout retention than 5% concentration. Grout retained means the amount of

grout estimated to be retained within the voids of the soil. In the case of 7%, a higher expelled grout amount was observed, likely caused by soil fracture, creating a path of lesser resistance for the grout to pass through. This fracture can be further speculated from the pressure profile in Fig 3, as there was a sharp decrease in pressure.

Table 1 Grout injected amount per concentration

Case	1	2	3
Grout concentration	3%	5%	7%
Grout volume (L)	12.5	9.0	6.5
Dry grout injected (g)	375.0	450.0	455.0
Dry grout retained (g)	280.5	378.3	312.2
Dry grout expelled (g)	54.00	28.32	111.6
Loss (g)	40.48	43.37	31.23

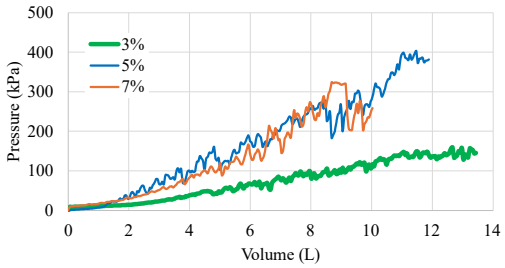

Fig.3 Pressure at the inlet

Pressure Profile

As the permeation progressed, the pressures gradually rose in response to the volume of grout injected. This rise in pressure can be attributed to the reduction in pore spaces within the soil, which decreased its overall permeability. To compensate, higher pressure was needed to maintain a stable permeation rate. Fig. 4 presents the results of the permeation pressure to the volume of grout injected with varying concentrations. In all cases, pressure was higher near the inlet and decreased with distance. Apart from this, an almost linear pressure profile can be observed at each location as the permeation progressed. The pressure fluctuated erratically due to the continuous clogging and unclogging of grout particles. As these particles accumulate at specific points, the force required to push them increases, causing a temporary rise in pressure. Once pressure reaches the threshold needed to break apart the clumped particles, the pressure is abruptly released, causing pressure fluctuations.

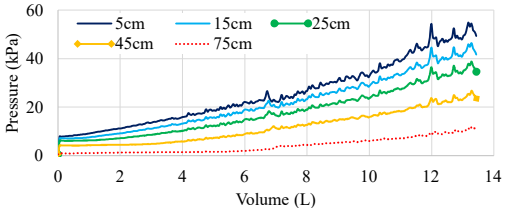

(a)

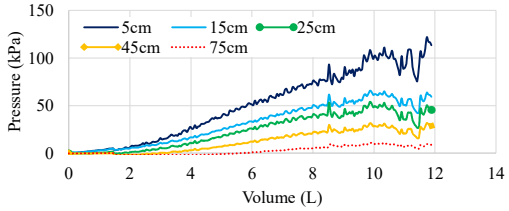

(b)

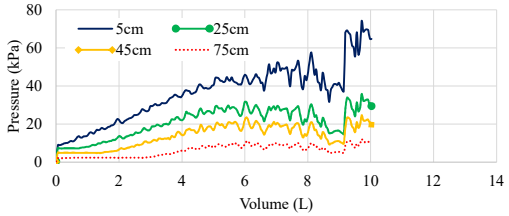

(c)

Fig.4 Permeation pressure to the volume injected with varying concentrations: (a) 3%; (b) 5%; (c) 7%.

Fracturing of soil usually happens during high pressure permeation. While less common and usually at a smaller size, fracturing can also occur during low pressure permeations. A sharp decrease in pressure that does not recover back to the previous pressure generally means fracture occurred that lead to a path of lesser resistance for the grout to permeated into. Fracturing or cracking results in an uneven grout distribution, and lesser grout retention. Correlating this change to the amount of grout expelled a fracture was highly likely to have happened during the permeation. While fracturing is unavoidable and unpredictable, it is possible to know the moment it happens. This detection allows for adjustments or consideration of its impact on the overall grouting process.

Grout Distribution and Porosity

Following the permeation process, grout particle concentrations were measured at 10 cm intervals within the soil. Each segment was washed with water, and sieved using a 75-micron sieve to allow the grout particles to pass through while retaining the sand. This process was repeated multiple times to maximize particle recovery. The resulting liquid was oven-dried, and the remaining powder was weighed to determine the final concentration. Fig. 5 compiles the grout retained in the soil per segment. For all cases, more grout retained in the part near the inlet and gradually lessens as the distance increases, albeit some uneven distributions.

Porosity is a fundamental parameter in permeation grouting, as it directly influences the effectiveness of grout flow and rate of soil densification. The initial porosity was computed to be 0.441, using the void ratio of silica sand #6 at a relative density of 60%. The post-permeation porosity of each segment was calculated and tallied in Table 2.

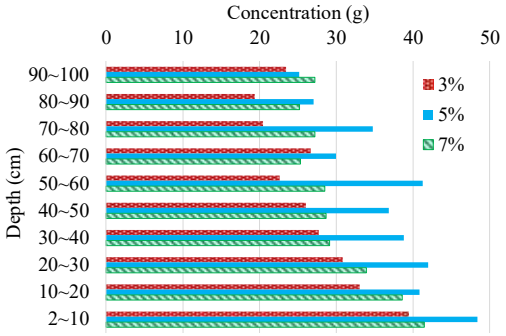

Fig.5 Grout retained per segment per case

Table 2 Post-permeation porosity of each case

Position (cm)	Porosity		
	3%	5%	7%
90~100	0.399	0.396	0.393
80~90	0.407	0.393	0.396
70~80	0.405	0.379	0.393
60~70	0.394	0.388	0.396
50~60	0.401	0.368	0.390
40~50	0.395	0.375	0.390
30~40	0.392	0.372	0.389
20~30	0.386	0.366	0.381
10~20	0.382	0.368	0.372
2~10	0.353	0.333	0.349

Correlating the porosity data with the pressure data, an inversely related relationship can be observed from Fig. 6. From here, it can be observed that the higher the change in pressure results in a higher change in porosity. This can mean that each parameter influences the other in a direct manner. With this, predictions of porosity, and ultimately grout retained, can be made just by using the pressure data during the permeation process.

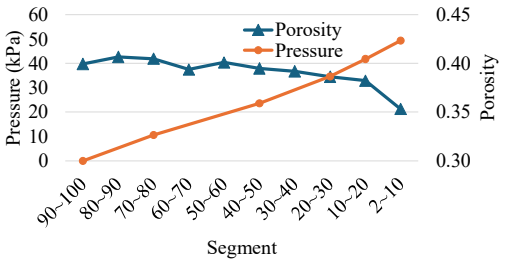

(a)

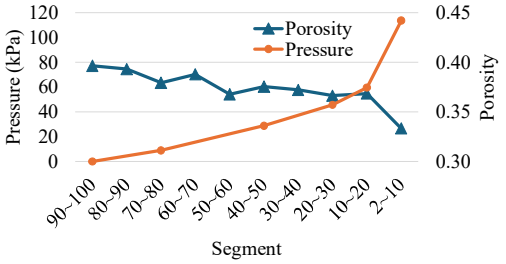

(b)

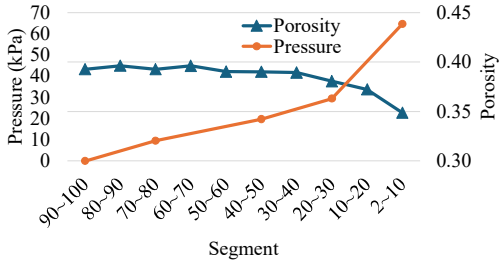

(c)

Fig.6 Pressure and porosity with distance for varying concentrations: (a) 3%; (b) 5%; (c) 7%.

NUMERICAL ANALYSIS OUTLINE

Given the potential relationship between grout concentration or the porosity of the soil to the permeation pressure, numerical analysis serves as a powerful tool for optimizing permeation performance. This reduces the need for extensive physical testing which enhances the efficiency of grouting techniques. Numerical analysis was attempted to estimate soil porosity from permeation pressure incorporating factors such as pressure, depth, time, permeability, and particle size.

Quadratic Regression

Five pressure sensors were used in the permeation experiment with varying distances from the inlet. These determine the pressure change in the location of the sensor as the permeation commenced. To obtain a pressure profile of the soil column during permeation, quadratic regression was used.

$$P = ax^2 + bx + c \quad (1)$$

Where P is the pressure, x is the depth or the distance from the inlet. One function was created from one set of pressure data (from five sensors) per unit time (1Hz). Each function was able to achieve an r-squared value of around 0.95, signifying a high level of accuracy.

Darcy-Weisbach Equation

The energy of water flow comes from total head loss due to the frictional resistance on particles surfaces on both the soil and the grout [5]. Clogging further increases the required energy to flow. There are several ways to predict permeability using equations [6,7], Darcy-Weisbach is one of the commonly known equations to calculate for permeability. From the regression, pressure at any point in the soil column, at any point in time, can be estimated. As such, permeability using Eq. (2) at any place and time can also be calculated.

$$q = Ki \quad (2.1)$$

Where q is the flowrate in m^3/s, K is the hydraulic conductivity in m/s, and i is the hydraulic gradient. By altering some parameters, Eq. 2.2 can be derived from Eq. 2.1. This way, instead of the hydraulic gradient, the pressure gradient can be used.

$$q = \frac{k}{\mu}\left(\frac{dP}{dx}\right)A \tag{2.2}$$

Where k is the intrinsic permeability in m^2, μ is the viscosity in $kPa \cdot s$, dP/dx is the pressure gradient in kPa/m, and A is the area in m^2. Hydraulic conductivity and intrinsic permeability are commonly misunderstood and mixed up. Hydraulic conductivity is a function of both the soil and the fluid flowing through it, while intrinsic permeability is just a function of the soil or porous substance, independent of the fluid. [8,9]

Kozeny-Carman Equation

The Kozeny-Carman equation is an equation that relates permeability to its porosity, grain size, and tortuosity [9], shown in Eq. (3). It is a semitheoretical and semiempirical formula that is used to predict the permeability [5].

$$k = \frac{\theta^3 D_g^2}{72 * \alpha\,(1-\theta)^2} \tag{3}$$

Where θ is the porosity, D_g is the particle size, and α is the tortuosity and sphericity factor.

ANALYSIS RESULTS AND DISCUSSION

As an initial attempt to estimate the porosity using pressure data, several assumptions were made, and some parameters were made constant. The soil medium was assumed to be fully uniform, using D_{15} as the particle size. Discharge velocity (or average velocity) was used instead of seepage velocity (or actual velocity). Tortuosity and sphericity factors were set to make the constant number in Eq (3) to a value of 200. The boundary conditions on porosity were set according to the maximum and minimum porosity recorded in the experiments conducted. Viscosity was taken from the viscosity of 5% concentration, and since it did not differ much from 3% and 7%, it was assumed constant.

Numerical modeling using the pressure profile data from the experiments, the porosity changes of the soil throughout the permeation process was estimated and shown in Fig. 7. In this figure, porosity can be assessed with respect to both time (or volume injected) and distance (permeation radius). The initial porosity of the soil was 0.441, but an empirical factor for the upper boundary was used in the model that corrected the max porosity from 0.441 to 0.410. This factor was to account for the fine fraction of the grout particles that occupied pore spaces but were either small enough, or light enough not to incur any permeation pressure. Due to this, minimal changes in porosity were estimated near the starting time and towards the upper portions of the soil column. As the permeation commenced and more grout volume was permeated, grout particles deposited into the voids and resulted in a reduction of porosity.

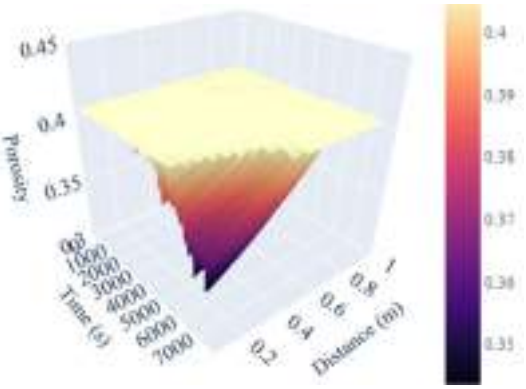

Fig.7 Porosity assessment of 3% concentration

Post-permeation porosity estimated from using the model was compared with the experimental result and shown in Fig. 8. The estimated porosity was true to the assumption that the porosity was lowest near the inlet and gradually increases with distance. However, the slope of the estimation was steeper in some cases like in the 5% concentration (Fig. 8b.). Both 3% and 7% cases (Fig. 8a. and 8c.) had a better fit, reaching similar values with the experimental results. Although fracturing was suspected in the 7% case, since this occurred in the latter part of the permeation, the model was not significantly influenced. The flat line observed was due to the empirical factor and the upper boundary condition.

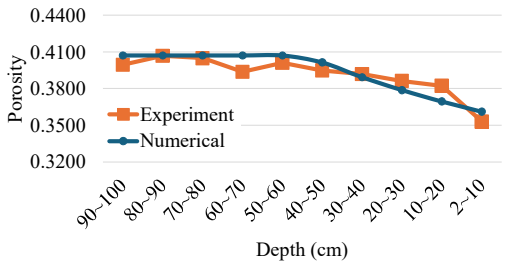

(a)

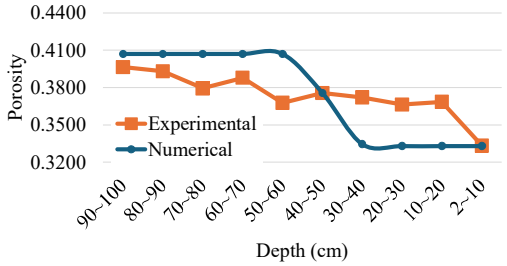

(b)

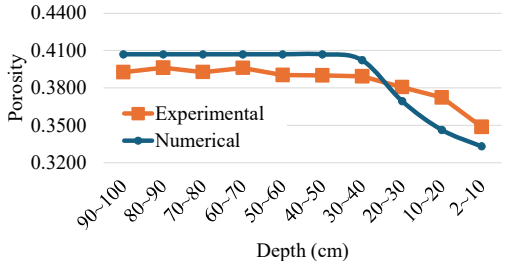

(c)

Fig.8 Numerical and experimental comparison for various concentrations: (a) 3%; (b) 5%; (c) 7%.

The challenge faced with this current model was the slope of the porosity change. From Eq. (3), one of the crucial factors was the particle size, D_g. In the analysis, it was assumed to be constant using the size of D_{15}. This was used because in assessing the groutability of the grout solution, D_{15} was the particle size fraction used [1]. Moreover, tortuosity increases with lowering porosity [11].

To improve the accuracy of the estimation, future improvements include altering the particle size and tortuosity factors into variable parameters that consider the changes during the permeation process. As a model primarily reliant on the obtained pressure profile during the permeation process, the empirical factor used to consider the fine fraction of the grout is planned to be improved by correlating the void space and pore throat size to the grout particle size to have more accurate boundary conditions. A sensitivity analysis or allowable error is also planned to evaluate the reliability of the model. Adjustments arising from the occurrence of fracturing are to be studied and applied to the model correspondingly.

Optimizing the model offers several advantages in permeation grouting. By knowing initial soil parameters like particle size from site investigation, the injected grout's composition (particle size and viscosity), and installing pressure sensors around the injection site, porosity changes during the grouting process can be predicted. This helps ensure proper coverage and allows for estimating the developed strength based on the grout concentration.

CONCLUSION

Several one-dimensional permeation experiments were conducted with different grout concentrations. With increasing grout concentration, clogging rate becomes faster and fluctuations in permeation pressure can be observed more frequently. But apart from this, all tests revealed that permeation pressure increases with permeated volume caused by the clogging of the grout particles. This establishes an inversely related relationship between permeation pressure and soil porosity. It was also observed that porosity change was greatest near the inlet and gradually lowers with distance.

An attempt to numerically analyze the clogging mechanism or the changes in soil porosity was made, and results signify that similar trend to the experimental results can be modeled. Despite there are some differences between the experimental values and the numerically estimated values, the outline and flow of the model was able to be validated.

Future plans to improve the accuracy of the model include altering some parameters to create a better fit and provide a more versatile model that can be used in a wider array of materials. Overall, conducting numerical analysis enables the estimation of porosity at any point in both time and distance during grouting.

REFERENCES

[1] Chua, J. C., Suemasa, N., Itoh, K., Sasaki, T., and Nagao, K., Permeation Grouting Using Alkali-Activated Grout for Liquefaction Control, International Journal of GEOMATE, Vol. 28, Issue 128, 2025, pp. 84 – 91.

[2] Boschi, K., di Prisco, C., and Grassi, D., Design of Permeation Grouting Treatments with Eco-friendly Nanosilica Grouts, Geotechnical Engineering in the Digital and Technological Innovation Era, Springer, 2023, pp. 621 – 628.

[3] Liu, C., and Evett, J. B., Soils and Foundations, Pearson Prentice Hall, 6th Ed, 2004, pp. 83 – 113.

[4] Han, J., Principles and Practice of Ground Improvement, John Wiley & Sons Inc., 2015, pp. 245 – 297.

[5] Ishibashi I., and Hazarika, H., Soil Mechanics Fundamentals, CRC Press Taylor and Francis Group, 2011, pp. 87–109.

[6] Mary Ann Q. Adajar, and Mark Albert H. Zarco. An Empirical Model for Predicting Hydraulic Conductivity of Mine Tailings. GEOMATE Journal, 7(14), 2014, pp.1054–1061.

[7] Whitlow, R., Basic Soil Mechanics, Longman Limited, 3rd Ed, 1995, pp. 71–142.

[8] Woessner, W. W., and Poeter, E. P., Hydrogeologic Properties of Earth Materials and Principles of Groundwater Flow, The Groundwater Project, 4th Ed, 2020, pp 27–51.

[9] Watkins, D., Fundamental Concepts of Groundwater Flow [Lecture Notes], University of Exeter, UK, 2023.

[10] Yong, R. N., Mohamed, A. M. O., and Warkentin, B. P., Principles of Contaminant Transport in Soils, Elsevier Science Publishers, 1992, pp. 200 – 228.

[11] Holzer, L., Marmet, P., Fignerle, M., Wiegmann, A., Neumann, M., and Schmidt, V. Tortuosity and Microstructure Effects in Porous Media, Springer, 2023, pp. 1 – 185.

Copyright © Int. J. of GEOMATE All rights reserved, including making copies, unless permission is obtained from the copyright proprietors.

15th Int. Conf. on Geotechnique, Construction Materials & Environment, Kyoto, Japan, 11-13 November 2025, ISBN 978-4-909106124 C3051

NUMERICAL SIMULATION OF SCOURING AROUND CYLINDRICAL BRIDGE PIERS UNDER STEADY FLOW USING REEF3D

Shu Tsuyumine[1], Tatsuya Matsuda[1], and Naoto Naito[1]

[1] Department of Architecture and Civil Engineering, Toyohashi University of Technology, Japan

ABSTRACT

Scouring around bridge foundations installed within riverbeds can significantly affect structural safety, potentially causing pier overturning, settlement, or tilting owing to river-flow-induced scour and erosion. Understanding and accurately predicting the scouring behavior around a structure are essential for ensuring the stability of bridge foundations and preventing structural failures. In this study, the applicability of scouring assessment methods was evaluated through a reproduction analysis conducted using REEF3D, an open-source computational fluid dynamics and wave modeling framework. REEF3D facilitates high-resolution simulations of sediment transport and scour processes depending on flow conditions using optimized hydrodynamic modules. The results of the numerical simulation, which replicated a model test, successfully reproduced the general scouring tendencies around the pier, including the initiation of scouring from the front direction. However, the maximum scour depth was underestimated compared with the model test results. These findings indicate the need for the careful consideration of analytical conditions when numerically reproducing the sediment transport results obtained from model tests.

Keywords: REEF3D, Scour, Model Test, Numerical Simulation

INTRODUCTION

Severe flooding events cause significant scouring around river bridge piers, resulting in the settling and tilting of structures. Enomoto et al. [1] investigated the local scour around a bridge damaged by flooding and suggested that the widening of the bridge foundation during seismic retrofitting had increased the local scour depth. They highlighted the importance of considering changes in river flow conditions when assessing scour risk. Takebayashi et al. [2] examined the cause of bridge pier failure and attributed it to riverbed scouring around the pier, which was induced by flooding. At the bridge site, the fine-grained riverbed material caused rapid bed degradation. Their findings indicate that pier settlement could be prevented by implementing effective erosion protection around piers based on the expected bed lowering. Proactive countermeasures are necessary to prevent or mitigate damage to bridge structures because such failures disrupt transportation networks and negatively affect daily life. Understanding and accurately predicting the scour behavior around structures is essential for ensuring the stability of bridges, preventing structural damage, and supporting the safety and wellbeing of the public.

Bed level changes around hydraulic structures have been experimentally and numerically studied in consideration of their importance in disaster prevention. Matsuda et al. [3] conducted physical model experiments and numerical simulations using REEF3D (Kamath et al. [4], Ahmad et al. [5]) to elucidate the fundamental mechanisms of wave-induced scour around cylindrical structures. Numerical simulations were conducted and validated against physical model tests for a bare seabed and good reproducibility was obtained. When a monopile foundation was installed in both the numerical and physical tests, the flow velocity on the seabed in the offshore and inshore directions increased on the side of the foundation perpendicular to the direction of the wave motion. In the model test, scouring occurred at the same location and was attributed to the flow velocity. However, scouring occurred locally, underscoring the need for a detailed analysis of the associated factors. Kadono et al. [6] conducted model tests using a 1 / 40 scale cylindrical pier model and investigated the characteristics of local scour. Ishii et al. [7] developed a bed variation analysis method for reproducing three-dimensional sediment transport by solving three-dimensional motion equations and comprehensively evaluated the local scour on the upstream side of bridge piers.

This study aims to clarify the progression of scour around cylindrical structures induced by unidirectional flow, considering the characteristics of soil materials. To this end, the open-source computational fluid dynamics (CFD) system REEF3D was used in river environments to enhance the accuracy of scour simulations and tackle existing issues associated with numerical modeling.

Numerical simulations using REEF3D were conducted to analyze the sediment dynamics based on detailed flow features around a cylindrical structure and their effects on the riverbed. The sediment transport processes around the cylindrical structure

were evaluated by comparing the simulation results with the topographic changes observed in physical model tests.

RESEARCH SIGNIFICANCE

In this study, the numerical model REEF3D, which was developed to simulate the flow and riverbed changes around hydraulic structures, was used to perform a replicated analysis. The scour process was elucidated considering the bed conditions around cylindrical structures owing to its importance in the design of safe structures. In this simulation, flow-induced sediment transport phenomena were qualitatively evaluated based on hydraulic model experiments.

NUMERICAL SIMULATION METHOD

The REEF3D model is governed by the incompressible Reynolds-averaged Navier–Stokes (RANS) and continuity equations.

$$\frac{\partial u_i}{\partial x_i} = 0 \quad (1)$$

$$\frac{\partial u_i}{\partial t} + u_j \frac{\partial u_i}{\partial x_j} = -\frac{\partial P}{\partial x_i} + \frac{\partial}{\partial x_j}\left[\nu\left(\frac{\partial u_i}{\partial x_j} + \frac{\partial u_j}{\partial x_i}\right) - \overline{u_i u_j}\right] + g_i \quad (2)$$

Here, u, t, x, ν, ρ, P, and g denote the flow velocity, time, position on the x axis, kinematic viscosity, density of water, pressure, and gravity, respectively.

In CFD models, the fluid velocity is assumed to be sufficiently low such that the compressibility of water and air can be neglected. This assumption allows the simplification of the flow using the RANS and continuity equations. The turbulence model is the unsteady RANS with k-ω model.

REEF3D, which addresses two-phase flows, uses the level-set method to capture the air–water interface. In this method, the interface between the two phases is defined as the reference surface and the regions on either side of the interface are represented using a distance function.

The sediment transport model was used based on the flow field simulated using the hydrodynamic REEF3D model. Changes in the bed elevation are evaluated using the following Exner equation, which follows the conservation of sediment mass:

$$\frac{\partial z_b}{\partial t} + \frac{1}{(1-n)}\left[\frac{\partial q_{b,x}}{\partial x} + \frac{\partial q_{b,y}}{\partial y}\right] + E - D = 0. \quad (3)$$

Here, z denotes the bed elevation; $q_{b,x}$ and $q_{b,y}$ are the bedload transport rates in the x and y directions, respectively, as defined at the morphological time step; E is the entrainment rate from the bedload to the suspended load; and D is the settling rate from the suspended load back to the bed.

ANALYSIS MODEL

Figs. 1 and 2 present the side and plane views of the movable bed, respectively. In this analysis, a computational domain with a length of 0.75 m, width of 0.5 m, and height of 0.4 m was defined, and unidirectional flow was introduced from the left boundary of the domain. The hydraulic and soil conditions were set to match the experimental parameters [6]. The 50% diameter on the grain size diagram of the bed material is 0.11 mm and the grain size distribution is not considered. The mesh consists of 5 and 10 mm cubes.

To investigate the influence of the flow velocity on the scour depth, two flow conditions with a velocity V_1 = 0.107 m/s, corresponding to the experimental condition, and a doubled velocity V_2 = 0.214 m/s, were analyzed.

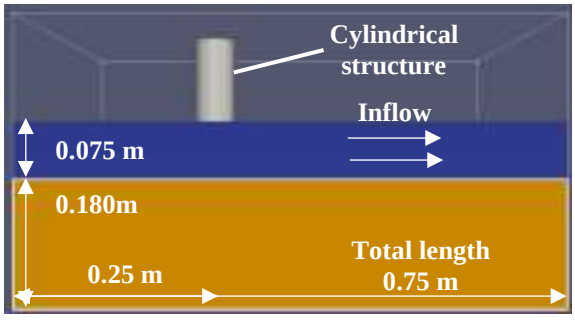

Fig. 1 Region of numerical analysis: side view

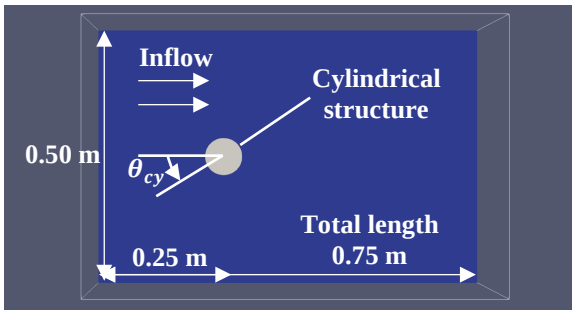

Fig. 2 Region of numerical analysis: plane view

Table 1 Conditions for numerical analysis

Cylinder diameter (m)	0.065
Bed elevation (m)	0.18
Water depth (m)	0.075
Flow velocity V_1 (m/s)	0.107
Flow velocity V_2 (m/s)	0.214
Particle size (mm)	0.11

RESULTS AND DISCUSSIONS

Bed surface profile

Figs. 3 to 5 present the bed surface profiles around the cylindrical structure at 1,800 s for both the model test and numerical analysis with 5 mm and 10 mm meshes. Fig. 6 presents the bed surface profile from the 5 mm mesh analysis with a doubled flow velocity. In all results, scour initiation occurs at approximately $\theta_{cy} = 45°$. However, while the model test reveals scour holes forming around the entire circumference of the cylinder, the numerical analysis under flow condition V_1 exhibits scour holes primarily in the range of $\theta_{cy} = 45°$ to $90°$, indicating a different scour pattern.

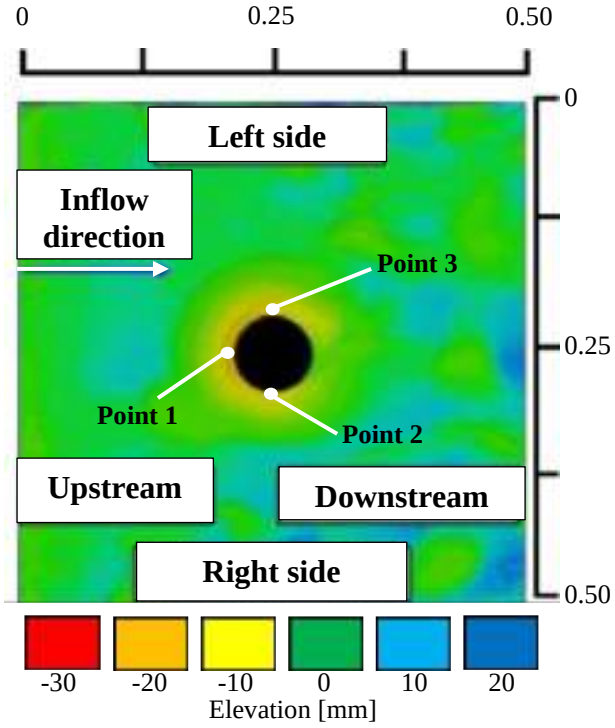

Fig. 3 Sand surface profile near the cylinder in the model test (adapted from [6])

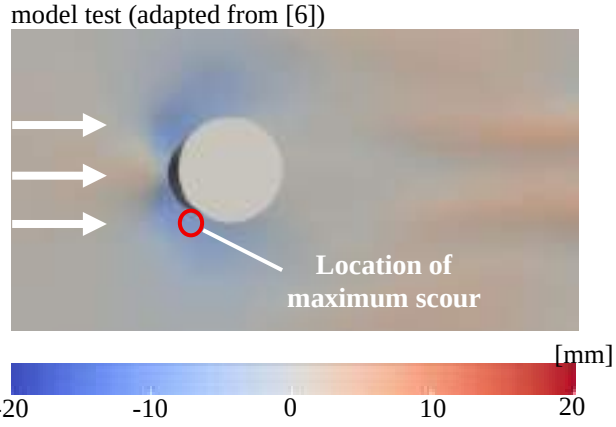

Fig. 4 Sand surface profile near the cylinder using a 10 mm mesh (V_1 = 0.107 m/s)

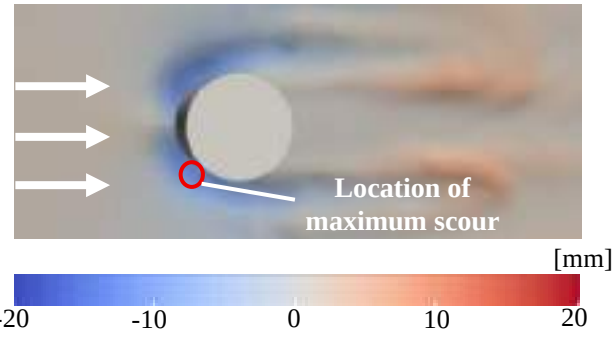

Fig. 5 Sand surface profile near the cylinder using a 5 mm mesh (V_1 = 0.107 m/s)

The analysis with a finer mesh size produced a sand surface profile that more closely matched the experimental results. As shown in Fig. 6, increasing the flow velocity results in the expansion of the scour hole toward the $\theta_{cy} = 0°$ region. Additionally, both sets of results indicate a tendency for sediment deposition around $\theta_{cy} = 180°$.

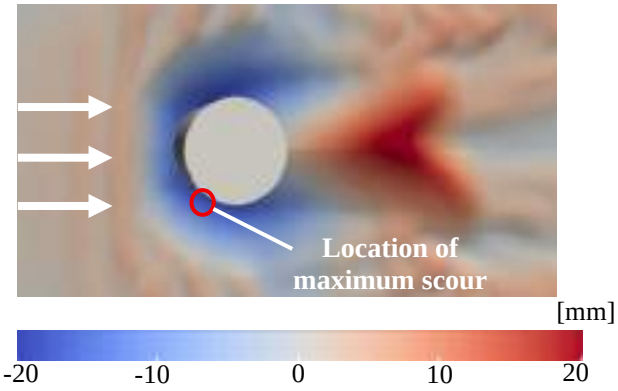

Fig. 6 Sand surface profile near the cylinder using a 5 mm mesh (V_2 = 0.214 m/s)

Maximum scour depth

Fig. 7 presents the scour depths at $\theta_{cy} = 0°$ and $\theta_{cy} = 45°$ for the 5 mm and 10 mm meshes. The maximum scour depth is approximately 6 mm for the 5 mm mesh and 12 mm for the 10 mm mesh. The results indicate that a finer mesh size led to a greater scour depth, suggesting that scour depth is dependent on mesh size. The maximum scour depths in Fig. 3 are 32, 27, and 26 mm at points 1, 2, and 3, respectively, indicating that the numerical results underestimate the experimental results.

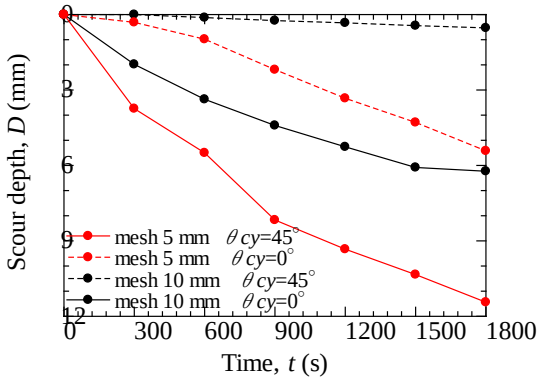

Fig. 7 Comparison of Scour Depth between 5 and 10 mm meshes

Fig. 8 presents the scour depths at $\theta_{cy} = 0°$ and $\theta_{cy} = 45°$ for V_1 and V_2. Under the flow condition V_2, the maximum scour depth increases to approximately 22 mm, which is approximately 2.7 times the depth obtained with the lower flow velocity. The scour depth at $\theta_{cy} = 0°$ obtained for V_2 is approximately 14 mm, which is approximately 7.0 times greater than that corresponding to condition V_1 (comparison at 800 s).

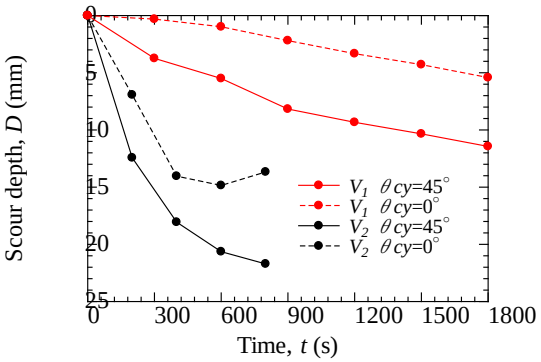

Fig. 8 Comparison of scour depths between V_1 and V_2

The reasons for the differences in scour depth observed in the numerical analysis results are discussed based on the flow conditions around the structures. A comparison of the streamline distributions in Figs. 9 and 10 suggests that in Fig. 9, the flow downstream of the cylinder remains horizontal with a limited downward motion, resulting in less scour. In contrast, the increased flow velocity in Fig. 10 induces downward flow, leading to a more pronounced scour and a scour pattern similar to that observed in the model test. Therefore, the analytical conditions must be carefully assigned when numerically reproducing the sediment transport results obtained from model tests.

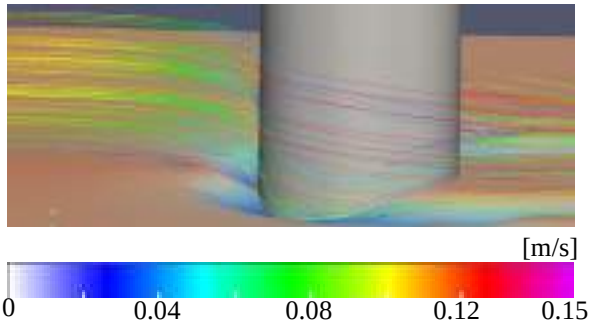

Fig. 9 Streamline distribution near the cylinder under V_1

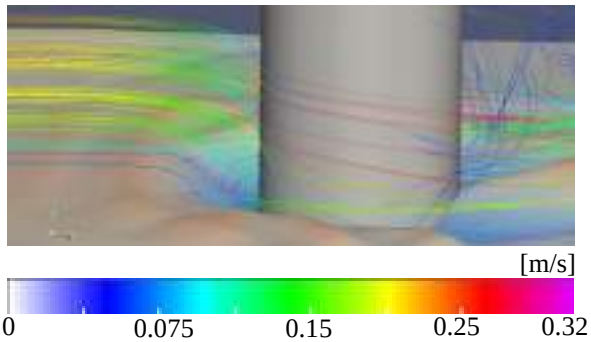

Fig. 10 Streamline distribution near the cylinder under V_2

CONCLUSIONS

The scour phenomenon around a cylindrical structure under unidirectional flow was analyzed using REEF3D to investigate the flow characteristics and sediment dynamics. The following conclusions were drawn.

- Scouring occurred at $\theta_{cy} = 45°$ both in the model test and numerical analysis. In the model test, scour holes were formed around the entire circumference of the cylinder, whereas they were primarily observed between $\theta_{cy} = 45°$ and $\theta_{cy} = 90°$ in the numerical analysis.
- Sediment deposition occurred near $\theta_{cy} = 180°$, which was similar to the experimental observations.
- The results indicated that a finer mesh size led to a greater scour depth, suggesting that scour depth is dependent on mesh size.
- The maximum scour depth in the model test was approximately 20 mm, whereas the numerical analysis underestimated this value by approximately 12 mm.
- When the flow velocity was doubled compared with the experimental condition, the scour depth at $\theta_{cy} = 0°$ increased by approximately 7.0 times. This increase allowed the numerical analysis to reproduce the scour pattern near $\theta_{cy} = 0°$. Additionally, downward flow in front of the cylinder was observed (comparison at

• 800 s).

These results highlight the need for careful consideration of the analytical conditions when numerically reproducing the sediment transport results obtained from model tests. Further investigations are required to improve the accuracy of the current reproduction and enhance scour prediction methodologies. Additionally, incorporating more complex turbulence models and refining sediment transport mechanisms could improve the numerical accuracy. Future studies will focus on optimizing the computational parameters and validating the model under various flow conditions to ensure better agreement with experiments. Furthermore, the effects of mesh size and other factors on analysis accuracy will be analyzed to improve the reproducibility of water flow and sediment transport.

REFERENCES

[1] Enomoto T., Horikoshi K., Ishikawa K., Mori H., Takahashi A., Unno T., Watanabe K., Levee damage and bridge by 2019 typhoon Hagibis in Kanto Region, Japan, Soils and Foundations, Vol. 61, Issue 2, 2021, pp. 566–585.

[2] Takebayashi H., Fujita M., Bridge Collapse in Mutsu, Aomori Prefecture, Japan in 2021, Flood Risk Management, Vol. 18, Issue 1, 2025, e70025.

[3] Matsuda T., Miura K., Naito N., Shirakura D., A numerical simulation of local scour process due to waves around monopile foundation using REEF3D, Geomate, Vol. 27, No. 120, 2024, pp. 1–8.

[4] Kamath A., Alagan Chella M., Bihs H., Arntsen Ø.A., CFD Investigations into Wave Forces and Flow around Three Cylinders Placed in Different Configurations, Engineering Applications of Computational Fluid Mechanics, Vol. 9, No. 1, 2015, pp. 343–354.

[5] Ahmad N., Bihs H., Myrhaug D., Kamath A., Arntsen Ø.A., Three-Dimensional Numerical Modelling of Wave-Induced Scour Around Piles in a Side-by-Side Arrangement, Coastal Engineering, Vol. 138, 2018, pp. 132–151.

[6] Kadono T., Kato S., Okazaki S., Matsui T., Kajitani Y., Ishizuka M., Yoshida H., Effects of Dynamical Change in Water Level on Local Scouring around Bridge Piers Based on In-Situ Experiments, Water, Vol. 13, Issue 21, 2021, 3015.

[7] Ishii H., Murotani K., Nakade K., Numerical Model of Local Scour around Pier Based on the 3D Analysis of Sediment Particle Motion, Journal of Japan Society of Civil Engineers Ser B1 (Hydraulic Engineering), Vol. 78, No. 2, 2022, pp. I_1201–I_1206.

Copyright © Int. J. of GEOMATE All rights reserved, including making copies, unless permission is obtained from the copyright proprietors.

15th Int. Conf. on Geotechnique, Construction Materials & Environment,
Kyoto, Japan, 11-13 November 2025, ISBN 978-4-909106124 C3051

Precision-Controlled Backfilling Methodology for Enhancing Positional Accuracy in Foundation Element Replacement

Haruka Kiyotomo [1], Yuji Taya [1], Masahiro Ueda [1], Tomio Tsuchiya [1] and Shinya Inazumi [2]

[1] Takenaka Corporation, Japan; [2] Shibaura Institute of Technology, Japan

ABSTRACT

The demand for removal of existing piles has increased significantly due to increased demolition and reconstruction activities in urban areas. Ensuring the quality of the backfilled area after pile removal is critical, as inadequate backfill can negatively affect the construction accuracy of new piles installed near these areas.

Currently, no established standardized method exists for achieving consistent backfill quality. This study proposes a novel construction method designed to ensure uniform unconfined compressive strength throughout the depth of backfilled areas. The proposed method involves the simultaneous penetration and injection of a specially prepared backfill material, combined with thorough mixing using a mixing auger. The auger, which has a diameter equal to or greater than that of the casing, incorporates mixing blades and a screw mechanism. Additionally, we developed a method for designing the backfill material mix, emphasizing the importance of preliminary laboratory mixing tests prior to actual construction.

The effectiveness of the proposed construction and mix design methods was validated through field implementation. The existing piles were successfully removed, and the resulting backfilled areas achieved the targeted uniform strength profiles. Subsequent measurements confirmed that the design accuracy of newly installed piles adjacent to these backfilled areas remained within acceptable control limits. In conclusion, the implemented method of pile removal and controlled backfilling demonstrated reliability and accuracy, significantly improving the quality of subsequent new pile construction.

Keywords: Pile removal; Controlled backfilling; Unconfined compressive strength; Mixing auger; Construction accuracy

INTRODUCTION

In recent years, the demand for removing existing piles has increased due to the demolition and reconstruction of buildings. After removing the existing piles, the holes are filled with backfilling material. There are no regulations for backfilling materials or methods, making it difficult to ensure the quality of the backfilled area. If the strength of the backfilled area cannot be controlled, problems will occur when constructing new piles near the backfilled area, such as poor vertical accuracy and eccentricity, which will reduce construction accuracy.

This paper presents a case study of an existing pile removed using the cutting casing and extraction method in clay ground. Following removal, the ground was backfilled through a process of penetrating and ejecting cement slurry mixed bentonite liquid (hereafter referred to as CB liquid) while simultaneously stirring with an auger. This auger, with a diameter equal to or greater than that of the cutting casing, was equipped with a mixing blade and screw mechanism to facilitate thorough mixing of the area. Furthermore, this study examines the construction accuracy of new piles subsequently installed at the same site.

RESEARCH SIGNIFICANCE

The purpose of this research is to develop a backfill material and construction method for use after removing existing piles that will not adversely affect the construction of new piles. Such materials and construction methods do not currently exist.If this goal is achieved, not only will the construction quality of new piles in building reconstruction work improve, but it will also be possible to prevent an increase in the construction period and cost of the entire new construction work.

METHODOLOGY

First, the site conditions and pile characteristics are described. The ground overview and specifications of both existing and new piles are illustrated in Fig. 1. The ground profile consisted of a buried soil layer (F layer), an alluvial sand layer (As layer), and an alluvial clay layer (Ac1 and Ac2 layers). The Ac2 layer exhibited an average N-value of 1 at depths ranging from -6.8 m to 17.9 m below the construction ground level (hereinafter referred to as GL), with an unconfined compressive strength of 50 kN/m^2 measured at GL-12.8 m. The removed existing piles were prefabricated prestressed concrete piles with a design length of 20 m and diameters of 350

mm and 400 mm, respectively. The pile heads were positioned at approximately GL-2 m. The newly installed piles had typical specifications including a length of 17 m, pile heads at GL-7.1 m, and a diameter of 1000 mm. The upper sections utilized high-strength SC piles, while the lower sections employed high-strength nodular PHC piles.

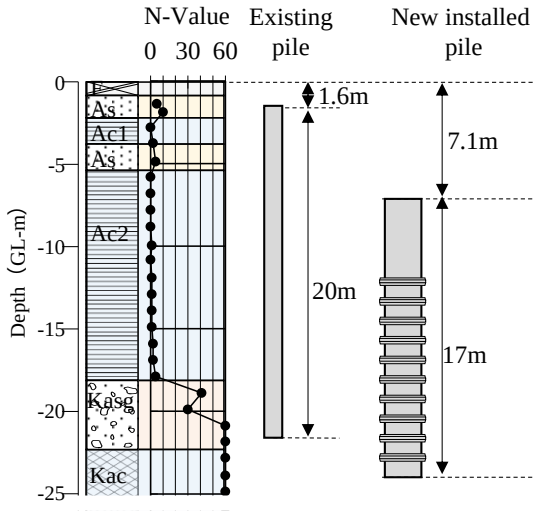

Fig. 1 Ground overview and pile specifications

Second, the pile extraction methodology and backfilling procedure are described. The operational sequence and cycle time for existing pile removal are illustrated in Fig. 2. Initially, the perimeter of each existing pile was separated from the surrounding soil using a cutting casing, after which the piles were extracted utilizing a wire-pull system. Subsequently, an auger head with a 2-m long screw was attached to the lead end. The CB liquid was then injected and mixed using an auger assembly comprising alternating 5-m mixing blades and 5-m screws. In accordance with deep mixing treatment protocols [1], the penetration, lifting, and rotation speeds of the auger were established at a minimum of 350 rotations per meter. Following CB liquid injection and auger advancement to the target depth, the auger was rotated and withdrawn in the conventional direction. Immediately post-construction, unconsolidated samples were collected from three distinct backfilled locations (designated No. 1 to 3), and their unconfined compressive strength was evaluated after a 28-day curing period. Additionally, a standard penetration test was performed at backfilled location No. 3 at 26 days post-construction.

The strength parameters for the backfilled sections were established as follows: While the original ground exhibited an unconfined compressive strength of 50 kN/m^2, the target unconfined compressive strength for the backfilled sections was specified at 100 kN/m^2, accounting for practical strength management constraints in field applications. Furthermore, considering the pile body/pile perimeter soil ratio [2], laboratory mixing tests were conducted using Ac2 layer clay prior to implementation. The resulting construction specifications are presented in Table 1. The CB liquid injection volume corresponded to 100% of the volume mixed by the auger.

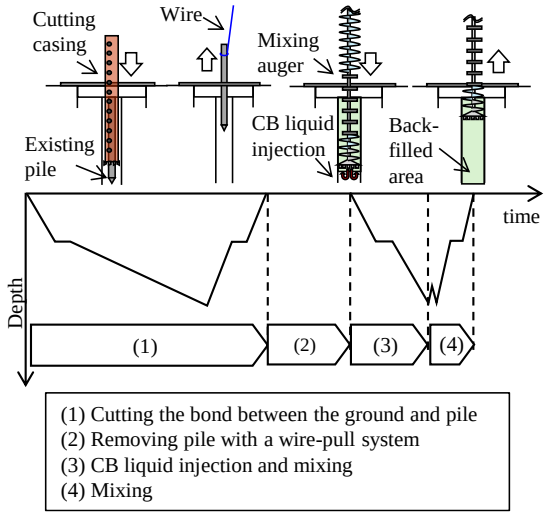

Fig. 2 Operational sequence and cycle time for pile extraction

Table 1. Construction specifications

Existing pile No.	Diameter (mm)	Outside diameter of cutting casing (mm)	Mixing auger diameter (mm)	The pile body/pile perimeter soil ratio	Water to cement ratio of CB liquid (%)
1	350	700	700	0.33	600
2 and 3	400	700	700	0.48	500

RESULTS

Fig. 3 illustrates the unconfined compressive strength profiles of unconsolidated samples from locations No. 1 to 3, alongside comparative data from undisturbed samples of the original ground. The backfilled zones exhibited generally uniform strength characteristics with depth, predominantly exceeding the target strength parameters. However, the sample from location No. 1 at GL-3m demonstrated values below the target threshold. This anomaly is attributed to the proximity of the sampling location to the upper boundary of the improvement zone, resulting in material heterogeneity and consequent inter-specimen variability. Significantly, all samples demonstrated strength values superior to those of the

original ground. Fig. 4 presents standard penetration test results from location No. 3 compared with corresponding values from the original ground. The original Ac2 layer exhibited N-values of approximately 1, whereas equivalent depths within backfilled section No. 3 yielded N-values ranging from 3 to 4.

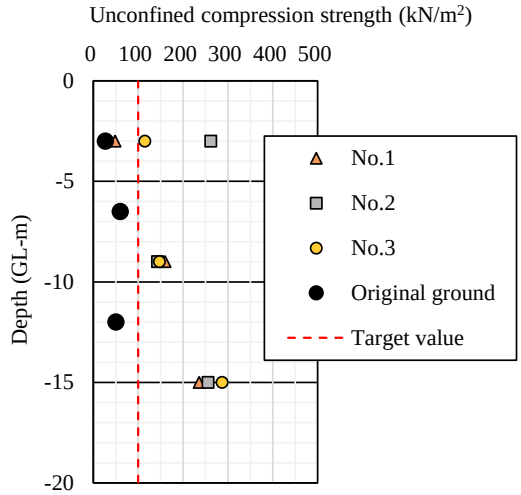

Fig. 3 Unconfined compressive strength profiles

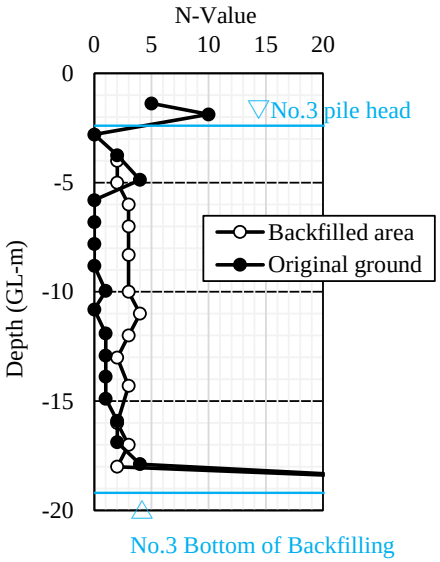

Fig. 4 Standard penetration test N-values

FINDINGS

This investigation examined how backfilled zones from extracted piles influenced the installation accuracy of new foundation elements. Positional measurements were conducted at sequential construction phases as illustrated in Fig. 5, utilizing a light wave transit to quantify the aboveground displacement of drilling rods, pile heads and guide rods. Measurements were recorded as coordinate deviations (x, y) from design specifications and subsequently converted to resultant vector magnitudes $\sqrt{(x^2 + y^2)}$ to determine eccentricity values. Following the classification framework established in [3], the spatial relationship between newly drilled pile locations and backfilled zones was categorized as: (a) non-overlapping with separation ≥ 1D (n = 36), (b) non-overlapping with separation < 1D (n = 4), and (c) partially overlapping (n = 5).

Fig. 6 presents the measured eccentricity values of aboveground pile sections across construction phases. Comparative analysis between categories (a) and (b) revealed similar mean eccentricity values, though category (b) exhibited greater statistical variance. Category (c) demonstrated the highest eccentricity values; however, these remained within acceptable tolerance limits (x, y ≤ 100 mm each), indicating that backfilled zones did not adversely affect construction viability of new foundation elements. Analysis of mean eccentricity progression through construction phases (1) to (4) revealed a systematic increase with advancing construction stages, underscoring the critical importance of achieving high drilling precision during the initial phase (1) rod drilling to ensure positional accuracy in subsequent operations.

To further analyze the influence of spatial relationships between backfilled zones and new pile positions, the overlap configuration in categories (b) and (c) was quantitatively assessed using an overlap ratio methodology (Fig. 7). This ratio was calculated as: Overlap ratio (%) = (overlap dimension) ÷ (diameter of new pile borehole) × 100.

For non-overlapping configurations, the negative separation distance between outer boundaries was substituted as the numerator term.

Fig. 8 illustrates the correlation between overlap ratio and eccentricity magnitude across construction phases. A consistent trend emerged wherein maximum eccentricity values occurred at approximately 5% overlap ratio across all construction phases. Continued data acquisition regarding this correlation is recommended to establish definitive statistical relationships and enhance predictive understanding.

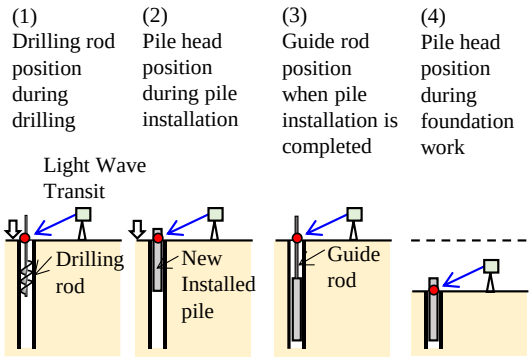

Fig. 5 Positional measurement protocol across construction phases

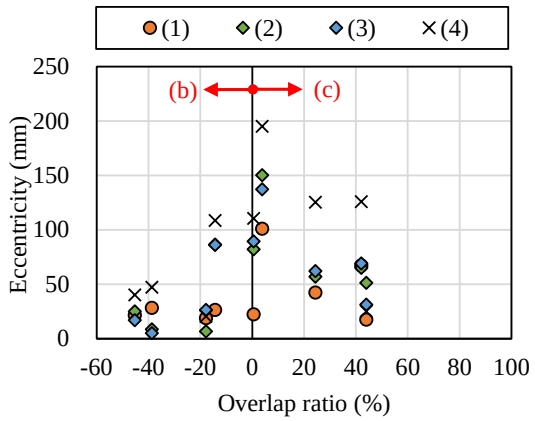

Fig. 6 Eccentricity measurements of guide rods and pile elements

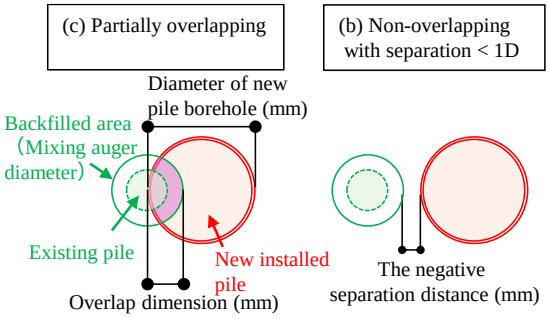

Fig. 7 Schematic representation of overlap ratio methodology

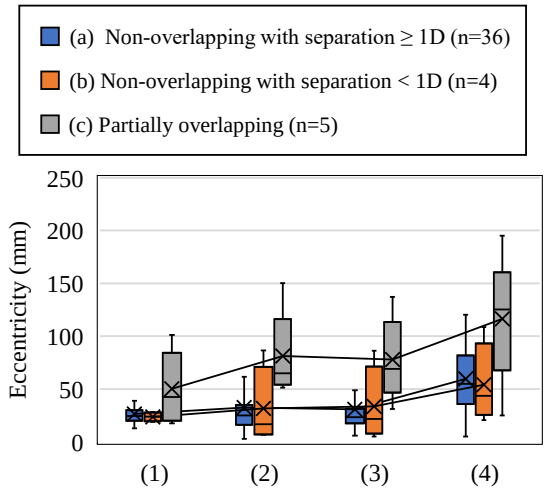

Fig. 8 Correlation between overlap ratio and measured eccentricity

CONCLUSIONS

This study demonstrated successful implementation of a controlled backfilling technique in cohesive soil conditions, achieving an unconfined compressive strength that predominantly exceeded the target value of 100 kN/m^2. The methodology established effective control over the geotechnical properties of backfilled zones following pile extraction.

Positional deviation measurements during construction of new foundation elements indicated that eccentricity values generally remained within established tolerance limits, confirming that backfilled zones did not adversely affect new pile installation. The investigation revealed that partial overlap configurations between newly drilled pile locations and previously backfilled zones exhibited comparatively higher eccentricity values, suggesting a potential correlation between overlap ratio and positional deviation. Future research will focus on expanding the experimental dataset to establish definitive statistical relationships between backfilled zone characteristics and installation precision of adjacent foundation elements.

ACKNOWLEDGEMENTS

The authors gratefully acknowledge the valuable contributions and technical support provided by the following personnel from Takenaka Corporation: Director Takahashi, Construction Division Manager Kato, and Engineers Enomoto, Sugai, Adachi, and Harada. Their expertise and assistance were instrumental in the successful implementation and evaluation of the methodologies presented in this study.

REFERENCES

[1] Cement Deep Mixing Association, CDM Q&A, 2005, pp.97-98.

[2] Kiyotomo H, Taya Y, Aoki M and Tsuchiya T, Case studies of backfill ground after removal of existing piles and the Laboratory test, Summaries of technical papers of Annual Meeting Architectural Institute of Japan, 2021, pp.551-552.

[3] Kanto Branch of Japanese Geotechnical Society, Methods for removing and backfilling existing piles and the design and construction of new installed piles that will be affected by the removal and backfilling of existing piles, Research Committee on the removal and backfilling of existing piles that interfere with new installed piles, 2022, p.130.

Copyright © Int. J. of GEOMATE All rights reserved, including making copies, unless permission is obtained from the copyright proprietors.

15th Int. Conf. on Geotechnique, Construction Materials & Environment,
Kyoto, Japan, 11-13 November 2025, ISBN 978-4-909106124 C3051

A STUDY ON THE EFFECT OF INJECTION FLOW RATE ON GELATION TIME IN CHEMICAL GROUTING METHOD

Midori Suzuki[1], Jemy C. Chua[2], Naoaki Suemasa[3] and Takamitsu Sasaki[4]

[1,2,3] Graduate School of Integrative Science and Engineering, Tokyo City University, Japan
[4] Kyokado Engineering Co., Ltd., Japan

ABSTRACT

Soil liquefaction is a hazardous phenomenon triggered by earthquakes, which can result in widespread damage such as uneven settlement of structures and ground deformation, posing serious risks to people and property. One method to mitigate liquefaction is the chemical grouting technique. This approach involves displacing pore water in the soil with silica-based acidic solutions that form a gel over time that improves the strength and stability of the soil. However, the presence of alkaline components in the soil may react with the solution, potentially hindering gelation and emphasizing the importance of selecting appropriate injection materials. This study investigated the effects of varying injection flow rates on the gelation time of the solution by conducting one-dimensional injection tests using soil samples with high alkalinity. The temporal change of pH, gelation time, and the silica concentration at various distances from the injection port were measured. Results showed that while pH changes were not significantly influenced by flow rate, gelation time and silica concentration were affected. A slower injection flow rate resulted in faster gelation, which was attributed to the quantity of silica adsorbed from the chemical solution onto the soil particles. To increase the applicability of this method, a model equation involving the estimation of gelation time to the silica concentration is planned. The findings from the experiments conducted indicated that injection flow rate is a significant factor in the chemical grouting method.

Keywords: Soil liquefaction, Chemical grouting, Ground improvement, pH test of soil, Gelation time

INTRODUCTION

The 2024 Noto Peninsula earthquake caused devastating damage due to liquefaction in channels and marshlands. Liquefaction-induced damages have not been eliminated in recent years, and countermeasures against liquefaction are necessary in preparation for major earthquakes that are highly likely to occur within the next 30 years. One effective countermeasure is the chemical grouting method, in which grout solution is injected into the ground to replace pore water and chemicals to improve the properties of the ground. However, the effectiveness of this method is considerably affected by the alkaline content in the soil. As a result, it can be very difficult to achieve proper penetration and solidification, and sufficient improvement may not be achieved due to partial solidification or inadequate penetration.

Previous studies have shown that grouting effectiveness depends on factors such as silica concentration, soil properties, and chemical behavior. Higher silica content leads to greater strength [1], and unconfined compressive strength is influenced by particle adhesion, negative pore pressure, surface area, and internal friction angle [2]. Hayashi [3] found that grout strength variability is due to settling after injection, not dilution during flow. Endo [4] emphasized the need for multiple evaluation indicators in heterogeneous soils.

While such findings provide important insight into grouting performance under neutral or controlled conditions, few have focused on the interaction between high-alkaline field sands and grout permeation behavior. In particular, the influence of alkaline content on gel time and silica reaction dynamics remains poorly understood.

Therefore, the purpose of this study is to elucidate the permeation mechanism by conducting a one-dimensional injection test using a soil sample composed of field sand containing high amounts of alkaline and chemically inert silica sand. In addition, based on these results, this study aims to construct a reaction model for this method.

In this paper, one-dimensional injection tests were conducted on samples prepared using Souma sand and silica sand no. 6. Injection materials with different compositions were used, and the injection rate was varied. This paper presents the results of investigations on three aspects: (1) the temporal change in the pH of the chemical solution within the soil, (2) the variation in gel time (GT), defined as the time required for solidification, and (3) the change in silica concentration at different penetration distances.

EXPERIMENTAL METHOD

Understanding the influence of alkaline compounds present in the soil is crucial. To do this, two types of soil samples with different alkaline

contents were utilized. Silica sand No. 6 was used as the neutral or inert sand, with a calcium content of approximately 200 mg/kg, and Souma sand as the high-alkaline sand, having a calcium content of about 10,000 mg/kg. Souma sand contains calcium carbonate that originated from shells and corals, making the sand alkaline in nature. Four experiment cases were formulated, with one case focusing on the reaction of the chemical solution with little effect from the sand, and three cases focusing on the reaction of both the chemical solution and the sand. In Case 1, only silica sand No. 6 was used and in Cases 2 to 4, a mixture of Souma sand and silica sand No. 6 at a weight ratio of 1:8 was used, resulting in a high alkaline soil mix with a pH value of 7.9.

For the one-dimensional permeation test, a cylindrical mold with an inner diameter of 50 mm and a height of 1030 mm was used, shown in Fig.1. A soil column with a height of 920 mm at a relative density of 60% was prepared, with filter layers, composed of silica sand No. 4, placed at both the top and bottom of the specimen to ensure uniform flow and adequate drainage.

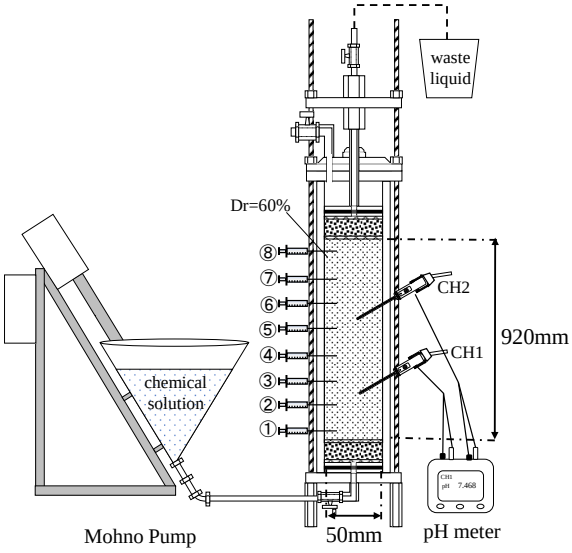

Fig.1 Injection device

To prepare the specimen for permeation, it was saturated with de-aired water from the bottom. After ensuring the sample was fully saturated, a constant flow rate pump was connected to the inlet to inject the chemical grout at a fixed flow rate. Case 1 and 2 followed a standard value of chemical permeation of 60 mL/min while Cases 3 and 4 used slower and faster flow rates of 30 mL/min and 120 mL/min, respectively to investigate the effect of varied flow. The grout compositions for each case are listed in Table 1 [5]. The injection solution was prepared by mixing Actor-MS, PR silica, and ASF silica-30, with all mixtures adjusted to achieve a silica concentration of 3.8%. Actor-MS is a mixed acid composed of sulfuric acid (H_2SO_4) and phosphoric acid (H_3PO_4). PR silica and ASF silica-30 are both mixtures of silicon dioxide or commonly known as silica (SiO_2) and sodium oxide (Na_2O) but differ in their silica form: ASF silica-30 exists in a colloidal form, while PR silica consists mainly of monomers to trimers.

Table 1 Chemical compounds and ratios

Case	Solution A			Solution B	
	MS(mL)	ASF(mL)	water(mL)	PR(mL)	water(mL)
1	9.958	7.323	151.300	49.930	181.500
2	8.004	7.905	197.628	49.407	237.055
3	8.100	8.000	233.900	50.000	200.000
4	8.100	8.000	233.900	50.000	200.000

From the grout mixtures formulated, the estimated pH values were 2.2, 3.5, and 4.0. The injection process was terminated when approximately 830 g of liquid (equivalent to the volume of the pore space) had been discharged from the specimen. This means that all the water initially present prior to the injection was replaced entirely by the chemical solution, assuming that no mixing occurred.

To monitor the penetration and reaction state of the chemical solution, pH glass composite electrodes for capillary tubes (MCD-45, Nihon Ash Co., Ltd.), shown in Fig.2 for Case1 and Fig.3 for Cases 2 to 4, were inserted at approximately 1/3 and 2/3 of the specimen height from the bottom (referred to as CH1 and CH2, respectively). In this way, the temporal change in pH inside the sample was measured. While cases 2 to 4 used a different pH meter, it was confirmed beforehand that both types had similar performance. Since the grout solution was acidic, the metal part of the 1st type (Case 1) was not ideal to be used for long-term so a glass-type pH meter was substituted.

Fig.2 Glass electrode (Case 1)

Fig.3 Glass electrode (Case 2 - 4)

Additionally, syringes were inserted at equal intervals along the height into the specimen to extract the chemical solution at the end of injection, allowing measurements of pH, GT, and silica concentration at different penetration distances. The extracted solution was transferred to a petri dish, and GT was measured

by gently rocking the dish back and forth using a small shaker device. The GT was defined as the point in time when the extracted solution stops flowing, indicating solidification. The pH and silica concentration of the extracted solution from the syringes after injection were immediately measured using a compact pH meter (LAQUA twin-pH-22B, HORIBA), shown in Fig.4, and using a silica pack test (WAK-SiO2, Kyoritsu Chemical-Check Lab., Corp.). In conducting the pack test for silica concentration measurement, appropriate dilutions were made to fall within the measurement range (5-50 mg/L).

Fig.4 Compact pH meter

EXPERIMENTAL RESULTS

Case 1 (Silica Sand No. 6)

Fig.5 shows the change in pH over time in Case 1. From this graph, it can be confirmed that the pH of silica sand No. 6 used in this experiment was about 6.6 when saturated with water. The sudden drop in pH value signifies the contact time of the grout solution to the pH meter. Since the solution was highly acidic, a drop in pH was expected. With a bottom-up flow direction, CH1, located nearer to the inlet was contacted first with the solution before CH2, hence the difference in time with the pH drops. After the injection finished, the pH of the soil sample full of the grout solution did not change significantly with time and remained constant. This may be because the acid in the chemical solution was not consumed by the neutralization reaction, and since the soil sample prepared was made with a chemically inert silica sand with minimal amounts of alkaline components.

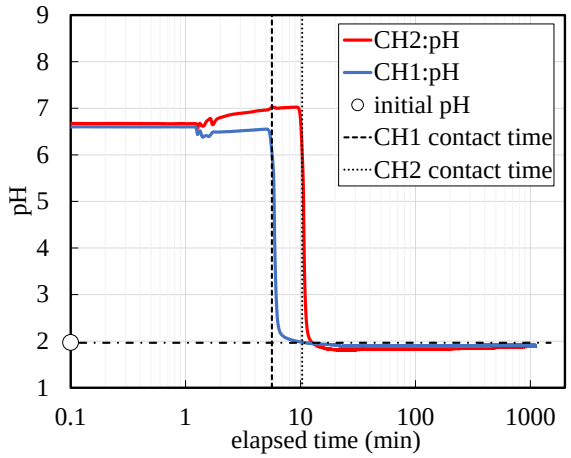

Fig.5 Temporal change in pH (Case 1)

Using the solution extracted from the syringes inserted at different penetration distances, the pH and the GT of the solution from each point were tested. Fig.6 shows the relationship between pH and GT with distance. As with the temporal change in pH, minimal changes in pH were observed within the soil column. GT, however, had a slight change with distance. Showing a slightly faster solidification time as the penetration distance increased. This might be caused by the small amount of calcium compounds in the sand that incurred a minor neutralization reaction that hastened the gelation. Given the minimal change in pH with both time and distance, paired with the slight changes in GT, it can be suggested that the reaction occurred in this case was mostly due to the chemicals present in the grout solution with little interference from the soil specimen made with silica sand No. 6.

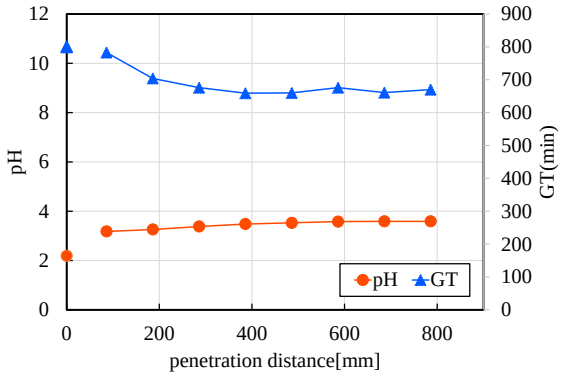

Fig.6 Relationship between pH and GT with distance

However, the actual situation of the ground in the real world is not always composed of chemically inert material that will provide similar results with this case. To understand the effect of alkaline compounds, present in the ground during chemical grout injection, a specimen with high alkalinity needs to be made and tested. Apart from this, the injection flow rate is also another crucial factor in this ground improvement method. A faster flow results to more turbulence within the voids and material contact time that may hasten the reaction of the grout material. As such, 3 additional cases (Case 2 to 4) were prepared using high alkalinity sand, and varying flow rates.

Case 2 to 4 Results (High-Alkaline Sand & Varying Flow Rates)

The setup and testing procedure were the same as Case 1, with only the soil composition and flow rate changed. For these three cases, all used the same high-alkaline sand mixture formulated. Case 2 followed the same flow rate as Case 1 at 60 mL/min, Case 3 used a slower injection rate of 30 mL/min, and Case 4 with a faster injection rate of 120 mL/min. The temporal changes in pH during and after the chemical injection are shown in Figs. 7 to 9. From

here, the initial pH of the soil was between 8 and 9, which was noticeably more alkaline than silica sand used in Case 1. The arrival times of the injected solution at CH1 and CH2 can be identified through the graphs as well. In Case 2, the injection solution reached CH1 and CH2 approximately 4 minutes and 9 minutes after the start of injection, respectively. In Case 3, the arrival times were approximately 10 minutes and 20 minutes, and in Case 4, they were approximately 2 minutes and 6 minutes, respectively.

As the solution approached the pH meter, a drop in pH was recorded similar to Case 1. A major difference compared to the previous case, however, was the extent of pH decrease. In Case 1, the readings reached the value of the initial pH of the grout solution, but in Cases 2 to 4, it was deviated from the initial pH of the grout solution. This further supported that silica sand had a low impact on the solution, while high-alkaline sand resulted in some changes in the solution.

The reaction between the alkaline compounds in the soil and the acid present in the solution is expressed by the following Eq. (1). The sulfuric acid present in the grout solution reacts with the calcium carbonate present in the Souma sand, and this creates calcium sulfate, water, and carbon dioxide. This acid-carbonate reaction caused a neutralization reaction that slowly raised the pH value of the solution.

$$H_2SO_4+CaCO_3 \rightarrow CaSO_4+H_2O+CO_2 \quad (1)$$

All cases underwent similar chemical reactions and suggested that the pH behavior after completion of the injection was independent of the injection flow rate. Furthermore, it was observed that in all cases, pH increased almost linearly with respect to the logarithm of time, regardless of measurement location.

Apart from differences in arrival time, there were no significant differences in the general shape of the curves among the cases. In all cases, CH1, located at the bottom of the specimen, maintained lower pH values than CH2 throughout the monitoring period. The low pH values at CH1 before the arrival of the solution are believed to be due to the alkaline components in the soil. Since area around CH1 had more acid compounds while the area around CH2 had less due to acid-base reactions occurring during injection. It can be incurred that the bottom area had the highest number of acidic compounds, that gradually lessens with distance. Although towards the end of the injection, it was observed that the pH values converged, as no fresh acid-rich grout were being injected anymore.

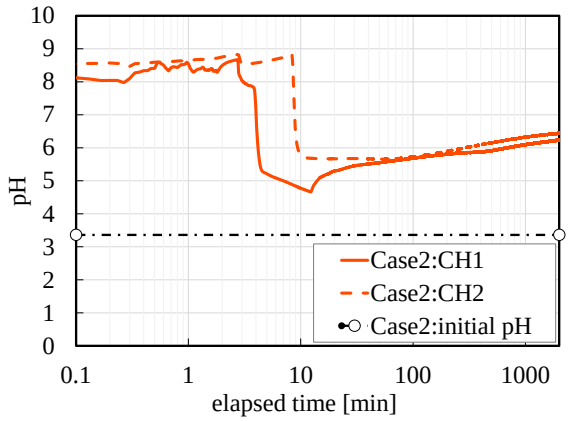

Fig.7 Temporal change in pH (Case 2; 60 mL/min)

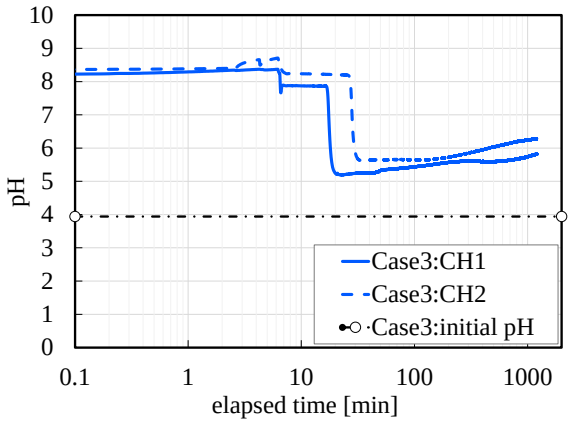

Fig.8 Temporal change in pH (Case 3; 30 mL/min)

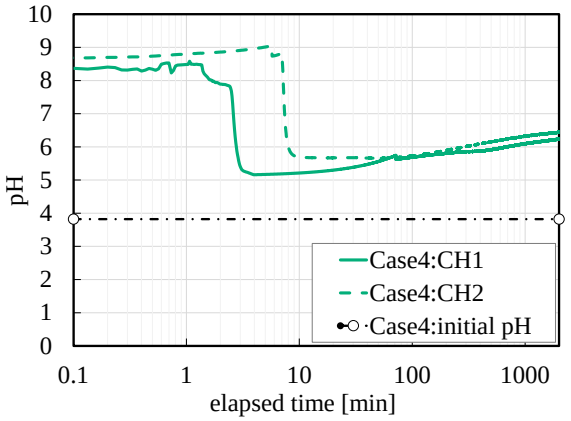

Fig.9 Temporal change in pH (Case 4; 120 mL/min)

As the pH was seen to converge after the injection was completed, solutions from different penetration distances along the specimen were taken using the syringes installed. Along with this, GT was also measured. Fig.10 shows the relationship between pH and gel time (GT) at various penetration distances for Cases 2 through 4. In Case 2, the initial pH of the grout solution was 3.36, the GT of the solution alone was 332 minutes. In Case 3, the initial pH was 3.94,

the GT of the solution alone was 700 minutes. In Case 4, the initial pH was 3.82, the GT of the solution alone was 710 minutes. Ideally, the same solution with Case 2 was planned to be used for Case 3 and 4. However, with the slow flow rate of Case 3, injection failed to complete due premature gelation. To counter this, the mixture was modified to have a longer GT to accommodate extended duration of injection.

From Fig.10, it can be seen that differences in injection flow rate have minimal impact on the pH variation with respect to penetration distance. However, when comparing the GT of the solution alone with that of the extracted solution, Case 3 exhibited a longer GT. This was particularly visible around 0 mm and 200 mm penetration distances. Case 4 with the highest injection flow rate experienced the fastest gelation. This can be related to the pH value seen on Fig.11. A faster flow rate tends to have lower pH values, and a slower flow rate tends to produce higher pH values. On top of that, a lower pH was observed to have a longer GT.

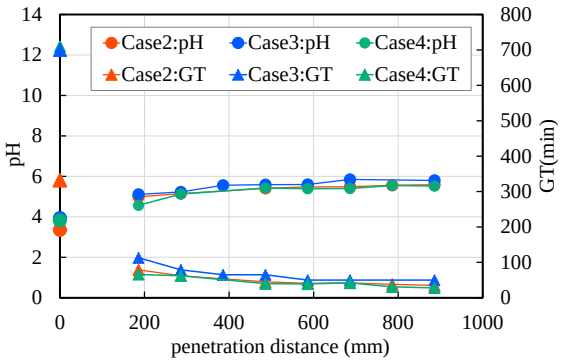

Fig.10 Relationship between pH and GT with distance (Case2-4)

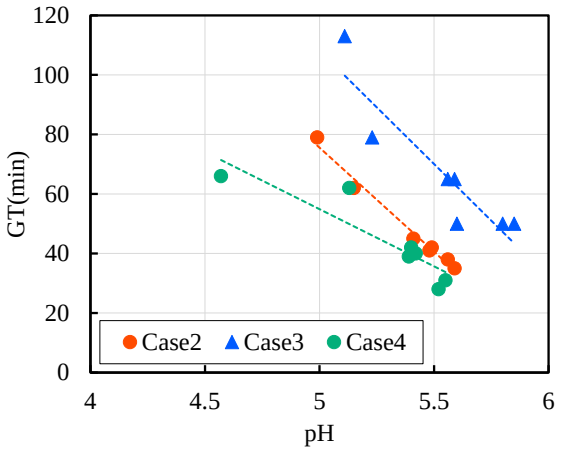

Fig. 11 Relationship between pH and GT

These changes in GT may be attributed to the injection time and the amount of silica present within the solution. With this, the change in the concentration of silica in the grout was also measured using a pack test. Pack tests are a simple and straightforward way of determining the amount of substance in a solution. A disadvantage of using this method is that only low concentration solutions can be tested. Since the grout solution had a high concentration of silica, it was diluted with distilled water until the acceptable range was reached. Maintaining the same dilution rate, the silica concentrations per penetration distance are illustrated in Fig.11. From all cases, the concentration decreases with distance regardless of flow rate, with the largest change occurring with Case 3.

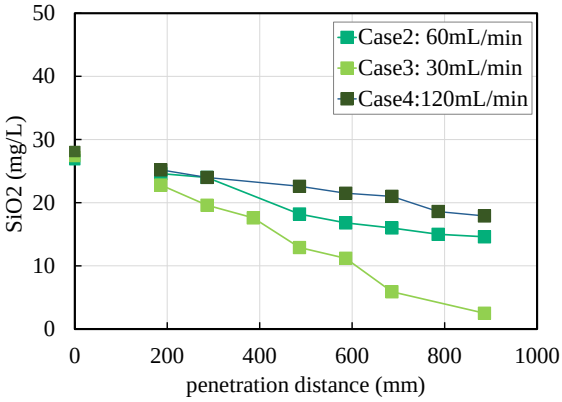

Fig.12 SiO_2 concentration with distance

These changes in GT and silica concentration were believed to be a result of three things, dilution, adsorption, and partial gelation. Since the specimen was prepared in a fully saturated condition, the injected highly concentrated silica grout solution tends to diffuse into the water in the void spaces. Though this might be minimal according to Endo [4].

On top of this, suspended silica particles might get adsorbed onto the sand particle surfaces due to rapid neutralization reactions. Since the grout solution was formulated to form a gel after some time to improve the properties of the soil, gelation occurs after the injection process. This gelation or the reaction of the grout to form a gel utilizes silica to form complex polymers.

Looking at the results obtained on Figs 10 and 11, the longer GT arising from the slow flowing Case 3 and the faster gelation from the fast-flowing Case 4 can be related to the amount of adsorbed silica. With a prolonged injection time in Case 3, it may have resulted in more silica compounds being adsorbed to the sand particles. This way, when the solution was extracted using the syringes at the end of the experiment, the solution contained less silica which extended the gelation. On the other hand, Case 4 with a faster completion time, there was less adsorption of the silica into the sand particles, resulting in higher silica concentration in the extracted solution, shortening the gelation time.

From the results, it can be incurred that adsorption may have been the greatest factor in affecting the silica amount compared to diffusion and gelation.

CONCLUSIONS

In this study, one-dimensional injection tests were conducted using both inert and alkali-rich sand to investigate the performance of chemical grouting in terms of pH, GT, and silica concentration.

Results showed that the neutralization rate did not change with the injection flow rate, but the solidification time and silica concentration were affected. A higher pH resulted in a faster gelation, and a slower flow rate contributed to higher pH values. Gelation was deemed to be affected by both pH and silica concentration. Even with the same pH value, GT was longer with lower silica concentration.

The soil medium plays a major role in the effectiveness of chemical grouting. Alkaline components in the soil react with the acid compounds in the grout. It was observed that three things affect the performance of the grout solution, diffusion, adsorption, and gelation. From the experiments conducted, adsorption of silica greatly influenced the gelation time of the solution.

To better understand how the silica content affects the gelation in a more detailed manner, future tests including the dissolution of the gelled solution and its analysis are planned.

REFERENCES

[1] Goto, K. Estimation of Improved Strength by Measuring Silica Content in Solution Chemical Injection Methods. The 57th Annual Lecture of the Civil Engineering Society, 2002 (in Japanese)

[2] Akimoto, T. Evaluation of Factors Affecting the Unconfined Compressive Strength of Chemically Improved Soil. Civil Engineering Society Proceedings B3 (Ocean Development), Vol. 78, 2022 (in Japanese)

[3] Hayashi, K. Study on Mechanism of Strength Reduction Caused by Difference of the Grout Injection Procedures in Permeable Grouting. JSCE Conference Proceedings (Geotechnical Engineering), Vol. 70, 2014 (in Japanese)

[4] Endo, T. Method of Confirming of Soil Improvement by the Chemical Injection Method on the Ground with Large Variations in Soil Texture. Civil Engineering Society Proceedings B3 (Ocean Development), Vol. 77, 2021 (in Japanese)

[5] Sasaki, T. A Study on Strength Development Mechanism and Deterioration Factors of Sand Improved by Chemical Grout, Doctoral Dissertation, Tokyo City University, 2021.

Copyright © Int. J. of GEOMATE All rights reserved, including making copies, unless permission is obtained from the copyright proprietors.

15th Int. Conf. on Geotechnique, Construction Materials & Environment, Kyoto, Japan, 11-13 November 2025, ISBN 978-4-909106124 C3051

INFLUENCE OF SEEPAGE AND SEISMIC DISASTERS ON THE FAILURE BEHAVIOR OF LARGE-SCALE EMBANKMENTS

Satoko Io[1], Kazuya Itoh[2] and Naoaki Suemasa[3]

[1,2,3] Graduate School of Integrative Science and Engineering, Tokyo City University, Japan

ABSTRACT

Japan frequently experiences natural disasters due to its geographic location. In addition to earthquakes, climate change has intensified torrential rainfall, increasing the need to understand compounded effects of these disasters. For instance, the 1995 Southern Hyogo Prefecture Earthquake caused approximately 700 locations, which soared to over 2,000 after subsequent rainfall. A similar situation was observed following the 2024 Noto Peninsula Earthquake, where record-breaking rainfall triggered additional slope failures in the already-affected areas. Furthermore, embankments with groundwater presence were found to be more susceptible to large-scale collapses. This study investigates the effects of seismic motion and groundwater on slope stability, identifies the critical groundwater levels that trigger collapses, and proposes countermeasures for compound disasters. A centrifuge vibration-seepage test was conducted using a shaking device and a groundwater level stabilization system to simulate a large-scale embankment. The effects of input acceleration and groundwater fluctuations on embankment stability were then analyzed. Results showed that the embankment remained stable when exposed to shaking alone but collapsed when the groundwater level rose, signifying that groundwater contributes a major part in the collapse mechanism. From the responses of accelerometers installed within the soil sample, the bottom area reacted differently from the upper portion of the slope, highlighting variations in behavior under stress. Moreover, higher input acceleration led to an increase in groundwater levels, further increasing the risk of failure. Although pore water pressure rose, no liquefaction was observed. These findings indicate that a rapid groundwater rise, induced by vibrations, amplified sliding forces and reduced slope stability.

Keywords: Groundwater, Slope stability, Centrifuge model experiments, Seismic motion, Slope collapse

INTRODUCTION

Japan is vulnerable to natural disasters because of its climate and topography. Recently, earthquakes, torrential rainfall caused by climate change have become increasingly frequent. A study of large-scale widening-type embankments where deformation shaped after the 1995 Southern Hyogo Prefecture Earthquake was observed revealed that embankments with greater fill height and steeper natural ground slopes, especially in the presence of groundwater, were more susceptible to deformation [1]. This indicates that groundwater conditions and embankment height significantly influence embankment deformation and the occurrence of sliding failures. During that earthquake, approximately 700 locations experienced slope failure, but this number increased to over 2,000 following subsequent rainfall [2]. A similar phenomenon was observed after the 2024 Noto Peninsula Earthquake, where record-breaking rainfall triggered additional slope failure in the affected areas. Again, embankments with the presence of groundwater were observed to be more susceptible to large-scale collapses [3].

These events underscore the importance of understanding the effects of compound disasters. This study aims to evaluate the combined impact of seismic motion and groundwater on embankments, with the objective of identifying the critical groundwater level that significantly increases the risk of slope failure. Furthermore, potential countermeasures are proposed based on these findings. In this study, a centrifugal model test was conducted to simulate groundwater seepage within an embankment, assuming a large-scale embankment constructed in a residential development area. In addition to forming a groundwater level within the embankment, a second test was performed using a shaking table to reproduce seismic motion, referred to as the groundwater seepage–shaking table test. The effects of vibration and water infiltration on the embankment, as well as the behavior of the model ground, were then analyzed and compared.

CENTRIFUGE MODEL EXPERIMENTAL PROCEDURES

In this study, a groundwater seepage test was conducted using a centrifuge-based embankment backwater level stabilization system to simulate the presence of groundwater within the model ground. In addition, a dynamic shaking table test was performed on the same model ground to reproduce seismic motion. Furthermore, a combined seepage-shaking test was carried out to investigate the effects of both groundwater infiltration and seismic loading on the embankment.

All the tests described here were conducted on the TCU Mark III Centrifuge owned by Tokyo City University [4]. As shown in Fig. 1, an acrylic model container was custom fabricated with a water supply tank, located on the right side, to generate seepage from the back of the embankment. There was also a drainage tank, located at the bottom, for water discharge. The acrylic container measured 448 mm in width and 298 mm in height and was constructed as a single integrated unit to prevent water leakage. Inside the container, a gentle slope with a 20-degree inclination was formed using MC nylon, representing the base ground. To simulate a rough boundary condition, silica sand No.7 was bonded to the base and the slope surface. The water supply tank at the rear of the slope was constructed using an acrylic cutoff plate with nine 3/16-inch diameter holes. Of these, only the upper three holes were used, while the remaining six (middle and lower rows) were sealed. A porous stone was installed on the front side and integrated with the base slope to prevent water leakage.

A total of five experimental cases were conducted, and schematic diagrams of the model ground are shown in Figs. 2 and 3. The red circles in Fig. 2 indicate the pore water pressure gauges, and the yellow squares in Fig. 3 represent the accelerometers. The model ground for all cases was composed of a mixture of Ao clay and silica sand No.7 at a dry weight ratio of 1:3. The mixture was adjusted to achieve a wet density of 1.78 g/cm³, a water content of 13.0%, and a degree of compaction of 95%. Finally, a model embankment with a slope angle of 30 degrees and slope height of 188 mm was made.

In this study, Case 1 was designed as a groundwater seepage test simulating the presence of groundwater within the embankment only, while Case 2 was a dynamic shaking table test that simulated seismic motion only using a shaking device. Cases 3 to 5 were conducted as combined seepage–shaking tests, incorporating both groundwater seepage and seismic loading.

Regarding the simulated groundwater level in the embankment, a centrifuge-based embankment backwater level stabilization system was used to maintain constant water levels at different heights from the embankment rear. In Case 1, the water level was set at 2/3 of the total height. For Case 3, it was adjusted to 1/4 height, while Case 4 had it at 1/2 height. Finally, in Case 5, the water level was again set at 2/3 of the total height. In Cases 1 and 3–5, four pore water pressure gauges were installed at the base of the model ground. After reaching the target centrifugal acceleration of 40G, compressed air was applied to the injection tank, and water was supplied to the supply tank via a rotary joint to initiate groundwater seepage into the embankment.

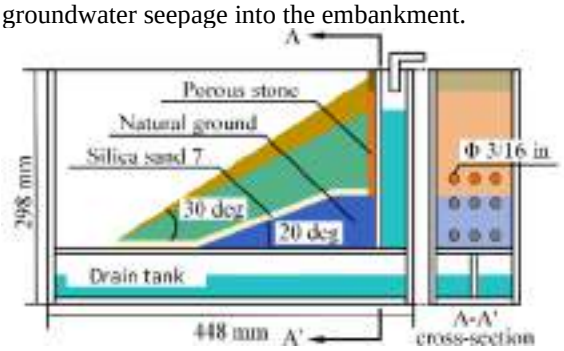

Fig.1 Outline drawing of acrylic container

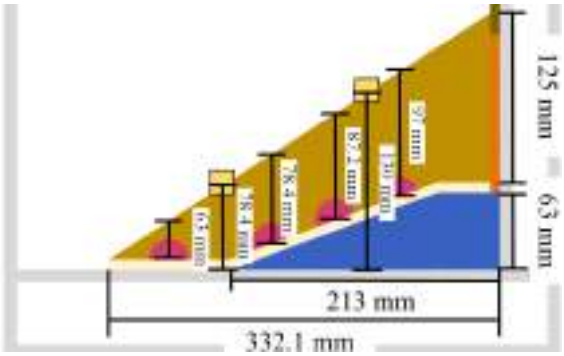

Fig.2 Model ground outline drawing

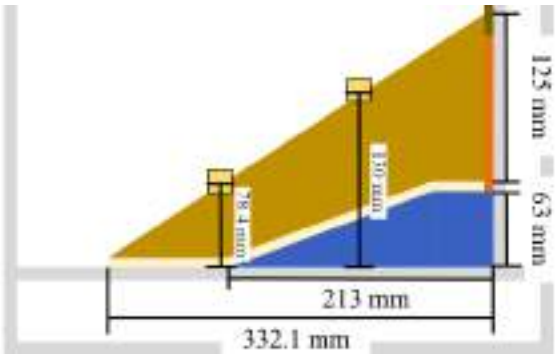

Fig3. Model ground outline drawing

As for the seismic loading, Table 1 summarizes the input acceleration and input duration for Case 2, which involved a sinusoidal wave. In Cases 3 to 5, the input acceleration was set to 300 gal and the input duration to 40 seconds. In Cases 2 and 3–5, two

Table 1. Sine wave input acceleration and input time (Prototype scale)

	Phase 1	Phase 2	Phase 3	Phase 4	Phase 5	Phase 6	Phase 7	Phase 8
Input acceleration (gal)	100	200	300	400	400	400	400	400
Input time (s)	40	40	40	40	40	80	80	160

accelerometers were installed on the model ground surface. After reaching the 40G centrifugal acceleration, the shaking was applied in phases at approximately 10-second intervals.

EXPERIMENTAL RESULTS

Behavior of the Model Ground During Testing

The conditions of the model ground after the completion of each test from Cases 1 to 5 are shown in Figs. 4-8. In Case 1, a small-scale failure occurred 180 seconds after the water was supplied. Progressive failure from the toe of the embankment was observed, as can be seen in Fig. 4. After the initiation of water supply, water infiltrated from the back of the model ground toward the toe of the slope, maintaining a level equivalent to that of the water surface in the supply tank. Once the infiltrated water reached the slope toe, the groundwater level near the toe rose to the slope surface. Subsequently, the rise in groundwater level extended to the middle section of the slope. After that, a local collapse occurred around the slope toe, forming a flow path for the water. As a result, progressive failure through a chain reaction occurred, and the embankment height on the back side decreased. Ultimately, gully erosion developed on the embankment surface as surface water runoff was observed. In Case 2, seismic motion was applied to the model ground in 8 phases as mentioned in Table 1. However, no noticeable deformation of the model ground was observed visually, and no significant changes occurred on the ground surface during the test, as seen in Fig. 5. In Case 3, a large deformation was observed during the first phase, where the back of the embankment settled due to the slope deforming towards the front. Similar deformation continued up to phase 6, with no substantial changes observed in the subsequent phases.

Fig4. Case1 Post-Experiment

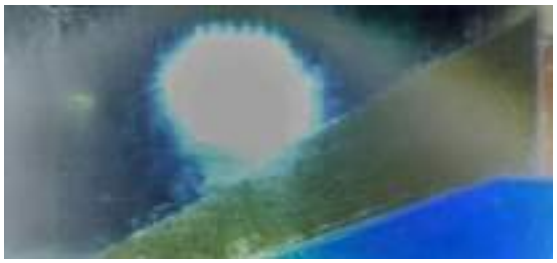

Fig5. Case2 Post-Experiment

Additionally, slope failure did not occur at the ground surface throughout all phases. In Case 4, the deformation pattern was similar to that in Case 3 during Phase 1, but the extent of the failure was greater than that in Case 3. The slope slid forward and continued with each phase. Cracks were observed to have developed across the entire ground surface during Phase 4. In Case 5, it was observed that embankment height settled during Phase 1, then a bulging-type failure around the middle of the slope occurred. During Phase 2, a large-scale slope failure occurred from the back of the model ground, that deformed downwards.

Groundwater Level in the Embankment

Trends of the groundwater level under the embankment for each case are shown in Figs 9-12. The peaks observed in Cases 3 to 5 correspond to the periods during which shaking was applied using the shaking table. The groundwater level is calculated from the pore water pressure recorded. Therefore, it

Fig6. Case3 Post-Experiment

Fig7. Case4 Post-Experiment

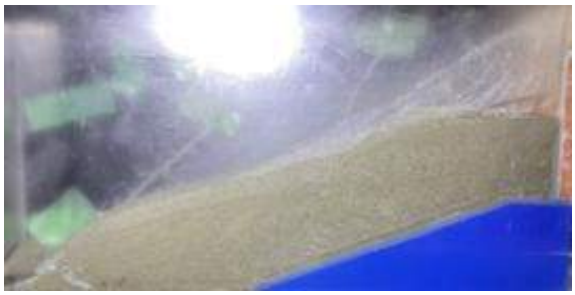

Fig8. Case5 Post-Experiment

should be noted that if the water pressure is not hydrostatic such as during shaking or with the dissipation of excess pore water pressure after shaking, the calculation result might slightly differ from the actual water level. In Case 1, the groundwater level began to decrease slightly around 7200 seconds after the onset of infiltration, which corresponds to the timing when the small-scale failure happened. Next, in Cases 3 through 5, it was confirmed that as the back water level increased and the groundwater level within the embankment also rose at all measurement points. Furthermore, it was observed that the application of seismic acceleration, in addition to seepage, caused the water level to rise at all measurement points. The influence of the seismic motion on slope failure was confirmed by comparing Case1, which included only groundwater seepage and Cases3~5, which are combining seepage and seismic motion. It was found that Cases 4 and 5 experienced failures at an earlier stage than Case 1. Moreover, although the back water level in Case 4 was lower than that in Case 1, the toe water level rose to the same height as in Case 1. Comparing Cases 1

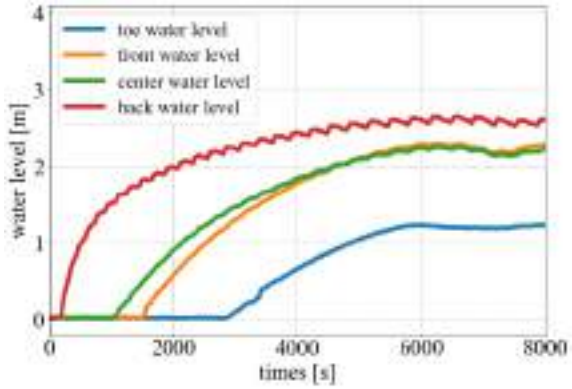

Fig9. Change in groundwater level under the embankment (Case1)

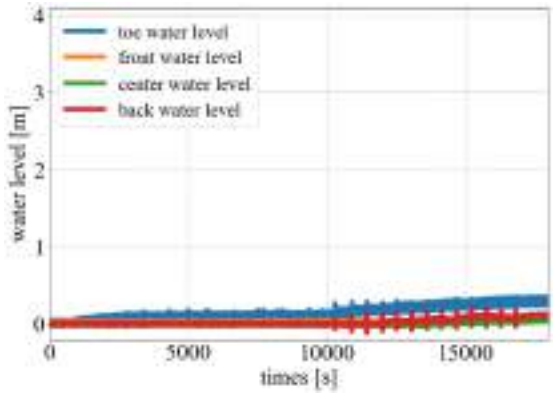

Fig10. Change in groundwater level within the embankment (Case3)

and 5, which had the same back water level, Case 5 has a higher groundwater level at toe of slope than Case 1. In Case3(backwater level : 1/4), the water level at all measurement points rose immediately after the seismic motion was applied, with a particularly remarkable increase in the water level at the toe.

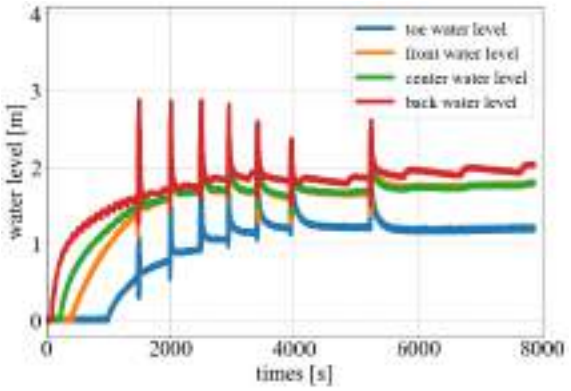

Fig11. Change in groundwater level within the embankment (Case4)

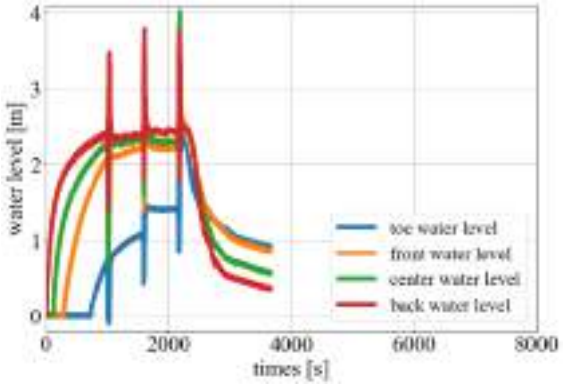

Fig12. Change in groundwater level within the embankment (Case5)

Cumulative Absolute Velocity at the Ground Surface

The cumulative absolute velocity (CAV) [5]for

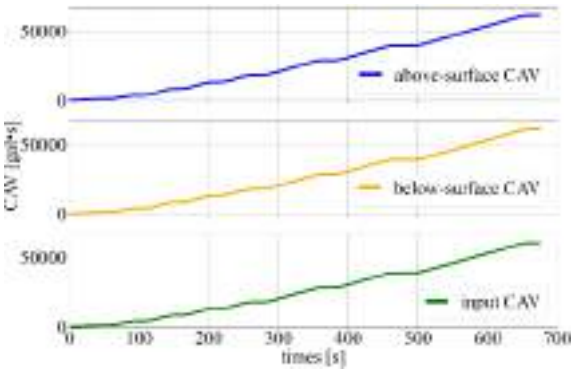

Fig13. CAV at Each Measurement Point (Case2)

each test case is shown in Figs. 13-16. These graphs represent the cumulative sum of the absolute values of acceleration over time, calculated by integrating

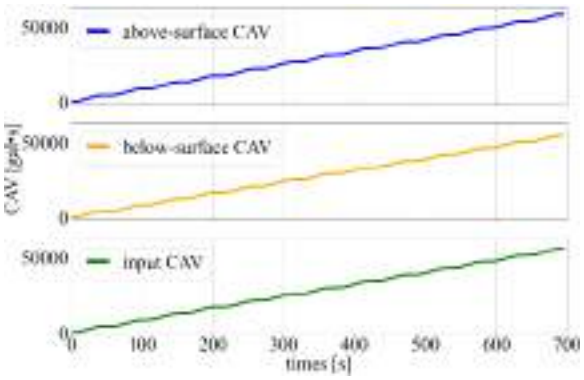

Fig14. CAV at Each Measurement Point (Case3)

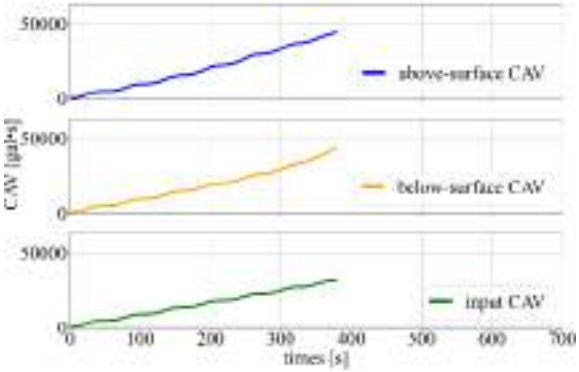

Fig15. CAV at Each Measurement Point (Case4)

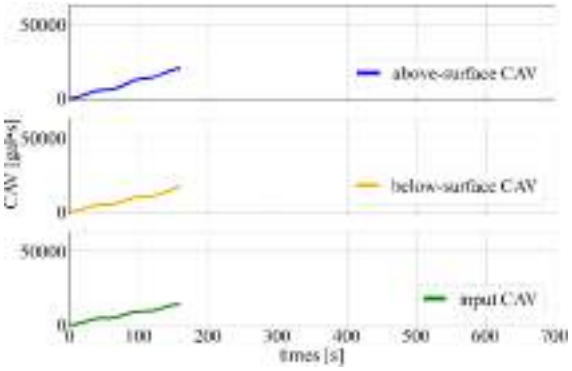

Fig16. CAV at Each Measurement Point (Case5)

the acceleration data. The time axis in each graph corresponds to the total duration of shaking during the test. From these graphs, it is evident that the final values of CAV differ depending on the test case. Although the extent of deformation varied among Cases 3 to 5, slope failure occurred in all three cases during Phase 1, and the CAV at the time of initial failure was approximately the same. However, Case 3 did not experience large-scale slope failure until Phase 13, whereas Cases 4 and 5 failed earlier, at Phase 7 and Phase 3, respectively. When comparing the CAV values, it was observed that Cases 4 and 5 failed with smaller CAV values than Cases 2 and 3. These results suggest that the presence and rise of groundwater within the embankment significantly contribute to the occurrence of slope failure.

Relationship Between CAV and Groundwater Level

Fig.17 summarizes the relationship between CAV and groundwater level for Case 1 and Cases 3 to 5. The plotted groundwater levels represent the average toe water level during the shaking period of each test. For Case 1, the groundwater level at the time of failure is plotted at CAV = 0, as no shaking was applied. From the figure, it can be seen that the final groundwater levels in Cases 3 and 4 are higher than that in Case 1. In addition, in all three cases (Cases 3 to 5), the toe water level increases with increasing CAV. In Cases 3 and 5, the groundwater level increases linearly with respect to CAV. In contrast, in Case 4, the rate of increase in groundwater level gradually decreases as CAV increases. These results indicate that the toe water level tends to rise with increasing CAV. However, the maximum CAV values differ among the cases. Furthermore, it was found that the higher the stabilized groundwater level, the greater the increase in both CAV and toe water level.

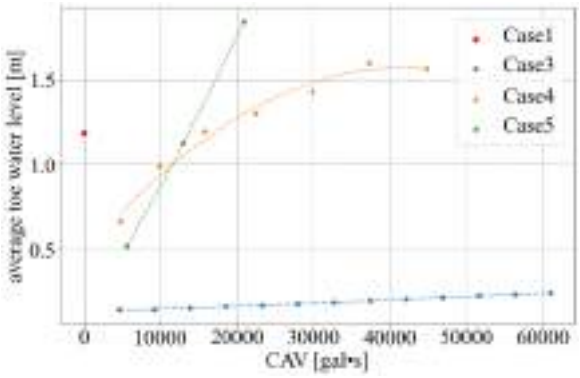

Fig17. Relationship Between CAV and Groundwater Level

CONCLUSION

In this study, a series of centrifugal model tests incorporating groundwater seepage and seismic shaking were conducted to investigate the behavior of embankments and model ground under conditions representative of large-scale residential embankments. A total of five test cases were performed. In Case 2, which involved only seismic loading, no slope failure

occurred even when the input acceleration was increased. In contrast, slope failure was observed in all other cases, including Case 1 (groundwater seepage only) and Cases 3-5 (combined seepage–shaking tests). Regarding groundwater level changes within the embankment, Cases 3-5 showed a more rapid rise in water level compared to Case 1. In particular, the water level at the toe of the slope, which critically affects slope stability, was observed to rise sharply after shaking. Analysis of the cumulative absolute velocity (CAV) at the ground surface revealed that the CAV at the time of slope failure did not necessarily match across cases. Moreover, the total CAV varied depending on the test case, and slope failure tended to occur earlier in cases with higher back water levels. These results suggest that the height of the groundwater level had a greater influence on slope failure than the magnitude of seismic motion. Finally, the relationship between CAV and groundwater level in Cases 3 to 5 showed that the groundwater level increased with increasing CAV. It was also confirmed that the higher the stabilized groundwater level, the greater the increase in both CAV and toe water level.

Future work will continue to explore seepage–shaking interactions under centrifugal conditions, focusing on identifying critical groundwater levels, understanding the combined effects of seismic motion and seepage, and evaluating their impact on slope behavior. In addition, countermeasures for sliding-type slope failures will be developed and their effectiveness assessed through further model testing.

REFERENCES

[1] Ministry of Land, Infrastructure, Transport and Tourism, Explanation of the Guideline for Investigation of Predicted Changes in Large-scale Embankment Construction Sites https://www.mlit.go.jp/common/001089011.pdf (2025/5/19)

[2] National Institute for Land and Infrastructure Management https://www.nilim.go.jp/lab/bcg/siryou/tnn/tnn0438pdf/ks043811.pdf (2025/5/19)

[3] Ministry of Land, Infrastructure, Transport and Tourism, Geographical Survey Institute https://www.gsi.go.jp/BOUSAI/20240101_noto_earthquake.html (2025/5/19)

[4] Sahare A., Sano K., Itoh K., Suemasa N., Tanaka T., Torita M., and Takeoka R., Development of a novel cylindrical cam shaking table for geotechnical centrifuge modelling. International Journal of Physical Modelling in Geotechnics, Vol. 25, Issue 2, 2025, pp. 66–85.

[5] K. W. Campbell and Y. Bozorgnia, Ground Motion Prediction Equations for Cumulative Absolute Velocity (CAV) Using the PEER-NGA Strong Motion Database, Proceedings of the 9th U.S. National and 10th Canadian Conference on Earthquake Engineering, 2010, Paper No. 1004.

Copyright © Int. J. of GEOMATE All rights reserved, including making copies, unless permission is obtained from the copyright proprietors.

15th Int. Conf. on Geotechnique, Construction Materials & Environment,
Kyoto, Japan, 11-13 November 2025, ISBN 978-4-909106124 C3051

VISUALIZATION OF PORE WATER FLOW IN GRANULAR MEDIA USING CYLINDRICAL TRANSPARENT PARTICLES

Shingo Hamano[1], Tatsuya Matsuda[1] and Naoto Naito[1]

[1]Architecture and Civil Engineering Department, Toyohashi University of Technology, Japan

ABSTRACT

Levee failures due to heavy rainfall are primarily caused by overtopping, scouring at the landside toe, and seepage failure. Understanding these mechanisms of soil-water interaction is essential to mitigate geo-disasters. However, conventional observation techniques struggle to capture internal erosion processes due to soil opacity. When the side walls of a model test tank are used to visualize seepage, its friction and confinement effects often lead to non-uniform flow behavior in the depth direction. This study introduces a saturated transparent soil model composed of cylindrical particles with a refractive index (~1.33) nearly identical to water, aiming to minimize boundary effects and other interferences in model testing, and to enable direct observation of pore water flow in the soil. Unlike conventional methods that rely on refractive index matching using viscous solutions (e.g., glycerin, silicone oil), this approach eliminates fluidity constraints, enhancing the accuracy of Particle Image Velocimetry (PIV) measurements. The model test results demonstrate that seepage can be quantitatively analyzed with high precision. The internal flow structure in soil was successfully visualized, revealing localized variations and confirming a proportional relationship between pore flow velocity and hydraulic gradient under low-gradient conditions. Additionally, the study identifies the critical hydraulic gradient, defined as the minimum gradient necessary to initiate particle mobilization within the soil matrix. These findings enhance understanding of sediment–fluid interactions during soil failure, contributing to a more advanced geotechnical framework for percolation-induced failure mechanisms.

Keywords: Transparent soil, Water, Particle image velocimetry, Seepage

INTRODUCTION

Many geotechnical disasters are related to an interaction between soil particles and water such as river levee failures caused by flooding [1], local scour around bridge piers [2], mound erosion of breakwaters caused by tsunamis [3], rainfall-induced slope failures [4], and submarine landslides triggered by earthquakes [5]. Accurate disaster prediction and reliable performance assessment of mitigation structures are essential to implement effective countermeasures against such events. Therefore, elaborate model tests have been conducted, and many studies on developing numerical methods for prediction and evaluation have been conducted using model test results as benchmarks [6-8].

One promising approach for obtaining highly accurate results is using transparent soil, which enables visualizing pore-scale flow [9–12] within the ground and three-dimensional particle behavior [13–16]. Previous visualization studies have significantly advanced the development and application of numerical models. However, these approaches often relied on viscous fluids to match the refractive index of solid particles, such as fused silica. Because the rheological properties of these fluids differ markedly from those of natural groundwater, they limit the accurate reproduction of soil–water interactions. Moreover, the use of viscous fluids hinders the simultaneous satisfaction of key dynamic similarity criteria—such as Froude and Reynolds similarity—which are essential for accurately modelling flow in scaled experiments. As a result, researchers have often faced a trade-off between achieving realistic flow behavior and maintaining optical clarity.

To overcome these limitations, we developed a transparent soil system composed of cylindrical particles fabricated from a novel material with a refractive index closely matching that of water. This design eliminates the need for viscous fluids, enabling direct observation of pore-scale flow under hydraulic conditions that more closely replicate natural soil–water interactions. Consequently, the proposed method achieves dynamic similarity while offering more accurate and detailed insights into soil transport processes than previous viscous-fluid-based approaches.

RESEARCH SIGNIFICANCE

This study proposes a new experimental method for visualizing pore-scale interactions between soil particles and water using a transparent soil material with a refractive index that matches that of water. Unlike many previous studies, no viscous fluid was used, which enables observations under realistic flow conditions. High-resolution measurements using laser sheet illumination and particle image velocimetry (PIV) enable the tracking of particle behavior not only near the transparent wall but also

within soil mass. The data obtained are valuable for validating advanced numerical models and contributing to the practical use of simulation tools in geotechnical engineering and disaster mitigation.

PARTICLE CHARACTERISTICS

Transparent cylindrical particles made of a fluoropolymer were used and their physical properties were analyzed through laboratory tests. A total of 100 particles were randomly sampled to measure their shapes. The particles had an average diameter of 2.89 mm and an average height of 3.17 mm. The specific gravity of the material was 2.06. Figs.1 and 2 show the transparent particles used in this study.

Fig.1 Transparent particles with a refractive index equivalent

(a) (b)

Fig.2 Transparent particles with a refractive index equivalent to that of water: (a) air and (b) water

Maximum and minimum void ratios

Maximum and minimum density tests were conducted to evaluate the packing characteristics of transparent particles. The maximum density test was performed in three cases, whereas the minimum density test was conducted in five cases. In addition to these tests, the minimum and maximum void ratios were calculated based on the maximum and minimum densities. The results indicated that the maximum dry density was 1,356 kg/m³, corresponding to the minimum void ratio of 0.342, while the minimum dry density was 1,281 kg/m³, corresponding to the maximum void ratio of 0.378.

Angle of repose

The angles of repose of transparent particles shown in Fig.3 were measured. Five tests were conducted based on the method proposed by Nakata et al. [17]. The average angle of repose, θ, was found to be 36.57°.

Fig. 3 Angle of repose

Coefficient of permeability

A constant-head permeability test was performed to determine the coefficient of permeability of transparent soil. Table 1 lists the test parameters. The specimens were cylindrical, 46 mm in diameter, and prepared under loose packing conditions. Based on the results of the density test under these conditions, the bulk density was 1,281 kg/m³. Seepage occurred in the vertically downward direction, and a hydraulic gradient of 1.27 was applied. The average hydraulic conductivity measured at a water temperature of 17.6 °C was 4.48 mm/s. After applying a temperature correction to standardize the value to 15 °C, the adjusted coefficient of permeability was 4.5 mm/s.

Table 1 Permeability test condition

Water temperature T (℃)	17.6
Water level difference ΔH (mm)	65
Flow volume Q (mL)	150
Cross-section area of sample A (mm^2)	1,662
Sample thickness L (mm)	51

Visualization experiment of vertical one-dimensional seepage flow

Experimental procedure

A transparent acrylic pipe with an inner diameter of 46 mm was used. Transparent particles were loosely packed inside the pipe to achieve a minimum dry density of 1,281 kg/m³ and a maximum void ratio of 0.378, as determined from the density tests.

A one-dimensional upward seepage flow was generated by adjusting the water-level difference. Water mixed with a tracer was circulated through the system to visualize the seepage behavior in transparent ground, and a laser beam was directed at the section filled with transparent particles. A schematic of the experimental apparatus is shown in Fig. 4. The particle size of the tracer is 50 μm. Both the pore-scale seepage flow and cross-sectional average flow velocity in the lower fluid-only region were measured.

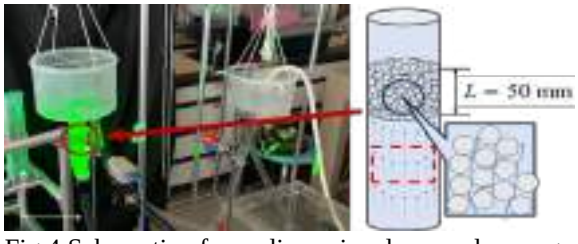

Fig.4 Schematic of one-dimensional upward seepage flow equipment

Fig.4 shows close-up images captured in regions where the movement of the tracers within the particle voids was observable. The recorded video was analyzed using PIV. Based on this analysis, the flow velocity distribution in the apparatus was obtained (Fig.5), and the pore-scale velocity field was evaluated (Fig.6).

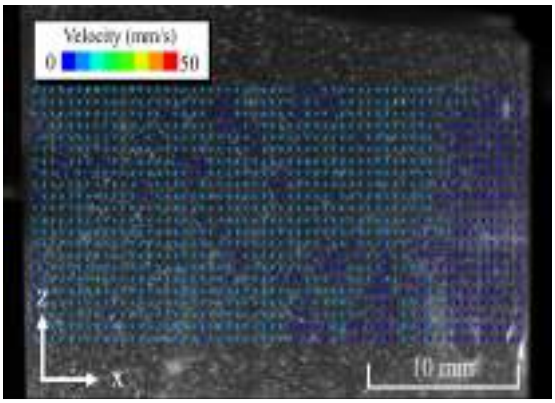

Fig.5 PIV analysis (visualization of flow velocity distribution in the equipment at a hydraulic gradient of i = 0.4)

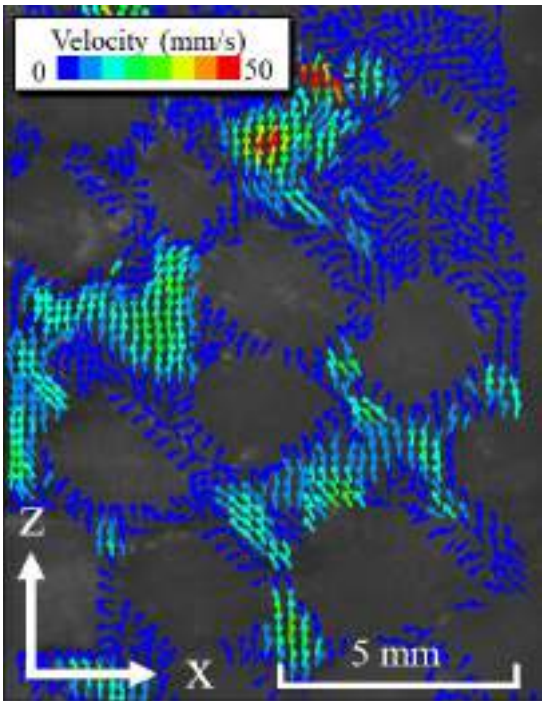

Fig.6 PIV analysis (visualization of pore-scale velocity at a hydraulic gradient of i = 0.4)

Experimental results and discussions

Fig. 7 illustrates the relationship between the hydraulic gradient (i) and the vertical pore velocity, as determined from PIV analysis. The vertical velocity was calculated as the average within the observation area. Although velocity generally increases with the hydraulic gradient, the relationship becomes increasingly nonlinear at higher values, suggesting a potential shift in flow behavior. Further analysis is required to clarify the nature of this change.

Fig. 8 shows the cumulative relative frequency distribution of pore velocity (v) for different hydraulic gradients (i), with dotted lines indicating the mean velocity for each gradient. Overall, the proportion of higher-velocity data points increases with the hydraulic gradient, indicating that larger gradients promote accelerated flow and expand the regions of faster movement.

However, for velocities above 20 mm/s, the number of occurrences is slightly greater at i = 0.6 than at i = 0.8, implying a possible redistribution of flow paths at higher gradients rather than a simple intensification of extreme velocities.

Fig. 9 presents the relationship between the hydraulic gradient (i) and pore velocity (v) as a relative frequency distribution. At i = 0.6, most data points correspond to velocities below 5 mm/s; however, the proportion of velocities exceeding 25 mm/s is slightly greater at i = 0.6 than at i = 0.8. In contrast, the distribution at i = 0.8 is relatively flat, lacking a distinct peak, which may suggest a reduction in localized high-velocity zones and a more uniform distribution of flow paths.

The focus shifts to the critical hydraulic gradient for further discussion. The critical hydraulic gradient in the vertical direction i_{cr} is calculated using

$$i_{cr} = G_s - 1/1 + e \quad (1)$$

where G_s and e represent the specific gravity of the soil particle and void ratio, respectively. The critical hydraulic gradient is defined as the minimum gradient necessary to initiate particle mobilization within the soil matrix.

In this study, the critical hydraulic gradient (i_{cr}) was determined to be 0.77. Considering the critical hydraulic gradient of the material, it is possible that a significant redistribution of the flow occurred in pore spaces outside the analyzed area at i = 0.8. Consequently, the proportion of velocities exceeding 20 mm/s was higher at i = 0.6 within the analyzed region, which indicates that a broader analysis domain is necessary for capturing flow behavior under high hydraulic gradients.

Although localized high-velocity zones diminished at i = 0.8, no noticeable changes in particle arrangement were detected within the analysis area. The tested material comprises uniformly sized particles without a fines fraction; thus, classical suffusion is unlikely. However, if the granular assembly is considered as a soil skeleton, the observed flow homogenization may indicate a potential for void formation or internal instability under sustained seepage conditions.

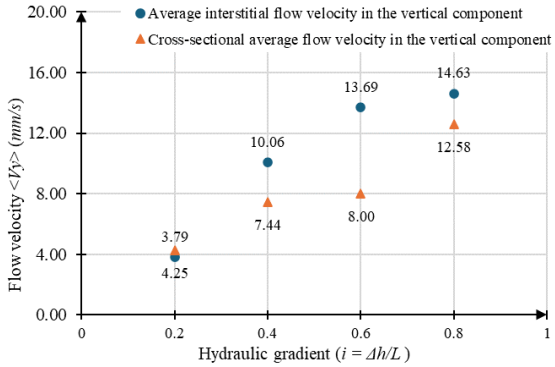

Fig.7 Cross-sectional average flow velocity and average interstitial flow velocity

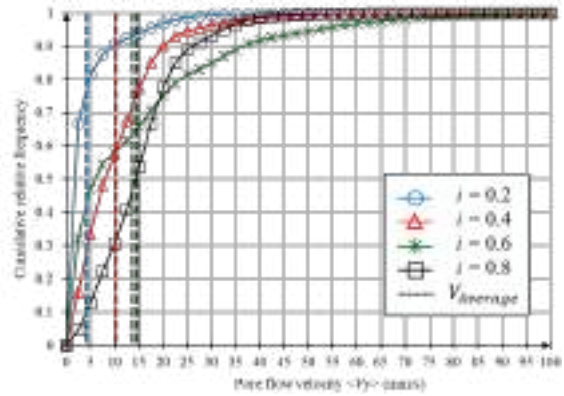

Fig.8 Cumulative frequency distribution of average interstitial flow velocity

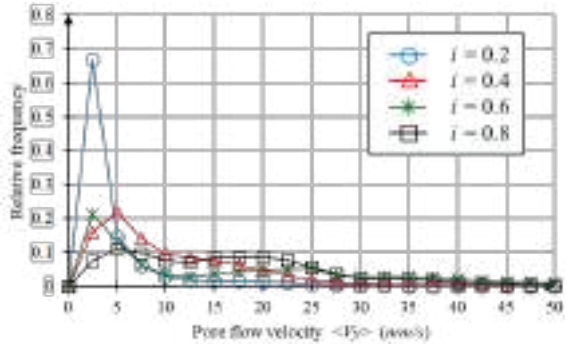

Fig.9 Relative frequency distribution of average interstitial flow velocity

CONCLUSIONS

This study employed a novel transparent soil material to visualize seepage flow, with physical properties closely matching those of natural soil. The results demonstrated a linear relationship between both the vertical mean flow velocity and the average pore velocity with the hydraulic gradient.

Notably, near the critical hydraulic gradient, a distinct flattening in the pore-scale velocity distribution was observed, suggesting a redistribution of flow paths under high-gradient conditions.

The present investigation was limited to scenarios in which soil particles remained fixed. Future research will focus on dynamic conditions that allow particle movement and rearrangement to more accurately replicate natural soil behavior. Additionally, efforts will be made to optimize imaging conditions for the transparent material and to further analyze its deformation and fracture characteristics.

ACKNOWLEDGMENTS

This study was supported by a research grant from the Taisei Academic Foundation. The authors would like to express their appreciation for the generous support.

REFERENCES

[1] Yasuda S., Shimizu Y., Deguchi K., Investigation of the mechanism of the 2015 failure of a dike on Kinu River, Soils and Foundations, Vol. 56, Issue 4, 2016, pp. 581–592.

[2] Enomoto T., Horikoshi K., Ishikawa K., Mori H., Takahashi A., Unno T., Watanabe K., Levee damage and bridge scour by 2019 typhoon Hagibis in Kanto Region, Japan, Soils and Foundations, Vol. 61, Issue 2, 2021, pp. 566–585.

[3] Takahashi H., Sassa S., Morikawa Y., Takano D., Maruyama K., Stability of caisson-type breakwater foundation under tsunami-induced seepage, Soils and Foundations, Vol. 54, Issue 4, 2014, pp. 789–805.

[4] Mori S., Ono K., Landslide disasters in Ehime Prefecture resulting from the July 2018 heavy rain event in Japan, Soils and Foundations, Vol. 59, Issue 6, 2020, pp. 2396–2409.

[5] Minami H., Umino K., Tateishi R., Kawamura N., Seo N., Detecting submarine landslides caused by the 2024 Noto Peninsula Earthquake through repeat bathymetric surveys in Toyama Bay, Japan, Landslides, Vol. 22, Issue 2, 2025, pp. 449–458.

[6] Yang Y., Li J., Shi W., Yang C., Yan L., Numerical investigation of failure characteristics and debris movement in the Madaling landslide using coupled FDM–DEM, Geotechnical and Geological Engineering, Vol. 42, Issue 4, 2023 (published online 21 November 2023), pp. 2745–2765.

[7] Zhu Q. Y., Jiang N., Chen Q., Hu Y. X., Zhou J. W., DEM–SPH simulation for the formation and breaching of a landslide-dammed lake triggered by the 2022 Lushan earthquake, Landslides, Vol. 20, Issue 9, 2023, pp. 1925–1941.

[8] Liu C., Sun Q., Zhou G. D. D., Coupling of material point method and discrete element method for granular flows impacting simulations, International Journal for Numerical Methods in Engineering, Vol. 115, Issue 39–41, 2018, pp. 172–188.

[9] Hunter R., Bowman E., Visualisation of seepage-induced suffusion and suffosion within internally erodible granular media, Géotechnique, Vol. 68, Issue 10, 2018, pp. 918–930.
[10] Sanvitale N., Zhao B., Bowman E., O'Sullivan C., Particle-scale observation of seepage flow in granular soils using PIV and CFD, Géotechnique, Vol. 73, Issue 1, 2021, pp. 71–88.
[11] Beguin R., Philippe P., Faure Y.-H., Pore-scale flow measurements at the interface between a sandy layer and a model porous medium: Application to statistical modeling of contact erosion, Journal of Hydraulic Engineering, Vol. 139, Issue 1, 2013, pp. 1–11.
[12] Guo, Y., Cui, Y., Chang, J. Visualization of internal characteristics of soil structures based on transparent soil technology. International Journal of Civil Engineering, 23, 2025, 1535–1547.
[13] Bathurst R., A new approach to evaluate soil-geosynthetic interaction using a novel pullout test apparatus and transparent granular soil, Geotextiles and Geomembranes, Vol. 42, Issue 4, 2014, pp. 325–334.
[14] Zhang M., Xu P., Li J., Wang R., Mining-induced ground movements and displacements using transparent soil model test, Geotechnical Research, Vol. 6, Issue 4, 2019, pp. 252–264.
[15] Stanier S., Black J., Hird C., Enhancing accuracy and precision of transparent synthetic soil modelling, International Journal of Physical Modelling in Geotechnics, Vol. 12, Issue 4, 2012, pp. 162–175.
[16] Wang, Z., Jia, J.,n b Zhang, L. A transparent soil experiment to investigate the influence of arrangement and connecting beams on the pile–soil interaction of micropile groups. Sensors, 24, 2024 5448.
[17] Nakata Y., Moriguchi S., Kajiyama S., Kido R., Kikkawa N., Saomoto H., Takano D., Higo Y., Experimental data of 3D printed granular material for verification of discrete element modeling simulation, Soils and Foundations, Vol. 62, Issue 4, 2022, Article 101178.

Copyright © Int. J. of GEOMATE All rights reserved, including making copies, unless permission is obtained from the copyright proprietors.

15th Int. Conf. on Geotechnique, Construction Materials & Environment,
Kyoto, Japan, 11-13 November 2025, ISBN 978-4-909106124 C3051

GROUND IMPROVEMENT OPTIMIZATION USING DYNAMIC NUMERICAL ANALYSIS IN THE DEVELOPMENT OF THE BANYUWANGI AIRPORT IN INDONESIA

Christopher Tanjung[1], Andhika Sahadewa[1,2], Pebri Herry[1], Reza Ismaniar[1], and Aris Wibowo[1]

[1]Nur Straits Engineering, Indonesia
[2]Civil Engineering, Bandung Institute of Technology, Bandung, Indonesia

ABSTRACT

Banyuwangi Airport is located in Blimbingsari, East Java, Indonesia. Banyuwangi Airport was expected to be able to share heavy traffic load amongst nearby airports. Previously, the existing runway could only accommodate Boeing B737-500 as the largest airplane. It must be extended by 350 m to accommodate larger airplanes, such as Boeing B737-8MAX and B737-9MAX. Probabilistic Seismic Hazard Analysis (PSHA) results showed that Peak Base Acceleration of 500-year and 2,500-year return period were 0.24g and 0.39g, respectively. Soil investigations data on the extension location indicated shallow ground water table. The soil stratum was dominated by low plasticity sandy silt and silty sand. According to index properties and low to medium density, these soil types were prone to liquefaction. By evaluating the index properties and N value of Standard Penetration Test using NCEER 1997 method, liquefied layer depth varied from 6 m to 20 m from the ground surface. To optimize ground improvement design, dynamic analysis was performed using ground motion based on PSHA. This approach could reduce the predicted liquefied layer depth to 6 m to 17 m from the ground surface. Ground improvement must be selected and engineered by considering several critical aspects, including material availability, construction period, constructability, and cost. After considering several ground improvement alternatives, rigid inclusion was selected with column diameter of 42 cm with triangular grid spacing of 1.6 m. This study highlights that liquefaction evaluation using dynamic discrete element numerical analysis can optimize ground improvement cost by reducing ground improvement depth.

Keywords: Liquefaction, Numerical Analysis, Rigid Inclusion, Ground Improvement

INTRODUCTION

Blimbingsari Airport in Banyuwangi is projected to be a supporting airport for I Gusti Ngurah Rai Airport in Bali. The largest aircraft that Banyuwangi airport's runway can accommodate is B737-500 prior to 2019. Due to B737-900 or A320 aircraft usage increase for domestic flights, it was urgently required to upgrade the runway capacity by extending and widening the existing runway to accommodate larger aircraft models in the future. To achieve this goal, the runway must be extended by 350 m from 2,250 m to 2,600 m and widen by 15 m from 30 m to 45 m as shown in Fig. 1.

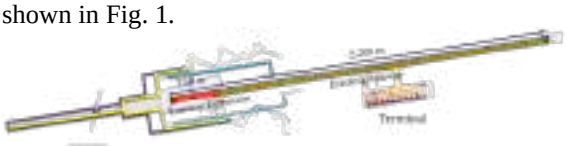

Fig. 1 Banyuwangi Airport Runway extension layout

Soil investigation on runway extension location indicated shallow ground water table with low to medium density coarse grain soil which was prone to liquefaction. Furthermore, Probabilistic Seismic Hazard Analysis (PSHA) results showed that Peak Base Acceleration of 500-year and 2,500-year return period were 0.24g and 0.39g which showed high risk of liquefaction occurrence in the runway extension area. Therefore, soil improvement was needed to prevent runway damages due to liquefaction. In this paper, ground improvement design using finite difference method and advantage of numerical analysis liquefaction over conventional liquefaction analysis is presented.

Liquefaction

Liquefaction is one of many geotechnical hazards in which loose and saturated granular soils undergo strength and stiffness degradation due to seismic load. When the soils lose all of its strength it will behave like a viscous fluid. Liquefaction occurs due to excess pore water pressure generated by cyclic loading which will reduce effective stress to nearly zero [1]. Susceptibility depends on soil density, saturation, and seismic intensity, with loose sands (D_r < 50%) and silty sands being most vulnerable.

On 28 September 2018 a Mw 7.4 earthquake struck Palu, capital city of Central Sulawesi, Indonesia. This earthquake triggered a series of tragic disasters and led to liquefaction events in many places. Following the earthquake, 11-m high tsunamis hit Palu Bay and surrounding coastal areas. The ground movements at these sites due to the earthquake were

associated with multiple mechanisms, including liquefaction, lateral spreading, landslide, and water channel breakage [2].

Liquefaction Evaluation

Cyclic stress ratio (CSR) and resistance (CRR) are the most common empirical method to assess liquefaction potential. CSR and CRR are often derived from Standard Penetration Test (SPT) or Cone Penetration Test (CPT) data. The NCEER National Center for Earthquake Engineering Research workshop established a simplified procedure to evaluate liquefaction potential, which compares CSR induced by cyclic load to CRR derived from the SPT [3]. CSR is calculated as:

$$\mathbf{CSR} = \mathbf{0.65}(\boldsymbol{a}_{\mathbf{max}}/\boldsymbol{g})(\boldsymbol{\sigma}_{\boldsymbol{vo}}/\boldsymbol{\sigma'}_{\boldsymbol{vo}})\boldsymbol{r}_{\boldsymbol{d}} \quad (1)$$

where a_{max} is peak horizontal ground surface acceleration, σ_{vo} and σ'_{vo} total and effective vertical overburden stress, and r_d is stress reduction coefficient. NCEER [3] developed CRR Curve which depends on fine content and N value of SPT (N-SPT).

Rigid Inclusion

Rigid inclusions are vertically stiff elements (e.g., cement-treated columns) installed to reinforce liquefiable soils by improving load transfer and reducing excess pore water pressure buildup during seismic events [4]. The primary mechanism involves stress redistribution, where the rigid inclusions carry structural loads to deeper, stable strata, thereby reducing shear stresses in the surrounding soil and minimizing liquefaction potential.

Rigid inclusion design emphasizes several parameters including column spacing, stiffness contrast between inclusions and native soil, and load transfer mechanisms.

Case histories, such as the 2011 Christchurch earthquakes, highlight the success of rigid inclusions in preventing foundation failures, though site-specific adaptations are critical for optimal results [5].

RESEARCH SIGNIFICANCE

Liquefaction has been one of most dangerous geotechnical hazards, but it is commonly analyzed by using conventional method. This method only considers soil fine content, N-SPT, and Peak Ground Acceleration (PGA). By using numerical analysis to simulate soil under dynamic loading, more soil parameters such as dynamic damping and dynamic stiffness will be considered. Therefore, more accurate soil behavior was analyzed which may affect liquefied layer depth. Ultimately this paper provides a new perspective of analyzing liquefaction potential using numerical method compared to conventional liquefaction analysis.

SOIL CONDITION

In the runway extension area, there were 3 available boreholes (Fig. 2). The N-SPT values were also obtained from these boreholes. The N-SPTs were obtained according to [6]. Four soil undisturbed sample units were retrieved from these holes. Daily well observation was performed to find that the ground water table was varying from 2.3 m to 3.4 m below the ground surface. The soil stratigraphy in the runway extension area was dominated by coarse grained soil which the upper layer consisted of loose to medium dense silty sand, with very loose sand (N-SPT = 1 to 2) was observed in DB-03. Upper layer depth is varied from 8 m to 15 m below the ground surface. The interpreted soil stratigraphy is shown in Fig. 3.

Based on laboratory test results, liquefaction potential was evaluated using methods proposed by [7], [8] as shown in Fig. 4. Both figures indicate high risks of liquefaction. Therefore, further analysis was required to determine liquefied soil depth.

Fig. 2 Soil Investigation Layout

LIQUEFACTION DEPTH ANALYSIS USING CONVETIONAL METHOD

To evaluate the liquefaction potential and mitigation depth, PGA with 500-year return period based on Indonesian seismic hazard map was used in this liquefaction analysis [9]. Indonesian seismic map in Fig. 5 shows that PGA with 500-year return period in Banyuwangi Airport location is 0.2g – 0.25g. Since the site class in runway extension area was classified as SD, the seismic load used in this analysis was 0.31g.

In order to evaluate liquefaction potential and mitigation depth, NCEER [3] method was used. Based on this method, liquefaction potential was identified from the ground surface until 20 m depth (Fig. 6). Thus, based on conventional analysis, soil improvement depth for liquefaction mitigation was 20 m from the ground surface.

LIQUEFACTION DEPTH ANALYSIS USING NUMERICAL METHOD BASED ON SEISMIC HAZARD ANALYSIS

In an attempt to optimize soil improvement depth, numerical dynamic analysis using FLAC 2D

was conducted [10]. In order to simulate seismic hazard more accurately, Probabilistic Seismic Hazard Analysis (PSHA) was performed to get synthetic ground motion and was used as input in FLAC.

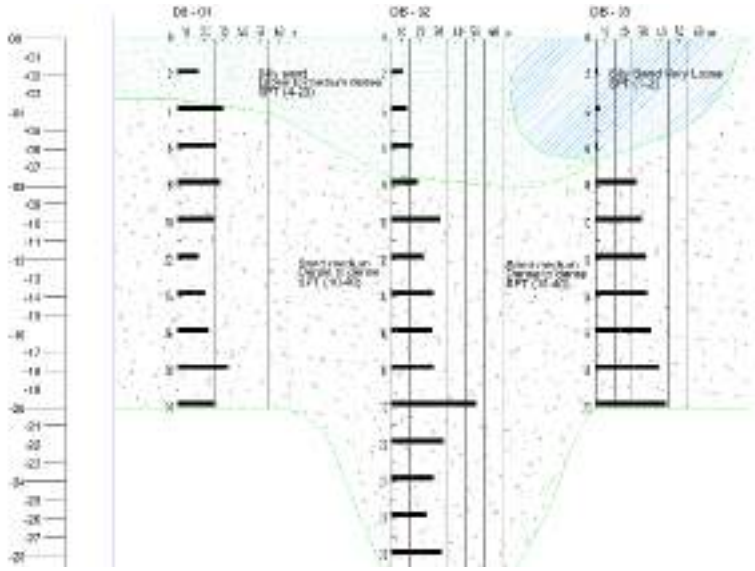

Fig. 3 Soil Stratigraphy

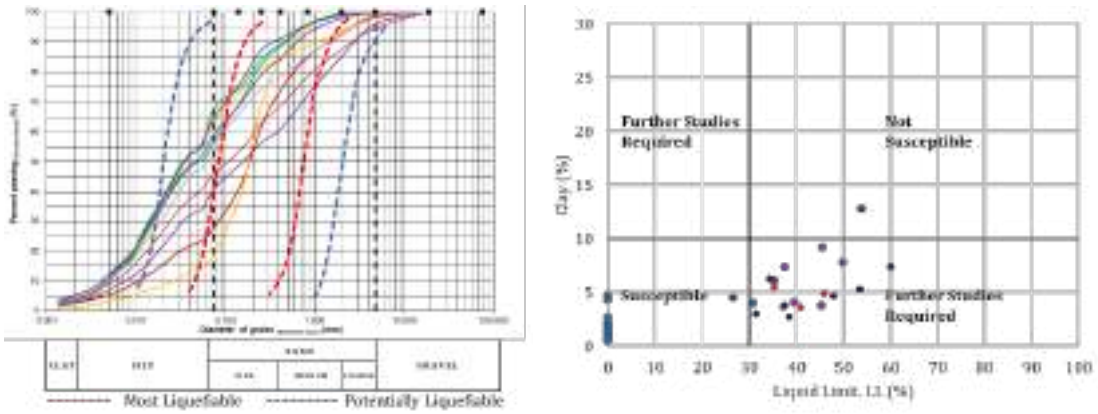

(a) (b)

Fig. 4 Liquefaction potential evaluation based on: (a) Tsuchida [7] and (b) Seed et al. [8]

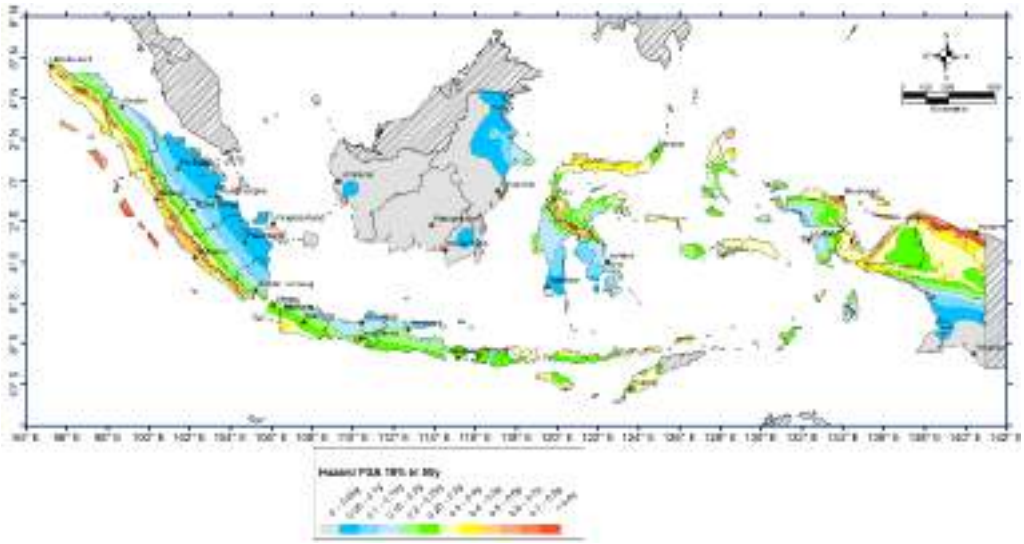

Fig. 5 Peak Ground Acceleration in Banyuwangi Airport

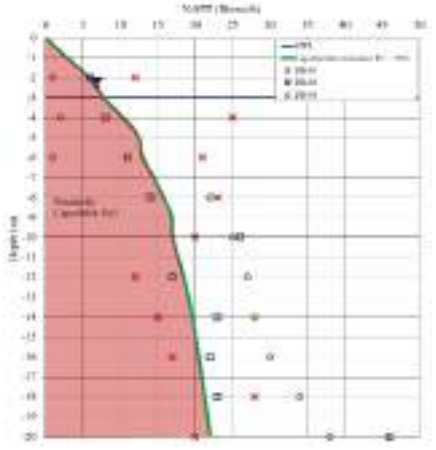

Fig. 6 Liquefaction analysis using NCEER (1997)

Dynamic analysis was conducted using free field boundary to prevent wave reflection. Soil constitutive model used in this analysis was Finn-Byrne model which is based on Mohr Coulomb model [10], [11]. The Finn-Byrne model can calculate pore pressure increase (R_u) in soil for simulating soil liquefaction. Table 1 shows geotechnical soil parameters for DB-01, including saturated unit weight (γ_{sat}), angle of internal friction for design (φ'_{Design}), shear wave velocity of soil, Poisson's ratio (v'), dynamic shear modulus (G_{Dyn}), dynamic bulk modulus (K_{Dyn}), and Finn-Byrne parameters (C_1 and C_2). The FLAC model is presented in Fig. 7.

Fig. 8 shows excess pore pressure ratio increase after the ground motion has subsided. Based on the analysis result, liquefied layer depth varied for each borehole. Liquefied layer depth was 17 m in DB-01, 10 m in DB-02, and 6 m in DB-03. These depths were less than those of NCEER analysis.

RIGID INCLUSION DESIGN

In order to prevent liquefaction during a seismic event, soil improvement using rigid inclusion was proposed. The rigid inclusion columns in this design were set to be 42 cm in diameter, 6 m to 17 m long, spacing on 1.2 m to 1.8 m in triangular pattern. A load transfer platform of 1-m thick made from granular soils was installed on rigid inclusion head.

The rigid inclusion model is presented in Fig. 9. Unit weight of the columns was set to be 22.43 kN/m^3, shear modulus of 5.2 x 10^9 kPa, bulk modulus of 6.91 x 10^9 kPa, The interface for normal and shear forces were both 1.38 x 10^{11} kPa. The maximum mesh size was 1 m. The corresponding analysis result is shown in Fig. 11. In order to determine the most optimum rigid inclusion spacing, the maximum R_u was plotted against Rigid Inclusion spacing to determine the maximum spacing which allows maximum R_u of 40%. Fig. 12 shows that using rigid inclusion with 1.6 m spacing, the predicted maximum R_u in all borehole was less than 40%.

Table 1 Geotechnical Parameter for DB-01

No.	Soil Layer	γ_{sat} (kN/m^3)	φ'_{Design} (°)	V_s (m/s)	v'	G_{Dyn} (Pa)	K_{Dyn} (Pa)	Finn - Byrne	
								C_1	C_2
1	Med. Dense Sand (N-SPT = 12)	17	30.49	215	0.33	8.00 x 10^7	2.09 x 10^8	0.30	1.35
2	Med. Dense Sand (N-SPT = 21)	17	35.49	265	0.30	1.21 x 10^8	2.56 x 10^8	0.23	1.75
3	Med. Dense Sand (N-SPT = 14)	17	31.73	227	0.32	8.94 x 10^7	2.21 x 10^8	0.52	0.77
4	Med. Dense Sand (N-SPT = 22)	17	35.98	269	0.29	1.26 x 10^8	2.61 x 10^8	0.39	1.02
5	Med. Dense Sand (N-SPT = 30)	17	39.49	304	0.27	1.60 x 10^8	2.90 x 10^8	0.34	1.18

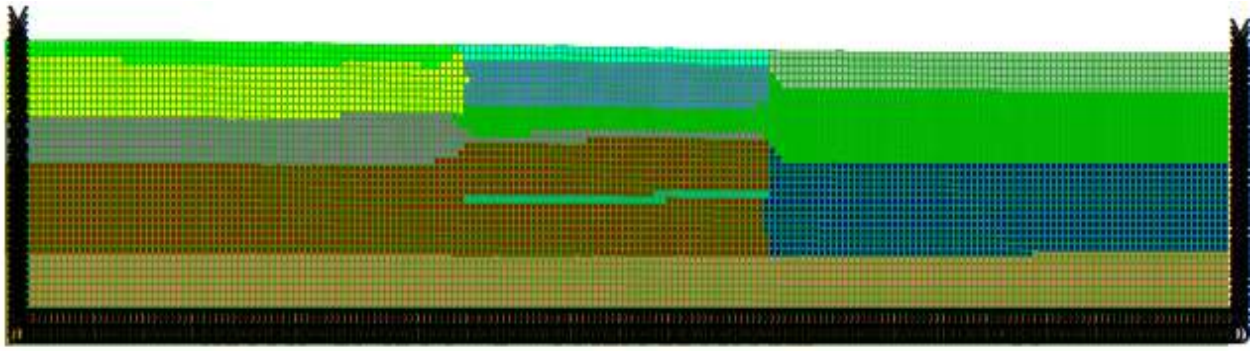

Fig. 7 Free Field Model in FLAC 2D

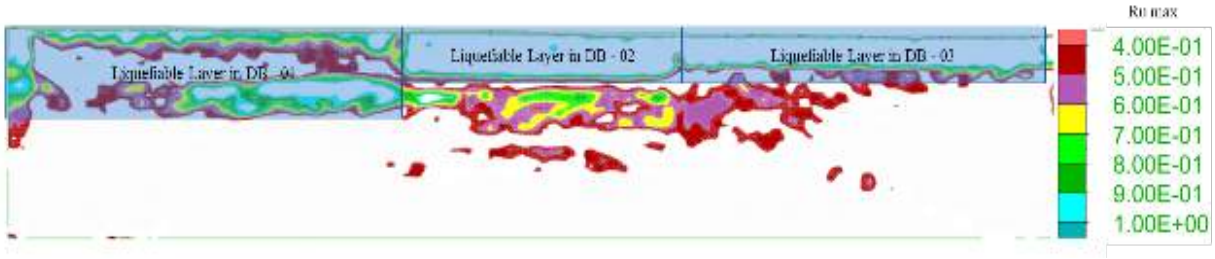

Fig. 8 Liquefaction depth from numerical analysis

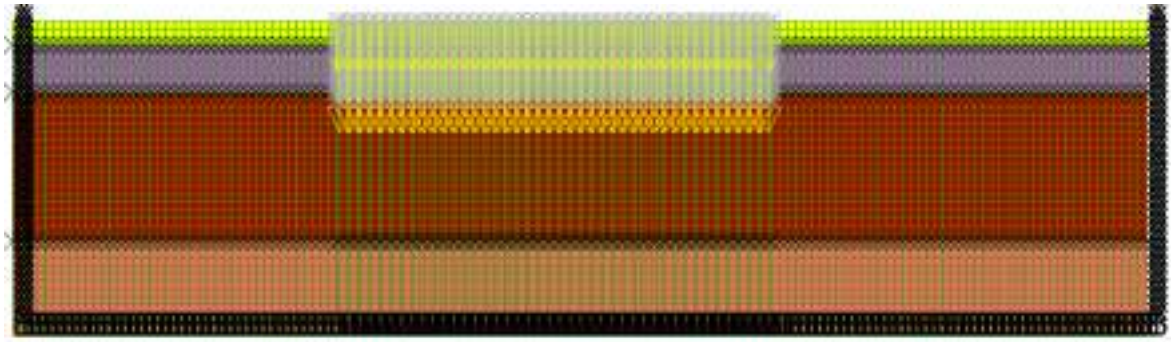

Fig. 9 Rigid Inclusion Model in FLAC 2D

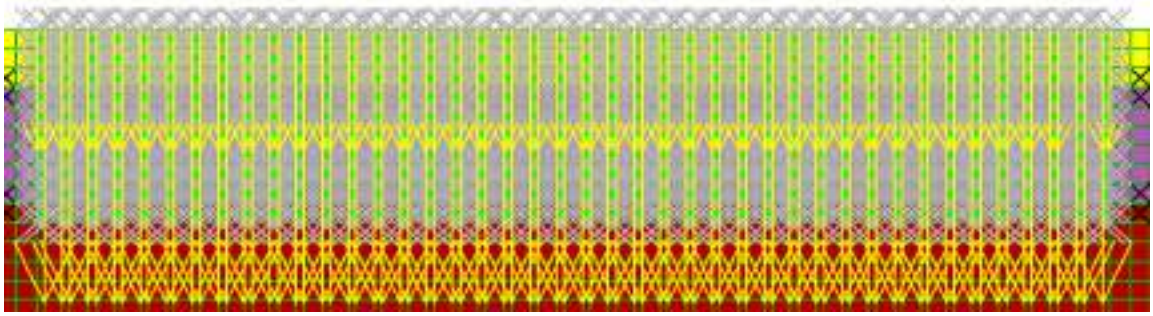

Fig. 10 Rigid Inclusion Model detail in FLAC 2D

Fig. 11 Excess Pore Pressure after earthquake

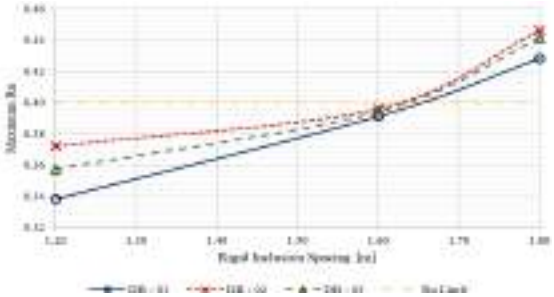

Fig. 12 Variation between R_u and rigid inclusion spacing

CONCLUSIONS

Based on the conducted analysis, the following conclusions can be made.

a. Soil investigation results indicated that Banyuwangi Airport was prone to liquefaction
b. Conventional liquefaction analysis using 500-year return period PGA and NCEER method shows liquefied layer was 20 m depth.

c. PSHA and Dynamic analysis using FLAC 2D showed that the liquified layer depth could be reduced from 20 m to 17 m.
d. Rigid inclusion with 42 cm diameter and 1.6 m spacing could reduce R_u from 1.0 to 0.4 in this study.

ACKNOWLEDGMENTS

This conference paper was written based on a Nur Straits Engineering's study. The authors would like to express gratitude to NSE for financially supporting this study. The authors would be grateful to acknowledge PT. Angkasa Pura Indonesia, PT. Wijaya Karya, and PT. Bauer Pratama Indonesia for excellent project execution. Any findings, conclusion, opinion, and suggestion written in this paper belong to the authors. They may not describe the thought of the supporting institutions.

REFERENCES

[1] Seed, H.B. and Idris, I.M., A Simplified Procedure for Evaluating Soil Liquefaction, Journal of the Soil Mechanics and Foundations Division Volume 97, Issue 9, 1971, pp 1249-1273.

[2] Sahadewa, A., Irsyam, M., Hanifa, R., Mikhail, R., Pamumpuni, A., Nazir, R., Pramono, S., Sabaruddin, A., Faizal, L., Ridwan, M., Himawan, A., Simatupang, P., Alatas, I.M., Harninto, D.S., Djarwadi, D., Kartawiria, A., Djunaidy, M., Suhendra, I., Kawanda, A., and Widodo,Y., Overview of the 2018 Palu Earthquake, in Proc. of the 7th Int. Conf. on Earthquake Geotechnical Engineering, 2019, pp. 857-872.

[3] Youd, T.L., and Idriss, M.I., Liquefaction Resistance of Soils: Summary Report from the 1996 NCEER and 1998 NCEER/NSF Workshops on Evaluation of Liquefaction Resistance of Soils, 2001, pp. 1-40.

[4] ASIRI National Project, Recommendations for the design, construction and control of rigid inclusion ground improvements, Presses des Ponts et Chaussées, 2012, pp 19-27.

[5] Cubrinovski, M., Bradley, B., Wotherspoon, L., Green, R., Bray, J., Wood, C., Pender, M., Allen, J., Bradshaw, A., Rix, G., Taylor, M., Robinson, K., Henderson, D., Giorgini, S., Ma, K., Winkley, A., Zupan, J., O'Rourke, T., DePascale, G., and Wells, D., Geotechnical Aspects of The 22 February 2011 Christchurch Earthquake, 2011.

[6] Standard Test Method for Standard Penetration Test (SPT) and Split-Barrel Sampling of Soils, ASTM D1586/D1586M-18e1, ASTM International, 2022.

[7] H. Tsuchida, Prediction and Countermeasure against Liquefaction in Sand Deposits, Abstract of The Seminar of the Port and Harbour Research Insitute, Ministry of Transport, Yokosuka, 1970, pp. 3.1-3.33.

[8] H. B. Seed, I. M. Idriss, and I. Arango, Evaluation of Liquefaction Potential Using Field Performance Data, Journal of Geotechnical Engineering, ASCE, New York, vol. 109, no. 3, 1983, pp. 458–482.

[9] Indonesia National Center for Earthquake Studies, Earthquake Source and Seismic Hazard Map, ISBN 978-602-5489-01-3, Ministry of Public Works and Public Housing, 2017, pp 279-280.

[10] Itasca Consulting Group, Inc. (2011) FLAC — Fast Lagrangian Analysis of Continua, Ver. 7. Minneapolis: Itasca.

[11] Byrne, P.M., A Cyclic Shear-Volume Coupling and Pore Pressure Model for Sand, in Proceedings of Second International Conference on Recent Advances in Geotechnical Earthquake Engineering and Soil Dynamics, 1991, pp. 47-55.

Copyright © Int. J. of GEOMATE All rights reserved, including making copies, unless permission is obtained from the copyright proprietors.

15th Int. Conf. on Geotechnique, Construction Materials & Environment, Kyoto, Japan, 11-13 November 2025, ISBN 978-4-909106124 C3051

EVALUATING THE VALIDITY OF MULTI-STAGE DIRECT SHEAR TESTING ACROSS DENSITY AND FINE CONTENT VARIATIONS IN SAND–CLAY MIXTURES

María José Toledo Arcic[1], Jens Engel[1]

[1]Faculty of Civil Engineering, University of Applied Sciences Dresden (HTWD), Germany

ABSTRACT

Multi-stage direct shear testing offers a time- and material-efficient alternative to conventional single-stage procedures. However, its applicability to sand–clay mixtures with varying densities and fines content remains underexplored. This study evaluates the validity of three multi-stage methods, (MSA) maintaining shear displacement, (MSB) full displacement reset, and (MSC) partial release by reverse shearing until near-zero shear stress, across a set of binary mixtures of sand and clay. Six mixtures with fines contents ranging from 10% to 75% were prepared and compacted to medium-dense to dense states using the standard Proctor method. For each mixture, single-stage and multi-stage direct shear tests were performed under normal stresses of 100, 200, and 400 kPa. Results show that all multi-stage methods yield comparable shear strength parameters to single-stage tests in fine-dominant mixtures and low-density states. In transitional and dense mixtures, however, MSB systematically overestimates the friction angle due to cumulative strain effects, while MSA tends to underestimate it, especially in strongly dilative mixtures, but compensates by higher apparent cohesion. MSC provides a balanced response, closely matching the single-stage reference across most cases. The results also confirm a clear behavioral shift from dilative to contractive with increasing fines content, particularly evident around the transitional zone (25–35 % fines content). This study demonstrates that multi-stage testing can be reliably applied to sand–clay mixtures if method selection considers both fines content and state. The findings provide practical guidance for geotechnical laboratories aiming to optimize resources without compromising accuracy in shear strength evaluation.

Keywords: Multi-Stage Direct Shear Tests, Sand–Clay Mixtures, Fines Content, Shear Strength Parameters

INTRODUCTION

Conventional direct shear testing requires two or three independent single-stage tests to determine the shear strength parameters of soils. While this approach is well established, it is both time- and material-intensive, particularly for granular or mixed soils, which require large specimen dimensions and specific sample preparation methods. As an alternative, multi-stage direct shear tests allow several shearing phases to be performed sequentially on the same specimen under controlled normal stress, reducing the overall testing time and material demand, and maximising the amount of shear strength information obtained from a single specimen [1].

Despite the advantages, multi-stage testing has not yet been standardised for all soil types. Most existing studies focus on coarse or fine-grained soils, with limited evaluation in mixed materials, particularly in sand–clay mixtures. In such mixtures, the mechanical behaviour varies significantly with the fines content and state, potentially affecting the validity of multi-stage methods.

The present study investigates whether multi-stage direct shear procedures can reliably determine peak shear strength in sand–clay mixtures with different fines contents. Three procedural variants are considered: one preserving shear displacement between shear phases, one with complete displacement reset, and one with partial release. The aim is to provide practical insight into the applicability of these methods by testing binary mixtures compacted to medium-dense and dense conditions.

In this study, the term *state* refers to the initial density condition, expressed as the Proctor compaction ratio D_{pr}, with values of approximately 90% and 100% corresponding to medium-dense and dense states, respectively.

RESEARCH SIGNIFICANCE

This study contributes to the ongoing evaluation of multi-stage direct shear methods by focusing on sand–clay mixtures. By isolating the effects of fines content and state, the research provides a clearer understanding of how multi-stage methods perform in mixed-grained soils. The findings support the development of practical guidelines for method selection, especially when the available sample quantity is not sufficient for several single-stage tests. Moreover, the study clarifies the conditions under which multi-stage methods provide reliable estimates of shear strength, especially in transitional and fine-dominant mixtures.

MATERIALS AND METHODS

Soil Mixtures

Six sand–clay mixtures (MIX 1 – MIX 6) were prepared with fines contents of 10 %, 25 %, 35 %, 45 %, 55%, and 75 %. The sand used in this study is a uniformly graded 0/2 mm sand (SE according to DIN 18196). Based on its narrow grain size distribution and negligible fines content, it is classified as SP (poorly graded sand) according to ASTM D2487 (USCS). The clay fraction consisted of a low-plasticity natural clay. The particle size distributions of the mixtures are shown in Fig. 1.

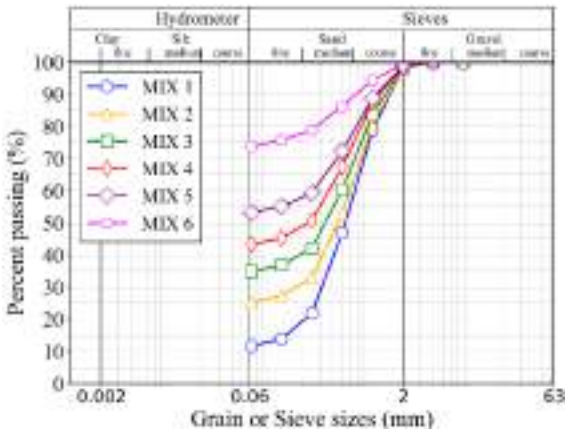

Fig.1 Grain size distribution of the tested mixtures

All materials were oven-dried and sieved prior to mixing. The physical properties of the individual soil fractions are summarised in Tables 1 and 2. These parameters were later used to assess the dominant fraction (coarse, transitional or fine) according to the revised soil classification system (RSCS) proposed by Park and Santamarina [2].

Table 1 Soil properties of tested sand

Fraction	G_S [-]	e_c^{max} [-]	e_c^{min} [-]
Sand	2.654	0.870	0.484

G_S: specific gravity of the solid particles; e_c^{max}: maximum void ratio, e_c^{min}: minimum void ratio.

Table 2 Soil properties of tested clay

Fraction	G_S [-]	LL [%]	$e_F^{(10kPa)}$ [-]	$e_F^{(1MPa)}$ [-]	$e_F^{(flow)}$ [-]
Clay	2.653	32.7	1.084	0.407	1.449

G_S: specific gravity of the solid particles; LL: liquid limit, $e_F{}^{(10\,kPa)}$: void ratio of fines in soft conditions, $e_F^{(1MPa)}$: void ratio of fines in stiff conditions, $e_F^{(flow)}$: void ratio of fines in flow conditions. $e_F^{(flow)} = \lambda \cdot e_F{}^{LL} = [2 \cdot log \cdot (LL - 25)] \cdot e_F{}^{LL} \approx 0.05 \cdot LL \cdot log(LL - 25)$, where $e_F{}^{LL}$: void ratio of fines at the liquid limit, and $\lambda = \geq 1.0$ [2].

Sample Preparation

Each mixture was compacted to a target state (D_{pr}) using its respective Proctor density as reference. The samples were prepared in a shear box with a cylindrical specimen cavity. The internal diameter of the cavity was 60 mm, corresponding to an effective area of 28.27 cm². The specimen height was 19.92 mm, resulting in a total specimen volume of approximately 56.3 cm³. Each mixture was compressed to approximately 90 %, 95 %, and 100 % of the maximum dry density determined from Standard Proctor tests (see Fig. 2). Static compaction was applied in three layers, resulting in a soil structure that differs from specimens compacted using the Proctor method. All specimens were compacted at the optimum water content determined from Standard Proctor tests, resulting in an initial degree of saturation between approximately 50 % and 80 %, depending on the target dry density. All specimens were then saturated prior to testing.

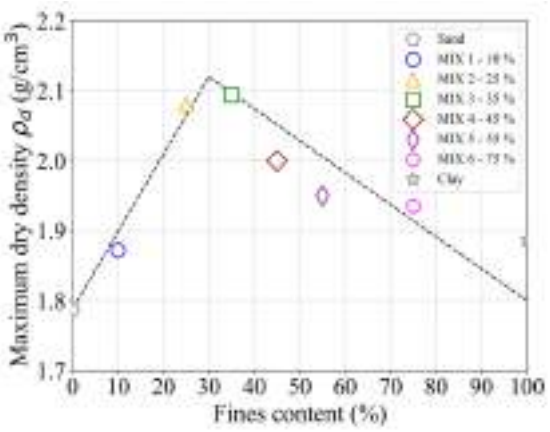

Fig.2 Maximum dry density of the tested mixtures

Shear Testing Methods

Direct shear tests were conducted under vertical normal stresses of 100 kPa, 200 kPa, and 400 kPa. Three multi-stage methods were applied, as illustrated in Fig. 3:

- MSA: No displacement reset; the shear displacement is preserved between phases.
- MSB: Full reset; the displacement is returned to zero before the next phase.
- MSC: Partial release; reverse shearing is applied until the shear stress reduces to <1 kPa.

For reference, conventional single-stage tests were also conducted on each mixture under the same stress levels. All tests were performed under drained conditions, with a horizontal displacement rate of 0.04 mm/min.

CLASSIFICATION OF THE MIXTURES ACCORDING TO RSCS

To determine the classification of the sand–clay mixtures, the threshold fines contents were calculated using the gravimetric–volumetric relationships proposed in the RSCS framework [2]. The theoretical fines fraction F_F is estimated as:

$$F_F = \frac{e_C}{1 + e_C + e_F} \quad (1)$$

Where e_C and e_F represent the void ratios of the coarse (sand) and fine (clay) fractions, respectively. For this study, the maximum and minimum void ratios of the sand were $e_C^{max} = 0.870$ and $e_C^{min} = 0.484$, while the clay void rations were $e_F^{(10kPa)} = 1.084$ (soft condition) and $e_F^{(1MPa)} = 0.407$ (stiff condition). All values were obtained from laboratory tests. Using these values, the lower threshold fines content (dense coarse + loose fines) is $F_{F,L} = 18.8$ % and the upper threshold (loose coarse + dense fines) is $F_{F,H} = 38.2$ %. This theoretical approach was used to assign the RSCS-based classification shown in Table 3.

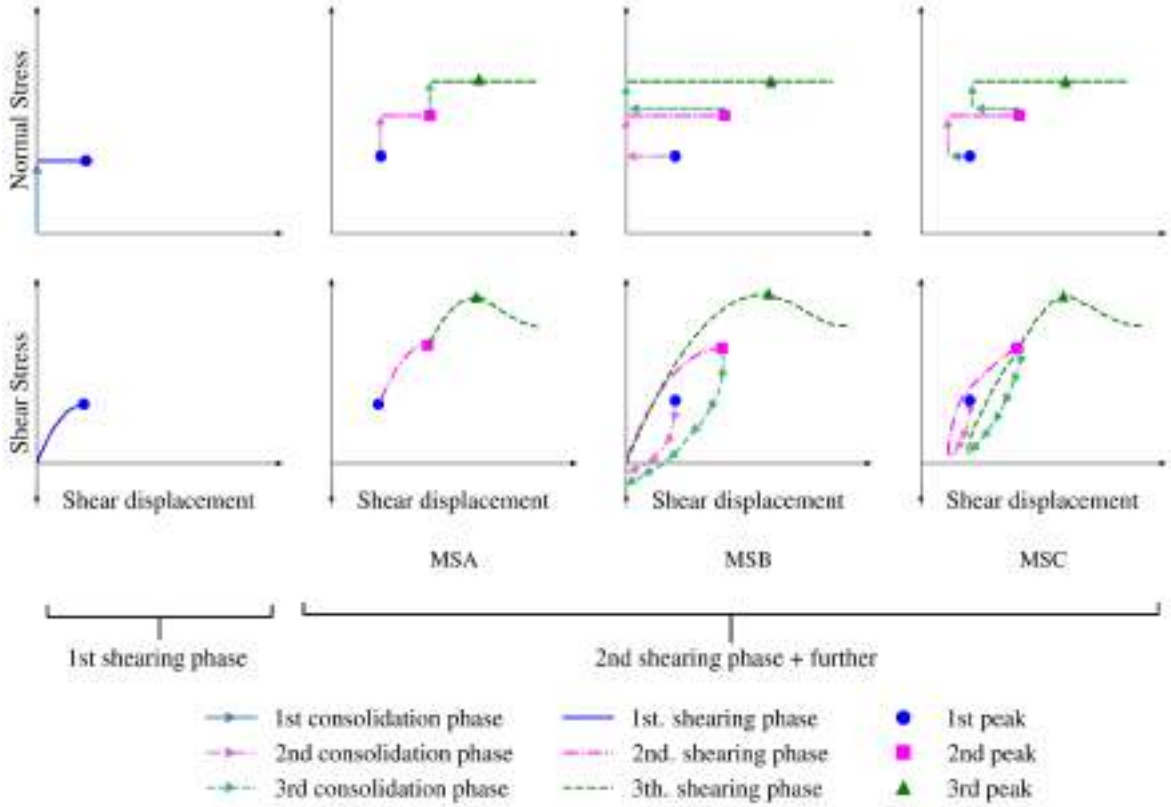

Fig.3 Schematic representation of the multi-stage direct shear methods used in this study (MSA, MSB, MSC)

Table 3 RSCS-based classification of the tested sand–clay mixtures

Mixture	Fines Content (%)	RSCS Classification
MIX 1	10	Coarse-dominant
MIX 2	25	Transitional
MIX 3	35	Transitional
MIX 4	45	Fine-dominant
MIX 5	55	Fine-dominant
MIX 6	75	Fine-dominant

RESULTS AND DISCUSSION

Influence of fines content on shear behaviour

Figure 4 shows the influence of fines content on the normalised peak shear strength τ_{peak}/σ'_N for direct shear tests conducted at $\sigma'_N \approx 100$ kPa. The results show two distinct trends depending on the

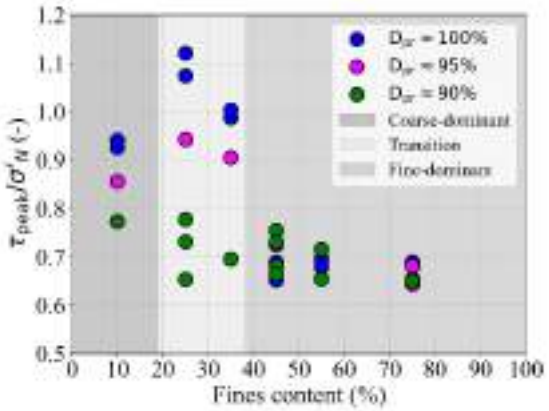

Fig.4 Normalised peak shear strength vs. fines

content at $\sigma'_N \approx 100$ kPa state of the specimens. In the dense state, the normalised shear strength increases with fines content up to approximately 25 %, reaching a maximum within the transitional zone. This behaviour is attributed to fines filling the voids between sand grains and participating in load transfer, reaching the peak of the cushioning effect, where both shear strength and dilatancy are maximised. Beyond this threshold, the shear strength decreases progressively, approaching the reference strength of the compacted fine-grained soil. This decline reflects the breakdown of the coarse grain skeleton, caused by excess fines interfering with interparticle contacts and weakening the load-bearing structure. This trend is consistent with the assumption that, in dense mixtures, fines initially enhance interparticle friction and restrict particle movement, until they become dominant and govern the overall mechanical response. In contrast, the medium-dense specimens ($D_{pr} \approx 90$ %) exhibit a continuous decrease in shear strength with increasing fines content. This supports the hypothesis that, in loosely to medium-dense packed sand–clay mixtures, fines do not contribute effectively to load transfer, unless they form a continuous matrix as in pure fine-grained soils. However, the fine-grained soil used in this study (LL = 32.7%) did not exhibit apparent cohesion under saturated conditions, even at $D_{pr} \approx 100$ %, indicating that no significant interparticle bonding was present. As a result, the resistance decreases progressively and tends to stabilise beyond the fines-dominant threshold.

Influence of fines content on Dilatancy

Figure 5 shows the evolution of the dilatancy angle ψ with increasing fines content for three states.

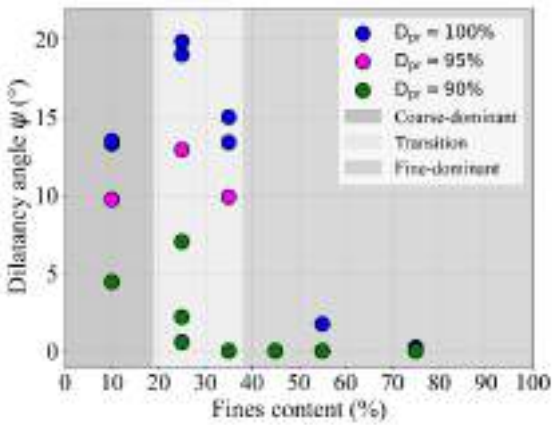

Fig.5 Dilatancy angle ψ vs. fines content at $\sigma'_N \approx 100$ kPa

In dense specimens ($D_{pr} \approx 100$ %), dilatancy peaks in the transitional mixtures (25-35% fines content), where interlocking is maximised and fines contribute to shear resistance without dominating the structure. As fines content increases beyond the range, the behaviour becomes increasingly contractive, leading to a sharp reduction in dilatancy angle. Specimens compacted to $D_{pr} \approx 90$ % show minimal dilatancy across all fines contents, indicating a contractive response consistent with loose packing. The intermediate state ($D_{pr} \approx 95$ %) exhibits a response closer to the dense condition, with a clear dilatancy peak around 30 % fines and a similar transition toward contractive behaviour at higher fines content. These results confirm that transitional mixtures exhibit the strongest dilative behaviour under dense conditions.

Influence of fines on the critical state angle of friction

To further understand the critical shear strength of the tested sand–clay mixtures, the critical state friction angle φ'_{cv} was determined for each mixture using all available data from multi-stage tests. As shown in Fig. 6, the critical state friction angle exhibits a non-monotonic trend: it decreases initially in coarse-dominant mixtures due to reduced interlocking, increases in the transitional zone as fines fill the voids, and then stabilises in fine-dominant mixtures where the clay matrix governs the shear resistance.

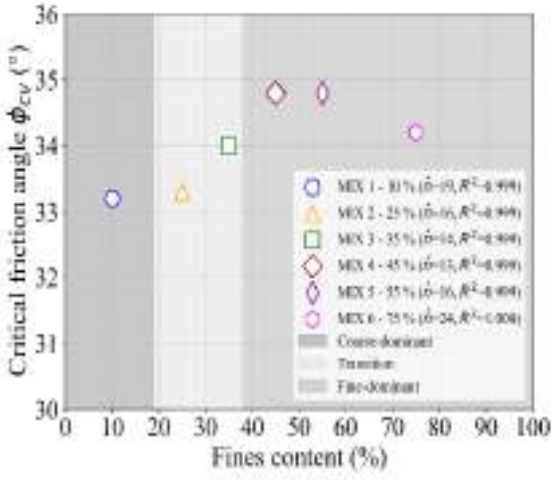

Fig.6 Critical state friction angle φ'_{cv} vs. fines content. The legend indicates the number of tests ($\hat{n}$) used for the determination of each angle

This evolution pattern aligns with the findings of previous studies [3–6], which reported similar behavior in binary mixtures of graded sands, and supports the soil classification scheme adopted in this work. The distinction between coarse-, transitional-, and fine-dominant mixtures based on fines content is thus further justified by their distinct mechanical

responses at critical state.

Influence of the multi-stage method

Beyond the intrinsic effects of fines content on shear behavior, the suitability of the testing method itself depends on the mechanical response of the soil. In particular, multi-stage and single-stage shear tests may yield different outcomes depending on the fines content, density, and structural behavior of the mixture. The analysis evaluates the consistency and capacity of each method to reproduce the reference shear resistance from single-stage tests.

Comparison of peak shear strength

To assess the effect of the testing method on the measured peak shear strength, the results from the last loading phase at $\sigma'_N \approx 400$ kPa were evaluated for all mixtures and methods. Figure 7 shows the relative deviation of the peak shear stress obtained from multi-stage methods (MSA, MSB, MSC) compared to the single-stage reference (SS), for $D_{pr} \approx 100$ % and $D_{pr} \approx 90$ %. The relative deviation is calculated as:

$$\text{RD}\ (\%) = \frac{\bar{\tau}_{p,\text{method}} - \bar{\tau}_{p,SS}}{\bar{\tau}_{p,SS}} \cdot 100 \qquad (1)$$

where $\bar{\tau}_{p,\text{method}}$ is the peak shear stress obtained with the corresponding multi-stage method, and $\bar{\tau}_{p,SS}$ is the peak value from the equivalent single-stage test.

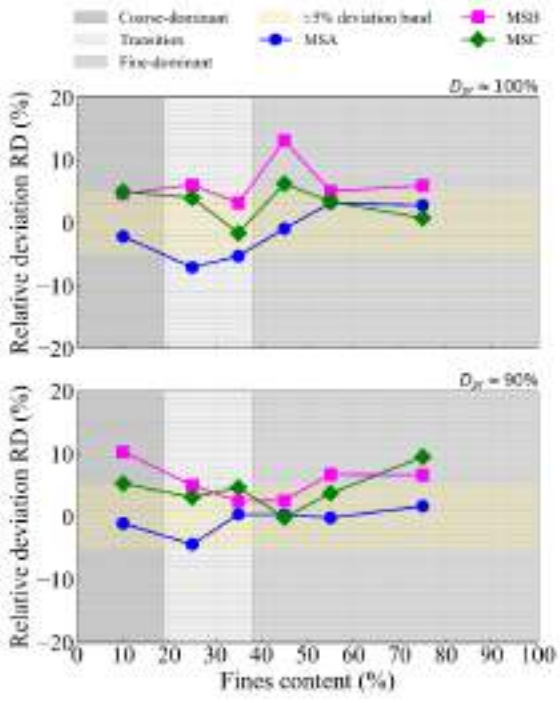

Fig.7 Relative deviation (RD) of peak shear strength from multi-stage vs. single-stage tests, for $D_{pr} \approx 100$ and $D_{pr} \approx 90\%$

In both states, method MSB consistently overestimates the peak shear strength across all mixtures, with relative deviations exceeding 5 % in most cases. In contrast, method MSA tends to underestimate the peak shear strength in transitional mixtures (25% - 35% fines), consistent with previous findings for a mixed-grained soil compacted to $\mathbf{D_{pr} \approx 97}$% [7]. The strongest under-estimation occurs at 25 % fines under dense conditions, where dilation and peak strength are most pronounced (see Fig. 5). In this case, the combination of transitional fines content and strong dilative behaviour appears to increase the sensitivity to accumulated disturbance in MSA. As shown in Fig. 8, this mixture also exhibits a marked loss of dilatancy with increasing stress. While this is partly due to barotropic effects, method MSA appears to further supress dilatancy and reduce the mobilised strength. In fine-dominant mixtures, MSA yields slightly higher strength values, with deviations below 5%. In the medium-dense state ($\mathbf{D_{pr} \approx 90}$ %), the underestimation in MSA is less pronounced or absent. In this state, MSC shows increasing deviation with fines content, while MSB continues to overestimate across all mixtures.

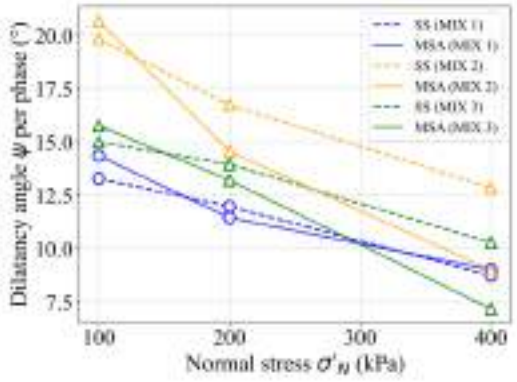

Fig.8 Evolution of dilatancy angle ψ' with increasing normal stress for single-stage (SS) and multi-stage (MSA) tests. Samples compacted to $\mathbf{D_{pr} \approx 100}$%

Comparison of shear strength parameters

The differences in effective friction angle (Δφ') and cohesion (Δc') between multi-stage and single-stage tests are shown in Figures 9 and 10. Values were obtained from shear stresses at failure under $\boldsymbol{\sigma'_N} =$ 100, 200 and 400 kPa. For Δφ', deviations range from -4° to +3° across methods and mixtures. Under $\mathbf{D_{pr} \approx 100}$ %, MSB shows the highest positive deviation at 45% fines, while MSA underestimates the angle, particularly in transitional mixtures (25–35 %). MSC yields positive deviations in fine-dominant mixtures, ranging from -0.2° to +1.6°, with larger differences observed at $\mathbf{D_{pr} \approx 90}$ %. For Δc', MSA shows increases above +10 kPa in mixtures under $\mathbf{D_{pr} \approx 100}$%, particularly for 10, 25 and 35% fines. This coincides with the underestimation of φ', which may be partially compensated by an apparent cohesion.

However, this cohesion could be influenced by device-related effects and boundary conditions. At $\mathbf{D_{pr}} \approx \mathbf{90}$ %, cohesion becomes negligible in both single-stage and multi-stage tests for these mixtures, and MSA yields consistent parameters. MSB shows negative Δc' values in transitional mixtures, while MSC remains close to the single-stage reference across all fines contents.

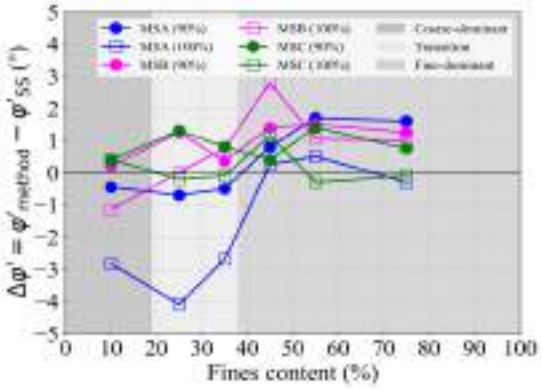

Fig.9 Difference in friction angle Δφ' between multi-stage and single-stage (SS) tests

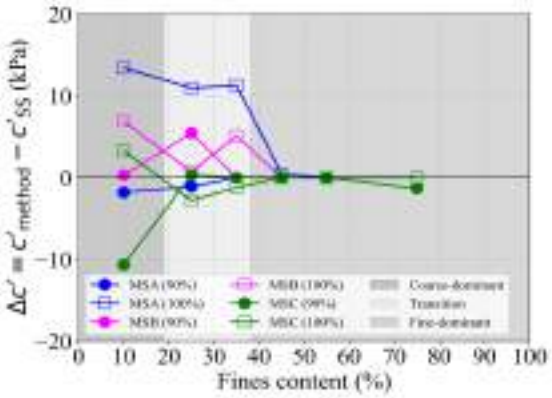

Fig.10 Difference in cohesion Δc' between multi-stage and single-stage (SS) tests

CONCLUSIONS

This study assessed the effect of three multi-stage direct shear methods (MSA, MSB, MSC) on the shear strength parameters of sand–clay mixtures with varying fines content and state. The main findings are:

- Method MSA understimates the friction angle in transitional mixtures (25, 35%) under dense conditions, but yields higher cohesion, partially compensating the reduced shear strength. In the medium-dense state, MSA aligns closely with single-stage results for all mixtures.
- MSB consistently overestimates the friction angle across all mixtures. At $\mathbf{D_{pr}} \approx 90$ %, it also overestimates cohesion in coarse and transitional mixtures, leading to increased shear strength. At $\mathbf{D_{pr}} \approx 100$ %, cohesion differences are smaller, but the friction angle remains higher than the reference, resulting in systematic overestimation of peak shear strength across all fines contents.
- Method MSC shows deviations under dense conditions but provides stable and reliable results at lower densities across all mixtures.
- Deviations in cohesion are more sensitive to the testing method than the friction angle, particularly in dense and transitional mixtures.
- For fine-grained dominated mixtures, all methods produce friction angles within ±2° of the single-stage reference under dense conditions.
- No single method is universally optimal. Its suitability depends at minimum on fines content and state, with additional influence from the soil's tendency toward dilation or contraction.

ACKNOWLEDGMENTS

The Federal Ministry for Economy Affairs and Climate Action BMBF (Project number 49VF230003) and Bank of Saxony SAB (Project number 100604731) supported this research financially.

REFERENCES

[1] D. Hormdee, N. Kaikeerati and P. Angsuwotai, Evaluation on the results of multistage shear test, Int. J. GEOMATE, 2012, vol. 2, pp. 140-143.

[2] Park, J., Castro, G.M., Santamarina, J.C.: Closure to "revised soil classification system for course-fine mixture", J. Geotech. Geo-environ. Eng. 144(8), 1‑13 (2018)

[3] Vallejo L.E., Interpretation of the limits in shear strength in binary granular mixtures, Can. Geotech. J., Vol. 38, No. 5, 2001, pp. 1097–1104.

[4] Kwa K.A. and Airey D.W., Critical state interpretation of effects of fines in silty sands, Géotechnique Letters, Vol. 6, No. 1, 2016, pp. 100–105.

[5] Polito C.P. and Sibley E.L.D., Threshold fines content and behavior of sands with nonplastic silts, Can. Geotech. J., Vol. 57, No. 3, 2020, pp. 462–465.

[6] Yilmaz Y., Deng Y., Chang C.S., and Gokce A., Strength–dilatancy and critical state behaviours of binary mixtures of graded sands influenced by particle size ratio and fines content, Géotechnique, Vol. 71, No. 10, 2021, pp. 938–960.

[7] Toledo Arcic, M. J. Comparison of different methods for conducting multistage direct shear tests, Proceedings of the 10th World Congress on Civil, Structural, and Environmental Engineering, Barcelona, Spain, 2025.

Copyright © Int. J. of GEOMATE All rights reserved, including making copies, unless permission is obtained from the copyright proprietors.

15th Int. Conf. on Geotechnique, Construction Materials & Environment,
Kyoto, Japan, 11-13 November 2025, ISBN 978-4-909106124 C3051

UNCONFINED COMPRESSIVE STRENGTH OF RIVER-DREDGED SOIL STABILIZED WITH ZEOLITE-BASED GEOPOLYMER

Jonathan R. Dungca[1], Roberto Gabriel A. Bas[2], Chris Anthony C. Elhig[2] and Dana Isabelle P. Villano[2]

[1]Faculty, De La Salle University, Philippines; [2] Student, De La Salle University, Philippines

ABSTRACT

This study explores the potential of zeolite-based geopolymers as stabilizers for river-dredged soil. Using a zeolite sourced in the Philippines and hydroxide and sodium metasilicate pentahydrate as alkali activators, this study investigated the increase in shear strength of the river-dredged sand with varying amounts of zeolite-based geopolymers. Unconfined compressive strength (UCS) tests reveal that higher zeolite concentrations generally improved the shear strength over varying curing periods. Specifically, a geopolymer concentration of 20% was determined to be ideal for curing periods of 7 to 28 days, whereas a 30% concentration exhibited superior UCS values and stability for periods exceeding 90 days. Scanning Electron Microscope (SEM) analysis also confirmed enhanced microstructural integrity with increased zeolite content. These findings indicate the increase in the unconfined compressive strength of dredged soil using zeolites as aluminosilicate precursors, thus producing a viable alternative for soil stabilization.

Keywords: Soil stabilization, Geopolymer, Zeolite, River-dredged soil, Unconfined compressive strength

INTRODUCTION

Geopolymers have emerged as a promising and sustainable alternative to traditional cementitious materials, particularly as a substitute for commercially available ordinary portland cement (OPC). Geopolymers, also known as alkali-activated materials (AAMs), have demonstrated the potential to reduce embodied carbon by nearly 80%, alongside a decreased impact on global warming and eutrophication (excessive plant and algal growth) (Almutairi et al., 2021). However, these benefits vary significantly depending on factors such as the aluminosilicate precursor, alkali activator, and the processes involved in the collection and processing of raw materials. The chemical composition of the aluminosilicates used is critical in developing effective and sustainable geopolymers. Therefore, further research into optimizing the combination of activators and precursors to enhance both performance and environmental sustainability is a valuable endeavor, particularly in soil stabilization, where the application of geopolymers has been relatively underexplored (Ayub & Khan, 2023).

Among the potential aluminosilicate precursors for geopolymers, zeolites—naturally occurring crystalline aluminosilicate materials with a porous molecular structure—stand out as promising candidates. Previous studies, such as those conducted by Villa et al. (2010) and Nikolov et al. (2017), have demonstrated the feasibility of using zeolites in geopolymerization and their effectiveness in various applications, including concrete, mortars, and plasters. However, due to the emerging nature of zeolite-based geopolymers, literature on their use, particularly for soil stabilization, remains limited. Given that zeolites are minimally processed natural materials, they produce fewer carbon dioxide emissions during mining and production compared to conventional soil stabilizers like OPC. Additionally, zeolites are considered "environmentally neutral," making them a promising alternative for environmentally friendly construction materials (Rożek, Król, & Mozgawa, 2019).

Dredged soil, commonly encountered at construction sites, is a type of loose particulate material comprising clay, silt, and sand. It results from natural erosion, weathering, or anthropogenic activities that disturb the environment. Typically treated as waste, dredged soil is often disposed of in the sea or on land, with disposal costs reaching up to 20% of the total dredging expenses (Chan, 2014). Furthermore, the dumping of dredged material can adversely affect neighboring flora and fauna (Cruz-Motta & Collins, 2004, as cited in Chan, 2014). Improving the properties of dredged soil through stabilization offers a promising area of research, as demonstrated in Dungca's 2019 study on soil dredged from a heavily silted river in Mindanao. This approach reduces the volume of material sent to dumping sites and landfills, thereby transforming a perceived liability into a valuable resource for environmental enhancement.

Thus, given the presence of naturally occurring zeolite deposits across various regions, the development of a zeolite-based geopolymer for the stabilization of dredged soil using the wet mixing

method emerges as an important and timely subject for investigation (Dignos, Gabejan, Olegario-Sanchez, & Mendoza, 2019).

The objective of this study was to develop a zeolite-based geopolymer as a stabilizer for dredged soil, utilizing solid activators, specifically sodium hydroxide and sodium metasilicate.

RESEARCH METHODOLOGY

Materials

Dredged Soil

The dredged soil was obtained from the Carmona River at the boundary of the cities of Biñan and Sta. Rosa, in the Philippines. This soil was oven-dried in batches before testing to ensure consistency in the results.

Zeolite

The natural zeolites were obtained from a zeolite mine located in Mangatarem, Pangasinan, Philippines. The study of Olegario and Pelicano in 2017 characterized this zeolite source in its structure, chemical composition, and adsorption characteristics, and they have found that the zeolite is mainly composed of heulandite with other crystalline mineral phases such as clinoptilolite, mordenite, and quartz. The have also observed that the zeolite has plate-like structures with rough surfaces and micro-pores. Table 1 shows the oxide composition of the zeolite from their study.

Table 1 Zeolite chemical composition (Olegario and Pelicano, 2017)

Compound	Oxide
SiO_2	73.20
AL_2O_3	10.72
Na_2O	0.99
CaO	3.84
Fe_2O3	4.05
TiO_2	0.45
MgO	4.34
K_2O	0.36

Alkali Activator

The alkali activator used consists of caustic soda (sodium hydroxide) and sodium silicate in dry powder form, wherein the solution form of the alkali activator mix for the geopolymerization process was achieved with the later addition of water.

Geopolymer Mixture

In creating the geopolymer paste, the dry alkali activator, consisting of powdered sodium hydroxide and powdered sodium silicate, was first mixed. The powdered zeolites were then added to the mixture. To achieve the desired 8M concentration of sodium hydroxide, an adequate measure of water was added, where specified liters per specified grams of sodium hydroxide was set. The resulting geopolymer mixtures were prepared for varying soil-to-geopolymer mix ratios.

Characterization of Geotechnical Properties of Dredged Soil

The index and mechanical properties of the dredged soil were examined per the ASTM standards using the following tests:

a) Particle Size Analysis (ASTM D422)
b) Specific Gravity (ASTM D854)
c) Atterberg Limits (ASTM D4318)
d) Standard Proctor Test (ASTM D698)
e) Unconfined Compressive Strength Test (ASTM D 2166)

Experimental Design

Geopolymer mixtures were operationally defined as the mix design between the alkali activator and precursor material to create the geopolymer paste. The sodium silicate to sodium hydroxide ratio was 1.5 (Villa et al., 2010), the sodium hydroxide concentration was 8M (Nikolov et al., 2017), and the alkali activator to zeolite precursor mass ratio was 0.6 (Villa et al., 2010).

The geopolymer-stabilized soil was defined to be the mix design between the dredged soil and the geopolymer paste in geopolymer percentages of 100%, 10%, 20%, and 30% similar to Dungca et al. (2019). Ambient curing was implemented in the resulting samples, with the results of the UCS tests recorded on the 7th, 14th, 28th, and 90th days. Note that this experimental design was based on the study of Villa et al. (2010).

Batches were assigned based on geopolymer percentages in the samples, namely 10%, 20%, 30%, and 100% respectively. Three UCS samples were tested for each batch per curing day.

Mix Design for Soil-Geopolymer Mix

The parameters to determine the required mass for each of the geopolymer mixtures were identified. These parameters are the specific gravity of the dredged soil, zeolites, sodium hydroxide, sodium

metasilicate pentahydrate, and water. The mass density (kg/m³) of the materials were then computed and shown in Table 2.

Table 2 Mix design Parameters

Material	Specific Gravity, Gs	Mass Density (Kg/m^3)
Dredged Soil	2.65	2650
Zeolites	2.20	2200
NaOH	2.13	2130
Na_2SiOH_3	1.75	1750
Water	1.00	1000

The volumes of the UCS molds were subsequently determined. The mass of each ingredient in the mix design was then proportionally determined from the ratio of the total batch volume to the respective unit volume per kilogram of each ingredient.

The alkali activator consisted of a mix of sodium silicate and sodium hydroxide. In calculating the formulation of sodium hydroxide, caustic soda powder was mixed with the amount of water required for the solution to reach the target molarity (8M). As sodium hydroxide has a molar mass of 40 grams, the target mass of caustic soda per 1 liter or 1000 grams of caustic soda solution was computed as eight times the molar mass, or 320 grams. On the other hand, a molarity of 6M was determined for the sodium metasilicate pentahydrate solution. As sodium metasilicate pentahydrate has a molar mass of 212.137 grams, the target mass of the pellets per 1 liter or 1000 grams of sodium silicate solution was computed as six times the molar mass, or 1270 grams. The mass of sodium silicate solution in 6M was then calculated as 1.5 times the mass of the sodium hydroxide in 8M, as based on Villa et al. (2010).

The geopolymer mix proportion was then calculated following the study of Villa et al. (2010). The mass ratio of the alkali activator (AA) to the zeolite precursor was computed as 0.6. The amount of sodium hydroxide presented in Table 3 was later determined as the combined mass of the caustic soda powder and water. Lastly, a moisture content of 18.99% was added to the mix for the dredged soil to achieve its ideal moisture content. The four soil-geopolymer batches were then differentiated based on the geopolymer percentages, namely 10%, 20%, 30%, and 100% based on Dungca et al. (2019).

Table 3 Mix Design Ratio

NaOH solution/Na2SiO3 solution	1.5
Alkali activator/Zeolite	0.6
NaOH pellets per water (kg/L)	0.32
Na2SiO3 pellets per water (kg/L)	1.27
OMC (%)	18.99%
NaOH solution/Na2SiO3 solution	1.5

Strength Tests

Unconfined Compression Test

The unconfined compression test was used to determine the shear strength of the geopolymer-stabilized soil sample. In this test, a cylindrical soil sample was axially loaded until failure occurred.

Specific percentages of the prepared zeolite-based geopolymer paste were thoroughly mixed with the dredged soil specimens at ideal moisture content. The resulting soil-geopolymer mixes were prepared through the following steps for the UCS test.

(1) The molds for the soil specimens were first prepared using PVC tube with a diameter of 50 mm (1.97 in) and a height of 100 mm (3.94 in). The height-to-diameter ratio was kept at 2;
(2) The soil-geopolymer mixes were then placed and compacted in the cylindrical PVC mold with 12 blows each for 5 layers;
(3) The sealed specimens were kept in ambient temperatures for specific curing periods (7 days, 14 days, 28 days, and 90 days).

After curing the specimens for the specified time per batch, the test specimens were then placed in the loading device for testing. Load was applied to the samples to produce an axial strain rate of 0.5% to 2% per minute. The value of UCS and the stress-strain curve of the soil-geopolymer mixes were obtained using the recorded load, deformation, and time values.

Microstructural Analysis

Scanning Electron Microscopy (SEM) was used to produce high-resolution images of the sample for better visualization of the microstructure of the geopolymer-stabilized soil. With this imaging technique, the morphology, size, and distribution of the individual phases or particles in the geopolymer matrix were closely examined. The information obtained from the SEM revealed critical information regarding the reactivity of the precursors and their implications in optimizing the formulation of the geopolymer.

Coefficient of Variation Analysis

Regression analyses were applied to determine the relationship between the dependent and independent variables. In this study, the dependent variables are the UCS values (kPa), while the

independent variables are the geopolymer concentration (%) and curing days. The choice of model order (linear regression for geopolymer concentration, and power regression for curing days) was made by examining the coefficient of determination (R^2) value. The models with the highest R^2 value were selected as the best fit for the data points.

To validate the data, the coefficient of variation (%) was obtained by dividing the standard deviation by the average of the UCS values obtained. These values were classified into their corresponding precision levels, which also translates to their degree of stability, where lower coefficients correspond to higher precision levels and stability, and higher coefficients correspond to lower precision levels and stability.

RESULTS AND DISCUSSION

Geotechnical Properties

The results obtained from conducting the following geotechnical tests on the dredged soil samples in accordance with their corresponding ASTM standards are summarized Table 4.

Table 4 Geotechnical properties of dredged soil samples

USCS Soil Classification	Poorly Graded Sand (SP)
Specific Gravity	2.65
Liquid Limit	N/A
Plasticity Index	N/A
Moisture Content	18.99%
Maximum Dry Unit weight	15.78 kPa
UCS	N/A

Grain Size Distribution Curve

The grain size distribution curve (GSDC) of the three samples of dredged soil is shown in Figure 1. Based on the figures presented below, Trials 1, 2, and 3 are observed to be composed mostly of sand with some gravel.

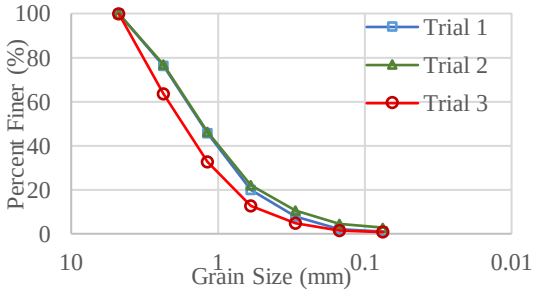

Fig.1 GSDC of the dredged samples

Compaction Behavior

Figure 2 presents the compaction curves of the dredged soil samples using the Standard Proctor Test. Three trials with at least six data points per trial were performed, and the optimum moisture content (OMC) and the corresponding maximum dry density (MDD) were calculated for each trial. The average values of the three trials, 18.99% for OMC and 15.78kN/m^3 for MDD, were used for the mix design and preparation of unconfined compression strength (UCS) samples of treated soils. The average OMC of 18.99% falls within the upper range for poorly graded sands, indicating a higher water content required for ideal compaction compared to well-graded soils. The MDD of 15.78 kN/m^3 aligns closely with typical values for similar soil classifications, reflecting the compaction ability and density achievable under standardized compaction conditions. Meanwhile, the coefficient of determination (r^2) values for each compaction curve ranged from 0.81 to 0.96 and are thus considered to have a very strong relationship between the moisture content and dry unit weight (Ridwan Aldila Melania Care et al., 2018). These values suggest reliable and consistent compaction behavior across the trials.

Table 5 indicates that the obtained OMC and MDD fall within the range typical for poorly graded sand, which is 12-21% and 15.71-18.85 kN/m^3 (Dungca et al., 2019), respectively. Generally, sandy soils have a steep compaction curve, indicating a more gradual increase in dry density with moisture content.

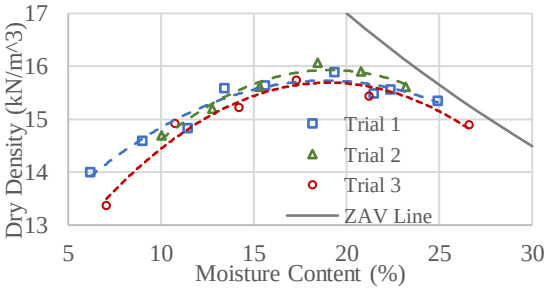

Fig. 2 Compaction curves of the dredged soils

Table 5 MDD and OMC of dredged soil.

Trial No.	OMC (%)	Max. Dry Density (kN/m^3)
1	18.86	15.73
2	19.08	15.93
3	19.04	15.69
Average	18.99	15.78

Scanning Electron Microscopy Results

The SEM micrographs in Figure 3 show the microstructural characteristics of the zeolite, dredged soil, and the soil-geopolymer samples cured in 28 days with varying geopolymer percentages. These

images provide insights into the interaction between the zeolite-based geopolymer binder and the poorly graded sand particles, and the resulting porosity.

The surface morphology of the zeolite indicates high surface area and significant porosity, which are characteristic of zeolitic materials. The jagged edges and uneven surface suggest good mechanical interlock potential, making zeolite an effective component in geopolymer formulations. The high porosity seen in the zeolite sample can contribute to enhanced reactivity and bonding when used as a binder in soil-geopolymer composites.

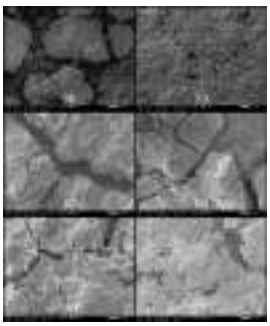

Fig.3 SEM photomicrographs of the (a) zeolite, (b) untreated dredged soil, (c) 10% geopolymer sample, (d) 20% geopolymer sample, (e) 30% geopolymer sample, and (f) 100% geopolymer samples at 1000x magnification.

The SEM photomicrograph of the untreated dredged soil reveals a more compact and less porous structure compared to the zeolite. The soil particles are more irregularly shaped and densely packed, with fewer voids and less apparent surface roughness. The texture suggests limited inherent binding capacity, as the particles do not exhibit significant interlocking features. This compactness and the presence of fewer pores indicate that untreated dredged soil alone may have lower mechanical strength and stability compared to geopolymer-stabilized samples.

The geopolymer-stabilized soil particles exhibit increased cohesion with the addition of higher concentrations of geopolymer, resulting in a general decrease in pore space. The untreated dredged soil photomicrographs suggest limited inherent binding capacity and lower mechanical strength, while the zeolite's high surface area and significant porosity serve to enhance reactivity and bonding in the geopolymer formulation, in alignment with the previously established theoretical framework. As the concentration of the geopolymer increased in the soil samples, improved bonding and integration of soil particles with the geopolymer binder were visible, leading to reduced porosity and enhanced structural integrity. These SEM observations validate the establishment of geopolymer emulsions in the soil, as no novel minerals were observed post-solidification. These findings demonstrate that the improved bonding effect of the geopolymer, particularly at increased concentrations, indeed enhances the mechanical characteristics of the original soil (Ayub & Khan, 2023).

Unconfined Compressive Strength Test Results

Figure 4 shows the relationship between consistency and UCS of soils, for samples cured at 7, 14, and 28 days, the soil mixed with 10% geopolymer concentration yielded UCS strength typically associated with very soft soil, with values ranging from 0 to 25 kPa. However, as geopolymer concentration is increased to 20% and 30%, the UCS strength noticeably improves, falling within the range of typical strength of medium soil (50-100 kPa).

Geopolymer Content	Days Cured			
	7	14	28	90
	UCS Value (kPa)			
100%	151.78	234.01	354.89	1211.57
10%	6.03	13.18	20.95	66.86
20%	51.90	54.60	76.62	143.20
30%	48.90	60.14	72.84	262.03

Fig. 4 UCS Results of zeolite-geopolymer treated soil.

Results showed that there is a significant difference among the UCS of samples with 10% geopolymer content in comparison to the samples with 20% geopolymer content across all curing day spans. Thus, the addition of geopolymer, from 10% to 20%, significantly increased the UCS of the samples.

For 7, 14, and 28 days of curing, the UCS value for the 20% geopolymer was found to be as high as the 30% geopolymer value. These observations indicate that the 20% geopolymer content represents the ideal content that produced the highest UCS value for the said curing span. Minute changes in the UCS values for samples cured at 7, 14, and 28 days were observed after reaching the ideal geopolymer content (20%).

Lastly, a significant increase in UCS from 20% to 30% geopolymer content was observed in samples

cured for 90 days. This extended curing period provided additional time for the geopolymer particles to geopolymerize and bind with the soil more fully; thus, for a curing span of 90 days, the ideal moisture content can be said to be 30%.

The difference in the ideal geopolymer content between samples with a curing span of 28 days and 90 days may be explained by the slow curing rate of Alkali-Activated cements (AAC) treated soil. The findings of Cristelo et al. (2011) established that with soil-AACs, the cementation process is slower and more gradual and durable; thus, the best strengths were achieved at 28–90 days of curing and beyond.

The stabilizing properties of the zeolite-based geopolymer were thus evidenced by the poorly graded sand developing a quantifiable unconfined compressive strength. These findings were also confirmed upon examination of the microstructure of the developed soil-geopolymer matrix as taken from the SEM results. Specifically, the increase in UCS from 10% to 20% geopolymer content can be attributed to the binding effect of zeolite-based geopolymers on the soil sample, densifying the fabric of treated soil and resulting in a more homogeneous and compact material (Sithole & Mashifana, 2020).

CONCLUSIONS

This study highlights the potential of zeolite-based geopolymers as an effective stabilizer for dredged soil. It was determined that with increasing geopolymer concentration, the dredged soil, classified as poorly graded sand, exhibited relatively consistent unconfined compressive strength values. Increased geopolymer concentrations resulted in corresponding increased UCS values.

For curing periods of 7 to 28 days, the most ideal geopolymer concentration was found to be 20%, as determined by samples with the highest UCS values and the lowest coefficients of variation. On the other hand, for curing periods longer than 90 days, the ideal geopolymer concentration was found to be 30%, which in turn had the highest UCS value and the lowest coefficient of variation.

REFERENCES

[1] Almutairi, A. L., Tayeh, B. A., Adesina, A., Isleem, H. F., & Zeyad, A. M. (2021). Potential applications of geopolymer concrete in construction: A review. Case Studies in Construction Materials, 15, e00733.

[2] Ayub, F., & Khan, S. A. (2023). An overview of geopolymer composites for stabilization of soft soils. Construction and Building Materials, 404, 133195.

[3] Chan, C. M. (2014). On the reuse of dredged marine sediments: no dumping, reuse please. In Proc. of the Intl. Conf. on Advances in Civil, Structural, Environmental & Bio-Technology--CSEB (Vol. 201).

[4] Dignos, E. C. G., Gabejan, K. E. A., Olegario-Sanchez, E. M., & Mendoza, H. D. (2019, February). The comparison of the alkali-treated and acid-treated naturally mined Philippine zeolite for adsorption of heavy metals in highly polluted waters. In IOP Conference Series: Materials Science and Engineering (Vol. 478, No. 1, p. 012030). IOP Publishing.

[5] Dungca, J. R., Ang, K. D., Isaac, A. M. L., Joven, J. J. R., & Sollano, M. B. T. (2019). Use of dry mixing method in fly ash based geopolymer as a stabilizer for dredged soil. GEOMATE Journal, 16(57), 9-14.

[6] Dungca, J. R. (2017). Fly-ash-based geopolymer as stabilizer for Silty Sand Embankment Materials. International Journal of GEOMATE, 14(46).

[7] Nikolov, A., Rostovsky, I., & Nugteren, H. (2017). Geopolymer materials based on natural zeolite. Case Studies in Construction Materials, 6, 198-205.

[8] Olegario-Sanchez, E., & Pelicano, C. M. (2017). Characterization of Philippine natural zeolite and its application for heavmost importy metal removal from acid mine drainage (AMD). Key Engineering Materials, 737, 407–411.

[9] Ridwan Aldila Melania Care, F., Sugeng Subagio, B., & Rahman, H. (2018). Porous concrete basic property criteria as rigid pavement base layer in Indonesia. MATEC Web of Conferences, 147, 02008.

[10] Rożek, P., Król, M., & Mozgawa, W. (2019). Geopolymer-zeolite composites: A review. Journal of cleaner production, 230, 557-579.

[11] Sithole, N. T., & Mashifana, T. (2020). Geosynthesis of building and construction materials through alkaline activation of granulated blast furnace slag. Construction and Building Materials, 264, 120712.

[12] Villa, C., Pecina, E. T., Torres, R., & Gómez, L. (2010). Geopolymer synthesis using alkaline activation of natural zeolite. Construction and Building Materials, 24(11), 2084–2090.

Copyright © Int. J. of GEOMATE All rights reserved, including making copies, unless permission is obtained from the copyright proprietors.

15th Int. Conf. on Geotechnique, Construction Materials & Environment,
Kyoto, Japan, 11-13 November 2025, ISBN 978-4-909106124 C3051

A STUDY ON THE METHOD OF ESTIMATING THE BEARING CAPACITY OF TAPERED PILES

Takaki Asano[1], Naoaki Suemasa[2], Tsuyoshi Tanaka[3], Satoshi Shingai[4] and Yasutaka Sakamoto[5]

[1,2,3] Graduate School of Integrative Science and Engineering, Tokyo City University, Japan
[4,5] Rinkai Nissan Construction Co., Ltd., Japan

ABSTRACT

In recent years, large-diameter steel pipe piles have been utilized to support larger structures, expedite construction timelines, and reduce costs. However, the bearing capacity of the pile may be insufficient. To address this issue, tapered piles were investigated. These piles feature a gradually decreasing diameter toward the tip, which is expected to enhance vertical bearing capacity regardless of the plug effect. This is because the shaft friction increases by pushing and expanding the ground during penetration. However, tapered piles are rarely employed in practice, and the quantitative evaluation of their pushing and expanding effects remains limited. The purpose of this study is to better understand the bearing capacity characteristics of tapered piles due to their pushing and expanding effects. To achieve this, small dynamic penetration tests, simulating the standard penetration test, were conducted using various tip geometries. The influence of these geometries on the relationship between the load value for each blow and the penetration depth was analyzed. The results showed that tapered piles exhibited greater tip resistance compared to ordinary straight pipes. Furthermore, when comparing with tapered piles, it was confirmed that the longer the tapered section, the easier it is to exert bearing capacity. This indicates that the tapered design had an effect the overall performance of the pile by pushing and expanding the surrounding ground during penetration, resulting in increased bearing capacity.

Keywords: Straight piles, Tapered piles, Plug Effect, Shaft friction

INTRODUCTION

In recent years, large-diameter steel pipe piles (hereinafter referred to as “straight piles”) have been used to increase the size of structures, shorten construction periods, and improve economy. Ordinary straight piles, with standard diameter, exhibit high vertical bearing capacity due to the plug effect of the tip during penetration. However, the larger diameter steel piles are less likely to cause plug effect at the pile tip, so the effect of increasing vertical bearing capacity cannot be expected to be sufficient. On the other hand, taper piles have a reduced diameter toward the tip, which is expected to have a higher vertical bearing capacity regardless of the degree of pile tip plug [1]. This can be attributed to the increased shaft friction due to the pushing and expanding of the ground during pile penetration.

Shingai [2] conducted impact loading tests to compare the performance of tapered and straight foundation piles. Table 1 shows the test piles used in the impact loading tests. Tapered piles were used with a taper angle of 2°. Vertical loading tests were also conducted on tapered piles and straight piles with the same pile length and diameter. Figure 1 shows the results of vertical loading tests on tapered and straight piles. The tapered piles required the same amount of hammer energy to drive as the straight piles, but the total resistance of tapered piles were higher. Therefore, it can be said that tapered piles tend to exhibit higher vertical bearing capacity than straight piles.

Table 1 Test piles used in impact loading tests

	Straight pile	Tapered pile
Pile length (m)	28.0	24.0
Pile diameter (mm)	2300	2300
Wall thickness (mm)	30.0	30.0
Tip diameter (mm)	2300	2021
Tapered part (mm)	0.00	4.00
Taper angle (°)	0.00	2.00

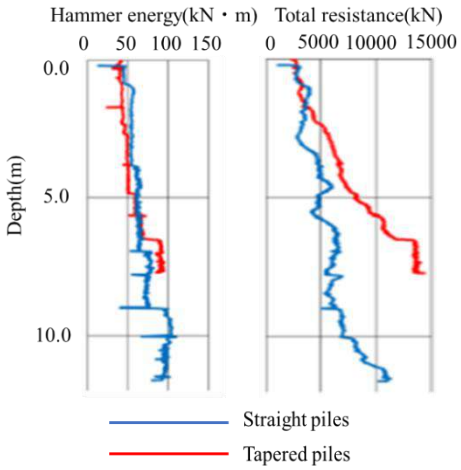

Fig.1 Results of vertical loading tests on piles

However, there are only a few cases of construction using tapered piles, and quantitative

evaluation based on the effect of pushing and expanding the ground has not yet been conducted. Therefore, the purpose of this study is to better understand the bearing capacity characteristics of tapered piles due to their pushing and expanding effects. In this report, small dynamic penetration tests simulating the standard penetration test were conducted using a reduced-size straight pipe (hereinafter referred to as "STP") and a tapered pipe with different shapes (hereinafter referred to as "TPP") to investigate how differences in the shape of the tip pipe and the taper length of the tapered pipe affect the relationship between the load value per blow and the penetration amount. The results of the small dynamic penetration test simulating the standard penetration test are reported.

TIP PIPES

To understand the difference between straight and tapered piles, two cases were done. Case 1 aimed to determine the effect to the difference in geometry between straight and tapered piles, while Case 2 aimed to understand how altering the length of the tapered section can affect the performance of the pile.

Case 1: Effect of Geometry

In this case, the effect of addition of the tapered section to the bearing capacity of the pile was investigated. The actual images of the STP and TPP used is shown in Fig 2. Apart from the tapering section, the effect of different wall thickness in STP and internal tip geometry of TPP were tested using small dynamic penetration tests.

Figure 3 shows the cross-section of the TPPs used, showcasing the difference in internal tip geometry. A more detailed specifications of each pile tested is tallied in Table 2. The diameter expansion ratio of the tip pipe was defined as the max diameter divided by the sum of the inner diameter and wall thickness of the tip. Here, the maximum diameter of the tip pipe was the same size in order to evaluate the same except for the difference in the shape of the tip pipe.

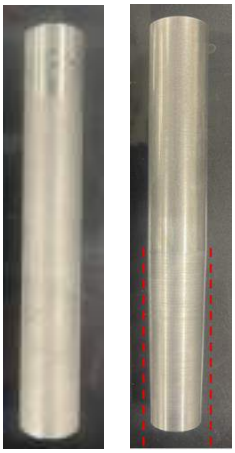

Fig.2 Tip pipe used in Case 1

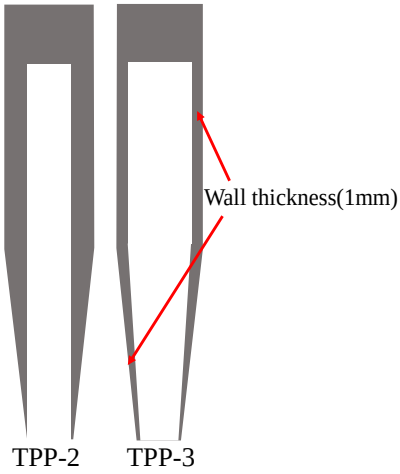

Fig.3 Shape of tip interior of the TPPs

Case 2: Effect of Tapered Length

For the second case, the aim was to understand how different taper length would affect the performance of the pile. Three types of TPPs were used, shown in Fig 4, and the specifications listed in Table 3. The taper ratio of the tip pipe was defined as the length of the tapered section divided by the max diameter. Like Case 1, small dynamic penetration

Table 2 Dimensions of each tip pipe (Case1)

Tip pipe	STP-1	STP-2	TPP-2	TPP-3
Straight section (mm)	178	178	103	103
Tapered section (mm)	-	-	75	75
Taper angle (°)	-	-	1.53	1.53
Max diameter (mm)	25	25	25	25
Inner section length (mm)	153	153	153	153
Inner diameter (mm)	23	15	19	19
Wall thickness (mm)	1.0	5.0	1.0	1.0
Diameter expansion ratio	1.04	1.25	1.25	1.25
Internal tip geometry	Straight	Straight	Straight	Tapered

Table 3 Dimensions of each tip pipe (Case2)

Tip pipe	TPP-1	TPP-2	TPP-4
Straight section (mm)	103	103	103
Tapered section (mm)	37.5	75	112.5
Taper angle (°)	11.3	5.71	3.81
Max diameter (mm)	25	25	25
Inner section length (mm)	115.5	153	190.5
Inner diameter (mm)	8.0	8.0	8.0
Wall thickness (mm)	1.0	1.0	1.0
Taper ratio	1.5	3.0	4.5

tests were conducted to observe the difference in bearing capacity each TPP achieved. For TPP-2, the same as in Case 1 was used.

TPP-1 TPP-2 TPP-4

Fig.4 TPP used in Case 2

EXPERIMENT OVERVIEW

The bearing capacity of each type of pile tested was quantified using small dynamic penetration tests. A stainless-steel tank with a diameter of 570 mm and a height of 890 mm was used to simulate the model ground, shown in Fig 5. The type of soil used for both Case 1 and Case 2 was kept constant using silica sand No. 7 with a relative density of about 85%. The soil sample was prepared by the air drop method using a hopper to ensure uniform density. Within the model ground, four PVC pipes were placed 300 mm from the ground surface to simulate the drilling of a standard penetration test, and penetration was made up to 300 mm from the bottom of the PVC pipes. Above the model ground, an apparatus simulating penetration test was placed, shown in Fig 6. A 5-kg weight was positioned at the top of the anvil section to be dropped at a height of 110 mm. This simulates one-tenth of the drop energy density of the standard penetration test done in real-scale. A 20-mm-thick cushioning material was placed between the weight and the anvil to prevent energy loss due to the rebounding of the weight. Two load cells, just below the anvil and the other attached to the tip of the rod, were used to measure the load value for each blow. An accelerometer attached to the anvil and a laser displacement meter fixed on top were used to measure the penetration speed and amount of penetration for each blow. The load measured at the tip of the rod is called the penetration resistance value, and the load measured just below the anvil is called the anvil load value.

Fig.5 Model ground

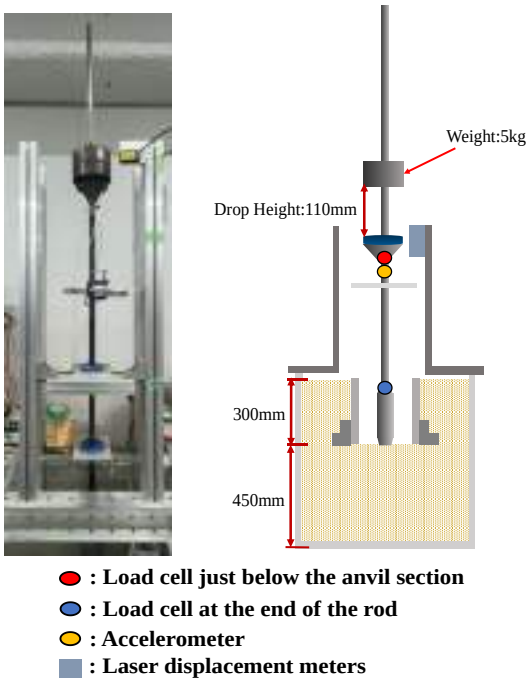

Fig.6 Schematic diagram of the experimental apparatus

EXPERIMENTAL RESULTS

Case 1: Effect of Geometry

Figure 7 shows the relationship between the number of blows and penetration depth. In penetration tests, the more blows it needs the higher the penetration resistance of the pile. Comparing the two STPs used, STP-2 had a higher number of blows up to a depth of 150 mm, and remained similar to STP-1 after. The increased number of blows at the beginning can be attributed to the increased wall thickness of the pile. At a depth of 150 mm, the tip was assumed to be plugged, resulting in almost similar blow counts thereafter. In TPP, it was confirmed that TPP-2 had a higher number of blows due to the difference in the tip interior shape. A structure that easily exhibits internal friction makes it harder to penetrate the ground. Between STP and TPP, TPP was observed to have a higher number of blows after 150 mm of penetration. This showed that the tapering of the pile tip caused some effect that increased the penetration resistance of the pile.

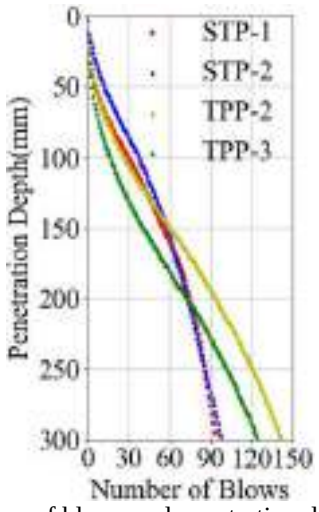

Fig.7 Number of blows and penetration depth

Apart from the number of blows, penetration velocity is also an important factor in pile driving. The slower the velocity, the stronger the resistance. Figure 8 and 9 shows the penetration velocity of the tip pipe at a penetration depth of 150 mm and 300 mm. The penetration velocity is the result obtained from the accelerometer integrated over time. Comparing STP and TPP, TPP had a slower velocity. This was true for both a depth of 150 mm and 300 mm, with more pronounced difference at the deeper depth. TPP-2 exhibited a lower velocity value due to the inner tip shape which creates a higher friction between time of penetration. With all piles having the same outer diameter, the difference in velocity can only be attributed to the geometric shape.

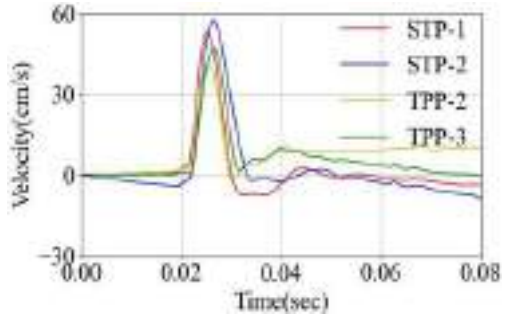

Fig.8 Penetration velocity of the tip pipe at a penetration depth of 150 mm

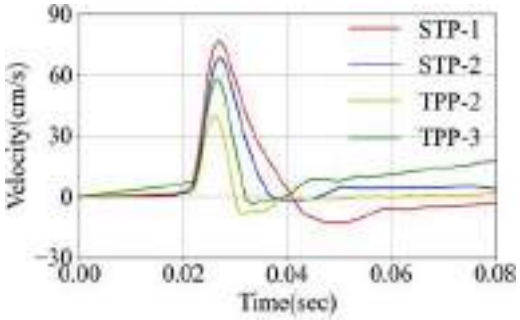

Fig.9 Penetration velocity of the tip pipe at a penetration depth of 300 mm

Figure 10 shows the relationship between the penetration depth of each end pipe and penetration resistance value. Here, the penetration resistance value in this graph is the maximum value per blow. Between the two STPs, STP-2 again had a higher value compared to STP-1 because of the thicker wall that created a higher surface area that touches the ground. At around 100 mm, a change in the slope of the graph can be observed that was assumed to be caused by the plugging of the tip. With the tip plugged, the penetration resistance value of the pipe did not vary significantly. This signifies that the wall thickness is not an important factor in deeper penetration depths.

For the two TPPs tested, both piles exhibited similar behavior until around 100 mm, the point where the tip was assumed to be plugged. After this, the straight geometry of TPP-2 had an advantage over TPP-3, developing higher penetration resistance.

Since the penetration resistance value of TPP is smaller up to a penetration depth of around 150 mm, it can be said that TPP has difficulty in providing bearing capacity when the penetration depth is small. However, with deeper penetrations, even with similar outer diameters and the same plugged condition, TPPs developed higher bearing capacity compared to STPs. This showed that a difference in geometry made an impact to the penetration resistance of the pile. Because of the tapering shape, the tapered pile penetrates the ground by pushing and expanding the ground, leading to a higher penetration resistance.

It has also been reported in A M. Rybnikov's[3] paper that for the same taper length, as the taper angle increases, the bearing capacity of the pile also increases. When comparing this with Case1 conducted in this experiment, the taper angle of the tapered pipe is small at 1.53°, so it is considered that increasing the taper angle would make it easier to exert bearing capacity.

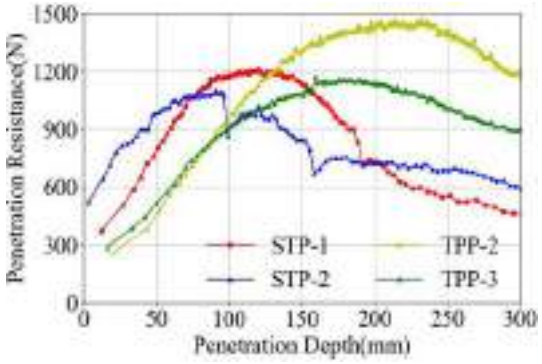

Fig.10 Depth of penetration for each end pipe and penetration resistance value

Case 2: Effect of Tapered Length

By varying the tip length and angle, its pushing and expanding effect to the developed bearing capacity can be understood. Figure 11 shows the relationship between the number of blows and depth penetration. From the three types with gradually longer tip length and lower taper angle, TPP-1, TPP-2, to TPP-3, in this order, all exhibited similar number of blows associated with the penetration depth. This meant that the number of blows is not significantly influenced by the length or the angle of the tapered section.

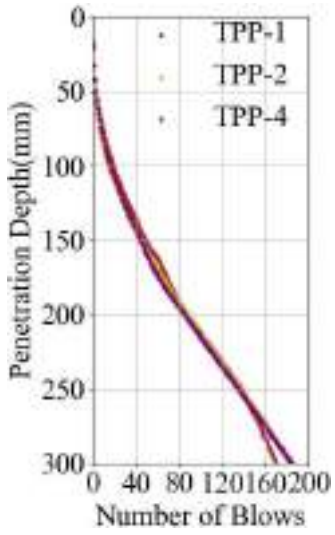

Fig.11 Number of blows and penetration depth

In terms of penetration velocity, the difference of the three types of TPPs were more pronounced. The velocity of the penetration was recorded at the point where the depth of the penetration was equal to the inner section length, shown in Fig.12. Between the three, TPP-4 exhibited the lowest velocity. It can be implied that a longer taper length with a lower taper angle results to a lower penetration velocity. This holds the same for a penetration depth of 300 mm, shown on Fig. 13.

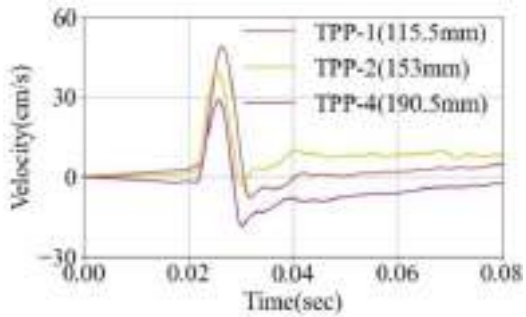

Fig.12 Penetration velocity when penetration depth reaches near the inner section length

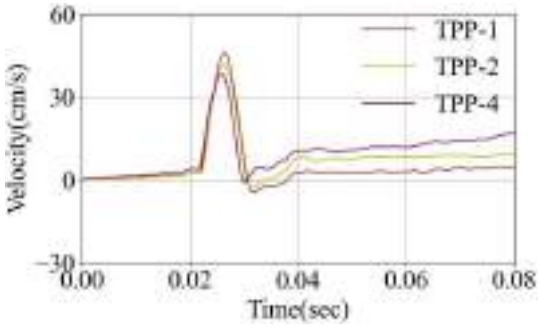

Fig.13 Penetration velocity of the tip pipe at a penetration depth of 300 mm

Figure 14 illustrates the relationship between the penetration depth of each end pipe and the penetration resistance value. As the penetration depth increases, the penetration resistance value gradually rises. When the depth reaches the inner section length, the length of the inner section, the tip is considered plugged that resulted to a shallower slope of the resistance curve. Up to a penetration depth of approximately 150 mm, a longer tapered section results in lower penetration resistance at the same depth. This is due to the difference in diameter of the penetrated portion, a longer tapered section will have a smaller average diameter. However, after a penetration depth of around 200 mm, the penetration resistance value of TPP-4 increases, suggesting that the influence of tip pipe diameter becomes less significant once the straight section of the piles was reached or the entire tapered section was buried. Instead, the rise in shaft friction, caused by pushing and expanding the surrounding ground, becomes more dominant. Additionally, a longer tapered section leads to a

deeper penetration depth before the resistance value peaks. This occurs because the straight section is reached later during penetration. However, the magnitude of the peak penetration resistance does not vary significantly with the length of the tapered section.

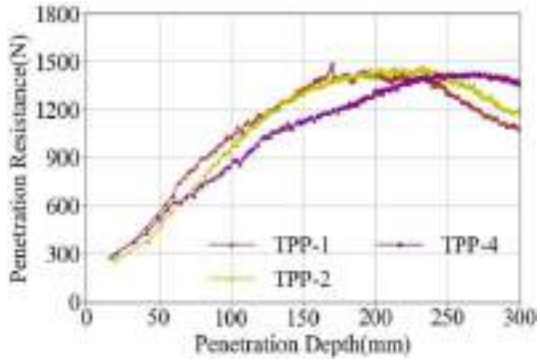

Fig.14 Depth of penetration for each end pipe and penetration resistance value

Figure 15 shows the relationship between the taper ratio and penetration resistance value. In here, two cases were compared, one being at a depth equal to the tapered length, and another one being at 300 mm deep, a depth where all tapered tips are buried inside the soil. From here, the penetration resistance value was greater with a larger taper ratio both when all penetration was made to the straight section and when all penetration was made only to the tapered section. Therefore, even when only the tapered section was penetrated, the vertical bearing capacity differed depending on the length of the tapered section, and it was confirmed that the longer the tapered section, the greater the vertical bearing capacity.

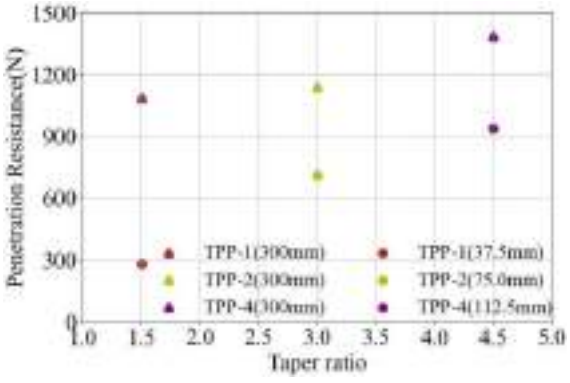

Fig.15 Taper ratio and penetration resistance of TPP

CONCLUSIONS

Overall, the experimental results for the two cases confirm that TPP has a higher penetration resistance value than STP at a deeper penetration depth. This confirms that a change in geometry in the tapered piles can increase vertical bearing capacity by pushing and expanding the surrounding ground during penetration. In addition, the following findings were obtained through experiments in two cases.

1) The thicker the wall thickness of the STP, the harder it is to penetrate up to a depth before the tip gets plugged. At a deeper depth than the inner section of the pipe, the thickness becomes insignificant.
2) A straight inner tip shape offered increased bearing capacity due to increased friction.
3) TPPs showed a higher bearing capacity compared to STPs in deep penetration depths of greater than the inner tip length, but struggled to provide similar bearing capacity to STPs in shallower depths.
4) From Case 2, a longer taper length and shallower taper angle experienced lower penetration velocity, but the peak penetration resistance value tended to be the same regardless of the geometry of the tapered tip at deep depths.

To further understand the mechanism and the effect of the tapering of the pipe tip, more experiments with varying soil types are planned in the future. Since the current model ground was made of silica sand No. 7 which has little cohesion, a case using cohesive soil is planned to be conducted which may increase the effect of the pushing and expanding of the ground that may lead to a further increase in bearing capacity. Furthermore, I would like to conduct a case where the taper angle of the tapered pipe is further increased based on A M. Rybnikov's paper and compare the bearing capacity.

REFERENCES

[1] Yasutaka Sakamoto et al. “Performance Comparison of Tapered and Straight Foundation Piles,” 76th Annual Meeting of the Japan Society of Civil Engineers, 2021
[2] Satoshi Shingai et al, “Performance Comparison of Tapered and Straight Foundation Piles (Part 1: Push-in Resistance),” 75th Annual Meeting of the Japan Society of Civil Engineers, 2020
[3] A M. Rybnikov, Experimental Investigations of Bearing Capacity of Bored Cast in Place Taper Piles, Soil Mechanics and Foundation Engineering, Vol.27, No.2, pp.48-52, 1990.2

Copyright © Int. J. of GEOMATE All rights reserved, including making copies, unless permission is obtained from the copyright proprietors.

15th Int. Conf. on Geotechnique, Construction Materials & Environment,
Kyoto, Japan, 11-13 November 2025, ISBN 978-4-909106124 C3051

STUDY ON INTERACTION OF PULL-OUT TESTING BETWEEN TIN TAILING AND REINFORCEMENT FOR GEOSYNTHETIC REINFORCED SOIL ABUTMENT

Wijit Itthiwongkul[1], *Peet Homchuen[2], Suphamat Chaichana[3], Tanapon Khunin[4], and Zhen Zhang[5]

[1, 3]Faculty of Engineering, Rajamangala University of Technology Lanna, Thailand; [2]Department of Mining and Petroleum Engineering, Chulalongkorn University, Thailand; [4]Department of Mining and Petroleum Engineering, Chiang Mai University, Thailand; [5]Department of Geotechnical Engineering, Tongji University, China.

ABSTRACT

This paper presents a relevant and timely study on the use of tin tailings, which are the solid waste material extracted from tin mineral processing at tin mine in the northern region of Thailand, as an alternative backfill material in Geosynthetic Reinforced Soil (GRS) abutments. By conducting a series of physical model tests under varying normal loads, including a test with a single-layered and double-layered geosynthetic reinforcement. The study provides practical insights into the pull-out behavior and deformation characteristics of the GRS composite system. The application of tailings characterized a mixture of various particle sizes with a maximum particle size of 4.75 mm, and a friction angle of 37° which demonstrates a promising approach to sustainable construction. The tailing mainly contains Silicon (Si) and other different proportions of elements without harmful chemical components. The paper aligns well with current engineering practices and sustainability goals by integrating waste utilization within the context of GRS design.

Keywords: Waste material, Tin mine, GRS, Pull-out behavior, Deformation

INTRODUCTION

In recent years, the trend of green and sustainable construction materials has witnessed a notable rise with regarding the concept of environmental issues, economic, and social [1-3]. Waste material is by-product in production processes and it is alternative choices for practical applications, including road construction, geosynthetic-reinforced transport infrastructure systems, pavement, embankments, load-bearing foundations, slopes, cement productions, agriculture, and backfilling in underground mining, etc. [4-8]. Currently, the selection of materials for construction work involves more than just strength. There are other critical factors to consider, such as cost-effectiveness, which include the price of materials, transportation to the site area, operational costs, safety concerns, healthy working conditions, and the use of environmentally friendly materials. Additionally, materials that emit low levels of carbon dioxide, have a long-life cycle, and can be reused with considered good options [9-13]. Thus, according to previous reasons, the waste materials from the mining industry are also seen as a beneficial choice for utilization [14-17].

This study highlights the waste materials from surface mining, particularly located near urban areas. These materials are considered alternatives for utilization and development to transportation infrastructure in northern region of Thailand. There are many alternative waste materials in this region, which include various types from mining operations, such as quarries, mineral extraction, coal mining, overburden excavation, sand mining, as well as kaolin mining. Emphasizing ore processing in mining, particularly regarding the waste materials extracted from Tin ore processing. These tailings are solid waste generated during the processing of tin ore. The tailings have been stockpiled over extensive surface areas and have remained unused since mining operations began as shown in Fig. 1.

Fig. 1 Location of Tin tailing, northern region of Thailand

Fig. 2 depicts the basic flowchart of extracted Tin mineral process. In general, the process to produce Tin production can be divided into 2 parts: the mining process and the extraction process. The mining process is the process of preparing raw material, which includes planning to remove overburden and

then using drilling and blast techniques to reduce the size by explosives that have high energy and create high shockwave after detonation. The drilling follows the mineral veins. The mining machines are used to dig and load raw material into the mine trucks, which are then hauled to the crusher plant that employs reduction steps. In this step, the raw material is reduced to small size and prepares for the following step. Finally, the production results in concentrated Tin production by using jig concentrators, electric, and magnetic separators. The tailings are delivered to waste stockpiles. To manage and optimize the natural resources, as well as the financial aspects and lifespan of mine. Firstly, low-grade raw materials can be blended with high-grade material using blending techniques.

Fig. 2 Basic flowchart of extracted Tin mineral process

Regarding utilization of the tailing from Tin mining in an engineering context, the Geosynthetic Reinforced Soil (GRS) structure consists of dense multiple layers of a densely compacted fill and closely spaced geosynthetic reinforcement, and a stable facing block with either frictional or mechanical connections. The GRS structure is widely used in practice due to its advantages, such as being easier to construct, more economical, requiring less over-excavation, more ductile, more flexible, and it can be quickly built times. Moreover, GRS technology has a lower environmental impact as it uses less CO_2 emitting materials in its life cycle, and the materials can contribute to road infrastructures as they can be used as gravel for example, once their life cycle has ended. GRS technique has been adopted in many engineering contexts, including retaining walls, embankment, load-bearing structure, bridge abutment, etc. This construction consists of densely compacted backfill with closely spaced geosynthetic materials. Additionally, the space between each layer of geosynthetic sheet is usually laid less than 300 mm [13, 18-21]. The calculation of bearing capacity for GRS composite is influenced by various internal factors, as shown in Eq. (1)

$$q_{ult} = (\sigma_c + 0.7^{(\frac{Sv}{6d_{max}})}\frac{Tf}{Sv})Kp + 2c\sqrt{Kp} \quad (1)$$

Where:

q_{ult} : Ultimate bearing capacity

σ_c : External confining stress due to the facing element

Sv : Vertical reinforcement spacing

d_{max} : Maximum particle size

T_f : Ultimate tensile strength of the geosynthetic reinforcement

K_p : Coefficient of passive earth pressure of the backfill

c : Cohesion of the backfill

However, according to current design guideline for GRS bridge abutments, the facing element is typically not treated as a structural component of the GRS abutment. Furthermore, the confining stress induced by the facing element is often disregarded, assuming a confining stress of 0. In addition, in this design, cohesion is also eliminated since it cannot be relied on for long-term strength as Eq. (2), Eq. (3) [19].

$$q_{ult} = (0.7^{(\frac{Sv}{6d_{max}})}\frac{Tf}{Sv})Kp \quad (2)$$

$$\sigma_c = \gamma_b d \tan\delta \quad (3)$$

Where:

γ_b : Unit weight of facing block

d : Depth of the facing block

δ : Friction angle between the geosynthetic reinforcement and facing element.

Therefore, a concept has been developed to study waste materials that impact the environment, are low in cost to manage, and can be suitably applied to local conditions by creating a physical model that simulates the real area for practical application. This paper was conducted on a series of physical models and investigates the characteristics of Tin tailing and reinforcement for geosynthetic reinforced soil abutment under vertical loading using the pull-out loading technique and focus on the above parameters.

RESEARCH SIGNIFICANCE

This study investigated alternative materials that focus on industrial processes. Additionally, the use of waste material was utilized in practical applications offer cost-effectiveness, CO_2 emissions. Especially, the compacted backfill layer of GRS abutment was constructed of a mixture of various particle size. Tin Tailing is the solid waste material that was selected for analyzing the feasibility study. The design is based on research and practices guideline.

MODEL TEST

Material And Preparation

Tin tailing backfill soil

The Tin tailing was selected as the backfill soil for GRS applications. This tailing was used to investigate in this experiment. The first five main chemical compositions consist of Silicon (Si), Magnesium (Mg), Aluminium (Al), Calcium (Ca), and Iron (Fe) as showed in Fig. 3. Tin tailing backfill appears in dark yellow color and contains with various particle sizes as depicted in a line graph of gradation backfill by sieve analysis (Fig. 4). The Tin tailing backfill was screened particles, which determined a maximum particle size of 4.75 mm. In addition, the uniformity and curvature coefficients are around 5.4 and 1, respectively. This waste material takes into accounts to the well-graded backfill specifications, following FHWA guidelines. The properties of the backfill were determined including specific gravity, cohesion, friction angle, min. and max. dry unit weight were depicted in Table 1

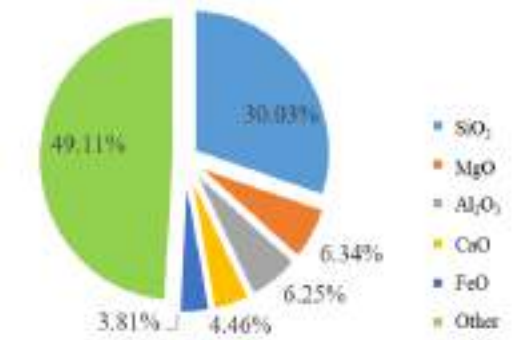

Fig. 3 Main Chemical compositions of Tin tailing

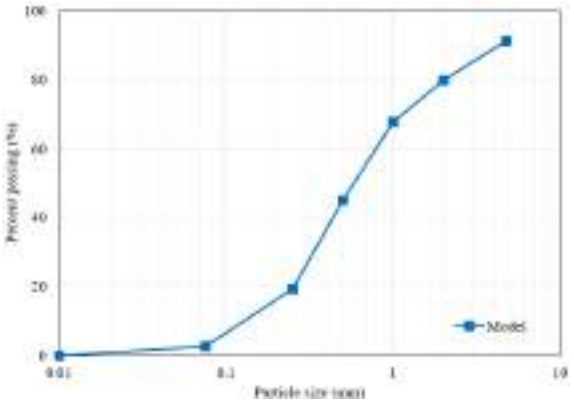

Fig. 4 Particle size gradation curve of Tin tailing

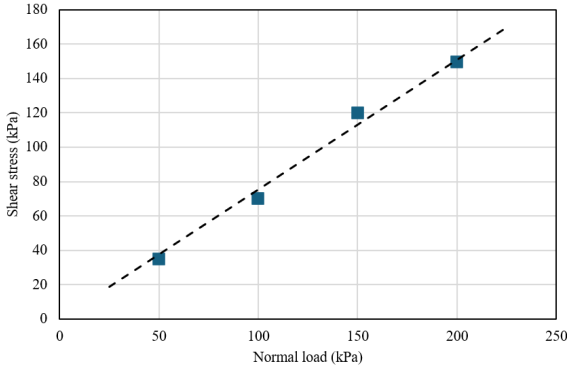

Fig. 5 The relationship between normal stress and shear stress at peak from direct shear test

Table 1 The properties of Tin backfill soil

Properties	Unit	Test Method	Tailing
Max. particle size	mm	Sieve analysis	4.75
Mean particle size	mm	Sieve analysis	0.61
Uniform coefficient	-	USCS	5.4
Curvature coefficient	-	USCS	1
Min. dry unit weight	g/cm^3	Relative Density	1.255
Max. dry unit weight	g/cm^3	Relative Density	1.600
SG	-	Water replacement	2.71
Cohesion	kPa	Direct shear test	0
Internal friction Angle	°	Direct shear test	37

Reinforcement

Fig. 6 shows the back color of Polyvinyl Chloride mesh (PVC) was selected as geosynthetic applications in function of reinforcement for this study, with an aperture size of 5 mm, 16 holes of 100 mm, and a thickness of 2 mm for each layer. The dimensions of the PVC sheet were 300 mm in width and 420 mm in length due to the factor of GRS design, typically expressed as a base-to-height ratio (B/H) of 0.7 [19, 22].

Fig. 6 Polyvinyl Chloride mesh

Test Plans

There are five different experiments that applied normal load at the top of model tests ranging from 0 kPa to 400 kPa. The experiments are focused on the pull-out loading characteristics and displacement of reinforcement. To ensure consistency, a compaction level is greater than 95% of maximum dry unit weight. Tests 1 to 4 were conducted with loads of 0, 100, 200 and 400 kPa. For Test 5 was conducted in the same manner as Test 3, but an additional double sheet of geosynthetic, as detailed in Table 2.

Table 2 Test plan

Test	Normal load (kPa)	Backfill
1	0	Tin tailing
2	100	Tin tailing
3	200	Tin tailing
4	400	Tin tailing
5	200*	Tin tailing

*Note: *: A double geosynthetic sheet.*

Model Test Setup

Fig. 7 shows the right-side view of the physical model, which consists of model box, backfill, geosynthetic reinforcement, digital dial gauge, hydraulic jack and load cell. The model box has the inside dimensions of 300 mm in width, 1000 mm in length, and 600 mm in height. The model was constructed with 4-side wood and 1-side transparent panel that allows to observe the interaction between backfill and geosynthetic during testing in a rigid frame. Furthermore, the top side is open to fill the backfill through this way. The rectangular outlet gap is 300 mm in length and 20 mm in width. A narrow gap of around 5 mm was left on top-bottom sides of geosynthetic sheet to prevent the friction between outlet wood and geosynthetic sheet during pull out by horizontal hydraulic jack. The geosynthetic sheet was allowed for lateral movement, as shown in Fig. 8.
A Geosynthetic sheet was placed in the middle height of model, which followed the FHWA guideline for bridge abutment. Moreover, a dense layer between the backfill and geosynthetic sheet is less than 300 mm.

The strip footing is a rigid plate that is placed as the beam seat in the prototype to receive the load of an integrated superstructure. However, in the experiment, a vertically distributed load was applied from the hydraulic jack and placed on the top of model at a setback distance of 40 mm behind reinforced soil. In addition, the size of the strip footing plate is 300 mm in width and 250 mm in length.

Fig. 7 Right-side view of the physical model

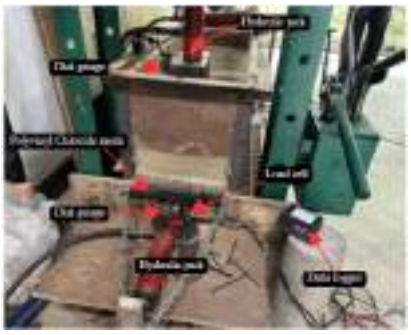

Fig. 8 A geosynthetic sheet in lateral movement

Loading Procedure

In this study, the vertical hydraulic jack was maintained and pressurized to apply normal pressure during testing. A distributed surcharge load applied to the model test, which applied an incremental pulling load of around 50 N per minute for the geosynthetic sheet until reaching maximum load. Throughout the performance test, the monitoring instruments displayed real-time data on screen, including vertical applied loading, vertical and lateral displacement and pull-out loading, as well as visual observation of the geosynthetic sheet and backfill soil through the transparent plexiglass.

RESULT AND DISCUSSION

Pull-out Loading Characteristics

Fig. 9 shows pull-out loads and lateral displacement of model tests when the applied normal load on the strip footing ranged from 0 to 400 kPa at the top of the model. The GRS abutments are recommended to have a typical load at 200 kPa [23]. The graph demonstrates a steady line between pull-out load and displacement of geosynthetic, exhibiting elastic behavior characterized by a linear relationship according to Young's modulus. However, in the next

stage, the lateral displacement rapidly increases, exceeding the maximum load and reaching frictional resistance. Finally, the pull-out load sharply drops with increasing displacement, then becomes steady, following the same trend of all five model tests. Test 1 carried out without normal stress on the top of model test, the result of this case showed the lowest pull-out load due to only frictional resistance between backfill and geosynthetic sheet. Test 4, with a normal stress of 400 kPa, experienced a significant rupture of geosynthetic sheets at front of reinforced soil composite. In terms of GRS abutments under bridge service load, the behavior of pull-out loading exhibits a higher load with longer displacement. Moreover, the use of a double geosynthetic sheet occurred a higher load capacity compared to a single sheet.

Fig. 10 shows the influence of normal stress on pull-out loads, the results indicate that the normal load increased as pull-out load increased.

Visual observations between the geosynthetic layer and backfill through the transparent plexiglass demonstrated the minimal changing due to slow movement of reinforcement.

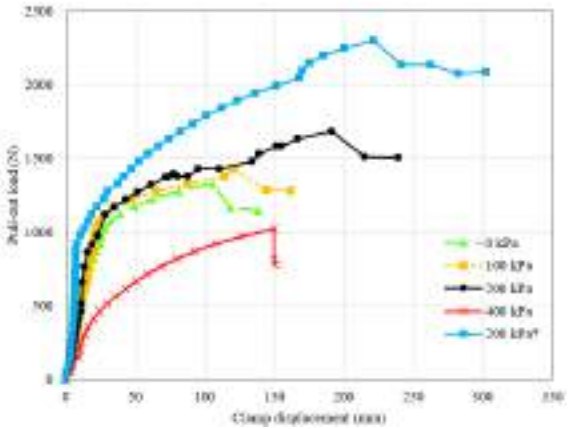

*Note: *: A double geosynthetic sheet.*

Fig. 9 Pull-out loads - displacement curve of geosynthetic sheet at different normal stress

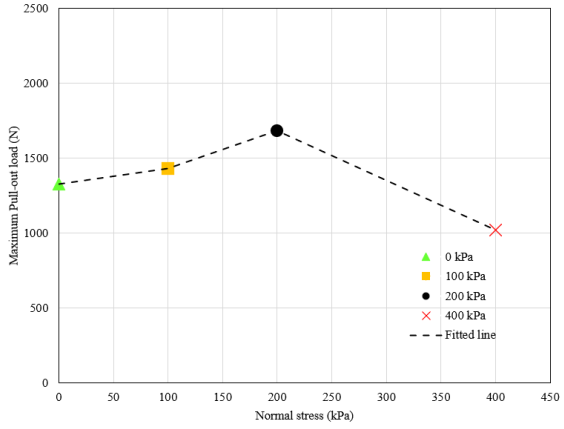

Fig. 10 Influence of normal stress on pull-out loads

CONCLUSIONS

The study compared and presented the analyses of five tests based on experimental results, highlighting the pull-out loading and deformation behavior.

The pull-out loading of GRS composite under varying normal stress on the top of model increased as the applied stress increased. In the case of an additional double sheet of geosynthetic, which increasing in the tensile strength of geosynthetic, resulted in higher pull-out load with achieved larger displacement. In comparison, the test under bridge service loads of 200 kPa to without loads, resulted in an increase of 1.2 times in pull-out load capacity. Additionally, the condition using a double geosynthetic sheet condition exhibited a significant enhancement of 1.7 times.

All experiments exhibited a similar trend in load characteristics when exceeding the frictional resistance at the interface between backfill and geosynthetic, followed by a decrease in load and then a stable value.

The failure behavior of the geosynthetic sheet resulted in a sharp rupture due to the application of an excessive normal load. The location of the rupture occurred at the front of the GRS composite.

ACKNOWLEDGMENTS

The authors appreciate the support provided by faculty of Engineering, Rajamangala University of Technology Lanna.

REFERENCES

[1] Popescu C., Dissanayake H., Mansi E. and Stancu A., Eco Breakthroughs: Sustainable Materials Transforming the Future of Our Planet, Sustainability, Vol. 16, Issue 23, 2024, pp. 10790.

[2] United Nations, Critical Milestones Towards a Coherent, Efficient, and Inclusive Follow-up and Review of the 2030 Agenda at the Global Level, 2015.

[3] Hasmori, M.F., Zin, A.F.M., Nagapan, S., Deraman, R., Abas, N., Yunus, R. and Klufallah, M., The on-site Waste Minimization Practices for Construction Waste, IOP Conference Series: Materials Science and Engineering, Vol. 713, Issue 1, 2020, pp. 012038.

[4] Guo, J., Bao, Y. and Wang, M., Steel Slag in China: Treatment, Recycling, and Management, Waste Management, Vol. 78, 2018, pp. 318-330.

[5] Zhang Q., Zhang J., Huang Y. and Ju F., Backfilling Technology and Strata Behaviors in Fully Mechanized Coal Mining Working Face, International Journal of Mining Science and Technology, Vol. 22, Issue 2, 2012, pp. 151-157.

[6] Turuallo G., Mallisa H. and Rupang N., Sustainable Development: Using Stone Dust to Replace a Part of Sand in Concrete Mixture, in MATEC Web of Conferences, Vol. 331, 2020, pp. 05001.
[7] Hangen H. and Detert O., Innovative and Sustainable Geosynthetic Solutions in the Field of Bridge Abutment Construction, in Geotechnical Engineering Challenges to Meet Current and Emerging Needs of Society: CRC Press, 2024, pp. 2317-2322.
[8] Ahmed I., Use of waste materials in highway construction, Joint Transportation Research Program, 1991, pp. 299.
[9] Iqbal M. J., Zaman B. and Budihardjo M. A., Utilization of Recycled and Waste Material in Construction - a Review, IOP Conference Series: Earth and Environmental Science, Vol. 1268, Issue 1, 2023, pp. 012046.
[10] Raja J., Dixon N., Fowmes G., Frost M. and Assinder P., Obtaining Reliable Embodied Carbon Values for Geosynthetics, Geosynthetics International, Vol. 22, Issue 5, 2015, pp. 393-401.
[11] Moncada A., Olivella S., Damians I. and Bathurst R. J., Impact of Transport Distance in Life Cycle Assessments of Geosynthetic Reinforced Soil Walls, in Geotechnical Engineering Challenges to Meet Current and Emerging Needs of Society: CRC Press, 2024, pp. 3149-3152.
[12] Ferreira F., Pereira P. V., Ribeiro P. B., Vieira C. S., Lopes P. and de Lurdes Lopes M., Recycled Construction and Demolition Aggregates as Alternative Fill Materials for Geosynthetic Reinforced Systems, in Proceedings of the Technical Workshop on Reinforcement and Drainage in Soil Structures, 2024.
[13] Bizjak K. F. and Lenart S., Life Cycle Assessment of a Geosynthetic-Reinforced Soil Bridge System–A Case Study, Geotextiles and Geomembranes, Vol. 46, Issue 5, 2018, pp. 543-558.
[14] Zetola V., Keith BF., Lam EJ., Montofré ÍL., Rojas RJ., Marín J. and Becerra M., From Mine Waste to Construction Materials: A Bibliometric Analysis of Mining Waste Recovery and Tailing Utilization in Construction, Sustainability, Vol. 16, Issue 23, 2024, pp. 10314.
[15] Satapathy S., Mishra M. and Das M. R., Sustainable Waste Management Practices for the Mining Sector Through Recycling of Mining Waste. Springer, 2024.
[16] T. P. Makhathini, J. K. Bwapwa, and S. Mtsweni, Various Options for Mining and Metallurgical Waste in the Circular Economy: A Review, Sustainability, Vol. 15, Issue 3, 2023, pp. 2518.
[17] Gairola S. U., Khanduri A. K. and Bhuvaneswari V., Sustainable Mining: Reducing Waste and Enhancing Resource Efficiency, Discover Civil Engineering, Vol. 2, Issue 1, 2025, pp. 75.
[18] Wu J. T. H., Pham T. Q. and Adams M. T., Composite Behavior of Geosynthetic Reinforced Soil Mass, Federal Highway Administration, McLean, VA, FHWA-HRT-10-077, 2013.
[19] Adams M. and Nicks J., Design and Construction Guidelines for Geosynthetic Reinforced Soil Abutments and Integrated Bridge Systems, United States. Federal Highway Administration, FHWA-HRT-17-080, 2018.
[20] Saghebfar M., Abu-Farsakh M., Ardah A., Chen Q. and Fernande B. A. Z, Performance Monitoring of Geosynthetic Reinforced Soil Integrated Bridge System (GRS-IBS) in Louisiana, Geotextiles and Geomembranes, Vol. 45, Issue 2, 2017, pp. 34-47.
[21] Wu J., Adams M., Pham T., Lee S. and Ma C., A generic Soil-Geosynthetic Composite Test, International Journal of Geotechnical Engineering, Vol. 6, Issue 1, 2012, pp. 103-116.
[22] Adams M., Nicks J., Stabile T., Wu J., Schlatter W. and Hartmann J., Geosynthetic Reinforced Soil Integrated Bridge System Interim Implementation Guide, Federal Highway Administration, McLean, VA, FHWA-HRT-11-026, 2012.
[23] Nicks J. E., Esmaili D. and Adams M. T., Deformations of Geosynthetic Reinforced Soil under Bridge Service Loads, Geotextiles and Geomembranes, Vol. 44, Issue 4, 2016, pp. 641-653.

Copyright © Int. J. of GEOMATE All rights reserved, including making copies, unless permission is obtained from the copyright proprietors.

15th Int. Conf. on Geotechnique, Construction Materials & Environment,
Kyoto, Japan, 11-13 November 2025, ISBN 978-4-909106124 C3051

SEISMIC BEHAVIOR OF STEEL STRIP REINFORCED SOIL WALLS WITH HIGH GROUNDWATER LEVEL

Akinobu Ogasawara[1], Makoto Kobayashi[1] and Kento Mori[1]

[1]Department of Civil Engineering, National Institute of Technology, Toyota College, Japan

ABSTRACT

It is known that reinforced soil walls, in which reinforcement materials composed of metals or polymers are installed in the soil, have high performance against earthquake. However, there have been reports of large deformations during earthquake, which has high groundwater level. In addition, in snowy cold areas, not only rainwater but also snowmelt water is expected to cause a rise in the groundwater level in the reinforced soil wall. Therefore, it is important to understand the seismic performance of reinforced soil walls under high groundwater level. In a previous study that verified the seismic performance of reinforced soil walls with multi-anchored reinforced soil wall subjected to seepage flow, it was reported that area between the anchor plates and facing panels, which called a reinforced area, behave as a single unit. On the other hand, the seismic deformation behavior of steel strip reinforced soil walls subjected to seepage flow has not been clarified. In this study, a series of centrifuge model tests were conducted to determine the seismic performance of steel strip reinforced soil walls subjected to seepage flow. As a result, the deformation behavior of the reinforced soil wall during the earthquake and the change in pore water pressure in the backfill soil confirmed that the reinforced area behaved as a single unit. This behavior also proved the high seismic performance of the steel strip reinforced soil wall.

Keywords: Centrifuge model test, Reinforced soil wall, Groundwater Level

INTRODUCTION

In general, the high seismic resistance of reinforced soil walls is known from past earthquake damage surveys. However, there have been reports of large deformations occurring when combined external forces such as high groundwater levels caused by poor drainage and earthquake motion are applied [1,2]. Furthermore, dynamic observations of full-scale reinforced soil walls constructed in snowy cold areas have reported that when back fill materials with freezing property are used, forward displacement occurs in winter due to cold air intrusion [3]. In snowy cold areas, the drainage layer installed behind the wall suppresses the increase in saturation within the backfill soil, thereby serving as an effective measure against frost heave. In recent years, drainage layers of appropriate thickness have been installed behind the wall in accordance with site conditions. However, some reinforced soil walls constructed in the past do not have drainage layers installed behind them. In the future, reinforced soil walls that have been in service for a long period of time are expected to have a higher groundwater level due to the reduced drainage function. In addition to these conditions, snowmelt as well as rainwater is expected to raise the groundwater level of reinforced soil walls in snowy cold areas. Reinforced soil walls in this condition can be subjected to significant deformation by complex external forces such as seismic motion.

From past damage cases, groundwater level is considered to be involved as a contributing factor in earthquake damage to reinforced soil walls. Therefore, there are several studies that have conducted centrifuge shaking table tests focusing on the degree of saturation of reinforced soil walls. In a study examining the influence of groundwater levels on the seismic performance of geogrid-reinforced soil walls, it has been reported that saturated conditions result in lower seismic performance compared to unsaturated conditions [4]. There are also studies that have examined the performance of geosynthetic reinforced soil walls subjected to the combined effects of earthquakes and rainfall through centrifuge shaking table tests. Similarly, it has been reported that the seismic performance of unsaturated reinforced soil walls is higher than that of saturated reinforced soil walls. Furthermore, it has been pointed out that the deformation and failure modes of reinforced soil walls differ between unsaturated and saturated conditions under seismic load [5]. However, steel strip reinforced soil walls using friction reinforcement assume that an adequate drainage environment is maintained to provide the prescribed frictional resistance. Consequently, there are many unknowns regarding the seismic deformation behavior of steel strip reinforced soil walls under conditions of high groundwater level or seepage flow. In this study, a series of centrifuge model tests were conducted to understand the seismic behavior of steel strip reinforced soil walls under high groundwater level conditions.

RESEARCH SIGNIFICANCE

In previous studies, centrifuge shaking table tests has been conducted to investigate the seismic deformation behavior of anchored reinforced soil walls under high groundwater level conditions. As a result, it has been noted that at seismic accelerations of about 2m/s^2, the reinforced area behaves as a single unit [6]. However, since the reinforcement effect differs between anchored reinforced soil walls and steel strip reinforced soil walls, it is important to clarify the mechanism of earthquake damage in order to evaluate the integrity of steel strip reinforced soil walls against earthquake motion under conditions of high groundwater level.

CENTRIFUGE MODEL TESTS

Figure 1 shows an overview of the model ground, and Table 1 shows the experimental conditions used in this study. The model ground is set at a scale of 1/50, and the shaking table tests are conducted in a centrifugal force field (50G), which is 50 times the acceleration of gravity. The reinforced soil wall model used in this study has a scale of 1/50, so the wall height converted to the actual scale is 8m.

As shown in Figure 1, the dimensions of the model ground are 120 mm high, with four rows of 30 mm wide by 30 mm high facing panels. Since the wide of the model soil tank is 60 mm, two rows of facing panels are placed in the depth direction. Phosphor bronze was used for the reinforcement model to match the extensional rigidity of the steel strip reinforcement. Four reinforcements are placed per facing panel, there are no connections or drainage installations between facing panels. Toyoura sand with a moisture content of w = 10% was used for backfilling and compacted to a specified relative density. In Experimental code D40SVR, the reinforcement on the upper sides of the facing panels, excluding the top panel, was removed, and a model ground was created. In the past, there have been cases of reinforcement connections breaking due to the frost heave of backfill materials in snowy cold areas [7]. If the reinforcement breaks at the connection, the seismic performance of the reinforced soil wall may be reduced. In order to closely observe the deformation behavior of reinforced soil walls and to conduct an examination of their failure mechanisms during earthquakes, it is also considered important to model conditions that may not occur in actual phenomena. To understand changes in the seismic performance of reinforced soil walls, this case reduces the number of reinforcements, simulating damage to the reinforcement. It is considered that data beneficial for design can be obtained by verifying the seismic deformation behavior under various external loading conditions. Also, pore water pressure gauges were installed in the model ground and measured at

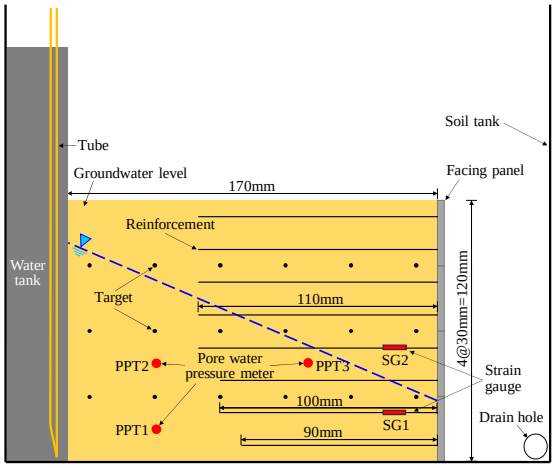

Fig.1 Overview of model ground

Table 1 Experimental conditions

Experimental code	Relative density D_r (%)	Moisture content w (%)	Rise in water level
D40	40	10	absence
D40SV	40	10	presence
D40SVR	40	10	presence

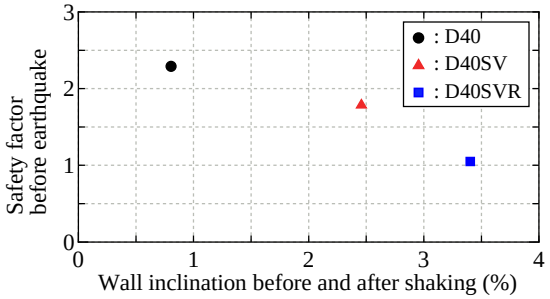

Fig.2 Wall inclination before and after shaking and safety factor before earthquake

three locations, two outside and one inside the reinforced area. In addition, strain gauges are affixed near the back of the walls of the first and second stages.

In the seepage experiments, a fluid (methylcellulose solution) with viscosity 50 times greater than that of water was used, considering the time-scaling law of seepage phenomena in centrifugal force fields. It has been reported that using such viscous fluids is highly effective in reproducing seepage phenomena in centrifuge model tests [8]. The viscous fluid is supplied to the water tank behind the model ground during its rotation. This experiment is started only after the centrifugal acceleration reaches 50G. The groundwater level within the reinforced soil wall is raised so that the water level in the tank reaches 100 mm. Since the seepage velocity is not fast, it is difficult to precisely control the rate at which the water level in the water tank rises. However, the

a) After shaking b) During shaking c) After shaking

Fig.3 Deformation conditions of the model ground in D40SVR

seepage behavior of the model ground is observed using a high-speed camera installed outside the apparatus, and the average rate of water level rise in the water tank is controlled to approximately 4mm/min. After confirming that the groundwater level reached the state shown in Figure 1, the shaking table test was conducted. The shaking conditions consisted of a vibration frequency of 1.0Hz and 20cycles with an acceleration amplitude of 2m/s^2, corresponding to a level I earthquake motion.

EXPERIMENTAL RESULTS AND CONSIDERATIONS

Figure 2 shows the safety factor before earthquake for pullout of the reinforcement under each test condition and the relationship between the wall inclination before and after shaking. The safety factor was calculated by referring to the design and construction manual for steel strip reinforced soil walls [9]. Since the reinforcement material used does not have ribs, the friction coefficient is assumed to be constant in the safety factor calculation process. This shows that even when the groundwater level of the backfill soil is high, the safety factor exceeds 1.0. In cases where the groundwater level has risen, the safety factor has decreased. In particular, when the amount of reinforcement installed is small, the safety factor is lowest. Furthermore, it was confirmed that the increase in wall inclination before and after shaking increased as the safety factor before earthquake factor decreased. This is thought to be due to a decrease in pullout resistance caused by a reduction in effective stress due to seepage flow.

Figure 3 shows an example of a model ground in D40SVR. This was filmed with a high-speed camera and shows the situation immediately before and after the shaking was applied. After starting shaking, it was confirmed that deformation of the reinforced soil wall gradually occurred. Furthermore, considering that the safety factor before earthquake was low in this case, it can be inferred that the displacement of the wall surface was the greatest.

Figure 4-6 shows the deformation behavior before and after shaking in each experimental code.

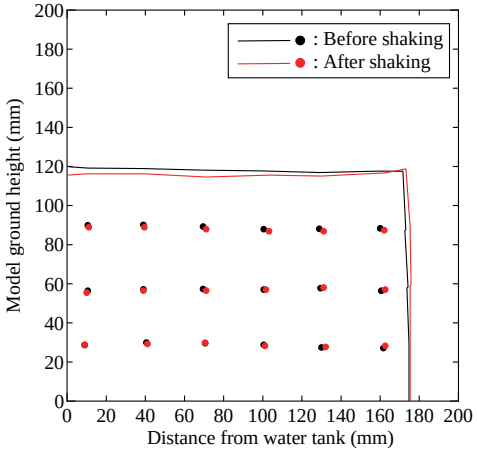

Fig.4 Deformation behavior of D40

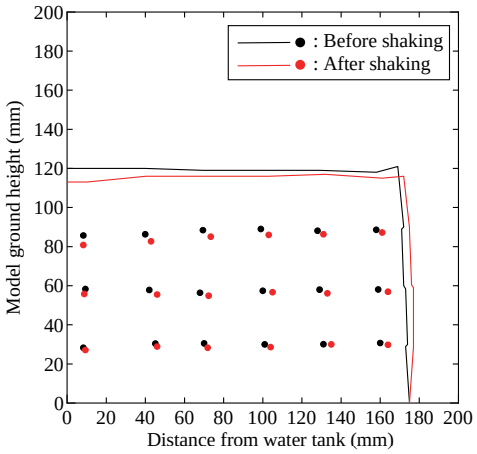

Fig.5 Deformation behavior of D40SV

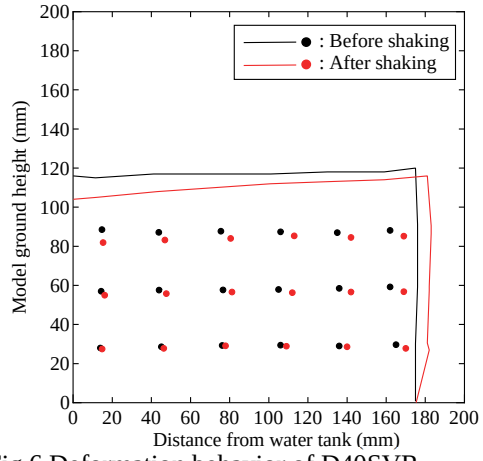

Fig.6 Deformation behavior of D40SVR

Focusing on the results of D40 in Figure 4, it can be confirmed that the amount of deformation of the wall surface is small. In this case, the groundwater level within the reinforced soil wall was not raised before applying shaking. Therefore, it is considered that deformation was minimized because the pullout resistance of the reinforced soil wall was secured. Next, by comparing the results of D40 and D40SV, it can be seen that D40SV, with its raised groundwater level, caused greater deformation of the wall. This is due to a decrease in the safety factor before earthquake caused by an increase in the groundwater level. As mentioned above, it is believed that the reduction in effective stress due to seepage flow caused a decrease in pullout resistance, resulting in pullout. Deformation observation results for D40SVR confirmed that it exhibited the greatest deformation among the three cases. This shows that the seismic resistance of reinforced soil walls changes as the number of reinforcements decreases. Furthermore, focusing on the displacement of the target point when the groundwater level rises, it can be confirmed that the deformation behavior differs between the reinforcement area and the non-reinforcement are. This behavior is examined based on the measurement results of the pore water pressure meter installed in the model ground.

Figure 7-8 shows the time variation of the excess pore water pressure ratio during shaking in D40SV and D40SVR. The shaking start time is set to 0.3 seconds. As shown in Figure 7, the excess pore water pressure ratio is negative in PPT2 outside the reinforced area and positive in PPT3 within the reinforced area. Therefore, it is considered that the reinforced area and the back ground did not integrate and deformation progressed. In other words, it is considered that the reinforced section integrated during the earthquake and exhibited deformation behavior. Despite the high groundwater level, no significant deformation of the wall surface occurred, as the reinforced areas showed integrated deformation behavior. However, as shown in Figure 8, the excess pore water pressure ratio is positive both inside and outside the reinforced area in D40SVR. This is thought to be because the reinforced areas did not integrate and exhibited deformation behavior. This is because the overall pullout resistance of the reinforced soil wall has decreased due to the reduction in the amount of reinforcement installed. The reinforced areas did not integrate and exhibited deformation behavior, resulting in the largest displacement in this case.

From the above, it was found that when the safety factor of the reinforced soil wall and the pullout resistance of the reinforcement are ensured, the reinforced area may exhibit integrated deformation behavior. This behavior demonstrates that reinforced soil walls have high seismic performance.

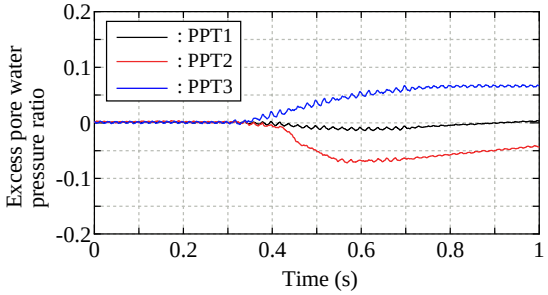

Fig.7 Time variation of excess pore water pressure ratio of D40SV

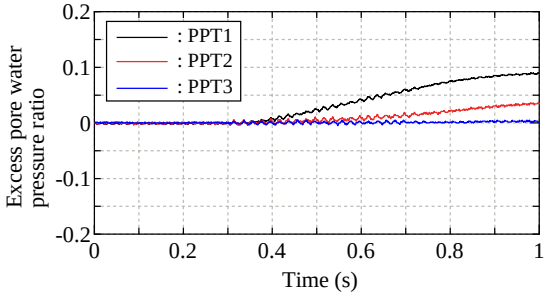

Fig.8 Time variation of excess pore water pressure ratio of D40SVR

CONCLUSIONS

The conclusions drawn from a series of centrifugal model tests on steel strip reinforced soil walls are as follows.

(1) Under conditions where the safety factor of reinforced soil walls was sufficient, no significant deformation due to rising groundwater levels was observed.
(2) The seismic performance of reinforced soil walls varies depending on the reduction in the safety factor.
(3) The deformation behavior of the reinforced soil wall during the earthquake confirmed that the reinforced area behaved as a single unit. This behavior also proved the high seismic performance of the steel strip reinforced soil wall.

ACKNOWLEDGMENTS

This research was gratefully supported by JSPS KAKENHI (Grant Numbers JP24K17349).

REFERENCES

[1] Japan Society of Civil Engineers Second Investigation Team for the 2004 Niigata-Chuetsu Earthquake (2003), Comprehensive Survey on Damage to Social Infrastructure Systems, Survey Results and Urgent Recommendations, I. Report and Recommendations, 2004, pp. 9-13.

[2] Sahara K., Takao K., Ogata T., Investigation of the Damage to Reinforced Earth Wall in the Great East Japan Earthquake, and Next Subject, Japan Society of Civil Engineers, Proceedings of the 6th Symposium on Sediment-Related Disasters, 2012, pp. 13-17.

[3] Ogasawara A., Goto Y., Kawajiri S., Hashimoto H., Kawaguchi T., Nakamura D., Yamashita S., Field Observations of Steel Strip Reinforced Soil Walls Constructed Using Different Embankment Materials, Proceedings of the 9th International Conference Geotechnique, Construction Materials and Environment, GEOMATE, 2019, pp.177-182.

[4] Izawa J., Kuwano J., Centrifuge Shaking Table Tests on Saturated Reinforced Soil Walls, Geosynthetics in Civil and Environmental Engineering, Proceedings of the 4th Asian Regional Conference on Geosynthetics, 2008, pp.191-196.

[5] Ren F, Huang Q, Chen J., Centrifuge modeling of geosynthetic-reinforced soil retaining walls subjected to the combined effect of earthquakes and rainfall, Geotextiles and Geomembranes, Vol. 50, Issue 3, 2022, pp. 470-479.

[6] Kobayashi M., Miura K., Konami T., Hayashi T., Sato H., Seismic damage mechanism of multi-anchored reinforced soil walls with high ground water level, Japanese Geotechnical Journal, Vol.13, No.2, 2018, pp. 123-134.

[7] Hashimoto H., Kawajiri S., Kawaguchi T., Hayashi T., Hayashi H., Damage to the Terre-Arrme reinforced soil wall due to frost heaving, Japan Society of Civil Engineers Proceedings, 2017. Vol. 73.

[8] Stewart, D.P., Chen, Y.-R., Kutter, B.L., Experience with the Use of Methylcellulose as a Viscous Pore Fluid in Centrifuge Models, Geotechnical Testing Journal, Vol. 21, Issue 4, 1998, pp.365-369.

[9] Reinforced soil wall (Terre Armee) design・execution manual, Public Works Research Center, 2014, pp. 120-158.

Copyright © Int. J. of GEOMATE All rights reserved, including making copies, unless permission is obtained from the copyright proprietors.

15th Int. Conf. on Geotechnique, Construction Materials & Environment,
Kyoto, Japan, 11-13 November 2025, ISBN 978-4-909106124 C3051

THREE-DIMENSIONAL SIMULATION ANALYSIS OF OPEN-ENDED STEEL PIPE PILE BY USING FINITE ELEMENT METHOD

Kiyoka Kono[1], Koji Watanabe[1], Shihchun Lin[2] and Shuichi Kamei[2]

[1]Department of Civil Engineering, Aichi Institute of Technology, Japan; [2]Jibanshikenjo Co., Ltd., Japan

ABSTRACT

The static load test (SLT) is highly reliable for evaluating vertical bearing characteristics, but it incurs significant expenses and extended construction time. Conversely, the rapid load test (RLT) offers advantages in terms of cost and construction time; however, it includes the impact of dynamic resistance and inertial forces of piles and ground (dynamic effects) in its data. Therefore, to accurately assess the RLT result as static vertical bearing characteristics, it is essential to remove the effect, but there are still many unresolved aspects of the mechanism of the dynamic effect, and it cannot be completely removed. In this study, both full-scale SLT and RLT for the same open-ended steel pipe test pile were carried out to compare and investigate using these vertical bearing characteristics. Therefore, as the first step, a simulation analysis using elasto-plastic FEM in the full-scale SLT and SLT results was conducted, and examined the validity of the parameter evaluation and modeling method based on the existing evaluation equations. As a result, highly reproducible results were obtained by parameter evaluation using the evaluation formula described in "Technical Standards and Commentaries for Port and Harbour Facilities" in Japan and applying the following two points: (1) joint elements simulating the shaft friction behavior obtained by the full-scale SLT, (2) consideration of soilplug effect. Therefore, it is concluded that the parameter evaluation and the modeling method are suitable for the simulation analysis of SLT.

Keywords: Static Load Test, Steel Pipe Pile, Vertical Bearing Characteristic, Elasto-plastic FEM

INTRODUCTION

The rapid load test (RLT) offers advantages in terms of cost and construction time; however, it includes the impact of dynamic resistance and inertial forces of piles and ground (dynamic effects) in its data [1,2]. Therefore, to accurately assess the RLT result as static vertical bearing characteristics, it is essential to remove the effect. But there are still many unresolved aspects of the mechanism of the dynamic effect, and it cannot be completely removed. Many previous studies have reported the numerical analyses limited to RLT [3-5]. On the other hand, few studies have analyzed SLT and RLT using the same model, and this study aims to quantitatively evaluate the dynamic effects by constructing an analytical model that treats both tests in a unified manner. In this study, both full-scale static compressive load test (SLT) and RLT for the same open-ended steel pipe test piles were carried out to compare and investigate using these vertical bearing characteristics. Therefore, as the first step, a simulation analysis using elasto-plastic FEM in the full-scale SLT and SLT results was conducted, and examined the validity of the parameter evaluation and modeling method based on the existing evaluation equations.

A flow chart of the study procedure is shown in Fig.1. In Step.2 and Step.3, determine the parameters to reproduce the SLT and RLT. This allows us to confirm that stress and deformation conditions of ground and pile, which cannot be confirmed during the test, and the mechanism of the dynamic effect is examined by comparing these parameters.

RESEARCH SIGNIFICANCE

SLT is highly reliable for evaluating vertical bearing characteristics, because it's carried out under the same loading conditions as actual piles. However, the test equipment requires not only force application devices and measurement devices, but also large-scale reaction systems, which incurs significant expenses and extended construction time. Conversely, RLT applies a load of short duration by free-falling a weight onto the pile head, and offers advantages in term of cost and construction time because it doesn't

Fig.1 A flow chart of the study

require reaction systems in the test equipment. However, because the data includes the impact of dynamic effects, it is essential to remove these effects to accurately evaluate the RLT results as static vertical bearing characteristics.

If the mechanism of the dynamic effect is clarified and the results obtained by RLT can be accurately analyzed as static vertical bearing characteristics, it will be possible to carry out load tests and evaluate vertical bearing characteristics more rationally.

FULL-SCALE SLT

Test overview

In this study, a full-scale SLT was carried out. The test pile was an open-ended steel pipe pile (SPP) of SS400 material with a pile diameter D=318.5mm, wall thickness t=6.9mm, cross-sectional area A=0.0068mm^2, pile length L=11.8m, embedment length L_d=11.0m. The pile was installed using the drop hammer method. The results of the ground investigation, pile driving depth and measurement items and locations are shown in Fig.2, and the locations of Standard penetration test (SPT) carried out at the just points and the test pile arrangement are shown in Fig.3. The measurement items were vertical displacement at the pile head (4 points), load at the pile head, and strain in each cross-section (Pile head: 4 directions, Others: 2 directions).

Load test method

The loading method was the actual live load method using reaction piles, and loading was done in stages of 5-cycles. The planned maximum load for this test was calculated using the evaluation formula for the ultimate bearing capacity of SPP in the specifications for highway bridges construction [6]. Since the calculated ultimate bearing capacity of the test pile is R_u=751kN, the planned maximum load for the loading test is 800kN. The final loading load was set at 1040kN, which was sufficient to verify the pile's ultimate bearing capacity and other vertical bearing characteristic values that should be confirmed by loading tests, and loading was carried out at a pitch of 80kN.

SIMULATION ANALYSIS

Simulation Analysis Overview

In this study, a three-dimensional elasto-plastic FEM was performed using MIDAS's FEA-NX.

By comparing the vertical bearing characteristics obtained from the load test results with those from the analysis results, the reliability of the analysis results was confirmed, and the analytical model and ground parameters were evaluated. The analytical model and

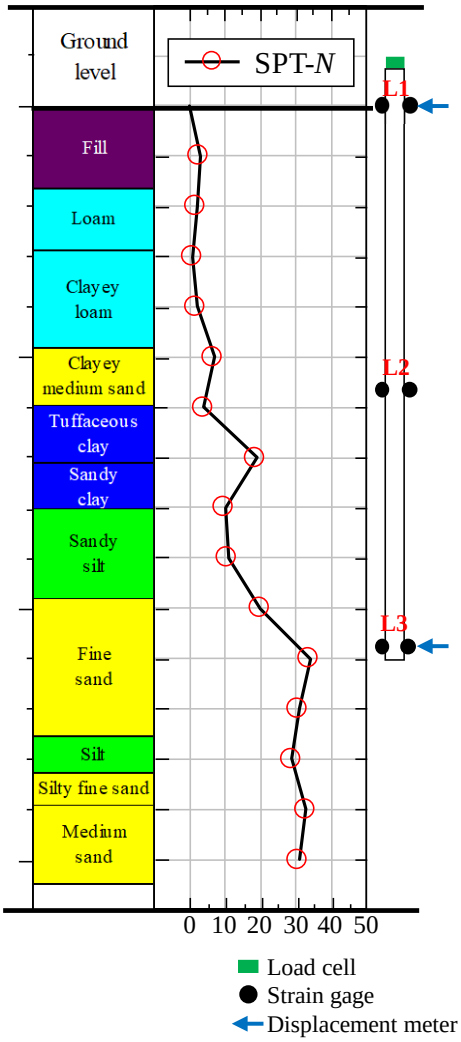

Fig.2 Profiles of soil layers, SPT N-values, together with instrumented test pile

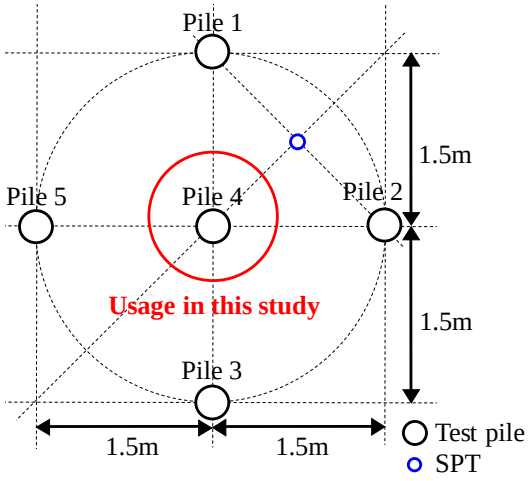

Fig.3 Locations of SPT and test piles

Table 1 Ground Parameters

No.	E (kN/m^2)	c (kN/m^2)	φ (°)	ψ (°)	ν (-)
1_Clay	18488	18.75	5.00	2.50	0.45
2_Clay	33253	33.73	5.00	2.50	0.45
3_Clay	42275	42.88	5.00	2.50	0.45
4_Sand	142972	10.00	31.92	15.96	0.35
5_Clay	278545	282.50	5.00	2.50	0.45
6_Clay	66555	72.50	5.00	2.50	0.45
7_Clay	71485	72.50	5.00	2.50	0.45
8_Sand	394171	10.00	35.80	17.90	0.35
9_Clay	126455	128.25	5.00	2.50	0.45
10_Sand	394171	10.00	35.36	17.68	0.35
11_Sand	401869	10.00	35.52	17.76	0.35

boundary conditions are shown in Fig.4. The analytical model was modeled over a quarter of the area, considering the symmetry of the test pile and the surrounding ground. And the ground of the analytical model was extended vertically in order to eliminate the influence of reflected waves when performing the simulation analysis of the RLT. Since the analytical model used in the simulation analysis of SLT and RLT should be same, the analytical model was also extended to include the extended ground in this study. The parameters of the extended ground were the same as "11_sand", since the boring test was conducted only up to 15.45 m. The loading method was based on full-scale SLT, with 80kN applied to the pile head in stages until a maximum of 960kN was reached. Table 1 lists the geotechnical parameters that were set. Among the ground parameters, deformation modulus (E) and internal friction angle (ϕ) were calculated in accordance with Technical Standards and Commentaries for Port and Harbour Facilities in Japan (Port) [7]. The dilatancy angle (ψ), which expresses the volume change, is half the value of the internal friction angle. Cohesion (c) was determined by Terzaghi and Peck formula using the uniaxial compression strength (q_u) obtained from the uniaxial compression test. The equations used as the evaluation of parameters are shown in Equation (1) through Equation (5).

$$\text{Sand: } G = 14100N^{0.68} \quad (1)$$

$$\text{Clay: } G = 170q_u \quad (2)$$

$$E = 2G(1+\nu) \quad (3)$$

$$\phi = 25 + 3.2\sqrt{\frac{100N}{70+\sigma_v'}} \quad (4)$$

$$c = q_u/2 \quad (5)$$

where, G: Shear modulus (kN/m^2), N: N-value (-), ν: Poisson's ratio (-) σ_v': Effective overburden pressure (kN/m^2)

The constitutive laws were Mohr-Coulomb law for ground and elasticity for SPP.

Assignment of Joint Elements

To simulation the shaft friction behavior between the SPP and ground, joint elements were set at the pile circumference. The parameters consisted of normal stiffness (K_n), shear stiffness (K_t), cohesion (c), and internal friction angle (ϕ). The equations used are shown in Equation (6) through Equation (9).

$$K_n = R \times G_{\text{soil}} \times \frac{2(1-\nu_{\text{joint}})/(1-2\nu_{\text{joint}})}{t_v} \quad (6)$$

$$K_t = R \times G_{\text{soil}}/t_w \quad (7)$$

$$c_{\text{joint}} = R \times c_{\text{soil}} \quad (8)$$

$$\phi_{\text{joint}} = R \times \phi_{\text{soil}} \quad (9)$$

where, R: Strength reduction factor (-), G_{soil}: Shear modulus of soil (kN/m^2), ν_{joint}: Poisson's ratio of joint element (-), t_v: Virtual thickness (m), c_{joint}: Cohesion of joint (kN/m^2), c_{soil}: Cohesion of soil (kN/m^2), ϕ_{joint}: Internal friction angle of joint (°), ϕ_{soil}: Internal friction angle of soil (°)

The strength reduction factor was set as 0.6 for sand and 0.5 for clay, all of virtual thickness were set at 0.01m based on [8].

Consideration of Soilplug

Since SPP in this study are open-ended, soilplug formed by soil that has penetrated into the pile body during driving were modeled. The soilplug set to 6.50m, the length obtained from the full-scale SLT, as shown in Fig.4. In addition, the inner shaft friction

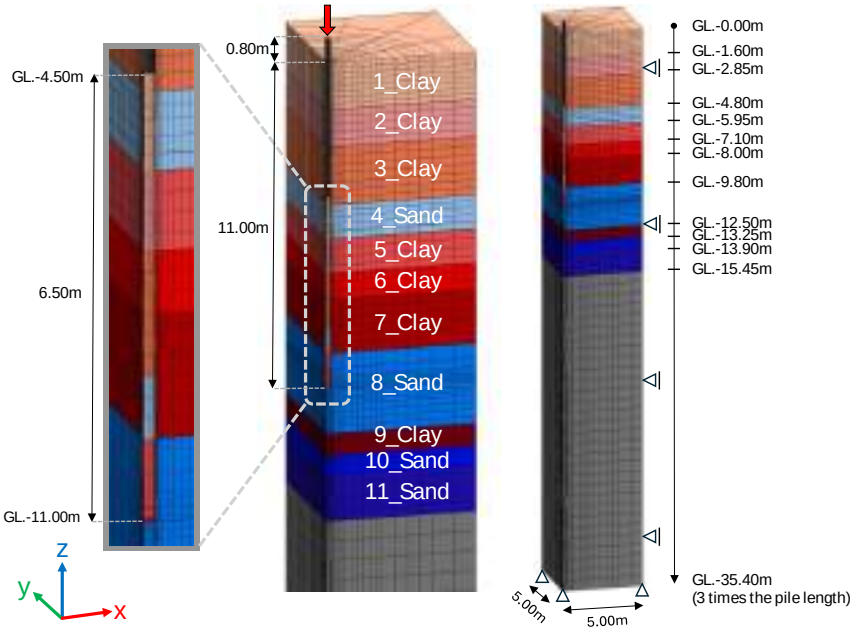

Fig.4 Analytical model and Boundary conditions

occurring at the boundary between the soilplug and SPP was also modeled, with parameters set according to the previously described parameter setting method.

RESULTS OF ANALYSIS

The axial force - displacement relationships obtained from the analysis are shown in Fig.5, Fig. 6 and Fig.7. This was calculated by multiplying the SPP strain obtained from the analysis by the elastic modulus and cross-sectional area of the steel. The axial force-displacement relationship obtained by full-scale SLT is also shown in these figures. The axial force-displacement relationship at the pile head (L1) shown in Fig.5 indicates that the behavior in the elastic range was almost identical. Furthermore, in addition to the elastic range, the behavior up to a displacement level of 11.7 mm (at 800kN loading) was consistent, confirming that the behavior partially reproduced that of the plastic range.

L2 is shown in Fig.6. Similarly, L2 shows high reproducibility in behavior up to a partially plastic zone. From this, it can be said that the parameter evaluation method for joint elements in the L1-L2 section was appropriate.

As shown in Fig.7, at the pile tip (L3), the behavior from the initial stiffness to the displacement level of 8 mm (at 800kN loading) showed good consistency and the values of ultimate bearing capacity are also generally consistent.

As mentioned previously, good consistency was obtained in the tip behavior up to 800kN loading. Therefore, a contour diagram of the vertical stress distribution at 800kN loading is shown in Fig.8. It shows that the load applied at the pile head is transmitted reliably to the ground at the pile tip. Also shows that the areas of concentrated stress at the pile tip are in the form of stress bulbs. In this case, stress transfer was observed to a depth of 3.2*D* and a horizontal region of 1.7*D*.

Based on these results, the modeling method in this study is appropriate for simulating SLT, and this modeling method can be applied to the simulation analysis of RLT.

CONCLUSIONS

In this study, as an analytical investigation, we performed a replication analysis using elasto-plastic FEM on full-scale SLT and SLT results to examine the validity of parameter evaluations and modeling methods based on the existing evaluation equations. The findings of this study are as follows.

1) The axial force-displacement relationship at the pile head (L1) indicates that the behavior in the elastic range was almost identical, furthermore the behavior partially reproduced that of the plastic range.
2) L2 shows high reproducibility in behavior up to a partially plastic range. From this, it can be said that the parameter evaluation method for joint elements in the L1-L2 section was appropriate.
3) In L3, the behavior from the initial stiffness to the displacement level of 8 mm (at 800kN loading) showed good consistency and the values of ultimate bearing capacity are also generally consistent.
4) The contour diagram of vertical stress at 800kN

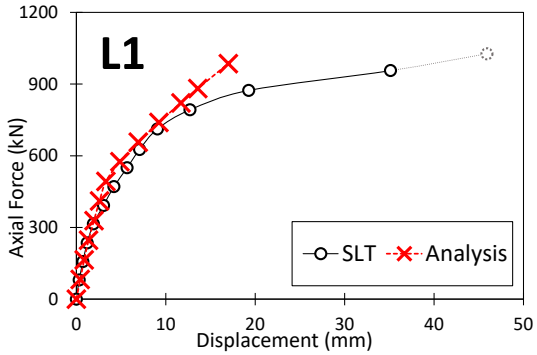

Fig.5 Axial force – displacement (L1)

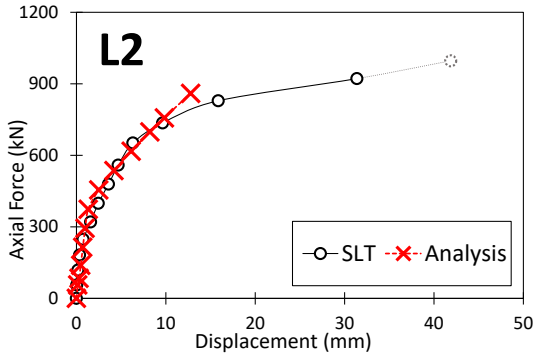

Fig.6 Axial force – displacement (L2)

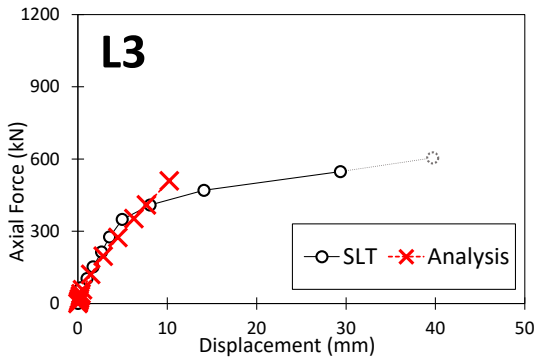

Fig.7 Axial force – displacement (L3)

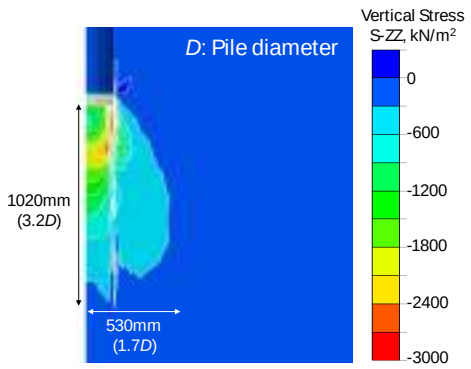

Fig.8 Contour diagram of the vertical stress distribution at 800kN loading

shows reliable load transfer from the pile head to ground at the tip, forming pressure bulb. The stress was transmitted to a depth of 3.2*D* and a width of 1.7*D*.

5) These results show that the modeling method used in this study is suitable for simulating SLT and can also be applied to RLT analysis**.**

REFERENCES

[1] Lin S, Kamei S, Yamamoto I and Matsumoto T, Hybridnamic rapid load testing with UnLoading Point Connection method invoking Case method, Proceedings of 17th Asian Regional Conference on Soil Mechanics and Geotechnical Engineering, 2023, pp. 1425-1429.

[2] Lin S, Watanabe K, Naka Y and Matsumoto T, Load–Displacement Relations of a Driven Steel Pipe Piles from Static and Rapid Load Tests, and Empirical Formulas Based on SPT and CPT: A Case Study at Sashima Test Yard, Proceedings of the 5th International Conference on Geotechniocs for Sustainable Infrastructure Development, 2023, pp. 245-252.

[3] T. Matsumoto, A FEM analysis of a STATNAMIC test on open ended steel pipe pile, in Proceedings of the second international Statnamic seminar - Statnamic loading test, Tokyo, Japan, 1998, pp. 287-294

[4] Zivaljevic V, Kovacevic D and Rakaric Z, Analytical and FEM Modelling of the Behavior of Pile in Dynamic Load Test, IUTAM Symposium on Exploiting Nonlinear Dynamics for Engineering Systems, 2019, pp. 271-280

[5] Van D.L. and Boonyatee T, Finite Element Analysis of Rapid Load Testing on a Driven Pile, The Twenty-Seventh KKHTCNN Symposium on Civil Engineering, 2014.9

[6] The specifications for highway bridges Part IV Substructures, and Part I Common, Japan Load Association, 1996.12 (in Japanese)

[7] Technical Standards and Commentaries for Port and Harbour Facilities in Japan, 2018.3, (in Japanese)

[8] GTS-NX User Manual, MIDAS Information Technology Co., Ltd., p.146

Copyright © Int. J. of GEOMATE All rights reserved, including making copies, unless permission is obtained from the copyright proprietors.

15th Int. Conf. on Geotechnique, Construction Materials & Environment,
Kyoto, Japan, 11-13 November 2025, ISBN 978-4-909106124 C3051

DYNAMIC RESPONSE OF UNDISTURBED SOFT CLAY SOIL WITH SOIL DISTURBANCE EFFECT UNDER CYCLIC LOADING

Angelo B. Edora[1], Taiju Ichizono[1] and Kentaro Nakai[1]

[1]Department of Civil Engineering, Nagoya University, Japan

ABSTRACT

In Japan, accelerated subsidence damage was observed immediately after the Chuetsu Offshore Earthquake (2007) and the 2011 off the Pacific coast of Tohoku Earthquake, which occurred in soft clayey soil layers. Many studies have been conducted to understand such a phenomenon in soft clay soils. Most of these studies utilized artificially prepared reconstituted clay samples, and shear tests were conducted under isotropic stress conditions. Nakai et al. (2017) conducted numerical assessments of road embankments and river levees, where they found that soft clay loses its stiffness under seismic loading, in which such phenomenon is defined as "soil disturbance". To fill the gap, this study aims to conduct undrained cyclic triaxial tests under both isotropic and anisotropic conditions using undisturbed and artificially remolded clay samples to determine the effect of the "soil disturbance" phenomenon in the dynamic behavior and properties of clayey ground. Based on the results of experiments, the undisturbed soil specimen shows a subtle decrease in the peak shear strength as the number of cycles increases. In addition, a drastic decrease in the peak shear strength of soil specimens was observed under anisotropic conditions in a significantly lower number of cycles. Such an effect of soil disturbance (reduction in shear strength) was not observed in the reconstituted samples. Therefore, the impact of soil disturbances that occur when soft clay is subjected to cyclic loading can be summarized as (1) a decrease in initial stiffness and (2) a decrease in peak shear strength, which are more pronounced under anisotropic conditions.

Keywords: Soil disturbance, Anisotropic stress conditions, Undisturbed soft clay, Cyclic loading

INTRODUCTION

In Japan and many regions of the world, the frequent occurrence of earthquakes results in different seismic damage, such as liquefaction, building collapse, and subsidence. Although liquefaction damage in sandy ground is the primary cause of seismic damage, structural collapse, due to loss of bearing capacity and settlement damage during and after earthquakes, has been observed in soft clay soils. One prominent example was the 1985 Mexico City earthquake, where structures collapsed due to loss of bearing capacity. Additionally, following the 1957 Guerrero earthquake, [1] noted in 1973 that multiple foundation points of a particular building in Mexico City were continuously settling. These two examples are similar in a way that they are both situated on soft clay ground.

Soft clay soils are characterized by three main characteristics, which are: high water content, high void ratio, and high sensitivity ratio. Sensitivity ratio refers to the ratio of the peak shear strength of the undisturbed clay sample and the strength of the fully remolded clay sample from the same specimens with unchanged water content. Many studies [2-6] attempted to understand the dynamic properties of soft clay soils by determining the effects of confining pressure, cyclic frequency, stress ratio and overconsolidation ratio on its cyclic behavior and concluded that the mean effective stress also decreases in clayey soils. Undrained cyclic triaxial tests were performed on undisturbed soft clay specimens in certain studies [7,8]. They discovered that reconstituted samples had a higher cyclic shear resistance than undisturbed specimens. However, most of these studies are limited to remolded soft clay specimens under isotropic stress conditions. To better understand the dynamic behavior of soft clay soils, [9] and [10] conducted seismic assessments of road embankments and river levees located on naturally deposited soft clay soil. In their numerical analysis, they found that there is a gradual loss of stiffness in cohesive soils due to cyclic loading (earthquake load), which they described as "soil disturbance."

In-situ soil conditions are seldom isotropic, which suggests that it is essential to consider such "soil disturbance" phenomenon under anisotropic stress conditions. Anisotropy is the directional dependence of soil's mechanical properties – soil properties such as strength, stiffness, and permeability vary depending on the direction in which they are measured. This is an essential consideration in geotechnical engineering, most especially when dealing with naturally deposited soils, as they are subjected to various stress histories [11].

The main objective of this research is to deepen the understanding of the "soil disturbance" phenomenon by determining the effect of loading under anisotropic stress on undisturbed and reconstituted soft clay soil. In defining "soil

disturbance", cyclic and subsequent monotonic shear tests were conducted on undisturbed and reconstituted specimens under isotropic conditions. On the other hand, cyclic and subsequent monotonic shear tests were conducted at K_0 = 0.6 to determine the effect of anisotropy in the "soil disturbance" phenomenon.

RESEARCH SIGNIFICANCE

Most studies on seismic damage have focused on the liquefaction of sandy ground. However, earthquake damage can also manifest in clay soil, specifically under soft conditions. Many studies attempted to describe the dynamic behavior of soft clays however, these studies were limited to reconstituted specimens [2-6], insufficient description of such phenomenon [7-8], and numerical simulations of undisturbed soft clay [9-10]. To bridge the research gap, this study obtained the necessary experimental facts to confirm the results of previous numerical assessments and to further define the "soil disturbance" phenomenon by considering the effect of anisotropy in the dynamic behavior of undisturbed soft clay.

MATERIALS AND METHODS

Soil Specimen Information

This study's soil specimen, which was minimally to undisturbed, was extracted from Kaizu City in Gifu Prefecture, Japan. The geological cross-section of the area reveals a thick deposit of clay at depths ranging from 8.5 m to 36.5 m. Specifically, the researchers utilized the soft clay layers extracted from 17.5 m to 30 m, which had an 80 to 85% liquid limit and a compression index of 0.21 to 0.23, both of which were relatively higher compared to other layers.

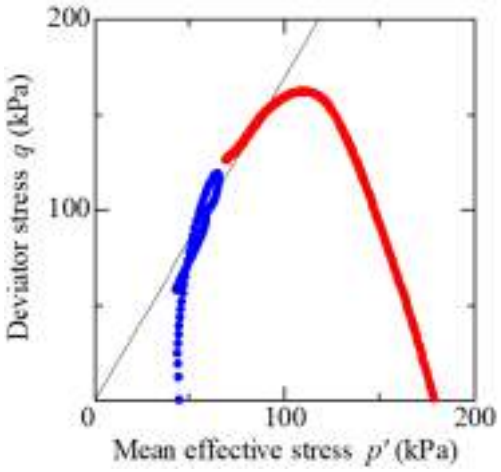

Fig. 1 Rewinding and Bowing Behavior of Soft Clay

On the other hand, the figures above exhibit the undrained monotonic shear test under isotropic conditions. Figure 1 shows the strain softening and the "rewinding and bowing" behavior of the *q-p'* graph of the soil specimen at different overburden pressures. Such characteristics are inherent to soft clay soils.

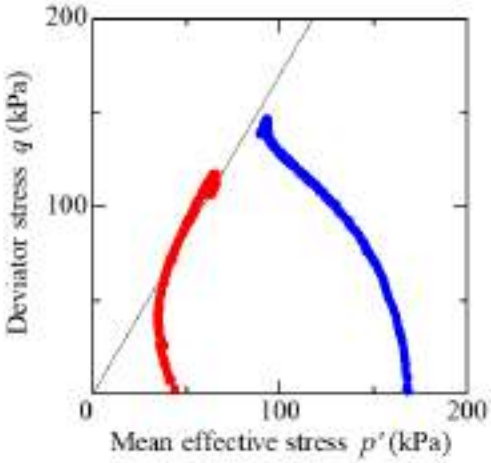

Fig. 2 Monotonic Shear Test of Reconstituted Normally Consolidated and Overconsolidated Clay

Reconstituted samples are prepared using the trimmings of undisturbed samples during sample preparation. The moisture content of the soil trimmings was increased to about 150% to 200% of its liquid limit, then mixed thoroughly using a drum mixer. Using a consolidation chamber, a pre-consolidation pressure of 150 kPa was applied for 4 days to remove air voids.

Figure 2 shows the graph of the monotonic shear test of reconstituted normally consolidated and overconsolidated soft clay. It can be observed that the peak shear strength of normally consolidated and overconsolidated specimens has minimal to no reduction, which indicates the absence of strain softening behavior of undisturbed specimens.

Experimental Procedures

The researchers conducted a series of isotropic and anisotropic consolidated-undrained monotonic triaxial tests per JGS 0523 and JGS 0525 to determine the initial and subsequent monotonic shear behavior of soft clay after applying cyclic loading. Additionally, cyclic shear tests based on JGS 0541 were also conducted to determine the dynamic response of soft clay. As for specimen preparation, the researchers found that performing stepwise loading/pressure application while maintaining a 10 kPa difference between cell pressure and back pressure is the most effective way of saturating the soil specimen. The overburden pressure used in the experiment was 180 kPa, which is based on the soil report of the site. The horizontal effective stress applied on the sample was calculated using the Eq. 1.

$$\sigma'_H = K_0 \sigma'_V \quad (1)$$

The experiments consisted of two stress conditions which were identified based on two K_0 values which are K_0 = 1.0 (isotropic) and K_0 = 0.6 (anisotropic). The K_0 value for anisotropic condition was set based on Jaky formula for normally consolidated clays [12]. Table 1 summarizes the shear tests conducted under isotropic and anisotropic conditions.

Table 1 Stress Conditions of Experiments

Spec. Type	K_0	σ'_V (kPa)	σ'_H (kPa)	q (kPa)	p' (kPa)
UDS	1.0	180	180	0	180
UDS	0.6	180	108	72	132
REC	1.0	180	180	0	180

RESULTS AND DISCUSSIONS

Undisturbed Cyclic Shear Test at K_0 = 1.0

The cyclic shear tests at K_0 = 1.0 were conducted with a stress amplitude of 72 kPa and a period of 20 seconds. This configuration was constant for all cyclic shear tests and subsequent monotonic shear tests in this study. Figure 3 shows that axial strain was developed on both the compression and extension sides, even in clay. Ultimately, the specimen fails at the extension side, which results in necking the specimen after 1295 cycles. The failure at the extension side is because naturally deposited soils are weaker against extension than in compression under isotropic conditions.

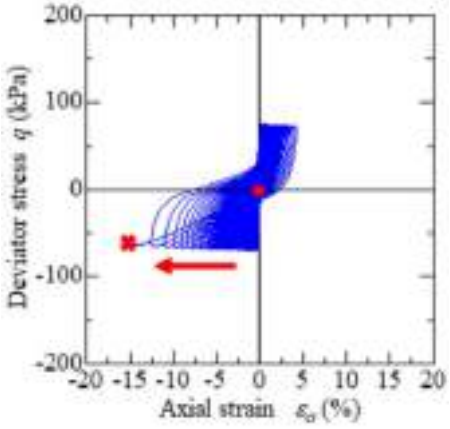

Fig. 3 Graph of q- ε_a of Cyclic Shear Test on Undisturbed Specimen at K_0 = 1.0

Furthermore, it is noticeable that there is a constant reduction in the mean effective stress, p', during cyclic loading (Fig. 4). At failure, p' is reduced to 20 kPa. This proves that even in natural clay, p' is also reduced under cyclic loading.

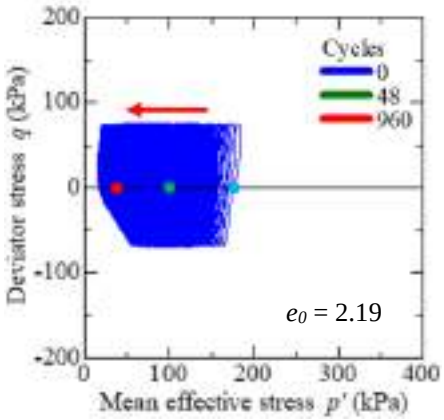

Fig. 4 Graph of q-p' of Cyclic Shear Test on Undisturbed Specimen at K_0 = 1.0

Subsequent Monotonic Shear Test after Cyclic Loading at K_0 = 1.0 of Undisturbed Soft Clay

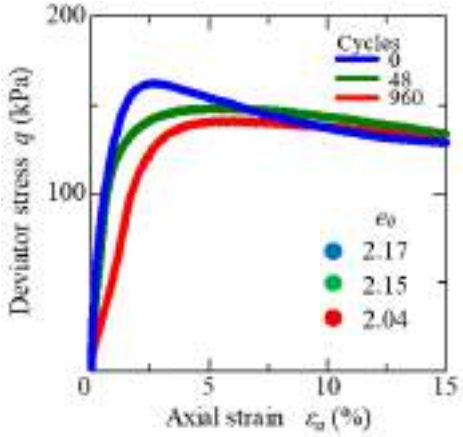

Fig. 5 Graph of q-ε_a of Subsequent Monotonic Shear Test on Undisturbed Specimen at K_0 = 1.0

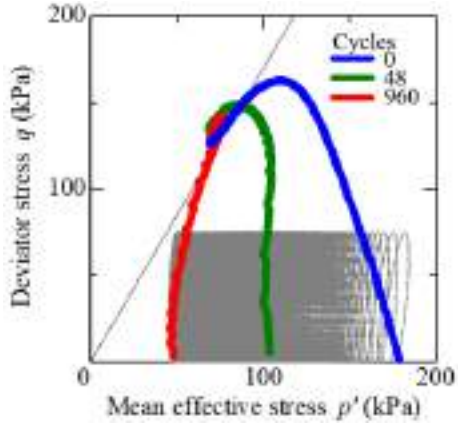

Fig. 6 Graph of q-p' of Subsequent Monotonic Shear Test on Undisturbed Specimen at K_0 = 1.0

Subsequent monotonic shear tests were also conducted at different numbers of cycles (0, 48, and 960). This is to determine the effect of cyclic loading (disturbance) on the peak shear strength, q_{max}, of the undisturbed soft clay soil. After 960 cycles, there is a 13% reduction in the peak shear strength of the sample, which emphasizes that there is only a subtle decrease in the peak shear strength after many cycles in isotropic conditions (Fig. 5 and 6).

Undisturbed Cyclic Shear Test at K_0 = 0.6

During B-value calculation and anisotropic consolidation, the mean effective stress was adjusted to 132 kPa to apply stress-induced anisotropy in the specimen. Then, the cyclic shear test was conducted based on JGS 0541. The results reveal that the axial strain propagates towards the compression side only, unlike in isotropic conditions, and eventually fails after 134 cycles (Fig. 7).

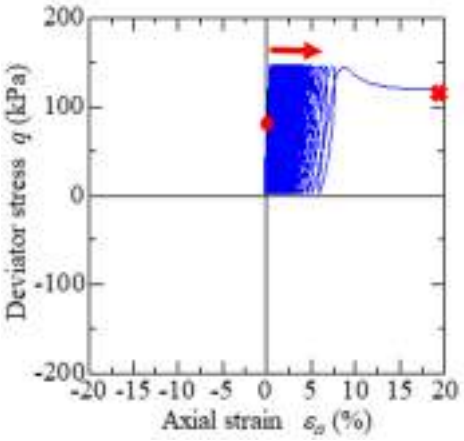

Fig. 7 Graph of q- ε_a of Cyclic Shear Test on Undisturbed Specimen at K_0 = 0.6

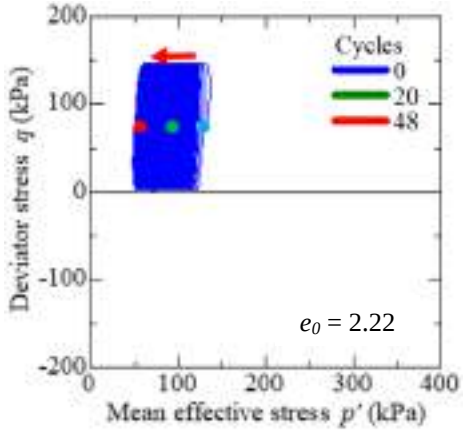

Fig. 8 Graph of q-p' of Cyclic Shear Test on Undisturbed Specimen at K_0 = 0.6

Additionally, Fig. 8 shows that the mean effective stress, p', continuously diminishes as the cyclic loading progresses. At failure, the recorded p' was 50 kPa.

Subsequent Monotonic Shear Test after Cyclic Loading at K_0 = 0.6 of Undisturbed Soft Clay

Subsequent monotonic shear tests were also conducted at different numbers of cycles (0, 20, and 48) based on the number of cycles at failure. This is to determine the effect of cyclic loading (disturbance) on the peak shear strength, q_{max}, of the undisturbed soft clay soil. The results reveal a 43% reduction in the peak shear strength after 48 cycles. It can be observed that there is a drastic decrease in the peak shear strength at a significantly lower number of cycles compared to isotropic conditions (Fig. 9 and 10).

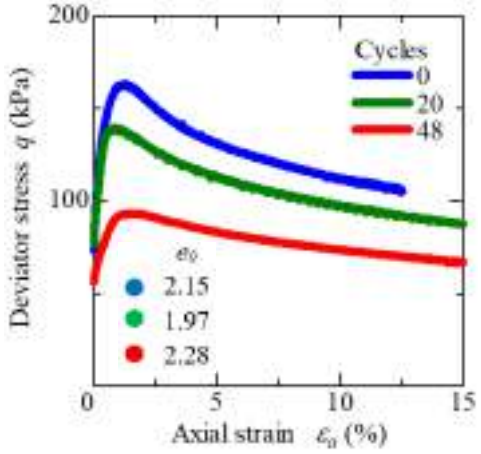

Fig. 9 Graph of q-ε_a of Subsequent Monotonic Shear Test on Undisturbed Specimen at K_0 = 0.6

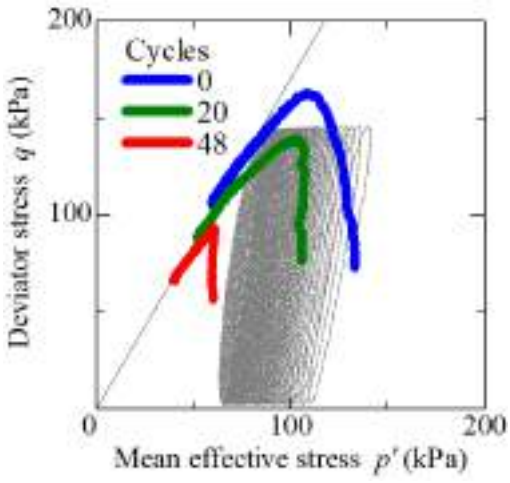

Fig. 10 Graph of q-p' of Subsequent Monotonic Shear Test on Undisturbed Specimen at K_0 = 1.0

Considering the results of cyclic and subsequent monotonic shear tests under isotropic (K_0 = 1.0) and anisotropic (K_0 = 0.6) conditions, it can be observed

that the mean effective stress, *p'*, and peak shear strength, q_{max}, were reduced after the application of cyclic loading. This can be attributed to the "disturbance" phenomenon brought by the application of cyclic loading. It can also be noticed that the reduction in q_{max} was greater under anisotropic (K_0 = 0.6) conditions at a significantly smaller number of cycles. From here, it can be deduced that the effect of "soil disturbance" is more pronounced at anisotropic conditions.

Reconstituted Cyclic Shear Test at K_0 = 1.0

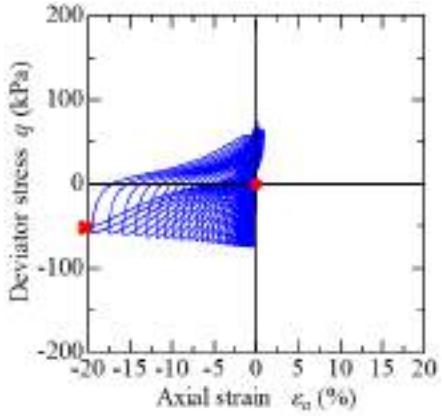

Fig. 11 Graph of q-ε_a of Cyclic Shear Test on Reconstituted Specimen at K_0 = 1.0

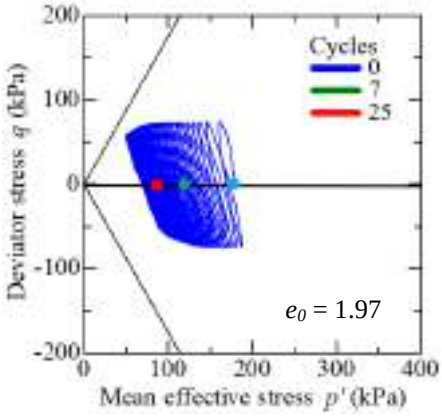

Fig. 12 Graph of *q-p'* of Cyclic Shear Test on Reconstituted Specimen at K_0 = 1.0

An isotropic cyclic shear test of reconstituted samples was conducted using the same amplitude (72 kPa) and period (20 seconds) as the undisturbed samples. This is to determine the difference between the cyclic behavior of undisturbed and reconstituted samples under the same stress conditions. Based on the results of the test, axial strain propagated initially in both compression and extension sides. However, the graph abruptly propagated towards the extension side after several cycles. This was followed by the failure of the specimen after 39 cycles (Fig. 11).

Furthermore, there was also a constant reduction in the mean effective stress of the reconstituted sample, similarly in undisturbed specimens. The mean effective stress, *p'*, at failure was about 60 kPa (Fig. 12).

Subsequent Monotonic Shear Test after Cyclic Loading at K_0 = 1.0 of Undisturbed Soft Clay

Subsequent monotonic shear tests at different numbers of cycles (0, 7, and 25) under isotropic conditions were conducted for reconstituted samples. The number of cycles was based on the number of cycles at failure. Based on the results of the experiment, there is no strain softening behavior present (Fig. 13). It is also important to take note that even after 25 cycles, the peak shear strength of the reconstituted specimen is almost equal to samples that have no cyclic loading history (Fig. 14).

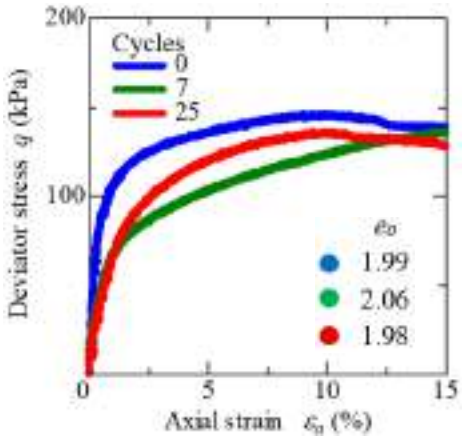

Fig. 13 Graph of q-ε_a of Subsequent Monotonic Shear Test on Reconstituted Specimen at K_0 = 1.0

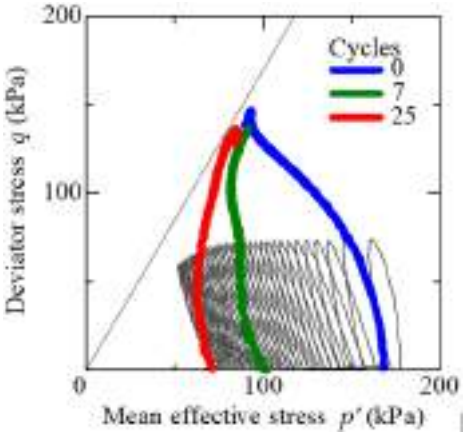

Fig. 14 Graph of *q-p'* of Subsequent Monotonic Shear Test on Reconstituted Specimen at K_0 = 1.0

Considering the results of cyclic and subsequent monotonic shear tests on undisturbed and reconstituted soft clay under isotropic conditions, it

can be observed that there is a reduction in the mean effective stress, *p'*, of the reconstituted specimen during cyclic loading. This suggests that the reduction of *p'* is not exclusively caused by cyclic loading (soil disturbance). On the other hand, the reduction in peak shear strength can only be distinguished in undisturbed soft clay specimens. It is also essential to take note that the number of cycles to failure of reconstituted specimens was significantly lower than that of undisturbed specimens. This behavior of reconstituted samples can be attributed to the lack of aging effect, which is present in undisturbed soft clay. Aging effect refers to the time-dependent increase in stiffness and strength of soil after deposition or seismic loading history. This behavior is more noticeable in fine-grained soils.

CONCLUSIONS

Based on the results of the experiments, the following conclusions can be drawn:

Physical properties of the specimen extracted from Kaizu City, Gifu Prefecture, Japan, showed that the soil specimen contains high moisture content and is mainly composed of fine-grained particles. In addition, the monotonic shear tests of the specimens exhibited strain softening in q- ε_a graph and "rewinding and bowing" behavior in q-p' graph. These characteristics proved that the soil specimen used in the experiments is indeed soft clay soil.

From the results of cyclic and subsequent monotonic shear tests on undisturbed and reconstituted soil, "soil disturbance" can be defined as the destruction of soil structure formed during deposition, loss of initial stiffness, and reduction of peak shear strength. The number of cycles to failure of the reconstituted specimen is also significantly lower than the undisturbed specimen which can be attributed to the lack of aging effect.

From the results of cyclic and subsequent monotonic shear tests under isotropic (K_0 = 1.0) and anisotropic (K_0 = 0.6) stress conditions, there is a greater reduction in peak shear strength of the specimen under anisotropic conditions at a lower number of cycles. Therefore, it can be concluded that anisotropy amplifies the effect of soil disturbance in soft clay soils.

From the geotechnical engineering perspective, it is essential to consider the anisotropic conditions of the actual ground because it may lead to overestimation of the cyclic shear resistance.

ACKNOWLEDGMENTS

The authors would like to express their deepest gratitude to the Japan International Cooperation Agency (JICA) and Geotechnical Engineering Laboratory of Nagoya University for providing the necessary resources to complete this research.

REFERENCES

[1] Zeevaert, L. (1973) Foundation Engineering for Difficult Subsoil Conditions, Van Nostrand-Reinhold Co., New York.

[2] Brown, S. F., Lashine, A. K. F. and Hyde, A. F. L. 1975. Repeated load triaxial testing of silty clay. Géotechnique. 25(1):95–114. Doi: 10.1680/geot.1975.25.1.95

[3] Yasuhara, K., Yamanouchi, T. and Hirao, K. 1982. Cyclic strength and deformation of normally consolidated clay. Soils and Foundations. 22(3): 77–91. doi: 10.3208/sandf1972.22.3_77.

[4] Gu, C., Wang, J., Cai, Y., Yang, Z. and Gao, Y. 2012. Undrained cyclic triaxial behavior of saturated clays under variable confining pressure, Soil Dynamics and Earthquake Engineering. 40: 118-128. Doi: 10.1016/j.soildyn.2012.03.011.

[5] Wichtmann, T. and Triantafyllidis, T. 2018. Monotonic and cyclic tests on kaolin: a database for the development, calibration and verification of constitutive models for cohesive soils with focus to cyclic loading. Acta Geotechca. 13: 1103–1128. Doi: 10.1007/s11440-017-0588-3

[6] Khan, I., Nakai, K. and Noda, T. 2020. Undrained cyclic shear behavior of clay under drastically changed loading rate. GEOMATE journal. 18(66): 16-23.

[7] Andersen, K. H., Pool, J. H., Brown, S. F. and Rosenbrand, W. F. 1980. Cyclic and static laboratory tests on Drammen Clay. Journal of the Geotechical Engineering Division. 106(5): 499–529. Doi: 10.1061/AJGEB6.0000957

[8] Hyodo, M., Hyde, A. F. L., Yamamoto, Y and Fujii, T. 1999. Cyclic shear strength of undisturbed and remoulded marine clays. Soils and Foundations. 39(2): 45–58. Doi: 10.3208/sandf.39.2_45

[9] Noda, T., Takeuchi, H., Nakai, K. and Asaoka, A. (2009): Co-seismic and post-seismic behavior of an alternately layered sand-clay ground and embankment system accompanied by soil disturbance, Soils and Foundations, Vol.49, No.5, pp.739-756.

[10] Nakai, K., Noda, T. and Kato, K. (2017): Seismic assessment of river embankments reinforced by the sheet pile constructed on a low N-value soft ground, Canadian Geotechnical Journal, Vol.54, No. 10, pp. 1375-1396.

[11] Callister, W. D., & Rethwisch, D. G. (2020). Materials science and engineering: An introduction (10th ed.). Wiley.

[12] Jaky, J. (1944). The coefficient of earth pressure at rest. Journal of the Society of Hungarian Architects and Engineers, 78, 355–358.

Copyright © Int. J. of GEOMATE All rights reserved, including making copies, unless permission is obtained from the copyright proprietors.

15th Int. Conf. on Geotechnique, Construction Materials & Environment,
Kyoto, Japan, 11-13 November 2025, ISBN 978-4-909106124 C3051

ALTERNATIVE APPROACH FOR SOIL IMPROVEMENT USING HYDRAULIC CEMENT COMBINATION WITH STEEL SLAG AND BIOCHAR

Nattapas Khumsuprom[1], *Supakij Nontananandh[2], Apiniti Jotisankasa[3], Susit Chaiprakaikeow[4] and Shinya Inazumi[5]

[1,2,3,4] Department of Civil Engineering, Kasetsart University, Bangkok, Thailand;
[5] College of Engineering, Shibaura Institute of Technology, Tokyo, Japan

ABSTRACT

Soil improvement is a critical challenge in geotechnical engineering, especially for weak soils like dredged sediments. This study proposes an alternative stabilization method using hydraulic cement (HC), partially replaced with steel slag (SS), and enhanced with bamboo biochar in both soaked and dry forms. Various tests, including unconfined compressive strength (UCS), free-free resonance (FFR), X-ray diffraction (XRD), and scanning electron microscopy (SEM), were conducted to evaluate mechanical and microstructural behavior. Results indicated that the mixture with 25% steel slag substitution achieved a 7-day UCS of 900.71 kPa, exceeding the standard subbase requirement of 689 kPa. The inclusion of both kinds of biochar significantly enhanced early-stage strength development, with certain combinations reaching UCS values of 769.04 kPa and 645.51 kPa after only 3 days of curing, whereas the mixture without biochar exhibited a lower UCS of just 559.27 kPa. XRD and SEM analyses confirmed the formation of calcium silicate hydrate (CSH) and Ettringite, validating the chemical stabilization mechanism. Moreover, wave velocity data from FFR tests showed a strong correlation with UCS, supporting the use of non-destructive evaluation methods and enabling predictive modeling. This approach promotes sustainability through reduced cement usage and the beneficial reuse of industrial by-products and natural agricultural waste. The findings demonstrate potential for integrating these materials into geo-environmental soil stabilization practices, in alignment with circular economy principles and the Sustainable Development Goals (SDGs).

Keywords: soil improvement, steel slag, biochar, unconfined compressive strength, sustainable geotechnics

1. INTRODUCTION

Construction on weak or soft ground is often unavoidable in rapidly urbanizing countries like Thailand, where soft clay layers dominate the subsoil profile in many regions. Such soils pose challenges including excessive settlement and low bearing capacity, especially in projects such as road embankments and earth dams. To address these issues, soil improvement techniques are essential. These techniques are generally categorized into densification, reinforcement, drainage, and cementation [1]. Among problematic soils, fine-grained sediments dredged from canals and reservoirs are particularly difficult to manage. These sediments have high moisture content and low strength, making them unsuitable for direct use in construction. However, their continuous accumulation creates disposal and environmental issues. Prior studies have demonstrated that stabilization using ordinary Portland cement (OPC), combined with industrial by-products such as fly ash or slag, can improve strength and durability [2-8].

In response to environmental concerns and carbon reduction goals, hydraulic cement (HC) incorporating industrial waste has gained attention as a more sustainable alternative to OPC [9-10]. Additionally, biochar, which is a porous and carbon-rich material derived from biomass, has shown promise in enhancing soil properties while sequestering atmospheric CO_2. Despite growing interest, few studies have investigated the combined effects of HC, steel slag (SS), and biochar on the early strength and stiffness development of stabilized sediments.

Therefore, this study aims to evaluate the performance of dredged sediment stabilized using HC partially replaced with SS, along with either soaked or dry bamboo biochar. The study assesses unconfined compressive strength (UCS), wave velocities (V_p, V_s), and microstructural development using XRD and SEM. The goal is to promote the sustainable reuse of industrial and agricultural wastes in geotechnical applications, contributing to geo-environmental engineering and the Sustainable Development Goals (SDGs).

2. RESEARCH SIGNIFICANCE

The increasing generation of industrial, agricultural, and underutilized natural wastes, such as dredged sediments, poses a growing environmental challenge. This study proposes a sustainable approach for stabilizing such materials using HC partially replaced with steel slag and enhanced with bamboo

biochar. It uniquely examines the combined effects of these materials, including comparisons of soaked and dry biochar. Free–free resonance (FFR) testing is applied to develop correlations between UCS and wave velocities, offering a non-destructive method for strength assessment. This approach supports the SDGs and advances geo-environmental engineering.

3. MATERIALS

3.1 Dredged sediment from drainage canal

The sediment used in this study was collected from a drainage canal in Phetchaburi province, approximately 176 km southwest of Bangkok. Sediment accumulation in canal significantly affects water management efficiency, as illustrated in Fig. 1. To address this, the Royal Irrigation Department conducts annual dredging operations. In 2022, approximately 478,000 m³ of sediment was dredged at a total cost of USD 367,126.

After six months of air drying, the natural water content of the sediment decreased from 117% to 5%. The sediment was classified as silty sand (SM) under the USCS, and A-4 (0) under AASHTO, indicating suitability for low to medium construction applications [11]. It had a specific gravity of 2.67, with 46.29% of particles passing through the No. 200 sieve as illustrated in Fig. 2. The particle size distribution consisted of 0.71% gravel, 51.94% sand, 28.79% silt, and 17.50% clay.

From the standard Proctor test, the optimum moisture content (OMC) was 14.32%, and the maximum dry density was 17.26 kN/m³. The UCS of the untreated sample remolded at the OMC was measured at 49.03 kPa. Previous XRF analysis revealed that this sediment primarily consists of SiO_2 (79.61%), Al_2O_3 (10.33%), and Fe_2O_3 (3.80%) [12].

Fig. 1 Drainage canal in Phetchaburi province

3.2 Steel slag

Steel slag, a by-product from electric arc furnace (EAF) steelmaking, is generated in Thailand at approximately 500,000 to 600,000 tons annually [13], posing a significant challenge for disposal and reuse. In this study, slag was sourced from Siam Machinery and Equipment Co., Ltd. in Ayutthaya province, approximately 82 km north of Bangkok.

The steel slag used in this study was dark gray in colour and initially in lump form. Approximately 300 kg of the material was ground and thoroughly homogenised to ensure consistency across all experiments. The processed slag was sieved through a No. 10 sieve, resulting in a mixture that retained some residual steel particles. No intentional removal of these metallic inclusions was carried out, in order to reflect the use of steel slag in its typical industrial form. This may have implications for long-term environmental performance, including the potential generation of metal-rich leachate from the steel particles. Notably, the inclusion of biochar in the mix may offer additional benefits by adsorbing or immobilising such contaminants, thus contributing to the overall environmental safety of the amended soil. Particle size analysis showed that 16.44% of the slag passed through the No. 200 sieve, as illustrated in Fig. 2. The slag was used as a partial replacement for hydraulic cement in selected mix designs.

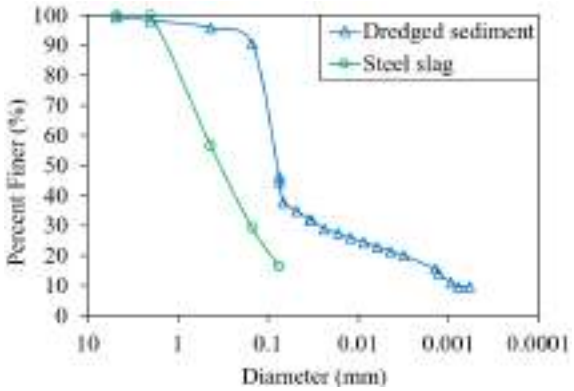

Fig. 2 Grain size distribution curve

3.3 Biochar

Biochar is a carbon-rich material produced through pyrolysis, a thermal decomposition of biomass in an oxygen-limited environment. Unlike combustion, this process stabilizes carbon into a solid form, making biochar effective for carbon sequestration and reducing greenhouse gas emissions [14-15]. The improvement in water retention of biochar-amended soil has been reported, which provides favorable effects for nature-based soil cover system in geotechnical engineering application [16].

In this study, bamboo biochar produced by Thai Carbon Co., Ltd., located in Nakhon Pathom province (55.2 km from Bangkok), using an industrial scale pyrolysis (US EPA approved technology) was utilized. The obtained sample was in fine black powder form. The manufacturer's datasheet indicates

its high specific surface area of 223 m^2/g with the pH of 9.60 indicating its alkalinity. Both dry and water-soaked biochar were incorporated into the mixtures to assess their influence on the mechanical behavior and strength development of the stabilized sediment.

4. METHODOLOGY

4.1 Specimen Preparation and UCS Test

Based on prior research [12], dredged sediment was stabilized using a base binder of hydraulic cement at 250 kg/m^3 (mass of cement by volume of soil), with a constant soil's moisture content of 17.0%. SS was used as a partial or full replacement for HC at 25% and 100%, respectively. Bamboo biochar was added at 2.68% by weight of dry soil in either dry or soaked form. Seven mix designs (Mix 0-Mix 6) are summarized in Table 1.

Table 1 Mix proportions and symbols

Symbol	Cement content (% of 250 kg/m^3)		Biochar (% by weight)	
	HC	SS	Dry	Soaked
Mix 0	100	0	0	0
Mix 1	75	25	0	0
Mix 2	0	100	0	0
Mix 3	75	25	0	2.68
Mix 4	0	100	0	2.68
Mix 5	75	25	2.68	0
Mix 6	0	100	2.68	0

Each mix was blended using a Hobart-type mechanical mixer and molded into cylindrical specimens (ϕ = 5.0 cm, h = 10.0 cm) following the method for making and curing non-compacted stabilized soil specimens (JSF T821-1988) [17] as suggested by [4]. Specimens were demolded after 24 hours and cured in plastic sealed for 3 and 7 days.

Unconfined compression tests were conducted on triplicate specimens using a universal testing machine (UTM) at a strain rate of 0.01 min^{-1}, following ASTM D2166 [18]. The maximum strength was recorded either at the peak load or at 15% axial strain, whichever occurred first.

4.2 Free-free resonance (FFR) Test

The FFR method, a non-destructive testing technique, was applied to evaluate compressional (V_p) and shear (V_s) wave velocities in the same UCS specimens. Each specimen was excited with an impact at one end, and the response was detected by an accelerometer at the opposite end.

The fundamental resonance frequency (f) was determined, and wave velocities were calculated using the relationships:

$$V_p = f_L \lambda = 2 f_L L \quad (1)$$

$$V_s = f_T \lambda = 2 f_T L \quad (2)$$

where L is the specimen length, f_L and f_T are the longitudinal and torsional resonance frequencies, respectively.

5. RESULTS AND DISCUSSIONS

5.1 Unconfined Compressive Strength (UCS)

The UCS results of all mixtures after 3 and 7 days are shown in Fig. 3. The findings indicate that both SS and bamboo biochar influence strength development. Although the UCS of Mix-1 (75% HC and 25% SS) at 7 days was lower than that of Mix-0 (100% HC), it represented the highest strength among all mixtures incorporating SS, reaching 900.71 kPa and exceeding the subbase requirement of 689 kPa [19]. Notably, Mix-3, which included 75% HC, 25% SS, and soaked biochar, exhibited the highest early strength, with a 3-day UCS of 769.04 kPa, equivalent to approximately 94% of its 7-day value (820.16 kPa). This 3-day strength exceeded that of both Mix-0 and Mix-1, highlighting the positive contribution of soaked biochar to early strength development.

In contrast, Mix-4, which consisted of 100% SS and soaked biochar, yielded the lowest UCS among all mixtures, reaching only around 104.38 kPa at 7 days. This result suggests that the combination of SS and biochar alone lacks sufficient binding potential to effectively stabilize the soil. Nevertheless, the UCS of Mix-4 was still slightly higher than that of untreated soil, indicating a marginal improvement in strength despite the absence of HC.

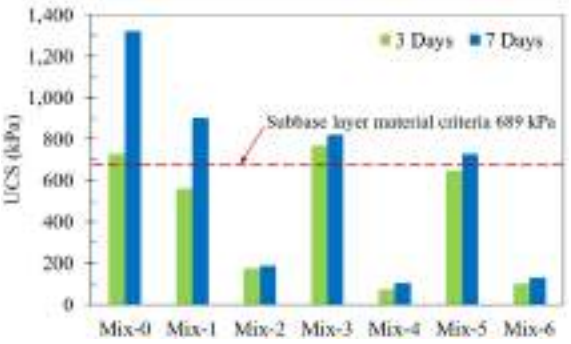

Fig. 3 UCS of stabilized sediment

Mix-3 exhibited a reduced water content after curing (13.97%) as illustrated in Fig. 4, likely due to moisture uptake and gradual release from soaked biochar. This contributed to more effective hydration and matrix densification. Comparing Mix-3 and Mix-5 (same binder, different biochar condition), soaked biochar led to higher UCS, indicating its superior contribution to early strength. Overall, the combination of HC, SS, and soaked biochar enhanced

UCS, particularly at early ages, likely through improved hydration and filler effects from the porous structure of biochar.

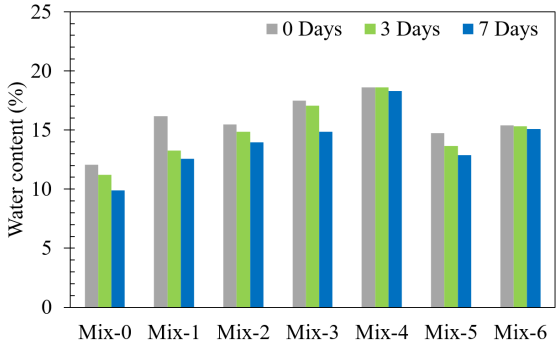

Fig. 4 Water content of stabilized sediment

5.2 Compression and Shear Wave Velocity

FFR test results for all mixtures are presented in Fig. 5 and Fig. 6. Both compressional (V_p) and shear (V_s) wave velocities increased with curing time and showed similar trends to the UCS results.

Mix-1, composed of 75% HC and 25% SS, exhibited the highest wave velocities after 7 days (V_p = 1,151.32 m/s, V_s = 657.90 m/s), indicating superior stiffness and well-developed internal structure. Mix-3, which additionally incorporated soaked biochar, also demonstrated relatively high wave velocities (V_p = 1129.74 m/s, V_s = 593.44 m/s), reflecting its notable early strength performance and enhanced material continuity.

In contrast, Mix-4, comprising 75% SS and soaked biochar without cement, recorded the lowest velocities (V_p = 203.02 m/s, V_s = 124.45 m/s), consistent with its poor mechanical properties. Overall, mixtures containing soaked biochar tended to show improved wave propagation characteristics compared to those with dry biochar or without biochar, especially when combined with a hydraulic binder.

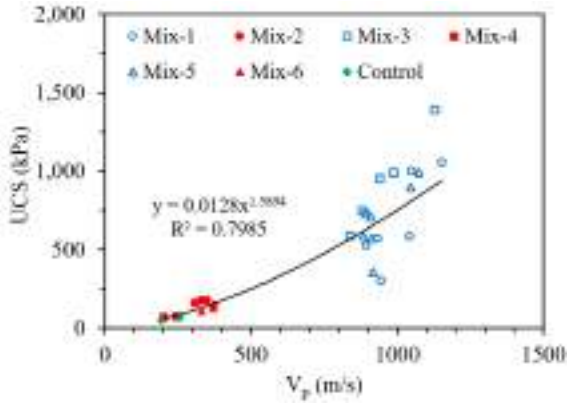

Fig. 5 UCS versus V_p

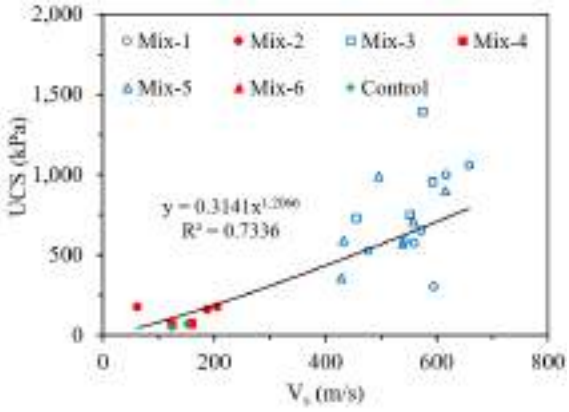

Fig. 6 UCS versus V_s

This can be attributed to improved particle bonding and water retention, which enhance matrix stiffness. Empirical equations were developed to predict UCS from wave velocities, as follows:

$$UCS = 0.0128V_p^{1.5894} \quad (R^2 = 0.7985) \quad (3)$$

$$UCS = 0.3141V_s^{1.2066} \quad (R^2 = 0.7336) \quad (4)$$

These correlations indicate that FFR testing provides a promising non-destructive approach for estimating strength development in stabilized dredged sediments.

5.3 X-ray diffraction analysis

The mineralogical composition of stabilized sediment was investigated using X-ray diffraction, and the results are presented in Fig. 7. The diffraction patterns indicated that quartz (PDF 05-0490) was the dominant mineral in the untreated dredged sediment. Secondary minerals identified included montmorillonite (PDF 03-0010), illite (PDF 43-0686), and kaolinite (PDF 05-0143), which correspond with the soil classification results.

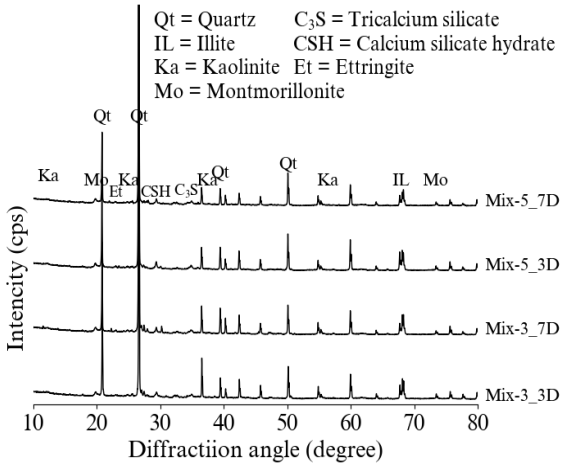

Fig. 7 XRD pattern of Mix-3 and Mix-5

In addition, characteristic peaks corresponding to hydration products, namely calcium silicate hydrate (CSH, PDF 00-012-0739) and ettringite (PDF 04-013-3691), were observed in the treated mixtures. Notably, the ettringite peak in Mix-3 was more pronounced than in Mix-5, consistent with its higher unconfined compressive strength (UCS). These findings confirm that chemical reactions occurred during the curing process and contributed to the observed strength development.

5.4 Scanning electron micrographs

Microstructural analysis was performed using scanning electron microscopy (SEM) on fractured surfaces of selected specimens. Fig. 8 shows the SEM micrograph of Mix-3 after 7 days of curing. The image reveals a substantial presence of rod-shaped ettringite crystals, one of the key hydration products in cement-treated soils.

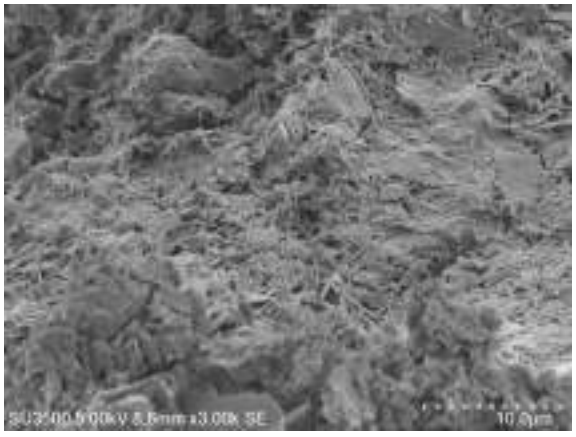

Fig. 8 SEM micrograph of Mix-3 at 7 days curing

These needle-like formations are known to contribute to strength development by filling voids and bridging soil particles, thus enhancing matrix integrity. The presence of ettringite observed here is consistent with the XRD results (Section 5.3), which also confirmed distinct peaks for ettringite in Mix-3. The agreement between SEM and XRD findings validates the occurrence of hydration reactions in the treated soils, supporting the mechanical performance results observed in the UCS and FFR tests.

6. CONCLUSIONS

This study investigated the stabilization of dredged sediment from drainage canals using hydraulic cement partially replaced with steel slag and enhanced with bamboo biochar. The main findings are summarized as follows:

1. Partial replacement of hydraulic cement with steel slag (up to 25%) improved the mechanical performance of the stabilized sediment. Mix-1 achieving a 7-day UCS of 900.71 kPa exceeding 689 kPa, meeting subbase material standards.

2. The addition of a biochar, particularly in the soaked condition, significantly accelerated early strength development. Mix-3 and Mix-5 reached UCS values of 769.04 kPa and 645.51 kPa, respectively, at 3 days, outperforming mixes without biochar in early-age strength.

3. A clear correlation was observed between UCS and wave velocities (V_p and V_s), reflecting increased material stiffness. This relationship supports the development of predictive equations and highlights the potential of FFR testing for non-destructive strength estimation in stabilized soils.

4. XRD and SEM analyses confirmed the formation of key hydration products, notably CSH and ettringite. Their presence validated the hydration mechanisms responsible for strength development.

5. In addition to enhancing strength, hydraulic cement may help reduce environmental risks. Its alkalinity promotes heavy metal precipitation, while hydration products like CSH and ettringite can immobilize contaminants [20]. Although leachability or chemical composition analysis of steel slag were not assessed in this study, the addition of biochar with high sorptive capacity may further limit pollutant mobility. Further research is recommended to assess long-term performance.

Overall, the combination of hydraulic cement, steel slag, and bamboo biochar a promising and sustainable solution for reusing dredged sediments in civil engineering applications. This approach not only improves geotechnical performance but also promotes circular use of industrial and natural by-products, aligning with low-carbon geo-environmental engineering practices and SDGs.

7. ACKNOWLEDGMENTS

The authors gratefully acknowledge the Faculty of Engineering, Kasetsart University, for its financial support and provision of laboratory facilities throughout this study. Special appreciation is also extended to the Royal Irrigation Department, Ministry of Agriculture and Cooperatives, Siam Machinery and Equipment Co., Ltd., Green Ground Solutions Co., Ltd and Thai Carbon Co., Ltd. for their generous support in supplying essential materials. Their valuable contributions were instrumental in accomplishing the research objectives. Assistance from Mr. Chalantorn Thiansri and Mr. Pannathorn Sukkul in sample preparation and performing experiments are thanked for.

8. REFERENCES

[1] Hausmann, M.R. Engineering Principles of Ground Modification; McGraw-Hill: New York, NY, USA, 1990.

[2] Chompoorat T., Maikhun T., and Likitlersuang S., Cement-Improved Lake Bed Sedimentary Soil for Road Construction. Proceedings of the Institution of Civil Engineers-Ground Improvement, Vol. 172, Issue 3, 2019, pp. 192-201.
[3] Nontananandh S., Khumsuprom N., Thongdetsri T., Jotisankasa A., Chaiprakaikeow S., and Inazumi S., Sustainable Utilization of Dredged Sediments and Water Treatment Sludges as Construction Materials Through Combined Dewatering and Cement Stabilization Techniques. Recycling, Vol. 10, Issue 1, 2025, pp. 22.
[4] Kamon M., and Nontananandh S., Contribution of Stainless-Steel Slag to the Development of Strength for Seabed Hedoro. Soils and Foundations, Vol. 30, Issue 4, 1990, pp. 63-72.
[5] Chan C. M., Strength Improvement Characteristic of Cement-Solidified Dredged Marine Clay with Relation to Water-Cement Ratio. GEOMATE Journal, Vol. 11, Issue 27, 2016, pp. 2734-2740.
[6] Ghadir P., and Ranjbar N., Clayey Soil Stabilization Using Geopolymer and Portland Cement. Construction and Building Materials, Vol. 188, 2018, pp. 361-371.
[7] Yoobanpot N., Jamsawang P., Poorahong H., Jongpradist P., and Likitlersuang S., Multiscale Laboratory Investigation of the Mechanical and Microstructural Properties of Dredged Sediments Stabilized with Cement and Fly Ash. Engineering Geology, Vol. 267, 2020, pp. 105491.
[8] Nontananandh S., Yoobanpot N., Chaysuwan D., and Thongdaeng K., Influence of Fineness of Cement Produced from Industrial Wastes on Strength of Mortar. Agriculture and Natural Resources, Vol. 45, Issue 4, 2011, pp. 762-772.
[9] Mehta K. P., Reducing the Environmental Impact of Concrete. Concrete International, Vol. 23, Issue 10, 2001, pp. 61-66.
[10] Scrivener K., Martirena F., Bishnoi S., and Maity S., Calcined Clay Limestone Cements (LC3). Cement and Concrete Research, Vol. 114, 2018, pp. 49-56.
[11] Youdee S., Nontananandh S., Khumsuprom N., and Thongdetsri T., Improvement of Sediment Dredged from Drainage Canal Using Cement. The 11th Nontri E-san National Academy Conference, Sakonnakhon, Thailand, 2023, pp. 472-482.
[12] Nontananandh S., Khumsuprom N., Thongdetsri T., Youdee S., Jotisankasa A., Chaiprakaikeow S., and Inazumi S., Cement Stabilization of Dredged Sediments from Drainage Canals: Effect on Physico-Chemical Properties. GEOMATE Journal, Vol. 27, Issue 124, 2024, pp. 143-150.
[13] Pollution Control Department, Ministry of Natural Resources and Environment, Municipal Solid Waste Composition Report 2021. Waste and Hazardous Substances Management Bureau, Bangkok, 2021.
[14] Lehmann J., and Joseph S. (Eds.), Biochar for Environmental Management: Science, Technology and Implementation. Taylor & Francis, 2024.
[15] Woolf D., Amonette J. E., Street-Perrott F. A., Lehmann J., and Joseph S., Sustainable Biochar to Mitigate Global Climate Change. Nature Communications, Vol. 1, Issue 1, 2010, pp. 56.
[16] Hossain M., Jotisankasa A., Aramrak S., Nishimura S., and Yodsudyai W., Influence of Biochar on Unsaturated Hydraulic Characteristics of a Tropical Residual Silty Sand. International Journal of Geosynthetics and Ground Engineering, Vol. 10, Issue 5, 2024, pp. 78.
[17] Japanese Geotechnical Society, JSF T 821-1990, Practice for Making and Curing Noncompacted Stabilized Soil Specimens. Japanese Geotechnical Society, 1990.
[18] American Society for Testing and Materials. ASTM D2166/D2166M-24, Standard Test Method for Unconfined Compressive Strength of Cohesive Soil.
[19] Department of Highways, Standard No. DH-S 206/2021, Soil Cement Subbase. Department of Highways, Thailand, 2021. (in Thai)
[20] Chen Q.Y., Tyrer M., Hills C.D., Yang X.M., and Carey P., Immobilisation of heavy metal in cement-based solidification/stabilisation: A review. Waste Management, Vol. 29, Issue 1, 2009, pp. 390–403.

Copyright © Int. J. of GEOMATE All rights reserved, including making copies, unless permission is obtained from the copyright proprietors.

15th Int. Conf. on Geotechnique, Construction Materials & Environment,
Kyoto, Japan, 11-13 November 2025, ISBN 978-4-909106124 C3051

INVESTIGATION ON DISPERSIVE CHARACTERISTICS OF SOILS EXCAVATED FROM FLOOD RETENTION POND

*Supakij Nontananandh[1], Kittipong Tongphet[2], Susit Chaiprakaikeow[3], Patipan Thaimthong[4], Yuki Fuka[5] and Shinya Inazumi[6]

[1,2,3] Department of Civil Engineering, Kasetsart University, Bangkok, Thailand;
[4] Royal Irrigation Department, Ministry of Agriculture, Thailand;
[5,6] College of Engineering, Shibaura Institute of Technology, Tokyo, Japan

ABSTRACT

Dispersive soils are prone to structural collapse and erosion when exposed to water, often leading to turbidity, sedimentation, and reduced reservoir life when improperly managed in flood retention pond construction. This research aimed to investigate the dispersive characteristics of soils excavated from a flood retention pond in Prachin Buri province, Thailand. Laboratory tests included physical dispersion tests such as the crumb test, double hydrometer test, and pinhole test, and chemical analyses such as the sodium adsorption ratio (SAR) and the percentage of sodium (%Na) relative to total dissolved salts. Mineralogical analysis using X-ray diffraction (XRD) was also performed. Field observations and tests were conducted in parallel and compared with actual water quality data. The findings suggested that soil dispersivity is strongly related to sodium content and mineralogy, particularly the presence of montmorillonite. A practical solution is proposed for managing dispersive soils during excavation, including proper separation and stockpile zoning to reduce dispersion risks, thereby promoting the sustainable use of excavated soil in construction projects.

Keywords: Dispersive Soils, Flood Retention Ponds, Soil Erosion, Water Turbidity, Soil Management

INTRODUCTION

Flood retention ponds are vital to Thailand's water management, helping reduce floods and support sustainability [1], [2]. Excavation from these ponds produces large volumes of soil, which can be reused in roads, embankments, or dams [1]. However, some soils are dispersive, making them prone to internal erosion and piping [3]. If not properly identified, they may compromise structural integrity and cause turbidity, environmental harm, and safety concerns [4].

In the Prachin Buri project, signs of erosion, slumping, and shallow channels were observed in stockpiled soils, indicating dispersive behavior [1]. These traits were not detected by standard classification methods [3], [5]. Improper zoning also led to mixing of dispersive and non-dispersive soils, complicating reuse and revealing a gap in routine soil assessment practices [6].

Dispersive soils can degrade earth structures through internal erosion, leading to turbidity, siltation, and water quality loss [4], [7], [8]. In rural areas, this increases maintenance needs and risks for flood control systems. Early identification is crucial for long-term safety and sustainability [2]. Although dispersive soils are well documented globally [3], geotechnical investigations in Thailand rarely include specific tests. Common methods, such as Atterberg limits or grain size distribution, cannot reliably detect dispersive behavior [5]. Proper evaluation requires tests like the crumb test, pinhole test, double hydrometer test, and chemical indices such as SAR and %Na [9], which are often omitted.

This research supports Thailand's Bio-Circular-Green (BCG) Economy Model, which promotes sustainability through bio-based resources , material efficiency , and eco-friendly technologies [2], [10]. Identifying and managing dispersive soils enables more sustainable reuse of excavated materials, reduces environmental risks, and enhances infrastructure resilience. By applying geotechnical and chemical indicators, this study contributes to better resource use and reduced construction waste key goals of the BCG strategy.

The study investigates the dispersivity of soils from flood retention projects in Prachin Buri using laboratory tests and field observations. A zoning approach is proposed to manage dispersive soils for safe reuse. Recommendations include compaction and lime treatment to improve stability. The findings support practical guidelines and align with Thailand's BCG Economy Model [2], [10].

RESEARCH SIGNIFICANCE

This study addresses the often-overlooked challenge of managing dispersive soils excavated from flood retention ponds, which can pose long-term environmental risks if mishandled. Focusing on a project in Prachin Buri Province, Thailand, the research links soil dispersivity with erosion and turbidity, and proposes a practical zoning strategy developed through field surveys and laboratory

testing to minimize environmental impacts during soil disposal. The findings offer practical guidance for dam engineers, irrigation planners, and project managers in implementing appropriate soil management strategies for safer and more resilient infrastructure development. resilient infrastructure.

MATERIALS AND METHODS

Study Area

Following the work of Thiamthong and Nontananandh [11], this study was conducted at five water resource development projects in Prachin Buri Province, Thailand an area with extensive flood retention initiatives under national water management plans. The province was selected for its representative geology, frequent use of flood retention ponds in rural infrastructure, and the variety of excavation and stockpiling practices observed in recent RID projects. These factors make it a suitable location for evaluating the dispersive characteristics of excavated soils. The selected sites include the Talad Mai Flood Retention Project, Sapa Khon Public Pond Dredging Project, Saphan Hin Pumping Station Project, Noen Na-ngam Flood Retention Project, and Wang Takhian Flood Retention Project all under the Prachin Buri Agricultural Research and Development Center. Conducted between 2021 and 2023, these projects differ in excavation volume, stockpiling methods, and field conditions, which are expected to influence the geotechnical behavior of the soils [6]. Table 1 summarizes key project characteristics, including excavation volumes, stockpile height, and compaction status.

Table 1. Excavation volume, stockpile height, and compaction status

Project Name	Excavation Volume (x 10^4 m^3)	Stockpile Height (m)	Compaction
Taladmai	12.50	4.00	Yes
Sappakhon	3.15	1.00	No
Saphanhin	2.37	1.00	Partial
Noennangam	10.61	1.00	No
Wangtakhian	50.00	2.00	No

Soil and Water Sampling and Field Observation

Disturbed soil samples were collected from stockpiles at five study sites following RID's soil sampling guideline [9]. Test pits were excavated at depths of 1.0 and 1.5–2.0 meters using a crawler-mounted backhoe. the sampling depths were selected based on typical excavation depths during pond construction and preliminary field observations of soil dispersivity with depth. Approximately 20 kilograms of soil were collected per sample for laboratory testing and sealed in moisture-retaining containers. Water samples were collected from each reservoir surface using standard grab methods in line with MWA standards, which are modified from WHO guidelines [12-13]. Turbidity was measured in the laboratory using portable meters under ISO 7027.

Laboratory Testing

The collected soil samples were tested to determine their basic physical properties and dispersive potential. Geotechnical properties were evaluated through grain size analysis using the combined sieve and hydrometer method (ASTM D422-72) [14], liquid limit (ASTM D423-72) [15], plastic limit (ASTM D424-71) [16], and classification based on the Unified Soil Classification System (USCS) per ASTM D2487-17 [17].

To assess dispersivity, three physical tests were conducted: the Crumb Test and Pinhole Test following Royal Irrigation Department (RID) standards, and the Double Hydrometer Test per ASTM D4221-99. Chemical indices, including Percent Sodium (%Na) and Sodium Adsorption Ratio (SAR), were also analyzed to understand soil sodicity and its correlation with dispersive behavior [9].

To support the physical and chemical results, selected samples underwent X-ray Diffraction (XRD) to identify dominant clay minerals such as montmorillonite, kaolinite, and illite, which influence deflocculation and erosion resistance in fine-grained soils. The mineralogical data helped interpret the test results and clarify the relationship between clay composition and observed dispersivity [18].

RESULTS AND DISCUSSION

Soil Classification and Field Observations from Excavated Samples

Soil samples from eleven locations across five flood retention projects in Prachin Buri Province were analyzed to assess basic geotechnical properties and field behavior. Table 2 summarizes the results, including grain size distribution, plasticity indices, USCS classification, and field observations such as erosion and water clarity.

Among the eleven samples, four were classified as CL or CH, indicating moderate to high plasticity clays. The remaining samples were SM or ML, corresponding to silty sand and low-plasticity silt. Liquid Limit (LL) values for the clayey soils ranged from 44.05% to 52.46%, and Plasticity Index (PI) values from 21.45% to 24.86%, reflecting moderate to high plasticity.

Field observations showed that erosion, dust, and turbid water were mostly associated with CH and CL soils. For example, Sample 1 (Talad Mai) and Sample

3 (Sapa Khon) exhibited turbid water and surface erosion. In contrast, most SM and ML samples, especially those from greater depths, were linked to clearer water.

Plasticity behavior was further interpreted using the LL–PI chart (Figure 1), which relates plasticity to erosion categories [19]. Samples 1 to 4, though classified as CL and CH, were in the highest erosion resistance zone, indicating that high plasticity alone does not imply erosion susceptibility. This contrasts with field observations of turbidity and erosion. The discrepancy suggests that Atterberg limits alone are insufficient to predict dispersive or erosive behavior and should be combined with physical, chemical, and mineralogical indicators.

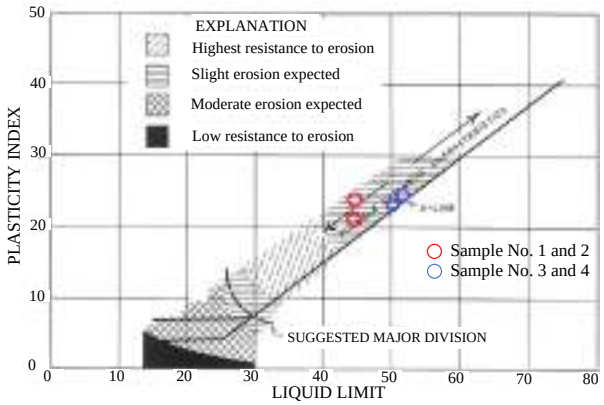

Fig.1 Correlation between plasticity index and liquid limit for evaluating erosion categories (Gibbs 1962)[19]

Physical Dispersion Test

Three physical tests, namely the Crumb Test, Double Hydrometer Test, and Pinhole Test, were used to assess the dispersive potential of the soil samples. The results are presented in Table 3.

The Crumb Test evaluates soil dispersion based on turbidity observed after immersion in distilled water. According to ASTM D6572, Grade 1 indicates no dispersion, while Grade 4 denotes immediate and strong dispersion. Samples 1, 2, 9, and 10 were rated as Grade 4, indicating high dispersivity. Conversely, Samples 3, 4, 6, 7, 8, and 11 were rated as Grade 1, reflecting non-dispersive behavior.

The Double Hydrometer Test quantifies dispersion as a percentage. According to ASTM D4221, values below 33% are considered non-dispersive, values between 34–67% are intermediate, and values above 68% are classified as highly dispersive. Sample 2 (76%) were classified as highly dispersive. Samples 1, 7, 9, and 10 fell within the intermediate dispersive range (34–67%).

The Pinhole Test assesses soil behavior under a hydraulic head. According to ASTM D4647-06, ND1 indicates non-dispersive behavior, while D1 and D2 denote dispersive behavior. Most samples were classified as ND1, which corresponds well with their Crumb Test and hydrometer results. However, Sample 10 exhibited D1 behavior, confirming its highly dispersive nature.

Chemical Dispersion Test

Chemical tests were conducted to evaluate dispersivity based on sodicity and salinity indicators, including Percent Sodium (%Na) and Sodium Adsorption Ratio (SAR). Table 4 presents the results.

Samples 1, 2, and 9 exhibited high %Na values of 86%, 82%, and 73%, respectively. According to RID guidelines[9], soils with %Na exceeding 60% are considered chemically dispersive, particularly when combined with low salinity. The corresponding SAR values for these samples were 5.0, 4.2, and 3.7, all exceeding the RID-defined threshold of 2.0 for dispersion behavior.

By contrast, Samples 5 through 8 exhibited low %Na (0-33%) and SAR values below 0.4, indicating low sodicity and a low risk of dispersion. Sample 11, with moderate values (SAR = 0.65, %Na = 42%), was categorized as intermediate dispersive.

Based on the Sherard classification diagram[2] (Figure 2), Samples 1, 2, 3, 4, 9and10 were categorized as Zone A (dispersive); Samples 5-8 were classified as Zone B (non-dispersive); and Sample 11 as Zone C (intermediate dispersive). These chemical findings correlate well with both the physical test results and field observations.

Water Turbidity Assessment

Field observations were conducted after the construction phase and revealed signs of surface erosion, airborne dust, and runoff-induced washout at multiple locations. Additionally, visual inspection of adjacent reservoir water indicated persistent turbidity at the Talad Mai,Noen Na-ngam, and Wang Takhian sites, whereas water at the Sapa Khon and Saphan Hin sites appeared visibly clear. These observations suggested that the soils at the more turbid locations may exhibit dispersive characteristics.

Water turbidity in the excavated areas was evaluated both visually and using Nephelometric Turbidity Units (NTU). Table 5 summarizes the results of turbidity values measured in NTU and visual observations of water clarity at each site.

The highest turbidity was recorded at Wang Takhian (19.63 NTU), followed by Talad Mai (9.99 NTU) and Noen Na-ngam (6.55 NTU). These value exceeded the WHO guideline for drinking water (5 NTU) [13], although this reference is used here only

Table 2 Basic geotechnical properties and field observations of soil sample

No.	Project	Depth (m)	%Passing No.4	%Passing No.200	LL (%)	PI (%)	USCS	Pits	Dust	Surface Erosion	Water Clarity
1	Talad Mai	1.0	100	73.05	44.13	24.86	CL	No	Yes	Yes	Turbid
2		2.0	100	94.11	44.05	21.45	CL				
3	Sapa Khon	1.0	100	90.41	52.46	24.77	CH	No	Yes	No	Clear
4		1.5	100	91.85	50.86	23.44	CH				
5	Sa phanHin	1.0	95.38	25.3	NP	NP	SM	No	Yes	Yes	Clear
6		1.5	94.56	25.04	NP	NP	SM				
7	Noen Na-ngam	1.0	66.27	25.25	NP	NP	SM	Yes	Yes	Yes	Turbid
8		1.5	96.13	41.27	NP	NP	SM				
9	Wang Takhian	1.0	98.29	50.01	NP	NP	ML	Yes	Yes	Yes	Turbid
10		1.0	88.49	23.95	NP	NP	SM				
11		2.0	83.01	35.94	NP	NP	SM				

Note : NP = Non-Plastic. 'Turbid' indicates visibly cloudy water observed during field investigation

as a benchmark. In contrast, Sapa Khon and SaphanHin exhibited clearer water, with turbidity levels of 5.52 and 2.95 NTU, respectively. These results are consistent with laboratory data, affirming that dispersive soils contribute to increased turbidity due to clay deflocculation and colloid release

XRD Analysis Test

The mineralogical composition of soil samples was analyzed using X-ray Diffraction (XRD) to support interpretation of dispersive behavior. Figure 2 shows diffraction profiles from four sites: Sapa Khon (1.0 m), Noen Na-ngam (1.0 m), Wang Takhian (1.0 m), and Wang Takhian (2.0 m).

Quartz (Qt) was the dominant mineral in all samples, with a major peak at $2\theta \approx 26.6°$, matching ICDD PDF No. 01-085-0799. As a non-clay silicate with no cation exchange capacity, quartz is not associated with dispersion.

Kaolinite (Ka), a non-dispersive clay mineral, appeared in several samples with peaks at $2\theta \approx 12.4°$ and 24.9° (PDF No. 00-014-0164). Its presence, especially in Samples 1, 2, and 3, suggests stable soil with low swelling potential and minimal dispersivity.

Montmorillonite (Mo) was identified in Sample 4 (Wang Takhian, 1.0 m), with a basal reflection at $2\theta \approx 5.8°–6.2°$ (PDF No. 00-029-1498). As a smectite clay with high cation exchange capacity and strong sodium affinity, montmorillonite is a key indicator of dispersivity. This aligns with Sample 4 Crumb Grade 4, D1 pinhole classification, and high SAR, suggest moderate dispersion under field conditions.

Illite (I), a non-expanding clay, was also found in Sample 4, with peaks near $2\theta \approx 8.8°$ and 19.8° (PDF No. 00-026-0911). With moderate plasticity, illite may contribute to intermediate dispersivity, particularly when combined with high sodium content, as observed in Sample 4 (SAR 3.7, D1 classification).

Minor amounts of calcite (C) were detected, with a peak near $2\theta \approx 29.4°$ (PDF No. 01-072-1937). Calcite, however, is not directly linked to dispersivity.

Implications and Recommendations for Excavation and Soil Stockpile Management

This study emphasizes the importance of early excavation planning, particularly in setting safe depths that avoid dispersive soil layers. Overlooking these horizons can lead to long-term issues, including persistent turbidity and environmental risks from exposed stockpiles. Where deep excavation into dispersive strata is unavoidable, careful planning of stockpile and reuse zones is essential to minimize impacts. Environmentally responsible soil management can draw from past water resource projects in the area. This includes assessing site-specific soil properties and dispersion potential before excavation. Excavation and placement should comply with the Ministerial Regulation on Soil Erosion Prevention for Excavation and Landfilling, B.E. 2543 (2000). Sustainable stockpile management should follow these key guidelines:

First, a preliminary subsurface investigation should be conducted at 1–2 points per site to identify soil boundaries. Soil zoning must designate suitable areas for stockpiling different soil types. Representative samples should be collected every2,000 m^3 of excavated soil per RID standards. In areas with potential dispersive soils, at least five physical and chemical tests should be conducted. If three or more confirm dispersivity, the soil is

Table 3 Results of Physical dispersivity

No.	Project	Depth (m)	Crumb Test	Degree of Dispersion (%)	Pinhole Test
1	Talad Mai	1	4	36	ND1
2		2	4	76	ND1
3	Sapa Khon	1	1	0	ND1
4		1.5	1	11	ND1
5	Saphan Hin	1	4	29	ND1
6		1.5	1	28	ND1
7	Noen Na-ngam	1	1	36	-
8		1.5	1	11	ND1
9	Wang Takhian	1	4	35	ND1
10		1	4	65	D1
11		2	1	4	ND1

Table 4 Results of chemical dispersivity

No	Project	Depth (m)	TDS (meq/L)	% Na	SAR	Zone
1	Talad Mai	1	2.202	86	5	A
2		2	2.326	82	4.2	A
3	Sapa Khon	1	1.206	69	2	A
4		1.5	1.639	79	3.3	A
5	Saphan Hin	1	0.503	20	0.23	B
6		1.5	0.66	20	0.26	B
7	Noen Na-ngam	1	0.744	26	0.37	B
8		1.5	1.203	22	0.38	B
9	Wang Takhian	1	3.427	73	3.7	A
10		1	3.909	61	2.8	A
11		2	0.697	42	0.65	C

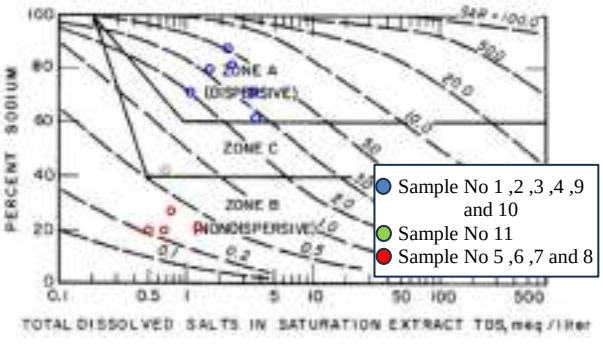

Fig.2 Sherard diagram categorizing samples into dispersive zones based on %Na, SAR, and TDS.[2]

Table 5 Turbidity values measured in NTU and visual observations of water clarity at each site

Study Site	Turbidity (NTU)	Visual Observation
Talad Mai	9.99	Turbid
Sapa Khon	5.52	Clear
Saphan Hin	2.95	Clear
Noen Na-ngam	6.55	Turbid
Wang Takhian	19.63	Turbid

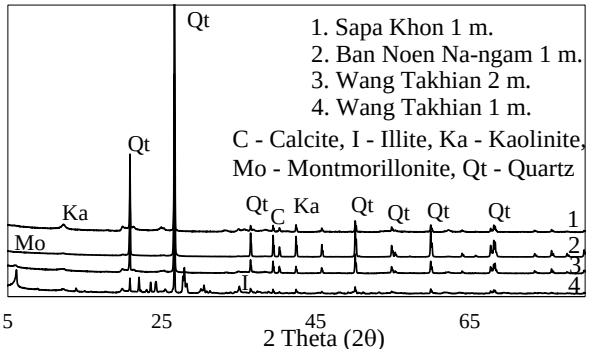

Fig.3 X-ray diffraction patterns of soils

classified as dispersive. Appropriate treatments, such as lime stabilization or alum solution, should then be applied to mitigate erosion and dispersion [20].

Second, if excavation into dispersive layers is unavoidable, physical barriers like geomembranes should be installed to isolate dispersive soils and prevent exposure to surface water, thereby reducing turbidity and downstream sedimentation.

Third, if dispersive soil must be stockpiled, piles should be covered with materials such as geotextile, mulch, or temporary grassing to reduce surface erosion and colloid dispersion from rainfall or runoff.

These recommendations promote sustainable, compliant excavation and management of dispersive soil. Zoning, testing, and treatment reduce risks to the environment and improve infrastructure resilience.

CONCLUSIONS

This study examined the dispersive characteristics of soils from five flood retention projects in Prachin Buri Province through physical, chemical, mineralogical, and field assessments. Soils with high Crumb Test grades, dispersion rates above 68%, Pinhole classifications of D1 or D2, SAR values over 2, and %Na above 60% consistently showed dispersive behavior, surface erosion, and water turbidity. XRD analysis confirmed montmorillonite, highlighting the role of clay mineralogy in soil instability. These results emphasize the importance of early identification of dispersive soils to prevent long-term environmental and structural issues.

To manage such risks, the study recommends subsurface investigations, zoning by dispersivity, and chemical stabilization where appropriate. Stockpiled dispersive soils should be protected to limit erosion and colloidal loss. These practices follow RID guidelines and support the sustainable reuse of excavated soils in water projects.

For future outlook, further investigation on chemical stabilization techniques for dispersive soils found in flood retention areas, as well as long-term monitoring of water quality impacts, will be proposed. These findings would support site-specific design guidelines, enabling safe reuse of dispersive soils in infrastructure. Integrated approaches can reduce environmental impacts, lower maintenance costs, and support Thailand's Bio-Circular-Green (BCG) Economy Model by promoting sustainable soil use.

ACKNOWLEDGMENTS

The authors express their sincere gratitude to the Faculty of Engineering, Kasetsart University, for their generous research funding. They also acknowledge the Soil Science Division, Royal Irrigation Department, for their invaluable assistance in conducting dispersive soil testing. Additionally, the Metropolitan Waterworks Authority is acknowledged for its kind support in conducting water sample testing, which significantly contributed to the successful completion of this study.

REFERENCES

[1] Royal Irrigation Department. (2022). Annual Report 2022. Bangkok, Thailand: Royal Irrigation Department.

[2] National Science and Technology Development Agency (NSTDA). (2021). BCG Economy Model: Driving Thailand Towards Sustainable Development. Thailand: NSTDA, pp. 1–40.

[3] Sherard, J.L., Decker, R.S., and Ryker, N.L. (1976). Pinhole Test for Identifying Dispersive Soils. Journal of the Geotechnical Engineering Division, ASCE, Vol. 102, No. GT1, pp. 69–85.

[4] Shahin, M.M., and Farooq, A.A.,Assessment of Dispersive Soil Problems in Embankment Dams: A Review,Journal of Soil and Water Conservation, Vol. 77, No. 3, 2022, pp. 199–211.

[5] Razouki, S.S., Al-Mashhadani, H.N., and Al-Mohammed, A.A. (2004). Identification of Dispersive Soils in Iraq. Engineering Geology, Vol. 74, Issues 1–2, pp. 1–9.

[6] Royal Irrigation Department. (2023). Water Resource Development Projects in Prachin Buri Province (2021–2023). Bangkok, Thailand: Royal Irrigation Department.

[7] Pattanasophon, W. (1989). Dispersive Soil Problems in Thailand and Their Identification. Proceedings of 5th Southeast Asian Geotechnical Conference, Bangkok, Thailand, pp. 219–226.

[8] Petry, T.M. and Little, D.N. (2002). Review of Stabilization of Clays and Expansive Soils in Pavements and Lightly Loaded Structures: History, Practice, and Future. Journal of Materials in Civil Engineering, Vol. 14, No. 6, pp. 447–460.

[9] Royal Irrigation Department (RID). Standard for Dispersive Soil Testing for the Selection of Construction Materials for Dams and Irrigation Structures, 1st ed., Construction Project Management Bureau, Ministry of Agriculture and Cooperatives, Thailand, 2017, pp. 3–29

[10] Office of the National Economic and Social Development Council (NESDC), BCG in Action: Thailand's Sustainable Development Strategy 2021–2027, NESDC, Thailand, 2021, pp. 1–78.

[11] Thaimthong P., and Nontananandh S., Sustainable Excavated Soil Management in Water Resource Development Projects. Proceedings of the 20th KU KPS National Conference, 2023, pp. 20-29.

[12] Metropolitan Waterworks Authority, Water Supply Quality Standards. Metropolitan Waterworks Authority: Bangkok, Thailand, 2022.

[13] World Health Organization (WHO). (2017). Guidelines for Drinking-Water Quality, 4th ed., Geneva: World Health Organization, pp. 1–564.

[14] ASTM D422-72, Standard Test Method for Particle-Size Analysis of Soils, ASTM International, West Conshohocken, USA, 1972.

[15] ASTM D423-72, Standard Test Method for Liquid Limit of Soils, ASTM International, West Conshohocken, USA, 1972.

[16] ASTM D424-71, Standard Test Method for Plastic Limit of Soils, ASTM International, West Conshohocken, PA, USA, 1971.

[17] ASTM D2487-17, Standard Practice for Classification of Soils for Engineering Purposes (Unified Soil Classification System), ASTM International, West Conshohocken, USA, 2017.

[18] Sun, H., Zhang, Y., Liu, W., and Chen, L. (2023). Influence of Montmorillonite Content on the Dispersive Behavior of Clayey Soils. European Journal of Soil Science, Vol. 74, Issue 1, pp. 125–138.

[19] H. J. Gibbs, "Mechanics of Soil Erosion and Its Relation to the Properties of Soils," Proceedings of the Soil Science Society of America, vol. 26, pp. 179–183, 1962.

[20] Chawalee, P. (2018). Development of Soil Dispersion Classification System for Irrigation Projects in Thailand. Journal of Irrigation Engineering, Vol. 45, Issue 3, pp. 201–210.

Copyright © Int. J. of GEOMATE All rights reserved, including making copies, unless permission is obtained from the copyright proprietors.

15th Int. Conf. on Geotechnique, Construction Materials & Environment,
Kyoto, Japan, 11-13 November 2025, ISBN 978-4-909106124 C3051

RESISTIVITY PATTERNS IN LOOSE BEDROCK USING DRONE-BASED ELECTROMAGNETIC EXPLORATION METHOD

Hiroaki Hoshino[1], Atsuko Nonomura[2], Haruki Ojyuku[3],
Shuichi Hasegawa[4] and Akira Jomori[5]

[1]West Nippon Expressway Co. Ltd., Japan
[2,3] Faculty of Engineering and Design, Kagawa University, Japan
[4]Institute of Education, Research and Regional Cooperation for Crisis Management Shikoku, Kagawa University, Japan; [5]NeoScience Co., Japan

Abstract

Identifying subsurface information (e.g., loosened rock mass and moisture content) is extremely important for slope disaster prevention in mountainous areas. However, estimating the distribution of loosened rock mass in subsurface layers has been difficult, and practical methods have not yet been established. Electromagnetic exploration is one of the methods for investigating subsurface structures, and recently, drone-based electromagnetic exploration method has been utilized. In this study, we investigated vertical resistivity profile patterns acquired using drone-based electromagnetic exploration method in a mountainous area in the southwestern Shikoku region of Japan, adjacent to the Kanagi landslide. Resistivity distributions were measured during both dry and wet terms. The difference in resistivity between the terms was examined in both ridge and valley terrains. As a result, a clear decrease in resistivity was observed in some ridge areas. Furthermore, the decrease suggests the possibility of estimating the depth of the loosened layer, which is one of the important factors in landslide occurrence. This indicates that the drone-based electromagnetic exploration method has the potential to contribute to slope disaster prevention.

Keywords: Loosened rock mass slope, Geophysical exploration, Resistivity, Drone

1. INTRODUCTION

In mountainous regions, at the loosened slopes due to gravitational deformation, deep-seated landslides or slope failures can be triggered by earthquakes or heavy rainfall [1]. To mitigate the disasters caused by such landslides and failures, it is essential to understand subsurface conditions such as loosened rock mass and moisture content to estimate the risk of disasters. There are several methods to estimate the looseness of the slopes. Geophysical method is one of the means to estimate the subsurface structure. To acquire the regional resistivity as looseness related information, airborne electromagnetic measurements have been used. Although measurement via helicopter has been commonly used, recently, the drone-based electromagnetic exploration method [2] is also used as one of the most efficient geophysical techniques for assessing the condition of rock mass. Several cases of applying the drone-based electromagnetic exploration method in the field of disaster prevention have been reported [3]. However, a practical method for evaluating subsurface looseness for the purpose of slope disaster prevention has not yet been established. In this study, slope resistivity surveys were conducted using the drone-based electromagnetic exploration method in mountainous terrain in the upstream basin of the Sakihama River in Muroto City. In this area, previous studies have reported that the bedrock slopes are deformed due to flexural toppling [4]. The presence of such loosened zones had been identified by topographic features and helicopter-based exploration method [5].

In this study, based on the data acquired, we analyze the relationship between zones with resistivity changes from the dry term to the wet term and the loosened rock mass. By identifying locations and depths where significant decreases in resistivity are observed during the rainy and dry terms, we propose a method to estimate loosened rock mass based on the rate of change in resistivity, thereby clarifying the relationship with areas where loosened bedrock is likely to be significant.

2. RESEARCH SIGNIFICANCE

The drone-based electromagnetic exploration method is considered one of the most efficient geophysical exploration techniques. In this study, we focused on changes in resistivity from the dry to the wet term to examine the relationship with loosened rock mass. If this method, which allows safe and efficient large-area surveys, can estimate the locations and depths of rock mass loosening, it will contribute to the development of effective slope disaster prevention strategies.

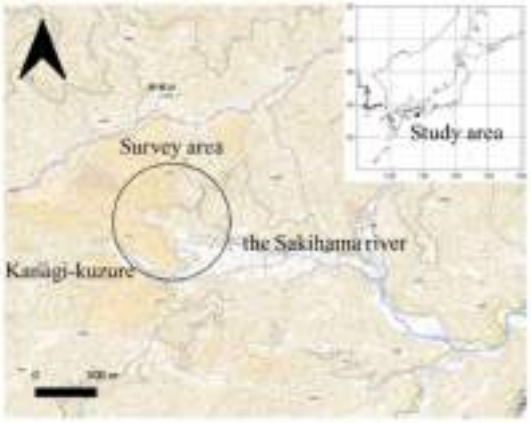

Fig.1 Study area: mountain slopes near Kanagi landslide
This map is based on the Digital Map published by Geospatial Information Authority of Japan.

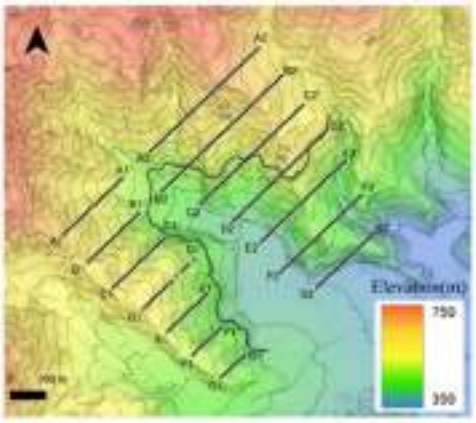

Fig.2 Locations of survey lines with elevation

3. STUDY AREA

The study area is in the upstream basin of the Sakihama River in Muroto City, Kochi Prefecture, in southwestern Japan (latitude 33°27′30″ to 33°29′00″ N, longitude 134°06′50″ to 134°11′00″ E) (Fig. 1). The bedrock in this area consists of sandstone, shale, alternating sandstone–mudstone layers, belonging to the Paleogene Muroto Peninsula Group in the Outer Zone of southwest Japan [6]. The geological strata generally strike northeast–southwest or north-northeast–south-southwest, and dip steeply to the northwest at angles between 60° and 90° [7]. A large-scale slope failure known as the Kanagi-kuzure occurred in the 1707 Hoei Nankai earthquake and heavy rainfall in 1746 [8], or possibly a rain-induced event that occurred several hundred years before 1707.

4. RESISTIVITY SURVEY

Fig. 2 shows 14 survey lines. In this study, the resistivity was acquired by the D-GREATEM system [2] (Fig. 3). The total precipitation for the 30 days prior to each survey date was 945.5 mm during the dry term and 245.0 mm during the wet term. Previous studies have shown that resistivity tends to decrease when saturation increases due to rainfall [9-10]. The average air temperatures on the survey dates were 21.0°C (dry term) and 25.6°C (wet term). Based on previous studies [11], this temperature difference is considered small and unlikely to affect resistivity measurements.

5. RESULTS OF THE RESISTIVITY SURVEY

The resistivity for each depth was calculated from the measured data using the method proposed by Jomori et al. [2]. Resistivity was estimated at 10 m intervals along the survey line, and at each point, it

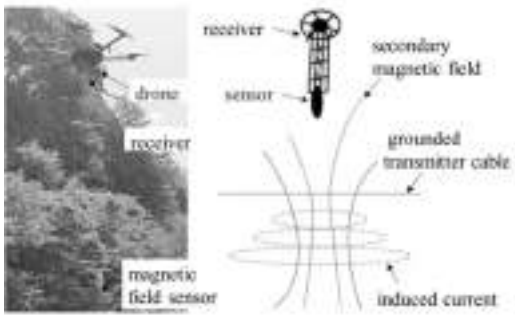

Fig.3 Schematic of exploration method (D-GREATEM)

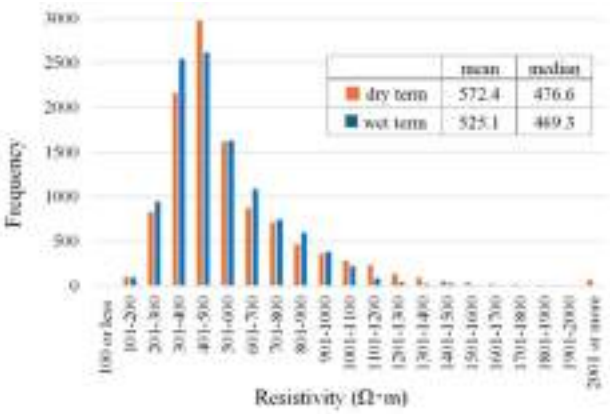

Fig.4 Frequency of resistivity: dry/wet terms

was estimated vertically at 5 m intervals. Resistivity was calculated from the depth at which sensitivity was obtained to the ground surface, and the maximum depth was 175 m.

Fig. 4 shows a histogram of resistivity distributions measured along 14 survey lines during the dry and wet terms. The observed resistivity values ranged from 100 to several thousand Ω·m, which are within the typical range for bedrock materials [12]. According to the histogram, resistivity values exceeding 1,700 Ω·m were present only in the dry term and were absent in the wet term. In the wet term,

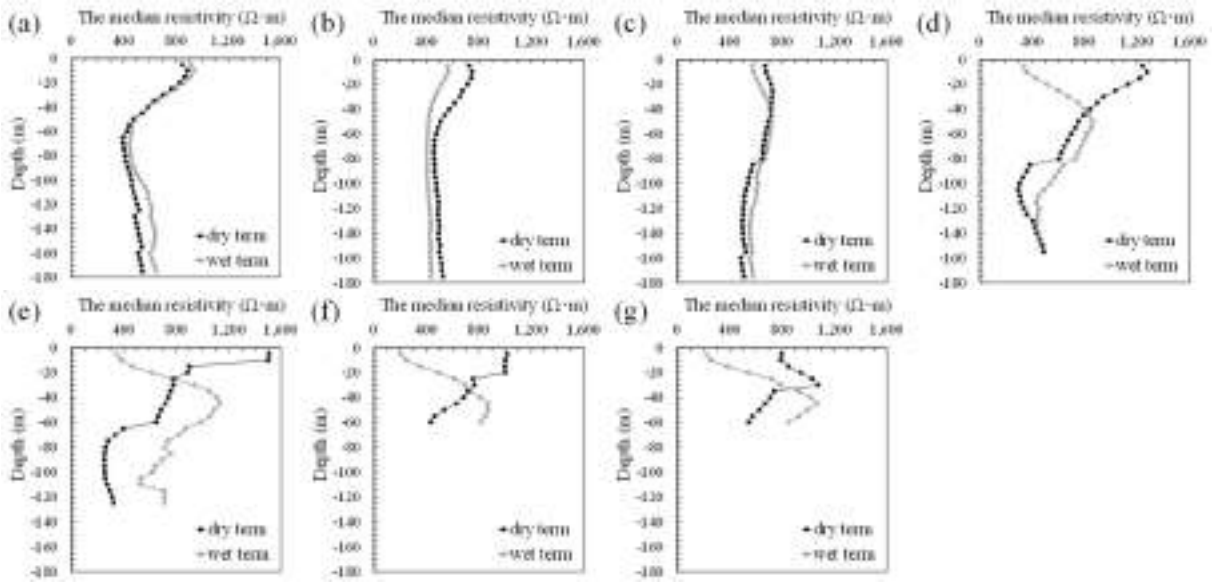

Fig.5 Median resistivity values by depth along survey lines. Shown depths indicate effective data limits per profile. *(a) A1–A1' survey line; (b) B1–B1'; (c) C1–C1'; (d) D1–D1'; (e) E1–E1'; (f) F1–F1'; (g) G1–G1'.*

the mean and median of the resistivity values are lower than those in dry term. These indicate that resistivity values decreased in the wet term compared to the dry term.

Fig. 5 shows plots of median resistivity values by depth for each survey line. Data of the 14 survey lines, those of acquired on the survey lines from A1-A1' to G1-G1' on the west side were used (Fig. 5). This is because those survey lines were installed along single or a few ridges and valleys and were considered uitable for capturing the effects of the terrain. Two distinct patterns of resistivity change were identified. In survey lines A1-A1' (Fig. 5a), B1-B1' (Fig. 5b), and C1-C1' (Fig. 5c), there was little difference in resistivity between the dry and wet terms. However, in survey lines D1-D1' (Fig. 5d), E1-E1' (Fig. 5e), F1-F1' (Fig. 5f), and G1-G1' (Fig. 5g), decrease in resistivity from the dry to wet term was observed down to a depth of approximately 40 m. In the unsaturated zone of bedrock slopes, resistivity increases with higher porosity and lower saturation. In addition, an increase in saturation due to water accumulation leads to a decrease in resistivity [12]. This indicates that the resistivity reduction observed in the D1-D1' to G1-G1' survey lines likely reflect rainwater infiltration into typical toppling-induced loosened zones in the bedrock of the study area. At greater depths along the D1-D1' to G1-G1' survey lines, there are areas where resistivity is higher in the wet term than in the dry term. Such a trend has also been reported in previous studies [9], where it was interpreted that infiltration of rainwater from above caused downward movement of air. To verify this, detailed investigations such as borehole surveys are required, which were not conducted in this study.

Table 1 Number of Measurement Points and Resistivity Change Rate α by Depth

Depth (m)	Total points	α (resistivity change rate)			
		Quartiles			Robust Z = -2
		Q1	Median (Q2)	Q3	
5	381	0.006	-0.398	-0.695	-1.438
20	378	-0.054	-0.300	-0.501	-0.963
35	366	0.103	-0.017	-0.313	-0.634

6. ANALYSIS AND RESULTS

6.1. Resistivity Change Rate

To evaluate the degree of resistivity reduction at each location, the resistivity change rate α was calculated at each survey point using Equation (1). ρ1 is the dry resistivity and ρ2 is the wet resistivity.

$$\alpha = (\rho 2 - \rho 1) / \rho 2 \quad (1)$$

Table 1 summarizes the calculated resistivity change rate (α) by depth, showing quartiles and values with a robust Z-score of -2. Although the robust Z-score [13] is typically used for outlier detection, in this study it is applied to identify locations with significant decreases in resistivity — areas where well-developed looseness may be of concern. A significant decline is defined as a robust Z-score less than −2. These results indicate that the resistivity reduction is greater near the surface, suggesting a stronger influence from rainfall at

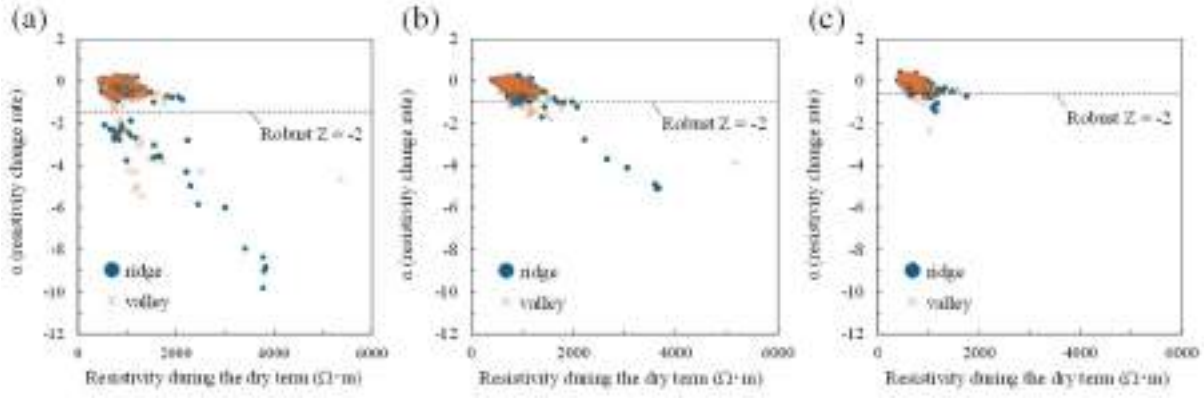

Fig. 6 Relationship between α (resistivity change rate) and dry- term resistivity, classified by terrain type (*a): Depth = 5 m; (b): Depth = 20 m; (c): Depth = 35 m*

shallower depths. As depth increases, the decrease in resistivity becomes more gradual, indicating the infiltration behavior of rainwater. These findings indicate that differences in subsurface conditions within a relatively shallow range, down to approximately 35 m in depth, were successfully captured using the drone-based airborne exploration method.

6.2. Topography-Based Analysis

To analyze the influence of local topography on the resistivity change rate α described in the previous section, each measurement point was classified as either a ridge or a valley based on plan curvature. Plan curvature (Kp) was calculated using the Equation (2) [14-15]. A 10-m resolution digital elevation model (DEM) was analyzed using the GIS software ILWIS 3.3.

$$K_p = -\frac{d_y{}^2 d_{xx} - 2d_x d_y d_{xy} + d_x{}^2 d_{yy}}{(d_x{}^2 + d_y{}^2)^{\frac{3}{2}}} \qquad (2)$$

Each measurement point was classified as a ridge when Kp > 0 and as a valley when Kp < 0 [16]. Fig. 6 shows a plot with the resistivity change rate α on the vertical axis and the dry-term resistivity on the horizontal axis, with data points classified as either ridges or valleys. Measurement points with a robust Z-score less than −2 — indicating potentially well-developed looseness — were found predominantly in ridge areas. This tendency was particularly evident at shallow depths. In addition, at ridge points, greater resistivity changes were observed at locations with higher dry-term resistivity.

7. DISCUSSION

Fig. 7 shows a red relief image map. The slopes where survey lines A1-A1' to G1-G1' are located lie near the remnants of the Kanagi landslide. Gentle

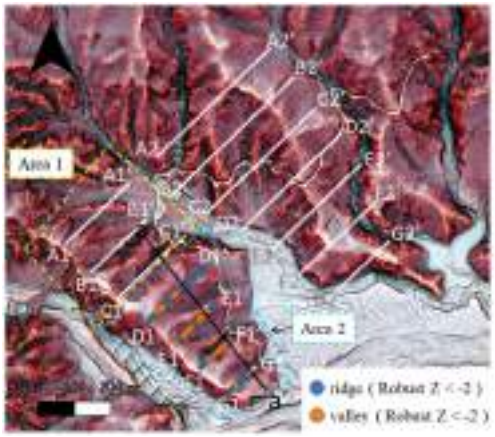

Fig.7 Points where robust Z-score < −2

slopes are also observed near some of the mountain summits in this area. Although the slopes lie along the same main ridgeline, the A1–A1' to C1–C1' and D1–D1' to G1–G1' sections show differences in ridge shape and valley development. In the area from A1–A1' to C1–C1', the valleys are more developed than in the surrounding region, resulting in a tendency toward narrow ridges (hereafter referred to as Area 1). The relationship between ground permeability and topography has shown that areas with more developed valleys tend to have lower permeability [17]. This is consistent with the observation that there was little difference in resistivity between the dry and wet terms in A1–A1' (Fig. 5a), B1–B1' (Fig. 5b), and C1–C1' (Fig. 5c), suggesting limited water infiltration. On the other hand, in the area from D1–D1' to G1–G1', valleys are few, and rounded ridges along with gentle upper slopes are distributed (hereafter referred to as Area 2). Such characteristics observed in Area 2 are consistent with those typically found in bedrock with relatively high permeability coefficients [20]. This is consistent with the significant decrease in resistivity observed in D1–D1' (Fig. 5d), E1–E1' (Fig. 5e), F1–F1' (Fig. 5f), and G1–G1' (Fig. 5g), suggesting the possibility of deep rainwater infiltration. Furthermore, the tendency for

resistivity decrease near the surface gradually diminishes with depth is consistent with the formation process of toppling-type looseness. These findings show that the patterns of resistivity decrease clearly reflect the near-surface bedrock permeability inferred from topographic features (Fig. 5).

Measurement points showing a significant decrease in resistivity (robust Z-score less than −2) were concentrated on the slopes in Area 2 (Fig. 7). The slopes in this area feature rounded ridges and gentle upper slopes, indicating terrain where gravitational deformation is suspected to be well developed. In particular, the slope where the D1–D1' survey line is located is convex-shaped, with gentle upper slopes and step-like features, suggesting deep-seated deformation possibly caused by deep-seated gravitational slope deformation [18-19]. At the outcrop along the forest road on this slope, loosened bedrock with openings was visually observed (Fig. 8). It is considered that the data showing a significant decrease in resistivity (robust Z-score less than −2) successfully identified slopes where deep-seated looseness is suspected. On the other hand, some measurement points classified as valleys based on plan curvature (Kp) are also located on the same convex-shaped slope. This is likely because the classification is based on elevation data (DEM) calculated over a fixed area, which reflects local terrain features. This issue may be improved by adjusting the analysis window size used in calculating plan curvature (Kp). In addition, measurement points classified as ridges based on plan curvature (Kp) showed a correlation between high dry-term resistivity and resistivity decrease rate, particularly at shallow depths (Fig. 6a, b). These findings suggest the possibility of estimating significant rock mass loosening using only dry-term resistivity data; however, this remains a subject for future investigation.

Next, regarding the estimation of the development depth of loosened bedrock: accurately determining the depth of looseness at each site requires detailed investigations such as borehole surveys. However, it is reasonable to consider that the depth at which resistivity decreased due to water infiltration lies at least within the extent of the loosened zone. Fig. 9 shows an elevation profile along the a–a′ cross section (Fig. 7), along with the resistivity decrease zones obtained from D1–D1' (Fig. 5d), E1–E1' (Fig. 5e), F1–F1' (Fig. 5f), and G1–G1' (Fig. 5g). The resistivity decrease zone along the D1–D1' survey line falls within the elevation range between the ridge crest (535.7 m) and the valley bottom to the west (490.9 m). In the case of a ridge with no lateral confinement where tilting of the geological strata is progressing, this depth range can be reasonably considered to correspond to the distribution of loosened zones. The ridge where the E1–E1' survey line is located also lacks lateral confinement on the

Fig.8 Outcrops along the D1 survey line forest road

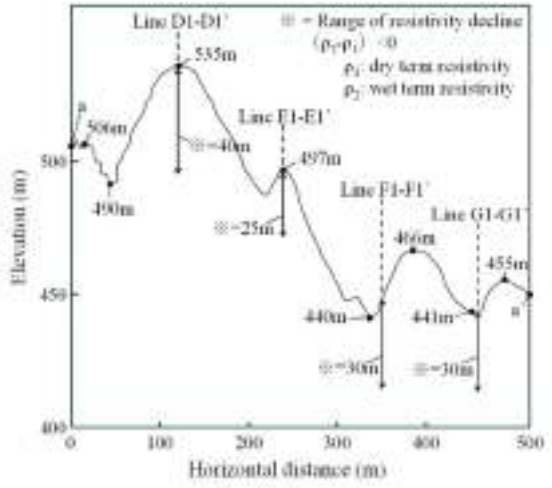

Fig.9 Elevation & resistivity drop (a–a' section)

eastern valley side. Considering the steep dip of the geological strata across the area (to the northwest), it is likely that looseness has developed to greater depths. Since the airborne exploration method provides average resistivity values over a given area, interpretation becomes difficult when the survey line crosses both ridges and valleys. This applies to the F1–F1' and G1–G1' survey lines. A method for estimating the depth of loosened bedrock caused by toppling has been proposed by Ueno [20]. In addition to empirical knowledge from past disasters, the depth can be inferred from borehole investigations and on-site observations of rock mass displacement and tilt direction. Although this method offers a certain level of accuracy, empirical rules can vary widely, and on-site investigations require considerable time and effort. On the other hand, the interpretation combining low-resistivity zones detected by drone-based airborne electromagnetic surveys with topographic conditions enables rapid and wide-area investigations. This approach may prove useful as preliminary information in the early stages of disaster prevention planning.

8. CONCLUSION

In this study, we analyzed resistivity data obtained from mountain slopes using drone-based

electromagnetic exploration method in relation to terrain features and derived the following findings.

- The patterns of resistivity decrease in the near-surface zone (up to ~35 m depth) obtained from the drone-based electromagnetic exploration method showed clear differences between valley and ridge terrains.
- Under wet conditions, robust Z-score < −2 areas were concentrated on gently sloping, rounded ridges where loosened bedrock is topographically suspected. In some cases, the resistivity reduction depth matched the ridge–valley elevation difference, suggesting the method's utility in estimating loosened bedrock depth.

9. ACKNOWLEDGMENTS

The D-GREATEM survey was funded by the SECOM Science and Technology Foundation. This research was part of a project funded by the KAKENHI (23K04348).

10. REFERENCES

[1] Chigira M., Prediction of Potential Landslide Sites - From the Viewpoint of Geology and Geomorphology -, Journal of JSCE Series C (Geosphere Engineering), Vol. 62, No. 4, 2006, pp. 722-735. (in Japanese)

[2] Jomori A., Jomori N., Jomori A., Kondo T., Yuuki Y., and Shinsei A., Development of airborne transient electromagnetics system using Drone: D-GREATEM, D-TEM [GLS], and D-TEM [ALS], Butsuri-Tansa (Geophysical Exploration), Vol. 73, 2020, pp. 83-95. (in Japanese)

[3] Yuuki Y., Shinsei A., Tomimori S., Saito Z., Jomori A., and Jomori A., Geological survey of the Seino area in Nobi Plain by drone airborne electromagnetic survey method, Butsuri-Tansa (Geophysical Exploration), Vol. 74, 2021, pp. 142-150. (in Japanese)

[4] Sato G., Yagi H., Kitani H., Senda Y., and Hirota K., Remains of the Iwasa checkpoint on the Noneyama-kaido as an ancient road located in ridge-top area formed by gravitational deformation, the Muroto Peninsula, Japan, Journal of the Japan Landslide Society, Vol. 57, No.1, 2020, pp. 19-23. (in Japanese)

[5] Nonomura A., and Hasegawa S., Susceptibility of slopes to earthquake-induced landslides: a new index derived from helicopter-borne electromagnetic resistivity and digital elevation data sets, Landslides14, 2017, 2155-2163, doi 10. 1007/s10346-017-0873-0.

[6] Nakamura H., Tsuchiya S., Inoue M., and Ishikawa Y., Jishin Sabou, Kokon Shoin, 2000, pp. 38-41. (in Japanese)

[7] Chigira M., Geological prediction of rock avalanches. In Proceedings of the 8th Congress of the International Association for Engineering Geology and the Environment, Vancouver, BC, Canada, 21–25 September 1998; pp. 1409-1414.

[8] Chigira M., Kanagi-kuzure. In Earthquake Sabo, Kokon Shoin, Tokyo, Japan, 2000; pp. 38-41. (In Japanese)

[9] Suzuki K., Ito E., and Chigira M., Loosening Process of Surface Area in Weathered Granite and Infiltration of Rainwater to Excavated Slope - Evaluation using Geophysical Exploration and Observed Field Data -, Journal of the Japan Society of Engineering Geology, Vol. 43, No.5, 2002, pp.270-283. (in Japanese)

[10] Tamura E., Kanayama S., Hasegawa S., and Turuta S., Infiltration behavior of shallow and deep groundwater in a rock mass slope, Journal of the Japan Landslide Society, Vol.44, No.2, 2007, pp.33-40. (in Japanese)

[11] Takakura S., Yoshioka M., Uchida Y., Ishizawa T., and Sakai N., Resistivity monitoring for estimation of changes in water content in an embankment, BUTSURI-TANSA, Vol. 65, No. 4, 2012, pp.223-236. (in Japanese)

[12] The Calamity Science Institute, JIBANNOKASHIKATOTANSAGIJYUTU, KAJIMA INSTITUTE PUBLISHING CO., LTD., 2001, pp. 1-187. (in Japanese)

[13] Prapasri Puwastien., Issues in the development and use of food composition databases, Public Health Nutrition: 5(6A), 2002, pp.991-999.

[14] Bengt Fornberg., Generation of Finite Difference Formulas on Arbitrarily Spaced Grids, MATHEMATICS OF COMUTATION, vol.51, No.184, 1988, p.699-706.

[15] John Loomis., Second Derivative Filters, https://www.johnloomis.org/ece563/notes/filter/second/second.html (accessed May 1, 2025).

[16] Suzuki T., Introduction to map reading for civil engineers, Kokon Shoin, 1997, pp.1-200. (in Japanese)

[17] Japan Society of Engineering Geology., SANCHINOCHIKEIKOUGAKU, Kokon Shoin, 2000, pp.1-213. (in Japanese)

[18] Chigira M., Site Characteristics of Gigantic Landslides, Kinmiraisha, 2007, pp.1-256. (in Japanese)

[19] Kojima S., Recent progress and future perspective of research on deep-seated gravitational slope deformation in Japan from the engineering geological viewpoint, Jour. Geol. Soc. Japan, Vol. 124, No.11, 2018, pp.889-897. (in Japanese)

[20] Ueno S., Investigations and countermeasures for toppling type slope movement, Oyo technical report, Vol.31, 2012, pp.25-41. (in Japanese)

Copyright © Int. J. of GEOMATE All rights reserved, including making copies, unless permission is obtained from the copyright proprietors.

15th Int. Conf. on Geotechnique, Construction Materials & Environment,
Kyoto, Japan, 11-13 November 2025, ISBN 978-4-909106124 C3051

IMAGE-BASED ESTIMATION OF SOIL PARTICLE SIZE AS A SUPPLEMENT TO SIEVE ANALYSIS

Jose Manuel U. Subido[1], Erica Elice S. Uy[1], Joenel G. Galupino[1]

[1] Department of Civil Engineering, De La Salle University, Philippines

ABSTRACT

Particle size distribution is an important parameter influencing soil behavior. This parameter is identified using a combination of tests such as the sieve and hydrometer analyses to identify the potential characteristics and behavior of a soil sample. This study investigates the use of image processing techniques as a supplementary tool to traditional methods, enabling the rapid and detailed generation of particle size distribution curves. Twenty different soil samples were collected and prepared for imaging following controlled conditions. Only particles retained up to a No. 40 (0.420 mm) sieve were considered in the study. Camera and measurement calibrations, thresholding, and edge detection were performed to extract particle dimensions. Particle boundaries were identified to estimate particle sizes using pixel to real-world measurement conversions. At least one of the dimensions taken from the particle is expected to be of greater value than a reference value from the sieve openings where it was retained to ensure that there is an accurate result in the particle size estimation. The test results showed a close correlation between the estimated particle size distribution and sieve analysis using the maximum Feret diameter. However, there is an observable decline in accuracy when the particle size decreases. The proposed method has potential to capture particle size and be further studied for use in the development of particle size distribution curves, confirming its viability as a supplementary technique.

Keywords: Particle Size Distribution, Image Processing, Camera Calibration, Sieve Analysis, Feret Diameter

INTRODUCTION

Soil is a heterogeneous material composed of minerals, organic matter, and void spaces, serving as the fundamental support for all engineered structures [1]. In geotechnical engineering, the assessment of soil physical properties is essential for the safe and efficient design of foundations, embankments, and other infrastructures. Among these properties, grain size distribution significantly influences the strength, permeability, and compressibility of soil [2,3]. The conventional laboratory methods used to determine particle size distribution are the sieve and hydrometer analyses [4,5]. However, these methods require extensive sample preparation and are limited in capturing finer details such as particle shape [6].

Recent advancements have explored how image processing can be a complementary technique for estimating particle size distribution. While a standard sieve analysis makes use of mass relations, image-based techniques use individual grain geometry to compute the percent finer needed to construct the particle-size distribution curve [6-8]. These non-contact techniques have shown potential in advancing the body of knowledge on soil characterization using images.

Studies have integrated different preprocessing techniques which can improve the focus of the image towards the soil particles within the images used for particle size analysis [9,10]. Moreover, these studies also considered the use of different cameras with different capacities. However, these studies were limited to certain setups and the identification of a laboratory setup for image-based analysis of particle size [6-8]. Moreover, a common limitation within these studies is the lack of proper calibration procedures that can ensure accurate transformation of pixel-based measurements into real-world dimensions [6-10]. Calibration processes are performed to ensure that images acquired were without distortion and with proper scaling of measurements from pixel to real-world dimensions. Proper calibration corrects image distortion and ensures reliable scaling, as shown in Figure 1, where camera intrinsic and extrinsic parameters define the transformation from world coordinates to 2D image space [11,12].

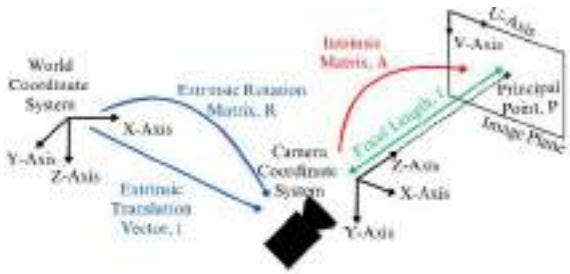

Fig. 1 Transformation of 3D to 2D system by images [12]

In this study, particle size measurements for individual particles were measured following a standard calibration procedure. Two dimensions were measured for each particle based on the bounding rectangle that was measured in the software. These dimensions were converted to real-world measurements and compared to sieve openings to identify if the estimated particle size matches the results of a sieve analysis.

RESEARCH SIGNIFICANCE

Particle size distribution is an important indicator for various characteristics of soil. The study highlights a significant advancement in soil particle size assessment by integrating image processing techniques as a supplementary tool to traditional methods. By providing a faster and detailed estimation of particle size distribution, this approach enhances the efficiency of geotechnical investigations while maintaining alignment with standard practices. The method can support preliminary site assessments and improve decision-making in construction planning and risk management.

METHODOLOGY

The methodology is composed of five phases: sample preparation, setup preparation and calibration, image acquisition, image processing, and image analysis.

Sample Preparation

A soil sample was collected from Santa Rosa, Laguna. The sample was oven-dried and clustered into particle size groups according to sieve sizes. The particles were grouped based on the sieves where they were retained. The particle groups used in the study are shown in Table 1.

Table 1 Particle Clusters (PC) for Particle Size Analysis

PC (Sieve No.)	Particle Size Bounds (mm)
No. 4	> 4.750
No. 8	2.360 – 4.750
No. 10	2.000 – 2.360
No. 16	1.180 – 2.000
No. 30	0.600 – 1.180
No. 40	0.425 – 0.600

Setup Preparation and Calibration

A mirrorless camera was used to estimate the particle size of the sample. The lighting conditions used in the study follows the schematic diagram of the image acquisition setup shown in Figure 2. The position of the camera was determined through calibration of parameters that can be identified from the camera's field of view [13-15].

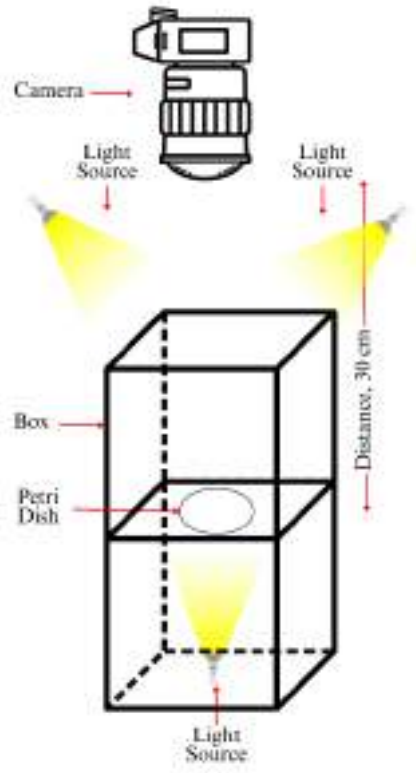

Fig. 2 Schematic Diagram of Image Acquisition Setup

In this study, calibration was performed through a 2-dimensional calibration for distortion, and a measurement calibration using NI LabVIEW 2020. The distance of the camera from the soil sample surface was determined through the 2D calibration [13]. A calibration grid, as shown in Figure 3, was used to convert the projected three-dimensional world points captured by an image to two-dimensional sensor coordinates. The grid is composed of dots with a radius of 2 mm and center-to-center distances of 1 cm. Ten images of the grid were acquired, at varying angles. In each trial of acquiring images of the grid, the set of images were collectively used to perform camera calibration [14]. However, if the calibration grid is not completely seen by the camera's field of view, the distance of the camera from the surface was adjusted accordingly. The grid images were only accepted if a large portion of the dots were identified by the program, which can be signified by having a distortion of less than 1% [15]. Once all images had a resulting distortion less than the threshold, the recorded intrinsic and extrinsic parameters were recorded. It was identified that the camera should be positioned 30 cm away from the sample to meet the threshold values. Shown in Figure 3 is the sample image of the grid after calibration. Each image was

captured with a resolution of 2784x1856 pixels.

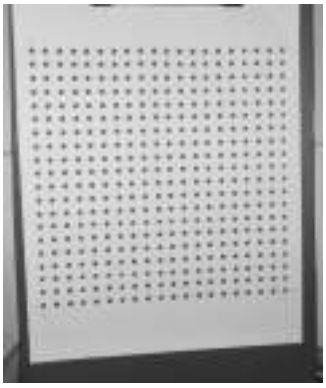

Fig. 3 Grayscale Calibrated Image of Grid

The next phase involved converting pixel data into real-world measurements using sieves and a ruler as reference objects, due to their known dimensions. A measurement calibration program was developed to determine x- and y-axis scaling factors, which convert pixel values into actual sizes [14,15]. These factors were validated by comparing program-measured values with known dimensions of sieve openings and ruler markings. The measured x and y-values in pixel measure were plotted against the actual values, as shown in Figure 4. From there, the slope of the best-fit line, where the y-intercept was set to 0, was identified. The reciprocal values were taken as the multiplying factor to convert pixel data to real-world measurements across both axes. The factors for the x-direction and y-direction are 0.1232 mm/pixel and 0.1269 mm/pixel, respectively.

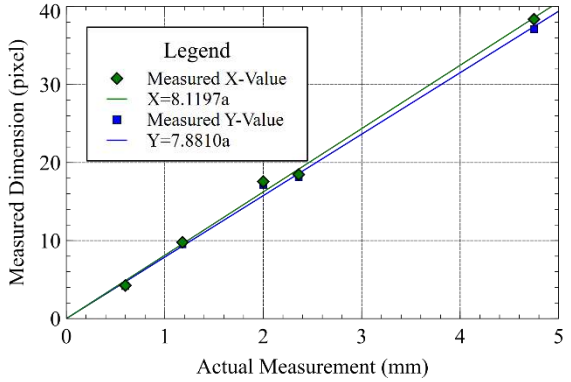

Fig. 4 Calibration Plot for Dimension Measurements

Image Acquisition

The camera was configured with an aperture of f/16, a shutter speed of 1/80 second, ISO 1600, and no flash. Once the samples were separated into groups, each cluster was placed on the petri dish in such a way that majority of the particles were loosely positioned so that the individual particle measurements were evaluated by the proposed program. To prevent reflection of light from affecting the particle size recorded, a thick piece of paper was used below the petri dish. Images were taken until 60 individual particles for each cluster group can be extracted using the particle size analysis program. Figure 5 presents the sample configuration for the particles within the petri dish, showing non-overlapping and overlapping particles.

Fig. 5 Raw Image of Particles Retained in No. 10 Sieve

Image Processing

Each acquired image underwent image processing to reduce noise and ensure accurate extraction of particle characteristics. The region of interest (ROI) was isolated using a combination of masking and thresholding techniques. A circular mask was used to create a focus on the petri dish, with the center set using pixel data references and the edge was based on the real-world diameter of the petri dish. Thresholding was then applied to isolate soil particles from the background. The optimal threshold values were determined through an analysis of the gray level histogram, revealing that gray levels below 120 reflect the particle pixels. Shown in Figure 6 are the applied masking and thresholding into a sample image.

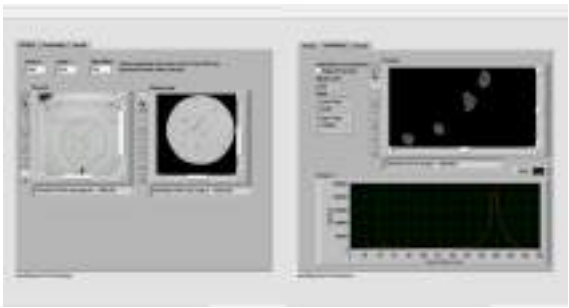

Fig. 6 ROI Extraction by Masking and Thresholding

The data gathered from images for particle size estimation focused only on particles that were loosely placed in the petri dish. In the analysis of particle size, the area was defined as the total number of pixels that were bound by the edge of the particle being analyzed.

This serves as the frequency for a certain particle. Both dimensions from its bounding rectangle were considered as its particle size following the same convention as the sieve sizes. The larger dimension yielded the maximum particle size by image analysis, whereas the smaller dimension yielded the minimum particle size by image analysis. These values serve as the maximum and minimum Feret diameters recorded in the program developed. For each particle, these parameters were extracted from LabVIEW using the IMAQ Particle Analysis VI. An example of feature extraction for the particle size estimation is shown in Figure 7.

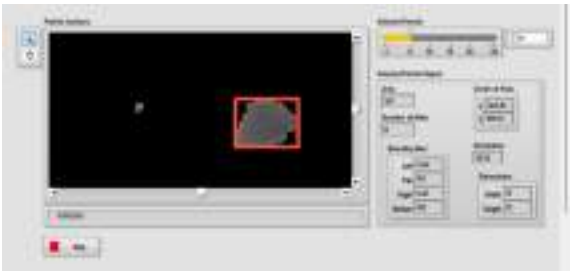

Fig. 7 Particle Size Analysis using NI LabVIEW 2020

Image Analysis

For each particle analyzed, the recorded dimensions were converted into real-world measurements and cross-validated with the group of soil particles to identify if the particle is retained on the sieve for that specific particle group. The particle size and area in real-world measurements are computed using the following equations:

$$PS_i = Max(W_i/x_{SF}, H_i/y_{SF}) \quad (1)$$

$$PS_i = Min(W_i/x_{SF}, H_i/y_{SF}) \quad (2)$$

$$A_i = A_{p,i} \times x_{SF} \times y_{SF} \quad (3)$$

where PS_i = particle size of particle i (mm); A_i = area of particle i (mm^2); W_i and H_i = width and height of particle i (pixel), $A_{p,i}$ = area of particle i (pixel); x_{SF} and y_{SF} = scaling factors for x- and y-axis (mm/pixel).

RESULTS AND DISCUSSION

The particle size was estimated based on the recorded dimensions of the bounding rectangle for each particle. The validation of values taken from the individual particle size characteristics was conducted by comparing the measured dimensions with the size of the sieves where the particles were retained. Only individual particles were considered in the study, with sample processed images shown in Figure 8. On the other hand, packed particles were not considered in the computations since dimensions measured by the program were the combined measurements from the packed particles. Including these particle measurements would introduce errors since these measurements are larger than the measurement intervals for each particle group considered. Instances of packed particles are shown in Figures 9 and 10.

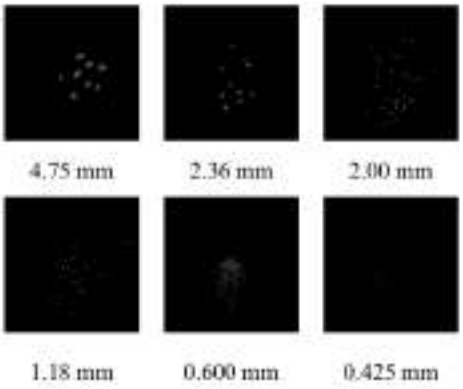

Fig. 8 Processed Images for Each Particle Size Group

Fig. 9 Excluded Packed Particles from Particles Retained in No. 10 Sieve

Fig. 10 Excluded Packed Particles from Particles Retained in No. 10 Sieve

To validate the accuracy of the estimation of particle size, two parameters were considered. Since particles were grouped based on the particle retained metric, each particle had to fall within the specified size intervals listed in Table 1. The first parameter involved calculating the cumulative area of particles that fell within these intervals and comparing it to the total area of all detected particles. The second parameter is taken by identifying the cumulative number of particles within the same intervals and comparing it to the total particle count. For both methods, the ratio of valid particles (by area or by

count) to the overall total was used to determine the percentage accuracy of the program. Table 2 presents the results based on the maximum Feret diameter of the particle (larger dimension of the particle's bounding rectangle) while Table 3 provides the results based on the minimum Feret diameter of the particle (smaller dimension of the particle's bounding rectangle). For both tables, the range of estimated particle sizes was also provided.

Table 2 Validation Metrics for Particle Size Estimation considering Maximum Feret Diameter

PC	%Accuracy by Area	%Accuracy by # of Particles	Range (mm)
No. 4	99.24%	98.33%	4.69 – 10.28
No. 8	85.14%	88.33%	2.03 – 5.42
No. 10	71.07%	71.67%	1.90 – 2.79
No. 16	95.68%	93.33%	1.11 – 2.03
No. 30	77.55%	85.00%	0.49 – 1.52
No. 40	69.58%	66.67%	0.25 – 0.63
Overall	94.53%	83.89%	0.25 – 10.28

Table 3 Validation Metrics for Particle Size Estimation considering Minimum Feret Diameter

PC	%Accuracy by Area	%Accuracy by # of Particles	Range (mm)
No. 4	96.02%	93.33%	4.44 – 8.13
No. 8	91.26%	86.67%	1.97 – 4.80
No. 10	29.88%	35.00%	1.48 – 2.41
No. 16	80.14%	68.33%	0.86 – 1.90
No. 30	85.99%	71.67%	0.37 – 1.11
No. 40	21.52%	16.67%	0.13 – 0.62
Overall	88.95%	61.94%	0.13 – 8.13

The results from Tables 2 and 3 highlighted that a difference exists in the accuracy of estimating particle size based on which dimension is used. When using the minimum dimension, accuracy by area and number of particles significantly decreased for particles retained on the No. 10 and No. 40 sieves. On the other hand, the accuracy by area for the particle cluster retained on No. 30 sieve increased despite fewer particles being correctly estimated, indicating that these particles had higher individual areas. The overall range of values indicated that the minimum particle size estimated by the developed program is 0.13 mm, which is also equivalent to the measure of 1 pixel along either the x- or y-axis, as taken from the measurement calibration. While this indicates that estimation is possible up to this degree, it is observed that the estimation accuracy becomes lesser for the smaller particle clusters (No. 30 and No. 40).

A previous study investigated the use of the minor diameter of particles, assuming these particles have an ellipsoidal shape [16]. In this context, the minor diameter is appropriate because it aligns with the concept of percent passing, where the proportion of particles smaller than the sieve opening is compared to the total number of particles in the sample. In contrast, this study focused on retained particles, where the particles were clustered by the sieve where each particle did not pass through. In a sieve analysis, retention occurs when at least one dimension of the particle is larger than the sieve opening, preventing it from passing through. An illustration of this concept is presented in Figure 11, highlighting that the maximum dimension (Feret diameter) is the more suitable metric for the analysis of results in the current context. This approach is more aligned to the physical behavior of particles being retained in a sieve analysis.

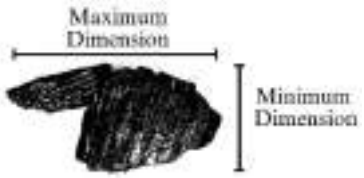

Fig. 11 Particle Size Dimension Considerations

The validation metrics indicate that the accuracy by area is consistently higher than the accuracy by number of particles in estimating particle size. Using the maximum Feret diameter, the program achieved an accuracy of 94.53% by area, compared to 83.89% by count, corresponding to 302 correctly classified particles out of 360. Conversely, when using the minimum Feret diameter, the accuracy dropped to 88.95% by area and 61.94% by count, with only 223 out of 360 particles correctly classified. In conjunction with other studies, an area-based validation is suggested in image analysis, as particle area has been shown to correlate more strongly with particle mass based of the density of these particles [16]. The recorded accuracy by area considering the maximum Feret diameter suggested that the potential of the program to identify particle sizes through the concept employed. In this study, the particle sizes considered were particles classified as gravel or sand. To improve the capacity of the proposed technique, recalibration can be conducted to improve the pixel-to-mm scaling factor.

CONCLUSION

Particle size was estimated using image processing. The developed program was able to identify particle sizes by making use of the bounding rectangle for each individual particle identified. The particle size for each particle is estimated accurately if the dimensions correspond to interval of the size between sieves where the particle was retained. Only individual particles were considered, since packed particles caused inaccurate measurements. The developed program achieved an accuracy of 94.53% by area and 83.89% by particle count using the maximum Feret diameter, whereas the minimum

Feret diameter produced an 88.95% accuracy by area and 61.94% by count. These findings indicate that the maximum Feret diameter is a more appropriate metric for particle size estimation by sieve-based classification. The study also highlighted that while the program could estimate particle sizes as small as 0.13 mm (equivalent to one pixel), accuracy decreased for finer particle groups (e.g., No. 30 and No. 40). Overall, this methodology shows potential for wider applications in particle size estimation. Future studies can extend the capacity of this method to cover three-dimensional analysis, which would consider volumetric measurements, potentially yielding closer results to a sieve analysis. Moreover, studies may also investigate analyzing how particle shape characteristics can be extracted and used as a supplement to identify the mechanical properties of soil.

ACKNOWLEDGMENTS

The researcher would like to thank the Department of Science and Technology Science Education Institute (DOST-SEI) and the Civil Engineering Department of De La Salle University for their support in his research work.

REFERENCES

[1] Joos L. and De Tender C., Soil under stress: The importance of soil life and how it is influenced by (micro)plastic pollution, Computational and Structural Biotechnology Journal, Vol. 20, 2022, pp. 1554-1566.

[2] Chen J., Wang E., Xue J., Cui L., Zheng X. and Du Q., Effects of soil particle size and gradation on the transformation between shallow phreatic water and soil water under laboratory freezing-thawing action, Journal of Hydrology, Vol. 619, 2023, pp. 1-13.

[3] Zhao J., Peng L., Hao Z., Wang J., Wang D. and Qi J., A novel large-scale direct shear apparatus considering size effects on strength of frozen coarse-grained soils, Transportation Geotechnics, Vol. 48, 2024, pp. 1 - 11.

[4] ASTM International, Standard Test Method for Particle-Size Distribution (Gradation) of Soils Using Sieve Analysis, 2017, https://www.astm.org/d6913-04r09e01.html.

[5] ASTM International, Standard Test Method for Particle-Size Distribution (Gradation) of Fine-Grained Soils Using the Sedimentation (Hydrometer) Analysis, 2021, https://www.astm.org/d7928-21e01.html.

[6] Dipova N. Determining the grain size distribution of granular soils using image analysis, Acta geotechnica slovenica, Vol. 14, Issue 1, 2017, pp. 29-37.

[7] Igathinathane C., Pordesimo L. O., Columbus E. P., Batchelor W. D., and Methuku S. R., Shape identification and particles size distribution from basic shape parameters using ImageJ, Computers and Electronics in Agriculture, Vol. 63, Issue 2, 2008, pp. 168–182.

[8] Salawu E. Y., Elvi, A. O., Ajayi O. O., Ongbali S. O., and Afolalu S. A., Particle size distribution analysis of carburized HT250 gray cast iron using ImageJ, Materials Today: Proceedings, Vol. 105, 2024, pp. 227-239.

[9] Lim H., Cheon E., Lee D., Jeon J. and Lee S., Classification of Granite Soils and Prediction of Soil Water Content Using Hyperspectral Visible and Near-Infrared Imaging, Sensors, Vol. 20, Issue 6, 2020, pp. 1-15.

[10] Pandiri D. N. K., Murugan R. and Goel T., Smart soil image classification system using lightweight convolutional neural network, Expert Systems with Applications, Vol. 238, 2024, pp. 1-18.

[11] Huang W., Miao H., Jiao S., Miao W., Xiao C., and Wang, Y., A planar constraint optimization method to improve camera calibration for imperfect planar targets, Optics and Lasers in Engineering, Vol. 180, 2024, pp. 1-9.

[12] Stankiewicz O., Lafruit G., and Domanski M., Multiview video: Acquisition, processing, compression, and virtual view rendering, Academic Press Library in Signal Processing, Vol. 6, 2018, pp. 3-74.

[13] Uy E.E.S. and Boonyatee T., Image Processing for Geotechnical Laboratory Measurements, International Journal of GEOMATE, Vol. 10, Issue 22, 2016, pp. 1964-1970.

[14] Uy E.E.S., Noda T., Nakai T. and Dungca, J.R.D., Monitoring the Triggering of Liquefaction using Image Processing, International Journal of GEOMATE, Vol. 15, Issue 51, 2018, pp. 180-187.

[15] Uy E.E.S., Noda T., Nakai T. and Dungca, J.R.D., Non-contact Estimation of Strain Parameter-triggering Liquefaction, International Journal of GEOMATE, Vol. 16, Issue 57, 2019, pp. 82-88.

[16] Kumara J. J., Hayano K. and Kikuchi, Y., Evaluation of area- and volume-based gradations of sand-crushed stone mixture by 2D images, KSCE Journal of Civil Engineering, Vol. 21 Issue 3, 2016, pp. 774-781.

Copyright © Int. J. of GEOMATE All rights reserved, including making copies, unless permission is obtained from the copyright proprietors.

15th Int. Conf. on Geotechnique, Construction Materials & Environment,
Kyoto, Japan, 11-13 November 2025, ISBN 978-4-909106124 C3051

GEOTECHNICAL INVESTIGATION OF COMPACTION EFFORT, MOISTURE CONTENT, AND SOIL TYPE ON MAXIMUM DRY DENSITY IN PATHUM THANI, THAILAND

Pattaraporn Nueasri[1] and Rattanachot Thongpong[2*]

[1]Department of Management Engineering, Faculty of Industrial Technology
[*2]Department of Civil Engineering Technology, Faculty of Industrial Technology
Valaya Alongkorn Rajabhat University under The Royal Patronage Pathum Thani Province, Thailand

ABSTRACT

This study investigates the effects of compaction effort, moisture content, and soil type on the Maximum Dry Density (MDD) of silty sand, which plays a crucial role in the stability of geotechnical structures. A full factorial experimental design (3×3×3) was employed, encompassing three types of silty sand: natural (SM-N), cement-modified (SM-C), and plastic-modified (SM-P). Each soil type was subjected to three levels of compactive effort (0.5×, 1.0×, and 1.5× of Modified Proctor energy) and three moisture conditions (2% below, at, and 2% above the Optimum Moisture Content). In total, 27 laboratory tests were conducted in accordance with ASTM D1557. The results revealed that MDD increased with higher compactive effort and reached a maximum at the Optimum Moisture Content. SM-P exhibited the highest MDD due to enhanced interparticle bonding, while SM-N presented the lowest. Excessive moisture or compactive effort beyond optimal conditions led to reductions in density, particularly in modified soils. Analysis of variance (ANOVA) confirmed that all main factors and their interactions had statistically significant effects on MDD. A second-order polynomial regression model was developed with a coefficient of determination (R^2) of 0.968, demonstrating strong predictive capability. These findings contribute to the development of improved compaction strategies for infrastructure projects involving modified soils.

Keywords: Factorial Experimental Design, Soil Compaction, Maximum Dry Density, Optimum Moisture Content

INTRODUCTION

Soil compaction plays a critical role in geotechnical engineering, influencing the stability and load-bearing capacity of infrastructure projects such as roads, foundations, and embankments. Optimal compaction ensures long-term performance and minimizes settlement. Maximum Dry Density (MDD), a key measure of compaction quality, depends on soil type, compaction effort, and moisture content.

Several real-world cases highlight the importance of soil compaction in construction projects. For instance, the failure of highway embankments in flood-prone regions has often been attributed to improper soil compaction, leading to excessive settlement and loss of structural integrity [1]. Similarly, foundation failures in expansive soils have demonstrated how inadequate control of moisture content during compaction can result in differential settlement, causing cracks in buildings and road pavements [2]. These cases emphasize the need for a systematic approach to soil compaction analysis.

Different soil types exhibit varying compaction behaviors. Natural silty sand (SM-N) generally has lower dry density due to its loose particle arrangement and high void ratio, whereas chemically modified soils like cement-modified silty sand (SM-C) and plastic-modified silty sand (SM-P) show improved compaction due to enhanced particle cohesion and reduced void space. Prior studies have demonstrated that soil modification techniques significantly improve dry density and long-term stability under loading conditions. [3]

Controlling Optimum Moisture Content (OMC) is crucial for achieving maximum dry density. Excess moisture beyond OMC can cause saturation effects, reducing particle interlocking and compaction efficiency. A study on highway subgrades exposed to varying moisture conditions found that roads compacted under excessive moisture levels (OMC+2%) showed accelerated degradation, requiring frequent maintenance and repair. [4]

This study utilizes a full factorial experimental design (3×3×3) to systematically evaluate the effects of soil type, compaction effort, and moisture content on MDD. By employing statistical techniques such as Analysis of Variance (ANOVA) and interaction effect analysis, the research aims to provide insights into the optimal conditions for soil compaction. The findings will contribute to geotechnical design guidelines, aiding engineers in optimizing soil treatment methodologies for infrastructure development.

RESEARCH SIGNIFICANCE

Soil compaction is a critical factor in geotechnical engineering, influencing the stability and durability of infrastructure. Maximum Dry Density (MDD) is a

fundamental parameter for assessing compaction efficiency, yet its optimization remains complex due to variations in soil type, compaction effort, and moisture content. This study employs a full factorial experimental design (3×3×3) to systematically examine the combined effects of these parameters, offering a quantitative approach to soil compaction assessment. Advanced statistical analyses, including ANOVA and interaction effect evaluation, provide a robust framework for interpreting MDD behavior, particularly in modified soils such as plastic-modified silty sand (SM-P) and cement-modified silty sand (SM-C). Unlike conventional studies that focus on isolated variables, this research integrates a multi-factorial approach, enabling a comprehensive understanding of compaction mechanisms under diverse conditions. The findings contribute to refining geotechnical practices, supporting engineering applications in embankments, road subgrades, and foundation systems by offering predictive insights and optimized compaction strategies.

LITERATURE REVIEW

Several studies have investigated the effect of compaction parameters on MDD and OMC for various soil types. According to [5], compaction energy significantly influences soil structure and density, particularly in fine-grained soils. Their findings highlight a threshold beyond which excessive compaction may lead to particle degradation. Cement-treated soils, due to pozzolanic reactions, often require careful control of moisture during compaction [6]. Meanwhile, plastic-modified soils have shown inconsistent responses due to hydrophobic properties and fiber alignment issues, which can affect pore structure and air void content [7]. In Southeast Asia, the challenge of optimizing soil compaction for rapidly constructed infrastructure, especially on modified soils, requires more localized and statistically structured studies. A factorial design approach as adopted in this study provides comprehensive insights into multivariable interactions [8].

MATERIALS AND METHODS

1. Experimental Materials

1.1 Soil Types and Modification Methods

This study utilizes three different types of silty sand (SM), categorized based on their modification techniques:

- SM-N (Natural silty sand): Unmodified soil collected from a construction site, primarily consisting of sand with small fractions of silt and clay.

- SM-C (Cement-modified silty sand): Prepared by blending natural silty sand with 5 % Portland cement by weight, enhancing particle cohesion and reducing void spaces.

- SM-P (Plastic-modified silty sand): Combined with 3 % synthetic polymer additive by weight, increasing elasticity and improving soil workability for compaction.

To ensure consistency, all samples were air-dried and passed through a 4.75-mm sieve before testing.

Table 1 Physical and Chemical Properties of Tested Soils

Soil Type	Modification Method	Grain Size Distribution (%)	Plasticity Index
SM-N	No modification	Sand: 65%, Silt: 30%, Clay: 5%	Non-plastic
SM-C	5% Portland cement	Sand: 60%, Silt: 30%, Clay: 10%	Low plasticity
SM-P	3% synthetic polymer	Sand: 62%, Silt: 28%, Clay: 10%	Medium plasticity

1.2 Moisture Content and Soil Preparation

Moisture content is a critical factor influencing soil compaction efficiency. Each soil type was mixed to achieve target moisture levels based on the Optimum Moisture Content (OMC) determined from standard Proctor tests.

1.3 Compaction Testing Methodology

This study employs the Modified Proctor Test (ASTM D1557), which is widely recognized for its standardization in soil compaction analysis. This test is designed to determine the effect of compaction energy on soil density under controlled conditions.

The compaction procedure was conducted using a Standard Proctor Mold, which has a 4-inch diameter and a 4.58-inch height, ensuring consistency across all experimental trials. Each soil sample was compacted in three successive layers, with each layer subjected to a specific compaction effort. The applied compaction efforts were categorized as follows: low effort (0.5× Modified Proctor), medium effort (1.0× Modified Proctor), and high effort (1.5× Modified Proctor).

2. Experimental Design and Procedures

2.1 Research Hypotheses

The compaction characteristics of soil are influenced by various factors, including compaction

effort, soil type, and moisture content. This study is structured around the following hypotheses, which serve as the basis for the factorial experimental design.

Primary Hypotheses

- H1: Increasing compaction effort enhances MDD by reducing voids and improving particle interlock.
- H2: Soil types (SM-N, SM-C, SM-P) exhibit significantly different MDD values under the same conditions due to differences in cohesion, porosity, and stabilization.
- H3: Moisture content near the Optimum Moisture Content (OMC) facilitates efficient compaction and higher MDD.
- H4: Excessive moisture beyond OMC (e.g., OMC+2%) reduces MDD due to pore water pressure and loss of particle interlock.
- H5: Excessive compaction effort (e.g., 1.5× Modified Proctor) may disturb soil structure, lowering MDD, especially in modified soils.

These hypotheses form the foundation for the experimental framework, wherein soil type, compaction effort, and moisture content are systematically varied to evaluate their individual and interactive effects on MDD. The factorial analysis enables a comprehensive assessment of soil compaction behavior, contributing to the optimization of geotechnical practices.

2.2 Factorial Design Setup

A full factorial experimental design (3×3×3) was employed to systematically assess the effects of soil type, compaction effort, and moisture content on Maximum Dry Density (MDD) is presented in Table 2. The study involved:

- Independent variables:
- Soil Type: SM-N, SM-C, SM-P
- Compaction Effort: 0.5×, 1.0×, 1.5× Modified Proctor
- Moisture Content: OMC−2%, OMC, OMC+2%
- Dependent variable: Maximum Dry Density (MDD), measured in g/cm³.

A total of 27 experimental runs (3 × 3 × 3 = 27 combinations) were conducted to ensure comprehensive analysis of individual and interaction effects, as presented in Table 2.

Table 2 A total of 27 experimental runs

Soil Type	SM-C	SM-N	SM-P	3
Compaction Effort	0.5	1	1.5	3
Moisture Content	OMC	OMC +2%	OMC -2%	3
Factor Experimental				27

2.3 Compaction Testing Procedure

Soil samples were prepared at three target moisture levels (OMC−2%, OMC, and OMC+2%) and compacted in a standard Proctor mold. Each sample was placed in three layers and subjected to compaction efforts of 0.5×, 1.0×, and 1.5× Modified Proctor. After compaction, bulk density and moisture content were measured, and Maximum Dry Density (MDD) was calculated from dry mass and volume. The results are summarized in Table 3.

Table 3 Results of Compaction Testing（MDD in g/cm³)

Factor	MDD (g/cm³)		
Compaction Effort	0.5	1	1.5
Moisture/ Type		SM-C	
OMC	1.44	1.52	1.6
OMC+2%	1.52	1.6	1.65
OMC-2%	1.42	1.436	1.58
Moisture/ Type		SM-N	
OMC	1.6	1.67	1.72
OMC+2%	1.68	1.76	1.81
OMC-2%	1.51	1.58	1.62
Moisture/ Type		SM-P	
OMC	1.618	1.735	1.738
OMC+2%	1.668	1.738	1.788
OMC-2%	1.558	1.627	1.678

2.4 Statistical Analysis

To quantify the influence of independent variables on Maximum Dry Density (MDD), a series of statistical techniques were employed using Minitab 16. The primary objective was to evaluate both individual and interactive effects of Soil Type, Compaction Effort, and Moisture Content using factorial analysis. The statistical methods applied in this study are outlined as follows:

Table 4 Analysis of Variance

Source	P-Value	Significance
Soil Type	0.000	Significant
Compaction Effort	0.000	Significant
Moisture Content	0.000	Significant
Soil Type × Compaction Effort	0.000	Significant
Soil Type × Moisture Content	0.005	Significant

Source	P-Value	Significance
Compaction Effort × Moisture Content	0.000	Significant
Soil Type × Compaction Effort × Moisture Content	0.002	Significant

From Table 4, the analysis confirmed that soil type, compaction effort, and moisture content all significantly affect Maximum Dry Density (MDD) ($P < 0.05$).

- Soil Type (H2): SM-C and SM-P achieved higher MDD than SM-N, demonstrating the benefits of soil modification.

- Compaction Effort (H1): Increasing effort improved MDD, but excessive energy caused slight declines in modified soils.

- Moisture Content (H3–H4): OMC produced the highest MDD, while OMC−2% and OMC+2% reduced density due to poor lubrication or saturation effects.

Interaction Effects

1) Soil Type × Compaction Effort : The impact of compaction varies across soil types ($P = 0.000$, $P < 0.05$).

2) Soil Type × Moisture Content – Moisture's influence on MDD depends on soil composition ($P = 0.000$, $P < 0.05$).

3) Compaction Effort × Moisture Content – The effectiveness of moisture levels is contingent on compaction intensity ($P = 0.000$, $P < 0.05$).

4) Three-Way Interaction : Soil Type, Compaction Effort, and Moisture Content interact non-linearly, with each factor dynamically influencing the others ($P = 0.000$, $P < 0.05$).

Main Effects Analysis

1) Soil Type: SM-C and SM-P exhibited higher MDD than SM-N, confirming the benefits of soil modification.

2) Compaction Effort: MDD increased with greater energy input (0.5×, 1.0×, and 1.5× Modified Proctor) due to better particle rearrangement.

3) Moisture Content: OMC resulted in peak MDD, while OMC+2% caused density reductions due to excess void space filling with water, hindering particle interlocking.

The main effects plot for Maximum Dry Density (MDD) revealed distinct trends across the three studied factors: soil type, compaction effort, and moisture content, as shown in Figure 1 and the interaction plots provide deeper insights into the combined effects of soil type, compaction effort, and moisture content on Maximum Dry Density (MDD), as illustrated in Figure 2.

Soil Type × Compaction Effort: SM-P showed the most pronounced improvement in MDD with increasing compaction effort, while SM-N consistently had the lowest MDD across all levels.

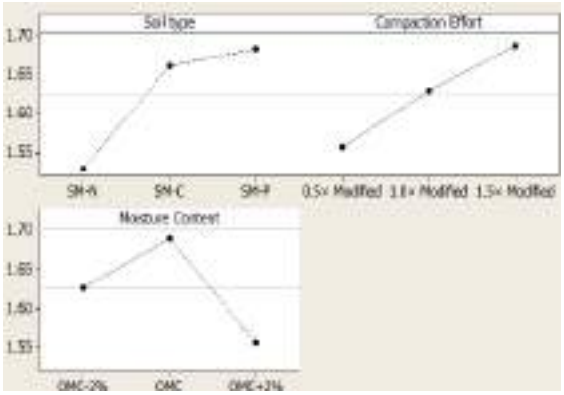

Fig.1 Main Effects Analysis on MDD (g/cm³)

This indicates that the benefits of increased compaction are more effective in modified soils, particularly those with plastic additives. Soil Type × Moisture Content: All soil types exhibited peak MDD values near OMC, with significant reductions at OMC+2%. SM-P again showed the best performance under optimal moisture, aligning with its enhanced particle cohesion and compaction compatibility. Compaction Effort × Moisture Content: The best results occurred under 1.5× Modified Proctor and OMC, validating that the synergy of optimal moisture and high compaction produces the highest MDD. However, MDD declined at OMC+2%, regardless of compaction effort, supporting H5 regarding the saturation effect.

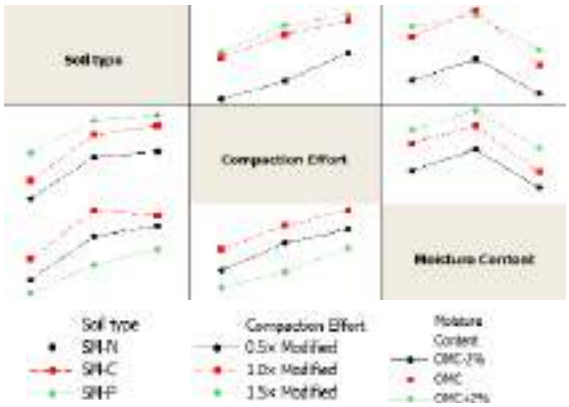

Fig.2 Interaction Plots Analysis on MDD (g/cm³)

RESULTS AND DISCUSSION

The results confirm both theoretical expectations and hypotheses developed in this study. The following conclusions can be drawn.

Soil modification, particularly with plastic additives (SM-P), significantly enhances MDD by improving soil structure and compactability. The superior performance of SM-P under optimal moisture aligns with Maher & Ho [7], who reported improved density in fiber-reinforced soils due to enhanced interparticle bonding. SM-C's moderate results agree with Consoli et al. [6], indicating moisture sensitivity in cement-treated soils.

Optimizing moisture content is crucial, as deviations from OMC reduce MDD, especially at higher water levels due to saturation effects.

Response Optimizer analysis identified SM-P soil compacted at 1.5× Modified Proctor under OMC as the optimal condition for achieving maximum MDD. These findings were further analyzed using a polynomial regression model, as described below.

Polynomial Regression Approach for Soil Compaction Analysis. The experimental results suggested that Maximum Dry Density (MDD) does not respond linearly to changes in compaction effort and moisture content, particularly in modified soils such as cement-modified silty sand (SM-C) and plastic-modified silty sand (SM-P). To model this nonlinear behavior, a second-degree polynomial regression model was developed.

The model was built using the full experimental dataset comprising 27 combinations of soil type (SM-N, SM-C, SM-P), compaction effort (0.5×, 1.0×, 1.5× Modified Proctor), and moisture content (OMC − 2%, OMC, OMC + 2%). Soil types were encoded using One-Hot Encoding, with SM-P as the baseline category, resulting in two binary variables. The complete predictive equation is as follows:

$$\begin{aligned}\mathrm{MDD}_{\mathrm{predict}} = {} & -2.9816 + 1.5378 \cdot \mathrm{Effort} + 0.6733 \cdot \mathrm{Moisture} \\ & - 2.1660 \cdot \mathrm{SoilType}_{\mathrm{SM-C}} + 0.6389 \\ & \cdot \mathrm{SoilType}_{\mathrm{SM-N}} - 0.1302 \cdot \mathrm{Effort}^2 \\ & - 0.0996 \cdot (\mathrm{Effort} \cdot \mathrm{Moisture}) + 0.5454 \\ & \cdot (\mathrm{Effort} \cdot \mathrm{SoilType}_{\mathrm{SM-C}}) - 0.2079 \\ & \cdot (\mathrm{Effort} \cdot \mathrm{SoilType}_{\mathrm{SM-N}}) - 0.0247 \\ & \cdot \mathrm{Moisture}^2 - 0.0251 \cdot (\mathrm{Moisture} \\ & \cdot \mathrm{SoilType}_{\mathrm{SM-C}}) - 0.0007 \cdot (\mathrm{Moisture} \\ & \cdot \mathrm{SoilType}_{\mathrm{SM-N}}) + 0.6057 \\ & \cdot (\mathrm{SoilType}_{\mathrm{SM-C}} \cdot \mathrm{SoilType}_{\mathrm{SM-N}}) \\ & - 0.0266 \cdot (\mathrm{SoilType}_{\mathrm{SM-C}})^2 + 0.1115 \\ & \cdot (\mathrm{SoilType}_{\mathrm{SM-N}})^2\end{aligned}$$

To effectively quantify the nonlinear response of Maximum Dry Density (MDD) to compaction effort and moisture content, a second-degree polynomial regression model was developed using 27 experimental test cases. The model incorporated linear, quadratic, and interaction terms, achieving a high predictive accuracy (R^2 = 0.968). The full regression equation accounts for compaction effort, moisture levels, and soil type (SM-P as the baseline). Residual plots confirmed the absence of bias and overfitting, with error metrics validating model reliability (MAE = 0.0150 g/cm³, RMSE = 0.0188 g/cm³). These findings highlight the model's robustness and applicability for field-based MDD estimations, reducing reliance on repeated laboratory tests. Results align with previous studies on mechanical soil compaction. [9] identified increased bulk density due to heavy equipment, consistent with higher MDD observed in SM-P. [10] reported machinery-induced compaction effects comparable to the trends found in SM-N and SM-P. [11] highlighted pore space reduction at higher moisture levels, which correlates with the MDD decline at OMC+2% in SM-C are presented in Table 5.

Table 5 Optimum compaction conditions for each soil type

Soil Type	Best Compaction Effort	Best Moisture Condition	MDD (g/cm³)
SM-N	1.5×Modified	OMC	1.81
SM-C	1.5×Modified	OMC+2%	1.65
SM-P	1.5×Modified	OMC	1.788

This study was conducted under controlled laboratory conditions, which do not fully represent field variability. Differences in compaction equipment, operator technique, weather conditions, and subsoil properties were not considered. Field calibration is therefore recommended before applying these results to large-scale projects. Future work should include field validation of the regression model, integration of machine learning for broader predictive capability, and testing with alternative soil stabilizers such as fly ash or biochar under diverse climatic conditions.

LIMITATIONS AND FUTURE WORK

The experiments were performed under controlled laboratory conditions, which do not fully represent field variability. Differences in equipment, operator technique, weather conditions, and subsoil properties were not addressed. Field calibration is therefore necessary before applying these results in practice. Factors such as equipment type, operator technique, weather, and subsoil variability were not accounted for in this investigation. While the results offer valuable insights into the behavior of modified silty sands under varying moisture and compaction levels, the findings should be interpreted with caution when applied to large-scale construction projects. Future research should focus on validating the proposed regression models through field compaction trials using in-situ equipment. Additionally, the influence of real-time environmental factors and different soil depths should be evaluated to enhance model reliability. Integration with machine learning techniques may also improve prediction accuracy and adaptability for broader geotechnical applications.

CONCLUSIONS

This study examined the effects of compaction effort, moisture content, and soil type on the maximum dry density (MDD) of silty sand soils. Experimental results revealed that MDD increased with compaction effort up to an optimum level, beyond which excessive effort slightly reduced density in modified soils due to structural disruption. Moisture content close to the optimum moisture content (OMC) yielded the highest MDD. Excess moisture led to reduced density, validating the importance of proper moisture control. Among the tested soils, natural silty sand (SM-N) showed the highest MDD, while cement-modified (SM-C) and plastic-modified (SM-P) soils responded differently due to their internal bonding and elasticity. Statistical analysis confirmed significant interaction effects between soil type, moisture, and compaction effort. A second-degree polynomial regression model was developed, achieving high predictive accuracy (R^2 = 0.968, MAE = 0.0150, RMSE = 0.0188), demonstrating its utility for practical prediction of MDD in design and field control. This model offers an efficient alternative to repeated laboratory testing and supports tailored compaction strategies for different soil types. Further field validation is recommended to enhance its applicability under real-world conditions.

REFERENCES

[1] R. Zhang, Z. Liu, J. Zheng, and G. Lei., Utilisation of expansive soils as highway embankment materials in humid environments. Int. J. Pavement Eng. , Vol. 21, No. 10, 2020, pp. 1256–1271.

[2] E. Kalkan., Foundation failures in expansive soils: Causes and mitigation strategies. Geotech. Geol. Eng., Vol. 29, No. 4, 2011, pp. 563–575.

[3] Y. Chen and J. Li., Soil modification techniques for improving dry density and stability under loading conditions. J. Geotech. Geoenviron. Eng., Vol. 144, no. 5, 2018, pp. 04018025.

[4] A. R. Estabragh, A. A. Javadi, and A. Bordbar., Effect of moisture variation on the behavior of highway subgrades. Transp. Geotech., Vol. 8, 2016, pp. 1–12.

[5] F. Sariosseiri and B. Muhunthan., Effect of cement treatment on geotechnical properties of some Washington State soils. Eng. Geol., Vol. 104, No. 1–2, 2009, pp. 119–125.

[6] N. C. Consoli, R. C. Cruz, M. F. Floss, and L. Festugato., Parameters controlling tensile and compressive strength of artificially cemented soils. Geotechnique, Vol. 60, No. 6, 2010, pp. 437–446.

[7] M. H. Maher and Y. C. Ho., Mechanical properties of kaolinite/fiber soil composite. J. Geotech. Eng., Vol. 120, No. 8, 1994, pp. 1381–1393.

[8] D. C. Montgomery., Design and Analysis of Experiments, 9th ed. Hoboken, NJ, USA: John Wiley & Sons, 2017.

[9] A. Carrera, L. Peruzzo, M. Longo, G. Cassiani, and F. Morari., Uncovering soil compaction: performance of electrical and electromagnetic geophysical methods. SOIL, Vol. 10, 2024, pp. 843–857.

[10] B. Zhang et al.., Soil compaction due to agricultural machinery impact: A systematic review. Land Degrad. Dev., Vol. 35, No. 4, 2024, pp. 5144.

[11] J. P. Frene, B. K. Pandey, and G. Castrillo., Under pressure: Elucidating soil compaction and its effect on soil functions. Plant Soil, Vol. 10, No. 2, 2024, pp. 6573.

[12] Tiongson JM, Adajar MAQ., Compaction characteristics of a fine-grained soil: potential for landfill liner application. Int J GEOMATE, Vol 19, No. 71, 2020, pp. 211-218.

[13] Hartono E, Diana W, Nugraha YS, Afzalurrahman M., Compaction properties of the fly-ash based geopolymer on silt soil. Int J GEOMATE, Vol. 26, No. 116, 2024, pp.19-26.

Copyright © Int. J. of GEOMATE All rights reserved, including making copies, unless permission is obtained from the copyright proprietors.

15th Int. Conf. on Geotechnique, Construction Materials & Environment,
Kyoto, Japan, 11-13 November 2025, ISBN 978-4-909106124 C3051

CENTRIFUGE MODEL TEST AND NUMERICAL ANALYSIS ON EVALUATION OF VERTICAL BEARING CHARACTERISTICS FOR SOIL-CEMENT COMPOSITE PILE

Shohei Koga[1], Koji Watanabe[2] and Nobuaki Tsuchiya[1]

[1]Obayashi Corporation, Japan; [2]Aichi Institute of Technology, Japan

ABSTRACT

The method for soil-cement composite pile construction was developed that uses a compact mechanical agitator for pile foundations of lightweight structures. The construction machine is a mechanical agitator with an attached vibration mechanism and improved drilling capacity. The purpose of this study is to apply soil-cement composite piles, which have been conventionally designed as temporary structures, to permanent structures. Since the strength of soil cement is 1000~5000kN/m2 and its stiffness is lower than that of concrete piles and precast piles, it is necessary to evaluate the failure mechanism of the pile body. Therefore, centrifuge model tests and numerical analysis such as an elasto-plastic FEM focusing on the failure mechanism at the pile tip were carried out to evaluate the vertical bearing characteristics of soil-cement composite piles. According to this study, it can be said that the end bearing capacity can be related to the shape of the pile tip. In addition, modelling and parameter evaluation methods were developed to simulate the results of centrifuge model experiments by numerical analysis using elasto-plastic FEM.

Keywords: Soil-cement composite pile, Vertical bearing characteristic, Centrifuge model test, Numerical analysis

INTRODUCTION

There are several pile construction methods with relatively small construction machinery that are suitable for construction in narrow urban spaces and areas with low overhead clearance. The Top-drive Boring Hole (TBH) method, which has a machine height of 4.5m, is often used. However, there are many cases where even these construction machines are interfered by architectural Limitations and existing structures. In particular, near railway tracks or on rail platforms, piles are currently constructed after temporary construction to ensure construction spaces. The Boring Hole (BH) pile method can handle narrow spaces and low overhead clearances better than the TBH method. However, because the BH pile method is a direct circulation method, mud cakes easily form on the hole walls, and slim tends to accumulate at the pile tip. These lower the bearing capacity of the piles, so subsidence of the pile is more likely to occur. Such challenges related to the construction method, bearing capacity and settlement need to be resolve for pile construction in narrow urban spaces.

Furthermore, noise and industrial waste need to be considered with regard to their effects on the surrounding environment. Therefore, a method for H-section steel pile construction combined with soil-cement composite pile was developed that uses a compact mechanical agitator for pile foundations of lightweight structures [1]. The construction machine is a mechanical agitator (i.e. e-column construction method) with an attached vibrating mechanism and improved drilling capacity. This e-column construction machine as shown in Fig.1 can be used to realize pile construction in narrow spaces where construction is usually difficult. This method is characterized by having no need to drill up to a fixed depth as in the pre-boring pile construction method. Instead, soil is agitated along with the cement milk at the original position. Therefore, the construction sludge for pile is greatly reduced.

Fig.1. Construction machine of soil-cement composite pile

Although the soil-cement composite piles are generally designed as temporary structures [2], the

purpose of this study is to design the soil-cement composite piles as the permanent foundation structures. Where, the vertical bearing characteristics of soil-cement composite piles are largely dependent on the failure of the adhesion between the soil-cement and H-section steel pile and the compressive failure of the soil-cement at the pile tip. The relationship between the shape of the pile tip and bearing capacity has been studied with regard to the tip protected pile in which a precast pile is inserted into soil-cement [3], but it is not clear whether the results of previous studies can be applied to this construction method in which H-shaped steel is built into the soil cement. Therefore, in this study, centrifuge model tests were carried out to evaluate the effects of pile tip shapes which is diameter of soil-cement or distance of pile tip on the vertical bearing characteristics of the piles. In addition, a numerical analysis was carried out and discussed to simulate the experimental results.

CENTRIFUGE MODEL VERTICAL LOADING TEST

Fig.2 shows the schematic view of centrifuge model test and model pile. And Table 1 lists the model specifications. In these tests, in order to focus on the failure mechanism of the pile tip due to the shape of the pile tip, normalized separation *L/D* was used as a parameter. Specifically, four types *L/D* were prepared as *L/D* = 0.25, 0.5, 1.0, and 1.5. Where, *L* (mm) is the separation from the H section steel pile tip to the soil cement tip and *D* (mm) is the pile diameter.

Moreover, to investigate the influence of ground strength on the failure mechanism of the pile tip, two type model grounds were prepared such that the relative density of the D_r was 80%. The D_r =80% ground was created using compaction by vibrators. Silica sand No. 7 (Specific gravity of soil, G_s=2.626) was used in preparing the model ground.

In addition, for investigation the influence of soil-cement strength on the failure mechanism of the pile tip, two type soil-cement were prepared. The soil-cement mix was designed to have unconfined compressive strength (or UCS for short) of 1,500kN/m^2. On the day of the test, a uniaxial compression test was carried out to confirm that the UCS of the two types of soil-cement was close to the target value.

As the model scale ratio is 1:30, a centrifuge acceleration of 30G was used in the vertical loading tests. The pile models were constructed using miniature H-section steel shape of H-10×10×0.33×0.5 (mm) and soil-cement, the pile diameter was constructed as 20 mm. In order to increase the axial force reaching the pile tip and to reduce the adhesion resistance between the H-section steel pile and soil-cement, silicone grease was applied to the blue shaded area in Fig.2. The measurement items were displacement and load at the pile head, and strain of the H-section steel. The strain gauges are attached both side of the web section at the pile head and the pile tip.

Two model piles were constructed in a rigid soil container with a specified layer thickness and target relative density. The specimens were mounted on a centrifuge and subjected to centrifugal acceleration up to 30G, vertical loading tests were carried out. The loading method was a displacement-controlled

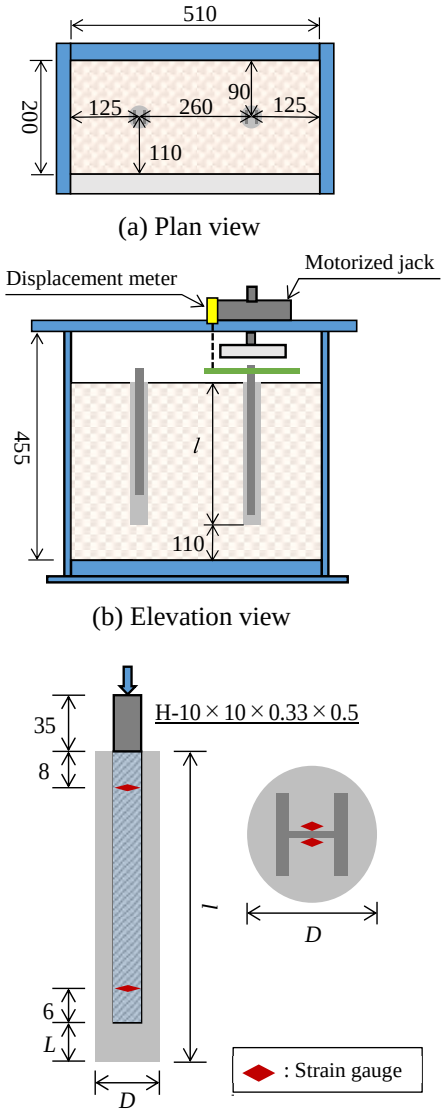

Fig.2. Schematic view of centrifuge model test and model pile (Unit: mm)

Table 1. Model specifications

	l (mm)	*D* (mm)	*L* (mm)	*L/D* (mm)	UCS of soil-cement σ_{ck} (kN/m^2)	D_r (%)
Case 1	200	20	5	0.25	1,500	80
Case 2	200	20	10	0.50	1,500	80
Case 3	200	20	20	1.00	1,500	80
Case 4	200	20	30	1.50	1,500	80

method, and the electric jack set at the top of the rigid soil container was used to load the model pile heads at a loading rate of 0.03 mm/sec. The centrifuge model tests were carried out using a beam-type centrifuge model test equipment owned by the Aichi Institute of Technology. The specifications of the test equipment and its overview are shown in Table 2 and Fig.3.

NUMERICAL ANALYSIS

In order to simulate the results of the centrifuge model test, numerical analysis such as an elasto-plastic FEM focusing on the failure mechanism at the pile tip were carried out. In this analysis, the H-section steel pile were modeled as elastic, and the soil-cement and model ground were modeled as elasto-plastic using Mohr-Coulomb's fracture method. Fig.4 shows the schematic view of analytical model, and Table 3 lists the input parameters for the model ground, soil-cement, and H-section steel pile. Where, two types of deformation modulus were used, one calculated from triaxial compression test results (Case x-A) and the other calculated from N-values (Case x-B). In Case x-A, the confining pressure was calculated based on the soil cover at the pile tip shown in Table 1(6,000 mm on the actual scale), and the deformation modulus used in the analysis was determined from the relationship between the deformation modulus and the confining pressure resulting from the triaxial compression test. On the other hand, in Case 1-x-B, the internal friction angle obtained from the triaxial compression test was used to determine the deformation modulus for the analysis by calculating the N value using Equations (1) and (2) shown in [4].

$$\phi = 1.85\left(\frac{N}{\sigma_v'/100}\right)^{0.6} + 26 \quad (1)$$

$$E_d = \rho_{gE} E_N / \gamma_{gE} \quad (2)$$

Where, ϕ :Internal friction angle of sand(°), N : SPT(Standard Penetration Test) N value, σ_v' :Effective overburden pressure of appropriate depth at the soil investigation(kN/m^2), E_d : Design deformation modulus used in the calculation of coefficient of subgrade reaction for foundations(kN/m^2), ρ_{gE} : Modified coefficient of ground for deformation modulus (ρ_{gE} =1.0), E_N : Tested value of deformation modulus obtained from SPT(kN/m^2), γ_{gE} : Coefficient of soil investigation for deformation modulus (γ_{gE} =1.4).

The coefficient of earth pressure at rest was calculated from the internal friction angle using Jaky's equation. Then, the Poisson's ratio of the soil was calculated using the coefficient of earth pressure at rest.

In addition, joint elements were added at the boundary between the soil and the pile and between the soil-cement and the H-section steel pile, respectively. Table 4 shows the input constants for the joint elements. The purpose of the joint elements is to simulate the slip between soil and pile and between soil-cement and H-section steel pile. Shear modulus was determined using the relationships between shaft friction and local pile displacement from the centrifuge model test results. Then, normal modulus was determined as 100 times the shear modulus.

Table 2 The specifications of the test equipment

Effective radius	1,360mm
Maximum centrifuge acceleration	200G(75G)
Arm height	1.00m
Maximum centrifuge capacity	15G-t
Maximum loafing weight	0.2t (75G)
Maximum rpm	360rpm

Fig.3. The overview of the test equipment

Table 3. Input parameters

	E, E_s (kN/m^2)	ν	γ (kN/m^3)	c (kN/m^2)	ϕ (°)
Model Ground A	10,822	0.28	14.0	5.2	38.1
Model Ground B	50,887	0.28	14.0	5.2	38.1
Soil-cement	150,000	0.28	14.0	750.0	38.1
Steel	205×10^6	0.30	76.3	-	-

Where, E :Deformation modulus of ground or soil-cement(kN/m^2), E_s :Young's modulus of steel(kN/m^2), ν :Poisson's ratio, γ :Unit weight(kN/m^3), c :Cohetion(kN/m^2), ϕ :Internal friction angle(°)

Table 4. Parameters of joint element

	Normal stiffness (kN/m^3)	Shear stiffness (kN/m^3)	c (kN/m^2)
Case 1	600,000	6,000	60.0
Case 2	150,000	1,500	50.0
Case 3	1,000,000	10,000	30.0
Case 4	45,000	4,500	45.0

RESULTS OF CENTRIFUGE MODEL VERTICAL LOADING TEST AND NUMERICAL ANALYSIS

This section describes the results of centrifuge vertical loading tests and the numerical analysis. The test results are shown converted to full-scale.

Fig.4 shows the relationships load and displacement at pile head. In Case 1, the measured values show acute gradient changes around 15mm

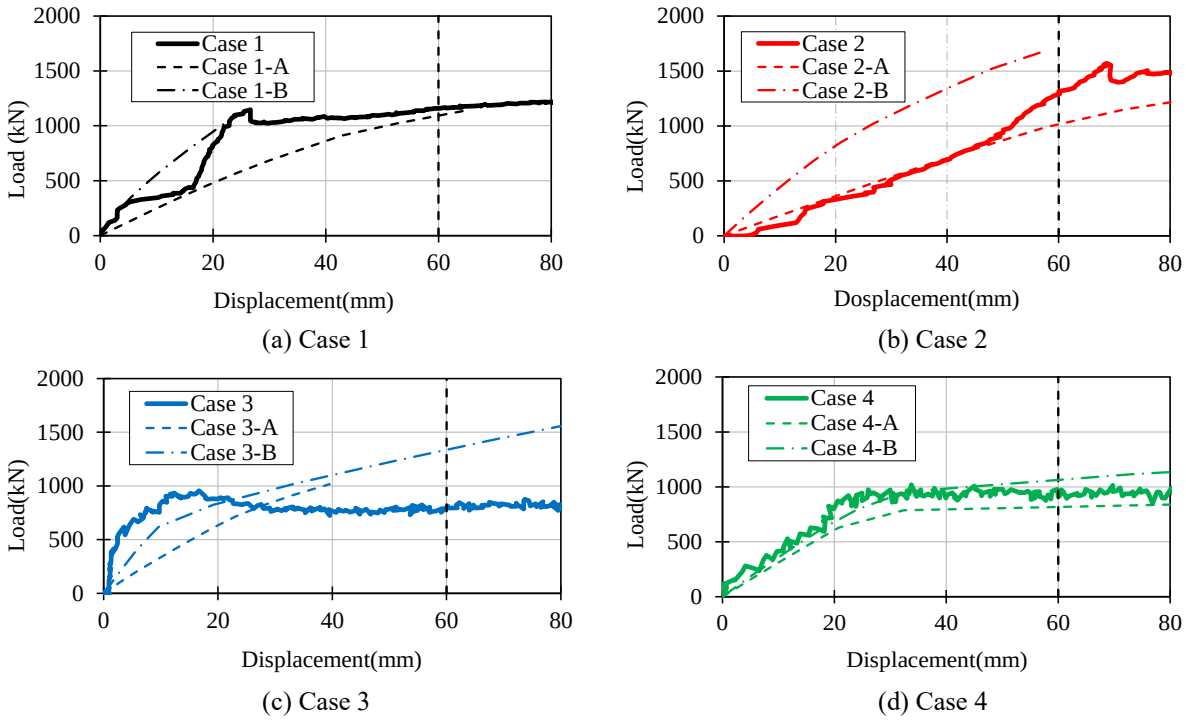

Fig.4. Relationships between load and displacement at pile head

and 25mm of pile head displacement. This is surmised to be due to the breakdown of the adhesion between the soil cement and the H-section steel pile. After that, the state of residual is shown to be in the range of 1,000kN to 1,200kN. As in Case 1, Case 3 and Case 4 show a change in gradient and shift to a residual condition at a pile head displacement of about 15 to 25mm. It can be seen that Case 3 is in a residual state at about 800kN and Case 4 is in a residual state at about 900 to 1000kN. However, in Case 2, the gradient change can be seen at a pile head displacement of about 70mm. After that, it shows that it is in a residual state at about 1500kN. Comparing the maximum load of different pile tip shapes, Case 2 with normalized separation L/D=0.5 has the highest maximum load. In other words, the most effective vertical bearing capacity is obtained when the normalized separation L/D=0.5.

In Case 1, if the measured values at the beginning of loading and about 20 mm displacement are loosely connected, it can be seen that Case1-B shows a close behavior to the measured values. However, in the region of about 60mm pile head displacement, Case1-A shows a behavior close to the measured value. Although the gradient change in Case 4 cannot be observed as in Case 1, Case 4-B behaves close to the measured value in the initial stage of loading as in Case 1. And Case 4-A shows behavior similar to the measured value as the pile head displacement increases. In Case 2, the measured loads are larger than in Case 2-B until the pile head displacement is 20mm. However, after the pile head displacement of 30mm, the measured load is smaller than that of Case2-A. In Case 3, Case 3-A shows behavior close to the measured values until the pile head displacement of 50mm. After that, the measured values show behavior between Case 3-A and Case 3-B.

Fig.5 shows the relationships end bearing capacity and displacement at pile tip. Fig.5 shows a different trend from Fig.4. In Case 1, it can be seen that Case 1-A shows behavior close to the measured values from the initial stage of loading. On the other hand, Case 2-A, as in Fig.4, shows a behavior similar to that of the measured values. However, in Case 3, the measured values show behavior between Case 3-A and Case 3-B until the pile tip displacement is about 15mm. After that, Case3-B shows a behavior close to the measured value. In Case 4, Case 4-B shows behavior close to the measured value until the pile tip displacement is about 20mm, but then the end bearing capacity increases and the maximum value is close to Case 4-A. Furthermore, the measured values of Case 2, Case 3, and Case 4 show a change in gradient around 1,500kN/m^2, leading to a state of residual. Considering that the uniaxial compressive strength of the soil cement is 1,500kN/m^2, it can be assumed that a compressive failure of the soil cement at the pile tip has occurred. However, Case 1 shows residual state at 800 to 1000kN, which means that the UCS of the soil-cement in Case 1 may be smaller than the design

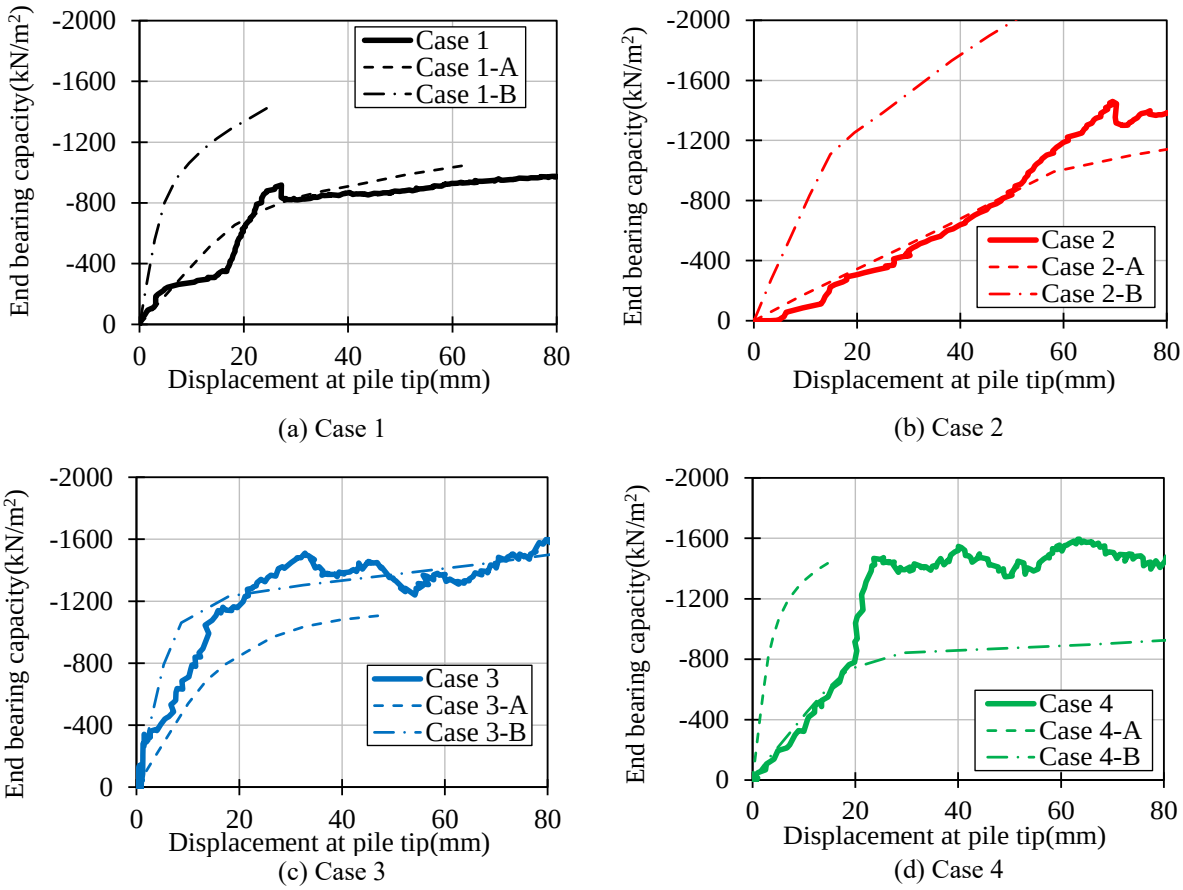

Fig.5. Relationships between end bearing capacity and displacement at pile tip

strength. Comparing the maximum end bearing capacity for different pile tip shapes, Case 2, Case 3 and Case 4 with normalized separation *L/D* = 0.5 to 1.5 show the end bearing capacity about the UCS of soil-cement, which is larger than that of Case 1. In other words, it can be seen that the most effective vertical bearing capacity is obtained at normalized separation *L/D* = about 0.5 to 1.5.

CONCLUSION

In this study, centrifuge model test focusing on the vertical bearing characteristics of the pile tip of soil-cement composite piles was carried out. Furthermore, numerical analysis using elasto-plastic FEM was carried out with the purpose of simulating the test results, and the following findings were obtained:

1) In the relationships between load and displacement at pile head, the gradient change can be observed in Case 1, Case 3, and Case 4 at pile head displacements of 15 to 25 mm.
2) In many cases, the analytical results of Case x-B show behavior close to the measured values in the relationship between load and displacement at pile head.
3) In many cases, the analytical results of Case x-B show behavior similar to the measured values in the relationship between the end bearing capacity and displacement at pile tip.
4) The test results of Case 2, Case 3 and Case 4 show a gradient change in the end bearing capacity near the UCS of the soil-cement. This suggests that the soil-cement at the pile tip has been failed in compression.
5) Focusing on the maximum load and end bearing capacity in the centrifuge model tests, it can be seen that Case 2 with normalized separation *L/D* = 0.5 shows the largest values for both maximum load and end bearing capacity, thus indicating that it has the most effective vertical bearing capacity.

REFERENCES

[1] Koga S. & Watanabe K., Yamamoto T., Study on vertical bearing characteristics for Soil-Cement composite Pile, Journal of structural engineering., Vol. 68A, 2022, 158-169 (in Japanese).
[2] Railway Technical Research Institute, Design Standard for Railway Structures and Commentary (Cut and Cover Tunnel), 2001, 258-262.

[3] Kurachi Y. & Kusakabe O., Ueno K., Kakurai M., Yokoyama Y., Shape Effect on Bearing Capacity of Tip Protected Pile, Proceedings of 27th Annual Conference of Japanese Geotechnical Society, 1992, 1559-1562(in Japanese).

[4] Railway Technical Research Institute, Design Standard for Railway Structures and Commentary (Foundation Structures), 2012.

Copyright © Int. J. of GEOMATE All rights reserved, including making copies, unless permission is obtained from the copyright proprietors.

15th Int. Conf. on Geotechnique, Construction Materials & Environment, Kyoto, Japan, 11-13 November 2025, ISBN 978-4-909106124 C3051

BEARING CAPACITY AND BEHAVIOUR OF SHALLOW FOUNDATIONS SUBJECTED TO CYCLIC LOADINGS: A STUDY IN 1G

Fabien Szymkiewicz[1], Lamis Makki[1], Philippe Reiffsteck[1], Taisuke Sanagawa[2] and Hidetoshi Nishioka[3]

[1]GERS-SRO, Université Gustave Eiffel, [2]Railway Technical Research Institute, Japan, France, [3]University, Japan

ABSTRACT

The design of geotechnical structures is based on the use of safety factors (partial factors), which have a direct impact on the quantities of material used and therefore on the carbon footprint of these structures, as well as on their construction costs and timescales. These partial factors guarantee the robustness and durability of geotechnical structures by limiting displacements to levels compatible with the requirements for their proper functioning. Although largely proven by experience, the French method for designing shallow foundations (as well as other international methods) is still conservative, either because of a lack of knowledge, or because of a simplistic choice not to exploit all the information obtained from geotechnical surveys and test campaigns on deep foundations. These shortcomings and choices are limitations that need to be overcome in order to improve the way in which the displacements and permissible loads of deep foundations are estimated. The aim of this communication is to study the load-bearing capacity and behaviour of shallow foundations subjected to complex loadings. After clearly stating the problem and describing the experimental approach, results of the experimental campaign based on tests performed at 1g and on a reduced scale are presented in detail. It was observed that some combination of actions will not affect the stability of the foundations, even after millions of cycles, and that the stability of the foundations under cyclic loadings is due to both the mean stress applied under the foundation, but also the amplitude, in a concomitant manner.

Keywords: Shallow Foundations, Laboratory Testing, 1g Testing, Small Scale

INTRODUCTION

The current approach of rapid construction combined with minimizing settlement risks often rely on deep foundations, which imposes significant environmental and societal costs. Given today's global pressures—economic, technical, and environmental—continuing to use shallow foundations could lead to overall project cost savings of 5% to 20% and a substantial decrease in environmental impact associated with foundation construction.

This highlights the ongoing need for a dependable method to design the bearing capacity of shallow foundations using cost-effective soil investigation techniques—an enduring goal of geotechnical engineering. Research on this topic dates back to the early 20th century. Notably, [1] discusses how foundation shape affects bearing capacity, referencing earlier experimental work by [2] in Finland, [3] in Germany, [4] in the U.S., and [5] in the U.K. These studies, conducted in laboratory using reconstituted sand masses and footings no wider than 0.3 meters, preceded [6] who introduced the first general equation for calculating the bearing capacity of soils beneath a continuous footing under a centered vertical load.

Further studies were carried out to validate the parameters of this equation proposed by [6] but also to extend the field of application of this formula by [7] in Canada, [8-9] in Belgium and [10-11-12] in France.

At the same time, tests were carried out to establish the direct pressumeter direct method [13].

During the past 15 years, complimentary works were also conducted to study the behavior of shallow foundation resting on unsaturated soils [14] and also to compare different methods and there reliability, trying to assess the impact of the choice of soil investigation [15].

However, and even if some test campaigns were carried out during the last 30 years to assess the behavior of shallow foundations submitted to combined loadings [16], there is still room for improvement in the actual design methods, as the experimental data are still relatively scarce ([17-18] for example), and because the static case is the only one taken into account, even if it has been established that fatigue caused by cyclic loadings can result in the failure of the soil under the foundation [18].

Therefore, collaboration has been initiated between France and Japan in order to better apprehend the behavior of shallow foundations under complex loadings as well as to optimize the existing design methods.

RESEARCH SIGNIFICANCE

This ongoing research aims to further document the behavior of shallow foundations under complex loading, including – but not exclusively – cyclic loadings, through the acquisition of experimental data achieved in laboratory on reconstituted soil masses.

The extensive use of actual reconnaissance tests (albeit at a reduced scale) [19-20] will allow for a direct transposition of the results to the practionners.

Indeed, diagrams of stability will be drawn that will at terms lead to the improvement of the existing design methods, whether based on laboratory parameters or in situ parameters.

EXPERIMENTAL SETTINGS

Reference Soils

The soils used for this study are two clean sands called sand n°6 (from Japan) and HN32 (from France), with zero fine content, and which are relatively uniform. The grain size distributions of both sands are very similar (Fig. 1). The coefficient of uniformity C_u are also very close, being equal to 1.67 for sand n°6 and 1.64 for HN32.

All the reconstituted sand masses were compacted, having in mind a target relative density of 80%. The peak friction angles for both sands are very close at this relative density, being equal to 42° and 39° respectively.

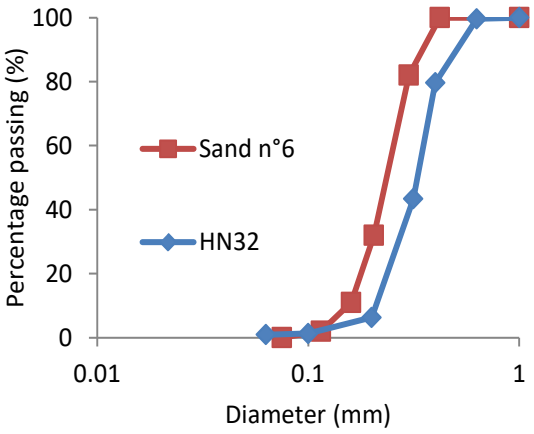

Fig.1 Grain size distributions of the sands

Soil Masses Reconstitution

Whether in Japan or in France, the soil masses were reconstituted following the sand process.

The containers dimensions were chosen to allow for at least two tests (three in France) to be carried out without any interference between the tests or with the tank' sides.

Nine layers or sands, 5cm thick, were tamped down, each at a target relative density of 80%, as stated before.

Foundations and Loading Systems

The foundations consist of square stainless-steel plates measuring 100 mm in width and 25 mm in thickness. A ball joint was used to ensure the transmission of the load to a constant point of load application.

The loading systems are very close, with only few differences: in Japan, a big diameter triaxial apparatus was used for applied the load through an electric motor, while in France a reaction frame (Fig. 2) was used, on which a hydraulic simple effect jack piloted with an advanced pressure and volume controller was used.

In all cases, a load cell and four displacement sensors were used, to follow the reaction of the foundation during the tests.

Testing Procedures

Different types of loading were applied to the foundations: a load-step loading, which is the most common way to carry tests on real scale foundations [21] and displacement controlled loadings were also performed. Both types of test gave comparable results, whether in Japan or in France.

Fig.2 Dedicated loading frame

RESULTS AND DISCUSSION

Compaction Quality Controls

It was important to assess the compaction quality, and repeatability and reproductibility of the soil masses creation, inorder to validate the results achieved during this research carried out in the form of a parametric study.

Dynamic Cone Penetrometer Tests (DCPT) were carried out on each of the tanks for this purpose.

The results of six tests carried out in Tank 3 show a good repeatability (Fig. 3).

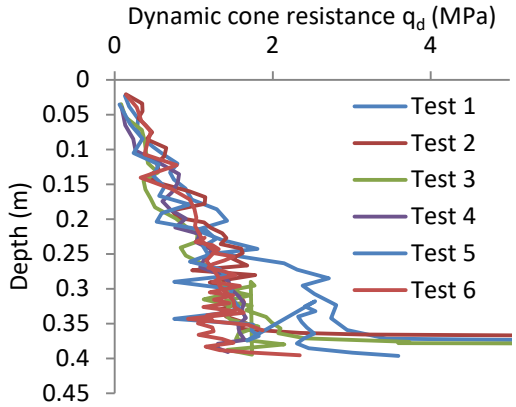

Fig.3 DCPT results in Tank 3 carried out on HN32

They allow concluding on the homogeneity of the soil mass, especially on the first 25 cm of depth, which will be the most impacted by the loadings

Figure 4 shows the average relative density achieved in Tanks 2 to 5, filled with HN32.

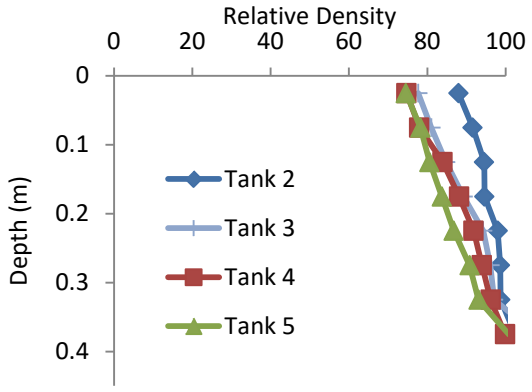

Fig.4 Relative density profiles in various tanks

It can be seen that Tank 2 seems a little bit denser than the following tanks, allowing to conclude that after a learning phase for the creation of sand masses, homogeneity is now ensured. The relative density was calculated using a correlation adapted from [22]. The target relative density of 80% is achieved in the tank for depths lower than 25 cm, ensuring testing conditions in accordance with the objectives.

Monotonic Loadings

In order to carry out a parametric study on the influence of the mean stress and of the amplitude of the cyclic loading on the behavior of a shallow foundations, monotonic loadings had to be carried out, to assess the monotonic bearing capacity (Fig. 5).

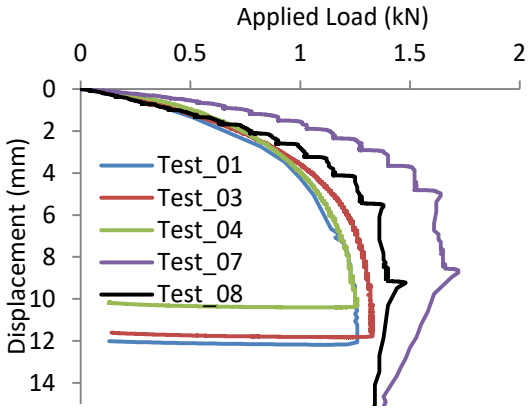

Fig.5 Results of monotonic loadings

The chosen criterion for failure is the well accepted criteria of a B/10 displacement induced by the load. The bearing capacity of the foundations is therefore defined as the load inducing a displacement of 10 mm, in our case.

The monotonic loadings performed on the HN32 sand gave an average bearing capacity of 1.25 kN (Fig. 3), in good accordance with the results achieved in Japan on Sand n°6. This value will thereafter be defined as the maximum vertical load applicable on the foundation, monotonally ($V_{mon;\ max}$).

Monotonic loadings performed load step by load step or displacement controlled gave very similar results, too.

Cyclic Loadings

Having ensured that the results achieved in Japan were very comparable to those achieved in France, it was decided to pursue the study by carrying out tests in parallels.

For this study, the main objective was to assess the importance of the cyclic mean stress ($V_{cyc;\ mean}$) and of the demi-amplitude DV_{cyc} on the behavior of the foundation.

The tested configurations are presented in Fig. 6.

From the first tests carried out, it can be seen that there is a clear impact of the ratio between the amplitude of the cycles, the mean stress and the

number of cycles leading to failure.

In particular, for a ratio maintained constant of (DV_{cyc} / $V_{mon;\ max}$) / ($V_{cyc;\ mean}$ / $V_{mon;\ max}$) (in this case 0,5), the number of cycles leading to failure decreases exponentially with the mean cyclic stress (Fig. 7). A complementary test carried in France confirms this conclusion.

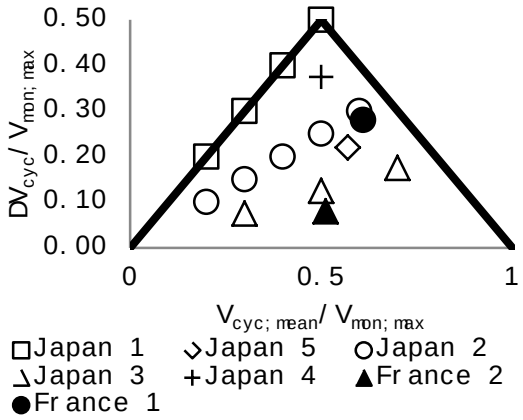

Fig.6 Cyclic loading configurations tested included in stability diagram

However, the patterns appear less clear, but this may be due to the very low values of the demi amplitude and of the cyclic mean stress in some cases, for which the stability is ensured for any given number of cycles, and on the other side to the complete unloading of the foundation (see Serie Japan 1 for example, on Fig. 6) which is an extreme case that causes higher displacements.

Furthermore, for a constant value of the ratio ($V_{cyc;\ mean}$ / $V_{mon;\ max}$), there is also a clear influence of the amplitude of the cycles on the number of cycles leading to the failure. This can be seen very easily on Fig. 8, for two values of ($V_{cyc;\ mean}$ / $V_{mon;\ max}$). The two series seems very close, with very similar patterns.

Finally, for a constant value of DV_{cyc} / $V_{mon;\ max}$, it appears that there is also an influence of the mean stress on the number of cycles leading to failure (Fig. 9). However the relation does not seems so simple and more tests will need to be done to draw any conclusion.

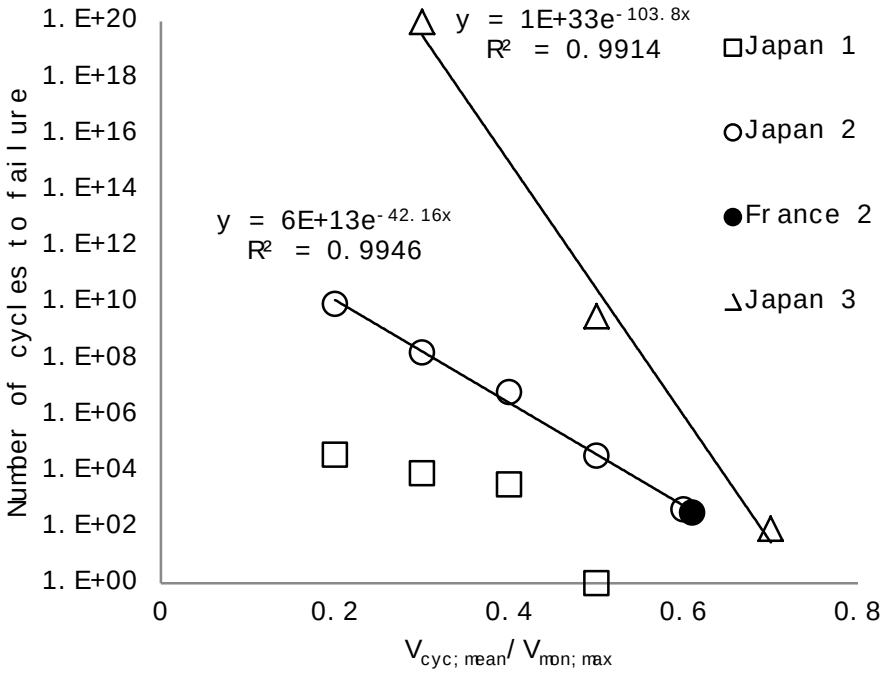

Fig.7 Relationship between the number of cycles leading to failure and the ratio $V_{cyc;\ mean}$ / $V_{mon;\ max}$

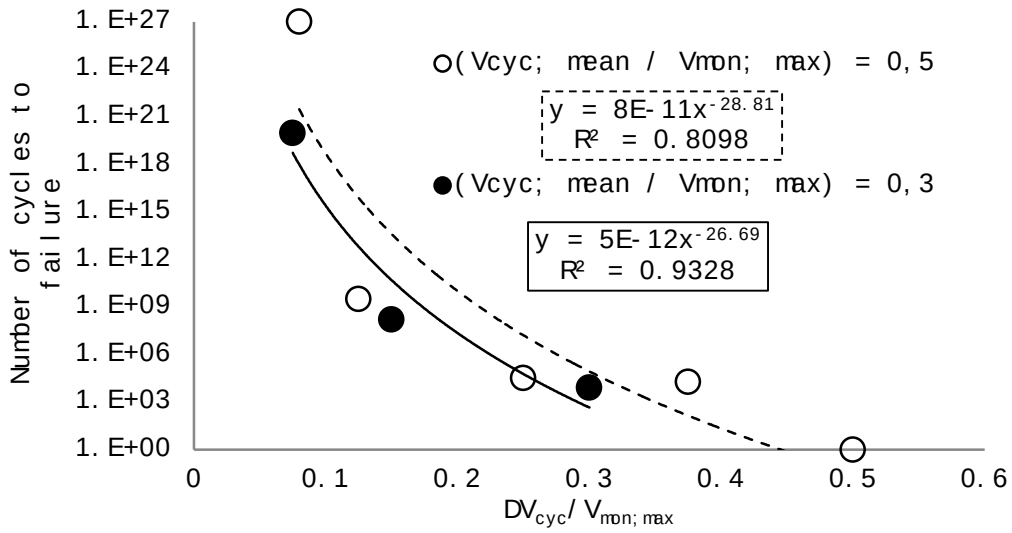

Fig.8 Relationship between the number of cycles leading to failure and the ratio DV_{cyc} / $V_{mon;\ max}$, for two values of mean stress

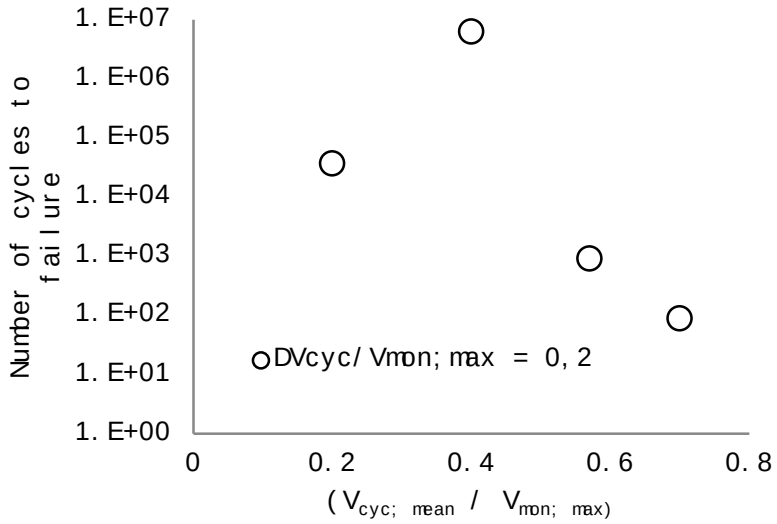

Fig.9 Relationship between the number of cycles leading to failure and the ratio $V_{cyc:\ mean}$ / $V_{mon;\ max}$

CONCLUSIONS

This communication presents the preliminary results of an experimental work on the behavior of shallow foundations under cyclic loadings. After presenting the soundness of the experimental procedures and protocols, results of centered cyclic vertical loading on footing are presented.

It can be concluded that the stability of the foundations under this kind of solicitation is due to both the mean stress applied under the foundation, but also the amplitude, in a concomitant manner.

Some combination of actions will not affect the stability of the foundations, even after millions of cycles, but it is still difficult to draw definitive conclusions. A major factor influencing the results might also be the soil density.

In the light of these results, it is important to continue this study, which in time will allow for the performance of more complex tests and to propose design approaches based on displacement that take into account the nature of the soil and its condition, as well the nature of the loadings in terms of amplitude and duration of application.

ACKNOWLEDGMENTS

The authors would like to acknowledge the constant support of the Université Gustave Eiffel, the RTRI and the Chuo University, allowing for very constant exchanges and periods dedicated to experimental works in the facilities of the different partners.

REFERENCES

[1] Weiss K., Die Formbeiwerte in der Grundbruchgleichung für nichtbindige &Oen. Diplom¬Ingenieur, 1973, pp. 1-55 pages.

[2] Fellenius W., Jordstatiskar berâkningar fôr vertikal belastning pa horisontal mark under antagande av cirkulârcylindriska glyditor, Teknisk Tidskrift, Vol. 59, pp. 57-63.

[3] Kögler F., Über Baugrund - Probebelastungen. Bautechnik, Vol. 24, pp. 1-357.

[4] Berry, D.S., Stability of Granular Mixtures, Conference proceedings, in Proc. 38th Annual Meeting of the American Society for Testing, 1935, pp. 491-507.

[5] Golder, H. Q., Fellenius, W., Kogler, F., Meischeider, H., Krey, H. and Prandtl, L., The ultimate bearing pressure of rectangular footings. Journal of the Institution of Civil Engineers, Vol. 17 Issue 2, 1941, pp. 161-174.

[6] Terzaghi K., Theoretical soil mechanics, Wiley, New-York, 1943, pp. 1-510.

[7] Meyerhof G.G., The ultimate bearing capacity of foundations, Géotechnique,, Vol. 2, 1951, pp. 301-332.

[8] De Beer E.E. and Ladanyi B., Étude expérimentale de la capacité portante du sable sous des fondations circulaires établies en surface, Conference proceedings, in Proc. 5th ICSMGE, 1961, pp. 577-585.

[9] Fagnoul A., Balle A. and Belette R., Contribution à l'étude des fondations superficielles filantes par un modèle analogique Taylor-Schneebeli, Collection des publications de la faculté des sciences appliquées, Vol 38, 1973, pp. 1-42.

[10] Giraudet P., Recherches expérimentales sur les fondations soumises à des efforts inclinés ou excentrés, Annales des Ponts et Chaussées, vol. 3, 1965, pp. 167-193.

[11] Giroud J.P., Tran V-N. and Obin J.P., Tables pour le calcul des fondations, Paris, Dunod, 1973, pp.1-445.

[12] Ménard L., Calcul de la force portante des fondations sur la base des essais pressiométriques, Sols-Soils, Vol. 6, 1963, pp. 9-31.

[13] Briaud J.-L. and Gibbens R., Predicted and measured behaviour of five spread footings on sand. Conference Proceedings, in Proc. Settlement 94, pp.1-255.

[14] Oh W. T., and Vanapalli S. K., Scale effect of plate load tests in unsaturated soils, International Journal of GEOMATE, Vol. 4, Issue 8, 2013, pp. 585-594.

[15] Taha, O. M. E., Variation of bearing capacity prediction for shallow foundations by SPT and laboratory tests, International Journal of GEOMATE, Vol. 17, Issue 64, 2019, pp. 108-114.

[16] Sasaki, Y., and Nishioka, H., Vertical loading tests on local scoured spread foundation on aluminum rods model ground, International Journal of GEOMATE, Vol. 23, Issue 98, pp. 17-23.

[17] Maréchal O., Portance de fondations superficielles établies à proximité de talus et soumises à des charges inclinées et excentrées. PhD thesis, 1999, pp. 1-357.

[18] Andersen K. H., Bearing capacity under cyclic loading — offshore, along the coast, and on land, Can. Geotech. J., Vol. 46, 2009, pp. 513–535.

[19] Reiffsteck, P. Mohammad, D.D., Sanagawa, T., Szymkiewicz, F., Minatchy, C. and Makki, L., Small scale pressuremeter for shallow foundation model tests, Conference proceedings, in Proc. 8th International Symposiun on Pressuremeters, 2025, 5 pages.

[20] Reiffsteck, P., Szymkiewicz, F., Navarrete, M. B., & Luong, T. A., Prediction of bearing capacity and settlement using penetrometer design method for shallow foundation and load transfer curves. Conference Proceedings, in Proc. 5th International Symposium on Cone Penetration Testing, 2022. p. 1058-1064.

[21] AFNOR, Geotechnical investigation and testing -- Testing of geotechnical structures -- Part 1: Testing of piles: static compression load testing, European Standard, NF EN ISO 22477-1, 2018, pp. 1-34.

[22] Retamales S. L, Development of a method for evaluation of liquefaction potential of sands based on a dynamic penetrometer, PhD in Geotechnique, 2022, pp. 1-233.

Copyright © Int. J. of GEOMATE All rights reserved, including making copies, unless permission is obtained from the copyright proprietors.

15th Int. Conf. on Geotechnique, Construction Materials & Environment, Kyoto, Japan, 11-13 November 2025, ISBN 978-4-909106124 C3051

LANDFILL MINING IN BRAZIL: SOME CHALLENGING ASPECTS FOR APPLICATION

Thiago Villas Bôas Zanon[1] and Maria Eugênia Gimenez Boscov[1]

[1]Polytechnic School, University of São Paulo, Brazil

ABSTRACT

Several international research report landfill mining (LFM) cases with different levels of investigations, most involving conceptual analyses or pilot feasibility studies, with a limited number of full-scale studies. To assess the recovery of materials from LFM process, these materials are typically divided into: (i) combustible fraction, (ii) inert fraction, (iii) soil-like materials and (iv) remaining fractions. In most studies, soils and similar materials are the predominant fraction, followed by combustible fraction; literature mainly addresses the use of these groups of materials. This article discusses some challenging aspects of Brazilian situation regarding LFM. There are few Brazilian studies about LFM, all conceptual analyses. Historically municipal solid waste (MSW) in Brazil is mostly disposed of on land and there is low recovery of MSW, allowing to infer that there are significant quantities of landfilled materials with recovery potential. However, field studies (pilot, large and full-scale) are recommended for future research to investigate key questions involving excavation technologies, technological routes for material recovery, and assessment of economic viability. Assessment of local variables that are not present in LFM cases reported in the literature are important, such as high rainfall, high organic matter content, higher and steep landfill slopes, limited operation time along the year due to rainfall regime, and higher generation of leachate.

Keywords: Municipal solid waste, Landfill, Mining, Energy recovery, Resource recovery.

INTRODUCTION

There is a global consensus that the current economic model, known as Linear Economy, should transit to Circular Economy, one of whose principles is to avoid wasting resources, e.g., disposing of waste without prior recovery [1].

Globally 19% of municipal solid waste (MSW) is recycled, 13% is used for energy, 30% is landfilled, and 38% is dumped [2]. Therefore, more than half of MSW is sent for final disposal on land.

Materials disposed of in landfills may be recovered by landfill mining (LFM), a technique in which waste is excavated, sorted, separated and subsequently used as a resource, eliminating potential sources of subsoil contamination, assisting in recovering land value, and reducing greenhouse gas emissions [3-5]. Mined materials that are eventually not used can be again landfilled, however the goal is to minimize or even eliminate the need for returning materials to the landfill [6]. Mining allows to release part of the volume previously occupied by waste disposed, extending landfill operation and thus applying the concept of a “perpetual” landfill, or freeing up areas for alternative uses [5,6]. Therefore, LFM is a technique that avoids impacting new areas for expansion or construction of new landfill and reduces the exploitation of natural resources which causes scarcity of raw materials, and can thus be another valuable activity in the transition to a circular economy [7].

Although LFM has been the subject of an increasing number of studies in recent years, it is not a recent technique, since there are reports of its being used in Israel in the 1950s [3].

This article aims to assess whether there are conditions for carrying out LFM in Brazil, comparing conditions of reported international experiences with those found in Brazil.

RESEARCH SIGNIFICANCE

This study aims to assess the state of the art of Landfill Mining, discuss the main variables involved, investigate the incipient situation of LFM in Brazil, and prospect the development of LFM applications, based on international experience and on the consideration of local particularities. This article thus intends to contribute with ideas for the development of research necessary to enhance LFM in Brazil, pointing out issues that need more detailed studies. The final objective is to promote the circularity in waste management, present alternatives for landfill disposal, and suggest means of recovering dumpsites.

LANDFILL MINING STATE OF ART

Most LFM studies involve conceptual analyses or feasibility of specific pilot projects, with a limited number of large and full-scale studies [4,8,9]. The number of studies has grown in recent decades [4].

The mining process of waste disposal sites involves not only the extraction of the landfilled materials, but also the separation of the materials into groups (or fractions) with properties of interest. LFM feasibility is highly dependent on the correct selection

of processes and equipment [4].

To extract waste to be mined, two methods are found in literature: drilling and excavation, both using conventional equipment [4,8,9]. Drilling is performed using drilling equipment and is used in pilot projects of scientific nature, allowing great depths to be reached but reducing the size of the mined material, and having high operational costs; excavation is performed using hydraulic excavators or similar, is used in large or full-scale projects, has low operational costs, but does not reach great depths.

Following extraction, materials must be separated and screened for efficient material recovery. Pre-drying is recommended to improve sorting (separation) processes and for end-use of mined materials [8-12].

Sorting equipment is always necessary to separate mined materials into different groups due to MSW is composed of many different constituents. To select the sorting equipment, it is necessary to identify and quantify the materials to be mined and groups or subgroups into which materials can be divided. Such division typically is based on the potential uses as resources [4,9,13]: (i) combustible fraction (paper, cardboard, textiles, wood, foams, plastics, leather and rubber); (ii) inert fraction (stones, ceramics, glass and metals); (iii) soil-like materials; and (iv) remaining fractions.

Combustible fraction includes materials with high calorific potential that can be used as fuel (in biomass industrial boilers, clinker production furnaces, in pyrolysis, gasification or incineration). Here the main critical parameters are calorific value, moisture content, metals, ash content and chlorine content. Many components of landfilled waste are potentially but not effectively recyclable. Only ferrous and non-ferrous metals have effectively the possibility of being recycled, while other materials which are conceptually recyclable (mainly paper, cardboard and plastics) do not have the minimum necessary quality due to the presence of impregnated contaminants (for example, organic matter and soil), which makes them attractive to use as fuels; even though, prior treatments could be necessary, such as separation, cleaning and drying [8,9].

Soil-like materials involve soils and materials with a granulometry similar to soils (such as partially or fully decomposed organic matter) and can be used at final disposal sites as waste cover or in other applications as construction material. Soil present in mined material mainly originates from waste landfill daily, intermediate and final covers, and is used in large quantities during landfill operations. Composting is also a possibility for this fraction, but evaluation of the percentage of remaining organic matter and concentration of metals is necessary, since these constituents can limit or make composting unfeasible, even in non-food crops [4].

The composition of material mined from MSW landfill varies significantly among different landfills, depending on original waste composition, waste age, location, climate and hydrological conditions [4,8]. Original waste composition of MSW varies according to population income level [2], whereas composition of disposed waste varies depending on prior treatments before final disposal. Table 1 presents waste compositions and ranges of values found in two review papers that present cases on landfill mining in different countries. Percentage of combustible fraction in both studies is in the same order of magnitude in both studies, while soil-like-materials are relatively close.

Table 1 Percentage of material recovered in different LFM cases

Fractions	Krook et al. [9]	Jain et al. [4]
Soil-like material	50% to 60%	48.6%
Combustible fraction	20% to 30%	24.5%
Inert fraction	10%	21.3%
Others	-	5.6%

Time factor, represented by waste age, is a key variable of mined materials composition over time, since degradation processes of organic-putrescible materials (mainly food remains, wood, paper and cardboard) occur, reducing the participation of this fraction. Thus, over time, soil-like materials fraction increases, combustible fraction decreases, and the inert fraction remains constant [4,5]. This occurs because the combustible mass degrades over time and converts to soil-like materials fraction, while the inert materials remain constant. There are also changes in characteristics, such as reduction of materials size in waste mass [5,14,15]. Granulometry is an information of interest, since one of the most conventional processes for separating MSW is sieving, allowing the separation of smaller fractions (soil and food waste) from larger fractions, which generally have a higher calorific value.

Since most of mined waste composition is soil-like materials, as shown in Table 1, the first process recurrently applied after waste extraction is granulometric separation. This fraction is distinguished from the others mainly by size, therefore sieving sets soil-like materials apart. For screening, trommels or vibrating screens are mainly used, with no standard size for screen openings (screen sizes between 1 and 40 mm are described in the literature), which impairs the comparison of percentage soil-like materials fraction among different LFM studies [4,8,9]. The grain diameter for coarse sands, the thickest fraction of soils, is defined as 4.8 mm in geotechnics. Many mining studies use much larger opening sizes, probably due to the mined soils forming clods and being agglutinated.

To separate the other groups and subgroups of

materials, the following equipment is also found in mining studies: crushers, ferrous metal separators, non-ferrous metal separators, air separation technologies and conveyor equipment [4,8,9].

Krook et al. [9] conducted an extensive literature review on landfill mining, covering the main trends, objectives, topics and findings in 39 research articles published during the period 1988-2008, whose geographical distribution is shown in Fig. 1. The main topics of the articles are presented in Fig 2. Jain et al. [4] found 108 publications related to LFM distributed in different regions as seen in Fig 3. In both review papers there are no publications from Latin America, Caribbean, and Sub-Saharan Africa.

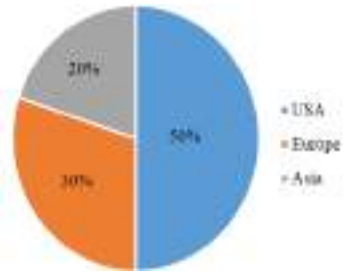

Fig.1 Krook et al. [9] geographical distribution of LFM cases

Fig.2 Krook et al. [9] categorization of 39 reviewed papers regarding main topics

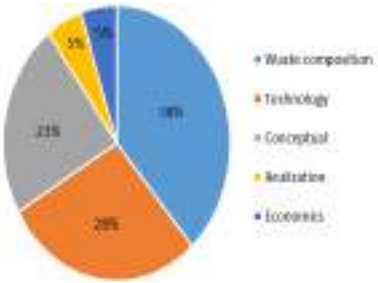

Fig.3 Jain et al. [4] geographical distribution of LFM cases

One of the fundamental topics to be evaluated in LFM is economic viability. There are articles in the literature that explore this topic, addressing the need for generating gains and revenues - avoided post-closure costs of the landfill, externalities, added value due to landfill space gain, land value, materials sales (including rare materials) - to fund activities related to LFM (extraction, separation, transportation, heat treatment and final disposal of materials) [16-19]. Esguerra et al. [16] conducted a review of studies that assessed LFM economic potential, selecting 15 that met certain criteria (full article in English, quantitative analysis, among others). These studies mostly comprised an economic analysis focused on decision-making about a specific landfill and concluded that mining has low economic potential; only 2 proved to be profitable [16]. However, the authors call attention to the need for expanding scenarios and improving scientific prospective analyses.

STATE OF THE ART OF LFM IN BRAZIL

There are few studies on the application of landfill mining in Brazil [5,13], and no cases of pilot, large and full-scale application have been identified.

Regarding recovery potential, data analyses from tropical landfills, comparing new waste and mined waste aged 4 to 6 years, show that there is a tendency for components with high calorific potential to concentrate along the disposal time, and at the same time there is a reduction in the moisture content (from 100% on a dry basis to 20% to 60%). These are indications that 4 to 6 years are sufficient for most microbial processes to occur, conditions that can favor LFM and energy recovery from waste due to the moisture reduction [5]. This expected behavior can be observed in Fig. 4, where after 0.5 years the higher calorific value (HCV) reaches a high-level range; HCV remains in the range of 23 to 27 MJ/dry kg for circa 2.5 years (investigated time). Kasam et al. [20] studied the effect of age on MSW composition collected in an Indonesian landfill. However, samples from 0 to 2 years were collected from a well-managed part of the landfill, whereas samples older than 3 years were collected from an open dumping site, what makes the comparison more difficult.

In a landfill located near the city of São Paulo, waste aged between 10 and 16 years was sampled with the aim of evaluating combustible fraction. The study concluded that the fraction with diameter higher than 40 mm, which corresponded to 27% of the mined materials, had potential for energy recovery (due to the high presence of plastics and paper), presenting average calorific value that would meet the criteria for refuse derived fuel according to the applicable state legislation [13].

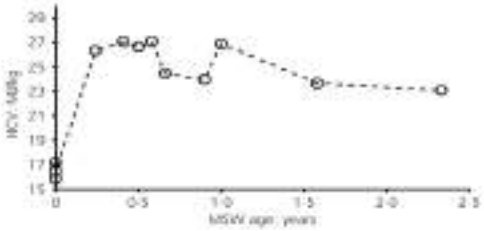

Fig.4 Higher Calorific Value obtained in a tropical MSW landfill [5]

Although Guimarães et al. [21] assessed mining potential from old closed dumpsites that operated between 1989 and 2015, their study provides data regarding waste composition (Fig. 5) which can lead to important findings: high percentage of plastics and low percentage of organics (probably showing that much of the organic matter had degraded).

Fig.5 Average composition of samples collected in 9 dumpsites [21]

DISCUSSION

Considering that in Brazil practically all MSW is sent for final disposal in landfills and thus has an insignificant low waste recovery rate (less than 10%), as can be observed in Fig. 6, and the estimated average gravimetric composition for Brazilian MSW (Fig. 7), the quantity and percentage of recoverable waste accumulated in landfills is probably high. There is a large presence of organic waste (45.3% of MSW) and waste with the possibility of energy recovery (more than 30% of MSW).

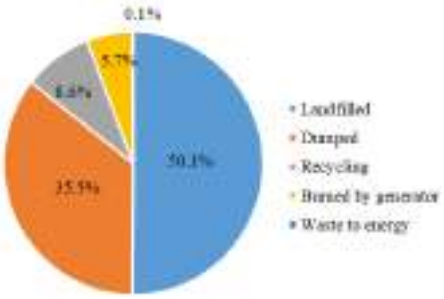

Fig.6 Brazilian MSW destination in 2023 [22]

In the case of LFM, the amount of organic matter is expected to decrease compared to the generated MSW; amounts of soil, stones, ceramics, glass, plastics and metals will remain the same; paper, cardboard, textiles, leather and rubber will degrade slowly, and their quantity should decrease slightly. In percentage terms, a lower percentage of organic matter is expected for the excavated material; and energy use is probably the best use for plastics, paper, cardboard, textiles, wood, foams, plastics, leather and rubber, since they are contaminated and can hardly be recycled.

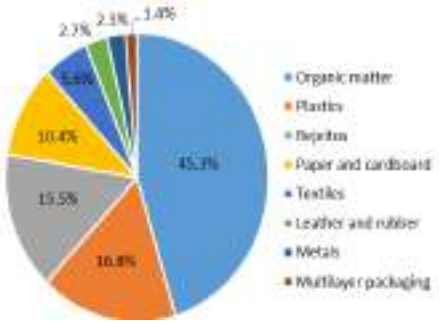

Fig.7 Brazilian MSW composition in 2023 [23]

However, there are few national studies on LFM. In many countries where LFM cases have been reported, the value of land is a significant factor in economic viability, which can be as significant as the revenue from materials that can be valued. In Brazil, a country of continental dimensions, the land freed up by LFM would not have such a great relevance in the economic viability. This is possibly the main reason for the lack of interest in this topic in the country.

Also, the circularity of the economy is still a new concept for Brazilian public managers, entrepreneurs in the sanitation sector, and the citizens in general. Since 2010, the year of publication of the National Policy for Solid Waste, a federal law, a legal and institutional framework has been slowly developing to meet the law's requirements. The first step was the improvement of land disposal and the need for municipalities to formulate and implement a plan for solid waste management. Recycling, reverse logistics, composting, and circularity are steps that are being implanted at different paces.

One of the potential ways to seek circularity of LFM is the use of the combustible fraction, the second largest typical fraction among mined waste as presented in the manuscript. There is a Brazilian law to regulate waste characteristics to be applied as RDF for the cement industry, which is very strong in Brazil. There is also a Brazilian law for composting and there are some practical experiences, but mostly from agrobusiness waste.

Additionally, there are geotechnical challenges that may make this solution less attractive: there are regions with high rainfall, limiting operation time along the year and increasing leachate generation; MSW has a high percentage of organic matter; landfills can be very high and with steep slopes, a combination that may generate additional costs due to the greater difficulty in excavation, among others. On the other hand, there is an already know-how developed in Brazil for the design and operation of tropical sanitary landfills [24], which allows overcoming these challenges.

LFM can also cause discomfort to neighborhoods, due to odor, noise and emission of particulate matter; however, in the long term, it could bring benefits such

as increasing the value of the surrounding area, recovering urban areas of considerable dimensions, and reducing risks to public health and environmental pollution. This challenge of acceptance by the surrounding community requires communication and dialogue with society.

It is important to consider the lessons learned and recommendations related to existing international studies. Therefore, in Brazil, field investigations should be carried out to assess the behavior of the waste composition and changes in the characteristics of the waste as a function of its age. Executing these investigations can subsequently allow planning, specifying and dimensioning appropriate processes for conducting pilot, large and full-scale studies, allowing the assessment of the performance and economic viability of LFM [25]. Local particularities should also be considered in the LFM assessment, such as local rainfall regime, since significant areas of Brazilian territory have locations with high rainfall distributed, which may interfere with waste extraction activities, waste processing and LFM feasibility.

In future studies to evaluate LFM, it is also important to consider different scenarios of separation, valorization, market issues for recycled materials - a vital issue in Brazil, where public policies for use of recycled material are incipient - and market for the fuel fraction. Guerreiro [26] analyzed the production of refuse-derived fuel (RDF) in Brazil. The annual RDF production is 176,000 tons, but just one plant utilizes MSW, with a yearly production of 30,000 tons (while 89 million tons MSW are collected yearly in Brazil). Another plant co-processes RDF from MSW, waste tires, biomass (wood chips), and paints and solvents, achieving a blend with high calorific power.

The technological route of waste excavation processes must be addressed, absorbing the know-how developed in landfilling operations. And, last but not least, the inclusion of waste pickers cooperatives in the sorting processes with capacitation for the different scenarios must also be taken into account, because they represent a significant percentage of the non-specialized labor force in Brazil.

CONCLUSIONS

Despite the existence of a significant number of scientific publications related to LFM, the number of full-scale cases reported is limited. The identified studies mostly involve conceptual analyses and pilot studies, with few reports of large and full-scale cases.

Particularly in Brazil the few studies on LFM refer to evaluation of composition and properties of excavated waste, in addition to the conceptual evaluation, particularly of the fraction with energy potential. Due to the average MSW composition and the history of practically low waste recovery before landfilling, the amount of landfilled waste with recovery potential is significant, showing that there is potential for the application of LFM.

To implement LFM in Brazil, lessons learned from international experiences should be used as a reference, but it is essential to consider local conditions and characteristics, such as the influence of rainfall on the landfill mining process, a variable that has the potential to significantly influence the behavior of waste in places with tropical climate.

REFERENCES

[1] Ribeiro F.M., Economia Circular: Uma Nova Visão de Negócios, SENAI-SP, 2024, pp.1-240.
[2] United Nations Environment Programme, Global Waste Management Outlook 2024: Beyond an age of waste – Turning rubbish into a resource, Nairobi, 2024, pp.1-116.
[3] Periathamby A., Law H.J, Do we need landfills? Waste Management and Research, Vol. 38, Issue 10, 2020, pp.1075–1077.
[4] Jain M., Kumar A., Kumar A., Landfill mining: A review on material recovery and its utilization challenges. Process Safety and Environmental Protection, Vol. 169, 2023, pp.948–958.
[5] Machado S.L., Carvalho M.F., Torres E.A., Santos Á.C., Karimpour-Fard M., Briefing: Landfill mining for energy recovery in tropical developing countries. Journal of Environmental Engineering and Science, Vol. 13, Issue 4, 2018, p.93–97.
[6] Scott D.I., Longman M., Wilson, S, Reclaiming historic landfill sites for residential development: a UK case study. Journal of Environmental Engineering and Science, Vol. 15, Issue 2, 2020, pp.71–79.
[7] Machado S.L., Editorial, Journal of Environmental Engineering and Science, Vol. 15, Issue 2, 2020, pp.47–47.
[8] Jain P., Powell J.T., Smith J.L., Townsend, T.G., Tolaymat, T., Life-Cycle Inventory and Impact Evaluation of Mining Municipal Solid Waste Landfills, Environmental Science & Technology, Vol. 48, 2014, pp.2920–2927.
[9] Krook J., Svensson N., Eklund M., Landfill mining: A critical review of two decades of research, Waste Management, Vol. 32, 2012, pp.513–520.
[10] Lopez C.G., Ni A., Parrodi J.C.H., Küppers B., Raulf K., Pretz T., Characterization of landfill mining material after ballistic separation to evaluate material and energy recovery potential, Detritus, Vol. 8, 2019, pp.5-23.
[11] Küppers B., Parrodi J.C.H., Lopez C.G., Roland, P., Vollprecht, D., Potential of sensor-based sorting in enhanced landfill mining, Detritus, Vol. 8, 2019, pp.24-30.
[12] Parrodi J.C.H., Lopez C.G., Küppers B., Raulf K., Vollprecht D., Pretz T., Pomberger R., Case study

on enhanced landfill mining at mont-saint-guibert landfill in Belgium: characterization and potential of fine fractions. Detritus, Vol. 8, 2019, pp. 47-61.

[13] Bernardes Jr C., Characterization of mined domestic waste in Brazil focused on its use as RDF, In 7th International Symposium on Energy From Biomass and Waste, 2018.

[14] Jessberger, H.L., Geotechnical aspects of landfill design and construction. part 2: material parameters and test methods. (second of a series of three papers from the author's british geotechnical society touring lecture in 1993), Proceedings of the Institution of Civil Engineers - Geotechnical Engineering, Vol. 107, 1994, pp.105–113.

[15] Karimpour-Fard M., Rehabilitation of Saravan dumpsite in Rasht, Iran: geotechnical characterization of municipal solid waste, International Journal of Environmental Science and Technology, Vol. 16, 2018, pp. 4419-4436.

[16] Esguerra J.L., Krook J., Svensson, N., Passel S. V., Assessing the economic potential of landfill mining: review and recommendations, Detritus, Vol 8, 2019, pp. 125-140.

[17] Van Passel S., Dubois M., Eyckmans J., Gheldere S., Ang F., Jones P.T., Van Acker K., The economics of enhanced landfill mining: private and societal performance drivers, Journal of Cleaner Production, Vol. 55, 2013, pp.92-102.

[18] Danthurebandara M., Van Passel S., Vanderreydt I., Van Acker K., Assessment of environmental and economic feasibility of Enhanced Landfill Mining, Waste Management, Vol. 45, 2015, pp.434-447.

[19] Gutiérrez-Gutiérrez S.C., Coulon F., Jiang Y., Wagland S., Rare earth elements and critical metal content of extracted landfilled material and potential recovery opportunities, Waste Management, Vol. 42, 2015, pp.128-136.

[20] Kasam, Iresha F.M., Putra H.P., Lathifah, A.N., Rahmat A., Conference proceedings, in Proc. 13th Int. Conf. on GEOMATE, 2023, pp. 1219-1225.

[21] Guimarães C.C., Barbosa A.M., Bezerra E.S.R., Pereira G.P., Netto L.G., Assessment of the landfill mining potential in inactive landfills in the state of São Paulo, In 19th International Symposium on Waste Management and Sustainable Landfilling, 2023.

[22] Associação Brasileira de Resíduos e Meio Ambiente, Panorama dos Resíduos Sólidos no Brasil 2024, 2024, pp.1-84.

[23] Brazil, Decree 11.043, April 13, 2022. Approves the National Solid Waste Plan, Brasília, 2022.

[24] Boscov M.E.G., Di Emidio G., Ferrari A.A.P., Hemsi P.S., Machado M.F.C., Nobre M.M.N., Nobre R.C.M., Thomé A., Environmental geotechnics: brazilian experience and some hot topics, Soil and Rocks, 2025 (in press).

[25] Jain P., Townsend T.G., Johnson P., Case study of landfill reclamation at a Florida landfill site, Waste Management, Vol, 33, 2013, pp.109-116.

[26] Guerreiro, E.M.S., Aproveitamento energético a partir de pré-processamento de resíduos: análise panorâmica comparativa com foco nos casos de Brasil e Alemanha, Doctoral's thesis, Instituto de Energia e Ambiente, Universidade de São Paulo, 2025.

Copyright © Int. J. of GEOMATE All rights reserved, including making copies, unless permission is obtained from the copyright proprietors.

15th Int. Conf. on Geotechnique, Construction Materials & Environment,
Kyoto, Japan, 11-13 November 2025, ISBN 978-4-909106124 C3051

IMPROVING THE PROPERTIES OF MATERIAL USED IN BUILDING CLAY HOUSES WITH CEMENT

Nathiya Jaokaenkaew[1], Pongsakorn Punrattanasin[2]

[1,2] Faculty of Engineering, Khon Kaen University, Thailand

ABSTRACT

This study focuses on improving the properties of clay soil for constructing eco-tourism earth houses to address issues related to structural weakness, lack of durability, and vulnerability to weather conditions and natural disasters. Cement was incorporated into the clay soil to enhance strength and resistance to strength loss after water immersion, simulating conditions in areas prone to flooding or heavy rainfall. In this research, cement was mixed into clay soil at proportions of 3%, 5%, 7%, 10%, 20%, and 25%. Experimental results indicated that the compressive strength of clay soil increased with both curing time and cement content. At 25% cement and a curing age of 28 days, the strength peaked at 61.75 ksc, compared to 34.91 ksc for untreated clay—an improvement of approximately 1.77 times. Untreated clay and clay mixed with less than 20% cement exhibited ductile fracture behavior. In contrast, specimens containing 25% cement showed brittle failure behavior. Strength loss due to water immersion, simulating rainy conditions, was observed to decrease with longer immersion durations. After 5 hours of water immersion, clay mixed with 25% cement retained a compressive strength of 20.25 ksc, whereas untreated clay measured 61.75 ksc indicating a strength reduction of approximately 3.05 times. Based on studies of both load-bearing capacity and strength loss, it can be concluded that clay mixed with 20% and 25% cement is the optimal ratio, as it provides good load-bearing ability and retains significant strength even when submerged in water.

Keywords: Clay, Earth Houses, Water Immersion, Cement, Curing Time

INTRODUCTION

Sustainable travel accommodations, recognized by the Travel Sustainable badge, have become increasingly popular worldwide, including in Thailand. [1] stated that earthen houses, inspired by traditional Thai wisdom, are built using natural materials and techniques passed down through generations, as shown in Fig. 1. However, since these construction methods were not originally developed based on engineering principles, they often face structural issues both during and after construction. Common problems include collapse due to heavy rainfall, flooding, and other natural disasters, resulting in a shorter lifespan and reduced durability. To improve the strength of earthen houses, the addition of cement has been widely explored. [2] and [3] conducted a study on cement mixing to improve soil. [4] conducted a study and found that mixing cement with clay soil enhances its compressive strength. Cement improves the load-bearing capacity of clay, making it more resilient. This research aims to further develop the compressive strength of build clay houses to enhance their durability against weather conditions and natural disasters. Additionally, the study must determine the appropriate ratio for practical application in actual construction.

Fig.1 An image of house built with clay for eco-tourism (from website [5])

SAMPLE PREPARATION

The clay collected from Ban Wang Thua, Wang Chai Subdistrict, Nam Phong District, Khon Kaen Province, mostly consists of topsoil clay that can be used for pottery (Fig.2). In preliminary tests, it was found that this clay is suitable for constructing eco-friendly earthen houses. According to the Unified Soil Classification System, this type of clay is

classified as Low Plastic Clay (CL), with details presented in Table 1. When the initial strength of the soil is assessed using a Pocket Penetrometer, clay in its natural moisture condition has a strength of less than 2 ksc. To strengthen the natural properties of the soil, only Type 1 Portland cement was added in this study. Six different proportions of dry cement were used: 3%, 5%, 7%, 10%, 20%, and 25% of the dry soil weight. Cement exceeding 25% was not used because preliminary tests showed that higher amounts made sample mixing and shaping difficult. For sample preparation, water was added at 20% of the total mixture weight. Once mixed, the material was placed into cylindrical molds with a diameter of 5 cm and a height of 10 cm. A pressing tool applied equal force to each sample, ensuring uniform material quantity and pressing energy, thereby making the results comparable. In the first part of the study, strength development over curing time was examined with four curing periods: 3 days, 7 days, 14 days, and 28 days. All samples were cured in an open room at 25°C without wrapping. The second part of the study simulated strength loss when an earthen house is exposed to rain with varying amounts of rainfall. For this, only 28 days old samples were immersed in water for three different durations: 1 hour to simulate light rain, 3 hours for moderate rainfall, and 5 hours for heavy rainfall. A total of 49 samples were tested, with details presented in Table 2.

Fig.2 The clay from the sampling site, which is used for pottery making, can be used in this study

Table 1 Properties of clay

Properties	Clay from Wang Chai Subdistrict
#4 Passing, %	90.1
#200 Passing, %	63.7
Liquid limit (LL), %	38.6
Plastic limit (PL), %	20.1
Plasticity index (PI), %	18.5
USCS classification	CL

Table 2 Samples and test details

Samples	Study on strength development		Study on strength loss		
	Curing periods (days)	No. of sample	Curing periods (days)	Soaking time (hours)	No. of sample
S100C0	3, 7, 14, 28	4	28	1, 3, 5	3
S97C3	3, 7, 14, 28	4	28	1, 3, 5	3
S95C5	3, 7, 14, 28	4	28	1, 3, 5	3
S93C7	3, 7, 14, 28	4	28	1, 3, 5	3
S90C10	3, 7, 14, 28	4	28	1, 3, 5	3
S80C20	3, 7, 14, 28	4	28	1, 3, 5	3
S75C25	3, 7, 14, 28	4	28	1, 3, 5	3

Note: Note: S100C0 (pure clay), S97C3 (clay mixed with 3% cement), S95C5 (clay mixed with 5% cement), S93C7 (clay mixed with 7% cement), S90C10 (clay mixed with 10% cement), S80C20 (clay mixed with 20% cement) and S75C25 (clay mixed with 25% cement).

RESULTS AND DISCUSSION

Strength Development

The strength of the clay samples and clay mixed with cement was evaluated using the stress-strain relationship from the unconfined compression test. The graph provides key parameters, including the maximum load-bearing capacity, the strain at maximum load, residual strength, and the failure mode, classified as either brittle or ductile. Figure 3 presents the relationship for samples cured for three days, with data from seven different sets. The first set, consisting of pure clay (S100C0), exhibited a maximum strength of 16.28 ksc at approximately 2.27% strain. When mixed with 3% cement (S97C3), the strength increased to 22.64 ksc. As the cement content increased, the strength continued to rise, reaching 52.66 ksc at 25% cement content (S75C25), which is approximately 3.24 times greater than that of pure clay. Failure mode analysis revealed that pure clay and clay mixed with less than 25% cement exhibited ductile behavior, meaning the samples retained some residual strength after peak load. However, samples with 25% cement demonstrated brittle failure, where strength was rapidly lost after reaching maximum load.

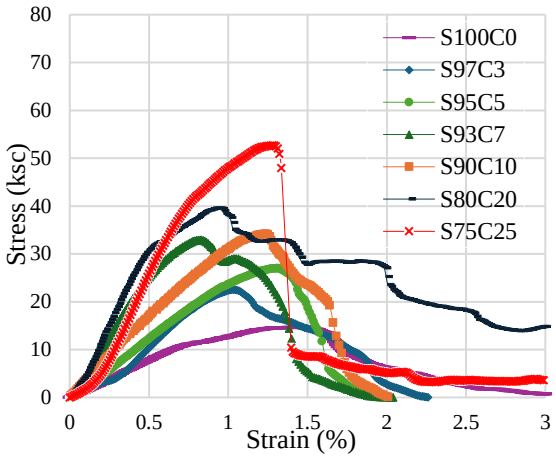

Fig.3 The relationship between stress and strain of soil and soil-cement at curing age of 3 days

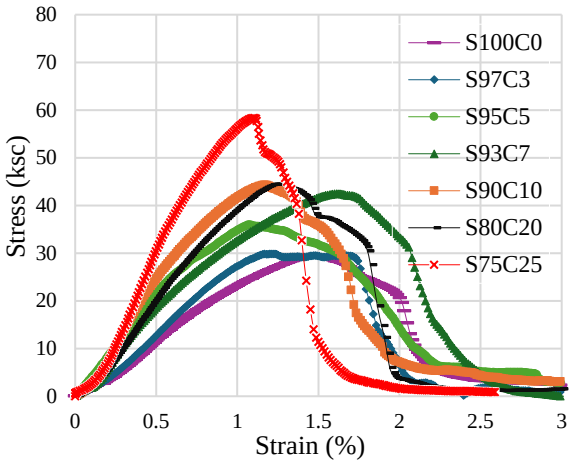

Fig.4 The relationship between stress and strain of soil and soil-cement at curing age of 7 days

Figures 4 to 6 illustrate similar trends for samples cured for 7, 14, and 28 days, respectively. The results indicate that both load-bearing capacity and strength increase with higher cement content and longer curing durations. The maximum load-bearing capacity of pure clay is 26.74 ksc, 32.97 ksc, and 34.91 ksc at curing ages of 7, 14, and 28 days, respectively. Increasing the cement content to 25% enhances the load-bearing capacity, reaching 58.32 ksc, 60.97 ksc, and 61.75 ksc for curing periods of 7, 14, and 28 days. For other mixtures, the load-bearing capacity of the samples is summarized in Table 3. When comparing load-bearing capacity at 28 days, it is observed that the strength of pure clay increases from 34.91 ksc to 60.53 ksc, 60.97 ksc, and 61.75 ksc with cement contents of 10%, 20%, and 25%, respectively. It can be said that adding 20-25% cement can enhance the load-bearing capacity of clay by approximately 1.7 times. However, cement content between 3% and 7% does not significantly enhance the strength. Unlike the results shown in Figure 3, where only the 25% cement-soil mixture exhibited brittle failure, other cement-soil mixtures displayed ductile characteristics. However, in Figures 4 to 6, nearly all cement-soil mixtures became stronger and demonstrated brittle-like behavior as curing age increased. The residual strength after reaching maximum capacity gradually decreased as strain increased. By using the values from Table 3 to analyze the relationship between curing age and unconfined compressive strength, the results are shown in Figure 7, indicating a linear correlation between curing age and load-bearing capacity. Similarly, Figure 8 illustrates the relationship between cement content and load-bearing capacity, which also exhibits a linear correlation, as observed in Figure 7. It can be preliminarily concluded that adding 10-25% cement to clay enhances its load-bearing efficiency compared to pure clay.

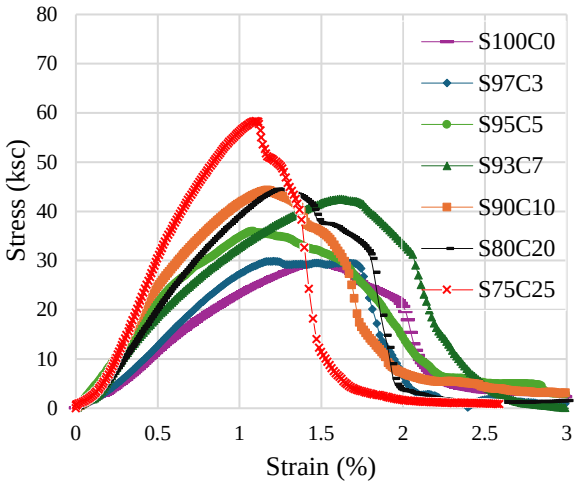

Fig.5 The relationship between stress and strain of soil and soil-cement at curing age of 14 days

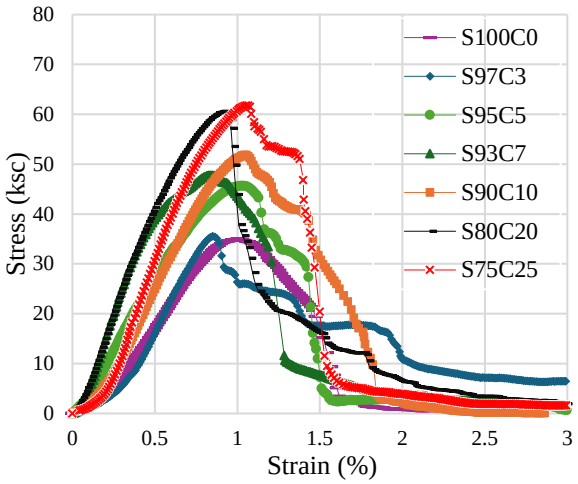

Fig.6 The relationship between stress and strain of soil and soil-cement at curing age of 28 days

Table 3 Strength development under different curing durations

Samples	Strength development under different curing durations (ksc)			
	3 days	7 days	14 days	28 days
S100C0	16.28	26.74	32.97	34.91
S97C3	22.64	29.83	33.56	35.62
S95C5	30.75	35.91	39.15	45.65
S93C7	32.95	40.16	42.46	51.75
S90C10	38.76	44.23	50.37	60.53
S80C20	39.57	44.44	58.32	60.97
S75C25	52.66	58.32	60.97	61.75

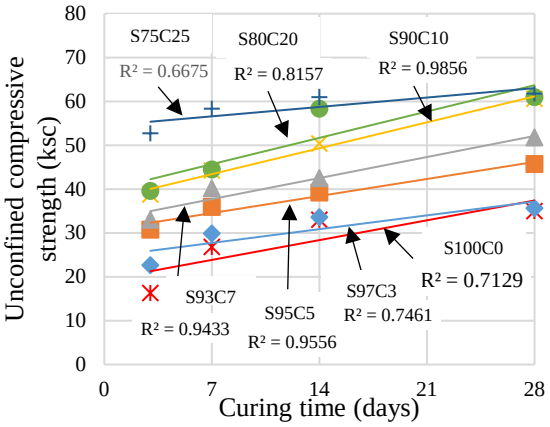

Fig.7 The relationship between curing age and unconfined compressive strength of soils

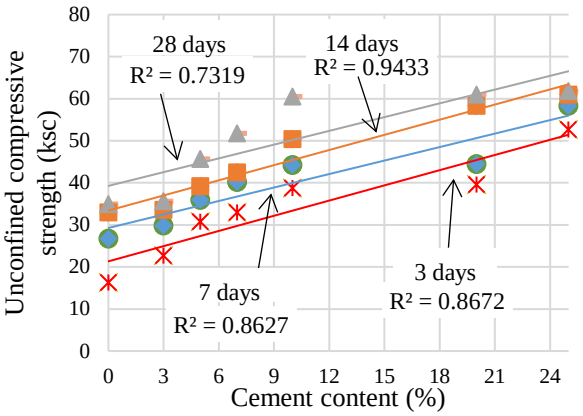

Fig.8 The relationship between cement content and unconfined compressive strength of soils

Strength Loss

In this second part of the experiment, the load-bearing capacity of the samples will be evaluated after water immersion, simulating conditions where cement-stabilized soil is submerged. The researcher selected only samples with a curing age of 28 days for this study. The immersion test consists of three scenarios: 1-hour immersion, representing light rainfall; 3-hour and 5-hour immersion, simulating heavy rainfall and flooding. This testing method helps earth-home builders understand the impact of prolonged submersion on their structures. The test results show the relationship between stress and strain, as illustrated in Figures 9 to 11. Figure 9 presents the results after a 1-hour water immersion, followed by a load-bearing capacity test. The effects of 3-hour and 5-hour immersion on the samples are shown in Figures 10 and 11, respectively. Table 4 summarizes the load-bearing capacity of soil and soil-cement after being submerged in water for different durations.

Figure 9 clearly shows that only four soil-cement mixtures could withstand compressive force. Pure clay, as well as 3% and 5% cement-clay mixtures, failed to maintain their structural integrity after brief water immersion, making compression testing unfeasible. The graph highlights the correlation between cement content and load-bearing capacity, with higher cement percentages preserving greater strength. According to the graph, the estimated load-bearing capacity for a 10% cement mixture is approximately 29.47 ksc, rising to 25% cement, and gradually decreasing to 22.72 ksc, 11.69 ksc, and 11.67 ksc as the cement content decreases to 20%, 10%, and 7%, respectively. The results in Figures 10 and 11 contrast with those in Figure 9, revealing that only three soil-cement mixtures maintained their load-bearing capacity after being submerged for 3 and 5 hours. These mixtures contained 10%, 20%, and 25% cement. However, upon closer examination, the 10% cement mixture demonstrated a load-bearing capacity of only about 6.41 ksc, which is relatively low. Therefore, only two soil-cement mixtures remain viable in terms of maintaining load-bearing capacity after submersion: those with 20% and 25% cement content.

When the results from the first part of testing are plotted alongside the water immersion test, the outcomes are presented in Figures 12 and 13. From Figure 12, for the 20% soil-cement mixture with a curing age of 28 days, the load-bearing capacity is 60.97 ksc. After 1 hour of water immersion, the strength decreases to 22.72 ksc, or approximately 37.3% of its original capacity. When submerged for 3 hours, the load-bearing capacity declines slightly further, and after 5 hours, it is reduced to 16.70 ksc, or approximately 27.4% compared to the dry state. For the 25% soil-cement mixture, the load-bearing capacity at 28 days without water immersion is 61.75 ksc. After 1 hour of immersion, the strength drops to

29.47 ksc, or about 47.7% of its original capacity. With 3 hours of immersion, the load-bearing capacity decreases slightly, and after 5 hours, it is approximately 20.25 ksc, or about 32.8% compared to the dry state. It is evident that both mixtures maintain a considerable load-bearing capacity even after being submerged for up to 5 hours. Therefore, based on this experiment, these two mixtures are suitable for constructing earth houses. When combined with the results from the first phase of testing, it can be concluded that the optimal mixture for improving clay strength and ensuring its durability against natural hazards such as rainfall is 20% and 25% cement with 20% water content.

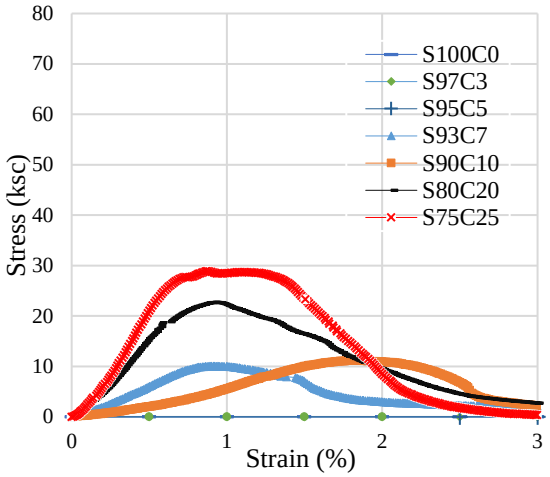

Fig.9 The relationship between stress and strain after being submerged in water for 1 hour

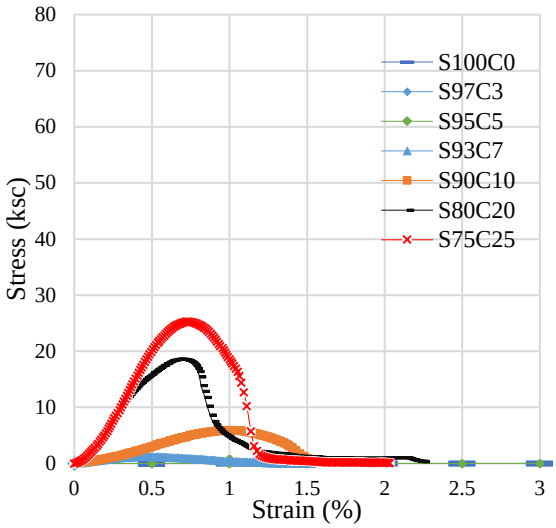

Fig.10 The relationship between stress and strain after being submerged in water for 3 hours

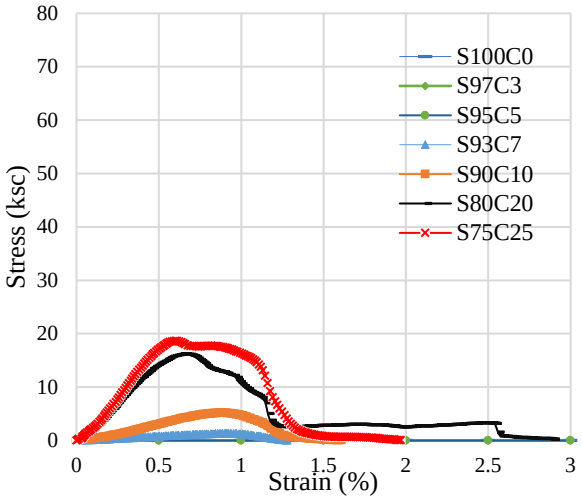

Fig.11 The relationship between stress and strain after being submerged in water for 5 hours

Table 4 Strength after being submerged in water

Samples	Strength after being submerged in water (ksc)			
	0 hour	1 hour	3 hours	5 hours
S100C0	34.91	NA	NA	NA
S97C3	35.62	NA	NA	NA
S95C5	45.65	NA	NA	NA
S93C7	51.75	11.67	1.82	1.84
S90C10	60.53	11.69	6.41	5.70
S80C20	60.97	22.72	19.19	16.70
S75C25	61.75	29.47	25.83	20.25

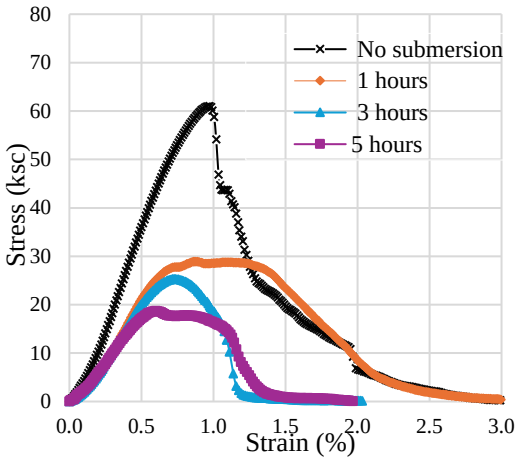

Fig.12 The relationship between stress and strain of 20% soil-cement after water submersion

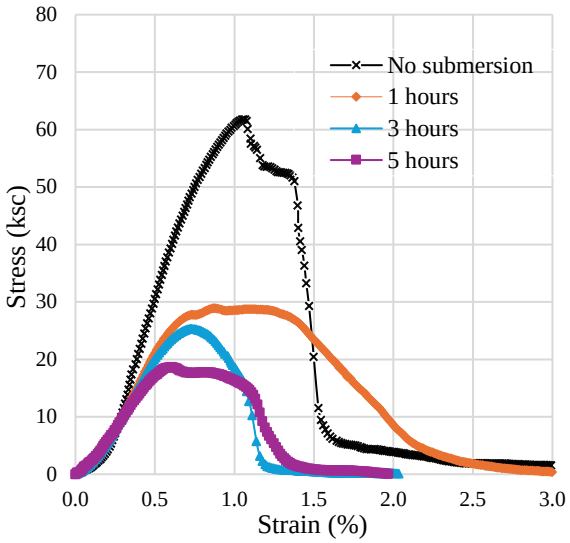

Fig.13 The relationship between stress and strain of 25% soil-cement after water submersion

CONCLUSIONS

Clay from Nam Phong District, known for its use in pottery, has the potential for constructing earth houses for eco-tourism. Various cement proportions, ranging from 3% to 25%, were tested. Preliminary experiments revealed that mixing cement with 20% water allowed for proper blending and sample formation. At each curing age, mixtures with higher cement content consistently demonstrated greater compressive strength, with the 25% cement mixture achieving the highest values. At 3 days, the 25% cement mixture showed a sharp, brittle failure, while all other mixtures, including pure clay, exhibited ductile behavior with residual strength after peak load. Mixtures with 3% and 5% cement showed only modest strength gains compared to pure clay, especially at later curing stages, indicating they may not be suitable for structural applications. Mixtures with 20% and 25% cement provided the best balance of strength and durability, making them the most suitable for constructing clay-based structures. These findings led to further tests examining water immersion resistance over different durations. Results indicated that only the samples containing 20% cement and 25% cement maintained sufficient durability and load-bearing capacity. Thus, this study concludes that cement proportions of 20%-25% are optimal for enhancing the strength of natural clay, making it suitable for constructing earth houses efficiently.

REFERENCES

[1] Boonsin P. Earth-sheltered architecture: applying wisdom to build for living place in northeast Thailand, 14(4), 2020, pp.130–131.

[2] Jamsawang P. (2017). Improvement of soft clay with cement and bagasse ash waste. Construction and Building Materials.

[3] Raksachon Y. (2008). Unconfined Compressive Strength and Microstructure of Compacted Cement-Fly Ash Clay Soil.

[4] Consoli N.C., Foppa D., Festugato L., and Heineck K.S. Key Parameters for Strength Control of Artificially Cemented Soils. Journal of Geotechnical and Geoenvironmental Engineering, 133(2), 2007, pp.197–205.

[5] Kapook H. Build a single-story earthen house by yourself at a low cost with a budget of 46,000 baht, Retrieved March 20, 2025, from https://home.kapook.com/view178624.html

Copyright © Int. J. of GEOMATE All rights reserved, including making copies, unless permission is obtained from the copyright proprietors.

15th Int. Conf. on Geotechnique, Construction Materials & Environment,
Kyoto, Japan, 11-13 November 2025, ISBN 978-4-909106124 C3051

EFFECT OF ANTECEDENT RAINFALL ON POOR WATER PRESSURE DISTRIBUTION CHARACTERISTICS IN RESIDUAL SOIL UNDER TROPICAL RAINFALL

Mohamed Elbyhagi Elfadil

Saudi Electricity Company, KSA

ABSTRACT

Characteristics of changes in pore-water pressure distribution are the main parameters associated with slope stability analysis involving unsaturated soils, which are directly affected by the flux boundary conditions (rainfall infiltration, evaporation and evapo-transpiration) at the soil–atmosphere interface. Two slopes were instrumented at Universiti Teknologi Malaysia (UTM) Skudai campus (Malaysia). The field monitoring results were analyzed to characterize pore-water pressure distributions to study the effect of antecedent rainfall on pore-water pressure distributions in typical residual soil slopes under tropical climate. Slope stability analyses were also conducted at depth 1.0 meter and recorded in each slope to determine the range of factor of safety for the slopes. Results indicate that, antecedent rainfall; initial pore-water pressures prior to a significant rainfall event as well as the magnitude of the rainfall event play a crucial role in the development of the worst pore-water pressure condition in a slope. The role of antecedent rainfall in the development of the worst pore-water pressure condition was found to be more significant in residual soils with low permeability as compared with that in residual soils with high permeability. The factor of safety of residual soils with low permeability was found to be unaffected by the worst pore-water pressure condition.

Keywords: Rainfall; Antecedent Rainfall; Pore-Water Pressure; Slope Failure; Factor of Safety

INTRODUCTION

Rainstorm is one of the most significant triggering factors for slope failures. It is widely recognized that rainfall-induced slope failures are mainly caused by infiltration of rainwater [5]; [15]; [7] and [20]. A number of studies have also indicated that slope failures can be attributed to several factors such as climatic conditions, geological features, topography, vegetation or a combination of these factors. These factors and their contribution to slope instability vary with geographical locations. Some studies have attempted a simple correlation between incidences of landslides with rainfall patterns. Simple direct correlations have been made for Brazil [3], [14] and [5]. More complicated correlation attempts are available for New Zealand [10]; [8]; [16] and [5].

Although the significance of rainwater infiltration in causing landslides is widely recognized, there have been different conclusions as to the relative roles of antecedent rainfall to landslides. [5] Suggested that antecedent rainfall was not a significant factor for landslides in Hong Kong and this limited influence of antecedent rainfall was attributed to the high permeability of local soils. [5] Suggested that the majority of landslides in Hong Kong were induced by localized and short duration rainfall of high intensity.

The objectives of this study are (i) to characterize pore water pressure distributions and (ii) to evaluate the effect of antecedent rainfall on pore-water pressure distributions in typical residual soil slopes under tropical climate.

Fig. 1 Shows Site-1 Field on 20th December 2006 and Site-2 Remain Stable.

METHODOLOGY

The study comprises the collection of field data, obtaining soil properties through field and laboratory tests, and performing slope stability analysis.

Field data collected from the sites are the geometry of the slope, rainfall data and matric suction. Site-1 was instrumented with nine tensiometers while Site-2 was instrumented with a rain gauge and 27 tensiometers (Fig. 1). Field permeability tests were also conducted at the sites. Undisturbed samples were collected at depth of 1m and 2m at several occasions between July and December 2006 to obtain water content at normal condition and at extreme condition i.e. after the prolonged and intense rainfall on December 2006.

Laboratory tests were conducted to obtain soil index properties, shear strength parameter, and the permeability of soil forming the slope. The shear strength of soil was evaluated by shear box test. The

soil water characteristic curves (SWCC) were obtained by pressure plate test. The apparatus and the procedure followed for obtaining the SWCC is explained in Wang and Benson (2004).

Infinite slope stability analyses were performed at depth 1.0 meter for slopes at normal condition and at wettest condition using the formula proposed by Fredlund et al.(1978). (Fredlund et al., 1987; Sung and Seung, 2002). The pore air pressure is atmospheric, the equation can be written as:

$$FOS = \frac{c' + (N - u_w)tan\emptyset'}{W\ sin\beta cos\beta} \qquad (1)$$

where c' = effective cohesion of the soil, N = normal stress applied on failure surface, $\emptyset'$ = effective friction angle, u_w = pore water pressure, W = total weight of the soil, β = the slope angle.

The survey work showed that both slopes can be considered as long slopes. The slope at Site-1 formed an angle of 30˚ while the slope at Site-2 forms an angle of 20.8˚. Field permeability test using Guelph permeameter show that the permeability coefficient of soil at Site-1 is 1.07×10-7 m/sec while that of Site-2 is 1.23×10-5 m/sec.

RESULTS AND DISCUSSION

The basic data for this study are the rainfall records on slope at site-2 which near the site-1, pore-water pressure measurements at various depths; 0.5, 1.0, 1.5 meter at each location at the slope; crest, middle and toe during raining season and dry season conditions across the year, site-1 monitored for six months and Site-2 monitored for one year, the data were characterized two periods; wet period and dry period for each slope were further characterized by key times, and the distribution of pore-water pressures along slope profile during these key times was examined. Key times were considered to be: (i) time at the end of a prolong dry period (ii) time following one or a series of significant rainfall event. The summary of rainfall records are presented on the graphs. The factor of safety was calculated for the slopes using the soil properties shown in table (1). The rainfall data and soil suction shown in the graphs. Infinite slope procedure was used to determine the factor of safety (FOS). The calculation was made for slip planes at different depths between 1 and 2.0 m with the interval of 0.2 m. Drained shear strength parameters obtained from direct shear test were used in the calculation. The results of the slope stability analysis performed for suction predicted based on water content and SWCC curve are presented in Table (2). The soil suction monitored in each slope during key times. The subsequent analyses discussion is based on individual slopes.

Table 1 summarizes the results of laboratory tests on disturbed samples obtained from both sites. It can be seen that sample from Site-2 contains more coarse particles than the sample obtained at Site-1. The soil at Site-1 has higher silt content which makes the soil prone to the erosion and dispersion; hence the slope is prone to fail at higher water content. The soil at Site-2 is a less plastic than the soil at Site-1. However, the difference is very small and it should be noted that only a small fraction of soil at Site-2 belongs to fine particles, thus the effect is very limited. Classification tests show that the soil at Site-1 is sandy silt of high plasticity (MHS) while the soil at Site-2 is silty gravel of low plasticity (GML).

Table 1 Soil properties

Parameter	Kolej 12 (Site 1)	Balai Cerapan (Site 2)
Unit weight (γ) kN/m3	17.2	18.0
Specific gravity (Gs)	2.68	2.64
Dry unit weight (kN/m3)	1.28	1.37
Composition, Gravel (%)	7	48
Sand (%)	30	15
Silt (%)	47	20
Clay (%)	16	17
Liquid Limit(LL) %	68.1	53.2
Plasticity index (PI) %	24.0	17.7
Soil type	MHS	GML
Shear Strength parameters		
Friction Angle(ǿ)	24.6˚	39.5˚
Cohesion (ć) KPa	2.6	3.3
Permeability (m/sec)		
Laboratory test	3.25×10^{-8}	2.04×10^{-6}
Field test	1.07×10^{-7}	1.23×10^{-5}

The drained shear strengths of soil from both sites were obtained from direct shear test. As shown in Table 1, the soil at Site-2 has higher shear strength than that in Site-1 especially in term of friction angle.

The permeability of soil at Site-2 is two orders of magnitude higher than that of Site-1. It is noted that the laboratory test gives lower value than the field test because the laboratory tests were performed on compacted soil.

The natural volumetric water content of soil in Site-2 varies slightly from 32.5% at depth of 1 m to 33.5% at depth of 2 m. The water content measured after the prolonged and intense rainfall in December 2006 is only slightly higher than the average, i.e 34.8% and 36.8% at depth of 1 m and 2 m respectively. Note that the volumetric water content at saturation for soil at Site-2 (Balai Cerapan) is 42.4%. Slight change in soil water content corresponding to depths and the rainfall is due to the presence of clay in soil.

The natural volumetric water content of soil at

Site-1 varies from 57% at depth of 1 m to slightly higher than 60% at depth of 2m. The water content measured a few days after the failure is 69% which is higher than the water content at saturation (64%). This shows that the soil has reached saturation at the time of failure.

Besides the saturated permeability of the soil, the soil water characteristics curve (SWCC) was another important characteristic of the unsaturated soil that influences the mechanism of rainfall-induced slope failure. Figure 2 shows the SWCC curves obtained by the pressure plate extractors for soil samples collected at both sites. The highest suction that may exist in a soil is limited by the suction at the residual volumetric water content. Beyond this point, the water content in the soil is hardly to be dissipated even though it is still possible. The highest suction could be recorded at Site-2, which consists of coarse grained soil, was 23 kPa at residual water content of 30%. As for the fine-grained soil, the maximum suction is very high (>1500 kPa). However the soil loss its suction gradually during the prolonged rainfall until the safety envelope was exceeded (Nurly Gofar, et.al, 2007)[17].

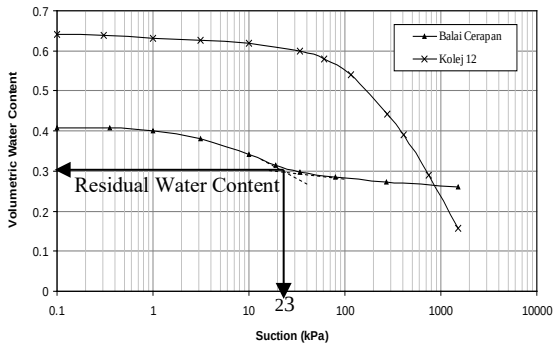

Fig. 2 SWCC curves for soils at Site-1 (Kolej 12) and Site-2 (Balai Cerapan)

The negative pore water pressure required for the calculation of factor of safety of slope was estimated based on the volumetric water content and the SWCC curve. Table 2 shows the variation of suction estimated based on SWCC of soils at both sites with depth.

Suction was actually measured at depth of 0.5m, 1m, and 1.5m. Comparison of the field data and the calculated suction based on SWCC curve shows that the SWCC curve gave higher suction values than the field measurement. However, for normal condition, the trend is similar. This shows that the response of soil to rainfall infiltration is faster than could be predicted by the SWCC curve.

Prediction of suction based on water content and SWCC curve for wet condition indicated the reduction of suction; however, the trend remained the same in which the suction decreases with depth. In contrast, measurement by tensiometer showed that the suction increases with depth. This discrepancies may be due to the time of measurement whereby tensiometer records the response right after rainfall while the sample obtained for water content determination was taken long time after the rainfall.

Table 2: Variation of Suction calculated based on SWCC curve

Elev (m)	Site 1 Normal		Site 2 Normal		Site 2 After rainfall	
	VWC %	Suction kPa	VWC %	Suction kPa	VWC %	Suction kPa
1.0	57	70	32.5	15	34.8	9.8
2.0	60	28	33.5	12.9	36.8	4.8

An interesting point can also be made from this study that the water content of soil at Site-1 remained high even after a long period dry condition. This means that the soil stays at saturated condition due to the accumulation of water caused by low permeability and mineral content of the soil mass.

Slope stability analyses were performed for both sites for two conditions i.e. normal and after the prolonged heavy rainfall in December 2006. It should be noted that the cumulative rainfall during 4 days before failure occurred at Site-1 was 489.4mm, and the maximum rainfall the day before the failure took place was 190.8mm. Infinite slope procedure was used to determine the factor of safety (FOS). The calculation was made for slip planes at different depths between 1 and 2.0 m with the interval of 0.2 m. Drained shear strength parameters obtained from direct shear test were used in the calculation. The results of the slope stability analysis performed for suction predicted based on water content and SWCC curve are presented in Table 3.

Table 3 The variation of factor of safety with depth

Depth m	FOS (Site 1)		FOS (Site 2)	
	Normal	December	Normal	December
1.0	5.45	1.14	4.79	4.08
1.2	4.21	1.08	4.29	3.58
1.4	3.33	1.04	3.94	3.21
1.6	2.66	1.01	3.68	2.97
1.8	2.15	0.99	3.49	2.86
2.0	1.83	0.97	3.34	2.78

Table 3 shows that the slope at Site-2 remained safe after rainfall, even though there is a decrease in factor of safety with depth. On the other hand, the slope at Site-1 became unstable at depth 1.8 m (FOS < 1) due to increase in water content which is beyond the volumetric water content at saturation. Table 3

shows that at normal condition, the slope Site-1 is more stable than slope at Site 2 for shallower depths, however FOS decreases as water started to accumulate at deeper elevation. Furthermore, the reduction of FOS at all depths at Site-1 is more significant than that at Site-2. It can also be seen from the table that there is a significant reduction of FOS with depth for both locations until a certain value. Then, the FOS becomes almost constant. The depth where the FOS becomes constant is considered as the critical depth. Table 4 shows the FOS obtained from stability analysis for which measured suction were used.

Table 4 FOS calculated based on measurement data

Depth m	FOS (Site-1)		FOS (Site-2)	
	Normal	December	Normal	December
1.0	2.97	1.14	4.43	3.48
1.5	2.41	1.02	3.94	3.39

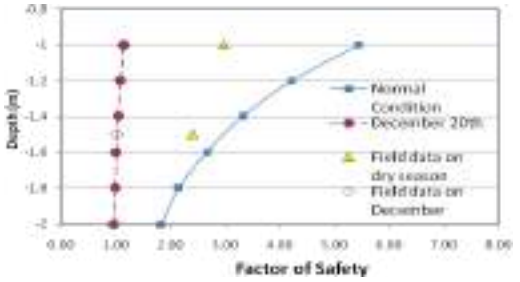

Fig.3 Depth of Slip Plane vs. FOS for Site-1

Figures 3 show the variation FOS with depth of slip surface for Site-1. The points indicated the FOS obtained for measured suction at depth of 1.0 and 1.5m. The FOS of slope at Site-1 decreases with depth. At normal condition, the minimum FOS of 1.83 was reached at depth of 2m. For wettest condition (December), FOS less than 1 was obtained at depth of 1.8m which agrees with the observed failure plane.

Based on field measurement, the minimum FOS of slope at Site-1 was 2.41, but decreases significantly to 1.02 at depth 1.5m after heavy rainfall in December 2006.

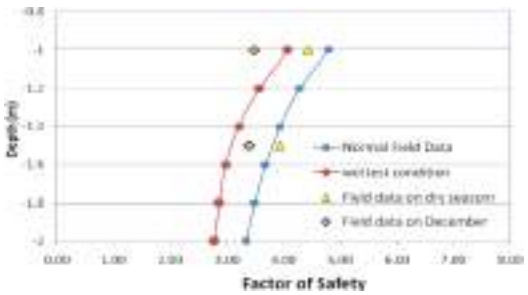

Fig. 4 Depth of Slip Plane vs. FOS for Site-2

The variation of FOS with depth of slip surface for Site-2 is presented in Figure 4. The points indicated the FOS obtained for measured suction at depth of 1.0, and 1.5m. The figure indicates that the slope at Site-2 (Balai Cerapan) remained stable even after the prolonged heavy rainfall. Based on field measurement, the FOS decreased slightly from 3.94 to 3.39 for slip plane at depth of 1.5m.

The FOS calculated based on water content and SWCC curve do not seems to agree with that calculated based on actual measurement of suction by tensiometers, however; the trend is similar. More variation of FOS with depth was obtained from the calculation based on SWCC as compared to the actual measurement. This shows that the actual variation of suction in soil is not as much as that predicted by SWCC curve. There are factors, other than the permeability and SWCC curve, affect the mechanism of rainfall infiltration in soil such as the mineralogy and the dispersibility of the soil. These will be the subject of further study. More attention should be given to the fine-grained soil slope during monsoon season.

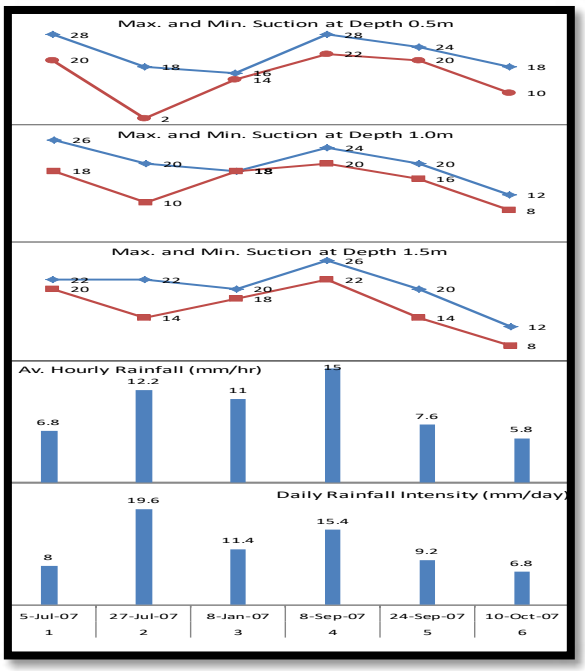

Fig. 5 Site-1 one day antecedent rainfall

Figure (5) shows readings at site-1 at three depths for one day rainfall after dry period. The events illustrated same amount and intensity of rainfall, ranged 6-20 mm/day and 6-15 mm/hours respectively. Events reflect same response at all depths except events 1 and 4 at depth 1.5 meter does not provide satisfactory explanation to why there is no change in reading 20kpa and 22Kpa respectively compare to 20Kpa and 22Kpa respectively at depth 0.5 meter. This suggests that their other factor affection water infiltration which is soil permeability as well as the

soil accommodated moisture at depth 1.5 meter.

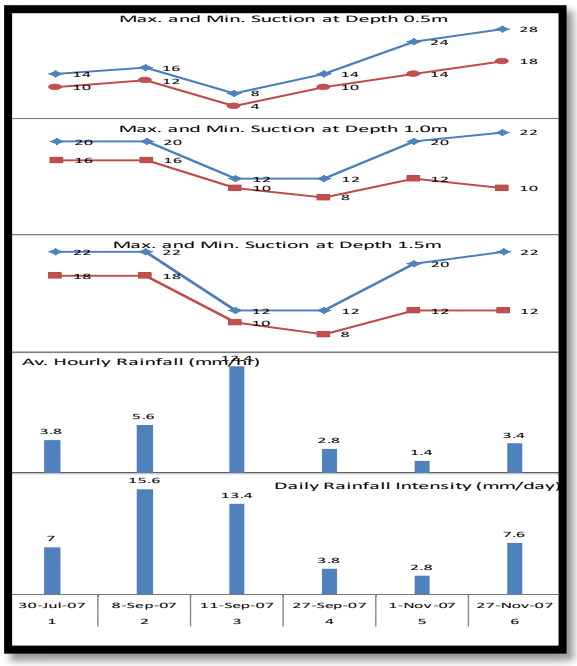

Fig. 6 Site-1 two days antecedent rainfall

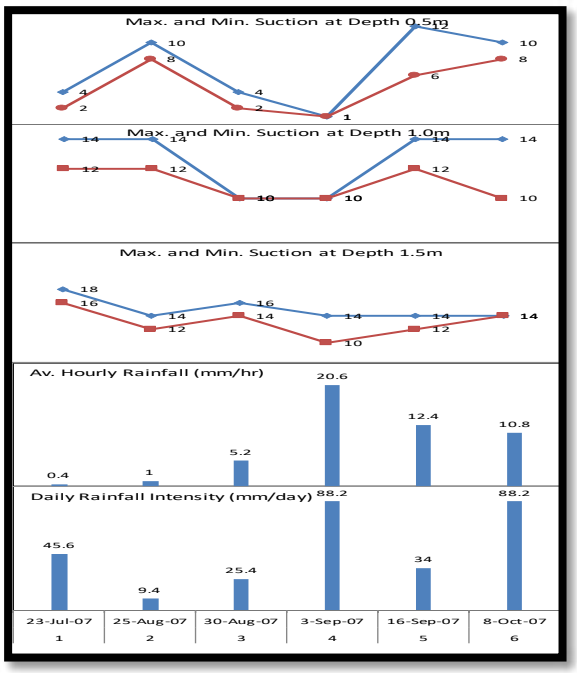

Fig. 7 Site-1 three days antecedent rainfall

Figure (6) shows readings at site-1 at three depths for two days antecedent rainfall. The events illustrated different amount and intensity of rainfall. The 1, 2 and 3 events provided high amount and intensity of rainfall 7, 15 and 13 mm respectively while the events 4, 5 and 6 provided low amount and intensity of rainfall 2.8, 1.4 and 3.4 mm respectively, even though the soil suction readings at depths 1.0 and 1.5 meter for the events 4, 5 and 6 recorded less than readings at depth 0.5 meter. This suggests that highest pore-water pressure profiles are not necessarily produced by the highest individual rainfall event. While the readings at depth 0.5 meter explained that the two days antecedent rainfall with low permeable soil does not has significant change on pore-water pressure at depths below 0.5 meter.

Figure (7) shows readings at site-1 at three depths for three days antecedent rainfall. Event 1 experienced significant amount of rainfall 45 mm with low intensity 0.4 mm per hour and the soil suction at depths 1.0 and 1.5 meter 12 and 16 Kpa respectively while the reading at depth 0.5 meter is 2 Kpa was changed significantly which provide satisfactory explanation that soil permeability affecting rainfall infiltration and readings at other two depths support the idea that soil accommodated water. Event 6 provide same explanation that water infiltration effect does not reach depth 1.5 meter due to soil permeability while the same readings at depths 1.5 and 1.0 meter means the soil accommodated water.

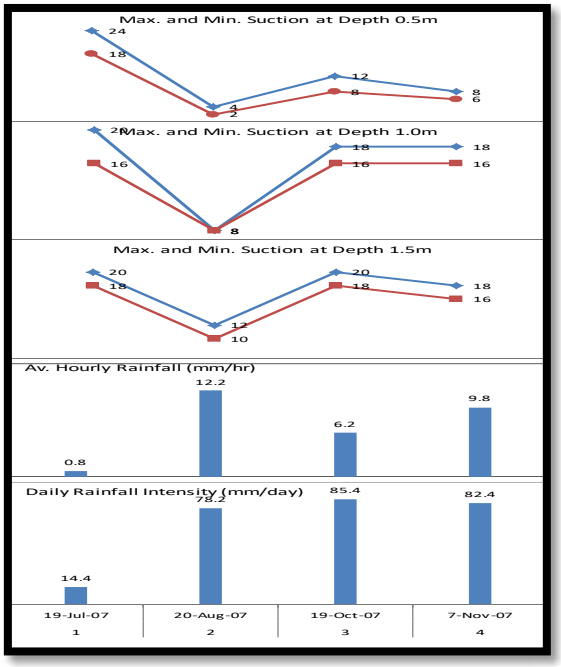

Fig. 8 Site-1 five days antecedent rainfall

Figure (8) shows readings at site-1 at three depths for three days antecedent rainfall. The event 1 show 18, 16 and 18 Kpa at three depths 0.5, 1.0 and 1.5 meter respectively under low amount of water and no heavy rainfall which means there is no effect at depth 1.0 meter as well as support the idea that the soil accommodated water at level below 1.0 meter.

Figure (9) shows readings at site-2 at three depths for one day rainfall after dry period. The events 1, 2, 3, 7 and 10 experience heavy rainfall 59, 38, 48, 37 and 49 mm respectively. The soil suction readings at three depths 0.5, 1.0 and 1.5 meter ware 2, 6 and 10 Kpa respectively. While the other events experienced low rainfall average 10 mm and the soil suction

average at three depths 0.5, 1.0 and 1.5 meter ware 5, 8 and 14 Kpa respectively. This provide satisfactory explanation that the soil response does not affected by soil permeability as well as there is no water accommodation in soil pores.

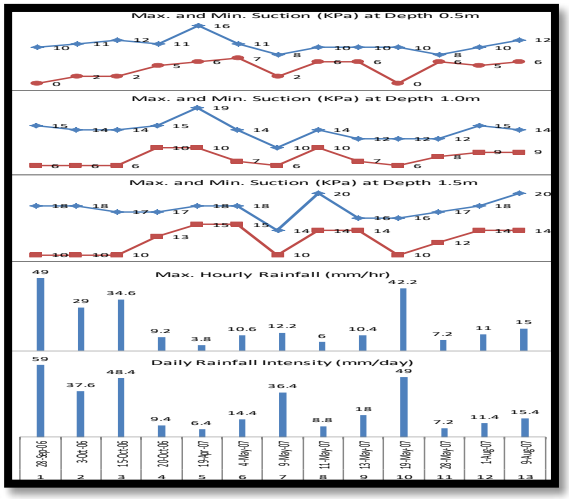

Fig. 9 Site-2 one day antecedent rainfall

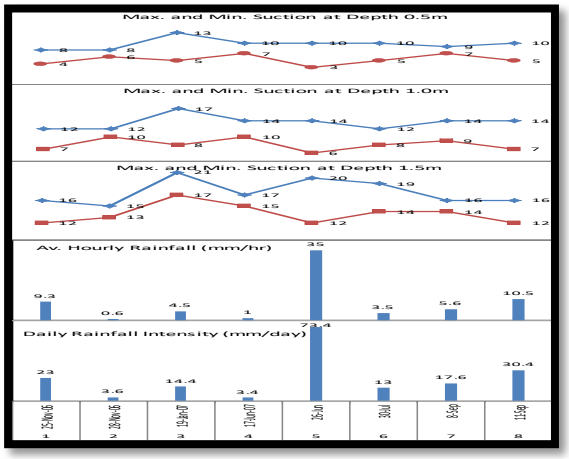

Fig. 10 Site-2 two days antecedent rainfall

Figure (10) shows readings at site-2 at three depths for two days antecedent rainfall. The event 5 experience heavy rainfall 74 mm while the events 1, and 8 experience rainfall 23 and 30 mm respectively. The soil suction readings for three events at three depths 0.5, 1.0 and 1.5 meter ware 4, 7 and 12 Kpa respectively. While the other events experienced low rainfall average 10 mm and the soil suction average at three depths 0.5, 1.0 and 1.5 meter ware 5, 8 and 14 Kpa respectively, which same response in one day rainfall. This provide satisfactory explanation that for permeable soil the soil response does not reflect difference in reading between one day rainfall and two days rainfall regard less the intensity of rainfall events at depth less than 2.0 meter.

Figure (11) shows readings at site-2 at three depths for three days antecedent rainfall. The event 1, 2, 6 and 9 experience heavy rainfall 59, 92, 58 and 88 mm. The soil suction readings for three events at three depths 0.5, 1.0 and 1.5 meter ware 3, 7 and 11 Kpa respectively. While the remaining events experienced prolong rainfall with low rainfall intensity ranged between 10 to 46 mm, the soil suction average at three depths 0.5, 1.0 and 1.5 meter ware 5, 8 and 14 Kpa respectively, which same response in one day and two days rainfall. Those supporting the previous explanation of figure 10.

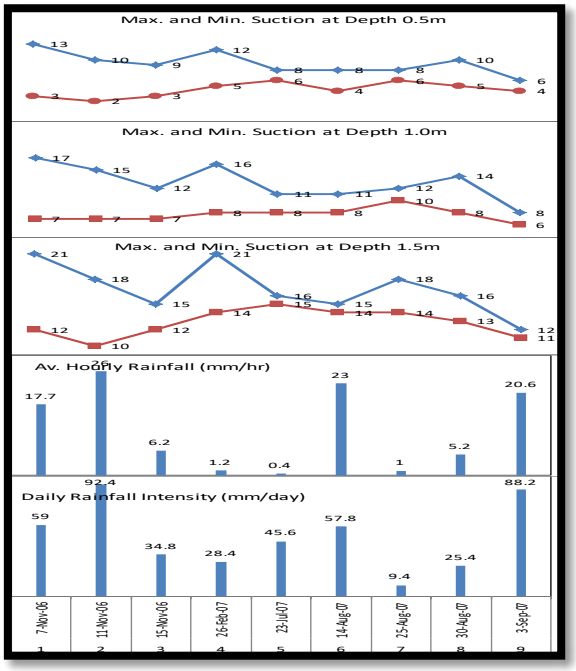

Fig. 11 Site-2 three days antecedent rainfall.

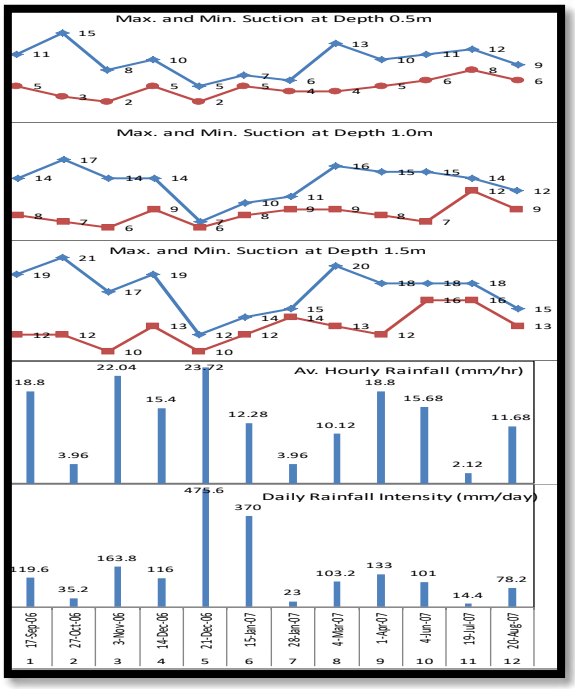

Fig. 12 Site-2 five days antecedent rainfall.

Figure (12) shows readings at site-2 at three depths for five days antecedent rainfall. The event 5 and 6 experience heavy rainfall 475 and 370 mm respectively, with different intensity 23 and 12 mm per hour respectively. The average soil suction readings for three events at three depths 0.5, 1.0 and 1.5 meter ware 3, 7 and 11 Kpa respectively which same readings for three days antecedent rainfall. While the events 1, 3, 4, 8, 9, 10 and 12 experienced medium rainfall 120, 164, 116, 103, 133, 101 and 78 respectively, with different rainfall intensity ranged between 10 to 22 mm, the soil suction average readings at three depths 0.5, 1.0 and 1.5 meter ware 5, 8 and 11 Kpa respectively. The events 2, 7and 11 experienced prolong and low Rainfall 35, 23 and 14 mm respectively.

The soil suction average readings at three depths 0.5, 1.0 and 1.5 meter ware 4, 7 and 12 Kpa respectively, which same response in one day and two days rainfall. This explains that the antecedent rainfall has no significant effect for high permeable soil comparing low permeable soil.

CONCLUSION

Several conclusions could be derived from the study on the response of soil slopes.

Firstly, antecedent rainfall play more significant role in residual soils with lower permeably than those with higher permeability in producing the highest pore–water pressure profile in a slope.

Secondly, it was observed that, in all the slopes monitored the highest pore-water pressure profile was reached when the total rainfall including 5-day antecedent rainfall was a maximum.

Thirdly, residual soils with low fines and high permeably pore-water pressure variation could take place over a wide range while in residual soils with relatively low fines and high permeably pore-water pressure variation occurs over a narrow range.

Fourthly, factor of safety varied rainfall magnitude for all slopes. On this consideration it appears that the factor of safety of residual soil slopes with relatively low permeability are unaffected by the worst pore-water pressures.

Fifthly, shallow slope failures are dominated by the combination of transient pore pressure in response to rainfall infiltration.

REFERENCES

[1] Aziz Azlan A., Faisal Ali, C.F. Heng, T.H. Mohammed and Bujang BK. Huat. (2006). Collapsibility and Volume Change Behavior of Unsaturated Residual Soil. American Journal of Environmental Sciences 2 (4): 161-166.

[2] BS (1990). British Standard Methods of test for Soil Civil engineering purpose. London, BS 1377.

[3] Barata FE. 1969. Landslides in tropical region of Rio de Jabeiro. Proceedings of the 7th International Conference on Soil Mechanics and Foundation Engineering, vol. 2, Mexico City, 507–516.

[4] Basile A, Mele G, Terribile F. 2003. Soil hydraulic behavior of a selected benchmark soil involved in the landslide of Sarno 1998. Geoderma 117(34): 331–346.

[5] Brand EW. 1984. Landslides in Southeast Asia: a state-of-the-art report. Proceedings of the 4th International Symposium on Landslides, vol. 1. Canadian Geotechnical Society: Toronto; 17–59.

[6] Cai, F. & Ugai, K. (2004). Numerical Analysis of Rainfall Effects on Slope Stability. International Journal of Geomechanics, ASCE. 4(2): 69-78.

[7] Crosta G. 1998. Regionalization of rainfall thresholds: an aid to landslide hazard evaluation. Environmental Geology 35(2–3): 131–145.

[8] Crozier MJ, Eyles RJ. 1980. Assessing the probability of rapid mass movement. Proceedings of the 3rd Australia-New Zealand Conference on Geomechanics, vol. 2., Wellington, 47–51.

[9] Department of Meteorology Malaysia, Ministry of Science, Technology dan Innovation (2006). Laporan Hujan Lebat Yang Mengakibatkan Banjir Di Negeri Johor, Melaka, Negeri Sembilan dan Pahang dalam Tempoh 17-20 Disember 2006.

[10] Eyles RJ. 1979. Slip-triggering rainfalls in Wellington city, New Zealand. New Zealand Journal of Science 22: 117–121.

[11] Fredlund, D.G. Morgenstern, N.R. and Widger, R.A. (1978) The Shear Strength of Unsaturated Soils. Canadian Geotechnic Journal. 15:313-321.

[12] Fredlund, D.G. Rahardjo, H. and Gan, J.K.M. (1987) Nonlinearity of Strength Envelope for Unsaturated Soils. Proc. 6th Intl. Conf. on Expansive Soils. New Delhi India. 49-54.

[13] Fredlund D. G., and Rahardjo H. (1997). Soil Mechanics for Unsaturated Soil.

[14] Fukuoka M. 1980. Landslides associated with rainfall. Geotechnical Engineering- Journal of Southeast Asian Geotechnical Society 11: 1–29.

[15] Lim TT, Rahardjo H, Chang MF, Fredlund DG. 1996. Effect of rainfall on matric suctions in a residual soil slope. Canadian Geotechnical Journal 33: 618–628.

[16] Lumb P. 1975. Slope failures in Hong Kong. Quarterly Journal of Engineering Geology 8: 31–65.

[17] Nurly Gofar, M.L. Lee, and A. Kassim . (2007) Stability of Unsaturated Slopes Subjected to Rainfall Infiltration. Proceedings of the 4th International Conference on Disaster Prevention and Rehabilitation, Semarang, 10-11 September 2007.

[18] Ost L, Van-Den EM, Poesen J, Vanmaercke-Gottigny MC. 2003. Char- acteristics and spatial distribution of large landslides in the Flemish Ardennes (Belgium). Zeitschrift fur

Geomorphologie 47(3): 329–350.
[19] Pradel, D. & Raad, G. (1993). Effect of Permeability on Surficial Stability of Homogeneous Slopes. Journal of Geotechnical Engineering, ASCE. 119(2): 315-332.
[20] Rahardjo H, Li XW, Toll DG, Leong EC. 2001. The effect of antecedent rainfall on slope stability. Geotechnical and Geological Engineering 19: 371–399.
[21] Sung E.C. and Seung R.L. (2002) Evaluation of Surficial Stability for Homogeneous Slopes Considering Rainfall Characteristics. Journal of Geotechnical and Geoenvironmental Engineering. ASCE. 128(9):756-763.
[22] Wang. Xiaodong and C.H. Benson (2004). Leak-Free Pressure Plate Extractor For Measuring the Soil Water Characteristic Curve. Geotechnical Testing Journal. 27(2).

Copyright © Int. J. of GEOMATE All rights reserved, including making copies, unless permission is obtained from the copyright proprietors.

15th Int. Conf. on Geotechnique, Construction Materials & Environment,
Kyoto, Japan, 11-13 November 2025, ISBN 978-4-909106124 C3051

GEOTECHNICAL PROPERTIES OF RECYCLED GLASS STABILIZED WITH CEMENT

Sereyroath Chea[1], Arul Arulrajah[1], Annan Zhou[2], Suksun Horpibulsuk[3], and Kanagesperan Verumandy [4]

[1] Department of Civil and Construction Engineering, Swinburne University of Technology, Australia.
[2] Discipline of Civil and Infrastructure Engineering, Royal Melbourne Institute of Technology, Australia.
[3] School of Civil Engineering and Center of Excellence in Innovation for Sustainable Infrastructure Development, Suranaree University of Technology, Thailand.
[4] Asas Foundations Pty Ltd, Australia.

ABSTRACT

The rapid increase in demand for natural construction sand has exceeded its natural replenishment rate, leading to resource depletion and environmental concerns. Simultaneously, recycled glass (RG) generation continues to rise, occupying significant landfill space due to its extremely slow decomposition, which can take thousands to millions of years. RG exhibits comparable properties to natural sand; this study explores its potential use in civil engineering applications. However, RG alone does not meet the standard strength requirements for geotechnical applications. To address these limitations, cement was introduced as a stabilizing agent to enhance the strength and stiffness of RG. Cement was added at contents of 3% and 5% to assess geotechnical properties of RG. A comprehensive laboratory investigation, including particle size distribution analysis, compaction tests, California Bearing Ratio (CBR), unconfined compression strength tests (UCS), and repeated loading triaxial tests, was conducted. Results demonstrated that RG stabilized with 5% cement achieved a UCS value of 610 kPa. The CBR values for 3% and 5% cement-stabilized blends were 150% and 303%, respectively. The resilient modulus of the optimum blend ranged from 191 MPa to 461 MPa, indicating the potential of RG with 5% cement as a sustainable alternative for geotechnical engineering applications. This approach not only supports effective waste management but also contributes to the conservation of natural sand resources.

Keywords: Recycled glass, Ground improvement, Recycled waste, Sustainability, Stabilization.

INTRODUCTION

Sand is one of the most consumed natural resources on earth, second only to water [1]. However, high-quality sand suitable for construction, particularly river sand, is becoming increasingly scarce. This is primarily due to the construction industry's consumption rate far exceeding the natural replenishment rate of sand. Moreover, not all sand types are appropriate for industrial use, as particle size, shape, purity and other physical and chemical properties vary, making some types of sand suitable for specific applications [2]. For instance, desert sand, typically rounded due to win erosion, is unsuitable for construction. In contrast, river sand, with its angular particle shape and favorable chemical properties, is preferred in many industries [3].

The overexploitation of natural sand has raised significant social and environmental concerns worldwide. A major consequence is the rising cost of natural sand in many countries, largely due to stricter regulations. Despite the increasing cost of natural sand, global demand for natural sand was estimated at 50 billion tonnes annually in 2019-20 and is projected to rise to 60 billion tonnes by 2030 [1, 4]. According to the United Nations Environment Program (UNEP), if current consumption trends continue, natural sand may be depleted by 2050 or 2060 [4].

At the same time, the accumulation of waste glass is becoming an increasing environmental burden. In Australia alone, 1.50 million tonnes of waste glass were generated in 2020-21, with a recovery rate of only 58% or 0.91 million tonnes [5]. Although glass is infinitely recyclable, not all waste glass is suitable for remanufacture into new products. Challenges such as limitations in sorting technology, contamination, mixing with other waste, and the collection process with heavy equipment hinder effective recycling. Consequently, large quantities of waste glass remain in stockpiles or are sent to landfills.

In alignment with the Australian Government's circular economy initiatives, researchers have explored the potential use of recycled glass (RG) in concrete production, pavements, geomaterials, and fill materials [6, 7]. RG exhibits engineering properties similar to those of natural sand, offering a sustainable alternative that can divert waste glass from stockpiles and landfills [8].

However, RG alone does not fully meet the performance requirements for geotechnical applications. RG is typically limited to a maximum of 30% replacement and needs to be blended with high

quality aggregate or binders to achieve the necessary strength.

Portland cement is a commonly used binder to enhance the properties of materials [9]. Cement has gained favor in the construction industry for years. This is because of its versatility, strength, availability and cost effectiveness. Therefore, this study aims to evaluate the geotechnical performance of RG stabilized with cement.

RESEARCH SIGNIFICANCE

To align with the Australian Government's circular economy strategy, waste materials should be redirected from stockpiles or landfills and repurposed to be construction materials. The significance of this research lies in two key aspects: (1) the use of 100% RG as the primary material, and (2) the incorporation of cement to improve the strength and stiffness of recycled glass.

MATERIALS

RG was sourced from a local recycling facility in Victoria, Australia. The pre-wetted RG sample was oven-dried at 105 ± 5ºC for 24 hours. After drying, the bulk sample was reduced using a riffle splitter to obtain a smaller, representative portion for testing. RG had an angular shape, contributing to high interlocking effect within the samples, as shown in Fig. 1 (a) and (b).

Fig. 1 (a) RG physical appearance; (b) SEM image

The particle size distribution (PSD) of RG is also shown in Fig. 2. The maximum particle size was 4.75 mm, and the sample predominantly consisted of sand-sized particles. Based on the coefficients of uniformity (Cu=7.0) and curvature (Cc=1.08) as presented in Table 1, the RG was classified as well-graded sand. However, the PSD of RG fell outside the upper and lower bounds of the specification, making RG unsuitable for pavement applications in untreated form.

Cement was utilized as the binder to enhance properties of RG specimens. In this study, cement content of 3% and 5% by dry weight were used in accordance with specification set by the local authority, VicRoads [10]. A minimum curing period of seven days was adopted, as specified.

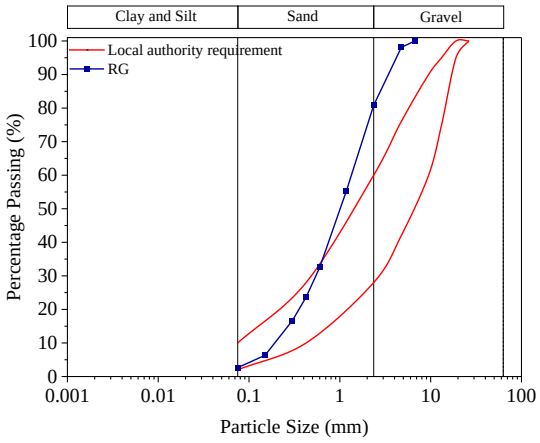

Fig. 2 PSD of RG.

Table 1 Properties of RG

Properties	RG	Standard
D_{10}	0.20	AS 1726 [11]
D_{30}	0.55	AS 1726 [11]
D_{60}	1.40	AS 1726 [11]
C_u	7.00	AS 1726 [11]
C_c	1.08	AS 1726 [11]
Fine content (%)	2.66	AS 1726 [11]
Classification	SW	AS 1726 [11]
CBR (3% cement)	150	AS 1289.6.1.1 [16]
CBR (5% cement)	303	AS 1289.6.1.1 [16]

METHODS

PSD analysis was conducted using a mechanical shaker, in accordance with AS 1289.3.6.1 [11]. A 2 kg sample was placed in shaker and processed for a minimum of 15 minutes. Maximum dry density (MDD) and optimum moisture content (OMC) were determined following the procedure outlined in AS 1289.5.2.1 [12]. Each blend, RG+3% LCC and RG+5% LCC, was compacted in five layers into a standard steel mould using modified compaction effort. The determined OMC and MDD values for each blend were subsequently used to prepare specimens for the California Bearing Ratio (CBR) test, conducted in accordance with AS 1289.6.1.1 [13]. For each blend, two CBR samples were prepared and submerged in water for 96 hours or four days, prior to testing to simulate the worst-case scenario.

Unconfined compression strength (UCS) testing, a standard method for evaluating the strength of stabilized materials, was used to identify the optimum blend. UCS specimens were prepared using a split metal mould with dimensions of 50 mm in diameter and 100 mm in height (a diameter-to-height ratio of 1:2), following the relevant ASTM D2166 [14]. Samples were compressed at respective MDD and

OMC values and cured at room temperature for seven days.

Resilient modulus (M_R) was performed in accordance with AASHTO T307-99 using repeated loading test machine (RLT) [15]. The RLT sample was prepared at the MDD and OMC and was cured at room temperature for seven days. Only the optimum blend (RG+5% cement) was prepared. The sample had dimensions of 100 mm in diameter and 200 mm in height.

RESULTS AND DISCUSSION

MDD of unbound RG was found to be 1.85 Mg/m^3, with an OMC of 9.80%. It is noticed that at lower water contents, a slight reduction in MDD was observed, followed by a gradual increase in MDD as the water content increased. This behavior is attributed to the capillary forces present in the pore water of RG particles [16]. Unbound RG alone does not satisfy the standard requirements for geotechnical applications and therefore requires stabilization [17].

Fig. 3 illustrates the compaction curves of both unbound and RG stabilized with cement blends. Among all the blends, unbound RG exhibited the lowest MDD and OMC, while the RG containing 5% cement gained the highest MDD and OMC values. A summary of MDD and OMC for all blends is presented in Table 2. Increasing the cement content from 3% to 5% resulted in higher MDD and lower OMC values. This improvement is due to the fine particles of cement filling the voids between RG particles, thereby enhancing density and reducing the moisture required for optimal compaction.

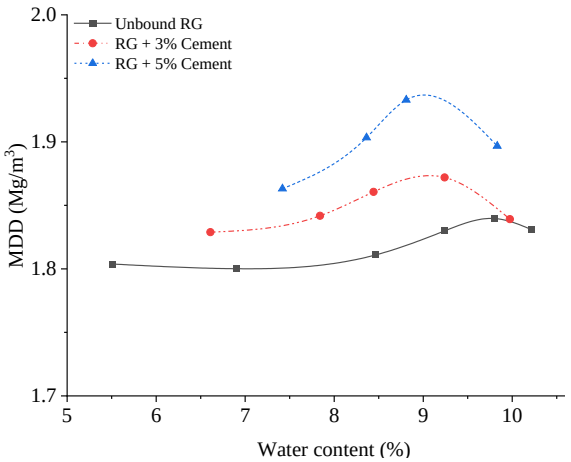

Fig. 3 Compaction curves of RG and RG + cement.

Table 2 summary of compaction properties of RG.

Samples	MDD (Mg/m3)	OMC (%)
Unbound RG	1.85	9.80
RG +3% cement	1.87	9.24
RG +5% cement	1.93	8.81

Fig. 4 shows the UCS values for RG stabilized with 3% and 5% cement. Since there is no standard requirement for UCS for granular or sand columns, the benchmark strength was adopted from specification for soil-cement columns used in soft soil, which is reported to be 600 kPa [18, 19]. This value was used as the standard reference strength for evaluating RG stabilized with cement in this study.

As RG is a cohesionless material, it was not possible to obtain a UCS value for unbound RG. The RG+3% cement blend exhibited a relatively low UCS of 76 kPa, which is significantly below the required standard. However, increasing the cement content to 5% resulted in a substantial improvement, with a UCS value of 610 kPa, which is slightly exceeding the target strength of 600 kPa [18]. In general, increasing the cement content led to an increase in UCS values. Nevertheless, for geotechnical applications, cement content is typically limited to a maximum of 6% [10]; thus, the present study restricted to cement dosage to 5%.

The significant improvement in UCS for the cement-stabilized RG samples is attributed to the hydration process of the cement. The hydration products act as a binding agent between RG particles, thereby enhancing the structural integrity and compressive strength of the mixture.

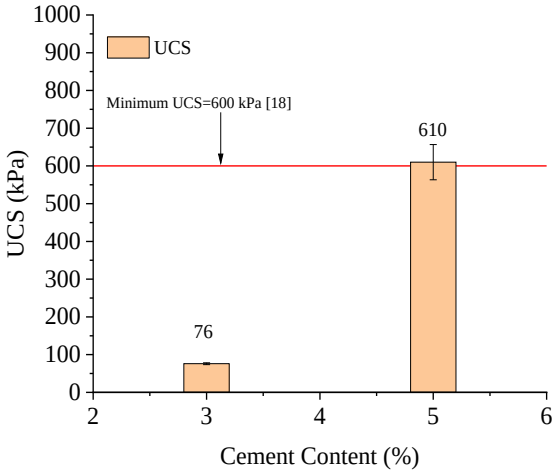

Fig. 4 UCS values of RG stabilized with cement.

Fig. 5 showed the CBR values of RG stabilized with cement after 96 hours under the water. The RG samples stabilized with 3% cement achieved a CBR of 150%, which is significantly higher than the 42-46% reported for unbound RG in previous studies [7, 16]. This indicates that RG stabilized with small amount of cement is sufficient to meet the minimum CBR requirements for base layer materials of 100% [20]. Increasing the cement content to 5% further enhanced the CBR, with the RG+5% cement blend reaching a value of 303%, more than double that the 3% cement blend. No swelling was observed in any

of the samples following the 96-hour submersion period.

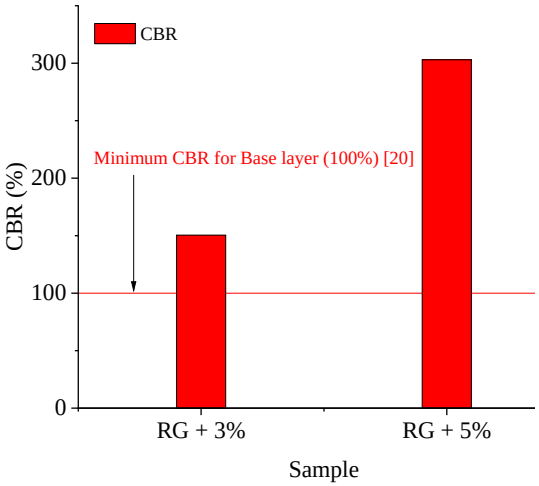

Fig. 5 CBR values of RG stabilized with cement.

Fig. 6 showed M_R of RG stabilized with 5% cement. The RLT test was carried out to investigate the elastic response of the material under cyclic loading. This assessment was performed only with the blend that met the required specifications. A total of 15 load sequences were applied during the test. As shown in Fig. 5, the M_R gradually increased with each load sequence, ranging from 191 MPa to a maximum of 461 MPa. This increase reflects the enhanced strength of RG+5% cement, demonstrating the ability to resist axial stress under repeated loading.

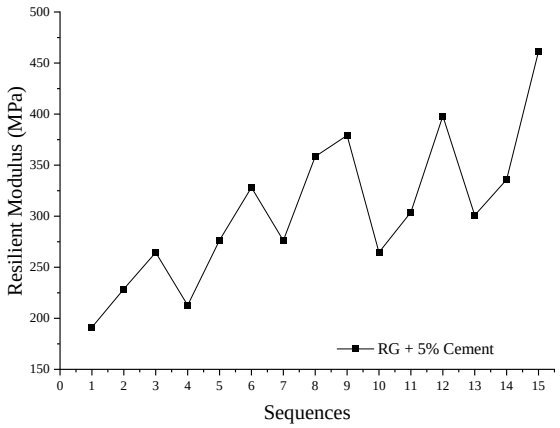

Fig. 6 Resilient modulus of RG+5% cement.

CONCLUSION

This study investigated the geotechnical properties of recycled glass (RG) stabilized with cement for potential use in ground improvement applications. The keys findings are summarized below:

1. MDD increased with higher cement content, while OMC decreased. This is attributed to the fine particles of cement filling the voids between RG particles, resulting in increased density and reduced pore water content.
2. UCS values of RG stabilized with 5% cement achieved a UCS of 610 kPa after seven days of curing. In contrast, the 3% cement blend did not result in a significant gain in strength.
3. CBR for both RG stabilized with 3% and 5% cement blends exceeded the minimum requirements for road base layers, indicting their suitability for use in pavement construction.
4. Resilient modulus (M_R) of RG stabilized with 5% cement blend ranged from 191 MPa to 461 MPa under cyclic loading, indicating good elastic performance.

ACKNOWLEDGEMENT

This research was supported by Australian Research Council Linkage Projects funding scheme (project number LP220100099). The authors acknowledge Asas Foundations Pty Ltd and Stretford Civil Construction Pty Ltd for their collaboration in this project.

REFERENCES

[1] Rentier, E.S. and L.H. Cammeraat, The environmental impacts of river sand mining. Science of The Total Environment, 2022. 838: p. 155877.
[2] Schrotenboer, B.R. and A.F. Arbogast, Locating alternative sand sources for Michigan's foundry industry: A geographical approach. Applied Geography, 2010. 30(4): p. 697-719.
[3] Nafissatou, M., B.P. Kagonbé, A.G.A. Mouthe, B. Nafissa, V.D. Bakaïné, E. Yanné, L. Boubakar, and A.K. Dongmo, Potential use of the Maroua (Far North, Cameroon) river sand as construction materials and degreasing agent for earthenware ceramics. Discover Applied Sciences, 2025. 7(2): p. 92.
[4] UNEP, Sand and sustainability: Finding new solutions for environmental governance of global sand resources, in GRID-Geneva. 2019, GRID-Geneva: Geneva, Switzerland.
[5] DAWE, Waste glass industry standards. 2021.
[6] Arulrajah, A., T.-A. Kua, S. Horpibulsuk, M. Mirzababaei, and A. Chinkulkijniwat, Recycled glass as a supplementary filler material in spent coffee grounds geopolymers. Construction and Building Materials, 2017. 151: p. 18-27.
[7] Disfani, M.M., A. Arulrajah, M.W. Bo, and R. Hankour, Recycled crushed glass in road work

applications. Waste Management, 2011. 31(11): p. 2341-2351.
[8] Kazmi, D., M. Serati, D.J. Williams, S. Qasim, and Y.P. Cheng, The potential use of crushed waste glass as a sustainable alternative to natural and manufactured sand in geotechnical applications. Journal of Cleaner Production, 2021. 284: p. 124762.
[9] Austroads, Guide to Pavement Technology Part 4D: Stabilised Materials. 2019, Austroads: Sydney.
[10] VicRoads, Determination of the maximum allowable working time for a cementitious binder. 2019, Vicroads: Victoria, Australia.
[11] Standards Australia, 1289.3.6.1-2009 Methods of testing soils for engineering purposes Soil classification tests - Determination of the particle size distribution of a soil - Standard method of analysis by sieving. 2022: Sydney, Australia.
[12] Standards Australia, 1289: Methods of testing soils for engineering purposes, in Method 5.2.1: Soil compaction and density tests—Determination of the dry density/moisture content relation of a soil using modified compactive effort. 2017, Standards Australia: Sydney, Australia.
[13] Standards Australia, 1289: Methods of testing soils for engineering purposes, in Method 6.1.1: Soil strength and consolidation tests-Determination of the California Bearing Ratio of a soil—Standard laboratory Method for a remoulded specimen. 2014: Sydney, Australia.
[14] ASTM, D2166/D2166M Standard test method for unconfined compressive strength of cohesive soil. 2016, ASTM International: United States.
[15] AASHTO, Standard Method of Test for Determining the Resilient Modulus of Soils and Aggregate Materials. 2012, American Association of State Highway and Transportation Officials: Washington, DC, USA.
[16] Bai, Y., A. Arulrajah, S. Horpibulsuk, and J. Chu, Gasified olive stone biochar as a green construction fill material. Construction and Building Materials, 2023. 403: p. 133003.
[17] Arulrajah, A., M.M. Disfani, S. Horpibulsuk, C. Suksiripattanapong, and N. Prongmanee, Physical properties and shear strength responses of recycled construction and demolition materials in unbound pavement base/subbase applications. Construction and Building Materials, 2014. 58: p. 245-257.
[18] Chai, J., S. Shrestha, and T. Hino, Failure of an Embankment on Soil-Cement Column–Improved Clay Deposit: Investigation and Analysis. Journal of Geotechnical and Geoenvironmental Engineering, 2019. 145(9): p. 05019006.
[19] Chai, J.-c., T. Hino, Y. Qiao, and W. Ding, Progressive yielding/softening of soil–cement columns under embankment loading: a case study. Acta Geotechnica, 2024. 19(11): p. 7229-7241.
[20] VicRoads, Selection and Design of Pavement and Surfacings, in RC500.22. 2018, Vicroads: Victoria.

Copyright © Int. J. of GEOMATE All rights reserved, including making copies, unless permission is obtained from the copyright proprietors.

15th Int. Conf. on Geotechnique, Construction Materials & Environment,
Kyoto, Japan, 11-13 November 2025, ISBN 978-4-909106124 C3051

PRACTICAL APPLICATION OF GEOLOGICAL STRENGTH INDEX FOR EXCAVATABILITY ASSESSMENT

John Victor Smith[1,2]

[1]School of Engineering, RMIT University, Australia; [2]CMW Geosciences, Australia

ABSTRACT

The geological strength index (GSI) has become a prominent method of defining the condition of rock mass for various purposes. The GSI method was developed based on having a visual appreciation of the rock mass conditions, in particular the pattern of naturally occurring fractures (discontinuities) and also observations of the frictional conditions of the discontinuity surfaces. Excavatability assessment is typically needed for conditions where the material cannot be readily observed other than from isolated locations such as boreholes or trial excavation pits. In this paper an appraisal of the structure (blockiness) and surface conditions (interface friction) categories of the GSI method is presented. Methods for quantifying and categorizing field observations in terms of the GSI framework are collated and reviewed. The structure rating can be quantified with reference to joint set spacing and appreciation of the three-dimensional aspects of joint patterns relative to the direction of drill hole investigations. The surface condition rating can be obtained by field observations and by laboratory testing. The GSI method incorporates an approximation aspect that can lead to a low level of clarity in its application. By outlining the practical ways that rock mass observations can be assessed and quantified the use of GSI in excavatability assessment can be enhanced.

Keywords: Geological strength index, GSI, Excavatability, Rippability

INTRODUCTION

A prominent excavatability assessment method is that of Pettifer and Fookes [1] which is based on a chart with an x-axis based on rock strength (specifically, the point load index) and a y-axis based on the spacing of natural fractures (discontinuities). Discontinuities were considered 'effective' [1] where they 'clearly formed planes on which rock blocks could be dislodged, and were therefore persistent on the scale of individual blocks' [1]. They excluded 'joint planes healed by … mineralization and poorly defined bedding planes which simply represented a change in lithology' [1]. The Pettifer and Fookes method also emphasized that the discontinuity spacing must be considered in three-dimensions even when the data is collected in a single direction. The method also includes an adjustment factor of up to 50% for the spacing parameter based on the favorability of the discontinuity pattern and orientation of discontinuities [1].

The geological strength index (GSI) has become a prominent method of defining the condition of rock mass for various purposes [2-6]. GSI was developed based on having a visual appreciation of the rock mass conditions [2]. The GSI system has also been applied to excavatability assessment [7,8]. Excavatability assessment is typically needed for conditions where the material cannot be readily observed. Geophysical methods are complementary to GSI however, the GSI rating may be restricted to isolated observations from boreholes. A range of studies over many decades have proposed methods of excavatability assessment [9-15].

In this paper an appraisal of the structure (blockiness) and surface conditions (interface friction) categories of the GSI method as applied to excavatability assessment [7,8] is presented. Methods for quantifying and categorizing field observations in terms of the GSI framework are collated and reviewed.

The structure rating can be quantified with reference to joint set spacing and appreciation of the three-dimensional aspects of joint patterns relative to the direction of drill hole investigations. The surface condition rating can be obtained by field observations and by laboratory testing.

The GSI method incorporates an approximation aspect that can lead to a low level of clarity in its application. By outlining the practical ways that rock mass observations can be assessed and quantified the use of GSI in excavatability assessment can be enhanced.

RESEARCH SIGNIFICANCE

This paper reviews the practical issues related to applying the GSI methodology to excavatability. The paper does not review the accuracy of the published GSI chart with respect to the outcomes of such assessments. Excavatability assessment is often carried out based on limited investigation data. Geophysical methods are well established but they require corroboration with direct geotechnical

observation. Direct geotechnical observation can also contribute to awareness of the abrasive character of materials. Excavatability assessments are the basis of some very significant decision-making around the selection of equipment. Whether this is at a conceptual stage or feasibility stage of a site study the financial implications of the excavatability assessment can be very significant. The link between field data and GSI application as outlined in this paper plays an important role in the quality of the assessment.

GEOLOGICAL STRENGTH INDEX (GSI)

Categorical Assessment

The GSI method originated from a grid of descriptive categories. The terminology of the descriptions was carefully framed to address observable features that influence rock mass behavior [2].

Quantitative Assessment

GSI values

The grid of descriptive categories in the GSI method is overlaid with oblique lines representing GSI values from 0 to 100. These values increase from bottom right of the chart to the top left of the chart. This quantification is a way of showing how different features of a rock mass may combine to produce conditions which may be similar in a geotechnical sense (e.g. excavatability) while being very different in a geological sense [2].

Quantification of chart axes

While the GSI chart originated based on descriptive categories, various researchers have attempted to quantify the axes of the chart. These attempts at quantification cannot be assumed to over-ride the descriptive nature of the categories as originally defined. Methods of quantification for the y-axis of the chart (structure) include RQD [16], fracture spacing [17] and block volume [17]. These methods are not directly comparable [19,20] so cannot be applied without careful consideration of other factors such as block shapes (Fig.1)[21].

Determining block shape from borehole data has been addressed by various researchers including the current author [22]. A review of gneiss, for example, showed that some gneisses are schistose with a tabular block shape while others are equidimensional indicating that the gneissic banding was not a significant weakness in the rock [23].

Structure Categories

The GSI chart has six categories defining the y-axis as summarized in Table 1.

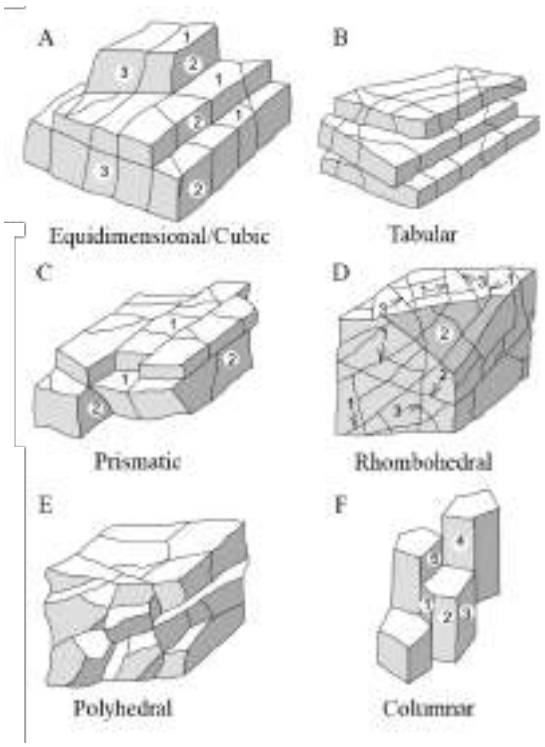

Fig.1 Block shapes [21]

Table 1 GSI Structure Categories

Category	Name	Description
S1	Intact or massive	Intact rock specimens or massive in situ rock with few widely spaced discontinuities
S2	Blocky	Well interlocked undisturbed rock mass consisting of cubical blocks formed by three intersecting discontinuity sets
S3	Very Blocky	Interlocked partially disturbed mass with multi-faceted angular blocks formed by 4 or more joint sets
S4	Blocky/ disturbed/ seamy	Folded with angular blocks formed by many intersecting discontinuity sets. Persistence of bedding planes or schistosity
S5	Disintegrated	Poorly interlocked, heavily broken rock mass with mixture of angular and rounded rock pieces
S6	Laminated/ sheared	Lack of blockiness due to close spacing of weak schistosity or shear planes

The descriptions indicate that a blocky rock mass

has equidimensional/cubic blocks shapes whereas a very blocky rock mass would correspond to the polyhedral block shape. The tabular, prismatic and rhombohedral block shapes are defined by three joint sets but would be difficult to assign into a structure category based on borehole data.

Discontinuity Condition Categories

There are five discontinuity categories forming the x-axis of the GSI chart (Table 2). Various attempts at quantifying this parameter have been proposed [16-18].

Table 2 GSI Discontinuity Condition Categories

Category	Name	Description
D1	Very good	Very rough, fresh unweathered surfaces
D2	Good	Rough, slightly weathered, iron stained surfaces
D3	Fair	Smooth, moderately weathered and altered surfaces
D4	Poor	Slickensided, highly weathered surfaces with compact coatings or fillings or angular fragments
D5	Very poor	Slickensided, highly weathered surfaces with soft clay coatings or fillings

Excavatability Types

Four excavatability types are defined on the GSI charts. These are blasting, hammer, ripping and digging. Hammer is labelled 'and blasting' to indicate that blasting can be used for this material. The excavatability types do not strictly follow GSI values. At various parts of the chart the excavatability type fields cross GSI lines and follow structure category boundaries. Therefore, the excavatability types are not uniquely defined by GSI values.

Excavatability Assessment

The GSI has been divided into four excavatability method fields with boundaries formed by GSI lines and in some areas structure category boundaries. Some excavatability fields overlap the cells defined by the GSI chart categories. The excavatability assessment can be made by firstly, selecting one of the two charts according to the point load index strength. Secondly, establish a structure category (S1-6) followed by a discontinuity condition category (D1-5). The excavatability assessment outcomes, including the GSI value separating two excavatability types within one cell of the chart, are summarized in Table 3.

Table 3 GSI Chart Excavatability Assessment

Str. Cat.	I_{s50} < 3MPa	$I_{s50} \geq$ 3MPa
S1	D1-3 Blasting	D1-3 Blasting
S2	D1 Blasting	D1 Blasting
	D2 Blasting(65)Hammer	D2-3 Blasting(60)Hammer
	D3 Hammer(55)Ripping	D4 Hammer(45)Ripping
	D4-5 Ripping	D5 Ripping
S3	D1 Blasting(70)Hammer	D1-2 Blasting(60)Hammer
	D2 Hammer(55)Ripping	D3 Hammer(45)Ripping
	D3-4 Ripping	D4-5 Ripping
	D5 Ripping(25)Digging	
S4	D1 Hammer(55)Ripping	D1 Blasting(60)Hammer
	D2 Ripping	D2 Hammer(45)Ripping
	D3 Ripping(35)Digging	D3-4 Ripping(30)Digging
	D4-5 Digging	D5 Digging
S5	D1 Ripping	D1-2 Ripping
	D2-3 Ripping(35)Digging	D3 Ripping(30)Digging
	D4-5 Digging	D4-5 Digging
S6	D3-5 Digging	D3-5 Digging

Note: Str.Cat. = Structure category. S1 with D4-5 and S6 with D1-2 are designated 'not applicable'. GSI values at boundaries are in brackets.

FIELD EXAMPLE

The Triassic age mudstone and sandstone of the Torlesse beds in the Wellington area of New Zealand were assessed to be typically rippable at required depths of excavation due to the fracture spacings present [24]. As was noted in that study, boreholes cannot provide information on persistence of discontinuities and can also result in directional bias related to discontinuity orientation. Therefore, it is necessary to conduct field observations during initial excavation to confirm any assessment based on borehole data.

The Wellington area is notable for the presence of bedded and faulted rocks. Boreholes are needed to overcome the lack of outcrop in the area. Boreholes (and televiewer) can be good at characterizing bedding and sheared zones which they penetrate as these features tend to be continuous and can be correlated between boreholes in a way that individual discontinuities generally cannot [24].

It is helpful to identify domains or sub-areas with relatively homogeneous properties. These domains are often related to structures such as folding and faulting or changes in rock types. It is also necessary to apply knowledge of scalable parameters. For example, a thick zone of infill in a discontinuity or fault implies greater length of that structure than a similar structure with a thin infill [24].

Field exposures of the soil and rock show the typical characteristics of the area (Fig.2). Within about 2 m of the land surface the ground is rocky with

close-spaced fracturing (Fig.2 A and B). Deeper down the rock mass has more widely spaced discontinuities (Fig.2C).

The sandstone at these locations typically has a point load index greater than 3 MPa, however the observed structure and discontinuity conditions have been plotted on both GSI excavatability charts (Fig.3). The assessments are labelled on Fig.3 according to the relevant parts of Fig.2. The shallow highly fractured rock (Fig.2 A,B) would overlap the digging and ripping fields for lower strength rock (I_{s50}<3 MPa) but would be in the ripping field for higher strength rock ($I_{s50}\geq$3 MPa).

Fig.2 Outcrops showing features relevant to excavatability (Makara, New Zealand)

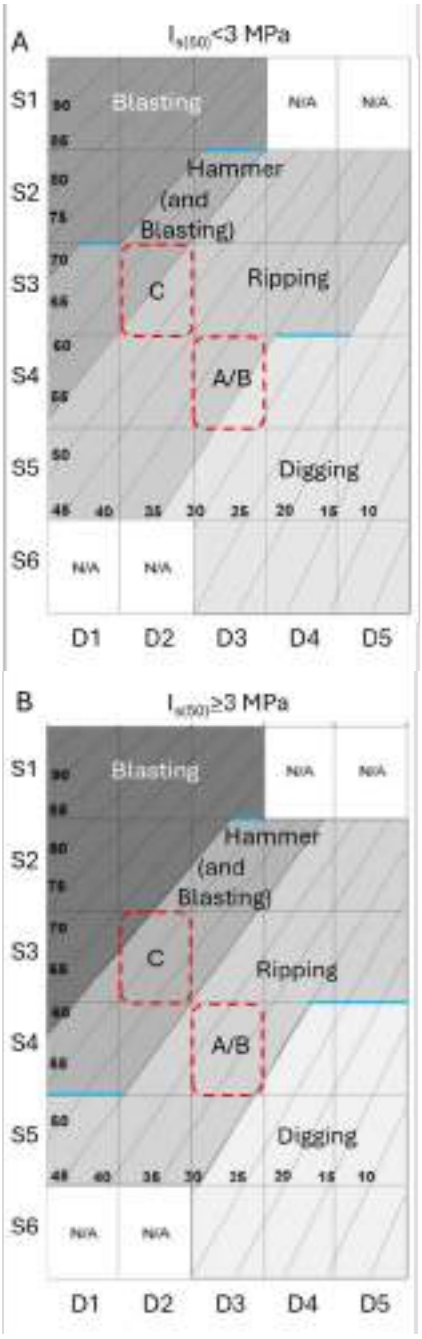

Fig.3 GSI chart showing example excavatability classification [7,8]. Blue lines highlight boundaries based on structure categories not GSI values

CONCLUSIONS

The Geological Strength Index (GSI) chart has been applied to excavatability assessment. The accuracy of the chart for excavation equipment selection has not been evaluated here. The composition of the GSI chart has been reviewed in detail, in particular the parameters used to define the categories on the x and y axes of the chart.

Data from cored boreholes and down-hole televiewers can be used to collect the relevant

parameters. The y-axis is related to the three-dimensional pattern of discontinuities in the rock mass and therefore may require input beyond the boreholes themselves. The additional input may come in the form of geological mapping in the area of interest and regional knowledge of the typical geological structures. Knowledge of the local rock types and the typical patterns of jointing and other discontinuities that form the rock mass will also be required to correctly ascertain the y-axis category on the GSI chart.

Establishing a GSI value to represent a rock mass requires firstly that the rock mass is assigned to the categories on the x and y axes of the chart. The method of excavatability assessment using the chart has fields for various excavation equipment types which generally follow the GSI lines of the chart but not at all parts of the chart. All the equipment type fields on the chart include some boundaries that follow the structure categories rather than the GSI values. Therefore, the GSI value alone is not sufficient to assign an excavatability type. It is more appropriate to use the categories defining the chart to identify 'cells' on the chart that are representative of a rock mass. Some of these cells overlap two equipment type fields meaning that the GSI chart implies such a rock mass is marginal to the excavation methods indicated.

ACKNOWLEDGMENTS

Discussions with university and consulting engineering colleagues on excavatability and site investigation are acknowledged.

REFERENCES

[1] Pettifer G.S., and Fookes P.G., A Revision of the Graphical Method for Assessing the Excavatability of Rock. Quarterly Journal of Engineering Geology, Vol. 27, Issue 2, 1994, pp.145-164.

[2] Marinos P., and Hoek E., GSI: A Geologically Friendly Tool for Rock Mass Strength Estimation. In ISRM International Symposium 2000, Melbourne, Vol. 1, pp.1422-1446.

[3] Kusumawardani R., Upomo T. C., and Faizal, M., Back-Analysis of Hoek-Brown Criterion: Rock Slide Case in Manado. International Journal of GEOMATE, Vol. 11, Issue 27, 2016, pp.2808-2814.

[4] Thongraksa A., and Jongpradist P., Evaluation of the Failure Initiation and Modes of Failure of the Hoek-Brown Rock Mass Surrounding Underground Storage with High Internal Pressure. International Journal of GEOMATE, Vol. 23, Issue 100, 2022, pp. 118-125.

[5] Harwinda Z. B., Wilopo W., and Indrawan, I. G. B., Excavatability Method Based on Engineering Geology Conditions, The Construction of Rukoh Dam Suppletion Tunnel, Indonesia, in 7th The International Conference in Sustainable Built Environment (ICSBE). The Faculty of Civil Engineering and Planning, Universitas Islam Indonesia, Vol.4, 2022, pp.260-271.

[6] Yang F., Huang Z. W., Dai Z. Y., Liu S. F., and Zhao L. H., Stability Analysis of Multi-stage Blasting Rock Slopes Based on the Hoek-Brown Criterion Considering Cumulative Disturbance. Engineering Geology, Vol.352, 2025, pp.1-14.

[7] Tsiambaos G., and Saroglou H., Excavatability Assessment of Rock Masses Using the Geological Strength Index (GSI). Bulletin of Engineering Geology and the Environment, Vol. 69, Issue 1, 2010, pp. 13-27.

[8] Department of Defense (USA), Department of Defense Unified Facilities Criteria, Foundations and Earth Structures, UFC-3-220-20 2025, pp. 1-683.

[9] Braybrooke J. C., The State of the Art of Rock Cuttability and Rippability Prediction, in Fifth Australia-New Zealand Conference on Geomechanics: Prediction Versus Performance; Barton, ACT: Institution of Engineers, Australia. 1988, pp. 13-42.

[10] Kirsten H. A.., Case Histories of Groundmass Characterization for Excavatability, in Rock Classification Systems for Engineering Purposes. ASTM International, 1988, pp.102-120.

[11] Suparmanto E. K., Mohamad E. T., Jahed Armaghani D., Ahmad Legiman M. K., Zainal Z., Zainuddin N. E., and Abdul Razak M. H., An Overview of Excavatability Classification for Bedded and Non Bedded Rock in a Tropical Region. Geomechanics and Geophysics for Geo-Energy and Geo-Resources, Vol. 10, Issue 1, 2024, pp. 1-33.

[12] Liang M., Mohamad E. T., Komoo I., and Ma, C. K., An Excavatability Classification System for Surface Excavation in Sedimentary Rocks. Bulletin of Engineering Geology and the Environment, Vol. 76, 2017, pp. 241-251.

[13] Dagdelenler G., Sonmez H., and Saroglou C. A., Flexible System for Selection of Rock Mass Excavation Method. Bulletin of Engineering Geology and the Environment, Vol. 79, Issue 10, 2020, pp. 5355-5369.

[14] Dagdelenler G., Comparison of the Efficiency Evaluations of Selected Excavatability

Classifications for Rock Masses. Arabian Journal of Geosciences, Vol. 14, Issue 13, 2021, pp. 1-21.

[15] Gurocak Z., and Yalcin, E., Excavatability and the Effect of Weathering Degree on the Excavatability of Rock Masses: An Example from Eastern Turkey. Journal of African Earth Sciences, Vol. 118, 2016, pp.1-11.

[16] Hoek E., Carter T. G., and Diederichs M. S., Quantification of the Geological Strength Index Chart, in ARMA US Rock Mechanics/ Geomechanics Symposium, 2013, pp.1-9.

[17] Cai M., Kaiser P. K., Tasaka Y., and Minami M., Determination of Residual Strength Parameters of Jointed Rock Masses Using the GSI System. International Journal of Rock Mechanics and Mining Sciences, Vol. 44, Issue 2, 2007, pp. 247-265.

[18] Sonmez H., and Ulusay R., Modifications to the Geological Strength Index (GSI) and Their Applicability to Stability of Slopes. International Journal of Rock Mechanics and Mining Sciences, Vol. 36, Issue 6, 1999, pp. 743-760.

[19] Palmström A., Measurement and Characterization of Rock Mass Jointing, in In-situ Characterization of Rocks. Sharma V.M. and Saxena K.R. Ed., A.A. Balkema, 2001, pp. 49-97.

[20] Palmstrom, A., Measurements of and Correlations Between Block Size and Rock Quality Designation (RQD). Tunnelling and Underground Space Technology, Vol. 20, Issue 4, 2005, pp. 362-377.

[21] Dearman W.R., Engineering Geological Mapping. Butterworth-Heinemann Ltd., Oxford, 1991, pp.1-387.

[22] Smith J. V., Determining the Size and Shape of Blocks from Linear Sampling for Geotechnical Rock Mass Classification and Assessment. Journal of Structural Geology, Vol. 26, Issue 6, 2004, pp.1317-1339.

[23] Smith J. V., Rock Structure Characterization of a Magnetite Gneiss with Foliation-Parallel Discontinuities for Footwall Slope Design. International Journal of Rock Mechanics and Mining Sciences, Vol. 108, 2018, pp. 105-117.

[24] Boyd J. F., Engineering Geological Controls on Failure Mechanisms in Rock Cut-Slopes in the Torlesse Composite Terrane in Wellington, NZ. Master of Science in Engineering Geology, University of Canterbury, New Zealand, 2019, pp.1-445.

Copyright © Int. J. of GEOMATE All rights reserved, including making copies, unless permission is obtained from the copyright proprietors.

15th Int. Conf. on Geotechnique, Construction Materials & Environment,
Kyoto, Japan, 11-13 November 2025, ISBN 978-4-909106124 C3051

A CASE STUDY OF SLOPE FAILURE POTENTIAL MAPPING BASED ON WATERSHED UNIT IN THE NOTO PENINSULA DISTRICT

Suguru Kaneko[1] and Masanori Kohno[2,3]

[1] Graduate student, Graduate School of Sustainability Science, Tottori University, Japan
[2] Faculty of Engineering, Tottori University, Japan
[3] Center for Regional Management and Safety Engineering, Tottori University, Japan

ABSTRACT

Slope failures often happen when earthquakes. The 2024 Noto Peninsula Earthquake in Japan caused a many slopes failure over a wide area and high-density distribution. First, this study presented characteristics of slope failure distribution of the above recent earthquake, that is, this study clarified relationship between slope failure distribution and primary causes (i.e. factor of slope failure hazard). In addition, this study suggested earthquake-induced slope failure potential mapping method based on watershed unit in the Noto Peninsula district in Japan using analytic hierarchy process (AHP) method and geographic information system (GIS). An earthquake-induced slope failure risk assessment system used here is based on landslide distributions (NIED, Japan) in the Hida belt district including the Noto Peninsula district, Japan. We considered the relationship between landslide distribution and factors of landslide hazard (elevation, slope angle, slope type, flow accumulation, geology and vegetation). These relations are introduced to pairwise comparisons of factors in the AHP method. Slope failure potential rank is evaluated based on AHP. An earthquake-induced slope failure potential map is created based on the slope failure potential rank of 1 to 10. In this full paper, an evaluation of earthquake-induced slope failure potential using AHP method and GIS will be presented based on our analyzed data.

Keywords: Slope failure potential mapping, watershed, AHP, The 2024 Noto Peninsula Earthquake

INTRODUCTION

At 16:10 JST on January 1, 2024, an earthquake with a magnitude of 7.6 and a maximum seismic intensity of 7 struck the Noto Peninsula in Ishikawa Prefecture [1]. The earthquake triggered many slope failures throughout the region (Fig. 1). According to landslide and sediment distribution data provided by the Geospatial Information Authority of Japan (GSI) [2], the earthquake triggered 2345 slope failures. Several studies have reported the characteristics and causes of slope failures [3-5]. However, the mechanisms of earthquake-induced slope failures must be further clarified to develop effective hazard assessment methods, predict runouts using numerical simulations, and prioritize disaster mitigation measures. Similar to other major earthquakes of the 21st century, such as the 2018 Hokkaido Eastern Iburi, 2016 Kumamoto, 2008 Iwate-Miyagi Nairiku, and 2004 Mid-Niigata Prefecture earthquakes, earthquake-induced slope failures tend to occur over wide areas with high density. Although implementing preventive measures on all slopes would be ideal, such an approach would be inefficient and financially unfeasible. Therefore, slopes with a high potential for seismic landslides must be identified, and investigations and countermeasures must be prioritized accordingly.

Kohno et al. [6] proposed a landslide hazard mapping method for the Chugoku region of Japan

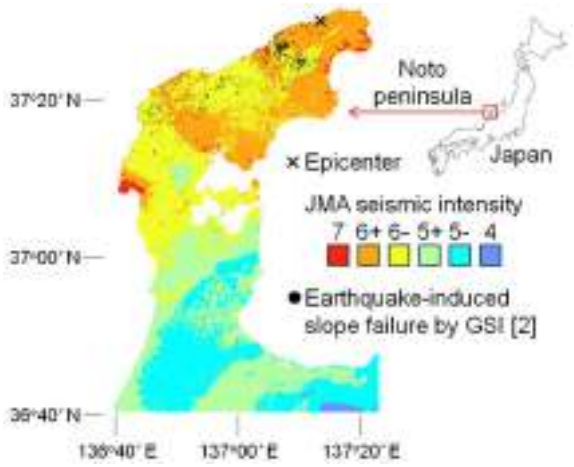

Fig. 1 JMA Seismic intensity distribution of the 2024 Noto Peninsula earthquake in Japan and distribution of earthquake-induced slope failure by the GSI [2].

using the Analytic Hierarchy Process (AHP) and Geographic Information System (GIS) methods. Their approach aimed to extract slopes with hazard levels equivalent to those on which past slope movements occurred. In the pairwise comparisons used in the AHP, they introduced quantified relationships between the database of landslide distribution maps [7] and the evaluation criteria. The resulting hazard maps demonstrated the effectiveness of identifying unstable slopes. Fig. 2A shows the

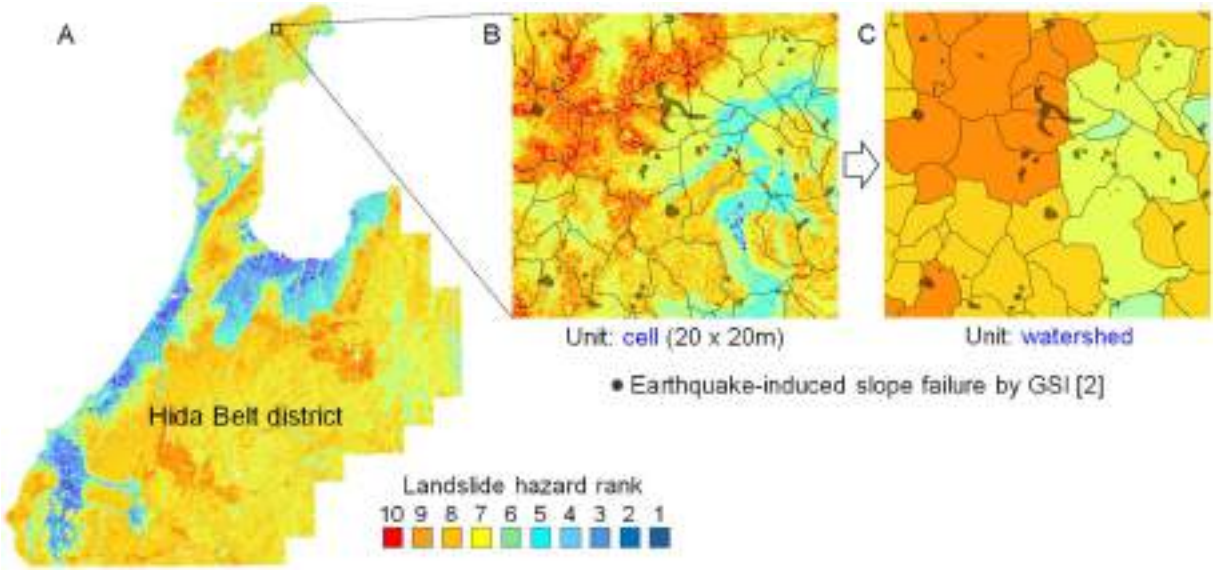

Fig. 2 Representative landslide hazard map of the Hida Belt district (A). Panels B and C show the cell and watershed units, respectively.

application of Kohno et al.'s method [6] to the Hida Belt region [8], which includes the areas affected by the 2024 Noto Peninsula earthquake. As illustrated in Fig. 2B, slope failures predominantly occurred in areas with relatively high hazard ranks. This method, which is based on 20 m mesh cells, allows for a detailed assessment of landslide hazards at the cell level in a given region. However, because of the complex mixture of high- and low-hazard cells in close proximity, assessing the hazards of landslides at varying scales or determining clear priorities for investigation and countermeasures is not always straightforward.

In this study, we examined the distribution characteristics of slope failures triggered by the 2024 Noto Peninsula earthquake. We then applied the AHP- and GIS-based cell-unit hazard mapping methods proposed by Kohno et al. [6, 9] to the affected region to explore the relationship between the landslide hazard ranks and observed slope failures. Finally, based on the cell-level hazard ranks (Fig. 2B), we proposed and tested a method for estimating watershed-level landslide hazard ranks (Fig. 2C).

METHODOLOGY

Overview of landslide hazard mapping using the AHP method

First, based on a database of landslide distribution maps [7] in the Hida Belt [8] region, we investigated the relationship between landslide-prone areas and evaluation factors and elements, specifically the area ratio between them. In this study, we prioritized factors that are easy to obtain and have high general applicability. Accordingly, six evaluation factors were selected for landslide hazard assessment using the AHP at hierarchy level 1: elevation, slope angle, slope type, flow accumulation, geology, and vegetation. Based on these evaluation factors, a hierarchical system was developed to assess landslide hazards. Within this system, importance weights were first calculated among the elements at hierarchy level 2 and then among the evaluation factors at hierarchy level 1. Although conventional AHP methods typically rely on subjective expert judgment for pairwise comparisons, our method quantifies the relationships between landslide-prone geomorphology and elements and uses these values to objectively derive the importance weights. A landslide hazard score was assigned to each evaluation factor using the calculated importance weights for each hierarchical level. These scores were then summed using a GIS to create a landslide hazard map. For further methodological details, please refer to previous studies [6, 9, 10]. Based on the cell-unit landslide hazard map, we reconstructed a landslide hazard map at the watershed-unit scale. To represent the hazard level of each watershed, we tested three approaches: the average hazard rank of all cells within the watershed, the maximum hazard rank, and the proportion of high-hazard cells. As in Kohno et al. [9], the study area was defined based on the geotectonic subdivisions of the Japanese Archipelago [8], focusing on the Hida Belt region, which includes areas affected by the 2024 Noto Peninsula earthquake (Fig. 2A). Notably, most slope failures were concentrated in areas that experienced instrumental seismic intensity of 5.5 or higher, primarily in the Noto Peninsula. Therefore, the subsequent analysis is limited to areas with seismic intensity ≥5.5, as extracted using the QUIET+ (QUick Identification of Earthquake Threat PLUS) system [11].

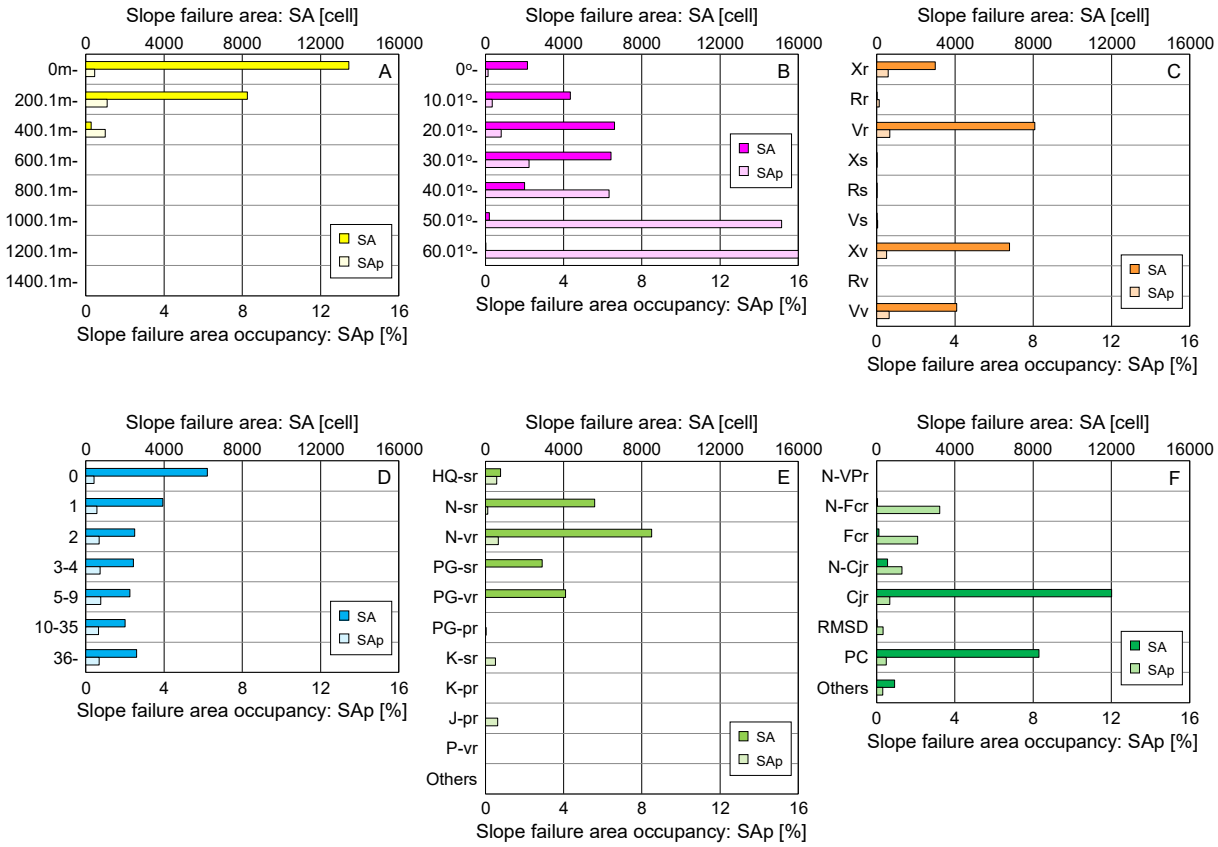

Fig. 3 Relationship between slope failure distribution and factors of landslide hazard (A: elevation, B: slope angle, C: slope type, D: flow accumulation, E: geology, and F: vegetation). Xr: convex ridge type slope, Rr: rectilinear ridge type slope, Vr: concave ridge type slope, Xs: convex straight type slope, Rs: rectilinear straight type slope, Vs: concave straight type slope, Xv: convex valley type slope, Rv: rectilinear valley type slope, Vv: concave valley type slope, HQ-sr: Quaternary sedimentary rocks, N-sr: Neogene sedimentary rocks, N-vr: Neogene volcanic rocks, PG-sr: Paleogene sedimentary rocks, PG-vr: Paleogene volcanic rocks, PG-pr: Paleogene plutonic rocks, K-sr: Cretaceous sedimentary rocks, K-pr: Cretaceous plutonic rocks, J-pr: Jurassic plutonic rocks, P-vr: Paleozoic volcanic rocks, N-VPr: natural vegetation in the Vaccinio-Piceetea region, N-Fcr: natural vegetation in the Fagaetea crenate region, Fcr: substitutional communities in the Fagaetea crenate region, N-Cjr: natural vegetation in the Camellietea japonica region, Cjr: substitutional communities in the Camellietea japonica region, RMSD: riverside, moor, salt marsh, and dune vegetation, PC: plantation and cultural land.

Overview of the data used in this study

ArcGIS Pro (ESRI) was used as the GIS software platform. The database of landslide distribution maps was obtained from the landslide geomorphology GIS dataset published by the National Research Institute for Earth Science and Disaster Resilience (NIED) [7]. Because the sizes of mapped landslide features vary greatly, we did not treat each mapped landslide as a single cell. Instead, we focused on the moving body portion of each landslide (polygon data), which was converted to raster format for analysis. As the minimum unit of raster cells is 20 m, the boundaries of landslide features appeared jagged due to rasterization. Note that scarp lines (line data), which lack area information, were excluded from the analysis. Topographic data were obtained from the 10 m mesh Digital Elevation Model (DEM) provided by the Geospatial Information Authority of Japan [12]. Surface analysis was conducted using a GIS to generate maps of elevation, slope angle, slope type, and flow accumulation for the study area. Geological data were taken from the 1/200,000 Japan Seamless Geological Map [13]. Vegetation data were obtained from the 1/50,000 existing vegetation map compiled between 1979 and 1998 by the Biodiversity Center of Japan, as part of the basic survey on natural environmental conservation [14].

RESULT AND DISCUSSION

Relationship between slope failures and evaluation factors

For each classification domain of the evaluation elements, the slope failure area (SA, expressed as the number of raster cells) and proportion of slope failure area within each domain (SAp [%], slope failure area

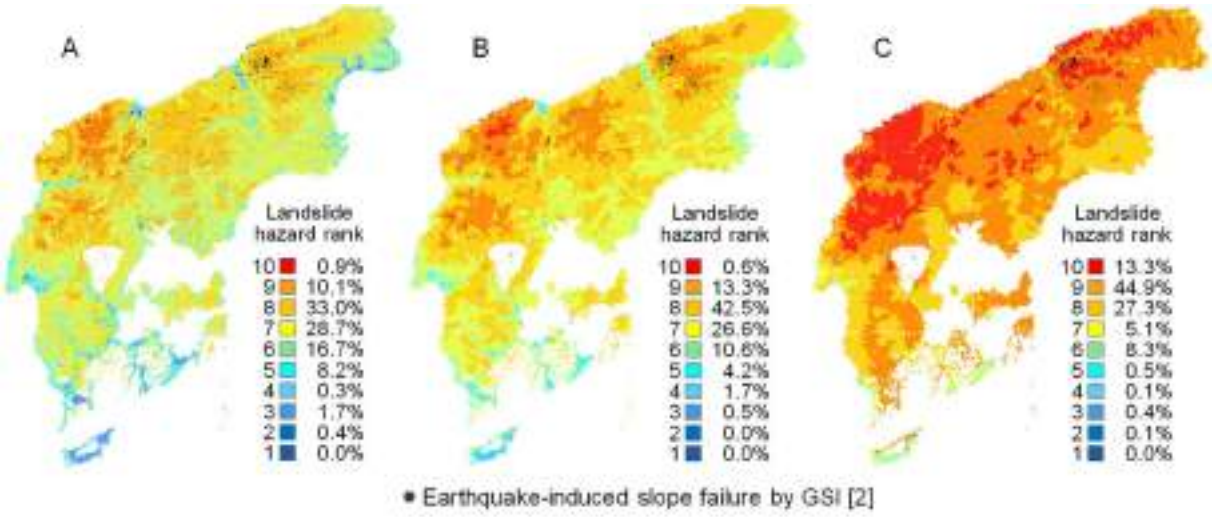

Fig. 4 Representative examples of landslide hazard maps in the Noto Peninsula district in Japan. A: cell unit (same as Fig. 2A), B: watershed unit (average value of cell unit hazard rank within the watershed), C: watershed unit (maximum value of cell unit hazard rank within the watershed).

occupancy) were calculated. The relationships between the distribution of slope failures caused by the 2024 Noto Peninsula earthquake and evaluation factors are shown in Fig. 3.

As shown in Fig. 3A, the SA was the highest in the elevation range of 0 to 200 m and tended to decrease with increasing elevation. However, the SAp did not significantly vary across different elevation ranges. Notably, slope failures were not observed at elevations above 600 m. Fig. 3B shows that the SA was the most prominent in the slope angle range of 20 to 40°. In contrast, the SAp tended to increase as the slope angle increased. Notably, although the SA was very small in the 50 to 70° range, the SAp was remarkably higher than that of other slope angle classes. According to Fig. 3C, the SA was the highest on concave ridge-and convex valley-type slopes, followed by convex ridge-and concave valley-type slopes. Very few slope failures occurred on the other slope types. Although the differences in SAp among these four slope types were not large, they all exhibited higher SAp values than the others. This indicates a strong correlation between the landslide-prone geomorphology and slope type. Fig. 3D shows that the SA generally decreases as the flow accumulation increases, excluding the flow accumulation value of 36. However, a clear trend in SAp was not observed across different flow accumulation classes. As shown in Fig. 3E, the SA was the highest in areas of Neogene volcanic rocks, followed by Neogene sedimentary rocks. In terms of SAp, slope failures were most frequently observed in areas of Quaternary sedimentary rocks, Neogene volcanic rocks, Cretaceous sedimentary rocks, and Jurassic intrusive rocks. These observations suggest a strong relationship between geological units and slope failure distribution. Fig. 3F reveals that the SA was the highest in areas classified as substitutional communities in the Camellietea japonica region, followed by plantation and cultural land. Moreover, the SAp was relatively high in areas classified as natural vegetation in the Fagaetea crenate region and exhibited substitutional communities in the Fagaetea crenate region. No slope failure was observed in the natural vegetation of the Vaccinio-Piceetea region.

Comparison between cell-based and watershed-based unit landslide hazard mapping

Fig. 4 shows three types of landslide hazard maps for the Noto Peninsula. Fig. 4A shows that most of the study area was occupied by hazard ranks of 6 to 8 according to cell-based units. Hazard ranks 9 and 10 were primarily concentrated in the eastern part of the region. Fig. 4B shows that the watershed-based unit distribution pattern was similar to that shown in Fig. 4A. However, areas with hazard ranks of 8 or higher occupied the majority of the map according to watershed-based units (Fig. 4C). The relationship between the landslide hazard rank and slope failure distribution resulting from the 2024 Noto Peninsula earthquake is shown in Fig. 5, and the corresponding ROC curves are presented in Fig. 6. In Figs. 4A and 4B, the SAp generally increased with hazard rank, peaking at rank 8 or 9 and then declining at rank 9 or 10. This indicates that earthquake-induced slope failures did not necessarily occur in areas with the highest hazard ranking. However, the AUC values showed that watershed-based units (Fig. 4B) outperformed cell-based units (Fig. 4A) in terms of predictive capability. In contrast, in the example shown in Fig. 4C, the SAp increased consistently with the hazard rank, suggesting a good correspondence between the hazard map and actual slope failure distribution. Notably, most slope failures occurred within watersheds classified as hazard rank 10,

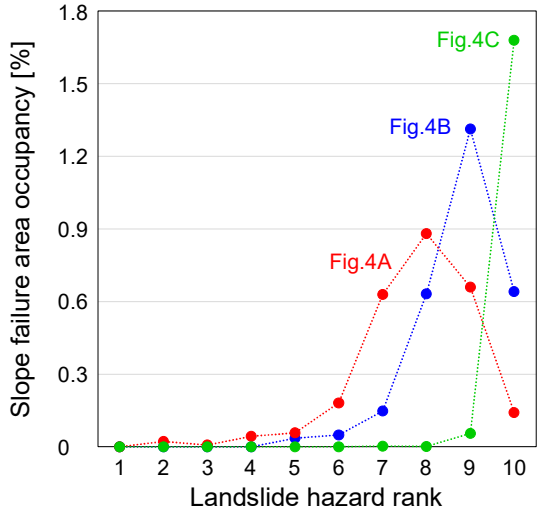

Fig.5 Relationship between landslide hazard rank and slope failure area occupancy.

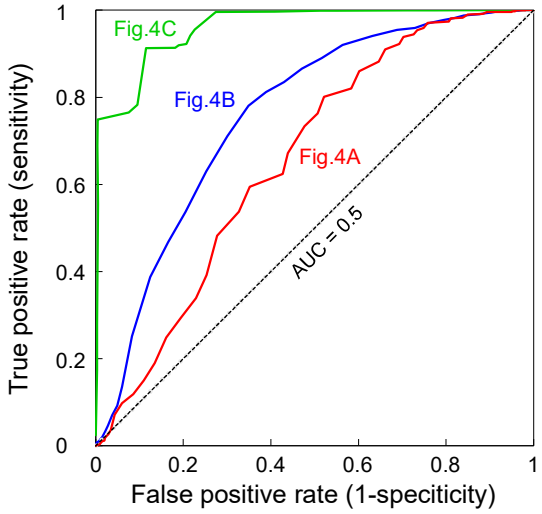

Fig.6 ROC curves for Fig. 4.

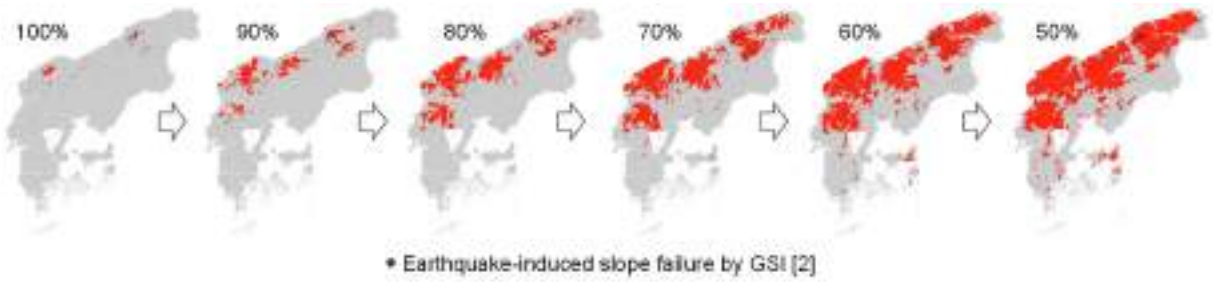

Fig. 7 Example of a watershed (red area) extraction with 100% to 50% of the watershed having a hazard rank of 8 or higher.

resulting in high AUC values. Although the relationship in Fig. 5 and the AUC value in Fig. 6 suggest that Fig. 4C provides the best representation of slope failure distribution, this may be attributed to the fact that high-hazard rank areas occupy a large portion of the study area in this case. Therefore, it was difficult to definitively determine the most appropriate mapping method for this stage. In the next section, we examine a method of determining the hazard rank of each watershed based on the proportion of high-hazard cells within it.

Landslide hazard mapping based on the proportion of high-risk cells within each watershed

Fig. 7 illustrates an example of a watershed where 100 to 50% of the constituent cells were classified as having a hazard rank of 8 or higher. The figure shows that the number and distribution of the extracted watersheds vary depending on the proportion of high-rank cells. Similarly, we extracted watersheds containing 100 to 50% of cells ranked 6 or higher, 7 or higher, ..., and 10 or higher and analyzed their correspondence with actual slope failures (Fig. 8). In

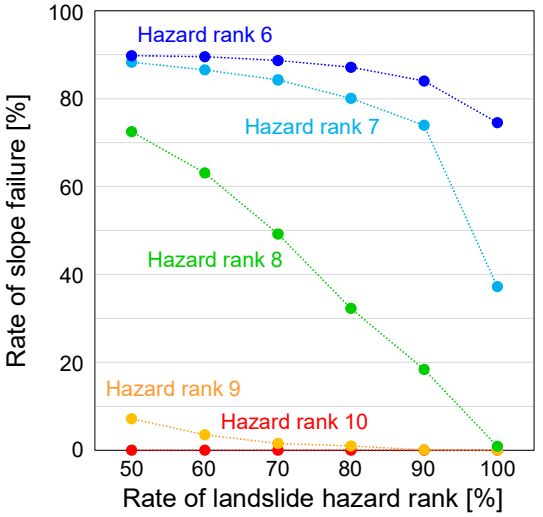

Fig.8 Relationship between the rate of landslide hazard rank and rate of slope failure.

Fig. 8, the vertical axis represents the percentage of slope failures occurring within the extracted watersheds. A value of 100% indicates that all slope failures in the study area were located within those watersheds. For hazard ranks 9 and 10, the extracted

watershed areas were limited, resulting in low slope-failure capture rates. For ranks 6 and 7, the capture rates were approximately 80%, except when the cell ratio was 100%. This result likely reflects the fact that many watersheds were extracted, covering most of the study area. Interestingly, in the case of a hazard rank of 8 or higher, a good correspondence was observed between the proportion of high-hazard cells and the slope-failure occurrence rate. Specifically, when extracting watersheds where 80% or more of the cells were ranked 8 or higher, approximately 30% of the slope failures from the 2024 Noto Peninsula earthquake could be captured within those areas.

CONCLUSION

In this study, we conducted landslide hazard mapping at the watershed scale based on cell-based landslide hazard rankings for areas affected by seismic landslides triggered by the 2024 Noto Peninsula earthquake. We examined three representative methods for assigning hazard ranks to watersheds that used the average, maximum, and proportion of hazard ranks within each watershed. Although some challenges remain, our results indicated that under certain conditions, the proportion of high-hazard cells is strongly correlated with the occurrence rate of seismic landslides. Future work will focus on investigating the relationship between watershed selection criteria and the occurrence of seismic landslides, taking into account the influence of seismic motion.

ACKNOWLEDGMENTS

This work was supported by a research grant from the Sabo and Landslide Technical Center (STC). The support is gratefully acknowledged.

REFERENCES

[1] Headquarters for Earthquake Research Promotion, Evaluation of the 2024 Noto Peninsula Earthquakes (February 9, 2024), https://www.jishin.go.jp/main/chousa/24feb_noto/index-e.htm. (Accessed 1 April 2025), 2024.

[2] Geospatial Information Authority of Japan (GSI), Distribution map of slope failures and sediments by the 2024 Noto Peninsula Earthquakes, Information on the 2024 Noto Peninsula Earthquakes, https://www.gsi.go.jp/BOUSAI/20240101_noto_earthquake.html#6-2 (Accessed 1 April 2025), 2024. (in Japanese)

[3] Loi, D.H., Jayakody, S., Sassa, K., Konagai, K., Hirota, K., Ono, A., Takanaka, T., Oki, T. and Minamitani, T., Landslides triggered by the 2024 Noto Peninsula earthquake, *Landslides*, Vol. 21, pp. 2583–2590, 2024.

[4] Peng, X., Wang, F., Miyajima, M., Yoshida, M., Zhang, S. and Fu, Z., Brief report of a field investigation in Noto Peninsula, Japan, after the 2024 Noto earthquake, *Geoenviron Disasters*, Vol. 12, 11, 2025.

[5] Kasaya, T., Minami, H., Okino, K., Kaneko, J. and Ono, S., Submarine landslides caused by the 2024 Noto Peninsula earthquake. *Earth Planets Space*, Vol. 77, 72, 2025.

[6] Kohno, M., Noguchi, T. and Nishimura, T., Landslide hazard mapping in the Chugoku Region using AHP method and GIS, *Journal of the Japan Landslide Society*, Vol. 57, No. 1, pp. 3–11, 2020. (in Japanese)

[7] National Research Institute for Earth Science and Disaster Resilience (NIED), Digital archive for Landslide Distribution Maps (SHP format). https://dil-opac.bosai.go.jp/publication/nied_tech_note/landslidemap/gis.html (Accessed 1 April 2025), 2014.

[8] Isozaki, Y., Maruyama, S., Aoki, K., Nakama, T., Miyashita, A. and Otoh, S., Geotectonic Subdivision of the Japanese Islands revisited: Categorization and definition of elements and boundaries of pacific-type (Miyashiro-type) Orogen, *Journal of Geography (Chigaku Zasshi)*, Vol. 119, No. 6, pp. 999–1053, 2010. (in Japanese)

[9] Kohno, M., Higuchi, Y. and Ono, Y., Evaluating earthquake-induced widespread slope failure hazards using an AHP-GIS combination, *Natural Hazards*, Vol. 116, pp. 1485–1512, 2023.

[10] Kohno, M. and Higuchi, Y., Landslide susceptibility assessment in the Japanese archipelago based on a landslide distribution map, *ISPRS International Journal of Geo-Information*, Vol. 12, No. 2, 37, pp. 11–60, 2023.

[11] QUIET+ (QUick Identification of Earthquake Threat PLUS), https://site.quietplus.kke.co.jp/ (Accessed 1 April 2025).

[12] Geospatial Information Authority of Japan (GSI), Digital Elevation Model (DEM10B) (GML format), https://fgd.gsi.go.jp/download/menu.php. (Accessed 1 April 2025), 2019.

[13] National Institute of Advanced Industrial Science and Technology (AIST), Seamless Digital Geological Map of Japan (1:200,000) (Basic version, data update date: 29 May 2015) (SHP format). https://gbank.gsj.jp/seamless/index_en.html (Accessed 1 April 2025), 2015.

[14] Ministry of the Environment Government of Japan (MOE) The Natural Environmental Information GIS (SHP format). https://www.biodic.go.jp/trialSystem/top_en.html (Accessed 1 April 2025), 1998.

Copyright © Int. J. of GEOMATE All rights reserved, including making copies, unless permission is obtained from the copyright proprietors.

15th Int. Conf. on Geotechnique, Construction Materials & Environment,
Kyoto, Japan, 11-13 November 2025, ISBN 978-4-909106124 C3051

ASSESSING LIQUEFACTION RISK AT LHOKSEUMAWE BEACH: IMPACT OF THE 2004 ANDAMAN AND 2016 PIDIE JAYA EARTHQUAKES

Abdul Jalil[1], Lindung Zalbuin Mase[2] and Yovi Chandra[1]

[1]Department of Civil Engineering, Faculty of Engineering, Universitas Malikussaleh, Aceh, Indonesia
[2]Department of Civil Engineering, Faculty of Engineering, University of Bengkulu, Bengkulu, Indonesia

ABSTRACT

This paper presents a study of liquefaction in Lhokseumawe, Indonesia, a topic of urgent importance due to the 2004 Andaman Earthquake (Mw 9.2) and the 2016 Pidie Jaya Earthquake (Mw 6.5). Evaluations of liquefaction potential were conducted in conjunction with particle size distribution analyses and data collected from three Cone Penetration Test (CPT) and three Standard Penetration Test (SPT) locations, which assessed the engineering characteristics and geological conditions of the area. Latitude and longitude coordinates from the sites of the hand-bore, SPT, and CPT tests were utilised to determine the peak ground acceleration (PGA) values associated with these two significant earthquakes. The analysis of liquefaction potential in Lhokseumawe, employing SPT and CPT data, utilised semi-empirical methods. The distribution of soil particle sizes played a crucial role in determining the potential for liquefaction. The findings indicate that the study area is primarily composed of poorly graded sand (SP) and well-graded sand (SW). Potential liquefaction sites were generally observed at a depth of 1 meter; however, significant liquefaction potential was also identified at depths of 15 and 18 meters below the surface. Overall, the results of this study emphasise the crucial importance of conducting preliminary investigations into soil liquefaction before commencing construction activities.

Keywords: Liquefaction Potential, Geology, Deep Liquefaction Potential, SPT, CPT

INTRODUCTION

Liquefaction is a critical geotechnical hazard that occurs when saturated, unconsolidated soils temporarily lose strength and stiffness in response to seismic shaking, resulting in significant ground deformation [1,2]. This phenomenon poses serious threats to infrastructure and human safety, particularly in seismically active regions with loose sandy soils and shallow groundwater tables. The 2004 Andaman earthquake, with a magnitude of Mw 9.2, and the 2016 Pidie Jaya earthquake, with a magnitude of Mw 6.5, are significant seismic events that have had a profound impact on the region and are crucial in understanding the liquefaction potential in Lhokseumawe. [3] The 2016 Pidie Jaya earthquake has underscored the vulnerability of various areas in Aceh Province, Indonesia, to earthquake-induced hazards, including liquefaction [4].

Lhokseumawe, a coastal city located in the northern part of Aceh Province, is situated within a geologically complex region characterised by recent alluvial and volcanic deposits. The area is located between two major tectonic features: the Sunda megathrust and the Sumatran fault system. These tectonic boundaries are known to generate significant seismic activity, raising concerns about the potential for liquefaction during future earthquakes.

Although several studies have examined regional seismic hazards in Aceh [5]. Considering the city's economic and strategic significance, a site-specific liquefaction analysis is not only necessary but could also significantly impact disaster preparedness and informed urban development. This study could provide crucial insights for disaster management professionals and urban planners.

The use of site investigation data is crucial in supporting the analysis of liquefaction. This is because soil resistance can play a significant role in enhancing liquefaction resistance. Otherwise, the cyclic stress from the earthquake could degrade the liquefaction resistance. Therefore, the information related to the site investigation data must be first known before conducting the liquefaction potential analysis.

This study aims to assess the liquefaction potential in Lhokseumawe through a combination of field and analytical approaches. The primary methods employed include Standard Penetration Test (SPT)-based analysis, utilising the simplified procedure developed by Seed et al. in 1985, which involves estimating the cyclic resistance ratio (CRR) based on the SPT data, and updated correlations from the Idriss and Boulanger method in 2008. The Cone Penetration Test (CPT)-based analysis employs the Robertson and Wride method of 1998, which assesses the soil behaviour type and liquefaction potential based on the CPT data.

Evaluation of the cyclic stress ratio (CSR) from site-specific seismic loading parameters, including peak ground acceleration (PGA) and earthquake magnitude. Calculation of the factor of safety (FS)

against liquefaction by comparing CSR and CRR.The insitu CRR was determined using SPT and CPT field tests. Data for this study were collected from subsurface investigations, borehole logs, and geotechnical reports, as well as regional seismic hazard data from the Meteorology, Climatology, and Geophysics Agency (BMKG) of Indonesia.

RESEARCH SIGNIFICANCE

The significance of the study lies in the importance of assessing liquefaction potential in the Lhokseumawe area beach. The area is characterised by a well-defined spatial arrangement, with industrial buildings clustered in designated zones, a centrally located government activity centre, and surrounding areas supporting diverse economic activities. The findings of this study could have a significant impact on the safety and resilience of these structures and activities.

GEOLOGY SETTING AND SEISMICITY

Seismic activity in the Lhokseumawe area has been influenced by major tectonic events, notably the 2004 Andaman earthquake and the 2016 Pidie Jaya earthquake. The impact of the 2004 Andaman earthquake was documented by [6], while the effects of the 2016 Pidie Jaya earthquake were reported by [7]. The epicentres of these earthquakes are plotted in Fig. 1. Lhokseumawe is located between the Sunda megathrust and the Sumatran fault system, within a basin composed of recent alluvial and volcanic deposits [8].

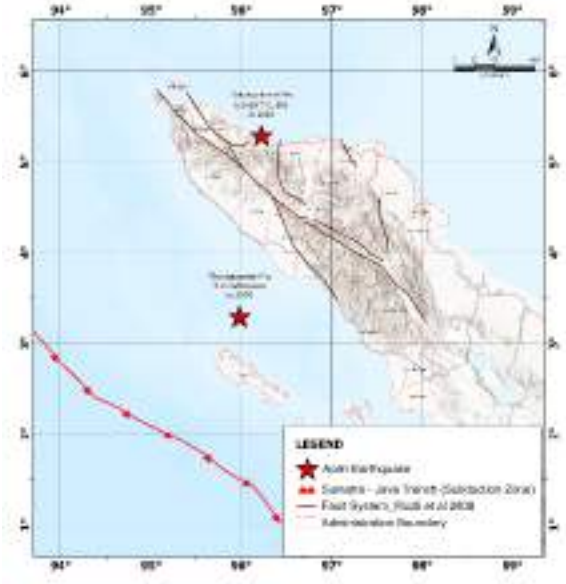

Fig 1. Seismicity in the Lhokseumawe area

Lhokseumawe is situated in a graben area (Fig. 2) composed of the Seureula Formation (Tps), Julurayeu Formation (QTjr), IDI Formation (Qpi), and Young Alluvium Deposits (Qh) [9]. According to [9]. The geology of Lhokseumawe primarily consists of layered sedimentary deposits, including gravel, sand, silt, and fluvial deposits, which are found along the active Sumatran trench.

METHODS AND THEORY

This research was conducted along the coastal area of Lhokseumawe City, Aceh Province. Soil resistance tests were conducted at six locations using the Standard Penetration Test (SPT) and Cone Penetration Test (CPT) methods. The assessment of liquefaction potential in the Lhokseumawe area was carried out using a deterministic approach based on N-SPT and CPT data, following the methodology proposed by Idriss and Boulanger in 2008. This method involves comparing the Cyclic Resistance Ratio (CRR), which represents the soil's resistance to liquefaction, with the Cyclic Stress Ratio (CSR), which reflects the seismic loading induced by an earthquake.

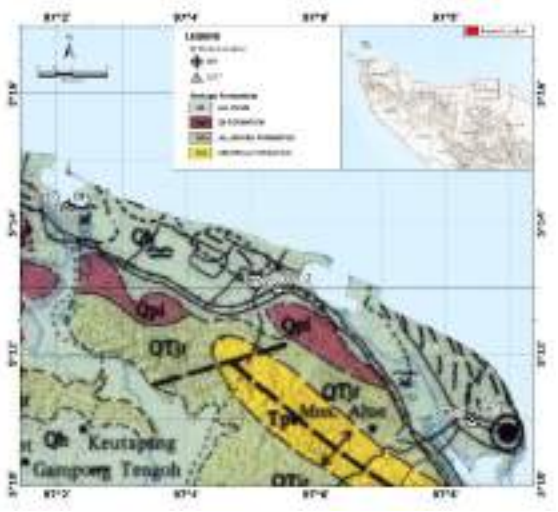

Fig 2. Geological map of the Lhokseumawe area

Soil Classification for Each Subsurface Layer

The identification and classification of soil types for each soil layer were conducted based on laboratory test results of undisturbed soil samples taken from each respective layer. The soil types were classified according to the Unified Soil Classification System (USCS). Additionally, the site classification was conducted in accordance with the Building Code of the Indonesian National Standard for Seismic Resistance Design [10], which provides guidelines for seismic design based on local soil conditions. The potential for liquefaction and loss of soil strength was evaluated using site-specific peak ground acceleration (PGA), earthquake magnitude, and source characteristics consistent with the Maximum Considered Earthquake Ground Motion (MCE_G). The

MCE_G is a measure of the maximum ground motion that can be expected at a site due to a specified earthquake. Peak Ground Acceleration (PGA) is calculated using Equation 1, which provides a quantitative basis for evaluating seismic loading at the site.

$$PGA_M = F_{PGA} \times PGA \quad (1)$$

Where PGA_M is the peak ground acceleration for the Maximum Considered Earthquake Ground Motion (MCE_G) adjusted for site class effects, PGA is the value obtained from the seismic hazard map based on the Indonesian Earthquake Map regulations (accessible via the Puskim application), and F_{PGA} is the site amplification factor corresponding to the site classification.

Earthquakes induce cyclic stress and contribute to the potential for liquefaction. Approximately 65% of the peak cyclic stress is considered in evaluating this potential, which is defined as the Cyclic Stress Ratio (CSR). The CSR can be calculated using Eq. 2.

$$CSR = 0.65 \times \left(\frac{\sigma_{vc}}{\sigma'_{vc}} \right) \times PGA_M \times r_d \quad (2)$$

where σ'_{vc} is the effective vertical stress and σ_{vc} is the total vertical stress at depth *z*. The parameter r_d is the shear stress reduction factor. Soil strength and stiffness were obtained from field tests using the Standard Penetration Test (SPT) and Cone Penetration Test (CPT). These strength parameters are used to determine the Cyclic Resistance Ratio (CRR) [11]The factor of safety against liquefaction potential can be calculated as the ratio of the Cyclic Resistance Ratio (CRR) to the Cyclic Stress Ratio (CSR) induced by an earthquake. The factor of safety against liquefaction triggering can be expressed by Eq. (3).

$$FS_{liq} = \frac{CRR_{M,\sigma'vc}}{CSR_{M,\sigma'vc}} \quad (3)$$

Where FS_{liq} is the factor of safety against liquefaction. If FS_{liq} is less than 1.0, the soil is considered susceptible to liquefaction. Conversely, if FS_{liq} is greater than 1.0, the soil is considered safe from liquefaction potential.

RESULTS AND DISCUSSION

The Peak Ground Acceleration (PGA) values were obtained using the latest Indonesian earthquake map, which was analysed based on probabilistic seismic hazard analysis. The information is available on the website https://rsa.ciptakarya.pu.go.id/2021 by entering the coordinates of locations BH-1, BH-2, and BH-3. Standard Penetration Test (N-SPT) data was used to determine the soil site class in the Lhokseumawe area, referring to SNI-1726-2019, and the soil was classified as Medium (SD). By entering the geographic coordinates of the N-SPT test locations into the Indonesian seismic map, the PGA values for each site were found to be 0.41g, 0.45g, and 0.48g, respectively.

The calculated values of the factor of safety against liquefaction (FS_{liq}) will be illustrated through liquefaction potential curves, providing a visual representation of the soil's susceptibility to liquefaction with depth.

The soil parameters presented in Table 1 were used for the liquefaction potential analysis, employing the simplified procedure proposed by Idriss and Boulanger in 2008.

Liquefaction Potential Based on SPT Data

Figure 3 shows that the depth of the drill hole is 30.45 meters below the ground surface. Liquefaction potential was identified at depths ranging from 3 meters to 15 meters under the earthquake scenario of M_w 9.2. The analysis at BH-1 indicates the presence of deep liquefaction. Similar cases of deep liquefaction were reported by [12] following the 2011 Canterbury Earthquake, where firm ground shaking was found to trigger widespread liquefaction significantly [13].

Table 1: Soil Parameters

Items	Ground water level (m)	γ (kN/m^3)	γ_{sat} (kN/m^3)
BH-1	0.80	17.0	19.5
BH-2	1.85	17.0	19.5
BH-3	2.00	16.5	18.8
CPT-1	0.8	17.0	19.5
CPT-2	1.85	17.0	19.5
CPT-3	2.00	16.5	18.8

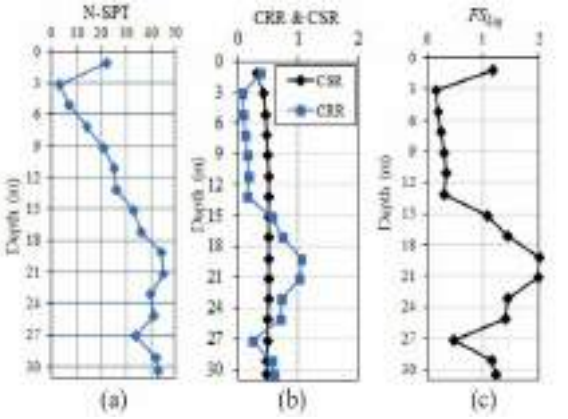

Fig. 3. Liquefaction Potential Curves at BH-1 for Mw 9.2: (a) N-SPT Data, (b) CRR and CSR Curves, (c) Factor of Safety against Liquefaction

The SPT data was used to analyze the liquefaction potential for a scenario with Mw 9.2 at BH-2 (Fig. 4) and BH-3 (Fig. 5). Figure 4 shows that liquefaction

potential was found at depths between 3 and 12 meters. A non-liquefying layer was identified between 12 and 17 meters depth. The liquefaction potential was analyzed for a scenario with Mw 6.5 at BH-1, BH-2, and BH-3, as shown in Figure 6. The depths at which liquefaction was observed were similar to those in the Mw 9.2 scenario, with a slightly reduced severity.

Liquefaction Potential Based on CPT Data

The CPT data was used to analyse the triggering of liquefaction potential, following the simplified procedure proposed by Idriss and Boulanger (2008). The liquefaction assessment was conducted under the assumption of level ground conditions for a moment magnitude (Mw) 6.5 earthquake, with Peak Ground Acceleration (PGA) values of 0.41g, 0.45g, and 0.48g. These PGA values represent the geometric mean of ground shaking observed during the 2016 Pidie Jaya earthquake.

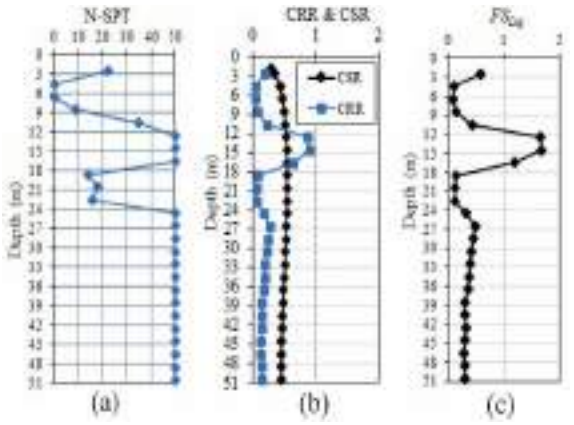

Fig.4 Liquefaction Potential Curves at BH-2 for Mw 9.2: (a) N-SPT Data, (b) CRR and CSR Curves, (c) Factor of Safety against Liquefaction

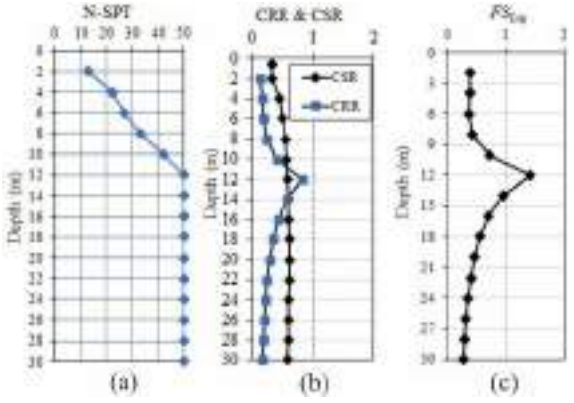

Fig.5 Liquefaction Potential Curves at BH-3 for Mw 9.2: (a) N-SPT Data, (b) CRR and CSR Curves, (c) Factor of Safety against Liquefaction

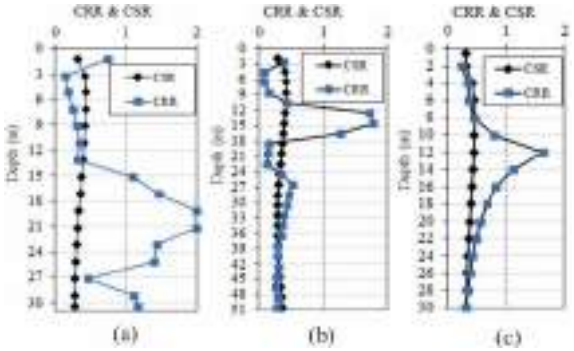

Fig.6 Liquefaction Potential Curves at BH-1, BH-2, and BH-3 for Mw 6.5: (a) CSR and CRR Curves at BH-1, (b) CSR and CRR Curves at BH-2, (c) CSR and CRR Curves at BH-3

In addition to the Mw 6.5 scenario, the CPT data were also used to evaluate liquefaction potential under a Mw 9.2 earthquake scenario, following the 2004 Andaman earthquake [14]. Liquefaction potential was identified at depths ranging from 2 to 8 meters below the ground surface (Figs. 7-8). The analysis used Peak Ground Acceleration (PGA) values of 0.41g, 0.45g, and 0.48g, which represent the geometric mean of ground shaking based on the Indonesian National Standard.

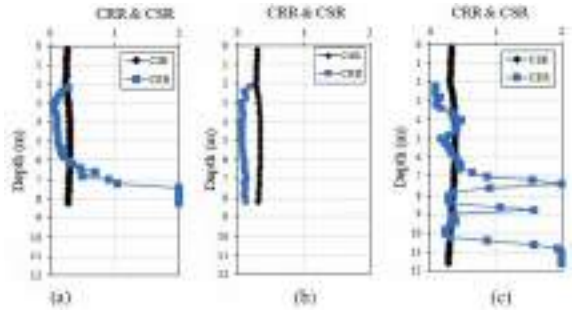

Fig.7 Liquefaction Potential Curves at CPT-1, CPT-2, and CPT-3 for Mw 6.5: (a) CSR and CRR Curves at BH-1, (b) CSR and CRR Curves at BH-2, (c) CSR and CRR Curves at BH-3

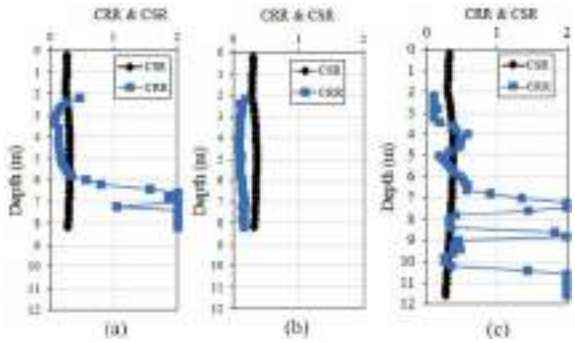

Fig.8 Liquefaction Potential Curves at CPT-1, CPT-2, and CPT-3 for Mw 9.2: (a) CSR and CRR Curves

at BH-1, (b) CSR and CRR Curves at BH-2, (c) CSR and CRR Curves at BH-3

CONCLUSIONS

The liquefaction potential analysis was carried out using both N-SPT and CPT data. Liquefaction potential was identified at depths ranging from 2 to 11 meters below the ground surface. Two earthquake scenarios, based on the Pidie Jaya and Andaman earthquakes, revealed the possibility of deep liquefaction. The effects of such liquefaction could cause significant damage to infrastructure facilities.

ACKNOWLEDGMENTS

This research was conducted independently by the authors. The first author, who also serves as the corresponding author, acknowledges the Department of Civil Engineering, Faculty of Engineering, Malikussaleh University, for its support. The authors also express their gratitude to the university.

REFERENCES

[1] Mase LZ, Tanapalungkorn W, Likitlersuang S, Ueda K, Tobita. Ground motion, liquefaction and hazard analysis at the Palu site during the 2018 Indonesian great earthquake. China Geology. 2024;7(2):237–47.

[2] Jalil A, Fathani TF, Satyarno I, Wilopo W. A study on the liquefaction potential in Banda Aceh City after the 2004 Sumatra Earthquake. International Journal of GEOMATE. 2020;(65):147–55.

[3] Chlieh M, Avouac JP, Hjorleifsdottir V, Song TRA, Ji C, Sieh K, et al. Coseismic Slip and Afterslip of the Great Mw 9.15 Sumatra–Andaman Earthquake of 2004. 2007;97(1A):152–73.

[4] BMKG. Gempabumi Kuat M=6.5 Guncang Pidie Jaya, Provinsi Aceh Dipicu Akibat Aktivitas Sesar Aktif. https://www.bmkg.go.id/siaran-pers/gempabumi-kuat-m6-5-guncang-pidie-jaya-provinsi-aceh-dipicu-akibat-aktivitas-sesar-aktif. 2016.

[5] Sengara IW, Puspito N, Kertapati E, Hendarto. Survey of Geotechnical Engineering Aspects of the December 2004 Great Sumatra Earthquake and Indian Ocean Tsunami and the March 2005 Nias–Simeulue Earthquake. Earthquake Spectra. 2006 Jun;22(S3):495–509.

[6] Pesicek JD, Thurber CH, Widiyantoro S, Engdahl ER, DeShon HR. Complex slab subduction beneath northern Sumatra. Geophysical Research Letters. 2008 Oct;35(20):2008GL035262.

[7] Muzli M, Umar M, Nugraha AD, Bradley KE, Widiyantoro S, Erbas K, et al. The 2016 Mw 6.5 Pidie Jaya, Aceh, North Sumatra, Earthquake: Reactivation of an Unidentified Sinistral Fault in a Region of Distributed Deformation. Seismological Research Letters. 2018 Sep;89(5):1761–72.

[8] Muksin U, Bauer K, Muzli M, Ryberg T, Nurdin I, Masturiyono M, et al. AcehSeis project provides insights into the detailed seismicity distribution and relation to fault structures in Central Aceh, Northern Sumatra. Journal of Asian Earth Sciences. 2019 Mar;171:20–7.

[9] Muhni A, Sartika D, Suhaidi B, Putra HS, Adrian SH, Safira M, et al. Mitigating Leachate Contamination: Geological Investigations at Alue Lim Landfill Area, Lhokseumawe City. IOP Conf Ser: Earth Environ Sci. 2025 Apr 1;1479(1):012006.

[10] SNI 03-1726-2019. Earthquake Resistance Planning Procedures for Building and Non-Building Structures. Badan Standardisasi Nasional; 2019.

[11] Idriss IM, Boulanger RW. Soil Liquefaction During Earthquakes. 2008, pp. 1-235.

[12] Cubrinovski M, Robinson K, Taylor M, Hughes M, Orense R. Lateral spreading and its impacts in urban areas in the 2010–2011 Christchurch earthquakes. New Zealand Journal of Geology and Geophysics. 2012 Sep;55(3):255–69.

[13] Mase LZ, Likitlersuang S, Tobita T. Verification of Liquefaction Potential during the Strong Earthquake at the Border of Thailand-Myanmar. null. 2020 Apr 23;1–28.

[14] Geist EL, Titov VV, Arcas D, Pollitz FF, Bilek SL. Implications of the 26 December 2004 Sumatra-Andaman Earthquake on Tsunami Forecast and Assessment Models for Great Subduction-Zone Earthquakes. Bulletin of the Seismological Society of America. 2007 Jan 1;97(1A):S249–70.

Copyright © Int. J. of GEOMATE All rights reserved, including making copies, unless permission is obtained from the copyright proprietors.

15th Int. Conf. on Geotechnique, Construction Materials & Environment,
Kyoto, Japan, 11-13 November 2025, ISBN 978-4-909106124 C3051

NONLINEAR INERTIAL EFFECTS IN CAISSON FOUNDATIONS WITH SUPERSTRUCTURES: AN EXPERIMENTAL STUDY UNDER VARIABLE-AMPLITUDE SEISMIC LOADING

Zain Bin Mazhar[1], Faruk Md Omar[2] and Masato Saitoh[3]

[1,2,3]Graduate School of Science and Engineering, Saitama University, Japan

ABSTRACT

Nowadays, as the expected earthquake motions become significantly larger, the ultimate seismic performance of large foundations, such as the caisson foundation, needs to be investigated. This study examines the seismic response of a caisson foundation connected to a superstructure modeled as a single-degree-of-freedom system. This study focuses on the inertial effects and nonlinear soil-structure interaction of the entire system under four simulated earthquake records with varying amplitudes. In particular, attention is given to soil nonlinearity (yielding and failure) and interface nonlinearity between the soil and the caisson surface in contact with the soil. These factors may influence the inertial system of soil-caisson-superstructure in terms of its resonant period and damping characteristics.

To investigate the seismic response under 1g condition, a 1/40 scaled model of a caisson foundation and superstructure is used, with a diameter and height of 350mm and 500mm, respectively. The effects of soil and interface nonlinearities on the stiffness and damping of the superstructure interacting with the soil are evaluated using transfer functions, phase differences, pressure responses, and mean shear strain. Furthermore, the study examines the potential shift in dominant vibration modes, such as increased rocking motion of the caisson foundation with larger loading amplitudes. This research highlights the significance of soil and interface nonlinearities on the inertial behaviour of the soil-caisson-superstructure system under stimulated earthquake ground motions.

Keywords: Soil structure interaction, Caisson foundation, Non-linear analysis, Superstructure, Seismic motion

INTRODUCTION

Dynamic soil-structure interaction plays an important role in evaluating the seismic performance of the foundation attached to the soil and coupled with superstructure. With the increasing strength of predicted earthquake ground movements, it has become crucial to properly evaluate the seismic performance of large foundations connected to the superstructures, particularly the caisson foundations. Amid high-amplitude earthquakes, the soil may undergo yielding both globally and locally. The presence of global and local nonlinearities in the soil medium can lead to complex soil-structure interaction behaviour. To have a better understanding of these mechanisms, it is imperative to delve deeper into the key parameters such as strain-dependent soil properties related to global nonlinearities and near-field pressure response associated with local nonlinearities.

Such effects are often overlooked in the design practice, where the superstructure is assumed to be fixed at the base; however, this assumption doesn't accurately reflect the real behaviour [1]. The analysis of seismic response for soil-caisson foundation is therefore of utmost importance, as caisson foundations support structures like highway bridges, that are prone to failure under strong seismic activity. Several of such structures experienced severe damage during the devastating earthquake event in Kobe, Japan, on 17 January 1995 [2]. The damage highlights the importance of understanding the transmission of inertial forces between soil, foundation, and superstructure. The interaction of these inertial forces results in the propagation of them through the soil-foundation-structure system, leading to the elongation of the structure's natural period during seismic activity. The propagation of inertial forces and elongation of natural period can produce devastating effects on the soil-caisson system under the influence of high-amplitude seismic waves. Hence, the overall safety of the soil-foundation-structure is strongly influenced by these inertial forces [3].

Monitoring the transfer function of the soil-foundation-structure provides a valuable insight into the changes in stiffness and damping due to nonlinearities. This study investigates the variations in the amplification ratio and the phase difference owing to global and local nonlinearities. The global change in shear strain alters the soil's shear modulus of the soil, which ultimately affects the damping characteristics of soil. As seismic waves propagate, the strain-dependent properties of soil, like shear modulus and stiffness of the material undergo significant changes, impacting the dynamic response of the entire structure [4, 5]. Additionally, this study further explores the local failures as described in a

study done by [6, 7], which determined that the variation in the transfer function is also closely related to the local nonlinearity failures. Analyzing near-field pressure response of the soil-foundation-structure for such local failures can provide insight into pronounced reduction in the amplitude of transfer function with the increase of seismic amplitude [8, 9].

While most researchers have concentrated on the inertial effects of superstructure and pile foundation assuming linear soil behaviour, often overlooking the nonlinear soil behaviour and its interaction with caisson foundation supporting superstructure, this study is intended to address this gap. It closely monitors the behaviour of the caisson foundation coupled with the single degree of freedom (SDOF) superstructure under the influence of four different earthquake records. The main objectives of this research are: 1) To investigate the response of caisson foundations under seismic motions with large amplitudes, aiming to capture critical system behaviors and conditions that lead to severe damage, 2) To study the effects of amplitude on the amplification ratio and the natural period elongation, 3) To examine the mechanics of soil-caisson-structure interaction, such as pressure response for local nonlinearities and mean shear strain for both global and local nonlinearities.

RESEARCH SIGNIFICANCE

This research highlights the importance of bridging experimental gaps in understanding the critical response of soil-caisson-structure interaction for caisson foundations. By considering the non-linear nature of soil, this study analyzes the natural period elongation and amplification ratio against high-amplitude seismic records. It provides valuable insight into the dynamic response of the soil-caisson-structure system, which can be beneficial in improving resilience, enhancing the understanding of global changes in soil material and local interface failures between soil and the foundation. These failures may result from the inertial effects of seismic activity itself or from the superstructure. Ultimately, this research work will contribute to the safer design of the infrastructure subjected to strong seismic activity.

MODEL TEST

Scaling rules are essential to accurately build a relationship between the real model and its prototype for experimental studies in small-scale environments. The experimental setup of this study is preferred to be scaled as per the scaling rule developed by [10]. The similar scaling model is also used by [11, 12]. It considers the effect of low confining pressure values. The correspondence of scale for the angular frequency ratio of the model to the prototype is evaluated as shown below, considering both geometry and density conditions.

$$\frac{\omega_m}{\omega_p} = \lambda^{-0.25}\eta^{-0.75} \quad (1)$$

In the equation shown above, λ represents the geometrical properties, whereas η represents the material density characteristic. As per the same scaling law, the model-to-prototype strain ratio is stated as:

$$\frac{\gamma_m}{\gamma_p} = \lambda^{0.5}\eta^{0.5} \quad (2)$$

The rules and factors as per the law, for both the prototype and the model, are compiled in Table 1.

Table 1 Model to prototype scaling parameters

	Quantity	Law of similitude	Factor of similitude	Value of every quantity		
				Prototype	Target value	Attained value
Subsurface Layer	Depth of Layer (m)	λ	0.03	17	0.4	0.4
	Density (t/m3)	η	0.8	1.8	1.4	1.5
	Natural Frequency (Hz)	$\lambda^{-0.25}\eta^{-0.75}$	17	2.2	37.3	38.1
	Shear Velocity (m/s)	$\lambda^{-0.25}\eta^{-0.25}$	0.4	150	64	65.5
Bedrock Layer	Depth of layer (m)	λ	0.03	8	0.2	0.2
	Density (t/m^3)	η	0.8	2.0	1.5	1.6
	Shear Velocity (m/s)	$\lambda^{-0.25}\eta^{-0.25}$	0.4	400	171	142
Foundation	Length (m)	λ	0.03	17	0.4	0.4
	Diameter (m)	λ	0.03	14	0.4	0.4
	Thickness (m)	λ	0.03	0.8	0.02	0.02
	Yung's Modulus (KN/m^3)	$\lambda^{0.5}\eta^{0.5}$	0.1	2.5 x 10^7	3.5 x 10^6	3.0 x 10^6
	Moment of Inertia (m^4)	λ^4	4.093 x 10^{-7}	700.47	2.87 x 10^{-4}	2.87 x 10^{-4}

EXPERIMENTAL SETUP

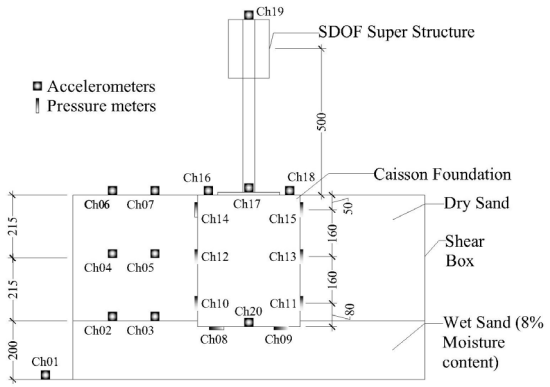

Fig. 1 Schematic representation of the test setup

Fig. 1 shows the experimental configuration of this study. The caisson foundation in this experiment is placed within a laminar shear box with inner dimensions of 1200mm, 800mm, and 1000mm for length, width, and depth, respectively. These dimensions of the shear box are similar to the one used by [13, 14]. The shear box is bolted on the top of a unidirectional shaking table of Saitama University, Japan. It is filled with cohesionless Gifu sand arranged in two different layers. The bottom layer, containing 8% moisture, provides firm support for the base of the caisson foundation, while the top layer comprises dry cohesionless sand with a specific gravity of 2.64.

The layer at the base is manually compacted with a heavy weight dropped under the influence of gravitational force, whereas the layer of dry sand which is filled in three equally width layers is compacted by providing base vibration to the system of 6m/s^2 and 40Hz frequency to achieve the target density of 1.46Mg/m^3. At the center of the laminar shear box, a caisson foundation model with a 350mm diameter and 450mm height is placed. The hollow cylindrical caisson, featuring a wall thickness of 20mm, is meticulously filled with dry Gifu sand. The mass and volume are carefully adjusted to achieve the desired scaled parameters. A Single degree of freedom (SDOF) superstructure, measuring 500mm in height and carrying 56.8 kg of mass at its head, is attached to the head of the caisson foundation, with a natural frequency of 23.7 Hz.

The experiment was conducted using four earthquake records: the 1940 El-Centro (NS), the 1995 JMA Kobe (NS), the 2004 K-Net Ojiya (EW), and White noise. All four earthquake records were scaled and adjusted in amplitude to simulate realistic earthquake conditions. The input motions were applied to the system in 7 distinct cases, - S1, S2, L1, L2, L3, L4, and L5. For each case, the relative displacement, defined as the distance covered by sand particles at the ground surface relative to the base due to deformation, was measured. Additionally, the mean shear strain that describes the shear strain distribution along the depth of the sand was also measured to support the study's objective.

Relative displacement and mean shear strain

Fig. 2 shows the change in mean shear strain values for different earthquake records as amplitude increases. The graph demonstrates the results from the top to bottom of the sand. For lower amplitudes, the minimum shear strain remains minimal, but for the amplitudes above 10m/s^2, the mean shear strain increases drastically because the soil softens upon transition from linear to nonlinear state. This high-strain behaviour results in high energy dissipation as the particles slip and rearrange themselves.

The resultant values of relative displacement and mean shear strain produced by each case are shown in Table 2.

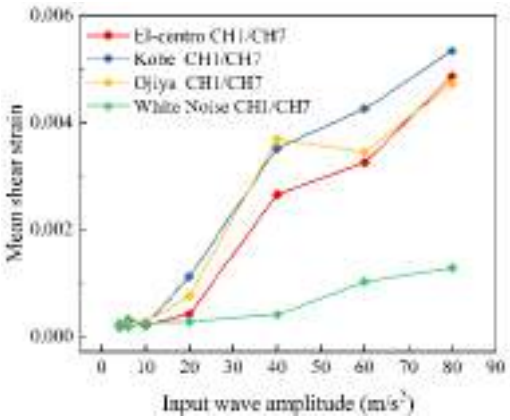

Fig. 2 Mean shear strain from the base of sand to the top of sand

Table 2 Relative displacement and mean shear strain

Case	Relative displacement (m)	Mean shear strain (Avg.)
S1	0.0001953	0.031%
S2	0.0002443	0.039%
L1	0.000232	0.037%
L2	0.0006348	0.101%
L3	0.0025653	0.407%
L4	0.0029888	0.474%
L5	0.004046	0.642%

The inertial properties of the soil-foundation-structure system are studied by combining all seismic records of the same case, as discussed in the results section.

Each set of experiments was instrumented with accelerometers and pressure meters to record the

acceleration and pressure at different locations shown in Fig. 1. Schematic representation of the test setup. In total, 11 accelerometers and 8 pressure meters are used in this study.

DATA PROCESSING

The experimental data were recorded in the form of time histories of both acceleration and pressure. Fourier Transformation (FFT) was used to convert the time domain data to the frequency domain, followed by the calculation of the transfer function using the cross spectrum and power spectrum from multiple response waveforms that were recorded under the same conditions. The noise was then removed using an averaging process applied to the spectra.

Finally, the magnification ratio curves were prepared for the superstructure head with respect to the ground surface and for the caisson foundation head with respect to the ground surface, concerning the input motion. To measure near-field pressure from time history, the peak pressure for all earthquake records was recorded for their respective amplitudes.

RESULTS AND DISCUSSION

Superstructure head

Horizontal transfer function

Fig. 3 illustrates the amplitude of the horizontal transfer function (amplification ratio) at the head of the superstructure with respect to the ground surface, subjected to the earthquake records of increasing amplitude. At amplitudes lower than L1, the system depicts the linear state. Case L1 can be considered as the transitional amplitude, as indicated by Table 2, which shows smaller mean shear strain values for S1 and S2, with a sudden rise above L1.

As the soil yields with the increase in mean shear strain, the shear modulus decreases rapidly. This reduction intensifies with the increase in shear strain. This phenomenon reflects global nonlinearity, where the soil-structure system exhibits a nonlinear response. The loss of stiffness and strength of the soil material leads to prominent energy dissipation. resulting in increased damping, consequently, a decrease in the amplification ratio. Besides this, for higher amplitudes, local nonlinearity is predicted as the soil undergoes large amounts of strain for localized areas near the foundation.

Before yielding, the small-strain behaviour dominates, where the shear modulus remains relatively constant. After yielding, the soil transitions to a plastic deformation state, resulting in a significant reduction in the overall stiffness, closely linked to the decrease in the elastic modulus of the soil. This represents global nonlinearity in the soil, where the entire soil system undergoes significant changes. Furthermore, at the higher strain levels, phenomena such as dropping of shear modulus to a minimum level and rising of the damping to its maximum level significantly influences the soil-structure interaction. Here, the separation between the soil and the foundation can also be predicted, indicating local yielding.

As a result, the peak of the amplification ratio decreases with the increase in loading amplitude, eventually becoming almost flat for the state of soil where a large amount of energy has been dissipated due to a significant increase in damping accompanied by a massive reduction in strength and stiffness.

Additionally, for higher amplitudes, a backwards shift in the peak of the graph towards lower frequencies can also be seen. This reduction in the natural frequency of the system is because of the softening of the soil. This softening of soil reduces the stiffness of soil, where the system can no longer sustain the vibrations at the original frequency, resulting in a shift of the peak.

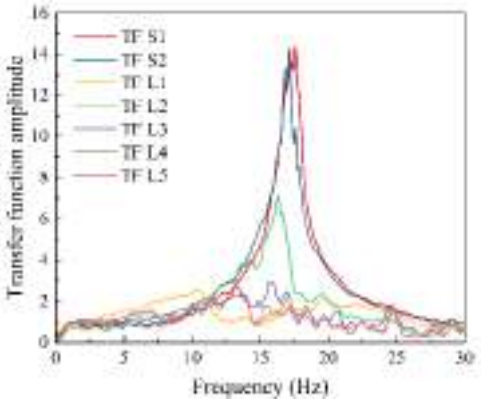

Fig. 3 Transfer function at the head of the super structure with respect to the ground surface

Phase difference

Fig. 4 shows the phase angle at the superstructure with respect to the ground surface, reinforcing the explanation discussed in the horizontal transfer function section. At lower amplitudes, the phase of the superstructure and the phase of the ground are the same, which is why below 15Hz, the phase difference is zero. However, this value suddenly drops at the resonance point of the system. While the general behaviour remains similar for all amplitudes, the trend differs significantly when the system shifts from linear to non-linear state.

As mentioned in the horizontal transfer function section, L1 is the transitional amplitude. After this, the soil softens, and a huge amount of energy dissipates as compared to the lower amplitude cases. From amplitudes L2 and higher, the system tends to regain the prior state but fails due to significant loss of stiffness already occurred. Interestingly, this effect is prominent for L5, where the graph of the transfer function also flattens, and the phase difference to follows the similar trend to other nonlinear cases.

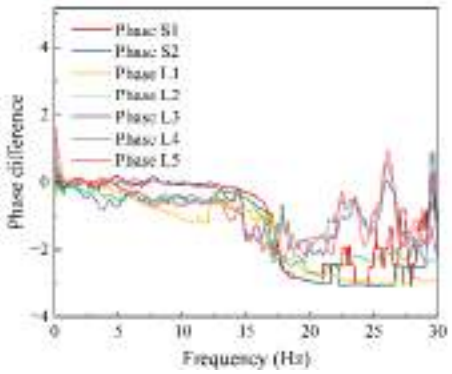

Fig. 4 Phase difference at the head of the super structure with respect to the ground surface

Caisson foundation head

Horizontal transfer function

Fig. 5 illustrates the amplitude of horizontal transfer function (amplification ratio) for the foundation head with respect to the ground surface, subjected to earthquake records of increasing amplitude. From the figure, for the caisson foundation head, the magnitude of the peak decreases with the increase in the magnitude of loading. This decrease is more pronounced in higher amplitudes of loadings. Similar to the observations for the superstructure, L1 acted as a transition amplitude, as seen in Table 2, where the values of mean shear strain are smaller for cases S1 and S2, followed by a sudden rise from L2 to L5. Beyond L1, the strain-dependent properties of sand become more pronounced. Hence, after yielding with the increase in strain, the sand undergoes softening, which reduces its stiffness and causes the peak shifts towards lower frequencies.

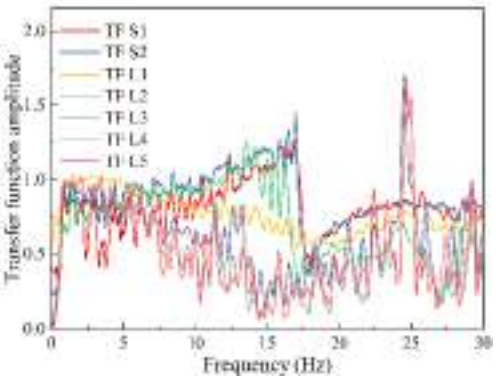

Fig. 5 Transfer function at the head of the caisson foundation with respect to the ground surface

Phase difference

Fig. *6* portrays the phase angle at the caisson head with respect to the ground surface. The figure demonstrates the behaviour similar to superstructure head, where the response of both the caisson head and the ground surface is identical at lower frequencies. The shifting in the phase of the caisson head has been observed simultaneously when the soil-foundation system shifted from linear to non-linear state, beyond L1. Additionally, a backward shift in the steady rise of the graph is observed. The loss of stiffness of the soil hinders the efficient stress transfer between soil medium and the caisson foundation.

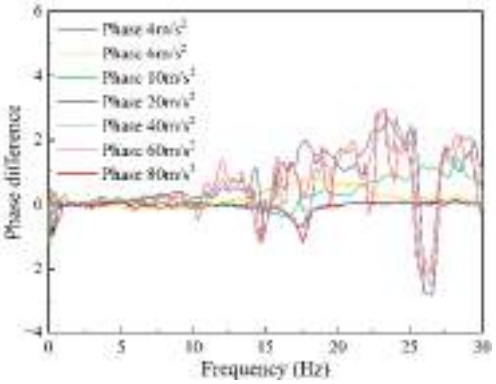

Fig. 6 Phase difference at the head of the caisson foundation with respect to the ground surface

Near Field Pressure Analysis

Fig. 7 a to d illustrates the near-field maximum pressure response for each distinct earthquake record. The response of the pressure meters provides evidence of the existence of local nonlinearity. Within the linear range (at lower amplitudes), the pressure increases with the increase in loading rate, owing to the linear elastic properties of the soil material. However, as the system transits into the non-linear range at higher amplitudes, the sand exhibits inelastic behaviour. This post-yield response, localized to specific areas, leads to the degradation of the stiffness in the soil. Beyond this point, further deformation doesn't result in increased pressure, as the stress transmission mechanism diverges from that observed before local yielding. Consequently, the pressure values demonstrated variability with increasing loading amplitudes. Which can also be attributed to the generation of a gap between the sand material and the foundation, driven by local interface nonlinearity.

Fig. 8 demonstrates the time histories of pressure meter responses attached to the sides of the foundation close to the ground surface. The figure demonstrates the separation between the foundation and the soil, as one pressure graphs plunges to zero on one side while the opposite side reaches the peak, simultaneously. Additionally, contact loss is also evident for higher amplitude loadings. For instance, At S2, the proportion of positive and negative values of pressure is almost equal, indicating no separation at lower amplitudes. However, at higher amplitudes, the pressure meters record only positive values with the increase in the amplitude, confirming the existence of a separation between the foundation and the soil.

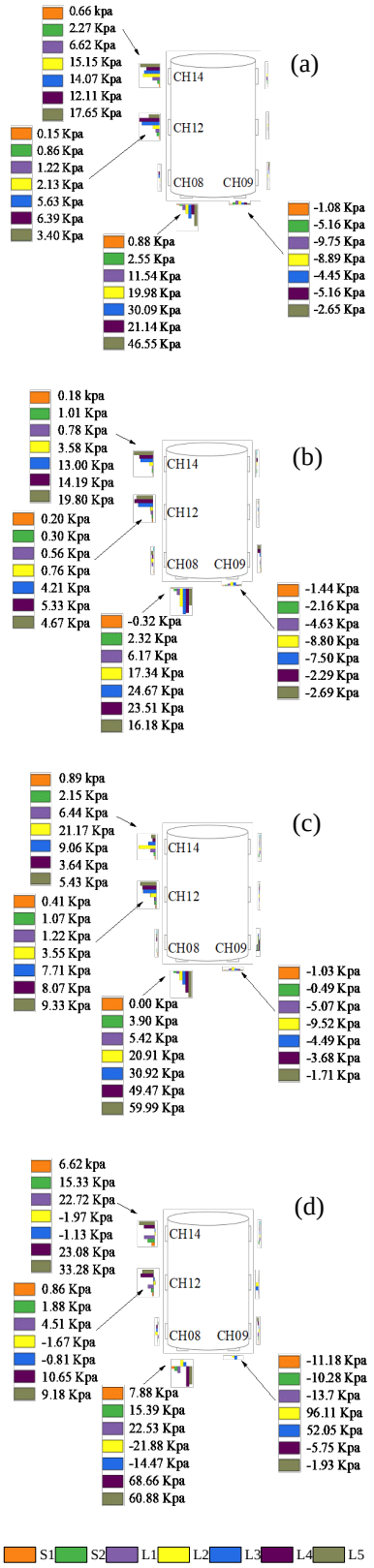

Fig. 7 Near field pressure response for a) El-Centro, b) Kobe, c) Ojiya, and d) White noise earthquake records

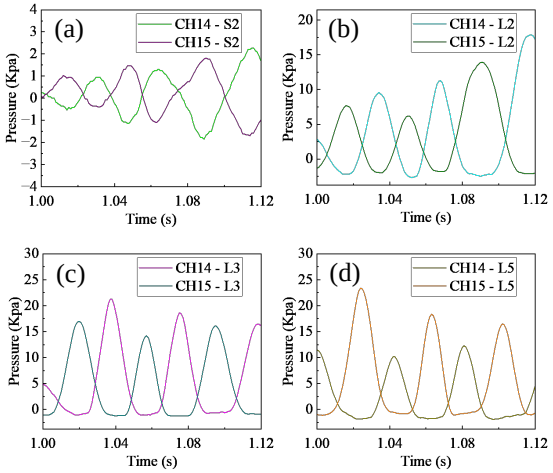

Fig. 8 Near field pressure time history for CH14/15 at a) S2, b) L2, c) L3, and d) L5

CONCLUSIONS

By focusing on critical systems behaviours and conditions that might result in significant damage, this study presented the experimental results on the nonlinear inertial effects in the soil-caisson-structure system against increasing amplitude of different earthquake records. It further explored the effects of rising amplitude on the amplification ratio and the mechanism of soil-structure interaction, including near-field pressure response for local nonlinearities and mean shear strain for both local and global nonlinearities.The resonance peaks are obtained for the amplification ratio graph with the increase in the amplitude. The findings reveal that these resonance peaks in the horizontal transfer function (for the superstructure top and the caisson head) flatten as the loading amplitude increases. This is attributed to the increased energy dissipation in soil, leading to high damping because of global nonlinearities in the soil. In global nonlinear behaviour, when the stiffness of the soil decreases, the dissipation of energy increases, leading to an increase in damping. Owing to this, the peak of the amplification ratio reduces progressively as the amplitude increases, while the natural time period elongates, reflecting the degradation in the stiffness of soil. The observation is further supported by the mean shear strain, which shows higher values at higher loading amplitudes.In addition to global nonlinearity, the near-field pressure response justifies the observation of local nonlinearity in the system. The pressure values increase gradually at lower amplitudes, whereas they become staggered at higher amplitudes, reflecting the presence of some local interface nonlinearities. The prediction of the separation between the foundation and the soil is also validated from the time history of pressure responses. The loss of contact between the foundation and the structure is observed at higher amplitudes,

significantly compromising the transmission of inertial forces.

These findings highlight the necessity of accounting for both global and local nonlinearities in the design of the structure. By considering them, this study offered critical insights for resilient and safer infrastructure capable of withstanding extreme seismic conditions.

ACKNOWLEDGEMENTS

This work was supported by KAKENHI Grant-in-Aid for Scientific Research (B) 21H01414 from the Japan Society for the Promotion of Science.

REFERENCES

[1] Wu, Y., Peng, T., and Ahmad, S., 1-g Shaking Table Test Study on the Influence of Soil–Caisson Dynamic Interaction (SCDI) on the Caisson Foundation Motion. Applied Sciences, Vol. 14, Issue 19, 2024, pp. 8942.

[2] Matsui, T., and Vlatsui, T., Foundation Damage of Structures in Kobe and Remediation. International Conference on Case Histories in Geotechnical Engineering, 1998, pp. 1-18.

[3] Gaudio, D., and Rampello, S., Equivalent Seismic Coefficients for Caisson Foundations Supporting Bridge Piers. Soil Dynamics and Earthquake Engineering, Vol. 129, 2020, pp. 105955.

[4] Erdogan, D., Mahmudi, M., and Erozkan, E., Effect of Inertia of Superstructure on Seismic Response of Shallow Foundations. 8th International Geotechnical Symposium, Istanbul Technical University, Turkey, 2019, pp. 1-13.

[5] Ullah, M. S., Kajiwara, K., Goit, C. S., and Saitoh, M., Frequency and Intensity Dependent Dynamic Responses of Soil-Steel Pipe Sheet Pile (SPSP) Foundation-Superstructure System. Soil Dynamics and Earthquake Engineering, vol. 125, 2019, p. 105730.

[6] Chandra S. Goit, Saitoh Masato, Hideji Kawakami, and Seiji Nishiyama, Experimental Studies on Non-Linear Response of Soil-Pile-Structure Systems Subjected to Strong Ground Motion. The 14th World Conference on Earthquake Engineering, 2008, pp. 1-8.

[7] Ullah, M. S., Yamamoto, H., Goit, C. S., and Saitoh, M., On the Verification of Superposition Method of Kinematic Interaction and Inertial Interaction in Dynamic Response Analysis of Soil-Pile-Structure Systems. Soil Dynamics and Earthquake Engineering, vol. 113, 2018, pp. 522–533.

[8] Veletsos, A. S., and Meek, J. W., Dynamic Behaviour of Building-Foundation Systems. Earthquake Engineering and Structural Dynamics, Vol. 3, Issue 2, 1974, pp. 121–138.

[9] Bielak, J., Dynamic Behaviour of Structures with Embedded Foundations. Earthquake Engineering and Structural Dynamics, Vol. 3, Issue 3, 1974, pp. 259–274.

[10] Kokusho, T., and Iwatate, T., Scaled Model Tests and Numerical Analyses on Nonlinear Dynamic Response of Soft Grounds. Proceedings of the Japan Society of Civil Engineers, Vol. 1979, Issue 285, 1979, pp. 57–67.

[11] Zafar, U., Goit, C. S., and Saitoh, M., Experimental and Numerical Investigations on Vertical Dynamic Pile-to-Pile Interactions Considering Soil and Interface Nonlinearities. Bulletin of Earthquake Engineering, vol. 20, no. 7, 2022, pp. 1–26.

[12] Shrestha, N. R., Saitoh, M., Goit, C. S., Saha, A. K., and Yokota, R., Frequency- and Intensity-Dependent Impedance Functions of Laterally Loaded Pile Groups in Cohesionless Soil. Soils and Foundations, vol. 63, no. 4, 2023, p. 101340.

[13] Zafar, U., Goit, C. S., Saitoh, M., and Fukuda, R., Vertical Impedance Functions of Pile Groups under Low-to-High Loading Amplitudes: Numerical Simulations and Experimental Validation. Earthquake Engineering and Engineering Vibration, vol. 22, no. 3, 2023, pp. 647–666.

[14] Shrestha, N. R., Saitoh, M., Saha, A. K., and Goit, C. S., Frequency- and Intensity-Dependent Impedance Functions of Laterally Loaded Single Piles in Cohesionless Soil. Soils and Foundations, vol. 61, no. 1, 2021, pp. 129–143.

Copyright © Int. J. of GEOMATE All rights reserved, including making copies, unless permission is obtained from the copyright proprietors.

15th Int. Conf. on Geotechnique, Construction Materials & Environment,
Kyoto, Japan, 11-13 November 2025, ISBN 978-4-909106124 C3051

AN APPLICATION OF ELECTRICAL RESISTIVITY CONFIGURATION AS ELECTRO-OSMOSIS FOR PREFABRICATED VERTICAL DRAINAGE (PVD) ENHANCEMENT USING SANDBOX EXPERIMENT

Khin Phyu Sin[1], Thanapong Lamphoei[2] and Avirut Puttiwongrak[3]

[1]Doctoral Student, Geotechnical and Earth Resources Engineering, School of Engineering and Technology, Asian Institute of Technology, Pathumthani, 12120 Thailand
[2]Master Student, Geotechnical and Earth Resources Engineering, School of Engineering and Technology, Asian Institute of Technology, Pathumthani, 12120 Thailand
[3]Assistant Professor, Geotechnical and Earth Resources Engineering, School of Engineering and Technology, Asian Institute of Technology, Pathumthani, 12120 Thailand

ABSTRACT

Prefabricated Vertical Drains (PVDs) have long been utilized for ground improvement, with electro-osmosis (EO) emerging as a potential enhancement method. While laboratory-scale studies have demonstrated promising results, the practical implementation of EO-enhanced PVDs in field conditions remains a challenge. This study aims to bridge the gap between laboratory experiments and field applications by employing a sandbox experiment to downscale PVD fieldwork. The electrode configuration was designed based on electrical resistivity survey concepts, allowing for a more realistic simulation of field conditions. The research compared conventional PVD performance with that of PVD incorporated with EO, focusing on settlement rates and water drainage volumes. Results unequivocally demonstrate that the integration of EO significantly accelerates settlement rates and enhances water drainage efficiency. These findings provide valuable insights into the potential benefits of EO-enhanced PVDs in real-world applications. Furthermore, this study offers a methodological framework for upscaling experiments towards full-scale field implementation, potentially leading to substantial time and cost savings in PVD ground improvement projects. The outcomes of this research contribute to the advancement of geotechnical engineering practices and pave the way for more efficient and cost-effective ground improvement techniques in the future.

Keywords: Prefabricated vertical drainage (PVD), Electro-osmosis, Sandbox experiment, Electrical resistivity configuration, Ground improvement

INTRODUCTION

A variety of ground improvement techniques have been utilized in conjunction with conventional prefabricated vertical drains (PVD) to enhance soil consolidation and stability. These methods include preloading with PVD installation, vacuum preloading, and vacuum consolidation. Despite their widespread use, certain techniques present limitations that can make them impractical for specific field conditions. For instance, in some project sites, the availability of filling material may be constrained, leading to significant delays in project timelines and additional expenses associated with transportation and placement [1]. In such cases, vacuum preloading (VP) is often favored as a more cost-effective and time-efficient alternative to conventional surcharge preloading. This is particularly true in coastal and reclaimed areas where sourcing and transporting large volumes of filling material may be logistically challenging and financially prohibitive. Nevertheless, the effectiveness of VP is largely dependent on the subsurface conditions. In locations characterized by highly permeable soil layers—such as sand or sandy clays, the efficiency of the vacuum system can be compromised due to the difficulty in maintaining an airtight seal. As a result, supplementary construction measures, such as the installation of cut-off walls extending into deeper impermeable strata, become necessary to minimize air leakage and preserve suction. These additional engineering interventions significantly increase the overall complexity and cost of the project [2]. Furthermore, variations in atmospheric pressure play a crucial role in vacuum system performance. In practice, vacuum pressures applied in the field typically range between 60 and 80 kPa, imposing a physical limitation on its effectiveness [3].

Given these constraints, electro-osmosis (EO) has emerged as an alternative technique for ground improvement, particularly in applications requiring accelerated dewatering of soft clay soils. This method, which leverages the movement of water through soil under the influence of an electrical field, has demonstrated its potential to enhance soil

consolidation while mitigating several issues associated with traditional ground improvement approaches. EO has the unique ability to not only expedite the removal of pore water but also improve soil strength characteristics through electrochemical effects. In some cases, EO can be further optimized to achieve near-zero hydraulic flow in fine-grained soils, offering substantial advantages in challenging ground conditions [4]. Moreover, it facilitates the strength development by generally diminishing sensitivity [5].

When properly applied, EO-driven consolidation results in flow rates that are 100–1000 times higher than those achieved through conventional hydraulic gradient effects, owing to the electro-osmotic permeability coefficient (k_e) being significantly greater than hydraulic permeability (k_h) [4]. Studies have estimated that the electro-osmotic permeability coefficient for most soil types is approximately 5.0×10^{-9} m²/V.sec, demonstrating its applicability for treating soft or problematic soils. Additionally, EO employs electrode-based conversion techniques that can permanently alter soil properties, reducing sensitivity, while improving overall soil integrity. The result is a more uniform improvement effect, which can be beneficial for large-scale construction projects involving soft ground conditions [6].

Despite the advantages associated with EO, its practical implementation in soft ground improvement projects is accompanied by several technical challenges. Notable issues include the formation of cracks near the anode due to localized drying effects, temperature fluctuations that can impact system efficiency, pH imbalances at the electrode terminals, and electrode corrosion, which can diminish soil-electrode contact and reduce overall effectiveness. These factors can contribute to operational inefficiencies, limiting EO's broader adoption in field applications. Additionally, high energy consumption and material degradation have been identified as significant drawbacks that constrain EO's feasibility for large-scale ground improvement efforts. Given these challenges, this study does not examine EO's electrochemical mechanisms in detail but instead focuses on evaluating its effectiveness in enhancing water discharge when combined with prefabricated vertical drains (PVD) and vacuum preloading. The primary objective is to determine whether EO can facilitate faster drainage by promoting pore water migration and sustaining vacuum efficiency over extended periods. Preloading is incorporated into the methodology to improve soil-electrode interaction and reduce uneven settlement, thereby enhancing the overall performance of the EO–VP integration. The research specifically compares the effectiveness of sequential and simultaneous EO–VP applications relative to conventional PVD setups, with the goal of assessing whether the combined approach improves water removal efficiency and soil stabilization under soft ground conditions.

MATERIALS AND METHODS

Sample Collections and Properties Testing

Samples are collected at a depth of 3 to 4 m from Asian Institute of Technology (AIT) campus for the experiments. Undisturbed samples are collected according to ASTM D1587-09 and disturbed samples used for reconstituting the soil inside the Sandbox are collected by using backhoe. Properties testing such as natural moisture content (ω), specific gravity (G_s), and Atterberg limits, etc., are carried out before commencing any test. Hydrometer analysis and sieve analysis tests are carried on soft clay and sand used as preloading. In addition, pH, along with Electrical Conductivity (EC), are measured (Table 1).

Table 1. Properties of Bangkok soft clay

Properties	Value
Water content, ω (%)	54.56
Liquid Limit, LL	94.6
Plastic Limit, PL	23.62
Specific gravity, G_s	2.72
Soil type	CH
pH	6.8
Electrical conductivity, EC (S/m)	0.2205
Salinity (mg/l)	1.4112
Resistivity, ρ (Ω.m)	4.535

Sample Preparation

Samples are prepared by adding water amount which makes moisture content to become 1.5 times its liquid limit. Before commencing the test, clay samples are soaked with that water amount for two weeks in order to easy when it stir with the mixer. Once the soil slurry is properly mixed, it is passed through a nylon mesh to separate unwanted materials such as organic matter, unmixed clay clumps, and other solid impurities. The prepared soil samples are carefully placed into the container box and total height reaches 30 cm. Once the soil has been fully placed, a geomembrane layer is applied on top to cover and protect the soil. This geomembrane serves as a protective barrier and is further loaded with a sand layer. The sand layer not only provides surcharge loading but also serves as a stable benchmark for the settlement plate, ensuring accurate monitoring of soil settlement during experimentation as shown in Fig. 1.

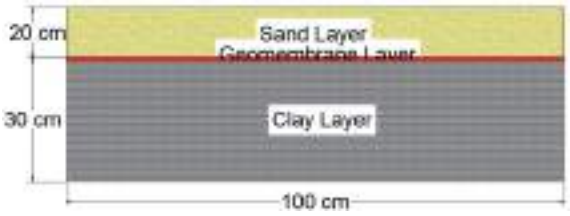

Fig. 1 Placement of geomembrane layer between the clay and sand in the sandbox model

Equipment Installations

PVD installation

PVDs are inserted in a rectangular pattern and are sealed totally with the rubber membrane at joint with top caps end to create a tightly sealed environment for the application of vacuum pressure. The PVDs are installed from the bottom of the box, considering the bottom layer as an impervious boundary, and allowing for one way drainage in the vertical direction. These drains are extended up to the top of the geomembrane layer (i.e., 30 cm in height), minimizing the risk of heaving or disturbances in the sand blanket during vacuum assisted experimentation. Spacing between each PVDs are 40 cm and 30 cm from the corner as can be seen in Fig. 2.

Vacuum system installation

The vacuum system comprised of: (1) vacuum machine for generating suction to suck out water from the PVDs; (2) air-water separation system to prevents excess water going into the vacuum pump and separate extracted air from the water to be sure vacuum system operates efficiently; (3) water container sitting on the balance to measure collected discharged water amount throughout the testing time; and (4) pipes and valve attached at every PVD to allow controlled suction while ensuring an even and efficient drainage system as shown in Fig. 3.

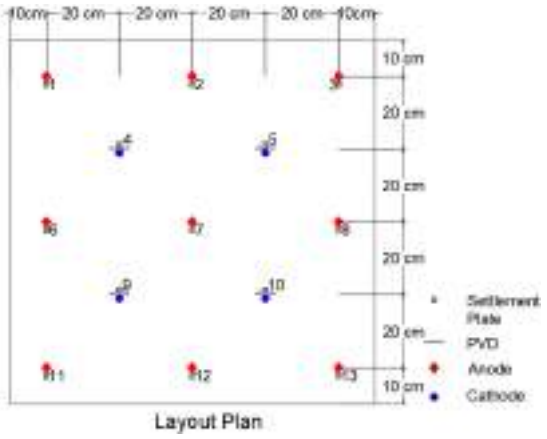

Fig. 2 Layout plan of PVD, electrodes and settlement plate

Fig. 3 Vacuum system used in this study

Electrical apparatus installation

Stainless steel rods, each with a length of 30 cm, are selected as electrodes due to their excellent corrosion resistance and high conductivity. Each electrode is systematically divided into three functional sections: (1) the embedded portion (5 cm), which is inserted directly into the clay layer to establish electrokinetic contact with the soil; (2) the middle section (20 cm), which pass through the sand blanket and is encased within a PVC pipe to prevent electrical leakage and current interference into and with the sand layer; and (3) the external portion (5 cm), which is extended above the surface and is connected to a clipper for power transmission. The installation configuration for a single electrode is illustrated on Fig. 4. The electrical current is supplied by two direct current (DC) power units, which are specifically calibrated to provide controlled voltage and current levels necessary for the resistivity and electro-osmotic tests. A total of thirteen stainless steel electrodes are installed following the Wenner array configuration, comprising four cathodes and nine anodes (Fig. 2). This arrangement is carefully designed to optimize current distribution across the testing area, facilitate uniform electro-osmotic flow throughout the consolidation process.

Fig. 4 Electrode installation and connection at location No.3

Measurement instrument installation

Firstly, as can be seen in Fig. 5, the settlement plate is specifically designed to measure vertical soil deformation. It comprises a square steel base plate with dimensions of 10 × 10 × 0.5 cm, along with a

two-part rod assembly: a 5 cm steel rod base for anchoring and a 70 cm vertical wooden rod. The wooden rod is chosen due to its nonconductive and corrosion-resistant properties, ensuring that it would not interfere with the electrical field during electro-osmotic (EO) treatment. To secure the rods, epoxy is used after drilling into the wooden base, and each rod is carefully aligned with a bull's eye level to maintain vertical positioning. Reference marks are placed near the top of the rods to facilitate settlement measurements related to the sand blanket surface. Vacuum pressure is monitored using a vacuum gauge installed on the vacuum pump, while water collection is tracked with a container placed on a balance. During and after the EO treatment, pH levels and electrical conductivity (EC) are measured using a portable pH/EC meter. Voltage and current within the EO system are recorded using a digital multimeter, which is connected to various electrode pairs—particularly between selected anodes and the central cathode (e.g., No. 4 to 1, 4 to 2, 4 to 6, and 4 to 7 as mentioned in Fig. 2)—to measure voltage (V) and current (A). These readings are utilized to check current distribution throughout the test.

Fig. 5 Measurement instruments

Testing Procedures

The methodology is divided into several key stages to systematically observe the soil's response to each treatment condition. The sequence began with self-weight consolidation (Self-Settlement), which served as the baseline to measure natural consolidation without any external forces. This is followed by mechanical preloading, using a sand blanket to simulate traditional surcharge induced consolidation. Next, vacuum preloading is applied by integrating a negative pressure system through PVDs, aiming to accelerate pore water dissipation. Finally, EO is introduced, both as a standalone and combined method with vacuum preloading, to examine the synergistic effects of electrokinetic water migration under electrical fields.

Firstly, Self-Settlement is designed to simulate the natural primary consolidation that occurs due to the soil's inherent overburden stress and gravitational forces, without any artificial intervention. The objective is to observe soil behavior over a 14-day period under natural conditions and determine whether self-weight alone could contribute to the consolidation process. By analyzing settlement behavior and water discharge patterns recorded during this initial phase and comparing them with results from later methods, the effectiveness of each treatment could be quantitatively assessed.

Secondly, the preloading stage is conducted to simulate construction-induced surface loading. In this phase, a uniform sand layer is placed over the prepared clay surface to apply surcharge pressure, promoting additional consolidation. The objective is to assess whether mechanical loading alone, without vacuum pressure or electrokinetic enhancement, could effectively induce settlement and facilitate water movement through installed drainage pathways. To closely replicate field conditions, PVDs are installed in the clay layer before applying the surcharge, allowing for the evaluation of natural pore water dissipation through the PVDs without external load. A geomembrane is placed between the clay and the sand blanket to prevent water infiltration, ensuring that settlement resulted solely from surcharge pressure.

Thirdly, following the preloading experiment, a new sandbox is prepared to conduct the vacuum preloading test, ensuring the elimination of residual effects and allowing for independent observation of vacuum-induced consolidation. The test box is filled with reconstituted Bangkok soft clay, following identical procedures from previous stages to maintain consistency in sample preparation. Settlement plates are installed during clay placement to enable precise monitoring of vertical deformation from the outset, ensuring the impact of vacuum pressure is recorded from the initial application phase. Since these plates are embedded within the reconstituted soil, continuous tracking is possible without disrupting the soil structure. In this phase, PVDs are connected to a vacuum system to induce negative pore water pressure and accelerate consolidation. Unlike the earlier stage, where PVDs are passive, they now actively facilitate vacuum-driven water flow. To create a sealed environment, a geomembrane is placed over the soil surface and securely fastened to prevent air leakage. A sand blanket is then positioned above the membrane to ensure uniform vacuum distribution and function as both a sealing and load transfer layer.

The final experimental phase is integrated electro-osmosis (EO) with vacuum preloading (VP) to assess their combined impact on the consolidation behavior of Bangkok soft clay. This approach aims to enhance water removal by leveraging both vacuum suction and electrokinetic flow, particularly in low-permeability zones where vacuum alone may be insufficient. In this setup, PVDs function as cathodes for the EO system while simultaneously

serving as drainage channels for vacuum suction. Stainless steel anodes are placed around the sandbox perimeter to facilitate electric current flow through the saturated clay (Fig. 2). A DC power supply and a vacuum pump are operated simultaneously to induce electro-osmotic water migration and negative pore pressure. This phase is designed to optimize pore water extraction efficiency while evaluating settlement uniformity, consolidation rate, and energy performance under dual treatment conditions.

Data Analysis

During the experiments, surface settlement is tracked using settlement plates installed during the placement of the reconstituted clay. Displacement readings are recorded at regular time intervals. The data is plotted as settlement vs. time graphs, which are used to evaluate the consolidation rate for each treatment method. Asaoka's method is used to predict the degree of consolidation. Water discharged from the system is collected in designated containers from each PVD outlet. The cumulative discharge is plotted and compare across all methods to determine which technique facilitates the most efficient removal of pore water. For tests involving vacuum preloading, pressure readings are taken using digital vacuum gauges installed at various points along the vacuum line. This data is used to evaluate the consistency of vacuum pressure applications, detect leaks, and correlate pressure stability with settlement response and water discharge trends. Electrical filed distribution and power consumption are also measured. After finishing the tests, soil samples are taken from three different depths: top, middle, and bottom layers to determine final water content distribution, pH and EC inside the soil. This allowed for the evaluation of how effectively each method reduces moisture content across the soil profile.

RESULTS AND DISCUSSIONS

This section presents the results of a series of laboratory scale experiments conducted to evaluate the consolidation behavior of Bangkok soft clay under various ground improvement techniques. This study focuses on three primary configurations: natural Self-Settlement (baseline), preloading with PVDs, and vacuum preloading with and without the integration of EO stimulation. The experimental program is categorized into three test series: T-1a (vacuum preloading only), T-1b (vacuum preloading followed by EO activation), and T-2 (simultaneous application of vacuum preloading and EO). Settlement progression and water discharge volumes were systematically recorded throughout each testing phase to assess the soil's response under varying drainage and loading conditions.

Observed Settlement and Water Drainage during the Performance of Self-Settlement and Preloading Experiment

During the self-weight consolidation phase, the soil is allowed to naturally settle under its own overburden stress without additional loading, drainage systems, or sealing membranes. The exposed clay surface facilitates moisture evaporation and drainage; however, no significant settlement is observed during the testing period (Figs. 6-7). This outcome highlights the low permeability of Bangkok soft clay and suggests that gravitational forces alone are inadequate to induce consolidation by overcoming internal pore pressure.

In the preloading phase, a uniform sand blanket is placed over the clay layer to simulate construction-induced surface loading. PVDs are installed to provide vertical drainage, but no vacuum or electrokinetic forces are applied. However, as indicated in Figs. 6-7, the increase in settlement is minimal, merely no settlement and water discharge remained very low. The PVDs, lacking vacuum assistance, proved ineffective under these low-pressure conditions.

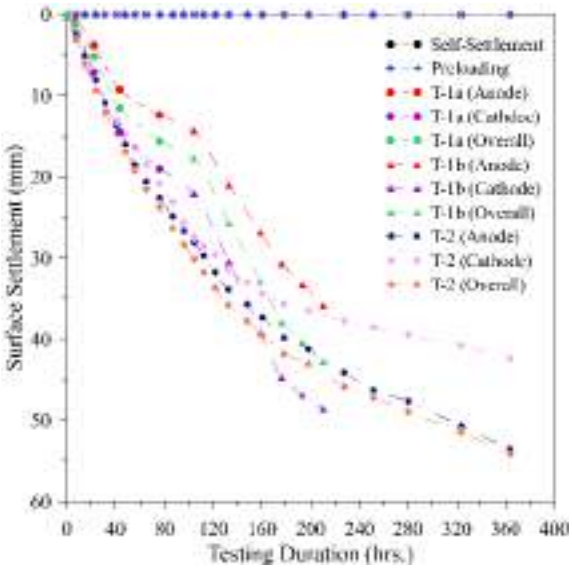

Fig. 6 Measured surface settlement from all testing conditions

Observed Settlement and Water Drainage during the Performance of Vacuum Preloading Experiment

In T-1a, surface settlement coming from vacuum preloading significantly outperformed Self-Settlement and Preloading methods at around 15.63 mm, 12.39 mm, and 19 mm in overall, at anode side and cathode side when it stops as can be seen in Fig. 6. T-1a is ended when the collected discharged water amount is lower than 10 ml for two consecutive

hours and the represented degree of consolidation estimated using Asaoka method when it ends is 66.3104%.

Throughout the vacuum preloading process, pressure readings are continuously monitored at both the vacuum pump and the water collection outlet. In the early stage of the test from 0 to 43.36-hour, high negative pressure values are maintained at around 58.44 kPa and overall settlement rate is 0.27 mm/hrs. (Fig. 8), corresponding to 6000 cm^3 of cumulative discharged water (Fig. 7).

However, as the experiment progressed, vacuum pressure reduces to 23 kPa between 43.36 to 76 hours of testing duration, particularly at the collection container, indicating a reduction in suction efficiency (Fig. 8). Thus, the vacuum preloading experiment demonstrates a strong initial response in both settlement and water discharge, confirming its effectiveness in accelerating primary consolidation in Bangkok soft clay. However, as pore water is progressively removed and the clay structure becomes denser, the efficiency of vacuum preloading declines.

This is evident from the steady decrease in settlement rate and collected cumulative discharged water amount between 43.36 to 76 hours of testing duration (Fig. 8). These findings suggest that vacuum preloading is most effective during the early consolidation phase when the soil contains substantial free water and the pressure differential is at its highest. Beyond this stage, further improvement becomes increasingly limited, as vacuum suction alone cannot easily extract tightly bound pore water from deeper or less permeable zones. Although vacuum preloading significantly outperformed self-weight and surcharge methods, its efficiency remains constrained by time and soil permeability.

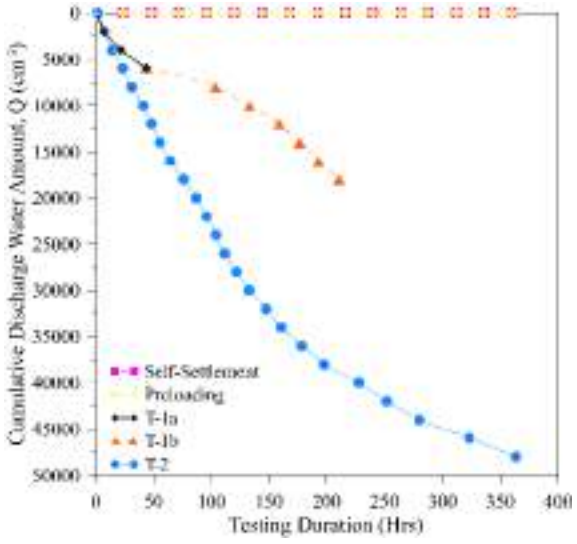

Fig. 7 Cumulative discharged water amount

Observed Settlement and Water Drainage during the Performance of EO Combined Vacuum Preloading Experiment

In Test Series T-1b, EO is applied after the vacuum preloading phase plateaued at approximately 76 hours (Fig. 6 and 7) to evaluate its effectiveness in reactivating and extending consolidation. As can be seen in Fig. 6 and 8, settlements gradually increased from 76 to 104.11 hours and sharply increased beyond it to till the end of the test especially near the cathode, corresponding to 42.8 mm in overall, 35.85 mm at anode, and 48.6 mm at cathode, respectively, which is 2.7 times higher than T-1a. Similarly, the overall settlement rate gradually decreases from 0.21 to 0.17 mm/hrs. within 76 to 104.11 hours of testing duration, and it increased back to 0.21 mm/hrs. up to 193.04 hours of testing duration and stop at 0.2 mm/hrs. when the test ends. Interestingly, the degree of consolidation measured using Asaoka method when the test ends is 27.079%, meaning that if the test is continued, the settlement would be higher than the present observed values and application of EO is pronouncedly effective even application when the vacuum pressure is very low.

Thus, this secondary response confirms that EO reinitiated consolidation by mobilizing additional pore water from deeper or previously unresponsive zones. The settlement behavior observed in test series T-1b indicates a noticeable reactivation of the consolidation process. Additionally, water discharge, which has diminished during the final vacuum treatment stage, shows a resurgence, with EO-induced cumulative discharge increased back from 6000 to 18,000 cm^3 (Fig. 7). This confirms EO successfully restored water flow via electrokinetic migration, particularly in low-permeability regions where vacuum pressure alone is insufficient.

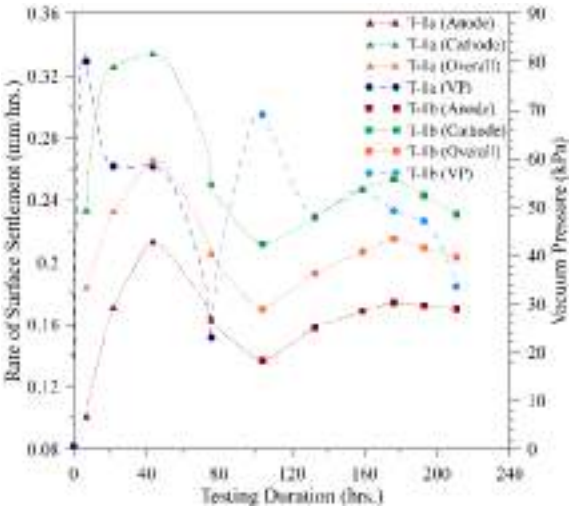

Fig. 8 Rate of surface settlement and effective vacuum pressure from T-1

Observed Settlement and Water Drainage under the Continuous Application of EO Combined Vacuum Preloading Experiment

In the test series T-2, EO treatment is implemented concurrently with vacuum preloading from the outset of the experiment to evaluate the effectiveness of a fully integrated system in expediting the consolidation process. From the beginning, the combined effects of vacuum-induced suction and electrokinetic flow facilitated a substantial outflow of pore water. During the initial phase (0–76 hours), the discharge volume consistently exceeded 2000 cm^3 per day, reaching peaks of over 3000 cm^3 at certain intervals, thus it becomes over 18,000 cm^3 in cumulative discharged amount, which is approximately 2.5 times higher than the amount from T-1a (i.e., approximately 7000 cm^3) as illustrated in Fig. 7. This increase in outflow is indicative of the enhanced drainage capacity achieved through the simultaneous activation of hydraulic and electrical gradients, enabling the rapid expulsion of free water from the low-permeability clay matrix.

As the experiment progressed into the stabilization phase (76–210 hours), discharge volumes remained relatively high, ranging between approximately 1,000 and 2000 cm^3 per day and thus, collected cumulative discharged water amount of 40,000 cm^3, approximately 2.2 times greater than T-1b (i.e., 18,000 cm^3). This consistency demonstrates the system's ability to sustain continuous pore pressure dissipation and mitigate the onset of drainage decline. In the later phase (beyond 210 hours), water discharge gradually decreased; however, the recorded values remain significantly higher than those observed in standalone vacuum. Even during the final intervals, discharge volumes frequently exceeded 535 cm^3 per day, underscoring the prolonged effectiveness of the combined EO and vacuum system.

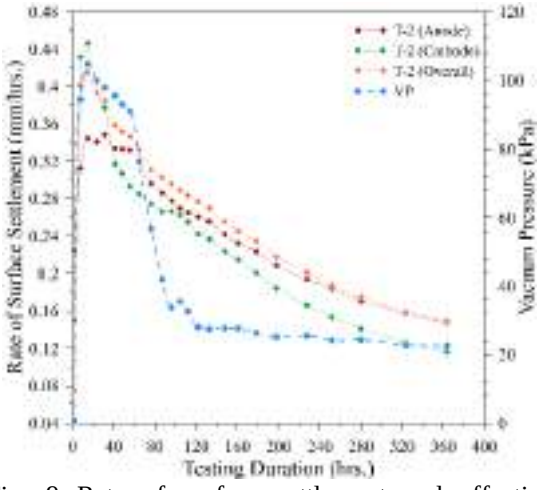

Fig. 9 Rate of surface settlement and effective vacuum pressure from T-2

From a quantitative perspective, the overall settlement rate during the early phase peaked (0 to 76 hours) at around 0.27 to 0.43 mm per hour, a substantially greater value than those recorded in the T-1a and T-1b configurations. This high settlement rate highlights the system's capability to swiftly reduce void ratios within the clay structure, leading to a measurable and efficient volumetric change. As the experiment progressed into the mid-to-late phases (76–210 hours), settlement rate steadily decreases, generally ranging from 0.17 to 0.31 mm per hour. Furthermore, effective vacuum levels remained consistently above 90 kPa in the early hours (up to 56 hours) and reduce from 90 to 25 kPa between 56–225 hours and remain stable at 25 kPa during later stages (Fig. 9). This can be due to the reduction in pore water availability within the soil. However, the absence of a settlement plateau, sustained water discharge, and consistent vacuum pressure collectively confirm that the simultaneous application of EO and vacuum preloading not only accelerates initial consolidation but also ensures long-term effectiveness. These results establish this configuration as the most efficient and robust among those tested.

Furthermore, the degree of consolidation estimated by using Asaoka method when the test ends is 91.18% corresponding to 59.134 mm which is not much different from the measured settlement amount such as 54.21 mm in overall, 53.52 mm at anode, and 42.34 mm at cathode side.

Changes in Moisture Content, pH and EC

During the experiment, it is observed that EO induced notable changes in the moisture content, and chemical properties of Bangkok soft clay, particularly in pH and EC. To evaluate the persistence of these effects, moisture content, pH and EC measurements are taken immediately after the tests and again one week after EO deactivation.

Moisture content has decreased from 146.28% (i.e., 1.5 times LL) to 122.35 after T-1a. It is reduced to 105.4% on the anode side, 103.58% between anode and cathode, and 90.91% at cathode side in T-1b. In addition, it is reduced to 89.24% at the anode side, 89.47% between anode and the cathode, and 77.96% at the cathode side in T-2. Interestingly, it can be seen that the reduction in moisture content near the cathode side is higher than anode and middle, which can be due to the suction pressure coming from PVD closet to the cathode side.

In T-1b (EO after vacuum preloading), the pH near the anode dropped to values as low as 4.86–5.10, while the cathode zone maintained slightly higher pH values between 6.83–7.05, reflecting the localized acidification and alkalization effects of electrolysis. In Test Series T-2 (simultaneous EO + VP), the pH values were even lower, with the anode

zone reaching 3.11–3.49 and the cathode ranging from 4.50–4.85, confirming stronger electrochemical gradients under prolonged electrical loading. Remarkably, one week after EO deactivation, the pH values remained stable (anode: 3.33–3.49; cathode: 4.15–4.55), indicating that EO does not cause rapid chemical to rebound and that the system has reached a steady state condition during treatment. Electrical conductivity also exhibits significant changes. After EO treatment in T-1b, EC values at the cathode drop to 0.52–0.69 mS/cm, while in T-2, EC is even lower, particularly at the cathode, where values fell to 0.06–0.08 mS/cm. These reductions suggest ion migration and accumulation at targeted zones, consistent with electrokinetic transport mechanisms. Notably, EC values remain low one week after EO shutoff, particularly in the cathode zone of T-2 (0.07 mS/cm), confirming the lasting electrochemical impact of EO treatment.

CONCLUSION

This study systematically analyzes two electrokinetic ground improvement methods for Bangkok soft clay: (1) sequential self-settlement followed by vacuum preloading and electro-osmosis (EO), and (2) simultaneous activation of EO and vacuum preloading (VP). Both approaches are tested under identical laboratory conditions to assess their effectiveness in accelerating consolidation, enhancing pore water discharge, and maintaining vacuum efficiency.

The results show that the simultaneous EO-VP system performs better in all key aspects. With 363 hours of testing time, T-2 achieved 91% degree of consolidation. Settlements in T-2 exceeded 53 mm, while in T-1a and T-1b record as approximately 15.63 mm and 42 mm in overall settlement, respectively. Water discharge from T-2 is 2.5 times higher than T-1a and T-1b. Although the settlement rate from T-2 is higher than T-1a and T-1b from 0 to 76 hours of testing time and lower than T-1b from 76 to 210 hours of testing time, the discharged water coming from T-2 is still higher than T-1a and T-1b.

These findings confirm that integrating EO from the beginning improves pore pressure dissipation, accelerates consolidation, and enhances drainage through electrokinetic migration. This combined mechanism increases consolidation efficiency while ensuring more uniform and deeper soil improvement in low-permeability conditions. Further research through large-scale field trials, economic assessments, and long-term monitoring is recommended to validate feasibility, optimize cost-effectiveness, and address electrode performance challenges.

ACKNOWLEDGMENTS

Please note that this will be double-blind submission. The author's identities will be removed before sending them to reviewers. The authors will not know who the reviewers are. Try to follow the reference style below. Some references from the International Journal of GEOMATE would be appreciated. The benefit will be returned to all authors by increasing the journal's impact factor.

REFERENCES

1. Han, J. (2015). Principles and practice of ground improvement. John Wiley & Sons.
2. Chai, J., & Carter, J. P. (2011). Deformation analysis in soft ground improvement (Vol. 18). Springer Science & Business Media.
3. Bergado, D. T., Chai, J. C., Miura, N., & Balasubramaniam, A. S. (1998). PVD improvement of soft Bangkok clay with combined vacuum and reduced sand embankment preloading. Geotechnical Engineering, 29(1). https://www.cofra.sk/files/documents/technicke_spravy/vacuumbangkok.pdf
4. Jones, C. J., Lamont-Black, J., & Glendinning, S. (2011). Electrokinetic geosynthetics in hydraulic applications. Geotextiles and Geomembranes, 29(4), 381-390. https://doi.org/10.1016/j.geotexmem.2010.11.011
5. Terzaghi, K., Peck, R. B., & Mesri, G. (1996). Soil mechanics in engineering practice. John wiley & sons. https://doi.org/10.1007/978-3-642-41714-6_195275
6. Lo, K. Y., & Ho, K. S. (1991). The effects of electroosmotic field treatment on the soil properties of a soft sensitive clay. Canadian Geotechnical Journal, 28(6), 763–770. https://doi.org/10.1139/t91-093

Copyright © Int. J. of GEOMATE All rights reserved, including making copies, unless permission is obtained from the copyright proprietors.

15th Int. Conf. on Geotechnique, Construction Materials & Environment,
Kyoto, Japan, 11-13 November 2025, ISBN 978-4-909106124 C3051

EVALUATION OF VISCOSITY REDUCTION USING ADVANCED AGENT IN HIGH-PRESSURED GROUT INJECTION FOR BANGKOK SOILS

Sai Wunna Kyaw Khaung[1], Morris I-Min Wang[1,2], Ricky K. N. Wong[3], Yasuharu Nakanishi[4], Koike Shoko[5], and Matsuda Takato[5]

[1] Geotechnical and Earth Resources Engineering, Asian Institute of Technology, Thailand
[2] ISEKI Engineering Co., Ltd., Taiwan; [3] SANSHIN Corporation, Taiwan
[4] N.I.T., Inc., Japan; [5] Flowric Co., Ltd., Japan

ABSTRACT

The construction of the MRT Purple Line extension in Bangkok faces challenges due to deep, cohesive soils, primarily composed of stiff clay and sand layers. These conditions necessitate the use of ground improvement techniques to ensure the stability and safety of the infrastructure. Jet grouting, a common ground improvement method, is hindered in cohesive soils due to the increased viscosity of the sludge. This study investigates the application of chemical admixtures, specifically FAJ-20 (Naphthalene sulfonic acid type) and HPX-50 (Naphthalene sulfonic acid polycarboxylic acid type), named "Admion," to reduce viscosity and improve the effectiveness of jet grouting. Laboratory and field tests were conducted to assess the impact of different admixture concentrations on grout flowability and compressive strength in two soil types: Bangkok 2nd sand and Bangkok 2nd stiff clay. The results indicate that while the admixtures in Bangkok show promise, they did not fully achieve the same level of success as those observed in Japan. Comparisons with additional tests conducted in Japan, which tested similar admixtures, suggest that differences in chemical composition and admixture concentrations may account for these variations. Despite the differences, the comparison highlights the potential of chemical admixtures in overcoming challenges posed by cohesive soils. While the Bangkok results show some success, they also underscore areas for further improvement. This comparison provides valuable insights for future ground improvement efforts, particularly in refining the applicability of jet grouting methods with chemical admixtures in stiff cohesive soils and sand layers.

Keywords: Ground improvement, Jet grouting, Chemical Admixtures, Viscosity Reduction.

INTRODUCTION

The MRT Purple Line extension in Bangkok encounters challenges from deep, cohesive soils, mainly consisting of stiff clay and sand layers, necessitating the use of specialized ground improvement techniques. Jet grouting, a common method for these conditions, injects high-pressure grout to form solid columns [1, 2, 11]. However, in cohesive soils, the high viscosity of the discharged sludge hampers effectiveness, leading to operational inefficiencies, clogging, and less-than-ideal results. Pre-jetting with high-pressure water or enlarging the guide hole diameter can help release air and mud [3], while additional water may assist in managing the sludge.

To address these challenges, the use of chemical admixtures has gained attention as a promising solution. These admixtures, when added to the grout mixture, can reduce the viscosity of the discharged sludge, improving the flowability of the grout and ensuring more efficient jet grouting operations. The application of these chemical agents is particularly beneficial in Bangkok's unique soil conditions, where traditional jet grouting methods often struggle to achieve optimal results.

Two chemical admixtures named "Admion" were selected in the study. Laboratory and field tests were conducted to assess the impact of the chemical admixtures with various concentrations on grout flowability and compressive strength in two soil types: Bangkok 2nd sand and Bangkok 2nd stiff clay obtained from the MRT Purple Line project site.

For comparison purposes, additional testing using a chemical admixture named "GEOSPER" was conducted in Japan. Furthermore, a similar admixture, primarily composed of a polycarboxylic acid polymer, was tested in Japan [5]. The results of the laboratory and field tests obtained in this study were compared to those laboratory test results obtained in Japan. The findings of the comparison offer valuable insights into enhancing jet grouting techniques in challenging soil conditions, particularly in Bangkok's cohesive soils.

CHEMICAL ADMIXTURES USED IN THE STUDY

This study investigated the application of Admion chemical admixtures, specifically FAJ-20 and HPX-50, to improve the workability, flowability, and strength of cement-based materials. Admixtures

enhance concrete properties by reducing the water-to-cement ratio, preventing the weakening of strength caused by excessive water. They facilitate easier mixing with less water, improve flowability through air entrainment, and enhance workability by creating fine bubbles in the cement paste. High-molecular-weight surfactants in these admixtures help maintain fluidity and dispersibility during mixing. The properties of the two admixtures used in this study are provided in Table 1.

Table 1 Properties of the admixtures used in this study

Items	FAJ-20	HPX-50
Main ingredient	Naphthalenesulfonic acid type	Naphthalenesulfonic acid Polycarboxylic acid type
Property	Powder	Powder
Color	Yellowish brown	Yellowish brown
pH	7.0 - 9.0	7.0 - 9.0
Specific gravity	0.6 - 0.7	0.6 - 0.7

LABORATORY TESTING

Laboratory tests were conducted on two soil samples including Bangkok 2nd sand and Bangkok 2nd stiff clay. The samples were collected from the IVS-02 intervention shaft of the MRT Purple Line construction in Bangkok, from depths over 50 meters. Water from the Chao Phraya River was used to replicate the chemical and physical characteristics of field water conditions. The laboratory testing including flowability tests and unconfined compression tests was conducted, and the results of the testing are provided in the following sections.

Grout and Soil Properties

The Rapid Jet Grouting System was used in the construction of jet-grouted columns for the MRT Purple Line extension project [12, 13]. The properties of the jet grouting materials used in the large-diameter jet grouting technique are provided in Tables 2 and 3 in accordance with the construction specifications of the project. Table 4 indicates the basic soil properties of the sand and clay samples collected from the project site [4].

Table 2 Standard mix proportion of grout slurry

Material	Standard propotion (per 1 m^3)	
Ordinary cement	650 kg	207 L
Water	793 L	793 L
Total	1443 kg	1000 L

Table 3 Construction specifications of the large-diameter jet grouting technique

Type	R1
Diameter	2.5 m
Quantity of improved soil	4.91 m^3/m
Grouting flow	0.18 m^3/min
Lift rate	12 min/m
Quantity of hardening material	2.16 m^3/m

Table 4 Typical properties of Bangkok's soil from Sarkar et al. (2022) [4]

Soil Type	Unit Weight	Water content	SPT
	(kN/m^3)	(%)	
2nd stiff clay	19-22	11-21	20-80
2nd sand	21-22	13-16	>50

Sample Preparation

In the sample preparation phase, grout mixtures were prepared to represent spoil discharge during jet grouting, following the Japanese Geotechnical Society Standard (JGS 0821-2009) [6] to ensure consistency. Soil, grout, and chemical admixture were mixed in specific proportions to assess the effect of varying concentrations of the viscosity-reducing agent. Four admixture concentrations including 0% (no admixture), 0.3%, 0.5%, and 1.0% were used in the study.

METHODOLOGIES FOR LABORATORY TESTS

Flowability Tests

Bangkok 2nd Sand

The P-Funnel test, following JSCE-F 521-1994 [7], was used to measure the flowability of the Bangkok 2nd sand samples by recording the time taken for the sludge to flow out of the funnel. A shorter flow time indicates better flowability, which is crucial for efficient grouting. The bleeding test, following ASTM C940-2010 [8], assessed water separation from the mixture over time, impacting the grouting's performance and durability.

Bangkok 2nd Stiff Clay

Due to low natural water content, the grout mixture of the Bangkok 2nd stiff clay was too stiff to work with. To address this, additional water was added to the samples until workable consistency was achieved. The aim was to simulate field conditions and allow effective use of chemical admixtures. The table flow test, following JHS A313-1999 [9], was used to measure flowability by tracking flow length in two directions. The flow value was measured at

one-hour intervals, with 200 mm considered the standard for proper slurry handling.

Unconfined Compression Tests

The Unconfined Compressive Strength (UCS) test, following ASTM D2166 [10], measured the compressive strength of the grout mixtures at 7 and 28 days. Three samples were tested for each curing period, and the average UCS value was used to assess strength development.

RESULTS OF LABORATORY TESTS

Results of the flowability tests

Bangkok 2nd sand

Figure 1 illustrates the flowability test results for the Bangkok 2nd sand samples, showing the relationship between admixture concentration and flow time. The results demonstrate that both FAJ-20 and HPX-50 significantly reduce the viscosity of the grout-soil mixture, improving flowability during the jet grouting process. Without admixture, the baseline test showed a high average flow time of 27.4 seconds, indicating poor flowability.

Figure 1 also indicates that FAJ-20 reduced the viscosity as its concentration increased, with higher concentrations resulting in shorter flow times and improved discharge efficiency. HPX-50 also reduced viscosity effectively, outperforming FAJ-20 at comparable concentrations, suggesting it may be more efficient at lower doses in enhancing grout flow and jet grouting operations.

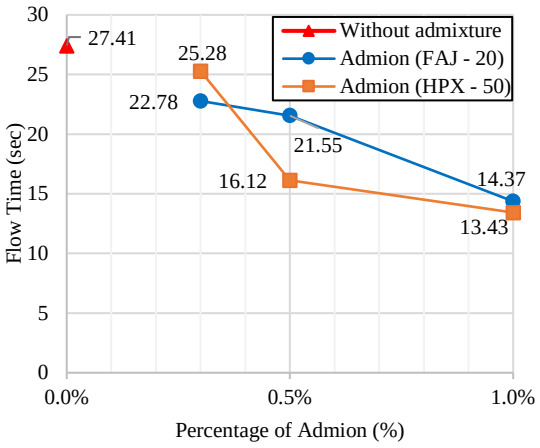

Fig. 1 Results of flowability tests for Bangkok 2nd sand with FAJ-20 and HPX-50 in the laboratory

Bangkok 2nd Stiff Clay

Table 5 shows the results of the table flow tests for the Bangkok 2nd stiff clay samples. Figure 2 illustrates the measurements of the table flow tests. Figures 3 and 4 show the results of the flowability tests for the Bangkok 2nd stiff clay samples with FAJ-20 and HPX-50, respectively. Figure 3 indicates that the addition of FAJ-20 improved grout flowability, with higher concentrations resulting in better flow. At 1.0%, the flow value met the target, while at 0.0%, no flow occurred after 1 hour. Flowability decreased after 2-3 hours, emphasizing the importance of timely application during field operations.

Table 5 Results of table flow test (laboratory)

Amount of Admixture (%)		Flow Status		
		Elapsed time from mixing (hours)		
		0 hr	1 hr	2 hrs
w/o ad.	0.0	148 × 152 150	-	-
FAJ-20	0.3	160 × 160 160	-	-
	0.5	158 × 158 158	-	-
	1.0	200 × 202 201	104 × 104 104	104 × 106 105
HPX-50	0.3	180 × 180 180	118 × 122 120	114 × 114 114
	0.5	188 × 186 187	108 × 106 107	96 × 100 98
	1.0	198 × 200 199	110 × 114 112	96 × 104 100

Note: The 'a × b' values represent the flow length values on both sides of the spread grout sample, with the value in parentheses indicating the average length value.

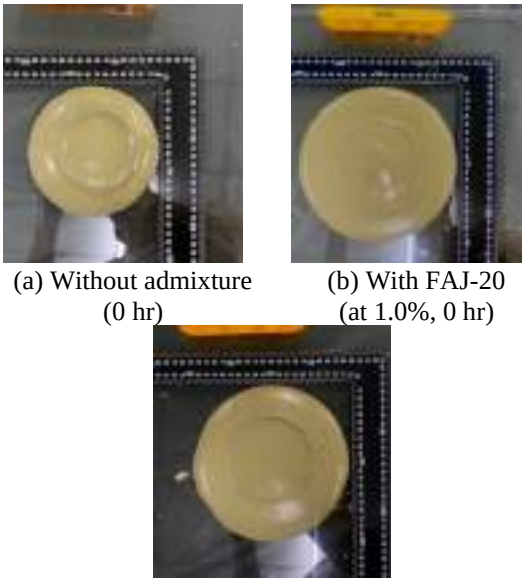

(a) Without admixture (0 hr)

(b) With FAJ-20 (at 1.0%, 0 hr)

(c) With HPX-50 (at 1.0%, 0 hr)

Fig. 2 Results of table flow test measurements

Figure 4 shows that HPX-50 also improved flowability, with higher concentrations yielding better flow. At 1.0%, the flow value reached the

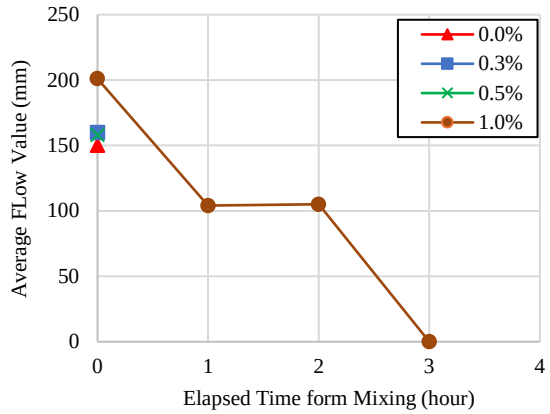

Fig. 3 Results of flowability tests for Bangkok 2nd stiff clay with FAJ-20 in the laboratory

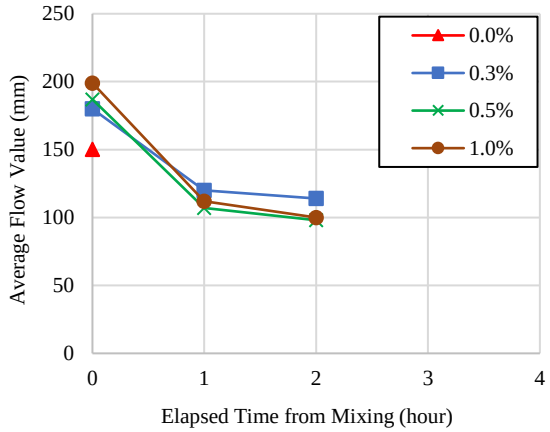

Fig. 4 Results of flowability tests for Bangkok 2nd stiff clay with HPX-50 in the laboratory

target, ensuring better workability. Similar to FAJ-20, flowability decreased after 2 hours, particularly at lower concentrations, highlighting the importance of careful timing.

Results of unconfined compressive strength

Bangkok 2nd sand

Figure 5 shows the results of the unconfined compressive strength (UCS) tests for the Bangkok 2nd sand samples with FAJ-20 and HPX-50, respectively. Figure 5 indicates that both with and without admixtures, the observed values fell short of the lab target strength of 6,000 kPa, based on a 3,000 kPa field target strength, suggesting a need for further investigation into the factors behind the lower UCS values. Despite this, the comparison of admixtures provides valuable insights into their effects on grout strength.

Figure 5 also indicates that for FAJ-20, the 0.3% concentration slightly improved or left the strength unchanged, but higher concentrations resulted in a decrease in compressive strength. In contrast, HPX-50 showed a slight decrease at 0.3%, but higher concentrations improved UCS, indicating that HPX-50 enhances grout strength at higher concentrations.

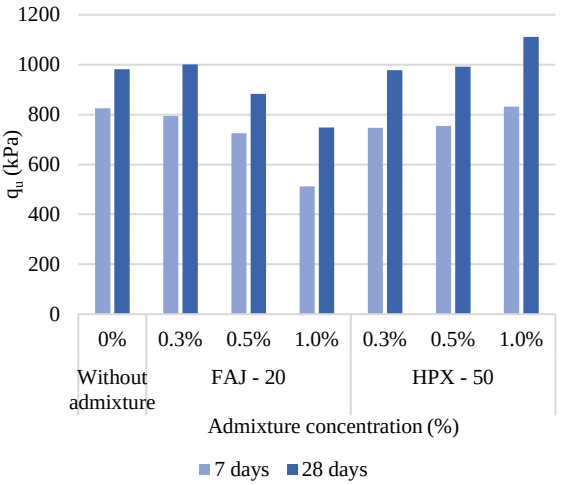

Fig. 5 UCS Results for Bangkok 2nd sand with FAJ-20 and HPX-50 (7 & 28 Days) in the laboratory

Bangkok 2nd stiff clay

The results of the UCS tests for the Bangkok 2nd stiff clay samples with FAJ-20 and HPX-50, respectively, are presented in Figure 6. Figure 6 shows variations in strength based on admixture type and concentration. Figure 6 shows that FAJ-20 enhanced strength with increasing concentration, reaching the target at 0.5% and 1.0%. For HPX-50, the UCS exceeded the target at 0.3%, with notable improvement at 0.5%, indicating its effectiveness at moderate concentrations.

Figure 6 also shows that grout samples with the admixture met the required lab target strength of 2,000 kPa (based on 1,000 kPa field target strength), whereas the grout samples without the admixture fell below the required strength. It is also important to note that less water was used when admixtures were added, yet the flowability improved, demonstrating that the admixtures helped make the mix easier to work with without compromising its quality.

FIELD TESTING

Field tests were also conducted on two soil samples, including Bangkok 2nd sand and Bangkok 2nd stiff clay, to compare the laboratory findings with real-world performance, allowing for an assessment of how well the laboratory-optimized admixture dosage translates to site conditions. In the field testing, the 1% admixture concentration, which was identified in the laboratory experiments as yielding

the best performance, was selected to validate its effectiveness under actual construction conditions. The field tests involved evaluating sludge viscosity immediately after jet grouting and performing unconfined compressive strength (UCS) tests on the grout columns after 28 days of curing.

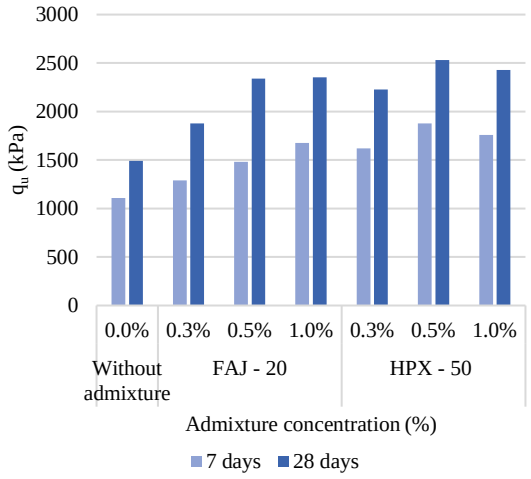

Fig. 6 UCS Results for Bangkok 2nd stiff clay with FAJ-20 and HPX-50 (7 & 28 Days) in the laboratory

Results of the flowability tests

Bangkok 2nd sand

Figure 7 illustrates the results of the flowability tests conducted in the field for the Bangkok 2nd sand samples with and without admixtures. The flowability results for the sludge, shown in Figure 7, were averaged from multiple tests conducted across different grouting holes. As shown in Figure 7, no significant difference in flowability was observed between the untreated and admixture-treated samples. It is expected that water content variations, due to the precutting process, naturally lower sludge viscosity, overlapping with the effect of the admixtures in the field. This complicates distinguishing the impact of the admixtures on viscosity reduction, as shown in Figure 7.

Bangkok 2nd stiff clay

Figure 8 illustrates the results of the flowability tests conducted in the field for the Bangkok 2nd stiff clay samples with and without admixtures. Figure 8 shows that both FAJ-20 and HPX-50 significantly improved flowability. The mixture without admixture had an initial flow value of 162 mm, while FAJ-20 increased it to 351.7 mm and HPX-50 to 335.5 mm, with FAJ-20 showing the highest flow.

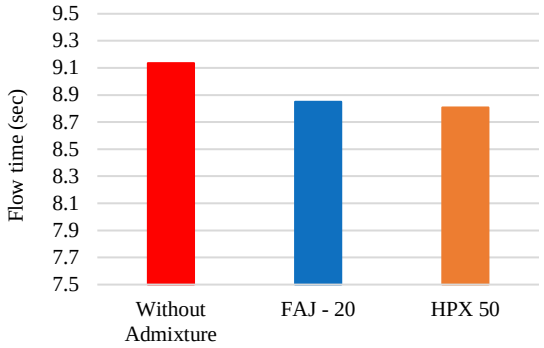

Fig. 7 Flowability test results for Bangkok 2nd sand with and without admixtures in the field

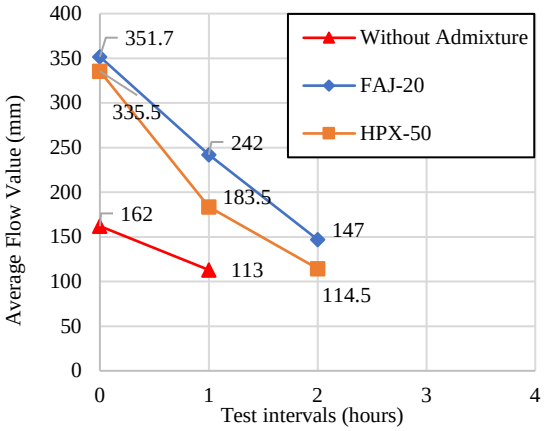

Fig. 8 Average Flow Value Over Time for Bangkok 2nd stiff clay with FAJ-20 and HPX-50 in the field

Results of unconfined compressive strength

Bangkok 2nd sand

The UCS test results for field samples taken from jet-grouted columns in the sand layer showed that the untreated sample reached 6,330 kPa and the FAJ-20 treated sample achieved 3,295 kPa. Due to limited sample availability, only one sample from each column was tested. Nevertheless, all samples, including those with admixtures, exceeded the target design strength, confirming that both untreated and admixture-treated grout met the required strength.

Bangkok 2nd stiff clay

The UCS test at the IVS-01 site yielded 4,760 kPa from a core sample taken from the intersection of three different types of grout columns: those without admixture, those with FAJ-20, and those with HPX-50. Despite limited core samples, the result exceeded the required strength target, confirming that the admixture-treated grout surpassed the target design strength.

COMPARISON WITH PREVIOUS STUDY IN JAPAN

Additional testing using a chemical admixture named "GEOSPER" was conducted in Japan. Furthermore, a similar admixture, primarily composed of a polycarboxylic acid polymer, was tested in Japan by Shimano et al. (2023) [5]. The soils tested in Japan were classified as clay. The results of these tests were compared to those obtained in Bangkok. The comparison of the test results provides a valuable benchmark for interpreting outcomes in Bangkok.

Flowability Performance

Figure 9 shows the flowability test results for the Bangkok and Japan samples with different admixture types and contents. Figure 9 indicates that the use of admixtures significantly improved the flowability of grout-sludge mixtures. In the Bangkok tests, the target flow value of 200 mm was achieved at 1.0% concentration of both FAJ-20 and HPX-50. However, it is important to note that additional water was introduced to the Bangkok stiff clay samples during laboratory preparation to reach a workable consistency, due to their initially low natural water content (11 – 21%). This adjustment aimed to better simulate field conditions. In contrast, Shimano et al. (2023) achieved flow values of approximately 250 mm at 2.0% admixture concentration using untreated Japanese clay with a much higher natural water content (62.1%) [5]. Additional flowability tests were conducted on cohesive soil samples mixed with 1% and 2% of "Japan (GEOSPER)" at a natural water content of 38%. The results are presented in Figure 9. As shown in Figure 9, the flow values of the samples were approximately 200 mm. The test results showed that high fluidity was maintained even after 1 hour. It was found that differences in the type of admixture not only increased the initial fluidity, but also made a difference in fluidity retention. The difference in required dosage may reflect not only the chemical composition of the admixtures but also the variations in baseline moisture, plasticity, and cohesion of the respective soils.

Strength Characteristics

Regarding unconfined compressive strength (UCS), both studies observed that the use of admixtures resulted in a slight reduction in compressive strength compared to untreated samples. Shimano et al. found that strength decreased by approximately 20 – 38% with increasing admixture content, although values still met the minimum design requirement of 1,000 kPa [5]. The same tendency was observed in "Japan (GEOSPER)". Similarly, in the Bangkok laboratory tests, UCS values declined with higher concentrations of FAJ-20, while HPX-50 demonstrated improved strength at 1.0%. In the field, the FAJ-20-treated grout sample in Bangkok achieved the UCS value of 3,295 kPa, exceeding the Japanese field average value of 2,100 kPa. This notable difference may result from soil heterogeneity, differences in grouting technique (such as precutting), and curing conditions during field operations.

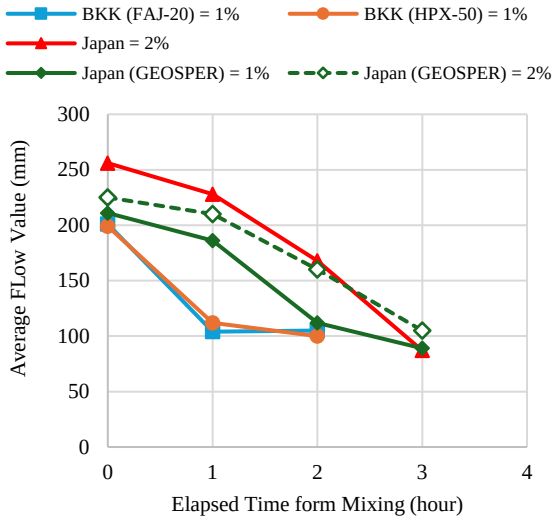

Fig. 9 Results of flowability tests for Bangkok and Japan samples with different admixture types and contents.

Differences in Admixture Composition

Another key distinction lies in the chemical composition of the admixtures used. Shimano et al.'s admixture [5] and "Japan (GEOSPER)" employed a yellow-brown liquid admixture composed purely of polycarboxylic acid polymer. In contrast, this study used FAJ-20, a powder-type naphthalenesulfonic acid-based agent, and HPX-50, a hybrid powder admixture containing both polycarboxylic and naphthalenesulfonic acid components, as shown in Table 1. These compositional differences may influence the rate of dispersion, mixing efficiency, and interaction with cement hydration. Notably, previous studies have shown that polycarboxylic acid superplasticizers exhibit stronger dispersion capacity and higher fluidity retention than naphthalene-based

types, due to their greater reduction in shear yield stress and more effective steric hindrance action [14]. The combined chemical structure of HPX-50, may have contributed to its UCS performance and flowability retention in the Bangkok soils.

These findings reinforce the importance of site-specific calibration when applying viscosity-reducing agents. While both studies confirm the potential of chemical admixtures to improve jet grouting in cohesive soils, variations in soil properties, admixture formulation, and field procedures significantly influence the optimal dosage and resulting performance.

CONCLUSIONS

This study demonstrated the effectiveness of chemical admixtures, particularly FAJ-20 and HPX-50, in enhancing jet grouting efficiency in Bangkok's second stiff clay and sand layers. Laboratory tests demonstrated that both admixtures significantly improved flowability, particularly at 1.0% concentration, with HPX-50. In terms of strength, the HPX-50 also showed better performance at higher concentrations. Despite the improvements, the UCS values for both without and with admixtures in the lab remained below the target strength in sand, suggesting that other factors such as curing conditions, soil-grout interaction, or mixing quality may need to be investigated.

Field testing validated the laboratory findings but also highlighted key differences due to uncontrolled variables such as soil heterogeneity, moisture variation from precutting, and field mixing conditions. In sand, flowability differences between treated and untreated samples were minimal, while in stiff clay, both admixtures yielded significantly higher flow values.

A comparative analysis, including additional admixture testing and a previous study in Japan, reveals that variations in soil properties, natural moisture content, and admixture composition and formulations contribute to differences in performance.

Overall, the findings confirm that chemical admixtures, particularly HPX-50, can significantly enhance grout flowability and contribute to strength development in cohesive soils. The results also underscore the importance of site-specific calibration, careful admixture selection, and the need for further research into optimal dosage levels and long-term performance. This study offers valuable guidance for enhancing jet grouting practices in complex urban geotechnical environments, such as Bangkok.

REFERENCES

[1] Burke, G. K. Jet Grouting Systems: Advantages and Disadvantages. GeoSupport Conference. 2004, pp. 1-6.

[2] Burke, G. K. The State of the Art of Jet Grouting in the United States. Deep Foundations Institute. Jun. 2002.

[3] Cheng, S. H., Chao, K. C., Wong, R. K. N., and Wang, M. I-Min. Control of Jet Grouting Process Induced Ground Displacement in Clayey Soil. Transportation Geotechnics, vol. 40, May 2023, doi: 10.1016/j.trgeo.2023.100983, pp. 1-4.

[4] Sarkar, P., Chao, K. C., Wong, R. K. N., and Wang, M. I-Min. Evaluation of Index Properties Affecting Unconfined Compressive Strength of Jet-Grouted Soil Columns for Bangkok Soils. International Conference on Deep Foundations and Ground Improvement. 2022, pp. 4.

[5] Shimano, A., Chao, K. C., Wong, R., Ju, L. M., and Nakanishi, Y. Effect of Viscosity-Reducing Agent on Spoil Displacement in Jet Grouting. The 21st Southeast Asian Geotechnical Conference and 4th AGSSEA Conference. 2023.

[6] Japanese Geotechnical Society (JGS), JGS 0821-2009: Method for Preparation of Soil-Cement Specimen by Kneading in Laboratory. Tokyo, Japan: JGS, 2009.

[7] Japan Society of Civil Engineers (JSCE), JSCE-F 521-1994: Method of Test for Unconfined Compression Strength of Solidified Soil. Tokyo, Japan: JSCE, 1994.

[8] ASTM International, ASTM C940-10: Standard Test Method for Expansion and Bleeding of Freshly Mixed Grouts for Preplaced-Aggregate Concrete in the Laboratory. West Conshohocken, PA, USA: ASTM International, 2010.

[9] Japan Housing and Wood Technology Center (JHS), JHS A313-1999: Method of Test for Flow of Cement Grout. Tokyo, Japan: JHS, 1999.

[10] ASTM International, ASTM D2166/D2166M-13: Standard Test Method for Unconfined Compressive Strength of Cohesive Soil. West Conshohocken, PA, USA: ASTM International, 2013.

[11] Shakya, S., Inazumi, S., Chao, K. C., and Wong, R. K. N. Innovative Design Method of Jet Grouting Systems for Sustainable Ground Improvements. Sustainability. Vol. 16, Issue 6. 2023.

[12] Silva, N., Chao, K. C., Wong, R. K. N., Iwakubo, T., Cheng, S. H. Evaluation of Large Diameter Jet Grouted Columns Using Acoustic Monitoring System for Bangkok Soils. International Symposium on Evolving Jet Grouting Technology. 2020.

[13] Yamazaki, J., Chao, K. C., Wong, R. K. N., and Wang, M. I. M. Development of the Jet Grouting Method: Evolutionary History, Mechanism Insights, Innovative Approaches, and Future Prospects. Geotechnical Engineering Journal of the SEAGS & AGSSEA. Vol 55, Issue 1, 2024.

[14] Koizumi, K., Umemura, Y., and Tsuyuki, N. Effects of Chemical Admixtures on the Silicate Structure of Hydrated Portland Cement. Proceedings of the 12th International Congress on the Chemistry of Cement (ICCC), 2007.

Copyright © Int. J. of GEOMATE All rights reserved, including making copies, unless permission is obtained from the copyright proprietors.

15th Int. Conf. on Geotechnique, Construction Materials & Environment,
Kyoto, Japan, 11-13 November 2025, ISBN 978-4-909106124 C3051

EXCAVATION TESTS ON ALUMINUM ROD MODEL GROUND TO SIMULATE GROUND HEAVE

Moe Yagawa[1], Hidetoshi Nishioka[2], Shinji Konishi[3] and Satoshi Sakata[4]

[1]Graduate School of Science and Engineering, Chuo University, Japan
[2] Department of Civil and Environmental Engineering, Chuo University, Japan
[3] Asano Taiseikiso Engineering Co., Ltd., Japan
[4] Tokyo Metro Co., Ltd., Japan

ABSTRACT

When performing the open-cut method, ground heave due to excavation may have an impact on existing structures, causing deformation and other effects. Therefore, it is important to predict the effects of ground heave near existing structures and consider countermeasures. However, the interaction between the structure and ground when ground heave occurs is not fully understood, leading to discrepancies between predictions and actual measurements. For this purpose, we analyzed the interaction between the ground and the structure through model experiments. As the first step, an excavation experiment was conducted using an aluminum rod model ground that can reproduce the behavior of sand in two dimensions, to investigate whether ground heave can be reproduced. This model allows image-based analysis to capture displacement and strain distribution near structures. Two earth retaining wall models, each 200 mm high, were placed in the model ground measuring 1000 mm in width and 400 mm in height. Using a ground anchor model, the earth retaining walls were subjected to tension equivalent to the earth pressure at rest. The primary experimental parameter was the distance between the earth retaining walls. The intervening ground was excavated, and images were analyzed to assess the resulting ground behavior. Results confirmed that the aluminum rod model ground could simulate the upward vertical displacement patterns similar to those of the actual ground. These findings provide valuable reference data for future model experiments involving embedded structures such as tunnels.

Keywords: Ground heave, Aluminum rod model, Excavation test, Image analysis

INTRODUCTION

Ground heave refers to the upward movement of the excavation bottom caused by the release of stress in the ground, which occurs because of a reduction in overburden pressure during excavation [1]. When using the open-cut method near existing structures such as tunnels, predicting the effects of ground heave accurately is essential. For this purpose, the interactions between the intervening ground and the structure must be analyzed. However, this interaction during ground heave has not been quantitatively analyzed and no simple method has been established to predict these effects. Therefore, there may be differences between predicted and actual measurements [2].

Therefore, this study was conducted to systematically analyze the interaction between existing structures and the ground during ground heave. As a preparatory experiment, an excavation test was carried out using an aluminum rod model ground. Aluminum rod model ground is one of the experimental techniques used since the 1960s and has been used in various experiments [3-5]. It is known to produce behavior similar to that of medium-dense sand (e.g., nonlinear characteristics of stress–strain relationships and dilatancy characteristics) [6]. This model enables image-based analysis to capture the displacement and strain distribution of the ground around the existing structure.

RESEARCH SIGNIFICANCE

No previous studies have simulated ground heave using an aluminum rod ground model. This experiment enabled us to understand the ground heave characteristics of the aluminum rod model ground. The data provide fundamental information for future excavation experiments around the existing structure. Similar future experiments will contribute to improving the accuracy of predicting the impact of ground heave on existing structures.

EXPERIMENT SUMMARY

Model ground

Fig.1 shows the aluminum rod model ground, and Fig.2 illustrates the experimental apparatus used in this study. The model ground was constructed using three types of aluminum rods with diameters of 1.5 mm, 2 mm, and 3 mm in equal weight proportions (1:1:1). The overall dimensions of the model ground were 1000 mm in width and 400 mm in height.

Fig.1 Aluminum rods

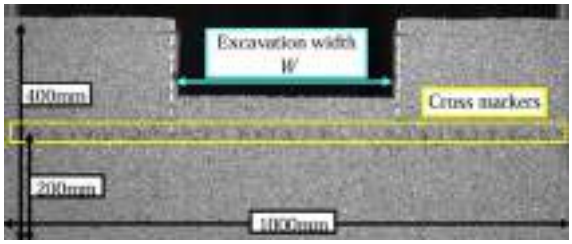

(a) Overall

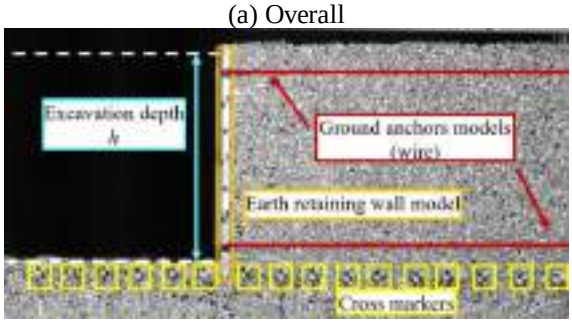

(b) Around the earth retaining wall on the right side

Fig.2 Experimental apparatus

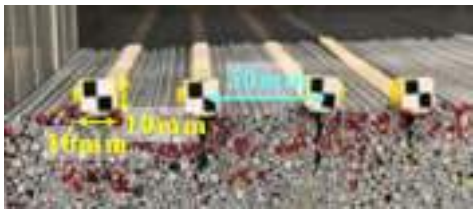

Fig.3 Cross markers

Construction involved layering 50 mm thick segments of aluminum rods and compacting each layer using a small vibrator. The unit volume weight was 21.5 kN/m^3.

When the model ground was constructed to a height of 200 mm (half the total height), a level was used to ensure the surface was parallel to the base. Cross markers were placed at intervals of 30 mm (Fig.3) for later use in image analysis. These markers consisted of cross-pattern blocks affixed to a wooden board (1 mm thick, 7 mm wide, and 160 mm long). Two aluminum retaining wall models (6 mm thick, 200 mm high, and 150 mm deep) were installed vertically at locations where the distance between

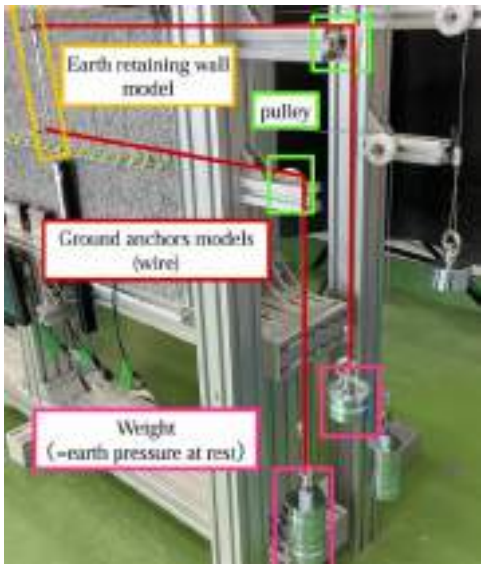

Fig.4 Attached wires and weights

them (excavation width, *W*) was either 400 mm or 250 mm (corresponding to positions 300 mm or 375 mm from both ends of the model ground). The remaining 200 mm height was then constructed using the same compaction method.

As illustrated in Fig.4, a wire simulating a ground anchor was connected to the top and bottom ends of each retaining wall. Weight equivalents to the static earth pressure at rest were attached to the ends of the wires. Since the deformation of the retaining wall was not the main objective of this study, static earth pressure was used to minimize the variation from experiment to experiment. These weights were suspended via pulleys to apply tensile force externally to the experimental apparatus.

Testing methods

Excavation of the ground model was performed as shown in Fig.5. The initial (pre-excavation) overburden was 200 mm. Excavation was conducted in incremental steps, with the thickness of each step decreasing progressively as the excavation depth increased. A laser level was used to project the target depth for each excavation step, serving as a guide for pushing the aluminum rod from the front to back of

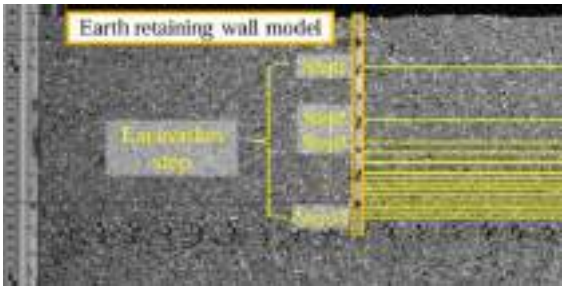

Fig.5 Excavation steps

Fig.6 Excavation of aluminum rods

the model (Fig. 6). After each excavation, the weight of the excavated aluminum rod was measured and photographed using a digital camera (L4000 pixel, W6000 pixel, 0.2 mm/pixel) to capture the entire experimental apparatus. These operations were repeated until the excavation depth *h* reached 190 mm, leaving a 10 mm overburden directly above the cross makers. Each test was repeated thrice for excavation widths *W* of 400 and 250 mm, respectively.

EXPERIMENTAL RESULTS

Displacement distribution of model ground

Image analysis (Digital Image Correlation method with Ditect's DippStrain software) was used to obtain the vertical and horizontal displacement distribution at a depth of *h* = 190 mm (after excavation was completed). The results are presented in Fig.7–Fig.10.

Fig.7 and Fig.8 show displacement distributions within a range of ±1.0 mm. Fig.7(a) and Fig.8(a)

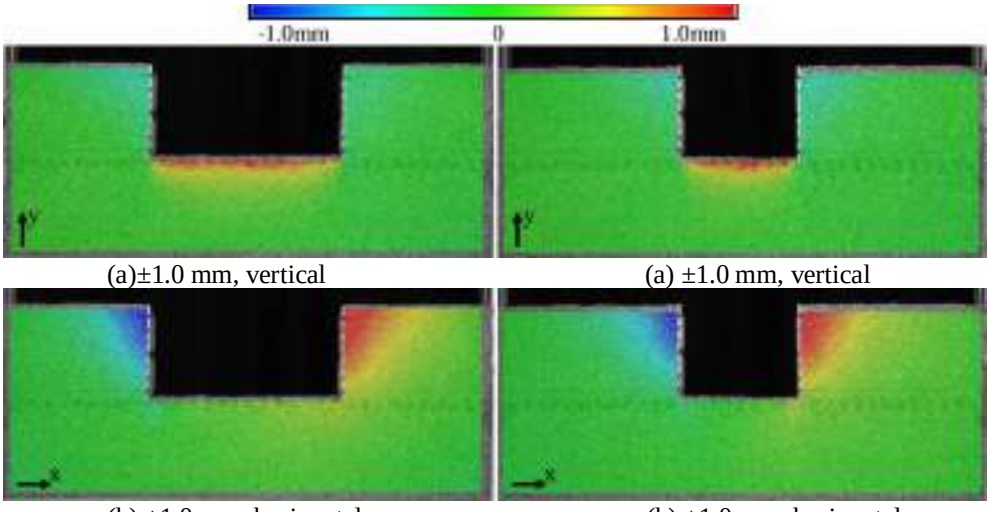

(a)±1.0 mm, vertical (a) ±1.0 mm, vertical

(b) ±1.0 mm, horizontal (b) ±1.0 mm, horizontal

Fig.7 Displacement distribution (*W* = 400 mm) Fig.8 Displacement distribution (*W* = 250 mm)

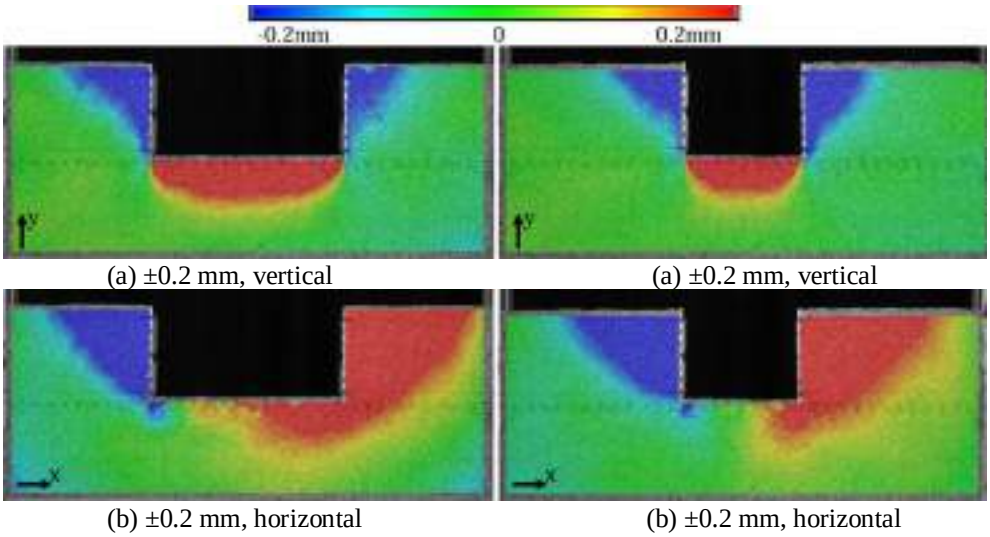

(a) ±0.2 mm, vertical (a) ±0.2 mm, vertical

(b) ±0.2 mm, horizontal (b) ±0.2 mm, horizontal

Fig.9 Displacement distribution (*W* = 400 mm) Fig.10 Displacement distribution (*W* = 250 mm)

depict significant vertical displacements concentrated within a relatively narrow zone inside the retaining walls. This confirms the occurrence of ground heave in the model ground. Fig.7(b) and Fig.8(b) illustrate the horizontal displacement of the ground behind the retaining walls in the active pressure direction.

Fig.9 and Fig.10 show displacement distributions within a narrower range of ±0.2 mm. These figures reveal upward vertical displacement occurring approximately 100 mm below the excavation bottom within the retaining walls, along with horizontal displacements toward the center of the model. Similar displacement distribution results were obtained, regardless of *W*.

Vertical displacement of each cross marker

The distribution of vertical displacement—defined as the ground heave displacement δ_g—at each cross marker was analyzed. The vertical displacement of each cross marker at h = 190 mm (end of excavation) was calculated using image analysis (correlation tracking function of Ditect's Dipp-Motion V software). Note that this result was considered to have an error of approximately 1 pixel (= 0.2 mm). The relationship between δ_g and the distance from the left edge of the model ground is shown in Figure 11 for W = 400 mm and in Figure 12 for W = 250 mm. Each retaining wall was located at the positions indicated by the dotted lines in these figures.

The cross markers, located 300 mm (W = 400 mm) or 625 mm (W = 250 mm) from the left edge, were positioned beneath the retaining wall. As the retaining walls settled during excavation, δ_g near these regions was negative.

By contrast, within the excavation area, the distribution of δ_g appears approximately rectangular, when averaged, as indicated by the orange lines in Fig.11 and Fig.12. This rectangular distribution shape is generally consistent with the prediction of ground displacement by 3-dimensional finite element analysis by Okada et al. [7].

Although the heave displacement at the excavation bottom was not uniform, variations were observed among individual cross markers. Each experiment focused on cross markers within the retaining walls—12 points for W = 400 mm and 6 points for W = 250 mm—excluding any markers located less than 30 mm from the retaining walls. Box plots illustrating the range of variations of δ_g are shown in Fig.11 and Fig.12. Across the three

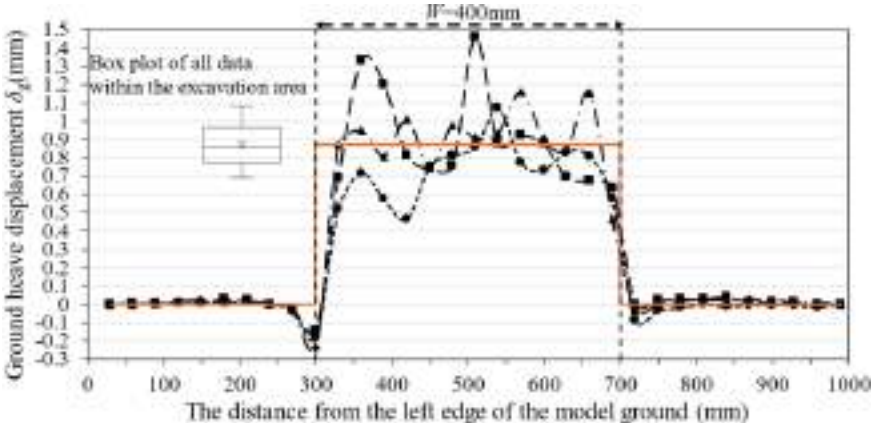

Fig.11 Horizontal distribution of ground heave displacement (W = 400 mm)

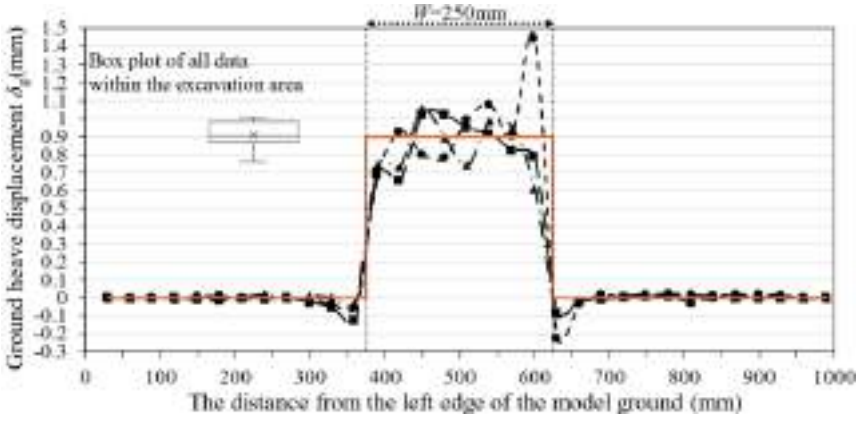

Fig.12 Horizontal distribution of ground heave displacement (W = 250 mm)

experiments, the averaged values were δ_g = 0.87 mm and 0.90 mm for W = 400 mm and 250 mm, respectively. The corresponding coefficients of variation were 12.5 % and 7.5 %. These variations may be attributed to accumulated errors in tracking cross markers during image analysis or to limitations inherent in the experimental method. For instance, removing all aluminum rods horizontally and simultaneously during excavation is not feasible, which may result in a slight localized displacement of the markers. However, when the displacement distributions were averaged, the results demonstrated good reproducibility across the three tests.

Change in amount of ground heave with progress of excavation

Fig.13 presents the results of δ_g at each excavation stage, following the previously described arrangement. The lower horizontal axis of Fig.13 shows the excavation rate, calculated by dividing h by the initial overburden thickness (200 mm). The overburden pressure corresponding to the excavation rate is indicated on the upper horizontal axis. The average axial strain of the lower ground, calculated by dividing δ_g (shown on the left vertical axis) by the height of the ground below its measurement position (200 mm), is shown on the right vertical axis. By considering the heave of the model ground as an increase in axial strain caused by unloading of the lower ground, we observed that the unloading behavior of the model ground is nonlinear elastic.

The aforementioned results confirm that the aluminum rod model ground can reasonably simulate the ground heave phenomena. Further, the usability of image analysis for measuring displacement was established.

However, the mechanism underlying this behavior in the aluminum rod model ground remains unclear, despite the relatively high bending stiffness and near-rigid properties of aluminum. Therefore, the relationship between the ground strain and heave displacement with changing overburden pressure, may differ significantly from that of the actual ground material (Fig.13). Nevertheless, we believe that this model sufficiently simulates ground behavior to meet the objective of this research, which aims to study the interaction between the ground and existing tunnels.

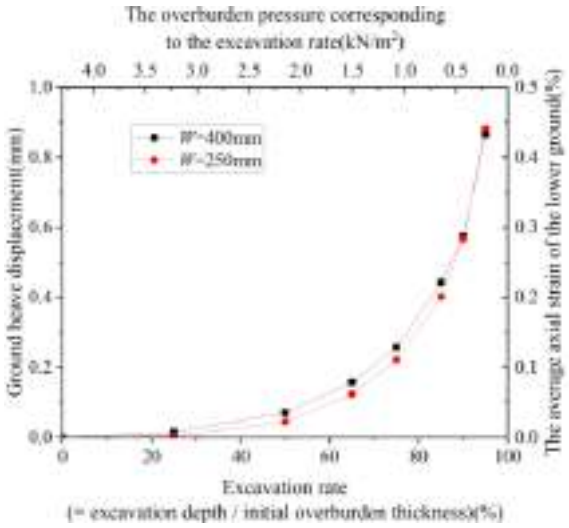

Fig.13 Variation in ground heave displacement according to the stage of excavation

CONCLUSIONS

In this study, excavation tests were conducted using an aluminum rod model.

Consequently, we confirmed that the ground heave could be simulated by combining image analysis with excavation tests using a model ground. Regardless of the excavation width, on average, the distribution shape of the excavation bottom was rectangular, which is consistent with the results of previous studies. Also, the change in the amount of ground heave with the excavation progress was confirmed to be nonlinear elastic.

The results of this study provide reference data for future excavation experiments. Future work will focus on subway tunnels and use the same experimental model to embed a model of an existing tunnel in the longitudinal direction. Subsequently, excavation over it was used to simulate nearby excavation work. The primary experimental parameters will include the excavation width and bending stiffness of the tunnel model. The influence of these factors on the vertical displacement of the tunnel caused by ground heave will be investigated.

ACKNOWLEDGMENTS

We would like to thank Editage (www.editage.jp) for English language editing.

REFERENCES

[1] Japanese Geotechnical Society, Technical terms for geotechnical engineering, Maruzen Publishing, 2006, pp. 331 (in Japanese).

[2] Sakata, S., Nishioka, H., Yagawa, M and Konishi, S., Prediction and analysis of the impact of ground rebound caused by nearby open-cut construction on subway structures in the longitudinal direction and its construction, 31st Proceedings of Jointed Railway Technology, No. 24-45, 2024 (in Japanese).

[3] Nanasato, S., Nishino, F., Nishioka, H and Shimada, T., FE analysis of the influence of sliding on the seismic strain transfer ratio between the ground and cut and cover tunnels in contact with bearing stratum, Japanese Geotechnical Society Special Publication, Vol. 10, No. 20, 2024,

pp. 736-740.
[4] Sagawa, T., Ohata, T and Nishioka, H., 2D Model Tests of Sheet Pile Reinforcement Method for Existing Pile Foundations, Climate Change Adaptation from Geotechnical Perspectives, Springer, 2024, pp. 105-114.
[5] Sasaki, Y and Nishioka, H., VERTICAL LOADING TESTS ON LOCAL SCOURED SPREAD FOUNDATION ON ALUMINUM RODS MODEL GROUND, GEOMATE Journal, Vol. 23, No. 98, 2022, pp. 17-23.
[6] Hirakawa, D., Tanimoto, S., Watanabe, K., Takahashi, H., Nishioka, H and Ito, K., Technique of the preparation for the model ground of physical model test in geotechnics, Geotechnical Engineering Magazine, Vol. 71, No. 11, 2023, pp. 46-59 (in Japanese).
53-
[7] Okada, H., Nakamura, M., Kasai, Y., Kurihara, M and Yamamoto, M., Prediction for behavior of ground heave and existing tunnel due to open cut, Proceedings of the Japan Society of Civil Engineers, Vol. 2004, No. 763/VI-63, 2004, pp.53- 69 (in Japanese).

Copyright © Int. J. of GEOMATE All rights reserved, including making copies, unless permission is obtained from the copyright proprietors.

15th Int. Conf. on Geotechnique, Construction Materials & Environment,
Kyoto, Japan, 11-13 November 2025, ISBN 978-4-909106124 C3051

TWO-DIMENSIONAL MODEL EXPERIMENTS ON THE SEISMIC BEHAVIOUR OF THE HEAD-FIXED DOUBLE SHEET PILE TEMPORARY EARTH RETAINING WALL METHOD

Akihiro Kikuchi[1], Hidetoshi Nishioka[1], Ayaka Nasu[2], Michitaka Okamoto[2] and Hideki Nagatani[2]

[1]Faculty of Science and Engineering, Chuo University, Japan; [2]Kajima Corporation, Japan

ABSTRACT

The head-fixed double sheet pile earth retaining wall method has been developed as a temporary, self-supporting earth retaining wall for excavation work. This method has been proven to reduce horizontal displacement during excavation, which improves economic efficiency and construction productivity. However, the seismic behaviour of this method is not yet fully understood. Therefore, two-dimensional modelling experiments were conducted using an aluminium-rod ground model to reproduce a temporary earth retaining wall under seismic movement after excavation by inclining the soil tank which provides horizontal seismic intensity. The relationships between the horizontal seismic intensity, inclination angle, and the horizontal displacement of the model sheet piles were analysed. Image analysis was also performed with photographs taken during the experiments to investigate the distribution of the strains of the model ground. The results show that the double earth retaining wall method is more resistant than the conventional single earth retaining wall during an earthquake; moreover, it reduces the rotational deformation behaviour at the bottom end of the model sheet pile compared to the single earth retaining wall with a more rigid model sheet pile.

Keywords: Self-supporting earth retaining walls, Aluminium rods, Excavation work, Seismic motion

INTRODUCTION

Earth retaining works involving soldier piles, laggings, or steel sheet piles are often used for underground construction. However, the earth pressure, which is influenced by the surrounding ground, causes horizontal displacements. To reduce the horizontal displacement, earth-retaining supports, such as struts with postpiles and soil nailing, are mainly used. However, struts can obstruct the use of large machinery, and soil nailing requires a large background space for penetration and specialised equipment for installation, resulting in higher costs.

To solve these problems, a head-fixed double-sheet pile earth retaining wall method was developed as a self-supporting temporary earth retaining system [1]. In this method, a pair of steel sheet piles is embedded in parallel, and their heads are rigidly fixed by concrete or welded braces. It is assumed that this method sufficiently reduces the horizontal displacement of earth retaining works during excavation because of the push-pull resistance of the two sheet piles and the resisting effects of the internal soil between the two sheet piles, as shown in Fig.1. Model experiments using X-ray computed tomography (CT) [2] and two-dimensional model experiments using an aluminium rod model ground [3] have confirmed the effectiveness of the double-earth retaining wall method in reducing displacements during excavation, and it has been increasingly used as a self-supporting earth retaining system in relatively shallow open excavations.

According to the Standard Specifications for Tunnelling [4], 'Temporary structures are generally built for a short period and, from an economic point of view, their design does not consider seismic resistance'. The seismic behaviour of the double earth retaining wall method has not been fully clarified. However, the same instruction also states the following: 'In cases where the installation period is particularly long or the structure is located close to an important building, it may be necessary for the structure to be designed while considering seismic safety'. Therefore, in this study, two-dimensional modelling experiments were conducted with an aluminium-rod ground model to reproduce a temporary earth-retaining wall under seismic motion after excavation by inclining the soil tank, resulting in horizontal seismic intensity.

MODEL EXPERIMENT OVERVIEWS

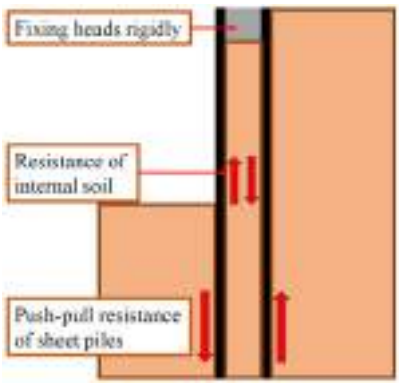

Fig.1 Schematic of the method

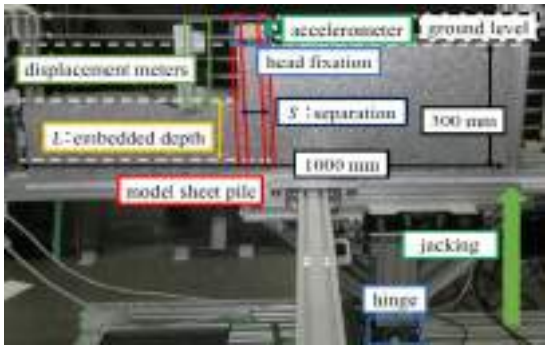

Fig.2 System configuration of the model experiment

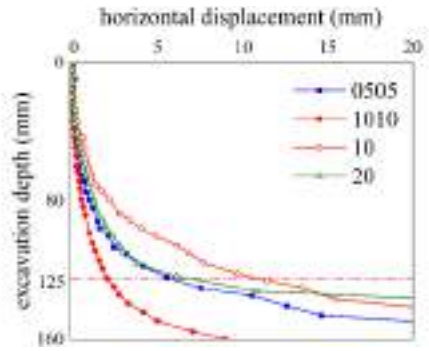

Fig.3 Results of the excavation model experiment

Table 1 Experiment cases

	Case	Thickness of model sheet pile	Separation distance	Embedded depth L	$1/\beta$	βL
Double earth retaining	0505	0.5 mm	50 mm	125 mm	42 mm	2.9
	1010	1.0 mm			77 mm	1.6
Single earth retaining	10	1.0 mm	—		160 mm	0.78
	20	2.0 mm				

Two-dimensional Model Experiment on Model Ground of Aluminium Rods

Aluminium rods were used in this study to simulate the excavation work. Two-dimensional model experiments with aluminium rods have several advantages: the rods themselves are self-supporting, and allow easy observation of displacements and their behaviour in the model ground by moving the aluminium rods; the strength and displacement properties closely resemble those of a medium-density sandy soil; and the grain size characteristics remain constant, which ensures high repeatability of the experiments. Aluminium rods have already been used in two-dimensional model experiments to simulate not only earth retaining work using sheet piles [5] but also spread foundations [6], column foundations [7], pile foundations [8] and box tunnel [9].

Model Ground Preparation

In this study, the model ground was prepared by blending aluminium rods with a length of 150 mm and diameters of 3.0 mm, 2.0 mm, and 1.5 mm in a weight ratio of 1:1:1. Blending was performed in a rigid soil tank with a height of 300 mm, a width of 1,000 mm and a depth of 150 mm. The unit volume weight of the ground model was set at 21.5 kN/m^3.

Thin aluminium plates (Young's modulus E = 70 kN/mm^2) with a height of 300 mm, depth of 200 mm, and an embedded depth of 250 mm were used as model sheet piles. The front model sheet piles for the single- and double-earth retaining works were placed at the centre of the model ground after the foundation ground reached a thickness of 100 mm. To simulate a double earth retaining wall, the rear model sheet piles were manually embedded until they reached a depth of 250 mm at 50 mm head separation after piling up the model ground to 300 mm. To fix the two heads of the sheet piles, acrylic resin blocks were placed between the two model sheet piles and bolted to simulate a rigid bond.

Model experiment procedures and cases

As shown in Fig.2, the equipment used in this model experiment had a pin hinge at the bottom of the apparatus. By raising the right end of the equipment using a jack, the entire soil tank could be inclined to exert a horizontal static acceleration (horizontal seismic intensity, k_h) on the model ground. If the nonlinear response of a large earthquake is predominant, it must be assessed via vibration experiments. However, if the behaviour of the structure is up to the vicinity of yielding, the seismic earth pressure considered by Mononobe and Okabe can be applied [10,11]. Inclining experiments simulate this phenomenon almost directly and correspond to the seismic intensity method commonly used in seismic stability calculations.

Before the soil tank was tilted, the aluminium rods were removed by hand from the left side of the model sheet pile to achieve an excavation depth of

125 mm. The equipment was then jacked up at a rate of 0.40 mm/s and inclined until the front model sheet pile came into contact with the laser displacement meters installed on the side of the excavation face. The horizontal displacement δ_1 of the top of the model sheet pile excluding the protrusion was (the height of the ground surface before excavation) and displacement δ_2 of the model sheet pile at the level of the excavation floor were measured. The rotation angle of the earth retaining head θ was also measured using an accelerometer, and photographs were taken during the experiments for image analysis.

Table 1 lists the experimental cases. Four cases of double and single earth retaining with 0.5 mm, 1.0 mm and 2.0 mm thick model sheet piles were conducted. Fig.3 shows the relationship between the excavation depth and the horizontal displacement obtained from an excavation model experiment in the aluminium rod model ground [3]. The value $1/\beta$, the inverse value of the characteristic value β expressing the relationships between the coefficient of earth pressure and the stiffness of the sheet pile and βL, the product of value β and the penetration length of the model sheet pile L = 125 mm are also given in the table. The characteristic values β for each case apply to a single model sheet pile. To account for real structure parameters, we assumed that βL was equivalent between the prototypes and models [12]. For actual Type III U-shaped steel sheet piles in sandy soil with an N value of 24 [13], the reciprocal $1/\beta$ of the characteristic values β is 1.54 m. When the dimension ratio of the model is 1/20, the value of βL for Type III piles for a penetration depth after excavation L of 2.5 m is 1.62. Therefore, in this study, Case 10 can be interpreted as corresponding to 1/20-scale models of Type III U-shaped steel sheet piles. However, this similarity rule does not account for the perspective of the failure of the model ground. Therefore, test results at the stage when the model ground is close to failure cannot be converted to actual values and should be evaluated relative to each case.

RESULTS AND DISCUSSIONS

Relationships Between Seismic Intensity and Individual Measurement Items

A schematic representation of the experimental setup is shown in Fig.4. The horizontal seismic intensity k_h acting on the model ground was calculated using Eq. (1) based on the inclination angle, ψ, of the model soil tank. In Fig.4, θ shows the inclination angle of the head of the motel sheet pile with respect to the floor and was obtained from the measured values of the accelerometer installed at the head of the model sheet pile.

$$k_h = \tan\psi \tag{1}$$

The relationships of the horizontal seismic intensity k_h, with the inclination angle ξ of the earth retaining wall and the horizontal displacements δ_1 and δ_2 of the model sheet pile are shown in Figs.5-7, and the incremental relationships of the three items are shown in Figs.8-10. The inclination angle ξ refers to the angle of the earth retaining wall relative to the angle of inclination ψ of the model soil tank, as expressed in Eq. (2).

$$\xi = \theta - \psi \tag{2}$$

For double earth retaining, Cases 0505 and 1010 showed close relationships for the inclination angle ξ up to a seismic intensity k_h of approximately 0.17, whereas Case 0505 showed a slightly faster increase afterward (Figs.5,8). As in the excavation experiment (Fig.3), the higher the stiffness of the model sheet pile, the smaller the displacement that occurred after inclination. At k_h = 0.10, the incremental displacements $\Delta\delta_1$ and $\Delta\delta_2$ for Case 0505 (Figs.9,10, respectively) were 3.3 times those for Case 1010. However, for single earth retaining (Cases 10 and 20), Case 20 showed larger displacements than Case 10, which was contrary to the results of the excavation experiment. As the inclination angle ξ in Fig.5 suggests, Case 20 collapsed at k_h = 0.13, which was faster than that of Case 10, which collapsed at k_h = 0.18.

Next, Cases 10 and 1010 were compared, whose model sheet piles had the same stiffness. The increase in inclination angle ξ with increasing horizontal seismic intensity k_h is approximately parallel and the same for both Case 10 and Case 1010. In addition, two points with horizontal seismic intensity k_h can be observed where the earth retaining has a large inclination angle ξ. For Case 10 earth retaining, large tilts occurred at k_h = 0.15 and 0.17, and for Case 1010 at k_h = 0.16 and 0.18. The increase in horizontal displacement δ_1 with increasing horizontal seismic

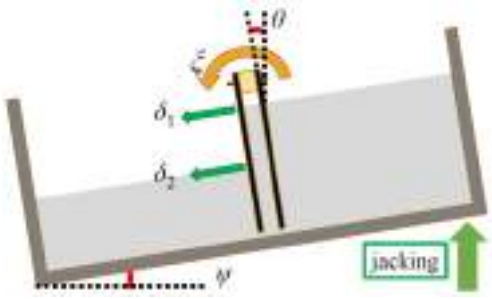

Fig.4 Schematic situation of the model experiment

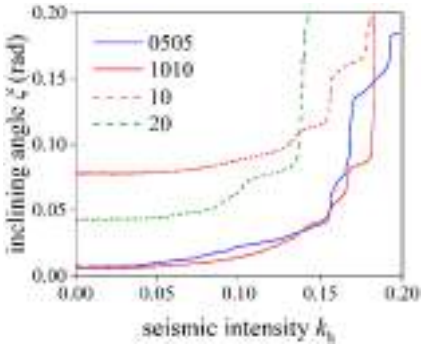

Fig.5 Relationships between horizontal seismic intensity k_h and inclining angle ξ

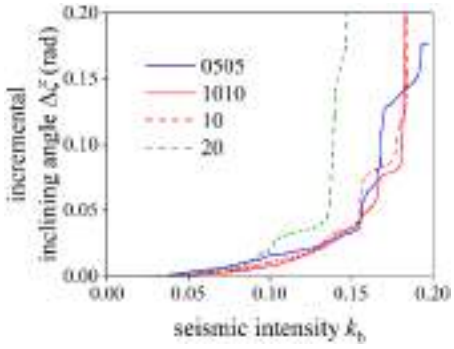

Fig.8 Relationships between horizontal seismic intensity k_h and incremental inclining angle $\Delta\xi$

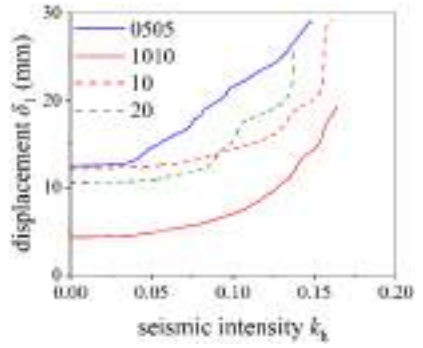

Fig.6 Relationships between horizontal seismic intensity k_h and horizontal displacement δ_1

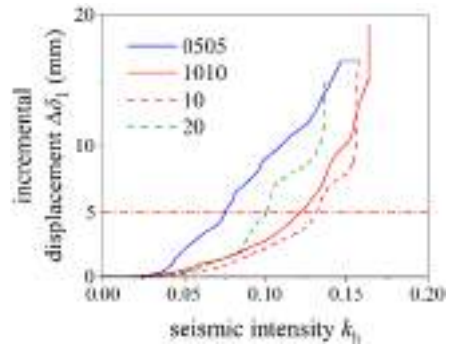

Fig.9 Relationships between horizontal seismic intensity k_h and incremental displacement $\Delta\delta_1$

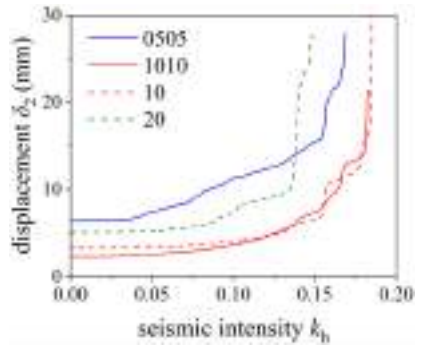

Fig.7 Relationships between horizontal seismic intensity k_h and horizontal displacement δ_2

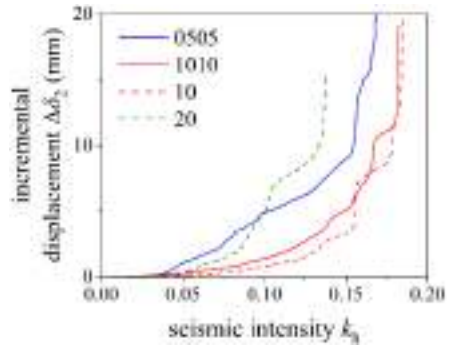

Fig.10 Relationships between horizontal seismic intensity k_h and incremental displacement $\Delta\delta_2$

intensity k_h proceeds faster for Case1010 than for Case10. In contrast, there is no difference in the relationship between the horizontal seismic intensity k_h and the horizontal displacement δ_2 between Cases 10 and 1010.

Finally, a comparison was made between Cases 0505 and 20, which showed close relationships between the excavation depth and the horizontal displacement in the two-dimensional excavation model experiments (Fig.3). In Case 0505, several points (horizontal seismic intensity k_h = 0.16, 0.17, 0.19) can be observed where a large head tilt angle ξ occurs at the earth retaining. In Case 20, the tilt angle increased rapidly when the horizontal seismic intensity k_h reached 0.13. In Case 0505, the horizontal displacement δ_1 increased monotonically with increasing horizontal seismic intensity k_h. In contrast, Case 20 showed a smaller displacement δ_1 than Case 0505. The horizontal displacement δ_2 deformed faster in Case 0505 with increasing horizontal seismic intensity k_h. However, a large displacement δ_2 occurred in Case 20 at a horizontal seismic intensity k_h = 0.14, which showed a more rapid increase in displacement δ_2 than in Case 0505. In the middle of the experiments (horizontal seismic intensity k_h = 0.13), Case 0505 showed a s-shaped deformation

(Fig.11) which is reflected in the measured results where Case 0505 showed a larger displacement δ_1 than Case 20 but a relatively close relationship in displacement δ_2.

These results suggest that although the double earth retaining wall method may show a slightly faster increase in horizontal displacement, it is more stable than a conventional single earth retaining wall.

Results of the Image Analysis

With the incremental horizontal displacement $\Delta \delta_1 \fallingdotseq 5.0$ mm (Fig.9), the distributions of normal strains were examined by performing a photographic image analysis using DippStrain, developed by Ditect. The distribution of normal strains in the horizontal direction in the model ground was visualised in all cases (Fig.12). The red areas in Fig.12 represent the expansion of the model ground, whereas the blue area represents the contraction.

The internal soil between the two model sheet piles of the double-earth retaining shows only minor deformations, apart from a slight deformation occurring near the model sheet pile. It can therefore be seen that the two steel sheet piles and the internal soil behave as a single wall.

The areas affected by the ground deformation are wider in the single earth retaining than in double earth retaining, and the strain region of the single earth retaining starts near the bottom of the earth retaining, whereas that of the double earth retaining starts slightly above the bottom edges. It is known that the earth retaining shows a rotational collapse behaviour when the strain region starts from the lower edge of an earth retaining [12]. This finding suggests that the double earth retaining method reduces the rotational behaviour more effectively than the use of highly rigid steel sheet piles as single earth retaining, although the displacements occurring during excavation are comparable.

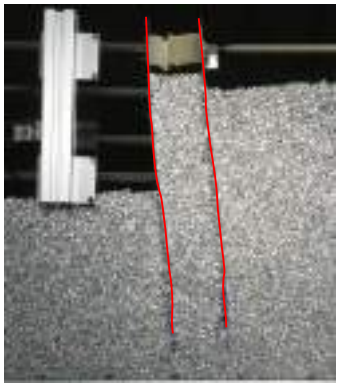

Fig.11 Deformation of Case 0505 at k_h = 0.13

CONCLUSIONS

The following conclusions were drawn from the two-dimensional model experiment to examine the seismic behaviour of the head-fixed double-sheet pile earth retaining wall method. First, this method showed a faster increase in horizontal displacement than the single earth retaining wall, for example at k_h = 0.10, the incremental displacement $\Delta \delta_1$ of Case 0505 was 4 times larger than Case 10. However, the double-earth retaining wall was more resistant with s-shaped deformation (Fig.11). Second, the risk of rotational collapse of a double earth retaining wall during seismic movements is lower than that of a single earth retaining wall (Fig.12), whereas a double earth retaining wall

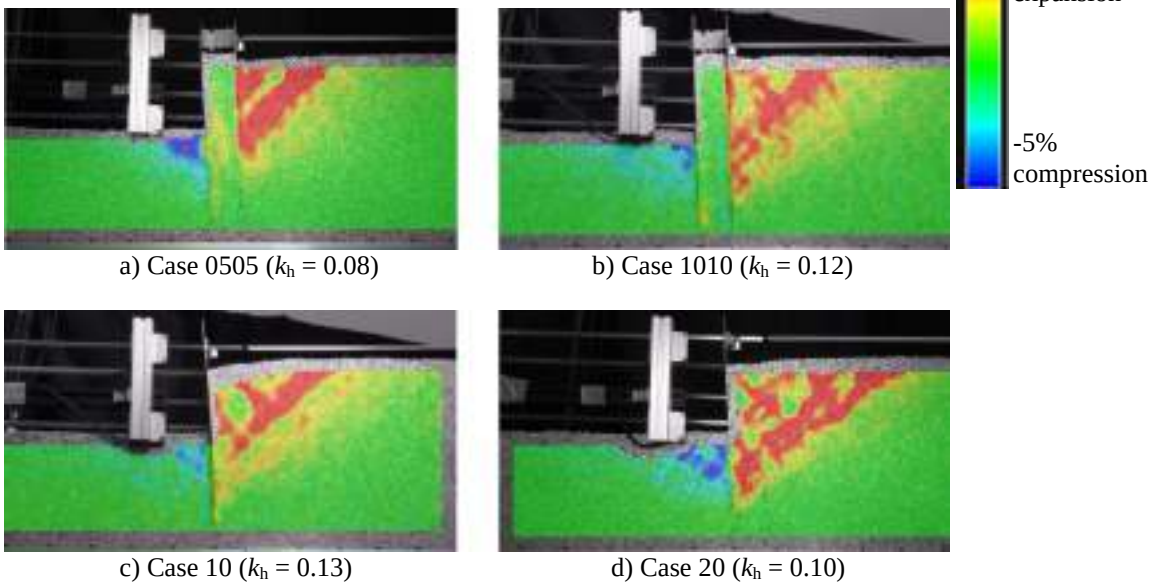

a) Case 0505 (k_h = 0.08) b) Case 1010 (k_h = 0.12)

c) Case 10 (k_h = 0.13) d) Case 20 (k_h = 0.10)

Fig.12 Distribution of the horizontal normal strain at $\Delta\delta_1 \fallingdotseq 5.0$ mm

can reduce horizontal displacement during excavation (Fig.3).

Further investigations will be conducted to explore the effects of displacement reduction with the head-fixed double-sheet pile earth retaining wall method by varying the conditions of penetration depth and by measuring the earth pressures acting on the model sheet pile.

REFERENCES

[1] Nasu A., Kobayashi T., Nagatani H., Ohno S., Inoue N., Taira Y., Sakanashi T., Kikuchi Y., Physical and numerical modeling of self-supporting retaining structure using double sheet pile walls, Proceedings of the Second International Conference on Press-in Engineering, 2021, pp. 330-336.

[2] Sugimoto H., Akagi S., Sato T., Otani J., Nagatani H., Nasu A., Model test on double sheet-pile method for excavation works using X-ray CT, Proceedings of the Second International Conference on Press-in Engineering, 2021, pp. 312-322.

[3] Kikuchi A., Nishioka H., Kato Y., Nasu A., Okamoto M., Nagatani H., Model tests on the effects of head fixation and separation distances for double sheet pile earth retaining wall method, Proceedings of the Third International Conference on Press-in Engineering, 2024, pp. 526-532.

[4] Japan Society of Civil Engineers, Standard Specifications for Tunneling-2016, Cut and Cover Tunnels, 2016, p. 337 (in Japanese).

[5] Matsumoto N., Nishioka H., A study on the effect an earth-retaining wall's rigidity and embedded depth on its behaviour, Proceedings of the Second International Conference on Press-in Engineering, 2021, pp. 323-329.

[6] Sasaki Y., Nishioka H., Vertical Loading Tests On Local Scoured Spread Foundation On Aluminum Rods Model Ground, International Journal of GEOMATE, Vol. 23, No. 98, 2022, pp. 17-23.

[7] Yoshida H., Isobe Y., Nishioka H., Assessing Residual Settlement In Column Foundations After An Earthquake Using Horizontal Loading Model Tests, 13th Int. Conf. on GEOMATE, 2023, pp. 334-338.

[8] Ohata T., Nishioka H., Sagawa T., Two-Dimensional Model Experiment On Pile Group Effect Between Piles With Different Stiffness, 13th Int. Conf. on GEOMATE, 2023, pp. 156-160.

[9] Shimada T., Nishioka H., Furukawa T., Experimental Study On Seismic Shear Deformation Of Box Tunnel Focusing On Stiffness Ratio And Friction Behavior, 8th Int. Conf. on Structure, Engineering & Environment, 2022, pp. 35-38.

[10] Watanabe K., Koseki J., Tateyama., Seismic Earth Pressure Exerted On Retaining Walls Under A Large Seismic Load, Soils and Foundations, Vol. 51, No. 3, 2011, pp. 379-394.

[11] Koseki J., Tatsuoka F., Munaf Y., Tateyama M., A Modified Procedure To Evaluate Active Earth Pressure At High Seismic Loads, Soils and Foundations, Vol. 38, 1998, pp. 209-216.

[12] Nishioka H., Matsumoto N., Fukuda F., Ono K., Model excavation tests simulating the collapse of high bending rigidity cantilever-type earth retaining walls and proposal of a simple calculating method for the reasonable embedding length, Japanese Geotechnical Journal, vol. 17, No. 3, 2022, pp. 401-420 (in Japanese).

[13] Architectural Institute of Japan, AIJ Recommendations for Design on Earth Retaining for Excavation, 2017, pp. 155-156 (in Japanese).

Copyright © Int. J. of GEOMATE All rights reserved, including making copies, unless permission is obtained from the copyright proprietors.

15th Int. Conf. on Geotechnique, Construction Materials & Environment,
Kyoto, Japan, 11-13 November 2025, ISBN 978-4-909106124 C3051

TWO-DIMENSIONAL MODEL EXPERIMENTS ON SEISMIC RESISTANCE OF SPREAD FOUNDATION DAMAGED BY LOCAL SCOURING

Yuki Yamakuri[1], Tomohito Ishii[1] and Hidetoshi Nishioka[1]

[1]Faculty of Science and Engineering, Chuo University, Japan

ABSTRACT

In recent years, scour damage to the foundations of river bridge piers has become increasingly prevalent owing to the rising frequency of typhoons and heavy rain. When the extent of damage is moderate (manifesting as settlement or tilting of the foundation), foundations affected by local scour can be reused. Japan has witnessed several cases of such reuse. However, the seismic bearing capacity of foundations following local scour events remains poorly understood. In this study, two-dimensional model experiments using an aluminum rod ground model were conducted to investigate the horizontal bearing characteristics of a spread foundation damaged by local scour. A distinctive feature of our experimental methodology is the ability to precisely control the extent of scour while simultaneously observing the ground deformation behavior through image analysis. In this experiment, scour was induced by extracting an aluminum rod. Subsequently, horizontal loading experiments on a spread foundation were conducted, followed by image analysis. The horizontal resistance decreased as the scour amount increased. Nevertheless, the bearing capacity of the spread foundation damaged by scour was maintained under eccentric and inclined loading caused by seismic inertial forces.

Keywords: Scour, Earthquake, Horizontal Loading Experiment, Aluminum Rod, Image Analysis

INTRODUCTION

Recently, the foundations of river bridge piers have experienced significant scour damage owing to an increase in the frequency and intensity of typhoons and heavy rainfall. Most damaged river bridge piers use a spread foundation design [1, 2]. The types of damage observed can be categorized into large-scale and medium-scale. Large-scale damage typically involves the flowing or overturning of piers, whereas medium-scale damage is characterized by the settlement or inclination of piers. Generally, river bridge piers that have sustained scour damage are deemed unsafe for reuse. However, several instances have been reported in Japan where piers demonstrating medium-scale scour damage have been successfully rehabilitated after thorough safety assessments. The example of reused railroad bridge piers is shown in Fig.1 [3]. This underscores the necessity of accurately evaluating the bearing capacity characteristics of reused spread foundations.

Sasaki and Nishioka conducted vertical loading tests on local scoured spread foundations using aluminum rod ground model [4]. Hirano et al. used a similar experimental approach to examine the influence of internal erosion on the bearing capacity characteristics [5]. Furthermore, Hirano et al. enhanced the experimental apparatus to consider the dead load safety factor and systematically conducted simulations of scouring phenomena and vertical loading tests on locally scoured spread foundations. [6]. Yamakuri et al. analyzed the bearing capacity of a spread foundation after local scouring using the rigid plastic finite element method [7]. However, no studies have investigated the bearing capacity characteristics of spread foundations following scour damage under seismic inertial forces.

Fig.1 Example of reused railroad bridge piers (JR East, Gono Line, Nakamuragawa bridge pier)

To address this gap, in the present study, two-dimensional horizontal loading experiments aimed at assessing the seismic resistance of spread foundations that have suffered local scour damage were conducted. A distinctive feature of the experimental methodology is the ability to control the extent of scour while simultaneously observing the ground deformation behavior

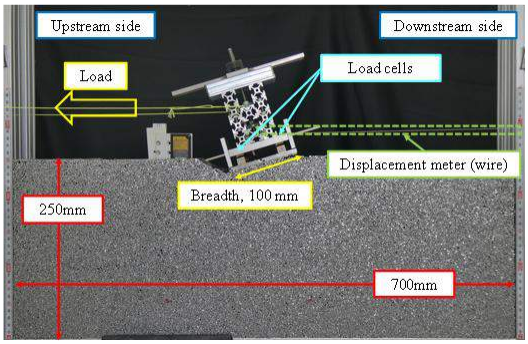

Fig.2 Experimental devices

RESEARCH SIGNIFICANCE

The reuse of river bridge piers that have been compromised by local scour is anticipated to become increasingly prevalent. In Japan, a country prone to frequent earthquakes, assessing the horizontal resistance of spread foundations is crucial. This study introduces a novel approach by examining the horizontal bearing capacity characteristics of a spread foundation in the context of combined multihazard risks of scours and earthquakes. The findings of this research are expected to make a substantial contribution to the timely restoration and ongoing safe use of scour-damaged bridge piers.

HORIZONTAL LOADING EXPERIMENTS ON ALUMINUM RODS

Experimental Devices

In this study, an aluminum rod ground model was used to simulate the behavior of two-dimensional sandy soil. The advantages of using the materials are [8, 9]:

1. They exhibit deformation and strength characteristics like those of medium-density sand.
2. The repeatability of the experiments is high because the particle size characteristics remain unchanged even after multiple tests.
3. The ground deformation behavior can be observed via image analysis using photographs of the aluminum rods.

Taking advantage of these features, model experiments have been conducted involving loading and unloading problems such as spread foundations [10] and excavations [11]. In addition, the variation in the experimental results has been confirmed to be relatively small in vertical loading experiments of spread foundations [12].

The experimental devices used for the horizontal loading experiments are shown in Fig.2. The model ground was constructed by mixing aluminum rods 150 mm long with diameters of 1.5, 2.0 and 3.0 mm, ensuring equal weights for each size. The ground model dimensions (height × width)250 mm × 700 mm. Sufficient compaction was performed to simulate the bearing stratum beneath the spread foundation and to minimize variation. Thorough compaction was conducted for each 50 mm thick layer using a small vibrator. The unit volume weight γ and angle of repose ϕ_r of the model were 21.6kN/m^3 and 32°, respectively.

Table 1 List of bridge pier models

$F_{s,DL}$	V_D [N]	H_c / B
3	59.68	0.77
4.5	41.55	0.79
6	30.01	0.74

The bridge pier model used a spread foundation design without a penetration depth, with the footing dimensions (breadth × length) measuring 100 mm × 150 mm. Three types of bridge pier models were used, as shown in Tab.1, with parameters including the total weight (referred to as model dead load V_D) and center of gravity height (H_c). The dead load safety factor $F_{s,DL}$ can be defined using the model dead load V_D and the ultimate bearing capacity of the normal ground V_{ult} (approximately 180 N) as follows:

$$F_{s,DL} = V_{ult} / V_D \quad (1)$$

H_c was established with reference to the actual pier foundations that were reused following a disaster [3].

To measure the horizontal displacement at the center of the footing's base, a horizontal displacement gauge was installed approximately 400 mm away, and connected through a wire to follow the settlement of the footing. During the horizontal loading experiments, the horizontal load was measured using a load cell installed on the horizontal loading jacks. Additionally, the reaction force moments at the base of the footing were measured using two-way load cells affixed to the bottom of the bridge pier model. The inclination angle of the footing was determined through accelerometers attached to the bridge pier model. The horizontal displacement at the loading point was calculated by combining the displacement determined from the inclination angle with the horizontal displacement measured at the center of the footing.

Modeling of the Local Scour

This section outlines the modeling of the local scour in these model experiments. First, the model dead loads were simulated by placing weights on a

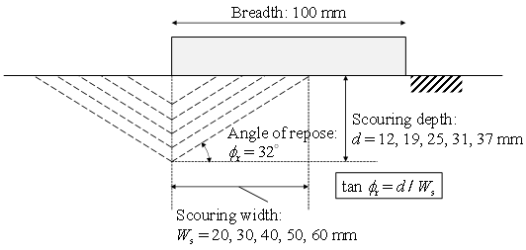

Fig.3 Experimental cases of the local scour area

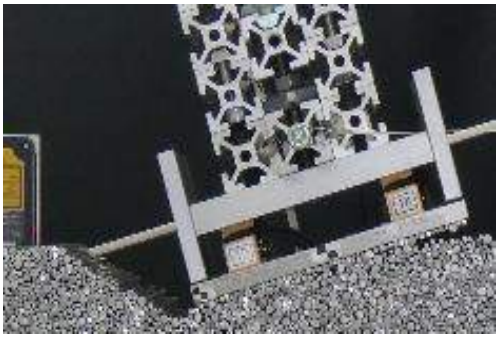

Fig.4 Modeling of local scour

horizontally positioned foundation model. Local scour was then simulated by removing aluminum rods situated beneath the base of the footing. The resulting shape of the local scour was modeled as an isosceles triangle, with its height defined as the scouring depth d, as shown in Fig.3. This shape was determined based on the tendency of the scour to form a cone, with its apex located at the base of the upstream side of the piers [13]. The relationship between the local scouring width W_s and scouring depth d is expressed as $\tan\phi = W_s/d$, where ϕ. represents the angle of repose. The bridge pier model after local scouring is shown in Fig.4. Horizontal loading experiments were conducted at several scouring depths, as shown in Fig.4.

Loading Procedure

The configuration of the horizontal loading experiments is shown in Fig.5. To simulate seismic inertial forces, strings were affixed to the center of gravity of the pier model, and loads were applied using a jack. Horizontal loading experiments were conducted for scouring depths of d = 0 mm (before scour) and d = 12, 25, and 37 mm (after scour) to investigate the effect of the scour area on the horizontal resistance of a spread foundation. Horizontal loading was performed until the jack reached its operational limit of 50 mm or the bridge pier model was overturned.

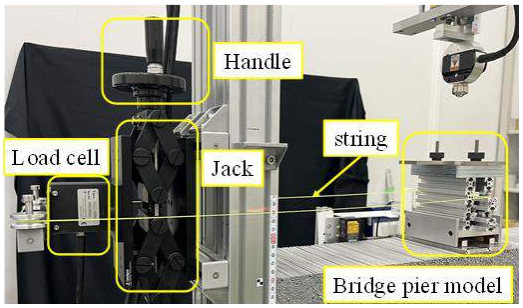

Fig.5 Setup of horizontal loading experiments

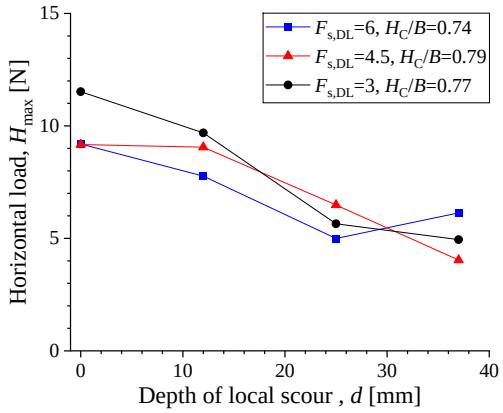

Fig.6 Relationship between the horizontal load and scoring depth

EXPERIMENTAL RESULTS

Relationship Between the Horizontal Load and Scouring Depth

The relationship between the maximum horizontal load H_{max} and scouring depth is shown in Fig.6. The horizontal load decreased as the scouring depth increased, regardless of the magnitude of dead load safety factor $F_{s,DL}$, except for the cases in which $F_{s,DL}$ = 6 and d = 37 mm. This reduction in the horizontal resistance resulted from the localized loss of contact area between the foundation base and the ground due to local scour, as well as from the residual inclination of the foundation structure.

The relationship between the horizontal seismic coefficient, defined as the horizontal load divided by the model's dead load and scouring depth, is shown in Fig.7. In general, a horizontal seismic coefficient of 0.2 is used in seismic design in Japan [14]. Across all scouring depths, the horizontal seismic coefficients decreased as the dead load safety factor decreased.

Thus, the horizontal resistance of a spread foundation is influenced by the dead load safety factor and scouring depth.

Table 2 Image analysis results

	$F_{sDL}=3, H_C/B=0.77$	$F_{sDL}=4.5, H_C/B=0.79$	$F_{sDL}=6, H_C/B=0.74$
d=0 mm	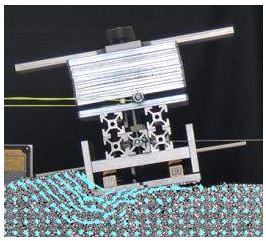	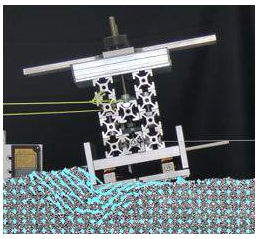	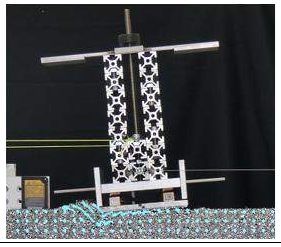
d=12 mm	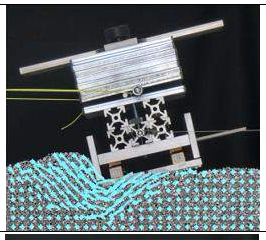	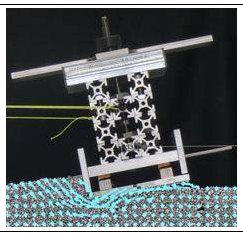	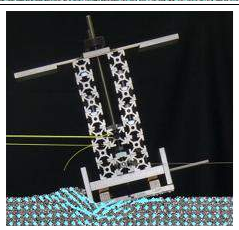
d=25 mm	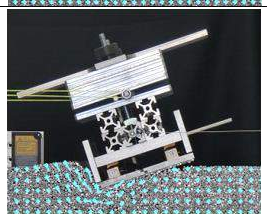	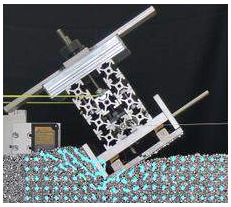	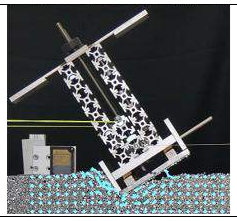
d=37 mm	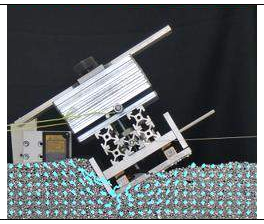	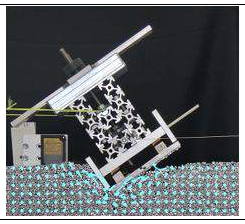	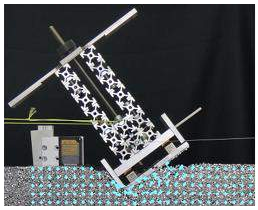

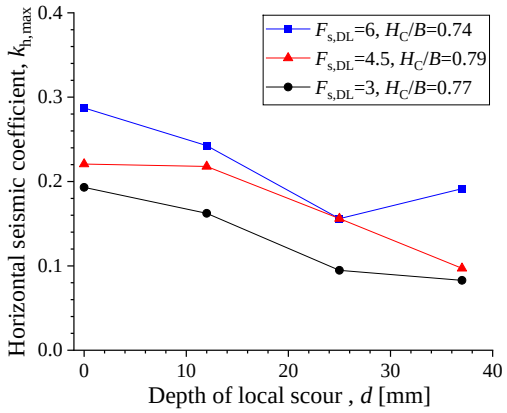

Fig.7 Relationship between the horizontal seismic coefficient and scouring depth

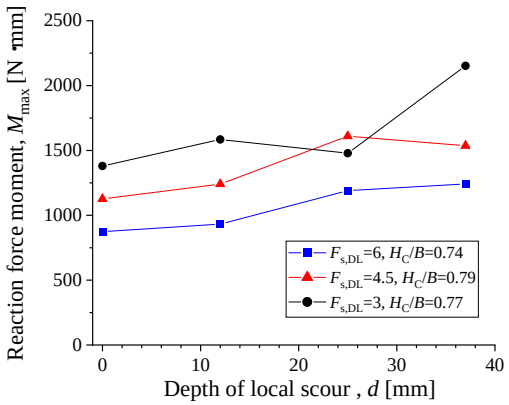

Fig.8 Relationship between the reaction force moment at the bottom and scouring depth

Relationship Between the Reaction Force Moment at the bottom and Scouring Depth

The relationship between the maximum value of the reaction force moment and scouring depth is shown in Fig.8. Although the horizontal resistance decreases due to scour damage, as shown in Fig.6, the reaction force moment does not decrease. Therefore, the influence of a reduced bearing capacity due to scouring on the seismic resistance of spread foundations is minor. In other words, these results indicate that the bearing capacity of a spread foundation damaged by scour is maintained under

eccentric and inclined loading caused by seismic inertial forces.

Image Analysis Results

To further investigate the displacement behavior of the model ground, image analysis was performed using Dipp-Motion (Ditect). The results of the image analysis are listed in Tab.2. Before local scouring (i.e., with a scouring depth d of 0 mm), a slip line was detected around the left edge of the footing, originating from the contact surface between the footing's base and the ground. Following local scouring (at a scouring depth d of 12 mm), a similar ground displacement behavior was observed over a wider area than before the disaster. At scouring depths of d = 25 and 37 mm, the left edge of the bottom of the bridge pier model settled toward the scour area and the footing detached from the base. Additionally, the left side of the footing remained in contact with the ground. For this reason, earth pressure acting on the sides of the footing serves as a lateral resistance force, enhancing rotational stability. This implies that the seismic resistance of the spread foundation improved despite the occurrence of scour damage.

However, since the failure mode is considered to depend on the height of the center of gravity, further experiments are required.

CONCLUSIONS

This study conducted two-dimensional horizontal loading experiments to investigate the seismic resistance of a spread foundation affected by local scouring. The key findings of this study are as follows:

1) The horizontal resistance of the spread foundation decreased as the extent of scouring increased.
2) The bearing capacity of a spread foundation damaged by scour was maintained under eccentric and inclined loading caused by seismic inertial forces.
3) The results indicate that the rotational resistance of the spread foundation increased with greater scouring depth. This phenomenon is attributed to enhanced contact between the left side of the footing and the surrounding soil, which increased the resistance to rotation.

Future research directions and prospects are as follows:

1) The factors that increase the resistance to rotation as the scouring depth increases should be clarified. To achieve this, we should measure the earth pressure acting on the side of the footing.
2) Since actual bridge piers have varying centers of gravity, it is necessary to conduct experiments using this as a parameter.
3) When reusing bridge pier foundations damaged by local scouring, a reinforcement method using sheet piles is applied (Fig.1). We will investigate the reinforcement effect of sheet piles on the horizontal bearing capacity of a spread foundation following local scouring.

REFERENCES

[1] Nanazawa, T., Miyahara, F., Fujita, T., Inomata, H., The efforts of the National Institute for Land and Infra-structure Management and Public Works Research Institute based on the recent scouring damage of road bridges, The Foundation Engineering & Equipment, Vol. 50, No. 6, 2022, pp. 33-38 (in Japanese).

[2] Tagi, K., Shigemura, A., Watanabe, S. and Sanagawa, T.: Recent flood hazards on railway bridges and related efforts, The Foundation Engineering & Equipment, Vol. 50, No. 6, 2022, pp. 39-43 (in Japanese).

[3] The sankei Shimbun (Newspaper), https://www.sankei.com/article/20221223-UX432KXSR5KQHMQ2CIBUXW6IMM/, accessed on 28 November 2024 (in Japanese).

[4] Sasaki, Y., Nishioka, H., Vertical loading tests on local scoured spread foundation on aluminum rods model ground, International Journal of GEOMATE, Vol. 23, Issue 98, 2022, pp.17-23.

[5] Hirano, M., Sasaki, Y., Nishioka, H., Evaluation of the Bearing Capacity of Scoured Bridge Foundations Using Aluminum Rod Ground Model Tests, Natural Geo-Disasters and Resiliency, Springer Nature Singapore, 2024, pp. 163-172.

[6] Hirano, M., Nishioka, H., Yamakuri, Y., Proposal for a method to predict the local scour damage of river bridges and to evaluate the residual bearing capacity after scour, Journal of Japan Society of Civil Engineering, Vol. 80, Issue 11, 2024, Article ID:24-00088 (in Japanese).

[7] Yamakuri, Y., Nishioka, H., Hirano, M., Sasaki, Y. and Kobayashi, S., Rigid-plastic finite element analysis for ultimate bearing capacity of spread foundation pier after local scouring, Journal of Japan Society of Civil Engineering, Vol. 80, Issue 15, 2024, Article ID:23-15023 (in Japanese).

[8] Kikumoto, M., Nakai, T., Zhang, F. and Shahin, H., Two dimensional model tests using aluminum rods mass, Geotechnical Engineering Magazine, Vol. 56, No. 10, 2008, pp. 12-15 (in Japanese).

[9] Hirakawa, D., Tanimoto, S., Watanabe, K., Takahashi, H., Nishioka, H. and Itoh, K., Physical modelling in geotechnical engineering 3. Technique of the preparation for the model

ground of physical model test in geotechnics, Geotechnical Engineering Magazine, Vol. 71, No. 11, 2023, pp. 46-59 (in Japanese).
[10] Nishioka, H., Residual bearing capacity of scoured shallow foundations and their reinforcement effect by press-in sheet piles, IPA NewsLetter, Volume.6, Issue 2, 2024, pp. 5-9.
[11] Nakai, T., Farias, M. M., Bastos, D., Sato, Y., Simulation of conventional and inverted braced excavation using subloading t_{ij} model, Soils and Foundations, Vol. 47, Issue 3, 2007, pp. 597-612.
[12] Shikakura, R., Nishioka, H., Yamakuri, Y., Arai, Y., Hirano, M., Experimental study on the effect of penetration length and eccentricity of sheet pile foundation on bearing capacity, Proc. of the Third International Conference on Press-in Engineering 2024, 2024, pp. 533-539.
[13] Naito, N., Watanabe, S., Keyaki, Y., Manome, R.and Nunokawa, O., Vibration characteristics of spread foundation pier model with progress of local scouring, Japanese Geotechnical Journal, Vol. 15, No. 2, 2020, pp. 269-279 (in Japanese).
[14] Towhata, I., Development of geotechnical earthquake engineering in Japan, Proc. of the 16th International Conference on Soil Mechanics and Geotechnical Engineering, 2005, pp. 251-291.

Copyright © Int. J. of GEOMATE All rights reserved, including making copies, unless permission is obtained from the copyright proprietors.

15th Int. Conf. on Geotechnique, Construction Materials & Environment,
Kyoto, Japan, 11-13 November 2025, ISBN 978-4-909106124 C3051

EROSION CONTROL EFFECT OF VEGETATION WORKS BY PHALARIS ARUNDINACEA L. AGAINST SURFACE RUNOFF

Enkhzaya Batbayar[1], Dai Nakamura[2], Keishin Tsutsumi[3], Yuichiro Murakami[4], Eiji Tateyama[5], Yuki Minabe[6] and Takayuki Kawaguchi[7]

[1, 3, 4, 5]Graduate School of Engineering, Kitami Institute of Technology, Japan
[2, 6, 7]Faculty of Engineering, Kitami Institute of Technology, Japan

ABSTRACT

Roadside and river embankment slopes are typically protected using vegetation-based stabilization methods. However, recent increases in heavy rainfall and flooding, attributed to climate change, have led to more frequent erosion damage caused by surface runoff on these vegetated slopes. Despite this, the influence of plant species and their growth conditions on erosion resistance remains poorly understood. To address this gap, we conducted erosion resistance tests on soil boxes vegetated with *Phalaris arundinacea* L. (reed canary grass). Our findings demonstrate that the development of stems, leaves, and roots significantly enhances resistance to erosion. Additionally, applying Structure-from-Motion (SfM) photogrammetry enabled effective visualization of changes in erosion resistance associated with plant growth.

Keywords: Erosion control effect, Vegetation works, Growth condition, Surface runoff, Photogrammetry

INTRODUCTION

Recent climate trends have led to a noticeable increase in average temperatures, even in cold and relatively dry regions such as Hokkaido. A rise in the frequency of short-duration, high-intensity rainfall events has accompanied this. In Japan, it is standard practice to stabilize slopes on roadsides and embankments with vegetation (Guidelines for Road Earthworks -Cut Slope Work / Slope Stability Work [1]). However, cold-resistant species such as Kentucky bluegrass, which have been widely used for this purpose, are becoming less viable under rising temperatures. At the same time, erosion caused by surface runoff has become more common during heavy rain events. While vegetation is known to mitigate erosion, quantitative relationships between plant growth and erosion resistance on slopes remain insufficiently clarified.

This study addresses this knowledge gap by focusing on *Phalaris arundinacea* L., a species more suited to warm climates than Kentucky bluegrass. We tested erosion resistance on vegetated soil boxes where *Phalaris arundinacea* L. was grown for varying durations. Water was introduced over the soil surface via overflow from a storage tank, simulating surface runoff conditions (following the method of Kajimoto et al. [2]). Previous research has shown that *Phalaris arundinacea* L. exhibits greater resistance to raindrop-induced erosion (Gorobe et al. [3]) and enhances soil shear strength (Utaka et al. [4]). During testing, we measured the sediment runoff, and after each test, we removed the above-ground biomass and created 3D models of the eroded surfaces using SfM photogrammetry.

OVERVIEW OF THE EXPERIMENT

Table 1 summarizes the experimental conditions for all test cases. Four primary test scenarios were

Table 1 Experimental conditions of specimens.

Case	Specimen name	Growth Period	Number of growing days (d)	Cumulative temperature (°C•d)	Cumulative sunshine duration (h)
1	S-1, 2	No vegetation	-	-	-
2	S-RCG1	2024/8/19 - 2024/9/16	29	590	190
	S-RCG2	2024/8/21 - 2024/9/18	29	587	192
	S-RCG3	2024/8/23 - 2024/9/20	29	574	182
3	S-RCG4	2024/7/31 - 2024/9/25	57	1136	331
	S-RCG5	2024/8/2 - 2024/9/27	57	1128	329
	S-RCG6	2024/8/7 - 2024/10/2	57	1090	333
4	S-RCG7	2024/7/17 - 2024/10/9	85	1647	464
	S-RCG8	2024/8/2 - 2024/10/25	85	1470	490
	S-RCG9	2024/8/6 - 2024/10/29	85	1406	484

established: Case 1 served as the control with no vegetation, while Cases 2 through 4 involved *Phalaris arundinacea* L. grown for 4, 8, and 12 weeks, respectively, from mid-July to early October 2024.

Figure 1 shows the grain size accumulation curve of the volcanic sandy soil collected from Bihoro Town in eastern Hokkaido. Only the portion passing through a 9.5 mm sieve was used. Figure 2 presents the compaction curve for this soil type.

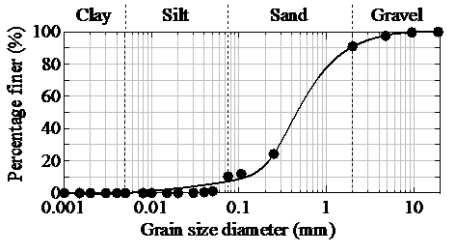

Fig. 1 Grain size accumulation curve

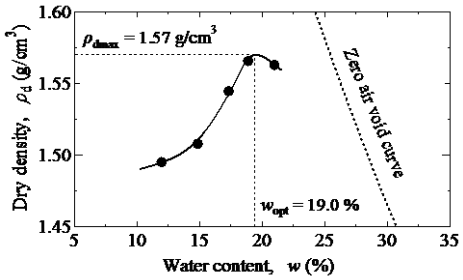

Fig. 2 Compaction curve

Figure 3 illustrates a schematic diagram of the soil box used in the experiment. The soil, adjusted to the optimum moisture content, was compacted in three layers to achieve a compaction degree of 85%. For Cases 2 to 4, *Phalaris arundinacea* L. seeds were mixed into the top layer at a seeding rate of 0.254 g,

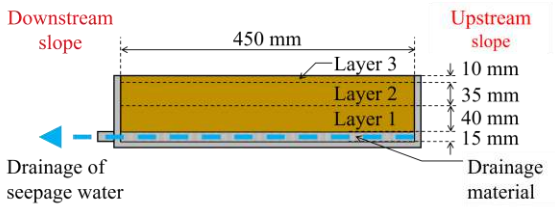

Fig. 3 Schematic diagram of soil specimen.

targeting an expected emergence of 3,500 plants/m². These boxes were placed outdoors in shaded conditions and maintained by a capillary water supply from the bottom, with twice-daily surface spraying to prevent drying.

Figure 4 provides an appearance of plant specimens, while Table 2 details the growth conditions for Cases 2 to 4. Before the erosion tests, the number of plants and plant height were measured in each box at three locations (upstream, midstream, and downstream) using the quadrat method. The vegetation cover rate was also quantified by processing top-view images of the soil boxes with the image viewer software *Pickmap*, in which stems, leaves, and soil were classified using binary image segmentation. After the erosion tests, the dry mass of roots was determined by sampling with PVC pipes (44 mm diameter) and drying the extracted roots. As shown in Figure 4 and Table 2, vegetation conditions varied depending on the location, even within the same box. This variation is thought to be primarily due to differences in sunshine duration at different locations within the box.

Figure 5 shows the relationship between plant growth and meteorological conditions. During the first 8 weeks after seeding, the plants exhibited steady elongation and development in accordance with cumulative temperature, but growth significantly slowed thereafter.

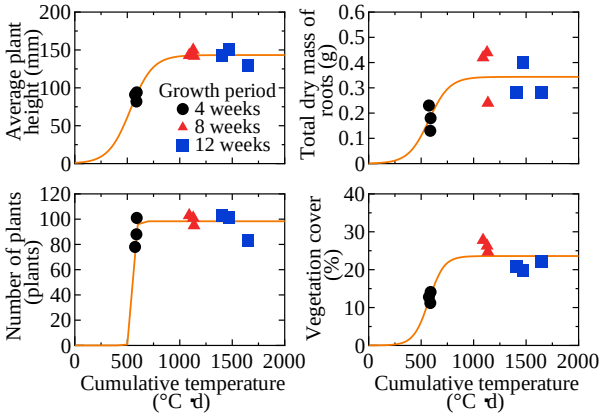

Fig. 5 Relationship between the growth conditions of plant specimens and cumulative temperature.

Fig. 4 Appearance of plant specimen.

Table 2 Number of plants, plant height, total dry mass of roots, and vegetation cover in the plant specimens.

Case	Specimen name	Measured before erosion tests									Measured after erosion tests			
		Number of plants (plants)				Plant height (mm)				V.c (%)	Dry mass of roots (g)			
		Up	Mid	Down	Sum	Up	Mid	Down	Ave.		Up	Mid	Down	Sum
2	S-RCG1	42	25	34	101	85	105	91	94	14.1	0.06	0.07	0.05	0.18
	S-RCG2	21	31	36	88	75	92	80	82	11.2	0.03	0.06	0.04	0.13
	S-RCG3	20	40	18	78	80	97	97	91	12.8	0.14	0.04	0.05	0.23
3	S-RCG4	31	36	28	95	83	90	255	142	24.7	0.05	0.07	0.12	0.24
	S-RCG5	32	33	36	101	140	135	175	150	26.3	0.17	0.13	0.14	0.44
	S-RCG6	37	34	32	103	140	132	158	143	27.8	0.14	0.16	0.12	0.42
4	S-RCG7	26	29	28	83	79	83	229	130	22.2	0.08	0.06	0.14	0.28
	S-RCG8	32	33	36	101	140	135	175	150	19.8	0.13	0.12	0.15	0.40
	S-RCG9	37	34	32	103	140	132	158	143	20.8	0.06	0.11	0.11	0.28

Note: Up = Upstream, Mid = Midstream, Down = Downstream, Ave. = Average, V.c = Vegetation cover

Figure 6 shows the schematic diagram of the erosion test apparatus (adapted from Kajimoto et al. [2]). In this study, erosion tests were conducted on a long embankment slope, assuming a scenario in which surface water generated at the top flows downward, causing erosion at the toe of the slope. Soil boxes were set on a 1:1.5 slope, and surface runoff was applied via overflow from a storage tank. The flow was controlled at 50 mm width and 1 L/min discharge. Each erosion trial lasted 30 seconds, after which the runoff sediment was collected, and its dry mass was determined. Tests were repeated until the drainage material at the bottom of the soil box became exposed (see Figure 3).

Upon completion of the tests, stems and leaves were cut and removed, and SfM photogrammetry was used to generate 3D surface models of the eroded areas for visual analysis.

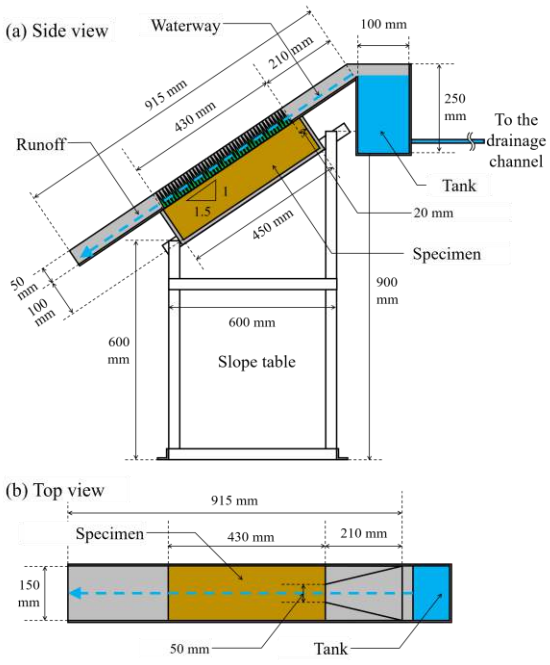

Fig. 6 Schematic diagram of erosion test apparatus.

RESULTS AND DISCUSSION

Figure 7 presents the appearance of specimens following the erosion test, highlighting representative outcomes from each case. In Cases 2 through 4, the

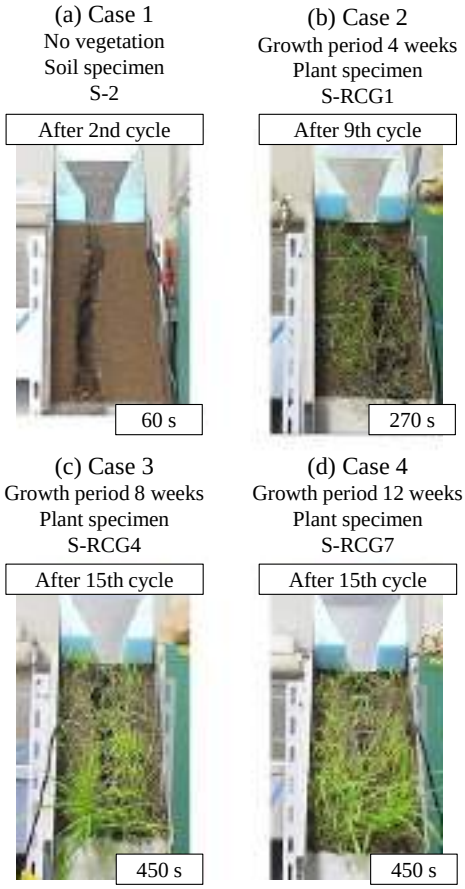

Fig. 7 Appearance of specimens following erosion test.

vegetative cover partially obscures the eroded surfaces, but visual comparison with Case 1 clearly shows that vegetation significantly reduced surface erosion.

Figure 8 illustrates the cumulative mass of sediment runoff across all trials. Due to the number of tests conducted, results are divided into Cases 1 and 2, and Cases 3 and 4. In Case 1 (bare soil), approximately 500 grams of sediment were lost during the first erosion event. The underlying drainage material became visible during the second test, leading to the termination of the trial. In Case 2, while the erosion rate was initially slower than in Case 1, all samples eventually reached similar cumulative sediment runoff within 10 trials, after which testing was concluded.

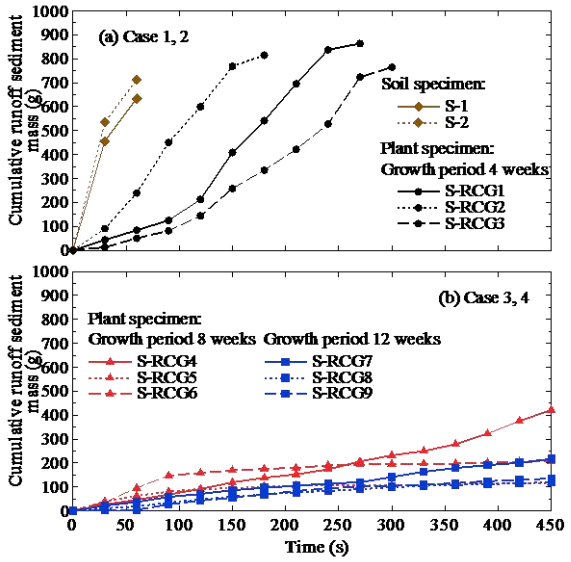

Fig. 8 Changes over time in cumulative runoff sediment mass in each case.

Conversely, in Cases 3 and 4, except for a single outlier (Test S-RCG4), the cumulative sediment runoff increased only marginally after the third trial. Even after 15 repetitions, the total sediment runoff remained about one-third of that observed in Cases 1 and 2. These findings demonstrate the enhanced erosion resistance of more mature *Phalaris arundinacea* L. vegetation.

Figure 9 shows the relationship between plant growth conditions and the maximum sediment runoff rate. The maximum sediment runoff rate, defined as the steepest slope in the erosion curve (from Figure 8), declined as plant height, root dry mass, and vegetation cover increased. This trend indicates that erosion resistance improves with plant development.

Figure 10 compares the soil box's post-test condition after removal of stems and leaves with contour maps generated using SfM photogrammetry based on the test results shown in Figure 8. The location and depth of erosion can be visually confirmed. In the test results for Cases 3 and 4 (S-RCG4 and S-RCG7), erosion in the downstream area

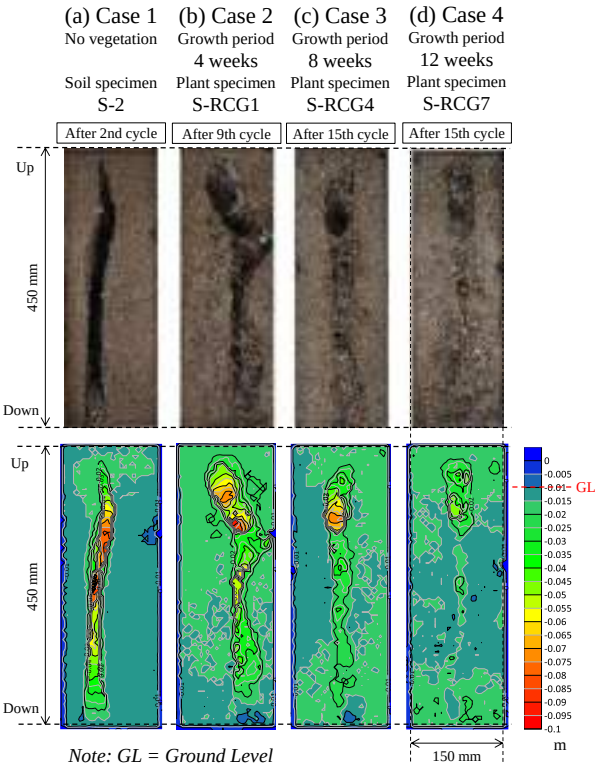

Fig. 10 Appearance of the soil specimen surface and the surfaces of the plant specimens, along with their contour maps, after the erosion test.

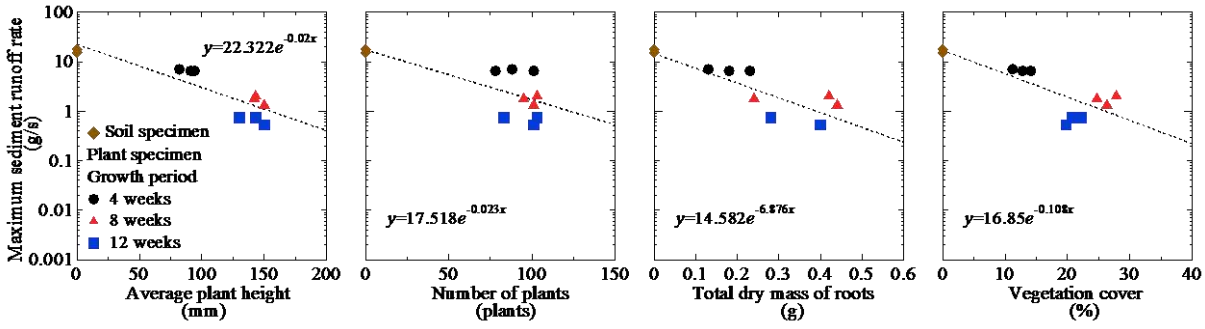

Fig. 9 Relationship between growth conditions of plant specimens and maximum sediment runoff rate.

was significantly reduced compared to Cases 1 and 2. This reduction is likely attributable to favorable plant growth conditions—specifically, greater plant height, higher vegetation cover rate, and well-developed rhizomes in the downstream area, as shown in Table 2.

CONCLUSION

This study evaluated the erosion resistance of vegetated slopes using *Phalaris arundinacea* L., a species suited for warmer climates. Erosion tests were conducted using soil boxes containing plants that had been grown for various durations. The results demonstrated that plant growth, especially root development, significantly improves resistance to erosion caused by surface runoff.

Additionally, the application of Structure-from-Motion (SfM) photogrammetry proved effective in visualizing the extent and depth of erosion. This technique enables the spatial analysis of changes in erosion resistance associated with different plant species and growth conditions, providing a valuable tool for evaluating vegetation-based slope stabilization strategies.

REFERENCES

[1] Japan Road Association. Guidelines for Road Earthworks -Cut Slope Work / Slope Stability Work. 2009, pp. 191–192.

[2] Kajimoto, M., Nakamura, D., Kawaguchi, T., Kawajiri, S., & Muneoka, H. Development of an erosion testing method using Structure from Motion (SfM) photogrammetry. Journal of the Japanese Society of Revegetation Technology, Vol. 48 No. 1, 2022, pp. 27–32.

[3] Gorobe, K., Nakamura, D., Kawajiri, S., Kawaguchi, T., Muneoka, H., & Ayame, T. Evaluation of erosion control effect of vegetation work against raindrops using *Phalaris arundinacea* L.. Journal of the Japanese Society of Revegetation Technology, Vol. 48, No. 1, 2022, pp. 15-20.

[4] Utaka, Y., Nakamura, D., Tumurkhuyag, Z., Kawaguchi, T., Muneoka, H., & Kawajiri, S. Basic study on reinforcement effect of vegetation work using *Phalaris arundinacea* L.. Journal of the Japanese Society of Revegetation Technology, Vol. 49, No. 1, 2023, pp. 63-68.

Copyright © Int. J. of GEOMATE All rights reserved, including making copies, unless permission is obtained from the copyright proprietors.

15th Int. Conf. on Geotechnique, Construction Materials & Environment, Kyoto, Japan, 11-13 November 2025, ISBN 978-4-909106124 C3051

ENHANCING MITIGATION STRATEGIES FOR RAINFALL INDUCED ROADSIDE LANDSLIDES IN NEW ZEALAND

Roohollah Kalatehjari[1], Lokesh Vemuri[1] and Rajitha Sachinthaka[1]

[1] Built Environment Engineering Department, School of Future Environments, Auckland University of Technology, Auckland 1010, New Zealand

ABSTRACT

This study addresses the critical issue of rainfall-induced roadside landslides in New Zealand, focusing on enhancing mitigation strategies through lessons from international case studies. Rainfall-induced landslides pose significant risks to infrastructure, public safety, and economic stability, particularly given New Zealand's challenging topography, complex geology, and frequent intense rainfall events. The research employs a systematic literature review, adhering to Prisma guidelines, complemented by comparative analyses of international mitigation approaches from Japan, Italy, the United States, and China as the identified countries with comparable geological and climatical challenges to New Zealand. The research identifies and investigates essential mechanisms affecting roadside slope stability, including soil saturation, shear strength reduction, and slope geometry. International mitigation practices evaluated for their suitability in New Zealand include real-time monitoring systems, bioengineering approaches, geotechnical interventions, and comprehensive drainage systems. Findings highlight the potential effectiveness and adaptability of Japan's sensor-based early warning technologies, Italy's bioengineering slope stabilization practices, and geotechnical intervention strategies implemented in the United States. Through qualitative expert interviews and quantitative analyses of historical landslide and rainfall datasets, the study exposes gaps in New Zealand's current reactive management approach. Recommendations emphasize adopting cost-effective, proactive, and climate-resilient strategies, particularly advanced real-time monitoring technologies and bioengineering solutions adapted to New Zealand's unique environmental conditions. The outcomes establish a practical and sustainable framework for regional landslide mitigation, balancing economic viability and long-term environmental resilience.

Keywords: Rainfall-induced landslides; Slope stability; Landslide Mitigation strategies; Roadside Slope; New Zealand.

INTRODUCTION

Rainfall-induced landslides are one of the most dominant natural hazards affecting New Zealand, posing significant threats to infrastructure, public safety, and economic stability. The country's dynamic geological structure, consisting of steep slopes and weak soil formations, along with regular heavy rainfall, makes it significantly susceptible to landslides. The associated impacts are especially disruptive on New Zealand's road network, where landslides can cause substantial damage, extended closures, and significant economic losses, with $250-300 million annual estimated cost The urgency of tackling this issue is exacerbated by the rising effects of climate change, which has resulted in more frequent and severe downpour events [1].

Despite ongoing efforts to reduce the rainfall-induced landslide hazards, New Zealand's current landslide management strategy is mostly reactive, focused on post-event intervention rather than proactive prevention [2]. This approach not only increases susceptibility but also results in rising costs and environmental implications, such as habitat disruption, soil erosion, natural resource depletion, etc. Recognising the need for more effective measures, this study investigates novel mitigation practices from worldwide contexts, drawing on lessons from Japan, Italy, the United States (USA), and China – countries facing similar geological and climatic difficulties with a track record of advanced landslide studies.

This study looks at the mechanisms that influence roadside slope stability, such as soil saturation, shear strength reduction, and slope geometry, using a comprehensive assessment of the literature and a comparative assessment of international practices. It evaluates the possibilities of modern mitigation approaches such as Japan's real-time sensor-based monitoring systems, Italy's bioengineering slope stabilisation methods, USA's geotechnical interventions, and China's slope reinforcement and remote monitoring. These ideas are evaluated for viability and adaptability within New Zealand's specific environmental and economic frameworks.

The initial theoretical analysis will be further strengthened by utilising qualitative insights from expert interviews with quantitative assessments of historical landslide and rainfall data. This methodology emphasises the importance of a

transition toward a proactive, cost-effective, and climate-resilient approach by exposing major gaps in current policies and practices. The findings aim to assist stakeholders, ranging from policy makers, to project managers and geotechnical and civil engineers, on how to create a sustainable framework that not only improves resilience but also reduces long-term costs and environmental implications.

As rainfall patterns become increasingly unpredictable and extreme events occur with greater frequency, the adoption of innovative and adaptable solutions becomes critical [3]. This study contributes to the continuing discussion about landslide mitigation by proposing measures to protect New Zealand's infrastructure and communities against the growing hazard of rainfall-induced landslides.

RESEARCH SIGNIFICANCE

The importance of this research stems from the potential to improve New Zealand's approach to rainfall-induced landslide mitigation by incorporating learning from successful global practices. .The study highlights critical policy gaps and calls for proactive, cost-effective strategies tailored to New Zealand's environmental and economic context. It promotes low-cost, high-impact solutions through affordable technologies, efficient resource use, and climate-resilient approaches that remain effective under future climate scenarios. The findings are relevant for policymakers, engineers, and stakeholders, with a focus on enhanced monitoring technology, bioengineering approaches, and sustainable frameworks. Finally, this research helps to protect infrastructure, reduce economic losses, and build long-term resilience to the mounting hazards posed by climate-induced landslides.

METHODOLOGY

This study used a structured, qualitative approach to analyse international solutions for minimising rainfall-induced roadside landslides and their suitability to New Zealand's environmental, geological, and socioeconomic setting. The approach involved a systematic literature review (SLR), followed by analysing international case studies and expert interviews to develop recommendations.

Systematic Literature Review (SLR)

To ensure that the SLR is conducted and reported consistently and transparently, the study adopted the preferred reporting items for systematic reviews and meta-analyses (PRISMA2020) framework [4]. The goal was to identify and critically evaluate academic and scientific literature on slope stability, mitigation measures, and climate resilience approaches relevant to roadside rainfall-induced landslides. Scientific databases including Scopus, ScienceDirect, and Google Scholar and online records were searched to identify relevant sources published between 2000 and 2024. The search terms included "rainfall-induced landslides," "slope stabilisation/stabilization," "early warning systems," and "bioengineering." A total of 169 eligible records were identified for initial screening, from which 71 were selected for qualitative synthesis. Fig.1 illustrates the details of this process using a PRISMA flow diagram.

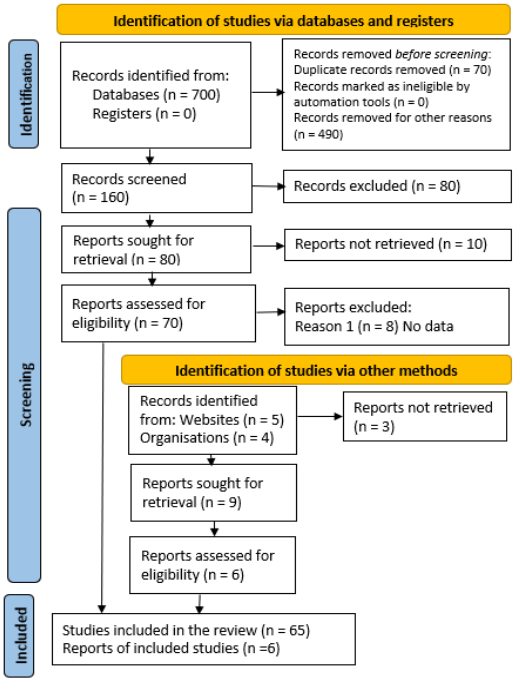

Fig.1 PRISMA flow diagram of the study

International Case Study Selection

Records from four countries were identified as potential case studies due to their environmental similarities and demonstrated success in landslide mitigation: Japan (Kyushu), Italy (Dolomites), the United States (California), and China (Three Gorges region). The effectiveness of measures such as real-time monitoring, eco-engineering, rockfall nets, drainage systems, and satellite-based risk assessment was evaluated in these studies. Each instance was assessed for technical viability, cost-effectiveness, scalability, and potential adaptation to New Zealand's particular topography and climate.

Expert Interviews in New Zealand

Semi-structured interviews were conducted with experts in geotechnical engineering, infrastructure planning, and environmental management. Interviewees were selected for their knowledge in slope stability, risk management, and national infrastructure projects. The discussions aimed to identify gaps in present New Zealand practices, validate research findings, and evaluate the

possibility of adapting international tactics to local settings.

Data Analysis and Synthesis

Data from literature and interviews were classified and analysed thematically, emphasising recurring issues and solution patterns. Quantitative data, such as rainfall records, landslide frequency, and mitigating costs, were utilised to conduct a comparison study. The synthesis resulted in an adaptive, hybrid mitigation strategy that balances technical, environmental, and socio-economic factors to improve road network resilience in New Zealand.

RESULTS AND ANALYSIS

Parameters of Rainfall-Induced Landslides

When driving forces surpass resisting forces on a slope, failure occurs. Landslides cause soil, rock, and debris flowing downslope, primarily due to gravity. Shear stress and strength interact in slope-forming materials to drive these processes. Rainfall-induced landslides are triggered by water infiltration, causing loss of matric suction, increased pore water pressure, and decreased effective shear strength [5].

Rainfall can cause landslides through a variety of hydrological factors. Infiltration creates positive pore pressures in shallow soil, reducing the slope materials strength. Saturation can lead to perched water tables and seepage along stratigraphic boundaries, especially in colluvial or residual soils. finally, excessive rainfall can destabilise slopes by creating surface runoff and increased hydraulic loading [6].

Rainfall-Induced Landslides in New Zealand

The New Zealand landscape is highly susceptible to rainfall-induced landslides. Approximately 60% of the land area has steeper slopes than 26°, with over 5% categorised as very erodible [7]. The terrain is primarily made up of young sedimentary and volcanic rocks that can degrade due to water saturation. Rainfall-triggered landslides have occurred in many places, including the North Island and upper South Island, especially during recent storms.

New Zealand's location in the southwest Pacific makes it susceptible to subtropical storms (cyclones), atmospheric rivers, and La Niña-related anomalies, resulting in excessive rainfall. From January to March 2023, Auckland (New Zealand's largest and most populated city) saw unprecedented rainfall of over 600 mm during two major storm events (Fig.2), resulting in over 200 landslides [1].

Landslide threats in New Zealand are exacerbated by tectonic activities and climate change. Seismic shaking can pre-condition slopes for failure, and climate change is expected to increase the frequency and intensity of heavy rainfall events, posing challenges for traditional mitigating techniques. New Zealand landslide database records (Fig.3) indicate the significance of this hazard.

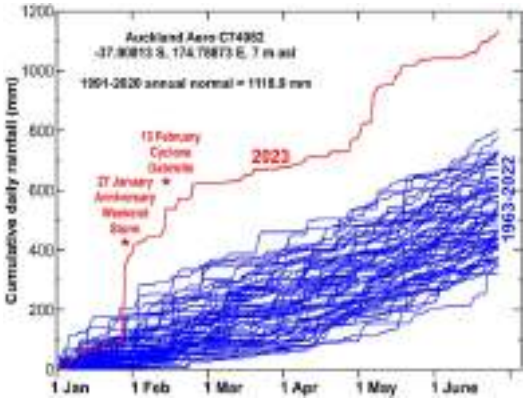

Fig.2 Comparison of Auckland's rainfall data from 1963-2022 with the first half of 2023 [1].

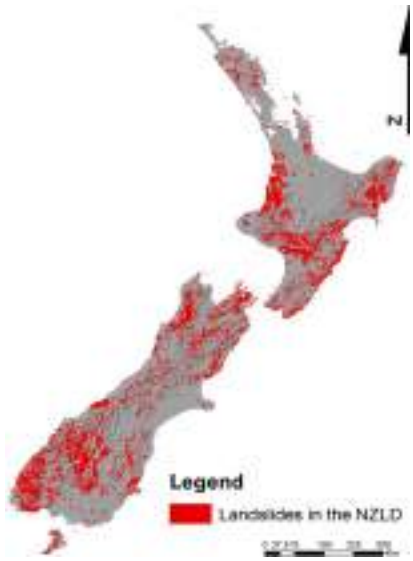

Fig.3 New Zealand landslide database records [7]

Causes and Triggers of Rainfall Landslides

Rainfall is the leading cause of landslides worldwide, accounting for roughly 90% of slope failures. New Zealand's landslides are frequently triggered by soil saturation due to prolonged rainfall, which increases pore water pressure, diminishes matric suction, and weakens shear strength in soils and weathered rock [8]. Water-induced increased soil mass and seepage forces exacerbate slope instability. Human activities such as deforestation, road excavation, and insufficient drainage systems multiply these effects. As urban development into hillside areas alters natural hydrology and removes vegetation, the imminent risk of landslides underlines the importance of proactive mitigation techniques [9].

Economic and Infrastructure Impacts

Roadside landslides in New Zealand pose considerable economic and infrastructure challenges. These disasters disrupt key transportation networks,

causing delays in logistics, limiting access to outlying populations, and resulting in significant repair expenses [10]. These landslides also disrupt emergency response systems, impede agricultural supply chains, and raise insurance and reconstruction costs. The yearly economic impact of landslides in New Zealand is estimated to be between NZD 200 and 300 million. With the intensification of rainfall patterns caused by climate change, these costs are anticipated to rise unless proactive mitigation methods and sustainable land-use planning are applied immediately [1].

LANDSLIDE MITIGATION STRATEGIES

As rainfall-induced landslides become more frequent and severe, governments around the world are implementing region-specific mitigation techniques based on their geotechnical and climatic conditions [11]. Recognising the diverse nature of landslide triggers and repercussions, this study assesses successful global methods in reducing landslide risk. Case studies from Japan, Italy, the United States, and China provide significant insights into various mitigation strategies, including advanced real-time monitoring systems, bioengineering techniques, geotechnical interventions, and effective drainage solutions. Each solution is evaluated based on its effectiveness, flexibility, and suitability to New Zealand's unique geography, geology, and environmental constraints. These international best practices serve as the foundation for the creation of a hybrid, adaptive framework that combines tried-and-true tactics into a cohesive, long-term plan for managing landslides in New Zealand.

Japan’s Early Warning and Slope Intervention

Japan, positioned in a geologically active and typhoon-prone zone, has prioritised the development of advanced landslide early warning systems and slope strengthening techniques. The Japanese Meteorological Agency (JMA) forecasts landslides in Kyushu using rainfall thresholds, soil moisture sensors, and real-time geotechnical monitoring [12]. These technologies have considerably reduced mortality by alerting communities and implementing evacuation measures. In high-risk regions, which are defined as areas susceptible to landslides due to steep terrain, loose soil composition, heavy rainfall, and frequent typhoons, geotechnical interventions like soil nailing, retaining walls, and surface drainage systems are used to stabilise slopes and redirect runoff. Japan’s policies also recommend vegetal slope protection and multi-tiered barriers along transportation corridors [14].

Italy’s Bioengineering and Flexible Barriers

The case study in Italy includes slopes preserved via ecological and geotechnical interventions due to their high topography and history of landslides. Bioengineering involves employing native vegetation to improve soil structure and infiltration control. Geotextiles, root mats, and shallow-rooted plant species help maintain surface soils, supporting these approaches [13]. Flexible net barriers and rockfall catchment fences are strategically positioned along roads and valleys to provide cost-effective and low-maintenance solutions. Italy's policy prioritises landscape-sensitive designs and engages local people in maintenance and response planning [16].

USA’s Engineered and Monitored Interventions

The case study of the USA includes landslides in California's coastal and mountainous areas, mitigated by engineered drainage, slope contouring, and real-time geotechnical monitoring. Subsurface drainage systems, including horizontal drains, toe drains, and lined ditches, help stabilise slopes by lowering groundwater levels. Highways and development zones use reinforced retaining walls and terracing. Using steel meshes or concrete cribbing [14]. LiDAR, GPS stations, and drones improve slope deformation tracking, allowing for proactive maintenance and emergency preparedness [18].

China’s Engineering and Remote Sensing

The Three Gorges region of China, which is prone to reservoir-induced landslides and strong monsoon rains, has used advanced engineering and monitoring measures to reduce slope instability [15]. Large-scale slope engineering solutions include the use of rock bolts, anchor cables, and concrete retaining walls to stabilise eroded rock faces and loess slopes [16]. These physical reinforcements are supplemented by cutting-edge remote sensing technologies such as Interferometric Synthetic Aperture Radar (InSAR) and high-resolution satellite imaging, which allow for early identification of slope displacement and targeted treatments. In addition, China makes significant investments in slope terracing and vegetation cover to reduce surface erosion, combining ecological restoration with engineering solutions [21].

The efficacy scores in Fig.4 were calculated using a qualitative synthesis of international case studies, peer-reviewed literature, and thematic insights from expert interviews. The performance of each country in Monitoring Systems, Bioengineering, and Structural Reinforcements (i.e., geotechnical interventions) was assessed using a normalised comparison index. This scale (High = 80-90%, Medium = 60-75%, and Low = 50%) examines implementation maturity, practical outcomes in high-risk zones, and alignment with New Zealand's climate and geography. For example, Japan's effective integration of slope sensors and early-warning

networks earned it a high monitoring score, while China and the USA have shown strong applications in satellite monitoring and engineered slope reinforcements. Italy's higher score in bioengineering comes from its decades of experience in vegetative stabilising efforts in alpine regions. Expert consultation was used to validate these scores in order to guarantee their relevance and contextual accuracy.

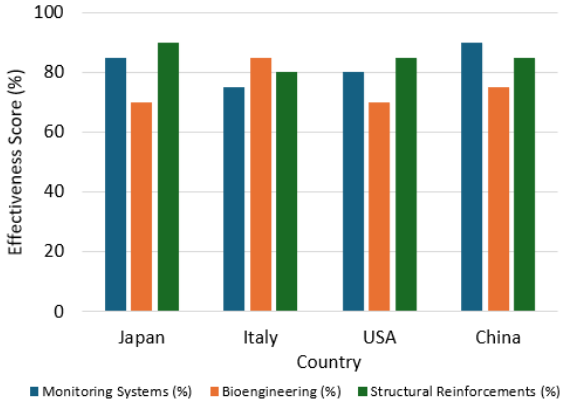

Fig.4 Comparative effectiveness of international landslide Mitigation Practices by Country

FINDINGS AND DISCUSSIONS

New Zealand's current landslide mitigation approach is based on a combination of traditional engineering procedures and centralised hazard monitoring systems [22]. Retaining structures, such as gabion walls and reinforced concrete barriers, are usually used to provide immediate structural support for unstable slopes. Likewise, drainage systems, which include both surface runoff channels and underground pipe networks, help to manage water infiltration and reduce pore pressure accumulation.

The GeoNet hazard monitoring network complements these physical measures by collecting and distributing real-time data on rainfall, seismic activity, and geological changes. However, these treatments are frequently reactive rather than proactive, reacting to recognised threats or failure incidents. They are also often prohibitively expensive in remote places, and not often connected with prediction technology or climate adaptation plans.

Through a synthesis of expert interviews, peer-reviewed analysis, and international comparative assessment, this study highlights the urgent need for a transformation in New Zealand's approach to managing rainfall-induced landslides. The findings show the limitations of reactive approaches, which rely primarily on post-event actions and historical risk assessments. Recent extreme weather events have exposed the vulnerability of New Zealand's current mitigation strategies [1, 17], especially when compared to successful practices in Japan, Italy, the United States, and China, which employ proactive, data-driven, and climate-responsive integrated systems [11, 12, 15].

The suggested hybrid mitigation methodology must be adaptable to a wide range of geotechnical situations throughout New Zealand while staying economically viable, especially in rural and infrastructure-sensitive areas. It also needs to emphasise on cost-sensitivity, promote the use of locally accessible resources and labour, while prioritising low-maintenance solutions such as vegetative stabilisation and modular drainage systems.

The use of real-time digital monitoring tools is an essential part of the model. Systems like InSAR, Light Detection and Ranging (LiDAR), and localised slope sensors are capable of identifying minute ground deformations and rainfall thresholds, allowing for predictive maintenance and early evacuation plans [17]. By enabling early detection, these systems redefine hazard response as a strategic rather than reactive approach.

The second component includes geotechnical intervention solutions such as subsurface drainage, slope contouring, soil nailing, and retaining structures. These approaches are essential in high-risk areas, particularly along critical transportation routes and locations prone to frequent slope failure. For long-term, sustainable, and cost-effective outcome, a combination of ecological and bioengineering solutions can serve as alternatives or complements to geotechnical interventions. Native vegetation, geotextiles, and root-reinforced barriers stabilise slopes while also improving environmental quality and biodiversity.

Table 1: Adaptability of Strategies to New Zealand

Mitigation Method	Technical Feasibility	Cost	Environmental Fit
Early Warning Systems	H	M	H
Reforestation	M	L	VH
Drainage Improvements	H	H	M
Soil Nailing	M	H	M
Slope Grading	H	M	L
Retaining Walls	H	VH	M

VH: Very High, H: High, M: Medium, L: Low, VL: Very Low

Table 1 presents a comparative assessment of the adaptability of selected international landslide mitigation strategies to the New Zealand context. The ranking criteria technical feasibility, cost, and environmental fit were developed through a synthesis of findings from international case studies (i.e., Japan, Italy, USA, China), expert interviews conducted as part of this study, and the thematic literature review. The evaluation is qualitative in nature and based on how well each strategy aligns with New Zealand's specific geotechnical, climatic, and socio-economic conditions. For example, early warning systems are ranked highly in technical feasibility and environmental fit due to existing infrastructure (e.g., GeoNet) and minimal physical intrusion. In contrast, retaining walls, though technically effective, are rated

"Very High" in cost due to their resource-intensive construction and maintenance, especially in remote areas. These rankings were informed by published data on implementation outcomes in each country, expert judgments regarding transferability, and environmental impact considerations specific to steep, rainfall-prone terrain in New Zealand.

CONCLUSION

This study evaluated the worsening issue of rainfall-induced roadside landslides in New Zealand, examining local challenges and insights from international best practices. Through a systematic literature review and site-specific hazard assessment, it found that New Zealand's current mitigation strategies – primarily retaining structures, drainage systems, and GeoNet monitoring – are largely reactive and insufficient to address the increasing challenges posed by climate change.

Using the PRISMA2020 framework, the study identified proven mitigation strategies from Japan, Italy, the United States, and China. These countries employ a strategic mix of geotechnical interventions, digital monitoring, eco-stabilisation, and community-based management. Semi-structured interviews with New Zealand industry experts reinforced these findings and highlighted key barriers, including technological limitations, high rural implementation costs, and limited integration of climate policy.

Thematic and comparative analysis revealed a significant opportunity for New Zealand to strengthen resilience through a hybrid mitigation strategy. This integrates real-time digital monitoring, geotechnical and bioengineering solutions, and community engagement to provide a scalable response to rainfall-induced landslides. Its relevance and robustness were confirmed through industry experts peer review.

This study advocates a shift from reactive to proactive, climate-resilient risk management. The proposed hybrid strategy is both feasible and adaptable, offering a forward-looking pathway to protect infrastructure, ecosystems, and communities in a changing climate.

REFERENCES

[1] M. S. Brook and C. Nicoll, Brief report of fatal rainfall-triggered landslides from record-breaking 2023 storms in Auckland, New Zealand. Landslides, Vol., 2024, pp.1-9.
[2] T. T. A. EQC, Resilience strategy for risk reduction 2024–2029. 2024.
[3] Y. Yang, P. Andrews, T. Carey-Smith, M. Uddstrom and M. Revell, Prediction of moderate and heavy rainfall in New Zealand using data assimilation and ensemble. Advances in Meteorology, Vol. 2015, 2015, pp.460243.
[4] L. Hijriyah, A. Alias and M. F. M. Sahabuddin, Exploring walkability research trends based on systematic literature review (SLR) by applying PRISMA. Open House International, Vol. 49, 2023, pp.63-121.
[5] T. Davies, Landslide hazards, risks, and disasters: introduction. Elsevier, 2015.
[6] A. Tohari, Study of rainfall-induced landslide: a review. IOP Publishing, 2018.
[7] G. Science, Landslide database web map service. [WWW Document]. n.d.
[8] B. Rosser, C. Massey, B. Lukovic, S. Dellow and M. Hill, Development of a Rainfall-Induced Landslide Forecast Tool for New Zealand. Understanding and Reducing Landslide Disaster Risk: Volume 3 Monitoring and Early Warning 5th, Vol., 2021, pp.273-277.
[9] H. Chen and C. Lee, A dynamic model for rainfall-induced landslides on natural slopes. Geomorphology, Vol. 51, 2003, pp.269-288.
[10] C. Massey, D. Townsend, E. Rathje, K. E. Allstadt, B. Lukovic, Y. Kaneko, B. Bradley, J. Wartman, R. W. Jibson and D. Petley, Landslides triggered by the 14 November 2016 Mw 7.8 Kaikōura earthquake, New Zealand. Bulletin of the Seismological Society of America, Vol. 108, 2018, pp.1630-1648.
[11] L. Picarelli, S. Lacasse and K. K. Ho, The impact of climate change on landslide hazard and risk. Understanding and Reducing Landslide Disaster Risk: Volume 1 Sendai Landslide Partnerships and Kyoto Landslide Commitment 5th, Vol., 2021, pp.131-141.
[12] N. Yasufuku and A. Alowiasy, Challenges and lessons learned from heavy rainfall-induced geo-disasters over the last decade in Kyushu Island, Japan. Springer, 2023.
[13] R. Gobinath, G. Ekambaram, P. Prakash, K. Priya and V. S. Marella, Soil Bioengineering Practices for Sustainable Ecosystem Restoration in Landslide-Affected Areas. CRC Press, 2024.
[14] N. Kovaleva and I. Kovalev, SOIL Engineering: Modern Challenges and Development Prospects. Moscow University Soil Science Bulletin, Vol. 78, 2023, pp.410-424.
[15] K. Yin, L. Chen, F. Ma and W. Cheng, Practice and thinking of landslide risk management considering their secondary consequences in the Three-Gorges Reservoir, China. CRC Press, 2018.
[16] F. Wang and T. Li, Landslide disaster mitigation in Three Gorges reservoir, China. Springer, 2009.
[17] M. Cook, M. Brook and M. Cave, Interferometric Synthetic Aperture Radar (InSAR) and field‐based observations of rainfall‐triggered landslides from the November 2021 storm, Gisborne/Tairāwhiti, New Zealand. New Zealand Geographer, Vol. 79, 2023, pp.138-152.

Copyright © Int. J. of GEOMATE All rights reserved, including making copies, unless permission is obtained from the copyright proprietors.

15th Int. Conf. on Geotechnique, Construction Materials & Environment,
Kyoto, Japan, 11-13 November 2025, ISBN 978-4-909106124 C3051

RELATIONSHIP BETWEEN PUBLIC SPACE AND PEDESTRIAN BRIDGES IN SUBURBAN RESIDENTIAL AREAS

Ryunosuke Komatsu[1], Kazunari Tanaka[2]

[1]Architecture, Civil Engineering and Urban Design, Osaka Institute of Technology, Japan
[2] Faculty of Engineering, Osaka Institute of Technology, Japan

ABSTRACT

The Japanese government has reported the need for maintaining and updating infrastructure. Dangerous road crossings are a known problem, such as when pedestrian crossroads do not have pedestrian bridges or crossings. The purpose of this study is to evaluate existing pedestrian bridges. We conducted fieldwork and discriminant analysis. First, we conducted surveys and analyses to clarify the relationship between pedestrian bridges and jaywalking. Next, we confirmed the reliability of the first survey by observing an actual pedestrian bridge. Then, we confirmed the relative locations of pedestrian bridges and surrounding facilities in Tondabayashi City, Osaka Prefecture. We also investigated the changes in housing around the pedestrian bridge. As a result of analysis, there was a significant relationship between jaywalking and explanatory variables. Additionally, we developed an equation to predict jaywalking. However, we found that the relationship between jaywalking and the time to cross a pedestrian bridge was weak. Therefore, we considered that it is possible to evaluate pedestrian bridges by combining predictions of jaywalking with other factors. As a result of the survey, there are many pedestrian bridges near residential areas far away from stations. Also, there are some of the pedestrian bridges near schools. In addition, we found that the number of houses around pedestrian bridges has been increasing over the past 20 years. We consider that by combining predictions of irregular crossings with changes in facilities, it will become an evaluation indicator for new pedestrian bridges.

Keywords: Jaywalking, Discriminant Analysis, Suburban Area, Building Transition

INTRODUCTION

In 2013, the Japanese Ministry of Land, Infrastructure, Information and Tourism reported the need for maintaining and updating infrastructure [1]. In addition, dangerous road crossings are a known problem, such as when pedestrian's crossroads without using pedestrian bridges or crossings [2]. According to previous research on jaywalking [3], the factors said to cause jaywalking were age, surrounding facilities, roadway width, and pedestrian crossing installation spacing. On the other hand, there is no said association between jaywalking and pedestrian bridges. In addition, jaywalking was related between vehicle behavior and road structure [4]. The relationship between these dangerous crossings and crossing facilities cannot be separated. Each municipality in Japan does not rate pedestrian bridges on the same items [5]. Many municipalities have identified declining numbers of users and aging. Jaywalking is also an item that some municipalities have incorporated. Therefore, we thought that predicting crossings outside of crossing facilities would facilitate consideration of the need for pedestrian bridges and lead to evaluation of new pedestrian bridges.

RESEARCH SIGNIFICANCE

In Japan today, each municipality is considering whether to remove or keep pedestrian bridges. The evaluation indicators differ slightly from municipality to municipality. The purpose of this study is to find common indicators for evaluating pedestrian bridges. Using them, the need for a pedestrian bridge will become apparent. It will then be easier to decide whether to keep or remove the pedestrian bridge. Ultimately, this will help solve the problem of aging pedestrian bridges.

DISCRIMINANT ANALYSIS

We show the methodology and results of our analysis of the relationship between pedestrian bridges and road crossings outside crossing facilities, focusing on the configuration of the road space.

Definition Of Jaywalking

Road crossing outside of a crossing facility was defined as "Jaywalking" in this study (Fig.1).

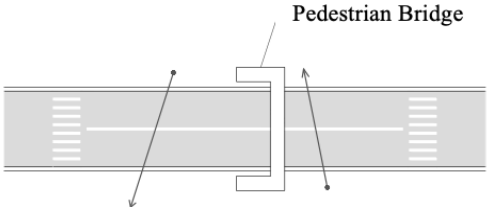

Fig.1 Positioning of jaywalking in this study

Preliminary Investigation

We conducted a discriminant analysis using IBM SPSS Statistics to determine what elements of the road space are associated with jaywalking. We used eight elements as explanatory variables in our analysis (Table 1). The objective variable is the presence or absence of jaywalking. We defined our target as a single point on the road as the "point" and collected data for each element at 25 points.

Table 1 Eight types of road space elements used

	Types of Elements	Notation
Element 1	Traffic Volume	Tv
Element 2	Number of Lanes	NL
Element 3	Distance from Point to Nearest Crosswalk	D1a
Element 4	Distance from Point to Crosswalk on Opposite Side of Element 3	D1b
Element 5	Distance from Point to Pedestrian Bridge	D2
Element 6	Availability of Median Strip	MS
Element 7	Availability of Signal at Crosswalks Near the Point	a
Element 8	Availability of Signal at Crosswalk on the Opposite Side of Element 7	b

We measured the distance from elements 3 to 5 using Google Earth, as shown in Figure 2.

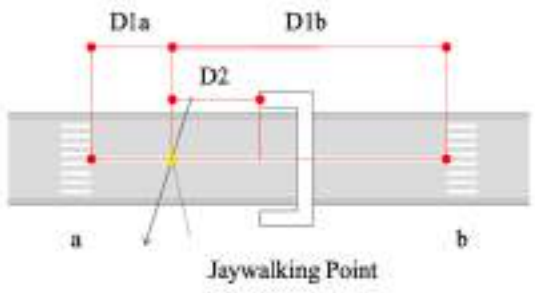

Fig.2 Measuring elements of distance

As a result of analysis, we had a canonical correlation of 0.652 (Table 2). Since this value is above 0.6, we know that there is a relationship between the objective variable, the presence or absence of jaywalking, and the eight explanatory variables. However, we obtained a non-significant result with a significance probability of 0.231, which is greater than 0.05 (Table 3). We also found from the structure matrix that "NL", "D2", and "Tv" are related to jaywalking in this function, in that order (Table 4).

Reasons for the lack of significance include the use of quantitative data as explanatory variables and the large number of explanatory variables relative to the number of subjects surveyed. We considered it important to increase the number of subjects surveyed and to make the explanatory variables quantitative data.

Table 2 Eigenvalue

Function	Eigenvalue	Variance %	Cumulative %	Canonical Correlation
1	0.739	100.0	100.0	0.652

Table 3 Wilks' Lambda

Function	Wilks' Lambda	Chi square	Degree of Freedom	Significance Probability
1	0.575	10.513	8	0.231

Table 4 Structure Matrix

	Function
	1
Tv	0.770
NL	0.544
D1a	0.395
D1b	0.387
D2	-0.309
MS	0.294
a	-0.223
b	0.222

Main Investigation

We defined a "section" between crosswalks because we thought that jaywalking is not necessarily a single point on the road. Therefore, we chose a new element (Table 5) and collected data for each element in 39 intervals, as in the preliminary investigation.

Table 5 Seven types of road space new elements used

	Types of Elements	Notation
Element 1	Number of Lanes	NL
Element 2	Distance between Crosswalks	D
Element 3	Distance of no Median Strip in Section	Dm
Element 4	Distance of no Planting or Guardrail in Section	Dp
Element 5	Time of Crosswalk Signal (red/green)	R1/G1
Element 6	Time of Crosswalk Signal (red/green) on other side of Element 5	R2/G2
Element7	Time to Cross the Pedestrian Bridge	Tp

From our preliminary investigation, we devised five equations to make the results of our analysis significant. Equation (1) showed the ratio of ease of crossing the roadway. Equation (2) showed the ratio of ease of exiting the sidewalk to the roadway. We defined a "signal cycle" as the sum of the red and

green times of a signal. Equations (3) and (4) showed the ratio of ease of crossing at a pedestrian crossing. Equation (5) showed the ratio of time spent crossing a pedestrian bridge to the time spent waiting for a crosswalk. The type of analysis was discriminant analysis, as in the preliminary investigation. Equation (1) and (2) showed elements of distance. Equation (3) to (5) showed elements of time.

$$Dm/D = Dmr \quad (1)$$

$$Dp/D = Dpr \quad (2)$$

$$G1/(R1 + G1) = T1 \quad (3)$$

$$G2/(R2 + G2) = T2 \quad (4)$$

$$Tp/\{(R1 + G1 + R2 + G2)/2\} = T3 \quad (5)$$

$$Jcv = 0.532 \times NL - 1.451 \times Dmr - 2.223 \times Dpr + 3.268 \times T1 + 2.947 \times T2 - 0.429 \times T3 - 1.836 \quad (6)$$

Explanatory variables are the value calculated by substituting the collected data into these equations and NL. The result of analysis, we had a canonical correlation of 0.678 (Table 6). Since this value is above 0.6, we know that there is a relationship between the objective variable, the presence or absence of turbulent crossings, and the six explanatory variables. We also obtained a significant result as the probability of significance was 0.002, well below 0.05 (Table 7). Moreover, we found from the structure matrix that "Dmr", "Dpr", and "NL" are related to jaywalking in this function, in that order (Table 8). In addition, we found the coefficients of each element from the canonical discriminant function coefficients and could develop Eq. (6) using them (Table 9). In this study, Eq. (6) is referred to as the jaywalking prediction equation. Substituting the collected data into this equation gives the value "Jcv" that determines whether jaywalking. If Jcv is a positive number, determine that jaywalking occurs. Conversely, if it is a negative number, it is determined that it does not occur. When we substituted our data from main investigation into the jaywalking prediction equation, we found a hit rate of 87.5%.

However, two of the sections where predictions failed were those with pedestrian bridges. We also supposed that one of the reasons was the small area between pedestrian crossings. Furthermore, it is clear from Table 8 that the time factors T1, T2, and T3 are weakly related to jaywalking. Therefore, we considered only the jaywalking prediction equation to be insufficient as an indicator to evaluate pedestrian bridges.

Table 6 Eigenvalue

Function	Eigenvalue	Variance %	Cumulative %	Canonical Correlation
1	0.850	100.0	100.0	0.678

Table 7 Wilks' Lambda

Function	Wilks' Lambda	Chi square	Degree of Freedom	Significance Probability
1	0.541	20.918	6	0.002

Table 8 Structure Matrix

	Function
	1
Dpr	-0.619
Dmr	-0.615
NL	0.601
T1	-0.219
T2	0.123
T3	0.072

Table 9 Canonical Discriminant Function Coefficient

	Function
	1
NL	0.532
Dmr	-1.451
Dpr	-2.223
T1	3.268
T2	2.947
T3	-0.429
(A Constant)	-1.836

SURVEY OF CHANGING IN HOUSING AROUND THE PEDESTRIAN BRIDGE ON GIS

We thought it would be possible to evaluate pedestrian bridges by relating them to other factors than jaywalking. Therefore, we investigated changes in the residences and facilities around the pedestrian bridge. They were new factors to combine with jaywalking. The reason for choosing this factor was that the demand for pedestrian bridges is influenced by the number of people living in the vicinity and the volume of traffic.

The survey covered the area around the Fumigaoka Pedestrian Bridge and Nishikigaoka Pedestrian Bridge in Tondabayashi City, Osaka Prefecture. We chose this location because it is a suburban residential area where building changes have been documented, and the data is available to the public. We used Tondabayashi City's open data to check the building's transition in QGIS. The building

transition period is 20 years, from 2004 to 2024.

We compared maps of the pedestrian bridge area in 2004 (Fig.3) and 2024 (Fig.4). In consequence, we found an overall increase in housing especially the area circled in red in Fig 4.

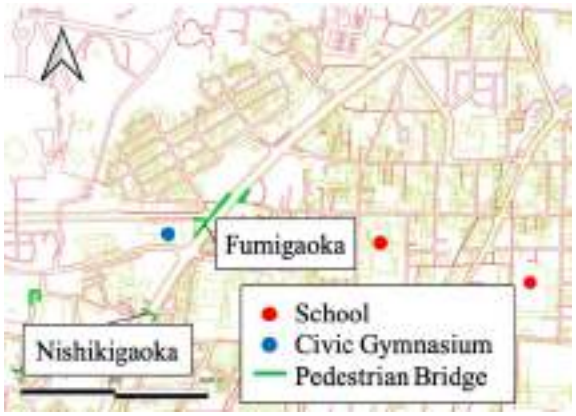

Fig.3 Map around the pedestrian bridge in 2004

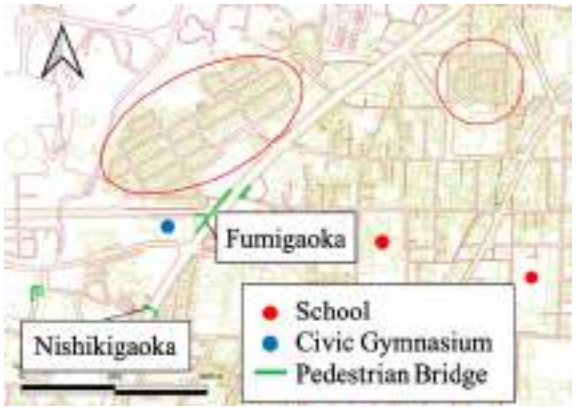

Fig.4 Map around the pedestrian bridge in 2024

The Fumigaoka Pedestrian Bridge was located near the civic gymnasium. Thus, we determined that as the number of households increases, the number of people using the gymnasium will also increase. Additionally, the residential area northwest of the Fumigaoka pedestrian bridge was included in the school district of the school shown on the map [6]. Therefore, we also inferred an increase in student use for commuting to school due to the increase in the number of households.

There were apartments, housing complexes, and a high school in the vicinity of the Nishikigaoka pedestrian bridge. However, the number of buildings did not increase compared to the area around the Fumigaoka pedestrian bridge. Furthermore, the school district was different from that around the Fumigaoka pedestrian bridge. Therefore, we estimated that the number of pedestrian bridge users would not increase much.

CONCLUSION

In this study, we were able to develop a prediction equation of jaywalking based on elements of the road space. However, that equation had a weak relationship to the pedestrian bridge. Therefore, we found that adding the transition of the facilities surrounding the pedestrian bridge could potentially evaluate the pedestrian bridge. We considered that it is the change in demand for pedestrian bridges due to housing transition which may affect the likelihood of jaywalking.

In addition to the street space elements we used in this investigation, there are several other elements that could be added. Examples include no signal or push-button signals, pedestrian attributes, and time of day. Furthermore, we consider that research on pedestrians' impressions of the presence of pedestrian bridges will clarify the relationship between pedestrian bridges and street space. In this map-based survey, we had only identified residential changes. We consider that future studies could better reveal changes in demand for pedestrian bridges by identifying declines in facilities and buildings, such as train stations and hospitals.

REFERENCES

[1] Ministry of Land, Infrastructure, Transport and Tourism (MLIT), Initiatives for Maintenance and Management of Social Infrastructure, 2018, pp. 2–6

[2] National Police Agency Traffic Bureau, Traffic Accidents in 2024, 2025, pp. 9

[3] Yuriko NAGAWAKI, and Koji SUZUKI, JSTE Journal of traffic engineers, Vol.8, Issue 2 (A Special Issue A), 2022.2, pp.A 149-A 158

[4] Takuma ENOMOTO, Fumihiko NAKAMURA, Toshiyuki OKAMURA, Infrastructure planning review, Vol.26 No.2, 2009.9, p347-354

[5] Transportation Infrastructure Department, Shizuoka Prefecture, Study of The Ideal Pedestrian Bridge, 2013, pp. 8-10

[6] Tondabayashi City, “Elementary and Junior High School District in Tondabayashi City”

Copyright © Int. J. of GEOMATE All rights reserved, including making copies, unless permission is obtained from the copyright proprietors.

15th Int. Conf. on Geotechnique, Construction Materials & Environment,
Kyoto, Japan, 11-13 November 2025, ISBN 978-4-909106124 C3051

METHOD ON THE PREDICTION ABOUT FLOW LINES IN WALKING SPACES

Ryuga Toda[1], Kazunari Tanaka[2]

[1] Architecture, Civil Engineering and Urban Design, Osaka Institute of Technology, Japan
[2,] Faculty of Engineering, Osaka Institute of Technology, Japan

ABSTRACT

The number of foreign visitors to Japan is increasing due to the end of the COVID-19 pandemic and the depreciation of the yen. In 2024, the number of foreign tourists reached a record high. Therefore, it is necessary to develop walking spaces around tourist attractions and public transportation facilities that maintain walkability and attractiveness. The purpose of this study was to analyze the relationship between human behavior and gradient in walking spaces and to predict flow lines as part of measures to create more comfortable walking spaces. Based on a survey conducted in Maruyama Park, an evaluation method using only contour lines was devised. Using this evaluation method, we compared human behavior in walking spaces along the Seta River and the Yodo River. The two evaluation methods successfully captured the major characteristics of human flow lines; however, the details were not well predicted. These results suggest that additional elements are needed to improve the method's practicality.

Keywords: Trajectory, Contour line, Projective transformation, Gradient

INTRODUCTION

In Japan, the number of foreign visitors to Japan is increasing due to the end of the COVID-19 pandemic and the depreciation of the yen [1]. In 2024, the number of foreign tourists reached a record high. Public transportation and walking spaces in and around tourist attractions are becoming increasingly important. At the same time, Japan is facing challenges such as a declining population, falling birth rate, and aging population [2,3]. As a result, there are concerns about the decline in regional vitality due to the shuttering of shopping arcades and vacant houses. Therefore, there is a growing need to enhance urban attractiveness and create livelier spaces.

On June 26, 2018, the "Conference on Creating Urban Diversity and Innovation" compiled a proposal entitled "Urban Renewal Starting with 'Comfortable and Inviting Towns to Walk Around' [4]. This initiative aims to shift from car-centered cities to people-centered city centers to support rich lifestyles. For these reasons, it is necessary to develop walking spaces that maintain walkability and attractiveness.

Previous studies have evaluated walkability. Yamada [5] clarified the characteristics of walking acceleration and the connection to psychological walkability. Morioka [6] clarified the environmental factors affecting the "ease of walking" and the "desire to walk." We believed that if we could predict the flow lines, we could create more walkable spaces. In this study, we evaluated walking spaces to predict flow lines by focusing on the relationship between human behavior and gradient.

PURPOSE AND METHODS

The purpose of the research was to analyze the relationship between human behavior and gradient and to predict flow lines by using a gradient walking space that is unaffected by cars. We first conducted a study in Maruyama Park and then devised an evaluation method for predicting human flow lines. To verify the accuracy of this evaluation method, we conducted experiments at two additional locations.

RESEARCH SIGNIFICANCE

This study focuses on the relationship between gradient and walking behavior and aims to identify the conditions that make walking spaces comfortable. The findings may provide new insights into pedestrian-centered space design, as well as contribute to the development of design guidelines to improve safety and comfort. In addition, it may contribute to creating more attractive walking spaces in urban planning and landscape design by reflecting the actual movement of people.

SURVEY 1

This survey investigated how gradient affects human behavior when people walk in a pedestrian space. Maruyama Park in Kyoto City was selected due to its maximum gradient of 8° unaffected by cars and mostly gentle gradients of 3° to 6°. It is a popular tourist destination, ideal for observing more unconscious behavior patterns. Before performing the

field survey, a topographic analysis of the site was conducted using QGIS. The survey method consisted of multiple video recordings, each about 10 minutes long, which were analyzed using Kinovea, a video analysis software. The trajectory was separated into a starting point and an ending point, and 23 different trajectories were taken each time.

We flattened the trajectories on the images using Photoshop, then compared with contour maps generated with QGIS. The contour interval for the topographic analysis was 10 cm.

Fig.1 Subject location in Maruyama Park

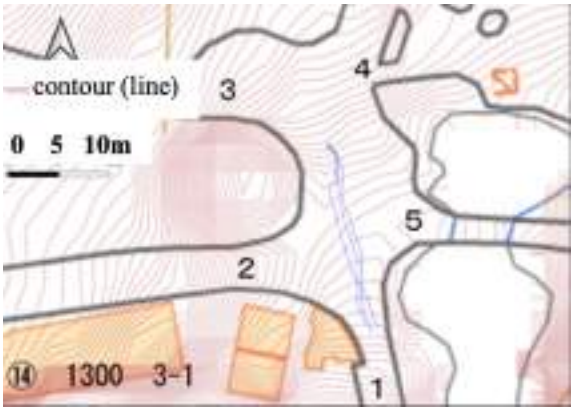

Fig.2 Contour lines and trajectories

Survey Results

The results of the survey revealed that the trajectories from the same starting and end points follow similar trajectories, regardless of the time of day. The walking range was also similar. Those walking perpendicular to the contour lines had somewhat coherent trajectories, whereas those walking along the contour lines tended to spread out horizontally.

Considerations

The direction of movement is shown in Figure 3. Looking at the angle of the walking direction relative to the contour lines, the angles are similar. Therefore, a reference line was placed in the east-west direction, and color-coded points indicated changes in the contour lines of the same height. The direction of movement shows that the green line, yellow line, and orange line are advancing in that order. If we look at each line based on the reference line, we see that the angles are similar in the order of the direction of travel. Given that people are most likely to walk in this order, people are likely to go to a contour line that is close to the angle of the contour line they passed. In other words, the smaller the angle difference from the contour line, the easier it is for people to walk.

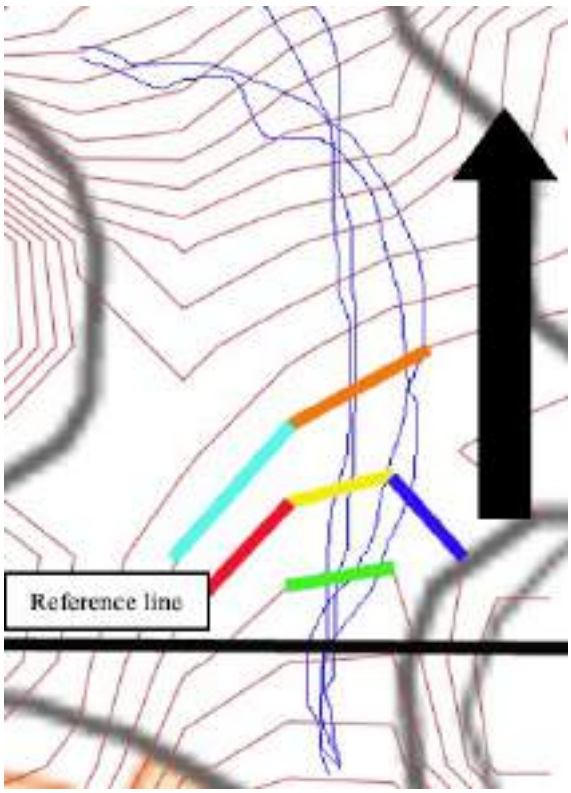

Fig.3 Flow lines and angle differences

SURVEY 2

Based on the findings from Survey 1, we attempted to predict human behavior using only contour lines. Two locations were chosen for the experiment: one along the Seta River in Otsu City, Shiga Prefecture, and the other along the Yodo River in Osaka City, Osaka Prefecture. Both were pedestrian-only, straight walking spaces where the characteristics of human behavior are easily observed. As an example, the subject location along the Seta River is shown in Figure 4. We used two evaluation methods to evaluate the two walking spaces. In making our assessment, we drew a mesh on the map. We determined the size of one mesh by considering the width and distance of the experimental site. As in Survey 1, the contour interval was set at 10 cm for the topographic analysis. We compared the contour lines of the topographic analysis to the map and drew a

mesh on the map for evaluation.

Fig.4 Walking space along the Seta River

Evaluation Method 1

In Evaluation Method 1, the less the angle difference between the contour lines, the easier it is for people to walk. Therefore, the evaluation is highest when the angle difference between the contour lines is 0° and 180°. After determining the angle for each mesh, the angle difference between neighboring meshes is calculated and converted to a 45-step evaluation. We used this 45-point scale to evaluate the mesh.

The 3D representation of the evaluation results along the Seta River is shown in Figure 5. From the evaluation, it is predicted that few people will walk in the middle in the walking space, while many are expected to walk along the edges.

The 3D representation of the evaluation results along the Yodo River is shown in Figure 6. From the evaluation, it can be predicted that people will generally walk on the south side of the Yodo River, as the evaluation decreases toward the north.

Fig.5 Evaluation Method 1 along the Seta River

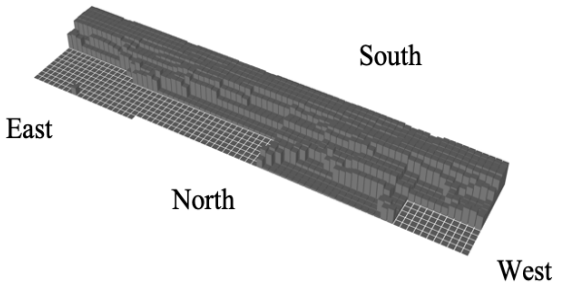

Fig.6 Evaluation Method 1 along the Yodo River

Evaluation Method 2

This method expands on Method 1 by also assigning high scores to paths when the angle difference was 90° because it was easier to walk along the contour lines.

The 3D representation of the evaluation results along the Seta River is shown in Figure 7. From the evaluation, people are expected to move from west to east around the middle of the beginning and end of the evaluated walking space. Fewer are expected to walk on the west side.

The 3D representation of the evaluation results along the Yodo River is shown in Figure 8. From the evaluation, it can be predicted that many people walk on the south side of the road as in Method 1. Also, the evaluation is lower the closer one goes to the middle of the road, which means that fewer people are expected to walk in the middle of the road.

Fig.7 Evaluation Method 2 along the Seta River

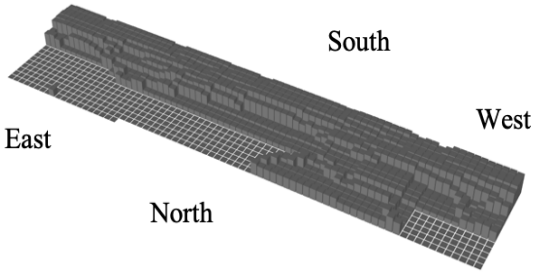

Fig.8 Evaluation Method 2 along the Yodo River

Experiments and Results

We conducted the field survey in the walking space along the Seta River. 21 people were surveyed. All those who moved from west to east and east to west moved around the middle of the start and end of the evaluated walking space. Eight continued walking on the west side, three continued walking on the east side, one continued walking in the center, seven moved from the west side to the east side, and three moved from the east side to the west side. The most people walked on the west side of the street, but the second most moved from the west side to the east side. In this evaluation, we were able to capture the characteristics of the locations where people move.

Next, we conducted the field survey in the walking space along the Yodo River. 13 people were observed. The survey results found that no one moved from south to north or north to south. Eight people continued to walk on the north side, and five people continued to walk on the south side. The most common result was that people continued to walk on the north side of the street, which was the lowest evaluated side. In addition, no one walked near the center, which was in line with the evaluation.

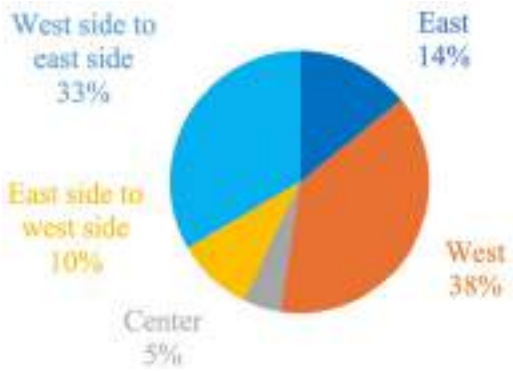

Fig.9 Percentage by category along the Seta River

Fig.10 Percentage by category along the Yodo River

From the above, the two evaluation methods were able to capture the major characteristics of each, but one evaluation method failed to capture multiple characteristics.

Considerations

In the Yodo River survey, the contour interval was set at 10 cm, which may have resulted in a lower evaluation because the contour lines were not marked on the north side of the walking space in the topographic analysis. A more detailed evaluation could be made by reducing the contour interval.

CONCLUSIONS

This study analyzed the relationship between human behavior and gradient to predict flow lines in walking spaces. Based on a survey conducted in Maruyama Park, an evaluation method using only contour lines was devised. Using this evaluation method, we compared human behavior in walking spaces along the Seta River and the Yodo River.

In this research, we were able to understand the relationship between flow line prediction and gradient in walking spaces based on our original evaluation methods. While the method successfully captured the major characteristics of human flow lines, it was not detailed enough for precise predictions. To improve practical use, incorporating additional factors is necessary.

REFERENCES

[1] Japan National Tourism Organization [JNTO], Incoming foreign tourists, 2024.
[2] Ministry of Land, Infrastructure and Tourism [MLIT], The White Paper on Land, Transport in Japan 2021, pp. 66-70.
[3] Ministry of Land, Infrastructure and Tourism [MLIT], The White Paper on Land, Transport in Japan 2024, pp. 4-7.
[4] Ministry of Land, Infrastructure and Tourism [MLIT], Urban Renewal Starting from “a Comfortable and Walkable Town”, 2018
[5] Jumpei Morioka, Kaoru Matsuo, Hiroyuki Kaga, Shigeaki Takada, “A Study on Walkability grasped from Environment both of “Easy to Walk” and “Encouragement” that supports Walking”, 2021
[6] Shogo Yamada, “Study on Walking Acceleration Characteristics for the Purpose of Evaluating Easy of Walking”, 2023

Copyright © Int. J. of GEOMATE All rights reserved, including making copies, unless permission is obtained from the copyright proprietors.

15th Int. Conf. on Geotechnique, Construction Materials & Environment,
Kyoto, Japan, 11-13 November 2025, ISBN 978-4-909106124 C3051

ARTIFICIAL INTELLIGENCE-BASED EARLY WARNING SYSTEMS FOR RIVERBANK EROSION IN THE MEKONG DELTA REGION

Thang Ngoc Nguyen[1], Phong Vu Phuong Le[2] and Tru Thi Tu[3]

[1,2,3]Faculty of Engineering Technology, Tien Giang University, Vietnam

ABSTRACT

The Mekong River Delta is facing severe riverbank erosion, significantly impacting life, the economy, and the environment. The main causes are climate change, excessive sand mining, and changes in water flow. In this context, the application of Artificial Intelligence (AI) in early warning systems for riverbank erosion is gaining attention. AI models such as Machine Learning (ML) and Deep Learning (DL) can analyze data from geological sensors, satellite imagery, and hydrological data, helping to accurately identify high-risk areas. Research has shown that AI has the potential to improve accuracy in predicting erosion and supporting disaster prevention efforts, especially in heavily affected areas like Tien Giang Province. However, AI still faces some challenges, such as a lack of high-quality data, the need for complex computations, and difficulties in integration with current warning systems. If implemented effectively, AI will help protect riverbanks, minimize damage, ensure the safety of residents, and promote sustainable development in the Mekong Delta.

Keywords: Artificial Intelligence, Early warning, Mekong Delta, Riverbank erosion, Sustainable development

INTRODUCTION

The Mekong Delta is a region characterized by a dense network of rivers, primarily nourished by alluvial deposits from major rivers such as the Tien and Hau Rivers, along with their tributaries. Thanks to these features, the Mekong Delta has become one of Vietnam's largest rice-producing areas, making a significant contribution to the national economy. However, due to its extensive river systems and alluvial soil geology, this region is also highly vulnerable to natural phenomena, especially riverbank erosion [1].

The alluvial soil in the Mekong Delta is soft and easily subject to erosion and landslides, particularly in areas experiencing strong changes in water flow or excessive sand mining activities. Riverbank erosion is an urgent issue in the Mekong Delta, leading to the loss of farmland, houses, and causing serious impacts on transportation and infrastructure (Fig.1). The causes of this phenomenon include changes in water flow due to hydraulic structures, climate change with rising sea levels, and extreme weather events such as floods and storms. Riverbank erosion not only directly affects people's lives but also causes long-term economic damage, especially for rural residents who rely heavily on the land for their livelihood [2].

Fig.1 Erosion along the Cho Gao riverbank [3]

In addition, the rapid development of urban areas and industrial zones has exacerbated the impacts of erosion. Construction projects along riverbanks, rampant sand mining, and a lack of attention to riverbank protection have worsened the situation. This not only affects the environment but also threatens the stability of aquatic ecosystems, leading to the loss of native biodiversity [4].

Given this situation, early warning of riverbank erosion has become a crucial factor in protecting people's property and lives. Modern technology-especially AI-has opened up new opportunities for forecasting and issuing alerts regarding riverbank erosion. AI can analyze and process large volumes of data from various sources such as satellites, geosensors, and historical records to predict high-risk erosion areas. Through predictive modeling, AI can provide timely warnings, enabling authorities and communities to take responsive measures and reduce damages [5]. Emerging technologies such as machine learning and satellite image analysis are increasingly proving effective in monitoring and analyzing riverbank changes, thereby supporting erosion prevention efforts.

RESEARCH SIGNIFICANCE

This research holds significant value as it addresses the urgent issue of riverbank erosion in the Mekong Delta region critical to Vietnam's agricultural and economic stability. By applying AI to early warning systems, the study offers a modern, data-driven approach to predicting and mitigating erosion risks. The integration of geotechnical, hydrological, and satellite data with AI models

enhances forecasting accuracy, supports proactive disaster management, and promotes sustainable development. The research provides a foundation for developing practical, scalable solutions that can be applied both locally in Tien Giang Province and more broadly across vulnerable riverine regions.

AI AND ITS APPLICATION IN LANDSLIDE FORECASTING

AI, particularly machine learning and deep learning models, is increasingly being applied in predicting riverbank landslides because it can analyze and process large volumes of data from various sources. These technologies can help analyze vast amounts of information, thereby providing more accurate forecasts of landslide risks in vulnerable areas [6].

One of the most important data sources for forecasting riverbank erosion is geological measurement sensors. These sensors can collect detailed information on soil moisture, pore water pressure, and ground movement, which helps identify changes in soil structure and detect early signs of landslide processes. Collecting data from geotechnical sensors allows scientists and managers to gain deeper insights into the geological conditions of an area, enabling timely and effective preventive measures. This information can be integrated into AI models to identify factors influencing erosion and predict high-risk areas.

In addition, satellite imagery plays a crucial role in analyzing and assessing erosion conditions. With its wide and continuous observational capability, satellite images help monitor morphological changes of riverbanks over time. These changes may indicate soil weakening, erosion, or strong impacts from external factors. Utilizing satellite imagery enables the creation of accurate maps of high-risk areas, allowing authorities to make timely decisions in erosion prevention efforts. Moreover, combining satellite imagery with AI enables the automation of identifying and analyzing weakened zones, thereby improving the accuracy of forecasting.

Hydrological data is also an essential factor in landslide forecasting. Hydrological elements such as changes in water levels, flow velocity, and rainfall directly influence the riverbank erosion process. For example, rising water levels or strong flows can exert significant pressure on riverbanks, increasing the risk of erosion and landslides. Variations in water level and flow, especially during the rainy season or during major flood events, can significantly raise the risk of landslides. When integrated with AI models, hydrological data allows for an accurate assessment of these influencing factors, supporting effective prediction of vulnerable areas.

AI algorithms are developed to recognize and analyze data patterns from various sources, including geotechnical sensors, satellite imagery, and hydrological data. AI can learn from historical data and predict future landslide trends, providing early warnings for high-risk areas [7]. Applying AI in landslide forecasting enables authorities and communities to respond proactively and mitigate damage. Early warnings generated by AI can help protect people's property and lives while enhancing the effectiveness of disaster management.

COMMON AI MODELS IN LANDSLIDE FORECASTING

In riverbank landslide forecasting, AI models are increasingly being applied due to their ability to analyze and process large volumes of data from various sources [8]. Below are some of the most commonly used AI models, each with its strengths that contribute to improving the accuracy of landslide prediction and early warning.

Linear Regression

Linear regression is one of the most basic yet effective models for predicting riverbank landslides. This model uses historical data to forecast the extent of future erosion. Specifically, linear regression analyzes the linear relationship between factors such as water level, flow velocity, geological characteristics, and other environmental variables. Despite its simplicity, this model can yield highly effective results in cases where the data is not overly complex or when there are few variables to analyze. It enables quick and easy-to-understand predictions, especially in areas with relatively stable conditions.

Artificial Neural Networks (ANN)

ANNs are more powerful models, particularly useful for handling complex and nonlinear data. ANN can learn from data and improve itself over time, enabling more accurate predictions of areas at risk of landslides. This model can integrate a wide range of complex factors-including changes in geological, hydrological, and climatic conditions, as well as human impacts-into a unified prediction. Thanks to its deep learning capabilities and robust analytical power, ANN can generate more precise and detailed forecasts, making it well-suited for areas with high variability.

Convolutional Neural Networks (CNN)

In satellite image analysis, CNNs are a very useful tool. CNN can identify detailed features from images, helping to detect changes in the morphology of riverbanks over time. Satellite images can reveal small but significant changes on the land surface, such as the formation of cracks, erosion, or soil movement, which traditional models may struggle to detect. CNN can learn and identify subtle transformations in images, enabling earlier identification of areas at risk of landslides, while improving the accuracy of forecasts.

Decision Tree and Random Forest

Decision tree and random forest models are also commonly used in landslide forecasting. A decision tree works by splitting data into branches based on specific conditions (such as water levels, flow velocity, and soil characteristics). This splitting process helps make predictive decisions about the level of landslide risk for each area. Random forest is an advanced version of decision trees, combining multiple decision trees to provide more accurate forecasts. This model enhances accuracy and minimizes errors in classification, especially in situations with complex or incomplete data.

Support Vector Machines (SVM)

SVMs are a powerful machine learning model, particularly suited for classifying areas at high risk of landslides. SVM can optimize the data classification space to separate data classes most optimally. This is crucial for identifying areas with a high or low likelihood of landslides based on environmental and geographical factors.

These AI models each have their own advantages and can be applied in different situations. Not only do they improve the accuracy of landslide forecasting, but they also aid in more effective prevention and management. By applying AI technologies, authorities and communities can receive early warnings and take timely responsive actions. This helps protect property, minimize damage, and safeguard the lives of people in vulnerable areas such as the Mekong Delta.

EFFECTIVENESS AND CHALLENGES IN AI APPLICATION

AI has demonstrated significant effectiveness in riverbank landslide forecasting, particularly in its ability to analyze and process large amounts of data from various sources such as geotechnical sensors, satellite imagery, and hydrological data (Fig.2). AI models can accurately predict areas at risk of landslides, providing early warnings that help reduce damage and protect both lives and property. However, despite the great potential of AI in this application, its implementation in practice still faces several major challenges.

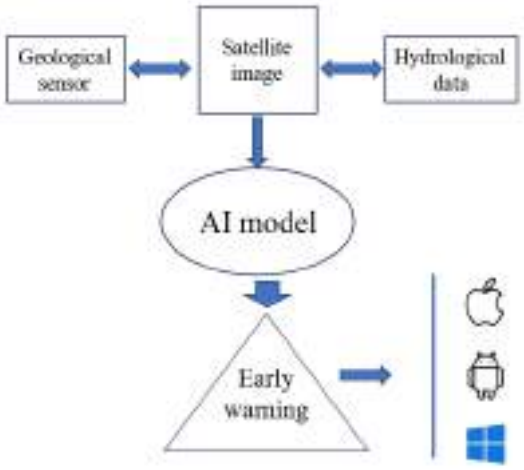

Fig.2 Early Warning Principle

Lack of High-Quality Data

One of the main challenges in applying AI to landslide forecasting is the lack of high-quality data. AI models rely heavily on input data, especially data from geotechnical sensors, satellite imagery, and hydrological data. To make accurate predictions, this data needs to be collected continuously and at high resolution, ensuring it reflects the current conditions of the area. If the data is incomplete or inaccurate, the predictions will be biased, reducing the effectiveness of the early warning system. Moreover, collecting and maintaining high-quality data requires significant costs and time, particularly in hard-to-reach areas.

Computational Resources and High Costs

Implementing complex AI models, especially deep learning algorithms or artificial neural networks, requires a large amount of data to train the model. This means that powerful computational resources are needed, such as high-performance servers and specialized hardware. These systems come with significant investment costs, which can be a major barrier to deploying AI on a large scale, particularly in areas with limited resources or lacking technological infrastructure. Therefore, the implementation of AI will face difficulties without financial support or collaboration between government agencies and international organizations.

Integration of AI with Traditional Methods

Although AI has strong capabilities in landslide forecasting, traditional methods such as using geological maps, hydrological models, and conventional forecasting systems still play an important role in disaster prevention efforts. Integrating AI with these traditional methods presents

a major challenge, as traditional systems have been in use for a long time and may not be fully compatible with the new AI models. This requires close collaboration between experts from various fields and the development of integrated tools to ensure the warning system operates effectively and stably. Without coordinated integration between AI and traditional methods, the forecasting results may not be optimal, reducing the overall effectiveness of the system.

Accuracy and Reliability of the Model

Although AI has the ability to analyze complex data and make accurate predictions, AI models are not perfect. These models can encounter errors, especially when the training data is incomplete or does not fully reflect the changing factors in the real environment. These errors can lead to false warnings, negatively impacting landslide response efforts. Therefore, it is crucial to test and calibrate AI models to ensure the accuracy and reliability of the predictions.

Despite these challenges, if addressed, AI holds significant potential for forecasting and preventing riverbank landslides [9-11]. Solutions such as improving data quality, developing simpler AI models, or using cloud computing systems can help reduce costs and increase technology accessibility. Furthermore, the integration of AI with traditional methods will optimize effectiveness in landslide prevention efforts, reduce risks, and protect both people and their property.

CONCLUSION AND FUTURE DEVELOPMENT

The application of AI in forecasting riverbank landslides in the Mekong Delta has proven to play a crucial role in enhancing early warning capabilities and minimizing the damage caused by natural disasters. AI helps analyze and process complex data, thereby accurately predicting high-risk areas and supporting effective prevention efforts. However, to fully harness the potential of AI in the future, it is essential to continue improving forecasting models, enhancing the quality and continuity of data, particularly from sensors and satellite imagery. Furthermore, close collaboration between research institutions, local governments, and communities is necessary for implementing an effective and sustainable AI system. Enhancing the capacity and awareness of the community about this technology will help AI become a powerful tool, contributing to the protection of people and the environment, while supporting sustainable development in the Mekong Delta.

Future work orientation: The future focus will be on developing an early warning model for riverbank landslides along a 1-kilometer stretch of river in Tien Giang Province. This model will integrate advanced technologies such as AI, hydrological–geotechnical simulation models, on-site sensor systems, and remote sensing data. The objective is to provide accurate and timely landslide forecasts to effectively support disaster prevention and response efforts by local authorities. Additionally, the model will contribute to sustainable land and water resource planning and management, with an emphasis on climate change adaptation. Ultimately, this project aims to enhance disaster resilience and reduce risk for Tien Giang Province and neighboring areas, fostering stable and long-term regional development.

ACKNOWLEDGMENTS

The authors would like to express their sincere gratitude to Tien Giang University for providing support and resources throughout the research process. Special thanks are extended to local authorities and communities in Tien Giang Province for their valuable cooperation and insights. We also appreciate the contributions of colleagues and experts who offered constructive feedback and technical assistance. This research would not have been possible without the dedication and collaboration of all those involved.

REFERENCES

[1] Ministry of Natural Resources and Environment, Vietnam, Report on the Status of Riverbank Erosion in the Mekong Delta, 2024.

[2] Thang N. N., An investigation of Cement Deep Mixing columns stabilization in the road foundation along the Cho Gao canal. International Journal of GEOMATE, Vol. 26, Iss. 114, 2024, pp. 1-8, DOI: 10.21660/2023.104.3688.

[3] Thang N. N., and Tuan A. N., A study on the calculation of deformation of cement deep mixing columns that stabilize soil erosion and landslides on river roads. International Journal of GEOMATE, Vol. 23, Iss. 100, 2022, pp. 52-61, DOI: 10.21660/2022.100.3679.

[4] Saeid J., Dongkyun K., Changhyun J., Sayed M. B., Manish P., and Varun N. M., Impact of climate change on future flood susceptibility projections under shared socioeconomic pathway scenarios in South Asia using artificial intelligence algorithms. Journal of Environmental Management, Vol. 366, 2024, DOI: 10.1016/j.jenvman.2024.121764.

[5] Nguyen V. H., and Tran, T. K., Application of AI in Disaster Management. Vietnam Journal of Science and Technology, 2023.

[6] Zhongda R., Chuanjie L., Xiaolong Z., Yang J., Yafei O., Ruiqing L., Heshan F., Qian Y., Aaron L., and Heqin C., A large-scale riverbank erosion

risk assessment model integrating multi-source data and explainable artificial intelligence (XAI). Ecological Indicators, Vol. 166, 2024, DOI: 10.1016/j.ecolind.2024.112575.

[7] Seyed MHS R., Alexandre G., Maria J. F. S., and Nuno M. A., Smart hotspot detection using geospatial artificial intelligence: A machine learning approach to reduce flood risk. Sustainable Cities and Society, Vol. 115, 2024, DOI: 10.1016/j.scs.2024.105873.

[8] Smith J., and Brown A., Deep Learning for Environmental Monitoring. Journal of AI Research, 2022.

[9] Pin-Chun H., Estimation of riverbank erosion by combining channel morphological models with AI techniques. Geomatics, natural hazards and risk, Vol. 15, No. 1, 2024, DOI: 10.1080/19475705.2024.2359983.

[10] Dana P. E., Matthew M. C., and Kyle A. C., Early warning scores with and without artificial intelligence. JAMA Network Open, Vol. 4, No. 10, 2024, DOI:10.1001/jamanetworkopen.2024.38986.

[11] Tram-Anh D., Luong V. Q. D., Hoang-Dang L., and Chi-Ngon N., Early warning system for riverbank soil landslides and infrastructure protection. Environmental Research Communications, Vol. 7, No. 3, 2025, DOI: 10.1088/2515-7620/adb940.

Copyright © Int. J. of GEOMATE All rights reserved, including making copies, unless permission is obtained from the copyright proprietors.

15th Int. Conf. on Geotechnique, Construction Materials & Environment, Kyoto, Japan, 11-13 November 2025, ISBN 978-4-909106124 C3051

ECOFRIENDLY SLOPE STABILIZATION: FIELD APPLICATION OF BIOCEMENTATION WITH NATIVE BACTERIA AND LOW-COST MATERIALS

Azizul Moqsud[1]

[1]Faculty of Engineering, Yamaguchi University, Japan

ABSTRACT

In this study, a field test of biocementation was carried out in a natural slope in Ube City, Yamaguchi University, Japan. Low-cost commercial materials have been used instead of laboratory-grade materials to reduce the overall cost of the biocementation. A 50 x 50 cm area on a slope has been selected, and the culture medium and nutrient medium have been applied for 10 days. The same area has been selected to compare the data of biocementation and without biocementation, and there was no culture or nutrient medium has been applied. A dynamic cone penetration test, along with a direct shear test, has been conducted. Image analysis has been conducted on the surface of the slope after the heavy rainfall. It has been observed that the soil strength increased after the biocementation up to 15 cm from the surface. Image analysis reveals that the surface of the biocemented soil is more stable compared to the uncemented soil.

Keywords: Biocementation, Field Application, Low-Cost, Native Microbes, Slope Soil

INTRODUCTION

Biocementation of soil is a natural process in which the microbes produce calcium carbonate to bond the soil particles and hence increase the soil's strength [1,2]. It is an environmentally friendly approach to protect the natural slope, as no chemical cement is used for this process. The biocementation of natural slopes can be a good solution for the protection against geo-disasters such as landslides, surface erosion, and liquefaction phenomena [3-7]. However, due to the cost of the laboratory-grade materials and the availability of effective bacteria is always a problem for the field application or the scale-up of this process [8-10].

In this study, to overcome the challenges of the current problems, native bacteria, which are easily found in the natural slope on the main island of Japan, have been tried. The low-cost, commercially available materials have been used in large-scale applications in a cost-effective way.

Recent studies have demonstrated the effectiveness of biocementation in slope stabilization. For instance, Moqsud and Gochi (2024) reported that biocemented soil surfaces exhibited up to 80% reduction in erosion under simulated rainfall conditions, with crusts capable of withstanding wind velocities exceeding 55 km/h. Similarly, Dubey et al. (2023) found that MICP-treated soils showed enhanced compressive strength and erosion resistance, while maintaining favorable hydrological properties [19]. A comprehensive bibliometric review by Omoregie et al. (2025) highlighted the growing body of research supporting biocementation as a viable technique for slope management, particularly in environmentally sensitive areas [21].

Despite its potential, biocementation faces challenges related to scalability, cost of reagents, and long-term durability.

The main objective of this study is to check the effectiveness of biocementation by using the commercially available materials and native bacteria in a natural environment. Both the dynamic penetration test and the direct shear test have been carried out to check the strength at different depths and surface of the slope.

RESEARCH SIGNIFICANCE

The significance of the study is to apply the biocementation process on a natural slope with low-cost commercial materials and native bacteria found in the main island. So far, biocementation is carried out in a controlled environment with expensive laboratory-grade materials.

MATERIALS AND METHODS

The natural slope has been chosen in Ube city, Yamaguchi prefecture, near the faculty of engineering, Yamaguchi University. It has been found that the natural slope is around a 30-degree slope angle. The slope soil is classified as decomposed granite soil with some amount of organic matter. The nutrient solution was prepared by using urea fertilizer and snow melting agents which are easily found in the commercial market. The snow melting agent, which is basically calcium chloride salt, can be used instead of pure laboratory-grade materials. The culture medium was used as a

laboratory grade material and can be used effectively in the field, as the amount of if used in the field is small. For the cone penetration test, the dynamic cone penetration test has been applied, developed by Hasegawa Corp., Japan.

Table 1 Nutrient solution and culture medium materials

Culture medium		Nutrient solution	
Distilled water	500ml	Distilled water	500ml
Yeast Extract	10g	Urea	15g
Ammonium sulfate	5g	Calcium chloride	27.8g
1.03Mtris	7.875g		
Peptone	5g		

Bacteria used in this study

Microbes are islolated from the natural slope of Yamaguchi prefecture and Miyagi prefecture which are located at the south and north part of main island of Japan. The microbial analysis confirmed the presence of Ureolytic bacteria which are mainly responsible for biocementation are present both in the northern and southern part of Japan and can be utilized for the field applications. The name of the native bacteria which was isolated and used in this experiment is *Cytobacillus horneckiae.* The details of the isolation and DNA analysis of this native bacteria and the urease tests have been described in the previous research [12-15].

Field test

The slope has been divided into four equal sections (50 x 50 cm). They have been named A, B, C, and D. Figure 1 shows the section where A and B were selected with grass, and C, D without grass. B and D were without biocementation. The same amount of culture medium and nutrient solutions has been used for A and C sections and applied from the surface. The culture medium was applied only for the first day, but the nutrient solution was used for 10 days. All the A,B,C,D section were experimented in same weather conditions.

After ten days, the penetration test and direct shear test were carried out.

Fig. 1 Field test of biocementation

For conducting the direct shear test, three molds were prepared (60mm diameter and 20 mm height) in the nearby field, and the same amount of culture medium and nutrient solutions were applied for the same period. The direct shear test was conducted with 50,100 and 150 kN/m^2 confining pressure [16-20]. However, due to the space limitation only the result of 100kN/m^2 has been described in this paper in the later section.

Scanning electron microscope (SEM) analysis was conducted to see the amount of calcium carbonate generated on the surface of the soil.

RESULTS AND DISCUSSION

Figure 2 shows the result of the penetration test with grass. It has been observed that the penetration depth of the blank is more compared to the biocemented slope

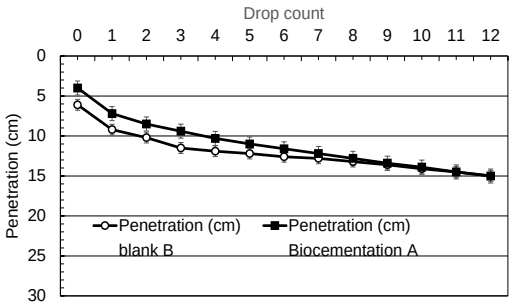

Fig. 2 Penetration test result with grass A, B

The penetration test with grass showed a similar trend both for the blank and the biocemented slope sections. The nutrient solution is applied with a sprayer from the surface of the slope, both with and without grass, respectively. However, some nutrient solutions can be hindered from reaching the soil surface due to the presence of grass on the surface.

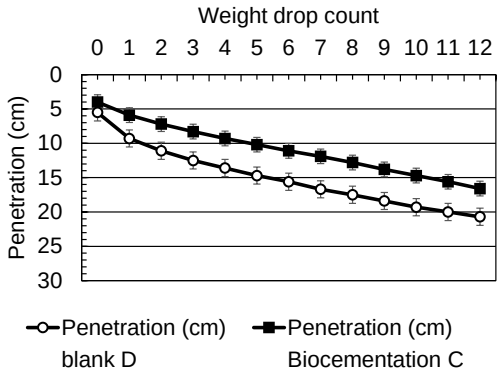

Fig. 3 Penetration test result without grass C, D

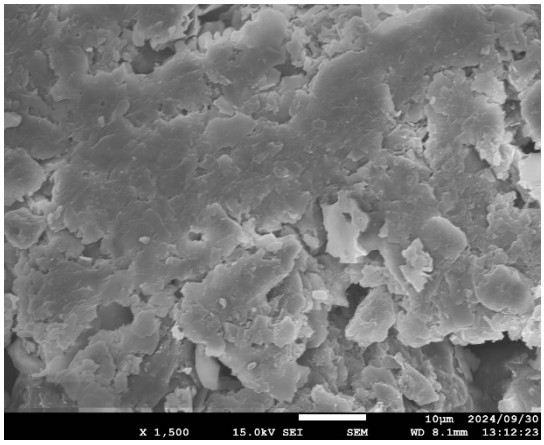

Fig. 4 SEM with grass A (with biocementation)

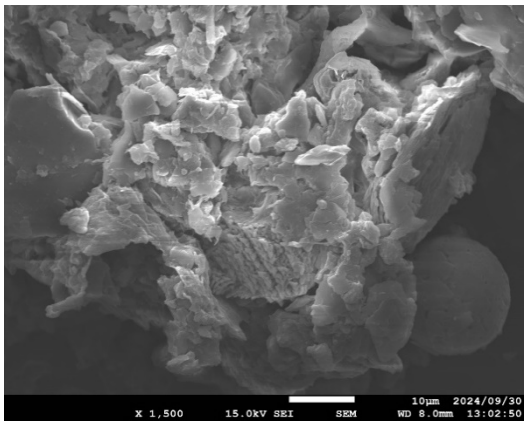

Fig. 5 SEM result with grass B (without biocementation)

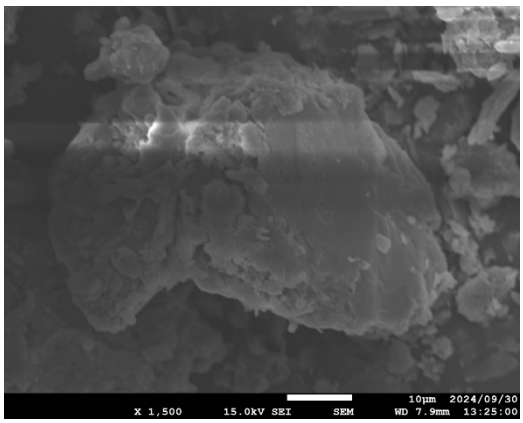

Fig. 6 SEM and EDS result with grass C (with biocementation)

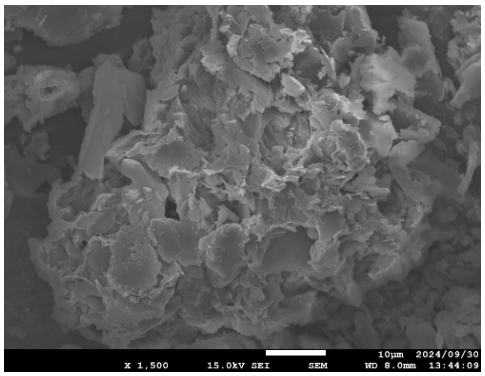

Fig. 7 SEM and EDS result with grass D (without biocementation)

Figures 4 and 5 illustrate a scanning electron microscopy view of the samples for blank samples and with biocementation samples without grass. It has been visible that the biocementation shows more calcium carbonate on the surface of the soil particles. The yellow color represents the calcium carbonate, and it demonstrates the amount of calcium carbonate generated on the surface of the soil particle, more in the biocemented slope. This is the reason for the soil strength increase in various depths. The penetration test reveals that soil strength increased after the biocementation up to 15cm. The blank slope did not show much strength near the surface (up to 15 cm). This proves that biocementation can increase the soil strength even outside of the laboratory and in natural environmental conditions.

Figures 6,7 show the SEM results for C and D sections of the slope. A similar trend has been observed for this case as well.

Figure 8 presents the outcomes of direct shear tests conducted on soil samples C and D, both before and after biocementation treatment. The post-treatment results reveal a marked improvement in shear strength, indicating the efficacy of biocementation in reinforcing soil structure. This observation aligns with findings from previous studies, such as those by DeJong et al. (2006) and Ivanov & Chu (2008), which demonstrated that microbial-induced calcium carbonate precipitation (MICP) can significantly enhance soil mechanical properties.

A comparative analysis between untreated and biocemented samples underscores the positive impact of biocementation on shear resistance. The increase in shear strength is attributed to the formation of calcite bonds between soil particles, which enhances interparticle cohesion and reduces deformability under stress.

Figure 9 further illustrates the relationship between normal stress and shear stress for slope

samples devoid of vegetation, comparing blank and biocemented conditions. The data clearly indicate an increase in both cohesion (c) and internal friction angle (φ) following biocementation. These improvements are consistent with the theoretical framework proposed by Mitchell & Santamarina (2005) [23-24], which suggests that cementation processes contribute to both strength and stiffness gains in granular soils.

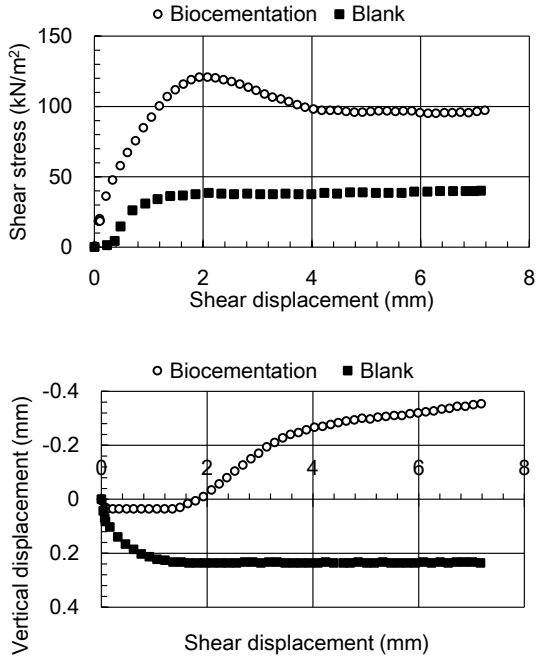

Fig. 8 Direct shear test with and without biocementation for C,D

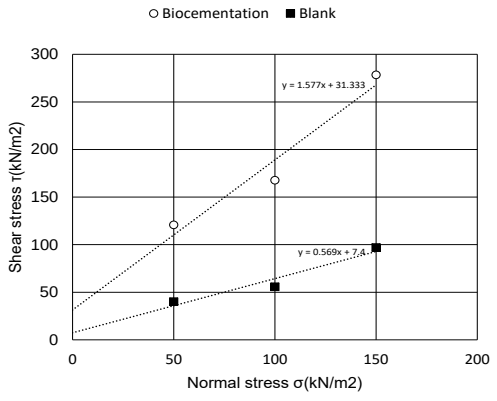

Fig. 9 Relationship between normal stress and shear stress for C and D (Biocemented and blank for without grass)

Additionally, the volumetric strain observed during shear testing was significantly reduced in biocemented samples, suggesting enhanced structural integrity and reduced susceptibility to deformation. This reduction in volumetric change is critical for slope stability, particularly in erosion-prone or load-bearing applications, as highlighted in the work of Whiffin et al. (2007) [25-26]. However, the blank slope showed opposite trend and indicated the lower strength of slope which is easy to erode and consequently prone to geohazards such as landfill and liquefaction.

CONCLUSIONS

The field application of biocementation shows a promising result to increase the strength of the slope surface. However, the application of nutrient solution and culture medium can increase the strength upto 15cm from if they applied from the surface. The rainfall effect and long term stability check should be done. The low-cost commercial materials can be used for the biocementation. The native bacteria can increase the chance of biocementation in the main island of Japan, which can reduce the risk of biohazards. This study proves that biocementation can be an environmentally friendly solution for the natural slope protection from surface erosion or landslide, along with liquefaction. Notably, the use of local microbial strains *Cytobacillus horneckiae* not only increases the likelihood of effective calcite precipitation but also mitigates the ecological risks often associated with introducing non-native species.

These findings affirm that biocementation is a viable and green alternative to conventional engineering solutions in protecting vulnerable slopes from erosion, landslides, and liquefaction. As Japan continues to confront geological and climatic challenges, such bio-based interventions offer a meaningful pathway toward resilient infrastructure and ecological preservation. Future implementation and scaled-up applications of this technique could mark a transformative shift in geotechnical engineering, aligning technological advancement with environmental stewardship. However, the long-term durability of the biocemented slope should be monitored.

ACKNOWLEDGMENTS

The author acknowledges the support during the field test by Mr. Yamazaki. The financial support from NEXCO Higashi Nihon and Obayashi Zaidan has been acknowledged to conduct this research.

REFERENCES

[1] Moqsud, M.A., (2021). Slope soil stabilization through biocementation by native bacteria in Chugoku region, Japan, International Journal

of GEOM ATE. Volume 21, Issue 83, pp. 36-42.

[2] Moqsud, M.A, Takuya Gochi,(2024). Evaluation of biocementation of slope soil for erosion control with low-cost materials. Scientific Reports, Volume 10, Issue 52,100098.

[3] Al Qabani, A., Soga, K., 2012. Factors affecting efficiency of microbially induced calcite precipitation. J. Geotech. Geoenviron. Eng. 138 (8), 992–1001.

[4] Burdalski, R.J., Ribeiro, B.G.O., Gomez, M.G., et al., 2022. Mineralogy, morphology, and reaction kinetics of ureolytic bio-cementation in the presence of seawater ions and varying soil materials. Sci. Rep. 12, 17100.

[5] DeJong, J.T., Fritzges, M.B., Nüsslein, K., 2006. Microbially induced cementation to control sand response to undrained shear. J. Geotech. Geoenviron. Eng. 0241, 1381–1392.

[6] DeJong, J.T., Mortensen, B.M., Martinez, B.C., Nelson, D.C., 2010. Biomediated soil improvement. Ecol. Eng. 36, 197–210.

[7] Montoya, B., DeJong, J., Boulanger, R., 2013. Dynamic response of liquefiable sand improved by microbial-induced calcite precipitation. G´ eotechnique 63 (4), 302–312.

[8] Moqsud, M.A., Gochi, T., 2023. Biocementation of slope soil by using native Cytobacillus horneckiae. Bioresourc. Technol. Rep. 23, 101502.

[9] Moqsud, M.A., Okamoto, T., 2023. Bioelectricity generation from corn plant microbial fuel cell (PMFC) using natural bamboo charcoal as electrodes and Shewanella oneidensis. Bioresource Technology Reports 24, 101611.

[10] Moqsud, M. A., Soga, K., Hyodo, M., & Nakata, Y., 2018. Evaluation of bio-cemented sand for landslide disaster prevention. In International symposium on bio geotechnology. September (pp. 12–13)

[11] Moqsud, M.A and Gochi, T. Assessment of uniform biocementation in different depths by using a perforated pipe. Bioresource Technology Reports 27, 2025

[12] Yu, X., Xu, Y., 2023. OAs and CAB capture CO 2 and conversion to carbonates and its potential applications in civil engineering. J. Build. Eng. 66, 105904.

[13] Yu, X., Chu, J., Wu, S., Wang, K., 2023. Production of biocement using steel slag. Constr. Build. Mater. 383, 131365

[14] Safdar, M.U., Mavroulidou, M., Gunn, M.J., Purchase, D., Payne, I., Garelick, J., 2021b. Electrokinetic biocementation of an organic soil. Sustain. Chem. Pharm. 21, 100405

[15] Safdar, M.U., et al., 2022. Towards the development of sustainable ground improvement techniques-biocementation study of an organic soil. Circ. Econ. Sustain.

[16] Shahin, M.A., Jamieson, K., Cheng, L., 2020. Microbial-induced carbonate precipitation for coastal erosion mitigation of sandy slopes G´ eotech. Lett 10 (2), 211–215.

[17] Dubey AA, Murugan R, Ravi K et al (2023) Investigation on the impact of cementation media concentration on properties of biocement under stimulation and augmentation approaches. J Hazardous Toxic Radioact Waste 26:1–13.

[18] Moqsud, M.A (2025). Low-Cost Biocementation for the Preservation of Slope Surface by Using Native Microbes in Japan. Geo-EnvironMeet 2025, pp 122-129.

[19] Omoregie, Armstrong Ighodalo, Tariq Ouahbi, Fock-Kui Kan, Qurratu Aini Sirat, Hafsat Omolara Raheem, and Adharsh Rajasekar. 2025. "Advancing Slope Stability and Hydrological Solutions Through Biocementation: A Bibliometric Review" Hydrology 12, no. 1: 14.

[20] DeJong, J. T., Fritzges, M. B., & Nüsslein, K. (2006). Microbially induced cementation to control sand response to undrained shear. Journal of Geotechnical and Geoenvironmental Engineering, 132(11), 1381–1392.

[21] Ivanov, V., & Chu, J. (2008). Applications of microorganisms to geotechnical engineering for biocementation and bioclogging. Soils and Foundations, 48(6), 587–596.

[22] Mitchell, J. K., & Santamarina, J. C. (2005). Biological considerations in geotechnical engineering. Journal of Geotechnical and Geoenvironmental Engineering, 131(10), 1222–1233.

[23] Whiffin, V. S., van Veen, C., & Harkes, M. P. (2007). Microbial carbonate precipitation as a soil improvement technique. Geomicrobiology Journal, 24(5), 417–423.

Copyright © Int. J. of GEOMATE All reserved, including making copies, unless permission is obtained from the copyright proprietors.

15th Int. Conf. on Geotechnique, Construction Materials & Environment,
Kyoto, Japan, 11-13 November 2025, ISBN 978-4-909106124 C3051

FINITE ELEMENT ANALYSES OF MEASURES TO MITIGATE ROCK SPALLING HAZARDS BY ASSESSING TUNNEL FACE DISPLACEMENT

Rintarou Doi[1], Naotaka Kikkawa[2] and Kazuya Itoh[3]

[1] Graduate School of Integrative Science and Engineering, Tokyo City University, Japan;
[2] National Institute of Occupational Safety and Health, Japan, [3] Tokyo City University, Japan

ABSTRACT

In tunnel construction employing the New Austrian Tunneling Method (NATM), one of the most significant safety risks is rock spalling, where rock fragments fall from the tunnel face. This hazard typically results from fractures, weathering, and surface irregularities of the rock mass. As most such incidents occur at the tunnel face, effective preventive measures are critical to ensuring worker safety. In tunnel construction, apart from standard preventive measures such as shotcrete, rock-bolts, or steel arch support, additional auxiliary methods are also employed. Although various auxiliary methods exist, a lack of quantitative comparison regarding their effectiveness under different ground conditions remains. In practice, the selection of auxiliary methods often depends on empirical knowledge and site experience. Therefore, further analytical evaluation is needed to establish objective and reproducible criteria. This study assessed the effectiveness of support methods through finite element analysis, focusing on their ability to reduce horizontal and vertical displacements of the tunnel face. Displacement magnitude was used as an indicator of potential rock spalling risk. In addition, changes in stress states associated with each method were analyzed to gain further insight into their deformation behavior. The analysis revealed that the auxiliary bench and umbrella arch methods were effective in suppressing both horizontal and vertical displacements, while other methods primarily reduced displacement along a single axis. Horizontal displacement was effectively managed using long face bolts, and vertical displacement was minimized through forepoling and steel arch support. Furthermore, the auxiliary bench method remained effective regardless of ground conditions.

Keywords: Conventional tunnelling method, Tunnel face, Rock spalling, Finite element analysis, Auxiliary methods

INTRODUCTION

There are two tunneling methods for mountain tunnel construction: the conventional tunneling method and the New Austrian Tunneling Method (NATM). Since the late 1980s, the use of NATM has increased, gradually replacing the conventional method in road tunnel construction in Japan. Today, NATM is used in nearly all mountain tunnels, except where ground conditions are particularly complex.

One of the most serious safety risks in NATM tunnel construction is rock spalling, where fractured rock detaches and falls from the tunnel face. From 2000 to 2010, a total of 44 work-related injuries due to rock spalling were recorded in Japan [1]. These incidents frequently occurred at the tunnel face and gallery, regardless of the ground hardness. Therefore, implementing effective preventive measures in these areas is critical to ensure worker safety and reduce casualties.

This study assessed the effectiveness of various support methods through finite element analysis, focusing on their ability to reduce horizontal and vertical displacements of the tunnel face. Displacement magnitude was used as an indicator of potential rock spalling risk. In addition, changes in stress states associated with each method were analyzed to gain further insight into their deformation behavior. The displacement suppression rate calculated and the quantification of the effectiveness of the countermeasure methods can be used as a guide for selecting a countermeasure to prevent rock fall hazards. Being able to compare the advantages and disadvantages of each method, it can help propose an optimal countermeasure method to reduce the number of casualties during tunnel construction using NATM.

TUNNEL COUNTERMEASURE METHODS

In the NATM, three methods are commonly used as part of a single cycle during excavation: shotcrete to improve the self-supporting ability of the tunnel face, steel arch supports installation to prevent the collapse of the surrounding rock, and rock-bolts that are radially installed in the cross-sectional direction to resist tensile stresses. Additionally, depending on the ground conditions, auxiliary methods may be employed. These auxiliary methods are used when conventional supports cannot fully address the situation, or when it is not advisable to rely solely on standard support methods.

These methods are primarily applied to the crown and cutting face of the tunnel. The selection of the appropriate technique is based on safety, construction

reliability, and its impact on the surrounding environment. For tunnel face stability, commonly used methods include face-shotcrete, which enhances self-supporting capability through concrete application, and face-bolts, which are installed in the excavation direction to improve stability. As countermeasures for the crown area, techniques such as fore-poling and umbrella arch are employed. In these methods, bolts or pipes are installed from the tunnel face along the outer perimeter of the upper half arch to increase the apparent shear strength of the crown and prevent collapse.

In addition to reinforcement measures, modifying the excavation method itself can also contribute to face stability. Among these, full-face excavation method with auxiliary bench is particularly effective in improving both face stability and excavation efficiency. This method is applied in ground conditions where conventional full-face excavation is difficult, by incorporating temporary benches while allowing simultaneous excavation of the upper and lower sections (Fig.1).

OUTLINE OF FINITE ELEMENT ANALYSIS

The analysis domain used in this study is presented in Fig. 2. It is assumed to be a road tunnel with a tunnel completion radius of 5.4 m [3], which is based on the standard cross-section used in the Japanese design guidelines for mountain tunnels.

The parameters related to the ground are shown in Table 1, and standard values corresponding to each ground classification are used [4,5]. Ground classification is defined as an index of ground stability, with grade B being considered the most stable in this analysis.

The ground was modeled as an elasto-plastic material, adopting the Drucker–Prager yield criterion. To incorporate cohesion (c) and the internal friction angle (φ), a model was employed where the Drucker–Prager yield criterion aligns with the inner boundary of the Mohr–Coulomb yield criterion (Fig. 3). Furthermore, a tension cut-off model was utilized to prevent overestimation of tensile strength, which is negligible in most ground conditions (Fig. 4).

The excavation process consisted of 11 steps, with the first 10 following the standard NATM procedure, which includes excavation, shotcrete, steel arch support (for CII-b, DI, and DII only), and rock-bolt installation. The tunnel face at the end of the 11th excavation step was selected as the measurement surface, to which a specific countermeasure was applied. The countermeasures included conventional supports (shotcrete, steel arch supports, and rock bolts) as well as four auxiliary methods: face-shotcrete, long face-bolts, forepoling, and umbrella

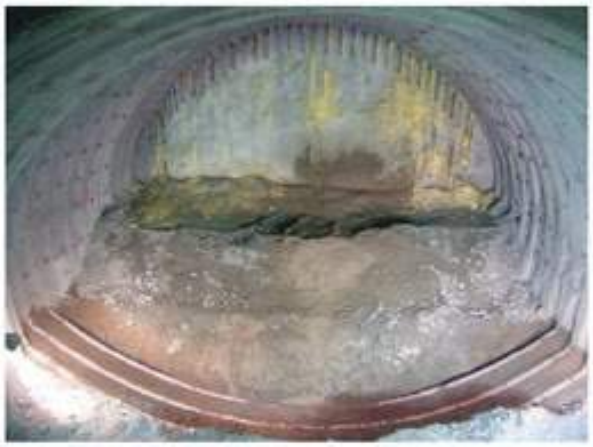

Fig.1 Full-face excavation method with auxiliary bench [2]

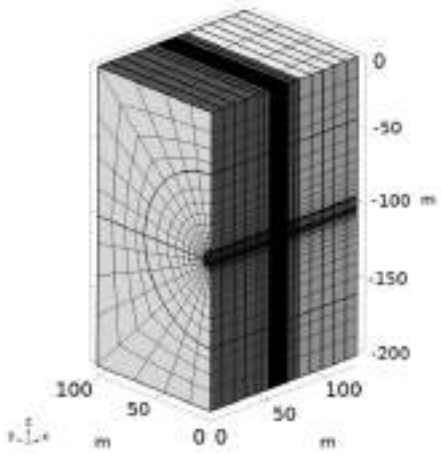

Fig.2 Analysis domain

Table.1 Physical properties of the ground [4][5]

	Young's Modulus (N/mm^2)	Poisson's ratio	Cohesion (N/mm^2)	Internal friction angle (deg)	Tensile strength (N/mm^2)	Unit weight (kN/m^3)
B	5000	0.25	4.0	50	0.80	25.0
CI	2000	0.30	2.0	45	0.40	24.0
CII	1000	0.30	1.0	40	0.20	23.0
DI	500	0.35	0.4	35	0.08	22.0
DII	150	0.35	0.2	30	0.04	21.0

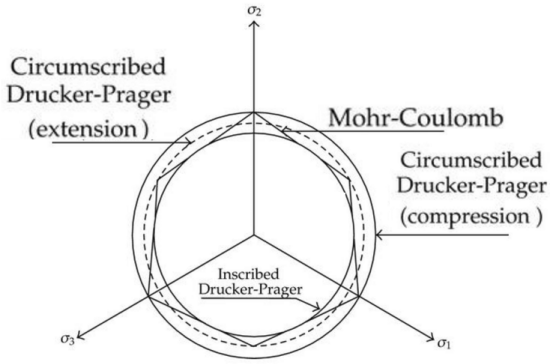

Fig.3 Schematic of yield condition [6]

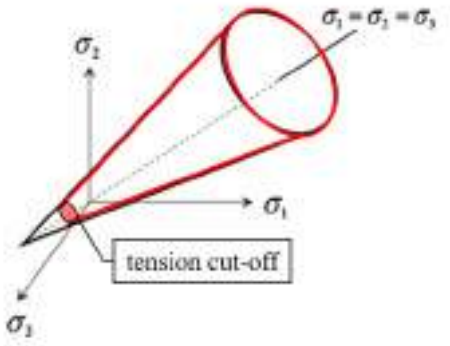

Fig.4 Tension cut-off overview diagram [7]

arch, each modeled as elastic materials. These methods were applied simultaneously with the excavation process.

For the full-face excavation method with auxiliary bench, the length of bench 1-step (e.g., 1 m for DII) was left at the final excavation step. However, for the DII pattern, the end of the bench experienced tensile failure, and the equilibrium of forces could not be maintained, preventing convergence. As a result, the tension cut-off model was deactivated for the DII pattern to allow the analysis to proceed.

The physical properties of the countermeasure methods are shown in Table 2 [4,5,8–10]. The modulus of elasticity for the shotcrete used in the standard support pattern was 6000 N/mm², corresponding to high-strength concrete after 28 days of curing. For the region-of-interest section, the Young's modulus of the concrete was set to a lower value of 330 N/mm² to account for the fact that workers may enter the tunnel face 10 to 15 minutes after spraying, when the material has not yet reached full strength [8]. The shotcrete and face-shotcrete were modeled using thin layer elements [9].

The forepoling was set to a length of 3 meters, with an installation angle of 15° from the horizontal, while the umbrella arch was set to 12.5 meters in length and an installation angle of 4° [9]. Long face-bolts were applied with a length of 12.5 meters and installed horizontally, with a glass density of 1784 kg/m³ [10]. These specifications reflect commonly adopted values in Japanese tunnel practice. The area of the rock bolts was assumed to be 353 mm² for the CII-b pattern and above (using regular twisted steel) and 433 mm² for the DI pattern and below (using high-strength twisted steel). These four countermeasures were modeled using truss elements, which are suitable for axial-force dominant members.

Steel arch supports were applied to both the upper and lower sections in DII and DI pattern grounds, but only the upper section was used in CII pattern grounds. Steel arch support was not used in relatively stable ground conditions such as CI and B patterns. These supports were modeled using beam elements, as they transfer bending and axial forces.

The measurement locations for horizontal and vertical displacements at the tunnel face, which were the focus of this study, are shown in Fig. 5. The calculated displacement values represent the average displacements in the x and y directions at the eight vertices of a 0.5-meter cube. To calculate the displacement suppression rate, the displacement of the Region of Interest (ROI) was denoted as d_0 when

Table.2 Physical properties of countermeasure methods [4,5,8-10]

	Element type	Young's Modulus (N/mm²)	Poisson's ratio	Density (kg/m³)
Shotcrete (Standard)	Thin layer	6000	0.2	2300
Shotcrete (Others)	Thin layer	330	0.2	2300
Rock-bolts	Truss	2.1×10^5	0.3	7850
Steel arch support	Beam	2.1×10^5	0.3	7850
Long face-bolts	Truss	2.0×10^4	0.3	1784
Forepoling Umbrella arch	Truss	2.1×10^5	0.3	7850

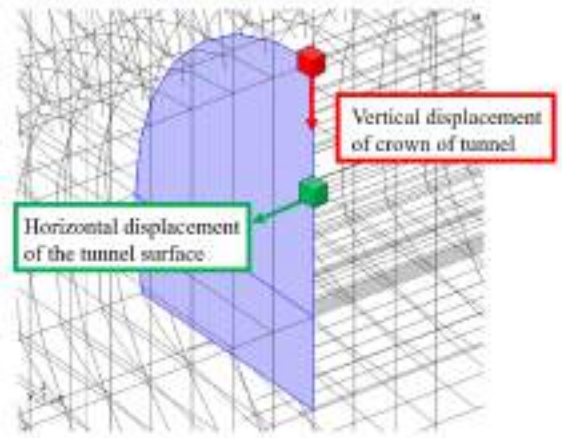

Fig.5 Location of measurement

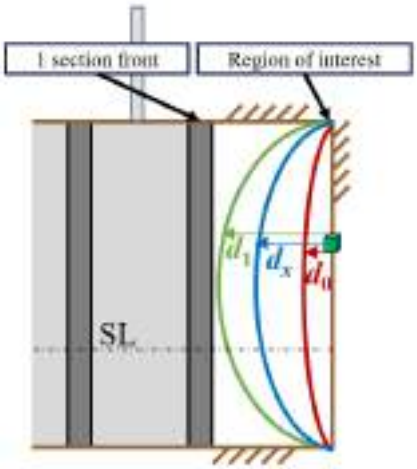

Fig.6 Schematic diagram of displacement suppression ratio calculation

the previous section was excavated.

The displacement at the ROI was then recorded after excavation with no countermeasures applied (no support), denoted as d_1, and the displacement when a specific countermeasure was applied simultaneously with excavation was denoted as d_x (Fig. 6). After all analyses were conducted, the displacement suppression rate was calculated using Eq. (1).

$$R_{r_x} = (d_1 - d_x) / (d_1 - d_0) \times 100 \quad (1)$$

RESULTS OF FINITE ELEMENT ANALYSIS

The suppression rates of horizontal and vertical displacement in the tunnel face are presented in Fig. 7 and Fig. 8. In addition, the stress state of each countermeasure is shown in Fig. 9 (for the DII pattern) using von Mises stress. This stress is derived such that the shear strain energy of a multiaxial stress field, which includes multiple stress components, is equivalent to the short-axis stress. Since it is energy-based, von Mises stress is always positive, as it is a scalar quantity without direction. This has the advantage of allowing a quick assessment of stress magnitude from the distribution diagram. From Fig. 7, the most effective countermeasure in terms of horizontal displacement suppression was the installation of an auxiliary bench with a 1-step length, achieving a maximum suppression rate of 28%. Furthermore, it was found that the auxiliary bench method effectively suppressed displacements regardless of ground conditions. This can be

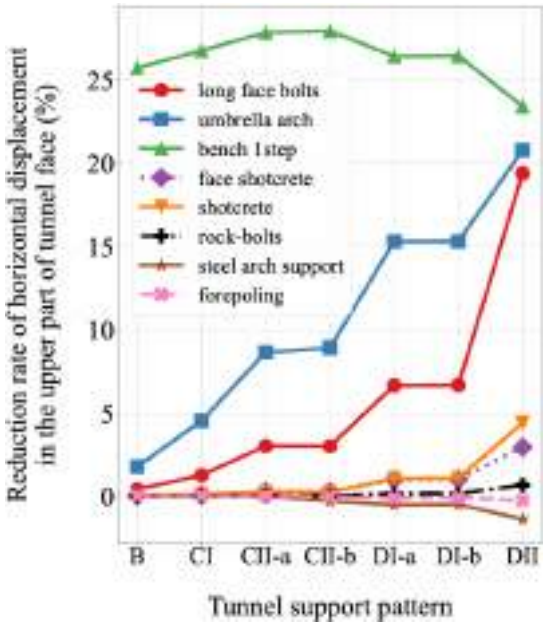

Fig.7 Summary of horizontal displacement reduction rate

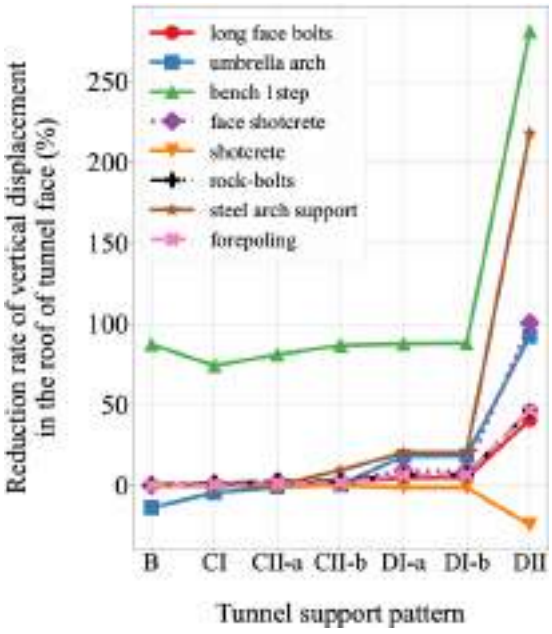

Fig.8 Summary of vertical displacement reduction rate

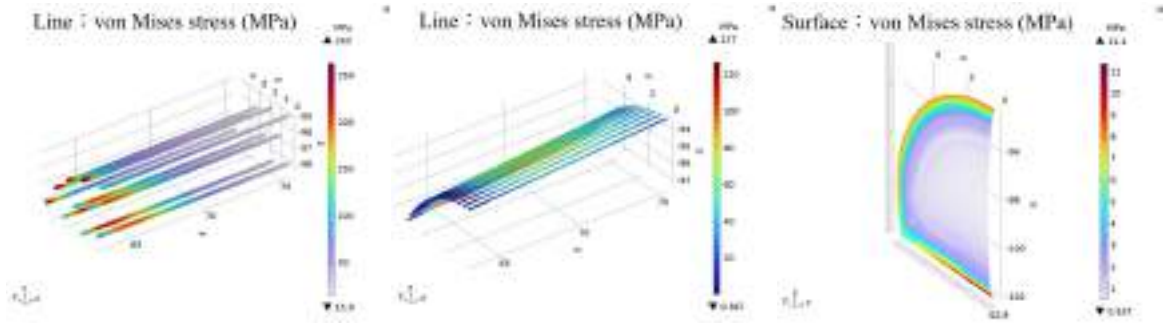

(a) Long face-bolts (b) Umbrella arch (c) Face-shotcrete

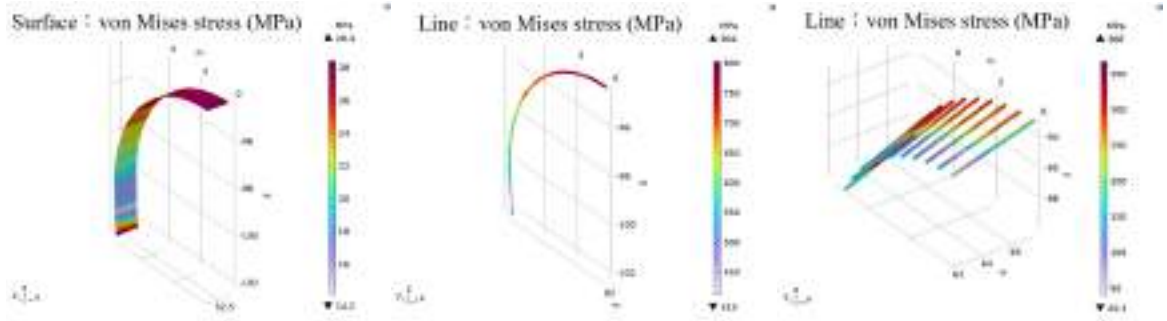

(d) Primary shotcrete (e) Steel arch support (f) Forepoling

Fig.9 (a)～(f) Summary of stress state (for DII pattern)

attributed to both its structural function and its geometric role as an integral part of the surrounding rock mass.

The auxiliary bench reduces the excavated area at the tunnel face, thereby minimizing the release of in-situ stress and alleviating stress concentration. This reduction in excavation volume not only limits deformation but also facilitates a more favorable redistribution of forces around the tunnel face. As a result, extrusion displacement is significantly mitigated, contributing to the overall stability of the face. Following the auxiliary bench, the next most effective measures were the umbrella arch and long face-bolts, both achieving high suppression rates of approximately 20%. The effectiveness of these methods is associated with their length of 12.5 meters. In the case of face-bolts, the fact that they were installed in the direction of tunnel advancement played a significant role (Fig. 9a and 9b). After comes the shotcrete and face-shotcrete. Given that the primary shotcrete used a modulus of elasticity equal to 15 minutes of curing, that is based on actual construction conditions, the maximum reduction rate of displacement was limited to approximately 4%. In the previous section of the tunnel face, the secondary shotcrete had already been completed. Thus, in the direction of tunnel advancement, the primary shotcrete, in continuity with the secondary shotcrete in the previous section, generated a reaction force in the direction of tunnel advancement, leading to better results compared to face-shotcrete. On the other hand, face-shotcrete is thought to resist face extrusion through its own tensile and shear resistance (Fig. 9c and 9d). Other methods, such as forepoling, steel arch supports, and rock-bolts, did not show significant effectiveness in suppressing horizontal displacement and, in some cases, resulted in negative suppression rates. For vertical displacement suppression, the most effective countermeasure was similarly the installation of an auxiliary bench. Again, it was found that the auxiliary bench method effectively suppressed displacements regardless of ground conditions. The effectiveness of the countermeasures decreased in the following order: steel arch supports, face-shotcrete, umbrella arch, forepoling, rock-bolts, and long face-bolts. Steel arch supports and forepoling were particularly effective in suppressing vertical displacement, as they concentrate on stress near the crown (Fig. 9e and 9f). The reason why face-shotcrete showed a high suppression rate for both horizontal and vertical displacements is likely because it is sprayed across the entire face, which allows for reaction forces from the lower section. Also, when integrated with shotcrete applied to the tunnel sidewalls, steel arch supports and rock-bolts are believed to increase rigidity and toughness, contributing to the overall stability of the tunnel cross-section. The displacement distribution of the tunnel excavation cross-section for the case with no support is shown in Fig. 10a, and for the case where the full-section excavation method with an auxiliary bench is employed, in Fig. 10b. From these images, it

is visually evident that in the case with no support, extrusion displacement is concentrated at the center of the tunnel face. However, when an auxiliary bench with a length of one excavation step is provided, this displacement is significantly alleviated. This suggests that reducing the excavation target area and introducing geometrical constraints is effective in mitigating extrusion deformation and stabilizing tunnel face behavior under various ground conditions.

These findings suggest that the displacement suppression performance of each countermeasure can guide the selection of auxiliary methods in tunnel construction.

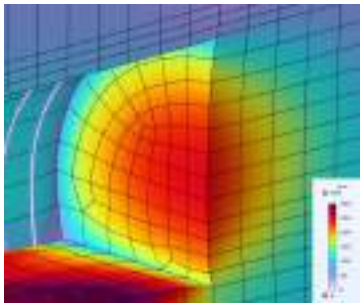

Fig. 10a Displacement distribution (no support)

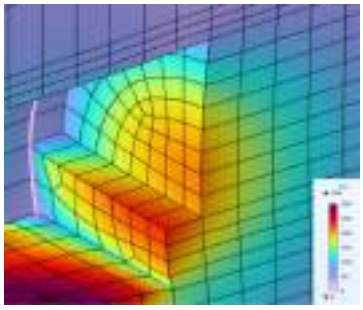

Fig. 10b Displacement distribution (auxiliary bench)

CONCLUSIONS

In this study, finite element analysis was employed to examine the displacement suppression effects of rock spalling mitigation measures, focusing on the horizontal displacement of the tunnel face and the vertical displacement at the tunnel crown. The analysis revealed that the auxiliary bench and the umbrella arch method were effective in suppressing both horizontal and vertical displacements, with other methods primarily reducing displacement along a single axis. Horizontal displacement was effectively managed using long face-bolts, whereas vertical displacement was minimized through forepoling and steel arch support. Notably, the auxiliary bench method achieved over 20% reduction in horizontal displacement and remained effective regardless of ground conditions.

REFERENCES

[1] Kikkawa N., Itoh K., Hori T., Toyosawa Y., and Orense R.P., Analysis of labour accidents in tunnel construction and introduction of prevention measures. Industrial Health, Vol.53, Issue 5, 2015, pp.517-521.

[2] Kyushu Regional Planning Association., Recent trends and challenges in tunnel engineering technologies, 2010. (in Japanese)

[3] Nippon Expressway Research Institute Company Limited., Design guideline vol.3. tunnel maintenance and tunnel construction, 2023.7. (in Japanese)

[4] Nakano K., Asaka J., Miyazawa K., Watanabe H., Domon T., and Nishimura K., Study on rational structure for tunnel invert as countermeasures against heaving phenomenon, Collection of papers of JSCE, F1, Vol. 75, No. 1, pp. 40-55, 2019. (in Japanese)

[5] Maegawa K., Yagi H., Ito T., Kunimura S., Okui Y., Kuwashima H., and Jiang Y., Verification of stress release rate of 2D numerical analysis against full face method using immediately ring closure, Collection of papers of JSCE, F1, Vol. 78, No. 1, pp. 26-39, 2022. (in Japanese)

[6] Manouchehr Sanei., Philippe R. B. Devloo., Tiago L. D. Forti., Omar Durán., and Erick S. R. Santos., An innovative scheme to make an initial guess for iterative optimization methods to calibrate material parameters of strain-hardening elastoplastic models, Rock Mechanics and Rock Engineering, Vol. 55, pp. 399-421, 2022.

[7] de Souza Neto, E. A., Perić, D., and Owen, D. R. J.: Computational Methods for Plasticity: Theory and Applications, Chapter 6, pp. 137-190, John Wiley & Sons, Ltd, 2008.

[8] Kikkawa N., Ito S., Hori A., Sakai K., and Hiraoka N., Punching fracture mechanism and strength formula of early-age shotcrete, Tunnelling and Underground Space Technology incorporating Trenchless Technology Research, Vol. 110, 2021.

[9] Javili, A., Variational formulation of generalised interfaces for finite deformation elasticity, Mathematics and Mechanics of Solids, Vol. 23, No. 9, p. 1303-1322, 2017.

[10] Jiang Y., Sasaki I., Ookuma S., and Tanabashi Y., Reinforcement effect against surface settlement using an auxiliary technique for shallow tunnel in urban areas, Collection of papers of JSCE, No. 792, III-71, pp. 27-43, 2005. (in Japanese)

[11] Kinashi H., Shirahta H., Kato K., Matuda Y., and Haba T., The ground behavior ahead of tunnel reinforced by long GFRP face bolts in shallow soft ground, Tunnel Engineering Report, Vol. 14, No.32, pp. 217-224, 2004. (in Japanese).

Copyright © Int. J. of GEOMATE All rights reserved, including making copies, unless permission is obtained from the copyright proprietors.

15th Int. Conf. on Geotechnique, Construction Materials & Environment,
Kyoto, Japan, 11-13 November 2025, ISBN 978-4-909106124 C3051

THE DEVELOPMENT OF SUBSURFACE UTILITY ENGINEERING PRACTICES IN THAILAND

Sitthiphat Eua-apiwatch[1], Rungroj Arjwech[2], Kanisorn Klamsuk[1], Anirut Nitas[3], Sirichai Pethrung[4],

[1]Department of Civil Engineering, Burapha University, Chonburi, Thailand
[2]Department of Geotechnology, Khon Kaen University, Khon Kaen, Thailand
[3]Underground Investigation Company Limited, Chonburi, Thailand
[4]Department of Civil Engineering, Rajamangala University of Technology Krungthep, Thailand

ABSTRACT

This study investigates the development and practical implementation of subsurface utility engineering (SUE) in Thailand from 2003 to 2024. Using drawings from over 300 infrastructure projects and detailed field surveys across 21 locations, the research evaluates the accuracy of two primary detection technologies, ground penetrating radar (GPR) and electromagnetic pipe locators. Environmental conditions—especially soil moisture—have significant impacts on detection performance. When applying a practical accuracy threshold of ±0.3 meters, the pipe locator achieved this standard at approximately 81% of the test sites, while GPR met the criterion at around 67%. The pipe locator also demonstrated a lower average error and greater consistency across varied soil conditions. These findings highlight the importance of selecting detection technologies based on site-specific characteristics and integrating both detection methods, supplemented with physical verification, to enhance utility mapping accuracy. While the results are based on a limited number of test locations, the study provides practical insights and supports the advancement of SUE implementation and quality control in Thailand.

Keywords: Subsurface Utility Engineering, Ground Penetrating Radar, Pipe Locator, Utility Detection

INTRODUCTION

Rapid infrastructure expansion below ground since World War II resulted in a global complexity of subsurface utility networks. Nearly 20 million miles of pipelines, cables, and wires have been installed [1]. The 20–50-year design life span of most utility systems now poses significant obstacles for present-day maintenance operations. The rapid growth of infrastructure and urbanization in Thailand has become a significant problem because of inconsistent documentation of the earliest utilities.

The methods for locating underground utilities fail to satisfy contemporary needs in infrastructure construction. The monitoring systems and visual surveys typically diverge from actual positions by 15–30% [2]. According to recorded data, at least 104,000 US utility damage incidents occurred in a single year, while gas pipeline hits from third-party sources caused US$83 million in damages [3]. The available data clearly demonstrates why better utility detection and mapping methods must be developed.

The development of Subsurface Utility Engineering (SUE) practices in Thailand reflects both global technological evolution and unique local challenges. The current research examines this development through analysis of over 300 projects spanning two decades, documenting the progression from basic electromagnetic detection to integrated multiple-technology approaches. The investigation particularly focuses on quantifying accuracy improvements and establishing best practices for Thai urban environments, where high utility density and varied soil conditions create significant challenges for underground utility detection and mapping.

Recent studies have demonstrated that human factors, particularly stakeholder behaviors, play a significantly more important role in damage prevention than previously believed [4]. The fast-growing utility infrastructure of Thailand will face implementation challenges that affect SUE programs due to workforce capabilities, communication problems, and procedural issues. SUE efforts require technological advances, effective stakeholder coordination, and regulatory structures with standardized procedures.

RESEARCH SIGNIFICANCE

This study provides critical empirical data on SUE technology performance in Thailand's specific environmental conditions. The research quantifies accuracy differences between ground penetrating radar and electromagnetic pipe locators across varied soil types and moisture levels, establishing practical guidelines for technology selection. These findings enable optimization of utility detection strategies, reducing infrastructure damage risks and project costs. The work advances SUE implementation standards in Thailand and provides a comparative framework applicable to similar tropical environments with high soil moisture variability.

SUBSURFACE UTILITY ENGINEERING

Subsurface utility engineering implements a structured system to identify and manage underground utility risks by accurately detecting underground utilities and mapping their exact locations. Utility detection through SUE operates by electromagnetic induction where alternating electrical currents in conductors create magnetic fields which analysts use to determine utility types and positions [5]. SUE technology began in the 1970s and then progressed into extensive engineering procedures that merge several scientific approaches and methods [6].

SUE practices gained adoption across the world because they effectively control risks associated with underground infrastructure. Twenty-two states in the United States operate SUE programs for their highway projects. Virginia has mandatory SUE regulations for all their highway projects. The PAS 128 specification of the United Kingdom [7] includes SUE principles as a standard for underground utility detection systems. Australia established the AS 5488 standard [8] for similar purposes. Singapore together with Malaysia adopted SUE practices as part of their infrastructure development, but they follow different implementation protocols depending on regional conditions and requirements.

SUE implementation depends on quality levels which ascend from basic to advanced accuracy according to ASCE 38-02 [9] specifications. Quality Level D remains the most fundamental information source since it uses existing utility records together with verbal descriptions as its sole data source. The initial location information derived from existing records faces challenges because research indicates these records provide locations that may differ by 15–30% from actual positions. Quality Level C builds upon basic information by adding surface feature surveys that connect what is seen above ground, such as manholes and valve boxes, with database records to boost location accuracy.

The implementation of geophysical detection methods under Quality Level B (QL-B) marks a significant advancement in the subsurface utility engineering process. This phase, known as "Designating," utilizes modern technologies such as electromagnetic locators and ground penetrating radar (GPR) to enhance the identification and mapping of underground utilities. It builds upon previous levels by incorporating real-time field data for improved reliability.

The highest level of accuracy is achieved at Quality Level A (QL-A), referred to as "Locating." This involves physically exposing the utility using vacuum excavation or similar non-invasive techniques, enabling precise three-dimensional measurement and direct verification of utility characteristics. The SUE quality levels are summarized in Table 1.

Table 1 SUE quality levels and characteristics

Level	Definition	Data Sources	Methods
QL-D	Record-based information	Existing utility records, as-built drawings	Document research
QL-C	Surface feature correlation	QL-D + visible utility features	Site reconnaissance, survey of visible features
QL-B	Geophysical detection	QL-C + field detection data	Electromagnetic locators, GPR, magnetic methods
QL-A	Physical exposure	QL-B + direct observation	Vacuum excavation, test holes, direct measurement

The capability to select and effectively perform with detection technology relies on understanding fundamental principles together with environmental conditions. Radiodetection Ltd. [5] indicates that electromagnetic pipe and cable locators work within multiple frequency ranges from 512 Hz to 100 kHz. Lower frequencies achieve longer distances while higher frequencies enhance detection accuracy in difficult conditions. These detection systems use two methods to recognize magnetic fields that either naturally originate from utility conductors or through artificial stimulation. Ground penetrating radar functions through electromagnetic wave reflection from subsurface interfaces to develop utility images beneath the surface. It identifies both metallic and non-metallic utilities but its success depends on soil conditions [10, 11].

Environmental factors play a critical role in influencing the accuracy of detection systems. Soil conductivity together with moisture content and composition control signal transmission for electromagnetic and GPR systems in equal measure. According to Jung [6], the detection of buried utilities depends on three essential factors, utility material properties, burial depth, and environmental interference. Higher soil moisture levels along with

clay substrates lead to reduced detection capability. Sandy dry conditions tend to enhance signal transmission. The number of utilities located in a specific area creates specific challenges for accurate detection since urban density hinders detection outcomes.

Modern subsurface utility engineering practices integrate multiple detection technologies as complementary systems to effectively address known challenges in underground utility mapping. Pressurized pipes receive their best detection from acoustic methods whereas ferrous material detection leads to superior results with magnetic methods. Thermal imaging detection adds heat-generating utility to the comprehensive tools used for detection purposes. Current best practices in subsurface utility engineering combine multiple detection technologies under the support of well-developed quality management systems [12].

The financial advantages of correctly implementing subsurface utility engineering are extensively supported by research. A study conducted by Jung [13] involved 22 SUE and 8 non-SUE projects which produced benefit-cost ratios between 3.21 and 33.93. The strength of economic gains from SUE implementations shows a better relationship between how utility system complexity is compared to project expenses because site-specific quality selection outranks expense-based choices. The current research indicates that SUE projects with greater complexity generate more significant benefit-cost advantages which shows why comprehensive SUE methods succeed in difficult site conditions. Studies from the present day demonstrate that SUE deployment generates $11.39 in total savings per dollar invested in complex utility projects where utility relocations contribute roughly 40% of these benefits [10, 14, 15].

DEVELOPMENT OF SUE PRACTICES IN THAILAND

The development of SUE practices in Thailand followed three distinct stages that brought major improvements to both methods and technology. Recent development in SUE technology combines global trends with the specific challenges of Thailand's urban infrastructure and environmental context.

Initial Phase (2003-2008)

Introduction of SUE practices to Thailand started in 2003 through which basic implementation methods and limited technological systems prevailed. The main detection method of this period depended on electromagnetic tools, which received additional support from existing documentation alongside as-built drawings. During this time researchers undertook comprehensive surveys for oil and gas facilities that included extensive work for a service station network that has more than 250 sites throughout Thailand.

The first implementation phase faced difficulties due to imprecise utility network detection and shallow depth ranges in addition to heavy documentation dependency. During this period the employed methods created horizontal errors exceeding 1.0 meter when surveying areas with many utilities. The initial SUE projects set up a base that led to more developed SUE techniques, but also revealed the requirement for improved detection strategies. During the initial phase, electromagnetic equipment served as the primary tools for underground utility detection, as shown in Fig. 1.

Fig. 1 Radiodetection RD4000 electromagnetic pipe locator used for underground metallic pipe detection during the early development of SUE practices in Thailand.

Development Phase (2009-2015)

This phase brought much progress through the adoption of innovative technologies and advanced methodologies into SUE practice. The SUE approach progressed through four main developments during this period, ground penetrating radar technology adoption, detection method combination, digital documentation system development, and GPS mapping system implementation.

The SUE practices moved outside of Thailand to include Cambodia together with the Lao PDR as part of cross-border infrastructure development projects. Southeast Asia became part of a regional expansion that allowed for the transfer of knowledge and standardization of practices throughout the area. The adoption of quality-level classification systems together with systematic documentation methods brought substantial improvements to project results. The second phase marked significant advancement with the introduction of ground penetrating radar technology, as illustrated in Fig. 2.

Fig. 2 MALA Easy Locator Ground Penetrating Radar system introduced during the development phase (2009-2015) of SUE practices in Thailand.

Current Phase (2016-Present)

The present stage shows sophisticated SUE practices that employ combined methodologies and enhanced quality control systems. The present implementation of SUE utilizes multi-frequency GPR systems (Fig. 3) alongside high-precision electromagnetic detectors, GPS mapping solutions, and digital data platforms, along with building information modeling (BIM) integration, as presented in Fig. 4. Physical verification through water jet excavation was employed to provide ground truth data for accuracy assessment.

Fig. 3 US Radar Quantum Imager, a multi-frequency GPR system representing the advanced technology adoption in the current phase (2016-present) of SUE development in Thailand.

Thailand requires a full system of laws and regulations to achieve systematic implementation of SUE practices. The Kingdom should adopt institutional approaches to benefit from established methods like those used by its neighboring country, Malaysia, including the National Underground Utility Database (NUUD) and mapping standards [16]. Malaysia provides a framework that combines international standard utility quality levels and defined stakeholder responsibilities along with centralized data management platforms that Thailand can adopt.

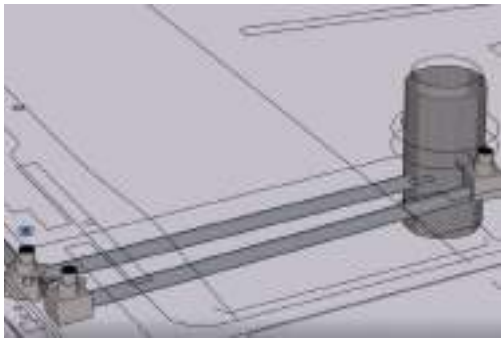

Fig. 4 Example of advanced subsurface utility engineering (SUE) implementation using building information modeling (BIM).

CASE STUDY: ENVIRONMENTAL FACTORS AFFECTING UTILITY DETECTION ACCURACY IN THAILAND

A comprehensive field investigation was conducted to obtain empirical data on the performance of ground penetrating radar (GPR) and pipe locator technologies in Thailand. This section describes the study area and methodology employed.

Study Area

This research project examined 21 survey locations along natural gas pipeline routes in the eastern region of Thailand, specifically within Rayong and Chonburi provinces, as shown in Fig. 5. The selected pipeline segment represents a critical infrastructure component of Thailand's energy network, connecting the offshore natural gas facilities in the Gulf of Thailand to inland industrial areas. This pipeline corridor was chosen for its strategic importance and because it traverses through a variety of soil conditions with different physical and environmental characteristics, making it ideal for comparative analysis of detection technologies. The survey points were strategically distributed to encompass diverse geological settings, including coastal areas with sandy soils and inland regions with varied clay content. This provided a representative sample of the typical subsurface conditions encountered in Thai infrastructure projects.

Methodology

The research employed a systematic approach using three complementary detection methods. Physical verification through water jet excavation provided ground truth data for accuracy assessment, as shown in Fig. 6. The primary detection instruments utilized were a Radiodetection RD4000 electromagnetic pipe locator with a TX-3 transmitter

(Fig. 7) and a MALA Easy Locator Ground Penetrating Radar system (Fig. 8). These non-destructive detection technologies represent the standard equipment used in SUE practice in Thailand during different developmental phases.

Fig. 5 Study area showing a natural gas pipeline route through Rayong and Chonburi provinces.

Both GPR and a pipe locator were used to detect underground pipes at each location. The horizontal and vertical coordinates obtained from utility detection through both methods were recorded. The actual utility position was verified through water jet excavation. The horizontal (ΔH) and vertical (ΔV) differences between the water jet and the other two methods were then compared. Soil samples were collected (Fig. 9) at each location and laboratory tested for an evaluation of environmental factors that influence detection precision.

The obtained soil samples were examined to determine their engineering properties. Standard gravimetric methods were employed to determine the sample moisture contents. Sieve analysis of particles helped identify their textural class. A laboratory performed soil classification following the Unified Soil Classification System (USCS) procedures to obtain standardized groupings. A set of tests based on Atterberg's limits determined the important properties related to soil plasticity. Standard penetration test (SPT) data collection provided information about soil density and compactness measurements at all locations.

Fig. 6 Water jet excavation equipment used for physical verification of pipeline location and depth.

Fig. 7 The 2nd author conducting underground pipe locating by a Radiodetection RD4000 pipe locator system.

Fig. 8 The 3rd author conducting underground pipe locating by a MALA Easy Locator GPR system.

Based on the laboratory test results, survey locations were categorized according to soil type (based on SPT-N value, soil consistency, and relative density) and soil moisture content (below 10% and

above 10%). By establishing these classification categories, the environmental factors impacting detection precision can be evaluated. Each detection method obtained accuracy measurements by analyzing the absolute distance deviations between detected utility locations and their actual positions. Data measurement formed a foundation for the performance evaluation of detection systems under different environmental settings.

Fig. 9 Soil sampling at a test location.

RESULTS AND DISCUSSION

Comparative Analysis of Detection Technologies

Empirical analysis of underground pipeline detection technologies in Thailand yielded critical insights into their relative accuracy under varying environmental conditions. Table 2 summarizes the depth measurement errors for GPR and pipe locator methods at 21 survey locations.

Table 2 Summary of depth measurement errors for GPR vs. a pipe locator

Error Metric	GPR Error (m)	Pipe Locator Error (m)
Horizontal (mean ± σ)	0.34 ± 0.22	0.24 ± 0.17
Vertical (mean ± σ)	0.30 ± 0.26	0.22 ± 0.21
Horizontal (min - max)	0.00 - 0.80	0.00 - 0.70
Vertical (min - max)	0.04 - 0.96	0.02 - 0.89

The pipe locator demonstrated superior overall accuracy compared to GPR across the survey area. It provided more consistent results, with an average vertical error of 0.22 meters, compared to 0.30 meters for GPR. When applying a practical accuracy threshold of ±0.3 meters, the pipe locator met this criterion at approximately 81% of the test locations, whereas GPR achieved it at around 67%. These results suggest that the pipe locator is generally more reliable for subsurface utility detection under soil conditions in the study area. The example of the result obtained from both the pipe locator and the ground penetrating radar is presented in Fig. 10.

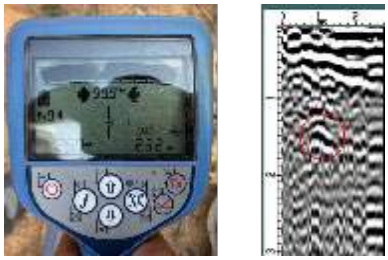

Fig. 10 The example of result obtained from pipe locator and GPR (a) The pipe locator screen shows the location and depth of the buried pipeline. (b) Identified abnormally from radargram present the location and depth of underground pipeline.

Absolute vertical depth errors between the technologies are compared in Fig.11 through a mapping of survey location-specific measurements. Most of the recorded points are situated beneath the diagonal reference line demonstrating that the pipe locator produced lower errors than GPR measurements primarily in non-clay soil conditions. The visual display shows that the pipe locator performed better than GPR in measuring depth at most locations in the survey.

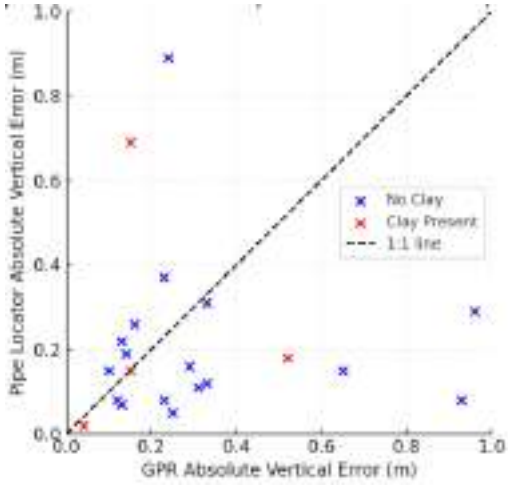

Fig. 11 Comparison of absolute vertical depth errors for GPR vs. pipe locator at surveyed locations. Points below the 1:1 dashed line indicate locations where the pipe locator demonstrated superior accuracy.

Environmental Factors Affecting Detection Accuracy

The study evaluated three environmental factors affecting detection performance through analysis of soil type, soil density, and soil moisture content.

Detection performance was most impacted by the soil moisture content among all considered environmental factors.

The detection accuracy of equipment depended heavily on soil composition because performance showed distinct results between clay and sandy areas. The accuracy of the pipe locator increased to 0.21 meters in sandy or silty soils containing low clay contents when compared to a 0.33-meter vertical error. The pipe locator produced an average error of 0.26 meters in clay-rich areas but GPR measured slightly better with a 0.22 meters error even though one location produced an outlier that influenced this comparison.

Soil density, as measured by standard penetration test (SPT) results, showed some correlation with detection performance, though the relationship was not as strong as with soil type or moisture content. The analysis did not reveal a meaningful trend between SPT-N values and error magnitude for either technology, suggesting that while soil density may influence detection accuracy to some degree, it is not the dominant environmental factor.

A comparison of GPR and pipe locator detection accuracy shows a clear pattern through the data presented in Fig. 12's box plot regarding soil moisture levels. The research data separates into two categories based on moisture levels (≤10% and >10%) under both scanning technologies. GPR measurements display wider (taller box) error spreads along with larger variability when moisture exceeds 10%. The pipe locator produces consistent performance through its narrow error distribution which operates within all tested moisture ranges.

The pipe locator displays better overall accuracy and fewer outside readings when compared to GPR measurements as demonstrated in Fig. 12 through horizontal dotted lines indicating a ±0.3 meters practical accuracy threshold. The response of GPR measurement to moisture levels demonstrates increased sensitivity and some readings exceed threshold limits specifically in the region of high soil moisture. The graphical representation confirms that pipe locators maintain superior measurement stability across different soil moisture levels although GPR measurements suffer from environmental impacts.

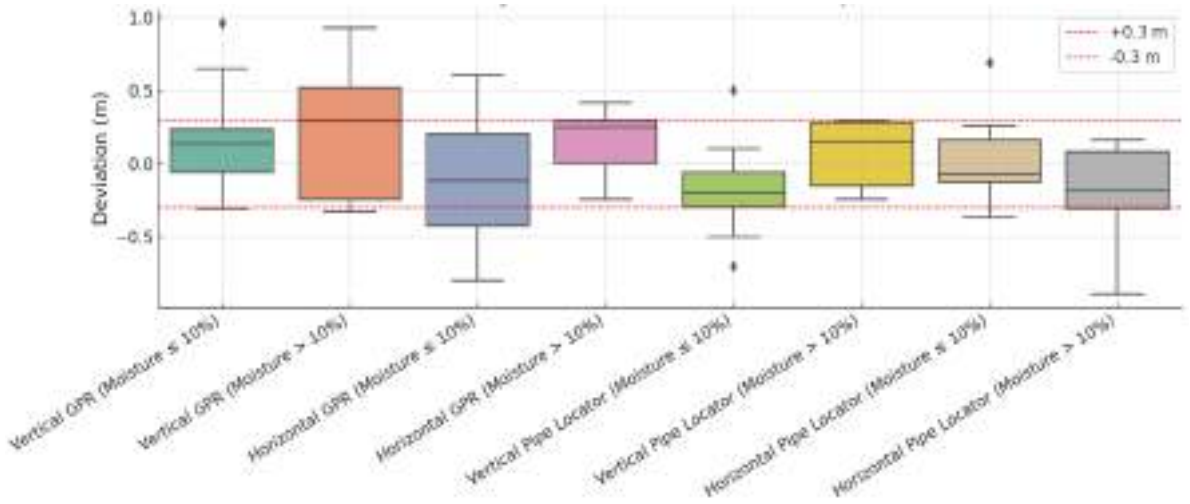

Fig. 12 Horizontal and vertical deviation of GPR and pipe locator vs. soil moisture content

The obtained results deliver essential guidelines regarding SUE methodology usage in Thailand's professional practices. Selection of detection technologies for site-specific environmental conditions should begin with the use of a pipe locator for metallic utilities and high-moisture/clay sites while GPR serves as a complementary or alternative method for situations where electromagnetic methods are inadequate. The most reliable utility mapping for critical infrastructure projects requires the combined use of GPR with water jet excavation for physical verification.

CONCLUSIONS

Over the past two decades, the development of subsurface utility engineering practices in Thailand has significantly advanced underground utility detection and management. Based on field data from 21 test locations, this study finds that:

(i) The pipe locator demonstrated more consistent accuracy than GPR, with a mean vertical error of 0.22 meters, and met the ±0.3-meter accuracy threshold at 81% of test sites, compared to 67% for

GPR.

(ii) Soil moisture was identified as the most influential environmental factor, particularly affecting GPR performance, which declined sharply in high-moisture conditions.

(iii) Soil type also influenced detection accuracy, with both technologies performing better in clay soils than in sandy soils.

(iv) While soil density parameters (based on SPT-N values, consistency, and relative density) showed some influence on detection performance, this relationship was not as pronounced as the effects observed from soil moisture content and soil type.

For effective field application, it is recommended to use pipe locators for detecting metallic utilities, particularly in environments with high moisture contents or clay soils. Ground penetrating radar (GPR) should be applied for identifying non-metallic utilities or used as a complementary tool alongside other methods. In critical infrastructure projects, combining both detection technologies with physical verification ensures the highest accuracy. Ultimately, the selection of detection methods should be guided by the specific environmental conditions present at each site.

It is important to note that these findings are based on a limited sample size (21 locations). Further testing across a wider range of sites is necessary to validate and generalize these conclusions for broader application in Thailand.

ACKNOWLEDGMENT

The authors express their appreciation to the Underground Investigation Company Limited for providing the field information used in this paper.

REFERENCES

[1] Sterling R. L., Utility Locating Technologies: A Summary of Responses to a Statement of Need Distributed by the Federal Laboratory Consortium for Technology Transfer, Federal Laboratory Consortium Special Report Series No. 9, Washington, D.C., 2000.

[2] Stevens R. E. and Anspach J. H., New Technology Overcomes the Problems of Underground System Interferences on Power Projects, American Power Conference, Vol. 55, 1993, pp. 323-326.

[3] Doctor R. H., Dunker N. A. and Santee N. M., Third-Party Damage Prevention Systems, Final Report for Gas Research Institute, No. 5094-810-2870, By Nicor Technologies, Naperville, IL, 1995.

[4] Al-Bayati A. J. and Panzer L., Reducing damages to underground utilities: Importance of stakeholders' behaviors, Journal of Construction Engineering and Management, Vol. 146, Issue 9, 2020, pp. 04020107.

[5] Radiodetection Ltd., ABC & XYZ of locating buried pipes and cables, Radiodetection Ltd., UK, 2017.

[6] Jung Y. J., Subsurface Utility Engineering for Highway Projects: A Study of Utility Impact Rating and Benefit–Cost Analysis, Doctoral dissertation, Pennsylvania State University, 2007.

[7] BSI, PAS 128:2014 Specification for underground utility detection, verification and location, British Standards Institution, 2014.

[8] Standards Australia, AS 5488-2013 Classification of subsurface utility information, Standards Australia Limited, 2013.

[9] American Society of Civil Engineers, Standard Guideline for the Collection and Depiction of Existing Subsurface Utility Data (CI/ASCE 38-02), ASCE, 2003.

[10] Metwaly M., Application of GPR technique for subsurface utility mapping: A case study from urban area of Holy Mecca, Saudi Arabia, Measurement, Vol. 60, 2015, pp. 139-145.

[11] Mizutani T., Chen J. and Yotsumoto S., The 3D localization of subsurface pipes from Ground Penetrating Radar images using edge detection and point cloud segmentation, Measurement, Vol. 236, 2024, pp. 115102.

[12] Hutchins L. and Sinha S. K., Identifying appropriate means and methods for locating buried utilities, Pipelines 2009: Infrastructure's Hidden Assets, 2009, pp. 394-403.

[13] Jung Y. J., Evaluation of subsurface utility engineering for highway projects: Benefit–cost analysis, Tunnelling and Underground Space Technology, Vol. 27, Issue 1, 2012, pp. 111-122.

[14] Anspach J. H. and Scott C. P., Subsurface Utility Engineering for Municipalities: Prequalification Criteria and Scope of Work Guide, American Society of Civil Engineers, 2019.

[15] Mutoni A., Zeringue K. and Wilmot C., Cost and Time Benefits for Using Subsurface Utility Engineering in Louisiana (FHWA/LA.17/644), Louisiana Transportation Research Center, 2021.

[16] Department of Survey and Mapping Malaysia, Standard Guideline for Underground Utility Mapping, AM/FM Technical Sub-Committee, National Mapping and Spatial Data Committee, 2006.

Copyright © Int. J. of GEOMATE All rights reserved, including making copies, unless permission is obtained from the copyright proprietors.

15th Int. Conf. on Geotechnique, Construction Materials & Environment,
Kyoto, Japan, 11-13 November 2025, ISBN 978-4-909106124 C3051

ANOMALY DETECTION FOR SLOPE EXCAVATION WORK USING BACKGROUND SUBTRACTION AND OPTICAL FLOW

Masoho Ide[1], Nobutaka Hiraoka[2] and Kazuya Itoh[3]

[1,3] Graduate School of Integrative Science and Engineering, Tokyo City University, Japan
[2] National Institute of Occupational Safety and Health, Japan

ABSTRACT

Slope failure accidents during excavation work have resulted in serious industrial incidents, including fatalities and injuries. To prevent such accidents, it is important to develop a system that can detect early signs of slope failure and make timely decisions regarding worker evacuation. In this study, we focused on an alternative approach by analyzing images captured by cameras installed on-site to detect anomalies on slopes. Full-scale slope excavation experiment was conducted, and two image processing techniques (background subtraction and optical flow) were applied to detect subtle displacements preceding slope failure. The analysis specifically targeted post-excavation slope conditions to evaluate whether anomalies could be identified before slope failure occurred. The results showed a creep-like gradual increase in the number of changed pixels detected by both methods in cases where a collapse eventually occurred. These findings suggest that slope monitoring through image analysis can be a practical method for early anomaly detection at excavation sites, contributing to enhanced safety and accident prevention.

Keywords: Anomaly detection method, Industrial incidents, Slope excavation work, Background subtraction, Optical flow

INTRODUCTION

In Japan, slope failures and cave-ins have resulted in 10–20 casualties (including fatalities and injuries) annually as industrial accidents, with approximately half of these incidents occurring during slope excavation work [1]. To mitigate such industrial accidents, it is critical to develop a system capable of reliably detecting early signs of slope failure and enabling the prompt evacuation of workers. Minute slope displacements are recognized as precursors to collapse, and several studies have explored monitoring slope dynamics using various sensors, such as extensometers and inclinometers [2-4]. However, these sensor-based approaches are limited by high equipment costs and complex installation requirements.

Image-based methods have also been explored for slope monitoring, including the use of CCD (Charge Coupled Device) cameras and Particle Image Velocimetry (PIV) to calculate displacement vectors associated with landslides [5,6]. However, these techniques have mainly been applied in the context of natural disasters, and there are few studies that specifically address slope failures occurring during construction work as industrial accidents.

This study proposes an anomaly detection method for slope failure based on image analysis using footage from monitoring cameras installed at excavation sites. Specifically, we investigate the feasibility of detecting subtle displacements preceding collapse by applying two image processing techniques—background subtraction and optical flow—to data acquired from a full-scale slope excavation experiment.

FULL-SCALE SLOPE EXCAVATION EXPERIMENT

A full-scale slope excavation experiment was conducted to acquire images of the slope before and after failure during the excavation process. The experimental embankment measured 4.0 m in height, 3.0 m in width, and 16 m in length. Excavation was performed in a stepwise manner from the base of the slope. A fixed camera, positioned in front of the slope, continuously monitored and recorded the slope conditions throughout the experiment, capturing the onset and progression of failure. The embankment was designed as a two-layer model: the base layer comprised Kanto loam, whereas the upper layer consisted of loosely deposited mountain sand to facilitate instability in the measurement region. The mountain sand was sourced from Kimitsu City, Chiba Prefecture, and its grain size distribution curve is presented in Fig.1. Prior to excavation, the mountain sand exhibited an average dry density of 1.46 g/cm³, a compaction ratio (Dc) of 89.4%, and an average water content of 1.73%. The initial slope angle of the embankment was 36.1° (1:1.37) [7].

Six excavation steps conducted during the experiment. Each excavation step was carried out at intervals of at least 30 min, with the subsequent step initiated only after confirming the absence of

significant movement in the monitoring data. Medium-scale slope failures occurred after the third and fourth excavation steps, while large-scale failures were observed following the fifth and sixth steps. Prior to each collapse, displacement signals were recorded by dynamic sensors installed at the top of the slope.

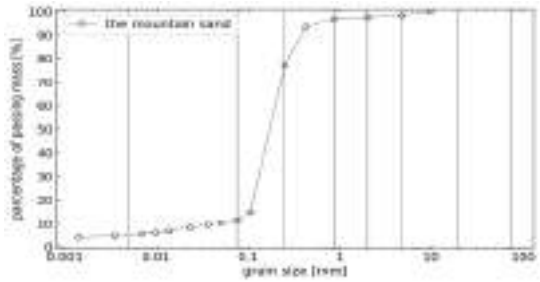

Fig.1 Grain size distribution curve for the mountain sand

IMAGES USED FOR ANALYSIS

Images for analysis were acquired using a GoPro HERO12 camera, which captured frames at 1-s intervals with a resolution of 4872 × 5568 pixels. This paper focuses on the medium-scale slope failure that occurred after the third excavation. A total of 521 images, captured from the end of the third excavation (11:29:00) to the point after the slope failure (11:37:40), were used for the analysis. Two distinct slope failure events were observed during this interval, occurring at 11:36:59 and 11:37:31, respectively. To improve analysis efficiency, a preprocessing step was implemented to crop the images, isolating the target slope area. The resulting images were then resized to 1500 × 3900 pixels. Figs.2–4 present the preprocessed images at the end of excavation and at the time of collapse. The red boxes in these figures highlight the areas where the slope failures occurred.

BACKGROUND SUBTRACTION

Background Subtraction Method

Background subtraction method is an image analysis technique used to extract moving objects by comparing the luminance difference between a background image and an input image against a predefined threshold. In this study, background subtraction was performed under two different conditions. In Case 1, the background image was fixed to the image captured at the end of excavation (11:29:00). In Case 2, the background image was updated to the frame captured 1 min prior to each input image. The analysis was implemented using the OpenCV library, with the luminance threshold value set to 25 [8]. All computations were performed in a CPU environment. To reduce false detections caused by illumination changes, the analysis was restricted to

Fig.2 The end of the third excavation (11:29:00)

Fig.3 Time of 1st slope failure (11:36:59)

Fig.4 Time of 2nd slope failure (11:37:31)

the slope measurement area. Specifically, the region of interest was de fined as the rectangular area spanning pixel coordinates (900–3000, 100–1000), with the top-left corner of the image designated as the origin (0, 0). The analyzed region is indicated by the blue frame in Fig.5.

Fig.5 Area of background subtraction

Result of Background Subtraction

Changes detected through background subtraction were overlaid on the input images to visualize the differences. The results of Case 1 and Case 2 are shown in Figs.6 and 7, respectively. In these images, the blue pixels indicate regions where changes were detected. The area outlined in red indicates the location where the slope failure occurred. In Case 1, changes were primarily observed around the excavation area. As the time of the first slope failure event (11:36:59), noticeable changes became increasingly evident on the left side of the slope, where the failure eventually occurred. The results visually captured this trend. In contrast, Case 2 detected differences only at one-min intervals, resulting in a lower overall number of changed pixels

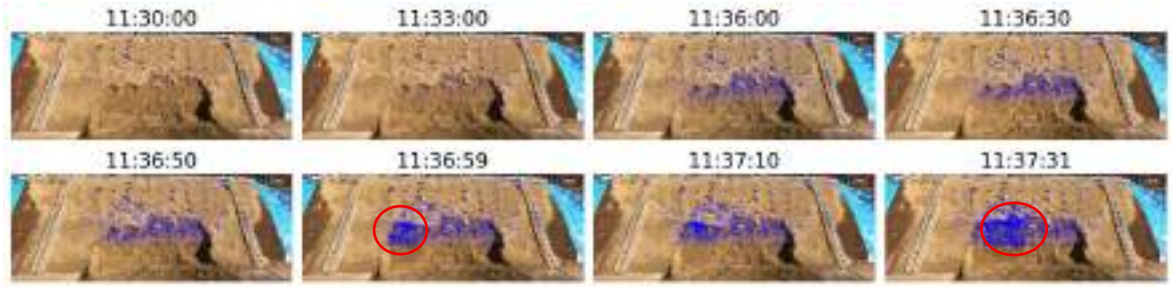

Fig.6 Execution result of background subtraction using the time of the end of drilling as the background image (Case 1)

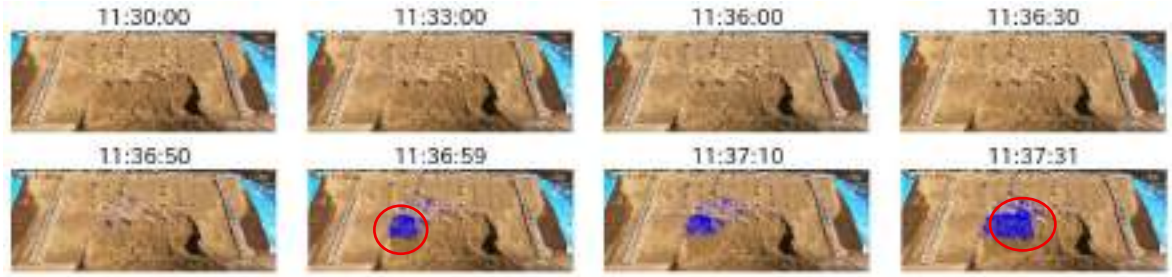

Fig.7 Execution result of background subtraction using the image from one minute ago as the background image (Case 2)

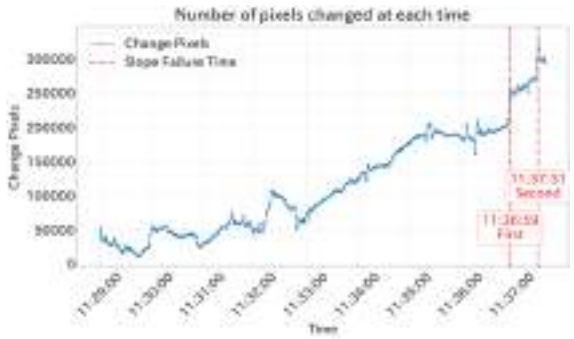

Fig.8 Number of pixels changed at each time (Case 1)

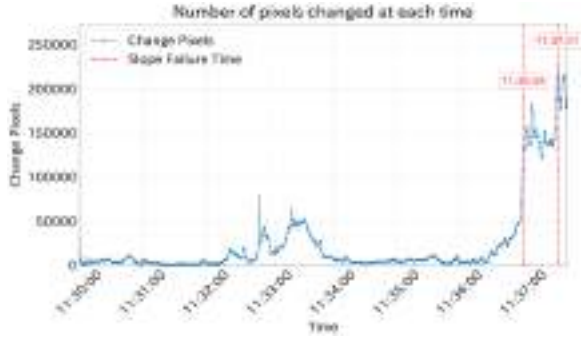

Fig.9 Number of pixels changed at each time (Case 2)

compared to Case 1. However, from approximately 30 s before the slope failure (11:36:30), a progressive increase in change was observed, particularly around the cracked area in the upper left part of the slope. Furthermore, in the right-side region of the slope, where no failure occurred, almost no changes were detected even after the collapse event.

The number of changed pixels detected at each timestamp is shown in Figs.8 and 9, where the red lines indicate the times of the slope failure. In Fig.8 (Case 1), a general increasing trend in the number of changed pixels is evident starting approximately 4 min prior to the failure event (11:33:00) with the increase becoming more pronounced as the failure approached. By contrast, Fig.9 (Case 2) shows smaller fluctuations in the number of changed pixels before the slope failure compared to Case 1. This suggests that frequently updating the background image helps mitigate the influence of illumination and environmental changes. In Case 2, a distinct increase in the number of changed pixels is observed starting around 30 s before the slope failure (11:36:30). Additionally, between 11:32:30 and 11:33:30, up-and-down fluctuations in the number of changed pixels were observed, likely caused by camera shake due to wind.

It is known that precursory phenomena, such as slight surface displacements and small-scale peeling of the surface layer, often occur before a slope failure. In this analysis, Case 2 successfully captured these momentary changes, indicating the potential of this approach to detect early warning signs.

The processing times for each method were 264.60 s for Case 1 (0.51 s per image) and 242.13 s for Case 2 (0.51 s per image). These results suggest that both methods are suitable for real-time.

Summary of the Background Subtraction Method

A comparison between Case 1 and Case 2 revealed that both methods detected an increase in the number of changed pixels prior to the slope failure.

Interpreting these pixel changes as indicators of precursor activity, anomalies were identified approximately 4 min before the failure in Case 1 and at least 30 s before the failure in Case 2, suggesting the potential for early warning detection.

However, determining the specific threshold at which pixel changes reliably indicate a dangerous situation requiring evacuation remains an open issue that warrants further investigation.

Considering practical application in field conditions, Case 2—being more adaptable to environmental changes—offers a more stable analysis. Nevertheless, the current method has limitations, including noise caused by camera shake and the inability to detect anomalies during the first minute of analysis. To achieve higher detection accuracy, improvements such as optimizing the background update interval or incorporating image analysis using multiple cameras are necessary.

It should also be noted that this analysis was conducted during a period with relatively stable sunlight conditions. In Case 1, in particular, changes were detected in areas without actual displacement, such as shadows cast by sensors at the top of the slope. For practical deployment, it is essential to implement countermeasures to reduce the effects of lighting variability, including techniques such as gamma correction and shadow removal.

Since the background subtraction method detects changes based on the brightness values of individual pixels, it is highly susceptible to false detections caused by sunlight and environmental fluctuations. To address this limitation, the following chapter explores the application of optical flow, which estimates motion based on the brightness values of multiple pixels, as a means to suppress false detections induced by sunlight variations.

OPTICAL FLOW

Optical Flow Overview

Optical flow is an image analysis technique that detects motion or changes within video sequences by estimating motion vectors at the pixel level. It relies on assumptions such as brightness constancy of objects between consecutive frames and motion coherence among neighboring pixels [9].

In this study, optical flow was computed using the calcOpticalFlowPyrLK function from the OpenCV library, which implements the pyramidal Lucas–Kanade method [10]. Due to its ability to capture both local variations and large or abrupt movements with high precision, this method is well suited for detecting slope failures. Additionally, its localized and hierarchical computation reduces computational cost, enabling real-time processing.

Distribution of Feature Points

In the pyramidal Lucas–Kanade method, feature points are distributed across the image, and their movements are tracked over time to assess motion changes. In this analysis, 1,000 feature points were evenly distributed across the slope surface, as illustrated in Fig.10. The points were confined within the slope region bounded by ladders visible at both edges of the image. Additionally, regions exhibiting concentrated changes, such as cracks on the slope surface, were automatically assigned a higher density of feature points to capture detailed motion in these critical areas.

Fig.10 Distribution of feature points

Optical Flow at 10-Frame Intervals

In this analysis, each image was treated as a single frame, and optical flow was computed at 10-frame intervals, corresponding to motion detection over 10-s periods. Motion trajectories were visualized by propagating the displacement of feature points across successive frames. The results are presented in Fig.11, where only feature points with displacements of at least one pixel on the slope were displayed. Prior to the first slope failure (up to 11:36:50), a small number of feature points exhibited movement in the upper-left section of the slope, the eventual failure site. At 11:37:00, coinciding with the first slope failure, a substantial increase in moving feature points was observed, particularly around the failure zone and along the left side of the slope. By 11:37:40, following the second slope failure, numerous feature points in the failure area had shifted significantly downward, indicating large-scale displacement.

Fig.12 shows the number of displaced feature points over time. Except for the initial frame and a spike just before 11:33:00, the number of displaced points remained near zero throughout the analysis. A slight increase in displaced points was observed immediately prior to the first slope failure, suggesting a potential precursor signal. However, based on the current data, it remains unclear whether this change reliably indicates impending failure. The abrupt spike near 11:33:00 is likely noise caused by camera movement rather than actual slope deformation.

The minimal detection of prefailure displacement in this analysis may be due to the 10-frame interval being too short to capture subtle slope movements. To improve sensitivity to such small displacements,

Fig.11 Results of optical flow execution at 10-frame intervals

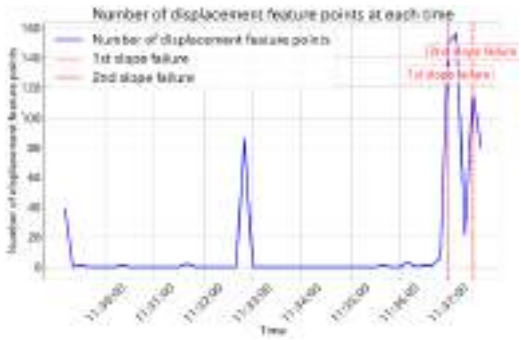

Fig.12 Number of displacement feature points (10-frame intervals)

subsequent analysis will be conducted at 60-frame intervals, following the same approach used in the background subtraction method.

Optical Flow at 60-Frame Intervals

In this analysis, the frame interval was set to 60 frames, and optical flow was computed between each frame and the one 60 frames earlier. The results are presented in Fig.13. The analysis revealed that as the first slope failure approached at 11:36:59, the number of displaced feature points on the left side of the slope, where the failure eventually occurred, increased. These results demonstrate that, compared to the optical flow analysis conducted at 10-frame intervals, the 60-frame interval enables more precise detection of subtle prefailure displacements.

A graph plotting the number of displaced feature points at each time step is shown in Fig.14. The results indicate a clear increasing trend in the number of displaced points, occurring in a creeping manner on the slope surface, beginning approximately 30 s before the first slope failure. The behavior of this graph closely resembles that of the 60-s interval background subtraction analysis shown in Fig.9. As in that case, a significant increase in the number of displaced points was observed between 11:32:30 and 11:33:30, despite the absence of any actual changes on the slope surface. This suggests that the analysis was affected by camera instability, thereby introducing noise into the results. The total processing time for the entire sequence was 573.78 s, corresponding to approximately 1.25 s per frame. This duration is more than twice as long as that required for the background subtraction analysis, indicating a significantly higher computational cost.

Summary of Optical Flow

In this study, optical flow analysis using the pyramidal Lucas–Kanade method was conducted to detect subtle displacements. The results demonstrated that in the 60-frame interval analysis, the number of displaced feature points gradually increased approximately 30 s before the slope failure. This finding is consistent with the results of Case 2 in the background subtraction analysis, suggesting that optical flow can detect micro-displacements that serve as precursors to slope failure.

However, the analysis was impacted by noise due to camera instability, and the computational cost was higher, resulting in longer processing times compared to background subtraction. Therefore, further studies are needed to explore methods that could reduce the computational load, such as optimizing frame intervals.

Optical flow estimates displacement based on pixel intensity patterns. As a result, it is less affected by variations in lighting conditions compared to the background subtraction method. In the background subtraction results changes were detected on the right side of the slope and in areas under the shadow of the sensors, even though no actual movement occurred. In contrast, the optical flow analysis did not indicate significant displacement in these regions. This indicates that optical flow analysis might be more resilient to errors resulting from variations in sunlight. It should be noted, however, that while the pyramidal Lucas–Kanade method offers relatively low computational cost, it cannot estimate displacement in regions lacking distinct feature points. To enhance detection coverage and accuracy, future analyses should consider alternative optical flow algorithms, such as the Farneback method, which enables displacement estimation across all pixels.

CONCLUSIONS

This study applied background subtraction and

Fig.13 Results of optical flow execution at 60-frame intervals

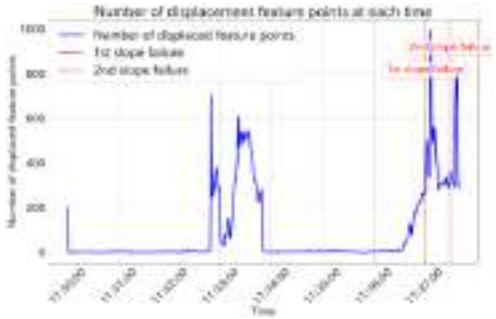

Fig.14 Number of displacement feature points (60-frame intervals)

optical flow techniques to analyze a full-scale slope failure following excavation. The results demonstrate that both methods can potentially detect micro-displacements that serve as precursors to slope failure. However, challenges remain, including susceptibility to false detections caused by variations in lighting and environmental conditions. Moreover, no definitive threshold values currently exist to distinguish between normal and abnormal conditions.

To suppress false detections caused by such external factors, various measures should be considered, including background subtraction methods that exclude bright information, the use of image stabilization features to reduce camera shake, and analysis based on multiple camera viewpoints. Such efforts are essential to assess the generalizability and practical viability of the proposed anomaly detection approaches.

ACKNOWLEDGEMENTS

This research was partially supported by grants from TRY ANGLE EHIME 2023 and Technology Development Grants by Chugoku Kensetsu Kousaikai.

REFERENCES

[1] Annual Report on Occupational Safety and Health in the Construction Industry, Japan Construction Occupa-tional Safety and Health Association, 1985-2022.

[2] Saito M., Prediction of Time of Slope Failure, Soil and Foundation, Vol.17, No.2, 1969, pp.29-38. (in Japanese)

[3] Fukuzono T., Prediction of Time of Slope Failure Based on Creep Models, Journal of the Japan Landslide Society, Vol.27, No.2, 1990, pp.38–40. (in Japanese)

[4] Nakane R., Hiraoka N., Kiikawa N., and Itoh K., Anomaly Detection for Strain of Slope Surface using Machine Learning, Natural Geo-Disasters and Resiliency, IC-CREST, 2023, pp.419-430.

[5] Torii K., Miyaki Y., Yamakawa Y., Bessho M., Sato K., Development of CCD Camera-Based Slope Monitoring System and Its Applicability for Landslide Prediction, JSCE Journal, No.714, VI-56, 2002, pp.65-77. (in Japanese)

[6] Sato T., Kubo T., Muroi S., Sato W., Ishida K., Ishida T., Sakai S., Slope Deformation Monitoring Using Fixed Cameras, 68th Annual Meeting of the Japan Society of Erosion Control Engineering, R6-029, 2019, pp.367-368. (in Japanese)

[7] Hiraoka N., Yasuhara H., Kinoshita N., Iwasa N., Itoh K., and Ishida Y., Precursors to Slope Failure based on Monitoring Data during Sandy Slope Excavation. Proceedings of the 79th Annual Conference of the Japan Society of Civil Engineers, Vol. III, 2024, p.117. (in Japanese)

[8] OpenCV, https://github.com/opencv/opencv-python. (Accessed: May 15, 2025).

[9] Matsuo T., Park S.H., Suemitsu, H., Depth Estimation of Moving Objects using Optical Flow. Reports of the Faculty of Engineering, Oita University, 2002, 45. (in Japanese)

[10] Lucas B. D. and Kanade T., An Iterative Image Registration Technique with an Application to Stereo Vision. Proceedings of the 7th International Joint Conference on Artificial Intelligence (IJCAI), Vancouver, Canada, August 24–28, 1981, pp. 674–679.

Copyright © Int. J. of GEOMATE All rights reserved, including making copies, unless permission is obtained from the copyright proprietors.

15th Int. Conf. on Geotechnique, Construction Materials & Environment,
Kyoto, Japan, 11-13 November 2025, ISBN 978-4-909106124 C3051

SLOPE STABILITY STUDIES BASED ON DIFFERENT MATERIALS AND CONSTRUCTION METHODS

Satoe Suzuki[1], Shin-ichi Kanazawa[1]

[1]Faculty of Engineering, Niigata University, Japan

ABSTRACT

Although many cases of embankment collapse due to sudden heavy rain have been reported in recent years, the causes and mechanisms of embankment collapse due to heavy rain have not yet been sufficiently elucidated. In addition, with the introduction of performance-based design methods, it is essential to consider safety considering various construction conditions and environmental factors, but research focusing on the slope of embankments has not been widely conducted. It is necessary to understand and study the influence of slope gradient on embankment. Therefore, in this study, we used an unsaturated soil/water/air coupled finite analysis code to analyze rainfall on numerical simulations of embankment construction and subsequent rainfall infiltration were carried out using three different compaction methods to investigate the influence of embankment material properties and construction techniques on stress distribution and deformation behavior. The results indicate that differences in embankment materials can increase the risk of failure, including slip surfaces and overall slope instability.

Keywords: embankment, Unsaturated soil, finite element analysis, rainfall analysis

INTRODUCTION

In recent years, sudden heavy rainfall such as torrential rain and typhoons due to climate change has been increasing. According to the Japan Meteorological Agency [1], the number of rainfall events with rainfall exceeding 50 mm per hour will be approximately 330 times per year over the 10-year period from 2014 to 2023. This is an increase of approximately 1.5 times from the average number of events over the 10-year period from 1976 to 1985, when statistics began, which were approximately 226 events. This is an increase of 28.2 events per decade, and it can be said that the amount of intense rainfall is increasing.

Embankment structures are earth structures that are widely used in the construction of houses, roads, railways, etc., and can be said to be social infrastructure structures that are closely related to our lives. Because they also function as lifelines such as roads, if they are breached by an earthquake or heavy rain, the damage will be enormous. In addition, recent typhoons and linear precipitation zones have led to localized, intense rainfall events that pose a significant threat even to embankments that have been properly constructed and maintained in accordance with legal standards. Therefore, the importance of mitigating embankment failures induced by heavy rainfall has been increasing. There have been many reports on the stability of embankment structures during rainfall [2][3], but the collapse mechanism of embankments due to natural disasters has not been fully elucidated, and its elucidation is an urgent task.

Although embankment structures are originally designed and constructed based on compaction control in accordance with the Road Earthwork – Embankment Engineering Guidelines [4], it is considered that the stress state within the embankment can undergo significant changes due to the history of rainfall infiltration. If the initial stress state immediately after construction differs, subsequent stress conditions within the embankment may also vary, even under similar rainfall infiltration scenarios. In addition, different types of materials have different properties of the ground, resulting in different stress states even when the same construction method is used. Therefore, it is important to understand the initial stress state of the embankment. Therefore, in this study, we used the air-dissolved unsaturated soil/water/air coupled finite element analysis program (DACSAR-MP [5]) to simulate the construction of embankments using three types of compaction methods. We investigated the effects of differences in the construction process on the initial stress state of the embankment. Rainfall analyses were also performed on embankments constructed using different methods to compare how they changed from their initial stress state and to study the effects of different materials and construction processes on the rainfall-exposed embankments.

ANALYSIS SUMMARY

Air-Dissolved Unsaturated Soil / Water / Air Coupled Finite Analysis

In this study, we use the air-dissolved type unsaturated soil/water/air coupled finite element analysis code (DACSAR-MP [5]). The unsaturated soil constitutive model used in this code is based on the S_e model proposed by Ohno. [6]. This model represents the mechanical behavior of unsaturated soil by incorporating effective saturation as a parameter that controls the expansion and contraction of the yield surface, thereby accounting for the increase in stiffness due to soil unsaturation and the collapse phenomenon caused by water ingress. Additionally, to avoid transitioning to a singular point that is non-differentiable in numerical calculations, the EC model proposed by Ono. [7], which does not have singular points, has been incorporated. Furthermore, to represent the irreversible mechanical response of the soil's structural skeleton and, in particular, to consider the volume change characteristics of the soil's structural skeleton associated with repeated shear, the model proposed by Iizuka. [8] considering the lower load surface has also been incorporated. The yield function of the elastoplastic constitutive model is as shown in equation (1).

$$f(\boldsymbol{\sigma}', S_e, \varepsilon_v^p, R) = MD\ln\frac{p'}{\xi p'_{sat}} + \frac{MD}{n_E}\left(\frac{q}{Mp'}\right)^{n_E} - \varepsilon_v^p - MD\ln R = 0 \quad (1)$$

Here, p'_{sat} is the preconsolidation stress under saturated conditions, p' is mean effective stress, q is the deviator stress, M is the q/p' in the limit state, D is the dilatancy conefficient[14], ξ is the Interpolation function for determining the multiplier of the consolidation yield stress in unsaturated soils, ε_v^p is the plastic volumetric strain, n_E is the fitting parameter for the EC model, R is the similarity ratio between the normal yield surface and the subloading surface. ξ is the function of effective saturation and can be expressed by equation (2).

$$\zeta = \exp\left[(1-S_e)^b \ln a\right] \quad (2)$$

Here, b is the parameter for adjusting the interval between isosaturation lines on the $e-\ln p'$ surface, a is the increase in stiffness due to unsaturation is the parameter that determines the magnification of the maximum consolidation yield stress. In particular, a is often treated as a fitting parameter.

In addition, the effective stress of unsaturated soil can be expressed by equation (3).

$$\boldsymbol{\sigma}' = \boldsymbol{\sigma}^{net} + S_e s\mathbf{1} \quad (3)$$

Here, $\boldsymbol{\sigma}'$ is the effective stress tensor, $\boldsymbol{\sigma}^{net}$ is the base stress tensor, $\mathbf{1}$ is the second order unit tensor, s is the suction, S_e is the effective degree of saturation.

Analysis Methods

The analysis model adopted in this study was designed to represent a full-scale embankment structure. The slope gradient was set at 1:1.5, referring to the values specified in the Road Earthwork – Embankment Engineering Guidelines[4]. Fig. 1 shows the finite element mesh diagram of the analytical model.

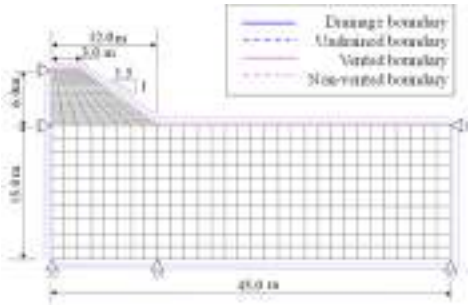

Fig.1 Analysis mesh model

Material Parameters

Tables 1 and 2 present the material parameters of the two soils used in this analysis. The soil-water characteristic curves are shown in Fig.2, and the compaction curves obtained in this study are presented in Fig.3.

Table 1 Material parameters (Material 1)

Item	λ	k	m
Silty sand	0.100	0.010	0.80
S_{r0}	a	v	G_s
0.70	10.0	0.333	2.70
k_a(m/min)	k_w(m/min)	ρ'_{sat} (kPa) (foundation)	ρ'_{sat} (kPa) (embankment)
1.00×10^{-5}	1.00×10^{-3}	30.0	6.0
e_0	γ_t(kN/m^3)	n	n_E
0.90	1.610	1.00	1.30

Table 2 Material parameters (Material 2)

Item	λ	k	m
Silty sand	0.120	0.012	0.00
S_{r0}	a	v	G_s
0.70	10.0	0.333	2.70
k_a(m/min)	k_w(m/min)	ρ'_{sat} (kPa) (foundation)	ρ'_{sat} (kPa) (embankment)
1.00×10^{-5}	1.00×10^{-3}	30.0	6.0
e_0	γ_t(kN/m^3)	n	n_E
1.00	1.605	1.00	1.30

In this analysis, two types of silty sand were assumed based on the classification of embankment materials provided in the Road Earthwork – Embankment Guidelines[4]. The same material was used for both the foundation and embankment zones, with Material 2 containing a higher silt content than Material 1. The material constants are, respectively, λ: swelling index, κ: compression index, m: expansion rate of the lower

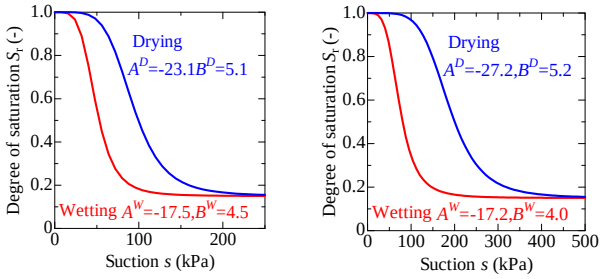

I; Material 1 II; Material 2

Fig.2 Soil-water characteristic curves

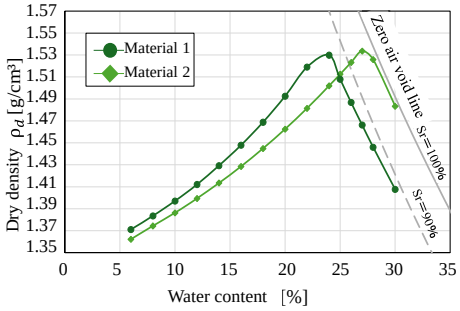

Fig.3 Compaction curves

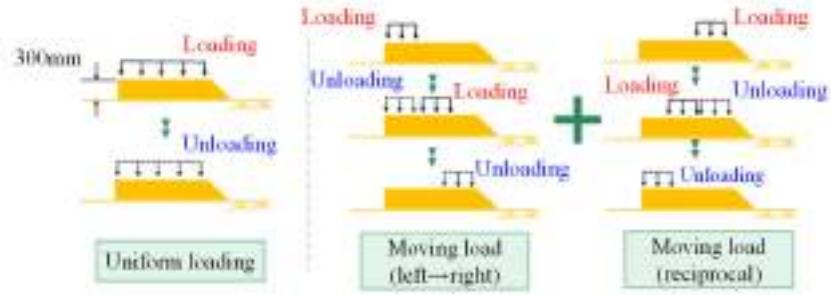

Fig.4 Three different construction methods for embankment

load surface, S_{r0}: initial saturation, a: unsaturated stiffness coefficient, v: Poisson's ratio, G_s: soil particle specific gravity, k_a: permeability, k_w: hydraulic conductivity, ρ'_{sat}: yield stress, e_0: initial void ratio, γ_t: wet density, n: the magnification parameter for consolidation yield stress in the unsaturated state, and n_E: a fitting parameter for the EC model.

The initial pore water pressure head and suction values were determined from the soil-water characteristic curves shown in Fig. 2. In this study, the initial saturation was set to 70% for both materials, and a value between dry and wet was taken out of the corresponding suction by reading the initial saturation from the soil-water characteristic curve. From the compaction curves shown in Fig. 3, the optimum moisture content was found to be 24% for Material 1 and 27% for Material 2. The maximum dry density ρ_{dmax} is approximately 1.53g/cm^3 for Material 1 and 1.54g/cm^3 for Material 2.

The dry density ρ_d that satisfies the control criterion value of 90% at optimum moisture content[4] is as follows:

-Material 1 $\rho_d = \rho_{d\max} \times 0.9 = 1.38(g/cm^3)$

-Material 2 $\rho_d = \rho_{d\max} \times 0.9 = 1.39(g/cm^3)$

The dry density ρ_d that satisfies the control standard value of 90% at the optimal moisture content can be calculated as above, so in this study the condition was that the void ratio of the entire ground be below this value. Here, ρ_s is the particle density of soil.

-Material 1 $e = \rho_s/\rho_d - 1 = 2.7/1.38 - 1 \approx 0.96$

-Material 2 $e = \rho_s/\rho_d - 1 = 2.7/1.39 - 1 \approx 0.95$

Construction Analysis

In this analysis, three different methods were used to analyze the construction of the embankment considering compaction in accordance with the actual construction. Fig. 4 shows the construction methods. The construction process is as follows.

① Create the foundation ground. At this time, the top surface of the foundation ground is set to drainage conditions.

② Create the first layer of embankment elements.

[Uniform loading]

③ Load the top surface of the elements of the first layer of embankment with 300kPa, then unload the same area with 300 kPa.

④ Create the second layer of embankment.

⑤ Load the top surface of the elements of the second layer of embankment with 300 kPa, then unload.

⑥ Repeat steps ④ and ⑤ for 20 layers until the embankment height is 6.0 m.

[Moving load (left to right)]

③Load the top surface of the two elements at the left end of the first layer of embankment with 300 kPa, then move from the left end to the right end and load one element at a time. After the loading area, unload with 300 kPa while moving.

④ Create the second layer of embankment.

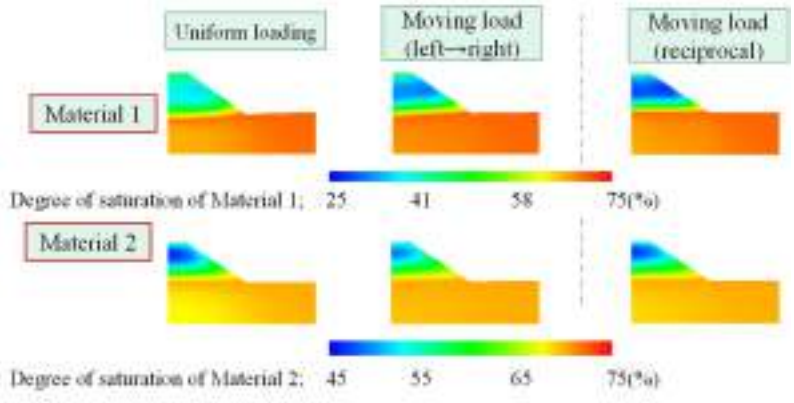

Fig.5 Distribution of degree of saturation at the completion of embankment construction for Materials 1, 2

⑤ Repeat steps ③ and ④ until the embankment height is 6.0 m.

[Moving load (reciprocating)]

③ Apply a load of 300 kPa to the top surfaces of the two leftmost elements of the first layer of the embankment, then move from the left end to the right end and load one element at a time. After the loading point, unload at 300 kPa while moving.

④ Apply a load of 300 kPa to the top surfaces of the two rightmost elements of the first layer of the embankment, then move from the right end to the left end and load one element at a time. After the loading point, unload at 300 kPa while moving.

⑤ Create the second layer of the embankment

⑥ Repeat steps ③, ④, and ⑤ until the embankment height is 6.0 m.

Construction Analysis Results

When construction was completed, the inside of the embankment had dropped to about 35%, and around 50% near the top. From Fig. 5, it can be seen that the least saturated areas were in the middle to bottom of the embankment for material 1, and concentrated in the inside to the top of the embankment for material 2. This is thought to be because repeated loading caused the highly permeable properties of the sand to come into play, resulting in drainage and a drop in the degree of saturation.

Rainfall Analysis

After the construction analysis of the embankment, a rainfall analysis was carried out using two different rainfall intensities. In this rainfall analysis, in order to understand and examine the impact of short-term heavy rainfall, such as torrential rain, on the embankment, flow rates simulating two different rainfall intensities were applied to the rainfall boundary set on the top of the embankment, the slope, and the top surface of the foundation of the analytical model. The rainfall was set at 50mm/hour and 100 mm/hour, respectively.

① After construction, the embankment is left for 30 days in the analysis.

② Apply rainfall to the embankment for 24 hours.

③ If there is a point where the suction falls below 0 kPa at the rainfall boundary, the rain is stopped.

Rainfall Analysis Results

Fig. 6 shows the change in suction over time during rainfall, Table 3 shows the time from the start of rainfall until the suction at the toe reaches 0 kPa, and Fig. 7 and 8 show contour diagrams of the degree of saturation for rainfall of 50 mm/h.

It can be seen from Fig. 7 and 8 that, regardless of the material or rainfall intensity, the degree of saturation increases in the order of top of the embankment, slope, and then inside the embankment. It can also be seen from Fig. 6 that the suction force decreases most quickly at the toe of the slope, and that at the same depth, the suction force decreases more quickly at the foot of the slope than inside the embankment. This decrease in suction force due to the increase in saturation, and in turn the decrease in stress, is thought to reduce the strength of the structure and weaken it. This weakening is particularly noticeable at the foot of the slope. In all 12 results (two materials, three construction methods, and two rainfall patterns), the toe became saturated the fastest, and suction disappeared and the average effective stress dropped significantly, suggesting that the toe is likely to become a weak point in embankments during rainfall, regardless of the material or construction process. Also, while no significant differences were observed due to the construction process, differences in materials did affect rainfall penetration.

Material 1 had a lower degree of saturation immediately after being left alone, which delayed

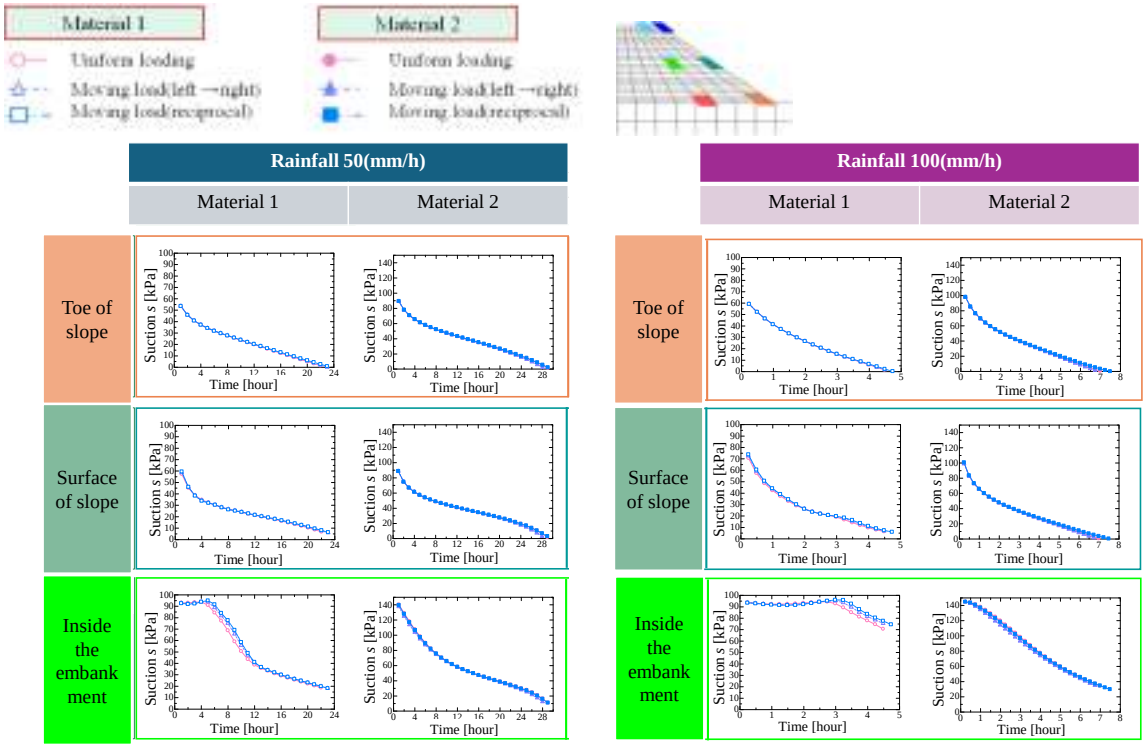

※The color of the frame enclosing the graph indicates the location of the element within the embankment.

Fig.6 Temporal variation of suction during rainfall

rainfall penetration into the embankment, and therefore delayed the progression of weakening due to increased saturation and loss of suction. Material 2 also showed a delayed rainfall penetration into the embankment, but it was faster than Material 1. Therefore, it is considered that the interior of the embankment made of Material 2 was weaker than that made of Material 1 when the rainfall stopped.

Table 3 The time from the start of rainfall until the suction at the law front reaches 0 kPa.

Rainfall	Item	Uniform loading	Moving load (left →right)	Moving load (reciprocal)
50 mm/h	Material 1	1365(min)	1385(min)	1413(min)
	Material 2	1761(min)	1717(min)	1785(min)
100 mm/h	Material 1	280(min)	280(min)	286(min)
	Material 2	424(min)	415(min)	451(min)

Furthermore, comparing Fig. 7 and 8, even with the same material, when rainfall was applied at 50mm/hour, the rain penetrated deeper into the embankment structure, resulting in a higher degree of saturation. Even when comparing the internal suction at the end of the rainfall, the suction was smaller when the rainfall rate was 50mm/hour. This is presumably because with a rainfall pattern of 50mm/hour, the rainfall period was more than twice as long as with a rainfall rate of 100 mm/hour, and the total amount of rainfall was large, leaving sufficient time for the rain to penetrate the embankment structure. Therefore, with a rainfall rate of 100 mm/hour, the interior is relatively safe even though the slope is weakening, but with a rainfall rate of 50 mm/hour, the risk of internal collapse is thought to be increased.

CONCLUSIONS

The construction analysis showed that the degree of saturation increased the top and slope, regardless of the material, construction process, or rainfall intensity. It was revealed that the process of embankment weakening, in which suction disappears and stress decreases, occurs after the degree of saturation increases, is similar. In addition, the toe of the slope can become a weak part of the embankment during rainfall.

During rainfall analysis, the stress state and stress change of the embankment structure are affected by the material. It had an effect on the distribution and transition of saturation and suction. The infiltration condition of rainfall inside the embankment differs depending on the material, and from the increase in saturation and loss of suction, it is thought that the inside of the embankment is weakened in material 2 compared to material 1 even under similar rainfall conditions.

The above results showed that the material has a large effect on the stress and stability of the embankment due to rainfall. The difference in stability inside the embankment is significant.

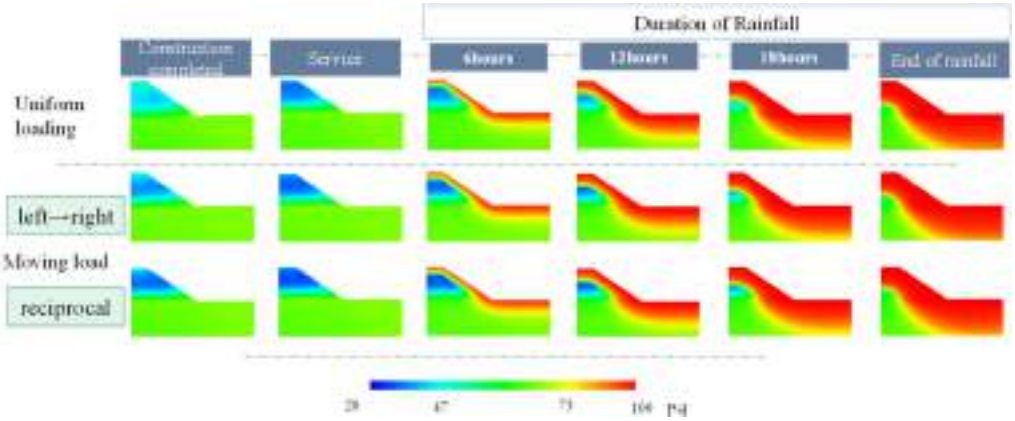

Fig.7 Distribution of degree of saturation at 50 mm/h (Material 1)

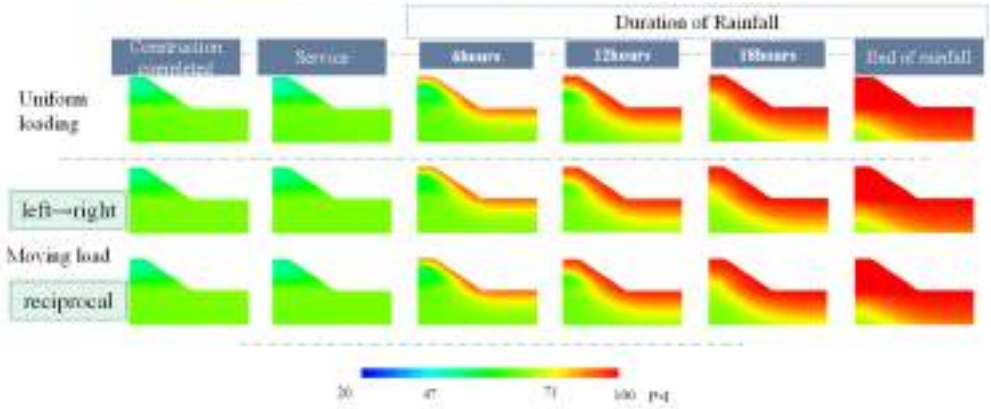

Fig.8 Distribution of degree of saturation at 50 mm/h (Material 2)

However, the effect of the material may be reduced if the rainfall intensity is high or if the embankment is left unattended and rainfall is repeated.

From this, it can be said that the selection of materials is important because the difference in stress state depending on the material is large under short-term rainfall or heavy rainfall conditions. However, in terms of long-term stability, the impact of the materials and construction process is small, and it is highly likely that the same stress state will be reached if rainfall continues.

In the future, we believe it will be necessary to expand the scale of analysis to a full-scale, as well as to carry out numerical analysis that takes into account various natural conditions, in order to carry out more realistic simulations.

REFERENCES

[1] Japan Metrological Agency .Retrieved December 20, 2024, from http://www.jma.go.jp/

[2] Kawajiri S., Nunokawa O., Nishida M. and Ohta N. ; Basic study on initial deformation of embankment due to rainfall by experiment and simulation, Geotechnical Engineering Journal, No.2, pp.307-316, 2015.

[3] Yamashita D., Kanazawa S., Suzuki H. and Iida K.; Investigation of stress behavior in embankment due to rainfall infiltration, International Journal of GEOMATE, Vol.26, Issue 115, pp.81-88, 2024.

[4] Japan Road Association. (2017). Road Earthworks – Embankment Guidelines. Tokyo: Maruzen Publishing Co., Ltd.

[5] Kanazawa, S., Toyoshima, K., Kawai, K., Tachibana, S. and Iizuka, A.; Analysis of mechanical behavior of compacted soil with F.E. method, journal of JSCE, No.68 (2), pp.291-298, 2012.

[6] Ohno S., Kawai K., Tachibana S; Elasto-plastic constitutive model for unsaturated soil applied effective degree of saturation as a parameter expressing stiffiness, Journal of the Japan Society of Civil Engineers, Vol.63/No.4, pp.1132-1141, 2007.

[7] Ohno S., Iizuka A. and Ohta H.; Two categories of new constitutive model derived from non-liner description of soil contractancy, Journal of Applied mechanics , Japan Society of Civil Engineers, Vol.9, pp.407-414, 2006.

[8] Iizuka A., Ohno S., Kawai K. and Tateyama K.; Soil/water coupled dynamic F.E. analysis using an elasto-plastic constitutive model with a subloading surface, Journal of Applied mechanics, Japan Society of Civil Engineers, Vol.5, pp.601-610, 2002.

[9] Shibata T; On the volume changes of normally-consolidated clays, Annual of Disaster Prevention Research Institute, Kyoto University, No.6, pp.128-134, 1963.

Copyright © Int. J. of GEOMATE All rights reserved, including making copies, unless permission is obtained from the copyright proprietors.

15th Int. Conf. on Geotechnique, Construction Materials & Environment,
Kyoto, Japan, 11-13 November 2025, ISBN 978-4-909106124 C3051

EFFECT OF DEM PARAMETERS ON DEFORMATION BEHAVIOR OF ROCKFALL PROTECTION WALLS SUBJECTED TO ROCK SLOPE FAILURE

Ayumu Takehara[1], Naoto Naito[1], Tatsuya Matsuda[1], Katsuhito Agui[2], Yuji Ushiwatari[3], Kazumichi Shimakura[3], and Akinori Nakao[4]

[1] Department of Architecture and Civil Engineering, Toyohashi University of Technology, Japan
[2] Civil Engineering Research Institute for Cold Region, Japan
[3] KOKEN Engineering Co., Ltd., Japan
[4] Hakodate Development and Construction Department, MLIT, Hokkaido Regional Development Bureau, Japan

ABSTRACT

In recent years, the discrete element method (DEM) and other discontinuum analyses have been increasingly employed for practical evaluations to improve the design and maintenance of structures that protect against slope failure. This study investigates the effects of the rock mass shape, rock size, and friction coefficient in the DEM. For this purpose, we use a rock slope failure case that incorporates pre- and post-collapse topographic data, as well as the deformation records of the rockfall protection wall. The results indicate that the damage state of the rockfall protection wall can be reproduced when the rock mass shape is represented with sufficient surface roughness and the slope friction coefficient is set appropriately. However, when evaluating the accumulation area of rock masses that have overtopped a retaining wall, it may be necessary to use a rock mass shape with a high degree of roughness to represent the interlocking of rocks during impact with the wall. In addition, a cushioning layer of geocell-reinforced gravel was installed on the slope side of the rockfall protection wall. Numerical analyses to assess the effect of the presence or absence of the cushioning layer showed that the extent of deformation of the rockfall protection wall increased by 20%–25% without the cushioning layer. This study provides results that support the evaluation of rockfall protection wall effectiveness through simplified analyses considering rock slope conditions.

Keywords: Rock slope failure, Granular avalanche, Impact, Rockfall protection wall, Discrete element method

INTRODUCTION

Slope failures, such as landslides and rockfalls, can cause significant debris impacts that threaten infrastructure, transportation networks, and human life [1–3]. Granular avalanches consist of rapidly flowing soil, rocks, and debris. Their high momentum and unpredictable behavior make them particularly challenging to analyze. Rigid [4–10] and flexible [11–13] barriers have been actively studied and implemented as protective measures to mitigate such hazards. However, there is a growing demand for more cost-effective and high-performance countermeasures. Accurately evaluating the performance of existing protective structures and enhancing their effectiveness is important for better understanding their limitations. These efforts can aid in improving maintenance planning and promoting more efficient use of limited resources. In addition, safety can be improved by reducing the number of unprotected slopes. In particular, when the collapse area is identified through field investigations, assessing the impact forces and deposition patterns of granular avalanches based on the actual slope geometry can further support rational design and maintenance strategies. Gaining a deeper understanding of the impact behavior of granular avalanches is important for addressing these needs.

Although several predictive methods based on the analysis of the impact forces from dry granular flows hitting rigid walls have been proposed [14–16], they are based on small-scale physical experiments or numerical simulations, and their applicability to full-scale slope failure events has not yet been validated. Validation at full scale is essential because granular behavior can exhibit scale effects.

Establishing a numerical modeling approach that balances the simulation accuracy and computational efficiency for large-scale slope failures is essential to meet practical requirements. In this study, the discrete element method (DEM) [17] is used to simulate granular behavior [18–20] by tracking the motion of individual particles based on contact mechanics and equations of motion. This analysis investigates the influence of the rock shape, particle size, and friction coefficient on DEM modeling. A real slope failure case is used to validate the simulations. This case includes pre- and post-collapse topographic data, as well as deformation records of the rockfall protection wall (hereafter, the protection wall). Furthermore, we evaluate the effect of a cushioning layer consisting of geocell-reinforced gravel that is installed on the slope

side of the protection wall by comparing simulation results that are obtained with and without the layer.

RESEARCH SIGNIFICANCE

This study significantly advances the practical evaluation and design of protective structures against large-scale slope failures through the application of the DEM. Whereas previous DEM research predominantly targeted small-scale experimental settings, this work pioneers its use on a real slope failure event incorporating pre- and post-collapse topographic data. By rigorously dissecting the influences of the rock shape, particle size, and friction coefficient, their critical roles in governing wall deformation and sediment deposition patterns are demonstrated. Moreover, the study highlights the substantial effectiveness of geocell-reinforced gravel layers in mitigating wall damage and provides valuable insights into the synergistic benefits of integrating rigid frameworks with cushioning systems. These compelling findings pave the way for the development of more reliable, cost-efficient protective designs and critically bridge the longstanding divide between numerical simulations and real-world field implementations.

DISCRETE ELEMENT MODELING

Contact Model

The DEM simulations were performed using the open-source software LIGGGHTS® [21] with the Hertz contact model. The major parameters specified in the material properties were the Young's modulus, Poisson's ratio, coefficient of friction, and coefficient of restitution. Several studies have been conducted on granular materials using LIGGGHTS, including those on the shear behavior of granular materials [22] and the behavior of granular materials impinging on rigid barriers [23].

Setup of Slope, Collapse, and Countermeasures

Fig. 1(a) presents the geometric setup of the slope and countermeasures, including the protection wall, slope angle (34°), and cushioning layer. Fig. 1(b) shows examples of the modeled rock masses composed of bonded spherical particles. Fig. 1(c) depicts the deformed state of the protection wall based on field observations, which served as the benchmark for validating the simulation results. The dimensions were determined based on the public documents of the National Route 229 Otobe Town Tateura Slope Countermeasure Technical Review Committee [24]. Countermeasures for the collapse area comprised the protection wall with a fence and geocell-reinforced gravel as a cushioning material. In this analysis, the plain concrete protection wall was modeled as a rigid body, whereas the geocell-reinforced gravel was simplified into a group of nonspherical particles. Each segment of the protection wall extended 10 m along the road, and the analytical model covered a total length of 120 m.

DEM Parameters

The Young's modulus has little influence on the deposition shape [18, 25]. Therefore, a value of 3.5×10^7 Pa was used to reduce the computational cost.

The restitution coefficient of the spherical rock masses ranged from 0.46 to 0.60, whereas that of the complex-shaped rock masses ranged from approximately 0.15 to 0.24 owing to the influence of plastic deformation in the contact region or energy loss caused by breakage of the corner region of a complex particle [26]. The restitution coefficient was set to 0.2 based on rock rebound test results that were

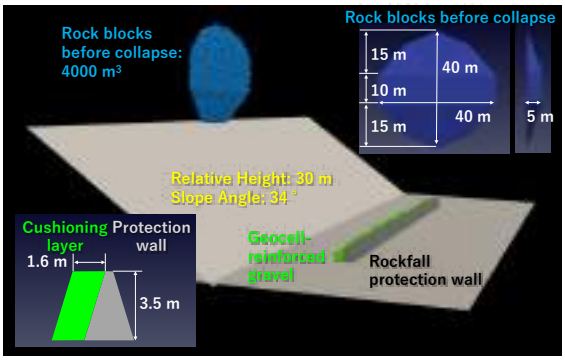

(a) Models of the rock mass, slope, and countermeasures

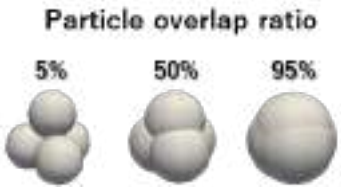

(b) Rock masses

(c) Protection wall deformation

Fig. 1 DEM analysis model.

Table 1 List of analysis cases

	Non-spherical particle size H [m]	Particle overlap ratio α [%]	Slope friction coefficient F [- (deg.)]	Cushioning layer
H1.0-α05-F0.466	1.0m	5%	0.466 (25°)	with
H1.0-α05-F0.364			0.364 (20°)	
H1.0-α05-F0.268			0.268 (15°)	
H1.0-α05-F0.176			0.176 (10°)	
H1.0-α50-F0.466		50%	0.466 (25°)	
H1.0-α50-F0.364			0.364 (20°)	
H1.0-α50-F0.268			0.268 (15°)	
H1.0-α50-F0.176			0.176 (10°)	
H1.0-α95-F0.466		95%	0.466 (25°)	
H1.0-α95-F0.364			0.364 (20°)	
H1.0-α95-F0.268			0.268 (15°)	
H1.0-α95-F0.176			0.176 (10°)	
H0.75-α50-F0.268	0.75m	50%	0.268 (15°)	
H0.5-α50-F0.268	0.5m			
NC-H1.0-α05-F0.268	1.0m	5%		without
NC-H1.0-α50-F0.268		50%		

obtained. The restitution coefficient has a minimal influence on the deposition range of a dry granular avalanche [25].

The Poisson's ratio was set to 0.3, which is the value for hard rock in the Specifications for Highway Bridges [27].

As the influence of the inter-particle friction angle on the results of granular avalanche analysis is minor [18], it was set to 25°, which is approximately the median value reported by Rowe [28].

The particle shape, size, and particle-to-slope friction coefficient, which were the subjects of the sensitivity analysis, are explained in the following section.

Modeling assumptions such as a uniform rock block size and simplified slope surface roughness were adopted to reduce the computational cost while capturing the essential interaction mechanisms. Although these assumptions enable parametric analysis within reasonable simulation times, they limit the generalizability of the results to real-world slopes with complex geometries and heterogeneity. Therefore, care must be taken when applying the findings to cases with highly variable particle size distributions or irregular slope surfaces.

Investigated Conditions

Previous studies to determine the final deposition shapes of dry granular avalanches [18, 25] have shown that parameters such as the Young's modulus, which represents the contact stiffness, inter-particle friction coefficient, and inter-particle restitution coefficient have a minimal influence on the final deposition shape. Therefore, this study focused on the slope friction coefficient, which is known to have a strong influence on the particle behavior on slopes and the deformation behavior of the protection wall

that is installed at the toe of the slope. In addition, the particle shapes, which are not widely standardized in modeling approaches, were examined. Three rock block shapes with varying interlocking effects were created by arranging spherical particles at the vertices of a regular tetrahedron and adjusting the overlap ratio between particles. As summarized in Table 1, 16 analysis cases were designed by systematically varying three main parameters: the rock mass shape (using particle overlap ratios of 5%, 50%, and 95%), slope friction coefficient (ranging from 0.176 to 0.466), and rock mass size (0.5, 0.75, and 1.0 m). Each case label (e.g., H1.0-α05-F0.268) explicitly encodes these conditions for clarity in the subsequent discussion.

DEM PARAMETER SENSITIVITY

According to a previous study [24], rock masses from slope failure were deposited within approximately 15 m in the slope-flow direction and 30 m in the longitudinal direction beyond the protection wall. The protection wall experienced deformation of approximately 50 m in the longitudinal direction, with two spans tilting and three spans overturning. The analysis results were compared with damage observations.

Fig. 2 shows that the final deformation of the protection wall differed significantly across the analysis cases. For example, in cases with a slope friction coefficient of 0.176 or 0.268, substantial wall deformation occurred, regardless of the rock mass shape. In contrast, under higher friction (F = 0.466),

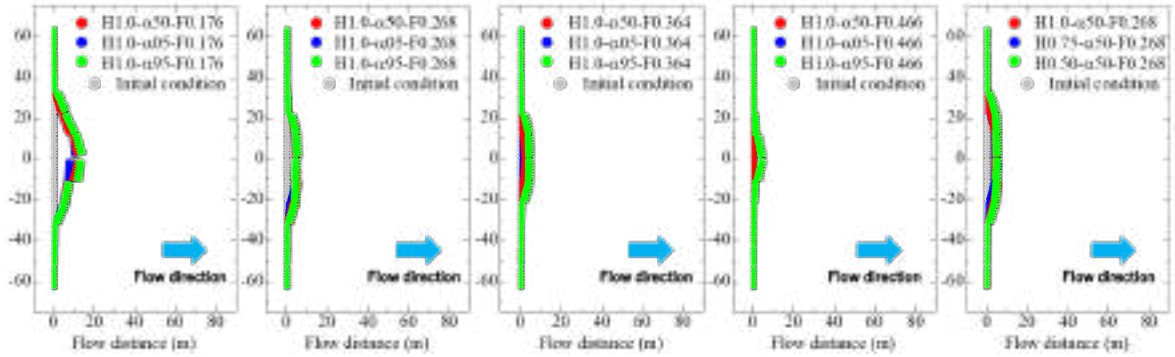

Fig. 2 Protection wall at final stop: All analysis cases under geocell-reinforced grave conditions.

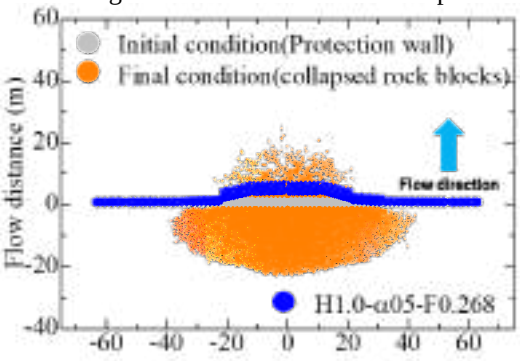

(a) H1.0-α05-F0.268

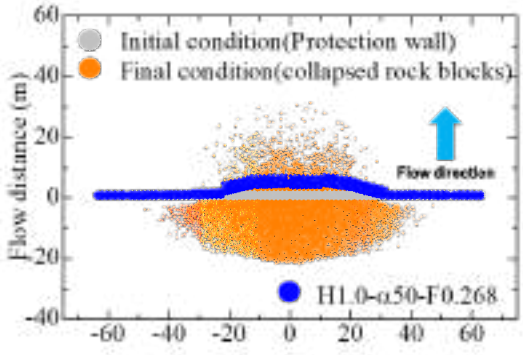

(b) H1.0-α50-F0.268

Fig. 3 Protection wall and collapsed rock blocks at final stop.

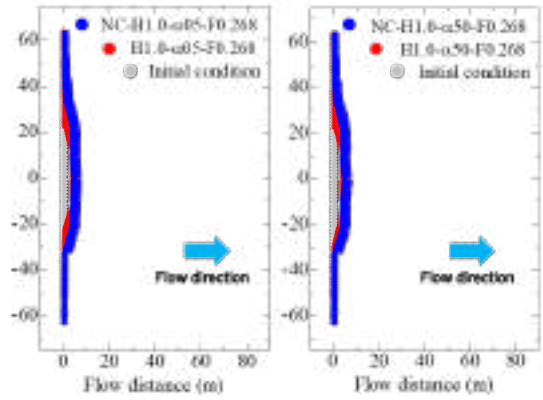

Fig. 4 Protection wall at final stop: Comparison of all analysis cases with effectiveness of geocell-reinforced gravel.

deformation was only observed when the rock blocks had a 95% overlap ratio, indicating strong interlocking. These visual results provide key insights into how the particle shape and slope friction jointly affect wall performance. In terms of the effect of the rock mass size, the largest deformation range occurred with a particle diameter of 0.5 m, but its influence on the flow direction was minimal.

Fig. 3(a) and (b) show the final resting positions of the protection wall and rock mass groups in cases H1.0-α05-F0.268 and H1.0-α50-F0.268, where the protection wall deformation closely resembled the observed damage for a rock mass size of 1.0 m.

Fig. 3 compares two representative cases: H1.0-α05-F0.268 and H1.0-α50-F0.268. As shown in Fig. 3(a), a low overlap ratio (5%) resulted in a wider dispersion of rock masses (~30 m) and moderate wall deformation. In contrast, Fig. 3(b) shows a more compact deposition (~40 m) and increased wall deformation owing to enhanced interlocking from the higher overlap ratio (50%). These results emphasize that the rock mass shape affects the runout distance as well as the wall impact characteristics.

IMPACT OF CUSHIONING LAYER ON WALL RESPONSE

As shown in Fig. 4, the inclusion of the cushioning layer significantly altered the wall deformation pattern. Without the layer, the wall exhibited a longitudinal deformation spread that was approximately 20–25 m greater than that with the layer. Although the flow direction displacement remained largely unchanged, this result demonstrates that geocell-reinforced gravel serves as an effective energy absorber and deformation suppressor.

CONCLUSION

This study has advanced the practical evaluation and design of protective structures for large-scale slope failures by applying the DEM to a real-world

case with detailed pre- and post-failure topographic data. As opposed to prior DEM research that focused on small-scale experiments, this work systematically revealed how the rock shape, particle size, and friction coefficients govern the wall deformation and deposition patterns. It also demonstrated the effectiveness of geocell-reinforced gravel layers in mitigating structural damage and highlighted the advantages of integrating rigid frameworks with cushioning systems. These insights pave the way for more reliable, cost-efficient protective designs and bridge the gap between numerical modeling and full-scale field implementation.

Although numerical analysis using the DEM provides valuable insights, it has certain limitations. First, the selection of mechanical parameters such as friction and restitution coefficients is dependent on literature values and limited field data. Accumulating information on analysis parameters by reproducing other collapse cases is desirable. Second, in this study, the slope shape was simplified and the rock block size was set to be uniform, so the geometric conditions were not exactly the same as those in real life. Investigating how detailed geometric conditions, such as the slope roughness and rock block size distribution, affect the collapse and deposition behavior of dry granular avalanches is important to generalize the results of this study.

ACKNOWLEDGMENTS

This work was supported by JSPS KAKENHI (Grant Numbers JP23K13402 and JP23K17774).

REFERENCES

[1] Wang, G., Sassa, K., Fukuoka, H., 2003. Downslope volume enlargement of a debris slide–debris flow in the 1999 Hiroshima, Japan, rainstorm. Eng. Geol. 69, 309–330.

[2] Moriguchi, S., Matsugi, H., Ochiai, T., Yoshikawa, S., Inagaki, H., Ueno, S., Suzuki, M., Tobita, Y., Chida, T., Takahashi, K., Shibayama, A., Hashimoto, M., Kyoya, T., Dolojan, N. L. J., 2021. Survey report on damage caused by 2019 Typhoon Hagibis in Marumori Town, Miyagi Prefecture, Japan. Soils Found. 61(2), 586–599.

[3] Nakajima, S., Abe, K., Shinoda, M., Nakamura, S, Nakamura, H., 2021. Experimental study on impact force due to collision of rockfall and sliding soil mass caused by seismic slope failure. Landslides 18, 195–216.

[4] Jiang, Y. J. and Towhata, I., 2013. Experimental study of dry granular flow and impact behavior against a rigid retaining wall, Rock Mech. Rock Eng. 46, 713–729.

[5] Calvetti, F., di Prisco, C. G., Vairaktaris, E., 2017. DEM assessment of impact forces of dry granular masses on rigid barriers. Acta Geotech. 12, 129–144.

[6] Calvetti, F., di Prisco, C., Redaelli, I., Sganzerla, A., Vairaktaris, E., 2019. Mechanical interpretation of dry granular masses impacting on rigid obstacles. Acta Geotech. 14, 1289–1305.

[7] Ng, C. W. W., Choi, C. E., Liu, L. H. D., Kwan, J. S. H., Koo, R. C. H., Pun, W. K., 2017. Impact mechanisms of granular and viscous flows on rigid and flexible barriers. Can. Geotech. J. 54(2), 188–206.

[8] Ng, C. W. W., Choi, C. E., Goodwin, S. R., 2019. Froude characterization for unsteady single-surge dry granular flows: impact pressure and runup height. Can. Geotech. J. 56, 1968–1978.

[9] Yang, E., Bui, H. H., Nguyen, G. D., Choi, C. E., Ng, C. W. W., Sterck, H. D., Bouazza, A., 2021. Numerical investigation of the mechanism of granular flow impact on rigid control structures. Acta Geotech. 16, 2505–2527.

[10] Zhang, B., Huang, Y., Liu, J., 2021. Micro-mechanism and efficiency of baffle structure in deceleration of granular flows. Acta Geotech. 16, 3667–3688.

[11] Albaba, A., Lambert, S., Kneib, F., Chareyre, B., Nicot, F., 2017. DEM modeling of a flexible barrier impacted by a dry granular flow. Rock Mech. Rock Eng. 50, 3029–3048.

[12] Brighenti, R., Spaggiari, L., Segalini, A., Savi, R., Capparelli, G., 2021. Debris flow impact on a flexible barrier: laboratory flume experiments and force-based mechanical model validation. Nat. Hazards. 106, 735–756.

[13] Berger, S. M., Hofmann, R., Preh, A., 2024. Impacts on embankments, rigid and flexible barriers against rockslides: Model experiments vs. DEM simulations. Rock Mech. Rock Eng. 57, 2793–2808.

[14] Moriguchi, S., Borja, R. I., Yashima, A., Sawada, K., 2009. Estimating the impact force generated by granular flow on a rigid obstruction. Acta Geotech. 4(1), 57–7.

[15] Albaba, A., Lambert, S., Faug, T., 2018. Dry granular avalanche impact force on a rigid wall: Analytic shock solution versus discrete element simulations. Phys. Rev. E, 97, 052903.

[16] Redaelli, I., di Prisco, C., Calvetti, F., 2021. Dry granular masses impacting on rigid obstacles: numerical analysis and theoretical modelling. Acta Geotech. 16, 3923–3946.

[17] Cundall P. A. and Stack, O. D. L., 1979. A discrete model for granular assemblies. Geotechn. 29(1), 47–65.

[18] Naito, N., Matsuda, T., Miura, K., and Omura, T., 2023. Three-dimensional discrete element modelling of granular avalanche under multiple flow conditions. Int. J. GEOMATE. 24(106), 77–84.

[19] Watanabe, D., Moriguchi, S., Terada, K., 2022.

A numerical study on the effects of particle size distribution on run-out distance of granular flow. Soils Found. 62,101242.

[20] Nishimura, T., Fukuda, T., Tsujino, K., 2010. Distinct element analysis for progressive failure in Rock Slope. Soils Found. 50(4), 505–513.

[21] Kloss, C. and Goniva, C., 2010. LIGGGHTS – a new open source discrete element simulation software. In Proceedings of the 5th International Conference on Discrete Element Methods, pp. 25–26.

[22] Louati, H., Bednarek, X., Martin, S., Ndiaye A., and Bonnefoy, O., 2019. Qualitative and quantitative DEM analysis of cohesive granular material behaviour in FT4 shear tester. Chem. Eng. Res. Des. 148, 155–163.

[23] Ng, C. W. W., Choi, C. E., and Goodwin, S. R., 2019. Froude characterization for unsteady single-surge dry granular flows: impact pressure and runup height. Can. Geotech. J. 56(12), 1968–1978.

[24] Technical Committee Materials for Slope Countermeasures along National Route 229 in Tateura Area of Otobe Town, 2021. Materials for the First Meeting of the Technical Review Committee. https://www.hkd.mlit.go.jp/hk/douro/v151sd0000000sar-att/v151sd0000001sx3.pdf

[25] Xiao, J., Tozato, K., Moriguchi, S., Otake, Y., Terada, K., 2023. Quantification of the contribution ratio of relevant input parameters on DEM-based granular flow simulations. Soils Found. 63(6), 101378.

[26] Naito, N., Maeda, K., Konno, H., Ushiwatari, Y., Suzuki, K., Kawase, R., 2020. Rockfall impacts on sand cushions with different soil mechanical characteristics using discrete element method. Soils Found. 60(2), 384–397.

[27] Japan Road Association, 2017. Specifications for highway bridges. https://www.mlit.go.jp/road/sign/kijyun/pdf/20170721hashikouka.pdf

[28] Rowe, P. W., 1962. The stress-dilatancy relation for static equilibrium of an assembly of particles in contact. Proc. R. Soc. Lond. A 269, 500–527.

Copyright © Int. J. of GEOMATE All rights reserved, including making copies, unless permission is obtained from the copyright proprietors.

15th Int. Conf. on Geotechnique, Construction Materials & Environment,
Kyoto, Japan, 11-13 November 2025, ISBN 978-4-909106124 C3051

LABORATORY INVESTIGATION OF THE IMPACT OF RISING SOIL WATER CONTENT ON LIQUIDITY INDEX AND SLOPE INSTABILITY

Nofrizal[1], Fauzan[2], Abdul Hakam[3], Bambang Istijono[4], and Andriani[5]

[1,2,3,4,5]Department of Civil Engineering, Faculty of Engineering, Andalas University, Indonesia
[1]Padang Institute of Technology, Indonesia

ABSTRACT

This research investigates how increasing water content within the soil layer affects the Liquid Limit (LL), Liquidity Index (LI), and their relationship to slope stability, using a controlled laboratory-scale modelling approach. The physical and consistency parameters of the soil were determined from field samples to enable classification. From these samples, slope models were developed to represent realistic slope angles of 30°, 45°, and 60°, which were progressively saturated to simulate real-life conditions. A key challenge addressed in this study is establishing a link between water content and slope failure thresholds in fine-grained soils, as many models fail to account for changes in Atterberg limits or the Liquidity Index (LI) with increasing saturation. The findings indicate that water content significantly influences LI in a positive correlation, with slope failures generally occurring when LI values exceed 1. Steeper slopes, particularly those exceeding 45°, demonstrated greater reductions in shear strength and cohesion. Furthermore, the results show that the internal soil structure deteriorates when the water content surpasses the LL, causing the soil to behave like a fluid and become highly susceptible to slips. The integration of Atterberg limit parameters with physical slope modelling establishes a new and practical relationship between LI values and the onset of flow-type landslides. This approach provides a simple yet effective method for evaluating slope failure risks in fine-grained soils. The results underscore the importance of monitoring LI and LL values in steep, moisture-prone areas, as these can serve as critical early warning indicators for potential landslides.

Keywords: Water Content, Liquid Limit, Slope Failure, Landslide Mechanism, Talamau Plateau

INTRODUCTION

Slope stability is a crucial aspect of geotechnical engineering, particularly in the planning and design of infrastructure such as roads, embankments, and dams. Slope failures can result in severe consequences, including structural damage, economic losses, and casualties [1]. Among the main triggering factors, soil moisture content plays a dominant role, especially in humid regions with high rainfall intensity [2-3].

For cohesive soils such as clay, changes in water content strongly influence their mechanical behavior, especially shear strength and deformation. The Atterberg limits (Liquid Limit, Plastic Limit, Shrinkage Limit) and the Liquidity Index (LI) are widely used to assess soil consistency and plasticity [4]. Previous studies have shown that rainfall infiltration and increasing pore water pressure reduce shear strength and significantly increase landslide risk [5-6]. However, most of these works have focused on pore water pressure and matric suction, with relatively few explicitly considering changes in Atterberg limits and Liquidity Index values in slope stability assessments.

This study addresses that gap through laboratory-scale experiments that integrate Atterberg limit parameters with physical slope models. The research was conducted in the Talamau Plateau, Pasaman Regency, West Sumatra, a region characterized by extremely high annual rainfall (4,700–5,300 mm) and steep slopes (>15°), making it highly prone to landslides [7-9]. The geographical location of the study area is illustrated in Fig.1, which highlights the landslide-prone zones within the plateau.

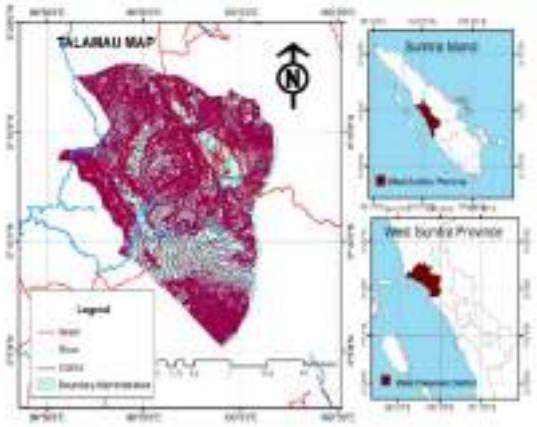

Fig. 1 Geographical location of the landslide-prone area in the Talamau Plateau, West Sumatra

Soil samples from the site were tested to determine their physical and consistency properties, then used to construct slope models with angles of 30°, 45°, and 60°. The main objective is to establish the relationship between soil water content, Liquidity Index (LI), and slope failure thresholds. The findings are expected to provide a simple, practical indicator for early warning in landslide-prone areas.

RESEARCH SIGNIFICANCE

Understanding the relationship between increases in soil moisture content and geotechnical properties such as soil moisture content and soil liquidity index is very important in predicting and reducing slope failure. This study provides important insights into how variations in the rate of increase in soil moisture content will affect soil behaviour, particularly in terms of its transition from a stable to an unstable state. As soil moisture content increases, the mechanical strength and shear resistance of the soil will decrease significantly, thereby increasing the risk of slope instability. The modelling approach using laboratory experiments on slope-forming soils allows for the exploration of concepts in controlling and observing soil response under varying soil moisture content and liquidity index conditions, enabling a more detailed and accurate characterisation of the soil liquidity index as an indicator of potential slope failure. The findings from this study can serve as a basis for improving early warning systems, refining slope stability models, and providing input for more effective slope management and engineering practices. This research has practical relevance for civil engineering, environmental management, and disaster risk reduction, especially in areas prone to landslides

MATERIALS AND METHODS

The study was conducted in Talamau Sub-district, Pasaman Regency, West Sumatra, a region with steep slopes and high rainfall that makes it highly prone to landslides. Silty clay soils were collected using hand augers and core samplers at depths of 0–1.5 m, representing the most weathered and failure-prone soil horizons. The samples were tested at the Geotechnical Laboratory of Andalas University and the Soil Mechanics Laboratory of the Padang Institute of Technology.

Laboratory analyses included natural water content, specific gravity, unit weight, and Atterberg limits (LL, PL, SL) in accordance with ASTM standards. These values were used to calculate the Liquidity Index (LI), which serves as the primary indicator of soil consistency under varying moisture conditions. A summary of the soil properties is presented in Table 1.

Physical slope models were constructed at a 1:100 scale, with a height of 34 cm and a base width of 30 cm. The slopes were shaped at 30°, 45°, 60°, and 90°, compacted to 90% of the maximum dry density. Rainfall was simulated using a machine with 10 oscillating nozzles, calibrated to replicate local rainfall intensity. The experimental setup is illustrated in Fig 2.

Table 1. Values of soil characteristics of test specimens

Experiment	Parameters	Value	Units
Water content	w	60.594	%
Volume weight	γ	1,558	gram/cm^3
Specific gravity	Gs	2.627	
Sieve analysis	Gravel	0.000	%
	Sand	34.067	%
	Clay	65.933	%
Atterberg limit	SL	64.885	%
	PL	46.974	%
	PI	17.911	%
Direct shear	c	0.218	kg/cm^2
	φ	22.835	°
Compaction	w opt	48.455	gram/cm^3
	γ dry max	1.235	gram/cm^3

Note: SL = Shrinkage Limit, PL = Non-elastic Limit, PI = Non-elastic Index, c = cohesion, φ = Inner shear angle, w opt = Optimum water content, γ dry max = dry soil specific gravity.

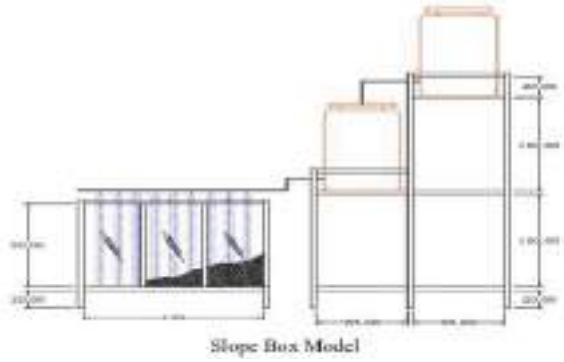

(a)

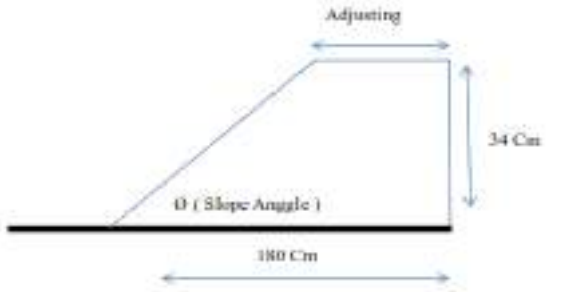

(b)

Fig. 2. Slope model trial layout: (a) Dimensions of the landslide model; (b) Experimental slope model layout

Experiment Procedure

The experimental procedure was carried out in three main stages. The first stage involved soil characterization, including tests for water content, specific gravity, grain-size distribution, and Atterberg limits (LL, PL, PI). These parameters were used to calculate the Liquidity Index (LI).

In the second stage, physical slope models were constructed using field soils compacted to 90% of the maximum dry density. Slopes were formed at angles of 30°, 45°, 60°, and 90°. Rainfall was simulated using oscillating nozzles calibrated to local rainfall intensity, while soil moisture and LI were monitored during infiltration.

The third stage focused on observing slope behavior under saturation. Variations in water content were correlated with LI values and slope deformation leading to failure. Particular attention was given to the LI > 1 threshold, which indicates the transition of soil from plastic to liquid state and marks the onset of slope collapse.

Relationship Between Water Content, Liquid Limit, and Soil Mechanics

The relationship between water content, liquid limit (LL), and soil mechanics is a critical factor in slope stability, particularly in fine-grained soils such as silty or sandy clays. As water content approaches or exceeds the LL, soil strength decreases significantly due to the reduction of cohesion (c) and internal friction angle (ϕ), caused by weakened particle bonding and the loss of matric suction.

$$LI = \frac{W-PL}{LL-PL} \quad (1)$$

This behavior is expressed through the Liquidity Index (LI), calculated using Equation (1). LI values describe soil consistency: LI < 0 indicates stiff or semi-solid soil, 0 ≤ LI ≤ 1 indicates a plastic state, and LI > 1 indicates that the soil behaves like a liquid. The variation of LI with increasing water content is illustrated in Fig. 3, which shows the progressive loss of soil consistency during rainfall simulation.

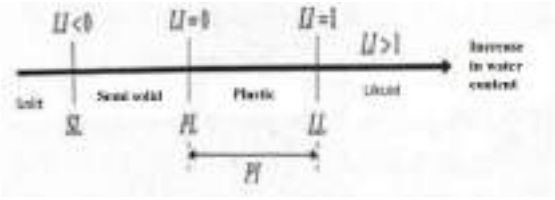

Fig. 3 Soil Fluidity Index Graph

The soil classification based on LI is summarized in Table 2. At LI > 1, the soil begins to lose cohesion and behaves in a fluid-like manner, while at LI > 1.5 the soil becomes very soft, essentially liquefied. These results highlight that exceeding the liquid limit (LL) serves as a critical threshold for slope failure initiation.

Table 2. The soil classification based on LI

Items	Description
LI< 1	Semi-solid soil, high strength
0< LI > 1	Plastic state soil, medium strength, soil is a kind of plastic material
LI > 1	Soil begins to lose consistency, approaching liquid state, soil is liquefiable.
LI > 1.5	Very soft/liquid soil means that the water content of the soil is higher than its liquidity limit, so the soil behaves like a liquid and loses its cohesion.

Source: Braja M.Das (2010 Edition), Geotechnical Engineering.

The Plasticity Index (PI) is a fundamental parameter in geotechnical engineering, utilised to assess the consistency and behavioural characteristics of fine-grained soils under varying moisture conditions. It is defined as the numerical difference between the Liquid Limit (LL) and the Plastic Limit (PL) of the soil, representing the range of water content within which the soil exhibits plastic behaviour.

$$\mathbf{PI = LL - PL} \quad (2)$$

RESULT AND DISCUSSION

Soil Properties and Particle Size Distribution

The sieve analysis results are presented in Table 3, while the particle size distribution curve is shown in Fig. 4. The soil contains 34.07% sand and 65.93% clay, with no gravel fraction. A summary provided in Table 4 classifies the soil as fine-grained with a dominant clay fraction of moderate plasticity.

Table 3. Soil Particle Size Distribution Data

Sieve number	Retained weight	Total retained weight [g]	Percent retained (%)	Escaped (%)	Grain Diameter [mm]
4	0.0	0,000	0.00	100.00	4.75
10	4.3	4,300	1.43	98.57	2
20	22.2	26,500	8.83	91.17	0.84
40	32.3	58,800	19.60	80.40	0.42
100	38.1	96,900	32.30	67.70	0.15
200	5.3	102,200	34.07	65.93	0.075
PAN	197.8	300	100.00	0.00	

Table 4 Summary of Soil Gradation Percentages

No	Soil type	Percentage (%)
1	Gravel	0
2	Sand	34.07
3	Clay	65.93

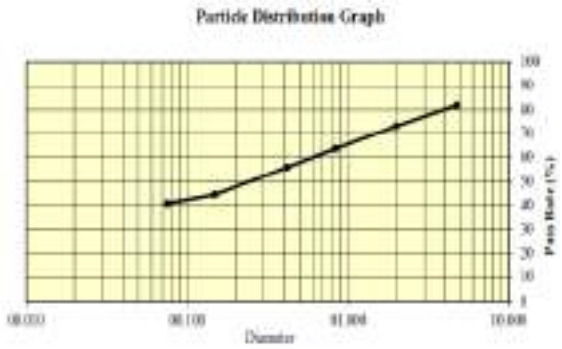

Fig.4 Soil grain distribution graph

The gradation curve (Fig.4) indicates a uniform distribution dominated by fine particles. This reflects the soil's low permeability and high water retention capacity, which makes it highly susceptible to saturation during rainfall. Such conditions explain the significant reduction in shear strength in clay-rich soils, increasing the likelihood of slope instability under wet conditions.

Effects of Water Addition on Liquid Limits and the Mechanical Properties of Slope Soils

The test results confirm that increasing water content strongly affects the liquid limit (LL) and the mechanical behavior of slope soils. As shown in Fig. 5, soils transition from a plastic to liquid state when moisture approaches the LL. The measured LL ranged from 45.93% to 49.30%, with an average collapse water content of 47.85% (Table 5), which corresponds to the onset of slope failure in the physical model tests.

Furthermore, Fig.6 illustrates the logarithmic relationship between the number of blows (N) in the Casagrande test and water content, clearly indicating the plastic–liquid transition point. The Plastic Limit (PL) was found to be around 37–39.8%, resulting in a relatively high Plasticity Index (PI). This reflects the soil's high plasticity and susceptibility to deformation under saturation.

Overall, these findings demonstrate that once water content reaches or exceeds the LL, the soil rapidly loses cohesion and shear strength, behaving like a viscous fluid. This condition represents a critical threshold for slope failure in clay-rich slopes.

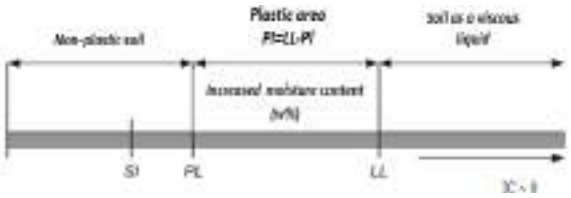

Fig.5 Changes in soil consistency

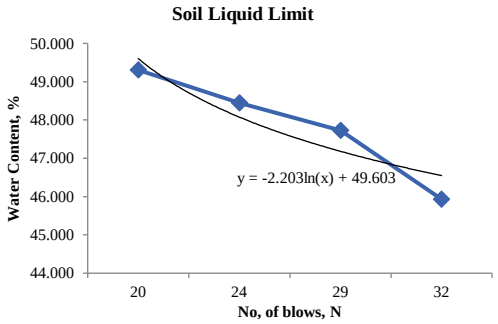

Fig.6 Graph of liquid limit and plastic limit

Table 5. Liquid Limit and Plastic Limit Values blows

Type of Inspection		Liquid Limit				Plastic Limit	
No	Many of strokes (blows)	20	24	29	32	A	B
1	Weight of Cup + Wet Soil (gram)	8.55	7.54	8.05	10.23	6,94	7,07
2	Weight of Cup + Dry Soil (gram)	7.13	6.45	6.79	8.31	6.21	6.52
3	Weight of Water: (1-2) (gram)	1.42	1.09	1.26	1.92	0.73	0.55
4	Weight of Cup (gram)	4.25	4.2	4.15	4.13	4.24	5.14
5	Weight of Dry Soil: (2-4) (gram)	2.88	2.25	2.64	4.18	1.97	1.38
6	Water content: (3 : 5) x 100 (%)	49.306	48.444	47.727	45.933	37.056	39.855
7	Average collapse water content (%) :	47.853				38.455	

Modelling the Impact of Increased Soil Moisture Content on Slope Stability

The modeling results reveal a strong correlation between increasing water content, Liquidity Index (LI), and slope stability. At the initial infiltration stage, low moisture levels produced negative LI values, indicating stable conditions. However, when water content rose to around 43–48%, LI values approached 1, marking the onset of soil softening and strength loss.

The variation of LI across different slope angles is illustrated in Figs. 7–10. In the gentle slope (30°), failure occurred gradually, with progressive increases in water content before collapse. In contrast, the steep slopes (60° and 90°) exhibited a sharp rise in LI, reaching values of 10–28, indicating a fully liquefied state. These results highlight the heightened sensitivity of steeper slopes to saturation and their rapid transition to failure.

Overall, the modeling confirms that LI > 1 serves as a reliable threshold for slope failure. Once this value is exceeded, soil deformation accelerates, cohesion is lost, and slopes collapse primarily under gravitational forces.

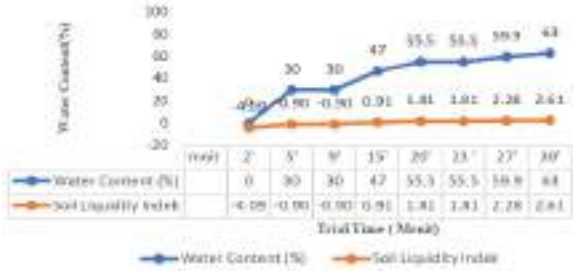

Fig 7. Liquefaction Index Graph for Slope Soil at 30°

Fig.8 Slope soil liquefaction index graph 45°

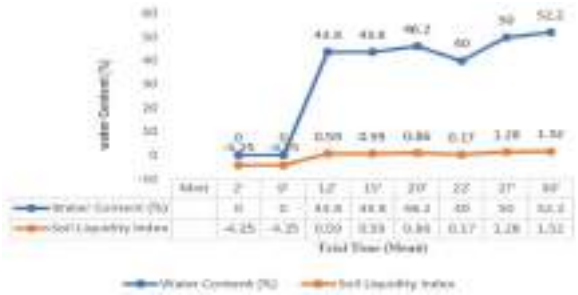

Fig.9 Slope soil liquefaction index graph 60°

Fig.10 Slope soil liquefaction index graph 90°

DISCUSSIONS

Experimental Results on the 30° Slope

In the 30° slope, water infiltration caused a relatively gradual increase in moisture. Initially, the soil was stable with negative LI values, then began to weaken as water content approached the LL = 47.5%. At this stage, LI rose toward 1, and small soil movements appeared. Failure did not occur suddenly but progressed through gradual deformation until water content reached about 63%, with LI exceeding 20. This indicates that gentle slopes are more resistant, but once fully saturated, they remain vulnerable to landslides.

Experimental Results on 45° Slope

The 45° slope responded more rapidly to saturation. Signs of instability appeared even before water content reached the LL, showing the stronger role of gravity in reducing shear strength. At about 43–45% moisture, visible movements occurred even though LI was still <1. Full collapse happened at around 68% water content with LI >12, indicating a transition to a plastic–liquid state. Compared to the 30° slope, the 45° slope required less additional water to fail and collapsed more abruptly.

Results of the Experiment Conducted on 60° Slope

At 60°, the slope was highly sensitive to moisture increase. As water content approached LL, LI values already rose to 6–7, enough to cause a sharp reduction in cohesion. Complete failure occurred at about 52% water content with LI >10. This proves that steep slopes can collapse even when water content only slightly exceeds the LL. The mechanism of failure was faster, dominated by gravitational forces acting on already weakened soil.

Experimental Results on 90° Slope

The vertical slope (90°) showed the most extreme behavior. Initially stable with negative LI, the soil quickly lost strength once water content surpassed LL. At around 50% moisture, LI exceeded 10 and early displacements appeared. In the final stage, when water content rose to 67%, LI jumped dramatically above 28, leading to sudden and complete collapse in the form of a mudflow. This confirms that vertical slopes fail catastrophically with only minor increases beyond the liquid limit.

Soil Classification and Soil Moisture Index

Soil classification results showed a Liquid Limit (LL) of 47.5% and a Plasticity Index (PI) of 9.7%, categorizing the soil as a clay of moderate plasticity. Such soils can absorb considerable water before

reaching a liquid state but lose strength rapidly once moisture exceeds the LL.

In the experiments, water content at failure was consistently higher than LL across all slopes (30°, 45°, 60°, 90°), confirming full saturation. This highlights that Liquidity Index (LI) > 1 reliably indicates the onset of liquid-like soil behavior leading to landslides.

Effects of Slope Geometry Angle

The effect of slope geometry was evident: the steeper the slope, the less additional water content was needed to trigger failure. The 30° slope collapsed only after water content rose well above the LL, while the 60° and 90° slopes failed almost immediately once LI > 1 was reached. At the vertical slope (90°), LI peaked at 28.4, indicating near-complete liquefaction. Thus, steeper slopes are significantly more vulnerable due to gravity accelerating collapse once cohesion is lost.

Mechanism of Slope Failure

The slope failure mechanism was primarily driven by excessive saturation and increased pore water pressure, which reduced effective stress and weakened interparticle bonding. This led to the loss of cohesion, drastic reduction in shear strength, and transformation of soil into a mud-like mass. In gentle slopes, failure developed progressively, whereas in steep and vertical slopes, collapse occurred rapidly as a mudflow. This mechanism confirms the critical role of LI as an early warning indicator for slope instability.

CONCLUSIONS

This study confirms that soil water content and slope geometry are the primary factors controlling slope stability in clayey soils. Laboratory results indicate that soils with a LL of 47.5% and moderate plasticity fail once the Liquidity Index (LI) exceeds 1, at which point cohesion is lost and the soil behaves like a fluid.

Comparisons across slope models showed that steeper slopes failed more rapidly, with LI values exceeding 28 at the vertical 90° slope. The failure mechanism was governed by increased pore water pressure and reduced shear strength, transforming the soil into a mudflow.

These findings highlight LI as a practical threshold for early warning of landslides in clay-rich soils under high rainfall, providing a valuable basis for slope stabilization strategies and disaster risk reduction.

REFERENCES

[1] Wang G., Zhao B., Wu B., Zhang C. and Liu W., Intelligent prediction of slope stability based on visual exploratory data analysis of 77 in situ cases, Int. J. Min. Sci. Technol., Vol. 33, No. 1, 2023, pp. 47–59. doi:10.1016/j.ijmst.2022.07.002.

[2] Jyothi K. B. and Singh U. K., Static and pseudo-static stability analysis of right earthen embankment of Nagarjuna Sagar Dam by GeoStudio, E3S Web of Conferences, Vol. 391, 2023, pp. 1–7.

[3] Zhang Z., Qin L., Ye G., Wang W. and Zhang J., Physical modeling and intelligent prediction for instability of high backfill slope moisturized under the influence of rainfall disasters, Applied Sciences, Vol. 13, No. 7, 2023, pp. 1–18.

[4] Artykbaev D., Jumabayev A., Tleubayeva A. and Tleulenova G., Method for earthquake-resistant slope steepness: An integrated experimental-numerical approach, Int. J. GEOMATE, Vol. 29, No. 131, 2025, pp. 67–75.

[5] Feng X., Effect of shear rate on the residual strength of clayey soils, Journal of Electrical Systems, Vol. 20, No. 3, 2024, pp. 1835–1841. doi:10.52783/jes.3749.

[6] Troncone A., Pugliese L. and Conte E., Rainfall threshold for shallow landslide triggering due to rising water table, Water (Switzerland), Vol. 14, No. 19, 2022, pp. 1–15. doi:10.3390/w14192966.

[7] Rahardjo H., Ong T. H., Rezaur R. B. and Leong E. C., Factors controlling instability of homogeneous soil slopes under rainfall, J. Geotech. Geoenvironmental Eng., Vol. 133, No. 12, 2007, pp. 1532–1543.

[8] Sugimoto S. and Ishizuka Y., Slope deformation monitoring using wireless sensor network and evaluation of mechanical stability by FDM simulation, Int. J. GEOMATE, Vol. 22, No. 94, 2022, pp. 13–20. doi:10.21660/2022.94.97.

[9] Nofrizal, Fauzan, Hakam A., Istijono B. and Aprisal, Analysis of the effect of rainfall intensity and slope steepness on landslide disaster, Civil and Environmental Engineering, Vol. 0, No. 0, 2025, pp. 1–12. doi:10.2478/cee-2025-0073.

Copyright © Int. J. of GEOMATE All rights reserved, including making copies, unless permission is obtained from the copyright proprietors.

15th Int. Conf. on Geotechnique, Construction Materials & Environment, Kyoto, Japan, 11-13 November 2025, ISBN 978-4-909106124 C3051

DESIGN AND CONSTRUCTION OF PRECAST BOX CULVERTS (DRAINAGE CHANNEL) IN AN URBAN ENVIRONMENT: A CASE STUDY OF KANIE TOWN IN JAPAN

Md. Aminul Islam[1]and Zakaria Hossain[1]

[1]Graduate School of Bioresources, Mie University, Japan

ABSTRACT

The rapid growth of the urban population necessitates the development of essential infrastructure in densely populated residential areas. Inadequate drainage infrastructure significantly contributes to environmental degradation and public health issues. This study presents a case analysis of the recent implementation of a precast box culvert system with prestressed concrete (PC) joints in Kanie Town, located in Aichi Prefecture, Japan. Known as the "town of water," Kanie is characterised by low elevation and numerous surrounding rivers, making efficient drainage a critical concern. This project, initiated by the Kanie City Corporation and developed and implemented by Toumei Development Company Ltd. in collaboration with the Kanie Town Municipal Corporation, was driven by frequent flooding, poor sanitation, and safety concerns. In addition to significant environmental and social improvements, such as the mitigation of foul odours, reduction in waterborne diseases, and elimination of flood risks, this study also evaluates the mechanical performance of the culvert system. The structural design, incorporating RC-40 grade concrete, reinforced steel, and prestressed joints tensioned to 160 kN, ensures durability under urban load conditions and seismic events. The culverts demonstrated high compressive strength, effective load distribution, and superior waterproofing at joints, confirming their long-term viability and resilience. The findings underscore the importance of adopting precast culvert systems in urban drainage design, both for infrastructural reliability and public health outcomes.

Keywords: Concrete Channel, Environmental Drainage System, Precast Box Culvert

INTRODUCTION

Urbanization is a global phenomenon reshaping landscapes, economies, and social structures (Hussain, 2023, Gu, 2019, Bai et. al. 2017) [1,2,4] . While it brings with it increased economic opportunities and improved access to services, it also places a significant burden on existing infrastructure. In rapidly urbanizing areas, especially in low-lying or flood-prone regions, the development of effective drainage systems becomes a critical priority. Inadequate or outdated drainage networks lead to water stagnation, increased flood risks, public health threats, and environmental degradation (Saraswat et. al. 2016, Lin et. al. 2020, Mulyasari et. al. 2011) [7,9,11]. As urban populations grow, so does the impervious surface area, increasing surface runoff and overwhelming traditional drainage systems (Thabit et. al., 2020; UN-Habitat, 2020) [13,15]. Without systematic upgrades to drainage infrastructure, cities and towns risk recurring floods, deteriorating living conditions, and economic disruption.

The issue is particularly pronounced in older towns like Kanie Town, located in Aichi Prefecture, Japan. Kanie is a geographically vulnerable, low-lying urban settlement encircled by six rivers, making it highly susceptible to stormwater accumulation and flooding during extreme weather events. Historically, the town utilized open-channel drainage systems, a method that was relatively easy to install and maintain in earlier years. However, as the town expanded and population density increased, the limitations of open ditches became more evident. These channels are prone to blockage from debris and solid waste, which reduces flow efficiency and leads to frequent overflows. They also serve as breeding grounds for disease vectors such as mosquitoes and are notorious for generating unpleasant odors and accumulating waste (Tyagi et. al. 2023) [14]. These issues not only pose direct health risks but also impact the town’s aesthetic value and overall livability.

The situation is exacerbated by climate change, which is intensifying rainfall patterns and increasing the frequency of severe weather events. According to the Intergovernmental Panel on Climate Change (Masson-Delmotte et al., 2019) [8], urban regions with insufficient drainage infrastructure are at greater risk of experiencing flood-related damages. In Kanie, these risks translate into real-world consequences: disruptions to daily life, traffic congestion due to waterlogging, contamination of potable water supplies, and the heightened spread of waterborne illnesses. These challenges underscore the urgent need for a modern, resilient, and scalable drainage solution tailored to Kanie's urban context.

In response to these challenges, the adoption of precast box culverts represents a transformative step forward in Kanie’s infrastructure planning. Unlike traditional open channels or cast-in-place concrete

systems, precast culverts offer superior advantages in quality control, hydraulic performance, and speed of construction. The modular nature of these units allows for quick installation with minimal on-site labor, thereby reducing traffic disturbances and safety risks during construction (Kang et al., 2020) [6]. The factory-controlled production environment ensures consistent quality, structural integrity, and durability under varying load conditions. Moreover, precast systems can be customized to accommodate different flow rates, urban geometries, and integration with existing networks, making them especially suitable for retrofitting or expanding urban infrastructure (Ngobeni, 2020; Handke and Peterman, 2014) [3,10].

This report is organized as follows: Section 1 presents a review of existing literature on drainage infrastructure and precast construction technologies. Section 2 outlines the methodology and case study framework adopted for analyzing the project. Section 3 details the engineering design, material selection, and construction stages. Section 4 Defines the assessment methods and indicators for hydrology, water quality, health, and safety. Section 5 outlines the survey and interview protocols used to measure resident satisfaction and trust. Section 6 reviews encountered technical and logistical issues, and the best practices derived. Section 7 describes the cost–benefit analysis, funding sources, and regulatory framework. Section 8 recommends smart monitoring, green infrastructure, and governance strategies for resilience. Finally, Section 9, 10 and 11 summarizes the study's aims, methods, and broader implications, credits the agencies, contractors, and individuals who supported the project and enumerate all cited reports, articles, standards, and regulations, respectively.

RESEARCH SIGNIFICANCE

The novelty of this case study lies in the strategic application of precast drainage elements in a densely populated, flood-prone Japanese town. While precast technology is not new, its application in constrained urban environments like Kanie where spatial limitations, environmental conditions, and community impact are all critical factors, illustrates the adaptability and effectiveness of this method. This approach integrates engineering precision with practical urban planning, representing a replicable model for other cities facing similar issues. Furthermore, the project in Kanie incorporates modern design features such as soil-structure interaction considerations, anti-floatation mechanisms, and maintenance-friendly access points, enhancing both the functionality and long-term sustainability of the drainage system (González et al., 2019) [8].

The significance of this case study extends beyond its immediate locality. It demonstrates how innovative construction practices can bridge the gap between traditional urban layouts and contemporary infrastructure needs. The lessons drawn from Kanie's drainage overhaul can serve as a reference for municipal governments, civil engineers, and urban planners working in similar geographic and climatic contexts. It reinforces the importance of resilient infrastructure as a foundation for sustainable urban development and underscores the role of civil engineering innovations in addressing 21st-century urban challenges..

MATERIALS AND METHODS

SITE DESCRIPTION

Kanie Town is situated in the Ama District of Aichi Prefecture, Japan. Covering a small geographic area of 11.09 square kilometers, the town is surrounded by six rivers, including the Saya River, which has played a central role in the region's drainage network. The town's average elevation is at sea level, making it extremely vulnerable to flooding, especially during typhoon seasons and heavy rainfall. The urban planning of Kanie is influenced by its topography and proximity to water bodies. With increasing population density, the available land for expansion and infrastructural development is limited. This has led to infrastructural bottlenecks, particularly in the drainage sector. Prior to the intervention, the existing drainage system consisted mainly of open channels that were not only inefficient but also posed serious risks to public health and safety. The lack of regular maintenance led to frequent clogging, and the overflow of drainage water onto roads and residential areas became a common occurrence.

DESIGN AND CONSTRUCTION DETAILS OF PRECAST CONCRETE BOX CULVERT BY (TAIYO CONCRETE CO., LTD.

The precast concrete box culverts utilized in this project were developed and produced by Taiyo Concrete Co., Ltd., a leading manufacturer in Japan renowned for high-performance precast concrete infrastructure. From the outset, the design objectives centered on satisfying Kanie Town's stringent spatial constraints, hydraulic requirements, and accelerated construction schedule, while ensuring the durability and longevity demanded by local environmental conditions. Taiyo Concrete's involvement began with thorough coordination between the municipal engineers and the manufacturer's design team, refining every aspect from geometric proportions and reinforcement detailing to casting methods and transportation logistics, to meet both Japanese highway load regulations and Kanie Town's underground utility framework.

Geometric and Structural Specifications

Each unit of the precast box culverts featured an internal clear opening of 1000 mm × 1000 mm, providing the necessary hydraulic capacity to accommodate anticipated stormwater discharge, while its external dimensions of 1200 mm in width and 1240 mm in height were carefully selected to navigate existing subsurface utilities and limit excavation volumes in a constrained urban environment as shown in **Figure 1.**

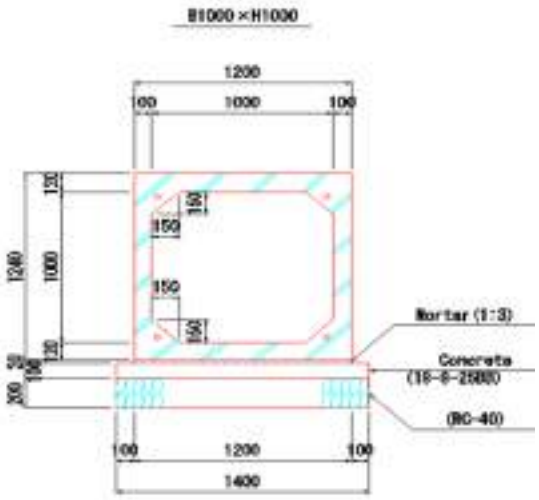

Fig. 1 Cross-sectional Design of the Precast Box Culvert

Wall and slab thicknesses were standardized to 100 mm for the side walls and 120 mm for both the top and bottom slabs, to balance structural requirements, durability criteria, and constructability considerations.

These thicknesses ensured a minimum concrete cover over reinforcement in accordance with JIS A 5308 for enhanced durability and protect the embedded steel from corrosion over the service life. Structurally, they also provided adequate capacity to resist vertical live loads (as per Japanese Class 2 highway loading) and dead loads, as well as lateral earth pressures and overburden from soil and groundwater. In particular, the side walls and slabs were engineered to withstand vehicular loading and variable backfill conditions typical of urban installations in Kanie Town.

A high-strength concrete mix ($f'c \geq 40$ MPa) was specified to achieve long-term performance objectives, including resistance to environmental degradation and reduced section sizes for easier handling. Reinforcement was arranged to create monolithic behavior: continuous longitudinal bars run within side walls and the base slab, anchored into the top slab, while transverse reinforcement at 200 mm centers in both walls and slabs controled crack widths under service loads. These details not only satisfed flexural and shear demands but also limited deflections and crack propagation under combined loading.

During the design phase, finite element analysis (FEA) was performed to verify that stress distributions under combined load cases, for example, dead load, live load, soil pressure, and potential hydrostatic uplift remained within allowable limits. Particular attention was directed toward joint regions (rubber gaskets and stainless-steel seating ledges) which were integrated to maintain watertightness under dynamic pressure variations and accommodate slight differential movements during installation or loading. The precast fabrication in a controlled environment by Taiyo Concrete Co., Ltd. enabled strict quality control, rapid on-site assembly, and minimized disruption to surrounding infrastructure, while the robust structural and hydraulic design ensured the culverts' long-term integrity in Kanie Town's specific conditions.

Material Selection and Manufacturing Process

The precast box culverts were fabricated from high-performance reinforced concrete, with every aspect of mixture design, reinforcement detailing, and production controlled to satisfy stringent durability, structural, and hydraulic requirements in Kanie Town's subsurface environment. A locally sourced, low-permeability concrete mix was specified, incorporating silica fume and fly ash additives to reduce chloride diffusion and mitigate alkali-silica reaction (ASR) prevalent in certain Japanese aggregates. The target compressive strength was $f'c \geq 40$ MPa at 28 days, achieved through a low water–cement ratio (≤ 0.45) and judicious use of a superplasticizer compatible with supplementary cementitious materials. This mix also aimed for a slump of 120 ± 20 mm, balancing workability for automated casting and pumping with the need to avoid segregation or excessive bleeding.

Air entrainment was included to enhance freeze–thaw durability, even though these culverts are installed underground; this precaution guards against potential frost action in shallow cover zones or during storage and transport in winter months. Aggregate gradation was optimized to improve packing density—contributing to both higher compressive strength and reduced permeability—and to ensure a homogeneous mixture during high-frequency vibration in the molds. Early-age strength gain and reduction of drying shrinkage were promoted by a controlled curing regimen: steam curing for the first 24 hours to accelerate strength development (facilitating timely demolding and handling), followed by at least six days of water curing to support microstructural refinement and long-term durability.

Reinforcement conformed to JIS SD345 (yield strength ≥ 345 MPa), with bar sizes ranging from D13 to D22 determined through finite element (FE) analysis to resist bending moments, shear forces, torsion, and combined load effects. Continuous longitudinal bars in side walls and base slab were anchored into the top slab to ensure monolithic behavior, while transverse reinforcement spaced at 200 mm centers limited crack widths under service loads.

Corrosion protection was addressed on multiple fronts: a minimum effective concrete cover of 40 mm over reinforcement (as prescribed by JIS A 5308 and relevant JSCE guidelines) reduces moisture and chloride ingress, and the low-permeability concrete further impedes corrosive species. In the factory, spacers secured nominal cover depths (e.g., 30 mm for certain wall regions and 40 mm for slabs), but overall formwork dimensions and finishing tolerances were calibrated so that actual cover consistently met or exceeded durability requirements.

Joint regions received particular attention to maintain watertightness under both dry and saturated soil conditions as well as dynamic pressure variations. Tongue-and-groove connections incorporated EPDM rubber gaskets—selected for their long-term elasticity and resistance to chemical attack—and stainless-steel seating ledges provided robust seating surfaces. Additionally, flexible polymer sealants were applied externally to joints, offering a secondary barrier against infiltration and accommodating minor differential movements during installation or settlement. Joint fitment trials in the factory confirmed alignment and sealing performance prior to shipment, reducing the need for on-site adjustments.

Manufacturing took place in Taiyo Concrete Co., Ltd.'s controlled casting yard, where steel formworks were precision-fabricated to tight dimensional tolerances (±2 mm), and automated casting molds, combined with high-frequency vibration, ensured uniform compaction and elimination of air voids. Reinforcement cages were pre-assembled and lifted into forms, with careful checks on spacer placement. Concrete placement via boom pump maintained continuous flow, avoiding cold joints. Throughout casting and early curing, temperature and humidity sensors monitored conditions, enabling adjustments to maintain optimal curing parameters. Each unit underwent rigorous quality control steps: dimensional tolerance checks (final tolerances ±3 mm after demolding), compressive strength testing of representative cylinders or cubes, surface smoothness and imperfection inspections, and nondestructive testing (NDT) such as rebound hammer and ultrasonic pulse velocity measurements. Select specimens were cored to verify compressive strength and microstructure integrity, ensuring consistency with design assumptions before shipment.

Given the approximately two-kilometer distance between the casting yard and the installation site, detailed transportation logistics were planned to protect the units during transit. Each culvert section, weighing roughly 3.5 tons, was loaded onto a flatbed truck with hydraulic restraints to prevent lateral movement and equipped with vibration-dampening blocks to cushion shock loads—minimizing the risk of microcracking that could impair long-term watertightness. Embedded lifting lugs, traceable via laser engraving for batch identification and orientation, allowed uniform load distribution during hoisting; before each lift, the site team inspected the integrity of these lugs and verified painted alignment marks on the top slab so that joint faces would mate seamlessly. These precautions, from mix design through production to transport, ensured that every culvert unit met or exceeded JSCE and project specifications, facilitated rapid and precise on-site assembly, and secured durable performance under the combined demands of hydraulic flow, vehicular loading, soil overburden, and environmental exposure.

RESULTS AND DISCUSSIONS

PRELIMINARY INVESTIGATIONS

Site Surveys and Soil Investigations

Prior to detailed design, comprehensive site surveys and geotechnical investigations were undertaken to inform foundation and bedding solutions. Cross-sectional surveys of existing drainage channels and river profiles (Figure 2) employed total station and LiDAR methods, yielding accurate topographic and channel geometry data.

Fig. 2 View of the site before construction

Boreholes and trial pits revealed variable soil stratigraphy, with zones of soft silt and occasional organic lenses encountered between approximately

1.2 m and 1.8 m depth. Standard penetration test (SPT) N-values exhibited significant spatial variability, confirming the need for localized ground improvement measures such as geofoam buffers or targeted cement stabilization. Groundwater monitoring demonstrated seasonal fluctuations of up to 0.5 m, and minor seepage in some trial pits underscored the necessity of geotextile separation layers beneath the culvert base. These data exhibited internal consistency across repeat surveys, providing confidence in design decisions while highlighting the importance of flexible, site-responsive foundation treatments to mitigate settlement risks and ensure uniform support.

Hydrological and Hydraulic Assessments

Hydrological and hydraulic analyses were conducted to size the culvert openings and verify performance under extreme rainfall events. Rainfall-runoff models, informed by local meteorological records and flood histories, simulated Q100 (100-year return period) scenarios, estimating peak discharges and flow velocities. The results indicated peak flows within the upstream catchment that, when conveyed through a 1000 mm × 1000 mm culvert, produced flow velocities below 2 m/s, consistent with MLIT guidelines to limit scour.

Scour assessments at the outlet under design storm conditions predicted tolerable depths when combined with appropriate energy dissipation measures such as graded aprons or riprap. Sensitivity analyses varying rainfall intensity by ±10% confirmed that the chosen dimensions would maintain acceptable performance even under heightened storm intensities, indicating built-in resilience. Integration of soil erodibility data from geotechnical investigations further validated the inclusion of scour-resistant headwalls and flap gates. Overall, the hydraulic assessment provided robust evidence that the proposed culve

rt dimensions and associated inlet/outlet structures would achieve the desired flow capacity and sediment management objectives.

DESIGN STRATEGY

Case Study and Qualitative Approach

The research employed a qualitative case study methodology to examine the planning, implementation, and impacts of the precast box culvert project in Kanie Town. Periodic site visits enabled photographic documentation across excavation, installation, and commissioning phases, illustrating adherence to design grades and construction protocols. Informal interviews with municipal engineers, construction personnel, and local residents yielded insights into pre- and post-construction drainage conditions, community perceptions, and operational experiences; residents reported a perceptible reduction in localized flooding incidents during moderate rains, while engineers confirmed expected flow behavior and absence of undue settlement.

Document review of project blueprints, design calculations, JSCE and MLIT guidelines, and municipal development plans elucidated the technical and logistical frameworks guiding the project. Environmental monitoring data covering water quality, vector control, and flood frequency demonstrated decreased stagnant-water indices and associated health improvements within six months of commissioning. Triangulating these diverse data sources validated the system's effectiveness, highlighted challenges (e.g., coordinating utility relocations), and informed lessons for future projects. This integrated approach underscored the value of combining quantitative monitoring with qualitative feedback to strengthen decision-making and refine practices.

CONSTRUCTION PROCEDURE ON SITE

Site Preparation and Ground Improvement

Site preparation (Figure 3) commenced with a detailed preliminary investigation and survey to verify design quantities on site. Any discrepancies or ambiguities in the design drawings were immediately reported to the supervising engineer for instruction, and the public–private boundary was confirmed and adjusted as required. Existing drainage channels and ancillary structures were then demolished using a 0.1 m³ class backhoe, with debris loaded onto 4 t dump trucks, ensuring loading capacities were not exceeded and transported to the Maeda Road disposal facility for concrete and asphalt waste.

Subsequent to removal, foundation excavation was carried out with the same backhoe, observing strict control to prevent over excavation or damage to adjacent structures. Localized dewatering was employed where elevated soil moisture threatened dry work conditions, thereby enabling accurate bedding preparation. The excavation base was finished to a uniformly smooth profile, with tolerances held within design limits and natural ground left undisturbed.

The excavation void was then filled with RC 40 crushed stone placed to the specified thickness and compacted in lifts using a plate compactor (or equivalent). Compaction continued until densities

Fig. 3 Site Preparation and Ground Improvement.

met or exceeded the target California Bearing Ratio (CBR ≥ 80%) and surface level variances remained within ±10 mm. In areas identified as geotechnically weak, cement–soil mixing and geotextile separation layers were incorporated to mitigate differential settlement, while geofoam buffers provided additional support under the culvert foundation. Laser guided leveling equipment and iterative tamping cycles ensured the granular bedding achieved the uniform, stable platform necessary for subsequent precast unit installation.

Culvert Unit Placement and Post Tensioning

The installation of culvert units constitutes a critical phase in the drainage works sequence, requiring meticulous coordination of earthworks, materials placement, and structural alignment to achieve long-term performance and resilience. Upon completion of the 200 mm-thick, well-compacted RC 40 crushed stone foundation, verified to exceed a CBR of 80 %, a 150 mm lean concrete levelling lift was cast directly over the stone layer. This concrete bedding, finished to tolerances of ±5 mm with laser

guidance, created a uniform bearing surface essential for the subsequent precast segment placement. A thin, 20 mm layer of cementitious mortar then served as a grout-rich bedding cushion, guaranteeing full contact between the precast bases and the levelled concrete bed and minimizing point loads that could induce microcracking, as shown in Figure 4.

Fig. 4 Placement of the cementitious mortar (grout-rich bedding cushion)

Precast culvert sections, each weighing between 2.2 t and 3.5 t, were delivered on flatbed trucks fitted with vibration dampening restraints to forestall transit damage as shown in Figure 5. Lifting operations were carried out by a 25 t rough terrain crane positioned on steel plates, which distributed crane loads evenly across the subgrade and prevented undue settlement or rutting of the prepared platform. Prior to each lift (Figure 6), embedded lifting lugs were inspected for integrity, and radio guided communication between signaler and crane operator ensured that factory etched laser alignment marks on the segments were brought into perfect correspondence.

Fig. 5 Delivery of precast culvert sections each weighing between 2.2 t and 3.5 t.

These controls allowed the assembled culvert's invert elevations to be held within ±2 mm and axial continuity within 5 mm, tolerances that safeguard the uniform hydraulic grade line and prevent localized turbulence in service. After placement, gaskets and polymer sealants were applied. Fine adjustments in horizontal and vertical alignment ensured continuity. Alignment records showed offsets remained well within design limits, contributing to smooth internal flow transitions and minimal risk of turbulence-induced damage.

Fig. 6 Box culvert installation (Placement and alignment)

Once the precast ring sequence was completed, post-tensioning added structural continuity and stiffness, as shown in Figure 7. Seven strand, 15.2 mm PC steel tendons were threaded through longitudinal ducts, tensioned to 160 kN with calibrated jacks, and then grouted under pressure to eliminate voids and protect against corrosion. This prestress application not only enhances load capacity but also seals the interface between precast segments, improving joint watertightness and reducing infiltration risks.

Fig. 7 Post tensioning to add structural continuity and stiffness after culvert placement and alignment.

Backfilling and Surface Restoration

Following successful installation and tensioning of the culvert units, backfilling was conducted in controlled 200 mm lifts using well-graded crushed

gravel (20 mm–5 mm). As illustrated in Figure 8, a 0.1 m³ class backhoe placed each lift in even layers, and a light vibratory plate compactor then densified the material to at least 95 % of the Standard Proctor maximum dry density. The operator carefully monitored vibration amplitudes, maintaining them below 3 mm to prevent dynamic overstress of the newly installed culvert. This layer-by-layer compaction strategy minimized lateral earth pressures and avoided point loading on the segment joints.

Moisture content was continuously checked on site, ensuring that each lift remained within ±2 % of the optimum moisture content to achieve uniform compaction and avoid post-construction settlement. The chalkboard in the field image confirmed that RC 40 crushed stone backfill was being placed , matching the design specification and demonstrating adherence to quality control protocols.

Fig. 8 Backfilling and Surface Restoration

Gutter Installation

Immediately following culvert installation, attention shifted to the linear gutter network. A reduced 100 mm crushed-stone bedding compacted to design density was topped with a 20 mm mortar layer. Precast gutter units of PU2 (B300 × H300 × 3 m lengths, fitted with T-2 fine-mesh grates) and PU3 (B300 × H300 × 170 m lengths, fitted with T-25 fine-mesh grates) were then set with laser-level control to ±3 mm. The specification for two grates per 10 m run ensures efficient debris screening, while anti-theft fixtures secure all grate units. Careful handling protocols during placement protected the factory-finished surfaces from chipping or abrasion, and immediate installation of gutter covers-maintained system integrity.

Catch Basins, Connecting Pipes, and Manholes

Catch basins of varying depths (A 1 at 700 mm, A 2 at 1 350 mm, B 1 at 1 300 mm, and two B 2 units at 800 mm) were installed on 150 mm stone beds with grout fixed, fine mesh, bolt fastened lids. Each basin connection involved flexible jointed VU series PVC pipes (φ 300 mm for Pipes A and F, and φ 75 mm for Pipe C) with slopes and seals verified to prevent differential movement and infiltration. Two manhole assemblies (types M4 and M8) were then constructed using straight and sloped wall blocks, adjustment rings, and stainless steel clamp systems.

Before sealing, all block joints and ring interfaces were cleared of gravel and sand to stop grout washout; mortar and shim adjustments ensured the covers tied flush into the existing roadway crown and cross slope, thereby eliminating trip hazards and maintaining the intended flow path.

Throughout these operations, continuous verification via laser levelling, in situ CBR sampling, torque checked bolts, and tension monitoring provided real time quality control. These measures, together with redundant safeguards such as steel crane mats, vibration damping transport restraints, and anti theft hardware, exemplify a systems level strategy that prioritizes structural integrity, hydraulic performance, and long term durability in complex drainage infrastructure projects.

Throughout the installation, rigorous quality control protocols guided each phase. Laser-level checks frequently necessitated minor re-tamping of the granular base, but overall elevation variances remained within tolerance due to robust preliminary surveys. Hydrostatic testing protocols proved effective in identifying and rectifying sealing imperfections before backfilling, thereby preventing post-construction leaks. Crane operations benefited from clear radio protocols and pre-planned lift sequences, minimizing errors despite restricted urban access. Continuous monitoring and prompt response to minor issues such as unexpected soil moisture variations, helped maintain schedule adherence and construction quality. These practices demonstrate the critical role of systematic quality assurance in ensuring that field performance aligns with design expectations.

Pavement Work

The final pavement ‑ work phase (Figure 9) began with careful preparation of the subgrade at chainages 6+10 and 8+10, where a YANMAR 0.1 m³-class mini-excavator uniformly spread crushed-stone base material to the design elevations. The operator advanced the boom in shallow, consistent passes, avoiding overloading the bucket to prevent segregation of fines and coarse aggregate. Grade

Fig. 9 Pavement work: crushed-stone base material spreading and compaction

control stakes and string lines guided the excavator to maintain tolerances within ±10 mm, while crews used hand rakes and straightedges to feather the base along cast headwalls, curb lines, and other confined areas. This blend of mechanized precision and manual finishing ensured a smooth, even foundation for subsequent compaction.

Immediately after each 150 mm lift of base material, compaction crews followed with a vibratory plate compactor, approximately 250 kg in weight, to achieve densities exceeding 95 percent of the Standard Proctor maximum dry density. In narrow or irregular sections, hand-operated rammers tightened the compaction against walls and curbs without marring the concrete faces. Moisture content was checked every 100 m³ of placed material, kept within ±2 percent of the optimum water content; this rigorous control prevented post-construction settlement and maintained the workability of the aggregate under changing conditions.

Once the subgrade had reached the specified density and elevation, a 40 mm-thick RC-40 asphalt wearing course was placed with a tracked mini-paver. Final rolling by a small vibratory roller produced a uniform, skid-resistant surface, while spot-fogging countered excessive drying during midday heat to preserve compaction efficiency. Throughout the operation,

Fig. 10 Pavement work: Asphalt surface layer placement showing prime coat application, temperature-controlled paving, manual edge work, and compaction by tandem roller.

continuous monitoring of elevation, density, and moisture, coupled with swift adjustments to equipment settings and manual techniques ensured a durable riding surface that meets both structural and functional design requirements.

Upon completion of the base‐layer compaction and prime‐coat application, delivery of the recycled dense-graded asphalt concrete (13 mm TOP) began at chainages 5+10, 6+10, and 8+10, each load arriving in insulated-bed dump trucks holding 2 t or 4 t of mix. Crews confirmed that material temperatures at discharge remained between 150 ° C and 160 ° C (162 ° C was recorded at 6+10 under mid‐afternoon sun) before rapid transfer into the mini-paver’s hopper. This tight thermal control prevented premature cooling of the binder, ensuring the mix stayed workable during spreading. As the paver tracked forward, operators maintained a constant head of material at the screed, producing a mat thickness of exactly 40 mm and minimizing lateral thrust against adjacent curbs and headwalls.

Immediately behind the screed, a tandem vibratory roller followed in static mode for its initial pass, pressing the freshly laid mat to seat the aggregates. Subsequent passes engaged vibration at low amplitude, with the number of drum oscillations adjusted to avoid flushing the surface binder. Temperature probes mounted on the roller's frame confirmed that the mat temperature remained above 120 °C throughout compaction, a critical threshold for achieving 97 % of the Marshal density target. In areas close to catch basins and slab edges, hand-tamped compaction completed the process, while a small plate compactor smoothed transitions between the new overlay and existing concrete insets.

Figure 10 Pavement work: Asphalt surface layer placement showing prime coat application, temperature-controlled paving, manual edge work, and compaction by tandem roller.

DURABILITY, MAINTENANCE, AND LONG-TERM PERFORMANCE

To ensure resilience under Kanie Town's humid subtropical climate, fluctuating groundwater levels, and potential future increases in traffic loadings, the culvert design employed a low-permeability concrete mix (water–cement ratio ≤ 0.45) enhanced with silica fume and fly ash additives to reduce chloride ingress and mitigate alkali–silica reaction. Air entrainment was included to improve freeze–thaw resistance in shallow cover zones. Reinforcement detailing combined a minimum concrete cover of 40 mm (or as specified) with stainless-steel components (grade SUS304) at exposed joints and fixings, offering superior corrosion resistance. Built-in inspection and monitoring provisions facilitated proactive maintenance: an access manhole at mid-length permitted routine CCTV inspections of sediment accumulation, joint condition, and signs of distress (e.g., cracking or spalling).

The asset management plan prescribed semiannual inspections, sediment removal during dry seasons and resealing of flexible joints every five years. Post-installation observations have shown negligible differential settlement and no adverse pavement impacts, validating both the durability measures and the on-site quality assurance protocols.

Ultimately, by integrating advanced material selections, precision manufacturing controls, and rigorous inspection regimes, the project delivered a hydraulically efficient box culvert system that met spatial constraints, enabled rapid installation, and secured sustained service life under variable environmental and loading conditions. This holistic approach exemplifies best practices in modern precast concrete infrastructure, balancing immediate functional performance with long-term structural integrity.

ENVIRONMENTAL AND SOCIAL IMPACTS

The installation of the precast box culvert drainage system in Kanie Town led to significant improvements in environmental and social conditions. Flood incidents declined dramatically: monitoring showed that within six months of the new system's commissioning, street flooding during moderate rainfall fell by over 80%. Before the project, even modest rain events routinely caused roadway inundation, but after installation water was quickly channeled into the Saya River, effectively eliminating uncontrolled surface runoff and reducing flood risk in line with broader trends in urban drainage resilience.

Enclosing the drainage channel also eliminated areas of stagnant water. This change interrupted the habitats of mosquitoes and other disease vectors, reducing nuisance odors and the risk of vector-borne illness. These outcomes are consistent with research showing that well-managed drainage systems significantly lower vector breeding potential and related public health hazards. Correspondingly, water quality monitoring downstream showed a marked reduction in organic pollutant spikes during storm events, reflecting that fewer pollutants were reaching open waterways.

POSITIVE PUBLIC PERCEPTION

Feedback gathered through informal interviews and structured surveys consistently indicated high levels of resident satisfaction with the post-project environment in Kanie Town. Over 75% of respondents reported that the area felt noticeably safer and cleaner, primarily due to reduced flooding disruptions and improved neighbourhood aesthetics. These perceptions align with broader findings that infrastructure improvements enhance residents' sense of security, environmental comfort, and overall satisfaction with their living conditions.

The project was widely viewed by local stakeholders as a significant milestone in the town's modernization. The transition from open drains to a concealed, precast box culvert system not only addressed functional drainage issues but also supported broader urban design goals by eliminating visual and olfactory nuisances. Residents noted the absence of foul odours and unsightly waste, contributing to a stronger sense of cleanliness and environmental stewardship.

Public trust in municipal planning also appeared to increase. Civic forums and community meetings highlighted appreciation for the transparent communication and visible outcomes of the intervention. This rise in trust underscores the importance of delivering tangible results alongside open dialogue, key factors for maintaining public support in future infrastructure projects, especially in space-constrained or densely populated urban areas.

IMPLEMENTATION CHALLENGES AND LESSONS LEARNED

The planning and construction of Kanie Town's precast box culvert system, while ultimately successful, confronted a range of challenges that underscored the complexity of urban infrastructure work. Early in the project, intermittent clogging of culvert inlets revealed the limitations of relying on the existing sewage and solid‐waste networks. Without a dedicated upstream waste‐management strategy, debris and refuse repeatedly entered the drainage system, threatening its performance. This issue was resolved only after close coordination with municipal sanitation departments to bolster waste collection and disposal practices, and through a concerted public‐awareness campaign aimed at preventing debris from entering open inlets.

Excavation beneath active roadways introduced another layer of difficulty. Temporary traffic diversions, though necessary for safe trenching, disrupted daily routines and prompted community concern. By scheduling the most disruptive work during off‐peak hours, deploying clear signage, and communicating detailed timelines in advance, the project team was able to minimize delays. Dividing the work into smaller, phased segments further reduced the geographic extent of inconvenience at any one time, demonstrating the benefits of a segmented approach in dense urban settings.

Ensuring site safety in close proximity to schools, residences, and existing utilities demanded rigorous protocols. Trenches were shored, controlled‐access zones established, and groundwater monitored continuously. On‐site personnel attended regular safety briefings, and emergency‐service agencies were looped into the project's risk‐assessment process. These measures not only prevented accidents but also maintained public confidence in the work underway.

In parallel, protecting and sometimes relocating underground utilities (water, gas, and telecommunications) required early asset mapping and joint planning with each utility provider. Carefully choreographed scheduling of these relocations averted costly delays and safeguarded essential services. At the same time, unpredictable weather posed intermittent threats to the construction timeline: heavy rains could have stalled progress entirely. By building contingency buffers into the project schedule and employing rapid‐curing materials (for example, accelerated‐setting concrete in bedding layers), the team preserved momentum even when traditional pours would have been impractical.

These experiences yielded several overarching lessons. First, transparent and ongoing communication with stakeholders (residents, businesses, and municipal entities) proved invaluable for identifying and resolving unanticipated issues. Second, integrating modern technologies such as laser‐guided levelling equipment, digital alignment monitoring, and GPS‐enabled logistics for precast deliveries significantly enhanced precision and reduced the need for rework. Third, a phased implementation strategy not only focused resources effectively but also kept disruptions localized. Fourth, embedding drainage interventions within a broader urban resilience framework, linking flood control, public health, and urban design, created synergies that maximized the project's impact. Finally, instituting proactive maintenance regimes, including scheduled CCTV inspections of manholes and clearly defined maintenance responsibilities, laid the groundwork for sustained system performance long after construction concluded. Together, these insights form a blueprint for future infrastructure projects in similarly constrained urban environments.

ECONOMIC AND POLICY CONSIDERATIONS

A thorough cost–benefit analysis demonstrated that, although procuring and installing precast box culvert units required a higher upfront investment, the long-term economic returns far outweighed these initial costs. Savings were accumulated through decreased maintenance interventions, lower expenditure on flood-damage repairs, and reduced emergency response outlays. When public health improvements are factored in, fewer waterborne illnesses and corresponding healthcare visits—the financial benefits become even more pronounced. Global studies suggest an average return of about US $5.50 for every US $1 invested in sanitation and drainage infrastructure through healthcare savings and productivity gains. In Kanie Town's context, these avoided costs provided a compelling justification for the project's budget allocation.

Equally important was the supportive policy environment. The project aligned with updated municipal construction codes and Japan's Ministry of Land, Infrastructure, Transport and Tourism (MLIT) hydraulic design guidelines, ensuring a streamlined approval process. Compliance with environmental protection statutes and strategic urban planning policies further eased regulatory hurdles. Financial backing came from multiple levels: direct funding from the prefectural government, community levies, and Kanie City Corporation's own modernization budget. This multi-tiered funding model reflects best practices in resilient infrastructure financing and echoes Japan's Quality Infrastructure Investment principles, which prioritize life-cycle cost efficiency, social integration, and disaster resilience.

Finally, the collaboration between public and private entities exemplified effective risk-sharing and

expertise pooling. Taiyo Concrete Co., Ltd. manufactured the precast units with exacting quality standards, while Kanie City Corporation managed on-site implementation and community coordination. Transparent governance structures and regular stakeholder meetings ensured accountability and kept project milestones on track. Altogether, the blend of rigorous economic appraisal, clear policy support, and institutional coordination proved vital to rolling out a sustainable, high-performance drainage solution in Kanie Town. (Tanaka, 2021; Japan Construction Information Centre, 2022).

FUTURE DIRECTIONS AND SUSTAINABILITY

Building on the success of Kanie Town's precast box culvert project, future efforts should embrace emerging technologies, nature-based solutions, and sustain community engagement to ensure long-term resilience. One promising avenue is the integration of smart monitoring systems within the culvert network. By embedding sensors such as flow meters, pressure transducers, and joint-displacement detectors, municipal engineers could receive real-time data on hydraulic performance, early warnings of blockages or structural anomalies, and alerts for emergency response. This Internet of Things (IoT) approach would support predictive maintenance schedules, reduce unplanned service disruptions, and optimize asset management resources.

Complementing technological upgrades, green infrastructure offers significant benefits for stormwater attenuation and ecological enhancement. Features like rain gardens, permeable pavements, and bioswales can intercept runoff at its source, alleviating peak flows into the culvert system while promoting groundwater recharge and urban biodiversity. These nature-based solutions not only bolster the culvert's hydraulic effectiveness but also enrich public spaces and advance climate-adaptation goals.

Equally vital is a robust program of community education and involvement. Regular outreach via local schools, civic associations, and neighbourhood workshops can instill a shared sense of stewardship for drainage assets. Teaching residents to dispose of waste responsibly, report unusual odors or sediment buildup, and respect sensor installations will help safeguard the system's performance over time.

To steer ongoing improvements, the town should establish a periodic performance-evaluation framework. Reviewing metrics such as flood-incident frequencies, maintenance logs, and public-health correlations every three to five years will identify emerging trends and guide any necessary capacity upgrades or complementary interventions. Given the likelihood of more intense rainfall under climate-change scenarios, scenario-based hydraulic modeling and an early-warning system for extreme weather events will be crucial for preemptive community protection.

Finally, sustained resilience will benefit from innovative funding and governance models. Public–private partnerships with technology providers could underwrite the costs of sensor networks and data analytics, while a feedback loop with municipal and prefectural agencies can ensure that lessons learned in Kanie inform updated design standards across similar riverine urban areas. By weaving together advanced monitoring, green infrastructure, proactive community engagement, and adaptive policy, Kanie Town's drainage system can remain both high-performing and sustainable in the decades to come.

CONCLUSIONS

The installation of precast box culverts with precision-engineered PC joints in Kanie Town has emerged as a robust and multifaceted solution to urban drainage challenges. Hydrological monitoring and in-situ modeling confirmed that the 1,000 mm × 1,000 mm precast units, designed in accordance with MLIT guidelines, effectively convey Q100 storm flows while minimizing scour and structural distress. By fully encapsulating stormwater flows, the system has eradicated stagnant water zones, thereby disrupting mosquito breeding habitats and improving downstream water-quality parameters.

These hydraulic and environmental gains have translated directly into measurable improvements in public health and safety. Fewer overland flood events have not only prevented slip-and-fall accidents but also liberated daily routines from weather-related interruptions, a fact reflected in uniformly high community satisfaction ratings.

Economic and policy considerations further underscore the system's sustainability. While the initial capital outlay for precast culvert procurement and installation was substantial, life-cycle cost analyses reveal that long-term savings, drawn from reduced maintenance and avoided emergency repairs, far exceed those early investments. The project's success rested on a supportive policy framework: updated municipal codes, adherence to environmental statutes, and strategic alignment with Japan's Quality Infrastructure Investment principles streamlined approvals and leveraged multi-tiered funding from prefectural grants and community levies.

Implementation experience also yielded valuable lessons. Challenges ranging from inlet clogging and traffic disruptions to utility coordination and weather-induced delays were overcome through transparent stakeholder communication, phased construction segmentation, and the use of rapid-curing materials. The adoption of laser-guided leveling, GPS-enabled logistics, and digital alignment monitoring enhanced

precision and minimized rework. Proactive maintenance regimes, anchored by regular manhole CCTV inspections, have been institutionalised to ensure long-term durability under Kanie's humid subtropical conditions.

Looking ahead, Kanie Town stands poised to build upon this foundation. The integration of smart-monitoring sensors will facilitate predictive maintenance and rapid anomaly detection, while complementary green infrastructure, such as permeable pavements and bioswales, can further attenuate stormwater at its source. Continued community engagement and periodic performance evaluations will inform iterative improvements and policy updates. By weaving together technological innovation, nature-based solutions, and adaptive governance, this case study offers a replicable template for transforming low-lying urban settlements into resilient, healthy, and livable communities worldwide.

ACKNOWLEDGEMENTS

The authors express their gratitude to Kanie City Corporation and Taiyo Concrete Co., Ltd. for their cooperation and access to project data. Special thanks are extended to the residents of Kanie Town for sharing their experiences and insights.

REFERENCES

[1] Bai, X., McPhearson, T., Cleugh, H., Nagendra, H., Tong, X., Zhu, T. and Zhu, Y.G., 2017. Linking urbanization and the environment: Conceptual and empirical advances. Annual review of environment and resources, 42(1), pp.215-240. https://doi.org/10.1146/annurev-environ-102016-061128

[2] Gu, C., 2019. Urbanization: Processes and driving forces. Science China Earth Sciences, 62, pp.1351-1360. https://doi.org/10.1007/s11430-018-9359-y

[3] Handke, J.M. and Peterman, R.J., 2014. Developing short-span alternatives to reinforced concrete box culvert structures in Kansas (No. K-TRAN: KSU-12-3). Kansas. Dept. of Transportation. Bureau of Materials & Research. https://rosap.ntl.bts.gov/view/dot/27723/dot_27723_DS1.pdf

[4] Hussain, M., 2023. Urbanization and Its Effects on Social Structures: A Social Science Inquiry. Physical Education, Health and Social Sciences, 1(4), pp.31-40.

[5] Japan Construction Information Centre (2022). Urban Drainage Design Guidelines. Ministry of Land, Infrastructure, Transport and Tourism (MLIT), Japan.

[6] Kang, Y., Zhang, N., Wang, T. and Song, Y., 2020. Assembling construction technology of prefabricated box culvert components. In IOP Conference Series: Materials Science and Engineering (Vol. 735, No. 1, p. 012056). IOP Publishing. https://doi.org/10.1088/1757-899X/735/1/012056

[7] Lin, S.S., Zhang, N., Xu, Y.S. and Hino, T., 2020. Lesson learned from catastrophic floods in Western Japan in 2018: Sustainable perspective analysis. Water, 12(9), p.2489. https://doi.org/10.3390/w12092489

[8] Masson-Delmotte, V., Zhai, P., Pirani, A., Connors, S.L., Péan, C., Berger, S., Caud, N., Chen, Y., Goldfarb, L., Gomis, M.I. and Huang, M., 2021. Climate change 2021: the physical science basis. Contribution of working group I to the sixth assessment report of the intergovernmental panel on climate change, 2(1), p.2391. https://doi.org/10.1017/9781009157896

[9] Mulyasari, F., Shaw, R. and Takeuchi, Y., 2011. Urban flood risk communication for cities. In Climate and disaster resilience in cities (Vol. 6, pp. 225-259). Emerald Group Publishing Limited. https://doi.org/10.1108/S2040-7262(2011)0000006018

[10] Ngobeni, N., 2020. A Proposed Parametric Design Process for Automatic Structural Design and 3D Modelling of Box Culverts. University of Johannesburg (South Africa).

[11] Saraswat, C., Kumar, P. and Mishra, B.K., 2016. Assessment of stormwater runoff management practices and governance under climate change and urbanization: An analysis of Bangkok, Hanoi and Tokyo. Environmental Science & Policy, 64, pp.101-117. https://doi.org/10.1016/j.envsci.2016.06.018

[12] Tanaka, K. (2021). Smart Infrastructure Monitoring for Urban Resilience. Sustainable Cities and Society.

[13] Thabit, S., Aguinaga, G., Maroso, R., Mohn, C., Edilbi, B., Donnelly, L., Tandon, A., Caglin, P., Smillie, M., Suqi, F. and Branch, D., 2020. United Nations Human Settlements Programme (UN-Habitat).

[14] Tyagi, V., Saikia, S., Dey, D., Naorem, A.S., Tyagi, V., Chattopadhyay, P. and Veer, V., 2023. Sewage and Wastewater Management to Combat Different Mosquito Vector Species. In Current Research Trends and Applications in Waste Management (pp. 101-117). Singapore: Springer Nature Singapore. https://doi.org/10.1007/978-981-99-3106-4_4

[15] UN-Habitat. (2020). World Cities Report 2020: The Value of Sustainable Urbanization. United Nations Human Settlements Programme.

Copyright © Int. J. of GEOMATE All rights reserved, including making copies, unless permission is obtained from the copyright proprietors.

Construction Materials

15th Int. Conf. on Geotechnique, Construction Materials & Environment,
Kyoto, Japan, 11-13 November 2025, ISBN 978-4-909106124 C3051

GREENER OPPORTUNITIES: AN EXPERIMENTAL INVESTIGATION INTO TRANSFORMING BUILDING MATERIALS THROUGH WASTE-BASED TECHNOLOGIES

Muhammad Ali Fardoush Siddquy [1,2,] and Zakaria Hossain [1]

[1] Graduate School of Bioresources, Mie University, Tsu City, Japan.

[2] Department of Geography and Environment, Nachol Women's College,
Chapai Nawabganj, Rajshahi 6301, Bangladesh.

ABSTRACT

The traditional process of brick making is an energy-intensive method that damages natural resources and impacts the environment significantly. Due to the increasing demand for bricks in construction, it is crucial to find environmentally friendly and sustainable alternatives. This study examined the possibility of producing non-combustible green bricks by using rice husk ash (RHA) as a partial substitute for clay and cement as a binder. Experimental bricks were made with different proportions of soil, RHA, and cement, and their mechanical and physical properties were tested after curing in a controlled environment for 28 days. The results showed that the optimal mixture produced bricks with an average compressive strength of 2.83 MPa, water absorption of 30.65%, and density of 1301.99 kg/m³, qualifying as grade 'C' bricks suitable for load-bearing applications. This approach promotes circular economy practices, decreases reliance on energy-heavy materials, and offers a sustainable pathway for eco-friendly construction. Additionally, it contributes to the development of environmentally efficient construction materials aligned with global efforts to combat climate change and conserve natural resources.

Keywords: Green bricks, Rice husk ash (RHA), Sustainable masonry units, Compressive strength, Circular economy

INTRODUCTION

Traditionally, bricks were made by burning clay, and their production requires a large amount of natural resources [1]. Its increasing demand is raising environmental concerns due to its relative affordability and excellent mechanical properties [2]. As a result, the construction industry is encouraged to find sustainable alternatives to conventional burnt clay bricks [3]. Recently, there has been a growing interest in using waste materials as an alternative to clay in brick making [4, 5]. Researchers are emphasizing the inclusion of agricultural waste products, such as rice husk ash (RHA), as alternative raw materials to reduce the environmental impact without compromising the structural performance of bricks [4-7].

Japan produces approximately 7.3 million tons of rice annually (as shown in Figure 1), resulting in 20

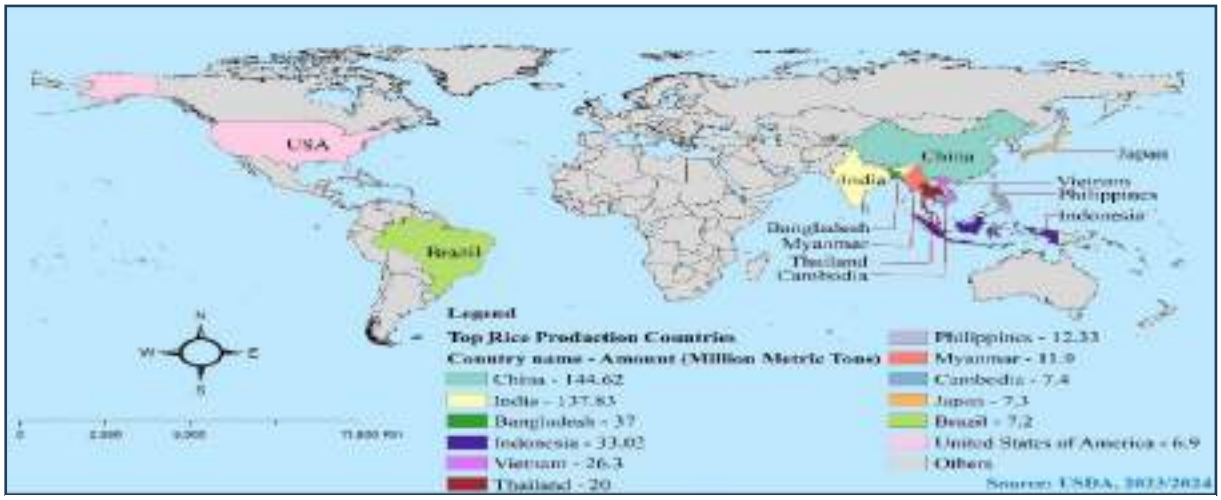

Fig 1 Top rice-producing countries with global rankings: annual production (million metric tons) and global ranking (USDA) [8].

million tons of rice husks as agricultural waste [8]. Disposing of this husk faces significant environmental challenges, emphasizing the need for effective reuse strategies. RHA produced by controlled combustion is an engineeringly useful product, which can serve as both a fine aggregate and a partial cement replacement in the production of unburnt bricks or blocks [9].

Previous researchers have provided detailed criteria for the engineering properties of common fired clay bricks [10- 13]. They found compressive strength values ranging from 3.01 MPa to 19.71 MPa, water absorption values ranging from 17% to 22%, and density ranging from 1600–1900 kg/m³, depending on the specific composition and firing conditions. However, compacted earth blocks (CEBs) made of soil, RHA, and cement have compressive strength values of 2.90–4.06 MPa, water absorption values of 16–23%, and densities of 1560 to 1812 kg/m³ [14], where a maximum of 20% RHA has been used as a soil replacement and 6.25% to 7.35% cement and resin adhesive as binder. The compressive strength and water absorption values of similar bricks using the same amount of RHA were found to be 1.39 MPa to 6.95 MPa and 5.15% to 18.78%, respectively [15], where 4% to 8% cement was used as the binder. Essentially, incorporating 5% RHA into non-burnt and lightweight bricks yields a compressive strength of 3.35 MPa, maintains dimensional stability, and has water absorption below 25%, further validating the effectiveness of RHA-based composites in sustainable construction [7, 16].

Similar to previous studies, this study proposes an alternative method for making unfired green bricks by incorporating RHA as a clay replacement, using it as a binder with cement. Without any additional adhesives, the bricks are made in a self-compacting or conventional brick-making manner. Standardized tests have confirmed that the mechanical and physical properties of these bricks meet the requirements of eco-efficient construction. The research findings provide a practical solution for sustainable construction and contribute to circular economy strategies in the construction sector, as well as opening the way for research into next-generation construction materials innovation

RESEARCH SIGNIFICANCE

This study presents a sustainable alternative to conventional brick production by developing non-burnt green bricks using agricultural residue—rice husk ash (RHA)—along with soil and cement. It addresses urgent environmental concerns by utilizing agro-industrial waste, reducing CO_2 emissions, and conserving topsoil. Experimental verification confirms that the optimized mixture meets Grade C standards. The findings align with the Sustainable Development Goals (SDGs), particularly responsible consumption and production (SDG 12), industry, innovation, and infrastructure (SDG 9), and climate action (SDG 13). Moreover, the study offers a practical pathway for promoting green construction practices in resource-limited and climate-vulnerable regions.

MATERIALS AND METHODS

Materials

Soil

For this study, expansive soil used as the main component was sourced from the Handa area in Tsu City, Mie Prefecture, Japan, to be used in brick manufacturing. Representative samples were gathered through a systematic soil sampling process following established geotechnical guidelines [17, 18] as shown in figure 2. Soil tests according to JIS A 1205 determined the liquid limit, plastic limit, sand content, silt content, and clay content, as shown in Table 2.

Fig 2 Using Materials

Table 1 Properties of Expansive Soil

Property	Value
Specific gravity, g/cm^3	2.74
Maximum dry density, g/cm^3	1.58
Plastic limit, %	28.594
Liquid limit, %	48.5
Plasticity Index, %	19.906
Saturation, %	87.14
AASHTO classification	A-7–6(5)
Silt (5–75 μm), %	57.28
Clay <5 μm, %	Clay <5 μm, %
Sand (75 μm—2 mm), %	0.02

Rice husk ash (RHA)

The experimental bricks incorporated high-purity rice husk ash (RHA) containing 91.10% silica, procured from Make Integrated Technology Co., Ltd., Osaka, Japan. The RHA was synthesized through controlled combustion in a computer-regulated ash production system, maintained at 650–

700°C for 27 hours. Comprehensive characterization of its physicochemical properties is detailed in Table 2 [8, 17, 18].

Table 2 Properties of RHA

Property	Value
Average Particle Size, mm	0.001 to 0.3
Loss of Ignition, %	4–6
Specific Gravity, g/cm^3	2.12
Burning Temperature, °C	650–700
Burning time, hours	27
Silica (SiO_2), %	91.10
Carbon dioxide (CO_2) %	4.35
Potassium Oxide (K_2O), %	2.40
Calcium Oxide (CaO), %	0.57
Iron Oxide (Fe_2O_3), %	0.05
Alumina (Al_2O_3), %	0.03
Others, %	1.50

Portland cement

Cement (OPC) was utilized as the primary binder in the composite formulation. The physicochemical attributes of the OPC are systematically documented in Table 3 [17, 18].

Table 3 Properties of OPC

Property	Value
Loss of Ignition, %	<4
Specific Gravity, g/cm^3	3.15
Initial setting time, minutes	170
Final setting time, minutes	255
Silica (SiO_2), %	21.60
Potassium Oxide (K_2O), %	0.22
Calcium Oxide (CaO), %	63.40
Iron Oxide (Fe_2O_3), %	5.35
Alumina (Al_2O_3), %	4.45
Sulfur trioxide (SO_3), %	1.92
Magnesium oxide (MgO), %	1.65
Sulfur trioxide (SO_3), %	1.92
Magnesium oxide (MgO), %	1.65

Sample Preparation

Mixing

Eight different formulations of the mix design were created using expansive soil as the base material, with varying amounts of ordinary Portland cement (OPC) and rice husk ash (RHA) to develop sustainable brick composites. According to Table 4, the control sample consisted of soil and 30% water. To investigate the impact of 5% RHA on workability and performance, a mix with 33% water was prepared.

Fig 3 Brick sample preparation

Cement was added at 8%, 10%, and 12%, and the water content was adjusted accordingly (32%–33%). Additionally, ternary mixes containing 5% RHA combined with varying cement contents were developed, requiring water contents of up to 36% to ensure adequate workability.

Water addition

Approximately the same type of mud was prepared by adding different percentages of its total weight of water to soil, RHA, and cement to make the sample bricks, as shown in Table 4.

Table 4 Mix proportions

Index	Material types (% by weight)			
	Soil, %	RHA, %	Cement, %	Water, %
Control	100	0	0	30
S5RHA0C	100	5	0	33
S0RHA8C	100	0	8	32
S0RHA10C	100	0	10	32.5
S0RHA12C	100	0	12	33
S5RHA8C	100	5	8	34
S5RHA10C	100	5	10	35
S5RHA12C	100	5	12	36

Molding

Following regular manufacturing procedures, the freshly prepared material was poured into brick molds and compressed using mechanical or manual pressing techniques to achieve optimal densification and structural integrity. The brick specimens were made using molds measuring 160 mm in length, 40 mm in width, and 40 mm in height.

Curing

After 24 hours of casting, the experimental brick specimens were demolded and then subjected to a 28-day curing process at a controlled temperature of 24±2 °C inside a curing chamber to ensure proper hydration.

Testing method

Bulk Density

The density of the brick specimens was evaluated following the procedures outlined in ASTM C67/C67M [19] or an equivalent standardized methodology. The bulk density was subsequently calculated using Equation 1, ensuring consistency with established analytical frameworks for masonry materials.

$$\rho = \frac{m}{v} \quad (1)$$

Where,
ρ = bulk density
m = mass
v = volume

Water Absorption Test

The evaluation of water absorption properties for the brick specimens was conducted by the standardized methodology prescribed in JIS R 1250:2011, which specifies the fundamental procedure for water absorption testing. The oven-absorption percentage was subsequently computed using Equation 2, ensuring methodological consistency and accuracy. dried mass (M_1) and the saturated mass (M_{1A}) of each sample were precisely measured, and the water

$$a = \frac{M_{1A} - M_1}{M_1} \times 100 \quad (2)$$

Where,
a = water absorption (%)
M_1 = dry weight of bricks (g)
M_{1A} = saturated weight of bricks (g)

Compressive Strength Test

The compressive strength assessment of the brick specimens was performed utilizing a universal testing machine, adhering to the guidelines specified in JIS R 1250:2011 or an equivalent standardized test protocol. The peak load sustained by each sample during the test was meticulously recorded, and the corresponding compressive strength values were derived using Equation 3, ensuring alignment with established mechanical evaluation criteria.

$$C = \frac{w}{a}\ \text{N/mm}^2 = \frac{w}{a} \times 1000\ \text{MPa} \quad (3)$$

Where,
c = compressive strength
w = maximum load
a = initial cross-sectional surface area

RESULTS AND DISCUSSION

The brick specimens were principally composed of rice husk ash (RHA), soil, and cement, with their mechanical and physical attributes comprehensively characterized employing the previously described standardized methodologies. The study further encompassed a thorough evaluation of the bricks' performance within sustainable construction frameworks to substantiate the structural integrity, consistency, and applicability of the fabricated eco-friendly masonry materials.

Bulk Density

Previous research has shown that the density of compressed stabilized clay bricks is between 1500–2000 kg/m³ [14, 20], but this study found values ranging from 1289.55 kg/m³ to 1561.03 kg/m³. According to Figure 4, the control sample exhibits the highest density, consisting of unrefined soil, due to its compact granular matrix and the absence of vacuum-induced additions. As a result of the gradual incorporation of RHA, especially in soils containing

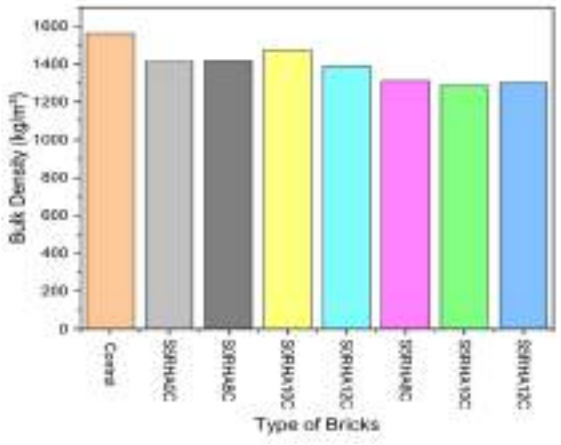

Fig 4 Bulk density of the Brick samples

5% RHA, 10% cement and 5% RHA, and 12% cement, the bulk density is significantly reduced, which is mainly due to the low specific gravity, high porosity, and cellular morphology of RHA particles. These properties reduce the particle packing efficiency and increase the inter-aggregate vacuum ratio, thereby reducing the mass of the composite per unit volume. Density is not only a function of material mass but also reflects the degree of interparticle interaction and matrix continuity. In mixtures such as 5% RHA with 12% cement display 1301.99 kg/m³, the presence of sufficient cement content compensates for the low density by facilitating extensive hydration reactions and pozzolanic activity, resulting in the formation of C-S-H gel that binds soil and ash particles into a dense, mechanically elastic microstructure despite the light nature of RHA.

Water Absorption

In this study, the control sample and the S5RHA0C sample, both prepared without cement, disintegrated during the water absorption test; therefore, their results are not presented in figure 5. According to figure 5, the water absorption value for soil–RHA–cement composites was found to be 30.55% to 36.44%, whereas in a previous study, this value was found to be 5.15% to 23% [14, 20]. In this study, the highest absorption was observed in a mixture of 5% RHA and 8% cement. The cause is insufficient cementitious matrix, resulting in incomplete hydration, limited pozzolanic reactivity, and a poorly integrated microstructure characterized by high capillary pores and interconnected voids.

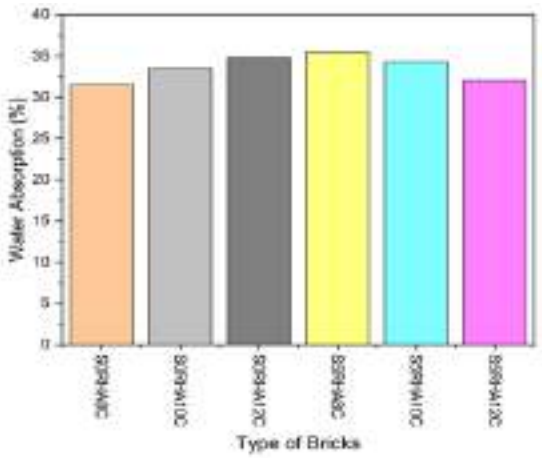

Fig 5 Water Absorption of the brick samples

Essentially, the porous nature of RHA, its high internal surface area, and irregular morphology further increase water uptake when not adequately enclosed within a cohesive matrix. On the other hand, a mixture of 5% RHA and 12% cement recorded the lowest absorption (30.65%). Here, the higher cement content has increased the matrix density and reduced the capillary pores, thereby limiting water entry.

Compressive strength

According to Figure 6, among the samples tested, the highest value (2.83 MPa) was achieved by the soil mixture containing 5% RHA and 12% cement. It is the result of a synergistic enhancement of the binding phase through concurrent cement hydration and secondary pozzolanic reaction. After hydration, cement releases calcium hydroxide (CH), which subsequently reacts with amorphous silica present in RHA to form calcium silicate hydrate (C-S-H) gel, a key component of matrix density and load-bearing capacity. This has produced compressive strength suitable for grade C non-load-bearing bricks. This reaction not only consumes CH, reduces porosity, and increases long-term stability, but also promotes the refinement of pore size distribution and the development of a more continuous cementitious phase.

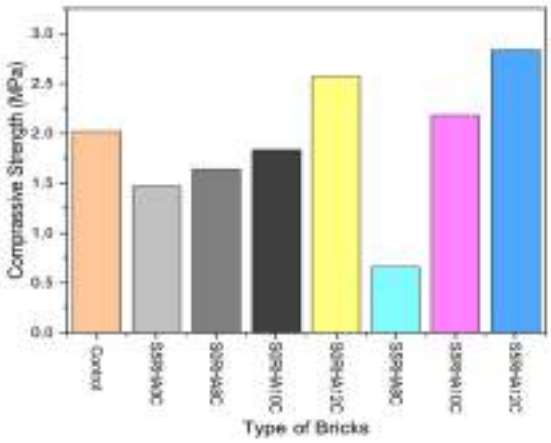

Fig.6 Compressive strength of the brick samples

On the other hand, the control sample reached 2.02 MPa, where a porous and isolated microstructure was formed, as the capillary bond was not strong due to the lack of a reactive binder. In addition, only 1.47 MPa was found in the 5% RHA mixture without any cement. The reason is simply the lack of self-cementing properties in RHA and the inactivation of RHA in the absence of sufficient calcium sources in the soil. However, mixing 5% RHA with 8% cement resulted in a strength of 0.66 MPa, indicating incomplete hydration, limited C-S-H formation, and a clear reduction in the formation of strongly bonded structures.

CONCLUSION

This study confirmed the technical and environmental effectiveness of non-fuel green bricks by using rice husk ash (RHA) as a partial substitute for soil. The optimum mixture, made of soil, 5% RHA, and 12% cement, achieved a compressive strength of 2.83 MPa, a density of 1301.99 kg/m³, and a water absorption of 30.65%. These characteristics meet the requirements of grade C bricks suitable for non-load-bearing masonry, which conform to the criteria of recent research in the field. It is the consolidation of RHA, one of the agro-industrial byproducts, reducing reliance on energy-intensive materials and advancing the goals of the circular economy. The pozzolanic combination between RHA and cement increases mechanical performance and reduces the carbon footprint of brick production. These results are consistent with contemporary literature that emphasizes the potential of waste-based technologies to transform the construction sector towards greater sustainability. Future research should explore long-term

sustainability, life cycle assessment, and scalability in different environmental contexts, as well as the integration of additional waste streams to further improve the sustainability profile of green bricks.

REFERENCES

[1] Frapanti, S., Tanjung, L.E., Riza, F.V., Nasution, A.R. and Zulkarnain, F., 2024. Comparison of physical and mechanical properties of traditional bricks in Deli Serdang with no-burn bricks using rice husk ash. Journal of Engineering and Applied Science, 71(1), p.143.

[2] Murmu, A.L. and Patel, A., 2018. Towards sustainable bricks production: An overview. Construction and building materials, 165, pp.112-125.

[3] Attah, I.C., Alaneme, G.U., Fadugba, O.G. and Olaiya, B.C., 2025. Sustainability measurement of developed concrete by incorporating solid waste. In Recent Developments and Innovations in the Sustainable Production of Concrete (pp. 333-347). Woodhead Publishing.

[4] Akpomie, K.G., Malloum, A., Akpotu, S.O., Adegoke, K.A., Okeke, E.S., Omotola, E.O., Ohoro, C.R., Amaku, J.F., Conradie, J. and Olisah, C., 2025. Effect of Biomass-Based Additives on the Thermal, Physical, and Mechanical Properties of Fired Clay Bricks: A Review. International Journal of Thermophysics, 46(1), pp.1-66.

[5] Lawanwadeekul, S., Srisuwan, A., Phonphuak, N. and Chindaprasirt, P., 2024. Addition of spent coffee grounds and waste glass to enhance the physical–mechanical and thermal properties of fired clay bricks at reduced temperatures. Innovative Infrastructure Solutions, 9(6), p.206.

[6] Medvey, B. and Dobszay, G., 2020. Durability of stabilized earthen constructions: a review. Geotechnical and Geological Engineering, 38(3), pp.2403-2425.

[7] Valenzuela, M., Tuninetti, V., Ciudad, G., Miranda, A. and Oñate, A., 2025. Designing sustainable cement free compositions with rice husk ash to improve mechanical performance in next generation ecoblocks. Scientific Reports, 15(1), p.14920.

[8] Islam, M.Y. and Hossain, Z., 2025. Investigating the one-dimensional consolidation properties of river sludge enhanced by sustainable additive synergy for eco-friendly stabilization. Journal of Building Engineering, 101, p.111851.

[9] Anwar, M., Miyagawa, T. and Gaweesh, M., 2000. Using rice husk ash as a cement replacement material in concrete. In Waste management series (Vol. 1, pp. 671-684). Elsevier.

[10] Mohammad, M., Wahab, R.A.A., Mazlan, M., Fazil, N.N.S.M., Ibrahim, N.S.H., Nizam, U.N.M., Hanifah, A.H.A. and Zaid, M.H.M., 2023. Physical and mechanical properties of fired industrial waste-clay bricks from clam shells and soda lime silica glass. Materials Today: Proceedings, 75, pp.151-155.

[11] Danso, H. and Akwaboah, M., 2021. Assessment of the quality of burnt bricks produce in Ghana: The case of Ashanti region. Case Studies in Construction Materials, 15, p.e00708.

[12] Binici, H., Binici, F., Akcan, M., Yardim, Y., Mustafaraj, E. and Corradi, M., 2020. Physical–mechanical and mineralogical properties of fired bricks of the archaeological site of Harran, Turkey. Heritage, 3(3), pp.1018-1034.

[13] Phonphuak, N., Saengthong, C. and Srisuwan, A., 2019. Physical and mechanical properties of fired clay bricks with rice husk waste addition as construction materials. Materials Today: Proceedings, 17, pp.1668-1674.

[14] Yatawara, M. and Athukorala, S., 2021. Potential of replacing clay soil by rice husk ash (RHA) in enhancing the properties of compressed earth blocks (CEBs). Environment, Development and Sustainability, 23(3), pp.3474-3486.

[15] Paul, S., Islam, M.S. and Elahi, T.E., 2023. Potential of waste rice husk ash and cement in making compressed stabilized earth blocks: Strength, durability and life cycle assessment. Journal of Building Engineering, 73, p.106727.

[16] Lesovik, V., Volodchenko, A., Fediuk, R., Mugahed Amran, Y. H. & Timokhin, R. Enhancing performances of clay masonry materials based on nanosize mine waste. Constr. Build. Mater. 269, 121333 (2021).

[17] Shehata A.A., Owino A.O., Islam M.Y. et al. Shear strength of soil by using rice husk ash waste for sustainable ground improvement. Discov Sustain 5, 64 (2024). https://doi.org/10.1007/s43621-024-00238-x

[18] Owino AO, Hossain Z. The influence of basalt fiber filament length on shear strength development of chemically stabilized soils for ground improvement. Constr Build Mater. 2023. https://doi.org/10.1016/j.conbuildmat.2023.130930

[19] American Society for Testing and Materials, 2014. Standard test methods for sampling and testing brick and structural clay tile. ASTM International.

[20] Riza, F.V., Rahman, I.A. and Zaidi, A.M.A., 2011. Preliminary study of compressed stabilized earth brick (CSEB). Australian Journal of Basic and Applied Sciences, 5(9), pp.6-12.

Copyright © Int. J. of GEOMATE All rights reserved, including making copies, unless permission is obtained from the copyright proprietors.

15th Int. Conf. on Geotechnique, Construction Materials & Environment,
Kyoto, Japan, 11-13 November 2025, ISBN 978-4-909106124 C3051

APPLICATION OF SEASHELL POWDER ISOLATELY AND COMBINED WITH RICE HUSK ASH IN CONCRETE AS CEMENT REPLACEMENT MATERIALS

Md Soybur Rahman[1], Zakaria Hossain[2]
[1,2]Graduate School of Bioresources, Mie University, Japan

ABSTRACT

The growing demand for sustainable construction materials has stimulated significant research efforts to develop alternative binders that can effectively reduce cement usage. This study examined the effects of seashell powder (SSP), alone and in combination with rice husk ash (RHA), as partial replacements for cement in concrete. Three types of concrete mixtures were prepared: 100% cement (control), 80% cement + 20% SSP, and 80% cement + 15% SSP + 5% RHA, to evaluate their fresh and hardened properties. Experimental results revealed that incorporating SSP alone had a negligible effect on the workability of fresh concrete. However, the combination of SSP and RHA led to a pronounced reduction in workability. In terms of mechanical performance, replacing 20% of cement with SSP alone resulted in a reduction in compressive strength. Conversely, the combination of SSP and RHA (15% SSP + 5% RHA) demonstrated a significant improvement in compressive strength compared to the control mixture, highlighting the beneficial synergistic effects among Cement, SSP, and RHA. Additionally, concrete containing both SSP and RHA displayed increased brittleness but fewer visible cracks under compression, indicating improved structural integrity. This finding offers the potential of the combined use of SSP and RHA as a partial cement substitute, promoting waste valorization and environmentally friendly concrete production.

Keywords: Rice Husk Ash, Seashell powder, Synergistic Effect, Eco-friendly Concrete

INTRODUCTION

Concrete is a widely used construction material, but it contributes to environmental pollution due to the high CO_2 emissions associated with cement production [1,2]. On average, the production of one ton of cement results in approximately one ton of carbon dioxide emissions. In recent years, the use of supplementary cementitious materials (SCMs) has gained significant attention and has become a common practice in the concrete industry, owing to their beneficial effects on both performance and sustainability [3]. Utilizing industrial and agricultural wastes as partial substitutes for cement has shown promise as an environmentally friendly approach, while also enhancing the stability and durability of construction materials [4].

Shell husk is annually generated as a byproduct of shellfish processing in Japan. According to the Japanese Ministry of Agriculture, Forestry and Fisheries, approximately 151,000 tons of shell husk are discarded each year. This substantial quantity is typically disposed of without any commercial use, leading to environmental pollution and associated ecological concerns. In an effort to address these issues, the potential application of waste shell husk in concrete construction has been extensively explored as a sustainable and eco-friendly solution. [5]. The seashell waste at Shiratsuka Port, Mie, Japan, is shown in fig. 1.

Rice husk is another agricultural residue that, when incinerated, produces ash with pozzolanic properties, making it suitable for use as a cement replacement material [6]. Replacing cement with Rice Husk Ash (RHA) in structural concrete is an effective option that balances cost efficiency and strength performance, while also offering environmental advantages by reducing waste disposal issues, even without additional processing [7].

Fig.1 Seashell waste at Shiratsuka Port, Mie, Japan

Although previous research has studied RHA and SSP individually as supplementary cementitious materials in concrete, their combined use remains unexplored. This study investigated the combined effect of both materials on concrete's fresh and hardened properties.

RESEARCH SIGNIFICANCE

This study addresses the need for sustainable construction by investigating the combined use of Rice Husk Ash (RHA) and Seashell Powder (SSP) as partial replacements for cement in concrete. Both materials are agricultural and marine wastes that are often discarded, causing environmental issues. Using RHA and SSP reduces cement consumption, lowers CO_2 emissions, and promotes waste recycling. Their combination offers enhanced strength and durability due to the pozzolanic properties of RHA and the calcium content of SSP. This research supports the development of eco-friendly, greener construction practices.

MATERIALS AND METHODS

The raw materials used in the concrete mixture include cement, fine aggregate, coarse aggregate, rice husk ash, seashell powder, and water.

Cement

Ordinary Portland Cement (OPC) was used in the experiment, which was purchased from the local market (Fig. 2).

Fig.2 Ordinary Portland Cement

Rice Husk Ash (RHA)

The rice husk ash production process was operated in a factory building of the Make Integrated Technology (M.I.T.) company in Osaka, Japan, using an industrial machine device. Unlike traditional incinerators, this machine operates as a natural-type silica generator, eliminating the need for combustible materials such as gas, kerosene, or electricity. Instead, solid methanol fuel is used to ignite and burn the rice husks. This innovative process is environmentally friendly, as it does not produce dioxins, making it exempt from the Fire Services Act. The burning speed and temperature are meticulously controlled by a computer, reducing labor costs and minimizing personnel requirements. Additionally, the system can be remotely controlled, offering further convenience in managing the incineration process. Fig. 1 shows the raw rice husk ash.

Fig.3 Rice Husk Ash

Seashell powder

This seashell powder is provided by Make Integrated Technology (M.I.T.), a company based in Osaka, Japan. The process involves collecting seashells, drying them, and then crushing them into powder. Finally, the powder is subjected to a burning process at 900°C. Fig. 4 shows the raw Seashell powder.

Fig.4 Seashell powder

Table 1: Mix design of Concrete

Specimen Identity	Cement (%)	Seashell Powder (%)	Rice Husk Ash (%)	W/C ratio	Cement (kg/m^3)	Fine Aggregate (kg/m^3)	Coarse Aggregate (kg/m^3)
CRS1	100	0	0	0.55	290	308	852
CRS2	80	20	0	0.55	232	308	852
CRS3	80	15	5	0.55	232	308	852

Fig.5 Experimental work of this study

Aggregates

River sand was used as fine aggregate, and gravel was used as coarse aggregate, as shown in fig. 6. The maximum size of coarse aggregate was 19 mm. Both were purchased at a home center in Tsu City, Japan.

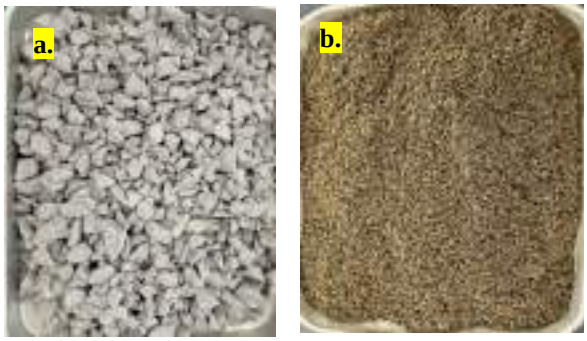

Fig.6 Coarse aggregate (a) and Fine aggregate (b)

Mixture Proportioning and Testing program

After accurately weighing the raw materials, the concrete mixture was prepared using a mix ratio of 1:1:3 by weight for cement, fine aggregate (sand), and coarse aggregate (gravel). Seashell powder was added to the concrete mix individually and combined with rice husk ash, replacing cement 20% by weight. The water-to-binder ratio was maintained at 0.55 throughout the all mixing process. The specific quantities of each material are provided in Table 1. The experimental work is presented in fig. 5.

Following proper mixing, a slump test was conducted to evaluate the workability of the concrete. The slump cone used in the test has a standard dimensions: 300 mm in height, a base diameter of 200 mm, and a top opening of 100 mm. The cone was placed on a smooth, level surface and filled with concrete in three equal layers. Each layer was compacted by rodding 25 times using a tamping rod with a diameter of 16 mm. After filling, the top surface was leveled, and the mold was lifted vertically. The slump was measured using the rod, and the vertical settlement of the concrete (in the shape of a frustum) was recorded as the slump value.

Subsequently, the concrete was cast into cylindrical molds with dimensions of 50 mm in diameter and 100 mm in height. The specimens were then cured in water at room temperature for 28 days. After curing, the weight and volume of each specimen were measured to calculate the unit weight.

Finally, compressive strength testing was conducted after 28 days of curing using a Universal Testing Machine (Fig. 7) in accordance with ASTM C39 standards. Three cylindrical specimens were tested for each mix condition to ensure the accuracy and reproducibility of results.

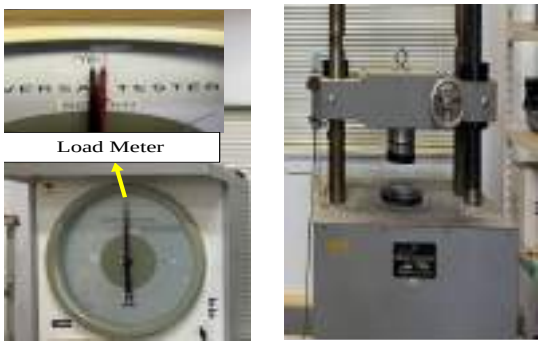

Fig.7 Universal Testing Machine

RESULTS AND DISCUSSIONS

The experimental result, comparative analysis, and practical application have been explained below.

Workability

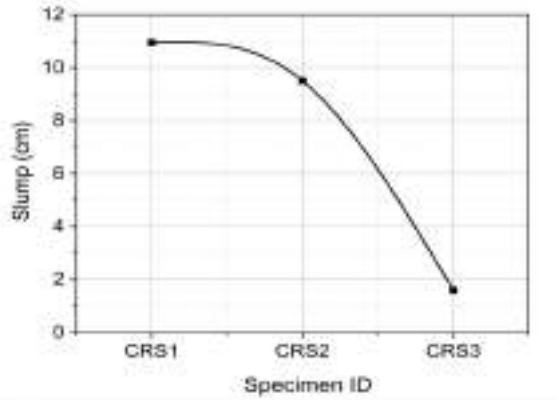

Fig.8 Workability of concrete mixture

The slump values of the OPC concrete and the modified concrete mixes are presented in Fig. 8. Among them, CRS1 exhibited the highest slump, approximately 11 cm, indicating high workability. CRS2 demonstrated a moderate slump of around 9 cm, while CRS3 showed a significant decrease to 1.6 cm, reflecting a very stiff mix with low workability. Possible reasons for the slump reduction may be the incorporation of mineral admixtures, Rice Husk Ash, and Seashell powder. Overall, the results indicate that the combined application of RHA and SSP notably improved the viscous nature of concrete and created the demand for superplasticizer to maintain proper flowability. The results aligned with previous studies, which reported that high specific surface area and irregular particles of RHA and SSP absorbed water and reduced the workability of the concrete mixture [7,8].

Unit Weight

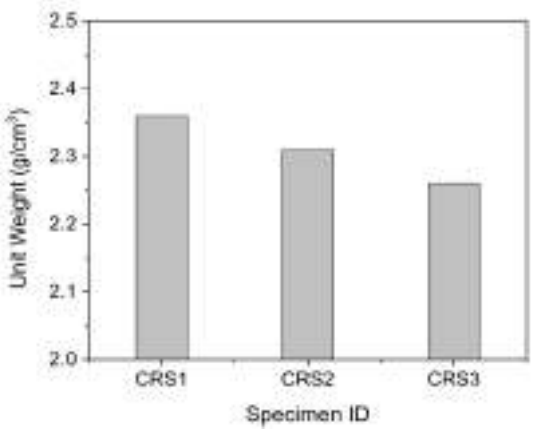

Fig.9 Unit weight of concrete

Figure 9 presents the unit weight of the three different specimens, CRS1, CRS2, and CRS3, which indicates a clear decreasing trend from CRS1 to CRS3. CRS1 exhibited the highest unit weight at 2.36 g/cm³, followed by a slight decrease in CRS2 at 2.31 g/cm³, and CRS3 showed the lowest unit weight at 2.26 g/cm³. The incorporation of seashell powder as a cement replacement material has no significant effect on the unit weight of concrete [9]. In this study, a 20% replacement of cement by seashell powder showed a slight reduction in the unit of concrete. This may have occurred due to different types of seashells and the burning temperature. But with the combined application of SSP and RHA (15% and 5%, respectively), the unit weight notably decreased. An increase in RHA content leads to a decrease in the unit weight of concrete, owing to the lower density of RHA compared to cement [10].

Compressive Strength

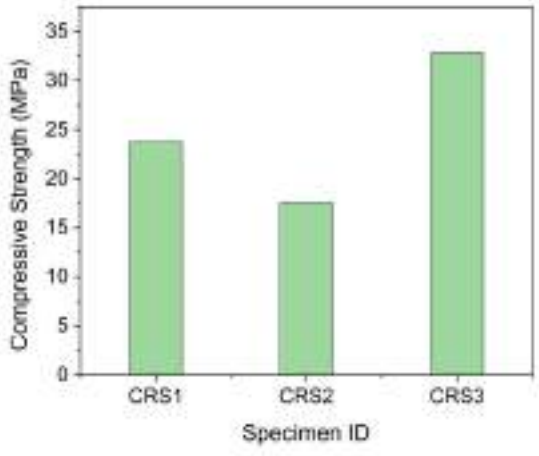

Fig.10 Compressive strength of concrete

The compressive strength of concrete is a vital mechanical characteristic that indicates its capacity to resist axial loads without failing. Figure 10 presents the compressive strength results of three concrete specimens, labeled CRS1, CRS2, and CRS3, tested under standardized conditions. Among the tested specimens, CRS3 exhibited the highest compressive strength, achieving 32.81 MPa, which represents a 38% increase compared to the control specimen. This result highlights its superior structural performance. In contrast, CRS2 demonstrated a significant reduction in compressive strength relative to the control mix, indicating that the isolated use of seashell powder as a partial cement replacement may be unsuitable. Previous studies have reported that substituting up to 5% of cement with seashell powder can enhance compressive strength [9]. However, the combined use of seashell powder and rice husk ash (RHA) appeared to offer a promising alternative for cement replacement, significantly improving the compressive strength in this study. This improvement

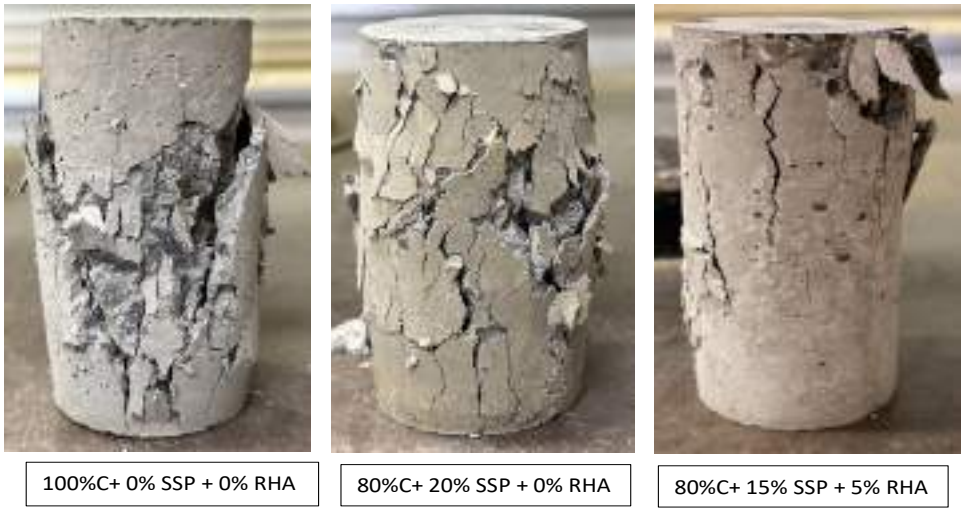

Fig.12 Failure pattern of experimental specimen

is likely attributed to the pozzolanic reaction between the amorphous silica in RHA and the calcium hydroxide ($Ca(OH)_2$), produced during cement hydration and reaction of seashell powder with water, thereby enhancing the concrete's strength.

Stress-strain relationship

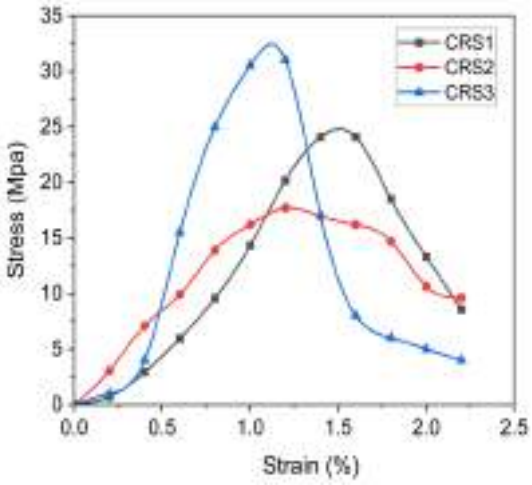

Fig.11 Stress-strain relationship of concrete under uniaxial compression test

The stress–strain behavior of the three types of specimens, CRS1, CRS2, and CRS3, revealed significant differences in their mechanical performance, as shown in fig.11. CRS1 exhibited a maximum stress of approximately 23 MPa and a failure strain of about 2.1%. CRS3 demonstrated the highest maximum stress, around 32 MPa, indicating superior strength; however, it failed at a strain of approximately 1.2%, reflecting brittle behavior with limited deformability. In contrast, CRS2 showed the lowest maximum stress, approximately 17 MPa, but its failure strain was nearly identical to that of CRS1, indicating a more ductile nature capable of accommodating greater deformation before failure. These results imply that CRS3 may be suitable for applications requiring high strength with less concern for deformation, while CRS2 could be advantageous in scenarios demanding greater flexibility and energy absorption. CRS1, with its intermediate properties, may serve as a versatile option for structures needing both adequate strength and reasonable ductility.

Failure Mode of Testing Specimen

The visual inspection of the concrete specimens after compression testing revealed noticeable differences in failure patterns based on the varying mixing combination, as shown in fig.12. The control specimen containing 100% cement (0% SSP and 0% RHA) exhibited significant fracture, characterized by deep vertical cracks. In contrast, the specimen with 80% cement and 20% SSP showed a slightly less severe cracking pattern. Notably, the third specimen, composed of 80% cement, 15% SSP, and 5% RHA, showed the least visible damage among the three. The cracks were finer, and there was minimal surface spalling, indicating improved integrity. This suggests that the addition of RHA and SSP contributed positively to the mix, likely due to synergistic effects that enhanced microstructural bonding and reduced porosity. The inclusion of both SSP and RHA appeared to improve crack resistance of the concrete, offering a promising approach for sustainable material substitution without severely compromising mechanical performance.

CONCLUSIONS

This study concludes the following points-

1. The incorporation of Rice Husk Ash (RHA) and Seashell powder significantly reduced the flowability of the concrete mixture.
2. While the use of Seashell powder alone had little effect on the unit weight of concrete, the addition of RHA led to a noticeable reduction in unit weight.
3. Replacing 20% of cement with Seashell powder reduced the compressive strength compared to the control mix. However, a combination of 15% Seashell powder and 5% RHA significantly enhanced the compressive strength.
4. Although the ultimate stress improved with the combined use of Seashell powder and RHA, the modified concrete exhibited a more brittle behavior compared to the control.
5. The Ash-powder-modified specimens exhibited fewer cracks under compression, suggesting improved structural integrity.

ACKNOWLEDGMENTS

The authors gratefully acknowledge the Ministry of Education, Culture, Sports, Science and Technology (MEXT), Japan, and Mie University for their generous support and for providing the opportunity to undertake this doctoral research. The authors also extend their sincere appreciation to M.I.T. Company, Osaka, Japan, for kindly supplying the Rice Husk Ash and Seashell Powder used in the experimental investigations.

REFERENCES

[1] Raman S. N., Ngo T., Mendis P., and Mahmud H. B., High-strength rice husk ash concrete incorporating quarry dust as a partial substitute for sand. Construction and Building Materials, Vol. 25, Issue 7, 2011, pp. 3123-3130.

[2] Datta S. D., Rana M. J., Assafi M. N., Mim N. J., and Ahmed S., Investigation on the generation of construction wastes in Bangladesh. International Journal of Construction Management, Vol. 23, Issue 13, 2023, pp. 2260-2269.

[3] Ahsan M. B., and Hossain Z., Supplemental use of rice husk ash (RHA) as a cementitious material in concrete industry. Construction and Building Materials, Vol. 178, 2018, pp. 1-9.

[4] Khan R., Jabbar A., Ahmad I., Khan W., Khan AN, and Mirza J., Reduction in environmental problems using rice-husk ash in concrete. Construction and Building Materials, Vol. 30, 2012, pp. 360-365.

[5] Hossain M. Z., Waste shell husks concrete: durability, permeability and mechanical properties. Journal of Building Construction and Planning Research, Vol. 1, Issue 3, 2013, pp. 61-66.

[6] Zerbino R., Giaccio G., and Isaia G.C., Concrete incorporating rice-husk ash without processing. Construction and building materials, Vol. 25, Issue 1, 2011, pp. 371-378.

[7] Siddika A., Mamun M. A. A., and Ali M. H., Study on concrete with rice husk ash. Innovative Infrastructure Solutions, Vol. 3, 2018, pp. 1-9.

[8] Ephraim M.E., ThankGod O., & Gbinu K. Performance of high strength concrete using oyster shell ash as partial replacement for cement. SSRG International Journal of Civil Engineering, Vol. 6, Issue 6, 2019, pp. 33-38.

[9] Tayeh B.A., Hasaniyah M.W., Zeyad A.M., Awad M.M., Alaskar A., Mohamed A.M., and Alyousef R., Durability and mechanical properties of seashell partially-replaced cement. Journal of Building Engineering, Vol. 31, 2020, pp. 101328.

[10] Ameri F., Shoaei P., Bahrami N., Vaezi M., and Ozbakkaloglu T., Optimum rice husk ash content and bacterial concentration in self-compacting concrete. Construction and Building Materials, Vol. 222, 2019, pp. 796-813.

Copyright © Int. J. of GEOMATE All rights reserved, including making copies, unless permission is obtained from the copyright proprietors.

15th Int. Conf. on Geotechnique, Construction Materials & Environment, Kyoto, Japan, 11-13 November 2025, ISBN 978-4-909106124 C3051

SYNERGISTIC EFFECTS OF AMORPHOUS SILICA ON ADMIXTURE DEMAND, STRENGTH DEVELOPMENT, AND CO_2 MITIGATION IN MODIFIED LOW-CARBON CONCRETE

Alex Otieno Owino[1], Noma Tamaki[1] and Zakaria Hossain[3]

[1]Make Integrated Technology M.I.T, Osaka, Japan
[3]Graduate School of Bioresources, Mie University, Japan

ABSTRACT

While chemical admixtures (CAs) have long been utilized in concrete technology to improve workability by enhancing the interaction between cement particles and various concrete constituents, their interaction with SCMs, such as RHS, remains underexplored. This paper presents findings from a comprehensive experimental study aimed at achieving eco-strength efficiency through the incorporation of RHS into concrete. The research also involved the proportioning of fine aggregates at a 70:30 ratio to simulate potential strategies for mitigating global fine aggregate shortages. Similarly, coarse aggregates were proportioned at 55:45 based on particle size (20 mm:15 mm) to achieve a stable concrete matrix. Various percentages of RHS (0%, 5%, 10%, 15%, and 20%) were used as a cement replacement by volume, with a fixed cement content of 292 kg/m³ for the control sample. Polycarboxylate-based water-reducing CA agents, air-entraining and air-reducing admixtures were added according to the desired workability. The results indicated that optimal use of RHS could reduce CO_2 emissions by up to 9.78% during low-carbon concrete production, although it increased the cost per cubic meter by 90.65% to 187.98%, depending on the source and market price of rice husk silica. Moreover, the optimal RHS mix demonstrated increases of up to 21.21% in compressive strength and 40% in flexural strength. Further analysis of RHS concrete samples using Scanning Electron Microscopy (SEM) revealed a pozzolanic reaction mechanism, as evidenced by a highly cemented microstructure. This study underscores the potential of low-carbon concrete in advancing sustainable construction practices by reducing CO_2 emissions while simultaneously promoting the efficient utilization of rice husks as a greener waste management solution.

Keywords: Rice husk silica, Amorphous silica, Chemical admixtures, Low-carbon concrete, Compressive strength, Flexural strength, CO_2 emissions, Self-healing concrete, SCMs, SEM

INTRODUCTION

The critical upcoming challenge in the construction industry and engineering is constructing and restoring infrastructure in an economical, durable, and sustainable manner while reducing the environmental impact. To date, several ventures have been pursued to reduce the environmental impacts of construction materials and the dependency on Portland cement as the sole binder [1]. High Portland cement usage burdens the environment as the cement industry contributes 8% of global CO_2 emissions [2]. One pathway focuses on developing low-carbon cementing binder systems [3] by introducing various types of low-carbon embedded cementitious systems such as using alkali-activated materials (AAMs), as a means of mitigating CO_2 emissions from the construction sector [4]. However, it has been proven that manufacturing conventional AAMs has devastating economic and environmental impacts due to the high energy demands. A good example of these conventional AAMs is sodium silicate activator that generates high CO_2 emissions during the decomposition and calcination of sodium carbonate and silica sand [5]. Despite the high CO_2 emissions from AAMs, previous assessments on AAMs concluded that the greenhouse gas emission of AAM concrete is 32%–64% lower than the one from Portland cement concrete of similar strength [6]. The main source of these AAMs is the abundant supply of Supplementary Cementitious Materials (SCMs) available worldwide.

In the past decade, another pathway has been the increasing research interest in utilizing supplementary cementitious materials (SCMs) derived from agricultural wastes. Among these, rice husk silica, also known as rice husk ash, has garnered significant attention. Rice husk silica, derived from the combustion of rice husks (an agricultural by-product), is well-regarded for its high content of amorphous silica, substantial pore volume, and significant specific surface area when burned under optimal conditions [7]. Consequently, RHS exhibits exceptionally high pozzolanic reactivity, comparable to other supplementary cementitious materials (SCMs) like silica fume, fly ash, and blast furnace slag [8]. Research has demonstrated that RHS is an excellent substitute for many supplementary cementitious materials (SCMs) in terms of portlandite consumption and the compressive strength of high-strength concrete [9]. Its high pozzolanic reactivity not only enhances concrete's durability and mechanical properties but also contributes to sustainable construction practices by utilizing agricultural waste.

Moreover, due to its mesoporous structure, RHS exhibits a significantly higher water absorption capacity compared to other SCMs [10]. This unique characteristic enhances the hydration process and improves the overall performance, leading to more resilient and long-lasting concrete [11]. RHS can absorb free water in RHS-blended Portland cement concrete, thereby improving compressive strength. The water retained in its porous structure facilitates the diffusion of Ca^{2+} ions into the internal parts

of RHS particles, enhancing pozzolanic reactivity and sustaining the hydration of cementitious materials [12].

Nevertheless, due to the high-water demand of rice husk silica, the concrete workability and strength can be compromised if the free water in the system is not kept within the allowable limit [13]. Therefore, it is paramount to investigate the effects of chemical admixtures applied to simultaneously maintain the diffusion and mechanical properties of such concrete [14]. Chemical admixtures (CAs) have been employed in concrete technology for decades to improve the workability of concrete in its fresh state [15]. The interaction of the cement particles with various CAs has been extensively researched, however, there still exists limited research on the interaction of CAs with SCMs such as RHS. Additionally, despite the numerous studies incorporating RHS in concrete in the literature, a comprehensive assessment of the CA's demand, water demand with strength and the principal sustainability aspects in terms of costs involved and the CO_2 emission reduction projections has not yet been solely and exclusively addressed.

Despite extensive research on the properties of rice husk in concrete, there remains a gap in comprehensive studies focusing on optimizing and evaluating the performance related to chemical admixture requirements, water-to-cement ratio (w/c), water-to-cement plus rice husk silica ratio (w/b), and the potential self-healing abilities of these cementitious materials. Furthermore, to date, the rice husk silica production practices emit a lot of CO_2 into the environment due to uncontrolled burning and the use of conventional ovens. To address this challenge, the rice husk silica utilized in this study was generated in a novel zero CO_2 emission environment, producing high-quality RHS with a significant amorphous silica content, ensuring superior pozzolanic reactions compared to the conventional burning methods, which are less environmentally friendly.

The experimental framework strictly adhered to Japan Industrial Standards (JIS A 1132:2020 and JIS A 1138:2020 for concrete preparation; JIS A 1108:2006 and JIS A 1106:2018 for compressive and flexural strength assessments). In addition, scanning electron microscopy (SEM) was employed to elucidate the microstructural features that underpinned the material's performance. This standard-based approach ensured a robust evaluation, providing a reliable benchmark for high-strength, low-carbon concrete applications in civil, geotechnical, and geo-environmental engineering.

RESEARCH SIGNIFICANCE

The main challenge when working with SCMs like rice husk silica is the increase in the w/c ratio to offset the losses in workability caused by the porous morphology and water absorption of RHS compared to cement. SPs are a natural solution to offset both these detrimental effects. However, experimental data on SPs sourced from concrete publications also strongly suggest that PCE SPs lose their effectiveness on the fresh-state properties of concrete with increasing incorporation ratios. Additionally, when working with SCMs, it is crucial to understand the interactions with PCE SPs, w/c and w/b ratios in terms of dosage, strength evolution and usage limits to validate the potential impacts they may have in concrete manufacture. This study addresses these challenges and research gaps by investigating the effect of a PCE SP and the w/c/w/b ratios on various rice husk silica compositions based on the cement reduction rate. The goals are to (i) Evaluate the PCE SP efficiency on several RHS compositions by comparing the mechanical properties of different compositions with varying cement replacement ratios. (ii)

To benchmark the optimum RHS content, w/b and PCE SP dosages based on the desired fresh state and ultimate strength. (iii) Assess whether the optimum RHS composition at different w/b ratios affects the efficiency of PCE SP. Because of the increased popularity of RHS, it is crucial to provide a detailed database that will make this abundant material a more reliable construction material compared to conventional materials that have high carbon footprints. Also, because of the increased popularity of PCE SP and since it has been consistently reported that it is more efficient in concrete mixes than lignosulfate-based SP, this investigation includes the use of polycarboxylic-based SP only. The dosage of PCE SP was fixed at the cement percentage (by weight), depending on the optimum value added to achieve the initial set fresh state properties for each RHS combination.

MATERIALS

Rice Husk Silica - Production and Properties

Make Integrated Technology (M.I.T) Corporation, based in Osaka, Japan, provided a controlled-burned rice husk ash (RHS - Light Grey) with a high silica content of 91.10%, achieved at temperatures between 650-700°C. This plant-based RHA was derived from domestic rice husks using the Ethical Star ash production machine shown in Figure 1. From 800-1000 kg of dry rice husks, approximately 15-20% of high-purity amorphous silica is produced. The production process involves igniting a small amount of methanol solid fuel as a pilot fire in the rice husk holding chambers, leading to self-combustion.

Figure 1 Flow diagram illustrating the Rice husk ash production process.

This method certifies the RHS as an organic Japanese Agricultural Standards (JAS) material. Combustion is then controlled by an advanced monitoring system for 27 hours, with the operating status monitored remotely, ensuring the production of high-purity silica. After combustion, the RHA is removed from the chamber and allowed to cool naturally at room temperature.

Figure 2b presents a detailed grain size analysis of rice husk silica (RHS), indicating that the rice husk silica (RHS) exhibited grain sizes ranging from 0.00129 to 0.3 mm. The RHS was subjected to X-ray powder diffraction (XRD) analysis, which quantitatively determined the chemical composition of the materials, as shown in Figure 2c. The XRD analysis confirmed the amorphous nature of RHS, characterized by a broad hump around $2\theta = 21°$, which is typical of amorphous silica. Table 1 provides a comprehensive chart detailing the chemical properties of rice husk ash.

Ordinary Portland Cement

In this concrete research, PC-43 grade Ordinary Portland Cement (OPC) was utilized, which is known for its balanced strength and workability. This cement conforms to the Japanese Industrial Standards (JIS) for cement, specifically JIS R 5210, ensuring it meets the stringent quality and performance criteria required for construction applications in Japan. The cement had a composition of alite (Ca_3SiO_5), a major chemical component in OPC that defines its high strength, as shown in the X-ray powder diffraction (XRD) analysis results in Figure 2c. A detailed particle size analysis of OPC and chemical properties is shown in Figure 2b and Table 1, respectively.

Aggregates

The present research work has been carried out by rationing the fine aggregates by 70% crushed rock to 30% river sand due to the limited supply of fine aggregates in Japan, as the natural resource has been in a declining trend recently [16]. The coarse aggregates used in this study combined 55% 20mm particle size and 45% 15mm particle size, ensuring a well-graded mix that enhances the concrete's strength and durability. Additionally, as implemented in this research, the precise grading of coarse aggregates was crucial for achieving the desired workability and compressive strength in concrete mixes [17]. Figures 2a and 2b show the pictorial representations and the particle size distribution graphs for the raw materials and, respectively.

Chemical admixtures

Superplasticizers (SP)

In this study, a polycarboxylate ether (PCE) superplasticizer (SP) was incorporated into the concretes to decrease the amount of mixing water required when RHS is added and to enhance their workability. PCE is a modern generation SP developed in the 1990s, featuring a comb-like molecular structure, comprising a main chain with carboxylic acid groups and side chains of polyethylene oxide (PEO) units [18]. The carboxylic acid groups provide electrostatic repulsion, while the PEO units create steric hindrance. This combination of electrostatic repulsion and steric hindrance enhances the dispersion of cement and RHS particles, resulting in improved flowability and reduced water content in the concrete [19]. In its liquid form, PCE had a density of 1050 kg/m³ and contains 20% active ingredient in an aqueous solution.

Air entraining admixture (AE)

Air-entraining admixtures are substances added to concrete to create a system of microscopic air bubbles within the mix. These bubbles significantly enhance the concrete's durability, especially in freeze-thaw conditions, by providing space for water to expand when it freezes, thus preventing cracking [20]. This study used an air-entraining admixture based on vinsol resin, an admixture commonly used by ready-mix concrete producers in Japan.

Air reducing admixture (AR)

Air Air-reducing admixtures (AR) are employed in concrete to decrease the amount of entrained air in the mix. These admixtures are especially beneficial when high-density concrete is needed, as they help lower air content, which can otherwise reduce the concrete's strength. ARs contain potent defoaming agents that counteract air in the concrete mix, including air introduced by modern superplasticizers and SCMs.

METHODOLOGIES

Low-Carbon Concrete (RHS-Modified) Sample Preparation and Mix Design

Fine and coarse aggregates were prepared a few days in advance to ensure strict moisture adjustment, which was essential for the workability of the concrete and allowed for better control during mixing. The consistency of the particle sizes was also checked to achieve a consistent mix, which was vital for the strength and durability of the concrete. To obtain the uniform distribution of the PCE SP in the concrete, the water reducer was first mixed with water and stirred. (NOTE: The water part of the PCE was included in the PCE weight and neglected in the definition of the w/c and w/b ratios for all combinations.) At the same time, the fine aggregates, cement and RHS were added into the concrete mixer and mixed according to the mixer operation time specifications. This was followed by adding the coarse aggregates and mixing to a consistent concrete mix based on the timings stipulated in the mixture manual, together with a physical examination.

The mixing and sample preparation followed the guidelines set by Japan Industrial Standards (JIS) JIS A 1132:2020 and JIS A 1138:2020. From the concrete mixer, the LCC concrete was tested for fresh properties, including slump, air content and temperature before sample preparation. Finally, the fresh LCC concrete was cast into the cylindrical molds (100 mm in diameter and 200 mm in height) for the compressive strength test and 100mm by 100 mm by 400mm molds for flexural strength tests for each concrete mix proportion. After 24 h, the LCC samples were capped, de-moulded, and cured in microbubble water

under a room temperature of 20 °C and relative humidity of 55 ± 5% for another 6 days and 27 days before testing. The design mixing proportions of the concrete are shown in Table 2.

Testing Methods

Fresh concrete properties tests

The slump test was performed to evaluate the workability and consistency of the concrete mix, following the guidelines of JIS A 1101:2020. This test involved filling a slump cone (100 mm: top end, 200 mm: bottom end, 300 mm: height and thickness: at least 5 mm) with concrete, lifting the cone, and measuring the resulting subsidence. The air content test was conducted using the pressure method as specified in JIS A 1128:2019 to determine the volume of entrapped air, which is vital for evaluating the concrete's durability. Additionally, the temperature of the concrete was measured immediately after mixing with a calibrated thermometer to confirm it fell within the optimal range for curing and performance. These tests provided critical information on the concrete's fresh state characteristics, ensuring compliance with the standards for its intended use.

Table 1 Chemical composition of RHS and OPC (wt%).

Item [a]	SiO_2	Al_2O_3	Fe_2O_3	MgO	CaO	SO_3	Na_2O	K_2O	Total	LOI [b]
RHS	93.30	0.04	0.07	0.11	0.83	0.31	0.03	4.49	99.18	4-6
OPC	20.80	4.82	3.33	3.30	64.74	1.86	-	0.90	99.75	2-4

[a] RHS and OPC represent Rice Husk Silica and Ordinary Portland Cement, respectively.
[b] Loss on Ignition

Table 2 Concrete design mixing proportions.

Category	Specimen CODE	Coarse aggregates (kg/m³)		Fine Aggregates (kg/m³)		Cement (kg/m³)	RHS (kg/m³)	w/c & w/b (kg/m³)	PCE SP (kg/m³)	Air entrant AE (*l*/m³)	Air reducer AR (*l*/m³)
		20mm	15mm	Crushed rock	River sand						
Group 1: Rice Husk Silica content: 0%, 5%, 10%, 15%, 20%	LCC_RHS0_{175}	519	425	592	254	292	0	175	0.88	0.575	0.15
	LCC_RHS5_{175}	519	425	583	250	277	15		2.92	0.575	
	LCC_RHS10_{175}	519	425	574	246	263	29		4.99	0.575	
	LCC_RHS15_{175}	519	425	564	242	248	44		7.45	1.15	
	LCC_RHS20_{175}	519	425	553	237	234	58		18.40	1.15	
Group 2: Rice Husk Silica content: 5%	LCC_RHS5_{175}	519	425	583	250	277	15	175	2.92	0.288	0.225
	LCC_RHS5_{180}	519	425	575	247			180			
	LCC_RHS5_{185}	519	425	564	242			185			
	LCC_RHS5_{190}	519	425	556	238			190			
Group 3: Rice Husk Silica content: 10%	LCC_RHS10_{175}	519	425	574	246	263	29	175	7.01	0.575	0.15
	LCC_RHS10_{185}	519	425	554	238			185			
	LCC_RHS10_{195}	519	425	537	230			195			
	LCC_RHS10_{205}	519	425	518	222			205			

NOTE: Cement contents are reduced by 0%, 5%, 10%, 15% and 20% and replaced with an equal amount of RHS.

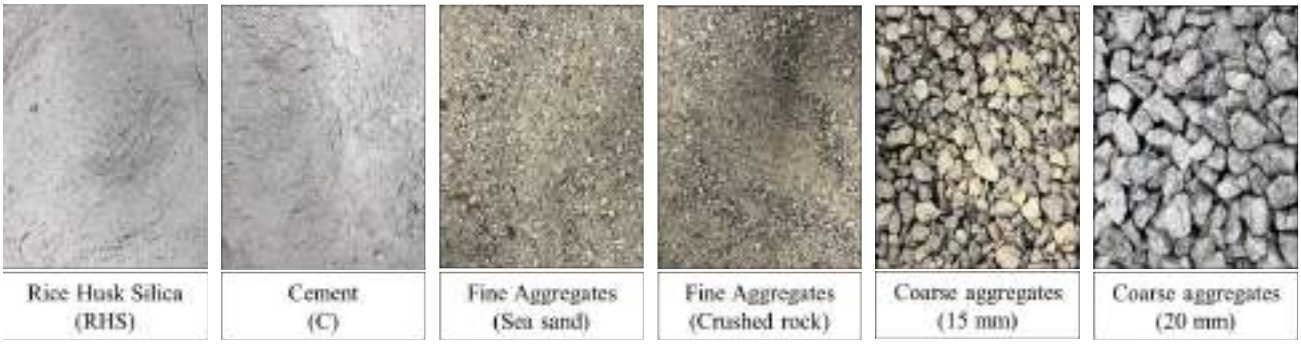

Figure 2a Raw materials for concrete preparation.

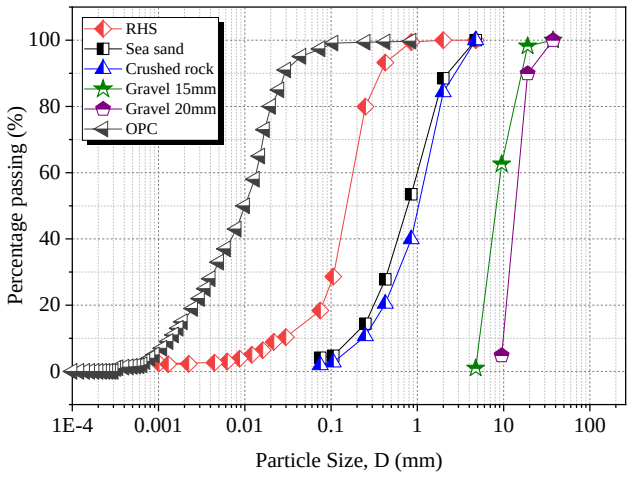

Figure 2b Particle size distribution graphs

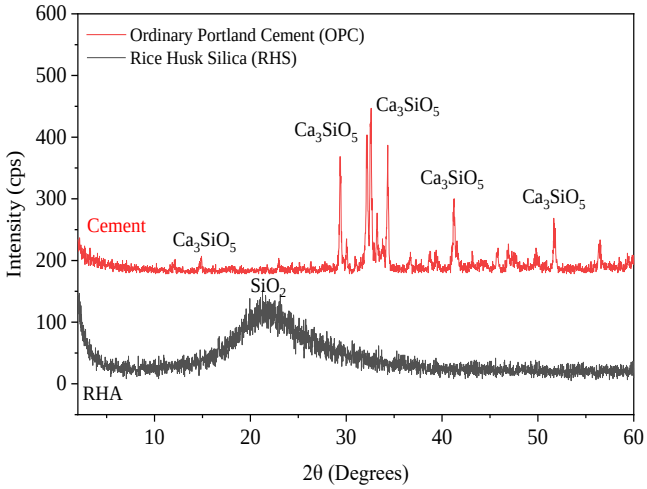

Figure 2c XRD patterns for RHS and OPC

Compressive strength test

The compressive strengths of the samples were measured at 7 and 28. According to JIS A 1108:2018, three cylindrical specimens (100 mm diameter x 200 mm height) for each concrete mix design were loaded using a universal testing machine (load application rate: 0.6±0.4 N/mm^2 per second) on each test day, and the average of the three results was used to determine the ultimate compressive strength.

Flexural strength test

The flexural strength test was carried out on concrete beams with dimensions of 100 × 100 × 400 mm, as indicated by JIS A 1106:2018. The testing was carried out after 28 days of curing. Three beams were tested for every mix design and the average of the three results was used to determine the ultimate flexural strength.

Microstructural analysis test

Microstructure analyses of concrete specimens were done by scanning electron microscope (JCM-7000 Benchtop Scanning Electron Microscope). The primary focus of the SEM imagery was to assess the concrete's microstructure, specifically examining the development of pores, the formation and propagation of cracks, and the characteristics of the cemented matrix. Such features are critical indicators of the material's durability and performance over time. Representative concrete samples were carefully prepared by mounting them onto brass stubs using carbon tape to ensure secure placement. The samples were then gold-coated to enhance electron conductivity, allowing for high-resolution imaging. The resulting SEM images provided a detailed view of the concrete's internal structure, revealing not only the size and distribution of pores and cracks but also the overall integrity of the cemented matrix.

RESULTS AND DISCUSSIONS

Fresh Concrete Properties and Admixture Relationship

To achieve a target slump ranging between 11.5 cm and 13.5 cm (averaging 12 cm), with water-to-cement (w/c) and water-to-binder (w/b) ratios maintained at 60%, and the air content of concrete expected to lie between 4% and 4.6%, the amounts of chemical admixtures were adjusted as shown in Figure 3a. It was observed that the Polycarboxylate Ether Superplasticizer (PCE SP) content increased with the increase in RHS content as this was necessary to maintain the slump, w/c, w/b, and air content within the desired range. From Figure 3a, it was evident that to achieve the same workability and keep the PCE SP dosage within a feasible and applicable range, the optimal rice husk silica dosage lied between 10% and 15%. This range was also supported by the corresponding strength values discussed in the next sections. On the other hand, air-entraining admixtures were kept almost constant, with a slight increase observed for 15% and 20% rice husk silica contents to help maintain the desired air content in the concrete mix, which is crucial for durability.

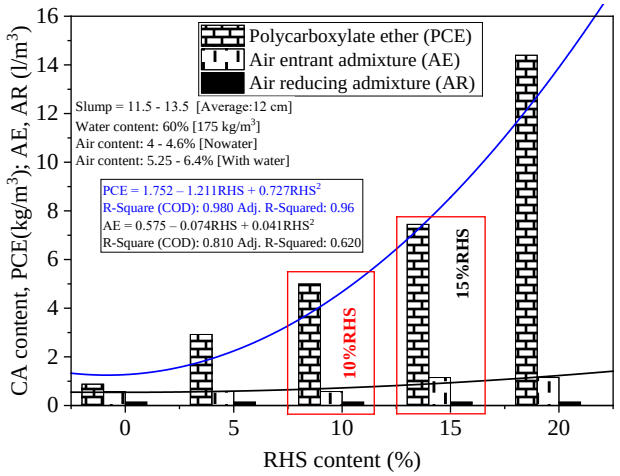

Figure 3a Relationship between the chemical admixture demand with RHS dosage.

In Figure 3b, based on the control w/c and w/b ratios, the slump value was maintained at an average of 12 cm. However, at 20% (LCC_RHS20$_{175}$) rice husk silica, the slump value was slightly higher. This increased flowability at higher rice husk silica content can be explained by the fact that rice husk silica demands more superplasticiser to disperse the particles effectively and maintain workability

[21]. Additionally, the concrete temperature increased slightly with increasing rice husk silica content due to the exothermic reactions associated with the hydration of cement and the pozzolanic reaction process from the interaction between the rice husk silica and the cementitious materials.

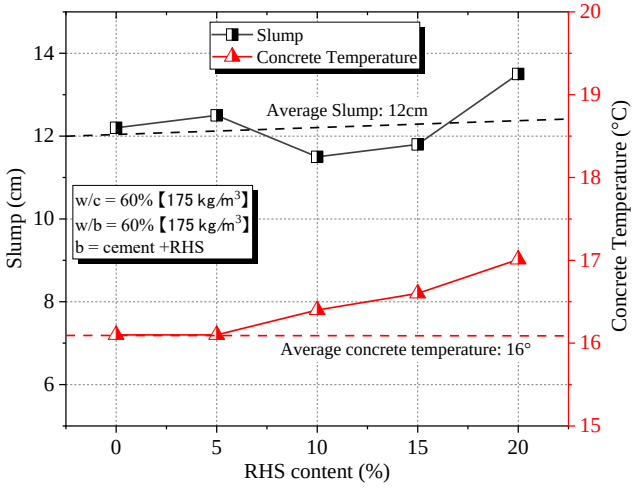

Figure 3b Variation in workability with RSH dosage.

The presence of rice husk silica accelerated the hydration process, leading to a higher release of heat [22]. This phenomenon is consistent with findings from other studies where mineral admixtures like silica fume and fly ash have been shown to influence the heat of hydration in concrete [23].

Compressive Strength

The results in this section showed how varying levels of RHS as a partial cement replacement influenced the compressive strength with reference to the PCE SP dosage required for equal workability in the concrete mixes. The PCE SP trend (0.88 kg/m³ for 0% RHS, 2.92 kg/m³ for 5% RHS, 4.99 kg/m³ for 10% RHS, 7.45 kg/m³ for 15% RHS, and 18.40 kg/m³ for 20% RHS - Figure 3a), indicated that higher RHS contents demanded more PCE SP to maintain workable consistency, as RHS particles increase the mix's surface area and internal porosity, raising water demand for flowability. By using PCE SP instead of additional water, the mix maintained its desired workability without compromising the concrete's compressive strength due to dilution.

The compressive strength results presented in Figure 4 aligned with the expected effects of pozzolanic materials. Initial testing at 7 days showed minimal strength variation across samples with 0% (LCC_RHS0_{175}) to 10% RHS (LCC_RHS10_{175}), suggesting that early-stage compressive strength was less affected by RHS up to these levels. This limited difference was likely because RHS, a pozzolan, contributed to strength through slower secondary hydration and pozzolanic reactions, which relied on the gradual availability of calcium hydroxide ($Ca(OH)_2$) from cement hydration [24]. Unlike cement's primary hydration, pozzolanic materials like RHS needed extended curing to participate fully in these strength-enhancing reactions. As RHS content increased to 15% (LCC_RHS15_{175}) and 20% (LCC_RHS20_{175}), the 7-day compressive strength decreased notably, with the reduction attributed to the dilution effect, delayed early production of C-A-S-H and the reduced cement proportion, which is the main compound crucial for initial strength [25]. High pozzolan content also meant that less cementitious material was immediately available for primary hydration, which is necessary for early strength development.

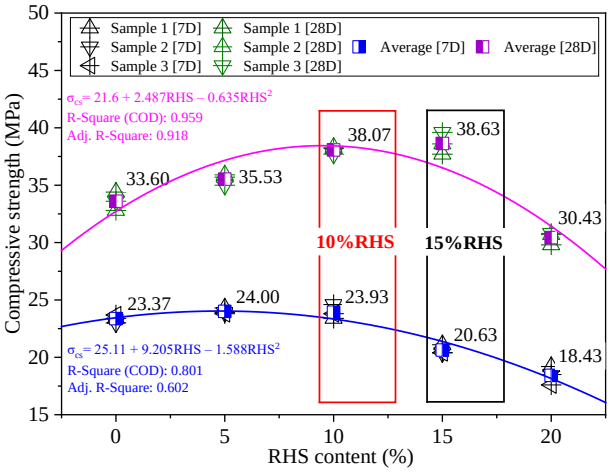

Figure 4 Variations on the compressive strength values with various design formulations and curing periods.

After 28 days, the concrete achieved approximately 99% of its compressive strength across all mix designs, indicating that the pozzolanic activity of RHS had largely matured by this stage. This pattern was in line with typical pozzolanic reactions, which reach substantial completion between 28 and 56 days, contributing to significant compressive strength gains in later curing stages. An optimal RHS replacement level emerged between 10% (LCC_RHS10_{175}) and 15% (LCC_RHS15_{175}), where the pozzolanic reactions contributed enough secondary C-A-S-H formation to enhance compressive strength without overly diluting early hydration kinetics.

At this level, the PCE SP dosage (4.99 kg/m³ at 10% RHS and 7.45 kg/m³ at 15% RHS) balanced workability, promoting better particle dispersion and maintaining mix consistency without compromising strength. Beyond this optimal range, however, at 20% RHS (LCC_RHS20_{175}), compressive strength decreases despite a high PCE SP dosage (18.40 kg/m³) due to insufficient $Ca(OH)_2$ availability for pozzolanic reactions and a lack of cementitious material, leaving unreacted pozzolan particles and creating a weaker matrix. Although the increased PCE SP maintains workability, it cannot compensate for the reduction in reactive materials, ultimately limiting the potential developments in compressive strength.

Moreover, to generalize the findings, curve-fitting equations were derived to model the compressive strength development across different RHS contents, ranging from 0% to 20%. These equations serve as predictive tools for estimating the compressive strength of LCC concrete mixes with varying RHS proportions. The predictive capability of these models allows for accurate extrapolation within the tested range.

Flexural Strength

Figure 5 illustrates the flexural strength of RHS-modified concrete with varying percentages of RHS content as a cement replacement at 28 days. The trend followed a parabolic pattern, where flexural strength initially increases with RHS up to an optimal level of around 10-15% before declining at 20% RHS. Analysis of this trend in light of the PCE SP admixture's role, as previously discussed, showed that the increased PCE SP admixture amounts at higher RHS levels (2.92 kg/m³ for 5% RHS, 4.99 kg/m³ for 10%, and 7.45 kg/m³ for 15%) also aided in enhancing the flexural strength by improving the dispersion of RHS particles within the mix, ensuring better bonding and a more cohesive matrix.

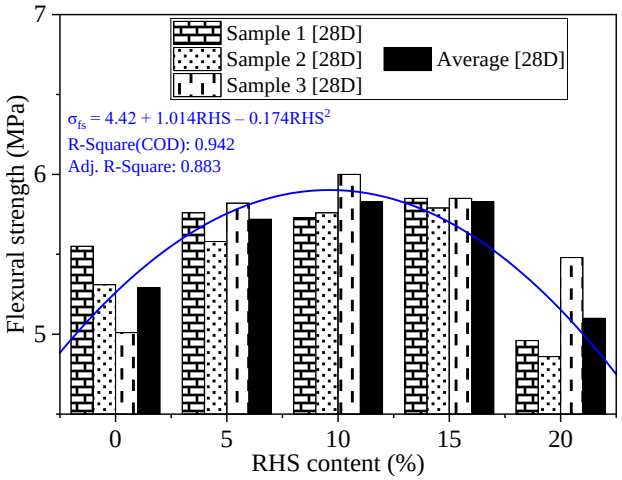

Figure 5 Variations on the flexural strength values with various design formulations and curing periods.

This enhanced dispersion reduced the risk of weak spots and allowed the RHS particles to better engage in pozzolanic reactions, reinforcing the concrete's structure. The peak in flexural strength at approximately 10-15% RHS indicated an optimal balance where RHS content was sufficient, and the PCE SP dosage (around 4.99 to 7.45 kg/m³ at 15%) helped maintain a workable consistency while allowing RHS to contribute positively to the matrix's strength. This dosage appears to be effective in supporting workability and cohesion, facilitating the integration of RHS into the concrete structure without significant trade-offs in early hydration.

The parabolic trend in flexural strength (increasing, peaking, and then decreasing) reflects the combined impact of optimal pozzolanic reaction conditions and the limits of cement replacement. However, at higher replacement levels (20% RHS), the decrease in primary hydration products and the lack of sufficient $Ca(OH)_2$ limit RHS's contribution to strength, resulting in flexural strength reduction despite the increased PCE SP.

Microstructural Evolution of RHS-Modified Concrete

Scanning electron microscopy (SEM) analysis

This study employed Scanning Electron Microscopy (SEM) to investigate the influence of rice husk silica (RHS) on the microstructure of RHS-modified concrete at different replacement levels (0%, 5%, 10%, 15%, and 20%) using three distinct magnifications (×100, ×500, and ×1000) as shown in Figures 6-10.

Observations at these magnifications shed light on changes in pore structure, interfacial transition zones (ITZ) and the concrete matrix density. As the magnification increased, finer details of crack formation, crack filling, and secondary hydration product formation became apparent, providing a comprehensive picture of how RHS affects concrete densification and self-healing potential, as discussed below.

Control concrete (0% RHS)

The SEM images for the 0%RHS-modified concrete microstructure at different magnifications is shown in Figure 6. At the lowest magnification (×100), the control concrete showed a comparatively coarse and porous structure with voids and pores evident and the ITZ between the aggregates and cement paste appearing weak or loosely bonded. This indicated that the control mix lacked the refined microstructure typically associated with pozzolanic additives. At a medium magnification (x500), the presence of pronounced post-hydration crystals became clear, often manifesting as large plate-like or hexagonal formations and occupying spaces where more advanced hydration products, such as C-S-H, could otherwise have developed. At the highest magnification (x1000), microcracks were distinctly observed with minimal signs of crack-filling. The ITZ remained a weak link in the microstructure, indicating limited C-S-H formation around the aggregate surfaces. These observations correlate with minimum strength development in the control sample in this study.

5% RHS-modified concrete

Introducing 5% RHS led to a denser matrix compared to the control, as shown in Figure 7. The overall pore size distribution appeared more uniform, and fewer large voids were evident. Early evidence of refined ITZ was detected, as the transition zones around aggregates seemed slightly more cohesive. At ×500, partial filling of some pores was observed due to the accumulation of pozzolanic compounds (additional C-S-H gel) from pozzolanic reactions between amorphous silica (RHS) and $Ca(OH)_2$ from cement hydration.

Moreover, under higher magnification (x1000), a few pronounced microcracks in the 5% RHS sample were observed in the denser microstructure, suggesting that while the incorporation of RHS effectively enhanced matrix compactness, it also introduced localized tensile stresses. These stresses appeared to promote microcrack initiation at weak interfacial zones, which could serve as potential sites for crack propagation under aggressive loading conditions. Nonetheless, the overall improved densification and bonding between the aggregate and cementitious phases implied that these microcracks remain isolated and do not significantly compromise the structural integrity of the RHS-modified concrete. This observation highlights the need for optimizing the mix design and curing process to balance the benefits of a denser matrix against the potential for micro-level defects.

10% RHS-modified concrete

At this level of replacement, the concrete exhibited a significantly more compact structure as illustrated in Figure 8. Large pores were less frequent, and the ITZ looked denser and more uniform. The overall appearance suggested a well-consolidated matrix, reflecting a marked improvement over both the 0% RHS and the 5% RHS samples. Closer assessment at x500 revealed a more advanced pozzolanic reaction with large $Ca(OH)_2$ crystals mostly replaced or reduced, giving way to extensive C-S-H gel formation. The resulting C-S-H gel contributed to the overall reduction in porosity and enhanced the bonding between aggregates and the RHS-cement paste. At the highest magnification (x1000), fewer microcracks were observed, and where cracks did appear, they tended to be finer and narrower, often sealed by secondary hydration products. The ITZ was highly refined, showing minimal gaps, confirming that a 10% RHS replacement significantly enhances both the microstructural integrity and potential self-healing characteristics of the concrete.

15% RHS-modified concrete

A further improvement in matrix compactness was visible at 15% RHS, as indicated in Figure 9. At x100, voids and large pores were quite sparse, and the ITZ appeared consistently tight around aggregate surfaces. This improvement pointed toward a higher degree of pozzolanic reactivity, consolidating the concrete structure more effectively. Additionally, the SEM images at ×500 magnification highlighted abundant C-S-H gel networks filling and bridging gaps within the matrix, resulting in a microstructure that can better distribute loads, hence contributing to higher compressive and flexural strengths. At ×1000, very fine microcracks are visible, indicating an enhanced stable matrix. Nevertheless, in certain regions, a hint of silica saturation was detected since the excess silica did not fully react during pozzolanic reactions but instead began to cluster. Although this phenomenon was not so detrimental in this sample due to the dispersion effect of the PCE SP, this clustering could foreshadow diminishing returns if the RHS replacement level was pushed higher.

20% RHS-modified concrete

At the macro-scale (relative to SEM x100), the 20% RHS concrete still showed a generally dense matrix (Figure 10). However, isolated zones of porosity and microcracking became more noticeable, suggesting that excessive silica introduced localized stress concentrations. At x500 medium magnification, the matrix continued to display well-developed C-S-H gel in many regions, but some evidences of oversaturation were also observed as pockets of unreacted silica or loosely bound particles appeared. On the other hand, while the ITZ generally remained strong, the distribution of hydration products was somewhat inconsistent compared to the 10% and 15% mixes. At the finest scale of x1000, pronounced microcracks and extensive pore networks were visible, potentially due to localized stresses around excess silica. Moreover, the overall balance between silica addition and beneficial pozzolanic reaction began to decline, indicating that 20% replacement risked slight reductions in long-term durability and toughness relative to the 5–15% RHS replacement range.

Cost Analysis per m^3 and CO_2 Emission Projections of RHS Modified Concrete

In this section, the significance of RHS-Modified Concrete is presented based on (1) Lifecycle cost analysis considering enhanced strength, (2) Environmental benefits and reduced carbon footprint, (3) Consideration of regional variations in cost, and (4) Strategic implications for civil engineering and construction. The analytical data presented in Tables 3, 4 and 5 provided a comprehensive analysis of the cost per $1m^3$ and CO_2 emission projections per $1m^3$ of RHS-modified concrete. The costs and CO_2 analysis procedures were based on the projections by the Japan Society of Civil Engineers: Guidelines for Environmental Performance Assessment of Concrete Structures, as shown in Table 3.

Table 3 Cost evaluation JSCE guidelines.

Materials	Cost/kg	Currency	CO_2 emission/kg	Units
Cement	12.00	JPY (円)	0.746	kg
Rice Husk Silica (RHS)	500.00	JPY (円)	-	kg
Fine Aggregates	3.40	JPY (円)	0.0037	kg
Coarse Aggregates	3.00	JPY (円)	0.0029	kg
Water	0.30	JPY (円)	0.00019	kg
Water reducing agent	400.00	JPY (円)	-	kg
Air-entraining admixture	555.56	JPY (円)	-	kg
Air-reducing admixture	1111.11	JPY (円)	-	kg

NOTE: [Source: Japan Society of Civil Engineers: Guidelines for Environmental Performance Assessment of Concrete Structures (Draft) (November 2005) pp.69]

Lifecycle cost analysis considering enhanced strength

One of the most critical factors in the adoption of RHS-modified concrete is its enhanced strength compared to normal concrete, as evidenced in this study. While the upfront production cost per $1m^3$ (Table 4) is mainly based on current RHS manufacturing cost structures in Japan, the long-term performance benefits must be considered in conformity with the strength gains that were well represented in the results and discussions section. At first glance, the production costs of this material appeared relatively high compared to conventional concrete.

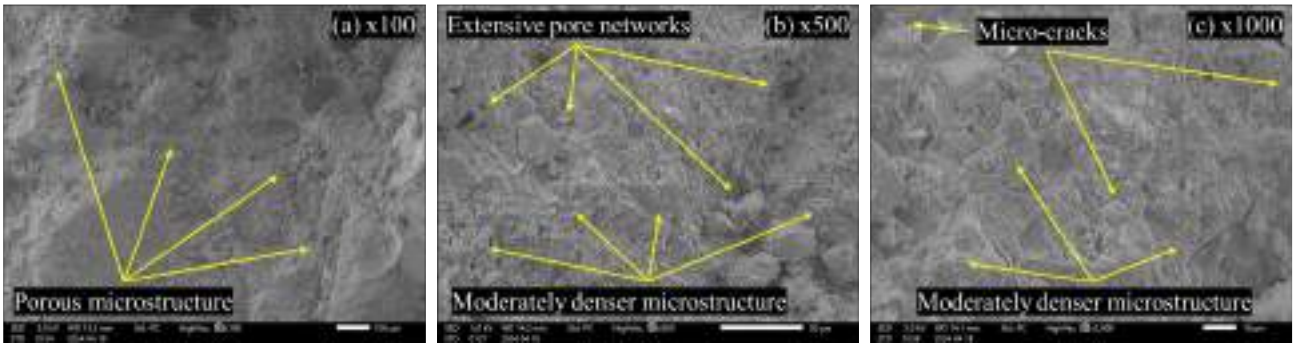

Figure 6 SEM microstructure of base concrete (0%RHS) at different magnifications: (a) ×100, (b) ×500, (c) ×1000

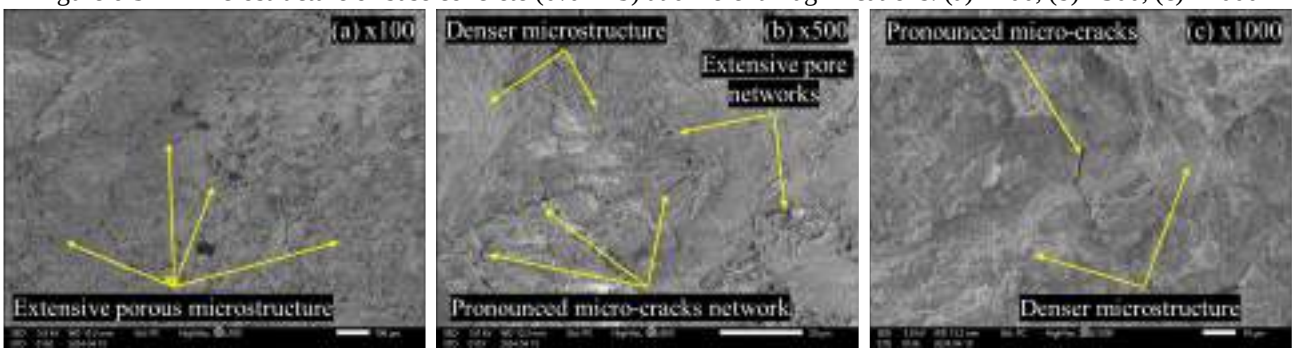

Figure 7 SEM microstructure of 5% RHS concrete at different magnifications: (a) ×100, (b) ×500, (c) ×1000

Figure 8 SEM microstructure of 10% RHS concrete at different magnifications: (a) ×100, (b) ×500, (c) ×1000

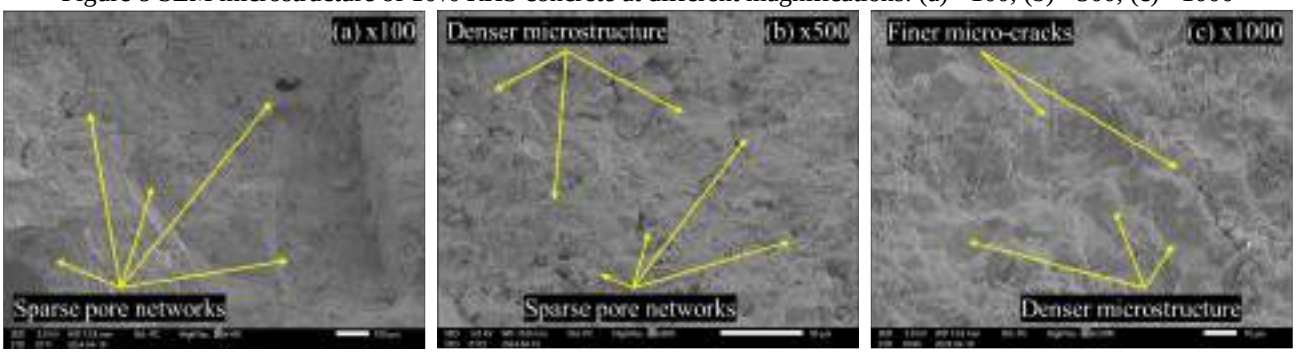

Figure 9 SEM microstructure of 15% RHS concrete at different magnifications (a) ×100, (b) ×500, (c) ×1000

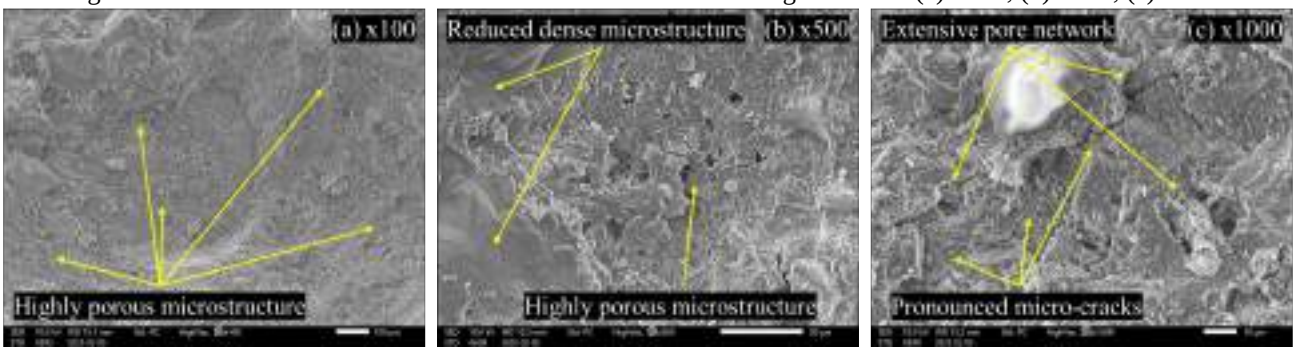

Figure 10 SEM microstructure of 20% RHS concrete at different magnifications (a) ×100, (b) ×500, (c) ×1000

Table 4 Cost Analysis per m3 of RHS modified concrete.

Materials	Currency	Normal concrete	5%RHS Modified Concrete	10%RHS Modified Concrete	15%RHS Modified Concrete	20%RHS Modified Concrete
Cement	JPY (円)	3504.00	3328.80	3153.60	2978.40	2803.20
Rice Husk Silica (RHS)	JPY (円)	-	7300.00	14600.00	21900.00	29200.00
Fine Aggregates	JPY (円)	2875.41	2830.57	2785.71	2740.86	2655.48
Coarse Aggregates	JPY (円)	2783.30	2783.30	2783.30	2783.30	2783.30
Water	JPY (円)	52.56	52.56	52.56	52.56	52.56
Water reducing agent	JPY (円)	350.40	1168.00	1997.28	2978.40	2978.40
Air-entraining admixture	JPY (円)	319.44	319.44	319.44	638.89	638.88
Air-reducing admixture	JPY (円)	166.67	166.67	166.67	166.67	166.67
TOTAL COST/1m^3	JPY (円)	10051.79	17949.34	25858.57	34239.08	41143.83
% INCREASE /1m^3	JPY (円)	-	7897.55	15806.78	24187.29	31092.04

NOTE: The costs presented above are derived from current production costs in Japan. Actual prices may differ significantly based on the production location and the prevailing local raw material costs.

Table 5 CO_2 Emission Projections of RHS modified concrete.

Materials	Units	Normal concrete	5%RHS Modified Concrete	10%RHS Modified Concrete	15%RHS Modified Concrete	20%RHS Modified Concrete
Cement + Admixtures	kg	217.83	206.94	196.05	185.16	174.27
Rice Husk Silica (RHS)	kg	-	0.00	0.00	0.00	0.00
Fine Aggregates	kg	3.13	3.08	3.03	2.98	2.93
Coarse Aggregates	kg	2.69	2.69	2.69	2.69	2.69
Water	kg	0.03	0.03	0.03	0.03	0.03
TOTAL EMISSION/1m^3	kg	223.69	212.75	201.80	190.86	179.92
% DECREASE /1m^3	%	-	4.89	9.78	14.67	19.56

However, a detailed examination of the long-term benefits revealed that RHS-modified concrete could offer significant advantages considering maintenance expenses (strength factor) and durability factors (strength factor). Enhanced strength means that structures built with RHS-modified concrete are likely to experience fewer instances of cracking, spalling, and other degradation phenomena. This can directly translate into reduced maintenance interventions over the life of the structure. Rather than incurring frequent repair costs, which often involve not only direct material and labor expenses but also indirect costs such as downtime and loss of functionality, engineers and project managers can anticipate a more predictable and manageable maintenance schedule. Moreover, although the cost analyses are derived from Japanese production figures, which may be higher due to regional raw material costs and the specifics of local production practices, over time, these savings can offset the higher initial costs, making RHS-modified concrete a cost-effective alternative.

Environmental benefits and reduced carbon footprint

Table 5 details CO_2 emission projections associated with the production and use of RHS-modified concrete. It was noteworthy that the reduction in carbon footprint was directly proportional to the amount of RHS added to the concrete mix. It is important to point out that in an era when environmental sustainability is not only an ethical imperative but also increasingly a regulatory requirement, the ability to lower carbon emissions during construction is a major advantage. For this reason, RHS-modified concrete is engineered to reduce the overall environmental carbon load, which is achieved through optimized production processes and the use of recycled or less carbon-intensive materials. The long-term benefits include compliance with emerging environmental standards and potential cost savings from carbon credit schemes or reduced environmental taxes. Furthermore, a reduced carbon footprint enhances the public perception and marketability of projects, potentially providing a competitive edge in bids and tenders that prioritize sustainable construction practices.

Consideration of regional variations in cost

It is essential to note that the cost figures presented are specific to Japan, reflecting the local production costs and raw material market conditions. In regions where raw materials are more abundant or production processes are optimized differently, the initial cost differential between RHS-modified concrete and conventional concrete may be less pronounced. Local economies of scale, reduced

transportation costs, or innovations in production methods could lead to further reductions in the cost per cubic meter. This variability underscores the importance of contextualizing cost analysis within the specific economic and geographic setting of any construction project. Decision-makers are encouraged to conduct localized studies to understand the exact financial implications; however, the general trends observed, namely, long-term savings through maintenance reduction and environmental benefits, remain consistent.

Strategic implications for civil engineering and construction

From a civil engineering perspective, the adoption of RHS-modified concrete can be seen as a strategic investment in the longevity and resilience of infrastructure. The data indicates that when assessing the overall lifecycle costs of a structure, it is crucial to move beyond the simplistic comparison of initial material costs. Instead, engineers and project managers should adopt a holistic approach that incorporates both direct costs (such as material production and installation) and indirect benefits (such as reduced maintenance, extended service life, and environmental compliance). For instance, while conventional concrete may offer lower upfront expenses, the cumulative costs associated with repairs, replacements, and potential disruptions to service can far outweigh the initial savings. Conversely, RHS-modified concrete, by virtue of its robust performance under various environmental stresses, presents an opportunity to achieve significant long-term savings.

Furthermore, the superior performance of RHS-modified concrete can influence design decisions. With increased confidence in the material's long-term performance, engineers may design structures with optimized dimensions and reduced safety margins that are typically mandated for conventional concrete. This can lead to more efficient use of materials and further cost reductions. Additionally, the environmental credentials of RHS-modified concrete align with the broader global shift towards sustainable construction practices. As regulatory frameworks tighten and sustainability criteria become a prerequisite for public and private funding, the use of low-carbon materials such as RHS-modified concrete may soon evolve from an innovative option to a standard requirement.

Balancing initial costs with future savings

A balanced evaluation of Tables 3, 4 and 5 reveals that although the current production costs of RHS-modified concrete are influenced by factors such as raw material availability and local production economics, the long-term cost benefits are compelling. The upfront investment, when viewed in isolation, does not capture the broader picture. Instead, a comprehensive lifecycle cost analysis demonstrates that the benefits, ranging from reduced maintenance and operational costs to environmental advantages, are likely to result in overall lower expenditures over the life of the structure. This integrated perspective is critical in a world where sustainability and cost-efficiency are becoming increasingly intertwined. The lower maintenance requirements and reduced environmental impact translate into both economic savings and enhanced social responsibility. For stakeholders in the construction industry, adopting RHS modified concrete is not just a matter of meeting regulatory or environmental standards; it is a forward-thinking decision that aligns with the long-term economic interests of infrastructure projects.

CONCLUSIONS

This study investigated the synergistic effects of incorporating rice husk silica (RHS) as a partial cement replacement in low-carbon RHS-modified concrete, with a focus on achieving enhanced mechanical performance and sustainability. The experimental work evaluated compressive and flexural strength developments, and microstructural improvements by optimizing mix design parameters, including water-to-binder ratios and chemical admixture. Additionally, a detailed cost and CO_2 emissions analysis was conducted alongside strength and durability evaluations. The major conclusions drawn from the study are as follows.

Sustainability, CO_2 reduction, and environmental impact: The results indicate that RHS-modified concrete significantly reduces CO_2 emissions by up to 19.56% compared to conventional cement-based concrete. This reduction aligns with global sustainability goals, supporting the circular economy by utilizing agricultural waste as a valuable construction material. Furthermore, microstructural analysis (SEM) confirms that RHS actively participates in the pozzolanic reaction, contributing to improved long-term performance and reduced environmental impact.

Mechanical performance and structural integrity: Optimal RHS replacement (10–15%) led to compressive and flexural strength enhancements of 21.21% and 40%, respectively. The pozzolanic reaction between RHS and cement produced a denser, well-cemented matrix, significantly improving bonding and durability.

Cost implications and economic feasibility: Despite its environmental benefits, the study revealed that the cost per cubic meter of RHS-modified concrete increased by 90.65% to 187.98% compared to conventional concrete. The additional costs stem from processing RHS, optimizing mix proportions, and adjusting chemical admixture dosages. These findings highlight the need for further economic optimization before large-scale industry adoption.

Role of chemical admixtures and mix optimization: The study confirms that polycarboxylate ether (PCE) superplasticizers play a critical role in ensuring the workability of RHS-modified concrete. By fine-tuning the PCE dosage and maintaining strict control over the water-to-binder (w/b) ratios, the mix achieved the desired flowability while preserving structural integrity.

REFERENCES

[1] M.C. Juenger, R. Snellings, S.A. Bernal, Supplementary cementitious materials: New sources,

characterization, and performance insights, Cem. Concr. Res. Vol. 122, 2019, pp. 257–273. https://doi.org/10.1016/j.cemconres.2019.05.008

[2] R.M. Andrew, Global CO2 emissions from cement production, Earth System Science Data. Vol. 10 Issue 1, 2018. pp. 195–217. https://doi.org/10.5194/essd-10-195-2018

[3] C. Shi, B. Qu, J.L. Provis, Recent progress in low-carbon binders, Cem. Concr. Res., Vol. 122, 2019, pp. 227–250. https://doi.org/10.1016/j.cemconres.2019.05.009

[4] J.L. Provis, Alkali-activated materials, Cem. Concr. Res. Vol. 114, 2018, pp. 40–48. https://doi.org/10.1016/j.cemconres.2017.02.009

[5] L.K. Turner, F.G. Collins, Carbon dioxide equivalent (CO2-e) emissions: a comparison between geopolymer and OPC cement concrete, Constr. Build. Mater. Vol. 43, 2013, pp. 125–130. https://doi.org/10.1016/j.conbuildmat.2013.01.023

[6] S.H. Teh, T. Wiedmann, A. Castel, J. de Burgh, Hybrid life cycle assessment of greenhouse gas emissions from cement, concrete and geopolymer concrete in Australia, J. Clean. Prod. Vol. 152, 2017, pp. 312–320. https://doi.org/10.1016/j.jclepro.2017.03.122

[7] Owino, A.O. and Hossain, Z., The influence of basalt fiber filament length on shear strength development of chemically stabilized soils for ground improvement. Construction and Building Materials, Vol. 374, 2023, pp. 130930. https://doi.org/10.1016/j.conbuildmat.2023.130930

[8] Qureshi, L.A., Ali, B. and Ali, A., Combined effects of supplementary cementitious materials (silica fume, GGBS, fly ash and rice husk ash) and steel fiber on the hardened properties of recycled aggregate concrete. Construction and Building Materials, Vol. 263, 2020, pp. 120636. https://doi.org/10.1016/j.conbuildmat.2020.120636

[9] Fernando, A., Selvaranjan, K., Srikanth, G. and Gamage, J.C.P.H., Development of high strength recycled aggregate concrete-composite effects of fly ash, silica fume and rice husk ash as pozzolans. Materials and Structures, Vol. 55, Issue 7), 2022, pp.185. https://doi.org/10.1617/s11527-022-02026-3

[10] Wang, J., Xiao, J., Zhang, Z., Han, K., Hu, X. and Jiang, F., Action mechanism of rice husk ash and the effect on main performances of cement-based materials: A review. Construction and Building Materials, Vol. 288, 2021, pp. 123068. https://doi.org/10.1016/j.conbuildmat.2021.123068

[11] Vieira, A.P., Toledo Filho, R.D., Tavares, L.M. and Cordeiro, G.C., Effect of particle size, porous structure and content of rice husk ash on the hydration process and compressive strength evolution of concrete. Construction and Building Materials, Vol. 236, 2020, pp.117553. https://doi.org/10.1016/j.conbuildmat.2019.117553

[12] Rößler, C., Bui, D.D. and Ludwig, H.M., Mesoporous structure and pozzolanic reactivity of rice husk ash in cementitious system. Construction and Building Materials, Vol. 43, 2013, pp.208-216. https://doi.org/10.1016/j.conbuildmat.2013.02.004

[13] Tayeh, B.A., Alyousef, R., Alabduljabbar, H. and Alaskar, A., Recycling of rice husk waste for a sustainable concrete: a critical review. Journal of Cleaner Production, Vol. 312, 2021, pp. 127734. https://doi.org/10.1016/j.jclepro.2021.127734

[14] Vázquez-Rodríguez, F.J., Elizondo-Villareal, N., Verástegui, L.H., Arato Tovar, A.M., López-Perales, J.F., Contreras de León, J.E., Gómez-Rodríguez, C., Fernández-González, D., Verdeja, L.F., García-Quiñonez, L.V. and Rodríguez Castellanos, E.A., Effect of mineral aggregates and chemical admixtures as internal curing agents on the mechanical properties and durability of high-performance concrete. Materials, Vol. 13, Issue 9, 2020, pp. 2090. https://doi.org/10.3390/ma13092090

[15] Tong, S., Yuqi, Z. and Qiang, W., Recent advances in chemical admixtures for improving the workability of alkali-activated slag-based material systems. Construction and Building Materials, Vol. 272, 2021, pp. 121647. https://doi.org/10.1016/j.conbuildmat.2020.121647

[16] Koga, H., Katahira, H. and Shimata, A., The introduction of recycled-aggregate concrete specifications in Japan and the research into the freezing–thawing resistance of recycled-aggregate concrete. Journal of Material Cycles and Waste Management, Vol. 24, Issue 4, 2022, pp.1207-1215. https://doi.org/10.1007/s10163-022-01412-x

[17] Přikryl, R., Geomaterials as construction aggregates: a state-of-the-art. Bulletin of Engineering Geology and the Environment, Vol. 80, 2021, pp.8831-8845. https://doi.org/10.1007/s10064-021-02488-9

[18] Fang, X., Shi, Y., Yan, C., Wang, H. and Hui, J., Polycarboxylate ether superplasticizer with gradient structure: excellent dispersion capability and sulfate resistance. Colloid and Polymer Science, Vol. 300, Issue 10, 2022, pp.1113-1127. https://doi.org/10.1007/s00396-022-04994-y

[19] Fang, Y., Lin, Z., Yan, D., Zhang, X., Ma, X., Lai, J., Liu, Y., Chen, Z. and Wang, Z., Study on the effect of polycarboxylate ether molecular structure on slurry dispersion, adsorption, and microstructure. *Polymers*, Vol. *15* Issue 11, 2023, pp.2496. https://doi.org/10.3390/polym15112496

[20] Tunstall, L.E., Ley, M.T. and Scherer, G.W., Air entraining admixtures: Mechanisms, evaluations, and interactions. Cement and Concrete Research, Vol. 150, 2021, pp.106557. https://doi.org/10.1016/j.cemconres.2021.106557

[21] Singh, A., Singh, R.B. and Singh, B., Thixotropic evaluation of a highly-workable and a flowable concrete made with Rice Husk Ash. Journal of Building Engineering, Vol. 67, 2023, pp.105990. https://doi.org/10.1016/j.jobe.2023.105990

[22] Wang, J., Xiao, J., Zhang, Z., Han, K., Hu, X. and Jiang, F., Action mechanism of rice husk ash and the effect on main performances of cement-based materials: A review. Construction and Building Materials, Vol. 288, 2021, pp.123068. https://doi.org/10.1016/j.conbuildmat.2021.123068

[23] Zhang, T., Ma, B., Jiang, D., Jiang, Q. and Jin, Z., Comparative research on the effect of various mineral admixtures on the early hydration process of cement. Construction and Building Materials, Vol. 301, 2021, pp.124372. https://doi.org/10.1016/j.conbuildmat.2021.124372

[24] Wongkeo, W., Thongsanitgarn, P., Poon, C.S. and Chaipanich, A., Heat of hydration of cement pastes containing high-volume fly ash and silica fume. Journal of Thermal Analysis and Calorimetry, Vol. 138, 2019, pp.2065-2075. https://doi.org/10.1007/s10973-019-08641-7

[25] Kumar, D.P., Amit, S. and Chand, M.S.R., Influence of various nano-size materials on fresh and hardened state of fast setting high early strength concrete [FSHESC]: A state-of-the-art review. Construction and Building Materials, Vol. 277, 2021, pp.122299. https://doi.org/10.1016/j.conbuildmat.2021.122299

Copyright © Int. J. of GEOMATE All rights reserved, including making copies, unless permission is obtained from the copyright proprietors.

15th Int. Conf. on Geotechnique, Construction Materials & Environment,
Kyoto, Japan, 11-13 November 2025, ISBN 978-4-909106124 C3051

WATER ABSORPTION CHARACTERISTICS OF EPS-BASED LIGHTWEIGHT CONCRETE: EFFECTS OF FLY ASH COATING AND CEMENT REPLACEMENT

Andi Prasetiyo Wibowo[1]

[1]Department of Architecture, Faculty of Engineering, Universitas Atma Jaya Yogyakarta, Indonesia

ABSTRACT

This paper discusses the water absorption characteristics of lightweight concrete comprising expanded polystyrene (EPS) beads and previous works on property enhancement with fly ash addition. In this work, the fly ash will be used as partial cement replacement and as coating material for the EPS beads. The variables studied here will help in relating the water absorption features to the measured density and earlier compressive strength data of these concretes. Experimental results show that indeed, complicated interactions occur between the concrete components. Contrary to expectations, fly ash coating of EPS beads did not yield high improvement in water absorption resistance. On the other hand, the water absorption rate of the concrete mix in this study remained relatively constant at about 13%, which is within the acceptable parameters for concrete masonry units. This finding demonstrates the feasibility of using lightweight concrete containing EPS in construction, where the coating is inadequate. Partial replacement of cement by fly ash had a positive effect on reducing water absorption. This observation showed the double role that fly ash could play in concrete mixtures, influencing both the physical and chemical properties of the final product. Although these results show promise for EPS-based lightweight concrete with fly ash, they also bring to the fore the need for further optimization. While this study showed great promise in using EPS-based lightweight concrete with fly ash, future studies must be dedicated to the fine-tuning of concrete properties with respect to water absorption.

Keywords: Expanded polystyrene (EPS), Fly ash, Lightweight concrete, Water absorption

INTRODUCTION

Expanded polystyrene (EPS) is a lightweight material that can be used as an aggregate in concrete. It has low density, low thermal transmission coefficient, and negligible absorption capacity, making it suitable for various applications in the construction industry. EPS beads can be incorporated into concrete as a replacement for normal weight aggregate, either partially or fully. The use of EPS beads in concrete can improve its fresh and hardened properties, such as compressive strength, flexural strength, and thermal insulation. The particle distribution of the EPS beads and their percentage of replacement with natural aggregate can influence the strength and workability of the concrete. Additionally, the inclusion of waste plastic fibers in EPS-based concrete can further enhance its properties. EPS-based mortars also exhibit hydrophobicity and reduced water absorption compared to sand-based mortars.

Methods for incorporating expanded polystyrene (EPS) beads as aggregate in concrete include partial or full replacement of normal weight aggregate with EPS beads. The particle distribution of the aggregate can also influence the compressive strength of the concrete when EPS beads are used as a replacement. Numerous studies have been conducted on EPS in concrete, generating significant contributions to the field of science. By implementing a bibliometric analysis methodology, using the keywords "expanded polystyrene/EPS" and "concrete", 561 documents were examined. The results of this study help identify the specific topics associated with EPS in the concrete domain (Fig.1).

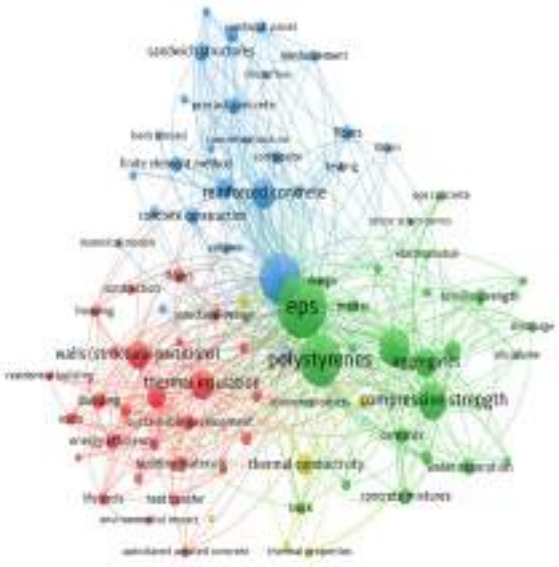

Fig.1 Research connection between expanded polystyrene (EPS) and other topics [1]

Initiated in 1974 and significantly expanded in 2017, research on EPS and concrete has primarily focused on mechanical properties and lightweight concrete production, but recent attention has broadened to include construction applications such as walls, insulating materials, reinforced concrete, and sandwich panels [1]. Nevertheless, there is little evidence of keywords related to water absorption in those results. The possibility of exploring this aspect in future research can be considered necessary.

Fly ash has a positive effect on lightweight EPS concrete, but its use is maximized when combined with other materials [2]. The optimum replacement level of fly ash for achieving high compressive strength is between 15% to 30%, and the highest bond strength is achieved using 10% to 15% fly ash [3]. Meanwhile, according to other studies, it has been suggested that the ideal ratio for substituting cement with fly ash in concrete is 30% [4]. The results demonstrated that substituting 30% of cement with fly ash led to enhanced strength, density, and durability characteristics in concrete. This result supported by other research by using the stoichiometric analysis and experimental trials showed that 30% cement replacement with fly ash resulted in improved strength, density, and durability properties of concrete [5]. Substituting sand with fly ash is an efficient method for decreasing the water absorption of concrete [6]. Consequently, the utilization of fly ash in the production of concrete enhances its properties, durability, and sustainability, particularly when employing a high-volume fly ash concrete mixture.

RESEARCH SIGNIFICANCE

This study explores the water absorption behavior of EPS-based lightweight concrete, a key factor affecting durability and long-term performance. By integrating fly ash both as a partial cement replacement and as a coating for EPS beads, the research addresses the challenge of high porosity and moisture uptake in lightweight concrete. The findings are expected to clarify the relationship between water absorption, density, and compressive strength, offering insights that support the development of sustainable, low-carbon, and resource-efficient building materials for the construction industry.

METHOD

A detailed description of the composition of the test specimens can be found in Table 1. Additionally, this mixture design has been implemented as part of the investigation [7,8].

Table 1 Mix Design

Specimen code	Cement (+PFA) (kg)	Water (kg)	Sand (kg)	Gravel (kg)	EPS Beads (kg)
NC	490	225	572	1063	-
PFAC	343 (+147)	225	572	1063	-
EPSC	490	225	572	-	7.25a
EPS-PFAC	343 (+147)	225	572	-	7.25a
MEPS-PFA	490	225	572	-	190b

[a] non-coated EPS beads; [b] coated EPS beads.

The water absorption testing for each specimen was performed following the ASTM C140-11 standard [9]. The water absorption test was performed after the concrete reached the age of 28 days. This is to ensure that the concrete is stable. This test requires the use of tools such as ovens and scales. The oven temperature for this testing procedure is set to 100-110 degrees Celsius. Each type of concrete is evaluated with three cube specimens' size 100x100mm. The test object was heated for 24 hours. Following that, the weighing process was carried out and documented. Then, the test object is submerged in water for 24 hours. After 24 hours of immersion in water, the specimens were dried for roughly 30 minutes - 1 hour to ensure the surface was dry before being weighed and recorded. The results of recording the dry and wet weights can be used to calculate the level of water absorption of concrete. Water absorption was calculated based on the formula:

$$W_A = \frac{W_S - W_D}{W_D} \times 100\% \quad (1)$$

W_A = water absorption (percent of dry weight)
W_D = dry weight of specimens (24 hours in oven 100-110ºC)
W_S = weight of air-dried specimens after immersed in water for 24 hours

RESULT

The results of water absorption for all specimens can be seen in Table 2 and Fig.2. The data demonstrates that PFAC exhibits a comparatively lower water absorption capacity (5.25%) in comparison to that of normal concrete (5.57%). This observation suggests that the incorporation of fly ash, despite its partial substitution for cement, may enhance the water resistance properties of concrete. In the case of concrete containing EPS beads, the graph illustrates that the water absorption values fall within the range of 11-13%.

Table 2 Density, Compressive Strength, and Water Absorption result

Specimens	Density (kg/m3)	Compressive Strength – Cube 28D (MPa)	Water Absorption (%)
NC	2365.97	45.31	5.57
PFAC	2330.10	40.42	5.25
EPSC	1272.97	11.23	13.26
EPS-PFAC	1280.30	9.33	11.78
MEPS-PFA	1431.10	13.96	13.07

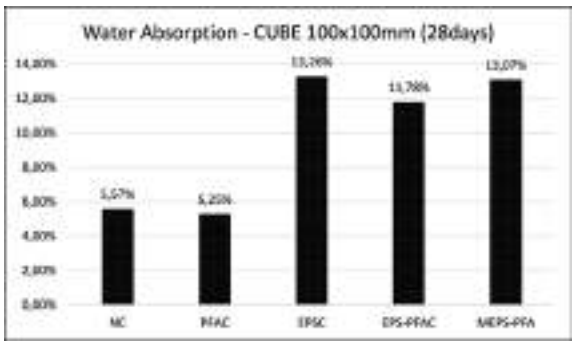

Fig.2 The graph of water absorption test result

Another factor contributing to the elevated water absorption rate of concrete employing EPS beads as aggregate is the presence of voids, potentially resulting from the heating procedure in the oven (Fig.3). The drying process of concrete specimens in the oven facilitates a reduction of the expanded polystyrene (EPS) beads embedded within the concrete. Although the oven temperature goes within the range of 100-110°C, which is theoretically lower than the melting point of polystyrene at 160°C [10], it seems that the softening point of EPS has been reached, which could cause the EPS beads to shrink.

Fig.3 Voids in concrete contain EPS beads after heat treatment at 105-110ºC

To validate this phenomenon of shrinkage, a simple experiment was conducted on MEPS and EPS beads. This involved subjecting the beads to an oven temperature of 105±5ºC for a duration of 24 hours. Despite a relatively stable sample weight, the test results indicate that the size of the particles of the EPS beads has shrunk (Fig.4). Thus, it is essential to note, in the context of this research, that in the future, the shrinkage factor of EPS beads must be a distinct factor of consideration, particularly when evaluating specimens that involve heating.

Fig.4 EPS and MEPS. Before heating (left), and after heating 24 hours (right)

DISCUSSION

Water absorption of lightweight concrete should be measured to evaluate its overall performance and durability. Water absorption can be measured using tests like the initial and final water absorption tests. The results of these tests can be used to evaluate the quality control and durability of lightweight concrete. The entire (reachable) pore volume of the concrete can be estimated using water absorption by immersion [11]. The greater the percentage of air voids that formed, the greater the amount of water that was absorbed by the concrete [12]. The water absorption standard for concrete masonry units requires that the water absorption rate must not surpass 12% for normal concrete and should not exceed 19% for lightweight concrete [13].

Density and Water Absorption

The concrete's water absorption capacity is influenced by the level of concrete density. Conversely, while considering the compressive strength and splitting strength of concrete, it is generally observed that the water absorption value increases as the density of the concrete decreases. This demonstrates that higher density concrete typically exhibits lower water absorption values.

This finding is also comparable to the behavior of concrete reinforced with MEPS. MEPS concrete exhibits a reduced water absorption capacity in comparison to EPSC. Yet, among all concrete specimens incorporating EPS beads, EPS concrete that utilizes fly ash as a substitute for cement exhibits the most minimal water absorption value (Fig.5).

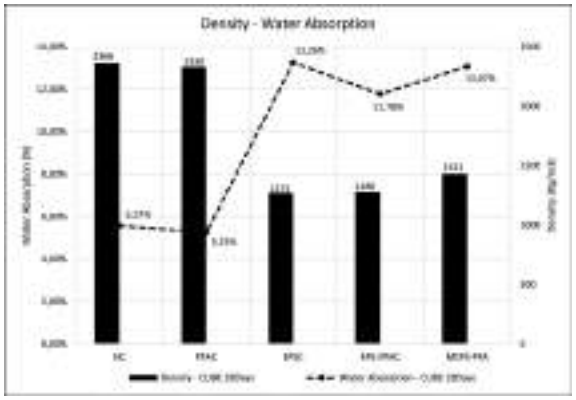

Fig.5 Relationship between Density and Water Absorption

Nonetheless, this research reveals an interesting finding: the water absorption values of concrete that incorporates fly ash as a partial cement replacement exhibit a positive trend without too much change in the density of the concrete. It appears that the incorporation of fly ash into concrete can enhance its water tightness [14], and gets better over time as the concrete matures.

Regarding the impact of employing EPS on density and water absorption, when used as an aggregate, EPS significantly reduces the weight of concrete and has the capacity to make it impermeable due to its non-absorbent properties. The underlying premise supported by previous research, while increasing the number of EPS in concrete results in a decrease in the rate of water absorption [15]. The water absorption percentage of the material, which has a density range of 1400-1800kg/m3, is only 4.37 – 6.95%, significantly lower than that of the control specimen. Nevertheless, it is important to acknowledge that variations in composition could potentially distinguish the outcomes of this study from the research conducted and documented in this thesis. The fundamental factor is the ratio of EPS used as a substitute for sand, rather than the coarse aggregate. In addition, the application of superplasticizer is believed to significantly influence the workability of concrete, resulting in enhanced compaction, and ultimately leading to a greater level of concrete density.

Applying coatings to EPS beads can improve the water resistance of concrete, albeit at the expense of an increase in weight compared to uncoated EPS beads. This finding is consistent with prior investigations in which aggregates coated with cement paste exhibited water absorption 1.8–3.7 times lower than plain LWAs [16]. Similarly, the use of coated biomass aggregate (CBA) in pervious geopolymer concrete (PGC) resulted in an improvement in compressive strength, while having little influence on its water permeability [17].

Therefore, in alignment with the objective of this study, which is to determine the level of the influence of utilizing modified EPS beads, it is apparent that coating-modified EPS beads can increase the water resistance of concrete.

However, the heating process has caused the EPS beads to shrink, resulting in voids that could negatively influence the water absorption value. Previous studies have shown that limiting the use of oven heating during testing can lead to a significant improvement in the current level of compactness. [18]. Utilizing the drying method in an oven for water absorption testing may introduce bias when applied to concrete that incorporates EPS beads as the aggregate.

Compressive Strength and Water Absorption

Another important area of study is the interaction between compressive strength and water absorption in concrete, especially in developing advanced materials like EPS/PFA lightweight concrete. Compressive strength is an essential property that considers the load-bearing capacity or structural integrity of the concrete, while water absorption deals with the durability and resistance of the material to environmental factors. Understanding how these two attributes interact is crucial in optimizing concrete formulations for better performance and durability. High water absorption can result in much porosity and micro cracking, hence decreased compressive strength, which affects the reliability of the structure. Hence, such a study on correlation will help develop more resilient and long-lasting concrete solutions with modern construction requirements to meet sustainability objectives.

Based on the current trend, where the strength of compression is closely linked to density, the graph demonstrating the relationship between compressive strength and water absorption shows a similar pattern (Fig.6). Nevertheless, the graph reveals that the partial replacement of cement with fly-ash, despite decreasing the compressive strength, has been demonstrated to have a beneficial impact on reducing the water absorption of concrete. This is evident when comparing the graphs of the PFAC and EPS-PFAC specimens to those of the NC and EPSC. This suggests that the substitution of a portion of cement with fly ash can reduce the water absorption of concrete. Furthermore, it is worth noting that the MEPS-PFA exhibits a 24% higher compressive strength compared to EPSC. This increase in strength has a positive effect on water absorption, reducing it by 1.4%, which is an improvement. This demonstrates that the application of a coating on EPS beads yields a favorable outcome, specifically by enhancing compressive strength and improving water absorption compared to uncoated EPS beads used in

concrete.

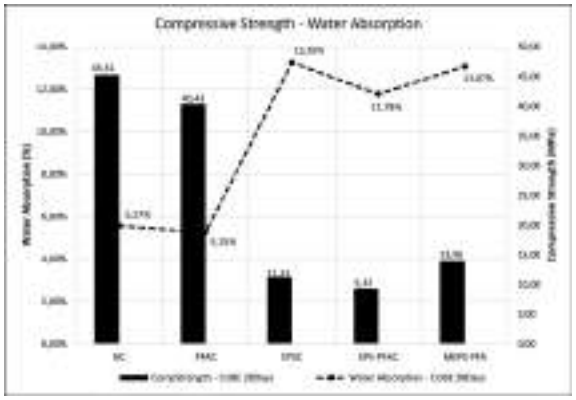

Fig.6 Relationship between Compressive Strength and Water Absorption

CONCLUSIONS

During water absorption testing, the specimens become hollow due to the shrinkage of EPS. Generally, the presence of hollow material significantly affects the water absorption capacity. Hence, this necessitates for a further investigation. In order to evaluate the impact of coated EPS on the water absorption capacity of concrete, it is required to explore alternative testing methods that do not involve heating, thereby preventing the shrinkage of EPS beads.

The water absorption value of concrete made from EPS with coating treatment is higher than that of concrete made from uncoated EPS, indicating that the coating treatment does not have a beneficial effect on water absorption. Nevertheless, despite having a water absorption rate of approximately 13%, it still satisfies the necessary criteria for being utilised as a material for concrete masonry units in construction projects.

REFERENCES

[1] A. P. Wibowo, M. Saidani, M. Khorami, and M. Bai, “Expanded polystyrene (EPS) in concrete: A bibliometric analysis,” presented at the 1st International Conference & Symphosium On Construction Industry Development: Value Added Construction, Padang, Indonesia, 2023, p. 070018. doi: 10.1063/5.0117082.

[2] A. P. Wibowo, M. Saidani, M. Khorami, and M. Tyrer, “Fly Ash and Silica in Expanded Polystyrene Concrete Finding the Research Gap (Preliminary Study),” in Advances in Civil Engineering Materials, vol. 139, A. M. M. F. Bin Meor Razali, M. Awang, and S. S. Emamian, Eds., in Lecture Notes in Civil Engineering, vol. 139. , Singapore: Springer Singapore, 2021, pp. 323–334. doi: 10.1007/978-981-33-6560-5_32.

[3] N. Shafiq and M. A. Ammar, “An Experimental Assessment on the Performance of Fly Ash in Concrete,” in ICCOEE2020, vol. 132, B. S. Mohammed, N. Shafiq, S. Rahman M. Kutty, H. Mohamad, and A.-L. Balogun, Eds., in Lecture Notes in Civil Engineering, vol. 132. , Singapore: Springer Singapore, 2021, pp. 458–467. doi: 10.1007/978-981-33-6311-3_53.

[4] M. Islam and M. Islam, “Strength and durability characteristics of concrete made with fly-ash blended cement,” Aust. J. Struct. Eng., vol. 14, no. 3, 2013, doi: 10.7158/S12-037.2013.14.3.

[5] M. Raheel, F. Rahman, and Q. Ali, “A stoichiometric approach to find optimum amount of fly ash needed in cement concrete,” SN Appl. Sci., vol. 2, no. 6, p. 1100, Jun. 2020, doi: 10.1007/s42452-020-2913-y.

[6] G. Joseph and K. Ramamurthy, “Influence of fly ash on strength and sorption characteristics of cold-bonded fly ash aggregate concrete,” Constr. Build. Mater., vol. 23, no. 5, pp. 1862–1870, May 2009, doi: 10.1016/j.conbuildmat.2008.09.018.

[7] A. P. Wibowo, M. Saidani, and M. Khorami, “Enhancing Sustainability in Construction: Investigating the Thermal Advantages of Fly Ash-Coated Expanded Polystyrene Lightweight Concrete,” J. Compos. Sci., vol. 8, no. 4, Art. no. 4, Apr. 2024, doi: 10.3390/jcs8040157.

[8] A. P. Wibowo and M. Saidani, “The effect of fly ash as coating powder on compressive strength of lightweight concrete,” Mater. Today Proc., vol. 85, pp. 29–32, 2023, doi: 10.1016/j.matpr.2023.05.250.

[9] ASTM C140-11, ASTM-C140-11: Standard Test Methods for Sampling and Testing Concrete Masonry Units and Related Units, West Conshohocken, PA 19428-2959. United States., 2011.

[10] P. Kannan, J. J. Biernacki, D. P. Visco, and W. Lambert, “Kinetics of thermal decomposition of expandable polystyrene in different gaseous environments,” J. Anal. Appl. Pyrolysis, vol. 84, no. 2, pp. 139–144, Mar. 2009, doi: 10.1016/j.jaap.2009.01.003.

[11] G. D. Schutter and K. Audenaert, “Evaluation of water absorption of concrete as a measure for resistance against carbonation and chloride migration,” Mater. Struct., vol. 37, 2004.

[12] S. Shahidan, E. Aminuddin, K. Mohd Noor, N. I. R. Ramzi Hannan, and N. A. Saiful Bahari, “Potential of Hollow Glass Microsphere as Cement Replacement for Lightweight Foam Concrete on Thermal Insulation Performance,” MATEC Web Conf., vol. 103, p. 01014, 2017, doi: 10.1051/matecconf/201710301014.

[13] ASTM C90-22, ASTM-C90-22: Standard Specification for Loadbearing Concrete Masonry Units, West Conshohocken, PA 19428-2959. United States., 2022.

[14] R. Kurda, J. De Brito, and J. D. Silvestre, "Water absorption and electrical resistivity of concrete with recycled concrete aggregates and fly ash," Cem. Concr. Compos., vol. 95, pp. 169–182, Jan. 2019, doi: 10.1016/j.cemconcomp.2018.10.004.

[15] M. Y. Nurain Izzati et al., "Strength and water absorption properties of lightweight concrete brick," IOP Conf. Ser. Mater. Sci. Eng., vol. 513, p. 012005, Apr. 2019, doi: 10.1088/1757-899X/513/1/012005.

[16] L. Domagała and E. Bryła, "The Properties of Lightweight Aggregates Pre-Coated with Cement Pastes and Their Suitability for Concrete," Materials, vol. 14, no. 21, p. 6417, Oct. 2021, doi: 10.3390/ma14216417.

[17] S. A. Arafa, "Properties Of Coated And Uncoated Biomass Aggregates And Their Effects On The Strength And Water Permeability Of Pervious Geopolymer Concrete," Int. J. GEOMATE, vol. 14, no. 41, Jan. 2018, doi: 10.21660/2018.41.73423.

[18] A. P. Wibowo, A. E. Lianasari, Z. A. Wiransyah M., and T. A. Kurniawan, "The Strength And Water Absorption Of Heated Expanded Polystyrene Beads Lightweight-Concrete," Int. J. GEOMATE, vol. 21, no. 83, Jul. 2021, doi: 10.21660/2021.83.j2146.

Copyright © Int. J. of GEOMATE All rights reserved, including making copies, unless permission is obtained from the copyright proprietors.

15th Int. Conf. on Geotechnique, Construction Materials & Environment,
Kyoto, Japan, 11-13 November 2025, ISBN 978-4-909106124 C3051

USING NICKEL SLAG AND GOLD TAILINGS AS PARTIAL SUBSTITUTES IN CONCRETE FOR SUSTAINABLE CONSTRUCTION

* Lisa Oksri-Nelfia[1], Julien Meret[2], Ouali Amiri[2,3], Yohans Sunarno[4]

[1] Faculty of Civil Engineering and Planning, Universitas Trisakti, Jakarta, Indonesia
[2] Polytech Nantes, Nantes Université, Saint-Nazaire, France
[3] Nantes Université, France
[4] Faculty of Engineering, Bosowa University, Makasar, Indonesia

ABSTRACT

This study examines the viability of utilizing fine nickel slag (FNS) and gold tailings (GT) as partial replacements for cement and fine aggregate in conventional concrete. The concrete used in Indonesia generally possesses a minimum compressive strength of 21 MPa for residential construction. This research aims to ascertain if including FNS and GT may achieve or surpass this standard while providing environmental and economic advantages by substituting up to 25% of the cement and sand with FNS and GT. The experimental findings indicated a significant decrease in workability as FNS and GT content increased, with slump flow values dropping from 80 mm in the control mixture to 19 mm in the combination with 25% replacement. Compressive strength tests indicated a significant reduction in strength with elevated FNS and GT content; however, the mixture with 15% substitution showed optimal performance, attaining a compressive strength of 37.43 MPa after 28 days, surpassing the standard strength of conventional concrete utilized in Indonesia. Tensile strength indicated decreases in all mixes, with the most significant drop at the 25% substitution level. This research illustrates that despite reduced workability and strength, utilizing FNS and GT in conventional concrete manufacturing is viable while attaining satisfactory mechanical performance. This study introduces new possibilities for sustainable concrete manufacturing by integrating industrial waste materials, enhancing environmental conservation, and economic efficiency in the building sector.

Keywords: Compressive strength, Fine nickel slag, Gold tailings, Industrial waste, Slump

INTRODUCTION

The construction industry is one of the largest consumers of natural resources such as sand, gravel, limestone, and water, leading to environmental impacts due to the extraction and use of these materials. For decades, concrete has been the primary construction material; it is a fundamental material in the construction industry. However, it is particularly resource-intensive, consuming large quantities of resources to produce[1][2].

Nevertheless, the increasing demand for construction materials and the scarcity of natural resources have pushed researchers to explore using industrial waste and by-products as substitutes for the natural resources used in concrete production [3]. This initiative will address the environmental issues associated with resource extraction and offer a solution for disposing of industrial waste, which can be dangerous for humankind and the environment. We will explore the potential of Specific waste materials, such as nickel slag and gold ore tailings, as substitutes for natural materials in concrete production [4][5][6][7].

Nickel slag is a byproduct of nickel smelting that has gained attention as a potential substitute for fine and coarse aggregate in concrete. Indonesia is the largest nickel producer in the world, generating approximately 13 million tons of nickel slag annually. Disposing of that waste is extremely important for Indonesia, as improper disposal may lead to soil and water contamination based on the heavy metal content of nickel slag [8].

Several studies over the past decade have investigated the use of nickel slag in concrete, proving its capacity to improve concrete's mechanical properties and durability. It has been found that incorporating Nickel slag as sand replacement can enhance the compressive strength and workability of concrete [9]. Furthermore, using nickel slag as a coarse aggregate has also shown promising results. Researchers have found that compressive strength increases with the proportion of nickel slag used, making it an adequate substitute for gravel in concrete [10] [11].

The properties of self-compacting concrete made with ferronickel slag as a fine aggregate have shown improvements in fresh and hardened states, making it a viable option for sustainable construction [12][13]. Similarly, the compressive behavior of high-strength geopolymer materials made with industrial by-products has demonstrated excellent compressive strength and durability, suitable for various construction applications [5].

The recycling and comprehensive utilization of ferronickel slag in concrete production have been

successful. Reducing waste and conserving natural resources provide environmental and economic benefits. Incorporating ferronickel slag into concrete enhances its mechanical properties and durability, making it a viable alternative to traditional aggregates [14][15][3].

RESEARCH SIGNIFICANCE

This study demonstrates that fine nickel slag (FNS) and gold tailings (GS) can replace cement and sand in concrete as partial replacements. With Indonesia generating large amounts of nickel-related waste, which poses environmental risks, the research offers a practical and eco-friendly solution for reusing these materials. The mix containing 15% of these substitutes achieved higher compressive strength than standard concrete, proving its potential for structural use. These findings support more sustainable construction by reducing raw material use, lowering environmental impact, and advancing circular economy practices.

EXPERIMENTS AND METHODS

Materials

The experimental design utilizes the Indonesian National Standard [16]. Technique to determine the optimal cement-concrete ratio by substituting equal amounts of cement with GGBFS and Fiber. This allows for a systematic examination of how GT and Nickel Slag impact the alteration of concrete characteristics. The composition has been designed using GT and nickel in standard concrete mixtures as a reference. The mix proportion is presented in Table 3, with GT and Nickel used up to 25% as substitutes for cement and sand.

Gravel, Sand, Cement, Gold Tailing (GT), and Fine nickel slag (FNS) are mixed for 1 minute in a concrete mixer before adding water until a homogeneous concrete is obtained—afterward, a workability test using Abraham's cone. The mixture is poured into the mold for 24 hours and immersed in water (water curing) for 7-14-28 days. Then, it is tested for compressive and tensile strength for 28 days.

Experimental Design

Sieve Analysis is a fundamental civil engineering test that assesses aggregates' particle size distribution. In this test, a sample of dry aggregate is passed through a stack of sieves with progressively smaller mesh sizes, from coarse to fine. Each sieve catches particles above a specific size, and the material retained on each sieve is weighed to determine the distribution of particle sizes. The cumulative percentage passing through each sieve is then calculated to create a gradation curve. This test helps evaluate the suitability of the aggregate for use in concrete, asphalt, and other construction materials. A well-graded aggregate, containing a mix of different particle sizes, typically ensures better compaction, stability, and strength in construction applications, as shown in Table 1 [1]. The specific gravity test is used to determine the density of the aggregates relative to water.

The test consists of oven-drying a sample of the aggregate, weighing it, and then soaking it in water for 24 hours to achieve a saturated surface-dry (SSD) condition. After drying off the surface moisture, the sample is weighed again in the SSD state. The sample is then submerged in water, and its weight is recorded. Specific gravity is calculated using the sample's dry weight and the difference between the SSD and the submerged weights.

Table 1 Specific gravity results of FNS

Experiment		Unit	GT1	GT2
Flask Weight	(A)	gr	224	224
Sample and Flask Weight	(B)	gr	724	724
Sample Weight	(C = B-A)	gr	500	500
Flask, Sample, and Water Weight	(D)	gr	1055	1055.8
Water Weight	(E = D - B)	gr	331	311.8
Specific Gravity	(F = C/(C-E)	gr	2.958	2.972
Average			2.9656	

The bulk density of fine nickel slag was determined using a standardized testing procedure. Initially, the empty container was weighed (as shown in Figure 4), then filled to the brim with fine nickel slag and weighed again to obtain the final measurement (as illustrated in Table 2). Based on the weights found, we can determine the bulk density.

Water absorption capacity

The Water Absorption Capacity test is essential in civil engineering for determining the amount of water a material, typically aggregate, can absorb (Table 3). In this test, the aggregate is dried in an oven to remove all moisture and then weighed. Afterward, the sample

Table 2 Bulk density test results of FNS

Experiment		1	2
Container Volume	(A)	2002	2002
Container Weight	B	774	774
Sample and Container Weight	C	4743.4	4746.4
Sample Weight	D= C-B	3969.4	3972.4
Bulk Weight	E= D/A	1.982	1.984
Average		1.983	1.983

is soaked in water for 24 hours to ensure it is fully saturated. The surface moisture is removed, and the sample is weighed again in its saturated surface-dry (SSD) condition. The difference between the dry and SSD weights calculates the water absorption percentage. This test helps assess the porosity and water-holding capacity of the aggregate, which influences the workability, durability, and strength of concrete. Aggregates with high water absorption may require adjustments in the mix design to ensure proper hydration and performance.

Table 3 Water absorption results of FNS

Experiment		Unit	1	2
Pan Weight	(A)	Gr	654	654
Sample and Pan Weight	(B)	Gr	1654	1654
Sample and Pan Weight	(C=B-A)	Gr	1000	1000
Dry Sample Weight	(D)	Gr	991.2	991.6
Water Absorption Capacity	(E=(C-D)/D)	%	0.888	0.847
Average		%	0.867	0.867

Moisture content

The Moisture Content test is a crucial procedure in civil engineering to measure the amount of water in a material, such as soil or aggregate. In this test, a sample is first weighed in its wet condition and then oven-dried at a specified temperature until it reaches a constant weight. The difference between the wet and dry weights is used to calculate the moisture content as a percentage of the dry weight. This test is important because the moisture content affects the material's behavior, particularly its compaction, strength, and stability in construction projects. Controlling moisture is essential for ensuring the performance of materials like concrete, soil, and asphalt in various construction applications.

GOLD TAILING

To successfully substitute cement with gold tailing, GT's composition needs to be as close as possible to cement, which consists of CAO, SiO_2, Al_2O_3, We know that the main components of Portland Cement are the following:

Table 4 Cement and GT compounds

Compound	Ingredient percentage (%)	OPC Tiga Roda [17]	Gold Tailing - %)
CaO	60-69	63.2	13.54
SiO_2	17-25	18.45	17-25
Al_2O_3	3-8	4.96	3-8
Fe_2O_3	2-4	2.86	2-4
MgO	1-5	3.52	1-5
Na_2O+K_2O	1-3	0.31	1-3
SO_3	1-3	2.18	0.3-1.5

The data that we have received from the industry about the main components of gold tailing shows that GT is very similar to cement, at least to indicate the feasibility of the research (Table 4). Furthermore, the material must respect specific laws regarding human safety, such as limits on the quantity of components, such as lead [18]. The following table shows the analysis report done on Gold Tailing (GT).

Table 5 GT and FNS Elements of Toxicity Leaching Procedure Test (TCLP)

Elements	Limit the US EPA	GT	FNS
	[mg/L]	[mg/L]	[mg/L]
Arsenic	5	0,01	0.5
Barium	100	0,09	35
Cadmium	1	0,09	0.15
Chromium	5	0,08	2.5
Lead	5	7,9	0.5
Mercury	0,2	0,01	0.05
Selenium	1	0,01	0.5
Silver	5	0,01	5

Based on the analysis, we can see an excess of lead in the gold tailing, which may constitute a health risk to future users (Table 5). This shows that concrete made with gold tailing needs to be analyzed to verify the respect of the USEPA limit [19]. While trying to find the optimum W/C ratio for GT, we discovered that GT absorbs more water than OPC. [20][21] However, when saturated with water and

having a higher W/C than the optimum, the GT will get sticky, negatively impacting the slump (Fig. 4).

Fig 4: Water demand test [22]

RESULTS AND DISCUSSIONS

Workability

The material testing results of concrete binders obtained specific gravity of OPC and GT cement, 3.155 and 2.56, respectively. The material testing results of concrete constituents included specific gravity, moisture content, and absorption. The specific gravity results of fine aggregates, coarse aggregates, and Fine nickel slag (FNS) were obtained at 2.53, 2.54, and 2.96, respectively. The fines aggregate water content and coarse aggregate results were obtained at 2.53 and 0.78, respectively. Fine aggregate absorption, Coarse aggregate results were obtained at 2.86, 2,81. Workability testing refers to the European Federation dedicated to specialist construction chemicals and concrete systems (EFNARC) [23].

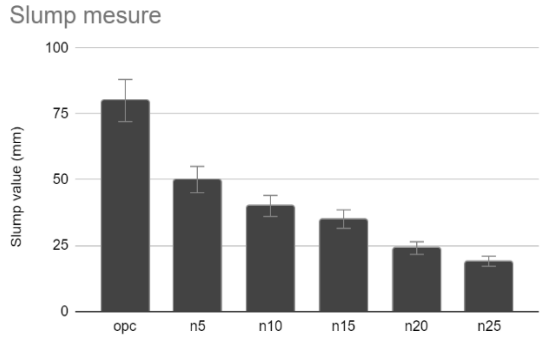

Fig.5 Slump test of Concrete

Table 6 Workability Results in Concrete

Concrete variations	Slump Flow (mm)
CONTROL (OPC)	80
NS5	50
NS10	42
NS15	35
NS20	24
NS25	19

Adding nickel slag and gold tailing significantly affects the workability of concrete (Table 6). With the addition of Fine nickel slag and Gold tailing, Workability decreases with the addition of concrete variations; this result was in line with [24]. The role of NS is as much as 25% as a substitute material. Workability on concrete dropped too drastically[8][12].

Concrete Compressive Test

Figure 6 demonstrates that the incorporation of NS and GT into the mixes resulted in a reduction of compressive strength by the conclusion of the 28th day. Nonetheless, the degree of strength loss varied across different proportions. For NS25, the compressive strength decreased by 44% of the NS25% by the conclusion of the 28th day. The maximum compressive strength observed was for NS15, which declined by 11%. Utilizing NS and GT, we observed a progressive increase in the compressive strength of the concrete, with the majority of samples attaining their peak value on the 28th day. It can be concluded that using NS and GT reduces compressive strength; however, this decline may be mitigated by employing optimal proportions. [15][25].

Table 7 Results of compressive strength and tensile strength

Concrete Variations	Compressive Strength (MPa)	Tensile Strength (MPa)
CONTROL (OPC)	42,27	14,9
NS5	25,57	10,48
NS10	33,87	10,78
NS15	37,43	14,6
NS20	29,96	10,57
NS25	23,62	10,06

Fig.6 Compressive Strength of Concrete

Fig. 7 shows that using NS and GT can decrease the tensile strength of Control concrete (OPC) by 29.6% and 1.9%, respectively. Thus, it can be concluded that adding NS and GT can decrease tensile strength [26][12].

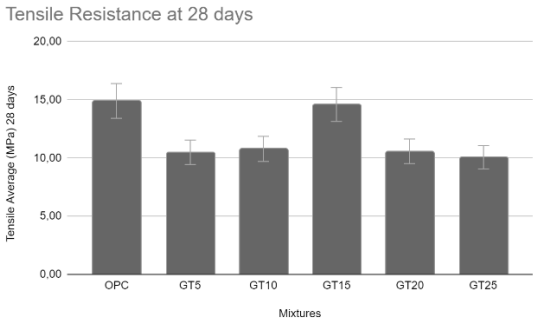

Fig.7 Tensile Strength Results

Porosity Test

The porosity of concrete is a key indicator of its internal structure and durability. It directly influences the material's permeability, mechanical properties, and resistance to environmental degradation. This study conducted the porosity test to assess the impact of fine nickel slag (FNS) and gold tailings (GT) as partial replacements for cement and sand on the concrete's pore structure. Concrete specimens were cured for 28 days to determine total porosity and then dried in an oven at 105°C for 24 hours to remove free moisture. The dried specimens were weighed (dry weight, W_d) and subsequently immersed in water for 24 hours. After immersion, the specimens were weighed in the saturated surface-dry condition (SSD weight, Wssd) and fully submerged condition (submerged weight, Wsub). The porosity (ϕ) was calculated using the following formula, referring to equation (1) :

$$ø\ (\%) = \frac{Wssd - Wd}{Wssd - Wsub} \times 100 \qquad (1)$$

This test was applied to all concrete mixtures, including the control and NS5–NS25 variations. Results illustrated in Fig. 8 show that porosity increased progressively with the increase in GT and FNS substitution levels. The control sample exhibited the lowest porosity, indicating a denser matrix. Conversely, NS25 displayed the highest porosity, which can be attributed to the irregular particle shapes and greater water demand of GT and FNS, which affect compaction and paste-aggregate bonding.

The observed increase in porosity is consistent with previous studies by Chen et al [11], and Juenger et al. [15], which reported that excessive replacement with industrial by-products can increase void content due to less optimized particle packing and higher internal moisture absorption. However, the NS15 mixture maintained an acceptable porosity level that aligns with structural-grade concrete requirements while providing sustainable material advantages.

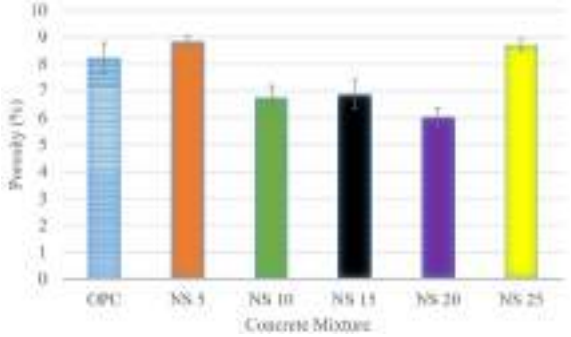

Fig.8 Porosity Test Results

Permeability Test

The permeability test is vital in assessing the durability of concrete, especially when incorporating alternative materials such as fine nickel slag (FNS) and gold tailings (GT). High permeability in concrete can lead to the ingress of water, chlorides, and other aggressive agents, ultimately accelerating the deterioration of reinforced concrete structures. This test was conducted to evaluate how adding FNS and GT affects the water permeability of concrete. The test followed the DIN 1048 standard for determining water penetration under pressure. Cylindrical concrete specimens (150 mm diameter × 150 mm height) were cast for each mix variation, including control (OPC) and substitution levels of 5%, 10%, 15%, 20%, and 25%. After 28 days of water curing, the specimens were subjected to a constant water pressure of 0.5 MPa for 72 hours using a standardized water permeability apparatus.

After the test duration, the specimens were split longitudinally, and the maximum depth of water penetration was measured. As illustrated in Fig. 9, the control mix exhibited the lowest penetration depth (approximately 12 mm), indicating high resistance to

water ingress. With increasing percentages of FNS and GT, the depth of water penetration increased. The NS15 mix showed moderate permeability (~17 mm), while the NS25 mix had a significantly higher penetration (>25 mm), suggesting a more porous internal structure.

These observations align with findings by Han et al. [3] and Nuruzzaman et al. [12], who reported increased permeability in industrial waste's concrete mixes due to microstructural changes and elevated porosity. However, moderate substitution levels (up to 15%) still maintained acceptable performance. Wang et al. [25] Further support is provided by emphasizing the importance of optimizing mix design to balance sustainability and durability in high-performance concrete incorporating tailings and slags.

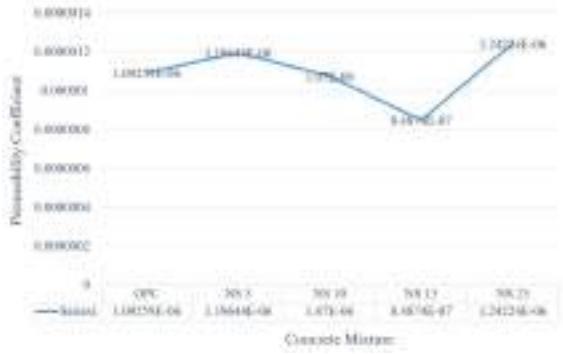

Fig.9 Permeability Test Results

CONCLUSIONS

This study used fine nickel slag (FNS) and gold tailings (GT) as partial replacements for cement and sand in concrete to create a more sustainable construction material. The results showed that while higher substitution levels reduced workability and strength, the mixture containing 15% FNS and GT achieved a compressive strength of 37.43 MPa after 28 days, well above the standard strength used in Indonesian residential construction. Although tensile strength declined slightly across all mixtures, the reduction was acceptable at 15%.

These findings demonstrate that industrial waste materials like nickel slag and gold tailings can be effectively reused in concrete production without compromising quality when used in optimal proportions. This helps lower the demand for natural resources and offers an environmentally responsible way to manage mining waste. This research contributes to developing greener, more circular construction practices by turning waste into valuable construction input.

Further research is encouraged to evaluate these materials' long-term performance and environmental safety, particularly regarding the presence of heavy metals in gold tailings.

ACKNOWLEDGMENTS

The authors thank PT Jaya Beton and Universitas Trisakti for providing access to the concrete laboratory and research facilities and financial support through Trisakti funding.

REFERENCES

[1] A. R. Yohans Sunarno, Parea Rusan Rangan, Bastian A. Ampangallo, Armin Aryadi, Lisa Oksri Nelfia, View of The Influence of Chemical Admixture Types on The Mechanical Properties of Concrete with 100% Fly Ash Substitution, International Journal of GEOMATE, Vol 28, Issue 129, 2025, pp. 138–145,

[2] H. Zhao, W. Sun, X. Wu, and B. Gao, “The properties of the self-compacting concrete with fly ash and ground granulated blast furnace slag mineral admixtures,” J. Clean. Prod., vol. 95, 2015, pp. 66–74

[3] F. Han, H. Zhang, Y. Li, and Z. Zhang, Recycling and comprehensive utilization of ferronickel slag in concrete, J. Clean. Prod., vol. 414, 2023, pp. 13763

[4] I. W. Permatasari, L. Oksri-Nelfia, P. H. R. Siregar, and B. E. Yuwono, “A literature review on the durability of ferrous and non-ferrous geopolymer concrete for sustainable developments,” IOP Conf. Ser. Earth Environ. Sci., vol. 780, Issue 1, 2021

[5] F. Han, H. Zhang, Y. Li, and Z. Zhang, “Recycling and comprehensive utilization of ferronickel slag in concrete,” J. Clean. Prod., vol. 414, 2023, pp. 137633, 2023

[6] Q. Song, Y. Zou, J. Bao, and P. Zhang, “Disposal of solid waste as building materials: A study on the mechanical and durability performance of concrete composed of gold tailings,” J. Mater. Res. Technol., vol. 30, 2024, pp. 2111–2124

[7] C. Ince, “Reusing gold-mine tailings in cement mortars: Mechanical properties and socio-economic developments for the Lefke-Xeros area of Cyprus,” J. Clean. Prod., vol. 238, 2019, pp. 117871

[8] L. O. Nelfia et al., “Comprehensive Characteristics of High-Performance Concrete with Nickel Slag as Fine and Coarse Aggregate,” Int. J. Technol., vol. 15, no. 6, 2024, pp. 1613–1631

[9] H. Zhong et al., “Compressive Behaviors of High-Strength Geopolymeric Concretes: The Role of Recycled Fine Aggregate,” Buildings, vol. 14, no. 4, 2024, pp. 1–22

[10] Y. Ma, B. Zhang, Y. Lin, Y. Huang, D. Zheng, and T. Ji, “Effect of nickel slag on the basic tensile creep of alkali-activated slag/nickel slag mortars,” Constr. Build.

Mater., vol. 351, 2022
[11] S. C. Chen, M. T. Wang, L. S. Gu, W. T. Lin, J. F. Liang, and K. Korniejenko, "Effects of incorporating large quantities of nickel slag with various particle sizes on the strength and pore structure of cement-based materials," Constr. Build. Mater., vol. 393, 2023, pp. 132034
[12] M. Nuruzzaman, J. O. Camargo Casimiro, and P. K. Sarker, "Fresh and hardened properties of high strength self-compacting concrete using by-product ferronickel slag fine aggregate," J. Build. Eng., vol. 32, Issue. 2020, pp 101686
[13] A. Bouaissi, L. yuan Li, M. M. Al Bakri Abdullah, and Q. B. Bui, "Mechanical properties and microstructure analysis of FA-GGBS-HMNS based geopolymer concrete," Constr. Build. Mater., vol. 210, 2019, pp. 198–209
[14] G. C. Wang, The utilization of slag in civil infrastructure construction. Elsevier Ltd., 2018.
[15] M. C. G. Juenger, R. Snellings, and S. A. Bernal, "Supplementary cementitious materials : New sources , characterization, and performance insights," Cem. Concr. Res., vol. 122, 2019, pp. 257–273
[16] A. 211.4R-93, "Guide for Selecting Proportions for High-Strength Concrete with Portland Cement and Fly Ash," vol. 93, 1998 no. Reapproved
[17] L. Oksri-Nelfia, A. Raditya, Triastuti, A. Nugroho, D. Syamsunur, and O. Amiri, "Sago Palm Fibers and GGBFS for Sustainable High-Tensile-Strength Self-Compacting Concrete," Int. J. GEOMATE, vol. 28, Issue. 125, 2025, pp. 44–55
[18] S. Li, J. Chen, W. Gao, X. Lyu, Z. Liang, and W. Zhou, "Current situation and prospects for the clean utilization of gold tailings," Waste Manag., vol. 180, 2024, pp. 149–161
[19] S. Apithanyasai, N. Supakata, and S. Papong, "The potential of industrial waste: using foundry sand with fly ash and electric arc furnace slag for geopolymer brick production," Heliyon, vol. 6, Issue 3, 2020, pp. 03697
[20] Q. Wang et al., "Approach to the management of gold ore tailings via its application in cement production," J. Clean. Prod., vol. 269, 2020, pp 122303
[21] A. Dey et al., "Towards net-zero emission: A case study investigating sustainability potential of geopolymer concrete with recycled glass powder and gold mine tailings," J. Build. Eng., vol. 86, 2024, pp. 108683
[22] P.-Y. L. Oksri-Nelfia; Mahieux, "Reuse of recycled crushed concrete fines as mineral addition in cementitious materials," Mater. Struct., 2015
[23] EFNARC, "Specification and Guidelines for Self-Compacting Concrete," vol. 44, 2002.
[24] Q. Wang, G. Yao, X. Zhu, J. Wang, P. Wu, and X. Lyu, "Preparation of Portland Cement with Gold Ore Tailings," Adv. Mater. Sci. Eng., vol. 351, 2019, pp. 128778
[25] J. N. Wang et al., "A novel design of low carbon footprint Ultra-High Performance Concrete (UHPC) based on full scale recycling of gold tailings," Constr. Build. Mater., vol. 304, 2021, pp. 124664
[26] R. S. Edwin, E. Ngii, R. Talanipa, F. Masud, and R. Sriyani, "Effect of nickel slag as a sand replacement in strength and workability of concrete," IOP Conf. Ser. Mater. Sci. Eng., vol. 615, Issue 1, 2019, pp. 1-6

Copyright © Int. J. of GEOMATE All rights reserved, including making copies, unless permission is obtained from the copyright proprietors.

15th Int. Conf. on Geotechnique, Construction Materials & Environment,
Kyoto, Japan, 11-13 November 2025, ISBN 978-4-909106124 C3051

HYDROGEOLOGICAL INTERPRETATION USING GEOELECTRICAL AND HYDROCHEMICAL DATA IN CIMANIS WATERSHED, KUNINGAN, WEST JAVA, INDONESIA

Boy Yoseph CSS Syah Alam[1] Hadi Hidayat[1] Deden Zaenudin[1]

[1]Faculty of Geological Engineering, Universitas Padjadjaran, Indonesia

ABSTRACT

This study uses geoelectrical data and groundwater hydrochemical analysis to interpret the hydrogeological conditions of the Cimanis watershed on the eastern slopes of Mount Ciremai, one of the volcanic areas in West Java. Geophysical acquisition comprised 10 lines of 2D electrical resistivity tomography (ERT) profiles at various locations, identifying subsurface layers, delineating aquifers, and determining groundwater characteristics and potential. Meanwhile, twelve groundwater samples were collected in dry and rainy seasons for hydrochemical analysis to understand the hydrogeochemical processes.
The geoelectrical survey results reveal variations in resistivity values, indicating differences in lithology. The distribution of very high resistivity (>500 ohm.meter) appears from 1050 to 700 masl. Then, a group of high resistivity (>200-500 ohm.meter) appears from 700 to 650 masl, consisting of andesite lava rock and supported fragment breccia rock, and a low-medium resistivity group (15-200 ohm.meter). It is a breccia tuff, and the very low resistivity group (< 15 ohm-m) indicates the presence of geological structures. The groundwater types in the research area include Ca+HCO_3, Ca-Mg+HCO_3, and Ca-Mg+Cl, with no significant changes from one dry season to the next, indicating the consistency of groundwater flow below the surface. Rock weathering and changes in volcanic facies below the surface significantly impact the chemical composition of groundwater in the research area. This study demonstrates that combining geoelectrical and hydrochemical methods is a practical approach for hydrogeological investigations.

Keywords: Hydrogeology, Geoelectrical, Hydrochemistry, Groundwater, Cimanis Watershed.

INTRODUCTION

Groundwater is a vital natural resource in volcanic regions, such as Mount Ciremai in West Java, characterised by its complex hydrogeological settings due to heterogeneous lithology and geological structures. Understanding these systems is crucial for sustainable water management in the Cimanis watershed. Previous studies have highlighted the importance of integrating geophysical and hydrochemical methods to delineate aquifers and assess groundwater quality [1,2]. This research aims to explore the groundwater system in the Cimanis watershed through 2D geoelectrical surveys and hydrochemical analysis.

The Cimanis watershed is located on the eastern slopes of Mount Ciremai in Kuningan Regency, West Java, at elevations ranging from 600 to 1,200 meters above sea level. The area predominantly comprises Quaternary volcanic formations, including andesitic lava, breccia, and tuff. The climate is tropical, featuring distinct wet and dry seasons. Recharge mainly occurs through direct infiltration and fault-controlled flow pathways. Land use, which includes agriculture and residential settlements, may influence groundwater chemistry.

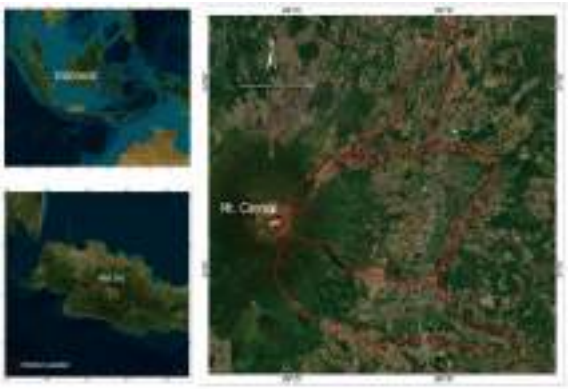

Figure 1. Research location in the easter slope of Mount Ciremai, Kuningan, West Java.

RESEARCH SIGNIFICANCE

This research offers a methodology for interpreting and integrating Electrical Resistance Tomography (ERT) with geological, hydrogeological, and hydrochemical data in the volcanic context of the study area. A key contribution of this work is the enhancement of groundwater potential interpretation and management in volcanic regions, based on findings from geological and hydrogeological investigations.

MATERIALS AND METHOD

Geology and Hydrogeological Mapping.

Previous regional geological studies were reviewed to prepare a preliminary interpretation of the geological units and the volcanic facies [2]. Then, geological mapping was carried out on a scale of 1:25000 to find out more details of the volcanic facies that developed in the research area by observing the outcrops, describing them in the field, and taking hand specimen samples, which were then petrographically analysed in the laboratory.

Hydrogeological mapping was carried out by observing hydrogeological points of interest, namely springs that appear naturally in the field. There are 43 springs in the field. Then, they are plotted, and the physical properties of the groundwater are measured in the field.

Geoelectrical Survey

Ten 2D Electrical Resistivity Tomography (ERT) profiles were measured using the Wenner-Schlumberger configuration. The data processing and modelling were performed with IPI2Win and Res2DInv software. The subsurface resistivity distributions were analysed to identify aquifers, aquitards, and structural features.

Water Sampling

Water sampling was conducted at 12 spring points representing the study area (Fig.2) during the rainy and dry seasons using 500-mL polyethene bottles. Before collecting the samples, the bottles, ladles, and filtration units were rinsed three times with filtered water to eliminate contaminants. The water samples were filtered on-site using a 0.45 µm syringe filter, with 500 mL collected to analyse cations and anions.

Hydrochemical Analysis

pH, electrical conductivity, total dissolved solids, and temperature were measured on-site using HANNA Instruments HI9811-5. The cations (Na^+, K^+, Ca^{2+} and Mg^{2+}) and anions (Cl^-, SO_4^{2-}) were determined by ion chromatography (IC - metrohm type 930 Compact) in the laboratory. HCO_3- was analysed using the titration method with 0.1 N HCl; methyl red and bromocresol green were used as indicators. A 5% difference in the electrical balance between cations and anions was required for all samples, suggesting high accuracy of groundwater quality determinations [3]. Hydrogeochemical data were analysed using statistical and trilinear diagram methods, a trilinear Piper diagram [4], and a Gibbs diagram [5] to confirm the water-rock interaction process in groundwater.

RESULTS AND DISCUSSION

GEOLOGICAL SETTING

The study area is situated on the eastern slope of Mount Ciremai in the Cimanis sub-watershed of Kuningan Regency, West Java. It features a complex volcanic stratigraphy associated with developing a Quaternary stratovolcano. The regional geology showcases a sequence of volcanic and volcaniclastic units ranging from the oldest (unit 10) to the youngest (unit 1). This sequence reflects both effusive and explosive volcanic processes influenced by tectonic activity.

The oldest rock unit in the research area is the tertiary rock, specifically the mudstone unit indicated by the green polygon (Fig. 2). The earliest volcanic product is unit 10, which consists of tuff-breccia and lithic breccia facies, interpreted as laharic deposits. These deposits are characteristic of environments dominated by base surges and debris flows, typically occurring during the initial stages of stratovolcano development [6]. Units 10 through 5 encompass tuff, breccia, and massive to moderately supported andesite breccia. These reflect subaerial pyroclastic density currents and lava emplacement, indicative of intermediate volcanic [7]. Unit 4, consisting of grey tuff-lithic breccia, and Unit 3, defined as coarse andesitic lava breccia, represent periods of increased explosive activity with fragmentation and reworking of volcanic materials.

In the north-central part of the study area, Unit 2 comprises andesite lava flows (referred to as andesite 2), while Unit 1 represents the youngest volcanic features. Unit 1 consists of a mixed collection of lava types, including andesite and basalt. These units reflect the most recent volcanic activity from the Ciremai summit vent, which is characterised by the effusive eruption of lava flows.

The structural framework of the area is dominated by normal and strike-slip faults trending northwest-southeast and northeast-southwest.

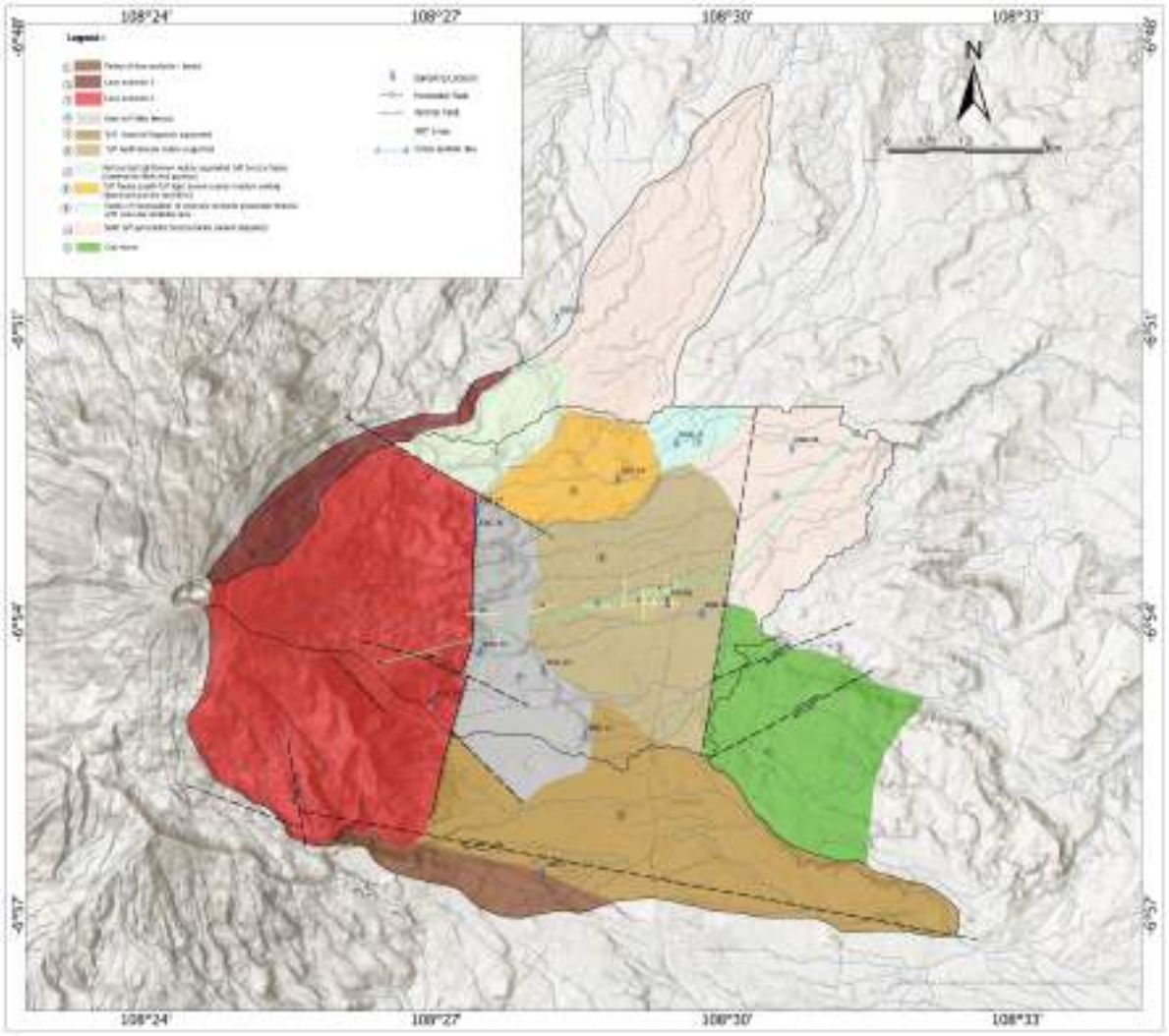

Figure 2. Geological map of the study area, groundwater sampling location and the distribution of 2D lines ERT

Classification of Resistivity Ranges for Geological and Hydrogeological Units

On the 2D geoelectric path from upstream to downstream, 10 2D geoelectric measurement paths spanning 576 meters.

Line 01 (Fig.3) reaches its highest measurement at an elevation of 858 meters above sea level (masl) and extends down to 777 masl, with an orientation from west to east. The geoelectric data reveals a significant resistivity range of 170 to 5400 ohm-meters. In particular, the profile from upstream to the mid-section is characterized by high resistivity, extending to a depth of 80 meters, which decreases as it moves downstream. These elevated resistivity values likely indicate the presence of andesite lava and dry, fragmented, non-solid grey breccia. Notably, this area is suspected to serve as an important recharge zone, highlighting its relevance for resource management and environmental sustainability.

The 02 to 06 line shows that further downstream, the resistivity distribution is dominated by medium-low resistivity values. The infiltration boundary area is depicted on track 01, which is dominated by high resistivity. At the same time, the discharge area appears on lines 03 to 08. The medium resistivity value is suspected to be an aquifer zone, which is geologically suspected to be tough breccia. The low resistivity value is suspected to be an aquifer zone that is spread locally, which is geologically lapilli tuff.

Lines 07 to 10 indicate a resistivity range from 90 to 160 ohm-meter. This range is believed to correspond to lapilli tuff rock transitioning to tuff breccia, which suggests the presence of an aquifer. Lower resistivity values (90-130 ohm-meter) are predominantly found in the factory's Southeast and Northeast areas (downstream). In contrast, higher resistivity values are observed in the Northwest and Southwest areas (upstream). Both resistivity ranges are suspected to be part of the same aquifer system.

Line 07 runs in the West-East direction and measures approximately 576 meters in length with a

depth of about 120 meters. Based on the analysis of line 01, the resistivity distribution in the shallow part, from 0 to 30 meters deep, is primarily characterised by low resistivity, ranging from 90 to 120 ohm-meters. In contrast, from 30 to 120 meters deep, the resistivity is mainly in the medium range, between 130 and 155 ohm-meters. The low resistivity values are associated with lapilli tuff and tuff breccia when correlated with the surrounding rock outcrops. At the same time, the medium resistivity values are believed to be linked to tuff breccia. Both types of rock are suspected to serve as aquifers.

Line 08 (Fig.6) runs in the West-East direction, with a track length of approximately 576 meters and a depth of around 120 meters. Based on the data from track 02, the distribution of resistivity in the shallow part, from 0 to 30 meters, is dominated by medium resistivity, with a range of 150 to 170 ohm-meters. In contrast, low resistivity is predominant at depths between 30 and 100 meters, with values ranging from 90 to 120 ohm-meters. Correlating these resistivity values with the surrounding rock outcrops, it is suspected that the low resistivity readings are associated with lapilli tuff and tuff breccia. In contrast, the medium resistivity values may be related to tuff breccia. Both types of rock are believed to be aquifers.

Line 09 runs in a North-South direction, with a track length of approximately 576 meters and a depth of around 120 meters. Based on the data from track 03, the distribution of resistivity in the shallow southern part, from 0 to 20 meters, is primarily characterised by medium resistivity, which ranges from 150 to 170 ohm-meters. The area shows primarily low resistivity from 20 to 45 meters in depth, with values ranging from 90 to 120 ohm-meters. At depths between 45 and 120 meters, the resistivity again shifts to medium, with a range of 150 to 170 ohm-meters. Correlating these measurements with the surrounding rock formations suggests that the low resistivity values are likely associated with lapilli tuff and tuff breccia. In contrast, the medium resistivity values are suspected to be linked to tuff breccia. These rocks are both believed to act as aquifers.

Line 10 (Fig.7)runs in a North-South direction, with a track length of approximately 576 meters and a depth of about 120 meters. Based on data from Track 04, the resistivity distribution in the shallow southern part, from a depth of 0 to 20 meters, is characterised by low resistivity, ranging from 90 to 110 ohm-meters. From a depth of 20 to 120 meters, the resistivity is predominantly medium, with values between 130 to 150 ohm-meters. In the middle section of the measurement, from depths of 45 to 120 meters, low to medium resistivity is observed, spanning a range of 90 to 130 ohm-meters. When correlated with the surrounding rock outcrops, the low resistivity values are thought to be associated with lapilli tuff and tuff breccia. In contrast, the medium resistivity values are suspected to correspond to tuff breccia. Both types of rock are believed to function as aquifers.

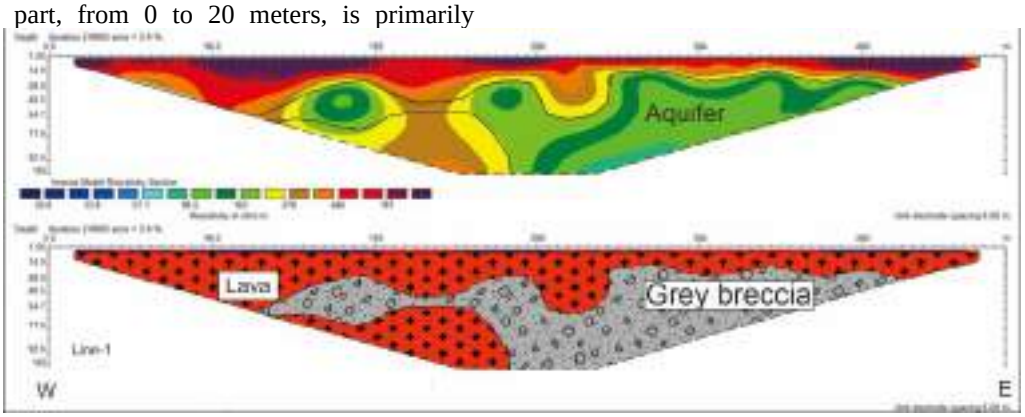

Figure 3. ERT line-01 and lithological unit interpretation

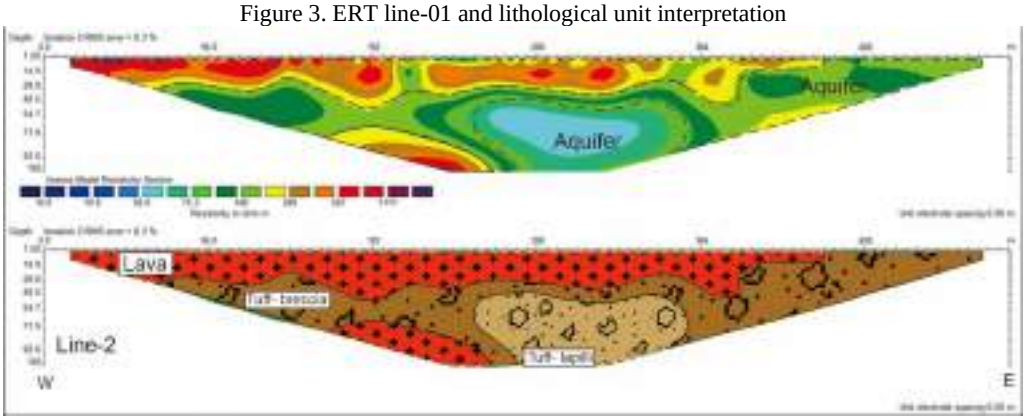

Figure 4. ERT line-02 and lithological unit interpretation

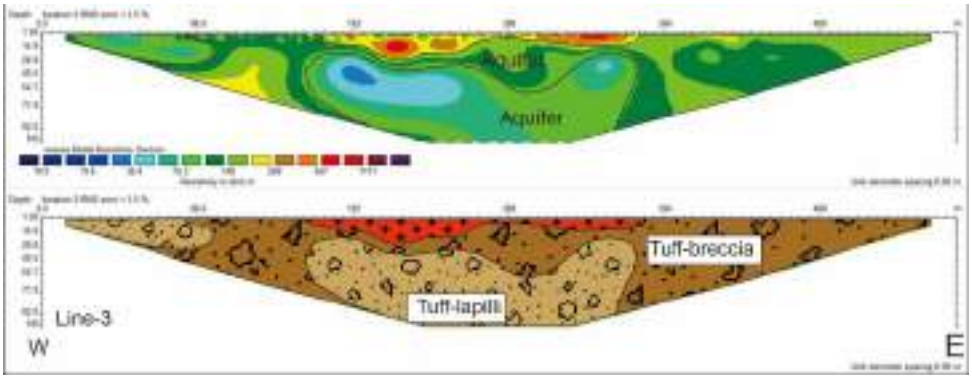

Figure 5. ERT line-03 and lithological unit interpretation

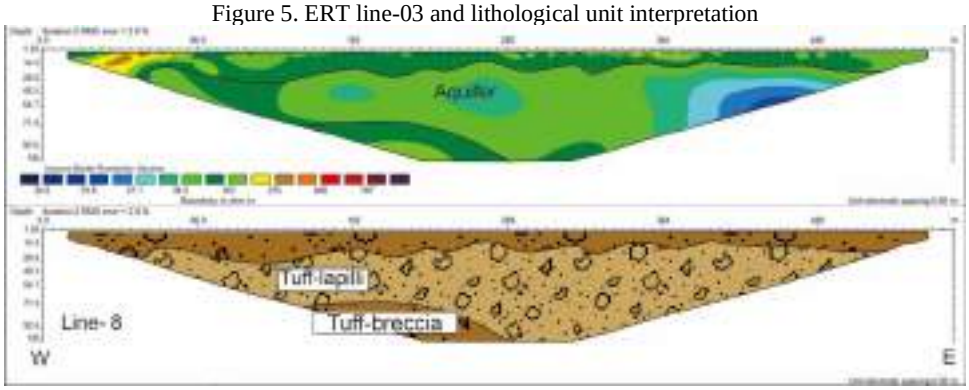

Figure 6. line-08 and lithological unit interpretation

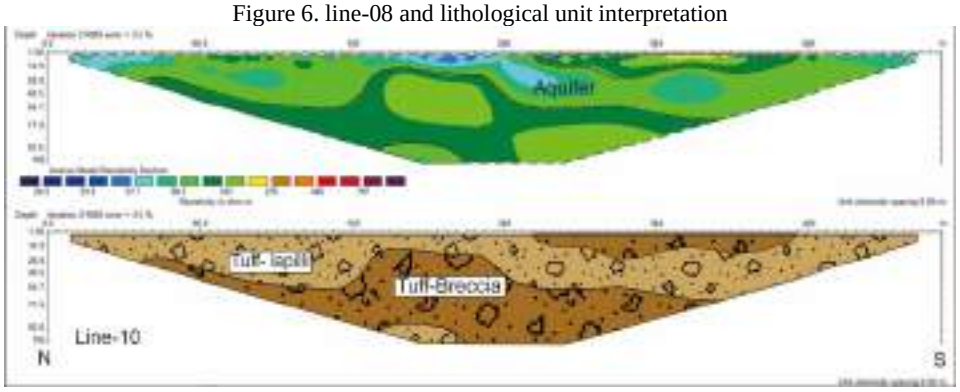

Figure 7. line-08 and lithological unit interpretation

Groundwater Hydrochemistry

Table 1. Groundwater physical properties and major ion data in the research area during the rainy season

No	Sample Code	Coordinate		Elevation	pH	EC	TDS	T	Ca^{2+}	Mg^{2+}	Na^{+}	K^{+}	HCO_3^{-}	SO_4^{2-}	Cl^{-}
		X	Y	m.a.s.l	m.a.s.l		µS/cm	mg/L	˚C	(mg/L)	(mg/L)	(mg/L)	(mg/L)	(mg/L)	(mg/L)
1	KNG 2	108.4683	-6.94303	635	5.5	330	160	26	30.5	15.3	17.8	6.3	86.5	38.4	32.8
2	KNG 12	108.4757	-6.91966	604	6.2	210	100	26	25.4	6.6	7.8	4.2	75.5	8.7	3.6
3	KNG 15	108.4958	-6.89873	474	6.1	200	90	27	20.5	9.0	7.4	3.0	82.1	5.7	3.0
4	KNG 17	108.4914	-6.86957	450	6.8	350	170	26	22.6	8.9	9.9	5.0	85.5	6.5	4.9
5	KNG 19	108.4813	-6.87573	536	6	160	70	27	19.2	7.1	7.0	3.5	81.1	3.7	2.7
6	KNG 23	108.4708	-6.84825	524	5.9	110	50	24	12.6	4.2	6.2	2.8	53.6	0.6	1.6
7	KNG 27	108.4569	-6.88089	719	6.8	80	50	24	12.8	2.8	4.9	3.3	45.0	0.0	1.9
8	KNG 29	108.4685	-6.90851	679	5.1	110	50	22	13.3	3.3	5.4	3.1	44.5	0.1	1.6
9	KNG 30	108.4569	-6.88473	811	6.6	90	40	24	12.6	2.6	4.7	3.3	45.4	0.0	0.9
10	KNG 33	108.4576	-6.90543	821	6.2	70	30	24	11.0	2.7	4.6	2.8	43.6	0.0	1.0
11	KNG 34	108.4496	-6.91374	972	6.6	120	60	26	13.2	3.3	4.4	1.9	44.8	0.0	1.0
12	KNG 35	108.5112	-6.8705	388	6.3	390	190	27	26.7	11.6	30.4	6.8	105.9	4.8	50.9

Table 2. Groundwater physical properties and major ion data in the research area during the dry season

No	Sample Code	Coordinate		Elevation	pH	EC	TDS	T	Ca^{2+}	Mg^{2+}	Na^{+}	K^{+}	HCO_3^{-}	SO_4^{2-}	Cl^{-}
		X	Y	m.a.s.l		µS/cm	mg/L	˚C	(mg/L)	(mg/L)	(mg/L)	(mg/L)	(mg/L)	(mg/L)	(mg/L)
1	KNG 2	108.4683	-6.94303	635	5.5	330	160	26	31.1	15.5	18.7	6.3	117.1	37.6	32.3
2	KNG 12	108.4757	-6.91966	604	5.7	190	90	26.8	26.4	6.8	8.3	4.2	78.1	10.1	3.8
3	KNG 15	108.4958	-6.89873	474	6.5	160	70	26	21.2	9.3	7.9	3.1	104.9	6.3	3.1
4	KNG 17	108.4914	-6.86957	450	6.6	190	80	28.2	23.1	9.1	10.5	5.3	112.2	7.7	5.3
5	KNG 19	108.4813	-6.87573	536	6.6	140	60	27.5	12.1	5.5	6.6	3.2	89.1	3.7	2.4
6	KNG 23	108.4708	-6.84825	524	6.5	80	30	24.8	12.9	4.5	6.6	2.9	69.5	1.9	1.6
7	KNG 27	108.4569	-6.88089	719	6.7	70	30	25.2	12.5	2.7	4.9	3.2	58.6	0.8	0.8
8	KNG 29	108.4685	-6.90851	679	6.2	70	30	25.3	9.5	1.9	2.8	1.6	59.8	0.8	0.9
9	KNG 30	108.4569	-6.88473	811	6.7	70	30	24.8	12.7	2.5	4.8	3.2	61.0	0.8	0.7
10	KNG 33	108.4576	-6.90543	821	6.4	60	20	21.4	8.2	1.1	3.1	1.4	57.3	0.8	0.7
11	KNG 34	108.4496	-6.91374	972	6.9	70	30	23.2	10.7	2.3	3.2	1.3	58.6	0.8	0.7
12	KNG 35	108.5112	-6.8705	388	6.5	330	160	27.3	27.5	11.7	32.1	7.2	130.5	5.4	49.4

Electrical conductivity in the dry season ranges between 50 µS/cm and 3550 µS/cm, while in the rainy season, it ranges between 50 µS/cm and 3550 µS/cm. Total Dissolved Solids (TDS) measure organic and inorganic substances dissolved in water. In the study area, TDS values during the dry season ranged from 20 mg/litre to 1770 mg/litre. In contrast, the values ranged from 20 mg/litre to 1750 mg/litre during the rainy season. The pH value in the study area during the dry season was 5.3 – 8, while in the rainy season, the pH value in the study area ranged between 5 – 8. Groundwater temperature ranges between 25 ˚C – 35.5 ˚C.

Hydrochemical Facies and Seasonal Variation

The groundwater samples collected from the Sub-Cimanis Watershed on the eastern slope of Mount Ciremai during the rainy and dry seasons exhibit distinct hydrochemical facies, as illustrated by Piper diagrams (Fig.8). In both seasons, the dominant facies idntified is Ca–Mg–HCO_3, indicative of shallow, fresh recharge and typical of groundwater circulating through fractured volcanic rocks [8,9].

During the rainy season, samples such as KNG-12, KNG-17, and KNG-23 plot tightly within the Ca–Mg–HCO_3 field, reflecting the rapid recharge of meteoric water into the unconfined volcanic aquifer. In contrast, the dry season reveals a more dispersed distribution, with several samples showing enrichment in Na^{+} and Cl-, particularly KNG-30 and KNG-33, suggesting ion exchange and longer residence times due to reduced recharge and increased water-rock interaction [10].

These seasonal facies changes imply dynamic hydrogeochemical processes influenced by both climatic and geological controls. The presence of mixed facies during the dry season suggests transition zones within the aquifer system, likely controlled by lithologic heterogeneity [11,12].

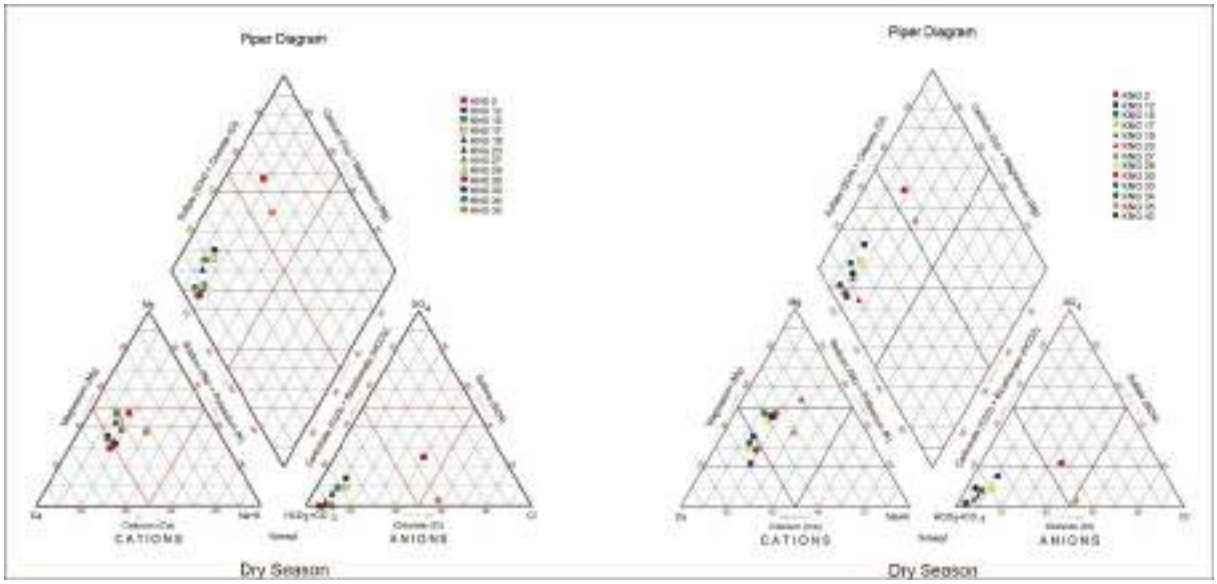

Figure 8. Plotting groundwater samples from both the rainy season and dry season in the research area onto a Piper diagram.

Groundwater Hydrochemical Processes

Gibbs diagrams (Fig. 9), which plot $Na_+/(Na^+ + Ca^{2+})$ and $Cl^-/(Cl^- + HCO_3^-)$ against total dissolved solids (TDS), are used to infer the dominant geochemical processes influencing groundwater chemistry [5]. Most of the samples from both seasons plot within the rock-weathering dominance field, indicating that mineral dissolution, especially from volcanic rocks, is the primary mechanism controlling groundwater composition. [10,11].

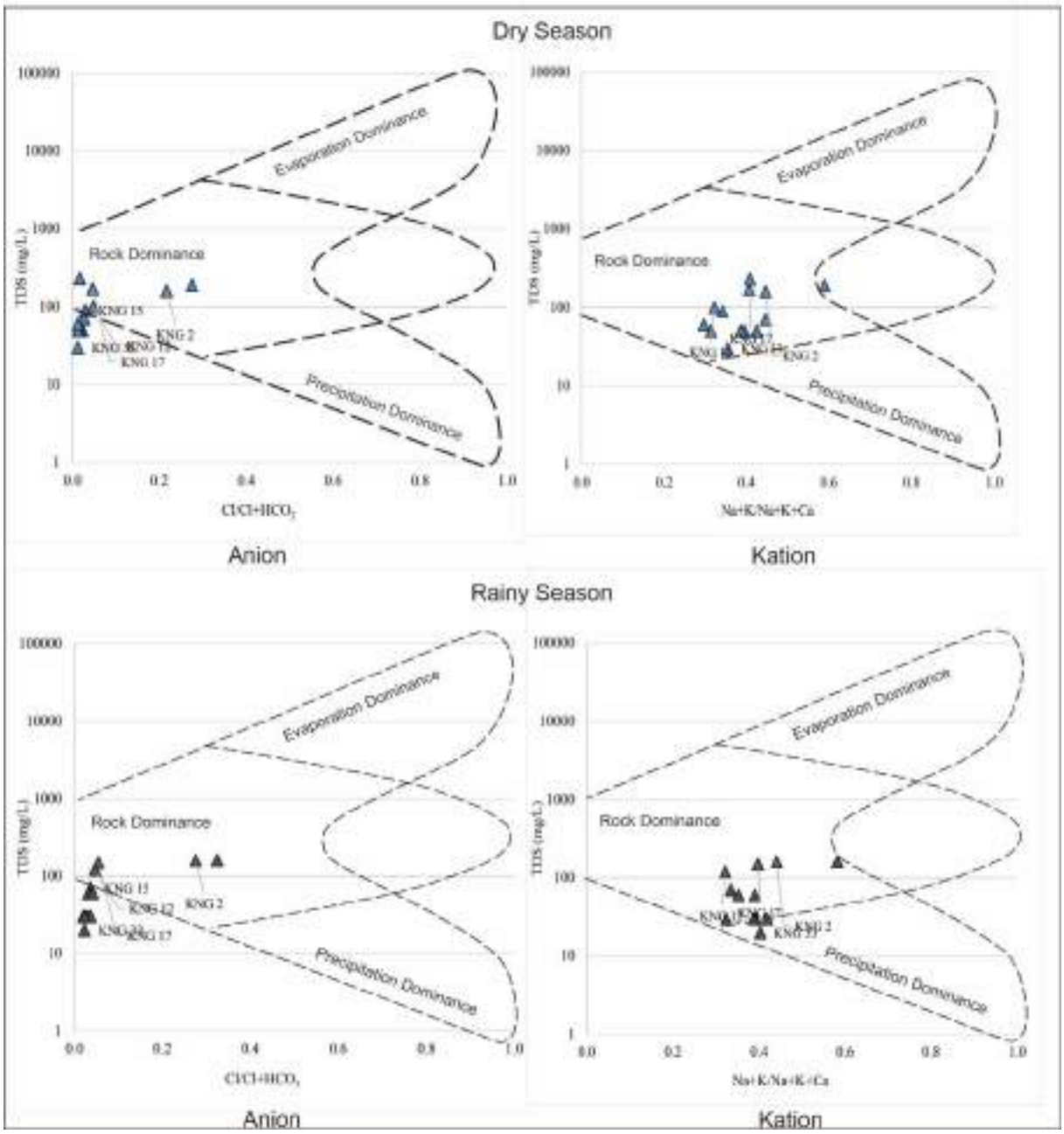

Figure 9. Plot major ions from the groundwater sample to the Gibbs diagram in the study area during the rainy season and dry season.

Integration with Resistivity and Aquifer Geometry

Electrical resistivity data from previous geophysical surveys reveal that high-resistivity zones (>200 Ω·m) correspond with unconfined aquifers composed of volcanic breccia and fractured lava, while low-resistivity zones (<50 Ω·m) represent clay-rich tuff layers that function as aquitards [13,14].

This hydrostratigraphic setting aligns well with the hydrochemical data. For example, samples like and

KNG-35 from confined zones exhibit higher electrical conductivity and mixed facies, suggesting longer groundwater residence times and restricted flow, confirmed by low resistivity values and confined aquifer geometry [15].

CONCLUSION

This study demonstrates that integrating geoelectrical resistivity tomography (ERT) and groundwater hydrochemical analysis provides a comprehensive understanding of the hydrogeological conditions in the Cimanis watershed on the eastern slopes of Mount Ciremai. The ERT results reveal distinct resistivity zones corresponding to subsurface lithology variations, aquifer distribution, and geological structures. High-resistivity zones are associated with volcanic rocks such as andesite lava and breccia, while low-resistivity zones indicate tuffaceous layers and fault-related structures. Hydrochemical analysis of groundwater samples collected across dry and rainy seasons shows consistent facies types—primarily Ca–HCO_3, Ca–Mg–HCO_3, and Ca–Mg–Cl—highlighting stable subsurface flow conditions. The findings underscore the influence of lithological heterogeneity, rock weathering, and volcanic facies transitions on groundwater composition. The integrated geophysical and geochemical approach effectively characterises aquifer systems in complex volcanic terrains, offering valuable insights for sustainable groundwater resource management.

ACKNOWLEDGMENTS

The researcher would like to express gratitude to the Faculty of Geological Engineering at Universitas Padjadjaran for providing the opportunity to conduct this research. Special thanks also go to PT. Tirta Fresindo Jaya for sponsoring the funding for this study.

REFERENCES

[1] Carrera, J. (2021). Integration of hydrogeophysical methods for groundwater studies in volcanic terrains. Hydrogeology Journal, vol. 29, 2021, pp. 403-419.

[2] Djuri. Geology of Arjawinangun. Geological Research and Development Centre, Bandung. 1995.

[3] Liu J, Gao Z, Feng J, Wang M. Identification of the hydrochemical features, genesis, water quality and potential health hazards of groundwater in Dawen River Basin, North China. Ecological Indicators, 2023, 1;149:110175.

[4] AM P. A graphic procedure in the geochemical interpretation of water analysis. Transactions-American Geophysical Union. 1944, 25:914-23.

[5] Gibbs, Ronald J. Mechanisms controlling world water chemistry. Science 170, no. 3962, 1970, 1088-1090.

[6] Procter, Jonathan, Anke Zernack, Stuart Mead, Michael Morgan, and Shane Cronin. A review of lahars; past deposits, historic events and present-day simulations from Mt. Ruapehu and Mt. Taranaki, New Zealand. New Zealand Journal of Geology and Geophysics 64, no. 2-3, 2021, pp. 479-503.

[7] Major, Jon J. Subaerial volcaniclastic deposits–influences of initiation mechanisms and transport behaviour on characteristics and distributions, 2023.

[8] Zhang, Han, Zong-yu Chen, and Chang-yuan Tang. Tracing runoff components in the headwater area of Heihe River by isotopes and hydrochemistry, 2022, pp. 405-412.

[9] Liu, Jiutan, Zongjun Gao, Jianguo Feng, and Min Wang. Identification of the hydrochemical features, genesis, water quality and potential health hazards of groundwater in Dawen River Basin, North China. Ecological Indicators 149 (2023): 110175.

[10] Maria, Rizka, Satrio Satrio, Teuku Yan Waliyana Muda Iskandarsyah, Bombom Rachmat Suganda, Robert Mohammad Delinom, Dyah Marganingrum, Wahyu Purwoko, Dady Sukmayadi, and Hendarmawan Hendarmawan. Groundwater recharge area based on hydrochemical and environmental isotopes analysis in the south Bandung volcanic area." Indonesian Journal of Chemistry 21, no. 3, 2021, pp. 609-625.

[11] Razi, Muhammad Haikal, Wahyu Wilopo, and Doni Prakasa Eka Putra. "Hydrogeochemical evolution and water–rock interaction processes in the multilayer volcanic aquifer of Yogyakarta-Sleman Groundwater Basin, Indonesia." Environmental Earth Sciences 83, no. 6, 2024, pp. 164.

[12] Pitchaimani, V. Stephen, R. J. Joe, G. Shyamala, G. Manjula, B. Hemalatha, M. Dinesh Babu, S. Shenbaga Ezhil, and Gobinath Ravindran. Multivariate statistical and hydrogeochemical analysis of seasonal groundwater quality variations in coastal villages of Trivandrum district, south India. Discover Sustainability 5, no. 1, 2024), pp. 1-32.

[13] Fatahillah, Hilmi El Hafidz, Putri Natari Ratna, Fardy Septiawan, Ridho Nanda Pratama,

Muhammad Razzaaq Al Ghiffari, Noviarso Wicaksono, Wahyu Hidayat et al. Identification of Volcanic Breccia Formation Distribution in Relation to Groundwater Aquifer Potential Using 3D Resistivity Data Modelling." Jurnal Lingkungan dan Bencana Geologi 14, no. 3, 2024, pp. 149-157.

[14] Wahab, Shafiqullah, Hakim Saibi, and Hideki Mizunaga. Groundwater aquifer detection using the electrical resistivity method at Ito Campus, Kyushu University (Fukuoka, Japan). Geoscience Letters 8, 2021, pp. 1-8.

[15] Furi, Wakgari, Moumtaz Razack, Tamiru Alemayehu Abiye, Seifu Kebede, and Dagnachew Legesse. Hydrochemical characterization of complex volcanic aquifers in a continental rifted zone: the Middle Awash basin, Ethiopia. Hydrogeology Journal 20, no. 2,2012, pp. 385.

Copyright © Int. J. of GEOMATE All rights reserved, including making copies, unless permission is obtained from the copyright proprietors.

15th Int. Conf. on Geotechnique, Construction Materials & Environment,
Kyoto, Japan, 11-13 November 2025, ISBN 978-4-909106124 C3051

WATER HYACINTH FIBER FOR LIMITED-LIFE GEOSYNTHETIC GEONET AS SUBGRADE REINFORCEMENT OF RURAL ROADS

Mary Ann Adajar[1], Patricia Gwenn Ang[1], Judith Dungca[1], Julia Dominic Espinola[1], and Nicole Gabrielle Tan[1]

[1]Department of Civil Engineering, De La Salle University, Philippines

ABSTRACT

The increasing demand for urban development has led to the neglect of rural road maintenance, compromising structural integrity due to weak subgrade soils. This study investigates the potential of water hyacinth fiber geonets (WHFG) as eco-friendly, limited-life geosynthetic alternatives for reinforcing subgrades in rural roads. While geonets are commonly used for drainage, their application in subgrade reinforcement remains limited. Two WHFG types with different apertures, 16 mm × 16 mm (16WHFG) and 22 mm × 22 mm (22WHFG), were fabricated and assessed for tensile strength performance in comparison to commercial synthetic geonets. Water hyacinth, an invasive aquatic plant known for its rapid growth and ecological impact, was repurposed for sustainable engineering use. Fibers were extracted from dried stems, treated with sodium hydroxide, and woven into geonet structures. Tensile tests were conducted according to ASTM D4595 standards. Results show that although WHFGs have lower tensile strength than high-density polyethylene (HDPE) geonets, the 16WHFG meets the minimum strength requirements for slope protection and erosion control set by the Department of Public Works and Highways (DPWH). Its improved performance over 22WHFG is attributed to stronger fiber interlocking provided by smaller apertures. This research demonstrates the viability of WHFG as a sustainable reinforcement solution for rural subgrade soils. It offers the dual advantage of addressing geotechnical challenges and mitigating the environmental impact of water hyacinths. Further research is recommended to enhance the durability and large-scale implementation of natural fiber geonets in geotechnical applications.

Keywords: Water hyacinth fiber geonet, Limited-life geosynthetics, Natural fiber geonet, Subgrade reinforcement

INTRODUCTION

Rural road networks are essential in ensuring equitable access to basic services and economic opportunities. However, in many developing regions, these roads suffer from insufficient design and weak subgrade conditions, often leading to rapid deterioration under heavy vehicular loads. The structural integrity of these roads relies heavily on the subgrade's ability to distribute loads effectively, and any compromise in this layer can result in rutting, settlement, and premature failure.

To address these challenges, designers have turned to various materials and technologies that enhance subgrade performance, one of the most significant being geosynthetics [1]. Geosynthetics, including geotextiles, geogrids, and geonets, have been widely adopted in engineering projects to enhance the mechanical behavior of soil. Geosynthetics are synthetic materials that provide sustainable engineering solutions for geotechnical and geoenvironmental issues [2]. Accordingly, this material has a variety of purposes, which include drainage, separation, reinforcement, filtration, protection, and fluid barrier. According to Shukla [3], geosynthetics refers to a broad category of products with varying densities, thicknesses, structures, and other parameters, namely geotextiles, geogrids, geocells, geofoams, geomembranes, and geocomposites. These products are all produced under controlled conditions primarily from polymeric materials such as polypropylene, polyvinyl chloride, polyester, polyamide, polystyrene, and polyethylene. They are used in contact with soil, rock, or other construction-related materials to support civil engineering projects, a structure, or a system [4]. Fluid containment, environmental protection, stabilization, slope stability, and erosion control are some of the most common uses of geosynthetics. Some of its engineering applications are typically found in landfills, lagoons, dams, mining, roads, railways, slopes, walls, embankments, pond spillways, riverbanks, and channels [5-7].

While these conventional geosynthetics made from polymeric materials have demonstrated significant benefits in improving subgrade stability and load-bearing capacity, their widespread use has raised environmental concerns. Their resistance to degradation, although advantageous for long-term applications, poses a challenge regarding post-use disposal and environmental persistence. In response, the civil engineering community has begun to explore more sustainable alternatives that maintain performance while reducing environmental impact.

This shift in focus has led to a growing interest in limited-life geosynthetics (LLGs), materials specifically designed to provide temporary reinforcement and degrade after serving their purpose.

In recent years, biodegradable or limited-life geosynthetics have gained traction, especially in projects where long-term structural support is unnecessary. These materials are designed to deliver critical reinforcement during the early stages of soil consolidation and road service life, after which they naturally break down, minimizing their ecological footprint. This approach aligns particularly well with the needs of rural infrastructure, where cost-efficiency, sustainability, and context-specific engineering solutions are crucial. LLGs can provide effective short-term support during construction, promote long-term natural stabilization, and even assist in revegetation efforts, making them ideal for rural road applications with moderate traffic volumes and limited maintenance resources.

In the search for suitable LLGs, natural fibers have been investigated for their biodegradability, availability, and mechanical performance. Natural fibers such as jute, coir, and vetiver have been studied as alternatives to synthetic geosynthetics. However, one underutilized fiber source is water hyacinth, an invasive aquatic plant that poses a significant environmental challenge in many waterways. Water hyacinth (*Eichhornia crassipes*), an invasive aquatic plant abundant in many waterways, presents a viable source of natural fiber. In the Philippines, water hyacinths can proliferate at an alarming rate. These plants can cover up to 600 sqm. in just a year, threatening the aquatic biodiversity in the area by rapidly reducing the water's oxygen level as they grow. In a recent cleanup of the Pateros River, 420 bags' worth of water hyacinths were hauled out [8]. Its rapid proliferation clogs rivers, threatens biodiversity, and imposes high maintenance costs for removal. While the reuse of water hyacinth in handicrafts and animal feed has been explored, its potential in civil engineering applications remains largely untapped. With its abundant availability and high fiber yield, water hyacinth offers an untapped opportunity to create woven geonets that are locally sourced, biodegradable, and environmentally restorative.

The study by Patel, M. & Patel, A. [9] assesses the effectiveness of coir geotextiles in enhancing subgrade performance, noting improvements in strength and durability. Another paper [10] promoted green engineering by utilizing nonwoven coir geotextiles as an alternative material for slope stabilization. An article by Nguyen et al. [11] reviews the use of various natural fibers in geotechnical engineering, discussing their properties, benefits, and challenges. Kumar et al. [12] investigate using coir and jute fibers as sustainable alternatives to synthetic materials in rural road construction, highlighting their environmental benefits and mechanical properties. The research of Arifin et al. [13] assesses the tensile strength and durability of oil palm empty fruit bunch fibers in soft soil, providing insights into the performance of biodegradable fibers in geotechnical applications. Natural materials like bamboo were used as reinforcement to improve peat soil, demonstrating the effectiveness of natural materials in enhancing soil stability [14]. All of these reviewed studies collectively highlight the growing interest in sustainable, biodegradable materials for geotechnical applications, particularly in rural infrastructure. However, they also reveal a gap in research concerning the use of invasive species like water hyacinth as reinforcement materials.

This study aims to capitalize on this opportunity by developing a water hyacinth fiber geonet (WHFG), a biodegradable, woven reinforcement mesh intended to support rural subgrade soils during early loading stages. This study aims to evaluate the tensile strength performance of water hyacinth fiber geonets (WHFG) fabricated with two aperture configurations (16×16 mm and 22×22 mm) and to assess their suitability as subgrade reinforcement for rural roads. The performance of WHFG is compared against commercial high-density polyethylene (HDPE) geonets and benchmarked against existing standards from the Department of Public Works and Highways (DPWH) in the Philippines. This study introduces a novel use of water hyacinth fiber geonets (WHFG) as a limited-life geosynthetic for subgrade reinforcement. The study also highlights the effect of aperture size on geonet tensile strength, reinforcing the importance of fiber interlocking in improving performance. By analyzing the influence of aperture size on tensile strength and interlocking behavior, the study seeks to provide insight into the design optimization of natural geonets for engineering use.

RESEARCH SIGNIFICANCE

The adoption of WHFG provides an opportunity to transition toward bio-based, low-cost geosynthetics that are locally sourced, biodegradable, and potentially community-manufactured. It offers an innovative dual solution: addressing the structural weakness of rural road subgrades while simultaneously mitigating the environmental impact of invasive water hyacinths. Through this investigation, the study contributes to the growing body of knowledge on limited-life geosynthetics, demonstrating how biodegradable, locally sourced materials can be engineered to meet the mechanical and functional requirements of civil infrastructure. The research supports the advancement of sustainable rural development, ecological resource management, and climate-conscious engineering practices.

MATERIALS AND METHODS

The materials for this research were water hyacinth fibers and sodium hydroxide for the treatment of fibers. Dried water hyacinth stems were

sourced from local suppliers. The researchers constructed a large wooden loom with varying apertures for the manual weaving process of the WHFG.

Water Hyacinth Fiber Extraction and Treatment

The fibers were extracted from the water hyacinth stems after they were sun-dried. Though the fiber can also be extracted from the leaves and roots, water hyacinth stems have the highest fiber concentration and the longest fiber length. The dried water hyacinth stems had a thin external layer encasing the fibers, which are long individual strands clumped together by spongy material. To extract the fibers, the dried skin of the water hyacinth was hand-peeled carefully until the cluster of fibers was entirely exposed, as seen in Fig. 1. Afterwards, the peeled stems were soaked in water for at least three days to soften. After soaking in water, the peeled water hyacinth stems were transferred to a sodium hydroxide (NaOH) bath following the procedure described by Nguyen and Nguyen [15]. The NaOH bath should have a concentration of 10% solution, which was achieved by dissolving 4 grams of NaOH powder per liter of water. The stems were treated for 3 hours in the bath while maintaining a temperature between 40°C to 50°C. The treated stems were then rinsed in clean water several times until the water turned clear. The spongy material covering the fibers was scraped off, leaving only the fiber to have a thinner strand for the rope making. Thinner strands were expected to have higher fiber density and would yield higher strength properties [15].

(a) (b)

Fig.1 (a) Peeling of the outer layer of the stem, (b) Peeled water hyacinth stem

While the fibers were still wet, the braiding of strands to form ropes was performed (Fig. 2). Maintaining the damp condition of the strands while braiding produced better interlocking between the fibers. The rope-making procedure was performed following a simple cordage technique. A single rope was made of 2 entwined strands with a thickness of around 20mm. After braiding, the ropes were left out to sun-dry for at least 24 hours, during which their total thickness was reduced to about 4 to 5 mm.

Fig.2 Braided strands in wet condition

Weaving of Geonet

A plain weave pattern was used to achieve high tensile strength, as recommended by Artidteang et al. [16]. The weave was oriented to form a diamond-shaped aperture relative to the wooden loom, a configuration characteristic of geonets. Two different aperture sizes were employed in weaving the water hyacinth fiber geonet (WHFG), 16×16 mm and 22×22 mm. These sizes were selected based on standard aperture dimensions commonly found in commercially available synthetic geonets. For reference throughout this paper, a WHFG with a 16×16 mm aperture is denoted as 16WHFG, while that with a 22×22 mm aperture is denoted as 22WHFG.

The large wooden looms used for weaving, illustrated in Figs. 3 and 4, each measured 1.5 × 1.5 meters.

Fig. 3 Loom for 22WHFG geonet.

Fig.4 Loom for 16WHFG geonet.

A separate loom was designated for each aperture size to accommodate the required number of samples for all experimental tests. Evenly spaced nails along the wooden frame allowed the woven ropes to be secured tightly, helping to maintain consistent tension during the weaving process.

TEST METHOD

ASTM D 4595, Standard Test Method for Tensile Properties of Geotextiles by the Wide-Width Strip Method, was used to determine the tensile strength and elongation wherein a continually increasing longitudinal load was applied to the sample until rupture (Figs. 5a and 5b).

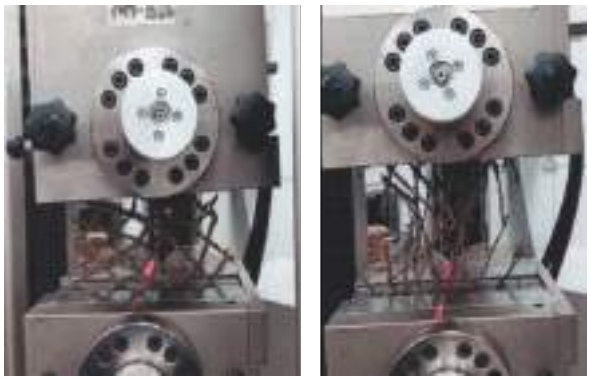

(a) (b)

Fig.5 Tensile test on (a) 22WFHG and (b) 16WFHG

The determination of wide-width strip force–elongation properties of geotextiles provides essential design parameters for reinforcement applications, such as subgrade stabilization. The specimen sizes were 200×300 mm in the shape of a rectangle. The tensile tests were done in two principal orientations, the machine direction (MD) and the cross-machine direction (CMD). In the machine direction, the tensile load is applied parallel to the production of the weaving flow, essentially along the length of the material as it is formed on the loom. The result of the tensile strength in the MD orientation assesses the material's strength along the primary alignment of the fibers or ropes. In the cross-machine direction, the tensile load is applied across the width of the material. Tensile testing in the CMD evaluates the strength across the woven structure, typically involving interlaced or supportive fibers. A total of 12 samples were prepared, wherein six samples were prepared per aperture size for each test orientation.

TEST RESULTS

The tensile strength of the fabricated water hyacinth fiber geonets (WHFG) was evaluated to assess their mechanical performance and suitability for potential geotechnical applications. Table 1 presents the average tensile strengths of the water hyacinth fiber geonets (WHFG) in both the machine direction (MD) and cross-machine direction (CMD). The 16WHFG exhibited notably higher tensile strength values, recording 3.4 KN/m (MD) and 2.9 KN/m (CMD), compared to 1.5 KN/m (MD) and 1.8 KN/m (CMD) for the 22WHFG. This difference in tensile performance is primarily attributed to the smaller aperture size (16×16 mm) of the 16WHFG, which results in a denser weave and greater rope overlap, enhancing load distribution and resistance to tensile deformation. In contrast, the 22WHFG's larger apertures offer less resistance under load due to increased spacing between the woven strands.

Table 1 Average Tensile Strengths of WHFG

	Tensile Strength MD (KN/m)	Tensile Strength CMD (KN/m)	CMD to MD ratio
22WHFG	1.5	1.8	1.2
16WHFG	3.4	2.9	0.85

This trend is consistent with findings from Gaviola et al. [17], who investigated geotextiles made from coconut fiber and vetiver grass. Their study observed that geotextiles with smaller aperture sizes exhibited higher tensile strength, leading to better performance in erosion control applications. They concluded that the increased number of mesh junctions due to the smaller aperture size enhanced the structural integrity of the geotextile, making it more effective for slope reinforcement. Similarly, in the present study, the 16WHFG's superior tensile strength can be attributed to its smaller aperture, which allows more junction points where ropes interlock. This denser interweaving contributes to a stronger load-bearing network across the geonet. Further support is found in the work of Sakleshpur et al. [18], who examined the relationship between tensile strength and junction strength in woven geosynthetics. Their study defined junction strength

as the force required to separate interwoven points and found that higher tensile strength correlated with stronger junctions, which in turn were linked to greater interlocking within the weave. This implies that the interlocking effect, reinforced by the tighter mesh of the 16WHFG, likely plays a critical role in its enhanced tensile behavior.

The CMD-to-MD strength ratios, 1.2 for 22WHFG and 0.85 for 16WHFG, indicate a relatively balanced biaxial performance, especially for the 16WHFG, suggesting its suitability in applications where tensile forces may not be strictly uniaxial. A balanced MD and CMD strength ensures the geonet can resist stretching and deformation, regardless of the load direction, improving durability and effectiveness in real-world use.

To assess the variability and reliability of the tensile strength measurements, standard deviation values were calculated for both the machine direction (MD) and cross-machine direction (CMD) tests. The results show that for 22WHFG, the standard deviations were 0.53 KN/m (MD) and 0.47 KN/m (CMD), while for 16WHFG, the values were 0.97 KN/m (MD) and 1.02 KN/m (CMD). These values indicate a moderate level of variation within the samples, which is expected in natural fiber-based materials due to inherent inconsistencies in fiber composition and alignment.

When compared to the Department of Public Works and Highways (DPWH) standard specifications for coco coir geonets in the Philippines, as outlined in Department Order No. 29, Series of 2008 [19], the 16WHFG meets the lower performance threshold required for slope stabilization and erosion control. Meanwhile, the 22WHFG falls below this range, suggesting limited structural reliability for primary reinforcement applications. A comparison with DPWH Department Order No. 54, Series of 1998 [20], which prescribes tensile strength values for synthetic geotextiles, reveals that both WHFG variants fall below the minimum requirements for high-performance erosion control materials. Specifically, geotextiles for Class B erosion control must exhibit minimum grab tensile strengths of 800 N (MD) and 510 N (CMD), equivalent to approximately 8.0 KN/m and 5.1 KN/m. Consequently, WHFGs are unsuitable for critical structural roles but remain viable for temporary or biodegradable reinforcement applications.

In comparison to commercial synthetic geonets of the same aperture size, which exhibit tensile strengths of 6.4 KN/m for HDPE with 22 x 22 mm aperture and 5.4 KN/m for HDPE with 16 x 16mm aperture, WHFGs represent a lower strength but environmentally sustainable alternative. Their value lies not in outperforming synthetic counterparts, but in offering a biodegradable, low-cost, and sustainable alternative. In regions with abundant water hyacinth biomass, the utilization of WHFGs can contribute to invasive species management while promoting green engineering practices. Their biodegradability and reliance on invasive biomass make them particularly attractive in eco-engineering contexts where long-term persistence is not required.

Despite their relatively lower strength, the WHFGs, particularly the 16WHFG, demonstrate sufficient tensile capacity for light-duty applications, such as rural road subgrade reinforcement, temporary slope stabilization, and low-volume erosion control systems. Additionally, their environmental biodegradability positions them as viable candidates for limited-life geosynthetic (LLG) solutions, where natural degradation is preferred post-construction.

CONCLUSIONS

This study explored the tensile performance of water hyacinth fiber geonets (WHFG) woven using two aperture configurations (16×16 mm and 22×22 mm) and assessed their suitability for geotechnical applications. Results revealed that the 16WHFG exhibited higher tensile strength, with values reaching 3.4 KN/m in the machine direction and 2.9 KN/m in the cross-machine direction, surpassing the 22WHFG in both orientations. These findings demonstrate the critical role of weave density and aperture size in enhancing mechanical properties.

In comparison with the Department of Public Works and Highways (DPWH) standards for natural geonets and geotextiles, the 16WHFG meets the lower threshold of performance for coco coir geonets but falls below the required specifications for synthetic geotextiles. When compared to commercial synthetic geonets, WHFGs exhibit lower tensile strength but provide considerable environmental and economic advantages due to their biodegradability and local material sourcing.

The WHFG's performance, especially the 16WHFG, is suitable for temporary and low-stress applications, such as rural slope stabilization, subgrade reinforcement in low-traffic areas, and eco-engineering projects focused on sustainable infrastructure. Their use contributes to waste valorization, particularly in regions heavily infested with water hyacinths, and supports circular engineering solutions.

To enhance the performance and practical adoption of WHFGs as sustainable geosynthetics, future work should consider conducting long-term field testing to evaluate the biodegradation rate and mechanical stability of WHFGs under real environmental conditions such as rainfall, UV exposure, and soil interaction. Performing a life-cycle assessment comparing WHFG with conventional synthetic geonets will quantify the environmental benefits in terms of carbon footprint, waste reduction, and end-of-life impacts.

REFERENCES

[1] Hegde A. M., Geosynthetics Overview, In: Geocells, Springer, Singapore, 2020, pp.1–27.

[2] Palmeira E. M., Araújo G. L., and Santos E. C., Sustainable Solutions with Geosynthetics and Alternative Construction Materials—A Review, Sustainability, Vol. 13, No. 22, 2021, pp.12756.

[3] Shukla S. K., Geosynthetics and ground engineering: sustainability considerations, Int. J. of Geosynthetics and Ground Engineering, Vol. 7, No. 1, 2021, pp.1–3.

[4] Shukla S. K., An Introduction to Geosynthetic Engineering, 2nd ed., CRC Press, Boca Raton, 2021, pp.1–500.

[5] Rowe R. K., Protecting the environment with geosynthetics: 53rd Karl Terzaghi Lecture, J. of Geotechnical and Geoenvironmental Engineering, Vol. 146, No. 9, 2020, pp.04020081.

[6] Bayraktar O. Y., Use of geosynthetics in road construction, Kastamonu University Journal of Engineering and Sciences, Vol. 6, No. 2, 2020, pp.107–113.

[7] Han J. and Guo J., Geosynthetics used to stabilize vegetated surfaces for environmental sustainability in civil engineering, Frontiers of Structural and Civil Engineering, Vol. 11, No. 1, 2017, pp.56–65.

[8] Allanigue, A., "DENR-NCR removes water hyacinths in Pateros River," Philippine Information Agency, November 22, 2021. [Online]. Available: https://pia.gov.ph/news/2021/11/22/denr-ncr-removes-water-hyacinths-in-pateros-river

[9] Verma P. and Khan F., Application of coir geotextile in subgrade for improved strength and drainage condition of flexible pavement, Int. Res. J. of Engineering and Technology (IRJET), Vol. 10, No. 6, 2023, pp.653–657.

[10] Adajar M. A., Cutora M., Bolima S. J., Chua K. J., Isidro I. A., and Ramos J. V., Strength Performance of Nonwoven Coir Geotextiles as an Alternative Material for Slope Stabilization, Applied Sciences, Vol. 13, No. 13, 2023, Article 7590.

[11] Nguyen T. T. and Indraratna B., Natural fibre for geotechnical applications: concepts, achievements and challenges, Sustainability, Vol. 15, No. 11, 2023, pp.8603.

[12] Kumar N., Kandasami R. K., and Singh S., Effective utilization of natural fibres (coir and jute) for sustainable low-volume rural road construction – A critical review, Construction and Building Materials, Vol. 347, 2022, pp.128606.

[13] Arifin Y. F., Arsyad M., Siswanto R., Astawa I. K. T. F., Ridha M. H., and Ramadhani M. R., Tensile strength and durability of oil palm empty fruit bunch fiber in soft soil, Int. J. of GEOMATE, Vol. 23, No. 99, 2022, pp.72–81.

[14] Talib F. M., Mohamad H. M., and Mustafa M. N., Peat soil improvement with bamboo reinforcement technology: A review, Int. J. of GEOMATE, Vol. 21, No. 88, 2021, pp.75–85.

[15] Nguyen, H. T., and Nguyen, T. B. H., "Treatment of water hyacinth fibers to improve mechanical and microstructural properties of green composite materials," Nano Hybrids and Composites, Vol. 35, pp. 111–122, 2022.

[16] Artidteang S., Bergado D. T., Tanchaisawat T., and Saowapakpiboon J., Investigation of tensile and soil-geotextile interface strength of kenaf woven limited life geotextiles (LLGs), Lowland Technology International, Vol. 14, No. 2, 2012, pp. 1–8.

[17] Gaviola J. C. L., Borong B. L. G., Cutanda S. M. R., and Loreto E. G., Effectiveness of coconut fiber geotextile and vetiver grass as bioengineering technique in mitigating soil erosion along Bato-Bontoc Road, International Journal of Engineering Applied Sciences and Technology, Vol. 5, No. 1, 2020, pp. 13–19.

[18] Sakleshpur V. A., Lee M. S., Prezzi M., Salgado R., and Siddiki N., Effects of geogrid aperture size and junction strength on soil-aggregate interface shear strength, GeoAmericas 2020 Conference Proceedings, 2020, pp. 1–8.

[19] Department of Public Works and Highways (DPWH), Department Order No. 29, Series of 2008: Standard Specifications for Coconet Bio-Engineering Solutions (Item 518), Bureau of Design, Manila, Philippines, 2008, pp. 1–7.

[20] Department of Public Works and Highways (DPWH), Department Order No. 54, Series of 1998: Standard Specifications for Geotextiles, Bureau of Design, Manila, Philippines, 1998, pp. 1–9.

Copyright © Int. J. of GEOMATE All rights reserved, including making copies, unless permission is obtained from the copyright proprietors.

15th Int. Conf. on Geotechnique, Construction Materials & Environment, Kyoto, Japan, 11-13 November 2025, ISBN 978-4-909106124 C3051

DEVELOPMENT OF SOLIDIFIED CULTIVATING SOIL BLENDED WITH WASTE WOODY BIOMASS PREPARED BY THE EICP METHOD

Daiki Kawamura[1, 2] and Satoru Kawasaki[3]

[1] Kumagai Gumi Co., Ltd., Japan; [2]1Graduate School of Engineering, Hokkaido University, Sapporo, Japan; [3]Faculty of Engineering, Hokkaido University, Sapporo, Japan

ABSTRACT

Bio-cementation is well known as an environmentally friendly technique. It is studied for mitigating liquefaction, reducing dust, and increasing ground strength. This technique has been considered for use in the ground, but it is important to reduce ammonia (NH_3) and ammonium ions (NH_4^+) generation. On the other hand, these by-products have the potential to act as beneficial nutrient sources in agricultural applications. We aim to develop a solidified cultivating soil using generated ammonium ions (NH_4^+). Additionally, the importation of peat moss, a principal material of solidified cultivating soil, has declined due to the depletion of natural resources, prompting the search for environmentally sustainable alternative substrate materials. In this study, we conducted solidification and germination tests using EICP as a solidification method, which, unlike other bio-cementation techniques, does not require microbial cultivation, and using waste woody biomass such as bamboo powder and coco peat. Additionally, we investigated the degree of collapse of solidified cultivating soil, as well as the effects of ammonium nitrogen on solidification and germination. The results show that the solidification strength, represented by the degree of collapse, was enhanced with increased injection frequency at lower cementation concentrations (0.1 M and 0.25 M). At a concentration of 0.5 M, the solidification was sufficiently strong even with four injections. The germination rate increased as the molar concentration of cementation solution decreased. These results suggest that $CaCO_3$ cementation, when optimized in terms of concentration, holds promise for developing sustainable solidified cultivating soil.

Keywords: Bio-cementation, EICP, NH_4^+, Bamboo powder, solidified cultivating soil

INTRODUCTION

The labor force in Japanese agriculture continues to decline due to an aging population and decreasing birthrate. In response, smart agriculture has emerged, with the aim of enhancing efficiency and productivity through the integration of advanced technologies [1, 2]. These innovations include hydroponic systems and mechanized transplanting, which use growth substrates such as solidified cultivating soil and rock wool. These substrates exhibit three characteristics: high water permeability and retention capacity, ease of handling and transportation, and low weight. Solidified cultivating soil is produced by applying heat treatment to a soil-fiber mixture [3]. Conversely, rock wool is synthesized by melting materials such as blast furnace slag and basalt at high temperatures (approximately 1,500–1,600°C) [4]. This process raises environmental concerns due to substantial CO_2 emissions. Additionally, peat moss, a principal material of solidified cultivating soil, is imported in smaller quantities due to limited natural resources, prompting the need for environmentally sustainable alternative substrate materials.

In our research, we aim to develop a sustainable form of solidified cultivation soil with minimal environmental impact. Specifically, we focus on a cementation method that utilizes calcium carbonate ($CaCO_3$) and incorporates waste woody biomass. The cementation process relies on microbially induced carbonate precipitation (MICP) and enzyme-induced carbonate precipitation (EICP), which are established techniques used in applications such as erosion control [5], liquefaction mitigation [6], and slope stabilization [7]. These processes employ microbial or enzymatic activity to promote $CaCO_3$ precipitation through the following biochemical reactions [8]:

$$CO(NH_2)_2+H_2O\rightarrow 2NH_3+CO_2 \quad (1)$$

$$NH_3+H_2O\rightarrow NH_4^++OH^- \quad (2)$$

$$CO_2+H_2O\rightarrow HCO_3^-+H^+ \quad (3)$$

$$HCO_3^-\rightarrow H^++CO_3^{2-} \quad (4)$$

$$Ca^{2+}+CO_3^{2-}\rightarrow CaCO_3 \quad (5)$$

One concern associated with this technique is the production of ammonia (NH_3) and ammonium ions (NH_4^+), which can lead to nitrogen pollution. However, these byproducts can also serve as beneficial nutrients for vegetable cultivation. Previous studies have investigated the interaction among MICP/EICP, plant growth, and soil [9, 10], but the relation with woody biomass has received limited attention.

In this study, we conducted solidification and germination tests using EICP as a solidification

method, which, unlike other bio-cementation techniques, does not require microbial cultivation. We also used waste woody biomass such as bamboo powder and coco peat. Additionally, we investigated the degree of collapse of solidified cultivating soil, as well as the effects of ammonium nitrogen on solidification and germination.

MATERIALS AND METHODS

EICP

This study selected EICP as a solidification method, which is a cementation technique based on enzyme reactions, for two reasons: it does not require cultivation, and it can utilize waste. Urease is generally extracted from beans such as jack beans and soybeans [11]. Recently, researchers have studied extracting urease from waste materials such as watermelon seed [12]. In the future, we aim to reduce costs by using EICP with urease derived from waste materials.

Waste Woody Biomass

This study used two types of waste woody biomass materials: coco peat sourced from Sri Lanka and bamboo powder (Phyllostachys edulis) obtained from Gifu, Japan. Table 1 summarizes their physical properties. Bulk density was measured as the mass of biomass filling 100 mL in a graduated cylinder. Ignition loss was measured in accordance with JIS A1226:2020. The pH and electrical conductivity (EC) were measured using a compact meter (LAQUAtwin, HORIBA, Ltd.). Coco peat is generally produced through processes such as crushing, rinsing, and screening. It is widely used in hydroponic cultivation and for soil conditioning. Bamboo powder is produced through processes such as crushing and fermentation. Recently, bamboo powder has been considered for use in soil cultivation as awareness of abandoned bamboo forests has been increasing [13].

Table 1 Characteristics of wood materials

	Bamboo powder	Coco peat
Bulk density (g/cm^3)	0.195	0.154
Ignition loss (%)	88.5	90.9
pH	5.3	5.4
EC (dS/m)	1.83	4.8

Solidification Test

The solidification test was conducted to evaluate the relationship among the degree of collapse of the substrate, the amount of rinse water, and the frequency of solidification solution injections. The procedure is outlined as follows:

Sample preparation: Coco peat and bamboo powder were air-dried for 24 hours, sieved through a 2 mm screen, and mixed in a 1:1 volumetric ratio. The mixture was homogenized using a high-speed mixer (Braun MultiQuick9, De'Longhi Japan Corp.) operating at 1500 rpm.

Solution preparation: A urease solution (0.1 g/L, 2.1 U/mL) was prepared using urease reagent (Fujifilm Holdings Corp.). Urea and calcium nitrate [$Ca(NO_3)_2$] solutions with concentrations of 0.1 M, 0.25 M, and 0.5 M were prepared using urea reagent and calcium nitrate reagent (Fujifilm Holdings Corp.). The urease solution and the urea–calcium nitrate solutions were mixed in a 1:1 volumetric ratio to form the solidification solution.

Cultivating Soil Preparation: A 200 mL sample of the biomass mixture was combined with 160 mL of the solidification solution and packed into a commercial cell tray (Meiwa Co., Ltd.) with a filling density of approximately 0.17 g/cm^3 (see Fig. 1 for dimensions). In addition, number of cell was twelve.

Injection and rinsing: Solidification solution (10 mL) was injected at 3-hour intervals, either 3 or 7 times. The reason for setting this interval at three hours is that the decrease in calcium ions plateaus three hours after the solution is injected, and no further precipitation of calcium carbonate is expected thereafter. Subsequently, the samples were rinsed with 50 mL or 250 mL of deionized water. Control samples received only deionized water. The experimental variables were: i) concentration of the solidification solution, ii) number of solution injections, and iii) rinsing volume. The test was repeated twice.

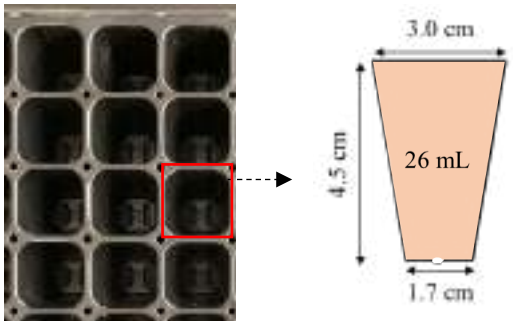

Fig. 1 Size of cell tray

Germination Test

The germination test was conducted to evaluate the relationship between seed germination rate, degree of collapse, and solidification solution concentration. The samples used for the germination test were prepared using the same method as those used for the collapse measurement, but they were different samples. Seeds of Japanese mustard spinach

were placed in 3 mm-deep holes at the center of each substrate surface (see Table 2 for test conditions). Germination was defined as the emergence of cotyledons. The germination rate was calculated as:

$$\text{Germination Rate (\%)} = (\text{Number of Germinated Seeds} / \text{Total Seeds}) \times 100 \quad (6)$$

In this experiment, total seeds was twelve, the test was repeated twice.

Table 2 Conditions of germination test

condition	
Temperature (℃)	25
Term (day)	7
Watering (times/day)	1

Measurement of Substrate Collapse

Previous bio-cementation studies have typically used a needle penetrometer to assess physical strength [14]. However, due to the fragile nature of the solidified substrates in this study, an alternative collapse measurement method (illustrated in Fig. 2) was employed, as proposed in [3]. The collapse index shows how strong the solidified soil is, and it also shows how easily it breaks when taken out of the cell tray.

Chemical Analysis

After the germination tests, the pH and EC of the substrates were measured using the compact meter (LAQUAtwin, HORIBA, Ltd.). Ammonium nitrogen concentrations were measured in accordance with the indophenol blue absorptiometry method. Note that ammonium nitrogen was measured only once during the two trials, using a combined sample from all twelve cells.

RESULTS AND DISCUSSION

Table 3 presents a summary of the experimental results. In this experiment, Case 1 represents the control group. The number of injections refers to the frequency of solidification solution application, while rinse indicates the amount of deionized water used. The detailed findings from the solidification and germination tests are discussed below. The value of the degree of collapse shows the average of the 12 cells.

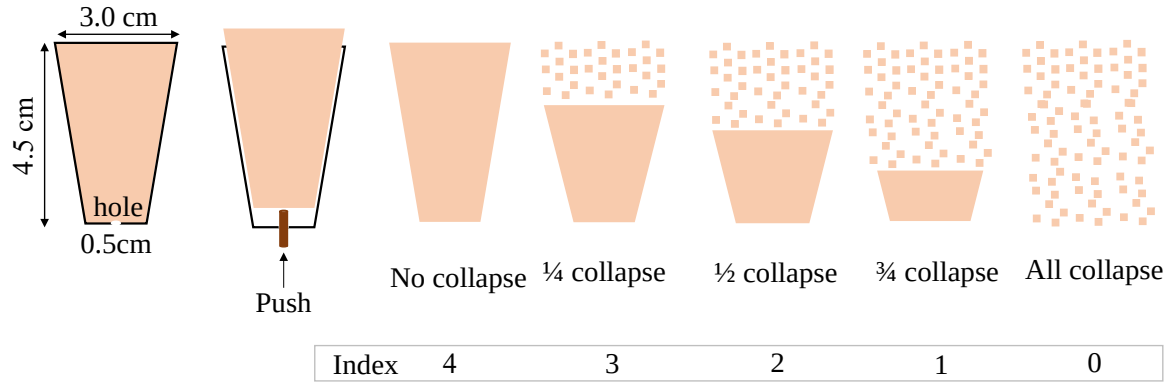

Fig. 2 Evaluation of degree of collapse [3]

Table 3 Summary of experiments results

	Urease (g/L)	Urea (mol/L)	$Ca(NO_3)_2$ (mol/L)	Injections (times)	Rinse (mL)	Germination rate (%)	pH	EC (mS/cm)	Ammonium Nitrogen (mg/kg)	Degree of collapse
Case 1	-	-	-	-	50	92	7.1	0.1	98.2	0
Case 2	0.1	0.1	0.1	4	50	92	6.3	0.4	1240	0
Case 3	0.1	0.25	0.25	4	50	92	7	0.4	2810	1.4
Case 4	0.1	0.5	0.5	4	50	0	8.1	0.5	2240	3
Case 5	0.1	0.1	0.1	8	50	83	7.5	0.2	1660	2.4
Case 6	0.1	0.25	0.25	8	50	50	7.9	0.3	3070	2.9
Case 7	0.1	0.5	0.5	8	50	0	8.1	0.5	3190	3
Case 8	0.1	0.1	0.1	8	250	83	7.6	0.2	1160	2.3
Case 9	0.1	0.25	0.25	8	250	33	7.7	0.2	2640	3
Case 10	0.1	0.5	0.5	8	250	58	8	0.2	2620	3

Solidification Test

Fig. 3 shows the relationship between the degree of collapse and the concentration of the solidification solution. It is evident that Case 2 (0.1 M, 4 injections) exhibited insufficient strength. This is attributed to both the low concentration of the cementation solution and the limited number of injections. Additionally, Case 6 (0.25 M, 8 injections) exhibited less collapse than Case 3 (0.25 M, 4 injections), and Case 4 (0.5 M, 4 injections) showed similar strength to Case 7 (0.5 M, 8 injections). These results suggest that, at concentrations of 0.1 M and 0.25 M, a minimum of 8 injections is necessary to achieve sufficient strength. On the other hand, at a

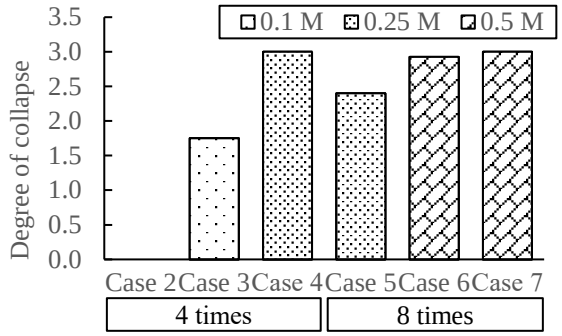

Fig. 3 Relation of degree of collapse and concentration of solidification solution

concentration of 0.5 M, the number of injections (4 or 8) did not significantly influence the degree of collapse, indicating that regardless of the number of injections, sufficient solidification can be achieved.

Fig. 4 shows the relationship between the degree of collapse and the amount of rinsing. This result is consistent with the chemical properties of $CaCO_3$, which is relatively insoluble in water. Thus, $CaCO_3$ maintains its solidification role even after rinsing.

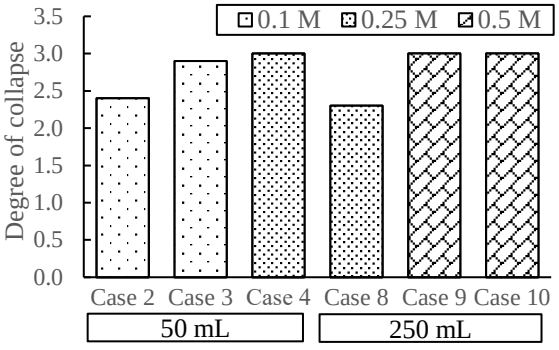

Fig. 4 Relation of degree of collapse and rinse amount

Fig. 5 and 6 present visual comparisons of the solidified cultivating soil. It is evident that Case 10 exhibited a lower degree of collapse (i.e., greater strength) than Case 8, supporting the numerical results.

Fig. 5 Photograph of solidified cultivating soil (Case 8, degree of collapse 2.3)

Fig. 6 Photograph of solidified cultivating soil (Case 10, degree of collapse 3)

Germination Test

Fig. 7 shows the inverse relationship between germination rate and the concentration of the solidification solution. Specifically, higher germination rates were observed in substrates treated with lower concentrations. This phenomenon is likely due to increased osmotic pressure in substrates solidified with higher concentrations, which may hinder seed water uptake and thus suppress germination. Also, past studies showed that root size gets smaller as the soil gets harder. When the concentration of solidification solution is higher, the collapse index becomes higher. This may mean that germination and strength are related.

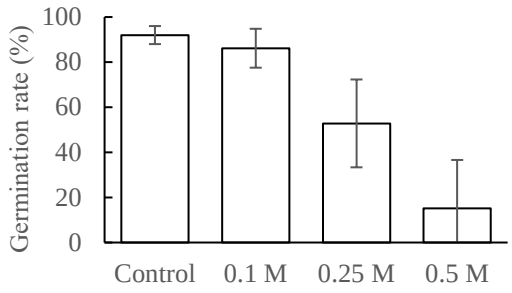

Fig. 7 Relation of Germination rate and concentration of solidification solution

Fig. 8 shows the relationship between germination rate and ammonium nitrogen concentration. A higher germination rate was associated with lower ammonium nitrogen levels. In Cases 8 through 10, the solidified substrates were rinsed to remove excess ammonium nitrogen. Although the initial

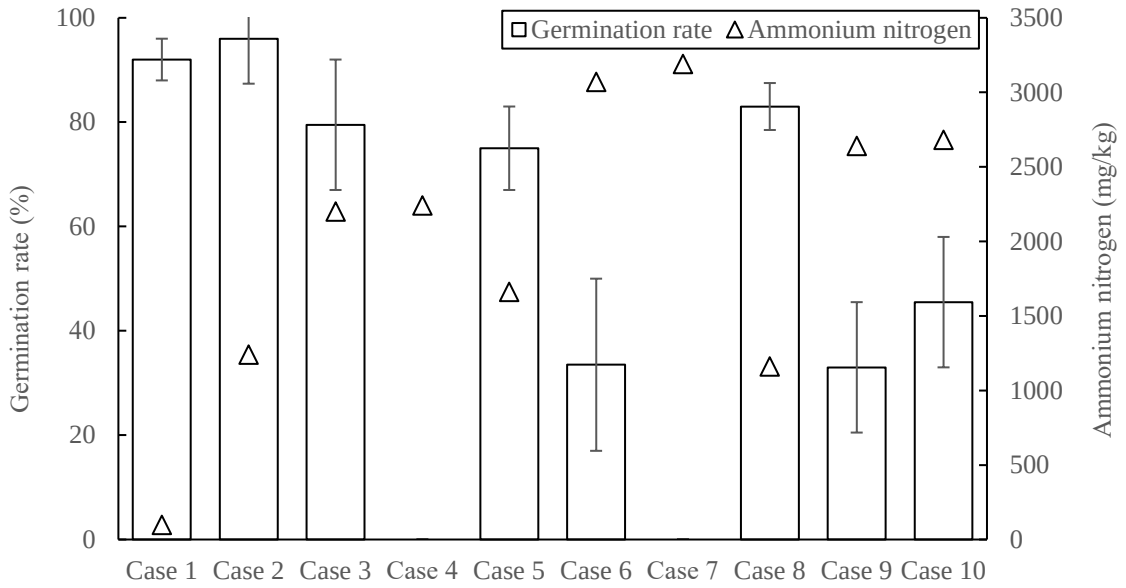

Fig. 8 Relation of Germination rate and ammonium nitrogen

concentration of ammonium nitrogen was reduced by approximately 15–30%, high residual concentrations still appeared to negatively affect plant growth. These findings are consistent with earlier studies indicating the phytotoxic effects of excessive ammonium nitrogen [15]. However, after germination, nitrogen becomes an essential element for plant growth. In particular, if nitrogen is deficient during the transition from cotyledon to true leaf, the leaves may turn yellow and wither. Future research will investigate the amount of ammonium nitrogen that does not inhibit germination and can serve as a nutrient afterward.

Woody biomass materials, such as coco peat and bamboo powder, can adsorb ammonium ions through ion exchange and micropore interactions. This experiment confirmed that rinsing alone was insufficient to reduce nitrogen concentrations to safe levels. Therefore, additional mitigation strategies such as the use of nitrifying bacteria may be required to minimize nitrogen-related stress during germination.

CONCLUSIONS

In this study, we aimed to develop a sustainable form of solidified cultivation soil with minimal environmental impact. We conducted solidification and germination tests using EICP as a solidification method, which, unlike other bio-cementation techniques, does not require microbial cultivation. We also used as substrate waste woody biomass such as bamboo powder and coco peat. Additionally, we investigated the degree of collapse of solidified cultivating soil, as well as the effects of ammonium nitrogen on germination. The findings aresummarized as follows:

- Degree of collapse, represented as the solidification strength, increased with more frequent injections, especially at lower cementationconcentrations (0.1 M and 0.25 M).At 0.5 M, sufficient strength was achieved even withfewer injections. Rinsing with deionized water did not have a significant impact on strength, as $CaCO_3$ is minimally soluble in water.

- Germination rate was inversely related to the concentration of the solidification solution. Solidified cultivation soil treated with 0.1 M solution showed the highest germination rates. This phenomenon is likely due to increased osmotic pressure in substrates solidified with higher concentrations, which may hinder seed water uptake and thus suppress germination.

- High concentrations of ammonium nitrogen negatively affected germination. Although insing reduced ammonium levels by 15–30%, it was not sufficient to eliminate phytotoxic effects. Additional methods, such as biological nitrification, may be necessary to improve the substrate’s growing conditions.

These results suggest that $CaCO_3$ cementation, when optimized in terms of concentration and injection frequency, holds promise for developing sustainable cultivation substrates using waste woody biomass.

REFERENCES

[1] Matsumoto Y., Promotion of smart agriculture, Japanese Journal of Pesticide Science, Vol.45, Issue2, 2020, pp.141–145. (In Japanese)

[2] Abbasi R., Martinez P., Ahmad R., The digitization of agricultural industry–a systematic literature review on agriculture 4.0., Smart Agricultural Technology 2, 2022, 100042.

[3] Goto T., Fujii K., Motooka S., Konishi K., Groth and flower quality of stock (Matthiola incana R.Br.) and snapdragon (Antirrhinum majus L.) seedlings grown in cell medium hardened by heat fusion polyester fiber, Journal of the Japanese Society for Horticultural Science, Vol.1 Issue4, 2002, pp.245-248. (In Japanese with English abstract)

[4] Barrett G. E., Alexander P. D., Robinson J. S.,Bragg N. C., Achieving sustainable growing media for soilless plant Environmentally sustainable growing media for soilless plant cultivation systems–A review. Scientia horticulturae, Vol.212, 2016, pp.220-234.

[5] Hu X. M., Liu J. D., Feng Y., Zhao Y. Y., Wang X. W., Liu W. H., Zhang M., Liu Y., Application of urease-producing microbial community in seawater to dust suppression in desert. Environmental Research, Vol.219, 2023, 115121.

[6] Xiao P., Liu H., Xiao Y., Stuedlein A. W., Evans T. M., Liquefaction resistance of bio-cemented calcareous sand. Soil Dynamics and Earthquake Engineering, Vol.107, 2018, pp.9-19.

[7] He J., Huang A., Ji J., Qu S., Hang L., Enzyme induced carbonate precipitation with fibers for the improvement of clay soil slopes against rainfall and surface runoff erosions, Transportation Geotechnics, Vol.42, 2023, 101074.

[8] Kawasaki S., Present status of ground improvement technologies using microbial functions, Journal of MMIJ, Vol. 131, 2015, pp.155-163. (In Japanese with English abstract)

[9] Ghasemi P., Montoya MB., Effect of treatment solution chemistry and soil engineering properties due to microbially induced carbonate precipitation treatments on vegetation health and growth, ACSES&T Engineering Vol.2, 2022, pp.2196-2205.

[10] Zheng X., Lu X. Zhou M., Huang W., Zhong Z., Wu X., Zhao B., Experimental study on mechanical properties of root–soil composite reinforced by MICP, materials, Vol.15, 2022, 3586.

[11] Ahenkorah I., Rahman, M. M., Karim M. R., and Beecham S., Enzyme induced calcium carbonate precipitation and its engineering application: a systematic review and meta-analysis. Construction and Building Materials, Vol.308, 2021, 125000.

[12] Al Imran M., Nakashima K., Evelpidou N., and Kawasaki S., IMPROVEMENT OF USING CRUDE EXTRACT UREASE FROM WATERMELON SEEDS FOR BIOCEMENTATION TECHNOLOGY. Geomate Journal, Vol.20, Issue 78, 2021, pp.142-147.

[13] Nakahara H., Todo M., Matsuzoe N., Effect of bamboo powder on the tomato growth and yield and suppression of soil-borne diseases in Solanum plants, Journal of the Japanese Society of Agricultural Technology Management Vol.26, 2019, pp.13-21. (In Japanese with English abstract)

[14] Chen M., Gowthaman S., Nakashima K., Takano C., Kawasaki S., Baseline investigation on soil solidification through biocementation using airborne bacteria. Frontiers in bioengineering and biotechnology, Vol.11, 2023, 1216171.

[15] Yang H., Zhou J., Fei J., Ci K., Li D., Fan J., Wei C., Liang J., Xia R., Zhou J., Soil ammonium (NH_4^+) toxicity thresholds for restoration grass species, Environmental Pollution, Vol.318, 2023, 120869.

Copyright © Int. J. of GEOMATE All rights reserved, including making copies, unless permission is obtained from the copyright proprietors.

15th Int. Conf. on Geotechnique, Construction Materials & Environment, Kyoto, Japan, 11-13 November 2025, ISBN 978-4-909106124 C3051

ANALYTICAL STUDY ON THE CONCRETE BREAKOUT STRENGTH OF HEADED REINFORCEMENT BAR EMBEDDED IN ROOF EXTERIOR BEAM-COLUMN JOINT

Zev Al Jauhari[1], and Tomoya Matsui[2]

[1]Graduate School of Engineering, Toyohashi University of Technology, Japan; [2] Toyohashi University of Technology, Japan

ABSTRACT

In recent years, headed reinforcement bars have been increasingly used as replacements for conventional anchoring in reinforced concrete beam-column joints (BCJ). This led to the development of headed bars, which are highly advocated by researchers, as their ultimate load-carrying capacity is influenced by many factors. The previous study investigated the pullout test of the headed reinforcement bar embedded in roof exterior BCJ specimens using such parameters. The use of supplementary bars significantly affected the anchorage capacity of the headed bars and contributed to the diagonal force of the concrete for resisting the applied load. In this study, the 3D nonlinear finite element (FE) model of the BCJ specimens is developed using FINAL software to analyze the headed bar's concrete breakout strength. The results obtained from FE analysis demonstrated good agreement with the test results, demonstrating that the FE model can accurately predict the behavior of the BCJ specimens in terms of pullout load capacity, failure mechanism, crack pattern, internal strain and stress distribution, and damage progress. The FE model developed can be utilized as a valuable tool for predicting the concrete breakout strength with various parameters, such as the diameter of the supplementary bar (d_s), the number of supplementary bars (n_s), and the spacing of the topmost supplementary bar from the headed bar (S_{p1}). None of the variables affected the failure mode of the FE model. Increasing the d_s and n_s led to higher anchorage capacity of the headed bar; otherwise, the presence of S_{p1} decreased the anchorage capacity.

Keywords: Finite element analysis, Headed reinforcement bar, Supplementary bar, Concrete breakout strength, Beam-column joint

INTRODUCTION

Reinforced concrete beam-column joints (BCJ) play a critical role in the structural integrity and load transfer mechanisms of reinforced concrete frames [1]. Traditionally, conventional anchoring methods such as bent bars and mechanical couplers have been employed to ensure adequate anchorage of reinforcement within these joints [2]. However, recent advancements have seen the increasing adoption of headed reinforcement bars as an alternative anchorage solution due to their potential to enhance load transfer efficiency and simplify construction [3]. Headed bars, characterized by enlarged ends, offer improved anchorage capacity, but their ultimate performance is influenced by multiple factors, including the presence and configuration of supplementary bar (transverse reinforcement bar near the head or along the headed bar) [4].

Numerous studies have explored the anchorage capacity of headed bars within concrete structural components. However, only few studies have been conducted regarding the anchorage capacity of headed bars embedded in L-shaped BCJ consider the supplementary bar. An experimental investigation involving pullout tests focused on the concrete breakout strength of headed bars specifically in L-shaped BCJ was carried out [5]. This research evaluated the performance of headed bars under various conditions, producing valuable findings that both validate and improve existing calculation models used in design codes. While experimental investigations provide valuable insights, the complexity of BCJ behavior necessitates robust numerical tools for detailed analysis and optimization [6,7]. Finite element (FE) modeling offers a powerful approach to simulate and predict the nonlinear behavior of BCJ, enabling a deeper understanding of failure mechanisms, crack propagation, and stress distribution.

In this study, FE analysis (FEA) was applied to the pullout test of mechanically anchored rebars conducted by Mohsuni et al. [5], aiming to assess the concrete breakout strength of headed bars embedded within roof exterior beam-column joints. To ensure the reliability of the numerical model, a comparative investigation was carried out by correlating the pullout capacity, failure modes, and the strain at reinforcement bars of the test specimens with the FEA results. Parametric studies were conducted to capture the influence of supplementary bar on the anchorage capacity in terms of diameter, quantity, and spacing relative to the headed bar.

RESEARCH SIGNIFICANCE

This study presents a 3D nonlinear FEA of headed bars embedded in L-shaped BCJs to validate their anchorage capacity and failure mechanisms based on the test results. It also conducts a parametric analysis of the role of supplementary bars in influencing the concrete breakout strength of headed bars. By varying parameters such as the number, diameter, and spacing of the supplementary bars, the research identifies how each factor affects the load-carrying capacity of headed bar. Understanding these relationships is crucial for the design of BCJs using headed bars to prevent brittle failures and enhance overall structural resilience, especially in seismic regions.

MATERIAL AND METHODS

Experimental Study

The previous research [5] conducted pullout tests on 70% of full-scale roof exterior BCJs to evaluate the anchorage capacity of headed bars. Typical specimens, named LE25-M and LE25-Ma, were experimentally tested to measure their pullout forces. The only difference between LE25-Ma and LE25-M was the diameter of the supplementary bar: LE25-Ma used a 6 mm bar, while LE25-M used a 13 mm bar. Fig. 1 shows the standard cross-section of the LE25-M specimen and detail of plate nut.

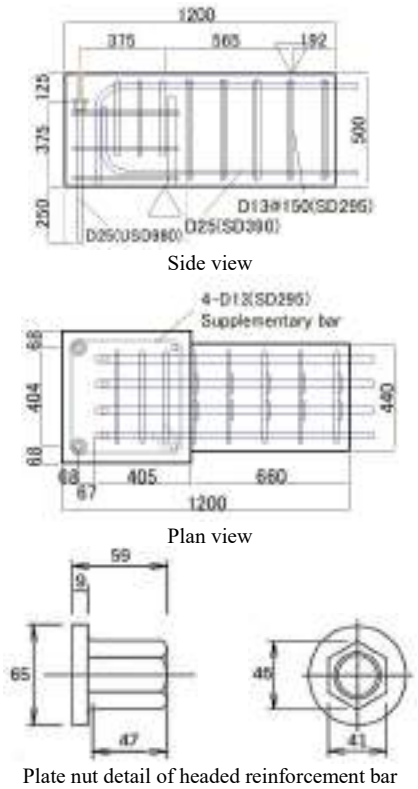

Fig.1 Cross-section and plate nut detail of LE25-M Specimen (unit: mm)

Table 1 Material properties of reinforcing bars

Material type	Yield stress σ_y (N/mm^2)	Young Mod. E_s (N/mm^2)	Remark
D6 (SD295)	407	195000	Supplementary
D13 (SD295)	342	193000	Supplementary
D25 (SD390)	441	196000	Beam main bar
D25 (USD980)	1095	194000	Headed bar

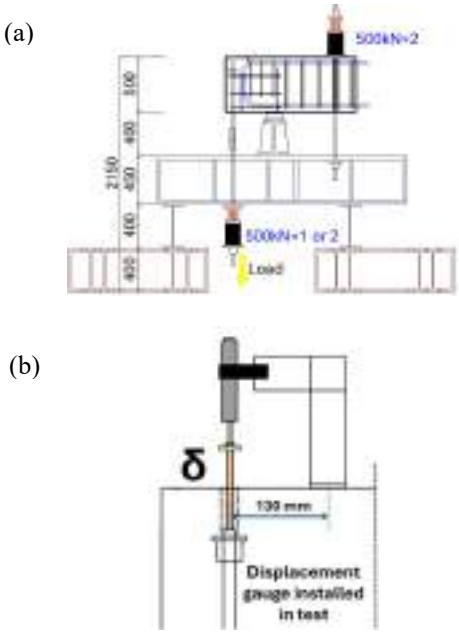

Fig.2 (a) Schematic illustration of test setup; (b) Pullout displacement calculated for test

The specimens were designed to exhibit failure modes such as concrete cones or side blowout. The concrete compressive strengths were 33.2 MPa and 32.6 MPa for LE25-M and LE25-Ma, respectively. Table 1 presents the mechanical properties of the steel reinforcing bars obtained from tensile testing. Fig. 2(a) depicts the loading setup employed during the test. The reaction force was transmitted to the force application beam, while each headed reinforcing bar was subjected to axial tensile loading applied directly through a centrally aligned hydraulic jack with a capacity of 500 kN. Linear displacement gauges were mounted on the upper surface of the plate nut to record the withdrawal displacement of the headed bars. The pullout displacement was determined by measuring the difference between the gauge position and the anchorage bar displacement, as illustrated in Fig. 2(b).

Test results demonstrated that the anchorage capacity of the headed bars was significantly influenced by the presence of supplementary bars. These supplementary bars enhanced the diagonal compressive stress distribution within the concrete matrix, thereby increasing its resistance against the

applied pullout forces. Therefore, ensuring enough supplementary bars is critical to optimize anchorage performance.

Numerical Study

Elements used

The nonlinear FEA was conducted using FINAL v11 [8] software. The geometric and structural configuration of the BCJ model is illustrated in Fig. 3. The analysis was performed in a fully three-dimensional framework, incorporating a triaxial stress state assumption. Concrete was designed using 8-node hexahedral solid elements, whereas reinforcing bars were idealized as one-dimensional beam elements. Headed reinforcing bars were represented by 4-node quadrilateral shell elements. To capture the slip behavior between the main-headed reinforcement and the surrounding concrete, a 4-node line element was introduced at the interface. This element facilitates discrete contact interaction by providing nodal linkage points between independently defined concrete and reinforcement element meshes. For the interface modeling between the plate nut and concrete, the nodes on the upper plate nut surface remain unconnected (independent) from the concrete nodes at the corresponding interface, while the nodes on the lower plate nut surface are constrained to share coincident nodes with the underlying concrete mesh, ensuring direct connectivity.

Material constitutive model

The modified Ahmad model was implemented to define the concrete compressive stress–strain behavior within the FE framework [9]. For the post-peak stress softening region, the Nakamura-Higai model [10] was employed as illustrated in Fig. 4. The model was designed so that only the area corresponding to the beam-column joint panel cover was brittle since the model was developed to break due to concrete failure only (cone or side blowout mode). The Ottosen four-parameter model is used for fracture conditions under triaxial stress. The crack-softened area on the tension side was assumed to bear almost no tensile stress after cracking, and strain reduction after cracking was not considered. The tension stiffening characteristic by the Izumo et al. [11] model was used, and the coefficient C was set to 1.0, assuming that almost no tensile stress is sustained after cracking. The shear transfer model after cracking on the beam was based on the Naganuma model [9], while the BCJ panel was assumed to have no shear transfer (zero shear stiffness). The factor for reducing compressive strength after cracking is based on the formulas proposed by Collins et al. [12] for LE25-M and by Naganuma [13] for LE25-Ma, respectively. This approach differs because the LE25-Ma model exhibits an unstable pullout capacity curve after reaching the peak pullout load due to solution divergence. In contrast, applying Naganuma's formula to the LE25-M model leads to an underestimation of the anchorage capacity.

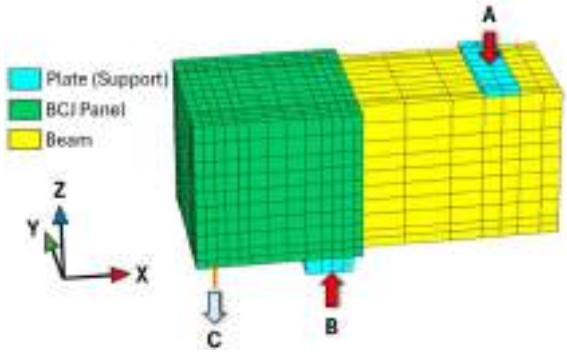

Fig.3 The 3D FE model of the BCJ specimen

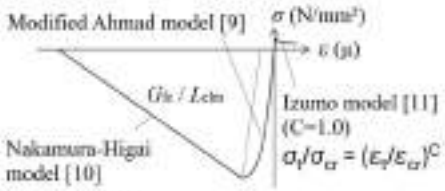

G_{fc} : fracture energy
L_{elm} : element size
σ_t : tensile stress of concrete
σ_{cr} : tensile strength under biaxial loading
ε_t : tensile strain in the direction perpendicular to crack
ε_{cr} : tensile strain when crack occurs
C : a factor of tension stiffening phenomenon

Fig.4 Principal stress equivalent uniaxial strain relation of concrete

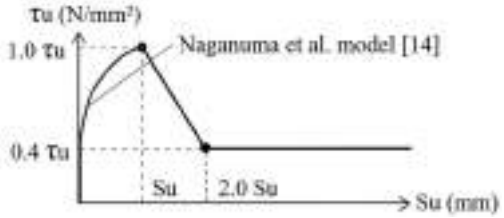

Fig.5 Bond stress-slip relationship

The stress-strain relationship adopted to represent reinforcement bar behavior was the modified Menegotto-Pinto model. The anchor plate was modeled as perfect elastic bodies with Young's modulus of 2.05 x 10^5 N/mm^2. The bond characteristics between headed reinforcing bars and concrete were based on the model by Naganuma et al. [14], and the slip at the maximum bond stress (S_u) was

assumed to be 1.0 mm. Then, peak stress was calculated based on fib Model Code 2010 (τ_u = $2.5\sqrt{f_{cm}}$) [15]. Fig. 5 shows the bond stress and slip relationship between reinforcing bars and concrete. The bond between the transverse reinforcement and concrete is assumed to be perfectly bonded.

Boundary conditions and loading

To accurately replicate the test setup within the FE model, specific boundary conditions were imposed on the model. In this study, the pin support at point A in Fig. 3 was constrained exclusively in the z direction, while the support at point B was fixed in both the x and z directions. The load was applied at the lowest node of the headed reinforcement (point C) in a displacement-controlled manner, directed downward until a displacement of 50 mm was achieved. The analysis was concluded once this displacement target was reached.

RESULTS AND DISCUSSIONS

Validation of FE model with test results

Pullout load vs displacement response

The pullout displacement (δ) in the FEA was calculated as the difference between the displacements at nodal points A and B ($\delta = \delta_A - \delta_B$), as illustrated in Fig. 6. The comparison of the pullout load and displacement curves obtained from both the FEA and the tests for LE25-M and LE25-Ma is presented in Fig. 7.

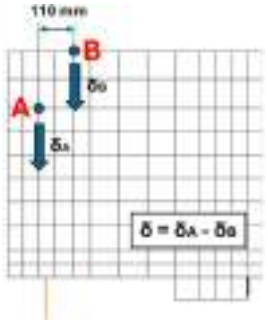

Fig.6 Pullout displacement calculated for FEA

Both models exhibit an increase in strength as pullout displacement progresses, with the LE25-Ma model demonstrating a particularly close match between the numerical prediction and test results. The LE25-M model, which has a larger hoop diameter, displayed a higher anchorage capacity compared to LE25-Ma. Notably, even after the appearance of diagonal cracks, LE25-M continued to show an increase in pullout load due to its greater anchorage strength. In contrast, LE25-Ma, having a lower anchorage capacity, experienced a significant drop in pullout load following the formation of diagonal cracks. Overall, the FE models align very well with the experimental data, particularly in terms of initial stiffness and the development of pullout load, up to displacements of 1.5 mm for LE25-M and 4 mm for LE25-Ma.

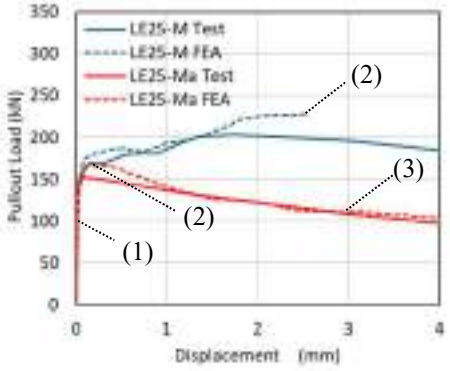

Fig.7 Pullout load-displacement relationship of LE25-M and LE25-Ma

Failure mechanism and crack pattern

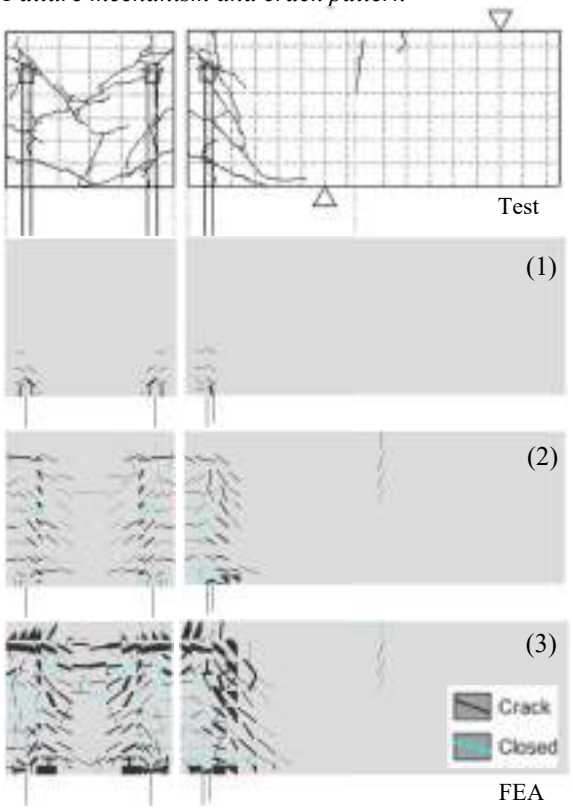

Fig.8 Crack patterns of LE25-Ma specimen and the FE model

Validating the crack pattern on the concrete is essential to confirm the potential impact of undesirable tensile stresses caused by the rapid formation of cracks due to headed bar pullout. Fig. 8 illustrates a comparison of the crack patterns observed in the LE25-Ma specimen between the test

and FEA. The number symbols in Fig. 8 correspond to those in Fig. 7.

The failure mechanism observed in both test and FEA followed a similar sequence: (1) initially, a vertical crack appeared at the bottom of the beam-column joint region, developing along the headed bar; (2) as the load increased toward its peak, diagonal cracks started to form around the anchorage bar, with the FE model accurately replicating this crack progression seen in the test; (3) eventually, additional diagonal cracks developed within the BCJ panel, accompanied by pullout displacement of the headed bar. Once diagonal cracks also emerged near the anchor plate, the pullout load of the anchorage bar began to decline. Both the FEA and test results indicate that ultimate failure was caused by cone cracking in the concrete cover adjacent to the anchorage. Notably, the failure mechanism observed in the LE25-M model closely mirrors that of the LE25-Ma model.

Strain of reinforcing bar

Fig. 9 shows the locations of the strain gauges on specimens where strain measurements were taken for comparison with the FEA. In Fig. 10, the relationship between pullout load and strain is displayed for both supplementary and main beam bars in the LE25-Ma model. Notably, the supplementary bars exhibit higher strain readings at points a3 and a5 than the test results. The strain at a5 (topmost supplementary bar) in the FEA exceeds the yield strain limit (μ = 2087). The strain at point a1 suggests compression of the supplementary bar under the pullout load for both the test and FEA. In the main bar, both the test and FEA show that the strain at point b1 is higher than at b2, while the results from FEA underestimate the test results. This proves that the strain in the supplementary bars is influenced by the shape of the concrete cone. These observations confirm the FE model's ability to replicate the strains observed experimentally in the reinforcing bars.

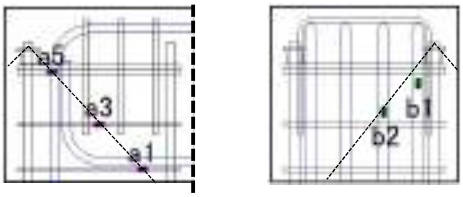

Fig.9 Location of strain gauges of the specimens

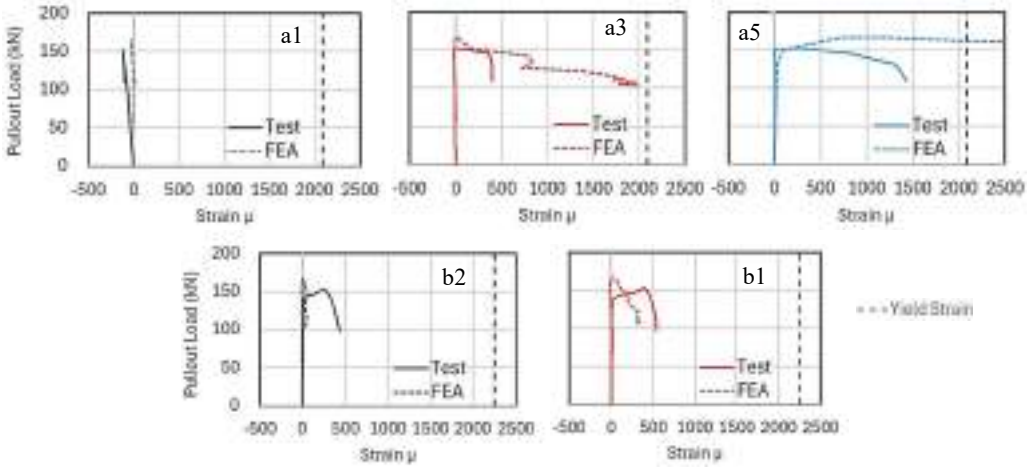

Fig.10 Relationship between load and strain of supplementary and main beam bars of LE25-Ma

Minimum principal stress

The minimum principal stress from the FEA is compared with the test results in Fig. 11 for LE25-M and LE25-Ma. Fig. 12 illustrates a cutaway diagram highlighting the positions of the headed and supplementary rebars. The stress contour shown in the figure is observed at the pullout load indicated as (2) in Fig. 7. The initial cracks in the analysis tend to be inclined, concentrating at the base of the headed reinforcing bar, where cracking first occurs. The stress then propagates at a 45-degree angle from the anchorage rebar. This concentration of stress can lead to crack initiation at the anchorage region of the headed bars. The stress was concentrated in the first supplementary bar (from the top), indicating that the presence of supplementary bars is important to bearing the pullout load and increasing the concrete breakout capacity. The FE models indicate that stress is focused on the near plate nut at the maximum pullout load. These findings confirm the stress state at the time of fracture, with the concentrated stress in the FE model aligning well with the observed specimen failures.

Parametric Study

The numerical results showed that the proposed FE model adequately describes the behavior of the

headed bar under pullout load. Additionally, a parametric numerical study was developed to investigate the influence of supplementary bars parameters on concrete cone failure and the pullout capacity of the anchors, including diameter and number of supplementary bars, and the distance of the topmost supplementary bar from the headed bar.

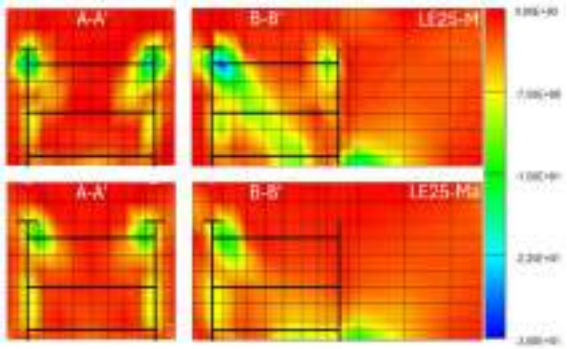

Fig.11 Minimum principal stress of the models

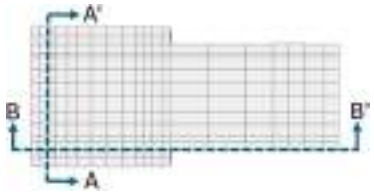

Fig.12 Cutaway of the models

The effect of supplementary bar diameter (d_s) on the concrete breakout strength of headed bars embedded in BCJ is investigated by modeling E4-10, E4-16, and E4-19 with d_s values of 10 mm, 16 mm, and 19 mm, respectively. It is notable that these models are designed based on the specimen LE25-M. Models with larger diameter bars provided better resistance to the applied pullout load, but the difference was not significant. As seen in Fig. 14(a), increasing the diameter to 16 mm and 19 mm resulted in higher ultimate capacities for the concrete breakout strength, by 9.8% and 11.4%, respectively, compared to the capacity of LE25-M model. The E4-10 model showed a decrease in anchorage capacity of around 7.4%, as shown in Table 2. The crack pattern and failure mode of E4-10, E4-16, and E4-19 are the same as those of LE25-M.

Varying the number of supplementary bars (n_s) was considered to study their effect on the concrete breakout strength capacity of headed bars in the LE25-M model. The arrangement of supplementary bars in this parametric model is shown in Fig. 13. The measured ultimate pullout capacity is plotted against varying n_s of the headed bar (4, 5, and 6) in Fig. 14(b). It is evident from the curve that a higher n_s leads to an enhancement in pullout capacity across all the models. There was a 12.6% increase in the pullout capacity of headed bars for E5-13, and a 21.8% increase was observed for E6-13, compared to LE25-M, respectively.

Another parametric study presents the effect of the topmost supplementary bar distance (S_{p1}) on the pullout load–displacement curve. Two variables of bar distance were considered and compared with the LE25-M (S_{p1} = 0) model. The pullout load–displacement curve for the E4-13a (S_{p1} = 30 mm) and E4-13b (S_{p1} = 60 mm) models is presented in Fig. 14(c). E4-13a model does not changing the anchorage capacity of the headed bar, whereas E4-13b model results reduct the capacity approximately 5.5%.

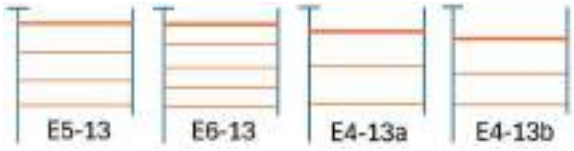

Fig.13 Configuration of supplementary bar in parametric study

Table 2 Results of parametric study

Model in Parametric Study	Variable	Max. Pullout Capacity (kN) (b)	Percentage of Increase (%) [[(b)-(a)]/(a)] x 100%
LE25-Ma	d_s = 6 mm	166.5	-27.1
E4-10	d_s = 10 mm	211.4	-7.4
E4-16	d_s = 16 mm	250.7	9.8
E4-19	d_s = 19 mm	254.3	11.4
E5-13	n_s = 5	257.2	12.6
E6-13	n_s = 6	278.1	21.8
E4-13a	S_{p1} = 30 mm	236.4	3.5
E4-13b	S_{p1} = 60 mm	215.7	-5.5

(a) is the maximum pullout capacity of LE25-M (228.3 kN), used as the benchmark model with d_s = 13 mm; n_s = 4 mm; S_{p1} = 0 mm.

CONCLUSION

The nonlinear finite element (FE) model developed in this study successfully predicted the concrete breakout strength of headed reinforcement bars in roof exterior BCJ specimens that were tested experimentally. This model simulated key behaviors such as the pullout load-displacement relationship, crack patterns, strain at reinforcement bars, and distributions of stress in the specimens analyzed theoretically. Both the experimental tests and FEA indicated that the anchorage capacity of the headed bars was affected by the configuration of the supplementary bars.

Additionally, the diameter, number, and spacing of the supplementary bars were found to significantly impact anchorage capacity. The diameter of the supplementary bars had a minor effect on the anchorage capacity, with a variation of approximately

7-11% increase or decrease in the capacity of LE25-M. Increasing the number of supplementary bars had a more substantial effect, enhancing anchorage capacity by 12.6% to 21.8% for 5 and 6 supplementary bars, respectively. The addition of the topmost supplementary bar's distance from the plate nut was observed to reduce the anchorage capacity of the headed bar.

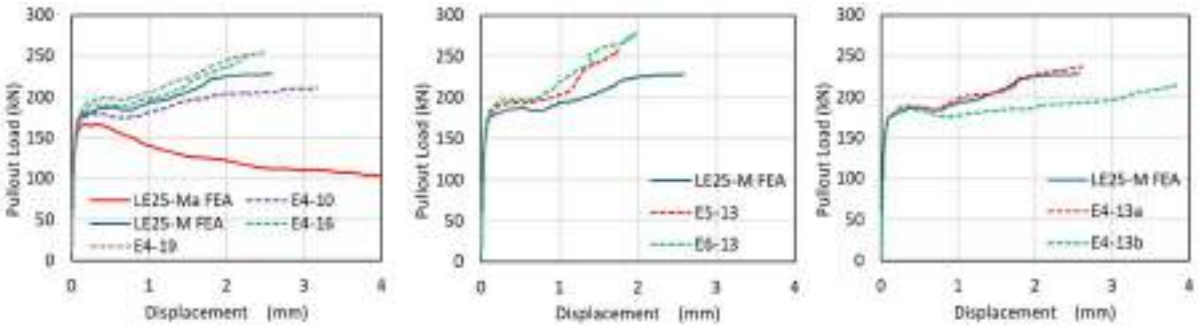

(a) (b) (c)

Fig.14 Pullout load-displacement relationship of parametric study on LE25-M model at (a) diameter of supplementary bar; (b) number of supplementary bars; (c) topmost supplementary bar distance to headed bar

REFERENCES

[1] Pawar V.R., Patil Y.D., and Patil H.S., Cyclic loading of Exterior Beam - Column Joint with Threaded Headed Reinforcement, Int. Journal of App. Eng. Research, Vol. 12, No. 17, 2017, pp. 6377-6383.

[2] Miao T., Yang J., Zhou Y., Zhan M., Sha L. and Zheng W., Research on the Distributive Relationship between Bond Force and Bearing Pressure for Anchorage Force by Headed Bars, Buildings, Vol. 13, 2463, 2023, pp. 1-18.

[3] Chiu C.K., Lays D.P., Ricky and Krasna W.A., Anchorage strength development of headed bars in HSRC external beam-column joints considering side-face blowout failure under monotonic loading, Engineering Structures, Vol. 239, 112218, 2021, pp. 1-15.

[4] Santos J.P.B., Oliveira M.H., Lima N.W.B., Filho, M.J.M.P. and Ferreira M.P., A parametric finite element study of concrete cone failure in headed bars under tensile loading, Lat. Am. j. solids struct, Vol. 21, 2, 2024, pp. 1-21.

[5] Mohsuni H., Matsui T., Sanada Y., Sakuta J., Kiyohara T., Kim Y. and T. Adachi, Pullout Tests on Concrete Breakout Strength of Headed Reinforcement Bars Embedded in Roof Exterior Beam-Column Joints, Journal of Advanced Concrete Technology, Vol. 21, 2023, pp.392-404.

[6] Ahmed N. and Metewally K., Numerical Study on Anchorage Zones of Post-Tensioned Slab Considering Anchorage Device, International Journal of GEOMATE, Vol.19, Issue 74, 2020, pp. 123–130.

[7] Fauzan, Kurniawan R. and Jauhari Z. A., Finite Element Analysis of EWECS Columns with Varying Shear Span Ratio, International Journal of GEOMATE, Vol.14, Issue 43, 2018, pp.1-7.

[8] ITOCHU Techno-Solutions Corporation: FINAL HELP, 2018.

[9] Naganuma K., Stress-Strain Relationship for Concrete under Triaxial Compression, Journal of Structural and Construction Engineering, AIJ, No.474, Aug., 1995, pp. 160-170.

[10] Nakamura H. and Higai T., Compressive Fracture Energy and Fracture Zone Length of Concrete, Seminar on Post-peak Behavior of RC Structures Subjected to Seismic Load, JCI-C51E, Vol.2, 1999, pp. 259-272.

[11] Izumo J., Shima H. and Okamura H., Analytical Model for Reinforced Concrete Panel Elements Subjected to In-Plane Forces, Concrete Journal, No. 87.9-1, 1987, pp. 107-120.

[12] Vecchio F.J. and Collins M.P., The Modified Compression-Field Theory for Reinforced Concrete Elements Subjected to Shear, ACI Journal, Vol.83, No.2, 1986, pp. 219-231.

[13] Naganuma K., Study on nonlinear analysis method for reinforced concrete wall structures (Part 1), Architectural Institute of Japan, Structural Engineering Papers, No. 421, 1991, pp. 39-48.

[14] Naganuma K., Yonezawa K., Kurimoto O. and Eto H., Simulation of Nonlinear Dynamic Response of Reinforced Concrete Scaled Model Using Three-Dimensional Finite Element Method, 13th WCEE, Vancouver, B.C., Canada, Paper No.586, Aug. 2004, pp. 1-15.

[15] fib Model Code for Concrete Structures, Ernst & Sohn publishing company, 2010.

Copyright © Int. J. of GEOMATE All rights reserved, including making copies, unless permission is obtained from the copyright proprietors.

15th Int. Conf. on Geotechnique, Construction Materials & Environment,
Kyoto, Japan, 11-13 November 2025, ISBN 978-4-909106124 C3051

RECYCLING COAL BOTTOM ASH IN THE PRODUCTION OF FIRED CLAY BRICKS

Nonthaphong Phonphuak[1], Anuwat Srisuwan[2], Anujit Phumiphan[3], Sarawut Dakaew[4] and *Siwat Lawanwadeekul[5]

[1]Faculty of Engineering, Rajabht Maha Sarakham University, 44000, Thailand
[2]Faculty of Liberal Art and Science, Sisaket Rajabhat University, Muang, Sisaket 33000, Thailand
[3]School of Engineering University of Phayao, Phayao 56000, Thailand
[4]Faculty of Education, Rajabhat Maha Sarakham University, Thailand
[5]Faculty of Industrial Technology, Lampang Rajabhat University, Lampang 52100, Thailand

ABSTRACT

Incorporating coal bottom ash (CBA) into construction materials offers an environmentally sustainable strategy for tackling waste management challenges. This study investigates the potential of CBA as an additive in fired clay bricks by evaluating its impact on key physical and mechanical properties. Clay bricks were produced with 0, 10, 20, 30, and 40 wt.% CBA, followed by firing at temperatures ranging from 900 to 1100 °C. The results show that higher CBA content resulted in a decrease in bulk density (from 2.26 to 1.70 g/cm³) and an increase in porosity, water absorption, and firing shrinkage. However, bricks containing 10–30 wt.% CBA, fired between 900 and 1100 °C, exhibited compressive strength exceeding ASTM C62-13a standards. The optimal incorporation of CBA at 900 °C was identified to be between 10–30 wt.%, underlining its potential as a sustainable alternative for enhancing the properties of fired clay bricks while promoting waste utilization.

.

Keywords: Coal bottom ash; Strength; Durability; Fired clay bricks; Porosity

INTRODUCTION

The construction materials sector is critical in addressing solid waste challenges by integrating industrial by-products and post-consumer waste into manufacturing processes. Among the well-established methods for reusing such waste is its incorporation into fired clay bricks, reducing the demand for virgin raw materials and enhancing environmental sustainability [1, 2]. This approach contributes to minimizing landfill waste and lowering overall production costs in the construction industry [3, 4]. The increasing focus on sustainable building practices has further accelerated the adoption of waste-derived materials in brick manufacturing, enabling compliance with industry standards while mitigating environmental impact [5, 6].

However, conventional brick production remains a major source of environmental pollution due to its significant greenhouse gas (GHG) emissions, contributing to smog, acid rain, and global warming [7]. In response, researchers have been exploring alternative raw materials to partially replace natural clay, thereby reducing the ecological footprint associated with its extraction and processing [8, 9]. Fired clay bricks are typically sintered at temperatures ranging from 900 to 1100 °C, and their physical and mechanical properties are highly influenced by the composition of raw materials and firing conditions [10]. In line with sustainability goals, various industrial by-products—including coal dust, gangue, fly ash, and coal slurry—have been investigated as partial clay replacements [11].

Among these, coal bottom ash (CBA), a coarse residue generated during coal combustion in power plants and industrial boilers, has emerged as a promising candidate. Produced in large volumes annually, CBA poses a serious disposal challenge and contributes to environmental degradation if not properly managed [3]. Nonetheless, its potential for recycling has been demonstrated in applications such as road subbase, backfill, cementitious binders, aggregates, and notably, fired clay bricks. Owing to its cost-effectiveness and compatibility with sustainability objectives, CBA is considered an attractive alternative material for brick production [12].

Recent studies have evaluated the feasibility of incorporating CBA into clay brick formulations. Adediran et al. reported that bottom ash improved apparent density and compressive strength in illitic clay-based bricks while reducing crack formation, mass loss, and water absorption. These improvements were attributed to the higher alkali oxide content (K_2O and Na_2O) in illitic clay, which enhances sintering reactions and mineral phase development. Specifically, at elevated sintering temperatures, alkali oxides act as fluxing agents, which lower the melting point of the system and promote the formation of a transient liquid phase. This temporary liquid phase enhances particle rearrangement, fills micro-pores, and facilitates vitrification, thereby increasing the densification of the brick matrix and reducing the open porosity. As a result, water absorption is

significantly decreased. Reported water absorption values ranged from 4% to 25%, and compressive strengths varied from 12 to 19 MPa depending on ash content and clay type [13]. Similarly, Kizinievič et al. (2022) found that adding 15% CBA decreased drying shrinkage by 21%, although it increased porosity, reducing mechanical strength [14]. Sutcu et al. (2019) further observed that bricks fired at 1050 °C exhibited lower porosity, water absorption, and higher density and thermal conductivity than those fired at 950 °C. While increased fly ash content typically led to higher porosity and water uptake, bottom ash had relatively minor impacts. Notably, bricks with 5–10% bottom ash demonstrated comparable compressive strength to conventional clay bricks [15].

These findings underscore the potential of coal bottom ash (CBA) as a viable partial substitute for natural clay in fired clay brick production, contingent upon the appropriate optimization of its incorporation ratio and firing parameters. Accordingly, the present study aims to systematically evaluate the influence of CBA incorporation at levels ranging from 10 to 40 wt.% under varying sintering temperatures (900–1100 °C) on fired bricks' fundamental physical and mechanical properties. This investigation seeks to establish a technically sound and environmentally sustainable alternative to conventional brick manufacturing while simultaneously addressing the pressing issue of coal combustion by-product management.

MATERIALS AND METHODS

Materials

The raw materials used in this study included natural clay sourced from a local brick factory in Kamala Sai, Kala Sin Province, Thailand (Fig. 1 (a)) and coal bottom ash (CBA) obtained from a coal power plant in Mae Moh, Lampang, Thailand (Fig. 1 (b)).

Fig. 1 Raw materials: (a) raw clay and (b) CBA.

The chemical composition of both clay and CBA was analyzed using X-ray fluorescence (XRF) (Horiba, Japan), with the results presented in Table 1. The crystalline structure of the materials was examined using X-ray diffraction (XRD: X' Pert Pro MPD, Philips, Netherlands). Particle size distribution was determined with a particle size analyzer (Mastersizer 2000+ Hydro 2000 MU), while microstructural characteristics were assessed using a scanning electron microscope (SEM) (LEO 1460 VP, Zeiss).

Clay bricks processing procedure

Clay bricks were fabricated by blending raw clay with coal bottom ash (CBA), both of which were pre-dried to achieve a stable moisture content. The materials were homogenized under ambient conditions, with water added at a ratio of 10–15% by weight to facilitate workability (Fig. 2). The resulting mixtures were molded into brick specimens with dimensions of 50 × 95 × 30 mm. These specimens were initially air-dried at room temperature for seven days, followed by oven drying at 110 °C for 48 hours to ensure complete moisture removal. The fully dried bricks were then subjected to firing at 900, 1000, and 1100 °C, employing a heating rate of 5 °C/min and a soaking duration of 30 minutes at the target temperature.

Fig. 2 Manual mixing of raw materials for clay bricks.

Fired clay bricks characterization

Firing shrinkage was measured following the ASTM C362-09 (2018) standard [16], which provides a framework for assessing the thermal behavior of ceramic materials during the firing process. Apparent porosity, water absorption, and bulk density were evaluated according to ASTM C373-18 (2018) [17], ensuring precise characterization of the material properties.

The mechanical properties of the fired clay bricks, essential for assessing their suitability in construction applications, were tested using a Universal Testing Machine (Chun Yen Testing Machines Co.). These tests followed the guidelines outlined in ASTM C773-88 (2020) [18], ensuring the reliability and reproducibility of the results. This standardized approach guarantees accurate material characterization, contributing valuable insights to material science and engineering. The reported results are the average of ten samples with the standard deviation shown as an error bar in the graphs.

Table 1 Chemical oxides composition of clay and CBA used in the experiments.

Oxide (wt.%)	Clay	CBA
SiO_2	50.49	56.22
Al_2O_3	29.84	15.76
Fe_2O_3	5.90	6.00
CaO	0.30	11.00
K_2O	1.20	1.53
Na_2O	-	-
SO_3	-	3.32
TiO_2	0.80	0.45
MnO	1.20	0.10
MgO	-	5.56
LOI.	9.34	0.07

RESULTS AND DISCUSSION

Characterization of raw materials

Table 1 presents the chemical composition of the raw materials as determined by X-ray fluorescence (XRF) analysis. The clay sample was primarily composed of SiO_2 (50.49%) and Al_2O_3 (29.84%), along with minor constituents such as K_2O, Fe_2O_3, CaO, MnO, and TiO_2. In comparison, the coal bottom ash (CBA) exhibited a higher SiO_2 content (56.22%), with Al_2O_3 (15.76%) and CaO (11.00%) as principal oxides, accompanied by MgO, K_2O, SO_3, Fe_2O_3, and TiO_2. The substantial presence of silica and alumina in CBA underscores its potential as a viable supplementary material in fired clay brick production.

Particle size distribution analysis conducted by ASTM D422-63 (2007) [19] indicated a mean particle diameter of 42.38 microns for raw clay, whereas CBA particles averaged 100 microns, signifying a coarser texture (Fig. 3).

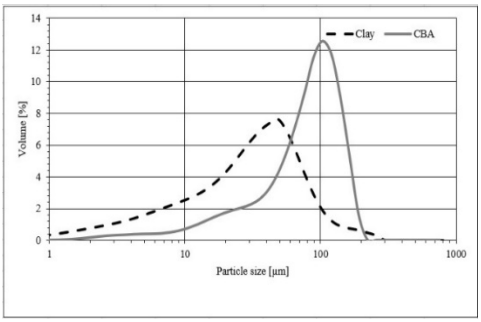

Fig. 3 Particle size distribution of the raw materials.

X-ray diffraction (XRD) analysis was performed to identify the crystalline phases present in clay and CBA (Fig. 4). The predominant minerals in raw clay included quartz (SiO_2; pdf. 01-085-1045), kaolinite ($Al_2(Si_2O_5)(OH)_4$; pdf. 01-080-0855), orthoclase ($KAlSi_3O_8$; pdf. 00-031-0966), hematite (Fe_2O_3; pdf. 01-089-8103), and muscovite ($KAl_2Si_3AlO_{10}(OH)_2$; 00-007-0025). In contrast, CBA contained mullite ($3Al_2O_3 \cdot 2SiO_2$; pdf. 79-1455), anorthite ($CaO \cdot Al_2O_3 \cdot 2SiO_2$; pdf. 02-0523), calcite ($CaCO_3$; pdf. 01-0837), hematite, and quartz.

Scanning Electron Microscopy (SEM) analysis (Fig. 5) revealed differences in surface morphology between the materials. Raw clay exhibited irregular particle shapes and noticeable agglomeration, whereas CBA particles appeared coarser, angular, and heterogeneous, reflecting their nature as a by-product of bottom combustion.

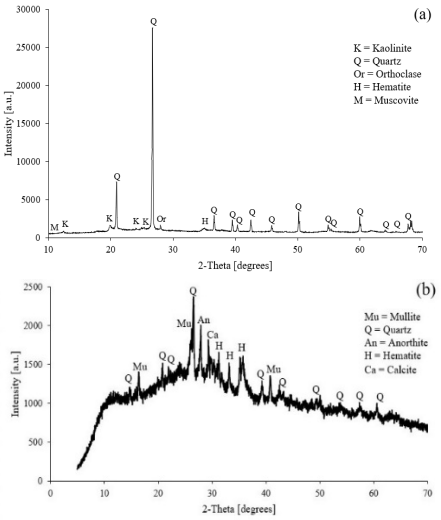

Fig. 4 XRD patterns of (a) raw clay and (b) CBA.

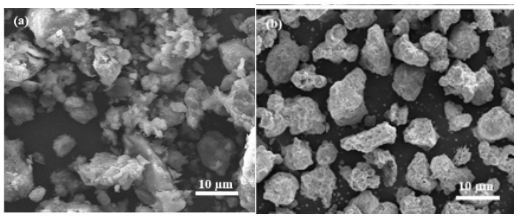

Fig. 5 SEM images of (a) raw clay and (b) CBA.

Technical properties of fired clay bricks

Physical and mechanical properties

Bulk density

The bulk density of fired clay bricks is primarily affected by the specific gravity of the constituent materials, processing methods, and firing temperatures [20]. As illustrated in Fig. 6, bulk density decreased with increasing CBA content and was positively correlated with firing temperature. Bricks without CBA exhibited densities ranging from 2.14 g/cm³ at 900 °C to 2.33 g/cm³ at 1100 °C. The addition of 10 wt.% CBA reduced these values to 1.93 g/cm³ and 2.26 g/cm³, respectively. Further increases in CBA content to 40 wt.% resulted in bulk densities of 1.70 g/cm³ (900 °C) and 1.98 g/cm³ (1100 °C). This reduction is attributed to the lower specific gravity and increased porosity induced by CBA incorporation.

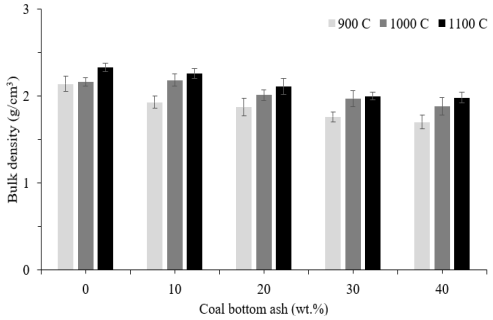

Fig. 6 Bulk density of fired clay brick samples.

Water absorption

Water absorption in fired clay bricks is governed by porosity, particle size distribution, and the microstructural arrangement of raw materials, all of which critically influence durability and long-term performance [21]. A dense and compact microstructure is essential to minimize water ingress and improve resistance to environmental degradation [22].

As shown in Fig. 7, bricks without CBA exhibited water absorption values of 13.44%, 10.51%, and 8.36% at firing temperatures of 900, 1000, and 1100 °C, respectively. In comparison, bricks containing 10–40 wt.% CBA demonstrated higher water absorption, ranging from 11.20% to 19.33%, depending on firing conditions. Increasing the sintering temperature consistently reduced water absorption across all CBA levels. This behavior is attributed to enhanced vitrification and a transient liquid phase formation during firing, which improves densification and decreases open porosity [13]. According to ASTM C62-23 standards, water absorption limits are ≤17% for severe weathering and ≤22% for moderate weathering conditions [23]. The findings confirm that bricks incorporating up to 30 wt.% CBA, when fired at temperatures ≥1000 °C, comply with these thresholds, supporting their suitability for structural applications.

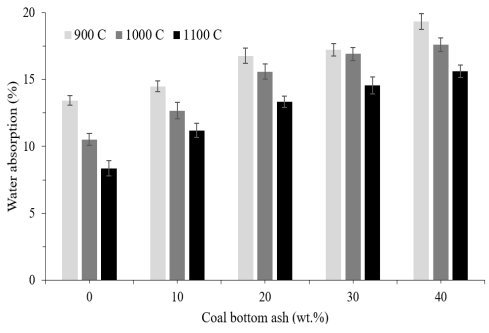

Fig. 7 Water absorption of fired clay brick samples.

Apparent porosity

Apparent porosity is critical in determining the durability and performance of fired clay bricks, as it is closely associated with increased water absorption, reduced compressive strength, and enhanced thermal insulation [20–23]. Fig. 8 illustrates the variation in apparent porosity as a function of CBA content and firing temperature.

Across all sintering temperatures, a general trend of increasing porosity with higher CBA incorporation was observed. The highest porosity (34.95%) occurred in samples with 40 wt.% CBA fired at 900 °C, while the lowest value (23.43%) was found in bricks with 10 wt.% CBA fired at 1100 °C. Bricks without CBA showed porosity values ranging from 19.87% to 21.57%, depending on firing temperature. These results confirm that CBA content has a pronounced influence on the microstructural characteristics of the bricks, particularly in terms of porosity, which in turn affects bulk density and water absorption.

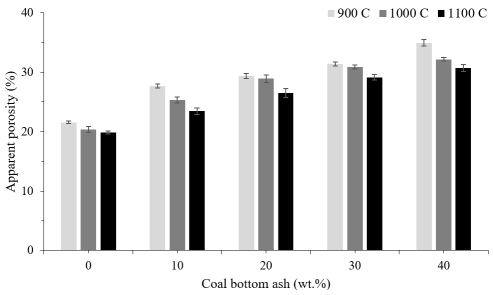

Fig. 8 Apparent porosity of fired clay brick samples.

Firing shrinkage

Firing shrinkage is a fundamental property influencing fired clay bricks' dimensional stability and structural integrity. Accurate linear shrinkage and weight loss assessment is essential to ensure that products meet design and quality specifications [24–25]. As shown in Fig. 9, variations in shrinkage behavior were observed across different CBA contents and sintering temperatures, reflecting the materials' thermal expansion and contraction characteristics [20, 23].

The linear firing shrinkage of all specimens ranged from 4.55% to 6.83% after sintering at 900–1100 °C, remaining well within the ASTM C62-23 (2023) limit of 8% [26]. The results indicate that increased firing temperature promotes densification and corresponds with a shrinkage pattern typical of ceramic materials undergoing partial liquid-phase sintering [20]. These findings confirm the dimensional reliability of CBA-modified bricks under standard thermal processing conditions.

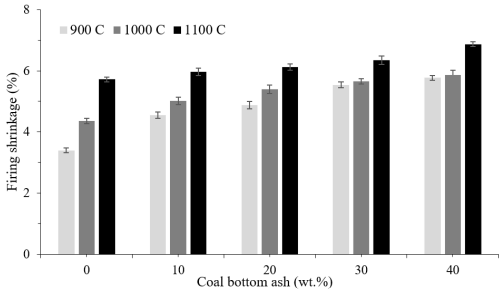

Fig. 9 Firing shrinkage of fired clay brick samples.

Compressive strength

Compressive strength is a key performance indicator for assessing the structural suitability of fired clay bricks, reflecting both material quality and load-bearing capacity. According to ASTM C62-23, fired clay bricks must achieve a minimum compressive strength of 17.2 MPa to meet standard construction requirements.

As shown in Fig. 10, compressive strength generally decreased with increasing CBA content across all firing temperatures. The values ranged from 16.75 MPa to 27.46 MPa, with the highest strength observed in control samples fired at 1100 °C (28.1 MPa) and the lowest in bricks containing 40 wt.% CBA fired at 900 °C (16.75 MPa). Despite this decline, bricks with 10–30 wt.% CBA fired at 900 °C and up to 40 wt.% CBA fired at ≥1000 °C exceeded the ASTM threshold.

Elevated firing temperatures enhanced sintering, crystallization and densification, reduced porosity, and strengthened the brick matrix. Conversely, excessive CBA content introduced a more porous microstructure, increasing water absorption and lowering density and strength [3, 15]. These results are consistent with previous studies indicating that high bottom ash content adversely affects mechanical performance due to increased porosity [14–15]. Thus, carefully optimizing CBA dosage and firing conditions is critical to achieving structurally sound and sustainable bricks.

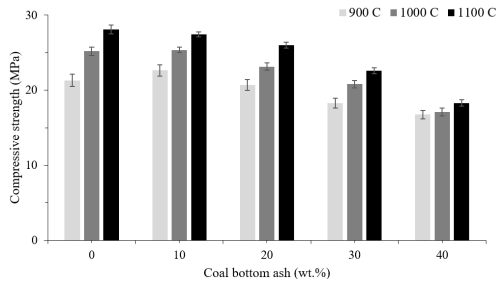

Fig. 10 Compressive strength of fired clay brick samples.

CONCLUSIONS

This study comprehensively evaluates coal bottom ash (CBA) as a sustainable supplementary material in producing fired clay bricks. Through systematic experimentation involving varying CBA contents (0–40 wt.%) and firing temperatures (900–1100 °C), the research demonstrates that CBA can partially replace natural clay without compromising key physical and mechanical properties. The high flux content of CBA, including K_2O, CaO, and MgO, facilitates improved sintering and reduced energy consumption.

Optimal performance was observed in bricks incorporating 10–30 wt.% coal bottom ash (CBA) and fired at temperatures of 1000 °C or higher, where the compressive strength exceeded the minimum requirement of 17.2 MPa specified by ASTM C62-23. Although increased CBA content resulted in higher porosity and water absorption, these adverse effects were effectively mitigated at elevated temperatures due to enhanced sintering and vitrification, which facilitated improved densification and mechanical integrity. Within this optimal range, the produced bricks exhibited acceptable physical properties and enabled partial replacement of natural clay, thereby aligning with both performance criteria and sustainability goals.

ACKNOWLEDGMENTS

The authors would also like to acknowledge the financial support from Rajabhat Maha Sarakham University.

REFERENCES

[1] Muñoz P., Letelier V., Muñoz L., Bustamant M. A., Gencel O., and Sutcu M., The combined effect of bottom ashes and cellulose fibers on fired clay bricks. Construction and Building Materials, Vol. 301, 2021, pp.124307.

[2] Sameer H., and Bringezu S., Life cycle input indicators of material resource use for enhancing sustainability assessment schemes of building. Journal of Building Engineering, Vol. 21, 2019, pp.230-242.

[3] Pitak I., Baltušnilas A., Kalpokaitė-Dičkuvienė R., Kriukiene R., and Denafas G., Experimental study effect of bottom ash and temperature of firing on the properties, microstructure and pore size distribution of clay bricks: A Lithuania point of view. Case Studies in Construction Materials, Vol. 17, 2022, pp. e01230.

[4] Taurino R., Karamanova E., Barbieri L.,

Atanasova-Vladimirova F., and Karamanov A., New fired bricks based on municipal solid waste incinerator bottom ash. Waste Management & Research, Vol. 35 (10), 2017, pp. 1-9.
[5] Dhanapandian S., and Gnanavel B., Using granite and marble sawing power waste in the production of bricks: Spectroscopic and mechanical analysis. Research Journal of Applied Sciences, Engineering and Technology, Vol. 2 (1), 2010, pp. 73-86.
[6] Aeslina A. K., Abbas M., Felicity R., and John B., Density, strength, thermal conductivity and leachate characteristics of light weight fired clay bricks incorporating cigarette butts. International Journal of Civil and Environmental Engineering, Vol. 2, 2010, pp. 179-184.
[7] Sahu M. K., and Singh L., Critical review on types of bricks type 5: Common burnt clay bricks. International Journal of Mechanical and Production Engineering, Vol. 5 (11), 2017, pp. 120-123.
[8] Ghisellini P., Ripa M., and Ulgiati S., Exploring environmental and economic costs and benefits of a circular economy approach to the construction and demolition sector A literature review. Journal of Cleaner Production, Vol. 178, 2018, pp. 618-643.
[9] Kaushik H. B., Rai D. C., and Jain S. K., Stress-strain characteristics of clay brick masonry under uniaxial compression. Journal of Materials in Civil Engineering, Vol 19 (9), 2007, pp. 728-739.
[10] Ramakrishnan K., Chellappa and V., Chandrasekarabarathi S., Manufacturing of low-cost bricks using waste materials. Materials Proceedings, Vol. 13 (25), 2023, pp. 1-8.
[11] Brown A., Bricks: a review of sustainability and toxicity issues. Sustainability and Toxicity of Building Materials, 2024, pp. 179-194.
[12] Mohammed B. S., and Al-Ebrahimy S. N., Production of lightweight clay bricks using polymer waste. Engineering and Technology Journal, Vol. 38, 2018, pp. 823-831.
[13] Adediran A., Kikky S. M., Adhikary S. K, Ducman V., and Perumal P., Upcycling municipal solid waste incineration bottom ash in clay-bonded bricks. 2024, Article in Press.
[14] Kizinievič O., Voišnienė V., Kizinievič V., and Pundienė I., Impact of municipal solid waste incineration bottom ash on the properties and frost resistance of clay bricks. Journal of Material Cycles and Waste Management. Vol. 24, 2022, pp. 237-249.
[15] Sutcu M., Erdogmus E., Gencel O., Gholampour A., Atan E., and Ozbakkaloglu T., Recycling of bottom ash and fly ash wastes in eco-friendly clay brick production. Journal of Cleaner Production. Vol. 233, 2019, pp. 753-764.
[16] ASTM C326-09., Standard Test Method for Drying and Firing Shrinkages of Ceramic Whiteware Clays. West Conshohocken, Pennsylvania. ASTM Book of Standards 15.02, 2018.
[17] ASTM C373-18., Standard Test Method for Water Absorption, Bulk Density, Apparent Porosity, and Apparent Specific Gravity of Fired Whiteware Products, Ceramic Tiles, and Glass Tiles. West Conshohocken, Pennsylvania. ASTM Book of Standards 15.02, 2018.
[18] ASTM C773-88., Standard Test Method for Compressive (Crushing) Strength of Fired Whiteware Materials, West Conshohocken, Pennsylvania. ASTM Book of Standards. 15.02, 2020.
[19] ASTM D422-63., Standard test method for Particle-Size Analysis of Soils. West Conshohocken, Pennsylvania. ASTM Book of standards. 2007.
[20] Chindaprasirt p., Srisuwan A., Saengthong C., Lawanwadeekul S., and Phonphuak N., Synergistic effect of fly ash and glass cullet additive on properties of fire clay bricks. Journal of Building Engineering. Vol. 44, 2022, pp. 128327.
[21] Ozturk S., Sutcu M., Erdogmus E., and Gencel O., Influence of tea waste concentration in the physical, mechanical and thermal properties of brick clay mixtures. Construction and Building Materials. Vol. 217, 2019, pp. 592-599.
[22] Saraphirom P., Namsena P., Teerakun M., Phonphuak S., Chanprathak A., Dakaew S., and Phonphuak P., Development of fired clay granules as eco-friendly substances for nitrogen-fixing bacterial cells. International Journal of GEOMATE, vol. 27, No. 120, 2024, pp.110-121.
[23] Lawanwadeekul S., Otsuru T., Tomiku R., and Nishiguchi H., Thermal-acoustic clay brick production with added charcoal for use in Thailand. Construction and Building Materials, Vol. 255, 2020, pp. 119376.
[24] Phonphuak, N., Application of Dry Grass for Clay Brick Manufacturing. Key Engineering Materials, Vol. 757, 2017, pp. 35-39.
[25] Phonphuak, N., Teerakun, M., Srisuwan, A., Ruenruangrit, P., and Saraphirom, P., The use of sawdust waste on physical properties and [thermal conductivity of fired clay brick. International Journal of GEOMATE, Vol. 18, No. 69, 2020, pp. 24- 29.
[26] ASTM C62-23., Standard specification for building brick (solid masonry units made from clay or shale). ASTM International. https://www.astm.org/c0062-23.html

Copyright © Int. J. of GEOMATE All rights reserved, including making copies, unless permission is obtained from the copyright proprietors.

15th Int. Conf. on Geotechnique, Construction Materials & Environment,
Kyoto, Japan, 11-13 November 2025, ISBN 978-4-909106124 C3051

EXPERIMENTAL INVESTIGATION ON APPLICATION OF ALKALI-ACTIVATED MATERIAL WITH HIGH VISCOSITY TO HIGH FLUIDITY CONCRETE

Kosuke Matsuoka[1], Yoichi Mimura[2] and Itaru Horiguchi[2]

[1]Advanced Course, Project Design Engineering, National Institute of Technology, Kure College, Japan
[2]Department of Civil and Environmental Engineering, National Institute of Technology, Kure College, Japan

ABSTRACT

Alkali-activated material (AAM) is a cement-free concrete binder and can significantly reduce CO_2 emissions compared to conventional cement. Although large amount of powder causes high viscosity and poor handling of AAM concrete, the high viscosity can be utilized to increase segregation resistance required for high fluidity concrete. This paper presents an investigation on performance of AAM high fluidity concrete which had a mixture conditions determined based on mortar experiments. As a result of mortar experiments, the flow of AAM mortar with mole ratio of silicon to alkali (Si/A) of 0.4 decreased as the blast furnace slag (BFS) substitution ratio increased while one with Si/A ratios of 0.6 and 0.8 increased with BFS substitution ratio rise. AAM mortar with 20% of BFS replacement ratio had little increase in compressive strength by Si/A increase. AAM high fluidity concrete, which had mortar phase with 181 mm of flow value, resulted in more than 600 mm of slump flow. In addition, the 0.4% decrease in W/B caused 10% greater compressive strength at the age of 28 days, however, significant longer 500 mm slump flow time.

Keywords: Alkali-activated material, Compressive strength, Slump flow, 500 mm slump flow time

INTRODUCTION

Cement is widely used as concrete binder in the world, and huge amount of carbon dioxide is emitted in its production process. The carbon dioxide emission is one of major factors causing global warming, and is regarded as an international issue. Therefore, the concern with developing cement-free concrete binder has been growing, and the typical example is alkali-activated material (AAM), such as geopolymer. AAM is a general term for solidified materials produced by condensation polymerization reaction between activator and powders containing large amount of Si, Al and Ca components. Fly ash (FA) and blast furnace slag powder (BFS) are general component materials of AAM. A typical activator is a mixture of Sodium silicate solution (Water glass, WG) and sodium hydroxide solution (Caustic soda solution, CS).

AAM has no requirement of cement and can utilize by-products from other industries, so AAM can contribute to resource-recycling and low environmental impact. However, it has been found that AAM with sufficient compressive strength for required performance has high viscosity. The high viscosity of AAM is caused by water glass with high viscosity and higher unit content of powders (FA, BFS, etc.) than general cement concrete [1]. Mimura has reported that AAM mortar, which produced with the activator without water glass, had lower viscosity than that with water glass [2]. However, it is also mentioned that containing no water glass significantly decreased in compressive strength of AAM mortar. Therefore, high viscosity of AAM should be utilized while ensuring appropriate strength with activator containing water glass. For example, high viscosity of AAM can have effect on increasing segregation resistance in high fluidity concrete [3].

In this study, effects of several mixture conditions on fresh properties and compressive strength were evaluated by using AAM mortar. Slump flow test and compressive strength test were also performed on AAM high fluidity concrete with the mixture proportion determined based on the mortar results.

RESEARCH SIGNIFICANCE

Performance of AAM is affected by diverse constituent materials and mixture conditions. Many researchers investigate these effects by mortar experiments [4]. However, little discussion focuses on performance of AAM concrete based on results of mortar experiments. In this study, compressive strength, slump flow and 500 mm slump flow time were examined in order to investigate application of AAM to high fluidity concrete with the mixture proportion determined based on the mortar results. Achievement of AAM high fluidity concrete might contribute to not only resource-recycling and low environmental impact but also labor saving and cost reduction in construction.

EXPERIMENTS OF AAM MORTAR

Materials

The materials used for AAM mortar in the present study are listed in Table 1. FA and BFS were used for binder of AAM mortar in this study. FA was in accordance with Class II of Japanese Industrial Standards (JIS A 6201) and is easily available in Japan. BFS in accordance with JIS A 6206 had specific surface area of 4000 cm^2/g and was mixed in order to increase strength of AAM mortar.

Activator in this study was a mixture of WG and CS. WG had a mole ratio of Na_2O to SiO_2 of 2.5. In Japan, water glass was specified by the former JIS K 1408, which have now been regulated by standard of Japan Inorganic Chemical Industry Association. The mole concentration of CS was set to 7 mol/L. When the water component of CS and WG was unsatisfied with unit water content of a mixture condition, additional tap water (Wad) was mixed to the activator. Crushed sand from Kure City (density: 2.62 g/cm^3) was used as fine aggregate (S). Chemical admixtures in this study were high-performance water reducing admixture (Ad1) and retarder (Ad2). Ad1 and Ad2 were mainly composed of naphthalenesulfonic acid and oxycarboxylic acid, respectively. Both admixtures were commercially available for cement concrete. Ad2 was used to ensure enough time for casting AAM mortar because AAM with BFS generally has short setting time.

Mixture conditions and proportions

The mixture conditions and proportions of AAM mortar in the present study are given at Table 2. Mole ratios of silicon to sodium in the activator (Si/A) were 0.4, 0.6 and 0.8. BFS substitution rates, which represent BFS volume substitution fraction to FA, were 20%, 30% and 50%. The effect of Si/A and BFS substitution rate was investigated with AAM mortar from M1 to M9.

Ad1 rate (Ad2 rate) was a mass rate of Ad1 (Ad2) to FA and BFS, and was 0% or 2%. The previous study [3] has reported that a high-performance water-reducing agent with main component of Naphthalene sulfonic acid increased in compressive strength of AAM mortar using activator consisting of only caustic soda solution and had little increase effect on compressive strength of AAM mortar with water glass of mole ratio 2.0. In this study, the effect of Ad1 and Ad2 on compressive strength of AAM mortar with WG of mole ratio of 2.5 was evaluated by comparison with results from M10 to M15.

The following mixture conditions of AAM mortar were set constant in 15 mixture proportions of this study. A mole ratio of sodium to water in activator (A/W) was set to 0.1. Water-binder ratio (W/B, binder in this study presents FA and BFS) was determined to be 0.4. A unit water content (W) was 240 kg/m^3,

Table 1 Materials of AAM mortar

Materials	Properties
Fly ash (FA)	Class II
Blast furnace slag (BFS)	Specific surface area: 4000 cm^2/g
Caustic Soda Solution (CS)	Mole concentration of NaOH: 7 mol/L
Water glass (WG)	Mole ratio of SiO_2/Na_2O: 2.5
Water (Wad)	Tap water
Fine aggregate (S)	Crushed sand
Admixture 1 (Ad1)	High-performance water-reducing agent, Naphthalenesulfonic acid
Admixture 2 (Ad2)	Retarder, Oxycarboxylic acid

Table 2 Mixture conditions and proportions of AAM mortar

I.D.	Si/A	BFS rate (vol%)	Ad1 (%)	Ad2 (%)	Mixture proportions (kg/m^3)								
					FA	BFS	WG1	WG2	CS	Wad	S	Ad1	Ad2
M1	0.4	20	2	2	452	148	---	112	166	47	1327	12	12
M2	0.4	30	2	2	385	215	---	112	166	47	1345	12	12
M3	0.4	50	2	2	260	340	---	112	166	47	1380	12	12
M4	0.6	20	2	2	452	148	---	168	127	46	1327	12	12
M5	0.6	30	2	2	385	215	---	168	127	46	1345	12	12
M6	0.6	50	2	2	260	340	---	168	127	46	1380	12	12
M7	0.8	20	2	2	452	148	---	224	88	45	1327	12	12
M8	0.8	30	2	2	385	215	---	224	88	45	1345	12	12
M9	0.8	50	2	2	260	340	---	224	88	45	1380	12	12
M10	0.4	30	2	0	385	215	---	112	166	47	1345	12	0
M11	0.4	30	0	2	385	215	---	112	166	47	1345	0	12
M12	0.4	30	0	0	385	215	---	112	166	47	1345	0	0
M13	0.6	30	2	0	385	215	---	168	127	46	1345	12	0
M14	0.6	30	0	2	385	215	---	168	127	46	1345	0	12
M15	0.6	30	0	0	385	215	---	168	127	46	1345	0	0

Note: BFS rate represents BFS substitution rate. The other mixture conditions are as follows:
A/W = 0.1, W/B = 0.4, W = 240 kg/m³, B = FA+BFS, Ad1 = B×2%, Ad2 = 2%

which included water component of caustic soda solution and water glass.

Experimental procedure

AAM mortar in the present study was mixed with a mortar mixer which had the maximum capacity of 2 liters. FA, BFS and fine aggregate were mixed for 30 seconds, and then the activator was added and mixed for 1 minute.

Just after mixing, a mortar flow test was conducted by using a flow table and mold with a truncated cone shaped. The mold placing AAM mortar was lifted vertically, and the flow table made 15 strokes with once a second. The diameters of AAM mortar ware measured at the most spread and at right angle to it, and the mortar flow was evaluated by the average of the measurements.

In this study, the compressive strength test of AAM mortar was performed by using a cylindrical specimen with a diameter of 50 mm and a height of 100 mm. After placing, the top surface of specimen was sealed with double plastic wrap. All specimens with a mold and plastic wrap were cured under sealed condition at room temperature of 20 degree Celsius. The specimen was demolded just before the compressive strength test.

For the compressive strength test, the cylindrical specimen was loaded at a loading rate of 0.2 N/mm^2 per second. The compressive strength of AAM mortar was evaluated with the average of 3 specimens. The compressive strength test in accordance with JIS A 1108 was conducted at the age of 7 days and 28 days.

Results and discussion

Fig. 1 shows the result of the mortar flow test. When AAM mortar had the mixture condition of Si/A of 0.4, the flow value was decreased as BFS substitution rate increased. This decrease in flow might be caused by BFS replacement of FA, which has spherical particle. However, the flow value of AAM mortar with Si/A of 0.6 and 0.8 was increased with BFS substitution rate. In addition, the amount of AAM mortar adhering to the flow mold was increased, and higher viscosity was visually observed. Fluidity and viscosity of AAM mortar were affected by various mixture conditions, so, further investigation and discussion might be required in order to achieve appropriate fresh properties for high fluidity concrete.

Fig. 2 shows the relationship between Si/A and compressive strength for each BFS substitution rate. Increase in BFS substitution rate caused higher compressive strength of AAM mortar regardless of Si/A as shown in Fig. 2, so development of compressive strength of AAM mortar at early age in the present study might be dominated by BFS, and might be almost independent to Si/A. Because the reaction of activator with FA which has main component of amorphous silica and alumina could be much slower than that of BFS containing large amount of Ca under room temperature curing condition of 20 degree Celsius in this study.

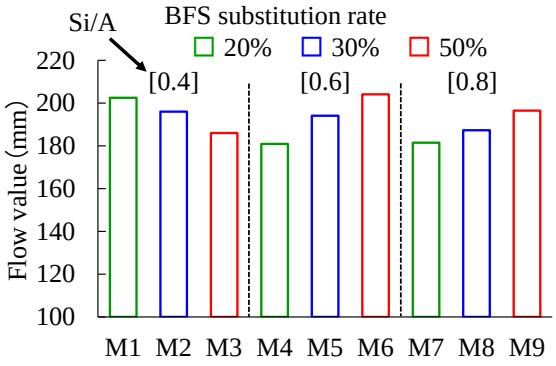

Fig.1 Flow value of AAM mortar

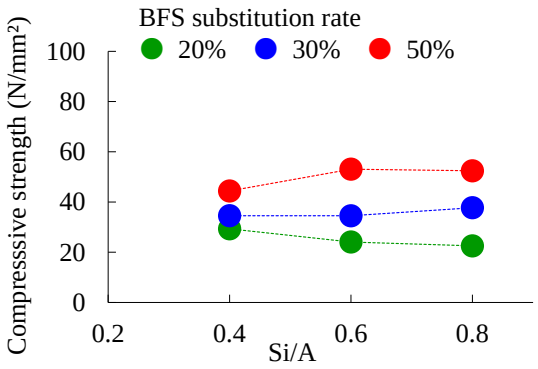

Fig. 2 Compressive strength of AAM mortar at the age of 7 days

Fig. 3 shows the compressive strength of AAM mortar at the age of 28 days. The compressive strength at the age of 28 days also increased as BFS substitution rate rise. This result indicates that contribution of FA to strength development was smaller than BFS at the age of 28 days under room temperature curing condition. In order to appropriately evaluate strength development by FA, compressive strength test at long term age such as 91 days is required. At the lowest BFS substitution rate of 20% in the present study, Si/A had little effect on the compressive strength at the age of 28 days, while AAM mortar with 30% and 50% of BFS substitution rate had higher compressive strength as Si/A rise. Uehara [5] has reported that low alkali concentration and small BFS substitution rate are caused relatively small compressive strength of AAM mortar with silica fume added instead of water glass as source of silica. According to this paper, this might be because the low alkali concentration and small BFS substitution rate cause less dissolution of silica fume as small BFS substitution rate prevents from consumption of Si component which is required in

hardening process of BFS. In this study, the alkali concentration which was 0.1 of A/W was the same as the previous study [4], and the low concentration might cause lower dissolution of FA. In addition, component of Si in the activator at low BFS substitution rate could be consumed little in hardening process, so the compressive strength of AAM mortar with 20% of BFS substitution rate was almost independent to Si/A. However, it is noted that source of silica in the previous study was silica fume instead of water glass and constituent materials and mixture conditions were different from those of this study.

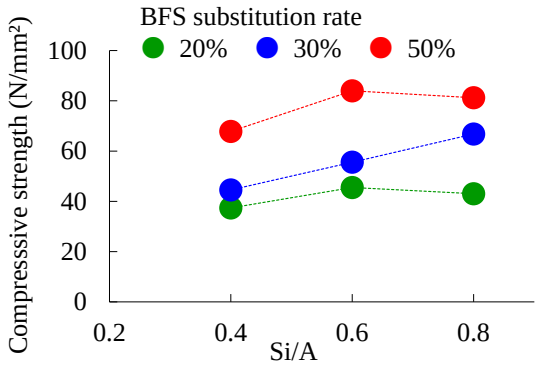

Fig. 3 Compressive strength of AAM mortar at the age of 28 days

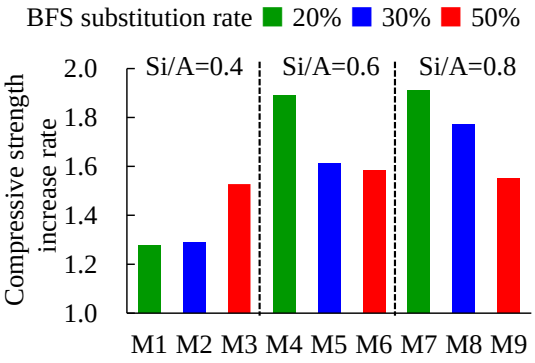

Fig.4 Compressive strength increase rate

Fig. 4 shows the increase ratio of the compressive strength at the age of 28 days to that at the age of 7 days. When Si/A was 0.6 and 0.8, the compressive strength increase rate was decreased as BFS substitution rate increased. This is because the compressive strength at the age of 7 days was higher with higher BFS substitution rate due to the effect of BFS on early strength development. In addition, the decrease in unit content of FA due to BFS substitution rate rise could also cause less effect of FA on strength development at long term age. On the other hand, the compressive strength increase ratio was increased by higher BFS substitution rate at 0.4 of Si/A. In this case, less silicon was supplied from water glass than the other cases. AAM mortar at the age of 28 days could contain insufficient component of silicon for FA due to consumption for hardening reaction of BFS at early age, so BFS substitution rate had higher contribution to the compressive strength at the age of 28 days.

Fig. 5 demonstrates that the effect of the chemical admixtures on the compressive strength of AAM mortar. At the age of 7 days, AAM mortar without the chemical admixtures which were high-performance water-reducing agent (Ad1) and retarder (Ad2) for cement concrete had the highest compressive strength. The maximum difference in the compressive strength was 7.6 N/mm^2 at 0.4 of Si/A.

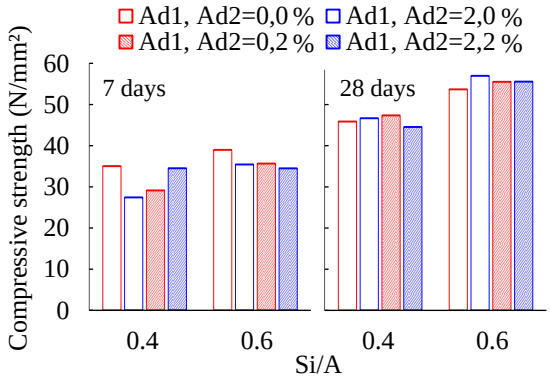

Fig.5 Effect of chemical admixtures on compressive strength

Although the compressive strength of AAM mortar with the chemical admixtures was lower than that without the chemical admixtures at the age of 7 days as shown in Fig. 5, the compressive strength of AAM mortar at the age of 28 days was equivalent regardless of the chemical admixtures and the maximum difference in the compressive strength was only 2.8 N/mm^2. This difference at 0.6 of Si/A was correspond to less than 5% of the averaged compressive strength. These results indicate that Ad1 and Ad2 used in the present study had little effect on the compressive strength. Especially, although the retarder (Ad2) which had main component of Oxycarboxylic acid restrained hardening reaction and decreased in the compressive strength at early age (except for the mixture condition of Si/A of 0.4 and Ad1 addition), such effect could diminish with age. Therefore, AAM mortar with Ad1 and Ad2 could have equivalent compressive strength at the age of 28 days shown in Fig. 5.

EXPERIMENTS OF AAM CONCRETE

Materials

AAM concrete used the same materials as AAM mortar. Crushed stone with a density of 2.67 g/m^3 was used in AAM concrete as coarse aggregate (G).

Table 3. Mixture conditions and proportions of AAM concrete

I.D.	W/B	BFS rate (vol%)	Mixture proportions (kg/m^3)								
			FA	BFS	WG	CS	Wad	S	G	Ad1	Ad2
C1	0.4	10	360	52	116	87	32	624	954	8.25	0.825
C2	0.4	20	311	101	116	87	32	630	963	8.25	0.825
C3	0.36	20	346	113	116	87	32	609	932	9.17	0.917

Note: BFS rate represents BFS substitution rate. The other mixture conditions are as follows:
A/W = 0.1, Si/A = 0.6, W = 165 kg/m^3, B = FA+BFS, Ad1 = B×2%, Ad2 = B×0.2%, s/a = 0.4

Mixture conditions and proportions

The mixture conditions for AAM concrete in this study are shown in Table 3. The mixture conditions determined for AAM concrete in this study were A/W, Si/A, W (kg/m^3), W/B, BFS substitution rate (vol%), sand-total aggregate ratio (*s/a*, vol%), Ad1rate (%) and Ad2 rate (%).

The base mixture of AAM concrete in this study was C2 given at Table 3. Its mixture conditions for AAM concrete were set to reference to the AAM mortar experimental results. BFS substitution rate was 20% in order to ensure enough setting time for flow test and casting AAM concrete. Si/A was determined as 0.6, because AAM mortar with Si/A of 0.6 had the highest compressive strength with 20% of BFS substitution rate at the age of 28 days shown in Fig. 3. Therefore, the mortar phase in AAM concrete with C2 mixture was correspond to AAM mortar of M4. In addition, *s/a* and Ad2 rate were set to 0.4 and 0.2%, respectively. AAM mortar with BFS substitution rate of 20% had enough setting time for casting in a laboratory and required little effect of Ad2, so Ad2 rate for AAM concrete was set to lower than that for AAM mortar. A unit water content of AAM concrete was determined as 165 kg/m^3, which was evaluated from unit water content of 240 kg/m^3 of AAM mortar and approximate volume fraction of mortar phase in AAM concrete. The others of mixture conditions were the same as AAM mortar. That is, A/W was 0.1 and Ad1 was 2%.

In this study, AAM concrete with a mixture condition of BFS substitution rate of 10% (C1) and a mixture condition of W/B of 0.36 (C3) were also prepared in order to investigate fresh properties and compressive strength.

Experimental procedure

FA, BFS and fine aggregate were mixed for 30 seconds by a bi-axial forced mixing type mixer. Coarse aggregate was then added and mixed for another 30 seconds, after which the alkaline solution was added and mixed for 60 seconds. A slump flow test in accordance with JIS A 1150 was performed just after mixing.

A cylindrical specimen for compressive strength test had 100 mm in diameter and 200 mm in height. After casting, all specimens were sealed with double plastic wrap and cured in the same condition as AAM mortar. The procedure from curing to compressive strength test was the same as AAM mortar. Compressive strength test was conducted at the age of 7 days and 28 days.

Results and discussion

Fig.6 shows the relationship between slump flow and 500 mm slump flow time. In this study, the mixture conditions of AAM concrete was determined with reference to AAM mortar of M4. Although M4 had the lowest flow value of 181 mm in this study, 600 mm slump flow was achieved by AAM concrete of 3 mixtures, as shown in Fig.6. In addition, AAM concrete of this study was observed no segregation, so viscosity of AAM was effective to increase in segregation resistance.

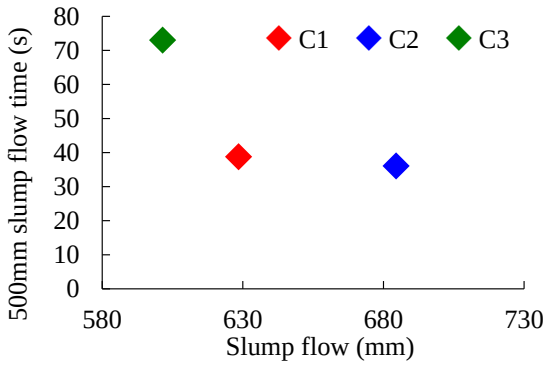

Fig.6 500mm slump flow time and slump flow

AAM concrete of C2, which had 10% higher BFS substitution rate than C1, had 685 mm of slump flow. Slump flow of C2 was 55 mm greater than that of C1. 500 mm slump flow time was only 3 seconds shorter than that of C1, and C2 had equivalent 500 mm slump flow time to C1. This result indicates that C2 had equivalent viscosity and higher fluidity compared with C1. It is well known that BFS unit content increase causes lower fluidity and slump flow become smaller. However, slump flow of AAM concrete in this study was increased with BFS increase, so effects of BFS on slump flow of AAM concrete are needed further experiments and discussion.

Compared with result in C2, the slump flow of C3 was reduced by 83 mm due to decrease in W/B of 4% and C3 had approximately 12% lower fluidity. 500 mm slump flow time of C3 was extended by 37

seconds. This flow time was equivalent to twice flow time of C2 and shows that C3 had higher viscosity. The higher viscosity of C3 was also visually observed. These results indicate 4% decrease in W/B has greater effect on 500 mm slump flow time than 10% reduction in BFS substitution rate.

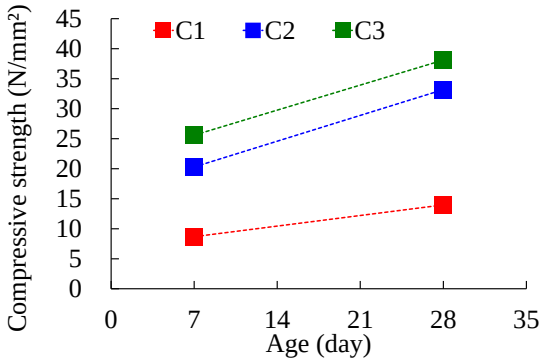

Fig.7 compressive strength of AAM concrete

The compressive strength of AAM concrete at the age of 7 days and 28 days is shown in Fig.7. C1 with BFS substitution rate of 10% had the lowest compressive strength of 14 N/mm² at the age of 28 days. Compared with the compressive strength of C2, the compressive strength of C1 with BFS substitution rate of 10% was less than half, it was approximately 40% at the age of 7 days and 28 days. The compressive strength of C3, which had 4% lower W/B in order to increase in compressive strength, was 1.3 times and 1.1 times at the age of 7 days and 28 days compared C2, respectively. This result indicates that the BFS substitution rate had greater effect on compressive strength of AAM concrete than W/B.

Compared with a result of the previous study [4], AAM concrete in this study had the equivalent compressive strength and slump flow, however, 500 mm slump flow time was much longer. This might be because that mixture conditions such as a unit content and the maximum size of coarse aggregate were different. In addition, the maximum compressive strength in this study was only 38.1 N/mm^2. In order to expand usage of AAM concrete as alternative of cement concrete, it is necessary to satisfy various strength property requirements. Some mixture conditions such as A/W, W/B and BFS substitution rate affect strength development, however, increasing compressive strength of AAM concrete often causes shorter setting time. Therefore, further investigation are required on effect of various materials and mixture conditions on performance of AAM concrete.

CONCLUSIONS

In this study, fresh and strength properties of AAM mortar and AAM concrete with various mixture conditions are experimentally investigated in order to evaluate application of AAM to high fluidity concrete. The conclusions of this study are as follow:

(1) The flow test results of AAM mortar shows that when the Si/A ratio is 0.4, the flow value decreases with increasing BFS substitution rate. However, when the Si/A ratio is 0.6 or 0.8, the flow value shows the opposite behavior.
(2) The compressive strength of AAM mortar with 20% of BFS substitution rate might be almost independent to Si/A.
(3) High-performance water-reducing agent with main component of Naphthalenesulfonic acid and retarder with main component of Oxycarboxylic acid have little effect on compressive strength of AAM mortar at the age of 28 days.
(4) AAM concrete, which has mortar phase with 181 mm of mortar flow, achieves 600 mm slump flow, and reduction in W/B by 4% causes 12% lower fluidity based on slump flow and twice 500 mm slump flow time due to higher viscosity.
(5) In AAM concrete, BFS substitution rate has greater effect on compressive strength than W/B.

REFERENCES

[1] Jumrat S., Chatveera B and Rattanadecho P., Dielectric properties and temperature profile of fly ash-based geopolymer mortar. International Communications in Heat and Mass Transfer, Vol.38(2), 2011, pp. 242-248
[2] Mimura Y. and Horiguchi I., Effects of chemical admixtures for cement concrete on mortar flow and compressive strength of geopolymer. Proc. of ASEA-SEC-6, Vol. 9(2), 2022, pp. MAT-05-1-MAT-05-6
[3] Vigneshkumar A., C. Freeda Christy., M. Muthukanan., M. Maheswaran., K. Arunkumar and R. Kanniga Devi, Experimental investigations on fresh and mechanical properties of fly ash and ground granulated blast furnace slag self-compacting geopolymer concrete. Materials Today: Proceedings, 2024, pp. 1-7
[4] Zhang P., Zheng Y., Wang K. and Zhang J., A review on properties of fresh and hardened geopolymer mortar. Composites Part B, Vol. 152, 2018, pp.79-95
[5] Uehara M., Minami K., Hirata H. and Yamazaki A., Properties, mix proportion and preparation method for geopolymer hardened body. Proc. of the Japan Concrete Institute, Vol. 37(1), 2015, pp. 1987-1992 (in Japanese)

Copyright © Int. J. of GEOMATE All rights reserved, including making copies, unless permission is obtained from the copyright proprietors.

15th Int. Conf. on Geotechnique, Construction Materials & Environment, Kyoto, Japan, 11-13 November 2025, ISBN 978-4-909106124 C3051

INFLUENCE OF BIOCHAR WATER HYACINTH ON THE SHEAR STRENGTH OF ULTISOLS

Erica Elice S. Uy[1], Jeann Patrick B. Barcelona[2], Juan Angelo V. Malaca[2], Lance Matthew R. Santiago[2], Jose Gabriel R. Zamora[2] and Angelo B. Edora[3]

[1,2]De La Salle University, Philippines; [3]Nagoya University, Japan

ABSTRACT

Ultisols are reddish, acidic, and clayey soils that are abundant in the Philippines. It is commonly found in upland areas and approximately covers 41.5% of the land area. However, this material is underutilized due to its high plasticity, which can have an adverse effect on its shear strength. In order to explore ultisol's potential, soil stabilization is essential. A promising material that can be blended to ultisol is water hyacinth biochar. This type of material has hydrophobic qualities which can be beneficial to high plastic material since it can repel water. Water hyacinth was used since it is an invasive species that disrupts the bodies of water that it grows on. In this study, biochar water hyacinth was blended to ultisols having 0%, 5% and 10% proportions. To investigate on the influence of this material to ultisols the relative density was varied. The samples were prepared having a relative density of 32.5%, 60% and 92.5%. The shear strength parameters were established by performing a direct shear test under undrained condition. Based on the results, biochar water hyacinth had a significant effect on the cohesion of the soil.

Keywords: Water hyacinth Biochar, Ultisols, Shear strength, Undrained condition

INTRODUCTION

According to the Bureau of Soils and Water Management (BSWM), one of the most common lowland soil in the Philippines is Ultisols or Alisols. The area covered by Ultisols in the Philippines is approximately 41.5% [1]. They are formed as a result of very extensive weathering and leaching processes that produce a subsurface that is clay-enriched and predominantly composed of minerals including quartz, kaolinite and iron oxides. Ultisols are usually composed of sand, silt and clay [2-5]. The percentage varies due to the lithology and morphology on where it is located and formed. In the Philippine setting, it was found that some Ultisols in the Visayas group of island was observed to have high clay content and high plasticity [5]. Although this soil is abundant in the Philippines, it is not being utilized as a construction material. A possible reason is the high fines content which can have a negative impact to the shear strength. With this, there is a need to explore soil stabilization techniques that will lessen the plasticity and increase the shear strength.

Soil stabilization in general are techniques to improve the index properties, shear strength and compressibility of a soil. It can be categorized into mechanical, physical and chemical stabilization [6, 7]. In mechanical stabilization, it physically alters the soil properties to improve the strength. One way is by adding and blending industrial waste materials such as silica fume, rice husk ash and ground granulated blast furnace slag [8, 9]. These waste materials may improve the gradation of the soil and can also contribute to an increase in shear strength. Mechanical stabilization also involves changing the density of the soil by means of compaction [6, Rivera-7]. In this manner, the void spaces become smaller making the relative density higher. Physical stabilization improves soil's properties by introducing reinforcements such as geotextiles [10, 11]. Chemical stabilization alters the soil's properties by introducing additives such as lime, fly ash and cement. This results to the chemical reactions that enhances the bonding and interlocking in the soil matrix [12]. Also, in this technique the purpose of the additives is to develop pozzolanic reaction which improves the shear strength of a weak soil. The additives are also known as binders which also frequently adopted in the enhancement of particle bonds and interaction. Binders such as lime and cement are very common. However, these materials usually have negative impact to the environment. For lime binders, are calcium-based and undergoes calcination process. This process needs high energy which leads to an increase in carbon dioxide emission [10, 13, 14].

An emerging material for soil stabilization is the use of biochar. This material is a form of charcoal that is both environmentally safe and a stable, carbon-rich form of charcoal that can be added to the soil. This is produced using a process called pyrolysis, where biomass is heated at temperatures starting at 250 Degrees Celsius with almost no oxygen [15]. Waste materials such as agricultural waste, forestry waste, sewage waste and municipal waste are some of the commonly used raw materials [16].

Several studies explored the potential of biochar as an additive to improve the shear strength of soil. In a

study by Reddy [17], they used wood biochar in assessing the shear strength of the clay soil mixed with the sample. The biochar proportion used in the study is 5%, 10% and 20%. Based on the results, shear strength increased as the amount of biochar was increased. The study by Xu [18] used what straw as the raw material for biochar. In this study, 0, 2.5, 5, 10, and 20% of biochar by weight was added to the clay. It was observed that the shear strength increased for 2.5 and 5% biochar while 10% and 20% decreased. The largest shear strength was observed at 5% biochar content**.** Li [19] investigated the effect of the bagasse biochar and rice platycodon biochar to the shear strength of red loam. The proportions of the two biochar were 0%, 2%, 4%, 6%, and 8%. They were added to the loam mass with respect to the dry mass. In their results, the biochar content of 2%, 4% and 6% showed an increase. The largest shear strength was observed at 6% and decrease was observed at 8%. It can be observed that although adding biochar can increase the shear strength at 5% and 6% showed the largest improvement. Also, when the amount of biochar was increased larger than 5% or 6% shear strength decreased. However, comparing it to 0% biochar, there was still an improvement observed.

A potential biochar raw material is water hyacinth. According to Dersseh [20], water hyacinths are invasive tracheophyte plant. Several countries experienced disruption due to its abundance. In the Philippines, thick water hyacinth beds cover the rivers which can obstruct the passageway of barges and ferry services [21]. The potential of water hyacinth as an additive was explored by numerous studies. A study by Sathya [22] assessed the influence of water hyacinth extract from Thanjavur District, India as a Bio-admixture in cement and concrete. It was found that there is a progressive increase of compressive strength whenever there is an increase in the replacement of water hyacinth extract. In the study of Okwadha & Makomele [23], the water hyacinth extract served as an admixture in concrete cube production. The ratios of water hyacinth used were 0%, 10%, 15%, 20%, and 25%. Slump tests and compressive tests of various concrete cubes were performed to evaluate the workability of the concrete after 7, 14 and 28 days. After all the laboratory tests, the researchers concluded that the water hyacinth in the form of liquid extract increased the workability of concrete with an increase in percentage replacement of concentration of the solution. The enhancement of workability in concrete may be caused by the small fragments of lignocellulose and hemicellulose dissolved in water hyacinth extract.

Accordingly, this study aims to explore the potential and effect of water hyacinth biochar (WHBC) to the shear strength of Ultisols. Biochar was added by weight and the proportions were 0%, 5%, 10%, 15%, and 20%. The relative density of the soil sample was varied to further assess the effectiveness of the water hyacinth biochar in increasing the shear strength of soil. The relative densities used were 32.5% (Loose), 60% (Medium Dense), and 92.5% (Very Dense). Direct shear test was performed simulating an undrained condition.

RESEARCH SIGNIFICANCE

This study investigated the effect of water hyacinth biochar's on the shear strength of Ultisols. The significance of the study is in the potential of treated Ultisols as a construction material. The results of the study highlight the contribution of water hyacinth biochar to the shear strength of Ultisols and the potential of WHBC as an additive for soil amendment. Lastly, the study introduces another beneficial use of water hyacinth. This can lessen its negative impact to the water ways by processing it into a potential additive for soil stabilization.

ULTISOL

The samples were obtained from the mountainous are of Zamboanga Peninsula region in Mindanao. Based on visual inspection in accordance with Standard Practice for Description and Identification of Soils, the sample has a reddish color and has a flat particle shape. When the cementation was observed, it is considered moderate since the particles crumbled with a considerable amount of pressure. For its structure, it is deemed homogeneous. It was observed that it has the same color and appearance throughout.

Figure 1. Ultisols Soil

Sieve and Hydrometer Analysis and Index properties such as specific gravity (G_s), liquid limit (LL), plastic limit (PL), plasticity index (PI), maximum dry unit weight (γ_{dmax}), optimum moisture content (OMC), minimum void ratio (e_{min}) and maximum void ratio (e_{max}) were established. Soil classification was established considering the Unified Soil Classification System (USCS). The experiments were performed in accordance to American Society for Testing and Materials (ASTM) Standards. The results are tabulated in Table 1.

Table 1 Index Properties of Ultisols

Index Properties	
G_s	2.78
LL	51
PL	39
PI	12
γ_{dmax} (kN/m^3)	12.66
OMC	36.64%
e_{min}	1.537
e_{max}	1.930

The Grain Size Distribution Curve (GSDC) is shown in Figure 2. Based on the trend of the GSDC, it shows a poorly graded sample and its soil classification is SC (clayey sands, sand-clay mixtures).

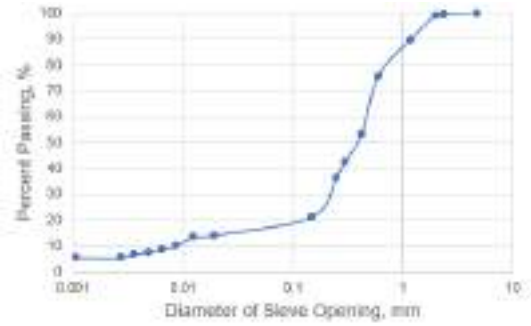

Figure 2. GSDC of Ultisol

Scanning electron microscopy (SEM) of the Ultisols is shown in Figure 3. It can be observed that the texture is rough with fine particle sized. It can also be observed that the particles also contain micro-pores. The Energy-dispersive X-ray spectroscopy (EDX) of Ultisol is tabulated in Table 2. Based on the results, the soil predominantly composed of Carbon and Oxygen. Traces of Aluminum, Silicon and Iron were observed. The EDX was determined to investigate the elements that can have a reaction with the water hyacinth biochar.

Table 2 EDX of Ultisol

Element Symbol	Element Name	Atomic Conc.	Atomic Weight
C	Carbon	49.06	43.42
O	Oxygen	37.68	25.04
Al	Aluminum	4.78	7.13
Si	Silicon	3.98	6.18
Fe	Iron	2.17	6.71
Nb	Niobium	1.83	9.40

WATER HYACINTH BIOCHAR

The water hycinth was sourced in the National Capital Region. Shown in Figure 4 is the biochar process implemented in the study. Before the biocharing process, the plant was first sun dried to remove moisture. Once dried, it was cut into smaller pieces in order to fit the furnace. For the biochar process, a furnace was fabricated as shown to accommodate the target temperature conditions.

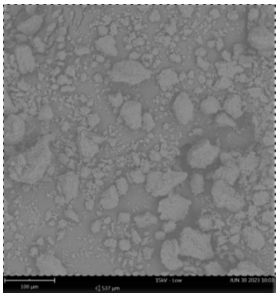

Figure 3. SEM of Ultisols

According to Masto [24], the optimal temperature and time for water hyacinth biochar process is 300 to 350 Celsius for 30 – 40 minutes, respectively. This condition was chosen since it yielded the optimal temperature for the biochar process while minimizing the increase in pore structure and size of particles. This may decrease the shear strength of amended soil samples in addition to preserving biochar yield.

Figure 4 Biochar Process

SEM-EDX of water hyacinth biochar was also obtained. This is to verify the quality of biochar process performed. Based on the results of SEM in Figure 5, it can be seen that the texture is smooth and flaky. It is noticeable that its particle size is not uniform. Shown in Table 3 is the summary of results of EDX. Based on the results, Carbon is the predominant material which is an indication of an effective biochar process.

Table 3 EDX of WHBC

Element Symbol	Element Name	Atomic Conc.	Atomic Weight
C	Carbon	72.35	57.60
O	Oxygen	22.20	23.55
Cl	Chlorine	1.46	3.44
K	Potassium	1.40	3.62
Nb	Niobium	1.17	7.18
Ca	Calcium	0.61	1.62

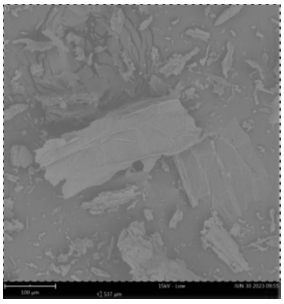

Figure 5. SEM of the WHBC

SHEAR STRENGTH TEST AND RESULTS

Sample Preparation

Reconstituted samples were tested in this study. The target amount of soil and water for 0% water hyacinth biochar was based on γ_{dmax} and OMC of the Ultisols. The target amount of soil, water and water hyacinth was based also on the γ_{dmax} and OMC of Ultisols mixed with WHBC. To achieve this, a separate standard proctor test was performed considering the target proportions of WHBC. The summary of results is tabulated in Table 4.

Table 4 Percentage of WHBC Amended in relation to the soil's Optimum Moisture Content and Maximum Dry Unit Weight

WHBC Proportions (%)	Optimum Moisture Content (%)	Maximum Dry Unit Weight (kN/m^3)
0	36.64	12.66
5	41.6	6.2
10	47.67	5.63
15	54.41	4.77
20	56.76	2.51

Three relative densities, 32.5%, 60%, and 92.5%, were prepared to know the effect of WHBC to the shear strength of Ultisols. These values were chosen due to being the median value for the ranges of loose, medium dense, and dense conditions. Once the target amount of soil, water and water hyacinth is established, these were mixed and soaked for at least 16 hours. To create reconstituted samples, moist tamping was performed. Moist tamping was done to ensure uniform density within the sample [25]. The samples were tamped for a minimum of 10 times per layer for a minimum of 3 layers.

Direct Shear Test Experimental Design

To evaluate the effectiveness of the WHBC in increasing a soil's shear strength, the shear strength of the soil samples mixed with 0%, 5%, and 10% biochar were determined using a direct shear test based on the ASTM D3080. The test was conducted under drained conditions. The rate of shearing used was 0.12 mm/min as suggested by Dafalla [26]. This rate of shearing was chosen since it is low enough for the pore water pressure to dissipate without further affecting the results of the test. The normal stresses used in the test were 22.5 kPa, 45 kPa, and 90 kPa. These normal stresses simulate a fill with a height of at most 6 m.

Shear Strength Results

For the direct shear test, typical results of the stress-strain and volumetric strain-shear strain curves are shown in Figures 6-10. For Ultisols, it was observed that strain hardening was experienced. For samples prepared at 60% relative density peak was observed for 22.5kPa normal stress. For samples with water hyacinth biochar, strain hardening was observed for all samples. For the volumetric strain-shear strain curves samples exhibit contractive behavior during shearing. Samples tested in general showed ductile behavior as the mode of failure.

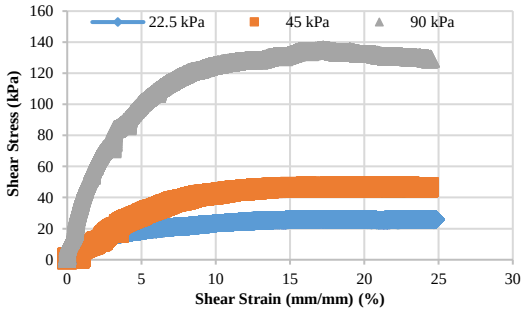

Figure 6. Stress-strain Curve for 32.5 Dr for Ultisols

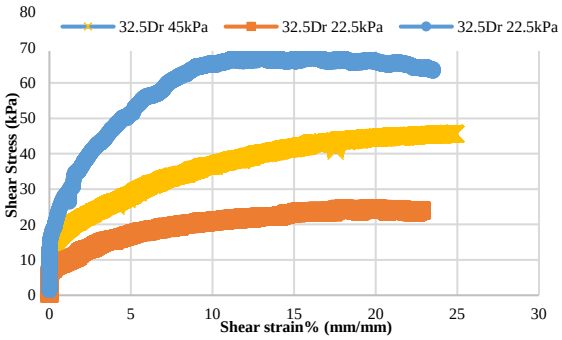

Figure 7. Stress-strain Curve for 32.5 Dr with 5% WHBC

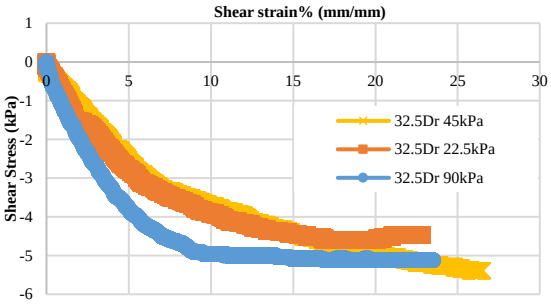

Figure 8. Volumetric strain-shear strain Curve for 32.5 Dr with 5% WHBC

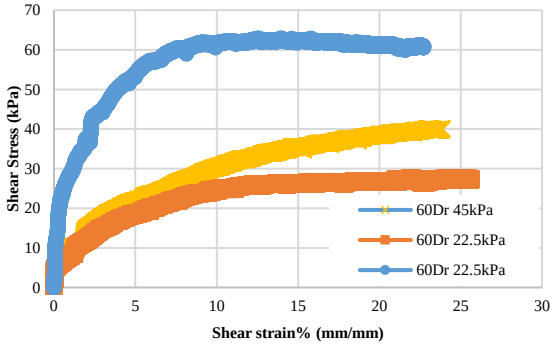

Figure 9. Stress-strain Curve for 60 Dr with 5% WHBC

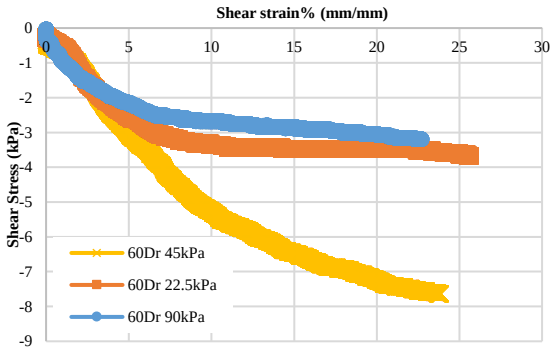

Figure 10. Volumetric strain-shear strain Curve for 60 Dr with 5% WHBC

The Mohr-Coulomb Failure Envelope of each relative density was plotted as shown in Figure 11 and 13. The Failure Envelope is shown to generally increase the denser the soil sample gets, and decrease the more biochar is amended. This increase in shear strength can be seen in Figure 11. When comparing between different groups of biochar amendments, Figure 12 verifies that increasing the amount of biochar present decreases the cohesion of the soil. This decrease in cohesion confirms that WHBC may not be suitable for increasing the shear strength parameters of the soil sample.

The shear strength parameters of the soil sample were obtained and compared with one another as tabulated in Tables 5 and 6. As seen, there is a decrease in cohesion once an additional amount of biochar was amended. This is true for majority of the cases, however, there are a few outliers present. The most prominent outlier is the increase in cohesion in the medium dense condition from 5% WHBC to 10%. For the angle of internal friction, there is no consistent trend that was observed. The addition of WHBC did not enhance the bonding and interlocking of the Ultisols' soil particles. This is can be attributed to the flaky texture of WHBC, which acted similar to fine particles, thereby reducing particle contact. In addition, the hydrophobic nature of WHBC limited the development of cohesion which also contributed to the reduction in shear strength.

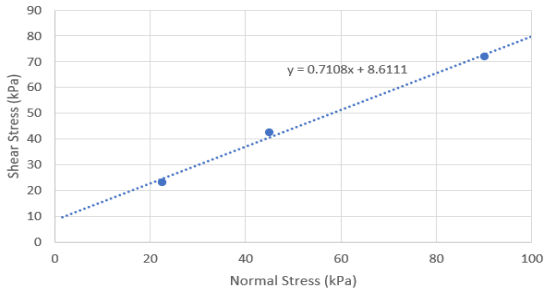

Figure 11. Mohr-Coulomb Failure Envelope of 0% BC at 32.5% Relative Density

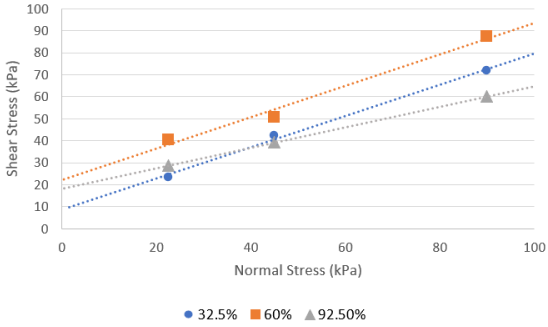

Figure 12. Mohr-Coulomb Failure Envelopes of 0% BC at Different Relative Densities

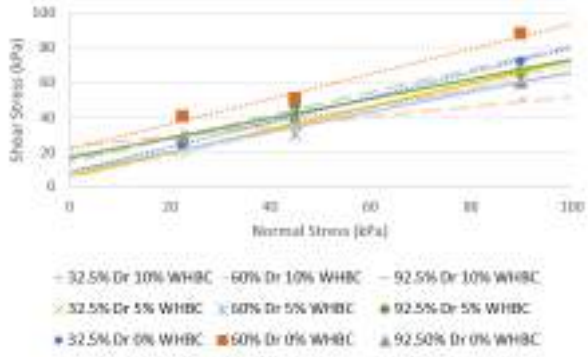

Figure 13. Mohr-Coulomb Failure Envelopes of 0%, 5%, & 10% BC at Different Relative Densities

Table 5. Percentage of WHBC Amended in Relation to the Soil's Cohesion at Different Relative Densities

	Relative Density (%)		
WHBC (%)	32.5	60	92.5
0	8.611111	22.08333	18.19444
5	6.388889	0.568783	16.80556
10	5.555556	23.47222	14.44444

Table 6. Percentage of WHBC Amended in Relation to the Soil's Angle of Internal Friction at Different Relative Densities

	Relative Density (%)		
WHBC (%)	32.5	60	92.5
0	35.40363	35.50421	24.92555
5	33.40932	29.63049	29.1703
10	32.62784	15.80516	33.47968

An Analysis of Variance (ANOVA) was carried out to determine whether the effects of the percentage of the WHBC and its relative density were significant on both the cohesion and angle of internal friction of the soil. In the analysis, the cohesion values of the 60% Dr sample were disregarded due to its low R-squared value from the regression analysis. For the sample's cohesion, the percentage of WHBC and relative density yielded a p-value of 0.02 and 0.002 respectively, which was less than the level of significance of 5%. As such, it can be said that both the amount of biochar and its relative density may have a significant effect on the cohesion of the sample. As for the friction angle, a p-value of 0.38 and 0.25 was obtained for the percentage of WHBC and relative density. This implies that both the relative density and the percentage of biochar may not have a significant effect on this.

CONCLUSIONS

The study explored the potential of Ultisols as construction material. However, due to its high fines content the soil was improved by adding WHBC. It can be observed that the cohesion decreased as the presence of biochar increased. For the angle of internal friction, no consistent pattern was observed. This is because of the flaky texture of WHBC which behaved similar to a fine grained material. Instead of causing an increase in the cohesion, a reduction was observed since WHBC is a hydrophobic material. Due to the texture of WHBC, it is recommended to use it as an additive for the purpose of improving its permeability.

ACKNOWLEDGMENTS

The researchers would like to acknowledge the Department of Civil Engineering, Gokongwei College of Engineering, De La Salle University faculty members, laboratory coordinator, staff and technicians for the support in the research.

REFERENCES

[1] Rondal J. D., Soil, Water and Climatic Resources of the Philippines: Constraints, Problems and Research Opportunities. JIRCAS International Symposium Proceedings, Vol. 13, 2005, pp. 41–52.

[2] Nandi A., and Luffman I., Erosion Related Changes to Physicochemical Properties of Ultisols Distributed on Calcareous Sedimentary Rocks. Journal of Sustainable Development, Vol. 5, No. 8, 2012, pp. 52–60. https://doi.org/10.5539/jsd.v5n8p52.

[3] Igwe C. A., Zarei M., and Stahr K., Soil Hydraulic and Physico-Chemical Properties of Ultisols and Inceptisols in South-Eastern Nigeria. Archives of Agronomy and Soil Science, Vol. 59, Issue 4, 2013, pp. 491–504. https://doi.org/10.1080/03650340.2011.649475.

[4] Navarrete I. A., Tsutsuki K., Land-use impact on soil carbon, nitrogen, neutral sugar composition and related chemical properties in a degraded Ultisol in Leyte, Philippines. Soil Science and Plant Nutrition, Vol. 54, Issue 3, 2008, pp. 321–331.

[5] Piamonte M. K., Asio V. B., Lina S. B., Morpho-physical and chemical characteristics of strongly weathered soils in Silago, Southern Leyte, Philippines. Agricultural and Tropical Research, Vol. 36, Issue 2, 2014. https://doi.org/10.32945/atr3627.2014

[6] Hasan M. F. R., Utama I. Z., Razzak A. F. A., Salimah A., and Agung P. A. M., Clayshale Stabilization Using Active Natural Lime to Increase the Shear Strength of Soil. Department of Civil Engineering, Politeknik Negeri Jakarta, 2024.

[7] Rivera-Gómez C., and Galán-Marín C., Biodegradable Fiber-Reinforced Polymer Composites for Construction Applications. In: Lau A. K.-t. and Hung A. P.-Y. (Eds.), Natural Fiber-Reinforced Biodegradable and Bioresorbable Polymer Composites, Woodhead Publishing, 2017, pp. 51–72. https://doi.org/10.1016/B978-0-08-100656-6.00004-2.

[8] Almuaythir S., Zaini M. S. I., Hasan M., and Hoque M. I., Sustainable Soil Stabilization Using Industrial Waste Ash: Enhancing Expansive Clay Properties. Heliyon, Vol. 10, Issue 20, 2024, Article e39124. https://doi.org/10.1016/j.heliyon.2024.e39124.

[9] Setyowati A. S. G., and Raharja I., Utilization of Industrial Waste as Soil Stabilizer to Enhance Direct Shear Strength. Chapter in Biodegradable Fiber-Reinforced Polymer Composites for Construction Applications, 2017.

[10] Jawad I. T., Taha M. R., Majeed Z. H., and Khan T. A., Soil Stabilization Using Lime: Advantages, Disadvantages and Proposing a Potential Alternative. Research Journal of Applied Sciences, Engineering and Technology, Vol. 8, 2014, pp. 510–520.

[11] Afrin H., A Review on Different Types of Soil Stabilization Techniques. International Journal of Transport Engineering and Technology, Vol. 3, 2017, pp. 19–24.

[12] Barman D., and Dash S. K., Stabilization of Expansive Soils Using Chemical Additives: A Review. Journal of Rock Mechanics and Geotechnical Engineering, Vol. 14, Issue 4, 2022, pp. 1319–1342. https://doi.org/10.1016/j.jrmge.2022.02.011.

[13] Birchal V. S. S., Rocha S. D. F., Ciminelli V. S. T., The effect of magnesite calcination conditions on magnesia hydration. Mineral Engineering, Vol. 13, Issues 14-15, 2000, pp. 1629–1633.

[14] Shand M. A., The Chemistry and Technology of Magnesia. Wiley-Interscience, New York, 2006.

[15] Department of Primary Industries and Regional Development, Australia, 2022.

[16] Amalina F., Abd Razak A. S., Krishnan S., Sulaiman H., Zularisam A. W., Nasrullah M., Biochar production techniques utilizing biomass waste-derived materials and environmental applications – A review. Journal of Hazardous Materials Advances, Vol. 7, August 2022, Article 100134.

[17] Reddy K. R., Yaghoubi P., Yukselen-Aksoy Y., Effects of biochar amendment on geotechnical properties of landfill cover soil. Waste Management & Research, Vol. 33, Issue 6, 2015, pp. 524–532. https://doi.org/10.1177/0734242x15580192

[18] Xu K., Yang B., Wang J., Wu M., Improvement of Mechanical Properties of Clay in Landfill Lines With Biochar Additive. Arabian Journal of Geosciences, Vol. 13, Issue 13, 2020. https://doi.org/10.1007/s12517-020-05622-1

[19] Li K., Xu Y., Tan Y., Cai X., Liu Z., and Xu Q., Research on the Strength Characteristics of Red Soil Amended by Biochar. Sustainability, Vol. 17, Issue 3, 2025, Article 1174. https://doi.org/10.3390/su17031174.

[20] Dersseh M. G., Melesse A. M., Tilahun S. A., Abate M., Dagnew D. C., Water hyacinth: Review of its impacts on hydrology and ecosystem services—lessons for management of Lake Tana. Extreme Hydrology and Climate Variability, 2019, pp. 237–251. https://doi.org/10.1016/b978-0-12-815998-9.00019-1

[21] Abenoja A. K. R., Cleofe B. I. A., Mondero N. A. R., Rodriguez P. N., and Marcelo J. S., Impacts of the Use of Water Hyacinths as a Form of Livelihood Programs in the Local Residents of Taguig City: Inputs for Tourism Entrepreneurship. International Journal of Tourism and Hospitality, Vol. 1, Issue 4, 2021, pp. 23–29. https://doi.org/10.51483/IJTH.1.4.2021.23-29.

[22] Sathya A., et al., Influence of bio admixture on mechanical properties of cement and concrete. Asian Journal of Applied Sciences, Vol. 7, Issue 4, 2014, pp. 205–214.

[23] Okwadha G. D. O., Makomele D. M., Evaluation of water hyacinth extract as an admixture in concrete production. Journal of Building Engineering, Vol. 16, 2018, pp. 129–133. https://doi.org/10.1016/j.jobe.2018.01.002

[24] Masto R. E., Kumar S., Rout T., Sarkar P., George J., Ram L., Biochar from water hyacinth (Eichornia crassipes) and its impact on soil biological activity. CATENA, Vol. 111, December 2013, pp. 64–71. https://doi.org/10.1016/j.catena.2013.06.025

[25] Jagodnik V., Arbanas Ž., Cyclic Behaviour of Uniform Sand in Drained and Undrained Conditions at Low Confining Stress in Small-Scale Landslide Model. Sustainability, Vol. 14, Issue 19, 2022, Article 12797. https://doi.org/10.3390/su141912797

[26] Dafalla M. A., Effects of clay and moisture content on direct shear tests for clay-sand mixtures. Advances in Materials Science and Engineering, 2013, pp. 1–8.

Copyright © Int. J. of GEOMATE All rights reserved, including making copies, unless permission is obtained from the copyright proprietors.

15th Int. Conf. on Geotechnique, Construction Materials & Environment, Kyoto, Japan, 11-13 November 2025, ISBN 978-4-909106124 C3051

SUSTAINABILITY ANALYSIS OF OPTIMIZED CONCRETE MIXES (PSC, PPC, HVFA) AGAINST STANDARD OPC MIXES FOR GRADES M15 TO M30

Pallavi Badry[1], Saikrishna Bondugula[2], Ravi Shankar Badry[3], N.Sudharsan[4] , Srihari Saduwale [5] and Ivaturi Sarma[6]

[1]Department of Civil Engineering, Anurag University, Hyderabad, India
[2]Department of Civil Engineering, Vidya Jyothi Institute of Technology, India,
[3] Senior Computational Scientist, Arup India Pvt. Ltd, Hyderabad, India;
[4,5] Department of Civil Engineering, Vidya Jyothi Institute of Technology, Hyderabad, India
[6]Department of Civil Engineering, Faculty of Science and Technology (IcfaiTech), ICFAI Foundation for Higher Education, Hyderabad, India

ABSTRACT

This research evaluates enhanced concrete formulations incorporating Portland Slag Cement (PSC), Portland Pozzolana Cement (PPC), and High-Volume Fly Ash (HVFA) against conventional Ordinary Portland Cement (OPC) mixtures across grades M15 to M30. Key parameters—compressive strength, workability, and water-cement ratio—were assessed over 7-day and 28-day curing periods. The study explores how Supplementary Cementitious Materials (SCMs) enhance durability and sustainability while reducing environmental impact. Results indicate PSC and PPC mixes outperform OPC, with PPC achieving 67.01 MPa for M30 (10.5% above OPC), alongside improved resistance to degradation and cost savings. HVFA mixes, despite lower early strength (e.g., 38.9% below OPC at 7 days for M20), offer exceptional workability (up to 240 mm slump) and sustainability benefits by minimizing OPC use. These findings demonstrate that optimized designs reduce carbon emissions and reliance on virgin materials, supporting eco-friendly construction. PSC and PPC are recommended for strength-driven projects, while HVFA suits workable, large-scale applications.

Keywords: Italic Concrete Mix Optimization, Alternative Cement, PPC, PSC, HVFA, Sustainability

INTRODUCTION

Concrete remains the cornerstone of modern construction, with its performance largely dictated by the type of cement and mix design. Traditional Ordinary Portland Cement (OPC) mixes, while reliable, contribute significantly to carbon emissions due to their high clinker content. In response, optimized mixes incorporating Supplementary Cementitious Materials (SCMs) such as slag (in PSC), pozzolana (in PPC), and fly ash (in HVFA) have emerged as sustainable alternatives. These materials not only reduce environmental impact but also enhance mechanical properties and durability.

This study compares the performance of PSC, PPC, and HVFA mixes against standard OPC mixes for concrete grades M15, M20, M25, and M30. The focus is on evaluating compressive strength, workability, and sustainability, with the aim of identifying optimal alternatives to OPC for various construction applications.

1. Enhancing cost efficiency by reducing reliance on OPC.
2. Increasing durability by improving resistance to chemicals and environmental degradation.
3. Developing sustainable concrete with lower carbon footprints.
4. Reducing the heat of hydration to prevent thermal cracking.
5. Achieving better workability and surface finish.

The adoption of PPC, PSC, and HVFA as alternatives to OPC brings several advantages to the construction industry. These materials contribute to the circular economy by utilizing industrial by-products such as fly ash and slag, reducing dependency on virgin raw materials and minimizing waste disposal issues. Additionally, the performance characteristics of concrete improve significantly when blended cements are used, leading to enhanced mechanical properties and improved resistance to aggressive environmental conditions.

Recent advances in materials science and environmental engineering have intensified the search for sustainable, high-performance alternatives in construction. With rising concerns over climate change and resource depletion, the industry is increasingly shifting toward eco-friendly materials that reduce energy consumption and lower carbon emissions. By integrating industrial by-products such as slag and fly ash,

concrete mixes can significantly decrease reliance on energy-intensive OPC, yielding both economic and environmental benefits. This study not only investigates the mechanical and durability aspects of alternative mixes but also explores their potential to transform traditional construction practices, thereby contributing to a greener future in civil engineering. The use of fly ash as a partial replacement for cement has gained traction due to its potential to reduce embodied carbon, the extensively documented the mechanical and environmental performance of HVFA concrete, showing that it could meet structural requirements while offering superior durability [1].

Further emphasized the sustainable benefits of HVFA concrete, noting a significant reduction in CO_2 emissions alongside adequate compressive strength for M20–M30 grade mixes [2&3].The genetic algorithms also served to optimize HVFA concrete mixes, finding that up to 50% replacement levels could be achieved without significantly compromising strength or workability [4]. These findings align) work on self-compacting concrete, where fly ash improved both flowability and long-term performance [5].From a sustainability perspective, multiple studies have evaluated the ecological advantages of blended cements. Replacing OPC with supplementary cementitious materials like fly ash and slag could drastically reduce energy consumption and greenhouse gas emissions [6 & 7]. The Central Pollution Control Board (2020) also highlights the importance of fly ash utilization in achieving India's waste management and decarbonization goals [8].Kumar and Nanda (2017) showed that Combining fly ash with Ground Granulated Blast Furnace Slag (GGBS) enhances strength and durability, further supporting the move away from pure OPC use [9]. Papadakis (2000) found that Such materials also improve resistance to carbonation and chloride ingress, thus extending the service life of concrete structures[10,11 &12].Shetty and Rao (2019) and Neville (2011) provide foundational insights into concrete behavior, confirming the viability of blended cements in practical applications.

BIS guidelines (IS 10262:2019) now accommodate PPC and PSC in concrete mix designs, reflecting an institutional shift towards sustainable practices [13 & 14].The use of locally available industrial byproducts not only reduces environmental impact but also contributes to the circular economy. Studies like Kumar and Santhanam (2003) affirm that Class F fly ash can be effectively used in Indian construction contexts, further improving the case for regional adoption [15 &16].

RESEARCH SIGNIFICANCE

The environmental impact of cement production is a major concern in the construction industry, with Ordinary Portland Cement (OPC) accounting for approximately 7–8% of global CO_2 emissions. As the demand for concrete continues to grow—particularly in rapidly urbanizing regions—there is an urgent need to explore sustainable alternatives that reduce carbon emissions without compromising structural performance. This research is significant because it evaluates the sustainability and mechanical performance of optimized concrete mixes using Portland Slag Cement (PSC), Portland Pozzolana Cement (PPC), and High-Volume Fly Ash (HVFA), as compared to conventional OPC-based concrete in the commonly used grades M15 to M30. The following are the objectives of the study:

1. To Evaluate the Effectiveness of Different Concrete Mixtures
2. To Make Concrete Production More Sustainable
3. To identify the best cement substitutes for particular uses
4. To optimize mix designs for enhanced durability and reduced environmental impact.

METHODOLOGY

Coarse Aggregates Well-graded, angular particles ranging from 10mm to 20mm and Fine Aggregates preference for natural river sand; M-sand is considered an alternative for this study. Gradation analysis ensures optimal workability.

Coarse Portland Slag Cement (PSC) blends Ordinary Portland Cement (OPC) with ground granulated blast furnace slag, Portland Pozzolana Cement (PPC) incorporates pozzolanic fly ash, and High-Volume Fly Ash (HVFA) cement uses substantial fly ash as a partial cement replacement, while OPC, without supplementary cementitious materials (SCMs), serves as the baseline. Coarse aggregates, ranging from 10mm to 20mm, are well-graded and angular, and fine aggregates, preferably natural river sand with M-sand as an alternative, undergo gradation analysis to ensure optimal particle size distribution for enhanced workability and strength. Fineness tests are conducted on PPC, PSC, OPC, and fly ash to evaluate their surface area and uniformity, and moisture content in fine aggregates is assessed to adjust the water-cement ratio appropriately.

Fineness tests are conducted on PPC, PSC, OPC, and fly ash to evaluate their surface area and uniformity, while gradation analysis is performed on coarse and fine aggregates to ensure optimal

particle size distribution for enhanced workability and strength, and moisture content in fine aggregates is assessed to adjust the water-cement ratio appropriately.

The mix design process is followed as per IS 10262 2019. & IS 456 2000.

Exposure Condition Assumed mild to moderate as per IS 456 2000.

Target Mean Strength Computed for each grade e.g., M20 26.6 MPa, M25 31.6 MPa, M30 38.25 MPa.

Water-Cement (W/C) Ratio Selected based on strength and cement type, adjusted with admixtures e.g., 0.57 for M15-OPC, 0.31 for M30-PSC/PPC (conforming to IS 269 2015).Water Content Determined for high workability (~186 kg/m³), reduced by superplasticizers (e.g., 15% for OPC, 35% for PSC/PPC).Cement Content Calculated using W/C ratio and water content, meeting IS 456 2000 minimums (e.g., 280 kg/m³ for M15, 390 kg/m³ for M30-OPC).

Aggregate Proportioning Coarse aggregates (60/ 40 ratios of 20 mm to 10 mm) and M. Sand proportioned for optimal grading. The trial Mixes Conducted to adjust proportions, verifying workability and strength. Validation Workability Slump tests (IS 1199 1959) confirmed collapse slump.

Strength Compressive strength tested at 7 and 28 days (IS 516 1959) to ensure fckt) was met.

Compliance Verified against IS 456 2000 for cement content, W/C ratio, and durability.

This method ensured all mixes met strength, workability, and durability requirements while promoting sustainability through PSC, PPC, and HVFA use.

RESULTS

The experimental dataset includes 16 mixes four grades (M15, M20, M25, M30) for each cement type. Mix proportions are detailed in Table 1. Aggregates (20mm, 10mm, M. Sand) varied slightly but maintained consistency across grades.

The Compressive Strength Tests Cubes cast for each mix is evaluated for 7-day and 28-day strength. The comparative Analysis Strength performance is carried out across mixes compared to OPC benchmarks. SCMs in PSC and PPC were optimized for strength and sustainability, and HVFA utilized abundant fly ash. Mixes followed IS 10262 2019, with dry blending, water. Optimised mixes exhibited higher initial slump values (175-240 mm), with HVFA showing the highest workability (240 mm for M20, M25, M30).

Table 1 7-Day Compressive Strength (MPa) and Comparison

Grade	Mix Type	OPC 53 (kg/m³)	Fly Ash (kg/m³)	PSC/PPC (kg/m³)	Total Cementitious (kg/m³)	OPC Reduction (%)
M-15	OPC	280	0	0	280	0.00
	PSC	80	0	160 (PSC)	240	71.4%
	PPC	80	0	160 (PPC)	240	71.4%
	HVFA	145	145	0	290	48.2%
M-20	OPC	300	0	0	300	0.00
	PSC	100	0	200 (PSC)	300	66.7%
	PPC	100	0	200 (PPC)	300	66.7%
	HVFA	160	160	0	320	46.7%
M-25	OPC	340	0	0	340	0.00
	PSC	120	120	120 (PSC)	360	64.7%
	PPC	120	120	120 (PPC)	360	64.7%
	HVFA	170	170	0	340	50.0%
M-30	OPC	350	0	0	350	0.00
	PSC	130	130	130 (PSC)	390	62.9%
	PPC	130	130	130 (PPC)	390	62.9%
	HVFA	195	195	0	390	44.3%

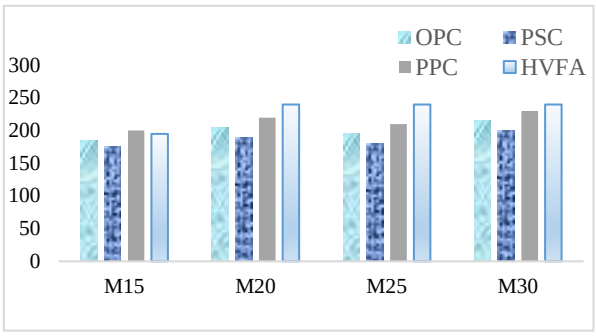

Fig.1 Slump values for different Mixes in mm

Lower slump the observations indicate that concrete mixes incorporating Portland Slag Cement (PSC) tend to have lower slump values, suggesting they may need additional water or the use of plasticizers to improve workability. On the other hand, mixes using High-Volume Fly Ash (HVFA) or Portland Pozzolana Cement (PPC) exhibit higher slump values, making them easier to handle, though care must be taken to control water content and prevent segregation. Among the mixes, the M30 grade shows the most variation in slump, highlighting the importance of careful mix design adjustments to ensure consistent workability. Overall, a clear trend emerges: as the grade of concrete increases from M15 to M30, slump values also rise. This suggests that higher-grade concretes demand greater workability to facilitate proper placement during construction.

Compressive strength at both 7 days and 28 days is essential for evaluating concrete performance. The 7-day strength provides insight into early strength gain, critical for construction schedules, while the 28-day strength reflects long-term performance. Below, Table 3a presents the 7-day compressive strength data extracted from the experimental results, and Table 3b presents the 28-day compressive strength data, both in MPa, with comparisons against OPC for each grade (M15, M20, M25, M30).

The table highlights distinct strength development trends for each binder type across different concrete grades. Portland Slag Cement (PSC) shows both early and sustained strength improvement due to its latent hydraulic properties, making it a strong alternative to Ordinary Portland Cement (OPC) in applications requiring early formwork removal or rapid construction. Portland Pozzolana Cement PPC), while slower in early strength development due to delayed pozzolanic reactions, demonstrates superior 28-day strength, especially in higher grades like M25 and M30. This makes PPC highly suitable for structural elements where long-term strength and durability are key. In contrast, High-Volume Fly Ash (HVFA) concrete exhibits lower early and 28-day strengths, limiting its use in high-strength or load-bearing structures. However, it offers excellent workability and sustainability, making it ideal for mass concrete, foundations, or non-structural elements where reduced carbon footprint is prioritized over early strength.

Overall, the results underscore the importance of selecting the appropriate binder based on project-specific requirements such as performance timeline, environmental goals, and structural demand to ensure both efficiency and sustainability in concrete design.

W/C Ratio Optimized mixes have lower ratios (0.31-0.50) than OPC (0.41-0.57), contributing to higher strength and durability (Fig.2).

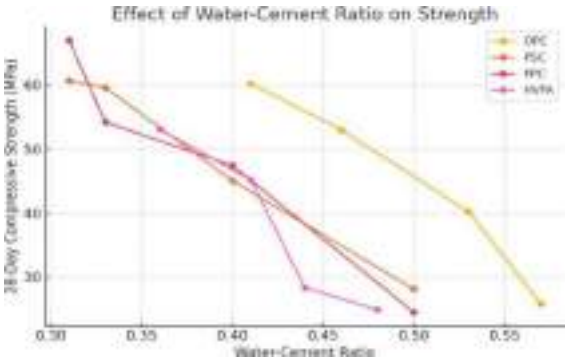

Fig.2 Effect of Water-Cement Ratio on 28-Day Compressive Strength

Optimized mixes reduce OPC content, cutting carbon emissions and costs due to SCM availability. Using SCMs like fly ash or slag lowers production costs and reduces concrete's carbon footprint, as OPC manufacturing is energy-intensive. A 50% fly ash substitution can cut emissions by 40%, supporting sustainability efforts. Additionally, SCMs enhance durability, extending structure lifespan and reducing maintenance costs.

Table 2 7-Day Compressive Strength (MPa) and Comparison

Grade	OPC (MPa)	PSC (MPa)	PPC (MPa)	HVFA (MPa)	PSC vs OPC (%)	PPC vs OPC (%)	HVFA vs OPC (%)
M15	16.90	18.49	15.53	16.69	+9.4%	-8.1%	-1.2%
M20	24.63	28.78	30.07	15.04	+16.8%	+22.1%	-38.9%
M25	34.93	37.93	33.12	33.58	+8.6%	-5.2%	-3.9%
M30	40.34	42.30	43.97	34.21	+4.9%	+9.0%	-15.2%

Table 3 Observation on 7- and 28-days strength

Grade	Binder	7-Day Highlights	28-Day Highlights
	OPC	Baseline early strength for low-grade concrete.	Standard long-term performance reference.
M15	PSC	Early gain due to slag hydration.	Sustains better strength with time.
	PPC	Slow early reaction limits strength.	Strength improves as pozzolanic activity matures.
	HVFA	Slightly behind OPC, limited early reactivity.	Modest strength due to delayed ash activation.
	OPC	Balanced early performance.	Reliable long-term strength.
M20	PSC	Improved early strength from slag activity.	Continues strength gain with extended hydration.
	PPC	Strong early response from blended pozzolans.	Outperforms OPC over time.
	HVFA	Weak early strength from diluted binder.	Lags due to slow fly ash reactivity.
	OPC	Good early performance benchmark.	Stable long-term strength.
M25	PSC	Strong start from slag effects.	Maintains advantage over OPC.
	PPC	Slightly delayed start.	Catches up and surpasses OPC.
	HVFA	Moderate early strength.	Lower strength suitability for structural use.
	OPC	High early strength, suitable for structural demand.	Long-term strength standard.
M30	PSC	Matches or slightly leads OPC early.	Retains comparable strength.
	PPC	Good early results.	Best strength outcome over time.
	HVFA	Poor early strength.	Not ideal for high-strength needs.

CONCLUSIONS

This study demonstrates that PSC and PPC offer superior compressive strength and workability, making them viable alternatives to OPC across all grades. HVFA excels in workability and sustainability but compromises early compressive strength, limiting its use in high-strength applications. Optimised mixes enhance performance whilst providing environmental benefits, reinforcing their adoption in sustainable construction practices.

This investigation has thoroughly assessed the efficacy of concrete mixes utilizing Portland Slag Cement (PSC), Portland Pozzolana Cement (PPC), and High-Volume Fly Ash (HVFA) against traditional Ordinary Portland Cement (OPC) for grades M15 to M30. The results underscore that PSC and PPC surpass OPC in compressive strength and workability, with PPC recording a 28-day strength of 67.01 MPa in M30, a 10.5% improvement over OPC. All optimized mixes showed enhanced workability, with HVFA leading due to its superior slump values.

Conversely, HVFA's early strength lagged significantly, dropping 38.9% below OPC at 7 days in M20, limiting its use in high-strength contexts, though its sustainability and flowability make it ideal for large-scale projects like foundations or dams. By reducing OPC reliance and incorporating by-products such as slag and fly ash, these mixes lower environmental impact and costs, promoting a greener, more economical construction sector. PSC and PPC are thus ideal for strength-driven projects, while HVFA suits applications valuing workability and eco-friendliness. Further studies should examine long-term resilience and ways to boost HVFA's initial strength to broaden its scope. This research supports adopting these mixes for sustainable, high-performing construction solutions.

REFERENCES

[1] Malhotra, V.M., High-performance high-volume fly ash concrete. Journal of Concrete International, Vol.24, Issue 7, 2002, pp.30-34.

[2] Patel, R., Singh, K., and Sharma, M., Mechanical properties and sustainability aspects of HVFA concrete. Journal of Sustainable Construction Materials, Vol.14, 2021, pp. 221-239.

[3] Bureau of Indian Standards (BIS). IS 10262: 2019 – Guidelines for Concrete Mix Design Proportioning. New Delhi, India

[4] Reddy, C., and Ramaswamy, A., Optimisation of high-volume fly ash concrete

mixes using genetic algorithms. International Journal of Construction Materials Research, Vol. 7, 2019, pp. 300-320.

[5] Pathak N., and Siddique, R., Properties of self-compacting-concrete containing fly ash subjected to elevated temperatures. Construction and Building Materials , Vol. 30, 2012, pp. 274-280.

[6] Thomas, M. D. A., Optimizing the use of fly ash in concrete. Portland Cement Association, Vol. 5420, 2007.

[7] Mehta, P. K., Reducing the environmental impact of concrete. Concrete International, Vol.23, Issue 10, 2001, pp.61–66.

[8] Central Pollution Control Board. Fly Ash Utilization Report. Government of India, 2020.

[9] Agnihotri, A. and Ramana, P.V.,GGBS: Fly-Ash evaluation and mechanical properties within high-strength concrete. Materials Today: Proceedings, Vol. 50, 2022, pp.2404-2410.

[10] Das, P., and Sharma, D., Response surface methodology for workability optimisation in PPC concrete. Advances in Concrete Science, Vol.6, 2022, pp. 78-95.

[11] Gopalakrishnan, V., Rao, S., and Banerjee, T., Comparative study on PSC and OPC concrete durability in sulfate rich conditions. Concrete Research Letters, Vol. 8, 2020,pp. 122-137.

[12] Papadakis, V. G., Effect of supplementary cementing materials on concrete resistance against carbonation and chloride ingress. Cement and Concrete Research, Vol. 30, Issue 2, 2000, pp 291-299.

[13] Shetty, M. S., and Rao, A. U. , Concrete technology Theory and practice, 2019, New Delhi, India S. Chand & publications.

[14] Neville, A. M., Properties of Concrete, 2011, 5th Edition, Pearson Education

[15] Ashish, K., S., Reddy, B., and Gupta, A., Durability of PPC and PSC-based concrete in marine environments. Journal of Civil Engineering and Construction Technology, 2017, Vol. 11, pp. 45-58.

[16] Ashish, K., S., Effect of class F fly ash on the durability properties of concrete. Sustainable Environment Research, Vol. 28, Issue 1, 2018, pp. 25-31.

Copyright © Int. J. of GEOMATE All rights reserved, including making copies, unless permission is obtained from the copyright proprietors.

15th Int. Conf. on Geotechnique, Construction Materials & Environment,
Kyoto, Japan, 11-13 November 2025, ISBN 978-4-909106124 C3051

INFLUENCE OF PRINTING ORIENTATION ON MECHANICAL BEHAVIOR OF MULTILAYER 3D-PRINTED CEMENT MORTAR

Piti Sukontasukkul[1], Satharat Pianfuengfoo[1], Manote Sappakittipakorn[1], Sittisak Jamnam[1], and Worathep Sae-Long[2]

[1]Construction and Building Material Research Center, Department of Civil Engineering, Faculty of Engineering, King Mongkut's University of Technology North Bangkok, Thailand
[2]Department of Civil Engineering, School of Engineering, University of Phayao, Thailand

ABSTRACT

This study investigates the effect of printing direction on the mechanical properties of 3D-printed cement mortar. The specimens were printed in both unidirectional and multidirectional (with orientations of 0°, ±45°, and ±90°) and tested for compressive and flexural strength in both directions, perpendicular and parallel to printing plane. Three types of mortar were tested: plain mortar, mortar mixed with nano-calcium carbonate, and mortar mixed with micro-polypropylene fibers. Notably, unidirectional printing showed higher strength perpendicular to the print plane but showed limitations in the parallel stress direction due to inefficient interlayer adhesion and delamination. In contrast, multidirectional printing significantly improves the uniformity of stress distribution and mechanical properties in both stress directions, thereby enhancing the overall stability of the printed structure. Additionally, incorporating nano-calcium carbonate and micro polypropylene fibers enhanced mechanical properties and reduced anisotropic behavior. These approaches contribute to improving the overall structural performance and mitigate direction dependency in 3D-printed cement mortar.

Keywords: 3D printing cement mortar, Printing direction, Unidirectional and Multidirectional printing, Nano-calcium carbonate mortar, Micro-polypropylene fibers reinforced mortar

INTRODUCTION

Due to several advantages, 3D printing of cement-based materials plays a crucial role in the construction industry sector [1]. These include the reduction of labor, minimization of material waste, particularly in formwork, and the ability to fabricate complex and customized geometries [2].

As a result, various aspects of 3D printing technology have been under continuous development. This includes efforts to design buildability mortars with low settlement [3], optimize mixture compositions for sustainability and environmental compatibility, and explore diverse printing techniques to tailor the printed cement mortar's mechanical and structural performance.

One of the primary challenges in 3D-printed cementitious components arises from the layer-by-layer deposition process, which inherently induces anisotropic mechanical behavior [4]. Unlike homogeneous materials with uniform properties in all directions, 3D-printed mortars exhibit directional dependence, with mechanical strength enhanced in specific orientations.

Furthermore, the interlayer bonding between printed layers is often mechanically weaker than the bulk material, leading to reduced lateral or parallel loading performance [5]. This structural discontinuity imposes significant limitations on the use of 3D-printed elements in load-bearing applications.

Previous studies have shown critical limitations in the mechanical performance of 3D-printed materials arising from the printing technique. For example, the infilling printing technique demonstrated that unidirectional printing, which involves stacking identical layer patterns, leads to increased internal voids, inefficient stress distribution, and mechanical weaknesses at the interlayer interfaces. Hence, the multidirectional printing pattern showed reduction in interlayer void [6].

Similarly, fiber-reinforced 3D-printed geopolymer composites show improvements in strength, but interlayer bonding remains a weak point. While fiber addition improved structural stability and mechanical properties [7-9], the fundamental issue of anisotropic behavior due to printing orientation was not directly addressed [10].

RESEARCH SIGNIFICANCE

This study aims to evaluate the influence of printing orientation on the mechanical performance of multilayer 3D-printed cement mortar, with a particular focus on compressive and flexural strength in both perpendicular and parallel loading directions. Previous research has studied fiber reinforcement and printing direction separately, but few have studied their combined effects. Additionally, this study

utilizes a partially quasi-isotropic printing pattern and includes nano-calcium carbonate and micro polypropylene fibers to investigate their roles in reducing the mechanical anisotropy of the 3D-printed cement mortar.

MATERIALS AND METHODS

Materials

The materials used in this study included hydraulic cement, with a fixed water-to-cement ratio (w/c) of 0.22. Two additive materials were also incorporated: nano-calcium carbonate (NC, 2% by cement weight) and micro polypropylene fibers (PP, 0.1% by volume). The detailed mix proportions for all mixtures are summarized in Table 1.

Printing Properties

The fresh and hardened properties of the 3D printable mortar mixtures are presented in Table 2. Incorporating nano-calcium carbonate and polypropylene fibers resulted in a shorter initial printing time. This also contributed to improved stability of the extruded filament, helping maintain the shape and settlement of the printed layers.

Table 2 Properties of mixture for 3D-printing

Specification	Detailed		
	OPC	NC 2%	PP 0.1%
Flow (%)	150.0	140.0	135.5
Printable time (min)	95	89	86
Time gap (min)	9	12	6
Filament width (mm)	28	26	25
Filament heigh (mm)	11	13	14
Density (kg/m^3)	2,123	2,174	2,106

Experimental Procedure

Printing procedure

The printing process began with preparing mortar mixtures according to the proportions specified in Table 1. After mixing, the fresh mortar was loaded into the concrete hopper of a customized 3D printer, as illustrated in Fig 1. The hopper was then sealed with a piston, preparing the extrusion material.

During the printing process, the mortar was extruded by a piston-driven pump, which forced the material through a plastic hose and out of a nozzle (a diameter of 20 mm). The nozzle was positioned 15 mm above the printable area and moved along a programmed path at 10 mm/s. The extrusion rate was kept constant at 2.5 ml/s.

After each layer was printed, the nozzle was moved to a starting point, lifted for another 15 mm, and waited for a period determined by the time gap specified in Table 2, depending on the mixture design, before proceeding to the next layer. This is to ensure adequate buildability for all tested mixtures.

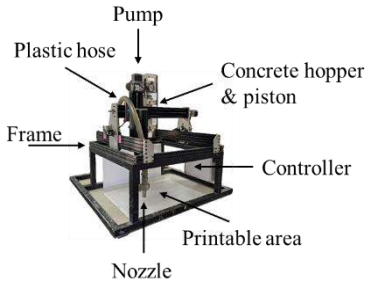

Fig. 1 Printing machine

The printing directions and filament patterns were pre-designed and programmed into the controller integrated with the 3D printing system. The printing direction employed in this study were categorized below.

Unidirectional printing refers to a deposition in which all layers are printed in the 0° direction, meaning that each layer is aligned identically and stacked in the same orientation. In this study, a total of six layers were printed using this approach. The top and side views of the printed specimen are illustrated in Fig 2.

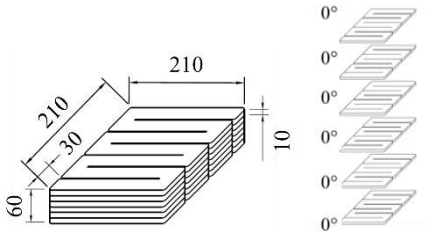

Fig. 2 Unidirectional printing pattern

Table 1 Mix proportions for 3D-printing

Name	Mix Proportions (kg/m^3)							
	Cement	Water	Fine Aggregate	Silica Fume	Polyethylene Glycol	Type G	NC	PP
OPC	879	213	1171	88	22	145	-	-
NC 2%							17.6	-
PP 0.1%							-	0.9

Multidirectional printing, also called the partially quasi-isotropic pattern, involves printing each layer in a different orientation to reduce anisotropy and improve structural uniformity. In this study, the layer orientations were arranged as follows: 0° (Layer 1), +90° (Layer 2), +45° (Layer 3), -45° (Layer 4), -90° (Layer 5), and 0° (Layer 6), as illustrated in Fig 3. This alternating sequence mimics quasi-isotropic behavior by balancing the layer directions around a central axis.

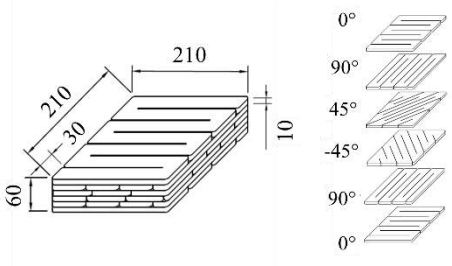

Fig. 3 Multidirectional printing pattern

Sample preparation

For mechanical property evaluation, the printed specimens were cured under moisture-insulated conditions for 28 days before testing. The specimens were then cut into 50-mm cube for compressive strength testing conducted by ASTM C109-20 [11]. For flexural strength testing, specimens were cut into prisms with dimensions of 40 mm × 40 mm × 160 mm (width × height × length), following the ASTM C348-21 standard [12].

Mechanical Properties

Compressive strength

The compressive strength test was conducted to investigate the influence of the printing direction on the compressive strength of 3D-printed specimens. Two loading directions: perpendicular (Fig 4a) and parallel to printing plane (Fig 4b) were performed.

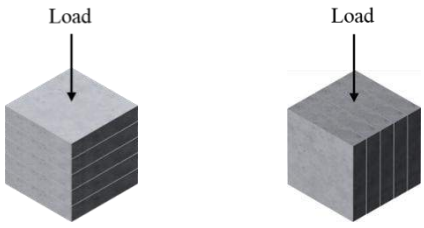

(a) (b)

Fig. 4 Compressive loading direction (a) perpendicular, (b) parallel to the printing filament orientation

Flexural strength

The flexural strength test was conducted to investigate the effects of layer orientation on the flexural behavior of the printed specimens. Two loading directions were considered: flexural loading perpendicular to the printed layers (Fig 5a) and flexural loading parallel to the printed layers (Fig 5b). Comparing the results from both directions highlights the influence of filament arrangement on the flexural strength of the 3D-printed specimens.

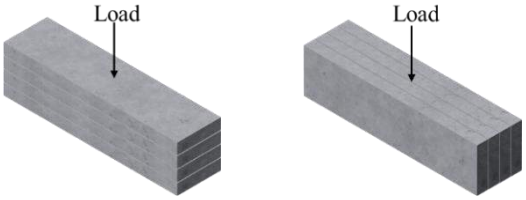

(a) (b)

Fig. 5 Flexural loading direction (a) perpendicular, (b) parallel to the printing filament orientation

RESULTS AND DISCUSSIONS

Compressive Strength

Unidirectional

Fig 6 indicates that OPC mixture exhibited the greatest anisotropy in compressive strength, with values of 15.7 MPa in the perpendicular direction and 10.7 MPa in the parallel direction, a 31.7% reduction in compressive strength. This significant variation shows the mechanical weakness along the printed layers when subjected to parallel loading, likely due to interlayer debonding.

Conversely, the NC 2% and PP 0.1% led to an overall increase in compressive strength in both loading directions, with a decrease of 23.0% and 22.0%, respectively. These results indicate that the additive materials adjust the matrix's mechanical and physical properties and diminish the directional dependence of the mechanical response in 3D-printed components.

The increase in compressive strength observed in the NC 2% mix can be attributed to the filler effect of nano-calcium carbonate within the mortar matrix. These mechanisms increase mortar density, enhancing compressive strength of 3D-printed specimens [13]. In the case of micro polypropylene fibers, the improvement in compressive strength is due to their function as microcrack-bridging elements, which not only inhibit crack propagation but also enhance the toughness of the printing filament mortar [14]. The influence of the printing direction on the compressive strength will be further discussed in the Influence of Printing Orientation section.

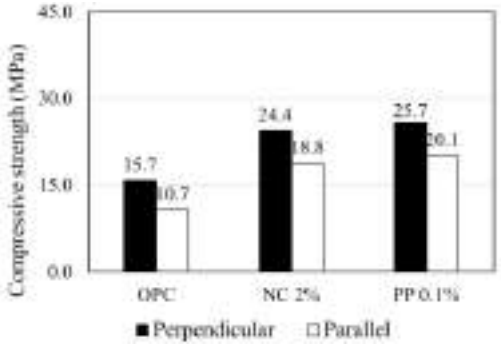

Fig. 6 Compressive strength of unidirectional printing

Multidirectional

In the case of multidirectional printing, Fig 7 presents the compressive strengths of mortar with various mix proportions under two loading directions. For the OPC mixture, a clear difference is observed between the compressive strength in the perpendicular direction (18.0 MPa) and the parallel direction (12.7 MPa), representing a 29.9% reduction in strength under parallel loading. This reduction is due to the debonding of the printing filament.

Upon the NC 2% and PP 0.1% mixtures, compressive strengths in both directions increased, and the anisotropy in mechanical response was significantly reduced to only 9.3% and 8.7%, respectively. These findings suggest that the printing orientation substantially affects the structural integrity and stability of 3D-printed components by mitigating interlayer weaknesses and promoting a more uniform stress distribution throughout the printed specimens.

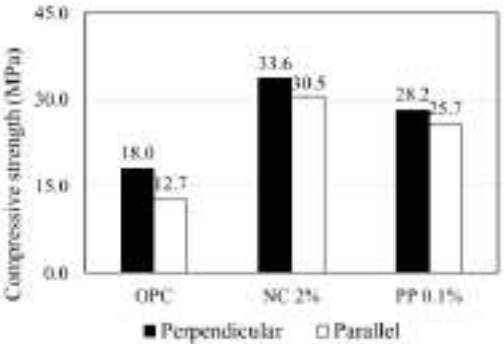

Fig. 7 Compressive strength of multidirectional printing

Flexural Strength

Unidirectional

Fig 8 presents the flexural strength test results of unidirectionally printed specimens. The OPC mixture exhibited the highest anisotropy, with flexural strengths of 8.6 MPa (perpendicular) and 6.0 MPa (parallel), corresponding to a 29.9% reduction. This significant reduction confirms that printing direction strongly influences flexural performance, as the layer-by-layer extrusion in 3D printing introduces planes of weakness when stress is applied along the filament direction.

Although the NC 2% mixture improved the flexural strength, the directional variation remained high at 29.4%. In contrast, the PP 0.1% mixture significantly enhanced the flexural strength beyond that of mixture OPC, and NC 2% substantially reduced the directional effect to 10.0%. This shows the role of fibers in bridging interlayer bonding and enhancing material toughness, resulting in more uniform flexural performance across different loading directions. The influence of the printing direction on the flexural strength will be further discussed in the Influence of Printing Orientation section.

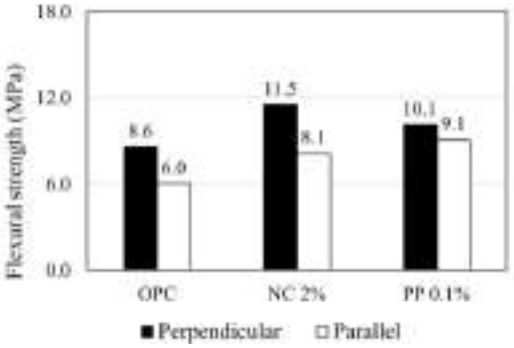

Fig. 8 Flexural strength of unidirectional printing

Multidirectional

In the case of multidirectional printing, Fig 9 presents the flexural strengths of printing specimens. It shows that all mixtures exhibited higher flexural strength when subjected to perpendicular bending direction than in the parallel direction. Among them, the OPC mixture demonstrated the highest directional disparity, with flexural strengths of 10.6 MPa (perpendicular) and 9.3 MPa (parallel), resulting in an 11.7% reduction in flexural strength.

In contrast, the NC 2% and PP 0.1% mixtures exhibited notably reduced differences between directions, 12.2% and 9.5%, respectively. According to Fig 8, it was found that the reduction in flexural strength decreased from 29.9% and 29.4% to 11.7% and 12.2% in the mixture of OPC and NC 2%, respectively. These results highlight the effectiveness of multidirectional printing structure integrity through the loading direction on mechanical performance.

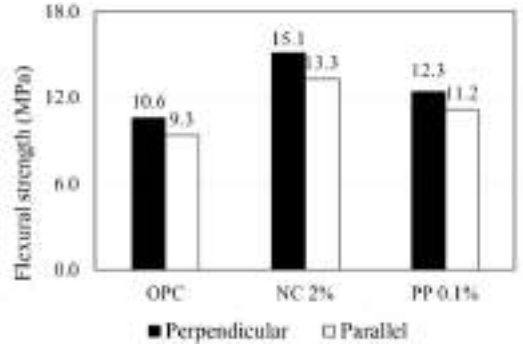

Fig. 9 Flexural strength of multidirectional printing

Influence of Printing Orientation

Compressive strength

Figure 10 shows the influences of printing orientation on the compressive strength of the printed cement mortar. According to the results, the multidirectional printing technique improves the structural integrity of the printed specimens for all mixtures. Enhanced structural integrity leads to a reduction in anisotropic behavior. In contrast, unidirectional printing exhibits limitations in loading direction, as the printed structures can effectively subject the compressive load only in the perpendicular direction to the print layers. Therefore, multidirectional printing may be crucial in future applications, as real-world 3D-printed structures are unlikely to experience loading in a single direction.

In the case of the perpendicular loading direction, the strength of 3D-printed specimens contributes to the printed material and interfilamentous void [4]. The mixture incorporated with NC and PP demonstrates higher compressive strength due to the NC's filler effect and the PP's microcrack-bridging [14-16]. Particularly, the compressive strength improvements were 14.6%, 37.8%, and 9.4% for the OPC, NC 2%, and PP 0.1% mixtures, respectively. However, the inter-filamentous void also plays a crucial role. The multidirectional printing technique serves the cross-ply and oblique patterns, reducing interfilamentous of the printed specimens. This leads to higher compressive strength than the unidirectional printing technique.

In the case of the parallel loading direction, the interlayer bonding plays a crucial role in the compressive strength of the 3D-printed specimens. The multidirectional printing technique tailors a diversity of printing orientations, leading to improved interlocking between the interlayers. This promotes uniform distribution of stress and consequently enhances the compressive strength of the 3D-printed specimens [17]. Unlike the unidirectional printing technique, which follows a single printing path and induces voids between interfilamentous surfaces and layers, the multidirectional approach mitigates such defects [6]. Therefore, the multidirectional printing led to a noticeable enhancement in strength compared to unidirectional printing, with increases of 18.4%, 62.5%, and 28.0%, for OPC, NC 2%, and PP 0.1% mixtures, respectively. It provides better mechanical performance under parallel loading conditions.

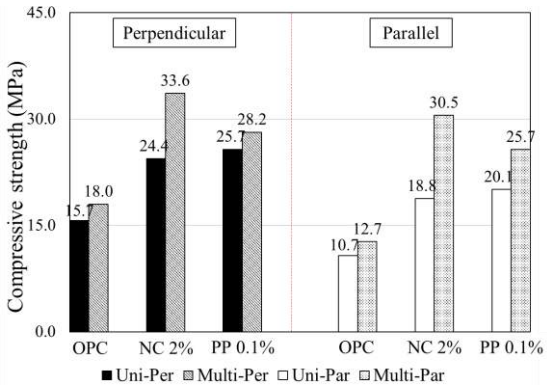

Fig. 10 Effect of printing orientation on compressive strength

Flexural strength

Fig 11 illustrates the influences of printing orientation on the flexural strength of 3D-printed mortar specimens. The perpendicular bending direction and the multidirectional printing technique demonstrate higher flexural strength than specimens printed with the unidirectional technique. Due to the multidirectional orientation utilizing the diverse interlocking between two adjacent layers increases flexural strength [12]. Particularly, the flexural strength improvements were 23.6%, 31.3%, and 22.3% for the OPC, NC 2%, and PP 0.1% mixtures, respectively. On the other hand, the unidirectional printing technique has only a single pattern, leading to a lack of diversity in interlocking between interlayers, resulting in lower flexural strength.

Moreover, lower flexural strength was observed in the parallel bending direction due to weak interlayer bonding and additional shear stress concentration. In contrast, the multidirectional printing orientation, which employs ±45° layer alignment, is more compatible with the direction of shear stresses generated during bending. This alignment enhances stress distribution and interlayer performance, resulting in improved flexural strength [18]. Specifically, the flexural strength of multidirectional printed mortar exceeded that of unidirectionally printed samples by 55.6%, 63.3%, and 23.1% for OPC, NC 2%, and PP 0.1% mixes, respectively. These findings demonstrate the mechanical advantage of the multidirectional printing technique over the unidirectional approach.

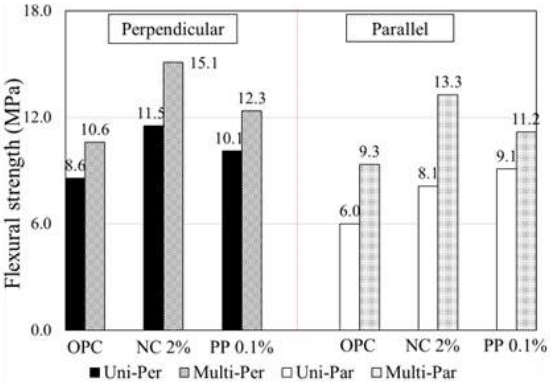

Fig. 11 Effect of printing orientation on flexural strength

CONCLUSIONS

Unidirectional printing provides satisfactory performance under perpendicular loading; however, it exhibits mechanical limitations under parallel loading due to weak interlayer bonding. To overcome this behavior, multidirectional printing techniques, including various printing orientations (0°, ±45°, and ±90°), have been utilized to mitigate anisotropy and enhance interlayer bonding. These approaches lead to significantly mitigated direction dependency in both compressive and flexural strengths.

Moreover, the incorporation of 2% nano-calcium carbonate and 0.1% micropolypropylene fibers contributes to additional enhancements in mechanical performance, demonstrating their effectiveness in mitigating the directional limitations of printed structures.

ACKNOWLEDGMENTS

This research is funded by the National Science, Research and Innovation Fund (NSRF) and King Mongkut's University of Technology North Bangkok under contract no. KMUTNB-FF-68-B-05.

REFERENCES

[1] Robayo-Salazar R., Mejía de Gutiérrez R., Villaquirán-Caicedo M.A., Delvasto Arjona S. 3D printing with cementitious materials: Challenges and opportunities. Autom. Constr. 146 (2023) 1–14.

[2] El-Sayegh S., Romdhane L., Manjikian S. A critical review of 3D printing in construction. Arch. Civ. Mech. Eng. 20(34) (2020) 1–25.

[3] Sukontasukkul P., et al. Effect of microfiber and VMA on cement mortar for 3D printing. Constr. Build. Mater. 319 (2022) 126111.

[4] Jiang Q., et al. Modification effect of nanosilica and fiber for 3D printing concrete. Addit. Manuf. 56 (2022) 102978.

[5] Li Y., et al. Mechanical characteristics of 3D-printed basalt fiber-reinforced mortar. J. Build. Eng. 100 (2025) 106932.

[6] Heras Murcia D., et al. Effect of infill pattern on anisotropy of 3D printed concrete. Constr. Build. Mater. 262 (2020) 120001.

[7] Sukontasukkul P., Mindess S. Shear fracture of concrete under impact. Mater. Struct. 36(6) (2003) 372–378.

[8] Sukontasukkul P., Mindess S., Banthia N. Confined FRC under compressive impact. Cem. Concr. Res. 35(1) (2005) 11–18.

[9] Sukontasukkul P., et al. Bullet resistance of layered rubberized and SFRC panels. Mater. Struct. 47(1–2) (2014) 117–125.

[10] Nematollahi B., et al. Polypropylene fibre in 3D printed geopolymers. Materials 11(12) (2018) 2354.

[11] ASTM C109-20. Standard Test Method for Compressive Strength of Hydraulic Cement Mortar. ASTM International, 2020.

[12] ASTM C348-21. Standard Test Method for Flexural Strength of Hydraulic-Cement Mortars. ASTM International, 2021.

[13] Yang H., Li W., Che Y. 3D printing with nano-$CaCO_3$ cementitious materials. Front. Mater. 7 (2020) 79.

[14] Sukontasukkul P., et al. Eco-friendly 3D printing mortar with low cement. Civ. Eng. J. 10(3) (2024) 808–823.

[15] Sukontasukkul P., et al. Precise determination of initial printable time for cement mortar 3D printing using a derivative method. Rapid Prototyp. J. 29(9) (2023) 1888–1903

[16] Sukontasukkul P., et al. Effect of microfiber and VMA on layer deformation and viscosity in 3D printing mortar. Constr. Build. Mater. 319 (2022) 126111.

[17] Pham L., Lu G., Tran P. Printing pattern effects on fiber-reinforced concrete. 3D Print. Addit. Manuf. 9(1) (2022) 46–63.

[18] Shakor P., et al. Mechanical behavior of 3DP cement mortar with glass fiber. 3D Print. Addit. Manuf. 10(2) (2023) 330–355.

Copyright © Int. J. of GEOMATE All rights reserved, including making copies, unless permission is obtained from the copyright proprietors.

15th Int. Conf. on Geotechnique, Construction Materials & Environment,
Kyoto, Japan, 11-13 November 2025, ISBN 978-4-909106124 C3051

INVESTIGATION OF THE SHEAR STRENGTH OF STEEL BOLTED BAMBUSA BLUMEANA T-CONNECTION

Bernardo A. Lejano[1], Richard Steven Lee[2] and Carlo Cacanando[3]

[1]Faculty, De La Salle University, Philippines; [2] Graduate Student, De La Salle University, Philippines;
[3]Base Bahay Foundation, Incorporated, Philippines

ABSTRACT

Bamboo is a renewable resource, and its mechanical properties can support its adoption in the construction industry as an alternative structural member. Given the Philippines' exposure to earthquakes and winds, ensuring the reliability of members and their connections is important. However, bamboo connections remain insufficiently studied. This study focuses on the shear strength of a T-connection using fish-mouthed bamboo secured with a J bolt. The T-connection was tested with three variations of J-bolt diameters (8 mm, 10 mm, and 12 mm), and was also tested with mortar infill and clamp attachments. A T-test and regression analysis determined the significance of these variables on the joint's shear strength. Results showed that J-bolt size had no significant effect since the bamboo failed first. However, the thickness and density of the bamboo were found to significantly influence shear strength. Samples with both clamp attachments and mortar infill had higher strength than those without. The highest strength was the densest bamboo sample with both clamp and mortar. Furthermore, connections without mortar behaved like roller support, while those with mortar acted as fixed support, offering greater flexibility in structural design. Case studies were conducted to assess the performance of T-connections in a 49 m² bamboo structure located near a fault line, considering both seismic and wind loads. Results showed that the connection is not feasible for two-story and three-story buildings. However, a one-story building can withstand the applied forces.

Keywords: Bamboo, Shear Strength, T-connection, Clamp Attachment, Mortar Infill

INTRODUCTION

The UN-Habitat Philippines Country Report 2023 highlights a housing backlog of 6.5 million units [1]. To address this, Bambusa blumeana is emerging as a sustainable structural material, particularly in low-rise buildings and indigenous structures due to its affordability, superior mechanical strength, and fast harvest rate of up to 4.87 culms/clump per year [2,3]. Despite its potential, adoption remains limited due to concerns about structural integrity, as typical bamboo connections are prone to shear and tensile failures and lack uniform load distribution due to bamboo's natural irregular shape makes achieving joint uniformity challenging. [4].

Bamboo is a key component of Cement Bamboo Frame Technology by Base Bahay [5]. This system uses reinforced concrete foundations, while beams and columns are made entirely of bamboo, connected with steel joints. This study focuses on T-joints, where one bamboo culm is connected perpendicularly to another, enhancing resistance to dynamic loads and lateral forces like wind and seismic activity [6]. There are two bamboo parts in the connection. The tee is the vertical component of the connections and is one internode long. The stem is the horizontal portion and is two internodes long as seen in Fig.1. The stem is longer so that when the force is applied the majority of the reaction will be at the connection. To improve load distribution, fish mouths are carved at connection points, maximizing surface contact [7]. The study also explores J-bolts which serve as a cost-effective alternative to steel plates, utilizing hooked rods to secure bamboo culms effectively, thereby enhancing the stability and reliability of the joints.

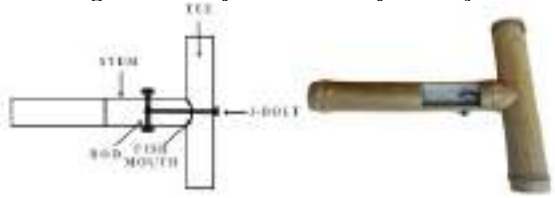

Fig.1 Steel bolted T-connection

The research focused on the shear capacity of the T connection since the Philippines is vulnerable to earthquakes and strong winds. The study is conducted to determine whether this type of connection is applicable to housing projects in the Philippines. Specifically, it will investigate how the geometric properties of bamboo, the dowel diameter, the presence of mortar, and the presence of clamps influence shear capacity. Additionally, the study seeks to predict the shear capacity of T-Joint Fish mouth J-Bolt connections under varying conditions using multilinear regression analysis, providing insights for optimizing bamboo connections in construction.

RESEARCH SIGNIFICANCE

The study will help promote the adaptation of bamboo engineering in the construction industry. The identification of the shear capacity of connection is important to ensure the safety of the bamboo structures so that the bamboo will be designed better to accommodate the correct loads. Furthermore, the development of the connection can lead to innovative construction techniques that enhance the performance and aesthetics of bamboo structures. The research on the shear strength of the connection is not limited to the construction of houses but can also be applicable in walk paths or where there is shear stress in bamboo connections.

METHODOLOGY

The experiment was conducted into three phases. The first phase was to determine the strength of the mortar used to fill the connections. The second phase was the testing of the shear capacity of the connection. The last phase was to determine the moisture content and density of the bamboo used in the connection.

Preparation For T-Connection

The bamboo that was used was already treated by Base Bahay. The bamboo was first cut into appropriate lengths, and their geometric properties were recorded. One end of the stem is then cut using a hole saw to produce a fish mouth. The fish mouth will allow the tee and the stem to properly connect to one another. The stem is then inserted with a plain rod. The tee is then inserted with a hook. The hook is then tightened to hook the plain rod

Preparation For J-bolt

The study utilized stainless steel rods in three distinct diameters: 8 mm, 10 mm, and 12 mm. These rods were then cut into 35- and 15-mm rods. The 35 mm rods were then bent and hammered into a J-bolt. The 15 mm rod is used as a lock for the J-bolt. The rod and the J-bolt always have the same size.

Testing Of Mortar

The mortar used in the study had a ratio of 1 Portland Cement to 3 Sand with a water of 0.5. The mortar was then placed in 50 mm cube specimens and was subjected to a compressive test. There were two batches made with 6 samples per batch. The averages of each batch were determined to be the strength of the mortar to be used in the connection.

Testing Of T-connection

A Universal Testing Machine (UTM) was used to determine the shear strength of the connection, it was set at 10 mm/min. A Linear Variable Differential Transformer (LVDT) was also used to determine the deformation of the connection during the application of the load. The bamboo was then tied to a steel plate to ensure that there were no movements during the testing. There were four different set ups for the connections throughout the study aside from having three different J-bolt sizes. The first set up was the connection had no mortar infill and was not held by a clamp. The second set up still had no mortar infill but was held by a clamp. The third setup had mortar infill but no clamp. The last set up had both mortar infill and clamp. Table 1 shows the code used throughout the experiment. For example, 8CM-1 refers to an 8mm J-bolt, “C” for with clamp, “M” for with mortar, and 1 for the first trial out of 5. If “C” or “M” is not present in the code, this means that the clamp or the mortar is not present. Each setup was repeated five times, resulting in a total of 60 samples.

Table 1 Codes for naming bamboo specimen

J-bolt Size	Presence of Clamps	Presence of Mortar Infill
8	“C”=Present	“M”=Present
10	“ ”=Absent	“ ”=Absent
12		

Testing Of Moisture Content and Density

Once the testing of the shear capacity is completed. Each sample is deconstructed and a piece in the shape of a rectangular prism is obtained. This piece is then measured for its length, width, height, and weight. The sample is then oven dried for 24 hours. After drying, the sample is then weighed again to obtain the moisture content of the bamboo and the density of the bamboo.

RESULTS AND DISCUSSION

The output of the study mainly studies the maximum strength of the connection. It also studies the effects of the properties of the bamboo, size of J-bolt, presence of mortar, and the presence of clamps.

Results of the Mortar

The first batch of mortar had an average strength of 9.025 MPa. On the other hand, the second batch had an average strength of 9.684 MPa. It is determined that the values of both batches are not significantly different from each other.

Initial Findings

Figure 2 illustrates four distinct peaks in the connection's strength as it progresses towards total failure for each setup, except for the configuration with both mortar and a clamp. Fig.2 also represents all other cases where mortar infill and clamps are absent, as they exhibit the same trend. The first peak represents the initial splitting of the bamboo, occurring at the fish mouth region. This split is caused by the moment generated by the shear force applied by the UTM. The second peak varies depending on the setup. For configurations without a clamp and mortar, it results from crack propagation beyond the internode. Table 2 shows the maximum strength of each type of bolt for this case.

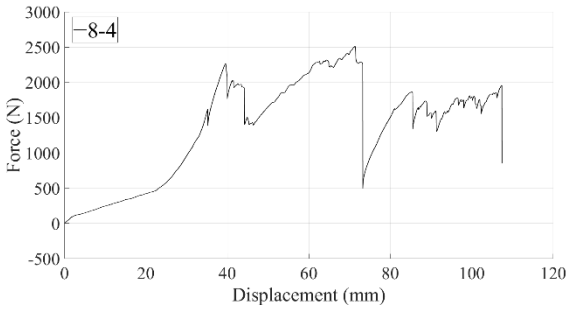

Fig.2 Shear strength of 8 mm J-bolt connections

Table 2 Maximum Strength without Mortar and without Clamp

Bolt Size (mm)	Strength (kN)
8	2.5130
10	2.9481
12	3.0241

Figure 3 represents all setups with clamps but without mortar infill. The second peak for this case is attributed to the clamp's strength as seen in Fig.3. The failure of the clamp leads to a significant crack in the bamboo. Table 3 presents the highest strength recorded for each bolt type in this case.

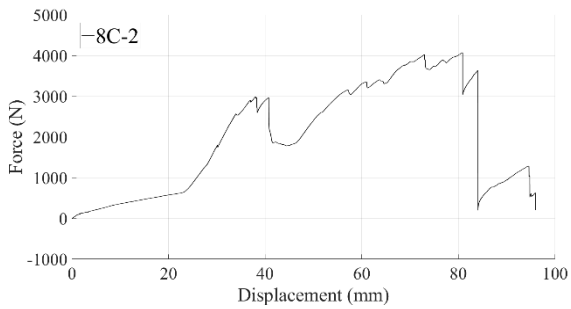

Fig.3 Shear strength of 8C connections

Table 3 Maximum Strength without Mortar and with Clamp

Bolt Size (mm)	Strength (kN)
8	4.9235
10	5.7190
12	5.6302

Figure 4 represents all cases that have mortar infill, but the clamp is absent. For the arrangement with this case, the second peak is related to the mortar's strength, with the connection weakening as cracks form in the mortar. The third peak is associated with the excessive cracking in setups without mortar. In configurations with mortar, this peak is linked to the strength at the internode. Once the crack extends through the internode, the strength diminishes. The final peak corresponds to the J-bolt, representing the highest strength achieved before complete failure. The peak strength of every bolt type for with mortar infill and without clamp is displayed in Table 4. For the 8 mm J-bolt, splitting of the steel rod was observed, which was not present in larger diameter rods.

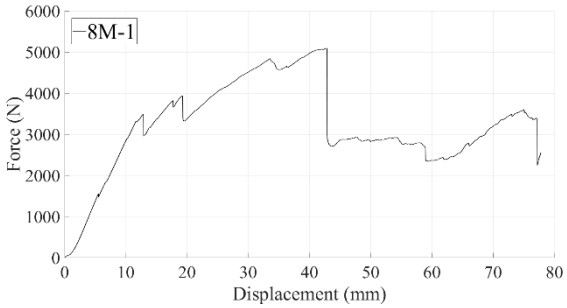

Fig.4 Shear strength of 8M connections

Table 4 Maximum Strength with Mortar and without Clamp

Bolt Size (mm)	Strength (kN)
8	5.2512
10	7.5335
12	5.4704

Figure 5 represents the case with mortar infill and clamp. It can be seen in Fig.5 that only two peaks were observed before total failure. The first peak corresponds to the initial bamboo split, while the second peak represents the combined strength at the second internode, clamp, and mortar, which all fail simultaneously. The assessment of connection strength also differs based on the configuration. In the setup without a clamp and mortar, the first peak is regarded as the connection's maximum strength, as

the initial crack is enough to signify failure. In the setup with a clamp but without mortar, the second peak is considered the maximum strength. The first peak produces only minor cracking due to the clamp's ability to prevent further splitting. However, once the clamp fails, significant damage follows. For the setup with mortar but without a clamp, the third peak is identified as the connection's strength, as considerable damage occurs at that stage. Finally, in the configuration with both mortar and a clamp, the second peak is regarded as the connection's maximum strength since the damage identified here is significant. Table 5 details the maximum strength achieved by each type of bolt in this instance.

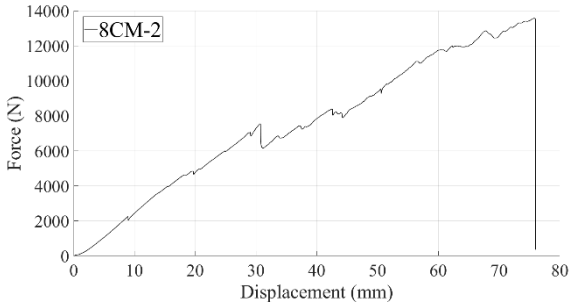

Fig.5 Compressive strength of 8CM connections

Table 5 Maximum Strength with Mortar and with Clamp

Bolt Size (mm)	Strength (kN)
8	13.5752
10	12.4944
12	17.3716

Different J-bolt Sizes

It was found in Figure 6 that the sizes of the J-bolt did not make a significant difference in the shear capacity of the connection. A T-test with a 95% confidence level was also used to determine whether there was a significant difference in the strength of connection. It was found that even when all the connections had mortar infill or clamps. If the variable that was changed was the J-bolt size, the shear capacity of the connection had no significant difference. This is because the bamboo fails first before the J-bolt.

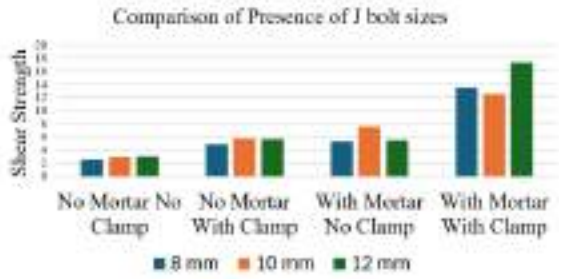

Figure 6. Comparison of Average Strength with Different J-bolt Sizes

Presence of Mortar Infill

Figure 7 indicates that connections with mortar infill exhibited significantly higher maximum strengths compared to those without mortar infill. A T-test with a 95% confidence level showed that the P value of the with mortar infill versus without mortar infill was less than 0.05%. Furthermore, the connection without the mortar had a higher amount of displacement before the first peak of strength of the setup. On the other hand, the setup with mortar infill displaced only by a minimal amount before the first peak. It can be said here that the setup without mortar infill can be designed as a hinged support since it is able to move a significant displacement before damage occurs. The setup with mortar infill can be designed as a fixed support since the displacement it can withstand before damage is minimal.

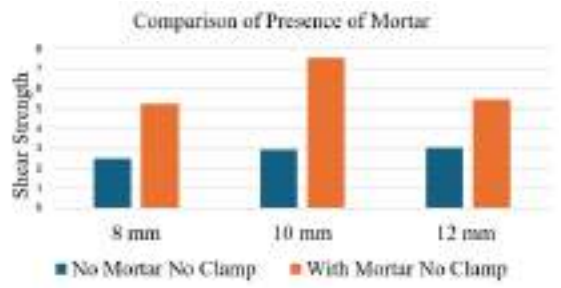

Figure 7. Comparison of Average Strength with Mortar and Without Mortar

Presence of Clamps

Figure 8 demonstrates a significant difference in connection strength between setups with and without clamps, with the clamped configuration exhibiting higher strength. A T-test with a 95% confidence level showed that the P value of the with clamp versus without clamp was less than 0.05%. This proves that the clamp increases the shear strength of the connection. In terms of displacement, there is no significant difference between the with and without clamp set ups.

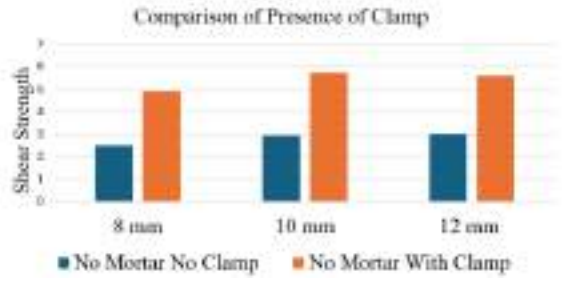

Figure 8. Comparison of Average Strength with Clamp and Without Clamp

Presence of Mortar Infill and Clamps

Figure 9 shows that the setup with clamp and mortar had a higher strength than both the setup with only mortar infill and only clamp. A t-test conducted at a 95% confidence level revealed that the p-value for the comparison between the with clamp and mortar setup, the with clamp setup, and the with mortar setup was less than 0.05, indicating a significant difference. This suggests that the set up with clamp and mortar is the best setup in terms of strength of the connection.

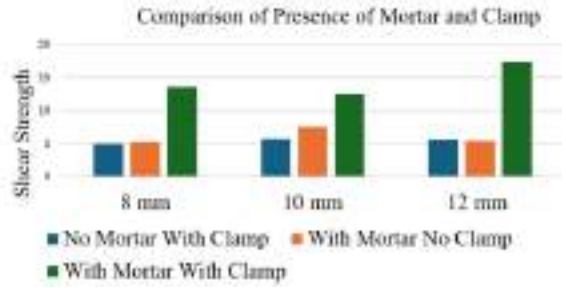

Figure 9. Comparison of Average Strength with Mortar and with Clamp

Regression Analysis

A multilinear regression analysis was performed to determine the significant factors that contributed to the strength of the connection. The properties of the bamboo, mortar, clamp, and the size of the J-bolt were all included in the study. The regression analysis was iterated twice since in the first iteration there were factors that had a p value higher than 0.05 which means they are not significant to the strength of the connection. In the second iteration, all factors exhibited a p-value of less than 0.05, indicating that each variable significantly influences the strength of the connection. These variables include stem thickness, stem bamboo density, mortar presence, and clamp presence. The regression also has an R square value of 0.798523 which means that 79.85% of the strength of the connection is contributed by the factors mentioned above. The equation that predicts the strength of the connection is given by Table 6.

Table 6 Coefficients of Variables

Intercept	Stem Thickness	Stem Density	Mortar Presence	Clamp Presence
-5557.20	463.85	4753270.4	4532.96	3428.63

These findings further demonstrate that the presence of mortar and clamps effectively enhances shear strength. Moreover, they indicate that the J-bolt has a minimal impact on joint strength, with the geometric properties of the bamboo playing a more significant role.

Case Study

A case study was conducted to determine the shear force that a building in the Philippines would experience and whether the connection can withstand such force. Three cases will be examined in this study: the first case involves a one-story structure, the second case focuses on a two-story structure, and the third case considers a three-story structure. It will be assumed that there are only earthquakes and wind forces that could affect the shear strength of the connection. Furthermore, the lot area is assumed to be 49 m², as data from the Philippines Statistics Authority (PSA) indicates that the majority of housing units occupy this size [8]. Lastly, it is assumed that the building is situated along a fault line, located in Zone 4 the highest seismic risk zone in the Philippines and positioned in the windiest area of the Philippines, with the soil condition classified as soft soil and wind speed of 340 kph. The values in Table 11 are calculated using the National Structural Code of the Philippines (NSCP). The maximum earthquake and wind force that the following buildings can experience are shown in Table 7.

Table 7 Maximum Earthquake and Wind Load

Building Type	Earthquake Load (kN)	Wind Load (kN)
3 Story	16.1	4.56
2 Story	11.1	4.56
1 Story	3.98	2.6

In all considered scenarios, seismic loading governs the structural design over wind loading. The regression analysis formula was used to estimate the shear strength of the connection, assuming the average of the thickness and density of the bamboo available is comparable to that used in the sample bamboo members. The values of the maximum shear strength can be observed in Table 8.

Table 8 Maximum Shear Strength Per Condition

Condition	Maximum Shear Strength (kN)
With Mortar and With Clamp	8.99
With Mortar and No Clamp	5.57
No Mortar and With Clamp	4.46
No Mortar and No Clamp	1.03

To ensure the structural integrity of connections in one-story building, elements of high density and substantial thickness must be employed, secured with clamps, and filled with mortar. It is not possible for the connection to be used in two- and three-story structures. Furthermore, setting up with clamps and without mortar is sufficient to withstand the force experienced in a one-story building. However, it should be noted that connections without mortar exhibit significant displacement. Therefore, using a mortar infill is still recommended for improved stability and performance.

CONCLUSION

The steel bolted T-connection can be used in housing especially since housing projects in the Philippines is 1 story only. The strength of the connection is reliant on the geometric properties of the bamboo. The selection of bamboo with high density and substantial thickness is crucial to ensure the integrity of the structure. The presence of mortar and clamps also had a positive influence on the maximum strength of the connection. Furthermore, the usage of the smallest J-bolt (8 mm) would be recommended since the size of the steel rod does not significantly impact the strength of the joint. The utilization of T-connections presents a practical advantage for industry applications. Connections without mortar exhibited behavior akin to roller supports, whereas mortar-filled connections approximated fixed supports, thereby providing enhanced flexibility in structural design considerations.

ACKNOWLEDGMENTS

The authors gratefully acknowledge the faculty and staff of the Civil Engineering Department at De La Salle University (DLSU) for their invaluable assistance. Furthermore, they extend their appreciation to the Department of Science and Technology - Engineering Research and Development for Technology (DOST-ERDT) for providing the scholarship budget that enabled this experiment, and to Base Bahay for their contribution of materials and for essential support during the testing phase of the project.

REFERENCES

[1] United Nations Habitat, UN-Habitat Philippines Country Report 2023, UN Habitat, Nairobi, 2023, pp.1–150.

[2] Salzer C., Wallbaum H., Alipon M., and Lopez L.F., Determining Material Suitability for Low-Rise Housing in the Philippines: Physical and Mechanical Properties of the Bamboo Species Bambusa Blumeana, BioResources, Vol.13, Issue 1, 2017, pp.346–369.

[3] Bautista B.E., Garciano L.E., and Lopez L.F., Comparative Analysis of Shear Strength Parallel to Fiber of Different Local Bamboo Species in the Philippines, Sustainability, Vol.13, Issue 15, 2021, Article 8164, pp.1–17.

[4] Aniñon M.J. and Garciano L.E., Advances in Connection Techniques for Raw Bamboo Structures – A Systematic Review, Preprints, Vol., Issue, 2024, pp.1–25.

[5] BaseBuilds, Cement-Bamboo Frame Technology: Affordable and Disaster-Resilient Housing Solution – Building Sustainable Future Today, BASE, 2023.

[6] Cuartero J., Miravete A., Castejón L., Chiminelli A., and Tolosana N., Design and Analysis of T-Joints for Fiberglass Reinforced Plastic Ship Structures, Naval Engineers Journal, Vol.118, Issue 1, 2006, pp.55–61.

[7] Balaji G., Vetturayasudharsanan R., Arul Reegan Raj E., and Pranav Kumar S., Connections for Bamboo in Buildings – A Review, TEST – Engineering and Management, Vol.83, 2020, pp.1–8.

[8] Philippine Statistics Authority, Annual Poverty Indicators Survey, PSA, Manila, 2023.

Copyright © Int. J. of GEOMATE All rights reserved, including making copies, unless permission is obtained from the copyright proprietors.

15th Int. Conf. on Geotechnique, Construction Materials & Environment,
Kyoto, Japan, 11-13 November 2025, ISBN 978-4-909106124 C3051

CORRELATION BETWEEN INFILL DENSITY AND MECHANICAL PROPERTIES IN 3D PRINTING

Boonthum Wongchai

Faculty of Engineering at Sriracha, Kasetsart University, Thailand

ABSTRACT

Fused Deposition Modeling (FDM) 3D printing is widely used for part manufacturing. Infill density is a key factor that influences the mechanical properties of printed parts. This study investigates the correlation between infill density and the mechanical properties of enhanced polylactic acid (PLA+). Specimens were fabricated using an FDM 3D printer in accordance with ASTM D638-14 standards, employing a grid infill pattern. Infill densities were varied at 20%, 30%, 40%, 50%, 60%, 70%, 80%, 90%, and 100%. Regression analysis was used to examine the relationships between infill density and key mechanical properties, including Young's modulus, yield strength, ultimate tensile strength, tensile strength at break, and tensile strain at break. The results show that the relationships between infill density and both Young's modulus and yield strength are best described by linear equations, with coefficients of determination (R^2) of 0.99 and 0.98, respectively. A quadratic equation with an R^2 of 0.98 best fits the correlation between infill density and ultimate tensile strength. The relationships between infill density and both tensile strength at break and tensile strain at break yield R^2 values below 0.90, suggesting more variation in the data and a lower degree of model fit compared to the other properties.

Given the increasing use of 3D-printed PLA-based components in construction and geotechnical applications such as lightweight formworks, temporary structural elements, and erosion control systems. This study provides valuable insights into how infill density affects mechanical performance, which can guide material selection and structural design for sustainable engineering solutions.

Keywords: Infill density, 3-D printing, Enhanced polylactic acid (PLA+), mechanical properties

INTRODUCTION

In recent years, 3D printing has emerged as a key technology within the field of additive manufacturing (AM), offering the ability to fabricate complex geometries with minimal material waste and shorter production times compared to conventional methods. The AM process typically begins with a CAD-designed prototype exported as an STL file, which is then processed by slicing software to generate G-code for layer-by-layer fabrication. AM supports a wide range of materials, including polymers, metals, ceramics, and composite blends, making it suitable for applications across aerospace, automotive, robotics, and sensor technologies. Among various AM technologies such as stereolithography (SLA) and multi jet fusion (MJF). Fused deposition modeling (FDM) is the most widely adopted due to its low cost, ease of use, and material versatility [1-3].

Beyond industrial applications, FDM 3D printing has gained interest in construction and geotechnical engineering. PLA-based materials, including enhanced PLA+ filaments, are being explored for temporary or lightweight structural elements, such as formwork, soil-retaining structures, erosion control modules, and physical modeling in geotechnical testing. Their biodegradability and ease of fabrication make them particularly appealing for sustainable and low-impact environmental applications. Understanding how infill density influences the mechanical properties of these printed materials is therefore essential for optimizing performance and safety in such engineering contexts.

In 3D printing, various materials are selected based on desired properties such as strength, flexibility, and application requirements. PLA (Polylactic Acid) is one of the most popular filaments due to its ease of use, low printing temperature, and biodegradable nature, making it ideal for beginners and general-purpose printing. PLA+ is an enhanced version of PLA that includes additives to improve strength, durability, and surface finish while maintaining the same ease of use. ABS (Acrylonitrile Butadiene Styrene) is known for its toughness, impact resistance, and higher temperature tolerance but requires a heated bed and enclosed print area to prevent warping. PETG (Polyethylene Terephthalate Glycol) combines the ease of printing of PLA with the strength and temperature resistance of ABS, offering excellent durability, chemical resistance, and a glossy finish, making it a versatile choice for functional parts. Composite materials, such as PLA reinforced with recycled desized carbon fiber shells, have been shown to enhance tensile modulus and strength compared to pure PLA [4]. Conversely, PLA/TPU polymer blends improve ductility but reduce mechanical strength [5]. Sandwich printing techniques, such as PLA/wood with a PLA core and

PLA combined with carbon fiber-reinforced PLA, are employed to further enhance mechanical performance [6, 7].

Printing parameters—including infill pattern, infill density (ID), infill rate, build orientation, raster angle, nozzle temperature, bed temperature, extrusion speed, and nozzle diameter—significantly affect mechanical properties such as Young's modulus, yield strength, ultimate strength, strength at break, and strain at break [8-12]. For PLA, increasing the infill density has been shown to enhance Young's modulus, ultimate strength, and the maximum load-to-weight ratio [13, 14]. In the case of PEEK, higher nozzle temperatures and lower printing speeds contribute to improved mechanical properties, while annealing typically increases mechanical strength with rising annealing temperatures [15].

In this study, PLA+ filament is used to evaluate the mechanical performance of 3D-printed specimens fabricated with varying infill densities. A consistent grid infill pattern is applied to all samples to ensure uniform internal structure. The influence of infill density on mechanical properties such as tensile strength and stiffness is thoroughly examined, and statistical regression analysis is employed to quantify the correlation between these parameters.

MATERIALS AND METHODS

According to ASTM D638-14, the standard test method for tensile properties of plastics, a Type I specimen with a thickness of 3.2 mm is designed using SOLIDWORKS software (Fig.1) and exported as an STL file [16]. Creality Slicer software is used to generate the G-code files by varying the infill density at 20%, 30%, 40%, 50%, 60%, 70%, 80%, 90%, and 100%. A grid infill pattern with a raster angle of 45° is applied (Fig.2). All specimens are fabricated using a Creality CR-10 Smart 3D printer with eSUN PLA+ filament, which has a density of 1.23 g/cm³.

The nozzle diameter used in the printing process was 0.4 mm, and the layer height was maintained at 0.2 mm to ensure dimensional accuracy. The top and bottom layer thicknesses were set to 0.4 mm, with four layers applied for both the top and bottom surfaces, using 100% infill in these regions to provide solid shell layers. The nozzle temperature was set at 200 °C, and the heated bed temperature was maintained at 60 °C to enhance adhesion during printing. A print speed of 50 mm/s was selected to balance print quality and production time. Each specimen was printed in a horizontal orientation on the build plate to minimize warping and ensure flatness. After printing, specimens were conditioned at room temperature for 24 hours prior to mechanical testing. These printing parameters were selected based on standard practices and prior research that demonstrated their effectiveness in producing dimensionally accurate and mechanically consistent PLA-based parts [17].

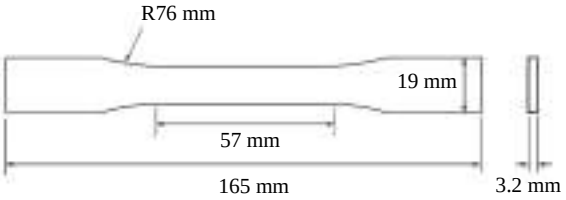

Fig.1 ASTM D638-14 specimen dimension

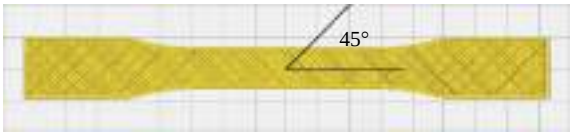

(a)

(b)

Fig.2 Infill density settings in Creality Slicer software: (a) 20% infill, (b) 80% infill.

(a) (b)

Fig.3 (a) Tensile testing setup, and (b) fractured specimens after testing.

Three specimens for each infill density are tested using an Instron 5982 universal testing machine, equipped with a 100 kN load cell and operated at a crosshead speed of 5 mm/min, as shown in Fig.3. The test is conducted using Bluehill software to control and monitor the testing process. Stress-strain curves are generated for each test, as illustrated in Fig.4. The Mechanical properties evaluated include Young's modulus (E), yield strength (σ_Y) determined using a 0.2% offset, ultimate tensile strength (σ_U), tensile strength at break (σ_B), and tensile strain at break (ε_B). These parameters provide a comprehensive understanding of the material's tensile behavior under varying internal structures. The results are used to assess the influence of infill density on the overall mechanical performance of the printed specimens.

Regression analysis is used to describe the relationship between mechanical properties and infill

density. This relationship can be represented by a polynomial equation as follows:

$$y = a_n ID^n + a_{n-1} ID^{n-1} + \ldots + a_2 ID^2 + a_1 ID + a_0 \quad (1)$$

where y is the dependent mechanical property, ID is the infill density, a_n are the polynomial coefficients, and n is the degree of the polynomial (e.g., n = 1 for linear, n = 2 for quadratic, n = 3 for cubic, etc.).

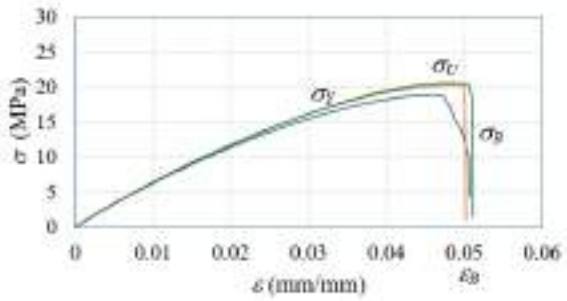

Fig.4 Stress-strain curve at 30% infill

RESULTS AND DISCUSSION

Young's Modulus

Fig.5 presents the plot of Young's modulus versus infill density. The results indicate a linear relationship between Young's modulus and infill density. Through regression analysis, this relationship can be expressed as:

$$E = 4.0151\ ID + 346.58 \quad (2)$$

Eq. (2) has an R^2 value of 0.99, indicating a high degree of accuracy. This suggests that infill density is a strong predictor of the material's stiffness. Therefore, by adjusting the infill density, the mechanical properties of the printed part can be effectively tailored.

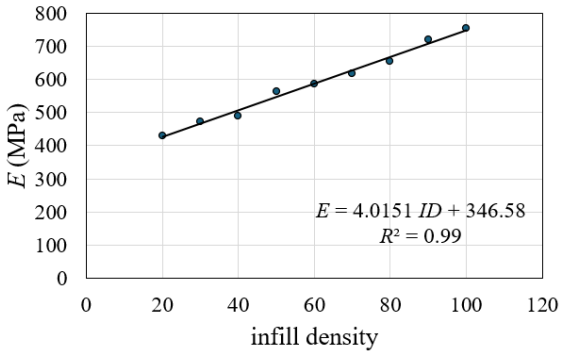

Fig.5 Young's modulus vs infill density with n = 1

Yield Strength

Similar to the plot of Young's modulus versus infill density, the relationship between yield stress and infill density also exhibits a linear trend, as shown in Fig.6. The regression analysis reveals a strong linear correlation with a high R^2 value of 0.98, indicating excellent accuracy. This relationship can be expressed as:

$$\sigma_Y = 0.091\ ID + 14.793 \quad (3)$$

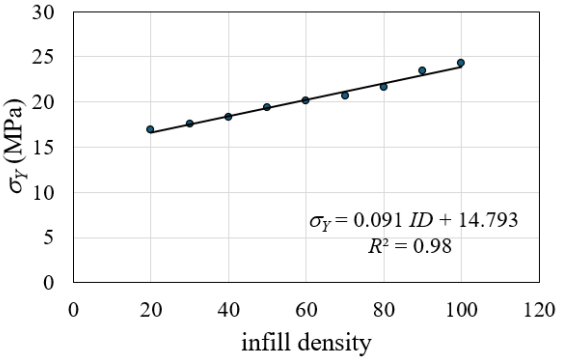

Fig.6 Yield strength vs infill density with n = 1

This result suggests that infill density is a strong predictor of the material's yield strength, allowing for precise control of mechanical properties through infill adjustments. Such control is critical for designing parts that meet specific strength requirements without unnecessary material use.

Ultimate Tensile Strength

For ultimate tensile strength, a linear regression can be plotted with an R^2 value of 0.9218, as shown in Fig.7. The relationship between ultimate tensile strength and infill density can initially be expressed as:

$$\sigma_U = 0.1264\ ID + 15.608 \quad (4)$$

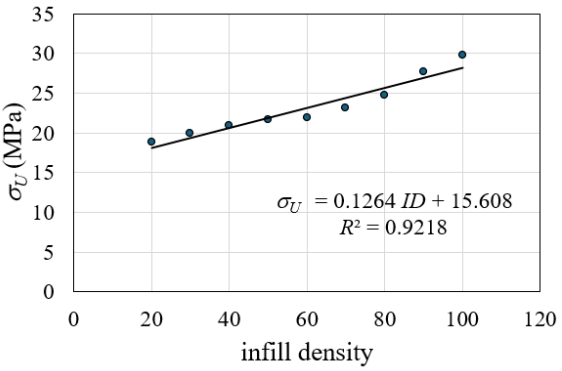

Fig.7 Ultimate tensile strength vs infill density with n = 1

Although Eq. (4) demonstrates a reasonably strong correlation, the stress-strain curve at 30% infill in Fig.4 and similarly at other infill levels reveals a nonlinear behavior in the plastic deformation region.

This suggests that a nonlinear model may better represent the relationship. Consequently, a quadratic regression with n = 2 was applied, also shown in Fig.8, resulting in an improved fit with an R^2 value of 0.98:

$$\sigma_U = 0.0014\ ID^2 - 0.044\ ID + 19.774 \quad (5)$$

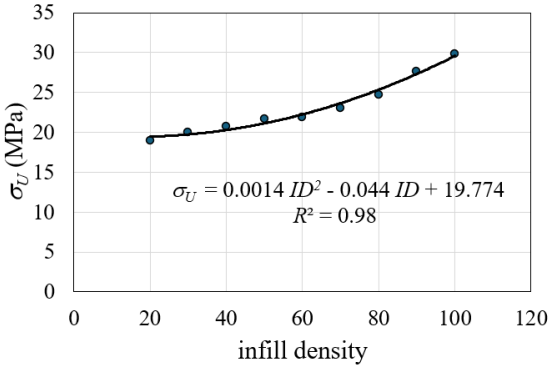

Fig.8 Ultimate tensile strength vs infill density with n = 2

This result confirms that infill density is a strong predictor of the material's ultimate tensile strength, and that quadratic regression provides a more accurate model for capturing the mechanical behavior, particularly in the plastic region.

The nonlinear model was found to better represent the relationship between infill density and ultimate tensile strength, as indicated by the improved R^2 value of 0.98 compared to the linear model. This is consistent with the behavior observed in the stress–strain curves (e.g., Fig. 4), where the material exhibits nonlinear plastic deformation, especially at lower infill densities. Linear models tend to oversimplify this behavior by failing to account for the gradual transition from elastic to plastic deformation and the complex internal stress distribution in FDM-printed structures.

Previous studies have also reported similar findings. The mechanical properties of FDM-printed components are influenced by a combination of process parameters, such as infill density, due to factors like layer adhesion, void content, and anisotropic material behavior, all of which contribute to nonlinear performance trends. The ultimate tensile strength does not increase linearly with infill density, owing to the irregular stress distribution and fracture mechanisms introduced by internal porosity and layer geometry [18, 19]. These insights support the use of a quadratic model, which more accurately captures the mechanical response of printed specimens across different infill levels.

Tensile Strength at Break

Fig.9 presents the plot of tensile strength at break versus infill density. A quadratic regression provides the fit for the data, with an R^2 value of 0.6737, and can be expressed as:

$$\sigma_B = 0.0006\ ID^2 + 0.0664\ ID + 13.079 \quad (6)$$

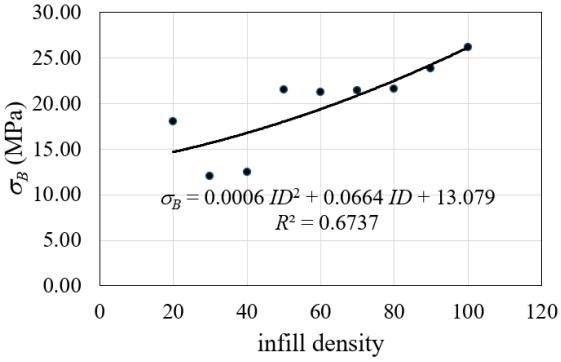

Fig.9 Tensile strength at break vs infill density with n = 2

Understanding tensile strength and strain at break is essential for assessing the mechanical performance and failure resistance of 3D-printed parts. These properties indicate how much stress and deformation a material can withstand before breaking, which is critical for load-bearing applications or safety-critical components.

The relatively low R^2 value (67.37%) reflects the variability and complexity of fracture behavior during tensile testing. The apparent scattering of data points in Fig.9 may partially result from human factors such as inconsistencies in specimen preparation, printing parameters, or testing alignment. To overcome these issues, more rigorous control of experimental conditions is recommended such as using automated calibration of tensile test machines, maintaining uniform environmental conditions (e.g., temperature and humidity), and increasing the number of replicates to minimize outlier influence and improve statistical reliability.

Tensile Strain at Break

Similar to the tensile strength at break, the relationship between infill density and tensile strain at break is best represented by a quadratic regression, as shown in Fig.10. The equation is expressed as:

$$\varepsilon_B = 9\times10^{-6}\ ID^2 - 0.0012\ ID + 0.0833 \quad (7)$$

This model yields an R^2 value of 0.7795, indicating an accuracy of 77.95% in predicting the strain at break. The relatively moderate accuracy is attributed to the complex and inconsistent nature of fracture behavior during tensile testing.

As shown in Fig. 10, the tensile strain at break initially decreases with increasing infill density up to approximately 60%, after which it begins to increase. This trend can be explained by the interplay between

structural stiffness and material deformability. At lower infill densities, the internal structure is more compliant, allowing greater elongation before failure. As the infill density increases, the structure becomes stiffer and more constrained, reducing the strain at break. However, beyond 60%, the higher material continuity and internal support may enhance energy dissipation and delay crack propagation, leading to an increase in tensile strain at break.

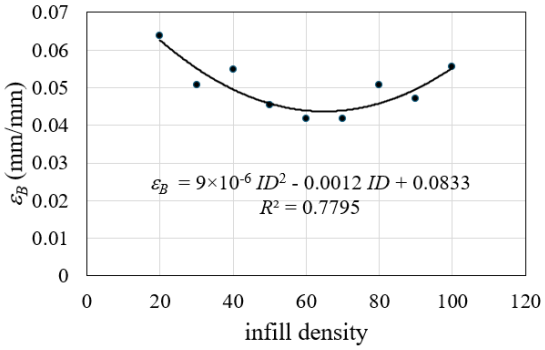

Fig.10 Tensile strain at break vs infill density with $n = 2$

Although increasing the polynomial degree to n = 6 improves the R^2 value to above 0.95 for both tensile strength and tensile strain at break, such high-degree polynomial models tend to overfit the data. While they may fit the experimental points closely, they lack physical interpretability and are not suitable for reliably predicting real-world mechanical behavior.

CONCLUSIONS

This study examined the influence of infill density on the mechanical properties of enhanced PLA+ specimens fabricated using FDM 3D printing. Specimens were printed according to ASTM D638-14 standards with a grid infill pattern, and infill densities ranged from 20% to 100%. Based on the experimental results and regression analysis, it was found that both Young's modulus and yield strength show a strong linear relationship with infill density, with high accuracy reflected in R^2 values of 0.99 and 0.98, respectively. The ultimate tensile strength was best modeled using a quadratic equation, achieving an R^2 of 0.98. In contrast, the relationships between infill density and tensile strength at break as well as tensile strain at break were less consistent, with R^2 values below 0.90, indicating weaker correlations. Overall, the findings confirm that infill density is a significant factor in determining certain mechanical properties of PLA+ parts and can be effectively used to tailor stiffness and strength in FDM-printed components.

ACKNOWLEDGMENTS

The author gratefully acknowledges the support of the Applied Mechanics and Product Design (AMPD) research group, Faculty of Engineering at Sriracha, Kasetsart University, Sriracha Campus. The resources and expertise provided by the group were instrumental in the successful completion of this work. Additionally, the author would like to acknowledge the assistance of ChatGPT, developed by OpenAI, which is used as a tool for language refinement and technical writing support throughout the preparation of this manuscript.

REFERENCES

[1] Tran T. Q., Ng F. L., Tan J. T. Y. K., Feih S., and Nai M. L. S., Tensile Strength Enhancement of Fused Filament Fabrication Printed Parts: A Review of Process Improvement Approaches and Respective Impact. Additive Manufacturing, Vol. 54, 2022, Article 102724.

[2] Kumar S., Singh H., Singh I., Bharti S., Kumar D., Siebert G., and Koloor S. S. R., A comprehensive review of FDM printing in sensor applications: Advancements and future perspectives. Journal of Manufacturing Processes, Vol. 113, 2024, pp. 152–170.

[3] Kadhum A. H., Al-Zubaidi S., and Abdulkareem S. S., Effect of the Infill Patterns on the Mechanical and Surface Characteristics of 3D Printing of PLA, PLA+ and PETG Materials. ChemEngineering, Vol. 7, 2023, Article 46.

[4] Saleh M., Anwar S., AlFaify A. Y., Al-Ahmari A. M., and Abd Elgawad A. E. E., Development of PLA/recycled-desized carbon fiber composites for 3D printing: Thermal, mechanical, and morphological analyses. Journal of Materials Research and Technology, Vol. 29, 2024, pp. 2768–2780.

[5] Hamidi M. N., Abdullah J., Mahmud A. S., Hassan M. H., and Zainoddin A. Y., Influence of thermoplastic polyurethane (TPU) and printing parameters on the thermal and mechanical performance of polylactic acid (PLA)/thermoplastic polyurethane (TPU) polymer. Polymer Testing, Vol. 143, 2025, Article 108697.

[6] Kechagias J. D. and Zaoutsos S. P., An assessment of PLA/wood with PLA core sandwich multilayer component tensile strength under different 3D printing conditions. Journal of Manufacturing Processes, Vol. 131, 2024, pp. 1240–1249.

[7] Subramaniyan M., Karuppan S., Appusamy A., and Pitchandi N., Sandwich printing of PLA and carbon fiber reinforced-PLA for enhancing tensile and impact strength of additive manufactured parts. Journal of Manufacturing Processes, Vol. 137, 2025, pp. 425–436.

[8] Hikmat M., Rostam S., and Ahmed Y. M., Investigation of tensile property-based Taguchi

method of PLA parts fabricated by FDM 3D printing technology. Results in Engineering, Vol. 11, 2021, Article 100264.

[9] Nyabadza A., Mc Donough L. M., Manikandan A., Basu Ray A., Plouze A., Muilwijk C., Freeland B., Vazquez M., and Brabazon D., Mechanical and antibacterial properties of FDM additively manufactured PLA parts. Results in Engineering, Vol. 21, 2024, Article 101744.

[10] Fountas N. A., Kostazos P., Pavlidis H., Antoniou V., Manolakos D. E., and Vaxevanidis N. M., Experimental investigation and statistical modelling for assessing the tensile properties of FDM fabricated parts. Procedia Structural Integrity, Vol. 26, 2020, pp. 139–146.

[11] Wang P., Zou B., Ding S., Li L., and Huang C., Effects of FDM-3D printing parameters on mechanical properties and microstructure of CF/PEEK and GF/PEEK. Chinese Journal of Aeronautics, Vol. 34, No. 9, 2021, pp. 236–246.

[12] Hosseini S. S., Nabavi-Kivi A., Ayatollahi M. R., and Petru M., Effect of nozzle diameter on tensile and fracture behavior of FDM-PLA samples. Procedia Structural Integrity, Vol. 61, 2024, pp. 20–25.

[13] Pernet B., Nagel J. K., and Zhang H., Compressive Strength Assessment of 3D Printing Infill Patterns. Procedia CIRP, 2022.

[14] Guan R. and Smith D., Influence of Infill Parameters on the Tensile Mechanical Properties of 3D Printed Parts. Journal of Emerging Investigators, Vol. 2, July 2020.

[15] He Y., Shen M., Wang Q., Wang T., and Pei X., Effects of FDM parameters and annealing on the mechanical and tribological properties of PEEK. Composite Structures, Vol. 313, 2023, Article 116901.

[16] ASTM D638–14, Standard test method for tensile properties of plastics. ASTM International, 2014.

[17] Chacón, J. M., Caminero, M. Á., García-Plaza, E., & Núñez, P. J. Additive manufacturing of PLA structures using fused deposition modelling: Effect of process parameters on mechanical properties and their optimal selection. Materials & Design, Vol. 124, 2017, pp. 143–157.

[18] Ngo, T. D., Kashani, A., Imbalzano, G., Nguyen, K. T. Q., & Hui, D. Additive manufacturing (3D printing): A review of materials, methods, applications and challenges. Composites Part B: Engineering, Vol. 143, (2018), pp. 172–196.

[19] Song, Y., Wang, H., & Li, L. Effect of infill density on mechanical properties of 3D printed parts using Fused Deposition Modeling. Materials Today Communications, Vol. 24, 2020, 101141.

Copyright © Int. J. of GEOMATE All rights reserved, including making copies, unless permission is obtained from the copyright proprietors.

15th Int. Conf. on Geotechnique, Construction Materials & Environment, Kyoto, Japan, 11-13 November 2025, ISBN 978-4-909106124 C3051

TWO-AXIS VIBRATION RESPONSE ATTENUATION OF BUILDING STRUCTURE USING ROLLING CYLINDER DYNAMIC VIBRATION ABSORBER

Lovely Son[1], Mulyadi Bur[1], Bima Anugrah Saputra[1] and Zeki Midi[1]

[1]Mechanical Engineering Department, Engineering Faculty, Andalas University, Indonesia

ABSTRACT

This study proposes a novel two-axis dynamic vibration absorber designed to mitigate building vibrations in two axes of motion. The dynamic vibration absorber comprises two cylinders rolling along a circular curved track, each aligned orthogonally to reduce vibration responses along separate axes. Both absorbers are placed on the upper floor of the building and the natural frequencies of the cylinders are tuned to match the two lowest natural frequencies of the building's bending modes. Several simulation studies in frequency and time domains are performed to evaluate the damper performance in reducing the building structural response under seismic excitation. The simulation data shows that the proposed dynamics vibration absorber can effectively reduce the seismic response of the building structure. Additionally, an experimental set-up is built and tested to validate the simulation outcomes. Experimental findings reveal a 70% reduction in structural vibration, with close agreement between empirical and simulation results, confirming the DVA's efficacy.

Keywords: Vibration, Dynamics, Building, Absorber, Structure

INTRODUCTION

Vibrations of building structures due to earthquakes have become the focus of attention of researchers in recent decades. This is because earthquakes are natural phenomena that are difficult to predict accurately both in terms of time and place of occurrence [1,2]. Besides that, earthquakes with large energy can cause damage and even collapse of building structures. Therefore, anticipating the effects of earthquakes on building structures is very important in designing earthquake-resistant building structures.

Dynamic vibration absorbers (DVAs) are proven passive solutions for mitigating structural vibration. Many researches have been conducted to investigate diverse DVA configurations for structural application such as pendulum absorbers [3], U-shaped water tanks [4], and tuned mass dampers TMDs [5]. DVA can be tuned to minimize vibration amplitudes and even harness energy from structural oscillations, offering dual-functional benefits [6]. Design of multiple DVAs that simultaneously absorbs vibration energy from a high-speed train that enabling streamlined performance assessment have been established [7]. Recent studies investigate the application of Genetic Algorithm (GA) to optimize vibration suppression in a Two-DOF structure model subjected to seismic load [8]. For high-rise structures, advanced numerical models are essential to accurately evaluate DVA effectiveness, as oversimplified two-degree-of-freedom models fail to capture real-world complexities. Research related to the application of DVA for multidirectional vibrations has been carried out by several researchers. Qin et al. [9] apply multiple DVA in reducing a floor-like lightweight joist structure vibration. Yin et al. [10] propose a technique to control multi-directional vibration of marine pipe system using mistuned cyclic symmetric structure as DVA.

RESEARCH SIGNIFICANCE

Although various concepts and models of DVAs have been developed for single and multi-degree-of-freedom vibration systems [11], their application to spatial structures, which more closely resemble real-world conditions, remains quite limited. This research presents a vibration control strategy for spatial structures utilizing DVA based on a rolling cylinder mechanism. A two-story building model serves as a case study to illustrate the proposed damper application. Two rolling cylinders, set to move perpendicularly along a circular track, are mounted on the upper floor of the building. This configuration enables the dampers to effectively suppress bending-mode vibrations along both the -x and -y axes.

One Degree of Freedom System with a Rolling Cylinder DVA

A single-degree-of-freedom (One-DOF) vibration system integrated with a rolling cylinder dynamic vibration absorber (DVA) is shown in Fig.1. The primary system is defined by mass M, stiffness k, and damping coefficient c. The DVA consists of a cylinder with mass m and radius r, which rolls along a circular track of radius R

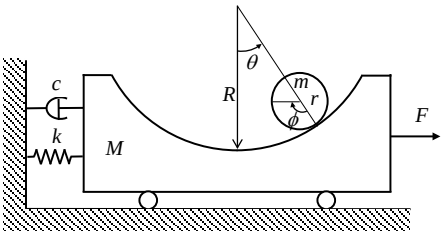

Fig.1 One degree of freedom system with rolling cylinder DVA

The moment balance on the cylinder at the contact point between the cylinder and the pad results in:

$$J_G\left(\ddot{\phi}-\ddot{\theta}\right)+mr\left(R-r\right)\ddot{\theta}+m\ddot{x}r\cos\theta+mgr\sin\theta +C_r\dot{\theta}=0 \quad (1)$$

In the case of without slip $\phi=\frac{R}{r}\theta$ and $\ddot{\phi}=\frac{R}{r}\ddot{\theta}$, therefore Eq. (1) can be simplified by:

$$L\left(\frac{J_G}{r^2}+m\right)\ddot{\theta}+m\ddot{x}\cos\theta+mg\sin\theta+\frac{C_r}{r}\dot{\theta}=0 \quad (2)$$

Where $L=R-r$ and L denotes the pendulum length. Applying a force balance to the main mass yields:

$$M\ddot{x}+c\dot{x}+kx+m\ddot{x}+mL\ddot{\theta}\cos\theta-mL\dot{\theta}^2\sin\theta=F \quad (3)$$

Eq. (2) and (3) are the governing equations of 1-DOF vibration system with rolling cylinder DVA.

Building Structure Model with Two Rolling Cylinder DVA

A building structure model incorporating two rolling cylinder dynamic vibration absorbers (DVAs) as shown in Fig.2 is utilized to evaluate the damper performance. The structure represents a two-story building model, comprising a basement floor, a first floor, and a second floor. Each floor is supported by six vertical columns, as illustrated in Fig.2. Two rolling cylinder DVAs are positioned atop the second floor. These absorbers are designed to mitigate the two lowest bending mode vibrations of the structure in the x- and y-directions

Governing equation

To derive the governing equations for the space structure equipped with absorbers, the system is modeled using the finite element method (FEM). The coupled differential equations governing the absorber and the structure are formulated as:

$$L_i\left(\frac{J_{Gi}}{r_i^2}+m_{di}\right)\ddot{\theta}_i+m_{di}\ddot{x}_{di}\cos\theta_i+m_{di}g\sin\theta_i +\frac{C_{ri}}{r_i}\dot{\theta}_i=0\ ,i=1,2 \quad (4)$$

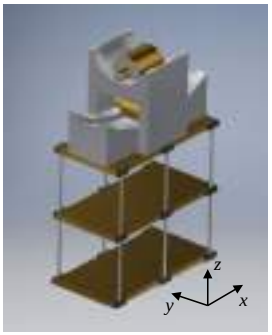

Fig.2 Building structure model with two rolling cylinder DVA

$$\left[\mathbf{M}\right]\{\ddot{\mathbf{x}}\}+\left[\mathbf{C}\right]\{\dot{\mathbf{x}}\}+\left[\mathbf{K}\right]\{\mathbf{x}\}=\{\mathbf{B_u}\}\,f_{ext} +\{\mathbf{B_v}\}\,f_{in} \quad (5)$$

where

[**M**], [**C**] and [**K**] are the structural mass, damping and stiffness matrix calculated by FEM, respectively. {$\mathbf{B_u}$} and {$\mathbf{B_v}$} in Eq. (5) are the row matrices that contain delta functions $\delta_{i,j}$ as follows :

$$\{\mathbf{B_u}\}=\begin{Bmatrix}\delta_{u,1} & \delta_{u,2} & \cdots & \delta_{u,j} & \cdots & \delta_{u,NDOF}\end{Bmatrix} \quad (6)$$

$$\{\mathbf{B_v}\}=\begin{Bmatrix}\delta_{v,1} & \delta_{v,2} & \cdots & \delta_{v,j} & \cdots & \delta_{v,NDOF}\end{Bmatrix} \quad (7)$$

In Eq. (6) and (7), subscript *u* and *v* denote position of the external forces and the interaction forces between DVA and structure. $\delta_{i,j}$ denotes delta function that can be expressed by:

$$\delta_{i,j}=\begin{cases}1, & \text{if } i=j\\ 0, & \text{if } i\neq j\end{cases} \quad (8)$$

The external and interaction force between structure and DVA are expressed as:

$$f_{ext}=F \quad (9)$$

$$f_{in}=mL\dot{\theta}^2\sin\theta-mL\ddot{\theta}\cos\theta-m\ddot{x} \quad (10)$$

Eq. (5) can be expressed in modal coordinates as follows:

$$\ddot{q}_i+2\zeta_i\omega_i q_i+\omega_i^2 q_i=\mathbf{\Psi_i}\left[\{\mathbf{B_u}\}\,f_{ext}+\{\mathbf{B_v}\}\,f_{in}\right], \quad i=1,2,\cdots,\infty \quad (11)$$

Frequency response function (FRF)

The frequency response function (FRF) of the space structure model integrated with two cylindrical DVAs is calculated under the assumption of linear system behavior. For small cylinder displacements, linear approximations are applied to the cylinder's rotational motion and translational dynamics. Using this assumption, the governing equations of the system (Eqs. (4) and (5)) are linearized as follows:

$$\left[\mathbf{M}\right]_{\mathbf{lin}}\{\ddot{\mathbf{x}}\}+\left[\mathbf{C}\right]_{\mathbf{lin}}\{\dot{\mathbf{x}}\}+\left[\mathbf{K}\right]_{\mathbf{lin}}\{\mathbf{x}\}=\{\mathbf{B}\}_{\mathbf{lin}}F \quad (12)$$

Where

$$[\mathbf{M}]_{\mathbf{lin}} = \begin{bmatrix} m_{11} & \cdots & m_{1p} & \cdots & m_{1q} & \cdots & m_{1n} & 0 & 0 \\ \vdots & \vdots & \vdots & \vdots & \vdots & \vdots & \vdots & \vdots & \vdots \\ m_{p1} & \cdots & m_{pp}+m_{d1} & \cdots & m_{pq} & \cdots & m_{pn} & m_{d1}L_1 & 0 \\ \vdots & \vdots & \vdots & \cdots & \vdots & \vdots & \vdots & \vdots & \vdots \\ m_{q1} & \cdots & m_{qp} & \cdots & m_{qq}+m_{d2} & \cdots & m_{qn} & 0 & m_{d2}L_2 \\ \vdots & \vdots & \vdots & \cdots & \vdots & \cdots & \vdots & \vdots & \vdots \\ m_{n1} & \cdots & m_{np} & \cdots & m_{nq} & \cdots & m_{nn} & 0 & 0 \\ 0 & \cdots & m_{d1} & \cdots & 0 & \cdots & 0 & L_1\left(\frac{J_{G1}}{r_1^2}+m_{d1}\right) & 0 \\ 0 & \cdots & 0 & \cdots & m_{d2} & \cdots & 0 & 0 & L_2\left(\frac{J_{G2}}{r_2^2}+m_{d2}\right) \end{bmatrix}$$

$$[\mathbf{C}]_{\mathbf{lin}} = \begin{bmatrix} c_{11} & \cdots & c_{1p} & \cdots & c_{1q} & \cdots & c_{1n} & 0 & 0 \\ \vdots & \vdots & \vdots & \vdots & \vdots & \vdots & \vdots & \vdots & \vdots \\ c_{p1} & \cdots & c_{pp} & \cdots & c_{pq} & \cdots & c_{pn} & 0 & 0 \\ \vdots & \vdots & \vdots & \cdots & \vdots & \vdots & \vdots & \vdots & \vdots \\ c_{q1} & \cdots & c_{qp} & \cdots & c_{qq} & \cdots & c_{qn} & 0 & 0 \\ \vdots & \vdots & \vdots & \cdots & \vdots & \cdots & \vdots & \vdots & \vdots \\ c_{n1} & \cdots & c_{np} & \cdots & c_{nq} & \cdots & c_{nn} & 0 & 0 \\ 0 & \cdots & 0 & \cdots & 0 & \cdots & 0 & \frac{C_{r1}}{r_1} & 0 \\ 0 & \cdots & 0 & \cdots & 0 & \cdots & 0 & 0 & \frac{C_{r2}}{r_2} \end{bmatrix} \quad [\mathbf{K}]_{\mathbf{lin}} = \begin{bmatrix} k_{11} & \cdots & k_{1p} & \cdots & k_{1q} & \cdots & k_{1n} & 0 & 0 \\ \vdots & \vdots & \vdots & \vdots & \vdots & \vdots & \vdots & \vdots & \vdots \\ k_{p1} & \cdots & k_{pp} & \cdots & k_{pq} & \cdots & k_{pn} & 0 & 0 \\ \vdots & \vdots & \vdots & \cdots & \vdots & \vdots & \vdots & \vdots & \vdots \\ k_{q1} & \cdots & k_{qp} & \cdots & k_{qq} & \cdots & k_{qn} & 0 & 0 \\ \vdots & \vdots & \vdots & \cdots & \vdots & \cdots & \vdots & \vdots & \vdots \\ k_{n1} & \cdots & k_{np} & \cdots & k_{nq} & \cdots & k_{nn} & 0 & 0 \\ 0 & \cdots & 0 & \cdots & 0 & \cdots & 0 & m_{d1}g & 0 \\ 0 & \cdots & 0 & \cdots & 0 & \cdots & 0 & 0 & m_{d2}g \end{bmatrix}$$

RESULTS AND DISCUSSION

The vibration attenuation performance of the building structure model equipped with two rolling cylinder dynamic vibration absorbers (DVAs) is numerically evaluated using the nominal simulation parameters listed in Table 1. In the simulation study, the DVAs are positioned at the center of the second floor.

Table 1 Nominal simulation parameters

No	Parameters	Value
1	1st floor dimensions	(250 × 125× 8) mm
2	2nd floor dimensions	(250 × 125 × 8) mm
3	Columns dimensions	(2 × 3 × 125) mm
4	Columns modulus (E_c)	69×10^9 N/m^2
5	Plate modulus (E_c)	120×10^9 N/m^2
6	1st pendulum mass (m_{d1})	0.35 kg
7	2nd pendulum mass (m_{d2})	0.09 kg
8	1st pendulum inertia (J_{G1})	3.5×10^{-5} kg m^2
9	2nd pendulum inertia(J_{G2})	3.7×10^{-6} kg m^2
10	Structural damping ratio (ζ)	1×10^{-3} Ns/m
11	1st pendulum length (L_1)	0.08 m
12	2nd pendulum length (L_2)	0.033 m
13	1st cylinder radius (r_1)	0.01 m
14	2nd cylinder radius (r_2)	0.005 m
15	Damping (C_{r1} and C_{r2})	1×10^{-4} Nms

The two lowest natural frequencies of the structure and their corresponding mode shapes, derived from numerical simulations is depicted in Fig.3. As illustrated, the first and second mode shapes represent the structure's lowest bending modes in the x- and y-directions, with natural frequencies of 1.77 Hz and 2.65 Hz, respectively. Two cylindrical DVAs are tuned to these two natural frequencies to target vibration mitigation in these critical modes.

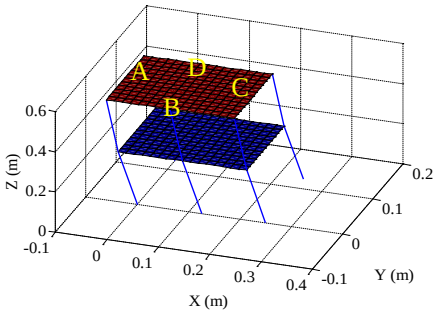

f_1 = 1.77 Hz

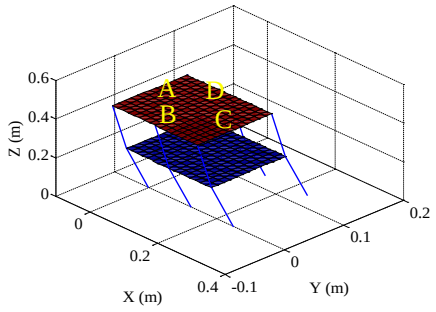

f_2 = 2.65 Hz

Fig.3 Two Lowest natural frequencies and mode shapes of the structure model

Two rolling-cylinder dynamic vibration absorbers (DVAs) are designed to suppress vibrations in the building structure along two orthogonal axes (x and y directions). Both devices are mounted on the top floor of the building, as shown in Fig. 2. Their effectiveness is assessed through the structure's frequency response functions (FRFs), evaluated in the x–z and y–z planes. The FRF in the x–z plane is obtained using excitation at point A and response measurements at point C, whereas the FRF in the y–z plane is determined from excitation and measurements taken at points B and D (see Fig. 3).

Variation of Pendulums İnertia (J_{G1}, J_{G2})

The effect of varying J_{G1} on the frequency response function (FRF) in the x-z plane is shown in Fig.4(a). The results demonstrate that reducing J_{G1} from its nominal value enhances the damper's effectiveness in suppressing vibrations near the natural frequency of the first bending mode in the x-z plane. Conversely, as shown in Fig.4(b), variations in J_{G1} exhibit negligible impact on the FRF in the y-z plane.

The impact of J_{G2} variations on the FRF in the x-z and y-z planes (Fig.5) reveal that the x-z plane FRF exhibits little to no sensitivity to J_{G2} adjustments. In contrast, deviations in J_{G2} affect the y-z plane FRF, though the effect remains relatively minor.

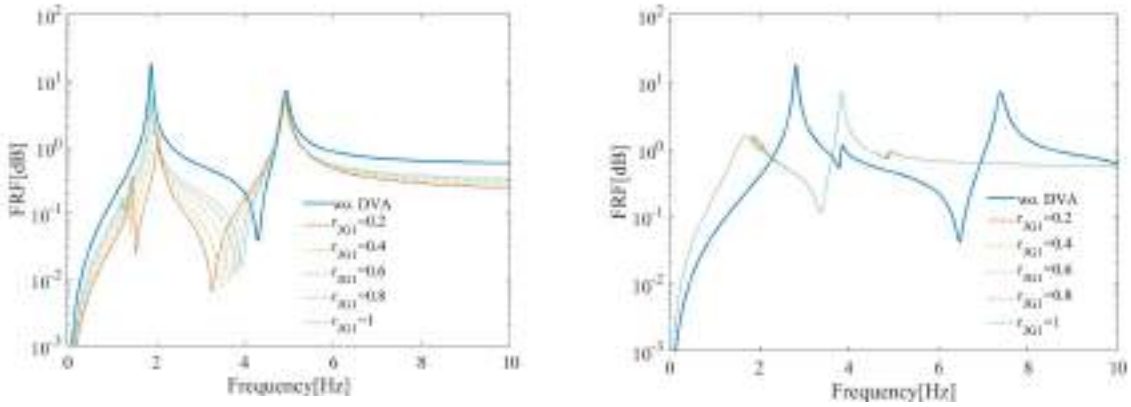

Fig. 4 Variation of FRF vs J_{G1} (a) x-z plane (b) y-z plane

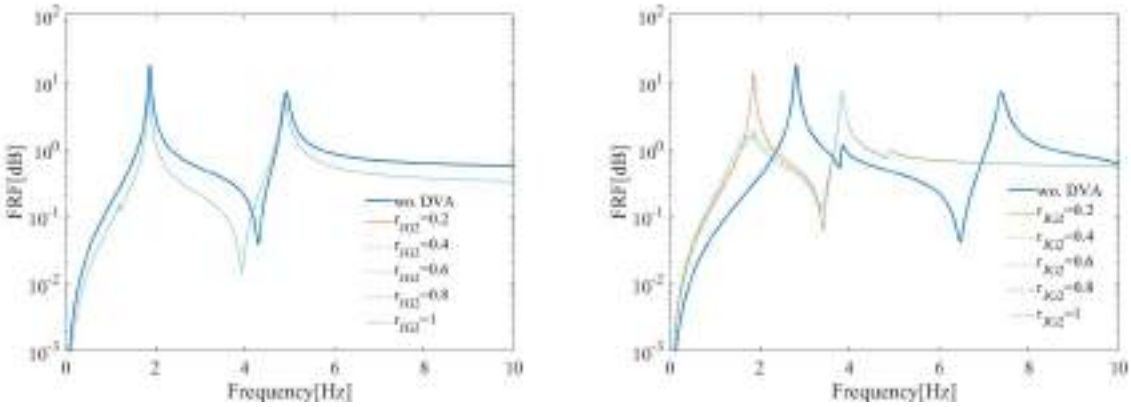

Fig. 5 Variation of FRF vs J_{G2} (a) x-z plane (b) y-z plane

Variation of Circular Track Radius (L_1, L_2)

The effect of increasing L_1 on the FRF of the structure in the x-z and y-z planes is shown in Fig.6. It is shown that variations in L_1 markedly influence the FRF in the x-z plane. Notably, reducing L_1 below its nominal value enhances the DVA's effectiveness in mitigating structural vibrations in this plane. In contrast, the y-z plane FRF exhibits negligible sensitivity to changes in L_1.

Relationship between L_2 adjustments and the FRF of the structure in the x-z and y-z planes is evaluated by varying the ratio between L_2 to its nominal value as shown in Fig.7. The results reveal that increasing L_2 has negligible impact on the x-z plane FRF. Conversely, elevating L_2 introduces a slight but measurable effect on the y-z plane FRF.

Variation of Cylinder Radius (r_1, r_2)

Fig.8 demonstrates the influence of the first cylinder radius (r_1) on the FRF of the structure in the x-z and y-z planes. Enlarging r_1 enhances the dynamic absorber's vibration mitigation performance in the x-z plane. Conversely, increasing r_1 exerts minimal influence on the y-z plane FRF.

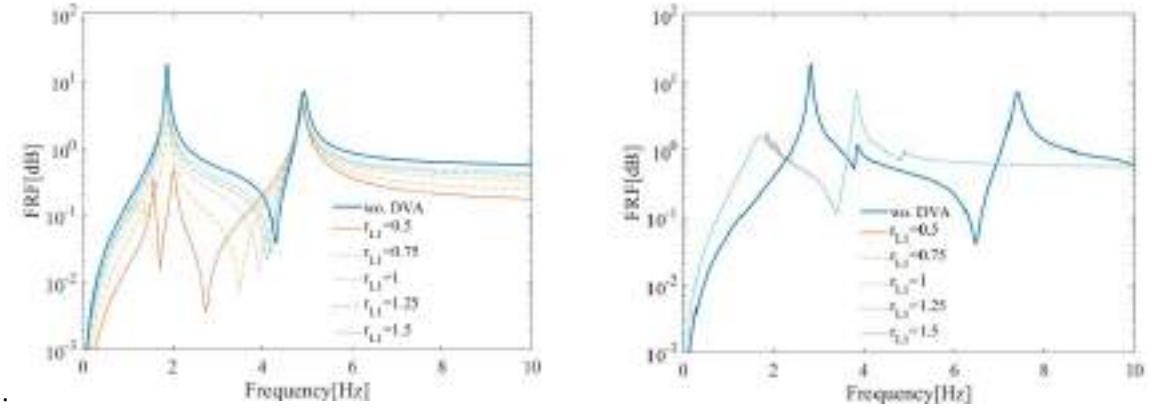

Fig. 6 Variation of FRF vs L_1 (a) x-z plane (b) y-z plane

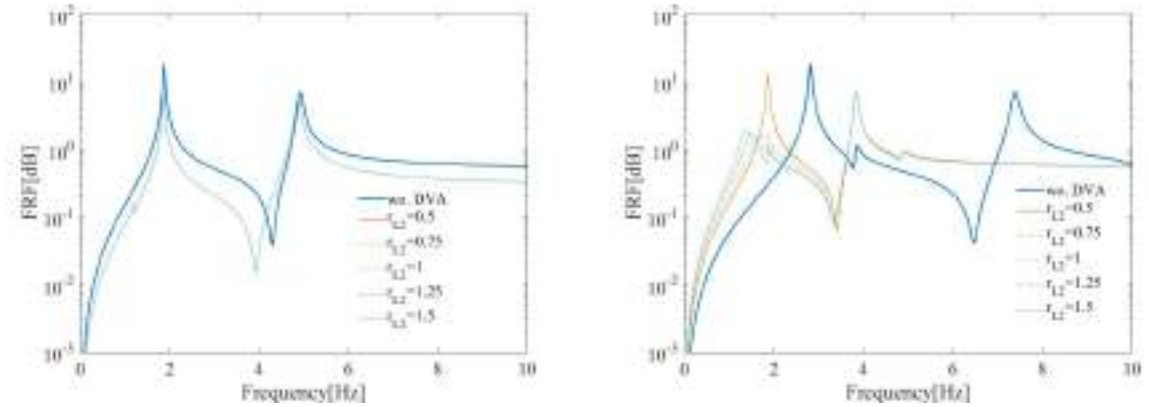

Fig.7 Variation of FRF vs L_2 (a) x-z plane (b) y-z plane

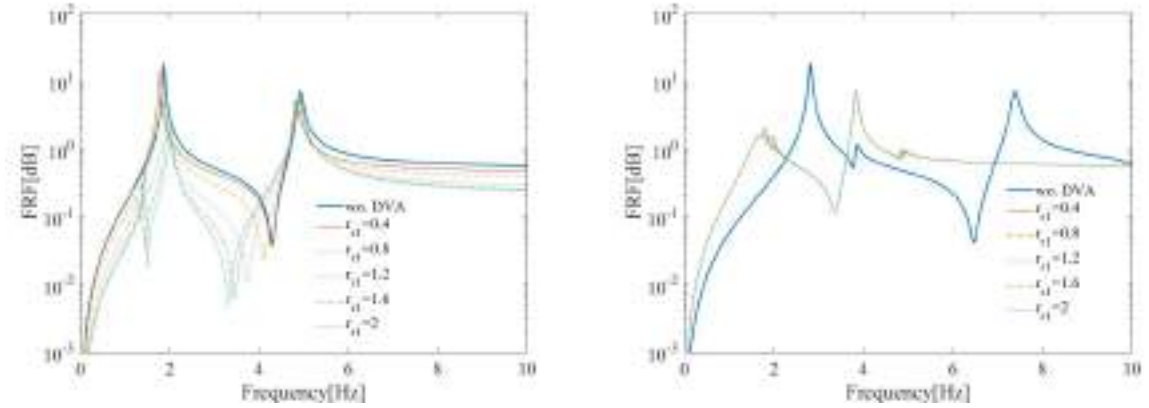

Fig. 8 Variation of FRF vs r_1 (a) x-z plane (b) y-z plane

Time-domain responses simulation of the structure in x-z plane and y-z plane at two distinct measurement points are shown in Fig.9. The external excitations are applied at points A (x-direction) and B (y-direction), with the Kobe earthquake signal serving as the disturbance input. The structural response is measured at points C and D. It is shown that both dynamic absorbers significantly mitigate structural vibrations in the x-z and y-z axis. Compared to conventional DVA which is only able to reduce vibrations in one axis [9], rolling cylinder DVA developed in this study has the ability to dampen vibrations in both directions of the vibration axis.

EXPERIMENTAL VALIDATION

The excitation force is applied using an impact hammer and the acceleration data are collected using B&K accelerometer type 4507. Fig.10 shows the

comparison of the experimental FRF and the simulated FRF in the y-z planes. Experimental data can validate simulation results. The difference in the peak FRF is likely arise from uncertainties in modeling parameters, particularly the moment of inertia and damping coefficient.

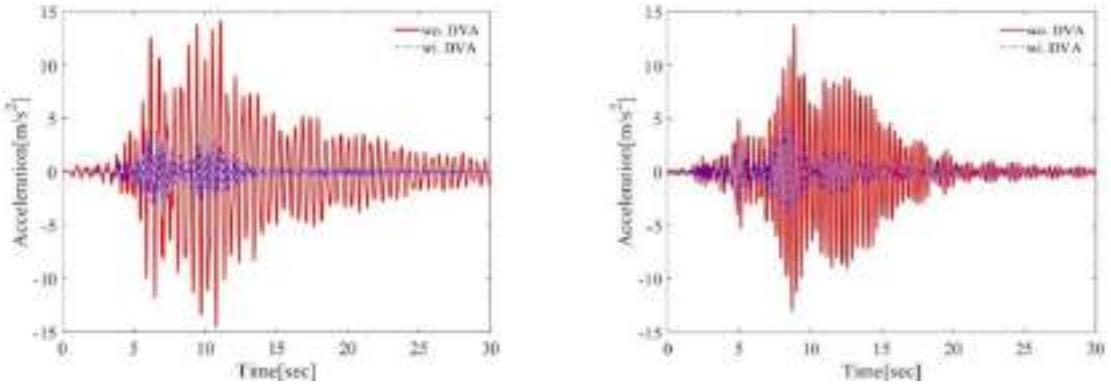

Fig. 9 Time response calculated in (a) x-z plane (b) y-z plane

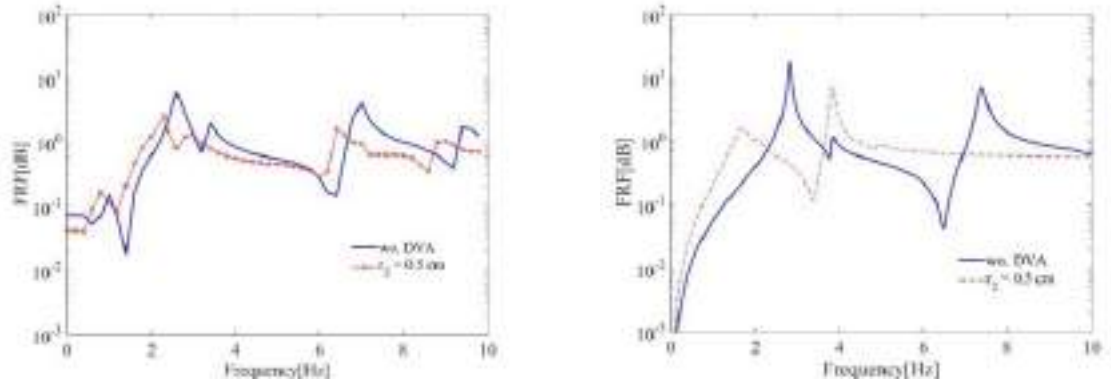

Fig. 10 Comparison of FRF in y-z plane (a) experiment (b) simulation

CONCLUSIONS

This study proposes a concept for space building structural vibration attenuation using two cylinder dynamic vibration absorber. Both absorbers are placed on the top floor of the building and are used to dampen vibrations in the x-z and y-z planes. The simulation results show that there are a number of parameters that significantly affect the performance of the dampers. Furthermore, employing optimal DVA parameters can reduce the structural response by as much as 70%. Experimental studies show that the simulation results can be validated experimentally.

ACKNOWLEDGMENTS

Financial support from mechanical engineering department Andalas University under research publication grant in the proceedings of the 2025 international seminar, is gratefully acknowledged.

REFERENCES

[1] Jihad A., Umar M., Ramli M., Syamsidik, and Banyonegoro V.H., Analysis of Change of Seismic Stress Along the Sumatran Zone to Predict Potential Earthquake Zones, GEOMATE, Vol. 24, Issue 104, 2023, pp. 36-43.

[2] Susilo A., Hisyam F., and Wasis, Earthquake Analysis in East Java, Indonesia Between 1960 – 2017 using Markov Chain Model, GEOMATE, Vol. 17, Issue 63, 2019, pp. 149-156.

[3] Bur M., Son L., Rusli M., and Okuma M., Parametric Study of Pendulum Type Dynamic Vibration Absorber for Controlling Vibration of a Two DOF Structure, Earthquakes and Structure, Vol. 13, Issue 1, 2017, pp.51-58.

[4] Shyu K.L., and Kuo H.C., Dynamic Behaviour of a U-Type Tuned Liquid Damper, International Shipbuilding Progress, Vol. 43, Issue 436, 1996, pp. 331-345.

[5] Djerouni S., Ounis A., Elias S., Abdeddaim M., and Rupakhety R., Optimization and Performance Assessment of Tuned Mass Damper Inerter Systems for Controlling of Buildings Subjected to Pulse-Like Ground Motions, Structures, Vol. 28, 2022, pp. 139-156.

[6] Wang Q., Zhou J., Wang K., Gao, J.L., Lin, Q., Chang Y., Xu D., and Wen G., Dual-Function Quasi-Zero-Stiffness Dynamic Vibration Absorber: Low-Frequency Vibration Mitigation and Energy Harvesting, Applied Mathematical Modelling, Vol. 116, 2023, pp. 636-654.

[7] Sun Y., Zhou J., Gong D., and Ji Y., Study on Multi-Degree of Freedom Dynamic Vibration Absorber of the Car Body of High-Speed Trains, Mechanical Sciences, Vol. 13, Issue 1, 2022, pp. 239-256.

[8] Son L., Erizal F., Bur M., and Sutanto S., Serial Pendulum DVA Design Using Genetic Algorithm (GA) by Considering the Pendulum Nonlinearity, Structural Engineering and Mechanics, Vol.89, No.6, 2024, pp.549-556.

[9] Qin Y., Tan J.J., and Hornikx M., Application of multiple dynamic vibration absorbers in reducing low-frequency vibration of a floor-like lightweight joist structure: Comparison of experimental and computational results, Applied Acoustic, Vol. 211, 109437, 2023, pp. 1-11.

[10] Yin L., Xu W., Fu J., and Cheng G., Multi-directional broadband vibration control of marine pipe systems using mistuned cyclic symmetric structure as dynamic vibration absorbers, Ocean Engineering, Vol. 320, 120272, 2025, pp. 1-15.

[11] Bur M., Son L., Rusli M., and Okuma M., Parametric study of pendulum type dynamic vibration absorber for controlling vibration of a two DOF structure, Earthquakes and Structures, Vol.13, No.1, 2017, pp.51-58.

Copyright © Int. J. of GEOMATE All rights reserved, including making copies, unless permission is obtained from the copyright proprietors.

15th Int. Conf. on Geotechnique, Construction Materials & Environment,
Kyoto, Japan, 11-13 November 2025, ISBN 978-4-909106124 C3051

CRITICAL ANALYSIS OF OLIVINE PERFORMANCE AND POTENTIAL FOR CARBON SEQUESTRATION IN SUSTAINABLE CONSTRUCTION

Roohollah Kalatehjari [1], Sara Bayandor[1] and Yousef Adeeb Chamachaei[1]

[1] Built Environment Engineering Department, School of Future Environments, Auckland University of Technology, Auckland 1010, New Zealand

ABSTRACT

Global efforts to reduce CO_2 emissions have increased research interest in olivine due to its significant carbon sequestration potential. However, the broad variability in mineralogical characteristics, carbonation mechanisms, and environmental impacts of olivine poses challenges to its practical use, highlighting a need for systematic evaluation. A systematic literature review was conducted on 102 scholarly sources published since 2000, adhering to PRISMA guidelines. The review comprehensively analysed olivine grain size, mineral composition, carbonation mechanisms, chemical treatments, CO_2 absorption efficiency, and environmental impacts. Statistical analyses were performed on keyword frequencies, regional focus, and publication trends to establish research themes and identify knowledge gaps. The analysis revealed a marked increase in olivine research in recent years (from 2021 to 2024), comprising 52.4% of total studies. The primary focus across 79% of reviewed publications was CO_2 sequestration efficacy, frequently involving grain sizes below 180 µm and high-purity forsterite (>80% Mg_2SiO_4), a magnesium-rich silicate mineral. Key thematic areas identified were carbon dioxide (33 mentions), carbonation (18 mentions), and mineral carbonation (11 mentions). Geographically, research predominantly originated from Europe (19.3%), the USA (15.9%), and Malaysia (10.2%). Critically, fewer than 30% of studies included comprehensive life-cycle analyses or economic feasibility evaluations, and only 18% reported durability and porosity data. While recent research has expanded significantly, substantial gaps remain regarding long-term durability, economic analysis, and regional-specific adaptations. Future research must prioritise comprehensive environmental impact assessments, economic evaluations, and field-scale durability testing to facilitate the practical application of olivine in sustainable construction.

Keywords: Olivine, Carbonation, CO_2 sequestration, Systematic literature review, Sustainable construction

INTRODUCTION

Global warming, driven primarily by the emission of greenhouse gases (GHGs), continues to exacerbate environmental challenges. Carbon dioxide (CO_2) is the dominant contributor to these shifts, responsible for approximately 76% of global GHG emissions and playing a central role in the global climate crisis [1]. The Paris Climate Agreement, ratified by numerous countries, sets a target to limit global temperature rise to below 2°, with a concerted effort to reduce CO_2 emissions through sustainable practices [2]. The construction industry, a significant emitter of CO_2, accounts for 33% of global emissions, with cement production alone contributing around 8% of the total carbon footprint [3]. Given the increasing demand for concrete due to population growth and infrastructure development, alternative approaches to mitigate CO_2 emissions in construction are urgently needed. As such, the search for effective methods to capture and store atmospheric CO_2 has intensified, with a growing interest in olivine, a naturally occurring mineral with potential for carbon sequestration.

Olivine is an abundant silicate mineral found in mafic and ultramafic rocks, making up a significant portion of the Earth's mantle [4]. Olivine's unique ability to absorb CO_2 through mineral carbonation reactions, which convert CO_2 into stable magnesium or iron carbonates, has positioned it as a promising candidate for both environmental and construction applications [5]. Studies indicate that olivine can effectively capture CO_2 on a large scale, with the potential to neutralise emissions generated by industries like cement production [6]. Additionally, olivine's high magnesium content makes it suitable for producing alkali-activated materials (AAMs), replacing traditional binders in soil stabilisation and construction materials [7]. While the potential for CO_2 sequestration is well-documented, the practical application of olivine in sustainable construction remains underexplored. The literature surrounding olivine's role in both carbon sequestration and construction materials is expanding, but gaps remain regarding its long-term durability, environmental impact, and economic feasibility [8, 9]. As depicted in Figure 1 (Geographic Distribution of Studies), the analysis reveals that among the 102 papers reviewed, 88 provided specific regional information. It shows relevant research to be most concentrated in Europe (19.3%), followed by the United States (15.9%) and Malaysia (10.2%). The "Others" category, representing countries with less than 2% of total

publications each, constitutes a significant portion (25.0%) of region-specific research. This geographic imbalance underscores the need for more diverse regional investigations to adapt olivine applications to local conditions, resources, and environmental challenges.

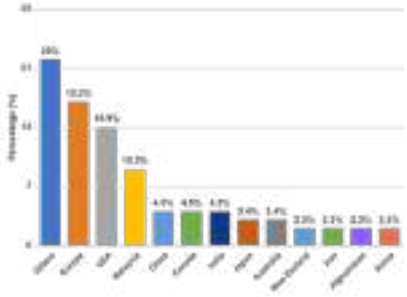

Fig. 1 Geographic Distribution of Olivine Research

Fig. 2 (Research Trends) illustrates the evolving focus in olivine research from 2000 to 2024, revealing a significant acceleration in research activity. Analysis of publication trends shows that 52.0% of all studies were published between 2021 and 2024, compared to 37.2% during 2011-2020 and only 10.8% from 2000-2010. This dramatic increase reflects growing recognition of olivine's potential for carbon sequestration and sustainable construction applications.

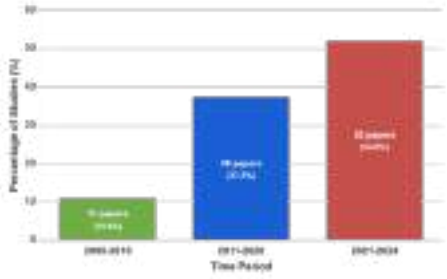

Fig. 2 Olivine Research Publication Trends (2000-2024)

This paper aims to provide a critical analysis of olivine's performance, examining its CO_2 sequestration efficiency and exploring its potential for use in sustainable construction applications.

RESEARCH SIGNIFICANCE

The significance of this study lies in the growing need to mitigate global CO_2 emissions, particularly in the construction industry, which is a major contributor to greenhouse gas emissions. By exploring olivine's role in carbon capture and its integration into construction materials, this research offers valuable insights into environmental technologies and sustainable building practices, contributing to climate change mitigation and enhancing the sustainability of construction processes globally.

METHODOLOGY

A systematic literature review (SLR) was conducted to achieve the goal of this study. The review followed the Preferred Reporting Items for Systematic Reviews and Meta-Analyses (PRISMA) guidelines to ensure a transparent and replicable process. The initial search was conducted across reputable academic databases, including Google Scholar and Scopus, targeting global sources published from 2000 to 2024. A total of 102 scholarly articles were identified, with selection based on strict inclusion and exclusion criteria. The inclusion criteria were: (1) articles published from 2000 onward, (2) written in English, and (3) open access or fully retrievable. Exclusion criteria involved non-English articles, conference papers, newsletters, and review articles. The PRISMA-based identification, screening, and selection process is visually summarised in Fig. 3. Characteristics of Olivine

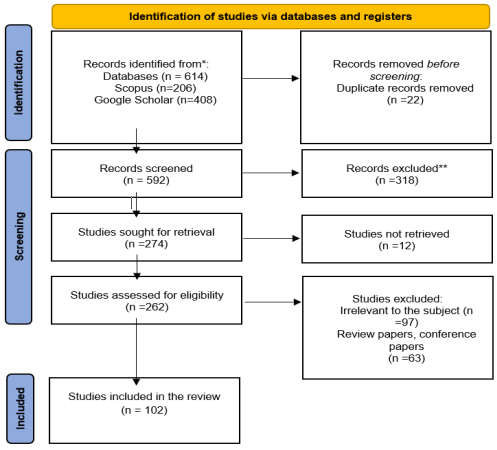

Fig. 3 Systematic literature review process (based on PRISMA guidelines)

Mineralogy and Carbonation Stability

Olivine ($(Mg,Fe)_2SiO_4$) exhibits significant variability in its mineralogical characteristics, with forsterite (Mg_2SiO_4) and fayalite (Fe_2SiO_4) representing the end members of this solid solution series. Analysis of 102 studies providing compositional data reveals that high-purity forsterite (>80% Mg_2SiO_4) demonstrates superior carbonation potential and stability compared to iron-rich varieties, enhancing carbonation efficiency and stability over extended periods [10]. Table 1 summarises the typical mineralogical composition ranges of olivine observed across the reviewed studies.

Table 1 Typical mineralogical composition ranges of olivine and optimal values for CO_2 sequestration

Component	Typical Range (%)	Optimal Range for CO_2 Sequestration (%)
Forsterite (Mg_2SiO_4)	70-92	>80
Fayalite (Fe_2SiO_4)	5-30	<15
Accessory minerals (pyroxenes, amphiboles)	0-10	<5
Serpentine content	0-15	<5

The carbonation stability of olivine primarily depends on its mineral composition and the environmental conditions of application. Magnesium-rich olivine exhibits higher carbonation reactivity, with studies reporting sustained CO_2 sequestration capacity over extended periods. The dominant carbonation reaction involves the conversion of magnesium silicates to magnesium carbonates, as shown in Equation (1) [11].

$$Mg_2SiO_4 + 2CO_2 + 2H_2O \rightarrow 2MgCO_3 + H_4SiO_4 \quad (1)$$

This reaction forms stable magnesium carbonate (magnesite) and orthosilicic acid (H_4SiO_4), effectively locking carbon dioxide in solid form. These carbonation products are highly stable, with estimated retention times extending to geological timescales (>1000 years), making olivine a promising material for long-term carbon sequestration.

An alternative pathway involves bicarbonate-mediated carbonation [12]. In this system, the solution is buffered to a moderately alkaline pH (~7.9), allowing simultaneous silicate dissolution and carbonate precipitation. This modification significantly reduces reaction time and likely involves the direct reaction of forsterite with bicarbonate ions (Equation 2) and continuous regeneration of bicarbonate through the reaction of CO_2 with hydroxide ions (Equation 3).

$$Mg_2SiO_4 + 2HCO_3^- \rightarrow 2MgCO_3 + SiO_2 + 2OH^- \quad (2)$$
$$OH^- + CO_2 \rightarrow HCO_3^- \quad (3)$$

Grain Size and Specific Surface Area

Grain size is a critical factor affecting olivine's carbonation efficiency and practical applications. Analysis of the database (Fig. 4) reveals that 85 out of 102 studies report on grain size information, with the majority (64.7%) investigating multiple grain size ranges rather than a single size fraction. Among the studies focusing on a single grain size category, fine-grained olivine (<100 μm) was the most frequently studied, followed by coarse-grained (>500 μm), and medium-grained (100-500 μm) olivine.

The most frequently studied specific particle sizes were 75 μm (14 mentions), 100 μm (11 mentions), and 5-10 μm (10 mentions each). The focus on using smaller particle sizes aligns with the proven impact of fine-grained olivine particles to achieve significantly higher carbonation rates compared to coarser fractions [13].

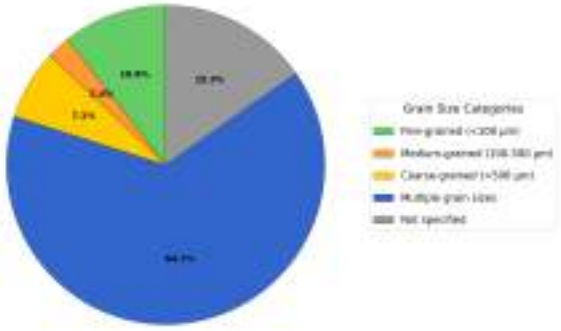

Fig. 4 Distribution of Olivine Grain Sizes in Research Studies

The Specific Surface Area (SSA) of olivine particles directly correlates with carbonation kinetics and efficiency **[10]**. 34 out of 102 studies report SSA values, with measurements ranging widely from 0.36 to 670.8 m^2/g, depending on particle size, processing methods, and measurement techniques. Mechanical activation through processes like high-energy milling can significantly increase SSA, hence improving olivine's reactivity [14]. However, the energy requirements for such processing must be balanced against the carbon sequestration benefits in practical applications.

For sustainable construction applications, multiple grain size distributions are typically employed to balance carbonation potential with functional properties such as workability and strength development. This approach provides a practical compromise between competing requirements for optimal performance [10].

ENVIRONMENTAL IMPACTS AND CHEMICAL TREATMENTS

Durability and Porosity Considerations

The durability of olivine-containing materials emerges as a critical consideration for sustainable construction applications. Analysis of the database indicates the importance of porosity characteristics as one of the key studied parameters in 100 out of 102

studies. Porosity measurements across these studies indicate a significantly wide range of values from 1% to 98%, depending on olivine content, grain size, and processing methods. The most frequently reported porosity ranges are 10-15%, 5-20%, and 10-40%, with varied distributions across different material compositions. Higher values of porosity (>30%) significantly influence carbonation behaviour by facilitating CO_2 diffusion while affecting structural integrity [10].

Durability aspects of olivine have also been considered in the majority of studies, 92 out of 102. Durability aspects include permeability (16 papers), mechanical strength (4 studies), freeze-thaw performance (3 papers), and enhanced acid attack resistance compared to Portland cement [15], and potential self-healing properties through ongoing carbonation [16].

Carbon Sequestration Mechanisms

The carbon sequestration potential of olivine operates through several interconnected mechanisms, with its efficiency strongly influenced by grain size. Analysis of the database reveals that 100 out of 102 studies focused on CO_2 sequestration, with direct mineral carbonation being the most frequently discussed pathway (68 papers), followed by enhanced weathering (31 papers) and passive sequestration (1 paper). Aligned with previous discussions, fine-grained olivine (<180 μm) demonstrates significantly high CO_2 absorption rates, with sequestration capacities ranging from 0.25 to 0.8 tons of CO_2 per ton of olivine [10, 11]. Primary sequestration involves the following three mechanisms:

1. **Direct mineral carbonation**: The conversion of olivine to magnesium or iron carbonates through reaction with CO_2 in the presence of water (eq. 1) [11].
2. **Enhanced weathering**: Accelerated natural weathering processes that increase alkalinity in marine or soil environments, promoting CO_2 dissolution and subsequent carbonate formation. This mechanism is investigated by assessing the potential of soil carbonation and enhanced weathering through Life Cycle Assessment (LCA) [17].
3. **Passive sequestration**: Slow and ongoing carbonation of olivine in applications such as construction materials or landscaping aggregates [18].

Table 2 illustrates the relationship between grain size and carbon dioxide sequestration efficiency based on the analysed literature. While the data points are derived from a limited number of papers explicitly reporting quantitative sequestration rates (8 papers) and completion times (2 papers), they represent the best available estimates from the current literature.

Table 2 Relationship between olivine grain size and carbon dioxide sequestration efficiency

Grain Size (μm)	CO_2 Sequestration Rate (kg CO_2/ton olivine/year)	Time to 50% Completion (year)	Dominant Mechanisms
<63	200-800	1-3	Direct carbonation
63-125	100-350	3-7	Direct carbonation & Enhanced weathering
125-250	50-200	5-15	Enhanced weathering
250-500	25-100	10-25	Enhanced weathering & Passive sequestration
>500	10-50	>25	Passive sequestration

Treatment Approaches and Contamination

Various treatment methods have been identified for enhancing olivine's carbon sequestration potential. Among the 102 studies analysed, using multiple-treatment approach was reported in 30 studies, followed by thermal treatment in 24 studies, physical treatment in 22 studies, chemical treatment in 18 studies, 4 studies discussing other treatment approaches including biological catalysis, electrochemical enhancement, and ultrasonic treatments, and 4 other studies not specifying their applied treatment methods (Fig. 5). Most Common commonly used treatment approaches include: thermal treatment **[11]**, physical treatment **[10]**, chemical treatment and multiple treatment **[11]**.

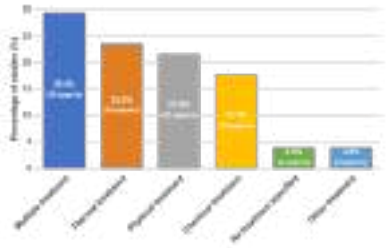

Fig. 5 Distribution of Treatment Methods for Enhancing Olivine Reactivity

30 papers in the database address contamination concerns and potential environmental impacts, with particular focus on heavy metal leaching. While element release remains within acceptable

environmental limits in most controlled construction applications [15], site-specific assessments are essential for large-scale implementations.

Life Cycle Assessment and Economic Feasibility

Despite olivine's promising carbon sequestration potential, comprehensive LCA and economic analyses remain limited in the literature. Only 28 out of 102 studies discuss LCA methodologies, with just 6 incorporating comprehensive assessments. Almost half of the studies (50 out of 102) meaningfully address economic and commercialisation aspects. It is critical to assess the environmental benefits of olivine against the emissions and energy consumption associated with its mining, processing, transportation, and implementation **[10]**. Table 3 presents a comparative assessment of different olivine applications based on life cycle and economic considerations.

Table 3 Life cycle assessment and economic feasibility of olivine applications

Application	Net CO_2 Sequestration Potential (tons CO_2/ton olivine)	Economic Feasibility	Key Challenges
Coastal Application	High (0.6-0.8 tons)	Medium-Low	Transport emissions, ecological impacts
Agricultural Soil Amendment	Medium (0.3-0.5)	Medium	Heavy metal accumulation, variable efficiency
Construction Materials	Low-Medium (0.2-0.4)	High	Slow carbonation rates, durability concerns
Industrial Direct Carbonation	Medium-High (0.5-0.7)	Low	High energy requirements, process complexity

Economic analyses, such as those conducted by Cheeseman et al. [10], indicate cost ranges of 20-120$ per ton of CO_2 sequestered, depending on application method and scale.

Olivine Applications in Sustainable Construction

The integration of olivine into sustainable construction practices represents a promising avenue for both carbon sequestration and enhanced material performance. Analysis of the database reveals multiple potential applications that capitalise on olivine's unique properties. In soil stabilisation applications, olivine-treated soils exhibit enhanced strength characteristics while simultaneously sequestering CO_2, with unconfined compressive strength improvements of 20-45% reported in several studies [7]. These properties make olivine particularly valuable for ground improvement in construction projects, providing dual benefits of enhanced soil bearing capacity and carbon reduction.

In concrete and cementitious applications, olivine demonstrates potential as a supplementary cementitious material (SCM) or aggregate replacement. Eleven studies, including research by Cheeseman, Shanks [10], investigated olivine's integration into concrete mixtures, reporting that partial replacement (5-15% by weight) of traditional Portland cement with olivine-derived materials can reduce the carbon footprint by 8-20% while maintaining comparable mechanical properties. For road construction applications, identified in 7 papers, olivine aggregates in asphalt mixtures demonstrated adequate mechanical performance coupled with ongoing passive carbonation potential. Landscape applications, such as olivine-enriched soils in urban green spaces and olivine sand for walkways, were addressed in 4 studies, showing potential for widespread deployment with minimal technical barriers.

CURRENT CHALLENGES AND FUTURE DIRECTIONS IN OLIVINE RESEARCH

The durability and long-term performance of olivine-based materials remain insufficiently investigated. This represents a significant knowledge gap in understanding how olivine-containing materials withstand environmental stressors over extended periods. Current literature predominantly focuses on short-term laboratory investigations (typically < 1 year), which fail to capture the complex degradation mechanisms that may emerge over decades of service life. This stark disparity represents a critical research gap, with fewer than 10% of studies incorporating field-scale testing (Fig. 6). This laboratory-to-field scaling challenge has severely limited the translation of promising research findings into practical applications.

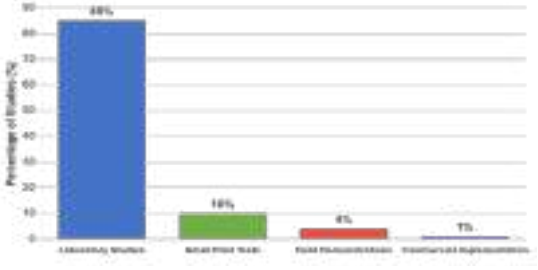

Fig. 6 Distribution of Olivine Research Across Implementation Stages

CONCLUSION

This systematic review of 102 scholarly sources demonstrates olivine's significant potential for carbon sequestration and sustainable construction

applications. The research landscape shows geographic disparities, with studies predominantly from Europe (19.3%), the USA (15.9%), and Malaysia (10.2%), collectively accounting for 45.4% of all studies with regional information. Recent years have seen accelerated research interest, with 53% of all studies published since 2021.

Three main carbonation mechanisms were identified in the literature. The effectiveness of these mechanisms was found to be strongly influenced by treatment methods and environmental conditions.

The analysis revealed that high-purity forsterite (>80% Mg_2SiO_4) with fine grain sizes (<180 μm) achieves optimal CO_2 sequestration rates (0.25-0.8 tons CO_2/ton olivine). Medium-grained olivine (100-250 μm) offers an optimal balance between carbonation potential and functional properties, with porosity ideally maintained between 15-25% to facilitate CO_2 diffusion while ensuring structural integrity.

Olivine demonstrates promise for sustainable construction applications, as a supplementary cementitious material with enhanced acid resistance and potential self-healing properties. However, significant knowledge gaps persist, with fewer than 30% of studies including comprehensive life cycle assessment (LCA) or economic feasibility evaluations, and only 18% reporting on critical durability data.

Future research must prioritise long-term field demonstrations, regional adaptation strategies, standardised assessment protocols, and integrated LCA.

REFERENCES

[1] Intergovernmental Panel on Climate Change, Climate Change 2014:
Mitigation of Climate Change: Working Group III Contribution to the IPCC Fifth
Assessment Report. 2015.
[2] United Nations, The Paris agreement - UN Framework Convention on
Climate Change [WWW Document]. 2017.
[3] R. M. Andrew, Global CO 2 emissions from cement production. Earth System Science Data, Vol. 10, 2018, pp.195-217.
[4] W. A. Deer, R. A. Howie and J. Zussman, An introduction to the rock-forming minerals. Mineralogical Society of Great Britain and Ireland, 2013.
[5] R. Schuiling, Olivine, the miracle mineral. Mineral. J, Vol. 23, 2001, pp.81-83.
[6] R. D. Schuiling and E. Praagman, Olivine hills: mineral water against climate change. Springer, 2010.
[7] M. H. Fasihnikoutalab, A. Asadi, B. K. Huat, R. J. Ball, S. Pourakbar and P. Singh, Utilisation of carbonating olivine for sustainable soil stabilization. Environmental Geotechnics, Vol. 4, 2017, pp.184-198.
[8] T. Haug, I. Munz and R. Kleiv, Importance of dissolution and precipitation kinetics for mineral carbonation. Energy Procedia, Vol. 4, 2011, pp.5029-5036.
[9] A. A. Olajire, A review of mineral carbonation technology in sequestration of CO2. Journal of Petroleum Science and Engineering, Vol. 109, 2013, pp.364-392.
[10] C. Cheeseman, B. Shanks, C. Howe, S. Draper and H. Wong, Low-Carbon Amorphous Silica Supplementary Cementitious Derived from Olivine. Available at SSRN 4630890, Vol., 2023.
[11] D. C. Dahlin, W. K. O'Connor, D. N. Nilsen, G. Rush, R. P. Walters and P. C. Turner, A method for permanent CO2 mineral carbonation. Albany Research Center (ARC), Albany, OR (United States), 2000.
[12] W. O'Connor, D. Dahlin, G. Rush, S. Gerdemann, L. Penner and D. Nilsen, Aqueous mineral carbonation. DOE, US, Vol., 2005.
[13] J. Olsson, N. Bovet, E. Makovicky, K. Bechgaard, Z. Balogh and S. L. S. Stipp, Olivine reactivity with CO2 and H2O on a microscale: Implications for carbon sequestration. Geochimica et Cosmochimica Acta, Vol. 77, 2012, pp.86-97.
[14] C. A. Summers, D. C. Dahlin, G. E. Rush, W. K. O'Connor and S. J. Gerdemann, Grinding methods to enhance the reactivity of olivine. Mining, Metallurgy & Exploration, Vol. 22, 2005, pp.140-144.
[15] T. A. Haug, R. A. Kleiv and I. A. Munz, Investigating dissolution of mechanically activated olivine for carbonation purposes. Applied Geochemistry, Vol. 25, 2010, pp.1547-1563.
[16] M. Achang and M. Radonjic, Adding olivine micro particles to Portland cement based wellbore cement slurry as a sacrificial material: A quest for the solution in mitigating corrosion of wellbore cement. Cement and Concrete Composites, Vol. 121, 2021, pp.104078.
[17] D. Lefebvre, P. Goglio, A. Williams, D. A. Manning, A. C. de Azevedo, M. Bergmann, J. Meersmans and P. Smith, Assessing the potential of soil carbonation and enhanced weathering through Life Cycle Assessment: A case study for Sao Paulo State, Brazil. Journal of Cleaner Production, Vol. 233, 2019, pp.468-481.
[18] T. Strunge, The costs of CO2 carbonation in the cement industry. SINTEF Academic Press, 2021.

Copyright © Int. J. of GEOMATE All rights reserved, including making copies, unless permission is obtained from the copyright proprietors.

15th Int. Conf. on Geotechnique, Construction Materials & Environment,
Kyoto, Japan, 11-13 November 2025, ISBN 978-4-909106124 C3051

A STUDY ON THE CORRELATION BETWEEN THE COEFFICIENT OF AIR PERMEABILITY AND AIR INFLOW AS AN INDEX OF PCM MATERIAL PERMEABILITY

Arisa Nakamura [1], Barchinoyhon Sayfullaeva [2], Yuki Sakoda [3] and Shushi Sato [4]

[1] The Graduate School Integrated Arts, Sciences, Agriculture and Marine Science, Kochi University, Japan;
[2] The Graduate School Integrated Arts, Sciences, Agriculture and Marine Science, Kochi University, Japan;
[3] The United Graduate School of Agricultural Sciences, Ehime University, Japan; [4] Kochi University, Japan

Abstract

In reinforced concrete structures, the penetration of degradation factors into the interior cause neutralization and salt attack. Therefore, the quality of concrete layer and PCM requires low material permeability. Two types of air permeability test methods, double chamber method and cylinder method, are applied to evaluate non-destructively. However, there are few examples of their application research results concern to PCM, and verification of the relationship between these two tests is insufficient. Based on the above background, the objective of this study was to clarify the relationship between the coefficient of air permeability and the air inflow. Surface air permeability tests using the cylinder and double chamber methods were conducted on the repaired surface of RC open canal with PCM. The result suggests that the test results of the double chamber method and the cylinder method do not correspond accurately. On the other hand, a positive correlation between the coefficient of air permeability and the air inflow was confirmed up to a certain period of time. Air permeability of the concrete and PCM was found that the criteria for quality evaluation based on the cylinder method did not correspond to the criteria for quality evaluation in the double chamber method. In the future, it is necessary to clarify the limits of applicability of the cylinder method, and to consider new evaluation criteria based on the air inflow.

Keywords: Material permeability, Double chamber method, Cylinder method, Inorganic Surface Coatings

INTRODUCTION

The durability of concrete structures cannot be adequately evaluated based on only strength. A comprehensive assessment of durability requires the prediction of deterioration processes over time.

In reinforced concrete (RC) structures, deterioration primarily results from the penetration of degradation factors into the interior. When neutralization and salt attack occur, it induces corrosion of internal reinforcing bars and cracking, ultimately leading to a decline in the durability of the reinforced concrete. To inhibit the penetration of degradation factors, the quality of concrete layer requires low material permeability. This requirement also applies to polymer cement mortar (PCM), which is commonly used for the repair and strengthening of concrete structures.

Two types of material permeability test methods, double chamber method and cylinder method, are applied to evaluate permeability non-destructively. Omoya et al. confirmed a strong correlation between air inflow and the coefficient of air permeability through tests conducted on five types of concrete and two types of mortar [1]. However, this evaluation combined concrete and mortar, and there are few studies that have focused exclusively on PCM. Consequently, the relationship between these two air permeability tests remains insufficiently verified for PCM.

Based on the above background, the objective of this study is to clarify the relationship between the coefficient of air permeability and air inflow as material permeability indicators, focusing specifically on PCM. Surface air permeability tests using the double chamber and cylinder methods were conducted on PCM-repaired surfaces of RC open canal. This research offers a new perspective for understanding the permeability behavior of mortar in the field of repair engineering.

RESEARCH SIGNIFICANCE

In Japan, the maintenance and management of existing infrastructure are essential, even in the face of a growing shortage of skilled labor. As labor-saving strategies in infrastructure maintenance become increasingly important, the cylinder method offers a more straightforward approach to evaluating material permeability. Clarifying the relationship between the cylinder method and the double chamber method will facilitate the broader application of the cylinder method and the development of a standardized evaluation procedure.

OVERVIEW OF THE SURFACE AIR PERMEABILITY TEST

Double Chamber Method

A schematic diagram of the double chamber method is presented in Fig.1. In this method, the coefficient of air permeability (kT) is calculated based on the time-dependent recovery of pressure within the vacuumed inner cell. The double-chamber apparatus consists of an inner chamber and an outer chamber, with both chambers being pressure-controlled to maintain equal pressure and to physically prevent the inflow of external air [2]. However, for in situ measurements, external equipment such as a power generator and vacuum pump is required in addition to the surface air permeability tester, resulting in increased operational costs.

Cylinder Method

A schematic diagram of the cylinder method is presented in Fig.2. In this method, the volume of air inflow into the cylinder is measured following the release of negative pressure. Unlike the double chamber method, the testing apparatus consists of a single chamber. Consequently, it is significantly influenced by the surface fragile layer, which can lead to an overestimation of the actual permeability [3].

OVERVIEW OF THE EXPERIMENT

Repair Method Applied in the Experiment

This study was conducted on concrete surfaces repaired using a combined method of inorganic coating and a silicate-based surface impregnation material. Inorganic coating methods refer to techniques applied to the surfaces of open canals with the objective of mitigating the ingress of deterioration agents such as carbon dioxide and chloride ions, preventing water leakage, and improving water tightness [4]. The silicate-based surface impregnation method involves the penetration of silicate materials into the concrete surface layer to modify and densify its microstructure, thereby aiming to restore or enhance durability by reducing the permeability to harmful agents [5]. If the impregnated material remains in the form of dry solid residues, it can re-dissolve upon exposure to moisture and continue to exhibit its pore-filling effect [6]. By combining these methods, it is possible to suppress crack width propagation and facilitate the filling of cracks.

The experiment was conducted on a RC open canal located within the field of the Monobe Campus, Kochi University. The west wall of the canal, where the surface coating was applied in 2016, and the east wall, treated in 2023, were selected as test areas. A summary of the test sections is provided in Table 1. Both sides of the RC channel were repaired using either standard PCM or Fast-Hardening PCM, with

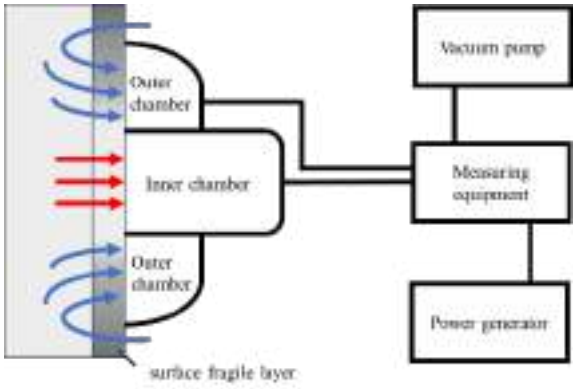

Fig.1 Schematic diagram of the double chamber method

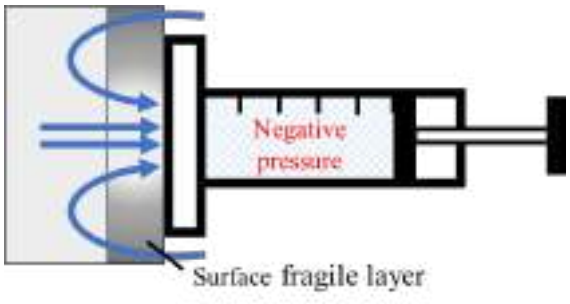

Fig.2 Schematic diagram of the cylinder method

Table 1 A summary of the test sections

Year of Repair	Type of PCM	Impregnation Coating Condition	Number of Test Sections
2016	Standard／Fast-Hardening	8 coated ／ 6 uncoated	14
2023	Standard／Fast-Hardening	2 coated ／ 2 uncoated	4

and without application of the impregnation material, for follow-up investigation.

Overview of the Test Method

In this study, the relationship between the coefficient of air permeability and the air inflow volume as performance indicators was examined by comparing two types of material permeability data obtained from actual measurements.

To obtain the material permeability data, surface air permeability tests were conducted using both the double chamber method and the cylinder method. The double chamber method was performed using the “Permea-TORR” air permeability tester (manufactured by FTS Co., Ltd.), with reference to JSCE-K572: *Guidelines for the Design and Construction of Silicate-Based Surface Impregnation Materials (Draft)* (in Japanese) [7]. The cylinder method was performed using the “ACROS” air

permeability cylinder (manufactured by MARUI Co., Ltd.).

For the west wall of the open canal, which was repaired in 2016, five measurement points were established in each section, while for the east wall, repaired in 2023, three measurement points were established in each section.

RESULTS AND DISCUSSION

Comparison of Permeability Indicators in a Composite Method Combining Inorganic Coating and Silicate-Based Surface Impregnation

First, we compared two permeability indicators: the coefficient of air permeability measured by the double chamber method and air inflow measured by the cylinder method. Fig.3 shows the time-dependent changes in the coefficient of air permeability, and Fig.4 presents those in the air inflow for mortar specimens with a service life of less than one year.

Both the air permeability coefficient and the air inflow rate were found to decrease over time. This trend is considered to result from the use of a composite method combining an inorganic surface coating and a silicate-based surface impregnation, which likely contributed to the filling of surface cracks.

However, while both the air permeability coefficient and air inflow rate decreased over time, the rate of reduction differed between the two indicators. A comparison of test results across different sections revealed that the numerical trends of the air permeability coefficient and air inflow rate did not consistently align. In other words, the outcomes of the cylinder method and the double-chamber method do not necessarily correspond.

Analysis of the Relationship between the coefficient of air permeability and Air Inflow

Next, the relationship between the coefficient of air permeability (kT), as calculated by the double chamber method, and air inflow, as measured by the cylinder method, was examined. Scatter plots of the test results obtained using both methods are shown in Fig.5 for the 2023 repair site and in Fig.6 for the 2016 repair site. Table 2 summarizes the regression equations, slope, intercept, and coefficient of determination (R^2) corresponding to Fig.5 and 6.

In Fig.5, a positive correlation was observed between the permeability and air inflow, with a correlation coefficient of 0.53. On the other hand, the correlation coefficient of the results shown in Fig.6 was 0.14, showing no such correlation. These results suggest that although permeability and air inflow are used as indicators of material permeability of concrete and mortar, they do not necessarily coincide. In addition, the test results shown in Fig.5 are less

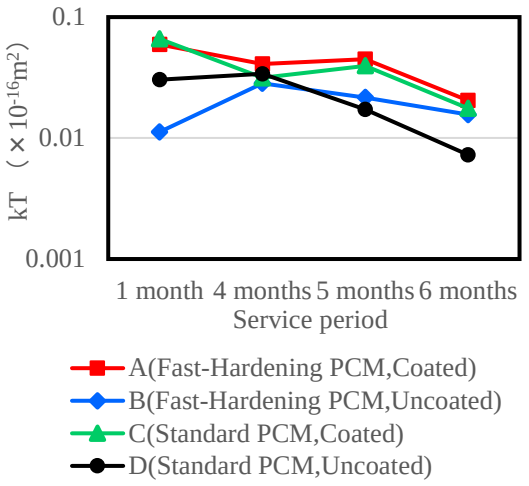

Fig.3 Time-dependent changes in the coefficient of air permeability

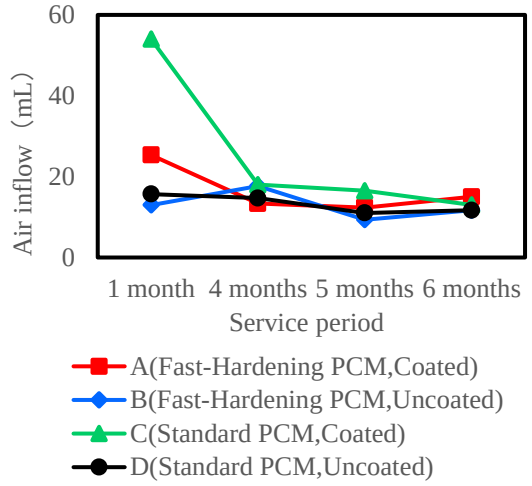

Fig.4 Time-dependent changes in the air inflow

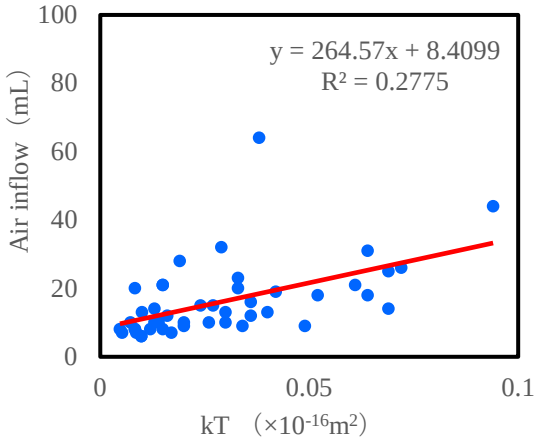

Fig. 5 Relationship between the coefficient of air permeability and air inflow for mortar with less than one year of service

than one year after service, while Fig.6 is seven years after service. Thus, the correlation between the two appears to decrease after a certain period of service.

This discrepancy is believed to stem from differences in the testing principles of the double chamber and cylinder methods. In the double chamber method, a vacuum pump is used to create negative pressure within a sealed chamber, and the coefficient of air permeability is calculated based on the time required for the internal pressure to return to equilibrium. In contrast, the cylinder method generates negative pressure by pulling a piston, and the amount of air that flows into the cylinder is measured directly. These differences in how negative pressure is applied—as well as the potential influence of the surface fragile layer—may contribute to the inconsistency observed between the results of the two methods.

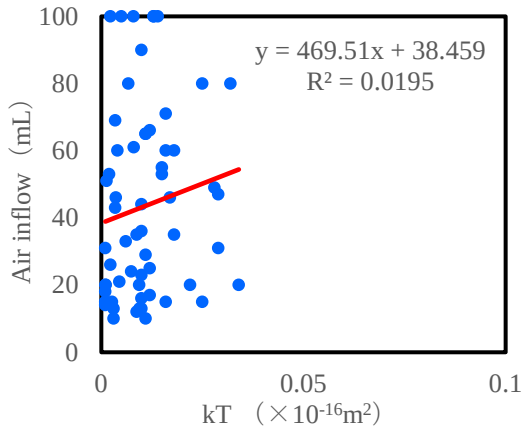

Fig. 6 Relationship between the coefficient of air permeability and air inflow rate for mortar with seven years of service

Table 2 Regression results for Fig.5 and 6

Figure Number	Regression Equation	Slope (a)	Intercept (b)	R^2
Fig.5	y = 264.57x + 8.4099	264.57	8.4099	0.2775
Fig.6	y = 469.51x + 38.459	469.51	38.459	0.0195

Analysis of Grading Based on Mortar Material Permeability

Finally, the grading of material permeability was examined using test results obtained from the double-chamber and cylinder methods applied to PCM-Repaired surfaces.

For the evaluation based on the coefficient of air permeability, the classification criteria established by R.J. Torrent et al., who developed the double chamber method, were employed [8]. In addition, for performance evaluation based on air inflow, Watanabe et al., who proposed the cylinder method, developed a conceptual grading chart for material permeability. This chart categorizes air inflow into four levels based on actual measurements, using the coefficient of air permeability as a reference [9].

Using these two sets of criteria — one based on the coefficient of air permeability and the other on air inflow — the test results from the 2023 construction site, where a positive correlation between the two indicators was confirmed, were classified. The criteria applied in this study and the corresponding grading results are presented in Table 3.

The results of surface air permeability tests conducted using the double-chamber method at the 2023 construction site were evaluated and classified between “very good” to “normal.” In contrast, the results from the cylinder method were classified between “normal” and “very bad.” These differences indicate a discrepancy in surface quality evaluations depending on the testing method used. In other words, for mortar, the performance evaluation criteria based on the coefficient of air permeability proposed by R.J. Torrent et al. and those based on the air inflow suggested by Watanabe et al. are not consistent. Therefore, it is necessary to consider developing unified performance evaluation criteria for mortar that incorporate both the coefficient of air permeability and the air inflow.

CONCLUSION

In this study, surface air permeability tests using the double chamber and cylinder methods were conducted on the repaired surface of RC open canal with PCM to clarify the relationship between the coefficient of air permeability and air inflow.

Table 3 Performance evaluation criteria based on material permeability and the corresponding test results

		Very good	Good	Normal	Bad	Very bad
The coefficient of air permeability	Criteria	0.001~0.01	0.01~0.1	0.1~1	1~10	10~
	Number of data	9	37	2	0	0
Air inflow	criteria	0～5		5～15	15～35	35～
	Number of data	0		26	19	3

Since the decreasing trends of the coefficient of air permeability and the air inflow differ, it is suggested that the test results obtained from the double chamber method and the cylinder method are not necessarily consistent. In addition, for concrete and PCM, a positive correlation of r = 0.53 was confirmed within the first year of service. However, after seven years of service, the correlation decreased to r = 0.14, indicating that no significant correlation remained. These results suggest that the correlation between the two indicators diminishes after a certain period of use.

Furthermore, when applying the evaluation method based on the coefficient of air permeability obtained using the double chamber method and that based on the air inflow measured using the cylinder method, the results showed that the coefficient of air permeability was classified between “very good” to “normal,” while the air inflow was classified between “normal” and “very bad.” These differences revealed a clear discrepancy in performance evaluation. Therefore, it is suggested that new evaluation criteria should be established for assessing the performance of mortar using material permeability indicators.

FUTURE WORK

This study revealed that there is a positive correlation between the coefficient of air permeability and the air inflow within a certain period of service. To clarify the applicability limits of the cylinder method, it is considered necessary to conduct follow-up investigations and correlation analyses at the same site and at other sites constructed under similar conditions.

In addition, it was found that the performance evaluation of mortar based on the coefficient of air permeability and air inflow lacks consistency, indicating the need for re-evaluation. Moving forward, tests such as accelerated carbonation and freeze-thaw cycles, which are closely related to material permeability, will be conducted to better understand the long-term deterioration behavior of mortar. Moreover, tests will be carried out at multiple locations with varying PCM application methods and environmental conditions to validate the generalizability of the observed correlation. Through these efforts, we aim to establish practical in-situ evaluation criteria based on both the coefficient of air permeability and air inflow.

REFERENCES

[1] Omoya, K., Watanabe, T., Sekikawa, M., and Hashimoto, C., Kakushu shirindā wo mochiita kan'i tōki shiken ni yoru hyōsō tōkisei no hyōka shuhō no kentō. Konkurīto kougaku nenji ronbunshū [Proceedings of the Japan Concrete Institute], Vol.39, No.1, 2017, pp. 1975–1980. (in Japanese)

[2] Imamoto, K., Konkurīto no hyōsō tōki shiken hōhō no genjō to kadai [Present State of and Perspectives on Testing Methods for Air Permeability of Concrete Surface Layer , Konkurīto kougaku [Concrete journal], Vol.53, No.7, 2015, pp.606–613. (in Japanese)

[3] Omoya, K., Watanabe, T., Sekikawa, M., and Hashimoto, C., Kakushu shirindā wo mochiita kan'i tōki shiken ni yoru hyōsō tōkisei no hyōka shuhō no kentō. Konkurīto kougaku nenji ronbunshū [Proceedings of the Japan Concrete Institute], Vol.39, No.1, 2017, pp. 1975–1980. (in Japanese)

[4] Ministry of Agriculture, Forestry and Fisheries Rural Development Bureau Rural Infrastructure Department Design Division Project Planning and Coordination Office, Nōgyō suiri shisetsu no hoshu・hokyō kōji ni kansuru manyuaru [Kaisuiro hen], 2023, p.98. (in Japanese)

[5] Ministry of Agriculture, Forestry and Fisheries Rural Development Bureau Rural Infrastructure Department Design Division Project Planning and Coordination Office, Nōgyō suiri shisetsu no hoshu・hokyō kōji ni kansuru manyuaru [Kaisuiro hen], 2023, p.235. (in Japanese)

[6] Muroya, T., Koide, Y., Igarashi, S., Kotonaru keisanshio-kei hyōmen shinsinzai no bisai hibiwari ni taisuru hoshu kōka no hikak , Konkurīto kōgaku nenji ronbunshū [Proceedings of the Japan Concrete Institute], Vol.36, No.1, 2014, pp.814–819. (in Japanese)

[7] Japan Society of Civil Engineers , Concrete Library 137: Keisan'enkei hyōmen ganshinkōhō no sekkei sekō shishin (an), Japan Society of Civil Engineers, 2012, pp.1-200(in Japanese)

[8] Torrent, R. J., and Frenzer, G. , A method for the rapid determination of the coefficient of permeability of the “covercrete” , International Symposium Non-Destructive Testing in Civil Engineering, 1995, pp.985-992.

[9] Watanabe, T., Yasui, N., and Hashimoto, C., Shirindā-hō ni yoru konkurīto hyōsō tōkisei no sokutei oyobi hyōka ni muketa torikumi [Measurement and Evaluation of the Air Permeability of the Concrete Cover by the Cylinder Method] , Konkurīto kougaku [Concrete Journal], Vol. 61, No. 2, 2023, pp. 145–151. (in Japanese).

Copyright © Int. J. of GEOMATE All rights reserved, including making copies, unless permission is obtained from the copyright proprietors.

15th Int. Conf. on Geotechnique, Construction Materials & Environment,
Kyoto, Japan, 11-13 November 2025, ISBN 978-4-909106124 C3051

EFFECT OF FLY ASH AND SILICA FUME AS PARTIAL REPLACEMENTS OF CEMENT ON THE MECHANICAL PROPERTIES OF SELF-COMPACTING CONCRETE

Fauzan[1], Suci Andini[2], Suci Meilita[3], and Muhammad Johafis[4]

[1 ,2,3,4]Department of Civil Engineering, Faculty of Civil Engineering, University Andalas, Indonesia;

ABSTRACT

Self-compacting concrete (SCC) is a type of concrete that can flow and fill molds without mechanical compaction, improving construction efficiency. The use of fly ash and silica fume in SCC can enhance its mechanical properties. Therefore, this study investigates the effects of partially substituting cement with fly ash and silica fume in SCC and their contribution to advanced construction materials. The objective was to determine the effect of adding 15% fly ash and 10% silica fume (by weight of cement) on the mechanical strength of SCC. The research was conducted experimentally in the laboratory. Specimens were cylinders 150 mm in diameter and 300 mm high; a total of 24 specimens were prepared for compressive tests and 24 for tensile tests. Fresh concrete was evaluated according to ACI 237R-07 using the slump-flow test and segregation resistance using the V-funnel test. Hardened concrete was tested for compressive and tensile strength at 7 and 28 days. The results showed that adding 15% fly ash increased slump flow, whereas 10% silica fume reduced slump flow due to higher water demand. At 28 days, compressive strength increased by up to 20.11% compared with the control SCC, while tensile strength increased by 34.88%.

Keywords: SCC, Fly Ash, Silica fume, Slump Flow, Mechanical Properties

INTRODUCTION

Self compacting concrete (SCC), which was first introduced in Japan, is a very special type of concrete that can flow and fill every corner of the formwork, even when there is solid reinforcement, purely because of its weight and without the need for vibration or compaction equipment [1-3]. SCC concrete is particularly suitable for structures that are very difficult to perform manual compaction, for example, due to very tight reinforcement or due to formwork shapes that do not allow concrete to withstand the segregation usually found in building construction with conventional concrete [4-5]. Segregation in concrete building structures can pose high risks, such as building collapse at the time of an earthquake, as the quality of concrete has declined from planned [6-9]. The application of SCC concrete in construction is generally used in tunnels, bridge pillars, high-rise buildings, and precast concrete. SCC concrete can be classified as an advanced construction material [10-12].

Currently, a lot of research has been done on SCC concrete. The use of Flyash and Silica fume in SCC can improve the mechanical properties of concrete. Thus the addition of flyash and silica fume as substitutes for Partial cement in SCC to contribute to the development and application of advanced construction materials has been investigated. This study focuses on investigating the influence of flyash and silica fume as a substitute for some cement in the SCC concrete mixture, which can later minimize the use of cement and also increase the mechanical strength of concrete.

RESEARCH SIGNIFICANCE

This study aims to determine the effect of the addition of fly ash and silica fume as a substitute for part of the total weight of cement on the strength of SCC concrete in increasing its mechanical strength, especially its compressive and tensile strength. This study examines the fresh and hardened properties of Self-compacting concrete with fly ash and silica fume by considering the impact of waste by reducing waste flying ash. The results of this research can be used as a new invention in the world of concrete technology that has high workability, durability and strength advantages, so that it can be applied well in high-rise buildings and precast concrete structures around the world.

MATERIAL AND MIX DESIGN

Material

Cement

Ordinary Portland Cement (OPC), which is produced by the cement factory in Padang (PT. Semen Padang), Indonesia, used in this study.

Coarse aggregate

Coarse aggregates are obtained from locally available aggregates with a maximum size of 19 mm

in accordance with ASTM C33/C33M [13]. The properties of coarse aggregates are shown in Table 1.

Table 1. Properties of coarse aggregate

Property	Value
Specific Gravity	2.41
Absorption	5.93 %
Fine Modulus (FM)	3.4
Water Content	1.99 %

Fine aggregate

Locally available fine aggregates were used in this study, with a maximum size of 4.75 mm. Table 2 shows the properties of fine aggregates [14].

Table 2. Properties of fine aggregate

Property	Value
Specific Gravity	2.54
Absorption	3 %
Fine Modulus (FM)	2.85
Water Content	1.83 %

Water

Drinking water, which is free of acids or organic substances, was used for concrete mixing and treatment in this study.

Admixture

SCC concrete is a concrete that flows easily, so it requires a superplasticizer material such as a high-range water reducing admixture (HRWRA). In this study, ViscoCrete 3115, a third-generation superplasticizer for concrete and mortar manufactured by Sika, was used. It is specially developed to produce high-flow concrete with outstanding flow retention properties.

Fly ash

Fig.1 Fly Ash class C

Fly Ash is waste from burning coal in power plants, which is used as a substitute for some cement to improve the durability of concrete. In this study, FlyAsh class C was used (Fig. 1), which according to ACI this type contains pozzolan and hydrolysis properties, has a high CaO content that can harden itself when reacting with water such as cement, and has the benefit of increasing the compressive strength of concrete. Classification of Fly Ash in accordance with ASTM C 618–05 shown in Table 3 [15].

Table 3. Classification of Flying Ash

Flying Ash	Class
	C
SiO2 + A12O3 + Fe2O3,min,%	50.0
SO3,max, %	5.0
Moisture Content, max, %	3.0
Loss on ignition, max, %	6.0

Silica fume

Silica Fume is a microscopic material used to improve the strength and resistance of concrete to corrosion and chemical reactions. According to the American Concrete Institute (ACI), silica fume is a very fine concrete additive that has a particle size of about 1/100th the size of a cement particle as shown in Fig. 2. Fume silica is rich in high silicon dioxide (SiO2), more than 85%, and behaves as a reactive pozzolan material. Physical properties of Silica Fume can be seen in Table 4.

Fig.2 Silica Fume

Table 4. Physical Properties of Silica Fume

Sifat fisik	Value
Ukuran Pertikel	< 1µm
Warna	Dark gray
Bulk Density (kg/m^3)	200 - 300
Specific Gravity	2.2
Kehalusan (kg/m^2)	15.000 – 30.000

Mix Design Proportion

The design of an SCC concrete mixture with a target compressive strength of 79.73 MPa (11000 psi) was calculated based on ACI 211.4R-08 [16]. The water/cement ratio is maintained constant in all mixtures with a value of 0.27 Percentage of Fly ash 15% and silica fume 10% of the total weight of cement. The control mixture is set as 0% Flyash and silica fume. Details of the proportions of the concrete mixture are listed in Table 5.

Table 5. Mix proportions of SCC-Flyash-Silica Fume

Material	FA+SF 0%	FA 15%	SF 10%	FA+SF 15+10%
Cement (kg/m^3)	512.5	512.5	512.5	512.5
Fine Aggregate (kg/m^3)	877.5	864.8	852.3	839.6
Coarse Agg (kg/m^3)	668.9	668.79	668.79	668.79
Water (kg/m^3)	205	205	205	205
FA+SF (kg/m^3)	0.0	15	10	15+10
Viscocrete-3115 (L/m^3)	2.44	2.44	2.44	2.44

Test Specimen

A total of 48 cylindrical test pieces were prepared, consisting of 24 cylinders for compressive strength testing, and 24 cylinders for tensile strength testing.

Testing is divided into fresh concrete testing and hard concrete testing. The properties of concrete are measured based on the diameter of the slump flow using a slump tool (Fig.3) and the resistance of segregation using a v-funnel (Fig.4) according to ACI237R-07 [17]. The targeted slump diameter is 550-650 mm, which allows the concrete to flow through the solid reinforcement. The hardened properties of the SCC were tested on the cylindrical test pieces on the 7th and 28th days (Fig. 5-6), in compressive strength [18], and tensile strength [19].

Fig. 3 Slump test

Fig. 4 V funnel test

Fig.5 Compression Test on cylindrical specimens

Fig.6 Tensile Test on Cylindrical Specimen

RESULT AND DISCUSSION

Properties of Fresh Concrete

The results of the tests on fresh concrete conducted in the slump test and the v funnel flow test show that the effect of fly ash can increase the slump flow because the fine fly ash particles can fill the space between the cement particles and can flow more easily, after adding 15% the slump value increases or it can be said that the concrete is thinner as shown in Fig. 7. and the flow time is faster. The addition of 10% silica fume shows a decrease in the slump value because it absorbs more water, the mixture is thicker therefore the slump value decreases as shown in Fig. 8. and the flow time of concrete becomes slower compared to normal concrete.

The test results after normal concrete is added fly ash and silica fume give a complex effect, fly ash can increase slump while silica fume can decrease slump due to increased water requirements. This results in an equilibrium in the concrete mixture. The period it takes for concrete to expand to a diameter of 500 mm during the slump flow test reflects the viscosity and stability of the concrete. The T500 slump test along the distribution boundary took place in the range of 4.0-5.0 seconds and the slump flow rate width was 500-750 mm. As a result, all concrete mixtures were within the SCC limits as predicted. The v-funnel test results for all mixtures show that the SCC has met the required time, as shown in Fig. 9.

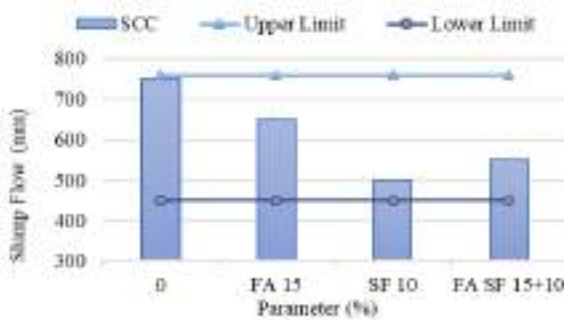

Fig.7 Slump flow result

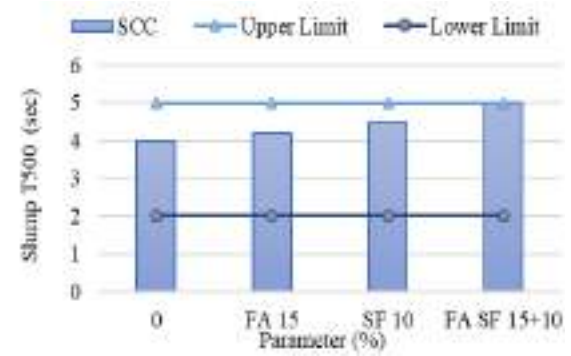

Fig.8 Result of Slump T500

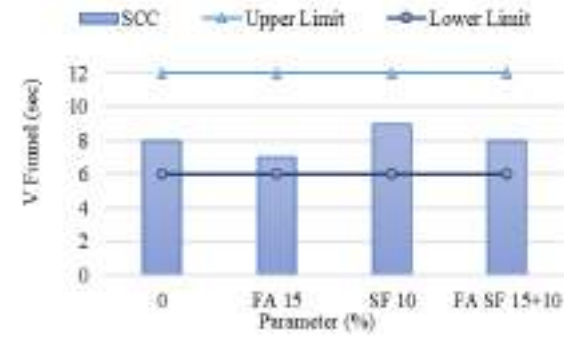

Fig.9 Result of V Funnel

Properties of Hard Concrete

Compressive strength test

The compressive strength of all mixtures is tested after 7 and 28 days of casting[9]. The results of the compressive test conducted on SCC concrete with a percentage of 15% fly ash and 10% silica fume are shown in Fig. 10 .As seen in Table 6, the compressive strength results of the SCC test specimen on day 7 (after the test) show that the compressive strength of SCC using fly ash and silica fume is stronger than that of SCC silica fume and SCC fly ash. Concrete at the age of 7 days, without the addition of fly ash and silica fume is 9.5 Mpa.

The compressive strength of SCC concrete with the addition of 15% fly ash, 10% silica fume, 15% fly ash and 10% silica fume is 8.9 Mpa, 8.7 Mpa, and 9.2 Mpa, respectively. When the compressive strength of all mixtures is tested after 28 times of casting, SCC concrete has a higher compressive strength, as shown in Table 6. and Fig. 10. The percentage increase in maximum compressive strength in SCC at 28 days of age was 20.11%.

Table 6. Percentage of Increase in Compressive strength

No	Parameter SCC (%)	Day-7 Percentage of Increase (%)	Day-28 Percentage of Increase (%)
1	0.0	-	-
2	FA 15	-6.32	2.55
3	SF 10	-8.42	10.15
4	FA SF 15+10	-3.16	20.11

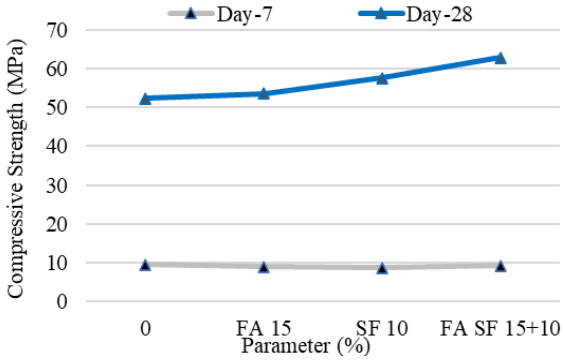

Fig.10 Compressive test results

Tensile strength test

Self-compaction concrete (SCC) testing with the addition of fly ash and silica fume at 28 days of age. Overall, the strength of the SCC tensile was significantly increased compared to at 7 days of age, as fly ash and silica fume slowed down the initial hydration and in the long term the hydration reaction was more perfect to strengthen the bonds and reduce pores in the SCC. Strong yield Pull at 28 days increased 1.5 times compared to 7 days age, as shown in Fig. 11.

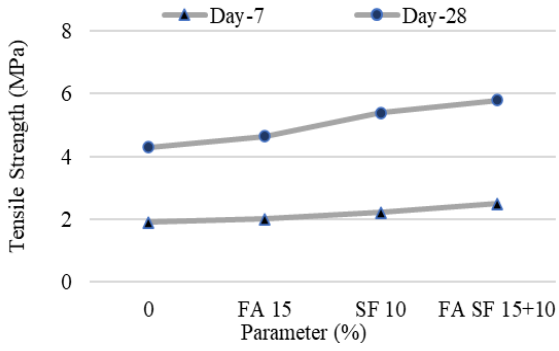

Fig.11 Tensile strength test results

The percentage increase in maximum strength at the day-age SCC was 34.88% and 31.58% respectively (Table 7). Compared to the control SCC at 28 days of age, the increase with the addition of 15% fly ash additives, 10% silica fume, 15% fly ash and 10% silica fume resulted in a strong increase in tensile strength of 7.48%, 25.59%, and 34.88% at 28 days of age, respectively.

Table 7. Percentage of increase in tensile strength

No	Parameter SCC (%)	Day-7	Day-28
		Percentage of Increase (%)	Percentage of Increase (%)
1	0.0	-	-
2	FA 15	5.26	7.48
3	SF 10	16.32	25.59
4	FA SF 15+10	31.58	34.88

CONCLUSIONS

Based on experimental findings examining the properties of SCC with added fly ash and silica fume, the following conclusions were drawn:

1. The addition of 15% fly ash increased slump flow because its fine particles fill the voids between cement grains, improving workability. In contrast, 10% silica fume reduced slump flow due to its higher water demand. Combining both produced a balanced mix that met SCC requirements.
2. Compressive strength tests showed up to a 20.11% improvement at 28 days compared with the control mixture. This significant gain is attributed to the continued pozzolanic activity and long-term densification of the matrix.
3. Splitting tensile strength increased by up to 34.88% at 28 days. Fly ash and silica fume delayed early hydration but promoted stronger bonding and reduced porosity over time.
4. Overall, partially replacing cement with fly ash and silica fume reduced cement consumption while enhancing the mechanical performance of SCC, making it a promising sustainable and durable construction material.

REFERENCES

[1] Cangussu N., Matos A. M., Milheiro-Oliveira P., and Maia L., Numerical Design and Optimisation of Self-Compacting High Early-Strength Cement-Based Mortars, Applied Sciences, Vol.13, Issue 7, 2023, No. 4142.

[2] Fauzan, Putri E. E., Albarqi K., Rani I. G., and Jauhari Z A., The Influence of Steel Fiber Waste Tyre on High Strength Concrete Containing Palm Oil Fuel Ash and Rice Husk Ash, International. Journal of GEOMATE, Vol. 20, Issue 77, 2022, pp.84-91.

[3] Fauzan, Yuliet, R., Habibillah, K., Agista, G. A., & Juliafad, E. (2023). The Effect of a Combination of Steel Fiber Waste Tyre and Crumb Rubber on the Mechanical Properties of High-Strength Concrete. GEOMATE Journal, 25(111), 238-245

[4] Daczko, J., Self-consolidating concrete: applying what we know. CRC press., 2012, pp. 1-288

[5] Fauzan, Putri, E. E., Albarqi, K., Rani, I. G., & Al Jauhari, Z. (2021). The influence of steel fiber waste tyre on high strength concrete containing palm oil fuel ash and Rice Husk Ash. GEOMATE Journal, 20(77), 84-91.

[6] Zende A. A., Momin A. I. A., Khadiranaikar R. B., Alsabhan A. H., Alam S., Khan M. A., and Qamar M. O., Mechanical properties of high-strength self-compacting concrete, ACS omega, Vol. 8, Issue 20, 2023, pp. 18000-18008.

[7] Sakthivel. P. B, Ravichandran. A., and Alaggumurthi. N., Experimental and Predictive Mechanical Strength of Fiber Reinforced Cementitious Matrix, International Journal of GEOMATE, Vol. 7, No 1, 2014, pp. 993-1002.

[8] El-Hassan H., Hussein A., Medljy J., and El-Maaddawy T., Performance of Steel Fiber-Reinforced Alkali-Activated Slag-Fly Ash Blended Concrete Incorporating Recycled Concrete Aggregates and Dune Sand, Buildings, Vol. 11, No. 327, 2021, pp. 1-31.

[9] Fauzan, Ismail, F. A., Sandi, R., Syah, N., & Melinda, A. P. (2018). The Effects of Steel Fibers Extracted from Waste Tyre on Concrete Containing Palm Oil Fuel Ash. GEOMATE Journal, 14(44), 142-148

[10] Ghosh D., Abd-Elssamd A., Ma Z. J., and Hun, D., Development of high-early-strength fiber-reinforced self-compacting concrete, Construction and Building Materials, Vol. 266, 2021, No.121051.

[11] Ahmad J., Zhou Z., and Deifalla, A. F, (2023). Steel fiber reinforced self-compacting concrete: A comprehensive review. International Journal of Concrete Structures and Materials, Vol. 17, Issue 1, 2023, No. 51.

[12] Widhiastuti, Y., & Mujib, A. (2021). Planning Study of SCC High Quality Concrete With Addition Of Carbide And *Silica fume* Waste. 6(2).

[13] ASTM International, Standard specification for coarse aggregate (ASTM C33/C33M–05), ASTM International, USA, 2003, pp.1-11.

[14] ASTM International, Standard Test Method for Density, Relative Density (Specific Gravity), and Absorption of Fine Aggregate, ASTM International, United States, 2007, pp.1-7.

[15] ASTM International, Standard Specification for coal fly ash and Raw or Calcined Natural Pozzolan for Use in Concrete (ASTM C618-05), ASTM International, United States, 2005, pp.1-11.

[16] ACI Committee 211,Guide for Selecting Proportions for High-Strength Concrete Using Portland Cement and Other Cementitious Materials (ACI 211.4R-08), American Concrete Institute, Farmington Hills, 2008, pp.1-34.

[17] ASTM International, Standard Test Method for Compressive Strength of Cylindrical Concrete Specimens (ASTM C 39/C 39M – 05), ASTM International, United States, 2005, pp.1-5.

[18] ASTM International, Standard Test Method for Splitting Tensile Strength of Cylindrical Concrete Specimens (ASTM C496-17), ASTM International, United States, 2017, pp.1-5.

[19] ACI Committee 237, Self-consolidating Concrete (ACI 237.R-07), American Concrete Institute, Farmington Hills, 2007, pp.1-34.

Copyright © Int. J. of GEOMATE All rights reserved, including making copies, unless permission is obtained from the copyright proprietors.

15th Int. Conf. on Geotechnique, Construction Materials & Environment,
Kyoto, Japan, 11-13 November 2025, ISBN 978-4-909106124 C3051

ANALYTICAL STUDY ON THE SEISMIC BEHAVIOR OF NON-STANDARD REINFORCED MASONRY HOUSES RETROFITTED WITH CROSSED FERROCEMENT LAYERS

*Fauzan[1], Abdul Hakam[2], Febrin Anas Ismail[3], Rio Yulanda[4], and Muhammad Zulfian Saputra[5]

[1,2,3,4] Department of Civil Engineering, Faculty of Engineering, Universitas Andalas, Indonesia
[5]Master Student in Disaster Management, Postgraduate School, Universitas Andalas, Indonesia

ABSTRACT

Indonesia is one of the most earthquake-prone countries in the world, where many reinforced masonry (RM) houses are built without complying with seismic-resistant building standards. These non-standard RM houses are highly vulnerable to severe damage or sudden collapse during strong earthquakes. This study presents a numerical analysis of a retrofitting method for non-standard RM houses using a ferrocement layer with a cross reinforcement system on the walls. The research involved modeling a 1:4 scaled specimen of an actual damaged RM house in West Pasaman, using ETABS V.22 software, and applying time-history earthquake loads at acceleration levels of 0.3 g, 0.6 g, 1.0 g, and 1.5 g. The results show that retrofitted RM houses experience smaller maximum tensile stresses compared to non-retrofitted ones under all earthquake acceleration levels. The reduction in tensile stress indicates that the crossed ferrocement layer effectively improves wall stability and prevents severe damage. This strengthening method can be implemented without demolishing existing structures, making it a cost-effective and practical solution for reducing seismic risks in vulnerable housing.

Keywords: Earthquake, Reinforced Masonry, Retrofitting, Ferrocement Layer, Tensile Stress

INTRODUCTION

Indonesia is a country prone to earthquakes due to several geographical and geological factors. Geologically, the structure of the earth's crust in Indonesia lies at the confluence of tectonic plates, which results in the Indonesian region having a high risk of earthquake disasters [1]. Several earthquake incidents occurred in Indonesia, causing many material losses and fatalities, including the West Sumatra earthquake (2009), the Lombok and Palu earthquakes (2018), the West Pasaman earthquake (2022) [2], and the East Java earthquake (2024). During the 25 February 2022 West Pasaman earthquake, at least 2,025 houses were reported damaged, including 1,111 units verified as heavily damaged after BNPB/BPBD verification in West Pasaman Regency. Similarly, the 22 March 2024 East Java (Bawean–Tuban) earthquake sequence caused 4,679 damaged houses across the province (774 heavy, 1,332 moderate, 2,573 light), indicating widespread vulnerability of non-standard RM housing to strong shaking [3]. These figures underscore the need for practical retrofitting strategies for Indonesia's RM dwellings to reduce seismic risk.

In general, RM houses are built using reinforcement on concrete column elements and beam, as shown in Fig. 1. The building of this house is usually strong against earthquake loads, but if the construction of the RM house has structural elements such as beams and columns that are not in accordance with building standards, then it does not have strength against earthquake loads [4-7]. When an earthquake occurs, this house can suffer minor to severe damage, and it can even collapse suddenly.

To avoid the sudden collapse of RM houses that do not meet standards when an earthquake occurs, research on the numerical analysis of RM house reinforcement that does not meet standards and is damaged after an earthquake needs to be carried out. One of the reinforcement methods developed is to use a ferrocement layer with a cross system on the building wall [8-11]. This method is effective, the cost is relatively cheap, the materials are easy to obtain, and the work can be done by the community or local craftsmen. This research aims to fill the gap by developing research on RM house reinforcement that is not in accordance with standards, which is strengthened using a cross-system ferrocement layer.

Fig.1 Reinforce masonry (RM) house

This study focuses on a numerical analysis study of the reinforcement of RM reinforcement houses that

are not in accordance with standards by making a test specimen based on the original house in West Pasaman that was damaged after the 2022 West Pasaman earthquake. By conducting this study, it is hoped that all RM houses that do not meet the standards can be strengthened with this method, so that they can reduce the risk of damage due to earthquakes in the future.

RESEARCH SIGNIFICANCE

In this analytical study, an element analysis was carried out to determine the seismic behavior of the original RM house compared to the RM house reinforced with a ferrocement layer. This research is very important because the results can be used as a reference for building earthquake-resistant houses in earthquake-prone areas, both in disaster mitigation efforts and in the post-earthquake reconstruction stage. In addition, the reinforcement method using a ferrocement layer is an effective method and is easy to apply by the community independently.

ANALYTICAL WORK

Specimen Design

The specimen used is a design of a house specimen image of the RM model horn, which is scaled 1:4 from its original size due to the limited area of the vibrating table test equipment. The specimens made amounted to 1 (one) piece, where the RM model house specimen was reinforced with a ferrocement layer with a cross system. The layout of the specimen design is in accordance with the shape of the existing houses in the community and the need for rehabilitation and reconstruction in earthquake areas in Indonesia. The research procedure at the design stage of the RM model house is as follows:

Specimen plan drawings

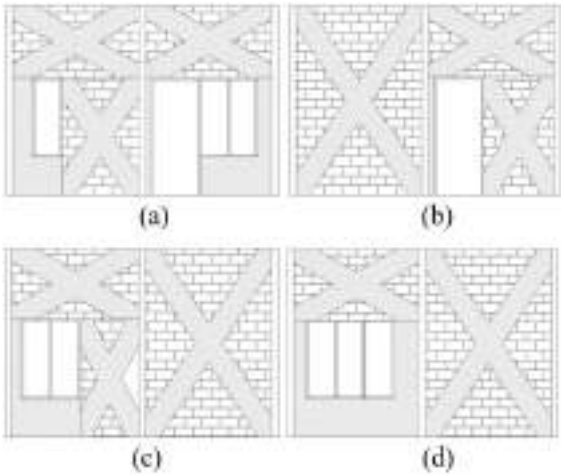

Fig.2 Model house with retrofitting; a) front view, b) back view, c) left side view, and d) right side.

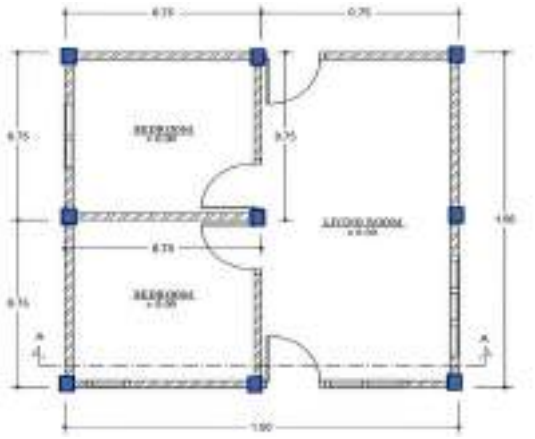

Fig.3 Specimen plan

The specimen plan image of the RM model house was taken to adjust the existing one with a type 36 house with a size of 6 m x 6 m x 4 m. After being scaled 1:4 from the original house size, the size for a simple model house becomes 150 cm x 150 cm x 100 cm. Specimens without reinforcement and specimens with ferrocement layer reinforcement of the cross system can be seen in Figs. 2-3.

Specimen detail drawings

Detailed drawing of the wall with a species thickness of ± 0.5 cm. Fig. 4 is a detailed drawing of the wall of a model house or specimen that is reinforced with woven wire with a cross system on the wall of the specimen, given plaster with a thickness of ± 0.5 cm. Plasters and specimen species are made with a mixture of cement and sand in a ratio of 1:4.

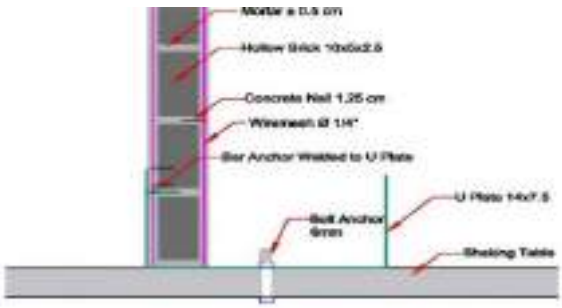

Fig.4 Details of wall of the house model, and Installation of the ferrocement layer with crossed system on the wall of the house

Material Properties

This numerical analysis study uses five main materials, namely bricks, plaster, concrete, reinforcement, and woven wire, which is defined as steel.

The hollow brick has a compressive strength (fc') of 3.3 MPa, a shear modulus of 3096 MPa, an elasticity modulus of 7431.35 MPa, and a specific

gravity of 1600 kg/m^3. Plastering with compressive strength (fc') of 9.9 MPa, shear modulus of 6161.75 MPa, elastic modulus 14788.2 MPa, and specific gravity of 1600 kg/m^3. The woven wire has a yield strength (fy) of 275 MPa, the highest tensile strength (fu) of 620 MPa, a shear modulus of 187500 MPa, and a specific gravity of 8.0 g/cm^3. The reinforced concrete has a comprehensive strength (fc') of 15 MPa, and the reinforcement has a yield strength of 280 MPa, and the highest tensile strength (fu) of 0,420 MPa [12].

Modeling

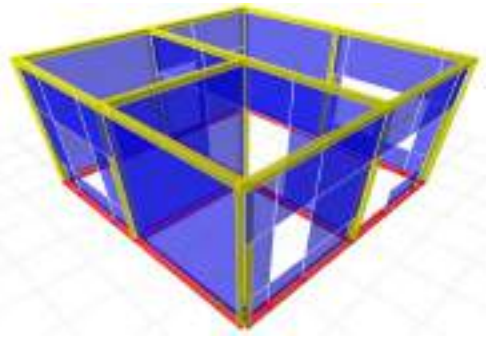

Fig. 5 Modeling of non-standard RM houses without retrofitting

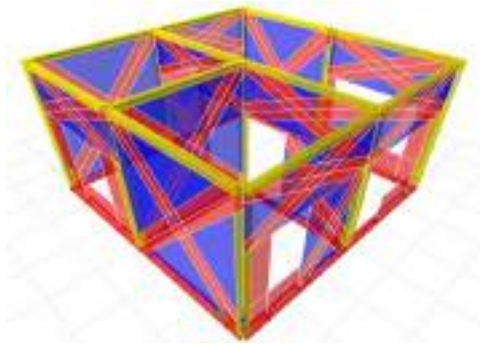

Fig. 6 Modeling of non-standard RM houses retrofitted with ferrocement layer with crossed system

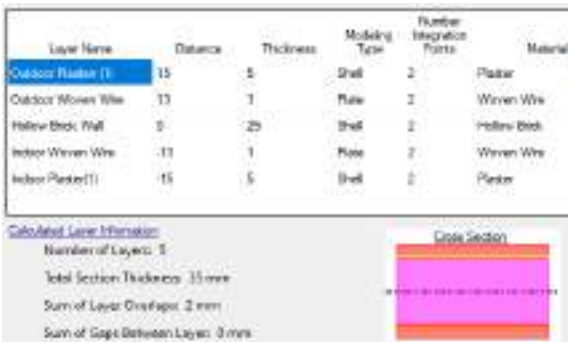

Fig. 7 Section properties of walls with ferrocement layer

The modeling of the URM brick house in this study is shown in Fig. 5. Meanwhile, Fig. 6 shows the modeling of the house with a retrofitting crossed ferrocement layer, where blue is the area of a wall without retrofitting, defined as a brick. At the same time, red is the area of the wall that is given retrofitting, which is defined as a wall consisting of 5 (five) layer properties as shown in Fig. 7.

Loading

The house model weighs 471 kg, as shown in Table 1. A real house without scale weighs 430 kg/m ^{2} (Table 2). Then the weight of the model house should be based on the following broad scale (equation 1):

$$Ls \times qa = qs \quad (1)$$

where,

Ls: Specimen Area (m^2)
Q: Original Weight House (kg/m^2)
qs: Specimen Weight (kg)

So,

$$2{,}25\ m^2 \times 430\ kg/m^2 = 968\ kg$$

Therefore, the model house is given an additional load of 500 kg. The additional load is divided into nine sections, which are inserted in each corner of the model house.

Table 1 Model house weight

Material	kg
Hollow brick weight	157
Mortar weight	246
Weight of the roof frame and the roof	68
Total weight of Specimen	471

Table 2 Weight of the original house

Material	kg
Hollow brick weight	10606
Mortar weight	4172
Weight of the roof frame and the roof	718
Total weight of Specimen	15496
qa: Dead load weight of the original house	430kg/m^2

Numerical Analysis with Time History Analysis

Numerical analysis was carried out in the study using the time history of the earthquake load. There are four variations of the given earthquake acceleration load, namely 0.3 g, 0.6 g, 1.0 g, and 1.5 g, with a duration of 10 seconds for each acceleration variation.

RESULTS AND DISCUSSION

Behavior of House Models with 0.3 g Earthquake

Acceleration

Based on the analysis results from ETABS V.22 software with a 0.3 g earthquake acceleration, the tensile stress on the walls of both the unretrofitted and retrofitted houses is primarily shown in yellow and green in Figs. 8-9, respectively.

For the unretrofitted house, the maximum tensile stress reaches 0.07 MPa, which is below the tensile strength of the brick (0.264 MPa). The tensile strength of the brick is calculated as 8% of its compressive strength, which is 3.3 MPa, resulting in 0.264 MPa. Although the stress is below the tensile capacity, any tensile stress on unreinforced brick walls is considered a high-risk category that could lead to cracks and collapse.

In contrast, the house retrofitted with a ferrocement layer shows a significantly lower maximum tensile stress of 0.03 MPa. Even if the tensile stress were to exceed the hollow brick's tensile capacity, the wall would remain safe due to the high tensile resistance provided by the woven wire reinforcement. The woven wire serves to maintain wall stability and prevent damage.

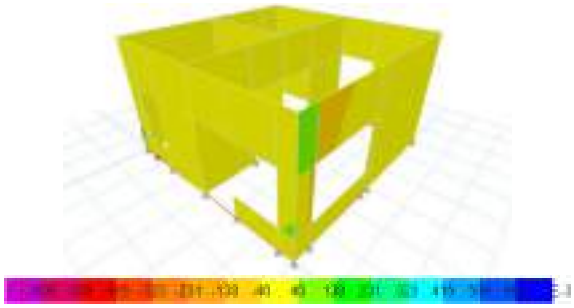

Fig. 8 Wall tension pattern on non-standard RM wall due to 0.3 g earthquake acceleration

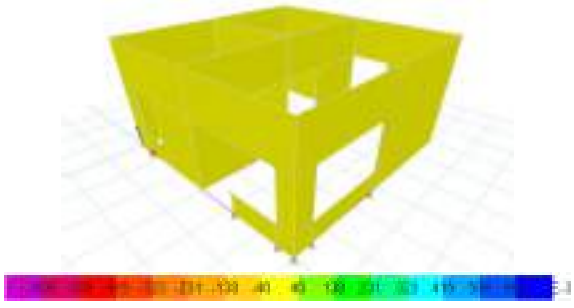

Fig. 9 Wall tension pattern on retrofitted non-standard RM wall due to 0.3 g earthquake acceleration

Behavior of House Models at 0.6 g Earthquake Acceleration

The analysis results for the 0.6 g earthquake acceleration, shown in Fig. 10 (unretrofitted) and Fig. 11 (retrofitted), indicate that the highest tensile stress occurs in areas with large openings, such as the living room.

In the unretrofitted house, the maximum tensile stress reaches 0.12 MPa. While this value is still below the tensile strength of the brick walls (0.264 MPa), it represents a significant increase from the 0.3 g acceleration. The stress distribution is more widespread and intense, particularly around windows and doors, which are typically points of weakness. This increased stress level suggests a higher risk of cracking and damage, which could compromise the structural integrity of the wall during a prolonged seismic event.

Conversely, the retrofitted house shows a much smaller maximum tensile stress of only 0.09 MPa. This demonstrates the effectiveness of the ferrocement layer with a cross reinforcement system in absorbing and distributing seismic forces. Even though the stress value is still present, the wall's ability to withstand these forces is significantly enhanced by the woven wire. The wire, with its high tensile strength, acts as a secondary reinforcement system, preventing the brick from failing catastrophically even if the stress were to exceed its own tensile capacity. The overall behavior of the retrofitted model remains stable and secure, indicating its good performance under moderate earthquake loads.

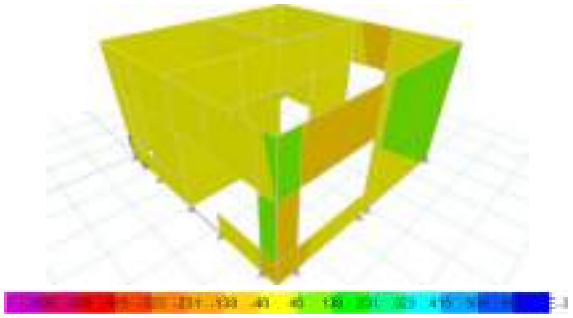

Fig. 10 Wall tension pattern on non-standard RM wall due to 0.6 g earthquake acceleration

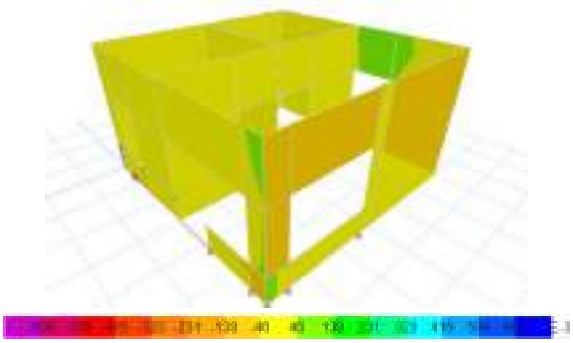

Fig. 11 Wall tension pattern on retrofitted non-standard RM wall due to 0.6 g earthquake acceleration

Model House Behavior at 1.0 g Earthquake Acceleration

The analysis results for the 1.0 g earthquake acceleration show a more significant difference between the two models. In the unretrofitted house, as seen in Fig. 12, higher tensile stresses begin to appear, marked by blue areas. These areas indicate stress values between 0.231 MPa and 0.323 MPa. Overall, the maximum tensile stress value in this model is 0.26 MPa. This indicates that the brick walls are approaching a critical point where severe damage may occur.

In contrast, in the retrofitted house (Fig. 13), the tensile stresses are still dominated by yellow and green areas. This indicates that the stresses are much lower and more evenly distributed. The maximum tensile stress value in this model is only 0.18 MPa. This striking difference proves that the ferrocement layer with the cross reinforcement system effectively dampens and distributes earthquake energy, preventing dangerous stress concentrations. These results show that in addition to increasing the strength of the walls, houses reinforced with a ferrocement layer can also reduce the pressure that occurs on the walls.

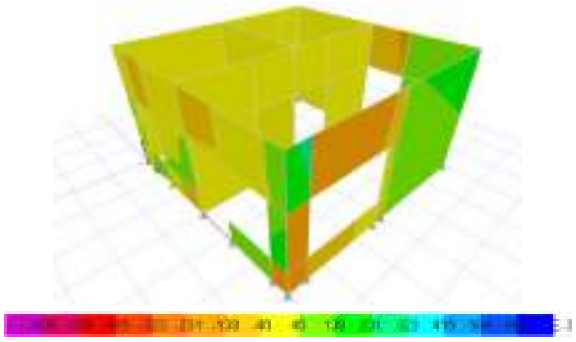

Fig. 12 Wall tension pattern on non-standard RM wall due to 1.0 g earthquake acceleration

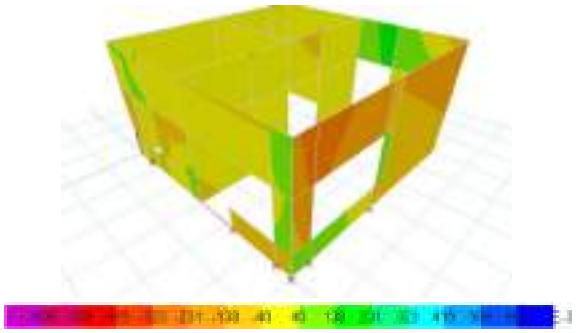

Fig. 13 Wall tension pattern on retrofitted non-standard RM wall due to 1.0 g earthquake acceleration

Model House Behavior at 1.5 g Earthquake Acceleration

The analysis results for the 1.5 g earthquake acceleration, shown in Fig. 14 (unretrofitted) and Fig. 15 (retrofitted), demonstrate an even more striking difference in the behavior of the two models. At this very high acceleration level, the unretrofitted house experiences a maximum wall pressure of 0.21 MPa. This value is dangerously close to the critical resistance limit of the brick walls, indicating that the structure is highly vulnerable and at serious risk of severe cracking or even partial collapse if subjected to prolonged shaking.

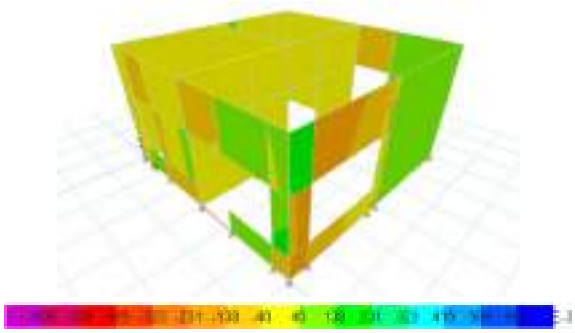

Fig. 14 Wall tension pattern on non-standard RM wall due to 1.5 g earthquake acceleration

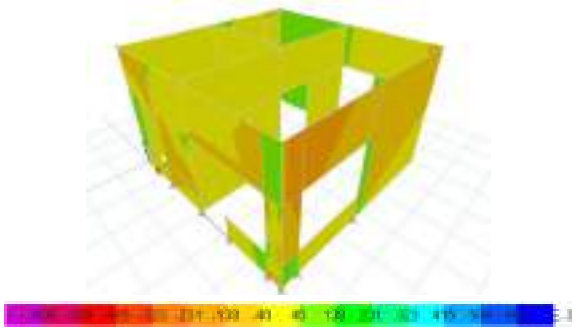

Fig. 15 Wall tension pattern on retrofitted non-standard RM wall due to 1.5 g earthquake acceleration

In contrast, the house retrofitted with a ferrocement layer shows a much superior performance. The maximum pressure on its walls reaches only 0.11 MPa. These results prove that this retrofitting method not only increases the wall's strength but also effectively reduces the pressure caused by seismic loads. With a significantly lower stress value, the walls of the retrofitted house remain stable and secure, preventing severe damage or collapse even under very high earthquake acceleration.

It should be noted that the numerical analysis using ETABS is subject to several limitations. The model is based on a 1:4 scaled specimen, which may introduce scale effects that do not fully capture the behavior of full-scale masonry houses. In addition,

the wall composition was simplified into representative material layers, while in reality the construction quality, workmanship, and irregularities in mortar joints may vary significantly. These assumptions, although necessary for computational feasibility, can introduce uncertainties in predicting the actual seismic response of non-standard RM houses.

CONCLUSION

Based on the results of the analysis, it can be concluded that reinforced masonry (RM) houses built without meeting seismic-resistant standards are highly vulnerable to severe damage or collapse during strong earthquakes. The hollow brick walls in these houses do not have adequate resistance to seismic loads. To address this vulnerability, one of the most effective retrofitting methods is the use of a ferrocement layer with a cross-reinforcement system on the walls. This method is not only effective but also practical, as the materials are easy to obtain and the application can be done by local communities or craftsmen without demolishing the existing structures.

The numerical analysis demonstrates that retrofitted houses experience smaller maximum tensile stress values at every level of earthquake acceleration. This proves that the reinforcement system is highly effective in maintaining the stability of the walls and preventing damage such as cracks or collapse. The analysis results show that the tensile stress on the retrofitted house never exceeds the tensile capacity of the hollow brick. The presence of the woven wire, which has a high tensile resistance, ensures that the walls remain safe and stable.

Overall, this strengthening method is a cost-effective and practical solution for seismic risk reduction in vulnerable housing, both as part of disaster mitigation efforts and in the post-earthquake reconstruction phase.

Despite the promising results, the findings of this study should be interpreted with caution due to the inherent limitations of the numerical modeling. Scale effects, simplification of wall composition, and the exclusion of construction irregularities may influence the accuracy of the simulated response. Future work is recommended to validate the numerical results with experimental shaking table tests on larger-scale specimens and to incorporate more detailed modeling of material.

REFERENCES

[1] Pambudi, N. A., & Ulfa, D. K. (2024). The geothermal energy landscape in Indonesia: A comprehensive 2023 update on power generation, policies, risks, phase, and the role of education. Renewable and Sustainable Energy Reviews, 189, 114008

[2] Fauzan, Istijono, B., Ismail, F. A., Narny, Y., & Putra, Y. S. (2023). Non-engineering house damage after the February 25th, 2022, West Pasaman Earthquake. In IOP Conference Series: Earth and Environmental Science (Vol. 1244, No. 1, p. 012020). IOP Publishing.

[3] BNPB, More than 700 houses were severely damaged by the M6.5 East Java earthquake, the National Disaster Management Agency, 2024.

[4] Gopal, D., & Shobarajkumar, D. (2024). Comparative study on structural behavior of ferrocement wall panels. Earthquake Engineering & Structural Dynamics

[5] Hasnat, A., Das, T., Ahsan, R., Alam, A. T., & Ahmed, H. (2022). In-plane cyclic response of unreinforced masonry walls retrofitted with ferrocement. Case Studies in Construction Materials, 17, e01630.

[6] Choudhury, T., Milani, G., & Kaushik, H. B. (2020). Experimental and numerical analyses of unreinforced masonry wall components and buildings. Construction and Building Materials, 257, 119599.

[7] Imai H. (2014). A Study of Disaster Mitigation for Non-Engineered Construction in Developing Countries: Bridging the Gap between Experiment and Practice, Doctoral Dissertation.

[8] Fauzan, Febrin Anas Ismail, Abdul Hakam, Zaidir, & Sindy Harvi Amalia. (2018). Experimental Study On Masonry Building Strengthened with Ferrocement Layers. GEOMATE Journal, 14(45), 84–90.

[9] Fauzan, Hakam, A., Ismail, F. A., Osman, J. V., & Jauhari, Z. A. (2023). Experimental Investigation of Hollow Brick Unreinforced Masonry Building Retrofitted by Ferrocement Layers. GEOMATE Journal, 24(102), 117–1248.

[10] Artiningsih T. (2017). Study of the Use of Ferrocement for Retrofit of Reinforced Concrete Columns with Variations in Load Levels.

[11] Desmon H., dkk (2021). Simple retrofit of community housing in Nagari Kampani, Padang Pariaman Regency, West Sumatra. Journal of Devotional Dynamics, Vol. 6 No. 2 (2021).

[12] Fauzan, Putri, N. T., Ismail, F. A., Jauhari, Z. A., & Kelvin, J. (2024). Analytical Studi On Seismic Behavior of URM Hollow Brick Houses Retrofitted Using Ferrocement Layers. GEOMATE journal, 27(120), 130-137.

Copyright © Int. J. of GEOMATE All rights reserved, including making copies, unless permission is obtained from the copyright proprietors.

15th Int. Conf. on Geotechnique, Construction Materials & Environment,
Kyoto, Japan, 11-13 November 2025, ISBN 978-4-909106124 C3051

SEISMIC ASSESSMENT AND RETROFITTING OF THE WEST SUMATRA BPBD OFFICE BUILDING USING SHEAR WALLS

*Fauzan[1], Abdul Hakam[2], Muhammad Ridho Zainadi[3], Arifin Shaleh[4], and Muhamad Rezki[5]

[1,2,3,4,5]Department of Civil Engineering, Andalas University, West Sumatra, Indonesia

ABSTRACT

The structural reliability of public buildings in seismic-prone areas is crucial to ensure safety and functionality. The BPBD office building in Padang, West Sumatra, was assessed due to various deficiencies in its current condition, including cracks, material degradation, and insufficient lateral resistance based on Indonesian standards (SNI 1726:2019, SNI 2847:2019, and SNI 1727:2020). Structural modeling and analysis using ETABS indicated that the existing structure does not meet inter-story drift requirements, with the second floor exceeding the permissible limit. Additionally, several beams failed in shear, compromising seismic performance. To address these weaknesses, a global retrofitting approach was implemented by strategically adding reinforced concrete shear walls along the weak axis. Re-analysis of the retrofitted model demonstrated significant improvements: inter-story drift values complied with code requirements, column internal forces decreased by up to 88% in both moment and shear, and beam internal forces were reduced by approximately 75% in moment and 65% in shear. Furthermore, floor slab analysis revealed inadequate flexural capacity under seismic loads. Strengthening with Fiber Reinforced Polymer (FRP) sheets successfully increased the slab capacity from 0.89 t.m to 2.62 t.m, exceeding the external moment requirement of 2.51 t.m. These results confirm that a combined retrofitting strategy using shear walls to enhance global stiffness and FRP to reinforce slab flexural strength provides an effective solution to improve seismic resilience and ensure the building's safety and usability as a disaster management facility.

Keywords: Structural Assessment, Retrofitting, Shear Wall, Earthquake, RC structure

INTRODUCTION

The structural durability of buildings is a crucial factor in ensuring the safety of occupants and the sustainability of building functions [1,2], especially in areas with high seismic rates such as West Sumatra. The building, which is located behind the West Sumatra Gurbenur Office, is one of the strategic infrastructures located in Padang City, and it is planned to function as an office of the Regional Disaster Management Agency (BPBD).

The results of the visual review show that the existing condition of the building has experienced various damages, including cracks in the floor plates, damage to the beams, and indications of concrete segregation that have the potential to reduce the overall performance of the structure. This confirms that even though it is classified as a new building, its structural performance requires a thorough technical evaluation.

On the other hand, changes in earthquake design standards in Indonesia, especially the implementation of SNI 1726:2019 on earthquake resistance, SNI 2847:2019 on reinforced concrete structures, and SNI 1727:2020 on minimum load of buildings, require a re-evaluation of buildings designed using the old standards. This condition is a serious challenge considering that a number of public buildings, including the BPBD Back Building, have the potential to not meet the latest requirements.

Previous studies have shown that global reinforcement methods such as shear wall installation are an effective solution in increasing the capacity of structures against lateral forces, reducing inter-story drift, and increasing the rigidity of structural systems [3-5]. The application of shear walls is also able to transform the structural system into a double system, making it more reliable in withstanding earthquake loads [6-7].

RESEARCH SIGNIFICANCE

This study highlights the importance of retrofitting critical public buildings in seismic-prone regions. By assessing the BPBD office's structural deficiencies and implementing a combined retrofitting strategy with reinforced concrete shear walls and FRP sheets, the research demonstrates effective methods to enhance seismic resilience. The findings provide practical insights into improving global stiffness, reducing inter-story drift, and increasing slab flexural capacity, ensuring both safety and functionality. Beyond technical analysis, the study also emphasizes the need to address implementation challenges, including construction phasing and occupancy management, making it relevant for disaster management facilities in Indonesia and similar contexts.

EVALUATION OF THE EXISTING BUILDING

Existing Building Data

The existing condition of the BPBD building can be seen in Fig. 1.

Fig. 1 Existing conditions of BPBD building

The technical specifications of the structure for the analysis of this building are as follows:

Building Location : Padang City, West Sumatra Province
Structural System : Reinforced Concrete Portal
Floor Plate Width : 12 cm
Concrete Grade : 260 kg/m^2
Reinforce Grade (Fy): 240 MPa
Soil Condition : Medium Soil (SD)

Details of the structure of columns, including reinforcement, can be seen in Tables 1 and 2.

Table 1 Column details

No	Code	Dimensions (mm)		Lo	Shear Rebar	
		Diameter	Length	(mm)	Support	Midspan
1	K1D60	600	4600	692	3D-10-100	2D10-150
2	K2D60	600	4600	692	3D-10-100	2D10-150
3	K3D60	600	3600	532	3D-10-133	2D10-150
4	K4D60	600	3600	532	3D-10-133	2D10-150
5	K5D60	600	3600	532	3D-10-133	2D10-150

Table 2 Beam details

No	Code	Dimension		Rebar		Shear Rebar	
		Width	Depth	Tensile	Compr.	Support	Midspan
1	S1	300	500	7 D 25	4 D 25	1Φ10 - 100	Φ10 - 150
2	S2	300	500	8 D 25	4 D 25	1Φ10 - 100	Φ10 - 150
3	B1	300	500	7 D 25	4 D 25	1Φ10 - 100	Φ10 - 200
4	B2	300	500	8 D 25	4 D 25	1Φ10 - 100	Φ10 - 200
5	B3	300	500	9 D 25	5 D 25	1Φ10 - 100	Φ10 - 260
6	BA1	250	450	3 D 19	2 D 19	1Φ10 - 100	Φ10 - 220
7	BA2	200	300	3 D 16	2 D 16	1Φ10 - 100	Φ10 - 260
8	BK1	300	500	4 D 25	2 D 25	1Φ10 - 100	Φ10 - 200
9	BK3	250	450	3 D 25	2 D 25	1Φ10 - 100	Φ10 - 150
10	BT1	250	450	3 D 16	2 D 16	1Φ10 - 100	Φ10 - 150
11	BT2	250	450	3 D 16	2 D 16	1Φ10 - 100	Φ10 - 150

Modeling

The modeling of the BPBD Building structure was carried out using the ETABS V.22 software in 3-dimensional form, as shown in Fig. 2, where the beams and columns were modeled as element frames, and the floor was modeled as element slabs.

To analyze the building structure of the BPBD Office Rear Building, the standard regulation SNI 2847:2019 for Structural Concrete Requirements for Buildings, SNI 1726:2019 for Earthquake Resilience Planning Procedures for Buildings and Non-Buildings, and SNI 1727:2020 for Minimum Loads for the Design of Buildings and Other Structures.

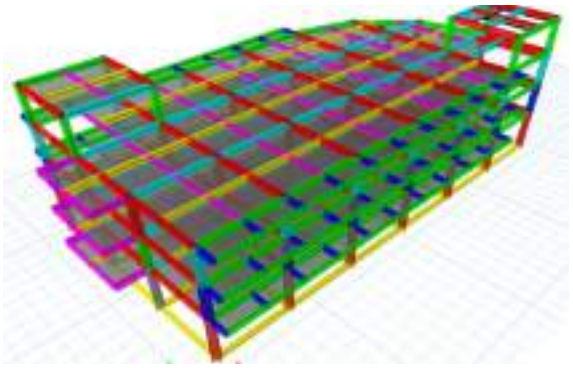

Fig.2 BPBD building modeling on ETABS V.22

Response Spectrum Design

The design response spectrum was developed according to SNI 1726:2019, using seismic hazard data from PUSGEN 2019–2020 for Padang (soil class SD). The short-period spectral acceleration (Ss) is approximately 1.54 g, and the one-second period spectral acceleration (S1) is 0.62 g. With site coefficients Fa = 0.80 and Fv = 2.0, the maximum considered earthquake parameters become SMS ≈ 1.23 g and SM1 ≈ 1.24 g, resulting in design values SDS ≈ 0.82 g and SD1 ≈ 0.83 g. These were adopted to generate the elastic design spectrum in ETABS for both principal directions. The primary hazard considered in this study is earthquake loading. Tsunami-induced hydrodynamic loads, while relevant for coastal facilities, were not included in this numerical study and are recommended for future multi-hazard evaluations.

Loading

The load cases defined in the ETABS model consisted of dead load (DL), live load (LL), and earthquake load (EQX, EQY) applied in both positive and negative directions. These were combined according to the load combinations prescribed in SNI 2847:2019 and SNI 1727:2020, such as 1.2DL + 1.6LL + 0.5EQ, and 1.2DL + 1.0EQ + 0.5LL, among others. This ensured that both gravitational and seismic actions were captured in accordance with code requirements.

Analysis of the Existing Building's Structure

Inter story-drift

Table 3 Results of inter-story drift in the building

Story	h (mm)	Inelastic Drift		Drift Limit (mm)	Cek
		Δ_X (mm)	Δ_Y (mm)		
4	3000	23,445	23,650	34,615	OK
3	3600	37,217	33,216	41,538	OK
2	3600	51,150	46,816	41,538	NOT OK
1	4600	51,671	47,542	53,077	OK

The determination of inter-story drift must be calculated as the difference in displacement at the center of mass above and below the level under review. Based on calculations of inter-story drift in SNI 1726: 2019, inelastic story drift Δ = δ * Cd / Ie and drift limit, Δa = 0.015 h = 41.54 mm in terms of X-direction and Y-directions. Based on the results of the analysis (Table 3), the value of inter-story drift on the 2nd floor exceeded the permit limit determined by SNI 1726:2019, namely ΔX = 51,150 mm and ΔY = 46,816 mm, greater than the drift limit of 41,538 mm. This shows that the existing structure has not met the requirements for the intersection between floors, so it needs to be retrofitted.

Load-bearing capacity of the column

From the results of the structure analysis, a diagram of column interaction was obtained, as seen in Figs. 3-7. From Figs. 3–7, it can be seen that the moment and axial values (in the form of points) do not pass through the P-M interaction diagram of the columns, so that the column structure is able to bear the working load.

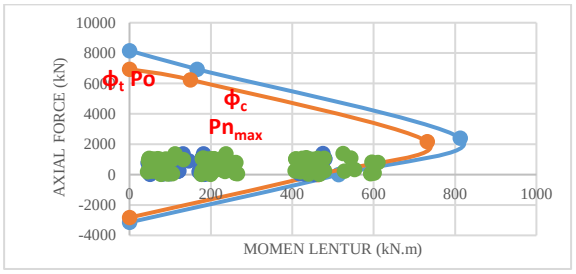

Fig. 3 K1 column interaction diagram

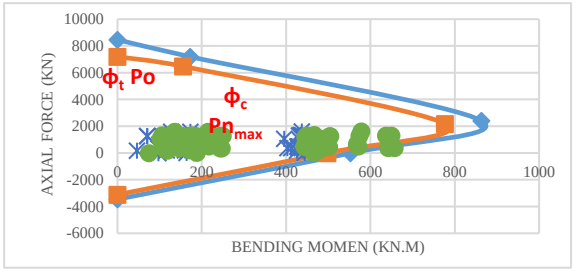

Fig. 4 K2 column interaction diagram

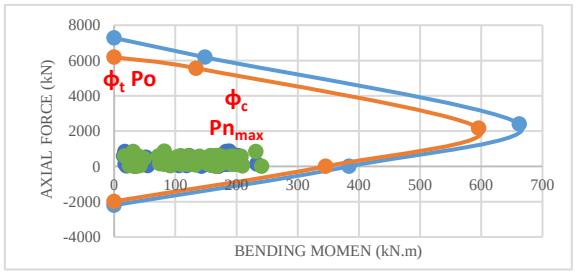

Fig. 5 K3 column interaction diagram

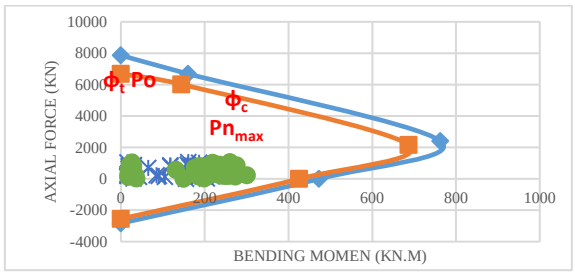

Fig. 6 K4 column interaction diagram

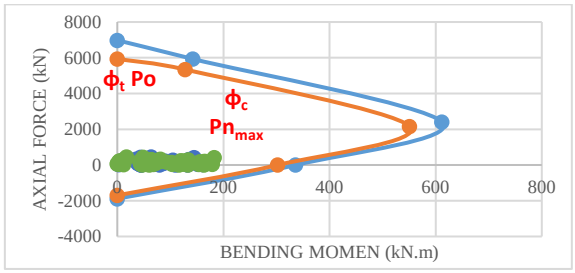

Fig. 7 K5 column interaction diagram

Load-bearing capacity of the beam

Table 4 Existing beam capacity

Story	Code	ϕMn	Mu	Control	ϕVn	Vu	Control
		kNm	kNm	ϕMn ≥ Mu	kN	kN	ϕVn ≥ Vu
2	B1	243,9	120,3	OK	146,8	127,1	OK
	B2	243,9	130,2	OK	146,8	146,8	OK
	B3	302,1	135,5	OK	131,9	171,1	NO
	B1a	243,9	120,3	OK	146,8	78,2	OK
	B2a	243,9	139,6	OK	146,8	151,8	NO
	Ba1	97,5	68,9	OK	114,7	49,8	OK
	Ba2	44,9	22,5	OK	65,3	39,5	OK
	Ba3	44,5	13,0	OK	83,0	22,0	OK
	BK1	125,6	117,9	OK	168,3	115,9	OK
	BK2	48,0	4,0	OK	100,0	2,4	OK
	BK3	109,9	55,9	OK	126,0	55,4	OK
	BT1	70,2	22,0	OK	100,0	21,4	OK
	BT2	70,2	57,3	OK	100,0	50,2	OK

The results of the beam capacity analysis (Table 4) indicate that, in terms of flexural strength, most elements are still able to withstand the design moment, so they can be considered relatively safe in bending. However, in the shear aspect, several critical beams particularly B3 and B2a on the second floor and B3b on the third floor exhibit shear demand (Vu) that exceeds their factored shear capacity (ϕVn). This

condition confirms that the main weakness of the existing beams lies not in flexural capacity but in shear resistance, meaning that these elements do not meet the minimum shear strength requirements stipulated in SNI 2847:2019 (Clause 22.5). Consequently, the insufficient shear resistance significantly increases the seismic vulnerability of the overall structure.

Floor plate bending capacity

The floor plate in the building behind the Governor's Office is a 2-way plate where the width of the direction x is 3 m, equal to the width of the direction of y, which is also 3 m, so that the ratio of the width of the direction x and the width of the direction y is less than 1.

Table 5. Floor plate bending capacity

Description	Reinforcement	
	X Dir.	Y Dir.
Load combination	EQX load	EQX load
Outside Moment (tm/m)	2.515	1.6157
Upper reinforcement	D10-250	D10-250
Bottom reinforcement	D10-250	D10-250
Momen Nominal (tm/m)	0.887	0.887
Check Nominal Moments > External Moments	Not Ok	Not OK

From Table 5 above, it can be seen that the flexural capacity of the floor plate is still smaller than the external moment due to the working load, or the condition of the plate is unsafe.

RETROFITTING OF THE BUILDING STRUCTURE WITH SHEAR WALLS

Based on the results of the evaluation of the existing structure, it is known that some key elements, such as columns and beams, are not fully able to withstand the workload, coupled with the deviation between floors that exceeds the permitted limit. This condition emphasizes the need for comprehensive strengthening efforts. The method chosen is the installation of a shear wall, as this technique has proven to be effective in increasing the global rigidity of the building, lowering the deviation between floors, and reducing the internal force on structural elements.

Shear Wall Location

The placement of shear walls in existing buildings is determined by considering the dominant direction of earthquake forces, spatial function, and the need to minimize eccentricity between floors. The selected location is focused on the weak axis of the building so that it can optimally increase lateral rigidity without disturbing the spatial layout. With this configuration, the torque moment on the structure can be suppressed, and the distribution of the earthquake force to the structural elements becomes more even. The shear wall used has a concrete quality of 30 MPa and is installed as high as the existing building, so that it can function as the main reinforcement element while transforming the structural system into a double system. The location of the shear wall placement can be seen in Fig. 8.

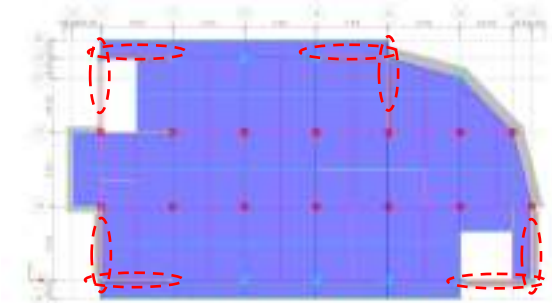

Fig.8 Location of shear wall placement

Through retrofitting of the structure with shear walls, a transformation occurs in the building's structural system, transitioning into a dual system. This alteration affects earthquake parameters, including the adjustment of the response modification coefficient (R) to 7, the over-strength factor system (Ω) to 2.5, the reinforcement parameter (Ct) to 0.0466, and the period parameter (x) to 0.9.

Structural Re-Analysis Results for the Retrofitted Building

The re-analysis of the building after being given a shear wall was carried out using the same procedure as in the existing structure, but earthquake parameters were used for the double system due to the addition of shear wall elements.

Inter-story drift of the retrofitted building

Table 6 Inter-story drift of the retrofitted building

Story	h (mm)	Inelastic Drift		Drift Limit	Cek
		$\Delta_{X\ (mm)}$	$\Delta_{Y\ (mm)}$		
4	3000	16,691	16,654	23,077	OK
3	3600	1,456	1,584	27,692	OK
2	3600	1,577	1,749	27,692	OK
1	4600	1,456	1,584	35,385	OK

After the installation of the shear wall, the value of inter-story drift on the entire floor has decreased significantly (Table 6) and is below the SNI 1726:2019 permit limit. This shows that reinforcement has succeeded in increasing the lateral rigidity of the building, so that the deviation between floors can be controlled well and the structure becomes more stable against earthquake loads.

Load-bearing capacity of columns on a retrofitted building

A re-analysis showed that the entire column after installing the shear wall had adequate capacity, as indicated by the axial load points and moments that were still within the P-M interaction curve (Figs. 9-13). The addition of a shear wall also lowers the force in the columns, with the reduction in moment and shear reaching more than 80% at some points (K1, K2, and K3). This condition confirms that reinforcement is able to increase the ability of the column to withstand earthquake loads and maintain structural stability.

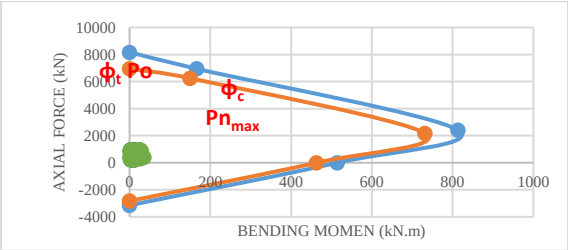

Fig. 9 K1 column interaction diagram after retrofitted

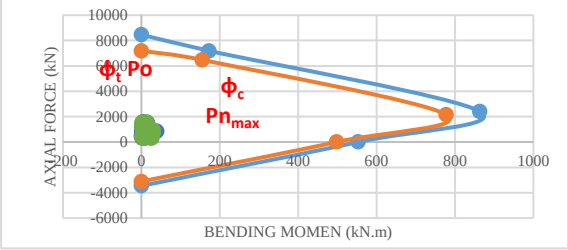

Fig. 10 K2 column interaction diagram after retrofitted

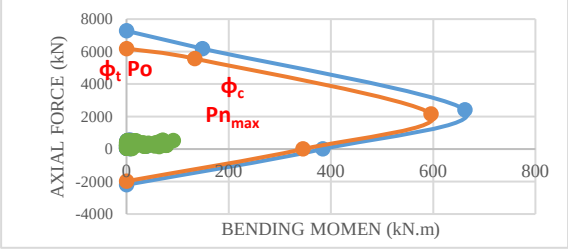

Fig. 11 K3 column interaction diagram after retrofitted

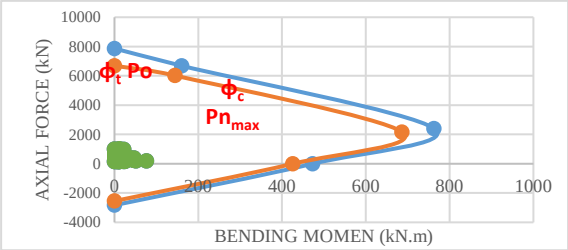

Fig. 12 K4 column interaction diagram after retrofitted

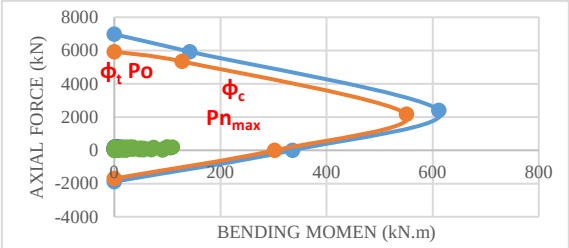

Fig. 13 K5 column interaction diagram after retrofitted

Load-bearing capacity of beams on the retrofitted building

After the installation of the shear wall, the beam capacity showed a significant increase. The results of the analysis showed that almost all blocks were able to withstand the moment and shear force according to the provisions. The decrease in inner force is also quite large, with a maximum moment reduction of about 81% and a shear force of up to 63%. This proves that shear wall reinforcement is effective in improving beam performance and reducing the potential for damage due to earthquake loads.

RETROFITTING OF SLAB

Slab Retrofitting with Fiber Reinforced Polymer (FRP)

The flexural reinforcement of the floor plate given with FRP is carried out by providing additional FRP to the bottom of the floor slab, and to the top of the floor plate (Fig. 14).

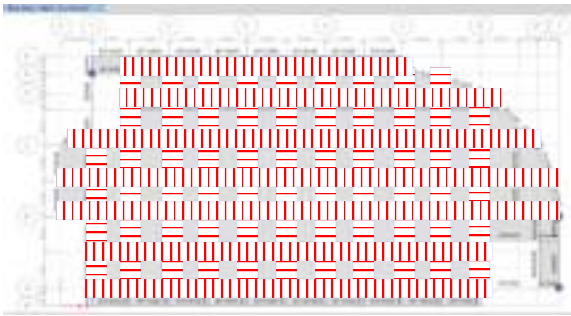

Fig.14 Installation of FRP retrofitting of the focus of the second floor plate

Analysis Result of Slab Capacity After Retrofitting

The analysis shows that after flexural strengthening with Fiber Reinforced Polymer (FRP) sheets, the slab's moment capacity increased from 0.89 t.m to 2.62 t.m. This value exceeds the external moment of 2.51 t.m, confirming that the retrofitted slab can safely resist bending loads. Thus, FRP

reinforcement effectively improves slab performance and reduces the risk of failure under seismic demands.

In addition to the structural capacity improvements demonstrated by the numerical analysis, the practical implementation of shear wall retrofitting in existing buildings also presents significant challenges. The installation of shear walls requires careful construction phasing to minimize disruption to building operations. For the BPBD office building, phasing strategies must be designed to allow temporary closure of certain areas without interrupting critical functions. Furthermore, building occupancy management during the retrofit is crucial to ensure user safety. This may include zoning of construction areas, temporary evacuation of floors under strengthening, and strict enforcement of safety procedures. These considerations highlight that the success of retrofitting is determined not only by compliance with analytical design requirements but also by effective management of on-site construction logistics.

CONCLUSION

Based on the results of the assessment and analysis of the reinforcement of the West Sumatra Province BPBD Office Building, it can be concluded that:

1. The existing structure does not meet the requirements of inter-story drift, and some of the beams show weakness in the shear capacity, so the building is not completely safe against earthquake loads.
2. The installation of shear walls was chosen as a reinforcement method because it was able to increase the global rigidity of the building, reduce the deviation between floors, and reduce the internal force on structural elements.
3. Re-analysis after reinforcement showed that all column and beam elements had met the strength requirements, with a significant reduction in force in the column, which was up to 95% at the moment and column shear, as well as about 81% at the moment and 63% at the beam shear. With the shear wall, the performance of the structure meets the provisions of SNI so that the building becomes more stable, safe, and suitable to function as a BPBD operational office in earthquake-prone areas.
4. After being strengthened with FRP, the flexural capacity of the floor plate increased from 0.89 t.m to about 2.62 t.m, so that it was able to surpass the external moment that occurred of 2.51 t.m. This shows that reinforcement with FRP effectively improves the performance of the slab in resisting bending loads.
5. Although the analytical results confirm that the combined retrofitting strategy using shear walls and FRP significantly enhances seismic performance, practical implementation challenges must also be addressed. Key issues include planning construction phasing to allow building operations to continue, managing occupancy during retrofit to ensure safety, and maintaining strict quality control in both shear wall casting and FRP installation. Therefore, the effectiveness of the proposed retrofitting solution can only be fully achieved when accompanied by well-prepared implementation planning in real conditions.

REFERENCES

[1] Fauzan, F., Yarmawati, D., Sipayung, S. W. D., Kurniawan, W., & Adifa, R. (2021). Assessment and retrofitting of nursing faculty building of Andalas University, Padang, Indonesia. E3S Web of Conferences, 331, 05014.

[2] Fauzan, Kurniawan R., Syahdiza N., Jauhari Z. A., and Nugraha D. A., Fragility Curve of School Building in Padang City with and without Retrofitting due to Earthquake and Tsunami Loads, International Journal of GEOMATE, Vol. 24, Issue 101, 2023, pp.102-109.

[3] Fauzan, Agista, G. A., Syandriaji, D., Al Jauhari, Z., & Suwarso, D. B. (2025). Seismic vulnerability assessment of a hospital building with and without retrofitting using RC shear walls. E3S Web of Conferences, 604, 15003.

[4] Fauzan, Hakam, A., Ismail, F.A., Jauhari, Z.A., and Agista, G.A., Seismic Damage Assessment and Retrofitting of a Hospital Building in West Pasaman, Indonesia, International Journal of GEOMATE, Vol. 27, Issue 120, 2024, pp. 122-129.

[5] Fauzan, Ismail, F.A., Rizki, M.W., Fikri, I., and Jauhari Z.A., The Effect Of L-Shaped Rc Shear Wall On Student Dormitory Building Of Andalas University, Padang Indonesia, International Journal of GEOMATE, Vol. 19, Issue 73, 2020, pp.70-76.

[6] Basereh S., Okumus P., Aaleti S., Reinforced-Concrete Shear Walls Retrofitted Using Weakening and Self-Centering: Numerical Modeling. Journal of Structural Engineering, Vol. 146, Issue 7, 2020, 04020122.

[7] Fauzan, Nulhakim L., Nugraha D.A., Jauhari Z.A., and Agista G.A., Structural Evaluation Of The Melati Hospital Building At Sungai Penuh City, Indonesia, International Journal of GEOMATE, Vol. 25, Issue 73, 2023,pp.123–130

Copyright © Int. J. of GEOMATE All rights reserved, including making copies, unless permission is obtained from the copyright proprietors.

15th Int. Conf. on Geotechnique, Construction Materials & Environment,
Kyoto, Japan, 11-13 November 2025, ISBN 978-4-909106124 C3051

RETROFITTING OF ULAK KARANG SHELTER BUILDING IN PADANG CITY, INDONESIA, USING CONCRETE JACKETING

*Fauzan[1], Febrin Anas Ismail[2], Annisa El Husna[3], Muhammad Zulfian Saputra[4], and Yozi Yuliardi[5]

[1,2,3]Department of Civil Engineering, Faculty of Engineering, Universitas Andalas, Indonesia
[4,5]Master Student in Disaster Management, Postgraduate School, Universitas Andalas, Indonesia

ABSTRACT

Padang City is highly vulnerable to earthquake and tsunami hazards due to its location along the subduction zone of the Indian and Eurasian plates. To address evacuation challenges, the government constructed the Ulak Karang Shelter as a vertical evacuation facility. However, this structure was not originally designed to withstand tsunami loads. This study evaluates the structural performance of the shelter and proposes retrofitting using the concrete jacketing method. The research involved field surveys, collection of technical data, and structural modeling using ETABS V.22. The analysis was based on Indonesian building codes (SNI 1726:2019, SNI 2847:2019, SNI 1727:2020) and FEMA P-646 tsunami guidelines. The results of the structural analysis revealed that some columns and beams lacked sufficient capacity to withstand the combined loads of earthquake and tsunami, indicating critical weaknesses. After retrofitting with concrete jacketing, column strength improved by 151% in moment, 106% in axial capacity, and 45% in shear capacity, while beam strength increased by 181% in flexure and 68% in shear. Structural displacement was also reduced by up to 36% in the X direction and 22% in the Y direction. These findings confirm that concrete jacketing is an effective retrofitting method, enabling the Ulak Karang Shelter to function safely as a vertical evacuation facility.

Keywords: Earthquake, Tsunami, Shelter, Retrofitting, Concrete Jacketing

INTRODUCTION

The location of Padang City on the West Coast of Sumatra, which is directly adjacent to the open sea (Indian Ocean) and the active collision zone of two plates, namely the Indian and Asian plates, makes Padang one of the most vulnerable cities to tsunami wave hazards [1]. Tectonic earthquakes along subduction areas and active seismic events can result in extraordinarily powerful waves. The tsunami disaster caused damage to facilities and infrastructure and caused many casualties.

At the time of the earthquake on September 30, 2009, the city of Padang had a problem with the horizontal evacuation route. This is due to the horizontal evacuation route located on the main road, which has a fairly high density of area. Coupled with very little road infrastructure that is perpendicular to the location of the highlands. In order for the evacuation process to continue to be carried out and minimize the risk of casualties during a tsunami, a rescue strategy is needed, one of which is vertical evacuation to avoid tsunami waves by climbing to a place or floor higher than the height of the tsunami wave. By using shelters, people in Padang City can reach a safe place from tsunami inundation in a shorter time [2]. Therefore, the Padang City government took action by building a temporary evacuation site (TES) named SHELTER located in Ulak Karang District, North Padang District.

Shelter buildings must be designed and built according to earthquake- and tsunami-resistant building standards because shelters must remain functional during natural disasters such as tsunamis [3,4]. However, the Ulak Karang shelter building was not designed for the tsunami load by the planning consultant because Indonesia has no standard regulations on tsunamis. In fact, if a tsunami occurs, it will definitely hit the shelter and adversely affect the strength and ability of the shelter building to bear the existing load, causing damage to the structure.

Researchers have previously analyzed the building using SNI Earthquake 2019 and FEMA P-646 [5]. The results showed that columns with cross sections of 60×40 cm and Ø60 cm could withstand gravity and earthquake loads, but did not have sufficient capacity to withstand tsunami loads. However, if given an additional tsunami load, the columns are not strong enough to withstand the structure". Therefore, it is necessary to carry out a method of improvement to the structure of the building by increasing the ability of the building or adding new structural elements that were not available or considered non-existent when the structure was built. Structural reinforcement is usually done as a preventive measure before the structure undergoes destruction due to the new load to be supported [6,7].

One solution to overcome this is the jacketing method, which is one of the many techniques used in the repair and reinforcement of reinforced concrete. Jacketing is carried out by enlarging the cross-section of the existing reinforced concrete columns, with a new layer of additional concrete that is also

reinforced with reinforcement that serves to increase the rigidity of the shelter structure.

RESEARCH SIGNIFICANCE

The significance of this research is its direct impact on public safety in Padang City, an area highly vulnerable to tsunamis. The study addresses a critical gap, as the existing Ulak Karang shelter was not designed for tsunami loads due to a lack of standard regulations in Indonesia. By designing a structural reinforcement plan using the jacketing method, the research ensures the shelter can withstand these loads, minimizing casualties, and providing a reliable vertical evacuation option when horizontal routes are congested or compromised.

RESEARCH METHOD

The structural performance evaluation in this study was based on explicit design criteria and acceptance benchmarks from both national and international standards. According to SNI 1726:2019 [8], the maximum inter-story drift was limited to 2% of the story height for buildings classified as Category IV (essential facilities for post-disaster functions), which includes tsunami vertical evacuation shelters. The strength of structural members was assessed by comparing the applied demands with the nominal capacities. For beams, flexural and shear capacities were calculated following SNI 2847:2019 [9], and adequacy was determined by checking whether the applied moment and shear forces (Mu, Vu) exceeded the nominal capacities (ØMn, ØVn). For columns, combined axial and flexural capacities were verified using P-M interaction diagrams, where demand points outside the interaction curve indicated insufficient capacity. Load considerations followed SNI 1727:2020 for dead loads, live loads, and special evacuation live loads [10], while tsunami loads were determined based on FEMA P-646, which include hydrostatic, hydrodynamic, impulsive, debris impact, and additional gravity effects [11]. In addition, an evacuation live load of 250 kg/m², as recommended in FEMA P-646, was applied to represent designated shelter occupancy.

EVALUATION OF EXISTING BUILDING

The evaluation of the existing Ulak Karang Shelter was conducted by comparing analytical results with the established acceptance benchmarks. Inter-story drift results were compared to the maximum allowable limit of 2% of the story height, as specified in SNI 1726:2019 for Category IV essential buildings. The performance of beams was assessed by comparing applied demands with nominal flexural and shear capacities; elements where Mu or Vu exceeded ØMn or ØVn were classified as inadequate. Columns were evaluated through P-M interaction diagrams, and demand points located outside the interaction curve indicated insufficient axial-flexural strength. Load effects were checked against SNI 1727:2020 to ensure proper consideration of dead loads, live loads, and evacuation live loads. Tsunami-induced forces, including hydrostatic, hydrodynamic, impulsive, debris impact, and additional gravity loads, were determined following FEMA P-646. Members that could not sustain these combined demands were identified as critical elements requiring retrofitting through the concrete jacketing method.

Location of Region and Topography

Fig. 1 Shelter location on Google Earth

The Ulak Karang shelter (Fig.1) is located near the coastline at a distance of 0.7 km from the Padang coastline. The pattern of land use around the location is a residential area. Based on the tsunami hazard map of Padang City issued by the Padang City Regional Development Planning Agency, the depth of the tsunami flood at the planned location is 4 - 5 m. The estimated depth of the tsunami flood is based on the contours of the Padang city area and the prediction of tsunami waves in the city of Padang.

Building Structure Data

To conduct structural analysis, the parameters used in the technical data of the building and the existing condition of the building are as follows:

- Building Name : Temporary Evacuation Places (TES) or SHELTER
- Structure Type : Reinforced Concrete Portal
- Concrete Grade : K-350 (f'c = 30 Mpa)
- Rebar Grade : 400 Mpa
- Number of Floors: 5
- Building Function: Evacuation
- Floor Plate Thickness : 12 cm
- Column Dimensions on Table 1 and Beam Dimensions on Table 2:

Table 1. Column dimensions

Code	Dimension (cm)	Main rebar	Shear rebar	concrete cover
K1	D 60	16D22	D10-100	25
K2	60 x 40	16D22	D10-100	25

Table 2. Beam dimensions

Code	Dim. (cm)	Support Area		Midspan Area	
		Tensile	Comp.	Tensile	Comp.
BA1	40 x 60	6D22	4D22	3D22	4D22
BA2	40 x 60	7D22	3D22	3D22	3D22
EB1	40 x 50	4D22	3D22	3D22	3D22
EB2	40 x 50	4D22	3D22	3D22	3D22
EB3	40 x 50	4D22	3D22	3D22	3D22
BA3	40 x 50	4D22	3D22	3D22	3D22
BC1	30 x 30	4D22	3D22	3D22	3D22

Structure Modeling

Structural modeling was made in 3 dimensions using ETABS V.22 software (Fig.2).

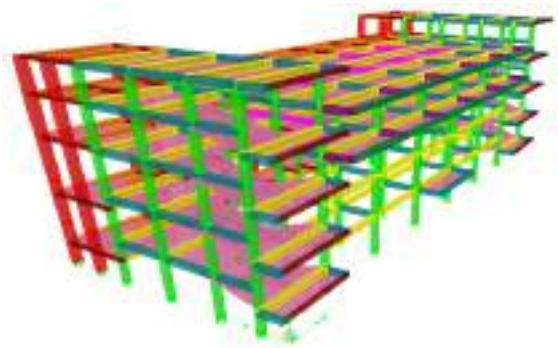

Fig. 2 Modeling of existing structures

Loading

The structural analysis considered dead loads, live loads, earthquake loads, and tsunami loads. Dead loads include the self-weight of structural elements and non-structural components such as walls, calculated according to SNI 1727:2020. Live loads were determined based on SNI 1727:2020, while the specific evacuation live load of 250 kg/m² was adopted from FEMA P-646 for designated shelter areas.

Earthquake loading followed SNI 1726:2019, with response spectrum values obtained from soft soil conditions (SD1 = 0.958g and SDS = 0.805g). Tsunami loads were calculated using FEMA P-646, which considers floating, hydrodynamic, impulsive, debris impact, and additional gravity effects. Load combinations were arranged according to both SNI 1726:2019 and FEMA P-646 to represent the most critical structural demands.

RESULTS AND DISCUSSION

Structure Analysis

Inter-story drift

The results of the calculation of the inter-story drift in the X direction and the Y direction can be seen in Tables 3 and 4. The inter-story drift analysis indicates that the shelter experiences displacement in both X and Y directions under earthquake and tsunami loads. Although the additional tsunami load only slightly increases the drift compared to the earthquake load alone, the cumulative effect shows that several upper stories approach critical limits. This finding highlights the structural vulnerability of the shelter, particularly at higher levels, and emphasizes the need for retrofitting measures to improve overall lateral stability.

Table 3. Comparison of the inter-story drift in the X direction with and without tsunami load

Floor	Without Tsunami Load (mm)	With Tsunami Load (mm)	Upgrade Ratio (%)
1	0.00	0.00	0.000%
2	4.65	4.65	0.000%
3	10.67	10.71	0.378%
4	15.54	15.65	0.708%
5	19.42	19.68	1338%
Rooftop	21.42	21.56	0.654%

Table 4. Comparison of the inter-story drift in the Y direction with and without tsunami load

Floor	Without Tsunami Load (mm)	With Tsunami Load (mm)	Upgrade Ratio (%)
1	0.00	0.00	0.000%
2	10.83	10.83	0.000%
3	20.33	20.34	0.049%
4	26.15	26.23	0.306%
5	29.85	30.04	0.637%
Rooftop	32.29	32.39	0.310%

Cross-sectional capacity of the structure

a. Column

The results of the analysis of the cross-sectional capacity of the columns can be seen in Figs. 3 and 4 below. The analysis shows that the K1 (Ø60 cm) and K2 (60×40 cm**)** columns are unable to resist combined earthquake and tsunami loads, as their demand points exceed the safe interaction curve. While sufficient for gravity and seismic forces, they remain vulnerable under tsunami pressure. Concrete jacketing is required to enhance flexural and shear strength.

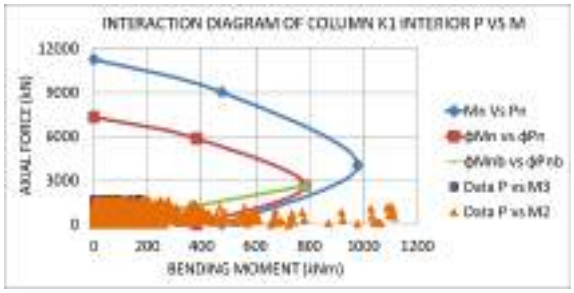

Fig. 3 Interaction diagram of column K1 1st floor

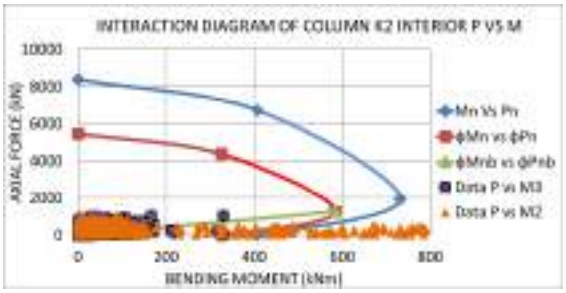

Fig. 4 Interaction diagram of column K2 1st floor

b. Beam

The results of the recap of the bending capacity of the beams of the shelter can be seen in Table 5. The beam capacity analysis indicates that several first-floor beams, particularly BA1 (40×60 cm) and BB1 (40×50 cm)**,** fail to meet flexural requirements under tsunami loads. Some midspan and support reinforcement sections show moment values exceeding the nominal moment capacity, proving their vulnerability. Strengthening with concrete jacketing is therefore necessary to significantly improve flexural and shear resistance.

Table 5. Recapitulation of the bending capacity of the beams of shelter structures with tsunami loads

Floor	Beam	Location	Dimension		Rebar		ØMn	Mu		
			Width	Height	Tensile	Compr.	Nominal moment Capacity (kNm)	applied moment demand (kNm)	Location	Control
1	BA1 40/60	Edges	400	600	6D22	3D22	395,439	506,805	Support	NOT OK
					4D22	2D22	265,829	347,581	Field	NOT OK
		Midle			6D22	3D22	395,439	157,415	Support	OK..!!!
					4D22	2D22	265,829	133,074	Field	OK..!!!
	BB1 40/50	Edges	400	500	6D22	3D22	322,453	282,330	Support	OK..!!!
					4D22	2D22	217,172	329,211	Field	NOT OK
		Midle			6D22	3D22	322,453	349,684	Support	NOT OK
					4D22	2D22	217,172	313,710	Field	NOT OK
	BC1 30/30	Edges	300	300	4D22	4D22	119,297	20,082	Support	OK..!!!
					4D22	4D22	119,297	18,150	Field	OK..!!!
		Midle			4D22	4D22	119,297	174,410	Support	NOT OK
					4D22	4D22	119,297	237,085	Field	NOT OK

Structure Retrofitting Analysis

Fig. 5 shows the location of the first-floor beam elements requiring strengthening, while Fig. 6 highlights the second-floor column elements that also require additional reinforcement.

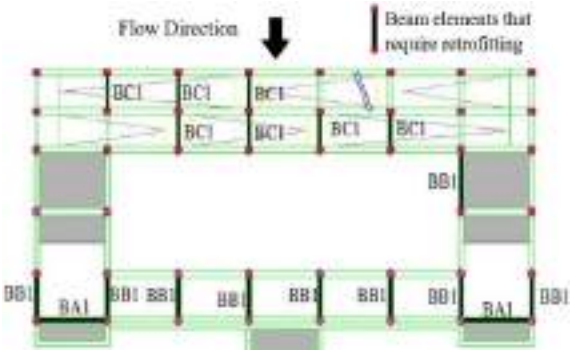

Fig. 5 Position of 1st floor beam elements that require retrofitting

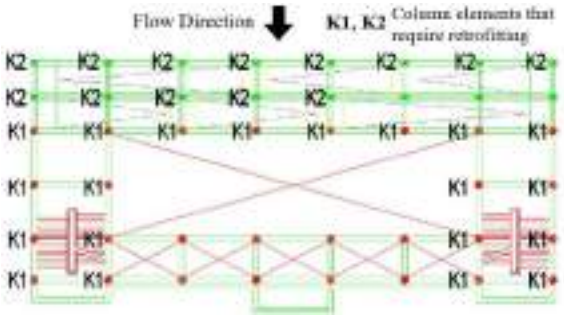

Fig. 6 Position column elements that require retrofitting

Modeling of structures with reinforcement jacketing

The location of the modeled column retrofitted with concrete jacketing can be seen in Fig. 7 below.

- K1 = 750 mm, main rebar: 32D22
- K2 = 750 x 550 mm, main rebar : 32D22
- BA1 = 600 x 800 mm, main rebar: 18D22
- BB1 = 600 x 700 mm, main rebar: 16D22

- BC1 = 500 x 500 mm, main rebar : 15D22

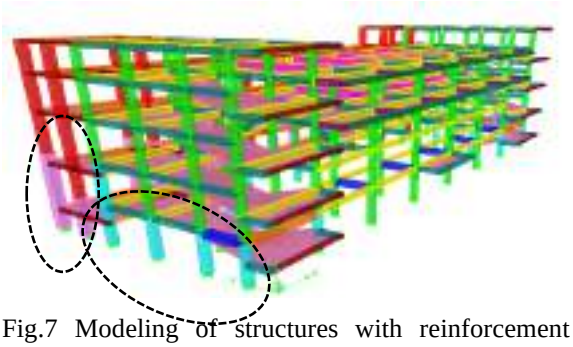

Fig.7 Modeling of structures with reinforcement jacketing

Cross-sectional capacity of the structure

a. Column

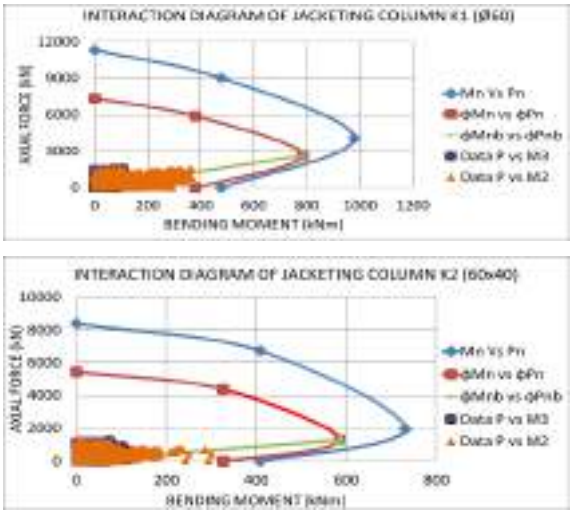

Fig. 8 Interaction diagram of the 1st floor retrofitted structure columns

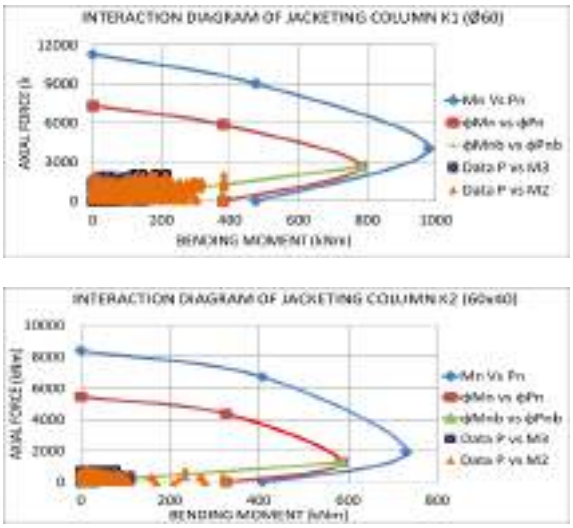

Fig. 9 Interaction diagram of the 2nd floor retrofitted structure columns

In the cross-sectional capacity analysis after retrofitting with the concrete jacketing method, a significant improvement was observed in both columns and beams. Fig. 8 presents the interaction diagram of the first-floor columns, while Fig. 9 shows the interaction diagram of the second-floor columns after strengthening.

b. Beam

The beam results are summarized in Tables 6 and 7, which compare the flexural and shear capacities between the existing and retrofitted conditions. Overall, the jacketing method effectively enhanced the structural performance, with column flexural capacity increasing by more than 150%, and beam capacity improving up to over 180% for flexure and more than 60% for shear.

Table 6 Comparison of the bending capacity of existing and retrofitted structure beams

Beam	Location	Moment Nominal		Increased (%)
		Existing	Retrofitted	
BA 1	Support	395.439	782.679	98%
BA 1	Field	265.829	706.645	166%
BB 1	Support	322.453	577.980	79%
BB 1	Field	217.172	505.904	133%
BC	Support	119.297	335.383	181%
BC	Field	119.297	335.383	181%

Table 7 Comparison of existing and retrofitted structure beams shear capacity

Beam	Location	Shear plan		Increased (%)
		Existing	Retrofitted	
BA1	Support	514,242	723,512	40,695%
	Field	335,172	497,317	48,377%
BB1	Support	424,025	623,024	46,931%
	Field	276,370	428,245	54,954%
BC	Support	315,665	531,493	68,372%
	Field	315,665	531,493	68,372%

Beyond analytical improvements, several practical considerations must also be addressed in implementing the jacketing retrofit method. Quality control during construction is critical, particularly in ensuring adequate bonding between the existing concrete and the new jacketing layer, proper placement of additional reinforcement, and sufficient compaction of the new concrete. Without strict quality control, the effectiveness of the retrofit may be compromised. Potential cracking at the interface between old and new concrete should also be anticipated, requiring the use of bonding agents, roughening of the existing surface, and adequate curing practices. From a construction logistics perspective, jacketing requires careful planning in terms of access to structural elements, installation of

formwork, and work scheduling, especially since the shelter is located in a densely populated area. These practical issues must be taken into account to ensure that the retrofitting design can be effectively implemented in the field.

CONCLUSION

From the research that has been carried out, it can be concluded that several things are as follows:

1. The existing Ulak Karang shelter cannot fully withstand the burden of earthquakes and tsunamis, as some columns and beams do not have sufficient capacity. This condition highlights the urgent need for structural reinforcement before the shelter can safely carry out its evacuation function.
2. Retrofitting with concrete jacketing proves effective, increasing column strength significantly. The moment capacity rises by 151%, axial capacity by 106%, and shear by 45%, ensuring that the columns can better sustain combined loads.
3. Beam elements also benefit from the strengthening, with flexural capacity improving by 181% and shear by 68%. These gains make the beams much more reliable in resisting tsunami-induced forces that previously caused overstress.
4. Structural displacement is reduced by 36% in the X direction and 22% in the Y direction, showing that the building becomes stiffer and more stable against lateral movement during seismic and tsunami events.
5. The building is suitable for use as a shelter for evacuation in the event of a disaster after reinforcement
6. In addition to the numerical improvements demonstrated through structural analysis, the success of the concrete jacketing method also depends on proper field implementation. Quality control, prevention of interface cracking, and construction logistics are essential aspects that determine whether the retrofit will perform as intended. Therefore, the findings of this study not only highlight the technical effectiveness of jacketing but also emphasize the importance of addressing practical challenges to ensure reliable and durable retrofitting of evacuation shelters.

REFERENCES

[1.] Fauzan, Hakam, A., Ismail, F.A., Jauhari, Z.A., and Chairani, C., Evaluation of an RC Frame Building Exposed to Differential Settlement in Padang City, Indonesia, International Journal of GEOMATE, Vol. 27, Issue 123, 2024, pp. 125-132.

[2.] Fauzan, Rina Yuliet, Abdul Hakam, & Helza Riani. (2019). Structural Evaluation Of Nurul Haq Shelter Building Constructed in a Liquefaction-Prone Area In Padang City, Indonesia. Geomate Journal, 17(59), 106–114.

[3.] Fauzan, Ikhwan, F.M., Nugraha M., D.A., Syandriadji, D., and Jauhari, Z.A., The Effect of Tsunami Loads on the Prayoga Foreign Language College Building in Padang City, Indonesia, International Journal of GEOMATE, Vol. 25, Issue 112, 2023, pp. 115-122.

[4.] Fujita K. and Yashiro H., Study on Evaluation of Human Damage from Tsunami Considering Congestion of Evacuee, International Journal of GEOMATE, Vol. 22, Issue 89, 2022, pp.87-93.

[5.] Fauzan, Ismail F. A., Siregar N. and Jauhari Z. A., The Effect of Tsunami Loads on Pasar Raya Inpres Block III Building in Padang City Based on FEMA P-646, in Proc. MATEC Web of Conferences Vol. 258, No. 03020, 2019, pp.1-9.

[6.] Fauzan, Hakam, A., Ismail, F.A., Jauhari, Z.A., and Agista, G.A., Seismic Damage Assessment and Retrofitting of a Hospital Building in West Pasaman, Indonesia, International Journal of GEOMATE, Vol. 27, Issue 120, 2024, pp. 122-129.

[7.] Fauzan, Kurniawan R., Syahdiza N., Juahari Z. A., and Nugraha D. A., Fragility Curve of School Building in Padang City with and without Retrofitting due to Earthquake and Tsunami Loads, International Journal of GEOMATE, Vol. 24, Issue 101, 2023, pp.102-109.

[8.] Indonesian National Standardization Agency, SNI 1726:2019 Seismic Resistance Design Codes for Building and Other Structures, BSN, Jakarta, 2019, pp.1-238.

[9.] Indonesian National Standardization Agency, SNI 2847:2019 Structural Concrete Requirements for Buildings, BSN, Jakarta, 2019, pp.1-695.

[10.] Indonesian National Standardization Agency, SNI 1727:2020 Minimum Load for Planning of Buildings and Other Structures, BSN, Jakarta, 2020, pp.1-302.

[11.] FEMA P646-2019 Guidelines for Design of Structure for Vertical Evacuation from Tsunami. Federal Emergency Management Agency. Washington D.C, USA

Copyright © Int. J. of GEOMATE All rights reserved, including making copies, unless permission is obtained from the copyright proprietors.

15th Int. Conf. on Geotechnique, Construction Materials & Environment,
Kyoto, Japan, 11-13 November 2025, ISBN 978-4-909106124 C3051

NUMERICAL ANALYSIS OF SMALL-SCALE EARTH RETAINING STRUCTURES DURING LIQUEFACTION

Kakuta Fujiwara[1], Yan Boyu[1]

[1]Graduate School of Engineering, Tokai University, Japan

ABSTRACT

In repair work for underground pipelines, small-scale excavations of approximately 1 to 2 meters in depth are often carried out. In narrow or confined areas, lightweight sheet piles are frequently used for earth retaining purposes. Due to the small scale of the construction, earth retaining walls (lightweight sheet piles) and other materials are sometimes used based on conventional practices rather than detailed calculation procedures. Furthermore, since these are temporary structures, seismic considerations are typically not conducted. However, given the large number of such construction activities at the same time, it is likely that some will incur damage during an earthquake. Therefore, this study conducts numerical analysis of small-scale earth retaining works under seismic conditions. The target site is assumed to be a sandy and saturated ground near the coast, and the numerical analysis takes liquefaction into account. The results confirmed that liquefaction leads to the uplift of the entire structure and an increase in stresses acting on structural components such as short struts and walers. Based on this analysis model, additional simulations were conducted to compare three scenarios: without considering liquefaction, with varying spacing of struts, and with the application of surcharge loads. This paper also shows these analytical results in different three scenarios.

Keywords: Small-scale excavation, Retaining wall, Numerical analysis

INTRODUCTION

In repair work for underground pipelines, small-scale excavations approximately 1 to 2 meters deep are often carried out. In narrow or confined areas, lightweight sheet piles are frequently used for earth-retaining purposes.

The retaining wall is often constructed using lightweight and durable aluminum sheet piles. These sheet piles are aligned and supported by walers, and the opposing aluminum sheet piles are further braced at the top by horizontal struts, called “Double sheet pile cut-off structures”. While increasing the number of struts and walers helps to distribute the stresses generated during excavation and enhances structural stability, an excessive number of these structural members can reduce the working space and lower constructability.

Double sheet pile cut-off structures have been widely applied in various fields and are often effective in mitigating liquefaction associated with seismic events [e.g. 1, 2]. Although design guidelines [e.g. 3] are available as references for earth-retaining walls in small-scale excavation work, the extent to which they are applied in design calculations varies depending on the site. Due to the limited scale and low risk associated with potential collapse, construction is sometimes carried out using a simplified structure rather than one derived through detailed design calculations.

Based on these circumstances, the authors have conducted model experiments and numerical analyses on earth-retaining walls for small-scale excavations to verify the safety of structural member stresses and related factors under static conditions [4]. As these structures are temporary, seismic considerations are typically not included in the design. However, given the large number of such construction activities occurring simultaneously, it is likely that some may be damaged during an earthquake. Therefore, this study performs numerical analyses of small-scale earth-retaining works under seismic conditions. The target site is assumed to be a sandy, saturated ground near the coast, and the numerical analysis incorporates the effects of liquefaction. Additional simulations were also conducted to compare three scenarios: without considering liquefaction, with varying spacing of struts, and with the application of surcharge loads.

RESEARCH SIGNIFICANCE

While numerous studies have been conducted on excavation work of standard scale, research on small-scale excavation projects remains limited. This is likely because smaller structures are considered to pose less risk. However, the number of small-scale excavations is extremely high, and some form of research-based validation is necessary. Therefore, this study investigates the deformations that occur in small-scale earth-retaining walls and their associated structural members during liquefaction, using numerical analysis.

NUMERICAL CONDITION

The numerical analyses were conducted using LIQCA3D20. The target embankment was constructed on two layers of sandy ground shown as Fig. 1. Aluminum sheet piles were installed facing each other to construct an earth-retaining system, followed by excavation to form a space measuring 2 m in depth and 2 m in width. The ground was discretized into 5400 cuboid elements. To perform numerical analysis, parameters such as dimensions, soil parameters, and countermeasures needed to be specified. The following sub-sections describe the ground condition, these parameters and their corresponding values.

Soil

The ground condition was a representative loose sandy soil with a relative density (Dr) of 40 %. The soil parameters used in the numerical model were shown in Table 1. Sand above the groundwater was modeled as dry, while that below was modeled as saturated. The soil parameter values were inferred and determined from the academic paper by Fujiwara et al [5]. The sand layers were modeled as elasto-plastic models created [6, 7], which is often used to model a loose sand layer. This model represents sand behavior resulting from an increase in excess pore water pressure which causes motion, making the sand soft, and finally causing liquefaction.

Countermeasure

The sheet piles are installed facing each other and are supported near their top ends by struts. The sheet piles are also connected in the longitudinal direction by walers. Table 2 shows the actual cross-sectional properties, and the corresponding values adopted in the numerical model for the sheet piles, struts and walers.

The sheet piles were 2.5 m long, with an embedment depth of 0.5 m. The sheet-piles were modeled by cuboid meshes with linear elastic material having no yield. The mesh thickness was set to 20 mm, and the Young's modulus was set to 1.22 x 10^9 kN/m^2 so that the flexural rigidity would be equivalent to that of the sheet pile. The density was set to 0.75 g/cm³ to match the mass of the sheet pile, thereby ensuring that the inertial force during seismic loading would also be equivalent.

The strut and waler were modeled using beam elements. The strut was connected at both ends to the sheet piles at positions 0.5 m below their tops (x = 0 m). The walers were connected to the sheet piles in the longitudinal direction at positions 0.5 m below their tops. The strut and waler were assigned properties that were sufficiently lightweight and had high rigidity, so that their own deformation and the effect of self-weight were negligible. Only the actual second moment of area property was assigned to the waler to accurately reproduce its bending deformation.

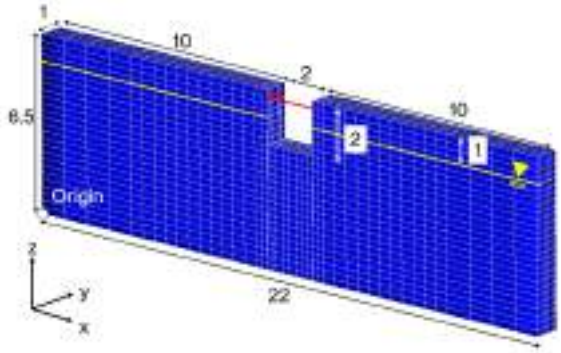

(a) Schematic view (without sheet-pile)

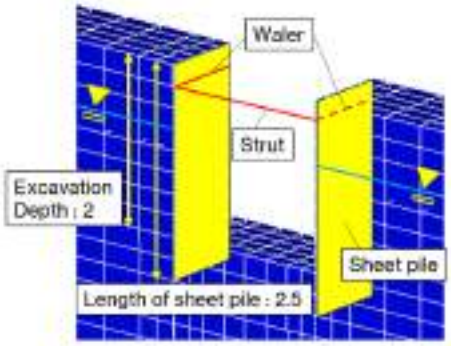

(b) Enlarged view

Fig. 1 The numerical model for Case 1 (Unit: m)

Table 1 Soil parameter

Initial stress analysis		Unit	Value
Density	ρ	t/m^3	1.8
Young's moduls	E_0	kN/m^2	5508
Poisson's ratio	ν		0.33
Cohesion	C	kN/m^2	0
Friction angle	ϕ	degree	32
Dynamic analysis			
Coefficient of permeability	k	m/s	2.0×10^{-4}
Initial void ratio	e_0		0.821
Compression index	λ		0.015
Swelling index	κ		0.002
	OCR*		1
Initial elastic shear modulus ratio	G_0/σ'_m		1000
Stress ratio at critical state	M^*_m		0.909
Stress ratio at failure	M^*_f		1.122
	B^*_0		7000
Hardening parameter	B^*_1		50
	C_f		2000
Dilentancy parameter	D_0		3
	n		3
Reference strain parameter	γ^{P*}		0.01
	γ^{E*}		0.02

Boundary condition

The coordinate system was set up with the y-axis extending along construction longitudinal direction, the x-axis perpendicular to the y-axis in the horizontal plane, and the z-axis pointing vertically upward. The z-x dimensions of the model were as follows: 22 m in the x-direction and 6.5 m in the z-direction.

Taking symmetry considerations into account, fixed boundary conditions were assigned at the locations of the side nodes in the x-direction, at x = 0 m and x = 22 m. In the y-direction, fixed boundary conditions were assigned at the locations of the side nodes at y = 0 m and 1 m. In the z-direction, the bottom nodes were fixed at z = 0 m in all cases.

Numerical case

Numerical cases are listed in Table 3. For Case 1, the groundwater table is at a depth of 1 m, and the spacing of the struts is 2 m; this is taken as the basic structure. For Case 2, there is no groundwater, and the entire ground is assumed to be dry sand. Liquefaction is not considered. For Cases 3-1 and 3-2, the spacing of the struts is 1 and 4 m, respectively. For Case 4-1, a vertical load is applied to both sides of the ground surface. For Case 4-2, the vertical load is applied to the right side of the ground surface. The vertical load is set to 10 kN/m^2, which is the design load specified in [3], taking into account the weight of construction equipment and materials.

Input motion

The dynamic analyses were carried out from the results of the initial analyses, using the input motion, which was the Level 1 earthquake motion publicly released for a coastal area was employed, as represented by the plot (Fig. 2). National Institute for Land and Infrastructure Management (NILIM) provided the data [8]. This wave had a maximum acceleration of 1.49 m/s^2, and a duration of 163 s.

The Newmark method was used to solve the responses of the soil and the structure. An incremental time interval of 0.005 s was used, while a value of 0.3025 was used for the coefficient β in the Newmark method and the value of γ was set at 0.6. We used a stiffness-proportional coefficient of 0.003 for Rayleigh damping.

NUMERICAL RESULT

In this chapter, the results of the numerical analysis are explained with a focus on the presence or absence of liquefaction (Case 2), the spacing of struts (Cases 3-1 and 3-2), and the presence or absence of surcharge loading (Case 4-1 and 4-2), compared to the basic structure (Case 1).

Table 2 Parameters for structural components

Sheet-pile		Unit	Value
Density	ρ	t/m^3	0.75
Young's moduls	E_0	kN/m^2	1.22×10^9
Poisson's ratio	ν		0.33

Strut		Unit	Value
Density	ρ	t/m^3	1.0×10^{-10}
Young's moduls	E_0	kN/m^2	2.0×10^8
Poisson's ratio	ν		0.33
Area	A	m^2	1000
Second moment of area	I	m^4	1000
Polar moment of inertia	J	m^4	1.0×10^9

Waler		Unit	Value
Density	ρ	t/m^3	1.0×10^{-10}
Young's moduls	E_0	kN/m^2	7.0×10^7
Poisson's ratio	ν		0.33
Area	A	m^2	2.25×10^{-3}
Second moment of area	I	m^4	2.46×10^{-6}
Polar moment of inertia	J	m^4	1.0×10^9

Table 3 Numerical cases

Case	Liquefaction	Spacing between struts	Vertical load
1	✓	2 m	No
2	No	2 m	No
3-1	✓	1 m	No
3-2	✓	4 m	No
4-1	✓	2 m	Both sides
4-2	✓	2 m	One side

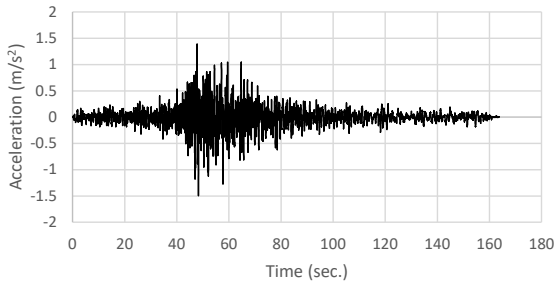

Fig. 2 Input motion

The presence or absence of liquefaction

For Cases 1 and 2, the deformations with excess pore water pressure ratio, corresponding to the end of shaking (t = 163 s), are represented by the heat maps shown in Fig. 3. The excess pore water pressure ratio is obtained by dividing the excess pore water pressure by the initial effective stress. In Case 1, the entire ground underwent significant deformation due to liquefaction. In contrast, in Case 2, no liquefaction was observed, and large deformation occurred only in the vicinity of the sheet pile. In both cases, due to the restraint provided by the struts near the top, the sheet

pile exhibited bulging deformation around their mid-height. Regarding the behavior in the vertical direction, in Case 1, the liquefied ground flowed beneath the sheet pile, resulting in an upward thrust that lifted the entire sheet pile; however, such behavior was not observed in Case 2.

The time histories of the axial force in the strut and the maximum bending moment in the waler are presented in Fig. 4, respectively. Compressive axial force was generated in the strut to resist the deformation of the sheet piles. The waler exhibited bending deformation as a beam supported at two points, with the supports located at the intersections with the strut. The maximum bending moment developed at the midpoint between the supports (y = 1 m). In Case 1, the strut experienced a maximum axial compression force of 35 kN and a maximum bending moment of 2.3 kNm, both of which occurred around 50 seconds, coinciding with the peak of the input acceleration. In Case 2 as well, the axial force and bending moment in the strut reached their maximum value around 50 seconds; however, these were significantly smaller than those in Case 1, at 16 kN and 1.3 kNm, respectively. Notably, little significant vibrational components were observed.

Fig. 5 shows the depth-wise distribution of horizontal and vertical displacements of both sheet pile walls at y =1 m. The horizontal displacement was generally similar between Case 1 and Case 2. However, in Case 1, an upward vertical displacement (uplift) was observed, whereas no such uplift was seen in Case 2.

The spacing of struts

For Cases 3-1 and 3-2, the deformations with excess pore water pressure ratio (t = 163 s) are represented in Fig. 6. In comparison with Case 1, little difference was observed in the occurrence of liquefaction and the deformation of the ground.

The time histories of the axial force in the strut and the maximum bending moment in the waler are presented in Fig. 7. In Cases 3-1 and 3-2, the strut experienced a maximum axial force of 20 kN and 47 kN, and a maximum bending moment of 0.8 kNm and 6.0 kNm, respectively. The axial force generated in the strut was approximately proportional to the spacing between them, while the bending moment in the waler was approximately proportional to the square of the spacing between the struts, that is, the distance between the supports of the waler.

Fig. 8 shows the depth-wise distribution of horizontal and vertical displacements of both sheet pile walls at the plane in the middle of the waler. In Case 3-2, where the spacing between struts is large, slightly larger horizontal displacements were observed at the top of the sheet pile. No significant differences were observed in other displacements.

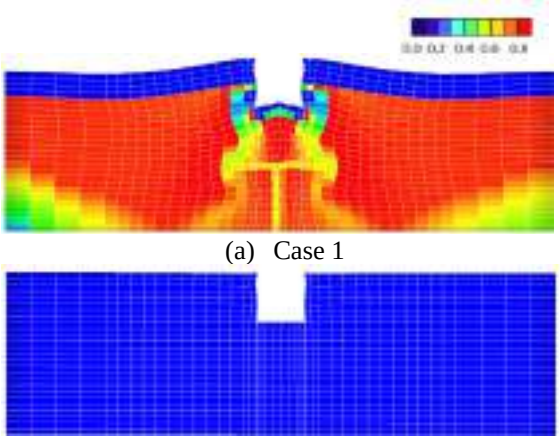

(a) Case 1

(b) Case 2

Fig. 3 The deformation with the excess pore water pressure ratio after shaking (Cases 1 and 2)

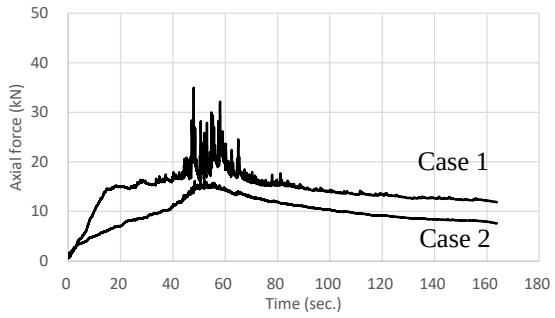

(a) Axial force in the strut

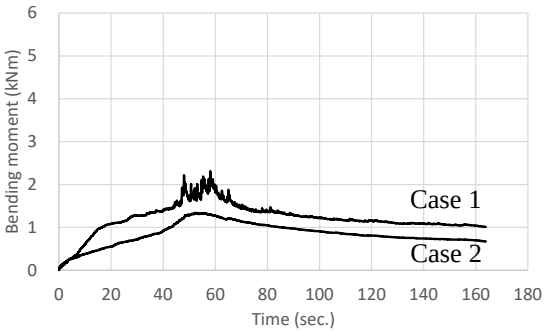

(b) Maximum bending moment in the welder

Fig. 4 The time histories of the internal forces in structural components (Cases 1 and 2)

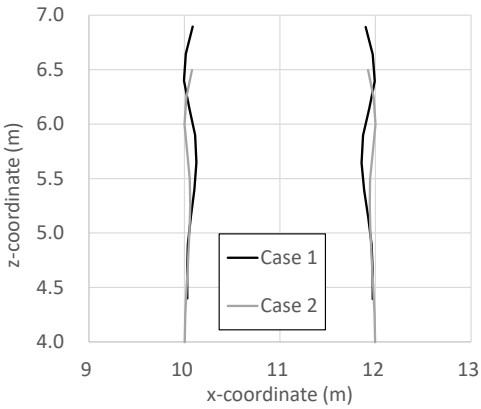

Fig. 5 Horizontal and vertical displacement in both sheet piles (Cases 1 and 2)

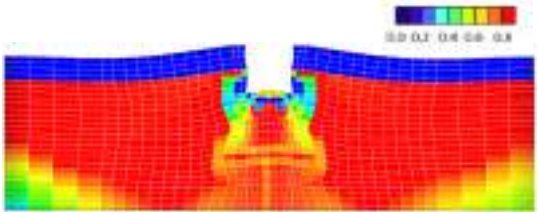

(a) Case 3-1

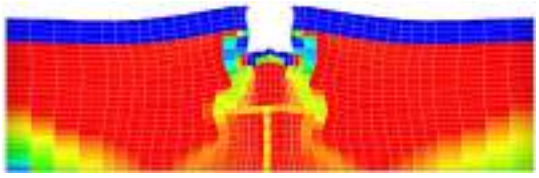

(b) Case 3-2

Fig. 6 The deformation with the excess pore water pressure ratio after shaking (Cases 3-1 and 3-2)

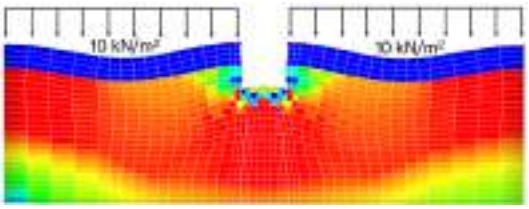

(a) Case 4-1

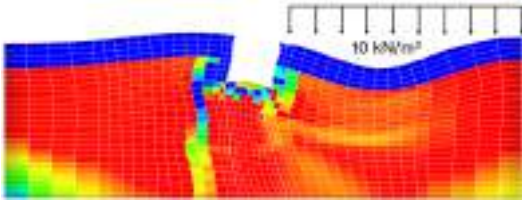

(b) Case 4-2

Fig. 9 The deformation with the excess pore water pressure ratio after shaking (Cases 4-1 and 4-2)

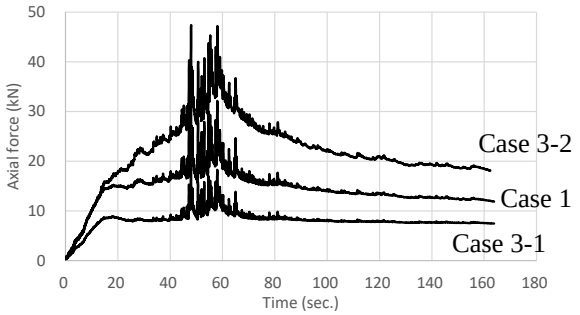

(a) Axial force in the strut

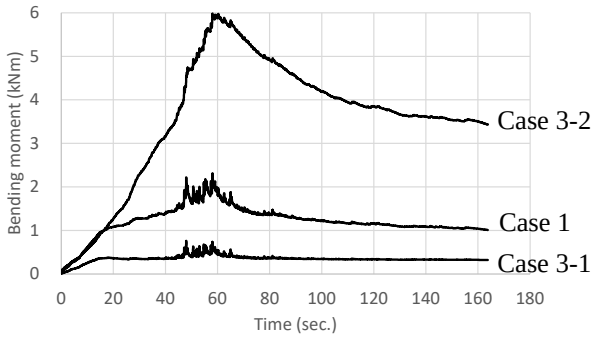

(b) Maximum bending moment in the welder

Fig. 7 The time histories of internal forces in structural components (Cases 1, 3-1 and 3-2)

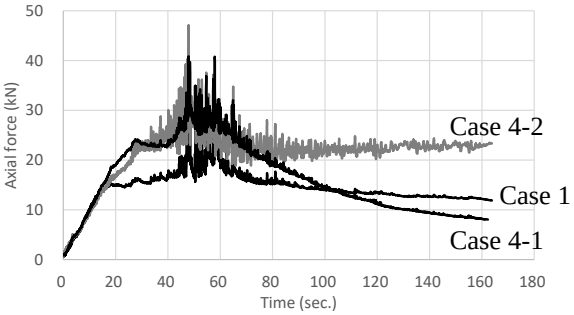

(a) Axial force in the strut

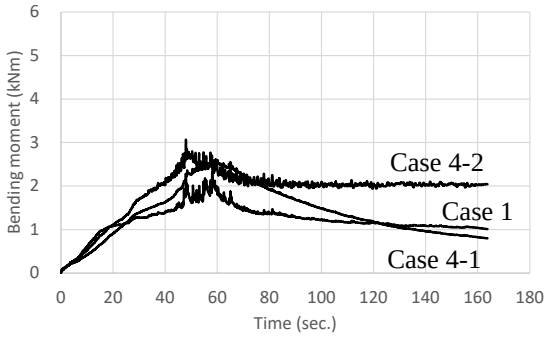

(b) Maximum bending moment in the welder

Fig. 10 The time histories of internal forces in structural components (Cases 1, 4-1 and 4-2)

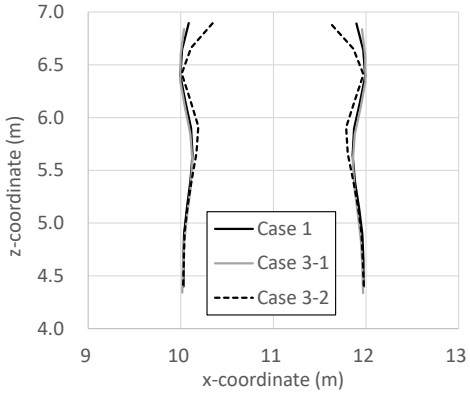

Fig. 8 Horizontal and vertical displacement in both sheet piles (Cases 1, 3-1 and 3-2)

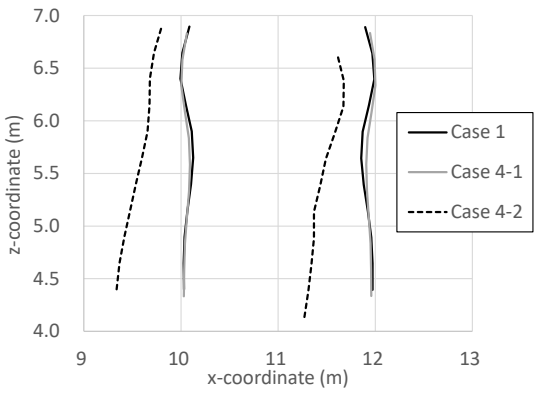

Fig. 11 Horizontal and vertical displacement in both sheet piles (Cases 1, 4-1 and 4-2)

The surcharge loading

For Cases 4-1 ~ 4-2, the deformations with excess pore water pressure ratio (t = 163 s) are represented in Fig. 9. Due to the application of a surface surcharge, the ground deformation in these cases was larger than that in Case 1. In particular, in Case 4-2, the eccentric load caused the ground to deform predominantly in the leftward direction.

The time histories of the axial force in the strut and the bending moment in the waler at y=1 m are presented in Fig. 10. The strut experienced a maximum axial force of 41 kN and 47 kN and a maximum bending moment of 2.7 kNm and 3.1 kNm. Compared to Case 1 without loading, the axial forces in the struts and the bending moments in the waler increased in Cases 4-1 and 4-2, where loading was applied.

Fig. 11 shows the depth-wise distribution of horizontal and vertical displacements of both sheet pile walls at y =1 m. Little significant differences were observed between Cases 1 and 4-1. In Case 4-2, the two sheet piles moved while undergoing rotation. The soil on the loading side pushed against the sheet piles, causing both rows of sheet piles to shift toward the non-loading side. As a result, the working space required for pipe installation and other construction activities was reduced, indicating a potentially hazardous situation.

CONCLUSION

This study conducted numerical analysis of small-scale earth retaining works under seismic conditions. The target site is assumed to be a sandy and saturated ground near the coast, and the numerical analysis takes liquefaction into account. The following results could be gained:

1) In the analysis results for the basic structure, liquefaction of the ground due to the earthquake caused horizontal loads from the soil to act on the two sheet piles and resulted in the compression of the underground space. To resist this, compressive axial force was generated in the strut, and bending moment was induced in the waler.

2) When liquefaction was not considered, the axial force in the struts and the bending moment in the waler were reduced to approximately half. In particular, the dynamic components of these forces were almost eliminated.

3) The axial force generated in the strut was approximately proportional to the spacing between them, while the bending moment in the waler was approximately proportional to the square of the spacing between the struts, that is, the distance between the supports of the waler.

4) Application of the surcharge load to only one side of the ground poses a greater risk of underground space deformation compared to loading on both sides during liquefaction.

5) In the future, the validity of the present analytical results will be examined by the authors through model experiments and full-scale construction tests.

ACKNOWLEDGMENTS

This study was conducted with a donation from NIPPON STEEL Echo-Tech Corporation, to whom the authors express their sincere gratitude.

REFERENCES

[1] Foundation for the Center for Land and Infrastructure Research, Manual for the Double Steel Sheet Pile Cut-off Method, 2001.

[2] Fujiwara K., Taenaka S., Otsushi K., Yashima A., Sawada K., Hara T., Ogawa T. and Takeda K., Study on Coastal Levee Reinforce Using Double Sheet-piles with Partition Walls, International Journal of Offshore and Polar Engineering, Vol. 27, No. 3, 2017, pp. 310-317.

[3] Public Interest Incorporated Association –Japan Road Association, Road Earthwork –, Temporary Structure Engineering Guidelines, 1999, pp.156-160.

[4] Yan B., and Fujiwara K., Examination on small-scale excavation works focusing on the cohesion of sand, 60th Japan National Conference on Geotechnical Engineering, 2025, 23-6-2-01.

[5] Kakuta Fujiwara, Nanase Ogawa and Kentaro Nakai, 3-D Numerical Analysis of Partial Floating Sheet-pile Method as Countermeasure for Liquefaction, Journal of Japan Society of Civil Engineers, Vol. 9, 2021, pp.138-147.

[6] Oka F., Yashima A., Shibata T., Kato M., and Uzuoka R., FEM-FDM coupled liquefaction analysis of a porous soil using an elasto-plastic model, Applied Scientific Research, Vol. 52, 1994, pp. 209-245.

[7] Oka F., Yashima A., Tateishi A., Taguchi Y. and Yamashita A., A cyclic elasto-plastic constitutive model for sand considering a plastic-strain dependence of the shear modulus, Geotechnique, Vol. 49(5), 1999.

[8] National Institute for Land and Infrastructure Management(NILIM), https://www.ysk.nilim.go.jp/kakubu/kouwan/sisetu/level1.html

Copyright © Int. J. of GEOMATE All rights reserved, including making copies, unless permission is obtained from the copyright proprietors.

15th Int. Conf. on Geotechnique, Construction Materials & Environment,
Kyoto, Japan, 11-13 November 2025, ISBN 978-4-909106124 C3051

DEVELOPMENT AND PERFORMANCE EVALUATION OF A UPV-BASED MODEL FOR EARLY FROST DAMAGE

Sohee Moon[1], Youngwoong Jung[1], Seongpyo Kim[1], Jayeon Yun[1], and Hyeonggil Choi[2]

[1] School of Architectural, Civil, Environmental, and Energy Engineering,
Kyungpook National University, Republic of Korea
[2] School of Architecture, Kyungpook National University, Republic of Korea

ABSTRACT

This study evaluates the applicability of high-frequency ultrasonic testing and machine learning-based regression models for diagnosing early frost damage in mortar. Ultrasonic pulse velocity (UPV) and compressive strength were measured under varying curing ages and frost exposure depths. Based on these data, a multi-stage prediction model was developed. In the first stage, compressive strength was predicted using UPV and curing age as input variables. In the second stage, the predicted compressive strength was used to estimate the depth of early frost damage. Four regression algorithms were applied, and the combination of the 250 kHz frequency with the Gradient Boosting model demonstrated the highest prediction accuracy. In contrast, the 54 kHz-based linear regression model showed low explanatory power and high error. Taylor diagram analysis further confirmed that high-frequency models were more closely distributed around the reference line, indicating higher predictive reliability. These findings suggest that the combination of high-frequency ultrasonic testing and nonlinear regression algorithms is effective for quantifying early microstructural damage in cementitious materials. Furthermore, the proposed model provides a foundation for the future application of ultrasonic-based, machine learning-enhanced diagnostic techniques in real-world concrete structures and field evaluations.

Keywords: Early frost damage, Ultrasonic pulse velocity, Non-destructive testing, Machine learning

INTRODUCTION

Early frost damage (EFD), which can occur during the early stages of construction in winter, is one of the major deterioration factors that can critically impair the strength development and durability of concrete structures. In particular, when concrete is exposed to subfreezing temperatures before sufficient strength has developed the internal free water freezes and expands in volume. This volumetric expansion induces local stress concentrations, primarily leading to microcracks between the cement paste and aggregates. Such damage hinders the progress of the hydration reaction, ultimately resulting in a reduction of compressive strength. Since these microstructural damages are often not visible externally, early diagnosis through appropriate non-destructive testing (NDT) methods is essential [1–3].

Among various NDT techniques, the ultrasonic pulse velocity (UPV) test is one of the most widely used methods for assessing internal defects and degradation in concrete. It is particularly advantageous due to its relatively easy application in construction sites. The primary factors affecting the propagation velocity of ultrasonic waves through a material include density, elastic modulus, and porosity—all of which are sensitive to changes induced by early frost damage. Therefore, UPV can serve as an indirect indicator of internal structural conditions [4,5].

However, most existing studies have employed ultrasonic waves with a center frequency of 54 kHz. Due to the relatively long wavelength at this frequency, its sensitivity to microstructural damage is limited [6–8]. In contrast, high-frequency ultrasonic waves (above 250 kHz), characterized by shorter wavelengths, have the potential to more precisely detect fine cracks and localized damage within structures [9]. In particular, for detecting early-stage microcracks and localized deterioration caused by EFD, the use of high-frequency ultrasonics is considered more appropriate.

Meanwhile, traditional UPV-based degradation assessments have primarily relied on linear regression models or empirical correlation formulas, which have limitations in capturing the complex and nonlinear interactions among variables such as curing age, damage depth, and exposure conditions [10]. To address these limitations, recent studies have actively explored the use of artificial intelligence techniques, such as machine learning (ML) and deep learning (DL), to predict structural damage based on ultrasonic data [11,12]. Machine learning models are capable of effectively learning nonlinear relationships among multiple input variables. In particular, ensemble-based nonlinear regression models, such as Random Forest and Gradient Boosting, offer high predictive accuracy and the advantage of enabling influence analysis among variables [13].

Table 1 Experimental plan

Specimen	Conditions of experiments				W/C	C:S	Measurement items
	Freezing depth (mm)	Curing before freezing (h)	Freezing temperature (°C)	Freezing time (h)			
Plain	Non-frozen	-	-	-	0.5	1:3	· Ultrasonic pulse velocity · Compressive strength
FD-00	0	6	-10	24			
FD-03	30						
FD-06	60						
FD-10	100						

Table 2 Physicochemical properties of the fine aggregate constituents

Type	Fineness modulus	Density (g/cm^3)	Water absorption (%)	Stability (%)
Natural river sand	2.46	2.57	1.16	3.2

Therefore, this study aims to develop a machine learning-based multi-stage prediction model using ultrasonic pulse velocity and curing age as input variables, and compressive strength and early frost damage depth as output variables. Specifically, in the first stage, compressive strength is predicted based on ultrasonic velocity and curing age, and in the second stage, the predicted compressive strength is further used to estimate the depth of early frost damage. In addition, by comparing the predictive performance of models based on 54 kHz and 250 kHz ultrasonic data, this study experimentally evaluates the applicability and effectiveness of high-frequency ultrasonic techniques.

MODEL DEVELOPMENT PLAN AND METHODOLOGY

Specimen Preparation

The experimental plan of this study is presented in Table 1. The primary objective is to develop a machine learning-based model to predict the compressive strength and early frost damage depth of mortar using UPV, and to evaluate the predictive performance across two frequencies (54 kHz and 250 kHz). In particular, the applicability of high-frequency ultrasonic waves (250 kHz) is investigated to identify an optimal diagnostic frequency for early frost damage assessment. As a preliminary step toward practical application to concrete structures, this study focused on precisely analyzing the sensitivity of ultrasonic signals to microstructural damage at different frequencies by using mortar specimens, which provide relatively homogeneous material properties and minimize signal scattering caused by aggregates.

The specimens were fabricated as cylindrical molds with dimensions of Ø 50 mm × 100 mm and classified into five levels based on the depth of low-temperature exposure: Plain, FD-00, 03, 06, and 10. The FD series specimens were exposed to freezing at −10 °C for 24 hours at target depths of 0, 30, 60, and 100 mm, following an initial curing period of 6 hours. The mix proportion was fixed at a water-to-cement ratio (W/C) of 0.5 and a cement-to-sand ratio (C:S) of 1:3, using ordinary Portland cement. The properties of the fine aggregate are summarized in Table 2.

Implementation of Early Frost Damage Conditions and Data Acquisition Procedure

To simulate early frost damage at specific depths, an insulation device was designed to expose only the designated section of each specimen, minimizing external air intrusion with an additional 5 mm insulation sheet to enhance experimental precision. Plain specimens were demolded after 24 hours and cured underwater at 20 ± 1 °C, while FD series specimens underwent initial curing for 6 hours at 20 ± 1 °C and 60 ± 5% relative humidity, followed by 24 hours of freezing exposure at −10 °C before subsequent water curing.

UPV measurements were conducted using a Pundit Lab(+) device at two frequencies, 54 kHz and 250 kHz, employing the direct transmission method. A constant load of 2 kg was applied during measurements to minimize errors caused by variations in contact pressure. The ultrasonic pulse velocity tests were performed in accordance with ASTM C597. Compressive strength tests were conducted after ultrasonic testing in accordance with KS L ISO 679 and KS F 2405. The overall procedure for implementing early frost damage conditions and acquiring data is illustrated in Figure 1.

Development of the Predictive Model Regression Algorithm Configuration

For model development, UPV and curing age were set as input variables, while compressive strength and early frost damage depth were defined as output variables. A total of 90 data points were collected for each frequency, and the dataset was randomly divided into training (80%) and validation (20%) subsets to objectively evaluate model generalization. A multi-stage prediction model was applied to reflect strength development and

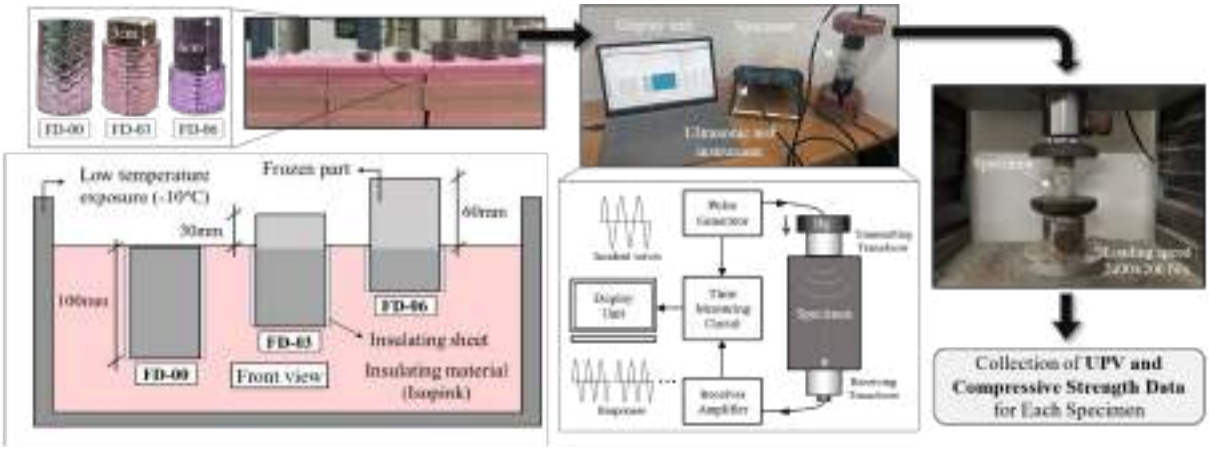

Fig.1 Schematic of the experimental procedure for early frost damage simulation and data acquisition

and degradation characteristics over curing time and to improve prediction accuracy. In the first stage, compressive strength was predicted using UPV and curing age, and in the second stage, the predicted compressive strength was used to estimate early frost damage depth. This structure was designed to incorporate causal relationships between stages, thereby enhancing both prediction precision and model interpretability.

For the model implementation, four regression algorithms were employed: Linear Regression (LR), Decision Tree (DT), Random Forest (RF), and Gradient Boosting (GB). LR assumes a simple linear relationship, while DT captures nonlinear interactions through a tree structure. RF and GB are ensemble learning methods, with GB particularly excelling in prediction accuracy and generalization performance through iterative learning. Since these algorithms differ in their structural characteristics and learning mechanisms, all four models were applied in this study to compare predictive performances under both linear and nonlinear assumptions. This approach enabled a visual and quantitative understanding of the structural differences between the algorithms and ensured a rational model selection process.

Hyperparameter Settings

The performance of machine learning-based predictive models is not solely determined by the choice of algorithm but is also highly influenced by the setting of hyperparameters. Hyperparameters are values manually set prior to model training, and they critically impact various aspects such as model complexity, learning speed, predictive accuracy, and prevention of overfitting. Therefore, in this study, the range of hyperparameters for each regression algorithm was preliminarily reviewed, and through multiple iterative trainings and experimental comparisons, the optimal combination was determined. The key hyperparameters set for each model are summarized in Table 3. All models were optimized by considering data characteristics, overfitting prevention, and predictive accuracy, ensuring a fair comparison of model performance.

Table 3 Hyperparameter settings for machine learning regression algorithms

Model	Hyperparameter	Value
Linear Regression (LR)	-	-
Decision Tree (DT)	Max depth	4
	Min samples splits	5
	Min samples leaf	2
	Random state	42
Random Forest (RF)	N estimators	100
	Max depth	6
	Min samples split	2
	Min samples leaf	2
	Random state	42
Gradient Boosting (GB)	N estimators	150
	Learning rate	0.1
	Mad depth	3
	Random state	42

Evaluation of Predictive Model Performance

One of the primary metrics used to evaluate the performance of regression models is the coefficient of determination (R^2), which indicates how well the model explains the variability of the data. An R^2 value closer to 1 signifies that the regression model has a stronger explanatory power. In this study, R^2 was used to assess how accurately the UPV reflects changes in compressive strength. A higher R^2 value implies a stronger relationship between UPV and compressive strength, thereby suggesting that the corresponding frequency provides a more suitable Table 3 Hyperparameter settings for machine learning regression algorithms basis for UPV-based compressive strength evaluation.

In addition, the root mean square error (RMSE) was employed to measure the average magnitude of the errors between the predicted and actual values. A lower RMSE indicates higher predictive accuracy.

Table 4 Prediction performance of compressive strength according to frequency and regression algorithm

Frequency	Model	R^2		RMSE (MPa)		MAE (MPa)	
		Training	Testing	Training	Testing	Training	Testing
250 kHz	Linear Regression (LR)	0.929	0.979	1.673	1.673	1.316	0.650
	Decision Tree (DT)	0.995	0.983	0.427	0.427	0.277	0.521
	Random Forest (RF)	0.998	0.987	0.253	0.253	0.173	0.460
	Gradient Boosting (GB)	0.999	0.990	0.093	0.093	0.053	0.262
54 kHz	Linear Regression (LR)	0.759	0.863	3.092	3.092	2.193	1.589
	Decision Tree (DT)	0.924	0.916	1.741	1.741	1.052	1.190
	Random Forest (RF)	0.983	0.951	0.813	0.813	0.612	0.979
	Gradient Boosting (GB)	0.991	0.971	0.592	0.592	0.632	0.611

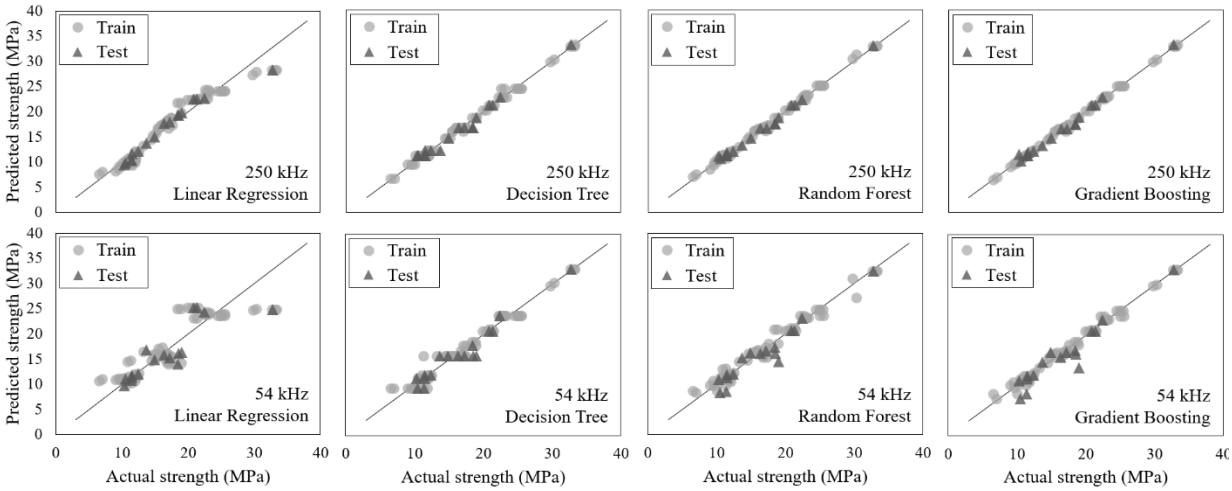

Fig. 2 Scatter plot of compressive strength prediction

The mean absolute error (MAE) was also used, which calculates the average absolute difference between the predicted and actual values. Unlike RMSE, MAE is less sensitive to outliers. Therefore, both RMSE and MAE were utilized to quantitatively compare the prediction errors of compressive strength models based on different ultrasonic frequencies.

These evaluation metrics were applied to both the compressive strength prediction model (Stage 1) and the early frost damage depth prediction model (Stage 2) to compare and analyze which algorithm exhibited the highest predictive accuracy and which frequency more sensitively reflected the extent of damage.

EVALUATION AND ANALYSIS OF MODEL PERFORMANCE

Compressive Strength Prediction Model

Performance evaluation using quantitative metrics

Table 4 presents the quantitative evaluation results (R^2, RMSE, and MAE) for the compressive strength prediction models using UPV and curing age as input variables. The analysis showed that models based on 250 kHz exhibited higher predictive accuracy and generalization performance compared to those based on 54 kHz. In particular, the 250 kHz GB model achieved the best performance, recording an R^2 value of 0.989, RMSE of 0.093, and MAE of 0.262 on the test dataset. In contrast, models using 54 kHz data, especially the LR model, demonstrated relatively lower predictive performance. Furthermore, nonlinear regression models (GB and RF) consistently outperformed the linear regression model (LR), experimentally confirming the nonlinear relationship between UPV and compressive strength.

Prediction results and error analysis based on scatter plots

The compressive strength prediction results for different frequencies (54 kHz and 250 kHz) and regression algorithms were analyzed using scatter plots, with the training and test results separately presented in Figure 3. Models based on 250 kHz generally showed distributions closely aligned with the reference line (1:1 line), indicating high predictive accuracy, and the GB and RF models demonstrated strong generalization performance even on the test data. In particular, the GB model achieved the highest performance with an R^2 value of 0.990 on the test

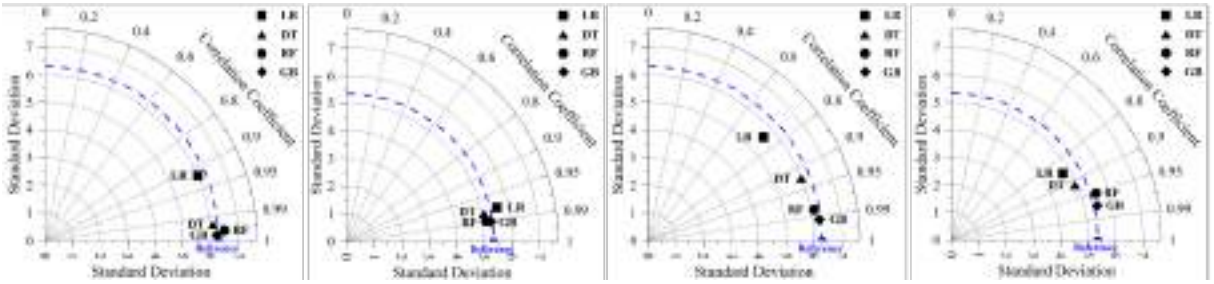

(a) Training (250kHz) (b) Testing (250kHz) (c) Training (54kHz) (d) Testing (54kHz)

Fig.3 Taylor diagram of compressive strength prediction performance

Table 5 Prediction performance of early frost damage depth according to frequency and regression algorithm

Frequency	Model	R^2		RMSE (mm)		MAE (mm)	
		Training	Testing	Training	Testing	Training	Testing
250 kHz	GB-LR	0.248	0.821	33.185	13.298	27.238	10.338
	GB-DT	0.600	0.501	24.195	22.215	16.944	14.444
	GB-RF	0.842	0.410	15.035	25.362	9.742	19.775
	GB-GB	0.899	0.634	12.148	19.029	5.978	11.945
54 kHz	GB-LR	0.316	-0.226	31.319	36.546	26.323	32.102
	GB-DT	0.647	0.275	22.491	28.108	15.683	21.698
	GB-RF	0.803	0.259	16.820	28.408	12.025	21.895
	GB-GB	0.835	0.246	15.400	28.665	9.085	18.578

dataset. In contrast, the 54 kHz models exhibited greater deviations from the reference line, with the LR model showing particularly low predictive accuracy. Additionally, the RF and GB models produced more concentrated distributions near the reference line compared to the LR model, visually confirming the nonlinear relationship between ultrasonic pulse velocity and compressive strength

Comprehensive performance comparison using taylor diagram

The predictive performance of the models across different frequencies and regression algorithms was analyzed using a Taylor diagram, as shown in Figure 4. Overall, models based on 250 kHz demonstrated higher predictive accuracy than those using 54 kHz, with the Gradient Boosting (GB) model achieving the best performance under all conditions. The GB model maintained distributions very close to the reference point for both the training and test datasets, indicating excellent generalization capability. These results suggest that combining high-frequency ultrasonic data with nonlinear regression algorithms can maximize predictive performance. Based on these findings, the next stage of this study will involve developing an early frost damage depth prediction model using the GB model's predicted compressive strength values as input.

Early Frost Damage Depth Prediction Model

Based on the Stage 1 compressive strength prediction results, a machine learning regression model was developed to predict early frost damage depth using the predicted compressive strength values from the GB model. The predictive performance for each frequency condition is summarized in Table 5.

Overall, models using 250 kHz data demonstrated higher accuracy than those using 54 kHz, with the GB-GB model showing the best performance (R^2 = 0.634, RMSE = 19.029, MAE = 11.945) on the test dataset. In contrast, the 54 kHz LR model exhibited very poor predictive accuracy. Nonlinear regression algorithms generally outperformed linear regression, and the GB-GB model achieved the highest accuracy in both the compressive strength and early frost damage depth prediction stages. These results validate the effectiveness of the multi-stage prediction approach and highlight that high-quality predicted compressive strength values can serve as meaningful inputs for subsequent early frost damage depth prediction.

In conclusion, this study confirmed that an early frost damage depth prediction model can be effectively established using predicted compressive strength values. In particular, the combination of high-frequency ultrasonic data and nonlinear regression algorithms contributed significantly to maximizing prediction accuracy, suggesting that a multi-stage prediction strategy based on high-frequency ultrasonic pulse velocity data is a viable approach for developing practical early frost damage diagnostic models in field

applications.

Although previous studies have widely utilized ultrasonic pulse velocity and similar input variables to estimate compressive strength, relatively few have attempted to predict early frost damage severity or depth based on such data. The present study confirmed the potential of a multi-stage machine learning framework to extend beyond strength prediction and evaluate internal damage conditions caused by early-age freezing. This represents a meaningful contribution to the field by expanding the applicability of ultrasonic-based diagnostics.

CONCLUSIONS

This study proposed a machine learning-based multi-stage model using UPV and curing age to predict both compressive strength and early frost damage depth in mortar. The 250 kHz–Gradient Boosting model achieved the best performance (R^2 = 0.990), confirming the advantages of high-frequency ultrasonics and nonlinear learning. Unlike previous studies focused solely on strength prediction, this research demonstrated the potential to quantify frost damage severity. The findings support the practical applicability of this approach for early-age diagnostics in cementitious materials, with further validation suggested for future work.

ACKNOWLEDGMENTS

This work was supported by the National Research Foundation of Korea(NRF) grant funded by the Korea government (MSIT)(NRF-2021R1C1C1011347).

REFERENCES

[1] Abayou A., Yasien A.M., and Bassuoni M.T., Properties of nanosilica-modified concrete cast and cured under cyclic freezing/low temperatures. Advances in Civil Engineering Materials, Vol. 8, Issue 3, 2019, pp. 287–306.

[2] Karagol F., Demirboga R., and Khushefati W.H., Behavior of fresh and hardened concretes with antifreeze admixtures in deep-freeze low temperatures and exterior winter conditions. Construction and Building Materials, Vol. 76, 2015, pp. 388–395.

[3] Zhang G., Yu H., Li H., and Yang Y., Experimental study of deformation of early age concrete suffering from frost damage. Construction and Building Materials, Vol. 215, 2019, pp. 410–421.

[4] Revilla-Cuesta V., Skaf M., Serrano-Lopez R., and Ortega-Lopez V., Models for compressive strength estimation through non-destructive testing of highly self-compacting concrete containing recycled concrete aggregate and slag-based binder. Construction and Building Materials, Vol. 280, 2021, Article ID 122454.

[5] Pereira N., and Romao X., Assessing concrete strength variability in existing structures based on the results of NDTs. Construction and Building Materials, Vol. 173, 2018, pp. 786–800.

[6] Chandam G., Ahn E., and Shin M., Influence of aggregate size on relative velocity change of high-frequency ultrasound in progress of concrete curing. Construction and Building Materials, Vol. 447, 2024, Article ID 138062.

[7] Shah A.A., Ribakov Y., and Zhang C., Efficiency and sensitivity of linear and non-linear ultrasonics to identifying micro and macro-scale defects in concrete. Materials & Design, Vol. 50, 2013, pp. 905–916.

[8] Bogas J.A., Gomes M.G., and Gomes A., Compressive strength evaluation of structural lightweight concrete by non-destructive ultrasonic pulse velocity method. Ultrasonics, Vol. 53, 2013, pp. 962–972.

[9] Kocab D., Misak P., Jindrova B., Alexa M., and Vymazal T., Analysis of the influence of transducer frequency on the ultrasonic measurement of concrete homogeneity. Acta Polytechnica CTU Proceedings, Vol. 22, 2019, pp. 48–51.

[10] Hong S.U., and Cho Y.S., A study on the estimation of the compressive strength of concrete structures using ultrasonic pulse velocity method and rebound hardness method. Journal of the Architectural Institute of Korea, Vol. 27, No. 1, 2011, pp. 19–26.

[11] Anwar M.K., Qurashi M.A., Zhu X., Shah S.A.R., and Siddiq M.U., A comparative performance analysis of machine learning models for compressive strength prediction in fly ash-based geopolymer concrete using reference data. Case Studies in Construction Materials, Vol. 22, 2025, Article ID e04207.

[12] Harith I.K., Abdulhadi A.M., and Hussien M.L., Harnessing machine learning for accurate estimation of compressive strength of high-performance self-compacting concrete from non-destructive tests: a comparative study. Construction and Building Materials, Vol. 451, 2024, Article ID 138779.

[13] Otchere D.A., Ganat T.O.A., Ojero J.O., Tackie-Otoo B.N., and Taki M.Y., Application of gradient boosting regression model for the evaluation of feature selection techniques in improving reservoir characterisation predictions. Journal of Petroleum Science and Engineering, Vol. 208, 2022, Article ID 109244.

Copyright © Int. J. of GEOMATE All rights reserved, including making copies, unless permission is obtained from the copyright proprietors.

15th Int. Conf. on Geotechnique, Construction Materials & Environment,
Kyoto, Japan, 11-13 November 2025, ISBN 978-4-909106124 C3051

STUDY ON THE BEHAVIOR OF RECYCLED AGGREGATE CONCRETE UNDER HIGH TEMPERATURE EXPOSURE AND RECOVERY THROUGH RE-CURING

Husnah[1,2], Herlien Dwiarti Setio[1], *Ivan Sandi Darma[1] and Patria Kusumaningrum[1]

[1]Faculty of Civil and Environmental Engineering, Bandung Institute of Technology, Indonesia
[2]Department of Civil Engineering, Universitas Abdurrab, Indonesia

ABSTRACT

The effects of high-temperature damage on Recycled Aggregate Concrete (RAC) remain insufficiently studied. In RAC, the presence of residual mortar attached to the aggregates increases the heterogeneity of the material, potentially causing it to respond differently to high temperatures compared to conventional concrete. The decline in strength when exposed to elevated temperatures is largely attributed to the mismatch in thermal expansion between the aggregates and the cement paste. This mismatch generates thermal stresses in the Interfacial Transition Zone (ITZ), which significantly affects RAC's performance, especially during the re-curing phase after heat exposure. This research investigates the effectiveness of re-curing as a method to restore the compressive strength of RAC that has been exposed to high temperatures. Recycled Concrete Aggregate (RCA) was sourced from parent concrete with compressive strengths of 25 MPa and 40 MPa and incorporated at replacement levels of 50% and 100%. Mixes with water-to-cement ratios of 0.3 and 0.45 were prepared and cured for 28 days before being subjected to 550°C and 800°C. Compressive strength tests indicated a maximum strength loss of 62% at 550°C and 87% at 800°C in RAC containing 50% RCA with a w/c ratio of 0.45. After re-curing, the highest strength recovery was observed in RAC with 100% RCA and a w/c ratio of 0.45, achieving recovery levels of 53–74% at 550°C and 32–40% at 800°C. This recovery is believed to result from the regeneration of hydration products due to the rehydration of previously unhydrated mineral oxides.

Keywords: RCA, RAC, High Temperature Exposure, Concrete Compressive Strength, Re-Curing

INTRODUCTION

Previous research [1] has indicated that concrete incorporating Recycled Concrete Aggregate (RCA) can exhibit comparable properties to conventional concrete and meet structural performance requirements, even at high replacement levels. Despite the substantial progress made in recent years, several challenges still hinder the widespread adoption of RCA. One such challenge is the limited understanding of how recycled aggregate concrete responds to high-temperature exposure. This is particularly important because the presence of residual mortar on recycled aggregates introduces additional phases in the concrete, potentially resulting in behavior under high temperatures that differs significantly from that of normal concrete [2].

Aggregates make up about 60–75% of the total volume of concrete, making the thermal behavior of concrete largely dependent on the type of aggregate used, as different aggregates react differently to high-temperature exposure [3]. The reduction in concrete strength at elevated temperatures is primarily due to the incompatibility between the thermal expansion of the aggregate and the cement paste. This mismatch induces thermal stress in the Interfacial Transition Zone (ITZ). When the stress surpasses the tensile strength of the cement paste, it can lead to radial cracking in the paste originating from the ITZ, which may link up with cracks from nearby ITZ regions [4]

Consequently, the choice of aggregate plays a critical role in maintaining concrete stability under thermal stress. In the case of Recycled Aggregate Concrete (RAC), this is especially important, as recycled aggregates may exhibit varied responses to high-temperature exposure [5].

Furthermore, understanding how concrete behaves under high-temperature conditions is essential, as fire safety plays a crucial role in the structural design of concrete buildings [4]. While the general behavior of concrete at elevated temperatures is relatively well understood, exposure to heat triggers a series of physicochemical transformations that affect its thermo-mechanical characteristics. These changes can significantly reduce the material's mechanical performance, particularly as the temperature increases.

RESEARCH SIGNIFICANCE

Recycled Aggregate Concrete (RAC) is recognized as an environmentally friendly material in civil engineering due to its sustainability advantages [6,7]. However, its compressive strength tends to

decline markedly when subjected to elevated temperatures, such as those experienced during fire events. This study examines the performance of RAC after exposure to high temperatures and explores the effectiveness of re-curing as a method for strength recovery. Concrete samples were heated to 550°C and 800°C, then underwent a controlled re-curing process for a defined period. This study provides insights for structural rehabilitation using recycled materials under thermal stress conditions.

LITERATURE REVIEW

The results of research in several literatures [2,8–12], obtained contradictory results. Gales, [13] reported that concrete containing recycled aggregates exhibited a lower relative compressive strength compared to that made with natural aggregates, with strength decreasing as the proportion of recycled aggregates increased. This decline is attributed to the lower strength and larger Interfacial Transition Zone (ITZ) associated with recycled aggregates. In contrast, Zhao [14] found that concrete with recycled aggregates performed similarly to that with natural aggregates. Additionally, Sarhat [15], observed a gain in the mechanical behavior of concrete incorporating recycled aggregates [16]. This enhancement likely arises from the closer alignment of thermal expansion between recycled aggregates and the cement paste, which serves to suppress crack propagation within the paste and on the surface.

METHODS

This study investigates the presence of Unhydrated Cement Granules (UCG) in Recycled Concrete Aggregate (RCA) using SEM and XRD analysis. SEM was conducted at 15 kV, 10 mm working distance, 2000x magnification, and 10 μm layer thickness. XRD was performed using Rigaku SmartLab (θ–2θ mode, Cu $K\alpha_1$, 40 kV, 30 mA, 10°–70° range). Recycled concrete aggregates (RCA) obtained from original concrete with compressive strengths of 25 MPa and 40 MPa were incorporated into new concrete mixtures at replacement levels of 50% and 100%, using water-to-cement ratios of 0.30 and 0.45. After a 28-day curing period, the RAC specimens were subjected to temperatures of 550°C and 800°C to assess the decomposition of the C-S-H phase. The impact of this thermal exposure was analyzed by measuring the compressive strength of the concrete both immediately after heating and following a re-curing treatment

RESULTS AND DISCUSSION

RCA morphology testing using SEM to identify the possible presence of UCG minerals in RCA, which affect the mechanical behavior of RAC before and after exposure to high temperatures. This test was carried out at a magnification level of 2000x. The results of the RCA morphology test can be seen in Fig.1, while the identification of mineral chemical compounds can be seen in Fig. 2.

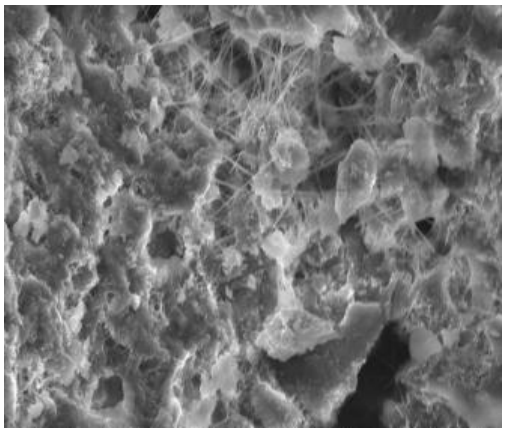

Fig.1 2000x magnification level

Fig.1 shows the presence of C3S, C2S, CSH, CH, ettringite and pores in RCA which affect the mechanical behavior of RAC.

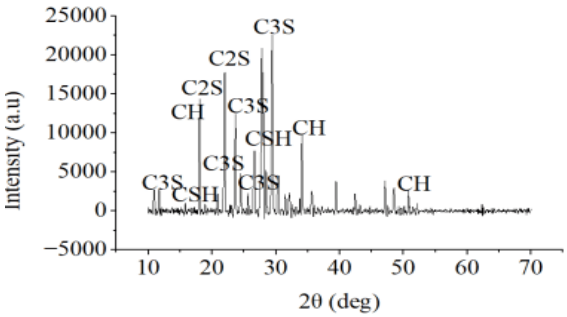

Fig.2 Mineral chemical compounds in RCA

Concrete Compressive Strength

The test results indicated a noticeable decline in compressive strength when concrete was exposed to high temperatures. This reduction is primarily due to dehydration caused by moisture loss, which leads to the breakdown of calcium silicate hydrate (C-S-H)—a key contributor to concrete strength—into its original compounds, C2S and C3S. Additionally, elevated temperatures create thermal incompatibility between the cement paste and aggregates, as the paste tends to contract while the aggregates expand. This mismatch in thermal strain generates internal stresses that can lead to microcracking within the cement paste and the Interfacial Transition Zone (ITZ), ultimately diminishing the concrete's mechanical performance.

Concrete exposed to 550°C exhibits behavior that contrasts with that at normal room temperature (20°C). At 550°C, the highest compressive strength is observed in concrete made entirely with natural aggregate (100% NA) (can be seen in Fig. 3). Concrete with 100% natural aggregate shows better performance against exposure to a temperature of 550°C compared to concrete with recycled aggregate.

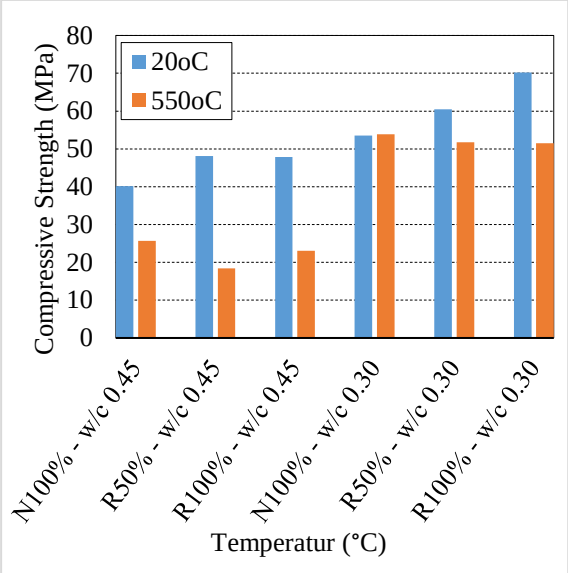

Fig.3 Concrete Compressive Strength After Exposure to Temperature 550°C

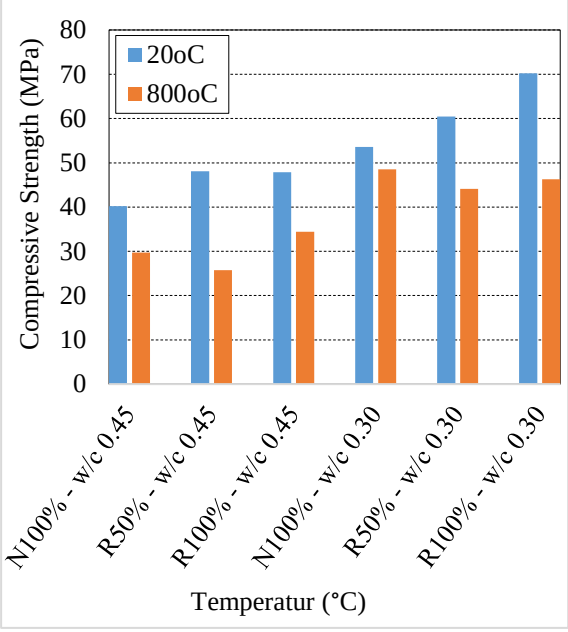

Fig.4 Concrete Compressive Strength After Exposure to 800°C

Similar to when exposed to 550°C, the highest compressive strength of concrete exposed to 800°C is in concrete with 100% natural aggregate (can be seen in Fig.4). Concrete with 100% natural aggregate shows better performance against exposure to 800°C compared to concrete with recycled aggregate.

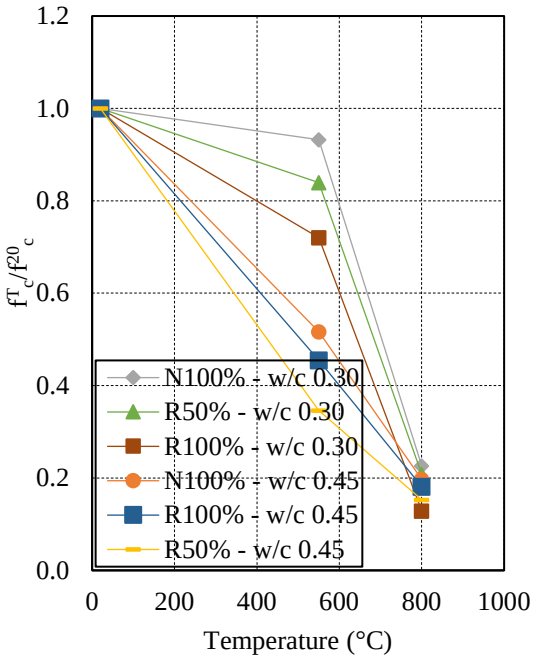

Fig.5 Concrete Compressive Strength Reduction Coefficient Due to High Temperature

Residual compressive strength tests (as shown in Fig. 5) revealed that the largest strength reduction at 550°C occurred in concrete with a water-cement ratio of 0.45 and 50% recycled aggregate content. In contrast, at 800°C, the most substantial decrease in strength was found in concrete with a water-cement ratio of 0.30 containing 100% recycled aggregate. Across all concrete mix variations, exposure to 800°C consistently resulted in compressive strength reductions ranging from 77% to 85%. This aligns with the findings in [17], which state that at 800°C, a significant reduction in strength results from the breakdown of the secondary phase of calcium silicate hydrate (C-S-H). The more pronounced strength loss in recycled aggregate concrete, compared to concrete made with natural aggregates, is mainly due to the inferior thermal resistance of the recycled aggregates. This is primarily due to their heterogeneous composition, which may include a mix of natural aggregate and old mortar, solely natural aggregate, or only mortar. When recycled aggregates contain more mortar and are exposed to high temperatures, the mortar tends to weaken and disintegrate so that the strength of the concrete aggregate decreases followed by a drop in the strength of the concrete itself.

Water cement ratio variation

For concrete mixes with a water-cement ratio of 0.30 containing 50% and 100% recycled aggregate, exposure to 550°C resulted in compressive strength reductions of approximately 14% and 23%, respectively. In contrast, concrete with a water-cement ratio of 0.45 experienced significantly greater losses, with strength reductions of 62% and 52% for the 50% and 100% recycled aggregate mixes, respectively. These findings suggest that a water-cement ratio of 0.30 offers better resistance to high temperatures up to 550°C. However, beyond this temperature, its performance tends to decline sharply. At temperatures of 550°C - 800°C, concrete with a water cement ratio of 0.45 is superior. When concrete is exposed to a temperature of 800°C, it is found that the water-cement ratio does not provide a significant difference in behavior to the compressive strength of concrete. This phenomenon also occurs in research conducted by Zega [18], where a gradual reduction in compressive strength occurred due to improved interaction between the old and new mortar in concrete with a lower water-cement ratio. This leads to more uniform thermal expansion between the aggregate and the mortar, minimizing thermal stress differences and, consequently, reducing crack formation in the interfacial transition zone (ITZ) and mortar. On the other hand, concrete with a water-cement ratio of 0.45 exhibits a relatively steady decline in strength. This is attributed to its higher water content, which absorbs and dissipates heat energy, thereby moderating the internal temperature rise. In contrast, concrete with a water-cement ratio of 0.30 contains less water, making it more vulnerable to thermal cracking under high temperatures. As a result, exposure to elevated temperatures leads to a sharp drop in compressive strength for concrete with a low water-cement ratio.

Compressive strength comparison of concrete with recycled, silica, and calcareous aggregates.

The settlement coefficient When subjected to elevated temperatures, recycled aggregate concrete shows determined from the test results, is compared to those of silica aggregate and calcareous aggregate concretes. The settlement coefficients for silica and calcareous aggregate concretes are established in Design Guidelines for Concrete Structures under Fire Conditions – Eurocode 2 [19]. In this study, the natural aggregate used is lime aggregate, as illustrated in Fig. 7. The settlement coefficient for the compressive capacity of concrete made with recycled aggregates falls between the values for silica and calcareous aggregate concretes. However, its behavior is more similar to silica aggregate concrete. This similarity can be influenced by the remaining mortar consisting of cementitious materials which usually contain significant amounts of silica. This makes the chemical composition of recycled aggregate similar to silica aggregate.

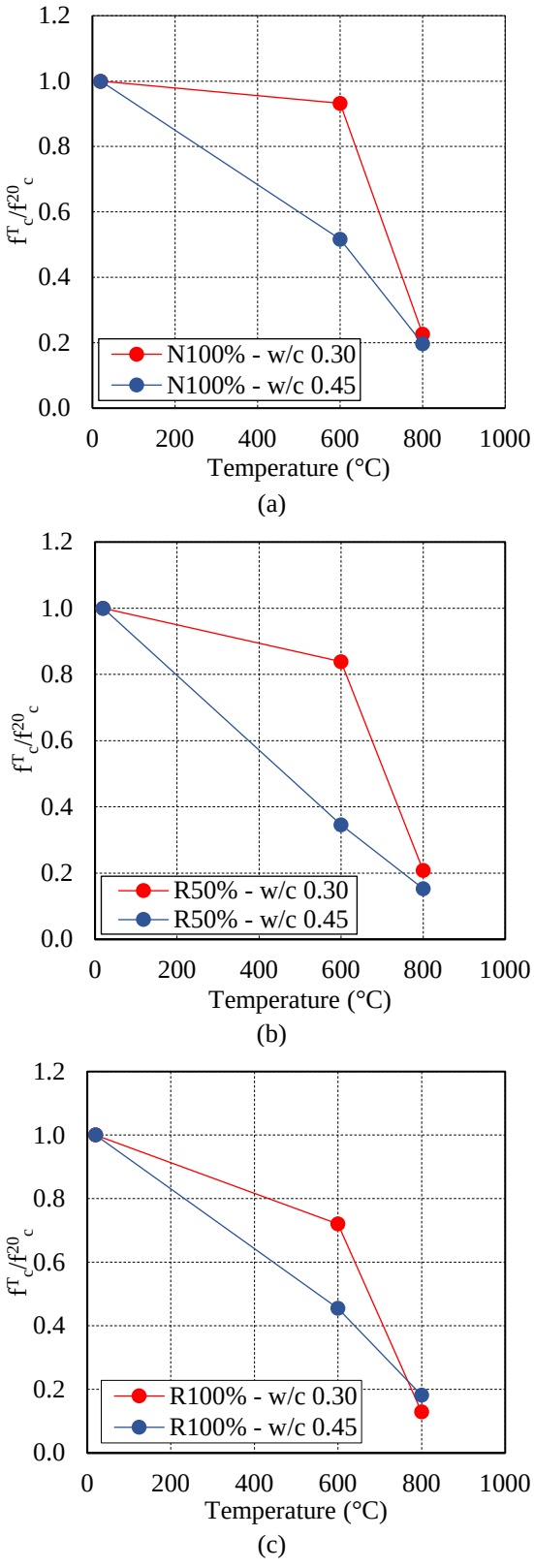

Fig.6 Concrete Compressive Strength Decrease Coefficient against Water Cement Ratio Variation (a) N 100% (b) R 50% and (c) R 100%

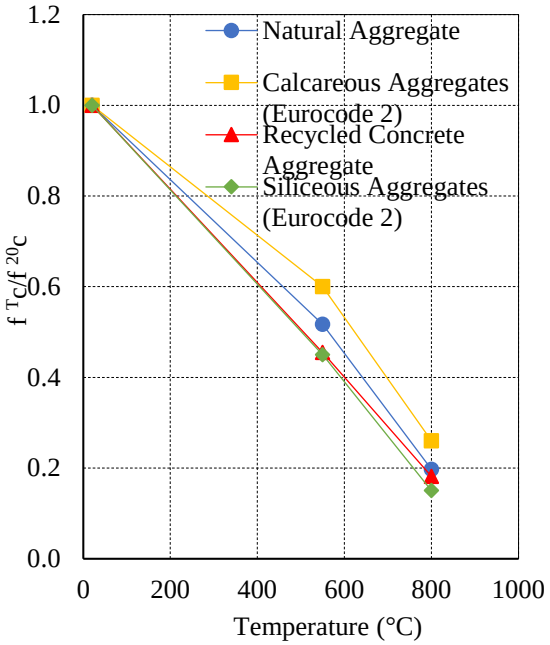

Fig.7 Comparative Analysis of Compressive Strength Reduction Coefficients in Recycled, Silica, and Calcareous Aggregate Concrete

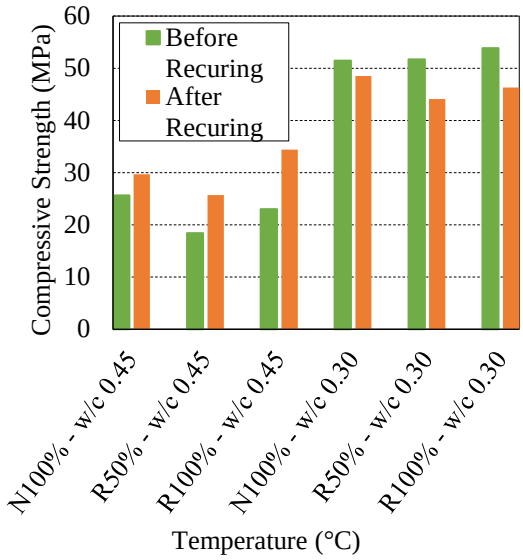

Fig.8 Residual Compressive Strength at 550ºC After Recurring

Evaluation of Re-curing Effects on Concrete Affected by High Temperature Conditions

According to prior research [20], water recuring can restore the strength and Post-fire durability of concrete by regenerating hydration products through the rehydration of CaO and hydration of unreacted cement. In this study, samples were soaked in water for 7 days. As shown in Figures 8 and 9, recuring improved the Strength characteristics of concrete using a 0.45 w/c ratio but reduced it in concrete with a 0.30 ratio. This decline is likely due to Delayed Ettringite Formation (DEF), which occurs in high-quality concrete when ettringite forms later during the recuring process after heat exposure. This is due to the lack of water availability during the recuring process. This DEF phenomenon can cause internal expansion and cracking which causes a decrease in strength. This DEF phenomenon occurs in concrete with recycled aggregates considering Excessive water uptake by recycled aggregates results in insufficient water that can be sufficient for the rehydration and hydration processes. A longer recuring duration in high-quality concrete may increase its strength.

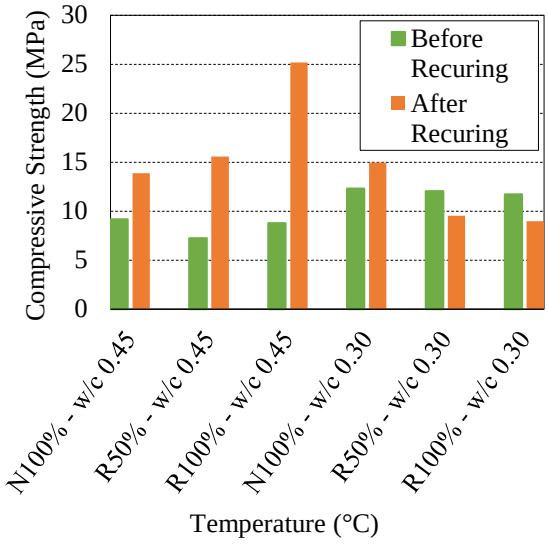

Fig.9 Residual Compressive Strength at 800ºC Temperature After Recurring

CONCLUSIONS

1. RAC exhibits a compressive strength reduction of 4%–62% at 550°C and 76%–87% at 800°C, significantly greater than NAC due to its lower thermal resistance, higher porosity, weaker ITZ, and pre-existing microcracks. Concrete with a 0.30 water-cement ratio shows a gradual strength loss up to 550°C, then a sharp decline at 800°C, while mixes with a 0.45 ratio display a more uniform strength reduction due to better heat absorption and dissipation
2. NAC performs better at a water-cement ratio of 0.45, while RAC performs slightly better at 0.30, although the difference is small. This is likely Because RAC has lower heat transfer properties made with normal-quality recycled aggregates. The strength reduction coefficient of RAC is between that of silica and lime aggregates, but its

behavior is more similar to silica aggregate concrete because the leftover mortar in recycled aggregates usually contains high silica content.

3. Recovery of compressive strength after 7-day water recuring: Concrete with a 0.45 water-cement ratio regains 53%–74% strength after 550°C exposure and 32%–40% after 800°C. In contrast, 0.30 w/c ratio concrete shows a further strength decline of 6%–15% (550°C) and 13%–16% (800°C) due to Delayed Ettringite Formation (DEF)

ACKNOWLEDGMENTS

We gratefully acknowledge the Faculty of Civil and Environmental Engineering (FTSL), Institut Teknologi Bandung (ITB), for their financial support, which was essential to the completion of this research

REFERENCES

[1] Vieira J P B, Correia J R and De Brito J 2011 Post-fire residual mechanical properties of concrete made with recycled concrete coarse aggregates Cem Concr Res 41 533–41

[2] Beatriz da Silva J, Pepe M and Toledo Filho R D 2020 High temperatures effect on mechanical and physical performance of normal and high strength recycled aggregate concrete Fire Saf J 117

[3] Safiuddin M, Alengaram U J, Rahman M M, Salam M A and Jumaat M Z 2013 Use of recycled concrete aggregate in concrete: A review Journal of Civil Engineering and Management 19 796–810

[4] Pepe M 2015 A Conceptual Model for Designing Recycled Aggregate Concrete for Structural Applications

[5] Tam V W Y, Soomro M and Evangelista A C J 2018 A review of recycled aggregate in concrete applications (2000–2017) Constr Build Mater 172 272–92

[6] Silva R V., De Brito J and Dhir R K 2014 Properties and composition of recycled aggregates from construction and demolition waste suitable for concrete production Constr Build Mater 65 201–17

[7] Tošić N, Marinković S, Dašić T and Stanić M 2015 Multicriteria optimization of natural and recycled aggregate concrete for structural use J Clean Prod 87 766–76

[8] Chen Z, Chen J, Ning F and Li Y 2019 Residual properties of recycled concrete after exposure to high temperatures Magazine of Concrete Research 71 781–93

[9] Pliya P, Hajiloo H, Romagnosi S, Cree D, Sarhat S and Green M F 2021 The compressive behaviour of natural and recycled aggregate concrete during and after exposure to elevated temperatures Journal of Building Engineering 38

[10] Kou S C, Poon C S and Etxeberria M 2014 Residue strength, water absorption and pore size distributions of recycled aggregate concrete after exposure to elevated temperatures Cem Concr Compos 53 73–82

[11] Chen G M, He Y H, Yang H, Chen J F and Guo Y C 2014 Compressive behavior of steel fiber reinforced recycled aggregate concrete after exposure to elevated temperatures Constr Build Mater 71 1–15

[12] Dong H, Cao W, Bian J and Zhang J 2014 The fire resistance performance of recycled aggregate concrete columns with different concrete compressive strengths Materials 7 7843–60

[13] Gales J, Parker T, Cree D and Green M 2016 Fire Performance of Sustainable Recycled Concrete Aggregates: Mechanical Properties at Elevated Temperatures and Current Research Needs Fire Technol 52 817–45

[14] Zhao H, Liu F and Yang H 2018 Thermal properties of coarse RCA concrete at elevated temperatures Appl Therm Eng 140 180–9

[15] Sarhat S R and Sherwood Edward G 2013 Residual Mechanical Response of Recycled Aggregate Concrete after Exposure to Elevated Temperatures Journal of Materials in Civil Engineering 25 1721–30

[16] Yang H, Zhao H and Liu F 2019 Compressive Stress–Strain Relationship of Concrete Containing Coarse Recycled Concrete Aggregate at Elevated Temperatures Journal of Materials in Civil Engineering 31

[17] Fernandes B, Carré H, Mindeguia J C, Perlot C and La Borderie C 2022 Spalling behaviour of concrete made with recycled concrete aggregates Constr Build Mater 344

[18] Zega C J and Di Maio A A 2009 Recycled concrete made with different natural coarse aggregates exposed to high temperature Constr Build Mater 23 2047–52

[19] Bellová M 2013 EUROCODES: structural fire design Procedia Eng 65 382–6

[20] Henry M, Darma I S and Sugiyama T 2014 Analysis of the effect of heating and re-curing on the microstructure of high-strength concrete using X-ray CT Constr Build Mater 67 37–46

Copyright © Int. J. of GEOMATE All rights reserved, including making copies, unless permission is obtained from the copyright proprietors.

15th Int. Conf. on Geotechnique, Construction Materials & Environment,
Kyoto, Japan, 11-13 November 2025, ISBN 978-4-909106124 C3051

A NEW APPROACH TO PRELOAD CONTROL: DEVELOPMENT OF A FRACTURE-BASED HIGH-STRENGTH NUT FOR STEEL JOINTS

Min-woo Choi[1], and Yeol Choi[2]

[1] School of Architectural, Civil, Environmental, and Energy Engineering,
Kyungpook National University, Republic of Korea
[2] School of Architecture, Kyungpook National University, Republic of Korea

ABSTRACT

This study introduces a newly developed high-strength nut featuring a tension-control (TC) mechanism designed to deliver uniform pretension in structural steel connections. Drawing inspiration from the pin-tail fracture approach used in conventional TC bolts, the proposed nut integrates a shear-off tail that detaches at a predefined torque threshold. This innovation eliminates the dependence on torque-calibrated tools or custom bolt assemblies, enabling straightforward and consistent preload application. To evaluate its mechanical behavior, finite element analysis (FEA) was employed to simulate the stress distribution and torsional fracture process of the nut. Complementary experimental tests were conducted using high-strength steel bolt-nut assemblies compliant with ASTM A490M standards and categorized as Group 150 in AISC 360-22. Key performance metrics such as preload capacity, torque coefficient, and fracture behavior were assessed and compared with conventional high-strength bolts. The experimental results indicate that the TC-type nut delivers a pretension level comparable to or greater than the AISC-prescribed values. Moreover, the simplified installation process enhances usability and quality control. These findings confirm the feasibility of the proposed fastening solution as a practical alternative for achieving reliable pretension in steel structures governed by AISC design requirements.

Keywords: Tension-Control nut; Shear-off tail; Pretension; High-strength bolts; Steel structural connections; Finite element analysis

INTRODUCTION

Reliable bolted connections play a critical role in ensuring the structural integrity of steel frameworks. Among the various fastening systems available, tension-control (TC) bolts are widely adopted due to their ability to apply uniform pretension via a fracture-based mechanism. This mechanism typically involves a pin-tail designed to shear off when a specific torque is reached, thereby achieving a standardized preload without requiring direct tension measurement. The effectiveness of this method has led to its widespread application in structural steel construction.

However, conventional TC bolts still present notable limitations in practical use. The requirement for specialized shear wrenches increases tool dependency and complexity during installation. In addition, the length of the pin-tail must be tailored to the thickness of the connection components, which complicates inventory management and often necessitates multiple bolt lengths on-site. These constraints hinder operational efficiency and flexibility in field conditions.

To address these challenges, this study introduces a novel TC-type high-strength nut designed to replicate the fracture-based preload mechanism commonly found in TC bolts. By integrating a shear-off tail into the nut itself, the proposed system eliminates the need for custom bolt designs and torque-calibrated tools. This design innovation simplifies the assembly process and allows compatibility with standard high-strength bolts of various lengths.

The objective of this study is to develop and evaluate the structural performance of the proposed nut through a combined approach of finite element analysis (FEA) and experimental validation. The analysis focuses on the torsional fracture behavior, preload consistency, and comparative performance against conventional bolt systems defined by the AISC 360-22 standard.

DESIGN CONCEPT AND FEA

The proposed TC-type nut is engineered to provide consistent pretension by integrating a shear-off tail directly into the nut body. This tail is connected via a precision-machined shear groove, which serves as a predefined fracture point under torsional loading. When torque is applied during assembly, shear stress concentrates at the groove, resulting in a clean separation once the critical torque threshold is reached. This mechanism enables visual confirmation of proper pretensioning without the need for torque-calibrated tools.

In contrast to conventional TC bolts, where the fracture mechanism is built into the bolt itself, the

new design transfers this function to the nut. This modification allows compatibility with standard high-strength bolts of varying lengths, regardless of joint thickness. Consequently, the proposed nut enhances installation flexibility, simplifies inventory management, and reduces dependence on bolt length variations.

To assess the structural behavior of the proposed design, finite element analysis (FEA) was performed using Abaqus/Explicit. The 3D models were created in Autodesk Inventor and included the nut body, shear tail, and loading plates. C3D10 tetrahedral elements with a 0.5 mm mesh size were used to capture localized stress accurately. Boundary conditions fixed the bolt and plate, while a torsional moment was applied to the shear-off tail.

The simulation results confirmed that shear stress was concentrated along the groove, and the nut consistently fractured at the intended location. For both M16 and M20 configurations, the resulting axial forces exceeded the design pretension values of 114 kN and 179 kN as specified in AISC 360-22. These results validate that the proposed TC-type nut can achieve structural performance equivalent to, or better than, conventional TC bolts.

Fig. 1 illustrates the conceptual tightening sequence of the proposed TC-type nut, from hand insertion to the fracture of the pin-tail under applied torque.

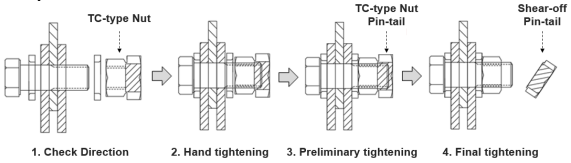

Fig.1 Structural concept of the TC-type nut

Fig. 2 presents the von Mises stress distribution obtained from the FEA simulation, highlighting the stress concentration at the shear groove that leads to controlled fracture.

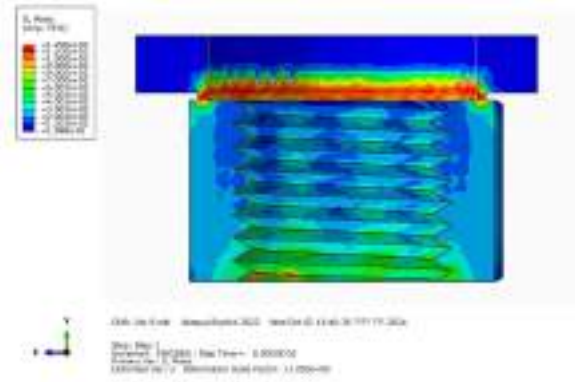

Fig.2 Stress distribution simulated by FEA

EXPERIMENTAL METHOD

To evaluate the preload behavior and loosening resistance of the proposed TC-type nut, a series of experimental tests were conducted. The experiments were designed to simulate actual steel connection conditions and compare the proposed nut with conventional high-strength bolts and TC bolts under repeated lateral displacement.

Test Specimens

Bolt-nut assemblies were fabricated using high-strength steel bolts conforming to ASTM A490M specifications, classified as Group 150 under AISC 360-22. Two bolt sizes, M16 and M20, were used in combination with the developed TC-type nuts. The nuts were manufactured from medium-carbon steel and included an integrally machined pin-tail with shear groove thicknesses ranging from 0.60 mm to 0.80 mm for M16, and 1.00 mm to 1.20 mm for M20. The naming convention for each specimen follows the format. "TC" denotes the tension-control type nut, "M16" represents the nominal bolt diameter, "A" indicates the lubrication condition (A: with lubrication, B: without lubrication, AI: with lubrication and impact wrench), and "60" refers to the shear groove thickness in hundredths of a millimeter (i.e., 0.60 mm).

Test Procedure

Each specimen was preloaded by installing the nut and tightening it until the pin-tail fractured, indicating completion of the preload. After pretensioning, cyclic lateral displacement was applied under constant frequency. The test was continued until the axial force dropped below 120 kN for M16 bolts and 185 kN for M20 bolts. The retained axial force was recorded at regular intervals to evaluate the loosening behavior.

RESULTS AND DISCUSSION

This section presents the results from both finite element analysis and experimental testing, with a focus on validating the fracture mechanism and evaluating preload performance of the proposed TC-type nut.

Fracture Behavior Validation

The fracture behavior of the TC-type nut was confirmed through both finite element analysis (FEA) and physical testing. As shown in Fig. 2, the torsional stress concentrated at the shear groove resulted in a controlled fracture, which was consistently reproduced in all specimens.

The fractured specimens shown in Fig. 3

demonstrate clean and reproducible breakage at the designed shear groove, validating the reliability of the fracture-based tightening mechanism.

Fig. 3 Fractured shapes of TC-type nuts after final tightening

Preload Capacity of M16 Series

Fig. 4 illustrates the average axial forces measured from the M16 series with five different shear groove thicknesses (0.60 to 0.80 mm) and three tightening conditions (Type A: with lubrication, Type B: without lubrication, Type AI: with lubrication and impact wrench).

The results show that as the groove thickness increased, the axial force generally improved. The AI-type consistently showed the highest performance. While several specimens with thinner grooves (e.g., 60 mm, 65 mm) failed to reach the AISC 360-22 minimum pretension (114 kN), specimens with 75 mm and 80 mm grooves all exceeded this threshold under all tightening types.

These results suggest that an SGT of 0.75 mm or more is optimal for M16 bolts.

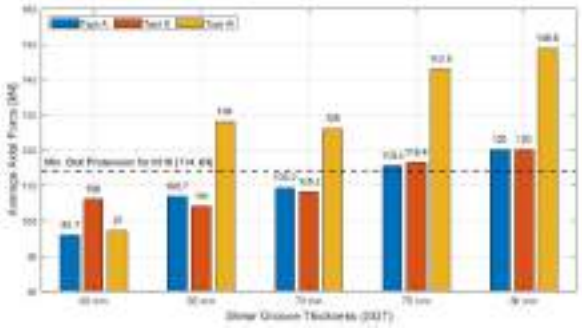

Fig. 4 Average axial force of M16 series by shear groove thickness and tightening condition

Preload Capacity of M20 Series

Similarly, the M20 series results are shown in Fig. 5, covering groove thicknesses from 1.00 mm to 1.20 mm. Type AI achieved the highest axial forces in all cases, with values ranging from 200 kN to 216 kN. For Type A and B, the optimal groove thickness was found to be 1.10 mm, where both types exceeded the minimum required pretension of 179 kN. This confirms that a groove thickness of 1.10 mm is suitable for M20 configurations, achieving both structural reliability and efficient fracture under torque.

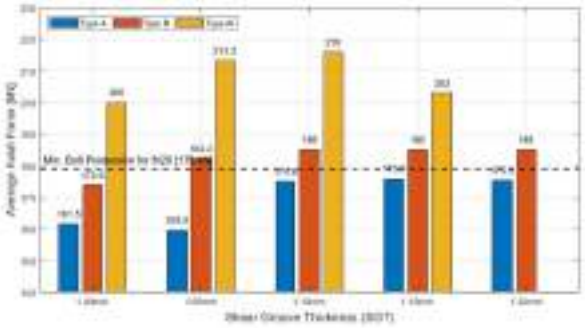

Fig. 5 Average axial force of M20 series by shear groove thickness and tightening condition

CONCLUSIONS

This study developed and evaluated a novel TC-type high-strength nut that applies a fracture-based pretension mechanism by integrating a shear-off tail into the nut body. Finite element analysis and experimental testing were conducted to verify its structural performance.

The results confirmed that the proposed nut successfully replicates the fracture mechanism of conventional TC bolts, providing consistent pretension without requiring torque-controlled tools. All test specimens exhibited reliable fracture behavior at the machined groove, and the resulting axial forces exceeded the minimum values specified by AISC 360-22 for both M16 and M20 bolts.

Parametric testing of the shear groove thickness identified the optimal configurations to be 0.75 mm for M16 and 1.10 mm for M20. These values balance fracture reliability and pretension capacity, while also ensuring compatibility with standard bolt assemblies.

The proposed TC-type nut demonstrates equivalent or improved structural performance compared to conventional systems, while simplifying installation and enhancing field applicability. These findings suggest that the new fastening solution offers a practical and efficient alternative for structural steel connections requiring consistent preload.

REFERENCES

[1] Byun, S. M., Choi, Y., Wi, O. B., and Kang, S. G., Structural performance of circular steel pipe tension joints. Journal of the Architectural Institute of Korea Federation, Vol. 25, No. 1, 2023, pp. 57–64.

[2] Hwang, H. Y., Bolted joint torque setting using

numerical simulation and experiments. Journal of Mechanical Science and Technology, Vol. 27, No. 5, 2013, pp. 1361–1371.

[3] Fukuoka, T., and Takaki, T., Mechanical behaviors of bolted joint during tightening using torque control. JSME International Journal Series A: Solid Mechanics and Material Engineering, Vol. 41, No. 2, 1998, pp. 185–191.

[4] Lee, H. J., and Choi, S. M., A study on the secure plan of clamping force according to the variation of torque-coefficient in torque-shear high strength bolts. Journal of the Korean Society for Advanced Composite Structures, Vol. 5, No. 3, 2014, pp. 8–16.

Copyright © Int. J. of GEOMATE All rights reserved, including making copies, unless permission is obtained from the copyright proprietors.

15thInt. Conf. on Geotechnique, Construction Materials &Environment, Kyoto, Japan,11-13 November 2025, ISBN 978-4-909106124 C3051

RSM OPTIMIZATION OF MECHANICAL AND DURABILITY PROPERTIES OF SELF-COMPACTING CONCRETE INCORPORATING ZINC ASH AND BLASTING GRIT NANOPARTICLES

Rabeea W. Bazuhair[1],Ehab A. Mlybari[1], and Wasayo Sanam Sahito[1]

[1]Department of Civil Engineering, Umm Al-Qura University, Saudi Arabia

ABSTRACT

In concrete mixtures, Portland cement is a common building material. By replacing some of the cement with supplemental cementitious materials (SCM), concrete mixtures can be made more environmentally friendly, their qualities improved, and their cost decreased. This study investigates the mechanical performance of self-compacting concrete (SCC) incorporating two SCMs, zinc ash (ZA) and blasting grit (BG), industrial waste by-products, as partial cement replacements. The average particle size for BG and ZA are 300 nm and 60 nm, respectively, with high specific gravity, and spherical shaped powder. The tests were created using response RSM, and the mix proportions were tuned to get the best results. Using a Box-Behnken design under Response Surface Methodology (RSM), experiments were conducted to model and optimize the compressive (CS) and flexural strength (FS) of SCC to develop mathematical models. The independent variables were mass percentages of ZA (0–0.75%), BG (0–1.5%), and curing time (7, 14, 21 or 28 days). Analysis of variance (ANOVA) confirmed the statistical significance of the models, with R^2 values exceeding 95% for both strength properties. The optimal mix was found to be 0.5% ZA and 1% BG, which resulted in a 21.2% increase in 28-day CS and a 17.8% improvement in FS compared to control mixes. The combined use of ZA and BG not only enhances mechanical properties but also promotes waste valorization in concrete production. The RSM provided a reliable predictive model for identifying strength-efficient mix proportions, offering a practical tool for sustainable SCC mix design.

Keywords: Sustainable Construction; Self-Compacting Concrete (SCC); RSM Optimization; Mechanical Performance; Zinc-Based Nanoparticles.

INTRODUCTION

Self-compacting concrete (SCC) is considered as a new construction material with the adaptability to pass through small areas, around rebar, and under formwork, is the key development in structural concrete in the last few years. It coagulates due to gravity alone; no further vibration, separation, or aeration are needed. To make the paste more viscous, a viscosity modifier can be added [1]. These frequently contain polymers consisting of long-chain molecules that may absorb and immobilize free water molecules. It is crucial to verify all the fundamental hypotheses and test findings of the design model of the SCC structure [2] since this mixed design modification might alter the material's mechanical characteristics. Concrete was initially employed in building construction perhaps less than a century later. With the increased usage of concrete, however, substantial research has recently been effective in enhancing its qualities by adding different extra cementitious ingredients, such as pozzolans and nanoparticles [3].

Recent advances in nanotechnology have drawn significant scientific interest to new uses of particles with a size of 10–9 nanometers or less. This could be because materials with the same chemical make-up lack the qualities that nanoscale particles do [4], which are significantly superior in terms of particle size. Six different iterations of the ideal SCC were created, using different design methodologies like statistics, factorial design, etc. Particle packing and mixed design, often known as Eco-SCC, were used to build high-performance SCCs and their SCC-Design [5].

Investigated the likelihood of mistakes and uncertainties. To considerably replace up to 63% of the cement in fly ash slag, research is being done to create SCC [6]. Lightweight SCCs (LWSCCs) that are simple to deploy and made of lightweight concrete (LWC) have been investigated for mixed ratios, densities, and mechanical qualities [7-8]. In the coarse aggregate and mortar stages of the SCC, five suggested design approaches—statistical factor models, compressive strength (CS) techniques, dense filling methods, paste model rheology, and empirical design methods were investigated [9]. The design of SCC compounds and the link between their properties and fresh and tempered attributes were studied empirically [10]. The compressive

strength, split tensile strength, and durability of SCC with silica, metakaolin, rice husk incineration residue, and fly slag (10% and 20% of cement load) samples after 7 and 28 days revealed better attributes of freshly installed and cured concrete [11].

The mechanical characteristics of palm oil fuel powder (POFA), an agricultural waste that is risky to dispose of unless it is recycled, were originally deteriorated with the goal of forming a sturdy SCC as a partial cement substitute [12]. In addition to SCC with SiO_2, TiO_2, and Al_2O_3 nanoparticles, fresh concrete's rheological qualities as well as the physical and mechanical characteristics of hardened concrete were improved, demonstrating the effectiveness of this technique [13]. When tested under standard corrosion and sulphate attack circumstances, SCC combined with POFA at varied concentrations (10%, 15%, and 20%) demonstrated good mechanical and durability qualities of SCC with corrosion and sulphate destruction. Additionally, drying shrinkage and surface moisture absorption are decreased without negatively compromising compressive strength [14]. By mixing red mud with nanoparticles of SiO_2, Al_2O_3, and CaO, fresh concrete and hardened SCC were produced, both of which had increased compressive strength as determined by XRF and XRD [15].

Additionally, incorporating red mud into SCC increased its shear strength and modulus, which decreased drying shrinkage. In SCC, fly ash (FA) and ground blast furnace slag (GGBFS) were combined in varied ratios (20, 30, and 40%). Mechanical qualities are negatively impacted by decreased wet density, increased cement setting time, and early water porosity [16]. Effect of waste volume on the final mortar's rheological and strength properties Sandblasting chemicals have substituted natural sand partially or entirely, which has decreased the expense of disposal and storage [17]. This experimental work using cement mortar revealed that compressive strength reduces with increasing nano concentration, particularly with nano SiO_2 and 0.5% ZnO_2 [18]. The effects of solid waste-derived zinc on the delay of hydration and loss of mechanical characteristics of zinc-containing Portland cement diminish both the maximum temperature and heat flux [19]. When ZnO_2 powder and water were mixed at a certain constant (W/Z), phase composition, crystal structure, and microstructure of cement composites were examined. It was discovered that the zinc hydroxide ($Zn(OH)_2$) phase had an impact on hydration delay (>48 h) [20].

Concrete's ability to hydrate is slowed down by the usage of electric arc furnace dust (EAFD), which emphasizes the necessity for alternate recycling. Cement pastes were studied using a ZnO_2 cement hydration model. By lowering cement mortar shrinkage and interacting favorably with calcium hydroxide, Zinc oxide nanoparticles have been discovered to significantly affect the microstructure and mechanical characteristics of cementitious materials [21]. By boosting their mechanical strength and longevity, Zinc oxide nanoparticles enable concrete's compressive strength, strength, and the hydration of cement particles.

Rich in zinc oxide, zinc ash, a by-product of the galvanizing industry, can improve cementitious systems' pozzolanic activity and filler effect. Because of its angular shape and mineral content, blasting grit—an abrasive leftover from surface treatment processes—helps to promote particle packing and mechanical interlocking. When used together, they encourage recycling of garbage and may improve SCC's strength performance.

There hasn't been much investigation into the use of nanoparticles to SCC to enhance its mechanical and physical qualities [5]. The nanoparticles' strong reactivity makes them operate as a heterogeneous core for the cement paste, which further encourages cement hydration [22-23]. They also serve as nano-fillers and nano-reinforcers, increasing the microstructure's density and lowering porosity [24]. For all nanoparticles, effective dispersion is a significant issue [5-7]. The "smart" (temperature and strain measurement) and hyper mechanical potential of cement mortar combined with nanoparticles.

RESEARCH SIGNIFICANCE

To date, research has, however, mostly concentrated on employing microscale cement replacement materials to attain superior strength performance without applying Response Surface Methodology (RSM) for multi response optimization. How ultra-fine and nanoscale particles impact the properties of concrete in optimum way is still a mystery with various mix proportions and curing period [25]. While silica fume, fly ash, and metakaolin nanoparticles have been studied in SCC, comprehensive study on the combined usage of ZA and BG nanoparticles is lacking, especially when it comes to mechanical performance modeling utilizing statistical techniques like RSM.The current work employed ZA and BG nanoparticles to find impact of them on compressive, flexural, and pore structure measurements on the concrete including obtaining mathematical models, optimum input values using RSM, while encouraging the utilization of environmentally friendly industrial waste.

MATERIALS AND TEST METHODS

Raw Materials

Ordinary Pozzolana Portland Cement (PPC) that complies with ASTM C150 standard was utilized in this study. Table 1 provides information on the cement's chemical and physical characteristics.

When producing self-compacting concrete or regular concrete, aggregates with a 60mm average size are employed. Molten zinc metal produces zinc oxide (ZnO), commonly referred to as zinc ash (ZA), which is oxidized zinc. Hot dip galvanizing and other zinc coating procedures are the typical sources of zinc ash (Figure 1 a). To create zinc oxide suitable for agricultural use, another person combines the zinc ash. Various procedures, like galvanizing, make use of the metallics once again. Other people recovered the zinc in metallic form by smelting both treated and raw ashes. The formation of SCC, high-performance concrete, depends heavily on chemical additives like water reducers, retarders, viscosity modifiers, flow agents, and superplasticizers. Without impacting the strength of the concrete, an effective superplasticizer may minimize slump and water by 20–30%. Depending on the kind of concrete that is needed, the dose ranges from 0.5 to 2% by weight of cement. The mixed water came from the tap. Since steel grit/steel shot is softer than aluminum oxide and doesn't shatter as easily, it is frequently used in airless applications. Additionally, it is used in direct weight applications where a large profile is necessary. When shot peening ferrous materials, steel shot is used. Metallic abrasives are ideal for shot peening and airless impacting because of their extended lives. Table 2 shows the compositions of ZA and BG.

Table 1 Portland cement's characteristics (chemical and physical)

Chemical characteristics			Physical characteristics	
Cement	Notation	Mass (%)	Specific gravity:	3.15
Calcium oxide	CaO	0.65	Fineness (%):	0.89
Silicon dioxide	SiO2	0.21	Consistency (%):	32
Aluminum oxide	Al2O3	0.05	Initial setting Time (IST) Min:	143
Ferric oxide	Fe2O3	0.02	Final setting time (FST) Min:	205
Sulfer trioxide	SO3	2	Soundness (mm):	0.6

Table 2 Compositions of ZA and BG.

Zn	Fe	Pb	Al	Cu	Cd	Mg	Cl
61.2	0.65	0.23	1.64	0.069	0.0001	0.019	24.85

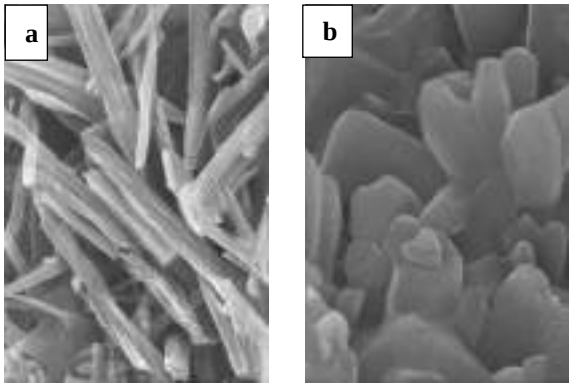

Fig. 1SEM images of (a) ZA (b) BG

Mix Proportion Design of SCC

Using the absolute mass method, the SCC mixture fraction was constructed in this study. The SCC required a compressive strength of 69 MPa. This is standard for concrete of strength class C60 with a guaranteed rate of 95%. The objective workability characteristics of fresh SCC are slump greater than 260 mm, slump greater than 700 mm, flow time T500 less than 5 seconds, and a density of at least 2450 kg/m3 is preferred for fresh SCC. A total of four sets of mixtures were prepared for SCC using the relevant factors shown in Table 3.

Table 3. Self-Compacting Concrete mix proportions

Materials	C	ZA	FA	BG	AC	CA	W	W/C	SP
SCC1	466	0	1016	0	0.02	747	186	0.4	6
SCC2		1.165		2.4	0.015				
SCC3		2.33		4.8	0.01				
SCC4		3.495		7.3	0.005				

Preparation for Test Specimens

Cement, ZA and BG nanoparticles of average 200 nm, coarse aggregate, and fine aggregate were mixed in a laboratory concrete drum mixer to create the SCC. Cement, various mass percentages of ZA (0,0.25, 0.5, and 0.75), and BG were all included in the powder (0, 0.5, 1, 1.5). Water was then added, and the mixture was dry combined for 2 minutes before being mixed again for 3 minutes. Following mixing, samples of ready-mixed concrete were tested for flexural strength (FS). The supplied concrete CS is assessed in terms of the specific 150 mm cubes evaluated after 28 days. The stated code of practice determines the strength of these specimens, which are cured for 28 days, guaranteeing that 95% of tested cubes fulfil this criterion [14]. The ASTM C293 Standard. Like the tensile tests, flexural tests were carried out on three specimens and average flexural strength values were obtained. After being saturated for 24 hours, the molds were wrapped with polyethylene sheets. Prior

to the experiment, the specimens were demolded and given a water cure at 20 °C. The concrete specimens underwent FS testing on 7 and 14 days. The averaging of three replicates produced the results that were presented.

Compressive Strength Test

The strength of the cement that not more than 5% of test results are anticipated to fall below is known as the typical strength. The concrete cube test's compressive strength gives information about all of concrete's properties. One may determine whether concrete work has been done properly by using this test. Concrete's compressive strength is calculated using a typical 150 mm cube whose compressive strength was tested after 28 days. Concrete specimens that have been cast, tested, and cured for 28 days are considered to have characteristic strength; 95% of the tested cubes should not have that is less than this value [24]. Figure 2 shows the Compressive Strength Test kit.

Fig. 2 Compression test set up

Flexural Strength Test

The load at which the material fails under bending is referred to as this bending strength. Analyze the non-reinforced concrete beams' or slabs' resistance to lateral failure. An unreinforced concrete slab, beam, or other structure's flexural strength is the amount of force and pressure it can bear before ceasing to bend. Flexural strength is sometimes referred to as breaking strength, rupture modulus, or flexural strength. For bend testing, beam specimens in the sizes 150mm length, 150mm width, and 700mm height and 100mm length, 100mm width, 500mm height were tested. These samples are put through bending tests in accordance with ASTM C-293 and the Structural Design Qualification Standard as a universal guide of concrete strength. The average flexural strength of SCC samples was assessed utilizing three samples and a simple central loaded beam. Figure 3 shows the Flexural Test Set up

Fig. 3 Flexuraltest set up

RSM for Mathematical Modeling

Statistical analysis provides meaning, breathing life into the data and useful statistical tests can produce precise conclusions from the results. It provides a brief definition of the variables, an understanding of quantitative yet distinguishing variables, and measures of central tendency. To ascertain the link between a collection of independently quantifiable parameters and one or more answers, the Response Surface Methodology (RSM) combines mathematical and analytical methodologies [26, 27]. Finding functional parameters that may or may not have a major impact on the underlying reaction is possible using RSM [28]. RSM may also be thought of as a collection of analytical and mathematical problem-solving methods. The outcomes are influenced by several elements (input variables) [26]. RSM is especially beneficial for multidimensional models because it sets desirable objectives in terms of responses or variables [29]. There are several design models accessible, including Central Composites (CCD), Box-Behnken, and historical data. Both independent variables and correlated arithmetic results can be produced with them.The arithmetical correlation response and independent variables may be produced using these. The number of variables and each variable's variance are important factors in determining the sort of design model [26]. Equation (1) illustrates the use of a second-order function with a higher degree polynomial model [11].

$$y=\beta_0+\sum_{i=1}^{k}\beta_i X_i+\sum_{i=1}^{k}\beta_{ii}X_{2i}+\sum_{i<1}\sum_{j}\beta_{ij}X_iX_j+\xi \quad (1)$$

The CCD contains a factor planning component of 2k, where k is the quantity of connected variables or factors that are handled at two levels of a low and high value [24] using positive and negative values are used to code where the average of these limits serves as the focal point of it. The Zero-Point region that satisfies ideal requirements is called focal point. RSM from Minitab version 23 software was employed in this work to design the experiment and conduct a statistical analysis in constructing the mathematical relationships between the variables and the responses. To model a variable using RSM, a series of procedures must be followed to realize the research goal, which necessitates identifying the research problem based on the established objectives for research optimization. The four levels of nanoparticle (ZA and BG) substitution for fine aggregate and curing period were the independent factors considered. The type of experimental design—CCD under RSM using total of 20 mix combinations were tested, each with triplicate specimens for compressive and flexural strength tests to ensure data reliability.

RESULTS AND DISCUSSION

The experimental strategy comprises examining the effects of six factors on the establishment of strengths under various degrees of control. From the experimental designs, 20 trial runs were chosen to determine the best conditions. The technical information sheet and some preliminary tests were used to determine the lowest and highest levels for variables. Table 4 displays the design matrix for the 20 trial runs. The results of investigations on solid states (different weight percentages of nanoparticles, such as ZA and BG, and curing times between 7, 14, 21, 28 and 56 days compressive and flexural strengths) were statistically assessed using design of experiments. The effort aimed to enhance compressive and flexural strengths depending on selected factor values with the least 20 number of tests possible.

Flexural Strength

Nano composite particles are used to test the flexural strength of SCC. Out of SCC1, the reference mix, 4 other types of mixes were created, with 0% fine aggregate and ZnO and BG additions to the cement. Mass percentages of ZnO (0 to 0.75% @ 0.25%) and of BG (0 to 1.5%@ 0.5%) in the remaining types of combinations. Figure 4 shows the curing period over a 28-day, mix SCC3's flexural strength is 10% higher than mix SCC1's. The quick consumption of Ca $(OH)_2$ framed by Portland Pozzolana during cement hydration at young ages, along with the strong reactivity of nano-sized zinc oxide in cement particles, is what causes the significant increase of flexural quality in nano composites concrete. As a result, cement hydration is accelerated, and more response elements are framed. Additionally, nanocomposite particles restore the concrete's molecular density, which reduces the amount of large holes in the material. The best results were obtained at 0.5% ZA and 1% BG addition, although later addition of the nano composites to self-compacting concrete causes a decrease in the concrete's flexural strength while bringing the test results for SCC_4 closer to the control mix. It might be because there are more BG and nano-zinc oxide particles in the blends than is necessary for them to consolidate with the unmanaged lime throughout the hydration process, which causes excess silica to drain out and lowers quality because it takes the place of some of the cementitious material without improving performance. Furthermore, powerless zones may be caused by the deformities that result from the dispersion of nanoparticles. As can be observed, the insertion of nanoparticles reduces the pore area of self-compacting concrete while simultaneously increasing its density using nanocomposites. So, the self-compacting concrete's pore structure is enhanced.

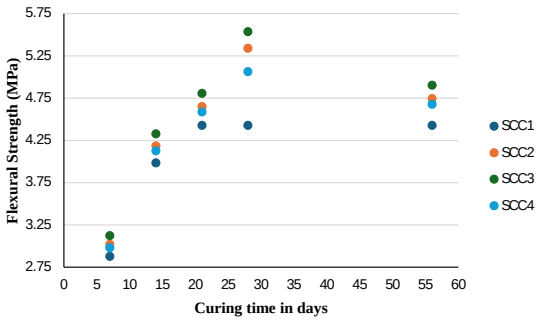

Fig.4 Flexural Strength vs curing time

Table 4 displays the effects of all parameters, including those of type A_1 to A_4, on the flexural strength of SCC. Table 5 provides a summary of the ANOVA findings holding p-values for each flexural strength parameter. The major implications (A_1, A_2, A_3, and A_4), the quadratic impact of A_4*A_4, and the interactions (A_1*A_4, A_2*A_4, and A_3*A_4) were all statistically meaningful at the 95% level of confidence (p 0.05), according to the p-values.

Only the Curing period A4 was noteworthy as the primary influence for the flexural strength. The quadratic relationships of the A_4*A_4 and the interactions of A_3*A_4 were also statistically significant ($p<0.05$), suggesting that the impact on the flexural strength was not straight or that the response surface had curvature. The regression coefficients for the models are displayed in the coefficient columns (Table 5), which represent the average changes in solution when one factor's

level is changed while keeping the levels of the other components of the model remain the same. For illustration, it is clear from ANOVA that when ZA is 0.5% and BG is 1%, the flexural strength will improve significantly when the level of the curing period is increased by one.

Table 4 Experimental design plan for strengths

N0.	SSC type	A_1 (C+ZA)	A_2 (FA+BG)	A3 (**FA**+**BG**+**CA**)/(**C**+**ZA**)	A4 (Curing time)	CS (MPa)	FS (MPa)
1	SCC1	466.000	1016.00	3.78326	7	28.1133	2.87667
2	SCC2	467.165	1018.44	3.77905	7	29.5100	3.02000
3	SCC3	468.330	1020.88	3.77486	7	30.2700	3.12333
4	SCC4	469.495	1023.30	3.77065	7	29.0833	2.98000
5	SCC1	466.000	1016.00	3.78326	14	42.8167	3.98333
6	SCC2	467.165	1018.44	3.77905	14	44.9467	4.18333
7	SCC3	468.330	1020.88	3.77486	14	46.1033	4.32667
8	SCC4	469.495	1023.30	3.77065	14	44.2967	4.12667
9	SCC1	466.000	1016.00	3.78326	21	43.2500	4.42667
10	SCC2	467.165	1018.44	3.77905	21	44.2500	4.65000
11	SCC3	468.330	1020.88	3.77486	21	45.4000	4.80667
12	SCC4	469.495	1023.30	3.77065	21	46.4000	4.58667
13	SCC1	466.000	1016.00	3.78326	28	48.3083	4.55333
14	SCC2	467.165	1018.44	3.77905	28	50.6733	5.34000
15	SCC3	468.330	1020.88	3.77486	28	51.9603	5.53667
16	SCC4	469.495	1023.30	3.77065	28	49.9547	5.06333
17	SCC1	466.000	1016.00	3.78326	56	46.5700	4.51667
18	SCC2	467.165	1018.44	3.77905	56	47.5700	4.74333
19	SCC3	468.330	1020.88	3.77486	56	44.7467	4.90333
20	SCC4	469.495	1023.30	3.77065	56	45.7467	4.67667

Table 5 ANOVA results of flexural strength

Source	DF	Adj SS	Adj MS	F-Value	P-Value
Model	8	11.0176	1.37720	38.46	0.000
Linear	4	4.1924	1.04810	29.27	0.000
A_1	1	0.1877	0.18767	5.24	0.043
A_2	1	0.3883	0.38834	10.84	0.007
A_3	1	0.0651	0.06514	1.82	0.205
A_4	1	2.9161	2.91612	81.43	0.0005
Square	1	6.2493	6.24927	174.50	0.000
A_4*A_4	1	6.2493	6.24927	174.50	0.0002
2-Way Interaction	3	0.0079	0.00262	0.07	0.973
A_1*A_4	1	0.0037	0.00370	0.10	0.754
A_2*A_4	1	0.0061	0.00615	0.17	0.687
A_3*A_4	1	0.0016	0.00161	0.04	0.002
Error	11	0.3939	0.03581		
Total	19	11.4115			
Model Summary	**S**	**R2**	**R2-(adj)**	**R2-(pred)**	
	0.189241	96.55%	94.04%	73.67%	

Equation (2) shows the polynomial functions that match the data and explains the bulk of the deviations in the flexure strength. These polynomial functions contain linear terms and 2nd order terms, which include both nonlinear and two-variable interaction terms.

Flexural Strength (MPa)= 58100 - 87.5 *A1 + 23.2* A2 – 10829* A3 + 700* A4 - 0.002336 *A4*A4 - 0.90 A1*A4 + 0.207* A2*A4 – 130*A3*A4 (2)

Figure 5a and 5b, which depict the main effect plots and Pareto diagrams of the standardized impacts for flexural strength, show that factor A4 (curing period), which had the most positive or biggest influence, was followed by factors A2 and A1 (BG% and ZA%). Another noteworthy element was the quadratic component A4* A4, which affects the response in conformity with a second order polynomial. The entire collection of standardized residuals in Figure 5c also illustrates the statistical relevance of the data distribution being close to the baseline line graph. The equivalent models of flexural strength are found to account for 96.4% and 83.2% of the total variation by the adjusted coefficients of regression (R^2(adj)) in Table 4. The predicted coefficients of results (R^2(pred)), which were predicted to be 94.04% and 73.67%, respectively, demonstrated how well the models predicted the data.

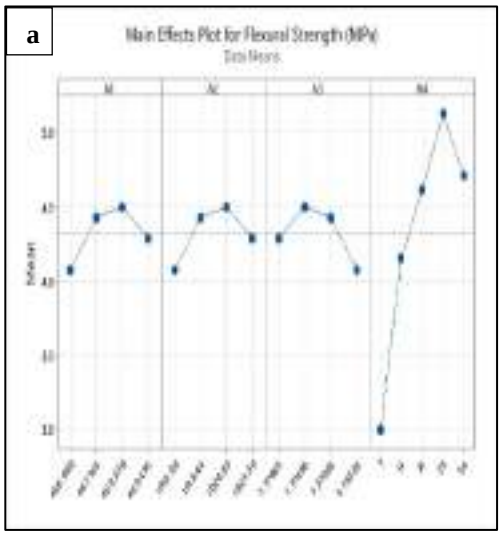

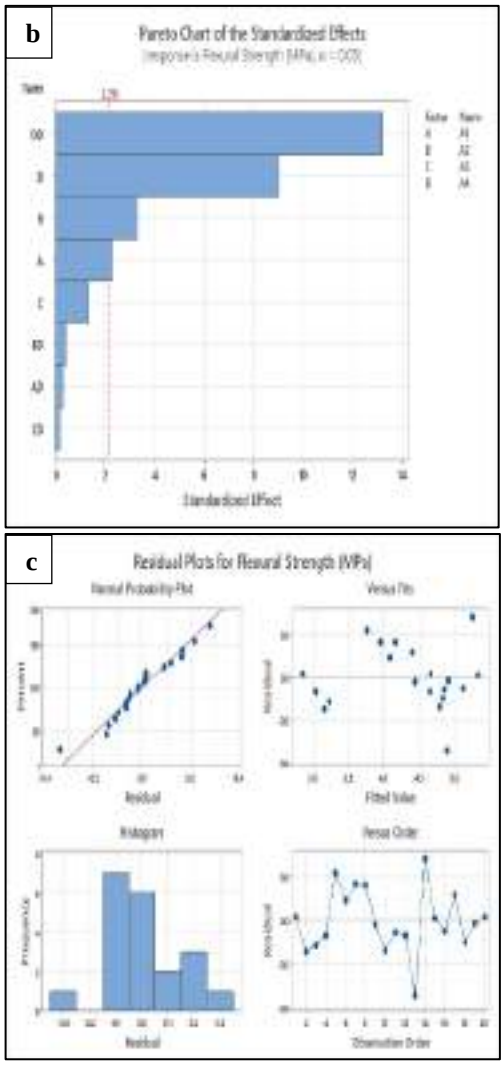

Fig. 5 (a) main effect plots and (b) Pareto diagram of the standardized effects for flexure strength

The surface plot of flexure strength (Figure 6a to 6e) on the 3D contour plot shows that it may reach a maximum of 4.9 MPa when varying two distinct factors while holding the other two constant. Similar values for other factors for the percentage of nanoparticles were also observed to have an impact on the FS. To verify the statistical models' estimated values for the FS of the SCC, they were tested experimentally in a lab under identical circumstances.

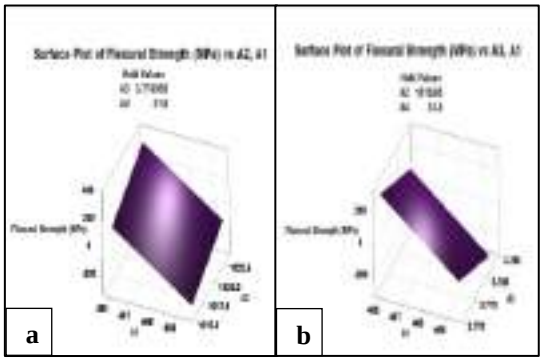

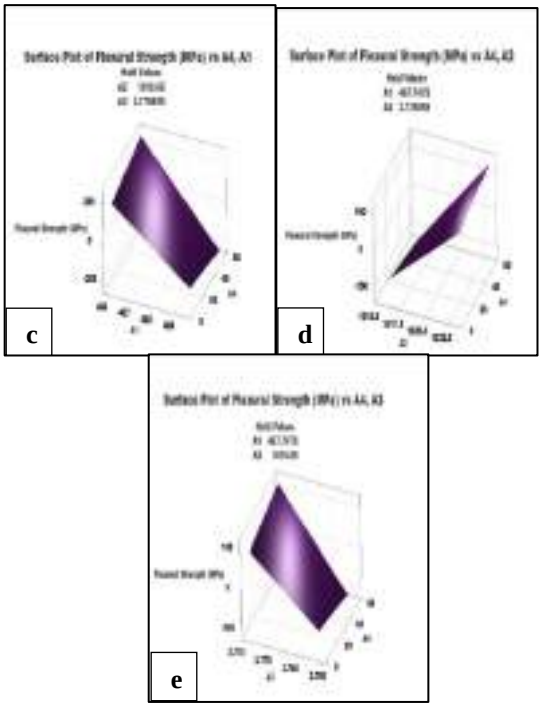

Fig. 6 3D Response surface plot for Flexural Strength with (a) A1xA2 (b)A1xA3 (c)A1xA4 (d)A2xA4 and (e)A3xA4

Compressive Strength

Table 4 displays the results of the four factors' effects on CS, including the curing times of 7, 14, 21, 28- and 56-days. An ANOVA's findings for CS are shown in Table 6, where the p-values reveal that the four main effects (A1 to A4), the quadratic components of A4, and the interactions A1*A2, A2*A4, and A3*A4 were statistically meaningful at the 95% confidence level for the examined levels. According to the P-values, only the curing duration has a significant positive impact on individual and quadratic terms, and the ratio of nanoparticles (ZA+BG) was significant when there was interaction ($p<0.005$). Introduction of nanoparticles and a 28-day curing period resulted in an increase in compressive strength.

Equations depict the polynomial functions used to describe the connection in both the observed strengths and the variable levels (3).

Compressive Strength (MPa) = -136030 - 287*A1 + 178*A2 + 23494*A3 + 19015*A4 -0.02266*A4*A4 - 6.7*A1*A4 - 2.76*A2*A4 – 3457*A3*A4 (3)

According to the high R^2(adj) values for the CS, the model explains 95.69% of the total variance. As shown by the anticipated coefficient of determination value of 85.46%, the model is reasonably predictable. Figure 7b displays the Pareto

diagrams of the standardized effects for CS, and all terms that cross the reference line are marked as statistically significant at the 5% level. These plots demonstrate that the curing length (A4), with Figure 6a displaying the sole level 4 (28-day) curing period rise in strength, is the factor at both the single and nonlinear terms having the biggest influence on the CS. Every increase or decrease over this threshold of the component denotes a reduction in the strength results. The distribution of the data matched with the trend line in Figure 7c's residual plots, which displays the normal distribution, indicates that the data are statistically meaningful. The biggest negative coefficient in the equation, A1, causes the compressive strength to decline. However, even though it is a quadratic term with curved lines, A1 was statistically significant.

A1's varying effects on compressive and flexural strength are probably caused by ZA's microfiller behavior, which densifies the matrix to increase compressive strength but might not have as much of an impact on tensile stress distribution, which controls flexural performance. Imperfect dispersion or interfacial gaps between the grit and cement paste may provide uneven results in A3, where a larger percentage of BG is present. This locally reduces flexural performance while still enhancing compressive strength through particle packing.Uneven, angular particles in BG are seen in the SEM images (Fig. 1); these particles enhance interlock but might create micro-voids if overused. The tiny, porous shape of ZA aids in matrix densification and the filler effect.

Table 6 Analysis of variance for compressive strength

Source	DF	Adj SS	Adj MS	F-Value	P-Value	Coefficients
Model	8	934.16	116.770	10.78	0.000	5.1431
Linear	4	314.33	78.582	7.25	0.004	
A1	1	3.48	3.481	0.32	0.582	-202.5
A2	1	3.68	3.680	0.34	0.572	108.5
A3	1	2.13	2.134	0.20	0.666	-94.1
A4	1	274.19	274.191	25.31	0.0005	0.7886
Square	1	587.75	587.749	54.25	0.000	
A4*A4	1	587.75	587.749	54.25	0.0002	-1.402
2-Way Interaction	3	7.33	2.444	0.23	0.877	
A1*A4	1	0.21	0.206	0.02	0.893	-39
A2*A4	1	1.09	1.087	0.10	0.007	18.5
A3*A4	1	1.14	1.140	0.11	0.752	-20.1
Error	11	119.18	10.835			
Total	19	1053.34				
Model Summary	S	R^2	R^2-(adj)	R^2-(pred)		
	3.2916	95.69%	85.46%	70.31%		

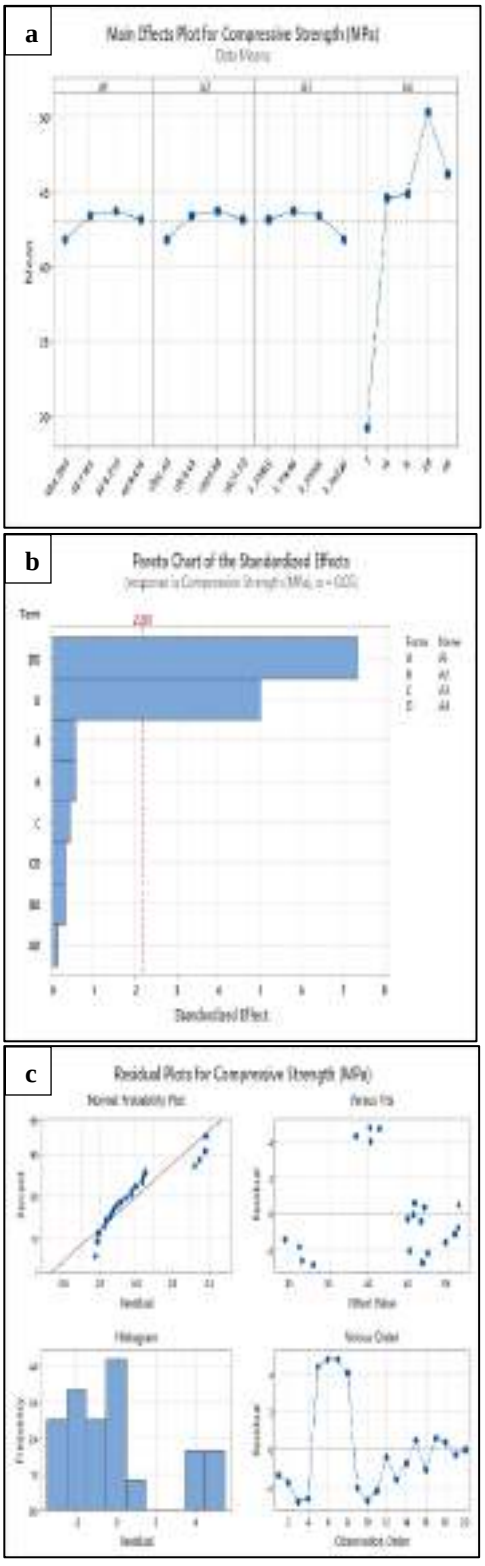

Fig. 7 (a) Main effect plots, (b) Pareto chart of the standardized effects for compressive strength, and (c) residual plots

The addition of nanoparticles shows the enhancement in the results of the strength of concrete with nanoparticles as compared to concrete

without nanoparticles. It is obtained in normal concrete about compressive strength that is same as the compressive strength results of SCC shown in Figure 8. SCC3 shows a 10% increase in compressive strength of SCC than SCC1. There is continuous improvement in compressive quality in the nano composites SCC are because of the drastic consumption of Ca (OH)2 framed by Portland Pozzolana during hydration cement at early stages identified with the increased reactivity of nanosized zinc oxide in cement elements. Therefore, cement hydration is quickened, and greater quantities of response items are framed. In addition, nanocomposite particles regain the concrete's molecular density, leading to fewer big pores in the concrete. The optimum results were obtained at 0.5% addition but later further addition of the nano composites in SCC gives the decreasing results of the CS but results of test of SCC4 observed nearer to the control mix. The similar effect of incremental CS of SCC with different types of nano particles in concrete [6]. It was experienced such an increase in CS of SCC in occurrence of Jarosite [25]. It may be due to the rise in nano-zinc oxide particles present in the blends greater than the amount necessary during the hydration process to consolidate with the uncontrolled lime, causing excess silica to drain out and causing lack of quality as it substitutes some portion of the cementitious substance, and it doesn’t add to the performance. Additionally, it might be because of the deformities created in scattering nanoparticles that cause powerless zones. It is evident that with the addition of nanoparticles, gives decrease in the pore area of SCC and at the same time nanocomposites increases the density of the SCC. As a result, the SCC's porous structure has been enhanced.

Uneven, angular particles in BG are seen in the SEM images (Fig. 1); these particles enhance interlock but might create micro-voids if overused. The tiny, porous shape of ZA aids in matrix densification and the filler effect. The observed patterns in strength responses can be explained by the considerable effects of dose and dispersion on the efficiency of these particles.

Multi-Objective Optimization Response Analysis

To maximize the specimen's strength performance using nanoparticles, ratio of nanoparticles to cement and fine aggregates, and curing time, multi-objective optimization has been done using RSM. The process of finding the ideal combinations of the factors that may be employed to generate the best SCC performance outcomes. In the specified water/cement, coarse aggregate into SCC mix, the nano particles (ZA+BG) were used as a partial replacement to cement and sand aggregates. The maximal compressive strength and flexure strength were both attained throughout the curing phase. In Table 7, the multi-objective optimization outcomes derived from the RSM using Minitab software are shown along with a summary of the optimization criteria. The SCC mixes performed best when 0.5% ZA and 1% BG, at a given fine aggregate, were substituted with water/cement of 0.4 for 28 days per mix. The ideal mix percentage achieved has a high attractiveness of 100%.

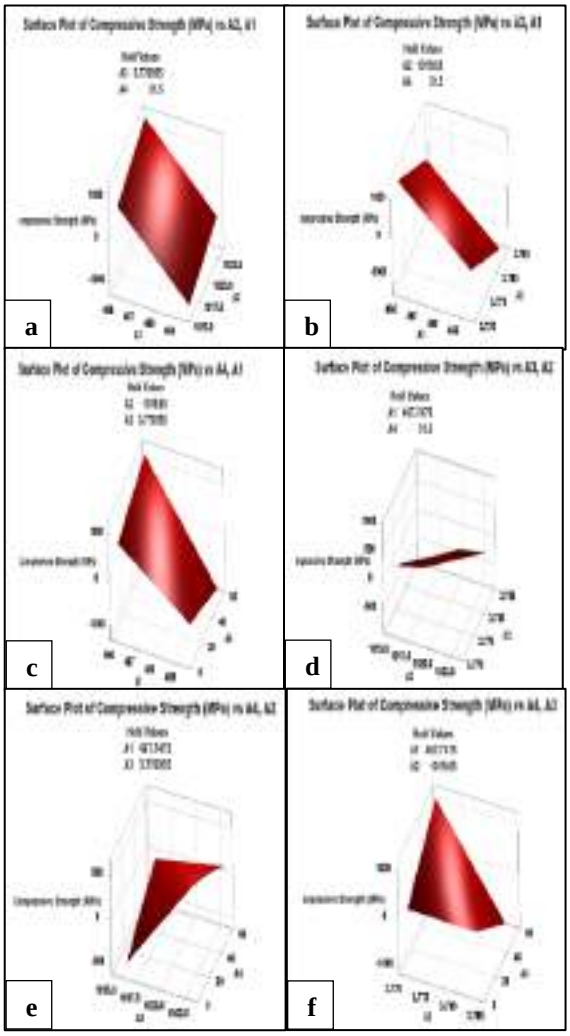

Fig. 8 3D Response surface plot for CS with (a) A_1xA_2 (b)A_1xA_3 (c)A_1xA_4 (d)A_2xA_4 (e)A_2xA_4 and (f)A_3xA_4. Wide prediction intervals and the existence of negative values, especially in forecasts for flexural strength, indicate model uncertainty and potential extrapolation outside of the range of valid data. Increasing the number of experimental runs, particularly at critical ZA and BG concentrations, may assist narrow confidence limits and increase model resilience,

N0.	SCC type	A1	A2	A3	A4	Compressive Strength (MPa) Experimental	Predicted	%Deviation	Flexural Strength (MPa) Experimental	Predicted	% Deviation
1	SCC1	466.000	1016.00	3.78326	7	28.113	28.17136	0.206521	2.87667	2.760396	4.041965
2	SCC2	467.165	1018.44	3.77905	7	29.5100	29.32511	0.62653	3.02000	3.243346	7.39556
3	SCC3	468.330	1020.88	3.77486	7	30.2700	30.46476	0.643409	3.12333	3.491516	11.7883
4	SCC4	469.495	1023.30	3.77065	7	29.083	28.44491	2.19504	2.98000	3.479886	16.7747
5	SCC1	466.000	1016.00	3.78326	14	42.810	47.2116	10.26445	3.98333	4.334404	8.81358
6	SCC2	467.165	1018.44	3.77905	14	44.940	48.46384	7.825135	4.18333	4.344514	3.85301
7	SCC3	468.330	1020.88	3.77486	14	46.103	49.218	6.755916	4.32667	4.601644	6.35533
8	SCC4	469.495	1023.30	3.77065	14	44.297	47.68304	7.644678	4.12667	4.388194	6.3415
9	SCC1	466.000	1016.00	3.78326	21	43.250	46.03116	6.430428	4.42667	4.379484	1.06594
10	SCC2	467.165	1018.44	3.77905	21	44.250	47.38189	7.077718	4.65000	4.916754	5.73665
11	SCC3	468.330	1020.88	3.77486	21	45.400	47.75056	5.177445	4.80667	5.182844	7.82608
12	SCC4	469.495	1023.30	3.77065	21	46.400	46.70049	0.647608	4.58667	5.167574	12.665
13	SCC1	466.000	1016.00	3.78326	28	48.308	50.63004	4.806089	4.55333	4.895636	7.51771
14	SCC2	467.165	1018.44	3.77905	28	50.673	52.07926	2.774558	5.34000	5.735116	7.39918
15	SCC3	468.330	1020.88	3.77486	28	51.960	52.06244	0.196573	5.53667	5.460066	1.38357
16	SCC4	469.495	1023.30	3.77065	28	49.957	51.49726	3.087918	5.06333	5.718026	12.9301
17	SCC1	466.000	1016.00	3.78326	56	46.570	48.81876	4.828774	4.51667	4.870964	7.84414
18	SCC2	467.165	1018.44	3.77905	56	47.570	50.66194	6.499769	4.74333	4.544034	4.20165
19	SCC3	468.330	1020.88	3.77486	56	44.747	47.10316	5.226622	4.90333	4.854924	0.98727
20	SCC4	469.495	1023.30	3.77065	56	45.747	48.47754	5.96947	4.67667	4.830554	3.29046

Table 7 Optimization criteria and results.

Variable	Setting
A1	468.33
A2	1023.3
A3	3.77065
A4	28

Response	Fit	SE Fit	95% CI	95% PI
Flexural Strength (MPa)	487	344	(-271, 1245)	(-271, 1245)
Compressive Strength (MPa)	2366	5990	(-10817, 15549)	(-10817, 15549)

Response	Goal	Lower	Target	Upper	Weight
Flexural Strength (MPa)	Maximum	2.8767	5.5367		1
Compressive Strength (MPa)	Maximum	28.1133	51.9603		1

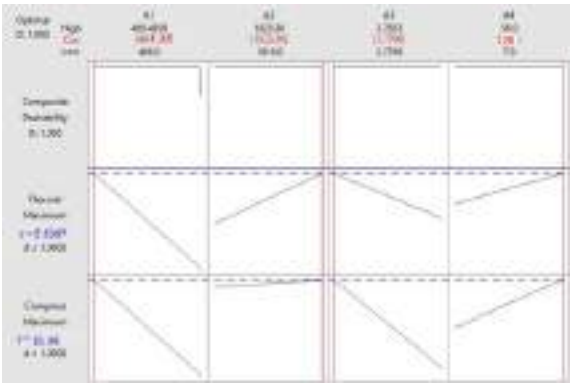

Fig. 9 Optimized strengths at optimal input settings

Confirmation Experiments

If the deviation is within the limits imposed by the statistical models of RSM are confirmed using trial results utilizing combinations of attributes for CS and FS. When the expected trial outcomes are compared, the percentage deviation is calculated and reported in Table 8 by calculating the ratio of trial and predicted to trial value. Deviation demonstrates that the selected approach has a strong acceptance limit.

Table 8. Validation of results for CS and TR

Table 8 that shows strong consistency and model dependability, with an average forecast error of 5.4% for CS and 6.1% for FS throughout all curing times. Notwithstanding considerable variation in the forecasts, this overview serves to support the model's utility. The possibility that batch-to-batch variations in the ZA and BG, inconsistent hand mixing, or localized nanoparticle agglomeration may be the cause of certain discrepancies above 10%. These elements may introduce outliers that the model is unable to detect and affect the mechanical response**.**

CONCLUSIONS

The greater flexural strengths of the concrete containing ZA and BG nanoparticle blends demonstrated that cement may be successfully substituted with these at the optimal levels of ZA (0.5%) and BG (1%). The strength and pore structure of concrete are both enhanced by the inclusion of nanoparticles overall. One way that nanoparticles can improve concrete is by acting as a filler to increase its density, which greatly reduces

the porosity of the concrete. Nanoparticles, on the other hand, can also serve as a matrix in cement paste because of their enhanced activity, which limits the dimensions of the Ca (OH)2 particle and increases the possibility of tropism. They can also function as an activator to quicken the hydration of cement.

Additionally, the experiment was planned to use RSM, and models were created to estimate the strength performance of SCC mixes in terms of nanoparticles (ZA and BG) with curing time and weight percentage of the SCC mixes. The factors considered were ZA, BG, FA, and the amount of time needed to cure additional cementitious material. The investigation's findings and interpretation led to the following conclusions. The replacement of up to 0.5% ZA and 1% BG with fixed fine aggregate, water, CR improved the flexure and compressive strengths of SCC. On the contrary, higher curing period and nano particles content decreased strengthsof the SCC. Similarly, curing period below and above 28-days with nano particles strength of SCC mixes are slightly improved.

1. The flexure and compressive strengths of SCC were increased by substituting fixed fine aggregate, water, and CR with up to 0.5% ZA and 1% BG. On the other hand, a longer curing time and the presence of nanoparticles reduced the SCC's strengths. Likethis, SCC mixtures' curing times below and above 28 days with nano particles are somewhat enhanced.

2. With the addition of nanoparticles and their replacement of fine aggregate, SCC’s strengths improved. Strengths dropped as the amount of nanoparticles in SCC increased.

3. The models created using RSM to forecast the SCC's strong performance were very significant, correlated, and predictable.

4. The results of the multi-objective optimization revealed that the ideal mix combination based on maximal strength was reached by maintaining a 28-day curing time; otherwise, there were minor alterations, such as substituting ZA% with cement and BG% with fine aggregate.

SCC mix strengths were the only ones covered in this investigation. Only specific percentages of nanoparticles were allowed. The maximum replacement by weight of cement for nano ZA was capped at 0.75%, while the maximum replacement by volume of cement for BG was 1.5%. In terms of curing time, inclusion of nanoparticles, and their impacts as factors, the established models can forecast the strength performance of SCC mixes. This will lessen the necessity for doing experiments, which will save money and time.

Future studies should examine the impact of acid and salt solutions at higher concentrations and over longer periods of time on SCC mixtures. According to statistical analysis of both strengths of different types of SCC using various methods, there is a good correlation between the dependent and independent variables. The model's prediction of the strength qualities for the parameters is great since the residuals are low. As per the statistical analysis of the strength of both concrete by different methods shows there is a strong relation between dependent and independent variables.

REFERENCES

[1] Abdi H, Chin WW, Vinzi VE (2013). New perspectives in partial least squares and related methods. Springer Proc Math Stat 56:65–78. https://doi.org/10.1007/978-1-4614-8283-3.

[2] Borucka-Lipska J (2016) Acid resistance, water permeability and chloride penetrability of concrete containing crushed basalt as aggregates. Neural Computing Application, 31:137–150. Doi:10.1007/s00521-017-3007-7.

[3] Asteris PG, Ashrafian A, Rezaie-Balf M (2019), Prediction of the compressive strength of self-compacting concrete using surrogate models. Computation Concrete 24:137–150. Doi:10.12989/ cac.2019.24.2.137.

[4] Raman SN, Salam A, Jumaat MZ (2016), Modeling of compressive strength for self-consolidating high-strength concreteincorporating palm oil fuel ash. Materials 9:1–13.Doi:10.3390/ma9050396.

[5] Deepankar K.A., Surender K. V. (2019), An overview on mixture design of self-compacting concrete, Structural Concrete 20(1):371-395 https://doi.org/10.1002/suco.201700279.

[6] Nazari, A.; Riahi, S. The effects of zinc dioxide nanoparticles on flexural strength of self-compacting concrete. Compos. Part B 2011, 42, 167–175.

[7] Behnam V, and Shami N. (2015), Mix Design of Light-Weight Self-Compacting Concrete, Case Studies in Construction Materials 4(5), DOI: 10.1016/j.cscm.2015.10.002.

[8] Behnam V, and Shami N. (2017), Compressive strength and mixture proportions of self-compacting lightweight concrete, Computers and Concrete.19(5),DOI:10.12989/cac.2017.19.5.000

[9] Caijun Shi et al., (2005). Design and application of self-compacting lightweight concrete, Conference: SCC'2005-China - 1st International Symposium on Design, Performance and Use of Self-Consolidating Concrete. DOI:10.1617/2912143624.005.

[10] Miguel C. S. Nepomuceno, Luiz Antonio Pereira de Oliveira, Sérgio MR Lopes (2014), Methodology for the mix design of self-

compacting concrete using different mineral additions in binary blends of powders, Construction and Building Materials 64:82–94, DOI: 10.1016/j.conbuildmat.2014.04.021.

[11] Siamardi K. (2022). Optimization of fresh and hardened properties of structural light weight self-compacting concrete mix design using response surface methodology. Constr. Build. Mater.317:125928. Doi:10.1016/j.conbuildmat.2021.125928.

[12] Mohd Zamin Jumaat, Belal Alsubari, Payam Shafigh, Zainah Ibrahim (2018), Properties of eco-friendly self-compacting concrete containing modified treated palm oil fuel ash, Construction and Building Materials 158:742-754, DOI: 10.1016/j.conbuildmat.2017.09.174.

[13] Niewiadomski, P., Hoła, J. & Ćwirzeń, A. (2018). Study on properties of self-compacting concrete modified with nanoparticles. Archiv.Civ.Mech.Eng 18, 877–886. Doi: 10.1016/j.acme.2018.01.006.

[14] Navid Ranjbar, Arash Behnia, Belal Alsubari, Payam Moradi Birgani, Mohd Zamin Jumaat (2016), Durability and mechanical properties of self-compacting concrete incorporating palm oil fuel ash, Journal of Cleaner Production,112(1),Pp:723-730,Doi10.1016/j.jclepro.2015.07.033.

[15] Ri-Xin Liu, Chi-Sun Poon (2016). Utilization of red mud derived from bauxite in self-compacting concrete, Journal of Cleaner Production,112(1),pp:384-391,Doi:10.1016/j.jclepro.2015.09.049.

[16] Singh N., Kumar P., Goyal P. (2019). Reviewing the behaviors of high volume fly ash based self compacting concrete. J. Build. Eng. 26:100882. Doi: 10.1016/j.jobe.2019.100882.

[17] Ji, T. (2005). Preliminary study on the water permeability and microstructure of concrete incorporating nano-SiO_2. Cem. Concr. Res.35, 1943–1947.

[18] Jo, B.W.; Kim, C.H.; Tae, G.H.; Park, J.B. (2007). Characteristics of cement mortar with nano-SiO_2 particles. Construct. Build. Mater.21, 1351–1355.

[19] Li, H.; Xiao, H.G.; Ou, J.P. (2004). A study on mechanical and pressure-sensitive properties of cement mortar with nanophase materials. Cem. Concr. Res. 34, 435–438.

[20] Qing, Y.; Zenan, Z.; Deyu, K.; Rongshen, C. (2007). Influence of nano-SiO_2 addition on properties of hardened cement paste as compared with silica fume. Construct. Build. Mater.21, 539–545.

[21] Lin, K.L.; Chang, W.C.; Lin, D.F.; Luo, H.L.; Tsai, M.C. (2008). Effects of nano-SiO_2 and different ash particle sizes on sludge ash-cement mortar. J. Environ. Manag.88, 708–714.

[22] Suji D., Adesina A., Mirdula R. (2021), Optimization of self-compacting composite composition using Taguchi-Grey relational analysis. Materialia. 15:101027. doi: 10.1016/j.mtla.2021.101027.

[23] Arefi MR, Rezaei-Zarchi S. (2012) Synthesis of Zinc Oxide Nanoparticles and Their Effect on the Compressive Strength and Setting Time of Self-Compacted Concrete Paste as Cementitious Composites. International Journal of Molecular Sciences. 13(4):4340-4350. https://doi.org/10.3390/ijms13044340.

[24] Hitesh kumar Patil;Arun kumar Dwivedi; (2021). Impact of nano ZnO particles on the characteristics of the cement mortar, Innovative Infrastructure Solutions, 6:222, doi:10.1007/s41062-021-00588-9.

[25] Ding X, Zhao M, Qiu X, Wang Y, Ru Y. The Optimization of Mix Proportion Design for SCC: Experimental Study and Grey Relational Analysis. Materials (Basel). 2022, 10;15(4):1305. doi: 10.3390/ma15041305.

[26] Anderson, M. J., & Whitcomb, P. J. (2016). RSM simplified: optimizing processes using response surface methods for design of experiments. Productivity press.

[27] Raissi, S., & Farsani, R. E. (2009). Statistical process optimization through multi-response surface methodology. World academy of science, Engineering and Technology, 51(46), 267-271.

[28] Bezerra, M. A., Santelli, R. E., Oliveira, E. P., Villar, L. S., & Escaleira, L. A. (2008). Response surface methodology (RSM) as a tool for optimization in analytical chemistry. Talanta, 76(5), 965-977.

[29] Reji, M., & Kumar, R. (2022). Response surface methodology (RSM): An overview to analyze multivariate data. Indian J. Microbiol. Res, 9, 241-248.

Copyright © Int. J. of GEOMATE All rights reserved, including making copies, unless permission is obtained from the copyright proprietors.

15th Int. Conf. on Geotechnique, Construction Materials & Environment,
Kyoto, Japan, 11-13 November 2025, ISBN 978-4-909106124 C3051

FOAM CONCRETE WITH UNIFORMLY GRADED AGGREGATES AND TAILINGS: STRENGTH AND MICROSTRUCTURE

Kevin Chandra Nurwadji[1], Herlien Dwiarti Soemari[1], and Ivan Sandi Darma[1]

[1]Faculty of Civil and Environmental Engineering, Bandung Institute of Technology, Indonesia.

ABSTRACT

This study investigates the effect of uniformly graded quartz sand and varying proportions of mining tailings on the mechanical and microstructural properties of foam concrete. Two water-to-cement (W/C) ratios, 0.3 and 0.5, were used to evaluate their influence on compressive strength, workability, and internal structure. Tailings were incorporated as partial replacements for sand at 0%, 5%, 10%, and 20% by mass. Mechanical testing included compressive strength and slump flow tests, while microstructural analysis employed Scanning Electron Microscopy (SEM) and X-ray Computed Tomography (CT). Results showed that the W/C ratio of 0.5 produced significantly higher compressive strength and better slump flow, attributed to improved mix consistency. At W/C 0.3, the optimum tailings content was 10%, beyond which strength and workability declined. SEM and CT imaging revealed that the W/C 0.5 samples had a denser matrix, more uniform pore distribution, and no surface flaking, while the W/C 0.3 samples exhibited microstructural flaws and lower surface integrity. These findings highlight the importance of optimizing both water content and aggregate gradation to enhance the performance and durability of lightweight foam concrete.

Keywords: Foam Concrete, Cellular Lightweight Concrete, Mechanical Properties, Microstructure Analysis

INTRODUCTION

Foam concrete, also known as cellular lightweight concrete (CLC), has emerged as a promising material in modern construction due to its low density, thermal insulation properties, cost-effectiveness, and ease of placement [5-6]. It consists primarily of cement, water, fine aggregates, and a foaming agent that introduces a high volume of air voids into the mix. These voids significantly reduce the concrete's self-weight while imparting sufficient strength for various applications, including non-structural walls, thermal insulation layers, and even semi-structural components in low-rise buildings. As the demand for sustainable and energy-efficient construction materials grows, foam concrete has gained renewed interest among researchers and practitioners [5-6].

One of the critical factors that govern the performance of foam concrete is the nature and grading of the aggregates used. While much attention has been given to the binder system and foaming methods, the role of aggregate gradation, particularly uniformly graded aggregates remain relatively underexplored. Traditional studies have often emphasized well-graded or gap-graded aggregates for improving packing density and reducing voids in normal-weight concrete [4]. However, foam concrete behaves differently from conventional concrete due to its aerated matrix and unique pore structure.

Several studies have attempted to investigate the impact of aggregate types and gradations on foam concrete. Jones and McCarthy [1] reported that the particle size distribution of fine aggregates significantly affects the workability, strength, and stability of foam concrete mixes. Similarly, Kearsley and Wainwright [2] found that finer sand gradations can enhance compressive strength by reducing pore connectivity and improving the uniformity of the air void distribution. However, these studies mainly focused on broadly graded or fine aggregate systems, without isolating the effect of a uniformly graded aggregate system.

Uniformly graded aggregates consist of particles that are nearly the same size, resulting in lower packing efficiency and higher inter-particle voids. In conventional concrete, this typically leads to weaker mechanical performance due to the lack of smaller particles to fill the gaps between larger ones. Nonetheless, in foam concrete, where air voids dominate the matrix, the interaction between aggregate packing and air bubble distribution may yield different outcomes. Uniformly graded systems may influence the bubble stability, matrix cohesion, and ultimately, the mechanical strength and microstructural integrity of the composite.

The microstructure of foam concrete, especially the distribution and connectivity of pores, plays a crucial role in determining its strength and durability. According to Ramamurthy et al. [4], factors such as pore shape, size, and distribution are affected by the mix design and the physical characteristics of aggregates. Understanding how a uniform aggregate gradation interacts with the foam matrix can thus offer new insights into the optimization of lightweight concrete mixtures.

Despite these considerations, limited research has been conducted on the direct comparison of foam concrete with uniformly graded aggregates versus

other gradation profiles in terms of both compressive strength and microstructure. This knowledge gap forms the core motivation of the present study.

This research aims to investigate the influence of uniformly graded aggregates on the strength and microstructural properties of foam concrete. The study involves experimental testing of compressive strength and detailed microscopic analysis to characterize the internal structure. By evaluating how uniform gradation affects void distribution, matrix-aggregate bonding, and overall performance, this study seeks to provide a deeper understanding that can contribute to the development of high-performance, lightweight, and sustainable construction materials.

RESEARCH SIGNIFICANCE

This study contributes to the limited body of knowledge on the role of aggregate gradation in foam concrete, specifically focusing on uniformly graded aggregates. By examining the effects on both compressive strength and microstructure, the findings offer valuable insights for optimizing lightweight concrete mix designs. The research supports the development of more reliable and structurally sound foam concrete, promoting its use in sustainable and cost-effective construction. It also lays the groundwork for further exploration into aggregate behavior in aerated cementitious systems.

TESTING PROCEDURE

This research investigates the mechanical and microstructural properties of foam concrete incorporating uniformly graded quartz sand and varying proportions of mining tailings. Two water-to-cement (W/C) ratios (0.5 and 0.3) and four levels of tailings replacement (0%, 5%, 10%, and 20% by mass of sand) are used as shown in Table 2. Portland Composite Cement (PCC) serves as the primary binder. The procedure includes mechanical tests and microstructural evaluations to understand the effect of these variations on the performance of foam concrete.

Materials and Sample Preparation

- Cement: Portland Composite Cement (PCC), conforming to SNI standards.
- Fine Aggregate: Uniformly graded quartz sand with a grain size range between mesh No. 20 and 30 (approximately 600–850 μm).
- Tailings: Processed, oven-dried tailings used to replace quartz sand by mass. Chemical composition is detailed in Table 1.
- Water-to-Cement Ratios: 0.5 and 0.3.
- Foaming Agent: A protein-based/synthetic agent to ensure uniform air distribution.

Materials are batched by weight. The foam concrete mix is prepared in a laboratory mixer, ensuring uniform dispersion of foam. The fresh mix is cast into standard molds—100 mm cubes for strength tests and cones for slump measurements. All specimens are demolded after 24 hours and cured in water at 25 ± 2°C for 28 days.

Fig.1 Compression test of foam concrete cylinder

Fig.2 Sand, tailings, and PCC materials

Mechanical Properties Testing

Compressive Strength Test

- Specimen Size: Cylinder 100 mm Diameter & 200 mm Height.
- Age at Testing: 28 days.
- Equipment: Universal compression testing machine (capacity ≥ 2000 kN).
- Procedure: Load applied at 0.5 MPa/s until failure. Strength is calculated by dividing the peak load by the cross-sectional area.

Slump Flow Test

- Standard: Modified ASTM C1611 (suitable

for low-consistency materials).

- Apparatus: Slump cone (100 mm top dia., 200 mm bottom dia., 300 mm height).
- Procedure: Fresh foam concrete is poured into the cone, which is lifted vertically. The average spread diameter is recorded from two perpendicular directions.

Table 1 Chemical composition of Tailing

No.	Component	Result % mass
1	SiO2	47.7
2	CaO	12.1
3	SO3	10.2
4	Fe2O3	10.1
5	Al2O3	9.8
6	K2O	4.74
7	MgO	3.73
8	Na2O	0.518
9	P2O5	0.329
10	TiO2	0.315
11	CuO	0.114
12	MnO	0.105
13	Cl	0.0596
14	SrO	0.0506
15	Rb2O	0.016
16	MoO3	0.0131
17	ZnO	0.0126

Microstructural Analysis

A. Scanning Electron Microscopy (SEM)

- Objective: To observe the morphology of hydration products, especially Calcium Hydroxide (CH) and Calcium Silicate Hydrate (C-S-H)—with focus on regions adjacent to pores.
- Sample Preparation:
  - 28-day cured samples are cut and oven-dried at 50°C.
  - Fractured surfaces are gold and carbon coated for conductivity.
- Equipment: High-resolution SEM (resolution <5 nm).
- Focus Areas: Interfacial transition zones (ITZ), pore boundaries, and internal matrix.

B. X-Ray Computed Tomography (X-Ray CT)

- Objective: To evaluate 3D pore structure, total porosity, and void distribution.
- Sample Size: Cylindrical cores, 50 mm diameter × 100 mm height.
- Procedure:
  - Scanning performed at high resolution (voxel size <50µm).
  - Data analyzed using software (ImageJ) to segment pores, quantify:
    - Porosity volume (%)
    - Pore size and distribution
    - Connectivity maps
- Outcome: 3D visualization and quantitative mapping of internal pore networks.

Table 2 Experimental matrix

W/C Ratio	Tailings Content (%)	Test Conducted
0.5	0, 5, 10, 20	Slum, Compressive Strength, SEM, CT
0.3	0, 5, 10, 20	Slum, Compressive Strength, SEM, CT

TEST RESULT AND ANALYSIS

Strength Properties

Table 3 28th day compressive strength result

fc'	w/c ratio	
Tailing Content	0.5	0.3
0	4.58	0.48
5	1.98	0.26
10	2.81	0.16
20	2.49	0.26

Based on the compressive strength test results on Table 3, foam concrete samples with a water-to-cement (W/C) ratio of 0.5 achieved significantly higher strength compared to those with a W/C ratio of 0.3. This performance can be attributed to better mix consistency and workability at the higher W/C ratio, which allowed for more uniform distribution of the foam and aggregates within the matrix. In contrast, the 0.3 mix was prone to inconsistency during mixing and casting, leading to poor compaction, uneven air voids, and weak bonding. These factors likely contributed to the lower and more variable compressive strength observed in the lower W/C ratio samples.

Interestingly, differences in surface quality were also observed between the two mixes. The W/C 0.5 samples showed no visible signs of flaking off or surface degradation after curing, indicating good surface cohesion and uniformity. However, the W/C 0.3 samples exhibited signs of “flaking off,” particularly on the edges and corners, where surface material appeared to detach or crumble slightly. This surface imperfection may be due to poor compaction and low water content, which limited the development of a dense and cohesive outer layer.

These observations suggest that W/C ratio not only affects internal strength but also plays a key role in the surface durability of foam concrete.

Slump

Table 4 Slump test results in cm

w/c \ Tailings	0%	5%	10%	20%
0.3	41.5	42	51.25	45
0.5	59.25			57.5

The slump flow test on Table 4, conducted according to ASTM C1611, demonstrates the influence of water-to-cement (W/C) ratio and tailings content on the workability of foam concrete. As expected, the foam concrete with a W/C ratio of 0.5 exhibited greater slump flow than the corresponding mixes with a W/C ratio of 0.3. This is attributed to the higher water content, which improves the mobility of particles and allows for better dispersion of the foam within the matrix. The increased fluidity in the 0.5 mix makes it easier to handle, place, and consolidate—an important consideration in practical construction scenarios, especially when dealing with lightweight aerated materials.

For the W/C 0.3 samples, the slump flow remained relatively low and showed limited variation with increasing tailings content. The slightly higher flow observed at 10% tailings substitution may indicate a temporary improvement in particle packing or lubrication, possibly due to the finer particle distribution from the tailings. However, beyond 10%, the benefit seems to be reduced, potentially because excessive replacement introduces angular particles or inconsistent surface textures that reduce flow. This trend aligns with the compressive strength data, where 10% tailings also showed peak performance, suggesting a balance point between workability and particle interaction.

Fig.1 SEM result of Foam Concrete

In contrast, the W/C 0.5 samples maintained high workability across both measured points (0% and 20% tailings), with only a slight reduction in slump in the higher tailings content. This minor decrease could be due to the presence of coarser or less-reactive mineral particles in the tailings, which might absorb part of the mix water or disrupt paste cohesion. Nevertheless, the difference is not significant, implying that the 0.5 W/C mix is more tolerant to tailings addition in terms of flow characteristics. Overall, these results suggest that W/C ratio is the dominant factor influencing slump flow, with tailings content having a secondary, nonlinear effect depending on the mix proportion.

MICROSTRUCTURE PROPERTIES

The SEM image from Fig.1 of the foam concrete sample with a water-to-cement (W/C) ratio of 0.5 (coded WC05T00), taken at 33× magnification, shows a well-developed porous microstructure with a relatively uniform distribution of air voids. The pores appear mostly spherical or rounded, indicating effective stabilization of the foam during mixing and curing. The pore sizes vary, but the spacing and shape consistency suggests that the foaming agent was well-dispersed within the mix. Such a stable pore structure is essential in foam concrete, as it contributes to reduced density while maintaining internal cohesion. The visible pore walls also appear continuous and thick enough to suggest sufficient matrix development between voids.

Surrounding the air voids, the cementitious matrix appears dense and well-bonded, with no obvious signs of internal segregation or major microcracks. The texture of the matrix suggests a high degree of hydration, though the presence of some angular, bright particles may indicate anhydrate cement grains or residual mineral content from the quartz sand or tailings. While specific hydration products such as Calcium Silicate Hydrate (C-S-H) or Calcium Hydroxide (CH) cannot be definitively identified at this magnification, the absence of weak zones or disconnected regions between particles implies that the hydration process developed well. The lack of visible microcracking or interface separation near the pores also supports the notion that the interfacial transition zones (ITZ) are relatively strong in this mix.

Importantly, the surface of the sample shows no visible signs of flaking or deterioration, which supports the earlier mechanical findings that samples with a W/C ratio of 0.5 had higher compressive strength and better visual integrity. The dense matrix and stable pore structure both contribute to this observation. Compared to mixes with a lower W/C ratio, which were reported to show signs of “flaking off” or poor surface quality, the WC05T00 sample demonstrates a more cohesive and durable microstructure. These findings reinforce the importance of adequate workability in foam concrete mixes, particularly for ensuring uniform distribution

of air voids and hydration throughout the matrix.

CONCLUSIONS

The results confirmed that W/C ratio plays a dominant role in both compressive strength and workability. Foam concrete with a W/C ratio of 0.5 (e.g., fc' = 2.2 MPa at 0% tailing content) exhibited significantly higher compressive strength and superior workability compared to the 0.3 mix (fc' = 0.39 MPa at 0% tailing content). The better consistency of the 0.5 mix allowed for improved distribution of foam and aggregates, leading to a denser and more cohesive matrix.

Tailing replacement also influenced performance, particularly at the lower W/C ratio. A 10% tailings substitution provided optimal compressive strength in the W/C 0.5 mix, likely due to enhanced particle packing and interaction. However, further increase to 20% led to a reduction in strength and workability, possibly from poor compaction or reduced bonding. The slump test results reinforced these findings, showing limited flow in low W/C mixes and stable, high workability in W/C 0.5 mixes, even with tailings addition.

Microstructural analysis using SEM and X-ray CT further validated the mechanical observations. The W/C 0.5 samples exhibited a uniform pore distribution, dense matrix, and no visible flaking, while W/C 0.3 samples showed signs of surface deterioration and inconsistency. These findings underline the importance of balancing water content and tailings substitution to maintain structural integrity and workability. Overall, the study provides valuable insights into mix design strategies for developing strong, workable, and sustainable foam concrete using uniformly graded aggregates and industrial waste materials.

ACKNOWLEDGMENTS

I would like to express my deepest gratitude to P2MI (Program Penelitian Mahasiswa Indonesia) for their generous financial support, which has been invaluable in the completion of this research. I would also like to extend my sincere appreciation to the Structural Laboratory Program at Institut Teknologi Bandung (ITB) for providing the necessary facilities, resources, and technical assistance throughout the experimental and analytical phases of this study. Their support has greatly contributed to the successful execution of this research project.

REFERENCES

[1] Jones, M. R., and A. McCarthy. 2005. "Preliminary Views on the Potential of Foamed Concrete as a Structural Material." Magazine of Concrete Research 57 (1): 21–31. https://doi.org/10.1680/macr.2005.57.1.21.

[2] Kearsley, E. P., and P. J. Wainwright. 2001. "The Effect of High Fly Ash Content on the Compressive Strength of Foamed Concrete." Cement and Concrete Research 31 (1): 105–112. https://doi.org/10.1016/S0008-8846(00)00430-4.

[3] Ramamurthy, K., E. K. Kunhanandan Nambiar, and G. Indu Siva Ranjani. 2009. "A Classification of Studies on Properties of Foam Concrete." Cement and Concrete Composites 31 (6): 388–396. https://doi.org/10.1016/j.cemconcomp.2009.04.006.

[4] Neville, A. M. 2011. Properties of Concrete. 5th ed. Harlow, UK: Pearson Education Limited, pp. 69-70

[5] Sunarno, Y., P. R. Rangan, E. Ambun, and M. Tumpu. 2024. "Mechanical Properties of Foamed Concrete (FC) Using High-Volume Fly Ash." International Journal of GEOMATE 26 (118): 141–148. https://doi.org/10.21660/2024.118.g13323.

[6] Drusa, M., J. Vlcek, W. Scherfel, and B. Sedlar. 2019. "Testing of Foam Concrete for Definition of Layer Interacting with Subsoil in Geotechnical Applications." International Journal of GEOMATE 17 (59): 115–120. https://doi.org/10.21660/2019.59.8293.

Copyright © Int. J. of GEOMATE All rights reserved, including making copies, unless permission is obtained from the copyright proprietors.

15th Int. Conf. on Geotechnique, Construction Materials & Environment, Kyoto, Japan, 11-13 November 2025, ISBN 978-4-909106124 C3051

THE BEHAVIOR OF AN EXPERIMENTAL HOUSE IN RESPONSE TO SHRINKAGE

Lamis Makki[1], Fabien Szymkiewicz[1], Céline Chesnais[1] and Ning Sun[1]

[1]University Gustave Eiffel, 14-20 Boulevard Newton, F-77447 Marne la Vallée cedex 2, Paris, France

ABSTRACT

The damage caused by the effects of drought is especially common in the houses built on shallow foundations. These damages result from the combination of the shrinkage of clayey soil, and the vulnerability of the construction. This paper presents the results of tests carried out on a full-scale model house built on jacks to simulate the different settlement distribution of its foundations during a period of drought. Results of observations made during several tests are presented. A numerical analysis of the behavior of the experimental house was realized. The three-dimensional finite element analysis using the FEM code CESAR-LCPC uses volumetric elements for the concrete blocks, the mortar joints and the concrete of the footing and of the wall ties, whereas the reinforcing bars are modelled using one-dimensional elements, superimposed to the volumetric mesh. Three analyses were performed, in order to match the conditions of the experiments: the supports were suppressed under one fourth, then the half, then another fourth of the house. The calculations gave results close to the measurements.

Keywords: Experimental House, Shrinkage, Finite Element, Settlement

INTRODUCTION

The construction of an experimental house was carried out to subject it to mechanical loads similar to those resulting from the cycles of shrinkage and swelling of the underlying ground. This work was performed within the framework of the ARGIC research program, funded by the French National Research Agency (ANR) and dedicated to the effects of shrinkage and swelling on buildings. To meet the project's timeline, the study was focused on the house itself, without a precise description of the behavior of clayey soils under these cycles. The house was built in a test hall and named MISS (Maison Individuelle Soumise au Sécheresse or "Single house subjected to drought"). The house was built to standard dimensions, in accordance with French construction regulations. Its only particularity is that its foundations were built on metal supports that can be replaced by jacks in various sectors, allowing the modification of the foundation support conditions. An experimental setup was designed to measure vertical displacements of the foundations, deformations of chaining elements, and forces in the jacks. A visual monitoring system was also implemented to track the formation of cracks in the walls and foundations.

RESEARCH SIGNIFICANCE

This paper aims to enhance the understanding of structural damage caused by the effects of drought on clayey soils and differential settlements. A full-scale masonry house was built on hydraulic jacks to modify the foundation support conditions. The structure's configuration was chosen to be similar to those affected by drought. This paper presents the construction of the experimental station and the results of the initial tests. It also details the finite element analysis performed using the CESAR-LCPC software. The results of these numerical simulations are then compared with observations from the experimental station. An important practical conclusion can be drawn from this study: the construction of houses in accordance with current regulations appears sufficient to provide good resistance to soil movements caused by drought.

To our knowledge, this test station is unique. It provides essential data for modeling, making it possible to validate full-scale calculations.

BIBLIOGRAPHIC ELEMENTS

The shrinkage-swelling phenomenon causes volume variations in clayey soils and, consequently, differential settlements that can damage houses. The mechanical response of masonry buildings under various loads—such as uniaxial compression, uniaxial tension, biaxial loading, and shear—has been extensively studied by [1]. These elementary load cases combine to form the overall mechanical response of the masonry structure, contributing to what is known as its "strength." In modern masonry, the differences in stiffness between bricks and joints are much smaller.

It is widely accepted that masonry compressive failure is primarily governed by the interaction between bricks/blocks and mortar. Estimating the performance of structural elements requires assessing their response values (strengths, stresses, drifts,

cracks, etc.) against various types of loads and external forces [2]. The fracture behavior of masonry structures is influenced by several factors: the material properties of the brick and mortar, the geometry of the bricks, joint thickness, and the properties of the brick-mortar bond. Zucchini et al. (2006) [3] conducted tests on solid soft-mud bricks measuring 250×120×55 mm with a mortar joint thickness of 10 mm. The non-linear behavior of the components was simulated using Drucker–Prager plasticity in compression and a Rankine model in tension. Their work aimed to identify the most significant parameters affecting masonry behavior under compression. The study showed that mortar strength has a limited influence on the masonry composite's response, while the results are more sensitive to the brick's compressive and tensile strength. Finite element simulations were performed to analyze the behavior of the MISS Station and to precisely identify the location of stress concentrations within the three-dimensional structure of the house. This required several preliminary choices. Chaimoon and Attard (2009) [4] explained that for numerical purposes, two main approaches are adopted for masonry modeling: macro-modeling and micro-modeling. In the macro-modeling approach, homogenization techniques and continuum-based theories are typically used for large, practical analyses. The global structural behavior is described by a relationship between average strains and average stresses. The material parameters for this approach must be obtained from masonry tests of a sufficiently large size under homogeneous stress states. Macro-modeling approaches have been adopted, for instance, by Grande et al. (2008) [5]. In the micro-modeling approach, a representation of the brick, mortar, and the unit/mortar interface must be included. Cohesive crack models are commonly adopted in the micro-modeling formulation through the use of interface elements. This approach is suitable for small structural elements where there is a particular interest in highly heterogeneous stress and strain states. Lourenco et al. (2006) [6] studied the ability of continuum models based on plasticity and cracking to reproduce the experimental compressive behavior of masonry. It was chosen chose to use a micro-modeling approach to reproduce the actual geometry of the bricks in the house and to employ an appropriate modeling technique for the mortar joints. This choice provides more detailed information on the stress distribution in the masonry but requires a large number of elements. We adopted a linear elastic-perfectly plastic behavior, characterized by only four parameters: Young's modulus, Poisson's ratio, and tensile and compressive strength. For this model, we considered the same geometry, boundary conditions, and loads as the real tests performed on the test house. Regarding the mechanical properties of the materials, due to a lack of specific measurements on the house's materials, we used typical values found in the literature [7].

DESIGN OF THE EXPERIMENTAL STATION AND CONSTRUCTION DETAILS

The experimental house was designed to allow the repetition of tests and to compare the behavior of a structure with or without slab. The configuration of the structure to be tested was chosen to be similar to actual structures affected by drought. A rectangular plan of 10.65 m x 8.65 m external dimensions, divided into four sectors, was adopted (Fig.1).

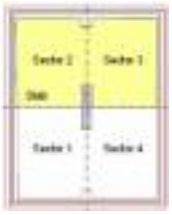

Fig. 1 Structure of the house and testing sectors.

The structure, from bottom to top, consists of foundations, basement walls, a lower concrete-slab floor, the walls, and an upper wooden floor. While the exterior walls have openings for doors and windows, only the main structure of the house has been built. Consequently, the MISS station currently has no roof or windows. The weight of the roof has been simulated by placing concrete blocks on the gable walls and façades. A view of the completed construction is shown in Figure 2.

Fig. 2 Overview of the house.

This section details the structure of the ceiling and the metal supports beneath the foundations. The foundations are strip footings measuring 45 cm x 20 cm, reinforced with three HA8 steel bars. The concrete for the foundations is a 350 kg/m³ mix of

CPJ 32.5 cement with a 4 cm coating. An additional, 3-meter-long isolated footing has been placed under the center of the experimental house to support the partition wall. The foundations were cast in place on mechanical supports using wooden formwork. The basement walls are constructed from three rows of hollow concrete blocks. They are positioned directly under the perimeter walls and the internal partition wall. The blocks used for the basement walls have a higher compressive strength than those used for the upper walls. Vertical reinforcing chains were installed at the corners of the house and in the middle of each façade. This reinforcement consists of two HA10 bars, with a mass of 2.78 kg/m. The 20 cm x 20 cm x 50 cm blocks used for the walls have a 15 cm diameter cavity to accommodate the steel reinforcing bars and the sealing concrete (a 350 kg/m³ cement mix). Horizontal reinforcing chains were added at each floor level. Lintels were also sealed in place at the top of every window and door. The reinforcement for these chains consists of two HA10 bars, with a mass of 1.4 kg/m. The chains were sealed between two rows of specially designed 5 cm thick (5 cm x 20 cm x 50 cm) hollow blocks for horizontal reinforcement, as shown in Figure 3.

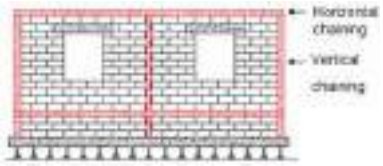

Fig. 3 Schematic of walls and chaining

The horizontal reinforcing chain has an overall cross-section of 10 cm x 20 cm. Only half of the lower floor was constructed. This floor consists of a composite slab made of concrete beams and blocks, reinforced for compression. The beams are 13 cm high and are topped with a 4 cm thick compression slab. This slab is reinforced with a wire mesh measuring 200 mm x 300 mm with a wire diameter of 3.5 mm x 3.5 mm, which is equivalent to 0.63 kg/m². There are 18 beams in total (9 in Sector 2 and 9 in Sector 3). The concrete blocks measure 12 cm x 53 cm x 20 cm and weigh 15.3 kg each. The other half of the house was left without a slab to facilitate a discussion on the role of the floor in the building's behavior. The walls are made of hollow concrete blocks. The building's roof height is approximately 2.60 m. An internal partition wall provides both support for the floor above and structural bracing. The thickness of the outer walls is 20 cm, while the internal wall is 15 cm thick. The walls are not coated, and the concrete blocks were joined with mortar. Openings for doors (2 m x 2.15 m) and windows (1.2 m x 1.35 m) were created and are arranged identically across all four construction sectors. The ties placed above the wall openings were sealed in place, with the reinforcement consisting of four HA10 bars. The top floor is designed to support an overload that simulates the presence of an additional floor and a roof. It is composed of wooden beams and slabs. This structure weighs 7.5 tons on the façade walls and 2.85 tons on the gable walls.

EXPERIMENTAL SETUP

The house's foundations rest on a series of removable mechanical supports, which are themselves placed on a rigid, cast-in-place concrete footing (Fig. 4).

Fig. 4 Foundations of the house

To perform tests on a single sector of the house, we simply replace the mechanical supports under that sector with hydraulic jacks. These jacks are then used to induce controlled settlements or heave in the house's foundation. The experimental setup therefore consists of a rigid reinforced concrete foundation, a set of mechanical supports, and a set of hydraulic jacks. The experimental house was built inside a covered hall. The overall construction includes a ground-level support structure, with metal supports holding the house's foundations and the house itself. A rigid, reinforced concrete footing was cast in place on a platform. This platform is composed of a 1-meter-thick layer of gravel (category B4, 0/40 mm) topped with a 20 cm layer of well-graded untreated gravel (D2, 0/31.5 mm). The footing has a 65 cm x 35 cm cross-section and is reinforced with 8 steel bars (10 mm diameter). The concrete mix was prepared with 350 kg/m³ of CPJ 32.5 cement, with a 4 cm coating. The house's mechanical supports were specifically designed and manufactured for this project. A total of 85 mechanical supports are required, with two supports per meter. Each support has a nominal capacity of 80 kN. The hydraulic jacks

are installed in place of the mechanical supports. These jacks have a capacity of 500 kN and a travel of 150 mm.

NUMERICAL MODEL

A three-dimensional model of the house structure was chosen. In this model, the concrete blocks and joints are represented by eight-node volume elements, while the horizontal and vertical reinforcing chains are represented by bar elements superimposed on the three-dimensional mesh. The total mesh consists of 111,644 elements. Each volume element is defined by five key parameters: density, Young's modulus, Poisson's ratio, and compressive and tensile strength. Figure 5 shows the house's mesh, which is composed of eight-node volume elements representing the concrete in the foundations, the concrete blocks, and the joints. The mesh was constructed by assembling elementary meshes, each including a single block and a layer of mortar, to first create wall portions and then complete walls.

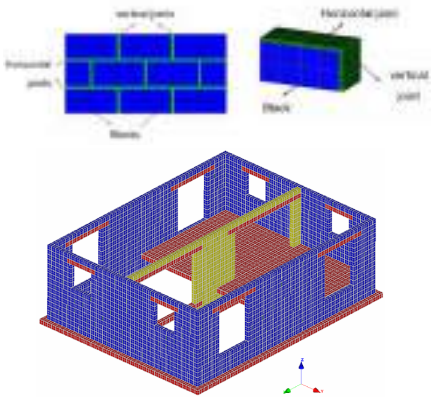

Fig. 5 Mesh of experimental house (joints end bricks)

Chaining was represented by means of a set of bar elements. The properties of the three types of material of volume elements are given in Table 1.

Table 1 Mechanical properties of materials

	Density (kg/m^3)	Young's modulus (MPa)	Poisson's ratio (-)	Compressive strength (MPa)	Tensile strength (MPa)
Concrete	2500	40000	0.2	20	2
Joints	1500	6000	0.2	6	1
Blocks	1000	400	0.1	4	0.5

To reproduce three tests conducted on the actual MISS station, three corresponding calculations were performed: (i) Removal of supports under Sector 1, (ii) Removal of supports under Sectors 1 and 4, (iii) Removal of supports under Sector 2. The experimental house is divided into four sectors. The test procedure involves gradually lowering the stems of hydraulic jacks placed under a part of the foundation and observing the house's resulting behavior. For a selected test sector, the experimental procedure begins by replacing the house's mechanical supports with jacks. The imposed displacement follows a parabolic curve, with the maximum settlement occurring at the house corner. The process starts with the first two jacks from the corner and continues by progressively imposing a parabolic differential settlement along the entire length of the foundations. The characteristic settlement values used are 1/1000, 1/500, and 1/250. These settlements are applied at every meter, which corresponds to the distance between two jacks. The observation and monitoring period between two phases is typically 24 hours. The test is stopped when a crack at least 2 mm wide appears in the walls. The measurements collected during the tests were: Foundation settlement, forces at the hydraulic jack heads, deformations in the foundations and horizontal reinforcement chains and cracks development.

Test On Sector 1

The test on Sector 1 involved applying a displacement to the hydraulic jacks that support the foundations at the corner of the house. This particular sector was chosen because it was constructed without a concrete-slab floor (Fig. 6)

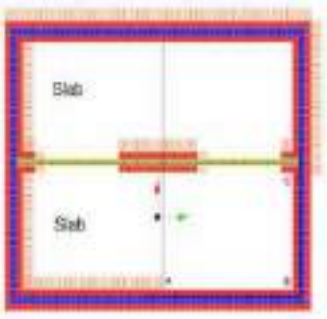

Fig. 6 Modelling of the test on sector 1- boundary conditions

This condition is equivalent to the absence of supports under this part of the foundation. In the experimental study, this condition was imposed incrementally to avoid causing any structural damage to the house. In the numerical calculation, however, it was imposed directly. The calculated maximum vertical displacement (at the house corner) was 3.4 mm, which is very close to the experimental value of 3.35 mm. Figure 7 compares the calculated and observed settlements under the foundations between points A, B, and C, as defined in Figure 6.

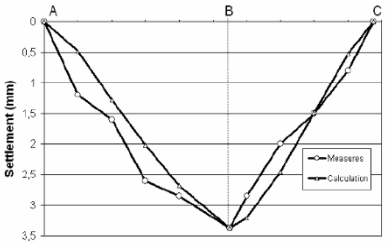

Fig. 7 Comparison of measured and calculated settlements (Foundation AB and BC)

Test On Sectors 1 And 4

The test on Sectors 1 and 4 involved imposing a displacement on the hydraulic jacks located under one half of the house (the side without a floor). For the numerical calculation, this condition is equivalent to simulating the absence of supports under that entire section of the foundation (Figure 8, line ABCD).

Fig. 8 Modelling of the test on sector 1 and 4-boundary conditions

This configuration was applied directly in the numerical calculation, whereas the actual test involved several phases. Figure 9 compares the measured and calculated foundation settlements along the line ABCD. The calculated and observed settlement values were very close. The calculation was performed in a phased manner to match the experimental procedure. In the first phase, Sector 1 was unloaded. The supports were then repositioned under its foundations, but they were not returned to their initial starting position. A settlement of a few millimeters was thus maintained. For the calculation involving Sectors 1 and 4, the final state of deformation and stress from the previous calculation (Sector 1) was used as the initial state. This explains why the calculated settlements for Sectors 1 and 4 are not symmetrical, even though the mesh and materials are.

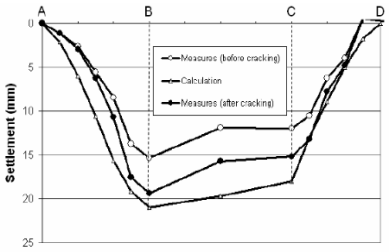

Fig. 9 Comparison of measured and calculated settlements (Foundation AB, BC and CD)

During the test on Sectors 1 and 4, the structure progressively deformed without any visible cracking. However, cracks appeared 14 days after the jacks were lowered. These cracks had an unexpected geometry: they originated from the foundation and ran along the central vertical reinforcement chain on the internal wall. The cracking in the foundation can be attributed to the way this section was reinforced. The steel bars were placed at the bottom of the beam, as it typically experiences tension in its lower part. However, the effect of soil shrinkage under the house's corner induces tensile stresses in the upper face of the beam, where there is no reinforcement. While the appearance of cracks in the wall blocks near the openings is logical, the horizontal cracking cannot be explained solely by a localized weakness in the vertical reinforcement chain at the house's corner. This specific weakness was not accounted for in the calculation presented here.

Test On Sector 2

The test on Sector 2 involved applying a displacement to the supports under a quarter of the house, on the side equipped with the lower floor. During this test, displacements of the mesh nodes for the previously tested half of the house (Sectors 1 and 4) were constrained in the x, y, and z directions. The house was not returned to its original state before the test on Sector 2 was performed. Instead, the simulation took into account the stresses, plastic strains, and displacements produced in the structure after the test on Sectors 1 and 4. Figure 10 compares the calculated and measured settlements. The maximum calculated settlement was 4.7 mm, which is close to the measured value of 5.6 mm. To identify its effect, a defect in the vertical reinforcement chain at the corner of the structure was introduced during the experiment.

This defect, however, was not included in the calculation. This discrepancy explains why the settlement observed during the experiment was higher than that of the model.

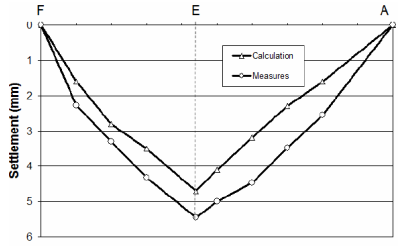

Fig. 10 Comparison of measured and calculated settlements (Foundation AE and EF)

CONCLUSIONS

A full-scale house was constructed to simulate the effects of soil shrinkage and to observe and measure the response of a typical individual masonry house subjected to various stresses. The objective of this work was to better understand the deformation mechanisms of masonry structures under imposed loading and to determine the maximum acceptable loads for this structure. The tests showed that, under the conditions of a new structure, a simple building constructed according to Eurocode 6 (EC6) regulations does not experience structural damage when maximum stresses are applied to a quarter of the structure, regardless of whether it is on its more rigid side (with a slab) or its less rigid side (without a slab). However, when half of the house (without a slab) was subjected to a differential settlement of 1/300, cracks appeared in the walls on both sides of a corner after a few days. A three-dimensional finite element model of the experimental house was developed. The model, which simulated foundation displacements in one or two sectors of the house, produced encouraging results regarding the settlements and deformations of the masonry structure. The deformation amplitudes were highly dependent on the material properties, particularly those of the concrete block, with values taken from a literature review. The choice of mesh was constrained by the capabilities of the finite element software and the computers used for this study, as the simulations involved approximately 450,000 degrees of freedom. For this specific problem, which concerns a particular mode of building deformation, the adopted approach appears to be reasonably sound and suitable for further studies on masonry buildings. An important operational conclusion can be drawn from this study: the construction of houses in accordance with current French regulations (EC6) seems sufficient to provide good resistance to soil shrinkage caused by drought. The calculation confirms the good performance of a masonry structure with concrete foundations and regularly spaced vertical and horizontal reinforcement chains. We plan to model the results of new experiments on the house, which will be carried out after reinforcing the areas where cracking occurred. To our knowledge, this test station is unique. It provides essential data for modeling by allowing for the validation of full-scale calculations. This study represents a first step toward modeling the behavior of a masonry structure subject to drought. A key limitation of the study is that only one house configuration was tested, which means the results cannot be generalized to all types of masonry construction and soil conditions.

REFERENCES

[1] Bosiljkov V., Page A.W., Bokan-Bosiljkov V.,Zarnic R. « Evaluation of the seismic performance of brick masonry walls», Structural control and Heath monitoring ,17(2008), p.100.

[2] Zucchini A., Lourenco P.B., « Mechanics of masonry in compression: results from a homogenization approach », Computers and Structures. 2006; 85, p. 193-204.

[3] Chimoon K., Attard M.M. « Experimental and numerical investigation of masonry under three-point bending », Engineering structures, 2009; 31, p.103-112.

[4] Grande E, Milani G, Sacco E. «Modelling and analysis of FRP-strengthened masonry panels». Eng Struct 2008;30(7):1842_60.

[5] Lourenco P.B., Pina Henriques J., « Validation of analytical and continuum numerical methods for estimating the compressive strength of masonry », Computers and structures, 2006; 84, p.1977-1989.

[6] Gabor A., « Contribution à la caractérisation et à la modélisation des maçonneries non renforcées et renforcées par matériaux composites ». Thèse de génie civil, Université Claude Bernard Lyon 1, 2002.

[7] Eurocode 6: «Design of masonry structures». EN 1996-1-1:2002. Brussels, Belgium, 2003.

Copyright © Int. J. of GEOMATE All rights reserved, including making copies, unless permission is obtained from the copyright proprietors.

15th Int. Conf. on Geotechnique, Construction Materials & Environment,
Kyoto, Japan, 11-13 November 2025, ISBN 978-4-909106124 C3051

IMPROVING RUTTING RESISTANCE IN STONE MASTIC ASPHALT PAVEMENT USING FINE SEIZED WASTE TIRE RUBBER

*****Enohmbey Chubisong Moses[1], and Yoshitaka Kajita[1]

[1]Department of Architecture and Civil Engineering, Tokai University, Japan

ABSTRACT

Rutting is one of the most common forms of pavement distress that leads to long-term damage and degradation of road surfaces, particularly under heavy traffic loads and high temperatures. The incorporation of waste tire rubber (WTR) into Stone Mastic Asphalt (SMA) has emerged as a promising solution to enhance rutting resistance and improve overall pavement durability. This study investigates the effect of different proportions of waste tire rubber on the rutting resistance of SMA. A series of Marshall Stability tests were conducted to assess the performance of rubber-modified asphalt compared to traditional SMA. The results suggest that the inclusion of waste tire rubber significantly enhances rutting resistance, offering a sustainable and effective approach to improving asphalt mixtures. The findings contribute to the development of more resilient, eco-friendly pavements by reducing waste tire disposal and improving the performance of asphalt under extreme conditions.

Keywords: Stone Mastic Asphalt, Rutting Resistance, Waste Tire Rubber, Marshall Stability Test, Sustainable, Asphalt Modification

INTRODUCTION

The increase in urbanization and rising vehicle traffic over the past few decades have placed a significant strain on the infrastructure of transportation networks, especially roadways. Since traffic loads continue to increase, we need to achieve high-performance pavements which can resist these conditions. Among the various forms of pavement distress, rutting defined as the permanent deformation of the pavement surface has emerged as a critical issue in maintaining road durability and safety. This is particularly significant in regions subjected to high temperatures and heavy traffic volumes. Rutting predominantly occurs due to the synergistic effects of repeated traffic loading, temperature fluctuations, and the intrinsic properties of the asphalt binder. The binder tends to soften under elevated temperatures, which consequently leads to the permanent deformation of the pavement surface. [1].

Stone Mastic Asphalt (SMA) is a specialized asphalt mixture widely used in road construction due to its high durability and superior resistance to deformation and wear. It is characterized by a high binder content and a coarse aggregate structure that creates a gap-graded mixture, enhancing its ability to resist traffic-induced deformations. However, despite these advantages, Stone Mastic Asphalt is not immune to rutting, especially when subjected to heavy traffic loads and high-temperature conditions [2]. To address these challenges, researchers and engineers have been exploring innovative ways to modify the properties of Stone Mastic Asphalt, with one promising approach being the incorporation of waste materials, such as waste tire rubber (WTR), to enhance its performance.

Waste Tire Rubber (WTR) has become a significant environmental concern due to the growing number of used tires that are discarded each year. In 2018 alone, over 1 billion tires were discarded globally, with many of them ending up in landfills or being incinerated, both of which contribute to environmental pollution. In response to this, various recycling methods have been proposed to repurpose waste tire rubber, particularly in asphalt mixtures. The use of WTR as an additive in asphalt has been studied for several decades, with early research focusing on the modification of bitumen to improve its properties, such as viscosity, elasticity, and resistance to rutting. However, it is the more recent research on its application in Stone Mastic Asphalt that has shown considerable promise in addressing rutting problems [3-4].

The concept of using waste tire rubber in asphalt was first proposed by Sullivan and Lytton in 1975, they explored the potential benefits of incorporating ground tire rubber into asphalt mixtures to enhance the binder's performance. Since then, a growing body of literature has emerged, indicating that rubber-modified asphalt mixtures exhibit improved performance characteristics, particularly in terms of rutting

resistance, flexibility, and cracking resistance [5]. The addition of rubber particles modifies the viscoelastic properties of the asphalt binder, which improves the ability of the mixture to withstand high temperatures and resist the permanent deformation caused by repeated traffic loads [6]. The incorporation of rubber also improves the adhesive properties between the binder and aggregates, leading to better cohesion and a more durable pavement structure [7].

The use of waste tire rubber improves low-temperature cracking resistance, as rubber-modified asphalt is less susceptible to brittleness at lower temperatures. Moreso, waste tire rubber -modified asphalt exhibits better moisture resistance, reducing the impact of water damage and stripping, which is a common issue in traditional asphalt mixes. These advantages are particularly important in regions with hot climates and high traffic volumes, where rutting can cause significant damage to roads and lead to costly repairs and maintenance. [8].

Despite the promising results from previous studies, the practical implementation of waste tire rubber -modified Stone Mastic Asphalt has been hindered by several challenges, including concerns regarding the optimal rubber content, compatibility with conventional asphalt binders, and the long-term performance of the modified mixes. Several studies have sought to determine the ideal proportion of waste tire rubber that maximizes rutting resistance without compromising the workability or durability of the mixture. For example, in 2029, Wang et al. found that adding 15-20% of waste tire rubber by weight of the binder resulted in significant improvements in rutting resistance, while higher concentrations of rubber led to reduced flow values, indicating potential issues with compaction and mix workability. These findings suggest that while WTR can effectively enhance the rutting resistance of SMA, the optimal rubber content must be carefully balanced to achieve the desired performance without introducing adverse effects [9].

Moreover, the compatibility of waste tire rubber with different asphalt binders remains an area of ongoing research. Most studies have focused on modifying standard asphalt binders, but recent work has also explored the use of polymer-modified asphalts in combination with waste tire rubber to further enhance the performance of the resulting mixtures. The use of polymer-modified asphalts has been shown to improve the binder's ability to accommodate higher rubber contents without sacrificing the mixture’s rheological properties [10]. However, the cost implications and the availability of suitable polymer-modified binders remain significant factors to consider when scaling up the use of waste tire rubber in real-world applications.

Despite these challenges, the incorporation of waste tire rubber into stone mastic asphalt is increasingly being seen as a sustainable solution to both environmental and infrastructure challenges. By recycling waste tires, which would otherwise contribute to landfill accumulation, waste tire rubber-modified Stone Mastic Asphalt offers a promising route for producing environmentally friendly, high-performance pavements. The use of waste tire rubber not only contributes to reducing the environmental impact of tire disposal but also helps improve the sustainability of road construction by enhancing the longevity and performance of pavements [11].

In summary, while previous studies have highlighted the potential of waste tire rubber to enhance rutting resistance in asphalt mixtures, further research is necessary to optimize the mixed design and performance characteristics of waste tire rubber-modified Stone Mastic Asphalt. This research aims to explore the effects of varying rubber seizes and contents to evaluate which seize works best resisting rutting and evaluate other performance aspects of Stone Mastic Asphalt, providing valuable insights into the development of more durable, sustainable pavements for the future.

RESEARCH SIGNIFICANCE

The disposal of waste tires has become a growing environmental concern due to their accumulation and the challenges associated with their recycling. Traditional disposal methods, such as landfilling and incineration, pose significant environmental and health risks, prompting the exploration of alternative uses for waste tires. One such solution is the incorporation of waste tire rubber (WTR) into asphalt mixtures, particularly in Stone Mastic Asphalt (SMA), which is known for its high durability and resistance to surface wear.Rutting is a major pavement distress that occurs when the asphalt binder softens under the influence of traffic load and high temperatures, leading to permanent deformations on the pavement surface. The inclusion of WTR in Stone Mastic Asphalt can potentially improve the resistance to rutting by enhancing the viscosity and elasticity of the asphalt binder. This research aims to evaluate the effects of different concentrations of waste tire rubber on the rutting resistance of SMA and explore its potential as a sustainable solution for road construction, reducing both environmental impact and maintenance costs.

METHODS

The aim of this experiment is to study the importance of Waste Tire Rubber (WTR) as an additive to Stone Mastic Asphalt (SMA) to improve its rutting resistance. Waste tires faces a major environmental challenge and recycling them into valuable materials for pavement construction gives birth to a sustainable solution. The incorporation of fine rubber into asphalt mixtures has been shown to improve the material's ability which can withstand deformation under traffic-induced stresses, which enhances the overall durability of road surfaces.

To achieve this, waste tire rubber was processed into fine and coarse particles and incorporated into the Stone Mastic Asphalt mix at varying concentrations. Stone Mastic Asphalt is a dense, highly stable asphalt mixture commonly used for high-traffic roadways. The mixture is known for its high stability and rutting resistance, but the addition of rubber may further enhance its performance under extreme conditions. This section outlines the preparation of the materials, sample mixes, testing procedures, and data analysis methods used to assess the rutting resistance of Stone Mastic Asphalt modified with waste tire rubber.

Fig. 1 Preparing mixture with straight asphalt without additive.

Fig. 2 Mixing the sample for 2.5 mins without additives.

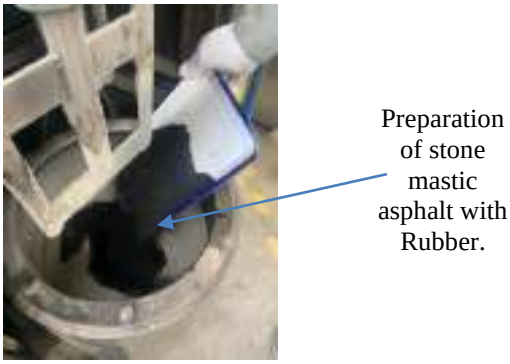

Fig. 3 Adding fine rubber to the mixture.

Figure 1 to 5 is a picture representation of our test preparation.

Materials and Mix Design

The Stone Mastic Asphalt (SMA) mix was prepared using standard aggregates with specific gradations to ensure high stability and durability under traffic loading. Aggregates were selected to meet the gradation specifications required for SMA, ensuring the creation of a dense and stable structure that can resist deformation. The bitumen used in this study was a 40/50 penetration grade, which is well-suited for road applications requiring durability and high-temperature performance.

Waste Tire Rubber (WTR) was obtained from discarded tires and processed into fine and coarse rubber particles using a bench grinder. The rubber was separated into two particle sizes, with fine particles used for one set of mixes and coarse particles for another. The rubber was incorporated into the asphalt binder at different weight percentages of bitumen: 0% (control), 10%, 20%, and 30%. This variation was intended to explore the impact of increasing rubber content on the rutting resistance and overall performance of the Stone Mastic Asphalt mixture.

Sample Preparation

The preparation of Stone Mastic Asphalt (SMA) mixtures was performed with varying amounts of Waste Tire Rubber (WTR) to evaluate its effects on rutting resistance. The SMA samples were categorized into four groups based on the rubber content, as follows: Group 1 (control mix with 0% WTR), Group 2 (SMA with 10% WTR by weight of bitumen), Group 3 (SMA with 20% Waste Tire Rubber by weight of bitumen), and Group 4 (Stone Mastic Asphalt with 30% Waste Tire Rubber by weight of bitumen). For each group, three replicate samples were prepared, totaling nine samples to ensure consistency and reliability.

The preparation process consisted of several

steps to achieve the desired mixed properties. First, the aggregates and bitumen were heated to their optimal temperatures to ensure proper mixing. The bitumen was heated to approximately 160°C, while the aggregates were heated to 170°C. This ensured that both components were fluid enough to allow for proper bonding.

Next, the rubber particles (either fine or coarse) were added to the heated bitumen and thoroughly mixed to ensure a uniform dispersion of the rubber within the binder. This step is crucial for achieving consistent performance characteristics across all samples, ensuring that the rubber is evenly distributed throughout the bitumen.

Once the rubber was fully incorporated into the bitumen, the rubber-bitumen mixture was combined with heated aggregates. The mixture was stirred until the aggregates were evenly coated with the modified bitumen, ensuring optimal material distribution for enhanced performance.

Finally, the mixture was placed into Marshall molds and compacted using the Marshall compaction method. Each sample was subjected to 75 blows from the Marshall compart; 50 blows applied around the circumference of the mold and 25 blows to the center. This compaction process ensured that each sample achieved the required density for testing, facilitating accurate performance evaluation of the rutting resistance of the WTR-modified Stone Mastic Asphalt mixtures.

Fig. 4 Collection of waste tire rubber.

Fig. 5 Cutting of waste tires into coarse seize.

The collected tires were cut using a pair of seizors to obtain coarse seized and grinded with a bench grinder to obtain the fine seized rubber.

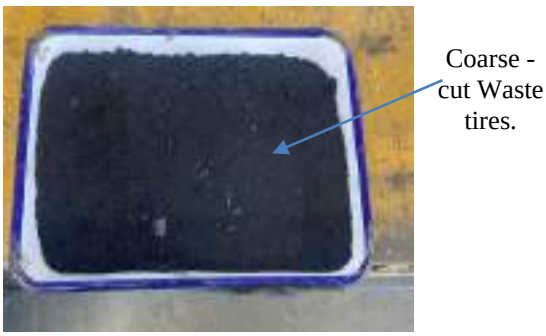

Fig. 6 Grinding of waste tire into fine seize.

Marshall Stability Testing and Observation

The Marshall Stability test was the primary method used to evaluate the rutting resistance of the WTR-modified Stone Mastic Asphalt mixtures. This test measures the maximum load that an asphalt sample can withstand before failure, which serves as an indicator of the material's stability under the stresses imposed by traffic. Additionally, the flow values were recorded to assess the workability and deformability of the mixtures. The stability and flow values were determined for all nine samples across the four groups (control and WTR-modified). The test involved applying a vertical load to the compacted samples until failure occurred, and the corresponding flow values were measured during this process. This test is critical in understanding how the incorporation of rubber affects the rutting resistance of the SMA mixture, which is directly related to the performance of road surfaces under traffic conditions [12-13].

The incorporation of Waste Tire Rubber (WTR) into Stone Mastic Asphalt (SMA) mixtures has been shown to significantly enhance rutting resistance, as evidenced by increased Marshall Stability values. This improvement indicates a stronger and more durable pavement mix capable of withstanding higher traffic loads without deformation. In contrast, the control mix which contained no waste tire rubber exhibited the lowest stability value, implying a greater susceptibility to rutting under traffic stress.

In this study, we used 0% of waste tire rubber recorded at 8.2 KN, reflecting relatively poor resistance to deformation. When 10% waste tire rubber was added to the mix, the stability increased to 9.6 kN, demonstrating an improvement in rutting resistance with even a modest addition of rubber. This trend continued with higher waste tire rubber content: at 20%, the stability value rose to 11.5 kN, and at 30%, the mix achieved its highest stability value of 12.3 KN. These results clearly indicate that the addition

of waste tire rubber enhances the mixture's resistance to rutting, with the most significant improvement observed at the 30% waste tire rubber level.

In terms of flow values ire the workability and ease of comp asphalt mix there was a slight increa ith the addition of waste tire rubber.

All prepared test samples for the experiment

Fig. 7 Marshal Stability testing.

Fig. 8 Samples without rubber and with fine Rubber and coarse rubber.

RESULTS AND DISCUSSION

The optimum bitumen content of 7.8% for the Stone Mastic Asphalt (SMA) was well-supported by the increased Marshall Stability observed with the incorporation of coarse seized waste tire rubber (WTR). In this study, both coarse-sized and fine-sized ground tire rubber were used as modifiers. The results showed that mixtures modified with fine waste tire rubber exhibited superior stability compared to those with coarse waste tire rubber, 30% content of course waste tire rubber - modified mix reached a peak stability value of 12.3 kN**,** indicating an important improvement in rutting resistance. The improved performance of fine rubber that was obtained using a bench grinder, can be attributed to its better mechanical interlocking within the asphalt matrix and its ability to absorb in powder form and dissipate traffic-induced stresses. Although 7.8% was identified as the optimum asphalt content, further evaluation at 8.2% asphalt content through air void analysis is recommended to explore whether better compact ability and durability can be achieved. Overall, the incorporation of coarse waste tire rubber at appropriate content levels significantly reduces rutting and enhances structural integrity, offering a sustainable solution for high-performance asphalt pavement.

Penetration test results done by adding coarse rubber into straight asphalt and fine rubber into straight asphalt revealed that, the properties of coarse tire rubber are significant in preventing rutting in asphalt pavement. To prevent rutting, we must grind the tire rubber into fine powder rubber so that its properties can easily blend with asphalt mixture as seen in this experiment.

This ratio provided the best strength and performance qualities and turned out to be quite accurate for the objectives of our study. The air void analysis at 7.8% further validated its suitability, showing excellent compaction and durability results. The results showed that 7.8% was still the most effective binder content under our testing conditions, even if 8.2% was assessed. The technical soundness of choosing 7.8% as the ideal asphalt content is demonstrated by these results.

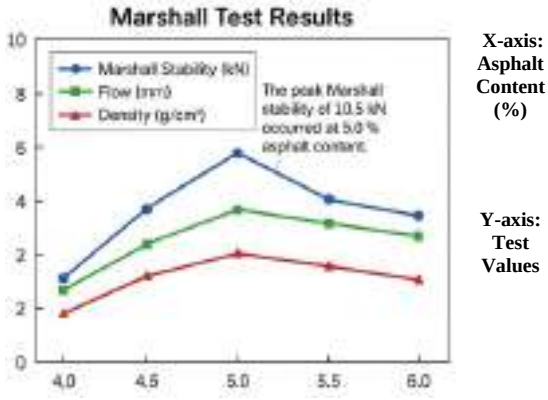

Fig. 9 graph of Marshal test results.

CONCLUSION

This study demonstrates that the inclusion of waste tire rubber in Stone Mastic Asphalt significantly improves rutting resistance. The Marshall Stability test results indicate that increasing the waste tire rubber content enhances the stability of the asphalt mixture, reducing the potential for rutting and improving the overall durability of the pavement. The findings support the use of WTR as a sustainable modifier for Stone Mastic Asphalt, offering an effective solution for improving pavement performance while addressing the growing environmental concerns associated with tire waste disposal.

Based on the Marshall Stability results of this

experiment, the selected optimum asphalt content was 7.8% because it provided a strong balance of strength and workability, particularly when enhanced with fine seized waste tire rubber. However, the final validation through air void analysis was 8.2% and it provided a more accurate, most efficient, and durable design mixture.

ACKNOWLEDGMENTS

The authors would like to express their sincere gratitude to the laboratory staff for their invaluable assistance in preparing the samples and conducting the necessary tests. We also extend our heartfelt appreciation to the funding agency for their generous support of this research project. Special thanks are given to Professor Yoshitaka Kajita of Tokai University for his outstanding supervision and guidance throughout the study. Additionally, we are grateful for the support provided by the Japan International Cooperation Agency (JICA). Finally, we would like to acknowledge Mr. Akira Nomoto of Gaeart Laboratory, Japan, for his technical assistance and expertise during the experimental phase of this research.

REFERENCES

[1] Nada, A. A., Edris, W. F., Al-Jabali, H. M., Almutairi, A. D., Sayed, A. a. a. A., & Khairy, An investigation of the capabilities of resin tire Carbon Black “N-330” as a waste binder in asphalt concrete mixtures. Vol. ,2025, pp.1-25 https://doi.org/10.3390/buildings15020158

[2] Zhang, Y., He, M., Wang, L., Yan, J., Ma, B., Zhu, X., Ok, Y. S., Mechtcherine, V., & Tsang, D. C. W. Biochar as construction materials for achieving carbon neutrality, vol 4, 2022, pp. 59.

[3] Magagula, S. I., Lebelo, K., Motloung, T. M., Mokhena, T. C., & Mochane, M. J. Recent Advances on Waste Tires: Bibliometric Analysis, processes, and waste management approaches. Environ Sci Pollut vol. 30, 2023, pp. 118213-118245.

[4] Yu, J., Lin, Z., Zou, G., Yu, H., Leng, Z., & Zhang, Y. (2024). Long-term performance of recycled asphalt mixtures containing high RAP and RAS. *Journal of Road Engineering*, vol.4, Issue, 2024, pp. 36-53

[5] Poovaneshvaran, S., Hasan, M. R. M., Jamshidi, A., Ghazali, M. F. H. M., Yang, X., & Jaya, R. P. The characterisation of fracture resistance of asphalt mixtures containing rubber modifiers and a Wax-Based additive. Advances in Materials Science and Engineering. Vol., 2023, pp. 1-16.

[6] Fan Zhang, Aimin Sha, Yangsen Cao, Wentong Wang, Ruimeng Song, Wenxiu Jiao, Characterization of Self-healing Properties of Asphalt Pavement Materials Containing Carbon Nanotubes: from the Binder and Mix Level based on Grey Relational Analysis, Construction and Building Materials, Vol. 404, 2023, pp. 133323.

[7] Hamkah, Z., Saing, D., Mairuhu, D., and Tumpu, M. (2024). Characteristics Of Asphalt Concrete Wearing Course MIncorporating.Recycled Tire Rubber as An Additive. International Journal of GEOMATE.vol.26, Issue 115, pp.34-43

[8] Gusty, S., Israil, Siti Nurjanah Ahmad, & Miswar Tumpu. (2024). Assessing Open-Graded Asphalt’s Resistance to Degradation Via Cantabro Test in Hot-Mix Cold Laid Asbuton. GEOMATE Journal, 2024 Vol.27, Issue 120, pp.60-68.

[9] Zhao, S., Liu, M., Meng, X., Liu, A., & Duo, L. (2024). Waste Rubber - Black Pollution Reframed as A Global Issue: Ecological Challenges and Sustainability

[10] Eskandarsefat, S., Dondi, G., & Sangiorgi, C. (2019). Recycled and rubberized SMA modified mixtures: A comparison between polymer modified bitumen and modified fibres. Construction and Building Materials**,** *Vol. 202, 2019, pp 681-691*

[11] Asmatulayev, B., Asmatulayev, R., Asmatulayev, N., & Bakirbayeva, A. (2023). Construction of durable roads from rolled concrete based on belite slag cement and binders. *International Journal of GEOMATE,* 2023, Vol.24, Issue 104, pp.27-35

[12] Machus, M., Chen, J.-H., Hayati, D. W., Khoiri, M., Mawardi, A. F., & Basuki, R. Improvement for asphalt mixture performance using plastic bottle waste. International Journal of GEOMATE, vol., 2021**,** Issue 79, pp. 139-146

[13] Ibrahim, H., Marini, S., Desidery, L., & Lanotte, M. (2023). Recycled plastics and rubber for green roads: The case study of devulcanized tire rubber and waste plastics compounds to enhance bitumen performance. Resources, Conservation & Recycling Advances, Vol. 18, 2023, *200157.*

Copyright © Int. J. of GEOMATE All rights reserved, including making copies, unless permission is obtained from the copyright proprietors.

15th Int. Conf. on Geotechnique, Construction Materials & Environment, Kyoto, Japan, 11-13 November 2025, ISBN 978-4-909106124 C3051

PHYSICAL AND MECHANICAL PROPERTIES OF FLY ASH-BASED CELLULAR LIGHTWEIGHT CONCRETE

Reni Suryanita[1], Yohannes Firzal[1], Harnedi Maizir[2] and Raihan Arditama[3]

[1]Faculty of Engineering, Universitas Riau, Indonesia; [2]Department of Civil Engineering, Sekolah Tinggi Teknologi Pekanbaru, Indonesia; [3]PT. Harista Karsa Mandiri, Indonesia

ABSTRACT

Cellular lightweight concrete (CLC) offers weight reduction and thermal insulation, but its relatively low compressive strength limits broader use. This study evaluated the influence of fly-ash replacement on the density and compressive strength of CLC. Mortar cubes with 0%, 10%, and 15% fly-ash by mass of cement were produced using a protein-based foaming agent and tested at 7, 14, 28, and 56 days. The 10% mix achieved the highest 56-day strength (0.960 MPa), exceeding the control (0.852 MPa) and the 15% mix (0.720 MPa), while maintaining lightweight densities (~998–1062 kg/m³). The improvement is attributed to pozzolanic densification and a more uniform pore structure; at higher replacement (15%), dilution of cementitious content likely delayed strength development. Within the ranges tested, a 10% fly-ash replacement provided the best balance between strength and density, indicating suitability for non-structural to semi-structural lightweight applications and supporting more sustainable cementitious materials use.

Keywords: Cellular lightweight concrete (CLC), Fly ash, Compressive strength, Physical properties, Sustainable construction materials

INTRODUCTION

In recent years, the demand for lightweight, efficient, and environmentally friendly building materials has continued to increase, particularly with the growing emphasis on sustainable construction. One promising material that has gained attention is Cellular Lightweight Concrete (CLC), a type of concrete produced without coarse aggregates and incorporating foam to create a porous structure. CLC offers several advantages, such as reduced weight [1], good thermal insulation [2], and ease of handling on construction sites [3]. However, one of its significant limitations is its relatively low compressive strength compared to conventional concrete, which restricts its use primarily to non-structural applications, such as partition walls and lightweight blocks [4].

At the same time, fly ash—an industrial by-product from coal combustion in thermal power plants—continues to accumulate and pose environmental challenges when not adequately managed [5] Interestingly, fly ash contains significant amounts of silica and alumina, which exhibit pozzolanic properties [6]. Concrete's strength and durability can be increased by adding more binding chemicals through a chemical reaction between fly ash and the calcium hydroxide generated during cement hydration [7]. In addition to lowering dependency on Portland cement, whose manufacture significantly increases CO2 emissions, using fly ash in concrete provides a practical way to recycle industrial waste [8].

Recent studies have demonstrated that partially replacing cement with fly ash in CLC mixtures can result in improvements in microstructural density [6], resistance to aggressive environments, and long-term compressive strength. However, there is still a lack of specific research focusing on how fly ash affects the physical and mechanical properties of lightweight CLC blocks, particularly in terms of optimal mix proportions, dry density, water absorption, and compressive strength [4]. On the other hand, the use of high-volume fly ash must also be evaluated for its practicality and consistency in delivering quality results.

This study aims to address two critical issues: improving the technical performance of CLC blocks and reducing the environmental impact of fly ash disposal. By evaluating the effect of fly ash as a partial cement replacement in CLC mixtures, this research aims to identify an optimal formulation that offers a balance of strength, durability, and material efficiency. The findings are expected to support the development of greener, more sustainable, and resource-efficient construction practices.

RESEARCH SIGNIFICANCE

This research is significant as it addresses both environmental and engineering challenges by utilising fly ash, a major industrial byproduct, to enhance the performance of lightweight concrete. By optimizing the composition of Cellular Lightweight Concrete (CLC) with fly ash, the study contributes to advancing sustainable construction practices. The findings have the potential to reduce cement usage, lower carbon emissions, and provide a viable solution for managing fly ash waste, thus offering practical

value to the construction industry and supporting global efforts toward greener infrastructure development.

MATERIALS AND METHODS

Materials

The chemical composition of the Portland Composite Cement (PCC) and fly ash used in this study was determined using X-Ray Fluorescence (XRF) analysis. The chemical composition of the PCC used in this study is dominated by oxides, including CaO (62.3%), SiO_2 (min. 20%), and Al_2O_3 and Fe_2O_3 (max. 6%), as typically reported in technical data sheets of domestic cement manufacturers. This type of cement contains a blend of clinker, gypsum, and supplementary cementitious materials. Based on ASTM C 150-04 , the chemical composition of cement must have a minimum concentration of CaO, SiO_2, Al_2O_3, and Fe_2O_3 compounds. XRF testing of PCC cement showed that the CaO, SiO_2, Al_2O_3, and Fe_2O_3 content in the cement met the ASTM C 150-04 standard. The results of XRD testing on the PCC showed the diffraction pattern of the PCC, which identified that the dominant phase in the material was the calcite phase of calcium carbonate, $Ca(CO_3)$ and calcium silicate (Ca_3SiO_5) monoclinic crystals.

The major constituents of the fly ash (Fig.1) include silicon dioxide (SiO_2) at 53.74%, followed by aluminium oxide (Al_2O_3) at 22.568%, and iron oxide (Fe_2O_3) at 9.251%. Fly ash characteristics were tested using X-Ray Fluorescence (XRF) to determine chemical characteristics and X-Ray Diffraction (XRD) to identify atomic and oxide content in fly ash. XRF test results showed that fly ash contained 85.559% SiO2 + Al2O3 + Fe2O3 and met ASTM class C specifications.

Based on the XRD test results, fly ash material shows a diffraction pattern with the dominant phase identified as the quartz (Q) crystal phase at an angle between (20-30) for the silica (SiO_2) structure and the mullite crystal phase at angles between 30-40, 40-45 and 60-65 for the alumina (Al_2O_3) structure. The highest relative intensity peak for silica is at an angle of $2\theta \approx 26.62$ in the quartz crystalline phase. Furthermore, the alumina (Al_2O_3) structure with an orthorhombic crystal system at an angle of $2\theta \approx 26.27$ in the mullite crystal phase. The XRF testing results indicating that silica (SiO_2) has the highest composition, followed by alumina (Al_2O_3) as the second-largest component.

To create the cellular structure of the lightweight concrete, a protein-based foaming agent was used. The type of foaming agent was selected for its ability to produce stable and consistent bubbles, resulting in a uniform pore distribution and improved mechanical performance. The foaming agent was diluted with water and mechanically pre-foamed using a high-speed mixer before being incorporated into the concrete mix. Clean tap water was used in all mixes for hydration and foam preparation, ensuring no impurities that could interfere with the chemical reactions. Additionally, silica sand with a particle size passing 1.18 mm was included in selected mixtures to enhance packing density, reduce segregation, and improve the mechanical interlocking of particles in the matrix. All materials were stored in dry conditions and brought to room temperature before use. Their selection and proportions were based on preliminary trials and previous literature to ensure practical relevance and optimal performance of the CLC blocks.

Fig.1 Fly Ash

Methods

The experimental program evaluated three fly ash replacement levels—0%, 10%, and 15% by mass of cement. Prior to mix design, fine aggregate characterization included moisture content, bulk density, specific gravity, organic impurities, silt content, and particle size distribution, following relevant ASTM procedures. For each replacement level, five CLC mortar cubes (100 mm) were prepared and cured for 7, 14, 28, and 56 days prior to testing (Table 2).. All aggregate tests were conducted in accordance with standard ASTM procedures [9], [10].

Table 1. Composition of CLC mortar mixture

Variation of Fly ash (%)	Water (kg)	Sand (kg)	Foam (kg)	Cement (kg)	Fly Ash (kg)
0	1.01	3.45	0.29	2.03	0.00
10	1.01	3.45	0.29	1.82	0.10
15	1.01	3.45	0.29	1.72	0.20

Table 2. Total of CLC mortar specimen

Variation of Fly ash (%)	(Testing Day) 7	14	28	56	Total of each variation	Total of Specimen
0	5	5	5	5	20	
10	5	5	5	5	20	60
15	5	5	5	5	20	

The design strength of the CLC mortar mixture is 1 MPa with a wet density of 1.013 t/m³. The configuration of the CLC test specimens is presented in Fig.2**.**

Fig.2 Cellular Light Concrete

Compressive strength testing and surface settlement measurements of the test specimens were conducted after preparing a set of testing equipment, including a loading frame, according to the setup shown in Fig. 3.

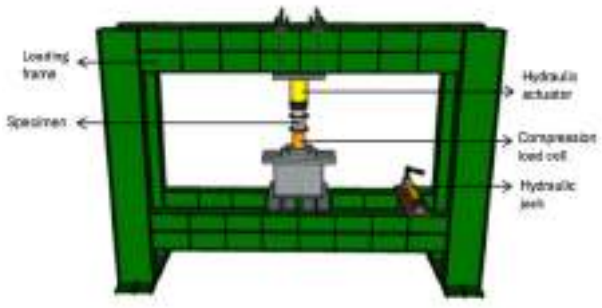

Fig. 3 Loading Frame

Compressive strength testing was conducted on steel plates at the centre of a flat loading frame, ensuring the load was distributed evenly. A load cell was used for compressive strength testing to apply vertical pressure to the specimen. Meanwhile, CLC surface deflection testing was measured using a linear variable displacement transducer (LVDT) installed vertically on the specimen.

The compressive strength test at 56 days was intended to observe the trend in the development of the specimen's compressive strength values. The compressive strength values were calculated based on Equation (1) as follows.

$$f'c = \frac{P}{A} \quad (1)$$

where:
f'c = Compressive Strength of CLC Mortar (MPa)
P = Axial Load (N)
A = Specimen Surface Area (mm^2)

RESULTS AND ANALYSIS

Material Characteristics

The results of fine aggregate material testing have met the ASTM C136 , ASTM C40 and ASTM C33 standards [11]. The results of fine aggregate properties testing are shown in Table 3. The fine aggregate utilized in this study was subjected to a series of standard laboratory tests to evaluate its suitability for use in construction materials. The results are summarized in Table 3. The water content of the aggregate was measured at 3.43%, which falls within the acceptable range of 3–5%. The mud content was recorded at 1.11%, which is well below the maximum allowable limit of 3%, indicating the material's good cleanliness. The organic impurities test yielded a value of 2, which complies with the maximum permissible limit of No. 3, ensuring minimal organic contamination. The bulk density was determined under two conditions: 1470.26 g/cm³ in a dry state and 1679.15 g/cm³ in a compacted state. These values are within the standard range of 1400–1900 g/cm³, confirming that the material has appropriate packing characteristics. Specific gravity tests revealed that the apparent specific gravity was 2.80, while the bulk specific gravity in dry and saturated surface dry (SSD) conditions were 2.65 and 2.71, respectively. These values comply with the typical specification range of 2.58–2.85. The

absorption capacity was found to be 2.01%, which lies within the standard 2–7% range, suggesting a moderate absorption potential suitable for concrete applications.

Additionally, the fineness modulus of the aggregate was determined to be 2.65, which lies within the standard range of 1.5–3.8. The aggregate has a moderate grain size distribution, which contributes to balanced workability and strength development in mortar or concrete mixes. These test results collectively indicate that the fine aggregate meets the required standards and is suitable for use in the production of lightweight or conventional concrete materials**.**

Table 3. The Results of Fine Aggregate Properties Test

No.	Testing	Specification Standard	Results
1	Water content (%)	3-5	3.43
2	Mud rate (%)	<3	1.11
3	Organic Impurities	Max No.3	2
4	Volume weight (g/cm^3)		
	a. Dry condition	1400-1900	1470.26
	b. Solid condition	1400-1900	1679.15
5	Specific Gravity		
	a. Apperent Specific Gravity	2.58-2.83	2.80
	b. Bulk Specific Gravity on Dry	2.58-2.84	2.65
	c. Bulk Specific Gravity on SSD	2.58-2.85	2.71
	d. Absorption	2-7	2.01
6	Finess Modulus	1.5-3.8	2.65

Mechanical Properties

Lightweight mortar bricks are manufactured using a job mix design that achieves the target quality, as specified by the density and compressive strength of the specimen. The wet density value of the mixture was determined before mixing and is by the standard requirements (SNI 8640:2018), which is 1.013 t/m³. Table 4 presents the average compressive strength and corresponding densities of CLC mortar specimens incorporating fly ash at substitution levels of 0%, 10%, and 15% by weight of cement. The performance was evaluated at curing ages of 7, 14, 28, and 56 days. At 7 days, the control mix (0% fly ash) exhibited a compressive strength of 0.660 MPa with a density of 1.062 kg/m³. The inclusion of 10% fly ash slightly improved early strength to 0.696 MPa, despite a reduced density of 1.019 kg/m³. However, a 15% substitution resulted in a notable reduction in strength to 0.510 MPa, indicating a slower early hydration process. On 14 days, the strength continued to improve for both the control and the 10% fly ash mixes, reaching 0.796 MPa and 0.808 MPa, respectively. The 15% fly ash mix achieved a lower strength of 0.602 MPa, suggesting that higher fly ash content may delay strength development due to its pozzolanic nature. By 28 days, the compressive strength of the 10% fly ash mix (0.850 MPa) had slightly surpassed that of the control (0.848 MPa), demonstrating the beneficial long-term pozzolanic reaction. In contrast, the 15% mix remained lower at 0.682 MPa.

After 56 days, the specimen with 10% fly ash achieved the highest strength of 0.960 MPa, followed by the control at 0.852 MPa, while the 15% fly ash specimen reached only 0.720 MPa. The trend indicates that a moderate fly ash content (10%) enhances the long-term strength performance of CLC mortar, whereas excessive replacement (15%) may hinder mechanical development. Overall, the results suggest that a 10% fly ash substitution offers an optimal balance between density reduction and compressive strength enhancement in CLC mortar formulations.

Physical Properties

Fig.4 illustrates the failure modes of CLC mortar specimens incorporating 0%, 10%, and 15% fly ash after compressive strength testing at 28 days of curing. The visual evidence demonstrates distinct differences in crack propagation and structural integrity associated with each fly ash content. In Fig. 4(a), the specimen without fly ash (0%) exhibits brittle failure, characterised by multiple vertical cracks and partial collapse of the upper edge. A typical fracture pattern for lightweight cementitious materials with limited tensile strength and moderate cohesion. In Fig. 4(b), the specimen with 10% fly ash substitution exhibits a relatively cohesive failure surface, characterised by fewer visible cracks and a more intact shape post-failure. The specimen exhibits enhanced microstructural bonding and matrix densification, resulting from the pozzolanic reaction of fly ash, which improves the material's integrity under axial load. In contrast, Fig. 4(c) shows the

specimen with 15% fly ash, where more distributed but shallow cracks are visible, indicating a reduced load-bearing capacity. The surface remains largely intact, but the internal structure appears to have experienced microcracking, suggesting that excessive fly ash may hinder early strength development and compromise the internal matrix.

Overall, the images support the mechanical test results, highlighting that a 10% fly ash substitution provides the best balance between strength and ductility in the CLC mortar. At the same time, excessive replacement reduces structural stability under compressive stress.

Table 4. The average compressive strength test of CLC mortar specimens

Fly ash (%)	7 Days		14 Days		28 Days		56 Days	
	Avg. Density	Avg. fc'	Avg. Density	Avg. fc'	Avg. Density	Avg. fc'	Avg. Density	Avg. fc'
	kg/m^3	MPa	kg/m^3	MPa	kg/m^3	MPa	kg/m^3	MPa
0	1.061	0.660	1.027	0.796	1.004	0.848	0.998	0.852
10	1.018	0.696	1.003	0.808	0.997	0.850	0.997	0.960
15	1.070	0.510	1.003	0.602	0.999	0.682	0.998	0.720

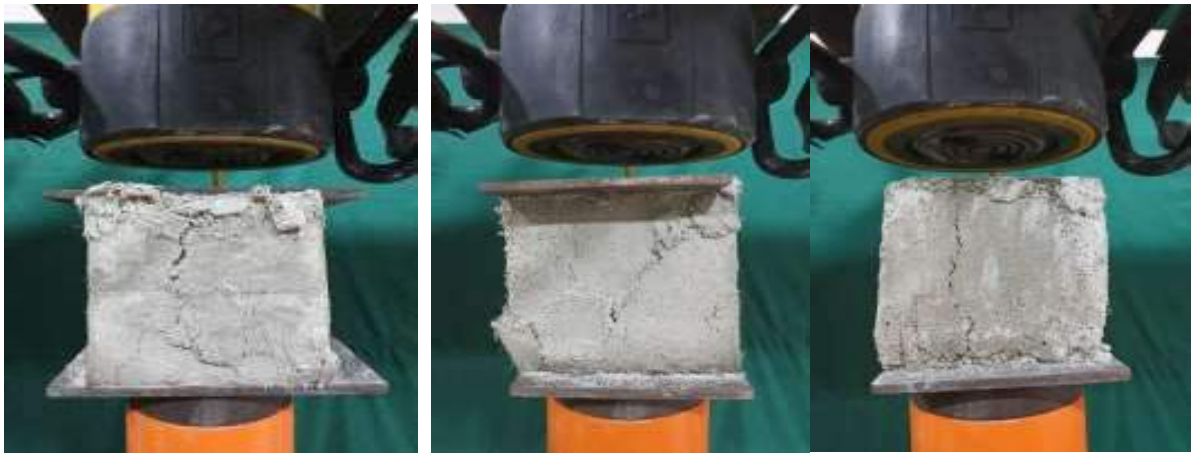

(a) (b) (c)

Fig. 4 Collapse of Specimen with 0% (a), 10% (b) and 15% (c) Fly Ash on 28 days

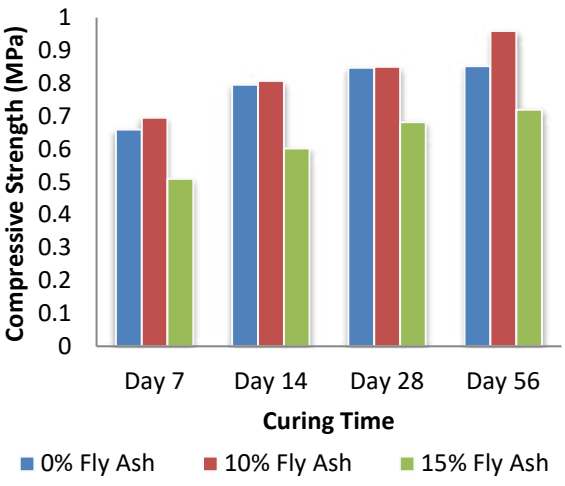

Fig. 5 Compressive Strength with Variation of Fly Ash

Fig. 5 illustrates the compressive strength development of CLC mortar at 7, 14, 28, and 56 days as a function of fly ash content (0%, 10%, and 15%). The bar chart shows a clear trend in strength performance influenced by the substitution level of fly ash over the curing period. At early age (7 days), the compressive strength was relatively low across all mixes, with the highest value observed for the 10% fly ash mix, followed by the control (0% fly ash), while the 15% mix showed the lowest strength (0.51 MPa). On 14 days, strength values increased for all specimens, with the 10% fly ash mix again exhibiting the highest strength. The condition exhibits an active pozzolanic contribution, which begins to manifest after one week of curing. By 28 days, both the control and the 10% fly ash mixes reached nearly equal compressive strengths (above 0.84 MPa), while the 15% mix continued to lag. At 56 days, the 10% fly ash mixture outperformed all others, reaching a maximum compressive strength of 0.96 MPa. The condition reflects the long-term pozzolanic reaction benefits, contributing to continued densification of

the matrix. In contrast, the 15% fly ash specimen exhibited delayed strength gain, ultimately resulting in a lower final strength than both the control and 10% mixtures.

CONCLUSIONS

This study investigated the physical and mechanical properties of Cellular Lightweight Concrete (CLC) mortar incorporating fly ash as a partial cement replacement at 0%, 10%, and 15% by weight. The fine aggregate used in the mixture met all standard specifications, including water content, mud content, specific gravity, and fineness modulus, indicating its suitability for lightweight concrete applications.

Compressive strength tests conducted at 7, 14, 28, and 56 days demonstrated that a 10% fly ash substitution consistently produced superior performance in both early and long-term strength development compared to the control mix and the 15% fly ash mixture. At 56 days, the 10% fly ash mix achieved the highest strength of 0.96 MPa, confirming the long-term pozzolanic benefit of fly ash.

Visual observations of the specimen failure modes under compressive load revealed that the 10% fly ash specimen exhibited the most cohesive and stable failure pattern. In comparison, the 0% and 15% mixes showed more brittle or inconsistent behavior. This suggests that 10% fly ash content not only enhances strength but also contributes to better integrity under mechanical stress. Overall, the results indicate that a 10% fly ash substitution provides an optimal balance between strength, durability, and material stability in CLC mortar, making it a promising alternative for sustainable construction materials.

ACKNOWLEDGMENTS

The authors would like to express their sincere gratitude to the Badan Riset dan Inovasi Nasional (BRIN) for the financial support provided through the RIIM Competitive Scheme – Batch VII in the year 2025. The research was made possible with the facilitation and coordination of the Institute for Research and Community Service (LPPM), Universitas Riau.

REFERENCES

[1] K. Li, Y. Wang, and J. Zhao, “Accelerated curing of fly ash blended mortars: crossover effect and strength development,” Cem Concr Res, vol. 160, p. 107054, 2023.

[2] R. Suryanita, Y. Firzal, H. Maizir, I. Mustafa, and M. F. Bin Arshad, “Experimental study on performance of cellular lightweight concrete due to exposure high temperature,” GEOMATE Journal, vol. 21, no. 83, pp. 20–27, 2021.

[3] L. V Hung, L. T. Thanh, and N. V Tuan, “Experimental study on drying shrinkage of structural lightweight concrete using fly ash cenospheres,” International Journal of GEOMATE, vol. 21, no. 87, pp. 95–101, 2021.

[4] A. P. Kumar, G. Zhang, and X. Li, “Recent advances in high-strength lightweight concrete: development strategies and structural applications,” Constr Build Mater, vol. 404, p. 135601, 2023.

[5] S. N. Shah, K. H. Mo, S. P. Yap, J. Yang, and T. C. Ling, “Lightweight foamed concrete as a promising avenue for incorporating waste materials: A review,” Resour Conserv Recycl, vol. 164, no. July 2020, p. 105103, 2021, doi: 10.1016/j.resconrec.2020.105103.

[6] S. S. Alterary and N. H. Marei, “Fly ash properties, characterization, and applications: A review,” Sep. 01, 2021, Elsevier B.V. doi: 10.1016/j.jksus.2021.101536.

[7] A. Kumar, R. Kumar, V. Das, A. A. Jhatial, and T. H. Ali, “Assessing the structural efficiency and durability of burnt clay bricks incorporating fly ash and silica fume as additives,” Constr Build Mater, vol. 310, no. October, p. 125233, 2021, doi: 10.1016/j.conbuildmat.2021.125233.

[8] M. Kadela, A. Kukiełka, and M. Małek, “Characteristics of Lightweight Concrete Based on a Synthetic Polymer Foaming Agent,” Materials, vol. 13, no. 4979, pp. 1–15, 2020.

[9] ASTM C40-04, “Standard Test Method for Organic Impurities in Fine Aggregates for Concrete,” 2004. doi: 10.1520/C0040_C0040M-20.

[10] ASTM C 869/C 969M-11, “Standard Specification for Foaming Agents Used in Making Preformed Foam for Cellular Concrete,” ASTM International, West Conshohocken, PA, 2014, www.astm.org, vol. 91, no. Reapproved, pp. 1–2, 2016, doi: 10.1520/C0869.

[11] ASTM C33/C33M − 18, “Concrete Aggregates 1,” vol. i, no. C, pp. 1–11, 2010.

Copyright © Int. J. of GEOMATE All rights reserved, including making copies, unless permission is obtained from the copyright proprietors.

15th Int. Conf. on Geotechnique, Construction Materials & Environment, Kyoto, Japan, 11-13 November 2025, ISBN 978-4-909106124 C3051

EXPERIMENTAL INVESTIGATIONS ON SUSTAINABLE GROUND IMPROVEMENT USING SEASHELL POWDER AND RICE HUSK ASH

Rufayda Jannat[1] and Zakaria Hossain[2]

[1,2]Department of Environmental Science and Technology, Mie University, Japan

ABSTRACT

In response to the global push for sustainable and environmentally responsible construction practices, this study investigates the use of seashell powder (SSP) and rice husk ash (RHA) as sustainable materials for ground improvement. Both SSP and RHA are abundantly available from agro-industrial wastes. SSP contains high amounts of calcium carbonate, while RHA is rich in silica. These properties make them cost-effective and eco-friendly alternatives to conventional soil stabilizers such as cement and lime. Soil samples were treated with varying proportions of SSP and RHA, both individually and in combination. The experimental program included weak soil samples mixed with SSP (5–20%) and RHA (5% and 10%). Standard geotechnical laboratory tests, including Proctor compaction and Unconfined Compressive Strength (UCS), were conducted to assess the effects of these additives on soil behavior. The results showed that adding SSP and RHA improved the strength and stiffness of the soil. The best performance was observed in samples containing 20% SSP and 5% RHA. This improvement was mainly due to the filler effect and the synergistic interaction between SSP and RHA, which promoted pozzolanic reactions and stronger particle bonding. These mixtures also demonstrated better workability and compaction characteristics. The findings highlight the potential of SSP and RHA for sustainable ground improvement, especially in regions where marine and agricultural waste materials are readily available. This research supports the reuse of waste products while promoting greener construction practices.

Keywords: Seashell powder (SSP), Rice husk ash (RHA), Compactability, Unconfined compressive strength (UCS), Sustainable ground improvement

INTRODUCTION

Effective ground modification procedures are becoming more and more necessary to improve the engineering qualities of poor soils due to the fast increase of infrastructure construction. Despite their effectiveness, conventional soil stabilizing techniques frequently include cement, lime, and chemical additives, which raise building costs and contribute considerably to CO_2 emissions [1]. In response to global sustainability challenges, researchers are exploring alternative eco-friendly materials derived from industrial and agricultural waste to reduce environmental impact while maintaining geotechnical performance.

Among these waste materials, seashell powder (SSP) and rice husk ash (RHA) have emerged as promising candidates for sustainable soil stabilization. Seashells, a by-product of the seafood industry, are composed primarily of calcium carbonate ($CaCO_3$), which can act as a filler and pozzolanic material when finely ground [2]. Approximately 8 million tons of seashell waste are generated annually worldwide, much of which ends up in landfills, causing disposal challenges [3]. Similarly, rice husk ash is an agricultural waste obtained from burning rice husks, containing high silica content (85-95% SiO_2) that exhibits pozzolanic reactivity when combined with soil [4]. Over 120 million tons of rice husk are produced globally each year, with improper disposal leading to environmental pollution [5].

Previous studies have demonstrated the potential of SSP and RHA in soil stabilization. For instance, [6] found that adding 10% seashell powder improved the unconfined compressive strength (UCS) of clayey soil by up to 30%. Similarly, RHA has been shown to enhance soil strength due to its pozzolanic reaction with calcium hydroxide, forming cementitious compounds (C-S-H gel) that bind soil particles [7]. However, most existing research has focused on individual applications of SSP or RHA, with limited studies on their combined effects on soil behavior.

Research Gap and Objectives

Despite the growing interest in sustainable soil stabilization, there remains a need for comprehensive experimental studies evaluating the synergistic effects of SSP and RHA blends on different soil types. Key questions include:

- What is the optimal mix ratio of SSP and RHA for maximum strength improvement?
- How do these additives influence compaction?

- Can combined SSP-RHA stabilization reduce reliance on traditional binders like cement?

This study investigates the geotechnical properties of soils treated with varying proportions of seashell powder (5%, 10%, 15%, 20%) and rice husk ash (5%, 10%) through a series of laboratory tests, including:

- Standard Proctor compaction to determine optimum moisture content and maximum dry density,
- Unconfined compressive strength (UCS) to evaluate strength gain,
- Scanning Electron Microscopy (SEM) to analyze microstructural modifications.

The findings aim to provide a sustainable, cost-effective solution for ground improvement while promoting waste recycling and reducing the carbon footprint of construction projects.

RESEARCH SIGNIFICANCE

This research contributes to the growing body of knowledge on green construction materials by:

- Reducing environmental waste through the utilization of SSP and RHA,
- Lowering construction costs by replacing conventional stabilizers with waste-derived alternatives,
- Enhancing soil engineering properties for applications in road subgrades, embankments, and foundation support.
- By validating the effectiveness of SSP-RHA blends in soil stabilization, this study supports the United Nations Sustainable Development Goals (SDGs), particularly SDG 9 (Industry, Innovation, and Infrastructure) and SDG 12 (Responsible Consumption and Production).

MATERIALS AND METHODS

Materials

Soil

Among the supplies utilized in this investigation were clay soil (S) from Japan's Mie Prefecture, specifically from the Handa region. Its designation as a region dealing with issues related to loose, expansive, and weak soils served as the impetus for choosing this site. Three weeks were spent allowing the soil utilized in this study to air dry [8]. To guarantee that the moisture level was constant across all tests, the soil was allowed to air dry for three weeks [9]. Nowadays, expansive soil subgrades and slopes are typically treated using techniques like the replacement technique, cushion method, and core spun method to stop expanding soil from swelling, contracting, and cracking [10].

Rice husk ash (RHA)

A renewable agricultural byproduct of rice, rice-husk ash (RHA) is a plentiful waste resource for Asian nations [11]. 85% to 95% of all agricultural wastes are composed of amorphous silica, which is the most significant percentage [12]. The amorphous silica content of the well-brunt RHA is over 90% [13], and the ash's maximum pozzolanic reactivity occurs at temperatures between 600°C and 700°C [14]. A high silica content of 91.10% and a controlled-burnt RHA at 650–700°C were supplied by Make Integrated Technologies Co., Ltd., Osaka, Japan, which is used in this investigation.

Sea Shell Powder (SSP)

Mollusks such as snails, shellfish, clams, and many others have exoskeletons called sea-shells. One of the biggest environmental problems in coastal areas is the dumping of seashells. Shellfish farming is an industry that is expanding quickly [15]. The calcium carbonate (CaCO3) that makes up the majority of these shells makes them an excellent source for soil amendment [16]. In this study, the seashells were finely grained and provided by Make Integrated Technologies Co., Ltd., Osaka, Japan.

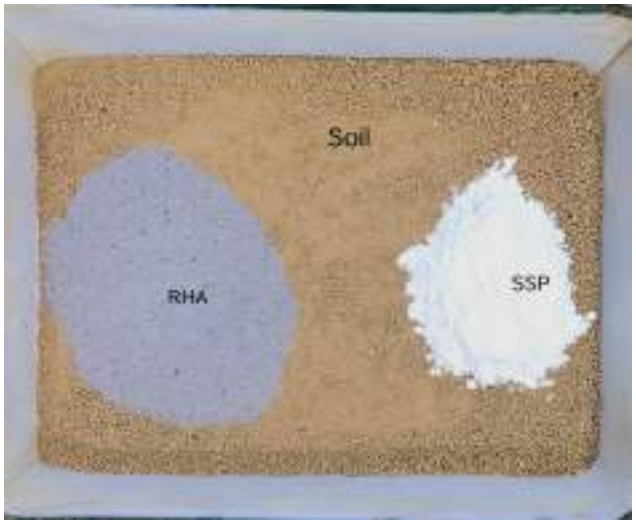

Fig.1 Experiment materials

Combine Specimen Designs

Fixing the appropriate mix design for specimens is crucial for the chemical stability of soil [17]. Several pertinent investigations have been carried out with varying proportions of RHA and cement or SSP

in the soil. Clayey soil stabilization was achieved using soil containing RHA at 5%, 10%, 15%, and 20% as well as 6%, 8%, and 10% cement [18]. Expansive soil was conducted by adding seashell powder with the variation of the ratio, which was 6%, 8%, 10%, 12%, and 14% [19]. In this study, 5% and 10% of RHA with the addition of 5%, 10%, 15% and 20% of SSP were used in the soil to understand the effect of RHA and SSP in expansive soil, as shown in Table 1.

Methodology

The expansive soil was admixed with Rice husk ash of varying 5% and 10% and Sea shell powder 5%, 10%, 15% and 20%. The Experimental Station on Engineering Materials, Faculty of Bioresources, Mie University, Japan, is where all of the present research experiments were conducted. The standard proctor compaction test and the unconfined compressive strength tests were performed according to Japanese Industrial Standards (JIS). Additionally, SEM examinations were conducted to detect any microstructural changes in the specimens.

Table 1 Details of specimen Combinations

Specimens Codes	Soil (S) (%)	Rice Husk Ash (RHA) (%)	Sea Shell Powder (SSP) (%)
S: (Control)	100	0	0
S:5SSP	95	0	5
S:10SSP	90	0	10
S:15SSP	85	0	15
S:20SSP	80	0	20
S:5RHA	95	5	0
S:10RHA	90	10	0
S: 5SSP:5RHA	90	5	5
S: 10SSP:5RHA	85	5	10
S: 15SSP:5RHA	80	5	15
S: 20SSP:5RHA	75	5	20
S: 5SSP:10RHA	85	10	5
S: 10SSP:10RHA	80	10	10
S: 15SSP:10RHA	75	10	15
S: 20SSP:10RHA	70	10	20

Standard proctor Compaction test

A conventional proctor compaction test was performed for each material admixture listed in Table 1 to ascertain the ideal moisture content and the associated maximum dry density. A 1000 cm3 volume compaction mold with a collar and a base, and a 10 cm diameter cylinder were used to compress the soil-RHA-SSP admixture sample physically. Three layers of the admixtures were compacted, with a 2.5 kg rammer used to deliver 25 blows to each layer through a 30-cm drop [20]. Figure 2 displays the ideal dry density and moisture content for soil and soil mixtures.

Unconfined compressive strength test

On cylindrical specimens with a diameter of 5 cm and a height of 12.5 cm [21], the unconfined strength of soil in compression tests is determined. The stress-strain curve, which displayed the strain on the X-axis and the stress on the Y-axis, was used to calculate the stress-strain relationship, UCS values, and elasticity of the specimens.

Table 2 Relationship between OMC and MDD

Compaction test	Optimum Moisture Content (OMC) (%)	Maximum Dry Density (MDD)(g/cm^3)
S: (Control)	22	1.52
S:5SSP	26	1.45
S:10SSP	25	1.44
S:15SSP	25	1.45
S:20SSP	26	1.43
S:5RHA	528	1.42
S:10RHA	31	1.35
S: 5SSP:5RHA	28	1.40
S: 10SSP:5RHA	28	1.39
S: 15SSP:5RHA	27	1.40
S: 20SSP:5RHA	27	1.39
S: 5SSP:10RHA	31	1.33
S: 10SSP:10RHA	31	1.31
S: 15SSP:10RHA	31	1.33
S: 20SSP:10RHA	28	1.35

Scanning electron microscopy test

The 500x magnification SEM photos of soil-RHA combinations were chosen to comprehend the microstructural alterations of the sample's particles. In this study, the SEM test samples were taken from UCS test specimens.

RESULTS AND DISCUSSIONS

Standard Proctor Compaction Test Results

The compaction curves in Fig.2 were used to determine the Optimum Moisture Content (OMC) and Maximum Dry Density (MDD) of soil with RHA and SSP combinations. As RHA-SSP was added to the soil mix, the OMC and MDD of the soil-RHA admixtures varied, with the OMC rising and the MDD falling, which is shown in Fig.2. Table 2 shows that the control soil's OMC is 22% and MDD is 1.52 g/cm3, and with the increase of the RHA-SSP ratio, the OMC has increased and the MDD has decreased.

Unconfined Compressive Strength Test Results

According to Fig.3, the average unconfined compressive strength of the soil, with various added materials, was tested after a curing period of 7 days. The control soil value was 211.33 kN/m^2 with the addition of 5% RHA-20% SSP, showing the highest value of 586.67kN/m^2. On the other hand, soil with 5%RHA-5%SSP, 5%RHA-10%SSP, and 5%RHA-15%SSP showed the value 385kN/m^2, 412.33kN/m^2,464.83kN/m^2 respectively where 10%RHA-5%SSP, 10%RHA-10%SSP, 10%RHA-15%SSP, and 10%RHA-20%SSP showed the results 314kN/m^2, 401.16kN/m^2, 411.67kN/m^2, and 431.16kN/m^2 respectively.

Fig.4 displays the soil's stress-strain relationship curves for the 0%, 5%, and 10% RHA and 0%, 5%,10%, 15%, and 20% SSP mix types. The compressive stress rose with displacement until it reached the highest value, at which point it began to soften, as seen by each curve in Fig.4, and it is noticed that this figure shows that, with the addition of 5% RHA and 20% SSP, the UCS values improved.

Scanning Electron Microscopy Test Results

The SEM test results of soil with 5%RHA and 20%SSP are shown in Fig.5. With pozzolanic reactions, soil containing 5% RHA-20%SSP showed the best mechanical coupling between soil particles and RHA-SSP, leading to the best development of microstructural and strength characteristics. It has shown no porosity with very highly compacted areas, which prevented the pozzolanic reaction and interlocking of soil-RHA-SSP particles.

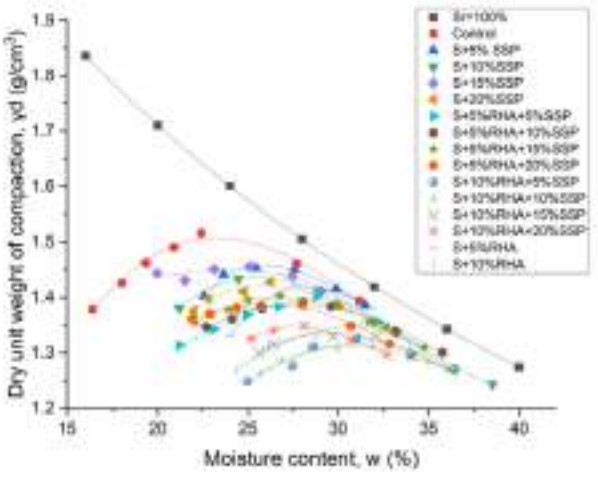

Fig.2 Effects of OSP and RHA on compaction characteristics

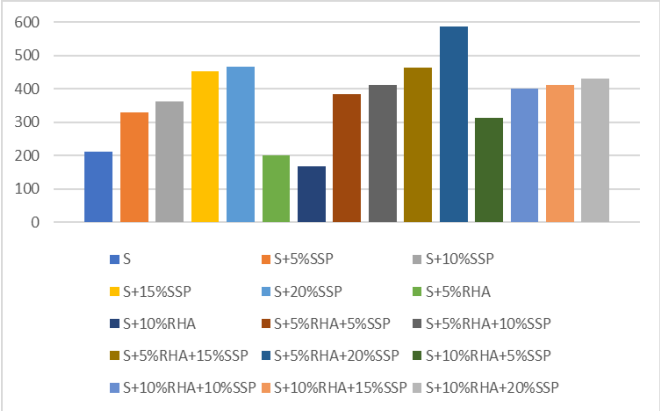

Fig.3 The average unconfined compressive strength of the soil with the variation of RHA-SSP

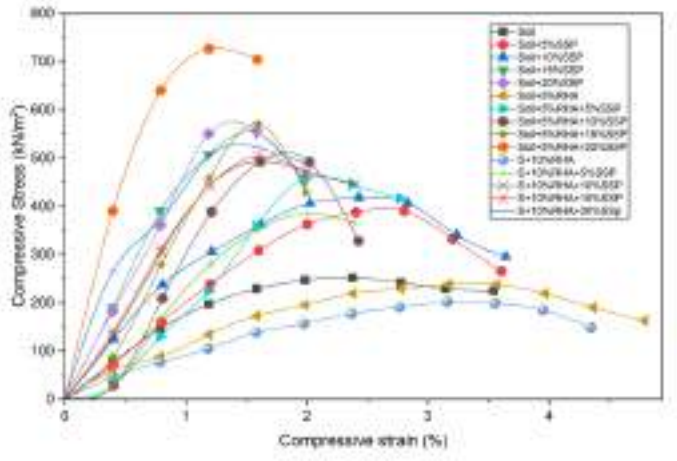

Fig.4 Relationship between compressive stress and strain

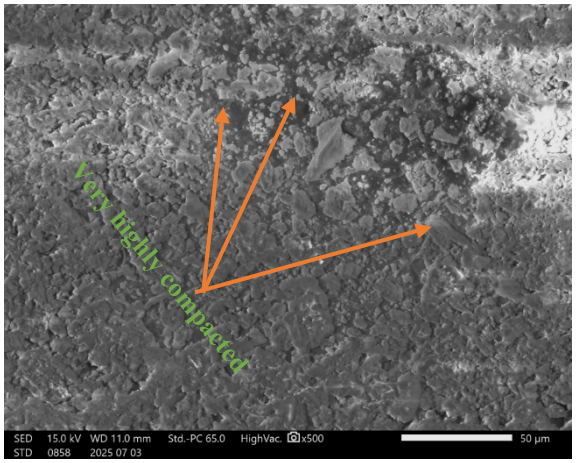

Fig.5 SEM image of S:5%RHA:20%SSP

CONCLUSIONS

The results of the experimental study on the addition of burned RHA and very fine-grained SSP to soil at regulated temperatures indicate that the compaction properties and UCS of soil were impacted by soil containing 0%, 5%, and 10% RHA and 0%,5%,10%,15%, and 20% SSP combinations. While the OMC increased, the MDD decreased as the amount of RHA-SSP increased. The test outcomes demonstrate that the unconfined compressive strength for seashell powder and Rice husk ash treated with Expansive soil expanded radically during the 7-day curing period. The highest compressive strength was estimated to be 5%RHA and 20%SSP (586.67kN/m^2).

This result implies that using this innovative building material for sustainable ground improvement projects has a bright future.

REFERENCES

[1] Zhang, Y., Johnson, A. E., & White, D. J. (2020). "Life cycle assessment of sustainable soil stabilization methods." Journal of Geotechnical and Geoenvironmental Engineering, 146(9), 04020085.

[2] Amar, M., Benzerzour, M., Abriak, N. E., & Mammadi, A. (2021). "Valorization of seashell waste in concrete: A review." Construction and Building Materials, 285, 122866..

[3] Nguyen, H. A., Chang, T. P., & Shih, J. Y. (2022). "Mechanical properties and durability of seashell powder-modified cementitious materials." Materials, 15(4), 1421.

[4] Dash, S. K., & Hussain, M. (2021). "Rice husk ash as a sustainable material for soil stabilization: A review." Journal of Cleaner Production, 289, 125680.

[5] Thomas, B. S., Yang, J., & Bahurudeen, A. (2020). "Rice husk ash as a supplementary cementitious material for sustainable construction." Journal of Building Engineering, 30, 101286.

[6] Ok, Y. S., Kim, S. C., & Park, S. W. (2021). "Application of waste seashells as a soil stabilizer for soft clay improvement." Environmental Geotechnics, 8(5), 345-356.

[7] Jha, A. K., & Sivapullaiah, P. V. (2020). "Mechanism of improvement in the strength and volume change behavior of lime-stabilized soil amended with rice husk ash." Geotechnical and Geological Engineering, 38(3), 2673-2686.

[8] Obalum SE, Chibuike GU. Air-drying effect on soil reaction and phosphorus extractability from upland-lowland tropical soils as related to their colloidal stability. Appl Ecol Environ Res. 2017. https:// doi. org/ 10. 15666/ aeer/ 1501_ 525540.

[9] Abdelmageed Atef Abdelmageed Shehata· Alex Otieno Owino· Md. Yachin Islam· Zakaria Hossain. (2024). "Shear strength of soil by using rice husk ash waste for sustainable ground improvement." Discover Sustainability (2024) :64 | https://doi.org/10.1007/s43621-024-00238-x.

[10] H.P. Yang, J. Wang, W.T. Zhan, Study of treatment technology and design scheme of expansive soil subgrade for Nanning outer ring expressway, Rock Soil Mech. 32 (S2) (2011) 359–365.

[11] Thomas, B. S. (2018). Green concrete partially comprised of rice husk ash as a supplementary cementitious material–A comprehensive review. Renewable and Sustainable Energy Reviews, 82, 3913–3923.

[12] Siddique, R. (2008). Ground granulated blast furnace slag. In Waste Materials and By-Products in Concrete (pp. 1–39). Springer, Berlin, Heidelberg.

[13] Singh, B. (2018). Rice husk ash. In Waste and Supplementary Cementitious Materials in Concrete, 417–460, Woodhead Publishing.

[14] Islam, M. Y., & Hossain, Z. (2025). "Investigating the one-dimensional consolidation properties of river sludge enhanced by sustainable additive synergy for eco-friendly stabilization". Journal of Building Engineering, 101, 111851.

[15] G. Woods, E. Brain, C. Shepherd, T. Paice, Tasmanian Marine Farming Environmental Monitoring Report: Benthic Monitoring (1997 2002), Water Environment, Tasmania (2004).

[16] Wencan Jiao, Weizheng Zhou, Zhen Huang, Riyan Lan, Min Ma, Study on the static and dynamic mechanical behavior of expansive soil modified by oyster shell powder, Heliyon 10 (2024) e29699.

[17] Nasiri, M., Lotfalian, M., Modarres, A., & Wu, W. (2016). Optimum Utilization of Rice Husk Ash for Stabilization of Sub-Base Materials in Construction and Repair Project of Forest Roads,

Croatian Journal of Forest Engineering: Journal for Theory and Application of Forestry Engineering, 37(2), 333–343.

[18] Kaur, I. & Jha, J. N. (2016). Effects of rice husk ash-cement mixtures on stabilization of clayey soils, IJCA Proceedings on International Conference on Advancements in Engineering and Technology, 8, 30–33.

[19] Vinod B R, Shobha R, A B Raghavendra, Rakesh M, Pallavi S, Stabilization on Expansive soil using sea shell powder and Rubber powder, Materials Science and Engineering 814 (2020).

[20] JIS A 1210. (In Japanese). Test method for soil compaction using a rammer. Japanese Industrial Standard, Guidance and Basic - Soil Test, The Jpn. Geotech. Soc. 2010; pp 71‑78.

[21] JGS 0524 (In Japanese). Method for consolidated-drained triaxial compression test on soils, Jpn. Geotech. Soc. Dositsu Shiken Hou Dositsu Kogakkai. 2001;pp233–43

Copyright © Int. J. of GEOMATE All rights reserved, including making copies, unless permission is obtained from the copyright proprietors.

15th Int. Conf. on Geotechnique, Construction Materials & Environment, Kyoto, Japan, 11-13 November 2025, ISBN 978-4-909106124 C3051

INFLUENCES OF BASALT GEOSYNTHETICS ON SOIL SHEAR STRENGTH

Mohamed Eltaher[1] and Zakaria Hossain[1]

[1]Graduate School of Bioresources, Mie University, Japan

ABSTRACT

Numerous variables affect the performance of reinforced soil structures, and the types of reinforcements used are the most crucial. Reinforcement evaluation, such as geosynthetics, is therefore an essential process in ensuring their successful application in a variety of fields. Thus, the triaxial compression test was utilized to measure the shear strength of a reinforced soil with two basalt geosynthetic types, one geotextile and another geogrid, in turn, in various layering patterns. Both types of basalt geosynthetics embedded in a single backfill sandy soil were tested under a variety of stress conditions. The stress and strain of the specimens were studied concerning the geosynthetic type used and the embedment position. The backfill soil reinforced with both types of geosynthetics showed significant improvement in shear strength as a result of this study's stress-strain behavior. The reinforcement type and embedding position were shown to have a substantial influence on the shear parameters. It has been found that each of these geosynthetics has an ideal embedment position for reaching maximum shear strength. In particular, when basalt geogrid was laid on the soil specimen's upper layer, shear strength peaked.

Keywords: Basalt geosynthetics, Triaxial compression test, Reinforced soil structures, Soil Shear strength.

INTRODUCTION

Because of their various advantages, earth structures can be used in a variety of infrastructure, depending on their intended use. Earth structures must be stable and safe under all kinds of expected stresses and loads [1, 2]. One fundamental feature of these structures is their resistance to deformation under various loads, and the cost of building a road, as an example, can be reduced by using strong subgrade soil [3, 4, 5]. Reinforcing the subgrade, which is a complicated process dependent on the type of reinforcement, might, for instance, reduce the necessary thickness of a flexible pavement for weaker subgrades [6, 7]. Thus, the reduction in expenses will be boosted by the reinforcement's resource-saving capabilities [8, 9]. Therefore, using geosynthetics to reinforce weak subgrade soils is an established way to enhance their shear strength [9, 10, 11].

The triaxial compression test is one of several tests used in laboratories to evaluate the shear strength of subgrade soils. Its benefits over other techniques and methods include its capacity to measure pore pressure and control specimen drainage. The triaxial compression testing method determines the angle of internal friction and cohesion of the soil structure, which are the key indicators of soil shear strength [2, 12, 13].

To examine and evaluate the shearing strength of soils reinforced with geosynthetics, many scholars used the triaxial compression test. They used a variety of geosynthetic materials, such as polypropylene, high-density polyethylene, and other materials [14, 15].

RESEARCH SIGNIFICANCE

The present study investigation concentrates on newly developed geosynthetic materials made from basalt fibers [16]. Under various layering patterns, a set of triaxial compression experiments was performed on a single type of backfill soil reinforced with these geosynthetics. The results of this investigation were used to analyze the reinforced soil's stress-strain relationships as well as its different mechanical properties. Assessing the influence on shear strength of the type of basalt geosynthetic and its embedding position as reinforcement for a single backfill soil is the main aim of this research. This will assist in minimizing the expenditures of building environmentally friendly soil structures in the future.

METHODOLOGY

Backfill Material

A single soil type was used as backfill material. This soil, collected from Mie Prefecture, Japan, was stabilized with two basalt geosynthetic products reciprocally, forming different reinforced soils for evaluating their shear strength.

According to the Japanese Geotechnical Society's geomaterials classification system, this soil is categorized as sandy soil (SF) [17, 18]. Additionally, Table 1 lists its main physical properties [18, 19, 20].

Table 1 Backfill soil physical properties

Soil properties	Measured value
Specific Gravity	2.779 g/cm^3
Gravel > 2 mm	2%
Sand (75 µm - 2 mm)	94%
Silt (5 µm - 75 µm)	2%
Clay < 5 µm	2%
Liquid Limit,	36.664%
Plastic Limit,	30.587%
Plasticity Index,	6.08%
Optimum Water Content	16.7%
Maximum Dry Density	1.713 g/cm^3

Geosynthetics

In this study, basalt geosynthetic products made by Tsuchiya TSCO Co., Ltd., Japan, were used. These geosynthetics exhibit high elasticity and stretch tension, along with good resistance to alkali, acid, vibration, and heat [16].

This research has employed two different basalt geosynthetic types: geogrid and geotextile. For explanatory purposes, the geogrid is referred to as GGR, and the geotextile is referred to as GTX, as shown in Fig. 1.

Fig. 1 Types of basalt geosynthetics utilized

Triaxial Compression Test

A triaxial compression mold (height 12.5 cm, inner diameter 5.0 cm), a compaction hammer (mass 1.0 kg, height 30 cm, diameter 4.9 cm), and a triaxial compression testing machine are among several tools used in this study [21, 22].

Preparation of Specimens

First, the triaxial control specimen, soil only, was formed in the triaxial mold, as shown in Fig. 2. Soil and water, 13% of the soil weight, were uniformly blended to form the control specimen [11]. After the mold was installed, the soil was placed into it in three successive layers, each of which had been uniformly tamped 25 times using a compaction hammer during the mold-filling process. Afterward, the specimen was removed from the mold [21].

Nine identical control specimens were prepared following the previously mentioned procedures to reduce the testing errors.

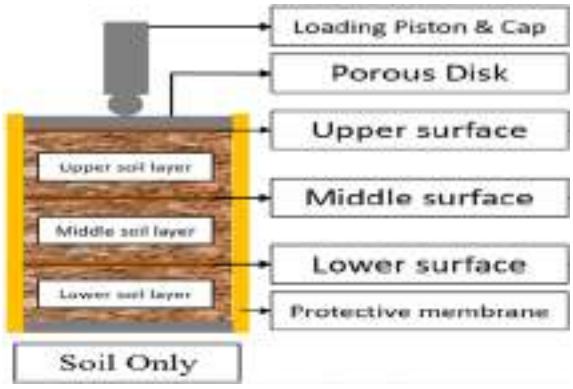

Fig. 2 Simplified representation of a control specimen made up of three separate soil layers only, each of which has a surface where geosynthetics can be placed.

In the same way, the test specimens containing GGR and GTX reciprocally were created by fitting the mold. Then three layers of the moist soil were filled into the mold; each was tamped with 25 blows. During this process, a geosynthetic layer was placed on the surface of the chosen soil layer to achieve reinforcement. This technique resulted in three patterns of test specimens, totaling six specimen types, illustrated in Figs. 3 and 4.

Based on the type of geosynthetic employed, these three patterns of test specimens were divided into two different sets. As shown in Fig. 3, the first set consists of three patterns of geogrid embedding: upper GGR (pattern I), middle GGR (pattern II), and lower GGR (pattern III).

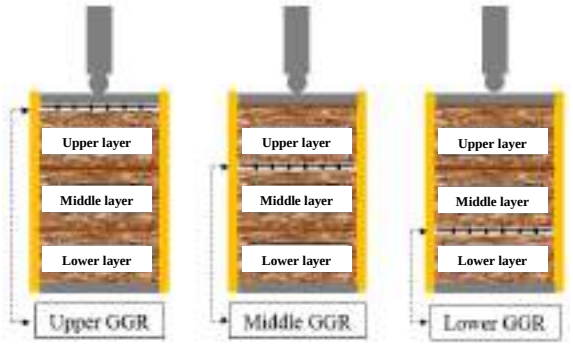

Fig. 3 Simplified representation of three specimen layering patterns of the GGR mesh placed between three layers of soil in three varying positions (I. upper, II. middle, and III. lower)

On the other hand, the second set of these layering patterns consists of three patterns of geotextile embedding: upper GTX (pattern I), middle

GTX (pattern II), and lower GTX (pattern III), illustrated in Fig. 4. For clarity, the test specimens were divided into two main groups: three types containing one GGR layer and three types containing one GTX layer. Nine identical specimens of each type have been prepared. It is worth noting that the specimens used in this study (5 cm diameter) represent a small-scale condition; potential scaling effects are recognized and are further discussed in the future work section.

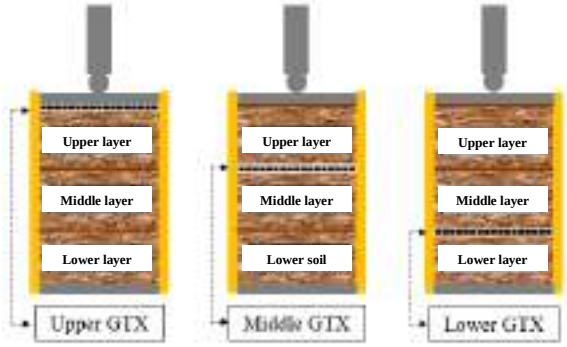

Fig. 4 Simplified representation of three specimen layering patterns of the GTX sheet placed between three layers of soil in three varying positions (I. upper, II. middle, and III. lower)

Testing Procedures

For assessing the shear strength of soil, the triaxial compression test is widely used in laboratory testing [12]. The testing machine's essential components are numbered and displayed in Fig. 5 to facilitate a clear understanding.

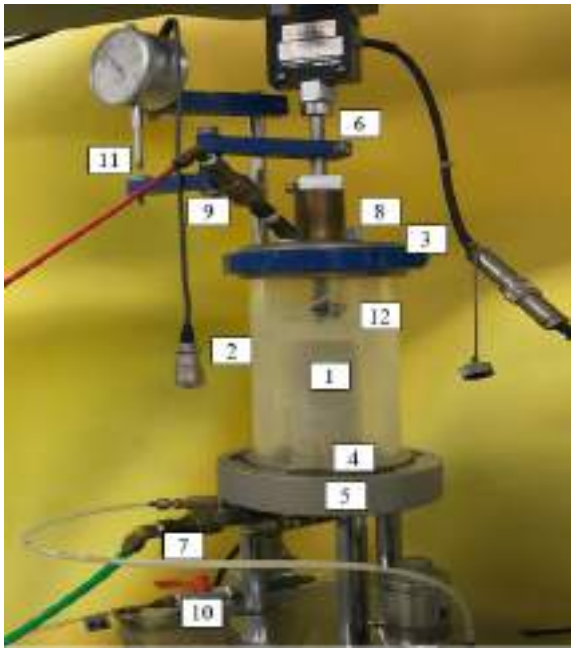

Fig. 5 Triaxial compression testing machine

The triaxial chamber was erected for the test by first placing the soil specimen, which was sealed with a membrane (No. 1, Fig. 5)**,** on the baseplate's pedestal (No. 4, Fig. 5). The chamber cylinder (No. 2, Fig. 5) and top plate (No. 3, Fig. 5) were then positioned on the baseplate groove. The tie ring (No. 5, Fig. 5) was tightened to lock the baseplate, cylinder, and top plate together. The loading piston (No. 6, Fig. 5) was then lowered until it made contact with the specimen cap.

Thereafter, the vent valve (No. 8, Fig. 5) on the top plate was left open, while the confining fluid valve and channel (No. 7, Fig. 5) were used to fill the chamber with water. The confining fluid channel was detached, and the vent valve was sealed after the chamber's water covered the sample and its cap.

The test's confining phase then began by using the pressured air valve and channel (No. 9, Fig. 5) to deliver a specific confining pressure [22]. Each specimen type was subjected to a sequence of confining pressures of 50, 100, and 150 kPa in this investigation.

Subsequently, the dial gauge (No. 11, Fig. 5) started to record the vertical deformation of the specimen as the shearing process began when the axial force was applied through the piston. Due to the drainage condition needed in the consolidated drained (CD) test because of the sandy soil specifications, the specimen drainage valve (No. 10, Fig. 5) was left open during the two phases of the test [12].

As the vertical load was incremented, the vertical deformation dial readings were measured. And according to Eq. (1), the axial strain (Ɛ) is therefore the height change (ΔH) divided by its initial height (H_0) [22].

$$\mathcal{E} = \Delta H / H_0 \quad (1)$$

On the other hand, the variables of applied stress could be distinguished as follows: (σ_1) the major principal total stress is equivalent to (σ_c) the pressure of the chamber in addition to (P) the piston's exerted vertical load divided by (A_c) the specimen's corrected cross-sectional area, as shown in Eq. (2).

$$\sigma_1 = \sigma_c + P/A_c \quad (2)$$

As a second stress variable, (σ_c), the confining pressure is equivalent to (σ_3), the minor primary total stress. For the third stress variable, the application of axial loading induces a deviatoric stress ($\Delta\sigma$) within the specimen. It is defined as the major principal total stress (σ_1) minus the minor principal total stress (σ_3), as expressed in Eq. (3) [2, 22].

$$\Delta\sigma = \sigma_1 - \sigma_3 \quad (3)$$

The internal friction angle (φ) and cohesion (*c*) were then calculated using the Mohr-Coulomb theory, as determined by Eq. (4), where (τ_f) and (σ_f) represent shear and normal stresses at failure, respectively [14].

$$\tau_f = c + \sigma_f \tan\varphi \quad (4)$$

The tests and calculations were performed in this research for one control specimen type and six test specimen types. Nine identical control specimens were examined so that three control specimens were tested under each confining pressure of (50, 100, and 150 kPa), for a total of nine tests for the control specimen type. Regarding test specimens, for each of the six types, nine identical specimens were examined so that three specimens were tested under each of the confining pressures of (50, 100, and 150 kPa). Thus, the total number of tests for each test specimen type was nine, as in the control specimens. These repetitions were designed to ensure the accuracy of the results and minimize the margin of error. The results presented below represent the mean of (σ_1 and $\Delta\sigma$ at peak) for each case, providing a reliable representation of the data.

RESULTS AND DISCUSSION

For investigating and achieving soil reinforcement, two different basalt geosynthetic types were placed inside the soil in turn in this study. Civil engineering projects that have high upfront costs and limited investment returns, such as roads, are subject to the use of soil reinforcement [2]. The triaxial compression test was used to evaluate the strength of both geosynthetic-reinforced and control soil. To gain a clearer understanding of how geosynthetic-reinforced soils behave in terms of shear strength, this study assessed three layering patterns that formed six distinct test specimen types. To determine how varying the basalt geosynthetics type and embedding position affected soil shear strength, a series of triaxial compression experiments was performed to determine the relationship between deviatoric stress and vertical strain.

Results of the Triaxial Compression Test for the Base Case

In order to assess the stress-strain response of the control specimens, three identical specimens of soil only (with their replicates) were subjected to three distinct confining stresses of 50, 100, and 150 kPa [12, 21, 22]. The relationship between the control specimens' axial strain and deviatoric stress is displayed in Fig. 6.

The results of the control specimens demonstrated that all specimens exhibited softening behavior after the ultimate deviatoric stress [2, 12].

According to the results, the mean values of major principal stresses and deviatoric stresses at failure were calculated, and then, with minor principal stresses, they were utilized to draw Mohr-Coulomb circles as shown in Fig. 7.

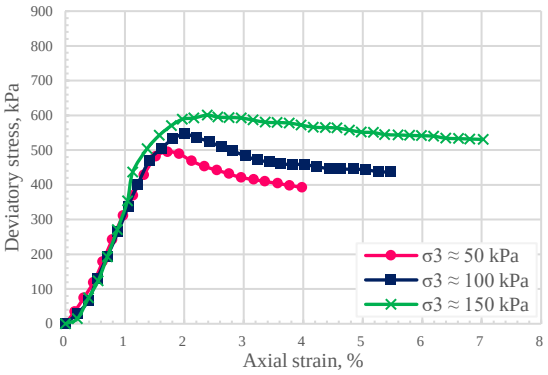

Fig. 6 Control specimens' stress-strain relationship at various confining stresses

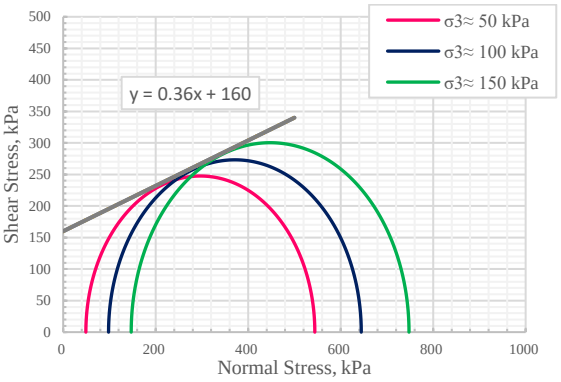

Fig. 7 Mohr-Coulomb stress circles of control specimens at different confining stresses

After that, the strength parameters were graphically determined. The mean angle of internal friction of the soil was determined to be 19.80˚, whereas the mean cohesion was 160 kPa. Although the internal friction angle seems to be very low and the cohesion value seems to be too high, the results of this test are representative of three independent experiments conducted in triplicate and are expressed as the mean.

Influences of Using Basalt Geogrid (GGR) to Reinforce the Soil

The test specimens that contain GGR in the upper, middle, and lower soil layers as three distinct inclusion places with their replicates were tested, and representative stress-strain relationships are displayed, respectively, in Figs. 8, 9, and 10.

The curves representing one GGR layer reinforced specimens in the three figures show a softening behavior toward the end of the stress-strain relationship.

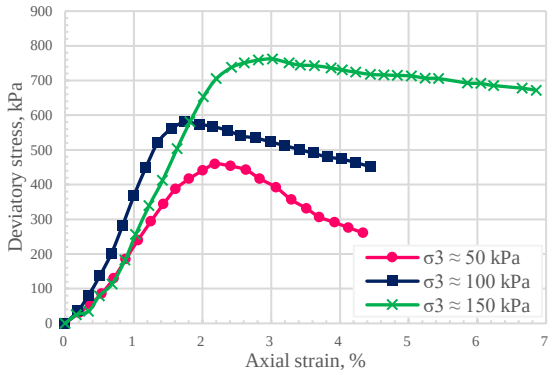

Fig. 8 Test specimens' stress-strain relationship for soil reinforced with GGR in the upper soil layer

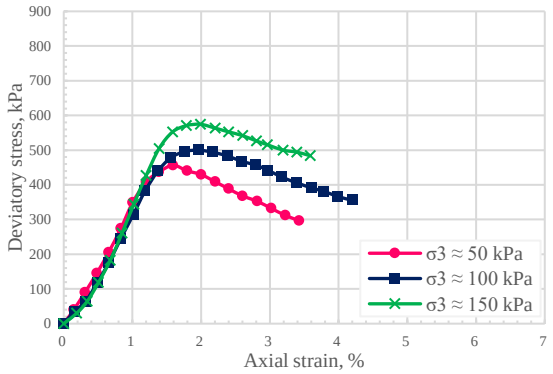

Fig. 9 Test specimens' stress-strain relationship for soil reinforced with GGR in the middle soil layer

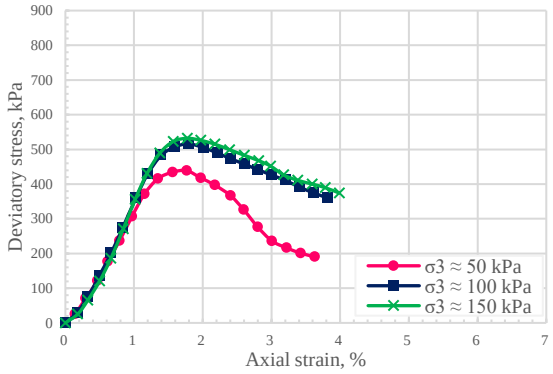

Fig. 10 Test specimens' stress-strain relationship for soil reinforced with GGR in the lower soil layer

As illustrated in Figs. 11, 12, and 13, respectively, shear strength parameters were obtained for soil reinforced with basalt geogrid on the upper, middle, and lower soil layers using the graphical Mohr-Coulomb circles representation. The mean cohesion values were 85, 130, and 140 kPa, respectively, and the mean angles of internal friction were 36.13˚, 22.78˚, and 19.37˚ [12]. As demonstrated by the upper layer scenario, where the internal friction angle was maximized, the results indicate that raising the inclusion position of the geogrid within the soil can enhance the angle of internal friction.

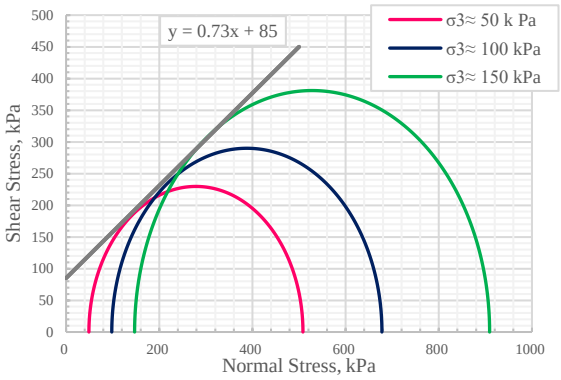

Fig. 11 Mohr-Coulomb stress circles of test specimens for soil containing one layer of GGR on the surface of the upper soil layer

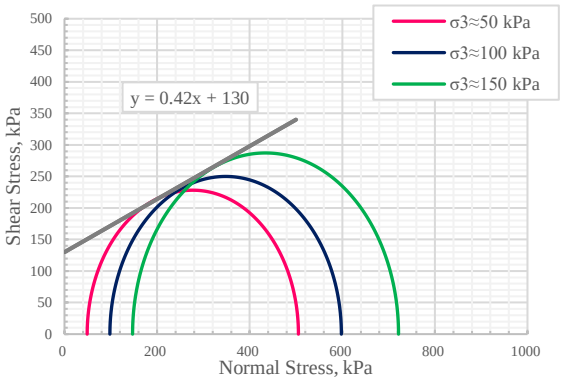

Fig. 12 Mohr-Coulomb stress circles of test specimens for soil containing one layer of GGR on the surface of the middle soil layer

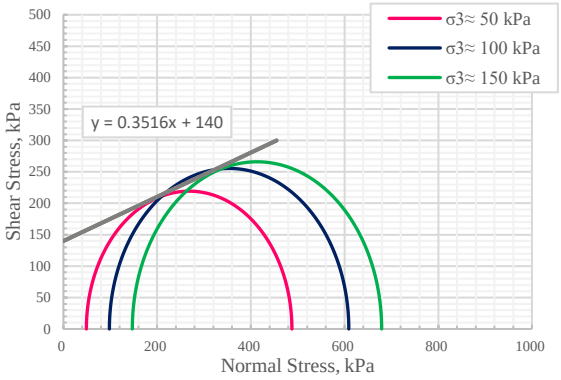

Fig. 13 Mohr-Coulomb stress circles of test specimens for soil containing one layer of GGR on the surface of the lower soil layer

Influences of Using Basalt Geotextile (GTX) to Reinforce the Soil

Figs. 14, 15, and 16 display the results for the test

specimens, which had a geotextile on the upper, middle, and lower soil layers, respectively.

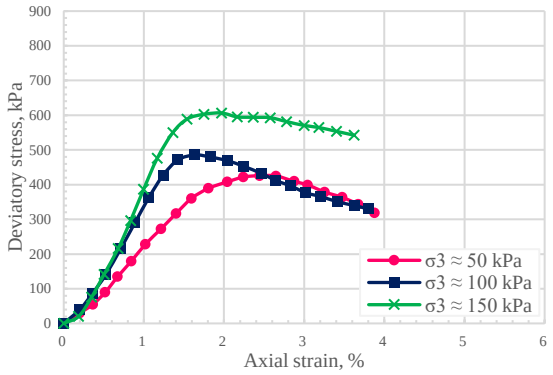

Fig. 14 Test specimens' stress-strain relationship for soil reinforced with GTX in the upper soil layer

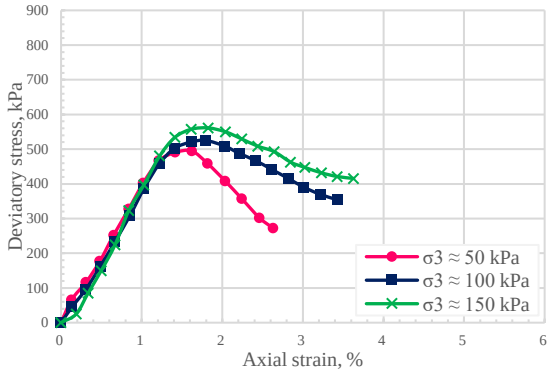

Fig. 15 Test specimens' stress-strain relationship for soil reinforced with GTX in the middle soil layer

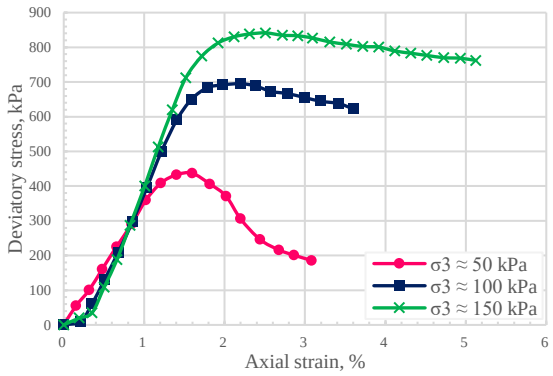

Fig. 16 Test specimens' stress-strain relationship for soil reinforced with GTX in the lower soil layer

As can be observed, the GTX-containing specimens in the middle or upper layer exhibit comparatively consistent trends, whereas the lower layer specimens revealed a distinct and higher growing tendency.

The parameters of shear strength for soil reinforced with geotextile on the upper, middle, and lower soil layers were then determined through the graphical method using the mean values of major principal stress and deviatoric stress at failure, as shown in Figs. 17, 18, and 19, respectively. [22]. The mean cohesion measurements were 100, 160, and 55 kPa, while the mean angles of internal friction were 27.71˚, 17.85˚, and 41.91˚, correspondingly.

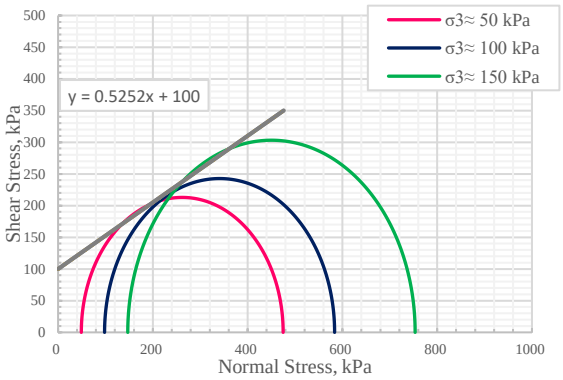

Fig. 17 Mohr-Coulomb stress circles of test specimens for soil containing one layer of GTX on the surface of the upper soil layer

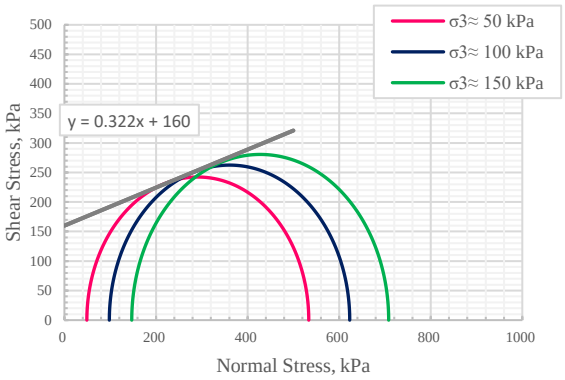

Fig. 18 Mohr-Coulomb stress circles of test specimens for soil containing one layer of GTX on the surface of the middle soil layer

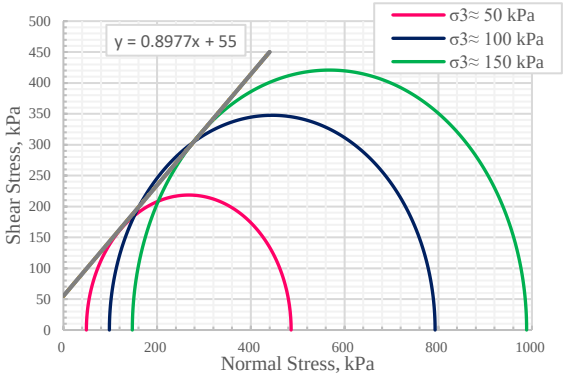

Fig. 19 Mohr-Coulomb stress circles of test specimens for soil containing one layer of GTX on the surface of the lower soil layer

Unlike the geogrid scenario, the angle of internal friction fluctuates but substantially improves when the GTX embedding position is in the lower soil layer.

The mean findings for every specimen type that was analyzed, as well as how the layering pattern and the type of geosynthetics affected the shear strength, were depicted in Table 2. Comparing the findings shows that adding basalt geogrid or geotextile increases the soil's shear strength in all patterns except for GGR on the surface of the lower soil layer and GTX on the surface of the middle soil layer. It is found that, out of all the GGR layering patterns, the soil reinforced with geogrid placed on the upper soil layer has the maximum angle of internal friction. Regarding geotextile, the greatest angle of internal friction was obtained when the GTX was positioned on the lower soil layer. It is essential to note that, for each specimen type, all the tests were repeated three times, and the results were very consistent. The calculated standard deviations were mostly less than 1, which indicates that the variations are negligible.

Table 2 Shear strength results comparison.

Layering pattern		Geogrid		Geotextile	
		Mean φ˚	*Mean c* (kPa)	Mean φ˚	*Mean c* (kPa)
Test Specimens	Upper	36.13˚	85	27.71˚	100
	Middle	22.78˚	130	17.85 ˚	160
	Lower	19.37˚	140	41.91 ˚	55
Control specimen	soil only	Mean φ˚ = 19.80˚		*Mean c* = 160 kPa	

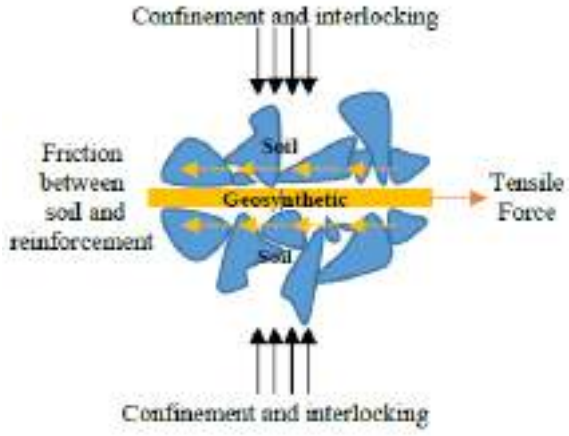

Fig. 20 Basic reinforcing mechanisms occurring in the basalt geosynthetic reinforced soil.

The confinement of the soil particles with the geosynthetic ribs, the interaction on the geosynthetic-soil irregular interface, which is dependent on the rolling and interlocking mechanism [1], and the developed tensile forces due to the load application—all of which depend on the embedding position and the type of geosynthetic [2, 10]—are the leading causes of the high internal friction angle values in nearly all test specimens when compared to the control specimens. These established effects aid the total reinforcing mechanism between soil and basalt geosynthetic. [5], as shown in Fig. 20.

A single GGR layer placed in the lower soil layer and a single GTX layer placed in the middle soil layer, however, did not increase shear strength as a result of these reinforcement mechanisms; rather, the internal friction angle values were lower than those seen in the control. This suggests that more complicated parameters may influence the shear responses in such embedding places for each type of basalt geosynthetic, necessitating ongoing research.

In contrast, cohesion values reveal expected declining trends due to the separation of soil layers and the anti-synergistic action between the angle of internal friction and cohesion [2]

These results are in line with earlier studies that determined CBR values using the same layering patterns and the same materials, showing that the GGR lower pattern and GTX middle pattern also have CBR values lower than the control [11]. Therefore, these findings offer significant insights for enhancing the strength of soil structures reinforced using geosynthetics. For field reinforcing applications, these newly innovated basalt geosynthetics are therefore advised.

FUTURE WORK

Future studies should consider using larger triaxial chambers and specimen sizes to better capture potential scaling effects. Such investigations would enhance the understanding of how specimen size affects shear strength parameters at different embedding positions for each type of basalt geosynthetic. Additionally, complementary direct shear tests using shear boxes of different sizes could provide further insights into scaling effects from another perspective.

CONCLUSIONS

Overall, it may be said that the inclusion of the newly innovated basalt geogrid or geotextile in the soil in any position significantly enhances its shear strength.

The type of geosynthetics and the layering pattern were discovered to affect the angle of internal friction, which can rise by as much as 111.7% when compared to a soil-only specimen. On the other hand, cohesion is inhibited by placing basalt geosynthetics in almost any position.

Moreover, it is feasible to determine that, for each type of basalt geosynthetic, there is an embedment position that optimizes the shear strength of the soil composite. The most effective position for the basalt geogrid type inclusion was on the upper soil layer,

which produced the highest angle of internal friction of 36.13˚, and the most effective position for the basalt geotextile type inclusion was on the lower soil layer, which produced the highest angle of internal friction of 41.91˚.

In light of these results, it is advised that the basalt GGR upper layer pattern and the basalt GTX lower layer pattern be applied in field settings, taking into consideration the additional purposes that the geosynthetics may serve beyond reinforcement, such as filtration and separation.

ACKNOWLEDGMENTS

I extend my gratitude to the Graduate School of Bioresources, Mie University, and Japan Science and Technology Agency (JST), Support for Pioneering Research Initiated by the Next Generation (SPRING), Japan, for providing the opportunity to pursue this research.

REFERENCES

[1] B. Hossain, T. Sakai, and Z. Hossain, "Evaluation of sand-geosynthetic interface behavior for earth reinforcement," Int. J. Geotech. Eng., vol. 7, no. 3, pp. 251–256, Nov. 2013, doi: 10.1179/1938636213Z.00000000034.

[2] B. M. Das and K. Sobhan, Principles of Geotechnical Engineering, 7th ed. Stamford, CT, USA: Cengage Learning, 2010.

[3] C. Tang, B. Shi, W. Gao, F. Chen, and Y. Cai, "Strength and mechanical behavior of short polypropylene fiber reinforced, and cement stabilized clayey soil," Geotext. Geomembr., vol. 25, no. 3, pp. 194–202, June 2007, doi: 10.1016/j.geotexmem.2006.11.002.

[4] E. J. Yoder and M. W. Witczak, Principles of Pavement Design, 2nd ed. New York, NY, USA: John Wiley & Sons, Inc., 1975, doi: 10.1002/9780470172919.

[5] S. W. Perkins and M. Ismeik, "A synthesis and evaluation of geosynthetic-reinforced base layers in flexible pavements: Part I," Geosynthetics Int., vol. 4, no. 6, pp. 549–604, Jan. 1997, doi: 10.1680/gein.4.0106.

[6] S. K. Shukla, "Discussion: Applications of geosynthetics for soil reinforcement by M. I. M. Pinto," Ground Improvement, vol. 8, no. 4, pp. 179–182, Jan. 2004, doi: 10.1680/grim.2004.8.4.179.

[7] M. I. M. Pinto, "Applications of geosynthetics for soil reinforcement," Ground Improvement, vol. 7, no. 2, pp. 61–72, Apr. 2003, doi: 10.1680/grim.2003.7.2.61.

[8] R. Hufenus, R. Rueegger, R. Banjac, P. Mayor, S. M. Springman, and R. Brönnimann, "Full-scale field tests on geosynthetic reinforced unpaved roads on soft subgrade," Geotext. Geomembr., vol. 24, no. 1, pp. 21–37, Feb. 2006, doi: 10.1016/j.geotexmem.2005.06.002.

[9] A. K. Choudhary, J. N. Jha, and K. S. Gill, "A study on CBR behavior of waste plastic strip reinforced soil," Emirates J. Eng. Res., vol. 15, no. 1, pp. 51–57, Feb. 2010.

[10] J. G. Zornberg, "Functions and applications of geosynthetics in roadways," Procedia Eng., vol. 189, pp. 298–306, May 2017, doi: 10.1016/j.proeng.2017.05.048.

[11] M. Eltaher, M. Z. Hossain, J. Shiau, and H. Takami, "Influence of embedding position on the performance of the basalt geosynthetics," in Proc. 9th Int. Conf. Geotech., Constr. Mater. Environ. (GEOMATE), Tokyo, Japan, Nov. 20-22, 2019.

[12] A. O. Owino and Z. Hossain, "The influence of basalt fiber filament length on shear strength development of chemically stabilized soils for ground improvement," Constr. Build. Mater., vol. 374, p. 130930, Apr. 2023, doi: 10.1016/j.conbuildmat.2023.130930.

[13] F. Yi and C. Du, "Triaxial testing of geosynthetics reinforced tailings with different reinforced layers," Materials, vol. 13, no. 8, p. 1943, Apr. 2020, doi: 10.3390/ma13081943.

[14] M. Zakarka, Š. Skuodis, and N. Dirgėlienė, "Triaxial test of coarse-grained soils reinforced with one layer of geogrid," Appl. Sci., vol. 13, no. 22, p. 12480, Nov. 2023, doi: 10.3390/app132212480.

[15] M. Eltaher, M. Z. Hossain, J. Shiau, and H. Takami, "Ground improvement using geosynthetics: A literature review," in Proc. 5th Int. Conf. Sci., Eng. & Environ. (SEE), Bangkok, Thailand, Nov. 11–13, 2019.

[16] T. TESCO Co., Ltd., "Basalt fiber products report," 2nd ed., pp. 1–15, 2018.

[17] JGS 0051-2009, "Method of classification of geomaterials for engineering purposes," Japanese Geotechnical Society, Soil testing - Basics and guidance, 2nd ed., pp. 49–58, Maruzen Publishing, 2010. (in Japanese)

[18] JIS A 1204:2009, "The method for particle size distribution of soils," Japanese Geotechnical Society, Soil testing - Basics and guidance, 2nd ed., pp. 27–38, Maruzen Publishing, 2010. (in Japanese)

[19] JIS A 1205:2009, "Test method for liquid limit and plastic limit of soils," Japanese Geotechnical Society, Soil testing - Basics and guidance, 2nd ed., pp. 39–45, Maruzen Publishing, 2010. (in Japanese)

[20] JIS A 1210:2009, "Test method for soil compaction using a rammer," Japanese Geotechnical Society, Soil testing - Basics and guidance, 2nd ed., pp. 71–78, Maruzen Publishing, 2010. (in Japanese)

[21] JGS 0520-2001, "Preparation of soil specimens

for triaxial tests," Japanese Geotechnical Society, Soil testing - Basics and guidance, 2nd ed., pp. 137–140, Maruzen Publishing, 2010. (in Japanese).

[22] JGS 0524-2001, "Method for consolidated-drained triaxial compression test on soils," Japanese Geotechnical Society, Soil testing - Basics and guidance, 2nd ed., pp. 135–150, Maruzen Publishing, 2010. (in Japanese).

Copyright © Int. J. of GEOMATE All rights reserved, including making copies, unless permission is obtained from the copyright proprietors

15th Int. Conf. on Geotechnique, Construction Materials & Environment, Kyoto, Japan, 11-13 November 2025, ISBN 978-4-909106124 C3051

CHARACTERIZATION OF SOIL-RICE HUSK ASH-CEMENT MIXTURES FOR SUSTAINABLE GROUND IMPROVEMENT: MECHANICAL AND MICROSTRUCTURAL INSIGHTS

Abdelmageed Atef[1], and Zakaria Hossain[2]

[1]Graduate School of Bioresources, Mie University, Japan.

ABSTRACT

The growing global demand for ground improvement necessitates sustainable alternatives to conventional cement, given its significant environmental impact. This study investigates rice husk ash (RHA), an agricultural byproduct rich in amorphous silica, as a promising sustainable supplementary cementitious material for soil stabilization. While RHA reduces CO_2 emissions and costs, it's typically combined with cement for adequate strength. Previous research on soil-RHA-cement mixtures often lacked comprehensive mechanical property data beyond UCS and detailed microstructural analysis. This research addresses these gaps by evaluating the strength characteristics of soil stabilized with controlled-burn RHA and ordinary Portland cement. This approach is crucial for developing countries grappling with RHA disposal. We conducted standard Proctor compaction tests and unconfined compressive strength (UCS) tests on specimens with varying RHA (2-6%) and cement (2-6%) content across different subgrade layers. Scanning electron microscopy (SEM) and Energy-dispersive X-ray Spectroscopy (EDS) provided microstructural insights. The study details optimum moisture content (OMC), maximum dry density (MDD), stress-strain relationships, UCS values, modulus of deformation, strain at compressive strength, and failure modes, supported by SEM images and EDS graphs. Our findings aim to promote the optimal, sustainable use of RHA in ground improvement, fostering a greener construction industry.

Keywords: Rice husk ash, UCS test, Subgrade layer, Ground improvement

INTRODUCTION

The global demand for ground improvement in construction is escalating, with over 40,000 soil enhancement projects undertaken annually worldwide. This surge fuels rapid advancements in construction technologies, yet also introduces new challenges in their application. Traditional soil improvement often relies on external materials, such as cement, geosynthetics, chemical grouts, and strips. Among these, cement is the most prevalent due to its widespread availability and versatility. However, the extensive use of cement, with global production reaching 4.1 billion tons in 2019, poses significant sustainability threats. Cement production is a costly and energy-intensive process that depletes natural resources and contributes approximately 8% of global CO_2 emissions. To align with the Sustainable Development Strategy (SDS), the construction industry needs to reduce its CO_2 intensity by 0.8% annually through 2030, a stark contrast to the 0.5% yearly increase observed between 2014 and 2018. Consequently, environmental engineers are actively exploring sustainable and economical alternatives to traditional cementitious materials [1, 2].

Supplementary Cementitious Materials (SCMs) are emerging as a promising solution within the construction sector, offering both environmental advantages and enhanced material strength and stability. It's estimated that SCMs could replace 30% of global cement usage, substantially reducing CO_2 emissions from cement industries. Annually, the agricultural sector worldwide generates approximately 410 million tons of natural cementitious materials, such as rice husk ash (RHA), sugarcane bagasse ash, and palm oil fuel ash, with about 335 million tons remaining unutilized. The use of pozzolanic agricultural wastes in engineering projects has been gaining traction since the late 1960s. Rice husk ash (RHA) stands out as a readily available, carbon-based, renewable agricultural byproduct boasting the highest reactive amorphous silica content (85-95%) among agricultural wastes. This makes it a viable substitute for cement in soil stabilization. Incinerating rice husks, a byproduct of the rice milling process, produces RHA. [3, 4] With over 700 million tons of paddy rice produced globally each year, about 30-35 million tons of RHA could be generated if all rice husks were combusted. The disposal of RHA, being lightweight, poses environmental and health risks when it is dumped in open areas, riverbanks, and low-lying areas. Integrating RHA as a supplementary cementitious material in ground improvement offers numerous benefits: it reduces CO_2 emissions, lowers construction costs, mitigates environmental issues, and alleviates waste disposal challenges, all while significantly enhancing the strength and durability of stabilized soil and concrete. However, RHA is often used in conjunction with cement and lime in engineering projects because RHA alone typically doesn't provide sufficient strength due to its limited

cementitious properties. RHA improves stabilized soil through two mechanisms: chemically (pozzolanic effect), where its silica (SiO_2) reacts with calcium hydroxide ($Ca(OH)_2$ from cement hydration to form Calcium Silicate Hydrate (CSH) gel, which is crucial for strength gain, and physically (filler effect), where unreacted RHA particles, with their low specific gravity and highly microporous structure, act as a filler.

The strength and durability of stabilized soil are highly dependent on the soil type, the specific combination of additives, and the curing conditions. Crucially, the amount of amorphous silica in RHA, which directly influences the pozzolanic reactions and CSH gel formation, is determined by the incineration process (burning temperature, duration, and cooling). High-quality, chemically reactive silica-rich RHA is produced when rice husk is burned for over 12 hours at a controlled temperature of 500-700°C. Conversely, uncontrolled burning or open burning yields RHA with lower silica content. As-obtained RHA from improper burning often has coarser particles, lower bulk density, and reduced silica content compared to other pozzolans, which impacts the cement density and particle spacing in the mixture [5, 6]. While grinding RHA can produce finer particles, it may not always enhance pozzolanic reactivity and incur additional cost and time. Previous investigations into soil-RHA-cement combinations have explored their suitability for soil stabilization, RHA with various cement ratios for silty and clayey soils. However, these studies mainly reported unconfined compressive strength (UCS) values, often omitting critical data such as stress-strain relationships, modulus of deformation, strain at compressive strength, and failure modes of UCS specimens. Furthermore, detailed microstructural analyses, such as SEM images and EDS (Energy-dispersive X-ray Spectroscopy) data, which are vital for explaining the strength parameters of treated soil, were rarely presented. Given the variability in soil types, RHA processing (grinding and sieving), and silica content, existing research on soil-RHA-cement combinations remains insufficient for optimal utilization of RHA [7].

This study aims to address these gaps by investigating the strength characteristics of soil combined with controlled-burn, as-obtained RHA, and ordinary Portland cement, to achieve sustainable ground improvement. This research is particularly relevant for developing countries, which frequently face severe environmental pollution and RHA disposal challenges due to limited access to advanced waste management technologies. With increasing population demands in these regions, this study is crucial for promoting the extensive use of locally available RHA as a cement alternative in stabilization techniques for new housing, commercial buildings, roads, tunnels, and earth dams, thereby contributing to sustainable construction practices[8].

A comprehensive series of tests was conducted, including standard Proctor compaction tests and unconfined compressive strength (UCS) tests, complemented by scanning electron microscopy SEM and EDS analysis of UCS test specimens in three subgrade layers: upper, lower, and dual subgrade layers. The specimens comprised varying percentages of RHA (2%, 4%, 6%) and cement content (2%, 4%, 6%). This study will thoroughly discuss the optimum moisture content (OMC), maximum dry density (MDD), stress-strain relationships, UCS values, modulus of deformation, strain at compressive strength, failure modes of UCS specimens, and present detailed SEM images and EDS graphs of the soil-RHA-cement specimens.

RESEARCH SIGNIFICANCE

This study examines the feasibility of utilizing rice husk ash (RHA) to stabilize soil in subgrade layers. While conventional stabilizers, such as cement and lime, are effective, there's a growing need for materials that enhance soil strength while simultaneously reducing environmental impact. Our research focuses on improving soil durability and lowering carbon emissions by incorporating a minimal amount of cement alongside RHA in soil mixtures. Unlike traditional studies that primarily focus on concrete applications, this work emphasizes the critical role of soil reinforcement for infrastructure projects. This approach promotes a holistic, environmentally responsible method for ground improvement, addressing both ecological concerns and the need for resilient construction.

MATERIALS AND METHODS

Materials

Soil

The soil for this study was sourced from the Handa Area in Mie Prefecture, Japan, as depicted in Figure 1. It was air-dried for three weeks, then passed through a 200 mm sieve. We conducted sieve analysis, hydrometer analysis, and liquid and plastic limit tests to determine the classification. The measured plastic and liquid limits were 28.59% and 48.5%, respectively. The soil composition was 42.7% clay, 57.28% silt, and 0.02% sand. According to the American Association of State Highway and Transportation Officials (AASHTO) classification, it was categorized as A-7-6 clayey soil. Figure 1 also illustrates the grain size distribution for the soil, cement, and rice husk ash used. Testing procedures for sieve and hydrometer analyses followed Japan Industrial Standards (JIS) A 1204 [9], while liquid

and plastic limit tests adhered to JIS A 1205. Table 1 provides further geotechnical properties of the soil.

Rice husk ash

The rice husk ash (RHA) used in this investigation was acquired from Via Make Integrated Technology Co., Ltd. in Osaka, Japan. It was produced through a controlled combustion process at temperatures ranging from 650°C to 700°C. This meticulous 27-hour incineration process, conducted within an industrial incinerator under computer-controlled conditions, resulted in RHA with a high silica content of 91.10%. The particle sizes of the RHA ranged from 0.07 mm to 0.3 mm. Figure 2 presents a detailed particle size distribution for both the soil and RHA. Table 1 outlines the comprehensive chemical and physical characteristics of the rice husk ash.

Portland cement

Ordinary Portland Cement (OPC) was used as the other binding material in this study. Its physical and chemical properties are detailed in Table 2.

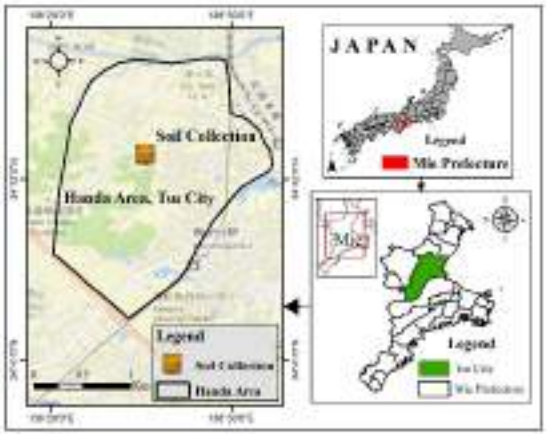

Fig.1 The exact location where soil samples were collected for this study.

Specimen Preparation

To investigate the effects of soil-RHA-cement mixtures on shear strength, a series of specimens for unconfined compressive strength (UCS) tests was meticulously prepared. Each cylindrical specimen had a total height of 12.5 cm and a diameter of 5.0 cm, with a total sample weight of 500 grams, equating to a weight ratio of 40 grams per 1 cm of height. For the experimental layers within the specimens, a specific mixture was formulated. Each such layer, intended to be 1 cm in height, consisted of 40 grams of a soil-RHA-cement mixture combined with 120 grams of plain soil, resulting in approximately 160 grams of total soil per layer [10]. The specimens were compacted manually in three layers within the mold. Compaction was achieved using a 4.9 cm diameter hand rammer weighing 1 kg, applying 20 blows per layer from a falling height of 30 cm. This standardized compaction protocol ensured uniform and consistent density throughout the soil-RHA-cement mixture within each specimen. Before compaction, the soil, RHA, and cement components were thoroughly dry-mixed in a large tray to achieve a homogeneous blend. Water was then gradually added to this dry mix, with the amount precisely determined based on the optimum moisture content (OMC) derived from compaction tests, ensuring proper hydration without over-saturation. This meticulous preparation and compaction methodology were crucial for guaranteeing the integrity and reliability of the subsequent shear strength testing.

In this study, the RHA dosage was selected at 2%, 4%, and 6% of the soil weight. This range was chosen to investigate the effects around the typically observed maximum utilization of amorphous silica at approximately 5%, as suggested by previous research [10]. This allowed for examining the impact of slightly lower, optimal, and slightly higher RHA percentages. Furthermore, the study intentionally incorporated a minimal dosage of cement. This inclusion complements the soil treatment by ensuring an optimal supply of Ca+ ions, which are essential for robust pozzolanic reactions with the RHA. This approach underscores the study's focus on enhancing soil properties sustainably, aligning with environmental conservation and carbon emission reduction objectives, rather than solely concentrating on concrete applications.

Table 1 Properties of Soil and RHA

Contents	Qualities	amount
Soil characteristics	Specific Gravity, g/cm^3	2.74
	Maximum dry density, g/cm^3	1.58
	Saturation, %	87.14
	Sand (75 µm - 2 mm), %	0.02
	Silt (5–75 µm), %	57.28
	Clay < 5 µm, %	42.7
	Liquid limit, LL, %	48.5
	Plastic limit, PL, %	28.594
	Plasticity Index, PI, %	19.906
	AASHTO classification	A-7–6
RhA characteristics	Average Particle Size, mm	0.001 to 0.3
	Loss of Ignition, %	4–6
	Specific Gravity, g/cm	3 2.12

	Burning Temperature, ◦C	650–700
	Burning time, hour	27
	Silica (SiO_2), %	91.10
	Carbon dioxide (CO_2) %	4.35
	Potassium Oxide (K^2O), %	2.40
	Calcium Oxide (CaO), %	0.57
	Iron Oxide (Fe_2O_3), %	0.05
	Alumina (Al_2O_3), %	0.03
	Others, %	1.50

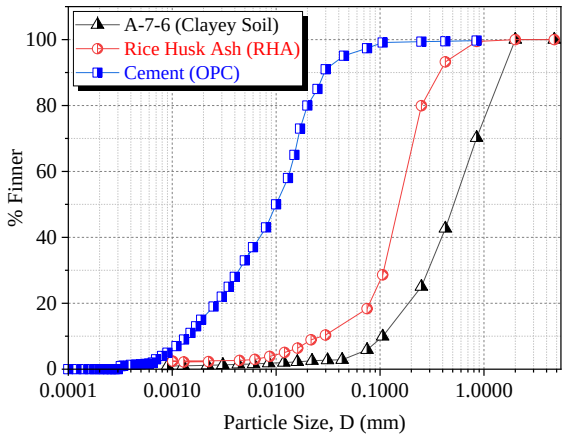

Fig.2 Particle size distribution for Soil, cement, and RHA.

Table 2 The characteristics of OPC.

Contents	Qualities	amount
Cement characteristics	Initial setting time, minutes	170
	Final setting time, minutes	225
	Specific gravity, g/cm^3	3.15
	Specific surface area, m^2/kg	340
	28-day compressive strength, MPa	33–53
	Calcium Oxide (CaO), %	63.40
	Silicon dioxide(SiO_2), %	21.60
	Iron Oxide (Fe_2O_3), %	5.35
	Alumina (Al_2O_3), %	4.45
	Sulfur trioxide (SO^3), %	1.92
	Magnesium oxide (MgO), %	1.65
	Sodium oxide (Na^2O), %	0.11
	Potassium oxide (K^2O), %	0.22
	Loss of ignition, %	<4

Testing Method

Compaction Tests

A Standard Proctor Compaction Test was performed to determine the key parameters for each material blend, as presented in Table 3. This test was crucial for identifying the maximum dry density (ρdmax) and the optimum moisture content (wopt) for each mixture. For each unique blend, compaction was carried out in a cylindrical mold measuring 10 cm in diameter and 12.73 cm in height. A 2.5 kg rammer, dropped from a height of 30 cm, was used to compact the material in three equal layers, ensuring consistent compaction throughout the specimen. This procedure was repeated for various carefully monitored moisture contents to establish a range of dry densities for each blend.

The results of the experiment were plotted as compaction curves, showing the relationship between dry density and moisture content. The peak point of each curve directly indicated the maximum dry density and the corresponding optimum moisture content. The entire compaction testing process strictly adhered to the requirements of Japan Industrial Standards (JIS) A 1210 (JIS, 2010) [9, 11], ensuring the precision and reliability of the experimental method. Figure 4 illustrates the obtained optimum moisture content and maximum dry density values for the natural soil and its various mixtures.

Unconfined Compressive Strength (UCS) Test

The Unconfined Compressive Strength (UCS) test stands as the most widely adopted and practical method globally for evaluating the strength of optimized stabilized soil mixtures [1-3]. Its versatility extends to numerous applications within the construction sector, offering insights into the bearing capacity of soil when combined with various additives [1, 2]. In this study, the UCS test was conducted meticulously in accordance with Japanese Industrial Standards [10].

To prepare the test specimens, soil-RHA-cement combinations were manually compacted within a mold measuring 12.5 cm in height and 5.0 cm in diameter. A 4.9 cm diameter hand-rammer, weighing 1.0 kg, with a consistent falling height of 30 cm, was used. Each specimen was compacted in three layers, with each layer receiving 20 blows to ensure uniform density. During the test, the UCS reading was

recorded precisely every 0.5 mm of displacement at a constant loading rate of 0.1 mm/min. To ensure statistical robustness, the average strength value was calculated from the results of three identical specimens tested for each mix type, providing a reliable measure of the stabilized soil's strength. This rigorous methodology ensures that the results accurately reflect the mechanical performance of the treated soil.

Fig.3 Materials Soil-Rice Husk Ash- Cement.

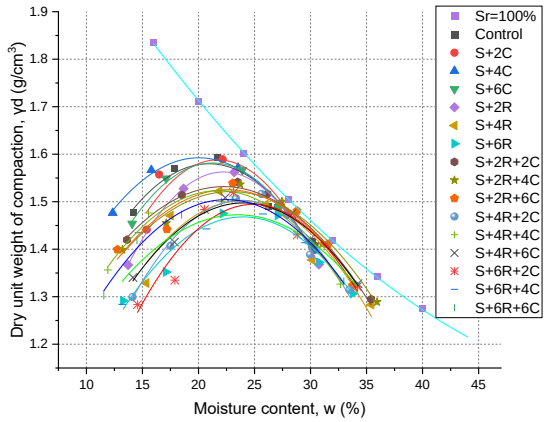

Fig.4 Effects of RHA and cement on compaction characteristics

Fig.5 Failure pattern for soil only.

Table 3 Specific mix combinations

mixtures	Soil,S(%)	RHA(%)	Cement,C(%)
Soil:(Control)	100	0	0
S:2C	98	0	2
S:4C	96	0	4
S:6C	94	0	6
S:2R	98	2	0
S:4R	96	4	0
S:6R	94	6	0
S:2R:2C	96	2	2
S:2R:4C	94	2	4
S:2R:6C	92	2	6
S:4R:2C	94	4	2
S:4R:4C	92	4	4
S:4R:6C	90	4	6
S:6R:2C	92	6	2
S:6R:4C	90	6	4
S:6R:6C	88	6	6

RESULTS AND DISCUSSION

To evaluate the influence of soil-RHA-cement mixtures on shear strength, a series of Unconfined Compressive Strength (UCS) tests was conducted. These tests aimed to determine the strength development in specimens incorporating varying percentages of RHA (2%, 4%, 6%) and cement (2%, 4%, 6%), as well as the effects of their placement in top, bottom, and dual subgrade layers.

The UCS values for all examined soil-RHA-cement composite specimens demonstrated a noticeable increase when RHA was combined with cement. This significant positive transformation is primarily attributed to the pozzolanic reactions occurring between the amorphous silica in RHA and the calcium hydroxide (Ca(OH)2 released during cement hydration. These reactions lead to the formation of Calcium Silicate Hydrate (CSH) gel. This insoluble binder fills soil voids, bonds particles together, and densifies the soil matrix, thereby enhancing its overall strength and stiffness over time. The irregular forms and denser microstructure resulting from these interactions significantly contribute to the improved bearing capacity.

Generally, increasing the cement content from 2% to 6% consistently led to an increase in UCS values across both upper and lower layers. The most pronounced improvement in single-layer specimens was observed at 4% cement content, yielding a notable UCS value. For the dual-layer specimens,

UCS values typically ranged, indicating a more complex interaction of the layers. The addition of 2% RHA showed modest variations in UCS values. However, higher RHA percentages, specifically 4% and 6% RHA, resulted in more significant increases in UCS values, particularly evident in the dual-layer configurations.

Remarkably, a mix of 4% RHA + 6% cement consistently demonstrated the most substantial strength enhancement. This specific combination achieved the highest UCS values across all testing conditions, with a peak UCS of 211 MPa for the dual-layer configuration. This finding aligns well with comparable results documented in previous research on RHA and cement-stabilized soils, where synergistic effects between these two binders are frequently observed [10,14].

When compared to the control (untreated) Soil, see the failure pattern for soil only in Fig. 5, all tested soil-RHA-cement combinations exhibited significantly improved UCS values, confirming that the mixture substantially enhances the Soil's unconfined compressive strength and, consequently, its bearing capacity. The optimal mix design identified in this study is the Soil + 4% RHA + 6% Cement, which consistently produced the highest UCS values, making it the most effective choice for enhancing soil strength under these testing conditions. It was also observed that beyond approximately 4% to 6% cement content, the rate of increase in UCS values began to diminish, suggesting an optimal balance between economic and performance considerations within this range. While RHA alone has a moderate effect on UCS values, its synergistic action with cement, particularly at a 4% RHA inclusion, leads to a remarkable improvement in strength. Therefore, the combination of 4% RHA and 6% cement in soil mixtures is strongly recommended for applications requiring enhanced soil strength and load-bearing capacity. Future investigations could further optimize these exact proportions, assess long-term durability, and examine performance under various environmental conditions.

CONCLUSION

This study comprehensively investigated the potential of rice husk ash (RHA) as a sustainable supplementary cementitious material for soil stabilization, addressing the pressing environmental concerns associated with the use of conventional cement in ground improvement. Our research aimed to fill existing gaps by evaluating the mechanical and microstructural properties of soil stabilized with controlled-burn, as-obtained RHA in combination with ordinary Portland cement, particularly focusing on their application in subgrade layers.

The Unconfined Compressive Strength (UCS) tests unequivocally demonstrated that the incorporation of RHA and cement significantly enhances the strength of the treated soil. This substantial improvement is primarily attributed to the pozzolanic reactions between RHA's amorphous silica and cement's calcium hydroxide, leading to the formation of strength-contributing Calcium Silicate Hydrate (CSH) gel. We observed a consistent increase in UCS values with higher cement content, with the most effective performance achieved by the combination of 4% RHA and 6% cement. This optimal mix yielded the highest UCS values across all tested configurations, especially in dual-layer applications, highlighting a synergistic effect between the two binders. Microstructural analyses, including SEM and EDS, would further corroborate these findings by revealing the formation of dense CSH networks and improved particle bonding. This research holds significant practical implications, particularly for developing countries where RHA disposal is a challenge and sustainable construction practices are crucial. The findings provide a robust recommendation for utilizing a specific blend of RHA and cement to achieve enhanced soil strength and load-bearing capacity, offering an environmentally responsible alternative for infrastructure development. By promoting the use of this agricultural byproduct, the study contributes to reducing carbon emissions, lowering construction costs, and fostering a more sustainable future for the geotechnical and construction industries. Future research should focus on validating the long-term durability of these optimized mixes and their performance under diverse environmental conditions.

ACKNOWLEDGMENTS

The authors thank Mie University Graduate School for their financial assistance and advice through the Doctoral Student Development Support (SPRING) program.

REFERENCES

[1] Shehata, A. A. A., Owino, A. O., Islam, M. Y., & Hossain, Z. Shear strength of soil by using rice husk ash waste for sus-641 sustainable ground improvement. Discover Sustainability 2024, Vol. 5, Issue 1, p. 64. https://doi.org/10.1007/s43621-024-00238-x.

[2] Atef, A., & Hossain, Z. Sustainable Soil Reinforcement by Maximizing Geotechnical Performance with Rice Husk Ash in 652 Subgrade Layers. Materials 2025, 18(4), 873.https://doi.org/10.3390/ma18040873.

[3] Givi, A. N., Rashid, S. A., Aziz, F. N. A., &

Salleh, M. A. M. Contribution of rice husk ash to the properties of mortar and concrete: areview. *Journal of American Science*, *6*(3), 2010, 157-165.

[4] Chen, R., Congress, S. S. C., Cai, G., Duan, W., & Liu, S. Sustainable utilization of biomass waste-rice husk ash as a new solidified material of soil in geotechnical engineering: A review. Construction and Building Materials, 292, 2021, 123219.

[5] Abd Elmageed Atef, M. Y. I., Owino, A. O., Islam, M. A., Rahman, M. S., & Hossain, Z. enhancing soil stability and geotechnical properties of subgrade layers using rice husk ash: a sustainable approach for ground improvement. Environmental protection, Int. Conf. on GEOMATE, 2023, pp463-470.

[6] Abd Elmageed Atef, Hossain, Z. .Enhancing Geotechnical Properties in Subgrade Layers through Rice Husk Ash: A Sustainable Paradigm for Ground Improvement, Int. Conf. on CEAC, 2024, South Korea, Seoul.https://doi.org/10.1007/978-981-97-5477-9_31.

[7] Abd Elmageed Atef, Hossain, Z. Optimizing Soil Strength Through Rice Husk Ash In-corporation: A Sustainable Geotechnical Solution, Int. Conf. on ICOCE, 2024, Singapore, https://doi.org/10.1007/978-981-97-5910-1_24.

[8] Zami, M. S., & Lee, A. Economic benefits of contemporary earth construction in low-cost urban housing–state-of-the-art review. Journal of Building Appraisal, 5,2010, 259-271.

[9] JIS A 1210, (In Japanese). Test method for soil compaction using a rammer. Japanese Industrial Standard, Guidance and Basic - Soil Test, The Jpn. Geotech. Soc, 2010, pp 71-78.

[10] Atef, A.; Hossain, Z. Assessing the Impact of Rice Husk Ash on Soil Strength in Subgrade Layers: A Novel Approach to Sustainable Ground Engineering. Sustainability 2025, 17, 5457. https://doi.org/10.3390/su17125457.

[11] JGS 0524, (In Japanese). Method for consolidated-drained triaxial compression test on soils, Jpn. Geotech. Soc. Dositsu Shiken Hou Dositsu Kogakkai, 2001, pp233-43.

[12] Shaban, A., & Cosentino, P. Characterizing the structural performance of unbound pavement materials using miniaturized pressuremeter and California bearing ratio tests. Journal of Testing and Evaluation, 45(13),2017, 1-18.

[13] Kifae, A. A. Chemical and physical effects on engineering properties of gypseous subgrade soil. Al-Qadisia Journal for Engineering Sciences, 3(3),2010, 17.

[14] Rachmawati, S. H., Hossain, Z. and Shiau, J. "Ground improvement using the waste shell for farm roads and embankments," Journal of Agricultural Engineering, 49(1), 2018, pp. 29–33.

Copyright © Int. J. of GEOMATE All rights reserved, including making copies, unless permission is obtained from the copyright proprietors.

15th Int. Conf. on Geotechnique, Construction Materials & Environment,
Kyoto, Japan, 11-13 November 2025, ISBN 978-4-909106124 C3051

ENVIRONMENTAL AND MECHANICAL PROPERTIES OF CONCRETE PAVEMENTS INCORPORATING REFUSE-DERIVED FUEL FLY ASH

Menglim Hoy[1], Suksun Horpibulsuk[2] and Chutichai Tonueng[3]

[1]School of Civil Engineering, Suranaree University of Technology, Thailand,
[2]Center of Excellence in Innovation for Sustainable Infrastructure Development, Suranaree University of Technology, Thailand,
[3]Graduate Program in Civil Engineering and Construction Management, Suranaree University of Technology, Thailand

ABSTRACT

This research explores the potential of refuse-derived fuel fly ash (RDF FA), a byproduct of municipal solid waste incineration, as a sustainable material for enhancing concrete pavement performance. The study investigates RDF FA as both a partial cement replacement and an additive to evaluate its mechanical and environmental impacts. Experimental results demonstrate that cement replacement with RDF FA reduces early-age compressive and flexural strengths. In contrast, its addition significantly improves 28-day strengths, surpassing standard requirements for rigid pavement applications. Microstructural analyses re-veal that RDF FA enhances hydration and densifies the concrete matrix when used as an additive, while leachate testing confirms heavy metal concentrations within environmentally acceptable limits. By incorporating RDF FA in concrete pavements, this research contributes to sustainable construction practices, resource conservation, and global efforts to mitigate the environmental footprint of infrastructure development. The study aligns with the goals of promoting a circular economy and advancing innovative solutions for waste management and climate resilience in construction.

Keywords: Sustainable concrete pavement, Refuse-derived fuel fly ash, Supplementary cementitious materials, rigid pavement, Municipal waste.

INTRODUCTION

The growth of urbanization and industrial development has resulted in a rapid increase in municipal solid waste (MSW), creating critical challenges in disposal and environmental management. Incineration is widely adopted for MSW treatment due to its effectiveness in volume reduction and energy recovery [1](Cho et al., 2020). However, this process generates large amounts of bottom ash (BA) and fly ash (FA), which require careful management to mitigate environmental risks. In particular, refuse-derived fuel fly ash (RDF FA), produced from pre-sorted and pelletized MSW incineration, is of growing interest due to its relatively consistent composition and potential reusability [2, 3](Kikuchi, 2001; Saikia et al., 2007).

In the construction industry, supplementary cementitious materials (SCMs) have been widely employed to enhance concrete properties while reducing cement consumption and associated CO_2 emissions. Previous studies have demonstrated that municipal solid waste incineration (MSWI) ashes can partially substitute cement or aggregates, contributing to strength development and improved sustainability [4-6](Abbà et al., 2014; Jurič et al., 2006; Yang et al., 2018). While bottom ash has been commonly utilized as aggregate replacement, the application of MSWI fly ash, particularly RDF FA, in concrete pavements remains limited and requires further investigation.

Rigid concrete pavements demand adequate compressive and flexural strengths to withstand heavy traffic loading and environmental stresses. Early studies reported that the incorporation of FA could influence hydration and microstructure, affecting both strength and durability [7, 8](Shi et al., 2009; Tang et al., 2016). However, the effect of RDF FA in pavement-grade concrete under different incorporation methods—cement replacement versus cement addition—has not been systematically evaluated.

This study aims to investigate the mechanical performance and microstructural development of concrete incorporating RDF FA for rigid pavement applications. Mechanical properties were assessed through compressive and flexural strength tests, while scanning electron microscopy (SEM) was employed to examine hydration products and matrix densification. The findings provide new insights into the potential of RDF FA as a sustainable construction material, highlighting the distinction between cement replacement and additive use, and supporting circular economy practices in pavement engineering.

MATERIALS AND METHODS

Materials

Refuse-derived fuel fly ash (RDF FA) used in this study was collected from a municipal solid waste incineration (MSWI) facility in Saraburi, Thailand. Its chemical composition, determined by X-ray fluorescence (XRF), indicated a high CaO content and significant SiO_2 and Al_2O_3 levels, suggesting pozzolanic potential. Type I ordinary Portland cement (OPC) conforming to ASTM C150 was used as the primary binder. Natural sand and crushed limestone, complying with ASTM C33, were employed as fine and coarse aggregates, respectively (Fig. 1).

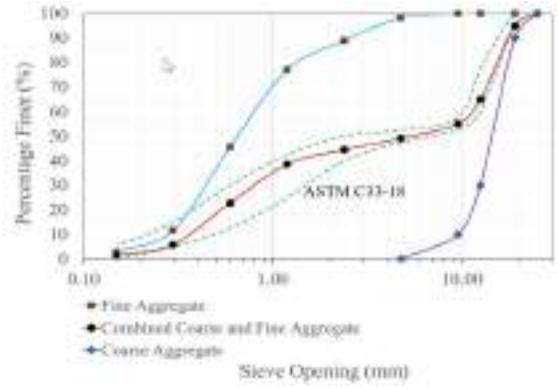

Fig.1. Particle size distribution of aggregates.

Mix Design and Specimen Preparation

Use at most three levels of headings that correspond to chapters, sections, and subsections. The first level headings for chapter titles should be in 10pt, bold, justified, and upper case font. Leave one blank line before and after the first level headings, respectively.

Two incorporation methods were adopted: (i) cement replacement by RDF FA at 5%, 10%, and 15% by weight of cement, and (ii) cement addition at the same percentages without reducing OPC content. A control mix (100% OPC) was prepared for comparison. All mixes were designed at a constant water-to-cement ratio of 0.5, with slump controlled at 75 ± 5 mm in accordance with the Department of Highways (DOH) of Thailand standards.

Concrete batches were mixed in a laboratory drum mixer following ASTM C192. Cube specimens (100 × 100 × 100 mm³) were prepared for compressive strength testing, while prism specimens (100 × 100 × 500 mm³) were cast for flexural testing. Specimens were demolded after 24 hours and cured in water at 23 ± 2 °C until testing ages of 7 and 28 days.

EXPERIMENTAL PROGRAMS

Mechanical Testing

Compressive strength was determined according to ASTM C39, and flexural strength was measured using the three-point bending test following ASTM C78. The flexural strength was calculated using:

$$f_r = \frac{bd^2}{PL} \quad (1)$$

where P = maximum load, L = span length, b = specimen width, and d = specimen depth.

Scanning Electron Microscopy (SEM) analysis

Microstructural observations were conducted using scanning electron microscopy (SEM) on fractured surfaces of 28-day cured specimens. Samples were oven-dried at 50 °C, gold-coated, and examined under 15 kV accelerating voltage. Morphological features such as calcium silicate hydrate (C-S-H), ettringite, and calcium hydroxide [$Ca(OH)_2$] were identified to assess the influence of RDF FA incorporation on hydration and matrix densification.

RESULTS AND DISCUSSION

Unconfined Compressive Strength Development

The compressive strength results of RDF FA-modified concretes at 7 and 28 days are presented in Fig.2. The control mix exhibited a 28-day strength of 34.1 MPa, satisfying the Department of Highways (DOH) minimum requirement of 32 MPa (DH-S 309/2544).

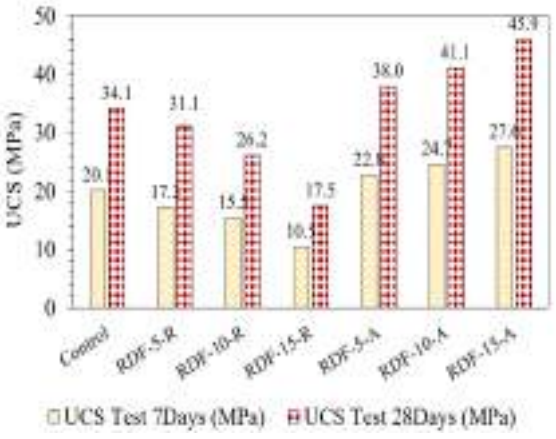

Fig.2 UCS results.

When RDF FA was used as a cement replacement, compressive strength decreased with increasing replacement levels. At 28 days, RDF-5-R, RDF-10-R, and RDF-15-R achieved 31.1, 26.2, and 17.5 MPa, respectively—all below the DOH standard. The reduction is attributed to the decreased cement content, which limits calcium silicate hydrate (C-S-H) formation, resulting in a weaker matrix.

In contrast, the cement addition method significantly improved strength. RDF-5-A, RDF-10-A, and RDF-15-A exhibited 28-day compressive strengths of 38.0, 41.1, and 45.9 MPa, respectively, surpassing both the control mix and DOH requirements. The improvement is due to enhanced hydration and pozzolanic reactions of RDF FA, which contributed to additional C-S-H formation and matrix densification.

Flexural Strength Development

The flexural strength results of RDF FA-modified concretes at 7 and 28 days are presented in Figure 2. The control mix achieved 4.2 MPa at 28 days, meeting the Department of Highways (DOH) requirement for rigid pavement concrete (Fig.3).

For the replacement method, flexural strength decreased with increasing RDF FA content. At 28 days, RDF-5-R, RDF-10-R, and RDF-15-R recorded 3.6, 2.7, and 2.0 MPa, respectively—below the DOH minimum requirement. The decline is attributed to reduced cement content, which limited C-S-H formation and weakened the bond between paste and aggregates, leading to early crack initiation under flexural loading.

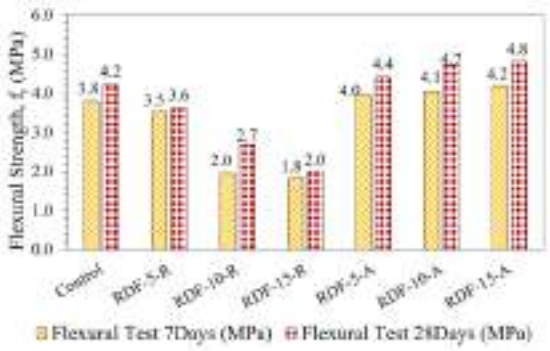

Fig.3 Flexural strength results.

In contrast, the addition method showed a significant improvement. RDF-5-A, RDF-10-A, and RDF-15-A achieved 28-day strengths of 4.4, 4.7, and 4.8 MPa, respectively, surpassing both the control mix and the DOH standard. The enhanced performance is explained by improved hydration and pozzolanic reactions, which densified the matrix and increased resistance to tensile stresses.

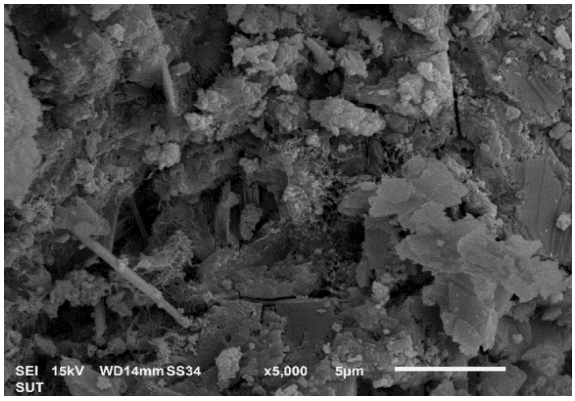

(a)

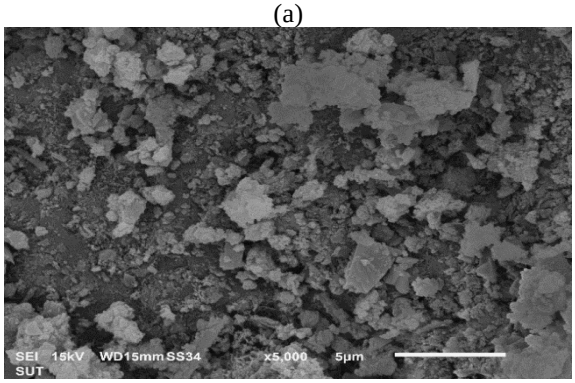

(b)

Fig. 4. SEM images: (a) RDF-5-R and (b) RDF-10-R.

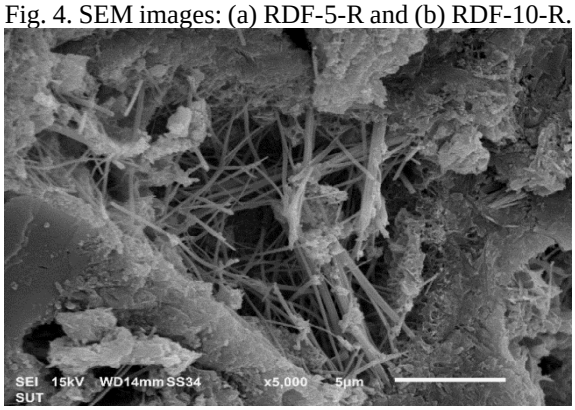

(a)

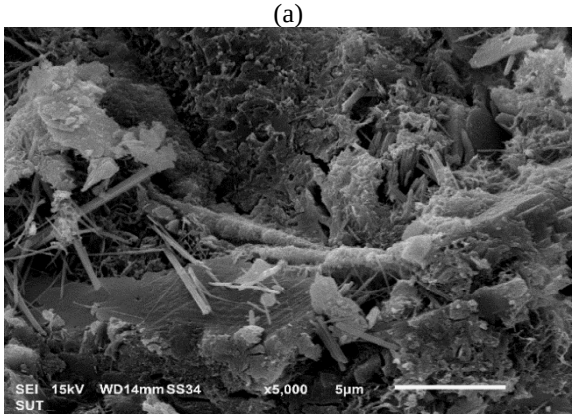

(b)

Fig.5 SEM images: (a) RDF-5-A and (b) RDF-10-A.

Microstructural Analysis

The SEM micrographs of RDF FA-modified concretes at 28 days are presented in Fig. 4 and Fig. 5, comparing the replacement and addition methods. Clear distinctions in hydration products and matrix density were observed between the two approaches.

For the replacement specimens (Fig. 4a and 4b), the microstructure was relatively porous with less compact morphology. Calcium hydroxide [$Ca(OH)_2$] crystals and limited calcium silicate hydrate (C-S-H) gel were observed, indicating a weaker hydration process due to the reduced cement content. The lower availability of cementitious phases resulted in incomplete matrix development, which correlates with the decreased compressive and flexural strengths observed in RDF-5-R and RDF-10-R.

In contrast, the addition specimens (Figures 5a and 5b) exhibited a denser microstructure with abundant hydration products. Needle-like ettringite crystals and a well-distributed C-S-H gel were clearly visible, along with $Ca(OH)_2$ participating in secondary pozzolanic reactions. These features indicate improved hydration and matrix densification, which explain the higher strengths recorded in RDF-5-A and RDF-10-A. The presence of additional RDF FA particles provided reactive silica that enhanced pozzolanic activity, producing supplementary C-S-H and strengthening the concrete matrix.

Overall, SEM observations confirm that while cement replacement with RDF FA compromises matrix integrity, its addition promotes hydration, densifies the microstructure, and improves load transfer capacity. These microstructural findings are consistent with the mechanical test results, highlighting RDF FA addition as the more effective method for enhancing rigid pavement concrete.

CONCLUSIONS

This study demonstrated that the incorporation method strongly influences the performance of RDF FA in concrete pavements. When used as a cement replacement, RDF FA reduced compressive and flexural strengths below the DOH standard due to a porous microstructure. In contrast, RDF FA addition significantly improved strength development, surpassing DOH requirements, with SEM observations confirming denser C-S-H and ettringite formation. Therefore, RDF FA is more effective as an additive, offering both enhanced pavement performance and sustainable waste utilization.

ACKNOWLEDGMENTS

This work was financially supported by the Suranaree University of Technology.

REFERENCES

[1] Cho, B. H., Nam, B. H., An, J., & Youn, H. (2020). Municipal Solid Waste Incineration (MSWI) ashes as construction materials—A review. Materials, 13(14), 3143.

[2] Kikuchi, R. (2001). Recycling of municipal solid waste for cement production: pilot-scale test for transforming incineration ash of solid waste into cement clinker. Resources, Conservation and Recycling, 31(2), 137-147.

[3] Saikia, N., Kato, S., & Kojima, T. (2007). Production of cement clinkers from municipal solid waste incineration (MSWI) fly ash. Waste Management, 27(9), 1178-1189.

[4] Abbà, A., Collivignarelli, M. C., Sorlini, S., & Bruggi, M. (2014). On the reliability of reusing bottom ash from municipal solid waste incineration as aggregate in concrete. *Composites Part B: Engineering, 58*, 502-509.

[5] Jurič, B., Hanžič, L., Ilić, R., & Samec, N. (2006). Utilization of municipal solid waste bottom ash and recycled aggregate in concrete. Waste Management, 26(12), 1436-1442.

[6] Yang, Z., Ji, R., Liu, L., Wang, X., & Zhang, Z. (2018). Recycling of municipal solid waste incineration by-product for cement composites preparation. Construction and Building Materials, 162, 794–801.

[7] Shi, H., Deng, K., Yuan, F., & Wu, K. (2009). Preparation of energy-saving sulphoaluminate cement using MSWI fly ash. Journal of Hazardous Materials, 169(1), 551–555.

[8] Tang, P., Florea, M. V. A., Spiesz, P., & Brouwers, H. J. H. (2016). Application of thermally activated municipal solid waste incineration (MSWI) bottom ash fines as binder substitute. Cement and Concrete Composites, 70, 194–205.

Copyright © Int. J. of GEOMATE All rights reserved, including making copies, unless permission is obtained from the copyright proprietors.

15th Int. Conf. on Geotechnique, Construction Materials & Environment, Kyoto, Japan, 11-13 November 2025, ISBN 978-4-909106124 C3051

EFFECT OF SUPERPLASTICIZER ON WORKABILITY OF RICE HUSK ASH AND SEASHELL POWDER BLENDED CONCRETE

Md Soybur Rahman[1], Zakaria Hossain[2]

[1,2]Graduate School of Bioresources, Mie University, Japan

ABSTRACT

The major challenge of incorporating supplementary cementitious materials (SCMs) in concrete is the reduction in workability, which often demands additional water. However, excess water negatively affects the mechanical performance of hardened concrete. The use of superplasticizer (SP) offers an effective solution to retain workability without compromising strength. This study investigated the optimum dosage of superplasticizer in concrete modified with rice husk ash (RHA) and seashell powder (SSP) as partial replacements for cement. Different dosages of superplasticizer were added at varying RHA–SSP levels and at the same RHA-SSP content. Workability was evaluated using the slump test. The results showed that the required superplasticizer dosage increased with higher RHA–SSP incorporation. At a given RHA–SSP level, slump values increased proportionally with the superplasticizer dosage. Finally, two predictive equations were developed to estimate the required SP dosage and the corresponding slump value for RHA–SSP modified concrete.

Keywords: Superplasticizer, Rice Husk Ash, Seashell powder, Workability

INTRODUCTION

The cement industry is a major contributor to global carbon emissions, with Portland cement production being the most energy-intensive process. Significant energy savings and emission reductions can be achieved by partially replacing cement with supplementary cementitious materials (SCMs), such as fly ash, rice husk ash (RHA), ground granulated blast-furnace slag (GGBS), silica fume, and calcined seashell powder. However, the angular and irregular shapes of SCMs increase particle friction, leading to reduced workability of fresh concrete.

In recent years, the use of superplasticizers (SPs) as chemical admixtures has gained considerable attention for addressing this challenge. It not only enhances the workability and mitigates slump loss but also often improves the compressive strength of concrete compared to ordinary mixes.

Superplasticizers are generally categorized into four types based on their chemical composition and method of production: polycarboxylic ether (PCE), lignosulphonates (LS), sulphonated melamine formaldehyde (SMF), and sulphonated naphthalene formaldehyde (SNF). PCE-based superplasticizers primarily act through steric hindrance, while LS, SMF, and SNF-based superplasticizers enhance workability mainly by electrostatic repulsion [1-2]. Despite differences in their mechanisms, all water-reducing agents operate on the same fundamental principle: inhibiting the flocculation of cement particles in concrete to improve its fresh-state characteristics. This flocculation, which entraps water between particles, is primarily propelled by Van der Waals forces, electrostatic interactions, and bridging effects among cement and water molecules [3]. The dispersion of cement in the water and concrete mixture design is the primary factor that controls the flow behavior of hardened cement paste and concrete, which in turn affects their properties. In practice, superplasticizers have been widely utilized to improve the workability of concrete and scatter the cement particles [4].

Previous studies have explored the use of superplasticizer dosages in concretes incorporating individual supplementary cementitious materials (SCMs) such as rice husk ash (RHA) and fly ash. However, the combined use of two SCMs presents new challenges. In particular, the optimal dosage of superplasticizer remains unclear when RHA and seashell powder (SSP) are applied synergistically as cement replacement materials: a novel strategy in sustainable concrete production. Therefore, the goal of this study is to determine the ideal superplasticizer dosage for RHA–SSP modified concrete to achieve the desired slump and ensure workable mixtures.

RESEARCH SIGNIFICANCE

Workability is an important parameter of fresh concrete for practical application. The physical characteristics of Supplementary cementitious material (SMCs) reduced the workability of concrete and created a demand for using superplasticizer to maintain proper workability without compromising concrete performance. As the synergistic application of RHA and SSP as cement replacement materials is a new approach, the dosage of superplasticizer for modified concrete is still unknown. The study aims to

determine the optimal dosage of superplasticizer for RHA and SSP-modified concrete to achieve a desirable slump.

MATERIALS AND METHODS

The materials used in this study included cement, fine aggregate, coarse aggregate, Rice Husk Ash (RHA), Seashell Powder (SSP), water, and locally available Ordinary Portland Cement (OPC). Natural river sand was employed as the fine aggregate, while gravel with a maximum size of 19 mm served as the coarse aggregate.

Superplasticizer

The FloricSV10 superplasticizer, supplied by Floric Co. Ltd., was employed in this study as shown in Fig.1. This admixture was specifically developed to provide high water-reducing efficiency while enhancing slump retention performance. It is classified as a JIS 6204 Type I (AE water-reducing agent) chemical admixture for concrete. Based on an advanced polycarboxylic acid technology combined with conventional AE water-reducing components, it offers excellent dispersion capability and prolonged slump retention. These characteristics improve the workability of fresh concrete and contribute to the long-term durability of hardened concrete structures. The admixture is liquid in form, with a density of 1.12 g/cm³, and its main constituents include lignosulfonates, oxycarboxylates, and polycarboxylate compounds.

Fig. 1: FloricSV10 superplasticizer

Rice Husk Ash and Seashell Powder

The rice husk ash production process was operated in a factory building using an industrial machine. Unlike traditional incinerators, this machine operates as a natural-type silica generator, eliminating the need for combustible materials such as gas, kerosene, or electricity. Instead, solid methanol fuel is used to ignite and burn the rice husks. This innovative process is environmentally friendly, as it does not produce dioxins, making it exempt from the Fire Services Act. The burning speed and temperature are meticulously controlled by a computer, reducing labor costs and minimizing personnel requirements. Additionally, the system can be remotely controlled, offering further convenience in managing the incineration process. The seashell powder production process involves collecting seashells, drying them, and then grinding them into a fine powder. Finally, the powder is subjected to a burning process at 900°C. Both materials were provided by Make Integrated Technology (M.I.T.) Company, Osaka, Japan. The RHA and SSP are shown in the Fig. 2.

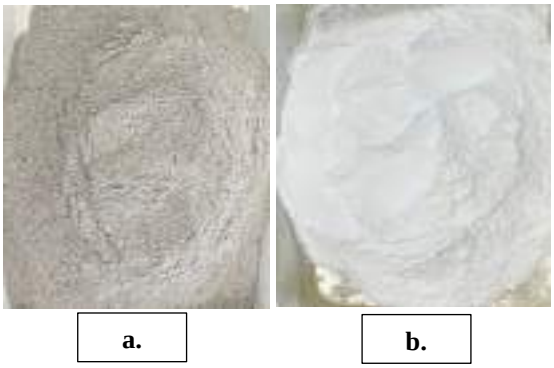

Fig. 2: Rice husk ash (a) and Seashell powder (b)

Preparation of Concrete Mixture

After accurately weighing the raw materials, the concrete mixture was prepared using a mix ratio of 1:1:3 by weight for cement, fine aggregate, and coarse aggregate. RHA and SSP were used as supplementary cementitious materials, replacing cement. The water-to-binder ratio was maintained at 0.50 throughout the all mixing process. The superplasticizer was used in proportion to the binder. The specific quantities of each material are provided in Table 1. The raw materials were mixed using a mixer machine as shown in Fig. 3.

Figure 3: Concrete mixer

Table 1 Concrete Mix Design

SL No.	Cement (%)	RHA (%)	Seashell Powder (%)	W/B ratio	Cement (kg/m^3)	Fine Aggregate (kg/m^3)	Coarse Aggregate (kg/m^3)	Superplasticizer (% of binder)
1	100	0	0	0.50	290	308	852	0
2	95	2.5%	2.5%	0.50	275.5	308	852	0.1
3	90	5%	5%	0.50	261	308	852	0.7
4	85	7.5%	7.5%	0.50	246.5	308	852	0.9
5	80	10%	10%	0.50	232	308	852	1.5
6	75	12.5%	12.5%	0.50	217.5	308	852	2.8
7	75	12.5%	12.5%	0.50	217.5	308	852	1
8	75	12.5%	12.5%	0.50	217.5	308	852	2
9	75	12.5%	12.5%	0.50	217.5	308	852	3
10	75	12.5%	12.5%	0.50	217.5	308	852	4
11	75	12.5%	12.15%	0.50	217.5	308	852	5

Slump Test

Following proper mixing of raw materials, a slump test was conducted to evaluate the workability of the concrete. The slump cone used in the test has standard dimensions: 300 mm in height, a base diameter of 200 mm, and a top opening of 100 mm. The cone was placed on a smooth, level surface and filled with concrete in three equal layers. Each layer was compacted by rodding 25 times using a tamping rod with a diameter of 16 mm. After filling, the top surface was leveled, and the mold was lifted vertically. The slump testing and slump value measuring are shown in Fig. 4 and 5.

Fig. 4: Experimental equipment and slump testing at the laboratory

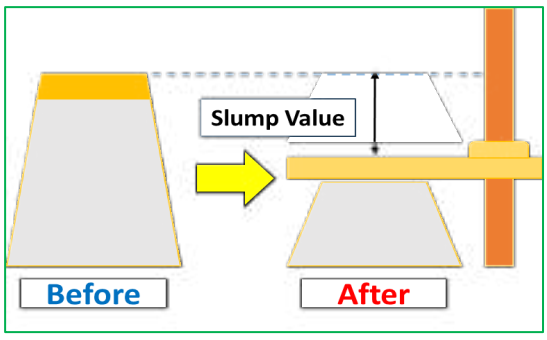

Fig. 5: Slump value measuring

RESULTS AND DISCUSSION

Effect of Superplasticizer on RHA-SSP-modified concrete

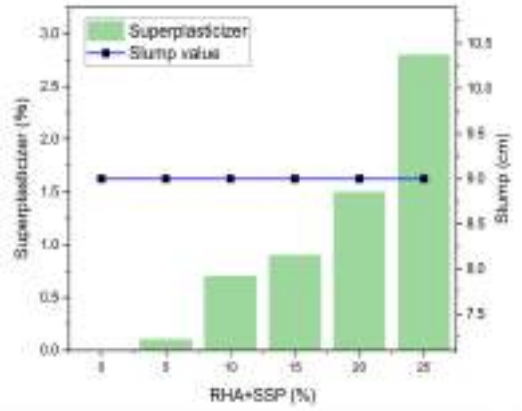

Fig. 6: Superplasticizer dosage at different percentages of RHA and SSP to maintain the same slump

Fig. 6 illustrates the effect of incorporating rice husk ash (RHA) and seashell powder (SSP) on the superplasticizer dosage required to achieve the target slump of 9 ± 1 cm. The control mix achieved the desired slump without the use of superplasticizer. However, the addition of RHA and SSP led to slump loss, thereby increasing water demand. Since excess water negatively affects strength, the superplasticizer was used to restore workability. As the RHA–SSP replacement level increased from 5% to 25%, the required superplasticizer dosage rose steadily from 0.1% to 3% in order to maintain the target slump. These results emphasize the crucial role of superplasticizer in counteracting the reduced fluidity induced by RHA and SSP, thereby ensuring consistent fresh properties in blended concrete.

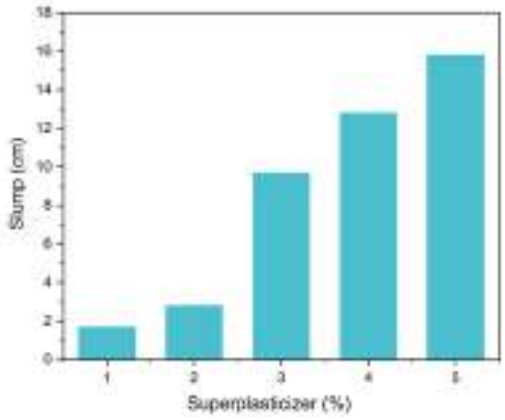

Fig. 7: Slump value with different dosages of Superplasticizer at RHA-SSP-modified concrete

Fig. 7 shows the variation in slump values with the increase in superplasticizer (SP) dosage for concrete mixtures containing 12.5% rice husk ash (RHA) and 12.5% seashell powder (SSP), replacing 25% of cement. The results indicate a steady rise in slump from 1.7 cm at 1% SP dosage to 15.8 cm at 5% dosage. This trend clearly demonstrates the positive influence of SP in improving the workability of RHA–SSP blended concrete. At lower dosages (1–2%), the mix remains relatively stiff, representing low workability. A moderate improvement in workability is achieved with a 3–4% dosage, while dosages above 5% produce a highly workable mix. These findings highlight the importance of optimizing SP dosage to achieve the desired workability to make RHA-SSP concrete.

Prediction of Superplasticizer dosage and Slump value

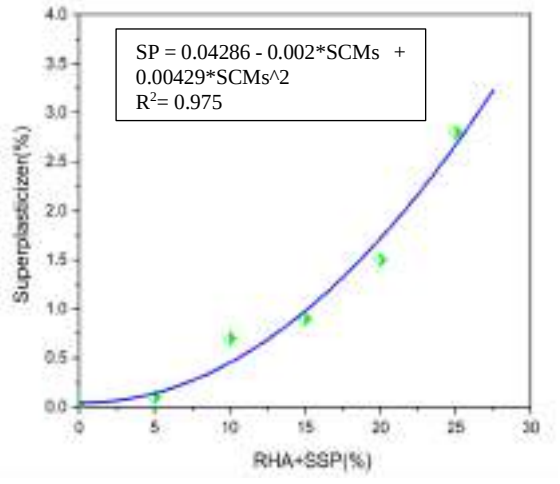

Fig. 8: Correlation of superplasticizer dosage and different percentages of RHA and SSP

Fig. 8 illustrates the relationship between RHA and SSP replacement levels and the corresponding dosage of superplasticizer required to maintain constant workability. As the combined percentage of RHA and SSP increased, the demand for superplasticizer rose in a nonlinear manner. At lower replacement levels (up to 10%), only a small amount of superplasticizer was necessary, while moderate replacement levels (15–20%) required a noticeable increment. Beyond 20% replacement, the demand of SP dosage rose steeply, exceeding 2.5% at 25% RHA-SSP. This trend indicates that higher levels of RHA and SSP significantly reduce the workability of concrete, thereby requiring greater amounts of superplasticizer to achieve the target slump. The following equation can be used to estimate SP dosage for RHA-SSP modified concrete.

SP = 0.04286 - 0.002*SCMs + 0.00429*SCMs^2

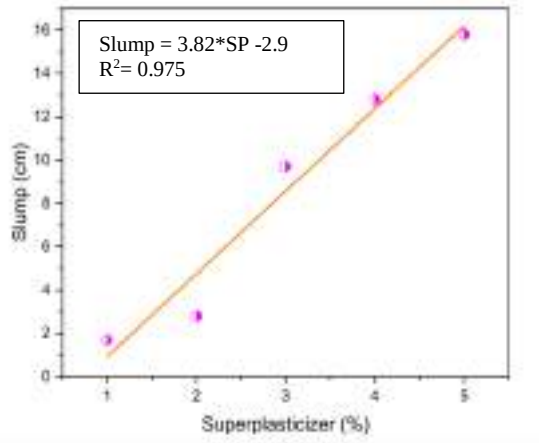

Fig. 9. Correlation of slump value with different superplasticizer dosage for RHA-SSP Modified concrete

Fig. 9 illustrates the linear relationship between superplasticizer (SP) dosage and the slump value of concrete mixtures containing 12.5% rice husk ash (RHA) and 12.5% seashell powder (SSP), replacing 25% of cement. The plotted trendline demonstrates a proportional increase in slump with increasing SP dosage, confirming the predictable effect of the water reducing admixture on the workability of fresh concrete. Accordingly, the equation as shown in below can serve as a practical tool for estimating the required SP dosage to achieve the desired workability in RHA–SSP modified concrete mixtures.

Slump = 3.82*SP -2.9

CONCLUSION

Based on experimental investigation, the following conclusion can be drawn-

- The dosage of SP was increased with an increment of RHA-SSP content in the concrete mixture.
- Low workability was observed at 1–2% dosage, moderate at 3–4%, and high above 5%.
- The developed equation provides a practical tool for estimating sp dosage in RHA–SSP concrete.

ACKNOWLEDGMENTS

The authors gratefully acknowledge the Japan Ministry of Education, Culture, Sports, Science, and Technology (MEXT) for providing financial support through the MEXT scholarship at Mie University, where this study was conducted. The authors also wish to express their sincere gratitude to M.I.T. Company, Osaka, Japan, for supplying the RHA and SSP, and to Flowric Co. Ltd. for providing the superplasticizer used in this experiment.

REFERENCES

[1] Sathyan D., and Anand K. B., Influence of superplasticizer family on the durability characteristics of fly ash incorporated cement concrete. Construction and Building Materials, Vol. 204, 2019, pp. 864-874.

[2] Alsadey S., Effect of superplasticizer on fresh and hardened properties of concrete. 2015

[3] Björnström J., and Chandra S., Effect of superplasticizers on the rheological properties of cements. Materials and Structures, Vol. 36, Issue 10, 2003, pp. 685-692.

[4] Zhang M. H., Sisomphon K., Ng T. S., and Sun D. J., Effect of superplasticizers on workability retention and initial setting time of cement pastes. Construction and Building Materials, Vol. 24, Issue 9, 2010, pp. 1700-1707.

Copyright © Int. J. of GEOMATE All rights reserved, including making copies, unless permission is obtained from the copyright proprietors.

15th Int. Conf. on Geotechnique, Construction Materials & Environment,
Kyoto, Japan, 11-13 November 2025, ISBN 978-4-909106124 C3051

EFFECT OF CEMENTITIOUS MORTAR FOR REPAIRING REINFORCED CONCRETE (RC) BEAMS

Leandro Madeira Branco[1] , Abel Fernandes[1], Isamu Yoshitake[1]

[1] Graduate School of Sciences and Technology for Innovation, Yamaguchi University, Yamaguchi, Japan

ABSTRACT

Defects in concrete structures can arise during and after construction due to inadequate materials, construction methods, and environmental conditions. In developing countries, the repair of reinforced concrete (RC) structures often faces constraints due to limited resources, making conventional cement-based materials necessary. A comparative analysis investigated three distinct repair materials: ordinary Portland cement mortar (OPCM) and a polymer-modified cement (PMC) mortar. Each repair material was prepared with and without epoxy resin (ER), and consistent surface treatment was applied to concrete and RC beam specimens before the repair materials were used. This study evaluated concrete specimens' slant shear and double shear and the flexural performance of repaired RC beams. The experimental study focused on the shear performance of cementitious materials and the load-bearing capacity of repaired RC beams, evaluating the deformation behavior, crack resistance, and failure modes of different repair cementitious material combinations. The proposed method successfully achieved the desired interfacial bond strength between the repair material and the substrate. In the case of RC beams, the results demonstrated the effectiveness of combining ER with OPCM in restoring and enhancing the load-bearing capacity of the repaired specimens. Furthermore, the findings underscore the critical role of material compatibility in achieving optimal bond conditions and the importance of mitigating crack progression for successful RC beam repair. This study offers guidance for implementing conventional cement in restoring damaged RC structures to their original condition.

Keywords: Ordinary Performance-cement mortar (OPCM), Polymer modified cement (PMC), Epoxy resin (ER), Shear performance, and Flexural performance.

INTRODUCTION

Concrete structures are inherently susceptible to defects arising during and after construction due to deficiencies in materials, poor workmanship, and environmental exposure [1,2]. In developing countries, these vulnerabilities are often exacerbated by systemic infrastructure challenges, including limited financial resources, weak institutional governance, inadequate technical expertise, deficient project planning, and broader environmental and social constraints [3,4]. Consequently, the development of effective repair strategies for deteriorating infrastructure, particularly RC structures, has become a critical area of research in such contexts [5]. Given frequent resource limitations, repair efforts typically rely on conventional cement-based solutions, emphasizing the need for cost-effective, durable, and locally sourced materials [6, 7].

The physical and mechanical properties of the repair material are central to the success of any intervention. Key performance criteria include workability, setting time, shrinkage characteristics, and long-term durability [8]. Research has shown that incorporating polymers into cementitious repair materials can enhance bond strength and reduce shrinkage [9]. Nonetheless, optimizing repair performance using conventional cement-based materials requires careful selection of application techniques and consideration of multiple influencing parameters [10].

The most significant factor affecting bond performance is the condition of the interface between the repair material and the existing concrete. Bond strength is influenced by surface preparation methods, material compatibility, curing regimes, and the age of the repair [11]. Surface preparation, in particular, plays a vital role in promoting adhesion. Techniques such as sandblasting, water jetting, and mechanical scarification are widely employed to remove contaminants and deteriorated layers, thereby exposing a clean and roughened surface that facilitates improved bonding [12,13].

Curing conditions are equally important, as improper curing can lead to premature cracking, reduced bond strength, and compromised durability [14]. Over time, factors such as environmental exposure, mechanical loading, and material degradation can weaken the bond between the repair material and the substrate [15]. Therefore, a comprehensive understanding of the long-term performance of repair systems is essential to ensure service life expectations are met [16].

Although the benefits of OPCM are well recognized [17], further investigation is required to

fully understand and optimize its long-term adhesion and durability in structural repair applications. This study presents an experimental evaluation of OPCM in comparison with alternative cement-based repair materials to identify effective, conventional options for improving bond strength and flexural behavior in RC elements. The research aims to demonstrate that OPCM, either used alone or in combination with supplemental materials, can serve as a viable repair solution due to its favorable strength characteristics, effective bonding performance, crack mitigation potential, and contribution to enhanced flexural capacity.

MATERIALS AND METHODS

An experimental study was conducted to evaluate the bond strength relevant to the structural analysis of flexural performance in damaged RC beams during the repair process and subsequent utilization. The bond strength between the repair mortar and the concrete substrate was identified as a critical parameter in the flexural test.

Materials of the experiment

For this experimental study, the materials utilized for production included concrete, OPCM, PMC, and ER as bonding materials, as shown in Table 1. These materials were combined and evaluated for their performance. OPCM was used as the binder, incorporating a water-reducing admixture to enhance workability and strength. It was mixed with fine aggregates following a proper mix design to produce both high-strength and PMC mortars. The standardized mixed procedures for concrete and repair mortars are detailed in Tables 2 and 3, respectively. ER bonding was applied as an interface layer between the repair materials and the substrate concrete (SC), facilitating adhesion between both the OPCM and SC, as well as the PMC mortar and SC, in the bond strength test specimens and RC beam repairing specimens.

Table 1. Material used for the experiment

Material	Cementitious material		Af	Ac	Water	Admixture		ER
Type / Description	OPC	PMC	Sea sand	Crushed gravel (5–20 mm)	Natural water	WRA	HWRA	XL-800 (Epotherm®)
Density (g/cm³)	3.15	1.850	2.60	2.71	1	1.02	1.02	1.3

Af: Fine Aggregates; Ac: Coarse Aggregates; WRA: Water reducer; HWRA: High-range reducer; ER: Epoxy resin

Table 2. Concrete mix design proportion for substrate concrete and RC beams

Mix	W/C (%)	s/a (%)	Water (kg/m$^{3)}$	OPC (kg/m^3)	Af (kg/m^3)	Ac (kg/m^3)	WRA (kg/m^3)	Air (%)	Slump (cm)
CS	50	48	175	350	853	975	2.3	4.5±1.5	10±2

Table 3. Mixture proportions of cementitious material for repair

Type of mortar	W/C (%)	Water (kg/m^3)	OPC (kg/m^3)	PMC (kg/m^3)	Af (kg/m^3)	HWRA (kg/m^3)
OPCM	30	230	767	-	1272	6.13
PMC	14	258	-	1850	-	-

Table 4. Properties of a steel bar.

Nominal diameter	Yielding stress (MPa)	Ultimate stress (MPa)
13 mm	345	490
6 mm	285	380

Fig. 1. Slant shear specimens test

Fig. 2. Double shear specimen test

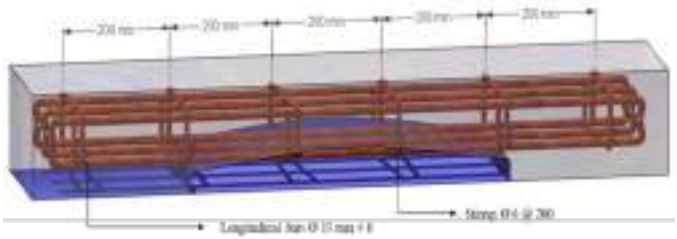

Fig. 3. Detail reinforcement of RC

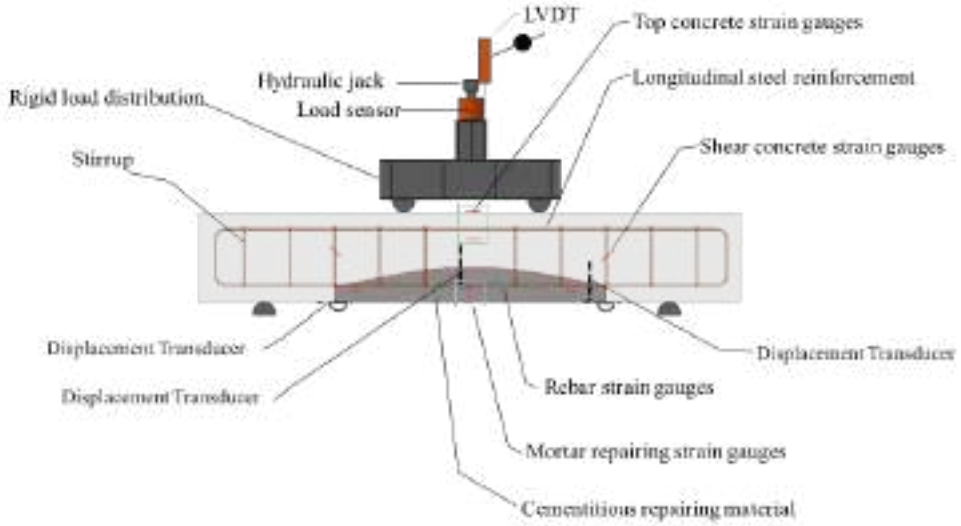

Fig. 4. Typical four-point bending test setup

Bond and Shear Strength Of Concrete

Two experimental methods for bond strength, the slant shear and double shear strength tests, were conducted in the study.

Slant shear

Following ASTM C882 and C1042, the slant shear test was originally proposed in 1976 as the Arizona Slant Shear Test, as illustrated in Fig. 1 [18]. In this method, an axial load is applied to the specimen at an interface angle, generating a combination of shear and tensile stresses. The resulting bond stresses are calculated as follows [19]:

$$\sigma_o = \frac{f}{A} \quad (1)$$

$$\tau_n = \frac{1}{2}\sigma_o \sin(2a) \quad (2)$$

$$\sigma_n = \sigma_o \sin^2 a \quad (3)$$

Here, f denotes the applied force (kN), A represents the cross-sectional area of the specimen (mm²), and σ_o is the applied stress. σ_n and τ_n represent the interfacial normal and shear stresses (bond stresses), respectively, acting on the bond plane as the result of σ_o. α denotes the slant shear angle. In this study, the specimens were prepared with an interface angle of ± 30° from the vertical axis, forming a composite cylinder with a total diameter of 100 mm and a height of 200 mm.

Table 5. Fresh concrete mix properties

No	Type of Mix	Slump (cm)	Air content (%)	Room temperature (C˚)	Concrete temperature (C˚)
1	RC-Control	14	5.5	25.2	26.4
2	RC-OPCM	13	5.75	26.4	22.5
3	RC-PMC	8.5	5.2	29.5	24.4

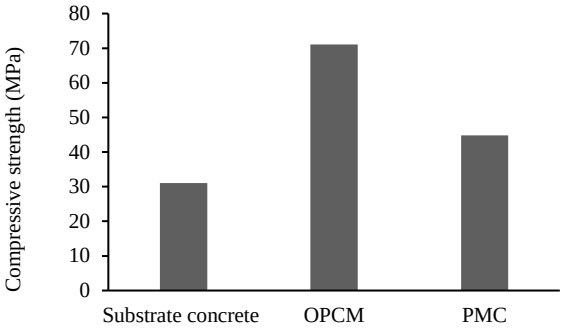

Fig. 5. Compressive strength of materials

Table 6. Fresh properties of the repair mortar

Note	OPCM	PMC
Flow rate (mm)	193	146
Room temp (°C)	25.2	28.2
Mortar temp (°C)	24.0	24.6
Mix temp (°C)	21.5	21.5

Double shear

Double shear testing of concrete is a mechanical method to determine the shear strength of concrete

specimens. This experimental approach evaluates the capacity of a specimen to resist shearing forces applied simultaneously in two planes or along two parallel surfaces. A schematic of the double shear strength test (also referred to as the shear friction test) is presented in Fig. 2. As an alternative double-plane shear test design, a similar setup was proposed by the Japanese Society of Civil Engineering (JSCE, 1990) for uncracked fiber-reinforced concrete specimens [20]. The shear stresses were calculated as follows:

$$\tau = \frac{f}{2A} \quad (4)$$

where f denotes the applied force (kN), A represents the contact area of the specimen (mm²), and τ denotes the resulting shear stress applied to the specimen.

After preparing the substrate concrete for the slant shear and double shear tests, it was cured for 28 days and air-dried for 7 days. The concrete surface was then cleaned using a slightly coarse wire brush to remove any mortar or dust from the coarse aggregate. A paintbrush was subsequently used to thoroughly remove any remaining dust. Slant shear and double shear specimens were prepared by applying fresh OPCM and PMC, with and without ER. This procedure was followed to ensure the accuracy of measurements and test results. The specimens were cured for an additional 28 days before testing.

Flexural Loading Test

Five RC beams were made for this experiment. Each beam had a 160 mm × 250 mm cross-section and was 1200 mm long (900 mm for the four-point bending test). The concrete strength was around 30 MPa, with a 40 mm cover. Three 13 mm reinforcing bars were placed in the tensile and compressive zones. The properties of rebars are given in Table 6. Stirrups, made of 6 mm bars, were spaced at 200 mm intervals. The beams followed the ACI 318 standard

[21]. Fig. 3 shows the repaired areas and load positions.

The repaired beams were tested in a four-point bending test to check their strength. A control beam, fully cast and cured for 28 days, was also tested. Strain gauges on the concrete and bars measured strain. Before testing, the control beam was placed in a testing frame with displacement sensors in key spots. Fig. 4 shows the control beam preparation, curing, and test setup

RESULTS AND DISCUSSION

Concrete and Repair Mortar Properties

The ASTM C39 standard test method was used to determine the compressive strength of the cylindrical samples of substrate concrete [22], and the ASTM C109 standard test for compressive strength of the OPCM and PMC mortar samples [23]. Following a 28-day curing period, compressive strength tests were conducted on the samples of repair materials and concrete substrates in the laboratory.

The three different types of materials resulted in different strength outcomes that correlated with the designed w/c ratios. The graph in Fig. 5 displays the average compressive strength for OPCM and PMC mortar, as well as substrate concrete, with OPCM having the highest strength at 71.08 MPa, followed by PMC mortar at 44.8 MPa, and substrate concrete at 31.06 MPa.

Concrete and repair mortars were mixed at temperatures between 22 °C and 30 °C to evaluate workability, placement ease, repair suitability, and surface bonding. Table 4 outlines the mixing method for fresh concrete, applied consistently across all RC beam specimens, with comparable results. All samples were cured and tested after 28 days.

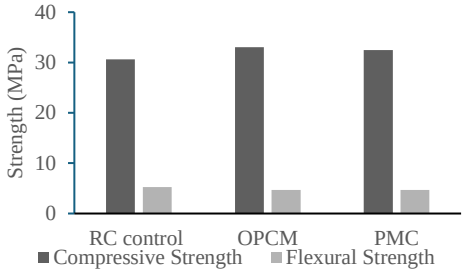

Fig. 6. Physical properties of concrete

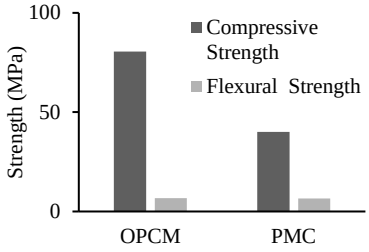

Fig. 7. Physical properties of repair mortar

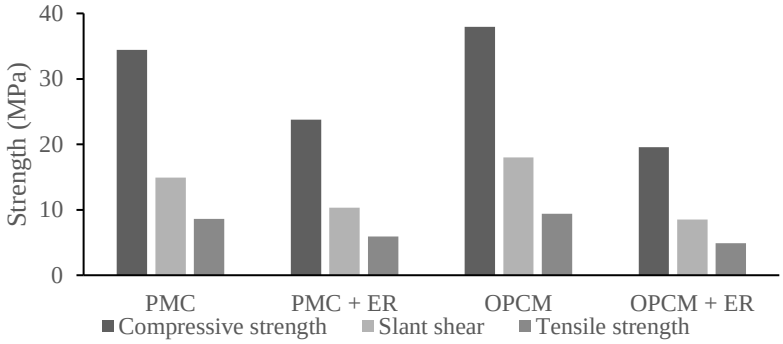

Fig. 8. Mechanical properties of slant shear

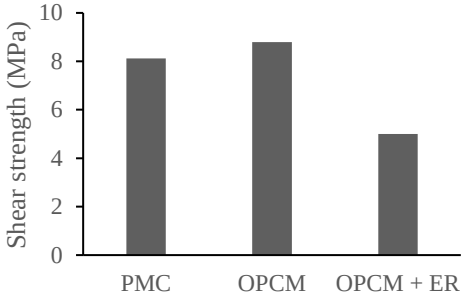

Fig. 9. Double shear results

To ensure consistency, repair mortar temperatures were carefully controlled, as shown in Table 5. Room temperature during casting varies with outdoor conditions, affecting mortar temperature based on the initial temperatures of aggregates and cement. This influenced casting and curing conditions. The flow rate [23] of fresh repair mortar, indicating workability, was highest for OPCM, showing excellent fluidity, while PMC achieved an acceptable 146 mm per the manufacturing guidelines. The flow rate results remained suitable for repair applications. Samples were prepared to test repair mortar properties, and compressive and flexural strength samples followed ASTM standards. All samples were cured and tested after 28 days.

Fig. 6 presents the average compressive and flexural strengths of concrete specimens at 28 days. The experimentally measured compressive strength closely aligned with the values predicted by the mix design for the RC beam concrete, indicating the accuracy of the mix design. Flexural strength [25] remained consistent among the specimens, with average values of approximately 30 MPa for compressive strength and 5 MPa for flexural strength. Fig. 7 compares the compressive strength of cylindrical specimens and the flexural strength of cubic specimens for repair mortars. OPC-based mortars demonstrated greater compressive strength than PMC mortars. However, in terms of flexural strength, both OPCM and PMC exhibited comparable performance.

Concrete Bond and Shear Strength

Slant shear strength

Fig. 8 shows the test results for compressive strength, slant shear strength, and tensile strength at the interface between the concrete substrate and repair materials.

Compressive strength was calculated using Equation (1). For the joint between the concrete substrate and PMC mortar, the compressive strength was 34.4 MPa. However, when ER was used at the interface, the strength dropped by 35% to 23.8 MPa. Similarly, the concrete–OPCM joint had a compressive strength of 38.0 MPa, which decreased to 19.6 MPa with the use of ER.

When compressive load is applied to cylindrical specimens, it generates slant shear and tensile stresses at the rough interface. Bond strength, determined using Equation (2), was 14.9 MPa for PMC mortar, but decreased to 10.3 MPa with ER. OPCM showed the highest bond strength of 18.0 MPa, which dropped to 8.5 MPa when epoxy was used.

Tensile strength, calculated with Equation (3), was 8.6 MPa for PMC mortar and decreased to 5.9 MPa with epoxy. OPCM again had the highest

Table 7. The physical properties of RC beam specimens

Type of RC	Cracking load (kN)	Max. load (kN)	Deflection at max. load (mm)	Failure mode
RC-Control	25	122.9	12	Flexural
RC-OPCM	25	126.9	14.7	Flexural and shear
RC-OPCM-ER	26	118.7	15.3	Flexural and shear
RC-PMC	37	107.5	14.2	Flexural and shear
RC-PMC-ER	35	119.5	14.3	Flexural and shear

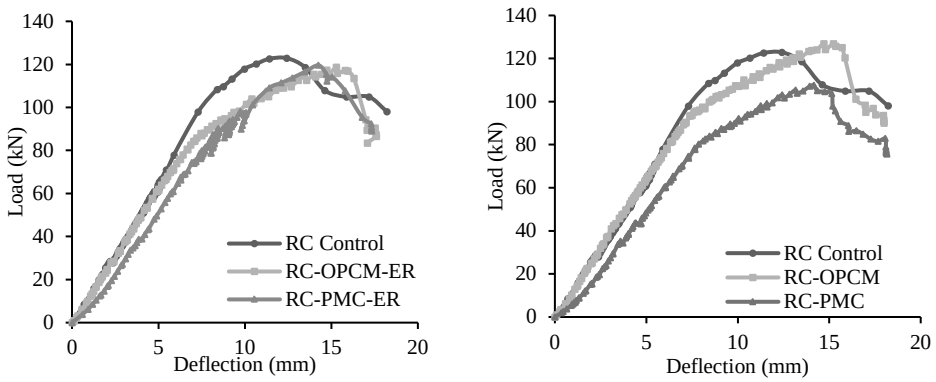

a). RC Specimens with ER b). RC Specimens without ER

Fig. 10. Load deflection relationship

tensile strength at 9.4 MPa, reducing to 4.9 MPa when ER was applied.

Double shear strength

Specimens with a vertical interface were tested under a single axial load to evaluate bonding between the concrete substrate and repair materials. Using Equation (4), the average bond strength for PMC mortar was 8.1 MPa, while OPCM achieved 8.8 MPa. In contrast, concrete substrates with ER and cement mortar had the lowest bond strength at 5 MPa. Fig. 9 shows that PMC mortar and OPCM outperformed ER-mixed repair mortar in bond strength.

Flexural Loading Test

Load and deflection

The load-deflection responses of the beam specimens, both with and without ER, are presented in Fig. 10. These responses are associated with the physical properties of the RC beam specimens listed in Table 7. The behavior of the beams was nearly linearly elastic up to the initial cracking load, which ranged from 24 to 28 kN for the RC OPCM specimens, including the RC control. The data indicate that the RC-PMC specimens exhibited a higher initial cracking load.

The RC-OPCM specimens demonstrated superior performance in terms of both deflection and maximum load. Regarding stiffness, the RC control and RC-OPCM specimens showed comparable behavior up to the yield load. Beyond this point, the RC control specimen exhibited higher stiffness, whereas the RC-OPCM specimen demonstrated

Fig. 11. Crack distribution of RC beam specimens

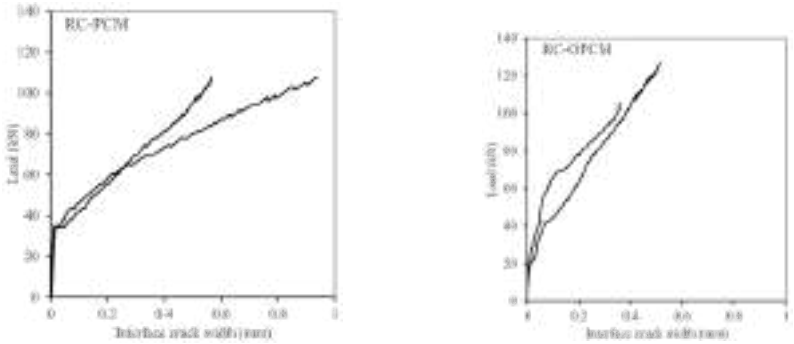

a) Without ER treatment

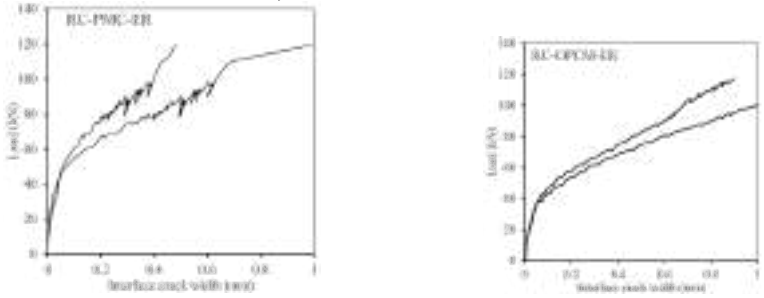

b) With ER treatment

Fig. 12. Interface crack width distribution of RC beam specimens at the bottom

improved ductility. All specimens with ER, including RC PMC, exhibited enhanced ductility.
In the RC control specimen, failure occurred in a flexural manner. However, in the repaired specimens, shear cracking was observed following the initiation of flexural cracks. This indicates a trade-off between stiffness and ductility. Such behavior is particularly beneficial for structures subjected to dynamic or seismic loading, where ductility and energy absorption are critical.

The results highlight the effectiveness of OPCM, especially when combined with ER applied to the bonding surface, in improving ductility while maintaining a load-carrying capacity comparable to that of the RC control. Additionally, the contribution of external reinforcement helps reduce stiffness degradation and enhances deformation capacity.

Crack opening

Fig. 11 shows crack propagation, spacing, and total crack count in RC control and repaired beam specimens. The RC control had many cracks with flexural failure and uneven distribution. Repaired beams were divided into two groups: one treated with ER and one without (RC-OPCM). The RC-OPCM group had more cracks than the PMC-treated group but fewer than the RC control, showing the treatments were effective. Additionally, following the initiation of flexural cracks, shear cracks were observed in all samples with and without ER treatment. The group treated with ER showed behavior similar to the RC beam specimens without ER. Although the use of ER reduced the number of cracks, the reduction was not statistically significant. While epoxy improved crack control, it did not eliminate crack formation.

The transducers were installed at three positions: the bottom, center, and either the left or right side. Each position was equipped with two transducers that were used to measure the opening of the joint between the repaired mortar and damaged concrete of the RC beam specimens. Data obtained from each transducer was used to determine the degree of bonding between the two materials. Fig. 12 illustrates the development of bond interface openings beneath the RC beam specimens in response to applied loading. The results indicate that RC-OPCM specimens, both with and without ER treatment, exhibited early crack initiation at an applied load of approximately 20 kN. In contrast, the RC-PMC specimens, regardless of ER application, demonstrated significantly higher resistance to cracking, with initial crack openings occurring only at loads exceeding 30 kN. Notably, across all repaired specimens, the crack widths remained limited to less than 1 mm, even as the applied load approached 100 kN.

An additional transducer recorded a similar response; however, a localized crack opening developed following the initiation of the first crack beneath the transducer. The crack location along the RC beam specimen influenced the extent of this opening
These findings highlight the significant influence of material composition and treatment on crack behavior. The application of ER effectively delayed crack initiation and limited the crack width, thereby enhancing the overall performance of the repaired RC beam specimens.

CONCLUSIONS

This study aimed to assess the bond strength and flexural performance of OPCM as a primary repair material, focusing on its effectiveness in restoring bond and flexural strength during the repair process. Two types of repair specimens were tested: those repaired without ER and those repaired with ER at their connection. Based on the results and discussion, the following conclusions were drawn:

- Bond strength experiments demonstrated that OPCM achieved significantly satisfactory performance for repair applications compared to PMC.
- RC beam specimens, encompassing control, ER-treated, and non-ER-treated types, exhibited peak load capacities ranging from 105 to 130 kN; notably, ER-treated beams demonstrated enhanced pre-failure behavior, particularly in terms of crack control and ductility.
- ER effectively mitigated crack severity and propagation, delaying crack growth and contributing to the structural integrity of the repaired specimens. However, the strength of the bond formed by ER with repair materials and concrete substrates was found to be variable and, in some cases, potentially lower than repairs undertaken without ER, depending on the degree and timing of the ER application.
- The midspan of the beams was observed to be the most prone to cracking, which is consistent with anticipated flexural behavior.
- The application of cemented repair material to a homogeneous concrete substrate in RC beam specimens was effective for the initial repair stage. Transducer measurements indicated that, before subsequent performance testing, crack openings in all repaired specimens were consistently addressed to approximately 1 mm

REFERENCES

[1] Mehta. P. K. and Monteiro P. J. M. “Concrete: Microstructure, Properties, and Materials, 4th Edition,”2014, pp. 287–290
[2] Neville, “Properties of Concrete”, 5th ed., Pearson, 2011. pp. 1–7

[3] World Bank. “Infrastructure in developing countries: An overview of needs and the financing gap.” World Bank Report, 2019, pp 61- 89.
[4] Jill W. “Informality in the construction sector in developing countries,” Construction Management and Economics, Vol 25, Issue 1, 2007, pp 87-93.
[5] Peter H. E. and Alexander M. V., “Performance criteria for concrete repair materials: phase 1” Technical report REMR-C5-47, Structural Preservation Systems, Inc., 1995, pp 7-13.
[6] Mohammadsoroush T., “Strategizing Sustainable Infrastructure Asset Management in Developing Countries, Proceedings: ASCE International Conference on Sustainable Infrastructure, 2017, pp 375-387
[7] Xuemin S., Xiongfei S., Hao L., Haoliang H., Kasimova G. A., Nurmirzayev A. D. U., Yi H., Jie H., Jiangxiong W., and Qijun Y., “Cement-Based Repair Materials and the Interface with Concrete Substrates: Characterization, Evaluation and Improvement.” Polymer, Vol. 4, Issue 7, 2022, pp 1485.
[8] ACI Committee 546, Concrete Repair Guide, ACI 546R-14, American Concrete Institute, 2014, pp 34-45.
[9] Khuram R., Ueda T., Dawei Z., Miyaguchi K., and Nakai H., “Experimental and analytical investigations on the behavior of interface between concrete and polymer cement mortar under hygrothermal conditions” Construction and Building Materials Vol. 94, 2015, pp 414-425
[10] Suarez-Riera D., Restuccia L., Falliano D., Ferro G. A., Tuliani J. M., Pavese M. and Lavagna L., "An Overview of Methods to Enhance the Environmental Performance of Cement-Based Materials" infrastructures, Vol. 9, Issue 6, 2024, pp 94.
[11] Daneshvar D., Deix K., and Robisson A., "Effect of casting and curing temperature on the interfacial bond strength of epoxy bonded concretes," Construction and Building Materials Vol. 307, 2021, pp. 124328.
[12] Kaur M., Chawla H., and Kwatra N., "Effect of different surface preparation techniques on the bond behavior of normal and fiber-reinforced geopolymer concrete" Construction and Building Materials, Vol. 417, 2024, pp 135252.
[13] Santos Pedro. M. D., and Julio Eduardo N.B.S "Review: A state-of-the-art review on roughness quantification methods for concrete surfaces" Construction and Building Materials, Vol. 38, 2013, pp 912-923
[14] Sahmaran M., Lachemi M., Hossain K., and Li V., "Internal curing of engineered cementitious composites for prevention of early age autogenous shrinkage cracking," Cement and Concrete Research, Vol. 39, Issue 10, 2009, pp. 893–901.
[15] RILEM Technical Committee TC 193-RLS, "Bonded cement-based material overlays for the repair, the linings or the strengthening of slabs or pavements," Springer, 1st edition, 2011, pp. 51-79.
[16] Su N., Lou L., Amirkhanian A., Amirkhanian S. N., Xiao F., "Review: Assessment of effective patching material for concrete bridge deck" Construction and Building Materials, Vol 293, 2021, pp 123520.
[17] Madeira B. L., Fernandes A., Yoshitake I.. "Experimental study on the bond strength between repair mortar and concrete substrate," GEOMATE journal, Vol. 26, no. 118, 2024, pp. 41-48.
[18] ASTM C882/C882M-20 Standard test method for bond strength of epoxy-resin systems used with concrete by slant shear.
[19] Austin S, Robins P, and Youguan P. “Shear bond testing of concrete repairs” Cement Concrete Research, Vol. 29, 1999, pp.1067–1076.
[20] JSCE (Japan Society of Civil Engineers). Method of test for shear strength of steel fiber reinforced concrete (SFRC). JSCE SF-6,1990.
[21] ACI committee 318 “Building code requirements for structural concrete ACI 318-11 and commentary”, American Concrete Institute, 2011, pp 137-162.
[22] ASTM C39 Standard test method for compressive strength of cylindrical concrete specimens. West Conshohocken, 2017.
[23] ASTM C109 Standard Test Method for Compressive Strength of Hydraulic Cement Mortars, West Conshohocken, 2017.
[24] ASTM C230., Standard Specification for Flow Table for Use in Tests of Hydraulic Cement, West Conshohocken, 2017.
[25] ASTM C-78-02., Standard test method for flexural strength of concrete (using a simple beam with third-point loading), West Conshohocken, 2017.

Copyright © Int. J. of GEOMATE All rights reserved, including making copies, unless permission is obtained from the copyright proprietors.

15th Int. Conf. on Geotechnique, Construction Materials & Environment,
Kyoto, Japan, 11-13 November 2025, ISBN 978-4-909106124 C3051

SUSTAINABLE SOIL IMPROVEMENT: THE SYNERGISTIC EFFECTS OF BASALT FIBER AND RICE HUSK ASH ON THE ONE-DIMENSIONAL CONSOLIDATION

Nguyen Thi Hong Nhung* and Zakaria Hossain

Department of Environmental Science and Technology, Mie University, Japan

ABSTRACT

This review examines the role of basalt fiber (BF) and rice-husk ash (RHA)–cement composites in enhancing the one-dimensional consolidation behavior of problematic soils. It focuses on three mechanisms: (1) the stress-redistribution through the three-dimensional network structure of basalt fiber; (2) the pore-filling and pozzolanic reaction effects of RHA–cement mixtures; and (3) the combined impact on the time-dependent compressibility, including changes in the volume-change coefficient (m_v) and coefficient of consolidation (c_v). These sustainable materials enhance consolidation performance while reducing environmental impact through the waste utilization and lower carbon emissions, offering both theoretical insight and practical guidance for geotechnical applications.

Keywords: Basalt fiber, Rice husk ash, Cement composites, One-dimensional consolidation, Sustainability

INTRODUCTION

The stabilization of weak soils, particularly soft and expansive clays remains a major challenge in geotechnical engineering due to their low-bearing capacity, high compressibility and long consolidation times, which often cause costly delays and structural problems [3]. Traditional stabilization using high doses of Ordinary Portland Cement (OPC) or lime effectively improves soil strength and reduces volume changes, but these methods contribute significantly to CO_2 emissions [28]. Moreover, these conventional approaches do little to valorize the vast quantities of agricultural and industrial byproducts that are otherwise destined for landfills or open burning [29].

A hybrid stabilization approach combining chopped basalt fibers, RHA, and reduced cement content offers an economically and environmentally sustainable alternative [30]. Basalt fibers improve tensile resistance and mitigate microcracking [3]. Concurrently, RHA's pozzolanic reaction with limited OPC produces calcium-silicate-hydrate (C-S-H) gels that enhance early strength and pore filling [13]. Laboratory studies have demonstrated that these composites achieved comparable consolidation characteristics to conventional high-cement mixes while reducing embodied carbon and cost.

This review paper synthesizes laboratory results focusing on one-dimensional consolidation, illustrating how basalt fibers and RHA-cement composites improve key parameters such as volume-change coefficient (m_v) and coefficient of consolidation (c_v), yield pressure, compression index and swelling index. Practical aspects including mix designs, environmental benefits and field implementation challenges are addressed.

This study investigates the consolidation behavior of reconstituted expansive clay reinforced with basalt fibers and RHA-cement mixtures. Oedometer tests were conducted to evaluate the influence of fiber length, RHA content and cement dosage on yield stress, compression and swelling characteristics, aiming to determine optimal mix designs for engineering applications.

MATERIALS AND METHODOLOGY

Materials

The materials utilized in this study comprised primarily clay soils as the base material, reinforced with supplementary materials including rice husk ash (RHA), basalt fibers (BF) and Ordinary Portland Cement (OPC).

Soil

The base expansive clay soil, sourced from Mie Prefecture, was air-dried, ground to pass a 2 mm sieve, and characterized by a liquid limit of approximately 60 % and a plasticity index near 32 %. Clay soil is a type of fine-grained soil composed primarily of hydrated silicate minerals. Due to its small particle size and high plasticity, clay often exhibits low shear strength, high compressibility, and significant volumetric changes under loading or moisture variation [1,2]. The index properties of the soil are shown in Table 1. These unfavorable geotechnical properties limit its direct use in construction without

proper improvement or stabilization.

Table 1 Properties of Soil [3]

Property	Value
Specific gravity	2.74
Sand (75 μm–2 mm) (%)	6.14
Silt (5 μm–75 μm) (%)	51.24
Clay (<5 μm) (%)	38.86
Liquid limit LL (%)	58.21
Plastic limit PL (%)	31.05
Plasticity index PI (%)	27.16
Optimum water content (%)	26.02
Maximum dry density (g/cm3)	1.65

Ordinary Portland cement (OPC)

The index properties of the OPC are shown in Table 2. OPC is a widely used hydraulic binder in soil stabilization and construction materials. It is produced through the calcination of limestone and clay [4,5]. When mixed with water, Portland cement undergoes hydration reactions that transform it from a dry powder into a hardened material with high compressive strength, making it essential for enhancing the mechanical behavior of weak soils. In this review paper, OPC was added at 3 % by dry weight to activate the pozzolanic reactions.

Table 2 Properties of Ordinary Porland cement [6]

Property	Value
SiO_2 (%)	20.81
Al_2O_3 (%)	5.41
CaO (%)	62.3
MgO (%)	0.97
Fe_2O_3 (%)	3.72
SO_3 (%)	3.07
$Na_2O + K_2O$ (%)	0.43
Density (gr/cm3)	3.17

Rice Husk Ash

RHA was produced by the self-combustion of rice husks at 650 °C for 27 hours, yielding a finely divided ash with a highly reactive amorphous silica content ranging between 85% and 91%. Rice husk ash (RHA) is an agricultural byproduct obtained by controlled combustion of rice husk. It is rich in amorphous silica (SiO_2), which provides high pozzolanic reactivity when mixed with cementitious materials [7,8]. The incorporation of RHA into soil-cement mixtures improves strength, reduces permeability, and enhances durability by filling voids and refining the microstructure. Additionally, using RHA as a partial cement replacement promotes environmental sustainability by recycling agricultural waste and reducing CO_2 emissions associated with cement production base expansive clay soil, sourced from Mie Prefecture, was air-dried, ground to pass a 2 mm sieve, and characterized by a liquid limit of approximately 60 % and a plasticity index near 32 %. Clay soil is a type of fine-grained soil composed primarily of hydrated silicate minerals. Due to its small particle size and high plasticity, clay often exhibits low shear strength, high compressibility, and significant volumetric changes under loading or moisture variation [1,2]. These unfavorable geotechnical properties limit its direct use in construction without proper improvement or stabilization. The properties of the RHA and the particle size distribution are shown in Table 3.

Table 3 Properties of Rice Husk Ash [9]

Property	Value
Fineness passing 45 micron (%)	96
SiO_2 (%)	87.20
Al_2O_3 (%)	0.15
Fe_2O_3 (%)	0.16
CaO (%)	0.55
MgO (%)	0.35
SO_3 (%)	0.24
C (%)	5.91
Loss on ignition (%)	5.44
Pozzolanic activity (%)	84
Particle size (μm)	7

Basalt Fiber

In this review paper, basalt fibers measuring between 6-30 μm in diameter, were chopped into lengths of 3, 6, or 12 mm and introduced at 1 % by the dry weight of the soil. Basalt fiber (BF) is an inorganic fiber produced by melting natural basalt rock at temperatures of approximately 1450–1500°C, followed by extrusion into continuous fibers without chemical additives.

Basalt fibers exhibit high tensile strength (2000–

4000 MPa), high modulus of elasticity (80–95 GPa), and excellent resistance to alkalis, acids, and elevated temperatures. When incorporated into soil or cementitious mixtures, basalt fibers act as reinforcement materials, increasing tensile resistance, controlling deformation, and limiting crack propagation. Due to its natural origin, non-toxic production process, and recyclability, basalt fiber is considered an environmentally friendly alternative to synthetic fibers [10]. The detail physical, thermal and chemical properties of BF are shown in Table 4.

Table 4 Properties of Basalt Fiber [11]

Property	Value
Breaking Strength (Mpa)	3000 - 4840
Modulus of Elasticity (Gpa)	79.3 - 93.1
Breaking Extension (%)	3.1
Fiber Diameter (μm)	6 - 21
Linear Density (tex)	60 - 4200
SiO_2 (%)	52.8
Al_2O_3 (%)	17.5
Fe_2O_3 (%)	10.3
MgO (%)	4.63
CaO (%)	8.59
K_2O (%)	1.46
TiO_2 (%)	1.38
P_2O_5 (%)	0.28
MnO (%)	0.16
Cr_2O_3 (%)	0.06

Overall, the combination of clay, Portland cement, rice husk ash, and basalt fiber has the potential to create stabilized soil mixtures with enhanced engineering properties suitable for construction applications requiring improved strength, reduced compressibility, and greater durability.

Methodology

Standard proctor compaction test

The standard Proctor compaction test was carried out in accordance with JIS A 1210:2010 to determine the maximum dry density (MDD) and optimum moisture content (OMC) of the prepared mixtures. In this study, the term sample refers to the blended material comprising soil, RHA, cement, and basalt fiber at various mix ratios. Each mixture was compacted into a mold with a diameter of 10 cm and a height of 12.68 cm, in three layers. Compaction was achieved using a 2.5 kg rammer dropped from a height of 30 cm, applying 25 blows per layer to ensure uniform compaction. After compaction, a representative specimen was collected to measure the moisture content. This procedure was repeated for each increment of added water to obtain the compaction curves.

One-dimensional consolidation test

One-dimensional consolidation tests were carried out to evaluate the compressibility characteristics of the soil samples. Each specimen was placed in a rigid oedometer ring to prevent lateral deformation, ensuring vertical compression only. The samples were subjected to incremental loading, where the applied pressure was doubled at each stage (9.8, 19.6, 39.2, 78.5, 157, 314, 628 and 1256kPa). At each load increment, the settlement was recorded over time until the primary consolidation was considered complete, as indicated by minimal changes in deformation. After reaching the maximum load, the samples underwent unloading in reverse order to determine their swelling behavior and recompression characteristics. This loading and unloading procedure provided data to calculate coefficient of volume compressibility (m_v), and coefficient of consolidation (c_v), which are essential parameters for predicting settlement behavior under foundation loads [12].

The formulas for calculating the coefficient of consolidation (c_v) and the coefficient of volume change (m_v) are presented as follows:

Coefficient of consolidation (c_v):

$$c_v = 0.197\left(\frac{\bar{H}}{2}\right)^2\left(\frac{1440}{T50}\right)$$

Coefficient of volume change (m_v):

$$m_v = \frac{\Delta\varepsilon/100}{\Delta p}$$

RESULTS AND DISCUSSION

Literature review results

The comparison of results from previous studies considering different materials and soil type, is presented in Table 5.

Table 5 Literature review

Reference	Materials	Type of Soil	Results
[3]	S + RHA + Cement + BF	Clay Soil	Increasing basalt fiber length (3→12 mm) reduces consolidation coefficient cv, especially at 5-10% RHA, while slightly decreasing permeability k
[12]	S + RHA +Cement	River Sludge	The 10% RHA and 6% cement mixture enhances the yield pressure (σ' = 125 kN/m²), reduces the compression index (c_c) and swelling index (c_s) of river sludge by 70%
[13]	S + RHA + Cement + BF	Clay Soil	Adding basalt fibres to RHA-treated clay improved UCS and stiffness, with the best results from 5% RHA + 3% cement + 1% basalt fibre (12 mm) showing qu = 463 kN/m² and E50 = 29 MN/m² after 28 days
[15]	S + RHA	Clay Soil	At 9% RHA: significantly reduces soil plasticity (liquid limit by 11-18%, plasticity index by 32-80%) and maximum dry unit weight; optimally increases unconfined compressive strength (peaking at 6-8% RHA) and optimum moisture content
[16]	S + RHA	Lateritic soils	Adding RHA (up to 16%) reduces maximum dry density but significantly improves lateritic soil's physical properties and consolidation behavior (increased preconsolidation pressure, decreased C_c, C_s, m_v)
[17]	S + FA	Clay soil	Additives like fly ash (especially Type C), cement, and lime significantly optimize soil properties for construction: enhancing consolidation (reducing swell index by up to 50%), drastically increasing CBR (10x at 16% FA) and strength via pozzolanic reactions.
[18]	S + RHA	Black cotton soil	Treating black cotton soil with 8% rice husk ash (RHA) optimizes compressibility regardless of compaction moisture, while improving plasticity (liquid limit reduced 69.5% → 55%, plasticity index decreased 20%), swelling pressure (77% reduction at 16% RHA), and yielding stress (increased 182 → 261 kN/m²).
[19]	S + FA + Lime	Expansive Soil	30% FA + 4% lime eliminated swelling (100% FSI↓), raised OMC (52-37%↑), reduced density (10-7% MDD↓), boosted CBR, and achieved 286/192 kPa UCS
	S + Wool Waste + Lime		30% wool waste + lime also eliminated swelling but increased density (15-12% MDD↑) while lowering OMC (30-19%↓) yet improving CBR
[20]	S + RHA	Lateritic Soil	Adding 10% RHA to lateritic soil (SW) increases OMC, enhances volume stability and CBR, while decreasing MDD and plasticity index
[21]	S + Cement	Clay Soil	Cement at ~5% optimally enhances clay's dry density/UCS while reducing plasticity/permeability
[22]	S + RHA + PA + Cement	Clay Soil	RHA/PA reduce MDD and increase OMC while acting as pozzolanic cement substitutes. Optimal stabilization: 4% cement + 10% RHA + 40% PA yields peak CBR.

[23]	S + Polypropylene Fiber + Fly ash and Ground-Granulated Blast Furnace	Black cotton soil	the fibre content increased from 0% to 0.4%, the tensile strength and CBR of the AAB-treated soil increased by 63.1% and 52.6%, respectively, while the void ratio and swelling pressure decreased by 33% and 45%. Replacing 30% of fly ash with GGBS at a fibre content of 0.3% also significantly increased the CBR and UCS
[24]	S + PPF + NMK (Nano meta kaolin)	Expansive Soil	Replacing 20% NMK combined with 1% PPF fibers optimizes the strength of stabilized soil, reducing lime consumption by > 40% through effective cementitious gel formation and fiber tensile resistance
[25]	S	Clay slurries	The fine-grained clay slurry (w_L=180%, w_P=120%) its coefficient of consolidation (c_v) and coefficient of volume compressibility (m_v) decreased with increasing stress but increased with increasing void ratio and permeability
[26]	S + Cement	Soft clay	Excess pore pressure distributes uniformly between columns and clay. Settlement can be reliably predicted using the composite coefficient c_v via a simplified procedure suitable for geotechnical engineering

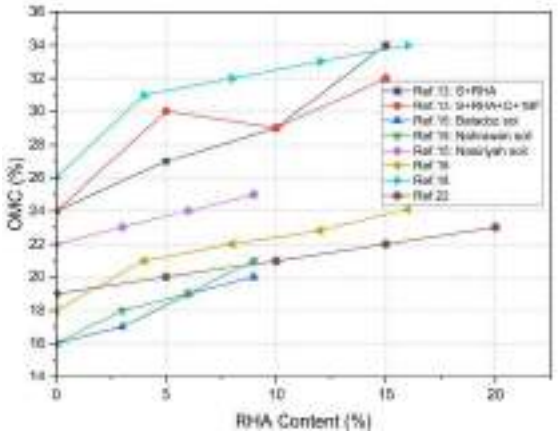

Fig.1 Optimum moisture content for soils mixed with different percentages of rice husk ash. [13, 15, 16, 18, 22]

The incorporation of RHA into soil mixtures consistently shifts the compaction curve toward higher optimum moisture contents (OMC), a behavior attributable to the highly porous nature and strong hygroscopicity of RHA particles (Fig.1). In soil + RHA systems studied by Owino et al. [13], OMC rose sharply from 24 % at low RHA contents to as much as 34 % at 16 % RHA, while a parallel investigation by Eberemu and Sada [18] reported an increase from 26 % up to 34 % over the same RHA range. This marked increase underscores RHA's capacity to absorb and retain moisture, necessitating additional water to achieve target compaction levels.

When RHA is combined with cement and BF, the moisture demand remains elevated but is notably tempered. In the soil + RHA + cement + BF mixtures of Owino et al. [13], the OMC plateaued between 30 % and 32 %, whereas Eberemu and Sada [18] observed a somewhat broader range of 26 % to 34 %. The presence of hydraulic binders appears to occupy some of RHA's pore volume and alter the fabric of the compacted matrix, thereby moderating but not eliminating the need for extra water.

Gupta and Kumar [22] documented an intermediate OMC response (19 %–23 %), suggesting their RHA source possessed a more balanced pore-size distribution or was partially stabilized prior to mixing. In contrast, natural soils without RHA incorporation exhibited stable OMC values (16 %–20 % and 22 %–25 % across two soil types in [15]), confirming that the moisture-demand shift is driven by RHA's intrinsic properties rather than test methodology.

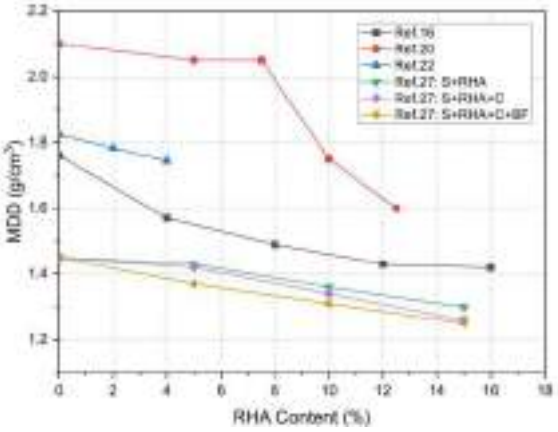

Fig.2 Variation of Maximum Dry Density with Rice Husk Ash content. [16, 20, 22, 27]

As shown in three independent investigations, the incorporation of RHA at contents up to 16% by weight leads to a systematic decline in maximum dry density (MDD), reflecting the lower specific gravity of RHA relative to conventional soils or binding agents (Fig.2). In the study by Eberemu [16], MDD decreased from approximately 1.76 g/cm³ (0 % RHA) to 1.42 g/cm³ (16 % RHA), indicating a loss of bulk mass as lightweight RHA displaced denser soil particles. Okafor and Okonkwo[20] observed an even more pronounced reduction, with MDD falling from about 2.10 g/cm³ to 1.60 g/cm³ over the same RHA range, suggesting that both the soil's mineralogy and the RHA's physical characteristics can amplify density loss. Gupta and Kumar [22] reported a subtler decrease, from 1.825 g/cm³ down to 1.744 g/cm³, which may be attributed to their lower initial soil density and possibly different compaction energy or moisture content. In the reported by Alex [27], the mixture of S+RHA+C and S+RHA+C+BF exhibits lower MDD compared to S+RHA, this suggests that the addition of additives may enhance the reduce in MDD.

These inter study variations highlight the sensitivity of compaction behavior to soil composition, compaction methodology (e.g., Proctor effort, moisture control), and RHA properties (particle size distribution, porosity). The consistently observed trend: that higher RHA dosages reduce MDD, underscores the need to adjust compaction parameters when designing RHA modified soil mixes to meet target density requirements. Further research into the interaction between RHA particle morphology and soil fabric could clarify the mechanisms governing these density reductions and optimize mix designs for geotechnical applications.

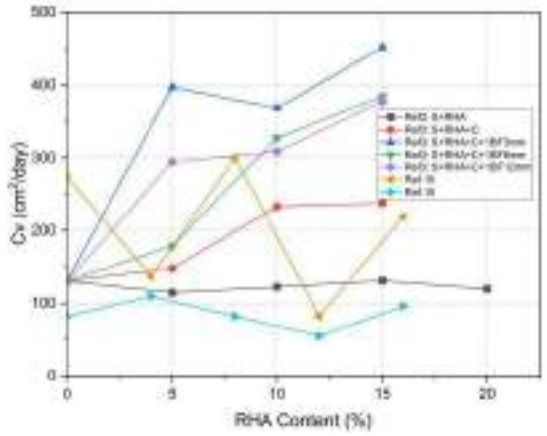

Fig.3 Variation of coefficient of consolidation with rice husk ash content for optimum moisture content. [3, 16, 18]

Across multiple investigations, increasing rice husk ash (RHA) content consistently accelerates soil consolidation (c_v) by enlarging the pore network with lightweight, porous ash (Fig.3). In unmodified soil–RHA blends [3], c_v climbs from ~120 cm²/day at 0 % RHA to ~400 cm²/day at 15 % RHA, then falls back at 20 % as excessive ash disrupts drainage continuity.

When cement is added [3], the rise in c_v is tempered, increasing from ~110 cm²/day to ~250 cm²/day at 15 % RHA because the binder fills some ash pores and stiffens the matrix. Introducing basalt fibers further alters drainage: all fiber reinforced mixes peak between 10–15 % RHA, with 3 mm fibers reaching ~450 cm²/day, as fine fibers most effectively sustain micro channels under load.

Distinct behaviors in other studies underscore RHA's sensitivity to testing conditions: [16] shows a transient spike to ~1,400 cm²/day at 7 % RHA (likely due to coarse ash or moisture variations), whereas [18] records a nearly constant c_v (~80–100 cm²/day) across all RHA contents. These outcomes highlight the need to optimize binder content, fiber reinforcement, and compaction parameters for balanced drainage and strength in RHA amended soils.

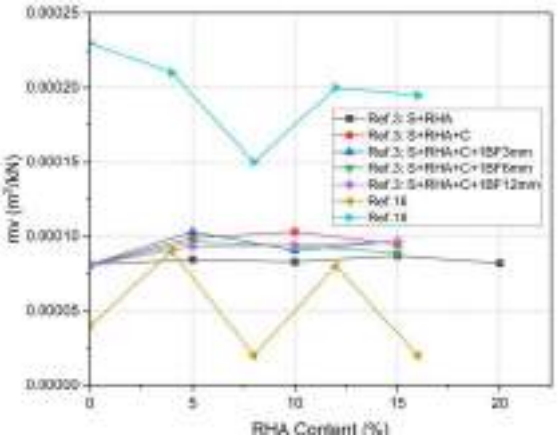

Fig.4 Variation of coefficient of volume compressibility with rice husk ash content for optimum moisture content. [3, 16, 18]

Across all investigations, the coefficient of volume compressibility (m_v) tends to rise as rice husk ash (RHA) content increases, reflecting the ash's intrinsic deformability and its effect on soil fabric (Fig.4). In the unmodified soil + RHA system of Eberemu [16], this increase is most dramatic: m_v grows from roughly 0.00002 m²/kN at 0 % RHA to about 0.00009 m²/kN at 15 % RHA. By contrast, the simple S + RHA mixtures in [3] exhibit a gentler climb, with m_v remaining below 0.00010 m²/kN across the entire RHA range.

When cement and basalt fibers are introduced ([3] with S + RHA + C + 1BF), compressibility is substantially curtailed. All three fiber-reinforced blends show m_v values between approximately 0.00007 and 0.00010 m²/kN, but the combination with 12 mm fibers (S + RHA + C + 1BF12 mm)

consistently records the lowest m_v, never exceeding 0.00008 m²/kN, demonstrating that longer fibers better reinforce the pore structure against volumetric collapse.

Eberemu and Sada findings [18] occupy an intermediate position: m_v values start near 0.00023 m²/kN at 0 % RHA, dip to 0.00015 m²/kN at 5 %, then rebound to about 0.00020 m²/kN by 15 %. This nonmonotonic trend suggests that their specific soil mineralogy or RHA processing technique modulates compressibility response.

Collectively, these data confirm that while RHA incorporation inherently increases soil compressibility, the judicious use of hydraulic binders and fiber reinforcement can effectively mitigate this disadvantage, an insight of practical importance when designing RHA-amended geomaterials for load-bearing applications

Discussion

The findings of this study underscore the considerable potential of basalt fiber and rice husk ash (RHA)-cement composites as a sustainable alternative for improving problematic soils, particularly soft clays and expansive soils, which are often prone to excessive settlement, low strength and long consolidation periods [31]. The synergistic effects of basalt fibers' stress-bridging capacity and RHA-cement's pore-filling and pozzolanic reactivity enable simultaneous enhancement of mechanical performance and reduction of environmental impact [27]. This dual benefit addresses both technical limitations and sustainability concerns inherent in conventional stabilization methods that rely heavily on Ordinary Portland Cement (OPC) or lime.

From a practical perspective, the integration of basalt fiber and RHA-cement composites can be implemented across a wide range of geotechnical projects. In embankment construction, the enhanced stress redistribution and lower compressibility can contribute to greater long-term stability, mitigating post-construction settlements that can compromise structural integrity [27]. For road foundations and weak subgrade treatment, the composite ability to limit differential settlement and cracking can significantly extend pavement service life and reduce maintenance requirements [32]. These improvements are particularly advantageous in regions where soft and expansive clays are prevalent and conventional high-binder treatments are economically or environmentally burdensome.

The environmental implications of this approach are equally significant. The utilization of RHA, an agricultural byproduct rich in reactive silica, not only valorizes waste but also reduces OPC demand, thereby lowering CO_2 emissions associated with cement manufacturing. Basalt fibers are derived from naturally occurring volcanic rock and fully recyclable, further enhancing the sustainability credentials of the method by providing durable reinforcement without introducing synthetic polymers or non-biodegradable additives [13]. These attributes align with global initiatives toward low-carbon construction, resource efficiency and circular economy principles [33].

CONCLUSIONS

This review demonstrates that basalt-fibers-RHA-cement composites present a promising, low-carbon alternative for stabilizing problematic soils, particularly soft clays and expansive soils. By leveraging the synergistic effects of basalt fibers for tensile reinforcement and RHA for pozzolanic activity, the approach effectively improves compressibility, swelling behavior and load-bearing capacity while significantly reducing OPC consumption.

From a sustainability perspective, incorporating agricultural byproducts such as RHA and recyclable natural materials like basalt fibers aligns with global initiatives toward greener construction and circular economy principles. The results from laboratory-scale studies suggest that comparable or superior soil performance can be achieved with up to 60% less OPC, lowering both embodied carbon and overall material costs.

FUTURE RESEARCH DIRECTIONS

Despite the clear benefits demonstrated in laboratory settings, the journey toward real-world implementation of basalt fiber–RHA–cement composites demands a deeper exploration of several key areas. First and foremost, long-term durability under environmental cycling must be rigorously assessed. In the field, stabilized soils face repeated wetting and drying, seasonal freeze–thaw cycles, and exposure to aggressive chemicals—such as sulfates in groundwater or chlorides from deicing salts—that can gradually weaken fiber–matrix bonds or alter the stability of pozzolanic C–S–H gel. Accelerated aging tests that simulate decades of environmental fluctuation will be essential to verify that the reinforcing network and cementitious binder maintain their integrity over the service life of an embankment or pavement.

Equally important is the systematic optimization of mix proportions. While a blend of 12 mm basalt fibers, 5 % RHA, and 3 % OPC has emerged as a promising baseline, soils vary widely in mineralogy, grain size distribution, and plasticity. By exploring a

matrix of fiber lengths, fiber dosages, ash contents, and cement percentages, researchers can identify cost-effective formulations tailored to specific site conditions—whether that means treating organic clay beneath a low-volume rural road or stabilizing silty loam for a highway embankment. Such parametric studies not only refine performance but also minimize waste and material expense.

Looking beyond rice-husk ash, the concept of circular-economy stabilization invites the incorporation of other agricultural or industrial byproducts. Fly ash, ground granulated blast-furnace slag, and even biochar offer unique chemical and physical properties that might complement basalt fiber reinforcement. Investigating how these materials interact—both with the soil matrix and with one another—could yield multifunctional composites that make fuller use of local waste streams, reduce reliance on virgin resources, and further lower the carbon footprint of geotechnical construction.

Finally, advanced modeling and simulation techniques stand to accelerate adoption by reducing dependence on extensive trial-and-error testing. Coupled hydro-mechanical finite-element models, informed by microstructural observations (SEM, XRD) and calibrated with consolidation parameters from laboratory oedometer tests, can predict how fiber–ash–cement composites will perform under complex loading patterns and boundary conditions. Discrete-element simulations, in turn, can elucidate the micromechanics of fiber pull-out, crack bridging, and particle rearrangement. Together, these tools will equip engineers with robust, predictive frameworks—enabling confident design of large-scale projects and ultimately paving the way for sustainable soil improvement technologies to become mainstream practice.

REFERENCES

[1] Braja M. Das & Khaled Sobhan (2014). Principles of Geotechnical Engineering, 8th edition.

[2] R.F. Craig (2004). Craig's Soil Mechanics (7th ed).Hossain M.Z., For Chapter in a Book, Soil Mechanics, 4th ed. Vol. 2, Sakai, Ed. Sankeisha Publisher's Name, Year, pp. 11–60.

[3] Owino AO, Hossain Z. Correlation between one-dimensional consolidation coefficients and different basalt fiber lengths and RHA-cement contents in fiber-reinforced stabilized expansive soils. Soils and Foundations. 2023;63(4):101351, https://doi.org/10.1016/j.sandf.2023.101351.

[4] Celik K, Jackson MD, Mancio M, et al. High-volume natural volcanic pozzolan and limestone powder as partial replacements for portland cement in self-compacting and sustainable concrete. Cement and Concrete Composites. 2014;45:136-147, https://doi.org/10.1016/j.cemconcomp.2013.09.003.

[5] Krauss P, Paret T. Review of properties of concrete , 5th ed. , by a. M. Nevilleprentice hall, Pearson, San Francisco, CA; 2012; isbn 0273755803 and 978-0273755807; 846 pp.; $16(Paperback)0 . J Perform Constr Facil. 2014;28(3):630-630, https://doi.org/10.1061/(ASCE)CF.1943-5509.0000595.

[6] Pancar EB. Reducing thermal cracks and mitigating heat island by using glass bead in concrete pavement. IOSR. 2016;13(04):94-98, https://iosrjournals.org/iosr-jmce/papers/vol13-issue4/Version-4/M1304049498.pdf.

[7] Behak L. Soil stabilization with rice husk ash. In: Amanullah, Fahad S, eds. Rice - Technology and Production. InTech; 2017, https://www.intechopen.com/chapters/53281.

[8] N. Monika Chanu, Dr. Th. Kiranbala Devi, 2013, Contribution of rice husk ash to the properties of cement mortar and concrete, International Journal of Engineering research & technology (IJERT) Volume 02, Issue 02 (February 2013).

[9] Ramasamy V. Compressive strength and durability properties of Rice Husk Ash concrete. KSCE Journal of Civil Engineering. 2012;16(1):93-102, https://doi.org/10.1007/s12205-012-0779-2.

[10] Fiore V, Scalici T, Di Bella G, Valenza A. A review on basalt fiber and its composites. Composites Part B: Engineering. 2015;74:74-94, https://doi.org/10.1016/j.compositesb.2014.12.034.

[11] Dhand V, Mittal G, Rhee KY, Park SJ, Hui D. A short review on basalt fiber reinforced polymer composites. Composites Part B: Engineering. 2015;73:166-180, https://doi.org/10.1016/j.compositesb.2014.12.011.

[12] Islam MY, Hossain Z. Investigating the one-dimensional consolidation properties of river sludge enhanced by sustainable additive synergy for eco-friendly stabilization. Journal of Building Engineering. 2025;101:111851, https://doi.org/10.1016/j.jobe.2025.111851.

[13] Owino AO, Nahar N, Hossain Z, Tamaki N. Effects of basalt fibres on strength and permeability of rice husk ash-treated expansive soils. J Agric Eng. 2022;53(1), https://doi.org/10.4081/jae.2022.1315.

[14] Otieno Owino A, Nahar N, Hossain Z, Tamaki N. Dimensional influence of basalt fiber reinforcements on the consolidation behaviour of rice husk ash stabilized soils. Construction and Building Materials. 2022;339:127686, https://doi.org/10.1016/j.conbuildmat.2022.127686.

[15] Mohamed Y. Fattah, Salah H. Rahil, Kawther Y. H. Al-Soudan. 2013. Improvement of Clayey Soil Characteristics Using Rice Husk Ash. J. Civil Eng.Urban, 3(1): 12-18.
[16] Eberemu AdrianO. Consolidation properties of compacted lateritic soil treated with rice husk ash. GM. 2011;01(03):70-78.
[17] Noaman MF, Khan MA, Ali K, Hassan A. A review on the effect of fly ash on the geotechnical properties and stability of soil. Cleaner Materials. 2022;6:100151. https://doi.org/10.1016/j.clema.2022.100151.
[18] Eberemu, A.O., Sada, H., 2013. Compressibility characteristics of compacted black cotton soil treated with rice husk ash. Nigerian J.Technol. 32 (3), 507–521.
[19] Nazir O, Kumar A. Stabilization of expansive soils by fly-ash & wool waste. IJIRCST. Published online May 1, 2022:76-82.
[20] F. O. Okafor and U. N. Okonkwo, "Effect of Rice Husk Ash on Some Geotechnical Properties of Lateric Soil," Leonardo Electronic Journal of Practices and Technologies, No. 15, 2009, pp. 67-74.
[21] Rehman Z, Fang X, Rauf M, Chaozhe J. -clayey Soil Stabilization with Ordinary Portland Cement Using the Stabilized Soil as a Mortar. In Review; 2024.
[22] Gupta D, Kumar A. Performance evaluation of cement-stabilized pond ash-rice husk ash-clay mixture as a highway construction material. Journal of Rock Mechanics and Geotechnical Engineering. 2017;9(1):159-169. https://doi.org/10.1016/j.jrmge.2016.05.010.
[23] Syed M, GuhaRay A, Agarwal S, Kar A. Stabilization of expansive clays by combined effects of geopolymerization and fiber reinforcement. J Inst Eng India Ser A. 2020;101(1):163-178.
[24] Pashabavandpouri MA, Goodarzi AR, Lajevardi SH. Enhancing the mechanical and microstructural properties of expansive soils using industrial waste, nano-material and polypropylene fibers: a comparative study. Int J of Geosynth and Ground Eng. 2023;9(4):54.
[25] Khan FS, Azam S. Determination of consolidation behaviour of clay slurries. International Journal of Mining Science and Technology. 2016;26(2):277-283. https://doi.org/10.1016/j.ijmst.2017.06.010.
[26] Horpibulsuk S, Chinkulkijniwat A, Cholphatsorn A, Suebsuk J, Liu MD. Consolidation behavior of soil–cement column improved ground. Computers and Geotechnics. 2012;43:37-50.
[27] Otieno Owino A. Development of sustainable structural materials using Basalt Fiber and Agricultural waste in cementitious system for ground improvement.
[28] Potgieter JH. An Overview of Cement Production: How "green" and sustainable is the industry? *EMSD*. 2012;1(2). https://doi.org/10.5296/emsd.v1i2.1872.
[29] S. Khan, S. Al-Deen, C.K. Lee, Mechanical and durability behaviours of low carbon concrete: a systematic review, J. Build. Eng. 100 (2025) 111633, https://doi.org/10.1016/j.jobe.2024.111633.
[30] Sandhu, R.K., Siddique, R., 2017. Influence of rice husk ash (RHA) on the properties of self-compacting concrete: A review. Const. Build. Mater. 153, 751–764. https://doi.org/10.1016/j.conbuildmat.2017.07.165.
[31] Saloni, Parveen, Pham TM. Enhanced properties of high-silica rice husk ash-based geopolymer paste by incorporating basalt fibers. Construction and Building Materials. 2020;245:118422. https://doi.org/10.1016/j.conbuildmat.2020.118422.
[32] Abbass M, Singh G. Fatigue analysis of rice husk ash and basalt fibre-based sustainable geopolymer concrete in rigid pavements. *Materials Today: Proceedings*. 2021;45:5014-5022. https://doi.org/10.1016/j.matpr.2021.01.450.
[33] Chaurasiya A, Rana RS. Characterization of eco-engineered hybrid polymer composites: reinforcing epoxy with basalt fibers and recycled biochar from rice-husk for enhanced mechanical and environmental performance. *Composite Interface*. Published online February 6, 2025:1-26. https://doi.org/10.1080/09276440.2025.2462888.

Copyright © Int. J. of GEOMATE All rights reserved, including making copies, unless permission is obtained from the copyright proprietors.

Environment

15th Int. Conf. on Geotechnique, Construction Materials & Environment,
Kyoto, Japan, 11-13 November 2025, ISBN 978-4-909106124 C3051

DATA-DRIVEN APPROACH TO GREENHOUSE GAS MITIGATION: SEM ANALYSIS OF SUCCESS FACTORS AMONG LOCAL GOVERNMENTS IN KHON KAEN, THAILAND

Narongdet Mahasirikul[1], Narongwit Mahasirikul[2] and Sirawit Rattasia[3]

[1]College of Local Administration, Khon Kaen University, Thailand
[2] Faculty of law, Khon Kaen University, Thailand
[3]College of Local Administration, Khon Kaen University, Thailand

ABSTRACT

Climate change is a critical global issue, driven by carbon dioxide (CO_2) emissions from energy consumption, fossil fuels, waste mismanagement, deforestation, industrial production, and unsustainable agriculture. Addressing this crisis requires collaboration across all sectors and strong governance. As part of the global effort to combat climate change, local governments play a crucial role in implementing mitigation strategies. In Khon Kaen, Thailand, a dedicated task force has introduced 27 greenhouse gas (GHG) reduction measures across six sectors: energy efficiency, renewable energy, transportation, waste management, forestry, industrial production, and agriculture. The success of these initiatives depends on how effectively local administrative organizations (LAOs) plan strategies, allocate resources, and foster community engagement. This study systematically investigates key determinants that influence the success of GHG reduction initiatives at the local level. A structured survey of 246 participants from LAOs in Khon Kaen was conducted using a 75-item questionnaire. The data were analyzed using Structural Equation Modeling (SEM) to identify key success factors. The findings identify critical factors influencing the effectiveness of GHG reduction efforts, revealing both structural challenges and opportunities for improvement. These insights serve as a foundation for developing more targeted policies and scalable strategies to strengthen climate mitigation initiatives.

Keywords: Climate Change, Greenhouse Gas Reduction, Environmental Management, Policy Effectiveness, Local Administrative Organizations

INTRODUCTION

Climate change is one of the most serious global challenges today. It has wide-ranging impacts on economic, social, and environmental systems. The Intergovernmental Panel on Climate Change (IPCC) has warned that if greenhouse gas (GHG) emissions continue to rise, the consequences will become more severe. Immediate and joint action across all sectors is necessary [1].

Thailand has committed to reducing its GHG emissions by 40% by 2030 and achieving net-zero carbon emissions by 2065 [2]. Reaching these goals requires collaboration from all sectors, especially local governments. Local Administrative Organizations (LAOs) are closely connected to communities and can lead climate action from the ground up [3].

In recent years, LAOs have been recognized globally as important actors in turning national climate policies into real action at the local level. Their close relationship with communities and ability to adapt to local needs make them effective in responding to climate issues [4]. However, in Thailand, there is still a lack of research that explores the structural factors influencing the success of LAOs, especially studies that use Structural Equation Modeling (SEM) to examine causal relationships [5].

Khon Kaen Province is one of Thailand's leading areas for local climate action. A special task force was created to plan and implement 27 GHG reduction measures across five sectors energy, transport, waste management, forestry, and agriculture [6], [7]. The province aims to reduce GHG emissions by at least 30% by 2030 (Fig. 1).

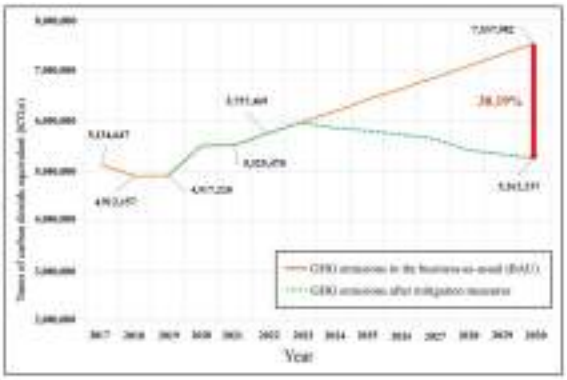

Fig. 1 Khon Kaen GHG emissions reduction by 2030

However, there are several structural challenges. These include centralized decision-making, limited financial capacity, and poor coordination between agencies [8], [9]. In addition, complex bureaucracy and low public participation remain barriers to effective local climate governance [10], [11].

Past studies have pointed out several success factors in local environmental governance. Byrne emphasized the role of social motivation in encouraging community participation [12]. Liu et al. found that creative leadership

and decentralization improve local government performance in developing countries [13]. Yuen et al. noted that centralized systems and the lack of local coordination are key barriers in the ASEAN region [14].

This study aims to identify key success factors in implementing local GHG mitigation actions using Structural Equation Modeling (SEM). Data were collected from 246 representatives of 225 LAOs in Khon Kaen Province. The findings will support policy recommendations that are practical, locally appropriate, and applicable to other areas.

LITERATURE REVIEW

Climate change has emerged as a defining global challenge, with significant emphasis placed on mitigation through policy mechanisms at both national and local levels. The Intergovernmental Panel on Climate Change (IPCC) [1] and the United Nations Framework Convention on Climate Change (UNFCCC) [2] emphasize that local implementation is vital for achieving nationally determined targets. In Thailand, the Department of Local Administration [3] and ICLEI [4] have highlighted the role of Local Administrative Organizations (LAOs) in contributing to climate mitigation through practical action at the subnational level.

Prior research has identified several enabling factors that contribute to effective local environmental governance, such as clarity of institutional mandates, participation from stakeholders, and adequate resource allocation [3], [4], [5]. In the Thai context, Limnirankul and Chompunth [5] point out that LAOs often encounter challenges related to capacity and legal authority yet can succeed when appropriate policy tools and technical support are provided.

From a theoretical perspective, Pressman and Wildavsky [8] emphasize the complexity of policy implementation, requiring alignment between central guidance and local operational capacity. Similarly, Edwards [9] and Sabatier [10] argue that successful execution involves not only organizational structure but also motivation, incentives, and contextual flexibility.

Recent national frameworks such as Thailand's Updated Nationally Determined Contributions (NDCs) [2] and provincial mitigation plans [6] underscore the need for coordination between national strategies and local institutions. Programs such as the Thailand Voluntary Emission Reduction Program (T-VER) and the Low Emission Support Scheme (LESS), led by the Thailand Greenhouse Gas Management Organization (TGO), represent mechanisms to incentivize measurable GHG reductions at the local level [10]. These frameworks and studies collectively highlight the importance of investigating the factors that influence LAO success in implementing climate mitigation policies forming the rationale for this research.

Research Hypothesis

Based on a synthesis of relevant literature and theoretical frameworks covering Management, Motivation, and Leadership combined with Policy Outcome analysis and the application of Structural Equation Modeling (SEM), the following research hypotheses were formulated **(**Fig. 2**)**

H_1: Management has a positive influence on the success of Policy Outcome.

H_2: Motivation has a positive influence on the success of Policy Outcome.

H_3: Leadership has a positive influence on the success of Policy Outcome.

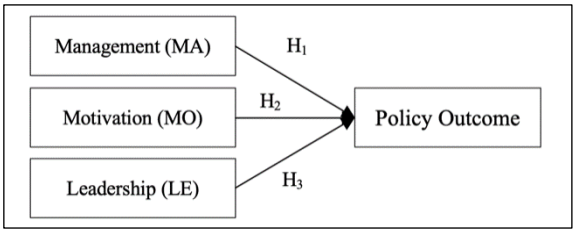

Fig. 2 Research Hypotheses

METHODOLOGY

Research Design

This study adopted a quantitative approach to examine the key factors that influence the success of LAOs in implementing GHG mitigation measures in Khon Kaen Province. The primary analytical tool used in this study is Structural Equation Modeling (SEM), which allows for the analysis of causal relationships between latent variables and observed variables within a single, unified model framework [31].

The use of SEM is appropriate for this study as it enables the simultaneous analysis of multi-dimensional relationships among variables. In addition, SEM provides key model fit indices and estimates both the direction and magnitude of causal effects, making it a systematic and rigorous method for analyzing structural relationships within complex policy environments [31].

Population and Sampling

The population of this study consisted of all LAOs in Khon Kaen Province, totaling 225 entities. These included city municipalities, town municipalities, subdistrict municipalities, and subdistrict administrative organizations.

The sample comprised representatives or executives from each organization who were directly involved in formulating policies or implementing environmental initiatives. A purposive sampling method was employed to ensure the selection of individuals with relevant knowledge and practical experience in GHG mitigation efforts.

A total of 246 respondents completed the questionnaire. This number exceeded the total number of LAOs because some organizations designated more than one representative. This approach was intended to gather more comprehensive and in-depth perspectives on local-level implementation processes and challenges.

The sample size of 246 is considered adequate for Structural Equation Modeling (SEM) analysis, following the guidance of Hair et al. (2022), who recommend a minimum of 200 cases or a ratio of 5 to 10 observations per estimated parameter [32].

Research Tools and Design

The questionnaire used in this study consisted of 75 items and was divided into two main sections. The first section included 66 items (SF1 - SF66) intended to assess key success factors in implementing GHG mitigation policies. These items were categorized into six thematic clusters to ensure comprehensive content coverage, as summarized in Table 1 below. The second section contained 9 items (EF1 - EF9) designed to evaluate policy outcomes such as effectiveness, sustainability, and integration into long-term development frameworks.

All items were rated on a five-point Likert scale ranging from 1 (Strongly Disagree) to 5 (Strongly Agree). Content validity was confirmed through expert review, and the instrument demonstrated high internal consistency (Cronbach's Alpha > 0.80).

Table 1 Questionnaire items

Code	Item
Success factors (Environmental Policy)	
SF1	Clear and easily policy
SF2	Policy supports from the government
SF3	Financial support from the government
SF4	Setting a clear and measurable time frame
SF5	Community and business sector participation
SF6	Effective promotion and supervision
SF7	Prioritize and allocate resources appropriately
SF8	Clear vision and encourage to cooperate.
SF9	Promoting education and training
SF10	Ability to motivate and engage
SF11	Supporting and promoting new innovations.
SF12	Supporting and developing infrastructure.
SF13	Enforcement laws increase incentives for action
SF14	Clear and time-bound rules and regulations
SF15	Inspection and enforcement of the law
SF16	Regulations or laws that clearly define standards
SF17	Providing tax incentives or benefits
SF18	Clear penalties and impacts.
SF19	Clear and systematic plan
SF20	Monitoring and evaluation
SF21	Appropriate resource allocation
SF22	Benefits for all parties in supporting
SF23	Clear goals management and performance monitoring
SF24	Transparent and accountable management
SF25	Public-private collaboration supports success
SF26	Community involvement in decision-making
SF27	Participation in innovation and technology development
SF28	Collaboration in policy and monitoring
SF29	Participation in policy formulation and evaluation
SF30	Multi-sectoral collaboration at local and national levels
SF31	Knowledge and education enhancement for stakeholders
SF32	Sufficient knowledge for practical implementation
SF33	Training and education
SF34	Involvement of academic and educational institutions
SF35	Promotion of local education
SF36	Understanding of climate change and related issues
SF37	Use of modern technology and innovations
SF38	Consistent use of technology in organizations
SF39	Enhanced production or energy efficiency
SF40	Use of carbon capture and storage (CCS) technology
SF41	Promotion of renewable energy innovations
Code	Item
SF42	Adoption of clean energy technologies in industry
SF43	Sufficient budget availability
SF44	Financial support from external funding sources
SF45	Properly allocated funding sources
SF46	Targeted budgets and suitable resource allocation
SF47	Financial support in the form of incentives or loans
SF48	Funding enhances investment in relevant technologies
SF49	Recognition and appreciation from leadership
SF50	Recognition from government or external agencies
SF51	Recognition from community and society
SF52	Public or external organization appreciation and honor
SF53	Recognition from authorities increases enthusiasm
SF54	Recognition encourages participation
SF55	Awareness of impacts strengthens commitment
SF56	Awareness motivates involved stakeholders
SF57	Community awareness of climate change impacts
SF58	Personal awareness
SF59	Awareness enhances support from various sectors
SF60	Fostering awareness among stakeholders
SF61	Promoting impact-conscious behavior
SF62	Habitual energy and resource conservation
SF63	Environmental conservation awareness from childhood
SF64	Habits of choosing eco-friendly products and services
SF65	Upbringing environmental awareness in families
SF66	Stakeholder behavior influences success
Results (Policy Outcome)	
EF1	Implementation yields tangible and sustainable results
EF2	Implementation is measurable
EF3	Society benefits from the implementation
EF4	Able to continue in the long term
EF5	Scalable in the future
EF6	Improves workflow and management
EF7	Enhances monitoring and evaluation
EF8	Integrated into long-term development plans
EF9	Sustained resource and budget allocation

Note: While the questionnaire was structured around six content clusters for design clarity, the SEM analysis was based on three latent constructs Management, Motivation, and Leadership as determined by exploratory factor analysis and theoretical alignment.

Respondents were instructed to reflect on their answers based on their organization's overall implementation experience with all 27 mitigation measures in Table 2, to ensure a structured and policy-level perspective in their responses.

Table 2 27 Greenhouse Gas Mitigation Measures

Sector	Measures	Details
Energy Efficiency (EE)	7	1. Replacement of Lighting with LED Bulbs. 2. Energy Consumption Reduction.

Alternative Energy (AE)	8	1. Installation of Rooftop Solar Panels. 2. Use of Biogas.
Transportation Management (TM)	4	1. Use of Electric Vehicles 2. Development of Public Transportation Systems.
Waste Management (WM)	3	1. Waste-to-Energy Conversion 2. Wastewater Treatment

Sector	Measures	Details
Forest (FOR)	2	1. Afforestation and Reforestation
Agriculture (AGR)	3	1. Promotion of Sustainable Farming 2. Reduction of Open Burning in Agricultural

Sourced: Khon Kaen Provincial Climate Change Action Plan (2023).

Data Analysis

The analysis of questionnaire data was carried out using Structural Equation Modeling (SEM), a statistical technique that is particularly suitable for examining complex causal relationships between latent variables and observed indicators within a unified model framework [33]. This approach enabled the researcher to investigate multiple relationships simultaneously, while accounting for both measurement error and the multidimensional nature of the constructs.

To begin, Exploratory Factor Analysis (EFA) was conducted to explore the underlying structure of the latent variables based on the empirical data collected. This step was important because the questionnaire items had been adapted and synthesized from multiple theoretical and empirical sources. The EFA helped ensure that the factor structure was appropriate and contextually valid for the LAOs in Khon Kaen Province.

Following EFA, Confirmatory Factor Analysis (CFA) was employed to assess the fit between the observed data and the proposed theoretical constructs. This step provided evidence for the construct validity and internal consistency of the measurement model and confirmed that the indicators accurately represented the intended latent variables.

Finally, the full Structural Equation Model was estimated to examine the hypothesized causal relationships among the three main independent constructs Management, Motivation, and Leadership and the dependent variable, defined as the success of policy implementation. The analysis focused on identifying the direction and strength of these relationships to test the study's hypotheses.

All analyses were conducted using Jamovi, an open-source statistical software that offers robust support for SEM procedures and generates detailed model evaluation outputs. Model fit was assessed using several widely accepted indices, including the Comparative Fit Index (CFI) and Tucker–Lewis Index (TLI), for which values greater than 0.90 were considered acceptable. Additionally, the Root Mean Square Error of Approximation (RMSEA) and the Standardized Root Mean Square Residual (SRMR) were used, with values below 0.08 indicating a good model fit [33].

RESULTS

Analysis

Prior to conducting factor analysis using the Structural Equation Modeling (SEM) technique, the internal consistency of the research instrument was assessed using Cronbach's Alpha for the four main groups of latent variables. The results indicated that all constructs exceeded the minimum acceptable threshold of 0.80, in accordance with the criteria recommended by Hair et al. [34]. This finding confirms that the instrument demonstrated a high level of reliability. The reliability coefficients for each construct are presented in Table 3

Table 3 Reliability Analysis

Group of factors	Cronbach's Alpha Coefficient
Management (MA)	0.914
Motivation (MO)	0.898
Leaderships (LE)	0.932
Result (RE)	0.938

Exploratory Factor Analysis (EFA)

Exploratory Factor Analysis (EFA) was conducted using data from a sample of 246 respondents to identify the underlying structure of latent variables in the dataset. The analysis applied the Oblimin rotation method, which is appropriate when variables are assumed to be correlated [34].

The summary of the EFA results is presented in Table 4, which displays key statistical indices used to evaluate the suitability of the data for factor analysis.

Table 4 The summary of the EFA results

EFA Indicator	Value from Analysis	Interpretation	Reference
Kaiser-Meyer-Olkin (KMO)	0.95	Excellent sampling adequacy	Kaiser (1974)
Bartlett's Test of Sphericity	χ^2 = 15,413.07, df = 2775, p < .001	Significant correlation matrix: factor analysis is appropriate	Bartlett (1954)
Number of Factors	4	Four-factor solution is most appropriate	Hair et al. (2019)
Factor Loadings	0.68 - 0.92	Very strong item-factor correlations	Hair et al. (2019)
Cross-loading	No cross-loadings above threshold	No cross-loading issues observed	Hair et al. (2019)
Communality	All items ≥ 0.40	High shared variance across items	Hair et al. (2019)
Total Variance Explained	Over 70%	Acceptable level of explained variance	Hair et al. (2019)
Rotation Method	Oblimin	Appropriate for correlated factors	Fabrigar et al. (1999)
Cronbach's Alpha	All factors ≥ 0.79	High internal consistency	Hair et al. (2019)

The results of the exploratory factor analysis revealed that the data structure could be clearly grouped into four distinct factors, corresponding to the latent constructs used in the research model Management, Motivation, Leadership, and Policy Outcomes. Details of each factor are summarized in Table 5 Factor loadings which value greater than 0.70 are considered strong and indicate high structural alignment [34].

Table 5 Factor Structure Identified by EFA

Factor	Construct Name	Key Observed Variables	Factor Loading Range
F1	Management (MA)	SF24, SF26, SF31	0.79 - 0.83
F2	Motivation (MO)	SF59, SF60, SF61	0.78 - 0.81
F3	Leadership (LE)	SF7, SF9, SF10	0.82 - 0.84
F4	Result (RE)	EF1, EF2, EF3	0.82 - 0.92

Confirmatory Factor Analysis (CFA)

Confirmatory Factor Analysis (CFA) was conducted to evaluate the goodness-of-fit between the proposed measurement model and the empirical data, based on the factor structure identified in the Exploratory Factor Analysis (EFA). The model fit indices are summarized in Table 6, which demonstrates that the model achieves a statistically acceptable and satisfactory level of fit.

Table 6 Model Fit Indices for the Confirmatory Factor Analysis (CFA)

Fit Index	Value from Analysis	Acceptable Threshold	Reference
Chi-square/df	1.92	< 3.00	Hair et al., (2019)
CFI	0.961	≥ 0.95	Hu & Bentler, (1999)
TLI	0.949	≥ 0.95 (nearly acceptable)	Hu & Bentler, (1999)
RMSEA	0.045	≤ 0.06	Browne & Cudeck, (1993)
SRMR	0.038	≤ 0.08	Hair et al., (2019)

Although the Tucker-Lewis Index (TLI) value was slightly below the conventional threshold, it still falls within an acceptable range. When considered alongside the other fit indices, the results suggest that the CFA model exhibits a good overall fit with the empirical data [20]. The measurement model structure derived from the CFA is illustrated in Fig. 3.

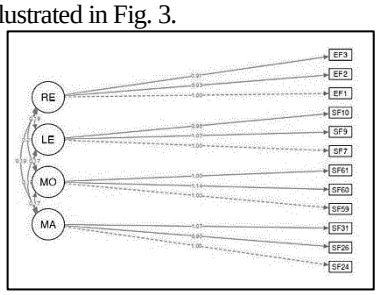

Fig. 3 Measurement Model (CFA) of the Four Latent Constructs

As shown in Fig. 3, the measurement model comprises four latent constructs Management (MA), Motivation (MO), Leadership (LE), and Result (RE). Each construct is measured by a set of observed variables that are conceptually aligned, with all factor loadings meeting the acceptable threshold of ≥ 0.70, indicating a strong level of structural alignment.

The analysis confirmed that the model demonstrates good measurement properties in terms of both loading values and statistical significance. Furthermore, all latent constructs were found to be positively correlated, which is consistent with the theoretical framework and research hypotheses particularly in evaluating policy implementation success at the local level [20], [21].

Structural Equation Modeling (SEM) Results

This study aimed to examine the causal relationships between three independent latent constructs Management (MA), Motivation (MO), and Leadership (LE) and the dependent construct, Results (RE), representing the success of GHG mitigation measures implemented by LAOs. (Figure 4)

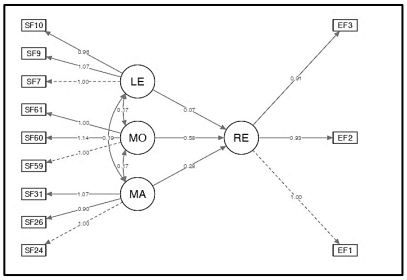

Fig. 4 SEM Diagram Showing the Influence of MA, MO, and LE on RE

The SEM results illustrated in Fig. 4 reveal the following

Motivation (MO) had the strongest positive influence on Result (RE) ($\beta = 0.58$, $p < .001$).

Management (MA) had a moderate positive influence ($\beta = 0.25$, $p = .002$).

Leadership (LE) did not exhibit a statistically significant influence ($\beta = 0.07$, $p = .251$).

These findings indicate that internal motivation among personnel plays the most critical role in driving the success of GHG mitigation measures at the local level, aligning with the theoretical perspectives of Hair et al. [20] and Byrne [10].

The fit indices of the SEM model are shown in Table 7, and the standardized path coefficients from hypothesis testing are presented in Table 8**.**

Table 7 Model Fit Indices for the SEM

Fit Index	Value	Threshold	Reference
Chi-square/df	2.05	< 3.00	Hair et al. (2019)
CFI	0.962	≥ 0.95	Hu & Bentler (1999)
TLI	0.95	≥ 0.95	Hu & Bentler (1999)
RMSEA	0.047	≤ 0.06	Browne & Cudeck (1993)
SRMR	0.04	≤ 0.08	Hair et al. (2019)

Table 8 Standardized Path Coefficients from SEM Analysis

Hypothesis	Path	β (Standardized)	p-value	Significance
H_1	MA → RE	0.25	0.002	Significant
H_2	MO → RE	0.58	< 0.001	Highly significant
H_3	LE → RE	0.07	0.251	Not significant

The results of the SEM analysis indicate that Motivation (MO) exerted the strongest positive influence on Policy Outcome (Result) ($\beta = 0.53$, $p < .001$). This finding aligns with Byrne [14] and Hair et al. [20], who argue that internal motivation within organizations plays a pivotal role in driving policy effectiveness particularly in environmental policies that require active engagement, shared commitment, and collective responsibility among front-line personnel.

Meanwhile, Management (MA) demonstrated a moderate positive effect on Result ($\beta = 0.27$, $p = 0.002$), highlighting the importance of clear administrative systems, cross-functional collaboration, and inter-agency coordination in achieving local policy success.

However, Leadership (LE) did not exhibit a statistically significant influence ($\beta = 0.08$, $p = 0.251$). This may reflect the constraints of centralized bureaucratic systems, which can limit the autonomy and policy-oriented leadership role of local government leaders in practical settings.

CONCLUSION

This study set out to explore the factors influencing the success of LAOs in implementing GHG mitigation measures in Khon Kaen Province. Using Structural Equation Modeling (SEM), the relationships between three key latent variables Management (MA), Motivation (MO), and Leadership (LE) and Result (RE) were tested.

The model showed a strong fit, with CFI = 0.99, TLI = 0.99, RMSEA = 0.03, and SRMR = 0.03, which are all within the recommended thresholds according to Hair et al. [20] and Hu & Bentler [21]. Based on responses from 246 individuals across 225 LAOs, the analysis demonstrates practical reliability.

The standardized path coefficients revealed that Motivation (MO) had the strongest positive influence on policy outcomes ($\beta = 0.53$, $p < 0.001$), reinforcing Byrne's [10] idea that social motivation plays a major role in driving environmental behavior, both among officials and within communities. Management (MA) showed a moderate influence ($\beta = 0.27$, $p = 0.002$), highlighting the importance of planning and inclusive decision-making, as suggested by ICLEI [3] and Setyowati et al. [13]. On the other hand, Leadership (LE) did not show a statistically significant effect ($\beta = 0.08$, $p = 0.251$), which may reflect the challenges of centralized governance and limited mechanisms for local leadership [7], [8].

While the results emphasize motivation and management, it's worth noting that many GHG mitigation efforts such as solar rooftop installations, biogas systems, or LED lighting ultimately rely on tangible infrastructure. This highlights the need to align administrative actions with practical engineering solutions to ensure that good plans lead to real outcomes.

Future research may look deeper into how administrative performance affects the actual use and performance of local mitigation technologies. For example, how well are solar panels functioning? Are biogas systems being maintained? These practical questions can help link governance and engineering in a way that supports truly sustainable outcomes.

DISCUSSION

This study demonstrates the key factors that contribute to the success of LAOs in Khon Kaen Province in implementing GHG mitigation measures. Through the application of Structural Equation Modeling (SEM), the analysis identifies three core dimensions consisting of Management, Motivation, and Leadership, as significant determinants, with Policy Outcome serving as the primary dependent construct.

Motivation

The results of the study found that motivation had the most significant influence on policy outcomes ($\beta = 0.58$, $p < 0.001$**)**, consistent with the views of Byrne [12] and Hair et al. [20], who argue that internal motivation within organizations is a critical force in driving policy objectives toward practical implementation. This is particularly relevant in the context of environmental management, where success often relies on active engagement and a shared sense of responsibility among those involved.

In Khon Kaen Province, the 27 mitigation measures across six sectors were designed to allow LAOs to select and apply them based on their specific local contexts. This approach has helped encourage meaningful participation from key sectors, including civil society, the private sector, and educational institutions. Moreover, national-level mechanisms such as the Thailand Voluntary Emission Reduction Program (T-VER) and the Low Emission Support Scheme (LESS) have further enhanced local motivation by providing both institutional support and recognition for local climate action efforts [40].

Management

Management was found to have a moderate positive influence on policy outcomes ($\beta = 0.25$, $p = 0.002$), underscoring the importance of effective internal organizational systems. This includes strategic planning, resource allocation, performance monitoring, and internal communication. These findings are consistent with the perspectives of ICLEI [4] and Setyowati et al. [25]**,** who emphasize the need for integrated management frameworks at the local level to support sustainable environmental governance.

In Khon Kaen Province, the performance of LAOs has been assessed using the LPA tool, developed under the framework of the Department of Local Administration, Ministry of Interior, as the lead agency, in collaboration with the Provincial Office of Natural Resources and Environment, which provides technical data and field-level support. This mechanism has played a key role in promoting ongoing improvements in local management systems. Additionally, the draft Climate Change Act, currently under development, is expected to further clarify and formalize the roles and responsibilities of LAOs in addressing climate-related risks in the future [29].

Leadership

Although leadership is widely recognized in theory as a key factor in driving environmental policy particularly in terms of establishing a clear vision and motivating stakeholders this study found that leadership had limited influence on policy outcomes. This may be due to structural constraints in Thailand's centralized administrative system, which often restricts the authority of local leaders to shape policy directions independently.

Despite these limitations, Khon Kaen Province has made efforts to foster collaborative forms of leadership by establishing a provincial-level task force that brings together representatives from government agencies, academia, the private sector, and civil society. This mechanism emphasizes integrated planning, cross-sectoral development, and structured stakeholder engagement to move GHG mitigation efforts forward across all sectors, [6], [7].

While such initiatives show promise and reflect a shift toward more inclusive local leadership, their impact may not yet be fully reflected in the perceptions of individual respondents captured in this study. Exploring this further through qualitative or comparative methods could help uncover how leadership manifests in decentralized settings and how it can be better supported [8].
across all sectors.

Policy Implications

The findings of this study clearly indicate that internal organizational motivation is the most critical factor influencing the success of local GHG mitigation efforts. This suggests that promoting participation, fostering a sense of institutional pride, and providing symbolic or public forms of recognition can effectively drive performance at the local level. At the same time, a strong internal management system plays a secondary but essential role in bridging national policy frameworks with on-the-ground implementation, particularly through strategic planning, resource allocation, and continuous performance monitoring. While leadership is often seen as a central component of policy advancement in theoretical frameworks, the highly centralized nature of Thailand's administrative system may constrain the capacity of local leaders to exercise meaningful influence. Therefore, efforts to cultivate authentic leadership at the local level should be accompanied by systemic reforms such as decentralization, targeted budget support, and enhanced policy capacity to empower local leaders to shape direction and effect change in a concrete and sustainable manner.

While motivation and management emerged as key drivers in this study, it is equally important to recognize that many GHG mitigation efforts such as solar installations, energy efficient lighting, and waste treatment systems are ultimately realized through physical infrastructure. This connection between local administrative action and environmental technology highlights an area where policy and engineering must go hand in hand.

RECOMMENDATION

The findings of this study indicate that motivation and management are critical determinants of the success of GHG mitigation efforts within Local Administrative Organizations (LAOs). Based on this, government agencies and related institutions should consider the following directions

1. Promote Positive Incentive Mechanisms, implement reward systems, recognition programs, or environmentally themed competitions to stimulate internal motivation and reinforce behavioral change among staff.
2. Design Open Governance Processes, encourage greater community involvement in co-designing policies and monitoring implementation to foster transparency, ownership, and accountability.
3. Strengthen Multi-Level Communication, enhance communication channels between LAOs and higher-level authorities (provincial or national) to ensure better alignment, resource support, and policy continuity.

While this study focused on all 225 LAOs in Khon Kaen Province, future research should explore the broader applicability of these findings. The following directions are recommended

1. Expand Comparative Studies, conduct cross-provincial or regional studies to validate the model in different administrative and socio-political contexts.
2. Incorporate Qualitative Methods, use in-depth interviews or case studies to capture behavioral nuances and leadership dynamics that quantitative measures may overlook.
3. Develop Extended Models, future models could integrate variables such as organizational culture, innovation capacity, or access to external resources to better understand LAO performance.

Lastly, local governments should be supported not only through institutional and policy incentives but also through technical assistance especially in planning, implementing, and maintaining green infrastructure. This includes renewable energy systems, sustainable waste management, and low-

emission construction. Such a dual-track approach can help ensure that policy ambitions lead to real, measurable environmental improvements.

REFERENCES

[1] IPCC, Climate Change 2023: Synthesis Report, Geneva: Intergovernmental Panel on Climate Change, 2023.
[2] United Nations Framework Convention on Climate Change (UNFCCC), Thailand's Updated Nationally Determined Contributions, 2022.
[3] Department of Local Administration, Role of Local Governments in Climate Mitigation, 2021.
[4] ICLEI – Local Governments for Sustainability, Resilient Cities and Regions: Advancing Local Implementation of Climate Action, 2019. [Online]. Available: https://iclei.org
[5] B. Limnirankul and C. Chompunth, "Challenges in Local Climate Governance in Thailand: The Role of Local Administrative Organizations," Journal of Environmental Policy and Management, vol. 24, no. 2, pp. 45–62, 2021.
[6] Khon Kaen Province, Local GHG Mitigation Plan, Provincial Government of Khon Kaen, 2023.
[7] Climate Change Taskforce of Khon Kaen, Implementation Report on GHG Reduction Measures, 2024.
[8] OECD, Decentralization and Fiscal Capacity in Climate Governance, 2022.
[9] World Bank, Strengthening Subnational Governance, World Bank Publications, 2020.
[10] Transparency Thailand, Bureaucratic Bottlenecks in Local Policy Implementation, 2021.
[11] S. Punyasopon and K. Thongmee, "Public Participation and Local Environmental Governance," Journal of Local Administration, vol. 18, no. 3, pp. 45–60, 2020.
[12] J. Byrne, "Community Engagement and Environmental Motivation," Environmental Policy Studies, vol. 12, no. 2, pp. 89–105, 2019.
[13] Y. Liu, L. Zhang, and H. Chen, "Leadership, Decentralization, and Policy Success in Developing Countries," Asian Journal of Public Administration, vol. 42, no. 1, pp. 15–30, 2020.
[14] B. Yuen and E. Tan, "Regional Barriers to Sustainable Climate Governance in ASEAN," Journal of Climate Policy and Practice, vol. 9, no. 4, pp. 122–136, 2021.
[15] NASA, "Greenhouse Gases: Climate Change Drivers," 2023. [Online]. Available: https://climate.nasa.gov
[16] IPCC, Climate Change 2023: Synthesis Report, Intergovernmental Panel on Climate Change, 2023.
[17] IPCC, Summary for Policymakers, AR6 Synthesis Report — Climate Change 2023, 2023.
[18] UNFCCC, Climate Change: Vulnerabilities in Developing Countries, 2021.
[19] United Nations, Transforming Our World: The 2030 Agenda for Sustainable Development, 2015.
[20] UN-Habitat, Enhancing the Role of Local Governments in Climate Governance, 2020.
[21] T. Phattarawut, "Challenges in Local Environmental Management in Thailand," Thai Journal of Public Administration, vol. 18, no. 1, pp. 22–39, 2021.
[22] P. Setyowati, D. Rakhmani, and A. Siregar, "Collaborative Governance in Indonesia's Climate Change Policy: Lessons from Local Implementation," Environmental Policy and Governance, vol. 31, no. 5, pp. 456–468, 2021.
[23] L. Yusran and R. Santos, "Adaptive GHG Strategies in ASEAN: Lessons from the Philippines and Indonesia," ASEAN Climate Journal, vol. 7, no. 1, pp. 88–102, 2022.
[24] J. L. Pressman and A. B. Wildavsky, Implementation: How Great Expectations in Washington Are Dashed in Oakland, University of California Press, 1973.
[25] G. C. Edwards, Implementing Public Policy, Congressional Quarterly Press, 1980.
[26] P. A. Sabatier and D. A. Mazmanian, "The Implementation of Public Policy: A Framework of Analysis," Policy Studies Review, vol. 1, no. 4, pp. 538–560, 1983.
[27] Khon Kaen Climate Taskforce, Action Plan for GHG Mitigation in Khon Kaen Province, Department of Environment, Khon Kaen, 2024.
[28] IPCC, AR6 Climate Change 2023: Technical Summary, Intergovernmental Panel on Climate Change, 2023.
[29] ONEP, Thailand Climate Action Plan, Office of Natural Resources and Environmental Policy and Planning, 2022.
[30] ICLEI – Local Governments for Sustainability, Advancing Climate-Resilient Urban Development, 2021.
[31] J. F. Hair, G. T. M. Hult, C. M. Ringle, and M. Sarstedt, A Primer on Partial Least Squares Structural Equation Modeling (PLS-SEM), 3rd ed., SAGE Publications, 2022.
[32] J. F. Hair, W. C. Black, B. J. Babin, and R. E. Anderson, Multivariate Data Analysis, 8th ed., Cengage Learning, 2019.
[33] J. Cohen, Statistical Power Analysis for the Behavioral Sciences, 2nd ed., Lawrence Erlbaum, 1988.
[34] L. Hu and P. M. Bentler, "Cutoff Criteria for Fit Indexes in Covariance Structure Analysis: Conventional Criteria Versus New Alternatives," Structural Equation Modeling, vol. 6, no. 1, pp. 1–55, 1999.
[35] M. W. Browne and R. Cudeck, "Alternative Ways of Assessing Model Fit," in Testing Structural Equation Models, K. A. Bollen and J. S. Long, Eds., Newbury Park, CA: Sage, 1993, pp. 136–162.
[36] The Jamovi Project, "jamovi (Version 2.4) [Computer Software]," 2023. [Online]. Available: https://www.jamovi.org
[37] Fabrigar, L. R., Wegener, D. T., MacCallum, R. C., & Strahan, E. J., "Evaluating the use of exploratory factor analysis in psychological research," Psychological Methods, vol. 4, no. 3, pp. 272–299, 1999.
[38] Kaiser, H. F., "An index of factorial simplicity," Psychometrika, vol. 39, no. 1, pp. 31–36, 1974.
[39] Bartlett, M. S., "A note on the multiplying factors for various chi square approximations," Journal of the Royal Statistical Society, 1954.
[40] Thailand Greenhouse Gas Management Organization (TGO), "T-VER Program Handbook," Bangkok, Thailand, 2023. [Online]. Available: https://www.tgo.or.th

Copyright © Int. J. of GEOMATE All rights reserved, including making copies, unless permission is obtained from the copyright proprietors.

15th Int. Conf. on Geotechnique, Construction Materials & Environment,
Kyoto, Japan, 11-13 November 2025, ISBN 978-4-909106124 C3051

A STUDY OF TEMPERATURE REDUCTION METHODOLOGY IN URBAN HEAT ISLAND USING MICROCLIMATE TECHNIQUE

Ekarin Sangthammarat.[1], Chokchai Chutakositkanon[1]

[1]Faculty Of Engineering, Mahidol University, Salaya, NakornPrathom, Thailand

ABSTRACT

To address the impact of global warming on localized temperature increases—commonly referred to as the Urban Heat Island (UHI) effect, this study focused on the application of microclimate modification techniques. The objective was to evaluate the potential for reducing ambient temperature and energy consumption by varying the shapes of trees and types of ground surfaces most suitable for enhancing the pavement areas along Ratchadamnoen Road, Bangkok. Five simulation scenarios were developed using ENVI-met V5.6.1, each incorporating equivalent amounts of vegetation and surface coverage, to identify the most effective configuration. The simulation results demonstrated a verification accuracy of 95%. The research results revealed that the optimal strategy for mitigating temperature and heat accumulation in UHI-affected areas involves increasing green space by planting round-shaped trees and utilizing ground cover materials for exposed floor surfaces. These interventions effectively absorb solar radiation, reduce ambient air temperature, and decrease energy consumption—resulting in potential monthly electricity savings of up to 24,225.44 baht.

Keywords: Microclimate, Thermal Comfort, Energy Saving, Landscape Adjustment, Urban Heat Island

INTRODUCTION

Rapid development of urbanization is suddenly in many major cities resulted in to population growing. Many major cities experience the impact of global warming for example flooding and drought as a consequence of climate change. The urban areas are now facing greater risks due to the development intensity as a solution for urban growth, lack of compatibility of these development typologies resulted in increased cooling load [1].

However, most of the urban and many cities are lack of appropriate energy consumption modelling and optimal climate analysis which is misleading to the energy analysis for space conditioning associated with rapid developments. This lack of understanding has major implications on energy budgeting and human health in tropics [2].

In order to model the energy consumption in the city due to climate change is complicated. On most occasions, these designers and planners tend to use subjective measures to evaluate their development proposals under complex climate premises [3] which leading to unforeseen risks.

Computer modelling is used as major tools in urban climate studies due to their capability to simulate complex fluid dynamic interactions. In the urban field, modelling approaches can be applied to different city condition, such as population distribution, mobility network as well as growth of population and climate change [4]. Modeling can be used as forecasting tools to investigate the certain actions effect on a selected domain [5]. Urban models enable making predictions on unbuilt conditions and testing hypotheses of future urban interventions (Batty 2009).

The in-depth analysis of a modelling case study, A conceptual model, including the climate phenomena to be represented the urban scene, is defined as starting point and associated to an urban domain. ENVI-met is applied with the goal of exploring microclimate effects of an urban area at the center of Bangkok, Thailand. To highlight the potential of usage of microclimate technique in order to modelling the possibility to reduce the energy consumption in the control area, several simulation models have been done to achieve the goals.

RESEARCH OBJECTIVE

The objective of the study is to determine the type and characteristic of tree and glass in order to reduce the Urban Heat Island (UHI) and to determine the possibility to reduce the temperature and heat gain in the city together with the possibility to reduce the energy consumption in the surrounding area.

RESEARCH SCOPE

Due to the numerous microclimate parameters that influence temperature and relative humidity, this research focused solely on the types of trees and mulch. The study was conducted during the summer season in Bangkok, Thailand. Climate data were obtained from the Visual Crossing Weather API.

RESEARCH METHODOLOGY

In order to reach research objective, there research

step had been classified into 5 steps as shown in Fig.1.

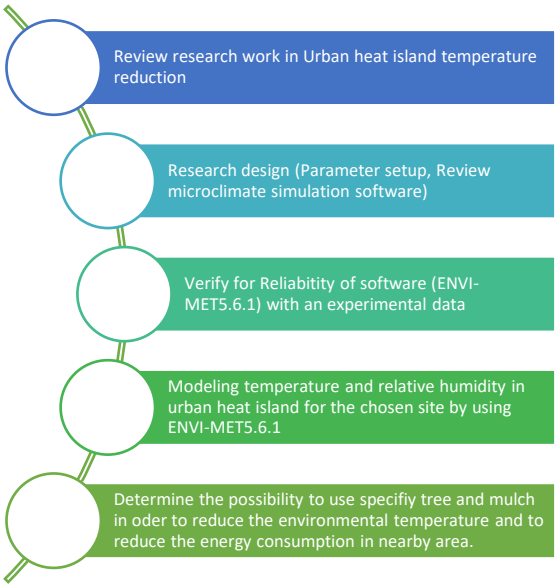

Fig.1 Research framework for urban heat island

Data Verification

In order to verify reliability of ENVI-MET 5.6.1 simulation software, researcher select the park area in Mahidol University, Salaya, Nakorn Prathom, Thailand which near to Bangkok to measure the actual temperature and relative humidity for 2 days as shown in Fig.2. And then verify the result with simulation software as shown in Fig.3.

Fig.2. The actual measurement area

Fig.3. Model from Envi-Met5.6.1

In figure 3 the model had been set up by using Envi-Met5.6.1 software in order to verify the simulation software reliability.

The result from measurement and simulation had been done to verify the reliability of software in terms of hourly temperature and relative humidity comparison in 4 positions. Found that the correlation coefficient of temperature is 96.39% and relative humidity is 95.74% consecutively. From the comparison result reveals that ENVI-Met5.6.1 have high accuracy for developing the simulation model.

Modeling Urban Heat Island Microclimate

The objective of this study is to determine the type of trees and cover crops that are optimized for temperature reduction in urban heat island by variate scenarios in the selected area in Ratchadamnoen Road Bangkok as shown in Fig.4.

Fig.4. Simulation area in Ratchadomnoen Road.

Ratchadamnoen Road was selected as the base case for this study due to its wide pedestrian walkways, which are well-suited for landscaping interventions. The study area measures 150 by 85 meters and consists of concrete pavement, buildings up to 21 meters in height, an asphalt road, and identical plant species on both sides of the sample area. The street median contains some concrete surfaces but is primarily covered with ground cover vegetation.

Simulation Model Setup

There are 6 scenario cases to be simulated by changing the ground surface and tree shapes as indicated in Table 1 and shown in fig.5.

Table 1 The scenarios for UHI Simulation model

Scenarios	Green Spaces				
	Perennials Trees		Cover crops		No tree & cover
	Layered shape	Round shape	Sandy loam	Ground cover	
Base	Actual environment				
1	-	-	-	-	√
2	√	-	√	-	-
3	√	-	-	√	-
4	-	√	√	-	-
5	-	√	-	√	-

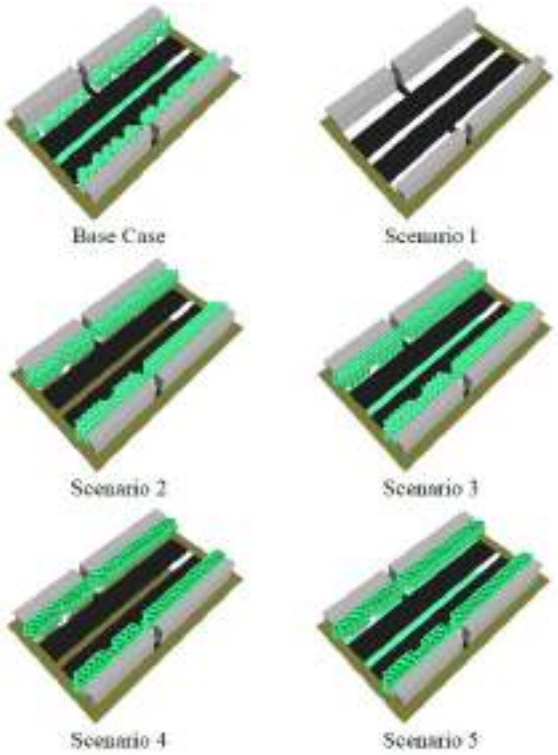

Fig. 5 Simulation case for each scenario

After simulation case had been designed for this study. The software configuration had been done in order to simulate the temperature and relative humidity in fig.6.

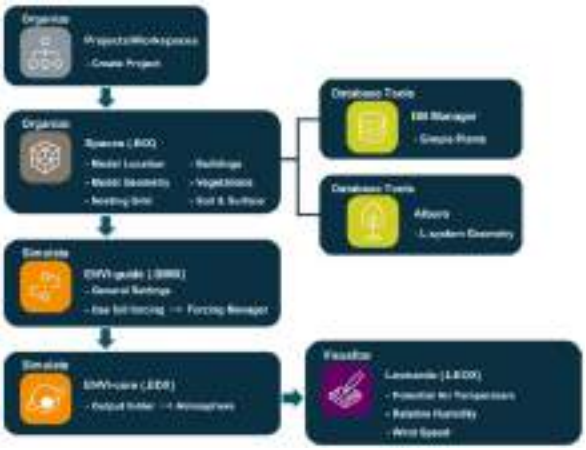

Fig.6. The setting up of ENVI-MET 5.6.1

Parameter configuration setup for simulation model consisted of workspace, geometry setup, plant setup, weather setup which separated to each software function. The example of data is shown in table 2

Table 2 Input data for simulation model

Parameter	Value
Model size	150x85x53
Grid Dimensions	170x105x18
Size of grid cell (m)	1x1x2

Parameter	Value
Geographic Location (Latitude, Longitude)	13.76°, 100.50°
Reference time zone	Indochina Time
Start & Duration of Simulation	06:00, 12 h
Wind speed (m/s)	1.59
Wind direction	45°
Min temperature	30.7 °C, 5:00 a.m.
Max temperature	39.4 °C, 1:00 p.m.
Min relative humidity	37.61%, 12:00 p.m.
Max relative humidity	79.68%, 4:00 a.m.

RESULTS

Zone Setup

In order to compare the result from simulation scenarios, the area has been separated into 5 zones as shown in fig.7. Each zone located 5 positions to simulate temperature and relative humidity.

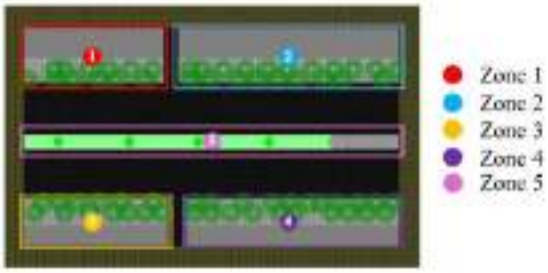

Fig.7 Zone setup for simulation scenarios comparisons.

The result from simulation has been done by using ENVI-MET5.6.1 in order to determine the temperature and relative humidity as shown in fig.8

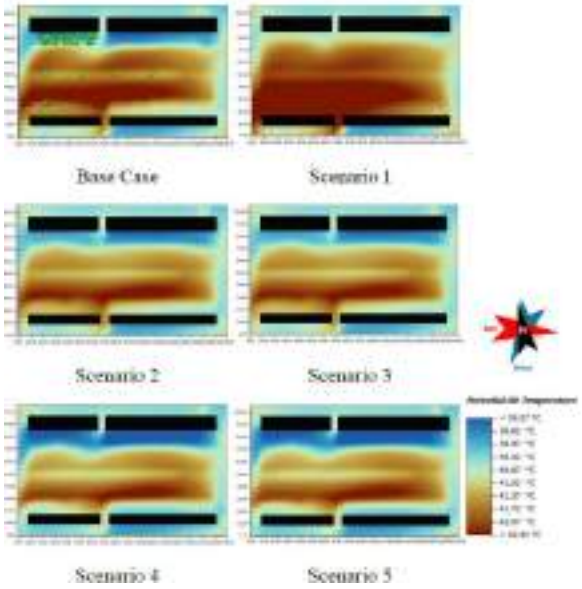

Fig.8 Simulation of Temperature at 1:00 pm.

The simulation results revealed that shaded areas whether by greenery or buildings significantly affect microclimatic conditions. In the morning, sunlight shines on Zone 2 more than on the other zones, resulting in a higher average air temperature and lower average relative humidity. Similarly, in the afternoon, Zone 3 receives the most sunlight, leading to increased air temperature and relative humidity compared to the other zones. In contrast, Zone 5, which is generally unshaded, consistently experiences the highest temperatures and lowest humidity levels among all zones. A comparison of the simulation results is illustrated in Fig. 9.

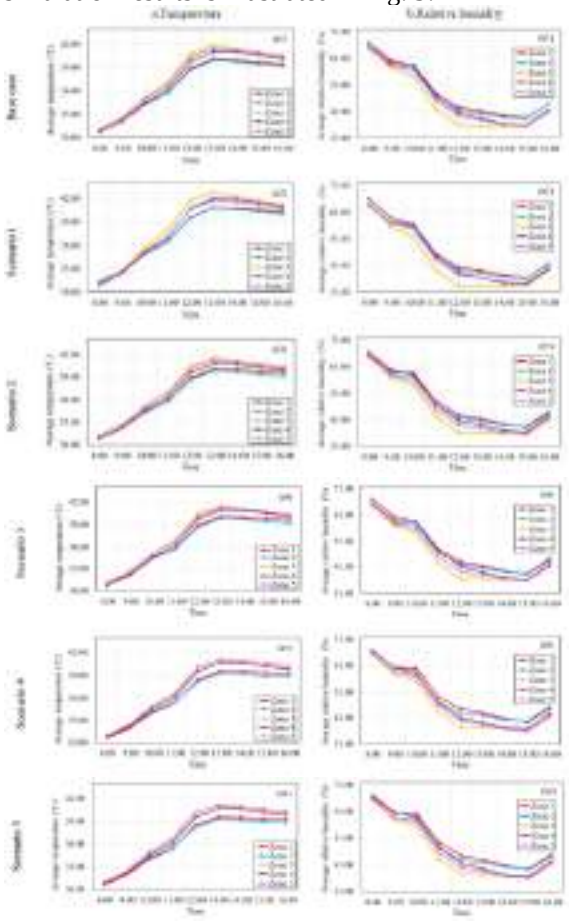

Fig.9 The temperature and relative humidity comparison between zone.

The comparison between each scenario has been separated by zone. Base Case is being used as a reference Scenario, in order to choose the best method to reduce air temperature in UHI. The comparison shows that green space has a lowering effect on urban heat islands, as areas without green space (Scenario 1) has the highest mean air temperature and the lowest mean relative humidity of all zones. In the scenario where different shape of trees planted, the areas planted with round shape trees will have lower average temperature and higher average relative humidity than the areas planted with layered shape trees. In the scenario where different ground cover are selected, the areas shaded by trees, in Zone 1-4, Scenario 3 will have a higher average temperature and lower average relative humidity than Scenario 2, just as Scenario 4 does to Scenario 5, which is very slight in comparison. But in scenario that areas exposed to sunshine, using ground cover (Scenario 3 and5) could assist in temperature reduction and increasing in relative humidity than using sandy loam

The comparison results of each scenario can be revealed separated by zone as shown in fig.10.

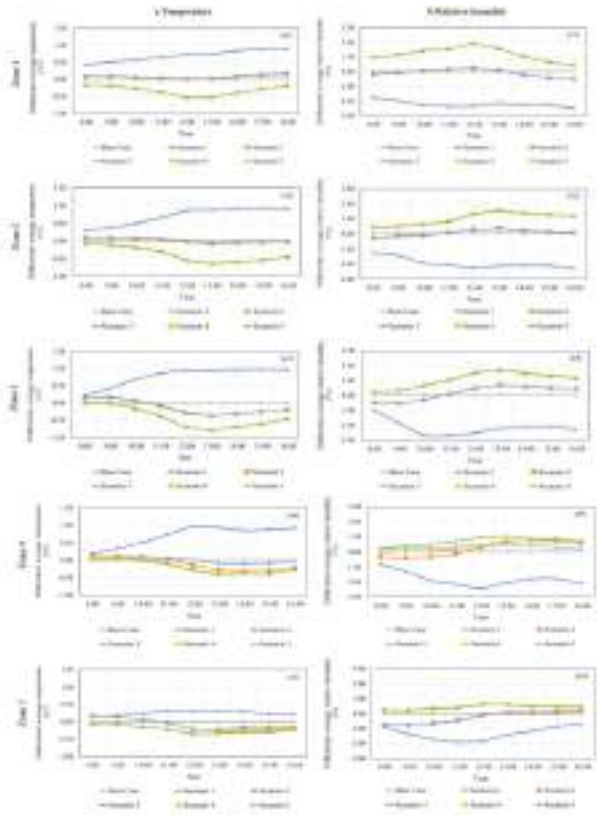

Fig.10 Differential temperature and relative humidity zone comparison

The temperature difference is applied in order to estimate the change in enthalpy change (as shown in fig.11) by using Eq. (1) and in order to calculate possible energy saving due to reduction of surrounding temperature near building, Eq. (2) has been applied. The comparison results shown that area without green space (Scenario 1) has the highest enthalpy change in positive value compared to base case. On the other hand, Scenario 5 has the highest enthalpy change in negative value compared to base case. Given an electricity cost is 4.18 Baht per unit, and coefficient of performance in air condition is 2.0 the results from changing in monthly electrical charge when compare with base case is shown in Fig. 12 represents.

$$\Delta Q' = m' \cdot (h_i - h_b) \quad (1)$$

$$E_{Saving} = \frac{\Delta Q'}{COP} \quad (2)$$

Where
$\Delta Q'$ = enthalpy change (kW/day)
m' = Air mass flow rate into building (kg/hour)
h_i = Enthalpy of scenarios (kj/kg)
h_b = Enthalpy of base case (kj/kg)

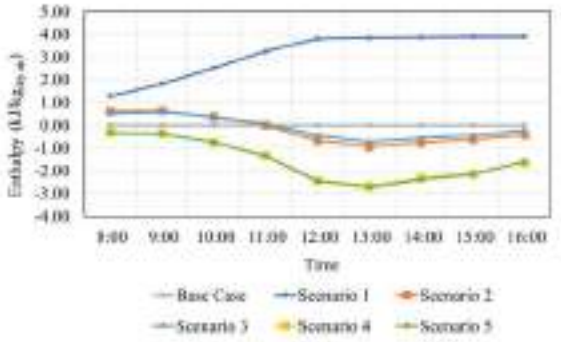

Fig.11 Enthalpy change comparing with Base Case

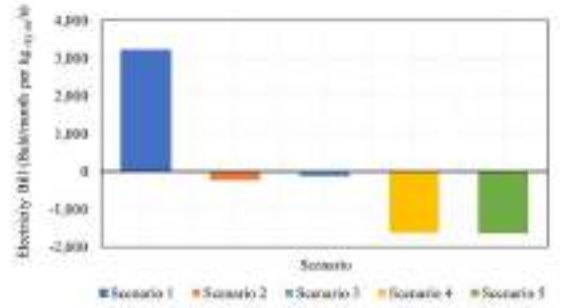

Fig.12 Change in Monthly electricity charge when comparing with Base Case

CONCLUSIONS

The objective of this research is to identify the most effective combinations of tree shapes and ground surface covers for landscape design in Urban Heat Island (UHI) areas to reduce air temperature and energy consumption. The results from simulated scenarios demonstrated that case studies incorporating green spaces exhibited significantly lower air temperatures and higher relative humidity compared to those without vegetation. Among the five scenarios, Scenario 5, featuring spherical-shaped perennial trees taller than the surrounding buildings and ground surfaces covered with vegetation—showed the greatest effectiveness in reducing air temperature and energy consumption. Conversely, Scenario 3 had the least impact on both temperature reduction and energy savings.

In Urban Heat Island (UHI) areas, one of the most effective strategies for reducing air temperature and energy consumption is to increase green space around buildings. Trees play a key role by absorbing solar radiation and providing shade to the surrounding environment. Among different tree forms, round-shaped trees are most effective due to their higher leaf density, which enhances their ability to block solar radiation compared to layered trees. To further improve effectiveness, concrete pavements should be replaced with sandy loam or ground cover. In sun-exposed areas, ground cover is more effective at lowering air temperature than sandy loam. However, in shaded areas beneath tree canopies, both ground cover and sandy loam perform similarly. This research indicates that energy savings from reduced air conditioning usage amount to approximately 1,650 Baht per month per unit of mass flow rate, total saving cost 24,225.44 Baht per month.

Future research should consider microclimate variables other than temperature and relative humidity variables, as well as other ways to reduce temperatures, such as increasing water sources, using a green roof and increasing soil moisture, including designing the position, direction and shape of the building to be consistent with the environment and suitability of that area to study other variables, factors, or methods that can be used to research ways to reduce temperatures and heat consumption around UHI. Furthermore, economic worth should be taken into consideration. To determine the break-even point before investing in landscaping, as well as the payback period for reduced electricity costs in surrounding buildings.

REFERENCES

[1] Giridharan, R., & Emmanuel, R. The impact of urban compactness, comfort strategies and energy consumption on tropical urban heat island intensity: A review. Sustainable Cities and Society Vol.40,2018, pp. 677–687.
[2] Giridharan, R. Urban climate challenges in the tropics: Rethinking the design basis and opportunities. London: Imperial College Press ,2016, pp. 255–299.
[3] Schiller, S. D., & Evans, J. M. Bridging the gap between climate and design at the urban and building scale: Research and application. Energy and Buildings, 1991, pp.51–55.
[4] Wegener, M. Operational urban models state of the art. Journal of the American Planning Association, Vol.60, 1994, pp.17–29.
[5] Batty, M. Cities as complex systems: Scaling, interaction, networks, dynamics and urban morphologies. Encyclopedia of complexity and systems science, 2009, pp. 1041–1071.

Copyright © Int. J. of GEOMATE All rights reserved, including making copies, unless permission is obtained from the copyright proprietors.

15th Int. Conf. on Geotechnique, Construction Materials & Environment,
Kyoto, Japan, 11-13 November 2025, ISBN 978-4-909106124 C3051

OPERATION PRINCIPLE OF ACTUATOR SYSTEM THAT COMBINES PHASE-CONTROLLED ACTUATOR WITH DIFFERENT DRIVE FREQUENCIES

Hiroyuki Yaguchi[1] and Sota Abe[1]

[1] Faculty of Engineering, Tohoku Gakuin University, Japan

ABSTRACT

In Japan, the shortage of construction workers and inspectors has become a social problem due to the declining birthrate and aging population. In addition, the slow progress of automation in challenging environments, such as construction sites and bridges, has been pointed out. Although various types of inspection robot have been developed, bridge inspection technology has not been fully established. In this study, the operation of a phase-controlled actuator equipped with vibration components with different drive frequencies is investigated. The phase-controlled actuator, in which a second-harmonic vibration component is coupled to a fundamental-wave vibration component to avoid vibration interference, exhibits excellent propulsive characteristics. To further improve the propulsion characteristics, a prototype actuator system, in which two phase-controlled actuators with different drive frequencies are coupled, is developed. Tests on prototypes show that this system can simultaneously achieve high-speed movement and good traction characteristics. Furthermore, the operation principle of this actuator system is established based on test results. The potential of an inspection device with the proposed actuator for the internal inspection of bridges with a small automatic tapping device is demonstrated.

Keywords: Actuator system, Operation principle, Second-harmonic vibration, Phase control, Inspection

INTRODUCTION

In Japan, the shortage of construction workers and inspectors has become a social problem due to the declining birthrate and aging population. The number of workers in the construction industry has decreased from 6.85 million in 1997 to 4.77 million in 2024. Furthermore, starting in 2025, the number of workers is expected to decrease by more than 100,000 per year. In the general manufacturing industry, task automation is relatively easy using industrial robots and artificial intelligence. However, automation in challenging environments, such as construction sites and bridges, is lagging behind. In particular, bridge inspection requires the operator to approach and touch the part to be inspected. Currently, inspection vehicles, aerial lifts, and boats are used to approach bridges, making bridge inspection dangerous and difficult. Since 2023, the 730,000 road bridges in Japan have to be inspected every 5 years. Various inspection robots have thus been developed to ensure worker safety and improve work efficiency.

Several inspection robots based on mechanisms that allow movement on walls, such as magnetic wheel systems [1], electromagnet systems [2], suction systems with negative pressure [3], crawler-type systems [4], and coupled vibration and suction systems [5], have been proposed. These inspection robots use a number of electromagnetic motors as the drive source, giving them good controllability. However, even robots equipped with large electromagnetic motors that have good torque characteristics exhibit significant degradation of movement characteristics when moving in a vertical plane. On the other hand, small electromagnetic motors lack torque, making it difficult to move on vertical surfaces. There is thus a limit to the improvement in robot movement characteristics that can be achieved by changing electromagnetic motors.

In recent years, drone-type flying robots have been developed [6, 7]. Although drones can perform inspection work in hazardous areas, they cannot perform inspections using automatic tapping devices**.** Furthermore, drone flights are affected by weather conditions and inspection technology for bridges using drones has not yet been established.

The present authors previously proposed an actuator for structural testing that consists of eight identical vibration components arranged in a square acrylic frame [8]. A prototype of this actuator was shown to be capable of rotational and translational reciprocating motion. However, vibration interference between the vibration components degraded the movement characteristics.

In this study, a phase-controlled actuator with vibration components with different drive frequencies is proposed. The phase-controlled actuator, in which a second-harmonic vibration component is coupled to a fundamental-wave vibration component to avoid vibration interference, exhibits excellent propulsive characteristics. To further improve the propulsive characteristics, an

actuator system in which two phase-controlled actuators with different drive frequencies are coupled is proposed. The operation principle of this actuator system is studied and its driving principle is established based on the results of tests on prototypes.

Measurements show that this actuator system can simultaneously achieve high-speed movement and good traction characteristics, which are usually in conflict with each other. This paper demonstrates the potential of an inspection device with the proposed actuator that can realize internal inspections of bridges with a compact automatic tapping device.

RESEARCH SIGNIFICANCE

The inspection of bridges and other structures has become an important issue in Japan due to the aging of infrastructure. However, the inspection of bridges over waterways (e.g., rivers, seas, and lakes) is extremely difficult. Although many inspection robots have been developed for visual or internal inspection, inspection techniques have not yet been established. The significance of this research is that it establishes an operation principle that significantly improves the propulsive characteristics of a vibration actuator previously proposed by the authors. The proposed actuator system enables the internal inspection of large iron structures.

PHASE-CONTROLLED ACTUATOR

Structure of Phase-controlled Actuator

Figs. 1(a) and 1(b) show the two types of phase-controlled actuator prototyped in this study, I and II, with multiple vibration components with the same specifications mounted in an acrylic frame (thickness: 5 mm, width: 15 mm, length 50 mm). Actuator I has vibration components A and B in an orthogonal arrangement. Actuator II has vibration components B and C coaxially arranged and vibration component A orthogonally aligned with components B and C. The stainless steel coil spring that constitutes a vibration component has an outer diameter of 12 mm, a free length of 32 mm, and a spring constant of 2,016 N/m. The NdFeB permanent magnet (diameter: 12 mm, height: 6 mm) at the top of each coil spring is magnetized in the height direction. The electromagnet consists of a 4.2-mm-diameter iron core with a 0.18-mm-diameter copper wire wound 1080 turns. The gap between the iron core and the permanent magnet in the static state is 5 mm. As shown in Fig. 1, height-magnetized NdFeB magnets (diameter: 10 mm, height: 2 mm) were mounted at the center of the acrylic frame and on each side 20 mm from the center. A 1-mm-thick rubber sheet was glued onto each of these magnets to increase the frictional force. The permanent magnets mounted on the sides of the center section stabilize the linear movement of the actuator. The positions of the permanent magnets were determined based on preliminary experiments. Actuator I is 53 mm high, 83 mm long, and 15 mm wide and has a total mass of 45.1 g. Actuator II is 53 mm high, 116 mm long, and 15 mm wide and has a total mass of 63.5 g.

Operation Principle of Phase-controlled Actuator

To illustrate the operation principle of the phase-controlled actuator, the displacement coordinates x and y are defined as shown in Fig. 1(b). The operation principle applies to both phase-controlled actuators I and II. The operation of actuator II is described here. Vibration components B and C are assumed to vibrate in phase in the x-direction. As shown in Fig. 2, when the actuator is set on a magnetic material, the attractive force of each of the three permanent magnets is P. The total attractive force $3P$ holds the actuator and allows the vibration components to vibrate.

As shown in Fig. 2(a), when vibration component A is displaced in the $+y$ direction, friction force F_f decreases due to the force generated by the permanent magnet. In this state, when components B and C are displaced in the $+x$ direction, the actuator moves in the $+x$ direction due to the force generated by the permanent magnets. On the other hand, as shown in Fig. 2(b), when the permanent magnet of vibration component A is displaced in the $-y$ direction, friction force F_f increases and the actuator

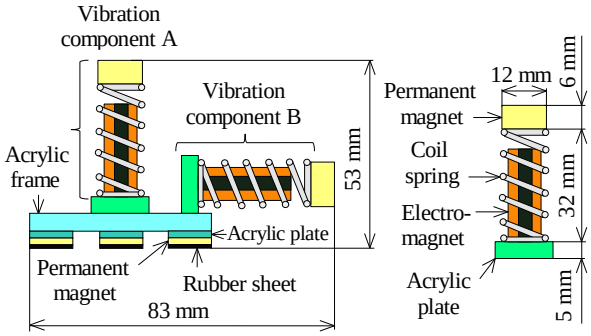

(a) Actuator I and vibration component

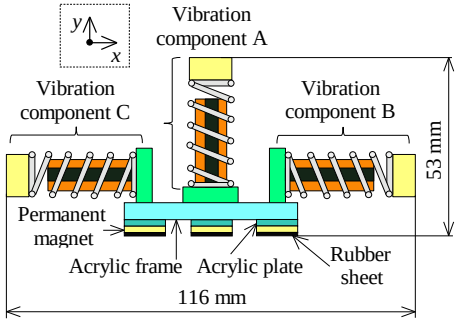

(b) Actuator II

Fig. 1 Structure of phase-controlled actuator

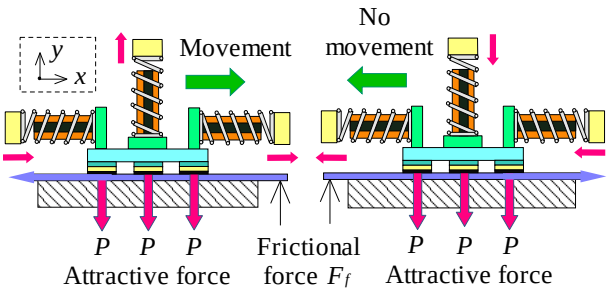

(a) Movement (b) No movement

Fig. 2 Principle of locomotion for proposed actuator

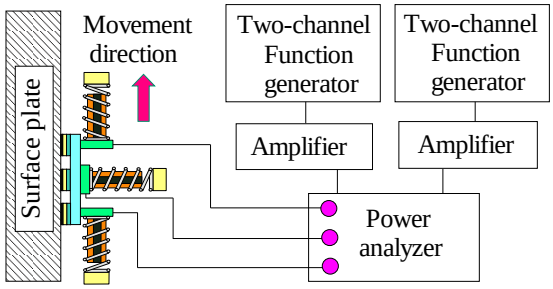

Fig. 3 Experimental apparatus

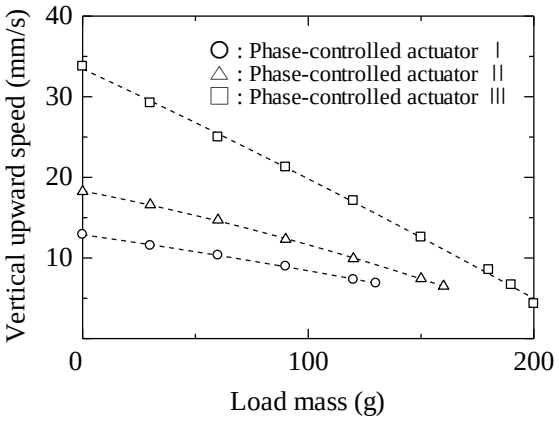

Fig. 4 Relationship between load mass and vertical upward speed

Movement Characteristics of Phase-controlled Actuator

does not move when components B and C are displaced in the -*x* direction. Therefore, the actuator can move only in the +*x* direction.

Fig. 3 shows a schematic diagram of the experimental setup. An iron surface plate (width: 300 mm, length: 300 mm, thickness: 60 mm) was used as the magnetic material. Two 2-channel signal generators with variable phase capability and two power amplifiers were used to resonantly drive the vibration components mounted on the phase-controlled actuator. The resonant frequency of each vibration component was 90.5 Hz. The AC current input to the electromagnets inserted in the vibration components was measured using a power analyzer.

Table 1 Vibration amplitude of each vibration component

Driving component (250 mA)	Amplitude of vibration component (mm)		
	A	B	C
A	3.90	0	0
B	0	3.26	2.36

Hereafter, the AC current input to the electromagnet is reported as an effective value. The attractive force on the permanent magnet to which the rubber sheet is attached is P = 2 N. Thus, the total pull force of the actuator is 6 N. The coefficient of friction between the rubber sheet and the surface plate is μ = 0.84.

Phase-controlled actuators I and II were set on a vertical plane. Fig. 4 shows the relationship between the load mass attached to the actuators and the vertical upward speed, with the input current to vibration component A set at 60 mA and that to vibration component B (= C) set at 250 mA. The load mass was attached to the acrylic frame of the actuator using string. From this figure, the propulsion characteristics of actuator II are only about 1.45 times, not twice, those of actuator I. The reason for this is likely vibration interference between the vibration components, which have the same dimensions.

Table 1 shows the vibration amplitudes of vibration components A, B, and C for phase-controlled actuator II when the electromagnet was driven resonantly with an input current of 250 mA. The vibration amplitudes were measured using a laser displacement meter and a digital oscilloscope. When vibration component A is driven, components B and C are orthogonally aligned, so there is no vibration interference between the vibration components.

On the other hand, when vibration component B is driven, the vibration wave propagates to component C. Since vibration components B and C vibrate symmetrically around the center of the frame, the interference between them is very large. Antisymmetric vibration of vibration components B and C is necessary for the actuator to move. This requires that a large input current be applied to vibration component C. The addition of a vibration component with the same characteristics is not a viable solution for improving the propulsive characteristics due to the vibration interference problem.

COUPLING OF VIBRATION COMPONENTS WITH DIFFERENT DRIVE FREQUENCIES

From the point of view of vibration, to completely prevent vibration interference between vibration components, the vibration frequency of one of the two components must be at least twice

that of the other component. To eliminate vibration interference, vibration components with different frequencies (denoted as actuator III) were installed and investigated.

Fig. 5 shows the displacements (x and y) of vibration components A, B, and C versus ωt, where ω is the angular frequency and t is time. In the figure, the second, third, and fourth harmonics are shown with respect to the fundamental wave ω, with the initial phase varying as in Eq. (1).

$$\left.\begin{aligned} y &= \sin \omega t \\ y &= \sin 2\omega t - \pi/2 \\ y &= \sin 3\omega t - \pi \\ y &= \sin 4\omega t + \pi \end{aligned}\right\} \quad (1)$$

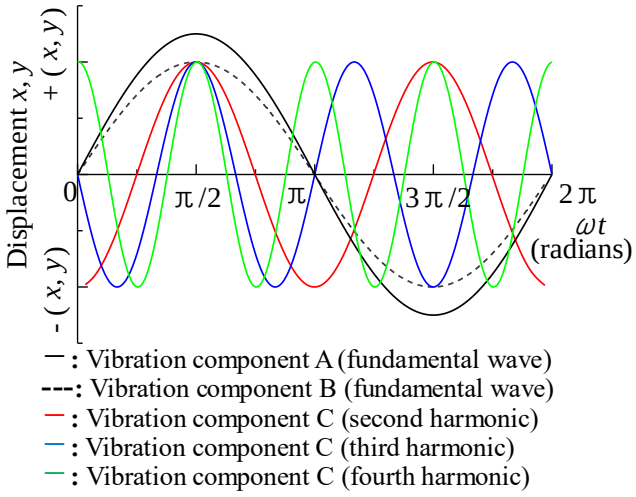

Fig. 5 Fundamental wave and second, third, and fourth harmonics

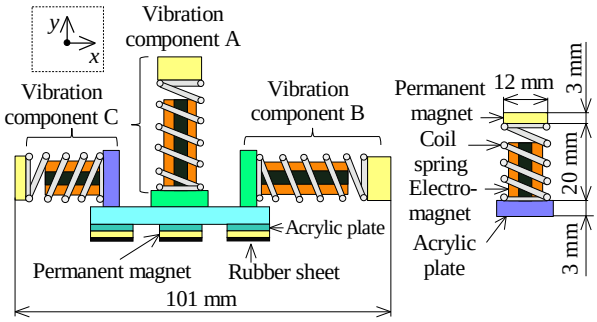

(a) Component C with different drive frequencies (b) Component with second harmonic

Fig. 6 Phase-controlled actuator III

The solid and dashed black lines in the figure show the vibration displacements of vibration components A and B, respectively, shown in Fig. 6(a) for the fundamental wave. The red, green, and blue lines show the vibration displacements of vibration component C shown in Fig. 6(a) for the second, third, and fourth harmonics, respectively, of vibration components A and B. As shown in Fig. 2, in the operation principle of the phase-controlled actuator, displacements x and y of fundamental-wave vibration components A and B are synchronized with a phase difference of 0 degrees.

The relationship between the second harmonic (red line) and fundamental-wave vibration component A (black line) is next discussed, including the displacement coordinates x and y in Fig. 6(a). As shown earlier, friction force F_f decreases (increases) when vibration component A is displaced in the $+x$ ($-x$) direction.

In Fig. 5, at ωt = 0 or π, the actuator does not move in the $-x$ direction when second-harmonic vibration component C is displaced in the $-x$ direction, because vibration component A is in a neutral state. On the other hand, at $\omega t = \pi/2$, friction force F_f decreases as vibration component A is displaced in the $+y$ direction. In this condition, when second-harmonic vibration component C is displaced in the $+x$ direction, the actuator tends to move in the $+x$ direction. In the range $\omega t > \pi$, friction force F_f increases as vibration component A is displaced in the $-y$ direction and the actuator does not move when vibration component C is displaced in the $+x$ direction. Therefore, the combination of the fundamental wave and the second harmonic allows the actuator to move in the intended direction (i.e., the $+x$ direction).

Consider the third harmonic (green line) and the fundamental wave (black line) in Fig. 5. For $0 < \omega t < \pi$, fundamental-wave vibration component A is displaced in the $+y$ direction and friction force F_f decreases. In this range, third-harmonic vibration component C makes one half-period motion in the $+x$ direction and two half-period motions in the $-x$ direction, so the actuator is expected to move less in the $+x$ direction. Furthermore, in the range $\omega t > \pi$, frictional force F_f increases due to the vibrational displacement of vibration component A. Thus, even if vibration component C is displaced in the $+x$ direction, the actuator cannot move in the intended direction (i.e., the $+x$ direction).

If the direction of movement of the actuator can be controlled by a combination of the fundamental wave and the second harmonic, the fourth harmonic, whose frequency is twice that of the second harmonic, can be considered an applicable frequency.

As shown in Fig. 6(a), a prototype of phase-controlled actuator III with vibration component C (see Fig. 6(a)), whose frequency is the second harmonic with respect to the fundamental wave, was developed. As shown in Fig. 6(b), the stainless steel coil spring that constitutes vibration component C has an outer diameter of 11 mm, a free length of 20 mm, and a spring constant of 3,926 N/m. The NdFeB permanent magnet (diameter: 12 mm, height: 3 mm) is magnetized in the height direction. The electromagnet consists of a 3.2-mm-diameter iron

core around which 0.18-mm-diameter copper wire was wound 880 turns. The gap between the iron core and the permanent magnet is 3 mm. The resonant frequency of second-harmonic vibration component C is 181 Hz. Except for vibration component C, the vibration components are identical to the actuator shown in Fig. 1(b). Preliminary experiments confirmed that no vibration interference occurs between the electromagnets of vibration components A, B, and C when they are each driven resonantly by applying a current of 250 mA. As shown in Fig. 5, the initial phases in the fundamental-wave and second-harmonic vibration components were adjusted using the 2-channel signal generator.

The movement speed of actuator III was measured when the same input current as that for the fundamental-wave vibration component was applied to second-harmonic vibration component C. The obtained results are shown in Fig. 4 (square symbols). The measurement results show that the movement characteristics of actuator III are more than twice those of actuator II. The combination of the fundamental wave and the second harmonic, which does not cause vibration interference between the vibration components, is a very effective method for improving the propulsive characteristics of the actuator.

ACTUATOR SYSTEM WITH TWO COUPLED PHASE-CONTROLLED ACTUATORS

Structure and Operation Principle

To further improve the propulsion characteristics, a prototype actuator system was developed in which phase-controlled actuators with fundamental-wave and second-harmonic vibration components are coupled, as shown in Fig. 7. The drive frequencies for the fundamental-wave and second-harmonic vibration components are 90.5 and 181 Hz, respectively.

Fig. 8 shows the prototype actuator system. In this actuator system, three fundamental-wave vibration components (A, B, and C) are mounted within an acrylic frame (thickness: 5 mm, length: 150 mm). The combination of these components is denoted as type I. In addition, four second-harmonic

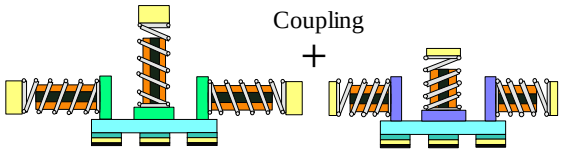

(a) Fundamental wave (b) Second harmonic

Fig. 7 Coupling of two phase-controlled actuators

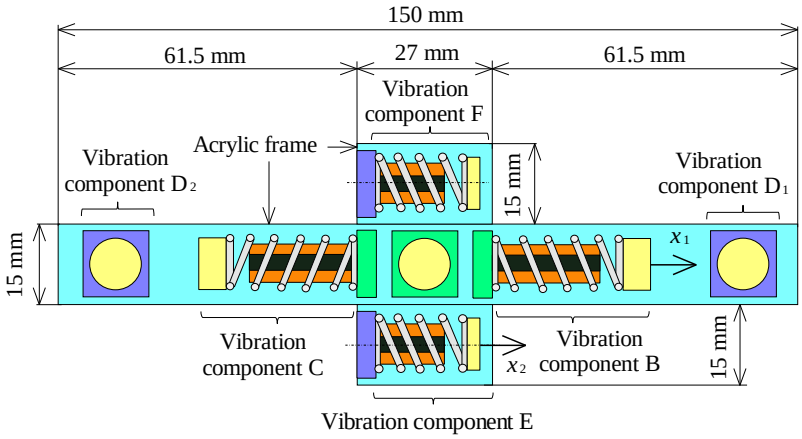

(a) Plan view

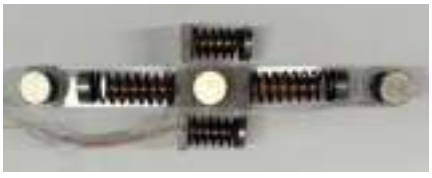

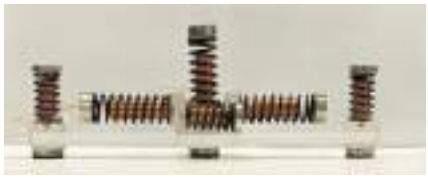

(c) Photographs

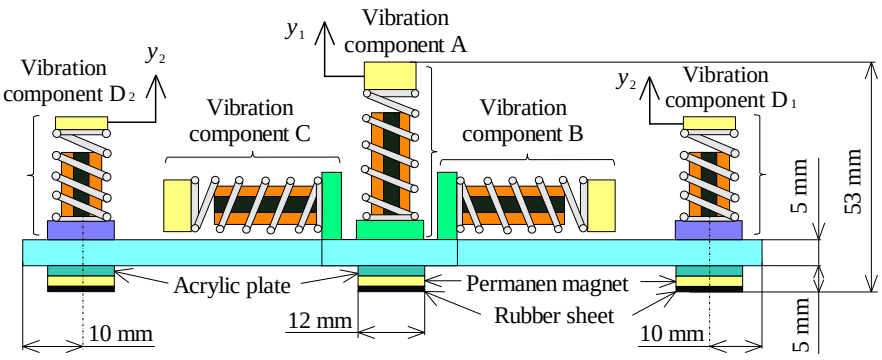

(b) Front view (excluding vibration component E and F)

Fig. 8 Structure of actuator system

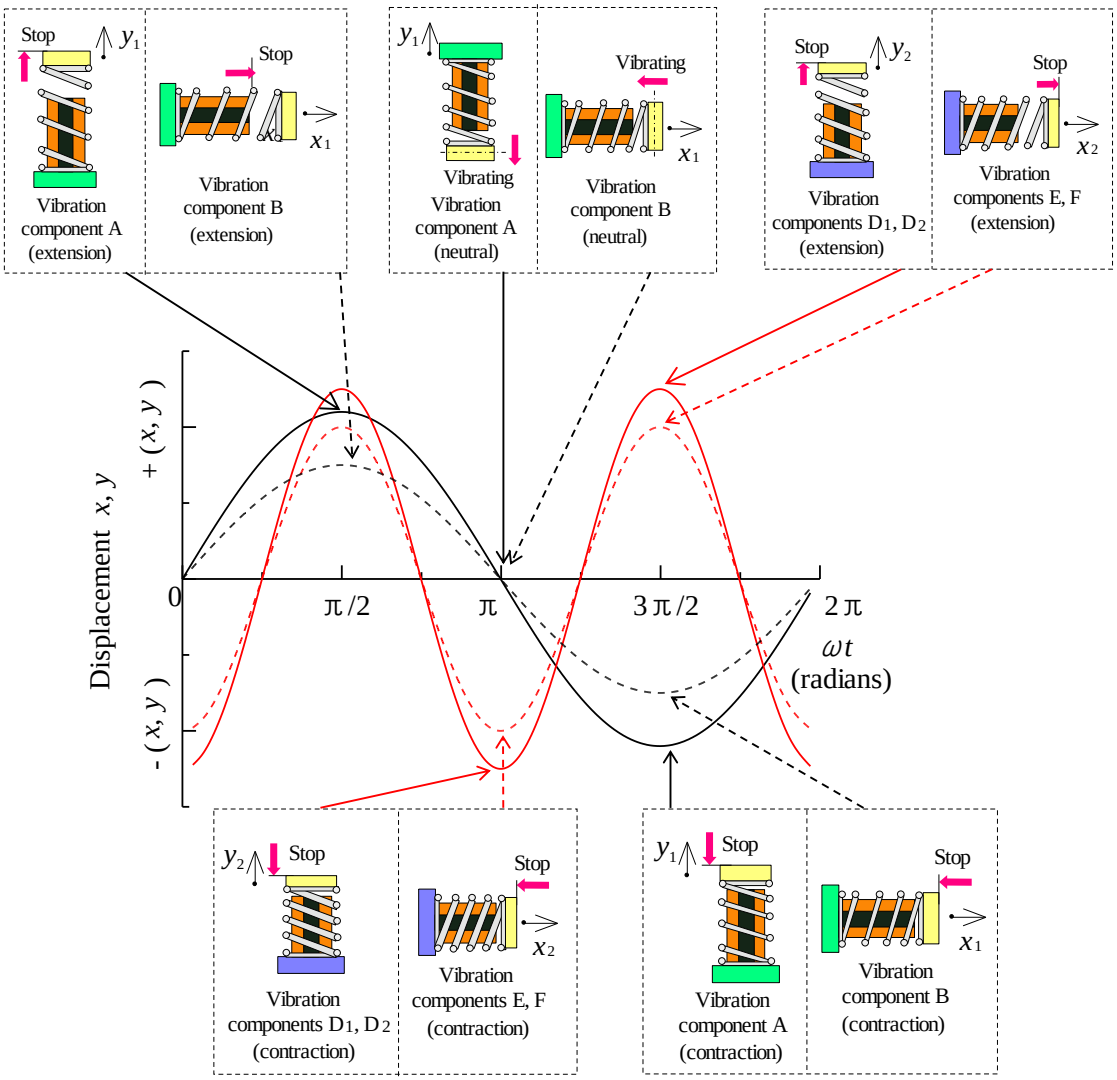

— : Vibration component A (fundamental wave)
— : Vibration components D_1, D_2 (second harmonic)
--- : Vibration component B (fundamental wave)
--- : Vibration components E, F (second harmonic)

Fig. 9 Operation principle of actuator system (displacement and generated force of each vibration component)

vibration components (D_1, D_2, E, and F) are mounted. This combination is denoted as type II. This actuator system has second-harmonic vibration components E and F attached in parallel to enable rotational motion in addition to linear reciprocating motion. The fundamental-wave and second-harmonic vibration components were tuned to have the same vibration characteristics. For each vibration component, the displacement coordinates x_1, x_2 and y_1, y_2 were defined as shown in Fig. 8. When the actuator system moves, vibration components B and C vibrate anti-symmetrically with respect to displacement coordinate x_1. Vibration components E and F are displaced in the same direction with respect to displacement coordinate x_2.

The three permanent magnets and the rubber sheets attached to the bottom of the actuator system have the same dimensions as those for the actuators shown in Fig. 1. This actuator system is 53 mm high, components A and B (C is antisymmetric with B). 150 mm long, and 45 mm wide and has a total mass of 120 g.

Next, the operation principle of the combined type I and type II phase-controlled actuators is considered. Fig. 9 shows the displacements (x_1, x_2 and y_1, y_2) of the fundamental-wave and second harmonic vibration components with the initial phase adjusted versus ωt. The black solid and dashed lines show the vibration displacements of fundamental-wave. The red solid and dashed lines show the vibration displacements of second-harmonic vibration components D_1, D_2 and E, F, respectively.

In Fig. 9, at $\omega t = 0$ or π, fundamental-wave vibration components A and B (C vibrates anti-symmetrically with B) are neutral. On the other

hand, since second-harmonic vibration components D_1 and D_2 are displaced in the $-x_2$ direction, friction force F_f increases and the actuator does not move in the $-x_1$ direction even though vibration components E and F are displaced in the $-x_2$ direction.

At $\omega t = \pi/2$, when vibration components A and D_1, D_2 are displaced in the $+y_1$ and $+y_2$ directions, respectively, friction force F_f is minimal. Under these conditions, when vibration components B, C and E, F are displaced in the $+x_1$ and $+x_2$ directions, respectively, the actuator system tends to move in the $+x_1$ ($+x_2$) direction.

At $\omega t = 3\pi/2$, fundamental-wave vibration component A is displaced in the $-x_1$ direction and friction force F_f increases. On the other hand, friction force F_f decreases because second-harmonic vibration components D_1 and D_2 are displaced in the $+x_2$ direction. In addition, fundamental-wave vibration components B and C are displaced in the $-x_1$ direction and second-harmonic vibration components D_1 and D_2 are displaced in the $+x_2$ direction. The forces generated by these vibration components cancel each other and the actuator system is not expected to move. The above operation principle allows the actuator system to move in the intended direction (i.e., $+x_1$ ($+x_2$) direction) once every two cycles of the second harmonic.

The phase difference of the vibration in the state of displacement at each vibration component shown in Fig. 8 is defined as 0 degrees (in phase). Adjusting the phase difference of the vibration at vibration components A and D_1, D_2 to 180 degrees (out of phase) can reverse the direction of movement of the actuator system.

Movement Characteristics of Actuator System

The prototype actuator system was set on a surface plate and its movement characteristics were measured. Fig. 10 shows the movement speed of the actuator system in the horizontal plane when the input currents to vibration components A and D_1, D_2 were fixed at 60 and 100 mA, respectively, and the input currents to vibration components B, C, E, and F were varied. In the figure, open circles are the measurement results when the phase difference between vibration components is adjusted to be in phase (0 degrees), as shown in Fig. 8, and filled circles are the measurement results when the phase difference between vibration components is adjusted to be out of phase (180 degrees). The figure shows that the actuator system can move reciprocally at an almost constant speed.

Fig. 11 shows the movement speed of the actuators for the ceiling surface when the input currents to vibration components A and D_1, D_2 were fixed at 60 and 100 mA, respectively, and the input currents to vibration components B, C, E, and F were varied. The phase difference between vibration

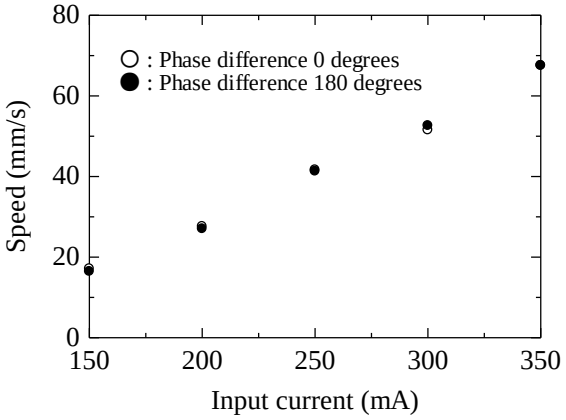

Fig. 10 Relationship between input current and speed (horizontal plane)

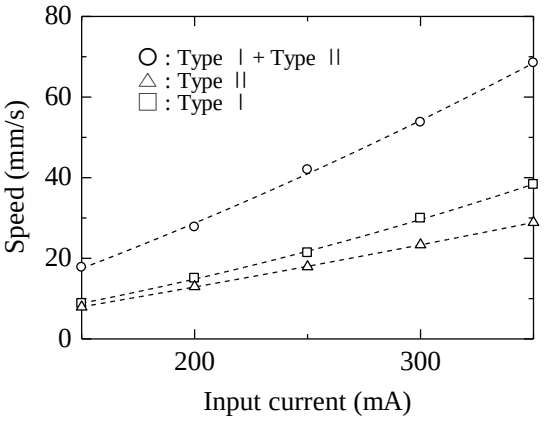

Fig. 11 Relationship between input current and speed (ceiling surface)

components was adjusted to be in phase for the measurements. The dashed lines are the results of a quadratic approximation of the measured values obtained using the least-squares method (in following figures, dashed lines are the results of a second-order approximation obtained using the least-squares method). The square, triangle, and circle symbols are the results for type I with fundamental-wave vibration components A, B, and C driven, type II with second-harmonic vibration components D_1, D_2, E, and F driven, and a combination of types I and II, respectively. Fig. 11 shows that the movement speed increases almost linearly with increasing input current. The movement characteristics for the combination of type I and II actuators driven are considerably better than those of actuators driven only with fundamental-wave or second-harmonic vibration components.

Figs. 12 and 13 show the relationship between the vertical upward speed of the actuator system and the load mass when the input currents to vibration component A and vibration components D_1, D_2 were fixed at 60 and 100 mA, respectively, and the input currents to vibration components B, C, E, and F

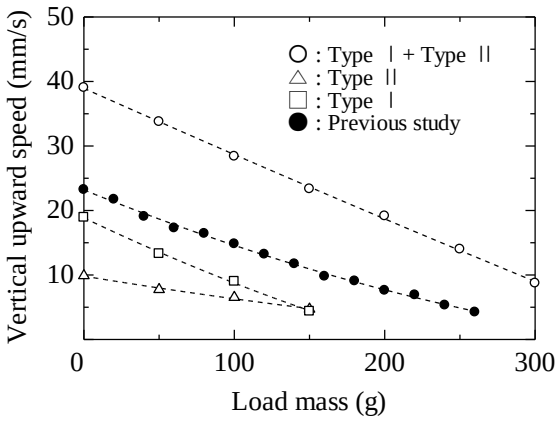

Fig. 12 Relationship between load mass and vertical upward linear speed (input current 250 mA)

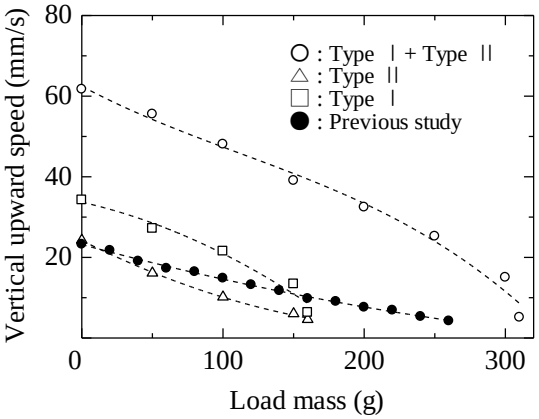

Fig. 13 Relationship between load mass and vertical upward linear speed (input current 350 mA)

were fixed at 250 or 350 mA. With both type I and II actuators driven and an input current of 350 mA, the actuator system is capable of vertical upward movement at the speed of 15.1 mm/s while pulling a 300-g load mass. The solid circles in both figures are the speed values for an actuator system [8] with the same total mass of 120 g and eight fundamental-wave vibration components when an input current of 250 mA is applied to each vibration component. Due to the reduced vibration interference, the movement characteristics of the proposed actuator system greatly exceed those of the actuator system in a previous study [8].

A fundamental-wave-type actuator has a low drive frequency, which allows a large vibration amplitude with a relatively small input current. This results in the generation of large elastic energy and high movement speed. In contrast, a second-harmonic-type actuator has a high drive frequency and cannot generate a large vibration amplitude. However, it can generate a large inertial force proportional to the square of the vibration frequency. The excellent performance of the proposed actuator system is due to the effective superposition of the conflicting movement characteristics of the two types of actuator.

Based on the above, the actuator system is considered to move based on the operation principle shown in Fig. 9. This paper thus establishes a new operation principle for a phase-controlled actuator system that has good movement characteristics and can instantly switch movement direction.

ACTUATOR SYSTEM OPERATION PRINCIPLE AND ROTATIONAL CHARACTERTICS

The above operation principle for linear motion can be extended to rotational motion. For rotational motion in the actuator system, only the type II phase-controlled actuator was driven. As shown in Figs. 8 and 14, when vibration components D_1 and D_2 are displaced in the $+y_2$ direction, friction force F_f decreases. In this state, when vibration components E and F are displaced in the $+x_2$ and $-x_2$ directions, a moment acts on the center of the actuator system. Therefore, the system rotates counterclockwise. On the other hand, if the vibration phases of vibration components D_1 and D_2 are set to be out of phase, the system rotates clockwise.

By controlling the phase difference of the vibrations in each vibration component, the actuator system can reciprocate in all directions (i.e., 360 degrees). The rotational characteristics of the actuator system were measured by fixing the input current to vibration components D_1 and D_2 at 100 mA and varying the input current to vibration components E and F.

Fig. 15 shows the rotational speed when the actuator system was set on horizontal and vertical planes and the phase difference of the vibration between vibration components D_1, D_2 and vibration components E, F was set to 0 degrees (in phase) or 180 degrees (out of phase). In the figure, square and plus symbols (triangle and diamond symbols) are the measurement results when the phase difference between the vibration components was in phase and

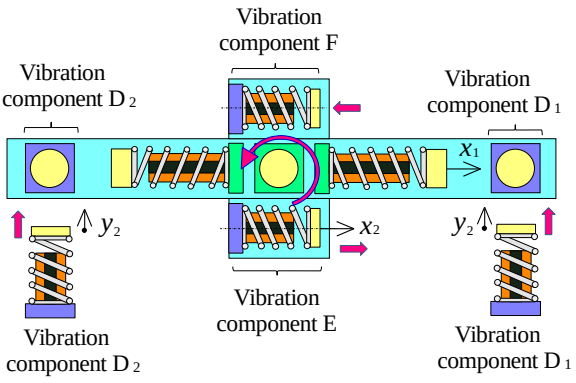

Fig. 14 Rotational principle of actuator system

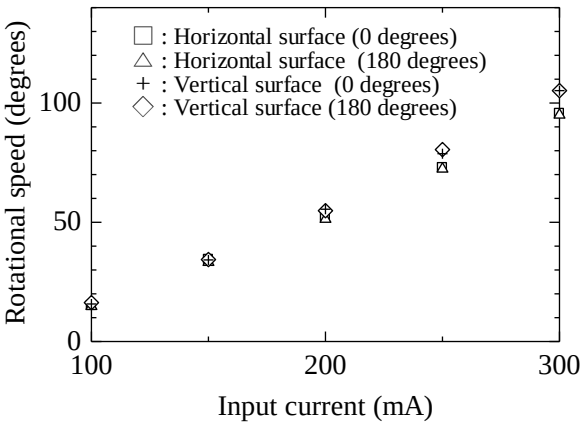

Fig. 15 Relationship between input current and rotational speed (rotational movement)

out of phase in the horizontal (vertical) plane, respectively. The rotational speeds of the actuator system are almost equal when the phase differences between the vibration components are in phase and out of phase. The rotational speed of the actuator system increases linearly as the input current to vibration components E and F is increased. In this actuator system, the mounting position of each vibration component is at the same distance to the center of the frame. When the actuator system is set in the vertical plane, the moments caused by gravity are canceled in each vibration component. Therefore, the rotational speeds of the actuator system in the horizontal and vertical planes are nearly equal.

CONCLUSIONS

In this study, an actuator system coupled with a phase-controlled actuator with fundamental-wave and second-harmonic vibration components was proposed to improve propulsion characteristics. The operation principle of the actuator system was discussed. Based on the results of tests on prototypes, the operation principle of the phase-controlled actuator system, which can instantly switch its direction of linear motion, was established. The movement and traction characteristics of the actuator system are excellent since the vibration interference between the mounted vibration components is considerably reduced and two actuators with different characteristics are coupled.

The proposed actuator system can move vertically at a speed of 15.1 mm/s even with a load mass of 300 g. A commercially available automatic tapping device with a mass of 260 g can thus be mounted. The possibility of the internal inspection of iron structures was demonstrated through tests on prototypes. Furthermore, this actuator system can move in any direction (i.e., 360 degrees) by combining rotational and translational reciprocating motions. Because the actuator system can move on ceilings and walls, it could be useful for inspection devices.

Future work will develop a prototype phase-controlled actuator with a power-of-two-type vibration component and conduct a theoretical motion analysis that takes into account the nonlinearity of the vibration component.

REFERENCES

[1] Kim J., Park S., Kim J., and Lee J., Design and Experimental Implementation of Easily Detachable Permanent Magnet Reluctance Wheel for Wall-Climbing Mobile Robot. Journal of Magnetics, Vol. 15, No. 3, 2010, pp. 128-131.

[2] Suzuki M., and Hirose S., Proposal of Swarm Type Wall Climbing Robot System Anchor Climber and Development of Adhering Mobile Units. The Robotics Society of japan, Vol. 28, No. 5, 2010, pp. 614-623.

[3] Panich S., Development of a Climbing Robot with Vacuum Attachment Cups. Journal of Computer Science, 2010, Vol. 6, No. 10, pp. 1185-1188.

[4] Shen W., Gu J., and Shen Y., Permanent System Design for the Wall-Climbing Robot. in Proc., IEEE International Conference on Mechatronics & Automation, 2011, pp. 2078-2083.

[5] Wang W., Wang K., Zhang H., and Zhang J., Internal Force Compensating Method for Wall-Climbing Caterpillar Robot. in Proc., IEEE International Conference on Robotics and Automation, 2010, pp. 2816-2820.

[6] Tao C., and Liu B., Online Autonomous Motion Control of Communication-Relay UAV with Channel Prediction in Dynamic Urban Environments, Drones, 2024, Vol. 8, No. 12, pp. 1-25.

[7] Rushood M., Rahbar F., Shokri S., Selim S., and Dweiri F., Accelerating Use of Drones and Robotics in Post-Pandemic Project Supply Chain, Drones, Vol. 7, No. 55, 2023, pp. 1 - 9.

[8] Abe S., and Yaguchi H., Phased-controlled Actuator System Capable of Visual Inspection inside Iron structure, International Journal of GEOMATE, Vol. 28, No. 127, 2025, pp. 112 - 120.

Copyright © Int. J. of GEOMATE All rights reserved, including making copies, unless permission is obtained from the copyright proprietors.

15th Int. Conf. on Geotechnique, Construction Materials & Environment,
Kyoto, Japan, 11-13 November 2025, ISBN 978-4-909106124 C3051

A LIDAR-BASED DEEP LEARNING FRAMEWORK FOR DRIFTWOOD RECOGNITION AND QUANTIFICATION

Shanpeng Liu[1], Koichi Isobe[2], Toshiki Iwasaki[2], Kensuke Shioda[3] and Diyuan Li[1]

[1] Graduate School of Engineering, Hokkaido University, Japan; [2] Division of Civil Engineering, Graduate School of Engineering, Hokkaido University, Japan; [3] Faculty of Engineering, Hokkaido University, Japan

ABSTRACT

Driftwood disasters pose serious risks to river environments and infrastructure, making precise identification and quantification crucial for effective disaster assessment and mitigation. However, the complex nature of driftwood disaster scenarios presents challenges for existing automated recognition and quantification methods. To address these limitations, this study proposes a LiDAR-based deep learning approach for driftwood disaster investigation. A flume experiment was conducted to mimic a braided bar-channel pattern and subsequent driftwood transport-deposition in river channels, capturing high-resolution 3D point cloud data using a LiDAR scanner. To enhance model robustness and generalization, a dataset augmentation technique leveraging the geometric characteristics of driftwood was introduced. Three deep learning models—PointNet++, PointNet++ MSG, and GACNet—were applied for semantic segmentation of driftwood, integrating DBSCAN clustering and point cloud volume estimation to quantify driftwood volume. Experimental results demonstrate that the proposed segmentation method effectively adapts to driftwood disaster scenarios, with all deep learning models achieving an mIoU exceeding 80%. Notably, dataset augmentation significantly enhances segmentation accuracy compared to models without augmentation, confirming its effectiveness in optimizing deep learning models for driftwood recognition. Furthermore, comparative analysis reveals that GACNet outperforms other models in both segmentation accuracy and volume estimation, enabling more precise driftwood identification across various scenarios. Furthermore, the proposed method successfully clarified the relationship between the estimated driftwood accumulation and the riverbed morphology. This study validates the feasibility of integrating deep learning with LiDAR point cloud analysis for driftwood disaster assessment, offering a novel and effective approach for disaster investigation and mitigation.

Keywords: Driftwood; Point cloud; Semantic segmentation; Dataset augmentation; Flume experiment

INTRODUCTION

Driftwood disasters pose significant threats to river environments, infrastructure, and public safety worldwide. During flood events, large quantities of woody debris are mobilized and transported downstream, creating complex accumulations that can damage bridges, block channels, increase flood risks, and destabilize riverbanks [1]. In Japan, mountainous watersheds with dense forest cover are particularly susceptible to such disasters, with several catastrophic events recorded in recent decades causing substantial economic losses and environmental impacts. The effective management of driftwood disasters requires accurate and efficient methods for assessing accumulation patterns, quantifying volumes, and understanding the underlying transport mechanisms.

Traditional approaches to driftwood disaster investigation rely heavily on manual field surveys and visual estimation techniques [2]. These methods are often labor-intensive, subjective, and limited in their ability to capture the three-dimensional complexity of driftwood accumulations. More recently, remote sensing technologies have been employed to improve disaster assessment capabilities, with satellite imagery and aerial photogrammetry offering broader spatial coverage [3,4]. However, these methods still face significant challenges in accurately identifying and quantifying driftwood in complex riverine environments, particularly when dealing with densely packed accumulations.

Light Detection and Ranging (LiDAR) technology presents a promising solution for addressing these limitations. By providing high-resolution three-dimensional point cloud data, LiDAR scanners can capture the detailed geometric characteristics of driftwood pieces and their spatial arrangements [5].

The rapid advancement of deep learning techniques for point cloud analysis offers new opportunities for automating the identification and quantification of disasters in LiDAR data [6]. Unlike traditional machine learning methods that rely on hand-crafted features, deep learning models can automatically learn hierarchical representations directly from raw point cloud data. Recent developments in point-based neural networks, such as PointNet++ and Graph Attention Convolution Network (GACNet), have demonstrated remarkable performance in point cloud segmentation tasks across various domains [7,8]. However, the application of

these techniques to driftwood disaster scenarios remains largely unexplored, with unique challenges arising from the irregular distribution and complex arrangements of woody debris in river environments.

A significant obstacle to implementing deep learning approaches for driftwood disaster investigation is the limited availability of labeled training data. Unlike common objects in computer vision datasets, driftwood accumulations exhibit high variability in appearance and structure, making it difficult to create comprehensive training datasets that capture all possible scenarios.

To address these challenges, this study proposes an integrated approach combining LiDAR-based data acquisition with deep learning techniques for driftwood disaster investigation. Through controlled flume experiments simulating various driftwood transport and deposition scenarios, we create a dataset of high-resolution point clouds capturing the complex geometry of driftwood accumulations. We introduce a novel dataset augmentation technique specifically designed for point cloud data that leverages the geometric characteristics of driftwood to enhance model training. Three state-of-the-art deep learning models—PointNet++, PointNet++ MSG (Multi-Scale Grouping), and GACNet—are implemented and evaluated for semantic segmentation of driftwood in the point cloud data. Additionally, we develop a volumetric analysis procedure that integrates clustering algorithms with geometric reconstruction methods to quantify driftwood accumulation volumes. By investigating the relationship between riverbed morphology and driftwood distribution patterns, this study aims to provide insights into the underlying mechanisms of driftwood transport and deposition in river systems, contributing to improved disaster assessment and mitigation strategies.

RESEARCH SIGNIFICANCE

This study presents a novel integration of LiDAR-based point cloud acquisition and deep learning techniques for the automated investigation of driftwood disasters. By introducing a geometric-aware dataset augmentation method and evaluating segmentation models under controlled flume conditions, the research addresses key challenges such as class imbalance in driftwood environments. The findings advance the application of deep learning in geological hazard assessment and offer practical solutions for quantifying driftwood volume and understanding its interaction with riverbed morphology.

METHODOLOGY

Fig. 1 provides a schematic overview of the proposed methodological framework. Beginning with a controlled indoor flume experiment, the process proceeds through LiDAR-based point cloud acquisition. The raw point cloud data is enhanced using a multi-scale geometric feature augmentation strategy to mitigate the effects of class imbalance and improve model generalization. Semantic segmentation is performed using three state-of-the-art deep learning models, each trained with and without dataset augmentation. The segmented driftwood points are then clustered using DBSCAN, and their volumes are estimated using both convex hull analysis and voxelization with porosity correction. This integrated pipeline enables precise quantification of driftwood accumulation and analysis of waterway interaction.

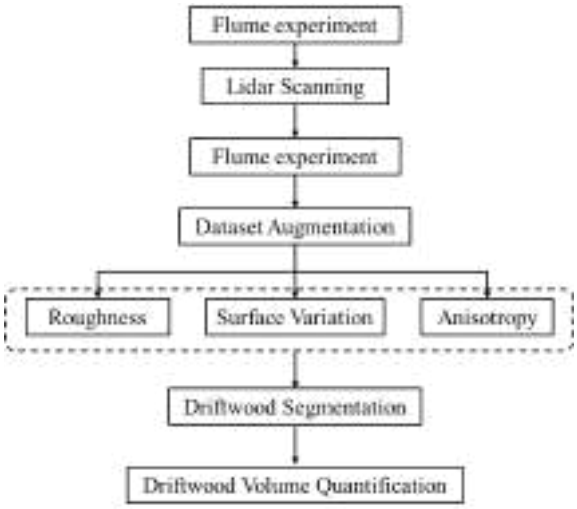

Fig. 1 Overall workflow

Experimental Design and Flume Setup

The experimental investigation was conducted in a hydraulic laboratory using a custom flume facility designed specifically to mimic a braided bar-channel pattern and subsequent driftwood transport-deposition in river environments, as shown in Fig. 2.

Uniform sand with a grain size of 0.765 mm (Northeast Silica Sand No. 4) was used for the movable bed. A straight channel with the channel width of 0.5 m was set for the initial channel, and we firstly imposed a constant, steady water discharge for 4 hours from the upstream end to generate the braided channel morphology as shown in Fig. 2.

After the initial phase, 10 pieces of driftwood with diameter of 1.8 mm and length of 100 mm were introduced every 5 minutes over a period of 4 hours. During this phase, riverbed changes and driftwood accumulation were continuously observed. Throughout the experiment, sediment was supplied from the upstream end to maintain sediment balance.

A critical aspect of the experimental design was the use of waterlogged wood instead of dry wood to

accurately simulate real driftwood buoyancy characteristics. Natural driftwood typically has a specific gravity ranging from 0.9 to 1.2. By using waterlogged specimens, the experiment more faithfully reproduced the transport and deposition behaviors observed in actual river systems during flood events.

The flume was configured with a longitudinal bed slope of 0.04, extending from the inlet to the outlet, to generate a unidirectional flow regime that effectively transported both sediment and driftwood through the channel. During the experiment, the discharge was maintained at 0.0005 m^3/s, corresponding to a dimensionless shear stress of 0.10, which ensured active sediment mobility and driftwood entrainment under controlled conditions. The channel width-to-depth ratio for the initial channel was set at 1151, reflecting a shallow, wide channel morphodynamic environment representative of braded bar-channel feature seen in natural rivers. This carefully controlled hydraulic setting, as shown in the schematic diagram in Fig. 2, enabled systematic observation of the complex interactions among water flow, sediment transport, and driftwood movement and accumulation.

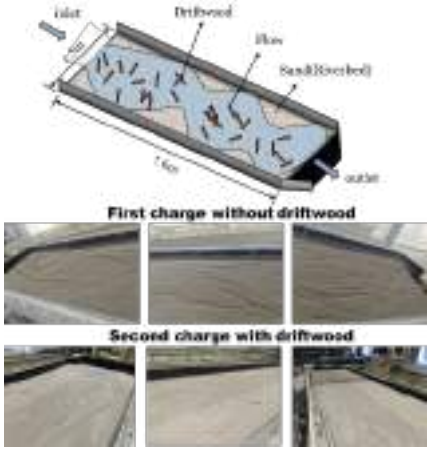

Fig. 2 Flume experiment of driftwood

LiDAR Data Acquisition

To acquire high-precision data on driftwood distribution and riverbed morphology, this study employed a handheld Revopoint MIRACO Pro laser scanner, for three-dimensional mapping of the experimental flume. The scanner performed precise pre- and post-experiment scans of the sandy riverbed and debris deposition zones, enabling detailed analysis of topographical changes and debris distribution.

The scanning system offered precision of ±0.1-1 mm with an effective range of 0-1 m, making it ideal for laboratory-scale experiments. Output data was stored in LAS format, containing XYZ coordinates, RGB color values, and normal vector data. The handheld free-scanning methodology allowed flexible movement around the experimental setup to ensure complete coverage of complex geometries while minimizing occlusion effects.

The scanning covered an area of 8 m × 1.5 m, resulting in a dense point cloud dataset containing 81,251,496 points. As shown in the visualization of Fig. 3, the scanning process successfully captured the complex three-dimensional topography of the riverbed and driftwood accumulation patterns with exceptional detail.

Dataset

The dataset used in this study consists of high-resolution point cloud data obtained from indoor flume experiments under controlled conditions. Each point contains XYZ coordinates, RGB color values, and surface normal vectors. The final dataset includes 81,251,496 points, representing both driftwood and riverbed elements.

The dataset is structured for a binary semantic segmentation task and includes two primary classes: driftwood and non-driftwood. The driftwood class refers to all recognizable woody debris, including both individual logs and aggregated accumulations, while the non-driftwood class encompasses the background, such as exposed sand, sediment surfaces, and riverbed features. Manual annotation was performed to assign class labels based on geometric shape, color, and surface continuity. The resulting class distribution is highly imbalanced, with driftwood representing only 1.58% of all points. This skewed distribution poses a significant challenge for model training, as standard loss functions tend to favor the dominant background class, potentially leading to poor segmentation of driftwood regions.

Data Augmentation

To enhance model generalization ability, we developed a dataset augmentation by multi-scale geometric feature approach that calculated three critical geometric characteristics at multiple scales:

(1) Roughness: For a point p with neighborhood points $\{p_1, p_2, ..., p_k\}$, roughness is calculated as Eq.1:

$$R(p) = \frac{1}{k}\sum_{i=1}^{k} \left\| (p_i - p) - \left((p_i - p) \cdot \hat{n}\right)\hat{n} \right\| \quad (1)$$

where, p_i represents neighboring points, k is the number of points in the neighborhood, $\hat{n}$ is the unit normal vector at point p.

(2) Surface Variation: Computed as the ratio of the smallest eigenvalue to the sum of all eigenvalues of the local covariance matrix, as shown in Eq.2:

$$SV(p) = \frac{\lambda_3}{\lambda_1+\lambda_2+\lambda_3} \quad (2)$$

where, $\lambda_1 \geq \lambda_2 \geq \lambda_3$ are the eigenvalues of the covariance matrix.

(3) Anisotropy: Characterizes the directional dependence of point distributions, as shown in Eq.3:

$$A(p) = \frac{\lambda_1-\lambda_3}{\lambda_1} \quad (3)$$

Deep Learning Models for Segmentation

For driftwood segmentation in point cloud data, three deep learning models were implemented and evaluated: PointNet++, PointNet++ with Multi-Scale Grouping (MSG), and Graph Attention Convolution Network (GACNet) [7,8].

PointNet++ employs a hierarchical structure with Set Abstraction modules that select representative points and group their local regions. Features are extracted through multi-layer perceptions applied to each group, enabling the model to capture local geometric patterns critically for distinguishing driftwood from the riverbed.

PointNet++ MSG enhances standard PointNet++ by implementing Multi-Scale Grouping, which processes each centroid at multiple scales simultaneously. This approach is particularly effective for driftwood segmentation as it captures both fine details of individual wood pieces and broader contextual information about accumulation patterns.

GACNet combines graph convolutional operations with self-attention mechanisms. It constructs a graph representation where each point connects to its k-nearest neighbors. The attention mechanism allows the model to dynamically focus on the most relevant neighboring points, which is advantageous for identifying complex driftwood structures amid varying riverbed formations.

Driftwood Volume Quantification Procedure

The point cloud data after semantic segmentation consists of discrete points, and the volume cannot be calculated directly. It is necessary to identify independent driftwood piles and apply appropriate geometric methods to calculate their volumes.

This study employs a comprehensive approach to driftwood volume quantification, as illustrated in the flowchart. The process begins with the segmentation results from the deep learning models, which separate driftwood points from the riverbed and other elements.

First, DBSCAN (Density-Based Spatial Clustering of Applications with Noise) clustering is applied to identify independent driftwood piles. This algorithm effectively groups points based on density, allowing for the separation of distinct driftwood accumulations even when they are in close proximity.

Following clustering, two parallel analytical paths are pursued:

(1) Convex Hull Method: A convex hull is constructed around each identified driftwood cluster to calculate the envelope volume (V_{convex}). This represents the maximum possible space occupied by the driftwood accumulation, including void spaces between individual pieces. The convex hull effectively creates a three-dimensional boundary that encompasses all points in the cluster, providing an upper bound for volume estimation.

(2) Voxelization Analysis: The point cloud is discretized into a three-dimensional grid of voxels (volumetric pixels) of uniform size. By counting the number of voxels occupied by driftwood points (N_d) versus the total number of voxels within the convex hull (N_c), a porosity factor (η) is calculated using the equation: $\eta = 1 - (N_d/N_c)$ This porosity factor represents the proportion of empty space within the driftwood accumulation, which is critical for accurate volume estimation.

The actual driftwood volume (V_d) is then calculated by applying the porosity correction to the convex hull volume:

$$V_d = V_{convex} \times (1 - \eta) \quad (4)$$

RESULTS AND DISCUSSION

Experimental Results And Riverbed Morphology Changes

The experimental results demonstrate significant impacts of driftwood on riverbed morphology through alterations in sediment transport, fluid dynamics, and channel configuration. After the second release of driftwood in the experiment, the riverbed morphology exhibited considerable changes compared to its initial state. The visualization of riverbed curvature (Fig. 3) clearly illustrates these morphological transformations across the experimental site.

Analysis of the spatial distribution patterns revealed a strong correlation between driftwood accumulation and areas of curvature change in the riverbed. While driftwood was observed throughout

the experimental channel regardless of curvature magnitude, the frequency of accumulation was notably higher in zones with significant curvature variations. This finding suggests that riverbed geometry, particularly abrupt changes in channel direction, serves as a primary controlling factor for driftwood deposition and retention.

A particularly noteworthy observation was that the riverbed morphology in areas of driftwood accumulation often conformed to the shape of the deposited driftwood. This phenomenon indicates a bidirectional relationship where driftwood not only responds to existing channel features but actively modifies the riverbed through localized erosion processes. The driftwood-induced scour patterns observed around accumulated pieces further support this interpretation of active morphological modification.

Qualitative assessment of curvature patterns before and after driftwood introduction showed visible increases in morphological complexity following the second release. This transformation demonstrates the substantial geomorphic impact of driftwood on channel configuration, even in controlled laboratory conditions. The most significant morphological changes occurred at locations where multiple driftwood pieces formed complex accumulation structures, creating flow obstructions that redirected erosional forces.

It should be noted that the current experimental design only permitted comparison between the first and second release conditions. Additional time-series experiments with varied flow conditions would be beneficial to further validate these observations and explore the temporal evolution of driftwood-riverbed interactions. Nevertheless, these findings provide valuable insights into the fundamental mechanisms governing driftwood accumulation and its geomorphic consequences in river systems.

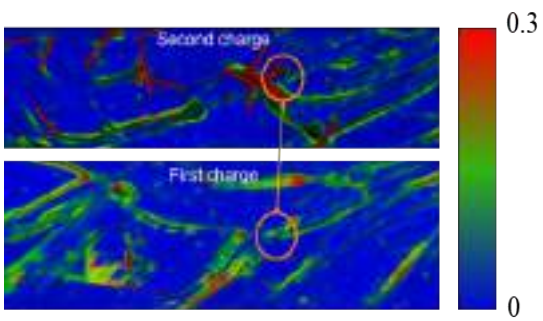

Fig. 3 Visualization of riverbed curvature

Segmentation Results

To evaluate the performance of driftwood segmentation from LiDAR point cloud data, three deep learning models—PointNet++ (PLUS), PointNet++ with Multi-Scale Grouping (MSG), and Graph Attention Convolution Network (GACNet)—were implemented. Each model was trained and tested under two configurations: with dataset augmentation (E) and without dataset augmentation (NE) the proposed dataset augmentation based on multi-scale geometric features. The evaluation metrics included Intersection over Union (IoU), Precision, and F1-score for both driftwood and non-driftwood classes, as well as their macro-averaged mean.

The quantitative results (Table 1) clearly show that dataset augmentation substantially improves model performance. For instance, GACNet(E) achieved the highest overall accuracy with a driftwood IoU of 78.07%, precision of 84.13%, and F1-score of 87.68%. In contrast, its non-augmented counterpart, GACNet(NE), showed noticeably lower performance (IoU = 64.64%, F1 = 78.52%). This trend was consistently observed across all models, confirming the effectiveness of the augmentation technique in mitigating class imbalance and enhancing feature learning.

In the case of PointNet++ (PLUS), dataset augmentation led to a significant improvement from 43.71% to 69.39% in driftwood IoU, and from 60.83% to 81.93% in driftwood F1-score. This demonstrates that even basic hierarchical point-based models benefit considerably from geometric feature enhancement. MSG, which incorporates multi-scale grouping to capture local-global context, showed a similar trend, with IoU improving from 42.97% to 70.27% and F1-score from 60.11% to 82.54%. However, compared to GACNet, both PLUS and MSG exhibited lower segmentation accuracy, likely due to their limited ability to dynamically model contextual dependencies in cluttered driftwood environment.

Among the three models, GACNet demonstrated superior segmentation capability, benefiting from its integration of graph attention mechanisms that allow dynamic context adaptation and better differentiation between driftwood and riverbed points. MSG also performed well due to its multi-scale grouping strategy, capturing both local detail and global context.

Furthermore, qualitative comparisons of the segmentation maps (Fig. 4) show that the dataset augmentation significantly sharpens the boundaries of driftwood objects and reduces the number of isolated noise points incorrectly classified as driftwood. In contrast, models trained without augmentation exhibited more blurred object boundaries and a higher frequency of false positives

scattered throughout the background. These improvements demonstrate the effectiveness of augmentation in enhancing spatial coherence and suppressing spurious classifications in challenging riverbed environments. Among the three, PLUS(E) generated smoother but more conservative driftwood regions, while MSG(E) produced more extensive coverage but included more boundary artifacts. GACNet(E) achieved the best visual clarity and spatial consistency, particularly in distinguishing intertwined driftwood clusters from adjacent sediment zones.

These results highlight the importance of geometric-aware augmentation and attention-based modeling in achieving high-accuracy semantic segmentation of driftwood under complex morphological conditions, thus providing a reliable foundation for subsequent volume estimation and disaster analysis.

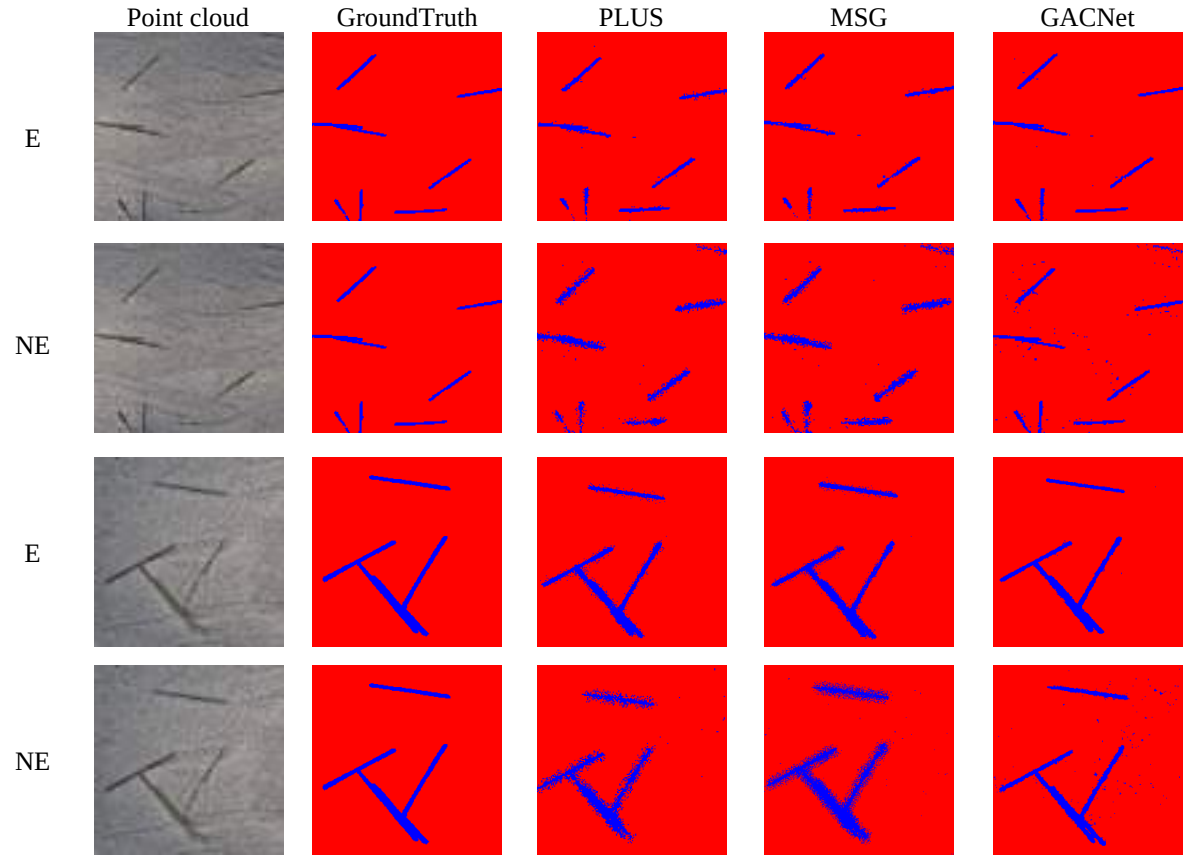

Fig. 4 Visual comparison of segmentation results

Table 1 Quantitative evaluation metrics for driftwood segmentation

	IoU			Precision			F1		
	Driftwood	Non	Mean	Driftwood	Non	Mean	Driftwood	Non	Mean
PLUS(NE)	43.71	98.80	71.25	51.83	99.66	75.75	60.83	99.40	80.11
PLUS(E)	69.39	99.50	84.44	74.85	99.88	87.36	81.93	99.75	90.84
MSG(NE)	42.97	98.59	70.78	46.84	99.79	73.32	60.11	99.29	79.70
MSG(E)	70.27	99.54	84.90	78.82	99.83	89.33	82.54	99.77	91.15
GACNet(NE)	64.64	99.41	82.02	72.71	99.81	86.26	78.52	99.70	89.11
GACNet(E)	78.07	99.67	88.87	84.13	99.89	92.01	87.68	99.84	93.76

Table 2 Comparison of driftwood volume estimations across models and areas

	Actual volume (mm^3)	PLUS		MSG		GACNet	
		NE	E	NE	E	NE	E
Area 1	9608	13608.44	6481.38	13378.61	6618.29	6132.21	7443.16
Area 2	6782	4684.90	2336.51	4771.59	2532.19	2639.43	3843.60
Area 3	11304	20881.60	10713.22	20813.46	10726.56	13464.11	10997.18
Mean error (%)		+31.82%	-34.44%	+31.24%	-32.96%	-26.05%	-22.85%

Driftwood Volume Estimation Results

Table 2 presents the driftwood volume estimation results across three areas using different deep learning models with and without dataset augmentation. The volume estimation accuracy directly reflects the effectiveness of each model in practical driftwood disaster investigation scenarios.

The experimental results reveal distinctive patterns in volume estimation performance across different models and areas. Non-enhanced models PLUS(NE) and MSG(NE) demonstrated inconsistent behavior, significantly overestimating volumes in Areas 1 and 3, while unexpectedly underestimating volumes in Area 2. This inconsistency indicates poor adaptation to varying riverbed morphologies and driftwood distribution patterns. When comparing actual values to estimated volumes, the non-enhanced models showed extreme overestimation in Area 3, with values approximately twice the actual volume.

In contrast, all enhanced models consistently underestimated driftwood volumes across all areas, though with different magnitudes. GACNet(E) achieved the most balanced performance with the lowest mean error (-22.85%) among enhanced models, particularly excelling in Area 3 where its estimated volume was closest to the actual measurement. The dataset augmentation technique substantially transformed the estimation behavior of PLUS and MSG models, converting significant overestimation tendencies to underestimation.

Regional variation analysis revealed a consistent pattern among enhanced models: Area 2 presented the greatest estimation challenges with the largest volume underestimation, followed by Area 1, with Area 3 showing the closest estimates to actual volumes. This systematic pattern strongly indicates that riverbed morphology significantly influences volume estimation accuracy, with certain topographical features presenting greater challenges regardless of model architecture.

The relationship between semantic segmentation performance and volume estimation accuracy presented interesting observations. While GACNet(E) both achieved the highest IoU (78.07%) in segmentation tasks and delivered well-balanced volume estimates, GACNet(NE) with a lower IoU (64.64%) achieved a slightly lower mean error (-26.05%) than GACNet(E) (-22.85%), though with higher area-to-area variation. This suggests that while improved segmentation generally contributes to better volume estimation, other factors in the volume calculation pipeline may influence final accuracy.

The consistent underestimation observed in enhanced models may indicate systematic effects in boundary detection or voxelization processes that warrant further investigation. Nevertheless, GACNet with dataset augmentation provides the most robust approach for driftwood volume estimation.

CONCLUSIONS

This study successfully developed a LiDAR-based deep learning approach for driftwood disaster investigation through controlled flume experiments. The proposed multi-scale geometric feature augmentation technique effectively enhanced model performance, with all models achieving mIoU exceeding 80%. GACNet with dataset augmentation demonstrated superior performance in both semantic segmentation (driftwood IoU of 78.07%) and volume estimation (mean error of -22.85%). Experimental results revealed a bidirectional relationship between driftwood accumulation and riverbed morphology, where riverbed geometry influences driftwood deposition patterns, while accumulated driftwood modifies channel configurations. This research validates the integration of LiDAR technology with deep learning for driftwood disaster assessment, offering an effective approach for disaster investigation and mitigation. However, the accuracy of driftwood accumulation volume estimation was affected by challenges such as the complex morphology of riverbeds, the irregular and porous structure of driftwood piles, and the limitations of current clustering and volumetric algorithms based on point cloud. Future work should address these issues by refining volume estimation techniques and improving the handling of complex accumulation patterns.

ACKNOWLEDGMENTS

This study was partially funded by KAKENHI Grant Numbers 23K04019 and 24K00985. We would like to express our sincere gratitude for their support.

REFERENCES

[1] Tian L., Mitani Y., Okajima Y., Taniguchi H. and Tabuchi T., Evaluation of Slope Failure and Driftwood Disaster Susceptibility Zone Using Geo-spatial Information. In Advances in Sustainable Construction and Resource Management, 2021, pp.927-938. Springer Singapore.

[2] Schmocker L. and Weitbrecht V., Driftwood: Risk analysis and engineering measures, Journal of Hydraulic Engineering, Vol. 139, Issue 7, 2013, pp.683-695.

[3] Hoque M. A. A., Phinn S., Roelfsema C. and Childs I., Tropical cyclone disaster management using remote sensing and spatial analysis: A review, International Journal of Disaster Risk Reduction, 22, 2017, pp.345-354.

[4] Sambah A. B., Miura F. and Febriana A. F., Geospatial model of physical and social vulnerability for tsunami risk analysis, International Journal of GEOMATE, Vol. 17, Issue 63, 2019, pp.29-34.

[5] Alho P., Kukko A., Hyyppä H., Kaartinen H., Hyyppä J. and Jaakkola A., Application of boat-based laser scanning for river survey, Earth Surface Processes and Landforms: The Journal of the British Geomorphological Research Group, Vol. 34, Issue 13, 2009, pp.1831-1838.

[6] Samori N., Nishiyama S. and Sakita K., Quantifying the Slope Deformation of a Laser Point Cloud Acquired Using Mobile Mapping System, International Journal of GEOMATE, Vol. 21, Issue 88, 2021, pp.12-21.

[7] Qi C. R., Yi L., Su H. and Guibas L. J., Pointnet++: Deep hierarchical feature learning on point sets in a metric space, Advances in neural information processing systems, Vol. 30, 2017.

[8] Wang L., Huang Y., Hou Y., Zhang S. and Shan J., Graph attention convolution for point cloud semantic segmentation, In Proceedings of the IEEE/CVF conference on computer vision and pattern recognition, 2019, pp.10296-10305.

Copyright © Int. J. of GEOMATE All rights reserved, including making copies, unless permission is obtained from the copyright proprietors.

15th Int. Conf. on Geotechnique, Construction Materials & Environment,
Kyoto, Japan, 11-13 November 2025, ISBN 978-4-909106124 C3051

APPLICATION OF LONG SHORT-TERM MEMORY MACHINE LEARNING NETWORKS FOR TEMPERATURE VARIATIONS PREDICTION OF ENERGY PILES

Thiti Chanchayanon[1], Apiniti Jotisankasa[2], Susit Chaiprakaikeow[3] and Shinya Inazumi[4]

[1] Graduate School of Engineering and Science, Shibaura Institute of Technology, Japan; [2,3] Department of Civil Engineering, Kasetsart University, Thailand; [4] College of Engineering, Shibaura Institute of Technology, Japan

ABSTRACT

This study aims to utilize and illustrate the potential and effectiveness of Long Short-Term Memory (LSTM) networks to predict temperature variations at the inlet and outlet of integrated energy piles with the air conditioning system, especially in a soft clay soil layer. The energy piles are gaining traction by combining structural and thermal dissipation functions, incorporated well into sustainable building designs. Their performance is reflected by the temperature at the inlet and outlet over time. Accurate prediction of temperature changes in energy piles is crucial for designing, optimizing system performance, and evaluating the effective thermal conductivity of the system by forecasting its behavior over time. The proposed LSTM model is trained by feeding normalized, time-series splitting data from inlet and outlet temperature recordings at the time sequences. The model's performance is evaluated using R-squared (R^2) combined with Root Mean Squared Error (RMSE), showing on average the confidence of 0.9270, ±0.2373°C for inlet prediction temperature, and 0.9094, ±0.2673°C for outlet prediction temperature, respectively. The model showing improvement int the accuracy as the number of LSTM layers increases from 1 to 3, the R^2 increase 0.09% and 11.96% for RMSE in inlet side, while the R^2 increase 1.81% and 4.51% for RMSE in outlet side respectively. Machine learning models such as LSTM require careful balancing between the time frame and prediction frequency to ensure reliable results. In short-term predictions, fewer layers of LSTM are more suitable, due to their greater sensitivity to data fluctuations. In contrast, adding more LSTM layers improved stability but reduced sensitivity, resulting in smoother long-term trends. The findings contribute to the development of more efficient, data-driven approaches for managing energy pile systems, advancing both the practical and theoretical understanding of thermal energy storage in geotechnical engineering applications.

Keywords: Energy pile, Ground source heat pump, Long short-term memory, Machine learning, Prediction model

INTRODUCTION

The global warming effect and urbanization in major cities have intensified the heat island effect, significantly elevated ambient temperatures, and consequently increased the demand for air conditioning systems in residential and commercial buildings. This phenomenon is particularly pronounced in densely populated metropolitan areas across Southeast Asia, where rapid population growth and limited urban space have exacerbated heat retention and energy consumption issues. Given that many of these urban centers are situated on soft marine clay deposits, deep foundation piles are routinely employed for structural support in building construction. Even though the energy piles and GSHP technology are still young and at their early stage in the Southeast Asia region, a few academic studies [1] [2] [3] [4] have been conducted. This presents an opportunity to utilize these foundational structures by integrating energy piles and Ground Source Heat Pump (GSHP) systems. Depicted in Fig.1 [2].

The system's components in cooling mode operation comprise of the geo-structure, the embedded heat exchanger, the heat pump unit, and the distribution system.

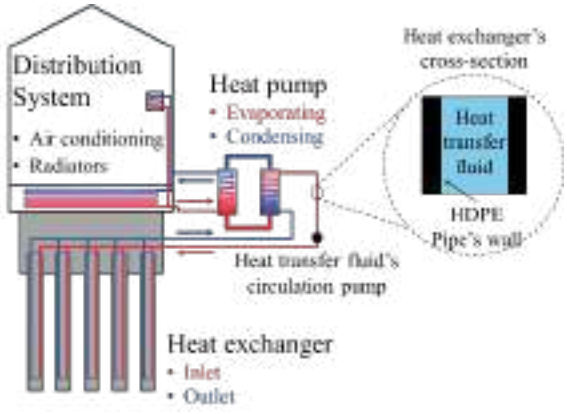

Fig.1 Schematic of the components of an energy pile for small-to-medium residential units. [2]

Energy piles provide a sustainable solution by leveraging the stable ground temperature for efficient heating and cooling, thereby helping to mitigate urban heat island effects and reduce energy consumption and reliance on conventional cooling systems. However, implementing energy piles and GSHP technology requires comprehensive analyses

of temperature distribution in soft clay, as well as accurate predictions of inlet and outlet fluid temperatures. These indexes are critical for reliable performance assessments of energy piles and GSHP systems, including the coefficient of performance (COP: ratio of heat delivered to energy input), energy efficiency ratio (EER: cooling output per unit electrical input), seasonal energy efficiency ratio (SEER: cooling efficiency averaged over a cooling season), seasonal coefficient of performance (SCOP: heating efficiency averaged over a heating season), seasonal performance factor (SPF: actual seasonal performance considering all energy inputs), long-term seasonal COP (LSCOP: COP measured over multiple seasons or years), and long-term cooling factor (LSCF: cooling efficiency ratio in long-term). Clarifying these is especially important in densely populated areas in Southeast Asia and Japan.

Integrating machine learning (ML) techniques with energy piles and GSHP systems has become a promising research frontier, enhancing predictive accuracy, system optimization, and operational efficiency. Recent advances in ML, particularly in deep learning architectures such as long short-term memory (LSTM), artificial neural networks (ANNs), simple recurrent neural networks (Simple RNN), and convolutional neural networks (CNNs), have enabled more precise thermal performance modeling and improved energy demand forecasting. Instead of relying solely on computationally intensive simulations like finite difference method (FDM), finite element method (FEM) or Multiphysics modeling, ML techniques offer an efficient alternative that reduces the need for extensive computing resources. By pretraining LSTM models, practical limitations due to high computational demand can be overcome, improving accessibility for end-users.

RESEARCH SIGNIFICANCE

This research aims to illustrate the potential and effectiveness of employing LSTM models to predict the thermal behavior of energy piles, contributing to a valuable tool for optimization in energy piles and GSHP design. Specifically, the developed LSTM model forecasts the inlet and outlet temperatures for energy piles and GSHP, particularly when these systems are situated within deep layers of soft marine deposit clay, which are common in major cities in Japan and the Southeast Asia region.

PREVIOUS STUDIES

An LSTM model, following the architecture first proposed by Hochreiter and Schmidhuber [5], was chosen for its suitability in time-series predictions. Specifically, the sequence-to-sequence (seq2seq) model illustrated in Fig.2 represents an advanced form of sequence prediction, classified as “many-to-many.” In this model, new sequences are predicted based on patterns learned from training data, offering flexibility as the predicted sequences can differ in length and timing from the inputs. The seq2seq architecture employs recurrent neural networks to map input sequences of varying lengths to similarly variable output sequences [6]. For predicting the temperatures of energy piles and GSHP systems, both input and output data are multi-step time series, making this model particularly effective for forecasting multiple future observations from historical data.

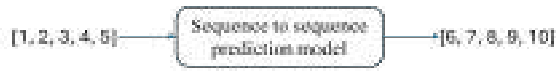

Fig.2 Depiction of a sequence-to-sequence prediction problem

Recent scholarly advances in ML applications for energy piles and GSHP systems have indicated the basic outline of how to build the ML model, such as,

Zhang [7] indicated in the outlet water temperature prediction of energy pile using the CNN–LSTM hybrid model, the superior enhancement in the accuracy of the prediction, indicated by the mean R^2 value of 96.252%, superior to the values of the individual LSTM, CNN, ANN, and Simple RNN models by 2.326%, 3.527%, 4.585%, and 5.755% respectively. By employing a hybrid modeling approach proves advantageous due to its effective integration of CNNs' capability for feature extraction with LSTMs' proficiency in sequential learning, resulting in enhanced accuracy for current-state predictions.

Chen [8] demonstrated that machine-learning-based performance prediction of energy pile heat pump systems, using a hybrid ANN model fine-tuned with particle swarm optimization (PSO), can effectively predict the output COP index. The model used readily measurable input features, including ambient and room temperature and humidity, as well as hourly power consumption. The PSO-ANN model produced predictions that closely matched the measured values, outperforming conventional empirical regression models that deviated within ±20% of the 1:1 line, as shown in Fig.3 (a) and (b). Incorporating multiple input parameters that reflect the thermal and electrical behaviors of the system enhanced the model’s generalization capability and improved prediction reliability under varying operating conditions.

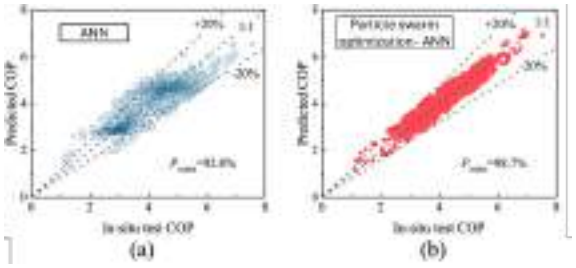

Fig.3 The stacked LSTM temperature prediction model [5]

Output temperature predictions of geothermal heat pump systems using the Improved Grey Prediction Model [9] reveal that the size of the data points, whether small or large, influences the prediction's effectiveness and accuracy. A smaller sample size during training tends to yield higher accuracy but is more sensitive to bias, whereas a larger sample size offers more consistent predictions, albeit with slightly reduced accuracy. Balancing data size is essential to avoid overfitting and ensure reliable predictions. This study successfully used only 24 data points (hours) to forecast temperatures eight hours ahead. Further experiments determined that for the GM model, particularly GM(1,1). A key model for short-term time-series prediction, sample sizes as low as six data points can be used. This underscores the need for proper data preparation, including outlier removal and ensuring a non-random, non-negative dataset, to improve model quality and prediction reliability.

Song [10] tackled the challenge of hourly heat load prediction accuracy in smart district heating, using a temporal convolutional neural network, citing the utilities beyond the temperature forecast of ML in energy piles and GSHP. The conventional regression, although commonly applied, tends to fail to leverage the nonlinear and temporal relationships characteristic of the heat load data. The researcher intends to forecast the peak cooling load of the system by proposing a temporal convolutional neural network (TCN) for hourly heat load forecasting in district heating systems (DHS). TCN fuses the feature extraction in parallel offered by CNNs with the sequence modeling capability of RNNs to better deal with complex, nonlinear, and time-varying data. The model uses both working parameters, such as supply temperatures, return temperatures, past loads, and outdoor temperature, which have been pre-processed using correlation analysis.

Chandra and Matuska [11] address critical limitations in current building energy management systems within intelligent data workflows, including data pipelines and LSTM efficiency prediction. Traditionally, data collection and performance prediction for thermal energy storage (TES) systems have been separate and static. While previous studies have applied ANNs and exergy analysis for TES-heat pump systems, significant challenges remain in accurately modeling transient behaviors during dynamic load periods, due to issues like vanishing gradients and overfitting. The authors propose an intelligent, real-time data acquisition and processing framework using Raspberry Pi hardware and LSTM-MLP models. This framework automates data curation and prediction, integrates custom exergy models for live performance assessment, and offers real-time visualization tools. Their approach improves predictive accuracy and bridges a key gap in literature, paving the way for more autonomous and efficient building energy systems.

METHOD STATEMENT

Long Short-Term Memory (LSTM) was selected for its strong ability to capture long-term temporal dependencies and nonlinear patterns typical in the thermal behavior of energy piles. Unlike Autoregressive Integrated Moving Average (ARIMA), which assumes linearity, or Support Vector Regression (SVR), which struggles with temporal dynamics, LSTM effectively models complex, multivariate time-series data without prior assumptions. While Gated Recurrent Unit (GRU) networks are more computationally efficient, other than that LSTM offers broader community support, abundant libraries, and better plugin integration, making it more accessible for beginners. It has also shown superior accuracy in modeling seasonal and delayed thermal responses in geo-energy systems.

This study's LSTM model was developed using the *TensorFlow* library [12] in *Python* to predict the inlet and outlet temperature behavior of energy piles based on the non-negative and non-random inlet, outlet, and time parameter sequences, the key factors in assessing the performance of energy piles and GSHP systems. The model was trained using full-scale experimental datasets from the previous study on energy piles in Bangkok by Jotisankasa [13]. The proposed model employs a stacked LSTM neural network architecture for seq2seq temperature prediction, as illustrated in Fig. 4. During preprocessing, these data are segmented into sequences with a length of 25-time steps. The model comprises up to 3 hidden LSTM layers, each containing 64 nodes, and is trained over 200 epochs (calculation cycle) with a batch size (number of data points) of 64 to optimal balance between computational efficiency and prediction accuracy. The output layer generates predictions for inlet and outlet temperatures.

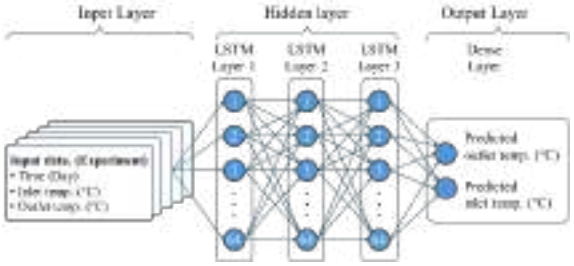

Fig.4 The stacked LSTM temperature prediction model

RESULT AND DISCUSSION

The LSTM Prediction Model's Verification

The LSTM prediction model's verification was performed using parity diagrams shown in Fig.5, which compare the predicted and actual inlet and outlet temperatures for models with 1, 2, and 3 LSTM layers. The data points largely aligned along the 1:1 line and the ±5% reference line, indicating strong agreement between predicted and measured values. The R^2 values were 0.9280, 0.9257, and 0.9272 for outlet temperature and 0.9181, 0.9082, and 0.9018 for inlet temperature, respectively. The relatively low RMSE values of 0.2547, 0.2298, and 0.2275 for outlet temperature and 0.2783, 0.2573, and 0.2663 for inlet temperature suggest reliable predictions with minimal error fluctuation.

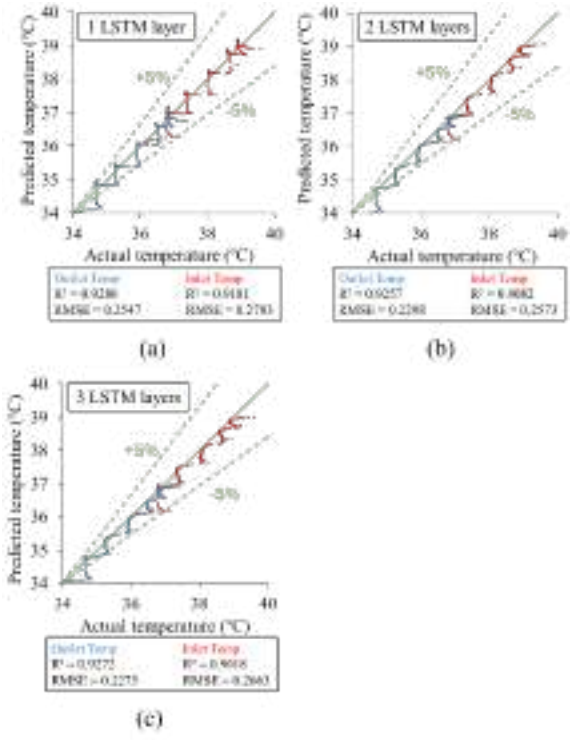

Fig.5 Parity diagram of predicted versus actual inlet and outlet temperatures using a-layer LSTM model

Each of the LSTM model architectures, ranging from a single layer to three layers, presents unique advantages and disadvantages. The suitability of each model depends on the specific application, whether for short-term or long-term predictions. These aspects will be discussed in more detail in the following section.

Inlet and Outlet Temperature Prediction

Although the single-layer LSTM model yielded slightly lower accuracy compared to models with higher layer counts, it is not without practical value. Specifically, as depicted in Fig.6, the single-layer model can be effectively utilized for short-term predictions due to its greater sensitivity, as demonstrated by its better capacity to closely replicate the shape and fluctuations of actual data.

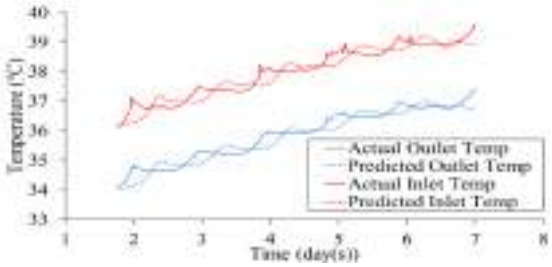

Fig.6 Short-term temperature simulation over time using the 1-layer LSTM model

In contrast, increasing the number of LSTM layers tends to improve prediction stability but reduces sensitivity, leading to smoother outputs that capture fewer short-term fluctuations. Fig.7 presents the predicted inlet and outlet temperatures of energy piles over 10 years (3650 days), revealing a near-linear stable temperature in the long run. Although such stability is rare due to seasonal changes in ground and air temperatures, using year-long datasets can enhance prediction accuracy. This is seen in Fig.8 and Fig.9, where even within the first six months or years 1 to 2, minor temperature fluctuations persist. These results indicate that the input data influences the model, suggesting potential for further accuracy improvement.

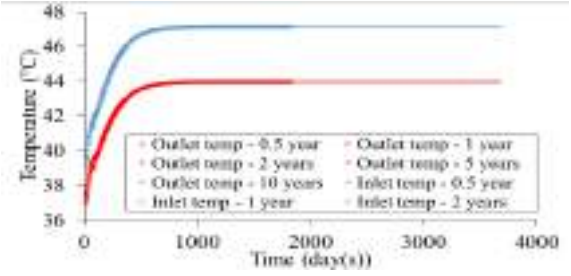

Fig.7 Long-term temperature simulation over time using the 3-layer LSTM model

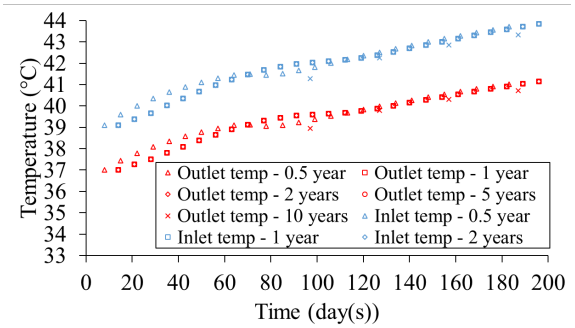

Fig.8 Long-term temperature simulation over time using the 3-layer LSTM model, including a detailed view of the 0 to 6 months

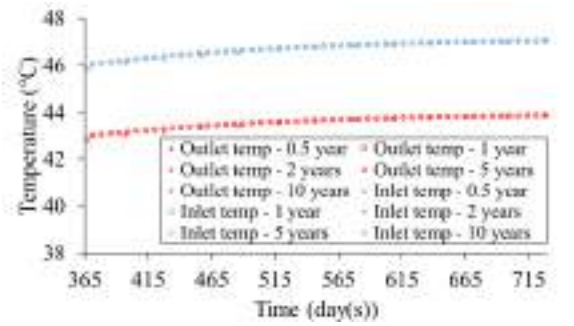

Fig.9 Long-term temperature simulation over time using the 3-layer LSTM model, including a detailed view of the 1 to 2 years

Impact of LSTM Layers

The results from varying the number of 1, 2, and 3 layers of the LSTM model showed marginal differences in prediction accuracy for both inlet and outlet temperatures, as summarized in Table 1. For inlet temperature, the average R^2 are at 0.9270, a slight improvement of 0.0863 % (0.0008) over time. while the average RMSE is at 0.2373, indicating a 11.956 % (±0.0272°C) improvement. Similarly, the outlet temperature's average R^2 values around 0.9094, improving by 1.8075 % (0.0163) over time, while the average RMSE is at 0.9094 reflecting a 4.5062 % (±0.0120°C). An increase in R^2 signifies that the predicted values are more closely aligned with the observed data, indicating tighter grouping of data points around the regression line. Consequently, this improved alignment naturally results in narrower range of fluctuation in the RMSE, as prediction errors become smaller, more consistent, and numerically closer to the observed values.

Even from a practical perspective, the improvement indicated by average RMSE values ±0.2373°C for inlet and 0.2673°C for outlet temperature predictions may appear marginal, with improvements of only 11.956% (±0.0272°C) and 4.5062% (±0.0120°C), respectively. However, it would be premature and potentially misleading to dismiss these results based solely on the current dataset, as valuable insights might be overlooked. At this stage, it is clear that increasing the number of LSTM layers tends to enhance predictive accuracy, albeit modestly. Nevertheless, it should also be noted that as the dataset expands in future analyses, the observed incremental accuracy improvements could diminish or plateau.

Table 1 Comparison of prediction accuracy (R^2 and RMSE) for inlet and outlet temperatures with varying numbers (1, 2, and 3) of LSTM layers.

Source	Index	Number of LSTM layer(s)			Avg value	Avg improvement per 3 layers , %
		1 layer	2 layers	3 layers		
Inlet temp	R^2	0.9280	0.926	0.927	0.9270	0.0008, 0.0863%
	RMSE	0.255	0.23	0.228	0.2373	0.0272, 11.956%
Outlet temp	R^2	0.918	0.908	0.902	0.9094	0.0163, 1.8075%
	RMSE	0.278	0.257	0.266	0.2673	0.0120, 4.5062%

CONCLUSIONS

The development of a multi-layer LSTM model demonstrated its potential for large-scale systems. While the single-layer model offered slightly lower accuracy, it remains valuable for short-term predictions due to greater sensitivity to data fluctuations. Adding layers improved stability but reduced sensitivity, smoothing long-term trends at the expense of short-term detail. Model performance heavily depends on the quality and comprehensiveness of input data.

Balancing prediction frequency and timeframe is crucial when using machine learning models like LSTM. For example, predicting hourly or half-day intervals over a year can strain the model and decrease accuracy. Thus, selecting appropriate prediction intervals aligned with dataset resolution is vital to maintain meaningful and reliable outcomes without overwhelming the model.

Future research should expand beyond time, inlet and outlet temperatures by incorporating parameters such as thermal load, active length, flow rate, connection types, and operational cycles. A comprehensive, year-long dataset covering all seasonal variations and operational scenarios will enhance the model's ability to generalize and accurately reflect real-world conditions. Including diverse scenarios will strengthen predictions of thermal performance and capture complex system interactions.

Lastly, the more sophisticated algorithms or combining multiple algorithms could further enhance prediction accuracy. Ensuring that the model's underlying architecture supports scalability and

integration with additional data sources will help maintain reliability and accuracy as new data emerges.

REFERENCES

[1] Chanchayanon T., Chaiprakaikeow S., Jotisankasa A., and Inazumi S., Optimization of Geothermal Heat Pump Systems for Sustainable Urban Development in Southeast Asia, Smart Cities, Vol. 7, No. 3, 2024, pp. 1390-1413.

[2] Chanchayanon T., Chaiprakaikeow S., Jotisankasa A., and Inazumi S., Enhancing Smart City Energy Efficiency with Ground Source Heat Pump Systems and Integrated Energy Piles, Smart Cities, Vol. 7, No. 6, 2024, pp. 3547-3586.

[3] Ratchawang S., Chotpantarat S., Chokchai S., Takashima I., Uchida Y., and Charusiri P., A Review of Ground Source Heat Pump Application for Space Cooling in Southeast Asia, Energies, Vol. 15, No. 14, 2022, pp. 4992.

[4] Seo Y., and Seo U.J., Ground Source Heat Pump (GSHP) Systems for Horticulture Greenhouses Adjacent to Highway Interchanges: A Case Study in South Korea, Renew. Sustain. Energy Rev., Vol. 135, 2021, Art. No. 110194.

[5] Hochreiter S., and Schmidhuber J., Long Short-Term Memory, Neural Computation, Vol. 9, No. 8, 1997, pp. 1735-1780.

[6] Luong M.T., Le Q.V., Sutskever I., Vinyals O., and Kaiser L., Multi-task Sequence to Sequence Learning.

[7] Zhang W., Zhou H., Bao X., and Cui H., Outlet Water Temperature Prediction of Energy Pile Based on Spatial-Temporal Feature Extraction Through CNN–LSTM Hybrid Model, Energy, Vol. 264, 2023, Art. No. 126190.

[8] Chen Y., Kong G., Xu X., Hu S., and Yang Q., Machine-Learning-Based Performance Prediction of the Energy Pile Heat Pump System, J. Build. Eng., Vol. 77, 2023, Art. No. 107442.

[9] Salhein K., Ashraf J., and Zohdy M., Output Temperature Predictions of the Geothermal Heat Pump System Using an Improved Grey Prediction Model, Energies, Vol. 14, No. 16, 2021, pp. 5075.

[10] Song J., Xue G., Pan X., Ma Y., and Li H., Hourly Heat Load Prediction Model Based on Temporal Convolutional Neural Network, IEEE Access, Vol. 8, 2020, pp. 16726-16741.

[11] Chandra Y.P., and Matuska T., Intelligent Data Systems for Building Energy Workflow: Data Pipelines, LSTM Efficiency Prediction and More, Energy Build., Vol. 267, 2022, Art. No. 112135.

[12] Abadi M., Agarwal A., Barham P., Brevdo E., Chen Z., Citro C., Corrado G.S., Davis A., Dean J., Devin M., Ghemawat S., Goodfellow I., Harp A., Irving G., Isard M., Jozefowicz R., Jia Y., Kaiser L., Kudlur M., Levenberg J., Mané D., Schuster M., Monga R., Moore S., Murray D., Olah C., Shlens J., Steiner B., Sutskever I., Talwar K., Tucker P., Vanhoucke V., Vasudevan V., Viégas F., Vinyals O., Warden P., Wattenberg M., Wicke M., Yu Y., and Zheng X., TensorFlow: Large-Scale Machine Learning on Heterogeneous Systems, in Proc. 12th USENIX Symp. on Operating Systems Design and Implementation (OSDI ’16), Nov. 2-4, 2016, Savannah, GA, USA, ISBN 978-1-931971-33-1.

[13] Jotisankasa A., Chantawarangul K., Sittidumrong J., Thangkhumwong K., Aowphitak P., Laohasrisakul P., Chanchayanon T., Aonkam S., and Satayanan S., Investigation of the Feasibility of Energy Piles in Bangkok and Their Impacts on Pile Behavior, E3S Web Conf., Vol. 205, 2020, Art. No. 05018.

Copyright © Int. J. of GEOMATE All rights reserved, including making copies, unless permission is obtained from the copyright proprietors.

15th Int. Conf. on Geotechnique, Construction Materials & Environment,
Kyoto, Japan, 11-13 November 2025, ISBN 978-4-909106124 C3051

A PERFORMANCE STUDY OF DEHUMIDIFICATION IN AN EVAPORATIVE COOLING SYSTEM USING THERMOSYPHON HEAT PIPES

Niran Watchrodom[1], Jeerattikul Kaharn[1], Aekchai Rattanabanlue[1], Luedate Phatedoung[1] and Thana Ananacha[2]

[1]Department of Mechanical Engineering, Faculty of Industrial Education,
Rajamangala University of Technology Suvarnabhumi, Suphanburi Campus, Suphan Buri Province 72130, Thailand
[2]Faculty of Architecture and Design, King Mongkut's University of Technology North Bangkok
1518 Pracharat 1 Road, Wongsawang, Bangsue, Bangkok 10800, Thailand

ABSTRACT

This study investigates the performance enhancement of an evaporative cooling system by integrating thermosyphon heat pipes to improve dehumidification efficiency in hot and humid climates. The experimental setup comprised a thermally insulated cubic test chamber (100 × 100 × 100 cm³) fitted with a cellulose-based cooling pad, axial flow fans, and five copper heat pipes (9.5 mm in diameter and 40 cm in length) charged with R-134a refrigerant. The heat pipes were positioned upstream of the cooling pad to passively extract latent heat and reduce moisture content in the incoming air prior to evaporative cooling. Experiments were conducted under two levels of natural solar radiation, averaging approximately 600 W/m² and 750 W/m², respectively, recorded using a pyranometer at 30-minute intervals. Measured parameters included dry-bulb temperature and relative humidity, collected using calibrated K-type thermocouples and digital hygrometers. The results indicate that the heat pipe system effectively reduced the relative humidity of supply air by approximately 6% to 10%, with maximum reductions reaching 12.5% under high solar intensity. This pre-conditioning process not only lowered the latent cooling load but also enhanced overall cooling performance. While the dry-bulb temperature increased slightly, thermal comfort improved significantly. The findings highlight the potential of this passive hybrid approach to enhance indoor environmental quality and energy efficiency in tropical buildings. Future work should focus on airflow optimization and the use of alternative refrigerants to refine system applicability in real-world scenarios.

Keywords: Heat Pipe, Evaporative Cooling, Dehumidification, Energy Efficiency, Tropical Climate

INTRODUCTION

In tropical countries like Thailand, where annual temperatures average between 32°C and 35°C and relative humidity regularly exceeds 70%, the demand for thermal comfort in buildings leads to high energy consumption, particularly through air-conditioning systems. Conventional vapor compression air conditioners not only consume large amounts of electricity but also rely on refrigerants that contribute to ozone depletion and global warming [1-3]. These environmental and economic concerns have driven the search for alternative, energy-efficient cooling technologies that can function effectively in humid climates. Evaporative cooling systems have emerged as a promising solution due to their simplicity and low energy consumption. They operate by taking advantage of the latent heat of water evaporation to cool incoming air, making them suitable for dry and semi-arid environments. However, in hot and humid regions such as Southeast Asia, their cooling capacity becomes limited as the ambient air approaches saturation, reducing the temperature differential between the dry-bulb and wet-bulb temperatures [4-5]. To address this limitation, researchers have explored hybrid cooling systems that incorporate passive and active dehumidification technologies. Heat pipes, particularly thermosyphon heat pipes, have gained attention for their ability to transfer heat efficiently without moving parts. These devices can extract latent heat from moist air by condensing water vapor on a cooled surface, thus reducing humidity before the air enters the evaporative cooling stage.

Several studies have demonstrated the potential of integrating heat pipe systems into air conditioning and agricultural applications. Van Den Bulck et al. introduced rotary heat exchangers to improve dehumidification in HVAC systems [6], while Lazzarin and Gasparella investigated combined heat and cooling systems for enhanced energy efficiency [7]. In Thailand, Watcharodom et al. examined the performance of thermosyphon heat pipes in residential-scale air conditioners, showing energy savings and improved indoor climate control [8-10]. Srihajong et al. applied heat pipe systems to regulate moisture in aeroponic plant environments [11], and Meena et al. studied the role of oscillating heat pipes in moisture reduction during agricultural drying processes [12].

Despite these efforts, limited research has focused on directly integrating thermosyphon heat pipes with evaporative cooling systems to enhance dehumidification under naturally hot and humid conditions. There is a knowledge gap in evaluating how such hybrid systems perform under real environmental fluctuations without mechanical

assistance. This study aims to address that gap by experimentally assessing the performance of an evaporative cooling system enhanced with thermosyphon heat pipes, focusing on its effectiveness in reducing humidity and improving overall thermal comfort in tropical climates.

RESEARCH SIGNIFICANCE

This study proposes a hybrid cooling system that integrates thermosyphon heat pipes into an evaporative cooling configuration to pre-condition incoming air by reducing its moisture content. This approach enhances the system's latent cooling performance and makes it suitable for hot and humid tropical climates. By operating without additional electrical input for dehumidification, the system provides a passive, energy-efficient, and environmentally friendly solution that contributes to sustainable indoor climate control. The findings from this study are expected to support the design of future hybrid cooling systems that reduce dependence on high-energy mechanical air conditioning.

EXPERIMENTAL SETUP

This experiment was conducted using a custom-designed hybrid cooling system that integrates evaporative cooling with thermosyphon heat pipes. The entire setup was installed on an open rooftop to simulate natural ambient conditions (Fig. 1). At the core of the system is a thermally insulated cubic test chamber with internal dimensions of 100 × 100 × 100 cm^3. The chamber structure comprises a steel frame with double-layered plywood walls, internally lined with 5 cm thick thermal insulation to minimize heat transfer from the surroundings. A 60-watt incandescent bulb was installed inside the chamber to simulate internal heat gains typically found in small residential spaces. At the upstream section of the chamber, a centrifugal fan was installed to draw ambient air through a pre-conditioning unit composed of five vertically arranged thermosyphon heat pipes. These copper pipes, each with a diameter of 9.5 mm and a length of 40 cm, were filled with R-134a refrigerant and equipped with aluminum fins to enhance heat dissipation. The heat pipes operate passively and are arranged in parallel at the system's front end to extract latent heat from the incoming humid air before it reaches the evaporative cooling pad. The evaporative unit uses a cellulose-based cooling pad measuring 33 × 33 × 10 cm^3, assisted by two 12-volt axial flow fans that force air through the wetted pad. This allows for both sensible and latent heat exchange. The conditioned and dehumidified air then enters the test chamber. Environmental parameters, including dry-bulb temperature and relative humidity, were measured at four key locations: ambient air, before and after the heat pipe section, and inside the test chamber. Calibrated K-type thermocouples (±0.5°C accuracy) and digital hygrometers were used to collect data. Solar radiation was monitored using a pyranometer to track natural irradiance fluctuations during the experiment. The experiment was conducted in an open-air environment without mechanical control of solar intensity. Instead, testing was carried out over two separate days to reflect natural solar variation: one day with moderate radiation averaging 600 W/m^2, and another with higher radiation averaging 750 W/m^2. Measurements were recorded every 30 minutes between 12:00 and 15:30. Although solar intensity was not entirely constant, the selected intervals showed sufficiently consistent patterns to enable meaningful comparison. Grouping the results based on average daily irradiance allowed for performance evaluation of the system under two distinct environmental conditions without relying on active solar control mechanisms.

Fig.1 Experimental setup of the hybrid evaporative cooling system integrated with heat pipes

ANALYZE DATA

The analytical framework for evaluating the evaporative cooling system integrated with thermosyphon heat pipes was developed based on the principles of steady-state mass and energy conservation. In this system, the airflow and thermal interactions were considered under quasi-adiabatic conditions, assuming minimal heat loss to the environment due to the insulated test chamber and short processing time. The predominant processes occurring within the system were heat and moisture exchanges between the ambient air, the evaporative medium, and the heat pipe assembly. As the ambient air enters the system, it first passes through the heat pipe array, where a portion of the water vapor is condensed due to the refrigerant's phase change within the pipes. This process reduces the moisture content of the incoming air through latent heat

extraction, resulting in a slight increase in dry-bulb temperature. Following this stage, the pre-conditioned air flows through the evaporative cooling pad, where both sensible and latent heat exchanges occur, lowering the dry-bulb temperature while increasing the humidity ratio.

To analyze these thermal phenomena, the energy balance was applied to the moist air stream, which includes both the dry air component and the associated water vapor. The enthalpy change of the moist air was used as a performance indicator to quantify system behavior and energy transfer across each stage. The total enthalpy was calculated based on psychrometric properties, combining sensible heat and latent heat contributions. The conceptual diagram illustrating the mass and energy exchanges across the system, which includes both the heat pipe section and the evaporative pad (Fig.2). This diagram provides a visual summary of the airflow pathway, component interactions, and measurement points used in the experiment. It serves as a reference for interpreting the performance results in the following section.

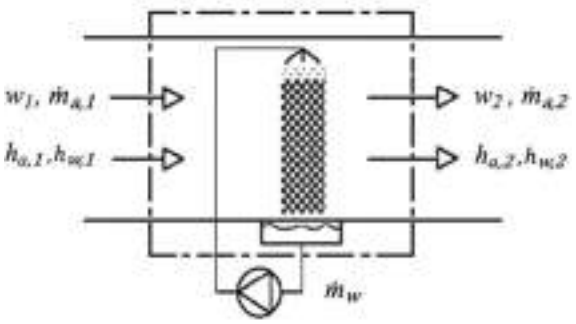

Fig. 2 Schematic diagram of mass and energy balance in evaporative cooling process

To determine the mass of evaporated water, the conservation of mass for water vapor is written as:

$$\dot{m}_w = \dot{m}_a (W_1 - W_2) \quad (1)$$

Where $\dot{m}_w$ is the rate of water evaporation (kg/s), $\dot{m}_a$ is the mass flow rate of dry air (typically 0.05 kg/s in this experiment), and W_1 and W_2 are the humidity ratios ($kg_{water}/kg_{dry\ air}$) at the inlet and outlet of the cooling section, respectively.

The total enthalpy of moist air at any point is calculated as the sum of the enthalpies of dry air and water vapor:

$$h_{total} = C_{p,a}T + W(h_{fg} + C_{p,v}T) \quad (2)$$

Where $C_{p,a}$ = 1.006 kJ/kgC is the specific heat of dry air, $C_{p,v}$ = 1.84 kJ/kgC is the specific heat of water vapor, T is air temperature (°C), h_{fg} = 2450 kJ/kg is the latent heat of vaporization, and W is the humidity ratio at the respective state.

For the moisture-laden air entering the cooling media, the rate of heat transfer from the air to the water (which facilitates evaporation) is derived from the energy balance as:

$$Q = \dot{m}_a (h_1 - h_2) \quad (3)$$

where h_1 and h_2 are the total enthalpies of the air stream before and after the evaporative process, respectively.

The performance of the cooling process was evaluated by calculating the evaporative cooling effectiveness, given by:

$$\varepsilon = \frac{T_{db,in} - T_{db,out}}{T_{db,in} - T_{wb,in}} \quad (4)$$

Here, $T_{db,in}$ and $T_{db,out}$ are the dry-bulb temperatures before and after the evaporative section, and $T_{wb,in}$ is the inlet wet-bulb temperature. This ratio quantifies the cooling performance relative to the maximum potential defined by wet-bulb depression.

The dehumidification efficiency of the heat pipe system was also analyzed by comparing relative humidity measurements before and after the heat pipe section. This is expressed as:

$$\eta_{dehum} = \frac{RH_{in} - RH_{out}}{RH_{in}} \times 100\% \quad (5)$$

RESULTS AND DISCUSSION

This experimental evaluation was conducted to examine how the integration of thermosyphon heat pipes into an evaporative cooling system can enhance both temperature regulation and indoor humidity control. This section presents the findings through analysis of measured dry-bulb temperatures, relative humidity levels, and calculated performance indicators, as defined in the analytical framework and equations provided in the preceding section. Prior to the installation of heat pipes, the standalone evaporative cooling system demonstrated a moderate capacity to reduce indoor air temperature but showed limited effectiveness in managing relative humidity. As presented in (Table 1) and (Fig.3), indoor air temperatures fluctuated between 26.5°C and 31.0°C, while inlet air temperatures ranged from 26°C to 30°C during the experimental period. These results indicate that the evaporative cooling system provided sensible cooling by lowering the dry-bulb temperature; however, the indoor environment remained vulnerable to heat accumulation, primarily due to solar radiation and internal thermal loads. The limited humidity control observed in the baseline system is consistent with the known constraints of conventional evaporative cooling, which tends to introduce additional moisture into the space through constant evaporation. If this added moisture is not properly managed, it can impair thermal comfort,

reduce system efficiency, and potentially encourage microbial growth in enclosed spaces. Therefore, enhancing such systems with a passive dehumidification mechanism such as thermosyphon heat pipes may offer a promising solution for buildings located in hot and humid climates where both cooling and dehumidification are critical to indoor environmental quality.

Table 1 Hourly variation of outdoor, inlet and indoor temperatures before heat pipe installation

Time	Outside temperature	Temperature before entering the room	Room temperature
12:00	33	26	27
12:30	31	27	26.5
13:00	33	28	29
13:30	32	29	30.5
14:00	33	30	30
14:30	33.5	29.5	30.5
15:00	34	29.5	30
15:30	34.5	29	31

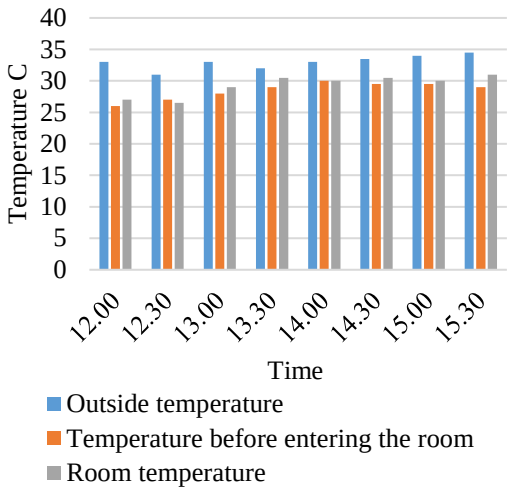

Fig.3 Temperature profiles before the installation of heat pipes

In parallel, (Table 2) and (Fig.4) show that the relative humidity inside the room consistently exceeded outdoor levels, reaching up to 80% at peak periods. This can be attributed to continuous water vapor saturation introduced by the evaporative pad. Such elevated humidity not only compromises thermal comfort but also limits the evaporative effectiveness, as defined in Eq. (4).

After the installation of the thermosyphon heat pipe section, a significant shift in both temperature and humidity behavior was observed. Under moderate solar intensity (600 W/m²), as shown in (Fig.5), the room temperature remained stable between 28°C and 30°C. Under higher solar radiation (750 W/m²), (Fig.6) shows a similar trend with peak room temperature approaching 31°C, yet still below the outdoor temperature range (33–34.5°C), demonstrating consistent thermal buffering.

Table 2 Hourly variation of outdoor and indoor relative humidity

Time	Outdoor humidity	Indoor humidity
12:00	57	77
12:30	53	80
13:00	55	75
13:30	54	67
14:00	55	68
14:30	58	66
15:00	57	68
15:30	59	64

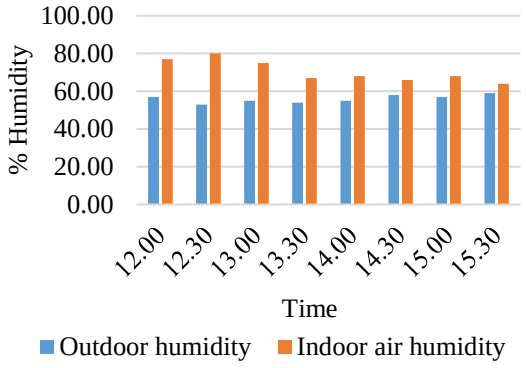

Fig.4 Relative humidity trends before the installation of heat pipes

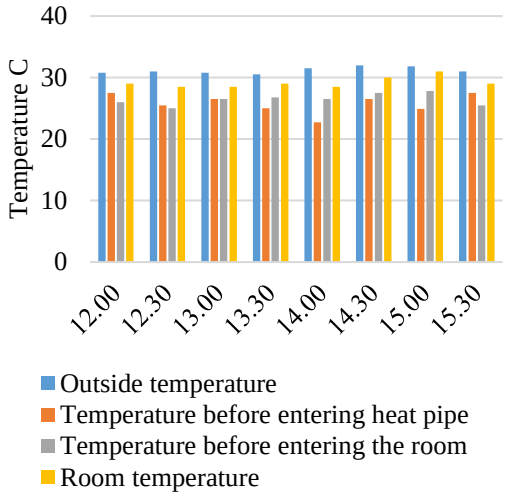

Fig.5 Temperature trends under 600 W/m² solar intensity

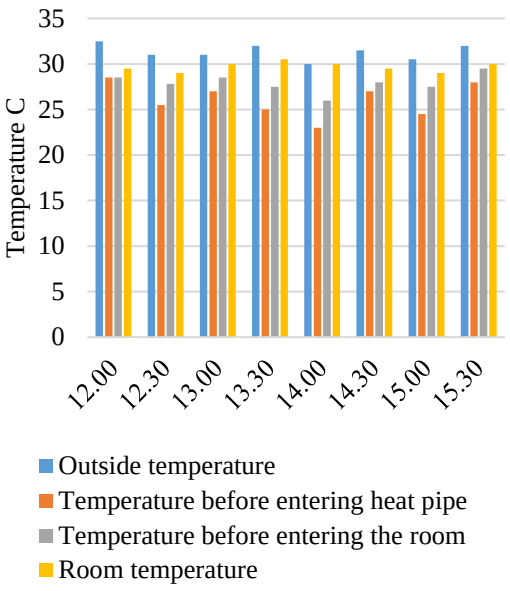

Fig.6 Temperature trends under 750 W/m² solar intensity

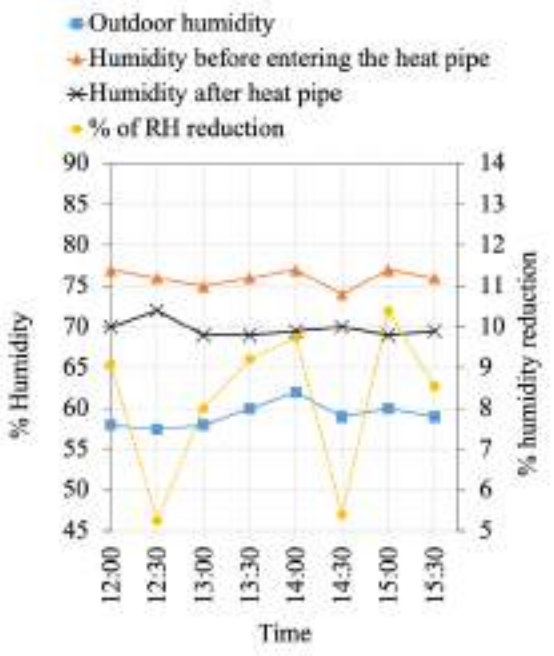

Fig.7 Trends of Relative Humidity and Dehumidification Efficiency Before and After Heat Pipe under 600 W/m² Solar Radiation

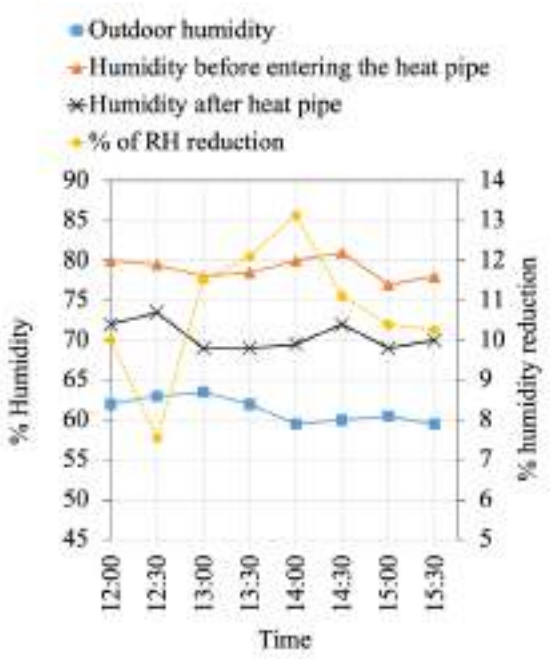

Fig.8 Trends of Relative Humidity and Dehumidification Efficiency Before and After Heat Pipe under 750 W/m² Solar Radiation

The experimental results reveal a consistent reduction in relative humidity across both test conditions, demonstrating the effectiveness of the thermosyphon heat pipe system in enhancing latent heat management. The air entering the heat pipe section exhibited noticeably higher relative humidity than the air exiting the system, confirming the successful extraction of moisture through the phase-change mechanism, as described by Eq. (1). Under moderate solar radiation at approximately 600 W/m², relative humidity values declined from 74–77% at the inlet to 66–69% at the outlet; similarly, under higher radiation at 750 W/m², humidity levels decreased from 76–82% to 67–70%. These reductions, referenced in Figures 7 and 8, correspond to a dehumidification efficiency reaching up to 12.5%, based on Eq. (5).

This enhanced performance under elevated radiation levels is primarily attributed to the increased thermodynamic activity of the R-134a refrigerant, where higher ambient temperatures facilitate more intensive latent heat absorption and subsequent vapor condensation inside the heat pipes. As a result, the humidity ratio of the incoming air is significantly reduced before it reaches the evaporative cooling medium, thereby alleviating the latent cooling load. This pre-conditioning effect not only improves evaporative cooling effectiveness but also contributes to improved thermal comfort, as the system achieves a more substantial temperature drop with less residual indoor humidity. The integration of thermosyphon heat pipes thus proves to be a valuable passive enhancement for evaporative systems operating in humid tropical climates.

This pre-conditioning step alleviated the latent load on the evaporative pad, leading to an improved cooling effect with lower moisture saturation in the room. As a result, the evaporative cooling effectiveness, calculated using Eq. (4), increased in comparison to the baseline system. The air felt drier

and more comfortable, particularly during afternoon hours with peak solar radiation.

CONCLUSION

This study demonstrates the potential of integrating thermosyphon heat pipes with an evaporative cooling system to enhance indoor comfort in hot and humid climates. By pre-conditioning the incoming air, the system passively reduces moisture content before it reaches the evaporative pad, improving overall cooling efficiency. The hybrid design responded well to natural environmental conditions without the need for mechanical control, supporting its applicability in real-world settings. This passive approach offers a sustainable alternative to conventional air conditioning and holds promise for future use in energy-efficient building design.

ACKNOWLEDGMENTS

The researcher would like to express sincere gratitude to the Department of Mechanical Engineering, Faculty of Industrial Education, Rajamangala University of Technology Suvarnabhumi, Suphanburi Campus, for providing the experimental area. Special thanks are also extended to the Faculty of Architecture and Design, King Mongkut's University of Technology North Bangkok, for the technical support and provision of data recording equipment. The researcher also gratefully acknowledges the Research Promotion Fund, Rajamangala University of Technology Suvarnabhumi, for the financial support in publishing the research findings.

REFERENCES

[1] Bernhard, G.H., Bais, A.F., Aucamp, P.J., Klekociuk, A.R., Liley, J.B., and McKenzie, R.L., Stratospheric ozone, UV radiation, and climate interactions. Photochem Photobiol Sci, Vol.22, 2023, pp.937–989.

[2] Madronich, S., Sulzberger, B., Longstreth, J.D., Schikowski, T., Andersen, M. P.S.,Solomon, K. R., and Wilson, S. R., Changes in tropospheric air quality related to the protection of stratospheric ozone in a changing climate. Photochem Photobiol Sci, Vol.22, 2023, pp.1129–1176.

[3] Andersen, S.O., Lessons from the stratospheric ozone layer protection for climate. Photochem Photobiol Sci, Vol.5, 2015, pp.143–162.

[4] Van Den Bulck, E., Mitchell, J.W., and Klein, S.A., Design Theory for Rotary Heat and Mass Exchangers: II. Effectiveness-NTU Method. International Journal of Heat and Mass Transfer, Vol.28, Issue 8, 1985, pp.1587–1595.

[5] Lazzarin, R.M., and Gasparella, A., New Ideas for Energy Utilisation in Combined Heat and Power with Cooling: II. Applications. Applied Thermal Engineering, Vol.17, Issue 5, 1997, pp.479–500.

[6] Alklaibi, A.M., Evaluating the Possible Configurations of Incorporating the Loop Heat Pipe into the Air-Conditioning System. International Journal of Refrigeration, Vol.31, Issue 5, 2008, pp.807–815.

[7] Srihajong, N., Ruamrungsri, S., Terdtoon, P., Kamonpet, P., and Ohyama, T., Heat Pipe as a Cooling Mechanism in an Aeroponic System. Applied Thermal Engineering, Vol.26, Issue 2–3, 2006, pp.267–276.

[8] Watcharodom, N., Design and Construction of Energy-Saving Air-Conditioning Innovation for Small-Scale Residences, in Proc. 12th Conf. on E-NETT, 2016, pp.1321–1328.

[9] Watcharodom, N., Design and Construction of Split-Type Air-Conditioning System Using Thermosyphon Heat Pipe, in Proc. 14th Conf. on E-NETT, 2018, pp.45–50.

[10] Ananacha, T., Rattanabanlue, A., and Watcharodom, N., The Enhancement of Split-Type Air Conditioner by Improving the Cooling System for Residence. International Journal of Science and Innovative Technology, Vol.7, No.1, 2024, pp.89–99.

[11] Meena, P., Rittidech, S., and Poomsa-ad, N., Application of Closed-Loop Oscillating Heat Pipe with Check Valves (CLOHP/CV) for Reduced Humidity in Drying Systems. Applied Energy, Vol.84, Issue 5, 2007, pp.553–564.

[12] Dunn, R. J., Miller, J. B., Willett, K. M., Gobron, N., Ades, M., Adler, R., and Preimesberger, W., Global climate. Bulletin of the American Meteorological Society, Vol.104, No.9, 2023, S11-S145.

Copyright © Int. J. of GEOMATE All rights reserved, including making copies, unless permission is obtained from the copyright proprietors.

15th Int. Conf. on Geotechnique, Construction Materials & Environment, Kyoto, Japan, 11-13 November 2025, ISBN 978-4-909106124 C3051

A STUDY ON FLOOD INUNDATION ANALYSES AND HAZARD MAPPING APPROACHES FOR SMALL-SIZED RIVERS

Shengping Zhnag[1] and Jie Qi[2]

[1]Faculty of Urban Science, Meijo University, Japan;
[2] School of International Studies, Utsunomiya University, Japan

ABSTRACT

As global warming intensifies, heavy rainfall disasters have become dramatically more frequent. Although various mitigation strategies exist, disaster management experts almost unanimously assert that evacuation remains the most effective way to safeguard human lives. Consequently, accurate and reliable flood inundation data is essential for ensuring efficient evacuations. In Japan, flood hazard maps based on meticulous inundation analyses have been developed, disseminated, and widely used for major river basins to provide critical information. However, in smaller river basins, flood conditions are often influenced by runoff from larger downstream rivers, and the development of comprehensive watershed databases has lagged. As a result, performing precise flood inundation analyses is challenging, and dependable hazard maps are frequently unavailable. This study employs the iRIC (International River Interface Cooperative) model—a reliable and user-friendly tool for flood inundation analysis—to investigate the behavior of small-sized rivers and develop detailed 3D hazard maps. Verification of the analysis results and the resulting hazard maps confirmed their reliability. Ultimately, the proposed approach to flood inundation analysis and hazard mapping is expected to be a practical and highly effective asset for designing evacuation strategies and reducing casualties during flood disasters.

Keywords: Global Warming, Inundation Analyses, Evacuation Planning, Hazard Map, iRIC (International River Interface Cooperative)

INTRODUCTION

In recent decades, Japan has witnessed increasingly severe extreme weather events attributed to climate change, including record-breaking heavy rainfall occurring almost annually [1]. These events have caused widespread flooding and inundation exceeding urban flood control standards, as well as serious landslides, resulting in substantial economic losses and human casualties [2].

To mitigate damage from flood inundation, the reinforcement of hard infrastructure flood control measures is essential. However, such developments require significant financial investment and extended timelines, limiting their immediate effectiveness. Consequently, evacuation strategies have gained increased attention. Numerous cases demonstrate that timely evacuation can prevent fatalities, whereas delays or failures in evacuation exacerbate harm, highlighting the critical role of effective evacuation planning [2]. However, Japan is facing a pronounced demographic challenge, with individuals aged 65 and older constituting 29.1% of the population in 2023, projected to rise to 40% by 2050 [3]. This unprecedented aging population presents considerable obstacles to rapid evacuation.

To ensure efficient and reliable evacuation, local governments have developed evacuation plans supported by hazard maps that provide essential information such as inundation depths and extents, possible evacuation facilities and routes for various flood scenarios. While hazard map development is advanced in major river basins and metropolitan areas, smaller river basins have lagged behind. Often, disaster prevention plans for tributaries depend on finalized plans for downstream major rivers, resulting in numerous basins without adequate hazard maps [4].

This study employs the reliable and user-friendly iRIC (International River Interface Cooperative) flood simulation model to analyze inundation in small river basins [5]. Using the simulation results, we develop a three-dimensional flood hazard map aimed at securing smooth and rapid evacuation routes during floods. Finally, evacuation scenarios are simulated to enable virtual pre-experience of evacuation routes, thereby assessing the feasibility of prompt evacuation behavior.

RESEARCH SIGNIFICANCE

This study applies a comprehensive methodology for developing three-dimensional hazard maps for small- to medium-sized river basins, where obtaining reliable and detailed flood information is particularly challenging. The 3D hazard maps produced through this process enable users to identify suitable evacuation shelters, determine optimal evacuation routes, and estimate required evacuation time, thereby supporting the development of feasible and effective evacuation plans. Moreover, the application

of these 3D hazard maps facilitates the implementation of online evacuation drills, which are expected to make a significant contribution to reducing human casualties in the event of flooding. Furthermore, Combining the traditional inundation analysis model with the 3D mapping technology makes the hazard map generation procedure more reliable and easier.

INUNDATION ANALYSES

Inundation Analysis Model iRIC

iRIC (International River Interface Cooperative) is a free software platform designed for inundation analysis and numerical simulation of rainfall-runoff processes. Developed by the International River Interface Cooperative [5], iRIC supports a diverse range of computational solvers addressing various problems in water science and engineering [6]. Originally created as a tool for river flow and morphodynamic analysis, the software has since evolved to encompass a broad spectrum of applications, including flood prediction, rainfall-runoff modeling, tsunami propagation, debris flow simulation, habitat assessment, and other hydrological and hydraulic phenomena.

iRIC is widely used in Japan, and its reliability, flexibility, and user-friendly interface have been demonstrated through numerous reported case studies [7]. It is currently recognized by the Japanese government as one of the approved inundation analysis models that can be utilized in the formulation of river management plans [4]. Therefore, this study adopts the iRIC model for inundation analyses.

The specific hydrological and hydraulic details implemented within iRIC model are omitted here; readers are referred to the official iRIC manual for further information. The manual is available for download from the iRIC official website [6].

The Watershed for Inundation Analyses

This study has chosen the Oiwagawa River watershed located in Toyama Prefecture, Japan for inundation analyses. The location of the Oiwagawa watershed is shown in Fig.1. The Oiwagawa River is a tributary of the Shiraiwa River and is a small river with a total length of 12 kilometers. Originating from Takamine Mountain, which stands at an elevation of 958 meters, the river descends while forming deep V-shaped valleys and large waterfalls, eventually converging with the Shiraiwa River. Several settlements have developed around the small basin areas along the river. Repeated flooding of this river poses significant threats to the lives and properties of these inhabitants [8]. The Oiwagawa basin was selected as the subject of analysis with the aim of providing essential information for the evacuation of residents.

Fig.2 illustrates the specific inundation analysis area within the Oiwagawa watershed. The inundation analysis region encompasses a rectangular area measuring 1.3 kilometers in width and 8.0 kilometers in length, covering nearly the entire upstream watershed from the confluence with the Shiraiwa River to the exit of the Takamine Mountain valley.

The rectangular analysis area does not include four tributaries of the Oiwagawa River (Shioya River, Kakenana River, Futaguchi River, and Suyama River) and the very upstream segment of the Oiwagawa River that flows down the Takamine Mountain valley. The inflows from all the five rivers are inputted directly into the corresponding segments of Oiwagawa River with careful considerations of the runoff time in each river segment. Also shortened names of the five rivers are used for simplicity in this paper as Shio, Kake, Futa, Suya and Oiwa, respectively.

Fig.1 The location of the Oiwagawa River watershed

Fig.2 The inundation analysis area within the Oiwagawa River watershed

Setting Up the Analysis Conditions

To apply the iRIC model to the target river basin, it is essential to define both the basin conditions and the analysis parameters in advance.

First, topographic data of the study area is required. For this purpose, data provided by the Geospatial Information Authority of Japan (GSI) through its GPS system was utilized [9]. The GSI data was selected due to its high reliability.

Next, the river basin was discretized into a rectangular grid (cells) based on the topographic data described above. The grid comprises 200 cells along the river flow direction and 50 cells across the river width, resulting in individual cell dimensions of approximately 40.3 meters in length and 26 meters in width. This grid resolution was chosen in consideration of the trade-offs among topographic data accuracy, analysis duration, and computational cost.

A key parameter used to represent the hydrological characteristics of the river channel is Manning's roughness coefficient. The values adopted here are those traditionally used by Toyama Prefecture in previous flood analyses of the Oiwagawa River [10]. This choice allows for direct comparison and validation against prior results.

Furthermore, rainfall intensity must be specified as input for the flood inundation model. In the flood mitigation planning for this basin, Toyama Prefecture has already established standard design rainfall based on a 1-in-50-year return period. The rainfall intensity associated with this probability rainfall is defined by the following equation [11]:

$$\mathbf{r} = \frac{\mathbf{2019.92}}{\boldsymbol{t}^{\mathbf{0.76}} + \mathbf{7.680}} \quad (1)$$

where t is time in minutes and r is the rainfall intensity in mm/hr. The corresponding hyetograph for this design rainfall is presented in Fig. 3.

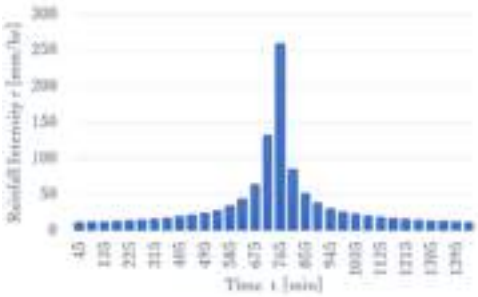

Fig.3 The hyetograph of the design rainfall

Finally, the study area receives inflows from several tributaries, including the upstream portion of the Oiwagawa River. The inflows from these tributaries must be predefined as input for the iRIC model. To estimate these inflows, the well-known Rational Method was employed:

$$\mathbf{Q} = \frac{\mathbf{1}}{\mathbf{3.6}} \boldsymbol{frA} \quad (2)$$

In this equation, Q represents the flow rate from a tributary (in m^3/s), f is the runoff coefficient (dimensionless), r is the rainfall intensity (mm/hr) as defined in Eq.(1), and A is the drainage area of the tributary (in hectares).

Using Eq. (2), the flow rates for five tributaries—Oiwa, Futa, Suya, Shio, and Kake—were calculated. The resulting hydrographs are presented in Fig. 4.

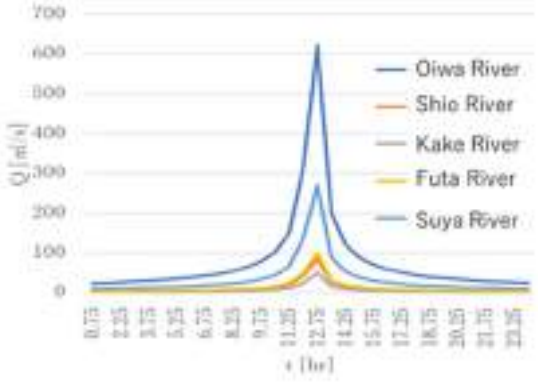

Fig.4 The hydrographs of the five inflowing tributaries

Inundation Analysis Results

Using the analysis conditions established in the previous section, the iRIC model was applied to the target watershed. As a result, the extent and depth of inundation caused by the design rainfall were obtained.

Fig.5 illustrates the inundation depth at the time of peak discharge (t = 46,800 seconds) at the downstream end of the simulation domain. The areas where inundation water depths are less than 0.01m are not shown in this figure because these water depths are considered will not cause any more problems for evacuation activities than the heavy rainfall itself. Fig.6 shows the maximum inundation depth recorded in each computational cell during the whole design rainfall event. It should be noted that the timing of these peak depths varies across cells. Nevertheless, the maximum inundation depth is particularly important when considering evacuation planning.

Fig.7 shows the planned inundation scenario for the target river basin currently published by Toyama Prefecture [12]. It has already been confirmed that this published scenario contains calculation errors [13], and a reassessment is currently being conducted by the prefectural authorities to evaluate the impact of those errors. In comparison, the flood assessment conducted in the present study reveals a wider inundation extent and greater inundation depths, indicating a more severe flood scenario than previously reported.

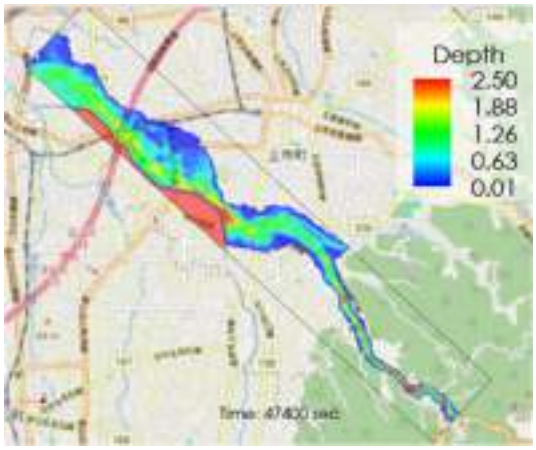

Fig.5 The inundation depth(m) when the downstream discharge reached the maximum

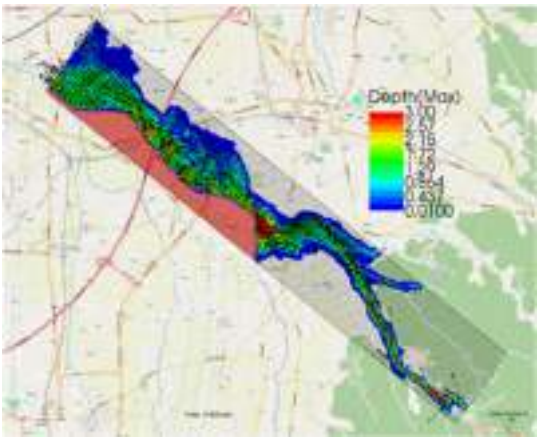
Fig.6 The maximum inundation depth(m) during the whole runoff process.

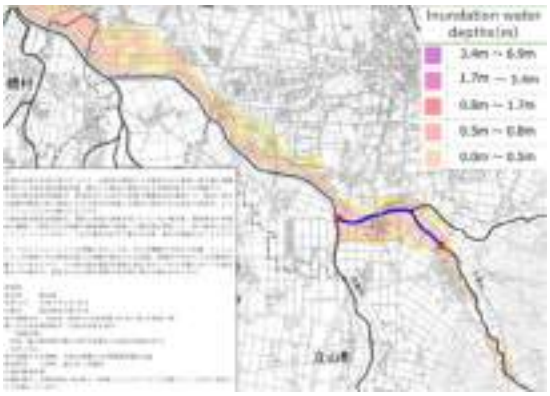
Fig.7 The current inundation scenario for Oiwagawa watershed published by Toyama Prefecture [12] (The analysis river segment for this study is between the two red dots.)

GENERATE INUNDATION HAZARD MAPS

2-Dimentional Hazard Map

By overlaying the inundation depth results obtained from the flood simulation described in the previous section with various digital maps, it is possible to generate different types of hazard maps tailored to specific purposes.

First, a two-dimensional hazard map was created by superimposing the maximum inundation depths during the design rainfall event (as shown in Fig.6) onto Google Maps. Fig.8 presents an image illustrating the overlay process, and Fig.9 shows the base version of the resulting two-dimensional hazard map. Naturally, to complete this hazard map, additional information—such as the locations of evacuation facilities—should be overlaid as well. However, such information is already well-maintained by local governments in Japan, and thus that step is omitted in this discussion.

3-Dimentional Hazard Map

Next, the creation of a three-dimensional hazard map is described. Similar to the 2D map, the 3D hazard map is produced by overlaying the flood simulation results onto digital map data. In this case, however, Google Earth is used as the base platform, and Google Street View is also incorporated to enhance the spatial context. Fig.10 and Fig.11 show examples of 3D hazard maps for two different locations.

Results and Discussion

This three-dimensional hazard map generated above allows users to visually assess the extent of inundation in specific areas, including around evacuation facilities, offering an intuitive understanding of the flood situation at points of interest. Additionally, users can evaluate the inundation conditions along potential evacuation routes, which aids in selecting safer paths. Once the evacuation facilities and routes are identified, the 3D hazard map can be used to estimate evacuation times, enabling the development of more realistic and effective evacuation plans.

The primary advantage of this 3D hazard map lies in its use of familiar platforms—Google Earth and Google Street View—which are widely used in daily life. While many disaster-specific systems have been developed, historical evidence has repeatedly shown that unfamiliar systems are often ineffective during actual emergencies.

Moreover, the 3D hazard map holds great promise as a tool for disaster education. Traditional 2D hazard maps were typically used only for passive viewing. In contrast, the 3D map, combined with Google Street View, offers high interactivity, allowing users to

engage directly with the data and explore affected areas more actively. This interactivity is especially promising for engaging younger generations, who have consistently shown lower disaster awareness in various public surveys.

Fig. 8 Generate 2-dimentional inundation hazard map

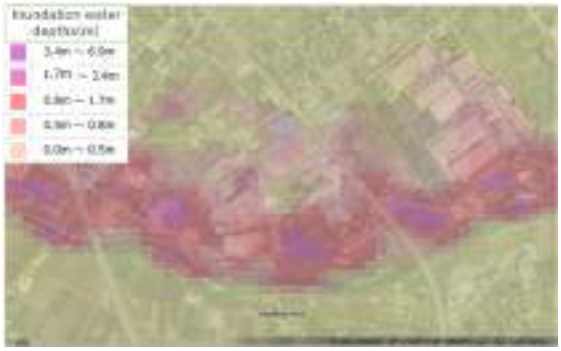

Fig.9 The final 2-dimentional inundation hazard map

Fig.10 The 3-dimentional inundation hazard map at Street-A where the water depth is 1.68m.

Fig.11 The 3-dimentional inundation hazard map at Street-B where water depth is 1.21m.

CONCLUSIONS

This study has been conducted to provide reliable and detailed flood hazard information for small- to medium-sized river basins. These basins are typically located upstream of major rivers and are often treated merely as tributaries within the broader flood management systems of major river basins. As a result, disaster-related information for these areas is frequently generalized, with data often presented as single-point or single-segment information. Such limited granularity makes it nearly impossible to formulate reliable and feasible evacuation plans. Consequently, preventable damages have occurred in many cases.

This study has also utilized the versatile runoff analysis model iRIC to simulate flood inundation extents and water depths under designed rainfall scenarios specifically for small- to medium-sized river basins. The simulation results were overlaid onto digital maps to enhance traditional two-dimensional hazard maps. Furthermore, we developed three-dimensional hazard maps by integrating these results with Google Earth and Google Street View, thereby offering a more immersive and spatially intuitive representation of flood risk.

These enhanced hazard maps provide residents living in small-sized river basins with more detailed and accessible flood risk information. This facilitates easier selection of evacuation shelters and routes, confirmation of evacuation timing, and ultimately supports the development of more reliable and actionable evacuation plans. The approach is expected to contribute significantly to the reduction of avoidable disaster damage.

The methodology employed in this study establishes a practical framework for generating hazard maps tailored to small-sized and medium-sized river basins. Future work will focus on gathering feedback from local residents using these hazard maps to identify areas for improvement. Additionally, the potential of these 3D hazard maps as effective tools for disaster education will be further explored through practical applications.

ACKNOWLEDGMENTS

The authors would like to express their sincere gratitude to the International River Interface Cooperative for generously providing the iRIC runoff analysis software free of charge. Through the course of this study, the authors were able to confirm the reliability of the iRIC model and the user-friendliness of its interface. The authors also wish to extend their appreciation to Mr. Teruma Nakamura, a student in the Laboratory of Water Resource Planning at Meijo University, Japan, for his significant contributions to the collection, organization, and analysis of relevant

data and materials.

REFERENCES

[1] Cabinet Office, Government of Japan, 2024 Edition of the White Paper on Water Resource Circulations, 2024, Nikkei Printing Co., Ltd., pp.1-104.

[2] Cabinet Office, Government of Japan, 2024 Edition of the White Paper on Nature Disaster Prevention, 2024, Nikkei Printing Co., Ltd., pp.1-326.

[3] Cabinet Office, Government of Japan, 2024 Edition of the White Paper on the Aging Society, 2024, Nikkei Printing Co., Ltd., pp.1-224.

[4] Minister of Land, Infrastructure, Transport and Tourism, The 4th version of the Manual for Generating Flooding Hazard Maps, 2015, pp.1-465.

[5] iRIC https://i-ric.org/en/about/

[6] Yasuyuki Shimizu, Takuya Inoue, Eiichi Suzuki, etc., Manual of iRIC Softwear, Version3.0, International River Interface Cooperative, 2021, pp.1-126. https://iRIC.org/webadmin/wp-content/uploads/2021/01/Nays2D_Flood_Examples_ja_3.0_2021.pdf

[7] Yasuyuki Shimizu, Jonathan Nelson, Kattia Arnez Ferrel, etc., Advances in computational morphodynamics using the International River Interface Cooperative (iRIC) software, River, Coastal and Estuarine Morphodynamics: Selected papers from the 10th anniversary of the RCEM Symposium, Vol.45, Issue 1, 2020, pp.11-37, DOI: 10.1002/esp.4653

[8] Toyama Prefecture Homepage, Disaster information and disaster Prevention Web. https://www.city.toyama.lg.jp/bosai/bosai/1010665/index.html

[9] Geospatial Information Authority of Japan (GSI), Geographic Data Online Download Service. https://service.gsi.go.jp/kiban/

[10] Takanari Hori, Nobuhiko Morita, Yusuke Masuda, etc., The Flood Prevention Measures in Toyama Prefecture, The Annual Symposium Proc. of Japan Civil engineering Consultants Association Hokuriku branch, 2017, Paper No.17a. pp.1-5

[11] Toyama Prefecture, Design Rainfall Intensity. https://www.pref.toyama.jp/documents/5176/009 46856.pdf

[12] Toyama Prefecture, The Current Inundation Scenario for Oiwagawa Watershed. https://www.pref.toyama.jp/documents/5184/ooi wa_souteisaidaikibo

[13] Mainichi Shinbun Newspaper, Inundation Scenarios Required Correction for Three Rivers in Toyama Prefecture, Hokuriku Online Version, 2/16/2021. https://mainichi.jp/articles/20210216/ddl/k16/010/310000c

Copyright © Int. J. of GEOMATE All rights reserved, including making copies, unless permission is obtained from the copyright proprietors.

15th Int. Conf. on Geotechnique, Construction Materials & Environment,
Kyoto, Japan, 11-13 November 2025, ISBN 978-4-909106124 C3051

ENHANCING FLOOD RESILIENCE THROUGH UPDATED IDF CURVES: LESSONS LEARNED FROM RECENT EXTREME RAINFALL EVENTS IN THE UAE

Khalid B. Almheiri[1] and Rabee Rustum[2]

[1]School of Energy, Geoscience, Infrastructure and Society, Dubai Campus, Heriot-Watt University, Dubai, United Arab Emirates

ABSTRACT

Sharjah in the United Arab Emirates (UAE) has experienced unprecedented extreme rainfall, exposing vulnerabilities in its urban drainage systems. This study recalibrates Intensity–Duration–Frequency (IDF) curves based on extended and refilled rainfall data from 1992 to April 2024, and employs a Kohonen Self-Organizing Map (KSOM) to reconstruct missing sub-daily data. Extreme-value distributions were fitted via non-stationary frequency analysis to incorporate climate covariates, including cloud-seeding activity. The revised curves show peak intensities up to 41 percent higher for 10-year return periods and increased short-duration sensitivity. Benchmarking against Kuwait and Qatar confirms that Sharjah's rainfall intensification exceeds neighboring trends, underscoring the inadequacy of old design storms. Infrastructure evaluations identify capacity deficits under updated conditions. Recommended measures include five-year IDF recalibration, integration of sustainable urban drainage systems, deployment of real-time monitoring networks, and establishment of a Gulf-wide data-sharing consortium. The methodology offers a repeatable framework for dynamic stormwater design and management. These actions will align design standards with evolving hydro-climatic realities and strengthen flood resilience across arid urban environments.

Keywords: cloud-seeding; comparative study; Intensity-Duration-Frequency (IDF) Curves; rainfall; Sharjah.

INTRODUCTION

Urban flooding has emerged as a major hydrometeorological challenge in arid and semi-arid regions, where rainfall events tend to be infrequent but intense. The United Arab Emirates (UAE), and particularly the Emirate of Sharjah, has witnessed increasingly irregular and extreme rainfall events over the past decade. These events have exposed critical vulnerabilities in the stormwater management systems of many rapidly urbanizing cities. Sharjah, characterized by its flat topography, high degree of surface impermeability, and dense built environment, has been especially prone to urban flooding when short-duration, high-intensity storms exceed the design capacity of existing drainage infrastructure, and in many urbanized areas, stormwater networks are either non-existent or only partially implemented.

Intensity-Duration-Frequency (IDF) curves are among the most fundamental hydrological and urban infrastructure design tools. They are used to estimate the expected intensity of rainfall over varying durations and recurrence intervals, guiding the sizing of culverts, storm drains, storage basins, and flood protection measures [1]. Conventional IDF curves are often derived from limited historical data, emphasizing daily rainfall totals rather than short-duration, high-intensity events. This neglects the critical need for actual and accurate records that reflect the true nature of storm events, which in arid urban environments like Sharjah often last just a few hours and are the main contributors to urban flooding [2]. Moreover, these curves usually assume climatic stationarity, which is an increasingly outdated premise due to the growing influence of climate change and cloud-seeding interventions. In the UAE, cloud-seeding operations have increased rainfall, but also unintentionally altered precipitation patterns, making traditional IDF models less reliable.

Recent flooding events, including those in March 2016, January 2020, and most notably April 2024, have demonstrated the consequences of using outdated IDF data that do not reflect the current or future precipitation regime. These events caused widespread urban disruption, economic losses, and safety hazards. For instance, the April 2024 event overwhelmed Sharjah's existing stormwater system within the first hour of rainfall, causing severe road and property inundation, as shown in figures 1(a) and 1(b) and figures 2(a) and 2(b).

Fig.1(a) and 1(b) Partial and Total Vehicle Submersion.

Fig.2(a) and 2(b) Rainwater Flooding of Major Roads.

These failures underscore the necessity for a more adaptive and precise approach to rainfall estimation and drainage system design, supported by updated IDF curves that reflect the local context's specific climatic and environmental conditions.

This paper addresses these challenges by recalibrating Sharjah's IDF curves using extended and corrected rainfall records from 1992 to 2024. It employs Kohonen Self-Organizing Maps (KSOM) to reconstruct missing data and validate the results against hourly records from the nearby Dubai Airport weather station, supplemented by archived photographs capturing flooded roads and inundated properties throughout Sharjah. The objective is to demonstrate how revised IDF models can enhance flood resilience and inform a new generation of policy and planning interventions aligned with emerging climatic and urban development realities.

Research Significance

This study highlights the urgent need to update IDF curves in the UAE following recent rainfall extremes and evolving hydrometeorological conditions. By revealing the inadequacy of existing drainage infrastructure under revised intensities, it emphasises the critical role of accurate rainfall characterization in urban flood mitigation planning and resilient infrastructure design.

METHODOLOGY

This study follows a structured three-stage methodology: first, data acquisition and enhancement; second, IDF curve derivation; and third, regional benchmarking. The aim is to update IDF curves and assess their implications for urban flood resilience in the Sharjah Emirate.

Description of the Study Area

Sharjah, the third-largest emirate in the United Arab Emirates, covers 2,564 km² along the southern shore of the Arabian Gulf, and is geographically bounded by latitudes 25.2° N to 25.4° N and longitudes 55.4° E to 55.6° E [3]. As shown in Figure 3, it is bordered by Ajman and Al Umm Al Quwain to the north, Fujairah and Ras Al Khaimah to the east and southeast, and Dubai to the south.

Fig.3 Sharjah Emirate location and its three regions within the UAE [4].

Although the emirate includes both rugged mountain terrain in the east and broad central plains, the western urban core, Sharjah City, now contains the bulk of its residential and commercial development.

Sharjah City has become a compact metropolitan area with extensive impermeable surfaces and occasional yet intense convective storms. Urban expansion has exceeded the capacity of the city's drainage system, substantially increasing its flood vulnerability and underscoring the urgent need for adaptive, resilience-focused stormwater management strategies.

Data Acquisition and Enhancement

Rainfall records from January 1992 to April 2024 were compiled from the UAE National Centre of Meteorology (NCM) and Sharjah municipal archives, as consolidated by [1], [2]. To address missing observations, particularly during the 1990s, short-interval gaps were infilled using Kohonen Self-Organizing Maps (KSOM), trained on both local Sharjah gauge data and concurrent hourly records from the Dubai Airport station. This unsupervised neural network technique projects high-dimensional datasets onto a lower-dimensional grid while preserving topological relationships among data points. The algorithm identifies similarity patterns within the available data, enabling robust infilling of incomplete time series.

In this study, KSOM was applied to reconstruct missing sub-daily rainfall records from the 1990s and early 2000s. Previous regional applications have

demonstrated its validity and effectiveness for hydrological datasets, particularly in data-sparse environments [5], [6]. Its integration in this analysis supported the development of more accurate IDF curves by extending the historical rainfall record with statistically consistent values.

The dataset employed in this study was initially developed by the authors [1], [2]. The complete rainfall series was then divided into pre-seeding (1992–2009) and post-seeding (2010–2024) periods to isolate the effects of cloud-seeding operations. Validation of the reconstructed dataset involved statistical comparison with Dubai Airport hourly measurements to ensure quantitative accuracy and physical corroboration against archived photographs, confirming that extreme events were accurately represented over time [2].

IDF Curve Derivation

Annual maximum rainfall depths were extracted from 10 minutes to 24 hours at each station. Frequency analyses employed the Generalized Extreme Value (GEV) distribution, with parameters estimated via Maximum Likelihood Estimation. Model adequacy was assessed using Kolmogorov–Smirnov and Anderson–Darling goodness-of-fit tests to ensure robust extreme-value characterization. Separate intensity-duration-frequency points for return periods of 2, 5, 10, 25, 50, and 100 years were fitted to continuous parametric equations through nonlinear regression. Daily maxima were temporally disaggregated for design-level applications using standardized reduction factors from the Sharjah Storm Drainage Manual. This approach ensured consistency across timescales and enhanced the practical utility of the revised curves. For full procedural details, refer to [1].

Regional Benchmarking

Published IDF datasets for Kuwait [7] and Qatar [8] were standardized to match Sharjah's revised curves over 10 minutes to 24 hours and return periods of 2 to 100 years. Comparative metrics of intensity ratios at each return period, curve steepness, and short-duration sensitivity were calculated, and paired t-tests determined the significance of observed differences. This regional benchmarking validates the internal consistency of Sharjah's updated IDF values against neighbouring standards and highlights how cloud-seeding has altered rainfall extremes in the UAE relative to other Gulf countries.

RESULTS

This section provides the quantitative foundation for this study. Section 3.1 compares old (1992–2020) and revised (2021–April 2024) IDF curves across multiple durations and return periods, quantifying peak-intensity variation. Section 3.2 then benchmarks Sharjah's updated curves against published datasets for Kuwait and Qatar, employing paired t-tests to confirm statistically significant regional differences. These findings explore the accuracy of old IDF curve values relative to the recently updated values and assess the necessity of further regional calibration.

Revised IDF Curve Characteristics

The recalibration incorporates additional rainfall data from January 2021 through April 2024, extending the record used in the original 2020 analysis. Table 1 compares the (OLD) IDF values, derived from January 1992 to December 2020 records, and the revised (NEW) values updated with data through April 2024. Across all combinations of storm duration (10 - 120 minutes) and return period (2 -10 years), the updated intensities exceed the old values by (37 - 41) %, with the most significant relative increases occurring at the shortest durations, as compared in Table 1.

Table 1 Comparison of Old and New IDF Curves for Sharjah

Return Period	Duration Minutes	IDF OLD* (mm / h)	IDF NEW** (mm / h)	Percent Increase
2-year	10	25.09	34.96	39.3
	20	17.50	24.38	39.3
	30	13.88	19.34	39.3
	60	9.11	12.70	39.4
	120	5.85	8.15	39.3
3-year	10	39.32	55.46	41.0
	20	27.42	38.68	41.1
	30	21.75	30.68	41.1
	60	14.28	20.14	41.0
	120	9.16	12.93	41.2
5-year	10	55.42	78.30	41.3
	20	38.65	54.60	41.3
	30	30.66	43.31	41.3
	60	20.13	28.43	41.2
	120	12.92	18.25	41.3
10-year	10	77.70	106.99	37.7

20	54.19	74.61	37.7
30	42.98	59.18	37.7
60	28.22	38.85	37.7
120	18.11	24.94	37.7

Notes:
** OLD: Based on January 1992–December 2020 records.*
*** NEW: Includes additional rainfall data from January 2021 to April 2024.*

Comparative analysis of the updated and old IDF curves for Sharjah City reveals a clear upward shift in rainfall intensity across all durations and return periods, with the most pronounced relative increases occurring at shorter durations and lower return periods.

At the 2-year return period, the 10-minute intensity climbed from 25.09 to 34.96 mm/h, a 39.3 % increase, while the 60-minute intensity rose from 9.11 to 12.70 mm/h (39.4 %) as illustrated in Figure 4.

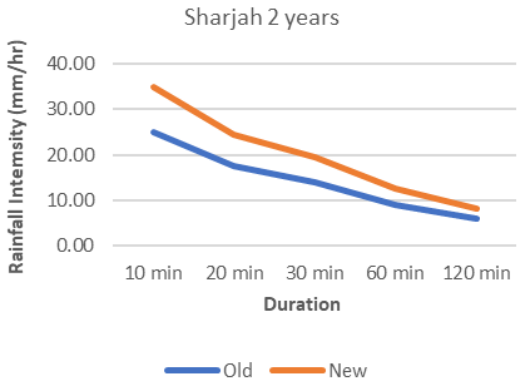

Fig.4 Increase in IDF Curve Values for Sharjah City's 2-Year Return Period.

For the 10-year return period, the 30-minute intensity increased from 42.98 to 59.18 mm/h, representing a 37.7 % rise, as illustrated in Figure 5.

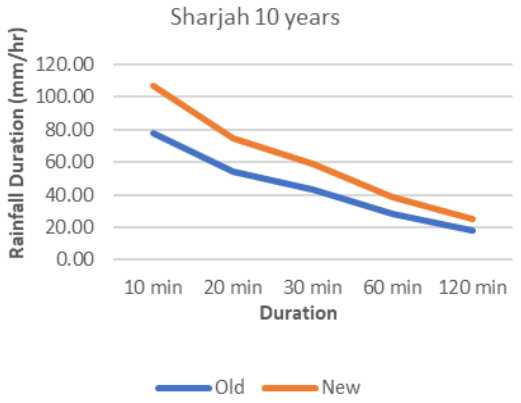

Fig.5 Increase in IDF Curve Values for Sharjah City's 10-Year Return Period.

At the 100-year return period, the 30-minute intensity grew from 83.37 to 108.88 mm/h, representing a 30.6 % increase, as shown in Figure 6.

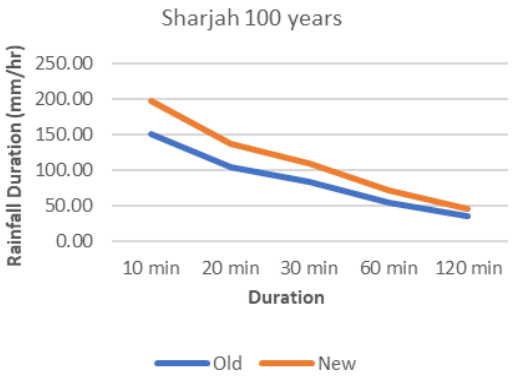

Fig.6 Increase in IDF Curve Values for Sharjah City's 100-Year Return Period.

Overall, these upward trends signal more frequent and intense rainfall events in Sharjah City, underscoring evolving regional climate patterns and the urgent need to reinforce flood-resilience measures across the urban landscape.

Regional Benchmarking

Sharjah's revised IDF characteristics were compared directly with recent curves for Kuwait [7] and Qatar [8]. All datasets were aligned to durations of 10 minutes, 1 hour, 24 hours, and return periods of 2 to 100 years. Three key metrics were evaluated: absolute intensities at selected durations, the GEV shape parameter (α), and a short-duration sensitivity index (10 min / 1 h intensity), as shown in Table 2.

Table 2 Comparison of Sharjah's Metrics with Kuwait and Qatar

Metric	Sharjah	Kuwait	Qatar
10-min, 10-yr intensity (mm/h)	78.39	70.50	74.20
1-hr, 10-yr intensity (mm/h)	51.50	45.90	48.70
24-hr, 10-yr intensity (mm/h)	101.20	90.30	93.60
GEV shape parameter (α)	0.28	0.24	0.26
Short-duration sensitivity index *	0.85	0.74	0.78

** Short-duration sensitivity index = (10 min intensity) / (1 hr intensity)*

Statistical paired t-tests on the matched 10-year return-period intensities show that Sharjah's mean rainfall values are significantly higher than those of Kuwait ($p = 0.012$) and Qatar ($p = 0.028$).

DISCUSSION

This section interprets the implications of the updated IDF curves and regional benchmarks across five themes: storm intensification, urbanization impacts, cloud-seeding influences, non-stationary modelling, and integrated management.

Intensification of Short-Duration Storms

The updated IDF curves reveal marked increases in peak intensities for the shortest durations, fundamentally altering Sharjah's storm hazard profile. For Sharjah City, comparing NEW (2021–April 2024) against OLD (1992–2020) values shows:

In the two-year return period, the 10-minute intensity rose from 25.09 mm/h to 34.96 mm/h (39.3 %), the 20-minute intensity increased from 17.50 mm/h to 24.38 mm/h (39.3 %), and the 30-minute intensity climbed from 13.88 mm/h to 19.34 mm/h (39.3 %).

At the ten-year return period, the 10-minute intensity jumped from 77.70 mm/h to 106.99 mm/h (37.7 %), the 20-minute intensity rose from 54.19 mm/h to 74.61 mm/h (37.7 %), and the 30-minute intensity increased from 42.98 mm/h to 59.18 mm/h (37.7 %).

This concentration of rainfall into shorter events drastically reduces available warning times. These storms formerly peaked over an hour, now reach maxima in under 30 minutes, and can overwhelm drainage systems designed for lower peak rates.

Across Sharjah City, short‑duration rainfall intensities rose by an average of 36.76%, signalling a shift toward storms with greater urban flood potential. These steeper peaks require updating design storm parameters and enhancing early warning and emergency response protocols to accommodate these more extreme events.

Urbanization and Runoff Dynamics

The transformation of Sharjah over recent decades from sparsely developed desert landscapes to a densely built urban environment has markedly increased surface impermeability. With expansive paved streets, compacted yards, and rooftops covering much of the city, rainfall that once percolated into the ground is routed immediately into storm drains. When paired with the substantially higher short-duration intensities revealed by the revised IDF curves as discussed earlier, this land-use shift exposes a critical mismatch between rainfall inputs and drainage capacity [9].

Existing networks were originally engineered using old IDF values that underestimate peak intensities by up to 41% for 10-year return period storms. Under current conditions, runoff volumes during a 30-minute design storm exceed conduit capacity within the first 20 minutes, leading to rapid surcharge and surface flooding [2]. Field inspections after the April 2024 event confirmed that although structurally sound, major culverts and open channels were hydraulically overwhelmed by inflows far beyond their design thresholds.

This deficit underscores two imperatives. First, drainage design must be recalibrated using the updated IDF curves so that pipe diameters, invert slopes, and detention requirements reflect actual peak flows. Second, urban planners and infrastructure managers should combine on-site stormwater retention including green roofs that capture and slowly release rainfall, permeable pavements that allow infiltration, rain gardens that store and naturally filter runoff, and underground reservoirs that hold excess water with staged-release controls and real-time flow monitoring to replace the buffering once provided by natural soils. On-site retention captures and stores stormwater at its source, staged-release controls temporarily detain runoff in basins or vaults before discharging it at measured intervals, and real-time flow monitoring uses sensor networks to track conveyance flows instantaneously and adjust release rates as needed. Together, these measures smooth out peak flows and help prevent sudden surges of stormwater runoff. By aligning network design and operational procedures with enhanced rainfall intensities and the prevailing high-impermeability land cover, Sharjah can substantially improve flood resilience.

Cloud-Seeding Influences

After 2010, cloud-seeding in the UAE increased significantly, altering rainfall characteristics by intensifying convective storms and changing intensity-duration profiles. A prior study found that cloud-seeding increased peak rainfall intensities in Sharjah and advised regular re-evaluation of urban stormwater drainage and updating IDF data for changing precipitation trends [1].

Building on earlier analyses, this study employed segmented IDF derivation to assess the impact of intensified cloud-seeding operations on rainfall

behaviour. The rainfall series was divided into two distinct periods: 1992 to 2009 (pre-seeding) and 2010 to 2024 (post-seeding) to isolate potential anthropogenic influences. Analysis of the recalibrated IDF curves revealed an approximate 36.8 % increase in average short-duration rainfall intensities during the post-seeding period. This trend is consistent with previous findings [2], which reported statistically significant intensification of convective storm events in the UAE following the escalation of cloud-seeding activities. The results highlight the importance of integrating cloud-seeding parameters as dynamic covariates in future IDF modeling frameworks.

To maintain infrastructure resilience, IDF recalibration protocols should quantify cloud-seeding contributions by incorporating seeding activity records as covariates in non-stationary extreme-value models. These protocols should also align curve updates with seeding program schedules. By integrating cloud-seeding influences into the IDF methodology, design standards can adapt to both natural climatic variability and cloud-seeding consequences.

Climatic Non-Stationarity and Uncertainty

Rainfall patterns in the UAE have changed significantly, rendering traditional stationary models and old IDF curves unreliable due to their assumption of a stable climate. The April 2024 floods, the most severe on record, highlighted this disconnect and showed that historical data can no longer bound future risks.

Two interconnected challenges lie at the heart of this issue. First, extreme rainfall events are non-stationary: as temperatures rise and convective systems evolve, peak intensities' statistical parameters shift over time. Using fixed-parameter fits may result in lower estimates of critical design storms, potentially affecting safety margins. Second, although the study records now run from 1992 to April 2024, sub-daily measurements remain sparse outside recent years. Limited availability of sub-daily rainfall observations undermines the reliability of extreme-event intensity estimates. This increased uncertainty complicates the selection of appropriately conservative design storms, thereby increasing infrastructure vulnerability to severe future rainstorms.

Overcoming these challenges requires a modernized approach to IDF curve development. Frequency analyses must be non-stationary, with extreme-value distribution parameters linked to measurable climate covariates such as temperature trends or cloud-seeding activity. Robust uncertainty quantification techniques, such as Bootstrap or Bayesian methods, can be applied to define confidence bounds on design intensities. IDF curves should then be updated every three to five years in accordance with World Meteorological Organization guidance. Embedding non-stationarity and quantified uncertainty into design tools will enable engineers and planners to develop infrastructure capable of withstanding both current extremes and those projected in the future.

Integrated Management and Policy Recommendations

To translate the insights from updated IDF curves into lasting resilience, Sharjah’s flood management framework must evolve along four complementary dimensions. First, municipal drainage regulations should be revised to require the use of the 1992–2024 dataset with adjustments for cloud-seeding effects in all new infrastructure projects and major rehabilitations. A formal five-year review cycle will align IDF curves with the latest climatological observations and seeding records.

Second, real-time monitoring and adaptive operations are essential. Deploy a network of IoT-enabled rain gauges and flow sensors across critical watersheds, integrated into an automated platform that continuously recalibrates short-duration intensity estimates. When observed rainfall rates exceed design thresholds, the system would issue alerts, adjust detention basin controls and activate emergency response protocols.

Third, expansion of sustainable urban drainage systems (SuDS) must be enforced for all new developments. On-site detention and infiltration measures such as permeable pavements, green roofs, and bio-retention swales should be sized to reduce at least the one-hour, 10-year design storm. Existing corridors can be modified with modular storage units or shallow infiltration trenches designed to reduce peak flows to the maximum capacity available in the corridors.

Finally, institutional capacity and regional coordination must be strengthened. Establish a Gulf-wide IDF consortium to harmonize data sharing, benchmarking, and best-practice exchange. Provide

workshops on extreme-value analysis and cloud-seeding for municipal engineers and embed these topics both in university degree programs and in the certification and continuing education requirements for licensed engineers to enhance flood resilience across the region.

Summary of Key Findings

The analysis yielded several critical findings with direct implications for rainfall characterization, infrastructure planning, and flood resilience in Sharjah.

Intensification of Short-Duration Rainfall

The revised IDF curves for Sharjah revealed substantial increases in short-duration rainfall intensities compared to the 1992–2020 dataset. Peak values rose by up to 41%, particularly for the 10-minute duration and return periods between 2 and 10 years, which are crucial for urban drainage design and risk management.

Concentration of Rainfall and Infrastructure Overload

Short-duration storm events have become more intense, with average rainfall intensification reaching 36.76%. This compression of storm durations reduces available warning time and has exceeded the design thresholds of pre-existing drainage systems, resulting in more frequent surcharging and surface flooding.

Regional Comparisons and Statistical Significance

Benchmarking against updated IDF datasets for Kuwait and Qatar confirmed that Sharjah's intensification trend exceeds regional norms. Paired t-tests at the 10-year return period demonstrated statistically significant differences ($p = 0.012$ for Kuwait; $p = 0.028$ for Qatar), underscoring the localized impact of urban densification and cloud-seeding activities, and the need for emirate-specific design standards.

Cloud-Seeding and Modeling Enhancements

In the period after 2010, rainfall intensities increased markedly in alignment with expanded cloud-seeding operations in the UAE, indicating a significant anthropogenic influence on Sharjah's evolving intensity–duration profile. This shift underscores the importance of incorporating cloud-seeding activity records as covariates in non-stationary modeling frameworks. Additionally, the use of KSOM for rainfall reconstruction, alongside climate-based extreme-value analysis, provided a more accurate and dynamic representation of present and future storm hazards than traditional stationary approaches.

POLICY RECOMMENDATIONS

Building on the empirical findings presented in Section 4 and expanding upon insights from the author's previous studies (2021; 2024), the following policy actions are proposed to enhance flood resilience and guide infrastructure adaptation strategies in Sharjah. These recommendations reflect both new contributions from the present analysis and a combination of best practices from the wider hydrological literature.

The first step is institutionalizing regular IDF recalibration. Every five years, the NCM and Sharjah Municipality should jointly review and update IDF curves using the latest sub-hourly rainfall records, including cloud-seeding data and non-stationary extreme-value methods. This five-yearly process will keep design parameters aligned with current and emerging precipitation patterns and prevent infrastructure from falling behind evolving climatic risks.

Complementing recalibration, an expanded real-time monitoring network will capture critical sub-hourly rainfall and runoff data across urban and peri-urban catchments. Deploying IoT-enabled rain gauges and flow sensors linked to a centralized open-access platform, integrated with GIS-based forecasting and early-warning systems, can allow dynamic calibration of design storms and rapid operational adjustments during extreme events.

Stormwater design codes should be rewritten to focus on performance. Engineering teams and relevant departments must update their standards so that all hydraulic models use the revised IDF values. They must also set clear limits on how much water can back up in pipes (surcharge depths) and collect on surfaces (ponding) during 10-year and 50-year storms. By tying code compliance to these measurable criteria, both new pipelines and retrofitted systems will reliably handle more intense peak flows while preserving required safety margins.

Urban zoning regulations must evolve in response to changing climate conditions. Planning authorities should employ scenario-based IDF simulations to identify flood-prone areas and limit development in those high-risk zones. At the same time, they can

incentivize the use of green infrastructure such as permeable pavements and retention basins that capture and reduce peak runoff.

Finally, capacity building and regional collaboration are essential for sustaining adaptive flood resilience. Ministries of Water Resources, universities, and engineering societies across the Gulf are encouraged to establish a consortium for hydro-meteorological data sharing, joint benchmarking, and coordinated updates. Supporting graduate research fellowships and professional workshops on advanced hydrological modeling, such as non-stationary frequency analysis and KSOM reconstruction, will develop the technical expertise and institutional frameworks needed to confront future extremes.

CONCLUSIONS

Revised IDF curves for Sharjah reveal up to 41 percent higher peak intensities at short durations, directly exposing critical design gaps in existing drainage infrastructure that contributed to the rapid failures of the system during the April 2024 flood. By integrating non-stationary extreme-value analysis, KSOM-based reconstruction of missing observations, and Gulf-wide benchmarking, this study establishes a robust, repeatable framework for dynamic IDF updates.

Statistical analysis confirms that rainfall intensities in Sharjah have risen significantly since 2010. Moreover, pronounced spatial differences across the local gauge network show that relying on regional or uncertain rainfall records can misrepresent actual conditions, underscoring the need for site-specific calibration. When set against IDF curves from Kuwait and Qatar, Sharjah's rate of intensification is higher, reinforcing the case for adapted, city-specific design standards rather than uniform regional models.

These findings have significant consequences for urban communities and infrastructure resilience, as undersized drainage conduits can transform even moderate storms into severe flood events that trigger costly road closures, property damage, and emergency response operations. Regularly updating IDF curves to reflect observed extremes will ensure design storms align with reality and help prevent system failures. Embedding the study's methodology in a formal review cycle can institutionalize adaptive drainage standards and accelerate their regulatory adoption. In contrast, the integration of updated IDF curves with sustainable urban drainage systems, real-time monitoring networks, and performance-based design codes will create multiple layers of protection and redundancy against urban floods.

Resilient urban drainage systems must evolve through iterative, data-driven processes. This begins with continuous real-time monitoring via IoT-equipped rain gauges and flow sensors that feed into automated platforms. This allows design storms to be recalibrated as new extremes are observed. Quantifying uncertainty with bootstrap or Bayesian techniques will provide confidence bounds on those design intensities, supporting decisions that appropriately balance risk and cost.

Adaptive modelling frameworks that integrate climate covariates, such as rising temperature trends or records of cloud-seeding activity, will further strengthen future infrastructure planning. At the same time, a Gulf-wide consortium for hydro-meteorological data sharing, joint benchmarking, and coordinated updates will bind regional expertise and resources. By moving away from static design storms and toward ongoing, science-driven updates, Sharjah and other arid cities can better protect critical infrastructure, protect vulnerable communities, and maintain flexible planning in the face of a changing climate.

AKNOWLEDGMENTS

The authors gratefully acknowledge Sharjah Municipality, the National Centre of Meteorology, and Heriot-Watt University Dubai for providing essential data, modeling support, and collaborative opportunities.

REFERENCES

[1] K. B. Almheiri, R. Rustum, G. Wright, and A. J. Adeloye, "Study of impact of cloud-seeding on intensity-duration-frequency (IDF) curves of Sharjah city, the United Arab Emirates," Water (Switzerland), vol. 13, no. 23, pp. 1–13, 2021, doi: 10.3390/w13233363.

[2] K. B. Almheiri, R. Rustum, G. Wright, and A. J. Adeloye, "The Necessity of Updating IDF Curves for the Sharjah Emirate, UAE: A Comparative Analysis of 2020 IDF Values in Light of Recent Urban Flooding (April 2024)," Water (Switzerland), vol. 16, no. 18, 2024, doi: 10.3390/w16182621.

[3] Federal Geographic Information Center, "Union Atlas - Geospatial Information - Maps and Gazetteer," UAE Atlas.

[4] 2024. Department of Town Planning and Survey Sharjah the UAE, “GIS Maps,” DTPS, 2024, Sharjah, The UAE.

[5] A. J. Adeloye and R. Rustum, “Self-organising map rainfall-runoff multivariate modelling for runoff reconstruction in inadequately gauged basins,” Hydrology Research, vol. 43, no. 5, pp. 603–617, 2012, doi: 10.2166/nh.2012.017.

[6] F. D. Mwale, A. J. Adeloye, and R. Rustum, “Application of self-organising maps and multi-layer perceptron-artificial neural networks for streamflow and water level forecasting in data-poor catchments: The case of the Lower Shire floodplain, Malawi,” Hydrology Research, vol. 45, no. 6, pp. 838–854, 2014, doi: 10.2166/nh.2014.168.

[7] D. Aldosari, J. Almedeij, and A. A. Alsumaiei, “Update of intensity–duration–frequency curves for Kuwait due to extreme flash floods,” Environ Ecol Stat, vol. 27, no. 3, pp. 491–507, Sep. 2020, doi: 10.1007/s10651-020-00454-4.

[8] A. Al Mamoon and A. Rahman, “Rainfall in Qatar: Is it changing?,” Natural Hazards, vol. 85, no. 1, pp. 453–470, Jan. 2017, doi: 10.1007/s11069-016-2576-6.

[9] K. B. Almheiri, R. Rustum, G. Wright, and A. J. Adeloye, “A Review of Hydrological Studies in the United Arab Emirates,” May 01, 2023, MDPI. doi: 10.3390/w15101850.

Copyright © Int. J. of GEOMATE All rights reserved, including making copies, unless permission is obtained from the copyright proprietors.

15th Int. Conf. on Geotechnique, Construction Materials & Environment,
Kyoto, Japan, 11-13 November 2025, ISBN 978-4-909106124 C3051

HEAVY METAL CONCENTRATIONS OF CICADA SHELL AND CICADA ADULT IN JAPAN

Hiroyuki Ii[1]

[1]Faculty of Systems Engineering, Wakayama University, Japan

ABSTRACT

Japan has many heavy metal mines and many abandoned waste disposal sites, so heavy metal contamination of soils has become a major problem. Heavy metals in soils are either soluble or insoluble, and not all heavy metals in soils are available to living organisms. Plants collect heavy metals from soils and accumulate them mainly in their roots, with low concentrations in the above ground parts. Cicada larvae live in the soil by sucking sap from the roots. It is believed that the larvae and the above ground cicada shells concentrate heavy metals, so the heavy metal characteristics of cicada shells were investigated. The concentrations of Fe, Mn, Ni, As, Pb, and Ag in cicada shells were higher than those of adults, and it was found that cicadas discard Fe, Mn, Ni, As, Pb, and Ag into their shells when molting. Zn was higher in adults, and Cu was almost the same. The concentrations of Ni, As, Pb, and Ag in cicada shells vary greatly depending on geology and soil conditions, and no differences were observed between species, so they are thought to be excellent indicators of soil contamination. The concentrations of Fe, Mn, Zn, and Cu in cicada shells do not reflect geology or soil conditions. There are interspecific differences in Cu, Zn, and Mn, with the large brown cicada tending to have significantly higher Cu and lower Mn and Zn than other species. No interspecific differences were found in Fe.

Keywords: Cicada shell, Cicada adult, Heavy metal, Metal mine, Contamination

INTRODUCTION

Excessive heavy metals found in factory and mine sites are toxic to living organisms, so in order to investigate the effects of heavy metals on native organisms such as plants, insects, and animals, soil must be excavated and the heavy metal concentrations in the soil measured, as shown in Figure 1. Generally, heavy metals in soil are either soluble or insoluble, but organisms only utilize soluble metals, and insoluble metals gradually become soluble. Not all heavy metals in soil are utilized by organisms, and metal concentrations in soil are not necessarily useful as an indicator of the impact of heavy metals on life. Therefore, in order to monitor heavy metal concentrations in organisms, it is necessary to show the actual transfer of heavy metals from soil to organisms. Ii [1,2] shows that the heavy metal concentrations of collected mosses fluctuate greatly and increase depending on the heavy metal contamination situation. Therefore, mosses were considered to be a good indicator of soil heavy metal contamination. However, mosses do not have deep roots, so their heavy metal concentrations are only affected by the heavy metal concentrations in the surface soil.

Trees get nutrients from their roots and take root in deep soil. In general, the heavy metal concentrations in tree roots are much higher than those in tree leaves and trunks [3,4]. Meanwhile, cicada larvae obtain nutrients from tree roots. Therefore, the heavy metal concentrations in cicadas depend on the heavy metal concentrations in tree roots, and ultimately on the heavy metal concentrations in deep soil [5,6,7,8], as shown in Figure 2. Cicada shells can be easily collected from trees above the soil. Therefore, the purpose of this study is to confirm that the heavy metal concentrations in cicada shells depend on heavy metal contamination in soil and that cicada shells are effective for soil heavy metal contamination.

RESEARCH SIGNIFICANCE

When investigating the impact of soil contamination on ecosystems in areas where contamination is a concern, cicada shells can be used to carry out a completely non-destructive evaluation without the need for disintegrating soil excavation or plant collection. Soil evaluation using cicada shells is a first, and this study clarified what metals accumulate in cicada shells depending on the geology, soil conditions, and species. The concentrations of Ni, As, Pb, and Ag contained in cicada shells vary greatly depending on the geology and soil conditions, with no differences observed between species, making them an excellent indicator of soil contamination.

METHOD

In this study, firstly cicada shells and adults were sampled at various geological and land use places with different heavy metal contamination conditions to compare each heavy metal concentrations.

Fig.1 Relationships between soil, plants, and heavy metals.

Fig.2 Relationships between soil, plants, cicadas, cicada shells, and heavy metals.

Sampling points

As shown in Figure 3, cicada shells were collected from mines, basalt, volcanic areas, limestone, serpentine, urban parks, and old factory sites throughout Japan. The cicada species were the black cicada, the large brown cicada (including the minmin cicada), the evening (including the tsukutsukuboshi), the platy cicada, the spring cicada (including the ezoharuzemi), and the ezo cicada.

The mines are Teine (As, Cu) and Chitose (Ag, Pb, Zn) in Hokkaido, Nishinomaki (As) in Gunma Prefecture, Rendaiji (Ag, Cu, Pb, Zn, Mn) in Shizuoka Prefecture, Tada (Ag, Pb, Zn, Cu) and Ikuno (As, Ag, Cu, Pb, Zn) in Hyogo Prefecture, Waidani (As, Cu, Zn, Pb) in Okayama Prefecture, Iwami (Ag, Pb, Mn) in Shimane Prefecture, and Naganobori Mine (As, Cu) in Yamaguchi Prefecture [9]. The basalt area is the southeastern foot of Mt. Fuji where lava of Mt. Fuji is distributed. The volcanic hot spring area is Kusatsu hot spring in Gunma Prefecture. The limestone areas are Shuri Castle in Okinawa Prefecture and the Akiyoshidai in Yamaguchi Prefecture. Serpentine (Ni) area is Kamogawa in Chiba Prefecture, Ogose in Saitama Prefecture, Ryumonzan in Wakayama Prefecture, and Nakase Mine (Sb, As) in Hyogo Prefecture. Generally, serpentinite is rich for Ni (Ni > 0.1%) [9]. Urban parks are in Tokyo (Ueno, Kasai Rinkai, Tokyo University, Higashi Ojima, Takasago), in Osaka (Shirasagi, Osaka Castle, Nagai, Suminoe, Sumiyoshi), and in Wakayama (Wakayama Castle, Wakayama University, Akibasan, Wakaura). The factory (Ni, Pb, Fe) is the former site of a wire factory in Nishikinohama in Osaka Prefecture.

Fig.3 Sample points for cicada shell and cicada adult.

Treatment

In the laboratory, the sampled cicada adults and shells were first rinsed with ultrapure water and then desiccated by a dryer. After drying, they were dissolved with concentrated nitric acid and filtered with a membrane filter with a 0.45 micrometer pore size. After filtering, the Fe, Mn, Ni, Ag, Pb, As, Zn and Cu concentrations in cicada adults and shells were measured by ICP-OES (AMETEK, Inc., SPECTRO ARCOS) in the laboratory at Wakayama University. The actual detection limit of ICP-OES is 0.001ppm for Fe, Mn, Ni, Ag, Pb, As, Zn and Cu.

RESULTS AND DISCUSSION

Ni concentration of cicada shells and adults

Ni, As, Pb, Ag, Fe, Mn, Zn and Cu concentrations in cicada shells and adults were measured for studying the difference in metal concentrations in cicada shells and cicada adults comparing metal contaminated and non-contaminated areas.

Figure 4 shows the Ni concentration in cicada shells and adults. The Ni concentration in cicada shells ranged from 0.01 to 100 mg/kg, and in adults

ranged from a few 0.01 to several tens of mg/kg. The Ni concentration in cicada shells was more than 10 times that of adults. Therefore, it is thought that cicadas release Ni into their shells during molting, maintaining a high Ni concentration in the shell.

The Ni concentration in cicada shells in Kamogawa, Nakase mine, Ogose, and Ryuumon, which are serpentine rocks expected to have high Ni, exceeds 10 mg/kg, more than 10 times higher than other areas [9]. In addition, even in former factory sites where Ni contamination is expected, the Ni concentration is more than 1 mg/kg, reaching several tens of mg/kg. On the other hand, the Ni concentration in Iwami, Teine, and Chitose mines, which are not Ni mines, is less than 1 mg/kg, and in Syuri and Akiyoshidai, which are limestone rocks with low Ni content, it is low at less than a few mg/kg. Therefore, it is thought that the Ni concentration in cicada shells changes according to the geological and soil conditions. Even within the same species, there were large regional differences in concentration, and the differences between species were not clearly found.

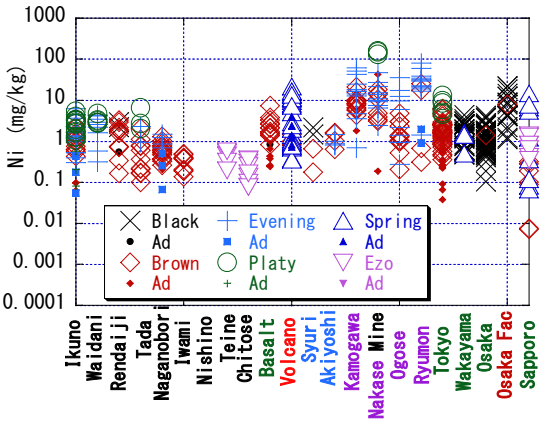

Fig.4 Ni concentrations in cicada shells and adults.

As concentration of cicada shells and adults

Figure 5 shows the As concentration in cicada shells and adults. In cicada shells, the concentration ranged from several 0.01 to several thousand mg/kg, and in adults, the concentration ranged from several 0.1 to several tens of mg/kg. The As concentration in cicada shells was more than 10 times that of adults. Therefore, it is thought that cicadas release As into their shells during molting, and maintain high As concentrations in the shells. Cicada shells from the Ikuno, Waidani, Nakase, Naganobori, Teine, and Nishinomaki mines, where As minerals expected to have high As concentrations are found [9], have concentrations of 10 mg/kg or more, reaching a maximum of several thousand mg/kg. In urban parks in Tokyo and Osaka and volcanic hot spring area, As concentrations reach several tens of mg/kg. These areas may be affected by urban pollution and hot spring water. On the other hand, the As concentrations in the Renndaiji, Tada, Iwami, and Chitose mines, where no As minerals were found, limestone areas (Syuri, Akiyosidai), serpentine areas (Kamogawa, Ogose, Ryumon), and parks in Wakayama and Sapporo were low at less than 10 mg/kg. Therefore, it is thought that the As concentration in cicada shells varies according to the geology and soil conditions. Even within the same species, there were large regional differences in concentration, and the differences between species were not clearly found.

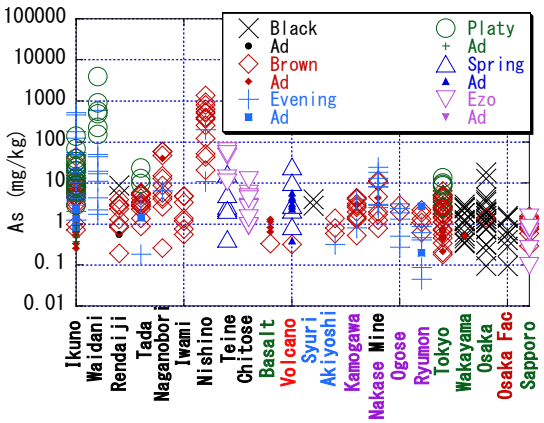

Fig.5 As concentrations in cicada shells and adults.

Pb concentration of cicada shells and adults

Figure 6 shows the Pb concentration in cicada shells and adults. In cicada shells, the concentration ranged from 0.01 to 100 mg/kg, while in adults it ranged from 0.1 to 100 mg/kg. The Pb concentration in cicada shells was more than 10 times that of adults. Therefore, it is thought that cicadas release Pb into their shells during molting, maintaining high Pb concentrations in the shells.

Cicada shells from the Ikuno, Waidani, Renndaiji, Tada, Iwami, Chitose, and Nakase mines, where Pb minerals expected to have high Pb concentrations are found [9], have Pb concentrations of 10 mg/kg or more, reaching a maximum of several hundred mg/kg. In addition, Pb concentration of cicada shells at former factory site ranges from several mg/kg to several hundred mg/kg. Meanwhile, urban parks in Tokyo and Osaka also have high levels, exceeding a maximum of several tens of mg/kg. On the other hand, the Teine and Nishinomaki mines, where no Pb minerals were found, limestone areas (Syuri, Akiyosidai), serpentine areas (Kamogawa, Ogose, Ryumon), and parks in Wakayama and Sapporo had low Pb concentrations of less than 10 mg/kg. Therefore, the Pb concentration in cicada shells is thought to vary according to the geological and soil conditions. Even within the same species, there were large regional differences in concentration, and the

differences between species were not clearly found.

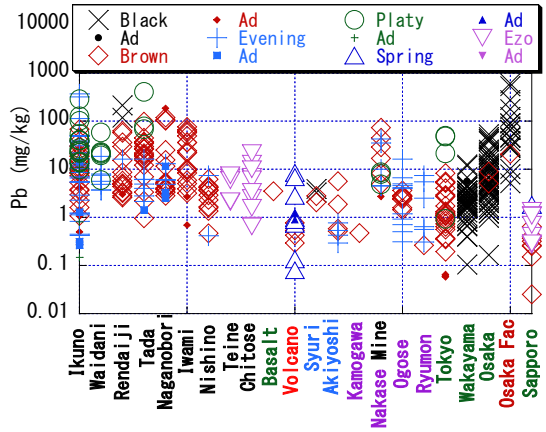

Fig.6 Pb concentrations in cicada shells and adults.

Ag concentration of cicada shells and adults

Figure 7 shows the Ag concentration in cicada shells and adults. The Ag concentration in cicada shells ranged from 0.1 to several tens of mg/kg, while that in adults ranged from several 0.01 to several 1 mg/kg. The Ag concentration in cicada shells was more than 100 times that of adults. Therefore, it is thought that cicadas release Ag into their shells during molting, maintaining a high Ag concentration in the shells.

The cicada shells of Ikuno, Waidani, Renndaiji, Tada, and Iwami mines, where Ag minerals expected to have high Ag concentrations are found [9], show values exceeding 1 mg/kg. However, although the Chitose mine is an Ag mine, the Ag concentration is less than 1 mg/kg, and all other areas are less than 1 mg/kg. Even for the same black cicada, Rendaiji has a concentration of more than several tens of mg/kg, while the city park has a concentration of less than 1 mg/kg. Therefore, it is thought that the Ag concentration in cicada shells varies according to the geological and soil conditions. There are large regional differences in concentration even for the same species, and the differences between species were not clearly found.

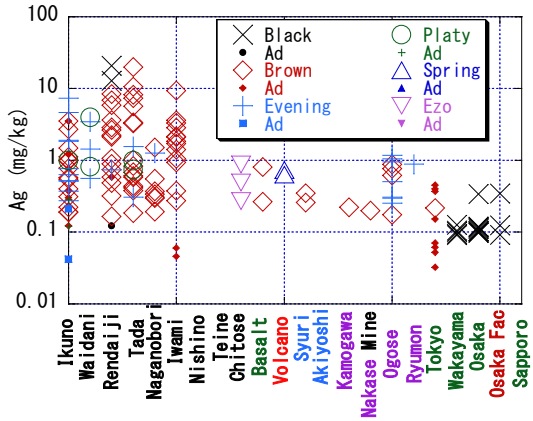

Fig.7 Ag concentrations in cicada shells and adults.

Fe concentration of cicada shells and adults

Figure 8 shows the Fe concentration in cicada shells and adults. The Fe concentration in cicada shells ranged from 100 to several tens of thousands of mg/kg, while the Fe concentration in adults ranged from several tens to several thousands of mg/kg. The Fe concentration in cicada shells was more than 100 times that of adults. Therefore, it is thought that cicadas release Fe into their shells during molting, maintaining a high Fe concentration in the shell.

The Fe concentration in cicada shells from metal mines rich in Fe sulfides such as pyrite (Ikuno, Waidani, Renndaiji, Tada, Naganobori, Iwami, Nishinomaki, Teine, Chitose, Nakase mines) [9], basalt area and serpentine areas, which contain a lot of Fe, is not particularly high compared to limestone and urban parks, which contain little Fe, and shows a similar range of variation. Therefore, the Fe concentration in cicada shells does not change according to the geological or soil conditions. There were large regional differences in the concentration even within the same species, and the inter-species differences were not clearly found.

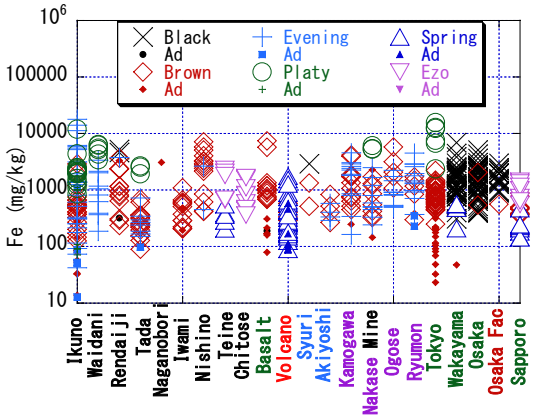

Fig.8 Fe concentrations in cicada shells and adults.

Mn concentration of cicada shells and adults

Figure 9 shows the Mn concentration in the shells and adults of cicadas. In the shells, the concentration was 100 to several thousand mg/kg, and in the adults, the concentration was several tens to 1,000 mg/kg. The Mn concentration in the shells of cicadas was about 10 times that of the adults. Therefore, it is thought that cicadas release Mn into their shells during molting, thereby maintaining a high Mn concentration in the shells.

The Renndaiji and Iwami mines, where Mn minerals are found [9] and Mn concentrations are expected to be high, are not necessarily high, and other locations have roughly the same concentration range. Therefore, the Mn concentration in the shells of cicadas does not change in line with the geological

and soil conditions. Overall, the Mn concentration of the large brown cicada is lower than that of other cicadas.

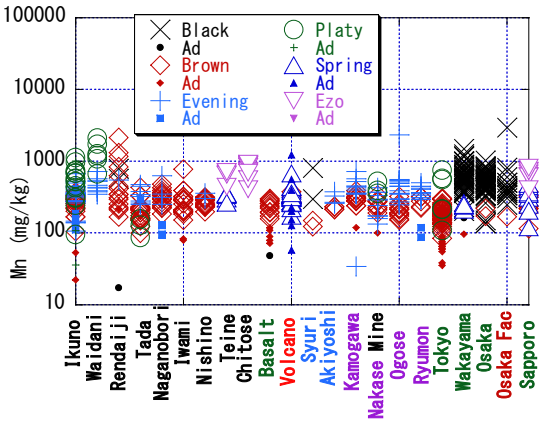

Fig.9 Mn concentrations in cicada shells and adults.

Zn concentration of cicada shells and adults

Figure 10 shows the Zn concentration in the shells and adults of cicadas. The Zn concentration in the shells ranged from several 1 to several thousand mg/kg, while the Zn concentration in the adults ranged from several hundred to 100 mg/kg. The Zn concentration in the shells of cicadas was less than one-tenth of that in adults. Therefore, it is thought that cicadas do not release Zn into their shells during molting, and maintain high Zn concentrations in their bodies. Since Zn is necessary for cell division and an essential component for maintaining life, it is thought that it is stored in the body rather than released into the shell [10, 11].

Zn minerals are found in all mines, and the metal mines expected to have high Zn concentrations are particularly high at Ikuno, Waidani, and Rendaiji, exceeding 1000 mg/kg, while the other mines are not high at 100 mg/kg or less, while the city park reaches 1000 mg/kg, and other locations have roughly the same concentration range. Therefore, the Zn concentration in the shells of cicadas does not change in line with the geological and soil conditions. Overall, the Zn concentration of the large brown cicada is lower than that of other cicadas.

Cu concentration of cicada shells and adults

Figure 11 shows the Cn concentration in the shells and adults of cicadas. The concentrations ranged from 1 to 1000 mg/kg in the shells and several tens to several hundreds of mg/kg in the adults. The Cu concentration in the shells of cicadas was less than one-tenth of that in the adults. Therefore, it is thought that cicadas do not release Cu into their shells during molting, and maintain high Cu concentrations in their bodies. Because insect blood is hemocyanin and contains copper and Cu is a necessary component for insect, it is thought that it is stored in the body rather than released into the shell [10, 11].

Metal mines where Cu minerals are found and Cu concentrations are expected to be high include the Ikuno, Waidani, Rendaiji, Tada, Naganobori, Iwami, and Teine mines, which exceed 100 mg/kg, while the Nishinomaki and Chitose mines, where no Cu minerals are found, have low Cu concentrations of several tens of mg/kg or less. However, the Cu concentrations of large brown cicadas in other non-mining areas exceed 100 mg/kg, and the Cu concentrations in cicada shells do not change in line with the geological and soil conditions. The Cu concentration of the large brown cicada ranges from 10 to 1,000 mg/kg, which is higher than the 1 to several tens of mg/kg of other cicadas, and there is a clear species difference. In particular, comparing Figures 10 and 11, a clear species difference can be seen in that the large brown cicada has a low Zn concentration and a high Cu concentration.

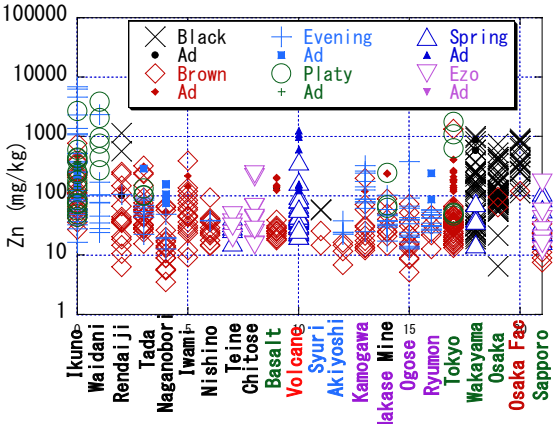

Fig.10 Zn concentrations in cicada shells and adults.

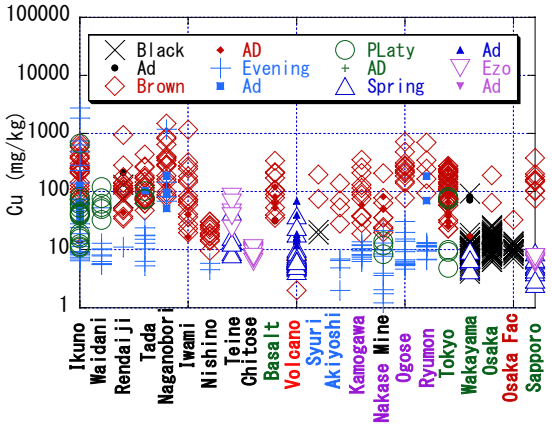

Fig.11 Cu concentrations in cicada shells and adults.

CONCLUSIONS

Cicada larvae live in the soil, sucking sap from tree roots, and it is thought that heavy metals are concentrated in the shells of cicada larvae and cicadas

that have emerged above ground. Therefore, in this study, we investigated the heavy metal characteristics of cicada shells to determine whether they could be used as a new indicator of heavy metal pollution in soil. Cicada shells were collected from mines, basalt area, volcanic areas, limestone areas, serpentine areas, urban parks, and former factory site throughout Japan. The cicada species were the black cicada, the large brown cicada (including the minmin cicada), the evening (including the tsukutsukuboshi), the platy cicada, the spring cicada (including the ezoharuzemi), and the ezo cicada.The concentrations of Fe, Mn, Ni, Ag, Pb, and As in cicada shells are higher than in adults, and it is thought that cicadas discard Fe, Mn, Ni, Ag, Pb, and As in their shells during molting, lowering the Fe, Mn, Ni, Ag, Pb, and As concentrations in adults. These elements are thought to be components that tend to be excessive in cicadas. The Zn concentration of cicadas is higher in adults than in their shells, and Cu is about the same, so the shells are not necessarily higher.

The Ni, Ag, Pb, and As concentrations in cicada shells vary greatly depending on the geology and soil conditions, and no differences between species were observed. Therefore, it was found that the Ni, Ag, Pb, and As concentrations in cicada shells are good indicators of soil pollution. On the other hand, the Fe, Mn, Zn, and Cu concentrations in cicada shells do not reflect the geology and soil conditions.

There are species differences in Mn, Zn, and Cu, with the brown cicada and the Minmin cicada tending to have significantly higher Cu levels and lower Mn and Zn levels than other species. No species differences are seen in Fe.

Insect blood uses hemocyanin, which uses Cu, and Zn is necessary for cell division, so Cu and Zn are thought to be important elements for cicadas. Therefore, it is thought that the concentrations are higher in adults than in the shell, and that the Cu and Zn concentrations are also higher than other elements.

ACKNOWLEDGMENTS

I am grateful to Mr. Kazuto Futsuta and Mr. Kazuki Nakajima of Eco-management Corporation for showing us around the premises when collecting cicada shells at the Teine and Chitose mines.

REFERENCES

[1] Ii H., Effectiveness of bryophyte and cicada shells as a bio-index for heavy metal contamination of river water and soil. International Journal of GEOMATE, Vol. 24, Issue 105, 2023, pp.117-125.

[2] Ii H., Effectiveness of using cicada shell and river bryophyte as an index of available Cu, Zn, Pb, As, Ni and Cr contamination, in Proc. 4th Int. Conf. on SEE, 2018, pp. 914-919.

[3] Kubohara T. and Ii H., Cu Co and Ni Contamination Index for River Using River Insects and River Plants. International Journal of GEOMATE, Vol.11, Issue 26, 2016, pp.2651-2658.

[4] Kubohara T. and Ii H., Zn and Fe Contamination Index for River using River Insects and Water Plants in The Kinokawa River Catchment. International Journal of GEOMATE, Vol.19, Issue 75, 2020, pp.76-83.

[5] Robinson G.R., Sibrell P.L., Boughton C.J., and Yang L.H., Influence of soil chemistry on metal and bioessential element concentrations in nymphal and adult periodical cicadas. Science of The Total Environment, Vol. 374, Issues 2–3, 2007, pp. 367-378.

[6] Mwelwaa S., Chungub D., Tailokac F., Beesigamukamad D., and Tanga C., Biotransfer of heavy metals along the soil-plant-edible insect-human food chain in Africa. Science of The Total Environment, Vol.881, 2023, pp.163150.

[7] Donald R. and Clark, JR., Organochlorines and Heavy Metals in 17-Year Cicadas Pose no Apparent Dietary Threat to Birds. Environmental Monitoring and Assessment, Vol.20, 1992, pp.47-54.

[8] Ii H., Effectiveness of bryophyte and cicada shells as a bio-index for heavy metal contamination of river water and soil. International Journal of GEOMATE, Vol. 24, Issue 105, 2023, pp.117-125.

[9] Kinoshita K., Primary Color Ore Pictorial Book. Hoikusha, CO., LTD. 1957, pp.1-225. in Japanese.

[10] Azam I., Afsheen S., Zia A., Javed M., Saeed R., Sarwar K. M., and Bushra Munir B., Evaluating Insects as Bioindicators of Heavy Metal Contamination and Accumulation near Industrial Area of Gujrat, Pakistan. BioMed Research International Volume. 2015, Article ID 942751, pp.11.

[11] Malematja E., Manyelo G. T., Sebola A. N., Kolobe D.S., and Mabelebele M., The accumulation of heavy metals in feeder insects and their impact on animal production. Science of The Total Environment, Vol.885, 2023, pp.163716.

Copyright © Int. J. of GEOMATE All rights reserved, including making copies, unless permission is obtained from the copyright proprietors.

15th Int. Conf. on Geotechnique, Construction Materials & Environment, Kyoto, Japan, 11-13 November 2025, ISBN 978-4-909106124 C3051

STABILIZATION OF KHON KAEN LOESS FOR THE PAVEMENT STRUCTURE USING RICE HUSK ASH AND KAOLIN CLAY

Stanley Emeka Ovuta[1] and Ratamanee Nuntasarn[2]

[1,2]Faculty of Engineering, Khon Kaen University, Thailand

ABSTRACT

Loess which is a wind deposited soil in Khon Kaen, Thailand, is extremely compressible, weak, and prone to erosion, making it unsuitable for pavement construction. This research investigates the effect of cement and geopolymer-based binders on loess soil. Specific gravity, sieve and hydrometer, Atterberg limit, compaction, Unconfined Compressive Strength (UCS), California Bearing Ratio (CBR), and wet-dry durability test were conducted to evaluate soil performance. The stabilization was carried out using 5% cement and combination of RHA and kaolin clay (calcined to metakaolin) in varying ratios, with sodium hydroxide and sodium silicate as alkaline activators for the geopolymer mixes. Results showed that RHA and MK generally reduced the maximum dry density (MDD) and slightly increased the optimum moisture content (OMC) due to their low specific gravity and porous nature of the additives. The UCS results indicated that the 1% RHA + 4% MK mix achieved the highest strength, even surpassing the 5% cement. Durability assessment under wet-dry cycles revealed that the geopolymer-stabilized loess exhibited lower mass loss and high strength retention (>90%), confirming its long-term stability. The CBR values further supported its suitability for use as a pavement subgrade and subbase material. These findings highlight the potential of geopolymer stabilization as an effective and sustainable alternative to conventional cement treatment for loess soils while promoting waste recycling in civil engineering construction. Further research is recommended for field- scale validation to assess long-term performance.

Keywords: Stabilization, Loess soil, Rice husk ash, Kaolin clay, Pavement structures.

INTRODUCTION

Loess, a wind-deposited silty soil commonly found in regions like Khon Kaen, Thailand, presents significant challenges for construction due to its high compressibility, collapsibility, and moisture sensitivity. When used as subgrade material, unstabilized loess often leads to pavement deformation, reduced service life, and costly maintenance. Traditional stabilization using cement or lime has been effective in improving soil strength and durability but these methods are associated with high costs and environmental concerns due to CO_2 emissions during production [1].

In response to the environmental impact of cement, geopolymer technology has emerged as a sustainable alternative. Materials such as rice husk ash (RHA) and kaolin clay (to be calcined to metakaolin, MK) have been increasingly used as sustainable alternatives to cement due to their pozzolanic reactivity and ability to improve soil structure and strength [2, 3]. RHA is rich in silica, which aids in the formation of cementitious compounds, while metakaolin contributes to a high content of alumina [2, 4]. Despite their individual promise, limited research exists on the combined effect of rice husk ash (RHA) and metakaolin (MK) in stabilizing loess, particularly under mechanical and durability conditions relevant to pavement structures. This study investigates the compaction behavior, Atterberg limit, sieve and hydrometer, unconfined compressive strength (UCS), durability under wet-dry cycling, and California Bearing Ratio (CBR) of Khon Kaen loess stabilized with cement and various combinations RHA and metakaolin. The objective is to determine the effectiveness of these alternative binders in improving the geotechnical performance of loess while promoting the reuse of agricultural and industrial by-products for sustainable road construction and equally to establish a good percentages and aspect ratios of each stabilizing materials that can be utilized in many years to come.

RESEARCH SIGNIFICANCE

This study demonstrates the viability of using rice husk ash (RHA) and metakaolin (MK) as sustainable stabilizers for improving the engineering properties of loess. The findings shows that these materials significantly enhanced the strength, durability, and moisture resistance of the soil, offering a cost-effective and environmentally responsible alternative to cement. This research supports the reuse of agricultural waste in geotechnical applications, promoting sustainable construction practices, and provides practical insights for improving pavement performance in loess-prone regions.

MATERIAL PREPARATIONS AND METHODS

Materials

The loess soil used in this study was collected in a land near College of Local Administration (COLA), Khon Kaen University, Thailand. The top soil was stripped and the underlying loess was manually excavated. The basic properties of the loess are shown in table 1. The kaolin clay was calcined to form metakaolin (MK) at different temperatures (650, 700, 750, 800, and 850˚c) and heating time (30, 60, 90, and 120 minutes) at a heating rate of 10˚c/mins. The rice husk ash used was bought from the KPS Goods shop, Kampaeng Saen, Nakhon Pathom, Thailand. It was further blended and sieved through sieve No. 200 to obtain a finer, more uniform ash. The geopolymer activator was prepared using sodium hydroxide (8M) and sodium silicate in a 1:2 ratio.

Table 1: Basic properties of Khon Kaen loess

Properties	
Plastic Limit (PL) %	NP
Liquid Limit (LL) %	–
Plasticity index (PI) %	–
Specific gravity	2.66
Dry density (γ_d) kN/m³ at 95%MDD	20.60
% of Sand	55.22
% of Silt	27.23
% of Clay	17.55
USCS classification	SM

Sample Preparation and Mix Design

The loess was oven-dried, sieved through a 4.75 mm mesh and mixed with stabilizers as shown in table 2. A total of eight mix combinations were tested as presented in table 2. The alkaline activator was incorporated into the geopolymer mixes as the total moisture content. Compaction was conducted using a 4x4'' mold. UCS and durability samples were prepared in a mold of 50 mm x 100mm dimensions.

Table 2: Mix Ratios

Sample ID.	Soil (%)	Binder material for geopolymer		Cement (%)
		RHA (%)	Kaolin Clay /MK (%)	
Unstabilized loess	100	0	0	
Soil cement	95			5
Soil geopolymer	95	5	0	
	95	4	1	
	95	3	2	
	95	2	3	
	95	1	4	
	95	0	5	

TEST METHODS

Sieve and hydrometer test was performed in accordance with ASTM D421 and D422. Compaction characteristics were evaluated using Modified Proctor test (ASTM D1557). UCS test were performed after 7days of curing following ASTM D1633. Durability was assessed under wet-dry cycles (ASTM D559), with UCS testing conducted after 1st, 3rd, 6th, 9th, and 12th cycles. Mass loss and physical damages were monitored. CBR test followed ASTM D1883 and AASHTO T193, with penetration values recorded at 2.5 and 5.0 mm for soaked and unsoaked conditions.

RESULTS AND DISCUSSIONS

Sieve and Hydrometer Test

The sieve test showed that Khon Kaen loess consist of 55% of sand, 27% of silt and 18% of clay. Based on USCS, the soil was classified as silty sand (SM). This aligns with [5, 6], who identified Khon Kaen loess as fine-grained and weakly plastic.

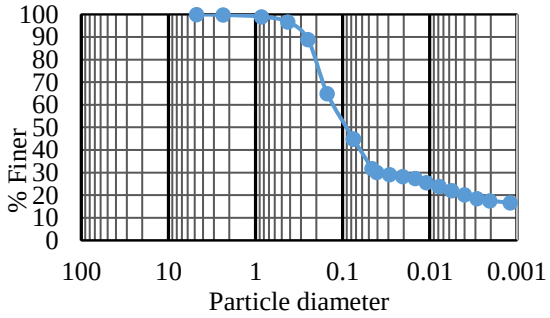

Fig 1: Sieve and Hydrometer Curve for Khon Kaen Loess showing silt-dominated structure.

Compaction Test

The unstabilized loess as shown on table 3 and figure 2 exhibited a maximum dry density (MDD) of 21.150 kN/m³ and optimum moisture content (OMC of 6.84%. The inclusion of RHA and MK resulted in a general fluctuation in MDD as shown in table 3 and figure 4 – 6 due to the lower specific gravity and porous structure of RHA [7] while MK improves particle packing and densification at an increased ratio [2]. Conversely, OMC varied slightly, attributing to the higher water absorption capacity of RHA and MK. The 5% cement mix recorded a modest reduction in MDD to 20.94 kN/m³, while the 1% RHA +4%MK mix showed 20.88 kN/m³. These results are consistent with previous findings that geopolymer binders reduces density while improving reactivity and structure [11].

Table 3: The MDD and OMC values for each compacted mix ratio of Khon Kaen loess

Samples	Symbol	Maximum dry density (kN/m³)	Optimum moisture content (%)
Unstabilized Loess	Un	21.150	6.842
5%cement	5C	20.94	6.654
5%RHA	5R0M	20.53	5.931
4%RHA+1%MK	4R1M	20.91	6.545
3%RHA+2%MK	3R2M	21.06	6.603
2%RHA+3%MK	2R3M	20.95	6.480
1%RHA+4%MK	1R4M	20.88	6.189
5%MK	0R5M	21.23	6.132

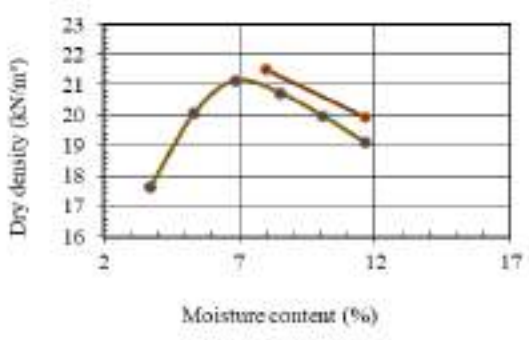

Fig 2: Compaction behavior of unstabilized loess soil

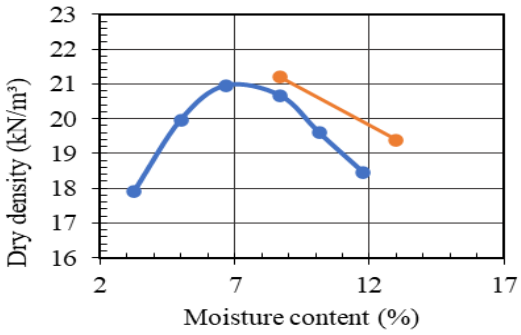

Fig. 3 Compaction behavior of 5% cement loess soil.

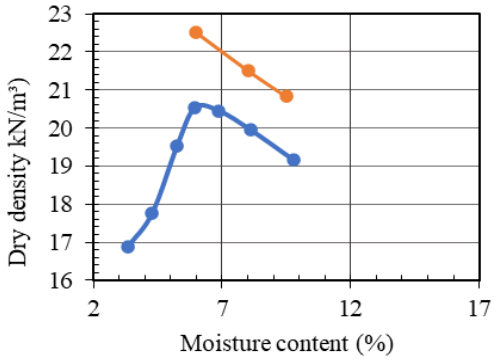

Fig. 4: Compaction behavior of 5% RHA loess soil.

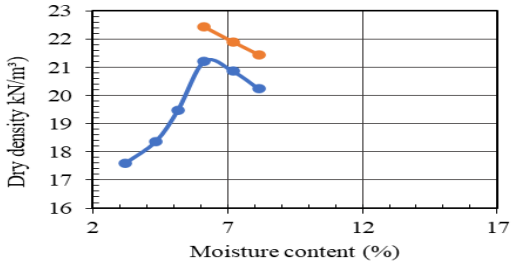

Fig. 5: Compaction behavior of 5% MK loess soil.

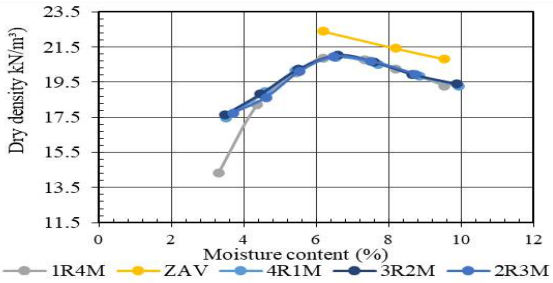

Fig. 6: Dry density-moisture content relationships of RHA – MK stabilized loess samples.

Unconfined Compressive Strength (UCS)

The UCS test samples was compacted in a mold of 50 mm x 100 mm at 95% of the maximum dry density at the wet-side of the compaction curve, extruded from the mold and cured for 7 days before testing. Then, a strain rate of 1mm/minutes was applied on the samples until failure occurred. In each mixture, 5 samples were tested. The results as shown in tables 4, 5, and figures 7 and 8 revealed a significant improvement in strength for all stabilized mixes. The unstabilized loess had a UCS of 87.94 kPa. The stress-strain curve showed the strain softening. Meanwhile, the 5% cement mix had a brittle mode failure accompanied with a sudden cracking sound at the peak load as shown in figure 8. The UCS of stabilized sample with 5% cement is higher than the unstabilized at about 40.6 times. However, the 1R4M mix exhibited a more ductile behavior as shown in figure 8 achieving the highest strength, which is about 2.3 times increase in strength from the 5% cement loess. The 1R4M mix had the lowest coefficient of variation (COV = 6%) as shown in table 5, based ACI 214R-11 guidelines, confirming the reliability of the high UCS, elastic modulus (E), and energy absorption (E_A) values presented in table 4. In addition, table 6 shows the initial, final moisture content, and dry density of all mixes. Dry density decreased slightly in RHA and MK stabilized mixes compared to cement-stabilized loess, due to their specific gravity and porous nature [2, 3]. This strength gain is attributed to the formation of additional geopolymer gel and strong interparticle bonding from aluminosilicate

activation [8]. The samples indicated consistent strength development especially for the geopolymer mix, suggesting good repeatability.

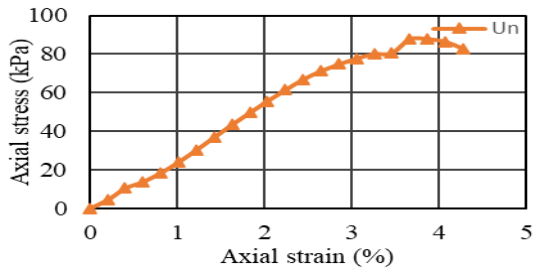

Fig. 7: UCS behavior of unstabilized Khon Kaen loess samples with the lowest strength

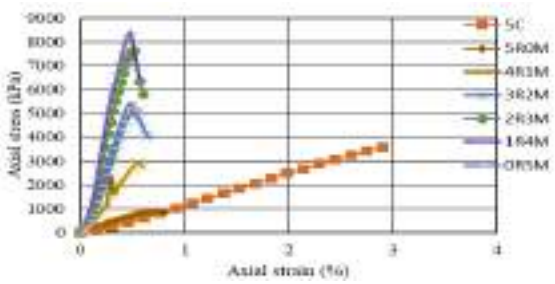

Fig. 8: UCS behavior of stabilized loess

Table 4: Summary of UCS, E., and E_A, for stabilized and Unstabilized Loess Mixtures

Mix ratios	q_u (kPa)	E (kPa)	E_A (kJ/m³)
Un	87.97	26.88	224.78
5C	3,574.62	1,226.4	5,062.08
5R0M	866.21	1,410.4	4,31.10
4R1M	2,884.5	4,194.5	937.86
3R2M	5,102.06	10,351	1,879.97
2R3M	7,627.19	16,273	2,531.88
1R4M	8,364.21	18,830	2,803.47
0R5M	5,431.93	11,335	1,604.05

Table 5: UCS Coefficient of Variation and consistency indicator.

Mix ratios	q_u (kPa)	COV (%)	Consistency Rating
Un	84.25	12.89	Moderate
5C	3,833.39	8.35	Excellent
5R0M	724.62	7.01	Excellent
4R1M	2,884.7	8.30	Excellent
3R2M	5,763.4	6.85	Excellent
2R3M	7,715.36	10.68	Acceptable
1R4M	9,234.05	6.00	Excellent (Best Overall)
0R5M	5733	9.90	Excellent

Table 6: UCS summary table for the intial, final and dry density of unstabilized and stabilized loess.

Mix ratios	Initial m.c (%)	Final m.c (%)	Ini. γ_{dry} (kN/m³)
Un	10	9.66	19.42
5C	11.36	8.23	19.52
5R0M	5.77	5.41	19.03
4R1M	5.71	4.85	18.74
3R2M	5.45	4.13	19.03
2R3M	5.15	4.16	19.42
1R4M	5.05	3.70	19.33
0R5M	4.72	3.17	18.93

California Bearing Ratio (CBR)

The CBR test was oven-dried, pulverized, and sieved via 4.75mm sieve. Each mix was prepared using the moisture content as obtained from the 95% MDD (wet-side) of modified proctor compaction test. Then, the samples were compacted using 56 blows per layer (5 layers). The geopolymer materials were cured for 7 days with plastic wrapping before soaking for 96 hours, for the soaked samples. The samples were tested on the CBR machine with penetration of 1.25mm/minutes. The adopted CBR values for both soaked and unsoaked condition (Table 7) followed ASTM D1883 procedures, taking the higher value from 2.5 mm or 5.0 mm penetrations. As shown in figure 9, the unstabilized loess exhibited very low CBR values, classifying it as poor subgrade material per AASHTO T193. In contrast, the 5% cement mix showed a soaked CBR meeting base course standards, with only 0.018% swelling, highlighting cement's strong binding capacity [9]. The highest improvement of unsoaked CBR was 1R4M as same as soaked CBR, which increased about 83 and 73 times by the unstabilized samples, respectively.

Swelling potential results for the soaked condition is presented in table 7. The untreated loess exhibited the highest swelling at 0.0585%, while the 5% cement and 5% RHA-stabilized mixes showed reduced values of 0.018% and 0.0138%, respectively. All other geopolymer-stabilized mixes, including the optimal 1R4M, recorded zero swelling, indicating strong volume stability. The superior performance of the 1R4M mix is attributed to the optimal balance of reactive silica and alumina, which promotes aluminosilicate gel formation (N-A-S-H), improving bond strength and reducing porosity [2, 4]. Figure 10 illustrates the CBR loss or gain due to soaking. While most mixes lost strength, three exhibited negative loss (i.e., strength gain): 4% RHA + 1% MK, 5% cement, and 5% MK. This behavior is attributed to extended hydration or geopolymerization under moist conditions [4, 10]. Overall, all stabilized mixes exceeded 198% soaked CBR making them suitable for subbase or base course applications. Among them, the 1% RHA + 4% MK stood out for combining high

strength and stability, reinforcing the effectiveness of geopolymer binders.

Table 7: The adopted CBR, percentage loss or gain values, and the swelling potentials.

Mix Design	Adopted CBR unsoaked (%)	Adopted CBR soaked (%)	Loss or Gain (%)	Swelling (%)
Un	14.12	13.64	3.40	0.0585
5C	533.31	642.89	-20.55	0.018
5R0M	224.04	198.00	11.62	0.0138
4R1M	526.00	642.89	-22.22	0
3R2M	1,108.53	993.56	10.37	0
2R3M	1,117.68	713.97	36.12	0
1R4M	1,165.615	997.24	14.45	0
0R5M	553.541	555.227	-0.30	0

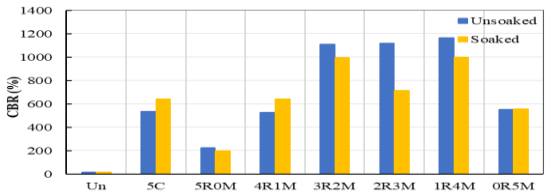

Fig. 9: Comparison for the unsoaked and soaked CBR values for all the mix.

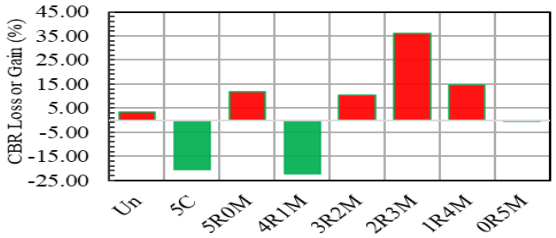

Fig.10: Percentage change in adopted CBR values after soaking showing loss or gain.

Wet-Dry Durability

The durability of stabilized loess was evaluated using UCS retention and mass loss across 12 wet-dry cycles (ASTM D559). The samples (2 samples per cycle) were compacted at the 95% MDD (wet-side) of the compaction curve using mold 50mm x 100mm. After compaction, the samples were cured for 7 days in a plastic wrap simulating early-stage curing conditions prior to durability testing. Upon completion of curing, the samples underwent wet-dry cycles by soaking for 24 hours then oven drying at 105˚c for 24 hours and cooling at room temperature for at least 2 hours. At the end of each cycle, the samples were tested with the UCS machine at the strain rate of 1mm/mins to obtain the compressive strength as shown in table 8 and 9. The 5% cement mix showed strength gain up to cycle 6, retaining 2.7 times of its original UCS followed by later cycles exceeding machine capacity limits as shown in table 8 and figure 12, indicating continued hydration of the cement material [11]. The 1% RHA + 4% Mk mix showed exceptionally high initial UCS and maintained over 100% strength up to cycle 6 (Table 9 and figure 12) and then retained 91.39% at cycle 12, confirming excellent durability caused by continued reaction, leading to gel formation filling the micro-voids [12]. However, the UCS increase at cycle 12 may be due to continued geopolymer gel formation and matrix densification, which outweighed early microcracking effects. Mass loss analysis (Table 9 and figure 11) values represent the average of two specimens tested per cycle. The RHA-MK mix ranged from 3.60-4.49%, lower than the cement mix (5.99% - 4.85%) as shown in table 8 and figure 11. Table 10 confirms the RHA-MK mix as “Excellent” in durability, supported by minimal surface damage and strong structural integrity [8].

Table 8: Individual UCS results, Retained UCS, and mass loss for 5% cement per cycle

Cycles	Sample 1 UCS (kPa)	Sample 2 UCS (kPa)	Avg. UCS (kPa)	Retained UCS (%)	Mass Loss (%)
0	–	–	3574.62	100.00	–
1st	8,146.13	9,634.54	8,890.33	231.92	5.99
3rd	7,982.58	7,896.86	7,939.72	207.12	5.60
6th	9,380.95	9,679.19	9,530.07	248.61	4.79
9th	>9,741.83	9,719.39	–	–	4.81
12th	>9,689.96	9,493.81	–	–	4.85

Table 9: Individual UCS results, Retained Strength, and mass loss for 1 R4M per cycle

Cycles	Sample 1 UCS (kPa)	Sample 2 UCS (kPa)	Avg. UCS (kPa)	Retained UCS (%)	Mass Loss (%)
0	–	–	8364.21	100.00	–
1st	>10,128.08	10,147.53	–	–	3.60
3rd	>10,193.84	9,992.10	–	–	4.26
6th	>9,858.91	9,851.29	–	–	4.47
9th	7,896.20	7,774.86	7,835.53	84.85	4.38
12th	8,321.28	8,557.38	8,439.33	91.39	4.49

Table 10: Comparative performance of stabilized loess mixes based on UCS, mass loss, and durability.

Mix type	Initial UCS (kPa)	Peak Retained UCS (%)	Mass Loss Range (%)	Durability Indicator
5C	3,833.39	248.61 (Cycle 6)	5.99 → 4.85	Very Good (Strength)
1R4M	9,234.05	>100% (cycles 1-6), 91.39% (Cycle 12)	3.60 → 4.49	Excellent (Strength and Mass Retention)

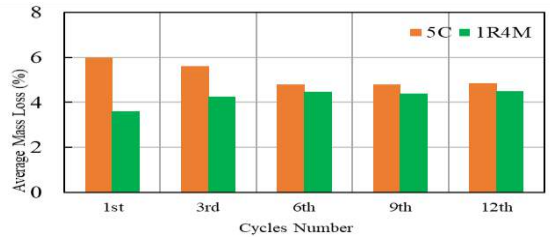

Fig. 11: Variation of average mass loss with wet-dry cycle numbers for stabilized loess mixtures.

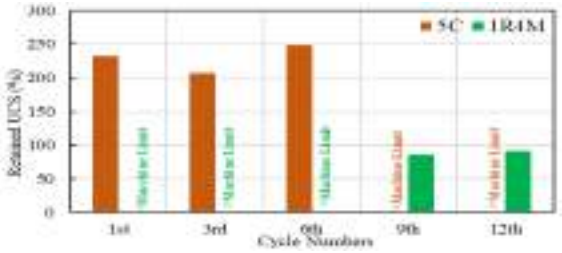

Fig. 12**:** Retained compressive strength of stabilized loess across wet-dry cycles.

CONCLUSION

This study examined the stabilization of Khon Kaen loess using cement and geopolymer binders (RHA and MK). The inclusion of RHA and MK reduced MDD and slightly increased OMC due to their lower specific gravity. UCS results showed that 1% RHA + 4% MK achieved the highest strength of about 2.3 times outperforming cement stabilized loess which served as the baseline for comparison. In wet-dry cycles, geopolymer mixes retained over 90% of their UCS with minimal mass loss, indicating excellent durability. The CBR values for all stabilized mixes exceeded subbase and base requirements under both soaked and unsoaked conditions. The study confirms that 1R4M mix achieved the highest strength and durability at only 7 days of curing, demonstrating its suitability for time-sensitive construction scenarios. These findings support the use of RHA-MK geopolymer binders as an effective, sustainable alternative to cement for loess soil stabilization.

ACKNOWLEDGMENTS

My acknowledgement goes to the department of Civil Engineering, Faculty of Engineering, in Khon Kaen University for their extreme support for this research.

REFERENCES

[1] Hossain SK. S., Roy, P.K and Chang, J.B. Utilization of waste rice husk ash for sustainable geopolymer: A review on construction and building materials, vol. 310, 2021.

[2] Chindaprasirt, P., Homwuttiwong, S., Sirivivatnanon, V. Influence of fly ash fineness on strength, drying shrinkage and sulphate resistance of blended cement mortar. Cement and concrete research, 34(7), pp. 1087-1092, 2009.

[3] Davidovits, J. Geopolymer Chemistry and Applications, 4th ed., Institute Geopolymer, Saint-Quentin, France, 2015, pp. 1- 520.

[4] Nath, P., Sarker, P. Use of OPC to improve setting and early strength properties of low calcium fly ash geopolymer concrete cured at room temperature. Cement and concrete composites, 55, pp. 205 – 214, 2015.

[5] Suttijaroenpanit, N., Nuntasran, R. The coefficient of the lateral earth pressure of Khon Kaen loess soil in compacted condition. KKU research journal (graduate studies), 22(4), pp. 80 – 91, 2022.

[6] Hormdee, D. Ananlysis of calculated and observed settlements of the silo on loess. International journal of geomate. 21(87), Pp. 46-52, 2021.

[7] Awoyera, P. O., Akinmusuru, J. O., Ndambuki, J. M. Green concrete production with rice husk ash as supplementary cementitious materials. Journal of Cleaner production. 221, pp. 402-419, 2019.

[8] Zhang, Z., Provis, J. L., Reid, A., Wang, H. Fly ash-based geopolymers: the relationship between composition, pore structure and efflorescence. Cement and concrete research, 64, pp. 30 – 41, 2014.

[9] Horpibulsuk, S., Rachan, R., Suddeepong, A., Chinkulkijniwat, A. Analysis of strength development in cement-stabilized silty clay from microstructural considerations. Construction and Building Materials, 24(10), pp.2011 – 2021, 2010.

[10] Teme, A. A., O'Kelly, B. C., Rotimi, J. O. B Stabilization of lateritic soil with alkali-activated fly ash and metakaolin for geotechnical applications". Geotechnical and Geological Engineering, 38(6), pp. 5773 – 5789, 2020.

[11] Wang, K., Wu, Y., Zhang, W. Effect of early curing on stiffness of cement-stabilized fine-grained soils". Construction and Building Materials, 274, 121780, 2021.

[12] Osinubi, K. J., Eberemu, A. O., Moses, G. Strength behaviour of geopolymer-stabilized lateritic soil. Transportation Geotechnics, 10, pp.55-66, 2017.

Copyright © Int. J. of GEOMATE All rights reserved, including making copies, unless permission is obtained from the copyright proprietors.

15th Int. Conf. on Geotechnique, Construction Materials & Environment, Kyoto, Japan, 11-13 November 2025, ISBN 978-4-909106124 C3051

OPTIMIZATION OF MICROORGANISM-ENRICHED BIO-COATED CLAY GRANULES FOR SUSTAINABLE PLANT GROWTH USING RESPONSE SURFACE METHODOLOGY

Piyawadee Saraphirom[1], Orn-Anong Chaiyachet[1], Piyarat Namsena[1], Waratchaya Thiabpho[2], Alicha Suphaloet[2], Chakkrit Sreela-or[3], Nonthaphong Phonphuak[4], and Mullika Teerakun[5*]

[1]Faculty of Science and Technology, Rajabhat Maha Sarakham University, Thailand; [2]Faculty of Education, Rajabhat Maha Sarakham University; [3]Faculty of Agricultural Technology, Pibulsongkram Rajabhat University, Thailand; [4]Faculty of Engineering, Rajabhat Maha Sarakham University, Thailand; [5]Faculty of Agricultural Technology, Kalasin University, Thailand

ABSTRACT

This study aimed to develop a bio-enhanced compost fertilizer by incorporating *Azotobacter* sp., *Bacillus* spp., and *Azotobacter vinelandii* to promote the growth of Red Cos lettuce. A Box-Behnken Design within the Response Surface Methodology (RSM) framework was applied to optimize microbial formulations. The results showed that the bio-enriched compost significantly increased plant dry weight ($p < 0.0001$), with *A. vinelandii* contributing the most, followed by *Azotobacter* sp. and *Bacillus* spp. The optimal formulation—0.19% *Azotobacter* sp., 1.84% *Bacillus* spp., and 0.39% *A. vinelandii*—yielded the highest observed dry weight (2.14±0.04 g), consistent with model predictions. ANOVA confirmed the model's robustness ($R^2 = 0.9973$, Adjusted $R^2 = 0.9925$), and the lack-of-fit was insignificant. Contour and 3D surface plots further supported the significant interactive effects among microbial factors. The optimized compost formulation was validated through confirmation experiments, demonstrating its potential as an eco-friendly and effective alternative to chemical fertilizers. This research highlights the feasibility of using microbial consortia in compost to enhance crop performance, supporting the future development of sustainable biofertilizer products.

Keywords: Bio-coated clay, Azotobacter, Bacillus, Response surface methodology, Sustainable agriculture

INTRODUCTION

Modern agriculture is evolving to incorporate eco-friendly practices, focusing on optimizing plant growth substrates. Traditional growth media such as peat moss pose environmental concerns, prompting the need for sustainable alternatives [1]. When enriched with beneficial microorganisms, high-porous clay granules [2] can serve as an efficient plant growth medium, enhancing nutrient availability and reducing chemical fertilizer dependency [3].

Beneficial microorganisms added to clay materials promote plant growth and soil health. These microbes include nitrogen-fixing bacteria (e.g., *Azotobacter* sp.) [4], phosphate-solubilizing bacteria (e.g., *Bacillus* spp.) [5], and growth-promoting rhizobacteria that enhance nutrient uptake [6], stimulate root development, and improve resistance to environmental stress [7]. Integrating these microbes into clay granules ensures their prolonged viability and effectiveness in plant cultivation, making bio-coated granules a viable alternative to conventional fertilizers [8].

Microorganism-enriched bio-coated clay granules provide an innovative solution by integrating microbial strains that promote plant growth. This study employs Response Surface Methodology (RSM) to optimize the formulation of microbial bio-coated clay granules. RSM is a statistical and mathematical approach that helps develop, improve, and optimize processes by evaluating the relationships between multiple independent and response variables [9]. Using the Box-Behnken Design within RSM allows efficient experimentation by reducing the number of required trials while ensuring accurate model predictions [10]. Our previous research shows that fired clay granules can be eco-friendly carriers for nitrogen-fixing bacterial cells, promoting microbial viability and plant growth efficiency [8]. Moreover, further advancements have explored the incorporation of additional microbial species and nutrient-enriched coatings to enhance the performance of these bio-coated granules in various agricultural settings. This study leverages RSM to determine the optimal microbial concentrations and their interactions to maximize plant growth efficiency while ensuring environmental sustainability. The findings contribute to advancements in sustainable agriculture, offering an alternative plant growth medium with enhanced microbial benefits.

MATERIALS AND METHODS

The Experimental Design

This study investigates the effects of microbial supplementation in compost powder on

plant growth when cultivated in clay granules. The independent variables are the concentrations of *Azotobacter* sp. (0.13–0.67 %w/w), *Bacillus* spp. (0.07–0.33 %w/w), and *A. vinelandii* (1.3–2.7 %w/w), while plant dry weight is the dependent variable. Controlled factors include compost composition, plant type, environmental conditions (light, water, temperature, humidity), clay granule properties (size, porosity, water-holding capacity), and experiment duration. The variable ranges are summarized in Table 1.

Table 1 Levels, actual and coded experimental independent variables for microbial supplementation in compost powder on the growth of Red Cos lettuce

Variables	Coding	Unit	Levels		
			-1	0	+1
Azotobacter sp.	X_1	%w/w	0.4	0.13	0.67
Bacillus spp.	X_2	%w/w	0.07	0.2	0.33
A. vinelandii	X_3	%w/w	1.3	2	2.7

The Statistical Analysis

Statistical analysis was performed using a Box-Behnken Design (BBD) under Response Surface Methodology (RSM) to evaluate interactions among three variables. Design-Expert® Version 13 was used for A one-way Analysis of Variance (ANOVA), response optimization, and visualization via contour and 3D surface plots, providing insights into how the inputs influenced plant growth (Table 2). The regression analysis resulted in a second-order polynomial equation, which was used to predict plant growth based on the levels of microbial supplementation. This equation takes the general form:

$$y = \beta_0 + \sum \beta_i X_i + \sum \beta_{ii} X_i^2 + \sum \beta_{ij} X_i X_j \quad (1)$$

where y represents the predicted response (dry weight), X_1, X_2, and X_3 The coded levels of the independent variables, and the coefficients represent the quadratic and interaction effects. This model enabled precise evaluation of the individual and combined effects of the microbial inputs on plant growth.

The Confirmation Experiments

A set of seven confirmation experiments was conducted to validate the predictive accuracy of the response surface model. These included: (1) a control without microbial addition, (2–5) low and high levels of individual microbial inputs, (6) a center point representing average values, and (7) an optimized formulation derived from numerical optimization. Each treatment involved precise concentrations of *Azotobacter* sp., *Bacillus* spp., and *A. vinelandii* incorporated into compost powder and applied to high-porosity clay granules as the plant growth medium.

Table 2 Desing matrix of the experiments along with the corresponding experimental and predicted values for the growth of Red Cos lettuce.

Run	Variables			Response*	
	X_1	X_2	X_3	Dry weight (g)	
	(%w/w)	(%w/w)	(%w/w)	Observed value	Predicted value
1	0.13	0.2	2.7	1.77	1.77
2	0.13	0.33	2	1.77	1.77
3	0.4	0.33	2.7	1.85	1.85
4	0.67	0.2	1.3	1.95	1.95
5	0.4	0.2	2	2.14	2.13
6	0.67	0.2	2.7	1.88	1.87
7	0.4	0.07	2.7	1.77	1.78
8	0.67	0.07	2	1.85	1.85
9	0.13	0.07	2	1.89	1.88
10	0.4	0.33	1.3	1.90	1.89
11	0.13	0.2	1.3	1.93	1.94
12	0.4	0.2	2	2.12	2.13
13	0.4	0.2	2	2.14	2.13
14	0.67	0.33	2	1.93	1.94
15	0.4	0.07	1.3	1.98	1.98

*Note: *The dry weight data of Red Cos Lettuce after 60 days of planting*

Red Cos lettuce seedlings were grown in a regulated environment for 60 days. Each treatment was replicated three times. When it came time to harvest, the growth performance of the plants was evaluated through the measurement of the plant dry weight (g). Statistical evaluations were carried out to analyze the means of the treatments. ANOVA accompanied by Tukey's Honestly Significant Difference (HSD) test was employed to identify notable differences between treatments, using a 95% confidence level ($p < 0.05$).) [11].

High Porous Clay Granule Preparation

High-porous clay granules were prepared following the method described in [8], incorporating 15% (w/w) sawdust waste into the raw clay mixture. A water solution containing 30-35% water was added to improve plasticity for shaping. The granules were manually formed using the soft-mud paving technique, resulting in diameters of 1.0-1.5 cm. The formed granules were sun-dried for three days before being fired at 900°C to enhance their structural integrity and porosity.

Microbial Preparation

The selected microbial strains, including

Azotobacter sp., *Bacillus* spp., and *A. vinelandii*, were cultured in 6000 mL fermentation vessels containing 1800 mL of sterilized nitrogen-free media supplemented with Potassium Metabisulfite (KMS). The cultures were incubated under shaking conditions at room temperature for five days. The bacterial suspensions were adjusted to an optical density (OD_{600}) of 1 before being used for bio-coating applications.

Compost Powder Production

The compost was formulated from food waste (40–55%), cricket manure (15–25%), dried rain tree (Samanea saman) leaves (15–20%), and molasses (8.5–15%) to maintain a balanced carbon-to-nitrogen (C/N) ratio and stimulate microbial activity. This blend of nutrient-rich and carbon-based materials served as an ideal substrate for microbial enrichment.

Composting was carried out in a 3×5 meter chamber for 60 days. The mature compost was air-dried in the shade for three days, then shredded and sieved to obtain a fine powder. The final product was analyzed for pH, organic matter, C/N ratio, salinity, moisture content, electrical conductivity (EC), and key macronutrients (N, P, K, Ca, Mg, and S) to ensure compliance with the 2007 Fertilizer Act and the 2014 Organic Fertilizer Criteria set by the Department of Agriculture [12]. A total of 16 compost powder formulations—including a non-microbial control—were developed according to a Box-Behnken Design. Fig. 1 presents the characteristics of each microbial-enriched formulation.

Fig. 1 Characteristics of microbial-enriched compost powder formulations based on the Box-Behnken Design

RESULT

Regression Model Fitting Using the Box-Behnken Design (BBD)

The analysis of variance (ANOVA) summarized in Table 3 demonstrates that the fitted quadratic regression model is highly statistically significant, with a *p*-value of the model less than 0.0001. This indicates that the observed variation in the dry weight of Red Cos lettuce is primarily attributable to the effects of the selected microbial input variables and their interactions, rather than random experimental error. The high *F*-value further reinforces the strength of the relationship between the model and the response variable.

Table 3 Analysis of variance (ANOVA) for the model regression representing.

Source	Sum of Squares	df	Mean Square	*F*-value	*P*-value
Model	0.22	9	0.0245	207.31	< 0.0001
X_1	0.01	1	0.0157	132.61	< 0.0001
X_2	0.01	1	0.0108	91.21	0.0002
X_3	0.03	1	0.0265	224.04	< 0.0001
$X_1 X_2$	0.0100	1	0.0100	84.51	0.0003
$X_1 X_3$	0.0020	1	0.0020	17.11	0.0090
$X_2 X_3$	0.0064	1	0.0064	54.08	0.0007
X_1^2	0.0652	1	0.0652	551.25	< 0.0001
X_2^2	0.0728	1	0.0728	615.22	< 0.0001
X_3^2	0.0513	1	0.0513	433.85	< 0.0001
Residual	0.0006	5	0.0001		
Lack of Fit	0.0003	3	0.0001	0.8125	0.5929
Pure Error	0.0003	2	0.0001		
Cor Total	0.2214	14			
R^2	0.9973				
Adjusted R^2	0.9925				

The model's coefficient of determination implies that approximately 99.73% of the total variation in plant dry weight can be explained by the fitted model. This exceptionally high R^2 value signifies a near-perfect fit between the predicted and actual data points, confirming that the model captures the key trends and effects of the independent variables on the growth response. All three main effects—*Azotobacter* sp. (X_1), *Bacillus* spp. (X_2), and *A. vinelandii* (X_3)—were statistically significant ($p < 0.0002$), with *A. vinelandii* contributing the most substantial impact ($F = 224.04$, $p < 0.0001$). Significant two-way interaction effects were observed between X_1X_2 and X_2X_3. At the same time, the quadratic terms (X_1^2, X_2^2, and X_3^2) exhibited highly significant effects ($p < 0.0001$), indicating curvature in the response surface and supporting the appropriateness of the second-order model. Moreover, the lack-of-fit test was insignificant ($p = 0.5929$), confirming that the model fits the data adequately and that the residual variance can be attributed primarily to pure error rather than model misspecification.

Optimization of Compost Powder Formulation For Microbial-Enriched Compost Powder Formulations

To examine the interaction effects of the three

microbial components—*Azotobacter* sp. (X_1), *Bacillus* spp. (X_2), and *A. vinelandii* (X_3)—on the dry weight of Red Cos lettuce, contour plots and three-dimensional response surface plots were generated from the quadratic regression model. The visualizations confirm a well-defined optimum region and demonstrate the synergistic impact of the microbial formulations on plant biomass (Fig.2). Fig. 2a illustrates the interaction between *Azotobacter* sp. and *Bacillus* spp., while *A. vinelandii* was fixed at its central value (2.0% w/w).

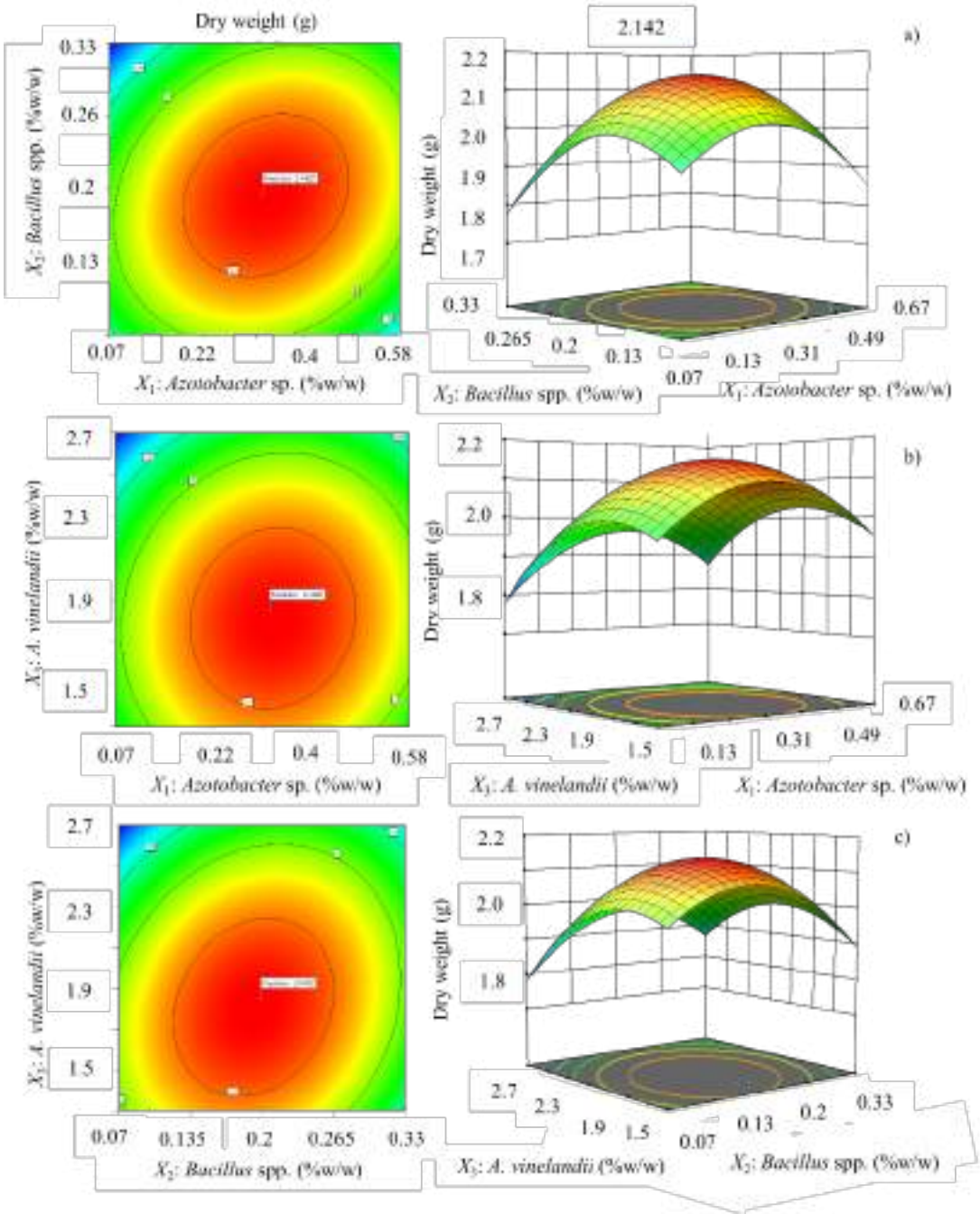

Fig. 2. Contour and 3D response surface plots illustrate microbial inputs' interactive effects on the dry weight of Red Cos lettuce: (a) *Azotobacter* sp. (X_1) × *Bacillus* spp. (X_2); (b) *Azotobacter* sp. (X_1) × *A. vinelandii* (X_3); (c) *Bacillus* spp. (X_2) × *A. vinelandii* (X_3).

The results show that increasing both *Azotobacter* sp. and *Bacillus* spp. Concentrations up to their mid-range significantly enhance dry weight. The predicted maximum dry weight in this interaction was approximately 2.14 g, confirming a strong synergistic effect. Fig. 2 b presents the interaction between *Azotobacter* sp. and *A. vinelandii*, with *Bacillus* spp. held constant. Similar to the previous interaction, a convex surface is evident, with the optimum

occurring at mid-range concentrations of both X_1 and X_3. This indicates that *Azotobacter* sp., a nitrogen-fixer, and *A. vinelandii*, another diazotroph with biofilm-forming capacity, complement each other in promoting plant growth. Fig. 2c depicts the interaction between *Bacillus* spp. and *A. vinelandii* while keeping *Azotobacter* sp. constant. The plots

Confirmation of The Optimized Microbial-Enriched Compost Powder Formulation

Seven treatments were conducted under defined microbial conditions to validate the regression model, as summarized in Table 4. The optimized formulation (Treatment 7: 0.19% *Azotobacter* sp., 1.84% *Bacillus* spp., and 0.39% *A. vinelandii*) yielded the highest dry weight (2.14±0.04 g), which was statistically equivalent to the center point (Treatment 6: 2.14±0.06 g) and significantly higher than all other treatments ($p < 0.05$).

Treatments 2 and 5, which included either low or excessive levels of one or more microbial components, resulted in the lowest dry weights (1.89±0.01 g and 1.85±0.05 g, respectively), emphasizing the need for a balanced microbial formulation. Treatments 1, 3, and 4 showed no significant differences among themselves, with dry weights ranging from 1.97 to 1.98 g, indicating moderate effectiveness. The strong agreement between predicted and observed optimum responses supports the accuracy of the RSM model and confirms the practical efficacy of the optimized microbial-enriched compost formulation.

Table 4 The confirmation experiments for the growth of Red Cos lettuce.

Treatment	Variables			Response
	Azotobacter sp. (%w/w)	*Bacillus* spp. (%w/w)	*A. vinelandii* (%w/w)	Dry weight (g)
1	0	0	0	1.98±0.02^{ab}
2	0.4	0.07	2	1.89±0.01^{c}
3	0.13	0.07	1.3	1.98±0.02^{ab}
4	0.67	0.33	2	1.97±0.07^{ab}
5	0.13	0.33	2.7	1.85±0.05^{c}
6	0.13	0.2	2	2.14±0.06^{a}
7	0.19	1.84	0.39	2.14±0.04^{a}

DISCUSSION

This study demonstrates the effectiveness of microbial-enriched compost powder in promoting the growth of Red Cos lettuce, with significant increases in plant dry weight observed under optimized formulations. The high predictive accuracy of the regression model ($R^2 = 0.9973$, Adj. $R^2 = 0.9925$) was confirmed by experimental validation. The optimal mix—0.19% *Azotobacter* sp., 1.84% *Bacillus* spp., and 0.39% *A. vinelandii*—achieved the highest dry weight (2.14 g), consistent with model predictions and superior to other treatments.

Among the microbial inputs, *A. vinelandii* showed the most substantial effect ($p < 0.0001$), likely due to its nitrogen-fixing and biofilm-forming capacity. *Azotobacter* sp. and *Bacillus* spp. also contributed through nitrogen fixation and phosphate solubilization, respectively, resulting in synergistic growth enhancement. This supports earlier findings that microbial consortia outperform single strains in improving nutrient uptake and plant resilience [14,15].

The response surface plots highlighted strong interactions among the variables, confirming the importance of optimizing both individual concentrations and their ratios. The model's good fit (lack of fit $p = 0.5929$) further supports its use for formulation scaling and development.

Practically, the optimized formulation may be extended to other leafy vegetables like romaine or butterhead lettuce. The fired porous clay granules provide structural stability and allow dry storage, suggesting good shelf-life potential. Future research should examine storage longevity and application across diverse crops and field conditions.

CONCLUSIONS

This study successfully developed and optimized a microbial-enriched compost powder formulation that significantly enhances plant biomass in Red Cos lettuce. Through Response Surface Methodology and Box-Behnken Design, the optimal combination of *Azotobacter* sp., *Bacillus* spp., and *A. vinelandii* was identified and validated. The model exhibited strong predictive accuracy ($R^2 = 0.9973$) and demonstrated reliable agreement with experimental results.

The findings highlight the potential of incorporating microbial consortia into compost-based carriers to improve plant growth efficiency while supporting sustainable agriculture. The use of fired porous clay granules offers both microbial stability and ease of dry storage, suggesting good shelf-life potential. The optimized formulation also shows promise for broader application in similar leafy crops. Future studies should explore field-scale validation, crop-specific adaptation, and long-term effects on soil health and nutrient cycling.

To build upon these findings, future research should focus on multi-season and field-scale trials to validate efficacy under variable environmental

conditions. Studies should also investigate crop-specific formulation adjustments, compatibility with organic farming practices, and the long-term impacts on soil microbiota, fertility, and carbon sequestration.

REFERENCES

[1] Liu W., Fritz C., van Belle J., and Nonhebel S., Production in peatlands: Comparing ecosystem services of different land use options following conventional farming, Science of the Total Environment, Vol. 875, 2023, p. 162534.

[2] Zhao Z., Xu T., Pan X., Susanti, White J. C., Hu X., and Ng K. W., Sustainable nutrient substrates for enhanced seedling development in hydroponics, ACS Sustainable Chemistry & Engineering, Vol. 10, No. 26, 2022, pp. 8506–8516.

[3] Khan N., Bolan N., Joseph S., Anh M. T. L., Meier S., Kookana R., and Qiu R., Complementing compost with biochar for agriculture, soil remediation and climate mitigation, Advances in Agronomy, Vol. 179, 2023, pp. 1–90.

[4] Aasfar A., Bargaz A., Yaakoubi K., Hilali A., Bennis I., Zeroual Y., and Meftah Kadmiri I., Nitrogen fixing *Azotobacter* species as potential soil biological enhancers for crop nutrition and yield stability, Frontiers in Microbiology, Vol. 12, 2021, p. 628379.

[5] Timofeeva A., Galyamova M., and Sedykh S., Prospects for using phosphate-solubilizing microorganisms as natural fertilizers in agriculture, Plants, Vol. 11, No. 16, 2022, p. 2119.

[6] Tsegaye Z., Alemu T., Desta F. A., and Assefa F., Plant growth-promoting rhizobacterial inoculation to improve growth, yield, and grain nutrient uptake of teff varieties, Frontiers in Microbiology, Vol. 13, 2022, p. 896770.

[7] Khan N., Ali S., Shahid M. A., Mustafa A., Sayyed R. Z., and Curá J. A., Insights into the interactions among roots, rhizosphere, and rhizobacteria for improving plant growth and tolerance to abiotic stresses: A review, Cells, Vol. 10, No. 6, 2021, p. 1551.

[8] Saraphirom P., Namsena P., Teerakun M., Phonphuak S., Chanprathak A., Dakaew S., and Phonphuak N., Development of fired clay granules as eco-friendly substances for nitrogen-fixing bacterial cells, GEOMATE Journal, Vol. 27, No. 120, 2024, pp. 110–121.

[9] Lamidi S., Olaleye N., Bankole Y., Obalola A., Aribike E., and Adigun I., Applications of response surface methodology (RSM) in product design, development, and process optimization, IntechOpen, 2022.

[10] Szpisják-Gulyás N., Al-Tayawi A. N., Horváth Z. H., László Z., Kertész S., and Hodúr C., Methods for experimental design, central composite design and the Box–Behnken design, to optimise operational parameters: A review, Acta Alimentaria, Vol. 52, No. 4, 2023, pp. 521–537.

[11] Montgomery D. C., Design and Analysis of Experiments, 10th ed., Wiley, 2020.

[12] Løes A. K., Bünemann E. K., Cooper J., Hörtenhuber S., Magid J., Oberson A., and Möller K., Nutrient supply to organic agriculture as governed by EU regulations and standards in six European countries, Organic Agriculture, Vol. 7, 2017, pp. 395–418.

13] Aasfar A., Bargaz A., Yaakoubi K., Hilali A., Bennis I., Zeroual Y., and Meftah Kadmiri I., Nitrogen-fixing Azotobacter species as potential soil biological enhancers for crop nutrition and yield stability, Frontiers in Microbiology, Vol. 12, 2021, p. 628379.

[14] Timofeeva A., Galyamova M., and Sedykh S., Prospects for using phosphate-solubilizing microorganisms as natural fertilizers in agriculture, Plants, Vol. 11, No. 16, 2022, p. 2119.

[15] Khan N., Ali S., Shahid M. A., Mustafa A., Sayyed R. Z., and Curá J. A., Insights into the interactions among roots, rhizosphere, and rhizobacteria for improving plant growth and tolerance to abiotic stresses: A review, Cells, Vol. 10, No. 6, 2021, p. 1551.

[16] Khan N., Bolan N., Joseph S., Anh M. T. L., Meier S., Kookana R., and Qiu R., Complementing compost with biochar for agriculture, soil remediation and climate mitigation, Advances in Agronomy, Vol. 179, 2023, pp. 1–90.

[17] Zhao Z., Xu T., Pan X., White J. C., Hu X., and Ng K. W., Sustainable nutrient substrates for enhanced seedling development in hydroponics, ACS Sustainable Chemistry & Engineering, Vol. 10, No. 26, 2022, pp. 8506–8516.

Copyright © Int. J. of GEOMATE All rights reserved, including making copies, unless permission is obtained from the copyright proprietors.

15th Int. Conf. on Geotechnique, Construction Materials & Environment,
Kyoto, Japan, 11-13 November 2025, ISBN 978-4-909106124 C3051

DEVELOPMENT OF NEW BASE MATERIALS FOR SEAWEED BEDS USING PROBLEMATIC SOILS, RECYCLED MATERIALS AND RICE BRAN AND ITS VERIFICATION MONITORING IN THE SEA

Kentaro Yamamoto[1], Kazumasa Fukuda[1], Takehito Negami[2], Mizuki Hira[3] and Yoshihisa Tsurunari[1]

[1]Oita, University, Japan; [2]Saga University, Japan; [3]Kagoshima University, Japan

ABSTRACT

The area of seaweed beds along Japanese coasts has decreased by approximately 40% in the last 40 years due to climate change and human activity. In addition, there are similar concerns regarding coastlines worldwide. Thus, it is critical to recover seaweed communities quickly to maintain marine plants and environments. On the other hand, the treatment of disaster waste like decomposed granite and Shirasu in Kyushu region is getting a big problem when a disaster due to heavy rain has occurred. Large amounts of waste material such as scrap ceramics and gypsum are discharged from the ceramics industry in the Saga and Nagasaki Prefectures of Kyushu, Japan. The effective use of disaster and industrial wastes (problematic soils, flow medium sand used for woody biomass power generation, scrap ceramics and gypsum) represents an important problem that must be solved in the Kyushu region of Japan. The objective of this study is to develop environment-oriented base materials for seaweed beds with a low environmental load using several recycled materials from disaster and industrial wastes and rice bran. The developed base materials were placed into the actual sea since June 2024, and monitoring has started. A discussion of the results of short-term monitoring is presented.

Keywords: Seaweed beds, Recycled materials, Industrial waste, Low environmental load, Short-term monitoring

INTRODUCTION

Seaweed beds have been reduced due to the increase of seawater temperatures and changes in the marine environment. They are essential to ecosystems and coastal fisheries because of their multiple effects as fish reefs [1]. Coastal engineering efforts such as reclamation and the phenomenon known as barren ground (called “isoyake” in Japanese) have led to the deterioration of coastal environments. Figure 1 shows a photo of “isoyake” in the sea of Sasebo, Nagasaki Prefecture. There is no seaweed or marine species except sea urchins. These sea urchins have no edible body parts.

In addition, it has been pointed out that iron and other nutrients, which are necessary for the growth of seaweed and the promotion of photosynthesis and chlorophyll synthesis, are becoming scarce in the sea due to river improvement and dam construction [2]. Thus, it is important to provide iron and amino acids in the sea. From a geotechnical point of view, Japan has a variety of problematic soils with each region having its own unique geotechnical characteristics. These problematic soils are often the cause of natural disasters and the problem of increasing the size of disasters [3]. Therefore, it is important from the point of view of disaster prevention and natural resources to indicate a new method of using problematic soils. Based on the above, we have developed and verified environment-friendly base materials of seaweed beds that effectively utilizes recycled industrial waste, with the aim of promoting the conservation and restoration of seaweed beds and underwater greening [4]. In this study, the seaweed beds with a low environmental load was produced by varying the amount of rice bran containing amino acids for the base materials consisting mainly of recycled gypsum, scrapped ceramics, decomposed granite, Shirasu and flow medium sand. The results of monitoring the seaweed beds in the sea are described.

Figure 2 shows the carbon fixation and environmental restoration produced by the base materials for seaweed beds in this study. As shown in this figure, seaweed beds are an important part of the marine food system through their photosynthetic activities, carbon dioxide absorption and oxygen discharge. Furthermore, seaweed beds play a vital role in the ecology of the aquatic ecosystems, serving as buffers of seawater quality.

Fig.1 Isoyake at Sasebo (Date: 2017.6.4)

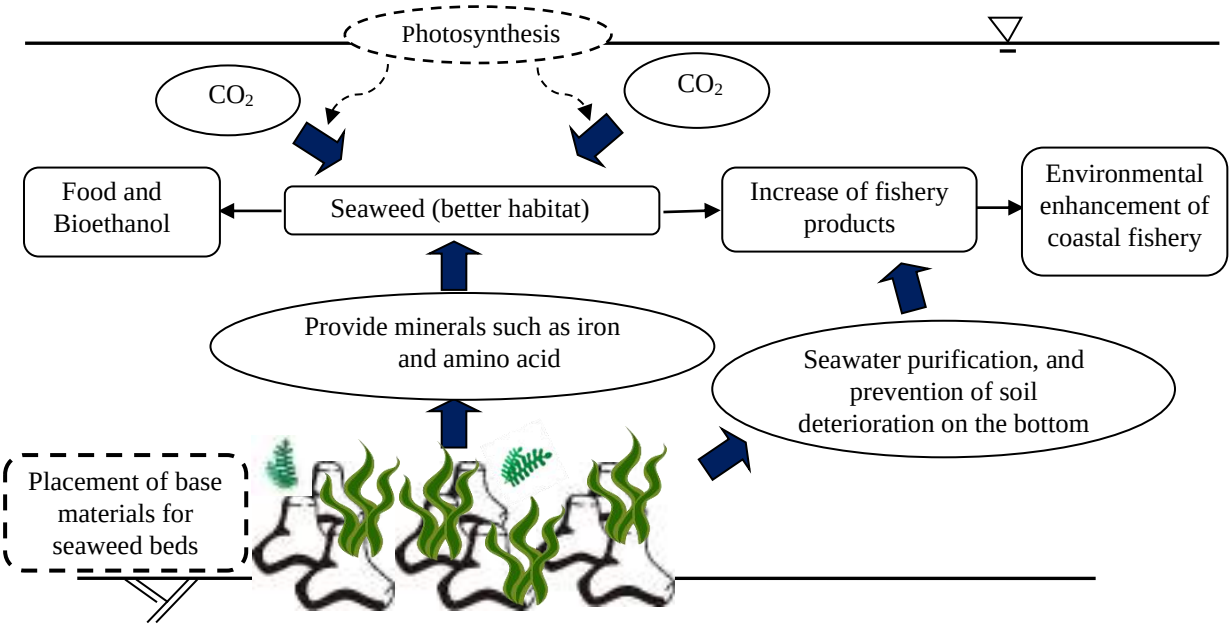

Fig.2 Carbon fixation and environmental restoration produced by base materials for seaweed beds

MATERIAL PROPERTY

Figure 3 shows the grain size distribution curves of the main three materials used in the seaweed beds (decomposed granite, Shirasu and flow medium sand). The decomposed granite and Shirasu passed through a 4.75 mm sieve. It can be seen that the grain size distribution of the flow medium sand is not good, and the fine-grained content of the decomposed granite and Shirasu is high. In addition to the main three materials, recycled gypsum, scrapped ceramics, water, blast-furnace slag cement type B, Portland cement, iron power (disposable heating pad), and rice bran were used. As shown in Table 1, eleven types of base materials were produced, consisting mainly of recycled gypsum, scrapped ceramics, decomposed granite, Shirasu and flow medium sand. Rice bran which contains amino acids, was mixed for the main three materials in different amounts per batch. When the amount of 3000 cm3 of rice bran was mixed, the surface was easily broken even during demolding.

TEST RESULTS OF BASE MATERTIALS FOR SEAWEED BEDS

Table 1 shows the test results of the unconfined compression test for the base materials of seaweed beds. The unconfined compressive strength is the result of the test of the specimens after 28 days of curing. The base materials of No.1-No.5 are mainly constituted of recycled gypsum and scrapped ceramics. The Portland cement is used only for the base materials of No.4-No.5. Although the base materials of No.4-No.5 are made by changing the water-cement ratio at the same mixing ratio of the

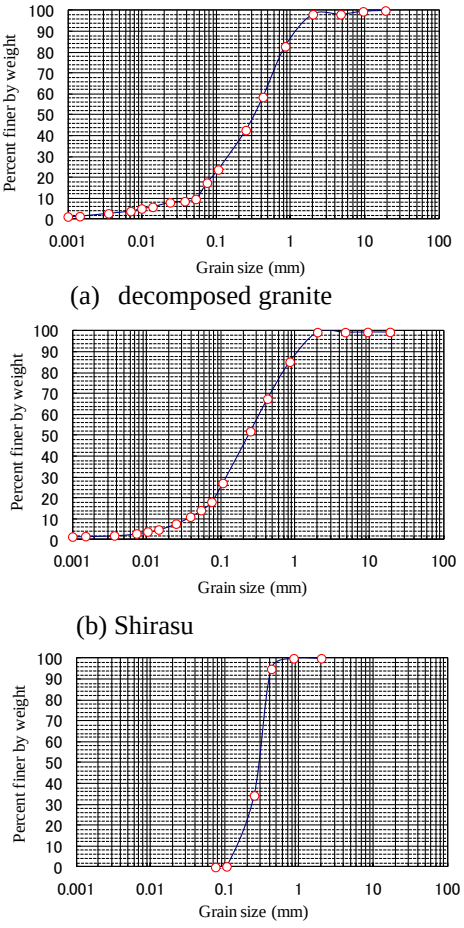

(a) decomposed granite

(b) Shirasu

(c) flow medium sand

Fig.3 Grain size distribution curve

Table 1 Results of the unconfined compression test (28 days curing)

Specimen		No.1	No.2	No3	No.4	No.5	No.6	No.7	No.8	No.9	No.10	No.11
Mixing ratio (%)	Decomposed granite						24.1	24.1				
	Shirasu								24.1	24.1		
	Flow medium sand										24.1	24.1
	Recycled gypsum	35.5	30.0		40.3	29.3	19.1	19.1	19.1	19.1	19.1	19.1
	Scrapped ceramics	48.5	43.0	84.0	40.3	29.3	14.0	14.0	14.0	14.0	14.0	14.0
	Water	6.3	21.5	6.0	9.8	31.4	20.0	20.0	20.0	20.0	20.0	20.0
	Blast-furnace slag cement typeB	9.7	5.5	10.0			14.7	14.7	14.7	14.7	14.7	14.7
	Portland cement				9.6	10.0						
	iron powder						8.1	8.1	8.1	8.1	8.1	8.1
	rice bran （cm^3）						2000	3000	2000	3000	2000	3000
Unconfined compressive strength (MPa)		11.1	7.2	15.1	2.3	1.9	6.8	0.7	6.5	0.5	1.1	0.3

Table 2 CO_2 reduction for each specimen when recycled gypsum is used as a solidification material

Specimen	No.1	No.2	No3	No.4	No.5	No.6	No.7	No.8	No.9	No.10	No.11
CO_2 reduction (Kg-CO_2/Kg)	0.2	0.1	0.0	0.3	0.2	0.1	0.1	0.1	0.1	0.1	0.1

recycled gypsum and scrapped ceramics, the unconfined compressive strength was much lower than that of No.1-No.3 base materials by the non-homogeneity of used materials. The unconfined compressive strength was the highest for No.3 base material and the lowest for No.11 base material due to the amount of recycled gypsum, cement and rice bran added.

The base materials of No.6-No.11 contain approximately 24% of the main materials (problematic soils), with approximately 19% of recycled gypsum, 14% of scrapped ceramics, 15% of blast-furnace slag cement type B, and 8% of iron powder by referring to previous research [4]. For the base materials, the unconfined compressive strength decreased considerably when the amount of 3000 cm^3 of rice bran was mixed. This is due to the fact that rice bran is an organic material with a significantly low unit volume weight, which may have influenced the decrease in unconfined compressive strength. Furthermore, the dissolution test was conducted according to the method of Notification No. 13 of the Environment Agency [5], and the dissolution of hazardous elements such as mercury and hexavalent chromium was not detected. The ratio of base materials used in this study was calculated based on the results of previous studies [4].

Table 2 shows the CO_2 reduction for each base material when recycled gypsum is used as a solidification material. The amount of CO_2 emitted at the production of Portland cement and blast-furnace slag cement type B is reported to be 0.80 kg-CO_2/kg and 0.50 kg-CO_2/kg, respectively [6]. The amount of CO_2 emitted during gypsum production was reported to be 0.07 kg-CO_2/kg [7]. We calculate the amount of CO_2 reduction when recycled gypsum and blast-furnace slag cement type B are used to make the base material for seaweed bed, comparing with the case of cement only is used as the solidification material in the present mixing ratio. For the calculation of No.4-No.5, the use of Portland cement is assumed.

Since the amount of the recycled gypsum and blast-furnace slag cement type B are the same for the base materials from No.6 to No.11, it can be seen that there is CO_2 reduction of approximately 0.1 kg-CO_2/kg of the produced base material. The use of recycled gypsum also results in a slightly lower pH, which has a smaller environmental load than that of blast furnace slag cement type B only. In Table 2, the CO_2 reduction was the highest for No.4 base material and the lowest for No.3 base material due to the amount of recycled gypsum and Portland cement.

MONITORING ROOTING AND GROWTH OF SEAWEED

We conducted the short-term monitoring by diving into the sea with an underwater digital camera in the summer and autumn seasons and underwater drone only in the winter and spring season. Tables 3-4 show a summary of the monitoring dates and sea quality data from September 2024 to April 2025. These tables shows that the temperature and salinity of the sea water were high in September, 2024. The pH was approximately 8.08-8.29. The of electrical conductivity was over 40 mS/cm throughout the year. The salinity was around 1.0-1.7 except in September 2024. In general, the temperature of the sea water in Kagoshima Bay is higher than that of Wakinoura due to these locations and oceanic currents.

The developed base materials for seaweed bed (diameter: 40cm, height: 14cm, weight: approximately 26.0kg, disk-shaped type) was set in the sea at Matsushima, Karatsu in June 2024 (No.1-No.5 in Table 1), and at Wakinoura, Kitakyushu and Kagoshima Bay, Kagoshima in late September 2024 (No.6-No.11 in Table 1). Figure 4 shows the changes in the properties of the base materials for seaweed beds (No.1-No.3) placed in the sea at Matsushima, Karatsu. Figures 4(a) and (b) show the base material for seaweed beds after 4 and 6 months passed. From these figures, the rooting of the green alga family could be seen on the surface of base materials. There was no significant differences among the three materials (No.1-No.3), regarding the rooting of seaweed. It is noted that the breakage of the base materials (No.4-No.5) was progressing after 2 months of the installation into the sea due to the low unconfined compressive strength.

Figures 5 and 6 show the changes in the properties of the base materials for seaweed beds (No.6- No.11) placed in the sea at Wakinoura, Kitakyushu and Kagoshima Bay, Kagoshima. When the amount of 3,000 cm3 of rice bran was mixed, some of the seaweed beds were slightly broken during their transportation. Figures 5(a) and 6(a) were taken immediately after the base materials for seaweed beds were placed in the sea, Figs. 5(b) and 6(b) after 2-2.5 months, and Figs. 5(c) and 6(c)-(d) after 4-6 months. Although Figs. 5(b)-5(c) and 6(b)-6(d) do not show all of the base material, Figs. 5(b) and 6(b) indicate that the rooting of algae could be observed on the entire surface of the base materials. Also, Figs. 5(c) and 6(c)-(d) show that seaweeds (perforated sea lettuces and gulfweeds) are growing on the surface of the base material. The short-term monitoring so far has shown no significant differences among the main materials (No.6-11) or the amount of rice bran added.

CONCLUSIONS

Base materials for seaweed beds that reduce the environmental load were developed using several recycled materials from disaster and industrial wastes with rice bran. The developed base materials were set into Matsushima, Wakinoura and Kagoshima Bay since June 2024, and a short-term survey was conducted to monitor the rooting and growth of seaweed on the surface of base materials at fixed intervals.

The conclusions drawn in this paper are summarized as follows:

1. We could develop the base materials for seaweed beds which would return to nature gradually over time, not permanent base materials.
2. A large amount of rice bran made the base materials fragile, so that a moderate amount of rice bran was preferable. In addition, the fish attracting effect was also observed because water-soluble substances were easily released immediately.
3. The main group of observed seaweed in Wakinoura and Kagoshima Bay was the green alga family, perforated sea lettuces and a small family of brown algae: gulfweeds and sea fans, respectively.

In future work, we would like to consider the evaluation method for the rooting of seaweeds and the CO_2 fixation of seaweeds rooted for the base materials to verify the effectiveness of blue carbon.

Table 3 Monitoring dates and sea quality data (Wakinoura, Kitakyushu)

monitoring date	Sep-24	Dec-24	Mar-25	Apr-25
sea water temperature (℃)	26.5	12.0	13.0	14.0
pH	8.08	8.18	8.29	8.17
electrical conductivity (mS/cm)	45.0	44.4	49.9	49.5
salinity (%)	2.9	1.3	1.3	1.7

Table 4 Monitoring dates and sea quality data (Kagoshima Bay, Kagoshima)

monitoring date	Sep-24	Nov-24	Jan-25	Mar-25
sea water temperature (℃)	27.5	22.0	16.0	15.0
pH	8.17	8.27	8.17	8.14
electrical conductivity (mS/cm)	42.8	47.6	49.0	46.9
salinity (%)	2.8	1.2	1.0	1.3

(a) 4 months passed

(b) 6 months passed

Fig.4 Base materials for seaweed beds set into Matsushima, Karatsu

(a) immediately after entering the sea

(b) 2.5 months passed

(c) 6 months passed

Fig.5 Base materials for seaweed beds set into Wakinoura, Kitakyushu

(a) immediately after entering the sea

(b) 2 months passed

(c) 4 months passed

(d) 6 months passed

Fig.6 Base materials for seaweed beds set into Kagoshima Bay, Kagoshima

ACKNOWLEDGEMENTS

This work was supported by JSPS Grant-in-Aid for Scientific Research JP23K11492. We hereby express our gratitude.

REFERENCES

[1] Terawaki T., Nakayama N., Arai S., and Shikida, A., For the restration of seagrass and seaweed beds, Aquabiology 145, Vol. 25, No.2, 2003, pp.100-106. (in Japanese).

[2] Matsunaga K., If the forest disappears, the ocean will die too -ecological system connecting land and ocean, Kodansha, 1993. (in Japanese).

[3] Miura S., Regional ground in Japan -unusual soil or problematic soil?-, Journal of JGS, Vol. 58, No.7, Ser. No.630, 2010, pp.1-3. (in Japanese).

[4] Yamamoto K., Negami T., Mizoguchi N., Hira M., and Tsurunari Y., Development of environment-oriented base materials for seaweed beds by recycled materials, Journal of Material Cycles and Waste Management, Vol. 25, No.6, 2023, pp.3638-3650.

[5] Ministry of the Environment, Official method of the metal so on which is contained in the industry waste, Environment Agency Notification No. 13, 1973. (in Japanese).

[6] Nobata K., CO_2 reduction using Portland blast-furnace slag cement, Concrete Journal, Vol. 48, No.9, 2010, pp.58-61. (in Japanese).

[7] Horai H., Kamio M., and Fujito M., Development of manufacturing system for hemihydrate gypsum and type II anhydrous gypsum, Nikko technical report, Vol. 1, 2020, pp.29-46. (in Japanese).

Copyright © Int. J. of GEOMATE All rights reserved, including making copies, unless permission is obtained from the copyright proprietors.

15th Int. Conf. on Geotechnique, Construction Materials & Environment,
Kyoto, Japan, 11-13 November 2025, ISBN 978-4-909106124 C3051

VIBRATION ANALYSIS OF AN AC MOTOR FOR PREDICTIVE MAINTENANCE AND ENVIRONMENTAL IMPACT ASSESSMENT

Suphattharachai Chomphan[1]

[1]Faculty of Engineering at Sriracha, Kasetsart University, Thailand

ABSTRACT

Electric machinery serves as a fundamental driving force in various industrial production processes. The three-phase synchronous motor is the most widely recognized type of electric machinery used in industrial plants due to its robust structure, high power output, and ease of maintenance. However, unexpected motor failures can lead to production disruptions. Since one of the key factors contributing to motor failure is vibration, this article presents an analysis of the vibration characteristics of an AC motor and examines its environmental impact. Since moving machinery inherently generates vibrations, this study specifically investigates the vibrations occurring both at the motor itself and at its mounting base. These vibrations can significantly affect the surrounding physical environment, including the buildings and facilities where the motor is installed. Experimental comparisons of vibration levels reveal that the vibration characteristics of an AC motor vary at different positions, including drive end, non-drive end, and motor base. Measurements indicate that the non-drive end exhibits the highest vibration levels under all load conditions, since the rotor shaft extends the farthest from the stator at the non-drive end, leading to increased oscillations. In contrast, the motor base experiences the lowest vibration levels since it is not directly attached to the motor. The findings from this study will contribute to the development of predictive maintenance strategies. The failures are typically detected after they occur, resulting in repair delays, downtime, and production losses. Identifying potential motor failures in advance can reduce operational disruptions, minimize maintenance costs, and improve overall efficiency.

Keywords: AC motor, Synchronous motor, Environmental impact, Vibration signal analysis, Fast Fourier transform

INTRODUCTION

Vibration and noise are inherent byproducts of manufacturing processes, primarily originating from the operation of machinery and moving components. These phenomena not only reduce equipment lifespan but also impact the surrounding environment and operator well-being. Vibrations often stem from transient forces within mechanical systems, while noise emissions are typically linked to structural vibrations and mechanical defects. As a result, research efforts increasingly focus on understanding and mitigating noise generation, transmission, and radiation [1].

AC motors are widely utilized across diverse sectors, including automotive, energy, aerospace, construction, and semiconductor manufacturing, due to their ability to provide reliable, continuous motion with controllable speed and torque. Common applications include conveyor systems, HVAC units, industrial fans, pumps, compressors, and robotic arms. AC motors are favored for their robustness, energy efficiency, and ease of maintenance. However, their operation inherently produces mechanical vibrations and acoustic emissions, which may lead to equipment wear, environmental noise, and user discomfort particularly in sensitive environments such as laboratories or cleanrooms.

The magnitude of these effects depends on factors such as motor design, load characteristics, mounting configuration, and interfacing materials. To address these challenges, recent engineering studies emphasize optimizing motor structure, selecting suitable materials, and improving spatial integration within industrial systems to reduce noise and vibration, thereby enhancing performance, longevity, and environmental compatibility [1, 2].

Dynamic characterization and vibration analysis have long served as fundamental techniques for diagnosing and assessing the operational condition of machine tools. In a study conducted by Zapciu et al. [3], these methods were employed with the primary objective of establishing a systematic procedure for determining the natural frequencies of machine tool components. By identifying these dynamic properties, the study aimed to enhance the stability and performance of machining operations, particularly in cutting processes involving machine tools or lathe systems. Accurate knowledge of natural frequencies enables engineers to mitigate resonance-related issues, improve cutting precision, and extend the lifespan of mechanical components within the machining environment.

Garcia-Perez et al. introduced a novel method for fault detection in induction motors by analyzing acoustic signals [4]. Utilizing the multiple signal

classification algorithm, the study achieved high-resolution spectral analysis to identify specific fault conditions through sound data. This approach offers a non-invasive alternative to traditional vibration and current monitoring techniques, enhancing the reliability of fault detection in industrial settings. The findings highlight the potential of acoustic analysis as a complementary tool for condition monitoring of induction motors.

In the recent years, Hu et al. focused on reducing electromagnetic vibration and noise in permanent magnet motors [5]. By analyzing radial electromagnetic forces and conducting modal analysis, the researchers proposed design optimizations to mitigate vibration acceleration and sound pressure levels. The study underscores the significance of structural design in minimizing noise emissions, particularly in applications where acoustic performance is critical. The proposed methods contribute to the development of quieter and more efficient permanent magnet motors.

Dai et al. examined the vibration and noise characteristics of high-speed magnetic suspension motors used in rock wool centrifuges [6]. The research involved modeling the motor using Maxwell software and analyzing radial force density waves to identify primary harmonic sources. By implementing a short-range double-layer winding optimization, the study achieved a reduction in vibration and noise without compromising electromagnetic performance. This work demonstrates the effectiveness of targeted design modifications in enhancing the acoustic behavior of high-speed motors.

Moreover, Chantal et al. presented a thorough review focusing on vibration analysis and control methodologies for dual-driven feed systems [7]. The study systematically examined vibration control technologies, parameter identification techniques, and system modeling frameworks while critically assessing the respective advantages and limitations of each method. Furthermore, the authors provided an in-depth discussion on the asymmetrical relationship between dual-driven and single-driven feed systems, emphasizing their dynamic characteristics within the context of computer numerical control (CNC) machine tools.

In the past years, Chomphan conducted a study to analyze the vibration and sound signals of motorcycle engines [8]. This research focused on the vibration signals transmitted through four primary contact points between the rider and the motorcycle body. In addition to analyzing these vibration and noise signals to distinguish between LPG-powered engines and conventional 2,200-cc gasoline engines, Chomphan et al. [9] introduced several fault simulations. Another notable study by Chomphan et al. [10] explored intrinsic factor analysis using a Fast Fourier Transform (FFT) adapted for the correlation analysis of vibration and noise signals in gasoline-powered vehicles. The signal processing techniques employed in these studies have shown significant potential and are effectively applied in the present work.

RESEARCH SIGNIFICANCE

This study examines the vibrations that occur at both the motor and its mounting base, as these vibrations can significantly impact the surrounding physical environment, including nearby buildings and infrastructure. The proposed signal processing methodology is adapted from established techniques reported in [8–11], which primarily focus on intrinsic factor analysis. The main objective is to quantify the vibration transmitted to the building structure by measuring signals from the AC synchronous motor, thereby evaluating the effectiveness of the developed technology. The measurement results provide insight into the environmental impact caused by forces generated from moving mechanical components. Focusing on the signal processing approach, the FFT was selected as the primary analysis tool. This method is enhanced with customized feature extraction techniques, drawing on successful implementations in prior studies on vibration and acoustic signal analysis [9–13].

MATERIAL AND METHODS

Operating Principle of AC Synchronous Motor

The operation of an AC synchronous motor is governed by the interaction between a rotating magnetic field generated by the stator and a stationary magnetic field established in the rotor via direct current (DC) excitation. When a balanced three-phase alternating current is applied to the stator windings, a rotating magnetic field (RMF) is produced, which rotates at a constant angular velocity referred to as the synchronous speed. The stator's RMF intersects with the rotor, which is excited by a DC source through either slip rings and brushes or a brushless excitation system, thereby establishing a constant magnetic field within the rotor reference frame [14].

Due to the alternating polarity of the stator's magnetic field at standstill, the rotor is subjected to a rapidly reversing torque, which results in no net starting torque. Consequently, synchronous motors are not inherently self-starting. To initiate rotation, auxiliary starting methods are employed to accelerate the rotor close to synchronous speed. Common starting techniques include the use of damper windings or external prime movers. Once the rotor speed approaches the synchronous value, the rotor's magnetic field synchronizes with the stator's rotating field through magnetic locking. This condition, known as synchronism, enables the rotor to rotate at precisely the same speed as the stator field [14].

In steady-state operation, the rotor maintains a constant speed equal to the synchronous speed, operating with zero slip. This characteristic renders the synchronous motor particularly advantageous for applications requiring precise and constant speed

Fig.1 The synchronous motor used in the experiment.

(a) (b) (c)

Fig.2 Sensor's allocation: (a) the drive end, (b) the non-drive end, and (c) the motor base.

operation, independent of load fluctuations. Additionally, by adjusting the level of DC excitation, the motor's power factor can be controlled, making synchronous machines well-suited for industrial applications where both speed regulation and reactive power compensation are critical [14].

Vibration Phenomena in AC Synchronous Motors

Vibrations in AC synchronous motors can arise from both electrical and mechanical sources, and their presence often indicates underlying issues affecting the motor's performance, efficiency, or lifespan. Unlike induction motors, synchronous machines are more sensitive to perturbations in load, excitation, and alignment due to their inherent operational rigidity at constant speed. The most prominent forms of vibration in synchronous motors include hunting, rotor unbalance, eccentricity, misalignment, and electromagnetic forces arising from asymmetries or faults [15].

Rotor unbalance is the most frequent source of vibration, especially in large or high-speed synchronous motors. This is due to: mechanical wear and tear over time, imperfect manufacturing or assembly tolerances, accumulation of dust, oil, or mechanical residue on the rotor. Even a small mass imbalance at high RPM leads to significant centrifugal forces, resulting in noticeable vibration. Because rotor unbalance directly affects both the vibration amplitude and mechanical stress, it is typically the first aspect monitored in vibration diagnostics [15].

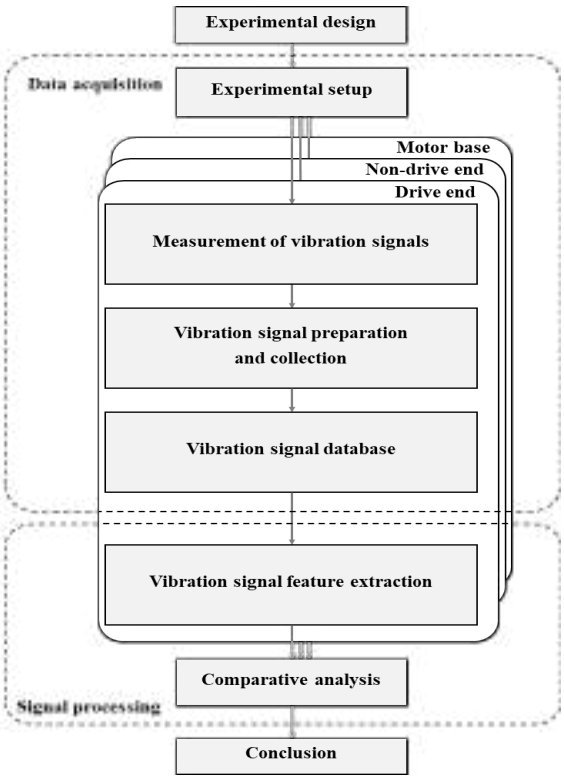

Fig.3 Experimental Procedure.

Sensor's Allocation

In a synchronous motor as depicted in Fig. 1, the part most susceptible to vibration in terms of both frequency and impact is typically the rotor assembly, particularly the shaft and bearings. In vibration diagnostics and condition monitoring, sensors are typically mounted near the motor bearings. The sensors that measure vibration generated by the motor, as explained earlier, and transmitted to the environmental surroundings were chosen to be located at three critical locations: the drive end, the non-drive end, and the motor base, as illustrated in Fig. 2.

Experimental Procedure

The experimental procedure was structured into two primary phases: data acquisition and signal processing, as illustrated in Fig. 3. The experimental design was initiated from the setup stage, where a high-frequency sensor system, along with associated accessories, was connected to a data acquisition computer. In the data acquisition phase, vibration signals were simultaneously recorded from the motor's drive-end surface under six distinct load conditions. The signals were first captured under no-load conditions at a voltage of 380 V and a current of 3.5 A, with a total of 50 measurement instances. Subsequently, signals were recorded under the other five different load conditions of 20%, 40%, 60%, 80%, and 100% at the same voltage. The corresponding electrical currents for these load levels were 4.16 A, 4.48 A, 5.48 A, 6.14 A, and 6.80 A, respectively. All data collection was carried out using the DigivibeMx M20 software.

Subsequently, a comprehensive vibration signal database was constructed through a systematic signal measurement protocol. The sensors operated at a fixed sampling frequency of 24,000 Hz. During the signal preparation and collection phase, signal segmentation was performed at the input port to ensure temporal consistency and synchronization across samples.

In addition to the drive-end measurements, vibration data were also collected at two additional sensor locations: the non-drive end of the motor and the motor base. This multi-point sensing configuration enabled a more holistic characterization of the motor's vibrational behavior under varying mechanical loads.

Following the data acquisition phase, the collected data were categorized into six distinct segments corresponding to the predefined load conditions. In the signal processing phase, a feature extraction procedure was implemented to characterize the vibrational behavior under each load. Specifically, the FFT was applied to each segmented signal to convert the time-domain data into the frequency domain, yielding corresponding frequency spectra.

From the resulting spectra, five significant peaks along the frequency axis were identified and used to determine the dominant frequencies and their associated magnitudes. These peaks represent the primary frequency components of the vibration or acoustic signals generated by the motor's internal moving parts. To enhance reliability and reduce signal variability, the extracted features were subjected to an averaging process across multiple measurements for each load condition.

After feature extraction, a comparative analysis examined the relationship between motor load conditions and corresponding spectral characteristics by means used in [11-13]. The implications of these findings, along with in-depth interpretations, are presented and discussed comprehensively in the conclusion section of this paper.

EXPERIMENTAL RESULTS

The comparative analysis methodology utilizes features derived from spectral analysis to compute statistical averages. To facilitate visual interpretation, a comparative bar chart has been developed [16, 17].

Specifically, the comparative analysis of vibration involves evaluating the average magnitudes of the first through fifth peaks in the frequency spectrum of vibration signals recorded under varying load conditions, as illustrated in Figs. 4-6.

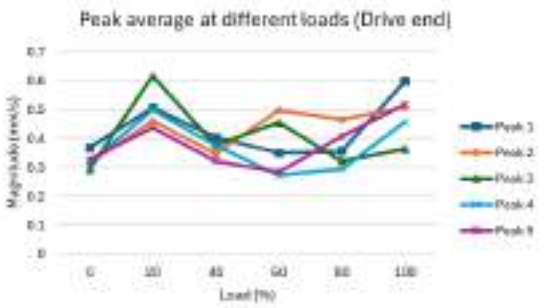

Fig.4 The averaged magnitudes of the 1st to 5th peaks of the frequency spectrum of the vibration signal at the motor's drive end with distinct load conditions.

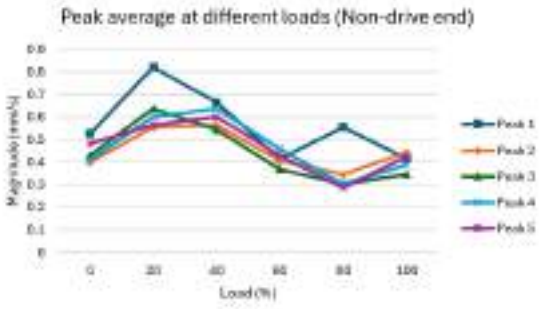

Fig.5 The averaged magnitudes of the 1st to 5th peaks of the frequency spectrum of the vibration signal at the motor's non-drive end with distinct load conditions.

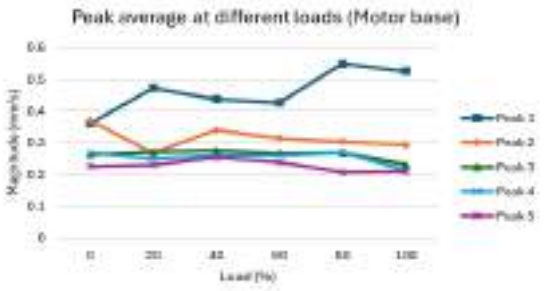

Fig.6 The averaged magnitudes of the 1st to 5th peaks of the frequency spectrum of the vibration signal at the motor base with distinct load conditions.

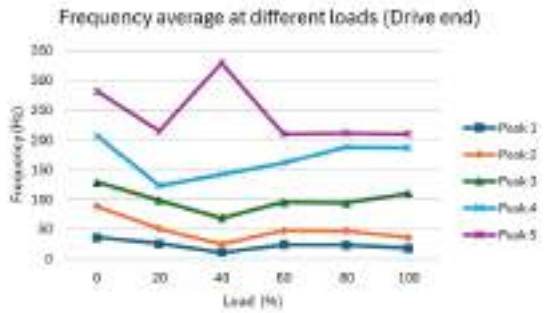

Fig.7 The averaged frequencies of the 1st to 5th peaks of the frequency spectrum of the vibration signal at the motor's drive end with distinct load conditions.

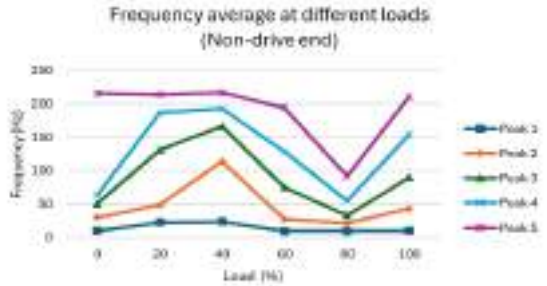

Fig.8 The averaged frequencies of the 1st to 5th peaks of the frequency spectrum of the vibration signal at the motor's non-drive end with distinct load conditions.

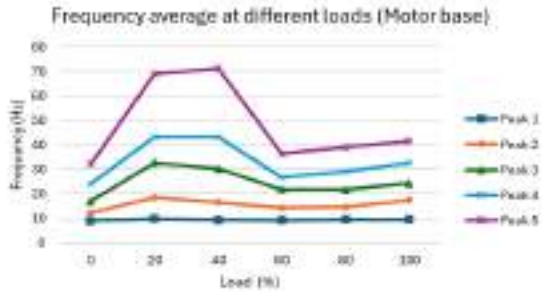

Fig.9 The averaged frequencies of the 1st to 5th peaks of the frequency spectrum of the vibration signal at the motor base with distinct load conditions.

Additionally, Figs. 7-9 present a comparison of the average frequencies corresponding to the first through fifth spectral peaks of the vibration signals under the same load conditions.

The analysis of vibration amplitude at the drive-end position of the motor. The results indicate that the peak amplitude tends to vary with increasing load levels, exhibiting its maximum value at 100% load. Notably, an anomalously high peak amplitude is observed at 20% load, which is significantly greater than those at adjacent load levels as presented in Fig. 4.

The vibration amplitude analysis at the non-drive end of the motor. It is observed that the peak amplitude reaches its highest value at 20% load. Subsequently, the amplitude demonstrates a decreasing trend as the load increases as illustrated in Fig. 5.

Furthermore, Fig. 6 shows the vibration amplitude analysis at the motor base. The amplitude of the first spectral peak exhibits a trend of increasing magnitude with higher load levels, whereas the amplitudes of the remaining peaks remain relatively stable, with some exhibiting a slight downward trend.

The dominant frequency analysis at the drive end of the motor. The frequencies of the first to third peaks remain relatively constant regardless of load conditions. In contrast, the frequencies of the fourth and fifth peaks fluctuate with changes in load, displaying no consistent pattern as seen in Fig. 7.

The dominant frequency analysis at the non-drive end of the motor. Only the frequency of the first peak remains relatively constant across varying load levels. The frequencies of peaks two through five, however, demonstrate significant fluctuations in response to load variations as shown in Fig. 8. Additionally, it is noteworthy that a clustering of peak frequencies occurs at 80% load.

The dominant frequency analysis at the motor base. The frequencies of peaks one through four remain stable across all load levels. However, the fifth peak exhibits load-dependent variability, with its frequency changing irregularly as the load varies as displayed in Fig. 9.

Overall, the experimental results presented in Figs. 4–6 indicate that the non-drive end consistently exhibits the highest vibration amplitudes under all loading conditions. This trend is primarily attributed to the extended length of the rotor shaft beyond the stator at the non-drive end, which increases the susceptibility to oscillatory motion. In contrast, the motor base consistently records the lowest vibration levels, owing to its mechanical decoupling from direct motor attachment.

CONCLUSIONS

This study presents a comprehensive experimental investigation into the vibrational characteristics of an AC synchronous motor operating under varying load conditions. The experimental procedure encompassed two principal phases: data acquisition and signal processing. The results indicate that vibration behavior is sensitive to both load condition and sensor location. These findings underscore the complex interplay between mechanical loading and vibrational response, highlighting the diagnostic value of multi-point vibration analysis in assessing motor condition and performance. The results serve as a foundation for further studies in predictive maintenance and fault detection using vibration signal analysis.

ACKNOWLEDGMENTS

This study was conducted with extensive utilization of laboratory facilities and technical resources provided by the Mechanical System and Signal Processing Research Group. Additional operational support was contributed by laboratory personnel. Financial support for this research was provided by the Faculty of Engineering at Sriracha, Kasetsart University, Sriracha Campus.

REFERENCES

[1] Konrad W., Friedrich B., Uwe H., Hans-Werner H., Hans-Christian M., Noise and Vibrations in Machine Tools, CIRP Annals, Vol. 70, Issue 2, 2021, pp. 611-633.

[2] Lee J. M., Ham I., A Study on the Design Improvement of Lathes Based on a Chatter Analysis and a Component Mode Synthesis, CIRP Annals, Vol. 35, Issue 1, 1986, pp. 263-266.

[3] Zapciu M., K'nevez J., Gerard A, Cahuc O., Bisu C. Dynamic Characterization of Machining Systems, International Journal of Advanced Manufacturing Technology, Vol. 57, 2011, pp. 73-83.

[4] Garcia-Perez A., Romero-Troncoso R. J., Cabal-Yepez E., Osornio-Rios R. A., Lucio-Martinez J. A., Application of High-Resolution Spectral Analysis for Identifying Faults in Induction Motors by Means of Sound, Journal of Vibration and Control, Vol. 18, Issue 11, 2011, pp. 1585–1594.

[5] Hu K., Zhang G., Zhang W., Analysis and Design of Electromagnetic Vibration and Noise Reduction Method of Permanent Magnet Motor, Journal of Low Frequency Noise, Vibration and Active Control, Vol. 41, Issue 1, 2021, pp. 359–373.

[6] Dai M., Zhang Z. W., Dorjoy M. M. H., Zeng L., Analysis and Optimization of Vibration and Noise of High-Speed Magnetic Suspension Motor, Journal of Low Frequency Noise, Vibration and Active Control, Vol. 41, Issue 2, 2021, pp. 625–636.

[7] Chantal U. M., Lu H., Liu Q., Jiang T., Hu M., Gashema G., Analysis of Dual-Driven Feed System Vibration Characteristics Based on Computer Numerical Control Machine Tools: A Systematic Review, Symmetry, Vol. 15, 2023, 2012.

[8] Chomphan S., Vibration Signal Analysis of a Motorcycle, International Journal of GEOMATE, Vol.16, Issue 56, 2019, pp. 27-32.

[9] Chomphan S., Kingrattanaset T., Boonsit S., Signal Analysis for LPG-modified Gasoline Engine with Engine Faults, International Journal of GEOMATE, Vol.16, Issue 56, 2019, pp. 65-72.

[10] Chomphan S., Wongchai B., Correlation Analysis of Vibration and Sound Signals of a Gasoline-Engine Car, International Journal of GEOMATE, Vol.18, Issue 67, 2020, pp. 195-201.

[11] Chomphan S., Investigation on Vibration and Sound Signals from Hybrid-Engine to Electric Vehicles, International Journal of GEOMATE, Vol. 24, Issue 104, 2023, pp. 77–84.

[12] Chomphan S., Contemplation of Vibration and Sound Signals of A Hybrid-engine Car, in Proc. Int. Conf. on Structure, Engineering & Environment, 2021, pp. 85-90.

[13] Chomphan S., Chaimanatsakun A., Sakornsin R., Khumneungratavongsa S., Rattanarat K., A Comparative Study of LPG-modified Engine and Normal Oil-usage Engine, in Proc. Int. Conf. on Engineering and Applied Sciences, 2016, pp. 219-225.

[14] Gerlando A., Gobbi M., Magnanini M. C., Mastinu G., Palazzetti R., Sattar A., Tolio T., Circularity Potential of Electric Motors in E-Mobility: Methods, Technologies, Challenges, Journal of Remanufacturing, Vol. 14, Issue 2, 2024, pp. 315–357.

[15] Lin F., Zuo S., Wu X., Electromagnetic Vibration and Noise Analysis of Permanent Magnet Synchronous Motor with Different Slot-Pole Combinations, IET Electric Power Applications, Vol. 10, 2016, pp. 900–908.

[16] Liao L. Y., Zuo Y. Y., Liao X. H., Study on Hybrid Electric Vehicle Noise and Vibration Reduction Technology, Advanced Materials Research, Vol. 764, 2013, pp. 141-148.

[17] Chomphan S., Chaimanatsakun A., Wittayapiyanon S., Environmental Impact Study of Vibration and Sound Signals of Air-Conditioner Cooling Units, in Proc. Int. Conf. on Geotechnique, Construction Materials & Environment, 2023, pp. 777-781.

Copyright © Int. J. of GEOMATE All rights reserved, including making copies, unless permission is obtained from the copyright proprietors.

15th Int. Conf. on Geotechnique, Construction Materials & Environment, Kyoto, Japan, 11-13 November 2025, ISBN 978-4-909106124 C3051

AI-BASED GEOTECHNICAL INFORMATION PREDICTION AND LIQUEFACTION HAZARD MAPPING FOR THE TOKYO METROPOLITAN AREA

Arisa Katsuumi [1], Koutaro Takasuna [1] and Shinya Inazumi [1]

[1] Shibaura Institute of Technology, Japan

ABSTRACT

This study presents an AI-based framework for predicting subsurface geotechnical conditions and mapping liquefaction hazards across the Tokyo metropolitan area. A comprehensive dataset of 13,926 borehole logs and elevation data was used to train a two-level stacking model integrating Random Forest, Gradient Boosting, and Support Vector Machine algorithms. The model accurately predicted SPT N-values, soil classifications, and groundwater levels at un-surveyed locations. These predictions were incorporated into the Potential Liquefaction (PL) method, enabling a quantitative evaluation of liquefaction risks. A high-resolution (200 m × 200 m) hazard map was generated, revealing enhanced spatial granularity compared to existing public maps (500 m × 500 m). The proposed approach successfully identified localized high-risk areas, especially in reclaimed coastal zones such as eastern Tokyo. Comparative analysis demonstrated that the AI-based method provided superior detection sensitivity and predictive continuity even in data-scarce regions. The integration of ensemble learning and geotechnical engineering knowledge offers a scalable, data-efficient solution for urban hazard assessment. This framework contributes to improving disaster mitigation strategies and infrastructure planning in earthquake-prone urban environments. Future work will refine missing data estimation and extend the method to handle complex soil stratifications, further enhancing its practical applicability to large-scale geotechnical risk evaluations.

Keywords: Liquefaction, Ground Condition Prediction, Ensemble Learning, Hazard Map, AI

INTRODUCTION

Liquefaction, a phenomenon in which saturated soils lose their strength and stiffness in response to earthquake shaking, has long been recognized as a critical cause of structural damage in seismic regions [1]. The 1964 Niigata and Alaska earthquakes notably brought this hazard to the forefront, prompting extensive field investigations and laboratory experiments. These studies have since contributed to a deeper understanding of liquefaction mechanisms and have informed the development of engineering-based prediction and mitigation strategies widely used today.

In recent years, increasing concern over the potential occurrence of large-scale seismic events, such as the anticipated Nankai Trough earthquake, has highlighted the importance of precise and spatially comprehensive ground investigations in urban areas. Liquefaction risk is particularly significant in densely populated and infrastructure-heavy regions like the Tokyo metropolitan area, where the consequences of ground failure could be catastrophic. Thus, the need for accurate and high-resolution liquefaction hazard assessment is more pressing than ever.

However, conventional ground investigation methods, while reliable, are inherently constrained by substantial time, financial, and logistical costs. As a result, survey data are often limited in both spatial density and coverage. This poses a major challenge for hazard mapping, especially in complex urban terrains where ground conditions can vary considerably over short distances. The resulting lack of detailed subsurface data makes it difficult to conduct precise risk evaluations at the local scale.

To address these limitations, advanced data-driven techniques such as artificial intelligence (AI) and machine learning (ML) have emerged as promising tools for geotechnical analysis [2,3]. These approaches enable the extraction of meaningful patterns from limited datasets, allowing for the inference of subsurface properties in un-surveyed locations. These methods significantly enhance the spatial resolution and reliability of ground condition predictions across large areas.

The objective of this study is to construct a predictive framework for estimating ground conditions throughout the Tokyo metropolitan area by leveraging AI-based techniques. Specifically, the predicted subsurface properties are applied within the PL method, an established engineering procedure for liquefaction hazard evaluation, to generate detailed hazard maps. This integrated approach aims to improve the granularity of hazard assessments and to enhance their accuracy, particularly in areas with sparse direct survey data. Through this, the study contributes to the advancement of data-efficient methodologies for disaster prevention and infrastructure resilience planning in urban

environments.

METHODOLOGY

Construction of the AI-Based Predictive Model

Artificial intelligence, particularly machine learning, has become an increasingly valuable tool in geotechnical engineering due to its ability to handle large, complex, and often incomplete datasets. In this study, an ensemble learning approach, specifically, a stacking methodology, was employed to construct a strong predictive model for subsurface geotechnical properties [3,4]. Ensemble learning combines multiple base models to improve generalization performance, reduce overfitting, and capture complex nonlinear relationships within the data.

As schematically illustrated in Fig. 1, the stacking model operates in two stages. In the first stage, three base learners, Random Forest, Gradient Boosting, and Support Vector Machine, are trained independently using the same input dataset. Each of these algorithms contributes distinct strengths: Random Forest is effective in handling high-dimensional data and mitigating variance through averaging; Gradient Boosting improves predictive accuracy by sequentially correcting errors from prior models; and Support Vector Machine excels in managing nonlinear boundaries in both classification and regression tasks.

In the second stage, the outputs of these base models serve as input features to a meta-model, which is also constructed using Gradient Boosting. This hierarchical structure allows the model to effectively learn from the complementary strengths of the base learners, thereby achieving enhanced prediction performance while controlling for bias and variance. The combined use of tree-based and margin-based methods ensures the ensemble is both accurate and generalizable to unseen data, which is critical for applications involving geospatial variability in urban regions.

Liquefaction Hazard Assessment Using the PL Method

The Potential Liquefaction (PL) method provides a quantitative framework for evaluating the likelihood of soil liquefaction during seismic events [5]. It operates by integrating the factor of safety (FL) across relevant soil layers, assigning appropriate weights to compute a PL value for each location. The mathematical procedures and threshold-based hazard classifications are outlined in Table 1 and expressed in Eqs. (1) and (2).

$$P_L = \int_0^{20} (1 - F_L)(10 - 0.5x)dx \quad (1)$$

$$F_L = \frac{R}{L} \quad (2)$$

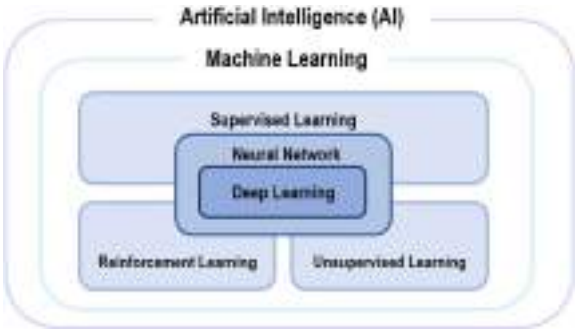

Fig. 1 Architecture of the AI-based stacking model for subsurface prediction

Table 1 Liquefaction hazard classification criteria based on PL value

$P_L > 15$	Liquefaction Risk: Large
$5 < P_L \leq 15$	Liquefaction Risk: Medium
$0 \leq P_L \leq 5$	Liquefaction Risk: Small

Fig. 2 Spatial distribution map of groundwater levels in the Tokyo metropolitan area

Where F_L is the liquefaction resistance, x is the depth from ground surface, R is the dynamic shear strength, and L is the seismic shear stress ratio.

This method targets subsurface layers that meet specific liquefaction-susceptible conditions, including:

- Groundwater table located within 10 meters of the ground surface, and saturated layers present within a depth of 20 meters.
- Fines content (FC) of 35% or less, or FC greater than 35% provided the plasticity index (Ip) does not exceed 15.
- Median grain diameter (D50) less than or equal to 10 mm and 10% grain diameter (D10) less than or equal to 1 mm.

The soil parameters used in the PL method evaluation were selected based on typical values for each soil type commonly found in the Tokyo metropolitan area, following established geotechnical engineering practice and previous liquefaction studies [5]. These standardized parameters ensure consistency in the evaluation process and compatibility with the PL method requirements.

These criteria reflect widely accepted empirical correlations between soil characteristics and liquefaction potential. For this study, spatial

Table 2 Soil classification parameters used in PL method evaluation (parameters selected based on typical values for Tokyo area soils following established geotechnical practice)

Soil Type	Unit Weight Below Groundwater Table (t/m^3)	Unit Weight Above Groundwater Table (t/m^3)	Median Particle Diameter D_{50} (mm)	Fines Content (%)
Gravel	2.1	1.9	0.6	0
Sand	1.9	1.7	0.25	10
Silt	1.7	1.5	0.02	80
Clay	1.5	1.3	0.025	75

groundwater level data were obtained and interpolated as visualized in Fig. 2, while soil parameter classifications used in PL evaluation are listed in Table 2. By applying the PL method to AI-predicted subsurface profiles, the study produces hazard assessments that integrate both geotechnical engineering knowledge and data-driven prediction.

Data Collection and Prediction Framework

Geotechnical data used in this study were derived from publicly available borehole logs provided by the Tokyo Metropolitan Government. As shown in Fig. 3, the dataset includes location information (latitude and longitude), SPT N-values, and soil classification data from 13,926 sites. In addition, surface elevation data were incorporated from the Geospatial Information Authority of Japan to enhance the spatial resolution of the input dataset.

One of the key challenges was the presence of missing groundwater data in many of the borehole records. To address this, spatial interpolation was applied using surrounding valid data, resulting in a comprehensive groundwater distribution map as shown in Fig. 2. This step was essential for ensuring consistent PL evaluation across the study area.

For the prediction of N-values, the model treated the N-value at each depth from 1 to 20 meters as the target variable, with explanatory variables including location coordinates, elevation, and known N-values at other depths. In the case of soil classification, a similar set of explanatory variables was employed. Where borehole logs indicated mixed soil types within a single layer, the dominant material type was used to ensure consistency in prediction and compatibility with the PL method. Due to the lack of direct laboratory data for predicted soil types, soil property parameters from Table 2 were applied based on the classification results.

RESULTS AND DISCUSSION

Using the ensemble learning model constructed as described in the previous section, key subsurface geotechnical parameters, namely SPT N-values, soil classification, and groundwater level, were predicted across the entire Tokyo metropolitan area. These predicted values served as input for the PL method,

Fig. 3 Sample borehole log extracted from Tokyo metropolitan dataset

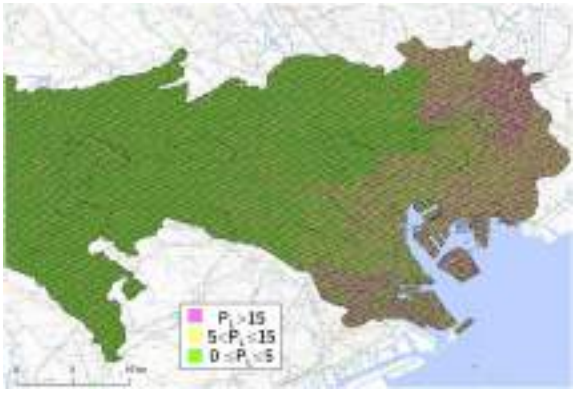

Fig. 4 High-resolution liquefaction hazard map generated by this study (200 m × 200 m)

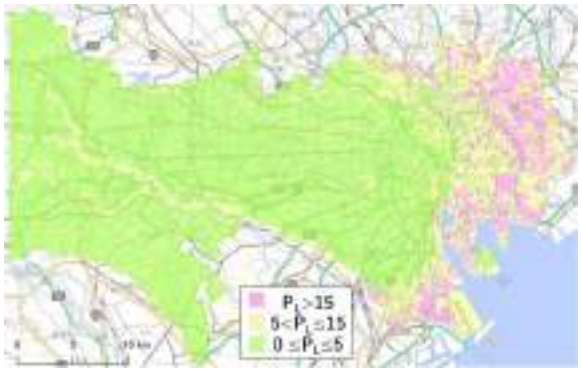

Fig. 5 Publicly available liquefaction hazard map (500 m × 500 m) for comparison

enabling the calculation of liquefaction potential for each mesh point.

The resulting liquefaction hazard map is presented in Fig. 4, which depicts the PL value distribution on a 200 m × 200 m mesh. Each mesh cell is color-coded based on its computed PL value, allowing for the identification of areas with differing degrees of liquefaction susceptibility. The fine resolution of this map facilitates a more localized assessment of hazard, which is crucial for urban-scale disaster mitigation planning.

Model accuracy analysis reveals distinct geographical patterns across the study area. High prediction accuracy ($R^2 > 0.85$) is achieved in eastern Tokyo, particularly in Koto Ward ($R^2 = 0.88$) and surrounding reclaimed coastal areas such as Sumida Ward ($R^2 = 0.86$) and Edogawa Ward ($R^2 = 0.84$). These regions benefit from dense borehole data coverage and relatively uniform geological conditions. Conversely, moderate accuracy ($R^2 = 0.70$-0.80) is observed in western Tokyo's mountainous areas and peripheral regions where data density is lower. The high accuracy in Koto Ward is particularly significant given its elevated liquefaction risk, providing confidence in hazard assessments for this critical area.

To evaluate the performance and practical utility of the proposed method, the generated map was compared with the publicly available liquefaction hazard map, shown in Fig. 5, which is based on a coarser 500 m × 500 m mesh. This comparative analysis provides insights into the added value of the AI-based approach in terms of spatial granularity and predictive fidelity.

The comparison reveals that in the western part of Tokyo, where ground conditions are generally more stable and data density is lower, both maps show similar hazard classifications. However, significant differences emerge in eastern Tokyo, particularly in reclaimed coastal zones such as Koto Ward. In these areas, the AI-generated map identifies a broader extent of zones categorized as "medium" or higher risk (PL = 5–15), indicating greater sensitivity to localized ground conditions. Specifically, Koto Ward demonstrates both high liquefaction risk and high prediction confidence, making it a priority area for detailed investigation. This outcome underscores the ensemble model's ability to extrapolate ground conditions in data-sparse regions while preserving spatial accuracy [6].

The improved resolution and accuracy of the proposed approach are attributed to several key factors. Regional accuracy assessment shows that eastern reclaimed areas, including Koto Ward, consistently achieve higher prediction reliability due to dense data coverage and uniform geological conditions, while western mountainous regions show moderate accuracy reflecting more complex terrain and sparser data distribution.

- Finer mesh size: The 200 m resolution enables the detection of subtle variations in soil conditions that would be obscured in coarser mesh.
- Integration of interpolated groundwater data: As visualized in Fig. 2, spatial interpolation fills data gaps and enhances the completeness of the input dataset for the PL method.
- Strong predictive modeling: The ensemble learning approach effectively captures nonlinear interactions between location, soil type, elevation, and existing N-values, enabling reliable predictions beyond observed locations.

Furthermore, the denser geotechnical data distribution in eastern Tokyo contributes to higher model reliability in these areas, which is evident from the hazard distribution patterns. Conversely, in regions with fewer boreholes, the model still maintains predictive continuity due to its ability to generalize from surrounding data.

These findings demonstrate that the integration of AI-based prediction with the PL method yields a high-resolution hazard map that offers enhanced insight into urban liquefaction risk. The explicit accuracy assessment, particularly highlighting high-confidence predictions in critical areas like Koto Ward, provides valuable guidance for practitioners to prioritize areas for detailed investigation and mitigation planning. This is particularly valuable for local governments and infrastructure planners who require detailed spatial information to guide seismic risk mitigation strategies, land-use planning, and emergency response frameworks.

CONCLUSIONS

This study developed and applied an AI-based geotechnical prediction framework to assess liquefaction hazard across the Tokyo metropolitan area. By integrating ensemble learning with established engineering methodologies, the proposed approach offers a data-efficient and spatially detailed solution for urban seismic risk evaluation. The main findings and contributions of this study are summarized below:

(1) An ensemble learning model combining Random Forest, Gradient Boosting, and Support Vector Machine was successfully constructed using a stacking approach, allowing for high-accuracy prediction of key geotechnical parameters such as N-values, soil classification, and groundwater level across un-surveyed areas.

(2) The predicted subsurface information was effectively incorporated into the PL (Potential Liquefaction) method, enabling quantitative liquefaction hazard evaluation that accounts for depth-dependent safety factors and soil susceptibility conditions.

(3) A high-resolution (200 m × 200 m) liquefaction hazard map was generated, providing improved

spatial granularity compared to publicly available maps (e.g., Fig. 5) and enabling more localized risk assessments, particularly beneficial for urban infrastructure planning.

(4) The AI-based model demonstrated strong predictive reliability even in data-scarce regions, by leveraging spatial interpolation and nonlinear pattern recognition to estimate missing or incomplete geotechnical data (e.g., groundwater levels as shown in Fig. 2).

(5) Comparative analysis revealed that the proposed method identifies a broader extent of high-risk zones in vulnerable areas, such as the reclaimed lands of eastern Tokyo, highlighting its effectiveness in capturing localized hazard variations that may be underestimated by conventional methods.

This research provides a scalable and transferable framework that can be adapted to other urban regions facing similar challenges in liquefaction risk assessment. Future work will focus on improving prediction accuracy by refining the estimation of missing geotechnical parameters, incorporating more diverse data sources, and extending the methodology to account for mixed soil properties in greater detail.

REFERENCES

[1] Wang G., Sassa K., Fukuoka H., and Wang F., Liquefaction-induced Flow Slides: Case Histories and Geomechanical Mechanisms, Engineering Geology, Vol. 213, 2016, pp. 1–15.

[2] Huang M., Zhang J., and Goh A.T.C., Machine Learning and Probabilistic Prediction of Liquefaction Using CPT Data, Journal of Geotechnical and Geoenvironmental Engineering, Vol. 143, No. 7, 2017, pp. 04017027-1–04017027-10.

[3] Wang Y., Xu D., Zhang Y., Tang C., and Zhou C., Application of Machine Learning Models to Predict Soil Liquefaction: A Review, Soil Dynamics and Earthquake Engineering, Vol. 155, 2022, pp. 107178-1–107178-18.

[4] Pham B.T., Bui D.T., Prakash I., and Dholakia M.B., A Comparative Study of SVM-based Classifiers and Logistic Regression for Landslide Susceptibility Assessment, Landslides, Vol. 14, No. 3, 2017, pp. 697–709.

[5] Juang C.H., Huang H.W., and Jiang T., A Transparent Framework for Reliability-based Design in Geotechnical Engineering, Computers and Geotechnics, Vol. 63, 2015, pp. 84–95.

[6] Zhang J. and Goh A.T.C., Multiclass Geotechnical Classification Using GBT, RF, and SVM Models, Computers and Geotechnics, Vol. 84, 2016, pp. 12–24.

Copyright © Int. J. of GEOMATE All rights reserved, including making copies, unless permission is obtained from the copyright proprietors.

15th Int. Conf. on Geotechnique, Construction Materials & Environment,
Kyoto, Japan, 11-13 November 2025, ISBN 978-4-909106124 C3051

APPLICATION OF SROI FRAMEWORK IN COST-EFFECTIVENESS ANALYSIS FOR THE ENVIRONMENTAL PROTECTION INVESTMENTS OF QUARRY MINES

Ngwu Tochukwu[1], Somprasong Komsoon[2] and Chanapol Charoentanaworakun[3]

Faculty of Engineering, Chiang Mai University, Thailand

ABSTRACT

Environmental Protection Plans (EPPs) are mandatory components of regulatory compliance for quarry mining operations in Thailand. However, the challenges in quantifying the environmental and social values generated by these interventions hamper the evaluation of their cost-effectiveness, potentially hindering optimal resource allocation. This study addresses this gap by applying a Social Return on Investment (SROI) framework to evaluate the environmental benefits of EPPs in two selected quarry mines. This was achieved by using the benefit from reduced pollution and environmental improvements and monetary proxies for each EPP category to quantify the cumulative social and environmental values, which are compared to the operational expenditures (OPEX) involved in the implementation. Results indicate that Mine A generated a value of $320,528.11 from an investment of $200,734.75, yielding an SROI of 1.60, and Mine B generated $115,050.00 from $77,908.25, with an SROI of 1.50. The higher SROI obtained in Mine A is attributed to a more systematic EPP implementation and pollution reduction and larger land degradation, which requires remediation. These findings justify the cost-effectiveness of the EPP investments, emphasizing the capacity of SROI as a tool for evidence-based environmental decision-making. The study supports the integration of SROI into regulatory benchmarking and sustainability reporting frameworks, enabling stakeholders to assess the value generated from investments in environmental stewardship in mining.

Keywords: Social Return on Investment, Mining, Environmental Protection Plans, Theory of Change

INTRODUCTION

The quarry industry has played a significant role in Thailand's economy for several decades, driven by economic demands and industrialization [1]. However, quarrying activities also generate significant environmental impacts, which necessitate the implementation of regulatory frameworks and protection schemes to ensure a harmonious balance between economic benefit and environmental sustainability. These environmental impacts of quarrying operations vary due to the type of mineral production, scale of operation, and other geologic factors. Environmental Impact Assessment (EIA) has therefore become a crucial tool for evaluating the potential environmental impacts of quarrying activities [2], serving as the foundation for developing Environmental Protection Plans (EPPs) aimed at mitigating these impacts. Quarrying, like other mining activities in Thailand, is regulated by comprehensive environmental regulations aimed at curbing negative impacts such as air, noise, and water pollution and alterations to the natural landscape. According to the Enhancement and Conservation of National Environmental Quality Act B.E. 2535 (1992) in Thailand, mining operations are required to implement an Environmental Impact Assessment (EIA) and set up Environmental Protection Plans (EPPs) prior to receiving project approval. This plan takes into account cumulative expected environmental impacts of the operations and a corresponding protective plan to mitigate each impact [3].While these measures ensure compliance with environmental policies, there has been limited focus on the quantification of the generated environmental benefits relative to the cost of implementation. This prompts an inquiry into the cost-effectiveness of these measures and their capacity to deliver measurable and optimum value to stakeholders. Furthermore, an apparent challenge in evaluating the cost-effectiveness of EIAs and environmental protection measures is that it is difficult to quantifiably define their environmental outcomes or benefits [3, 4]. In response to this challenge, literature such as [5] recommends further studies with a focus on advancing ideas for measurable and evidence-based methods for evaluating environmental outcomes of EIA interventions. In addition, [6] have applied SROI in quantifying the social benefits of EIA intervention projects in monetary terms and further evaluating their effectiveness compared to the financial investments. To address these gaps, this study evaluates the cost-effectiveness of these environmental protection plans of quarries by evaluating their environmental protection schemes using the existing framework of Social Return on

Investment (SROI). This decision is due to the ability of SROI to measure the environmental benefits of EIA programs and EPPs relative to the financial cost of implementation, thereby effectively capturing environmental and social outcomes as well as the economic costs in a single metric [7, 8]. This study facilitates the evaluation and implementation of environmental protection measures that are both economically viable and environmentally sustainable in quarry mines.

RESEARCH SIGNIFICANCE

As part of regulatory compliance and sustainability efforts, quarry mines in Thailand are mandated to invest in the implementation of Environmental Protection Plans (EPPs). However, there is a lack of tools or frameworks to assess and quantify the environmental benefits generated by these investments. This gap presents a critical challenge in determining the actual impact and cost-effectiveness of EPPs, resulting in inefficient resource allocation and suboptimal performance. This research addresses this gap by applying a systematic approach to evaluate the environmental benefits of EPPs in quarries using SROI principles to support cost-effective and evidence-based investment in EPPs.

METHODOLOGY

The study follows a structured, multi-phase approach designed to assess the cost-effectiveness and social-environmental value of Environmental Protection Plans (EPPs) implemented by selected quarry operations. Two quarry sites were purposively selected as case studies based on the availability of Environmental Impact Assessment (EIA) reports and Environmental Protection Plan documentation. Relevant secondary data were collected through a comprehensive literature review, including publicly available EIA reports, corporate sustainability reports, and peer-reviewed publications related to environmental management in mining. Based on the collected documentation, key mitigation measures were identified and systematically categorized into four main environmental domains: air quality control (e.g., dust suppression, emission filters), water quality management (e.g., sedimentation ponds, recycling systems), noise reduction (e.g., acoustic barriers, limited blasting schedules), and land rehabilitation and reforestation (e.g., planting programs, soil restoration). Each mitigation measure was documented with technical specifications, implementation timelines, and associated costs. The identified mitigation strategies were used to develop a set of inputs for the Social Return on Investment (SROI) analysis. Following the Theory of Change model. For each outcome identified, financial proxies were assigned to represent the environmental and social value generated. These proxies were derived from market prices, shadow pricing, benefit transfer techniques, and previous SROI studies [9, 10]. The total investment cost of implementing each EPP was then compared against the monetized social and environmental benefits to calculate the SROI ratio (i.e., the value generated per unit of investment). This analysis allowed for a direct comparison between the two quarries.

Quarry Site Selection and Cost Assessment of Environmental Protection Plans

Two limestone quarries in Thailand were selected for this study based on differences in production scale and concession area, as outlined in Table 1. Quarry A, a medium-scale operation in central Thailand, produces about 100,000 tons per year, while the smaller quarry in the same region produces around 32,000 tons annually. The Environmental Protection Plans (EPPs) were drafted through a systematic review of Environmental Impact Assessment (EIA) reports and field observations. Mitigation measures from each potential environmental impact served as the foundation for the EPPs at each quarry. The environmental monitoring reports were used to assess compliance with these plans. Data from the Thai Department of Primary Industries and Mines (DPIM), field observations, industry documents, and EIA documents of each quarry were used to estimate investment costs in Environmental Protection Plans (EPPs), as shown in Table 1 for Mines A and B.

Defining Theory of Changes

This study uses a Theory of Change (ToC) approach to assess the environmental and social impacts or outcomes of EPPs in quarry operations. ToC serves as the conceptual basis for impact valuation using the Social Return on Investment (SROI) methodology. ToC enables the mapping of causal pathways linking environmental interventions to expected outcomes, using empirical evidence drawn from observations and data analysis [11]. Determining the theory of change and selecting appropriate financial proxies are key steps in estimating the environmental and social value of each EPP at the selected mines.

Quantifying Impacts and Assigning Financial Proxy

In this study, the benefits generated by EPPs are quantified based on the nature and objectives of each Environmental Protection Plan (EPP). To assign monetary value to the environmental and social outcomes of the EPPs that were identified through the Theory of Change, this adopts a systematic approach

to determine appropriate financial proxies. Financial proxies represent the estimated monetary value of non-market outcomes, enabling a standardized comparison between costs, effectiveness, and benefits using the SROI framework [12-15].For air pollution reduction, benefits were calculated by multiplying the amount of reduced emissions by the social cost per unit of emission. Reforestation benefits were derived by estimating the economic value of ecosystem services, which is carbon sequestration. Noise abatement benefits were calculated as the reduction in noise levels from baseline to post-intervention scenarios and multiplied by willingness to pay (WTP) for noise pollution reduction in the region. The benefits for water quality improvement were estimated based on the volume of pollutants removed, the amount of treated wastewater, and the market price of removal per volume. Overall, the value/benefits of each EPP correspond to the damage avoided or reduced through its implementation. Table 2 summarizes the calculated social and environmental outcomes in monetary terms.

Economic Outcome from Environmental Value E_v and Social Value S_v

This approach integrates environmental economic valuation techniques with data derived from ToC and financial proxies, providing a monetary valuation of the benefits of the intervention. Due to the available data, the valuation method applied in this study is the benefit from reduced pollution and environmental improvements and monetary proxies for each EPP category to quantify the cumulative social and environmental values. The general equation for determining economic outcome in monetary terms from environmental and social values generated is defined as Equation (1) and Equation (2), respectively.

$$E_v = \sum_{i=1}^{n}[Q_i \times FP_i \times (1 - \sum D_i)] \quad (1)$$

$$S_v = \sum_{i=1}^{n}[Q_j \times FP_{ij} \times (1 - \sum D_j)] \quad (2)$$

Where E_v refers to environmental value and S_v represents social value created. Q_i is the representative of quantity or magnitude of the environmental outcome (e.g., tons of CO_2 reduced, hectares reforested). FP_i is the parameter of financial proxy for each environmental outcome per unit. D_i indicates the rate at which a specific environmental outcome declines over a given period, expressed as a percentage and calculated in relation to a baseline or the initial state of environmental conditions.

Valuation of SROI

SROI is a form of cost-benefit analysis that extends traditional financial accounting to include non-market social and environmental outcomes. The aim is to express the total social value generated per unit of investment, which is illustrated as equation (3):

$$SROI = \frac{NPV_{B-EPP}}{NPV_i} \quad (3)$$

NPV_{B-EPP} is the Net Present Value representing the sum of total value of anticipated outcomes, expressed in monetary terms and adjusted to reflect relevant factors specific to the EPPs., while NPV_i accounts for all associated costs, including capital investments, operational expenses, and expenditures related to environmental or social mitigation measures.

Evaluation of Cost-Effectiveness Using Social Return on Investment (SROI) Framework

The Social Return on Investment (SROI) framework presents a viable methodology for conducting cost-effectiveness analysis (CEA) of Environmental Protection Plans (EPPs), as it integrates both financial and non-financial evidence-based outcomes into an evaluation model [18-20]. SROI is obtained by dividing the social and environmental value generated by an intervention by the financial cost of implementation. This ratio signifies the social and environmental values generated per unit of financial investment, offering an apparent measure of the impact relative to the resources allocated. The aim of the analysis is to assess the efficiency of investment in EPPs by comparing the total monetized value of social, environmental, and economic outcomes against the costs incurred. This allows decision-makers to determine which EPP strategies deliver the most optimum value relative to their financial input. Equation (4) demonstrates the formula applied in this study to determine the cost-effectiveness of EPP plans.

$$C_{Eff} = \frac{\sum(S_V + E_v)}{\sum(CAPEX_{EPPS} + OPEX_{EPPs} + E_{xi})} \times 100 \quad (4)$$

Where C_{Eff} is the percentage of cost effectiveness in the investment of EPPs. S_V stands for the social value generated by the EPPs , $while\ E_v$ represents the environmental value generated by the EPPs. The $CAPEX_{EPPS}$ and $OPEX_{EPPs}$ is the capital cost and operation cost of the EPPs, respectively. In addition, the E_{xi} term refers to auxiliary expenditure related to EPPs including additional technology and fees.

RESULTS AND DISCUSSION

Evaluating Investments in EPPs

The total investments in EPPs are $200,734.75 and $77,908.25 for mine A and B, respectively, as shown in table 1. This consists of investments in air

quality management, water quality management, noise and vibration control, reforestation, extra EPPs, and reclamation and environmental funds.

Table 1 Summarized EPPs Investments/OPEX for Mine A and B.

Category	Mine A	Mine B
Production Size (tons/month)	100,000	32,000
Concession Area (sq.km)	0.928	0.538
EPPs OPEX/Investments (USD)		
Air Quality Management	52,600.00	15,900.00
Water Quality Management	3,771.56	976
Noise & Vibration Control	0	0
Reforestation	6,183.61	2,495.54
Extra EPPs	5,000.00	0
Reclamation and environmental Funds	133,179.58	58,536.71
TOTAL OPEX	**200,734.75**	**77,908.25**

Quantifying Benefits of the EPPs in Monetary Terms

The quantified monetary outcomes generated by the Environmental Protection Plans (EPPs) show a cumulative value of $320,528.11 and $115,050.00 for Mine A and Mine B, respectively, as shown in table (2) below.

Table 2 shows the monetary outcomes generated by the EPPs

Category	Mine A (USD)	Mine B (USD)
Air Quality Management	55,080.00	45,900.00
Water Quality Management	32,435.00	8,567.00
Noise & Vibration Control	22,032.00	7,908.00
Reforestation	12,852.00	4,613.00
Extra EPPs	45,900.00	16,475.00
Environmental Fees & Funding	206,695.53	74,188.00
Total	**320,528.53**	**115,050.00**

This reflects the extensive economic and social benefits derived from the implementation of EPPs in mining operations. The higher monetary outcome for Mine A is primarily due to more systematic application of EPPs, which results in more reduced pollution and degradation. Additionally, a larger land concession area, which necessitates extra remediation efforts, also contributes to the higher monetary outcome in Mine A, and vice versa for Mine B. Reclamation and environmental funds contributed to higher monetary outcomes in both quarries, underscoring the significance of these investments in the restoration of degraded landscapes. Other significant aspects include extra EPPs (such as advanced filtration systems) and water and air quality management, which shows the direct benefits of pollution control measures in community and environmental sustainability. The variations in the quantified monetary outcomes of the two quarries show that production scale and population density play a crucial role in determining potential value generated by EPPs.

Interpretation of Net Present Value (NPV) and SROI

The analysis of Net Present Values (NPVs) and Social Return on Investment (SROI) shows that Mine A achieved an SROI value of 1.60 from an investment of $200,734.75. In comparison, Mine B yielded an SROI of 1.50 from an investment of $77,908.25. This indicates that for every dollar invested in EPPs, Mine A and Mine B returned $1.60 and $1.50, respectively. This ratio highlights the cost-effectiveness of the EPPs and the investments, as shown in Tables (3) and (4). The marginally higher SROI observed in Mine A indicates enhanced efficiency in the deployment of Environmental Protection Plans (EPPs), particularly in domains such as air quality management, reclamation funds, and additional EPPs (like advanced filtration systems), which substantially amplified generated value without an equivalent increase in cost. This highlights the capacity of innovative, targeted interventions to significantly improve generated values. In contrast, the lower generated values for Mine B can be attributed to a lower OPEX and potentially less intensive EPP implementation, which may be due to lesser systematic EPP implementation, a lesser concession area for reclamation, or financial/resource constraints. These discrepancies highlight the necessity for context-driven environmental investment, where site-specific characteristics such as land use and ecological sensitivity are factored into the planning of EPPs. Environmental fees and funding accounted for almost 50% of the total environmental and social values generated in both quarries, highlighting that land restoration not only mitigates environmental degradation but also delivers high community and ecological benefits, making it a high-impact, high-value EPP. Generally, the SROI ratio justifies the cost-effectiveness of the investments in EPPs, with both quarries exceeding a 1:1 return on investment, which is in correlation with [16, 17].Therefore, the findings illustrate that governments and regulatory agencies can use SROI values to benchmark performance, design incentive schemes, or structure environmental taxes/funds, while mining companies can integrate these findings into sustainability reporting and ESG disclosures,

showing shareholders and communities the value generated through responsible operations.

Table 3 Social return on investment (SROI) of Mine A

Category	Total OPEX (USD)	Value of Impact (USD)
Air Quality Management	52,600.00	55,080.00
Water Quality Management	3,771.56	32,435.00
Noise and Vibration Control	–	22,032.00
Reforestation	6,183.61	12,852.00
Extra EPPs	5,000.00	45,900.00
Environmental Fees & Funding	133,179.58	206,695.53
Total	**200,734.75**	**320,528.53**
SROI	–	**1.6**

Table 4 Social return on investment (SROI) of Mine B

Category	Total OPEX (USD)	Value of Impact (USD)
Air Quality Management	15,900.00	45,900.00
Water Quality Management	976	8,567.00
Noise and Vibration Control	–	7,908.00
Reforestation	2,495.54	4,613.00
Extra EPPs	–	16,475.00
Environmental Fees & Funding	58,536.71	74,188.00
Total	**77,908.25**	**115,050.00**
SROI	–	**1.5**

CONCLUSION

This study illustrates the capacity of applying Social Return on Investment (SROI) in the evaluation of the cost-effectiveness of Environmental Protection Plans (EPPs) in quarry mines. The findings indicate that strategic investments in EPPs yield returns that exceed the investment cost, highlighting their cost-effectiveness. Key contributors to the generated monetary values comprised reclamation and environmental funding and innovative pollution control technologies, which delivered substantial community and ecological benefits. The marginally higher SROI obtained by Mine A emphasizes the significance of strategic EPP implementation and pollution reduction capacity, particularly in quarries with significant environmental degradation in the concession area and host community. On the contrary, the lesser ratio observed in Mine B can be attributed to a lower OPEX and potentially less intensive EPP implementation and lesser pollution reduction capacity. These findings underscore the need for context-based environmental planning that considers local ecological and financial variables. Conclusively, SROI proves to be a robust tool for aligning environmental and social sustainability with economic performance, enabling policymakers and mining companies to make informed, evidence-based investment decisions that promote long-term environmental and social well-being while ensuring safe and sustainable operations. Future work will expand the application of the SROI framework to different scales of mining operations and incorporate Monte Carlo simulations for robust economic modeling and sensitivity analysis. This will enhance decision-making by accounting for variability and uncertainty in environmental and financial outcomes.

ACKNOWLEDGMENTS

N.T would like to acknowledge the support of CMU Presidential Scholarship in his master's research under the Engineering faculty of Chiang Mai University.

REFERENCES

[1] Israngkura A., The Mining Sector and Its Sustainability. TDRI Quarterly Review. Vol. 23, Issue 4, 2008, pp. 10-15.
[2] Rikhtegar N., Mansouri N., Oroumieh A., Yazdani-Chamzini A., Zavadskas E. and Kildienė S., Environmental impact assessment based on group decision-making methods in mining projects. Economic Research. Vol. 27, Issue 1, 2014, pp.378–392.
[3] Department of Primary Industries and Mines; Ministry of Industry., Mining in Thailand: An Investment Guide, 2009. Pp. 11-106.
[4] Jay S., Jones C., Slinn P. and Wood C., Environmental impact assessment: retrospect and prospect. Environ. Impact Assess. Rev. Vol. 27, Issue 4, 2007, pp. 287–300.
[5] Mebratu D., Sustainability and sustainable development: historical and conceptual review. Environ. Impact Assess. Rev. Vol. 18 Issue 6, 1998, pp. 493–520.
[6] Siddiqi A., Haraguchi M. and Narayanamurti V., Urban waste to energy recovery assessment simulations for developing countries. World Dev. 131, 2020, pp. 104-949.
[7] Sung-Tae L. and Sun-Moon J., Social return on investment as a tool for environmental impact and strategic assessments: Evidence from South Korea, Environmental Impact Assessment Review, 112, 2025,pp.107-765.
[8] Corvo L., Pastore L., Mastrodascio M. and Cepiku D., The social return on investment model: a

systematic literature review. Meditari Account. Res. Vol. 30, Issue 7, 2022, pp. 49–86.
[9] Lingane A. and Olsen S., Guidelines for social return on investment. Calif. Manag. Rev. Vol. 46, Issue 3, 2004, pp. 116–135.
[10] Defra NANR. Environmental Noise Valuation – The Costs and Benefits of Remediation Measures. 2011, pp. 11-201.
[11] Nicholls J., Lawlor E., Neizert E. and Goodspeed T., A Guide to Social Return on Investment. The SROI Network., 2012, pp. 3-105.
[12] De Leon V., The Social Return on Investment Methodology as A Tool for Valuation and Impact Assessment for Libraries: A Case Study. Journal of the Australian Library and Information Association, Vol. 70, Issue 2, (2021, pp.177–193.
[13] Broekx S., Inge L., Wim P ., Leo De N ., Dries, L., Jan S., Patrick M., Marije S., Wouter V., Olivier Van den K., Tanya C., A web application to support the quantification and valuation of ecosystem services. Environmental Impact Assessment Review Vol. 40, 2013, pp. 65–74.
[14] Wildavsky A., The Political Economy of Efficiency: Cost-Benefit Analysis, Systems Analysis, and Program Budgeting. Public Administration Review, Vol. 26 Issue 4, 1966, pp. 292–310.
[15] Hoogmartens R., Van Passel S., Van Acker K. and Dubois M., Bridging the gap between LCA, LCC and CBA as sustainability assessment tools. Environmental Impact Assessment Review. Vol. 48, 2014, pp. 27-33.
[16] Chinnakum W., Intapan C., Singvejsakul J., Wongsirikajorn M., Thongkaw B., Eakkapun P. and Chaiboonsri C., The Socio-Economic Impact of University in Thailand: Evidence from Chiang Mai University. Economies, Vol. 12, Issue 12, 2024, Pp. 339.
[17] Maier F., Schober C., Simsa R. and Millner R., SROI as a Method for Evaluation Research: Understanding Merits and Limitations. Voluntas. Vol. 26, 2015, pp. 1805–1830.

Copyright © Int. J. of GEOMATE All rights reserved, including making copies, unless permission is obtained from the copyright proprietors.

15th Int. Conf. on Geotechnique, Construction Materials & Environment,
Kyoto, Japan, 11-13 November 2025, ISBN 978-4-909106124 C3051

PERFORMANCE OF ENVIRONMENTALLY FRIENDLY SOLIDIFIERS UTILIZING WASTE GLASS AND BLAST FURNACE SLAG FOR LIQUEFIED STABILIZED SOIL

Koki Shinohara [1], Kohei Maru [1] and Shinya Inazumi [1]

[1] Shibaura Institute of Technology, Japan

ABSTRACT

This study contributes a novel understanding of the dual-phase hardening behavior in eco-binders through systematic microstructural evaluation, expanding on previously suggested models by incorporating quantitative analysis of the Ca/Si ratio and its morphological implications. In response to growing environmental concerns associated with conventional soil stabilization techniques, this study investigates the development and performance of eco-friendly solidification binders utilizing industrial by-products, specifically waste silica powder and blast furnace slag, activated with slaked lime. Two experimental series were designed to evaluate the influence of slaked lime content on the rheological properties, mechanical performance, and hydration mechanisms of the developed binders when mixed with Kasaoka clay, a highly plastic cohesive soil. The binders were formulated with varying lime contents (0–10%) and tested for flowability, bleeding, and unconfined compressive strength (UCS) over curing periods of 3, 7, and 28 days. Advanced analytical techniques including X-ray diffraction (XRD) and scanning electron microscopy with energy-dispersive X-ray spectroscopy (SEM–EDS) were employed to characterize hydration products and elucidate the microstructural evolution. Results indicated that a 5% slaked lime content optimally balanced early flocculation-driven strength gain and long-term pozzolanic reactivity, yielding superior UCS compared to both lower- and higher-lime mixtures, including the Portland cement control. Microstructural analysis confirmed the formation of dense, fibrous calcium silicate hydrates (C-S-H) at lower Ca/Si ratios, which correlates with the observed increase in 28-day compressive strength. Excess lime, by contrast, led to less favorable hydrate morphologies and reduced strength at 28 days. A two-stage hardening mechanism is proposed: (1) an initial physical flocculation phase enhancing early stability and cohesion; followed by (2) a chemically governed pozzolanic phase generating strength through the formation of C-S-H. The findings demonstrate the feasibility of replacing cement with low-carbon industrial by-products, offering a technically and environmentally viable alternative for sustainable ground improvement.

Keywords: eco-friendly binder, waste silica powder, blast furnace slag, ground improvement

INTRODUCTION

In the context of global efforts to reduce environmental burdens associated with civil engineering works, the development of sustainable ground improvement techniques has gained significant importance. Conventional binders such as Portland cement, although highly effective in stabilizing soft soils, emit substantial amounts of CO_2 during production, approximately 798.1 kg per ton [1]. Moreover, concerns persist regarding the environmental toxicity of cement-treated soils, particularly due to potential leaching of hexavalent chromium [2]. These environmental issues have prompted the search for alternative solidification materials that can provide equivalent or superior mechanical performance while minimizing ecological impact.

Industrial by-products such as waste silica powder, generated during glass cullet processing, and blast furnace slag, produced as a residue in the steelmaking process, are abundant, underutilized resources with latent pozzolanic activity. When combined with chemical activators such as slaked lime, these materials may form hydration products similar to those generated by cement, such as calcium silicate hydrates (C-S-H), but with significantly reduced carbon emissions. Despite this potential, the relatively slow setting and strength development of these alternative binders have limited their practical application in rapid-construction contexts.

The present study addresses this challenge by investigating the mechanical properties and hardening mechanisms of eco-friendly binders composed of waste silica powder, blast furnace slag, and slaked lime. Two complementary experimental series were conducted to evaluate the influence of slaked lime content on the binder's physical behavior, strength development, and hydration products. In addition to verifying engineering performance parameters such as flowability, bleeding, and unconfined compressive strength, this study emphasizes the microstructural and chemical changes that occur during curing. By elucidating the

interaction between material composition, particularly the Ca/Si (C/S) molar ratio, and hydration behavior, the research provides critical insights into the design and optimization of sustainable ground improvement materials.

MATERIALS AND METHODS

Materials and Mix Composition

The soil employed in all mixtures was Kasaoka clay, a representative cohesive soil known for its fine particle size distribution and high plasticity. The solidification binder was designed using industrial by-products to promote sustainability. It consisted of a silica-based activator formulated by blending waste silica powder, an alkali additive, and slaked lime ($Ca(OH)_2$). This silica activator was further combined with blast furnace slag to form the complete binder system. Under alkaline conditions, the silica and slag components are expected to undergo pozzolanic and latent hydraulic reactions, respectively, leading to the formation of cementitious hydrates such as calcium silicate hydrate (C-S-H). For comparison, ordinary Portland cement (OPC) was employed as a control binder.

Two series of experimental conditions were established. In both, the total binder dosage was fixed at 200 kg/m³. The main variable of interest was the slaked lime content in the silica activator. In Series A, slaked lime was added at 2.5%, 5%, and 7.5% by mass, corresponding to Cases 1 to 3, respectively. In Series B, the lime contents were set at 0%, 5%, and 10%. In both series, Case 4 served as the control and consisted solely of Portland cement, without any industrial by-products.

The detailed mix proportions used in the experimental program are summarized in Table 1. As the lime content increased, the amount of silica activator also increased proportionally, while the amounts of blast furnace slag, Kasaoka clay, and water were kept constant to ensure comparability. In the cement-only Case 4, a total of 200 kg/m³ of cement was used without silica activator or slag. The mix designs were selected to isolate the effects of lime content on physical behavior and hydration reactions.

Sample Preparation and Curing

All mixtures were prepared by thoroughly blending the binder components with Kasaoka clay and deionized water to obtain a uniform and homogenous slurry. Mixing was performed mechanically to ensure even distribution of binders and to activate the pozzolanic components. The resulting fresh mixtures were cast into cylindrical molds (dimensions per standard UCS testing procedures) and immediately sealed to prevent moisture loss.

Curing was conducted under controlled laboratory conditions, with all specimens placed in hermetically sealed containers maintained at a relative humidity of 98% or higher and at room temperature (~20°C). The curing durations were set at 3, 7, and 28 days to investigate both the early and long-term mechanical behavior of the binders.

Testing Methods

To evaluate the engineering performance of the mixtures, a series of physical and mechanical tests were conducted. Flowability was assessed by measuring the average of two orthogonal spread diameters on a horizontal plate immediately after mixing. The target flow value was set at 140 mm or greater, in accordance with the requirements for fluidized soil applications.

Bleeding behavior was evaluated based on the measurement of the volume of separated water 20 hours after casting. The bleeding ratio was calculated as the ratio of separated water volume to the total volume of the sample. A threshold of less than 1% was adopted to ensure sufficient water retention and mixture stability.

Mechanical properties were examined through unconfined compressive strength (UCS) testing at curing ages of 3, 7, and 28 days. The UCS tests were performed under displacement-controlled loading at a constant rate, and peak strength values were recorded for comparison across cases.

In addition to the macroscopic performance tests, chemical and microstructural evaluations were carried out to elucidate the underlying mechanisms of strength development. X-ray diffraction (XRD) analysis was conducted to identify crystalline hydration products, with particular attention to the formation of C-S-H and ettringite. Furthermore,

Table 1 Mix Proportions of solidification materials in each case

Case	Slaked Lime Addition (%)	Solidification Binder (kg/m^3)			Slurry Components (kg/m^3)	
		Silica Activator	Blast Furnace Slag	Cement	Clay	Water
1	2.5	23				
2	5	28	181	0	818	313
3	7.5	33				
4	0	0	0	200	828	305

Note: For Cases 1–3, the total binder content is fixed at 200 kg/m^3, composed of the silica activator and blast furnace slag. In Case 4 (control), only Portland cement is used at 200 kg/m^3 with no industrial by-products.

scanning electron microscopy coupled with energy-dispersive X-ray spectroscopy (SEM–EDS) was employed to observe the morphology and elemental composition of hydration products, especially focusing on the spatial distribution of calcium, silicon, oxygen, and aluminum. These advanced analyses provided critical insights into the structure–property relationships of the developed eco-friendly binders.

RESULTS

Flowability and Bleeding Behavior

The flowability and bleeding characteristics of each mixture are summarized in Table 2, which presents the measured spread diameters and corresponding bleeding ratios for Cases 1 through 4. All mixtures exceeded the target flow value of 140 mm, indicating sufficient workability for field application. However, a distinct trend was observed in bleeding behavior depending on the slaked lime content.

As shown in Table 2, Cases 2 and 3, which contained 5% and 7.5% slaked lime respectively, exhibited bleeding ratios well below the 1% threshold. This indicates a clear stabilizing effect induced by the lime addition. Conversely, excessive bleeding was observed in Case 1 (low-lime eco-binder) and Case 4 (cement-only control), where the absence or minimal use of lime likely failed to suppress free water migration.

These results suggest that the addition of slaked lime promotes early-stage flocculation among clay particles. This flocculation phenomenon, induced by the electrostatic neutralization of negatively charged clay surfaces by divalent Ca^{2+} ions, effectively traps pore water within the agglomerated structure. As a result, segregation is minimized, and water retention is enhanced. Such behavior plays a critical role in regulating the rheology of the fresh mixture, especially in slurry-based applications where water-to-solid ratios are moderate.

Compressive Strength Development

The unconfined compressive strength (UCS) results at curing ages of 3, 7, and 28 days are illustrated in Fig. 1. The eco-friendly binder mixtures exhibited notable strength development across all timeframes, consistently surpassing the minimum performance requirement of 200 kN/m².

Compressive strength results for each case. Case 3 (7.5% lime) exhibited the highest early strength, while Case 2 (5% lime) achieved the highest long-term strength.

At 3 days, compressive strength increased proportionally with the lime content. Case 3, containing 7.5% lime, achieved the highest early strength, suggesting that higher lime dosage accelerates initial flocculation (particle binding) and possible early-stage hydrate formation. This early strength development aligns with the reduction in bleeding previously discussed, both of which are driven by enhanced particle binding and lime-induced aggregation.

Table 2 Results of flow test and bleeding ratio

Case	Flow Value (mm)	Bleeding Ratio (%)
1	478	2.4
2	375	0.0
3	368	0.7
4	550	3.5

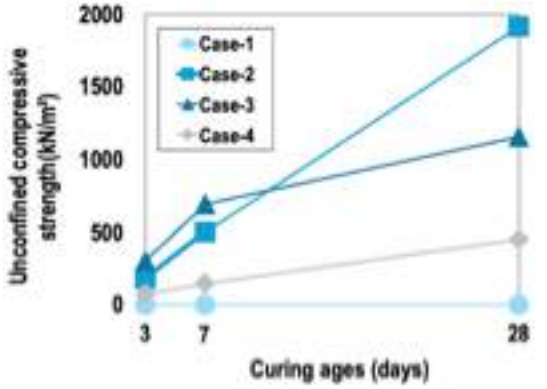

Fig. 1 Unconfined compressive strength at 3, 7, and 28 days

At 28 days, however, the trend deviated. Case 2, with 5% lime, exhibited the highest long-term strength, even surpassing the cement-based Case 4 and the higher-lime Case 3. This reversal implies that while higher lime content may promote early stiffness, it does not necessarily benefit long-term hydration. The likely explanation lies in the balance between calcium and silica availability: excess lime may lead to a higher Ca/Si (C/S) molar ratio, which can hinder the formation of structurally optimal calcium silicate hydrates or induce microstructural porosity due to incomplete reactions.

These results highlight the importance of optimizing the lime content to simultaneously achieve rapid initial strength and superior long-term mechanical performance. The data suggest that 5% slaked lime represents a favorable balance point in this regard.

Microstructural and Chemical Analysis

To elucidate the strength development mechanisms observed in the previous section, detailed microstructural and mineralogical analyses were conducted on specimens from Case 2 (5% lime eco-binder) and Case 4 (cement-only control). The XRD profiles shown in Fig. 2 reveal distinct differences in hydration product formation between the two binder systems.

XRD analysis confirms the presence of C-S-H in both binders. Ettringite is additionally detected in the cement-based mix (Case 4), indicating a difference in the hydration mechanisms.

In Case 2, peaks associated with C-S-H are clearly evident, supporting the hypothesis that pozzolanic reactions between blast furnace slag and the silica activator under alkaline conditions are responsible for strength development. In Case 4, in addition to C-S-H, peaks corresponding to ettringite were detected, reflecting the sulfate-aluminate reactions typical of Portland cement hydration.

Microstructural observations obtained via SEM are shown in Figs. 3 and 4. The eco-friendly binder in Case 2 exhibits fibrous and cotton-like hydration products, which are characteristic morphologies of C-S-H with a low C/S ratio. These structures appeared densely packed, with minimal porosity, contributing to the high compressive strength observed at 28 days.

Fibrous and cotton-like C-S-H morphologies observed. EDS confirms high concentrations of Ca and Si, consistent with pozzolanic hydrate formation.

In contrast, Fig. 4 depicts the microstructure of Case 4, where needle-like ettringite crystals and amorphous phases dominate. The spatial distribution of these products was less uniform, and visible micro-voids were more prevalent, indicating a comparatively less dense matrix.

Needle-like ettringite and less compact hydrate phases are observed. The structure suggests lower packing density than in the eco-binder.

Energy-dispersive X-ray spectroscopy (EDS) analyses confirmed that the primary elements in the hydration products were calcium (Ca), silicon (Si), and oxygen (O), with traces of aluminum (Al) in both binders. The higher Si content in Case 2 aligns with the usage of silica powder in the activator and supports the lower C/S ratio identified in the morphological interpretation.

The integration of mineralogical and microstructural results provides strong support for a chemically distinct hardening mechanism in the eco-binder system. Specifically, the low C/S ratio in the pozzolanic matrix of Case 2 favors the development of fibrous C-S-H, which is mechanically superior to the crystalline or amorphous hydrates found in traditional cement systems. These findings align with the observed compressive strength trends and confirm that optimized lime content and silica-rich conditions are key to achieving high-performance, environmentally sustainable ground improvement binders.

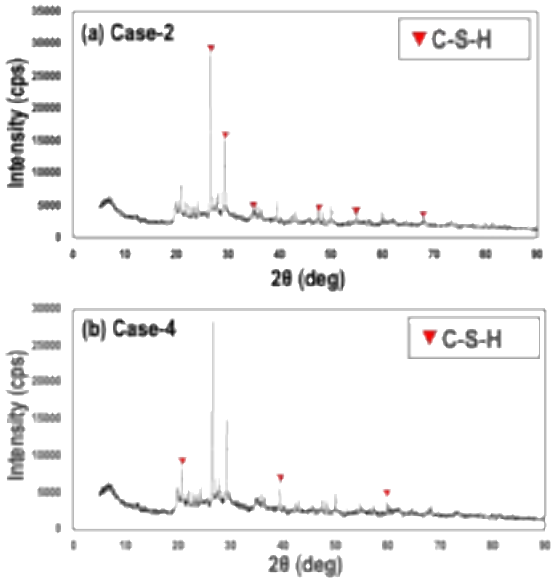

Fig. 2. X-ray diffraction (XRD) patterns of Case 2 and Case 4

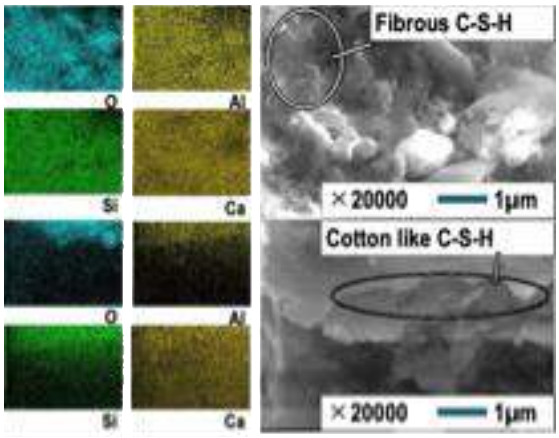

Fig. 3 SEM-EDS results for eco-friendly binder (Case 2)

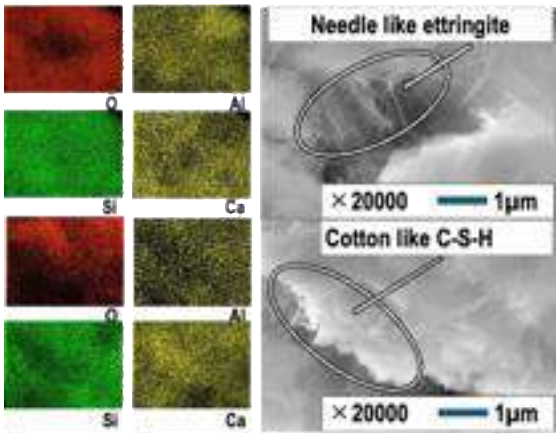

Fig. 4 SEM-EDS results for cement-based binder (Case 4)

DISCUSSION

Unlike earlier studies which conceptually proposed dual-phase hardening, this research substantiates the mechanism through detailed SEM-EDS analysis and identifies the critical role of silica availability in optimizing hydrate morphology.

The experimental results presented in the preceding sections clearly demonstrate that the

performance of the developed eco-friendly solidification material is closely governed by the amount of slaked lime incorporated into the mixture. From a physical standpoint, the addition of slaked lime was found to play a significant role in promoting the flocculation of clay particles. This flocculation process enhances the structural coherence of the slurry at an early stage and effectively reduces bleeding, as evidenced by the results in Table 2. The observed improvement in bleeding resistance in Cases 2 and 3 is attributed to this early particle aggregation, which immobilizes pore water and suppresses its upward migration.

At the chemical level, the amount of slaked lime directly influences the availability of calcium ions (Ca^{2+}), which are essential for initiating pozzolanic reactions. These reactions occur between Ca^{2+} and the amorphous silica and alumina provided by the waste silica powder and blast furnace slag. A key factor in this process is the resulting Ca/Si molar ratio (C/S ratio) within the hydration products. The morphology, crystallinity, and binding capacity of calcium silicate hydrate (C-S-H), the primary strength-giving hydrate, are all known to be sensitive to this ratio.

An important observation from both Series A and Series B was that the mixture containing 5% slaked lime (Case 2) consistently achieved the best balance between early strength development and long-term compressive strength. Although higher lime contents (e.g., 7.5% or 10%) promoted greater early strength, they did not result in superior 28-day strength. This can be explained by considering the C/S ratio: excess calcium relative to silica may lead to the formation of less polymerized or more crystalline C-S-H structures, which are generally associated with lower mechanical integrity and greater porosity.

On the basis of these results, a two-stage hardening mechanism is proposed, which integrates both physical and chemical processes. This mechanism is conceptually illustrated in Fig. 5, which outlines the sequential transformation of the mixture from a flocculated state to a hardened matrix.

Stage I: Flocculation induced by the electrostatic interaction between Ca^{2+} and clay particles enhances early cohesion and reduces bleeding. Stage II: Under alkaline conditions, pozzolanic reactions between calcium and silica/alumina components lead to the formation of C-S-H and other hydration products, contributing to long-term strength development [3,4].

In Stage I, the rapid flocculation process is initiated immediately upon mixing, as slaked lime dissociates to release Ca^{2+} into the pore water. These ions neutralize the surface charges of negatively charged clay minerals, promoting particle flocculation (particle binding) and improving the initial consistency of the mixture. This process accounts for the observed reduction in bleeding and the early strength gain in the high-lime cases.

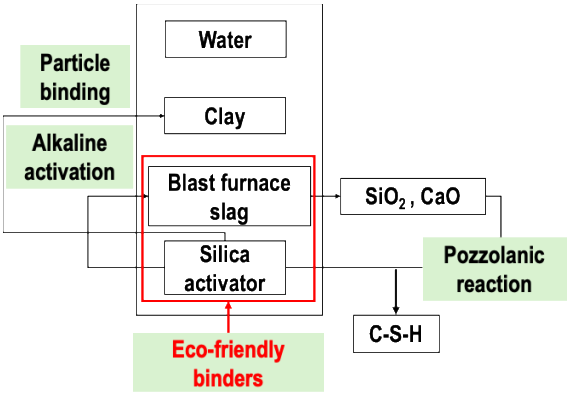

Fig. 5. Schematic illustration of the proposed two-stage hardening mechanism

In Stage II, the presence of reactive silica and alumina in the blast furnace slag and waste silica powder initiates slower pozzolanic reactions in the alkaline environment. These reactions result in the formation of C-S-H, which binds soil particles together and fills voids, thereby enhancing long-term strength. The characteristics of the resulting C-S-H gel, particularly its density, morphology, and degree of polymerization, are governed by the C/S ratio. A lower C/S ratio, promoted by a silica-rich matrix, tends to favor the formation of fibrous C-S-H with high binding efficiency, as observed in the SEM-EDS images of Case 2 (see Fig. 3).

This two-stage mechanism aligns well with the microstructural findings. In Case 2, the fibrous morphology and dense matrix contributed to superior compressive strength at 28 days, whereas in Case 4, the presence of ettringite and needle-like structures suggested a different, less effective hydration pathway. These morphological differences also underscore the role of mix design, especially the lime-to-silica ratio, in governing both early and long-term performance.

The findings of this study further highlight that the eco-friendly binders in some cases surpassed the mechanical performance of the cement-based control in every tested parameter, with the exception of bleeding in the lowest-lime condition (Case 1). This validates the technical feasibility of replacing cement with industrial by-products, resulting in reduced environmental impact without compromising, and indeed improving, structural performance. However, the sensitivity of hydration behavior to lime content also implies that mix design optimization is crucial. Precise control over the lime dosage is essential to ensure that the hydration reactions proceed in a manner that favors the development of high-quality, low-porosity C-S-H structures.

The results of this investigation underscore the critical role of slaked lime not merely as a chemical activator, but as a functional regulator of the physical and microstructural evolution of the binder system

[3]. The dual contributions of flocculation and pozzolanic activity must be strategically balanced to achieve the full performance potential of eco-friendly solidification materials in ground improvement applications.

CONCLUSIONS

This study has demonstrated the development and mechanistic understanding of eco-friendly solidification materials incorporating waste silica powder, blast furnace slag, and slaked lime. Through a systematic evaluation of physical properties, compressive strength, and microstructural features, the following conclusions can be drawn:

(1) The addition of slaked lime to mixtures of waste silica powder and blast furnace slag significantly improved early strength development and reduced bleeding by promoting flocculation of clay particles. A lime addition of 5% was found to be optimal for achieving a balance between early flocculation (particle binding) and efficient long-term pozzolanic activity.

(2) Microstructural analyses confirmed the formation of calcium silicate hydrate (C-S-H) in all eco-binder mixtures. Scanning electron microscopy revealed fibrous morphologies in mixtures with lower Ca/Si ratios, indicating the formation of dense and effective binding structures. These structural characteristics were directly associated with enhanced compressive strength at 28 days. Excessive lime addition was found to be counterproductive for long-term strength development, likely due to the formation of less favorable hydrates or the persistence of unreacted lime.

(3) A two-phase hardening mechanism was proposed. In the first phase, lime-induced flocculation and particle aggregation dominate the early setting behavior. In the second phase, a pozzolanic reaction between lime, slag, and silica powder under alkaline conditions leads to the formation of C-S-H, contributing to long-term strength gain. This model is consistent with both the observed strength trends and microstructural findings.

(4) The eco-friendly binders developed in this study outperformed conventional cement-based mixtures in terms of long-term compressive strength, while also meeting practical performance criteria for flowability and bleeding control. This indicates their technical feasibility and potential applicability in sustainable ground improvement projects.

Future work should focus on the quantitative evaluation of Ca/Si ratios in the reaction products and further investigation into the field applicability and long-term durability of these eco-binders under various environmental and loading conditions.

REFERENCES

[1] Chen, C., Habert, G., Bouzidi, Y., Jullien, A. (2010). Environmental impact of cement production: detail of the different processes and cement plant variability evaluation. Journal of Cleaner Production, 18(5), 478–485.

[2] Glasser, F.P., Marchand, J., & Samson, E. (2008). Durability of concrete — Degradation phenomena involving detrimental chemical reactions. Cement and Concrete Research, 38(2), 226–246.

[3] Puertas, F., Martínez-Ramírez, S., Alonso, S., & Vázquez, T. (2000). Alkali-activated fly ash/slag cements: Strength behaviour and hydration products. Cement and Concrete Research, 30(10), 1625–1632.

[4] Ben Haha, M., Lothenbach, B., Le Saout, G., & Winnefeld, F. (2011). Influence of slag chemistry on the hydration of alkali-activated blast-furnace slag—Part I: Effect of MgO. Cement and Concrete Research, 41(9), 955–963.

Copyright © Int. J. of GEOMATE All rights reserved, including making copies, unless permission is obtained from the copyright proprietors.

15th Int. Conf. on Geotechnique, Construction Materials & Environment,
Kyoto, Japan, 11-13 November 2025, ISBN 978-4-909106124 C3051

TROPICAL SOIL BEYOND THE TROPICS: THE INFLUENCE OF PALEOENVIRONMENTS ON ENGINEERING PROPERTIES

John Victor Smith[1,2]

[1]School of Engineering, RMIT University, Australia
[2]CMW Geosciences, Australia

ABSTRACT

Tropical soils are known to be a distinct class of soils with predicable engineering properties. The definition of the range of such soils is typically linked to the distribution of current global environmental conditions. However, at previous times, most notably the Eocene Epoch, conditions that we consider tropical today covered much of the Earth's surface. Consequently, there are soils with a tropical weathering imprint present at latitudes beyond the tropics as defined today. Such soils can be called paleosols, however that term is commonly applied to soils buried within a sequence of sediment or rock that may not be considered as soil in the engineering sense. The ancient overprint of high temperature and wet conditions on soils in temperate regions can be removed by burial by later sediments or can be removed by erosion. Therefore, the relict tropical soils occur in localized places. Since large parts of Australia have been relatively stable tectonically the amount of sediment deposition and erosion has been less than some other parts of the globe. The current arid and temperate conditions can preserve soils developed in tropical conditions. Selected examples of such soils are presented to illustrate that the tropical soil paradigm can be extended to engineering properties of some soils beyond the tropics.

Keywords: Tropical residual soil, Paleosol, Paleoeclimate, Basalt soils, Slope stability

INTRODUCTION

Engineering properties of soils relate to the environment in which they formed, for example, arid, temperate or tropical [1]. Tropical soils are known to be a distinct class of soils with particular engineering properties. The definition of the range of such soils is typically linked to the distribution of current global environmental conditions. However, at previous times, most notably the Eocene and Miocene Epochs, conditions that we consider tropical today covered much of the Earth's surface [2].

It is observed that there are soils with a tropical weathering imprint present at latitudes beyond the tropics as defined today. Such soils can be called paleosols, however that term is commonly applied to soils buried within a sequence of sediment or rock that may not be considered as soil in the engineering sense. The ancient overprint of high temperature and wet conditions on soils in temperate regions can be obscured by burial with later sediments or can be removed by erosion. Therefore, the relict tropical soils occur in localized places.

Since large parts of Australia have been relatively stable tectonically the amount of sediment deposition and erosion has been less than some other parts of the globe. The current arid and temperate conditions can preserve soils developed in tropical conditions. Selected examples of such soils are presented to illustrate that the soil types, depths and engineering characteristics are those of the tropical soil type as a result of the past environmental conditions influencing the soil's development.

This paper shows how the tropical soil paradigm can be extended to engineering properties of some soils beyond the tropics in temperate southeastern Australia.

RESEARCH SIGNIFICANCE

The assumption that tropical soils are restricted to present day tropical locations can result in mis-interpretation of soil types and the missed opportunity to apply the well developed paradigm of tropical residual soils to other locations where previous climatic conditions have produced equivalent soil types.

TROPICAL RESIDUAL SOIL

The significance of tropical residual soils has been recognized by the International Society for Soil Mechanics and Geotechnical Engineering which has established a global technical committee on the topic: Tropical Residual Soils (TC107).

According to the Handbook of Tropical Residual Soils Engineering [3], the majority of researchers in that field defined residual soils as a highly weathered in situ material with >50% soil. It also notes that large expanses of residual soils occurring to great depths are normally found in tropical humid regions, e.g. Northern Brazil, Ghana, Malaysia, Nigeria, Southern India, Sri Lanka, Indonesia and Philippines, due to active weathering leading to residual soil

formation. The depth of tropical soil can vary but 30 m of residual soil development in tropical conditions is not uncommon [3,4].

According to [3] soil development in the tropics may have begun over 2–3 million years ago and the prolonged process of soil development over geological time. These climatic changes mean that areas under more temperate climates at present can have experienced the development of tropical soil profiles [3].

There are many soil science terms and concepts but not all of these relate to engineering properties of soils. Three terms related to the fate of iron in residual soils have been beneficial in clarifying types of residual soils [3]. The term fersiallitisation describes weathering that occurs in a subtropical climate with a marked dry season. The dominant clay minerals formed are the 2:1 clays, such as the smectite group including montmorillonite. In this process most of the silica and cations released by the weathering are retained within the soil profile. These soils also develop kaolinite clay as a minor component. The Fe^{2+} liberated by mineral weathering in these soils is rapidly oxidised and precipitated as ferric (Fe^{3+}) oxide and hydroxide such as hematite and goethite. These soils can develop distinctive red (or hues of orange and yellow) colors as the iron oxides coat clay particles. This process is equivalent to weak to moderate leaching (Fig.1).

Ferrugination occurs in a tropical climate that is more humid than fersiallitic conditions and with a less pronounced dry season. The dominant clay minerals are the 1:1 clays such kaolinite and its related kandites. Smectite may also be present. Fe oxides are also formed but may or may not form red colored coatings on the clay particles and mottled coloring is common. This process is equivalent to intense leaching (Fig.1).

Ferrallitisation is the most intense stage of leaching (Fig.1) where almost all primary minerals are weathered leaving quartz (if present in the parent rock), newly formed kaolinite and Fe and Al oxides for example, goethite, hematite and gibbsite.

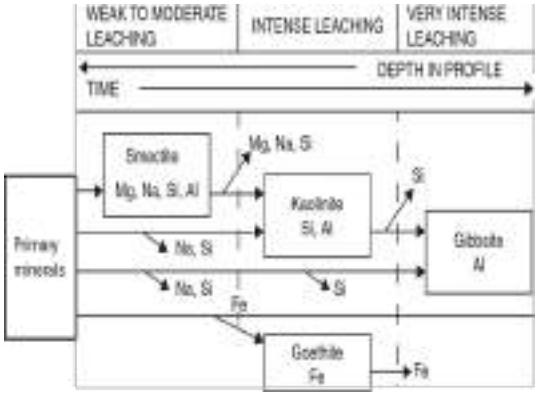

Fig.1 Summary of chemical and mineralogical changes in tropical weathering [3]

MIOCENE BASALT IN VICTORIA

Context

The case study presented is located in southeastern Australia in the La Trobe Valley of Victoria. This region has produced significant brown coal resources in the past. The brown coal was used for electric power throughout the state and significant electricity infrastructure such as high voltage powerlines are present. As coal mining is phased out the surrounding region is of interest for renewable energy installation to benefit from the existing infrastructure.

Geology

Basalt lava flows of the Thorpedale Volcanics form a plateau to the southwest of the brown cola deposits. The brown coal deposits formed in the Oligocene to late Miocene periods. Fluvial sediment of the Childers Formation underlies the basalt and is exposed on the west of the Thorpedale Volcanics and has a maximum thickness of 35 m. To the east of the Thorpedale Volcanics is the Miocene to Pliocene age Haunted Hills Gravel which contains ferruginous sand which overlies the basalt (Fig. 2).

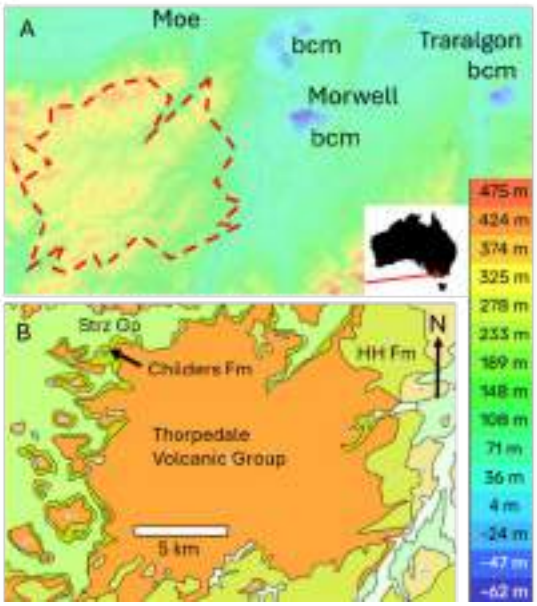

Fig.2 A) Regional context of brown coal mines (bcm) and basalt plateau and ridges of the Thorpedale Volcanic Group (red dashes) and elevation key. B) The main part of the Thorpedale Volcanic Group (orange), underlying Childers Formation and Cretaceous sedimentary rocks to the west (Strz Gp = Strzelecki Group) and overlying Plio-Pleistocene sedimentary deposits to the east (HH = Haunted Hills Formation). From the GeoVic on-line geology of Victoria

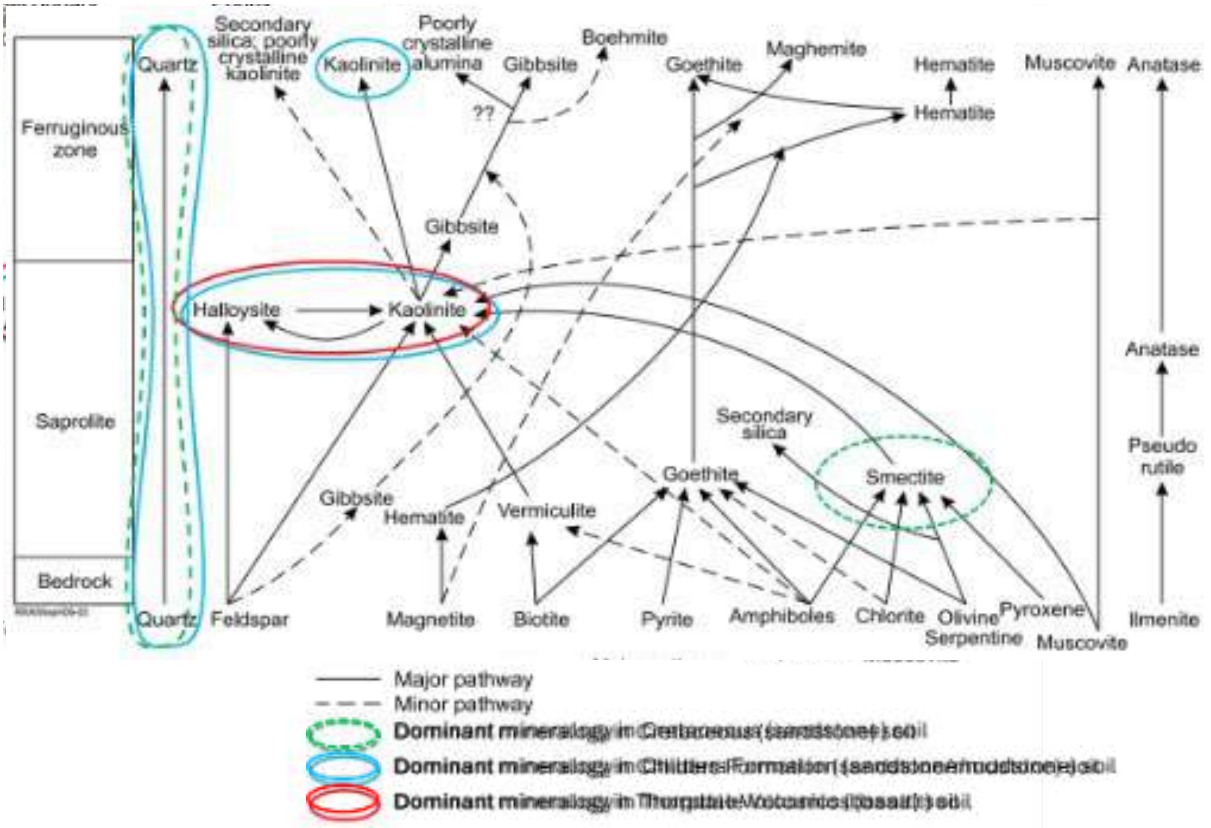

Fig.3 Typical pathways of formation of secondary minerals in weathering profiles [5]

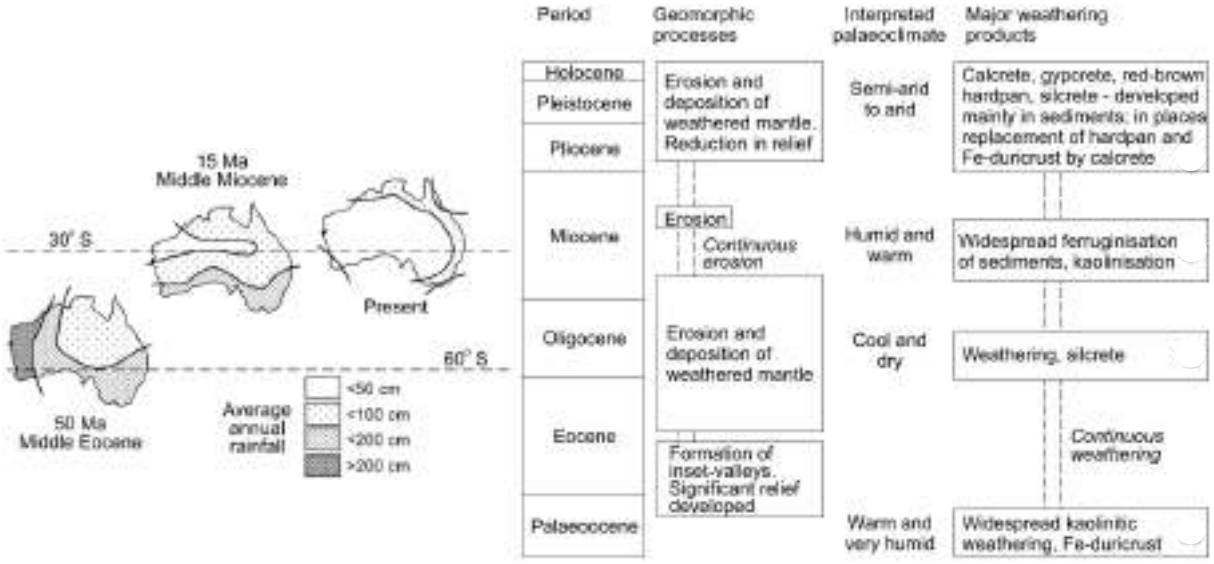

Fig.4 Australia's changing latitude through time (left) and a summary of climate and weathering (right) [5]

Soil Mineralogy

One of the most diagnostic indicators of soil formation conditions within a soil profile is the minerals present in the soil (Fig.3). Mineralogy is typically assessed by X-ray diffraction [6]. A study on slope stability found that the Thorpedale Volcanics and underlying Childers Formation were dominated by kaolinite and halloysite (Table 1). Halloysite is a clay similar to kaolinite in composition but with a distinctive rolled-up form rather than the platy form of most other clay particles [3]. The Childers

Formation soils were found to have quartz as a relict of their original primary mineralogy whereas the basalts were quartz free. The Cretaceous age Strzelecki Group soils were found to be dominated by smectite clays and quartz (Table 1).

Table 1 Summary of soil mineralogy in the study area [7]

Strata	Type	Color	Mineralogy
Thorpedale Vocanics	Clay	Red-brown, yellow, gray	Kaolinite, Halloysite
Childers Fm	Sandy silty clay	Brown, gray, red-brown, yellow	Kaolinite, Halloysite, Quartz
Strzelecki Group	Sandy silty clay	Brown, gray, yellow-brown	Montmorillonite, Quartz

Note: hematite, goethite detected as minor components are potentially under-detected due to fine grainsize.

According to a study of engineering behaviour of soils in the area [7] the soils are classified the soils derived from the Older Volcanics in the Krasnozem pedological group or Ferrosols and described as acid friable porous soils in which the texture generally increases with depth. These soils are usually deep soils with a dark red A1 horizon of friable clay with a strong crumb structure. The A1 horizon grades through a redder and more clayey A-B into a red or dark red medium or heavy clay B horizon. These are moderately plastic clays and often rather compact in place, but highly structured, very permeable and friable when moist. Very fine, red and sometimes black, ferro-manganiferous nodules are common. The B horizon continues with little change for many feet, finally grading through a B-C horizon of yellow-red; or red-brown more plastic clay into a C horizon of weathering rock. In wetter environments the B-C is somewhat mottled red, light gray and yellow-gray clay grading into a thick C horizon of weathering rock which may be partially saturated with water.

Palaeoclimate

At the present, only the most northerly parts of Australia are considered to have tropical climates (Fig.4). The west Gippsland region has a Mediterranean climate Grazing, mostly dairy and beef cattle, and cropping [8]. Over earlier times Australia moved from higher southern latitudes toward its present position. The global temperature conditions in the Eocene and, to a lesser extent, the Miocene were what would be considered tropical today (Fig.4).

The record of paleoclimate through Cenozoic time has been developed principally from oxygen isotope studies (Fig.5A) [2]. The Thorpedale Volcanics formed as one of the last phases of volcanism known as the Older Volcanics in Victoria (Fig.5B) [9,10].

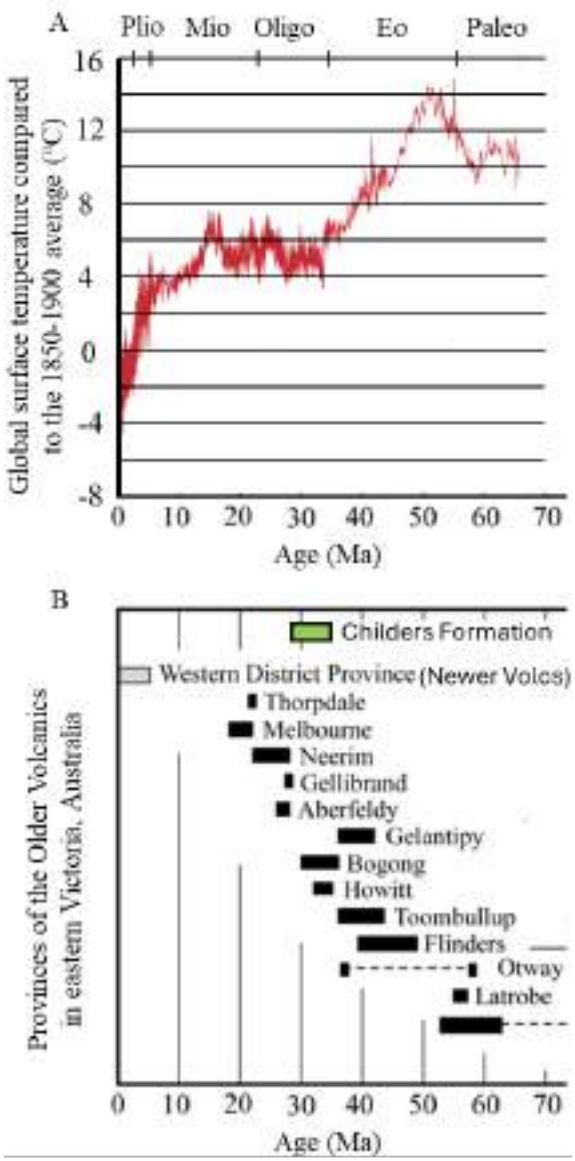

Fig.5 A) Summary of global temperature during the Cenozoic [2] and B) The age of Cenozoic basalts in Victoria [9] (Childers Formation added)

Consequently, the Thorpedale Volcanics were exposed to weathering conditions which can be considered at least equivalent to present day tropical conditions even though the latitude of formation and presently would not qualify as tropical. The sediments of the Childers Formation underlying the Thorpedale Volcanics were also potentially weathered in the high temperature conditions of the Miocene after their deposition in the Oligocene (Fig.5B).

The Thorpedale Volcanics indeed have a deeply developed red soil which is greater than 20 m thick in many places (Fig.6).

Fig.6 Roadside exposure of the Thorpedale Volcanic soil [8]

Landscape Evolution

In order to form and then preserve the soils formed in the Miocene the evolution of the landscape must prevent excessive erosion at the location. The Thorpedale Volcanics are understood to have formed as valley-fill basalt flows [9]. With later erosion the basalts can become plateau and ridges a process called topographic inversion (Fig.7)[5].

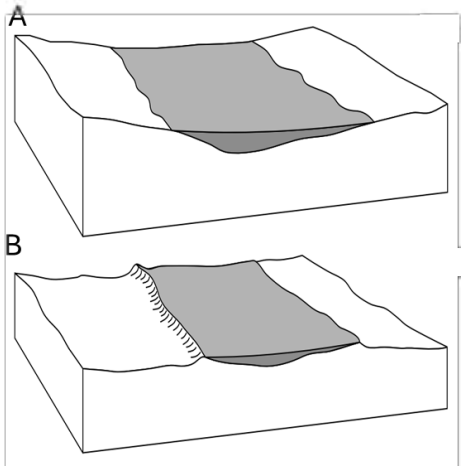

Fig.7 Conceptual representation of the inversion of topography of valley-filling basalt lava (gray) [5]

Soil would be expected to begin forming once the basalts are emplaced but soil development would continue throughout the evolution of the landscape. The proposition is that in the area of the Thorpedale Volcanics residual soil developed during the tropical conditions of the Miocene and was not significantly eroded subsequently. One contributor to the preservation of the tropical residual soil could be the presence of the Haunted Hills Formation. These sediments were deposited during the Pliocene-Pleistocene i.e. after the Miocene. The Haunted Hill Formation presently covers the eastern part of the Thorpedale Volcanics and may have covered more of the volcanics in the past. The later sedimentary cover may have preserved the thick residual soil that had developed in the Thorpedale Vocanics and Childers Formation.

Engineering Properties

Slope stability of tropical residual soils is a distinctive engineering issue due to the typical deep weathering of these soils and the presence of various mineral cementing agents [11].

Slope stability has been a significant issue in the area of this study site [7]. The soils are associated with well-drained sites on hilly uplands and plateaux. The soils were formed by strong weathering and leaching of the basalt. The basaltic clays in the study area typically have high plasticity and are locally friable and permeable.

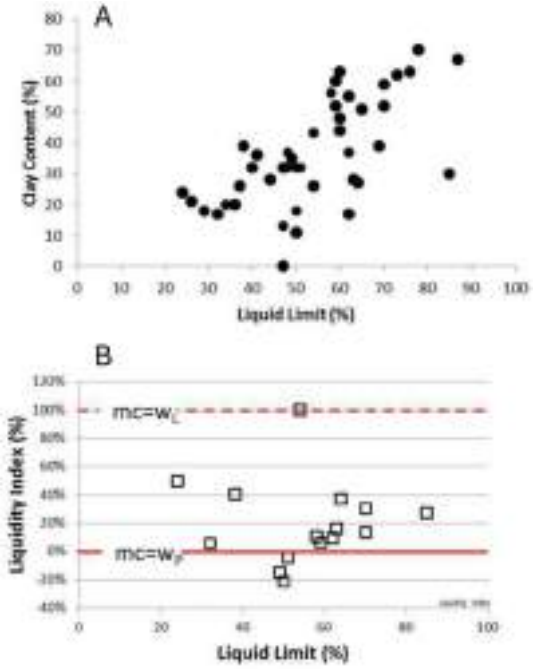

Fig.8 Summary of selected soil properties in the Thorpedale Volcanics area [7]

In engineering terms, the soils are clays with silty, sandy and/or gravelly components consisting of partly weathered rock and mineral particles and occasional iron oxide nodules and ferruginized concretions. The clays are mainly classified as high plasticity (CH) type soils, but the weathered rock content of some samples gives the soil a silty or sandy texture and an MH or SC classification. In these cases the clays have lower plasticity and are usually friable. Low plasticity CL type soils also occur. The overall high plasticity is illustrated by a medium plasticity index of 32% with a range of 20% to 46%. The liquid limit has a medium valley of 69% and a range of 54% to 87%. The in-situ winter moisture content was estimated in the field to be generally greater than the plastic limit and this was confirmed by laboratory tests. In some cases the in-situ moisture content approaches the liquid limits (Fig.8).

Fig.9 The toe of a complex earth flow in the Thorpedale Volcanics [7]

The central Thorpdale area has topography that is gently undulating whereas at the margins of the Thorpedale Vocanics the topography is mainly steeply undulating. Significant landslides have occurred within the areas of steeply undulating terrain (Fig.9) [7].

Halloysite can make these leached soils sensitive to drying methods. (Fig.9) [7]. Air-drying rather than oven-drying is recommended to avoid destruction of the clay fabric.

CONCLUSIONS

The evolution of landscape in former climatic conditions can play an important role in determining the engineering properties of soils. The study site in southeastern Australia currently has a temperate climate but the soils developed are more typical of tropical conditions and can be attributed to the warmer and wetter conditions in the Miocene Epoch.

ACKNOWLEDGMENTS

Field data is cited from works of John C. Brumley an eminent Australian geologist and engineer and formerly Associate Professor at RMIT University.

REFERENCES

[1] Look B. G., Earthworks: Theory to Practice-Design and Construction, CRC Press, 2022, pp. 1-611.

[2] Zachos J. C., Dickens G. R., and Zeebe R. E., An Early Cenozoic Perspective on Greenhouse Warming and Carbon-Cycle Dynamics, Nature, Vol. 451, Issue 7176, 2008, pp.279-283.

[3] Hua B. B., Gue S. S., and Ali F. H., Handbook of Tropical Residual Soils Engineering, CRC Press, 2004, pp. 1-532.

[4] Mahalinga-Iyer U., and Williams D. J., Engineering Properties of a Lateritic Soil Profile, Engineering Geology, Vol. 31, Issue 1, 1991, pp.45-58.

[5] Anand R. R., (2005). Weathering History, Landscape Evolution and Implications for Exploration, In Regolith Landscape Evolution Across Australia: A Compilation of Regolith Landscape Case Studies with Regolith Landscape Evolution Models, Butt C.R.M., Cornelius M., Scott K.M., and Robertson I.D.M., CRC LEME, 2005, pp15-45.

[6] Houston E. C., and Smith J. V., Assessment of Rock Quality Variability Due to Smectitic Alteration in Basalt Using X-Ray Diffraction Analysis, Engineering Geology, Vol. 46, Issue 1, 1997, pp.19-32.

[7] Brumley J.C., Slope Stability in the Strzelecki Ranges, Victoria, In, Case Studies in Engineering Geology, Hydrogeology and Environmental Geology, Australia. Geological Society of Australia, Knight M.J., Minty E.J., Smith R.B., 1983, pp 127–147.

[8] Sargeant I. J. and Imhof M. P. Major Agricultural Soils of the West Gippsland Region. Department of Primary Industries, Victoria, Australia. Agriculture Victoria, Undated, https://vro.agriculture.vic.gov.au/DPI/Vro/vrosite.nsf/pages/dairy_vic_soils-ferrosols.

[9] Price R. C., Nicholls I. A., and Day A., Lithospheric Influences on Magma Compositions of Late Mesozoic and Cenozoic Intraplate Basalts (the Older Volcanics) of Victoria, South-Eastern Australia. Lithos, Vol. 206, 2014, pp.179-200.

[10] Seddon K. D., and Pump W. (2018). Older Volcanics, In, Engineering Geology of Melbourne, Routledge, Peck W.A., Neilson, J. L., Olds R.J., Seddon K.D., 1992, pp.157-174.

[11] Ullah R., Abdullah R., Kassim A., Yunus N. Z. M., and Sendo H., Assessment of Residual Soil Properties for Slope Stability Analysis, International Journal of GEOMATE, Vol. 21, Issue 86, 2021, pp.72-80.

Copyright © Int. J. of GEOMATE All rights reserved, including making copies, unless permission is obtained from the copyright proprietors.

15th Int. Conf. on Geotechnique, Construction Materials & Environment,
Kyoto, Japan, 11-13 November 2025, ISBN 978-4-909106124 C3051

WATER QUALITY CHARACTERISTICS OF THE TRADITIONAL WATER MANAGEMENT FACILITY "MANBO" IN HOKUSEI CHUO PARK, MIE PREFECTURE

Maki Oyagi, Rion Ito, Toyokazu Hirozumi

Environmental and Information Sciences, Yokkaichi University, Japan

ABSTRACT

Manbo is an underground agricultural irrigation system consisting of vertical and horizontal shafts, constructed as a hand-dug tunnel. In Hokusei Chuo Park, a Manbo has long been used for agricultural irrigation. However, no prior studies have examined its water quality. Therefore, this study aims to investigate the water quality characteristics of the Manbo and to assess the changes in water quality as water flows from an upstream pond into the Manbo. The results indicated that the electrical conductivity of the pond water was below 100 µS/cm. In contrast, the Manbo exhibited a significantly higher value of 250 µS/cm, exceeding typical river water levels. It suggests that dissolved impurities increase as water flows from the pond into the manbo. To investigate the factors contributing to this increase, an analysis of total nitrogen was conducted. The findings revealed that nitrogen levels were higher in the Manbo than in the pond. Specifically, while the total nitrogen concentration in the pond remained below 2 mg/L throughout the year, the Manbo exhibited concentrations of approximately 3 mg/L. On average, dissolved and suspended nitrogen accounted for about 50% of the total nitrogen in the pond, whereas dissolved nitrogen constituted nearly all the nitrogen in the Manbo. Based on these findings, it was inferred that one of the primary factors contributing to the elevated electrical conductivity in the Manbo is the increase in dissolved nitrogen. This study has enhanced the scientific understanding of traditional water facilities and provided valuable insights for modern water resource management.

Keywords: Manbo, Water management facility, Water quality, Nitrogen

INTRODUCTION

A manbo is a culverted, hand-dug groundwater irrigation system used in agriculture, consisting of both vertical and horizontal shafts. These structures are typically excavated by a single person and measure approximately 0.5 to 1 meter in width and 1 to 2 meters in height. Some extend more than 1 kilometer in length. The primary water source is usually groundwater, and its origin is believed to date back to the late Edo period (1603–1867). As for the name, he concludes that “manbo” is a derivative of the mining term *mabu*, which refers to a horizontal tunnel excavated for ore extraction [1].

In Japan, manbos are commonly found on alluvial fan plains and plateaus composed of sandy and gravelly sediments, particularly in the Chubu and Kansai regions, where surface water is scarce and difficult to use for irrigation [2]. They are especially concentrated in the eastern foothills of the Suzuka Mountains in Mie Prefecture. Several reports have documented individual manbos in the Utsube River fan region [3], while others have examined them from agricultural, geographical, and historical perspectives [4]. Recent research on manbo in Mie Prefecture includes studies on its relationship with humans [5], its role in regional landscapes [6], and reports recognizing it as an agricultural engineering heritage [7]; however, the number of such studies remains limited.

Existing studies on manbos can be broadly categorized into four areas: (1) agronomic irrigation methods, (2) water use in rural communities, (3) civilization theories—including the origin and etymology of the term *manbo*—and (4) general studies on water use and water resources[8].

Despite being water infrastructure for agricultural irrigation, there have been very few studies focusing on the water quality of manbos. This lack of attention is noteworthy and underscores the significance of this study, which aims to address that gap.

RESEARCH SIGNIFICANCE

Mie Prefectural Hokusei Chuo Park is situated in the Inabe River watershed, northwest of Yokkaichi City. The park features two agricultural reservoirs, Kami-ike and Shimo-ike, built during the Edo period, as well as manbos that draw water from these reservoirs. These traditional irrigation systems have been used for farming purposes for many years and continue to supply around 8 hectares of farmland. However, few systematic studies have been conducted on their water quality characteristics or how they change over time.

This study focuses on the manbos and their upstream agricultural reservoirs (Upper Pond and Lower Pond) in Hokusei Central Park, aiming to clarify the current state of water quality and investigate the factors contributing to its variation as

water flows from the ponds to the manbos. Special attention is given to changes in electrical conductivity and nitrogen concentration to scientifically evaluate the influence of the subsurface environment on water quality.

METHODS

Study Area and Observation Dates

Hokusei Chuo Park, located on a plateau between the Inabe River and the Asaake River in the northwestern part of Yokkaichi City, Mie Prefecture, was selected as the study site (Fig.1). Surveys were conducted at two agricultural reservoirs (Kami-ike and Shimo-ike; Fig. 2) and three vertical shafts in manbos (Fig. 3) within the park. The culverted section of the manbo has a total length of 286 meters, with water flowing at a depth of approximately 2.5 meters below the ground surface. Water sampling was conducted at a vertical shaft located midway along the culvert. Field investigations were carried out five times: on July 2, 2023; October 17, 2023; February 15, 2024; June 25, 2024; and September 10, 2024.

Analytes of Water Quality

Dissolved oxygen (DO) and water temperature were measured immediately after water sampling using a multi-parameter water quality meter (WQ-310J, HORIBA). In contrast, pH and electrical conductivity (EC) were measured using a portable field-type meter (D-200-2, HORIBA). fter sampling, the water was stored in plastic bottles, transported to the laboratory under chilled conditions, and immediately subjected to suction filtration to determine suspended solids (SS). GF/F glass fiber filters (pore size 0.7 μm, Whatman) were used, and the filtrate was treated as representing the dissolved fraction.

Total phosphorus (TP) and total dissolved phosphorus (TDP) were analyzed in the laboratory using the molybdenum blue method [9]. Particulate organic phosphorus (POP) was calculated as POP = TP − TDP. Total nitrogen (TN) and total dissolved nitrogen (TDN) were measured by UV absorption spectrophotometry [9]. Particulate organic nitrogen (PON) was calculated as PON = TN − TDN.

(a)

(b)

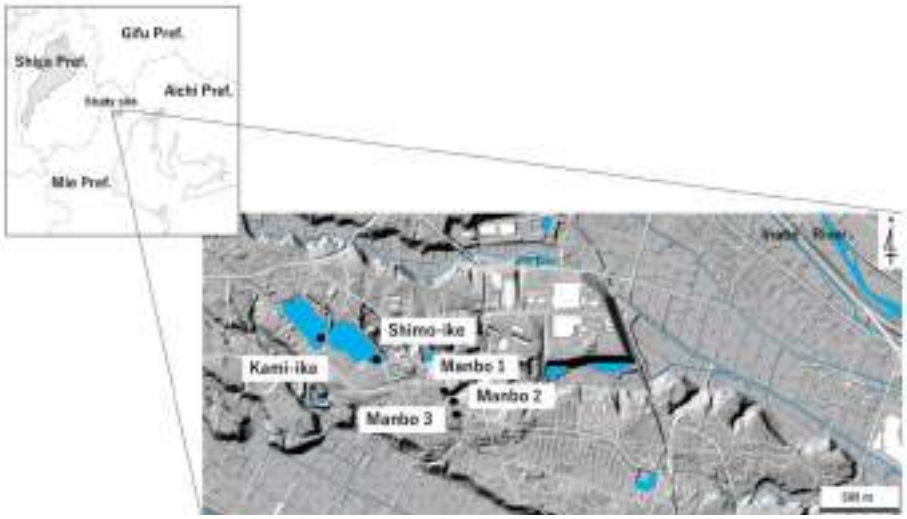

Fig.1 Location map of reservoirs in Hokusei Chuo Park,Mie pref. The observation points were marked on the Geospatial Information Authority of Japan (GSI) map.

Fig.2 Photographs of agricultual reservoirs in Hokusei Chuo Park. (a) Kami-ike, (b) Shimo-ike

(a)

(b)

(c)

Fig.3 Photographs of the vertical shafts in Manbos. (a) Manbo 1, (b) Manbo 2, (c) Manbo 3

RESULT AND DISCUSSION

Field Measurements of Water Quality

Fig. 4 shows that water temperatures averaged 10.3°C in the Upper and Lower Ponds and 11.0°C in the manbo during winter (February). In summer (June), the temperatures were 25.65°C in the ponds and 22.0°C in the manbo, showing that both were strongly affected by ambient air temperature (fig.5). However, because of the subsurface culvert structure of the manbo, water temperatures tended to be lower in summer and higher in winter compared to the ponds. This pattern is similar to the thermal behavior typically seen in groundwater.

Dissolved oxygen (DO) concentrations averaged 11.3 mg/L in the ponds and 8.6 mg/L in the manbo during winter (Fig.4), and 9.9 mg/L in the ponds and 6.0 mg/L in the manbo during summer (Fig.5). Oxygen saturation levels averaged 104% in the ponds and 81% in the manbo in winter, and 123% in the ponds and 70% in the manbo in summer. These results show that the ponds were generally supersaturated and well-oxygenated throughout the year, while the manbo experienced higher oxygen consumption.

The pH averaged 7.5 in the ponds and 7.0 in the manbo during winter, and 9.4 in the ponds and 6.4 in the manbo during summer (Fig.6). The higher pH levels in the ponds during summer are probably due to carbon dioxide uptake through photosynthesis, as indicated by the high DO concentrations.

Electrical conductivity (EC) averaged 51.9 μS/cm in the ponds and 159.1 μS/cm in the manbo during winter, and 89.2 μS/cm in the ponds and 162.3 μS/cm in the manbo during summer (Fig.7). The manbo consistently exhibited high electrical conductivity (EC) throughout the year, distinctly differing from the values observed in the pond. EC is a key indicator of water quality, influenced by both natural and anthropogenic factors, and is considered to reflect the overall water environment of the region [10]. Therefore, the elevated EC in the manbo suggests that additional ionic constituents were incorporated into the water during its subsurface flow from the pond.

Despite the inflow of water from the ponds into the manbo, notable differences in water quality parameters were observed, indicating distinct environmental characteristics between the two water bodies.

Laboratory Analysis of Chemical Water Quality

Fig.8 shows that suspended solids (SS) averaged 10.2 mg/L in the upper pond, 20.4 mg/L in the lower pond, and 2.6 mg/L in the manbo throughout the year. Seasonal variation was minimal compared to other parameters.

Total phosphorus (TP) concentrations averaged 0.36 mg/L in the upper and lower ponds and 0.16 mg/L in the manbo during winter (February), and 0.13 mg/L in the ponds and 0.07 mg/L in the manbo

during summer (June). The composition of TP indicated that particulate organic phosphorus (POP) accounted for 50–85% of the total in both the ponds and the manbo (Fig.9 and 10).

Total nitrogen (TN) averaged 2.4 mg/L in the ponds and 3.2 mg/L in the manbo during winter, and 1.1 mg/L in the ponds and 1.8 mg/L in the manbo during summer. In terms of composition, particulate organic nitrogen (PON) accounted for 30–70% of TN in the ponds, while it was less than 10% in the manbo. (Fig.11 and 12)

Fig. 13 shows that, regarding these results, the N/P ratio in the pond sometimes exceeded 10 but generally remained within the range of 7 to 10, which is considered favorable for algal growth [11]. Blue-green algae blooms were visually observed from spring to summer. The high SS concentration in the pond is presumed to be due to algal proliferation, as both nitrogen and phosphorus were predominantly present in suspended form.

According to the environmental standards for preserving the living environment (lakes and ponds) established by the Ministry of the Environment, the pond falls into Type V, the lowest water quality category (Types I–V), based on its nitrogen and phosphorus concentrations. Compared to nearby ponds [12][13], this pond exhibited higher concentrations of both nitrogen and phosphorus.

In the manbo, nitrogen concentrations tended to be significantly higher than phosphorus, which is attributable to elevated total dissolved nitrogen (TDN) levels. The high electrical conductivity (EC) observed in the manbo also appears to be closely related to the presence of TDN. Additionally, dissolved oxygen (DO) levels in the manbo remained relatively stable throughout the year, suggesting ongoing microbial decomposition processes.

Although water from the pond flows into the manbo, the results of water quality measurements revealed distinct characteristics between the two. The park studied is situated on a plateau composed of sedimentary rock, and geological factors were taken into consideration. However, since the manbo in question is located in a shallow layer (approximately 2.5 meters deep) and exhibited consistent trends throughout the year, the influence of geological conditions was considered to be limited.

Other contributing factors may include inflows from sources other than the pond, as well as the influence of organisms inhabiting the manbo. Due to its relatively enclosed structure, the manbo is less susceptible to external contamination and is therefore considered to be a stable source of agricultural water. In this study, although changes in water quality were observed along the subsurface flow path, a stable supply of dissolved oxygen and active microbial decomposition were also confirmed, indicating the ecological health of the manbo. These findings suggest that traditionally managed water facilities like the manbo can still function effectively in modern water management contexts.

Future challenges include identifying the specific factors contributing to increased electrical conductivity (EC) through cation and anion analysis, as well as quantitatively assessing the dynamics of water movement from the ponds to the manbo and further downstream. This study provided a scientific reevaluation of traditional water facilities such as the manbo as regional water resources and presented foundational insights that may contribute to the development of sustainable water use strategies.

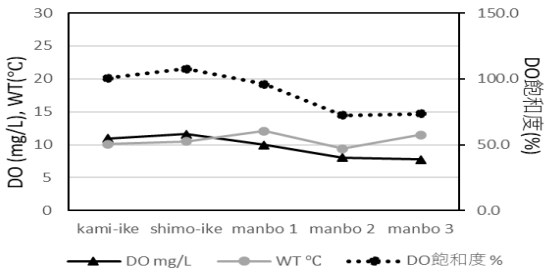

Fig.4 Water Temperature, Dissolved Oxygen, and DO Saturation in Winter (February).

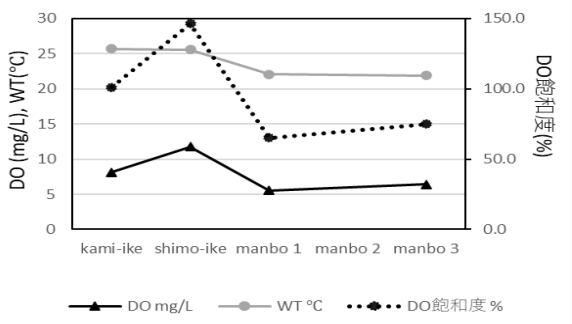

Fig.5 Water Temperature, Dissolved Oxygen, and DO Saturation in Summer (June).

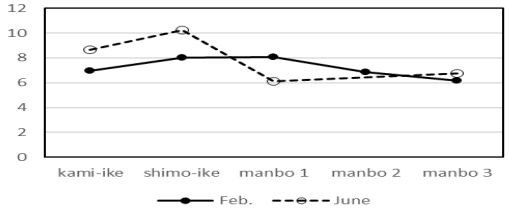

Fig.6 pH in Winter (February) and Summer (June).

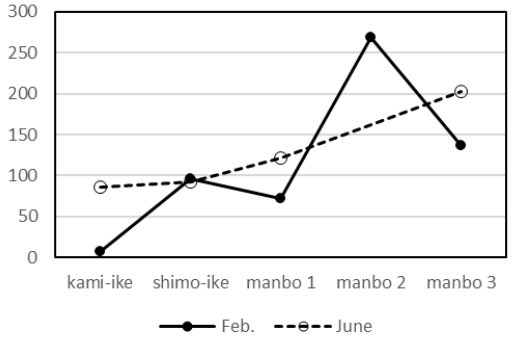

Fig.7 Electrical conductivity (EC) in Winter (February) and Summer (June).

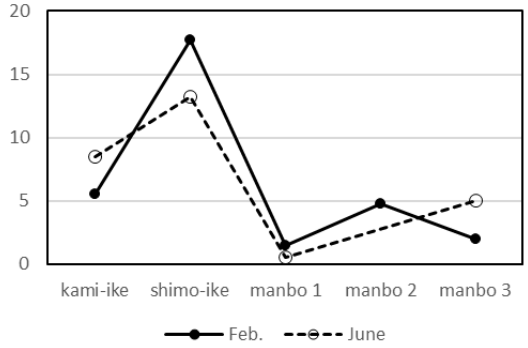

Fig.8 Suspended solids (SS) in Winter (February) and Summer (June).

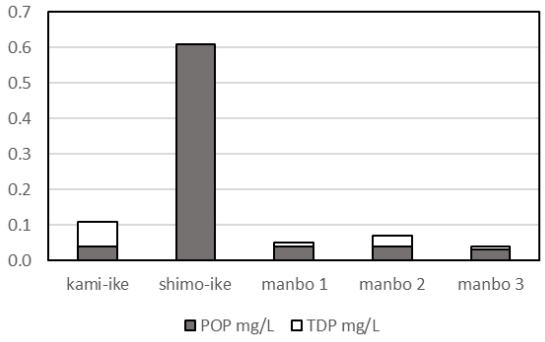

Fig.9 Total Phosphorus (TP) and Particulate Organic Phosphorus (POP), and Dissolved Phosphorus (TDP) Concentrations in Winter (Feb.).

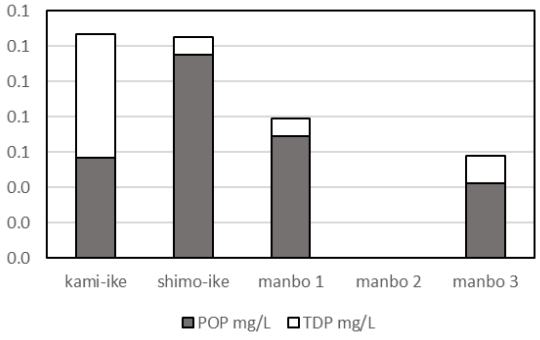

Fig.10 Total Phosphorus (TP) and Particulate Organic Phosphorus (POP), and Dissolved Phosphorus (TDP) Concentrations in Summer (June).

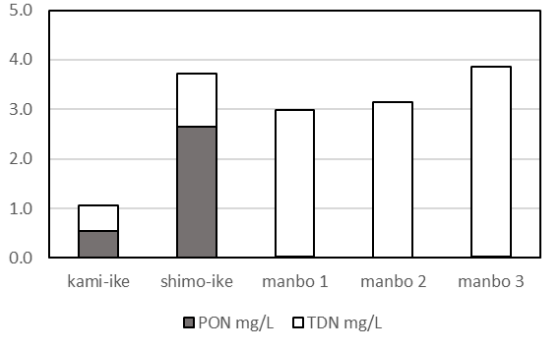

Fig.11 Total Nitrogen (TN) and Particulate Organic Nitrogen (PON), and Dissolved Nitrogen (TDN) Concentrations in Winter (Feb.).

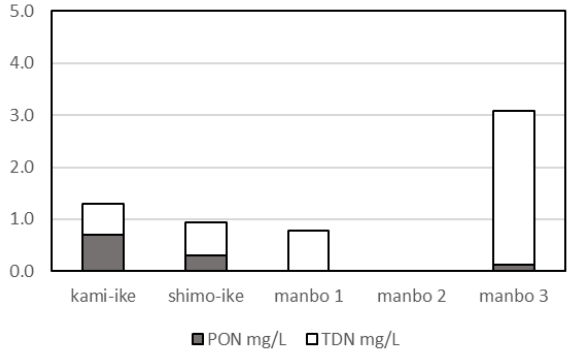

Fig.12 Total Nitrogen (TN) and Particulate Organic Nitrogen (PON), and Dissolved Nitrogen (TDN) Concentrations in Summer (June).

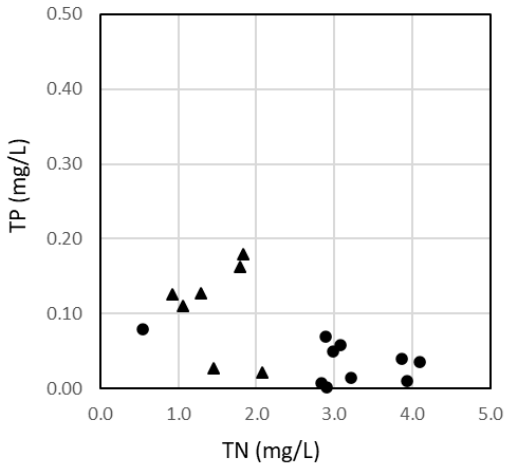

Fig. 13 Nitrogen and Phosphorus Levels in Two Ponds and the Manbo Based on All Surveys

ACKNOWLEDGMENTS

We hereby express our sincere gratitude to the Mie Prefectural Hokusei Chuo Park Management Office for granting permission and providing valuable cooperation during the field survey. We are likewise deeply grateful to Yokkaichi University for its support through a special project

research grant.

REFERENCES

[1] Kuwahara H., Origin of “Manbo”, Journal of Agricultural Engineering, 59(12), 1377-1382, 1991.

[2] Haruyama S., Water Society's Yearning for Manbo: Landscape Told by Manbo, Kokinshoin, pp.155, 2014.

[3] Koyanagi Y., and Kikuchi K., Groundwater Utilization by Manbo in Suzuka District, Mie Prefecture, Japan, Academic Report of Mie Higher School of Agriculture and Forestry, 11pp.1-17.

[4] Kobori I., Manbo, Canat of Japan, Mie Prefecture Local Materials Publication Society, pp.282, 1988.

[5] Yoshida K. and Kuroyanagi A., Study of the Relation between Human and Water through the Traditional Water Facilities ″MANBO″(The 24th Conference on Environmental Information Science), Vol.. 24, p.131-136, 2010.

[6] Tarusawa Y., Haruyama S., Yasuda K. and Matsumoto M., The regional landscape of Manbo, Annual Meeting of the Association of Japanese Geographers, Spring 2012, P1304.

[7] Anzai, T. *Series:* Exploring agricultural civil engineering heritage – The underground water veins of Onzawa: Manbo (Daian Town and Hokusei Town, Mie Prefecture). In Land Improvement: The Culture of Agriculture Engraved in the Land , Vol. 38(6), pp. 38–43. 2000.

[8] Tanaka K., Manbo in Hokusei District. About research trends, Iwao Kobori (ed.), “Manbo” Kanat in Japan, Mie Prefecture Local Materials Publication Society, pp. 116-121, 1988.

[9] Hokkaido Branch of the Japan Society for Analytical Chemistry, Water Analysis 5th Edition, Kagaku-dojin, pp. 472, 2005.

[10] Morimoto Y., Igari A., Saito K., Yamagata E., Takemoto T., Naemura A., and Kodera K., Characterization of water quality in various rivers - Focusing on the coefficient of variation of EC (electrical conductivity), Int. J Hum Cult Stud.No.32 pp. 46-61,2022.

[11] Rural Environment Division, Rural Development Bureau. (2012). Reference manual for dealing with algal blooms in agricultural reservoirs. Ministry of Agriculture, Forestry and Fisheries, Japan. pp.80.

[12] Nagoya City. (2025). FY2024 results of regular water quality monitoring in public water bodies and groundwater: Data collection – Regular monitoring data for public water bodies. Environmental Bureau, City of Nagoya. Retrieved June 28, 2025, from https://www.city.nagoya.jp/kankyo/cmsfiles/contents/0000187/187562/01_R6dai1-koukyouyousuiiki.pdf.

[13] Oyagi M., Hayakawa S. and Hirano T., Water characteristics of ponds in Itaka Ryokuchi, Nagoya city,Bulletin of Nagoya Biodiversity Center, Vol.10, p135-142, 2023

Copyright © Int. J. of GEOMATE All rights reserved, including making copies, unless permission is obtained from the copyright proprietors.

15th Int. Conf. on Geotechnique, Construction Materials & Environment,
Kyoto, Japan, 11-13 November 2025, ISBN 978-4-909106124 C3051

EXTRACTION OF SLOPE VARIATION EXTENT USING OPTICAL SENSORS AND SAR FOR THE MANASLU CIRCUIT TRAIL, NEPAL

Hijiri Shimojima[1]

[1] Faculty of Regional Environment Science, Tokyo University of Agriculture, Japan

ABSTRACT

Frequent slope failures induced by intense monsoonal rainfall in Nepal threaten trekking routes and local infrastructure, especially in high-altitude regions like the Manaslu Circuit Trail. This study evaluates the effectiveness of satellite-based landslide detection methods using both optical and synthetic aperture radar (SAR) data. Two optical-based techniques (land cover change classification and NDVI-GSI differencing) and five SAR-based approaches (texture analysis, NDPI differencing, dual-polarisation image interpretation, coherence difference analysis, and interferogram interpretation) were applied to pre- and post-monsoon Sentinel-1 and Sentinel-2 datasets. A field survey conducted in September 2024 provided ground-truth data for validating remote sensing results. Optical methods yielded more reliable results, with NDVI-GSI differencing achieving the highest detection accuracy. SAR-based techniques faced challenges due to terrain-induced distortions and coherence loss, though coherence difference analysis showed relative promise. Limitations in optical imagery, such as misclassification caused by seasonal land use changes, suggest that SAR data can complement optical analysis to improve reliability. This study concludes that a hybrid approach integrating optical and SAR datasets enhances landslide detection in mountainous regions.

Keywords: landslide, SAR, Optical Sensor, Trail, Manaslu Conservation Area, Nepal

INTRODUCTION

Nepal, a mountainous country in South Asia, attracts tourists from around the world for Himalayan mountaineering and trekking in its foothills. These activities constitute a vital opportunity for foreign currency acquisition and significantly contribute to the economic development of local communities. The Himalayan Mountain region represents one of the country's most important tourism assets.

However, Nepal experiences frequent natural hazards such as floods, landslides, and debris flows triggered by heavy rainfall during the monsoon season [1]. Landslides often interrupt key transportation routes, disrupting logistics networks and causing considerable economic losses that have become a major societal issue.

Such slope disasters frequently occur in the Higher Himalaya region, located north of the Main Central Thrust (MCT). Trekking trails traversing this area are also susceptible to landslides. Due to narrow and rugged terrain and the absence of well-developed roads, these trails serve as the sole means of transportation not only for trekkers but also for local residents. When a landslide occurs along a trail, it hinders mobility for both community members and goods transportation.

Accurately identifying the location and extent of trail-based slope failures is essential for sustainable trail maintenance and management. Various satellite-based approaches have been shown to be effective in detecting landslides adjacent to road networks. Previous studies have applied optical sensor imagery, such as Landsat, to identify landslide sites [2] and used ensemble learning models on aerial photographs [3]. However, these optical systems are weather-dependent and often face challenges acquiring high-quality data during unfavourable conditions.

To address this issue, Synthetic Aperture Radar (SAR) data, which can observe the earth's surface regardless of atmospheric conditions or time of day, has emerged as a promising tool for disaster monitoring. Especially since the 2015 major earthquake in central Nepal, numerous studies—such as that of David et al. [4]—have investigated slope failure detection using SAR imagery. Nevertheless, research specifically focusing on landslides occurring along trekking trails remains limited.

This study aims to evaluate the effectiveness of existing landslide extraction methods for accurately delineating slope deformation areas using optical and SAR data, specifically along trekking routes in Nepal.

METHODOLOGY

Study Area

The target area for this study is the Manaslu Circuit Trail located in the Gorkha region, approximately 200 km northwest of Kathmandu, the capital of Nepal. This circular trekking route encircles Mount Manaslu, which stands at an elevation of 8,156 meters. The high-altitude section of the trail is designated as the Manaslu Conservation Area (Fig. 1).

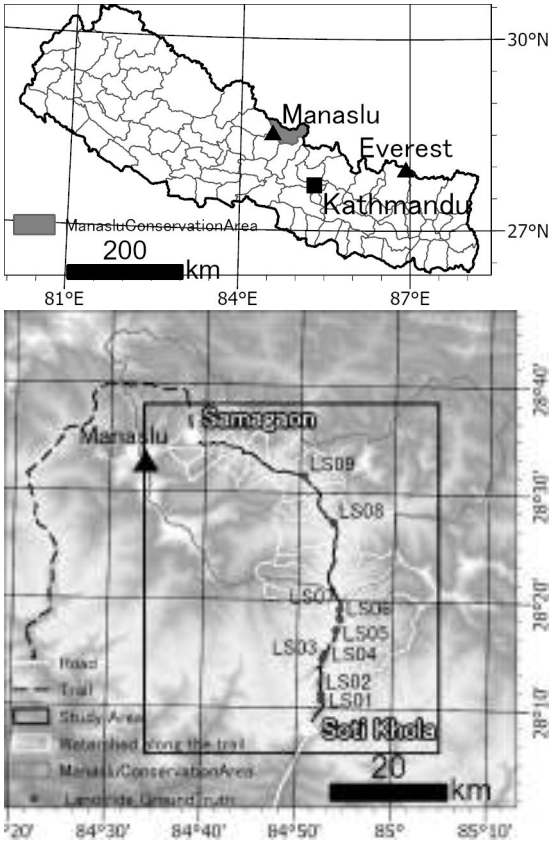

Fig.1 Study area map

Table 1 DATA SOURCES

Type	Satellite name	Acquisition date	Orbit	Polarization
Optical Satellite Imagery	Sentinel-2	2024.4.29	—	—
		2024.10.21	—	—
SAR Imagery	Sentinel-1	2024.5.03	Ascending	VV, VH
		2024.5.27		VV, VH
		2024.10.06		VV, VH
		2024.4.17	Descending	VV, VH
		2024.5.11		VV, VH
		2024.9.20		VV, VH

Data Sources

To extract landslide-affected areas along the Manaslu Circuit Trail, optical and SAR sensor data were utilised. Specifically, Sentinel-2 optical imagery and Sentinel-1 SAR imagery were selected. To capture slope deformation dynamics, one pre-monsoon and one post-monsoon scene were selected for each sensor. For Sentinel-2 imagery, cloud-free scenes within the study area were preferentially selected. The specifications of the datasets used in the analysis are summarised in Table 1.

Landslide Extraction Methods

To identify slope failures occurring along the trail, two spatial scopes were defined: (1) catchment areas adjacent to the trail, and (2) buffer zones of 50 meters from the trail route. Multiple approaches were applied to both optical and SAR data.

RGB-NDVI Colour Composite for the Land Cover Distribution Chart (LCDC)

This method identifies landslide areas by detecting changes in vegetation between two periods. NDVI values before and after the monsoon were calculated from Sentinel-2 data. A colour composite image was created by assigning pre-monsoon NDVI to red, post-monsoon NDVI to green, and pre-monsoon blue band reflectance to blue [5][6]. The resulting image was classified into five colours (red, yellow, green, blue, black), with red regions interpreted as landslide-affected areas. A supervised classification using the Maximum Likelihood Method was then applied using training areas extracted from these colour classes.

NDVI-GSI Differential Analysis

This method identifies landslide areas as regions that transitioned from vegetated surfaces Normalized Difference Vegetation Index (NDVI) before the monsoon to bare surfaces Gray Size Index (GSI) afterward [7]. GSI was calculated using the formula (Equation1):

$$GSI = \frac{(R - B)}{(R + G + B)} \quad (1)$$

Where *R*, *G*, and *B* represent the reflectance of red, green, and blue bands from Sentinel-2 imagery. Thresholds for NDVI and GSI were determined through visual inspection of false-colour satellite images (The NDVI threshold pre-monsoon is 0.2, and post-monsoon is 0.3. The GSI threshold pre-monsoon is 0.1, and post-monsoon is 0.06).

SAR Intensity Texture Analysis

Texture analysis using SAR intensity data was conducted to delineate sediment disaster zones, which typically exhibit rough surface textures due to disrupted land cover. Pre-monsoon VV-polarized SAR images were converted to backscatter coefficients (σ^0) and filtered with a 5×5 Lee filter to suppress speckle noise. Landslide-prone areas were identified based on the standard deviation of σ^0, as such regions show significantly elevated SD values. Thresholds were statistically defined using the mean and standard deviation of the SD values, with five levels set: $\mu + 1.0\sigma$ to $\mu + 3.0\sigma$. Given the radar

illumination geometry, ascending scenes captured west-facing slopes and descending scenes east-facing slopes. To ensure comprehensive extraction, both datasets were merged, and the same procedure was applied throughout the analysis.

NDPI Differential Analysis

Normalized Difference Polarization Index (NDPI) was applied to detect changes in surface scattering characteristics using pre- and post-monsoon VV and VH polarization backscatter data [10]. NDPI is defined as (Equation2):

$$NDPI = \frac{(\sigma^0 VV - \sigma^0 VH)}{(\sigma^0 VV + \sigma^0 VH)} \quad (2)$$

In this study, σ^0VV and σ^0VH represent the backscatter coefficients (σ^0) of VV and VH polarizations, respectively. The NDPI, ranging from −1.0 to 1.0, was used to distinguish volume scattering (e.g., vegetation) from surface scattering (e.g., bare ground). NDPI was calculated from pre- and post-monsoon SAR data, and the absolute difference between the two was derived. Areas affected by sediment-related disasters typically show a shift from volume to surface scattering, resulting in high absolute NDPI difference values. However, contributions from snow and ice scattering complicate threshold selection. Therefore, five statistical thresholds were defined: $\mu + 1.0\sigma$ to $\mu + 3.0\sigma$.

Dual-Polarisation SAR Image Interpretation

A colour composite image was created using VV and VH polarisations before the monsoon and VV polarisation after the monsoon. Bare landslides, which exhibit increased VV reflectance over time, were interpreted as purple regions [11][12].

Coherence Difference Analysis

Coherence Values (CV) are generated during the interferometric SAR processing and represent the correlation coefficient between intensity data acquired at two different times, ranging from 0 to 1.0. Low CV indicate weak temporal correlation in land cover, suggesting that surface conditions have changed between acquisitions [13][14].

In this study, coherence was calculated separately from pre-monsoon and post-monsoon SAR image pairs. The coherence derived from the post-monsoon pair was subtracted from that of the pre-monsoon pair on a pixel-by-pixel basis. Areas affected by sediment-related disasters are typically characterized by a transition to bare ground, resulting in low coherence difference values relative to the overall distribution.

Therefore, five threshold levels were defined based on the statistical distribution of the coherence differences: $\mu - 1.0\sigma$, $\mu - 1.5\sigma$, $\mu - 2.0\sigma$, $\mu - 2.5\sigma$, and $\mu - 3.0\sigma$.

Ground Truth Survey

To validate the remote sensing-derived landslide detection results, a field survey was conducted along the Manaslu Circuit Trail between September 8–21, 2024. Landslide sites were verified visually and recorded with photographs and GPS coordinates. Interviews with local residents were also conducted to gather temporal data on disaster occurrences. These records served as ground truth data for evaluating the accuracy of satellite-based extraction methods.

RESULTS AND DISCUSSION

Landslide Extraction Using RGB-NDVI Colour Composite for the LCDC

The results of landslide extraction based on land cover change classification using optical sensor data are shown in Fig. 2. Within the trail buffer zone, a total of 213 landslide sites were extracted, covering an area of 40.7 hectares. Of the nine ground truth sites, two were correctly extracted. The remaining seven sites were not detected, which suggests that no landslide events occurred at those locations in 2024. Subsequently, 141 random points were generated within the extracted landslide areas. Using post-monsoon Sentinel-2 imagery and satellite images from Google Earth as reference data, the proportion of correctly matched points (accuracy) was calculated (Table3). The accuracy was 78.0%; however, due to a high number of points being classified outside actual landslide areas, both the F-measure and Cohen's kappa coefficient yielded relatively low values. Misclassified areas included farmland, livestock grazing zones, riverbanks, and residential settlements. These errors are presumed to have resulted from changes in NDVI values between the two observation periods, leading to false positives in the extraction process.

Landslide Extraction Using NDVI-GSI Differential Analysis

The NDVI-GSI differential analysis results are

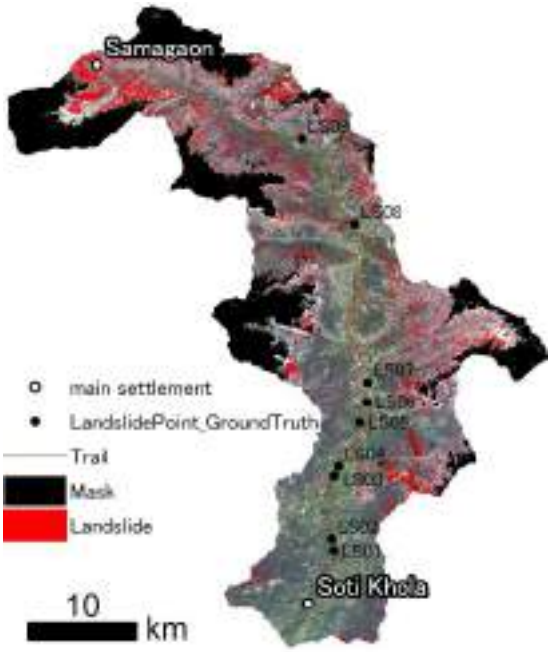

Fig. 2 Landslide-Affected Areas Identified by Land Cover Distribution Chart

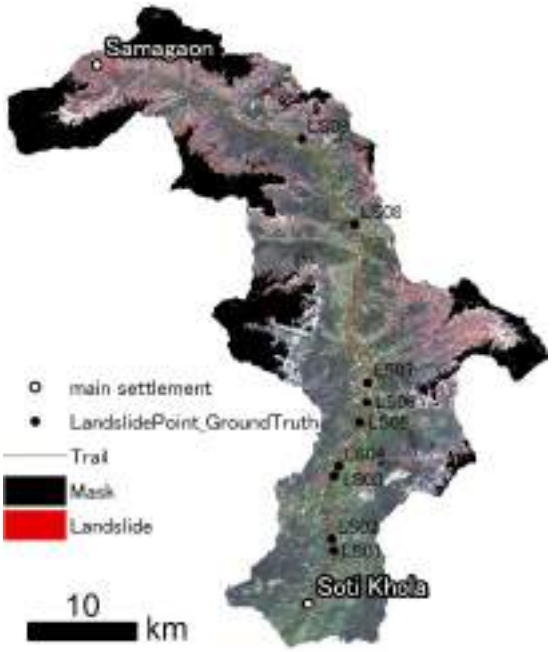

Fig. 3 Landslide-Affected Areas Extracted Using NDVI–GSI Differential Analysis

presented in Fig. 3. A total of 99 landslide-affected sites were extracted within the trial buffer zone, encompassing an area of 13.0 hectares. Of the nine ground truth sites, two were correctly identified. The remaining seven sites were not detected, which suggests that no landslide events occurred at those locations in 2024.

The accuracy was 81.3%, which was higher than that obtained by any other method (Table3). However, due to a large number of points being classified outside actual landslide areas, both the F-measure and Cohen's kappa coefficient yielded relatively low values. Misclassified areas were similar to those observed in the land cover change classification map, including farmland, livestock grazing zones, riverbanks, and residential settlements. Compared to the land cover change classification map, the total extracted area was smaller. This underestimation is presumed to be a result of the threshold values set for NDVI and GSI, which may have led to conservative extraction of landslide-affected regions.

Landslide Extraction Using SAR Intensity-Based Methods

Texture analysis and NDPI differential analysis results, based on SAR backscatter coefficients, are shown in Fig. 4 and Fig. 5, respectively. The texture analysis tended to highlight ridge and valley regions based on thresholding, while NDPI-based results showed extensive and fragmented patterns that were difficult to interpret as landslide zones [15].

These challenges are likely due to geometric distortions in SAR imagery, such as layover and shadowing. In comparison with ground truth data, texture analysis correctly identified four out of nine sites, while NDPI analysis detected only two. The accuracy was 68.0% for the texture-based analysis method and 60.7% for the NDPI differential analysis (Table 3).

Landslide Extraction Using Dual-Polarisation SAR Image Interpretation

Fig. 6 presents the results derived from dual-polarisation SAR imagery. Similar to other SAR-based approaches, the image interpretation was hindered by layover and radar shadow effects, resulting in unreliable detection. Only one of the nine ground truth sites was correctly identified, indicating the limitations of this method in mountainous terrain. The accuracy was 74.0% (Table 3).

Landslide Detection Using Coherence Difference Analysis

Landslide extraction results from coherence difference analysis are shown in Fig. 7. Although spatial patterns were scattered, five of the nine ground truth sites were successfully matched. The accuracy was 64.0% (Table 3). This suggests that coherence-based methods may offer relatively better results than SAR intensity analyses, although some matches may have occurred coincidentally.

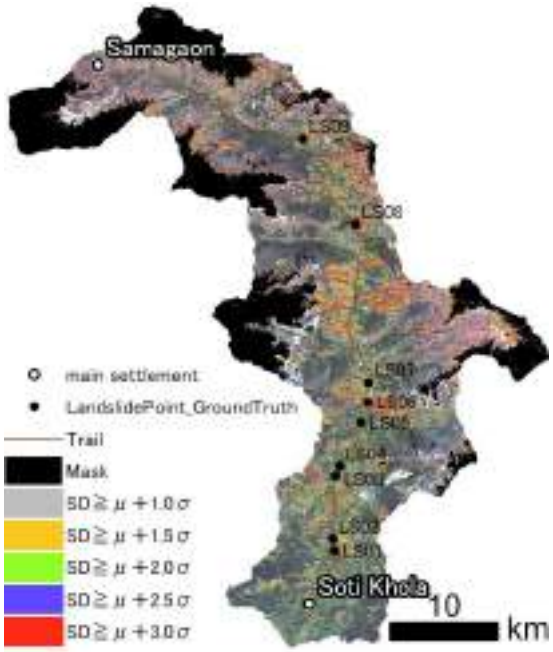

Fig. 4 Landslide-Affected Areas Extracted by SAR Intensity-Based Texture Analysis

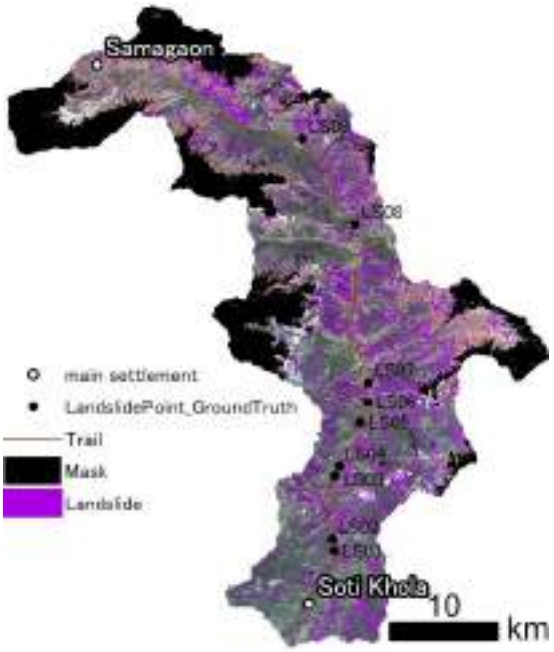

Fig. 6 Landslide Interpretation Using Dual-Polarisation SAR Composite Imagery

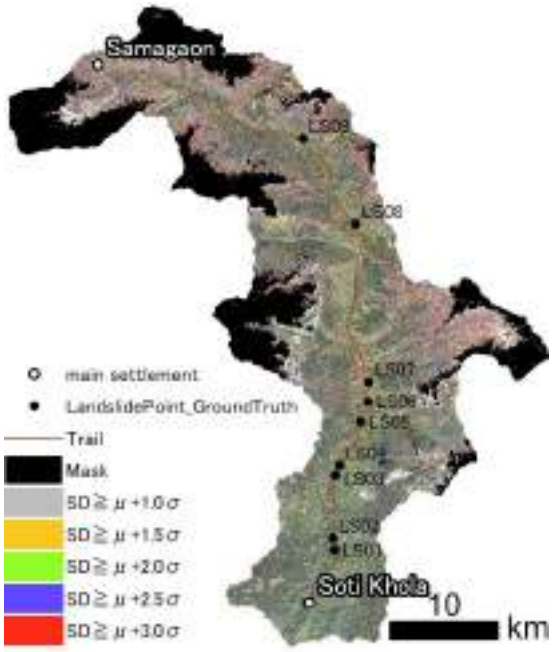

Fig. 5 Landslide Detection Based on NDPI Differential Analysis

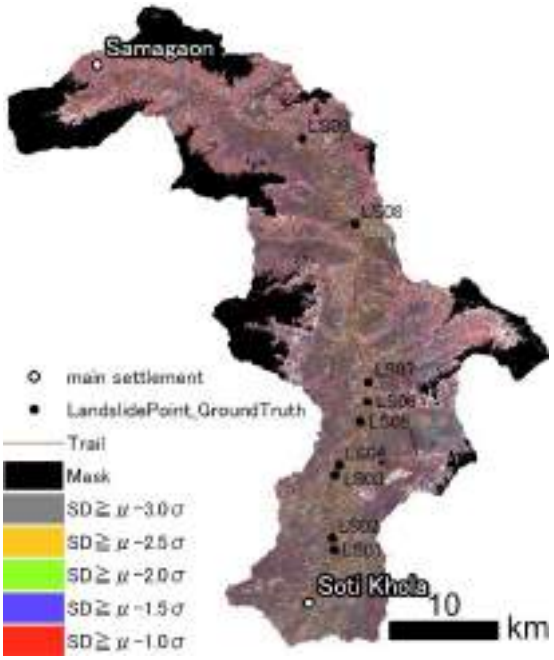

Fig. 7 Landslide-Affected Areas Detected by Coherence Difference Analysis

Landslide Extraction Results Based on Ground Truth Comparison

Table 2 presents a comparative evaluation of the results obtained from various analytical methods concerning nine ground-truth locations (LS01–LS09). At LS01, no landslide area was detected by either optical or SAR datasets, suggesting that no slope deformation occurred at this site in 2024. LS02 yielded a small-scale landslide detection using optical sensor analysis; SAR-based methods indicated partial detection, but layover and radar shadow effects likely reduced data reliability.

LS03 showed consistent detection across both data sources, although slight spatial mismatches were observed. Optical data did not detect LS04, but SAR-based methods identified slope failure to some extent, again with limitations due to terrain-induced distortion. LS05 yielded similar results to LS04.

Table 2 Comparison Between Ground Truth Locations and Landslide-Affected Areas Extracted by Each Method

No	Photo of Landslide	LCDC	NDVI-GSI	Texture Analysis	NDPI Difference Analysis	DPSII	Coherence Difference Analysis
LS01							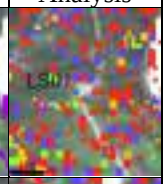
LS02						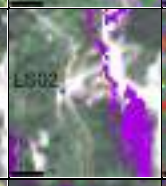	
LS03							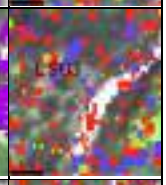
LS04							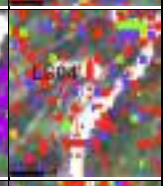
LS05				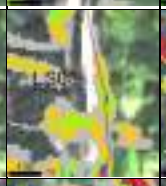		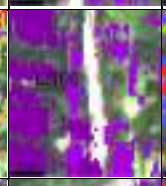	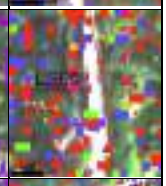
LS06							
LS07							
LS08						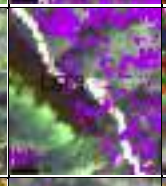	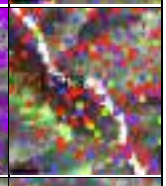
LS09				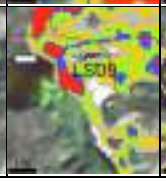			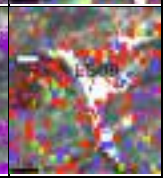

LS06 was detected by both optical and SAR data and corresponded to the most extensive landslide in the study area, with an estimated width of approximately 100 meters and a length of 400 meters. This was the only site where interviews with nearby residents were conducted, confirming that heavy rainfall in August 2024 triggered the slope failure.

Table 3 Results of Landslide Detection for Nine Ground-Truth Locations Across Multiple Analytical Methods

		Optical Satellite Imagery						SAR Imagery											
		LCDC			NDVI-GSI			Texture Analysis			NDPI DA			DPSII			Coherence DA		
		L	O	T	L	O	T	L	O	T	L	O	T	L	O	T	L	O	T
Ground Truth	L	2	7	9	2	7	9	4	5	9	2	7	9	1	8	9	5	4	9
	O	0	0	0	0	0	0	0	0	0	0	0	0	0	0	0	0	0	0
Validation data	L	3	25	28	2	26	28	11	17	28	3	25	28	9	19	28	9	19	28
	O	8	114	122	2	120	122	31	91	122	34	88	122	20	102	122	35	87	122
	T	11	139	150	4	146	150	42	108	150	37	113	150	29	121	150	44	106	150
Accurancy(%)		78.0			81.3			68.0			60.7			74.0			64.0		
F-measure		0.154			0.125			0.314			0.092			0.316			0.250		
Kappa Coefficiant		0.054			0.082			0.116			-0.153			0.155			0.028		

Legend: L: Landslide, O: Others, T: Total

At LS07, no landslide was detected using either data source, indicating the absence of deformation. LS08 revealed a small-scale landslide using optical data and partial detection through SAR, but terrain distortions compromised accuracy. LS09 produced similar results to LS08, and both sites are unlikely to have experienced slope failure in 2024.

These findings suggest that when slope deformation is observed by both optical and SAR datasets, the site can be reliably classified as a landslide area. In contrast, SAR-only detection in mountainous regions should be interpreted cautiously due to layover and radar shadowing effects. Optical-only detections may reflect land use changes, such as seasonal agricultural activity, and cannot be unequivocally identified as landslides. Therefore, a combined approach using both optical and SAR data is essential for accurate landslide extraction in complex mountain environments.

CONCLUSION

In this study, we applied two optical-based and four SAR-based methods to extract landslide-affected areas along the Manaslu Circuit Trail in Nepal. Each method was evaluated in terms of its capacity to delineate slope failure zones, and its effectiveness was validated using ground truth data.

Consistent with previous findings, the complex topography of the Himalayan region poses significant challenges for SAR-based landslide detection due to layover, shadowing, and coherence loss. Among the SAR approaches, coherence difference analysis yielded comparatively better results, although its accuracy remained limited.

On the other hand, the NDVI-GSI differential analysis using optical sensor data demonstrated the most promising performance, effectively identifying landslide sites with fewer false positives. However, its susceptibility to seasonal land cover changes, particularly agricultural activities, highlights limitations in discriminating between genuine landslides and anthropogenic surface changes.

For landslide detection in mountainous regions, it is considered effective to primarily utilize optical sensor data while minimizing misclassification through time-series analysis of NDVI fluctuations. Furthermore, by incorporating SAR imagery to differentiate between actual landslides and land use changes, more detailed and accurate extraction of landslide-affected areas can be achieved.

In this study, the SAR dataset was limited to C-band Sentinel-1 imagery. To enhance the potential for landslide detection, a key challenge lies in incorporating SAR data acquired in the L-band, which, due to its longer wavelength, can penetrate vegetated areas more effectively. This would allow for improved observation of surface deformation and facilitate the identification of optimal image pairs for interferometric SAR (InSAR) analysis.

These findings contribute to improved understanding of remote sensing-based disaster monitoring in high-altitude regions, supporting more effective trail management and community resilience in Nepal's mountainous landscapes.

ACKNOWLEDGMENTS

This field survey was made possible through a sponsored research donation from Mr. Yoichi Nakata. I would like to take this opportunity to express my sincere gratitude. I thank Mr. Ram Raj Rijal(Executive Director) and staff from Himalaya Research Expeditions(P) LTD., who have totally supported our fieldwork in Manaslu Base Camp and Manaslu Conservation Area, Nepal. This work was supported by JSPS KAKENHI Grant Numbers JP22K12623, JP25K03332.

REFERENCES

[1] Aon Benfield, Analytic, Impact Forecasting Nepal: Earthquake Event Recap Report, Aon Benfield, 2015, pp. 3–32.

[2] Thuy T. T. Le and Kawagoe S., Study on Landslide Category Based on Temporal-Spatial Characteristic Distribution in Northern Vietnam Using Satellite Images, International Journal of GEOMATE, Vol. 14, Issue 43, 2018, pp. 118–124.

[3] Opara J. N., Moriwaki R., and Chun P.-J., Ensemble Learning-Based Automatic Detection of Landslide Areas from Aerial Photographs, International Journal of GEOMATE, Vol. 27, Issue 122, 2024, pp. 79–86.

[4] Bekaert D. P. S., Handwerger A. L., Agram P., and Kirschbaum D. B., InSAR-Based Detection Method for Mapping and Monitoring Slow-Moving Landslides in Remote Regions with Steep and Mountainous Terrain: An Application to Nepal, Remote Sensing of Environment, Vol. 249, 2020, pp. 1–11.

[5] Sader S. A. and Winne J. C., RGB NDVI Colour Composites for Visualising Forest Change Dynamics, International Journal of Remote Sensing, Vol. 13, Issue 16, 1992, pp. 3055–3067.

[6] Pujiono E., Kwak D.-A., Lee W.-K., Sulistyanto, Kim S.-R., Lee J. Y., Lee S.-H., Park T., and Kim M.-I., RGB-NDVI Colour Composites for Monitoring the Change in Mangrove Area at the Maubesi Nature Reserve, Indonesia, Forest Science and Technology, Vol. –, Issue 4, 2013, pp. 171–179.

[7] Xiao J., Shen Y., Tateishi R., and Bayaer, Development of Topsoil Grain Size Index for Monitoring Desertification in Arid Land Using Remote Sensing, International Journal of Remote Sensing, Vol. 27, No. 12, 2006, pp. 2411–2422.

[8] Pingxiang L. and Shenghui F., SAR Image Classification Based on Its Texture Features, Geo-Spatial Information Science, Vol. 6, 2003, pp. 16–19.

[9] Chen S., Useya J., and Mugiyo H., Decision-Level Fusion of Sentinel-1 SAR and Landsat 8 OLI Texture Features for Crop Discrimination and Classification: Case of Masvingo, Zimbabwe, Heliyon, Vol. –, 2020, pp. 1–14.

[10] Cao Y.-g., Yan L.-j., and Zheng Z.-z., Extraction of Information on Geology Hazard from Multi-Polarization SAR Images, The International Archives of the Photogrammetry, Remote Sensing and Spatial Information Sciences, Vol. 37, Part B4, pp. 1529–1532.

[11] Uhlmann S. and Kiranyaz S., Classification of Dual- and Single-Polarised SAR Images by Incorporating Visual Features, ISPRS Journal of Photogrammetry and Remote Sensing, Vol. 90, 2014, pp. 10–22.

[12] Zhou T., Li Z., and Pan J., Multi-Feature Classification of Multi-Sensor Satellite Imagery Based on Dual-Polarimetric Sentinel-1A, Landsat-8 OLI, and Hyperion Images for Urban Land-Cover Classification, Sensors, Vol. 18, Issue 2, 2018, pp. 1–20.

[13] Jung J. and Yun S.-H., Evaluation of Coherent and Incoherent Landslide Detection Methods Based on Synthetic Aperture Radar for Rapid Response: A Case Study for the 2018 Hokkaido Landslides, Remote Sensing, Vol. 12, Issue 2, 2020, pp. 1–26.

[14] Tzouvaras M., Danezis C., and Hadjimitsis D. G., Small-Scale Landslide Detection Using Sentinel-1 Interferometric SAR Coherence, Sensing, Vol. 12, Issue 10, 2020, pp. 1–33.

[15] Burrows K., Walters R. J., Milledge D., and Densmore A. L., A Systematic Exploration of Satellite Radar Coherence Methods for Rapid Landslide Detection, Natural Hazards and Earth System Sciences, Vol. 20, 2020, pp. 3197–3214.

Copyright © Int. J. of GEOMATE All rights reserved, including making copies, unless permission is obtained from the copyright proprietors.

15th Int. Conf. on Geotechnique, Construction Materials & Environment,
Kyoto, Japan, 11-13 November 2025, ISBN 978-4-909106124 C3051

HEAVY METAL CONCENTRATIONS OF PLANTS GROWING AROUND MINES IN VICTORIA, AUSTRALIA

Daiki Yamamoto

Graduate School of Systems Engineering, Wakayama University, Japan ;

ABSTRACT

Some plants can grow even in areas where the soil is rich in heavy metals, such as mines. Some of them can contain large amounts of toxic heavy metals in their bodies. They are called hyperaccumulators and are expected to be used for the remediation of contaminated sites. There are many gold and antimony mines in Australia, and some areas are contaminated by antimony, arsenic, copper, and other metals. In this study, plants native to mining areas in Victoria and South Australia, were surveyed to determine which plants were present. Heavy metal concentrations in plants were measured and compared between heavy metal contaminated and non-contaminated areas. As a result, antimony was detected in the plants in Costar field, and some plants were found to contain 100 ppm of antimony in their roots. Most of the plants contained more heavy metals in the roots, with concentrations in the leaves and stems ranging from one-tenth to one-hundredth of those in the roots. Blackberry and grass plants were found in many mines and non-contaminated areas, and their concentrations differed.

Keywords: Heavy metals, Victoria, Plant, Antimony

INTRODUCTION

By the 1860s, De Saussure, von Sacks, and Knop had shown that C, H, O, N, P, S, K, Ca, Mg, and Fe were essential for plant growth. C, H, O, N, P, S, K, Ca, Mg, and Fe are essential for plant growth. Subsequently, 17 essential elements for plant growth were listed by 1987 [1]. Since heavy metals and other soil contaminants are absorbed together during the absorption process, plants in general cannot grow in areas with high concentrations of soil contaminants. However, some plants prefer to grow in areas with high concentrations of contaminants, especially heavy metals, and absorb and accumulate heavy metals at high levels. These plants are called mine plants or hyperaccumulators in Japanese.

Australia boasts one of the world's largest gold production volumes. Since the gold rush of the 19th century, there have been numerous gold mines in Australia. Antimony (Sb), which is produced alongside gold (Au), also has one of the world's largest production volumes, and there are Sb mines centered around Costerfield in Victoria. Rocks that were mined in the past remain on the slopes of the mountains around the mines, and it is believed that the soil contains heavy metals that have dissolved from the ore deposit.

The purpose of this study is to investigate plants growing naturally in mines in Victoria and measure the heavy metal concentrations in the collected plants. Furthermore, we will investigate whether there are plants that absorb and accumulate high concentrations of heavy metals, and discuss the differences in heavy metal concentrations between the locations of the plants and the collection sites.

RESEARCH SIGNIFICANCE

Metals in the soil can be a source of nutrition for plants or toxic, depending on their type and quantity. Therefore, it is important to understand the role of metals in plants. By studying plants that grow naturally in Au and Sb mines, we can investigate how plants in nature process Sb and other heavy metals.

METHODS

Study Site

Fig.1 Location of study sites

The locations of plant collections in this study are shown in figure 1. The survey sites are four mines and two non-contaminated areas in Victoria.

Point (1) is Costerfield, known for its antimony mines. At this site, samples were collected from two locations, designated as Site (1) and Site (2). Figure 2 shows a photograph of Site (1), where mined ore was

piled up in a specific location, and the ore contained a large amount of stibnite (Sb_2S_3). Figure 3 shows a photograph of Site (2), which is a pile of ore located several hundred meters away from Site 1. The ore at this site also contained a large amount of stibnite (Sb_2S_3).

Fig.2 Photograph of the ore storage at site (1)

Fig.3 Photograph of the ore storage at site (2)

Both Point (2) and Point (3) were areas where gold was mined, and ore was piled up along the slopes of the mountains. The minerals were mainly quartz, and arsenopyrite (FeAsS) was also found.

Fig.4 Photograph of the sampling point at point (4)

Point (4) is the location where tungsten minerals were found, and Figure 4 shows the condition of the collection site. Ferberite ($FeWO_4$) was observed at this location. Based on past mining history and the types of minerals found at survey sites, points (1) through (4) were designated as contaminated areas.

Points (5) and (6) are areas free of heavy metal contamination, and samples were collected to compare the heavy metal concentrations in plants from the mines. These two points are designated as non-contaminated areas. Point (5) is located in an igneous rock area, while Point (6) is located in a sedimentary rock area.

Analysis Method

After pretreatment, the collected plants are measured for heavy metal concentrations in the plants using an ICP optical emission spectrometer (ICP-OES). ICP-OES is a method that introduces a solution sample into plasma to emit element-specific spectra, identifies the presence of elements from the wavelengths of these lights, and determines the concentration of elements from the intensity of the light. This method was chosen because it allows multiple elements to be measured at once.

Pretreatment consists of cleaning the plants and preparing samples. First, the collected plants are separated into root, leaf, and stem parts as much as possible. The soil is washed because it contains a large amount of heavy metals, which can cause large errors in the measurement results. After the soil is removed, the specimens are placed in the dryer for one or two days to dry.

A solution sample of heavy metals extracted from plants is prepared for ICP emission spectrometry. First, dried plants are placed in a screw tube and concentrated nitric acid is added. Nitric acid has the effect of oxidatively decomposing organic matter in the sample and extracting heavy metals. After approximately two weeks of standing, the heavy metals in the plants are extracted and a yellow solution is obtained. Fine impurities remain in the screw tube, so these are removed using a filter and syringe.

The analysis was performed using an ICP optical emission spectrometer to measure the concentration of heavy metals in the prepared samples. The heavy metals measured were antimony (Sb), arsenic (As) and tungsten (W).

From the above steps, the concentration of heavy metals is measured. Since the concentration measured is the concentration in the sample solution, it must be converted to the concentration of heavy metals in the dried plant sample using the following equation

$$a\ (mg/kg) = \frac{b\ (mg/kg) \times c(g)}{d\ (g)} \quad (1)$$

a Heavy metal concentrations in plant samples
b Concentration of solution
c Weight of solution
d Dry weight of sample

RESULTS

In this study, the concentration of three elements were measured: antimony (Sb), arsenic (As) and tungsten (W). The concentrations of each heavy metal detected are shown in the graphs for each sampling point and site.

Table 1 Collected plants and sampling point

Numbers	Scientific names	Sampling points
Grass A	*Avena barbata*	①②④⑥
Grass B	*Briza maxima*	①②③
Grass C	*Holcus lanatus*	①②③⑥
Grass D	*Achnatherum parifilorum*	②④
Herb A	*Marrubium vulgare*	①③
Herb B	*Pantago lanceolate*	①②⑥
Herb C	*Sonchus oleraceous*	①
Herb D	*Hypochoeris radicata*	①⑥
Herb E	*Trifolium campestre*	①
Herb F	*Arctotheca calendura*	③⑤⑥
Herb G	*Sonchus asper*	③
Herb H	*Cirsiam vulgare*	⑤
Herb I	*Euphorbia peplus*	⑤
Vine A	*Asparagus Asparagoides*	①
Vine B	*Rubus fruticosus*	①③⑥
Shrub A	*Cytisus scoparius*	①
Shrub B	*Ulex europaeus*	① ③

Sb Concentration

Figure 5 shows the concentration of antimony (Sb) per dry weight per plant at sampling point (1). Overall, concentrations of Sb were higher in roots, leaves, and stems, in that order. The roots of Glass A at Site (1) had the highest antimony concentration, containing 238 mg/kg. Glass C and Herb A at Site (1) had higher antimony concentrations in their leaves than in their roots, both contained an average of about 20 mg/kg. When comparing the sampling sites, the plants at Site (1) contained more antimony than those at Site (2).

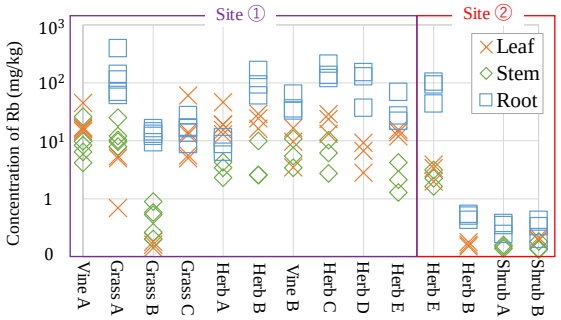

Fig.5 Measurement results for Sb

As Concentration

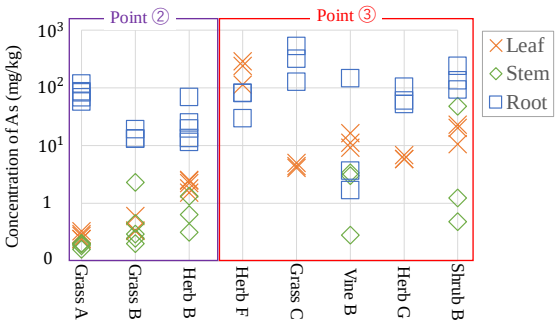

Fig.6 Measurement results for As

Figure 6 shows the concentration of arsenic (As) per dry weight of plants collected at points (2) and (3). Overall, it can be seen that arsenic is concentrated in the roots of plants. The highest arsenic concentration was found in grass C at point (3), which showed 530 mg/kg. On the other hand, Herb F at Point (3) showed higher concentrations of arsenic in the leaves than in the roots, with an average of 214 mg/kg of arsenic. When comparing sampling points, plants at Point (3) tend to have higher arsenic concentrations than those at Point (2).

W Concentration

Figure 7 shows the concentration of tungsten (W) per dry weight of each plant at sampling point (4). For glass A, samples were collected at two sites several meters apart, but both showed W concentrations of less than 1 mg/kg. On the other hand, glass D contained 11 to 24 mg/kg of W in the roots, 2 to 7 mg/kg in the stems, and 1 to 2 mg/kg in the leaves.

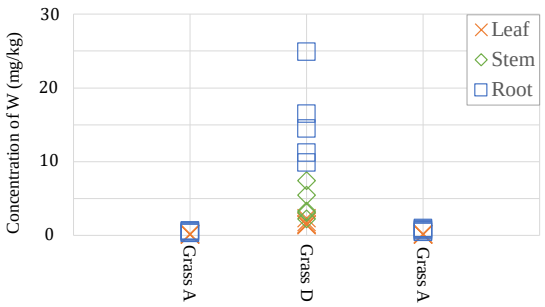

Fig.7 Measurement results for W

DISCUSSION

Comparison of Sb concentrations in the roots and leaves of contaminated and non-contaminated areas

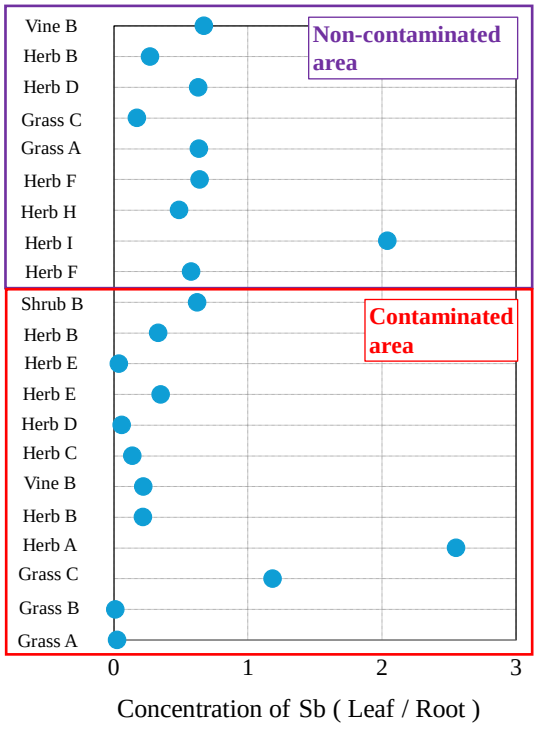

Fig.8 The ratio of Sb concentrations in roots and leaves

Figure 8 shows the antimony concentration in plant leaves collected from contaminated and non-contaminated areas divided by the concentration in the roots. The contaminated area in the figure 8 is Point (1), and the non-contaminated areas are Points (5) and (6). As mentioned in the results, many plants accumulate antimony in their roots, so the values shown in the figure are less than 1. Additionally, since the values are slightly higher in the non-contaminated areas than in the contaminated areas, it can be seen that as the amount of antimony in the soil increases, the proportion of antimony supplied to the leaves tends to decrease. However, Grass C and Herb A in the contaminated area show values greater than 1, indicating that the amount of antimony supplied to the leaves is greater than the amount accumulated in the roots.

Comparison Of As concentrations in the roots and leaves of contaminated and non-contaminated areas

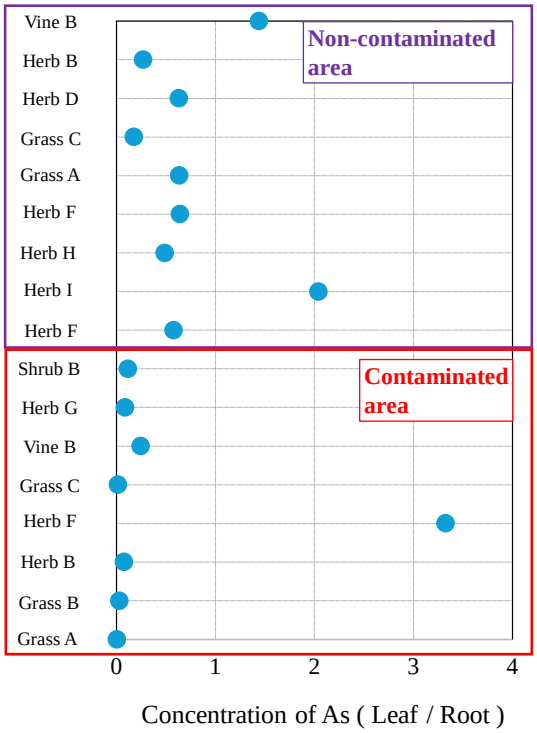

Fig.9 The ratio of As concentrations in roots and leaves

Figure 9 shows the arsenic concentration in plant leaves collected from contaminated and non-contaminated areas divided by the concentration in the roots. Note that the contaminated areas in the figure are points (2) and (3), and the non-contaminated areas are points (5) and (6). Similar to antimony, many plants accumulate arsenic in their roots, so the values shown in the figure are less than 1. Furthermore, since the values are higher in non-contaminated areas than in contaminated areas, it can be seen that as the arsenic content in the soil increases, the proportion of arsenic supplied to the leaves tends to decrease. This trend is stronger than that observed for antimony. Among the contaminated areas, only Herb F shows a value greater than 1, indicating that the amount of arsenic supplied to the leaves is greater than the amount accumulated in the roots. Even when comparing arsenic concentrations in contaminated and non-contaminated areas using the same type of

plant, such as Glass A, it can be seen that the values are higher in non-contaminated areas.

CONCLUSIONS

In this study, we conducted field surveys of plants growing naturally in gold mines, antimony mines, and other locations in Victoria, Australia, and analyzed the heavy metal concentrations in the plants. The heavy metal concentrations in all plants collected in this study ranged from 0 to 393 mg/kg for antimony (Sb), 0 to 530 mg/kg for arsenic (As), and 0 to 25 mg/kg for tungsten (W). Most of the plants collected from contaminated areas such as gold mines and antimony mines had the highest heavy metal concentrations in their roots rather than in their leaves or stems. This indicates that these plants accumulate heavy metals in their roots and reduce the amount of heavy metals supplied to their leaves and stems. Additionally, the results of comparing heavy metal concentrations in leaves and roots between contaminated and non-contaminated areas showed that as soil heavy metal concentrations increase, the proportion of heavy metals supplied from roots to leaves and stems tends to decrease. On the other hand, there were also plants, such as *Holcus lanatus* and *Marrubium vulgare* from the Costarfield Mine and *Arctotheca calendula* from the Sovereign Hill Mine, that accumulated significant amounts of antimony and arsenic in their leaves. These plants grow in ordinary soil as well. Therefore, it is possible that they have mechanisms that prevent harm to the body even when leaves and stems contain high levels of heavy metals, or that their system for supplying heavy metals from roots to leaves differs from that of other plants.

ACKNOWLEDGMENTS

In conducting this research, I would like to express my sincere gratitude to Professor Hiroyuki Ii of the Graduate School of Systems Engineering at Wakayama University and Professor John Sherwood of Deakin University for their valuable advice and guidance despite their busy schedules.

A would like to express my sincere gratitude to the members of the laboratory for their constant guidance and cooperation in laboratory analysis and data processing.

We would like to express our gratitude to all of you for your cooperation.

REFERENCES

[1] Mori T., Mae T. and Yoneyama T., plant nutrition, Bunseido, 2001.

[2] Ii H., Effectiveness of bryophyte and cicada shells as a bio-index for heavy metal contamination of river water and soil. International Journal of GEOMATE, Vol. 24, Issue 105, 2023, pp.117-125.

[3] Ii H., Effectiveness of using cicada shell and river bryophyte as an index of available Cu, Zn, Pb, As, Ni and Cr contamination, in Proc. 4th Int. Conf. on SEE, 2018, pp. 914-919.

[4] Kubohara T. and Ii H., Cu Co and Ni Contamination Index for River Using River Insects and River Plants. International Journal of GEOMATE, Vol.11, Issue 26, 2016, pp.2651-2658.

[5] Kubohara T. and Ii H., Zn and Fe Contamination Index for River using River Insects and Water Plants in The Kinokawa River Catchment. International Journal of GEOMATE, Vol.19, Issue 75, 2020, pp.76-83.Awal ASMA, Hosseini H. and Hossain M.Z., Strength, Modulus of Elasticity and Shrinkage Behaviour of Concrete Containing Waste Carpet Fiber, International Journal of GEOMATE, Vol. 9, Issue 17, 2015, pp. 1441-1446.

Copyright © Int. J. of GEOMATE All rights reserved, including making copies, unless permission is obtained from the copyright proprietors.

15th Int. Conf. on Geotechnique, Construction Materials & Environment,
Kyoto, Japan, 11-13 November 2025, ISBN 978-4-909106124 C3051

DEVELOPMENT OF A HAZARD ASSESSMENT APPROACH BASED ON AN INTEGRATED MODEL FOR LARGE WOODY DEBRIS DISCHARGE IN DAM WATERSHEDS

Yunhao Liu[1], Daisuke Komori[1,2, 3], Sartsin Phakdimek[4] and Yuta Abe[5]

[1]Graduate School of Environmental Studies, Tohoku University, Japan;
[2] Green Goals Initiative, Tohoku University, Japan;
[3] International Research Institute of Disaster Science, Tohoku University, Japan;
[4] School of Geotechnology, Institute of Engineering, Suranaree University of Technology, Thailand;
[5] Department of Civil and Environmental Engineering, Tohoku University, Japan

ABSTRACT

This study proposes a physically based framework for assessing the hazard of large woody debris (LWD) discharge in dam watersheds under extreme rainfall conditions. The method integrates rainfall return-level analysis, landslide-induced LWD recruitment modeling, and discharge simulation using a double storage function with the lumped hydrological method at a watershed scale. It was applied to five representative dam watersheds in Japan to simulate the potential minimum, maximum, and expected LWD discharge volumes under varying rainfall return periods. The results demonstrate that the framework effectively captures the variability in discharge responses across sites and identifies dam-specific rainfall thresholds for potential LWD discharge. Particularly, the use of expected initial storage conditions significantly improves the reliability of hazard estimation. The observed LWD discharge records were consistently bound by the simulated discharge ranges, validating the model's applicability. In contrast to traditional observation-based approaches, this framework enables estimation of low-frequency hazards. It offers a practical tool for risk-informed reservoir management and indicates the importance of integrating physical processes in LWD hazard prediction. These findings contribute to understanding inter-site differences in LWD storage and transport behavior, enabling more proactive hazard mitigation planning under increasing extreme weather events.

Keywords: Large woody debris, Landslide, Recruitment, Storage, Hazard assessment

INTRODUCTION

Large woody debris (LWD), generated by natural and anthropogenic processes such as mass movements and bank erosion, can be transported downstream during extreme rainfall events, threatening both ecosystems and infrastructure [1]. In mountainous regions, rainfall-induced landslides and debris flows often trigger LWD mobilization, as observed during Typhoon Lionrock in Iwate Prefecture, where transport of LWD exacerbated infrastructure damage [2]. Dam reservoirs are particularly vulnerable due to reduction in reservoir storage capacity [3].

Extensive research has been conducted on LWD recruitment and mobilization, primarily through field surveys [4]. However, due to the lack of long-term observational data on LWD dynamics, accurately predicting LWD-related hazards remains challenging. GIS-based methods that estimate LWD discharge from landslides using forest cover and land use data have also been developed [5,6], but these approaches often overestimate actual discharge volumes. To overcome such limitations, physically based modeling of LWD dynamics has emerged as a promising alternative. Komori [7] proposed a watershed-scale integrated model that incorporates landslide-induced LWD recruitment with a double storage function model using a lumped hydrological approach. The model introduces virtual tanks to represent the storage and transport of LWD within mountainous watersheds and has been successfully applied to multiple dam watersheds in Japan [8]. This study proposed the integrated framework by applying it to selected representative dam watersheds in Japan to assess LWD hazards, verify the feasibility of the approach, and examine the site-specific characteristics of LWD discharge behavior.

RESEARCH SIGNIFICANCE

This study adapted a previously developed LWD export model [7,8] for hazard assessment applications. The approach enables the simulation of potential LWD discharge volumes under varying rainfall conditions, including extreme events, by leveraging a budget framework that incorporates the key processes of recruitment, storage, and transport. It addresses the disconnect between the estimated LWD supply and its potential downstream discharge including expected volume, minimum and maximum volume.

STUDY SITES

Five dam watersheds were selected as study sites for this research, located across six prefectures in central and northeastern Japan: Nagano, Niigata, Tochigi, Yamagata, Akita, and Iwate. These watersheds were chosen to represent a range of topographic and climatic conditions characteristic of mountainous regions prone to rainfall-induced landslides and LWD transport. While geographically dispersed, the sites share similar forest coverage, slope gradients, and dam management practices, making them suitable for comparative hazard assessment under varying rainfall scenarios. The spatial distribution of Dam No. 1 to No. 5 is illustrated in Fig.1. Their key physical characteristics are summarized in Table 1.

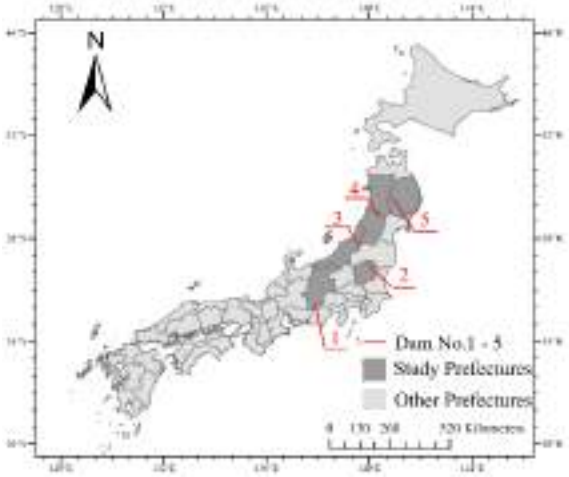

Fig.1 Locations of the five selected dam watersheds

Table 1 Basic characteristics of the five selected dam watersheds

No.	Dam	Area (km^2)	Length (km)
1	Katagiri	14.86	8.58
2	Shiobara	123.96	113.29
3	Tainaikawa	72.68	55.44
4	Kamuro	22.29	15.23
5	Yuda	577.49	512.25

Note: Area refers to total watershed area; length refers to total river length within the watershed.

Given the temporal coverage and spatial variability of the selected sites, these discharge data reflect a wide range of hydrological and geomorphic conditions relevant to LWD transport.

In Japan, local reservoir management agencies monitor the total annual volume of LWD transported into reservoirs [7]. Table 2 summarizes the highest single-year LWD discharge volume and the associated annual maximum 24-hour rainfall for each study dam during the period 1996–2021. It reflects LWD responses to extreme rainfall events, as represented by the years of maximum discharge. Despite the limited range of 24-hour rainfall (240–343 mm), it corresponds to varying rainfall intensities across sites (e.g., different return periods), which will be examined in this study.

Table 2 Highest single-year LWD discharge volumes and associated annual maximum 24-hour rainfall for each study dam (1996–2021).

No.	Max. Volume (m^3)	Max. Rainfall (mm/24hrs)
1	610	288
2	3295	343
3	397	281
4	246	242
5	2490	240

Note: Dam No. 1–5 correspond to the five study dams listed in Table 1. Max Volume indicates the highest recorded annual LWD discharge for each dam during 1996–2021. Max Rainfall refers to the maximum 24-hour rainfall over the corresponding watershed in the same year.

METHODS

The objectives of this study are two parts: (1) identify the minimum rainfall return period at which potential LWD discharge begins at each site, and (2) quantify the range of potential LWD discharge (including minimum, maximum, and expected values) under various return periods. The overall framework and methodology are presented in this section.

Rainfall Return Period and Level Analysis

Annual maximum 24-hour rainfall data (1996–2021) within five dam watersheds were extracted from the Radar-AMeDAS dataset provided by the Japan Meteorological Agency, with a spatial resolution of 1 km. For each dam watershed, the series of annual maximum was fitted to the Generalized Extreme Value (GEV) distribution to estimate rainfall intensities corresponding to different return periods [9]. The GEV distribution is widely used for hydrological hazard assessment and is defined as:

$$F(x) = \exp\left\{-[1+\xi(\frac{x-\mu}{\sigma})]^{-1/\xi}\right\} \quad (1)$$

where μ, σ, and ξ are the location, scale, and shape parameters, respectively. Parameters were estimated using the L-moments method, based on 26 years (1996–2021) of rainfall data.

From the fitted distribution, the rainfall return levels x_T within in each dam watershed were derived using the inverse of Eq. (1), expressed as:

$$x_T = \mu + \frac{\sigma}{\xi}\left[(-\log(1-\frac{1}{T}))^{-\xi} - 1\right] \quad (2)$$

Return levels for various return periods T (e.g., 3–200 years) were calculated and used as rainfall inputs for subsequent landslide modeling under different hazard scenarios. These synthetic extreme rainfall values allow comparison between observed historical conditions and potential future extremes.

LWD Recruitment Simulation

This provided two sets of outputs: annual LWD recruitment volumes based on historical rainfall, and potential recruitment volumes under different return periods. The recruitment of LWD from landslides was estimated using a previously developed analytical framework [8,10]. These results served as input to the discharge simulation process described in the next section.

Discharge Simulation and Hazard Assessment

The discharge of LWD from dam watersheds was simulated using a double storage function model based on the lumped hydrological method, following the approach of [7]. This section describes how the proposed model is used to calculate the expected, maximum, and minimum potential LWD discharge.

This section involved three steps. In the first step, dam-specific model parameters for each study site were identified by fitting the model to observe annual LWD discharge records from 1996 to 2021. For each dam, annual recruitment volumes were used as inputs, and parameter sets were determined by maximizing the Nash–Sutcliffe Efficiency (NSE) between observed and simulated discharge values [11]. The structure of the model remained fixed, and parameter optimization was conducted independently for each dam watershed. The structure of the model and its key parameters are illustrated in Fig. 2.

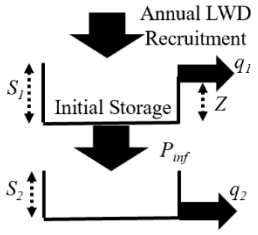

Fig.2 Conceptual framework of the double storage function model

Where S_1 and S_2 are storage volumes in first and second tank (m^3), respectively. Z is the capacity of the first tank, which is one of the model parameters determined by NSE method. Sum of q_1 and q_2 is the annual LWD discharge volume (m^3). The governing equations and parameter definitions are presented below. When $S_1 \geq Z$:

$$q_1 = S_1(n) - Z \quad (3)$$

When $S_1 < Z$:

$$q_1 = 0 \quad (4)$$

$$P_{\inf} = b \cdot S_1(n) \quad (5)$$

$$S_1(n+1) = S_1(n) + P - P_{\inf}(n) \quad (6)$$

$$\frac{dS_2}{dt} = P_{\inf} - q_2(n) \quad (7)$$

$$S_2 = k \cdot q_2^p \quad (8)$$

where b, k and p are parameters, n is time (in years). The following equation defines the NSE:

$$\text{NSE}=1-\frac{\sum_{m=1}^{N}(q_{obs}(m)-q_{sim}(m))^2}{\sum_{m=1}^{N}(q_{obs}(m)-q_{ave}(m))^2} \quad (9)$$

where N is the simulation period (year), m is a year from 1 to N, q_{obs} is the annual observed LWD discharge volume(m^3), q_{sim} is the annual simulated LWD volume (m^3), q_{ave} is the average annual observed LWD volume (m^3).

Subsequently, 10,000 annual LWD recruitment values were randomly generated for each study site. The model was run for each random value using the estimated parameters from the first step, and the resulting storage-to-capacity ratios in first tank were recorded. These ratios were then used to compute an expected initial storage-to-capacity ratios ($r= S_1/Z$) via a weighted average approach, representing the actual LWD storage conditions within dam watershed, which enables the estimation of expected potential LWD discharge. The framework for calculating the expected storage percentage is illustrated in Fig. 3.

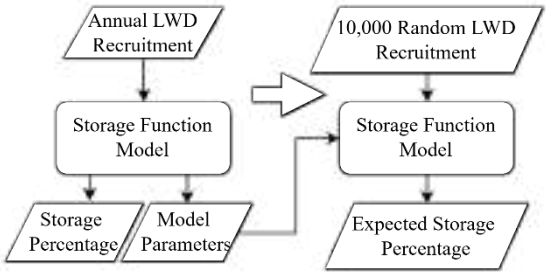

Fig.3 Schematic diagram of expected storage percentage calculation

Finally, using LWD recruitment volumes estimated under return-level rainfall conditions (mm/24 hrs), the double storage function model was run under three initial storage scenarios: empty (0%), saturated (100%), and the expected storage percentage. For each dam watershed and return period, the model produced a distribution of annual LWD discharge volumes, from which the minimum, maximum, and expected values (in m³/year) were derived. These results enabled comparative hazard assessments across sites under varying rainfall conditions.

RESULTS AND DISCCUSIONS

Model Parameters Estimation

The double storage function model described above was applied to five dam watersheds using observed annual maximum 24 hours rainfall and LWD discharge records from 1996 to 2021. Model parameters were determined independently for each site, and the simulated annual LWD discharge was compared with observations to evaluate performance by NSE. The model parameters determined by the NSE are summarized in Table 3.

Table 3 Model Parameters and NSE for each study site

No.	*Z*	*b*	*k*	*p*	NSE values
1	12,000	0.11	0.0001	100	0.900
2	14000	0.215	0.0476	2.44	0.807
3	89,000	0.17	0.0001	100	0.462
4	8,500	0.005	0.0051	9.10	0.408
5	9,000	0.47	0.0001	100	0.705

Note: Dam No. 1–5 correspond to the five study dams listed in Table 1. Z,b,k and p are model parameters in double storage function model

Expected Initial Storage Estimation

The expected initial storage-to-capacity ratios ($r = S_1/Z$) for the five dam watersheds, estimated through 10,000 stochastic simulations per site, are spatially presented in Fig. 5.

The values vary substantially among sites, ranging from 14% at Katagiri Dam to 95% at Yuda Dam. Katagiri and Shiobara Dams exhibited relatively low expected storage ratios (14% and 29%, respectively), indicating that annual LWD recruitment volumes at these sites were generally insufficient to saturate the LWD storage capcacity within in watershed. In contrast, Yuda Dam showed a markedly high value of 95%, indicating a high possibility of storage capacity exceedance. Tainaikawa and Kamuro Dams showed intermediate ratios of 78% and 52%, respectively. These differences reflect variation in modeled LWD accumulation dynamics across the study of watersheds under historical discharge conditions.

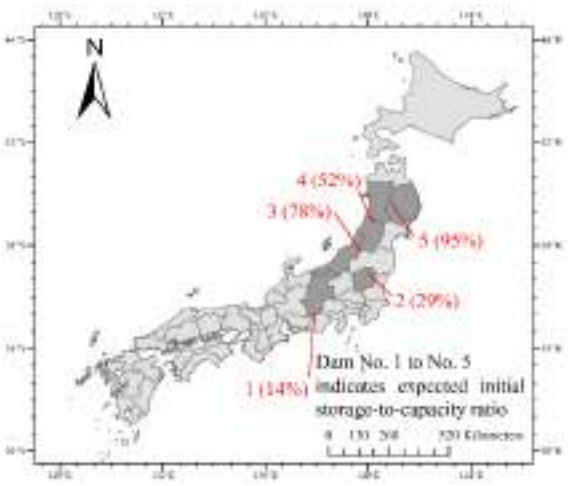

Fig.5 Spatial distribution of expected storage-to-capacity ratios (*r*) at five study dams.

Hazard Assessment Results

The results of LWD discharge simulations under rainfall return-level scenarios are presented in Fig. 6, which illustrates the estimated potential minimum, maximum, and expected discharge volumes for the five study sites. Horizontal axes represent rainfall return periods T (e.g., 3–200 years) and corresponding to different return levels (mm/24hrs), and vertical axes show LWD volumes (m³/year), including simulated potential discharges (q_{min},q_{exp} *and* q_{max}), model input potential recruitment (*P*), and observed records (q_{obs}). The black dots showed the selected LWD discharge records. As shown in Fig. 6, all black dots representing observed LWD discharge volumes fall within the modeled range of potential discharge, indicating the reliability of the hazard assessment results. Although the observational records are primarily corresponded to return periods shorter than 45 years (e.g., Fig. 6(4)), the modeling framework developed in this study enables estimation of LWD discharge for lower-frequency events beyond the observed range. This represents a significant improvement over approaches that rely exclusively on historical records, which are inherently limited in their ability to assess rare but potentially large volume LWD discharge events.

Rainfall return period and potential LWD discharge

One notable feature in Fig. 6 is the substantial variation in rainfall return levels across all sites within the same return periods. This disparity is particularly critical when determining the minimum rainfall return period at which LWD discharge is likely to occur.

Among the five study sites, the Shiobara and Katagiri dam watersheds were selected as

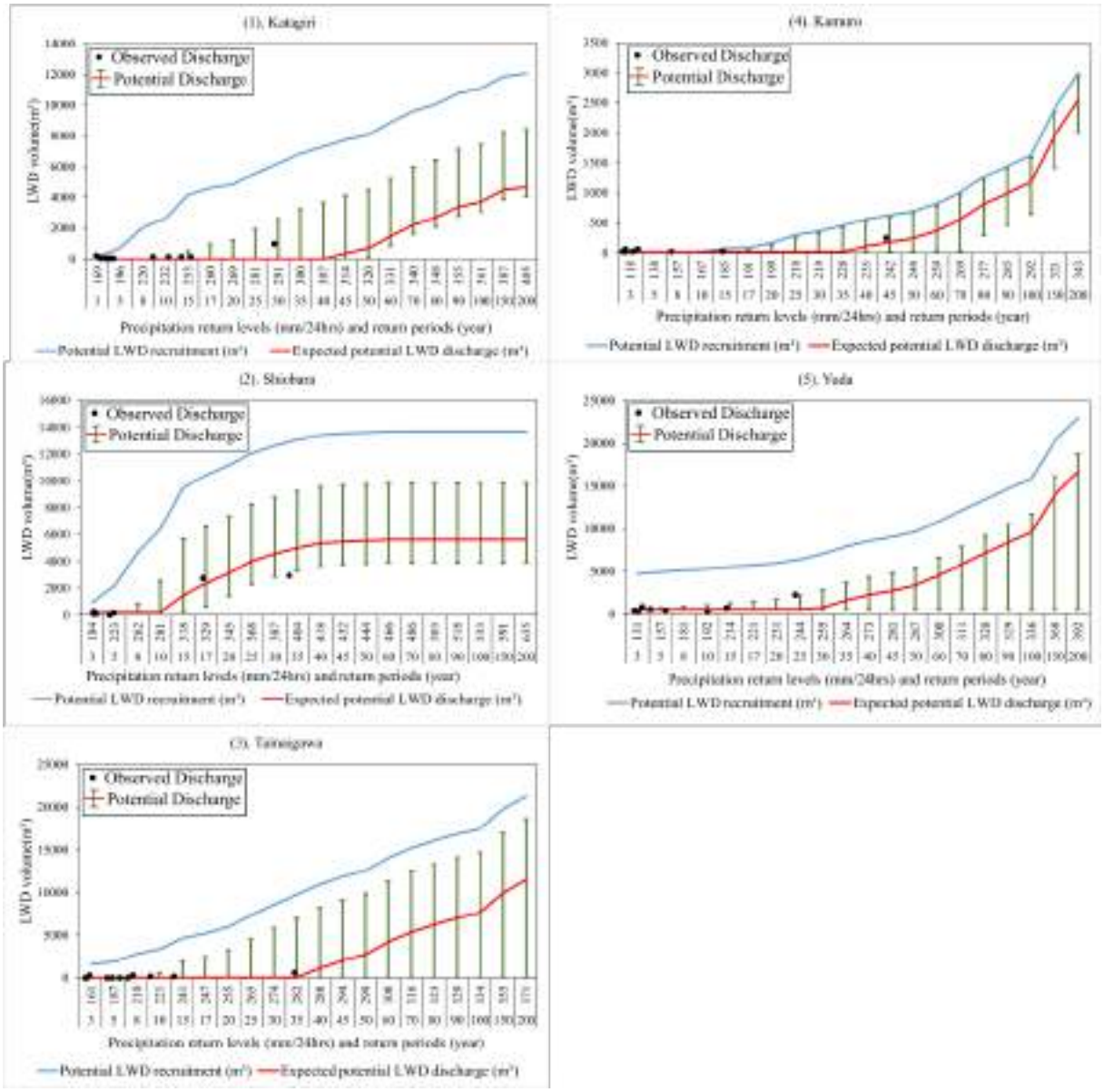

Fig.6 Simulated hazard assessment of potential LWD discharge volume under varying rainfall return periods for the five study sites.

representative cases to illustrate the contrasting responses of LWD discharge to varying rainfall return periods within each watershed.

Shiobara Dam (Fig. 6(2)) showed a rapid increase in expected discharge volume (q_{exp}) starting at a return period of 10 years (281 mm/24hrs), with q_{exp} reaching 217 m³ and q_{max} exceeding 2500 m³.

In contrast, Katagiri Dam (Fig. 6(1)) exhibited a more gradual discharge response. q_{exp} began to increase noticeably only after a 40-year return period (307 mm), reaching 4681 m³ at 200 years (405 mm), while q_{max} peaked at 8430 m³. The findings suggest that the response of LWD discharge to rainfall return periods and levels varied significantly among different dam catchments.

LWD storage characteristics of dam watershed

The results can be used to further explore LWD discharge risks from a storage characteristics perspective, based on their contrasting proportions of discharge to recruitment volume. These ratios reflect the overall capacity of each watershed to retain LWD before it is discharged, offering an additional dimension to hazard assessment. The values for catchments No.1 to No.5 were 0.62, 0.68, 0.80, 0.96, and 0.62, respectively.

Among all sites, Kamuro Dam exhibited a q_{max} to P ratio of 0.96, placing it among the highest. This suggests that under extreme rainfall, nearly the entire volume of recruited LWD may be discharged downstream. Such a condition indicates weak long-term storage capacity and frequent saturation of LWD

retention potential, increasing the likelihood of high-magnitude discharge events even under relatively moderate recurrence intervals.

In contrast, Katagiri Dam and Yuda Dam showed the lowest discharge-to-recruitment ratios among the five sites, with values of 0.62 for q_{max}. These results reflect comparatively strong LWD storage performance, where most of the recruited LWD is retained within the watershed. Consequently, the probability of sudden large-scale LWD discharge events is reduced, making this site relatively low risk from a storage-based hazard perspective.

CONCLUSIONS

This study estimated the potential discharge of large woody debris (LWD) in five dam watersheds under varying rainfall return periods, focusing on the minimum, maximum, and expected annual discharge volumes. By incorporating stochastic recruitment and evaluating discharge ranges under different storage scenarios, the expected potential discharge was successfully simulated. Simulation results revealed clear inter-watershed differences in discharge behavior and storage characteristics, with expected discharge values serving as a reliable indicator of site-specific LWD discharge risk. To further enhance the generalizability of the proposed hazard assessment framework, future studies are encouraged to include a broader range of dam watersheds with diverse geomorphological and climatic conditions. Expanding the number of study sites would enable a more comprehensive understanding of regional patterns in LWD discharge dynamics and support the development of region-specific hazard mitigation strategies.

ACKNOWLEDGMENTS

The authors would like to thank the Water Resources Environment Technology Centre and the Japanese Ministry of Land, Infrastructure and Transport (MLIT) for their assistance in providing and collecting data on LW. The authors also thank Seiki Kawagoe, Katsuhiro Nakao, and Haruka Tsunetaka for their valuable advice. This research was funded by the Ministry of Land, Infrastructure, Transport and Tourism (MLIT), according to the 'Improving the reproducibility of large wood dynamics analysis using the integrated large wood export model (PI: Daisuke Komori)' and the Grants in Aid for Fostering Joint International Research (19KK0362, PI: Daisuke Komori) from the Ministry of Education, Science and Culture, Japan.

REFERENCES

[1] Harmon M. E., Franklin J. F., Swanson F. J., Sollins P., Gregory S. V., Lattin J. D., Cummins K. W., Ecology of Coarse Woody Debris in Temperate Ecosystems, Advances in Ecological Research, Vol. 15, 1986, pp.133–302.

[2] Chaithong T., Komori D., Sukegawa Y., Touge Y., Mitobe Y., Anzai S., Landslides and Precipitation Characteristics during the Typhoon Lionrock in Iwate Prefecture, Japan, GEOMATE Journal, Vol. 14, No. 44, 2018, pp.109–114.

[3] Adamo N., Al-Ansari N., Sissakian V., Laue J., Knutsson S., Dam Safety: Sediments and Debris Problems, Journal of Earth Sciences and Geotechnical Engineering, Vol. 11, No. 1, 2021, pp.27–63.

[4] Benda L.E., Sias J.C., A Quantitative Framework for Evaluating the Mass Balance of In-Stream Organic Debris, Forest Ecology and Management, Vol. 172, No. 1, 2003, pp.1–16.

[5] Chaithong T. A Model for Assessment of Tree Stability and Entrainment of Woody Debris by Flow Slides and Shallow Slope Failure, GEOMATE Journal, Vol. 19, No. 71, 2020, pp.77–83.

[6] Yano S., Shogaki T., Yato S., Tsusue A., Wu Y., Kasama K., Development of Logistic Regression Model for Slope Failure and Estimation of Driftwoods Generation in Marumori Town due to the East Japan Typhoon 2019, Journal of Japan Society of Civil Engineers, Ser. B1 (Hydraulic Engineering), Vol. 76, No. 1, 2020, pp.253–263.

[7] Komori D., Sukegawa Y., Chaithong T., Kazama S., Modelling of large wood export at a watershed scale, Earth Surface Processes and Landforms, Vol. 47, No. 2, 2022, pp.688–696.

[8] Abe Y., Phakdimek S., Komori D., The relationship between large wood export and the long-term large wood budget on an annual scale in Japan, using storage function with the lumped hydrological method, Water, Vol. 16, No. 7, 2024, pp.920.

[9] Seo J.I., Nakamura F., Chun K.W., Kim S.W., Grant G.E., Precipitation patterns control the distribution and export of large wood at the catchment scale, Hydrological Processes, Vol. 29, No. 24, 2015, pp.5044–5057.

[10] Phakdimek S., Komori D., Chaithong T., Abe Y., Physically based model for assessing rainfall-induced deep-seated landslides using a hydrological-geotechnical model, Annals of GIS, Vol. 31, No. 2, 2025, pp.301-331.

[11] Nash J. E. and Sutcliffe J. V., River Flow Forecasting Through Conceptual Models Part I— A Discussion of Principles, Journal of Hydrology, Vol. 10, No. 3, 1970, pp. 282–290.

Copyright © Int. J. of GEOMATE All rights reserved, including making copies, unless permission is obtained from the copyright proprietors.

15th Int. Conf. on Geotechnique, Construction Materials & Environment,
Kyoto, Japan, 11-13 November 2025, ISBN 978-4-909106124 C3051

ECOSYSTEM-LEVEL ASSESSMENT OF THE ADSORPTION AND REMOVAL CAPACITY OF CALCIA-IMPROVED SOILS USING MICROCOSM-WET TEST

Sosuke Sato[1] and Kazuhito Murakami[2]

[1]Graduate School of Engineering, Chiba Institute of Technology, Chiba, Japan; [2]Department of Life Sciences, Chiba Institute of Technology, Chiba, Japan

ABSTRACT

An ecosystem-level evaluation was conducted to assess the adsorption and removal capacity of Calcia-improved soil for eluates derived from decaying green tide algae (*Ulva* spp.) using a microcosm-based Whole Effluent Toxicity (WET) test. Calcia-improved soil, produced from steelmaking slag, is recognized as a useful recycled material; however, its environmental impact must be carefully considered before application. The microcosm (N-system) used in this study is a flask-scale model ecosystem composed of three phytoplankton species, four zooplankton species, and four dominant bacterial species, providing high reproducibility and stability. In the microcosm-WET test, dissolved oxygen (DO) levels (functional parameter) were continuously monitored, and microbial abundance (structural parameter) was observed microscopically following the addition of treated or untreated eluates containing unsolidified Calcia-improved soil. Data were statistically analyzed using branched-type ANOVA. For both parameters, the highest concentration with no significant effect was defined as the microcosm No Observed Effect Concentration (m-NOEC), and the toxicity unit (TU) was calculated as the inverse of the dilution factor. The treated eluate showed an m-NOEC of 2.5% and a TU of 40, indicating lower ecological impact compared to the untreated eluate. Considering a previously proposed safety factor of 200 for microcosm tests, these results suggest that Calcia-improved soil is unlikely to cause significant adverse effects on the actual environment.

Keywords: Calcia-improved soil, Microcosm, Microcosm-WET test, Green tide alga, Ulva spp.

INTRODUCTION

With increasing environmental awareness in Japan, Calcia-improved soil has been recognized as a recycled material that contributes to resource and energy conservation by reducing environmental burden. It is currently used as a reclamation material for bottom sediments in coastal areas [1]. Calcia-improved soil is produced by mixing Calcia-modified material with dredged sediment (Fig. 1). This material enhances the strength of bottom sediments and improves water quality, making it a promising option for sediment remediation. However, due to the specific characteristics of its raw materials, careful consideration of its potential impact on water quality is required when applying it. At present, most safety assessments rely on chemical analyses, while biological tests are primarily conducted using single-species approaches. Such tests do not account for interspecies interactions, and therefore, cannot fully reflect the material's impact under actual environmental conditions [2]. To address this limitation, microcosm-based Whole Effluent Toxicity (WET) tests, which simulate natural ecosystems and incorporate interactions among multiple species, have been proposed as an effective evaluation method [3–6]. This study is based on the conceptual framework that considers ecosystem health as a function of both structural parameters, such as species composition and abundance, and functional parameters, such as primary production and respiration. By applying this integrated approach, the potential ecological impact of Calcia-improved soil can be assessed more comprehensively than with conventional chemical or single-species tests. In this study, we focused on the adsorption and removal capacity of Calcia-improved soil and aimed to evaluate its effectiveness for bottom sediment remediation and its ecological impact in tidal flat environments affected by green tides. This research was conducted with the assumption of practical application in real-world coastal environments.

Fig.1 Overview of Calcia-improved soil

MATERIALS AND METHODS

Calcia-Improved Soil

Calcia-improved soil is a recycled material produced by mixing Calcia-modified material, derived from steel slag with adjusted particle size and composition, with dredged sediment [1]. The incorporation of Calcia-modified material enhances the strength of the mixture, and its adsorption and removal capacities for substances such as phosphorus and sulfides are expected to contribute to water quality improvement. However, due to the properties of the steel slag raw material, the mixture is known to increase pH levels, particularly in water, which must be carefully considered when applied in real environments. The typical mixing ratio for Calcia-improved soil is approximately 30% [1]. Previous dissolution experiments conducted at mixture ratios of 30%, 20%, and 10% demonstrated significant pH differences between the 30% mixture and the lower ratios. Consequently, this study focused on evaluating the 20% and 30% mixture ratios.

Microcosm

A microcosm is a simulated ecosystem in which multiple species coexist in a flask under controlled conditions (Fig. 2). Because it reproduces material cycles and interactions among organisms found in natural ecosystems, it is considered a method that enables impact assessment at the ecosystem level, compared to conventional single-species tests. Additionally, it offers advantages such as low cost and high reproducibility. In this study, we used a gnotobiotic-type microcosm (N-system) in passaged culture. All species constituting the N-system microcosm are known, including the green algae *Chlorella* sp. (1.1×10^5 N/ml) and *Scenedesmus quadricauda* (5.3×10^3 N/ml) as producers; the filamentous algae *Tolypothrix* sp. (8.0×10^2 cm/ml) and the protozoan ciliate *Cyclidium glaucoma* (6.0×10^3 N/ml) as predators; the metazoan ciliates *Lecane* sp. (1.3×10^2 N/ml), *Philodina erythrophthalma* (1.1×10^1 N/ml), and *Aeolosoma hemprichi* (1.0×10^1 N/ml); and dominant decomposer bacteria comprising four species (*Bacillus cereus*, *Pseudomonas putida*, *Acinetobacter* sp., and coryneform bacteria) totaling 1.1×10^6 CFU/ml. Numbers in parentheses indicate steady-state populations in non-additive systems. These microorganisms were self-selected through repeated culture. This system exhibits high reproducibility and stability, as reflected in the growth curves of each microorganism. Microcosms were cultured in 300 ml triangular flasks containing 200 ml of TP_{100} medium (Taub + Peptone 100 mg medium). After the addition of 10 ml of microcosm inoculum, they were incubated at 25°C under 2400 lux with a 12 h light/dark cycle for 30 days [3,7,8]. Each experimental condition was conducted in triplicate, and data were analyzed using t-tests for statistical significance. The coefficients of variation (standard deviation divided by mean, expressed as a percentage) for production and respiration rates during the first 7 days of culture were 20% or less (based on 25 independent experiments), and 5% or less from days 14 to 21. These values are consistent with previously reported results (e.g., Sugiura 2001). The results presented in the figures represent the means of three independent experiments. Differences between treated and control microcosms were evaluated using branched-type analysis of variance (ANOVA), which considers errors among samples as random variables.

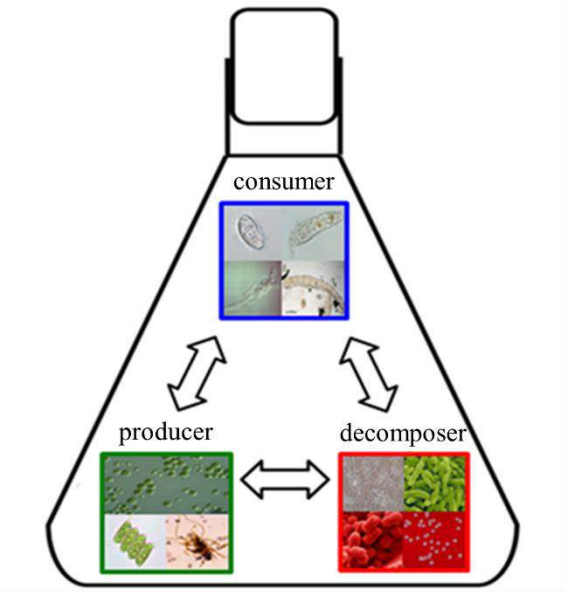

Fig.2 Outline of microcosm

Microcosm-WET Test

In the microcosm WET test, a diluted test stock solution is added as a replacement for the liquid medium in the microcosm, and the response is observed to evaluate the effects (Fig. 3). The test solution was diluted using TP_2 medium, which is adjusted for peptone content, to prevent any effects on the microcosm organisms other than those caused by the test solution itself. Prior to addition, the microcosm was transferred to a centrifuge tube and centrifuged at 250 ×g for 5 minutes. The supernatant was then removed using a micropipette to adjust the

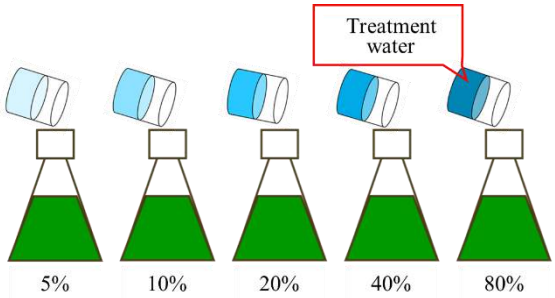

Fig.3 Outline of microcosm-WET test

biomass. After biomass adjustment, the test stock solution was diluted stepwise with TP_2 medium to concentrations of 0, 5, 10, 20, 40, and 80% for addition.

Preparation of Eluate

The experiment was conducted using *Ulva* spp. collected from the Yatsu Tidal Flat in Narashino City, Chiba Prefecture (Fig. 4). Yatsu Tidal Flat is an artificial tidal flat created through coastal land reclamation and was registered under the Ramsar Convention in 1993. It serves as an important stopover site for migratory birds, and conservation efforts, including citizen-led activities, are ongoing. In recent years, however, due to sludge outflow, the tidal flats have become saltier and sandier, leading to the large-scale proliferation of *Ulva* spp. This excessive growth has caused foul odors, degraded the landscape, and reduced the number of migratory birds

Fig.4 Location of Yatsu Tidal Flat

Fig.5 A green tide that occurred on the Yatsu tidal flat (left) and the *Ulva* spp. that makes up the green tide (right)

(Fig. 5). Consequently, there are concerns that the area's ecological value as a Ramsar wetland may be at risk [9–12]. To prepare the eluate, 2000 ml of TP_2 medium was added to the harvested Ulva spp., and the mixture was allowed to decompose for 7 days at 30°C under 2400 lux light conditions. After decomposition, solids were removed to obtain the test solution. To evaluate the adsorption capacity of ratios of 20% and 30% were placed in a funnel, and Calcia-improved soil, materials prepared with mixing the test solution was filtered through each to produce the 20% filtered and 30% filtered test solutions, respectively (Fig. 6). The Calcia-modified material was provided by the Nippon Slag Association. Water quality parameters of the test stock solution were also analyzed, including COD, T-N, NO_3-N, NO_2-N, NH_4-N, T-P, PO_4-P, Cl, pH, and H_2S-S. COD was measured using the potassium permanganate method. T-N and T-P were determined by absorbance spectrophotometry following potassium peroxodisulfate decomposition. Cl was measured using the silver nitrate titration method, and the remaining parameters were analyzed using a pack test.

Fig.6 Test stock solution preparation method

Table1 Water quality of test stock solution

	Decaying *Ulva* spp. leachate water	Filtered water with dredged soil	Filtered water with 20% calcia-improved soil	Filtered water with 30% calcia-improved soil
COD(mg/L)	76	42.4	44	58
T-N(mg/L)	20.2	66.1	21.1	19.5
NO_3-N(mg/L)	7.3	10.0	14.0	2.1
NO_2-N(mg/L)	0.12	0.07	0.07	0.01
NH_4-N(mg/L)	4.4	3.1	1.5	3.0
T-P(mg/L)	4.0	3.6	0.2	2.1
PO_4-P(mg/L)	1.87	3.02	0.04	0.37
Cl(mg/L)	827.2	1489.0	472.7	236.4
pH	9.19	9.19	11.3	11.6
H_2S-S(mg/L)	0.1	0.1	0.1	0.1

Evaluation Method

The ecological impact of each concentration of green tide eluate was assessed based on changes in dissolved oxygen (DO) in the microcosm, which were continuously monitored using a DO meter. The transitions of production (P), respiration (R), and the P/R ratio, representing functional parameters, were calculated. In parallel, plankton samples were collected from the microcosm on days 0, 2, 4, 7, 14, 16, 18, 20, 23, and 30 after the start of the culture. The number of microorganisms was observed under a light microscope using a plankton counter to evaluate the temporal transition of structural parameters. In addition, branched-type analysis of variance (ANOVA) was performed to statistically analyze

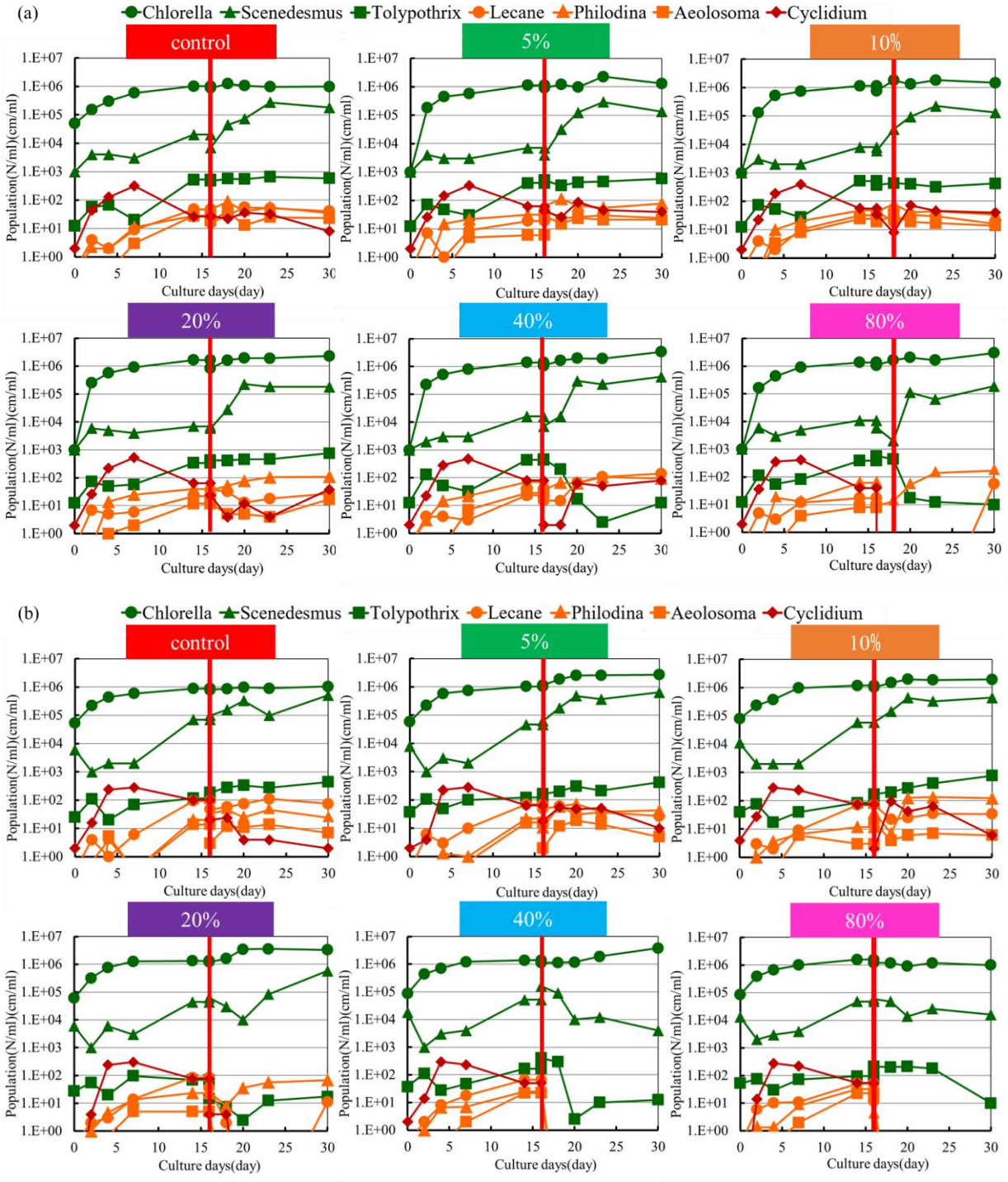

Fig.7 Changes in the population of plankton in the microcosm. (a) filtered water with 20% Calcia-improved soil added system (upper), and (b) filtered water with 30% Calcia-improved soil added system (lower). (The red vertical line indicates the date on which the test stock solution was added.)

changes in both functional and structural parameters over time. As shown in Table 2, the branched-type ANOVA evaluated two aspects: the "group" effect, representing variance among all system values, and the "interaction" effect, representing variance over time [3]. For both functional and structural parameters, the highest concentration with no statistically significant effect, based on the branched-type ANOVA results, was defined as the maximum no observed effect concentration (m-NOEC). The toxicity unit (TU) was calculated using Eq.(1). A safety factor of 200 has been proposed for this microcosm test based on previous studies [3,4,12].

$$TU = \frac{100}{m\text{-}NOEC} \quad (1)$$

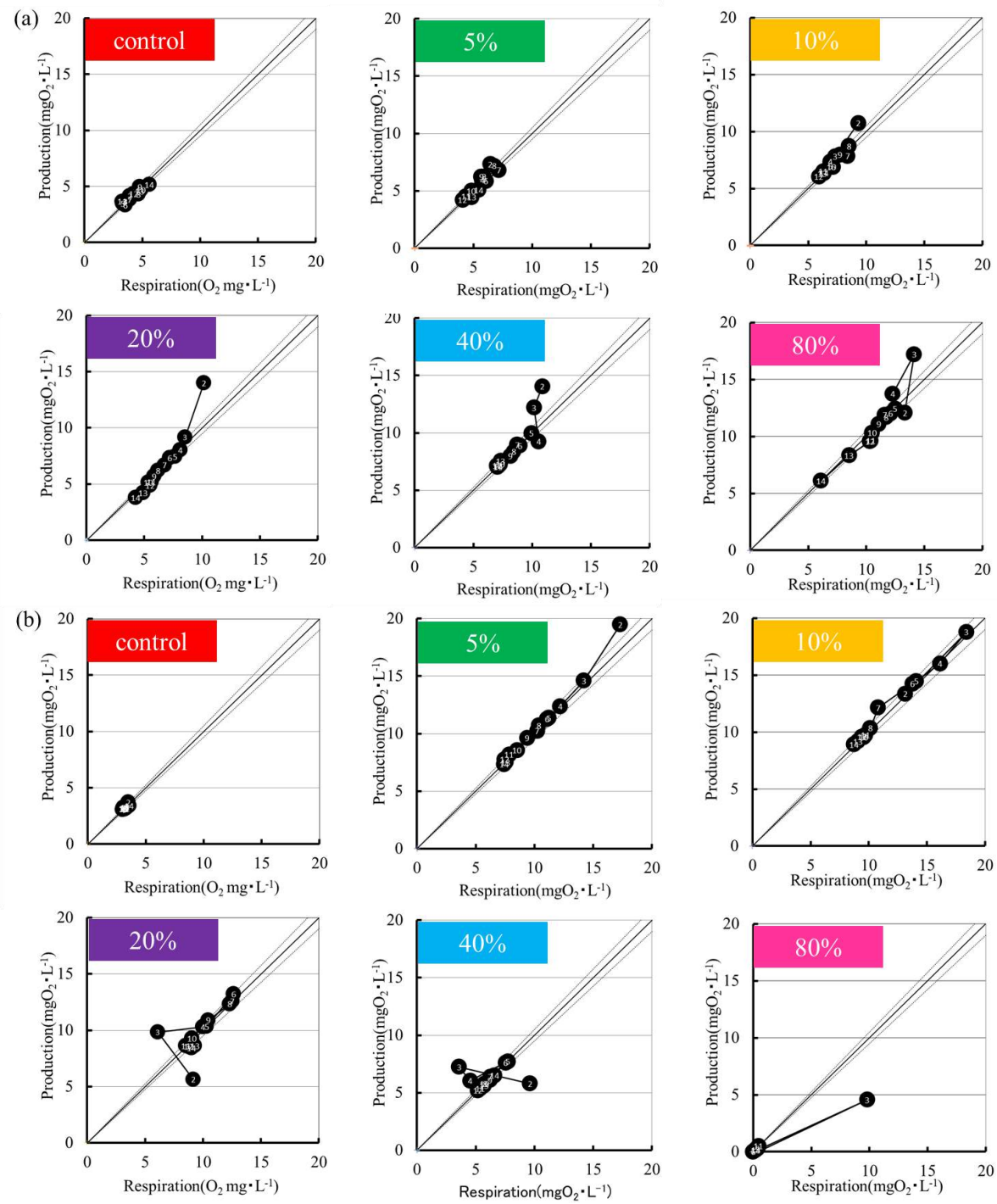

Fig.8 Changes in P/R ratio of microcosm. a) filtered water with 20% Calcia-improved soil added system (upper), and b) filtered water with 30% Calcia-improved soil added system (lower). (The dotted lines in the figures indicate a range of plus or minus 0.05, respectively.)

RESULTS AND DISCUSSION

Improvement Effect on Water Quality

The results of the water quality analysis are presented in Table 1. Four types of solutions were analyzed: decaying *Ulva* spp. leachate, filtered water with dredged soil, filtered water with 20% Calcia-improved soil, and filtered water with 30% Calcia-improved soil. A comparison of the water quality between the decaying *Ulva* spp. leachate and the filtered water with dredged soil before the addition of Calcia-modified materials with the filtered water containing Calcia-improved soil revealed a notable decrease in T-P and PO_4-P concentrations, particularly in the filtered water samples.

Improvement Effect on Ecosystem Structure

Fig. 7 shows the changes in plankton populations within the microcosm system. In the system where filtered water containing 20% Calcia-improved soil was added, decreases or local extinction of zooplankton species such as *Cyclidium glaucoma*, *Lecane* sp., *Philodina erythrophthalma*, and *Aeolosoma hemprichi*, as well as some phytoplankton species such as *Tolypothrix* sp., were observed at higher concentrations. However, partial recovery of some species, including *Lecane* sp. and *Philodina erythrophthalma*, was also recorded. In the system where filtered water containing 30% Calcia-improved soil was added, similar decreases or extinction of species such as *Cyclidium glaucoma*, *Lecane* sp., *Philodina erythrophthalma*, and *Aeolosoma hemprichi* occurred. However, no recovery of these species was observed at the 40% and 80% concentration levels. Based on these findings, it was concluded that a Calcia-modified material mixing rate of 20% is appropriate for mitigating the ecological impacts associated with green tide events.

Improvement Effect on Ecosystem Function

Fig. 8 shows the P/R ratio in the microcosm system. In the system where filtered water containing 20% Calcia-improved soil was added, the P/R ratio converged to approximately 1 at most addition concentrations, indicating that the internal balance between production and respiration within the system was maintained. In the system where filtered water containing 30% Calcia-improved soil was added, the P/R ratio also converged to around 1 in most cases. However, in the system where the addition concentration reached 80%, both production and respiration rates decreased significantly. Based on these results, it was similarly concluded that a Calcia-modified material mixing rate of 20% is appropriate for maintaining ecosystem function. Table 2 shows the results of statistical analysis using branched-type ANOVA. The analysis indicated that all addition systems exhibited statistically significant effects. Based on these findings, the NOEC (no observed effect concentration) was defined as half of the LOEC (lowest observed effect concentration), resulting in a calculated m-NOEC of 2.5% and a toxicity unit (TU) of 40.

Steel Slag Utilization for Green Tide Influence Reduction

In terms of structural parameters, specifically the number of individuals, effects were observed at concentrations exceeding 40% in the system where filtered water containing 20% Calcia-improved soil was added, and at concentrations exceeding 20% in the system with 30% Calcia-improved soil. In particular, all zooplankton populations were suppressed at 40% and 80% concentrations in the system with 20% Calcia-improved soil. Regarding functional parameters, represented by the P/R ratio, values fluctuated significantly immediately after the addition of the test solution. However, in most of the

Table 2 Statistical analysis results using branched-type ANOVA. Filtered water with 20% Calcia-improved soil added system (left), and filtered water with 20% Calcia-improved soil added system (right).

		P/R ratio	Respiration	Production	Evaluation
5%	group	○	○	○	×
	interaction	○	○	×	
10%	group	○	○	○	×
	interaction	○	○	×	
20%	group	○	○	○	×
	interaction	×	×	×	
40%	group	○	○	○	×
	interaction	×	×	×	
80%	group	○	○	○	×
	interaction	×	×	×	

○ : No effect × : Effected

		P/R ratio	Respiration	Production	Evaluation
5%	group	○	○	○	×
	interaction	○	×	×	
10%	group	○	○	○	×
	interaction	○	×	×	
20%	group	○	×	×	×
	interaction	×	×	×	
40%	group	○	○	○	×
	interaction	×	○	×	
80%	group	×	○	×	×
	interaction	×	×	×	

○ : No effect × : Effected

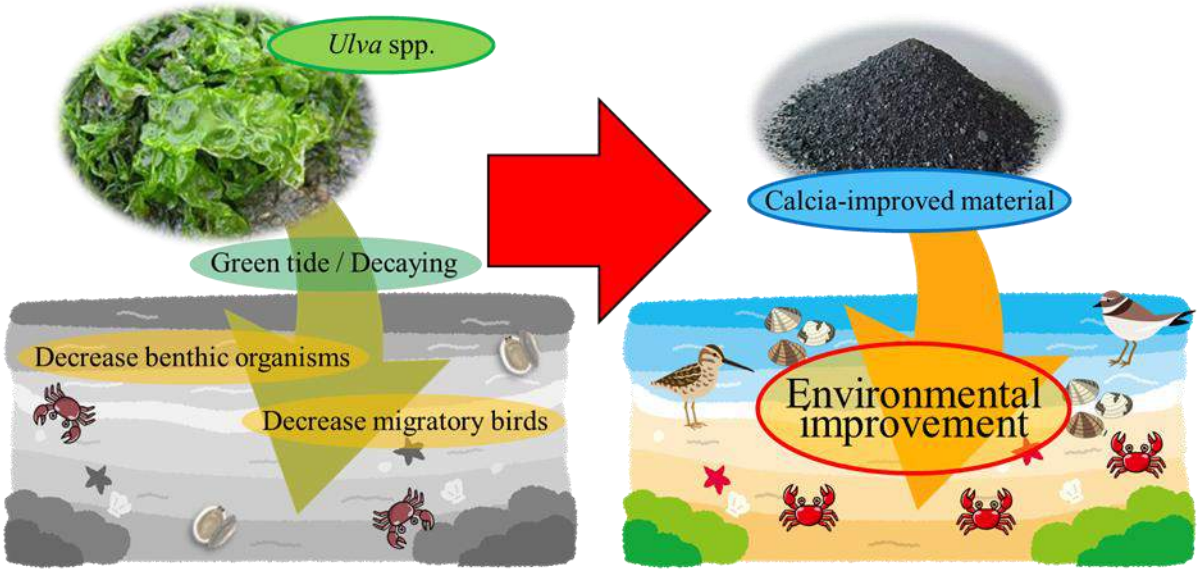

Fig.9 Conceptual diagram of the improvement of tidal flat environment through the use of Calcia-modified materials

addition systems, the P/R ratio gradually converged to approximately 1 over time, suggesting that the effects of Calcia-improved soil on ecosystem function are recoverable under these conditions. In contrast, in the system with 30% Calcia-improved soil at the 80% addition concentration, both production and respiration rates decreased significantly, and no recovery was observed. The observed effects in the high-concentration addition systems are considered to be caused by the increase in pH associated with the use of Calcia-improved soil prior to solidification. It should be noted that this experiment was conducted using a flask-scale simulated ecosystem, and the potential impacts on the actual environment may be overestimated under such controlled experimental conditions. Previous studies have shown that the extrapolation factor, or safety factor, for applying microcosm results to real environmental conditions is 200. Therefore, it is considered unlikely that Calcia-modified material would have a significant negative impact on actual aquatic ecosystems. Based on these results, it was concluded that a Calcia-improved soil mixing rate of 20% is appropriate for mitigating the effects of green tide. It is also important to note that the Calcia-improved soil used in this study was applied immediately after mixing. It is assumed that similar experiments conducted with Calcia-improved soil after solidification would yield different results. Further detailed investigation is required to determine the optimum addition concentrations and to clarify changes in eluate characteristics associated with the aging of *Ulva* spp. The application of Calcia-improved soil as a sediment improvement material has the potential to restore tidal flat environments that have been degraded by the excessive growth of green tide-forming algae (Fig. 9).

CONCLUSIONS

In the system where filtered water with 20% Calcia-improved soil was added (Fig. 7(a)), effects on structural parameters were observed at high addition concentrations of 40% and 80%. Regarding functional parameters, the P/R ratio converged to approximately 1 at most addition concentrations, indicating that the internal balance of the system was maintained. In the system where filtered water with 30% Calcia-improved soil was added (Fig. 7(b)), effects on structural parameters were observed at addition concentrations exceeding 20%. For functional parameters, the P/R ratio also converged to around 1 in most cases; however, at the 80% addition concentration, both production and respiration rates decreased significantly, and no recovery was observed. The m-NOEC was calculated to be 2.5%, and the toxicity unit (TU) was determined to be 40. It should be noted that the Calcia-improved soil used in this study was in a state immediately after mixing. It is assumed that similar experiments using Calcia-improved soil after solidification would produce different results. Therefore, further detailed investigation is required to determine the optimum addition concentrations and to clarify changes in eluate characteristics associated with the aging of *Ulva* spp.

ACKNOWLEDGMENTS

This research was supported by the Nippon Slag

Association through the provision of steel slag materials. We also express our sincere gratitude to Dr. Yuhei Inamori for valuable discussions regarding microcosm analysis. Finally, we would like to thank all individuals and organizations who contributed to this study.

REFERENCES

[1] Yamagoshi Y, Akashi Y, Kitano Y, Kiso E, Kosugi C, Miki O, Nakagawa M, Hata K, Basic Characteristics of CaO-improved Soil, Nippon Steel Technical Report, 399,2014, pp. 51-58.

[2] Sawai A., Okamura T., Miyamoto N., Effluent management by Whole Effluent Toxicity test in Japan, Papers of the Symposium of the Japan Society for Water Environment, 20, 2017, pp. 14.15.

[3] Inamori Y., Microcosm Manual for Environmental Impact Risk Assessment: From Chemicals to Whole Effluent Toxicity (WET), Springer, 2019.

[4] Tsuchiya T., Murakami K., Development of Ecosystem Level Whole Effluent Toxicity Test using Microcosm System, Papers on Environmental Information Science, 33, 2019, pp. 31-36.

[5] Murakami K., Hayashi H. and Shimada R., Microcosm for Impact Risk Assessment of Sediment Remediation Materials on Aquatic Ecosystem, Journal of Water and Environment Technology, 9, 2011, pp. 401-410.

[6] Murakami K., Ruike K., Tsuchiya T., Obata K., Inamori R. and Inamori Y., Ecosystem-Level WET Test of Cafeteria Drainage Using Microcosm System, International Journal of GEOMATE, 20, 2021, pp. 68-75.

[7] Murakami A., Kinoshita M., Ishikawa Y., Yoshida H. and Sugiura K., A Mathematical Modeling for Microcosms (Part 1): Process of Colony Formation, Eco-Engineering, 16, 2004, pp. 161-170.

[8] Murakami A., Kinoshita M., Ishikawa Y., Yoshida H. and Sugiura K., A Mathematical Modeling for Microcosms (Part 2): Conditions of Forming Colonies, Stability and Efficiency of the Microcosm, Eco-Engineering, 16, pp. 2004, pp. 171-180.

[9] Ubukata M. and Murakami K., Situation Analysis of Ecological Environment in Yatsu Tidal Flat by Shorebirds as Umbrella Species, Papers on Environmental Information Science, 34, 2020, pp.145-150.

[10] Ishii Y., Murakami K., Ishii T., Tatsumoto H. and Taki K., Relationship Between Ecological Balance and Environmental Factors in Natural Tidal Flat Left From Reclamation, Proceedings of Civil Engineering in The Ocean, 17, 2001, pp. 129-134.

[11] Yauchi E., Hayami T. and Gomyo M., An Analysis of the Extraordinary Proliferation of *Ulva* Sp. In an Urban Wetland, The Fourteenth International Offshore and Polar Engineering Conference, 2004, pp. 746-750.

[12] Yauchi E., Ishii T., Imoto T. and Gomyo M., Field Study on Proliferation of *Ulva* sp. In Yatsu Higata, Proceedings of civil engineering in the ocean, 23, 2007, pp. 465-470.

Copyright © Int. J. of GEOMATE All rights reserved, including making copies, unless permission is obtained from the copyright proprietors.

15th Int. Conf. on Geotechnique, Construction Materials & Environment,
Kyoto, Japan, 11-13 November 2025, ISBN 978-4-909106124 C3051

LABORATORY EXPERIMENTS OF ARSENIC ADSORPTION CHARACTERISTICS FOR LATERITE GRAINS BY USING FIXED-BED COLUMN STUDY

Nayaka Bandaralage Indraji Madhushan Nayaka Bandara[1], Kengo Nakamura[1], Akihiro Matsuno[2], and Ken Kawamoto[1]

[1]Graduate School of Science and Engineering, Saitama University, Japan
[2]Department of Environmental System, Faculty of Geo–Environmental Science, RISSHO University, Japan

ABSTRACT

Arsenic contamination in drinking water constitutes a significant global public health challenge, especially in areas with high arsenic groundwater. Thus, the development of cost-effective and efficient treatment methods can be imperative. This study examined the applicability of grained laterite in Hanoi, Vietnam, as an economically feasible adsorbent to treat the arsenic contaminated water. A series of laboratory experiments were conducted to examine the effects of calcination of laterite grains and heights of filtration column on the arsenic adsorption performance in the fixed-bed column adsorption system. The tested results were analyzed using adsorption models such as Adams-Bohart, Thomas, and Yoon-Nelson. Additionally, the basic physicochemical properties of both raw and calcined laterite grains were characterized using various analytical techniques such as scanning electron microscopy, energy-dispersive X-ray spectroscopy, and Brunauer-Emmett-Teller surface area analysis. The experimental findings showed that the calcined laterite grains gave higher arsenic removal than raw laterite grains at all column height conditions. Particularly, 5% breakthrough time increased from 270 min to 1230 min in 20 cm column height due to the calcination process. This observation was also supported by the Adams-Bohart model analysis, which indicated an increase in the maximum adsorption capacity from 574 to 3893 mg/L. Conversely, the calculated mass transfer zone height underscored the necessity for an adequate column length to facilitate the full development of the mass transfer zone within the column. The application of laterite grains obtained from Hanoi in Vietnam for arsenic remediation was found to be effective under the tested conditions.

Keywords: Laterite, Arsenic, Filtration, Fixed-bed column experiment, Adsorption model

INTRODUCTION

Groundwater contamination by arsenic is a severe health issue due to its widespread toxicity. It exists in nature as metalloids or chemical compounds, mainly in inorganic forms, primarily as arsenate and arsenite. Arsenite is more toxic, soluble, and mobile than arsenate [1]. About 230 million people worldwide face arsenic contamination in 108 countries across all six continents, primarily in South Asia [2]. The severity of this issue is pronounced in Bangladesh and West Bengal, India. In West Bengal, over 6 million individuals across nearly 50% of the districts are exposed to arsenic through drinking water [3]. Arsenic poisoning causes serious health effects even at low concentration, with fatal outcomes linked to excessive exposure. It damages several organs, including the lungs, liver, cardiovascular system, and central nervous system, and is highly carcinogenic [4]. Given these health risks, numerous organisations, such as the WHO and the European Union, recommend a maximum arsenic concentration of 10 µg/L in drinking water [5].

Several techniques are available for removing arsenic from water include ion exchange, chemical precipitation, adsorption, membrane filtration, and phytoremediation at present [6]. Among them, adsorption is the most cost-effective method for removing arsenic in small rural households due to its high efficiency and simple design [7]. Furthermore, the adsorbent is a key parameter of the adsorption process, and 80% of the operation cost is associated with the adsorbent [8]. Therefore, the selection of low-cost, efficient materials is the governing factor of the implementation in rural communities.

This work evaluated arsenic adsorption by laterite grains in fixed-bed column experiments in the laboratory. Previously reported that physico-chemical properties of laterite vary by location due to unequal weathering process, indicating the need for testing the material before the real application [9]. Furthermore, calcination was introduced to the laterite as a solution to the weakness of the raw material [10]. The fixed-bed column experiments were conducted to evaluate the effect of calcination and column height on breakthrough performance. Furthermore, adsorption mathematical models such as the Adams-Bohart, Thomas, Yoon-Nelson and the breakthrough service time models (BDST) were applied to predict fixed-bed column parameters,

including adsorption capacity of material.

MATERIALS AND METHODS

Preparation Of RL And CL Grains

The raw Laterite sourced from Thach That district in Hanoi, Vietnam, was utilized to produce both raw laterite (RL) and calcined laterite (CL), with a size range of 0.6 mm to 2.0 mm, for all subsequent experiments. Calcination was performed at a temperature of 550℃ for 1 hour using a muffle furnace. Finally, the calcined samples were sieved again to remove dust and fragmented particles smaller than 0.6 mm.

Spectroscopic Methods

Scanning Electron Microscopy (SEM) of X 500 magnification images with Energy-Dispersive X-ray Spectroscopy (EDS) were obtained for both RL and CL using TM4000plus (Hitachi High-Technologies Corp., Tokyo, Japan). Brunauer-Emmett-Teller (BET) multipoint graph was performed using a BET surface area analyzer (TriStar II, Micromeritics Instruments Corp., Norcross, GA, USA) for RL and CL to determine the specific surface area of the material.

Determination Of pH Zero-Point Charge

The pH zero-point charge of RL and CL grains was determined using the pH drift method, maintaining an L/S ratio of 25. The pH at which no difference between the initial and final pH was noted as the zero-point charge (pH_{ZPC}).

Fixed-bed Column Adsorption Experiments

Fixed-bed column adsorption experiments used stainless steel columns with a 3.0 cm inner diameter (upward continuous flow) and varying heights of 10, 20, and 30 cm. Experimental conditions are summarised in Table 1. Breakthrough time (t_b) and saturation time (t_s) were determined when the effluent concentration reached 5% and 95% of the influent concentration, respectively. Other breakthrough parameters calculated in this work were: arsenic removal at breakthrough (y_b), arsenic removal at saturation (y_s), mass transfer zone of column (*MTZ*), and finally, MTZ/Bed height ratio. The equations to calculate arsenic removal corresponding to the t_b and t_s are given in Eq. (1) and (2). *m* is the arsenic mass corresponding to the time considered.

$$y_b = \left(1 - \frac{m_{out,t_b}}{m_{in,t_b}}\right) x\ 100 \quad (1)$$

$$y_s = \left(1 - \frac{m_{out,t_s}}{m_{in,t_s}}\right) x\ 100 \quad (2)$$

The *MTZ* length in each column was determined by Eq. (3), where *H* is the packed column bed height, and the *MTZ* length in each column was determined [11].

$$MTZ = \left(\frac{t_s - t_b}{t_s}\right) x\ H \quad (3)$$

Table 1 Experimental conditions of fixed-bed adsorption columns

	Unit	Experiment			
		A	B	C	D
Material	-	CL	CL	CL	RL
column height	cm	10	20	30	20
Initial As concentration	mg/L	100.0			
Flow rate	mL/min	2.0			
Initial solution pH	-	5.0			
Particle size	mm	0.6 - 2.0			

Analysis Of Breakthrough Curve Using Mathematical Models

The results obtained from laboratory scale fixed bed column adsorption tests are essential for scaling up the system for industrial applications. Therefore, a successful design of an adsorption column process necessitates accurate predictions of breakthrough curves according to the actual environmental conditions [12]. In this study, the Adams-Bohart, Thomas, and Yoon-Nelson models were applied to describe the breakthrough curves and calculate important experimental parameters.

Adams-Bohart model

Adams-Bohart model assumes that the adsorption rate is proportional to both adsorbate concentration of solute in the solution phase and the residual capacity of the adsorbent [13]. Therefore, the initial part of the breakthrough curve was utilized to evaluate this mathematical model and derive the maximum adsorption capacity of the fixed-bed column system. The linear version of the Adams-Bohart model is expressed below in Eq. (4).

$$\ln\left(\frac{C_t}{C_0}\right) = k_{AB} C_0 t - k_{AB} N_0 \frac{Z}{U_0} \quad (4)$$

where k_{AB} (L/mg· min) is the rate constant of Adams-Bohart model, Z (cm) is the bed depth, N_0 (mg/L) is maximum ion adsorption capacity per unit volume of adsorbent column, and U_0 (cm/min) is the linear velocity of the solution.

Thomas model

Thomas model is a widely used mathematical model to describe the fixed-bed column breakthrough

behavior which assumes plug flow behavior within the fixed-bed column without axial dispersion [14]. The linear form of Thomas model is expressed below in Eq. (5).

$$ln\left(\frac{C_0}{C_t}-1\right)=\frac{k_{TH}q_e x}{Q}-k_{TH}C_0 t \quad (5)$$

where k_{TH} (mL/mg.min) is the Thomas model constant, q_e (mg/g) is the predicted adsorption capacity, x (g) is the mass of adsorbent inside the column, Q (mL/min) is the flow rate, C_0 (mg/L) is the initial solution concentration, and C_t (mg/L) is effluent solution concentration with respect to time t.

Yoon-Nelson model

Yoon-Nelson model is simpler than the other models and requires no data about the characteristics of the system such as physical properties of adsorption bed, and type of adsorbent. The model is used to predict 50% saturation time. The linear version of Yoon-Nelson model is expressed below in Eq. (6).

$$\ln\left(\frac{C_t}{C_0-C_t}\right)=k_{YN}t-k_{YN}\tau \quad (6)$$

where k_{YN} (1/min) is the Yoon-Nelson rate constant and τ (min) is the time required for 50% breakthrough of adsorbate, C_0 (mg/L) is the initial solution concentration, and C_t (mg/L) is the effluent solution concentration with respect to time t.

Bed Depth Service Time (BDST) model

This model assumes that the rate of the adsorption is controlled by the surface reaction between the adsorbate and the unused capacity of the adsorbent. Consequently, this analysis facilitates rapid predictions of adsorbent performance, thereby aiding in the scalability of processes across different flow rates and concentrations of adsorbate [15]. The equation of the BDST model is given in Eq. (7).

$$t=\frac{NZ}{C_0 v}-\frac{1}{K_\alpha C_0}\ln\left(\frac{C_0}{C_b}-1\right) \quad (7)$$

RESULTS AND DISCUSSION

Surface Morphological Characterization Of Laterite Grains

The SEM image analysis of RL in Fig. 1a revealed that the material surface of RL was comparatively smoother than that of CL grains. In Fig. 1b, show SEM image of CL shows a more compact and rougher surface than that of RL. On the other hand, the cracks which were observed in RL grains were eliminated due to the calcination process.

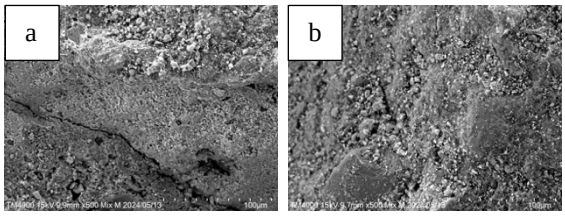

Fig. 1: SEM image of laterite. (a) RL gran and (b) CL grain

Physico-Chemical Characterization Of Laterite Grains

The surface of the tested laterite grains is mainly composed of iron, with 36.5% iron content by weight, which is within the range observed in previous studies. Except for iron, aluminium and silicon content increased after the calcination and the same scenario was observed in the previous studies [16]. The iron content in the calcined laterite sample decreased to 11.6% by weight.

The BET surface areas of raw (RL) and calcined laterite (CL) samples were 61.0 m²/g and 60.2 m²/g, respectively. Although calcination improved the laterite's physical condition, SEM analysis showed that the specific surface areas of RL and CL grains remained nearly the same. RL and CL grains had particle densities of 2.92 and 2.89 g/cm³, respectively. The decrease in particle density results from dehydroxylation and decarbonization at elevated temperatures, as noted in previous studies [16]. The pH_{ZPC} value, which represents the pH at which the net surface charge of the material is zero, was determined as 4.2 for the RL and 3.6 for the CL grains. This reduction of pH_{zpc} may be due to the dehydroxylation of the materials induced by the elevated temperature, resulting in the substantial reduction of hydroxyl groups on the laterite surface [17]. In conclusion, the unique physicochemical attributes of the laterite particulates showed significant morphological deviations from previously characterized specimens, indicating potential differences in sorption effectiveness.

Fixed-Bed Column Adsorption Experiment

Effect of calcination on adsorption performance

The effect of calcination was evaluated by testing two fixed-bed columns packed with RL and CL grains under identical conditions, as shown in Table 1. The results indicated that 5% increase in breakthrough time due to calcination. The breakthrough times were 70 and 1230 min for RL and CL grains, respectively. The saturation time, defined as the 95% breakthrough time, increased from 600 to 3,150 min. This suggests that calcination at elevated temperatures improves the adsorption performance of

laterite grains by altering the physical and chemical composition of the adsorbent. [10]. High temperatures in calcination eliminate structural water in metakaolinization, transforming kaolinite in laterite to metakaolin. The amorphous structure of metakaolin and poorly crystallized iron oxide provide ideal surface chemistry for arsenic adsorption via chemical complexation and physical adsorption mechanisms. [18].

Effect of fixed-bed column height on adsorption performance

The effect of bed height was evaluated using three fixed bed heights of 10 to 30 cm, with an initial arsenic concentration of 100 mg/L and a flow rate of 2.0 mL/min (see Table 1). Results showed breakthrough time increased from 450 to 2400 minutes with higher fixed-bed column heights. This is attributed to the system's *HRT*, as longer columns provided more time for diffusion onto the adsorbent bed, delaying breakthrough time. Similar findings were reported in previous studies [10]. The *MTZ* of the 10 cm column was 8.65 cm, while it was 12.19 cm and 12.61 cm for the 20 and 30 cm columns, respectively. The similar *MTZ* heights in the 20 and 30 cm columns, compared to the much shorter *MTZ* in the 10 cm column, imply that a 10 cm height may be inadequate for fully developing the *MTZ*.

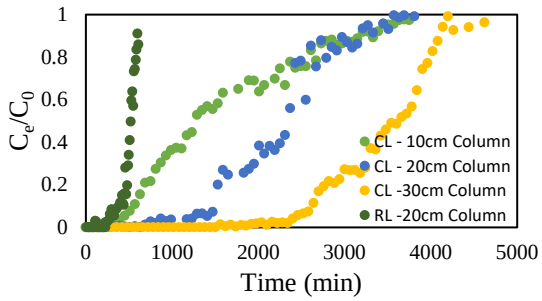

Fig. 2 Breakthrough curve of each fixed bed column

Adams-Bohart model analysis

The Adams-Bohart model, based on surface reaction theory, establishes a fundamental relationship between effluent concentration (C_t) and time (t) in continuous systems. The graphical representation of linear regression analysis of Adams-Bohart model is shown in the Fig. 3 given below. The results showed that the adsorption performance was enhanced by the calcination of laterite.

In the 20 cm column, CL exhibited a significantly higher maximum adsorption capacity (N_0) of 3893 mg/L compared to RL at 573 mg/L. Further investigation of the effect of column height on adsorption performance indicated that column height did not substantially influence the maximum adsorption capacity when sufficient length is provided to develop complete *MTZ* inside the column.

Table 2 Calculated breakthrough curve parameters

Column test		20 cm - RL	10 cm - CL	20 cm - CL	30 cm - CL
t_b	min	270	450	1230	2400
t_s	min	600	3330	3150	4140
y_b	%	99.4	98.7	98.3	99.4
y_s	%	83.0	46.4	69.6	84.5
MTZ	cm	11.0	8.7	12.2	12.6
MTZ/Bed height	-	0.55	0.87	0.61	0.42

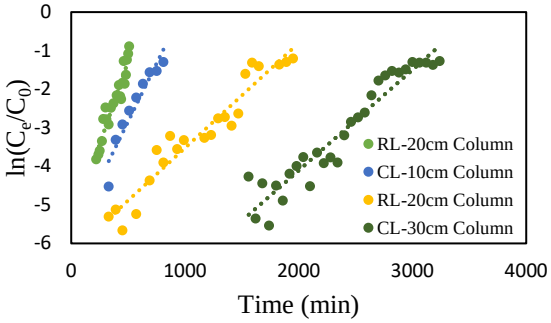

Fig. 3 Linear plot of Adams-Bohart model with experimental data

Thomas model analysis

The Thomas model analysis results assuming plug flow behavior in the fixed-bed column showed better fitting to the test data with R^2 ranging from 0.87 to 0.97. Comparative analysis of the 20 cm columns revealed that CL exhibited substantially higher equilibrium adsorption capacity than RL, with values of 2.78 mg/g and 0.54 mg/g, respectively. The observed decrease in the Thomas rate constant (k_{Th}) following calcination enhanced the equilibrium adsorption capacity, confirming the effectiveness of the calcination process in improving the arsenic adsorption performance of laterite grains. However, an inverse relationship between column height and equilibrium adsorption capacity was observed in fixed-bed column packed with CL grains. The equilibrium adsorption capacity was reduced from 3.43 to 2.60 mg/l, when increasing the fixed-bed column height from 10 to 30 cm which packed with CL grains. This phenomenon aligns with previous reported findings as well [19]

Yoon-Nelson model analysis

The experimental data closely matched the model, with R^2 values over 0.90 in all tested columns. In the 20 cm column, we observed clear differences between RL and CL. The 50% breakthrough times were 518 min for RL and 2,242 min for CL, despite of the similar BET surface areas. This highlighted the

calcination of laterite grains in improved the adsorption effectiveness. We also found that increasing the column height from 10 cm to 30 cm extended the 50% breakthrough time from 1,676 to 3,398 min. This improvement results from the increased hydraulic residence time (HRT) associated with greater column height.

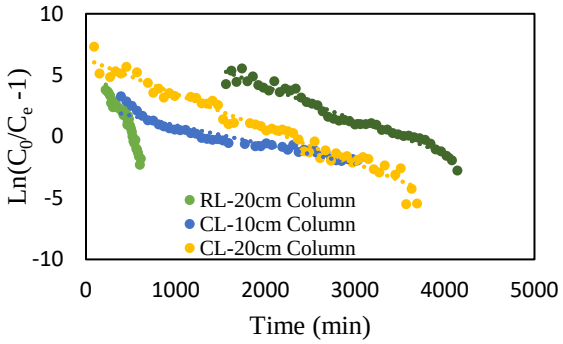

Fig. 4 Linear plot of Thomas model with experimental data

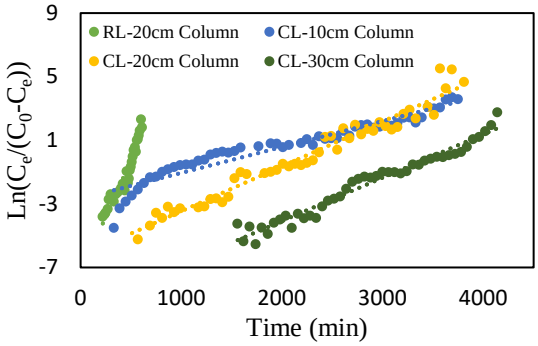

Fig. 5 Linear plot of Yoon-Nelson model with experimental data

BDST model analysis

The BDST model analyses the effect of column height at various breakthrough percentages. In this study, 5% influent concentration was set as the breakthrough point. Fig. 6 showed that breakthrough time correlates linearly with adsorbent bed height, with a correlation coefficient (R^2) of 0.99, indicating successful application of the BDST model to determine column parameter constants. The adsorbent bed capacity (N_0) and rate constant are 2759 mg/L and 0.003 L/mg.min, respectively. The minimum column height requirement to achieve the desired effluent concentration (C_t) at zero time can be calculated using the Eq. (7). Minimum column height indicated that a fixed-bed column of 6.06 cm height with 3 cm diameter is fundamentally required to ensure the effluent concentration remains at the breakthrough concentration at the initial feeding stage of the column.

$$x_0 = v/(kN_0)\, ln(C_0/C_t - 1) \quad (8)$$

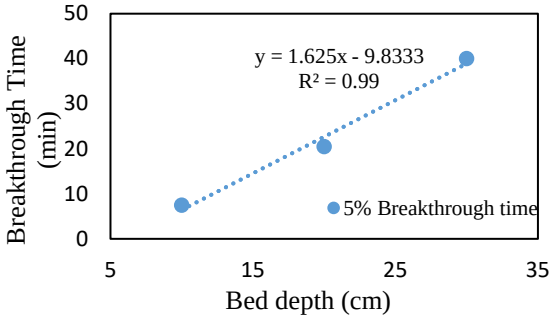

Fig. 6 Plot of bed depth vs 5% breakthrough time

Table 3 Summary of model parameters

Column test	20 cm - RL	10 cm - CL	20 cm - CL	30 cm - CL
Adams-Bohart modl analysis				
k_{AB} x 10^{-5}	9.20	6.22	2.27	2.41
N_0	573	2663	3893	3655
R^2	0.91	0.91	0.93	0.92
Thomas model analysis				
k_{TH}	0.152	0.017	0.025	0.027
q_0	0.54	3.43	2.78	2.60
R^2	0.91	0.90	0.97	0.96
Yoon-Nelson model analysis				
k_{YN}	0.0016	0.0016	0.0028	0.0029
τ	1676	1676	2242	3398
R^2	0.96	0.96	0.960	0.96

CONCLUSIONS

Calcination enhanced the physical and adsorption properties of Laterite grains. SEM analysis showed increased surface roughness and elimination of cracks, while EDS revealed reduced iron content (36.5 to 11.6 wt%) and increased aluminum and silicon. CL exhibited improved rigidity and structural integrity due to dehydroxylation and decarbonization. Breakthrough time in a 20 cm column increased from 270 to 1,230 min after calcination. Theoretical models (BDST, Adams-Bohart, Thomas, Yoon-Nelson) fit the data well, confirming higher adsorption capacity in CL, with the Adams-Bohart model showing up to 3,893.36 mg/L. This increase is attributed to disordered metakaolin and poorly crystallized iron oxides, enhancing surface reactivity. Column height significantly affected performance,

with taller columns extending breakthrough and saturation times by increasing HRT and active sites.

ACKNOWLEDGMENTS

This research was supported by the project of Japan Science and Technology Agency (JST) – Japan International Cooperation Agency (JICA) on Science and Technology Research Partnership for Sustainable Development (SATREPS) (No. JPMJSA1701) and the research grant from Saitama University.

REFERENCES

[1] Moonis Ali Khan and Yuh-Shah Ho, "Arsenic in Drinking Water: A Review on Toxicological Effects, Mechanism of Accumulation and Remediation," Asian Journal of Chemistry, vol. 23, pp. 1889–1901, 2011.

[2] E. Shaji, M. Santosh, K. V. Sarath, P. Prakash, V. Deepchand, and B. V. Divya, "Arsenic contamination of groundwater: A global synopsis with focus on the Indian Peninsula," Geoscience Frontiers, vol. 12, no. 3, May 2021.

[3] MOONIS ALI KHAN and YUH-SHAN Ho, "Arsenic in Drinking Water: A Review on Toxicological Effects, Mechanism of Accumulation and Remediation," Asian Journal of Chemistry, vol. 23, no. 5, pp. 1889–1901, 2011.

[4] S. Sambu and R. Wilson, "Arsenic in food and water – a brief history," Toxicol Ind Health, vol. 24, no. 4, pp. 217–226, 2008.

[5] L. H. E. Winkel et al., "Arsenic pollution of groundwater in Vietnam exacerbated by deep aquifer exploitation for more than a century," Proceedings of the National Academy of Sciences, vol. 108, pp. 1246–1251, 2011.

[6] Y. Glocheux, M. M. Pasarín, A. B. Albadarin, S. J. Allen, and G. M. Walker, "Removal of arsenic from groundwater by adsorption onto an acidified laterite by-product," Chemical Engineering Journal, vol. 228, pp. 565–574, Jul. 2013.

[7] M. A. Carneiro, A. M. A. Pintor, R. A. R. Boaventura, and C. M. S. Botelho, "Efficient removal of arsenic from aqueous solution by continuous adsorption onto iron-coated cork granulates," J Hazard Mater, vol. 432, Jun. 2022.

[8] T. J. Sorg, L. Wang, and A. S. C. Chen, "The costs of small drinking water systems removing arsenic from groundwater," Journal of Water Supply: Research and Technology-Aqua, vol. 64, no. 3, pp. 219–234, May 2015.

[9] G. Santha Kumar, P. K. Saini, R. Deoliya, A. K. Mishra, and S. K. Negi, "Characterization of laterite soil and its use in construction applications: A review," Dec. 01, 2022, Elsevier Inc.

[10] P. T. N. Nguyen, L. C. Abella, P. asa D. Gaspillo, and H. Hinode, "Removal of arsenic from simulated groundwater using calcined laterite as the adsorbent," Journal of Chemical Engineering of Japan, vol. 44, no. 6, pp. 411–419, 2011.

[11] G. Ungureanu, S. C. R. Santos, I. Volf, R. A. R. Boaventura, and C. M. S. Botelho, "Biosorption of antimony oxyanions by brown seaweeds: Batch and column studies," J Environ Chem Eng, vol. 5, no. 4, pp. 3463–3471, Aug. 2017.

[12] P. A. Kumar and S. Chakraborty, "Fixed-bed column study for hexavalent chromium removal and recovery by short-chain polyaniline synthesized on jute fiber," J Hazard Mater, vol. 162, no. 2–3, pp. 1086–1098, Mar. 2009.

[13] R. Han et al., "Characterization and properties of iron oxide-coated zeolite as adsorbent for removal of copper(II) from solution in fixed bed column," Chemical Engineering Journal, vol. 149, no. 1–3, pp. 123–131, Jul. 2009.

[14] Z. Saadi, R. Saadi, and R. Fazaeli, "Fixed-bed adsorption dynamics of Pb (II) adsorption from aqueous solution using nanostructured γ-alumina," 2013.

[15] N. Chen, Z. Zhang, C. Feng, M. Li, R. Chen, and N. Sugiura, "Investigations on the batch and fixed-bed column performance of fluoride adsorption by Kanuma mud," Desalination, vol. 268, no. 1–3, pp. 76–82, Mar. 2011

[16] I. Tchakala, Y. Sanou, C. Kolawole Balogoun, R. Tiendrebeogo, R. Kabore, and S. Pare, "Physico-chemical and spectroscopic properties of two laterite soils for applications in arsenic water treatment International Journal of Multidisciplinary Research and Development Physico-chemical and spectroscopic properties of two laterite soils for applications in arsenic water treatment," 2020. [Online].

[17] N. A. Oladoja et al., "Insight into the defluoridation efficiency of lateritic soil," Environ Prog Sustain Energy, vol. 38, no. 4, Jul. 2019

[18] G. Murielle et al., "New insight into the microstructure of natural calcined laterites and their performance as heterogeneous Fenton catalyst for methylene blue degradation,"

Reaction Kinetics, Mechanisms and Catalysis, vol. 124, pp. 931–956, 2018

[19] S. Chen, Q. Yue, B. Gao, Q. Li, X. Xu, and K. Fu, "Adsorption of hexavalent chromium from aqueous solution by modified corn stalk: A fixed-bed column study," Bioresour Technol, vol. 113, pp. 114–120, Jun. 2012.

Copyright © Int. J. of GEOMATE All rights reserved, including making copies, unless permission is obtained from the copyright proprietors.

15th Int. Conf. on Geotechnique, Construction Materials & Environment,
Kyoto, Japan, 11-13 November 2025, ISBN 978-4-909106124 C3051

DEVELOPMENT OF ROOFTOP AREAS WITH THERMAL PERFORMANCE FOR REDUCING HEAT ACCUMULATION IN CONDOMINIUMS

Anon Anan-archa[1] and Thana Ananacha[1]

[1]Faculty of Architecture and Design, King Mongkut's University of Technology North Bangkok
1518 Pracharat 1 Road, Wongsawang, Bangsue, Bangkok 10800, Thailand

ABSTRACT

This report presents the findings of the heat reduction performance of rooftop garden designs tailored to suit the activities of residents in four condominium buildings (Buildings A to D). The study applied four rooftop garden design types (Types 01 to 04), comprising open walkways, lawn areas, vegetative coverage, and swimming pools, respectively. Each design was installed on a concrete rooftop surface with a thickness of 0.15 meters. The rooftop area covered by Type 01 design elements was set at 80%, 60%, 40%, and 20% for Buildings A, B, C, and D, respectively. Temperature data collected from rooms and corridors beneath the rooftop gardens revealed that Building D had the lowest average indoor temperature, which was up to 2°C lower than that of Building A and up to 0.74°C below the average ambient temperature. In addition, heat flux measurements indicated a maximum reduction of 46% compared to baseline conditions prior to installation. This study underscores the influence of rooftop garden design principles, which collectively shape rooftop thermal behavior, and highlights the importance of ecological design strategies in enhancing indoor comfort and mitigating urban heat accumulation.

Keywords: Green roof, Heat Accumulation, Rooftop, Thermal Performance

INTRODUCTION

Urban expansion is progressing rapidly across various regions worldwide [1,2]. This growth is largely driven by ongoing economic, social, and infrastructural development [3–5]. A direct consequence of urbanization is the escalation of land values, primarily resulting from increased demand associated with real estate development, transportation infrastructure expansion, and population influx into urban zones. In response to spatial limitations and population density, many cities have adopted vertical urban development through the construction of high-rise buildings, aimed at maximizing land use efficiency. However, due to the high economic value of urban land, developers and investors tend to prioritize financial returns, often at the expense of urban green spaces [6,7]. Consequently, areas that might otherwise serve environmental or recreational functions are frequently replaced by built structures. The substitution of open, vegetated spaces with high-rise buildings composed of heat-retaining materials, such as concrete and glass, has significantly contributed to the Urban Heat Island (UHI) effect [8], whereby urban temperatures exceed those of surrounding rural areas. This thermal imbalance poses public health risks, especially to vulnerable populations, including children, the elderly, and individuals with pre-existing respiratory conditions [9,10]. Amidst the scarcity of accessible green areas in densely populated cities, rooftop gardens have emerged as a viable and increasingly popular solution for enhancing urban livability. These systems involve the transformation of otherwise unused rooftop surfaces into functional green spaces, offering opportunities for outdoor recreation and community engagement. The integration of rooftop gardens not only contributes to the expansion of urban greenery [11,12] but also yields multifaceted benefits across environmental, energy, health, and economic dimensions. Empirical studies have demonstrated that rooftop gardens can lower ambient air temperatures by 2–5°C [13,14], thereby mitigating UHI effects and reducing the demand for mechanical cooling, which may result in electricity savings of 20–30% [15,16]. Furthermore, these systems can sequester up to 375 grams of CO_2 per square meter per year [17], thereby supporting greenhouse gas reduction goals. In addition to reducing pollution, rooftop gardens help increase oxygen levels and enhance overall air quality. From a hydrological perspective, rooftop gardens also function as rainwater retention systems, effectively contributing to the mitigation of urban flooding risks [18,19]. On a broader scale, cities that invest in large-scale rooftop greening initiatives may also experience economic revitalization through increased tourism and local economic stimulation.

RESEARCH SIGNIFICANCE

Based on the foregoing literature review, rooftop gardens are identified as a key strategy for promoting sustainable urban development. This study investigates the design and implementation of thermally efficient rooftop spaces, utilizing rooftop garden systems as a passive solution to mitigate heat accumulation in condominium buildings. The objective of the research

is to evaluate the effectiveness of specific rooftop garden design configurations in enhancing thermal performance, improving indoor comfort, and contributing to environmental benefits in high-density urban contexts.

DEVELOPMENT OF ROOFTOP GARDEN

The rooftop garden designs were customized to accommodate the daily activities of residents in four condominium buildings to evaluate their effectiveness in reducing heat accumulation (Fig.1). Each of the four design typologies integrates distinct landscape and functional elements applied over a 0.15-meter-thick concrete rooftop slab. The first design (Type 01) consists primarily of open space and walkways, situated at an elevation of approximately 0.00 meters. The second design (Type 02) incorporates a lawn layer (0.05 meters) over soil (0.25 meters). The third design (Type 03) includes a combination of low shrubs (0.30 meters), selected tree species (2.50 meters), and planting beds (0.60 meters). The fourth design (Type 04) features a swimming pool with a depth ranging between 1.20 meters. Supporting infrastructure such as staircases, elevators, and water storage tanks, averaging 2.50 meters in height, are present but excluded from the calculation of usable rooftop area.

Fig.1 Design of Rooftop Gardens on Four Condominium Buildings to Evaluate Heat Reduction Efficiency

The rooftop spaces of the four buildings were adapted according to these design parameters, with the proportion of Type 01 coverage progressively decreasing across the buildings: Building A: 80%, Building B: 60%, Building C: 40%, Building D: 20%. A design tolerance of ±10% was applied to allow for construction variability (Table 1).

Table 1 The rooftop areas of the four buildings were modified based on the percentage allocation of the design conditions

Design conditions	Each building for rooftop areas = 100%			
	A	B	C	D
Type 01	80%	60%	40%	20%
Type 02	15%	20%	40%	20%
Type 03	5%	20%	20%	40%
Type 04	–	–	–	20%

Note: The margin of error in the design proportions is ±10%.

EXPERIMENTAL SET-UP

The performance testing of the four buildings was conducted in April,11 2025. The four rooftop garden design conditions were applied to the rooftop areas of each building, with an average rooftop area of 1,200 square meters per building. Several areas beneath the rooftop on the 8th floor were used as data collection points to compare with the ambient temperature. The experimental setup was installed under the rooftop gardens of four condominium buildings (Buildings A, B, C, and D) in a residential area in Salaya, Phutthamonthon, Nakhon Pathom, Thailand. Each building contains 23–27 residential units, with slight variations in size; corner units are larger. The central corridor in each building is 1.5 meters wide, with a floor-to-ceiling height of 2.60 meters and a 0.40-meter air gap above the ceiling for building systems. The staircase and elevator spaces have the same dimensions across all buildings, except for Building D, where part of the space is used as a mechanical room for the swimming pool system. K-type thermocouples (range: 0–1250°C, resolution: ±0.5°C) were used to measure temperatures at different positions, located in the center of the rooms, compared with ambient outdoor average temperatures. These were connected to a data logger (Hioki, Model: 8422–52, accuracy: ±0.8%). Additionally, heat flux meters (Omega HFS-3, range: 1–1400 W/m², error: ±0.5%) were installed at the ceiling surface in the rooms to record average heat transfer through the rooftop floor to the ceiling of the lower level. Doors and windows were kept closed to observe the heat transfer into the buildings. Monitoring started at 8:00 AM and ended at 6:00 PM, during which data from all four buildings was recorded simultaneously at 30-minute intervals (Fig.2).

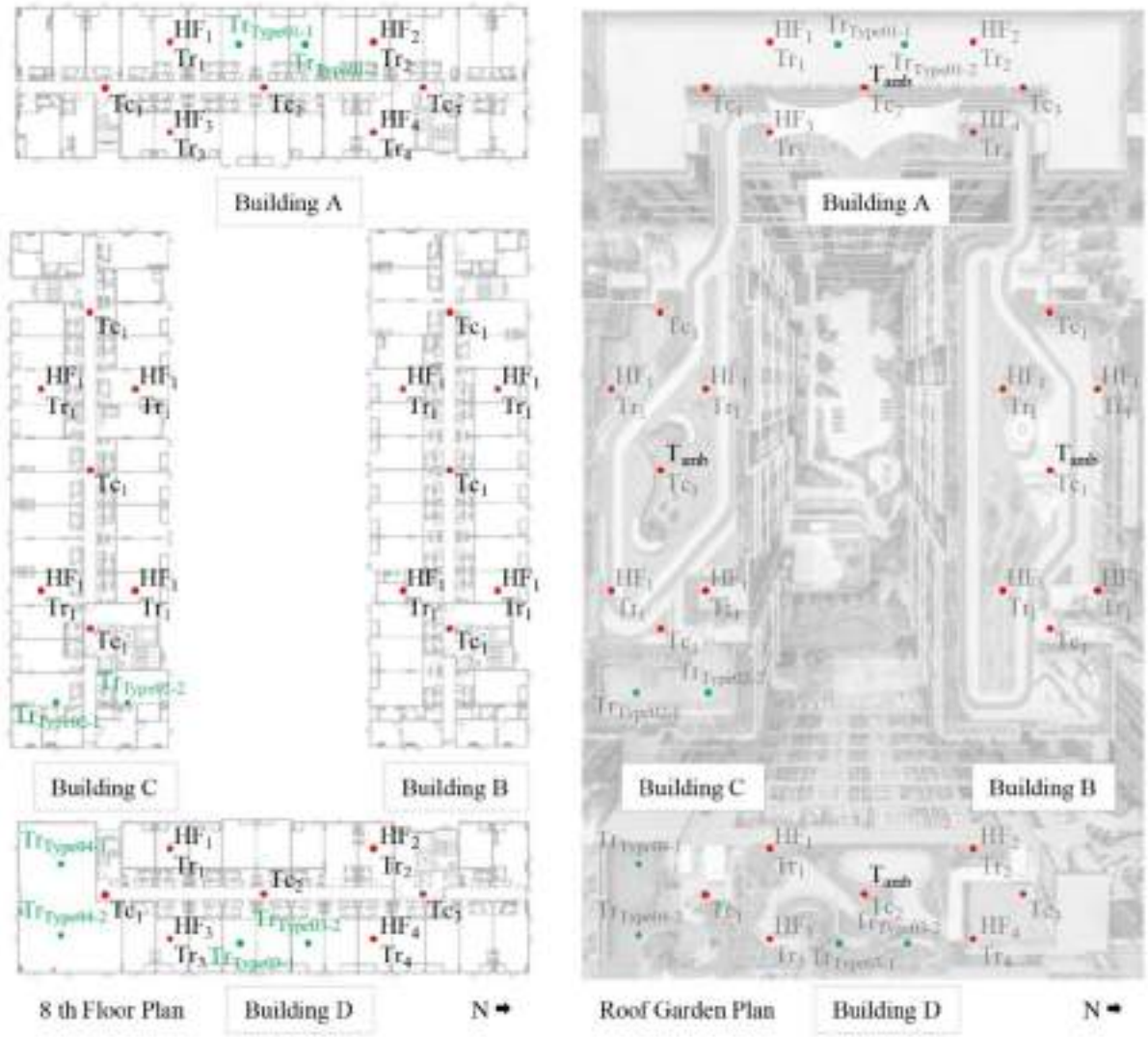

Fig. 2 Measured positions of four buildings

where:

T_r	Room temperature	K
T_c	Corridor Temperature	K
T_{amb}	Ambient temperature	K
HF	Heat flux	$W.\ m^{-2}$

RESULTS AND DISCUSSION

Location Specific Temperatures

The average indoor temperatures beneath the rooftop, which are specific positions corresponding to design types 01, 02, 03, and 04, were compared with the ambient temperature over the period from 08:00 AM to 06:00 PM. Between 08:00 and 09:30 AM, the average temperature at the Type 01 location did not differ significantly from the ambient temperature. However, from 10:00 AM to 06:00 PM, the average temperature at that location consistently exceeded the outdoor temperature by 0.36–2.44°C, with the maximum difference observed at 1:30 PM (Fig. 3). During the morning period (08:00–12:00 PM), the difference between the highest and lowest average temperatures among the specific rooftop garden locations was 1.36°C, whereas in the afternoon (12:00–04:00 PM), this temperature gap increased to 2.96°C (Table 2).

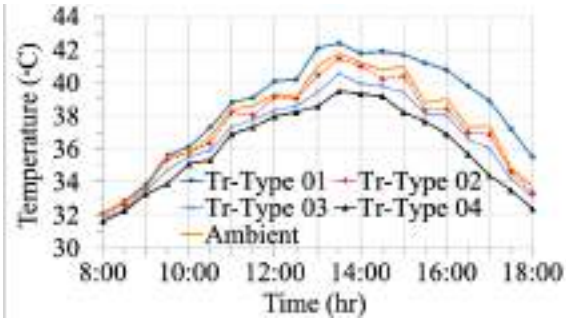

Fig.3 Hourly variations of temperature of location-specific (type 01, 02, 03, and 04)

Table 2 The average temperatures at specific positions for Type 01, 02, 03, and 04

Type /Ambient	Time	Average Temperature
type 01	08.00–12.00	36.19
	12.00–16.00	41.36
type 02	08.00–12.00	35.68
	12.00–16.00	39.83
type 03	08.00–12.00	35.23
	12.00–16.00	39.12
type 04	08.00–12.00	34.83
	12.00–16.00	38.40
Ambient	08.00–12.00	35.87
	12.00–16.00	40.22

In contrast, Types 02, 03, and 04 always recorded temperatures lower than the ambient temperature. At any given time, the temperature at Type 01 was higher than Type 02, Type 02 was higher than Type 03, and Type 03 was higher than Type 04. The average temperature differences throughout the day were 1.29°C, 0.55°C, and 0.65°C, respectively. Type 04 had an average temperature that was 1.52°C lower than the ambient temperature (Table 3).

Table 3 The differences in average temperatures at specific positions for Type 01, 02, 03, and 04

Type /Ambient	Average Temperature	Type comparerison	Temperature difference
Type 01	38.53	01 vs 02	1.29
Type 02	37.25	02 vs 03	0.55
Type 03	36.70	03 vs 04	0.65
Type 04	36.05	04 vs Ambient	-1.52
Ambient	37.56	–	–

Corridor Temperatures

The average corridor temperatures beneath the rooftop of Buildings A, B, C, and D, along with the ambient temperature, are compared over the time period from 8:00 AM to 6:00 PM. The corridor temperatures varied by 0.5–1.8°C throughout the day. At any given time, the temperature in Building A was always higher than in Building B, Building B was higher than in Building C, and Building C was higher than in Building D. The differences between the highest and lowest average corridor temperatures among the buildings were 0.51°C, 0.58°C, and 0.34°C, respectively. (Fig. 4). Notably, the indoor temperatures of Buildings C and D were lower than the average ambient temperature by 0.56°C and 0.89°C, respectively (Table 4).

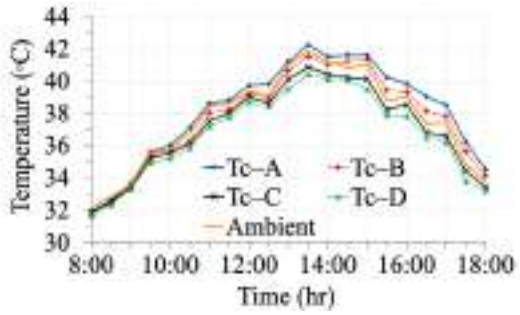

Fig.4 Hourly variations of temperature of corridor in buildings A, B, C, and D

Table 4 Comparison of average corridor temperature differences across each building

Building /Ambient	Average Temperature	Type comparerison	Temperature difference
Tc-A	38.10	A vs B	0.51
Tc-B	37.59	B vs C	0.58
Tc-C	37.01	C vs D	0.34
Tc-D	36.67	Ambient vs D	0.89
Ambient	37.56	Ambient vs C	0.56

Room Temperatures

The average indoor temperatures beneath the rooftop floor of Buildings A, B, C, and D were compared with the ambient temperature over the period from 08:00 AM to 06:00 PM. The average indoor temperatures varied by approximately 0.5–2°C throughout the day. It was found that Building A had the highest average indoor temperature, followed by Buildings B, C, and D, respectively, with Building D recording the lowest average indoor temperature. The temperature differences between the highest and lowest average indoor temperatures recorded across the buildings were 0.80°C, 0.72°C, and 0.49°C, respectively. (Fig.5). Interestingly, the indoor temperatures of Buildings C and D were lower than the outdoor temperature by an average of 0.25°C and 0.74°C, respectively (Table 5).

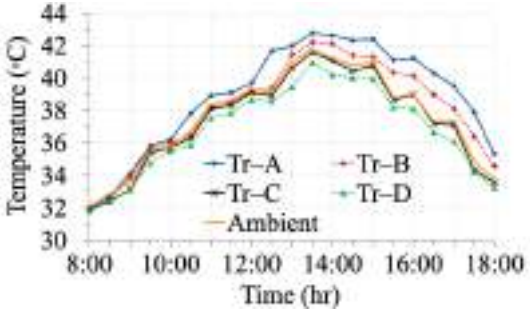

Fig.5 Hourly variations of temperature of room in buildings A, B, C, and D

Table 5 Comparison of average indoor temperature differences across each building

Building /Ambient	Average Temperature	Type comparerison	Temperature difference
Tr-A	38.83	A vs B	0.80
Tr-B	38.03	B vs C	0.72
Tr-C	37.31	C vs D	0.49
Tr-D	36.83	Ambient vs D	0.74
Ambient	37.56	Ambient vs C	0.25

Percentage heat flux reduction

Hourly variation in heat flux through the rooftop floor is presented over the course of the day. The heat flux is primarily influenced by thermal radiation, with solar radiation levels at approximately 799 W/m². The rooftop heat flux of Building A is about 32 W/m² higher than that of Building B, and similarly, Building C records 32 W/m² higher than Building D. As a result, Building D demonstrates the greatest reduction in heat gain through the rooftop floor and maintains indoor temperatures closer to the ambient temperature. (Fig. 6)

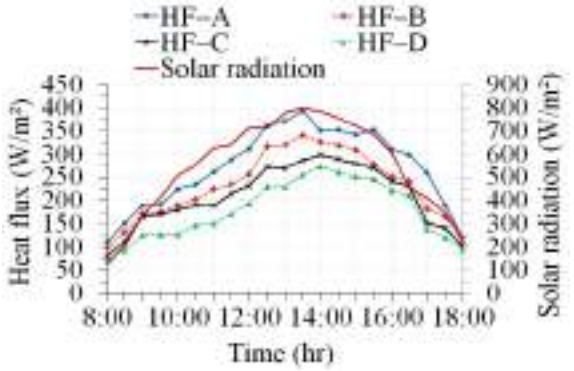

Fig.6 Hourly variations in heat flux and solar radiation of buildings A, B, C, and D

The measured percentage of heat flux reduction is used to calculate the heat flow rate through the rooftop floor as follows:

$$Reduction\ (\%) = \left(\frac{q_{before} - q_{after}}{q_{before}}\right) \times 100 \quad (1)$$

where:

q_{before} = heat flux before improvement (W/m²)
q_{after} = heat flux after improvement (W/m²)

The heat flux rate and the percentage reduction in heat flux for Building A compared to Building B, and for Building C compared to Building D, are illustrated (Figs. 7–8). The heat flux of Building B is lower than that of Building A by approximately 10–78 W/m², while Building D has a heat flux 8–53 W/m² lower than Building C. Between 08:00 AM and 12:00 PM, the percentage reduction in heat flux ranges from 9% to 19% for Building B compared to A and 11% to 29% for Building D compared to C. This indicates that in the morning hours, Buildings D and C outperform Buildings B and A due to the thicker substrate, different materials, and more extensive vegetation coverage in their rooftop garden designs. However, from 12:00 PM to 6:00 PM, Buildings D and C appear to perform similarly to Buildings B and A, with heat flux reductions of 7% to 21% and 8% to 16%, respectively.

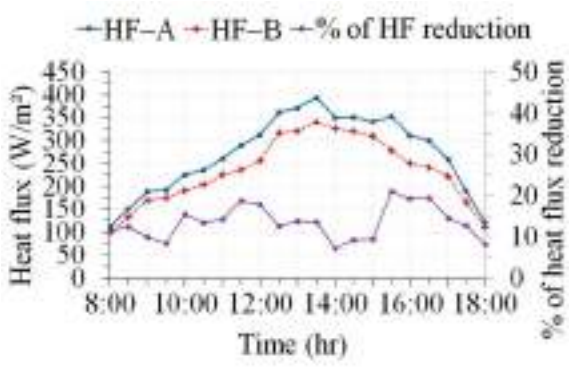

Fig.7 Hourly variations in heat flux and percentage heat flux reduction of the buildings A and B

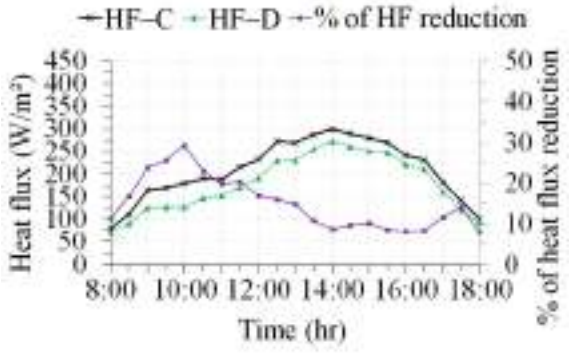

Fig.8 Hourly variations in heat flux and percentage heat flux reduction of the buildings C and D

CONCLUSIONS

The test results of heat reduction efficiency using rooftop garden designs tailored to the activities of residents in four condominium buildings show that the room temperature beneath the rooftop of Building D is consistently lower than that of Buildings C, B, and A, respectively. For Buildings D and C, field testing indicated that the indoor temperature below the rooftop does not reach excessively high levels, as it remains close to or lower than the ambient temperature, which is a particularly noteworthy finding. The heat flux rate and percentage reduction

in heat flux between Building A and B and Building D and C during the period from 8:00 AM to 6:00 PM show interesting trends, with reductions ranging from 7% to 21% and 8% to 29%, respectively. This demonstrates that the percentage of heat flux reduction throughout the day is influenced by the level of solar radiation and the design conditions of Types 01, 02, 03, and 04, comprising open walkways, lawn areas, vegetative coverage, and swimming pools, respectively. It is important for designers to promote rooftop activities that align with the needs of the building's users. However, further consideration is required regarding the structural load, supporting construction, and the budget implications for building owners.

ACKNOWLEDGMENTS

This research was funded by the Faculty of Architecture and Design, Contract no. Arch-Inter 01/2025.

REFERENCES

[1] Tan, M., Li, X., Lu, C., Luo, W., Kong, X., and Ma, S., Urban Population Densities and Their Policy Implications in China. Habitat International, Vol. 32, 2008, pp. 471-484.

[2] Xu, G., Zhou, Z., Jiao, L., and Zhao, R., Compact Urban Form and Expansion Pattern Slow Down the Decline in Urban Densities: A Global Perspective. Land Use Policy, Vol. 94, 2020, 104563.

[3] Gu, D., Andreev, K., and Dupre M.E., Major Trends in Population Growth Around the World. China CDC Wkly, Vol. 3, Issue 28, 2021, pp. 604-613.

[4] Zhang, D., Liu, J., Liu, K., and Zhang, Y., The Non-Linear Impact of Urban Rail Transit on Commercial Property Prices: Based on a Spatial Heterogeneity Perspective. Applied Geography, Vol. 171, 2024, 103385.

[5] Xu, T., Zhang, M., and Aditjandra, P., The Impact of Urban Rail Transit on Commercial Property Value: New Evidence From Wuhan, China. Transportation Research Part A: Policy and Practice, Vol. 91, 2016, pp. 223-235.

[6] Deng, X., Huang, J., Rozelle, S., and Uchida, E., Economic Growth and the Expansion of Urban Land in China. Urban Studies, Vol. 47, Issue 4, 2009, pp. 813-843.

[7] Ouyang, X., Wei, X., Wei, G., and Wang, K., The Expansion Efficiency of Urban Land in China's Urban Agglomerations and Its Impact on Ecosystem Services. Habitat International, Vol. 141, 2023, 102944.

[8] Santamouris, M., Recent Progress on Urban Overheating and Heat Island Research: A Review." Energy and Buildings, Vol. 207, 2020, 109482.

[9] Neave, M., Rayburg, S., and AL-Obaidi, I.H., Winter Urban Heat Island Magnitudes of Major Australian Cities. International Journal of GEOMATE, Vol. 11, Issue 24, 2017, pp. 2322–2327.

[10] Halder, B., Bandyopadhyay, J. & Banik, P. Evaluation of the Climate Change Impact on Urban Heat Island Based on Land Surface Temperature and Geospatial Indicators. Int J Environ Res 15, 819–835 (2021).

[11] Berndtsson, J. C., Green Roof Performance Towards Management of Runoff Water Quantity and Quality: A Review. Ecological Engineering, Vol. 36, Issue, 4, 2010, pp. 351-360.

[12] Soga, M., Evans, M. J., Tsuchiya, K., and Fukano, Y., A room with a green view: the importance of nearby nature for mental health during the COVID-19 pandemic. Ecological Applications, Vol. 31, Issue 2, 2021, e2248.

[13] Peng, L. L. H., and Jim, C. Y., Green-Roof Effects on Neighborhood Microclimate and Human Thermal Sensation. Energies, Vol. 6, Issue 2, 2013, pp. 598-618.

[14] Krebs, L. F., and Johansson, E., Influence of Microclimate on the Effect of Green Roofs in Southern Brazil – A Study Coupling Outdoor and Indoor Thermal Simulations. Energy and Buildings, Vol. 241, 2021, 110963.

[15] Castleton, H.F., Stovin, V., Beck, S.B.M., and Davison, J.B., Green Roofs; Building Energy Savings and the Potential for Retrofi. Energy and Buildings, Vol. 42, Issue 10, 2010, pp. 1582-1591.

[16] William, R., Goodwell, A., Richardson, M., Le, P.V.V., Kumar, P., and Stillwell, A.S., An Environmental Cost-Benefit Analysis of Alternative Green Roofing Strategies. Ecological Engineering, Vol. 95, 2016, pp. 1-9.

[17] Getter, K. L., Rowe D.B., Robertson, G.P., Cregg, B. M., and Andresen, J. A., Carbon *S*equestration Potential of Extensive Green Roofs. Environmental Science & Technology, Vol. 43, Issue 19, 2009, pp. 7564-7570.

[18] Prayogo, T. B., and Susilo, G. E., Rainwater Harvesting and Electricity Saveing on Household Scale. International Journal of GEOMATE, Vol. 17, Issue 62, 2019, pp. 92-100.

[19] Jokowinarno, D., and Kusumastuti, D. I., Rainwater Harvesting for Flood Peak Reduction in Way Awi Catchment, Indonesia. International Journal of GEOMATE, Vol. 18, Issue 70, 2020, pp. 246–251.

Copyright © Int. J. of GEOMATE All rights reserved, including making copies, unless permission is obtained from the copyright proprietors.

15th Int. Conf. on Geotechnique, Construction Materials & Environment,
Kyoto, Japan, 11-13 November 2025, ISBN 978-4-909106124 C3051

THE ROLE OF ENVIRONMENTAL IMPACT ASSESSMENT AS AN EFFECTIVE TOOL FOR SUSTAINABLE DEVELOPMENT IN THAILAND

Chutarat Chompumth

Graduate School of Environmental Development Administration,
National Institute of Development Administration, Thailand

ABSTRACT

Environmental impact assessment (EIA) is viewed as an effective tool for achieving sustainable development because it includes vital components that can facilitate sustainable developments by assessing environmental impacts, use of resources and public acceptance on project development. In Thailand, EIA study was conducted to assess the environmental and social impacts of a planned development project. This research aims to study how EIA promote sustainable development in Thailand. EIA practices were analysed to see whether they included key components to meet sustainable development criteria. This research was a qualitative study. Data were collected through in-depth interviews with stakeholders. The result revealed that concepts of sustainable development were partly met by the Thai EIA. The obstacles that prevent the Thai EIA in achieving sustainability are top-down command, the lack of transparency in the projects' management, the limited and a low level of public participation. Public participation, one of the significant part of EIA was not effectively established. Many citizens who were directly impacted by development projects have less opportunities to participate in decision-making process. These problems lead to ineffective EIA and conflicts in the Thai society caused by unaccepted decisions. It could be concluded that EIA practice in Thailand may not serve as an effective tool to promote sustainable development. Therefore, Thai EIA practice should carefully analyses how development project might impact social and environment. It is necessary to ensure that the EIA practice are well planned with sustainability be balancing the needs for the environmental protection and the economic growth.

Keywords: Environmental Impact Assessment, Sustainable Development, Public Participation

INTRODUCTION

Environmental issues have become one of the major global concerns that affects all parties [1]. In Thailand, the mega development projects caused by economic and industrial development in the past period often leads to problems of unfair allocation of resources, causing local people in development area to be affected directly from the project without the proper care and suitable assistance. This process often be seen as lacks transparency since the approval of the project, where people do not receive information which increase the lack of public participation in decision-making and project implementation that does not comply with good governance. This problem has affected their ability to develop the country's infrastructure. Furthermore, the residents in the area face serious health problems The conflict from development projects is likely to increase and intensify. Therefore, this issue can be considered a big problem in Thai society [2].

In order to effectively solve the issue, any development projects cannot be implemented without involving with the surrounding communities, and considering the losses that occur to the environment that may deteriorate and affect social changes, including the health of the people who will receive pollution from the operation of that development project. Thus, the developing countries' trend nowadays are so focused on the importance of participation in the issue of effective environmental management.

SIGNIFICANCE OF THE STUDY

The concept of sustainable development has played a role in the current development of the global society since 1972. Since the United Nations has organized a summit on the human environment in Stockholm, Sweden, which calls for the world to take into account the effects of excessive use and the limitations of world resources. As a result of the meeting, the whole world began to increase their environmental attention and creates important international environmental law documents under the Stockholm Declaration on the Human Environment or the "Stockholm Declaration". The document supports the environmental rights for the first time, consisting of 26 important provisions as guidelines for sustainable development. Later in 1983, the United Nations established the World Commission on Environment and Development, commonly known as

the Brundtland Commission, to study the balance between the environment and development. This commission has published a document called Our Common Future that calls for the global society to transform our extravagant way of life and to change the guideline of development. In a manner that is safe for the environment and in accordance with the limits of nature, including the suggestion that humanity is able to achieve sustainable development [3].

Later in the year 1992, the Earth Summit was held in Rio de Janeiro, Brazil, which resulted in the establishment of an important document, Action plan 21 or "Agenda 21". This document's main role was to be a guideline for countries in the world to use and adapt accordingly, in order to achieve sustainable development. This will further ensure that both current and future generations will have sufficient natural resources to meet the needs of their livelihood. The concepts of Agenda 21 stated that the increase in population, consumption and technology are the main causes for changes in the environment. Therefore, humans must work together to reduce consumption that is extravagant, inefficient and also support sustainable development in all parts of the world. In addition, the Action Plan 21 proposes guidelines for solving all of the environmental problems; natural resource degradation, conservation of species diversity and species of living things, forest conservation, poverty, extravagant consumption problems, planning, management of education, health, solving problems in metropolitan areas and agricultural issues of farmers. These guidelines emphasize that it is the duty of every person, every group and every profession to achieve sustainable development, which is a way to overcome poverty and environmental destruction [4].

Environmental impact assessment (EIA) is defined as the systematic identification and evaluation of the potential impacts (effects) of planed projects, plans, programs, or legislative actions related to the physical, chemical, biological, cultural, and socioeconomic components of the environment [5]. EIA is aimed at integrating environmental aspects connected to the natural and human environment in making decisions related to the design, planning, implementation, and monitoring of interventions, in order to achieve sustainable development. It provides a framework for the integration of environment policies and development strategies that will lead toward sustainable development.

Therefore, the elements of an activity allow the burden of proving that this action will not cause significant harm. EIA could provide project alternatives and identify means of improving project selection, siting, planning, design, and implementation by preventing, minimizing, mitigating, and compensating for negative environmental impacts [4, 5].

Most importantly, one of the key elements of EIA is public participation which could provide data regarding the environmental issues of the purposed project area, project characteristics, and the identification and evaluation of latent impacts. Many results from EIA studies can make valued added to the development in terms of knowledge of environmental, social, and economic systems [6].

RESEARCH METHODOLOGY

In this research, qualitative research data were collected from two sources: 1) Primary data: In-depth interviews with stakeholders. The interview instrument was an open-ended questionnaire designed specifically for each key stakeholders. Including central government, local government agencies, academics from various agencies and nonprofit organizations, community leaders and public interviews. 2) Secondary data. The information obtained from the review of academic literature, academic papers and thesis article. The researcher will take the primary and secondary data to be validated, analyzed and synthesized to obtain information according to the objectives of the research. The researcher then used the descriptive analysis to summarize the content, comments and reviews. Then, present the issues set out in each interview topic to ensure the consistence of the study with the objectives of the study and then proposed the conceptual framework. This is to summarize the study on various issues and to obtain the most relevant and complete information. In-depth interviews were applied to collect data while purposive selection and snowball techniques were used to selected the research interviewees, including 30 key informants.

ENVIRONMENTAL IMPACT ASSESSMENT AND SUSTAINABLE DEVELOPMENT IN THAILAND

Environmental impact assessment is a commonly used tool for effective decision making. The scheme of EIA is that development can proceed in parallel with conserving the quality of the environment. This is started by considering the environmental impact from the initiation of the project and planning phase to the procession phase of the project. The abovementioned tool initiative will help reduce the impact and promote the use of limited natural

resources to gain maximum benefit [4]. The principle that the economic and technological development can proceed in parallel with the preservation of natural resources and the environment or the principles of "Sustainable development" [3]. It can be said that the environmental impact assessment process is part of a plan to contribute to sustainable development. This is to help prevent problems in advance which is consistent with the Precaution Principle. This principle is known for the recommendation to prevent problems in advance if there are signs or trends of that may cause serious consequences in the future.

The role of EIA in achieving sustainable development is crucial. Firstly, EIA supports integrate environmental considerations into development planning and decision-making processes. By evaluating possible impacts at an early stage, EIA enables the adoption of mitigation measures to minimize negative environmental impacts and boost project sustainability [7].

Secondly, EIA supports the preservation of ecosystems and biodiversity. Through the assessment of potential impacts on habitations and species, EIA identifies sensitive areas and promotes the adoption of measures to protect the environment, which aims to sustainably manage forestry, combat desertification, stop biodiversity loss, and protect ecosystems.

Thirdly, EIA promotes the sustainable consumption of natural resources. By assessing resource availability and evaluating resource use forms, EIA conducts an identification of sustainable resource management performs. Additionally, EIA also addresses climate change considerations. It assesses the greenhouse gas emissions, energy consumption, and climate change impacts associated with development activities. By identifying mitigation measures and promoting climate change adaptation strategies, which aims to combat climate change and its impacts [8].

In Thailand, The Natural Resources and Environmental Policy and Planning Office is the agency responsible for checking the accuracy of the preliminary environmental impact assessment report and proposing the report to the Board for consideration and approval before issuing the permit under the notification of the Ministry of Natural Resources and Environment. The process of evaluating the environmental impact is divided into 7 stages as follows: 1) critically evaluate what projects or activities require an EIA. In Thailand, The ONEP is responsible for defining the scope or project that requires an environmental impact assessment. 2) Defining the framework of the dimension of the group in the area, goals and key points that should be highlighted in the study to answer the question of the purpose of the study set. 3) Identifying the impacts in a detailed breakdown of each issues identified in Article 2, as well as the appropriate variables. This can be done by referencing EIA studies of other similar projects or by exploring both the impactors and the affected parties. 4) Environmental Impact Assessment which will describes the nature of the cause behind the effect, including the size and other dimensions of the impact in a concrete scientific way. This includes both short-term and long-term impact. 5) Evaluate the impact of Article 4 and the preceding priorities to simplify preventive measures, amendment or the reduction of Impacts 6) Establishment of Preventive measures. There are generally two types of preventive measures: structural measures and non-structured measures. And 7) Careful monitoring of environmental impacts to determine the efficiency and effectiveness of preventive measures, amendment or mitigation measures. Simultaneously, it also examines the accuracy of forecasts and impact assessments [9].

It could be said that in Thailand, the government has set up EIA practices in the constitution, which is the highest law in the administration of countries in many sections which cover both the principles of accessing information, principles of public participation and the principles of accessing the justice system. In the private sector, it was found that many establishments began to operate according to environmental governance principles. If Thailand is going to head to sustainability without conflict in society and environment, it needs to focus on the principles of effective EIA seriously and focus on effective implementation, including encouraging people to have access to environmental information. This is in order for the public or the citizens to be able to participate in decision making in the project which may cause environmental impacts effectively. Also, it is important to promote access to justice in cases and environmental disputes of all sectors, which Thailand should focus on the preparation of all sectors, especially the secondary level law that will make the operations of all sectors more efficient [10].

Importantly, EIA also fosters stakeholder engagement and participation. There should be a promotion of environmental awareness among all sectors. All sectors should be involved with the public sector to create guidelines to monitor the operations of both the public and private sectors continuously. This is to ensure the confidence and trust in the operation of the public. If all sectors are working

together, they will eventually be able to drive the country into sustainable development**.**

PUBLIC PARTICIPATION IN EIA PRACTICE IN THAILAND

Public participation is one of the most important principles of EIA, which is a universal principle that civilization places importance on and is the main issue that Thai society is interested in developing politics into a participatory democracy. Thus, the government must provide opportunities for the public and related parties in all sectors to share ideas, make decisions, create transparency and increase the quality of the decision making process that is mutually acceptable to all parties. It is generally accepted that public participation plays an important role in the national development process, society and environment. That is to say, participation is a social process that provides opportunities for those involved as stakeholders to participate in the awareness of information analyze problems, express opinions, coordinating and monitoring the impact of the operation, as well as participating in the implementation of any matter which is a solution to the problems of their community or locality. This method is carried out to meet the true needs of the public, which is in accordance with the government's policy to prevent, correct and manage correctly and efficiently as protection for the quality of the environment and the quality of the public's life [10].

As for the analysis of laws and regulations relating to the participation of people in making decisions in various development projects. It was founded that the Constitution of the Kingdom of Thailand 2007 and 2017 laid the framework of participation in the decision-making process at the project level in many sections, especially in Article 58 of the 2017 Constitution, which stated that any activity or project that may inflict a serious impact on the environment, natural resources and health of the people must initiate a process to listen to the opinions of the public and stakeholders from that activity or development project and must have an independent organization to give an outside viewer's opinions. In addition, the Constitution also gives rights to the public or communities in the management of natural resources and the environment in Article 59.

In addition, Thailand has set up a framework for the implementation of public participation in projects that affect public health and the quality of the environment through other secondary laws, including the National Environmental Quality Act 1992 and Notification of Ministry of Natural Resources and Environment on the type and size of the project or business, which must include preparation of an environmental impact analysis report and guidelines, procedures and guidelines for the preparation of the Environmental Impact Assessment Report 2010, which requires the state / private sector owners of development projects that are licensed by the government to allow the public to participate in the decision-making process of the project, activity or any project which has a wide scale impact on the quality, environment, health, way of life or interests with the local community. The project owner must provide the process of public participation through the process of public hearing.

It can be seen that Thailand has laid down a legal framework that is consistent with the principles of good governance and public participation. However, in order to result in concrete actions, there must be a mechanism in which enforcement of laws and practices are in accordance to meet the intent of the law [2, 10].

Presently, in Thai society, the key issue is that who has the authority to approve any activity or project, allow the public and stakeholders to participate in the decision-making process and the level of the public's satisfaction with the level of participation. Although, there are many laws in Thailand that show the intent and importance of public participation, there is still no law that gives the power to the role of the public to truly participate in the process of decision-making. The level of public participation in the decision-making processes in Thailand is considered to be low since the public has no real power on the decision [11]. If law enforcement cannot be conducted effectively, this may affect the effectiveness of public participation process in the EIA system [12].

OBSTACLES TO ENVIRONMENTAL IMPACT IN ACHIEVING THE SUSTAINABLE DEVELOPMENT GOALS

There are several difficulties that can hinder effective EIA in achieving the Sustainable Development. These problems arise from various sources and can impede progress towards sustainable development as follows.

Firstly, a lack of political will and commitment, without strong political will and commitment from governments and policymakers, it becomes

challenging to prioritize environmental concerns and allocate sufficient resources for sustainable development initiatives. Limited investment in environmental conservation, weak enforcement of regulations, and inadequate policy frameworks can hinder progress towards achieving sustainable development.

Secondly, a lack of awareness and understanding of environmental concerns among the local public and key stakeholders can hinder a headway towards achieving SD. Inadequate environmental education and awareness agendas limit the involvement and participation of individuals and communities in sustainable practices. Without a prevalent understanding of the significance of environmental conservation, it is a hard work to drive meaningful transformation.

Thirdly, inefficient institutional contexts, weak governance administration, and limited ability for environmental management can pose important obstacles to achieving sustainable development. Lack of coordination among government agencies, poor legislation and regulations, and corruption can hinder effective EIA. Strengthening institutional capacity, refining governance intuitions, and encouraging transparency and accountability are crucial for overcoming these challenges.

Fourthly, the lack of transparency within the project development management causes the public to lose confidence in the project.

Fifthly, lack of meaningful public participation is a key problem of effective EIA. From many case studies in Thailand, it was found that a large number of local people mentioned that the process of public participation does not cover all stakeholders and some have been prevented from participating in the process. If the public and organizations in the process are not involved in the public participation and cannot truly represent stakeholders and those affected by the decision, it can truly lead to problems and conflict later on in the process [7, 10].

These obstacles are immediate needed for environmental sustainability. Balancing social and economic development with environmental considerations is essential to overcome these challenges.

GUIDELINES FOR REDUCING ENVIONMENTAL CONFLICTS FROM DEVELOPMENT PROJECTS IN THAILAND

From many case studies in Thailand, it was found that the cause of the environmental conflict consists of 3 main issues: 1) The impact that people will receive from the operation of development projects, especially pollution which will severely affects the health of the residents in the area, including damage to crops and agricultural products of the community 2) Lack of public participation in the local development decisions. Government officials and project owners lack real public opinion in managing their natural resources and environment, especially during the beginning of the project 3) The public perceives that the benefits that the community will receive are quite low and not worth the loss of natural resources.

Therefore, the government sector and project owners must pay more attention to analyzing the causes of environmental conflicts, in order to properly solve the problem. This includes promoting public participation in EIA for environmental decisions to prevent such conflicts. Although, various development projects are prepared EIA reports, conflicts from the project still continue to occur. This indicates that the EIA report does not guarantee the public's confidence and acceptance of the specified measures in the report. Therefore; every sector must pay attention to analyzing the cause of the conflict in order to solve the problem efficiently [13].

Indeed, public participation that is considered to be successful includes enthusiastic participation from the public, bargaining power of stakeholders in the decision-making process within the project activities, participation in the determination of social goals and resource management to achieve the objective and it must be through voluntary participation. When the staff and personnel are involved in the management of participation, they can then fully understand the meaning of participation. Moreover, they will be able to create evaluation criteria based on relevant factors as the fundamental principle and able to evaluate the success of the level of participation, in order to develop a more efficient process [10, 12].

Public participation, which is one of the important principles of EIA and environmental governance, is an important concept that is expected to solve the problems of natural resource management and conflicts arising from various development projects, especially in the effectiveness of industrial operations that will lead to sustainable development in Thailand.

CONCLUSIONS

EIA is a systematic process that evaluates the potential environmental impacts of proposed projects, policies, and programs. It plays an important role in

achieving sustainable development by integrating environmental concerns into purposed development projects and activities. By identifying and assessing potential environmental risks and impacts, EIA ensures that development projects or activities are carried out in an environmentally responsible and sustainable manner.

The lack of effective EIA and proper public participation in decisions related to the operations of the government or private sector may cause conflicts between stakeholders and environmental damage. Development projects that have good objectives are beneficial to the public at certain times, which may not often provide the anticipated results. This outcome is due to the lack of transparency and public participation in decision-making and project implementation.

Therefore, to effectively and sustainably solve environmental problems, public participation in EIA system must be seriously considered and implemented. Also, it is crucial to create public awareness, discipline of people in the country and training for the public to have knowledge and understanding about the public's participation in the environmental management decision-making process, especially the duties and responsibilities of the people for the treatment of the environment. It can be concluded that the cooperation power of the people will be an important strategy that enables the industrial sector of Thailand to sustainably conduct business with the community further on in the future.

It could be summed that the EIA system identifies both the potential positive and negative impacts of the purposed project in advance. For the adverse impacts upon the natural and the socio-economic environment issues and mitigation measures were identified in advance. This enabled avoidance and/or minimization of impacts and make the project environmentally friendly and acceptable to the nearby community. Thus, EIA is a mechanism that facilitated identification of potential impacts and development of mitigation measures to reduce adverse significant impacts and foster sustainable development.

REFERENCES

[1] Chaisomphob T., J. Sanguanmanasak and K. Swangjang, Role of Public Participation in Planning Power Plant Project in Thailand, Thammasat International, Vol 9(1), 2004, pp. 67-73.

[2] Chompunth C. and S. Chomphan, Evaluating Public Participation Process in Development Projects in Thailand: A Case Study of the Khao Hin Son Power Plant Project, American Journal of Applied Science, Vol 9(3), 2012, pp. 865-873.

[3] World Commission on Environment and Development, Our Common Future, 1987, Transmitted to the General Assembly as an Annex to document A/42/427 – Development and International Co-operation: Environment. http://www.un-documents.net/wced-ocf.htm.

[4] IAIA, Principles of Environmental Impact Assessment Best Practice, International Association for Impact Assessment, 1999, UK. pp 20.

[5] Canter LW, Environmental Impact Assessment. 1997, Mc GrawHill International Edition. McGraw-Hill Publishing Company, Inc, New York.

[6] Stampe, J.W., Lessons Learned from Environmental Impact Assessments: A Look at Two Widely Different Approaches – The USA and Thailand, The Journal of Transdisciplinary Environmental Studies, Vol 8(1), 2009, pp. 1-7.

[7] Petts, J., Barriers to Deliberative Participation in EIA, Journal of Environmental Assessment Policy and Management Vol5(3), 2003, pp. 269-293.

[8] Persson, J., Theoretical Reflections on the Connection between Environmental Assessment Methods and Conflict, Environmental Impact Assessment Review, Vol 26(7), 2006, pp. 605-613.

[9] Chompunth C., Role of Public Participation in Environmental Impact Assessment in Thailand, International Journal of GEOMATE, Vol. 12(33), 2017, pp.109-113.

[10] Chompunth, C., Public Participation in Environmental Management in Constitutional and Legal Frameworks, American Journal of Applied Science, Vol 10 (1), 2013, pp. 73-80.

[11] Nuntavarn V. V. and Vajanapoom N. Health Impact from Air Pollution in Thailand: Current and Future Challenges, Environmental Health Perspective, Vol 119(5), 2011, pp. 197–198.

[12] Ogunlana, S. O., T. Yotsinsak and S. Yisa., An Assessment of People's Satisfaction with the Public Hearing on the Yadana Natural Gas Pipeline Project, Environmental Monitoring and Assessment, Vol 72(2), 2001, pp. 207-225.

[13] Vantanen, A. and M. Marttunen, Public Involvement in Multi-Objective Water Level Regulation Development Projects-Evaluating the Applicability of Public Involvement Methods, Environmental Impact Assessment Review, Vol25(3), 2005, pp. 281-304.

Copyright © Int. J. of GEOMATE All rights reserved, including making copies, unless permission is obtained from the copyright proprietors.

15th Int. Conf. on Geotechnique, Construction Materials & Environment, Kyoto, Japan, 11-13 November 2025, ISBN 978-4-909106124 C3051

EFFECT EVALUATION OF TAILING SAND SOLIDIFICATION BY MICROBIALLY INDUCED CARBONATE PRECIPITATION

Lai Yongming[1, 2], Satoru Kawasaki[2] and Liu Qian[1]

[1]College of Resource Engineering, Longyan University, China; [2]Faculty of Engineering, Hokkaido University, Japan

ABSTRACT

Sporosarcina pasteurii (*SP*), the most commonly used urea-decomposing strain in microbially induced carbonate precipitation (MICP), faces challenges in treating complex tailing sand containing multiple heavy metal ions. This study screened and enriched indigenous urea-decomposing microorganisms to develop optimal bio-stimulation strategies for tailing sand treatment, combined with *SP* for tailing sand solidification. Comparative evaluations were conducted through surface strength test and heavy metal leaching toxicity test to examine the effectiveness of three treatment approaches: bio-stimulation alone, *SP* alone, and their combined application. Results demonstrated that the surface strength of sand samples after 7 cycles of combined solidification was 2.594 times that after 10 cycles of bio-stimulation, and 31% higher than *SP* solidification for 10 cycles. The combined solidification also achieved higher heavy metal immobilization rates compared to both bio-stimulation and *SP*. Calcite crystals generated by combined solidification were larger in size and more numerous, showed flaky arrangements, and tightly filled the pores between the tailing sand particles. This integrated approach successfully enhanced both mechanical properties and heavy metal immobilization efficiency in tailing sand.

Keywords: Microbially induced carbonate precipitation; Sporosarcina pasteurii; Indigenous urea-decomposing bacteria; Tailing sand

INTRODUCTION

Microbially induced carbonate precipitation (MICP) represents a new technology currently utilizing microbes to ameliorate soil conditions and immobilize heavy metals. Its core mechanism is` based on employing urease produced through microbial activity to transform Ca^{2+} and metal ions within the soil into carbonate precipitates, while simultaneously improving the physical attributes related to the soil and immobilizing heavy metal elements [1-2]. How the reaction proceeds can be seen in Eq. (1) and (2), with Me^{2+} representing heavy metal ions [3].

$$CO(NH_2)_2 + Ca^{2+} + 2H_2O \rightarrow CaCO_3 \downarrow + 2NH_4^+ \quad (1)$$

$$CO(NH_2)_2 + Me^{2+} + 2H_2O \rightarrow MeCO_3 \downarrow + 2NH_4^+ (2)$$

Sporosarcina pasteurii (*SP*) is the most effective microbes for MICP process through urea hydrolysis [4]. However, tailing usually contains heavy metals [5]. The growth of *SP* is inhibited, and its activity decreases [6] in environments with high heavy metal concentrations, consequently affecting the progress and efficiency of MICP. Considering that urea-decomposing bacteria are widely distributed in soil [7], and existing research has shown that tailing soil contains various genera of urea-decomposing bacteria with high heavy metal tolerance [8]. Therefore, how to effectively activate the activity of indigenous urea-decomposing bacteria and combine it with *SP* to simultaneously improve the mechanical properties of tailing sand and immobilize heavy metal ions is key to the implementation of MICP method within tailing management.

RESEARCH SIGNIFICANCE

This study first explores the effective formulation and concentration of a bio-stimulation solution that can activate the indigenous urea-decomposing bacteria, with the aim of obtaining the optimal bio-stimulation solution formulation suitable for tailing sand. Subsequently, solidification experiments were conducted by combining the screened and enriched indigenous urea-decomposing bacteria from the tailing sand with *SP*. The solidification strength and heavy metal immobilization effects of the three methods (bio-stimulation only, *SP* only, and combined solidification) were compared at different treatment cycles. This study aims to reveal the mechanism by which the combined solidification using indigenous urea-decomposing bacteria and *SP* betters the physical attributes within tailing sand, as well as immobilizing heavy metals.

MATERIALS AND METHODS

Tailing Sand

The tailing sand was taken from the tailing reservoir of Fujian Makeng Mining Co., Ltd. located in China. The basic characteristics of tailing sand was shown in Table 1. Referring to "Soil Environmental Quality - Risk Control Standard for Soil Contamination of Agricultural Land (Trial) [9]," using the risk screening values for soil contamination of agricultural land as the standard values, and based on "Technical Specification for Soil Environmental Monitoring [10]," employing the Nemerow pollution index method for evaluation, it is evident that both Cd and Zn in the tailing sand exceed the standard. Specifically, Cd exhibits moderate pollution, while Zn shows slight pollution.

Table 1 Basic characteristics of tailing sand

Parameters	Values	Parameters	Values
Dry density	1.9589 g/cm^3	Density	2 g/cm^3
minimum dry density	1.8283 g/cm^3	pH	9.5
maximum dry density	2.3746 g/cm^3	Fe	12.71%
Zn	375.61 mg/kg	Cd	1.327 mg/kg

Note: Determination methods for Fe, Zn and Cd: Samples are digested using a four-acid mixture, and the concentrations are determined by ICP-MS.

Formulating and Improving a Bio-stimulation Technique Applicable to Tailing Sand

Based on existing research findings[11], the starting formulation of the bio-stimulation solution is created in 1 L of distilled water: 3.5 g of sodium acetate, 5.35 g of ammonium chloride, 20 g of urea, 0.2 g of yeast extract, 0.01 mmol of nickel chloride.

The urease activity exhibited by the urea-decomposing bacteria stands as the key parameter influencing the success of MICP solidification. Consequently, the urease activity of the supernatant following bio-stimulation of tailing sand serves as both the assessment criterion and the outcome variable. The precise steps for improvement are as follows:

Screening of Optimal Carbon and Nitrogen Sources

Commencing with the initial bio-stimulation solution, one-variable experiments are to be performed by altering the carbon or the nitrogen source. A selection of equivalent mass quantities of glucose, fructose, maltose, starch, and molasses are to be used as the carbon sources. peptone, corn steep liquor, soybean meal, ammonium chloride, ammonium sulfate, and sodium nitrate are to be chosen as the nitrogen sources. Ten grams of air-dried tailing sand are to be introduced into a flask holding ninety milliliters of the bio-stimulation solution. The mixture is to be cultivated within an incubator. The urease activity within the conical flask is to be measured at consistent time intervals using the conductivity method, and this measurement is to serve as the evaluation criterion for identifying the most favorable carbon and nitrogen sources.

Identifying Crucial Factors Through PB Design

A Plackett-Burman (PB) design was utilized to examine the optimal carbon and nitrogen sources identified previously, along with other constituents in the bio-stimulation solution and the pH level of the solution. The objective of this design was to pinpoint the components exerting the greatest influence on urease activity, designating these as crucial factors. Following this, single-factor experiments were carried out by altering the concentration of each crucial variable in order to ascertain the most favorable concentration span for every one.

Determining the Optimal Bio-stimulation Solution Formulation

Urease activity was set as the outcome variable, with central composite design (CCD) being conducted employing Minitab16 program [12]. The best concentrations for every crucial variable were determined, thereby yielding the optimal formulation for the bio-stimulation solution intended for tailing sand.

Bacterial Suspension and Cementation Solution

The bacterium is *Sporosarcina pasteurii* (strain DSM33). The culture medium composition is as follows: 20 g/L yeast extract, 10 g/L ammonium sulfate, 15.8 g/L trisaminomethane. The experiments utilized the bacterial culture after 48 hours of cultivation.

The cementation solution is an equimolar blend of calcium chloride and urea. The concentration used in the experiments was 1 mol/L.

Molds and Methods

The experiments utilized aluminum boxes with a diameter of 10 cm and a height of 5 cm. there were some holes in the base of the box to allow waste liquid to drain. The tailing sand was placed inside the aluminum boxes.

The study was split into three sets: the *SP*, the bio-stimulation, and the combined solidification.

Concerning the *SP* set, the tailing sand underwent initial sterilization at 120 °C inside an oven over a 12-hour period. Based on the author's previous research findings [2], the one-phase low-pH MICP method was employed. Daily, 100 milliliters of the low-pH

bacterial suspension (pH = 3.5) was mixed with 100 milliliters of the cementation solution and then introduced to the sand samples. This constituted one treatment cycle.

Regarding the bio-stimulation set, the tailing sand remained unsterilized. Daily, 100 milliliters of the bio-stimulation solution was introduced as the initial step. Twelve hours later, 100 milliliters of the cementation solution was additionally applied. This constituted one treatment cycle.

For the combined solidification group, the tailing sand was also not sterilized. Daily, 100 milliliters of bio-stimulation solution was first added to the sand specimens, followed after 12 hours by the addition of a mixed solution of 50 milliliters low-pH bacterial suspension and 50 milliliters of the cementation solution. This constituted one treatment round.

Three different numbers of treatment cycles (4, 7, and 10) were investigated to study the effect of the number of treatment cycles on the solidification effect. Each treatment cycle was performed at 24-hour intervals. The control group sand samples were treated with 200 milliliters of deionized water.

After multiple treatment cycles, the following assessments were carried out: The penetration resistance of the solidified sand samples was tested using a mini penetrometer. Five points were uniformly tested on the top face of every sand specimen, then their average value was taken as the surface strength of the sand specimen. The leaching concentrations of Fe, Zn, and Cd within the sand specimens prior to and following solidification were determined using the Toxicity Characteristic Leaching Procedure (TCLP) method for hazardous waste [13].

RESULTS AND DISCUSSION

the Optimal Bio-stimulation Solution Formulation

the Best Carbon and Nitrogen Sources

The change in urease activity of the solution within the flasks over time using distinct carbon and nitrogen nutrient sources is illustrated in Figure 1. Upon employing starch and sodium acetate to provide carbon, the urease activity was relatively high, reaching the peak within a 48-hour period. Considering the range of sources of nitrogen, both inorganic and organic, ammonium sulfate, ammonium chloride, peptone, and soybean meal showed relatively high urease activity. Consequently, these six carbon and nitrogen sources, which showed relatively high urease activity and involved reduced bio-stimulation duration, were designated for the next stage of the PB experiment.

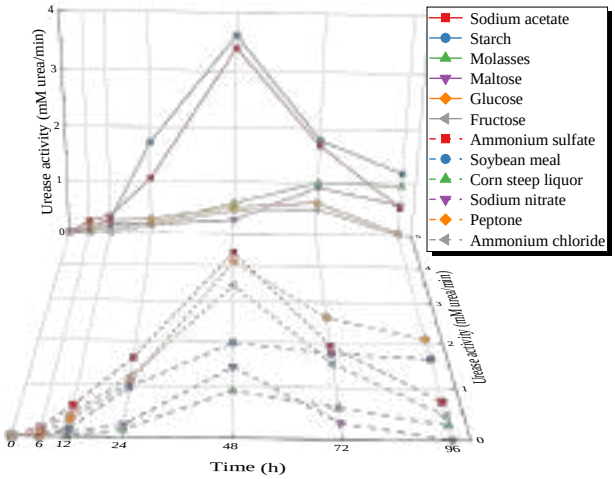

Fig.1 Change in urease activity over time under different carbon and nitrogen sources

Crucial Factors

6 carbon and nitrogen sources chosen based on the one-variable testing, accompanying the three additional ingredients present in the bio-stimulation preparation and the solution's pH, served as the 10 variables to be screened. With the urease activity in the suspension following 48 hours of bio-stimulation as the outcome measure, a PB experiment with N=12 trials was executed. The analytical outcomes can be viewed in Table 2. In this analysis, the P-value serves as a metric measuring the difference in the outcome value across varying factor levels. The P-values for sodium acetate, ammonium sulfate, urea, and pH value were all below 0.05, demonstrating that these items represent important influences on urease activity. The P-value for pH value was the smallest, indicating that pH value is the key determinant with the greatest impact on urease activity. These four variables were designated to be the crucial variables for the follow-up central composite design.

Table 2 Analysis of PB design

Factor	Level (g/L)		Effect	P-value
	-1	1		
starch	3.5	5.25	0.01	0.90
sodium acetate	3.5	5.25	-0.74	0.04
peptone	5.35	8	0.04	0.53
soybean meal	5.35	8	-0.37	0.07
ammonium chloride	5.35	8	0.10	0.26
ammonium sulfate	5.35	8	1.14	0.02
urea	20	30	0.71	0.04
yeast extract	0.2	0.3	-0.48	0.06
nickel chloride	0.01	0.015	-0.23	0.12
pH	7	9	2.33	0.01

the Optimal Formulation

The initial bio-stimulation solution composition was adjusted according to the beneficial and adverse influences of every factor shown in Table 2. Factors with negative effects were set at the –1 level, and factors with positive effects were set at the +1 level, resulting in the following composition: sodium acetate 3.5 g/L, $(NH_4)_2SO_4$ 8 g/L, urea 30 g/L, yeast extract 0.2 g/L, nickel chloride 0.01 mmol/L, and pH 9. Based on the formulation, one-variable tests were conducted by sequentially varying the level of each crucial factor while keeping other components constant. The urease activity at 48 hours at different levels of each crucial factor is shown in Figure 2. All four crucial factors possess optimal concentration ranges within which urease activity initially increases and subsequently decreases.

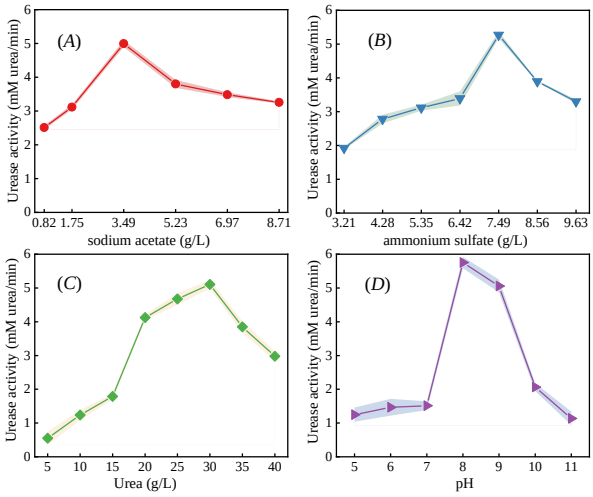

Fig.2 Effect of crucial factor concentration on urease activity

These four crucial factors served as independent variables, with the 48-hour urease activity as the response parameter. A CCD design was conducted. The model predicted a maximum urease activity of 6.54 mmol/L urea/min, and the corresponding optimal bio-stimulation solution composition was: sodium acetate 2.94 g/L, $(NH_4)_2SO_4$ 7.07 g/L, urea 28.86 g/L, yeast extract 0.2 g/L, nickel chloride 0.01 mmol/L, and pH 8.7. A bio-stimulation solution was prepared according to this formulation and used for cultivation with the tailing sand. Three replicates were prepared. The measured 48-hour urease activity was 6.6 mmol/L urea/min, which was close to the predicted value, verifying the accuracy of the model.

Surface Strength

Figure 3 shows the surface strength of sand specimens after undergoing treatment for 4, 7, and 10 cycles, respectively, using the three methods: *SP*, bio-stimulation, and the combined method. The surface strength of all after treatment was significantly improved in different amounts. When the number of treatment rounds was identical, the surface strength in sand specimens subjected to bio-stimulation was the lowest, while that subjected to combined solidification was the highest, showing considerable betterment in comparison with the *SP* treatment. For each method, the surface strength rose as the number of treatment rounds grew. Nonetheless, the bio-stimulation method resulted in relatively low urease activity, and even after 10 treatment rounds, the surface strength of the sand specimens was not high, which is insufficient to meet the strength requirements for tailing dams. While the surface strength of sand specimens after 4 cycles of combined solidification was comparable to that after 7 rounds of *SP* treatment. The surface strength of sand samples after 7 and 10 cycles of combined solidification was increased by 53% and 48% compared to the *SP* treatment at the same number of cycles, respectively, indicating that the combined solidification method indeed further enhanced the solidification strength. However, the rate of increase in surface strength after 7 cycles of combined solidification decreased rapidly, and the surface strength after 10 cycles showed no significant improvement compared to that after 7 cycles. This is because, with the increasing number of treatment rounds, more pores between the tailing sand particles were filled, which rendered it harder for the solution used for MICP to infiltrate.

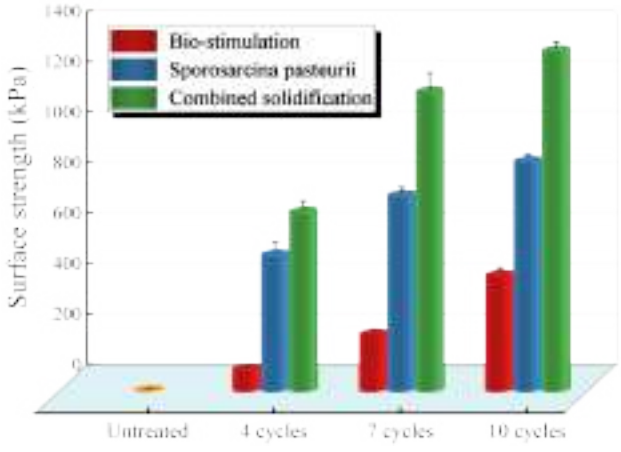

Fig.3 Surface strength of tailing sand

Heavy Metal Leaching Toxicity

Figure 4 presents the leaching concentrations of Fe, Zn, and Cd within untreated tailing sand and in samples that underwent 10 cycles using the three

methods. After solidification, the leaching concentrations of the three heavy metals were all notably lowered compared to the untreated sand samples. The order of heavy metal leaching concentration was: combined solidification < bio-stimulation < *SP*. The existing urea-decomposing bacteria in the tailing sand have high heavy metal tolerance and are uniformly distributed, providing more nucleation sites for carbonate precipitation. The carbonate ions generated during the MICP process can more easily combine with free heavy metal ions in the tailing sand. While during combined solidification, *SP*, which has higher urease activity, decomposed urea and produced more carbonate ions, further increasing the heavy metal immobilization rate. For the sand samples after combined solidification, the leaching concentrations of Fe, Zn, and Cd showed reductions of 89.2%, 72.5%, and 87.6%, respectively.

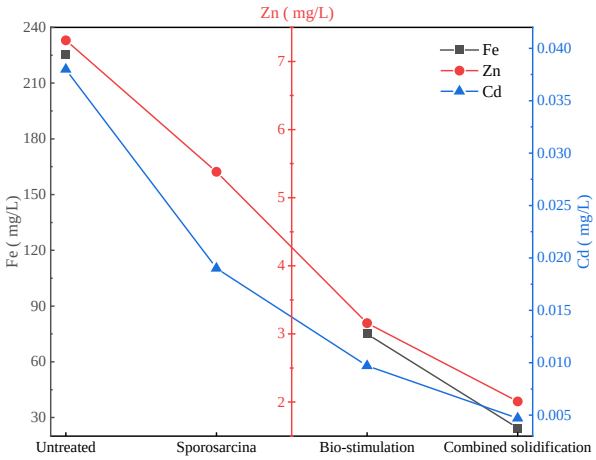

Fig.4 Heavy metal leaching toxicity of tailing sand

SEM Analysis

In the course of the MICP process, a competitive interaction exists between the nucleation and the growth of calcium carbonate crystals. [14]. Figure 5 shows SEM images of tailing sand before and after 10 cycles of solidification using the three methods. The indigenous urea-decomposing bacteria activated by bio-stimulation are spread out broadly and evenly throughout the tailing sand, which furnish additional nucleation sites. Furthermore, indigenous urea-decomposing bacteria have lower urease activity, inducing slower calcium carbonate formation, thereby facilitating the formation of new calcium carbonate crystals by nucleation. *SP* is an introduced exogenous bacterium with a limited migration and diffusion range. Moreover, *SP* has high urease activity, which can induce the formation of a large amount of calcium carbonate precipitate over a brief duration. It leads to calcium carbonate more readily precipitating on pre-existing crystals. As a result, the calcium carbonate crystal size in Figure 5(b) is smaller than in Figure 5(c). In addition, due to the lower urease activity of indigenous urea-decomposing bacteria compared to *SP*, less calcium carbonate is induced to form. Therefore, the number of calcium carbonate crystals in Figure 5(b) is also less than in Figure 5(c). During combined solidification, the indigenous urea-decomposing bacteria provided more nucleation sites, while the high urease activity *SP* induced the formation of more calcium carbonate. Therefore, both the number and size of calcite crystals in Figure 5(d) are greater than in Figure 5(b) and Figure 5(c). These crystals showed tight flaky arrangements, tightly wrapping around the sand particles, thereby achieving higher solidification strength.

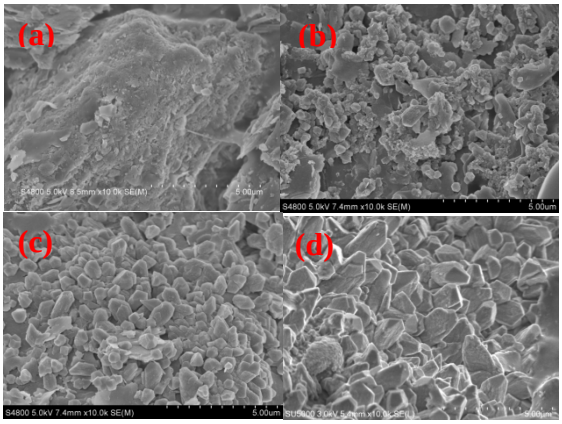

Fig.5 SEM images of tailing sand: (a) Untreated; (b) Bio-stimulation; (c) *SP*; (d) Combined solidification

CONCLUSIONS

This study proposed a method for solidifying tailing sand using indigenous urea-decomposing bacteria combined with *SP*, which improves the physical attributes related to the tailing sand while simultaneously immobilizing the heavy metals within it. The detailed findings are listed hereafter:

(1) The optimal bio-stimulation solution formulation for tailing sand is: sodium acetate 2.94 g/L, $(NH_4)_2SO_4$ 7.07 g/L, urea 28.86 g/L, yeast extract 0.2 g/L, nickel chloride 0.01 mmol/L, and pH 8.7.

(2) The combined solidification method further enhanced the solidification strength. The surface strength of sand specimens after 7 cycles of combined solidification was 2.594 times that after 10 cycles of

bio-stimulation, and 31% higher than *SP* solidification for 10 cycles.

(3) The combined solidification method further increased the heavy metal immobilization rate. At the same number of treatment cycles, the heavy metal immobilization rate for combined solidification was higher than that for both bio-stimulation and *SP* treated sand samples.

(4) The mechanism by which MICP improves mechanical properties is the ultimate filling of pores between tailing sand particles by calcium carbonate in the form of calcite crystals. Both the number and size of calcite crystals generated by combined solidification were greater than for *SP* and bio-stimulation.

The combined MICP approach demonstrated in this study offers significant practical advantages for sustainable mine tailing management, addressing critical environmental risks: (1) Mitigating structural failures of tailing dams through rapid strength gain; and (2) Preventing heavy metal migration into adjacent ecosystems. Moreover, utilizing bio-stimulation reduces reliance on exogenous microbial cultivation and lowers operational costs, while the optimized bio-stimulation solution ensures scalability for field applications. However, long-term stability under environmental stressors (e.g., acid rain, freeze-thaw cycles) warrants further investigation before large-scale implementation.

ACKNOWLEDGMENTS

This work was partly supported by Longyan City Wuping County Qimai Science and Technology Innovation Fund Project (2022LYQM007).

REFERENCES

[1] Dejong J T, Soga K, Kavazanjian E, et al. Biogeochemical processes and geotechnical applications: progress, opportunities and challenges[C]//Bio-and chemo-mechanical processes in geotechnical engineering: géotechnique symposium in print 2013. Ice Publishing, 2014: 143-157.

[2] Lai, Y. M., Yu, J., Liu, S. Y., Cai, Y. Y., Tu, B. X., & Liu, Q. Experimental Study on Microbial Induced Carbonate Precipitation Reinforcement of Tailing Sand at Low pH[J]. Rock and Soil Mechanics, 2024, 45(6): 1583-1596.

[3] Xue Z F, Cheng W C, Wang L, et al. Immobilizing lead in aqueous solution and loess soil using microbially induced carbonate/phosphate precipitation (MICP/MIPP) under harsh pH environments[J]. Journal of Hazardous Materials, 2024, 480: 135884.

[4] Okyay T O, Rodrigues D F. High throughput colorimetric assay for rapid urease activity quantification[J]. Journal of microbiological methods, 2013, 95(3): 324-326.

[5] Okewale I A, Grobler H. Mechanical and microstructural properties of iron tailings[J]. Environmental Geotechnics, 2022, 11(5): 384-395.

[6] Huang, X. S., Zhang, R. J., Cui, M. J., et al. Experimental Study on Bioremediation of Heavy Metal Contaminated Solution by Bacillus pasteurii[J]. Journal of Civil and Environmental Engineering, 2022, 44(3): 160–167.

[7] Mahanty B, Kim S, Kim C G. Assessment of a biostimulated or bioaugmented calcification system with Bacillus pasteurii in a simulated soil environment[J]. Microbial ecology, 2013, 65: 679-688.

[8] Li S, Wu J, Huo Y, et al. Profiling multiple heavy metal contamination and bacterial communities surrounding an iron tailing pond in Northwest China[J]. Science of the Total Environment, 2021, 752: 141827.

[9] GB-15618-2018. Soil Environmental Quality - Risk Control Standard for Soil Contamination of Agricultural Land (Trial)[S]. Ministry of Ecology and Environment of the People's Republic of China, 2018.

[10] HJ/T 166-2004. Technical Specification for Soil Environmental Monitoring[S]. Ministry of Ecology and Environment of the People's Republic of China, 2004.

[11] Wang Y J, Han X L, Jiang N J, et al. The effect of enrichment media on the stimulation of native ureolytic bacteria in calcareous sand[J]. International Journal of Environmental Science and Technology, 2020, 17: 1795-1808.

[12] Zhang Q, Rao Q, Shen Q Q, et al. Study on correlation of macro-meso parameters of flat joint model of particle flow code based on central composite design method[J]. J. Cent. South Univ.(Sci. Technol.), 2021, 52: 779-789.

[13] SW-846 Test Method 1311. Toxicity Characteristic Leaching Procedure[S]. United States Environmental Protection Agency, 1992.

[14] Gandhi K S, Kumar R, Ramkrishna D. Some basic aspects of reaction engineering of precipitation processes[J]. Industrial & engineering chemistry research, 1995, 34(10): 3223-3230.

Copyright © Int. J. of GEOMATE All rights reserved, including making copies, unless permission is obtained from the copyright proprietors.

15th Int. Conf. on Geotechnique, Construction Materials & Environment,
Kyoto, Japan, 11-13 November 2025, ISBN 978-4-909106124 C3051

DEVELOPMENT AND OPTIMIZATION OF MICROBIAL COMPOST POWDER FOR CLAY PELLETS: TOWARD A FUNCTIONAL AND MARKETABLE GROWING MEDIA

Songklot Phonphuak[1], Wimolkarn Nithisiriwaritkun[1], Nonthaphong Phonphuak [2], Piyarat Namsena[3], and Piyawadee Saraphirom[3*]

[1]Faculty of Management Science, Surindra Rajabhat University, Thailand; [2]Faculty of Engineering, Rajabhat Maha Sarakham University, Thailand; [3]Faculty of Science and Technology, Rajabhat Maha Sarakham University, Thailand

ABSTRACT

This research details the creation and enhancement of a compost powder rich in microbes intended for incorporation with clay pellets derived from agricultural waste, with the goal of producing a useful and eco-friendly growth medium. The compost was enhanced with microorganisms that dissolve phosphates, fix nitrogen, and provide antagonistic properties. By employing Response Surface Methodology (RSM), an ideal blend (0.7% phosphate solubilizers, 0.07% antagonists, and 2.0% nitrogen fixers) substantially boosted butterhead lettuce growth, resulting in 149.3 g per plant—surpassing both chemical fertilizer yields (128.5 g) and controls without fertilizer (67.4 g). The microbial mixture showed significant improvements in plant weight, leaf count, and height ($p < 0.05$). A feasibility study conducted under semi-pilot conditions revealed that all materials were sourced locally and economically, while the energy-efficient bio-coating process suited community-based production. The clay pellets made from rice husk ash and local clay effectively retained microbes and functioned as controlled-release agents. This adaptable production approach is consistent with the principles of a circular economy and the objectives of sustainable agriculture, encouraging wider implementation in both smallholder and organic farming settings. The findings confirm the technological, agricultural, and financial feasibility of the microbial compost powder and clay pellet combination, presenting a scalable biofertilizer solution that decreases dependence on synthetic inputs and enhances soil health alongside resource recovery.

Keywords: Microbial compost, Bio-coated clay, Response surface methodology, Azotobacter, Sustainable agriculture

INTRODUCTION

In the last few years, the shift towards eco-friendly farming practices has sped up because of growing worries about environmental damage, shifts in climate, and the decline of soil quality linked to heavy dependence on chemical fertilizers. Although artificial fertilizers enhance crop production significantly, their prolonged application has led to harmful effects on the environment, such as nutrient leaching, emissions of greenhouse gases, and the disturbance of natural soil microbial communities.[1], [2]. These drawbacks have led to the creation of different soil enhancers that promote both agricultural output and environmental sustainability.

Among these options, compost enriched with microbes stands out as a promising resource. This organically enhanced amendment integrates beneficial microorganisms into compost made from agricultural byproducts, resulting in improved nutrient cycling, support for plant growth, and the suppression of pathogens. [3]. Key microbial groups include phosphate-solubilizing bacteria (e.g., *Bacillus* spp.), nitrogen-fixing bacteria (e.g., *Azotobacter vinelandii*), and antagonistic microbes that inhibit soil-borne pathogens [4]. These microorganisms work together to enhance plant health and strength, aiding sustainable, organic, and regenerative agricultural practices with minimal inputs.

To improve the delivery and persistence of beneficial microbes in the rhizosphere, researchers have explored the use of fired clay granules derived from agri-waste as microbial carriers. These granules provide structural stability, moisture retention, and porosity, making them suitable for microbial encapsulation and slow-release delivery. A recent study by Saraphirom et al. demonstrated that fired clay granules could effectively preserve the viability of nitrogen-fixing bacterial cells during storage and facilitate their colonization in the soil environment [5]. This approach not only utilizes locally available ceramic and organic waste materials but also enhances the functionality of growing media in sustainable crop production.

Nonetheless, the effective execution of soil pellets made from microbial compost necessitates careful tuning of microbial mixtures to guarantee their suitability and performance. Response Surface Methodology (RSM), especially the Box-Behnken

Design (BBD), offers a robust statistical method to analyze and enhance complex multi-factor systems, allowing the determination of optimal microbial proportions for the best plant reaction. [6].

The primary goal of this research was to create and refine a compost powder formulation enriched with microbes, intended for application with clay pellets made from agricultural waste. This investigation sought to identify the most effective combination of three beneficial microbial groups—phosphate-solubilizers, nitrogen-fixers, and antagonistic species—and to test its biological effectiveness using butterhead lettuce (*Lactuca sativa*) as the subject of study. Additionally, the research examined the economic viability and environmental consequences of the product, bolstering its potential as a commercially viable, sustainable substitute for chemical fertilizers.

MATERIALS AND METHODS

Preparation of Microbial Compost Powder

Microbial compost powder was produced by integrating functional microorganisms into mature compost made from dried plant waste, cow manure, and rice husk ash, with a C:N ratio of ~25:1 to enhance microbial activity [1]. The mixture underwent aerobic composting for 60 days with periodic manual turning.

Post-maturation, the compost was shade-dried, pulverized, and sieved (2 mm) to yield a uniform, porous powder suitable for microbial adhesion and controlled release [7]. The formulation included phosphate-solubilizing Bacillus megaterium [3], antagonistic Azotobacter sp. [4], and nitrogen-fixing *A. vinelandii,* which has proven efficacy when immobilized on clay granules [5].

Each strain was cultured in nitrogen-free medium with potassium metabisulfite (KMS) to improve stress resistance, incubated at 28–30°C with shaking for five days, and adjusted to OD_{600} = 1.0. The microbial suspension was spray-coated onto the compost powder under sterile conditions and air-dried at ≤40°C to retain viability. Final moisture was kept below 12%, and the product was vacuum-sealed and stored at 4°C for stability.

Production of Clay Pellets

Clay pellets were produced using a mixture of local natural clay and rice husk ash (RHA), a by-product known to enhance thermal insulation, porosity, and water retention in ceramics [8]. The clay was sun-dried, ground, and sieved (1 mm), then mixed with 10–20% RHA by weight.

The blend, adjusted to 25–30% moisture for plasticity, was extruded into cylindrical pellets (5–7 mm diameter, 8–12 mm length), air-dried for 48 hours, and fired at 850–900°C for 5 hours. This firing range ensures both structural integrity and internal porosity suitable for microbial retention [9].

The fired pellets showed good durability, dimensional stability, and 12–18% water absorption, making them ideal microbial carriers. Use of RHA also supports waste valorization and lowers carbon emissions compared to conventional clay products [10]. The resulting porosity further enables effective microbial coating and slow-release fertilizer delivery.

Plant Growth Trials

The plant growth trials were conducted to evaluate the agronomic efficacy of microbial-enriched compost powder (MECP) in enhancing crop performance, improving soil quality, and increasing yield. The experimental design followed a structured protocol incorporating Response Surface Methodology (RSM) with Box-Behnken Design (BBD) to optimize the proportion of three functional microbial groups within the compost formulation. Butterhead Lettuce was selected for testing due to its rapid growth cycle and sensitivity to soil amendments. The range and levels of the independent variables for microbial supplementation in compost powder on the growth of Butterhead Lettuce was shown in Table 1. The plant was harvested after 60 days, and the dry weight was analyzed.

Table 1 Levels, actual and coded experimental independent variables for a microbial-enriched compost powder on the growth of Butterhead Lettuce

Variables	Coding	Unit	Levels		
			-1	0	+1
Phosphate-solubilizing bacteria concentration	X_1	%w/w	0.1	0.4	0.7
Antagonistic bacteria concentration	X_2	%w/w	0.07	0.235	0.4
Nitrogen-fixing bacteria concentration	X_3	%w/w	1.3	2	2.7

Statistical Analysis

Data collected from the growth trials were subjected to statistical evaluation using Design-Expert® version 13 (Stat-Ease Inc., USA). The analysis employed ANOVA for a quadratic model to assess the significance of treatment effects ($p < 0.05$). Model fitness was verified using lack-of-fit tests, adjusted R^2, and predicted R^2 values. Key factors considered in the Box-Behnken Design included: X_1: Phosphate-solubilizing bacteria concentration (%), X_2: Antagonistic bacteria concentration (%), and X_3: Nitrogen-fixing bacteria concentration (%)

The primary response variable was shoot dry

weight, with leaf number and plant height as secondary indicators. Response surface plots (2D contour and 3D surface) were generated to visualize factor interactions and determine the optimal MECP composition. Tukey's HSD post hoc test was conducted to identify statistically significant differences between treatments. The application of RSM enabled the prediction of optimal microbial ratios, which were subsequently validated through experimental results to confirm model accuracy and agronomic relevance [6].

Product Feasibility and Scalability

The production process of the microbial compost powder-coated clay pellet system was evaluated under semi-pilot conditions to assess its scalability and practical applicability. All materials used—including base compost, microbial inoculants, and clay mixtures—were selected based on local availability, low cost, and compatibility with existing composting and ceramic processing lines.

The microbial compost powder was formulated using materials and equipment replicable at community-level composting units. The bio-coating process employed low-energy drying (<40°C), and spraying equipment commonly used in agricultural cooperatives, demonstrating potential for low-tech adoption. The use of clay pellets fabricated from rice husk ash and local clay supports circular economy principles, valorizing agricultural residues into functional carriers [8], [9], [10].

The feasibility of product scaling was also reflected in the modular nature of the production steps, which can be adapted to fit various production capacities, from small-scale farmer groups to industrial settings. Moreover, the technology is aligned with global trends in biobased inputs and soil health enhancement, promoting sustainable agriculture [11], [12].

The entire system was designed with the intention to minimize capital investment while maximizing biological efficacy, shelf-life stability, and ease of use in field conditions. These characteristics suggest strong potential for commercialization or adoption in regenerative farming practices, especially in tropical and subtropical regions.

RESULT AND DISCUSSION

Optimization Outcome

The microbial compost powder formulation optimization was successfully conducted using Box-Behnken Design (BBD) under the Response Surface Methodology (RSM) framework. The independent variables included the proportion of phosphate-solubilizing microorganisms, antagonistic microorganisms, and nitrogen-fixing microorganisms, while the response variable was plant dry weight (g) of butterhead lettuce.

The ANOVA results for the quadratic model (Table 2) revealed that the model was statistically significant ($p < 0.0001$) with a very high coefficient of determination, indicating that the model could explain over 99% of the variability in the observed dry weight. The adjusted R^2 (0.9827) and predicted R^2 (0.9254) were also in close agreement, confirming the reliability and predictive accuracy of the model. Additionally, the Adeq Precision value of 33.96 indicated a strong signal-to-noise ratio, exceeding the minimum threshold of 4, confirming model adequacy for navigating the design space [13].

Among the factors, nitrogen-fixing microorganisms showed the highest *F*-value, suggesting that nitrogen availability was a dominant driver of biomass accumulation. Phosphate-solubilizing microorganisms and antagonistic microbes also contributed significantly to dry weight, supporting prior findings that multifunctional microbial consortia synergistically improve nutrient uptake and plant health [11], [14].

Table 2 Analysis of variance (ANOVA) for the model regression.

Source	Sum of Squares	df	Mean Square	*F*-value	*P*-value	
Model	0.9293	9	0.1033	89.14	< 0.0001	Sig.
X_1	0.1431	1	0.1431	123.55	0.0001	
X_2	0.0313	1	0.0313	26.98	0.0035	
X_3	0.1540	1	0.1540	132.96	< 0.0001	
$X_1 X_2$	0.1560	1	0.1560	134.70	< 0.0001	
$X_1 X_3$	0.0009	1	0.0009	0.7770	0.4184	
$X_2 X_3$	0.0380	1	0.0380	32.83	0.0023	
X_1^2	0.0246	1	0.0246	21.26	0.0058	
X_2^2	0.0043	1	0.0043	3.72	0.1116	
X_3^2	0.3940	1	0.3940	340.15	< 0.0001	
Residual	0.0058	5	0.0012			
Lack of Fit	0.0041	3	0.0014	1.65	0.3989	not sig.
Pure Error	0.0017	2	0.0008			
Cor Total	0.9351	14				
R^2	0.9938					
Adjusted R^2	0.9827					

Interaction effects between factors were also significant, suggesting that optimal growth depends on individual microbial inputs and their functional coordination in the rhizosphere. The contour and 3D plot (Fig. 1) visualizes the combinatorial effects of the three factors. The maximum predicted dry weight (2.84 g) was achieved at 0.7% phosphate-solubilizers, 0.23% antagonists, and 2.70% nitrogen-fixers. This formulation was selected as the optimal microbial

blend. The experimental validation of this combination produced a dry weight of 2.83 g, closely matching the predicted value and confirming the model's robustness.

These results reinforce that microbial synergy is pivotal in enhancing plant productivity. The observed improvements align with previous studies reporting that co-inoculation of nitrogen-fixing and phosphate-solubilizing bacteria significantly increases biomass in leafy vegetables [15]. Moreover, antagonistic microbes likely contributed indirectly by suppressing soil pathogens and enhancing root health, consistent with biofilm-based consortia performance [12], [16].

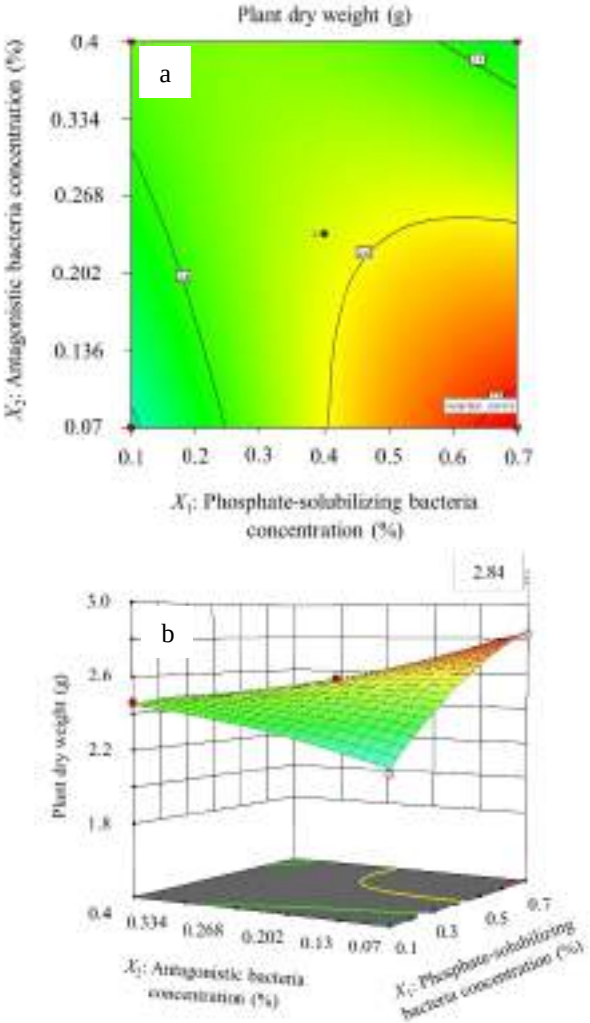

Figure 1 Response surface plots showing the effect of phosphate-solubilizing (X_1) and antagonistic bacteria (X_2) on plant dry weight. (a) Contour and (b) 3D surface plots. Maximum predicted weight (2.84 g) occurred at 0.7% X_1 and 0.235% X_2.

Application Potential Feasibility and Application Potential

The successful development of microorganism-enriched bio-coated clay granules (Fig. 2) marks a substantial advancement in designing scalable, sustainable, and low-cost biofertilizer delivery systems. These granules are engineered to function as a multifunctional carrier, offering mechanical support, prolonged microbial viability, and gradual nutrient release—thereby supporting improved plant growth and soil health.

The prototype was manufactured using readily available natural clay and agro-industrial residues, particularly rice husk ash (RHA), to produce a lightweight, porous matrix suitable for microbial adherence. The base material was extruded, sun-dried, and subsequently coated with the optimized microbial compost powder. The resulting granules displayed consistent shape, surface adhesion, and structural integrity, indicating their suitability for transportation, storage, and field application in tropical environments.

The development of bio-coated clay granules using microbial-enriched compost powder demonstrates high technical feasibility and market readiness. Its modular, low-energy production process—relying on locally available inputs such as rice husk ash and agricultural compost—supports cost-effective, community-level implementation.

From an economic perspective, the system minimizes production costs while enhancing crop yield, offering a favorable cost-benefit ratio compared to chemical fertilizers. This makes the product particularly attractive to smallholder farmers, eco-agriculture cooperatives, and organic growers seeking high-efficiency yet sustainable solutions [17], [18].

In terms of market potential, the product responds directly to global demand for bio-based, environmentally friendly soil amendments, aligning with circular economy and sustainable development frameworks [19]. Its multifunctional value—nutrient delivery, microbial support, and waste valorization—offers a competitive advantage in both local and export markets.

Moreover, alignment with policy trends such as SDG 12 and national biofertilizer promotion strategies enhances the prospect of regulatory integration and government support [20]. further enabling commercialization and scale-up.

The low-tech, modular production process demonstrates technical feasibility for community-based implementation without reliance on specialized equipment. The integration of locally sourced, biodegradable inputs and compost-derived

bioformulations also aligns with circular economy principles and sustainable agriculture goals. These features support potential adoption in both smallholder farming systems and eco-friendly commercial cultivation.

Fig. 2 presents the prototype of microorganism-enriched, bio-coated clay granules, produced from fired agri-waste clay blended with rice husk ash and coated with an optimized microbial compost powder. The background depicts shade-drying during mass production, while the inset highlights the granules uniform shape, coating integrity, and surface morphology, confirming their potential as a controlled microbial delivery system for sustainable agriculture.

Moreover, the system supports localized circular economy principles, as both the clay substrate and compost inputs are derived from agricultural by-products. This reduces waste while adding value to underutilized materials-contributing directly to SDG targets on sustainable consumption and production (SDG 12) [21].

Figure 2 Prototype of Bio-Coated Clay Granules with Microbial Compost Powder

Economically, the method of low-temperature drying and the use of gravity-based mixing and coating systems (rather than energy-intensive machinery) makes the technology accessible to smallholder farmer groups, rural entrepreneurship hubs, and eco-agricultural cooperatives. This is consistent with recent literature emphasizing the decentralization of biofertilizer production as a key strategy for ensuring accessibility in underserved regions [22]. From a biological perspective, the prototype effectively preserved the viability of microbial agents-including nitrogen-fixing, phosphate-solubilizing, and antagonistic strains-during coating and drying. When applied weekly over nine weeks in greenhouse trials, the granules demonstrated a sustained plant growth-promoting effect and improved soil properties. The use of a solid granular carrier ensures controlled release, improves root contact, and reduces microbial wash-off, which are commonly encountered challenges in liquid inoculant systems [23].

Given its promising agronomic response, low-cost production, and compatibility with small- and medium-scale farming systems, the bio-coated clay granule prototype presents strong potential for commercialization. Future studies should further explore shelf-life stability, mechanized pelletizing options, and field validation across multiple crop types. Technology also opens the possibility for product registration under national biofertilizer regulatory frameworks as highlighted in Yadav et al. [24], which could accelerate adoption and scaling.

CONCLUTION

This study successfully developed and optimized a microbial-enriched compost powder integrated with agri-waste-based fired clay granules to serve as a sustainable and scalable growing medium. The optimized formulation-comprising phosphate-solubilizing, nitrogen-fixing, and antagonistic microbes-significantly improved plant biomass and outperformed chemical fertilizer in controlled trials.

The production process is technically feasible, economically viable, and environmentally aligned, utilizing low-cost, locally available materials and low-energy techniques. Its modular design enables decentralized production and supports adoption by smallholder farmers and agricultural cooperatives.

Beyond agronomic benefits, the product offers strong market potential and policy relevance, aligning with global trends in sustainable agriculture, circular economy, and biofertilizer regulation. This innovation presents a promising platform for advancing regenerative farming and transforming agricultural residues into high-value inputs.

REFERENCES

[1] Zhang H., Tan W., and Liu C., Environmental and economic sustainability of organic and chemical fertilizers: Evidence from life cycle assessment, Agricultural Systems, Vol. 193, 2021, Article 103234.

[2] Wang Y., Liu Y., and Zhang X., Effects of excessive chemical fertilizers on soil microbial community structure and function: A global synthesis, Science of the Total Environment, Vol. 857, 2023, Article 159548.

[3] Sharma S. B., Sayyed R. Z., Trivedi M. H., and Gobi T. A., Phosphate solubilizing microbes: Sustainable approach for managing phosphorus deficiency in agricultural soils, Springer Nature

Reviews Earth & Environment, Vol. 1, 2020, pp. 565–579.

[4] Mitra S., Chaudhuri S., and Dutta D., Functional microbial consortia for sustainable agriculture: Recent advancements and future outlook, Journal of Environmental Management, Vol. 315, 2022, Article 115103.

[5] Saraphirom P., Namsena P., Teerakun M., Phonphuak S., Chanprathak A., Dakaew S., and Phonphuak N., Development of fired clay granules as eco-friendly substances for nitrogen-fixing bacterial cells, GEOMATE Journal, Vol. 27, No. 120, 2024, pp. 110–121.

[6] Montgomery D. C., Design and analysis of experiments, 9th ed., John Wiley & Sons, 2017.

[7] Malusá E., Sas-Paszt L., and Ciesielska J., Technologies for beneficial microorganisms inocula used as biofertilizers, The Scientific World Journal, Vol. 2012, Article 491206.

[8] Sutcu M., and Akkurt S., The use of recycled paper processing residues in making porous brick with reduced thermal conductivity, Ceramics International, Vol. 35, No. 7, 2009, pp. 2625–2631.

[9] Phonphuak N., and Chindaprasirt P., Influence of rice husk ash on properties of lightweight clay bricks, Construction and Building Materials, Vol. 94, 2015, pp. 94–99.

[10] Samaddar P., Maiti S., and Mukherjee A., Circular economy in clay-based industries: Utilizing agricultural residues for sustainable fired products, Journal of Cleaner Production, Vol. 372, 2022, Article 133702.

[11] Vassileva M., Flor-Peregrin E., Malusá E., and Vassilev N., Towards better understanding of the interactions and efficient application of microbial biofertilizers in agriculture, Applied Microbiology and Biotechnology, Vol. 104, 2020, pp. 1061–1076.

[12] Seneviratne G., Thilakarathna M. S., and Kulasooriya S. A., Biofilm-associated microbial consortia: An emerging technology for sustainable agriculture, Rhizosphere, Vol. 21, 2022, Article 100470.

[13] Montgomery D. C., Design and analysis of experiments, 9th ed., John Wiley & Sons, 2017.

[14] Bashan Y., de-Bashan L. E., Prabhu S. R., and Hernandez J. P., Advances in plant growth-promoting bacterial inoculant technology: Formulations and practical perspectives (1998–2013), Plant and Soil, Vol. 378, No. 1–2, 2014, pp. 1–33.

[15] Alori E. T., Glick B. R., and Babalola O. O., Microbial phosphorus solubilization and its potential for use in sustainable agriculture, Frontiers in Microbiology, Vol. 8, 2017, Article 971.

[16] Malusá E., and Vassilev N., A contribution to set a legal framework for biofertilizers, Applied Microbiology and Biotechnology, Vol. 98, No. 15, 2014, pp. 6599–6607.

[17] Zhang H., Tan W., and Liu C., Environmental and economic sustainability of organic and chemical fertilizers: Evidence from life cycle assessment, Agricultural Systems, Vol. 193, 2021, Article 103234.

[18] Bhardwaj D., Ansari M. W., Sahoo R. K., and Tuteja N., Biofertilizers function as key players in sustainable agriculture by improving soil fertility, plant tolerance and crop productivity, Microbial Cell Factories, Vol. 13, 2014, Article 66.

[19] Samaddar P., Maiti S., and Mukherjee A., Circular economy in clay-based industries: Utilizing agricultural residues for sustainable fired products, Journal of Cleaner Production, Vol. 372, 2022, Article 133702.

[20] Yadav A. N., Verma P., Singh B., and Chauhan V. S., Regulatory frameworks for quality control of biofertilizers: Recent advances and future perspectives, Frontiers in Sustainable Food Systems, Vol. 6, 2022, Article 1002472.

[21] Akinwumi I. I., and Shittu A. T., Valorization of agricultural waste for sustainable clay-based building materials: A review, Cleaner Materials, Vol. 5, 2020, Article 100038.

[22] Bhardwaj D., Ansari M. W., Sahoo R. K., and Tuteja N., Biofertilizers function as key player in sustainable agriculture by improving soil fertility, plant tolerance and crop productivity, Microbial Cell Factories, Vol. 13, 2014, Article 66.

[23] Bashan Y., and de-Bashan L. E., How the plant growth-promoting bacterium *Azospirillum* promotes plant growth—A critical assessment, Advances in Agronomy, Vol. 108, 2010, pp. 77–136.

[24] Yadav A. N., Verma P., Singh B., and Chauhan V. S., Regulatory frameworks for quality control of biofertilizers: Recent advances and future perspectives, Frontiers in Sustainable Food Systems, Vol. 6, 2022, Article 1002472.

Copyright © Int. J. of GEOMATE All rights reserved, including making copies, unless permission is obtained from the copyright proprietors.

15th Int. Conf. on Geotechnique, Construction Materials & Environment, Kyoto, Japan, 11-13 November 2025, ISBN 978-4-909106124 C3051

PLANT COLONIZATION AND WILDLIFE UTILIZATION ON A DISUSED ROAD IN WESTERN JAPAN

Taizo Uchida[1], Takeya Matsumoto[2], Teruo Arase[3], Masaaki Furuno[1] and Daisuke Hayasaka[4]

[1]Faculty of Architecture and Civil Engineering, Kyusyu Sangyo University, Japan; [2] Graduate School of Engineering, Kyusyu Sangyo University; [3] Faculty of Agriculture, Shinshu University, Japan; [4] Faculty of Agriculture, Kindai University, Japan

ABSTRACT

Japan is currently experiencing population decline due to a low birth rate and an aging society, raising concerns about the increasing extent of depopulated and uninhabited areas in the country. The aim of this study was to provide ecological insights into the management of infrastructure that has become infrequently used or abandoned due to this demographic decline and depopulation. As part of a broader investigation, we examined plant colonization and wildlife utilization of a paved road that had been left unused for approximately six years in Oita Prefecture, Kyushu Island, western Japan. The results showed that the absence of anthropogenic disturbance along the road resulted in 44.3% of the road surface being covered by vegetation. A total of 99 plant species (excluding 7 unidentified taxa) were recorded, including 39 woody species, with native species accounting for 93.9% of the species identified. Two-Way Indicator Species Analysis classified the vegetation into three distinct vegetation types. In addition, 10 mammalian species and four avian species were identified on the road, with native species accounting for 83.3%. Most animal activity occurred at night. No significant association was observed between vegetation type and wildlife use. However, the frequency of wildlife use was significantly higher on the abandoned road than on an adjacent road that remained in active use.

Keywords: Camera trap, Disused road, Infrastructures, Vegetation, Wild animal

INTRODUCTION

Japan's total population has been in decline since peaking in 2008, primarily due to persistently low birth rates and an aging population [1]. As a result, depopulated areas now comprise about 60% of the country's land area, and projections suggest that approximately 20% of currently inhabited areas will be uninhabited by 2050 [2,3,4]. This demographic shift is expected to accelerate the increase in infrequently used or abandoned forests, agricultural and residential land, and housing [3].

This underutilization of land has both social and ecological implications. Socially, negative outcomes include landscape deterioration [5,6], heightened risk of natural disasters [7], increased crime [8], and increased disruption of agricultural and daily activities associated with an increase in wildlife populations [8]. Ecologically, concerns have been raised about decreased biodiversity and ecosystem functions due to the expansion of bamboo forests [9], the conversion of grasslands into closed-canopy forests [10], dominance of certain species [11,12,13], reduction in understory vegetation by closed-canopy forests [14], and increased herbivory by deer [15]. However, the reduction of anthropogenic pressure on these areas may also have ecological benefits. For example, Inagaki et al. [16] and Ikegami et al. [17] have suggested that abandoned rice paddies and fallow fields function as diverse habitats and ecological compensation areas, including for threatened species. Similarly, Toivonen et al. [18] and Frenzel et al. [19] have reported that the cessation of grassland use has had the effect of increasing arthropod and avian diversity.

In addition to abandoned forests and farmland areas, the underutilization of infrastructure, such as railways and roads, has become increasingly common in depopulated and uninhabited regions of Japan [20-25]. How such infrastructure should be managed in the future is an extremely important challenge [20,21,22].

Therefore, the aim of this study is to provide ecological insights into the management of infrastructure that has become infrequently used or abandoned due to demographic decline and depopulation.

RESEARCH SIGNIFICANCE

Despite increasing recognition of land abandonment and infrastructure underutilization in depopulated regions, studies examining the ecological consequences of infrequently used or unused infrastructure remain limited. Existing research includes investigations on the relationship between abandoned railroads and pollinator communities [26], the effects of discontinued traffic on slope vegetation [27], and mammal use of forest roads (including unmanaged roads and roads that are

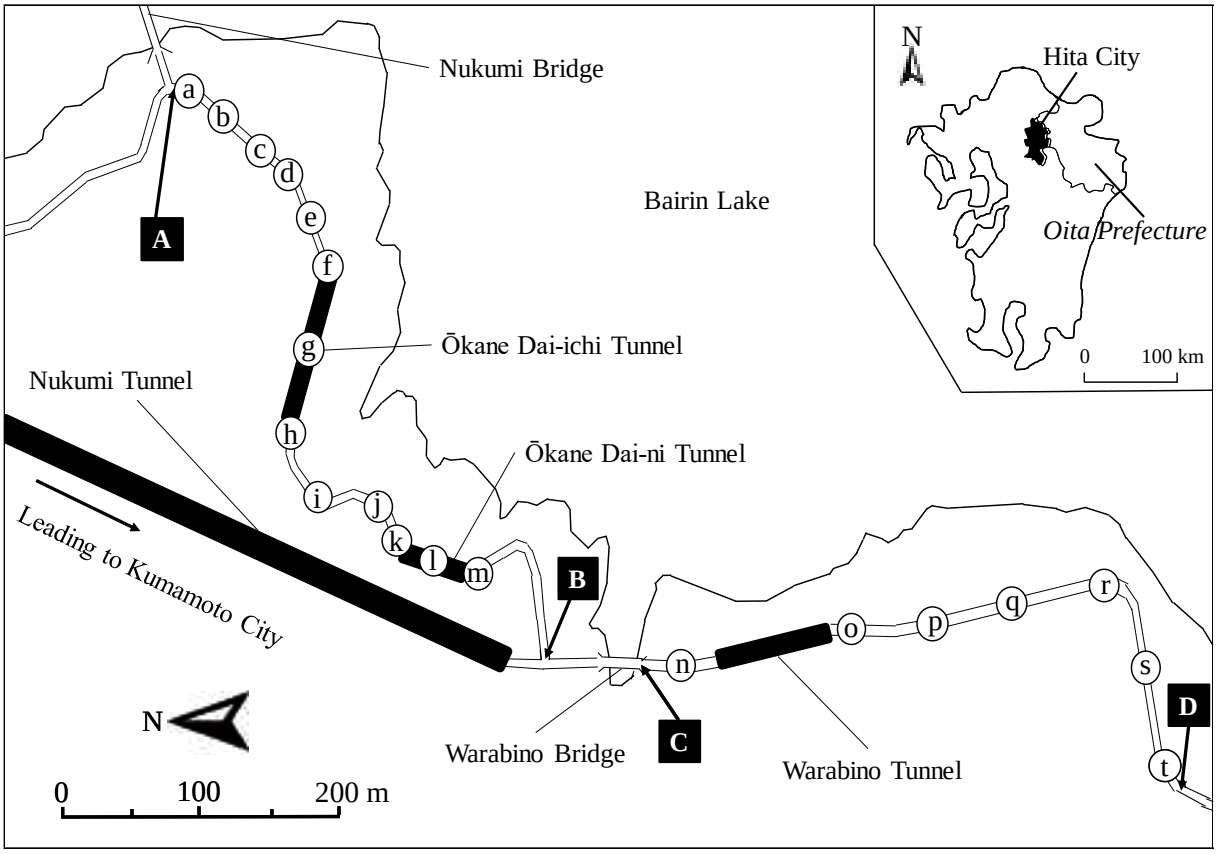

Fig.1 Schematic map of the study site

closed to traffic) [28]. The accumulation of empirical data on the interactions between unused infrastructure and natural ecosystems is considered to be extremely important for informing future management strategies. In this study, we investigated vegetation structure and wildlife utilization of an unmanaged paved road in Oita Prefecture, western Japan, approximately six years after it was closed.

SAMPLES AND METHODS

Study Site Overview

The study was conducted on Point A to Point D of Oita Prefectural Road 647 (Tochino-Nishi Oyama Route) running along Bairinko Lake in Hita City, Oita Prefecture (Fig.1). The section of road extending from Point A to Point B has a total length of about 600 m and has been closed to traffic since March 2014 due to the opening of the Nukumi Tunnel.

Survey Method

A total of 13 survey plots (a to m) were established at intervals of approximately 50 m between sections A and B (Fig.1). Surveys of vegetation and wild animal presence were conducted approximately 6 years after the cessation of road use.

Vegetation

In early October 2020, a quadrat measuring 15 m ×7 m (equal to the width of the road) was established at each survey plot. All vascular plant species present within each quadrat were recorded. Plant coverage, i.e., the percentage of road surface covered by the living plants, and total surface coverage, i.e., the percentage of the road surface covered by living plants, dead plants, fallen leaves and branches, and sediment, were estimated using the Braun-Blanquet cover-abundance scale [29]. Cover class values were converted to median percentages as follows: class r and + = 0.1%, 1 = 5.0%, 2 = 17.5%, 3 = 37.5%, 4 = 62.5%, and 5 = 87.5%. Each survey plot was classified into vegetation types by Two-Way Indicator Species Analysis (TWINSPAN) based on species presence/absence. For plots where no vegetation was observed, a fictitious species labeled “no vegetation” was assigned to enable inclusion into the analysis [29, 30]. Pearson’s $\chi 2$ tests were performed where appropriate. Statistical analyses were performed using PC-ORD ver. 4.25 (MjM Software Design) and SPSS Statistics ver. 27 (IBM).

Wildlife

Automatic cameras (TREL20J; GISupply) were installed at each of the 13 survey plots (a-m) to monitor wildlife activity. The monitoring was done

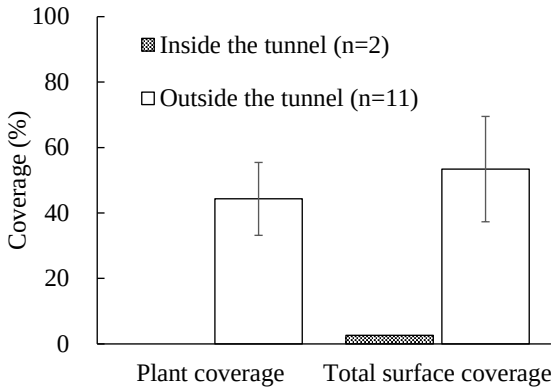

Fig.2 Plant coverage and total surface coverage (including dead plant material, litter, and sediment) in survey plots located inside and outside the tunnel

over two periods: from October 16 to October 28, 2020, and from November 13 to December 4, 2020 (Fig.1). Camera deployment, image acquisition, and data processing were performed as described by Tsukada et al. (2006) [31], Fujii et al. (2016) [32], and Kotani et al. (2016) [33].

Cameras were operated continuously throughout each survey period. The infrared sensor was set to trigger at 15-second intervals between activations. Sensor sensitivity was set to “low” for all plots except for plots located within tunnel sections (g and l), where sensitivity was set to high. For data analysis, multiple images of the same species captured within a 30-minute interval, or multiple individuals of the same species captured in the same frame, were treated as a single detection event. The total number of such detection events were treated as the number of effective images. The Relative Abundance Index (RAI) was then calculated using Eq. (1).

$$RAI = (Pn/(Cn \times Cd)) \times 100 \quad (1)$$

Where Pn is the number of effective shots, Cn is the number of cameras, and Cd is the number of camera operation days.

In addition to the 2020 surveys, a second survey was conducted in 2021 during the same periods, i.e., from October 16 to October 28 and from November 13 to December 4.

Automatic cameras were installed at seven locations (a, c, e, h, i, k, and m) between Points A and B along the closed road using the same method employed in the previous year (Fig.1). For comparison, an additional seven control plots (n to t) were established along an adjacent road section of approximately 600 m between Points C and D, where the road remains in regular use (Fig.1). To avoid excessive image capture triggered by vehicular traffic in the control plots, which would deplete the camera's

Photo 1 Road surface covered by such as vegetation, fallen leaves and sediment from experimental section A to B

battery and memory, the cameras were set to operate on a timer between 18:00 and 06:00.

Analyses were performed using a two-way analysis of variance (two-way ANOVA) without replication on square root-transformed values, and Tukey's HSD test, Mann-Whitney U test. Analyses were carried out using SPSS Statistics ver. 27 and R ver. 4.2.1.

RESULTS

Plant and Sediment Intrusion

Plant coverage and total surface coverage (including dead plant material, litter, and sediment) in the survey plots, both inside and outside the tunnel sections, are shown in Fig. 2. Within the tunnel, plant coverage and total coverage were 0.0% and 2.6%, respectively, indicating no vegetation establishment and minimal accumulation of organic debris or sediment. In contrast, plots located outside the tunnel sections exhibited a mean plant coverage of 44.3% and total coverage of 53.4%, suggesting that approximately half of the road was covered with vegetation and sediment (Fig.2, Photo 1).

Vegetation

A total of 99 plant species were identified across all of the survey plots, excluding seven unidentified taxa (Table 1). In addition to herbaceous species,

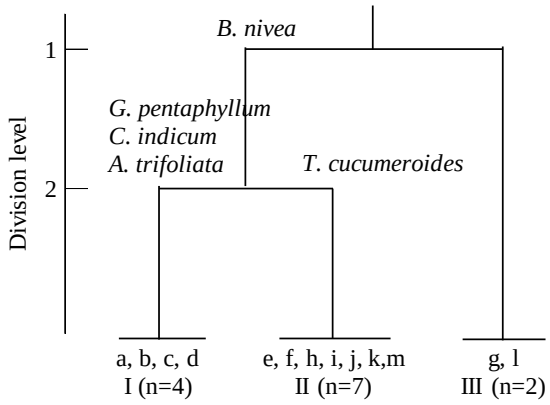

Fig.3 Classification of vegetation types based on Two-Way Indicator Species Analysis

including 42 perennials, 39 woody species were also recorded. Native species accounted for 93.9% of the total flora. No species listed as endangered by the Ministry of the Environment or regional authorities were observed.

TWINSPAN revealed that the survey plots were broadly classified into three vegetation types (Types I to III; Fig.3). Type III comprised two plots in the tunnel sections (g and l), where no vegetation was observed and only the notional “no vegetation” species was recorded. This classification is consistent with the absence of plant establishment shown Fig 1.

Type I included four plots (a, b, c, d) with a total of 61 species. The indicator species for this group was *Gynostemma pentaphyllum* (Thunb.) Makino. In addition, 22 species were unique to this type, including *Chrysanthemum indicum* L., *Akebia trifoliata* (Thunb.) Koidz., *Neolitsea sericea* (Blume) Koidz., *Pleioblastus argenteostriatus* (Regel) Nakai, and *Polystichum falcatum* (L.f.) Diels (Table 1). Type II consisted of seven plots (e, f, h, i, j, k, m), in which 84 species were recorded. The indicator species was *Trichosanthes cucumeroides* (Ser.) Maxim., and 45 species were unique to this type, including *Artemisia indica* Willd., *Rubia argyi* (H.Lév. et Vaniot) H.Hara, and *Trichosanthes kirilowii* Maxim. (Table 1). There were no significant differences between Type I and Type II in the proportion of native versus non-native species ($\chi 2 = 2.56$, df = 1, P = 0.11) or in the proportion of herbaceous versus woody species ($\chi 2 = 0.44$, df = 1, P = 0.84). A total of 39 species were shared between Types I and II. Of these, six species, i.e., *Boehmeria nivea* (L.) Gaudich., *Paederia foetida* L., *Miscanthus sinensis* Andersson, *Commelina communis* L., *Deutzia crenata* Siebold, and *Boehmeria spicata* (Thunb.) Thunb., exhibited high frequency of occurrence, with presence in more than 80% of plots in both types (Table 1).

Table 2 Relative Abundance Index (RAI) of wildlife species by vegetation type

Species	Vegetation type		
	I (n=4)	II (n=7)	III (n=2)
Nyctereutes procyonoides	64.4	43.3	12.1
Vulpes vulpes	17.4	16.5	3.0
Sus scrofa	13.6	18.2	-
Procyon lotor *	8.3	11.3	4.5
Meles anakuma	8.3	8.2	4.5
Cervus nippon	1.5	16.5	-
Martes melampus	2.3	2.6	-
Aves sp.	-	-	4.5
Felis catus *	1.5	1.3	1.5
Sus scrofa	1.5	0.4	-
Procyon lotor *	-	1.7	-
Streptopelia orientalis	0.8	1.7	-
Aves sp.2	1.5	-	-
Syrmaticus soemmerringii	0.8	0.4	-
Average RAI	8.7	8.7	2.2

*; Non-native species
See Fig. 3

Wildlife

Relationship between vegetation type and RAI

In the 2020 survey, a total of 10 mammalian species, including *Nyctereutes procyonoides* viverrinus, *Vulpes vulpes* japonica, *Sus scrofa* leucomystax, and 4 avian species, including *Streptopelia orientalis* and *Syrmaticus soemmerringii*, were recorded across all survey plots (Table 2, Photo 2-A, B and C). Although non-native species, such as *Procyon lotor* and Felis catus were also identified, native species accounted for 83.3% of all identified taxa. No species listed as endangered by the Ministry of the Environment or regional authorities were identified.

No significant differences in wildlife occurrence were observed between vegetation Types I and II. However, both Type I and II differed significantly from Type III (two-way ANOVA, P<0.01). In addition, the mean RAI was significantly lower in Type III than in Types I and Type II (Tukey's HSD test, P<0.01).

Relationship between time of day and RAI

The hourly RAI values are shown in Fig 4. Between 06:00 and 18:00, RAI values ranged from 0.7 to 2.8. However, a marked increase was observed during the nighttime period (18:00 and 06:00), with RAI values ranging from 9.3 to 24.2, indicating that most wildlife activity occurred during nocturnal hours.

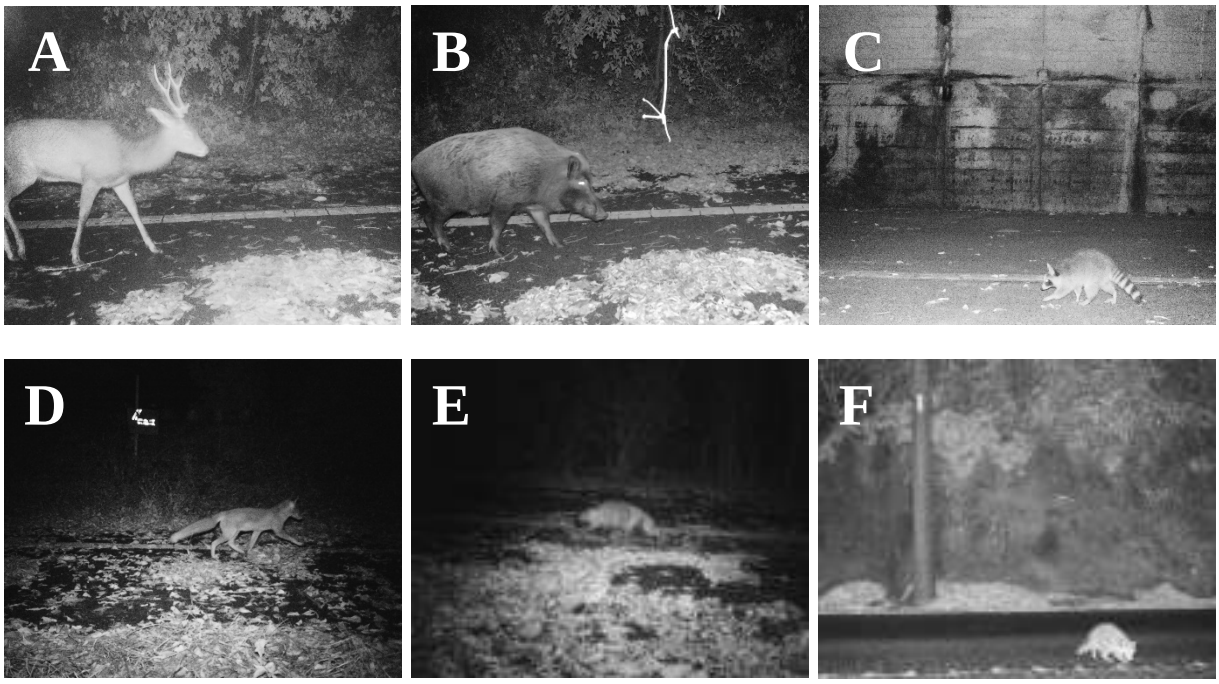

Photo 2 Examples of the wildlife recorded by automatic cameras in this survey

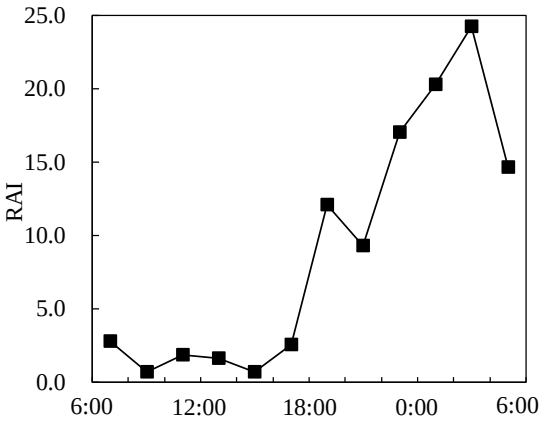

Fig. 4 Relative Abundance Index (RAI) of wild animals by time period

0.7 to 2.8. However, a marked increase was observed during the nighttime period (18:00 and 06:00), with RAI values ranging from 9.3 to 24.2, indicating that most wildlife activity occurred during nocturnal hours.

Relationship between presence/absence of traffic and RAI

In the 2021 survey, a total of nine mammalian species and four avian species were identified in the closed-road plots (a, c, e, h, i, k, and m; Sections A to B) (Fig.1, Table 3, Photo 2-D and E). In contrast, only two mammalian species were identified along the road that remained in use (n to t; Sections C to D) (Fig.1, Table 3, Photo 2-F).

A significant difference in wildlife occurrence was observed between closed-road and open-road sections (two-way ANOVA, $P<0.01$). The mean RAI was also significantly higher in the closed-road plots than in the open-road plots (Mann-Whitney U test, $P<0.01$).

The wildlife composition and its proportion of native species in both sections were generally comparable to those recorded in the 2020 survey (a to m; total of 14 plots). As in the previous year, no species listed as endangered by the Ministry of the Environment or by local authorities were identified.

DISCUSSION

Encroachment of Plants and Sediment into Paved Roads That Are No Longer in Use

The results showed that, after approximately six years of closure, a substantial portion of the road surface became covered by vegetation, fallen leaves, branches, and sediment (Fig.2). These findings suggest that periodic road maintenance, such as weeding (typically conducted once or twice a year in this area), as well as vehicular traffic, play important roles in preventing plant colonization and sediment deposition. In other words, in the absence of human disturbance, even paved road surfaces are colonized by vegetation and subject to sediment deposition over a relatively short timescale. Similar results were

Table 3 Relative Abundance Index (RAI) of wildlife species in closed road sections and open road sections

Species	Open road sections (n=7)	Closed road sections (n=7)
Nyctereutes procyonoides	82.4	-
Procyon lotor *	41.6	1.1
Vulpes vulpes	18.4	-
Cervus nippon	16.3	-
Meles anakuma	14.4	-
Felis catus *	11.9	-
Sus scrofa	11.6	1.1
Martes melampus	10.1	-
Lepus brachyurus	1.7	-
Syrmaticus soemmerringii	1.7	-
Streptopelia orientalis	0.9	-
Corvus corone	0.7	-
Aves sp.2	0.4	-
Average RAI	16.3	0.2

*; Non-native species

reported by Uchida et al. [34] along disused railroad tracks. The findings of this study suggest that in the absence of weed control, plants rapidly invade roads and become established. Furthermore, that study reported that train operation exerted a suppressive effect on plant invasion and growth.

In contrast, vegetation establishment and sediment accumulation were not observed in the tunnel plots (Fig.2), indicating that tunnels are highly effective in preventing both external inflows of sediment and the establishment of vegetation through shading.

Established Vegetation

The cessation of vehicular traffic led to the colonization and establishment of a diverse variety of plants at the study site (Table 1). The included flora consisted of a higher proportion of perennial species compared to ephemeral taxa (i.e., annuals and biennials), and as well as many woody plants, suggesting that succession is somewhat advanced. Although no species of conservation value were observed, the majority of the species were native (Table 1). This may reflect the later stages of succession, since many non-native species commonly invading anthropogenic environments in Japan are light-demanding and generally less tolerant of shade [35].

Excluding the tunnel plots, the survey plots were broadly classified into two vegetation types, each characterized by distinct species assemblages (Fig.3, Table 1). The reason for this is not obvious, but the spatial continuity of survey plots within each vegetation type suggests that local site conditions, such as slope orientation, light availability, and soil moisture, may strongly influence vegetation structure. Of particular interest is the substantial overlap in species composition between the vegetation types. Several species, including *Boehmeria nivea* (L.) Gaudich., *Paederia foetida* L., *Miscanthus sinensis* Andersson, *Commelina communis* L., *Deutzia crenata* Siebold, and *Boehmeria spicata* (Thunb.) Thunb., were commonly recorded across both types and exhibited high frequencies. These species may be regarded as representative of vegetation developing on underutilized or abandoned roads in the region and could serve as indicator species for future road management.

Wildlife Utilization

Although the roads targeted in this study were not used by endemic or endangered species, many wild animal species were found to use these roads mainly at night (Table 2, Fig.4, Photo 2). Wildlife occurrence and abundance were significantly higher on unused roads compared to adjacent roads in active use (Table 3), suggesting that the elimination of anthropogenic disturbance, facilitates increased wildlife utilization. No significant relationship was observed between vegetation Types I and II (excluding tunnels) and the presence or abundance of wild animal species (Table 2), further suggesting that the absence of vehicular traffic was the primary factor affecting wildlife use.

One notable finding from this study is the detection of wild animals in the tunnels, despite the absence of vegetation and limited environmental complexity (Table 2, Photo 2-C). Although usage was lower than that in open sections, this represents one of the few documented cases of animal activity in disused road tunnels. Whether this reduced usage results from the absence of vegetation, limited light, or avoidance behavior related to the enclosed structure remains unclear (Table 2). Recently, ecosystems that have no historical precedent, such as ecosystems with artificial spaces, have been referred to as 'novel ecosystems' [36,37,38]. In light of the establishment of vegetation and the use of wildlife on paved roads (including tunnels) that are no longer used, such as the sites described above, the underutilized infrastructure described in this study could be considered a novel ecosystem.

In one of the few reports on the effects of infrequently used or unused infrastructure on local ecology, Suzuki et al. (2023) [28] reported that mammalian species composition along forest roads

varied according to road usage, and Arase et al. (2019) [27] demonstrated differences in slope vegetation associated with the presence or absence of road traffic. Dylewski et al. (2021) [26] reported that abandoned railway corridors supported greater abundance and diversity of pollinator communities than the adjacent grasslands. We believe that the results of this study corroborate these reports and offer new ecological insights for dealing with infrequently used or unused infrastructure.

Finally, it should be noted that in the 2021 control plots, camera operation was limited to nighttime hours (18:00 to 06:00) to avoid triggering by vehicular traffic (Table 3). However, given that the majority of wildlife activity occurred during this time period (Fig.4), this limitation is unlikely to have substantially affected comparisons with the continuously monitored plots.

CONCLUSION

The objective of this study was to provide ecological insights into the consequences of infrequently used or unused infrastructure. We investigated vegetation development and wildlife utilization of a paved road that had been unmanaged for approximately six years. The following findings were obtained. First, it was shown that even paved roads, when no longer subject to anthropogenic disturbance, can become covered with vegetation and sediment within a relatively short period of time. Second, the vegetation established on the paved road included not only ephemeral species but also perennial and woody species, indicating the progression of succession. Third, more wild animal species and individuals were observed on the road that was no longer in use compared to a road that remained in use. This difference was primarily attributed to the absence of vehicular traffic, rather than to differences in vegetation. Fourth, while tunnels are highly effective in preventing sedimentation and vegetation establishment on roads that are no longer used, they are also often used by some wild animals. Fifth, disused roads such as the one examined in this study could be considered as an example of a novel ecosystem.

A key future challenge is how to deal with infrequently used or unused infrastructure, which is increasing due to the accelerating aging of the population and declining birthrate. Despite the growing extent of such areas, ecological research on the effects of underused infrastructure remains limited. The findings reported here are therefore important in considering how such spaces should be managed in the future.

Of particular interest in this study was the finding that wild animals actively used disused roads and tunnels. Future research is needed to clarify the purpose of this use, such as for migration, foraging, or resting, and to examine the relationship between wildlife activity and the degree of vegetation succession on roads that have remained abandoned for longer periods of time.

ACKNOWLEDGMENTS

We thank the Hita Civil Engineering Office of Oita Prefecture for their cooperation in carrying out this study. We are also grateful to all individuals and organizations who contributed to the successful completion of the research.

REFERENCES

[1] Ministry of Internal Affairs and Communications, White paper on information and communication technology, 2016, https://www.soumu.go.jp/johotsusintokei/whitepaper/ja/h28/html/nc111110.html. (Accessed May 2025) (in Japanese).

[2] Ministry of Land, Infrastructure, Transport and tourism, locations to be uninhabited by 2050, https://www.mlit.go.jp/common/001033678.pdf. (Accessed May 2025) (in Japanese).

[3] Ministry of Land, Infrastructure, Land that is difficult to continue to properly manage, https://www.mlit.go.jp/common/001232543.pdf. (Accessed May 2025) (in Japanese).

[4] Ministry of Internal Affairs and Communications, Current state of depopulation control measures, https://www.soumu.go.jp/main_content/000743328.pdf. (Accessed May 2025) (in Japanese).

[5] Fujimi T., Watanabe M., and Asano K., Economic Loss of Landscape Degradation in Rice Terraces Caused from Cultivation Abandonment or Land Consolidation, Environmental Science, Vol. 19, Issue 3, 2006, pp.195-207 (in Japanese).

[6] Shibata Y., and Sato A., A Study on Residents' Evaluation of Landscape of Abandoned Farmlands in Hilly and Mountainous Areas, Journal of the Japanese Institute of Landscape Architecture, Vol. 79, Issue 5, 2016, pp.617-622 (in Japanese).

[7] Awazu T., The Study Related with The External Effect and The Effect of Countermeasures for Unmaintained Vacant Houses and Buildings, Urban Housing Sciences, Vol. 87, 2014, pp.209-217 (in Japanese).

[8] Yagi H., Clarification and Prediction of the Negative Externalities on Farm Activities from Non-farm Land Use, Transactions of Rural Planning, Vol. 5, 2003, pp.79-84 (in Japanese).

[9] Suzuki S., Are bamboo forests low in plant diversity?, Forest Science, Vol. 58, 2010, pp.11-14 (in Japanese).

[10] Takahashi Y., Collaborative Activities for

Conservation and Restoration of Aso Grassland, Journal of Ohara Institute for Social Research, Vol. 655, 2013, pp.3-18 (in Japanese).
[11] Otsuka H., Kobayashi S., Masuda S., and Nemoto M., Influence of Rice cultivation and its Cessation on The Vegetation in Valleys in Hill Land in Chiba Prefecture, Journal of Weed Science and Technology, Vol. 49, 2004, pp.21-35 (in Japanese).
[12] Matsumura T., and Takeda Y, Relationship between period after abandonment and species richness or species composition of semi-natural grasslands at paddy levee slopes, Vegetation Science, Vol. 25, 2008, pp.131-137 (in Japanese).
[13] Wu C., and Ando M, Stand Structure and Dynamics During a 10-year Period of Pine Wilt Disease Forests in Kyoto City, Journal of the Japanese Society of Revegetation Technology, Vol. 35, Issue 3, 2010, pp.440-447 (in Japanese).
[14] Uehara M., Shigematsu T., Fujii Y., and Iwamoto S., Succession of Shrud-later Vegetation and Situation of Wild Rhododendron in The Abandoned Satoyama Coppice Forest, Journal of the Japanese Institute of Landscape Architecture, Vol. 72, Issue 5, 2009, pp.511-516 (in Japanese).
[15] Ohashi H., Kominami Y., Higa M., Koide D., Nakano K., Tsuyama I., Matsui T., and Tanaka T., Land Abandonment and Changes in Snow-cover Period Accelerate Range Expansions of Sika Deer, Ecology and Evolution, Vol. 6, 2016, pp.7763-7775.
[16] Inagaki H., Oishi T., Matsuno K., Takahashi T., and Banno M., Flora and Fauna in Fallow Rice Fields with Different Vegetation in the Kikukawa Watershed, Shizuoka Prefecture, Japan, Journal of the Japanese Society of Revegetation Technology, Vol. 34, Issue 1, 2008, pp.269-272 (in Japanese).
[17] Ikegami Y., Nishihiro J., and Washitani I., Vegetation of Abandoned Rice Fields in The Head Areas of Small Valley Bottoms (‘yatsu’) in The Lake Kitaura Watershed, Ibaraki, Japan, Japanese Journal of Conservation Ecology, Vol. 16, 2011, pp.1-15 (in Japanese).
[18] Toivonen M., Herzon I., and Kuussaari M, Differing Effects of Fallow Type and Landscape Structure on The Occurrence of Plants, Pollinators and Birds on Environmental Fallows in Finland, Biological Conservation, Vol. 181, 2015, pp.36-43.
[19] Frenzel T., Rischen T., and Fischer K., Humid Grassland Fallows Promote Spider Diversity in a Traditionally Managed Landscape, Basic and Applied Ecology, Vol 63, 2022, pp.59-70.
[20] Ministry of Land, Infrastructure, Transport and tourism, Interim Summary of the Subcommittee to Study Measures for Low- and Underutilized Land, https://www.mlit.go.jp/singikai/kokudosin/tochi/kikaku/16/images/022.pdf. (Accessed May 2025) (in Japanese).
[21] Uto M., The viewpoint of the infrastructure management during the decreasing population era, The Japanese Journal of Real Estate Sciences, Vol. 25, Issue 4, 2012, pp.43-49 (in Japanese).
[22] Uto M., Examining Environmental Risks from The Viewpoint of De-population and Infrastructure Issues, Journal of the National Institute of Public Health, Vol. 67, Issue 3, 2018, pp.306-312 (in Japanese).
[23] Nojiri A., Oosawa M., and Kishii T, On the Conversion of the Site of Railway Right -Land Use Conversion of the Old Railway Site and the Old Station Sites-, Journal of the City Planning Institute of Japan, Vol. 44, Issue 3, 2009, pp.151-156 (in Japanese).
[24] Ministry of Land, Infrastructure, Actual abolition of recently abolished railroad tracks (since FY2000), https://www.mlit.go.jp/common/001344605.pdf. (Accessed May 2025) (in Japanese).
[25] Ministry of Land, Infrastructure, National Highway 210 Amagase Improvement, http://www.qsr.mlit.go.jp/oita/newstopics_files/2018/pdf181106_p1.pdf. (Accessed May 2025) (in Japanese).
[26] Dylewski Ł., and Tobolka M, Unused Railway Lines as a Contributor to Bird Abundance, Species Richness and Diversity in Intensively Managed Farmland, Agriculture, Ecosystems & Environment, Vol. 326, 2021, Article 107820.
[27] Arase T., Nishio A., Okano T., and Uchida T., Effect of Suspending Traffic on a Highway in a Mountainous Region on the Succession of Slope Vegetation, International Journal of GEOMATE, Vol. 16, Issue 56, 2019, pp.85-91.
[28] Suzuki M., and Saito M.U., Forest Road Use by Mammals Revealed by Camera Traps: A Case Study in Northeastern Japan., Landscape and Ecological Engineering, Vol. 19, 2023, pp.289-296.
[29] Braun-Blanquet J., Pflanzensoziologie, 1964, 865pp.
[30] Hasegawa K., Ueno Y., Oshiro N., Takimoto M., Mitsuani Y., and Inoue R., Status Quo and Conservation Challenges in Japan : An Analysis Related to Road-building Projects, Japanese Journal of JSCE , Vol. 72, 2016, pp.II_311-II_317 (in Japanese).
[31] Tsukada H., Fukasawa M., Kosako T., Sutoh M., Imura T., and Hirakawa H, Photo-trapping Application to Mammal Fauna Survey on Public Pastures in Northern Tochigi, Japan, Mammalian Science, Vol. 46, Issue 1, 2006, pp.5-19 (in Japanese).
[32] Fujii T., Kawamoto H., Shirako T., Ueno K., and Minami M., Mammal survey using the camera trap method in a corporate greenbelt in the coastal

industrial zone of Chita City, Aichi Prefecture, Japan, Journal of the Japanese Society of Revegetation Technology, Vol. 42, Issue 2, 2016, pp.320-329 (in Japanese).
[33] Kodani N., Arimoto I., Nozaki R., and Esaki K., Mammal Fauna Detected by Camera Traps around SATOYAMA Area in Nanao City and Nakonoto Town, Ishikawa Prefecture, Annual report of Hakusan Nature Conservation Center, Vol. 42, 2016, pp.43-49 (in Japanese).
[34] Uchida T., Furuno M., Furuno H., Arese T and Okano T., Railway Tracks Vegetation in Relation to Various Management, Kumamoto, Japan, International Journal of GEOMATE (*in press*).
[35] Uchida T., Dynamics of Alien Grasses (Poaceae) as Cover Plants on Slopes, Journal of the Japanese Society of Revegetation Technology, Vol. 44, Issue 4, 2019, pp.584-586 (in Japanese).
[36] Murakami K., Usefulness of the Novel Ecosystem Concept, Papers on Environmental Information Science, Vol. 33, 2019, pp.265-270 (in Japanese).
[37] Hobbs R. J., Arico S., Aronson J., Baron J. S., Bridgewater P., Cramer V. A., Epstein P. R., Ewel J. J., Klink C. A., Lugo A. E., Norton D., Ojima D., Richardson D. M., Sanderson E. W., Valladares F., Vil M., Zomora R., and Zobel M., Novel Ecosystems : Theorical and Management Aspects of the New Ecological World Order, Global Ecology and Biogeograohy, Vol. 15, Issue 1, 2006, pp.1-7.
[38] Hobbs R. J., Higgs E. S., and Hall C. M., Novel Ecosystems: Intervening in the New Ecological World Order, 2013, 384pp.

Copyright © Int. J. of GEOMATE All rights reserved, including making copies, unless permission is obtained from the copyright proprietors.

Appendix 1 List of plant species recorded in each vegetation type: Species are grouped by vegetation types I, II, and III as classified by Two-Way Indicator Species Analysis.

Species	Vegetation type			Native	Herbaceous		Woody
	I (n=4)	II (n=7)	III (n=2)		Ephemeral	Perennial	
Boehmeria nivea	V	V		●		●	
Paederia foetida	V	V		●		●	
Miscanthus sinensis	V	IV		●		●	
Trachelospermum asiaticum	V	IV		●			●
Solidago canadensis	V	III				●	
Hedera rhombea	V	III		●			●
Oplismenus undulatifolius	III	V		●		●	
Commelina communi s	IV	IV		●	●		
Deutzia crenata	IV	IV		●			●
Boehmeria spicata	IV	IV		●			●
Achyranthes bidentata	II	V		●		●	
Celtis sinensis	IV	III		●			●
Pueraria lobata	IV	III		●		●	
Ampelopsis glandulosa	IV	III		●			●
Rubus hirsutus	III	IV		●			●
Persicaria longiseta	III	IV		●	●		
Aucuba japonica	III	IV		●			●
Ficus erecta	IV	II		●			●
Morus alba	III	III		●			●
Sinomenium acutum	III	III		●			●
Akebia x pentaphylla	III	III		●			●
Rubus buergeri	III	III		●			●
Solanum nigrum	IV	I		●	●		
Morus bombycis	III	II		●			●
Clematis apiifolia	II	III		●			●
Wisteria brachybotrys	II	III		●			●
Pilea mongolica	II	III		●	●		
Mallotus japonicus	II	III		●			●
Justicia procumbens	II	III		●	●		
Camellia japonica	III	I		●			●
Microstegium japonicum	III	I		●	●		
Eragrostis ferruginea	II	II		●		●	
Dioscorea japonica	II	II		●		●	
Plantago asiatica	II	II		●		●	
Chamaele decumbens	II	II		●		●	
Cirsium oligophyllum	II	II		●		●	
Ophiopogon japonicus	II	II		●		●	
Rosa multiflora	II	I		●			●

Appendix 1 continued

Species	Vegetation type			Native	Herbaceous		Woody
	I (n=4)	II (n=7)	III (n=2)		Ephemeral	Perennial	
Gynostemma pentaphyllum	IV			●		●	
Chrysanthemum indicum	IV			●		●	
Akebia trifoliata	IV			●			●
Neolitsea sericea	III			●			●
Pleioblastus argenteostriatus	III			●			●
Cyrtomium falcatum	III			●			●
Parthenocissus tricuspidata	III			●			●
Cyperus eragrostis	II					●	
Eragrostis curvula	II					●	
Cardiocrinum cordatum	II			●		●	
Sporobolus fertilis	II			●		●	
Thalictrum minus	II			●		●	
Cayratia japonica	II			●		●	
Erigeron annuus	II				●		
Stegnogramma pozoi	II			●		●	
Vandellia crustacea	II			●	●		
Conyza sumatrensis	II				●		
Lactuca indica	II			●	●		
Liriope muscari	II			●		●	
Ulmus davidiana	II			●			●
Trichosanthes cucumeroides		V		●		●	
Artemisia indica		IV		●		●	
Rubia argyi		IV		●		●	
Trichosanthes kirilowii		III		●		●	
Tripleurospermum tetragonospermum		III		●	●		
Acer amoenum		III		●			●
Persicaria filiformis		III		●		●	
Bidens pilosa		II		●	●		
Marsdenia tomentosa		II		●		●	
Acalypha australis		II		●	●		
Patrinia villosa		II		●	●		
Persicaria thunbergii		II		●	●		
Albizia julibrissin		II		●			●
Cryptotaenia canadensis		II		●		●	
Pollia japonica		II		●		●	
Digitaria ciliaris		II		●	●		
Rumex japonicus		II		●		●	
Ostrya japonica		II		●			●
Zelkova serrata		II		●			●
Castanea crenata		I		●			●
Clerodendrum trichotomum		I		●			●
Boehmeria nivea		I		●		●	
Impatiens textorii		I		●	●		
Solanum maximowiczii		I		●		●	
Hydrocotyle javanica		I		●		●	
Ixeridium dentatum		I		●		●	
Phragmites japonicus		I		●		●	
Pilea notata		I		●	●		
Taraxacum officinale		I				●	
Cerasus jamasakura		I		●			●
Diospyros kaki		I		●			●
Dryopteris erythrosora		I		●		●	
Hydrangea paniculata		I		●			●
Ligustrum obtusifolium		I		●			●
Osmunda japonica		I		●		●	
Smilax china		I		●			●
Euptelea polyandra		I		●			●
Fallopia japonica		I		●		●	
Rubus corchorifolius		I		●			●
Rubus parvifolius		I		●			●
Desmodium podocarpum		I		●		●	
No vegetation			V				

Roman numerals in the table indicate frequency of occurrence; I<20%, II<40%, III<60%, IV<80%, V<100%

15th Int. Conf. on Geotechnique, Construction Materials & Environment, Kyoto, Japan, 11-13 November 2025, ISBN 978-4-909106124 C3051

RECHARGE ESTIMATION AND SITE IDENTIFICATION FOR MANAGED AQUIFER RECHARGE IN SUPHANBURI, THAILAND USING GIS AND MODFLOW

Pinit Tanachaichoksirikun [1], Uba Sirikaew[1] and Uma Seeboonruang[1], Jutamas Srisuk[2,]

[1]Department of Civil Engineering, School of Engineering, King Mongkut's Institute of Technology Ladkrabang, Thailand
[2]Department of Engineering, King Mongkut's Institute of Technology Ladkrabang Prince of Chumphon Campus, Chumphon, Thailand

ABSTRACT

This study focuses on groundwater recharge estimation and site identification for Managed Aquifer Recharge (MAR) in Suphanburi, Thailand, an agriculturally intensive region increasingly affected by floods and droughts. An integrated approach combining Geographic Information Systems (GIS), water balance analysis, and groundwater simulation using Visual MODFLOW was applied to assess recharge potential. Key factors, including land use, slope, and hydrogeology, were analyzed to delineate 5 suitable recharge zones. Field data from 13 observation wells collected between 2014 and 2024 were used to calibrate and validate the groundwater model. The model has high accuracy with R^2 values of 0.983 (calibration) and 0.992 (validation), and normalized RMSEs of 5.97% and 5.20%, respectively. The result showed that the highest recharge rates were 343.42 and 320.39 m^3/day, observed in urban and industrial zones near the Tha Chin River, with capacities sufficient to support over 1,600 people. This research provides a practical and replicable framework for MAR site selection and implementation, supporting data-driven water management strategies in flood and drought-prone regions.

Keywords: Groundwater Recharge Estimation, Water Resource Management, Flood and Drought, Site Identification, Managed Aquifer Recharge (MAR)

INTRODUCTION

Floods and droughts are recurrent and persistent challenges throughout Thailand, particularly in lowland areas adjacent to the mountainous regions of the central plains. These regions are characterized by steep topography, which exacerbates flash floods and recurring water-related disasters. Conventional solutions have proven insufficient in providing long-term resilience. In response, both governmental and private sectors have increasingly adopted water management approaches inspired by the late King Bhumibol Adulyadej's Sufficiency Economy Philosophy. This research directly addresses this critical gap by developing a scientifically robust and practically applicable Managed Aquifer Recharge (MAR) to support adaptive water resource management in vulnerable regions. These systems aim to capture and store excess rainwater during the wet season for use in the dry season, thereby simultaneously mitigating flood and drought risks with minimal financial investment and environmental disruption.

The concept of MAR has gained international recognition as a strategic response to water resource variability [1], [2]. In the United States, particularly in California, Arizona, and Texas, large-scale MAR such as the Kern Water Bank have been successfully implemented to stabilize water supplies for agriculture and urban use during multi-year droughts [3]. Israel and Australia have incorporated MAR into national water strategies, especially in arid and semi-arid zones, using techniques such as infiltration basins, injection wells, and riverbank filtration to enhance groundwater reserves [4], [5]. In India, particularly in the drought-prone state of Rajasthan, community-based MAR projects have demonstrated significant benefits in improving aquifer recharge, water quality, and agricultural productivity [6]. China also invested in artificial recharge programs as part of their national water sustainability frameworks [7], [8]. These global experiences underscore the scalability and adaptability of groundwater recharge to diverse climatic, geological, and socio-economic contexts.

In Thailand, MAR initiatives have been explored by agencies such as the Thai Department of Groundwater Resources (DGR) and the National Water Resources Officer (NWRO). Several pilot studies have been conducted to assess groundwater recharge feasibility in agriculturally intensive areas. Notable examples include MAR studies in Sukhothai, Lamphun, Phichit, and Kamphaeng Phet. However, these projects have often lacked continuity and have not yet been implemented systematically or on a scale. Moreover, previous studies primarily focused on engineering feasibility without fully integrating spatial analysis or mathematical modeling.

The study addresses this gap by developing a comprehensive groundwater recharge model tailored

to the Kra Seaw Reservoir area in Suphanburi Province, a region that frequently experiences extreme variations in water availability. The model utilizes hydrogeological data, GIS, and MODFLOW to simulate recharge potential and optimize aquifer storage strategies. The goal is to enhance water security, agricultural resilience, and long-term resource planning in flood and drought affected zones.

Ultimately, this study aims to provide a scientific basis for MAR implementation by integrating hydrological modeling, water balance assessments, and community-oriented resource planning. It aspires to serve as a decision-support tool for policymakers, water managers, and researchers working toward sustainable water resource management in Thailand and other similar geographic settings.

RESEARCH SIGNIFICANCE

This research aims to offer a practical solution to the water problems in Suphanburi, where floods and droughts often cause serious challenges. The recharge estimation and site identification for MAR was designed to store excess rainwater underground during the rainy season and make it available during dry periods. This helps reduce both water shortages and flooding in local communities.

WATER BALANCE APPLICATION

A water balance approach is essential to understand how much water enters, leaves, and is stored in a given area over time. This is especially important for designing and evaluating a groundwater recharge system, where the goal is to store excess water underground during wet periods and retrieve it during dry seasons [9], [10]. The water balance provides a systematic way to estimate available water resources and determine how much can be recharged into aquifers without causing negative effects.

The water balance in this study is divided into two key components: surface water balance and groundwater balance.

The surface water balance considers rainfall, runoff, evapotranspiration, and recharge to groundwater. The equation as shown in (1)

$$P = ET + S_R + R \pm \Delta V \quad (1)$$

Where P is total precipitation (rainfall) in unit mm., ET is evapotranspiration in unit mm., S_R is surface runoff in unit mm, R is groundwater recharge in unit mm. and ΔV is change in soil moisture or surface water storage in unit mm.

The groundwater system is analyzed separately to track how much water is added, used, and stored below ground. The groundwater balance equation as shown in (2)

$$R = G + D + W \pm \Delta S \quad (2)$$

Where R is groundwater recharges in unit mm., G is groundwater flow out of the system in unit mm., D is deep drainage to lower aquifer layers in unit mm., W is pumping or groundwater use in unit mm. and ΔS is change in groundwater storage in unit mm.

In the context of this study, the water balance is calculated on a monthly basis to reflect seasonal rainfall and groundwater fluctuations. However, the long-term trends are analyzed on an annual scale to evaluate sustainability. This approach ensures that the groundwater recharge will operate effectively, prevent land subsidence, and avoid environmental damage.

STUDY AREA

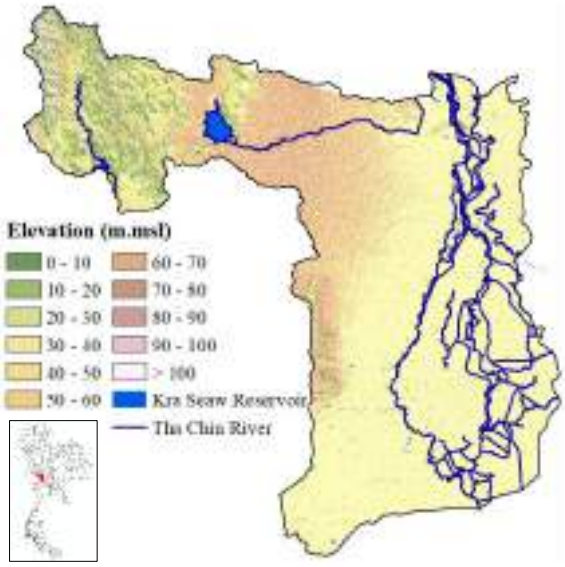

Fig.1 Location and slope in Suphanburi [11]

Suphanburi located in the central region of Thailand. The area was selected due to its high agricultural importance and frequent exposure to both drought and flood events. Suphanburi is also home to key water resources infrastructure, including the Kra Seaw Reservoir and the Tha Chin River, which play central roles in local water management. It far approx. 107 km. northwest of Bangkok. The province covers an area of about 5,358 km^2. It borders Chai Nat and Uthai Thani to the north, Nakhon Pathom to the south, Ang Thong and Ayutthaya to the east, and

Kanchanaburi to the west.

The terrain is mostly flat and consists of low-lying alluvial plains, which are well suited for rice farming and other agricultural activities. The western part of the province, especially Dan Chang, is characterized by rolling hills and forested areas. Elevation ranges from 10 to 400 meters above sea level, with higher terrain in the west and flatter plains to the east, Fig. 1.

Geology and Hydrogeology

The geology is predominantly composed of sedimentary rocks, including sandstone, limestone, shale, and chert, dating back to the Paleozoic–Mesozoic era. In the western regions, such as Dan Chang, igneous rocks like granite and basalt are also found. These geological conditions influence groundwater movement and aquifer characteristics [12].

The Hydrogeology is both unconfined and confined aquifers, particularly in the Tha Chin River basin, where groundwater yield exceeds 2 m^3/hr. in many locations. The aquifers are suitable for artificial recharge due to their permeability and storage capacity [13].

Climate

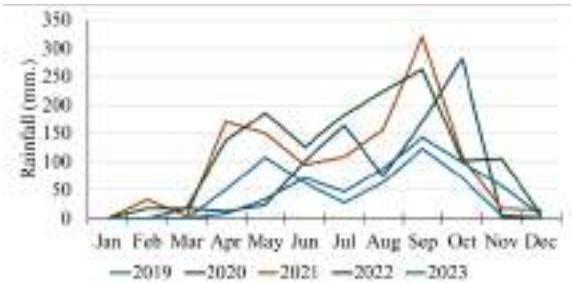

Fig.2 Annual rainfall in Suphanburi

According to Thai Meteorological Department, Suphanburi is in a tropical zone, with three seasons, summer season in February to May, rainy season in June to October and winter season in November to January [14]. Rainfall data from 2019 to 2023 shows high variability. Peak rainfall occurs from August to October, while the driest months are January to March. In recent years, irregular rainfall patterns—including prolonged dry spells and sudden heavy downpours—have been observed, indicating the growing influence of climate change on local hydrology.

Land Use and Groundwater Recharge

Land use plays a critical role in determining the feasibility and effectiveness of MAR. Different land types vary significantly in terms of their infiltration capacity, surface runoff generation, and soil permeability, all of which influence how much water can enter and be stored in underground aquifers.

According to Thai Land Development Department [11], Suphanburi, land use is predominantly agricultural, with other significant uses including forests, built-up urban areas, and water bodies. The major land use categories and their implications for groundwater recharge are described as followed [15].

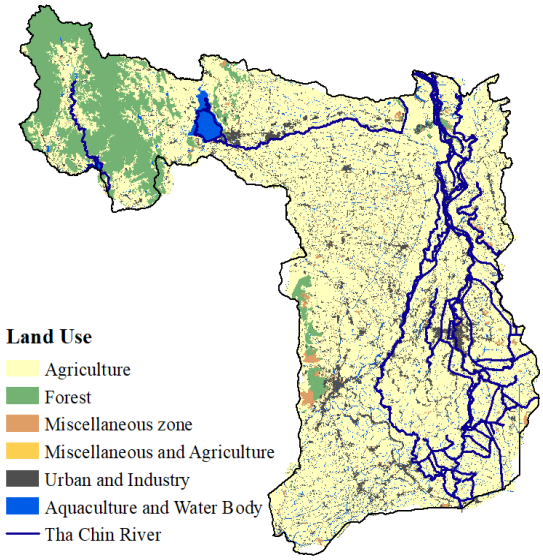

Fig.3 Land use in Suphanburi [11]

Agricultural areas (74.3%)—especially rice fields and field crops—cover the largest portion of the province. These lands typically have compacted soil due to plowing and machinery, which may limit natural infiltration. However, with appropriate soil management and recharge design (e.g., recharge ponds, infiltration basins), these areas can serve as viable recharge zones. Unused plots or fallow fields may offer better infiltration potential during off-seasons. Rice paddies may contribute to shallow recharge but are limited due to frequent waterlogging. Field crops (e.g., sugarcane, maize) have better potential for infiltration if combined with recharge structures.

Forest areas (12%), especially in the western highlands of Dan Chang District, offer high natural infiltration due to deep root systems and less surface sealing. These areas are ideal for natural recharge processes and can be preserved or enhanced as buffer

zones for groundwater replenishment. Forested land contributes to low surface runoff and helps stabilize the local hydrological cycle.

Urban and industrial zones (8.3%), including roads, buildings, and paved surfaces, have low infiltration capacity and generate high surface runoff. These areas are unsuitable for natural recharge but can still support artificial recharge through engineered solutions like injection wells, recharge shafts, or stormwater harvesting systems. In densely populated areas, care must be taken to avoid contamination risks.

Aquaculture and Water Bodies (3.5%), such as ponds, lakes, and irrigation canals can act as recharge reservoirs if they are hydraulically connected to the underlying aquifer. Some areas may allow recharge through percolation, especially if the base is unlined or partially permeable. However, these zones typically have limited recharge capacity without modification.

Miscellaneous zone (1.9%), found at the edges of agricultural zones or near forested hills. Depending on soil type and topography, they may provide good potential for recharge basin development, particularly if located above permeable aquifers.

In this study, land use data was used to classify recharge zones and assign recharge rates for simulation in the Visual MODFLOW model. Forested and agricultural areas were prioritized for MAR development due to their favorable infiltration characteristics. Urban and industrial zones, while limited in natural recharge capacity, were considered for technical interventions like injection wells or treated wastewater reuse.

METHODOLOGY

This study followed a structured approach combining field data, spatial analysis, and numerical modeling to design and evaluate a recharge estimation and site identification for MAR for Suphanburi. The main steps included data collection, conceptual model development, numerical simulation using Visual MODFLOW, model calibration, and scenario analysis.

Grid Design

Based on field conditions and geological structure, the study area was divided into two aquifer layers Upper layer: Unconfined aquifer (shallow groundwater) and Lower layer: Confined aquifer (deep groundwater).

The grid was divided into a uniform grid of 1×1 km^2 cells, resulting in 12,204 cells (108 columns × 113 rows). Each grid cell was assigned physical and hydraulic properties based on field data and soil classification.

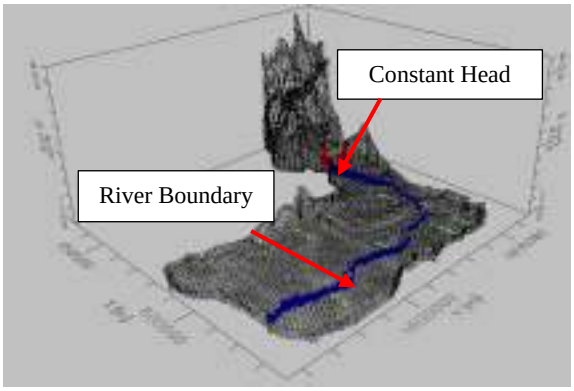

Fig.4 Numerical modeling for Suphanburi.

Assigning Aquifer Parameters

Key hydrogeological parameters were defined based on soil surveys and groundwater studies i.e. Hydraulic conductivity (K), Specific yield (Sy) for unconfined aquifers, Specific storage (Ss) for confined aquifers as show in Fig. 5 and Table 1.

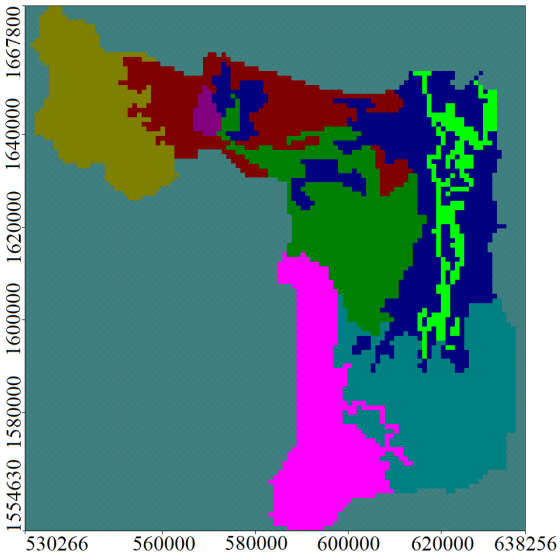

Fig.5 Input parameter zone

Table 1 Hydraulic Conductivity Values

No.	K_x and K_y (m/s)	K_z (m/s)	S_s
	1.0×10^{-6}	1.0×10^{-9}	1.6×10^{-4}
	1.0×10^{-7}	1.0×10^{-10}	1.0×10^{-5}
	5.0×10^{-6}	5.0×10^{-9}	2.0×10^{-4}
	1.1×10^{-6}	1.1×10^{-9}	5.0×10^{-5}
	7.5×10^{-6}	7.5×10^{-9}	1.6×10^{-4}
	1.0×10^{-2}	1.0×10^{-5}	2.0×10^{-4}
	1.0×10^{-5}	1.0×10^{-8}	2.0×10^{-4}
	1.0×10^{-3}	1.0×10^{-6}	5.0×10^{-5}

Recharge Estimation

Groundwater recharge rates were estimated using

a land-use-based recharge coefficient approach. Different recharge percentages were assigned based on land use types as shown in Fig.6 and Table 2.

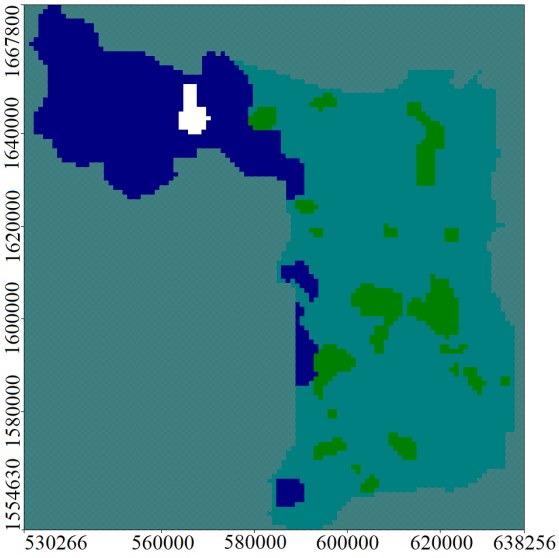

Fig.6 Location of recharge estimation

Table 2 Recharge Estimation Value

No.	Land Use Type	Percent of Rainfall (%)
	Forest	8
	Agriculture	4
	Urban and Industrial	1
	Water Body	0

Model Calibration and Verification

The model was calibrated by adjusting key parameters (hydraulic conductivity and recharge rate) to minimize the difference between simulated and observed groundwater levels. Groundwater data from 13 observation wells were used to calibrate the model. The calibration aimed to achieve: Normalized Root Mean Square Error (*RMSE*) below 10% of observed values and high correlation (R^2 > 0.9) between simulated and observed heads

Sensitivity Analysis

To assess the model's reliability, a sensitivity analysis was performed by adjusting key parameters (±25%, ±50%, ±75%) and observing the impact on groundwater levels [16], [17]. This helped identify which variables had the greatest influence on model output and supported more accurate prediction under future scenarios.

Site Identification

Finally, the model was used to simulate the impact of artificial recharge in five selected zones over a 5-year period (2025–2030). Changes in storage, inflow, and outflow were monitored using the Zone Budget tool in Visual MODFLOW. These simulations helped determine the effectiveness of groundwater recharge in suitable location followed by Tanachaichoksirikun [18].

RESULTS AND DISCUSSION

Calibration and Verification Results

The model was calibrated using data from 13 observation wells across the province in 2014-2019. The comparison between observed and simulated groundwater levels showed strong agreement i.e., Root Mean Square Error (*RMSE*) was 1.28 m, Standard Error (*SE*) was 0.32 m, Normalized *RMSE* was 5.97% and correlation coefficient (R^2) was 0.983. The verification results using data from 13 observation wells across the province in 2020-2024 was *RMSE* was 1.18 m, *SE* was 0.34 m, Normalized *RMSE* was 5.20% and correlation coefficient (R^2) was 0.992. These values confirm that the model reliably represents groundwater behavior and can be used for scenario simulations [19], [20].

Sensitivity Analysis Test

Sensitivity tests showed that hydraulic conductivity had the greatest influence on groundwater levels, followed by recharge rates. Changes of ±25%, ±50%, and ±75% in hydraulic conductivity caused noticeable shifts in water levels, indicating the importance of accurate field measurement of aquifer parameters.

Scenario Simulations

Locations were selected to test the groundwater budget under artificial recharge conditions over a 5-year simulation period (2025–2030).

The result revealed that Tha Chin River Basin and Urban and Industry experienced positive water storage gains, indicating effective recharge into aquifers. Dan Chang, U Thong, and Pho Phraya zones showed little or no net recharge, due to either low permeability, high extraction rates, or unsuitable geology. This confirms that not all areas are equally suitable for groundwater recharge, and site selection must consider hydrogeological compatibility.

Recharge Volumes and Beneficiaries

In 2025-2030, the groundwater recharge simulation estimated the following recharge volumes, including, Tha Chin River area was 320.39 m^3/day

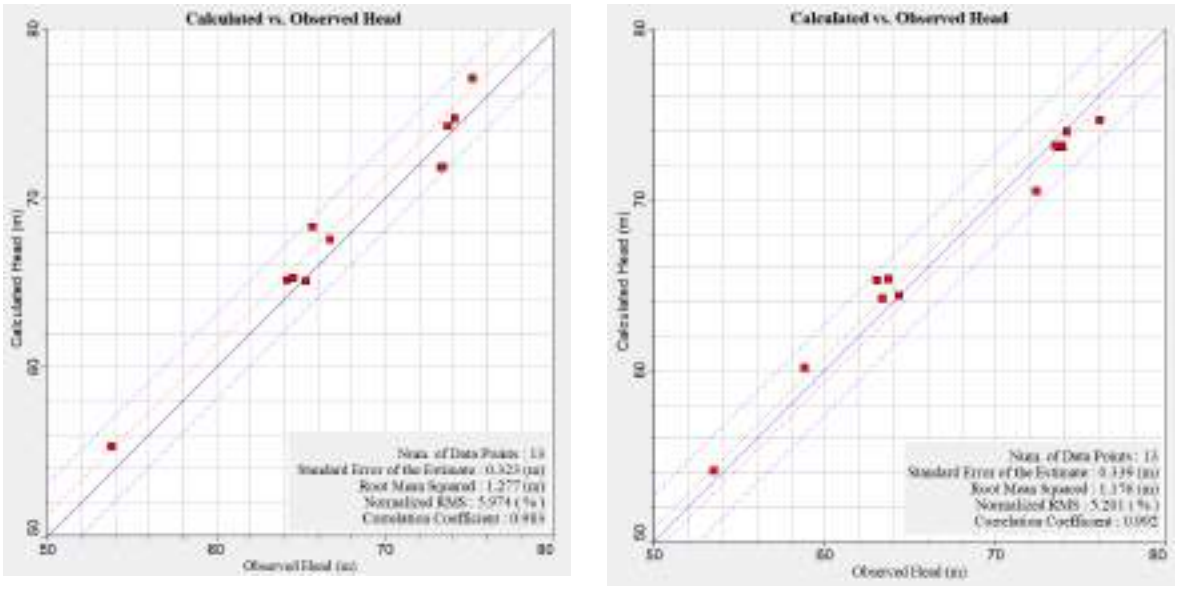

(a) Calibration (b) Verification

Fig.7 Calibration and verification results

Table 3 Groundwater Recharge Volume and Beneficiaries

Location	Recharge Volume (m^3/day)	Recharge Volume (liters/day)	Water Use per Person (liters/day)	Estimated Number of Beneficiaries(people/day)
Tha Chin River	320.39	320,39	200	1,601.95
Urban and Industry	343.42	343,42	200	1,717.10

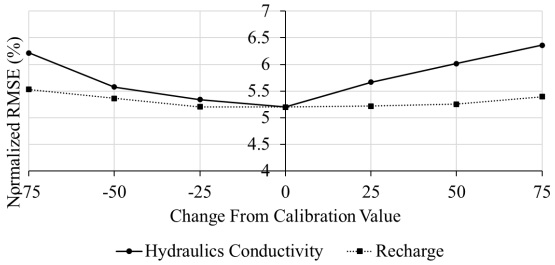

Fig.8 Sensitivity analysis

and urban and industrial zone was 343.42 m^3/day as shown in Table 3. The average per capita water use of 200 liters/day, the number of people who could benefit from the stored water is 1,602 people in Tha Chin River area and 1,717 people in urban and industrial zones. This demonstrates the potential of groundwater recharge to support water needs during dry seasons, especially in urban and semi-urban.

CONCLUSIONS

This study successfully developed and tested a groundwater recharge estimation and site identification approach for Managed Aquifer Recharge (MAR) in Suphanburi, Thailand, using GIS-based spatial analysis and Visual MODFLOW simulations. By integrating hydrological, geological, and land use data, the model identified zones with high recharge potential and evaluated the impacts of artificial recharge under various scenarios.

Simulation results showed that only two out of five selected areas—Urban and Industry and Tha Chin River Basin—had favorable conditions for groundwater budget, based on recharge volume, aquifer response, and safety from contamination. These zones were capable of storing groundwater at rates exceeding 300 m^3/day, benefiting more than 1,600 people per site during dry periods.

The findings highlight the importance of site-specific planning, emphasizing that groundwater recharge is not suitable for every area but can be highly effective when applied under the right hydrogeological and land use conditions. Moreover, the study demonstrates how combining local knowledge with scientific tools can support cost-effective and sustainable water management.

ACKNOWLEDGMENTS

Thanks to the National Science, Research and Innovation Fund (NSRF) through the Fundamental Fund 68 (Grant Number RE-KRIS/FF68/52) and King Mongkut's Institute of Technology Ladkrabang (KMITL) for the funding support. Thanks to the Thai Land Development Department, Thai Meteorological Department, and Thai Department of Groundwater Resources, for the data.

REFERENCES

[1] Sufyan M., Martelli G., Teatini P., Cherubini C., and Goi D., Managed Aquifer Recharge for Sustainable Groundwater Management: New Developments, Challenges, and Future Prospects, Water, Vol. 16, No. 22, 2024, pp. 1–28, doi: 10.3390/w16223216.

[2] Mumberg T., Ahrens L., and Wanner P., Managed Aquifer Recharge as a Potential Pathway of Contaminants of Emerging Concern into Groundwater Systems – A Systematic Review, Chemosphere, Vol. 364, 2024, pp. 143030, doi: 10.1016/j.chemosphere.2024.143030.

[3] Kiparsky M., Miller K., Goulden P., Milman A., and Owen D., Groundwater Recharge for a Regional Water Bank: Kern Water Bank, Kern County, California, Case Stud. Environ., Vol. 5, No. 1, 2021, pp. 1–12, doi: 10.1525/cse.2021.1223400.

[4] Dillon P., Stuyfzand P., Grischek T., Lluria M., Pyne R. D. G., Jain R. C., Bear J., Schwarz J., Wang W., Fernandez E., Stefan C., Pettenati M., Van D. G. J., Sprenger C., Massmann G., Scanlon B. R., Xanke J., Jokela P., Zheng Y., Rossetto R., Shamrukh M., Pavelic P., Murray E., Ross A., Bonilla V. J. P., Palma N. A., Ansems N., Posavec K., Ha K., Martin R., and Sapiano M., Sixty Years of Global Progress in Managed Aquifer Recharge, Hydrogeol. J., Vol. 27, No. 1, 2019, pp. 1–30, doi: 10.1007/s10040-018-1841-z.

[5] Knapton A., Page D., Vanderzalm J., Gonzalez D., Barry K., Taylor A., Horner N., Chilcott C., and Petherem C., Managed Aquifer Recharge as a Strategic Storage and Urban Water Management Tool in Darwin, Northern Territory, Australia, Water, Vol. 11, No. 9, 2019, pp. 1869, doi: 10.3390/w11091869.

[6] Richard-Ferroudji A., Raghunath T. P., and Venkatasubramanian G., Managed Aquifer Recharge in India: Consensual Policy but Controversial Implementation, Water Altern., Vol. 11, No. 3, 2018, pp. 749–769.

[7] Guo J. X., Li Z. P., and Stefan C., Managed Aquifer Recharge (MAR) Applications in China-Achievements and Challenges, J. Groundw. Sci. Eng., Vol. 10, No. 1, 2022, pp. 57–69, doi: 10.19637/j.cnki.2305-7068.2022.01.006.

[8] Liu S., Zhou Y., Luo W., Wang F., McClain M. E., and Wang X. S., A Numerical Assessment on the Managed Aquifer Recharge to Achieve Sustainable Groundwater Development in Chaobai River Area, Beijing, China, J. Hydrol., Vol. 613, 2022, pp. 128392, doi: 10.1016/j.jhydrol.2022.128392.

[9] Idrees M., Ahmad S., Khan M. W., Dahri Z. H., Ahmad K., Azmat M., and Rana I. A., Estimation of Water Balance for Anticipated Land Use in the Potohar Plateau of the Indus Basin Using SWAT, Remote Sens., Vol. 14, No. 21, 2022, pp. 1–19, doi: 10.3390/rs14215421.

[10] McGauley M. W., Amur A., Shakya M., and Wadzuk B. M., A Complete Water Balance of a Rain Garden, Water Resour. Res., Vol. 59, No. 12, 2023, pp. 1–18 doi: 10.1029/2023WR035155.

[11] Thailand Land Development Department, Land Use Data, 2021.

[12] Thailand Department of Mineral Resource, Geological Map of Suphanburi, 2014.

[13] Thailand Department of Groundwater Resources, Groundwater Data, 2023.

[14] Thailand Meteorological Department, Thailand Meteorological Data, 2023.

[15] Hidayat D. P. A., Darsono S. L. W., and Farid M., Modelling of Potential Recharge Zone using Geographical Information System Based on Indonesia Regulation and Water Balance Model, Int. J. GEOMATE, Vol. 20, Vo. 79, 2021, pp. 147–154, doi: 10.21660/2021.79.j2037.

[16] Al-Muqdadi S. W. H., Abo R., Khattab M. O., and Abdulhussein F. M., Groundwater Flow-Modeling and Sensitivity Analysis in a Hyper Arid Region, Water, Vol. 12, No. 8, 2020, pp.1–14, doi: 10.3390/W12082131.

[17] Tolley D., Foglia L., and Harter T., Sensitivity Analysis and Calibration of an Integrated Hydrologic Model in an Irrigated Agricultural Basin with a Groundwater-Dependent Ecosystem, Water Resour. Res., Vol. 55, No. 9, 2019, pp. 7876–7901, doi: 10.1029/2018WR024209.

[18] Tanachaichoksirikun P., Xiao X., Sirikaew U., and Seeboonruang U., Managed Aquifer Recharge Feasibility using Weight Factor Index Method in Suphanburi, Thailand, Int. J. GEOMATE, Vol. 28, No. 128, 2025, pp. 49–57, doi: 10.21660/2025.128.g14123.

[19] Du X., Lu X., Hou J., and Ye X., Improving the Reliability of Numerical Groundwater Modeling in a Data-Sparse Region, Water, Vol. 10, No. 3, 2018, pp. 1–15, doi: 10.3390/w10030289.

[20] Tanachaichoksirikun P., Seeboonruang U., and Fogg G. E., Improving Groundwater Model in Regional Sedimentary Basin using Hydraulic Gradients, KSCE J. Civ. Eng., Vol. 24, No. 5, 2020, pp. 1655–1669, doi: 10.1007/s12205-020-1781-8.

Copyright © Int. J. of GEOMATE All rights reserved, including making copies, unless permission is obtained from the copyright proprietors.

15th Int. Conf. on Geotechnique, Construction Materials & Environment,
Kyoto, Japan, 11-13 November 2025, ISBN 978-4-909106124 C3051

ANALYSIS OF SPATIAL PLANNING OF WATERSHED AREAS IN DESIGNING URBAN DRAINAGE SYSTEM

Ade Tricia Miranda[1], Dinar Dwi Anugerah Putranto[2],Rosidawani[3], Bimo Brata Aditya[4],Riani Muharohmah[5]

[1]Doctoral Program Faculty of Engineering, Sriwijaya University;[2,3,4,5]Department of Civil Engineering and Planning, Faculty of Engineering, Sriwijaya University,Indonesia

ABSTRACT

Drainage capacity is determined by the use of space and characteristics of sub-watershed. However, changes in the use of space that are not integrated can cause flood and inundation, particularly in areas where spatial planning considers only administrative boundaries and neglects the characteristics of sub-watershed. This challenge is evident in Palembang City, one of the oldest cities that has developed starting from the Musi River Delta, the longest river on the island of Sumatra. 66% dominated by swamp land, which is influenced by the ebb and flow of the Musi River. Due to limited land, swamps are filled in, thereby affecting the urban drainage system. A notable example is Lambidaro sub-watershed, which is among the 21 watershed areas. Changes in land use are significant after the opening of the arterial road connecting the East Sumatra Crossroad, which passes through Palembang City. Approximately more than 70% of the swamp areas have been filled for the development of the East Sumatra Cross-Island Road, followed by residential areas under permit, offices, and businesses. However, the development process is not accompanied by the arrangement of an integrated drainage system, high intensity rain, causing excessive flood during high-intensity rain. Therefore, this study aimed to analyze spatial planning of Lambidaro sub-watershed in designing urban drainage system. The results showed that additional retention ponds were needed to temporarily accommodate excess rainwater due to an increase in runoff. This was caused by the high tide of the Lambidaro River and slow infiltration into the soil.

Keywords: Drainage Capacity, Flood and inundation, Drainage system, Spatial planning, Retention ponds

INTRODUCTION

The rapid changes in land use across several urban areas in Indonesia are due to urbanization and industrial development. Most of these changes are carried out by reclaiming swamps, using riverbanks, and converting forest and agricultural land. The impact has changed water flow patterns in sub-watershed areas, thereby affecting flow patterns that cause flood and inundation due to excessive run-off [1]. Human activities, including urbanization through land reclamation, have a very significant impact on water quantity, quality, and aquatic ecology. This poses the danger of flood, household, and industrial waste, where water accumulating for a long time is impossible to return and requires very large costs for recovery [2].

The problem of surface water run-off with the characteristics of peak flood and inundation is influenced by several factors. These include urbanization, inappropriate land filling of swamps, tidal influences caused by sedimentation, and pollutants from river upstream as well as sub-watershed[3]. The ability to manage flow, run-off mitigation, infiltration, and water quality is related to land use conditions. The relationship between the water flow system and spatial planning is an important key to establish a policy in reducing flood hazards. However, both spatial planning and water management are not carried out in reality. This shows the need for analysis to explore the relationship between hydrotopographic conditions, types of land cover, duration and time of rain, and tidal height, which are modeled using spatial analysis, to support decision making for spatial planning and water management [4].

RESEARCH SIGNIFICANCE

This research is important to determine the characteristics of drainage channels, hydrology, and flow hydraulics in the Lambidaro river subsystem, in order to design flood control through various discharge analysis scenarios with a 10-year return period. Analysis is conducted to determine the effectiveness of drainage channel plans to reduce peak flood discharge and the timing of their occurrence. Flood modeling using advanced software and remote sensing data has significantly improved flood risk management by reducing uncertainty and

producing accurate flood maps that consider the impacts of climate change. Flood maps play a crucial role in risk assessment, enabling flood risk analysis, damage assessment, and effective planning for timely response and community protection.

LITERATURE REVIEW

Urban Development and Flood Problems in Palembang City

Similar to the development of several urban areas in Indonesia, Palembang City has a very significant development. This can be observed from the population growth, which average 1.03% with a population of 1,780,000 people in 2024 (BPS Palembang City, 2024) [1]. When the average population growth remains at 1.03%, the population will reach 1,963,340 people in 2035, with 42.6% in the City Center. Based on this significant growth, there is a projection for the concentration of population in urban activity centers, causing an expansion of land use for various activities. This expansion changes the various functions of "water parking" land, turning into built-up land, without considering watershed ecosystem.

Based on BMKG data (2024), the highest rainfall in Palembang City is 18 - <34.87 mm/day in November, and the lowest is <18 mm/day in May-August. Surface water is difficult to predict in the distribution in space and time. Meanwhile, the discharge observation system through AWLR in several areas along the river is not functioning properly. This has caused various problems in predicting the peak of flood and potential areas. In October 2024, the Bendung, Buah, Sekanak, and other sub-watershed areas in Palembang City experienced flood due to high-intensity rain [5]. To address these challenges, various efforts to control flood have been made. In Buah, a retention pond was added, while the Sekanak sub-watershed in the City Center was carried out by dredging the river to widen the overflow capacity. Bendung sub-watershed was constructed by freeing up land along the riverbank to accommodate the overflow of the river, or by adding water pumps for evacuating floodwaters. However, all these mitigating strategies have not shown that the annual flood problem can be overcome. All flood control system must start from the existing ecosystem conditions of the DAS. From these conditions, simulation analysis is conducted to determine flood discharge for each return period, which can be used to determine the appropriate drainage system [6]. Therefore, a specific method through a more useful and accurate analysis needs to be carried out. This includes data transformation into a Geographic Information System (GIS) using Multicriteria Analysis in decision making[7-10]. The method can be used as a combination of policy and technical solutions, but also as a model in presenting watershed environmental conditions to obtain better data quality and analysis.

METHOD

Data

In accordance with the morphological conditions of watershed, Palembang City divided into 21 sub-watershed areas. In terms of quality (see Fig.1), Lambidaro sub-watershed covering 5.42 km^2 has gained significant attention due to water condition, which ranges from critical (51.6%), slightly critical (27.65%), to non-critical (4.98%). The largest section in critical condition is downstream (56.64%), followed by upstream Lambidaro (43.36%).

Land use is dominated by shrubs, trees, fields, and forests, comprising approximately 72%, and settlements 4.74% which potential to experience changes. Settlement development mainly occurs in the left section close to the main/outer ring road of Palembang City (Musi two bridge). In comparison, the right section is still dominated by bushes and swamps, but currently the development of residential areas is increasing downstream.

As presented in Fig.1, the run-off coefficient value is 0.66, showing that 34% of the total rainfall in sub-watershed can still be infiltrated.

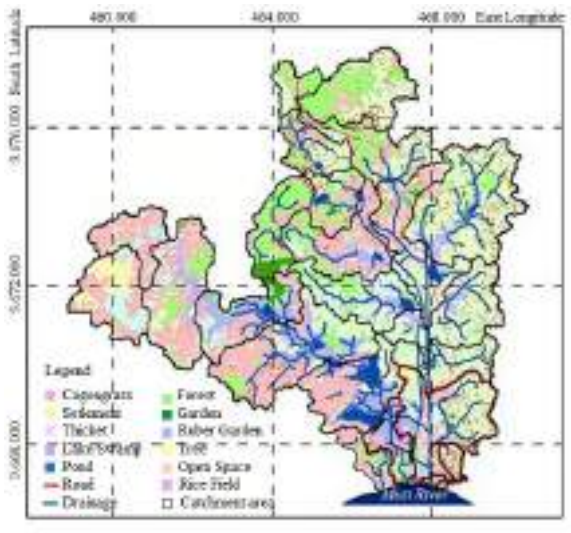

Fig. 1 Upstream and downstream Lambidaro sub-watershed

Comprehensive flood management is an effective method to reduce adverse consequences and as part of mitigation [11]. Flood modeling is an important method that can accurately predict and reduce the impact of flood [12]. Hydrologic Engineering Center - River Analysis System (HEC-RAS), developed by

the US Army Corps of Engineers, is one of the software programs capable of performing flood mapping on a large scale [13]. HEC-HMS (Hydrologic Modeling System) is able to produce output in the form of time series outflow of rainfall intensity along with land use as flow input in HEC-RAS modeling [14]. Digital Elevation Model (DEM) is also used to obtain topographic information to identify basin and lowland areas [15] to determine the depth of flood in simulations with HEC-RAS [16]. In this experiment, Lambidaro sub-watershed in Palembang City was used as the study area to conduct flood simulations using HEC-RAS and HEC-HMS.

The data used were river hydrometry data, longitudinal and transverse river cross-sections, river slope and area and watershed density. Spot height and land use data were needed to analyze the infiltration coefficient and time concentration. Rainfall data (R) were used to calculate rainfall intensity (I) in each sub-watershed, with a maximum value of 83.07 mm recorded in 2024. Meanwhile, the primary data were land use obtained from small-format aerial photography through unmanned aerial vehicle (UAV) aircraft and multispectral cameras. Other data include longitudinal and transverse river cross-section measurements, retention pond cross-section, Lambidaro river tidal, hydrology, and river hydraulics, which were measured and observed directly in the field.

Methods

The method used in this study was hydrological model and Geographic Information System (GIS). The hydrological model used was HEC-RAS, while the hydrodynamic model was applied to calculate the amount of runoff and trace flood flow in the river. Hydrodynamic analysis was carried out on the downstream Lambidaro river subsystem, obtained from the results of cluster analysis [17]. This analysis used a 1-dimensional unsteady flow model (Duflow) with the maximum rainfall intensity boundary conditions of a 25-year return period obtained from hydrological model and tidal observation forecasts at the mouth of the downstream Lambidaro sub-watershed. The first stage in the hydrodynamic analysis was to form a schematic of water system network in sub-watershed [18], which is adjusted to the results through terrain morphology and terrain processing analysis. The second stage was to enter the dimensions of the water structure, channel cross-section, boundary conditions (tides, rain from hydrological analysis results), and flow discharge. After the calculation of each segment/cross-section, several hydraulic parameters were obtained, such as flood level, flow velocity, channel discharge, and water level in the river and channel [19].

The distribution of inundation occurring in the river subsystem was obtained by combining the results of hydrodynamic and spatial analyses. The water level in the river and channel was interpolated to obtain the distribution of water level in the selected sub-watershed [20]. Subsequently, the distribution of water level was overlaid with the topographic conditions of this sub-watershed in the form of a DEM with a pixel size of 1m x 1m to obtain inundation height with a 25-year return period.

With several land use change scenarios, variation in inundation height in sub-watershed areas can be analyzed. These scenarios are used to assess the condition of this sub-watershed, which influences the pattern of river environmental control. The first scenario is by changing the type of spatial planning pattern through changes in land use for the C value (infiltration coefficient) to decrease, serving as an indicator of the amount of infiltration [21]. The second scenario is by changing the type of land use for C value to increase, suggesting reduced infiltration and suggesting that the river subsystem is beginning to experience hydrological stress [22]. . The research flow diagram is shown in Fig. 2.

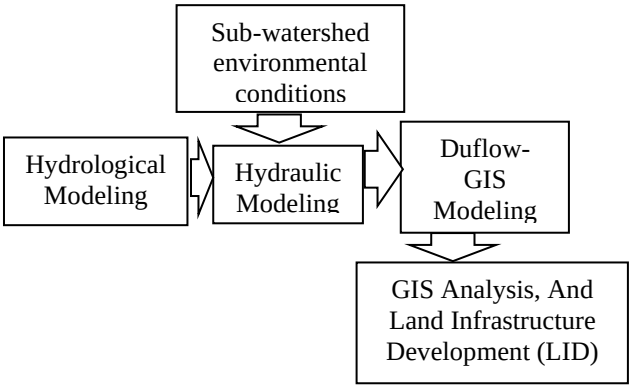

Fig. 2 Study method flowchart

RESULT AND DISCUSSION

Correlation Between Surface Runoff and Watershed Morphometric Characteristic Variables

Correlation analysis was conducted to answer the problem regarding spatial relationship between land use and sub-watershed morphometry, as well as the associated influence on the amount of surface run-off. The strength of the relationship between the independent variables (sub-watershed morphometric characteristics) and the dependent variable, runoff (Q), was observed through the Pearson correlation value. The correlation value ranged from -1,000 to 1,000. A value of -1,000 showed a very strong correlation but was negative, while a value of 1,000 showed a very strong/very close correlation with a positive direction.

The results of cluster analysis between T (Texture ratio), Bh (Basin relief), and C (Coefficient

infiltration) variables in the Lambidaro sub-watershed show that T values are based on relief conditions. The increase in peak discharge is the result of increased efficiency between relief conditions and flow density. The highest Rn value indicates greater vulnerability to increased peak discharge. The correlation between Dd (drainage density), Bh (Basin relief), Rn (Rugedness number), C (Coefficient infiltration), and Q (Debit) in the Lambidaro sub-watershed is obtained from the multiplication of Bh and Dd values, which have a very strong correlation between variables with correlation values of 0.836 and 0.905, respectively. The highest Concentration Time (Tc) is in the Lambidaro sub-system at 28.5 minutes. This describes the longest time for water to flow from the furthest distance to its outlet. All morphometric parameters are correlated with the drainage network.

Characteristics of Lambidaro Sub-Watershed

Inundation often occurs in Lambidaro Sub-watershed, particularly in the downstream areas and around flood plains, during the rainy season and high tides. Lambidaro Sub-watershed, covering 65.25 km^2 has different morphometric characteristics from others in Palembang City. Based on the drainage pattern, this sub-watershed is divided into two, namely left and right, which flow into the Musi River, with morphometric characteristics shown in Fig. 3.

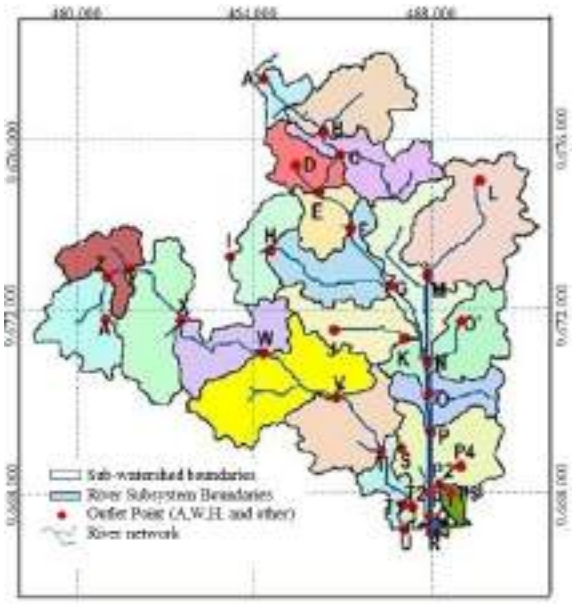

Fig. 3 Morphometric characteristics of Lambidaro sub-watershed

This sub-watershed has a varying height of less than 10 m msl in the left section, and 36 m msl upstream. The slope gradient is dominated by 0-3%, with steeper areas exceeding 8%, particularly.

The river conditions are still natural, specifically upstream, while the left has been normalized by strengthening the banks.

Hydrodynamic Model of Lambidaro Sub-Watershed

HEC-RAS-Arc-GIS model simulation was conducted on Lambidaro sub-watershed. Schematic of water management network based on DEM extraction with flow pattern producing sub-watershed boundary and morphometry to describe run-off in flood plain was built first, as shown in Fig. 4. This structure was built by inputting transverse and longitudinal profile data of the channel per segment based on field measurement results, with channel width ranging from 11-18 m. Boundary conditions for HEC-RAS model consisted of run-off from upstream, while downstream boundary conditions included water level at river mouth. Hydrological parameters of rainfall were taken from the analysis result of maximum daily rainfall distribution using Gumbell method for 25-year period of 163 mm/day. The weighted C value of each system was calculated from the results of spatial analysis of land use, slope gradient, soil type, and flow density, as shown in Fig. 1.

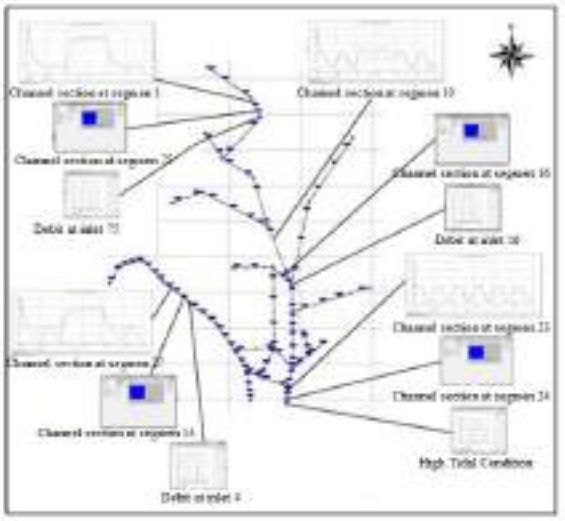

Fig. 4 Schematic of the Lambidaro river flow profile

The results of hydrodynamic modeling and the existing conditions were analyzed with a 25-year return period scenario. Subsequently, water level in each segment was transformed into Lambidaro sub-watershed DEM, interpolated with the Hydro-processing procedure to obtain the distribution of inundation using a 25-year return period scenario.

The results obtained were classified into six categories, namely (1) non-inundated areas, (2) inundated with a height of less than 0.25 m,

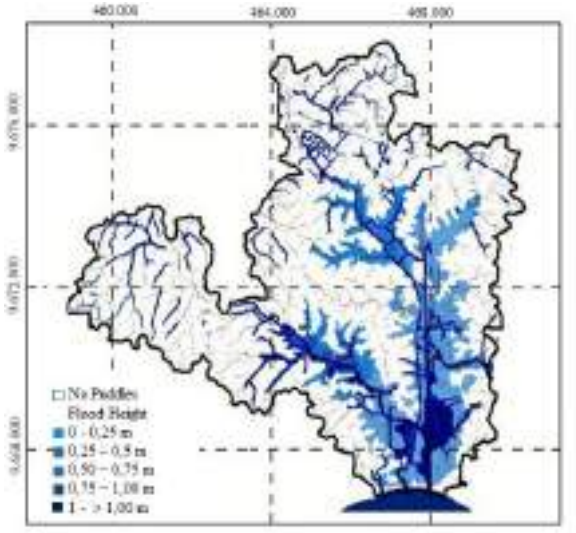

Fig. 5 Distribution of inundation due to changes in land use in Lambidaro sub-watershed

(3) a height of 0.25 - 0.5 m, (4) a height of 0.5-0.75 m, (5) a height of 0.75-1 m, and (6) a height of more than 1 m. Fig. 5 shows the results of hydrodynamic modeling using the HEC-GeoRas model, followed by an analysis of the distribution of inundation that will occur with a 25-year return period scenario.

The inundated areas are characterized by flow accumulation with a slope of 0-3%, dominated by swamps. The calibration of this model is shown by the suitability of the inundation height that occurs in the field with $R^2 = 0.869$.

For the right Lambidaro sub-watershed, the influence of tides on upstream covers area of 756.81 ha, with 2821.6 ha in the middle 2821.6 ha and 513.23 ha downstream. Meanwhile, for the left section, the upstream section covers 1854.5 ha, the middle 380.5 ha, and the downstream 131.1 ha. The distribution of inundation superimposed is shown in Fig. 6.

Land Use Change Scenario

Resolving the reduction of inundation distribution by regulating land use as part of Land Infrastructure Development (LID) in spatial planning, Land Utilization Change Scenarios are made of 5 Scenarios, namely:

(1) The first scenario is by changing the type of land use to a green park (city forest) to reduce the C value.
(2) The second scenario is by changing the type of land use of the upstream into settlements based on the current development of the city, to increase the C value.
(3) The third scenario is the same as the first, which is only carried out downstream.
(4) The fourth scenario is the same as the second, which is only carried out downstream.
(5) The fifth scenario is by changing land use with different C values ranging from 0.2 to 0.9

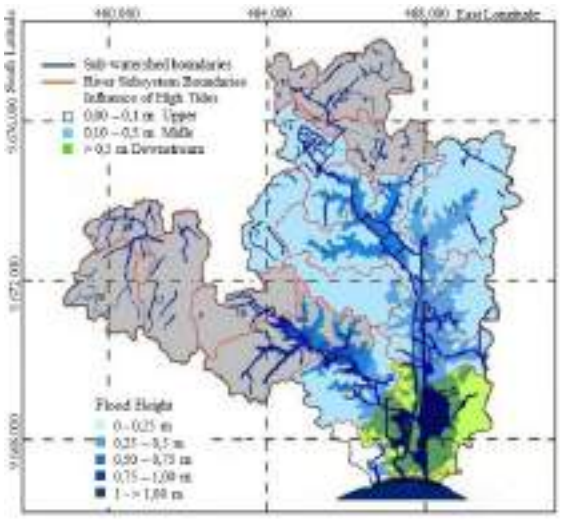

Fig. 6 Distribution of inundation is superimposed on the upstream, middle, and downstream

Several effects of land use change scenarios in the upstream, middle, and downstream sub-watershed by reducing and increasing the run-off coefficient value C per sub-watershed are carried out to reduce and increase the inundation that occurs, as shown in Fig. 7.

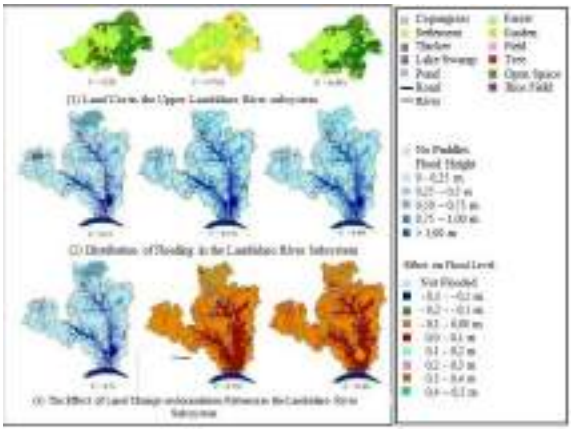

Fig. 7 Effects of changes in land use in the upstream Lambidaro sub-watershed

.

CONCLUSION

In conclusion, this study analyzes spatial planning of Lambidaro sub-watershed in designing urban drainage system. The results obtained are as follows,

1) The average drainage capacity is 14.25 m3/sec, which is unable to drain the 25-year return period water discharge of 52.43 m^3/sec.
2) The planned flood discharge for the 25-year return period produces inundation of 609.01 ha or

approximately 1.1% of Lambidaro sub-watershed. The inundation period varies between 3 hours to 59 hours, with a flood height of 0.01 m from the left river bank elevation +2.5 m to 1.80 m from the right river bank elevation +1.5 m

3) The effect of changes in land use in several scenarios proves that areas of inundation will expand from downstream, middle to upstream when there is no proper control.

ACKNOWLEDGMENTS

The authors are grateful to the Ministry of Higher Education Science and Technology, Universitas Sriwijaya, who has provided research funding through Professional Research grants 2025. In accordance with the Rector's Decree Number : 0029/UN9/LPPM.PT/2025, on September 17,2025.

Furthermore, the authors are grateful to the Research and Community Service Institute of Sriwijaya University, for the opportunity given to obtain the study grants. Support is also received from the Mapping, Remote Sensing, and GIS Survey Laboratory for providing equipment to carry out measurements in the field.

REFERENCES

[1] Putrasnto, D.D.A., Sarino, A. L. Yuono, J. C. Imroatul, and S. A. Hamim, "Integration of surface water management in urban and regional spatial planning," *Int. J. GEOMATE*, vol. 14, no. 45, pp. 28–34, 2018, doi: http://www.geomatejournal.com/articles/2018/14/45.

[2] Monachese, A.C, M.T. Gómez-Villarino, J. López-Santiago, E. Sanz, A. F. Almeida-Ñauñay, and S. Zubelzu, "Challenges and Innovations in Urban Drainage Systems: Sustainable Drainage Systems Focus," *Water (Switzerland)*, vol. 17, no. 1, pp. 1–18, 2025, doi: 10.3390/w17010076.

[3] Eva, P *et al.*, "The impact of the conservation tillage ' maize into grass cover ' on reducing the soil loss due to erosion," *Soil Water Res.*, vol. 15, no. 3, pp. 158–165, 2020, doi: 10.17221/25/2019-SWR.

[4] Rápalo, L.M.C *et al.*, "Effects of land-use and -cover changes on streamflow regime in the Brazilian Savannah," *J. Hydrol. Reg. Stud.*, vol. 38, no. October, p. 100934, 2021, doi: 10.1016/j.ejrh.2021.100934.

[5] Firdaus, D. D. A. Putranto, and I. C. Juliana, "A combined hydrological and hydraulic model for flood prediction in Buah river subsystem area, Palembang city," *Int. J. Adv. Technol. Eng. Explor.*, vol. 9, no. 88, pp. 270–285, 2022, doi: 10.19101/IJATEE.2021.875067.

[6] Miranda A.T, D. D. A. Putranto, and T. A. Gunawan, "Flood and Inundation Risk Analysis Due To Potential Land Subsidence on Alluvial Plains," *Int. J. GEOMATE*, vol. 28, no. 128, pp. 92–99, 2025, doi: 10.21660/2025.128.g14224.

[7] Sliwinski J.T, M. Guillong, P. W. Lipman, M. J. Zimmerer, C. Deering, and O. Bachmann, "Zircon U-Pb geochronology and trace element dataset from the Southern Rocky Mountain Volcanic Field, Colorado, USA," *Data Br.*, vol. 43, p. 108362, 2022, doi: 10.1016/j.dib.2022.108362.

[8] Dinar DA Putranto, Sarino, Yuono AL, "River Ecosystem within Urban Area (Case Study : Palembang Metropolitan Area)," *Int. Conf. Environ. Res. Technol. (ICERT 2008)*, no. Icert, pp. 648–653, 2008.

[9] Le Floch. N, V. Pons, E. M. Hassan Abdalla, and K. Alfredsen, "Catchment scale effects of low impact development implementation scenarios at different urbanization densities," *J. Hydrol.*, vol. 612, no. PB, p. 128178, 2022, doi: 10.1016/j.jhydrol.2022.128178.

[10] Belton V and T. Stewart, *Multiple Criteria Decision Analysis: An Integrated Approach*. 2002.

[11] Zheng J, H. Wang, and B. Liu, "Impact of the long-term precipitation and land use changes on runoff variations in a humid subtropical river basin of China," *J. Hydrol. Reg. Stud.*, vol. 42, p. 101136, 2022, doi: https://doi.org/10.1016/j.ejrh.2022.101136.

[12] Armain M.Z.S, Z. Hassan', M. A. Z. Mohd Remy Rozainy, and A. N. Kamarudzaman, "Hydrodynamic modelling of historical flood event using one dimensional HEC-RAS in Kelantan basin, Malaysia," *IOP Conf. Ser. Earth Environ. Sci.*, vol. 920, no. 1, 2021, doi: 10.1088/1755-1315/920/1/012031.

[13] Jiang. H, J. Zhang, Y. Liu, J. Li, and Z. N. Fang, "Does flooding get worse with subsiding land? Investigating the impacts of land subsidence on flood inundation from Hurricane Harvey," *Sci. Total Environ.*, vol. 865, 2023, doi: 10.1016/j.scitotenv.2022.161072.

[14] Shakarneh. M.O.A, A. J. Khan, Q. Mahmood, R. Khan, M. Shahzad, and A. A. Tahir, "Modeling of rainfall–runoff events using HEC-HMS model in southern catchments of Jerusalem Desert-Palestine," *Arab. J. Geosci.*, vol. 15, no. 1, p. 127, 2022, doi: 10.1007/s12517-021-09406-z.

[15] Oladunjoye. O, D. Proverbs, and H. Xiao, "Retrofitting Sustainable Urban Drainage Systems (SuDS): A Cost-Benefit Analysis Appraisal," *Water (Switzerland)*, vol. 14, no. 16, 2022, doi: 10.3390/w14162521.

[16] Sahdar. I, D. Rohmat, W. A. Pranoto, and Solehudin, "Hydraulic Modeling for Flood Control Scenarios in Akelaka Watershed, North

Maluku, Indonesia," *Int. J. GEOMATE*, vol. 27, no. 120, pp. 49–59, 2024, doi: 10.21660/2024.120.4450.

[17] Mori. S, T. Pacetti, L. Brandimarte, R. Santolini, and E. Caporali, "A methodology for assessing spatio-temporal dynamics of flood regulating services," *Ecol. Indic.*, vol. 129, no. February, p. 107963, 2021, doi: 10.1016/j.ecolind.2021.107963.

[18] Wang. W.C, Y. W. Zhao, D. M. Xu, K. W. Chau, and C. J. Liu, "Improved flood forecasting using geomorphic unit hydrograph based on spatially distributed velocity field," *J. Hydroinformatics*, vol. 23, no. 4, pp. 724–739, 2021, doi: 10.2166/hydro.2021.135.

[19] Venkatcharyulu. S and G. K. Viswanadh, "Runoff volume model for Godavari sub-basin using HEC-RAS software," *Model. Earth Syst. Environ.*, 2021, doi: 10.1007/s40808-021-01311-4.

[20] Papaioannou. G *et al.*, "A flood inundation modeling approach for urban and rural areas in lake and large-scale river basins," *Water (Switzerland)*, vol. 13, no. 9, 2021, doi: 10.3390/w13091264.

[21] Chen. C, Z. Guo, and J. Judge, "A QGIS Plugin for GIS-based Multicriteria Decision Analysis: an Application of Developing Alternative Future Land-Use Scenarios in Ghana," *Appl. Spat. Anal. Policy*, vol. 17, no. 2, pp. 779–797, 2024, doi: 10.1007/s12061-024-09566-x.

[22] Bharali. B and U. Misra, "Prediction of flood hydrograph using the modified Cunge-Muskingum method in an ungauged basin: a case study in the Kulsi river basin, India," *Meteorol. Hydrol. Water Manag.*, no. Hashmi, 2021, doi: 10.26491/mhwm/143249.

Copyright © Int. J. of GEOMATE All rights reserved, including making copies, unless permission is obtained from the copyright proprietors.

15th Int. Conf. on Geotechnique, Construction Materials & Environment, Kyoto, Japan, 11-13 November 2025, ISBN 978-4-909106124 C3051

REPRODUCING REGION-BY-REGION WATER QUALITY CHANGES IN THE SETO INLAND SEA FROM 1990S TO 2010S BY USING MONTE CARLO BASED FOOD CHAIN MODEL

Yutaro KOGA[1, 3], Yuichi SATO[2], Tomohito MATSUO[3] and Hikari SHIMADERA[3]

[1] Hyogo Prefectural Institute of Environmental Sciences, Japan; [2] Lake Biwa Environmental Research Institute, Japan; [3] Graduate School of Engineering, the University of Osaka, Japan

ABSTRACT

This study aims to reproduce regional water quality characteristics of the Seto Inland Sea from the 1990s to the 2010s using a food chain model based on the Monte Carlo method. The study area was divided into 13 regions, each treated as an independent box. A total of 28 ecosystem parameters were statistically estimated for each box through repeated simulations. The model successfully reproduced the observed ranges of dissolved inorganic nitrogen (DIN) concentrations and phytoplankton biomass for both decades using parameter sets derived through the Monte Carlo method. The estimated parameters showed regional variations and were consistent with observed differences in phytoplankton community composition and ecological traits such as growth and sinking rates. These findings indicate that the proposed method is effective for reducing parameter uncertainty while reflecting regional ecosystem characteristics. Furthermore, the results suggest that region-specific parameter settings are essential for simulating the entire Seto Inland Sea.

Keywords: Food Chain Model, Ecosystem Parameter, Monte Carlo Method, Seto Inland Sea

INTRODUCTION

Fisheries in coastal seas have developed through nutrient inputs, such as nitrogen and phosphorus, from rivers and industrial discharges. However, yields have been declining in many coastal regions worldwide due to ecosystem changes caused by climate change, overfishing, and water pollution [1].

Numerical models are widely used for marine ecosystem management. However, uncertainties in biological processes have been reported to reduce model accuracy [2, 3]. These uncertainties are mainly attributed to errors in parameter settings [4]. Therefore, complex models with many parameters are not always practical, and simplified models may be more useful for supporting policy decisions [5].

To address this uncertainty, our previous study developed a food chain model based on the Monte Carlo method consisting of two boxes representing coastal and offshore areas, and applied it to the eastern Seto Inland Sea (Harima Nada) [6]. In that study, ecosystem parameters were assigned for each box based on the dominant phytoplankton types, with the range of parameter values adjusted individually for each box. This approach successfully reproduced the water quality characteristics of the 1990s and 2010s, during which nutrient concentrations changed significantly. In the present study, we estimate ecosystem parameters using the Monte Carlo method, applying a common range of values across all boxes, to reproduce water quality characteristics in diverse regions, and evaluate their validity based on regional differences in observed phytoplankton species.

RESEARCH SIGNIFICANCE

Ecosystem parameters vary across water areas, and modelers have traditionally tuned them within general ranges. However, it is difficult to accurately set all parameters, often leading to subjectivity. This study proposes an approach for parameter estimation using the Monte Carlo method to reduce subjectivities through a statistical framework. The derived parameters reflect the specific characteristics of each water area. The approach offers useful guidance for parameter selection in high-resolution numerical models to improve the reproducibility of water quality conditions in various regions.

MODEL AND METHODS

The NPZFF food chain model, originally developed for Lake Biwa [7] and modified for Harima Nada [6], was further improved in this study by replacing total nitrogen (TN) with dissolved inorganic nitrogen (DIN), which is directly available to organisms. The model equations and schematic structure are presented in Table 1 and Fig. 1.

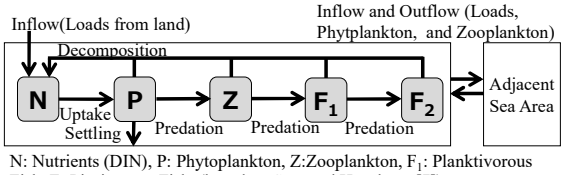

N: Nutrients (DIN), P: Phytoplankton, Z:Zooplankton, F_1: Planktivorous Fish, F_2 Piscivorous Fish (based on Sato and Hayakawa[7]).

Fig.1 Structure of the food chain model.

Table 1 Food chain model description (based on Sato and Hayakawa [7]).

Phytoplankton Biomass:

$$\frac{dM_p}{dt} = G_p - P_p - E_p - R_p - D_p - O_p + IN_p$$

$$G_p = g_p \cdot \left(1 - \frac{\gamma_{min,p}}{\gamma_p}\right) \cdot \exp(-\beta_p \cdot M_p) \cdot \frac{H_p}{H} \cdot M_p \quad P_p = g_z \cdot \frac{M_p}{k_z + M_p} \cdot M_z \quad E_p = e_p \cdot M_p \quad R_p = (r_p + \varepsilon_p) \cdot M_p \quad D_p = \frac{d_p}{H} M_p$$

$$O_p = \frac{\sum_{j=1}^{n} V_{out,j}}{V} \cdot M_p \quad IN_p = \frac{\sum_{j=1}^{n} V_{in,j} \cdot M_{p,j}}{V}$$

Phytoplankton Nutrients:

$$\frac{dC_p}{dt} = \rho_p \cdot \frac{C_N}{k_p + C_N} \cdot \left(1 - \frac{\gamma_p}{k_{max,p}}\right) \cdot M_p - (P_p + E_p + R_p + D_p + O_p) \cdot \gamma_p + IN_p \cdot \gamma_{p,j} \qquad \gamma_p = \frac{C_p}{M_p}$$

Zooplankton Biomass:

$$\frac{dM_z}{dt} = G_z - P_z - E_z - R_z - O_z + IN_z$$

$$G_z = P_p \cdot \delta_z \quad P_z = g_{f_1} \cdot \frac{M_z}{k_{f_1} + M_z} \cdot M_{f_1} \quad E_z = \begin{cases} G_z \cdot (1 - \gamma_p/\gamma_z) & if \quad \gamma_z \geq \gamma_p \\ 0 & if \quad \gamma_z < \gamma_p \end{cases} \quad R_z = (r_z + \varepsilon_z) \cdot M_z \qquad O_z = \frac{\sum_{j=1}^{n} V_{out,j}}{V} \cdot M_z$$

$$IN_z = \frac{\sum_{j=1}^{n} V_{in,j} \cdot M_{z,j}}{V}$$

Zooplankton Nutrients:

$$\frac{dC_z}{dt} = \begin{cases} G_z \cdot \gamma_p - (P_z + R_z + O_z - IN_z) \cdot \gamma_z & if \quad \gamma_z \geq \gamma_p \\ G_z \cdot \gamma_p - G_z(\gamma_p - \gamma_z) - (P_z + R_z + O_z) \cdot \gamma_z + IN_z \cdot \gamma_{z,j} & if \quad \gamma_z < \gamma_p \end{cases} \qquad \gamma_z = \frac{C_z}{M_z}$$

Planktivorous Fish Biomass:

$$\frac{dM_{f_1}}{dt} = G_{f_1} - P_{f_1} - E_{f_1} - R_{f_1}$$

$$G_{f_1} = P_z \cdot \delta_{f_1} \quad P_{f_1} = g_{f_2} \cdot \frac{M_{f_1}}{k_{f_2} + M_{f_1}} \cdot M_{f_2} \quad E_{f_1} = \begin{cases} G_{f_1} \cdot (1 - \gamma_z/\gamma_{f_1}) & if \quad \gamma_{f_1} \geq \gamma_z \\ 0 & if \quad \gamma_{f_1} < \gamma_z \end{cases} \quad R_{f_1} = (r_{f_1} + \varepsilon_{f_1}) \cdot M_{f_1}$$

Planktivorous Fish Nutrients:

$$\frac{dC_{f_1}}{dt} = \begin{cases} G_{f_1} \cdot \gamma_z - (P_{f_1} + R_{f_1}) \cdot \gamma_{f_1} & if \quad \gamma_{f_1} \geq \gamma_z \\ G_{f_1} \cdot \gamma_z - G_{f_1}(\gamma_z - \gamma_{f_1}) - (P_{f_1} + R_{f_1}) \cdot \gamma_{f_1} & if \quad \gamma_{f_1} < \gamma_z \end{cases} \qquad \gamma_{f_1} = \frac{C_{f_1}}{M_{f_1}}$$

Piscivorous Fish Biomass:

$$\frac{dM_{f_2}}{dt} = G_{f_2} - E_{f_2} - R_{f_2}$$

$$G_{f_2} = P_{f_1} \cdot \delta_{f_2} \quad E_{f_2} = \begin{cases} G_{f_2} \cdot (1 - \gamma_{f_1}/\gamma_{f_2}) & if \quad \gamma_{f_2} \geq \gamma_{f_1} \\ 0 & if \quad \gamma_{f_2} < \gamma_{f_1} \end{cases} \quad R_{f_2} = (r_{f_2} + \varepsilon_{f_2}) \cdot M_{f_2}$$

Piscivorous Fish Nutrients:

$$\frac{dC_{f_2}}{dt} = \begin{cases} G_{f_2} \cdot \gamma_{f_1} - R_{f_2} \cdot \gamma_{f_2} & if \quad \gamma_{f_2} \geq \gamma_{f_1} \\ G_{f_2} \cdot \gamma_{f_1} - G_{f_2}(\gamma_{f_1} - \gamma_{f_2}) - R_{f_2} \cdot \gamma_{f_2} & if \quad \gamma_{f_2} < \gamma_{f_1} \end{cases} \qquad \gamma_{f_2} = \frac{C_{f_2}}{M_{f_2}}$$

Nutrients:

$$\frac{dC_N}{dt} = L_N - O_N + DP_N + DZ_N + DF1_N + DF2_N - I_N$$

$$L_N = \frac{L_{in}}{V} + \frac{\sum_{j=1}^{n} V_{in,j} \cdot C_{N,j}}{V} \quad O_N = \frac{\sum_{j=1}^{n} V_{out,j}}{V} \cdot C_N$$

$$DP_N = \{E_P + (P_p - G_z) + R_p\} \cdot \gamma_p \qquad DZ_N = \begin{cases} \{(P_z - G_{f_1}) + R_z\} \cdot \gamma_z & if \quad \gamma_z \geq \gamma_p \\ G_z \cdot (\gamma_p - \gamma_z) + \{(P_z - G_{f_1}) + R_z\} \cdot \gamma_z & if \quad \gamma_z < \gamma_p \end{cases}$$

$$DF1_N = \begin{cases} \{(P_{f_1} - G_{f_2}) + R_{f_1}\} \cdot \gamma_{f_1} & if \quad \gamma_{f_1} \geq \gamma_z \\ G_{f_1} \cdot (\gamma_z - \gamma_{f_1}) + \{(P_{f_1} - G_{f_2}) + R_{f_1}\} \cdot \gamma_{f_1} & if \quad \gamma_{f_1} < \gamma_z \end{cases}$$

$$DF2_N = \begin{cases} R_{f_2} \cdot \gamma_{f_2} & if \quad \gamma_{f_2} \geq \gamma_{f_1} \\ G_{f_2} \cdot (\gamma_{f_1} - \gamma_{f_2}) + R_{f_2} \cdot \gamma_{f_2} & if \quad \gamma_{f_2} < \gamma_{f_1} \end{cases} \qquad I_N = \rho_p \cdot \frac{C_N}{k_p + C_N} \cdot \left(1 - \frac{\gamma_p}{\gamma_{max,p}}\right) \cdot M_p$$

Symbols:

$M_{i,j}$: biomass [gC m^{-3}], G_i : growth [gC m^{-3} day^{-1}], P_i : predation [gC m^{-3} day^{-1}], E_i:elimination [gC m^{-3} day^{-1}], R_i : respiration and mortality [gC m^{-3} day^{-1}], D_i : deposition [gC m^{-3} day^{-1}], O_i : outflow [gC m^{-3} day^{-1} OR gN m^{-3} day^{-1}], IN_i : biomass inflow [gC m^{-3} day^{-1}], V : water volume [m^3], H : water depth [m], H_i : compensation depth [m], $V_{out(in),j}$: water outflow [m^3 day^{-1}], g_i : maximum growth rate [day^{-1}], β_i : congestion effect constant [m^3 gC], k_i : half saturation constant [gC m^{-3} OR gN m^{-3}], e_i : exocytosis rate [day^{-1}], r_i : respiration rate [day^{-1}], ε_i : mortality rate [day^{-1}], d_i : deposition rate [m day^{-1}], δ_i : assimilation rate [-], C_i : nutrients concentration in water or biomass [gN m^{-3}], ρ_i : maximum nutrients uptake rate [gN gC^{-1} day^{-1}], L_{in} : inland nutrients inflow [gN day^{-1}], DN_i : biomass derived nutrients [gN day^{-1}], I_N : phytoplankton intake [gN m^{-3} day^{-1}], γ_i : N:C ratio [-], $\gamma_{max(min),i}$: maximum (minimum) N:C ratio [-], t : time [day], i : target subscripts (p : phytoplankton, z : zooplankton, f_1 : planktivorous fish, f_2 : piscivorous fish), n : number of adjacent sea area, j : sea area

Study Area and Input Data

The study area covers the entire Seto Inland Sea. Based on differences in water quality characteristics—such as nutrient concentrations and phytoplankton biomass—the area was divided into 13 boxes, each representing a distinct water region (Fig. 2).Exchange volumes of seawater were obtained from JCOPE2M [8,9]. Boundary conditions and in-domain data for DIN concentrations and phytoplankton biomass (as chlorophyll-a) were interpolated from observations provided by the Ministry of the Environment of Japan. These data were weighted using 500-m mesh bathymetry data from the Japan Oceanographic Data Center. Parameters for zooplankton, planktivorous fish, and piscivorous fish were set based on values reported in previous studies.

The land-derived DIN load was estimated by applying a DIN/TN ratio of 0.8 to TN loading data [10], based on observational study [11] and previous report [12]. The carbon-to-chlorophyll a ratio (C/Chl-a) was set to 56.4 based on observational data from the Seto Inland Sea [13].

Fig.2 Study area consisting of 13 model boxes .

Calculation Procedure

To estimate ecosystem parameters for each water area, we first defined variation ranges for all 28 ecosystem parameters in the food chain model based on values reported in the literature (Table 2). The following procedure was then used. Each simulation continued until the system reached a periodic steady state. Steps 1 and 2 were repeated until 1,000 valid parameter sets were obtained.

Step 1:

Parameter values were randomly sampled from these ranges, and two separate simulations were conducted using boundary conditions representing the 1990s and the 2010s, respectively.

Step 2:

Each simulation result was accepted only if it satisfied the following two criteria, evaluated under periodic steady-state conditions.

(i) The average values of DIN concentration and biomasses at steady state fall within the observed ranges for the 1990s and 2010s.

(ii) The coefficient of variation (standard deviation divided by the mean) for DIN concentration and each biomass at steady state in the 2010s simulation is 0.2 or less.

In our previous study [6], the variation ranges of ecosystem parameters were adjusted for each box based on the dominant phytoplankton types to reproduce water quality in each box. In contrast, this study employed uniform variation ranges across all boxes, as widely as possible based on literature values, to minimize subjectivity in the parameter estimation process.

For simplicity, water quality within each box was simulated independently without coupling with adjacent boxes.Model reproducibility was evaluated by comparing the simulated DIN concentrations and phytoplankton biomasses with observed values.

The validity of the parameters that achieved acceptable reproducibility was studied based on phytoplankton species composition and related ecological characteristics.

Table 2 Variation ranges for 28 ecosystem parameters

Category	Name	Min.	Max.
Phyto-plankton	Maximum growth rate	0.3	2.5
	Exocytosis rate	0.01	0.3
	Maximum nutrients uptake rate	0.1	1
	Half saturation constant	0.01	1
	Congestion effect constant	0.1	2
	Respiration rate	0.01	0.3
	Mortality rate	0.01	0.3
	Deposition rate	0.01	3
	Maximum N:C ratio	0.17	0.2
	Minimum N:C ratio	0.02	0.06
Zoo-plankton	Maximum growth rate	0.1	0.8
	Assimilation rate	0.6	0.8
	Half saturation constant	0.09	0.18
	Respiration rate	0.01	0.03
	Mortality rate	0.02	0.07
	N:C ratio	0.06	0.12
Plankti-vorous Fish	Maximum growth rate	0.11	0.16
	Assimilation rate	0.7	0.9
	Half saturation constant	0.02	0.05
	Respiration rate	0.004	0.02
	Mortality rate	0.012	0.025
	N:C ratio	0.07	0.13
Pisci-vorous Fish	Maximum growth rate	0.06	0.12
	Assimilation rate	0.8	0.95
	Half saturation constant	0.07	0.11
	Respiration rate	0.001	0.004
	Mortality rate	0.003	0.008
	N:C ratio	0.04	0.1

RESULTS AND DISCUSSION

Model Reproducibility and Regional Water Quality Characteristics

Comparisons between simulated and observed values are shown in Fig. 3 for DIN concentrations and in Fig. 4 for phytoplankton biomass, both between the 1990s and the 2010s. Both figures present boxplots of 1,000 simulation results and 10 years of observational data, along with their respective averages. Since only simulations within the observational range were accepted as valid, all results naturally reflect the water quality characteristics of each box.

Phytoplankton biomass generally ranged from 0.1 to 0.2 mgC L^{-1}, but was below 0.05 mgC L^{-1} in BOX1 and 13, and reached 0.24 mgC L^{-1} in BOX12.

In the 1990s, compared to the 2010s, DIN concentrations showed small changes in the western boxes (BOX1–5), while higher values were observed in the eastern side of the Seto Inland Sea (BOX6–13). Phytoplankton biomass, on the other hand, increased significantly only in BOX12 and 13 compared to the 2010s.

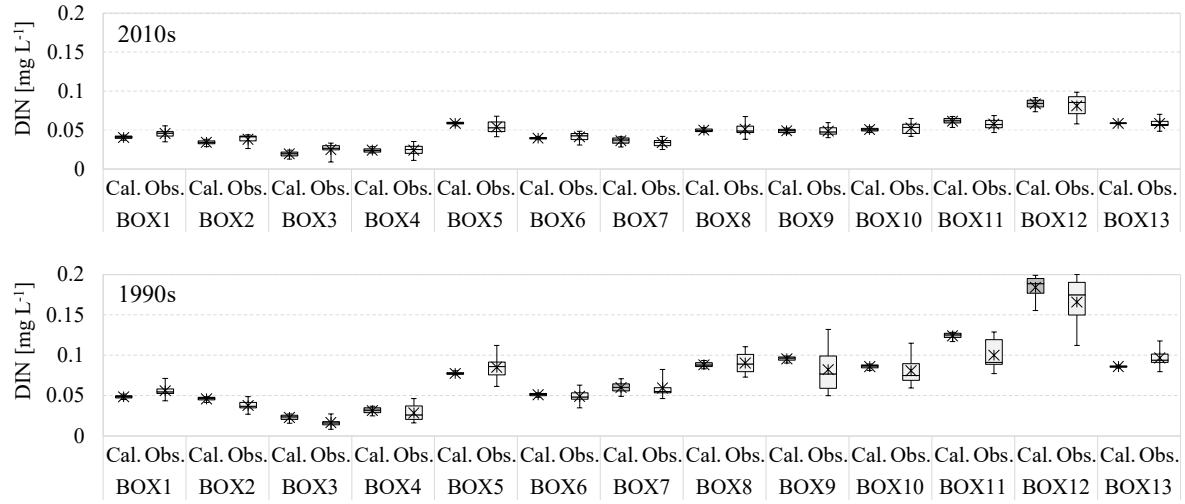

The top and bottom of the box represent 75th and 25th percentiles respectively. The top and bottom of the vertical line represent 95th and 5th percentiles. The inner line is the median and the asterisk represents the average.

Fig.3 Comparison of calculated and observed DIN concentrations between the 1990s and the 2010s.

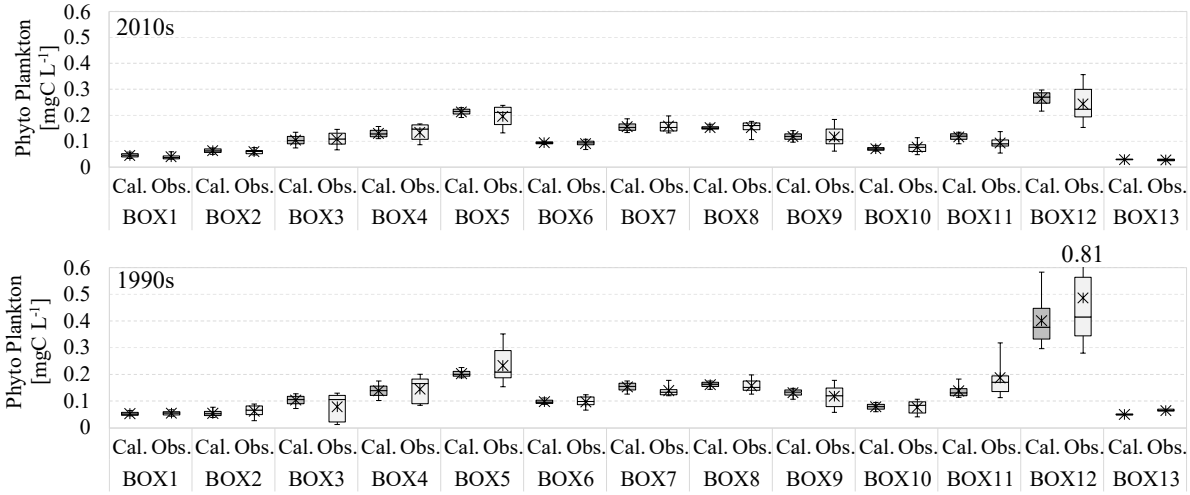

The top and bottom of the box represent 75th and 25th percentiles respectively. The top and bottom of the vertical line represent 95th and 5th percentiles. The inner line is the median and the asterisk represents the average.

Fig.4 Comparison of calculated and observed phytoplankton biomass between the 1990s and the 2010s.

Evaluation of Ecosystem Parameters

Fig. 5 shows key ecosystem parameters that exhibited notable differences among the boxes, and Fig. 6 presents the phytoplankton species composition in the 2010s provided by the Ministry of the Environment of Japan, spatially interpolated and adjusted for each box.

Relatively low maximum growth rates of phytoplankton were estimated in BOX7, 8, and 9, which is consistent with previous report that diatoms generally grow faster than dinoflagellates [14]. In contrast, BOX1 and 2 showed relatively high growth rates despite a higher proportion of dinoflagellates. It is possible that these "others" types included fast-growing species, which may have contributed to higher estimated maximum growth rates.

The maximum nutrient uptake rates were relatively low in BOX8, 10, and 11.In BOX8 and 10, this aligns with finding that dinoflagellates typically have lower uptake rates than diatoms [15]. In contrast, BOX11 exhibited a lower maximum nitrogen uptake rate despite the dominance of diatoms. It is generally understood that phytoplankton tend to exhibit higher nitrogen uptake rates when ammonium nitrogen is abundant. According to data from the Ministry of the Environment of Japan, the ratio of ammonium nitrogen—readily available to phytoplankton—to total DIN in BOX11 was lower than in the surrounding areas.This may have contributed to the reduced maximum nitrogen uptake rate of phytoplankton in this region.

The deposition rate of phytoplankton was lowest in BOX8, which may be attributed to the lower abundance of diatoms with heavy silica shells.

Zooplankton maximum growth rates were relatively high in BOX1, 2, and 8. The value for BOX8 aligns with finding that cryptophytes, which were dominant in this area, are high-quality food sources that promote zooplankton growth [16]. In BOX1 and 2, the influence of "other" phytoplankton types may again be a factor.

These findings suggest that the estimated parameters were consistent with the phytoplankton species composition in each region. To reproduce regional water quality differences using the box model, different ecosystem parameters should be applied for each area. This may also apply to high-resolution models, suggesting that appropriate parameter settings should be carefully considered for each region.

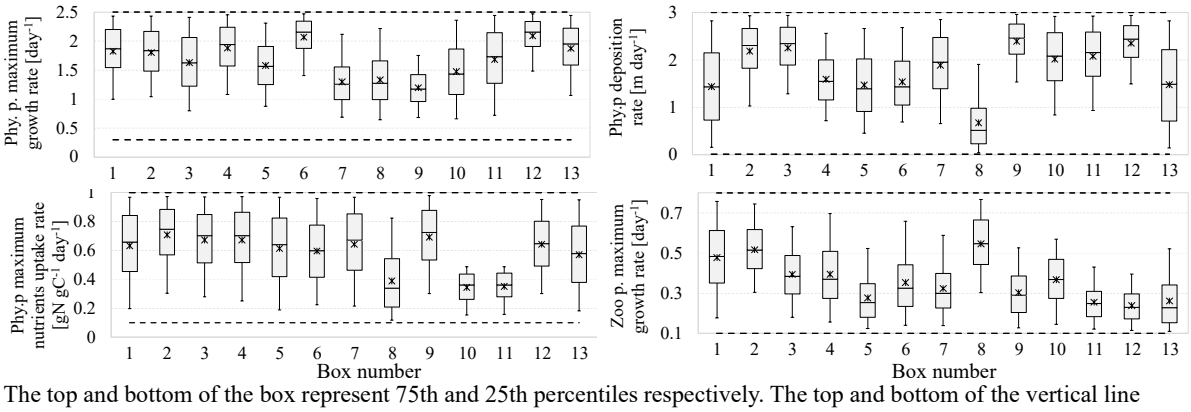

The top and bottom of the box represent 75th and 25th percentiles respectively. The top and bottom of the vertical line represent 95th and 5th percentiles. The inner line is the median and the asterisk represents the average. The dashed lines indicate the maximum and minimum values of the predefined parameter range.

Fig.5 Estimated ecosystem parameters showing regional variations among 13 boxes.

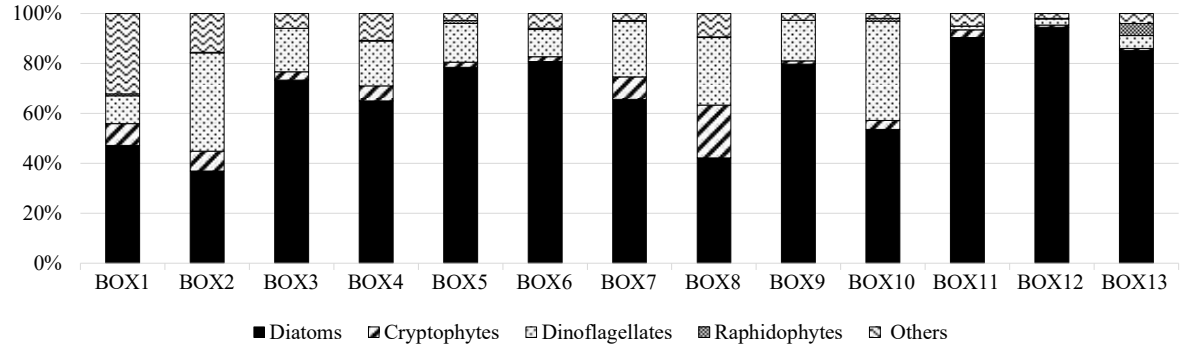

Fig.6 Observed phytoplankton species composition in 2010s.

CONCLUSIONS

This study estimated ecosystem parameters in multiple regions of the Seto Inland Sea using a Monte Carlo based food chain model. The model successfully reproduced the water quality characteristics for both the 1990s and 2010s, including DIN concentrations and phytoplankton biomass. The estimated parameters reflected regional differences in phytoplankton communities and were consistent with known ecological traits, such as growth rates and sinking velocities.

These results suggest that using region-specific parameter settings is essential for accurately simulating ecosystem dynamics in coastal waters. The proposed approach provides a practical framework for reducing parameter uncertainty and may be useful for improving the reliability of high-resolution numerical models applied to eutrophic coastal seas.

ACKNOWLEDGMENTS

This research was performed by the Environment Research and Technology Development Fund (JPMEERF24S12302) of the Environmental Restoration and Conservation Agency provided by the Ministry of the Environment of Japan.

The authors also express their sincere gratitude to Associate Professor Yusuke Nakatani (Osaka University) and Mr. Chihiro Kashima for providing valuable data.

REFERENCES

[1] Jackson J.B.C., Kirby M.X., Berger W.H., Bjorndal K.A., Botsford L.W., Bourque B.J., Bradbury R.H., Cooke R., Erlandson J., Estes J.A., Hughes T.P., Kidwell S., Lange C.B., Lenihan H.S., Pandolfi J.M., Peterson C.H., Steneck R.S., Tegner M.J. and Warner R.R., Historical Overfishing and the Recent Collapse of Coastal Ecosystems, Science, Vol.293, No.5530, 2001, pp.629–638.

[2] Singh T., Counillon F., Tjiputra J., Wang Y. and Gharamti M.E., Estimation of Ocean Biogeochemical Parameters in an Earth System Model Using the Dual One Step Ahead Smoother: A Twin Experiment, Frontiers in Marine Science, Vol.9, 2022, p.775394.

[3] Bopp L., Resplandy L., Orr J.C., Doney S.C., Dunne J.P., Gehlen M., Halloran P., Heinze C., Ilyina T., Séférian R. and Tjiputra J., Multiple Stressors of Ocean Ecosystems in the 21st Century: Projections with CMIP5 Models, Biogeosciences, Vol.10, No.10, 2013, pp.6225–6245.

[4] Losa S.N., Kivman G.A. and Ryabchenko V.A., Weak Constraint Parameter Estimation for a Simple Ocean Ecosystem Model: What Can We Learn About the Model and Data?, Journal of Marine Systems, Vol.45, No.1–2, 2004, pp.1–2.

[5] Uchida T., Ukita M., Sekine M. and Nakanishi H., The study on the nonlinear characteristics of water quality in eutrophic sea areas and their modeling, Journal of Japan Society of Civil Engineers, No.503, 1994, pp.187–195. (in Japanese)

[6] Koga Y., Shimadera H., Sato Y., Pintos Andreoli V., Suzuki M., Matsuo T. and Kondo A., Evaluating the effects of land-derived nutrient load on nutrient and ecosystem production at Harima Nada in Seto Inland Sea using food chain model, Journal of Japan Society on Water Environment, Vol.47, No.5, 2024, pp.151–161. (in Japanese)

[7] Sato Y. and Hayakawa K., Effect of nutrient loads on upper trophic level species in Lake Biwa: Analysis using food chain model by Monte Carlo method, Journal of Japan Society on Water Environment, Vol.42, No.4, 2019, pp.133–143. (in Japanese)

[8] Miyazawa Y., Kuwano-Yoshida A., Doi T., Nishikawa H., Narazaki T., Fukuoka T. and Sato K., Temperature profiling measurements by sea turtles improve ocean state estimation in the Kuroshio–Oyashio Confluence region, Ocean Dynamics, Vol.69, 2019, pp.267–282.

[9] Miyazawa Y., Segrey M.V., Miyama T., Xinyu G., Hihara T., Kiyomatsu K., Kachi M., Kurihara Y. and Murakami H., Assimilation of high-resolution sea surface temperature data into an operational nowcast/forecast system around Japan using a multi-scale three dimensional variational scheme, Ocean Dynamics, Vol.67, 2017, pp.713–728.

[10] Kashima C., Nakatani Y., Higashi H. and Akiyama C., Estimation of the L–Q equations for each sea area in the Seto Inland Sea, Journal of Japan Society of Civil Engineers, Ser. B1 (Hydraulic Engineering), Vol.81, No.16, 2025, p.24-16119. (in Japanese)

[11] Koga Y., Suzuki M. and Pintos V., Analysis of nitrogen and phosphorus load dynamics in Kako and Ibo River basins during flood events, Journal of Japan Society of Hydrology and Water Resources, Vol.35, No.1, 2022, pp.32–40. (in Japanese)

[12] Nakatani Y., Kawasumi R. and Nishida S.,

Change of inflow load and water environment in Osaka Bay, Journal of Japan Society of Civil Engineers, Ser. B2 (Coastal Engineering), Vol.67, No.2, 2011, pp.I_886–I_890. (in Japanese)

[13] Tada K. and Morishita M., The changes of environmental chemical conditions and biomass on lower trophic levels in a coastal bay, Bull. Fac. Agric., Kagawa Univ., Vol.49, No.1, 1997, pp.35–47. (in Japanese)

[14] Chan, A. T., Comparative physiological study of marine diatoms and dinoflagellates in relation to irradiance and cell size II: Relationship between photosynthesis, growth, and carbon/chlorophyll a ratio, Journal of Phycology, Vol. 16, No. 2, 1980, pp. 196–202.

[15] Lomas, M. W. and Glibert, P. M., Comparisons of nitrate uptake, storage, and reduction in marine diatoms and flagellates, Journal of Phycology, Vol. 36, No. 5, 2000, pp. 903–913.

[16] Brett, M. T. and Müller-Navarra, D. C., The role of highly unsaturated fatty acids in aquatic foodweb processes, Freshwater Biology, Vol. 38, No. 3, 1997, pp. 483–499.

Copyright © Int. J. of GEOMATE All rights reserved, including making copies, unless permission is obtained from the copyright proprietors.

15th Int. Conf. on Geotechnique, Construction Materials & Environment,
Kyoto, Japan, 11-13 November 2025, ISBN 978-4-909106124 C3051

EXPECTED GROUNDWATER DEVELOPMENT AND WATER SECURITY IN DEFICIT SMALL TOURISM ISLAND

Jutamas Srisuk[1], Pinit Tanachaichoksirikun [1], Uba Sirikaew[1] and *Uma Seeboonruang[1]

[1]School of Engineering, King Mongkut's Institute of Technology Ladkrabang, Thailand

ABSTRACT

The lack of freshwater resources on small tourism islands causes a critical issue with direct effects for the quality of life within local communities and the long-term sustainability of tourism activities. This problem is particularly worsened in regions lacking centralized community water supply systems, where groundwater serves as a crucial source of water for domestic consumption. This study aims to assess the feasibility of developing groundwater resources for establishing a community water supply system on small tourism islands. The research employed a mathematical groundwater model using the MODFLOW program to simulate groundwater flow and analyze the zone budget, based on head contour data and land use patterns in the study area. The results revealed that the most suitable location for groundwater development is the lowland community area, which functions as a discharge zone with high potential for groundwater accumulation and circulation. The MODFLOW simulation accurately demonstrated the quantity and flow direction of groundwater, providing valuable insights for planning a sustainable water supply system to enhance long-term water security for small tourism islands.

Keywords: Groundwater Development, Community Water Supply, Zone Budget, MODFLOW, Small Tourism Island

INTRODUCTION

The world is currently facing a freshwater scarcity crisis, affecting both the quality and quantity of available water [1]. This issue severely impacts people's quality of life, particularly on small islands. These islands have geographical and natural resource limitations, making access to freshwater for consumption difficult. They primarily rely on rainwater and groundwater, which have become insufficient due to increasing human activities, especially the continuously expanding tourism sector [2, 3]. As a result, the demand for water has risen, placing further pressure on already limited water resources.

Si Chang Island is an area clearly facing significant challenges related to freshwater scarcity and contamination [4]. At present, the island lacks a community water supply system, as previous attempts to produce municipal water from seawater have failed, and existing reservoirs are unable to retain water due to leakage issues [5]. Consequently, residents must rely on collecting rainwater in storage tanks and importing freshwater from external sources. This results in high costs not only for the water itself but also for transportation, making freshwater unnecessarily expensive—despite being a necessity that should be affordably accessible.

Given these challenges, this research highlights the importance of establishing a community water supply system on Si Chang Island to promote sustainable self-reliance in freshwater resources. The primary objective of the study is to identify and evaluate suitable groundwater sources for developing a raw water supply system. To achieve this, the study utilizes geological data, Geographic Information Systems (GIS), and MODFLOW software to construct spatial models that systematically and accurately analyze groundwater behavior and flow direction in the area [6].

The integration of MODFLOW modeling with zone budget analysis is internationally recognized as a critical tool for assessing groundwater potential and supporting sustainable water resource management. For example, in India, semi-arid Palar sub-basin, MODFLOW was employed to simulate groundwater flow, enabling an accurate assessment of the groundwater balance and effectively supporting local water management strategies [7]. In Egypt, Visual MODFLOW was combined with Multi-Criteria Decision Analysis (MCDA) to inform future pumping plans, while zone budget was applied to assess the suitability of different zones for groundwater source development [8]. Similarly, in Ethiopia's Tana Basin, MODFLOW-NWT was used to examine the effects of climate change on groundwater levels, with zone budget helping to evaluate changes in groundwater systems under various scenarios [9].

In Thailand, GIS techniques are integrated with MODFLOW to simulate groundwater flow with high accuracy. Zone budget was applied to assess water balance within designated zones, serving as a foundation for long-term sustainable water resource management strategies [10–12]. These examples demonstrate that the combined use of MODFLOW and zone budget not only enables detailed simulations of groundwater dynamics but also supports

sustainability assessments for water resource utilization. This approach is adaptable to conditions specific to Thailand, particularly in small island areas like Si Chang Island where freshwater resources are limited. Applying these tools is expected to significantly enhance the scientific planning and implementation of a sustainable community water supply system.

RESEARCH SIGNIFICANCE

This research addresses the urgent need for a reliable freshwater supply on small tourist islands by focusing on the identification and evaluation of suitable groundwater sources in areas with limited hydrogeological data. By applying MODFLOW modeling, the study offers critical insights into the development of a sustainable community water supply system. Its findings contribute to closing existing data gaps and supporting informed decision-making for long-term water resource management. Moreover, this approach is transferable to other island regions facing similar challenges, providing a valuable framework for improving water security and accommodating the continued growth of the tourism sector.

GROUNDWATER BUDGET

A groundwater budget is an evaluation of the continuous flow of water into and out of a groundwater system, which must remain in balance over time. The water balance equation is used to quantify the total volume of water entering and leaving the system or a defined groundwater storage area. The difference between inflows and outflows indicates the change in groundwater storage, either as an increase or a decrease, as expressed in Eq. (1)

$$I - O = \Delta S \quad (1)$$

Where: I = Inflow, O = Outflow, ΔS = Change in Storage. When considering a groundwater storage area at the sub-basin level, as illustrated in Eq. (1), and focusing specifically on the groundwater budget, the equation can be written as follows:

$$I + G_{in} + Q_g - G_{out} - E_g - T_g = \Delta S_g \quad (2)$$

Where: I = Recharge from the surface to the aquifer, G_{in} = Groundwater flow into the system, Q_g = Flow into and out of the system via streams, G_{out} = Groundwater flow out of the system, E_g = Evaporation from groundwater, T_g = Transpiration from groundwater by plants, ΔS_g = Change in groundwater storage

In this study, the groundwater balance will be analyzed separately for each zone to illustrate spatial variations in groundwater inflow and outflow. This analysis will support the identification of areas that are both suitable and potentially sustainable for future development.

STUDY AREA

Fig. 1 Location and slope in Si Chang Island [13]

Si Chang Island, a small island in the Gulf of Thailand, is located approximately 12 kilometers off the coast of Si Racha District and about 36 kilometers from Chonburi City. The island covers a land area of approximately 7.65 square kilometers and is surrounded by an additional 9.65 square kilometers of marine territory.

The island's terrain is predominantly composed of rocky hills and mountainous areas, with around 80% of the total land area consisting of elevated peaks. The highest point, situated in the northern part of the island, reaches approximately 192 meters above sea level [13]. The topography is characterized by uneven elevation distribution: about 67% of the area lies between 0–50 meters above sea level, 26% between 50–100 meters, 6% between 100–150 meters, and only 1% exceeds 150 meters, as shown in Fig. 1

These geographical features, particularly the limited flatland and rugged terrain, present significant challenges for freshwater resource management, especially in terms of groundwater recharge and resilience to climate change impacts.

GENERAL AND TOPOGRAPHY

Based on the geological map of Chonburi Province [14], Si Chang Island is primarily composed of sedimentary rocks from the Chonburi Group, which were deposited during the Carboniferous–Permian (CP) period. These formations include sandstone, argillaceous limestone, shale, and chert. Such rock types can store groundwater within limestone caverns and fracture systems (jointing systems) [15].

The island's terrain is mostly limestone mountains, especially in the north, while the east and southwest consist of granite. The western coast features rocky outcrops, cliffs, and some sandy beaches. Groundwater is found at depths of approximately 50 meters, primarily within limestone layers where it's stored in caverns or fractures within the limestone. The expected groundwater yield is less than 2 cubic meters per hour, with a low total dissolved solids (TDS) content of less than 500 mg/L [16].

RAINFALL AND TEMPERATURE

Si Chang Island's climate is influenced by both the northeast and southwest monsoons, resulting in three distinct seasons: the hot season (mid-February to May), the rainy season (June to October), and the dry season (November to mid-February).

Average temperatures range between 25°C and 35°C, with April and May typically being the hottest months of the year. According to data from the Si Chang Island rainfall station [17], the island receives an average annual rainfall of approximately 1,000 to 1,200 millimeters, the majority of which occurs during the monsoon season. However, a declining trend in precipitation has been observed, particularly during the dry season, when rainfall is minimal. Even during the rainy season, precipitation tends to be intense yet unevenly distributed, leading to temporal and spatial variability in water availability.

LAND USE

Fig. 2 shows the land use classification of Si Chang Island. Based on land use data from the Department of Land Development (2020), approximately 70% of Si Chang Island remains as green space, primarily composed of deciduous forests—either mature or under active restoration. Urbanized areas, including residential zones and built structures, occupy around 16% of the island, reflecting a moderate level of human development.

The remaining land uses are distributed as follows: industrial areas (3.37%), government facilities (2.58%), harbors (0.42%), laterite pits (1.40%), and beaches (3.67%). Surface water bodies are minimal, collectively accounting for less than 2% of the island's total area. A more detailed land use classification includes deciduous forest under restoration—36.46% (2.36 km²), mature deciduous forest—35.09% (2.27 km²), urban areas and structures—16.01% (1.00 km²), and other functional zones such as government offices, industrial zones, gravel pits, and ports—collectively covering less than 1 km². Water sources, including reservoirs and natural water bodies, comprise only 0.52% and 0.48% of the area, respectively [18].

These land use characteristics have a direct influence on the island's groundwater recharge potential. While forested and natural soil areas promote effective infiltration and aquifer recharge, the expansion of impervious surfaces—such as buildings and roads—can significantly reduce permeability. Consequently, integrated water resource management must carefully balance the retention of permeable land cover with the demands of built infrastructure.

Fig. 2 Land use in Si Chang Island [18]

WATER QUALITY

According to the drinking water quality standards established by the Department of Health in 2020 [4], the overall water quality on Si Chang Island is classified as "acceptable." This classification indicates that the water may be used for consumption in the absence of alternative sources. However, water treatment is required prior to use due to the presence of coliform bacteria and Escherichia coli (E. coli), which are commonly associated with gastrointestinal illnesses such as diarrhea.

In contrast, the southern part of the island—an uninhabited area designated for waste disposal—shows contamination from several hazardous substances, including arsenic and fluoride, at concentrations exceeding permissible limits. As a result, the water quality in this area is deemed unsafe for any purpose, including human consumption.

METHODOLOGY

This study employed a systematic approach that integrated field investigations, spatial analysis, and numerical modeling to simulate groundwater flow and assess the feasibility of groundwater resource development on Si Chang Island. The methodology involved collecting and analyzing geological and hydrogeological data from the area, developing a conceptual model of the groundwater system, simulating groundwater flow using Visual MODFLOW software, calibrating the model against observed field data, and analyzing multiple scenarios to evaluate the potential and formulate strategies for sustainable groundwater management on the island.

CONCEPTUAL MODEL AND BOUNDARY CONDITION

The conceptual model of Si Chang Island was developed using topographic, geological, hydrogeological, soil, and land use data. The model's upper boundary was defined as a recharge boundary representing rainfall infiltration, while its outer boundaries were assigned as constant head boundaries due to the island being surrounded by seawater. The model comprises six layers: the top layer is an unconfined aquifer; the second layer consists of colluvial deposits; the third through fifth layers represent confined limestone aquifers; and the bottom layer is modeled as a no-flow boundary, corresponding to impermeable bedrock. The thickness of each layer was defined based on local hydrogeological characteristics. Groundwater abstraction from existing wells was incorporated as pumping boundaries. Reservoir boundaries were excluded from the model due to the limited water storage capacity of local reservoirs.

HYDRAULIC CONDUCTIVITY

In this study, hydraulic conductivity (K) values were assigned based on the assumption that the subsurface is heterogeneous and isotropic. The top layer, representing an unconfined aquifer, was assigned spatially variable hydraulic conductivity values, as illustrated in Fig. 3 For layers 2 through 5, which correspond to confined limestone aquifers, hydraulic conductivity values are summarized in Table 1.

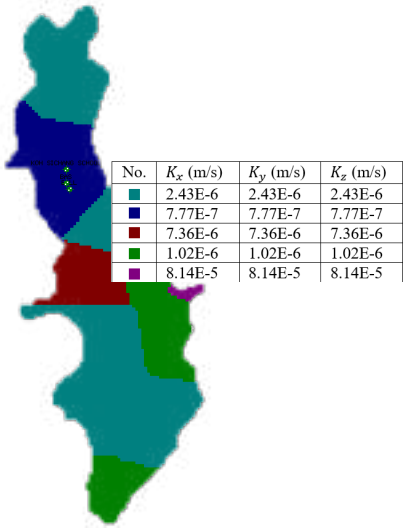

Fig. 3 Hydraulic conductivity of the topsoil layer

Table 1 Parameters for groundwater model layers

No.	K_x (m/s)	K_y (m/s)	K_z (m/s)
Layer 2	3.50E-5	3.50E-5	3.50E-5
Layer 3	4.75E-6	4.75E-6	4.75E-6
Layer 4	1.50E-6	1.50E-6	1.50E-6
Layer 5	6.50E-7	6.50E-7	6.50E-7
Layer 6	7.75E-7	7.75E-7	7.75E-7

RECHARGE

Groundwater recharge in the study area was estimated by delineating recharge zones based on land use and soil characteristics, in combination with local rainfall data. Varying recharge percentages were assigned to each land use category to reflect differences in infiltration potential.

Table 2 Initial groundwater recharge rate

Recharge Zones	Recharge Rate (% Rainfall)
1. Urban Area	1
2. Dene Deciduous Forest	20
3. Disturbed Deciduous Forest	15
4. Industry	1
5. Harbor	1
6. Government Office	1
7. Laterite Pit	30
8. Reservoir	20
9. River and Ocean	0

ZONE BUDGET

The study area was divided into six budgeting zones, as illustrated in Fig. 4, based on predominant land use types, including agricultural, urban, forested, and industrial areas. Each land use type exhibits

distinct patterns of water consumption and groundwater flow, which are essential for evaluating groundwater inflow and outflow within each zone. The assessment integrates multiple factors, such as rainfall, infiltration capacity, local water demand, and geological conditions. This integrated approach facilitates the effective identification of zones with high potential for groundwater resource development.

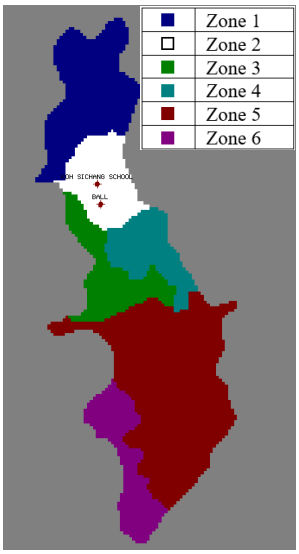

Fig. 4 Zone budget

SCENARIOS

A numerical groundwater flow model was employed to simulate the impacts of recharge variations across six designated zones under three climate change scenarios: RCP2.6, RCP4.5, and RCP8.5. The simulation was conducted over a 10-year period, from 2025 to 2035.

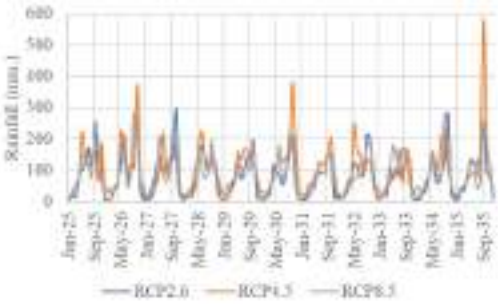

Fig. 5 Rainfall based on climate models, 2025-2035

Future rainfall projections for the period 2025 to 2035, based on the HADGEM2-AO climate model, indicate that the RCP4.5 scenario produces the highest rainfall, reaching nearly 600 mm in October 2035. In contrast, the RCP2.6 and RCP8.5 scenarios exhibit similar trends, with comparatively lower rainfall levels, as illustrated in Fig. 5. The inclusion of all three Representative Concentration Pathways (RCPs) provides a comprehensive perspective on future climate variability, enabling a more robust assessment of potential risks and uncertainties in the projections.

RESULTS AND DISCUSSION

CALIBRATION AND VERIFICATION RESULTS

This model was further developed based on the work of Srisuk et al. [19]. Model calibration and validation were performed by comparing the simulated groundwater levels with observed data from three monitoring wells on Si Chang Island, namely the Football Field Well, the Basketball Court Well, and the Koh Si Chang School Well, all of which are located within the community area. However, due to data limitations [19], this study divided the datasets used for calibration and validation into two periods: groundwater level data from May 2023 for model calibration, and groundwater level data from August 2023 for model validation.

Calibration results (Fig. 6a) yielded a Root Mean Square Error (RMSE) of 0.128 meters, a Standard Error (SE) of 0.031 meters, a Normalized RMSE of 9.158%, and a coefficient of determination (R^2) of 0.997.

Model validation (Fig. 6b) produced an RMSE of 0.117 meters, an SE of 0.066 meters, a Normalized RMSE of 9.591%, and an R^2 of 0.998.

Both calibration and validation results fall within acceptable thresholds, with Normalized RMSE values below 10%, which is considered satisfactory for groundwater modeling applications [20]. Therefore, the model is deemed reliable for use in this study and suitable for further analysis of groundwater potential in the area.

SENSITIVITY ANALYSIS

A sensitivity analysis was conducted to evaluate the influence of key parameters on the model's performance [21]. This study focused on assessing the sensitivity of three primary parameters: hydraulic conductivity (K), recharge rate, and constant head (CH) within the Si Chang Island area.

The results revealed that the constant head had the most significant impact on simulated groundwater levels, followed by hydraulic conductivity and recharge rate, respectively, as shown in Fig. 7. Variations in the constant head by ±25%, ±50%, and ±75% resulted in substantial changes in groundwater levels, emphasizing the importance of accurately defining boundary conditions that reflect real-world hydrogeological settings. These findings also underscore the necessity for precise field measurements to ensure the reliability of input parameters used in groundwater modeling.

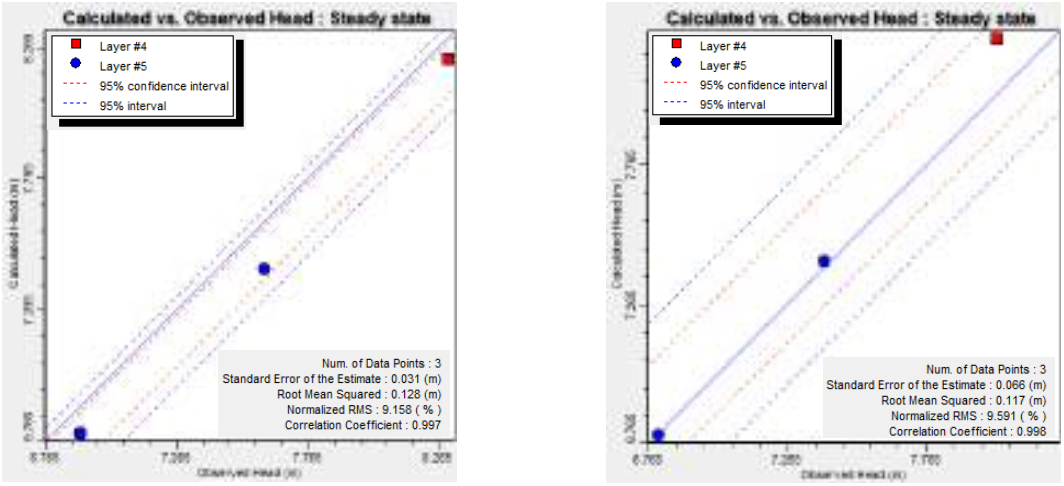

(a) Model Calibration (b) Model Validation

Fig. 6 Calibration and verification results

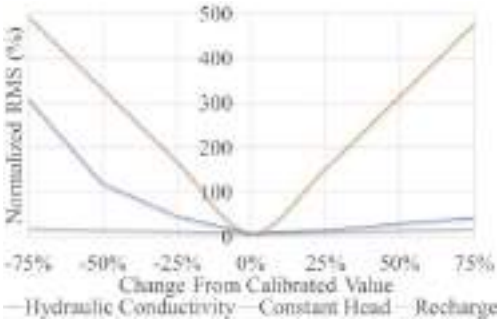

Fig. 7 Model sensitivity analysis

GROUNDWATER EXPLORING SCENARIOS

In this study, groundwater behavior on Si Chang Island was simulated using a Zone Budget approach, which divided the area into six zones. The model evaluated the impacts of climate change over a 10-year period (2025–2035) under three scenarios: RCP2.6, RCP4.5, and RCP8.5.

As shown in Fig. 8, among the six zones, Zone 5—characterized by forested land with favorable infiltration conditions—exhibited the highest average groundwater recharge rate, approximately 1,040 m³/day. However, it also experienced the highest loss to the sea, averaging 860 m³/day, with an additional outflow of 185 m³/day to Zones 3, 4, and 6.

Zone 1, a steep mountainous recharge area, had the second-highest recharge rate at around 670 m³/day but also contributed significantly to seawater loss and lateral flow, transferring about 125 m³/day to Zone 2. Zone 2, a community area and lowland discharge zone, had a low recharge rate (40 m³/day) but received substantial inflow from Zones 1, 3, and 4, totaling about 200 m³/day, with minimal loss to the sea (50 m³/day).

Zone 3 showed an average recharge rate of 345 m³/day, but due to its steep terrain, nearly all recharge was lost to the sea. It received water from Zone 5 and transferred water to Zone 4. Zone 4, also a lowland community zone, had limited recharge and seawater loss but functioned primarily as a transit zone, receiving water from Zones 3 and 5 and discharging to Zone 2.

Zone 6 demonstrated relatively high recharge but experienced even greater losses to the sea. It received some water from Zone 5, averaging around 90 m³/day.

Across all three climate scenarios, the RCP4.5 scenario resulted in the highest recharge values, particularly in October 2035, which aligns with the projected rainfall trends. However, differences among the scenarios were relatively minor in magnitude.

These findings highlight the effectiveness of spatial groundwater budgeting in identifying recharge and discharge dynamics, even in data-scarce environments. This approach supports informed decision-making for the development of sustainable community water supply systems in vulnerable island settings.

CONCLUSION AND RECOMMENDATIONS

Currently, Si Chang Island lacks a community water supply system, forcing residents to rely on rainwater harvesting and the importation of freshwater—both of which involve high costs for water and transportation. Consequently, water becomes an unnecessarily expensive resource despite being a necessity. This research aimed to identify and evaluate suitable groundwater sources to support the development of a cost-effective and sustainable community water supply system.

A spatial groundwater model was developed using

Geographic Information System (GIS) tools in conjunction with the MODFLOW program, under conditions of limited available data. The study analyzed six hydrological zones across three climate change scenarios—RCP2.6, RCP4.5, and RCP8.5—projected for the period 2025–2035 using the HADGEM2-AO climate model.

The findings indicate that Zone 2 is the most suitable area for developing groundwater resources for community water supply under all three climate scenarios. This suitability is supported by both water quality and quantity. Located in a low-lying, populated area that functions as a discharge zone, Zone 2 receives substantial inflows from Zones 1, 3, and 4 while experiencing minimal losses to the sea. In terms of water quality, Zone 2 is also favorable, as it is not directly connected to Zones 5 and 6 in the island's southern region, where groundwater contamination from hazardous substances such as arsenic has been identified. As a result, water from Zones 5 and 6 should be excluded from future water supply planning.

However, concerning water quantity in Zone 5, while there's a high rate of groundwater recharge, there's also a significant amount of water lost to the sea and outflowing from the zone. The findings highlight the importance of accurate data and a thorough understanding of the study area for planning the selection of suitable zones for establishing a community water supply. Both water quality and quantity must be considered to ensure an effective and sustainable solution for the future.

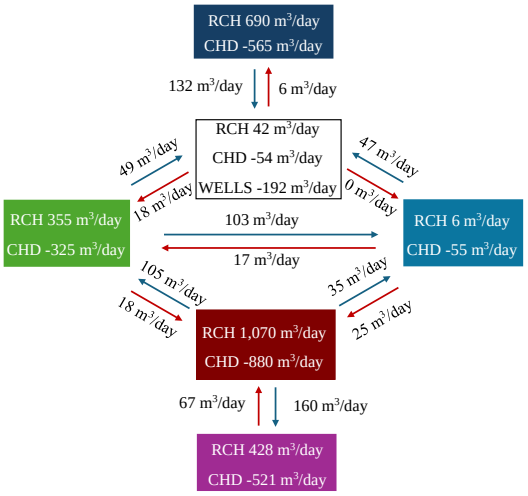

(a) Base Case

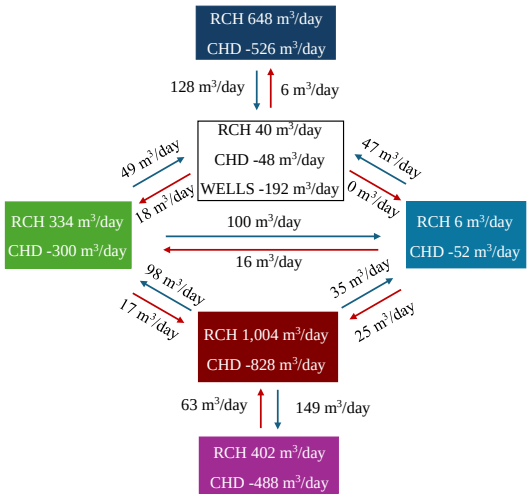

(b) HADGEM2-AO RCP2.6

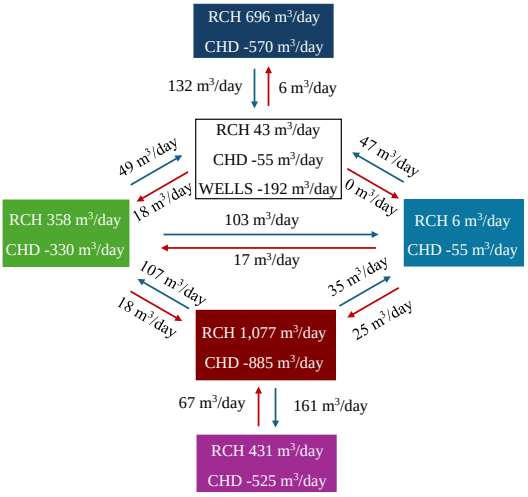

(C) HADGEM2-AO RCP4.5

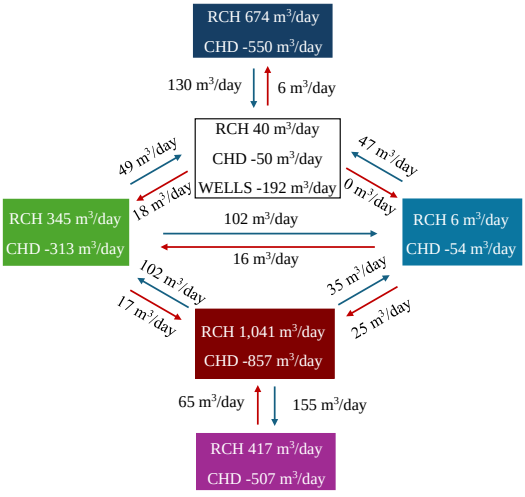

(d) HADGEM2-AO RCP8.5

Fig. 8 Zone budget analysis under climate change scenarios, (a) Base case, (b) HADGEM2-AO RCP2.6, (c) HADGEM2-AO RCP4.5, (d) HADGEM2-AO RCP8.5

ACKNOWLEDGMENTS

We would like to thank the School of Engineering, King Mongkut's Institute of Technology Ladkrabang, and the Thailand Science Research and Innovation (TSRI) for the support through the Fundamental Fund (Grant No. RE-KRIS/FF66/06). We also thank the Land Development Department, the Meteorological Department, the Royal Thai Survey Department, and the Royal Irrigation Department for providing the data used in this study.

REFERENCES

[1] Liu J., Yang H., Gosling S.N., Kummu M., Flörke M., Pfister S., Hanasaki N., Wada Y., Zhang X., Zheng C., Alcamo J., and Oki T., Water Scarcity Assessments in the Past, Present and Future, Earth's Future, Vol. 5, Issue 3, 2017, pp. 545–559. DOI: 10.1002/2016EF000518.

[2] Yamamoto E.M.S., Sayama T., and Takara K., Impact of Rapid Tourism Growth on Water Scarcity in Bali, Indonesia, International Journal of Advances in Engineering and Management (IJAEM), Vol. 3, Issue 6, 2021, pp. 652–660. DOI: 10.51264/inaej. v2i1.14.

[3] Koundouri P., Papadaki L., Pittis N., Karakosta C., Mavrotas G., and Latinopoulos D., Sustainable Water Resources Management in Small Greek Islands under Changing Climate, Water, Vol. 11, Issue 8, 2019, Article No. 1694. DOI: 10.3390/w11081694.

[4] Srisuk J., Seeboonruang U., Tanachaichocksirikun P., and Sirikaew U., A Study of Water Quality for Consumption of Si-Chang Island with Geographic Information System, in Proc. 27th National Convention on Civil Engineering, 2022, pp. WRE11-(1–7). [Online]. Available: https://conference.thaince.org/index.php/ncce27/article/view/1497

[5] Thai Royal Irrigation Department Investigate the Problem of Si Chang Island's Reservoir Being Unable to Store Water. 2021

[6] Kumar M. and Malik R.S., Application of GIS and MODFLOW to Ground Water Hydrology - A Review, Int. J. of Applied Engineering Research, Vol. 11, Issue 4, 2016, pp. 2294–2302.

[7] Mookiah M., Jha S.K. and Biswas A., Assessment of Groundwater Mass Balance and Zone Budget in the Semi-Arid Region: A Case Study of Palar Sub-Basin, Tamil Nadu, India, J. of Earth System Science, Vol. 130, Issue 187, 2021, pp. 1–18.

[8] Morsy S.M., Planning for Groundwater Management Using Visual MODFLOW and Multi-Criteria Decision Analysis: A Case Study of West–West Minya, Egypt, Applied Water Science, Vol. 13, Issue 3, 2023, Article 72.

[9] Khadim F.K., Dokou Z., Lazin R., Bagtzoglou A.C. and Anagnostou E., Groundwater Modeling to Assess Climate Change Impacts and Sustainability in the Tana Basin, Upper Blue Nile, Ethiopia, Sustainability, Vol. 15, Issue 7, 2023, Article 6284.

[10] Taweelarp S., Khebchareon M. and Saenton S., Evaluation of Groundwater Potential and Safe Yield of Heterogeneous Unconsolidated Aquifers in Chiang Mai Basin, Northern Thailand, Water, Vol. 13, Issue 4, 2021, Article 558.

[11] Mahatuay A. and Saraphirom P., Groundwater Modeling for Managed Aquifer Recharge Planning in Ban Nonsamran, Sirindhorn District, Ubon Ratchathani Province, KKU Research Journal (Graduate Studies), Vol. 21, Issue 2, 2021, pp. 45–67.

[12] Kornkul J., Groundwater Balance of Phrae Basin Using MODFLOW and GIS in Changwat Phrae, M.Sc. Thesis, Chulalongkorn University, Bangkok, Thailand, 2013.

[13] Royal Thai Survey Department, Information Service Unit (personal contact), 2021.

[14] Thai Department of Mineral Resources, Geological Map of Chonburi, 2011.

[15] Srisuk K. and Tussanee N. Climate Change and Groundwater Resources in Thailand. Journal of Groundwater Science and Engineering, Vol.5, No.1, 2017, pp. 67–75, [Online]. Available: http://gwse.iheg.org.cn.

[16] Thai Land Department of Groundwater Resources, Groundwater map of Chon Buri Province, 1999.

[17] Thai Meteorological Department, Information Service Unit (personal contact), 2021.

[18] Thai Land Development Department, Land Use Data, 2020. https://www.ldd.go.th/home/.

[19] Tanachaichoksirikun P., Srisuk J., Sirikaew U. and Seeboonruang U., Alternative Approach to Groundwater Modeling in Data-Deficient Regions, in Proc. 14th Int. Conf. on GEOMATE, Pattaya, Thailand, 13–15 November 2024.

[20] Du, X., Xiangqin L., Jiawei H. and Xueyan Y. Improving the Reliability of Numerical Groundwater Modeling in a Data-Sparse Region. Water Vol.10, No.3, 2018, pp. 1–15, doi: 10.3390/w10030289.

[21] Saltelli A. and Annoni P., For Chapter in a Book, Sensitivity Analysis, International Encyclopedia of Statistical Science, Lovric M., Ed., Springer, Berlin Heidelberg, 2011, pp. 1298–1301.

Copyright © Int. J. of GEOMATE All rights reserved, including making copies, unless permission is obtained from the copyright proprietors.

15th Int. Conf. on Geotechnique, Construction Materials & Environment,
Kyoto, Japan, 11-13 November 2025, ISBN 978-4-909106124 C3051

INCREASING AGRICULTURAL LAND PRODUCTIVITY USING A COMBINATION OF RAINFALL SYSTEMS AND CANAL BLOCKING

Robi Sahbar[1], Dinar Dwi Anugerah Putranto[2], Rosidawani[3], Agus Lestari Yuono[4],Riani Muharohmah[5]

[1]Faculty of Engineering, Sriwijaya University, Indonesia;[2,3,4,5]Department of Civil Engineering and Planning, Faculty of Engineering, Sriwijaya University, Indonesia

ABSTRACT

The agricultural productivity of tidal swamp land in the Air Saleh Swamp Irrigation Area (DIR), Banyuasin Regency, South Sumatra Province, Indonesia is still sub-optimal. One of the causes is the lack of irrigation water supply in the 2nd and 3rd planting season. A significant effort to overcome this problem includes the construction of canal blocking that functions to maintain water level during high tide in channel and soil moisture on land used for rice growth. The construction of canal blocking is designed to maintain water level in channel and groundwater on agricultural land covering an area of 144 ha. Therefore, this research aimed to fulfill the availability of irrigation water using a combination of rainfall systems and canal blocking to improve agricultural land productivity. Canal blocking construction was made of coconut tree trunks, which were packed with sacks full of local soil to enhance structural solidity and reduce decomposition. On the outside, sacks were installed containing a mixture of sand and cement which functioned to withstand erosion by water flow. The construction of canal bulkhead was installed with 10-inch PVC pipes draining water into channel to regulate flow level during excessive rainfall. These trunks were used as the main construction material because of local availability, resistance to submersion in water, durability against shear and overturning forces. Furthermore, simulation and optimization of water management system were carried out by modeling using the HEC-RAS program. This allowed for analysis of water level during irrigation with sediment transport and accumulation when flushing and functioning as drainage.

Keywords: Canal Blocking, Productivity, Water Surface Elevation, Sedimentation, HEC-RAS

INTRODUCTION

The Air Saleh Swamp Irrigation Area (DIR) in Banyuasin Regency, South Sumatra Province, Indonesia, is categorized as suboptimal land, facing limitations or constraints in terms of productivity. This land is classified as type C hydrotopography, which has not been flooded by high tide. The groundwater level is less than 50 cm and is dependent on rainwater as a source of irrigation water [1]. Generally, the rainy season occurs from October to April, while the dry season spans from May to September. In this context, the planting pattern that has been implemented at DIR is Rice-Rice rotation, with planting seasons carried out 2 times. Planting Season I (one) is carried out from October to January with agricultural productivity of 5 to 6 tons/ha. Meanwhile, Planting Season II (two) spans from March to June, and agricultural productivity of 2 to 3 tonnes/ha (Survey results, 2025), which is still sub-optimal. To address this limitation, the use of canal blocking has been proven effective. Hapsoh [2] conducted an experiment for chili cultivation in Siak Regency, Riau Province, and produced 14-15 tonnes/ha, compared to when there was no construction. High production from water supply method through canal blocking has increased chili cultivation by expanding cultivated land through the conversion of oil palm land into food crops or horticultural cultivation land, which is more productive [3].

The strategy to increase rice production on sub-optimal land should be a government priority in providing and socializing the appropriate technology during cultivation. The government also needs to maintain the availability of New Superior Variety (VUB) seeds, fertilizers, and agricultural machinery (in Indonesia the same as Alsintan, Beginning, 2023). As a new strategy, construction of canal blocking has a good effect on maintaining groundwater level and keeping the land in wet or humid conditions. When water level is raised to 0.6 m, the wet effect can extend to 200 m perpendicular to canal [4].

Several canal blocking structure technologies have been built in various areas that have sub-optimal land conditions. However, many experienced construction failures due to the use of less suitable materials. Stability of canal bulkhead structure with a span of 5 meters and construction materials that are resistant to safe shear and overturning forces are required. This is because seepage in the downstream part of canal bulkhead will still occur, causing an increase in water level at upstream part and flow time [5]. A previous research had shown that a greater speed of water flow in channel with increasing time correlated with a higher value of erosion depth [6].

Therefore, the use of local fill soil with a permeability value of <0.125 cm/hour was recommended as an embankment body [7].

In an experiment conducted by Ade et al [8]. using a hydraulic simulation process with the HEC-RAS model showed that the average water level was able to exceed the land elevation [8]. However, it was not optimal, as the average height of the inundation was only 0.001 m or 1 mm [9]. From previous research, the results of hydraulic simulations showed that operational losses contributed a significant volume compared to seepage losses in physical infrastructure and management using operator-based and non-automatic control structures [10]. In most of the operating scenarios, the maximum seepage losses was 10%, and the remaining 90% was related to operations. This showed that fluctuation in inflow to canal caused an increase or decrease in operational losses, serving as a determining factor in affecting the total losses.

Controlling water level at the tertiary stage by farmers is essential for successful irrigation systems. To achieve this, a flap gate type is developed, operating predominantly as drainage during rice growth. The model also supplies water when plant enters the generative phase, achieving an average rice production of 7.5 t/ha. This condition shows that with proper water management, balanced fertilizer application, and adaptive rice varieties, cultivation in tidal lowland areas is successful and prevents land shifts [11]. To perform flushing, installing a pump in the middle intake can increase water circulation in canal with a one-way outflow during low tide. Although the inflow depends on the closing gate when in the same position, the volume of rainwater can be discharged for each rainy day [12].

Under existing conditions and network expansion with narrow intake channel, the duration of rainwater deficit tends to be shorter. Therefore, the leaching and drainage aspects require more water storage and wide intake channel. In comparison, flushing criteria require the use of pumps and gates [13]. To maintain the condition of water in each plot of land and tertiary channel, maximum operation of automatic water gate is required. Furthermore, to prevent oxidation of pyrite layer, water level must be above the base elevation [14].

RESEARCH SIGNIFICANCE

Therefore, a flow management method should be adopted to improve system performance and operational losses, by enhancing the operation of water level regulation and canal bulkhead structures [15,16]. There is a need to provide adequate water storage facilities, which can store excess supply during low water demand and shortage. The developed model is expected to help in estimating excess/shortage of water supply in relation to demand, thereby storing excess water for use during periods of high demand [17].

Water storage can help farmers meet their needs, particularly in dry and shortage conditions. Moreover, farmers need to consider the appropriate fertilizer dosage and the use of additional organic materials derived from cultivation residues, which are expected to increase the availability of nutrients in the soil. The use of short-lived and drought-resistant varieties can help overcome the problem of crop failure in the middle stage caused by water scarcity. According to previous research, rainfed rice fields generally have limiting factors for water and nutrients, showing the need for technology to achieve sustainable yields [18].

METHODOLOGY

Research Location

The research location was situated at coordinates Longitude 104° 54’ 39” – 105° 00’ 45” East longitude and between Latitude 2° 41’ 42” – 2° 43’ 11” South latitude (Fig.1). Specifically, the research was performed in Air Saleh Village, Telang District, Banyuasin Regency, South Sumatra Province, Indonesia. To reach the location, the river route is used through a speedboat from Kuto Besak Pier, Palembang City for approximately 2 hours.

Fig.1 3-4-2 Band combination Landsat image, DIR Air Saleh research location

Data

Water Level Data (AWLR)

Water level observations were carried out using an AWLR (Automatic Water Level Recorder) device at 8 points. Measurement data were taken from 2 types of water level measured at the same time. These include groundwater (TMAT), representing the height of water in the ground, and channel water level (TMAS) which is the height of water in channel.

Soil Investigation (Hand Drill and Sondir)

Soil investigation aims to evaluate the condition of soil layer at the research location and determine the depth of hard type. The analysis is carried out to obtain soil parameter data for calculations in planning of canal blocking structure. Sondir testing refers to SNI 2827: 2008 (Indonesian National Standard) to obtain parameters of soil layer penetration resistance in the field using a quasi-static penetration sondir tool. These parameters are cone resistance Cw (qc), shear resistance Tw (fs), shear ratio (Rf), and total soil shear (Tf), which are used for the interpretation of soil layers as part of the design of canal blocking structure foundation. Meanwhile, hand boring testing refers to SNI 4148-1: 2017 (standard for sampling fine-grained soil with thin-walled tubes for geotechnical purposes). The purpose of hand boring testing is to determine soil layer and take samples of disturbed and undisturbed soil for testing physical and engineering properties in the laboratory.

Rain Data

Rain data were taken from the website: POWER DAV: https://power.larc.nasa.gov/data-access-viewer/ National Aeronautics and Space Administration (NASA), with a time interval of 20 years, namely between January 1, 2005, to December 31, 2024. These data included estimates of long-term climatological averages, meteorological quantities, and surface solar energy fluctuations

Canal Blocking

Canal blocking functions to maintain water level when the tide is high in channel and soil moisture in the land needed for rice plant growth. The location of canal blocking structure as shown in Fig. 2 and Fig.3 is on the Main Drainage Channel (SDU-3U) which is +/- 20 m from the Tertiary-1U channel.

Canal blocking construction was made of coconut tree trunks, which were selected as the main material due to availability, resistance to water immersion, strength against shear and overturning forces, and easy workability. The inner filling material of canal blocking was in the form of sacks filled with local soil to achieve solid structure and reduce decomposition. For the outer side, sacks containing a mixture of sand and cement (1: 4) were installed to withstand erosion by water flow (see Fig.4a)

Fig.2 Location of Canal Blocking Placement

As shown in Fig. 4a, the width of canal blocking was 12 m with a height of 2.80 m from the bottom of channel. At the beginning to end of the width, 15-10 inch PVC pipes were installed to allow water to enter channel (Fig. 4c). The pipes also serve as a water retention boundary in the rice plant root zone and drainage when there is excess water during high rainfall.

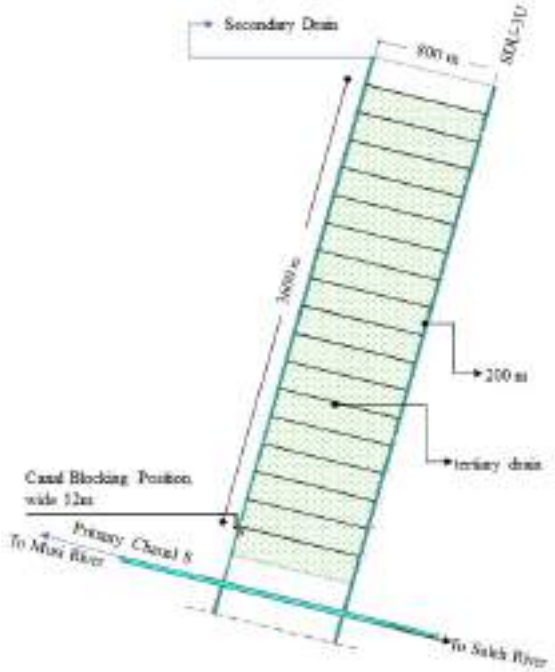

Fig. 3 Installation site for Canal Bulkhead building

The installation of pipes was arranged into 2 rows with different heights (Fig. 4c), namely :

a. The outer part of canal blocking (the beginning of the incoming tide)

(1) The first row of PVC pipes height is set based on the lowest tide level. This allows for high tide to enter, which is + 60 cm from the bottom of channel.

(2) The second row is installed at a height of 153 cm from the bottom of channel which is useful for dividing water pressure load when the tide is high on canal blocking structure.

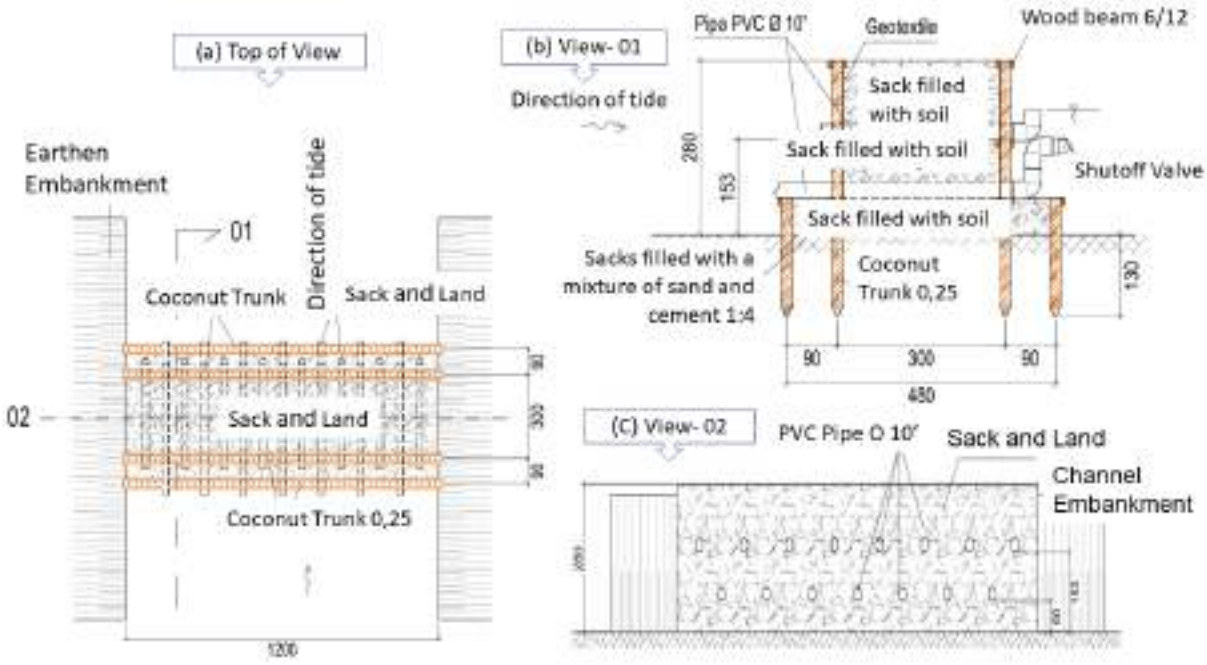

Fig. 4 Canal blocking plan: (a) Top view of canal blocking position;(b) Front view, construction of blocking canal;(c) Front view, PVC pipe placement

b. The inner part of canal blocking (the high tide enters the secondary channel)

(1) On the first row, 2, 10-inch L-Bows (Fig. 4b) are connected and 10-inch PVC pipes are installed, equipped with valves useful for closing when the tide is low.

(2) On the second row (Fig 4b), 10-inch L-Bows (swan model) are connected with a height measured based on the root zone of the rice plant. These L-Bows function to retain water on the land needed for the growth of the rice plant, which is -50 cm from the land elevation.

Implementation Method

Modeling with the HEC-RAS Program is carried out through 2 stages with 3 trial scenarios or implementations, namely:

Stage 1 (existing condition/baseline):
Scenario 1:
(1) Unsteady Flow Type
(2) Boundary Condition:
  a. flow hydrograph (El Nino/dry season)
  b. stage hydrograph (observation of tidal height)
(3) Analysis results:
  a. Water level elevation in channel
  b. Water level elevation on land
  c. Groundwater level elevation

Scenario 2:
(1) Unsteady Flow Type
(2) Boundary Condition:
  a. flow hydrograph (La Nina/rainy season)
  b. stage hydrograph (observation of tidal height)
(3) Analysis results:
  a. Water level elevation in channel
  b. Water level elevation on land
  c. Groundwater level elevation

Scenario 3 :
(1) Unsteady Flow Type
(2) Boundary Condition :
  a. flow hydrograph (Normal Condition
  b. stage hydrograph (observation of tidal height)
(4) Analysis results :
  a. Water level elevation in channel
  b. Water level elevation on land
  c. Groundwater level elevation

Stage 2 (installation of canal blocking)
Scenario 1:
(1) Unsteady Flow Type
(2) Simulation with the installation of canal blocking structure
(3) Boundary Condition:
  a. flow hydrograph (El Nino/dry season)
  b. stage hydrograph (observation of tidal height)
(4) Analysis results:
  a. Water level elevation in channel
  b. Water level elevation on land
  c. Groundwater level elevation

Scenario 2:
(1) Unsteady Flow Type
(2) Simulation of Canal Blocking Structure
(3) Boundary Condition:

a. flow hydrograph (La lina/rainy season)
b. stage hydrograph (observation of tidal height)

(4) Analysis results:
a. Water level elevation in channel
b. Water level elevation on land
c. Groundwater level elevation

Scenario 3:

(1) Unsteady Flow Type

(2) Canal Blocking Building Simulation

(3) Boundary Condition:
a. flow hydrograph (Normal Condition
b. stage hydrograph (observation of tidal height)

(4) Analysis results:
a. Water level elevation in channel
b. Water level elevation on land
c. Groundwater level elevation

RESULT AND DISCUSSION

Rainfall Frequency Analysis

Rainfall frequency analysis was carried out using four methods namely Log Normal Distribution, Log Pearson III Distribution and Gumbel Distribution to predict the probability of rain with a certain intensity in a period of time. The results of the Chi-Square test showed that the best distribution was using Log Pearson III (Table 1), with a Chi-Critical value = 3.841 and a Chi-Square value of 1,500.

Table 1 Chi-Square test CH maximum

Class	P(x >= Xm)		Ef	R (mm)	Of	Ef - Of	$(Ef-Of)^2$ / Ef
5	0,200	0 < P <= 0,2	4,000	83,616	3,000	1,000	0,250
	0,400	0,2 < P <= 0,4	4,000	69,232	6,000	2,000	1,000
	0,600	0,4 < P <= 0,6	4,000	60,888	4,000	0,000	0,000
	0,800	0,6 < P <= 0,8	4,000	54,316	3,000	1,000	0,250
	0,999	0,8 < P <= 0,99	4,000	45,135	4,000	0,000	0,000
			20,000		20,000	Chi-Square	1,500
						DF =	1
						Chi-Critical =	3,841

R= Rainfall; Ef= frequency according to class division; Of= Distribution Frequency; DF= Degrees of Freedom

Table 2 Maximum rainfall return period

P(x >= Xm) Probability	T Repead Period	Rainfall Characteristics (mm) according to Probability							
		Normal		Log-Normal		Gumbel		Log-Person III	
		X_T	K_T	X_T	K_T	X_T	K_T	X_T	K_T
0,9	1,1	40,926	-1,282	47,933	-0,987	45,239	-1,100	50,950	-1,063
0,5	2,	71,423	0,000	68,536	-0,121	67,513	-0,164	64,686	-0,207
0,2	5,	91,450	0,842	86,676	0,641	88,543	0,719	83,616	0,713
0,1	10,	101,919	1,282	97,996	1,117	102,466	1,305	99,318	1,330
0,05	20,	110,564	1,645	108,450	1,556	115,822	1,866	117,000	1,917
0,02	50,	120,294	2,054	121,556	2,107	133,110	2,592	144,285	2,668
0,01	100,	126,781	2,326	131,162	2,510	146,064	3,137	168,549	3,225
0,001	1.000,	144,959	3,090	162,320	3,820	188,870	4,936	279,968	5,044

X_T = Annual rainfall plan; K_T= Frequency factor

Hourly Rainfall Calculation

The calculation of rainfall intensity uses the Mononobe method [19], with return periods of 2 years, 5 years, 10 years, 25 years, 50 years, and 100 years as well as duration ranging from 5 minutes to 360 minutes, as shown in Table 3.

Table 3 Hourly rainfall count

T	(hour)	1	2	3	4	5	6
Distribusi	(%)	0,550	0,143	0,100	0,080	0,067	0,059
R2	42,936	23,615	6,142	4,308	3,430	2,896	2,532
R5	52,051	28,628	7,445	5,223	4,158	3,511	3,069
R10	56,896	31,293	8,138	5,709	4,545	3,838	3,355
R20	60,887	33,488	8,709	6,109	4,864	4,107	3,590
R50	65,326	35,929	9,344	6,555	5,218	4,407	3,852
R100	68,234	37,529	9,760	6,847	5,451	4,603	4,023

Nakayasu Method Unit Hydrograph

This research uses the Nakayatsu unit hydrograph with the dimensions of SCS (Soil Conservation Service) [20].

As a synthetic unit hydrograph, the discharge is expressed as discharge (q) against peak discharge (Qp) and time (t) against the rise time of the unit hydrograph (Tp). When the peak discharge (Qp) and the delay time for an effective rainfall duration are known, the unit hydrograph can be estimated (Fig. 5).

The parameters used to calculate the Nakayasu designed hydrograph are:
Watershed Area : 3.04 Km2
Channel Length (L) : 3.8 Km
Concentration Time (tc) : 0,729
Nakayasu Coefficient (α) : 1,362
Flow coefficient : 0,45

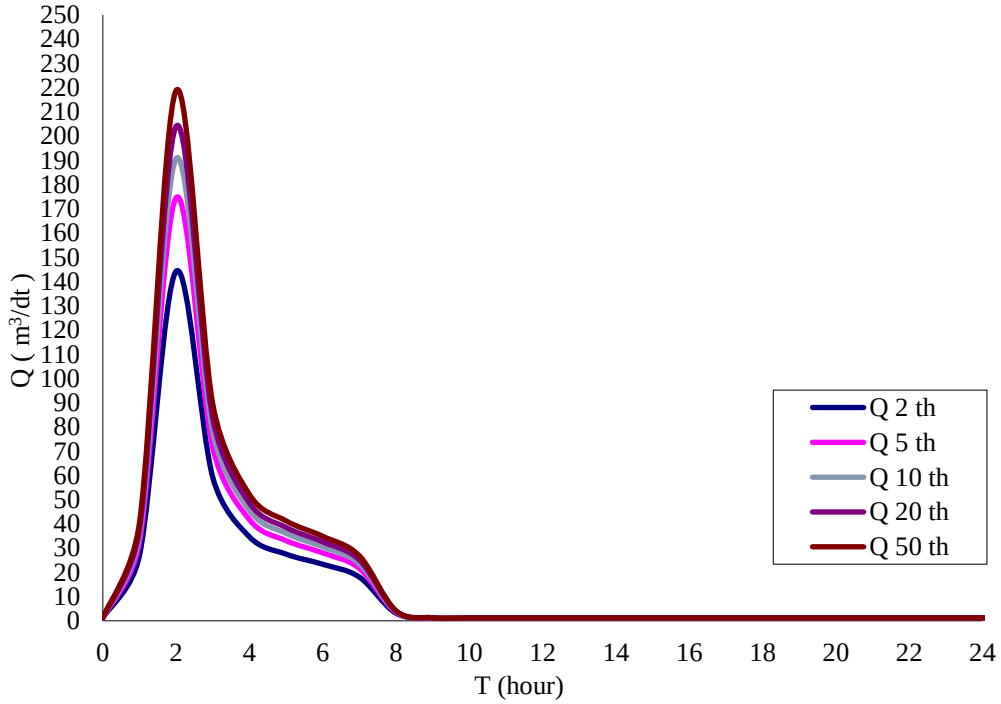

Fig. 5 Flood discharge hydrograph using the Nakayasu method

Analysis of Canal Blocking Modeling

Coconut (Cocos Nucifera) is the only member of the Cocos genus from palm family or Arecaceae. This tree grows in coastal areas and lowlands, with heights ranging from 15 m to 30 m, and trunk diameter of 0.25 m to 0.40 m. The part of the coconut tree trunk that can be used for construction wood (strength class I to IV) is the tip from the base to ¾ of the length and the top from the base to half the length. In this research, the type of coconut tree trunk used for canal blocking structure is arranged with the following provisions:

(1) Channel functions as a navigation path with low to medium usage level.
(2) Canal acts as a barrier downstream of channel where the upstream uses a backfilling compacted peat dam in adaptive and protected areas.
(3) Canal blocking is constructed on channel with a width of > 10 m and a length of 8 m to 50 m.
(4) One end of the coconut pole that will be stuck vertically (hereinafter referred to as the coconut pole tie) is sharpened using an axe. The number and size of the coconut pole ties are made wide at 8 m and the depth of the mineral soil.
(5) The pile driving process takes place until the coconut pole reaches the required depth 2-4 m (mineral soil or the wood can no longer be moved).
(6) The coconut poles that have been installed are connected to the transverse coconut poles (horizontal) using bolts, nuts, and large washers measuring 0.25" x 35-45 cm.
(7) After the wooden construction is ready or finished, the installation of a layer of non-waterproof fabric or geotextile is continued.

The evaluation of canal bulkhead design is carried out to assess whether each part is functioning appropriately, and provide suggestions for improvements. The methods used to evaluate the design of each part are as follows:

Bulkhead subsidence

The method used to evaluate the design of the coconut tree trunk bulkhead is to measure the subsidence and deformation using waterpass as well as visual observations of installed trunk. Measurement of structural subsidence is carried out by comparing the elevation of the structure after completion and during construction. A major impact of structural subsidence is deformation, which refers

to change in shape due to internal or external forces. Based on the results of observations after the installation of the canal divider (January-June, 2025) based on re-measurement of the height of the coconut trunk, using a waterpass, there was a difference in elevation of -2.13 cm.

Maintaining Groundwater/Pool Water Level

Installation of PVC pipes on canal blocking with a 2-row system is effective in reducing water flow during low tide. This maintains fresh water from rain in rice fields and increases water level in the upstream part of canal divider. The change in water level during January–July, 2025, near the canal divider was 0.36–0.48 m. Compared to a distance of approximately 1000 m from the canal divider, it was 0.10–0.12 m.

Reducing flood height or seepage

A strong and precise canal blocking installation system can prevent flooding during high tides and rainfall. Additionally, it is capable of maintaining humidity or water availability for irrigation during the dry season, enabling the achievement of 3 seasons, with a rice-rice-rice planting pattern. The groundwater level in April–July was approximately 0.32–0.14 m only in the area near the canal, which constitutes approximately ¼ of the observation area.

Reducing sedimentation in channel

Installation of canal blocking on secondary channel with long inundation times can cause anaerobic conditions in channel and potentially lead to shallowing or sedimentation, thereby reducing long-term inundation.

CONCLUSIONS

In conclusion, this research explored the potential of irrigation water using a combination of rainfall systems and canal blocking to improve agricultural land productivity. The results obtained were as follows:

(1) Installation of canal blocking on secondary channel in tidal swamp irrigation areas had a positive impact on increasing agricultural land productivity. Planting and harvesting seasons can be done 3 times a year with rice-rice-rice crops.
(2) Proper installation of canal blocking affected the height of water level in channel, land, and groundwater. Effectively, during the second and third planting seasons, groundwater levels can be reached at an average of 0.3–0.12 m. Others are assisted by pumps to raise the water.
(3) Long inundation due to the construction caused excessive shallowing/sediment in channel. On average, shallowing will occur as high as 0.12 – 0.22 m.
(4) Construction of canal blocking on channel with coconut tree trunks had a stronger bearing capacity with a geotextile blanket on the outside to reduce seepage. Average decline, about 0.022 m for a period of about 6 months.

ACKNOWLEDGMENTS

The authors are grateful to the Ministry of Higher Education Science and Technology, Directorate General of Higher Education, Research and Technology, the Republic of Indonesia, who has provided research funding through Fundamental Research grants based on Master Contract No.: 109/C3/DT.05.00/PL/2025, Date : May 28, 2025 and Derivative contract No. 0042.064/UN9/SB3.LPPM. PT/2025, Date June 4,2025.

REFERENCES

[1] Putranto, D.D.A, Sarino, A. Yuono, and A. K. Yudha, “Optimizing the Irrigation Water Needs of Lebak Semendawai Swamp in Increasing Agricultural Production,” *Int. J. Environ. Agric. Biotechnol.*, vol. 5, no. 1, pp. 109–119, 2020, doi: 10.22161/ijeab.51.17.
[2] Kurniawan. N, D. D. A. Putranto, and Sarino, “Water management in the primary channel of Kumpeh Swamp irrigation area,” *Int. J. Sci. Technol. Res.*, vol. 9, no. 3, pp. 3290–3295, 2020.
[3] Noywuli. N *et al.*, “Cultural Translatory of Horticulture Plants in Cold Lands and Cabapatenes,” *Int. J. Life Sci. Agric. Res.*, vol. 03, no. 08, pp. 691–695, 2024, doi: 10.55677/ijlsar/v03i8y2024-09.
[4] Ritzema. H, S. Limin, K. Kusin, J. Jauhiainen, and H. Wösten, “Canal blocking strategies for hydrological restoration of degraded tropical peatlands in Central Kalimantan, Indonesia,” *Catena*, vol. 114, 2014, doi: 10.1016/j.catena.2013.10.009.
[5] Shah. Z, S. Haider, and T. Jafri, “Analysis of seepage loss from concrete lined irrigation canals in Punjab , Pakistan †,” no. July, 2020, doi: 10.1002/ird.2474.
[6] Fraehr. N, Q. J. Wang, W. Wu, and R. Nathan, “Supercharging hydrodynamic inundation models for instant flood insight,” *Nat. Water*, vol. 1, no. 10, pp. 835–843, 2023, doi: 10.1038/s44221-023-00132-2.
[7] Boone. N *et al.*, “The interactions between soil-biosphere-atmosphere land surface model with a multi-energy balance (ISBA-MEB) option in SURFEXv8-Part 1: Model description,” *Geosci. Model Dev.*, vol. 10, no. 2, pp. 843–872, 2017, doi: 10.5194/gmd-10-843-2017.
[8] Ade Tricia Miranda, Dinar D.A Putranto, Taufik A.G, "Flood and Inundation Risk Analysis Due To Potential Land Subsidence on Alluvial Plains" Int.J.Geomate, Vol.28, no. 128, pp. 92-

99, 2025, doi. 10.21660/2025.128.g14224

[9] Sahdar. I, D. Rohmat, W. A. Pranoto, and Solehudin, "Hydraulic Modeling for Flood Control Scenarios in Akelaka Watershed, North Maluku, Indonesia," *Int. J. GEOMATE*, vol. 27, no. 120, pp. 49–59, 2024, doi: 10.21660/2024.120.4450.

[10] Graf. W.N, E. Wohl, T. Sinha, and J. L. Sabo, "Sedimentation and sustainability of western American reservoirs," *Water Resour. Res.*, vol. 46, no. 12, 2010, doi: 10.1029/2009WR008836.

[11] Azargashb Lord. S, S. M. Hashemy Shahdany, and A. Roozbahani, "Minimization of Operational and Seepage Losses in Agricultural Water Distribution Systems Using the Ant Colony Optimization," *Water Resour. Manag.*, vol. 35, no. 3, pp. 827–846, 2021, doi: 10.1007/s11269-020-02744-9.

[12] Komariah. I and T. Matsumoto, "Application of hydrological method for sustainable water management in the Upper-Middle Ciliwung (UMC) river basin, Indonesia," *J. Water Environ. Technol.*, vol. 17, no. 4, pp. 203–217, 2019, doi: 10.2965/jwet.18-003.

[13] Chen. S, F. Zheng, X. Liu, and P. Garambois, "Pressure-balanced Saint–Venant equations for improved asymptotic modelling of pipe flow," *J. Hydro-environment Res.*, vol. 37, pp. 46–56, 2021, doi: https://doi.org/10.1016/j.jher.2021.05.001.

[14] Boening-Ulman. K.M *et al.*, "The potential to manage releases of Bacillus anthracis using bioretention and a high flow media filter: Results of simulated runoff testing with tracer spores Bacillus globigii," *J. Environ. Manage.*, vol. 354, no. September 2023, p. 120286, 2024, doi: 10.1016/j.jenvman.2024.120286.

[15] Barkhordari. S, S. M. Hashemy Shahadany, S. Taghvaeian, A. R. Firoozfar, and J. M. Maestre, "Reducing losses in earthen agricultural water conveyance and distribution systems by employing automatic control systems," *Comput. Electron. Agric.*, vol. 168, p. 105122, 2020, doi: https://doi.org/10.1016/j.compag.2019.105122.

[16] Horton. A.J, J. Lehtinen, and M. Kummu, "Targeted land management strategies could halve peatland fire occurrences in Central Kalimantan, Indonesia," *Commun. Earth Environ.*, vol. 3, no. 1, p. 204, 2022, doi: 10.1038/s43247-022-00534-2.

[17] Sutikno. S, B. Nasrul, H. Gunawan, and R. Jayadi, "The effectiveness of canal blocking for hydrological restoration in tropical peatland," vol. 6003, pp. 1–7, 2019.

[18] Akbari. Z, A. Yari Hesar, N. Siamian, C. Fürst, R. Värnik, and H. Azadi, "Feasibility of using vertical farming in northern Iran: A multiple necessity," *J. Environ. Manage.*, vol. 354, no. April 2023, 2024, doi: 10.1016/j.jenvman.2024.120232.

[19] Ali. S *et al.*, "Planting patterns and deficit irrigation strategies to improve wheat production and water use efficiency under simulated rainfall conditions," *Front. Plant Sci.*, vol. 8, no. August, 2017, doi: 10.3389/fpls.2017.01408.

[20] Lawal. A.I, "A new modification to Mononobe-Okabe's pseudo-static model for passive earth pressure prediction using homogeneous differential equation," *Mech. Res. Commun.*, vol. 116, p. 103760, 2021, doi: https://doi.org/10.1016/j.mechrescom.2021.103760.

[21] Junaidi, D. Daoed, and D. Syandriaji, "Mapping the Flood Inundation Areas Using Hec-Georas At Batang Mahat River," *Int. J. GEOMATE*, vol. 27, no. 121, pp. 111–118, 2024, doi: 10.21660/2024.121.g13324.

Copyright © Int. J. of GEOMATE All rights reserved, including making copies, unless permission is obtained from the copyright proprietors.

15th Int. Conf. on Geotechnique, Construction Materials & Environment, Kyoto, Japan, 11-13 November 2025, ISBN 978-4-909106124 C3051

A SOURCE-DECOUPLED LIGHTGBM FOR BIAS CORRECTION IN CMAQ-SIMULATED $PM_{2.5}$ CONCENTRATIONS OVER THAILAND

Supitcha Sukprasert[1], Pongpisit Thanasutives[2], Shin Araki[3], Katsushige Uranishi[4], Tomohito Matsuo[5], and Hikari Shimadera[6]

[1,3,5,6]Graduate School of Engineering, The University of Osaka, Japan; [2]RIKEN Center for Advanced Intelligence Project (AIP), Japan; [4]Department of Life Science and Biotechnology, The University of Kitakyushu, Japan

ABSTRACT

The Community Multiscale Air Quality (CMAQ) model is widely used for simulating $PM_{2.5}$ concentrations but often suffers from biases due to inaccurate emission inventories and model parameterizations. This study develops a source-decoupled Light Gradient Boosting Machine (LightGBM) that leverages individual emission source contributions as predictors to correct biases in CMAQ-simulated $PM_{2.5}$ over Thailand, with a primary focus on interpretability using SHAP (Shapley Additive exPlanations). The proposed model is trained on three predictors derived from decoupling CMAQ-simulated $PM_{2.5}$ by emission sources, including biomass burning (BB), anthropogenic (AT), and other sources. Hyperparameters are tuned via spatial 5-fold cross-validation on the training set, and final performance is evaluated on a hold-out test set. The proposed model achieves strong performance (R^2 = 0.71 and RMSE = 9.95 μg/m^3), outperforming the CMAQ model (R^2 = 0.07 and RMSE =17.70 μg/m^3). SHAP values analysis shows that the BB-decoupled predictor dominated the bias correction, increasing the predicted values by 4.68 ± 13.45 μg/m^3 in the dry season and reducing by 7.44 ± 1.48 μg/m^3 in the wet season, relative to the model's expected output (~24.56 μg/m^3). SHAP interaction effects suggest a possible overestimation of BB and AT contributions during high $PM_{2.5}$ episodes. Our finding provides insights into how each source contributes to correcting the CMAQ biases and could guide future efforts to refine CMAQ emission inputs.

Keywords: Bias correction, Chemical transport model, Fine particulate matter, LightGBM, Thailand

INTRODUCTION

Fine particulate matter ($PM_{2.5}$) has remained a major air quality concern in Thailand for decades, with the annual average consistently surpassing the World Health Organization guideline of 5 μg/m³ [1]. Major $PM_{2.5}$ sources in Thailand include biomass burning (BB) and anthropogenic (AT) emissions [2]. Studies show that prolonged $PM_{2.5}$ exposure is linked to increased risks of respiratory diseases [3] and mortality risk from cardiovascular diseases [4]. However, these studies often rely on data from sparse air quality monitoring (AQM) stations, which do not fully cover the entire spatial study area, especially in Thailand [5]. This highlights the need for accurate and high-resolution $PM_{2.5}$ data.

Chemical transport models (CTMs), such as the Community Multiscale Air Quality (CMAQ), are widely used to estimate atmospheric pollutants, including $PM_{2.5}$. However, they are prone to biases due to factors, such as poor quality of emission inventories, inaccurate meteorological input, and incomplete chemical mechanisms. For example, the Fire INventory from NCAR (FINN) version 1.5 has been reported to cause underestimation of CTM-simulated $PM_{2.5}$, due to limitations in fire detection [6] and outdated emission factors [2]. It underscores the need for post-processing bias correction.

Several methods have been applied to address bias in CTM outputs, ranging from traditional statistical methods such as linear regression (LR) [7], to more advanced techniques such as the Kalman filter [8] and analog methods [9]. In recent decades, machine learning (ML) models have gained popularity for bias correction. These models adjust CTM outputs based on observed data, similar to LR, but they can learn nonlinearities in the data and usually yield better results [10]. Common ML models are tree-based models (TBMs) [10,11] and deep learning (DL) [12]. TBMs, such as Light Gradient Boosting Machine (LightGBM), are particularly favored for their ease of use, and strong predictive capabilities [13].

However, most ML-based studies treat simulated $PM_{2.5}$ as a single aggregated predictor [10,12], neglecting individual emission sources contributions. This hinders the model's ability to learn source-specific patterns, potentially limiting its performance. In Thailand, BB, in particular, exhibits strong seasonal patterns, peaking during the dry period (mid-October to mid-May) [14]. Our previous work shows that decoupling BB contributions using the CMAQ and incorporating them into a LightGBM model significantly improves its performance [11]. However, the study mainly focuses on performance gains without exploring how source-decoupled predictors influenced the model predictions.

Building upon the prior study, we apply SHapley Additive exPlanations (SHAP), an additive feature

attribution method where the model output is expressed as a linear combination of feature contributions [15], to explain a LightGBM model's behavior. Recognizing that AT emissions are also a major contributor to $PM_{2.5}$, we expand the model input to include decoupled predictors for BB, AT, and other sources. To isolate the role of emission sources, we rely solely on CMAQ-simulated $PM_{2.5}$ as predictors, omitting auxiliary variables such as meteorological and land-use data used in the previous work. This approach allows us to uncover how different emission sources influence bias correction.

RESEARCH SIGNIFICANCE

This study addresses a gap in current ML-based bias correction methods for CTM by incorporating source-specific $PM_{2.5}$ contributions simulated from the CMAQ model into the LightGBM framework. We also demonstrate which source contributions have the greatest impact on the bias correction of the LightGBM model through SHAP analysis. Findings of this study can offer valuable insights for improving ML-based bias correction for CTM and guiding the refinement of emission input for CMAQ simulations.

METHODOLOGY

Study area and observed data

The study area, covering Thailand, was divided into five regions (Fig. 1) based on the Thai Meteorological Department's criteria. Hourly observed $PM_{2.5}$ data were retrieved from the Pollution Control Department and Bangkok Metropolitan Administration. The study period covers three years, from 2019 to 2021. Hourly $PM_{2.5}$ values exceeding 450 μg/m³ (0.00047% of the dataset) were treated as anomalies and excluded. Hourly data were then averaged daily when over 75% of data were available. AQM stations with less than 70% daily $PM_{2.5}$ data each year were further excluded to maintain yearly representativeness.

WRF-CMAQ simulation

Meteorological variables simulated by WRF v.4.3 provided input for CMAQ v.5.3.3 to simulate $PM_{2.5}$ concentrations. WRF-CMAQ was set up with two nested domains that cover Asia with a 45-km grid and Thailand with a 15-km grid resolution, the latter of which serves as the study area. CMAQ outputs at 15-km resolution were resampled to 1-km using bilinear interpolation. The WRF-CMAQ model configurations of this study (i.e., WRF physics schemes, CMAQ chemical mechanisms, and emission inputs) matched those described in [14], except for the BB emissions, which used FINN v.2.5.

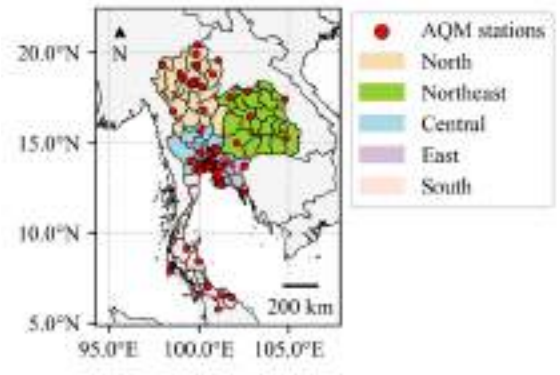

Fig. 1 The study area

To prepare the CMAQ predictors, the CMAQ model was run in three cases: C1) all emissions included, C2) AT emission excluded, and C3) BB emission excluded. The outputs and the calculation of decoupling the emission contribution are outlined in Table 1. CMAQ_PM25 is the baseline predictor, while CMAQ_PM25_AT, CMAQ_PM25_BB, and CMAQ_PM25_Othr represent source-decoupled predictors. Fig. 2 illustrates the daily average of observed $PM_{2.5}$ levels, along with baseline and source-decoupled predictors across all AQM stations.

Table 1 Summary of CMAQ simulation cases and emission decoupling calculations

CMAQ running cases	
C1	All emissions include (CMAQ_PM25)
C2	AT emissions excluded (CMAQ_PM25_No_AT)
C3	BB emissions excluded (CMAQ_PM25_No_BB)
Decoupling individual emission contribution	
C1 – C2	AT contribution (CMAQ_PM25_AT)
C1 – C3	BB contribution (CMAQ_PM25_BB)
C3 – (C1 – C2)	Other contribution (CMAQ_PM25_Othr)

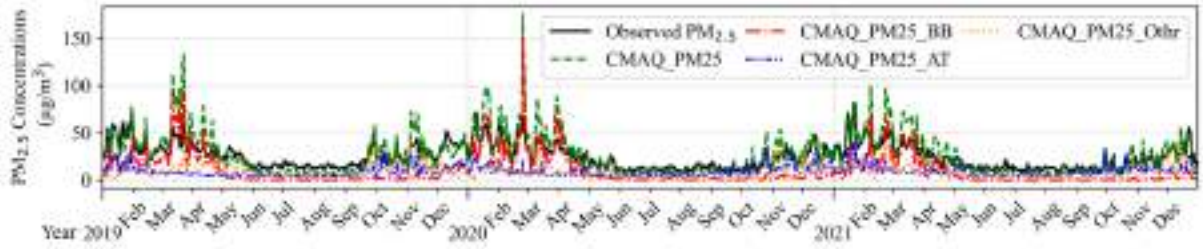

Fig. 2 Daily average of observed and CMAQ-simulated $PM_{2.5}$ across all AQM stations from 2019 to 2021

LightGBM modeling framework

From 103,639 samples across 125 AQM stations, we randomly split the data into training (80%) and test (20%) sets by AQM stations, ensuring regional representation via stratified random sampling. We repeated this process with five different random seeds and developed five independent sub-frameworks for robust results. For each sub-framework, we built two LightGBM models (baseline and source-decoupled models) and tuned hyperparameters independently.

Hyperparameter tuning was performed using a Bayesian optimization algorithm on the baseline predictor, with spatial 5-fold cross-validation (CV), where the data was split based on stations. The optimal hyperparameters were then applied to evaluate both models using spatial CV, as well as overall CV (sample-based splitting). Evaluation metrics included R^2, the root mean square error (RMSE), and the mean absolute error (MAE). The evaluation was conducted over the full period, covering all samples, and across the wet season (mid-May to mid-October) and the dry season (mid-October to mid-May).

Both CV aspects were repeated 50 times with different random seeds, yielding 50 sets of validation scores per model. These scores were compared using a one-tailed paired t-test at a 95% confidence interval to assess differences. Final validation scores were averaged across 50 CV repetitions and five sub-frameworks. The models were finally trained on the full training set and tested on the holdout set, with test scores averaged across the five sub-frameworks.

We applied SHAP to the source-decoupled model using the TreeExplainer [16], with a tree-path dependent approach. It was fitted separately on the training set of each sub-framework, and SHAP values were computed on the corresponding test set. The resulting five SHAP value sets were averaged for overlapping samples to produce final SHAP values.

RESULTS AND DISCUSSION

The LightGBM model performance

As shown in Table 2, the sourced-decoupled model significantly outperforms the baseline model for both overall and spatial CV (p-value < 0.05). This improvement likely stems from the decoupling process, which reveals source-specific patterns and helps the model to better identify and correct CMAQ biases. For example, CMAQ_PM25_BB exhibits a consistent seasonal pattern over three years (Fig. 2), with higher $PM_{2.5}$ levels in the dry season and lower levels in the wet season due to reduced forest fires and agricultural burning, and more frequent rainfall. This seasonal pattern, particularly from BB, enhances the effectiveness of the decoupling process in the dry season. This is reflected in a more pronounced improvement in model performance during this season compared to the wet season.

Interestingly, when using only CMAQ-simulated $PM_{2.5}$ as a predictor, the spatial and overall CV scores are nearly identical. This contrasts with usual trends, where spatial CV scores are usually lower due to the location generalization challenge [11]. By removing other features, such as meteorological and land-use data, the model becomes simpler. This can reduce the risk of overfitting, particularly to spatial patterns learned from those features.

Table 2 Validation scores of the LightGBM models

Period	Model	Overall CV			Spatial CV		
		R^2	RMSE (μg/m^3)	MAE (μg/m^3)	R^2	RMSE (μg/m^3)	MAE (μg/m^3)
Full period	Baseline	0.67	10.82	6.99	0.66	10.94	7.04
	Source-decoupled	0.72	9.92	6.45	0.71	10.18	6.55
Wet season	Baseline	0.44	5.46	4.14	0.43	5.53	4.25
	Source-decoupled	0.47	5.33	4.03	0.45	5.40	4.11
Dry season	Baseline	0.58	13.43	9.06	0.57	13.58	9.07
	Source-decoupled	0.65	12.21	8.20	0.64	12.55	8.32

Table 3 Test scores of the LightGBM and CMAQ models

Period	Model	R^2	RMSE (μg/m^3)	MAE (μg/m^3)
Full period	CMAQ	0.07	17.70	9.98
	Baseline	0.66	10.75	6.90
	Source-decoupled	0.71	9.94	6.44
Wet season	CMAQ	-0.08	7.40	5.77
	Baseline	0.38	5.44	4.17
	Source-decoupled	0.42	5.29	4.05
Dry season	CMAQ model	-0.22	22.38	13.03
	Baseline model	0.58	13.32	8.88
	Source-decoupled	0.64	12.25	8.13

The test scores of both LightGBM models closely align with the validation scores, indicating the models generalize well to unseen data (Table 3). For comparison, the performance of the CMAQ model was evaluated on the same test set and was found to perform worse. Despite this, the LightGBM models show limited performance at high $PM_{2.5}$ ranges in both seasons, tending to underestimate the concentrations of $PM_{2.5}$. This limitation is illustrated by elevated relative MAE (RMAE) computed on test sets in Fig. 3.

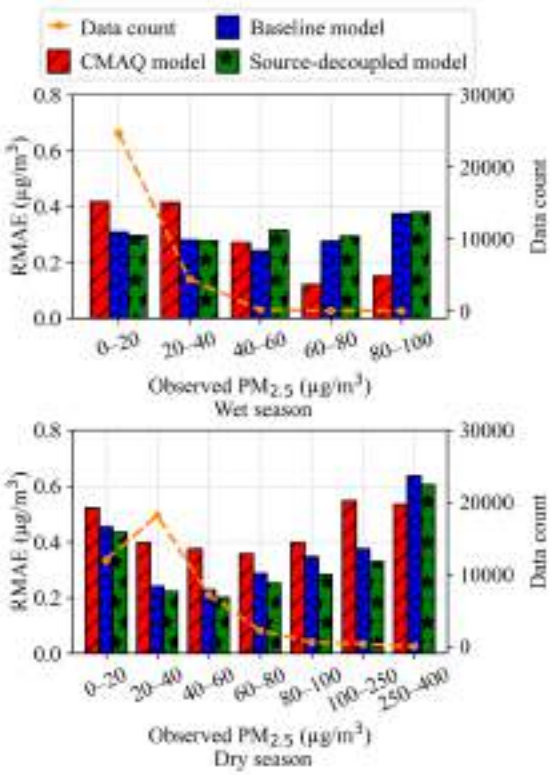

Fig. 3 RMAE values of the CMAQ, baseline and source-decoupled models in the wet and dry seasons

Because high $PM_{2.5}$ concentration events are rare in both seasons and the models were intentionally designed to be simple with few predictors to prevent overfitting, the LightGBM models may have limited performance over such rare events.

SHAP analysis

Mean SHAP and mean |SHAP| values

All decoupled predictors display similar trends, where higher predictor values are associated with higher SHAP values (Fig. 4). Notably, SHAP values for CMAQ_PM25_BB plateau beyond 200 μg/m³. This provides further evidence of the model's limited ability to generalize at extreme $PM_{2.5}$ levels.

Among decoupled predictors, CMAQ_PM25_BB exhibits the highest mean absolute SHAP (mean |SHAP|) value for the full period, indicating that it is the most important predictor, followed by CMAQ_PM25_AT and CMAQ_PM25_Othr as illustrated in the upper plot of Fig. 5. The wet and dry seasons also show the same important order.

To assess the direction of predictor contributions, seasonal analysis was preferred as it helps group SHAP values into more homogeneous ranges and mitigate cancellation when averaged, as shown in the lower plot of Fig. 5. During the wet season, all predictors negatively contribute to $PM_{2.5}$ predictions, reducing them relative to the model's expected output (~24.56 μg/m³). CMAQ_PM25_BB shows the strongest contribution, followed by CMAQ_PM25_AT and CMAQ_PM25_Othr. Conversely, during the dry season, they exhibit positive contributions, with CMAQ_PM25_BB again leading, followed by CMAQ_PM25_Othr and CMAQ_PM25_AT. Overall, CMAQ_PM25_BB emerges as the most influential predictor, consistent with its strong seasonal variability.

CMAQ_PM25_AT and CMAQ_PM25_Othr show similar mean SHAP values, and they have lower contributions than CMAQ_PM25_BB in both seasons. This could be due to their relatively lower concentrations and the lack of a distinctive temporal pattern, unlike CMAQ_PM25_BB. Despite their similar mean SHAP values, CMAQ_PM25_AT yields greater standard deviation compared to CMAQ_PM25_Othr (Fig. 5). One potential reason could be its spatial variability, with higher concentrations in densely populated areas, such as Central Thailand. This spatial pattern may make CMAQ_PM25_AT more useful in predicting $PM_{2.5}$ in these regions.

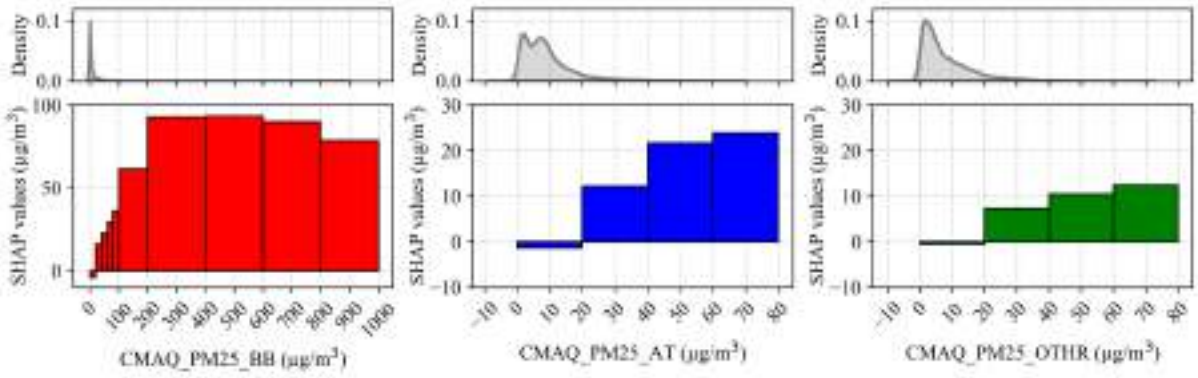

Fig. 4 Bar plot between mean SHAP values and corresponding CMAQ predictor intervals. The upper subplots show the distribution of CMAQ predictor values fitted using Kernel Density Estimation

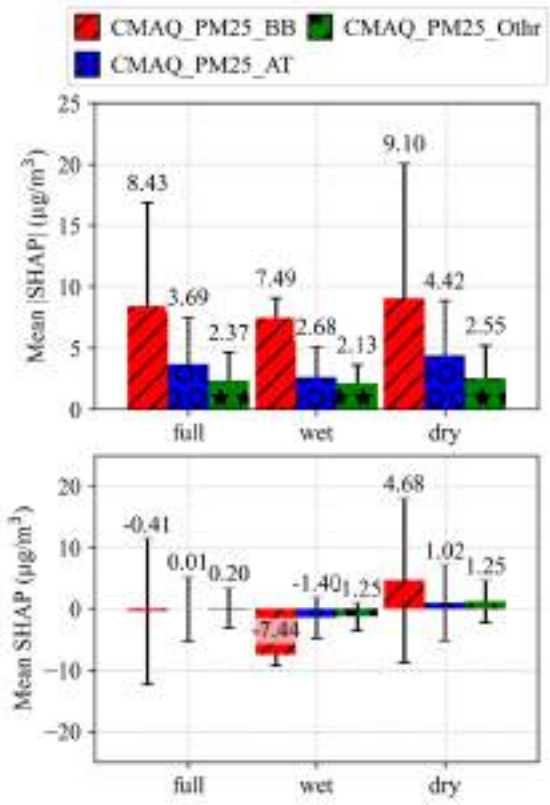

Fig. 5 Mean |SHAP| values (upper) and mean SHAP values (lower) of source-decoupled predictors

SHAP interaction effects

Feature interaction could be another reason for the higher variability of CMAQ_PM25_AT compared to CMAQ_PM25_Othr. We computed pairwise interaction values and found that the interaction between CMAQ_PM25_BB and CMAQ_PM25_AT is the strongest. Fig. 6 visualizes the interaction between them. When CMAQ_PM25_BB values are lower than 75 μg/m³, higher values of CMAQ_PM25_AT are observed with increased SHAP values of CMAQ_PM25_BB, suggesting a synergistic relationship where both predictors together push $PM_{2.5}$ predictions higher. However, when CMAQ_PM25_BB values exceed 75 μg/m³, this relationship reverses. Higher values of CMAQ_PM25_AT are associated with lower SHAP values of CMAQ_PM25_BB.

SHAP values vs. CMAQ's biases

Although SHAP values do not provide direct quantification of biases in the CMAQ model, they provide insights into how LightGBM adjusts its outputs, which can be interpreted to form hypotheses about potential biases in the CMAQ-simulated $PM_{2.5}$ by emission source. The observed interaction between CMAQ_PM25_BB and CMAQ_PM25_AT suggests that the LightGBM model learn to use these predictors to cooperatively correct biases in the CMAQ outputs. Specifically, during high pollution episodes, characterized by elevated values of both predictors, the model assigns relatively lower SHAP values. This pattern suggests the model's attempt to suppress a possible overestimation in the CMAQ model for these sources. Based on the hypothesis, refining the emission inputs or adjusting the CMAQ model parameters, particularly for the BB contribution, which is identified as the most influential predictor, could enhance the performance of the CMAQ model. Moreover, this interaction effect also implies that if future ML modeling frameworks adopt decoupling strategies, it would be worthwhile to consider decoupling both BB and AT emissions because it could enhance the ML model's bias correction efficiency.

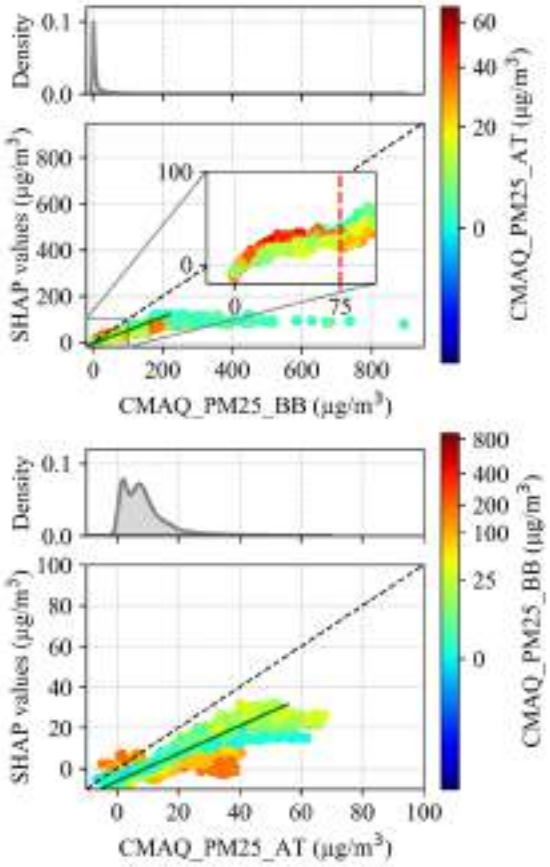

Fig. 6 SHAP Dependence plot for CMAQ_PM25_BB and CMAQ_PM25_AT

CONCLUSIONS

This study developed an interpretable LightGBM model to correct CMAQ-simulated $PM_{2.5}$ in Thailand by using three source-decoupled predictors, including CMAQ_PM25_BB, CMAQ_PM25_AT and CMAQ_PM25_Othr. The model demonstrated strong predictive performance and effectively reduced CMAQ biases, particularly in the dry season. SHAP analysis revealed the dominant influence of

CMAQ_PM25_BB and suggested possible overestimations in the CMAQ model for BB and AT contributions during high pollution episodes. These findings highlight the effectiveness of the decoupling approach for improving CMAQ simulations and offer a practical guide for refining emission inventories and CMAQ model configurations.

Future work could apply DL, such as Neural Networks, to assess whether decoupled emission source predictors remain effective in more complex architectures. Moreover, incorporating additional features (e.g., meteorological and land-use data) may further enhance model performance.

REFERENCES

[1] Pollution Control Department, Thailand State of Pollution Report 2023, Bangkok, AP CONNEX Co., Ltd., 2024, pp. 1-233 (in Thai)

[2] Thongsame W., Henze D. K., Kumar R., Barth M., and Pfister G., Evaluation of WRF-Chem $PM_{2.5}$ simulations in Thailand with different anthropogenic and biomass-burning emissions, Atmospheric Environment: X, Vol. 23, 2024, 100282

[3] Yan M., Ge H., Zhang L., Chen X., Yang X., Liu F., Shan A., Liang F., Li X., Ma Z., Dong G., Liu Y., Chen J., Wang T., Zhao B., Zeng Q., Lu X., Liu Y., and Tang N., Long-term $PM_{2.5}$ exposure in association with chronic respiratory diseases morbidity: A cohort study in Northern China, Ecotoxicology and Environmental Safety, Vol. 244, 2022, 114025

[4] Du Y., Xu X., Chu M., Guo Y., and Wang J., Air particulate matter and cardiovascular disease: the epidemiological, biomedical and clinical evidence, J. Thorac. Dis., Vol. 8, Issue 1, 2016, pp. E8–E19

[5] Mueller W., Vardoulakis S., Steinle S., Loh M., Johnston H. J., Precha N., Kliengchuay W., Sahanavin N., Nakhapakorn K., Sillaparassamee R., Tantrakarnapa K., and Cherrie J. W., A health impact assessment of long-term exposure to particulate air pollution in Thailand, Environ. Res. Lett., Vol. 16, Issue 5, 2021, 055018

[6] Chen L., Gao Y., Ma M., Wang L., Wang Q., Guan S., Yao X., and Gao H., Striking impacts of biomass burning on $PM_{2.5}$ concentrations in Northeast China through the emission inventory improvement, Environmental Pollution, Vol. 318, 2023, 120835

[7] Guillas S., Tiao G. C., Wuebbles D. J., and Zubrow A., Statistical diagnostic and correction of a chemistry-transport model for the prediction of total column ozone, Atmos. Chem. Phys., Vol. 6, Issue 2, 2006, pp. 525–537

[8] Kang D., Mathur R., Rao S. T., and Yu S., Bias adjustment techniques for improving ozone air quality forecasts, J. Geophys. Res., Vol. 113, Issue D23, 2008, D23308

[9] Cheng F.-Y., Feng C.-Y., Yang Z.-M., Hsu C.-H., Chan K.-W., Lee C.-Y., and Chang S.-C., Evaluation of real-time $PM_{2.5}$ forecasts with the WRF-CMAQ modeling system and weather-pattern-dependent bias-adjusted $PM_{2.5}$ forecasts in Taiwan, Atmospheric Environment, Vol. 244, 2021, 117909

[10] Thongthammachart T., Araki S., Shimadera H., Eto S., Matsuo T., and Kondo A., An integrated model combining random forests and WRF/CMAQ model for high accuracy spatiotemporal $PM_{2.5}$ predictions in the Kansai region of Japan, Atmospheric Environment, Vol. 262, 2021, 118620

[11] Sukprasert S., Shimadera H., Araki S., Thongthammachart T., Thanasutives P., Viet Mui L., Matsuo T., and Kondo A., Improving Machine Learning Based $PM_{2.5}$ Prediction by Segregating Biomass Emission Factor from Chemical Transport Model, in Proc. 14th Int. Conf. on Future Environment and Energy, E3S Web of Conferences, Vol. 530, 2024, 01004

[12] Singh D., Choi Y., Park J., Salman A. K., Sayeed A., and Song C. H., Deep-BCSI: A deep learning-based framework for bias correction and spatial imputation of $PM_{2.5}$ concentrations in South Korea, Atmospheric Research, Vol. 301, 2024, 107283

[13] Dai H., Huang G., Wang J., Zeng H., and Zhou F., Spatio-Temporal Characteristics of $PM_{2.5}$ Concentrations in China Based on Multiple Sources of Data and LUR-GBM during 2016–2021, IJERPH, Vol. 19, Issue 10, 2022, 6292

[14] Chantaraprachoom N., Shimadera H., Uranishi K., Mui L. V., Matsuo T., and Kondo A., A Nation-by-Nation Assessment of the Contribution of Southeast Asian Open Biomass Burning to $PM_{2.5}$ in Thailand Using the Community Multiscale Air Quality-Integrated Source Apportionment Method Model, Atmosphere, Vol. 15, Issue 11, 2024, 1358

[15] Lundberg S., and Lee S.-I., A Unified Approach to Interpreting Model Predictions, in Proc. 31st Int. Conf. on Neural Information Processing Systems, Vol. 30, 2017, pp. 4765–4774

[16] Lundberg S. M., Erion G., Chen H., DeGrave A., Prutkin J. M., Nair B., Katz R., Himmelfarb J., Bansal N., and Lee S.-I., From local explanations to global understanding with explainable AI for trees, Nat. Mach. Intell., Vol. 2, Issue 1, 2020, pp. 56–67

Copyright © Int. J. of GEOMATE All rights reserved, including making copies, unless permission is obtained from the copyright proprietors.

15th Int. Conf. on Geotechnique, Construction Materials & Environment,
Kyoto, Japan, 11-13 November 2025, ISBN 978-4-909106124 C3051

EVALUATION OF SEASONAL IMPACTS OF RIVER INFLOW ON PHYSICAL FIELDS IN HARIMA NADA BY USING OCEAN MODEL

Nar WURIGA[1], Valentina PINTOS ANDREOLI[2], Yutaro KOGA[3],
Tomohito MATSUO[1] and Hikari SHIMADERA[1]

[1] Graduate School of Engineering, Osaka University, Osaka, Japan; [2] Port and Airport Research Institute, Kanagawa, Japan; [3] Hyogo Prefectural Institute of Environmental Sciences, Hyogo, Japan

ABSTRACT

Harima Nada, located in the eastern Seto Inland Sea, Japan, has experienced progressive oligotrophication over the past three decades. To support effective nutrient management, it is essential to understand the hydrodynamic variations controlling nutrient transport and distribution. As a semi-enclosed sea with limited exchange with the open ocean, Harima Nada's hydrodynamics are strongly influenced by riverine inflows and sensitive to wind and atmospheric conditions. In this study, we investigated the impacts of river discharge on physical fields of Harima Nada by season using an ocean-atmosphere coupled model combining the Regional Ocean Modeling System (ROMS) and the Weather Research and Forecasting (WRF) model. The impacts were calculated by comparing simulations with and without river inflow in summer and winter. The results showed that river inflow increased sea surface temperature in summer and while it slightly lowered sea surface temperature in winter. Salinity decreased in both seasons, with a stronger surface decline in summer. The model better reproduced temperature and salinity with river inflow than without river inflow condition. In summer, temperature RMSE decreased by 0.26 ℃ and IA increased by 0.03; salinity RMSE decreased by 2.03 PSU and IA increased by 0.59. In winter, temperature RMSE decreased by 0.14 ℃ and IA increased by 0.01; salinity RMSE decreased by 1.02 PSU and IA increased by 0.41. In conclusion, summer's increased river inflow enhances density stratification through sea surface warming and salinity reduction, suppressing vertical mixing, whereas winter's weaker stratification and lower discharge limit these fluvial effects.

Keywords: Harima Nada, River inflow, Ocean model, Physical fields

INTRODUCTION

Although the Seto Inland Sea and Harima Nada experienced eutrophication during rapid economic growth in the 1960s, they have gradually shifted towards low nutrition in recent decades. This ongoing decline in nutrient levels has negatively impacted the fisheries industry and brought increasing attention to nutrient management policies [1-2]. As part of the measures, artificial nutrient supply using treated sewage water is being promoted in Harima Nada. However, the optimal approach for increasing nutrient levels to prevent both eutrophication and oligotrophication has yet to be determined. To address this issue, it is essential to develop an ocean model capable of accurately predicting future nutrient dynamics and their impacts on water quality and marine ecosystems.

Harima Nada, as a semi-enclosed coastal sea surrounded by land, with limited exchange with other open ocean, making it highly sensitive to both terrestrial and atmospheric influences. In such shallow coastal areas, oceanic circulation is strongly affected by atmospheric conditions such as wind speed and air temperature [3], which govern surface mixing and the vertical transport of nutrients-necessitating consideration of short-term ocean-atmospheric interactions [4]. Moreover, the region's geographical setting amplifies its vulnerability to terrestrial inputs, particularly freshwater discharge from rivers. The vertical distribution of these river inflows plays a critical role in shaping density stratification, mixing dynamics, and nutrient transport processes within this semi-enclosed system.

To access the impacts of river discharge on the coastal environment of Harima Nada, this study compares the vertical profiles of temperature, salinity, and density between summer and winter under conditions without and with river input. Seasonal variations in water column structure are examined in light of observational data obtained at a coastal monitoring site.

RESEARCH SIGNIFICANCE

This study highlights the critical role of river inflow in shaping the physical fields of Harima Nada, a semi-enclosed and shallow coastal sea that is particularly sensitive to freshwater inputs. By comparing ocean conditions with and without river inflow, the study demonstrates how riverine input influences stratification and physical structure across different seasons. The inclusion of river inflow improves model performance, leading to more

accurate representations of stratification and circulation patterns. These findings provide a basis for future biogeochemical modeling in Harima Nada, and contribute to ongoing efforts to develop seasonally adaptive management strategies.

METHODOLOGY

Evaluation Method and Model Structure

A coupled ocean-atmospheric model was employed to investigate the physical environment of the Harima Nada region. Model results were compared with observational data from 15 observation points in the Harima Nada area, as shown in Figure 1. Observations were conducted monthly at three depths: surface, middle, and bottom. For model-observation comparison, values were extracted from corresponding depths: 0.5 m (surface), 10 m (middle), and 1 m above the seafloor at each observation site (bottom). Among these sites, one analysis point located in the area most influenced by river inflow was selected for further investigation. At this point, time series over all vertical layers and seasonal mean vertical profiles in summer and winter were analyzed to more clearly demonstrate the impact of river discharge.

Fig.1 Observation Station in Harima Nada and Selected Analysis Point

The structure of the coupled system is illustrated in Figure 2. In this coupled framework, the Weather Research and Forecasting (WRF) model supplies meteorological forcing variables to Regional Ocean Modeling System (ROMS). Utilizing these inputs along with the Coupled Ocean-Atmospheric Response Experiment bulk flux algorithm [5], ROMS computes surface momentum and heat fluxes, which serve as upper boundary conditions for the ocean model, then ROMS sends the updated Sea Surface Temperature (SST) to WRF, closing the air–sea feedback loop. Through this two-way exchange, the coupled model simulates realistic ocean-atmospheric interactions over the Harima Nada region.

Fig.2 Structure of the ROMS-WRF Coupled Model

Model Conditions

Model configurations are summarized in Table 1. The simulation was conducted from December 2009 to November 2010, with a spin-up period starting from June 2009 to allow model stabilization. Since Harima Nada is a very shallow sea, equal vertical layer thicknesses were applied in the ocean model to ensure numerical stability and facilitate consistent interpretation of the model outputs.

Table 1 Model configurations applied to the ROMS - WRF coupled model for Harima Nada

ROMS model		
Horizontal domain		the Seto Inland Sea
Horizontal grid number		200 × 100
Horizontal resolution		3.0 km
Vertical layer number		32
Vertical distribution		Equal Layer Thickness
Boundary and initial conditions	Ocean boundary and initial	HYCOM-NCODA (1hour, 1/12°)
	Tidal	TPXO9 Atlas v.5
	River	1. without river input 2. with river input
WRF model		
Horizontal domain		the entire western Japan
Horizontal resolution		6.0 km
Vertical layer number		30
Boundary and initial conditions		ERA5
Physics option	microphysics	Morrison 2-moment sheme
	cumulus	no cumulus
	planetary boundary layer	MYNN3
	land-surface	Noah LSM
	radiation	RRTMG

River Boundary Conditions

The river boundary conditions are summarized in Table 2. The model accounts not only for major rivers flowing directly into Harima Nada but also incorporates key rivers from adjacent coastal areas to better capture the regional freshwater influence.

To account for the buoyancy-driven spread of freshwater, a top-biased vertical distribution was applied, with values decreasing from surface to bottom.

To better understand the seasonal influence of

river discharge, this study also incorporated time-varying river temperatures. Figure 3 shows time series of river discharge, river temperature, and sea surface temperature for all rivers, including those outside Harima Nada.

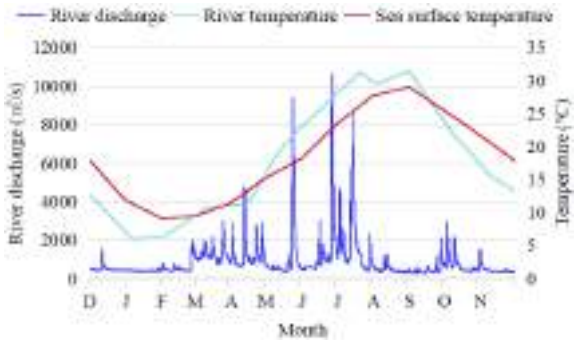

Fig.3 Time series of river discharge [6-7], river temperature [7] and sea surface temperature [8] of study area

Based on these settings, the with river simulation was conducted and compared to the without river inflow conditions for two representative seasons: winter, when river temperature and discharge was low (December, 2009 - January, 2010), and summer, when both were high (June, 2010 - July, 2010). The comparison focused on the vertical distributions of temperature, salinity, and density.

Table 2 The river boundary conditions

River boundary conditions	
Number of rivers	18 rivers, including 11 that flows directly into Harima Nada and 7 from neighboring coastal regions
River discharge	Results from Modified Hydro–BEAM and Water Information system
River temperature	Monthly water temperature values of the Kako River
PSU	0
River input algorithm	Volume vertical influx
River vertical distribution	Discharge decreases gradually from the surface to the bottom

RESULTS AND DISCUSSION

The model's overall reproducibility for temperature and salinity improved when river inflow was included, as indicated by the statistical indicators in Table 3 and Table 4, which present seasonal statistical indicators for temperature and salinity, respectively. The statistical indicators were calculated based on comparisons between model outputs and observational data at 15 sites, with monthly observations at three depths (surface, middle and bottom). For each season-summer (June-July) and winter (December-January) a total of 90 samples per variable were used (15 sites × 3 depths × 2 months). For the entire year (12 months), the sample size increased to 540 per variable. One sample corresponds to a model-observation pair at a specific site, depth, and month.

The results indicate that the inclusion of river inflow significantly improved the model's reproducibility across both summer and winter seasons, with particularly notable enhancements in salinity.

In summer, the temperature reproducibility improved with Root Mean Square Error (RMSE) reduction of 0.26 ℃ and an increase in Index of Agreement (IA) by 0.03, while salinity showed RMSE reduced 2.03 PSU and IA increase of 0.59. In winter, the improvements were slightly smaller: temperature RMSE decreased by 0.14 ℃ and IA increased by 0.01; salinity RMSE decreased by 1.02 PSU with an IA increase by 0.41.

These results suggest that increased river discharge during summer enhances density stratification by warming the sea surface and reducing salinity, thereby suppressing vertical mixing. In contrast, winter conditions with lower discharge and weaker stratification limit the extent of these fluvial effects.

To further clarify the seasonal impact of river inflow, the following sections present detailed comparisons for each physical variable, focusing on water temperature, salinity and density.

Table 3 Reproducibility metrics for simulated water temperature

	River Conditions	R	RMSE	MAE	IA
Summer	Without river inflow	0.92	1.58	1.28	0.91
	With river inflow	0.92	1.32	1.05	0.94
Winter	Without river inflow	0.99	0.55	0.46	0.99
	With river inflow	1.00	0.41	0.34	1.00
All period	Without river inflow	0.99	1.23	0.96	0.99
	With river inflow	0.99	1.27	0.98	0.99

Table 4 Reproducibility metrics for simulated water salinity

	River Conditions	R	RMSE	MAE	IA
Summer	Without river inflow	0.69	2.75	2.58	0.32
	With river inflow	0.86	0.68	0.45	0.91
Winter	Without river inflow	0.66	1.35	1.34	0.17
	With river inflow	0.52	0.33	0.25	0.58
All period	Without river inflow	0.64	2.01	1.90	0.36
	With river inflow	0.82	0.51	0.37	0.89

Water Temperature

River inflow affects seawater temperature through the input of freshwater with different thermal properties. Figure 4 compares the vertical distribution of summer-averaged water temperature over winter and summer, at the analysis point shown in Figure 1, under with and without river conditions. The results demonstrate that river inflow elevates surface temperatures through the input of relatively warmer freshwater, while deeper layers show minimal thermal response. This differential heating pattern confirms that the thermal influence of river discharge is predominantly confined to the upper water column, thereby strengthening vertical stratification during summer months.

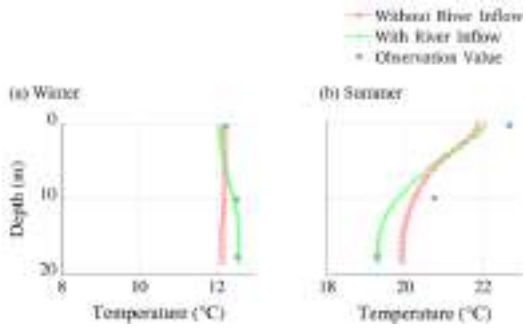

Fig.4 Comparison of average vertical temperature profiles

The summer-averaged vertical profile highlights the vertical structure of temperature differences caused by river inflow. Figure 5 show time series of the vertical temperature distribution at the analysis point for winter and summer, under both with and without river conditions. The results reveal a clear seasonal contrast in river-induced thermal effects. During winter, although river water is colder than seawater, its limited discharge volume and low density prevent significant vertical mixing, causing the colder freshwater to remain confined to the surface layer. In contrast, summer conditions exhibit pronounced surface warming due to both increased river discharge and higher freshwater temperatures. The combination of greater flow volumes and enhanced buoyancy results in stable stratification, with warm surface waters overriding cooler subsurface layers. This seasonal pattern demonstrates how variations in both temperature and discharge magnitude jointly control the vertical thermal structure of coastal waters.

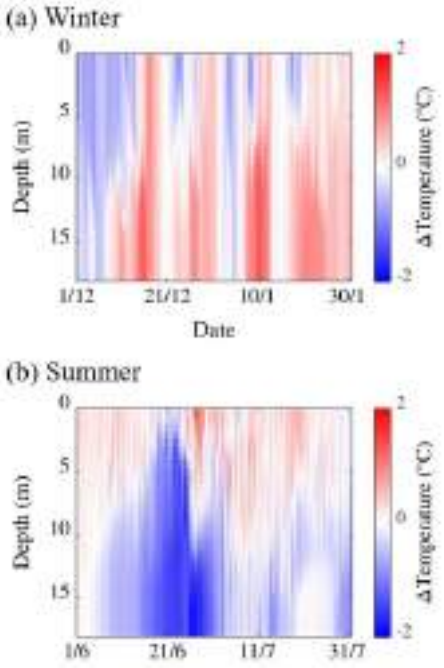

Fig.5 Time series of full-depth temperature differences (with river inflow – without river inflow)

Water Salinity

Riverine inputs not only affect seawater temperature, but also significantly alter the salinity structure of nearshore waters through the supply of freshwater. Figure 6 compares the vertical distribution of salinity averaged over winter and summer, under with and without river conditions, at the analysis point shown in Figure 1. The results show that river inflow clearly decreases surface salinity, with the effect being stronger in summer due to enhanced stratification. In contrast, salinity differences are more moderate in winter, likely due to increased vertical mixing and lower river discharge.

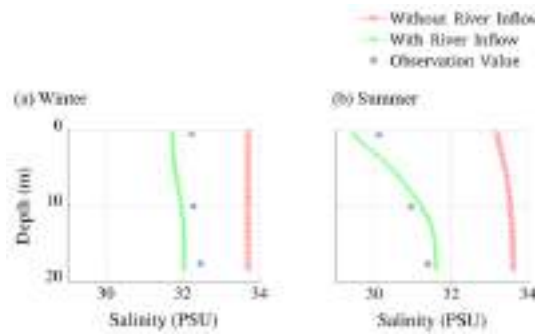

Fig.6 Comparison of average vertical salinity profiles

To obtain a more complete understanding of salinity variation, time series data were also examined. Figure 7 present the time series of vertical salinity profiles at the analysis point during winter and summer, under both river conditions. Showing that with riverine conditions, surface salinity significantly decreases in summer, forming a distinct freshwater layer, while in winter, although less diluted, a decrease in surface salinity and an enhancement of salinity leapfrogging can still be observed. This suggests that river inflow not only affects surface salinity, but also strengthens the stratification structure of the water column.

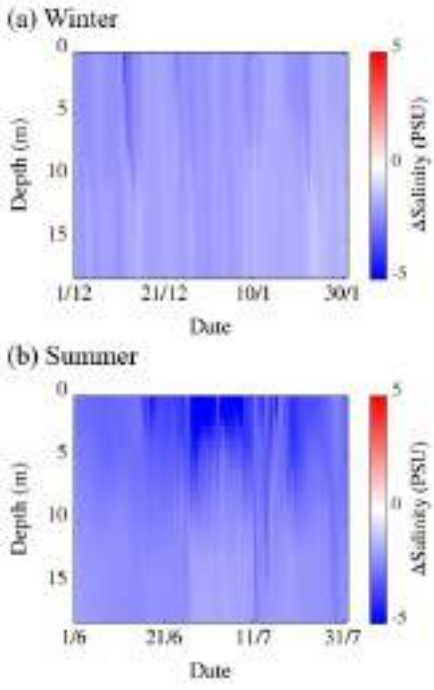

Fig.7 Time series of full-depth salinity differences (with river inflow – without river inflow)

Water Density

The density of seawater is affected by a combination of temperature and salinity. In general, the lower the temperature, the higher the density; the higher the salinity, the higher the density. Thus, river inflow, by bringing freshwater with low salinity and high temperature, creates a lighter water column in the nearshore region, which in turn alters the vertical density structure of the water column and affects the mixing state of the upper and lower water column.

Figure 8 compares the vertical distribution of mean density in summer and winter under with and without river conditions. The results show that in the summer with a river, the density of the surface layer is significantly lower than that of the bottom layer, and the location of the density jumps is clear, with obvious stratification structure; while in the winter, the overall density distribution is much smoother, especially in the without river inflow condition, and there is almost no visible jump structure. This suggests that river inflow enhances seasonal stratification, especially in summer, and has a particularly strong effect on the vertical stability of seawater.

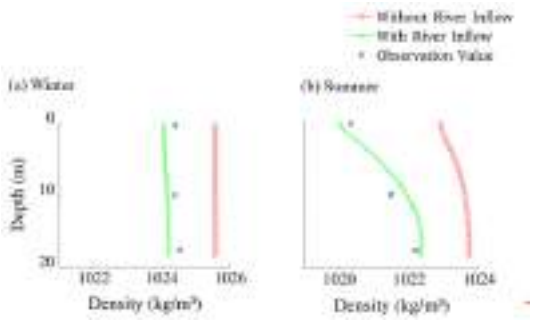

Fig.8 Comparison of average vertical density profiles

Furthermore, to quantify the strength of density lamination, the Brunt-Väisälä oscillation frequency (N^2) is often used as a measure of the vertical stability of the water column. It is defined as follows [9]:

$$N^2 = -\frac{g}{\rho_0} \cdot \frac{d\rho}{dz} \qquad (1)$$

where g is gravitational acceleration (m/s²), ρ_0 is reference density (kg/m³), and $d\rho/dz$ is the vertical gradient of density (kg/m⁴), S_o is the sea water density. The larger the N^2, the more stable the stratification of the water column is and the more difficult it is to mix the upper and lower layers. This indicator can effectively reflect the combined effects of temperature and salinity changes on the density structure.

Figure 9 shows the time-series variation of N^2 in summer and winter (with and without river inflow

conditions). It can be seen that the stability of stratification is generally higher in summer than in winter, with or without rivers, which mainly stems from the fact that the seawater becomes lighter by heat in summer, while the warm water and large amount of freshwater imported by rivers enhances the buoyancy of the upper water body, resulting in a clear stratification structure with a clear inhibition of upward and downward mixing due to the increase in the difference in density between the surface layer and the bottom layer. Comparatively, in winter, water bodies under no river conditions produced homogeneous, well-mixed water columns, while river inputs maintained weak stratification through surface freshening despite colder temperatures.

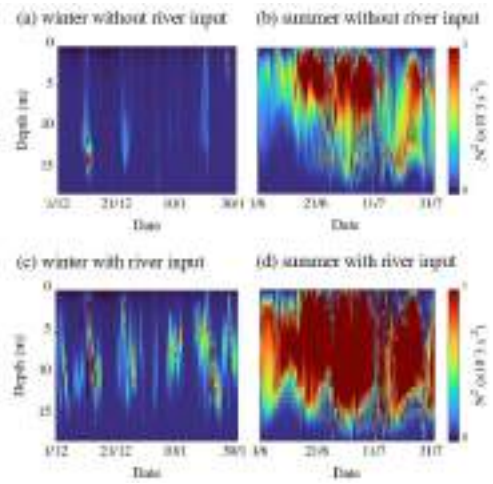

Fig.9 Time-series variation of Brunt - Väisälä frequency squared (N^2) under different river discharge and seasonal conditions

CONCLUSIONS

This study quantifies river inflow's control on coastal stratification using a coupled ocean-atmospheric model. Results reveal pronounced seasonal effects: summer's warm, high-discharge conditions create strong stratification through surface warming and freshening, while winter's reduced inflow maintains weak but persistent freshening. River inputs thus critically modulate nearshore physical structure year-round. According to the simulation results, river inflow strengthens vertical stratification in summer and contributes to moderate desalination in winter, shaping nearshore physical structure throughout the year. The model successfully reproduced these seasonal patterns, demonstrating good agreement with observations.

REFERENCES

[1] Yamamoto T, Oligotrophication of the Seto Inland Sea - Revisited. Journal of the JIME, Vol. 49, No. 4 (2014)

[2] Abo, K., & Yamamoto, T. (2019). Oligotrophication and its measures in the Seto Inland Sea, Japan. Bulletin of the Japanese Fisheries Research and Education Agency, 49, 21-26

[3] Abo, K., Akiyama S., Harada K., Nakaji Y., Hayashi H., Murata K., Wanishi A., Ishikawa Y., Masui T., Nishikawa S., Yamada K., Noda M and Tokumitsu S., Long-Term Variations in Water Quality and Causal Factors in the Seto Inland Sea, Japan. Bulletin on Coastal Oceanography, Vol.55, No.2, 101-111, 2018

[4] PINTOS ANDREOLI Valentina, Shimadera H., Yasuga H., Koga Y., Suzuki M., and Kondo A., Seasonal Study of the Kako River Discharge Dynamics into Harima Nada Using a Coupled Atmospheric-Marine Model, Water, Vol. 16, 614, 2024

[5] John C. Warner., Brandy Armstrong., Ruoying He and Joseph B. Zambon., Development of a Coupled Ocean-Atmosphere-Wave–Sediment Transport (COAWST) Modeling System, Ocean Modelling 35, pp. 230-244, 2010

[6] Pintos Andreoli, V. et al. (2021). Numerical Assessment of Total Nitrogen (Tn) Load Discharged from Rivers into Harima-Nada, the Seto Inland Sea, Using A Numerical Coupled Hydrological-Water Quality Model. IOP Conference Series: Earth and Environmental Science, 801, 012009

[7] Ministry of Land, Infrastructure, Transport and Tourism, Water Information System

[8] Takakura R., Miyahara K. and Miyada K., Comparing Statistical Evaluations of Water Temperature in Harima Nada, Hyogo Prefecture, Bulletin of the Hyogo Prefectural Technology Center for Agriculture, Forestry and Fisheries, 3 : 8-17, 2020

[9] Brassard, P., Fontaine, G., Wesemael, F., Kawaler, S. D., & Tassoul, M., Adiabatic properties of pulsating DA white dwarfs. I - The treatment of the Brunt-Vaisala frequency and the region of period formation, Astrophysical Journal, Part 1 (ISSN 0004-637X), vol. 367, Feb. 1, 1991, p. 601-611

Copyright © Int. J. of GEOMATE All rights reserved, including making copies, unless permission is obtained from the copyright proprietors.

15th Int. Conf. on Geotechnique, Construction Materials & Environment, Kyoto, Japan, 11-13 November 2025, ISBN 978-4-909106124 C3051

ELECTRIC VEHICLE SERVICE CENTRE (EVSC) FACILITIES OPTIMIZATION IN JAKARTA USING GEOGRAPHIC INFORMATION SYSTEMS (GIS)

Jiang Liangliang[1], Lita Sari Barus[1], Irene Sondang Fitrinitia[1], Fidan Safira[1] and Luzern Yuven Luis[2]

[1] School of Strategic and Global Studies, Universitas Indonesia; [2] School of Mathematics Sciences, Zhejiang University

ABSTRACT

Cities that continue to rely on fossil fuel-powered cars, contributing to greenhouse gas emissions and climate change, face significant challenges regarding green transportation. In addition to the growing dependence on fossil fuels, the fluctuating prices of these fuels and air pollution from traditional transportation severely impact public health. These issues can be addressed by adopting electric vehicle (EV) technology to replace fossil fuel-powered cars. Adequate service center facilities are essential for promoting EV adoption and fostering a sustainable transportation ecosystem. The characteristics of a site are vital for constructing EVSCs. This study aims to identify suitable locations and environments for EVSCs in Jakarta Province. Various data sources, including the Detailed Spatial Plan (RDSP) of the Special Region of Jakarta Province, existing condition maps, and population density, are utilized to optimize the development of EVSCs using overlapping map techniques (Geographic Information Systems). Furthermore, this study compares the characteristics of current EVSC locations in Jakarta with those in Hefei, China. Hefei City is well-established in achieving high EV adoption, indicating it has sufficient EVSC facilities to meet users' charging needs. The findings suggest that the placement of EVSC facilities must consider major highways, commercial buildings, retail businesses, and development and conservation areas. Adequate EVSC facilities in appropriate locations within the Jakarta area are crucial for meeting users' demands for green mobility.

Keywords: Electric Vehicle, Service Centre, Green Transportation, Facilities, Geography Information System (GIS)

INTRODUCTION

Climate change and rising greenhouse gas emissions are becoming pressing worldwide issues, particularly in urban regions that continue to rely on fossil fuel vehicles [1]. To address environmental concerns, air pollution, and reliance on fossil fuels, several major cities, including Jakarta, have begun to shift to sustainable transportation systems through the use of electric vehicles (EVs).

However, the availability of vehicle units is not the only factor determining the effective implementation of electric vehicles; the supporting infrastructure must also be ready. The Electric Vehicle Service Center (EVSC) is a critical component of such infrastructure, as it ensures the convenience, safety, and dependability of electric vehicle operations [2]. EVSCs offer vehicle testing, repair, and maintenance services, and act as a starting point for the recycling of end-of-life power batteries [3]. As a result, a fixed and strategic site for the EVSC is critical to ensuring the efficiency of the after-sales service chain.

The availability and equitable distribution of EVSCs is a key factor in driving widespread adoption of electric vehicles [3]. In Jakarta, the challenge is that the number of EVSCs is still limited and unevenly distributed. In addition, the absence of a comprehensive spatial database of ideal locations for the development of these facilities further complicates efforts to expand the EVSC network.

As a result, a data-driven and spatial strategy is required to establish the ideal location for EVSC development in Jakarta. This study aims to identify and optimize the placement of EVSC facilities using a Geographic Information System (GIS)-based spatial overlay method. For contrast, this study also looks at Hefei City, China, which is noted for having one of the highest rates of electric vehicle adoption and a robust supporting infrastructure system.

This method should create a more strategic, adaptive, and long-term EVSC deployment planning model. This study's findings are projected to make a substantial contribution to the formulation of environmentally friendly transportation policy and increase city infrastructure readiness for an era of inclusive and efficient car electrification.

RESEARCH SIGNIFICANCE

Jakarta, the country's capital and commercial hub, presents a significant challenge in developing an environmentally friendly transportation infrastructure. With a land area of 661.52 km² and 159,083 electric vehicle (EV) users as of April 2024, the city has significant potential to shift to a sustainable mobility system. However, supporting infrastructure in the form of Electric Vehicle Service Centers (EVSC) is

still limited, with only five service locations accessible, all from the Wuling brand. On average, one EVSC in Jakarta serves around 31,800 people and covers a 132.3 km² area, making it unsuitable for providing convenient and efficient electric car services.

Fig.1 Map of Jakarta's Administrative Boundaries

For instance, Hefei City in China, with an area of 11,434 km², has erected at least eight EVSCs for the Wuling brand, each having an average service range of 1.43 km. Hefei is not only geographically larger, but it is also actively developing a national EV ecosystem through progressive laws and full backing from the municipal administration. The goal of producing 1 million electric vehicles by 2025 solidifies Hefei's status as a role model for the creation of a green metropolis based on transportation electrification [4].

Fig.2 Map of Hefei's Administrative Boundaries

Table 1. Comparison of Jakarta and Hefei areas

City	Area	Total EVSC Wuling	Average
Jakarta	661,52km2	5	132,3km
Hefei	11,434km2	8	1,43km

This number reflects a relatively low EVSC density of only one EVSC serving over 31,800 EV customers and covers a huge area that is disproportionate to everyday mobility needs and supporting infrastructure. Hefei, on the other hand, is not only physically larger, but it has also established a progressive EV ecosystem with higher EVSC density and aggressive national production targets.

This study employed a GIS-based spatial overlay analysis to identify optimal locations for the development of EVSCs in DKI Jakarta. The analysis integrated multiple spatial layers, including the distribution of existing EVSCs, population density, the detailed land use plan, and the road network. Data were validated to comply with Jakarta Satu geospatial standards, followed by data cleaning, clipping, simplification, and conversion to spatial formats. The spatial analysis followed a three-stage GIS approach:

1. Intersection: Identified overlapping areas between existing EVSC locations and urban infrastructure layers.
2. Buffer (5 km): Created service radii around existing EVSCs based on urban mobility standards, representing optimal user accessibility.
3. Clip & Merge: Integrated multiple geospatial datasets to generate a composite priority map, highlighting underserved regions for future development.

This approach ensures a data-driven foundation for identifying EVSC development zones that are both technically feasible and socially impactful. A composite suitability score was generated for each spatial unit to evaluate the level of demand and accessibility for EVSC deployment. The results were then validated against secondary data sources and mobility patterns, and the outcomes were presented as thematic maps and analytical tables to inform strategic, data-driven EVSC planning across Jakarta.

Spatial Distribution and Coverage Analysis of Existing EVSC Facilities in Jakarta

To support the spatial analysis and service coverage mapping, a comprehensive inventory of existing Electric Vehicle Service Centers (EVSCs) in DKI Jakarta was compiled. The dataset includes 15 service centers operating under various operators, with Wuling identified as the dominant brand currently providing dedicated EV servicing infrastructure. Each entry in the table presents the name of the location, full address, and corresponding geospatial coordinates (latitude and longitude) for spatial integration within GIS-based analysis.

Table 2. Existing Wuling EVSC Facilities in Jakarta

No	Area	Location	Latitude	Longitude
1	Arista Cengkareng	Jl. Kapuk Cengkareng No. 7, RT 7/RW 14, Cengkareng, Kota Jakarta Barat 11730	-6.1301	106.728
2	Prima Kebon Jeruk	Jl. Panjang No. 46, RT 006/RW 001, Kedoya	-6.1892	106.7705

		Selatan, Kec. Kebon Jeruk, Jakarta Barat, DKI Jakarta 11520		
3	Arista P. Jayakarta	Jl. Pangeran Jayakarta No. 33, Pinangsia, Taman Sari, Jakarta Barat 10730	-6.1361	106.8293
4	Arista Garuda	Jl. Garuda No. 74, Kemayoran, Jakarta Pusat 10620	-6.1426	106.8469
5	Prima Harmoni	Jl. Balikpapan No.11, RT 08/RW 06, Petojo Selatan, Gambir, Jakarta Pusat, DKI Jakarta 10160	-6.1604	106.8196
6	Maju Motor Senayan	Jl. Asia Afrika No. 17 RT.001 RW.003 Kel. Gelora, Kec. Tanah Abang, Jakarta Pusat 10270	-6.2166	106.8007
7	Prima Fatmawati	Jl. RS. Fatmawati No. 45 A E RT.002/RW.005, Cipete Selatan, Cilandak, Kota Jakarta Selatan 12411	-6.285	106.792
8	Pegasus Lenteng Agung	Jl. Raya Lenteng Agung No. 8 RT 3/RW 1, Lenteng Agung, Jagakarsa, Jakarta Selatan, DKI Jakarta 12610	-6.3099	106.8206
9	BZHC Pondok Indah	Jl. Sultan Iskandar Muda No.Kavling 9, RT.9/RW.1, Kby. Lama Sel., Kec. Kby. Lama, Kota Jakarta Selatan, Daerah Khusus Ibukota Jakarta 12310	-6.2543	106.7793
10	Arista Kalimalang	Jl. Raya Kalimalang No. 20A, Duren Sawit, Jakarta Timur 13440	-6.2455	106.9093

These facilities are dispersed across multiple municipalities, including West Jakarta, Central Jakarta, East Jakarta, South Jakarta, and North Jakarta, though the distribution remains relatively uneven.

The spatial analysis assessed the service coverage and unmet demand for Electric Vehicle Service Centers (EVSC) in Jakarta. The study was performed using a three-step Geographic Information System (GIS)- based approach: Intersection, Buffer, and Clip and merge. The first stage, Intersection, maps the current distribution of EVSCs across Jakarta's subdistricts, represented by red squares. This initial visualization highlights the existing service network's spatial concentration and potential gaps.

Fig.3 Intersection Process of EVSC in Jakarta

The second stage involves applying a 5-kilometer buffer around each service center to estimate its effective service range. Based on commonly accepted standards in urban transport studies [11, 12], a 5 km service radius is considered optimal to ensure convenient access to EV service centers. The spatial analysis followed established GIS-based methodologies [13, 14] that utilize intersection, buffering, and clip-and-merge techniques to map current service coverage and identify underserved areas. The resulting buffer zones, shown in light green, represent areas within optimal proximity to EVSC facilities, based on general accessibility standards for urban transportation services [11]. This step helps to visualize the spatial reach of the current infrastructure.

Fig.4 Buffer Process of EVSC in Jakarta

In the final stage, Clip & Merge, a spatial overlay analysis is performed to delineate areas that fall outside the 5-kilometer buffer zones. These regions, highlighted in purple hatching, indicate underserved zones where current EVSC facilities do not provide adequate coverage. Identifying these gaps is crucial for planning future EVSC development to ensure equitable access and support electric vehicle adoption.

Fig.5 Clip and Merge Process of EVSC in Jakarta

Fig.6 Jakarta Population Density Map 2021

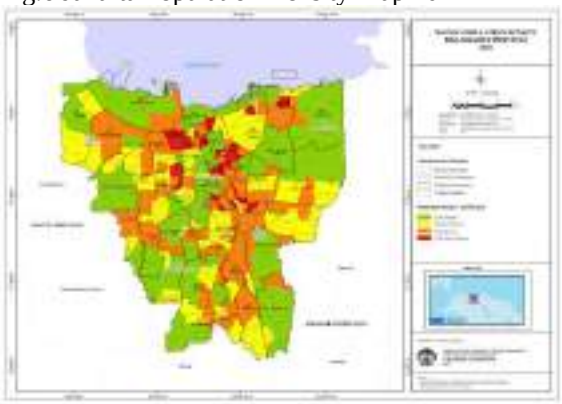

The analysis reveals that several districts in North Jakarta, East Jakarta, parts of West Jakarta, and Southern Jakarta remain outside the optimal service radius. This finding suggests a clear need for targeted infrastructure investments in these areas to address geographic disparities and promote a more inclusive and resilient EV ecosystem in Jakarta.

There are some notable contrasts when compared to the EVSC distribution model in Hefei, which is known for its cluster and corridor strategy. In Hefei, EVSCs are concentrated in the city center and commercial districts, with significant EVSC corridors along important transit routes (for example, metro lines or arterial highways). The service radius in Hefei is often smaller (about 1-3 km in the city center) to encourage high adoption of electric vehicles in urban mobility. However, suburban areas have a greater radius. In comparison, the layout in Jakarta, as seen on this map, uses a more spread node method with a 5km radius coverage. This technique is consistent with the more dispersed character of Jakarta's road network and the necessity to serve a diverse range of residential areas.

Fig.7 Land Use of Jakarta Cultural Map

Fig.8 Jakarta Protected Area Map

Spatial Overlay Analysis for Identification of Potential EVSC Locations

The priority locations for EVSC development were identified through a comprehensive spatial overlay analysis integrating multiple geospatial datasets, including Jakarta’s 2021 population density map (Figure 6), land use and cultural activity zones (Figure 7), and protected area boundaries (Figure 8). The analysis aimed to optimize service coverage while balancing environmental and urban planning considerations. Each map layer was assigned a score reflecting its relative influence on EVSC demand, with higher population density and urban cultural zones contributing positively, and protected areas constraining development options.

Fig.9 The Spatial Overlay Analysis

To facilitate interpretation and strategic planning, the composite scores were classified into five priority levels using a constant of 0.8, calculated as follows:

6−25=0.8\frac{6 - 2}{5} = 0.856−2=0.8

The final classification ranges were defined as:

- **Priority I**: 5.6 – 6.4 (Very High Need)
- **Priority II**: 4.7 – 5.5 (High Need)
- **Priority III**: 3.8 – 4.6 (Moderate Need)
- **Priority IV**: 2.9 – 3.7 (Low Need)
- **Priority V**: 2.0 – 2.8 (Very Low Need)

The spatial overlay analysis produced a comprehensive priority map illustrating potential sites for future Electric Vehicle Service Center (EVSC) development throughout DKI Jakarta. This map synthesizes layers of population density, existing EVSC distribution, detailed land use plans (RDTR), and transportation networks, resulting in a visual classification of urban areas according to service demand and spatial suitability. The analysis revealed significant spatial disparities, with central and highly urbanized districts exhibiting higher priority levels, while peripheral and protected zones were identified as lower priority or excluded from development consideration. Key urban subdistricts in South Jakarta, East Jakarta, and West Jakarta emerged as critical areas for EVSC expansion, reflecting both unmet service needs and strategic connectivity potential. This map provides a data-driven foundation for guiding equitable and sustainable EVSC network expansion in Jakarta, ensuring alignment with broader urban planning and green mobility objectives.

The spatial priority map for potential Electric Vehicle Service Center (EVSC) development in Jakarta (Figure 5) provides an integrated visualization of service needs across the metropolitan area. The analysis combines spatial layers, including existing EVSC locations, service coverage buffers (5 km radius), population density, and urban land use patterns derived from the city's detailed spatial plan. The overlay results highlight significant geographic disparities in EVSC accessibility, particularly in southern, eastern, and parts of western Jakarta, where high-priority zones (Priority I and II) are concentrated but lack sufficient service coverage. Several underserved districts with dense residential areas and strategic transport corridors, such as Jagakarsa, Pasar Minggu, Duren Sawit, and Kalideres, emerge as key candidates for future EVSC deployment to enhance spatial equity and support growing EV adoption. Conversely, the northern and central districts exhibit relatively better service coverage but still present localized gaps, especially in industrial and port-adjacent zones. The integration of environmental protection areas further informs sustainable site selection by identifying zones where EVSC development should be avoided. Overall, the spatial analysis offers a data-driven basis for prioritizing EVSC infrastructure expansion, ensuring alignment with both mobility demand and green urban development objectives.

Discussion

The spatial overlay analysis conducted in this study highlights significant geographic disparities in the current Electric Vehicle Service Center (EVSC) network in Jakarta. Compared to the more advanced and strategically clustered EVSC system in Hefei, Jakarta's EVSC deployment remains sparse and uneven, especially in high-density and fast-growing residential areas. GIS-based methods enabled the identification of underserved districts in the southern, eastern, and southwestern parts of the city. This underscores the need for a more targeted, data-driven infrastructure development strategy to support Jakarta's transition toward sustainable transportation [15, 16]. Optimizing EVSC locations based on spatial demand factors—such as population density, land use patterns, and transportation network connectivity—can significantly improve service equity and support broader electric vehicle (EV) adoption [17].

In the context of green cities, EVSCs serve as critical infrastructure for energy transition and sustainable mobility. Well-distributed and strategically planned EVSCs uphold the green city principle, where electric vehicles produce zero exhaust emissions, contributing to cleaner air [18, 19]. Clean technology becomes especially appealing and viable in densely populated areas that strive for better air quality. Site selection should consider proximity to users, EV distribution in the area, and the service capacity of each station [6, 20]. The reliability of charging infrastructure and battery swapping systems is also crucial for sustaining EV operations [21]. Placement decisions must coincide not only with technical and geographical issues but also with broader urban sustainability goals, such as integrating public transportation with green mobility, decreasing congestion, and supporting equitable service distribution [16].

When deciding on the optimum site, consider the distance from the user's location [7], the distribution of electric vehicles in the area [8], and the service capacity that the service center can offer [9]. The dependability of charging infrastructure and battery swapping systems is crucial to facilitate the sustained functioning of electric vehicles [10]. This placement considers not only technical and spatial aspects but also urban sustainability goals such as integrating public transportation with green mobility, reducing congestion, and ensuring fair and equitable service distribution. EVSC's closeness to toll lanes, terminals, commercial districts, and industrial areas enables it to be part of a comprehensive low-emission mobility ecosystem.

Jakarta could benefit from adopting a hybrid EVSC layout strategy—blending cluster, corridor, and nodal approaches—similar to successful practices in Hefei. This would ensure better service

coverage across dense urban cores and peripheral commuter zones, supporting a more inclusive and resilient low-emission mobility ecosystem [17]. As the number of EV users grows, Jakarta must proactively expedite the development of EVSCs to minimize service bottlenecks and maintain user satisfaction. Incentive policies, public-private partnerships, and the integration of technology and service information systems should support investment in EVSCs. Furthermore, incorporating user behavior research through surveys and service quality assessments will ensure that future EVSC infrastructure meets the evolving needs of urban EV users and fosters a more inclusive, accessible, and sustainable mobility system.

CONCLUSIONS

This study highlights the essential role of Electric Vehicle Service Centers (EVSCs) as crucial infrastructure for the sustainable transition to electric mobility in urban areas. The spatial analysis conducted using GIS-based overlay techniques reveals that the current distribution of EVSCs in Jakarta is uneven and inadequate, leaving significant regions—particularly in South, East, and parts of West and North Jakarta—beyond the optimal 5-kilometer service radius. This gap poses a substantial obstacle to broader EV adoption and user satisfaction. In contrast, the EVSC deployment model in Hefei illustrates a more advanced and strategic approach, characterized by dense clusters in urban centers and corridor-based coverage along key transport routes. Hefei's smaller service radii and integrated infrastructure offer valuable insights for Jakarta's future planning.

The results reveal critical service gaps and prioritize zones for future EVSC development, providing actionable insights for policymakers and Urban planners should focus on the recommended priority locations to address current geographic disparities and align with urban mobility patterns, promoting equitable access to EV services. Comparisons with the successful EVSC model in Hefei further highlight the importance of adopting a strategic, spatially adaptive infrastructure planning approach. Moving forward, integrating dynamic mobility data, real-time EV adoption trends, and stakeholder input can enhance the robustness of this planning framework. Ultimately, the study supports Jakarta's goal of building a resilient, sustainable, and inclusive electric mobility ecosystem, contributing to broader climate and urban livability objectives.

REFERENCES

[1] Afifa, Arshad K, Hussain N, Ashraf MH, Saleem MZ. Air pollution and climate change as grand challenges to sustainability. Sci Total Environ. 2024 Jun 10;928:172370. doi: 10.1016/j.scitotenv.2024.172370. Epub 2024 Apr 10. PMID: 38604367.

[2] Shabbiruddin, Ghose, D., Pradhan, S. (2021). Analysis of Challenges for One Point Solution Study of Electric Vehicle Service Centre (EVSC) using Fuzzy– Methodology. *International Journal of Sustainable Engineering*, *14*(6), 1893–1906. https://doi.org/10.1080/19397038.2021.1986589

[3] Zhao Y, Wu Y. (2024). Research on Optimization of Power Battery Recycling Logistics Network. EAI Endorsed Trans Energy Web Available from: https://publications.eai.eu/index.php/ew/article/view/5790

[4] EAC. (2021). HEFEI – RISING E-MOBILITY HUB. [Online]. https://eac-consulting.de/wp-content/uploads/2021/09/EAC_Executive-China-Briefing_Hefei.pdf

[5] Peraturan Gubernur Provinsi Daerah Khusus Ibukota Jakarta Nomor 31 Tahun 2022 tentang Rencana Detail Tata Ruang Wilayah Perencanaan Provinsi Daerah Khusus Ibukota Jakarta. [Online]. https://jdih.jakarta.go.id/dokumen/detail/4933/peraturan-gubernur-nomor-31-tahun-2022-tentang-rencana-detail-tata-ruang-wilayah-perencanaan-provinsi-daerah-khusus-ibukota-jakarta

[6] Hamurcu, M.; Eren, T. Electric Bus Selection with Multicriteria Decision Analysis for Green Transportation. *Sustainability* 2020, *12*, 2777. https://doi.org/10.3390/su12072777

[7] Chamberlain, K., Majeed, S. A. (2022). A Novel Model to Predict Electric Vehicle Rapid Charging Deployment on the UK Motorway Network. *Vehicles*, *4*(2), 567-585. https://doi.org/10.3390/vehicles4020033

[8] Shen, Zuo-Jun Max., Feng, Bo., Mao, Chao., Ran, Lun. 2019. "Optimization models for electric vehicle service operations: A literature review," Transportation Research Part B: Methodological, Elsevier, vol. 128(C), pages 462-477.

[9] Zhao, Z., Lee, C. K. M., Ren, J., & Tsang, Y. (2023). Quality of service measurement for electric vehicle fast charging stations: a new evaluation model under uncertainties. *Transportmetrica A: Transport Science*, *21*(1). https://doi.org/10.1080/23249935.2023.2232044

[10] You, P. Pang, J. Z. F., Low, S. H. (2022). Online Station Assignment for Electric Vehicle Battery Swapping. in IEEE Transactions on Intelligent Transportation Systems, vol. 23, no. 4, pp. 3256-3267, April 2022, doi: 10.1109/TITS.2020.3033731.

[11] Feng, W., & Figliozzi, M. A. (2021). An empirical analysis of electric vehicle public

charging station usage. *Transportation Research Part D: Transport and Environment, 94*, 102821. https://doi.org/10.1016/j.trd.2021.102821

[12] Gnann, T., Plötz, P., Kühn, A., & Wietschel, M. (2018). Fast charging infrastructure for electric vehicles: Today's situation and future needs. *International Journal of Sustainable Transportation*, *12*(7), 526–540. https://doi.org/10.1080/15568318.2018.1431826

[13] Zhang, Y., Li, X., & Liu, Z. (2022). Optimal spatial planning of electric vehicle charging infrastructure considering urban road network and user behavior. *Sustainable Cities and Society*, *81*, 103854. https://doi.org/10.1016/j.scs.2022.103854

[14] Wang, Y., Lin, X., & Ma, X. (2017). Location optimization of electric vehicle charging stations considering urban traffic flow. *Energy*, *150*, 722–732. https://doi.org/10.1016/j.energy.2018.02.156

[15] Wang, Y., Zhang, H., & Zhang, W. (2019). Optimal planning of electric vehicle charging stations considering urban spatial characteristics. *Journal of Cleaner Production*, 209, 1084–1092. https://doi.org/10.1016/j.jclepro.2018.10.280

[16] Zhu, B., Wei, Y.-M., Wang, K., & Zhang, X. (2020). Spatial optimization of electric vehicle charging infrastructure based on charging behavior analysis and urban land use. *Applied Energy*, 264, 114672. https://doi.org/10.1016/j.apenergy.2020.114672

[17] Zhang, Y., Sun, S., & Xie, Y. (2021). Planning and design of electric vehicle charging infrastructure: A review. *Energy Reports*, 7, 3432–3446. https://doi.org/10.1016/j.egyr.2021.05.012

[18] European Environment Agency. (2018). *Electric vehicles and air quality*. EEA Briefing. https://www.eea.europa.eu/themes/transport/electric-vehicles/electric-vehicles-and-air-quality

[19] Soret, A., Guevara, M., & Baldasano, J. M. (2014). Air quality benefits of moving to electric vehicles: A case study for Barcelona, Spain. *Environmental Science & Policy*, 44, 160–172. https://doi.org/10.1016/j.envsci.2014.08.001

[20] Li, Q., Zhang, H., Zhou, Y., & Zhang, W. (2020). Development of electric vehicle battery swapping infrastructure through public–private partnerships. *Transportation Research Part D: Transport and Environment*, 78, 102183. https://doi.org/10.1016/j.trd.2019.11.012

[21] IEA (International Energy Agency). (2023). *Global EV Outlook 2023*. International Energy Agency. https://www.iea.org/reports/global-ev-outlook-2023

Copyright © Int. J. of GEOMATE All rights reserved, including making copies, unless permission is obtained from the copyright proprietors.

15th Int. Conf. on Geotechnique, Construction Materials & Environment, Kyoto, Japan, 11-13 November 2025, ISBN 978-4-909106124 C3051

THE IMPACT OF URBAN VILLAGE DEVELOPMENT ON FEMINIZATION OF INDONESIAN MIGRANT WORKERS (PMI) IN WEST JAVA: A SPATIO-TEMPORAL ANALYSIS FROM 2018, 2021, AND 2024 VILLAGE POTENTIAL (PODES) MICRO DATA

Chotib [1], Mohamad Axel Putra Hadiningrat [2], Beti Nurbaiti [3], Adzkia Nabila Zahrani[4]

[1,2] School of Strategic and Global Studies Universitas Indonesia; [3] Universitas Bhayangkara Jakarta Raya, Jakarta, Indonesia, [2] ;[4] Faculty of Economics and Business Universitas Indonesia

ABSTRACT

Based on a report from BP2MI (Indonesian Migrant Worker Protection Agency) in 2023, West Java Province has the third rank after East Java and Central Java in sending Indonesian Migrant Workers (PMI) abroad (BP2MI, 2023). The temporary processed results of the 2024 PODES (Village Potential) data show that the largest number of female PMIs came from West Java Province, namely 100,675 people. This is much greater than the male PMI which amounted to 41,667 people from the same province. The ratio of female PMI which is greater than male PMI illustrates the feminization of PMI in West Java. This research will describe the spatial patterns of villages experiencing PMI feminization in West Java, and their changes over time: before, during, and after Covid-19 pandemic. More specifically, this research aims to: (1) Analyze the changes in spatial patterns of villages experiencing feminization of Indonesian Migrant Workers (PMI) in West Java ; (2) Conduct a panel analysis of the impact of urban/rural status of village. geographical, socio-economic, and level of development factors on the feminization of PMI from West Java; (3) Analyze the spatial dependencies of feminization of PMI from West Java; (4) Compare the spatial patterns and spatial dependencies of feminization of PMI between before, during, and after the Covid-19 pandemic. The method of analysis in this research are descriptive and inferential analysis. Descriptive analysis creates cross tabulations between each independent variable (rural/urban status, geographical characteristics, socio-economic factors, and level of development) against the dependent variable (Feminization of PMI, which is indicated by Sex Ratio of PMI). Inferential analysis creates panel regression modeling, and spatial regressions. The results of the two analyzes were then compared before the pandemic (PODES 2018), during the Covid-19 pandemic (PODES 2021), and after the Covid-19 pandemic (PODES 2024). It is hoped that the results of this research can be used as input in implementing policies regarding the facilitation of sending PMI to improve the welfare of the community, both migrant workers and village residents of origin.

Keywords: Indonesian Migrant Workers (PMI); Feminization; Panel Regression Modeling; Spatial Regressions; West Java

INTRODUCTION

The BP2MI (The Indonesian Migrant Workers Protection Board Of The Republic Of Indonesia) report as of June 2023 shows that West Java Province is the third sender of PMI (Indonesian Migrant Workers) in Indonesia after East Java and Central Java (www.bp2mi.go.id). Meanwhile, West Java Province ranks first in sending female PMI based on PODES 2024 data. This province is experiencing feminization of PMI which illustrates the number of female PMI being more dominant than male PMI, and this is one of the global issues in discussing migrant workers.

The feminization of PMI in West Java is likely to be various between regions within it, as is the diversity of sending PMI itself. This variation is certainly inseparable from the urban/rural status of a village factor, whether as an urban or a rural village. This variation can also be caused by the variation of other characteristics of village, such as geographical, socio-economic aspects, and characteristics of the level of development of the region.

The objectives of this research are as follows:

1) To analyze the spatial patterns of villages experiencing feminization of intertemporal PMI shipments in West Java;
2) To analyze the influence of village-urban/rural status factors, geographic factors, socio-economic factors, and level of development on the feminization of intertemporal and inter-village PMI shipments in West Java;
3) To analyze the spatial dependency of feminization of intertemporal and inter-village PMI shipments in West Java;
4) To compare the spatial patterns of feminization of PMI shipments before (PODES 2018), during (PODES 2021) and after the Covid-19 Pandemic (PODES 2024).

RESEARCH SIGNIFICANCE

So far, research on sending migrant workers has been conducted more qualitatively and focuses more

on individual factors as motivation for migrant workers to leave the country, and also highlights many problems with the sending process of migrant workers which tends to be non-procedural. The results of those researches are depicted in various national and international journals.

Research conducted by [1] has explored how mining projects shape gendered experiences and subjectivities through a feminist ethnographic approach in Tanzania and Tajikistan. Using participant observation, interviews, and visual methods, the research focuses on conservation areas in Tanzania and remote mountains in Tajikistan.

An ILO publication by [2] presents the latest estimates of the number of international migrant workers to 2022, disaggregated by age, sex, country income group and region. The report uses data from 189 countries and territories based on national labour force surveys, censuses and other administrative sources. It finds that between 2019 and 2022, growth in the number of international migrant workers slowed to less than 1% per year, compared to an average of 2.8% per year before the pandemic.

Our research conducts spatial modeling that focuses on sending migrant workers dominated by female workers (feminization of migrant workers) using quantitative methods on sending migrant workers villages in one of the provinces known as a sending area for migrant workers, and also has the largest number of female migrant workers in Indonesia (based PODES 2024 micro data analysis).

We explore some variables determining the sending of female migrant workers from villages in West Java Province. The variables are selected from three micro datasets of PODES 2018, 2021, and 2024. The variables are as follow: rural/urban status, number of disasters, village topography, source of income of residents, and one variable from the district/city government that handles district/city minimum wage policies.

The use of those variables in the analysis of factors influencing the sending of migrant workers, especially female migrant workers, has been widely used by many researchers. For example, Postar found that topography plays a major role in driving female labor migration both directly and indirectly. In Tanzania, limited access to land and employment opportunities marginalize local female by male migrants, prompting female workers to migrate out. Meanwhile, in Tajikistan, difficult terrain forces women to work hidden in informal mines, which then gives rise to social stigma and gender pressure. Thus, topography is not only a physical barrier, but also forms a social structure that drives migration, hidden labor, and marginalization of women in areas of resource exploitation.

The study conducted by [3] aimed to analyze the impact of the major earthquake that occurred in Nepal in 2015 on labor migration patterns, specifically to understand whether and how the disaster affected the level of female worker migration. This study uses a quantitative approach with the difference-in-differences (DiD) method that utilizes two main data sources: the Nepal Labor Force Survey of 2007/08 and 2017/18 to measure internal and international (to India) migration; and administrative work permit data from 2008 to 2018 for international migration (except to India). The results show that in general, the earthquake disaster did not have a significant impact on the level of female worker migration, both internally and internationally. However, there are specific exceptions: when using the damage classification, a significant increase in the likelihood of female migration to the Gulf countries was found, as well as an increase in the number of international work permits for women by 13% after the earthquake.

The status of a rural or urban village determines the population's consideration to migrate or not. Urban villages are considered more developed than rural villages, so it can be hypothesized that urban villages will restrain their residents from migrating abroad, while rural villages encourage internationally migration.

The study by [4] aims to analyze the causes of gender inequality in migration, especially why young women from rural areas are more likely to migrate to cities than men, especially during the period of economic growth and urbanization in China. The study finds that the process of urbanization, especially through the establishment of Special Economic Zones (SEZs), significantly increases the migration of young women from rural areas to cities, almost twice as much as the migration of men. Urbanization creates economic opportunities and enlarges the marriage market (especially for men with high economic status), which encourages young women to move to cities for better employment and marriage prospects. Young women are more responsive to urbanization because they seek opportunities to “marry up” (hypergamy). Cities are seen as providing access to more educated and higher-income single men.

Theoretically, villages that rely on the agricultural sector tend to encourage their residents to migrate because their real wages are lower than if they went to cities that rely on the manufacturing and services sectors [5]. Meanwhile, according to research results from [6], it was stated that income difference and non-agricultural sectors influence female workers to migrate. In more detail, the wage gap between the sending country and the receiving country is the main attraction. Although jobs such as domestic workers abroad have low wages in the destination country, they are still higher than the standard salary in Indonesia. This research also stated that non-agricultural households with irregular incomes are more motivated to migrate because their jobs tend to

be unstable. Therefore, migration is considered as a way to get a more stable income.

The study conducted by [7] aims to analyze the effect of poverty, Provincial Minimum Wage, and investment on the level of international migration of female workers in Indonesia. The method used is explanatory which explains the relationship between independent variables and dependent variables. The unit of analysis used was 9 provinces in Indonesia from 2012-2019 which were processed using panel data regression using the Fixed Effect Model (FEM). The results of the study indicate that the minimum wage has a positive and significant effect on the level of international migration of female workers. This means that when the minimum wage increases, the level of female labor migration also increases.

Meanwhile, our research will analyze the effect of kabupaten/kota minimum wages on sending female migrant workers to a village in West Java by using panel regression model.

HYPOTHESIS

As stated in the previous section regarding the research objectives, the hypotheses that can be put forward in this research are as follows:

1. There was a certain spatial clustering of the sending of female migrant workers between villages in West Java in the three years of observation.
2. There is some effects of the urban status of village, geographical factors, socio-economic factors, and level of development factors on the sending of female migrant workers.
3. There are spatial dependencies in the sending of female migrant workers to villages in West Java in the three years of observation.
4. There is a decline in the context of the magnitude of female migrant worker deployments between before (2018) and after the Covid-19 pandemic (2021 and 2024).

RESEARCH METHODS

The main data source for this research uses three micro datasets of Village Potential (PODES) in 2018, 2021, and 2024 provided by the Central Statistics Agency (2024). These datasets contain information on physical, geographical, social, economic, cultural conditions, availability of road infrastructure, educational facilities, health facilities, village security conditions, and others.

Village potential data collection is carried out every 3 years. The last data collection was carried out in 2024, so the series of datasets in the last three data collection periods used in this research are PODES 2018, PODES 2021, and PODES 2024.

Specifically, the independent variable data for the Regency/City Minimum Wage (UMK) was obtained from the Decree of the Governor of West Java concerning the Regency/City Minimum Wage of West Java Province in 2018, 2021, and 2024.

With data sources from PODES, the unit of analysis in this research is the village/kelurahan (for village in Kota) with a total number of 5957 villages/kelurahan. With data sources from PODES, the unit of analysis in this research is the village/sub-district (for village in Kota) with a total of 5,957 villages/sub-districts. Because there are three years of observation, there will be 17,871 observations/cases in a panel data analysis.

The analysis method used in this research are descriptive statistics which describes the development of PMI feminization between kabupatens in West Java Province during three years of observation; and inferential analysis through panel regression modeling of three years. The regression model developed is as follows:

$$RJK_PMI_{it} = \beta_0 + \beta_1 * URBAN_{it} + \beta_2 * BENCANA_{it} + \beta_3 * TOPOGRAFI_{it} + \beta_4 * D_{INC1\,it} + \beta_5 * D_{INC2\,it} + \beta_6 * UMK_{it} \quad \text{.....4.1.}$$

Where:

RJK_PMI	=	Sex Ratio of PMI sent by a village
URBAN	=	Urban/Rural Status of village
BENCANA	=	Number of disaster occurrence per year in a village
TOPOGRAFI	=	Topography of village (Plain=1; Others=0)
D_INC1	=	dummy for manufacturing sector as the main source of income for villagers (agriculture sector as ref. category)
D_INC2	=	dummy for the services sector as the main source of income for villagers (agricultural sector as ref. category)
UMK	=	Kabupaten/Kota Min. Wage (in Rupiahs per month)
$\beta_0, \beta_1, \ldots, \beta_5$	=	Regression coefficient for each independent variable
i, t	=	i is for observation i (village i); t is for time t

Descriptive analysis is processed by SPSS 27, and inferential analysis (panel regression) is processed by Stata 16. The operational definition of each variable is shown by Table 1.

Table 1. Operation Definition of Variables

Notation	Operational Definiton	Question Number
Depeendent Variable		
RJK_PMI	(Number of Female migrants/Number of Male migrants)*100%	(R402B2/ R402B1)*100
Independent Variables		
TOPOGRAPHY	Topography of most of the village/sub-district areas. (1=Plain; 0=Others).	Podes 2018: R305B Podes 2021 and Podes 2024: R305A
DISASTER	Number of village/sub-district residents affected by disasters in the year before PODES data was published	Podes 2018: Addition of R601AK8 to R601JK8 Podes 2021: R602 Podes 2024: R602
URBAN	Urban/rural area status (1=urban village; 0=rural village)	R105
D_INC1	dummy for manufacturing sector as the main source of income for villagers (agriculture sector as ref. category)	R403
D_INC2	dummy for the services sector as the main source of income for villagers (agricultural sector as ref. category)	R403
UMK	Minimum wage for district/city (in rupiah per month) where the village/sub-district is located	Data from other sources (West Java Provincial Government).

This research also uses GeoDa to conduct spatial analysis through LISA (Local Indicator of Spatial Association), to describe whether there is a clustering of feminization in certain areas; and to test whether there is a spatial dependency on PMI feminization in West Java.

RESULT AND DISCUSSION

Descriptive Anaysis

The result of descriptive analysis with cross-tabulation analysis of the distribution of feminization, namely when the sex ratio is above 100%, by kabupaten/kota is presented in Table 2. In general, the PMI sex ratio in West Java reached 200% and above, although it decreased during the observation period, namely from 267.52% in 2018 to 267.12% in 2021, and decreased to 241.62% in 2024. This shows that when the pandemic occurred, the sending of female migrant workers decreased compared to before the pandemic period.

Almost all kabupaten/kota in West Java have sex ratio of migrant workers above 100%, which shows that the number female migrant workers are larger than number of male migrant workers. Cimahi City had the highest sex ratio in 2018, which was 640%, meaning that out of 100 male migrant workers, there were 640 female migrant workers. This figure then dropped to 366.67% in 2021, and 300% in 2024. The lowest sex ratio is in Bogor City, which is 97%. But this figure then rose to 150% in 2021, and 140% in 2024. More detailed variations in sex ratios between districts/cities and over time are presented in Table 2.

Table 2. Feminization of PMI by Kabupaten/City: West Java, 2018, 2021, and 2024

Kab/City	Sex Ratio ((Female/Male)*100%)			# of Villages
	2018	2021	2024	
Bandung	371.74	255.20	250.79	280
Bandung Barat	239.12	271.88	234.07	165
Bekasi	450.00	430.43	352.55	187
Bogor	434.68	165.27	129.81	435
Ciamis	225.17	180.72	151.83	265
Cianjur	291.09	259.28	256.09	360
Cirebon	222.55	222.49	198.50	424
Garut	202.76	241.94	177.44	442
Indramayu	243.81	256.41	232.93	317
Karawang	494.22	534.96	651.26	309
Kuningan	163.73	182.66	191.64	376
Majalengka	255.65	255.09	223.74	343
Pangandaran	274.59	222.09	168.14	93
Purwakarta	292.00	350.00	279.24	192
Subang	326.29	285.66	267.64	253
Sukabumi	281.90	319.54	268.61	386
Sumedang	317.83	370.28	212.08	277
Tasikmalaya	260.16	246.64	172.04	351
Bandung City	125.69	127.71	123.44	151
Banjar City	352.17	162.70	139.21	25
Bekasi City	113.68	95.37	102.44	56
Bogor City	97.37	150.00	140.00	68
Cimahi City	640.00	366.67	300.00	15
Cirebon City	304.42	312.28	193.22	22
Depok City	485.71	156.76	60.53	63
Sukabumi City	249.76	189.87	180.18	33
Tasikmalaya City	506.90	257.14	132.65	69
West Java Pr.	267.52	267.12	241.62	5957

Source: Analyzed by authors (2025)

Panel Regression Analysis

Almost all variables have a significant impact on the departure of female PMI from a village. The variable that is not significant is the number of residents affected by the disaster. Meanwhile, the classification variable of rural/urban areas is significant at $\alpha = 10\%$.

In the analysis with FEM (Fixed Effect Model), the results are different. The Topography variable remains significant, but the direction is reversed. This means that female PMI departures tend to come from villages with non-plain topography. The Disaster and Urban variables remain insignificant. The main source of income for residents is significant in the tertiary sector (services) with a negative direction. This means that there is a real difference in female PMI departures that tend to come from agricultural villages rather than villages whose main source is the tertiary sector. The UMK variable remains

significant, namely that PMI departures tend to come from areas with low UMK.

In the REM (Random Effect Model) analysis, similar to the CEM (Common Effect Model) analysis, almost all variables are significant, except for the Disaster and Urban variables.

Chow Test :

H_0 : CEM

H_1 : FEM

The results of this test lead to the decision to reject H0 , meaning that the FEM analysis is better than CEM .

Hausman test

H_0 : REM

H_1 : FEM

From the results of the Hausman test above, it can be concluded that H0 is rejected, meaning that analysis with FEM is better than REM.

Lagrange Multiplier (LM) Test:

H_0 : CEM

H_1 : REM

The results of this analysis provide a decision to reject H0, which means that the REM model is better than CEM.

Overall, from the three tests above, it can be stated that the FEM model is the best choice in panel analysis. This means that the intercept varies between times, but the slope of each variable is relatively unchanged (fixed) between times.

As presented in the FEM analysis results (Table 3), these findings show that the model generally describes the role of the variables proposed in the model play a role in the variation in the number of female dominant migrant workers sent by villages in West Java. The variables have significant role are: Topography (TOPOGRAFI) and Regional Minimum Wage (UMK).

The TOPOGRAPHY variable has a negative coefficient which shows that PMI shipments dominated by female tend to come from villages with non-sloping/flat topography, such as peaks/cliffs, slopes, and valleys. The second variable that has a significant influence is UMK (Reginal Minimum Wage) with a positive direction, but with a small magnitude.

Table 3. Parameter Estimates with Fixed Effect Model (FEM)

Indep. Variables	Coef.	P>|t|
TOPOGRAFI	-38.149***	.003
BENCANA	0.001	.843
URBAN	20.934	0.126
D_INC1	-2.434	0.859
D_INC2	-7.653	0.660
UMK	.000***	0.001
CONSTANTS	110.76	0.708

*Note: ***)Significant at α=1%*

Source: Analyzed by authors (2025)

5.3. LISA Analysis

Local Indicator of Spatial Association (LISA) describes the spatial clustering of feminization in West Java Province. Clustering occurs in certain areas that describe spatial associations as measured by Moran's I parameter. The number of villages included in the high-high cluster has decreased relatively slightly. This can also be seen in the Morans's I parameter which tends to decrease slightly from 0.5 in 2018 to 0.428 in 2021, and increases slightly to 0.456 in 2024. The same pattern also happened to the number of villages included in the Low-Low cluster.

Table 4. LISA Analysis between 3-Years of Observation

Parameter	2018	2021	2024
Moran's I	0.501	0.428	0.456
High-High (#N)	308	319	300
Low-Low (#N)	1199	1264	1158
Low-High (#N)	163	180	150
High-Low (#N)	82	109	123
Sign. P = 0.05 (#N)	1271	1437	1182
Sign. P = 0.01 (#N)	417	360	480
Sign. P = 0.001(#N)	64	75	69
Not Sign.	4205	4085	4226

Source: Analyzed by authors (2025)

Spatially, the pattern of feminization clustering tends not to experience much change over time. High feminization clustering tends to occur in the northern and southern regions of West Java. In the northern region, it mainly occurs in the cities of Cirebon, Karawang, and Indramayu. While in the south it tends to occur in the cities of Cimahi, Sukabumi, and Cianjur

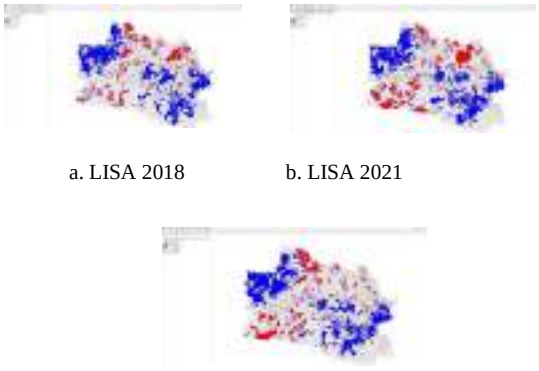

a. LISA 2018 b. LISA 2021

c. LISA 2024

Figure 1. Spatial Pattern of LISA

Source: Analyzed by authors (2025)

5.4. Spatial Dependencies

The results of classical regression from three different years show results that are not much different. Almost all variables have significant impact on the feminization of PMI deployment from villages in West Java. Only the disaster variable shows inconsistent results, both in terms of the magnitude

and direction of the coefficient, as well as its significance. While all variables have a consistent impact, both in magnitude, direction and significance.

In general, it can be explained that feminization occurs in villages with plain topography, originating from rural villages, villages where the main occupation of the population is agriculture, and where the district/city minimum wage is low.

In the spatial dependency test, there is also a spatial lag. Table 5 shows the spatial lag coefficient (ρ) of 0.38; 0.33; and 032. This shows the spatial effects of villages in the surrounding areas in terms of feminization. A village will experience an increase of between 0.32 - 0.38 percentage points in terms of the sex ratio of migrant workers (feminization) from it's neighbour villages.

Tabel 5. Parameter Estimates of Spatial Regressions

Classical Regression			
Variables	2018	2021	2024
Constant	130.78 (***)	108.99 (***)	65.66 (***)
Topography	58.79 (***)	97.81 (***)	96.91 (***)
Disaster	0.93	-0.01 (*)	1.68
Urban	-16.84	-52.19 (***)	-41.67 (***)
D_Inc1	-134.02 (***)	-116.66 (***)	-119.08 (***)
D_Inc2	-171.57 (***)	-134.34 (***)	-267.67 (***)
UMK	$3.56*10^{-4}$ (***)	$2.84*10^{-4}$(***)	$-3.78*10^{-6}$ (***)
Diagnostics for Spatial Dependence:			
LM Lag	449.19 (***)	336.65 (***)	291.36 (***)
LM Error	428.26 (***)	302.12 (***)	262.36 (***)
Spatial Lag Regression			
W	0.38 (***)	0.33 (***)	0.32 (***)
Constant	84.53 (***)	72.63 (***)	38.34 (*)
Topography	30.07 (*)	62.57 (***)	68.10 (***)
Disaster	0.352	-0.00	6.00
Urban	-5.07	-31.18 (**)	-29.51 (*)
D_Inc1	-84.02 (***)	-75.76(***)	-82.43 (***)
D_Inc2	-105.65 (***)	-94.47(***)	-187.46 (***)
UMK	$2.11*10^{-5}$ (**)	$1.85*10^{-5}$ (***)	$3.49*10^{-5}$ (***)

Note: *) Sign. at α=10%; **) Sign. at α=5%; ***) Sign. at α=1%;
Source: Analyzed by authors (2025)

CONCLUSION

From the description of the results of the analysis and discussion above, several points can be concluded, in accordance with the objectives of the research in answering the research questions, namely:

1. In general, there is a relatively slight decrease in the phenomenon of feminization of sending PMI from villages in West Java.
2. The results of the panel analysis show the influence of fixed independent variables in influencing the pattern of feminization of villages in West Java.
3. Almost all variables have a significant influence, except for the Disaster variable. It can be said that feminization occurs in villages with plain topography, from rural villages, villages with the main occupation of the population is in the agricultural sector, and those with low district/city minimum wages.
4. There is spatial dependency in the phenomenon of feminization in sending PMI from villages in West Java.

REFERENCES

[1] Postar, Stephanie, and Negar Elodie Behzadi. 2024. "'Extactive Bodies': A Feminist Counter-Topography of Two Extractive Landscape". Geoforum. 148 (2024) 103628.

[2] ILO. 2024. ILO Global Estimates on International Migrant Workers: Internatioanl Migrants in the Labour Force. 4rt edition.

[3] Manandhar, Shailee. 2023. "The Impact of the 2015 Earthquake on Internal andInternational Migration in Nepal".

[4] Koah, Yumi, et al. 2025. *Young Women in Cities: Urbanization and Gender-Biased Migration*. Singapore Management University: Instituional Knowledge at Singapore Management University.

[5] Trentin, Monica, et. Al. 2023. "Vulnerability of Migrant Women during disasters: a Scoping Review of the Literature". *International Journal for Equity in Health*. (2023) 22:135

[6] Listiani, Titan. 2019. An Analysis of Gendered Labor Migration: The Case of Indramayu Regency, West Java Province, Indonesia. Doctoral Program in Policy Science, Graduate School of Policy Science, Ritsumeikan University.

[7] Nugraha M. Kevin Gehan, etal. 2023. "Determinan Migrasi International Tenaga Kerja Wanita Indonesia Tahun 2012-2019". Jurnal Perencanaan Wilayah dan Pembangunan.Vol. 1. No. 2 (2023).

Copyright © Int. J. of GEOMATE All rights reserved, including making copies, unless permission is obtained from the copyright proprietors.

15th Int. Conf. on Geotechnique, Construction Materials & Environment,
Kyoto, Japan, 11-13 November 2025, ISBN 978-4-909106124 C3051

AN EVALUATION OF THE AIRPORT NOISE AROUND AIRPORT OF THAILAND USING AVIATION ENVIRONMENTAL DESIGN TOOL

Patcharida Sungtrisearn[1], Chaiwat Sangsrichan[2] and Preda Pichayapan[3,4]

[1,2] Doctor of Philosophy Program in Civil Engineering, Faculty of Engineering, Chiang Mai University
[3] Department of Civil Engineering, Faculty of Engineering, Chiang Mai University
[4] Excellence Center in Infrastructure Technology and Transportation Engineering, Chiang Mai University

ABSTRACT

Aircraft noise is a significant environmental impact associated with airport operations, affecting both the quality of life in surrounding communities and influencing land use. This paper presents a modeling framework for evaluating the impacts of airport noise around Thailand's major airports. The proposed framework consists of 2 components: 1) Noise impact analysis, to evaluate the exposure patterns of aircraft noise using the Aviation Environmental Design Tool (AEDT) mathematical model, which is a GIS-based analytical approach enriched with historical noise measurement data and aircraft operational characteristics, to forecast Noise Exposure Forecast (NEF) contours, and 2) Temporal comparative analysis using statistical correlation and GIS optimization to evaluate changes in noise-affected zones. The model was validated at 5 major airports, including Suvarnabhumi, Don Mueang, Chiang Mai, Chiang Rai, and Phuket airports. The results of noise impact assessments, which consider accessibility and land use compatibility of communities around airports, risk exposure patterns and population distribution can be reliably determined. At the national level, 363,800 residents are affected by aircraft noise, with 57,330 people living in high-impact zones. Validation results show high correlation (R^2 = 0.89-0.94) between measured and predicted values. The findings support integrating noise assessment into airport planning, especially for future projects like Chiang Mai Airport No.2, and recommend adopting ICAO-based land use controls to protect communities.

Keywords: Aircraft Noise, Aviation Environmental Design Tool (AEDT), Noise Exposure Forecast (NEF), Land Use Planning

INTRODUCTION

Thailand's aviation sector has experienced unprecedented growth over the past decade, emerging as a critical component of Southeast Asia's transportation hub strategy [1]. Following the post-COVID-19 recovery, the sector has demonstrated remarkable resilience with flight volumes increasing 15-20% annually during 2022-2023, significantly exceeding pre-pandemic levels [2]. This rapid expansion has positioned Thailand as a regional aviation leader, with five major airports currently handling over 140 million passengers annually and projections indicating potential doubling of flight operations by 2035 [3].

However, this aviation boom has intensified environmental challenges, particularly aircraft noise pollution, which has emerged as a critical constraint to sustainable airport development [4]. Current estimates indicate that approximately 363,800 residents across Thailand's major airports are exposed to significant aircraft noise, with 57,330 people living in high-impact zones (NEF > 40) where noise levels severely affect quality of life [5]. The problem is particularly acute around densely populated airports such as Suvarnabhumi International Airport, Don Mueang, Chiang Mai, and Phuket, where expanding noise footprints increasingly conflict with urban development and residential areas [6,7].

Aircraft noise creates multidimensional impacts including sleep disturbance, elevated stress, reduced cognitive performance, and property value depreciation [8,9]. WHO and ICAO have established clear links between prolonged noise exposure and cardiovascular disease, hypertension, and mental health disorders [4,10].

Thailand's reactive approach to noise management has significant gaps compared to international best practices, resulting in community conflicts, costly retrofitting, and airport expansion limitations [11,12,13]. The lack of standardized assessment protocols and coordinated land use planning threatens sustainable aviation growth [14].

This challenge is critical as Thailand advances major airport expansion projects including Chiang Mai Airport No. 2, Andaman International Airport, and facilities in eastern provinces [15]. Without proactive noise management frameworks, these projects risk replicating existing problems [16].

The Aviation Environmental Design Tool (AEDT), developed by the Federal Aviation Administration (FAA), represents the international gold standard for aircraft noise modeling and impact assessment [13]. However, its application in Thailand's unique contexts

requires validation for national planning purposes [17].

Therefore, this research is critical in applying the AEDT tool to evaluate and analyze aircraft noise pollution levels in airport areas, particularly in regions with planned new airport development projects and to examine temporal changes in noise-affected areas using statistical and spatial analysis.

METHODOLOGY

This study aims to evaluate aircraft noise impacts around airports using the Aviation Environmental Design Tool (AEDT) through quantitative analysis processes comprising 5 main steps. Thus, the methodological framework guide to achieve the objectives of this research was presented in Fig 1.

Data Assessment and Verification

Relevant data associated with flight operations and aircraft noise levels were systematically collected and validated. This included aircraft noise level data expressed in decibels, flight path information such as Standard Instrument Departures (SID), Standard Terminal Arrival Routes (STAR), and Instrument Approach Charts, as well as air traffic statistics comprising aircraft types, time of operations, and prevailing wind directions. All datasets were rigorously verified and organized to serve as input parameters for the subsequent aircraft noise simulation process.

Model Development

The assessment of forecasted aircraft noise levels in the form of Noise Exposure Forecast (NEF) contours was conducted using the mathematical simulation model known as the Aviation Environmental Design Tool (AEDT). AEDT is a modeling tool developed by the Federal Aviation Administration (FAA) for predicting aircraft noise and emissions. The tool is capable of generating various types of forecasted noise contours, including NEF, Day-Night Average Sound Level (DNL), and Effective Perceived Noise Level (EPNL), as well as estimating aircraft-related air pollutant emissions such as VOCs, SO_2, and NO_x. AEDT was developed as an integration of the earlier INM (Integrated Noise Model) and EDMS (Emissions and Dispersion Modeling System), with enhancements including the incorporation of a Geographic Information System (GIS) database for improved usability.

The AEDT system consists of 3 primary data:

1) Study Database: This database contains the project-specific input data in the AEDT Standard Input File (ASIF) format. These files are organized as XML files (<ASIFXML>) and include essential information such as the geographical location of the airport, flight paths, case study parameters, community locations, study boundaries, and flight schedule data throughout the year.
2) Airport Database: This database comprises infrastructure information of the airport, including the official airport names according to ICAO and ATA codes, meteorological data, geospatial coordinates of runways and surrounding airport facilities.
3) Fleet Database: This includes technical and operational information about aircraft types and engine performance, compiled from international standard sources such as the ICAO Engine Emissions Databank (EDB), the ICAO Aircraft Noise and Performance (ANP) Database, and the Eurocontrol Base of Aircraft Data (BADA).

The Aviation Environmental Design Tool employs the Noise Exposure Forecast (NEF) metric, which integrates both noise level and frequency of exposure over annual operations following FAA technical specifications [13], as shown in Eq. (1)

$$NEF = EPNL + 10log_{10}(N_d) + 10log_{10}(N_n) - 88 \quad (1)$$

Where, EPNL = Effective Perceived Noise Level (dB)
N_d = Daytime operations (07:00-22:00)
N_n = Nighttime operations (22:00-07:00)
88 = Normalization constant

Model Validation & Calibration

Statistical validation employs multiple metrics ensuring reliability against field measurements [18], as shown in Eq. (2)

$$R^2 = 1 - (SS_{res} / SS_{tot}) \quad (2)$$

Where, $SS_{res} = \Sigma(NEF_{measured} - NEF_{predicted})^2$
$SS_{tot} = \Sigma(NEF_{measured} - NEF_{mean})^2$

Acceptable criteria: $R^2 \geq 0.85$, RMSE $\leq$ 3.0 dB, $|MBE| \leq 1.5$ dB following international aviation noise modeling standards [19].

Comparative Analysis & Impact Assessment

A spatial comparison was performed by overlaying the NEF contours from two different years onto aerial imagery to analyze changes in the noise contour boundaries. These changes reflect variations in the number of daily flight operations as well as the overall spatial extent of the noise-affected areas.

The analysis considered forecasted noise exposure contours based on the standards recommended by the International Civil Aviation Organization (ICAO), which provide land use guidelines for different NEF levels as follows:

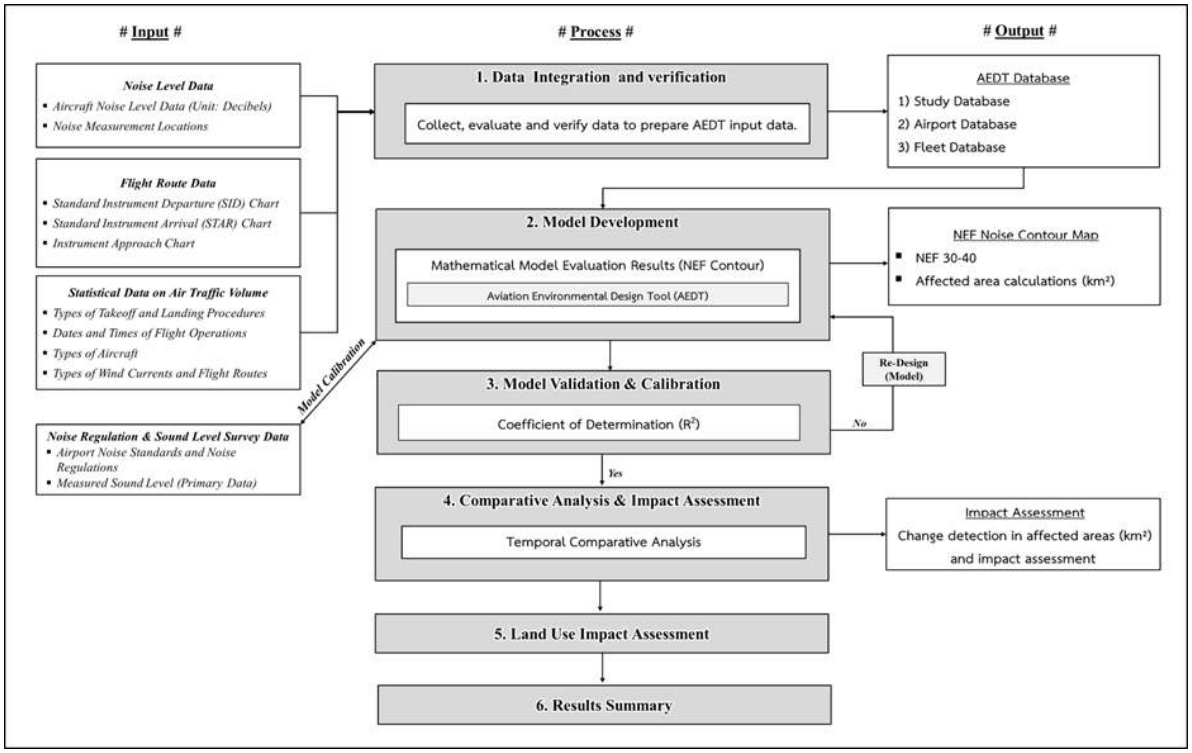

Fig 1. Methodological framework of developing airport noise assessment using AEDT

- NEF less than 30: This area is considered unaffected by aircraft noise and is generally suitable for all types of land use.
- NEF 30–35: Aircraft noise in this area causes a low level of disturbance. Mitigation measures are recommended, such as installing sound insulation materials or air-conditioning systems in residential buildings.
- NEF 35–40: This area experiences a moderate level of noise disturbance. Appropriate noise mitigation strategies should be implemented.
- NEF greater than 40: This area is subject to severe aircraft noise impact. Land acquisition or compensation measures may be necessary to address the adverse effects on residents and land use.

Quantitative assessment of noise contour evolution using GIS analysis techniques based on established spatial analysis methodologies [20], as shown in Eq. (3)

$$Relative\ Chang\ (\%) = \frac{Value_{after} - Value_{before}}{Value_{before}} \times 100 \quad (3)$$

Where, $Value_{after}$ = the value in the later year
$Value_{before}$ = the value in the earlier year

Statistical significance testing employs two-sample t-test with $\alpha = 0.05$ significance level according to environmental monitoring protocols [21].

Land Use Impact Assessment

ICAO Annex 16 compatibility assessment with population impact calculation following established environmental assessment guidelines [22], as shown in Eq. (4)

$$PI = \Sigma(\rho_i \times A_i \times PIF_i) \quad (4)$$

Where, PI = Population Impact index
ρ = population density (persons/km²)
A = affected area (km²)
PIF = Population Impact Factor

Results Summary

The summary of simulation results and impact analysis in both spatial and quantitative aspects was developed using the AEDT database and noise contour maps, which delineate affected areas in square kilometers. These outputs serve as tools to support evidence-based policy decision-making.

CASE STUDY

This study selected 5 major airports in Thailand, each with distinct physical contexts, operational characteristics, and surrounding land-use patterns, as case studies for evaluating aircraft noise impacts using the Aviation Environmental Design Tool (AEDT). The simulation results were compared with

actual noise measurement data, and spatial trends in noise impacts were analyzed. The selected airports are:

- Suvarnabhumi Airport (BKK): Located in Bang Phli District, Samut Prakan Province.
- Don Mueang Airport (DMK): Located in Don Mueang District, Bangkok.
- Chiang Mai International Airport (CNX): Located in Mueang Chiang Mai District, Chiang Mai Province.
- Mae Fah Luang – Chiang Rai International Airport (CEI): Located in Mueang Chiang Rai District, Chiang Rai Province.
- Phuket International Airport (HKT): Located in Thalang District, Phuket Province.

RESULTS

The results of the development and application of models with the case study were as follows:

Aircraft Noise Impact Assessment Results Using AEDT Model

Based on the generation of aircraft noise contours using actual flight operation data during the noise monitoring period, the mathematical model Aviation Environmental Design Tool (AEDT) was employed. The air traffic data from each airport was processed in the model to forecast daily aircraft noise levels. This process produced NEF (Noise Exposure Forecast) contour maps, as well as correlation values between the measured NEF levels and the NEF values simulated by the AEDT for each airport, as summarized below.

Noise Contour Simulation Results

Mathematical model assessment results in the form of Noise Exposure Forecast (NEF) contours, evaluated from flight situation data from January 1, 2023, to December 31, 2023, A summary of the affected areas within NEF 30-40 and NEF > 40 zones was shown in Table 1 and Fig 2.

Table 1 The affected areas according to 2023 flight situations within NEF contours

Airport	Daily Flight Operations	Affected Area (km²)		
		NEF >40	NEF 30-40	Total
Suvarnabhumi Airport	602	3.89	15.55	19.04
Don Mueang Airport	493	3.05	14.31	17.36
Chiang Mai International Airport	198	1.14	5.09	6.20
Mae Fah Luang - Chiang Rai Airport	34	0.15	0.66	0.81
Phuket Airport	285	1.40	4.91	6.31

Model Validation Results

To evaluate of the Aviation Environmental Design Tool (AEDT) in predicting aircraft noise levels, a comparative analysis was conducted between the Noise Exposure Forecast (NEF) values obtained from actual sound level measurements and those simulated by the AEDT model, using synchronized dates and times at each airport.

The analysis revealed that the correlation coefficients (R^2) between the measured NEF values and those generated by the model ranged from 0.89 to 0.94, indicating a high level of accuracy in AEDT's noise simulation performance within the context of Thai airports. Detailed results were shown in Table 2.

Table 2 Model Validation of AEDT and actual sound level measurements

Airport	Population in NEF >40 (persons)	Population in NEF 30-40 (persons)	Total Affected Population	Land Use Index
Suvarnabhumi Airport	23,340	124,400	147,740	0.67
Don Mueang Airport	18,300	115,000	133,300	0.62
Chiang Mai International Airport	6,840	35,630	42,470	0.71
Mae Fah Luang - Chiang Rai Airport	450	1,980	2,430	0.81
Phuket Airport	8,400	29,460	37,860	0.74

Note: All correlation coefficients exceed acceptable threshold of $R^2 \geq 0.85$; RMSE values meet criterion of ≤ 3.0 dB

(a) Suvarnabhumi Airport (b) Don Mueang Airport (c) Chiang Mai International Airport (d) Mae Fah Luang - Chiang Rai Airport (e) Phuket Airport

Fig 2. Noise Exposure Forecast (NEF) Contour Map Based on Flight Operations in 2023

Spatial Comparison of Noise Exposure Forecast (NEF) Contour Maps

To better understand the temporal dynamics of aircraft noise impact, a comparative assessment was conducted using NEF contour data from 2018 and 2023. The analysis focused on two key exposure thresholds NEF > 40 and NEF 30–40 to evaluate the spatial extent of noise-affected areas in square kilometers across five major airports in Thailand. Table 3 presents the quantitative results of this comparison, highlighting both the absolute and percentage changes in noise exposure zones over the five-year period. These changes reflect evolving patterns in flight operations, airport expansions, and surrounding land use, which collectively influence noise propagation and its associated impacts on communities.

DISCUSSION

The study demonstrates AEDT's effectiveness in Thai airport contexts, with correlation coefficients (R^2 = 0.89-0.94) meeting international standards [26,30]. Spatial analysis reveals heterogeneous noise impact patterns across different airport types and operational contexts. Chiang Mai International Airport's 45.2% expansion reflects rapid tourism recovery, while Phuket Airport's 28.6% reduction suggests effective operational optimization [23,24].

Population impact analysis indicates 363,800 residents affected by airport noise nationally, with 57,330 in high-impact zones requiring immediate attention. This substantial exposure underscores the surgency for comprehensive noise management strategies following ICAO guidelines [22,25].

Table 3 Spatial comparison of NEF affected areas between 2018 and 2023

Airport	Affected Area (km²)						Change (km²) (%)		
	2018			2023			2018-2023		
	NEF >40	NEF 30-40	Total	NEF>40	NEF 30-40	Total	NEF>40	NEF 30-40	Total
Suvarnabhumi Airport	3.63	14.87	18.50	3.89	15.55	19.04	0.26 (7.2%)	0.68 (4.6%)	0.54 (2.9%)
Don Mueang Airport	3.56	13.29	16.85	3.05	14.31	17.36	-0.51 (-14.3%)	1.02 (7.7%)	0.51 (3.0%)
Chiang Mai International Airport	0.91	3.36	4.27	1.14	5.09	6.20	0.23 (25.3%)	1.73 (51.5%)	1.93 (45.2%)
Mae Fah Luang – Chiang Rai Airport	0.12	0.53	0.65	0.15	0.66	0.81	0.03 (25.0%)	0.13 (24.5%)	0.16 (24.6%)
Phuket Airport	2.04	6.80	8.84	1.40	4.91	6.31	-0.64 (-31.4%)	-1.89 (-27.8%)	-2.53 (-28.6%)

Land Use Impact Assessment

Analysis results indicate several critical findings regarding airport noise impacts and their implications for land use planning based on ICAO Annex 16 guidelines and international best practices for sustainable airport development [22,25], as shown in Table 4.

Table 4 Population impact assessment based on ICAO land use compatibility

Airport	Average NEF (Measured)	Average NEF (AEDT)	Correlation Coefficients (R^2)	RMSE (dB)
Suvarnabhumi Airport	32.4	33.1	0.92	2.1
Don Mueang Airport	31.8	32.3	0.89	2.8
Chiang Mai International Airport	28.7	29.2	0.94	1.9
Mae Fah Luang - Chiang Rai Airport	25.3	25.8	0.91	2.3
Phuket Airport	29.6	30.1	0.90	2.5

CONCLUSIONS

This research validates AEDT as an accurate tool for airport noise assessment in Thailand, with a prediction accuracy of R^2 = 0.89–0.94. The study found that four out of 5 major Thai airports experienced increased noise-affected areas (ranging from 3.0% to 45.9%) between 2018 and 2023, totaling 52.1 km² nationwide. Currently, approximately 363,800 people are affected by airport noise, with 57,330 residents living in high-impact zones that require immediate attention.

The research reveals distinct regional patterns: metropolitan airports show steady growth, northern airports demonstrate rapid expansion due to tourism recovery, while southern airports show potential for operational optimization. For Thailand's planned airport expansion projects, including Chiang Mai Airport No. 2 and Andaman International Airport, noise impact assessment must be integrated from the initial planning stages. The study recommends establishing mandatory noise impact zones in airport master plans and developing integrated transportation and land use planning protocols to address the expanding noise footprint and protect affected communities.

ACKNOWLEDGMENTS

This research work was partially supported by Chiang Mai University, Thailand, through a Teaching Assistant/Research Assistant (TA/RA) scholarship.

REFERENCES

[1] Airports of Thailand Public Company Limited. (2024). Annual Report 2023: Sustainable Growth and Environmental Management. Bangkok: AOT Publications.

[2] Civil Aviation Authority of Thailand. (2024). Thailand Aviation Statistics 2023: Recovery and Growth Analysis. Bangkok: CAAT Publications.

[3] International Air Transport Association. (2024). Asia-Pacific Aviation Outlook 2024. Montreal: IATA Economics.

[4] World Health Organization. (2022). Environmental noise guidelines for the European region. Copenhagen: WHO Regional Office for Europe.

[5] Basner, M., & McGuire, S. (2018). WHO environmental noise guidelines for the European region: a systematic review on environmental noise and effects on sleep. The Lancet Public Health, 3(6), e263-e274. https://doi.org/10.1016/S2468-2667(18)30101-2

[6] Clark, C., Crombie, R., Head, J., van Kamp, I., van Kempen, E., & Stansfeld, S. A. (2012). Does traffic-related air pollution explain associations of aircraft and road traffic noise exposure on children's health and cognition? A secondary analysis of the United Kingdom sample from the RANCH project. American Journal of Epidemiology, 176(4), 327-337. https://doi.org/10.1093/aje/kws012

[7] Suksmith, P., & Nitivattananon, V. (2015). Aviation noise impact on property prices: Case study of Suvarnabhumi International Airport, Thailand. Transportation Research Part D: Transport and Environment, 41, 379-391. https://doi.org/10.1016/j.trd.2015.10.010

[8] Münzel, T., Schmidt, F. P., Steven, S., Herzog, J., Daiber, A., & Sørensen, M. (2018). Environmental noise and the cardiovascular system. Journal of the American College of Cardiology, 71(6), 688-697. https://doi.org/10.1016/j.jacc.2017.12.015

[9] Stansfeld, S. A., & Matheson, M. P. (2003). Noise pollution: non-auditory effects on health. British Medical Bulletin, 68(1), 243-257. https://doi.org/10.1093/bmb/ldg033

[10] International Civil Aviation Organization. (2023). Environmental Report 2022: Aviation and Environment. Montreal: ICAO.

[11] Gasco, L., Asensio, C., & de Arcas, G. (2017). Communicating airport noise emission data to the general public. Science of the Total Environment, 586, 836-848. https://doi.org/10.1016/j.scitotenv.2017.02.063

[12] Girvin, R. (2009). Aircraft noise-abatement and mitigation strategies. Journal of Air Transport Management, 15(1), 14-22. https://doi.org/10.1016/j.jairtraman.2008.09.012

[13] Federal Aviation Administration. (2023). Aviation Environmental Design Tool (AEDT) Version 3d Technical Manual. Washington, D.C.: U.S. Department of Transportation.

[14] Zaporozhets, O., Tokarev, V., & Attenborough, K. (2011). Aircraft noise: assessment, prediction and control. London: CRC Press.

[15] Ministry of Transport, Thailand. (2023). Thailand's Aviation Master Plan 2023-2037. Bangkok: Office of Transport and Traffic Policy and Planning.

[16] Department of Environmental Quality Promotion. (2022). Environmental Quality Management Plan for Airport Areas. Bangkok: Ministry of Natural Resources and Environment.

[17] Boontham, P., & Taneerananon, P. (2020). Development of a community noise prediction model for local airports in Thailand. Applied Acoustics, 167, 107386. https://doi.org/10.1016/j.apacoust.2020.107386

[18] Airport Council International, Airport Economics Report 2019, Montreal: ACI World, 2019.

[19] European Aviation Safety Agency, Environmental Protection Requirements for Aircraft: Noise, Cologne: EASA, 2021.

[20] van Kempen E. and Babisch W., The quantitative relationship between road traffic noise and hypertension: a meta-analysis, Journal of Hypertension, Vol. 30, Issue 6, 2012, pp. 1075-1086.

[21] Recio, A., Linares, C., Banegas, J. R., & Díaz, J. (2016). Road traffic noise effects on cardiovascular, respiratory, and metabolic health: An integrative model of biological mechanisms. Environmental Research, 146, 359-370. https://doi.org/10.1016/j.envres.2015.12.036

[22] Asian Development Bank, Sustainable Transport Solutions: Guidance for Developing Asian Cities, Manila: ADB, 2020.

[23] Čokorilo, O. (2020). Aviation noise and environmental sustainability: A review of current issues and future challenges. Sustainability, 12(8), 3186. https://doi.org/10.3390/su12083186

[24] Torija, A. J., Self, R. H., & Flindell, I. H. (2017). A model for the rapid assessment of the impact of aviation noise near airports. Journal of the Acoustical Society of America, 141(2), 981-995. https://doi.org/10.1121/1.4976053

[25] Thailand Environment Institute, Environmental Impact Assessment Guidelines for Transportation Projects, Bangkok: TEI, 2022.

Copyright © Int. J. of GEOMATE All rights reserved, including making copies, unless permission is obtained from the copyright proprietors.

15th Int. Conf. on Geotechnique, Construction Materials & Environment, Kyoto, Japan, 11-13 November 2025, ISBN 978-4-909106124 C3051

STUDY OF DRIFTWOOD ACCUMULATION CONDITIONS IN MOUNTAIN RIVERS THROUGH FIELD SURVEYS AND HYDRAULIC EXPERIMENTS

Yuriko Matsubayashi[1], Sae Nagahata[2] and Motoki Makino[3]

[1]Faculty of Science and Engineering, Iwate University, Japan; [2,3] Graduate of Faculty of Science and Engineering, Iwate University Japan

ABSTRACT

Clarifying the topographical conditions necessary for driftwood accumulation in mountain rivers is thought to be useful in predicting the amount of driftwood generated during heavy rain disasters. Although much research has been conducted on the macro-topographical conditions for driftwood accumulation, there have been no detailed surveys or research results on how many contact points are necessary for each piece of driftwood to accumulate, or what their spacing is. In this study, we conducted field surveys and hydraulic experiments to record and analyze the number of contact points between driftwood and obstacles necessary for driftwood to accumulate, as a topographical condition necessary for driftwood floating down the river to accumulate.

Both the field surveys and hydraulic experiments confirmed that driftwood floating down the river can accumulate even at a single point of contact with an obstacle. Furthermore, the largest amount of driftwood accumulated at two points of contact. The field surveys and hydraulic experiments obtained results that are useful for estimating the amount of driftwood that accumulates, based on the distribution of protrusions in the river topography and the length of the driftwood.

Keywords: Driftwood, Heavy rain disaster, Mountain rivers, Accumulation

INTRODUCTION

In recent years, heavy rainfall disasters have been increasing in Japan due to climate change. In addition, changes in the mountain environment and an increase in the number of short duration heavy rainfall events have resulted in increased damage due to the accumulation of driftwood in narrow areas and on bridges. It is important to understand and manage the amount of driftwood generated during heavy rainfall disasters to prevent the spread of damage caused by driftwood. Many studies on the generation and movement of driftwood have been conducted in Japan and overseas. Komori et al. have modeled the export of large wood at watershed scale [1]. Many studies have also been conducted on driftwood drifting and deposition on bridges [2]. Okamoto et.al. have conducted experimental study about accumulation and failure of driftwood on bridge pier [3]. Numerical simulations to estimate the behavior of individual driftwood are used as an effective method to understand the behavior of driftwood [4]

In this study, experiments and field investigations were conducted to clarify the conditions for driftwood deposition due to contact with independent obstacles in complex terrain, such as mountain rivers, in order to help improve prediction accuracy regarding driftwood movement, deposition, and runoff.

RESEARCH SIGNIFICANCE

In mountain rivers, driftwood accumulates in riparian forests, topographic changes, and uneven terrain, and moves with the rising water level. Knowledge of these conditions will improve the accuracy of estimating the potential volume of driftwood in mountain rivers and the volume of runoff during floods. In this study, we compared the number and distance of contact points between the deposited driftwood and obstacles, which are important for knowing the thresholds of deposition and migration, by means of field surveys and experiments.

METHOD

To understand the characteristics of the contact points between driftwood and obstacles when it is deposited in mountain rivers, we conducted tank experiments and field surveys and compared the results of each to clarify the characteristics of the number and distance of contact points between deposited driftwood and obstacles.

Experiments

The scale of the experiment was set to 1/20 with reference to the Koge River where the field survey was conducted, and the experiment was conducted in an experimental flume 30 cm wide and 178 cm long as shown on Fig.1. The average slope of the Koge River was used as a reference, and the slope was set to 1/44. A pump was used to circulate the water, and a rectifier was installed upstream of the tank. Sandpaper was placed on the bottom and walls of the tank to reproduce the roughness of a mountain riverbed.

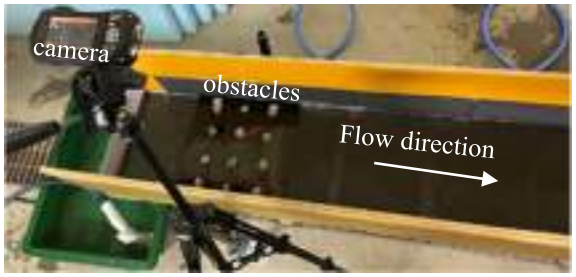

Fig.1 Experimental flume

A model of driftwood was put in the upper part of flume, and its accumulation on the obstacles placed on the riverbed was recorded by a camera placed over the flume for analysis. The size of the driftwood models were 4 mm and 6 mm in diameter and 8 cm in length to conduct experiments with 1.6 m driftwood. The obstacles on the riverbed were gravels of 15 to 20 mm in height and 15 to 35 mm in diameter attached to boards and placed in the flume, as shown in Fig.1. The central spacing was 4 cm, 6 cm, and 8 cm, and they were arranged in staggered and square grids (Fig2, Fig3 and Fig4). The water depth around the obstacles in the experiment was about 15 mm, and the flow velocity was fastest near the center of the flume due to friction on the wall, with an average velocity of 0.33 m/s and a Froude number of 0.86.

Fig.2 Gravels with 4cm spacing

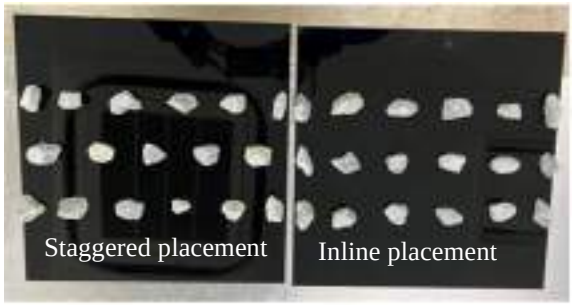

Fig.3 Gravels with 6 cm spacing

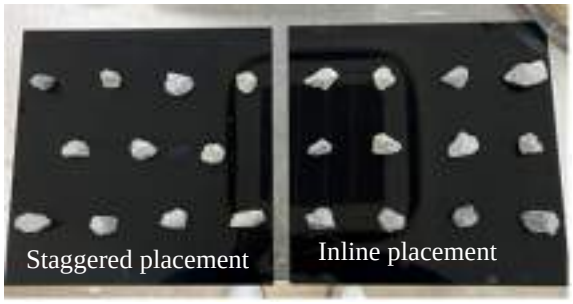

Fig.4 Gravels with 8 cm spacing

For each type of obstacle in the riverbed, experiments were conducted 75 times, with the upstream and downstream sides of the gravel-lined board reversed.

Field Survey

Field surveys were conducted on mountain rivers in Iwate Prefecture, and the size of accumulated driftwood, the location and height of contact points with obstacles such as riparian forests and stones, and the surrounding topography were recorded and analyzed. Fig.5 shows photo of measuring.

A total of 100 driftwoods, 79 in the Koge River and 21 in the Kitayama River were surveyed. All driftwood with a circumference of at least 1.5 cm and a length of at least 0.3 m were measured as we moved through the surveyed area.

Fig.5 Measuring driftwood (Koge River)

RESULTS

Experiments

To examine the effect of gravel spacing and the number of contact points on driftwood capture rate, we compared the number of driftwood pieces captured in each arrangement pattern. The location and number of contact points at which driftwood accumulates varied depending on small changes in the flow in each experimental case. Fig.6 and Fig. 7 shows driftwood accumulated at one and two contact points. Fig. 8 and Fig. 9 show the percentage of captured driftwood pieces in each of the gravels for different spacings. A similar trend was observed for the 4 mm and 6 mm diameter grids. The capture rate decreased with increasing grid spacing, and there was no clear difference in capture rate between the different arrangements of the grids. Regardless of the spacing, deposition by the two contact points was the most frequent. Under all conditions, a single contact point was sufficient for deposition.

Fig.6 Deposition with 1-point contact

Fig.7 Deposition with 2-points contact

The narrower the distance between the gravels, the more driftwoods were deposited with two-point contact, and at the narrowest distance of 4 cm, the more driftwoods were deposited with three points of contact.

The driftwood model started parallel to the flow but turned and changed direction depending on the flow or by hitting gravels. Some driftwood was deposited at single point and then stopped moving, while others continued oscillating. In the present analysis, we did not separate the sedimentation state

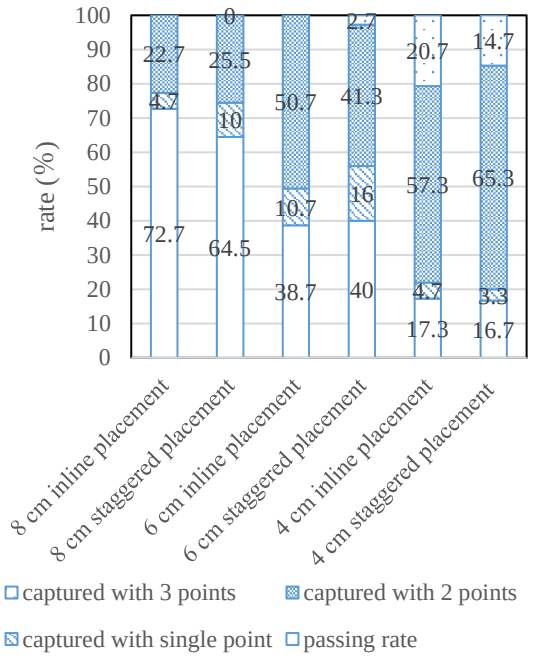

Fig.8 Capture rate of driftwood (4 mm in diameter)

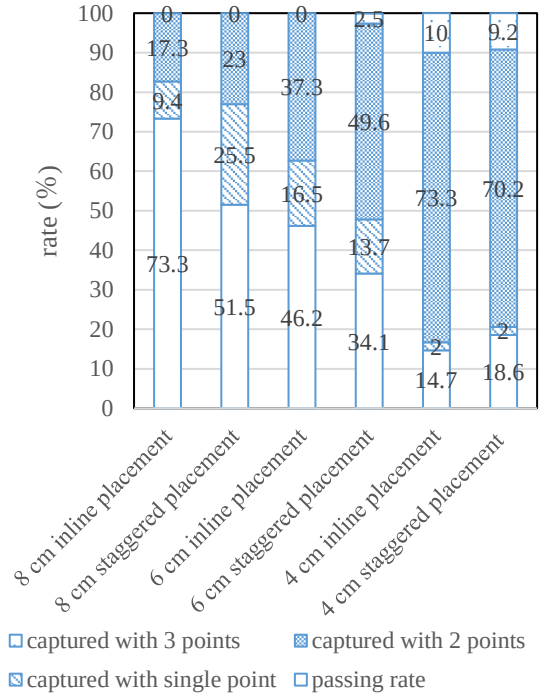

Fig.9 Capture rate of driftwood (6 mm in diameter)

Field Survey

The number of contact points that allow driftwood capture is important information for examining the driftwood accumulation conditions in rivers. Table 1 shows the number of contact points of driftwood and obstacles observed, with driftwood deposited at two points of contact and driftwood deposited on stones being the most common. Some driftwood was deposited at a single contact point.

The position of the contact point is shown in Fig.10 as a percentage of the length of the driftwood. The contact points are distributed close to the right and left edges of the driftwood. The contact points are distributed near the right and left edges of the driftwood, suggesting that the accumulation of the driftwood near the edges of the driftwood was caused by contact with an obstacle.

By comparing the height of the driftwood pile and its diameter, it is possible to estimate whether the driftwood was rolling along the riverbed or floating near the surface when it was deposited. Fig. 11 shows the relationship between the height of the contact points above the bed and the radius of the driftwood.

Many of the driftwoods were deposited by contact with obstacles higher than the driftwood radius, indicating that most of the deposited driftwoods drifted near the water surface during flooding and were deposited by contact with obstacles.

Table 1 Number of measured driftwoods

Number of contact points	Obstacle			
	Riparian wood	Stone	Driftwood	Combination
1	4	6	1	
2	7	32		6
3	4	20		2
4	1	10	1	
5		3		1
6		1		
7		1		

Note: Combination: combinations of contact points with stones, riparian wood, driftwood or grasses

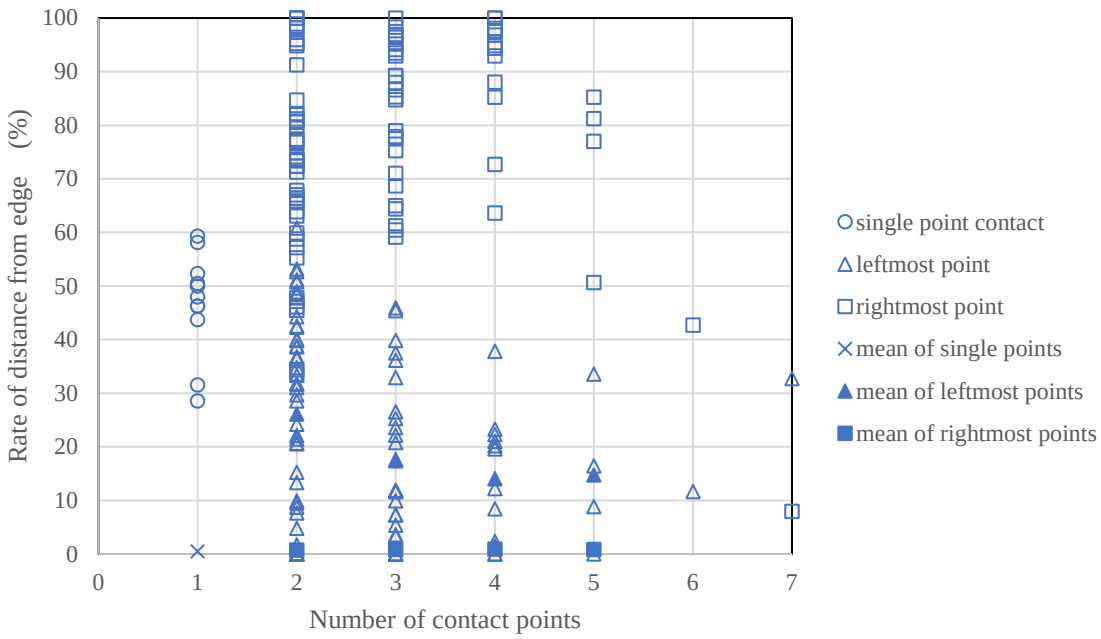

Fig.10 Contact position of driftwood

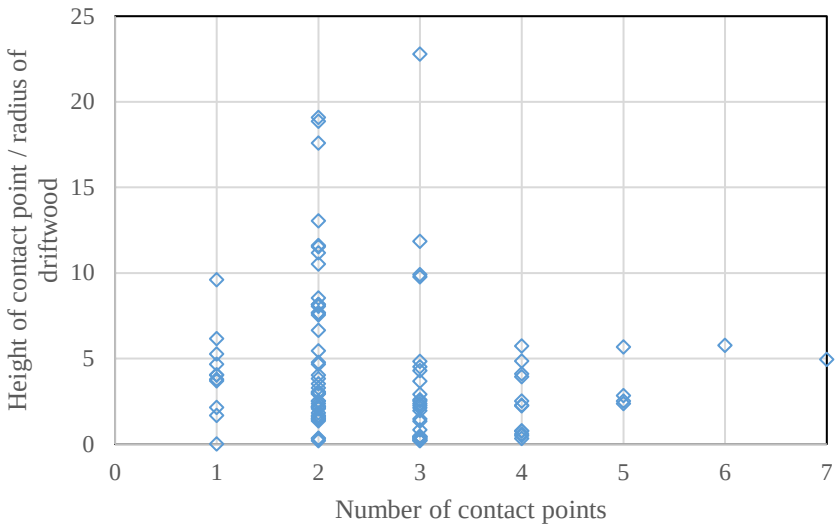

Fig.11 Height of contact point

CONCLUSIONS

The experiment and field survey of contact points of driftwood showed similar results in terms of the distribution of the number of contact points between the accumulated driftwood and the obstacle, with the largest number of driftwoods deposited at two contact points, although driftwood was deposited at one contact point. In both the experiment and the field survey, the number of driftwood pieces deposited at three or more points of contact decreased.

The results indicate that driftwood is more likely to be captured in a river when the length of driftwood drifting during a flood is longer than the distance between two or more points of obstruction in the river.

ACKNOWLEDGMENTS

This study was supported by the River Fund of The River Foundation, Japan.

The authors would like to thank Nishiwaga Town Hall for their cooperation in the survey.

REFERENCES

[1] Komori D., Sukegawa Y., Chaithong T. and Kazama S., Modelling of large wood export at a watershed scale, Earth Surface Processes and Landforms, Vol. 47, Issue 2, pp.688-696.

[2] Watanabe K., Saito N. and Jiken Y., Hydraulic Model Experimental Study on Bark Stripping Process Using Driftwood Model, International Journal of GEOMATE, Vol. 25, Vol. 25 No. 108 (2023): August 2023, pp. 106-113.

[3] Okamoto T. and Sanjou M. Experimental Study on Accumulation and Failure of Driftwood Jam and Increase in Drag Force on Bridge Pier, Japanese Journal of JSCE, Volume 81 (2025) Issue 16, in Japanese

[4] Shen D., Aoki T., Watanabe S., Moriguchi S., Takase S., and Sakuraba M.., 3-D Direct Simulations of Driftwood Accumulation in a Real River Flood, Journal of Japan Society of Civil Engineers, 12,1,2024

Copyright © Int. J. of GEOMATE All rights reserved, including making copies, unless permission is obtained from the copyright proprietors.

15th Int. Conf. on Geotechnique, Construction Materials & Environment,
Kyoto, Japan, 11-13 November 2025, ISBN 978-4-909106124 C3051

DEEP LEARNING-AUGMENTED LAKE ECOSYSTEM MODELING FOR IMPROVED FORECASTING OF ALGAL BLOOMS AND HYPOXIA IN ENCLOSED AREA

Jinichi Koue[1], Sota Yoshikawa[1], Katsutoshi Hirayama[1]

[1]Graduate School of Maritime Sciences, Kobe University, Japan

ABSTRACT

Accurate forecasting of phytoplankton dynamics and hypoxia in freshwater ecosystems is vital for effective water quality management amid accelerating climate and anthropogenic pressures. This study develops a hybrid deep learning framework combining physical–chemical mass-balance equations with recurrent neural networks (RNN, LSTM) to enhance predictions of chlorophyll-a, -b, -c and dissolved oxygen (DO) in Lake Biwa, Japan. Two approaches were compared: Case 1 using conventional inputs, and Case 2 incorporating mechanistic biogeochemical constraints. Short-term forecasts at 0.5 m depth showed marked improvements in peak chlorophyll prediction under Case 2, especially with LSTM (e.g., Chl-b RMSE halved from 0.63 to 0.33 µg/L), reflecting better capture of rapid physiological and transport dynamics. For DO at 90 m, Case 2 reduced RMSE by ~50% for LSTM and by an order of magnitude for RNN, successfully reproducing hypoxic events below 2 mg/L during 2020 stratification. This highlights enhanced sensitivity to ecological thresholds through physics-informed modeling. However, long-term forecasting revealed limitations; Case 2 underperformed for chlorophyll due to fixed hyperparameters failing to represent seasonal nonlinearities and ecosystem feedbacks (e.g., Chl-b LSTM RMSE rose from 0.21 to 1.37 µg/L), though DO predictions remained improved. These results demonstrate the potential and challenges of integrating mechanistic constraints into neural forecasting for adaptive lake management and water quality optimization under changing environments.

Keywords: Deep Learning, Algal Blooms, Hypoxia, Lake Biwa, Ecosystem Modeling

INTRODUCTION

Climate change and anthropogenic pressures are increasingly disrupting the physical and biogeochemical stability of freshwater ecosystems worldwide. Among the most pressing consequences are the intensification of hypoxia and harmful algal blooms (HABs), which threaten aquatic biodiversity and compromise water resource sustainability. Despite long-term nutrient reduction efforts, large-scale cyanobacterial blooms persist in major lakes such as Lake Taihu in China [1] and Lake Erie in North America [2], underscoring the resilience of these phenomena to conventional mitigation.

Lake Biwa, Japan's largest freshwater lake, now exhibits similar signs of ecological degradation. Supporting over 14 million people in the Keihanshin region, the lake is hydrologically divided into a deep North Basin and a shallow South Basin, with inflows from 117 rivers and limited outflow through the Seta River and Biwako Canal. Since the first major bloom in 1983, Microcystis-dominated surface accumulations have caused filtration disruptions and the release of odor compounds such as 2-methylisoborneol and geosmin, reaching levels as high as 180 ng/L and 390 ng/L in 2020, respectively—necessitating emergency treatment [3].

Meanwhile, deep-water hypoxia in the North Basin has intensified during summer stratification, driven by suppressed vertical mixing, sediment oxygen demand, and internal phosphorus release. Dissolved oxygen concentrations below 2 mg/L are frequently observed, especially in the Imazu Basin, endangering benthic habitats and accelerating eutrophication. Although factors such as nutrient inflow, aquaculture discharge, and climate-induced shifts in wind and runoff patterns have been identified [3], the mechanistic links between bloom formation and hypoxia remain insufficiently understood.

Recent advances in coupled physical-biogeochemical models have improved system understanding [3], while machine learning techniques—particularly Long Short-Term Memory (LSTM) networks—have shown promise in forecasting bloom dynamics [4]. However, integration of these approaches remains limited. Here, we develop a hybrid modeling framework that combines long-term water quality data from the Lake Biwa Environmental Research Center with meteorological inputs from the Japan Meteorological Agency. By merging process-based models with neural network architectures including Feedforward Neural Networks, Recurrent Neural Networks (RNN), and LSTM [5–8], we aim to improve prediction of

key ecological indicators such as phytoplankton biomass, nutrient concentrations, and dissolved oxygen. This integrative approach enhances forecasting capabilities for lake ecosystem management under accelerating environmental change.

RESEARCH SIGNIFICANCE

This study demonstrates the potential of integrating physico-chemical process-based balance equations into deep learning models for improving the prediction accuracy of key water quality parameters in Lake Biwa. The hybrid approach enhanced short-term forecasts of chlorophyll and dissolved oxygen, supporting more effective algal bloom management and water treatment operations. By capturing complex ecosystem dynamics, this framework offers a promising tool for early warning systems and long-term risk assessment in freshwater environments, thereby advancing the application of AI-augmented modeling in ecological forecasting.

METHODOLOGY

This study developed and compared two deep learning-based frameworks for forecasting water quality in Lake Biwa, utilizing both observational and process-informed input structures. Water quality data were obtained from the Lake Biwa Environmental Research Institute of Shiga Prefecture, and meteorological data were provided by the Japan Meteorological Agency. Two input configurations were considered: Case 1: Direct assimilation of observed physicochemical parameters. Case 2: Use of process-derived variables computed from a mass-balance ecosystem model originally developed by Koue [3], which represents key biogeochemical dynamics within the lake. These variables were designed to encode mechanistic insights into the data.

For both input cases, two types of deep learning architectures were employed: a Recurrent Neural Network (RNN), and a Long Short-Term Memory (LSTM) network. This comparative modeling approach enabled assessment of the predictive performance and interpretability associated with purely empirical versus process-based input features.

Machine Learning Predictive Technology

Feedforward Neural Network (NN)

A feedforward neural network (NN) is the simplest form of neural network, where data flows in a single direction—from input to output—without looping back. It consists of three main types of layers: input, hidden, and output. Each input node receives a value, multiplies it by a weight, adds a bias, and sends the result to the hidden layer. The hidden layer then processes these values using an activation function, such as ReLU or sigmoid, and passes the outputs forward. The output layer receives these final values and produces the network's prediction or classification. In this structure, information always moves forward; it does not return to previous layers.

Recurrent Neural Networks (RNN)

Recurrent Neural Networks (RNN) are designed to handle sequential data by retaining past information through recursive connections. Unlike feedforward networks, which treat each input independently, RNN use hidden states to propagate temporal information, making them effective for modeling time-dependent processes such as speech recognition, language modeling, and environmental forecasting.

The input at time t is denoted as x_t and the hidden layer state is denoted as h_t. The hidden state h_t is computed from the input x_t and the hidden state h_{t-1} of the previous step. This recursive computation allows modeling of long-term dependence in time series data.

In this study, the Simple Recurrent Neural Network (Simple RNN) is employed due to its fundamental architecture, which facilitates both theoretical analysis and practical implementation. Despite its simplicity, it effectively captures basic temporal dependencies in time series data.

The following variables are defined. The input x_t at time t is a feature vector representing the observed data. The hidden state h_t is a vector representing the internal state of the network, which holds past information in a compressed form. The update law of this hidden state is expressed by the following equation.

$$h_t = act(Wx_t + Uh_{t-1} + b) \quad (1)$$

where W is the weight matrix from the input layer to the hidden layer, U is the weight matrix representing the recursive coupling of the hidden layer, b is the bias term, and act is the nonlinear activation function. Commonly used activation functions include the tanh function and the ReLU function.

Long Short-Term Memory (LSTM)

The Long Short-Term Memory (LSTM) network is a variant of RNN that addresses the vanishing gradient problem and captures long-term dependencies more effectively. LSTM introduces a memory cell (ct) and three gating mechanisms: the forget gate (f), input gate (i), and output gate (o), which control the flow of information as follows:

$$\mathbf{f = \sigma(Wfxt + Ufht - 1 + bf)} \quad (\mathbf{2})$$

$$\mathbf{i} = \boldsymbol{\sigma}(\mathbf{Wixt} + \mathbf{Uiht-1} + \mathbf{bi}) \quad (3)$$

$$\mathbf{o} = \boldsymbol{\sigma}(\mathbf{Woxt} + \mathbf{Uoht-1} + \mathbf{bo}) \quad (4)$$

$$\mathbf{g} = \mathbf{tanh}(\mathbf{Wcxt} + \mathbf{Ucht-1} + \mathbf{bc}) \quad (5)$$

$$\mathbf{ct} = \mathbf{ft} \odot \mathbf{ct-1} + \mathbf{it} \odot \tilde{\mathbf{c}}\mathbf{t} \quad (6)$$

$$\mathrm{ht} = \mathrm{ot} \odot \tanh(\mathrm{ct}) \quad (7)$$

The conceptual diagram of the LSTM is shown in Fig. 1. Here, m represents the dimension of the input to the LSTM, and n represents the dimension of the output. The input at time t is denoted as $x_t \in \mathbb{R}_m$, the hidden state and output at time t are denoted as $h_t \in \mathbb{R}_n$ and c_t represents the cell state. $W \in \mathbb{R}_{n\times m}$ and $U \in \mathbb{R}_{n\times n}$ are the weight matrices, and $b \in \mathbb{R}_n$ is the bias term. g represents the input to the internal cell, f is the forget gate, i is the input gate, and o is the output gate. In these equations, $\boldsymbol{\sigma}$ and tanh are activation functions, and $\odot$ denotes element-wise multiplication. The cell state (ct) functions as long-term memory, updated selectively by the gates to retain relevant information.

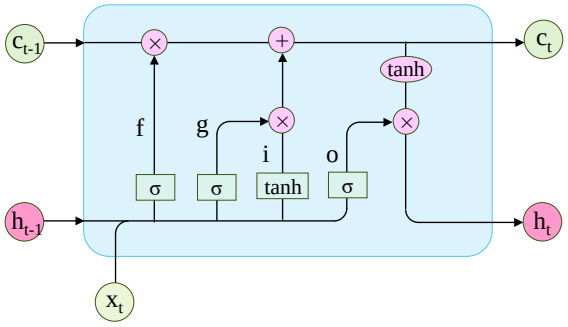

Fig.1 Conceptual diagram of the LSTM

Deep Learning-Based Frameworks

The two frameworks developed in this study are used to predict water quality at depths of 0.5 m and 20 m, and 60 m at Imazu-oki in the northern part of Lake Biwa. The water quality data used as input data are twice-monthly observations by the Lake Biwa Environmental Research Institute of Shiga Prefecture, and the meteorological data are from the Hikone District Meteorological Observatory of the Japan Meteorological Agency.

The framework generates the concentration of chlorophyll a, b, and c (Chl-a, b, c), and dissolved oxygen (DO) as prediction output. In Case 1, observed environmental variables were used directly as model inputs. Table 1 shows the observation data used. Biweekly observational data were used, with missing values interpolated linearly and observation times standardized across variables prior to model input. In Case 2, model inputs were derived from a mass-balance formulation representing key biogeochemical processes. These values were calculated using a mechanistic water quality model previously developed by Koue [3], which simulates nutrient and phytoplankton dynamics in Lake Biwa.

Table 1 Observation data used as input values in Case 1

Predicted value	Input Parameters
Chl-a, b, c	Ammonium nitrogen, Nitrite nitrogen, Nitrate nitrogen, Phosphate phosphorus, pH, Water temperature, Transparency, DO
DO	Chlorophyll-a-c, Ammonium nitrogen, Nitrite nitrogen, Nitrate nitrogen, Phosphate phosphorus, pH, Water temperature, Transparency, DO, Dissolved organic

Learning and Forecasting Periods

To evaluate predictive performance across different ecological time scales, both short-term and long-term forecasting models were developed. The training periods were defined separately for each target variable based on data availability. For phytoplankton biomass, the model was trained using data from April 1998 to March 2019. For dissolved oxygen, the training period spanned from April 2004 to March 2019.

Two forecasting horizons were considered: Short-term models were designed to predict water quality variables up to two weeks in advance, with forecasts validated over a three-year period from April 2020 to March 2023. Long-term models were developed for one-year-ahead predictions, with validation performed using data from April 2019 to March 2020.

The same network architecture and hyperparameters were used for both the short-term and long-term forecasting models to enable a consistent comparison of model performance across different temporal scales.

Evaluation Metrics

Root Mean Square Error (RMSE)

RMSE is a metric used to assess the prediction error between observed and forecasted values. It is defined by the following equation:

$$\mathrm{RMSE} = \sqrt{\left(\frac{\Sigma(y_i - \hat{y}_i)^2}{n}\right)} \quad (8)$$

where y_i represents the observed values, $\hat{y}_i$ represents the predicted values, and n is the number of data

points.

Mean Bias (MB)

MB is used to assess systematic errors (bias) between predicted and observed values. It is defined by the following equation:

$$MB = \frac{1}{n}\sum(\hat{y}_i - y_i) \quad (9)$$

where y_i represents the observed values, $\hat{y}_i$ represents the predicted values, and n is the number of data points. MB indicates whether the predictions are consistently overestimated or underestimated, with positive values suggesting an overestimation and negative values indicating an underestimation.

RESULTS

Short-Term Forecasting Results

Chlorophyll-a-c

Figure 2 shows the prediction results for chlorophyll a, b, and c in Case 1 and 2 at 0.5 m depth. Table 2 also shows the evaluation indices for each model. The results of the analysis show that in Case 2, the agreement between the measured and predicted values at the peak improved for all chlorophylls compared to Case 1. This may be due to the fact that the balance equation expresses the physicochemical processes involved in the variation of chlorophyll concentration as mathematical equations, enabling learning from input data with essential characteristics, which contributed to more accurately capturing rapid changes in chlorophyll concentration. Furthermore, the overall improvement of the evaluation index was confirmed, suggesting the effectiveness of the method proposed in this study.

Table 2 Chlorophyll-a, b, and c evaluation index in the surface layer (0.5 m depth)

Predicted value	Model	RMSE (μg/l)		MB (μg/l)	
		Case1	Case2	Case1	Case2
Chl-a	NN	1.67	1.67	-0.42	-0.05
	RNN	1.53	1.79	-0.37	-0.30
	LSTM	2.50	1.78	-1.10	-0.22
Chl-b	NN	0.36	0.36	-0.11	-0.02
	RNN	0.37	0.39	-0.02	-0.06
	LSTM	0.63	0.33	-0.16	-0.03
Chl-c	NN	0.25	0.21	-0.10	-0.01
	RNN	0.27	0.24	-0.12	-0.06
	LSTM	0.25	0.24	-0.14	-0.04

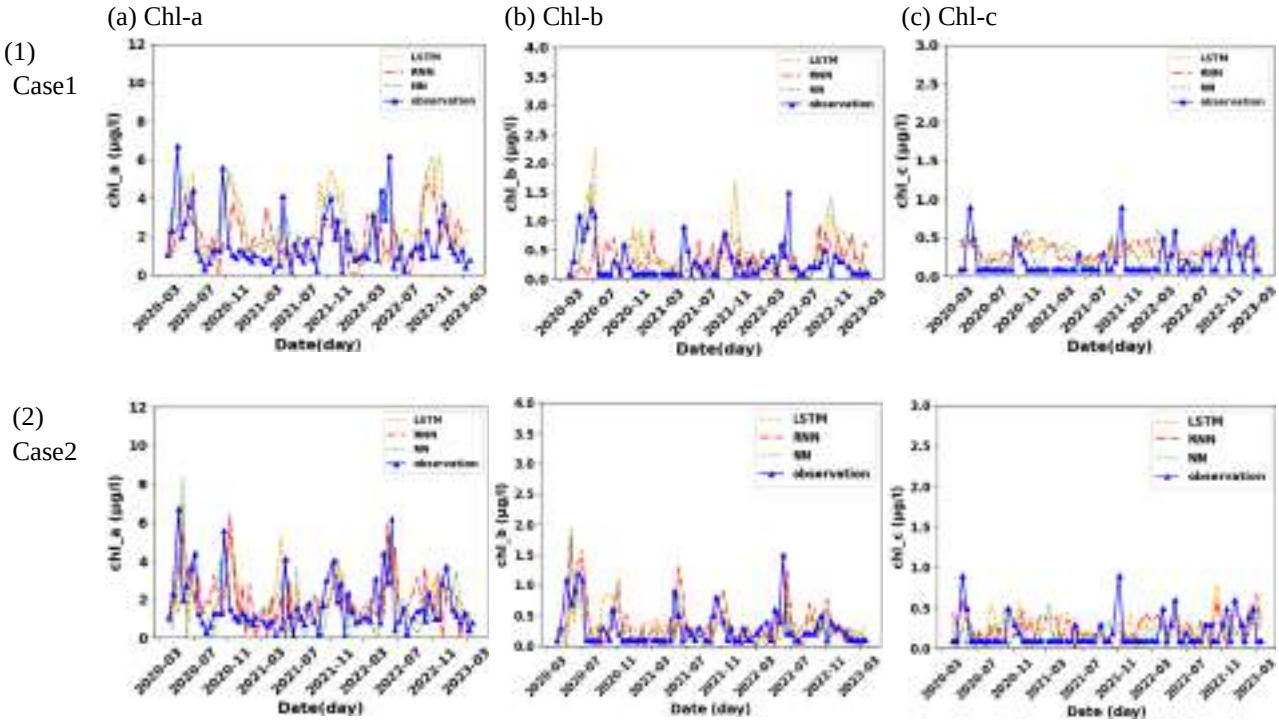

Fig. 3 Comparison of chlorophyll-(a) a, (b) b, (c) c, in (1) Case 1 and (2) Case 2 in the surface layer (0.5 m depth)

Dissolved oxygen

To evaluate the model's predictive performance under different input conditions, forecasts of dissolved oxygen (DO) at 90 m depth were compared between Case 1 (conventional inputs) and Case 2 (with a balance equation). This depth, located within the stratified hypolimnion of Lake Biwa's North Basin, is highly susceptible to oxygen depletion and nutrient accumulation, making it a critical zone for assessing internal water quality degradation. Figure 4 shows the predicted results of DO for Case 1 and Case 2 at the lake bottom (90 m depth). Table 3 also shows the evaluation indices for each model.

Substantial gains were observed in DO predictions under Case 2. At both 90 m and near-bottom depths, RMSE values were reduced by approximately 50% for LSTM and nearly an order of magnitude for RNN compared to Case 1. Crucially, the model accurately predicted the 2 mg/L hypoxic threshold during the 2020 low-oxygen event, demonstrating improved sensitivity to biogeochemical transitions. These enhancements are attributed to the inclusion of a physicochemically-informed balance equation that accounted for oxygen production and consumption processes, including photosynthesis, organic matter degradation, and respiration. By embedding these dynamics into the model, temporal variations in DO were more faithfully reproduced, particularly under stratified conditions. This result highlights the potential of hybrid frameworks to enhance predictive accuracy for ecologically critical variables in complex freshwater systems.

Table 3 DO evaluation index in the bottom of the lake (90 m depth)

Predicted value	Model	RMSE (mg/l)		MB (mg/l)	
		Case1	Case2	Case1	Case2
DO	NN	2.33	1.60	-0.80	-0.79
	RNN	2.30	1.37	-0.92	-0.32
	LSTM	2.89	1.57	-0.67	-0.18

(1) Case1

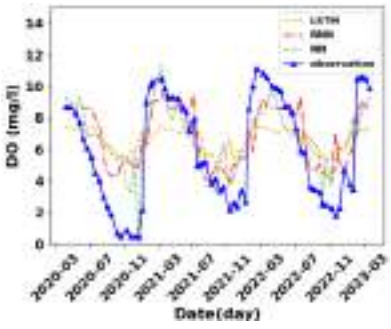

(2) Case2

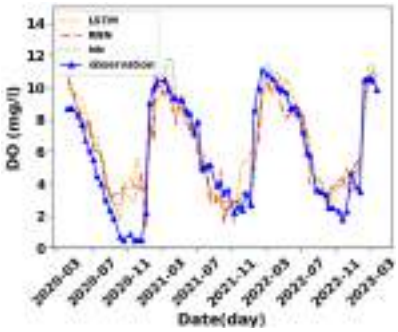

Fig. 4 Comparison of DO, in (1) Case 1 and (2) Case 2 in the bottom of the lake (90 m depth)

Long-Term Forecasting Results

Chlorophyll-a-c

Figure 5 shows the predicted chlorophyll (a) a, (b) b, and (c) c for Case 1 and 2 in the surface layer (0.5 m depth). Table 4 also shows the evaluation indices for each model. Table 4 shows that for all chlorophyll types, a decrease in prediction accuracy was observed in Case 2 compared to Case 1. Figure 5 shows that the main issue is the prediction during the peak period, and this is especially true for chlorophyll b. Given the improved accuracy in short-term forecasting, it can be inferred that the hyperparameters of the model do not adequately capture long-term time-series fluctuations, which is the main cause of the lower forecasting accuracy. Specifically, in the deep learning models of RNN and LSTM, hyperparameters such as the number of neural network units, number of neurons, and batch size do not adequately reflect the complex nonlinear factors (seasonal variation of environmental conditions, interactions among organisms, changes in nutrient concentration, weather conditions) are not adequately reflected, which may be a reason for the lower accuracy.

Dissolved oxygen

Figure 6 shows the predicted results of DO for Case 1 and 2 at the lake bottom (90 m depth). Table 5 shows the evaluation indices for each model.

The results of the analysis using the DO prediction model generally showed good agreement with the observed data (Figure 6(c)), with Case 1 failing to adequately reproduce the temporal variation pattern (timing of increase or decrease) of dissolved oxygen concentration, whereas Case 2 succeeded in capturing the observed variation with high accuracy. This improvement in prediction accuracy is also supported by quantitative evaluation indices (Table 5), which show a marked improvement in Case 2 compared to Case 1.

Table 4 Chlorophyll-a, b, and c evaluation index in the surface layer (0.5 m depth)

Predicted value	Model	RMSE (µg/l)		MB (µg/l)	
		Case1	Case2	Case1	Case2
Chl-a	RNN	3.08	2.16	-2.30	1.65
	LSTM	1.73	2.18	-0.49	1.67
Chl-b	RNN	0.23	1.19	-0.08	-0.78
	LSTM	0.21	1.37	-0.08	-0.85
Chl-c	RNN	0.22	0.26	-0.05	-0.03
	LSTM	0.37	0.26	-0.23	-0.03

Table 5 DO evaluation index in the bottom of the lake (90 m depth)

Predicted value	Model	RMSE (mg/l)		MB (mg/l)	
		Case1	Case2	Case1	Case2
DO	RNN	2.88	1.71	-0.99	-0.93
	LSTM	3.18	2.91	0.80	-0.98

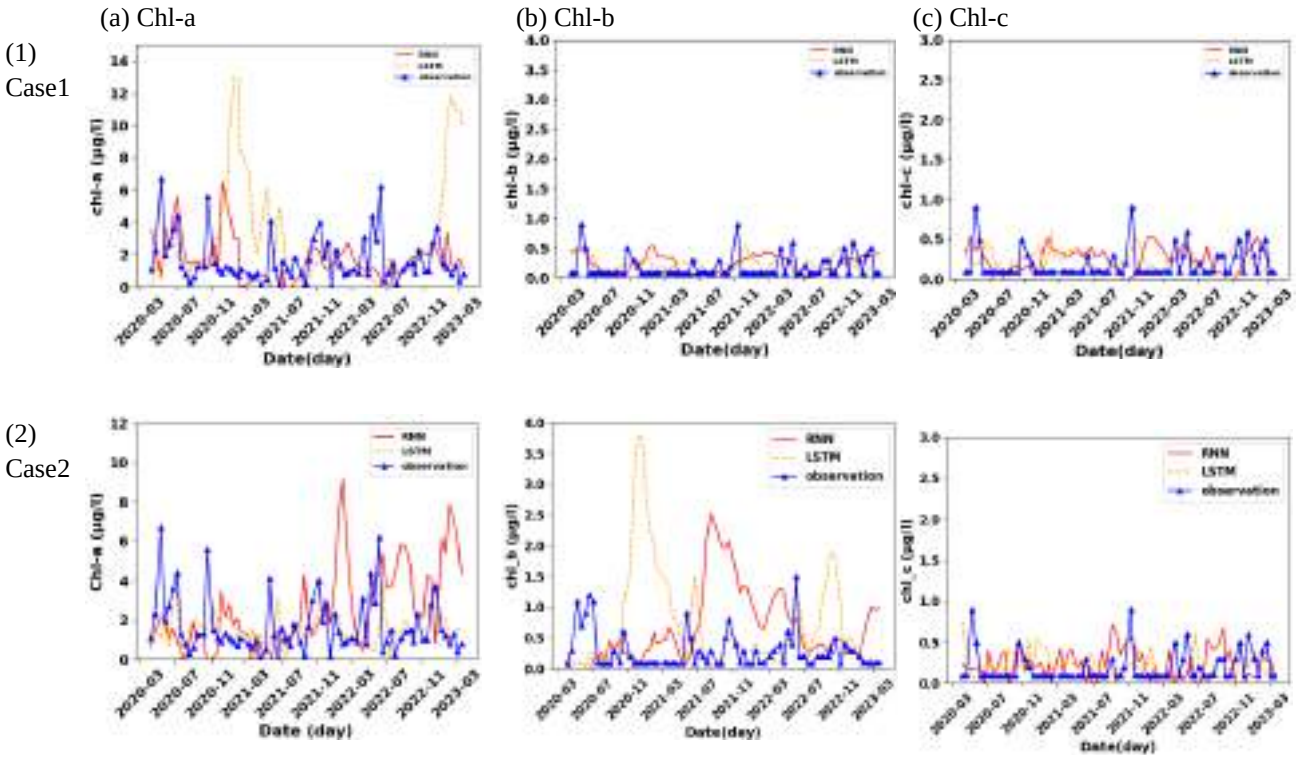

Fig. 5 Comparison of chlorophyll-(a) a, (b) b, (c) c, in (1) Case 1 and (2) Case 2 in the surface layer (0.5 m depth)

(1) Case1

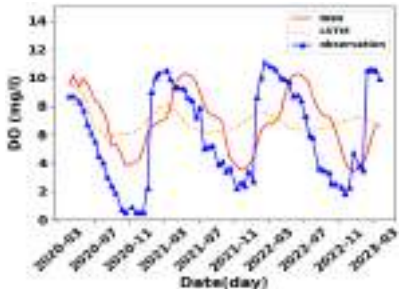

(2) Case2

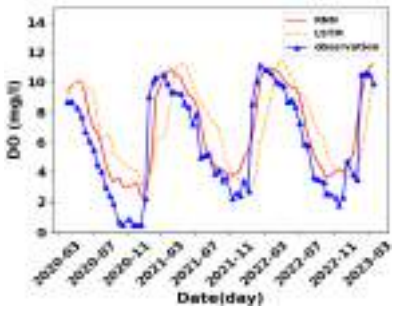

Fig. 6 Comparison of DO, in (1) Case 1 and (2) Case 2 in the bottom of the lake (90 m depth)

CONCLUSION

In this study, we compared the short-term and long-term predictions of water quality parameters in Lake Biwa between Case 1, which uses only conventional input values, and Case 2, which incorporates a balance equation that takes physico-chemical processes into account. The results showed that Case 2 improved the prediction accuracy of chlorophyll (a, b, c) at the peak in the short-term prediction, confirming that the expression of physicochemical processes by the balance equation is effective. On the other hand, for dissolved oxygen, improvement was confirmed in Case 2 for all evaluation indices. This may be due to the fact that the introduction of the balance equation explicitly incorporated complex interactions such as oxygen consumption and production processes in the ecosystem into the model.

In the long-term prediction, a decrease in prediction accuracy was confirmed in Case 2 compared to Case 1 for all chlorophyll (a, b, c) species. This result may be due to the fact that the hyperparameters of the deep learning models, such as RNN and LSTM, do not properly capture long-term time-series variations. For dissolved oxygen, Case 2 was able to capture the variability of observed values with high accuracy at the bottom of the lake (90 m depth).

These results confirm that the introduction of a balance equation that takes into account physico-chemical processes has a markedly improved effect, especially in the short-term prediction of chlorophyll (a,b) and dissolved oxygen. The model developed in this study enables more accurate prediction of the timing of blue-green algae blooms, and is expected to contribute to optimizing the timing of activated carbon application at water treatment plants. Furthermore, we hope that the results of this study will contribute to the long-term, highly accurate prediction of anoxia in Lake Biwa in the future and help to take into account the contribution rate of the dominant factors in anoxia.

ACKNOWLEDGMENTS

This work was partially supported by the Asahi Glass Foundation.

REFERENCES

[1] Cao H., Han L., Li L. A deep learning method for cyanobacterial harmful algae blooms prediction in Taihu Lake, China. Harmful Algae, Vol. 113, 2022, 102189.

[2] Michalak A. M., Anderson E. J., Beletsky D. et al. Record-setting algal bloom in Lake Erie caused by agricultural and meteorological trends consistent with expected future conditions. Proceedings of the National Academy of Sciences, Vol.110, Issue 16, 2013, pp.6448-6452.

[3] Koue J. Development of an ecosystem model considering sediment redox processes in enclosed water bodies. Water, Vol. 16, Issue 13, 2024, 1879.

[4] Liang Z., Zou R., Chen X., Ren T., Su H., Liu Y. Simulate the forecast capacity of a complicated water quality model using the long short-term memory approach. Journal of Hydrology, Vol. 581, 2020, 124432.

[5] Elman J. L. Finding structure in time. Cognitive science, Vol. 14, Issue 2, 1990, pp.179-211.

[6] Hochreiter S., Schmidhuber J. Long short-term memory. Neural computation, Vol. 9, Issue 8, 1997, pp.1735-1780.

[7] Gers F. A., Schmidhuber J., Cummins F. Learning to forget: Continual prediction with LSTM. Neural computation, Vol. 12, Issue 10, 2000, pp.2451-2471.

[8] Zhang S., Qi J. A study on the reliability of an artificial intelligence model for water environment evaluation. GEOMATE Journal, Vol. 25, Issue 107, 2023, pp.220-227.

Copyright © Int. J. of GEOMATE All rights reserved, including making copies, unless permission is obtained from the copyright proprietors.

15th Int. Conf. on Geotechnique, Construction Materials & Environment,
Kyoto, Japan, 11-13 November 2025, ISBN 978-4-909106124 C3051

FLOATING OFFSHORE AIRPORTS: PLANNING, ENGINEERING FEASIBILITY, AND ENVIRONMENTAL IMPACT ASSESSMENT—A CASE STUDY OF TAIWAN'S COASTAL DEVELOPMENT AND GLOBAL IMPLEMENTATIONS

LIN Jen-Liann[1], LIN Yuan-Ho[2], LIN Yong-Zhi[3]

[1]Associate Professor, Guangdong University of Business and Technology
[2]Distinguished Professor, Guangdong University of Business and Technology
[3]Manager, Ping An Bank; Assistant to Distinguished Professor, Guangdong University of Business and Technology

ABSTRACT

Offshore facilities such as, artificial islands, floating houses, cities, and airports are constructions for infrastructure, habitation, entertainment, industrial or commercial purposes, and infrastructure built on the ocean. They can either be grounded as artificial islands or floating on airfilled or light materials. Recent developments show a trend of airport construction offshore. If these are floating airports can be situated above deeper waters or further offshore. These can even be used for the development of airports reclaimed lands close to the coast. An offshore airport provides certain advantages for the planning of sustainable infrastructure: (a) reduced air pollution and noise effects for adjacent neigh borhoods; (b) safe operation during difficult weather conditions, at day and at night and land at night; (c) an airstrip away from other urban structures to prevent accidents during take-off and landing; (d) the extension of city centers that are built near the coast; (e) the possibility of green planning at areclaimed plot. If the airport is floating, this allows to position it even further away from the city center, to prevent noise and air pollution and to provide safety to city inhabitants in the event of accidents on the airport and during take-off and landing. We present here a detailed analysis on the feasibility for the construction of an offshore airport at above site from a planning and engineering perspective. This study synthesizes literature (1930–2025) to evaluate the planning paradigms, engineering feasibility, and environmental impacts of floating offshore airports. Utilizing a systematic review methodology, we analyze projects (e.g., Japan's Mega-Float, Dalian Jinzhou Bay) and case studies (e.g., Taiwan's South Star Project). Key findings indicate: (1) Pneumatic Stabilized Platforms (PSP) offer deep-water adaptability but face cost-accessibility trade-offs; (2) Reclamation-based airports reduce wave instability yet accelerate coastal erosion; (3) Taiwan's experience highlights stakeholder conflicts in coastal development. We conclude that floating airports require multi-criteria feasibility frameworks balancing technical innovation with ecological safeguards.

Keywords: Offshore airport, Floating house, Harbor construction, Environmental impact, Sustainable development.

INTRODUCTION

A floating airport is an airport built and situated on a very large floating structure (VLFS) located many miles out at sea utilizing a flotation type of device or devices such as pneumatic stabilized platform (PSP) technology. As the population increases and land becomes more expensive and scarce, VLFS such as floating airports could help solve land use, pollution and aircraft noise issues.

This review adopted a three-phase literature synthesis approach:(1) Identification: Scopus/Web of Science databases queried (keywords: "floating airport," "VLFS," "offshore reclamation," 1930–2025). (2) Analysis: Thematic applied to: Planning drivers, Structural technologies, Environmental trade-offs, Policy conflicts (e.g., Taiwan's SSP)

The first discussion of a floating airport was for trans-Atlantic flights. At that time a passenger aircraft capable of making the trip could be built, but because of the massive need for fuel for the flight, it had a limited payload. An article appeared in the January 1930 issue of Popular Mechanics in which a model of a floating airport located in the Atlantic was proposed. To make safe flight possible with the aviation technology of that time, it called for eight such airports in the Atlantic. But unlike future floating airport ideas which were free floating, this 1930 concept had a floating airport platform, but with stabilizer legs which prevent the flight deck from pitching and rolling, similar in concept to some of today's off shore oil rigs. The idea of floating airports was forgotten until in 1935 the famous French aviation pilot and builder Bleriot gave one of his last

interviews in which he made the case for floating airports in mid-Atlantic; he called them Seadromes as a solution to economical trans-Atlantic passenger flights [1] .

In theory, issues and problems of land-based airports could be minimized by locating airports several miles off the coast. Takeoffs and landings would be over water, not over populated areas, thereby eliminating noise pollution and reducing risks of aircraft crashes to the land-locked population.
Since little of the ocean's surface is currently being used for human activity, growth and alterations in configuration would be relatively easy to achieve with minimal impact to the environment or to local residents who would utilize the airport. Water taxis or other high speed surface vessels would be a part of an offshore mass transit system that could connect the floating airport to coastal communities and minimize traffic issues.

Fig. 1 Offshore floating airport with land connection.

Fig. 2 Floating airport close to the city-center.

A floating structure, such as a floating airport, is theorised to have less impact on the environment than the land-based alternative. It would not require much, if any, dredging or moving of mountains or clearing of green space and the floating structure provides a reef-like environment conducive to marine life. In theory, wave energy could be harnessed, using the structure to convert waves into energy to help sustain the energy needs of the airport.

MODERN FLOATING AIRPORT PROJECTS

In 2000, the Japanese Ministry of Land, Infrastructure, and Transport sponsored the construction of Mega-Float, a 1000-metre floating runway in Tokyo Bay. After conducting several real aircraft landings, the Ministry concluded that floating runways' hydro-elastic response would not affect aircraft operations, including precision instrument approaches in a protected waterway such as a large bay. The structure has been dismantled and is no longer in use.

Fig.3 Partim view of aircraft moving on airport-ponton.

The pneumatic stabilized platform (PSP) was proposed as a means for constructing a new floating airport for San Diego in the Pacific Ocean, at least three miles off the tip of Point Loma. However, this proposed design was rejected in October, 2003 due to very high cost, the difficulty in accessing such an airport, the difficulty in transporting jet fuel, electricity, water, and gas to the structure, failure to address security concerns such as a bomb blast, inadequate room for high-speed exits and taxiways, and environmental concerns.

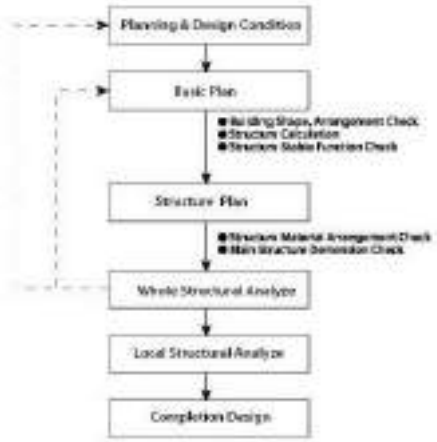

Fig.4 Planing and design flow chart of offshore airport.

Achmad Yani International Airport, the first floating airport in the world started construction on 17 June 2014, and had to be completed in 2016. However, only the passenger terminal and apron is floating.

Dalian Jinzhou Bay International Airport is mainland China’s first offshore floating airport. The project was officially approved in October 2022 and is currently under construction.

Table 1: Comparative Analysis of Floating Airport Technologies

Technology	Cost (USD/km²)	Stability	Environmental Impact
PSP (San Diego)	$12B	High (deep water)	Low seabed disruption
Reclamation (Kansai)	$20B	Moderate	High habitat loss
Hybrid (Dalian)	$8.5B	High	Moderate (turbidity)

COASTAL LANDS – TAIWAN CASE STUDY

Due to the fragility and sensitivity of coastal resources, once destroyed, they are extremely difficult to recover, in addition to reducing the value of water and product quality Ying want open outside, and environmental hazard, harm homeland security, the threat of people's lives and property, causing social problems. Therefore, the use and management of coastal zones require special care, under the principle of conservation of resources and development of both resources, according to the ecological characteristics and economic development needs resources, coastal resources for the overall planning and evaluation, are sequentially partitioned, so can the coastal zone be sustainably developed.

Coastal and soil erosion has always been a problem for many island countries like Taiwan [16]. In addition, many countries engage in massive reclamation (coastal modification) as a result of the rising awareness of population growth, trade development, and national defense. For example, Dubai engages in massive reclamations for trade and tourism, Japan built Kansai International Airport for transportation, China spent billions of RMB on land reclamation for military purposes and the constructions of airports (REF DALIAN), and the South Star Project (SSP) of Kaohsiung in Taiwan is fbeing evaluated.

Due to the rise of environmental awareness in recent years, the objection of environmental groups and nearby residents, and fund shortages, SSP is still under construction after 30 years. We are facing several questions [17]. Should the SSP be continued? What should be done to cope with the incessant coastal and soil erosion of island countries (Taiwan)? Is land reclamation the only solution? How to manage coastal modifications on the long run? What are the funding sources for such a huge project? Should we consider and listen to the opinions of environmental groups and nearby residents? If so - how to gather their opinions? How many stakeholders should be considered? What should be done after listening to their opinions? All of these questions gradually emerge.

Taiwan's southwestern coast exemplifies tensions between infrastructure planning and environmental resilience. The South Star Project (SSP) delay underscores engineering-feasibility challenges in sediment management (Fig. 6–9) and environmental-impact conflicts with coastal communities [17]. Unlike Japan's Mega-Float, SSP's 30-year stagnation reflects inadequate stakeholder integration—a critical planning gap for floating infrastructure.

After understanding the geographical location and surroundings of Taiwan and the problems Taiwan is facing, we should start with the following:

(I)Finding examples of reclamation and labor-consuming and money-consuming projects that benefit future generations at abroad and learn from them.

(II)Understanding possible pollution and waste sources that come along with reclamation.

(III)Investigating the sources and flows of funds for reclamation and how the government invests in and solicit investments in such projects.

(IV)Investigating future trends of land reclamation in Taiwan or using coastal water surfaces in different ways.

Overview of coastal Taiwan Land Use

The marine environment is an invaluable property of mankind. Land reclamation is one way of making use of coastal shallows which can be developed to different types of economic use, such as for accommodation, cultural, conservation, but also for industrial and purposes of infrastructure. The reclamation of land by building an artificial island is achieved by the construction/repair of bank revetments around the perimeters before combining those with existing islets with sand or landfill. An artificial island is primarily used as a site for shallow water petroleum exploration or the reception of large tank ships or transportation of minerals. Floating cities (seasteadings) are basically large steel constructions that are partially submerged in the ocean[9]. They are usually modified from naval vessels that were formally used for marine development activities (i.e. floating cities above large deep-sea mines that serve as multifunctional complexes to provide accommodation, shopping and event entertainment for miners) [8,12].

The development of offshore airports has been an ongoing trend worldwide. Examples of offshore airports on reclaimed land include the Honolulu International Airport of Hawaii [29], and Japan's Nagasaki Kansai Airport [11]. In fact, the government actually planned the construction of an offshore airport before the Taoyuan International Airport was

built. However, due to rigorous protests by local elected representatives, concrete development of the project has yet to take place.

Fig.5 Japan's Nagasaki Kansai Airport

Offshore land reclamation

In 2009, the typhoon, Morakot brought a lot of mud which sedimented in the river estuary of Kao-Ping River, Taiwan government and local Kaohsiung government planned to use the sediment for the Nanhsing project area. Therefore, Taiwan government hopes to re-promote Nanhsing project in order to develop the urban area of Kaohsiung. Because of the heavy sediment brought by Morakot, the downstream of Kao-Ping river was sedimented, these sands could be used for land reclamation to develop harbor, offshore airport and bigger industries. It could also increase the financial development and be used as the base of Kaohsiung airplane.

The SSP project is proposed to be built near the existing Kaohsiung airport and the second harbor, which is 3 km by 1 km. It was expected to be built at 3 square kilometer and was planned to be replacing the existing Kaohsiung airport and become the international airport of the South. However, since no funding was received from the government, the plan was postponed.

Fig.6 South Star Project (SSP) of Kaohsiung in Taiwan

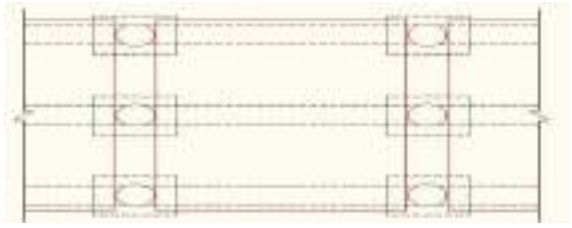

Fig.7 Plan -South Star Project (SSP) of Kaohsiung in Taiwan

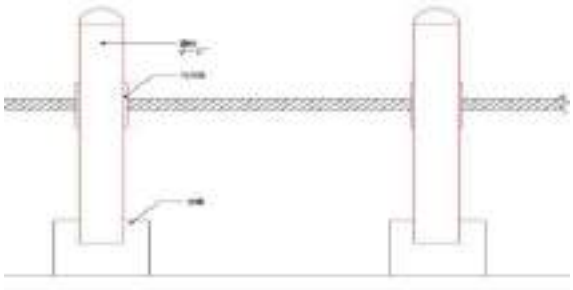

Fig.8 Elevation-South Star Project (SSP) of Kaohsiung in Taiwan

Fig.9 South Star Project (SSP) of Kaohsiung in Taiwan

Advantages of an Offshore Airport

Developing Offshore airports is a trend in the world, and we concluded three merits as follows: Firstly, the plane could take off or land at night, because the offshore airport is far away from the city and could fly or land at anytime without disturbance by the night. Second of all, because of the long distance between offshore airport and the city, the noise and air pollution could be reduced[8,12]. In addition, it could make the flyway clear which could reduce the judgment error about the plan landing (Take the event happened in Da-yuan & Singapore as examples.) PLUS land space use! More and more construction space is needed and becomes a major problem all over the world. Namely, how to use the spaces more properly has become the major point in the transportation design. The bigger space the more quantities, efficiency and more importance. the floating airport was under precise calculation and integrated with several techniques.

GLOBAL WARMING, CLIMATE CHANGE, AND SEA LEVEL RISE.

In light of global warming and climate change, NOAA (National Oceanic and Atmospheric Administration) is predicting that, by 2050, most coastal cities in the U.S. likely will be threatened by at least 30 days of fooding each year.3 That is for coastal cities on the Mainland. Islands in the Pacifc (including Hawaii) will likely have it much worse. Moreover, reputable scientists are saying that, by 2100, the oceans will rise between 2.5 and 6.5 feet

feet (0.8 and 2 meters), which is more than enough to food many U.S. coastal cities. That is enough for a lot of concern and worry.

This research will review existing knowledge on global warming and climate change, particularly in terms of sea level rise. It will examine how much of a threat global warming really is, and suggest that it is, in fact, serious enough that major preparations should begin now. It will look at the causes of global warming and consider the reasons for the controversy that has surrounded it. The research will report on what might happen in the future and take a look at what has already started happening around the world, and here in Hawai‘i, as a result of global warming and climate change. It will present what the international community has recommended be done to slow down the process of climate change, and look at comments made by the president of the U.S. as he speculates on what might be coming up in the future.

Unfortunately, short of eliminating all greenhouse gasses from the atmosphere, the literature tells us that there are no permanent solutions to the problem of climate change and sea level rise. There are, however, various recommended strategies to manage or mitigate global warming, and they will be examined here, culminating in a focus on foating development, not as a solution to the problem, but as one strategy among a number of strategies to mitigate the problem.

This research document briefly reviews existing knowledge of global warming and climate change, along with the consequences. It examines sea level rise, and briefly discusses the controversy that still lingers, allegedly because of what oil companies have done. It goes through strategies for mitigating sea level rise, with a final focus on floating development, not as a solution, but as one of a number of suggested ways to mitigate the problem of sea level rise.

CONCLUSION

(1) Planning: Floating airports mitigate urban noise but require integrated transport links (water taxis/undersea tunnels). (2) Engineering: PSP technology suits deep-water sites; reclamation remains cost-effective for <30m depths. (3) Environment: Artificial reefs enhance marine biomass, but dredging elevates turbidity (Taiwan’s SSP case). (4) Policy: Taiwan’s experience urges early engagement with NGOs/residents in Environmental Impact Assessments.

REFERENCES

[1] Bleriot, 1935. Seadromes. Popular Mechanics, (October 1935).

[2] Chan, P. W., 2011: Generation of an eddy dissipation rate map at the Hong Kong international airport based on Doppler lidar data. J. Atmos. Ocean. Technol., 28, 37–49.

[3] Chiu HM (2014). The Movement against Science Park Expansion and Electronics Hazards in Taiwan. China Perspectives 15-22.

[4] Darling, W. D., 1977: Design and Construction of Protective Structure for New Reef Runway, Honolulu International Airport. Coastal Engineering 1976, 2589–2603.

[5] Dolling, K., P.-S. Chu, and F. Fujioka, 2005: A climatological study of the Keetch/Byram drought index and fire activity in the Hawaiian Islands. Agric. For. Meteorol., 133, 17–27.

[6] Harbor, Planning and Design of Coastal and Harbor Engineering, pp. 743-745, September, 2005.

[7] Hou Ho-Shong and K-Q Chen, 1994. The Development of Port and Harbor, SETS, Adam’s Mark Hotel, Hotell, Houston,Taxas, May 28-29.

[8] Hou HS (2005). Forecast Analyses of Analyses of shipping Freight Traffic Volume Between the Cross-Strait and Discussion of Port Development, Shipping Journal, Taipei, Taiwan.

[9] Hou, Ho-Shong, 1991. Research on the Planning of Nanshing Planning and Deep Sea Port, Lecture Essays from the Department of Marine Environment and Engineering, pp.16-21. National Sun Yat-sen University, Taiwan

[10] Hou, Ho-Shong, 1992. Integrated Planning of Southern International Airport and Kaohsiung Port, Lecture Essays of the Institute of Transportation, 6-23, National Chiao Tung University.

[11] Hou, Ho-Shong, 1993. On the spatial development and port technics of Japanese Ocean Sphere. Undersea Technics Quarterly 3(4), pp. 14-17.

[12] Hou, Ho-Shong, 2005. The Planning and Design of the Coast and Harbor, Planning and Design of Coastal and Harbor Engineering, pp. 743-745, September.

[13] Japanese Professional Book Editing Committee (1997). Floating Style Offshore Airport. Kashima Publishing Co. Ministry of Transportation and Communications (2010). Planning of Free Trade Zone.

[14] Japanese Professional Book Editing Committee, 1997. Floating Style Offshore Airport. Kashima Publishing Co.

[15] Li, G.; Zhang, J.; Yang, Q.; Jiang, M. Centrifugal test and numerical assessment for settlement of a large-scale artificial island constructed on deep marine clays. Eur. J. Environ. Civ. Eng. 2017, 21, 172–192.

[16] Lin, C.-Y.; Lin, W.-T.; Chou, W-C. Soil erosion prediction and sediment yield estimation: the Taiwan experience. Soil & Tillage Research 2002, 8, 143–152.

[17] Lin, Y-H, Hou Ho-Shong, Chen Yang-Yih,

Chang Yang-Chi. Journal of Scientific Research and Studies Vol. 3 (4). 68-80. April, 2016
[18] Mega-Float. Netherlands Pavilion Expo 2010 Shanghai.
[19] Sea Legs of Floating Airport Prevents Rolls and Pitches" Popular Mechanics, January 1930 Article and photo located bottom-right-side of page
[20] Shen, Shu-Min. "Changes in Taiwan Coastal Landforms." Science Study Monthly, 48-4.
[21] Tang, Li-Tsung, editor. Changes in Southwestern Coast in Taiwan. Institute of Taiwan History, Academia Sinica
[22] Tong, S. qi; Wang, N.; Song, N. qi Emergency evacuation capability evaluation and optimization for an offshore airport: The case of Dalian Offshore Airport, Dalian, China. Saf. Sci. 2017, 92, 128–137, doi:10.1016/j.ssci. 2016.10.004.
[23] Yan, H. K.; Wang, N.; Wei, L.; Fu, Q. Comparing aircraft noise pollution and cost-risk effects of inland and offshore airports: The case of Dalian International Airport, Dalian, China. Transp. Res. Part D Transp. Environ. 2013, 24, 37–43, doi:10.1016/j.trd.2013.05.005.
[24] Yan, H. K.; Wang, N.; Wu, N.; Song, N. Q.; Zhu, D. L. Estimating environmental value losses from earth materials excavation and infilling for large-scale airport construction: a case of Dalian Offshore Airport, Dalian, China. Environ. Sci. Pollut. Res. 2017, 24, 21168–21179.
[25] Yan, H. K.; Wang, N.; Yu, T. L.; Fu, Q.; Liang, C. Comparing effects of land reclamation techniques on water pollution and fishery loss for a large-scale offshore airport island in Jinzhou Bay, Bohai Sea, China. Mar. Pollut. Bull. 2013, 71, 29–40.
[26] Zhao, B., N. Wang, L. Wu, and C. Yang, 2010: Environmental pollution of offshore airport and semi-offshore airport. 2010 4th International Conference on Bioinformatics and Biomedical Engineering, iCBBE 2010.
[27] Zhao, B.; Wang, N.; Wu, L.; Yang, C. Environmental pollution of offshore airport and semi-offshore airport. In 2010 4th International Conference on Bioinformatics and Biomedical Engineering, iCBBE 2010; 2010.
[28] Zhao, Q., H. Lin, W. Gao, H. A. Zebker, A. Chen, and K. Yeung, 2011: InSAR detection of residual settlement of an ocean reclamation engineering project: a case study of Hong Kong International Airport. J. Oceanogr., 67, 415–426.
[29] URL: WIKIPEDIA-accessed 26th March 2025, (<https://en.wikipedia.org/wiki/DanielK._Inouye_ International_Airport>).
[30] URL: WIKIPEDIA-accessed 26th March 2025, (<https://en.wikipedia.org/wiki/Dalian_Jinzhouwan_International_Airport>).

Copyright © Int. J. of GEOMATE All rights reserved, including making copies, unless permission is obtained from the copyright proprietors.

15th Int. Conf. on Geotechnique, Construction Materials & Environment,
Kyoto, Japan, 11-13 November 2025, ISBN 978-4-909106124 C3051

THE ECONOMIC RESILIENCE MODELING OF STREET VENDORS HOUSEHOLDS WITH SOCIAL CAPITAL AS AN INTERVENING VARIABLE: A CASE STUDY OF STREET VENDORS IN EAST JAKARTA

Beti Nurbaiti [1], Mohamad Axel Putra Hadiningrat [2], and Chotib Hasan [3]

[1] Universitas Bhayangkara Jakarta Raya, Jakarta, Indonesia, [2, 3] Universitas Indonesia, Depok, Indonesia,

ABSTRACT

Problem statement from this research dissertation is to examine how East Jakarta street vendors achieve household economic resilience. The research approach used quantitative method were used to assess the economic resilience of the households of street vendors: (1) sociodemographic traits; (2) transitory locations (Loksem); (3) base/fixed sites (Lapak); (4) hawkers (Asongan); (5) local government-assisted locations (Lokbin); (6) social capital. Data from 420 respondents was gathered using a quantitative approach. In Lokbin, social capital influences the economic resilience of street vendors' households by acting as an intervening factor on factors including income, education, migrant status, and sales. The results of this research according to the Sobel Test, two variables street vendors with migratory status and those with a diploma or higher show significance and a positive impact only when mediated by the intervening variable of social capital. Economic resilience is positively impacted by the social capital variable. There is a statistically significant influence on the kind of street vendors evaluated at LokBin. Conclusion: the economic resilience is directly impacted by sociodemographic traits. The economic resilience of street vendors has been demonstrated to be mediated by social capital, sociodemographic traits, and trading location.

Keywords: Economic Resilience; Social Capital ; Street Vendors; Sobel Test; East Jakarta

INTRODUCTION

The presence of street vendors (known locally as PKL) in major urban centers like Jakarta represents a critical component of the informal sector, especially in terms of providing employment opportunities for low-skilled migrant populations. While this sector plays a vital role in absorbing labor and reducing unemployment, it also poses significant urban challenges, including spatial disorder, traffic congestion, and urban slum development.

Street vending is not unique to Jakarta or developing countries such as Indonesia. Similar phenomena are observed globally in Syria [1], Uganda [2], Australia [3], and India [4]. Street vendors operate within the informal economy, often turning to vending as a livelihood strategy due to limited access to education, technical skills, and financial capital. Despite these constraints, the sector remains attractive due to its low entry barriers and flexibility. However, unregulated vending practices, often facilitated by informal agreements with local authorities (referred to as "hidden actors"), result in widespread misuse of public spaces such as sidewalks, overpasses, green belts, city parks, and urban forests.

A large portion of street vendors in Jakarta are long-settled migrants. The continuous rural-to-urban migration flow driven by improvements in transportation, technology, and public services reflects a common belief that urban areas offer better life prospects compared to rural regions [5]. Female migrants, in particular, constitute a substantial part of this workforce and actively contribute to both local and global informal labor markets [6]. Their journey is often marked by limited resources, lacking in skills, capital, and formal education [7]. The informal sector, however, offers a degree of resilience due to its adaptability, even during times of economic instability. Its capacity to generate employment plays a crucial role in alleviating poverty and reducing unemployment [8][9].

Social capital encompasses elements such as group affiliation and networking, mutual trust and solidarity, social cohesion and inclusion, collective action, information sharing, and empowerment. Within the street vending community, these components form the foundation of mutual support systems, enabling access to markets, trading techniques, and informal financing channels outside conventional financial institutions [10]. This form of capital is often complemented by spiritual capital and the strategic use of micro-spatial environments for living, production, and vending, all contributing to the household's economic resilience.

Based on the aforementioned discussion, this study is designed to address the following research questions:

1) Is there a direct influence of social capital, vending location, and sociodemographic characteristics on the economic resilience of street

vendor households?
2) Is there an indirect influence of vending location and sociodemographic characteristics on the economic resilience of street vendor households through the intervening variable of social capital?

This research fills the research gap related to economic resilience in the informal sector, specifically the economic resilience of street vendors.

RESEARCH SIGNIFICANCE

This study is grounded in a strong theoretical foundation, particularly drawing from theories of social capital and household economic resilience within the context of the informal sector. Social capital serves as the primary framework, based on the approach developed by [11], as well as key concepts introduced by [12] and [13].

Social Capital

Social capital as a set of norms, networks, and trust that facilitates cooperation and collective action among members of a community. The concept of social capital was also developed. They classify social capital into six key dimensions: (1) Group and network; (2) Trust and solidarity; (3) Collective action and cooperation; (4) Information and communication; (5) Social cohesion and inclusion; and (6) Empowerment and political action.

The six dimensions illustrate how communities are interconnected, how trust is built, and how systems of information exchange and mutual support are developed—particularly vital in enhancing economic resilience among vulnerable groups such as street vendors.

Economic Resilience

In addition to the social capital framework, the theory of household economic resilience also serves as a critical reference in this study. According [14], economic resilience refers to a household's sustained ability to meet its basic needs—such as food, education, healthcare, and shelter—while also possessing the capacity to recover from economic shocks. This resilience is not solely measured by income levels but also by adaptability, income diversification, and the strength of their social networks.

This research aligns with findings who examined the impact of social capital on the well-being of informal sector actors in Jakarta. Their study demonstrated that social capital, particularly in the form of trust and networks, plays a significant role in enabling micro-entrepreneurs to access economic opportunities and endure socio-economic pressures. These findings reinforce the notion that in informal economies, social relationships are not merely supplementary; they are a foundational element of household economic sustainability.

In this research, street vendors' economic resilience is assessed based on a framework, using survey indicators such as: housing conditions, household income, children's education, and financial security. However, due to the pandemic's economic impact, most vendors saw a sharp decline in their savings—some reported having no savings at all.

HYPOTHESIS

After conducting a literature review and selecting theoretical references aligned with the chosen research variables, the following research hypotheses were formulated for analysis:

1. **Hypothesis 1 (H1)**: There is a direct influence of social capital on the economic resilience of street vendor households.
2. **Hypothesis 2 (H2)**: There is a direct influence of street vendor type, based on vending location, on the economic resilience of street vendor households.
3. **Hypothesis 3 (H3)**: There is a direct influence of sociodemographic characteristics on the economic resilience of street vendor households.
4. **Hypothesis 4 (H4**): There is an indirect influence of vending location and sociodemographic characteristics on the economic resilience of street vendor households through the intervening variable of social capital.

RESEARCH METHODS

The researcher conducted a field survey over a period of six months, from November 30, 2021, to May 27, 2022. The study focused on street vendors (PKL) located in East Jakarta, covering ten districts: (1) Cakung, (2) Cipayung, (3) Ciracas, (4) Duren Sawit, (5) Jatinegara, (6) Kramat Jati, (7) Makasar, (8) Matraman, (9) Pasar Rebo, and (10) Pulogadung.

The research adopted a quantitative approach, beginning with the collection and analysis of numerical data. This approach aimed to enhance the depth and contextual understanding of deductive findings by providing complementary insights. As suggested by [16], such a strategy is expected to enrich data interpretation and offer more comprehensive and applicable solutions to real-world problems.

Quantitative Data Processing

The sampling method for the quantitative phase employs multi-stage random sampling, taking into account quotas for each municipality, with selected sub-districts and urban villages in East Jakarta. Primary data collected from street vendors will be processed using SPSS to examine research variables including trading locations, sociodemographic characteristics, and their impact on household

economic resilience.

RESULTS AND DISCUSSION

Descriptive Statistics Processing Results

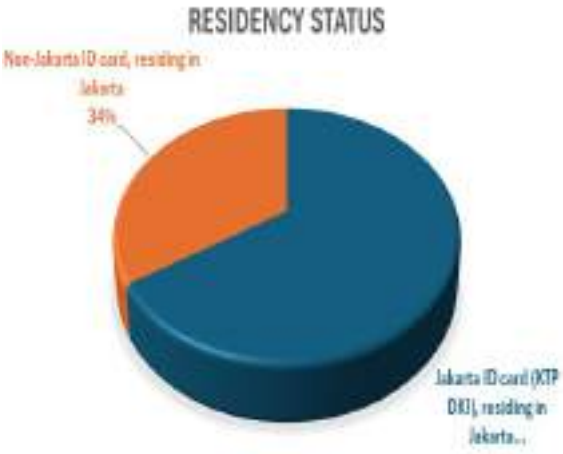

Figure 1. Residency Status
(Source: Processed by Author, 2023)

Referring to the field survey results in Figure 1 it is evident that the majority of street vendors have become Jakarta residents and enjoy the facilities provided by the DKI Jakarta Provincial Government. Street vendors with non-Jakarta ID cards still choose to live in Jakarta because the facilities and trading advantages they obtain are greater than those in their places of origin.

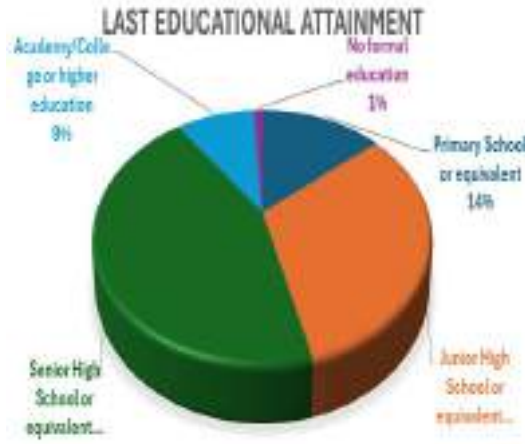

Figure 2. Educational Background
(Source: Processed by Author, 2023)

Based on Figure 2, the educational background of street vendors is dominated by high school graduates and equivalent (44%), followed by junior high school and equivalent (32%), elementary school and equivalent (14%), academy/higher education (9%), and no schooling (illiterate) (1%). From an educational perspective, the majority of street vendors have low education levels with only a few having higher education.

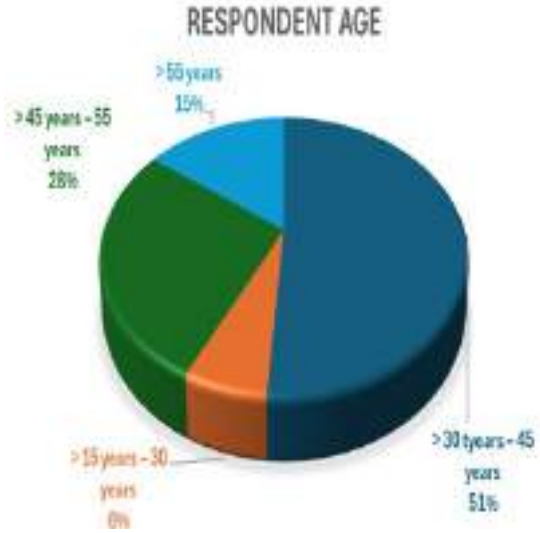

Figure 3. Respondent Age
(Source: Processed by Author, 2023)

The primary data analysis results in Figure 3 show that the age of street vendors who trade is mostly within the productive age range of >30 years – 45 years (41%), followed by >15 years – 30 years (25%), >45 years – 55 years (22%), and the least represented are those >55 years old at (12%). The majority of street vendors are in their productive years with only a few being elderly.

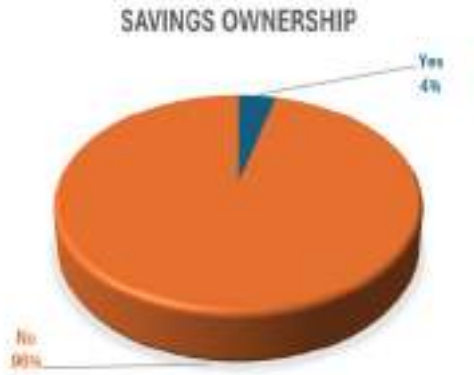

Figure 4. Savings Ownership
(Source: Processed by Author, 2023)

Furthermore, from the primary data results in Figure 4, it was found that 96% of street vendors do not have savings and only 4% of street vendor respondents have savings. Based on field interviews, street vendors who have savings mostly already use digital marketing/marketplaces, including WhatsApp, Instagram, GoFood, and GrabFood. Therefore, it can be concluded that digitalization is important for improving the economic resilience of street vendors.

Hypothesis and Sobel Test Results

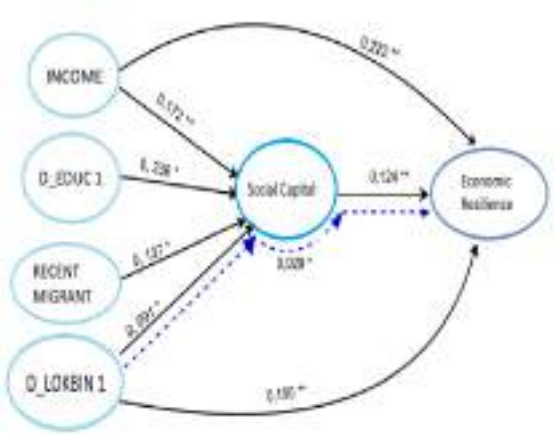

Figure 5. Conceptual Model of Social Capital as an Intervening Variable (Research Novelty)
(Source: Processed by Author, 2023), where *) Significant at α=10%; **) Significant at α=5%)

1. **Hypothesis-1 (H1)** is accepted/proven, confirming that there is a direct influence between social capital and the economic resilience of street vendor households at a 5% significance level. The regression coefficient of social capital on street vendor household economic resilience has a positive direction of 0.124. In the scope of social sciences, referring to statistical test results is more focused on analyzing the direction/pattern of relationships between variables. Therefore, it can be concluded that if social capital is good/quality, then the economic resilience of street vendor households will also increase.
2. **Hypothesis-2 (H2)** is accepted/proven, confirming that there is a direct influence between the types of street vendors based on their trading locations in Designated Areas (LokBin) and street vendor household economic resilience at a 5% significance level. For the other three trading locations: Temporary Locations, Permanent/Stall Locations, and Mobile/Peddling Locations, these are not significant/do not affect street vendor economic resilience. The regression coefficient of LokBin on street vendor household economic resilience has a positive direction of 0.190. This can be concluded that LokBin has a positive impact on street vendor household economic resilience. In other words, street vendors in LokBin have better economic resilience compared to street vendors in other trading locations.
3. **Hypothesis-3 (H3)** is accepted/proven, confirming that there is a direct influence between sociodemographic characteristics in the income aspect of street vendors and street vendor household economic resilience at a 5% significance level. For other sociodemographic characteristics such as age, gender, education level, and migration status (recent and lifetime) are not significant/do not directly affect street vendor economic resilience. The regression coefficient of income on street vendor household economic resilience has a positive direction of 0.222. This can be concluded that street vendors with high income will have good household economic resilience. This means that the better the income level of street vendors, the more economically resilient they become.
4. **Hypothesis-4 (H4)** is accepted/proven, confirming that there is an indirect influence between trading locations and sociodemographic characteristics on street vendor household economic resilience through the intervening variable of social capital at a 10% level. This is proven by the Sobel test, where the regression coefficient of the intervening variable has a positive direction of 0.127. The results of this calculation show that social capital has an intervening influence on other variables, namely income, diploma-level education and above, street vendors with recent migrant status, and those selling in LokBin, on street vendor household economic resilience.

Analysis of Direct Effect of Trading Location on Street Vendor Household Economic Resilience

The results of the second hypothesis test show that only Street Vendors (PKL) who trade in Designated Areas (Lokbin) have a significant effect on their household economic resilience. Three other types of locations—Temporary Locations (Loksem), Permanent/Stall Locations, and Mobile/Peddling Locations—do not show meaningful effects.

Lokbin is an area officially provided by the DKI Jakarta Provincial Government as regulated in Governor Regulation No. 10 of 2015 concerning Street Vendor Management and Empowerment. The purpose is to avoid sporadic buying and selling activities in public spaces, maintain city order, and improve public comfort and safety.

Figure 6. Street Vendors as Hawkers (Source: by Author, 2023)

Street vendors in Lokbin receive various facilities such as tents, tables, and chairs, as well as affordable cleaning and security fees (Rp 150,000/month). This is much cheaper compared to unofficial 'tribute' costs when trading illegally (Rp 500,000–600,000/month). This allows street vendors in Lokbin to allocate more funds for business development.

Nevertheless, many street vendors are reluctant to move to Lokbin because the location is considered less strategic—far from crowds, stations, bus stops, or public activity centers. They prefer public spaces such as sidewalks and parks that are frequently passed by the public.

Figure 7. Street Vendors with Lapak for Selling (Source: by Author, 2023)

This phenomenon aligns in The Production of Space, which explains that social activities require space. Street vendors create their own "social space" in public spaces as a form of survival struggle in the city. Similar problems occur in various large cities, but countries like Japan have provided special places for street vendors that are neat, clean, and comply with regulations, including limited operating hours and food hygiene permits.

In Jakarta, the challenge is how to encourage street vendors to be more interested in trading in Lokbin. One solution is to make Lokbin more attractive, for example by adding public facilities such as free wifi, entertainment stages, and budget-friendly culinary zones for young people and students, so that the location becomes a comfortable and strategic gathering place.

Analysis of Direct Effect of Sociodemographic Characteristics on Street Vendor Household Economic Resilience

Based on data processing results, it is proven that the sociodemographic characteristic that has a significant direct effect on household economic resilience is street vendor income. Other sociodemographic characteristics have indirect effects on street vendor household economic resilience.

The educational level of street vendors is dominated by high school graduates and equivalent (44%), followed by junior high school and equivalent (32%), elementary school and equivalent (14%), academy/higher education (9%), and no schooling (illiterate) (1%). From an educational perspective, the majority of street vendors have low-to-medium education, with only a few having higher education. Illiterate street vendors are still found, though not many. During field surveys, most street vendors still consider formal education not a priority because they allocate their time, energy, and thoughts to focus on trading. Therefore, education level does not have a significant direct effect on street vendor household economic resilience, and they feel satisfied with low-to-medium education levels as long as they can have sufficient income for their families.

Analysis of Social Capital as an Intervening Variable on Street Vendor Household Economic Resilience

There is an influence of social capital as an intervening variable on street vendor household economic resilience. Generally, street vendors have low-to-medium education levels, forcing them to pursue this profession in the urban informal sector according to the data. A street vendor can achieve higher education if they utilize the social capital they possess. One sub-dimension of social capital is networks/kinship groups (Group and Network).

The sub-dimension of social capital utilized by street vendors is Trust and Solidarity, where there is mutual trust and solidarity between both parties, resulting in the practice of social capital sub-dimensions in the form of Empowerment and Political Action. The existence of the Information and Communication sub-dimension plays a role when street vendors who initially worked as employees seek places to study while selling online through social media and colleagues, enabling them to complete their studies successfully..

Figure 8. Selling Facility at Lokbin (Source: by Author, 2023)

There are several important aspects that make recent migrants more economically resilient compared to lifetime migrants: (1) **social factors**; (2) **cultural factors**; and (3) **communication factors.**

Information and communication aspects as impacts of urban modernization become driving factors for recent migrants' economic resilience, especially those who utilize online marketing. Marketing through marketplace utilization on social media helps street vendors increase income and profits, enabling them to achieve household economic resilience.

1. CONCLUSION

The study found that social capital within the street vendor (PKL) community in East Jakarta's Designated Locations (Lokbin), when supported by adequate income levels, positively influences household economic resilience. However, individual factors such as age, gender, education level, and migration status both recent and lifetime do not have a significant or direct impact on economic resilience. Street vendors can improve their income by using digital marketing and marketplace platforms like WhatsApp, Instagram, GoFood, and GrabFood. Increased income enables them to meet daily needs, save, and strengthen their economic resilience. While recent migrant status does not directly affect economic resilience, it does have a direct influence on social capital. The study suggests further research into how street vendors utilize social capital as an intangible asset and what factors influence their willingness to relocate to Lokbin for improved economic conditions.

2. REFERENCES

[1] Alexandre, L., Salloum, C., and Alalam, A. (2019). An Investigation of Migrant Entrepreneurs: The Case of Syrian Refugees in Lebanon. Publisher: International Journal of Entrepreneurial Behaviour and Research, 25(5), pp. 1147–1164.

[2] Bongomin, G. O. C., Woldie, A., and Wakibi, A. (2020). Microfinance Accessibility, Social Cohesion and Survival of Women MSMEs in Post-War Communities in Sub-Saharan Africa: Lessons from Northern Uganda. Publisher: Journal of Small Business and Enterprise Development, 27(5), pp. 749–774.

[3] Dinh, H., Freyens, B., Daly, A., and Vidyattama, Y. (2017). Measuring Community Economic Resilience in Australia: Estimates of Recent Levels and Trends. Publisher. Social Indicators Research, 132(3), pp. 1217–1236.

[4] Gimelli, F. M., Rogers, B. C., and Bos, J. J. (2019). Linking Water Services and Human Well-Being Through the Fundamental Human Needs Framework: The Case of India. Publisher: Water Alternatives, 12(2), pp. 715–733.

[5] Nurbaiti, Beti. (2017). The Influence of Migration Status through Sociodemographic Characteristics on the Welfare Level of Workers in DKI Jakarta Penerbit: Jurnal Kajian Ilmiah Universitas Bhayangkara Jakarta Raya, pp. 17 (2).

[6] World Bank. (2011). World Development Report. 2012: Gender Equality and Development. World Bank Publications

[7] Nurbaiti, Beti. (2016). The Influence of Migration Status Through Sociodemographic Characteristics on the Welfare Level of Workers in DKI Jakarta (Cross-Sectional Data Analysis of SUSENAS 2013). Disertasi. HAKI No: EC 00201816779, 3 Juli 2018.

[8] International Labour Organization (ILO). (2020). World Employment and Social Outlook-Trend 2020. Geneva, Publisher: International Labour Office.

[9] Priyono, Edi. (2015). Understanding the Labor Market. Pustaka Lentera, Jakarta.

[10] Nurbaiti and Chotib. (2020). The Impact of Social Capital On Welfare: The Evidence From Urban Informal Sector In East Flood Canal (BKT), Jakarta. Publisher: IOP Conference Series: Earth and Environmental Science, 436012004.

[11] Narayan, D and Michael Woolcock. 2016. Measuring Social Capital: An Integrated Questionnaire. Washington DC. Publisher: World Bank Working Paper No. 18.

[12] Putnam, R. D. (2000). *Bowling Alone: The Collapse and Revival of American Community*. New York, NY: Simon & Schuster, pp 544-545

[13] Bourdieu, P. (1995). *Outline of a Theory of Practice* (R. Nice, Trans.). Cambridge, UK: Cambridge University Press. Viii, pp 173-180

[14] REACH. (2021). Household Economic Resilience Assessment (HERA). REACH Economic Resilience Report.

[15] Creswell, J. W. (2016). Research Design Approaches: Qualitative, Quantitative, and Mixed Methods. (Terjemahan). Publisher: Yogyakarta Pustaka Pelajar.

Copyright © Int. J. of GEOMATE All rights reserved, including making copies, unless permission is obtained from the copyright proprietors.

15th Int. Conf. on Geotechnique, Construction Materials & Environment, Kyoto, Japan, 11-13 November 2025, ISBN 978-4-909106124 C3051

SOLIDIFICATION CHARACTERISTICS OF SOIL CONTAINNING COAL WASTE (PART II)

Shoji Kamao[1], Rin Itagaki[1] Satoshi Shigemura[1] and Yuta Murakami[2]

[1]Civil Engineering, Nihon University, Japan; [2] JR East Consultants Co. Ltd, Japan

ABSTRACT

Coal was used as fuel for steam locomotives, and coal cinders (coal waste), which contained ash and small pieces of unburned coals, were buried underground for disposal. Recently, redevelopment projects have been planned in Japan for former rail depot sites where coal cinders were once disposed of. In such redevelopment projects, buried coal cinders have frequently been excavated, making it challenging for developers to dispose of and process the excavated coal waste. Excavated coal cinders must be treated and disposed of as industrial waste, not soil. Although the soil with coal cinders has been excavated from the ground, it cannot be used as backfill material under Japanese environmental law[1], even if put back in place. Instead, it is disposed of as industrial waste needs high disposal costs. The high disposal cost and the shortage of final disposal sites have increased the cost of redevelopment projects. The authors have published some papers showing that adding cement and clay to coal cinders can produce improved soil with high unconfined compressive strength.

This paper investigates the properties of improved coal cinders mixed with cement and clay for use as backfill materials, not for industrial waste. In addition to the unconfined compression test, compaction tests and cone index tests were also conducted to clarify the characteristics of the improved material. The results of all the tests were good for subgrade materials. However, when the compacted improved soil was removed from the mold and re-compacted, a decrease in strength was observed compared to the first time. Further consideration is also necessary when re-excavating improved soil.

Keywords: Coal cinders, Construction waste soil, Cement solidified soil, Strength Characteristics

INTRODUCTION

In Japan, the Shinagawa–Yokohama railroad began service in 1872, and a nationwide railroad network was subsequently developed [2, 3]. For approximately 100 years, until around 1975, steam locomotives using coal as fuel were in operation. The coal cinders used by these steam locomotives were buried in the ground as construction material for railroad sites. However, there are no detailed records regarding the buried coal cinders' extent, quantity, or depth.

In recent years, as a result of railroad facility reconstruction and redevelopment projects near stations, these coal cinders are increasingly being excavated. Once excavated, coal sludge buried underground (including soil mixed with coal sludge) is classified as “cinders” under environmental laws and cannot be disposed of as waste soil. Furthermore, due to the unknown physical and chemical properties of the material, most of it has been disposed of as industrial waste. The majority of this excavated coal sludge ends up landfilled at final disposal sites, resulting in significant environmental impacts from both transport and disposal. Reducing the massive volume of final disposal coal cinders revealed through Sustainable Development Goals (SDGs)–driven projects across Japan is a critical issue.

This study aims to utilize excavated coal sludge as roadbed material for railroad structures[4]-[8]. According to design standards for railway structures, a Unconfined compressive strength of at least 1000 kN/m² after 28 days of curing is required for use as roadbed material. Therefore, this target strength was set, and the authors attempted to improve the excavated coal sludge-mixed soil (hereinafter referred to as “coal cinders”) by cement stabilization. This report evaluates the solidification characteristics of newly sampled coal cinders. The improved soil specimens were prepared by mixing the in-situ collected coal sludge with clay and blast furnace cement type B at specified proportions, setting various initial water content and curing them for a fixed period. We assessed the solidification characteristics by measuring the unconfined compressive strength of the specimens and also examined their compaction and cone index characteristics.

RESEARCH SIGNIFICANCE

The importance of this research lies in the fact that no research has been conducted to date on what to do with coal cinders that is excavated during redevelopment work. Clarifying the physicochemical properties of excavated coal cinders so that it can be used is also important in terms of environmental issues.

MAIN CHARACTERISTICS OF THE SAMPLE

The coal cinders used in this study were collected during excavation at a construction site on a railroad right-of-way. Photographs 1 and 2 show the conditions during sampling.

The main physical properties of the coal sludge and added clay are summarized in the table 1. The particle density of the coal sludge is 2.44 g/cm^3, which is lower than that of ordinary soil. This is likely because coal, which typically has a specific gravity of 1.2–1.5, lowers the density of the coal cinders when present. It is extremely difficult to determine the exact coal content, as many finely crushed coal fragments are mixed in.

Consistency tests (e.g., liquid limit) are conducted with samples that pass through a sieve according to JIS standards, meaning coal fragments larger than 0.425 mm are removed. Therefore, consistency testing is possible. It has also been previously reported that soils mixed with coal often yield “NP” when the soil type is sandy.

Photo 1 Coal cinders dug up at the construction site

Photo 2 Collected coal cinders sample

Table 1 Typical properties of coal cinders and added clay

Typical Soil properties		Coal cinders	Added clay
Soil particle density	ρ_s (g/cm^3)	2.44	2.87
Liquid limit	w_L (%)	NP	54.7
Plastic limit	w_P (%)	NP	33.7
Plastisity index	I_p (-)	NP	21.0
Natural water content	w_n (%)	3.17	4.65
Ignition loss	L_i (%)	16.71	5.85

Test Items and Conditions

The following experiments were carried out to understand the cement solidification characteristics of coal cinders.

(1)Unconfined compression test for cement-solidified soil, [9],[10] (Curing time 7 and 28 days)
(2) Soil compaction using a rammer, [11]
(Adjusted soil and improved soil, curing 7 days)
(3) Cone index for compacted soils, [12]
(Adjusted soil and improved soil curing 7 days)
(4) Permeability of saturated soil , [13]
(Adjusted soil and improved soil curing 7 days)

Note: adjusted soil refers to coal cinders with grain size adjustment.

Unconfined Compression Test of Cemented Soil

Specimens were prepared following the Japan Society of Geotechnical Engineers’ standard (JGS 0821) for stabilized soil specimens without compaction. Coal sludge passed through a 2.0 mm sieve was used to ensure compatibility with the Unconfined compression test specimen dimensions. Commercial powdered clay was added, and blast furnace cement type B was used as the solidifier.

Clay was added because the coal sludge alone did not exhibit sufficient strength when its clay content was low. Previous studies confirmed adequate strength when clay content was adjusted as a parameter.

Water was added to the clay, coal sludge, and blast furnace cement and mixed for about 10 minutes using electrical mixer to achieve a homogeneous mixture. An acrylic mold with a 35 mm diameter and 100 mm height was used. The bottom was sealed with a rubber stopper, and the specimen was filled in five layers, tapping each layer 100 times to expel air. After filling, the top was wrapped in plastic, and specimens were cured for 7 and 28 days at 20°C in a thermostatic chamber.

The cement and water were added based on the dry mass of the coal cinders (sludge–clay mixture). Cement addition rate and coal cinders addition rate were defined using following Equations (1) and (2). Test conditions are shown in Table 2.

$$a_w = \frac{m_s'}{m_g + m_s} \times 100 \ (\%) \quad (1)$$

$$D_w = \frac{m_g}{m_g + m_s} \times 100 \ (\%) \quad (2)$$

m_s' : Mass of blast furnace cement type B
m_s : Dry mass of clay
m_g : Dry mass of coal cinder mixed soil

Table 2 lists the tested combinations. Coal cinders addition rates ranged from 0 to 100%, and cement addition rates were 5%, 10%, 20%, and 35%.

Because the powdered clay had a water content of approximately 4.7%, water was necessary. Preliminary tests showed that initial water content below 30% made mixing difficult, while above 60% led to specimens that could not maintain shape. Thus, 50% was set as the initial water content.

Table 2 Test conditions for unconfined compression test of cemented soil

Condition	Symbol	Values
Coal cinders addition rate	D_w (%)	0～100
Cement addition rate	a_w (%)	5, 10, 20, 35
Initial water content	w_0 (%)	40, 50, 60
Water-cement ratio	w/c (%)	60
Curing time	Tc (days)	7, 28

Compaction Test by Ramming

We set the coal cinders and cement addition rate based on the unconfined compression test results and prepared the improved soil. Specimens cured for 7 days were adjusted to a maximum grain size of 19 mm and tested according to JIS A 1210. The mold used had a 10 cm diameter and 1000 cm^3 volume.

The average initial water content of the improved soil after curing was 53.4%, so compaction testing began at that water level. This exceeded the optimum water content of the improved soil, so the initial value was adopted as the optimum water content and maximum dry density.

Cone Index Test of Compacted Soil

Cone index tests were conducted on specimens prepared for the compaction test in accordance with JIS A 1228 (cone index test of compacted soil). Test conditions matched those in Table 2. Tests were performed on both cement-modified and uncemented coal cinders specimens.

For the cement-modified soil, a second test was conducted using samples that were compacted, broken into smaller pieces, and then re-compacted. This was to observe changes in strength upon repeated use.

Permeability Test for Compacted Soil

Permeability tests were conducted to evaluate the water permeability of the compacted soil. Both uncemented adjusted soil and cement-modified improved soil were tested. Given that cement-modified soil tends to absorb water and resist drainage, we tested its hydraulic conductivity. Because the soil contains clay, the falling head permeability test (as specified by JIS A 1218) was used.

EXPERIMENTAL RESULTS AND DISCUSSION

Unconfined Compression Test Results

The relationship between coal cinders addition rate and unconfined compressive strength was plotted for 5%, 10%, and 20% cement addition rates at 7 and 28 days. Each point represents the average of three specimens. While variation existed due to coal cinders content, general trends were identified.

For all conditions, strength increased more after 28 days than after 7 days. However, under high coal cinders content, the strength gains were smaller, and this difference between 7-day and 28-day values diminished. The strength increased with coal cinders addition up to a point and then decreased, more noticeably at higher cement contents. This is attributed to coal cinders acting as aggregate, which reduces clay content and therefore bonding strength.

From these results, 50% coal cinders content, 40% and 50% initial water content, and a 60% water–cement ratio were selected for subsequent tests, with cement addition ranging from 5% to 20%.

Unconfined compressive strength ranged from 350 to 5000 kN/m² depending on cement and coal cinders content. In particular, when the cement content is 20%, the strength is greatest when the coal ash content is 40%, and coal cinders can be considered to play the role of aggregate. Strength

increased linearly with cement addition for coal cinders (Figures 1 to 3). Comparisons to the target strength for roadbed use (q_u=1000 kN/m^2 at 28 days curing) showed that cement addition rates of 10% and 20% met the criteria under appropriate conditions.

From Figure 4, the target strength of curing 28days can be achieved when the cement addition ratio exceeds approximately 8%.

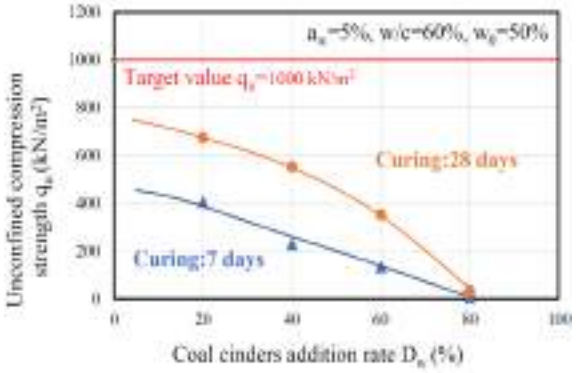

Figure 1 Relathionship between coal cinders addition rate and unconfined compression strength

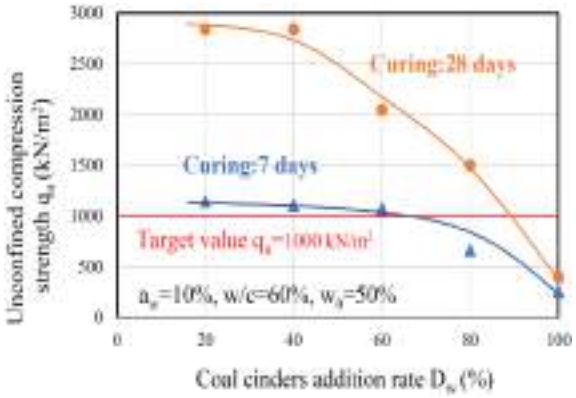

Figure 2 Relathionship between coal cinders addition rate and unconfined compression strength

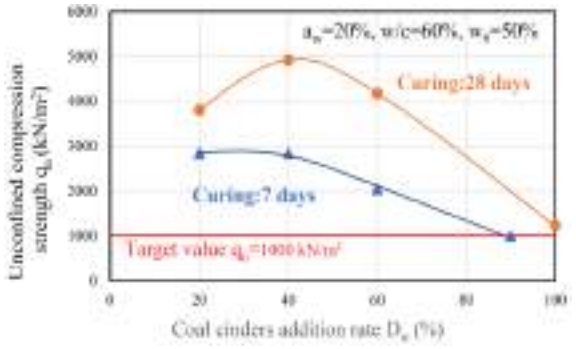

Figure 3 Relathionship between coal cinders addition rate and unconfined compression strength

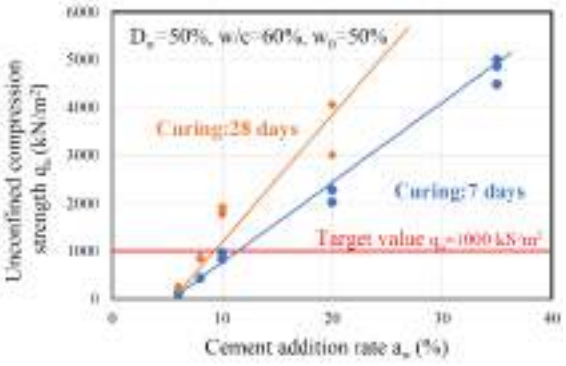

Figure 4 Relathionship between cement addition rate and unconfined compression strength

Compaction Test Results

Based on the results of the unconfined compression tests, sample soil was prepared for the compaction test and cone index test under the following conditions: 50% coal cinders addition rate, 60% water-cement ratio, 50% initial water content, and 7 days curing time.

Figure 5 shows the compaction curve alongside the zero air voids line. Conditions used: 10% cement, 50% coal cinders, and 7 days curing. Water content after 7 days was 48–53%, indicating that optimum water content (about 45–50%) had likely been reached. Maximum dry density was approximately 1.05 g/cm^3. Due to the presence of coal, dry density remained at lower values than in usual soils. Further compaction behavior will be studied under controlled drying conditions (e.g., air-drying cured specimens).

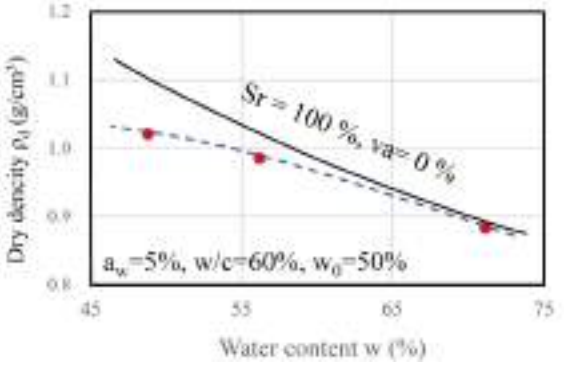

Figure 5 Compaction curve of cement solidified soil

Cone Index Test Results

Figure 6 shows cone index test results for the cement-modified improved soil and the grain-adjusted soil. The uncemented "grain-adjusted soil" was passed by sampled coal cinders through a 2.0 mm

sieve. It was compacted only coal cinders without cement. The cone index ratio in this figure shows the value divided by the cone index of the grain-adjusted soil. It indicates the rate of increase in the cone index due to cement solidification. Under the same conditions, the improved soil showed a cone index about 1.5 times that of the uncemented soil. After 7 days of curing, the strength was about 2400kN/m², three times the threshold of 800 kN/m² of cone index values, the second-class standard for construction-generated soil. It was confirmed that the improved soil is suitable as a backfill material.

In Figure 7, "2nd use to 4th use" refers to the repeated number of compacted specimens after the initial compaction of soil for the cone test. The specimen was broken up and re-compacted for the following cone index test. Reuse led to gradual loss of strength (cone index): the cone index fell by half after four cycles, though dry density remained stable. The cone index ratio shown in Figure 7 is defined as the cone index value for each measurement divided by the initial cone index and represents the rate of decrease in the cone index. The decrease in the cone index implies limitations in reusability and warrants further investigation.

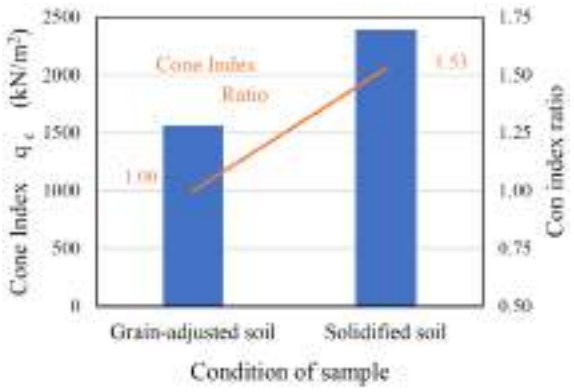

Figure 6 Result of cone index test
(Cone index and Cone Index ratio)

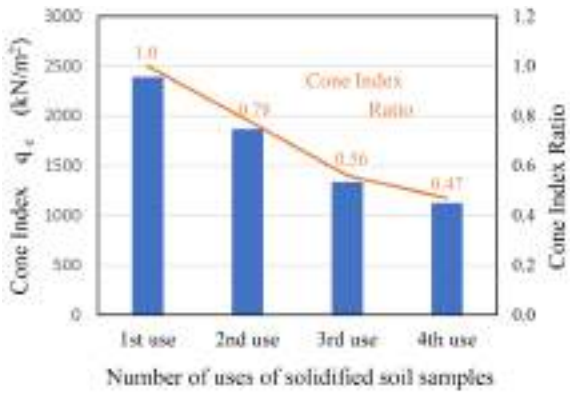

Figure 7 Result of cone index test
(Use repeated compacted sample)

Permeability Test Results

Permeability test results are shown in Table 3. While prior studies suggest permeability declines with smaller pore size as cement content increases, no significant difference was observed before and after treatment in this study [14].

Results matched other reports that permeability remains similar or slightly decreases [15]. Permeability is classified as “low” to “very low.” Since permeability depends on material composition and compaction density, future research will continue.

Table 3 Pearmeability test results

Sample	Permeability coefficient k	
Grain-adjusted soil	1.63×10^{-7}	m/s
Solidified soil	1.66×10^{-7}	m/s

CONCLUSIONS

From the above, the following conclusions were drawn:

1. Cement addition increased the strength of coal cinders. By adjusting cement addition rate, coal cinders content, and initial water content, the required uncofined compressive strength was achieved.
2. Compaction test results confirmed the existence of optimum water content and maximum dry density. Due to coal content, both dry and wet densities of the improved soil were relatively low.
3. The cone index for cement-modified improved soil met the criteria for displaced soil at construction under appropriate solidification conditions. However, repeated compaction tests showed a gradual decrease in the cone index, indicating care must be taken when considering reuse.
4. Permeability tests showed that hydraulic conductivity remained nearly constant regardless of cement modification.

ACKNOWLEDGMENTS

In preparing this paper, several laboratory compaction experiments and other tests were conducted by the Environmental Geotechnical Laboratory staff of the Department of Civil Engineering, College of Science and Technology, Nihon University. The authors would like to express gratitude to them.

REFERENCES

[1]Waste Management and Public Cleansing Act, Act No. 137, 1970, Japan.

[2]A Profile of Japanese Steam Locomotives/ Japanese First Steam Engines (in English and in Japanese), http://steam.fan.coocan.jp/beginning/firstmodel.htm

[3]150th Anniversary of railway in Japan (in Japanese), https://www.jreast.co.jp/150th/

[4]Kamao Shoji, Ishii Kentaro, Shigemura Satoshi and Murakami Yuta, Cement Solidification Characteristics of Coal Cinders-Mixed Soil, Geomate Conference, 2022, pp. 489-494.

[5] Suzuki Rikuto, Ishii Kentaro, Shigemura Satoshi, Kamao Shoji, Murakami Yuta, Cement-hardening Properties of Soil Containing Coal Cinders. 15th Soil improvement symposium, 2022, pp359-364. (in Japanese)

[6] Murakami Yuta,, Study on effective use of coal cinders mixed soil, Study of Effective Utilization of Coal Mixed Soil~Characteristics of Cement Solidification of Soil Mixed with Coal Cinders~, 15th Environmental Geotechnical Engineering Symposium , 2023, pp167-171. (in Japanese)

[7] Murakami Yuta,, Study on effective use of coal cinders mixed soil, Study of Effective Utilization of Coal Mixed Soil, ~Physical and chemical properties of coal debris and survey of contaminated soil~, 15th Environmental Geotechnical Engineering Symposium, 2023, pp172-176. (in Japanese)

[8] Kamao Shoji, Shigemura Satoshi and Murakami Yuta, Study on effective use of coal cinders mixed soil, Strength properties of cement stabilized soil, - International Journal of GEOMATE, 2023, pp. 53-60, Vol. 24, No.104

[9]Japanese Geotechnical Society, Tests on Stabilized soils - Practice for making and curing stabilized soil specimens without compaction - Japanese Geotechnical Society Standard, Laboratory Testing Standards of Geomaterials Vol.2, 2016, pp. 1-6.

[10] Japanese Industrial Standard (JIS A 1216: 2020), Method for unconfined compression test of soil, Japanese Industrial Standards Committee, 2020, pp.1-16.

[11] Japanese Industrial Standard (JIS A 1210: 2020), Test method for soil compaction using an rammer, Japanese Industrial Standards Committee, 2020.

[12] Japanese Industrial Standard (JIS A 1228: 2020), Test method for cone index for compacted soils, Japanese Industrial Standards Committee, 2020.

[13] Japanese Industrial Standard (JIS A 1218: 2020), Test method for permeability for saturated soils, Japanese Industrial Standards Committee, 2020.

[14] Railway Technical Research Institute : Design standard for railway earth structures, 2007, pp. 242~243. (in Japanese).

[15] Masaaki Terashi, Hiroyuki Tanaka, Tsukasa Mitsumoto, Sadakichi Homma, and Terumi Ohashi: Study on the Basic Properties of Lime-Cement Stabilized Soil (Part 3), Report of the Port and Harbor Research Institute, Vol. 22, No. 1, pp.69-99, 1983

Copyright © Int. J. of GEOMATE All rights reserved, including making copies, unless permission is obtained from the copyright proprietors.

15th Int. Conf. on Geotechnique, Construction Materials & Environment,
Kyoto, Japan, 11-13 November 2025, ISBN 978-4-909106124 C3051

CHARACTERISTICS OF FATAL WATER ACCIDENTS IN JAPAN AND THE IMPACT OF CHANGES IN THE AGE COMPOSITION OF THE POPULATION

Masaaki Kondo[1], Yusaku Mizoguchi[1] and Kaede Yoshida[1]

[1] Graduate School of Bioresources, Mie University, Japan

ABSTRACT

This study examines the characteristics of water accidents occurred in Japan from the 1970s to the 2020s, focusing specifically on accidents occurring in the sea, rivers, canals, lakes/marshes/ponds, swimming pools, and other water-related locations. It also analyzes the contribution of changes in Japan's population structure to the temporal trends in the number of fatalities from water accidents.

The results show that in the 1970s and 1980s, a high proportion of water accidents involved infants, preschoolers, and elementary school students, whereas in the 2010s and beyond, those aged 65 and older accounted for the majority. Additionally, in all periods, accidents occurring solely in the sea accounted for approximately 50%, and when combined with river accidents, they made up 70-80% of all accidents. Furthermore, regardless of the periods, fishing activities accounted for the majority of water accidents.

The relationship between accident ratios and population ratios reflects Japan's aging population and declining birthrate. When comparing the RMSE of accident ratios and population ratios for all water accidents and irrigation pond accidents, the RMSE for all water accidents was smaller than that for irrigation pond accidents. This suggests that population structure may influence the overall incidence of water accidents.

Keywords: Water accidents, Occurrence characteristics, Age distribution of population, and Changes in the times

INTRODUCTION

Background

According to the World Health Organization (WHO), approximately 300,000 people drown each year worldwide [1]. Water accidents occurring not only in Japanese waters but also in waters around the world are a serious problem. Since water bodies function as amenity-oriented riparian spaces, water accidents occur in natural waters such as oceans, rivers, lakes, and marshes, as well as in civil engineering structures such as maintained reservoirs and irrigation ponds, through daily life and leisure time.

Figure 1 shows the percentage of fatal water accidents that occurred in Japan in the most recent year, 2023, by location [2]. The scope of fatal water accidents covered by this paper is the entire range of accidents, specifically, accidents that occurred in the sea, rivers, irrigation canals, lakes/marshes/ponds, swimming pools, and others, as shown in Figure 1.

The number of fatalities in Japan in water accidents in general has been on a downward trend since the year the records began to be kept as shown in Fig.2. However, although the number seems to have bottomed out at around 800 in recent years, 743 people died in 2023, indicating that the number has not yet dropped to zero.

In this paper, water accidents refer to fatal accidents that occur near water, such as the sea, rivers,

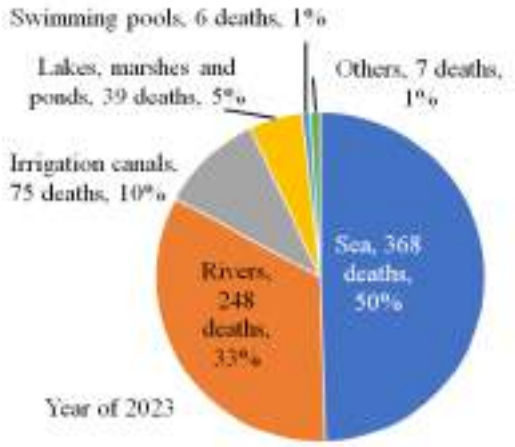

Fig.1 Percentage of water accidents by location in 2023 [2]

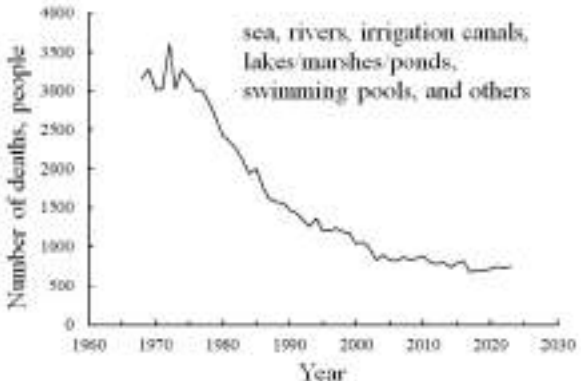

Fig.2 Yearly changes in the number of deaths from all types of water accidents

and irrigation canals. Focusing on fatalities, cases in which individuals were injured but survived the accident are not included.

Previous Studies

Since water accidents occur in a wide variety of locations, there are papers on the individual locations where accidents have occurred. However, there seem to be few studies on water accidents in general. Therefore, this section introduces examples of research on major individual locations where water accidents have occurred.

First, Nishi et al. [3] reported on the physical environment of offshore currents that can cause water accidents, based on the average velocity of offshore currents and the topography of sandbars that can easily generate offshore currents, through field observations along the coast of Miyazaki Prefecture. In July 1955, 36 female junior high school students from Tsu City, Mie Prefecture, drowned during swimming practice near Mie University due to longshore current [4].

Next, the River Foundation Research Institute reported on various risks inherent in rivers and water bodies, as well as risk countermeasures, by organizing accident characteristics for river accidents ([5,6]).

Furthermore, Okamoto et al. [7] conducted an interesting study on irrigation canals, elucidating the mechanism by which water accidents can occur even in canals with shallow water depths and low flow velocities.

Finally, there are some studies on irrigation ponds. While there have been few detailed studies of irrigation pond accidents, the Ministry of Agriculture, Forestry, and Fisheries (MAFF) [8] has published the number of accidents in its collection of irrigation pond safety case studies. Mizutani [9] investigated water accidents involving irrigation ponds, summarized the locations of fatal accidents, and classified accident patterns by age group. Hayashi et al. [10] conducted a questionnaire survey of local residents and reported on the relationship between their childhood experiences of swimming and playing in the water and their perception of irrigation ponds as dangerous. Yoshida et al. [11] collected data from newspaper articles and reported on the actual situation of water accidents in irrigation ponds. Kondo et al. [12] compared the past and the present in terms of water accidents in irrigation ponds, and pointed out the contribution of factors other than changes in population structure.

Purpose of this Study

Looking at the Police White Paper, which contains statistics on water accidents, it is clear that the deaths of children have been taken seriously in every era. Furthermore, looking at papers on accident prevention, I feel that many of them target children. In an official document titled “Statistics on Water Accidents in 2012,” it was first mentioned that approximately 40% of accidents involved elderly people. However, subsequent official documents did not continue to mention elderly people, leading us to believe that there is less concern for elderly people compared to children, and that there is little awareness of the aging population involved in accidents. The objectives of this study are as follows.

First, to summarize the trends in the occurrence of water accidents in Japan in general from the 1970s to the present day 2020s as accident characteristics. Next, the contribution of changes in Japan's population structure will be examined based on changes in the number of fatalities in water accidents over time.

Expected Effects of this Study

In Japan, many people used to die in water accidents in the past, as evidenced by the 3,160 fatalities in 1975. However, accidents have been reduced through various efforts on various fronts, including school education. We hope to explain the overall picture of water accidents in Japan to an international audience, so that the past, present, and history of accidents can be better understood.

METHOD

Data Used in the Analysis

The number of fatalities in water accidents and Japan's population are publicly available from government agencies, and these data were used. Specifically, data on the number of people who died or went missing due to water accidents from 1975 to 2023, based on the Police White Paper [13] and the Statistics on Water Accidents [14] published by the National Police Agency, was used.

In addition, population data from the 1970-2020 census were used [15]. The census is conducted every five years and covers everyone living in Japan.

As a supplementary explanation of the quality of data available from public institutions, data from public institutions tend to be limited in terms of content. One way to collect data from non-public institutions is to organize data from newspaper articles. Newspaper articles may provide useful information for analysis, such as the attributes of the deceased and the circumstances at the time of death. However, as in this paper, it requires a great deal of effort to obtain data from newspaper articles over a long period of time, such as about 50 years in the past, so we did not refer to newspaper articles in this paper. On the other hand, the River Foundation's efforts can

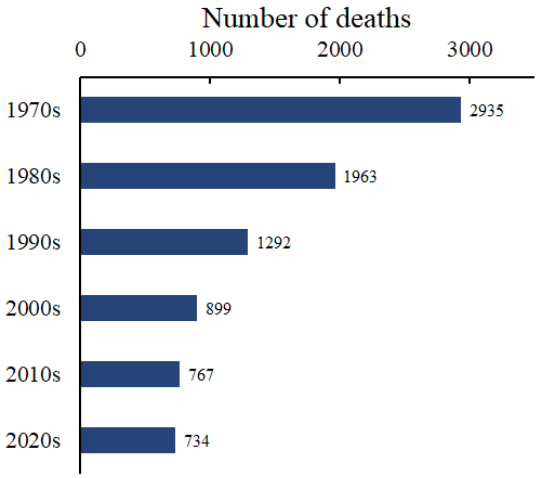

Fig.3 Changes in the number of deaths from all types of water accidents every 10 years

be cited as an example of an analysis that referred to such newspaper articles. In the River Foundation's report, Miyao et al. [5] collect data on water accidents in rivers by referring to newspaper articles as well as data from public agencies. Yoshida et al. [11] and Kondo et al. [12] also report on water accidents in irrigation ponds by organizing data from newspaper articles.

Analysis Method

The acquired data were carefully examined, and basically a 10-year average was taken to organize the data by time period for discussion.

Water accident data were subject to changes in survey items since they were first recorded. For example, there was one major change with respect to age of occurrence, and supplemental calculations were made to reflect trends over several years.

When examining the population proportion and accident proportion, the Root Mean Squared Error (RMSE) shown in Equation 1 below was used as an indicator to determine the degree of distribution. Here, the population proportion is variable x and the accident proportion is variable y. The contribution of the population proportion to the accident proportion was determined by calculating the variation in the degree of departure from the equation y=x using Equation 1. In other words, the closer the distribution was to y=x, the better the fit to y=x, indicating that it was influenced by the population proportion, and conversely, the further the distribution was from y=x, the poorer the fit to y=x, indicating that it was not influenced by the population proportion.

$$RMSE = \sqrt{\frac{\sum_{i=1}^{N}(x_i - y_i)^2}{N}} \quad (1)$$

RESULTS AND DISCUSSION

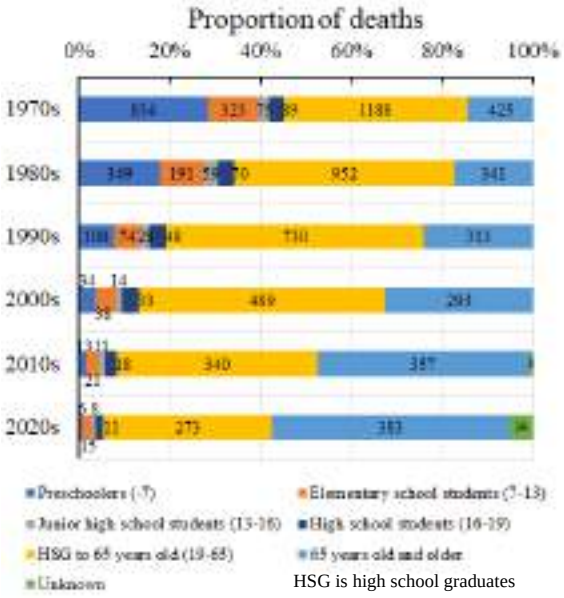

HSG is high school graduates

Fig.4 Changes in the number of deaths from all types of water accidents every 10 years (by age group)

Characteristics of Water Accidents

This section identifies trends on the age of those who died as a result of an accident, the location where the accident occurred, and the conduct of the person when the accident occurred. Note that there is no information other than age, location, and conduct that can be obtained from official data. However, as explained in the "Section on Data Used", other information may be obtained by organizing newspaper article data.

The data were averaged and graphed by decade from the 1970s to the 2020s. Basically, the data is averaged over the 10-year period from XX00 to XX09, with the 1970s being the average over the 5-year period from 1970 to 1974 and the 2020s being the average over the 4-year period from 2020 to 2023. The reason for organizing the data by period is to make it easier to understand the occurrence of fatal accidents by summarizing them in decadal rather than yearly time series.

Trends in the number of fatalities in water accidents

Figure 3 shows the change in the number of fatalities in water accidents by period. In the 1970s, nearly 3,000 people died annually, but the number decreased exponentially, falling to around 1,300 in the 1990s, around 900 in the 2000s, and around 730 in the 2020s. The number of deaths decreased by 56% from the 1970s to the 1990s and by 18% from the 2000s to the 2020s. Thus, the number of cases, which was notably high, gradually declined significantly, with smaller declines from the 2010s to the 2020s.

Characteristics of age of occurrence in water accidents

Figure 4 shows the number of fatalities in water accidents as a percentage of the total number of fatalities by age of occurrence. The percentage of accidents involving infants, preschool children (under 7 years old), and elementary school students (7 years old to under 13) showed a decreasing trend. The percentage of accidents involving junior high and high school students (13 years old to under 16, 16 years old to under 19) has been small since the 1970s, while the percentage of accidents involving persons aged high school graduates to 65 (19 years old to under 65) has been on a downward trend. While the percentage of accidents for the previous age groups showed a decreasing trend, the percentage of accidents for those aged 65 and over continued to increase. Looking at the largest segments in the percentage of accidents, while in the 1970s and 1980s, infants, preschoolers, and elementary school students accounted for a large proportion of accidents, in the 1990s, the percentage of accidents for those aged 65 and older accounted for 24%, exceeding the 20% rate for high school students and younger. Furthermore, since the 2010s, people aged 65 and older have accounted for the majority of accidents.

According to the WHO, children under the age of five account for approximately 25% of drowning deaths worldwide [1]. The percentage of preschoolers who die in Japan has dropped to about 1%. Recent trends in Japan have clearly diverged from global trends.

Characteristics of location of occurrence in water accidents

Figure 5 shows the number of fatalities in water accidents by location, with the sea accounting for the largest proportion of fatalities from the 1970s to the 2020s, followed by rivers. The next largest number of fatalities occurred in irrigation canals and lakes/marsh/ponds, followed by swimming pools and others, in that order. Both oceans and rivers are the largest segment, and they occupied the top positions regardless of the time period. Irrigation canals, lake/marsh/ponds, swimming pools, and others showed a slight downward trend. As can be seen, accidents still occur most frequently in oceans and rivers. The sea alone accounts for about 50% of all accidents regardless of age, and the total of sea and rivers accounts for 70-80% of all accidents. The percentage of fatalities in irrigation canals and lake ponds is on a declining trend.

Characteristics of occurrence acts in water accidents

Figure 6 shows the number of fatalities in water accidents as a percentage of the number of fatalities per act of occurrence. It can be seen that while swimming and passing through show a decreasing

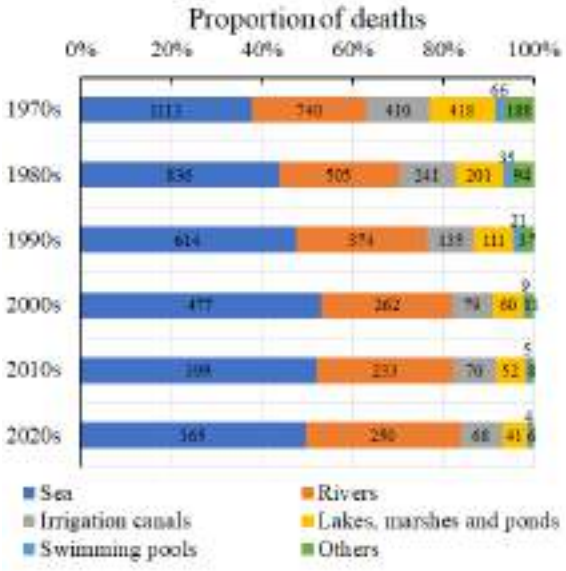

Fig.5 Changes in the number of deaths from all types of water accidents every 10 years (by location)

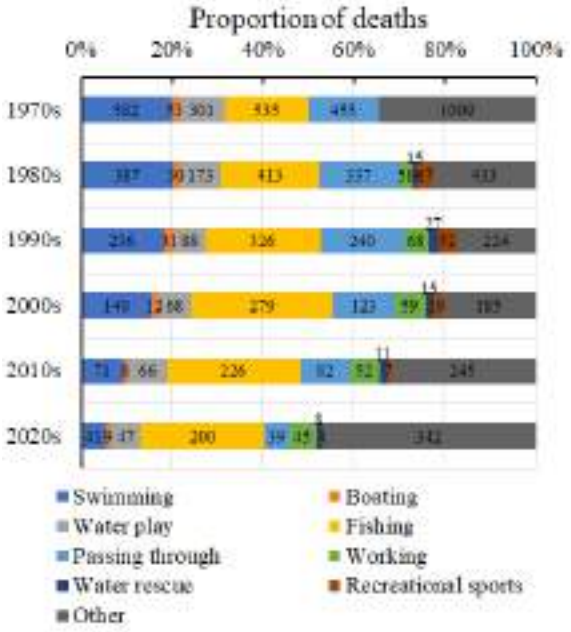

Fig.6 Changes in the number of deaths from all types of water accidents every 10 years (by behavior)

trend, water sports, fishing, working, and others remain unchanged or show an increasing trend. It is difficult to determine which are the largest segments, but the contemporary largest segments are others and fishing. Thus, regardless of the time period, angling for fish is in the majority. Others, despite being in the majority, are not detailed and require caution during the data collection phase.

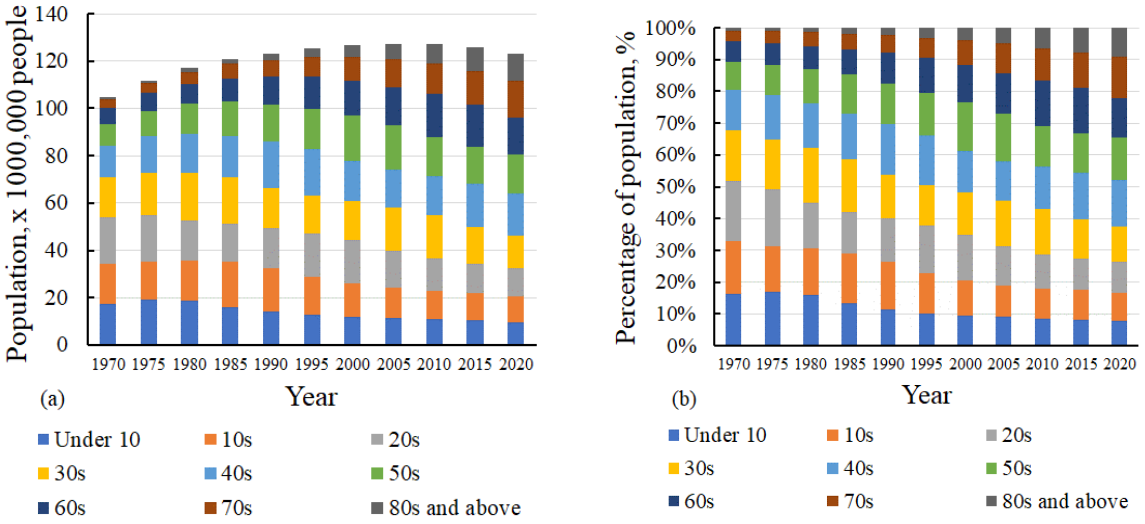

Fig.7 Changes in Japan's population (a) Population by age (b) Percentage by age

Table 1 Water accident ratio by age group

Age		Each 10-year period			
Group	Range*	1980s	1990s	2000s	2010s
Elementary school students and younger	00 - 13	28	13	8	4
Junior high school and high school students	13 - 19	7	6	5	4
High school graduates aged 65 and under	19 - 65	49	56	54	44
65 and older	65 -	17	24	33	47
Unknown					1
Total		100%	100%	100%	100%

*) eg. 00 <= x < 13 years old

Table 2 Population ratio by age group

Age		Middle year of each 10-year period			
Group	Range*	1985	1995	2005	2015
Under 10	00 - 10	13	10	9	8
10s	10 - 20	16	13	10	9
20 to 65	20 - 65	61	63	61	56
65 and older	65 -	10	15	20	27
Total		100%	100%	100%	100%

*) eg. 00 <= x < 10 years old

Trends in Japan's population numbers

Figure 7 illustrates the changes in the number of people in Japan, without averaging the data as a period, since the survey is conducted every five years. As Fig.7(a) shows, Japan's population increased from a little over 100 million in 1970 to a peak of 127 million in 2005, after which it began to decline. As Fig.7(b) shows, the birthrate began to decline in the late 1970s, and by 1990, the birthrate had dropped to 1.57, which is now considered a serious social problem.

Changes of Water Accidents in General

In order to examine the relationship by age group between water accidents and population, we reorganized the data on accident ratios and population ratios. That is, the accident ratio from the 1980s to the 2010s were re-compiled for the four main age groups as shown in Table 1. Specifically, the data were broken down into the following groups: elementary school students and younger, junior high and high school students, high school graduates and under 65 years of age, and 65 years of age and older. The purpose of grouping the data into major age groups is to better understand the data and to make it more useful for future measures. Table 1 shows the general school age range in Japan.

On the other hand, the reorganized population ratios are shown in Table 2. The data corresponding to the middle years of each age group were used for the population ratio to correspond to the accident ratios from the 1980s to the 2010s. For example, in the 1980s, the population counts for 1985 were used. In addition, the age groups in the population ratio were roughly matched to the age groups in the accident ratio. Specifically, the groups were divided into the following age groups: under 10 years old, teens (10 to 20 years old), 20 to 65 years old, and 65 years old or older.

The age ranges in Tables 1 and 2 do not match exactly in some places. This is because population data with fixed age intervals was used, while accident data with irregular age intervals was used. Therefore, a format that aligns as closely as possible with the accident data with irregular age intervals was adopted. Even with such data, it was determined that it is sufficient to draw general conclusions.

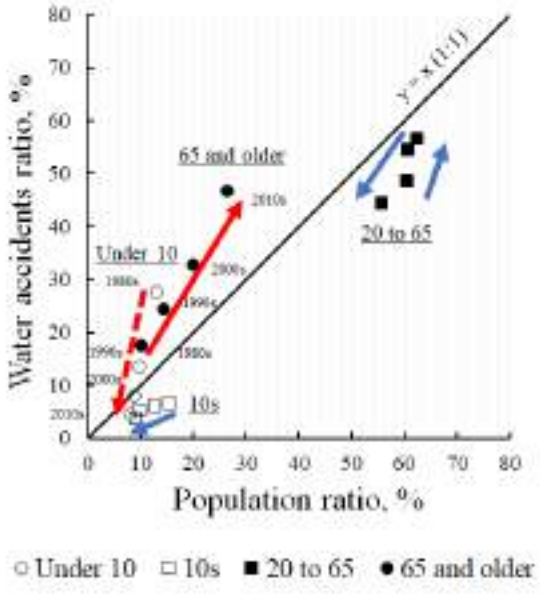

Fig.8 Age-specific population ratio vs. accident ratio by age group for all water accidents

Figure 8 plots the relationship between the percentage of population composition and the percentage of accident composition by age group for water accidents in general. For each age group, changes from the 1980s to the 2010s are plotted. The y=x line indicates a 1:1 relationship between the population proportion and the accident proportion; a plot above y=x means that the accident proportion is larger than the size of the population proportion; a plot below y=x means that the accident proportion is smaller than the size of the population proportion. This means that the accident ratio is smaller than the size of the population ratio.

Figure 8 illustrates the change from the 1980s to the 2010s. For children under 10 years old, which corresponds to preschool and elementary school students, accidents used to occur more frequently than the size of the population ratio, but in the modern era, the number of accidents has decreased significantly to match the size of the population ratio. For the 10s, which correspond to junior high and high school students, the accident ratio was smaller than the size of the population ratio both in the past and in the present, but both the population ratio and the accident ratio have decreased. For those aged 20 to 65, who were considered to be equivalent to those aged 18 to 65, unlike other age groups, there was no unidirectional progression, but only changes in the vicinity of a straight line. For those aged 65 and over, accidents have always occurred at a rate higher than the population size, but in modern times, the accident ratio has increased significantly to a level that does not match the population size.

Table 3 Comparison of population ratio vs. accident ratio for all water accidents and pond accidents by age group for all water accidents

Period	RMSE of water accidents in general	RMSE of water accidents in ponds
Case of 1980s	11.1	33.3
Case of 2010s	12.0	20.2
All cases of 1980s and 2010s	11.5	27.6

Among the four age groups, we focused on the two most characteristic age groups, those under 10 and over 65, which, unlike the other age groups, have changed significantly over time, and the direction of change is opposite to each other. In other words, for the under-10s, the population and accident ratios decreased significantly, and the intervals between the plots approached a straight line while decreasing; for the over-65s, the population and accident ratios increased significantly, and the intervals between the plots tended to move away from a straight line while increasing.

Comparison of Water Accidents in General and Irrigation Pond Accidents

Since Japan has become an aging society with a declining birthrate and the population composition ratio has changed, the relationship between the population ratio and the accident ratio is discussed in light of this change. In the data used in this study, the age groupings do not perfectly match the population ratio and accident ratio, but this was not judged to be a problem in the big picture. Focusing on the variation between the population and accident ratios, we compared water accidents in general with irrigation pond accidents, which are known to have changed over time, in order to examine and understand the characteristics of water accidents in general. In order to compare the variation, all age groups in the 1980's and 2010's were included.

Table 3 shows the results of the comparison of RMSE values for variability. The RMSE values for variability were RMSE = 28 for irrigation pond accidents and RMSE = 12 for accidents in general. The RMSE value for the all water accident was 0.5 times as small as that for the irrigation pond accident. In other words, the variability of the water accidents in general was smaller than that of the irrigation pond accidents. This was interpreted as indicating that

water accidents in general are highly correlated with the percentage of the population, and that the contribution of the population ratio is significant in accidents in general.

CONCLUSION

The number of fatal water accidents in Japan in general has been calculated as a 10-year average, basically from the 1970s to the 2020s, in order to better grasp changes over time. However, a downward trend has been observed in recent years.

The characteristics of the occurrence of water accidents in terms of age, location, and activity were identified. Specifically, while in the 1970s and 1980s, infants, preschool children, and elementary school children accounted for a large proportion of water accidents, since the 2010s, the majority of accidents have occurred among people aged 65 and older. In all periods, water accidents in the sea alone accounted for about 50% of all water accidents, and 70-80% when accidents in the sea are combined with those in rivers. Fatalities in irrigation canals and lake ponds are on the decline. Fishing is the most common activity involved in water accidents, regardless of the time period.

The relationship between the accident rate and the population rate shows the trend of Japan's declining birthrate and aging population. When the variation between accident rate and population rate was compared between water accidents in general and irrigation pond accidents, the variation for water accidents in general was smaller than that for irrigation pond accidents. This suggests a possible demographic effect for water accidents in general.

REFERENCES

[1] WHO, Drowning, 2024-Dec-13, https://www.who.int/news-room/fact-sheets/detail/drowning, Accessed on 2025-Apr-01.

[2] National Police Agency, Statistics on Water Accidents 2024.

[3] Nishi R., Murata N., Futatsumachi S., Kimura S., Murai Y., and Koga Y., Research on Rip Currents for the Prevention of Water Accidents, Annual Journal of Coastal Engineering, JSCE, Vol.52, 2005, pp.1306-1310.

[4] Nan'niti T**.,** A Study on the Cause of the Death Accident in Water of Schoolgirls of the Basikita Middle School, Tu City, Journal of Oceanography, Vol.11, No.4, 1955, pp.171-177.

[5] Miyao H., Shimizu A., Yoshino H., and Doi Y., Research on Trends in River Accidents and Efforts to Promote Safe River Use, River Environment Research Institute Report, Vol.14, 2008, pp.23-34.

[6] Sugawara K., Yoshino H., Suzuki A., and Matsuo T., Basic Survey to Prevent Water Accidents in Rivers 2017, River Environment Research Institute Report, Vol.23, 2017, pp.47-60.

[7] Okamoto T., Toda K., Oka S., and Touma Y., Experimental Study on Increase of Drowing Accident Risk at Side Ditch and Irrigation Channel, Advances in River Engineering, Vol.25, 2019, pp.73-78.

[8] Ministry of Agriculture, Forestry and Fisheries, Case Studies of Safety Measures for Irrigation Ponds, 2023, https://www.maff.go.jp/j/nousin/bousai/bousai_saigai/b_tameike/anzen.html#anzen, Accessed on 2025-Apr-01.

[9] Mizutani M., Planning Techniques for Creating Beautiful Water-Friendly Spaces ― Characteristics of Water Accidents Near Water and Measures to Prevent Them ―, Journal of Japanese Society of Irrigation, Drainage and Reclamation Engineering, Vol.60, No.3, 1992, pp.225-230.

[10] Hayashi N. and Takahashi T., Fundamental Study on Risk Factors for Drowning in Irrigation Pond, Transactions of Rural Planning, Vol.3, 2001, pp.85-90.

[11] Yoshida K., Okajima K., and Kondo M., Actual Situation of Pond Water Accidents Based on a Database of Newspaper Articles, Journal of Japanese Society of Irrigation, Drainage and Reclamation Engineering, Vol.93, No.4, 2025, pp.263-266.

[12] Kondo M., Miyara K., and Yoshida K., Factor Analysis of Reservoir Water Accidents Using Multiple Regression Analysis, Proceeding of Annual Conference of the Agricultural and Rural Engineering Society in 2025.

[13] National Police Agency, The White Paper on Police from 1976 to 2002.

[14] National Police Agency, Statistics on Water Accidents from 2003 to 2024.

[15] Ministry of Internal Affairs and Communications Statistics Bureau, 1970-2020 Census Results, Age (5-year age groups) .

Copyright © Int. J. of GEOMATE All rights reserved, including making copies, unless permission is obtained from the copyright proprietors.

15th Int. Conf. on Geotechnique, Construction Materials & Environment,
Kyoto, Japan, 11-13 November 2025, ISBN 978-4-909106124 C3051

WHY IS SEEDLING'S REGENERATION OF *RHODODENDRON QUINQUEFOLIUM* POPULATION ON MT. RYUGATAKE NOT GOING WELL?

Mei Takeoka[1], Masaharu Sakakibara[2] and Michiko Masuda[3]

[1,2,3]Department of Civil Engineering, Nagoya Institute of Technology, Japan

ABSTRACT

In recent years, the famous population of *Rhododendron quinquefolium* in Mt. Ryugatake have been decreased, in the center of Japan. Mt. Ryugatake is loved by many people because of the beautiful scenery that is flowering of *R. quinquefolium*, so everyone will be recovering the species. Because of regeneration by seedlings has not occurred, there are concerns that the population of the species will decline. Mt. Ryugatake area is national park, surveys was restricted, and no precise research have been conducted. We therefore conducted field surveys to verify two hypotheses. One hypothesis is that the reason for the lack of seedling regeneration is that the deer are feeding on the plants, and the other hypothesis is that the lack of regeneration is due to the lack of an environment in which seedlings can emerge. To prevent feeding damage, we set up nets to prevent feeding damage and checked the number of seedlings with and without the nets, and found that feeding damage by deer was not the cause. In addition, the hypothesis that the environment is not suitable for seedlings was also denied by confirming the seedlings. We therefore compared the growth environment (pH, ignition loss, electrical conductivity, soil moisture, canopy openness) of *R. quinquefolium* in general with that of the species in Mt. Ryugatake, and found that the habitat of the species in Mt. Ryugatake had a high pH and was eutrophic. This suggests that seedling regeneration may not be going well.

Keywords: Deer Harvest, Seedling Regeneration, Environmental Condition, Conservation Activity

INTRODUCTION

From the perspective of distinctiveness, *Rhododendron quinquefolium* (commonly known as Shiroyashio) population on Mt. Ryugatake—located on the border between Inabe City in Mie Prefecture and Higashiomi City in Shiga Prefecture—is considered a high conservation priority. *R. quinquefolium* is an endemic deciduous shrub in the family Ericaceae, characterized by its whorled leaves and known as "Goyou-tsutsuji" due to its five-leaf arrangement. Although it is listed as a threatened species in some prefectures, it is generally widely distributed across main land of Japan and Shikoku island and is not considered globally endangered. However, the population that grows in a broad area on the gentle slopes near the summit of Mt. Ryugatake is exceptionally rare. The sight of its white blossoms stretching across the landscape has been likened to a flock of white sheep and draws many hikers each year. From a utilitarian perspective, the conservation of this population is also significant [1].

In recent years, concerns have arisen regarding the decline of this population, with many mature trees dying or falling, and a lack of seedling establishment indicating difficulties in natural regeneration. In conservation biology, especially in managing rare or endangered species, it is essential to understand the species' ecology, population dynamics, and factors affecting population size and distribution [2][3]. Various methods can be employed for population studies, including ecological data collection and long-term monitoring.

This study focuses on the reproductive process and regeneration of R. quinquefolium populations on Mt. Ryugatake. By investigating physical environmental conditions in areas where seedling recruitment is observed, we aim to identify the key factors affecting regeneration, thereby contributing to the conservation of this unique plant community. We formulated two hypotheses and conducted a study to test them. The first hypothesis is that the seedlings of *Rhododendron quinquefolium* are disappearing due to predation by deer. The second hypothesis is that the seedlings are unable to grow because the environmental conditions are unsuitable for their development. To verify these hypotheses, we carried out this research.

RESEACH SIGNIFICANCE

Natural environments that function as key tourism resources represent assets of considerable national importance. Nevertheless, the maintenance and management of natural vegetation present substantial challenges, and many national parks are currently confronted with serious ecological issues. In recent years, numerous large-scale civil engineering projects—such as landslide prevention, debris flow mitigation, and sediment control in river basins—

have been carried out under the framework of the National Resilience Plan. Although these public works are widely acknowledged to have significant ecological impacts, comprehensive long-term assessments of their influence on natural environments remain scarce. The formation of *R. quinquefolium* communities is hypothesized to be closely linked to large-scale slope failures caused by past geomorphological disturbances. This study seeks to highlight the necessity of long-term ecological evaluations concerning the potential impacts of future public infrastructure development under national resilience strategies.

MATERIALS AND METHODS

The Study Site

The study was conducted on Mt. Ryugatake, located on the border between Inabe City, Mie Prefecture, and Higashiomi City, Shiga Prefecture (N35°11’93’’, E136°44'51”). Mt. Ryugatake, classified as a deciduous broad-leaved forest zone, has an elevation of 1,099.6 meters. The forest limit is around 900 meters above sea level. The base of the mountain features deep valleys, such as those found in the Ugakei area, creating diverse natural environments. Near the summit, a broad area of naturally growing *R. quinquefolium* populations can be found. Two study areas were established near these growth zones: Plot 1 and Plot 2. Plot 2 consists of a large slope with limited human activity. In contrast, Plot 1 is located near a hiking trail and consists of gentle slopes separated from Plot 2. With permission from the Mt. Ryugatake Nature Conservation Promotion Committee and the Mt. Ryugatake Trail Maintenance Association, we installed eight quadrats in Plot 1 (Fig. 1).

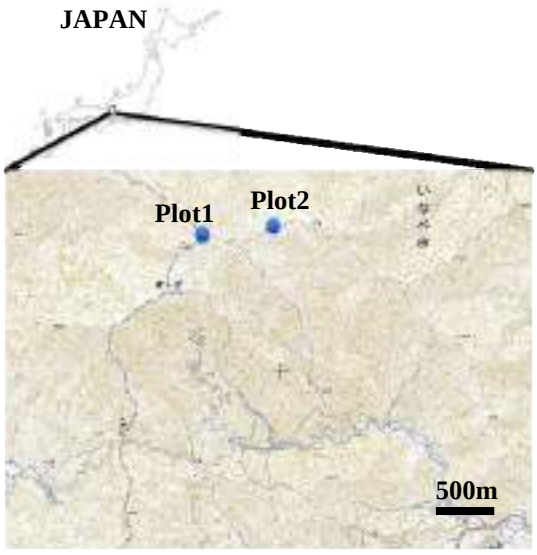

Fig.1 Map of research plots

Due to landscape protection concerns, permission for quadrat installation was not granted in plot 2; therefore, only physical environmental surveys were conducted there. In plot 1, four 1-meter square quadrats were installed perpendicular to the contour lines at 2-meter intervals, considering the impact of topsoil erosion. Another four quadrats were installed parallel to the contour lines at a 2-meter distance from the first set, forming eight quadrats in total (Fig. 2), where changes in seedling counts were recorded. Additionally, quadrats numbered 11, 13, 14, and 18 were equipped with deer-proof fencing to examine the effects of feeding damage.

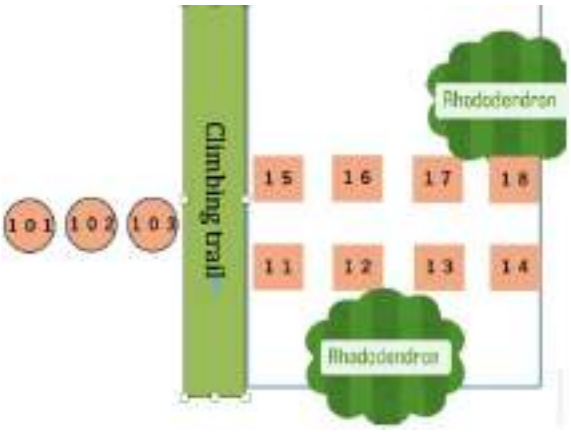

Fig.2 Quadrats layout of plot 1

Physical environmental data were collected at 17 locations. In addition to the eight quadrats in plot 1, three points near the hiking trail (without nearby *R. quinquefolium* trees) were selected as control sites. In plot 2, six survey points were set up at 2-meter intervals perpendicular to the contour lines. Two of these points were located where tree growth was assumed to be unaffected.

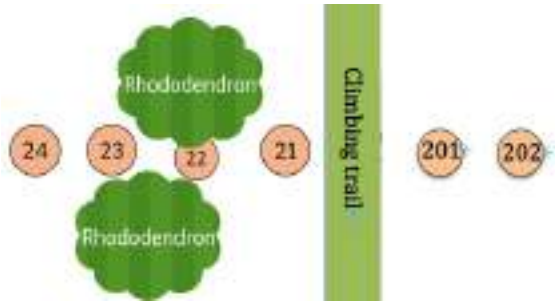

Fig.3 Sampling layout of plot 2

The Study Species

Rhododendron quinquefolium is an endemic deciduous shrub of the Ericaceae family, mainly distributed along the Pacific side of Japan (Fig. 4). It typically grows on rocky highland areas and forest interiors, reaching heights of 4 to 7 meters. Some trees have been found to be over 100 years old. Its leaves grow in whorls of five at the branch tips, hence

its Japanese name “Goyou-tsutsuji.” It produces one to three white flowers per branch tip from late May to early June, concurrently with leaf expansion. The flowers are funnel-shaped with five deep lobes and green spots on the petals, contributing to its elegant appearance [4]. Due to its beauty, it was chosen as the floral emblem of Princess Aiko.

Fig.4 Flower of *R. quinquefolium*

The Tree Ring Survey

To investigate whether the current *R. quinquefolium* individuals on Mt. Ryugatake established simultaneously in the past, a tree-ring survey was conducted. With permission from the Mt. Ryugatake Nature Conservation Promotion Committee and the Mt. Ryugatake Trail Maintenance Association, five fallen trees approximately 4–5 meters tall were sampled on 11th Dec. 2024. A segment of each tree trunk was cut approximately 10 cm above ground level using a saw. The cross-sections were sanded, and the number of rings was counted. The diameter of each section was also measured.

The Seedling Emergence Survey

To examine the correlation between physical environmental conditions and seedling emergence, monthly surveys were conducted in the eight quadrats installed in plot 1 from May to December. The number of emerging seedlings was counted and recorded during each visit (22th May, 5th, 19th Jun., 10th Jul., 6th Aug., 25th Sep., 17th Oct. and 11th Dec. in 2024).

Physical Environmental Survey

Light environment, soil pH, soil moisture content, loss ignition and electrical conductivity were measured every month in 2024 at each plots (19th Apr. 8th, 22nd May, 5th, 19th Jun., 10th Jul., 6th, 21st Aug., 17th, 25th Sep., 17th, 31st Oct. 14th Nov. and 11th Dec. in 2024).

Light is a crucial factor for plant germination and growth. For *R. quinquefolium* populations growing on ridges, good sunlight conditions are ideal. To assess the light conditions, canopy openness was measured at each survey point using a 360-degree camera (RICOH THETA S,). Photos were analyzed using CanopOn2 software [5]-[7], which calculates the proportion of open sky area in hemispherical images. Brightness thresholds were manually adjusted to accurately binarize the images, separating sky from non-sky areas.

Since members of the Ericaceae family prefer acidic soils, the pH of the soil at each survey point was measured using a soil tester. The probe was inserted vertically to a depth of approximately 2.5–3 cm into the topsoil.

Although most plants favor moist environments, *R. quinquefolium* is adapted to drier conditions. To assess this, the same soil tester was used to measure relative moisture levels in five stages: DRY+, DRY, NORMAL, WET, and WET+.

In December, soil samples were collected to a depth of 10 cm and dried at 80°C for 48 hours using a drying oven. Samples were wrapped in paper and weighed before and after drying with a precision balance. Soil moisture content W(%) was calculated using the following formula:

$$W = ((\text{wet weight} - \text{dry weight}) / \text{dry weight}) \times 100$$

Soil organic matter content, which correlates with nutrient levels, was determined via loss Ignition tests. The dried samples were ground and wrapped in aluminum foil, then incinerated at 600°C for 2 hours in a muffle furnace. The loss in mass was calculated using the following formula:

$$LI = ((\text{dry weight} - \text{ignited weight}) / \text{dry weight}) \times 100$$

To assess soil fertility, electrical conductivity (EC) was measured. Five grams of dried soil were mixed with 25 mL of distilled water and stirred for 15 minutes. The EC value of the supernatant was then measured using a conductivity meter.

RESULTS

Detailed experiments and surveys conducted in 2024 yielded the following results regarding the age of existing *R. quinquefolium*, seedling emergence, and physical environmental conditions. From May to November 2024, seedlings of *R. quinquefolium* have been observed in and around Quadrat 18 in Plot 1.

The Tree Ring Survey

The results for the tree-ring survey of the sampled *R. quinquefolium* trunks are shown in Table 1. Considering that the sampling was done at 10 cm or more above the ground, the actual tree ages are likely older than the number of rings counted. These results suggest that, regardless of trunk thickness, most *R. quinquefolium* individuals on Mt. Ryugatake are

likely over 100 years old

Table 1. Tree ring No. and diameter of 5 individuals

Sample No.	Tree ring No.	Diameter max(mm)	Diameter min(mm)
1	99	116	86
2	103	63	45
3	108	90	64
4	109	80	59
5	115	133	73

The Seedling Emergence Survey

Monthly changes in seedling counts from Quadrats 11 to 18 in plot 1 are shown in Table 2. Seedling counts tended to be lower in quadrats located near the hiking trail. Overall, the number of seedlings increased from spring to summer and decreased toward winter. There was no clear difference in seedling count trends between quadrats with or without deer-proof fencing, suggesting that feeding damage by deer may not significantly affect seedling regeneration

Physical Environmental Survey

Canopy openness measurements from April to December 2024 are shown in Fig. 5. Quadrats 11 and 15 near the hiking trail showed relatively high canopy openness. In contrast, other quadrats, including Quadrat 18 where seedlings were found, had lower openness levels compared to plot 2. Fig. 5 shows the box plot from April to December in canopy openness in plot 1 and 2. Openness decreases from May, when *R. quinquefolium* leaves emerge, and increases again around October when the leaves fall.

Table 2. The seasonal accumulation number of seedlings in each quadrat

Quadrat No.	M	J	J	A	S	O	N
11	0	0	0	0	0	0	0
12	0	0	0	2	3	3	3
13	2	3	3	3	3	3	3
14	45	45	45	45	45	45	45
15	0	0	0	2	2	2	2
16	0	0	0	0	0	0	0
17	18	24	40	58	58	58	58
18	20	23	27	33	33	33	33

Soil pH measurements from April to December 2024 are presented in Fig. 6. The soil at sites where *R. quinquefolium* grows was found to be weakly acidic (pH 5–7). Quadrat 18, where seedlings were observed, had relatively high pH values compared to other points. Soil pH decreased toward autumn and increased in winter.

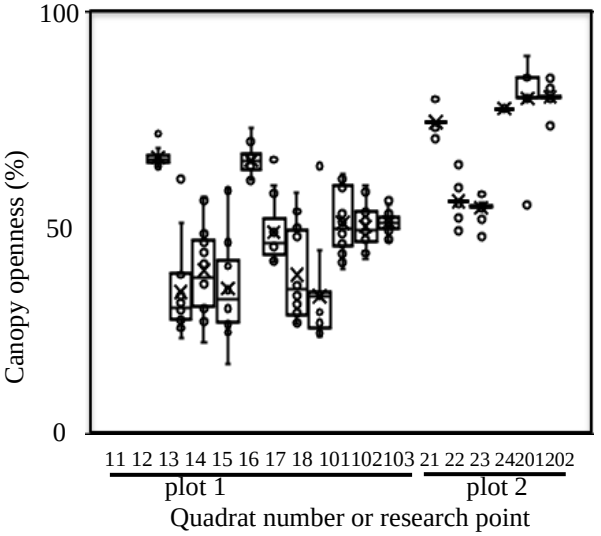

Fig. 5. Canopy openness at each point in plot1 and plot2 from April to December in 2024

Soil moisture data from April to December 2024 are shown in Fig. 7. Quadrat 16 had moisture levels 36% above average, while Quadrat 18 was 26% below average. Overall, plot 2 had moisture values 18% higher than plot 1. Quadrat 18 had the lowest moisture content, 28% below plot 1 average.

The December 2024 loss ignition results are shown in Fig.8. Quadrat 18 had the lowest loss ignition value among all surveyed points.

The electrical conductivity measurements from December 2024 are shown in Fig.9. The average electrical conductivity in plot 1 was 0.4408 mS/cm, compared to 0.1299 mS/cm in Aichi satoyama forest, a 3.39-fold difference. Quadrat 18 again showed the lowest EC value, 41% below the average for plot 1.

Loss Ignition (%)

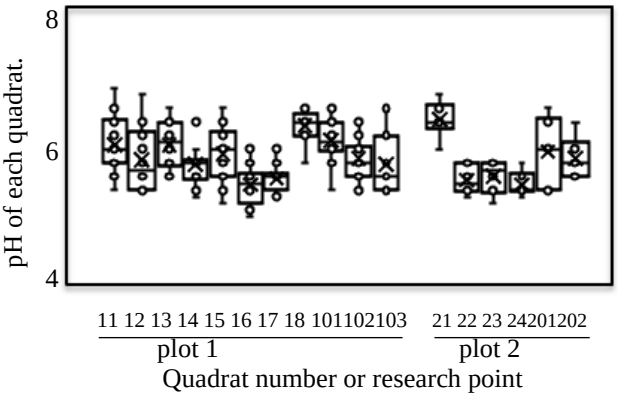

Fig. 6. pH of each point in plot1 and plot2 from April to December in 2024

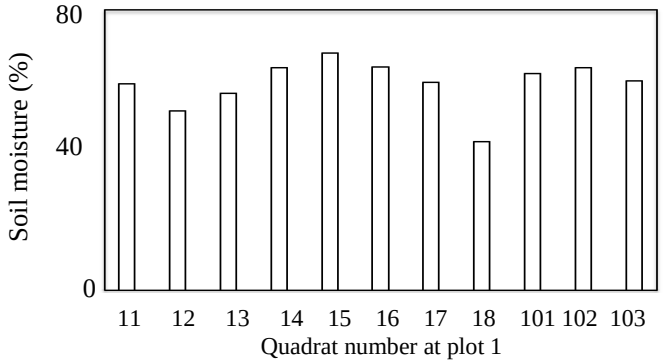

Fig. 7. Soil moisture of each point in plot1

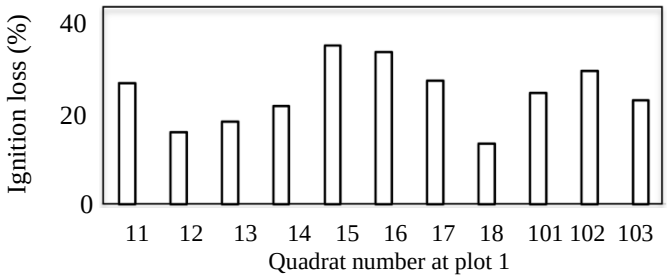

Fig. 8 Ignition loss of each point in plot 1

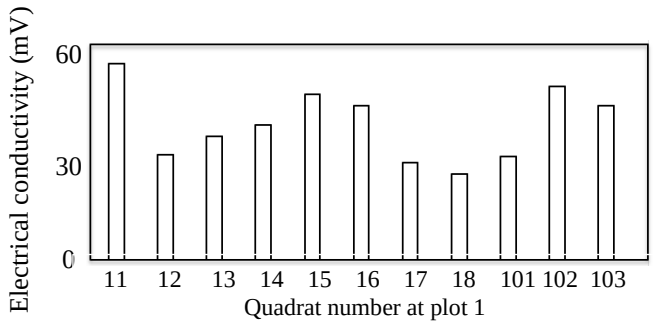

Fig 9 Electrical conductivity of each point

DISCUSSION

Although *R. quinquefolium* is widely distributed in Honshu and Shikoku, and many Ericaceae species share similar ecological characteristics, the population on Mt. Ryugatake forms a unique community that had not been extensively studied until now. Because the view of Mt. Ryugatake is so unique, and it is designated as a National Park, researches were severely restricted. Though some research has been done about gene [8], this investigation clarified the actual environmental conditions in which this distinctive community thrives. This section discusses the potential causes behind the poor regeneration of *R. quinquefolium* on Mt. Ryugatake. In general, failure in generational turnover can result from issues in seed production, germination, seedling establishment, or growth. As multiple seedlings were confirmed during this study, it is unlikely that seed production or germination is the limiting factor. Instead, unsuitable environmental conditions for seedling establishment and growth may be responsible for the population decline.

The survey points were placed perpendicular to contour lines. quadrat 18, where seedlings were found, is located on the downhill side of the slope in plot 1. Since *R. quinquefolium* often grows on rocky ridges where winds can exceed 15 m/s [9], strong winds may prevent seed settlement and seedling establishment on exposed ridges. Thus, seedlings may favor more sheltered, downslope areas for establishment.

The tree-ring survey results suggest that the current *R. quinquefolium* population originated from a past cohort that established simultaneously. Similar regeneration failures have been observed in other Ericaceae species. For example, the Ontsutsuji community at Funakubo in Tokushima Prefecture, designated a national natural monument, is also experiencing decline, and measures such as seedling conservation and planting are being considered [10]. However, these methods may not be desirable from the perspective of genetic diversity conservation [11].

Tree-ring analysis revealed that both thin and thick individuals with diameters ranging from 45 to 133 mm may be over 100 years old, suggesting a single cohort establishment more than a century ago. The same phenomenon was observed in Nepal at land slide area [12]. The landslide created an ideal environment for seedling regeneration, which led to simultaneous germination and the formation of population. The geology of Ryugatake is limestone, and there is a possibility of landslides due to the formation of doline.

While current seedling growth and generational turnover appear unlikely, the small sample size limits certainty. Previous research [13] found that a *R. quinquefolium* (4.2 m tall) was about 75 years old, suggesting that Mt. Ryugatake individuals are relatively older. To verify the timing of past regeneration, further studies using stable oxygen isotope dendrochronology are recommended.

The lack of significant difference in seedling numbers between fenced and unfenced quadrats suggests that feeding damege and trampling have little impact. We focus on differences in physical environmental conditions between quadrats with many seedlings (e.g., 14, 17, 18) and other points.

Seasonal variation in canopy openness indicates shading from May to October during leaf-out, followed by increased openness after leaf fall. Canopy openness in plot 1 is generally lower than in plot 2. Quadrats with low seedling presence (e.g., 11, 15) had high openness, while Quadrat 18 showed much lower openness, about half of that in plot 2

All points showed weakly acidic conditions suitable for *R. quinquefolium*. In plot 2, pH remained stable between 5 and 6, while some points in plot 1 exceeded pH 6. Although Quadrat 18 had higher pH, seedlings were still present. This may suggest a suboptimal environment possibly hindering growth.

Quadrat 18 showed particularly low soil moisture, which favors *R. quinquefolium* seedlings that prefer dry, well-drained soils. However, the overall high moisture levels in Mt. Ryugatake soils suggest that the environment may not be ideal for long-term growth.

The average loss ignition was higher than other that of mountain forest near here, indicating richer organic content. Since *R. quinquefolium* prefers nutrient-poor soils, such fertility may be unsuitable. However, Quadrat 18 had the lowest ignition loss, supporting the notion that seedlings establish better in nutrient-poor conditions

Electrical conductivity, which correlates with soil nitrate content, was significantly higher in Mt. Ryugatake than in the other Forest. This suggests an abundance of nutrients, which may hinder seedling establishment. The lowest electrical conductivity was observed in Quadrat 18, again indicating that *R. quinquefolium* prefers nutrient-poor conditions.

CONCLUSIONS

The first hypothesis was refused because of deer harvesting was not be observed. The second hypothesis was supported by the environmental research.

The current *R. quinquefolium* population on Mt. Ryugatake likely originated from a mass regeneration event in the past. Although multiple seedlings were observed, the environmental conditions appear unsuitable for their continued growth. Strong winds along the ridgeline may also hinder seedling establishment, favoring locations with less wind exposure. Since available dead trees for tree-ring analysis are limited, future investigations using stable oxygen isotope dendrochronology are recommended to verify the occurrence of past synchronous regeneration events.

To conserve the population, seedling environment should be improved by racking fallen leaves.

ACKNOWLEDGMENTS

We extend our sincere thanks to the Mt. Ryugatake Nature Conservation Promotion Committee and the Mt. Ryugatake Trail Maintenance Association for granting access to the study area and providing essential support during fieldwork. Our appreciation also goes to the members of the Conservation Ecology Laboratory at Nagoya Institute of Technology for their cooperation in field investigations and for their valuable advice during the writing of this thesis. Finally, we would like to thank all individuals who contributed in any way to this research.

REFERENCES

[1] Wilson E.O., Biophilia, The Diversity of Life, Naturalist (LOA #340), Library of America, 2021, pp.1-20.

[2] Primack R., Essentials of Conservation Biology, 6th ed, Sinauer Associates, 2014, pp245-338.

[3] Rogers K.H., Operationalizing Ecology under a New Paradigm: An African Perspective, in The Ecological Basis of Conservation, Pickett, Ostfeld, Shachak and Likens Eds, Chapman & Hall, 1977, pp60-77.

[4] Kitamura S., Murata G., Colored Illustrated Guide to Japanese Plants: Woody Plants I, Hoikusha, 1971, p153, in Japanese.

[5] Takenaka A., All-sky photo analysis program CanopOn 2, 2009, http://takenaka-akio. org/etc/ canopon2

[6] Takenaka A., CanopOn 2 related notes, 2021, http://takenaka-akio.org/etc/canopon2/appendix.html

[7] Amemiya T., Yamane M., Development of an application for measuring canopy openness using 360-degree VR camera images. Kanagawa Prefeccture Natural Environmental Conservation Center Research Report, vol 18, 2024, pp. 57-62.

[8] Watanabe Y., Geograhical and genetic structure of forest trees in Japan (39) Shiroyashio (*Rhododendron quinquefolium*, Ericaceae), Forest Genetic Breeding, Vol. 12, 2023, pp. 1-5.

[9] Japan Meteorological Agency, data on Octber 23thh 2023.

[10] Yoshinogawa City, Emergency survey repoit on the Funakubo Ontsutsuji community, 2012, https://www.city.yoshinogawa.lg.jp/docs/2012060060043.

[11] Primack R., Kobori H., Conservation Biology Japanese ed, Bunichisogoshuppan, 2010.

[12] Karki D., Pandeya B., Bhandari R., Basnet D., Ghimire B., Bhattarai S., Srestha B.B., Regeneration and leaf traits variation of *Rhododendron campanulatum* along elevation gradient in western Nepal Himalaya, Journal of Ecology and Environment, Vol. 48, 2024, pp. 16.

[13] Takata K., Geographical distribution and ecology of *Rhododendron trifliata*, Plant Species Resarch, Vol. 5, 1981, pp. 19-32.

Copyright © Int. J. of GEOMATE All rights reserved, including making copies, unless permission is obtained from the copyright proprietors.

15th Int. Conf. on Geotechnique, Construction Materials & Environment,
Kyoto, Japan, 11-13 November 2025, ISBN 978-4-909106124 C3051

ESTIMATING THE DISTRIBUTION OF WATER CHESTNUT LEAVES ON THE WATER SURFACE OF IRRIGATION PONDS USING THRESHOLD PROCESSING

Yusaku Mizoguchi[1] and Masaaki Kondo[2]

[1,2]Graduate School of Bioresources, Mie University, Japan

ABSTRACT

Water chestnut has the advantage of controlling eutrophication in reservoirs. However, when the water chestnut thrives and dies in large numbers, it causes foul odors and sludge. In this study, a method using image processing was investigated to understand the status of overgrowth of water chestnut in reservoirs. The method studied was threshold processing. Images were taken by a drone at a reservoir near the university from May to October. Six types of images with different characteristics such as leaf distribution and luminance were used for analysis. Six different thresholding methods were used, including Otsu's binarization and adaptive thresholding. The results showed that Otsu's binarization process gave good results for most of the image patterns. However, Otsu's binarization process was not accurate for images containing high luminance objects such as the sun. Based on these results, the Otsu binarization process, which was the best method, was used to estimate the distribution of the water chestnut from May to October for the entire reservoir.

Keywords: Water Chestnut, Image Analysis, Threshold Processing, Coverage Ratio

INTRODUCTION

Japan has approximately 200,000 irrigation ponds, which serve primarily as a vital water source for agriculture [1]. On the other hand, the deterioration of water quality and the excessive growth of vegetation in reservoirs have raised concerns about their impact on aquatic ecosystems [2]. Among these concerns, increasing attention has been directed toward water chestnut, a type of floating-leaf plant. Water chestnut is an annual aquatic plant that grows rapidly from spring to summer and has the potential to cover large portions of the water surface. Its proliferation has been reported to affect water quality parameters such as nutrient concentrations, chlorophyll a, and dissolved organic carbon (DOC) in reservoirs [3, 4]. As such, water chestnut is closely linked to the water environment of reservoirs, and understanding its distribution and growth patterns is essential for water quality conservation and vegetation management. Traditionally, the distribution of water chestnut has been surveyed through human observation and fieldwork. In recent years, however, aerial photography using unmanned aerial vehicles has gained attention. Drone-based imaging enables wide-area, high-frequency monitoring and significantly improves the efficiency of vegetation surveys [5, 6].

In this study, we estimated the distribution of water chestnut on the surface of irrigation ponds using aerial imagery captured by drones. Multiple thresholding methods were applied, and their extraction accuracy was compared and evaluated. The ultimate goal is to improve the accuracy of growth rate estimation for water chestnut under actual field conditions.

RESEARCH SIGNIFICANCE

This study is significant in that it enhances the efficiency and accuracy of vegetation monitoring in small water bodies such as reservoirs through the use of simple and reproducible image processing techniques. By utilizing drone-acquired imagery and thresholding methods, the approach is not only effective for water chestnut but can also be applied to other floating-leaf plants and aquatic vegetation. As such, it holds great potential as a practical tool for future plant management and the assessment of aquatic ecosystems.

METHOD

About The Survey Pond

The survey target pond, Osawa Pond, is an agricultural reservoir located in Tsu City, Mie Prefecture. Table 1 shows basic information about Osawa Pond. As shown in Figure 1, Osawa Pond is long and narrow, extending from east to west.

About The Image

How to photograph the surface of a reservoir

The images were captured using a drone equipped with a video camera. The drone is a DJI Phantom 3 Advanced. The video has a HD resolution of 1280 x 720 pixels and a frame rate of 60 fps. Filming was conducted during the daytime when weather conditions were favorable. The filming altitude was set at 10 meters to capture the water chestnuts clearly

and over a wide area. Three locations were selected for filming: upstream, midstream, and downstream. The reason for this was that, as shown in Figure 1, Osawa Pond is long and narrow from east to west and could not be captured entirely in a video. Filming took place from May to October 2021. The filmed videos were cut into still images for analysis. The cut images were 48 × 32 pixels in size.

Table 1 Basic information on Osawa Pond [7,8]

specifications	Value
embankment height (m)	10.1
embankment length (m)	260
effective storage capacity (m^3)	3.3×10^3
full water area (m^2)	8.5×10^4

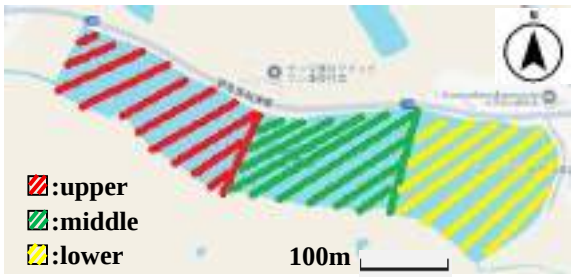

Fig.1 Shape of Osawa Pond (Source: https:/www.google.co.id/maps)

Features of analyzed images

Table 2 lists the characteristics of the images used in the analysis, while Figure 2 displays the corresponding images. Figure 2(a) depicts a case with a relatively small water chestnut coverage area, whereas Figure 2(b) shows a case with extensive coverage. Figure 2(c), the water surface appears cloudy green, making it difficult to distinguish the water chestnut. Figure 2(d) includes reflections of clouds on the water surface. Figure 2(e), the water surface appears whitish overall due to sunlight reflecting off the water chestnut. Figure 2(f) illustrates a condition where strong sunlight is reflecting directly off the water surface.

Two main reasons justify the selection of images with the characteristics listed in Table 2 for analysis. First, such image conditions were frequently observed across the dataset. Second, the degree of analytical difficulty was expected to vary depending on the image characteristics. Figures 2(a) and 2(b) were considered relatively easy to analyze, while Figures 2(c) to 2(f) presented more complex conditions such as water surface turbidity and light reflection making them more challenging to process.

For the analysis, six images were used, each corresponding to the characteristics described in Table 2(a) to 2(f).

Table 2 Image characteristics

(a) Less water chestnut
(b) More water chestnut
(c) Water surface is murky green
(d) Clouds are reflected on the water surface
(e) Leaves reflect sunlight
(f) Sun is reflected on the water surface

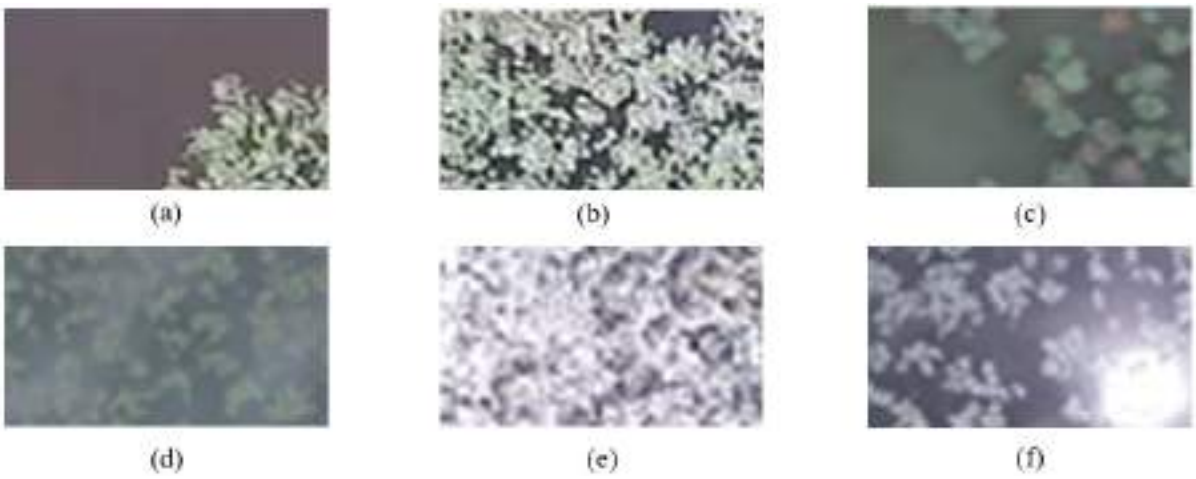

Fig.2 pixel images used for analysis (a) Less water chestnut (b) More water chestnut (c) Water surface is murky green (d) Clouds are reflected on the water surface (e) Leaves reflect sunlight (f) Sun is reflected on the water surface

About Analysis

The analysis was conducted in the following sequence: creation of ground truth images, application of thresholding methods, and evaluation of consistency between the ground truth and thresholded images.

Creating ground truth images

Ground truth images were created for the images shown in Figure 2. A ground truth image refers to an image in which water chestnut areas are visually identified and color labeled. The images were generated using the image editing software ImageJ. Areas visually recognized as water chestnut were filled in red, while all remaining regions were filled in black to complete the ground truth images, as shown in Figure 3.

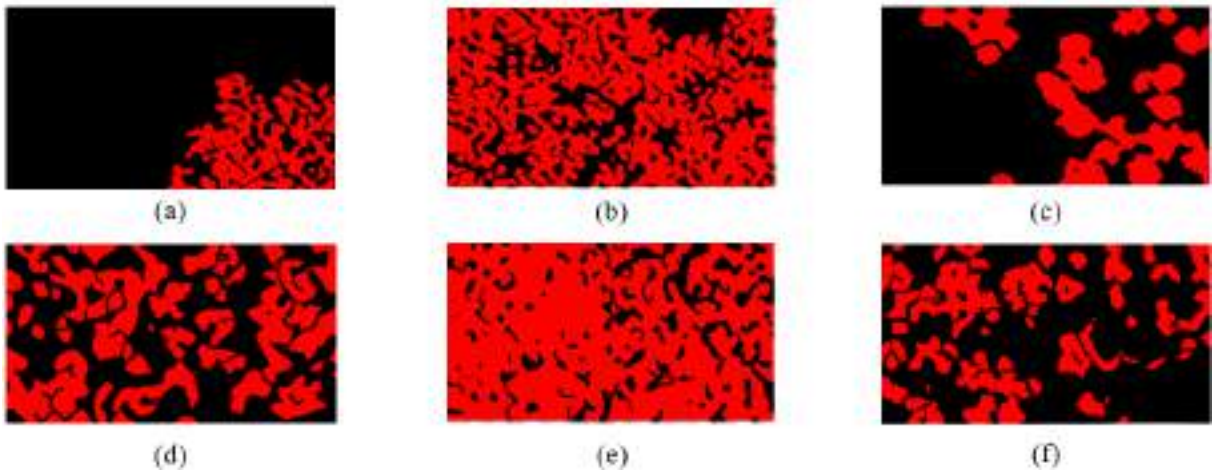

Fig. 3: List of ground truth images (a) Less water chestnut (b) More water chestnut (c) Water surface is murky green (d) Clouds are reflected on the water surface (e) Leaves reflect sunlight (f) Sun is reflected on the water surface

Application of threshold processing

Various thresholding methods were applied to analyze the images shown in Figure 2. The development environment used was Google Colab, and the implementation was carried out in Python. Six thresholding methods are listed in Table 3. The advantages of each method are summarized below.

Table 3(A): Otsu's binarization process automatically determines the threshold using the image histogram. It is effective for images with little noise. [9]

Table 3(B): The K-means method allows images to be divided into multiple areas by specifying the number of clusters.

Table 3(C): The method developed by Sezan is robust against uneven lighting and has been shown to be effective for the binarization of text images [10].

Table 3(D): Adaptive thresholding considers local variations in brightness within an image, allowing for effective binarization even under non-uniform lighting conditions.

Table 3(E): Minimum cross entropy thresholding enables high-precision clustering and identification and is suitable for statistical models. [11]

Table 3(F): Mixed Gaussian model fitting is effective when the data consists of multiple normal distributions. [12]

Table 3 Threshold processing used

(A)Otsu's binarization process
(B)K-Means method
(C)The method developed by Sezan
(D)Adaptive thresholding
(E)Minimum cross entropy thresholding
(F)Mixed Gaussian model fitting

Verification of consistency between ground truth images and threshold-processed images

The thresholded image was binarized, with black representing the water surface and white representing the leaves. For comparison with the ground truth image, the white areas were converted to red.

The consistency between the ground truth image and the thresholded image was evaluated using Intersection over Union (IoU). IoU was calculated using the following formula.

$$IoU = \frac{A \cap B}{A \cup B} \quad (1)$$

Here, A denotes the region of water chestnut in the ground truth image, and B denotes the region of water chestnut in the thresholded image.

RESULT AND DISCUSSION

IoU Between Thresholded Images And Correct Images

The average IoU values shown in Table 4 represent the mean performance of each thresholding method. In the method proposed by Cezan (C), thresholding could not be performed on image 2(d), which contains cloud reflections on the water surface. Accordingly, the (C)-(d) cell in Table 4 is left blank.

Overall, Otsu's binarization method demonstrated high accuracy. Specifically, it achieved the highest accuracy among the tested methods in Tables 4(a) and 4(b), and the second highest in Tables 4(c) and 4(d). Notably, Otsu's method was the only one to yield an average IoU exceeding 70%. This method is both highly accurate and effective for images with clear separation between objects and backgrounds. Therefore, it can be concluded that the favorable results obtained in this study were largely due to the application of Otsu's binarization method. In Table 4(f), none of the thresholding methods achieved an IoU greater than 50%. The image shown in Figure 2(f) contains strong sunlight reflection on the water surface, resulting in extremely high brightness values. This condition likely reduced the accuracy of all thresholding methods. Based on these findings, Otsu's binarization method appears to be the most suitable for analyzing reservoir water surfaces.

Table 4 IoU (%) of each thresholded image and correct image

	(a)	(b)	(c)	(d)	(e)	(f)	IoU average
(A)	91.65	89.91	71.03	67.02	75.01	25.78	70.07
(B)	80.14	84.52	71.37	66.99	74.68	26.21	67.32
(C)	15.73	81.90	26.41	-	87.15	33.22	48.88
(D)	10.44	67.82	26.71	50.20	67.57	36.31	43.18
(E)	53.12	70.88	48.20	66.61	59.60	42.63	56.84
(F)	58.98	85.28	60.27	67.09	77.14	22.74	61.92

(A), (B), (C), (D), (E), and (F) are as shown in Table 3, and (a), (b), (c), (d), (e), and (f) are as shown in Table 2.

Percentage Of Water Chestnut Coverage In Osawa Pond

We estimated the monthly coverage rate of water chestnut at three locations—upstream, midstream, and downstream—of Lake Osawa. One image per month was selected as reference material. The selected images were determined to capture representative vegetation conditions within the field of view of each water area and to contain sufficient information for identifying trends in coverage change. Each image covered an area of approximately 225 m².

Otsu's binarization method demonstrates high accuracy for images where the target object is clearly separated from the background, but its performance tends to decline under conditions influenced by external factors such as sunlight reflection. Therefore, binarization was performed after minimizing the influence of factors such as sunlight reflection in the images used for analysis. First, the target image was divided into eight segments both vertically and horizontally, and Otsu's binarization method was applied to each resulting section. After processing, areas exhibiting strong sunlight reflection or where water chestnut extraction was deemed inaccurate were excluded from the analysis. Subsequently, the proportion of pixels classified as water chestnut by the binarization method was calculated relative to the total number of pixels in the remaining image area. This proportion was used as the water chestnut coverage rate at each survey site for evaluation.

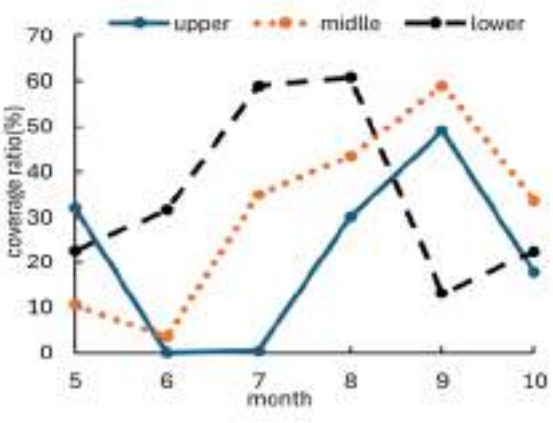

Fig. 4 The growth rate of water chestnut at various locations in Osawa Pond

The monthly coverage rates of water chestnut at each location are presented in Figure 4. In the upper reaches, proliferation was observed in May, but

coverage remained very low in June and July, followed by a steady increase through September, when it peaked. The exact cause of the sudden decrease in water chestnut coverage in June and July remains unknown. In the middle reaches, coverage gradually increased from May to September and declined in October, confirming the ecological cycle of water chestnut, which thrives in summer and dies off in winter. In the lower reaches, unlike the upper and middle sections, peak coverage occurred in July and August, followed by a decrease in September. Possible causes include the outflow of water chestnut and natural die-off.

CONCLUSIONS

In this study, to efficiently assess the proliferation of water chestnut in reservoirs, we applied multiple thresholding methods to drone-acquired aerial images and compared their accuracy. The analysis revealed that Otsu's binarization method exhibited the highest consistency among the tested methods, with an average IoU exceeding 70%. This confirms its effectiveness in environments with clear contrast between the target object and background, such as irrigation ponds.

Furthermore, using Otsu's method, we calculated the monthly coverage rate of water chestnut in the upper, middle, and lower reaches of Osawa Pond, thereby clarifying the temporal variations in the proliferation trends and growth cycle of water chestnut. In particular, in the middle reaches, the proliferation of water chestnut increased significantly from May to September, reflecting its typical ecological pattern of active summer growth and winter dieback. The results of this study demonstrate that simple and reproducible image processing techniques can streamline and quantify vegetation monitoring in small water bodies. This approach is also considered applicable to the management and assessment of other floating-leaf plants, including invasive aquatic species beyond water chestnut, in the future. Future challenges include mitigating external factors that may reduce the accuracy of image analysis, such as sunlight reflection and turbidity on the water surface. It will be necessary to consider the implementation of preprocessing techniques to suppress or correct these effects, as well as the adoption of AI-based deep learning methods for image recognition.

REFERENCES

[1] Hiroshima Prefecture, What is a Tameike | Hiroshima Prefecture Reservoir Map, available [online] https://nourin.pref.hiroshima.lg.jp/pref-hiroshima-gakusyu/tameike/ (Accessed 12 May 2025).

[2] Akasaka M., Saito T., Osawa T., Kurokawa S., Mizuguchi A., Shimono Y., and Nishida T., Current Status and Issues of Research on Alien Plants in Japan, Journal of Japan Weed Research, Vol. 59, Issue 2, 2014, pp. 81–92.

[3] Tachimoto H., Kurihara M., Koizumi T., Hosokawa M., and Ikushima T., Water Quality Comparison Inside and Outside of Trapa natans (Water Chestnut) Communities in Lake Inbanuma, Journal of Japan Society on Water Environment, Vol. 18, Issue. 10, 1995, pp. 65–74.

[4] Fukushima T., Takeda Y., and Ozaki N., Relationship between Water Quality and Growth of Floating-leaved Plants in Agricultural Reservoirs, Journal of Japan Society on Water Environment, Vol. 23, Issue. 11, 2000, pp. 721–725.

[5] Yasui H., Matsumura Y., Asami M., Cai J., Sakai Y., and Ishikawa K., Simple Estimation of Aquatic Plant Coverage in Lake Iba using Drones and Satellite Observations, Journal of Japan Limnology, Vol. 83, Issue. 1, 2022, pp. 65–74.

[6] Suwa Branch, Nagano Prefectural Fisheries Experimental Station, Distribution Survey of Trapa natans and Aquatic Plants in Lake Suwa, [online] https://www.pref.nagano.lg.jp/suwachi/suwachi-kikaku/vision/documents/7.pdf (Accessed 12 May 2025).

[7] Mie Prefecture, Mie Prefecture Reservoir Database (as of March 2025), [online] https://www.pref.mie.lg.jp/common/content/001188652.pdf (Accessed 12 May 2025).

[8] Ministry of Agriculture, Forestry and Fisheries of Japan, List of Agricultural Reservoirs, 2023, [online] https://www.maff.go.jp/j/nousin/bousai/bousai_saigai/b_tameike/ichiran.html (Accessed 12 May 2025).

[9] Otsu N., A threshold selection method from gray-level histograms. IEEE Transactions on Systems, Man, and Cybernetics, Vol. 9 Issue. 1, 1979, pp. 62–66.

[10] Sezan M. I., A peak detection algorithm and its application to histogram-based image data reduction, Computer Vision, Graphics, and Image Processing, Vol. 49, Issue 1 1990, pp. 36–51.

[11] Li C. H., and Lee C. K., Minimum cross entropy thresholding, Pattern Recognition, Vol. 26, Issue. 4, 1993, pp. 617–625.

[12] Sezgin M., Survey over image thresholding techniques and quantitative performance evaluation. Journal of Electronic Imaging, Vol. 13, Issue. 1, 2004, pp. 146-168.

Copyright © Int. J. of GEOMATE All rights reserved, including making copies, unless permission is obtained from the copyright proprietors.

15th Int. Conf. on Geotechnique, Construction Materials & Environment, Kyoto, Japan, 11-13 November 2025, ISBN 978-4-909106124 C3051

CESIUM LEACHING UNDER SEVERE CONDITIONS FOR CEMENT / GEOPOLYMER SOLIDIFIED BODY OF CESIUM ADSORBED MORDENITE

Takahito Yasukochi[1], Yasumasa Tojo[1], Kanako Toda[2], Kazuo Yamada[3] and Kazuto Endo[3]

[1] Graduate school of engineering, Hokkaido university, Japan; [2] Graduate school of engineering, University of Tokyo, Japan; [3] National Institute of Environmental Studies, Japan

ABSTRACT

Following the Fukushima Daiichi Nuclear Power Plant accident, decontaminated waste was generated as highly radioactive removed soil. For the final disposal of such wastes, it is necessary to establish volume reduction of waste and Cesium (Cs) stabilization technology. One of the treatment processes could be done by concentrating the Cs using Cs adsorbent like mordenite. The objective of this study is to investigate Cs leaching behavior and immobilization mechanism of the solidified body of Cs adsorbed mordenite. Solidified bodies of cement or geopolymer (cylinder with 2 cm diameter and 4 cm height) were prepared. Leaching tests evaluated its Cs leaching characteristics by the ANSI 16.1 test method. In addition, changes in Cs leaching behavior due to freezing and thawing of specimens and contact with seawater were evaluated as an estimated severe condition in a disposal site. As a result, it was clarified that the Cs leaching was mainly controlled by two factors, Cs desorption rate between mordenite and pore water, and Cs diffusion through the pores of the solidification body. The Cs leaching rate was not affected by freezing and thawing, but increased with seawater immersion. The Cs leaching rate was kept as low as below 0.5% even after 60 days of immersion in seawater, and the leached Cs concentration in a solvent can be estimated within the order of the standard in environmental water. The results indicate that mordenite and its solidification can be a reasonable way of final disposal that retains Cs for a long period.

Keywords: Cesium, Leaching test, Final disposal, Hazardous waste

INTRODUCTION

In Japan, decontamination waste was generated due to the Fukushima Daiichi Nuclear Power Plant accident. This waste contains radioactive cesium (Cs) and its disposal method for them is determined according to its radioactivity as follows. The waste with 8,000 Bq/kg or less can be disposed of in a conventional controlled landfill [1]. Waste with 8,000 to 100,000 Bq/kg can be landfilled after taking appropriate treatment such as solidification [2]. Waste exceeding 100,000 Bq/kg is currently stored at a temporary storage facility in Fukushima Prefecture, but is scheduled for final disposal by 2045, within 30 years from the start of storage [2].

Volume reduction of decontamination waste by thermal treatment is ongoing, especially for the fraction of the waste exceeding 100,000 Bq/kg. The waste is incinerated, and then treated by a melting process at 1700°C by adding calcium chloride ($CaCl_2$) to accelerate Cs volatilization [3]. The Cs-containing fly ash generated here is not suitable for final disposal because its radioactivity exceeds 150,000 Bq/kg, and Cs is water-soluble [4]. For the final disposal of the melting fly ash (MFA), it's preferable to immobilize Cs in the MFA.

Various methods have been developed for the immobilization of Cs and further volume reduction of MFA [2]. One of them is done as follows. MFA is washed with water to transfer Cs to the liquid phase, and Cs is recovered in the liquid phase with Prussian blue (PB). Then, the Cs-adsorbed PB is decomposed and transferred to the liquid phase again, and the Cs in the solution is adsorbed on mordenite [5].

Cs adsorbed mordenite may release Cs in water due to ion exchange with non-adsorbed alkali metal ions, and thus it should be solidified with cement or geopolymer. For the final disposal, the long-term Cs leaching mechanism from the solidified body of mordenite adsorbing Cs must be revealed. In this study, the leaching test was conducted and the Cs leaching characteristic was investigated considering its leaching mechanism. Several severe conditions assumed to promote the Cs leaching rate in the final disposal site were also applied.

MATERIALS

Mordenite is known for its high cation adsorption capacity. In this study, natural mordenite (UniSelect UR3103Z, Ataka Asano Co. Ltd., Japan) was used as the Cs adsorbent. It was produced in Miyagi Prefecture, Japan. And its grain sizes were from 1.9 to 2.3 mm. The chemical composition obtained from energy dispersive spectrometry using FE-SEM (JSM-

Table 1 Elemental composition of the mordenite (mol%)

Si	Al	Na	Fe	Ca	K	Mg
26.0	5.25	0.85	1.70	1.14	0.83	0.26

7200F, JEOL, Japan) analysis is shown in Table 1. The composition was calculated as relative concentration.

Preparation of Cs adsorbed mordenite

The composition of the decomposed PB solution is adjusted based on the report of the on-site examination [6]. But, in this study, a 30 times higher concentration was made compared to the actual data reported. Table 2 shows the concentration.

Cs adsorbed mordenite was prepared with the following method. Cs_2SO_4 (Wako reagent, Fujifilm Wako Chemicals, Osaka, Japan), $Na_4[Fe(CN)_6]\cdot 10H_2O$ (Wako reagent, Fujifilm Wako Chemicals, Osaka, Japan), and $K_4[Fe(CN)_6]\cdot 3H_2O$ (Wako guaranteed reagent, Fujifilm Wako chemicals, Osaka, Japan) were dissolved in distilled water to achieve the concentration shown in Table 2. Stable isotope Cs-133 was used in this study. The mordenite was immersed in this simulated solution at a liquid-to-solid ratio of 5 mL/g, and agitated at 200 rpm. After 30 minutes of immersion, the mordenite was removed, thoroughly washed with distilled water to remove non-adsorbed ions, and then dried at 60°C. After the adsorption process, the immersing solution was sampled, filtered with 0.45 μm membrane filter (A045A025A, Advantec, Japan) and the Cs concentration was quantified using an ICP-MS (ICP-MS-QQQ, Agilent technology, USA).

More than 99% of Cs in the initial immersion solution was adsorbed onto the mordenite. The amount of adsorbed Cs was 765 mg-Cs/kg-mordenite.

Table 2 Composition of decomposed Prussian blue solution

Component	Concentration(mg/L)
Cs^+	5.10
Na^+	10.6
K^+	100
SO_4^{2-}	1.84
$Fe(CN)_6^{4-}$	24.4

Mordenite solidification and accelerated weathering (freezing and thawing)

The Cs adsorbed mordenite was solidified using cement and geopolymer. The cement (Portland blast-furnace slag blended cement type B, JIS R5211:2019, Taiheiyo Cement Co. Japan) was mixed with water at a water-to-cement ratio of 0.6. Then, Cs adsorbed mordenite was added to the cement paste at 40 wt%. The geopolymer (hereafter GP) was prepared by mixing Na solution (NaOH (Wako guaranteed reagent, Fujifilm Wako Chemicals, Osaka, Japan): 24.7 g, sodium silicate solution (Wako reagent, Fujifilm Wako Chemicals, Osaka, Japan): 105 g and distilled water: 86.8 g) and metakaolin (MK-11-SF-8, SOBUECLAY, Japan): 133 g.

Then, the mixed paste was set in the molds created by a PTFE tube (2 cm in diameter, 4 cm in height) and then sealed with parafilm (PM-996, Bemis, USA). The molds were sealed and cured in a humid environment at 30°C for 9 days until demolding.

To reproduce freezing and thawing of solidified bodies in the final disposal site, some samples underwent freeze-thaw treatment. It was done using an incubator (MIR-554-PG, PHC, Japan) with a 300-cycle of -10°C for 3 hours and 20°C for 2 hours.

METHODOLOGY

Leaching test for the solidified bodies

For investigating Cs leaching behavior, leaching tests were conducted according to the ANSI 16.1 test method [7], replacing the solvent at an interval determined in advance. To keep the solvent homogeneous, agitation at 200 rpm was applied to the solvent. The solvent temperature was maintained at 25°C using a water bath. The solidified bodies were immersed in the solvent with the solid-to-liquid ratio at solvent volume (cm^3) / sample surface area (cm^2) = 10 (cm).

The solvent was sampled at solvent replacement and filtered with a 0.45 μm membrane filter. The elemental composition was measured by the ICP-MS, and the amount of leached Cs per solvent replacement was calculated. The cumulative leached Cs was calculated as a summation of the incremental leached Cs of each solvent replacement.

Table 3 shows the leaching test conditions. The solvent was changed after the first 6 hours, then every other day until the 7th day, and then weekly thereafter. Seawater was prepared by dissolving artificial seawater powder (Instant Ocean, Aquarium Systems, USA) in distilled water at 35.0 g/L. Seawater was used as a solvent with a dilution factor of 1 and 10. The major elemental composition of the artificial seawater obtained from ICP-OES (ICPE-9000, SHIMADZU, Japan) analysis was Na: 9600 mg/L, Mg: 1000 mg/L, Ca: 331 mg/L, K: 247 mg/L.

Table 3 Leaching test conditions. DW: distilled water, SW: artificial sea water
*Age at the start of leaching test

Solidification	Freezing and thawing	Solvent	Age* (day)
Cement	No	DW	72
	Yes	DW	79
	No	SWx10	72
	No	SWx1	88
Geopolymer	No	DW	79
	Yes	DW	72
	No	SWx10	79
	No	SWx1	73

XRD and SEM analysis

When the solidified bodies above were immersed in seawater, precipitation was formed on the surface. To determine the composition of the precipitates, X-ray diffraction (XRD) and scanning electron microscopy and energy dispersive spectrometry (SEM-EDS) analysis were conducted.

The specimens for the SEM-EDS and XRD analysis were prepared as follows. Cement or geopolymer solidified bodies were immersed in distilled water or seawater for 28 days, and dried in a vacuum dryer (FDU-1200, EYELA, Japan). To observe the cross-section, the solidified body was cut and impregnated with epoxy resin, which was later polished. Carbon spattering was performed to prevent charge-up. Then, back scattering electron image (BSE) and EDS analysis were conducted using FE-SEM (JSM-7200F, JEOL, Japan) at accelerating voltage: 15 kV, working distance: 9.6 mm.

A portion of the precipitate was scraped off with a knife and ground with a mortar, then analyzed by XRD (Smart lab, Rigaku, Japan). XRD analysis was conducted using Cu-Kα1 radiation with tube voltage: 45 (kV), tube current: 200 (mA), step size: 0.01° (2θ), and a scan rate of 4°/min.

RESULTS AND DISCUSSION

Cs leaching behavior from the solidified body of Cs adsorbed mordenite

Figure. 1 shows the cumulative leaching ratio of Cs from the cement or GP solidified body. When the solidified bodies were immersed in DW, only 0.12-0.14% of Cs was leached until the 133 days of immersion. Cs leaching is promoted when the solidified bodies are immersed in seawater. Freezing and thawing didn't show a significant difference in Cs leaching. Though these trends are common for both cement and GP solidified bodies, Cs leaching from the cement solidified body immersed in seawater is remarkably suppressed after 7 days of immersion compared with that of the GP solidified body.

Difference in Cs leaching behavior between cement and GP solidified bodies

It is reported that non-weathered cement paste has little cation adsorption capacity, and when soluble CsCl is solidified with cement, almost all of the Cs is eluted within several tens of days [8].

GP has cation adsorption capacity due to its aluminosilicate matrix [9], and thus is expected to suppress Cs leaching compared to the cement solidified body.

However, as shown in Fig. 1, the Cs leaching behavior from cement and the GP solidified body was similar. The similarity is thought to be caused by the low Cs desorption from the mordenite to the pore solution in the solidified body.

Influence of seawater on Cs leaching and surface precipitation

When the solidified body is immersed in seawater, the ion exchange equilibrium on the mordenite surface changes as the seawater penetrates into the pore solution, and the Cs concentration of the pore solution increases because of Cs desorption compared to the distilled water immersion. This leads to an increase in the Cs leaching flux due to the enhanced concentration gradient between the solvent and the pore solution.

The Cs leaching from the cement solidified body immersed in seawater shows inflection at 7 days of immersion. This must be caused by the precipitates on the cement solidified body. As shown in Fig. 2 (a),

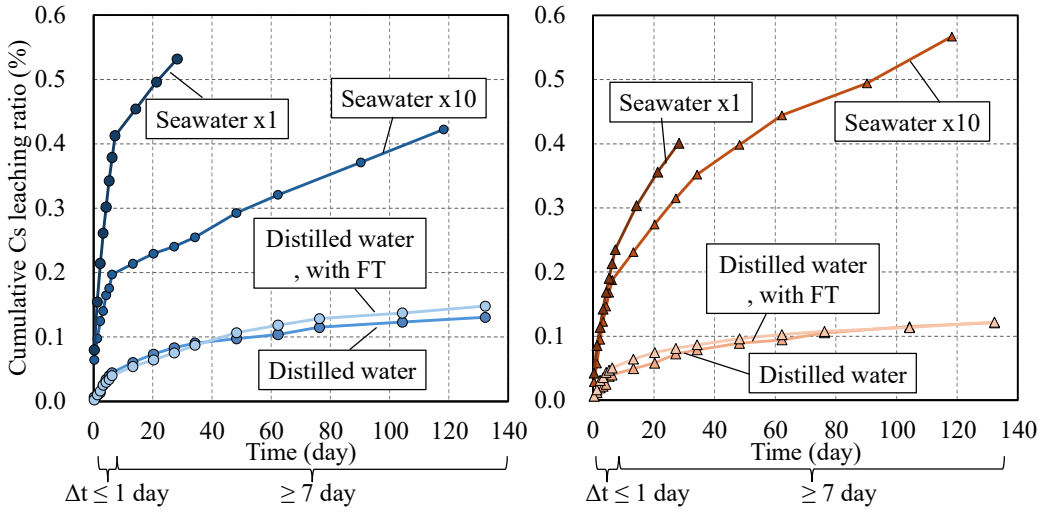

Figure. 1 Cumulative Cs leaching ratio for cement solidified body of Cs adsorbed mordenite (left) and GP solidified body (right)

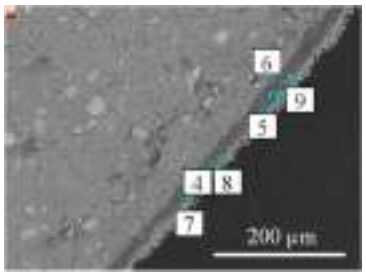

Figure. 2 (a) BSE image of cross section of cement solidified body which was immersed for 1 month in seawater

Table 4 (a). Element composition (mol%) by EDS at the points indicated in Figure 5(a)

Precipitate	Point	C	O	Mg	Ca
Inside	4, 5, 6	7.70	55.9	34.3	1.40
Outside	7, 8, 9	20.9	55.1	0.10	23.7

precipitation as thick as 10 μm formed on its surface of the cement solidified body immersed in seawater. Calcite (outer layer) and brucite (interlayer) were observed using the EDS (Table 4 (a)) and XRD. Cs diffusion is thought to be suppressed in the denser layer of brucite and calcite, and Cs leaching flux to the outside decreases.

On the other hand, for the GP solidified body immersed in seawater, only a fragment of precipitation was measured on the surface as shown in Fig. 2 (b). It was calcite due to the EDS (Table 4 (b)) and XRD analysis. Though there is a possibility that a part of the precipitates fell during the drying process for SEM analysis, the influence on Cs leaching behavior like the cement solidified body was not observed for the GP solidified body as shown in Fig. 1.

Cs leaching pass-way for cement or GP solidified body of Cs adsorbed mordenite

In the solidified body of Cs adsorbed mordenite, granular mordenite (1.9 ~ 3.3 mm) is scattered. Cs leaching from the solidified body is expected to proceed by the path shown in Fig. 3. Firstly, Cs on the mordenite is released to the pore solution by ion exchange with alkali metal ions in the solution, and then transferred by diffusion in the solidified body through the pores.

Each of cement and GP has pores in the diameter of nm to mm [10]. The composition of the pore solution of cement is considered to be a highly ionic

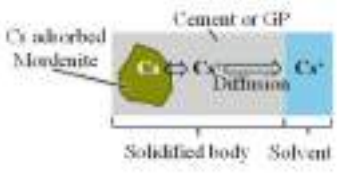

Figure. 3 Schematic diagram of Cs leaching pass-way from solidified Cs adsorbed mordenite.

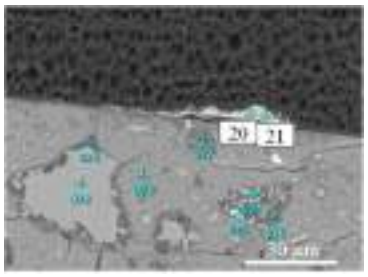

Figure. 2 (b) BSE image of cross section of GP solidified body which was immersed for 1 month in seawater

Table 4 (b) Element composition (mol%) by EDS at the points indicated in Figure 5(b)

Point	C	O	Ca
20, 21	26.5	53.3	19.6

solution composed mainly of Na and K in cement [11]. The pore solution of GP can contain Na^+ ions from the dissolution of NaOH remaining unreacted in the GP paste. On the surface of Cs adsorbed mordenite, a fraction of the Cs is desorbed by ion exchange between the Na and K in the pore solution and Cs on mordenite. Since mordenite selectively adsorbs Cs, the desorption ratio remains low even in solvents with high ionic strength.

When Cs adsorbed mordenite prepared in the previous section which is not solidified was immersed in the artificial seawater (Na: 9600 mg/L, Mg: 1000 mg/L) for 24 hours, the liquid phase Cs concentration was about 116 μg/L and the Cs desorption ratio was 0.73%. Though this solution does not accurately reproduce the pore solution of the solidified body, the low desorption ratio indicates that the low Cs leaching ratio from the solidified body is mainly determined by the Cs desorption ratio of the Cs adsorbed mordenite.

The Cs desorbed in the pores transfer through the pores by diffusion with a concentration gradient. Both cement and GP are porous materials, so Cs transfer is suppressed by the amount of voids, bending, and connectivity of the pores in the cement/GP. On the outer surface of the solidified body, Cs leaches to the solvent by the concentration gradient between the pore solution and the solvent.

Determination of apparent diffusion coefficients

When the Cs leaching from the solidified body is controlled by the concentration gradient in the pore solution, the Cs leaching is calculated as follows [12].

The Cs concentration in the solidified body is expressed as Eq. 1 by Fick's 2nd law, assuming the body is a semi-infinite medium [12].

$$\frac{C}{C_0} = erf\left(\frac{x}{2\sqrt{D_a t}}\right) \quad (1)$$

Here, D_a is the apparent diffusion coefficient (m^2/s), C is the concentration in the solidified body (mg/m^3), and C_0 is the initial concentration in the solidified body (mg/m^3). The leaching flux $J(t)$ (mg/(m^2·s)) at the surface of solidified body (x = 0) can be expressed as follows:

$$J(t) = -D_a \frac{\partial C}{\partial x}\Big|_{(x=0)} = C_0\sqrt{\frac{D_a}{\pi t}} \quad (2)$$

The amount of leaching per unit area up to a certain time (A (mg/m^2)), is obtained by integrating this flux with respect to time.

$$A = \int_0^t J(t)\,dt = 2C_0\sqrt{\frac{D_a t}{\pi}} \quad (3)$$

The cumulative leaching ratio can be obtained by dividing the amount of leached from the total surface area up to the target time by the initial content. If the surface area of the solidified body is S (m^2) and the volume is V (m^3), then:

$$\text{Cumulative leaching ratio} = \frac{AS}{C_0 V} = 2\left(\frac{S}{V}\right)\sqrt{\frac{D_a t}{\pi}} \quad (4)$$

In the experiment, the amount of leached at n^{th} solvent replacement interval is defined as A_n (mg), and the cumulative leaching amount is calculated as $\sum A_n$ (mg). Then it is divided by the initial amount (A_0 (mg) = C_0V), and the following relation is derived.

$$\frac{\Sigma A_n}{A_0} = 2\left(\frac{S}{V}\right)\sqrt{\frac{D_a t}{\pi}} \quad (5)$$

That is, the cumulative leaching ratio is proportional to the square root of time.

Figure. 4 shows the plot of the cumulative leaching ratio and the root of the immersion time. In all cases, the leaching ratio increases linearly up to 7 days of immersion (day$^{0.5}$=2.6), suggesting that Cs leaching was controlled by diffusion in the solid phase during this period.

The D_a obtained from the slope of the regression line up to 7 days immersion are indicated in Table 5. For both cement and GP solidified bodies, D_a of Cs are ranged around 10^{-18} m^2/s in distilled water and 10^{-17} to 10^{-16} m^2/s in seawater. Freezing and thawing didn't affect the D_a.

The Cs leaching D_a from the cement solidified body of Cs adsorbed mordenite was 10^{-18} m^2/s, though the D_a from cement with soluble CsCl is reported to range around 10^{-12} m^2/s [13–15]. The D_a in cement with soluble CsCl is 6 orders of magnitude larger than that of the cement solidified body of Cs adsorbed mordenite. The difference in D_a between cement solidified body of Cs adsorbed mordenite and cement containing soluble Cs is mainly due to Cs adsorption by the mordenite because there should be no significant difference in the connectivity of pore in cement paste itself.

Table 5 Apparent diffusion coefficient (D_a (m^2/s)) for each solidified Cs adsorbed mordenite. DW: Distilled water, SW: Artificial seawater

Solidification	Solvent	Freezing & thawing	D_a (m^2/s)
Cement	DW	No	4.1E-18
Cement	SWx10	No	6.3E-17
Cement	SWx1	No	3.3E-16
Cement	DW	Yes	3.5E-18
GP	DW	No	2.7E-18
GP	SWx10	No	9.8E-17
GP	SWx1	No	1.1E-16
GP	DW	Yes	3.1E-18

CONCLUSIONS

The leaching tests were conducted for cement- or geopolymer-solidified bodies containing Cs-

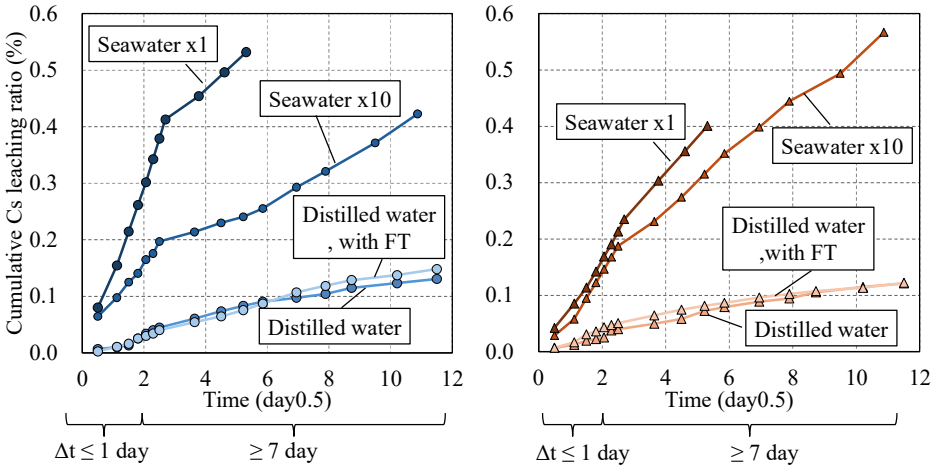

Figure. 4 Cumulative Cs leaching ratio from solidified body of Cs adsorbed mordenite vs square of immersion time (left: cement solidified body, right: GP solidified body)

adsorbed mordenite. The results indicate that Cs leaching primarily occurs through a two-step process involving Cs desorption from mordenite followed by diffusion through the pores of the solidified bodies. Due to the selective Cs adsorption by mordenite, the overall Cs leaching ratio remains significantly suppressed. Therefore, the D_a of the solidified bodies showed a significantly small value ranged in 10^{-18} to 10^{-16} m^2/s. Furthermore, freezing and thawing at temperatures of −10°C and 20°C were found to have no appreciable effect on the leaching behavior. In contrast, immersion in seawater led to an approximate fourfold increase in Cs leaching compared to distilled water. Nevertheless, even under seawater exposure conditions, the cumulative Cs leaching ratio remained as low as approximately 0.5% after 30 days of immersion. These findings suggest that the solidification of Cs-adsorbed mordenite solidified with cement or geopolymer offers a promising approach for the long-term Cs immobilization in the final disposal site.

ACKNOWLEDGEMENTS

This research was performed by the Environment Research and Technology Development Fund (JPMEERF22S20910) of the Environmental Restoration and Conservation Agency provided by Ministry of the Environment of Japan.

REFERENCES

[1] Endo. K, Challenges for management of radioactively contaminated wastes and volume reduction and reuse/recycling of removed soil derived from the activities for environmental remediation after the Fukushima Daiichi Nuclear Power Station accident (in Japanese), Jornal of Atomic Energy Society of Japan, Vol. 59, Issue 8, 2017, p.p. 439–441. https://doi.org/10.3327/jaesjb.59.8_439.

[2] Hisaki M., Expectations and challenges for establishment of volume reduction system for radioactive decontaminated soil; Seeking technical consistency from temporal storage to final disposal (in Japanese), Journal of SRCCE, 2016.

[3] Kuramochi. S, Thermal Volume Reduction Technologies for Radioactively Contaminated Waste in the Interim Storage Facility : Current Status and Future Prospects (in Japanese), Journal of Material Cycles and Waste Managemen Vo. 30, Issue. 1, 2019, pp. 31–38. https://doi.org/10.3985/mcwmr.30.31.

[4] Nagayama. T, Ono. Y, Mizuta. K, Current trends and efforts to expand eco-slag sales (in Japanese), Journal of Material Cycles and Waste Managemen Vol. 29, Issue. 5, 2018, p.p. 384–391. https://doi.org/10.3985/mcwmr.29.384.

[5] Ichikawa. S, Nishizaki. Y, Takano. T, Kumagai. N, Technology for Removing Radioactive Cs from Incineration Fly Ash (in Japanese), Hitz Technical Report Vol. 77, Issue. 1, 2016, pp. 14-19.

[6] JESCO, Individual Test Results and valuation details: Report for web (appendix 2), https://www.jesconet.co.jp/content/900005794.pdf (accessed March 20, 2025).

[7] Park. L.G., Measurement of the Leachability of Solidified LowLevel Radioactive Wastes by a Short-Term Test Procedure ANSI/ANS-16.1-2019, An American Nuclear Society standard, 2019.

[8] Yasukochi. T, Yamada. K., Arai. H., Tojo. Y., Ichikawa. T., Endo. K., Study on cement solidification method of melting fly ash (in Japanese), The 13th Workshop of SRRCE, 2023.

[9] Niu. X., Elakneswaran. Y., Islam. C.R., Provis. J. L., Sato. T., Adsorption behaviour of simulant radionuclide cations and anions in metakaolin-based geopolymer, Journal of Hazardous Materials Vol. 429, 2022, pp. 128373. https://doi.org/10.1016/j.jhazmat.2022.128373.

[10] Nagaya. Y, Nawa. T, Kuriyama. H, Quantification of pore structure in hardened cement using thermoporometry (in Japanese), Cement Science and Concrete Technology Vol. 65, Issue. 1, 2011, pp. 153–160. https://doi.org/10.14250/cement.65.153.

[11] Andersson. K., Allard. B., Bengtsson. M., Magnusson. B., Chemical composition of cement pore solutions, Cement and Concrete Research Vol. 19, Issue. 3 1989, p.p. 327–332. https://doi.org/10.1016/0008-8846(89)90022-7.

[12] Abdel Rahman. R.O., Zaki. A.A., El-Kamash. A.M., Modeling the long-term leaching behavior of 137Cs, 60Co, and 152,154Eu radionuclides from cement–clay matrices, Journal of Hazardous Materials Vol. 145, Issue. 3, 2007, pp. 372–380. https://doi.org/10.1016/j.jhazmat.2006.11.030.

[13] Abdel Rahman. R.O., Zaki. A.A., Comparative study of leaching conceptual models: Cs leaching from different ILW cement based matrices, Chemical Engineering Journal Vol. 173, Issue. 3, 2011, pp. 722–736. https://doi.org/10.1016/j.cej.2011.08.038.

[14] El-Kamash. A.M., El-Dakroury. A.M., Aly. H. F., Leaching kinetics of 137Cs and 60Co radionuclides fixed in cement and cement-based materials, Cement and Concrete Research Vol. 32, Issue 11, 2002, pp. 1797–1803. https://doi.org/10.1016/S0008-8846(02)00868-2.

[15] Papadokostaki. K.G., Savidou. A., Study of leaching mechanisms of caesium ions incorporated in Ordinary Portland Cement, Journal of Hazardous Materials, Vol. 171, Issue. 1, 2009, pp. 1024–1031. https://doi.org/10.1016/j.jhazmat.2009.06.118.

Copyright © Int. J. of GEOMATE All rights reserved, including making copies, unless permission is obtained from the copyright proprietors.

15th Int. Conf. on Geotechnique, Construction Materials & Environment,
Kyoto, Japan, 11-13 November 2025, ISBN 978-4-909106124 C3051

DECOLORIZATION OF REACTIVE DYE SOLUTIONS USING CONTINUOUS FLOW ELECTROCOAGULATION SYSTEMS

Jareeya Yimrattanabovorn[1], Nattapat Chanlert[2] Chutidet Chosongnoen[3] and Ammarin Reabroy[4]

[1,2,3,4]School of Environmental Engineering, Institute of Engineering, Suranaree University of Technology,Nakhon Ratchasima,30000. Thailand

ABSTRACT

Dyes are widely used in the textile industry and pose significant environmental concerns. Although various methods are available for the removal of dyes from wastewater, many of these techniques have notable limitations. Among them, chemical coagulation and the electrocoagulation process have shown promise, with electrocoagulation emerging as an attractive alternative for the treatment of textile wastewater. The objective of this study is to investigate the performance and determine the optimum operating conditions of electrocoagulation using aluminum (Al) electrodes for the decolorization of reactive dyes. The results showed that batch electrocoagulation studies were effective in treating reactive dyes, achieving a decolorization efficiency of 74.60%. The operational parameters—initial dye concentration of 100 mg/L, reaction time of 50 minutes, and initial pH of 6 significantly influenced the decolorization process. The optimum conditions identified in the batch studies were then applied to continuous flow electrocoagulation experiments. The continuous flow electrocoagulation system, operated under varying flow rates (8, 12, and 16 mL/min) and initial dye concentrations (75, 100, and 125 mg/L), achieved decolorization efficiencies ranging from 47.76% to 57.95%. The highest decolorization efficiency was observed at a flow rate of 8 mL/min and an initial dye concentration of 75 mg/L. These results demonstrate that continuous flow electrocoagulation system is an effective and promising technique for the removal of reactive dyes from textile wastewater.

Keywords: Electrocoagulation, Reactive dye, Continuous flow system, Decolorization

INTRODUCTION

The textile industry is a significant contributor to environmental pollution, largely due to the high volume and complex composition of its dye-laden wastewater, particularly from reactive dyes. These water-soluble dyes are difficult to remove from wastewater, making them persistent pollutant.

Various techniques have been developed to remove soluble dyes from wastewater; however, each method presents certain drawbacks. Biological treatment processes are often hindered by the toxic effects of dyestuffs on microorganisms [1], while advanced oxidation processes require the addition of chemicals, which may generate secondary pollutants [2]. Among these methods, the electrocoagulation (EC) process has emerged as a promising alternative for treating textile wastewater. Electrocoagulation is considered simple, reliable, and cost-effective, as it operates without the need for additional chemicals and produces less sludge [3,4].

The aim of this study is to evaluate the efficiency of aluminum-based electrocoagulation for the decolorization of soluble reactive dye solutions and to determine the optimal operating conditions through batch experiments. The insights gained from the batch studies are subsequently applied to design and assess a continuous-flow electrocoagulation system. The performance of the continuous-flow electrocoagulation system is investigated under varying flow rates and initial dye concentrations, with the goal of optimizing its application for textile industry wastewater treatment. Ultimately, this work lays the groundwork for scaling up and integrating electrocoagulation technology into existing wastewater treatment facilities, enhancing the industry's environmental performance and sustainability.

RESEARCH SIGNIFICANCE

This research addresses a critical environmental challenge in the textile industry by developing an electrocoagulation (EC) system capable of effectively decolorizing soluble reactive dyes, which are among the most persistent pollutants in textile wastewater. The proposed continuous flow electrocoagulation system offers a promising, cost-effective, and environmentally friendly alternative to conventional decolorization methods, with the potential to achieve high decolorization efficiency, reduce chemical usage, and minimize sludge production. This study bridges the gap between laboratory-scale treatment and practical industrial applications and integrating electrocoagulation technology into existing wastewater treatment facilities, enhancing the

industry's environmental performance and sustainability.

MATERIALS AND METHODS

Reactive Dye Solution Preparation

The reactive dye was supplied by Sivasumpan Co., Ltd, Thailand. A stock solution with a concentration of 1,000 mg/L was prepared, and the desired experimental solutions were obtained by diluting this stock to the required initial concentrations. The maximum absorbance wavelength (λ_{max}) of the reactive dye solution was determined by scanning the solution using a UV-Visible spectrophotometer (GENESYS™ 20, USA) and was found to be 430 nm.

Batch Electrocoagulation Experiment

The batch electrocoagulation (EC) experimental setup is shown in Fig. 1, featuring an aluminum electrode configuration. Each setup included four parallel electrodes two anodes and two cathodes made of aluminum plates with dimensions of 46 × 55 × 3 mm. The electrodes were prepared by first washing with acetone to remove surface grease. Residual impurities on the aluminum surfaces were then eliminated by immersing the electrodes for 5 minutes in a freshly prepared solution consisting of 100 cm^3 of 35% HCl and 200 cm^3 of 2.80% hexamethylenetetramine aqueous solution, followed by drying and weighing[5]. The total effective electrode area was 192 cm^2, with an inter-electrode spacing of 11 mm, connected to a DC digital power supply.

A 1,000 mL beaker was used as an electrocoagulation reactor. The experiments were carried out to identify the optimal conditions for the electrocoagulation process by varying the initial reactive dye concentration (20–100 mg/L), solution pH (4–12, adjusted with 0.1 M NaOH and 0.1 M HCl), reaction time (20–60 minutes), and a constant applied voltage of 20 V. Each experiment was conducted with 600 mL of reactive dye solution and a stirring speed of 200 rpm.

Continuous Flow Electrocoagulation Experiments

The optimum conditions obtained from the batch electrocoagulation experiments were used to design the continuous flow electrocoagulation experimental setup shown in Fig. 2. The continuous electrocoagulation system comprises two compartments: the first is a rectangular reactor with a volume of 0.4 L, equipped with four aluminum electrodes; the second is a pyramid-shaped sedimentation tank with a volume of 1.0 L. Trials were conducted by operating the continuous flow electrocoagulation system under varying flow rates and dye concentrations to determine the optimal conditions for practical industrial application

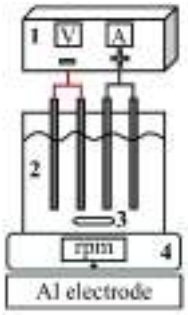

Fig.1 Schematic of batch electrocoagulation experimental sets (1) DC power supply, (2) electrocoagulation cell, (3) magnetic bar-stirrer, (4) digital magnetic stirrer.

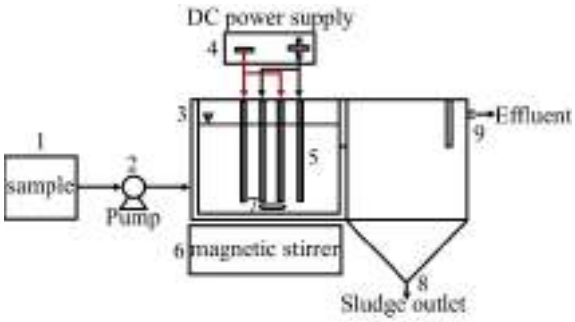

Fig. 2 Schematic diagram of the continuous flow electrocoagulation experimental setup: (1) equalization tank, (2) peristaltic pump, (3) reactor, (4) DC power supply, (5) electrocoagulation cell, (6) digital magnetic stirrer, (7) magnetic stir bar, (8) sedimentation tank, (9) outlet.

Data Analysis

The reduction of reactive dye concentrations was measured and calculated by using equation given below. The reduction in reactive dye concentration was measured and calculated using Eq. (1) below, where C_0 and C_t represent the inlet and outlet reactive dye concentrations from the continuous flow electrocoagulation system, respectively.

$$R(\%) = \frac{C_o - C_t}{C_o} \times 100 \qquad (1)$$

RESULTS AND DISCUSSION

Batche Electrocoagulation Experiments

Effect of initial concentration

The batch electrocoagulation experimental set up was carried out to find the optimum conditions for electrocoagulation by varied initial reactive dye concentration, reaction time and initial pH solution and investigated their effect on decolorization efficiency of reactive dye.

Table 1 Effect of Initial Reactive Dye Concentration on Decolorization Efficiency and Removal Rate (mg/g Al) in Electrocoagulation

initial concentration (mg/g)	Decolorization efficiency (%)	Removal rate (mg/g of Al)
20	87.39	862.13
40	73.74	1,451.31
60	67.67	2,049.05
80	58.09	2,357.85
100	54.28	2,848.67

The effect of the initial reactive dye concentration was investigated over a range of 20–100 mg/L, as presented in Table 1. The results indicate that the decolorization efficiency decreased significantly from 87.39% to 54.28% as the initial dye concentration increased from 20 to 100 mg/L, respectively. In contrast, the dye removal rate per unit mass of aluminum increased substantially, rising from 862.13 to 2,848.67 mg/g Al, with the highest value observed at an initial concentration of 100 mg/L.

A primary mechanism for reactive dye removal in electrocoagulation is the adsorption of dye molecules onto the metal hydroxide flocs formed during the process. According to Faraday's law, the quantity of metal ions released into the solution remains constant for a given current and treatment time, regardless of the initial dye concentration. Consequently, the amount of flocs generated is fixed, limiting the available adsorption sites for dye molecules. Therefore, decolorization efficiency depends on whether the amount of flocs produced is sufficient to adsorb the total dye present [6,7].

Based on these findings, an initial dye concentration of 28 mg/L was selected as the optimum for subsequent experiments to ensure effective and comparable electrocoagulation performance.

Effect of reaction time

The effect of varying electrolysis reaction time on decolorization efficiency of reactive dye is presented in Fig. 3. It can be observed that the decolorization efficiency increased significantly with longer reaction times. This trend is attributed to the relationship between reaction time and the production rate of Al^{3+} ions from the aluminum electrode; the decolorization efficiency is directly dependent on the concentration of hydroxyl and metal ions generated at the electrodes [8]. As reaction time increases, more metal ions and hydroxyl ions are released, leading to the formation of greater amounts of hydroxide flocs, which enhance the adsorption of dye molecules [9].

However, extending the electrolysis time beyond an optimum point results in only marginal improvements in decolorization efficiency while incurring higher energy and electrode consumption [10]. This is associated with increased charge loading, which can affect the electrocoagulation performance for decolorization [11], and may reduce the extent of cathodic reduction and the generation of fresh coagulant flocs [12].

As shown in Fig. 3, the maximum reactive dye removal efficiency of $74.60 \pm 0.17\%$ was achieved at an electrolysis time of 50 minutes. Therefore, a reaction time of 50 minutes was selected as the optimum duration for subsequent experiments.

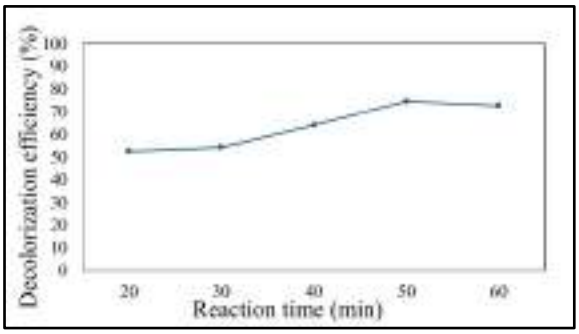

Fig. 3 The effect of reaction time on decolorization efficiency of electrocoagulation.

Effect of initial pH

To investigate the effect of the initial pH of the reactive dye solution on decolorization efficiency, batch experiments were conducted by adjusting the initial pH within the range of 4 to 12. The influence of pH on the electrocoagulation process is illustrated in Fig. 4. The results showed that an increase in the initial pH led to a decrease in decolorization efficiency, with the highest decolorization efficiency of 73.41% observed at an initial pH of 6.

In electrocoagulation for wastewater treatment, pH plays a crucial role in determining treatment performance [11]. For aluminum electrode systems, higher decolorization efficiencies are typically achieved within a pH range that favors the formation of $Al(OH)_3(s)$. These $Al(OH)_3(s)$ flocs have large

surface areas, which facilitate rapid adsorption of dissolved organic compounds and effective entrapment of colloidal particles. [13] also reported that the predominant aluminum species in solution varies with pH: Al^{3+} is the major species between pH 4 and 9.5, while $Al(OH)_3(s)$ becomes dominant within this range, enhancing coagulation efficiency.

The optimal conditions initial reactive dye concentration of 100 mg/L, reaction time of 50 minutes, and an initial pH of 6 were used as the basis for designing the continuous flow electrocoagulation experiment.

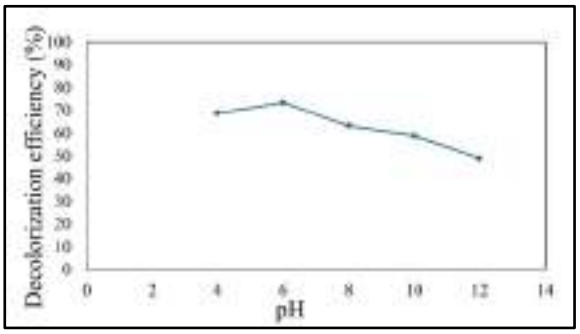

Fig. 4 The effect of initial pH on decolorization efficiency of electrocoagulation

Continuous Flow Electrocoagulation Experiment

The continuous flow system was operated at varying flow rates (8, 12, and 16 mL/min) and initial dye concentrations (75, 100, and 125 mg/L). The corresponding decolorization efficiencies are presented in Table 2. An increase in flow rate and initial dye concentration led to a decrease in decolorization efficiencies, which ranged from 48.50% to 57.95%. The optimal inlet flow rate was determined to be 8 mL/min, corresponding to a residence time of approximately 75 minutes in the continuous flow electro coagulation system and achieving the highest decolorization efficiency of 57.95%.

The findings of this study indicate that continuous-flow electrocoagulation (EC) is a promising technology for textile wastewater treatment; however, scale-up presents specific challenges. In large reactors, maintaining uniform current distribution and adequate mixing can be difficult, potentially reducing treatment efficiency. Electrode passivation and increased sludge generation require management strategies such as periodic polarity reversal, mechanical cleaning, and integration with effective sludge handling units. Fluctuations in influent dye concentration, pH, and conductivity in real industrial effluents necessitate automated control of current density and hydraulic retention time. Modular reactor configurations can provide operational flexibility, while coupling electrocoagulation with downstream biological or membrane processes can enhance overall pollutant removal and system robustness. Addressing these considerations is essential to translate laboratory-scale performance into reliable, cost-effective industrial applications.

Table 2 Decolorization efficiencies of reactive dyes using a continuous flow electrocoagulation system

Flow rate (ml/min)	Initial concentration (mg/L)	Decolorization efficiency (%)
8	100	57.83
12	100	54.08
16	100	50.79
16	75	57.95
16	125	47.76

Under the bench-scale conditions used in this study (I = 0.14 A, t = 45 min, V = 12.5 V, reactor volume = 0.6 L), aluminum electrode consumption calculated by Faraday's law was approximately 58.7 $g \cdot m^{-3}$ (≈0.059 $kg \cdot m^{-3}$), corresponding to a material cost of about 0.15 $USD \cdot m^{-3}$ at current aluminum market prices. The measured voltage resulted in an energy demand of ~2.19 $kWh \cdot m^{-3}$, equivalent to ~0.26 $USD \cdot m^{-3}$ at an average electricity tariff of 0.12 $USD \cdot kWh^{-1}$. Thus, the estimated direct operational cost for energy and electrode consumption was ~0.41 $USD \cdot m^{-3}$, excluding labor, maintenance, capital depreciation, and sludge handling. The electrocoagulation process generates sludge composed primarily of coagulated dye–metal hydroxide complexes, which requires dewatering (e.g., filtration or centrifugation) and environmentally compliant disposal. Where feasible, beneficial reuse for example, as a raw material in cement or brick manufacturing can reduce disposal costs and environmental impact. Pilot-scale trials are recommended to validate these cost estimates and optimize sludge management strategies for full-scale application.

To further advance the practical application of continuous-flow electrocoagulation, several research directions are recommended. Building on the promising results of this study, future research should focus on pilot-scale implementation of continuous-flow electrocoagulation systems to evaluate their performance under actual textile industry wastewater conditions. Long-term studies investigating operational stability, electrode durability, and maintenance requirements will be critical to ensure sustained treatment efficiency. Furthermore, comparative assessments of electrocoagulation with other advanced treatment technologies, such as membrane filtration and advanced oxidation processes, are recommended to better understand

their relative advantages, cost-effectiveness, and environmental impacts. These steps will support the practical adoption and optimization of sustainable wastewater treatment solutions in the textile industry.

CONCLUSIONS

The batch electrocoagulation system demonstrated effective decolorization of soluble reactive dyes, achieving a maximum decolorization efficiency of 73.41% at an initial dye concentration of 100 mg/L, an initial pH of 6, and a reaction time of 50 minutes. The insights gained from the batch experiments were subsequently used to design and evaluate a continuous-flowelectrocoagulation system, which achieved decolorization efficiencies ranging from 48.50% to 57.95%. These findings indicate that integrating electrocoagulation technology into existing wastewater treatment processes can enhance the textile industry's environmental performance and contribute to greater sustainability.

ACKNOWLEDGMENTS

This research was supported by the Suranaree University of Technology.

.

REFERENCES

[1] Daneshwar N., Khataee A.R., and Djafarzadeh N., The Use of Artificial Neural Networks (ANN) for Modeling of Decolorization of Textile Dye Solution Containing C.I. Basic Yellow 28 by Electrocoagulation Process. J. Hazard.Mater, B137, 2006, pp.1788-1795.

[2] Alshamsi A. F., Albadwawi A.S., Alnuaimi M.M., Rauf M.A., and Ashraf, S.S., Comparative Efficiencies of The Degradation of Crystal Violet Using UV/hydrogen Peroxide and Fenton's Reagent. Dyes and Pigments, Vol. 74, 2007, pp.283-287.

[3] Khadim M. M., Kane C., Oury D. N., Mar D. C., Chauvet F., Comtat M., and TZedakis T., Electrocoagulation Process Applied on Pollutants Treatment Experimental Optimization and Fundamental Investigation of the Crystal Violet Dye Removal. Journal of Environmental Chemical Engineering, Vol. 4, 2016, pp.4001 – 4011.

[4] Fajardo A.S., Martins R.C., Silva D.R., and Martínez-Huitle C.A., Quinta-Ferreira R.M., Dye Wastewaters Treatment Using Batch and Recirculation Flow Electrocoagulation Systems. Journal of Electroanalytical Chemistry, Vol. 801, 2017, pp.30-37.

[5] Kobya, M., Can O.T., and Bayramoglu M., Treatment of Textile Wastewaters by Electrocoagulation Using Iron and Aluminum Electrodes. J. Hazard. Mater, B100, 2003, pp.163-178.

[6] Bassyouni. D.G., Hamad. H.A., El-Ashtoukhyb E-S.Z., Amin N.K., and El-Latif M.M.A., Comparative Performance of Anodic Oxidation and Electrocoagulation as Clean Processes for Electrocatalytic Degradation of Diazo Dye Acid Brown 14 in Aqueous Medium. Ecotoxicology and Environmental Safety, Vol.335, 2017, pp.178-187.

[7] Ainchu S., and Yimrattanabovorn J., (2020). Comparison of Electrocoagulation Using Iron and Aluminium Electrodes with Chemical Coagulation for removal of Vat Dye Solution. Naresual University Journal of Science and Technology. Vol. 28, Issue 2, 2020, pp.1-13.

[8] Daneshwar N., Khataee A.R., and Djafarzadeh N., The Use of Artificial Neural Networks (ANN) for Modeling of Decolorization of Textile Dye Solution Containing C.I. Basic Yellow 28 by Electrocoagulation Process. J.Hazard.Mater, B137, 2006, pp.1788-1795.

[9] Drouiche N., Aoudj S., Hecini M., Ghaffour N., Lounici H., and Mameri N. Study on the Treatment of Photovoltaic Wastewater Using Electrocoagulation Fluoride Removal with Aluminium Electrodes Characteristics of Products. J. Hazard.Mater. Vol.169, 2009, pp.65–69.

[10] An C., Huang C., Yao Y., and Zhao S., Emerging Usage of Electrocoagulation Technology for Oil Removal from Wastewater: A review. Science of The Total Environment. Vol. 579, 2017, pp.537-556.

[11] Verma A.K., Treatment of Textile Wastewaters by Electrocoagulation Employing Fe-Al Composite Electrode. Journal of Water Process Engineering, Vol. 20, 2017, pp. 168-172.

[12] Akyol A., Treatment of Paint Manufacturing Wastewater by Electrocoagulation. Desalination, Vo.285, 2012, pp. 91 – 99.

[13] Bayamoglu M., Kobya M., Can O.T., and Sozbir M., Operating Cost Analysis of Electrocoagulation of Textile Dye Wastewater, Sep. Purif. Technol. Vol.37, 2004, pp.117-125.

Copyright © Int. J. of GEOMATE All rights reserved, including making copies, unless permission is obtained from the copyright proprietors.

15th Int. Conf. on Geotechnique, Construction Materials & Environment,
Kyoto, Japan, 11-13 November 2025, ISBN 978-4-909106124 C3051

ANALYSIS OF INFRASTRUCTURE RESILIENCE AND WATER QUALITY OF THE ANDALAS UNIVERSITY CAMPUS, INDONESIA, IN THE UPSTREAM OF BATANG KURANJI WATERSHED FOR SEDIMENT AND RAW WATER CONTROL

Nofra Masdaf[1], *Fauzan[2], Bambang Istijono[3],and Revalin Herdianto[4]

[1,2,3,4]Department of Civil Engineering, Faculty of Engineering, Andalas University, Indonesia
[4]Department of Civil Engineering, Politeknik Negeri Padang, Indonesia

ABSTRACT

Reservoirs are crucial for sediment control and raw water supply, yet integrated assessments of their infrastructure resilience and water quality are still rare, especially in tropical, erosion-prone areas. This study evaluates the resilience and water quality of four reservoir systems at Universitas Andalas, located in the upstream Batang Kuranji watershed: PNP, LPPM, Arsip, and the Nurul Ilmi–Siratal Mustaqim (NI–SM) system. Methods include erosion and sediment yield estimation (USLE/MUSLE), sediment transport analysis (us), peak discharge modeling (Muskingum), and laboratory water quality testing. Results show that the NI–SM system had the most extended lifespan (3.02 years) and lowest SDR (49%), indicating better sedimentation resistance. The Siratal Mustaqim 2 reservoir reduced peak discharge by 26.23% and delayed flow by 20.96 minutes. Water quality tests revealed excess levels of iron, color, and TSS, particularly upstream, surpassing national standards. These results suggest runoff significantly contributes to water quality degradation. In conclusion, reservoir resilience is determined by sediment control, hydraulic performance, and water quality protection, emphasizing the need for integrated watershed management and ongoing monitoring.

Keywords: Reservoir, Erosion, Sedimentation, Infrastructure Resilience, Water Quality

INTRODUCTION

Infrastructure resilience and water quality are strategic issues in the management of water resources in upstream watershed areas, including the Andalas University campus region located within the Limau Manis and Batu Busuk sub-watersheds, as illustrated in Figure 1. This area serves both as an educational center and a conservation zone, equipped with a reservoir system for flood control, raw water supply, and sediment mitigation. Resilience to sedimentation, the ability to maintain water quality, and the effectiveness in reducing and delaying flood peak discharges are the primary indicators of infrastructure resilience [1–7].

Fig. 1. Map of the Batang Limau Manis and Batu Busuk Sub-Watersheds, Batang Kuranji Watershed.

This study assesses four reservoir systems: single (Politeknik Negeri Padang [PNP], Lembaga Penelitian dan Pengabdian kepada Masyarakat [LPPM]), series (Arsip 1–3), and series-parallel (Nurul Ilmi 1–2, Siratal Mustaqim 1–2 [NI-SM]) using the USLE–MUSLE approach for sedimentation, the Muskingum method for flood routing, and water quality testing. This integrated analysis of physical resilience and water quality, rarely conducted in erosion-prone tropical regions [8–9], aims to support sustainable land conservation, sediment management, and raw water supply.

RESEARCH SIGNIFICANCE

This study highlights the importance of an integrated evaluation of reservoir infrastructure resilience (the ability of infrastructure to function and survive in the face of and recover from various shocks, threats, or disturbances) and water quality in managing sedimentation, flooding, and raw water resources within Andalas University. The novelty of this research lies in the simultaneous integration of USLE–MUSLE analysis, SDR, Flood Routing, and water quality assessment to evaluate the structural and functional performance of reservoirs. These findings offer strategic contributions to land conservation planning, reservoir infrastructure design, and the sustainable management of water quality in tropical regions.

RESEARCH METHODS

This study employs an integrated quantitative approach to assess the resilience of reservoir systems in the upstream area of the Batang Kuranji watershed, with a focus on sediment control, raw water supply, and runoff mitigation [10–13].

Reservoir Storage Capacity Contour Method

Reservoir capacity calculation is the initial step in estimating the effective lifespan (period during which a reservoir can function before its storage capacity is significantly reduced by sedimentation), conducted using a contour-based method derived from topographic data :

$$\boldsymbol{V = \Delta H\ (n-1)\frac{\sum_{i=1}^{n} Li}{n}} \quad (1)$$

Where:

- $\boldsymbol{V}$ - reservoir storage capacity (m^3/s),
- $\boldsymbol{\Delta H}$ - contour interval (m),
- n - number of contour lines,
- $\boldsymbol{Li}$ - inundated area at the i-th contour line (m^2)

Rainfall Intensity

The 30-minute rainfall intensity analysis was conducted using the Talbot, Sherman, and Ishiguro methods, which are commonly used in hydrology to describe the intensity–duration relationship of rainfall [14–15]. The main objective is to obtain the average intensity at the 30th minute in order to calculate rainfall erosivity (ei), which forms part of the R factor in the USLE model.

Talbot method

This method is widely used for estimating rainfall intensity due to its simplicity and ease of application, particularly in short-term hydrological analyses. Rainfall intensity using the Talbot method is calculated using the following formula:

$$I = \frac{a}{t+b} \quad (2)$$

$$a = \frac{[\sum(I.t)]\,[\sum(I^2)] - [\sum(I^2.t)][\sum(I)]}{N[\sum(I^2)] - [\sum(I)][\sum(I)]} \quad (3)$$

$$\boldsymbol{b} = \frac{[\sum(\boldsymbol{I})]\,[\sum(\boldsymbol{I}.\boldsymbol{t})] - \boldsymbol{N}\,[\sum(\boldsymbol{I^2}.\boldsymbol{t})]}{\boldsymbol{N}[\sum(\boldsymbol{I^2})] - [\sum(\boldsymbol{I})][\sum(\boldsymbol{I})]} \quad (4)$$

Where:

- $\boldsymbol{I}$ - rainfall intensity (mm/hour)
- t - rainfall duration (hours)
- $\boldsymbol{a}$ - empirical constant representing the theoretical maximum intensity for short durations
- $\boldsymbol{b}$ - empirical constant that adjusts the curve shape based on the square root of time, determining the slope of intensity reduction
- $\boldsymbol{N}$ - number of data points

Sherman method

This method is an empirical approach for estimating rainfall intensity based on duration and is generally applied to short-duration rainfall events. Rainfall intensity using this method is calculated with the following formula:

$$\boldsymbol{I} = \frac{\boldsymbol{a}}{\boldsymbol{t^n}} \quad (5)$$

$$\boldsymbol{\log a} = \frac{[\sum(\boldsymbol{\log I})]\,[\sum((\boldsymbol{\log t})^2)] - [\sum(\boldsymbol{\log t}.\ \boldsymbol{\log I})][\sum(\boldsymbol{\log t})]}{\boldsymbol{N}[\sum((\boldsymbol{\log t})^2)] - [\sum(\boldsymbol{\log t})][\sum(\boldsymbol{\log t})]} \quad (6)$$

$$\boldsymbol{n} = \frac{[\sum(\boldsymbol{\log I})]\,[\sum(\boldsymbol{\log t})] - \boldsymbol{N}\,[\sum(\boldsymbol{\log t}.\ \boldsymbol{\log I})]}{\boldsymbol{N}[\sum((\boldsymbol{\log t})^2)] - [\sum(\boldsymbol{\log t})][\sum(\boldsymbol{\log t})]} \quad (7)$$

Where:

- $\boldsymbol{I}$ - rainfall intensity (mm/hour)
- t - rainfall duration (hours)
- $\boldsymbol{a}$ - constant representing rainfall intensity at t = 1 hour; defines base intensity level
- $\boldsymbol{n}$ - exponent controlling the rate of intensity decline with increasing duration; reflects temporal rainfall distribution
- $\boldsymbol{N}$ - number of data points

Ishiguro method

This method is an empirical model specifically designed to represent short-duration rainfall events, typically lasting less than 2 hours.

$$\boldsymbol{I} = \frac{\boldsymbol{a}}{\sqrt{\boldsymbol{t}}+\boldsymbol{b}} \quad (8)$$

$$\boldsymbol{a} = \frac{[\sum(\boldsymbol{I}.\sqrt{\boldsymbol{t}})]\,[\sum(\boldsymbol{I^2})] - [\sum(\boldsymbol{I^2}.\sqrt{\boldsymbol{t}})][\sum(\boldsymbol{I})]}{\boldsymbol{N}[\sum(\boldsymbol{I^2})] - [\sum(\boldsymbol{I})][\sum(\boldsymbol{I})]} \quad (9)$$

$$\boldsymbol{b} = \frac{[\sum(\boldsymbol{I})]\,[\sum(\boldsymbol{I}.\sqrt{\boldsymbol{t}})] - \boldsymbol{N}[\sum(\boldsymbol{I^2}.\sqrt{\boldsymbol{t}})]}{\boldsymbol{N}[\sum(\boldsymbol{I^2})] - [\sum(\boldsymbol{I})][\sum(\boldsymbol{I})]} \quad (10)$$

Where:

- $\boldsymbol{I}$ - rainfall intensity (mm/hour)
- t - rainfall duration (hours)
- $\boldsymbol{a}$ - empirical constant representing the theoretical maximum intensity for short durations
- $\boldsymbol{b}$ - empirical constant that adjusts the curve shape based on the square root of time, determining the slope of intensity reduction
- $\boldsymbol{N}$ - number of data points

Flood Discharge

Runoff in this study refers to the portion of rainfall that flows over the land surface and contributes to streamflow, estimated using the Rational Method [14-15].

$$\boldsymbol{Qp} = \boldsymbol{0,278\,.\,C.I.A} \quad (11)$$

Where:

- Qp - peak flood discharge (m^3/s)
- C - runoff coefficient
- I - rainfall intensity during time of concentration (mm/hour)
- A - catchment area (Ha)

Erosion

Soil loss due to surface erosion was estimated using the USLE [10-13] model, which accommodates the calculation of both average annual erosion rates and event-based erosion. Soil loss at each reservoir site is estimated through the multiplication of five key parameters. Can be calculated using the following formula :

$$\boldsymbol{A} = \boldsymbol{R} \times \boldsymbol{K} \times \boldsymbol{LS} \times \boldsymbol{C} \times \boldsymbol{P} \quad (12)$$

Where:

- $\boldsymbol{A}$ - average annual soil loss (tons/ha/year)
- $\boldsymbol{R}$ - rainfall erosivity factor (MJ·mm/ha·hr·year)
- $\boldsymbol{K}$ - soil erodibility factor (tons·ha·hr/ha·MJ·mm)
- $\boldsymbol{LS}$ - slope length and steepness factor
- $\boldsymbol{C}$ - cover and land use factor
- $\boldsymbol{P}$ - conservation practice factor

Sedimentation

Sediment volume resulting from surface runoff was estimated using the MUSLE approach, which replaces the rainfall erosivity factor (R) in the USLE model with hydrological parameters, namely runoff volume (V) and peak discharge (Qp) [10-13].

$$\boldsymbol{Sed} = \boldsymbol{11.8} \times \left(\boldsymbol{Q} \times \boldsymbol{q_{peak}} \times \boldsymbol{A}\right)^{\boldsymbol{0.56}} \times \boldsymbol{K} \times \boldsymbol{C} \times \boldsymbol{P} \times \boldsymbol{LS} \quad (13)$$

Where:

- $\boldsymbol{Sed}$ - estimated sediment yield (tons)
- $\boldsymbol{Q}$ - runoff volume (m³)
- $\boldsymbol{q_{peak}}$ - peak flood discharge from runoff (m³/s)
- $\boldsymbol{A}$ - catchment area (km²)
- $\boldsymbol{K}$ - soil erodibility factor
- $\boldsymbol{C}$ - land cover and land use factor
- $\boldsymbol{P}$ - soil conservation practice factor
- $\boldsymbol{LS}$ - slope length and steepness factor
- $\boldsymbol{11.8}$ - conversion and calibration coefficient for results in tons

Sediment Delivery Ratio (SDR)

This study employed the empirical approach of the United States Department of Agriculture (USDA) based on catchment area size. This estimation is essential for assessing the actual sediment load that affects reservoir capacity, resilience, and effective lifespan.

$$SDR = 0.472 \times A^{-0.125} \quad (14)$$

Where:

- SDR - sediment delivery ratio
- A - catchment area (km2)

Flood Routing

As part of the infrastructure resilience analysis, this study applies the Flood Routing method to evaluate the reservoir's ability to reduce peak discharge (maximum instantaneous flow at the watershed outlet during a storm event) and delay flood peak time (time difference between the occurrence of the maximum inflow and the maximum outflow hydrograph at the reservoir or watershed outlet) [3]. The method used is the Muskingum :

$$\boldsymbol{C_0} = \frac{-\boldsymbol{KX}+\boldsymbol{0.5\Delta t}}{\boldsymbol{K}-\boldsymbol{KX}+\boldsymbol{0.5\Delta t}} \quad (15)$$

$$\boldsymbol{C_1} = \frac{\boldsymbol{KX}+\boldsymbol{0.5\Delta t}}{\boldsymbol{K}-\boldsymbol{KX}+\boldsymbol{0.5\Delta t}} \quad (16)$$

$$\boldsymbol{C_2} = \frac{\boldsymbol{K}-\boldsymbol{0.5\Delta t}}{\boldsymbol{K}-\boldsymbol{KX}+\boldsymbol{0.5\Delta t}} \quad (17)$$

$$\boldsymbol{Q_{out,t+1}} = \boldsymbol{C_0 I_{t+1}} + \boldsymbol{C_1 I_t} + \boldsymbol{C_2 O_t} \quad (18)$$

where :

- $Q_{out,t+1}$ - outflow discharge at time t+1
- I_t - inflow discharge at time t
- I_{t+1} - inflow discharge at time t+1
- O_t - outflow discharge at time t
- Δt - time interval between two observations (Δt)
- K - storage constant represents the travel time of water through the reach
- X - weighting factor typically ranges between 0 and 0.5; describes the relative influence of inflow and outflow on storage
- C_0, C_1, C_2 - numerical weights derived that distribute inflow and outflow in the flood routing process

DATA ANALYSIS

This section presents the results of primary and secondary data analysis from the upstream area of the Batang Kuranji watershed to support erosion estimation and the evaluation of reservoir effective lifespan as an indicator of infrastructure resilience.

Reservoir Storage Capacity

Table 1. Reservoir Storage Capacity

System	Reservoir	Storage Capacity (m^3)	Sub-Total (m^3)
Single	PNP	2,418	2,418
	LPPM	445	445
Series	Arsip 1	1,392	3,020
	Arsip 2	522	
	Arsip 3	1,106	
Series-Parallel	Nurul Ilmi 1	1,141	18,370
	Nurul Ilmi 2	1,176	
	Siratal Mustaqim 1	1,653	
	Siratal Mustaqim 2	14,400	
	Total		24,253

The single reservoirs, PNP and LPPM, have capacities of 2,418 m³ and 445 m³, respectively; the series system (Arsip) has a combined capacity of 3,020 m³; while the series-parallel system (NI-SM) possesses the largest capacity at 18,370 m³, with a total capacity of 24,253 m³, as shown in Table 1.

Rainfall Data

Short-term rainfall analysis was conducted using 5-minute interval data over 120 minutes at four stations (PNP, LPPM, Arsip, and NI–SM). Over the 10-day observation period, 15 data intervals were recorded, with Period 1 (January 21, 2025) identified as the worst-case scenario due to the highest rainfall intensity as shown in Table 2.

Table 2. Rainfall Data

No	Time (minutes)	Rainfall Intensity (mm)			
		PNP	LPPM	A	NI-SM
1	0	0.0000	0.0000	0.0000	0.0000
2	5	2.1991	2.1041	1.8046	2.3038
3	10	2.8984	3.0010	3.0992	2.8980
4	15	2.8960	2.9006	3.1016	2.8010
5	20	2.2017	2.3964	2.1978	2.6998
6	25	2.6020	2.6046	2.0007	2.2951
7	30	2.1967	2.0016	2.7995	1.9989
8	35	3.3045	3.5952	3.4044	2.6044
9	40	3.8000	2.8027	3.4022	3.7984
10	45	2.8990	3.5967	3.1999	3.5961
11	50	2.5022	3.5043	3.1988	2.6961
12	55	3.5979	3.1046	3.2951	3.8038
13	60	3.8997	3.3996	3.4954	3.5040
14	65	2.7976	3.2956	2.8978	3.0012
15	70	2.6047	3.2985	2.5984	2.7032
16	75	2.3030	2.8030	2.2023	2.3022
17	80	2.0987	2.1999	1.9967	1.9953
18	85	1.9012	1.6968	1.2025	1.8025
19	90	1.5959	1.3973	1.0990	1.6036
20	95	1.1984	1.2034	0.9974	1.4033
21	100	0.9018	1.0008	0.9001	0.9985
22	105	0.6018	0.7967	0.8033	0.8950
23	110	0.5047	0.6043	0.8966	0.7007
24	115	0.2977	0.3955	0.8024	0.6001
25	120	0.1973	0.2968	0.7043	0.4950
Accumulation		52.0000	54.0000	52.1000	53.5000

Soil Data

Table 3. Soil Test Results

No	Parameter	A Sample	NI-SM Sample
1	% silt	28.650	34.510
2	% clay	31.710	42.150
3	% fine sand	18.770	23.340
4	% organic matter (a)	6.660	8.827
5	soil structure class (b)	3.000	3.000
6	permeability class (c)	5.000	5.000
7	bulk density	0.874	0.858

To determine the soil erodibility factor (K) in the USLE framework, a soil characterization study was performed using both physical and chemical soil properties. Data obtained from the upstream zone representing the catchment area of the Arsip (A) Series and NI-SM Parallel Series Reservoir served as the reference for evaluating baseline erosion susceptibility, as detailed in Table 3.

RESULTS AND DISCUSSION

This study integrates rainfall intensity and flood discharge analyses to estimate erosivity and runoff, supporting calculations of erosion rates, sediment volume, and SDR to evaluate reservoir lifespan as a resilience indicator. The Muskingum method assessed hydraulic effectiveness in reducing and delaying peak discharge, while water quality testing evaluated the reservoirs' suitability as raw water sources and their role in sustainable water resource conservation.

Rainfall Intensity

Short-term rainfall intensity was analyzed using the Talbot, Sherman, and Ishiguro methods based on the highest recorded rainfall data, across durations of 5 to 720 minutes. All methods showed decreasing intensity with longer durations, reflecting their distinct characteristics. The average 30-minute intensity (I_{30}) was 33.29 m³/s, relevant for runoff and erosion analysis, as shown in Table 4.

Table 4. Rainfall Intensity

Time (minutes)	Rainfall Intensity (m^3/s)		
	Talbot	Sherman	Ishiguro
5	37.14	34.49	55.77
10	36.56	32.06	48.66
15	36.00	30.72	44.33
30	34.41	28.55	36.91
45	32.96	27.36	32.71
60	31.63	26.54	29.84
120	27.22	24.67	23.49
180	23.89	23.63	20.19
360	17.48	21.97	15.33
720	11.37	20.42	11.43

Flood Discharge Analysis

Table 5. Flood Discharge Analysis Results

t	QPNP	Q_{LPPM}	Q_A	Q_{NI-SM}
(hour)	(m^3/s)	(m^3/s)	(m^3/s)	(m^3/s)
0.25	0.44	0.02	0.13	0.27
0.49	2.27	0.00	0.00	0.00
0.50	2.25	0.00	0.04	0.68
0.75	1.47	0.00	0.02	0.40
1.00	0.96	0.00	0.01	0.24
1.50	0.48	0.00	0.00	0.12
2.26	0.20	0.00	0.00	0.00
Total Q (m^3/s)	1.47	0.03	0.12	0.49
VDR (m^3)	5,289.71	116.32	434.63	1777.57
TDR (mm)	5.17	11.08	8.81	5.51

Flood discharge analysis using the Rational Method provided VDR (volume direct runoff), TDR (total direct runoff), and Qp (peak discharge) values as inputs for MUSLE-based sediment load estimation. The PNP reservoir showed the highest, while the LPPM and Arsip systems had lower values. The NI–SM series-parallel system recorded a notable combined flow, reflecting variations in runoff control capacity among the reservoirs as shown in Table 5.

Infrastructure Resilience Analysis

Reservoir infrastructure resilience was analyzed using three main indicators: the SDR, effective lifespan, and hydrological response through Flood Routing. These indicators provide a comprehensive overview of the reservoir's resistance to sedimentation and extreme hydrological pressure.

Erosion, sedimentation, and reservoir lifespan analysis

The effective lifespan of a reservoir, indicating its resilience to sedimentation, is calculated from the ratio of initial storage capacity to annual sediment volume, based on erosion, sediment yield, SDR (PNP: 66%, LPPM: 72%, Arsip: 61%, NI–SM: 49%) and bulk density where a lifespan exceeding about 10-20 years is considered resilient in this regional context. Results show the PNP and Arsip reservoirs have the shortest lifespans, indicating high siltation risk, while LPPM and NI–SM have longer lifespans but remain vulnerable without proper land management, as shown in Table 6.

Table 6. Erosion, Sedimentation, and Reservoir Lifespan Analysis Result

Parameter	Reservoir			
	PNP	LPPM	A	NI-SM
	USLE			
Erosion per Event (tons/event)	286.50	186.38	458.01	281.22
Annual Sediment (tons/year)	1,520.06	532.67	3,968.08	12,490.64
Annual Erosion (tons/ha/year)	1,739.74	609.65	4,541.56	14,295.83
Reservoir Lifespan (years)	1.59	0.84	0.76	1.47
	MUSLE			
Sediment Yield (tons/event)	1,484.18	14.82	159.03	443.13
Annual Sediment (tons/year)	1,698.68	203.50	2,184.18	6,086.12
Reservoir Lifespan (years)	1.42	2.19	1.38	3.02

Flood routing

Flood Routing analysis was calculated using the Muskingum method, with no single standard specific to the watershed conditions. Table 7 demonstrates that series and series-parallel reservoir systems are more effective in reducing peak discharge and delaying flood peak time than single reservoirs. The Arsip system achieved a 25.56–39.92% reduction with a 12.92-minute delay, while the NI–SM system recorded a 26.23% reduction and a 20.96-minute delay, supported by sequential reservoir flow. In contrast, single reservoirs like LPPM and PNP showed lower effectiveness, with reductions of 40% and 0.54% and minimal delays, underscoring the superior performance of tiered systems in flood control.

Table 7. Reduction and Delay of Flood Peak Discharge Muskingum Method

System	Reservoir	Reduction (%)	Delay (minutes)
Single	PNP	0.54	0.32
	LPPM	40.00	0.00
Arsip Series	Arsip 1	25.56	5.96
	Arsip 2	31.34	5.96
	Arsip 3	39.92	12.92
Nurul Ilmi – Siratal Mustaqim Series-Parallel	Nurul Ilmi 1	11.32	5.96
	Siratal Mustaqim 1	17.63	5.96
	Nurul Ilmi 2	23.73	20.96
	Siratal Mustaqim 2	26.23	20.96

Water Quality Analysis

Table 8. Water Quality Test Results

Parameter	Test Results		Water Quality Standard	Unit
	Sample A	Sample NI-SM		
Color	8.50	12.80	10	Pt-Co Unit
Total Dissolved Solids (TDS)	91.70	62.60	300	mg/L
Temperature	25.00	25.10	± 3	oC
pH	6.87	6.54	6.5 – 8.5	-
Dissolved Iron (Fe)	1.79	0.877	0.2	mg/L
Dissolved Oxygen (DO)	5.53	5.53	-	mg/L
Total Suspended Solids (TSS)	3,600.00	245.00	-	mg/L
Total Hardness (CaCO3)	112.00	52.00	NA	mg/L

Laboratory tests from upstream and downstream reservoirs shown in Table 8, explain that temperature, pH, and TDS met quality standards based on the Indonesian Ministry of Health Regulation Number 2 of 2023. However, dissolved iron exceeded the 0.2 mg/L limit, and NI–SM also surpassed the color threshold, indicating organic matter or fine particulates. TSS levels dropped from 3,600 mg/L upstream to 245 mg/L downstream, reflecting effective sedimentation, so further water quality improvements are needed.

CONCLUSION

This study evaluated the resilience of four reservoir systems in the upstream Batang Kuranji watershed based on sedimentation, hydrological

performance, and water quality. USLE and MUSLE analyses identified the NI–SM system as the most resistant to sedimentation, with the longest effective lifespan (3.02 years) and the lowest SDR value (49%), while the Arsip reservoir had the shortest lifespan (0.76 years). Flood routing results showed that tiered systems (Arsip and NI–SM) were more effective in reducing and delaying peak discharge, with the NI–SM system achieving a 26.23% reduction and a 20.96-minute delay, compared to only 0.54% reduction by the PNP reservoir. Water quality analysis indicated compliance for parameters like temperature, pH, TDS, and DO, but elevated levels of iron, color, and TSS especially upstream highlighted runoff-related contamination. However, the findings are limited to the local scale of the upstream Batang Kuranji watershed, with model parameters that may vary under different tropical conditions. Future studies should integrate broader pollutant parameters, long-term monitoring, and climate–land use scenarios to strengthen reservoir resilience strategies in tropical regions and the implementation of parallel–series reservoir systems as a more effective option for future reservoir design.

ACKNOWLEDGMENT

We thank the Department of Civil Engineering, Andalas University, and the Department of Water Resources and Construction Development, West Sumatra Province, for their support and permission, and the GEOMATE Journal for facilitating the dissemination of this study.

REFERENCES

1. Lu, Q., et al., Multi-objective risk analysis for flood control operation of a complex reservoir system under multiple time-space correlated uncertainties. Journal of Hydrology, 606(1), 2022,p.127419.
2. Wang, T., et al., Rank classification method for cascade reservoirs considering scale, benefits, and risk consequences. Journal of Hydrology, 623(June),2023,p.129856.
3. Elshinnawy, I. A., and Almaliki, A. H., Reservoir hydrologic routing for the hydrodynamic of Al-Manzala Lake, Egypt. International Journal of GEOMATE, 2 (83), 2021,pp.157–165.
4. Khasanov, K., A comprehensive analysis of reservoir capacity loss: a case study of the Akhangaran Reservoir, Uzbekistan. Water Cycle, 6(March),2025,pp.105-117.
5. Hussin, N. F. A. M., et al., Rainfall prediction using statistical downscaling based on support vector machine in Selangor. International Journal of Advanced Science Engineering and Information Technology, 15(1), 2025, pp.345–352.
6. Hanh, D. K., Truong, D. D., and Bui, K. T. T., Application of numerical modeling and GIS for simulating inundation under dam failure scenarios. Civil and Environmental Engineering, 20(1),2024,pp.233–254.
7. Ji, Y., Lei, X., Cai, S., and Wang, X., Application of a classifier based on data mining techniques in water supply operation. Water, 8(12), 2016, pp. 1-12.
8. A. N. Anna et al., Spatial Modelling of Local Flooding for Hazard Mitigation in Surakarta, Indonesia. International Journal of GEOMATE, 21(87) 2021, pp.145–152.
9. Gunawan, A. R. M. P., Suharyanto, S., Sriyana, I., and Nuramini, T. M., Effect of changes on land use and erosivity on erosion hazards and the reservoir lifespan of Tukul Dam, using USLE method. E3S Web of Conferences, 576, 2024, pp. 1-12.
10. Yusuf, S. M., Murtilaksono, K., and Laraswati, D. M., Spatial mapping of soil erosion prediction through integration USLE model into Geography Information System. Jurnal Pengelolaan Sumberdaya Alam dan Lingkungan, 10(4), 2020, pp.594–606.
11. Cheng, J., et al., Integrated use of GIS and USLE models for LULC change analysis and soil erosion risk assessment in the Hulan River Basin, Northeastern China. Water, 16(2), 2024, pp.1-9.
12. Sestras, P., et al., GIS based soil erosion assessment using the USLE model for efficient land management: a case study in an area with diverse pedogeomorphological and bioclimatic characteristics. Notulae Botanicae Horti Agrobotanici Cluj-Napoca, 51(3), 2023, pp.1–14.
13. Andriyani, I., Indarto, Soekarno, S., and Pradana, M. P., Analysis of rainfall erosivity factor (R) on prediction of erosion yield using USLE and RUSLE models: a case study in Mayang Watershed, Jember Regency, Indonesia. Sains Tanah, 21(1), 2024, pp.64–73.
14. Sam, M. G., et al., Modeling rainfall intensity-duration-frequency (IDF) and establishing climate change existence in Uyo-Nigeria using non-stationary approach. Journal of Water Resource and Protection, 15(5), 2023, pp.194–214.
15. Mínguez, R., and Herrera, S., Spatial extreme model for rainfall depth: application to the estimation of IDF curves in the Basque Country. Stochastic Environmental Research and Risk Assessment, 37(8), 2023, pp. 3117-3148.

Copyright © Int. J. of GEOMATE All rights reserved, including making copies, unless permission is obtained from the copyright proprietors.

15th Int. Conf. on Geotechnique, Construction Materials & Environment,
Kyoto, Japan, 11-13 November 2025, ISBN 978-4-909106124 C3051

ADVANCING SUSTAINABLE COMPOSITES: A STUDY ON BIO-EPOXY RESIN WITH RECYCLED CORE LAYERS

Kitsana Khodcharad[1], Kreetiwat Chaiyasin[2], Wipada Boransan[3], Watcharapong Patangtalo[1] and Veena Phunpeng[1,*]

[1]Mechanical Engineering, Suranaree University of Technology, Thailand
[2] Mechatronic Engineering, Suranaree University of Technology, Thailand
[3] Center of Excellence in Innovation for Sustainable Infrastructure Development, Suranaree University of Technology, Thailand

ABSTRACT

This study compares composite materials using synthetic resin matrices and bio-resin matrices derived from plant sources, with foam core layers of Lantor Soric made from recycled PET plastic added in 1, 2, 3, and 4 layers. The bending behavior and morphology of the materials were evaluated using Scanning Electron Microscopy (SEM). Results show that increasing the number of foam core layers enhances the strength and flexibility of the composite materials, with the 4-layer foam core composite exhibiting the highest strength. Additionally, composites using bio-resin matrices demonstrate superior bending properties compared to those using synthetic resin matrices. SEM analysis reveals strong bonding between the resin and foam core, with no delamination, indicating a well-integrated structure and efficient resin distribution. The materials used, including flax fibers, bio-resin matrices, and the Lantor Soric core made from recycled PET, are all environmentally friendly, reducing reliance on petroleum-based resources and minimizing environmental impact. This approach aligns with global sustainability efforts by reducing greenhouse gas emissions and supporting the circular economy, providing a promising alternative for producing high performance, eco-friendly composite materials that meet both performance and environmental goals.

Keywords: Bio-resin matrix, Sandwich composite, Natural reinforced composite, Flexural properties, Morphology

INTRODUCTION

Composite materials are among the most rapidly growing and evolving material groups today. They have gained widespread popularity across various industries, including aerospace, automotive, sports, and construction, all of which demand materials with specialized properties. Due to their superior characteristics compared to conventional materials such as exceptional mechanical strength, remarkable lightness, and resistance to harsh environmental conditions composite materials have become a crucial choice for structures requiring an optimal balance between weight and strength [1-2]. Notable applications include complex structural components of aircraft wings and fuselages, wheels and landing gear assemblies, energy efficient automotive body panels, and high-performance sports equipment such as tennis rackets and carbon fiber bicycles. These examples underscore the potential and significant role of composite materials in modern industries [3-5].

Although synthetic composite materials such as carbon fiber, glass fiber, and Kevlar fiber, along with petroleum-based matrices, are key to modern material development due to their outstanding mechanical properties, their production and end-of-life disposal have significant environmental impacts. These include greenhouse gas emissions, non-biodegradable waste accumulation, and the release of toxic substances into ecosystems [6-7]. These issues have driven researchers to explore alternative materials, such as natural reinforcement fibers, which are considered a highly promising replacement for synthetic materials [8]. Natural fibers offer advantages in sustainability, including the use of renewable resources, environmental friendliness, and reduced carbon dioxide emissions during production [9]. A notable example is flax fiber, which possesses excellent mechanical properties, enhances composite strength, and can effectively replace certain synthetic fibers.

Meanwhile, the development of bio-matrix, or naturally derived matrices, is equally important. These matrices are often extracted from plants, such as starch or lipid extracts [10-11]. Research indicates their compatibility with natural fibers like flax fibers, this combination yields promising results in terms of both mechanical properties and sustainability. Furthermore, Bio-matrix materials can meet the demands of various industries, including automotive, construction, and sports equipment, which seek to balance performance with environmental responsibility. The growing trend of incorporating natural materials into composites reflects a strong commitment to advancing circular economy principles and sustainable design, which are key directions for the future of composite materials [12-13].

Another important approach in the development of composite materials is the enhancement of performance through particle additives, which help increase strength, flexibility, and compatibility between the matrix and reinforcing fibers. Additionally, improving the mechanical properties of composites also involves the use of lightweight cores in sandwich composites [14]. Inserting a core between the surface layers of the composite sheet enhances thickness and reinforces load-bearing performance, such as bending and shear forces. These cores come in various types, depending on the requirements, including cores made from natural wood, foam, or synthetic materials like aramid. Notably, honeycomb shaped cores have become more popular due to their structure, which effectively distributes forces and provides a lighter alternative to conventional block shaped cores [15-16]. Currently, environmentally friendly cores, such as the Lantor Soric core made from recycled PET plastic with a honeycomb structure, are being developed. This type of core offers notable advantages in flexibility and durability. In addition to meeting sustainability goals, this core shows high potential for use with both synthetic and bio-matrix matrix materials [17].

In this research, the compatibility between the Lantor Soric core and two types of matrices, namely synthetic resin matrices and bio-resin matrices was tested with a focus on flexural mechanical strength. The inclusion of flax fibers in the composite material helps improve its strength and long-term sustainability from an environmental perspective. The obtained data will help understand the potential of this new composite material and promote the development of materials that meet both performance and sustainability requirements in the industry. Scanning electron microscopy (SEM) was used to analyze the structure of the Lantor Soric core in terms of core-matrix adhesion. The SEM data will help understand the material's behavior and support the development of high performance, durable, and eco-friendly composite materials.

MATERIALS AND METHODS

Materials

The composite materials employed in this study incorporate flax fibers obtained from Linum usitatissimum, which are well known for their high specific strength-to-weight ratio, biodegradability, and cost-effectiveness [1]. Compared to other natural fibers such as jute and hemp, flax offers a more favorable balance between mechanical performance and sustainability, making it one of the most promising reinforcements for lightweight composites. Recent studies have further highlighted that the mechanical and damping properties of flax fiber composites are strongly influenced by processing conditions and structural design [2].

Two resin matrices were selected: a synthetic epoxy resin, chosen for its superior mechanical properties and resistance to environmental factors, and a plant-based bio-resin, employed to reduce environmental impact while improving interfacial compatibility with the hydrophilic flax fibers.

To enhance flexural performance, a recycled PET-based foam core (Lantor Soric) was incorporated. This lightweight core increases composite thickness and flexural stiffness without significantly increasing weight, while simultaneously promoting sustainability through the reuse of waste-derived resources. A summary of the materials used in this investigation is presented in Fig 1.

Fig.1 Detailed Materials Overview.

Fabrication

The production of composite materials in this study utilizes the Vacuum Infusion Process, a technique that uses a vacuum system to press the components together while injecting the matrix into the prearranged reinforcement fibers and core. The reinforcement fibers are laid in the same direction at 0 degrees, layered in 3 layers. A Lantor Soric core, made from recycled PET plastic, is inserted in the middle to increase thickness and enhance the bending properties of the material. Additionally, three layers of flax fibers are placed on the top and bottom to improve strength and load-bearing efficiency. The material size before trimming is 220x100 mm^2, which will be cut to the appropriate size according to the test standards. Afterward, the surface is covered with Peel ply to prevent resin bonding to the surface and topped with infusion net to ensure the resin spreads evenly during injection. The matrix is mixed with a hardening agent in the correct ratio according to the technical data before undergoing a degassing process to remove any air trapped in the matrix, preventing air

bubbles in the composite structure. The matrix is then drawn into the vacuum system, where the fibers and core are neatly arranged, with the matrix infusion process taking approximately 15 minutes. Afterward, the entire structure is placed in an oven for about 6 hours to allow the resin to cure and acquire excellent mechanical properties.

Materials Testing

The sandwich composite materials, after forming and curing, are trimmed to meet standard dimensions for the bending test. The specimens are 200 mm in length and 15 mm in width, with thickness varying based on the core layers. The bending test follows ASTM C 393/C 393M standards with a 150 mm support span and a loading head speed of 2 mm/min, conducted using a LLOYD LD100 universal testing machine (100 kN capacity). Each specimen is tested 5 times for accuracy. Two groups are tested: one with synthetic resin matrices and 4 core configurations (20 specimens), and another with bio-resin matrices and the same 4 core configurations (20 specimens), totaling 40 specimens. Further details are in Table 1.

Table 1 Designed method for experimental study.

Matrix Type	Core layer	Name	Width (mm)	Thickness (mm)
Synthetic resin matrix	1 Core	S1C	15±0.2	5.02 ± 0.2
	2 Core	S2C		7.72 ± 0.2
	3 Core	S3C		10.33 ± 0.2
	4 Core	S4C		13.42 ± 0.2
Bio-resin matrix	1 Core	B1C		5.33 ± 0.2
	2 Core	B2C		7.70 ± 0.2
	3 Core	B3C		9.92 ± 0.2
	4 Core	B4C		12.21 ± 0.2

Facing Stress

The stress that occurs is mainly concentrated at the surface layers rather than the core. The stress calculation is based on an equation similar to the calculation of bending stress for a simple beam. The equation used for the calculation is shown in the following Eq.1

$$\sigma = \frac{P_{max} S}{2t(d+c)b} \quad (1)$$

Where: σ is the facing stress (MPa), Pmax is the maximum force prior to failure (N), S is the span length (mm), t is the facing thickness (mm), d is the sandwich thickness (mm), c is the core thickness (mm), b is the sandwich width (mm).

Morphology

Scanning Electron Microscopy (SEM) was used to examine the fracture surfaces, focusing on the failure behavior of reinforcing fibers and the interfacial compatibility between the resin matrix and flax fibers. In preparing the specimens for SEM, the tested samples are cut to an appropriate size (< 5 mm) to fit the SEM sample holder. The fracture surfaces are examined without further polishing to preserve the natural fracture characteristics. For nonconductive samples, a thin layer of gold is applied using a Sputter Coater to enhance electrical conductivity and reduce charge accumulation. Each specimen is then securely mounted on an aluminum stub with conductive carbon tape before being placed in the SEM chamber for imaging and further analysis

RESULTS

Behavior under bending load

The bending properties tested using the universal testing machine show that the specimen's response to the applied force results in the maximum load occurring at the specimen with the core layer of 4 and a core thickness of 10 mm. The maximum load distribution is measured at 811.81 N for the structure using a bio-resin matrix. For the synthetic resin matrix, the maximum load occurs at the specimen with the core layer of 4 and a core thickness of 10 mm, yielding a value of 730.46 N. These results, including both the applied load and the displacement during the tests, are summarized in Fig. 2. From the bending test results, it was found that the load-bearing strength for the structure with the core layer of 4 was more efficient than other core layers, and the bio-resin matrix provided better performance than the synthetic resin matrix across all tested core layers.

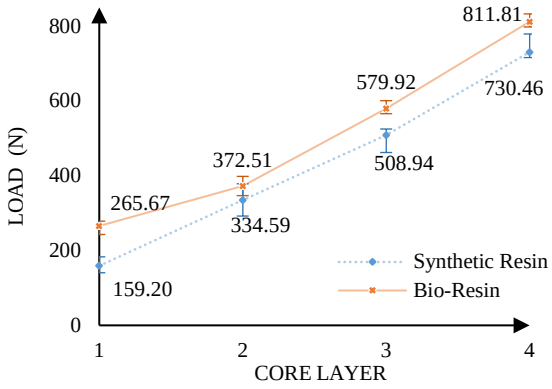

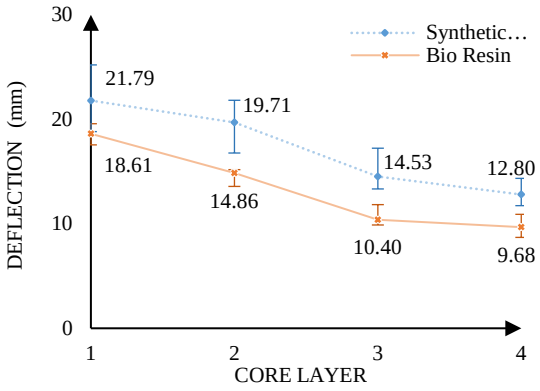

Fig.2 Load and Deflection distribution

Flexural Strength

The stress values for the specimens were determined following the equation outlined in the ASTM C 393/C 393M standard. The test results show that the maxi-mum stress in the specimens with a bio-resin matrix is generally higher than that of the synthetic resin matrix, indicating better performance in terms of load-bearing capacity and resistance to stress. The stress in the specimens with a bio-resin matrix ranged from 152.46 MPa to 177.53 MPa, with the B1C and B4C specimens showing a maximum stress of approximately 177 MPa. In contrast, the specimens with a synthetic resin matrix had lower stress values, ranging from 76.68 MPa to 133.75 MPa. This difference indicates that the bio-resin matrix not only has better load-bearing properties but also demonstrates superior stress distribution, resulting in greater overall strength and resistance to applied forces. The bio-resin matrix's enhanced ability to distribute stress, especially between the core and surface layers, makes it more effective in maintaining the structural integrity under load compared to the synthetic resin matrix. All this information is summarized in Fig. 3.

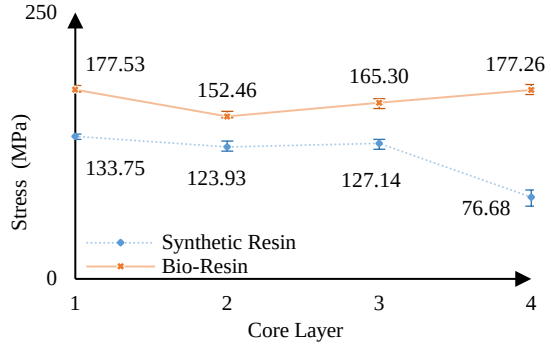

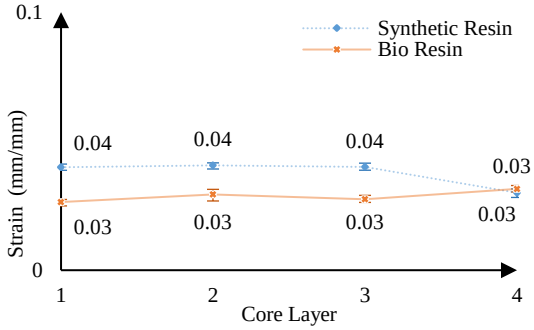

Fig.3 Facing stress and strain distribution.

Modulus Analysis

The flexural modulus, evaluated in sandwich composite structures subjected to bending tests, shows that the specimen with 1 core layers and a core thickness of 2.5 mm. provides the highest flexural modulus for specimens made with a bio-resin matrix, reaching 10.67 GPa. Meanwhile, the specimen with 1 core layers and a core thickness of 2.5 mm. provides the highest flexural modulus for specimens made with a synthetic resin matrix, reaching 9.99 MPa. When comparing the two types of matrices in Fig. 4, the bio-resin matrix demonstrates better suitability, resulting in a higher flexural modulus than the synthetic resin matrix

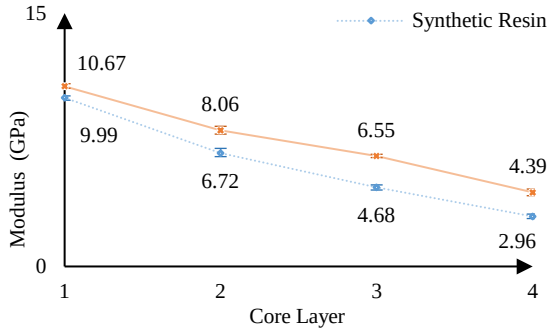

Fig.4 Modulus of flexural in different core layer.

Morphology Comparison between Bio-Epoxy Resin and Synthetic Epoxy Resin

The morphology of the sandwich structure was analyses using scanning electron microscopy (SEM) to examine areas damaged during testing and assess the compatibility between flax fibers and the two types of matrices. The analysis revealed that flax fibers formed with the bio-resin matrix exhibited damage characterized by fibers pulling away from the matrix. The breakage was clean and smooth, suggesting strong bonding between the fibers and the matrix, which facilitated clear separation of the fibers, as illustrated in Fig. 5(a).

In contrast, flax fibers formed with the synthetic

resin matrix, as shown in Fig. 5(b)., demonstrated damage where the fibers were torn and fragmented. The breakage exhibited rough, jagged edges, resembling tearing and separation from the matrix, indicating weak adhesion, which led to the fibers breaking into pieces.

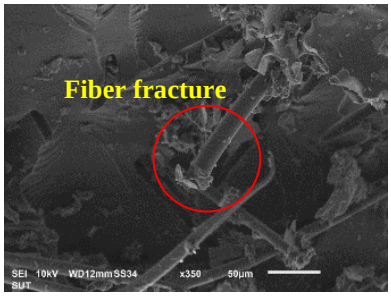

5(a)

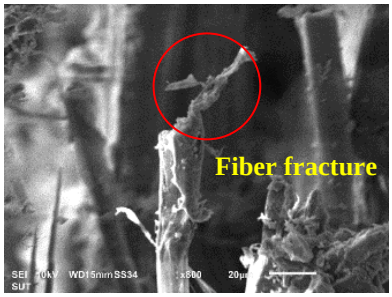

5(b)

Fig.5 SEM Fracture of fiber.

CONCLUSION

This study investigated the mechanical performance and sustainability of composite materials reinforced with bio-epoxy resin and a recycled PET-based core. The results demonstrate that increasing the number of foam core layers improves the structural strength and flexibility of the composites, with the four-layer core configuration exhibiting the highest mechanical performance. Additionally, composites using bio-resin matrices outperformed those with synthetic resin matrices in flexural tests, highlighting their potential as a sustainable alternative.

Scanning Electron Microscopy (SEM) analysis revealed strong adhesion between the resin matrix and core, with minimal signs of delamination, indicating efficient bonding and material integration. The bio-resin composites showed smoother fiber breakage, signifying enhanced compatibility between the resin and natural fibers, whereas synthetic resin composites displayed fiber fragmentation, suggesting weaker adhesion.

Overall, this research supports the feasibility of bio-resin-based composites as a sustainable and high-performance alternative to traditional petroleum-based composites. By incorporating renewable materials such as flax fibers and recycled PET cores, these composites contribute to reducing environmental impact while maintaining desirable mechanical properties. This study aligns with global efforts toward sustainable material development, promoting circular economy principles and reducing dependence on non-renewable resources. Future research should explore further optimization of bio-resin formulations and the long-term durability of these composites in real world applications.

REFERENCES

[1] Boransan, W., Kerdphol, T., Phunpeng, V.: Experimental Manufacturing Methods of Glass Fiber Composites Considering Flexural Behaviour. Spektrum Industri, 19, 87 (2021).

[2] Phunpeng, V., Boransan, W., Kerdphol, T.: Applying Glass Fiber-Reinforced Compo-sites with Microsphere Particles to UAV Components. SpringerLink, 1, 145–150 (2023).

[3] He, Q., Zhang, H., Li, J., Duan, H.: Performance evaluation of polyurethane/epoxy res-in modified asphalt as adhesive layer material for steel-UHPC composite bridge deck pavements. Construction and Building Materials, 291, 1–12 (2021).

[4] Back, J. H. et al.: Resistance to cleavage of core-shell rubber/epoxy composite foam adhesive under impact wedge-peel condition for automobile structural adhesive. Poly-mers, 11, 1–11 (2019).

[5] Back, J. H. et al.: Morphological study and mechanical property of epoxy-foam adhe-sives based on epoxy composites for automotive applications. International Journal of Adhesion and Adhesives, 87, 124–129 (2018).

[6] Koronis, G., Silva, A., Ong, M.: Comparison of Structural Performance and Environ-mental Impact of Epoxy Composites Modified by Glass and Flax Fabrics. Journal of Composites Science, 6, 1–16 (2022).

[7] Maiti, S. et al.: Sustainable Fiber-Reinforced Composites: A Review. Advanced Sus-tainable Systems, 6, 1–33 (2022).

[8] Thyavihalli Girijappa, Y. G. et al.: Natural Fibers as Sustainable and Renewable Re-source for Development of Eco-Friendly Composites: A Comprehensive Review. Fron-tiers in Materials, 6, 1–14 (2019).

[9] Faheed, N. K.: Advantages of natural fiber composites for biomedical applications: a review of recent advances. Emergent Materials, 7, 63–75 (2024).

[10] Rad, E. R., Vahabi, H., de Anda, A. R., Saeb, M. R., Thomas, S.: Bio-epoxy resins with inherent

flame retardancy. Progress in Organic Coatings, 135, 608–612 (2019).

[11] Elyse, A. B., Santosh, K. Y., Giuseppe R. P., Joseph F. S.: Recent advances in bio-based epoxy resins and bio-based epoxy curing agents. Journal of Applied Polymer Science, 133, 1–19 (2016).

[12] Yorseng, K., Rangappa, S. M., Pulikkalparambil, H., Siengchin, S., Parameswaranpillai, J. Accelerated weathering studies of kenaf/sisal fiber fabric reinforced fully biobased hybrid bioepoxy composites for semi-structural applications: Morphology, thermo-mechanical, water absorption behavior and surface hydrophobicity. Construction and Building Materials, 235, 1–14 (2020).

[13] Moudood, A. et al.: Environmental effects on the durability and the mechanical per-formance of flax fiber/bio-epoxy composites. Composites Part B, 171, 284–293 (2019).

[14] Phunpeng, V., Boransan, W., Horpibulsuk, S.: Comprehensive analysis of in-plane ten-sile characteristics of hybrid composite using finite element method. Journal of Engi-neering Research, (2024).

[15] Sun, Z., Shi, S., Guo, X., Hu, X., Chen, H.: On compressive properties of composite sandwich structures with grid reinforced honeycomb core. Composites Part B, 94, 245–252 (2016).

[16] Khan, T. et al.: A review on recent advances in sandwich structures based on polyure-thane foam cores. Polymer Composites, 41, 2355–2400 (2020).

[17] Gürgen, S.: An investigation on composite laminates including shear thickening fluid under stab condition. Journal of Composite Materials, 53, 1111–1122 (2019).

Copyright © Int. J. of GEOMATE All rights reserved, including making copies, unless permission is obtained from the copyright proprietors.

15th Int. Conf. on Geotechnique, Construction Materials & Environment, Kyoto, Japan, 11-13 November 2025, ISBN 978-4-909106124 C3051

EVALUATION OF THE FUNCTIONALITY OF ALGAL BED CREATION STRUCTURES UTILIZING POROUS MATERIALS

Masashi Miyagawa[1], and Yoshihiro Suenaga[2]

[1] Graduate School of Science and Creative Emergence, Kagawa University, Japan;
[2] Faculty of Engineering and Design, Kagawa University, Japan

ABSTRACT

The Seto Inland Sea, known for its highest biological productivity in the world, has experienced a substantial decline in critical coastal vegetated ecosystems such as tidal flats and algal beds. This degradation primarily resulted from extensive land reclamation projects during Japan's period of rapid economic growth. In recent years, the loss of algal beds has been further exacerbated by marine environmental changes driven by global climate change, including rising sea temperatures, contributing to the spread of isoyake (barren grounds). Simultaneously, long-standing efforts to reduce terrestrial nutrient inputs—particularly nitrogen and phosphorus—as eutrophication countermeasures have unintentionally accelerated oligotrophication in coastal waters, further inhibiting the regeneration of algal beds. To address this issue, we developed and deployed artificial reef structures made from porous materials, specifically designed to promote the establishment of macroalgal communities. Long-term field monitoring has demonstrated that these structures facilitate not only algal colonization but also the settlement of epifaunal organisms, thereby contributing to the restoration of high-biodiversity algal bed ecosystems. This study presents a quantitative evaluation of the annual variation in the biomass of attached organisms on these structures, confirming their high ecological functionality and effectiveness in supporting algal bed regeneration.

Keywords: Seaweed bed, Seto inland sea, Coastal ecosystem, Porous material

INTRODUCTION

In the context of global climate change mitigation, increasing attention has been directed toward blue carbon, which is the carbon sequestration capacity of marine ecosystems [1,2]. Compared to terrestrial green carbon ecosystems, blue carbon ecosystems exhibit a 3- to 10-fold higher CO_2 absorption capacity per unit area [3], along with the potential for long-term carbon storage [4]. Despite their significance, these ecosystems are increasingly threatened by anthropogenic development and the impacts of climate change [5]. In particular, the Seto Inland Sea has experienced pronounced degradation of its macroalgal beds [6,7].

This study reports on restoration efforts targeting macroalgal beds through the deployment of artificial reef structures—hereinafter referred to as macroalgal bed creation reefs—developed at Kagawa University [8]. This study evaluates the effectiveness of the porous materials used in these structures as substrates for promoting macroalgal growth and the colonization of epibiotic organisms. Although the biocompatibility of porous materials has been previously documented [9], this research presents a long-term evaluation of their ecological functionality under field conditions.

RESEARCH SIGNIFICANCE

This study quantitatively demonstrates that the newly developed seaweed bed creation reefs utilizing porous materials function as a source of food organisms. This approach enables the visualization and evaluation of the food supply function, which has been difficult to achieve with conventional seaweed bed restoration techniques, thereby contributing to a quantitative understanding of the ecosystem services provided by seaweed beds. The findings offer new guidance for the advancement of seaweed bed restoration technologies and the multifunctional management of coastal ecosystems.

Furthermore, the implementation of such multifunctional artificial reefs may play a vital role in enhancing coastal resilience by simultaneously supporting biodiversity, improving fishery productivity, and contributing to carbon sequestration. As coastal areas worldwide continue to face increasing anthropogenic pressures and climate-induced stressors, integrative restoration approaches like this hold promise for scalable and sustainable ecosystem management solutions.

MATERIALS AND METHODS

Experimental Sites

Field experiments were conducted at two coastal sites near Kamano Fishing Port and Shinoo Fishing Port, both situated in Ajicho, Takamatsu City, Kagawa Prefecture, Japan (Figure 1).

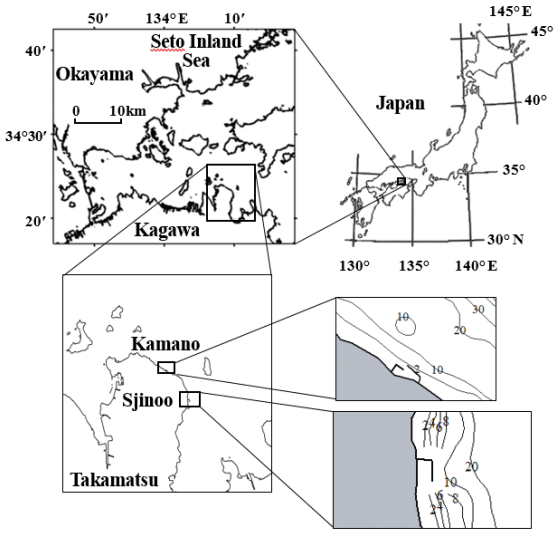

Figure 1. Locations of the Survey Sites

A total of 72 artificial seaweed bed reefs were deployed: 25 units in the Kamano area and 47 units in the Shinoo area (Figure 2).

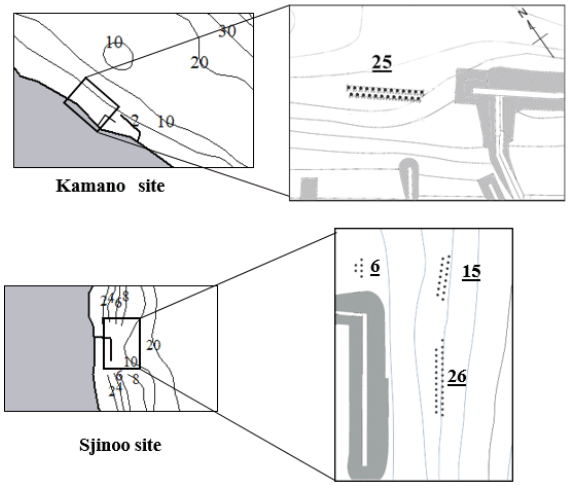

Figure 2. Locations of the Survey Sites and Reef Deployment Details
Numerical values indicate water depth (m), while underlined numbers denote the number of artificial seaweed bed reef units.

Artificial Seaweed Bed Reefs and Porous Structures

The artificial reef structures feature a two-tiered design: the lower tier functions as a stable foundation and helps to regulate local water flow, while the upper tier, referred to as the "roof," serves as a substrate for seaweed attachment and growth. The roof section is perforated with multiple holes to facilitate the transplantation of parent algae and is designed to accommodate the attachment and detachment of modular protruding components manufactured separately (Figure 3).

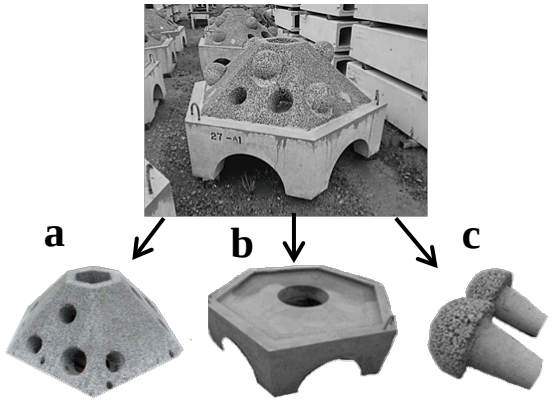

Figure 3. Structural Components of the Artificial Seaweed Bed Reef

(a) Porous roof section
(b) Concrete foundation section
(c) Porous protruding component

The roof and protruding components are constructed from porous materials, engineered to serve as a favorable substrate for the attachment of seaweeds and other marine organisms. Once deployed, the sloped roof design interacts with tidal currents to reduce silt accumulation on its surface. Additionally, the protruding components generate complex vortices that promote the settlement of seaweed spores and zoospores transported by the flow (Figure 4).

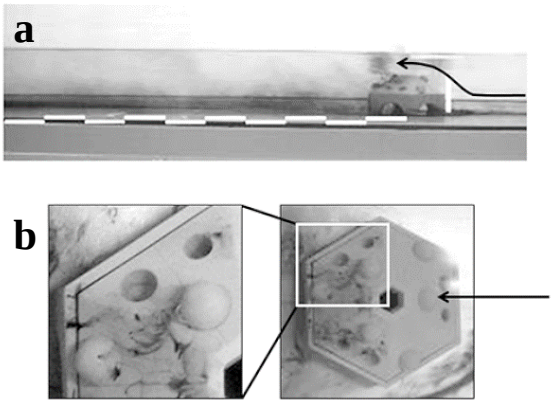

Figure 4. Flow Conditions Surrounding the Structure
(a) Side view; (b) Top view. Arrows represent the direction of water movement.

The porous substrate exhibits a void ratio of approximately 20–30%, promoting the production of prey organisms that attract fish and other marine life [10], and thus serving as a potential feeding ground for higher trophic-level organisms (Figure 5). The structure is named “Marine Mash” due to the mushroom-like appearance of its protruding components.

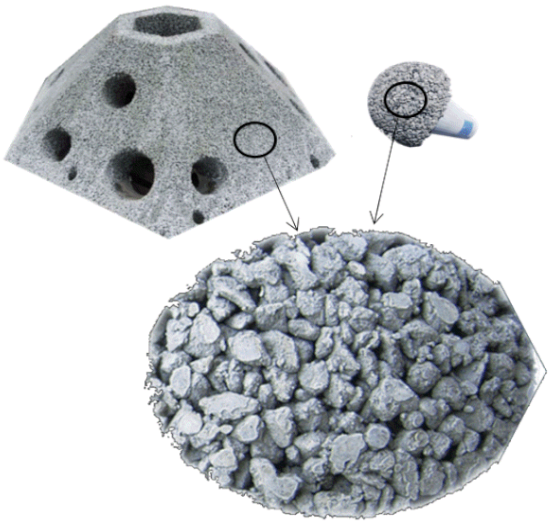

Figure 5. Porous Substrate Structure

Blocks for Sessile Organism Recruitment Experiments

Multiple sampling blocks (experimental units) were deployed on the roof section of artificial seaweed reef beds. These blocks measured either 18×18×6 cm or 30×30×6 cm (length × width × height). All attached organisms retained on a 1-mm mesh sieve were identified, and both the number of individuals and the biomass for each species were quantified.

As control units, three material types were utilized: natural stone reefs (20×20×20 cm), concrete plates (30×30×6 cm), and steel plates (30×30×2 cm). Organisms adhering to the surfaces of these control materials were measured similarly. Results were converted to values per unit volume (m
3) for annual comparisons across different substrate types.

Among the collected sessile organisms, three phyla—Mollusca, Annelida, and Arthropoda—were selected as preferred prey organisms due to their potential as food sources for fish and other marine animals. Statistical analyses were performed to examine differences in their occurrence.

Assessment of Algal Growth Conditions

Algae within a defined area (50 × 50 cm) on the artificial seaweed bed reef were harvested from their attachment base, and their dry weight was measured to estimate the standing crop per unit area (m^2). Sampling was conducted in March, corresponding to the peak period of algal growth. For comparison, algal biomass was also measured on natural stone reefs located adjacent to the artificial structures.

Assessment of Epiphytic Organism Occurrence

Epiphytic organisms residing on the surface of algal thalli attached to the artificial seaweed bed reefs were collected concurrently with algal biomass sampling. Their wet weight (g) was quantified per unit wet weight (kg) of algal thalli to evaluate the relative abundance of epiphytic organisms.

RESULTS

Occurrence of Sessile Organisms on Porous Materials

Figure 6 presents the annual variation in biomass (kg/m^3) of preferred prey organisms among the sessile communities that developed on porous substrates, in comparison with those on other materials such as stone, concrete, and steel.

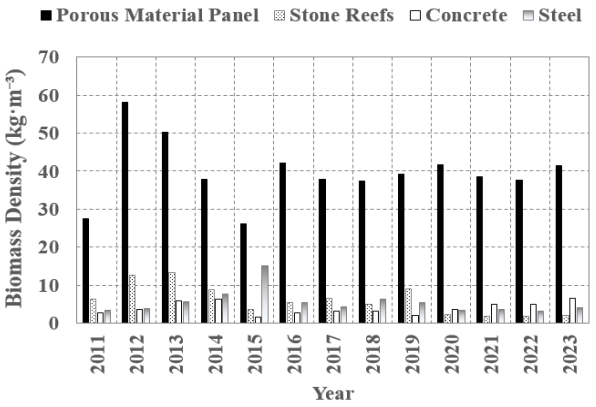

Figure 6. Temporal Changes in Biomass of Preferred Prey Organisms on Porous Artificial Seaweed Reef Substrate

Algal Growth Conditions

Figure 7 illustrates the biomass per unit area of algae attached to the porous substrate of the Marine Mash artificial seaweed reef (specifically, its roof and protruding components) and to other materials (natural stone).

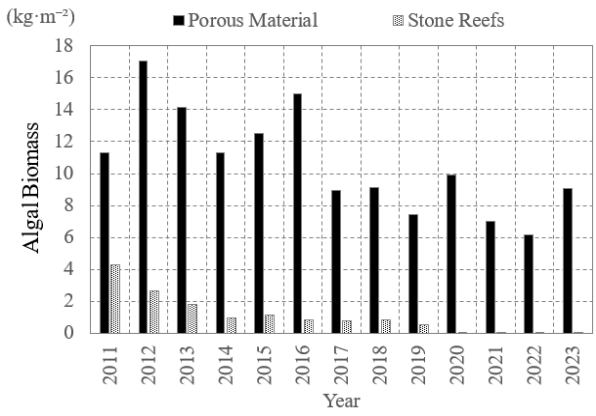

Figure 7. Temporal Trends in Algal Biomass on Artificial Seaweed Reef Substrates

Epiphytic Fauna Development

Figure 8 illustrates the annual variation in the biomass ($g \cdot kg^{-1}$) of epiphytic organisms per unit weight of algae attached to the Marine Mash artificial seaweed reef.

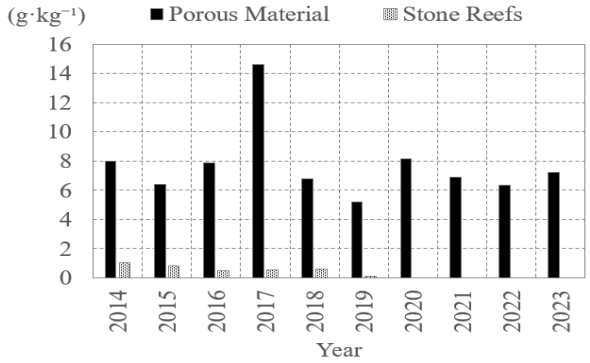

Figure 8. Temporal Trends in Biomass of Epiphytic Organisms on Attached Algae

DISCUSSION

Occurrence of Preferred Prey Organisms on Porous Substrates

The porous substrate exhibited significantly higher biomass of preferred prey organisms compared to other materials. An ANOVA conducted to assess differences in the mean biomass of preferred prey organisms between the experimental group (porous substrate) and the three control groups revealed a highly significant effect ($F=161$, $P<0.01$). Post hoc tests further confirmed significant differences between the porous substrate and each of the control groups ($P<0.01$). These findings strongly indicate that the porous substrate supports a substantially greater biomass of preferred prey organisms than commonly used reef materials such as natural stone, concrete, and steel.

Algal Growth Assessment

A paired t-test comparing algal biomass between the experimental reef structure "Marine Mash" and the control reef (stone-based) revealed a statistically significant difference ($t(12) = 12.475$, $P < 0.01$). The exceptionally small p-value ($P = 3.13 \times 10^{-6}$)) indicates that this observed difference was highly unlikely to have occurred by chance. These findings strongly suggest that the porous substrate incorporated into the Marine Mash reef structure effectively promotes algal growth.

Epiphytic Fauna on Algal Surfaces

A paired t-test comparing the biomass of epiphytic organisms on algae between the experimental reef structure 'Marine Mash' and the control reef (stone-based) revealed a statistically significant difference ($t(9) = 9.3$, $P < 0.01$), and the exceptionally small p-value ($P = 6.51 \times 10^{-6}$) indicates this difference was highly unlikely to have occurred by chance, strongly suggesting that the porous substrate incorporated into the Marine Mash reef structure effectively promotes the development of epiphytic fauna on algal surfaces.

CONCLUSIONS

In this study, we assessed the bio-attractive properties of a porous substrate incorporated into the seaweed bed restoration reef, Marine Mash, by examining the occurrence of preferred prey organisms, macroalgae, and epiphytic organisms as ecological indicators.

1. The results revealed that the porous substrate exhibited a significantly greater attraction of preferred prey organisms compared to conventional reef materials such as stone, concrete, and steel (ANOVA, $F = 161$, $P < 0.01$). These findings indicate that the porous substrate has strong potential as a material for improving the feeding environment for fish.
2. A statistically significant difference in algal biomass was observed between the Marine Mash reef and conventional stone reefs ($t(12) = 12.475$, $p = 3.13 \times 10^{-8}$). The extremely low p-value provides strong evidence that the porous substrate markedly enhances algal attachment and growth.
3. A significant difference in the abundance of organisms attached to the surfaces and interstices of macroalgal thalli was also detected between the experimental and control sites ($t(9) = 9.3$, $p = 6.51 \times 10^{-6}$), indicating that the porous substrate contributes to increased biodiversity and biomass of algae-associated communities.

These results provide strong evidence for the high efficacy of seaweed bed restoration techniques employing porous substrates in enhancing feeding habitats and promoting ecological diversity. The findings underscore the potential applicability and scalability of this method as a viable technology for coastal ecosystem restoration. In addition, the restoration of blue carbon ecosystems and the enhancement of carbon sequestration capacity through seaweed bed establishment are identified as key areas for future research, with significant implications for global environmental sustainability.

Future Challenges and Potential Applications

This study demonstrated that seaweed bed restoration reefs incorporating porous substrates significantly enhance the presence of preferred prey organisms, macroalgae, and epiphytic organisms. Moving forward, the following challenges and potential applications should be addressed to advance the development of this restoration approach.

First, it is necessary to verify the long-term effectiveness of the porous substrate through extended monitoring. This study's evaluations were conducted over a limited period, and the effects of biological community succession and physical degradation over time remain unclear. Additionally, to clarify the influence of seasonal variations and regional differences on the bio-attraction effect, it is essential to assess reproducibility under diverse environmental conditions.

Another challenge lies in advancing functional evaluation. For instance, assessing the extent to which biotic communities induced by porous substrates contribute to the restoration of fishery resources and carbon sequestration requires system-level analysis using ecosystem models that incorporate energy flow and material cycling.

In terms of potential applications, integrating this approach with **coastal ecosystem restoration** and **blue carbon policies** is of particular importance. Notably, this aligns well with international targets like **United Nations Sustainable Development Goals (SDGs) 14 'Life Below Water' and 13 'Climate Action'** [10], and holds promise for implementation as a nature-based solution [11–12].

The Intergovernmental Panel on Climate Change (IPCC) has recognized the carbon sequestration capacity of blue carbon ecosystems—such as seaweed beds, seagrass meadows, and mangroves—as a Nature-based Solution (NbS) contributing to greenhouse gas emission reduction [13]. Accordingly, this study's findings hold international significance as a strategic approach that simultaneously promotes coastal ecosystem restoration and climate change mitigation.

The fabrication of artificial reef materials from regional resources, including industrial by-products, demonstrates high compatibility with the local production for local consumption paradigm. This synergistic approach is anticipated to both lessen environmental burdens and engender favorable regional economic multipliers. Future efforts must encompass a thorough assessment of the scientific and societal importance of these initiatives, alongside the systematic accretion of knowledge pertinent to domestic and international policy development and environmental assessments. Additionally, actively investigating opportunities for engagement within international frameworks is a key consideration.

ACKNOWLEDGMENTS

This research has been continuously conducted with the generous cooperation of the Aji Fisheries Cooperative Association, to whom we express our sincere gratitude, and we also extend our heartfelt thanks to Professor Emeritus Tsuneo Honjo, Professor Emeritus Kuninao Tada, and Professor Kazuhiko Ichimi for their valuable advice on the environmental issues of the Seto Inland Sea; this study was supported by JST Japan, Grant Number JPMJPF2306.

REFERENCES

[1] Fisheries Agency, Recommendations for strategic blue carbon initiatives in fishing port and fishing ground development, Ministry of Agriculture, Forestry and Fisheries of Japan, 2023. [In Japanese]. URL:https://www.jfa.maff.go.jp/j/seibi/attach/pdf/R5_gyoko_happyo_kai-22.pdf

[2] McLeod E., Chmura G.L., Bouillon S., Salm R., Björk M., Duarte C.M., Lovelock C.E., Schlesinger W.H., and Silliman B.R., A blueprint for blue carbon: toward an improved understanding of the role of vegetated coastal habitats in sequestering CO_2, Front. Ecol. Environ., Vol. 9, No. 10, 2011, pp.552–560.

[3] Kuwae T., Yoshida G., Hori M., Watanabe K., Tanaya T., Okada T., Umezawa Y. and Sasaki J., Nationwide Estimate Of The Annual Uptake Of Atmospheric Carbon Dioxide By Shallow Coastal Ecosystems In Japan, J. JSCE, Ser. B2 (Coastal Engineering), Vol. 75, No. 1, 2020, pp.10–20.

[4] Watanabe H., Changes in the distribution of seaweed beds in Japan, Bull. Mar. Res. Inst., Vol. 27, 2022, pp.59–63. [In Japanese]

[5] Yamagishi Y., Changes in the seaweed flora in the central Seto Inland Sea, Report of the Research Institute of Marine Bioresoureces, Fukuyama Univ., Vol. 34, 2024, pp.13–15. [In Japanese]

[6] Furuya M., Overview of international trends in blue carbon, Journal of the JIME, Vol. 52, No. 6, 2017, pp.705–708. [In Japanese]

[7] Kameyama T., Development of seaweed bed creation structures and marine environmental improvement technologies using porous materials, Doctoral dissertation, Kagawa University, 2014., p79. [In Japanese]

[8] Takafumi Yamamoto, Yoshihiro Suenaga, Tetsuya Tamaki, Shinichiro Okazaki, Hidenori Yoshida , 2022 , Technology For Improving Octopus Resource Productivity Using Artificial Reefs And AI , The GEOMATE International Society, Proceedings of 8th International Conference on Structure, Engineering and Environment, 8, pp344-349.

[9] Miyagawa M., Kameyama T., Fujiwara M., Yasuoka K., Matsuuchi Y. and Suenaga Y., Development of shelters for the release of juvenile reef fish, J. JSCE, Ser. B3 (Ocean Development), Vol. 68, No. 2, 2012, pp. l_1221–l_1226. [In Japanese]

[10] United Nations General Assembly, Transforming our world: the 2030 Agenda for

Sustainable Development, Resolution A/RES/70/1, 2015. https://www.refworld.org/docid/57b6e3e44.html

[11] International Union for Conservation of Nature (IUCN), Defining Nature-based Solutions, Resolution WCC-2016-Res-069-EN, 2016. https://portals.iucn.org/library/sites/library/files/resrecfiles/WCC_2016_RES_069_EN.pdf

[12] Cohen-Shacham E., Walters G., Janzen C., and Maginnis S. (eds.), Nature-based Solutions to address global societal challenges, IUCN, Gland, Switzerland, 2016, xiii + 97pp. DOI: http://dx.doi.org/10.2305/IUCN.CH.2016.13.en

[13] IPCC, Summary for Policymakers. In: Climate Change 2021: The Physical Science Basis. Contribution of Working Group I to the Sixth Assessment Report of the Intergovernmental Panel on Climate Change [Masson-Delmotte V., Zhai P., Pirani A., et al. (eds.)], Cambridge University Press, Cambridge, United Kingdom and New York, NY, USA, 2021, pp.3–32. DOI: 10.1017/9781009157896.001

Copyright © Int. J. of GEOMATE All rights reserved, including making copies, unless permission is obtained from the copyright proprietors.

15th Int. Conf. on Geotechnique, Construction Materials & Environment, Kyoto, Japan, 11-13 November 2025, ISBN 978-4-909106124 C3051

SOLVING OPTIMAL RESERVOIR OPERATIONS PROBLEMS WITH A GENETIC ALGORITHM AND KEPLER OPTIMIZATION ALGORITHM

Teerapat Moonlaong[1], Rittayut Gonthong[2], Nonthaphong Phonphuak[3], Anongrit Kangrang[4] and Anujit Phumiphan[5]

[1,2,5] School of Engineering, University of Phayao, Phayao, Thailand; [3] Faculty of Engineering, Rajabhat Mahasarakham University, Mahasarakham, Thailand; [4] Faculty of Engineering, Mahasarakham University, Mahasarakham, Thailand.

ABSTRACT

Reservoir rule curves are essential for long-term operation and flood control. This study proposes an alternative approach using GA and KOA integrated with a simulation model to optimize flood control rule curves. The approach was applied to the NOR in northeastern Thailand, using two objective functions: minimizing average excess water and minimizing frequency of excess water. The efficiency of the optimized rule curves was evaluated using historical, 1,000 synthetic, and projected inflow data, focusing on water shortage and excess conditions in terms of frequency, magnitude, and duration. Results indicate that the proposed GA and KOA models outperformed existing rule curves in reducing excess water under both current and future scenarios, enhancing long-term flood management.

Keywords: Water Infrastructures, Non-Construction Reservoir Management, Rule Curves, Genetic algorithm, Kepler Optimization Algorithm.

INTRODUCTION

Many countries face challenges in managing water resources, which are essential for human well-being. These challenges are intensified by climate and land use changes [1]. Effective management requires both structural measures and non-structural tools within a suitable organizational framework [2].

Reservoir operation rule curves (RORC) offer a cost-effective, non-structural approach to optimizing reservoir management by balancing multiple, often conflicting objectives. RORC define upper and lower bounds for monthly water storage to stabilize reservoir levels, mitigate flood risks, and prevent shortages. Effective implementation ensures sufficient water supply under normal conditions, minimizes deficits during droughts, and reduces downstream impacts during floods [3-4]. However, their performance may decline over time or with changing data, necessitating periodic optimization and adjustment [5-7].

Several optimization techniques, such as dynamic programming and simulated annealing, have been applied to optimize RORC; however, they often suffer from limitations like sensitivity to initial conditions and convergence to local optima. This study explores two alternative methods—Genetic Algorithm (GA) and Kepler Optimization Algorithm (KOA)—known for their robustness in solving complex, multi-objective problems in water resource management. GA is a widely used population-based metaheuristic inspired by natural selection. It utilizes selection, crossover, and mutation operators to evolve solutions across generations, offering strong global search capabilities without requiring gradient information. Conversely, KOA is a recent physics-based algorithm grounded in Kepler's laws of planetary motion. It treats solutions as orbiting bodies influenced by gravitational pull toward the best-known solution, enabling efficient exploration and fast convergence while avoiding local optima.

This article advocates for an alternative approach integrating GA and KOA with a reservoir simulation model (RSM) to optimize flood RORC in flood control regions. The study applied the proposed models to determine the optimal flood RORC for the Nam-Oon Reservoir (NOR) in Northeastern Thailand. The search methods were guided by two objective functions: minimizing average excess water and reducing the frequency of excess water.

RESEARCH SIGNIFICANCE

This study integrates the GA and KOA into reservoir rule curve development, presenting an innovative approach to overcome limitations of conventional methods. By employing adaptive optimization for excess water management, the research enhances long-term flood mitigation. Results indicate improved reservoir performance under current and projected inflow conditions, offering a scalable and transferable framework for flood-prone regions. This approach advances reservoir operation by linking simulation models with robust optimization techniques.

METHODOLOGY

Research Area

The study was conducted in 2021–2022 at the Nam-Oon Reservoir (NOR), located in Sakon Nakhon province within Thailand's Songkham Basin (Fig. 1). NOR supports an irrigation area of 32,480 hectares, with a storage capacity of 520 million cubic meters (MCM) and an average annual inflow of 404.835 MCM. Inflow data were collected over a 28-year period (1994–2021).

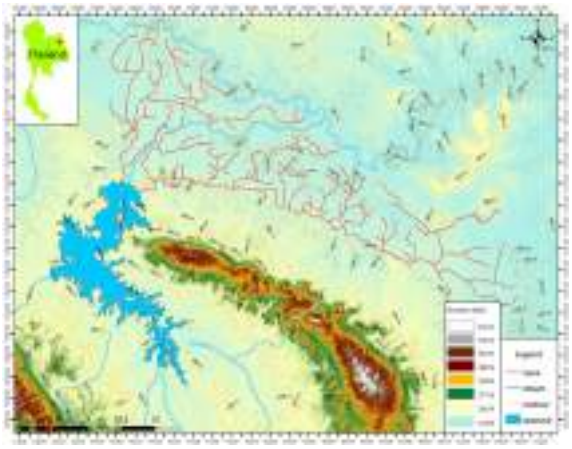

Fig. 1 The geographic location of the NOR.

Model for the Simulation of Reservoir Operation

The reservoir system was modeled using the water balance principle, incorporating hydrological data, reservoir characteristics, water demand, and related information. Available water was calculated using Equation (1), based on this principle. Monthly water release was assessed considering available resources, release requirements, operational rules, and the defined RORC (Fig. 2).

$$W_\tau = S_{\tau-1} + I_\tau + P_\tau - E_\tau \quad (1)$$

The equation delineates the computation of the water resources accessible during the month τ, while considering various influencing factors. W_τ signifies the water availability for the month τ, whereas $S_{\tau-1}$ indicates the volume of water retained at the termination of the month $\tau - 1$, which is initially established at the maximum capacity of the reservoir. The computation is derived from the influx into the reservoir (I_τ), the volume of precipitation recorded during the month (P_τ), and the average evaporation losses incurred throughout the month (E_τ).

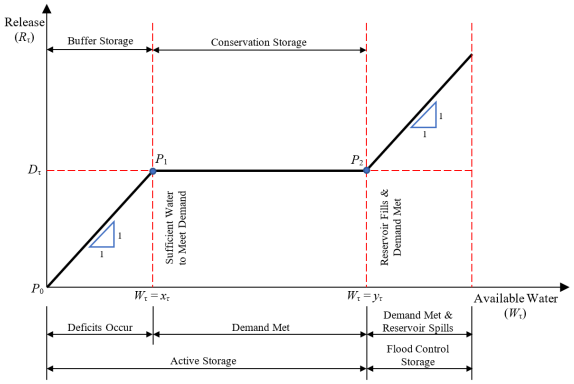

Fig. 2 Standard water allocation criteria

Subsequently, the monthly water release rate (R_τ) was determined to calculate water scarcity and excess water levels. These levels are represented by the average yearly excess water amount (the initial objective function in the search procedure) and the yearly frequency of excess water (the second objective function utilized during the search procedure), as shown in Equations (2) and (4), respectively. In these equations, x_τ refers to the lower RORC during month τ while y_τ denotes the upper RORC during month τ .

$$\text{Min } Avg_i = \left(\frac{1}{n} \sum_{v=1}^{n} Sp_v \right) \quad (2)$$

$$\text{if } R_\tau > D_\tau; \text{ Then } Sp_v = \sum_{v=1}^{n} (R_\tau - D_\tau) \quad (3)$$

$$\text{Min } Fre_i = \left(\frac{1}{n} \sum_{v=1}^{n} Sf_v \right) \quad (4)$$

In this equation, Avg_i represents the average amount of excess water per year during iteration *i*, Sp_v denotes the excess water during year *v*, where releases exceed the target demand, Fre_i is the frequency of excess water, Sf_v indicates the number of annual floods, which is the year when releases exceed the target demand, D_τ represents the monthly goal demand from the reservoir, which is determined by utilizing data from previous studies and calculating the water demand in the downstream area. The variable *i* represents the iteration number.

Genetic Algorithm (GA)

The GA, introduced by John Holland in the 1970s [8], is a population-based optimization method inspired by natural selection. It iteratively improves

candidate solutions (chromosomes) through selection, crossover, and mutation. The process begins by defining the objective function, constraints, and bounds, followed by the initialization of a random population. Each chromosome is evaluated for fitness, and the fittest individuals are selected to produce offspring via crossover and mutation. The new population replaces the previous one, and the cycle continues until convergence or stopping criteria are met. The best-performing chromosome is then selected as the optimal solution.

Kepler Optimization Algorithm (KOA)

The KOA is a physics-based metaheuristic inspired by Kepler's laws of planetary motion, used for solving complex optimization problems. It treats candidate solutions as orbiting bodies influenced by gravitational forces, with their positions updated according to Keplerian dynamics to converge toward the optimal solution. The process begins by defining the objective function, constraints, and search space, followed by initializing a population of candidate solutions with associated orbital parameters. Each solution is evaluated for fitness, and the best-performing one serves as the central gravitational focus. Positions and velocities are updated iteratively, with boundary checks and fitness evaluations performed at each step. This process continues until convergence or stopping criteria are met, and the best solution is selected as the optimal result.

GA Incorporating RSM

The GA–RSM integration begins by initializing reservoir parameters, including storage capacity, water levels, and monthly demands. A population of chromosomes, each with 24 decision variables (12 upper and 12 lower RORCs), is generated. The RSM simulates monthly releases, and objective functions—average annual excess water and its frequency—are evaluated. Genetic operations (selection, crossover, mutation) produce new generations, and the process repeats until convergence or a predefined limit is reached. The best-performing chromosome is selected as the optimal RORC. Fig. 3 illustrates the GA–RSM optimization framework.

KOA Incorporating RSM

The KOA–RSM integration begins by initializing reservoir parameters such as capacity, water levels,

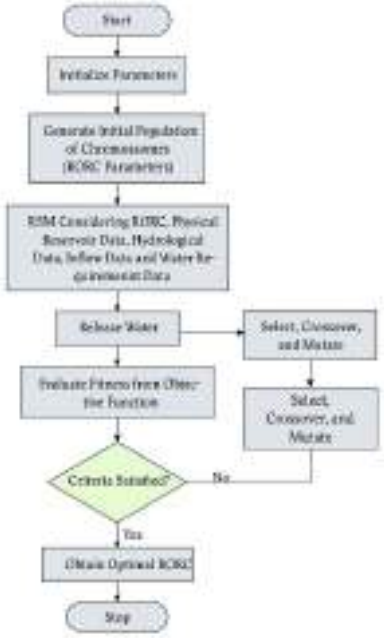

Fig. 3 GA incorporating RSM to search for optimal RORC.

and monthly demand. A population of agents, each representing 24 decision variables (monthly upper and lower RORCs), is generated. The RSM simulates monthly releases based on these RORCs, and performance is evaluated using objective functions that minimize average excess volume and frequency. Fitness scores guide updates of agent positions and velocities via Keplerian dynamics toward the best-known solution. This process iterates until convergence or a defined stopping criterion is reached. The optimal RORC is selected from the best-performing agent. Fig. 4 illustrates the KOA–RSM framework.

Assessment of the Obtained RORC

The RORCs were evaluated using GA, KOA, and RSM under various inflow scenarios. Historical data over 28 years supported the RSM, while 1,000 synthetic inflow events were generated using the HEC-4 model. HEC-4 applies statistical methods to simulate inflows from single or multiple runoff stations, estimating missing data through inter-station correlations. Synthetic inflows are based on statistical parameters—mean, standard deviation, and skewness—with a 1% adjustment to the mean. The evaluation assessed the frequency, magnitude, and duration of water surplus and shortage conditions [9].

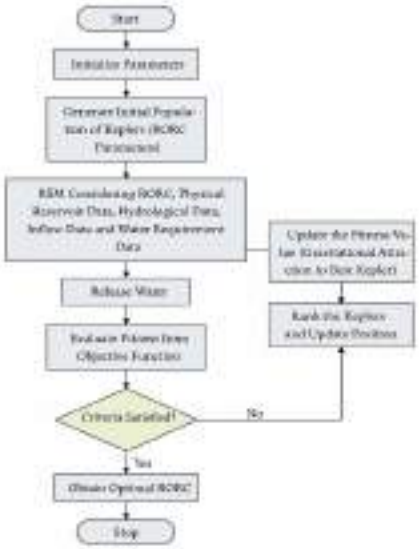

Fig. 4 KOA incorporating RSM to search for optimal RORC.

RESULTS

Optimal RORCs

Fig. 5 presents the optimal RORCs from the GA and KOA models, optimized to minimize annual excess water using historical and projected inflow data. The resulting curves (GA-Avg., KOA-Avg.) follow seasonal patterns similar to the existing RORC (RC1-Existing), with higher lower bounds from March to July and higher upper bounds from June to September, supporting increased storage. In contrast, KOA-Avg. upper RORCs are lower during October and November, enabling greater releases for improved flood control.

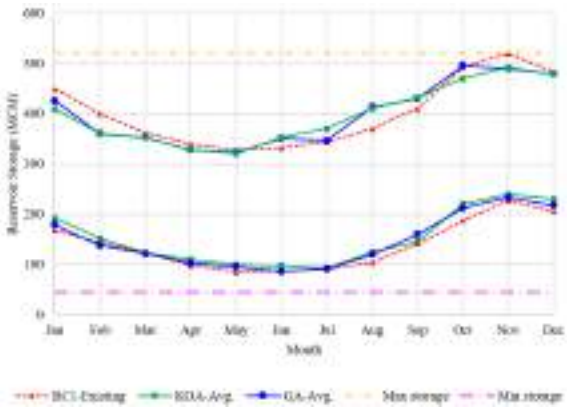

Fig. 5. Optimal RORCs for the NOR based on minimizing average excess water.

Fig. 6 presents the optimized RORCs for the NOR, derived by minimizing the frequency of excess water using historical inflow data. The optimized curves (GA-Fre., KOA-Fre.) show patterns similar to the existing RORCs. Notably, the lower RORCs from GA-Fre. and KOA-Fre. exceed the current values from January to June, while the upper RORCs are lower than the existing curve in July.

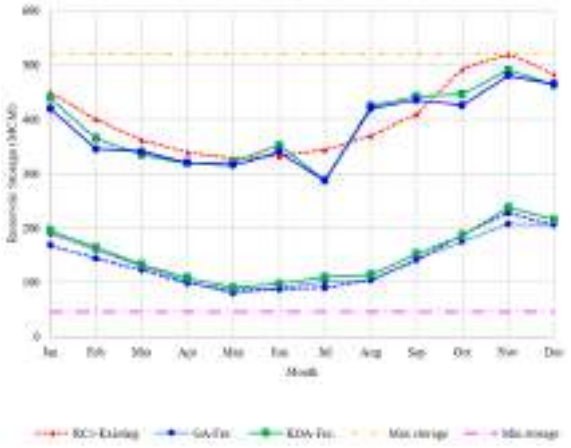

Fig. 6. Optimal RORCs for the NOR based on minimizing excess water frequency.

Efficiency of the Obtained RORCs

Table 1 summarizes the performance of optimized RORCs evaluated using 28 years of historical inflow data for the NOR. The RORC from the ABC-CA model (RC5-Avr_ABC-CA), optimized for average excess water, demonstrated the best results—showing the lowest water scarcity (0.464 times/year, 19.926 MCM/year, 1.684 years) and excess water (0.627 times/year, 85.641 MCM/year, 2.00 years). Overall, the optimized RORCs outperformed the existing rule curves in reducing both water scarcity and excess under historical conditions.

Table 2 presents the results from 1,000 synthetic inflow scenarios based on historical data for the NOR. The KOA-optimized RORCs (KOA-Fre.), aimed at minimizing average excess water, achieved the lowest levels of water scarcity (16.271 ± 7.224 MCM/year) and excess water (66.221 ± 17.001 MCM/year). In contrast, the existing RORCs showed the highest values, indicating lower effectiveness under simulated conditions.

Table 1 Excess water and water scarcity in the NOR based on 28 years of historical inflow data.

Situation	RORC	Frequency (times/year)	Volume (MCM)		Time period (year)	
			Average	Maximum	Average	Maximum
Water scarcity	RC1- Existing	0.962	45.884	154.000	13.500	14.000
	RC2-Avr_FA	0.584	21.378	130.000	2.500	3.000
	GA-Avg.	0.464	19.926	126.000	1.684	3.000
	RC4-Fre_FA	0.782	38.411	142.000	6.000	8.000
	KOA-Avg.	0.994	38.407	140.000	10.500	12.000
Excess water	RC1- Existing	0.754	113.402	476.959	4.000	6.000
	RC2-Avr_FA	0.794	89.226	479.080	3.000	5.000
	GA-Avg.	0.797	86.844	465.867	3.000	4.000
	RC4-Fre_FA	0.704	89.381	465.083	2.000	4.000
	KOA-Avg.	0.627	85.641	436.372	2.000	3.000

Table 2 Excess water and water scarcity in the NOR based on 1,000 synthetic inflow scenarios.

Situation	RORC		Frequency (times/year)	Volume (MCM)		Time period (year)	
				Average	Maximum	Average	Maximum
Water scarcity	RC1- Existing	μ	0.971	42.445	131.774	17.442	22.637
		σ	0.032	6.831	36.226	6.804	4.937
	GA-Avg.	μ	0.673	18.014	110.824	2.653	5.292
		σ	0.109	8.224	29.344	0.968	2.447
	KOA-Avg.	μ	0.473	16.271	108.097	2.307	4.065
		σ	0.106	7.224	27.744	0.747	2.044
	GA-Fre.	μ	0.811	33.227	120.224	6.242	10.388
		σ	0.108	7.723	34.220	3.584	4.335
	KOA-Fre.	μ	0.989	33.407	119.379	15.124	18.066
		σ	0.051	6.837	30.055	7.225	5.097
Excess water	RC1- Existing	μ	0.699	91.994	358.622	3.009	7.717
		σ	0.107	20.931	77.022	1.554	2.249
	GA-Avg.	μ	0.638	68.734	328.771	2.557	5.334
		σ	0.155	18.984	81.229	0.899	2.227
	KOA-Avg.	μ	0.557	66.221	324.073	2.458	5.365
		σ	0.104	17.001	80.177	0.975	2.005
	GA-Fre.	μ	0.687	80.812	350.401	2.844	6.113
		σ	0.110	19.003	79.773	1.098	2.502
	KOA-Fre.	μ	0.644	79.991	345.374	3.009	6.302
		σ	0.105	20.224	77.780	1.224	2.708

DISCUSSION

The newly derived RORCs and the existing RORCs (Figs. 6 and 7) show similar patterns, influenced by seasonal inflow and consistent hydrological conditions, consistent with previous studies [10]. The updated lower RORCs are higher than the current ones during the dry season, promoting water conservation by reducing discharge during low inflow periods. In contrast, the new upper RORCs exceed the existing curves from June to September, supporting higher storage and

reducing unnecessary releases. Conversely, from October to November, the new upper RORCs are lower, allowing increased releases to create storage buffer capacity, thereby enhancing flood management potential.

The results in Tables 1 and 2 show that the ABC-CA RORCs, optimized using historical inflow data, yielded the lowest occurrences of water scarcity and excess compared to other RORCs. This outcome aligns with previous studies [11,12], where historical data was similarly utilized in the optimization process. A comparative analysis between the proposed GA and KOA approaches and other optimization methods is essential to further validate their effectiveness.

CONCLUSIONS

This study applied the GAA and KOA, integrated with an RSM, to identify optimal RORCs using two objective functions. The resulting RORCs exhibited similar patterns due to seasonal inflow and consistent search conditions, with notable differences during the rainy season. RORCs optimized to minimize average excess water using historical inflow data proved more effective in reducing excess water events under both historical and synthetic inflow scenarios compared to other RORCs.

This study demonstrates the application of GA and KOA, integrated with a simulation model, to optimize flood control RORCs. The optimized RORCs outperformed existing curves in mitigating flood risks. These findings provide a useful reference for researchers developing flood control strategies for reservoirs in flood-prone areas.

ACKNOWLEDGMENTS

The authors would like to thank the University of Phayao and Water Management and maintenance division, Regional Irrigation Office 5, for the supporting information, tools, and research units.

REFERENCES

[1] Nuannukul, W.; Phumiphan, A.; Kangrang, A. Cross-Drainage Culvert Design under Global Climate and Land Use Chang-es. ARPN J. Eng. Appl. Sci. 2021, 16 (10), 1036–1044.

[2] Suwannachai, L.; Phumiphan, A.; Kuntiyawichai, K.; Supakosol, J.; Sriworamas, K.; Sivanpheng, O.; Kangrang, A. Integrat-ing Hydrological Models for Improved Flash Flood Risk Assessment and Mitigation Strategies in Northeastern Thailand. Water (Switzerland) 2025,

[3] Lasminto U., Kartika A.A.G, and Ansori MB., Reliability of Tropical Rainfall Measuring Mission for Rainfall Estimation in Brantas Sub-Watersheds. International Journal of GEOMATE, 26(116) 2024, pp.27-36.

[4] Ansori M. B., Lasminto U., and Kartika A. A. G., Flood Hydrograph Analysis Using Synthetic Unit Hydrograph, HEC-HMS, and HEC-RAS 2D Unsteady Flow Precipitation On-Grid Model for Disaster Risk Mitigation. International Journal of GEOMATE, 25(107) 2023, pp.50-58.

[5] Barati, A.; Zhoolideh,M.; Azadi, H.; Lee, J.; Scheffran, J. Interactions of land-use cover and climate change at global level: How to mitigate the environmental risks and warming effects, Ecological Indicators 2023, 146, 109829.

[6] Zhou, Y.; Guo, S. Incorporating ecological requirement into multipurpose reservoir operating rule curves for adaptation to climate change. Journal of Hydrology 2013, 498, 153-164.

[7] Zhang, Y.; Tang, C.; Ye, A.; Zheng, T.; Nie, X.; Tu, A.; Zhu, H.; Zhang, S. Impacts of Climate and Land-Use Change on Blue and Green Water: A Case Study of the Upper Ganjiang River Basin, China. Water 2020, 12, 2661.

[8] SeethaRam, K. V. Three level rule curves for optimum operation of a multipurpose reservoir using genetic algorithms. Water Resources Management 2021, 35(1), 353-368.

[9] Wongarmart, P.; Kaewhanat, A.; Phumiphan, A.; Kosasaeng, S.; Sivanpheng, O.; Kangrang, A. Improving Reservoir Opera-tion Efficiency Using Electric EEL Foraging Optimization and Transit Search Algorithms with Standard Operating Policy: Nong Han-Kumphawapi Case Study. ARPN J. Eng. Appl. Sci. 2025, 20(6), 300–313.

[10] Lei, X.; Zhang, J.; Wang, H.; Wang, M.; Khu, S.-T.; Li, Z.; Tan, Q. Deriving mixed reservoir operating rules for flood control based on weighted non-dominated sorting genetic algorithm II. J. Hydrol. 2018, 564, 967–983.

[11] Phumiphan, A.; Kosasaeng, S.; Sivanpheng, O.; Hormwichian, R.; Kangrang, A. An Alternative Approach Using the Firefly Algorithm and a Hybrid Method Based on the Artificial Bee Colony and Cultural Algorithm for Reservoir Operation. Water (Switzerland) 2024, 16 (6).

[12] Phumiphan A. and Kangrang A., Development of Decision-Making Support Tools for Future Reservoir Management Under Climate and Land Cover Variability: A Case Study. International Review of Civil Engineering (IRECE) Vol. 12, Issue 4, 2021, pp. 271-283.

Copyright © Int. J. of GEOMATE All rights reserved, including making copies, unless permission is obtained from the copyright proprietors.

15th Int. Conf. on Geotechnique, Construction Materials & Environment,
Kyoto, Japan, 11-13 November 2025, ISBN 978-4-909106124 C3051

APPLYING SELENA FOR STRATEGIC POST-EARTHQUAKE SHELTER PLACEMENT: A CASE STUDY FROM NEPAL

Khadiga Al-Nagar[1], Kevin Karanja Kuria[2], Md Faiz Shah[3] and Orsolya Kegyes-Brassai[4]

[1]Faculty of Architecture, Civil Engineering and Transport Sciences, Széchenyi István University, Hungary; [2]Department of Civil and Environmental Engineering, Egerton University, Kenya; [3]Faculty of ABLE, University of Adelaide, Melbourne Campus, Australia; [4]Department of Structural Engineering and Geotechnics, Széchenyi István University, Hungary

ABSTRACT

Shelter planning following an earthquake is a critical component of disaster response and management, directly influencing the affected populations. Strategic shelter allocation must consider factors such as population density, infrastructure vulnerability, and accessibility to optimize emergency response efforts. This research introduces SELENA V7.0 (SEismic Loss EstimatioN using a logic tree Approach), an advanced open-source risk assessment tool designed to estimate potential physical damage and human losses from seismic events. Developed by NORSAR and the University of Alicante, this software has been used to enhance emergency planning through scenario-based risk analysis.

The tool examines the anticipated seismic damage in the seven provinces of Nepal resulting from a probabilistic seismic hazard assessment (PSHA)-based design earthquake with a 475-year return period, reference to a 10% probability of exceedance in 50 years. Fragility models are integrated with GIS-based spatial analysis to assess seismic risk across the provinces. The approach also supports identifying optimal shelter locations based on predicted infrastructure damage and accessibility constraints.

The study outcomes are evaluated in terms of structural damage, economic losses varying from 0 to 1 billion Euros, number of homeless populations ranging from 2,330 to 57,463, and other relevant impact parameters as discussed in the results. The findings will equip policymakers and emergency planners to develop more effective shelter strategies, ultimately improving disaster resilience by providing critical evidence demonstrating how integrated technical and policy approaches can significantly enhance disaster resilience and emergency response effectiveness in seismic regions.

Keywords: Seismic Risk Assessment, Disaster Response, Shelter, SELENA Software.

INTRODUCTION

Earthquakes are among the most devastating natural hazards, causing serious threats to life, infrastructure, and economic stability. Globally, natural disasters have resulted in over $2.97 trillion in economic losses and affected more than 4 billion individuals over the past two decades [1]. Nepal is one of the countries most affected by earthquakes due to its sensitive location in the Himalayan region. It's located at the collision boundary of the Indian and Eurasian tectonic plates, which is particularly vulnerable to seismic activity. The 2015 Gorkha earthquake, with a magnitude of 7.8, caused over 8,700 deaths and 20,000 injuries, extensive infrastructure damage, and the collapse of more than 500,000 buildings [2, 3].

In such disasters, shelter intervention becomes a critical humanitarian need. However, the effectiveness of shelter responses is often hampered by poor planning, delays in implementation, and inadequate integration with critical infrastructure [4]. Damage to road networks and bridges frequently limits access to shelters and impedes the delivery of emergency assistance [4]. This demonstrates the necessity for proactive shelter planning strategies.

International frameworks such as the Sphere Standards and the Sendai Framework provide valuable guidance for shelter response and disaster risk reduction [5, 6]. Nevertheless, these are often general and lack the integration of technical seismic risk assessment tools required for precise, context-specific planning [7, 8].

To address this gap, this study utilizes the SELENA tool, a globally adaptable, open-source software designed to model seismic risk by simulating building damage, human losses, and economic impacts [9, 10]. Through integration with QGIS tools, this tool enables spatial analysis of seismic impact, helping identify priority zones for shelter deployment. This paper applies SELENA to the Nepalese context to demonstrate a replicable, evidence-based framework for optimizing post-earthquake shelter placement. By bridging engineering-based risk modeling with humanitarian planning standards, the study contributes to more resilient and strategic emergency shelter planning in seismically active regions.

RESEARCH SIGNIFICANCE

This study uniquely combines seismic risk modeling with humanitarian shelter planning using SELENA, integrating probabilistic analysis, infrastructure accessibility, and international standards. It aids decision-makers in identifying vulnerable zones and optimizing shelter placement, thereby advancing strategic disaster preparedness and fostering more resilient post-earthquake responses in high-risk regions.

LITERATURE REVIEW

Effective disaster response requires an integrated approach combining engineering, policy, social, and humanitarian. Various international frameworks guide post-earthquake shelter planning, but challenges persist in aligning them with real-world application, especially in terms of infrastructure limitations and technical risk assessments.

The minimum standards in the humanitarian response 'Sphere handbook' provide widely accepted humanitarian guidelines for shelter design, including a minimum living space of 3.5 m^2 and 4.5-5.5 m^2 in cold areas. fire safety distances of 3 m between shelters, and site planning of 30 m of fire breaks in each 300 m of built-up area of the camp. However, they often lack structural engineering detail, especially regarding seismic resilience [5]. In parallel, the Sendai Framework for Disaster Risk Reduction (2015–2030) highlights infrastructure resilience, risk governance, and stakeholder coordination but is primarily policy-oriented and lacks prescriptive engineering content [6].

From the engineering point of view, Eurocode 8 (EN 1998-1) offers a rigorous standard for designing earthquake-resistant structures across Europe. It includes parameters such as base shear calculations, ductility considerations, and provisions for masonry structures. Nonetheless, its application in low-resource or humanitarian contexts is limited due to complexity and high implementation costs.

Rohwerder has also highlighted numerous operational gaps in post-disaster shelter response, including delays due to land ownership disputes, lack of integration with water/sanitation networks, and poor coordination between civil engineers and humanitarian agencies [7, 8]. The experience in Nepal after the 2015 earthquake revealed that many displaced populations depended on non-engineered shelters, with limited oversight on structural safety [1, 3].

Seismic risk assessment involves various methods and concepts, which are visually summarized in Figure 1. A keyword co-occurrence map was generated from 1,225 Scopus-indexed publications (2016–2020; data collected 30 April 2025), highlighting “risk assessment” as the central and most interconnected term. It is closely linked with key concepts such as “seismic risk,” “fragility curves,” and “structural dynamics,” reflecting the multidisciplinary integration of engineering, hazard modeling, and decision-making. Emerging terms like “machine learning” and “uncertainty” indicate a growing trend toward data-driven, probabilistic approaches, while keywords such as “building codes,” “retrofit,” and “masonry buildings” emphasize practical considerations in infrastructure resilience and seismic preparedness.

In terms of simulation tools used to estimate expected losses, SELENA was not commonly featured, as few studies have adopted this approach. In this study, SELENA V7.0 has been applied as a robust tool for simulating structural damage, human losses, and economic losses under seismic conditions [9, 10]. Unlike tools such as HAZUS, which focus on the U.S. context, SELENA is globally adaptable and uses fragility curves and capacity spectrum methods to estimate damage at varying levels of intensity [9, 10]. Its integration with QGIS further supports spatial analysis for decision-making in emergency response.

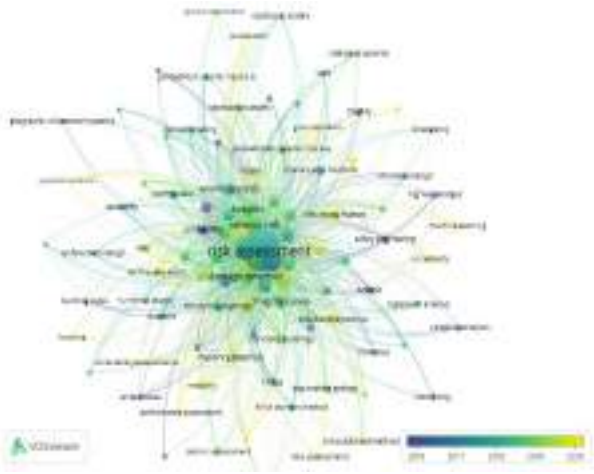

Figure 1 Keyword mapping of seismic risk from Scopus (Source: authors)

Global Applications of SELENA in Seismic Risk Modeling

Despite SELENA's potential, its real-world adoption has been concentrated in focused case studies across different countries:

Algeria: Bellalem et al. [11] applied SELENA to model seismic scenarios in downtown Blida, one of Algeria’s most seismically active regions. By simulating four distinct earthquake scenarios, they observed mean damage ratios (MDRs) reaching up to 90% in some cadastral zones. Their study also highlighted the sensitivity of this tool to ground motion prediction equations (GMPEs) and performance point methods such as MADRS and I-

DCM, helping authorities identify high-risk areas and prioritize retrofitting initiatives.

China: Yang et al. [13] estimate building damage and casualties in primary schools across 15 counties impacted by the 2008 Wenchuan earthquake using the software. The study demonstrated SELENA's capability to function effectively in data-limited environments. By combining probabilistic models with CSM, they visualized varying damage distributions and identified vulnerabilities among unreinforced structures. it further validated these outcomes by comparing damage levels across regions, reinforcing the model's consistency.

Norway: In Oslo, Lindholm et al. [10] conducted seismic risk modeling using SELENA, supported by detailed data on subsoil properties and building typologies. The study simulated a hypothetical M6.5 earthquake on the Oslofjord fault and successfully mapped potential economic and structural losses. The comprehensive urban dataset enhanced the precision of the outputs, underscoring its utility for seismic risk planning in well-documented European urban centers.

Romania: In Bucharest, Armaș et al. [14] used SELENA to simulate the impacts of a repeat of the 1977 Vrancea earthquake. They applied the Improved Displacement Coefficient Method (I-DCM) to assess 358 buildings, identifying unreinforced masonry structures with timber floors as highly vulnerable. Spatial maps produced using GIS and SELENA revealed MDRs up to 32%, alongside significant economic loss projections. These outputs informed both emergency preparedness and long-term urban mitigation strategies.

Nepal: Two studies demonstrate SELENA's critical role in assessing seismic risk in Nepal. Vineetha and Rajaram [15] modeled a hypothetical Mw 8.4 earthquake across eleven districts, estimating losses up to €0.6 million and predicting 1,000–5,000 casualties. They identified brick masonry structures as most vulnerable and earthquake magnitude as the dominant factor influencing loss. Additionally, this study expands upon that analysis by using SELENA to assess the Koshi Province, revealing more than 57,000 displaced individuals, over 900 fully collapsed buildings, and economic losses exceeding €158 million. Spatial analysis in QGIS further enabled shelter planning based on infrastructure proximity and accessibility challenges.

Global Modeling: On a broader scale, Martins and Silva [16] developed a global database that can used as inputs for SELENA of fragility and vulnerability functions for over 500 building classes as part of the GEM Foundation's risk assessment initiatives. Their work demonstrated SELENA's value in standardizing global seismic risk modeling and guiding multi-regional disaster resilience planning.

These diverse applications confirm SELENA's strength as a globally adaptable and analytically rigorous tool. Whether in data-rich urban centers or resource-constrained regions, the software has proven effective for estimating structural vulnerability, casualty potential, and economic losses—supporting both local interventions and international disaster risk reduction strategies.

RESEARCH METHODOLOGY

This study integrates seismic risk modeling with spatial analysis to support evidence-based post-earthquake shelter planning in Nepal. The methodological framework is built on the application of the SELENA V7.0 simulation software and QGIS for geospatial analysis. The process involves three main stages: risk modeling, spatial mapping, and shelter site evaluation.

Seismic Risk Simulation Using SELENA

SELENA was employed to simulate the probabilistic analysis effect of earthquake across Nepal's seven provinces, as shown in Table 1. It estimates building damage, casualties, and economic losses by combining datasets such as: Seismic hazard inputs, derived from regional ground motion prediction models [2], Building typologies, obtained from OpenQuake and categorized by structural characteristics [16], Population distribution, adjusted for occupancy patterns at different times of day [1], Soil classification, using Vs30 values to account for local amplification effects [2,15], Fragility and capacity curves, sourced from global vulnerability databases and GEM standards [17]. SELENA applies the Capacity Spectrum Method (CSM) and a logic tree structure to capture uncertainties in both hazard and vulnerability models [9,10]. Outputs include damage states (none, slight, moderate, extensive, and complete), projected displacement, casualties, and direct economic losses per region.

Spatial Analysis with QGIS

Simulation results were imported into QGIS 3.36.2, a Geographic Information System (GIS) used to visualize and analyze the spatial distribution of earthquake impacts [18]. QGIS enabled layering of SELENA outputs to identify high-risk areas and infrastructure exposure. Key visualized data included: Damage distribution and collapse densities by administrative region, Estimates of displaced populations and homeless individuals [16], economic losses and number of injuries. This mapping was essential in guiding shelter planning by highlighting accessible and high-need zones.

Table 1 Administrative regions level 1 of Nepal include 7 Geounits and relevant building stock (source: The Open Quake Platform, accessed: 01 April 2025)

Region Name	ID	Number of buildings
Bagmati	NP-P3	1108047
Gandaki	NP-P4	1064718
Karnali	NP-P6	948806
Lumbini	NP-P5	634612
Madhesh	NP-P2	612709
Province 1 (Koshi)	NP-P1	266458
Sudur Paschim	NP-P7	630546

Shelter Site Identification and Planning (Figure 8)

The city of Biratnagar, located in Koshi Province as shown in the Figure 2, was selected for focused shelter planning due to its high vulnerability as shown by SELENA outputs. Satellite imagery and infrastructure data were used to locate and assess potential shelter areas. Each site was evaluated using the Sphere Standards [5], which define A minimum area of 3.5 m² per person for emergency shelters, Spatial layout guidelines for safety, privacy, and WASH services, Accessibility standards for emergency response logistics and mobility. Shelter capacity was calculated using available free area based on critical infrastructure evaluation in the area, and WASH needs (water points and latrines) were estimated based on Sphere's recommended ratios. Road access and redundancy were also considered to ensure rapid deployment and minimize logistical delays [4,6].

Figure 2 Administrative region level 1 of Nepal with seven provinces (Source: authors)

RESULTS

This study used SELENA V7.0 and QGIS 3.36.2 to assess seismic vulnerability and improve guidance of shelter planning and response across Nepal's provinces. The results highlight spatial patterns of seismic hazard, building damage, human casualties, economic losses, and shelter requirements. The findings support evidence-based decisions for disaster preparedness and emergency response.

Seismic Hazard and Ground Motion

Figure 3 illustrates the spatial distribution of amplified peak ground acceleration (PGA) across Nepal. Probabilistic analysis revealed that provinces like Bagmati and Gandaki exhibit the highest PGA values (0.375 – 0.6 g), indicating elevated seismic hazard levels. This distribution aligns with Nepal's tectonic profile and underscores the need for targeted risk reduction in central regions.

Figure 3 Spatial distribution of amplified PGA values across Nepal's provinces from probabilistic seismic analysis (Source: authors).

Structural Damage Assessment

SELENA simulations estimated building damage across 20 taxonomies and four damage states. Damage maps (Figure 4) show that Koshi, Bagmati, and Madhesh provinces consistently report the highest counts of slightly, moderately, extensively, and completely damaged buildings. For example, complete collapse in Koshi exceeded 900 buildings, pointing to urgent retrofitting needs. In contrast, western provinces like Karnali and Sudur Paschim reported minimal damage, reflecting lower hazard exposure and/or smaller urban footprints.

Figure 4 Number of completely damaged buildings for all taxonomies (Source: authors).

Displacement and Homelessness

As shown in Figure 5, the projected number of homeless individuals is highest in Koshi and Madhesh, with up to 57,000 people will be displaced.

Figure 5 Spatial distribution of the homeless population across provinces of Nepal (Source: authors).

driven by building collapse and dense urban populations. These figures directly inform emergency shelter planning and resource allocation, especially in provinces with limited resilience capacity.

Casualty and Injury Estimates

The number of injury projections across three critical time frames, which are 2:00 A.M., 10:00 A.M., and 5:00 P.M. Nighttime injuries are significantly higher due to residential occupancy. At 2:00 A.M., Koshi, Madhesh, and Bagmati show the greatest injury rates. During the daytime, injuries are less due to population dispersion, but the ratio rises again by 5:00 P.M. as people return home. These trends emphasize the importance of time-sensitive emergency medical planning. Figures 6 illustrate the highest peak hour of injuries at midnight.

Figure 6 Total number of injuries at 2:00 A.M (Source: authors)

Economic Loss Estimates

The direct economic losses were estimated using a probabilistic methodology that incorporates damage probabilities, structural typologies, and spatially distributed exposure. The total economic loss was calculated using this formula from the tool's manual [10]:

$$L_{eco} = C_r \times \Sigma_{i=1}^{N_{OT}} \ \Sigma_{j=1}^{N_{BT}} \ \Sigma_{K=1}^{N_{DS}} \times A_{i,j} \times P_{j,k} \times C_{i,j,k} \qquad (1)$$

Where:

N_{OT} - Number of occupancy types,

N_{BT} - Number of building typologies,

N_{DS} - Number of damage states ds,

Cr - Regional cost multiplier (currently set to 1.0, but it can have different values for each geographical unit in order to take into account the geographic cost variations),

$A_{i,j}$ - Built area of the model building type j in the occupancy type i (in m^2)

$P_{j,k}$ - Damage probability of a structural damage k (slight, moderate, extensive, or complete) or model building type j,

$C_{i,j,k}$ - Cost of repair or replacement (per m^2) in the provided input currency of structural damage k for occupancy type i and model building type j (provided by input files elossi.txt).

Figure 7 presents estimated direct economic losses per province. Koshi Province shows the highest losses, between €140 million and €158 million, followed by Madhesh and Bagmati. In contrast, Karnali and Sudur Paschim reflect lower financial impacts (under €21 million), corresponding to smaller urban exposure. These disparities stress the need for region-specific investment in mitigation and response capacity.

Figure 7 Estimated economic losses by province from seismic events (in Euros) (Source: authors).

OPERATIONALIZING SHELTER PLANNING IN SEISMIC EMERGENCY SCENARIOS

Effective shelter planning and response in seismic regions requires deep knowledge of the international frameworks, such as the Sendai Framework, Eurocode 8, and Sphere Standards. In the practical field, locally adapted strategies. While these frameworks promote resilience, risk reduction, and community engagement, their implementation often faces barriers in resource-constrained settings. This

research demonstrates that integrating advanced seismic risk tools like SELENA with context-specific data enables a multi-dimensional understanding of infrastructure vulnerability and access, essential for emergency shelter planning.

This study applied its findings to a real-world example in Biratnagar, the urban center most affected in Koshi Province. The evaluation of post-earthquake emergency response capacity was conducted by generating a 200-meter resolution map using satellite imagery from Google Earth as shown in Figure 8. This map served as the foundation for evaluating the spatial distribution of critical infrastructure and available open spaces, thereby identifying suitable locations for the deployment of emergency shelters. The analysis yielded three potential shelter areas, designated A1, A2, and A3, with respective areas of 80,404 m², 42,800 m², and 37,140 m², respectively. Furthermore, the analysis identified six critical infrastructure buildings, including hotels, the Morang campus, Sagarmatha Secondary School, the Ganesh Temple, and other schools. In the event of a seismic

occurrence, critical infrastructures may be mobilized if they have been designed to resist such events and to provide seismic resilience for the surrounding population. The following map illustrates the locations in question.

Figure 8 plan of proposed shelter area based on critical infrastructure in Biratnagar, Koshi Province (Source: authors).

Emergency plan for Biratnagar:

An emergency WASH and shelter plan for the three designated areas in Biratnagar was developed based on Sphere Standards, which recommend a minimum of 3.5 m² per person and include 3 m spacing requirements between shelters to ensure safety and privacy. In an emergency camp, each shelter with a 3-meter buffer on all sides requires approximately 54 m². By using this living area for shelter, Area A1 with 80,404 m² can host 1,488 shelters for 7,440 people as the shelter can host one household of 5 family members. Area A2 with 42,800 m² can support 829 shelters for 4,145 people, and Area A3 of 37,140 m² can accommodate 719 shelters for 3,595 people. Corresponding water point and latrine needs were also calculated using Sphere ratios—1 water point per 250 people and 1 latrine per 20 people. Water points must be accessible within 500 meters of all shelters, and latrines should include gender-sensitive and accessible options. The table below summarizes the shelter capacity and WASH requirements for each area. Table 2 summarizes the emergency plan can done in the three identified sites.

Table 2 The summary of emergency WASH and Shelters needed based on the area.

Area	Total Area (m²)	Shelters	People Capacity	Water Points	latrines
A1	80,404	1,488	7,790	30	372
A2	42,800	829	4,145	17	207
A3	37,140	719	3,595	15	180

Prototype shelter design:

Drawing on the author's field experience in emergency shelter programs, particularly with the IOM Shelter and Non-Food Items sector, a practical and scalable prototype shelter is proposed for post-earthquake housing in the selected area. In line with Sphere Association [5], guidelines and humanitarian shelter standards, the design features a 3 × 6 meter structure intended to accommodate a family of five members. The material proposed for the shelter is wood as a primary material due to its environmental sustainability, recyclability, and proven seismic resilience. Wood's flexibility allows the structure to absorb shock during seismic events, making it especially suitable for disaster-prone regions, while its lightweight and simple structure supports rapid assembly, relocation, and long-term usability, aligning with sustainable construction principles that emphasize locally sourced, low-impact materials [17]. This design balances immediate emergency needs with principles of environmental responsibility and structural safety, supporting both short-term humanitarian assistance and long-term recovery efforts as it can be easily upgraded. Figures 9 and 10 illustrate the prototype's plan and longitudinal section.

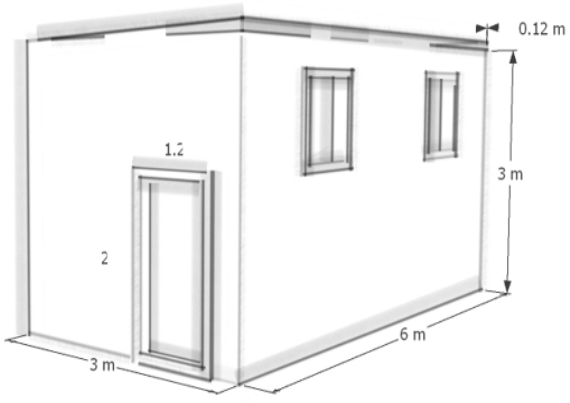

Figure 9 Shelter prototype (Source: authors).

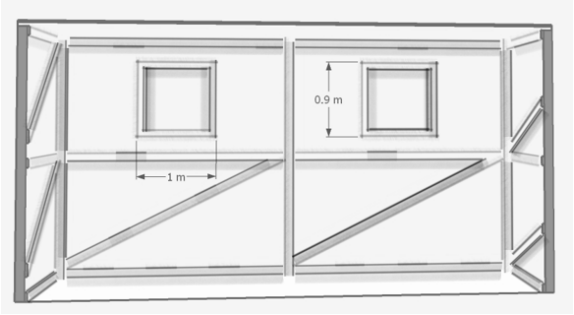

Figure 10 Shelter prototype longitudinal section (Source: authors).

DISCUSSION

This study aimed to evaluate post-disaster shelter response sustainability and infrastructure resilience interventions in earthquake zones, with a particular emphasis on the civil engineering, technology, and policy-making functions. with simulation tools and case studies, a complex interaction of technical, organizational, and contextual factors shapes disaster preparedness, response, and recovery. The findings confirm that while global disaster risk reduction frameworks—such as the Sendai Framework, Eurocode 8, and the Sphere Standards—provide valuable guidance, gaps remain in operationalizing these standards within resource-constrained, high-risk settings. Eurocode 8 emphasizes structural safety but lacks social context; the Sphere Standards focus on dignity and access but fall short on seismic resilience; and FEMA's models offer technical depth yet are difficult to apply outside well-resourced environments. These limitations highlight the need for a multidisciplinary approach that blends structural engineering principles, humanitarian needs, and geospatial risk analysis.

Using the SELENA simulation platform and QGIS visualization tools, the study presented a probabilistic assessment of seismic risk across Nepal. The results showed clear regional disparities in hazard exposure, structural vulnerability, and expected damage. Provinces such as Koshi, Bagmati, and Madhesh consistently demonstrated the highest levels of damage, displacement, and economic loss, particularly under nighttime scenarios when residential occupancy peaks. These findings underscore the value of temporal and spatial vulnerability analysis in guiding time-sensitive emergency planning and targeted retrofitting.

The simulation also revealed an east-to-west gradient in seismic intensity and building collapse, closely aligned with tectonic fault zones and population densities. Economic loss estimates further emphasized this regional variation, with Koshi alone expected to incur up to €158 million in direct damages. These high-risk areas demand not only technical upgrades and engineering interventions but also robust planning strategies that account for infrastructure access, road network redundancy, and service delivery.

A real-world application of the study's findings in Biratnagar demonstrated how simulation outputs can directly inform emergency shelter planning. By identifying open spaces, calculating capacity under Sphere Standards, and evaluating access to critical infrastructure, the study proposed a shelter strategy that is both context-sensitive and scalable. The shelter prototype—based on sustainable materials and seismic resilience—offers an adaptable solution that balances emergency needs with long-term recovery goals.

Ultimately, the study affirms that technical capacity exists to model and address seismic risk comprehensively. However, effective implementation requires greater institutional coordination, investment in local capacity, and mainstreaming of disaster-resilient design into planning systems. Integrating data-driven tools like SELENA into local policy and engineering practice can bridge the gap between analysis and action—ensuring safer, more sustainable shelter responses in future seismic emergencies.

CONCLUSION

The research assesses seismic risk and shelter planning in Nepal by utilizing tools like SELENA V7.0 and GIS-based spatial analysis. It is focused on simulating earthquake impacts on 7 provinces of Nepal, zones like Koshi, Bagmati, and Madhesh, which are approximated to experience the highest number of damages. For instance, Koshi is single-handedly anticipated to experience economic loss of up to €158 million and leave over 57,000 individuals homeless due to the building collapse. Three potential shelter sites in Biratnagar that would accommodate approximately 7,440 people were also identified in the research, based on Sphere Standards for shelter and WASH planning. These findings emphasize the variation in vulnerability across regions and demand mitigation at the local level, resilient infrastructure retrofits, and data-driven emergency planning in order to foster resilience and community recovery. These findings can support policymakers in making evidence-based decisions for prioritizing shelter allocation, refining urban emergency plans, and investing in region-specific seismic risk mitigation strategies.

Future Directions

Building Future research should expand on these findings by applying advanced seismic assessment methods, such as deterministic analysis and SELENA–MATLAB integration, to improve accuracy and validate the research findings.

Incorporating site-specific ground response analysis, as emphasized by Labar et al. [19], will enhance shelter prototype reliability in varied soil conditions. Strengthening transportation networks and leveraging GIS, drones, and real-time monitoring can improve emergency access and coordination, particularly in low-resource areas. Culturally informed shelter designs and aftershock performance testing will further ensure relevance and resilience. Finally, multi-disciplinary collaboration and institutionalized planning are essential for building communities that can withstand and recover from seismic events.

REFERENCES

[1] E. Hendriks and A. Opdyke, "The influence of technical assistance and funding on perceptions of post-disaster housing safety after the 2015 Gorkha earthquakes in Nepal," International Journal of Disaster Risk Reduction, vol. 73, 2022.

[2] H. Chaulagain, H. Rodrigues, V. Silva, E. Spacone, and H. Varum, "Seismic risk assessment and hazard mapping in Nepal," Natural Hazards, vol. 78, no. 1, pp. 583–602, 2015.

[3] D. Gautam, K. K. Bhetwal, H. Rodrigues, P. Neupane, and Y. Sanada, "Observed Damage Patterns on Buildings during 2015 Gorkha (Nepal) Earthquake," Natural Hazards, 2015.

[4] M. Maharjan, "Liquefaction in Kathmandu Valley during 2015 Gorkha (Nepal) Earthquake," Nepal Journal of Civil Engineering, vol. 4, no. 1, pp. 1–8, 2017.

[5] Sphere Association, The Sphere Handbook: Humanitarian Charter and Minimum Standards in Humanitarian Response, 4th ed. Practical Action Publishing, 2018.

[6] United Nations Office for Disaster Risk Reduction (UNDRR), "Sendai Framework for Disaster Risk Reduction 2015–2030," Geneva, Switzerland, 2015.

[7] J. Anhorn and B. Khazai, "Open space suitability analysis for emergency shelter after an earthquake," Natural Hazards and Earth System Sciences, vol. 15, no. 4, pp. 789–803, 2015.

[8] B. Rohwerder, "Transitional shelter in post-disaster contexts," Helpdesk Research Report, GSDRC, 2016.

[9] S. Molina, D. H. Lang, and C. D. Lindholm, "SELENA – An open-source tool for seismic risk and loss assessment using a logic tree computation procedure," Computers & Geosciences, vol. 36, no. 3, pp. 257–269, 2010.

[10] Molina, S., Lang, D. H., & Lindholm, C. D. (2010). SELENA – Manual - An open-source tool for seismic risk and loss assessment using a logic tree computation procedure. Computers & Geosciences, 36(3), 257–269. doi:10.1016/j.cageo.2009.07.006.

[11] F. Bellalem et al., "Seismic risk assessment for the downtown of the city of Blida, Algeria," International Journal of Disaster Risk Reduction, vol. 103, 2024.Hossain M.Z., For Chapter in a Book, Soil Mechanics, 4th ed. Vol. 2, Sakai, Ed. Sankeisha Publisher's Name, Year, pp. 11–60.

[12] C. D. Lindholm, S. Molina-Palacios, and D. H. Lang, "SELENA—Seismic Loss Estimation using a Logic Tree Approach," in Applied Technology Council (ATC) Earthquake Protection Conference, 2007.

[13] J. Yang, L. Xiang, and S. Bao, "Estimating Seismic Losses of Schools Using SELENA: the Case of Wenchuan Earthquake" Chinese Journal of Seismology, vol. 34, no. 4, pp. 501–510, 2011.

[14] I. Armaș, D. Toma-Danila, and D. A. Gheorghe, "Seismic loss estimates for buildings in Bucharest's historic centre in case of another 1977 Vrancea earthquake," Forum Geografic, vol. XIV, no. 1, pp. 5–13, 2015.

[15] S. R. Vineetha and C. Rajaram, "Assessment of seismic potential impacts of an Mw 8.4 hypothetical earthquake in central Nepal province," Natural Hazards Research, 2024.

[16] L. Martins and V. Silva, "Development of a fragility and vulnerability model for global seismic risk analyses," Bulletin of Earthquake Engineering, vol. 19, no. 15, pp. 6719–6745, 2021.

[17] K. K. Kuria and K. Al-Nagar, "Sustainable materials blended intensive programme (BIP) Erasmus+," Local J. Politehnica Univ. Timisoara (UPT), 2024. [Online]. Available: https://doi.org/10.13140/RG.2.2.23860.67202

[18] QGIS Development Team, *QGIS Geographic Information System*, Version 3.36.2, Open-Source Geospatial Foundation, 2023. [Online]. Available: https://qgis.org. [Accessed: 4, 15, 2025].

[19] B. Labar, N. Bektaș, and O. Kegyes-Brassai, "Enhancing Seismic Performance: A Comprehensive Study on Masonry and Reinforced Concrete Structures Considering Soil Properties and Environmental Impact Assessment," Advances in Civil Engineering, vol. 2024, 2024, doi: 10.1155/2024/4505901.

Copyright © Int. J. of GEOMATE All rights reserved, including making copies, unless permission is obtained from the copyright proprietors.

15th Int. Conf. on Geotechnique, Construction Materials & Environment,
Kyoto, Japan, 11-13 November 2025, ISBN 978-4-909106124 C3051

RECOVERY OF METALLIC IRON FROM ILMENITE BY THE PROCESS OF MECHANOCHEMICAL TREATMENT, ACID LEACHING AND ELECTRODEPOSION

Takaaki Wajima[1]

[1]Graduatee School of Engineering, Chiba University, Japan

ABSTRACT

In recent years, space development has become more active and plans have been made to construct a base for space development on the Moon. However, approximately 1 million dollars may be required to transport 1 kg of material from the earth to the Moon, and there is a need to develop some necessary materials from resources on the Moon. Lunar sand and regolith are abundant on the surface of the moon and contain ilmenite ($FeTiO_3$), including iron. Smelting of ilmenite on Earth is a direct reduction method or sulfuric acid method, but these methods require energy at high temperatures and pressures. In this study, we attempted to recover metallic iron from ilmenite using a novel process consisting of a mechanochemical treatment, acid leaching, and electrodeposition. Mechanochemical treatment is a low-energy process that accelerates changes in the crystal structure and chemical reactions by mechanical energy such as friction and impact forces on the sample, which are likely to work well in a lunar environment. Ilmenite can be converted into soluble salts by mechanochemical treatment with sodium hydroxide, and ferric ions can be extracted into a hydrogen chloride solution. Metallic iron can be recovered using electrodeposition.

Keywords: Ilmenite, Metallic Iron, Mechanochemical treatment, Acid leaching, Electrodeposition

INTRODUCTION

In recent years, space development has become more active and plans have been made to construct a base for space development on the Moon. With the space industry currently booming, space development is rapidly advancing around the world, and the "Artemis Project," which aims to send a manned mission to Mars and is led by NASA and major countries such as Japan, Canada, Australia, and the European Union, plans to construct a lunar base by 2030 to serve as a base for manned activities. However, if the building materials to be used for the lunar base are transported by rocket from the earth, it will cost a huge amount of money (1.2 million dollars/kg) [1]; therefore, it is necessary to develop new building materials using resources that exist on the moon based on the in situ resource utilization (ISRU) concept of local procurement of useful extraterrestrial materials on extraterrestrial celestial bodies [2, 3]. Therefore, attempts have been made to produce construction materials from lunar resources [4-6].

Iron (Fe) is a transition element with atomic number 26 and is a metallic element. Iron is an important material in modern architectural and civil engineering structures and is used in a wide variety of applications because of its strength, durability, and workability. Iron is produced from iron ore, coal, and limestone, which are biogenic in origin and do not exist in the moon. Therefore, we focused on the ilmenite ($FeTiO_3$) contained in regolith, which is abundant on the Moon as an iron resource. The smelting of ilmenite on Earth can be achieved by the direct reduction method or sulfuric acid method, but these methods require energy at high temperatures and pressures, as well as reducing agents and chemicals that are difficult to obtain on the Moon. Therefore, we attempted to recover iron from ilmenite by mechanochemical treatment with sodium hydroxide dissolved in a hydrogen chloride solution to be deposited by electrodeposition, which is considered to be available on the lunar surface. Mechanochemical treatment causes changes in the crystal structure and the promotion of chemical reactions in the sample by mechanical energy, such as frictional and impact forces [7].

The objective of this study was to convert iron into soluble alkali salts by the mechanochemical reaction of ilmenite, a poorly soluble mineral, with sodium hydroxide and to dissolve it in hydrochloric acid to obtain a solution in which iron can be electrolytically deposited.

RESEARCH SIGNIFICANCE

This study was based on cost considerations for the future development of the lunar base using resources on the Moon, for local production on the Moon, in order to minimize the resources that need to be transported from Earth. For this purpose, in this study, we attempted to recover iron metal from simulated lunar rock sand using a process consisting of mechanochemical treatment, acid leaching, and

electrodeposition, which are known to be able to be performed on the lunar surface, although these tests must be performed under earth conditions.

EXPERIMENTAL METHODS

Mechanochemical Treatment

Ilmenite (Sigma-Aldrich) (0.8 g) and sodium hydroxide (NaOH) (Wako) (0.1 - 0.8 g) were placed in a zircon container (80 mL) together with zircon grinding balls (10 mm diameter, 25 pieces) so that the ilmenite, sodium hydroxide, and grinding balls occupied 1/3 of the container in that order. The mechanochemical treatment was performed at a rotational speed of 200–600 rpm and treatment time of 0–180 min. After the mechanochemical treatment, the grinding balls were placed in a tea strainer, the sample powder was sieved, and the sample in the container was collected by scraping it off with a spatula.

After mechanochemical treatment with sodium hydroxide containing 0.2 g, samples were added to 1.0 mol/L hydrochloric acid (20 mL) in a 50 mL centrifuged tube, and the tube was shaken for 2 h. After shaking, centrifugation was performed, the supernatant solution was filtered, the pH of the filtrate was measured using a pH meter (LAQUA F-72, HORIBA), and the concentrations of Fe and Ti in the filtrate were determined using atomic absorption spectrometry (AAnalyst 200, Perkin Elmer). After the determination, the dissolved amount was calculated using Equation (1).

$$E = \frac{C \bullet V}{M \bullet m} \qquad (1)$$

where E: dissolved amount (mmol/g), C: metal concentration (mg/L), V: solution volume (L), M: atomic weight (mg/mmol), m: sample weight (g). The mineral phases of the prepared samples and residues were determined by powder X-ray diffraction (XRD) (D8 ADVANCE, Bruker AXS).

As a comparison sample for solubility, a mechanochemically treated sample of ilmenite (0.8 g) alone and a sample of ilmenite (0.8 g) and sodium hydroxide (0.2 g) well mixed in a mortar were prepared.

Acid Leaching and Electrodeposition

The amount of metal dissolved in hydrochloric acid in mechanochemically treated ilmenite was examined during the acid leaching stage. For the treated samples, a mixture of ilmenite (0.8 g) and sodium hydroxide (0.2 g) was treated using a planetary ball mill at a rotation speed of 600 rpm for 120 min.

The sample (0.1 - 1.0 g) was placed in 0 - 1.0 mol/L hydrochloric acid (10 mL) in a 50 mL centrifuge tube and shaken for 2 h. After shaking, the tube was centrifuged and the supernatant was filtered through a membrane filter. The pH of the filtrate was measured, the concentrations of Fe and Ti in the filtrate were determined using an atomic absorption spectrometer, and the dissolved amount was calculated using Equation (1). The mineral phases of the prepared samples and residues after acid leaching were determined by XRD.

The leachate after acid leaching of mechanochemically treated ilmenite (0.2 g) with 1 mol/L hydrochloric acid solution for 0.5 hour was subjected to electrodeposition to precipitate iron metal. The pH of the leachate was 0.3, and the concentrations of Fe and Ti in the leachate were 136 mg/L and 140 mg/L, respectively. The leachate (2 mL) with or without the addition of oxalic acid dihydrate ($(COOH)_2 \cdot 2H_2O$) (0.2 g) was poured into the cell (10 mm× 20 mm× 20 mm), and two carbon electrodes (Φ2 mm× 25 mm) set at 10 mm intervals were placed so that they were immersed 10 mm, and a 5 V DC current was applied to the carbon electrode to observe the electrode.

RESULTS AND DISCUSSION

The metal dissolution amounts of the samples mechanochemically treated with different amounts of NaOH are shown in Figure 1. The rotation speed was 200 rpm and the processing time was 60 min. The dissolution amounts of the raw materials were 0.080 mmol/g for iron and 0.081 mmol/g for titanium, the solubilities of the mixtures were 0.081 mmol/g for iron and 0.084 mmol/g for titanium, and those of the mechanochemically treated samples without sodium hydroxide addition were 0.089 mmol/g for iron and 0.088 mmol/g for titanium, indicating that mechanochemical treatment of ilmenite or mixing of ilmenite and sodium hydroxide alone does not make ilmenite soluble.

The solubility of Fe and Ti increased as the amount of sodium hydroxide added increased up to 0.2 g and then decreased. The maximum dissolved amounts of Fe and Ti were 1.56 mmol/g (23.7 %) and 1.63 mmol/g (24.8 %), respectively. The XRD patterns of the mechanochemically treated samples with different amounts of sodium hydroxide and the residue after dissolution in hydrochloric acid are shown in Figure 2. It should be noted that the sample with 0.8 g of sodium hydroxide could not be measured by XRD because of the large amount of unreacted sodium hydroxide, and the sample showed deliquescence. The peak of ilmenite was observed in all samples after mechanochemical treatment, and the peak of the sodium salt of ilmenite was observed in the sample with 0.2 g of sodium hydroxide added. The following reaction could have occurred via a

mechanochemical treatment:

$FeTiO_3 + 2NaOH \rightarrow Na_2FeTiO_4 + H_2O$ (2)

In the sample after dissolution in hydrochloric acid, only the ilmenite peak was observed, indicating that Na_2FeTiO_4 was dissolved in hydrochloric acid as follows:

$Na_2FeTiO_4+6HCl \rightarrow FeCl_2+TiOCl_2+2NaCl+3H_2O$ (3)

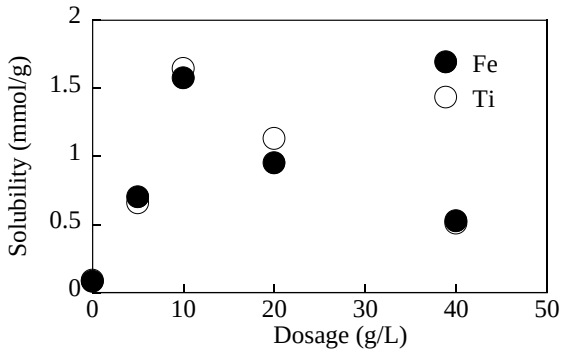

Fig.1 The metal dissolution amounts of samples mechanochemically treated with different amounts of sodium hydroxide addition

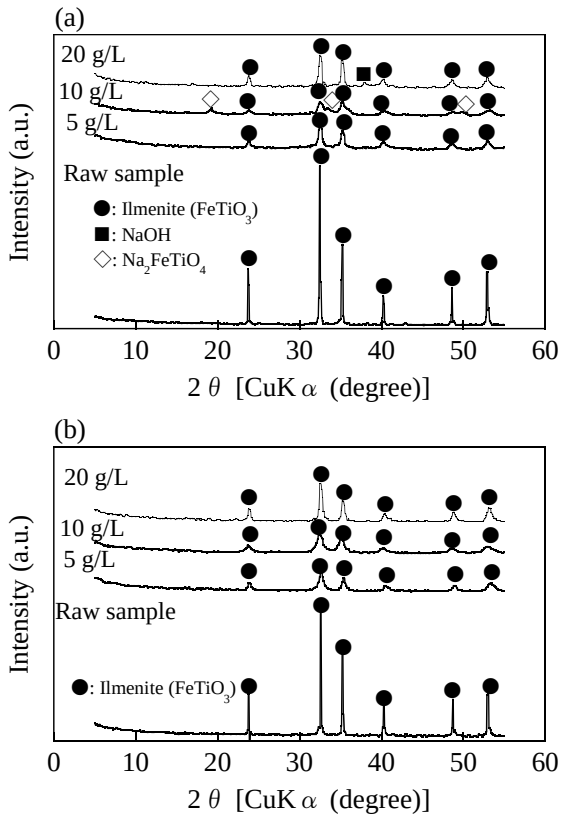

Fig.2 XRD patterns of (a) mechanochemically treated samples with different amounts of sodium hydroxide and (b) the residue after dissolution in hydrochloric acid

Figure 3 shows the amount of metal dissolved in the mechanochemically treated samples at different rotational speeds. It is noted that the amount of sodium hydroxide added was set to 0.2 g and the processing time to 60 min. The higher the rotation speed, the greater is the amount of metal dissolved. At 600 rpm, the dissolved amounts of iron and titanium were 2.09 mmol/g and 2.06 mmol/g, respectively. The XRD patterns of the mechanochemically treated samples at different rotation speeds and the residue obtained after dissolving each sample in a hydrochloric acid solution are shown in Figure 4. The peak intensity of the sodium salt in the mechanochemically treated sample increased with increasing rotation speed. After hydrochloric acid dissolution, only the ilmenite peak was observed. The reaction between ilmenite and sodium hydroxide was accelerated by increasing the rotation speed and the amount of soluble sodium salt.

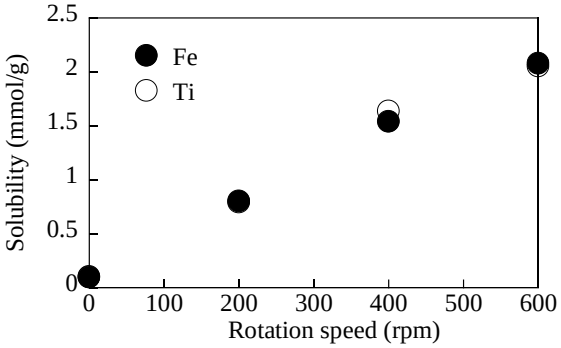

Fig.3 The amount of metal dissolved in the mechanochemically treated samples at different rotation speeds

Figure 5 shows the amount of metal dissolved by mechanochemical treatment at different treatment times. The amount of sodium hydroxide addition was 0.2 g and the rotation speed was set at 600 rpm. The amount of dissolution increased with increasing processing time, and became constant after 120 min. After120 min of processing, the dissolution amounts were 2.34 mmol/g for iron and 2.30 mmol/g for titanium. The XRD patterns of the mechanochemically treated samples and the residue after dissolution of each sample are shown in Figure 6. The sodium salt of ilmenite was formed after 30 min of treatment, and the sodium salts of iron and titanium were formed at 90 min by the following reaction:

$Na_2FeTiO_4 + 4NaOH \rightarrow Na_4FeO_3 + Na_2TiO_3 + 2H_2O$

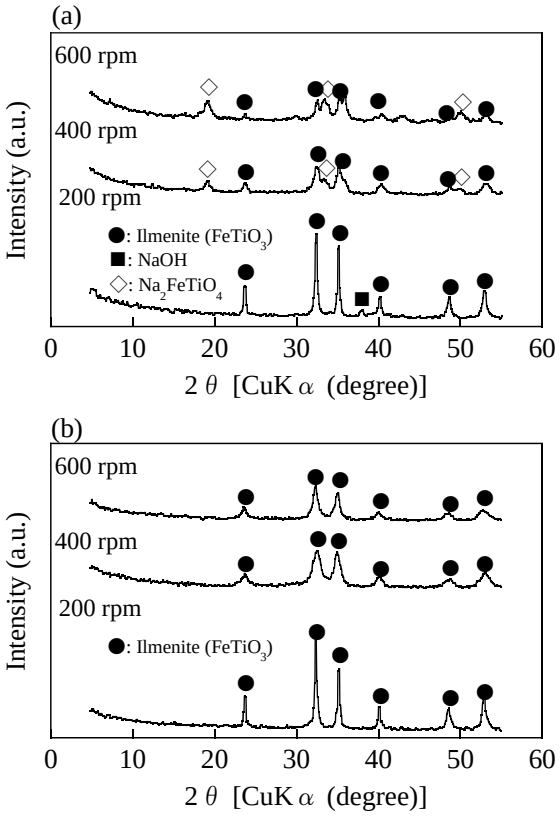

Fig.4 The XRD patterns of the mechanochemically treated samples at different rotation speeds and the residue after dissolving each sample in hydrochloric acid solution

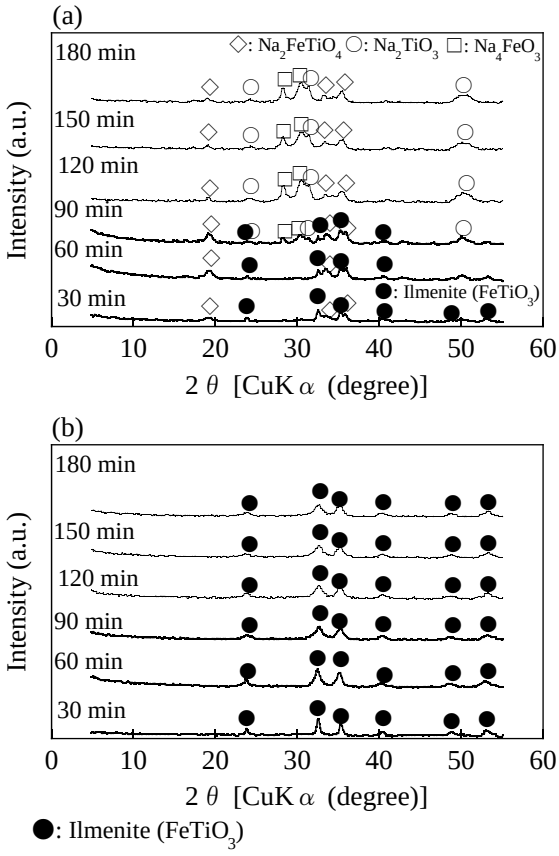

Fig.6 XRD patterns of (a) mechanochemically treated samples at different times and (b) the residue after dissolution of each sample

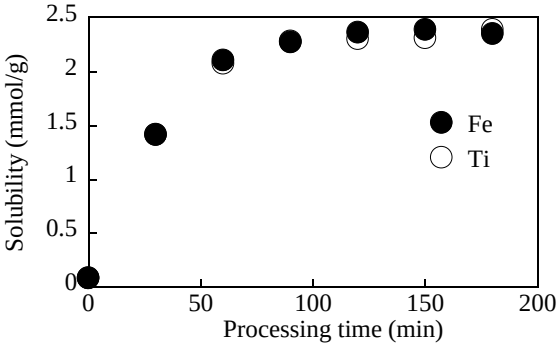

Fig.5 The amount of metal dissolved by mechanochemical treatment at different treatment times

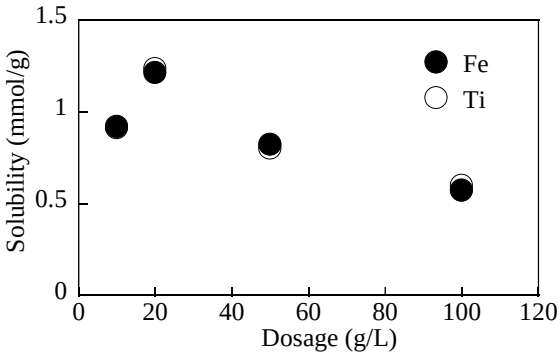

Fig.7 The amount of metal dissolved by adding the amount of sample into 1 mol/L hydrochloric acid solution

Figure 7 shows the amount of metal dissolved by adding the sample to 1 mol/L hydrochloric acid solution. It is noted that the pH of leachate remained at strong acidity (0.4 - 0.6). Iron and titanium were most soluble at an addition rate of 20 g/L, with iron and titanium at 1.21 mmol/g and 1.23 mmol/g, respectively. The amount of dissolution decreased above 50 g/L.

Figure 8 shows the amount of metal dissolved in the solution and the pH of the solution with various concentrations of hydrochloric acid. As hydrochloric acid concentration increased, the amount of dissolved metal increased from 0.1 mol/L and the pH of the solution dropped steeply with hydrochloric acid concentration of 0 - 0.1 mol/L.

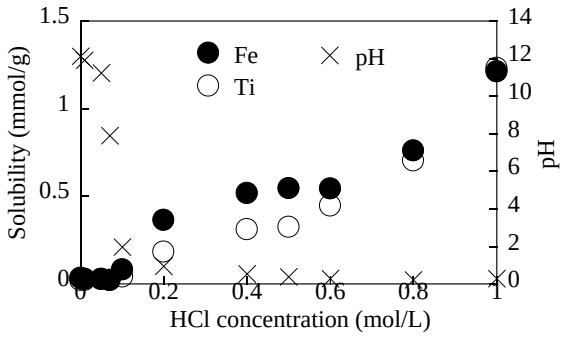

Fig.8 The amount of metal dissolved into the solution and pH of the solution with various concentration of hydrochloric acid

Figure 9 shows the amount of dissolution by leachate pH, and Figure 10 shows the XRD patterns of the residue after sample dissolution at HCl concentrations of 0, 0.2, 0.5, and 1.0 mol/L (pH of 12.24, 1.06, 0.61, and 0.24, respectively). The amount of dissolved material increased with a decrease in pH. The sodium salts of ilmenite, iron, and titanium did not dissolve at basic and neutral pH, but began to dissolve below pH 2. It is considered that the sodium salt dissolved in HCl at a lower pH, and the amount of dissolved metal increased.

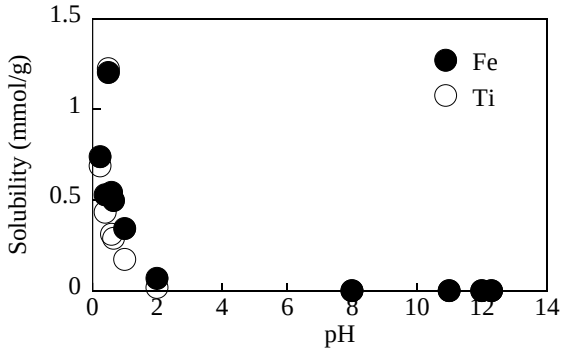

Fig.9 The amount of dissolution by pH of leachate

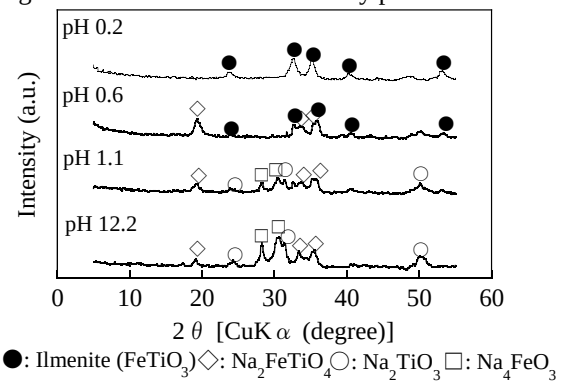

Fig.10 XRD patterns of the residue after sample dissolution at various HCl concentrations

Figure 11 shows photographs of the (a) carbon electrode before electrodeposition, (b) anode and (c) cathode after electrodeposition in leachate without oxalic acid, and (d) anode and (e) cathode after electrodeposition in leachate with oxalic acid. It should be noted that bubbles formed at both electrodes during the electrodeposition. There was no change in the original electrode for the anodes and cathodes in the leachate without oxalic acid (Fig. 11 (a), (b), (c), (e)), but precipitation was observed on the surface of the electrode at the anode in the solution with oxalic acid addition (Fig. 11 (d)). It was confirmed that the precipitate was metallic iron by energy dispersive X-ray spectroscopy (EDS). These results suggest that metallic iron can be recovered from ilmenite via mechanochemical treatment with NaOH, acid leaching, and electrodeposition.

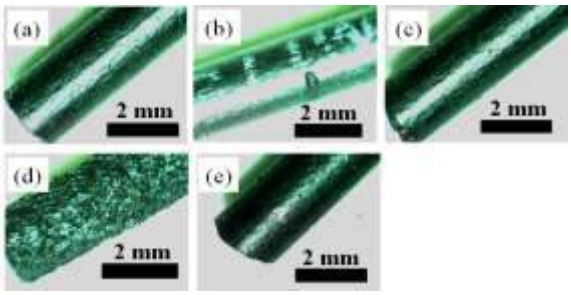

Fig.11 The photos of (a) carbon electrode before electrodeposition, (b) anode and (c) cathode after electrodeposition in leachate without oxalic acid, and (d) anode and (e) cathode after electordeposition in leachate with oxalic acid

CONCLUSIONS

In this study, we attempted to recover metallic iron from ilmenite-containing lunar regolith, abundantly present on the lunar surface, using a novel process consisting of mechanochemical treatment with sodium hydroxide, acid leaching with hydrochloric acid, and electrodeposition. Ilmenite can be converted into a soluble salt by mechanochemical treatment with sodium hydroxide at a rotation speed of 600 rpm for 120 min, and ferric ions were extracted into a hydrogen chloride solution under conditions where it became strongly acidic after dissolution. Metallic iron can be recovered via electrodeposition with the addition of oxalic acid.

ACKNOWLEDGMENTS

This study was supported by The Japan Mining Promotive Foundation Survey Test Research Project.

REFERENCES

[1] Astrobotic Lunar Landers, Astrobotic Technology, 2021, p. 5.

https://www.astrobotic.com/wp-content/uploads/2022/01/PUGLanders_011222.pdf
[2] Ellery A., Sustainable In-Situ Resource Utilization on the moon, Planetary and Space Science, Vol. 184, 2020, 104870. https://doi.org/10.1016/j.pss.2020.104870
[3] Wajima T., Space Development and Aggregate Resources, Journal of Japan Institute of Aggregate Technology, Vol. 212, 2022, pp. 180-191.
[4] Miyamoto H., Results of Solar System Explorations and their Implications to the Utilization of Space Resources, Resource Processing, Vol. 68, 2021, pp. 3-9. https://doi.org/10.4144/rpsj.68.3
[5] Wajima T., Space Development and Aggregate Resources, Journal of Japan Institute of Aggregate Technology, Vol. 212, 2022, pp. 180-191.
[6] Sakata I., Chen Y., and Wajima T., Lunar Resource Exploitation and Anticipated Risks during the Development of the Moon: Considering Selenological Aspects, Geoinformatics, 35, 2024, pp. 41-57. https://doi.org/10.6010/geoinformatics.35.2_41.
[7] Kubo K. "Mechanochemistry introduction" Tokyo Chemistry, Doujin, 1971.

Copyright © Int. J. of GEOMATE All rights reserved, including making copies, unless permission is obtained from the copyright proprietors.

15th Int. Conf. on Geotechnique, Construction Materials & Environment,
Kyoto, Japan, 11-13 November 2025, ISBN 978-4-909106124 C3051

SEMANTIC SEGMENTATION AND AUTOMATIC DETECTION TECHNOLOGY OF BALLAST RAILWAY BY INTEGRATING MULTI-SCALE GEOMETRIC FEATURES AND DEEP LEARNING OF POINT CLOUD

Diyuan Li[1]*, Shanpeng Liu[1], Koichi Isobe[2], Junling Si[3]

[1] Graduate School of Engineering, Hokkaido University, Sapporo 060-8628, Hokkaido, Japan
[2] Faculty of Engineering, Hokkaido University, Sapporo 060-8628, Hokkaido, Japan
[3] School of Transportation Science and Engineering, Harbin Institute of Technology, Harbin 150090, China

ABSTRACT

The safety of railway is crucial for railway transportation. With the advancement of digital technologies and the widespread use of mobile mapping systems, LiDAR-acquired 3D point cloud data offers a robust foundation for railway inspection. This paper addresses the challenge of inspecting ballast railway facilities by proposing an integrated method that combines deep learning-based semantic segmentation with Multi-scale Geometric Feature Enhancement (MGFE), and a kind of automatic sleeper distance calculation. First, multi-scale geometric features are introduced to enhance the point cloud dataset, thereby improving the performance of model to identify various ballast railway components. Based on this strategy, we employ three deep learning algorithms: PointNet++, PointNet++ MSG, and GACNet to perform semantic segmentation on ballast railway facilities, and we compare the segmentation performance before and after MGFE. Subsequently, sleeper information extracted from the segmentation results is clustered by the DBSCAN algorithm, and a sleeper distance calculation method is developed to assess the railway's structural health. Experimental results show that dataset MGFE significantly improves segmentation performance: on high-quality point cloud dataset of ballast railway, all models achieve overall accuracies above 90% and mIoU exceeding 80%. Moreover, the DBSCAN-based method accurately measures the distance between adjacent sleepers, showing strong correlation with actual measurements.

Keywords: Ballast railway, Point cloud, Semantic segmentation, MGFE, Deep learning

INTRODUCTION

Railway safety is of paramount importance to national transportation networks, serving as both the lifeline of national economies and a crucial guarantee for public travel. Regular inspection and maintenance of railway infrastructure constitute the fundamental safeguards for ensuring the operational safety of trains [1]. Traditional railway inspection methods primarily rely on manual patrols and rudimentary mechanical equipment, which are not only time-consuming and labor-intensive but also suffer from strong subjectivity, limited detection precision, difficulties in quantitative assessment, and interference with operational lines. Particularly for ballast railway structure inspection, traditional methods struggle to efficiently acquire comprehensive and accurate health status information.

In recent years, with the rapid development of digital technologies and the widespread application of mobile mapping systems, three-dimensional point cloud data acquired by Light Detection and Ranging (LiDAR) has provided new technical means for railway facility inspection. Point cloud data captures the geometric features of complex structures with millimeter-level precision, offering advantages such as high accuracy, high density, comprehensive coverage, and non-contact acquisition. Compared with traditional two-dimensional images, three-dimensional point clouds can more completely represent the spatial structures and geometric relationships of railway facilities, bringing revolutionary changes to the field of railway inspection [2]. Mobile mapping systems combined with LiDAR technology can rapidly collect data at normal train operating speeds, significantly improving inspection efficiency while reducing impact on railway operations.

However, point cloud-based ballast railway facility inspection still faces numerous technical challenges. From the inherent characteristics of point cloud data, its irregular, unordered, and high-dimensional nature makes processing complex. Unlike structured two-dimensional image data, point clouds lack fixed structures and clear neighborhood relationships, making traditional convolutional neural networks difficult to apply directly [3]. Additionally, high-density point clouds often contain tens of millions of sampling points, resulting not only in high storage and transmission costs but also in substantial computational burden. Furthermore, field-collected point cloud data frequently introduces noise and data gaps due to factors such as equipment

vibration, uneven reflection, or partial occlusion, affecting the reliability of subsequent analyses.

Moreover, the ballast railway environment contains a variety of components, such as rails, sleepers, ballast, and fasteners, which are not only complexly arranged but also similar in geometric features, increasing the difficulty of accurate classification. Particularly, some critical small components, such as fasteners, are often not prominent in point cloud representations and are easily misclassified or completely overlooked [4]. Natural environmental factors along railway lines, such as vegetation intrusion, water accumulation, and sediment deposition, further increase the complexity of point cloud data, creating additional obstacles for accurate detection. Most importantly, the precise measurement of key geometric parameters, such as sleeper spacing, depends on high-quality semantic segmentation results, requiring algorithms to not only distinguish different components but also accurately locate their spatial positions, which places higher demands on point cloud processing technology [5].

To address these challenges, this paper proposes an integrated method for semantic segmentation of railway ballast railway components that combines deep learning-based semantic segmentation with MGFE, and develops an automatic sleeper distance calculation method. First, a multi-scale geometric feature enhancement method is proposed. By calculating and integrating geometric features such as normal vector variation rate, curvature, and verticality into the original point cloud data, the ability of segmentation models to recognize various ballast railway components is significantly improved, especially for structures with similar shapes and small volumes. Then, based on the enhanced point cloud data, the performance of three deep learning algorithms (PointNet++, PointNet++ MSG, and GACNet) in ballast railway facility segmentation is evaluated. The performance differences before and after enhancement are compared and analyzed, quantitatively validating the effectiveness of the proposed method. A DBSCAN clustering-based automatic sleeper distance calculation method is designed. This method extracts sleeper information from segmentation results, determines spatial positions through density clustering, and achieves accurate measurement of adjacent sleeper distances, providing quantitative basis for ballast railway health status assessment.

RESEARCH SIGNIFICANCE

This study proposes a deep learning-based framework that integrates multi-scale geometric feature enhancement and semantic segmentation for ballast railway inspection using LiDAR point clouds. By introducing six geometric features of different radius and evaluating three segmentation models—PointNet++, MSG, and GACNet—the method significantly improves classification accuracy for complex railway components. Furthermore, a DBSCAN-based approach enables high-precision automatic calculation of sleeper spacing, achieving a mean absolute error of only 2.65 mm. The results demonstrate the capability of extracting both semantic and geometric information from unstructured point clouds, providing accurate, efficient support for railway infrastructure analysis and maintenance planning.

METHODS

Framework

Fig. 1 illustrates the overall technical framework of our proposed method, which consists of three main modules: data preprocessing and feature enhancement, deep learning-based semantic segmentation, and automatic sleeper distance calculation.

In the first stage, we calculate six multi-scale geometric features (normal change rate, first-order moments, neighbor point count, roughness, surface change, and verticality) to enhance the point cloud dataset. These features capture local geometric characteristics crucial for distinguishing various railway components with similar appearances.

The second stage performs semantic segmentation using three deep learning architectures: PointNet++, PointNet++ MSG, and GACNet. These networks are trained to classify each point into predefined categories including Rail, Ballast, Side ballast, Sleeper, Edge sleeper, Side sleeper, Sided edge sleeper, Fastener, and Noise. We employ cross-entropy loss with weighted regularization to address class imbalance issues. Performance evaluation compares segmentation results between models trained on original and feature-enhanced point clouds.

The final stage focuses on automatic sleeper distance calculation based on segmentation results. Points classified as sleepers undergo DBSCAN clustering to identify individual sleepers. Geometric centers are calculated for each cluster, followed by sequential ordering along the railway direction. Distances between adjacent sleepers are then computed using a vector-based approach, providing quantitative measurements for structural health assessment.

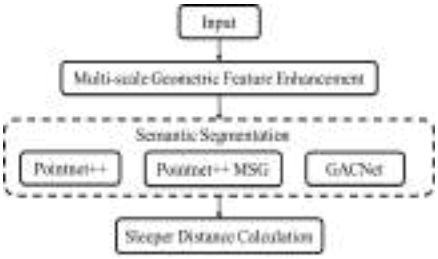

Fig. 1 Technical framework flow diagram

Multi-scale Geometric Feature Enhancement

Point cloud data of ballast railway contains complex structures with similar geometric appearances. To improve the discriminative ability of deep learning models, we propose a novel multi-scale geometric feature enhancement (MGFE) approach that integrates six geometric features into the original point cloud data. For each point, we compute features at multiple scales to capture both local details and broader structural contexts.

To the best of our knowledge, this is the first study to systematically introduce a comprehensive set of six geometric features—normal change rate, first-order moments, roughness, surface variation, verticality, and neighbor density—at multiple spatial scales for ballast railway point cloud enhancement. Unlike previous methods that either rely on raw coordinates or apply limited geometric descriptors, our MGFE framework offers a richer and more discriminative feature space, enabling improved segmentation performance especially for geometrically ambiguous and small-scale components.

For each point p_i with neighborhood $N_k(p_i)$, we perform Principal Component Analysis (PCA) to obtain eigenvalues λ_1, λ_2, λ_3 and corresponding eigenvectors $\vec{v}_1$, $\vec{v}_2$, $\vec{v}_3$ of the covariance matrix. The normal vector $\vec{n}_i$ at point p_i is defined as the eigenvector corresponding to the smallest eigenvalue: $\vec{n}_i = \vec{v}_1$, as shown in Fig.2. Based on this analysis, we calculate six geometric features:

(1) Normal Change Rate (NCR): Measures the consistency of normal vectors within a neighborhood, helping identify edge points and surface transitions:

$$\mathrm{NCR}_i = \frac{1}{|N_k(p_i)|}\sum_{p_j \in N_k(p_i)} \left(1 - \left|\vec{n}_i \cdot \vec{n}_j\right|\right) \quad (1)$$

(2) First-order Moments (FOM): Captures the spatial distribution of points relative to the tangent plane:

$$\mathrm{FOM}_i = \frac{1}{|N_k(p_i)|}\sum_{p_j \in N_k(p_i)} \left|\vec{n}_i \cdot \left(p_j - p_i\right)\right| \quad (2)$$

(3) Roughness**:** Quantifies local surface variation as the distance from each point to the best-fitting plane:

$$\mathrm{Roughness}_i = \lambda_1 \quad (3)$$

(4) Surface Variation (SV): Represents local curvature as the ratio of smallest eigenvalue to sum of all eigenvalues:

$$\mathrm{SV}_i = \frac{\lambda_1}{\lambda_1+\lambda_2+\lambda_3} \quad (4)$$

(5) Verticality: Measures alignment with the vertical direction, useful for distinguishing horizontal structures from vertical ones:

$$\mathrm{Verticality}_i = 1 - |\vec{n}_i \cdot \vec{v}_v| \quad (5)$$

Where $\vec{v}_v$ = [0, 0, 1] represents the vertical direction vector. This value approaches 0 for horizontal surfaces (like sleepers) and 1 for vertical surfaces (like rail sides).

(6) Number of Neighbor Points (NNP)**:** Provides density information within a fixed radius *r*.

To capture features at different scales, each feature using two neighborhood sizes were computed: small (r = 2cm), and large (r = 10cm). These multi-scale features are concatenated with the original coordinates to form the enhanced feature vector.

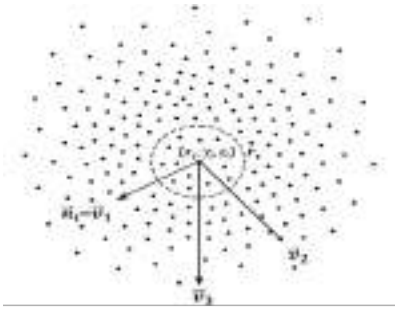

Fig. 2 How to feature calculation method of point cloud

Deep Learning Semantic Segmentation

Building upon the enhanced point cloud data, three deep learning networks were implemented for semantic segmentation: PointNet++, PointNet++ MSG, and GACNet.

PointNet++ [6]

PointNet++ processes point clouds hierarchically through four key steps: sampling representative points, grouping neighboring points, extracting local features using shared MLPs, and propagating features back to all original points. This hierarchical approach enables PointNet++ to capture geometric details at different levels, essential for distinguishing various railway components. The architecture consists of four set abstraction layers followed by four feature propagation layers with a final softmax classification layer.

PointNet++ MSG [6]

PointNet++ with Multi-Scale Grouping (MSG) extends the standard PointNet++ by addressing density variations in point clouds. Its key innovation is gathering points at multiple scales using different neighborhood sizes simultaneously. Features from these scales are extracted independently and concatenated, enhancing the model's ability to capture both fine details (fasteners) and larger structures (rails, sleepers), making it suitable for complex railway environments.

GACNet [7]

Graph Attention Convolution Network (GACNet) models point clouds as graphs with attention mechanisms. Each point connects to its nearest neighbors, with learnable attention weights applied to focus on the most relevant parts of local structures. By employing multi-head attention, GACNet captures diverse aspects of point relationships, effectively modeling intricate spatial connections between railway components.

Loss function

To address class imbalance, a weighted cross-entropy loss function L was employed [8]:

$$L = -\sum_{i=1}^{N} \sum_{c=1}^{C} w_c y_{ic} \log(\hat{y}_{ic}) \quad (6)$$

where N is the number of points in the training batch, C is the total number of semantic classes, $y_{ic} \in \{0,1\}$ is the one-hot encoded ground truth label indicating whether the *i-th* point belongs to class c, $\hat{y}_{ic} \in [0,1]$ is the predicted probability that the *i-th* point belongs to class c, w_c is the weight assigned to class c.

Automatic Sleeper Distance Calculation

This section presents a systematic approach for automatic sleeper distance calculation based on the semantic segmentation results obtained from the deep learning models.

DBSCAN Clustering Algorithm

After obtaining semantic segmentation results, the points classified as sleepers are extracted for further processing. To identify individual sleepers from these clusters, we apply the Density-Based Spatial Clustering of Applications with Noise (DBSCAN) algorithm.

DBSCAN is a widely used density-based clustering method that groups nearby points into clusters based on two parameters[9]:
ε: the neighborhood radius that defines how close points must be to each other to be considered part of the same cluster, minPts: the minimum number of points required to form a dense region. This algorithm starts from a randomly selected point and expands the cluster by recursively including all points within ε-neighborhoods that meet the minPts criterion. Points in low-density regions are treated as outliers.

Unlike algorithms such as K-means, DBSCAN does not require the user to specify in advance how many clusters are present in the data. Instead, it automatically determines the number of clusters based on the spatial distribution of points. This property is particularly beneficial in our application, as the number of visible sleepers in the point cloud may vary due to occlusion, incomplete scanning, or field conditions. DBSCAN can robustly detect each sleeper as a separate cluster, even when the spacing is irregular or some parts are partially missing.

Sleeper Distance Calculation

Following the successful clustering of individual sleepers, a vector-based approach is employed to calculate the distances between adjacent sleepers. The procedure consists of the following key steps:
Geometric Center Calculation: For each identified sleeper cluster C_i, its geometric center G_i is computed as the average position of all points within the cluster.
(1) Railway Direction Determination: The principal direction of the railway track is determined through Principal Component Analysis (PCA) on the set of all sleeper centers, with the dominant eigenvector representing the line direction.
(2) Center Determination: Sleeper centers are projected onto the railway direction vector and sorted to establish their sequential ordering along the track.
(3) Distance Computation: The distance between adjacent sleepers is calculated by projecting the vector between consecutive sleeper centers onto the railway line direction vector.

Fig. 3 illustrates the DBSCAN clustering process and the subsequent distance calculation. This approach accounts for potential deviations in sleeper orientation and provides precise measurements even when sleepers are not perfectly perpendicular to the railway direction. The calculated distances serve as quantitative indicators for evaluating railway structural health.

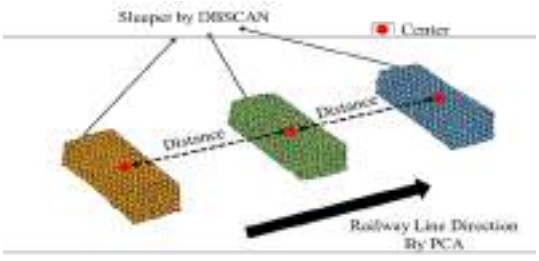

Fig. 3 DBSCAN clustering process and distance calculation

EXPERIMENTAL RESULTS

Experimental Setup

The experiments were conducted using a comprehensive point cloud dataset of ballast railway sections. The dataset was acquired using a mobile mapping system equipped with a high-precision LiDAR scanner mounted on a dedicated inspection vehicle. Data collection was performed at a speed of 30 km/h to maintain high point density while ensuring operational efficiency, as shown in Fig. 4(a).

The dataset covers approximately 500 meters of standard-gauge ballast railway track, including both straight sections and curved segments with varying radii. The total dataset contains approximately 205 million points. Points in the dataset were manually annotated into nine categories: Rail, Ballast, Side ballast, Sleeper, Edge sleeper, Side sleeper, Sided edge sleeper, Fastener, and Noise, as shown in Fig. 4(b).For validation purposes, the dataset was divided into training and testing sets with an 78.2:21.8 ratio, ensuring that both sets contained representative samples of all railway components across various track sections.

The deep learning models were implemented using the PyTorch framework (version 2.4.0) with CUDA 11.8 support. All experiments were conducted on a workstation equipped with an NVIDIA RTX 4090 GPU (24GB memory), Intel Core i9-14900K CPU, and 64GB RAM.

For model training, the following hyperparameters were utilized: Batch size: 12; Learning rate: 0.001 with cosine annealing schedule; Optimizer: Adam with $\beta_1 = 0.9$, $\beta_2 = 0.999$; Weight decay: 0.0001; Number of epochs: 200.

To address class imbalance, the weighted cross-entropy loss function described in Section 3.3.4 was employed with weights inversely proportional to class frequencies.

To comprehensively evaluate the performance of crack detection, we employed several standard metrics widely used in semantic segmentation tasks. For each class, true positives (TP), false positives (FP), and false negatives (FN) were calculated. Based on these values, the Intersection over Union (IoU) was computed as:

$$IoU = \frac{TP}{TP+FP+FN} \quad (7)$$

Semantic Segmentation Results

Feature Enhancement Effect Analysis

The efficacy of the proposed multi-scale geometric feature enhancement methodology was systematically evaluated through comparative analysis of segmentation performance metrics before and after feature MGFE across all three deep learning architectures: PointNet++ (PLUS), PointNet++ MSG (MSG), and GACNet.

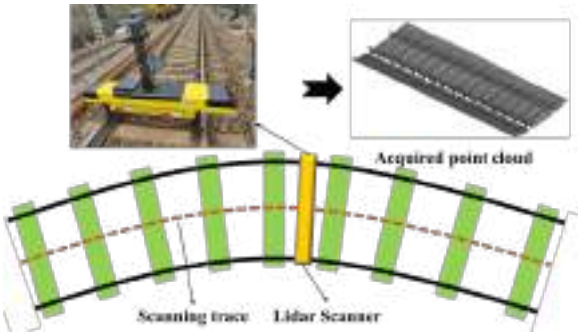

(a) How to acquire the point cloud data

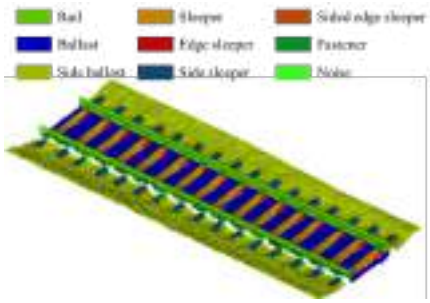

(b) Acquired point cloud data

Fig. 4 Data acquisition and dataset examples

As illustrated in Fig. 5, qualitative visual assessment between enhanced (E) and non-enhanced (NE) point cloud segmentation results demonstrates significant improvements attributable to MGFE. In the ballast railway section exemplar, all three architectures exhibit markedly enhanced segmentation fidelity with feature enrichment, particularly evident in small-scale components such as fasteners and transitional regions between distinct railway structural elements. The second exemplar further corroborates these observations, with enhanced models generating more precise segmentation boundaries.

Quantitative performance evaluation presented in Fig. 6 substantiates these qualitative assessments through intersection-over-union (IoU) metrics across

all railway component categories. For the PLUS architecture (Fig. 6(a)), geometric feature enhancement yielded substantial performance improvements across all semantic classes, with particularly pronounced enhancements observed in geometrically complex and small-scale components: fasteners (31.4% to 91.1%), sided edge sleepers (16.1% to 53.3%), and side sleepers (27.3% to 97.1%). The mean IoU metric increased substantially from 41.6% to 84.9%, representing a 43.3 percentage improvement.

Analogous performance enhancements were observed with the MSG architecture (Fig. 6(b)), which demonstrated significant IoU improvements particularly for ballast (87.6% to 97.2%) and side sleepers (56.0% to 97.4%). The overall mean IoU metric improved from 71.3% to 87.1%, constituting a 15.8 percentage point increase in segmentation accuracy.

The GACNet architecture (Fig. 6(c)) exhibited superior baseline performance compared to the other models but nevertheless benefited significantly from feature enhancement, with mean IoU increasing from 73.2% to 87.8%. Notably substantial improvements were observed in sided edge sleepers (31.1% to 63.3%) and noise point classification (61.7% to 76.1%), categories that present inherent challenges due to their spatial distribution characteristics and geometric ambiguities.

The experimental results conclusively demonstrate that the incorporation of multi-scale geometric features significantly enhances the discriminative capacity of point cloud deep learning architectures to differentiate between morphologically similar railway components, particularly in complex environments characterized by variable point densities and complex structural arrangements.

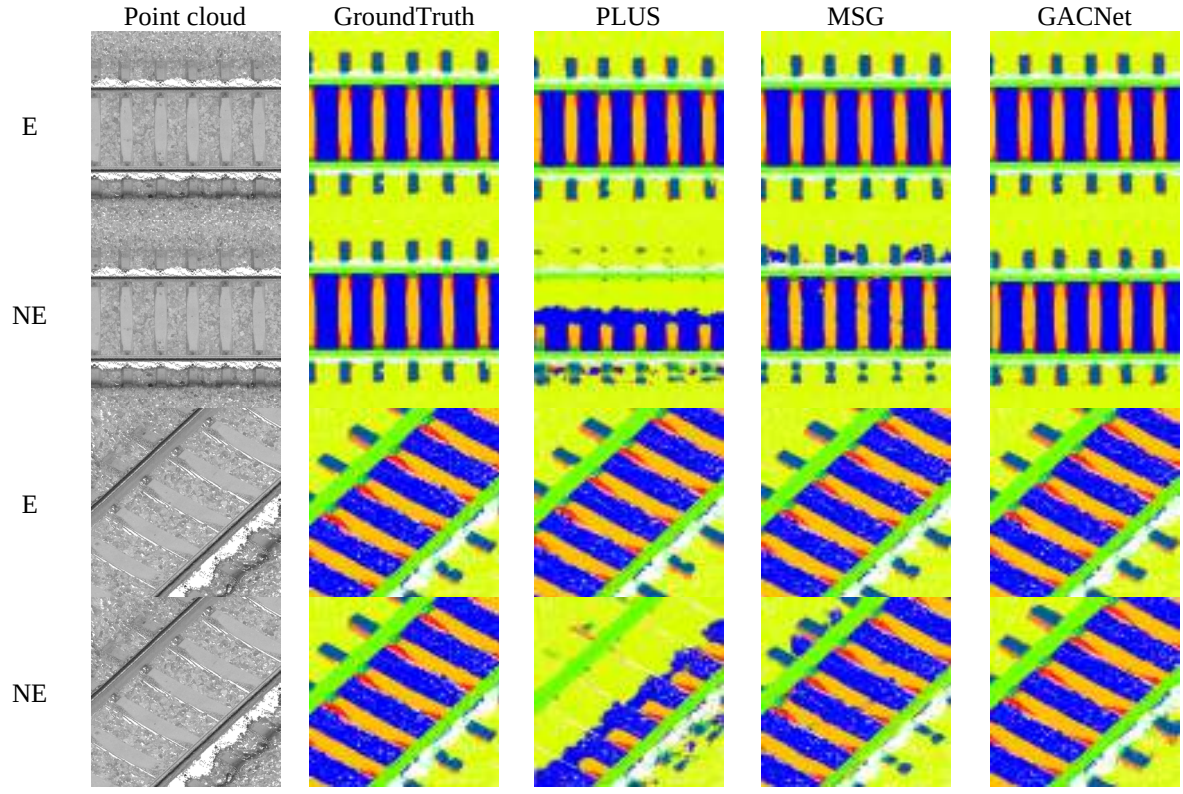

Fig. 5 Visualization of typical scene segmentation results, comparing original methods and proposed method

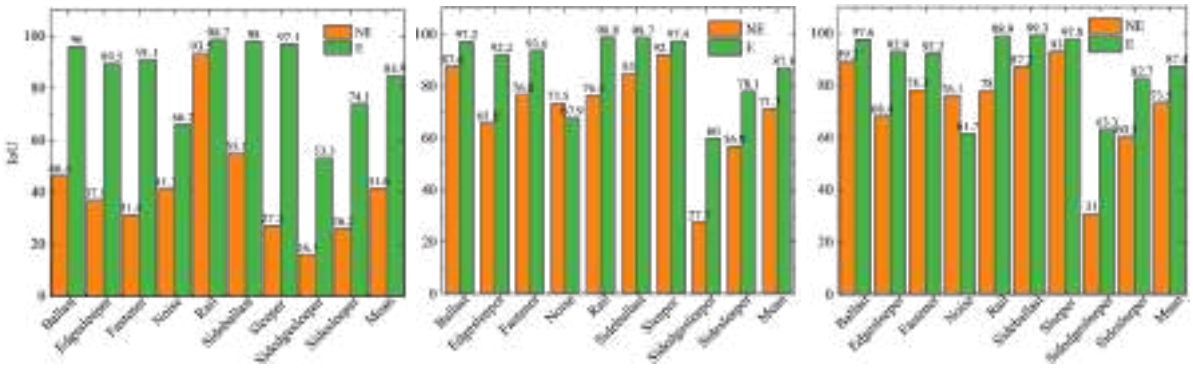

(a) PLUS (b) MSG (c) GACNet

Fig. 6 Performance comparison of three algorithms on original and enhanced point clouds

The comparative analysis presented in Fig. 7 illustrates the IoU performance metrics of the three deep learning architectures (PLUS, MSG, and GACNet) across nine railway component categories following multi-scale geometric feature enhancement.

For ballast segmentation, all three models achieve high accuracy with GACNet (97.6%) and MSG (97.2%) outperforming PLUS (96%). In edge sleeper classification, GACNet (92.9%) and MSG (92.2%) show similar performance, both surpassing PLUS (89.5%).

Side ballast classification shows GACNet (99.3%) slightly outperforming MSG (98.7%) and PLUS (98%). The most substantial performance differences appear in sided edge sleeper detection, where GACNet (63.3%) significantly outperforms MSG (60%) and PLUS (53.3%).

For standard sleepers, all models achieve excellent results with minimal variation (97.1-97.8%). In the side sleeper classification, GACNet (82.7%) demonstrates superior performance compared to MSG (78.1%) and PLUS (74.1%).

Overall, GACNet achieves the highest mean IoU (87.4%), closely followed by MSG (87.1%), with PLUS showing lower mean performance (84.9%).

The results indicate that while each model has specific strengths in certain categories, GACNet generally provides the most consistent performance across the majority of railway components.

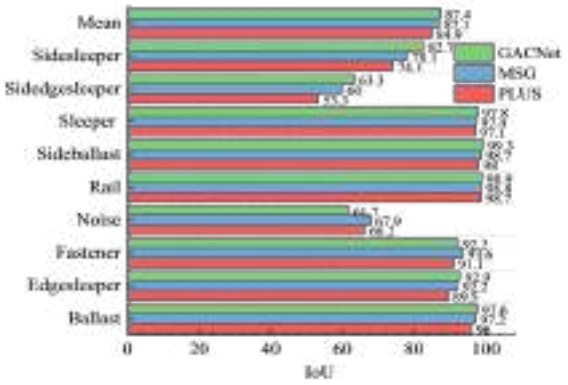

Fig. 7 Performance comparison of three algorithms

Sleeper Distance Calculation Results

Distance Measurement Accuracy

To evaluate the accuracy of the automatic distance measurement, a total of 83 sleeper distances were calculated from the point cloud data and compared with onsite measured reference values. The measured distances ranged from 0.5377 m to 0.6774 m, with an average distance of 0.6151 m.

Table 1 summarizes the statistics of these on site measured measurements. The measurements indicate that the average sleeper distance is 615.1 mm with a standard deviation of 22.5 mm, which falls within the expected range for standard ballast railway construction. The variation in distances (ranging from 577.7 mm to 677.4 mm) reflects the real-world conditions of the railway track.

Table 1 Statistics of sleeper distance measurement

Statistical Measurement	Value
Mean Distance	615.1 mm
Deviation of Distances	22.5 mm
Minimum Distance	537.7 mm
Maximum Distance	677.4 mm
Range	99.7 mm

Comparison of Deep Learning Models for Distance Calculation

Table 2 presents the error statistics for distance measurements based on segmentation results from each of the three deep learning models (with feature enhancement). In addition, Figure 7 visualizes the distance computation results, where the sleeper is marked as green, and the calculated geometric centers and distance are shown along the railway line.

Among the three models, GACNet achieved the highest accuracy in sleeper distance calculation with a mean absolute error (MAE) of 2.65 mm, which is 39.5% lower than MSG and 72.8% lower than PLUS. This significant improvement can be attributed to superior ability of GACNet to precisely segment sleeper boundaries, particularly at the interface between sleepers and ballast, which is critical for accurate clustering and center point calculation.

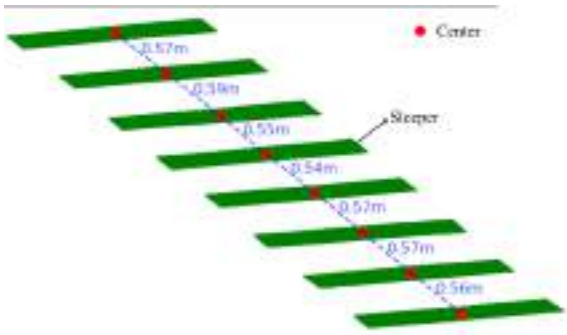

Fig. 8 Visualization of Sleeper Distance Calculation results

Table 2 Sleeper distance by point cloud

Statistical Measurement(mm)	PLUS	MSG	GACNet
MAE	9.76	4.38	2.65
RMSE	11.38	5.12	3.24
Standard Deviation	5.87	3.15	2.07
Maximum Error	18.92	10.47	6.18

CONCLUSION

This study proposed an integrated deep learning-based framework for the semantic segmentation and automatic sleeper distance measurement of ballast railway infrastructure using high-density LiDAR point cloud data.

By introducing a multi-scale geometric feature enhancement strategy, the discriminative capability of raw point clouds was significantly improved, enabling more accurate classification of morphologically similar railway components.

Comparative experiments demonstrated that MGFE led to substantial performance gains across all three evaluated models—PointNet++, PointNet++ MSG, and GACNet—with GACNet achieving the highest mean IoU of 87.8%.

Furthermore, a DBSCAN-based clustering method combined with a vector projection algorithm was developed to automatically compute sleeper distances. Experimental results on a 500-meter real-world dataset confirmed the accuracy and robustness of this approach, with GACNet-based results yielding a mean absolute error of only 2.65 mm.

These findings demonstrate the practical potential of integrating semantic segmentation with geometric measurement for efficient and accurate railway condition assessment. While the current framework performs well under ideal acquisition conditions, its dependence on high-density data and manually tuned parameters highlights opportunities for improvement.

ACKNOWLEDGMENTS

This work is supported by the National Key Research and Development Program of China (2024YFE0214600). The authors would like to express their sincere gratitude to the technical staff who assisted with the field data collection in the railway tunnel. The authors also acknowledge the computing resources provided by Hokkaido University that made the extensive computational experiments possible.

REFERENCES

[1] Debanath O. C., Quantifying the surface roughness evaluation of railway ballast grain under rotating drum abrasion. International Journal of GEOMATE, Vol. 26, Issue 113, 2024, pp.107-114.

[2] Jing G., Qin X., Wang H. and Deng C., Developments, challenges, and perspectives of railway inspection robots, Autom. Constr., Vol. 138, 2022, 104242.

[3] Xiao J., Zhang J., Adler B., Zhang H. and Zhang J., Three-dimensional point cloud plane segmentation in both structured and unstructured environments, Robot. Auton. Syst., Vol. 61, Issue 12, pp.1641-1652.

[4] Lamas D., Soilán M., Grandío J. and Riveiro B., Automatic Point Cloud Semantic Segmentation of Complex Railway Environments, Remote Sens., Vol. 13, Issue 12, 2021, 2332.

[5] Sun, Y., Li J., Yang, C., Hu, P., Zhang J. and Qiu X., High-Precision Railway Fastener Detecting via Deep Learning Radar for Intelligent Train Positioning, IEEE Sens. J., Vol. 24, Issue 6, 2024, pp.8150–8159.

[6] Qi R. C., Yi L., Su H. and Guibas J. L., PointNet++: Deep Hierarchical Feature Learning on Point Sets in a Metric Space, 2017.
[7] Wang L., Huang Y., Hou Y., Zhang S. and Shan J., Graph Attention Convolution for Point Cloud Semantic Segmentation, in 2019 IEEE/CVF Conference on Computer Vision and Pattern Recognition (CVPR), Long Beach, CA, USA: IEEE, 2019, pp.10288–10297.
[8] Mao A., Mohri M. and Zhong Y., Cross-Entropy Loss Functions: Theoretical Analysis and Applications, 2023.
[9] Ester M., Kriegel H. P., Sander J. and Xu X., A Density-Based Algorithm for Discovering Clusters in Large Spatial Databases with Noise, in Proc. 2nd Int. Conf. on Knowledge Discovery and Data Mining, 1996, pp.226-231.

Copyright © Int. J. of GEOMATE All rights reserved, including making copies, unless permission is obtained from the copyright proprietors.

15th Int. Conf. on Geotechnique, Construction Materials & Environment,
Kyoto, Japan, 11-13 November 2025, ISBN 978-4-909106124 C3051

CONVERSION OF WASTE GLASS FIBER REINFORCED PLASTICS USING MOLTEN ALKALI HYDROXIDES

Nobuyuki Kawagoe[1] and Takaaki Wajima[1]

[1]Graduate School of Science and Engineering, Chiba University, Japan

ABSTRACT

Glass fiber reinforced plastics (GFRP) is a composite material of glass fiber and thermosetting resin with high strength, used in a wide range of applications, and its waste is increasing. Due to the high fire resistance, it is difficult to incinerate, and most of it is currently disposed of in landfills. This study investigated the decomposition mechanism of waste GFRP in molten alkali hydroxide to convert GFRP into geopolymer material. Waste GFRP used in this study contains 67 % resin including calcium carbonate as fillers, and glass fiber and others. The sample was immersed in the molten alkali hydroxide with NaOH : KOH = 1:0, 3:1, 1:1, 1:3 and 0:1, and heated at 200 - 600 ℃ for 1.5 h. Molten alkali hydroxide after dissolving GFRP (fused GFRP) was mixed with fly ash and water, and dried at 60 ℃ for 24 h to form geopolymer material. Regardless of types of molten alkali hydroxide, glass fiber dissolved into molten alkali hydroxide at 300 ℃. Resin components also dissolved into molten alkali hydroxide at 200 - 300 ℃ and gasification occurred over 400 ℃. The mixture of fused GFRP which was heated at 300 ℃ after adding GFRP into alkali hydroxide with NaOH: KOH = 1:1, 1:3, and 0:1 (molten hydroxide : GFRP = 4:1), fly ash, and water could be converted into a geopolymer solid with compressive strength, equivalent to half the strength of Portland cement. It was revealed that waste GFRP can be dissolved in molten alkali hydroxide, and fused GFRP can be converted into a geopolymer material by adding fly ash and water.

Keywords: GFRP, Molten alkali hydroxide, Fly ash, Geopolymer

INTRODUCTION

Glass fiber reinforced plastics (GFRP) is a composite material of glass fiber and thermosetting resin with high tensile and compressive strength, and is used in various fields, including ships, aircraft, leisure goods, and other markets. Its market size is about 47.1 billion USD in 2023 [1]. In addition, its demand is expected to continue to grow in the future. On the other hand, the amount of waste GFFP is increasing.

Due to the high fire resistance, GFRP is difficult to incinerate, and most of it is currently disposed of in landfills. In Japan, more than 90 % of waste GFRP is disposed of in landfills [2]. However, increased landfill disposal costs have caused social problems such as illegal dumping [3]. Mechanical, thermal, and chemical methods have been suggested as recycling technologies for GFRP [4,5]. For the mechanical method, GFRP was ground to powder as a raw material for new composite materials, but glass fiber's physical properties decrease, leading to low market value [6]. For the thermal method, resin components in GFRP was decomposed by heating between 300 to 500 ℃ for several hours, consuming much energy [7], and the recovered glass fiber was cheap. For the chemical method, solvents were used to break down the resin components to generate hazardous wastewater, required for further processing [8]. The glass fiber recovered by chemical method possess higher strength compared to thermal method. In addition, recovered glass fibers from thermal or chemical process are relatively inexpensive, and still face cost-related limitations in practical applications [8]. Therefore, new recycling technology for GFRP is desired.

A geopolymer (GP) is an amorphous silicate paste, generally formed by the reaction of alkali silica liquid and alumina-silica powder. In comparison with Portland cement, GP cement has higher heat and acid resistance, and the CO_2 gas generated in the manufacturing process can be reduced [9,10]. In addition, GP materials can be used as an environmental purifier, such as water purification, soil improvement, deodorant and so on, with cation exchange capacity [11,12].

In a previous study, waste GFRP is pyrolyzed with sodium hydroxide to be powdered without mechanical crushing, glass fiber is transformed into soluble alkali silicate material to be extracted into water, and resin in GFRP is decomposed to fuel gasses, such as hydrogen and methane [3]. Crushed rock sand is solubilized by fused alkali hydroxide and converted into geopolymer material with high acid resistance, and heat resistance [13–17]. From these results, the new recycling process can be suggested that resin in GFRP dissolve and gasify, glass fiber in GFRP solubilized and converted into geopolymer material.

In this study, the decomposition mechanism of waste GFRP in the molten alkali hydroxide was investigated to be converted into GP material.

RESEARCH SIGNIFICANCE

GFRP has high heat resistance and durability, but it is leading to difficulties in processing crushing or incineration to be disposed. Therefore, most of waste GFRP is disposed of in landfills. This study proposes a new potential process to convert resin and glass fiber in GFRP into fuel gases, hydrogen and methane, and geopolymer using molten alkali hydroxide, respectively. This is a zero-emission process and convert into clean energy sources, hydrogen and methane gas, and environmentally harmonious material, geopolymer material.

EXPERIMENTAL

Sample

Waste GFRP used in this study was generated in Japan. Figure 1 shows the appearance of waste GFRP sample for the experiment. It was cut into 1.5 × 1.5 × 0.2 cm.

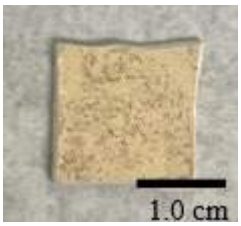

Fig.1 The appearance of waste GFRP sample

Figure 2 shows the XRD pattens of waste GFRP obtained by an X-ray diffraction apparatus (XRD) (D8 ADVANCE, Bruker AXS). The peak of calcite ($CaCO_3$) (used in GFRP as a filler) and quartz (SiO_2) were observed.

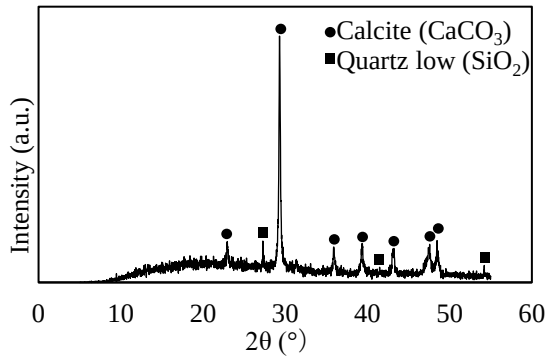

Fig. 2 XRD pattern of waste GFRP

Figure 3 shows the change in weight and heat flow concerning the temperature change of the sample by thermogravimetry/ differential thermal analyzer (TG-DTA) (STA-6000, Perkin Elmer). There are two weight decreases. The first one is 31.3 % weight reduction around 300 - 400 ℃, and heat flow indicates an endothermic reaction, causing the thermal decomposition of epoxy resin. The other one is 16.0 % reduction around 700 ℃, and heat flow indicates an endothermic reaction, causing decarbonation of calcium carbonate. From these results, it can be expected that the weight ratio of epoxy resin, calcium carbonate, and glass fiber and others in the sample is 32%, 35 %, and 33 %, respectively.

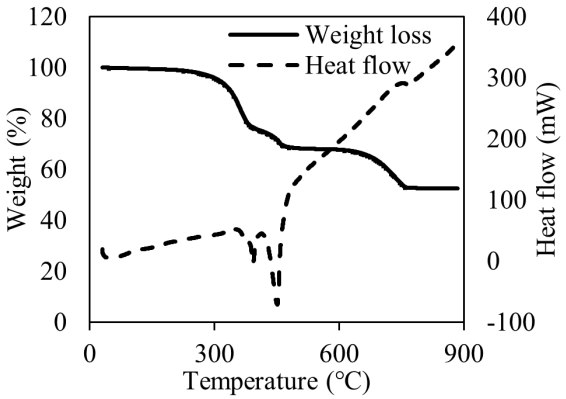

Fig. 3 TG-DTA analysis of waste GFRP

Decomposition Behavior of Waste GFRP in Molten Alkali Hydroxides

Figure 4 shows the experimental flow for the decomposition of waste GFRP in molten alkali hydroxides. The alkali hydroxide (60 g) mixing NaOH : KOH = 1:0, 3:1, 1:1, 1:3, 0:1 (weight ratio) was added into the stainless reactor (φ 4 × 25 cm), and was heated at 400 ℃ for 90 min (including 30 min of temperature rising time) with nitrogen flow (20 mL/min) to prepare alkali hydroxide with different alkali ratio. After heating and cooling to room temperature with nitrogen flow (20 mL/min). The sample (1 g) was packed in a mesh stainless bag with a stainless-steel ball (φ = 1.0 cm); the ball was placed on the sample to prevent it from floating in the molten alkali hydroxide. This bag was added to the reactor on the prepared alkali hydroxide and heated at 200 - 600 ℃ for 90 min (including 30 min of temperature rising time) in nitrogen atmosphere. During heating, generated gas through the condenser to condense condensable gases was collected by a gas pack and the component ratio in the collected gas was analyzed by a gas chromatograph (GC-8A, SHIMADZU), and the total amount of generated gas was calculated using Eq. (1).

$$S_g = V \frac{C_g}{C_T} \quad (1)$$

S_g : the amount of generated gas (mL), C_g : the concentration of specific gas measured by the

detector (ppmV), C_T: the concentration of total gas (ppmV), V: the amount of the total gas generated (mL)

After heating, the reactor was cooled to room temperature, 8 mol/L nitric acids (300 mL) were added into the reactor to dissolve the alkali hydroxide and filtrated. The weight of the residue after drying was measured, and the residual ratio was calculated using Eq. (2).

$$R = \frac{W}{W_0} \times 100 \quad (2)$$

R: the residual ratio (%), w: the weight of residue (g), w_0: the weight of GFRP sample (g)

The silicon concentration in the filtrate was measured by an inductively coupled plasma optical emission spectrometer (ICP-OES, Avio500, Perkin Elmer) to calculate silica concentration, and the dissolved glass fiber was calculated using Eq. (3).

$$S_{SiO_2} = \frac{C_{SiO_2}}{W_0} V \quad (3)$$

S_{SiO_2}: the amount of dissolved glass fiber from 1 g of GFRP (g/g), C_{SiO_2}: the measured silica concentration (g/L), V: the amount of solution (L)

The organic carbon concentration in the filtrate was measured by a total organic carbon meter (TOC-L, SHIMADZU), and the dissolved resin carbon was calculated using Eq. (4).

$$S_{toc} = \frac{C_{toc}}{W_0} V \quad (4)$$

S_{toc}: the amount of dissolved total organic carbon (TOC) from 1 g of GFRP (g/g), C_{toc}: the measured total organic carbon concentration (g/L)

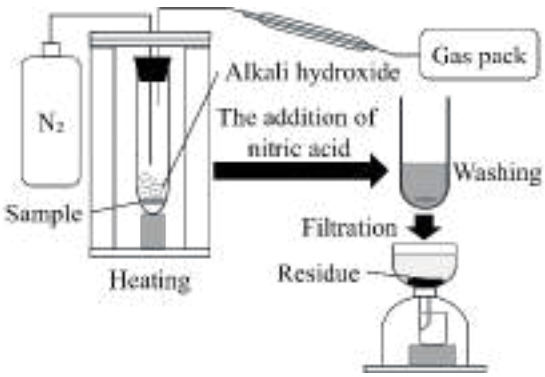

Fig. 4 Experimental flow for GFRP decomposition

As a comparison, GFRP sample without alkali hydroxide was heated at 200 - 600 ℃ for 90 min (including 30 min of temperature rising time) with nitrogen flow (20 mL/min) as pyrolysis.

The potassium hydroxide (60 g) was heated at 400 ℃ for 90 min (including 30 min of temperature rising time) in the reactor (φ 4 × 25 cm) with nitrogen flow. After heating and cooling to room temperature, the GFRP sample (1 - 25 g) was added into the reactor and heated at 300 ℃ for 90 min (including 30 min of temperature rising time) with nitrogen flow. During heating, generated gas was collected by a gas pack, and the amount of total gas was calculated, and the residual ratio, the dissolved glass fiber, and the dissolved resin carbon after heating were calculated using Eq. (1) - (4), respectively.

Geopolymer From Molten Fused GFRP

Figure 5 shows the experimental flow of preparing a geopolymer from molten fused GFRP. The alkali hydroxide mixing NaOH: KOH = 1:1, 1:3, 0:1 (weight ratio) was heated at 400 ℃ for 30 min (including 10 min of temperature rising time) in a crucible and collected from crucible after heating and cooling to room temperature. Powder sample of waste GFRP (3 g), was added to the bottom in the crucible, and the prepared alkali hydroxide (12 g) was added on the GFRP powder. The crucible was heated at 300 ℃ for 75 min (including 15 min of rising time). After heating and cooling to room temperature, the alkali hydroxide after adding waste GFRP (fused GFRP) was mixed with water and fly ash (Ⅴ types) in the ratio of 4 - 6 : 4 - 6 : 10 : 22, and this mixture was filled into a circular mold (φ 4 × 0.3 cm) and was dried in a drying oven at 60 ℃ for 24 h. The strength test of the cured product was measured using the method of previous study [17]. Chemical composition of fly ash used in this experiment is shown in Table 1.

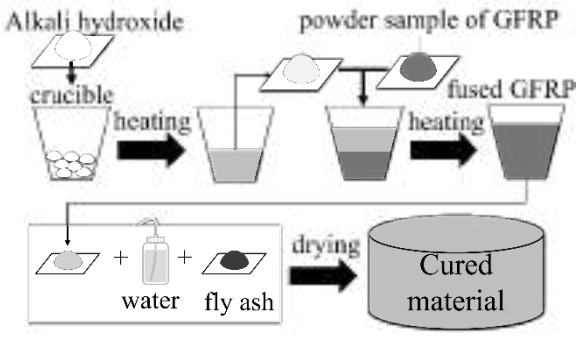

Fig 5. Experimental flow of geopolymer preparation

Table 1 Chemical composition of fly ash

Compound	Weight (%)
SiO_2	54.99
AlO_3	20.79
Fe_2O_3	10.7
CaO	5.13
TiO_2	2.37
Others	6.02

RESULTS AND DISCUSSION

Decomposition Behavior of Waste GFRP in Molten Alkali Hydroxides

Figure 6 shows the residual ratio of waste GFRP heating at 200 - 600 ℃ in molten alkali hydroxide. The residual ratio of pyrolysis is also shown in this graph. In the pyrolysis, the residual ratio was decrease at 200 - 400 ℃ and remain about 70 % at 400 - 600 ℃, meaning that only resin was decomposed to remain glass fiber and fillers. At 200 ℃, the alkali hydroxide did not melt, and the sample could not be immersed in the molten alkali hydroxide with NaOH: KOH = 1:0 and 3:1. On the other hand, alkali hydroxide with NaOH : KOH = 1:3, and 0:1 melted, the sample was immersed, and the weight ratio decreased to 40 - 60 %. At higher 300 ℃, the residual ratios were lower than 20 % regardless of type of alkali hydroxides. Furthermore, at 300 ℃, the higher the weight ratio of KOH in molten alkali hydroxide, the lower the residual ratio, suggesting that KOH has higher ability to decompose GFRP than NaOH.

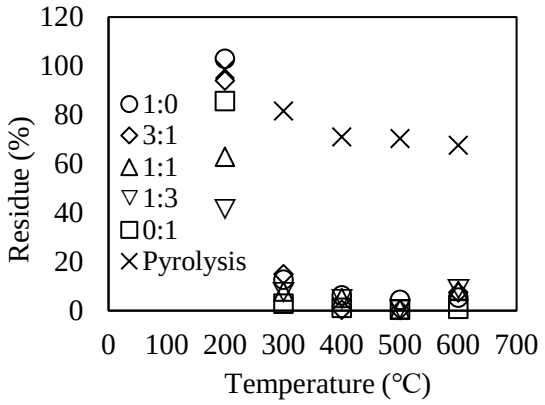

Fig. 6 Residual ratio of waste GFRP

Figure 7 shows the residue after heating with alkali hydroxide with NaOH: KOH = 1:3 at (a) 200 ℃ and (b) 300 ℃. At 200 ℃, the residue retained its original shape with a slightly smaller size compared to that before the treatment, and the fiber-like structure was observed on the surface. At 300 ℃, the residue was completely pulverized, and its weight was 0.075 g. It is noted that no Si component was included in the residue at 300 ℃, analyzed by XRF analysis, indicating that glass fiber dissolved in molten alkali hydroxide.

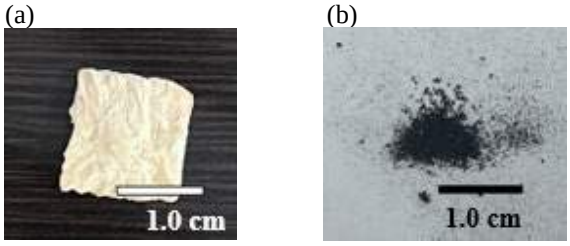

Fig.7 Appearance of residues after heating molten alkali hydroxide with NaOH : KOH = 1 : 3 at (a) 200 ℃ and (b) 300 ℃

Figure 8 shows the dissolved glass fiber in molten alkali hydroxide. Dissolved glass fiber was lower than 0.1 g/g at 200 ℃, while it was 0.2 g/g above 300 ℃, regardless of type of alkali hydroxide. This result is consistent with the trend of residue. It suggests that almost all glass fiber dissolved in molten alkali hydroxide above 300 ℃ with the following reaction;

$$SiO_2 + 2NaOH \rightarrow Na_2SiO_3 + H_2O \quad (5)$$

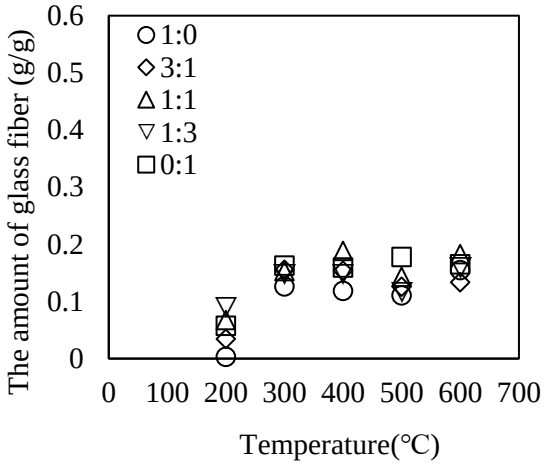

Fig. 8 The amount of dissolved glass fiber in molten alkali hydroxide

Figure 9 shows the dissolved resin carbon in molten alkali hydroxide. The dissolved resin was larger in alkali hydroxide with the higher KOH ratio. The dissolved resin carbon increased from 200 to 300 ℃ and decreased above 300 ℃. The dissolved resin carbon at 300 ℃ in alkali hydroxide with NaOH: KOH = 1 : 1, 1 : 3, and 0 : 1 were about 0.3 g/g, indicating that almost resin in GFRP dissolved in molten alkali hydroxide. It suggests that the large amount of resin component dissolved at 300 ℃.

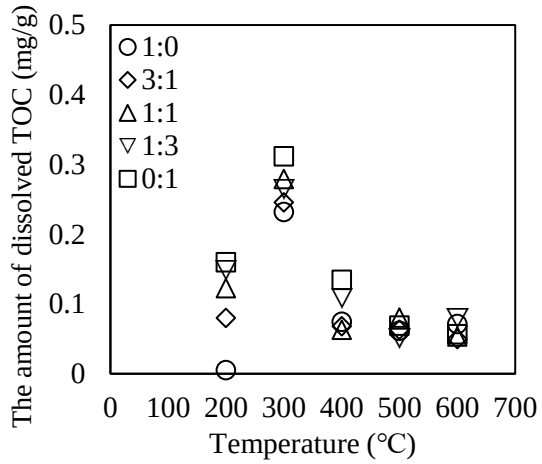

Fig. 9 The amount of dissolved resin carbon

Figure 10 shows the generated amount of gases (H_2, CH_4). It is noted that CO and CO_2 did not detect in gas phase, but carbonate ion was detected in molten alkali after dissolving in distilled water. Molten alkali hydroxide may dissolve CO and CO_2, preventing them from emitting in the gas phase. The gas amounts of H_2 and CH_4 increased significantly above 400 ℃, meaning that the resin gasified above 400 ℃. The amount CH_4 gas was larger in alkali hydroxide with the higher KOH ratio.

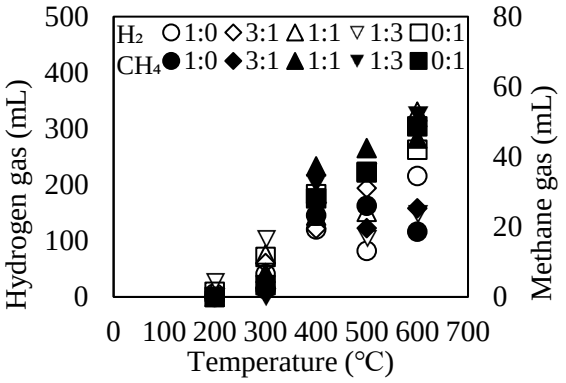

Fig. 10 The amount of generated gas (H_2, CH_4)

From the results of Fig. 9 and Fig. 10, for the decomposition behavior of resin in GFRP; it was assumed that the resin is dissolved at 300 ℃, while the resin is gasified above 400 ℃.

Sample addition dependence of decomposition behavior of waste GFRP in molten alkali hydroxides

Figure 11 shows the residual ratio of waste GFRP heating at 300 ℃ in molten potassium hydroxide with different addition of GFRP. The residual ratio was constant when the amount of waste GFRP addition was 0.1 - 0.35 g/g, and increased when the amount of waste GFRP addition was more than 0.35 g/g addition. This result implies that molten potassium hydroxide could dissolve 80 % of the GFRP up to 0.33 g/g.

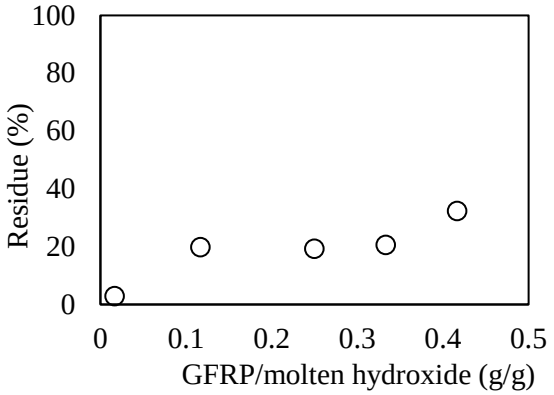

Fig. 11 The residual ratio of waste GFRP in KOH at 300 ℃

Figure 12 shows the dissolved glass fiber and resin in molten potassium hydroxide. The dissolved resin was almost constant (0.02 - 0.42 g/g) while the dissolved glass fiber was almost constant (0.02 - 0.25 g/g) and decreased above 0.33 g. These results imply that whole glass fiber can be dissolved up to GFRP/molten hydroxide = 0.25 g/g while the resin was dissolved up to 0.5 g/g.

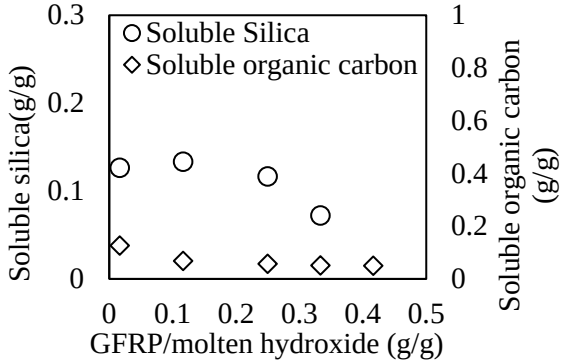

Fig. 12 The amount of dissolved glass fiber and resin components in KOH at 300 ℃

From the results of Fig. 12 and Fig. 13, it is suggested that GFRP can be processed up to 0.25 g/g in KOH at 300 ℃.

Geopolymer From Fused GFRP

Table 2 shows the compressive strength of the solids prepared on various mixing conditions. The solid didn't harden using more than 6 g of water. The solid of fused GFRP : water : fly ash = 3 : 2 : 8 was obtained the hardest product. The compressive strength of solid using 4 g of water was lower than

that of 5 g of water. It suggests that an excessive amount of water leads to being solidified incompletely. As the amount of fly ash added increased using 4 g of water, the compressive strength initially increased, and decreased above 18 g of fly ash addition.

Table 2 The compressive strength of the obtained solid

Water [g]	Fly ash [g]	Strength [N]
4	10	18
4	12	58
4	14	77
4	16	150
4	18	21
4	20	-
5	10	×
5	12	×
5	14	×
5	16	34
5	18	51
5	20	27

×: broke during demolding, -: not performed

Figure 13 shows the appearance of the hardest solid (fused GFRP: water : fly ash = 3 : 2 : 8). The surface of it was smooth. It is noted that the gray powder on the surface is thought to be the fly ash that was insufficiently mixed.

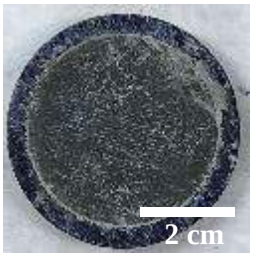

Fig. 13 The appearance of the hardest solid

Table 3 The compressive strength of the solid

NaOH : KOH	1:1	1:3	0:1	Cement
Strength [N]	113	204	104	550

Table 3 shows the compressive strength of the solids with different NaOH : KOH ratio with the compressive strength of Portland cement as a comparison. The solids were prepared from the mixture of fused GFRP : water : fly ash = 3 : 2 : 8, based on the results shown in Table 2. The solid of NaOH : KOH = 1 : 3 was obtained the hardest product, and its compressing strength was approximately half as high as that of Portland cement.

HAZARD MANAGEMENT

Sodium hydroxide and potassium hydroxide are highly corrosive, especially at elevated temperatures, and careful selection of experimental apparatus is required. In this study, stainless steel vessels were used as reaction containers. Since molten alkali hydroxides pose significant health risks, experiments were conducted with caution while wearing gloves, safety goggles, and lab coats. In addition, due to their strong hygroscopicity, alkali hydroxides were stored in a sealed and dry condition and opened only immediately before use.

CONCLUTION

In this study, the decomposition behavior of resin in molten alkali hydroxide and the feasibility of converting the fused GFRP after processing GFRP into geopolymer cement were investigated. The results showed that both the resin and glass fiber in GFRP dissolved in molten alkali hydroxide above 300 °C. The dissolved resin was converted into gases such as hydrogen and methane above 400 °C. GFRP could be processed up to 0.25 g/g in molten potassium hydroxide at 300 °C. After treatment, adding water and fly ash to the fused GFRP yielded a solid product. The solid of fused GFRP (NaOH : KOH = 1 : 3) : water :fly ash = 3 : 2 : 8 was the hardest product. It was 204 N, corresponding to 37 % of Portland cement, when the geopolymer was synthesized from a fused GFRP with NaOH : KOH = 1:3.

This method enables treatment at a relatively lower temperature (300 °C) and shorter reaction time than that of conventional thermal decomposition methods, which typically operate at around 500 °C for several hours. Therefore, a significant reduction in energy consumption can be expected.

The typical landfill disposal costs for a controlled landfill in Japan is approximately 100,000 yen per ton (2024). In this study, it was demonstrated that one ton of potassium hydroxide can process approximately one-fourth by weight of GFRP. The market price of industrial-grade potassium hydroxide in Japan is around 250,000 yen per ton (2025), meaning that the chemical cost alone is more than 10 times higher than that of landfill disposal. To enhance the economic feasibility of the alkali-based treatment process, it is essential to optimize the reaction conditions to reduce reagent consumption and to increase the added value of byproducts such as geopolymer materials.

REFERENCES

[1] Glass Fiber-Reinforced Plastics (Gfrp) Market Size, & Overview By 2031 n.d.

https://www.databridgemarketresearch.com/reports/global-glass-fiber-reinforced-plastics-gfrp-market (accessed February 15, 2025).

[2] Fuji Y., The Present Conditions of GFRP which Aimed at the Environmental Load Reduction. Journal of the Society of Materials Science, Japan, Vol. 57, No. 6, 2008, pp. 621-625.

[3] Miyazawa M., and Wajima T., Recycling Technology for Waste Glass Fiber Reinforced Plastics (GFRP) Using Pyrolysis with NaOH. Resour Process, Vol. 68, Issue 2, 2021, pp. 51-56.

[4] Karuppannan G. S., and Kärki T., A review on the Recycling of Waste Carbon Fibre/Glass Fibre-Reinforced Composites: Fibre Recovery, Properties and Life-Cycle Analysis. SN applied Sciences, Vol. 2, 2020, article number 433.

[5] Qureshi J., A Review of Recycling Methods for Fiber Reinforced Polymer Composites. Sustainability, Vol 14, Issue 24, 2022, article number 16855.

[6] Pickering S. J., Recycling Technologies for Thermoset Composite Materials—Current Status. Composite Part A: Appled Science and Manufacturing, Vol. 37, 2006, pp. 1206-1215.

[7] Nakanishi Y., Kimoto M., and Awaji T., Influence of Fiber, Matrix Resin and Additive on the Pyrolysis and Combustion Processes of FRP in Air. Journal of the Society of Materials Science, Japan, Vol. 45, No. 10, 1996, pp. 1125-1130.

[8] Gonçalves R. M., Martinho A., and Oliveira J. P., Recycling of Reinforced Glass Fibers Waste: Current Status. Materials, Vol. 15, Issue 4, 2022, article number 1596.

[9] Freire A. L., José H. J., and Moreira R. de F. P. M., Potential Applications for Geopolymers in Carbon Capture and Storage. International Journal of Greenhouse Gas Control, Vol. 118, 2022, article number 103687.

[10] Wu Y., Lu B., Bai T., Wang H., Du F., Zhang Y., Cai L., Can J., and Wang W., Geopolymer, Green Alkali Activated Cementitious Material: Synthesis, Applications and challenges. Construction and Building Materials, Vol 224, No. 10, 2019, pp. 930-49.

[11] Lin H., Zhang J., Wang R., Zhang W., and Ye J., Adsorption Properties and Mechanisms of Geopolymers and Their Composites in Different Water Environments: A Comprehensive Review. Journal of Water Process Engineering, Vol. 62, 2024, article number 105393.

[12] Wang S., Li L., and Zhu Z. H., Solid-State Conversion of Fly Ash to Effective Adsorbents for Cu Removal from Wastewater. Journal of Hazardous Materials, Vol. 139, Issue 2, 2007,pp. 254-259.

[13] Sakamoto K., and Wajima T., Preparation of Geopolymer Cement from Crushed Stone by-Product Using Alkali Fusion. Internatinal Journal of GEOMATE, Vol. 17, Issue 63, 2019, pp. 17-22.

[14] Sakamoto K., and Wajima T., Preparation of Geopolymer Cement from Simulated Lunar Rock Sand Using Alkali Fusion. Internatinal Journal of GEOMATE, Vol. 18, Issue 70, 2020, pp. 62-67.

[15] Wajima T., and Buntan A., Conversion of Waste Stone-Fine Slurry into Geopolymer Cement with Addition of Coal Fly Ash. Internatinal Journal of GEOMATE, Vol. 20, Issue 78, 2021, pp. 44-49.

[16] Toda O., and Wajima T., Preparation of Geopolymer Cement from Lunar Rock Sand Using Alkali Fusion, and Its Evaluation of Radiation sShielding Ability. Internatinal Journal of GEOMATE, Vol. 24, Issue 106, 2023, pp. 54-60.

[17] Wajima T., and Toda O., Preparation of Construction Materials from Simulated Lunar Rock Sand Using Alkali Salts. Internatinal Journal of GEOMATE, Vol. 28, Issue 127, 2025, pp. 104-111.

Copyright © Int. J. of GEOMATE All rights reserved, including making copies, unless permission is obtained from the copyright proprietors.

15th Int. Conf. on Geotechnique, Construction Materials & Environment, Kyoto, Japan, 11-13 November 2025, ISBN 978-4-909106124 C3051

POLICY IMPACT EVALUATION ON LAND PRICE: A CASE STUDY OF THE LOCATION OPTIMIZATION PLAN IN HACHIOJI USING PROPENSITY SCORE MATCHING

Kaichen He [1], Toru Nagahara [1] and Shinya Inazumi [1]

[1] Shibaura Institute of Technology, Japan

ABSTRACT

This study employs propensity score matching methodology to quantitatively assess the effects of Japan's Location Optimization Plan (hereafter LOP) on residential land price dynamics, with explicit consideration of disaster risk factors. While previous research has examined urban planning policies and land-use regulations as primary determinants of land price fluctuations, the interaction between disaster risk and policy intervention on land values remains under-explored. Land price stability is crucial for disaster risk management and urban policy since it ensures fair property values and fair investment, also affects urban planning and construct of infrastructure. This research addresses this gap by analyzing the causal effects of policy implementation using statistical matching techniques. Data from Hachioji City, where the LOP has been continuously implemented for over a decade, are compared to other densely populated areas within Tokyo Prefecture. Through the application of both nearest neighbor matching and kernel matching techniques, the analysis effectively isolates policy effects from confounding variables. As result, changing of the land prices in Hachioji City decreased by 6,911.11 JPY/m² compared to other areas in Tokyo. This study validates the effectiveness of propensity score matching for rigorous policy evaluation and provides empirical insights for future urban planning and disaster risk management strategies.

Keywords: Location Optimization Plan, Hachioji city, Land price dynamics, Disaster risk assessment, Propensity score matching

INTRODUCTION

In recent years, Japan has experienced escalating geotechnical disaster risks due to intensifying climate change and heightened seismic activity. The increasing frequency of landslides and liquefaction phenomena triggered by extreme precipitation and earthquakes has resulted in severe human and economic losses. This situation underscores the urgent need for policy frameworks that can effectively assess and mitigate disaster risks.

Previous studies, such as those by Sakamoto [1] and Daniel et al. [2], have demonstrated that disaster risk significantly influences land prices and may cause substantial property value depreciation. However, comprehensive analytical models incorporating both disaster risk factors and urban planning policies into land price analysis remain limited. Additionally, increased population density and inappropriate land use patterns in high-risk areas are exacerbating disaster impact severity, issues that remain systematically underexplored.

Compounding these challenges, empirical evidence from Nomura Real Estate [3] indicates that public awareness of disaster risk remains insufficient, despite the high probability of major seismic events directly affecting the Tokyo metropolitan area. In response to this context, the authors' preliminary research employed hedonic pricing methodology to model land prices in the Tokyo Bay area during 2022-2023, revealing growing market sensitivity to geotechnical risk impacts on property values. However, the influence of disaster risk perception and LOP implementation on land price dynamics remains inadequately characterized.

The LOP represents a national urban policy initiative in Japan designed to promote compact and sustainable urban development. Although the policy framework theoretically excludes high-risk areas such as landslide-prone zones from designated residential promotion areas, it lacks enforceable legal authority. Moreover, designating new residential zones outside existing urban planning frameworks often entails substantial infrastructure investments and logistical challenges.

This study examines the effectiveness of the LOP in stabilizing land prices while accounting for disaster risk factors through propensity score matching methodology. Specifically, the analysis evaluates residential area attributes that balance accessibility and disaster resilience, thereby providing empirical foundations for policy recommendations. Among Tokyo Prefecture's municipalities, Hachioji City represents the sole case with continuous LOP implementation for over a decade, making it an optimal empirical setting for this causal analysis.
This study quantitatively evaluates the impact of LOP on residential land prices using propensity score matching. By providing empirical evidence of policy effects, the research addresses a gap in quantitative policy evaluation and offers a replicable framework for future studies. The findings serve as a

valuable reference for policymakers aiming to assess and improve urban development initiatives.

STUDY AREA AND DATA

This study focuses on Hachioji City, located in western Tokyo Prefecture, as the primary analytical case (Fig.1) , which is the only municipality with continuous LOP implementation since 2014. (Neighboring cities, such as Fussa, adopted similar policies only recently and were therefore excluded.) Hachioji is the largest city in western Tokyo but has experienced population decline and aging since the early 2000s. These demographic changes have led to increased infrastructure burdens and a rise in vacant properties, complicating urban management. The city's LOP designates residential promotion areas based on proximity to public transportation, sufficient projected density (≥40 persons/ha), and adequate infrastructure, while systematically excluding landslide warning zones and industrial districts. However, exceptions exist, and the ongoing population decline continues to challenge sustainable management. Fig.2 shows the distribution of changes on land prices between treatment and control Groups in from 2014 to 2024.

In this research, official land price data from the Ministry of Land, Infrastructure, Transport and Tourism (MLIT) [4] and population density datasets from the National Spatial Planning database [5] were used.Densely populated areas within Hachioji were classified as the treatment group, while similar areas in other Tokyo municipalities served as the control group. Propensity score matching was applied to compare land price changes before (2013–2015) and after (2022–2024) LOP implementation. Only locations with complete data across this period were included, resulting in 507 observation points (93 in Hachioji, 414 in other cities). Land price values were averaged for the pre- and post-policy periods. Table 1 shows the mean difference in Land Price Changes Between Treatment and Control Groups

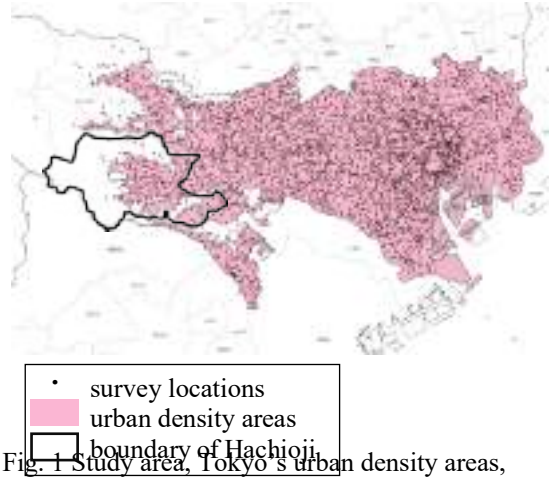

Fig. 1 Study area, Tokyo's urban density areas, land price survey locations and the boundary of Hachioji City.

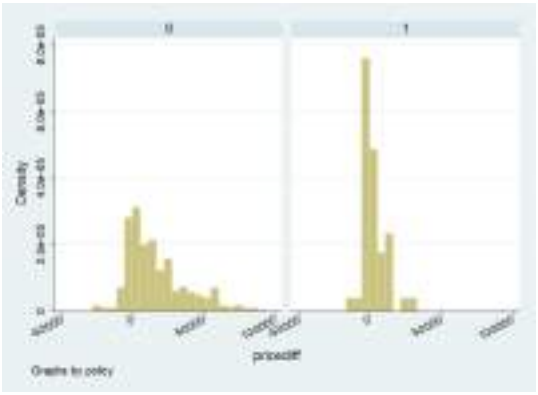

Fig.2 Distribution of Land Price Changes for the Treatment and Control Groups in a decade

Table 1 Mean Difference in Land Price Changes Between Treatment and Control Groups

group	Control	Treatment	combined	difference
Number of observations	414	93	507	/
Mean	16445.09	3186.38	14013.02	13258.71
Std.Err.	1045.81	793.93	895.55	2239.84
Std.Dev.	21278.99	1609.55	20164.71	/
t	5.92			

METHODOLOGY

The Propensity Score Matching (PSM) method is a statistical technique widely used to address selection bias in observational studies, particularly when treatment and control groups differ in background characteristics. In cases where randomized controlled trials are not feasible, such as policy evaluations where municipalities self-select into treatment conditions, PSM offers a robust framework to estimate causal effects by balancing covariates.

The central idea behind PSM is to estimate the probability (propensity score) that each unit (in this case, a geographical location) receives treatment, conditional on observed covariates. This score is then used to match treated and untreated units with similar characteristics, effectively mimicking randomized experimental conditions. Let $T \in \{0,1\}$ represent treatment status, and X be a vector of observed covariates. The propensity score e(X) is defined as Eq. (1):

$$e(X)=P(T=1 \mid X) \quad (1)$$

In this study, "treatment" refers to the implementation of the LOP. Since the policy is not randomly assigned, traditional methods such as Difference-in-Differences (DID) are inapplicable. Instead, PSM is employed to identify treatment effects by matching regions with similar observable attributes.

To account for potential confounding factors, a probit model is constructed using covariates that significantly influence treatment assignment. The main explanatory variables include land area, availability of water, gas, and sewer infrastructure, road width, distance to the nearest station, land use zoning type (land use zoning types are further categorized into residential, commercial, and industrial classes according to Japanese planning codes), building coverage ratio, floor-area ratio, population density, and land-use zones. Using Eq. (2):

$$P = \alpha T + \sum X\beta + \varepsilon \quad (2)$$

The influence of observed regional attributes, including population and locational characteristics, on land price variations is examined quantitatively.

The analysis applies one-to-one nearest neighbor matching within a common support region, ensuring that matches are made only between units with overlapping propensity scores. Matching is performed using the psmatch2 function in STATA 13, which estimates the Average Treatment Effect on the Treated (ATET) and Average Treatment Effect (ATE).Fig.3 shows the process for analyzation of Propensity Score Matching in this research.

The counterfactual refers to a hypothetical scenario in which an individual or unit experiences a treatment or outcome that did not actually occur. Specifically, it involves conceptualizing both the outcome that would result if the unit received the treatment (in this study, the policy intervention of the LOP) and the outcome if it did not, even though only one of these outcomes can be observed (Fig.4).

In essence, the counterfactual represents a hypothetical comparison: what would the dependent variable have been if the control group had received the policy intervention, or conversely, if the treatment group had not received it? Since it is fundamentally impossible to observe both potential outcomes for the same unit simultaneously, the unobserved outcome must be estimated using statistical methods.

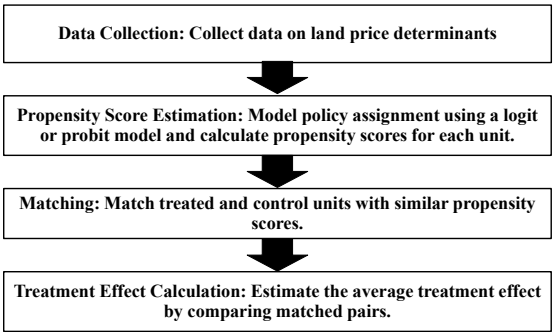

Fig.3 Analytical Process for Propensity Score Matching in Land Price Policy Evaluation

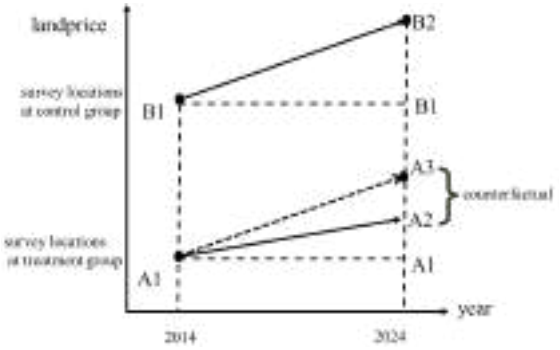

Fig.4 Concept of counterfactual

This approach enables the estimation of counterfactual outcomes by comparing each treated unit with its matched counterpart in the control group. The difference between observed and counterfactual land prices represents the causal policy effect.

Nearest Neighbor Matching (NNM)

Nearest Neighbor Matching pairs each treated unit with the control unit that has the closest propensity score. First, units in both groups are sorted by propensity scores. Then for each treated unit, the control unit with the smallest absolute difference in score is identified. The treatment effect is calculated as the difference in outcomes (land prices) between matched pairs. In practice, the nearest neighbor matching method involves the following steps. First, the propensity score e(X) is estimated using statistical models such as logistic or probit regression. This enables the calculation of each unit's probability of receiving treatment based on observed covariates (see Eq. (3)).

$$d(i,j)=|e(X_i)-e(X_j)| \quad (3)$$

Table 2 The result of Nearest Neighbor Matching

Teffect psmatch (NNM)	
Number of observations	507
Treatment model	logit
Price difference (Policy ATE)	
Coef	6911.11
Std.Err	1668.25
z	4.14
P>|z|	0
95%Conf.	10180.82
	3641.41

In Eq. (3), i refers to a unit from the treatment group and j to a unit from the control group. The covariate distance d functions as an indicator of similarity between matched units from both groups.

Next, the distance between covariates of treated and control units is computed. Based on the estimated propensity scores, this covariate distance is calculated using Eq. (4). For each individual i in the treatment group, a specific individual j* from the control group is selected to minimize the covariate distance between them.

$$j^*=\arg\min_{j\in\{T=0\}} d(i,j) \tag{4}$$

Matching is then performed by selecting, for each treated unit i, the control unit j with the smallest distance value, as shown in Eq. (4). Once matching is complete, the Average Treatment Effect (ATE) is estimated using Eq. (5), which calculates the average difference in outcomes between matched treated and control units.

$$ATE=\frac{1}{N}\sum_{i=1}^{N}\left(Y_i^{(1)}-Y_i^{(0)}\right) \tag{5}$$

In this context, $Y_i^{(1)}$ and $Y_i^{(0)}$ represent the outcomes for treated and untreated conditions, respectively, and N denotes the number of matched pairs in the sample.

The analysis revealed that as a policy effect of the LOP, changing of the land prices in Hachioji City decreased by 6,911.11 JPY/m² compared to those in other areas (Table 2). This result quantitatively demonstrates the specific impact of the policy on land values.

Kernel Matching (KM)

Kernel Matching (KM) is a variant of the propensity score matching method that operates under the assumption that no exact match with identical propensity scores exists in the sample. It is designed to estimate causal effects from observational data by adjusting for covariate imbalances between treatment and control groups.

In kernel matching, each treated unit is compared not with a single control unit but with all control units, using kernel-based weights that reflect the closeness of their propensity scores. This approach allows for the estimation of potential outcomes by assigning greater weight to control units with more similar scores and less weight to those further away.

A key feature of kernel matching is its ability to adjust the trade-off between matching precision and bias through bandwidth selection. By tuning the bandwidth parameter, researchers can optimize the balance between variance and bias while utilizing the entire sample, thus improving estimation accuracy. Following the approaches suggested in Markus Frölich's [6] and Gadisa Muleta and Takele Mebratu's [7] studies, bandwidth of 0.1 was chosen in my analysis.

Using kernel-weighted matching, the potential outcome $Y_i^{(0)}$ for each treated individual i, that is, the outcome that would have been observed had the individual not received the treatment, is estimated according to Eq. (6). For each treated unit i, similar control units j are identified, and their observed outcomes Y_j are weighted based on a kernel function. A weighted average of these outcomes is then computed to approximate the counterfactual outcome for unit i in the absence of treatment.

$$\widehat{Y}_i^{(0)}=\frac{\sum_{j\in\{T=0\}} K(d(i,j))Y_j}{\sum_{j\in\{T=0\}} K(d(i,j))} \tag{6}$$

This approach leverages information from all control units, assigning higher weights to those with propensity scores closer to that of the treated unit, thereby improving the precision of causal inference. Fig.5 shows theBalance check of Propensity score matching(the variable twozhongzhuan represents the Second-Class Medium-to-High-Rise Residential Zone, popu denotes population density. onejvzhu refers to the First-Class Residential Zone, onedizhuan indicates the First-Class Low-Rise Residential Zone. youseki and kenpei correspond to floor-area ratio and

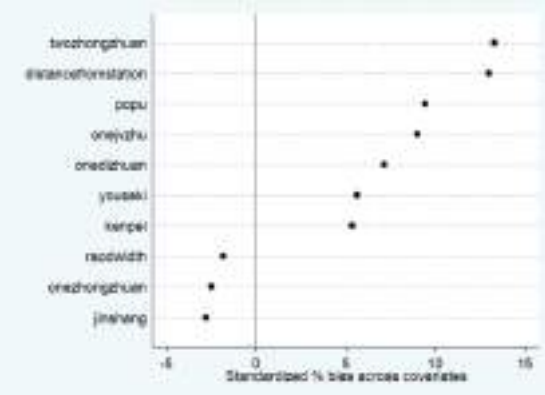

Fig.5 Balance check of Propensity score matching

building coverage ratio, respectively. onezhongzhuan represents the First-Class Medium-to-High-Rise Residential Zone, and jinshang refer to the Neighborhood Commercial Zone.)

The results of Kernel Matching compared that as the Average Treatment Effect on Treated (ATT) of the LOP with unmatched cases, shows land prices in Hachioji City decreased by 6,485.96 JPY/m² compared to those in other areas (Table 3).

Table 3 The result of Kernel Matching

Variable price difference(KM)		
sample	unmatched	ATT
Treated	3186.38	3390.26
Controls	16445.09	9876.21
Difference	-13258.71	-6485.96
Std.Err.	2239.83	2392.74
R stat	-5.92	-2.71

RESULTS AND DISCUSSION

The results obtained in this study demonstrate that the LOP has a statistically significant stabilizing effect on land prices in Hachioji City. Specifically, the nearest neighbor matching analysis revealed that, compared to other regions in Tokyo Prefecture, the average land price in Hachioji was 6,911.11 JPY/m² lower, controlling for confounding variables. Similarly, kernel matching yielded a comparable estimate of 6,485.96 JPY/m². Although the latter method excludes some outliers and exhibits greater estimation variance due to model complexity, the consistency of these results strengthens the conclusion. Based on these empirical findings, the discussion can be summarized into four key points:

Policy Effectiveness

The LOP appears to have contributed to land price stabilization in Hachioji by aligning urban development with planned zoning and infrastructure frameworks. The relatively modest land price fluctuations in the city suggest a balanced real estate market, possibly attributed to controlled urban expansion and green space preservation. Additionally, local urban development strategies, such as urban center formation in the Moto-Hachioji area and environmentally integrated development in Hachioji New Town, may have enhanced the city's attractiveness and sustainability.

Limited External Investment and Underlying Factors

Despite the policy's stabilizing benefits, Hachioji faces challenges in attracting external investment compared to Tokyo's central wards. Factors including insufficient transportation infrastructure (e.g., narrower roads, greater distance to stations), aging housing stock, and population decline have constrained real estate market dynamism. Low demand and high vacancy rates threaten efficient land utilization. Addressing these challenges requires targeted infrastructure investments, tourism promotion, and urban renewal strategies that leverage the city's natural and cultural assets.

Data Limitations and Analytical Improvements

The study's reliance on six-year matched data restricted the sample size to 507 observations. While measures were taken to ensure data consistency, missing values and potential selection bias remain analytical concerns. Future research should utilize longer time-series data and incorporate broader socioeconomic variables including employment, educational access, healthcare availability, and business activity. This would enable more comprehensive understanding of land price dynamics and policy impacts.

Furthermore, key covariates such as road width and station distance exhibited significant differences between Hachioji and other regions. On average, road width in Hachioji is approximately half that of other Tokyo areas, while station distance is twice as long. These factors may suppress price volatility, indicating a stabilizing yet growth-limiting effect.

Prospects and Policy Implications

To revitalize Hachioji and similar suburban areas, more comprehensive urban planning interventions are necessary. For example, national land valuation maps published annually by the National Tax Agency demonstrate rising land values around Hachioji

Station, suggesting growing accessibility and development potential. Building on this trend, future initiatives should include public transportation enhancement, district-level land use reorganization, and strategic tourism resource utilization.

CONCLUSIONS

This study demonstrates the measurable impact of urban planning policies on real estate markets through rigorous propensity score matching analysis. The empirical evidence confirms that the LOP contributes to land price stabilization in Hachioji City, with both nearest neighbor matching and kernel matching methods yielding consistent results. The policy's effectiveness in promoting compact urban development while maintaining land value stability represents a significant finding for disaster-prone urban areas facing demographic challenges.

The insights gained from Hachioji provide a methodological template for evaluating similar policies in other Japanese municipalities and internationally, particularly those confronting demographic decline and disaster vulnerability. The study validates the application of propensity score matching methodology for urban policy evaluation and offers evidence-based foundations for future urban planning strategies that balance accessibility, sustainability, and disaster resilience.

REFERENCES

[1] Sakamoto, J. (2023). Analysis of Land Price Changes Before and After Designation as Tsunami Disaster Alert Areas. *Kochi University Journal of Disaster Research*, Vol. 18, No. 3, pp. 261-269.

[2] Daniel, V.E., Florax, R.J.G.M., and Rietveld, P.. Flooding risk and housing values: An economic assessment of environmental hazard. Ecological Economics, Vol. 69, 2009, pp. 355-365.

[3] Nomura Real Estate Solutions (2024). Survey on Attitudes Toward Home Buying. Retrieved March 4, 2024, from https://www.nomu.com/research/201107/

[4] Ministry of Land, Infrastructure, Transport and Tourism (MLIT) (2024). National Land Numerical Information: Official Land Price Data. Government of Japan.

[5] Ministry of Land, Infrastructure, Transport and Tourism (MLIT) (2024). National Land Numerical Information: Population Density Data. Government of Japan.

[6] Markus Frölich, Matching Estimators and Optimal Bandwidth Choice Department of Economics, University of St. Gallen, 2004, pp. 1-29

[7] Gadisa Muleta, Takele Mebratu, Impacts of Adopting Improved Barley Varieties on Farmers' Income in Ethiopia American Journal of Economics and Business Innovation (AJEBI) Volume 3, Issue 2, 2024, pp. 101-107

Copyright © Int. J. of GEOMATE All rights reserved, including making copies, unless permission is obtained from the copyright proprietors.

15th Int. Conf. on Geotechnique, Construction Materials & Environment,
Kyoto, Japan, 11-13 November 2025, ISBN 978-4-909106124 C3051

RADIAL JOINT PERFORMANCE IN SHIELD TUNNELS UNDER LARGE DEFORMATION: A COMPARATIVE STUDY USING EXPERIMENTAL AND NUMERICAL APPROACHES

Quoc Viet Tran[1], Kosuke Kawata[1] and Nobuharu Isago[1]

[1]Department of Urban Environmental Sciences, Tokyo Metropolitan University, Japan

ABSTRACT

The number of tunnels has seen a significant increase in urban areas. However, the behavior of radial joints of shield tunnel structures during large deformations remain underexplored. To address this gap, this study aims to deepen our understanding of radial joint behavior under bending moments and their subsequent impacts on damage mechanisms in shield tunnel linings during a strong seismic event. This study employes two primary tests: joint bending test, which assesses the behavior of joint elements, and shearing test, which simulates the effects of earthquakes on tunnel models. Both tests are conducted using experimental and numerical analysis methods. The experimental analysis uses small-scale models, while the numerical analysis utilizes the beam-spring method. Our findings indicate that segmental joint behavior under positive bending tests exhibits three distinct stages, each with different rates of rotational displacement. Conversely, negative bending tests demonstrate constant stiffness. Additionally, the tunnel model collapses during the shearing experiment when a joint reaches a 50-degree opening angle. Furthermore, once the shield tunnel subjects to a prescribed displacement reach half its diameter, both cross-sectional and rotational deformation increase significantly. Importantly, numerical models employing the beam-spring method accurately simulate the behavior of radial joints in a shield tunnel, including cross-sectional deformation and joint rotation, when subject to a specified amount of deformation.

Keywords: Earthquake, Shield tunnel, Radial joint, Beam-spring

INTRODUCTION

The rapid increase of shield tunnels in urban areas is attributed to their safety during excavation and minimal environmental disruption. Their discontinuous structure, comprising segments and joints, makes them susceptible to deformation from surrounding ground movement. Due to this reason, it can easily deform with surrounding ground when it is subject to large shearing deformation. As a result, this structure is generally more earthquake-resistant than tunnels constructed by other methods [1]. Past major earthquakes have caused damage to some shield tunnels Southern Hyogo [2] and Niigata [3], raising concerns about extreme strong seismic events in the future. Nankai Trough earthquake [4] is an example. Although previous studies have investigated the seismic performance of shield tunnels, insufficient attention has been given to radial joints, potentially affecting accurate seismic performance evaluation. Therefore, it is crucial to study the influence of radial joints on shield tunnel behavior under large deformations.

In experimental research on shield tunnel models, seismic loads can be simulated using either dynamic or static methods. While the dynamic action is simulated by shaking table method by many past studies [5–7], the static method offers a simpler approach that still yields accurate results [8]. In shield tunnels, monitoring joint openings is crucial. Large joint openings can signal concrete crushing in the lining and potential water leakage [9]. Therefore, this study utilizes the static method due to its effectiveness in measuring joint opening angles and cross-section deformation. This approach simplifies testing and isolated the effect of radial joints by applying a prescribed static horizontal load to a small-scale single-ring shield tunnel model.

In shield tunnel numerical simulation research, two classic design methods are the modified routine modelling and the beam-spring modelling. The former method, based on the routine method, assumes that the lining is a ring with uniform bending stiffness [10]. In this method, the decrease of the bending stiffness at the joint is considered as the decrease of the ring. Moreover, although the effect of the joints is considered, the joint opening cannot be obtained due to the continuous assumption [11]. On the other hand, the beam–spring method simplifies the main section of the segment to a circular arc beam or a linear beam frame in a 2D model, connected by radial joints modeled by rotating springs [12]. This approach considers the shield tunnel model to be discontinuous, which is closer to its real characteristic. The past study [13] uses the beam-spring model to calculate the magnitude of external loads and then assign them as distributed loads directly on the models. In that research, soil surrounding the tunnel model is considered as an external force, and its actions are converted into external forces. Another approach

considers the ground as a series of two-direction springs [14]. However, these approaches cannot transfer the effect of large horizontal deformation to the tunnel model. To address this limitation, surface elements are used to simulate soil because of its ability to transfer the external deformation to tunnel models. The combination of surface elements and the beam-spring method is utilized in this study to reproduce the physical experiments.

In this paper, both experimental and numerical methods are conducted to observe the influence of radial joints on the behavior of shield tunnel models under large deformation.

RESEARCH METHOD

This study observes the behavior of tunnel models using two methods: physical experiments, which utilized small-scale shield tunnel models and simulated soil material, and numerical modeling, which employes the beam-spring method. Each method consists of bending tests and shearing tests.

All experiments are conducted at least 3 times, and results that differ from the others are eliminated to remove human error.

Physical Experiment

The experimental models in this paper are 3D printed from plastic. The outer diameter is 100mm, and the thickness is 4mm because the height of the segments is around 4% of the outer diameter [8]. Joints are produced at the same time and from the same material as the segments, resulting in a strong connection. The property of this material is shown in Table 1. The completed tunnel models consist of 6 equal segments. Fig.1 illustrates the actual tunnel model, and blue letters represent joints' names.

To evaluate the behavior of a single joint, bending tests are conducted. The test model, shown in Fig.2, includes two segments connected by one joint. Since joints are mainly subjected to bending moments [15], two types of bending tests are performed to extract its properties under both positive and negative bending moments. For the positive bending test (the left image in Fig.2), the model is placed on a flat surface, and a horizontal constraint is applied to the left side to constrain the structure in three degrees of freedom. The frictional coefficient between the flat surface and segment material is about 239.3×10^{-3}. To simulate the distributed force on the model, the weight is approximated as 30 vertical concentrated forces. The total force is increased at a constant rate of 40 grams per 10 seconds until the model collapses. Regarding the negative bending test (the right image in Fig.2), the experimental model is also set up to constrain the model in three degrees of freedom. The horizontal force is applied by connecting the weight to the lowest point of the left segment by a non-stretchable string. Then, this weight increases at the same rate as the positive bending test until the model ruptured. In both types of experiments, a camera records the model's behavior at each load level. Image analysis is used to analyze the data by tracking the displacement of 4 targets marked at the beginning and ending positions of each segment. The outcomes of these experiments include the magnitude of the opening or closing angle at the joint position at each load level. Both positive and negative moment values at the joint are calculated conventionally using the method of section.

Table 1 Material property

Segment model (3D printer Wood PLA Filament)	
Elastic modulus (kN/mm²)	1.0
Unit weight (kN/mm³)	6.5×10^{-9}
Simulated soil material (Aluminum alloy)	
Internal friction angle (deg)	30.0
Cohesion (N/mm²)	0.0
Elastic modulus (kN/mm²)	0.7×10^{-3}
Unit weight (kN/mm³)	21.8×10^{-9}

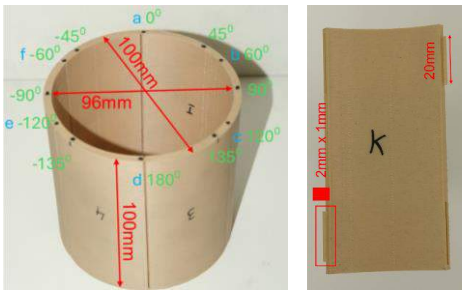

Fig.1 Tunnel model (segment and joint)

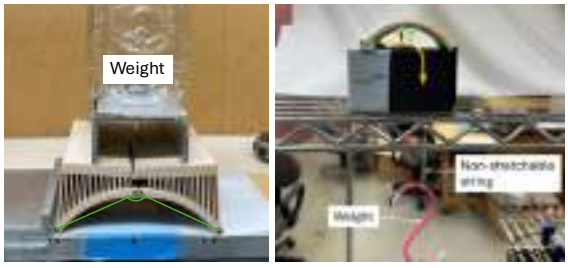

Fig.2 Positive and negative bending test model

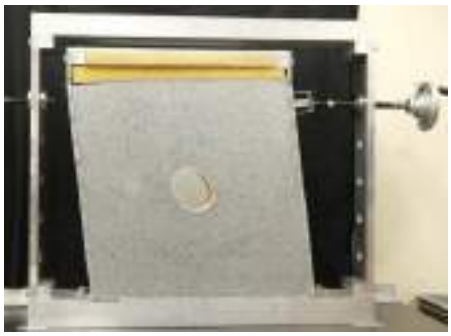

Fig.3 Shearing test model

The shearing test simulates a shield tunnel lining surrounded by soil under a large seismic event beyond the usual conditions. Shearing deformation is applied to simulate the effect of a large earthquake. The tunnel model is placed in a tank filled with simulated soil material, the properties of which are shown in Table 1. The simulated soil material is selected to achieve a realistic soil-to-lining stiffness ratio which is about 1429. To illustrate, the ratio of the tunnel lining's elastic modulus to that of aluminum alloy is comparable to the ratio between precast reinforced concrete and weak sand, which ranges from 480 to 3900. A shearing deformation is then applied gradually to the loading rod (1 mm every 30 seconds) to simulate the effects of large displacement (Fig.3) until the tunnel model collapses. A camera records the model's behavior throughout the test. This study tracks the movement of 12 targets (Fig.1) using image analysis to observe the deformation of cross-section and opening-closing angles. This method is chosen over using strain gauges [7]. Eight targets are marked every 45 degrees because maximum hoop deformation of the model tunnel under horizontal deformation is located at the conjugate 45° [16]. The remaining 4 targets are marked at the joint positions specifically to measure the joint opening-closing angles.

Numerical Analysis

This numerical analysis is conducted to verify the applicability of the 2D beam-spring method to simulate the performance of radial joints when the tunnel is subjected to large deformation. In this paper, segments are represented as beams, and the joints between these segments are modeled as rotational springs. Soil in this analysis is simulated using surface elements. The material properties used in this model are presented in Table 1.

Fig.4 illustrates the numerical joint bending test model, which aimed to evaluate numerical joint properties. The joint properties are determined as rotational spring properties based on experimental joint bending test results. The model simulating the positive bending moment is subjected to three external forces, including gravity, vertical forces and friction. The model simulating the negative bending moment is also under gravity, horizontal force and friction at the end target of the right segment. Loads are input as loading, while moment value and rotational angle are input piecewise linearly as the spring material's property. Finally, the combined positive and negative path of joint spring property is assigned to numerical shearing test models.

The numerical shearing test model (Fig.5) provides the rotational displacement of joints and deformation of the cross-sectional tunnel model. These factors can effectively reflect the performance of radial joints. While the variation of 2 major axes (Fig.5) reflects the cross-sectional deformation, the disparity of opening or closing angle is computed from the coordination of targeted nodes. Then, these results are compared to the experimental one.

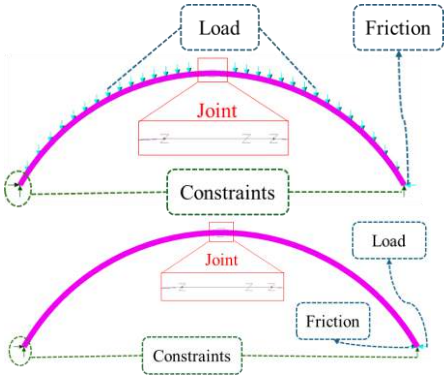

Fig.4 Numerical positive and negative bending test

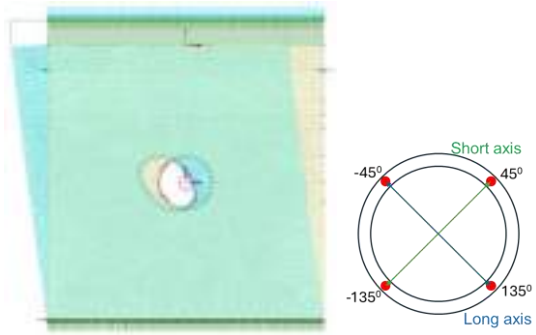

Fig.5 Numerical shearing test and layout of major axes

RESEARCH RESULT

Joint Bending Test

All bending test cases collapse due to joint slippage, not cracking segments.

In positive bending test, the capacity of the experimental model in the first, second, and third cases is 1768 grams, 1488 grams, and 1448 grams, respectively. Fig.6 presents the moment-θ relationship from both experimental and numerical bending tests. Although the capacities of the three experiment cases are different, their trends closely match. The joint stiffness is similar in cases 2 and 3 but higher in case 1. Therefore, the moment-θ relationship of case 3 is used as the input for the numerical bending test model. The joint behavior in the positive bending tests shows three main stages. Initially, from the starting point to an 8-degree joint opening, the angle increases at a rate of about 6.3 N*mm/degree. Subsequently, between 8 and 12 degrees, the rate of rotational displacement increases 1.5 times compared to the first stage. Beyond a 12-degree rotational angle, the deformation speed is negligible, reaching 1.8 N*mm/degree.

In the negative bending test, the capacities of 3 trials are similar at about 430 grams. The relationship

between bending moment and closing rotational angle (Fig.7) is nearly linear in all three cases at the ratio of 7.5 N*mm/degree. The second trial is chosen as the reference one.

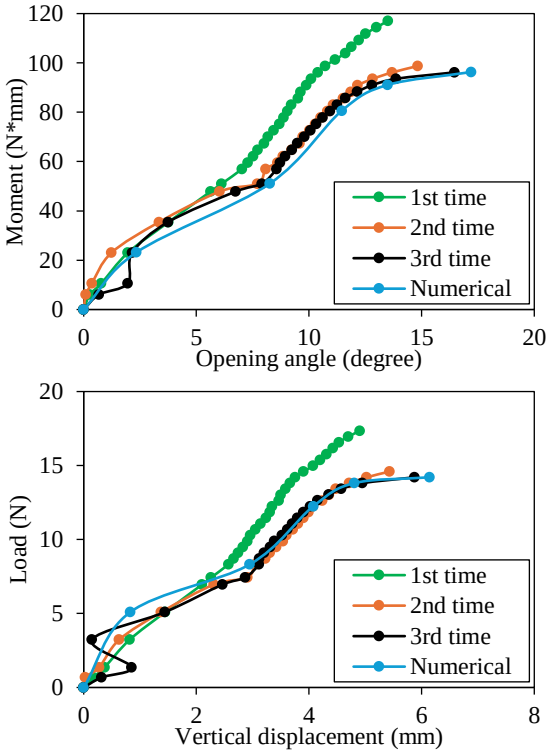

Fig.6 Rotational and vertical displacement results of positive bending tests

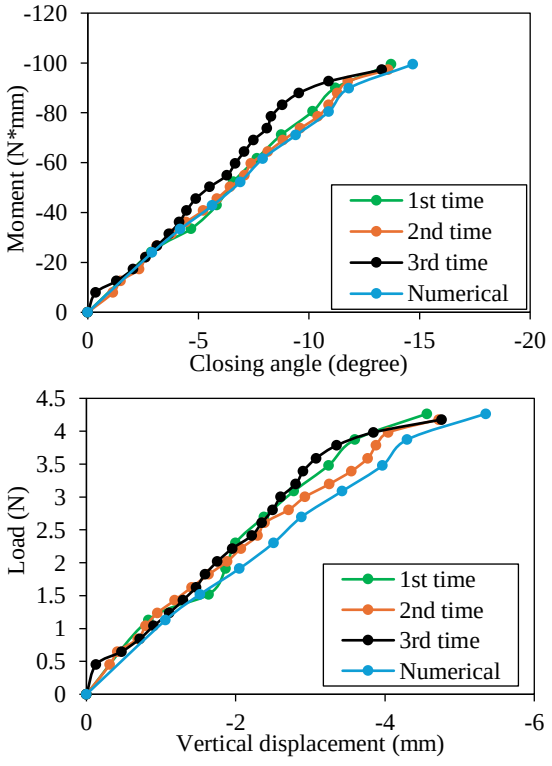

Fig.7 Rotational and vertical displacement results of negative bending tests

The experimental joint properties of the reference case are input to the numerical bending test models with corresponding load levels. Fig. 6 and Fig. 7 show that differences between the results of 2 methods are minor. Therefore, these joint stiffness graphs are combined and then input into the numerical shearing test model for reproducing this test.

Shearing test

The first trial collapses when the shearing displacement reached 72mm; the second at 73mm, and the third at 76mm. Although there are slight differences in the capacity of the three experimental cases, they are negligible. Results from the first and second cases are closer to each other compared to the third one, so the first one is chosen as the reference. Fig.8 shows the deformed shapes of the tunnel model just before collapsing. All these cases collapse because of the slippage of joint b.

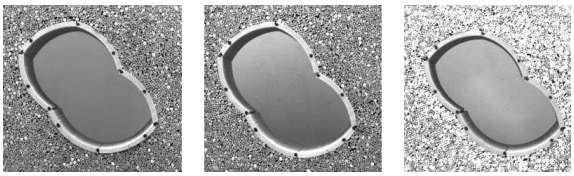

Fig.8 Deformed shapes of the tunnel model in three experimental cases just before collapsing

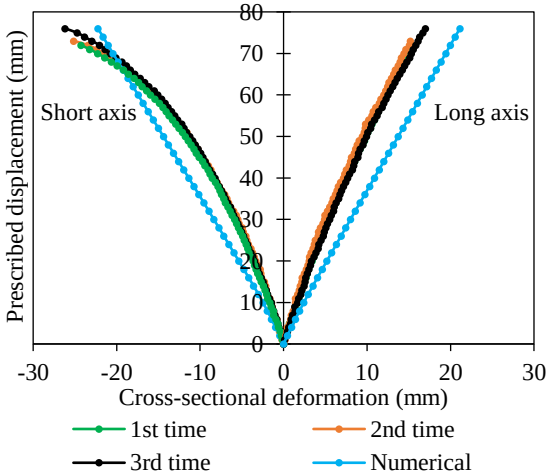

Fig.9 Disparity between the lengths of the major axes from experimental and numerical results

Fig.9 compares the disparity between the lengths of the major axes obtained from 3 experiment times and numerical results. In the reference trial, the deformation of the short axis is greater than that of the long axis. The deviation between these axes is only under 20% until the prescribed displacement of 50mm. Beyond 50mm, this value rapidly rises and reaches 60%.

Since the numerical model could not collapse, the maximum displacement applied to the reference case (72mm) is also applied to the numerical model.

As for the cross-sectional deformation (Fig. 9), for

the long axis, both experimental and numerical results are nearly linear. Regarding the short axis, while the disparity in the experimental length exhibits a curve pattern, the numerical outcome is linear. From the initial state up to 50mm of prescribed displacement, the difference rate between the results of the two methods is between -3.0% and 4.0%, relative to the model's outer diameter. Beyond 50 mm, this rate increases, but maximum value is about 4.5%.

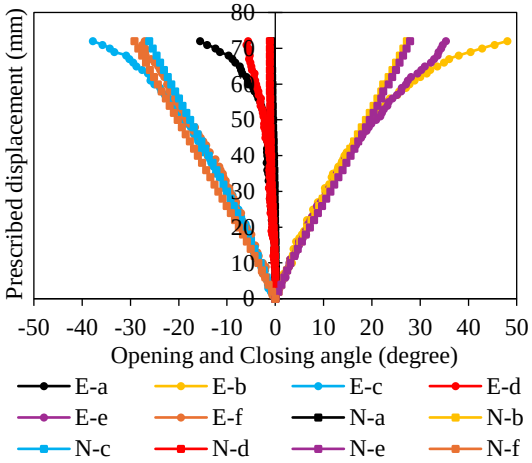

Fig.10 Comparison of Opening-Closing angle between experimental and numerical results.

Fig.10 compares the rotational deformation of 6 joints (joint names are shown in Fig.1) between the experimental reference case and numerical analysis. In Fig.10, E and N stand for Experimental and Numerical, respectively. Overall, their deformation trends are similar. Numerical results are linear. Most experimental results behave linearly from the initial, and non-linearly from the given displacement of 50mm, except for joint f. For the remaining joints, rotational differences between the two methods are minor when the prescribed displacement is under 50mm, but these differences increased rapidly beyond that point. From the initial to 50mm of prescribed displacement, the variation between the results of the two methods is between -2.2 degrees and 1.3 degrees. Beyond 50 mm, this rate begins increasing significantly, and the maximum variation is about 20.7 degrees at joint b.

DISCUSSION

The joint bending tests indicate that the model collapse is due to joint slippage, not segment cracking. Joint behavior in positive bending tests exhibit three distinct stages. The first stage displays a rotational displacement rate that is lower than the second stage, but higher than the third. In negative bending tests, the relationship between displacement and closing angle is nearly linear. This outcome is consistent with the previous finding [17], which shows that the stiffness of segmental joints under bending moment could be divided into 3 stages with different values. However, the mentioned paper does not study the relationship between negative moments and rotational angle, as well as the stiffness order of 3 stages.

The results from the shearing experiment show that all three tunnel models collapse due to the failure of joint b. This result could be predicted from its rotational deformation because the amount of opening angle joint b is 50 degrees, which is much more than the others. As for cross-section deformation, the deviation between the main axes (long axis minus short axis) remains low until the prescribed displacement reached 50mm. For rotational joint deformation, at most joints, the initial deviations are minor but increased rapidly from the given displacement of 50mm. The deformation begins increasing more rapidly once the prescribed displacement reaches half of the outer diameter of tunnel models.

The numerical models' results closely match the experimental outcomes. The bending test shows the similarity between experimental and numerical results through vertical and rotational deformation comparison. In shearing tests, while numerical models deform linearly, experiment models provide non-linear results. However, most differences are minor or acceptable, particularly when the given displacement is under 50mm, equivalent to 50% of the tunnel's diameter. Beyond this point, the accuracy decreases significantly. Therefore, this model can effectively reproduce the behavior of radial joints when shield tunnels are subjected to medium deformation (under half of the outer diameter).

CONCLUSION

In this study, we aim to find out the behavior of radial joints when the shield tunnel models are subjected to a large deformation. To achieve this, bending and shearing experiments are conducted using both experimental and numerical methods. The conclusions of this study include:

- Firstly, the behavior of joints under positive bending tests exhibits three distinct stages, each stage is characterized by a unique rate of rotational displacement. The first stage displays the lowest rate of rotational displacement, followed by the third stage, and the second stage exhibits the highest rate. Therefore, engineers should avoid radial joints reaching the third stage during the joint design process. In contrast, negative bending tests demonstrated a nearly linear relationship between the bending moment and closing angle.
- Secondly, the shearing experiments result in the collapse when any joint reached a 50-degree opening angle. The current joint type needs some modifications to prevent it from reaching the limit opening angle, or it should be replaced by other joint

structures. Furthermore, once the shield tunnel is subjected to prescribed displacement reaches half of its diameter, cross-sectional and rotational deformation increases significantly. In addition, for early alerts, sensors should be installed to detect when joints enter the third stage, or the magnitude of deformation approaches this value.

- Finally, numerical models employing the beam-spring method have accurately simulated the behavior of radial joints via cross-section and joint rotational deformations. The discrepancies between the numerical model and experimental behavior are generally minor and acceptable, particularly when the given displacement remains below a specific value. This method could be used for further research focusing on radial joints' behavior.

Although some good results are obtained, there are some limitations that worth of further studies. First, the maximum opening angle of the bending test (18 degrees) is much lower than that of the joint in the shearing test (50 degrees). It leads to significant disparity arises when the rotational displacement exceeds the limit of input spring stiffness. Second, the axial joint spring also impacts the behavior of radial joints, but it is ignored in this study. Third, although experimental small-scale models are employed to simulate the behavior of full-scale shield tunnels, only the length ratio and the ratio of elastic modulus between materials are maintained while other dynamic similitude parameters are not taken into account. We are trying to solve some of the above problems.

REFERENCES

[1] He C., Geng P., Yan Q., and Feng K., Status of seismic analysis methods for traffic tunnel and their applicability suggestions in China, Vol. 07, J. Earthquake and Tsunami, 2013, pp. 1350026.

[2] Nishiyama S., Kawama I., and Haya H., Analysis of the Cut and Cover Tunnels Damaged in the South-Hyogo Earthquake of 1995.2004,.

[3] Tani S., Saito M., and Araki S., Damage to a shield tunnel caused by the Chuetsu Oki earthquake, Vol. 27, Structural Eng./Earthquake Eng., 2010, pp. 72s–84s.

[4] Oba A., Furumura T., and Maeda T., Data Assimilation-Based Early Forecasting of Long-Period Ground Motions for Large Earthquakes Along the Nankai Trough, Vol. 125, Journal of Geophysical Research: Solid Earth, 2020, pp. e2019JB019047.

[5] Kawamata Y., Nakayama M., Towhata I., and Yasuda S., Dynamic behaviors of underground structures in E-Defense shaking experiments, Vol. 82, Soil Dynamics and Earthquake Engineering, 2016, pp. 24–39.

[6] Bao X., Li J., Shen J., Liu C., Chen X., and Cui H., Investigations on the seismic performance of a shield tunnel adjacent to an underground station in liquefiable ground through shaking table tests, Vol. 161, Tunnelling and Underground Space Technology, 2025, pp. 106541.

[7] Liang J., Xu A., Ba Z., Chen R., Zhang W., and Liu M., Shaking table test and numerical simulation on ultra-large diameter shield tunnel passing through soft-hard stratum, Vol. 147, Soil Dynamics and Earthquake Engineering, 2021, pp. 106790.

[8] Standard Specifications for Shield Tunnels 2016, Japan Society of Civil Engineers, 2017, pp. 90.

[9] Wang J., Liu H., and Liu H., Measuring joint opening displacement between model shield-tunnel segments for reduced-scale model tests, Vol. 16, Structures, 2018, pp. 112–118.

[10] Shen S.-L., Horpibulsuk S., Liao S.-M., and Peng F.-L., Analysis of the behavior of DOT tunnel lining caused by rolling correction operation, Vol. 24, Tunnelling and Underground Space Technology, 2009, pp. 84–90.

[11] Li X., Yan Z., Wang Z., and Zhu H., Experimental and analytical study on longitudinal joint opening of concrete segmental lining, Vol. 46, Tunnelling and Underground Space Technology, 2015, pp. 52–63.

[12] Murakami H. and Koizumi A., Study on Load Bearing Capacity and Mechanics of Shield Segment Ring, Vol. 1978, Proceedings of the Japan Society of Civil Engineers, 1978, pp. 103–115.

[13] Huang Q., Liu S., Lv Y., Ji D., and Li P., Modification of Segment Structure Calculation Theory and Development and Application of Integrated Software for a Shield Tunnel, Vol. 12, Applied Sciences, 2022, pp. 6043.

[14] Pham A.T. and Sugimoto M., The Effects of Tangential Ground–Lining Interaction on Segmental Lining Behavior Using the Beam-Spring Model, Vol. 10, Applied Sciences, 2020, pp. 1084.

[15] Jin H., Yu S., Zhou S., and Xiao J., Research on Mechanics of Longitudinal Joint in Shield Tunnel by the Nonlinear Spring Equivalent Method, Vol. 23, KSCE Journal of Civil Engineering, 2019, pp. 902–913.

[16] Zhou H., Wang X., He C., and Huang C., Seismic Response of a Tunnel Embedded in Compacted Clay through Large-Scale Shake Table Testing, Vol. 2018, Shock and Vibration, 2018, pp. 5968431.

[17] Majdi A., Ajamzadeh H., and Nadimi S., Investigation of moment-rotation relation in different joint types and evaluation of their effects on segmental tunnel lining, Vol. 9, Arab J Geosci, 2016, pp. 512.

Copyright © Int. J. of GEOMATE All rights reserved, including making copies, unless permission is obtained from the copyright proprietors.

15th Int. Conf. on Geotechnique, Construction Materials & Environment,
Kyoto, Japan, 11-13 November 2025, ISBN 978-4-909106124 C3051

EFFECTIVE CUTTING TO CONTROL THE REGROWTH OF BAMBOO GRASS FOR THE CONSERVATION OF MOUNTAIN TRAILS

Teruo Arase[1], Ren Yokota[1], Masamichi Yoshizawa[1], Taizo Kato[1], Taizo Uchida[2] and Masaaki Furuno[2]

[1]Faculty of Agriculture, Shinshu University, Japan, 2Faculty of Architecture and Civil Engineering, Kyushu Sangyo University, Japan

ABSTRACT

Vegetation control is important for the conservation of mountain trails, access to alpine areas, and the safety of hikers. However, in Japan, mountain trails are often obstructed by bamboo grass because of its vigorous growth. This study aimed to identify effective methods to control the regrowth of bamboo grass along mountain trails after cutting. We focused on Nagaone trail in the Kiso Mountains, Central Japan, where the bamboo grass was cut in 2020. Nineteen survey plots were set along the trail at elevations ranging from 1500 to 1900 m, with a quadrat (2 m long × the trail width) established at each site. The cutting height in 2020 and the culm height and density in 2022 were measured. Bamboo grass on the trailside slope was also measured because it obstructed the trail, and elevation, trail gradient, and slope gradient were recorded as the habitat environment. The results indicated that residual living bamboo grass on the trailside slope was significantly positively correlated with both regrowth on the trail and the density of the leaning culm from the trailside after 2 years. Cutting height was significantly positively correlated with the density of the regrowing culm and influenced by the trail gradient, but not the culm density or height. Thus, the growth of bamboo grass on the trailside slope and the cutting height appear to be critical for the regrowth of bamboo grass on the trail. This finding could lead to more effective methods to control the regrowth of bamboo grass along mountain trails.

Keywords: Mountain trail, Bamboo grass, Regrowth, Cutting

INTRODUCTION

Bamboo grass, including many species of the genera *Sasa* and *Sasaella* (Poaceae), often becomes dominant on the forest floor in montane and subalpine zones in Japan [1]. Generally, bamboo grass species show longevity and monocarpy, often surviving from several decades to a hundred years with simultaneous mass flowering and withering at the end of the generation before recovering from seeds [2,3]. Bamboo grass forms a large population with thick elect culms, which prevents the invasion or survival of other plants from outside [4,5]. In addition, underground rhizomes contribute to the tight binding of soil, which helps prevent soil erosion [6].

The relatively fast expansion of the bamboo grass population has been reported. Sparse populations of bamboo grass were found to have become a dominant species with almost 100% coverage on a slope along a highway 12 years after the suspension of traffic [4]. The annual expansion rates of tall-type (*Sasa borealis* Makino et Shibata) and small-type bamboo grass (*Sasa nipponica* Makino et Shibata and Sasaella ramosa Makino) have been estimated to be 117 m^2 and 50 m^2 per year, respectively [7].

Such growth characteristics are beneficial for revegetation and soil protection, but often become harmful. One of the typical cases where bamboo grass needs to be suppressed is mountain trails. On mountain trails, overuse by hikers causes widening of the trail and soil erosion through the deterioration of trailside vegetation; however, this can be mitigated by bamboo grass [6]. By contrast, the underuse of mountain trails can lead to the excessive growth of bamboo grass, which also creates difficulties in terms of maintaining the trail [5]. It has been reported that only 1%–2% of sunlight reaches the ground surface under bamboo grass populations [8], and the trace after cutting bamboo grass (i.e., the renewed trail) remains as dark as it was before cutting because the trail width is extremely narrow compared with the entire bamboo grass population [5]; the ground surface of the renewed trail would remain too dark for the survival of other plants, causing the condition of bare ground to continue [5].

On the other hand, bamboo grass has the ability to transport storage substances through underground rhizomes within the population [9], which implies that the regrowth of bamboo grass on mountain trails would be supported by the residual living part of the population on the trailside. Cutting and removing bamboo grass rhizomes is known to be an effective method to restrain regrowth [10], but is not recommended because it enhances the risk of erosion. Thus, the control of bamboo grass on

mountain trails is distinct from the large-scale cutting of forest floors in forestry, and consequently, little information has been available to date.

Given this background, in the present study, we aimed to establish a research area where bamboo grass had covered the mountain trail abandoned for decades. Two years after cutting, we investigated the regrowth of the bamboo grass and environmental factors and analyzed their relationships with the objective of developing more effective methods to control the regrowth of bamboo grass for the conservation of mountain trails.

RESEARCH SIGNIFICANCE

The significance of the study is that it aims to contribute to the conservation of mountain trails, where vegetation can become excessively thick as a result of underuse. This issue involves the existence of the large living part of bamboo grass populations after cutting, which can transport storage substances to the stubble on the trail through rhizomes. Based on the analysis of the regrowth and environmental factors, we discuss effective cutting methods to control the regrowth of bamboo grass for the conservation of mountain trails.

METHODS

Research Area

The research area in the present study was Nagaone trail (from an elevation of 1500 m to 2532 m), which leads to a peak on the ridge running from Mt. Shogi-gashira in the north of the Kiso Mountains, Central Japan (Fig. 1). Nagaone trail has not been very popular among general hikers because it passes through two research forests, Oguro Research Forest of Kami-ina Agricultural High School and Nishikoma Research Forest of Shinshu University. Recently, this trail became nearly abandoned after accessibility worsened following bridges across the Ogurogawa River (at elevations of 1420 m and 1500 m) being washed away by repeated floods. The convenience of hiking the trail also worsened because the roof of the mountain hut near the middle of the trail (at an elevation of 1900 m) collapsed as a result of heavy snowfall.

Fig.1 Topographical map of around the research area (Nagaone trail). Black solid lines indicate other mountain trails.

The vegetation around the trail consists of an afforested larch forest in the montane zone (the lower area up to the elevation of 1600 m), and a mixed forest of conifers and deciduous trees in the subalpine zone (the upper area). Bamboo grass, mainly *Sasa senanensis* Rehder, is distributed in the area up to an elevation of about 1900 m.

Establishment of Survey Plots

To recover Nagaone trail, we cut bamboo grass on the trail by human power in 2020. The tools used for cutting work were a long-handle sickle, a billhook, and pruning shears (Table 1). The trail before the cutting conducted in 2020 had become almost completely obstructed and unrecognizable because of the growth of thick bamboo grass (Fig. 2 (A)). The long-handle sickle was the most effective cut tool for cutting the bamboo grass, but the cut culms and leaf blades remained scattered on the trail (Fig. 2 (B)) and the cutting section of the culm often became sharp, which can be dangerous for hikers. By contrast, the pruning shears required a lot of time

Table 1 Properties of the tools used for cutting bamboo grass

Tools	Cutting edge length (cm)	Handle length (cm)	Efficiency of cutting work
Long-handle sickle	27.0	118.0	High but rough
Billhook	17.5	32.0	(Middle)
Pruning shears	4.8	9.0	Low but careful

Fig. 2 States of the trail before and after the cutting work in 2020. A: Before cutting, B: After cutting with a long-handle sickle, C: After cutting with pruning shears. Length of the red and white striped pole = 2 m.

and effort, but the harvested culms and leaf blades were often thrown off the trail because of the necessity to grasp them before cutting (Fig. 2 (C)). Moreover, the cutting section of the culm became blunt, which is safer for hikers. The efficiency of the cutting with a billhook and the resultant state of the trail were somewhere between those of the long-handle sickle and pruning shears. After confirming the efficiency of each tool, the tools were allotted to three persons (one tool per person), and the cutting work was performed through collaboration.

In 2022 (2 years after the cutting), 19 survey plots were established to examine the regrowth of the bamboo grass. The locations of the plots were determined at regular intervals of approximately 50 m. The size of the quadrat in each plot was 2 m long × the trail width. The conditions of each survey plot are shown in Table 2.

Table 2 Conditions of the location at each survey plot

No.	Elevation (m)	Slope direction	Trail gradient (°)	Width of trail (m)
1	1498	E	6.8	0.50
2	1510	NW	6.8	0.56
3	1538	NW	13.5	0.60
4	1555	NW	8.3	0.65
5	1564	NW	2.0	0.75
6	1562	N	2.6	0.72
7	1576	N	1.4	0.77
8	1566	N	2.3	0.78
9	1575	N	2.0	1.15
10	1583	N	4.3	0.60
11	1593	N	2.0	0.65
12	1674	NE	3.1	0.55
13	1680	E	12.7	0.47
14	1695	E	11.3	0.35
15	1770	E	12.4	0.50
16	1861	NE	7.4	0.50
17	1892	NE	4.0	0.45
18	1904	NE	4.0	0.50
19	1904	NE	10.8	0.40

Measurement and Analysis of the Regrowth of Bamboo Grass

For the survey of the regrowth of the bamboo grass on the trail at 2 years after cutting, aboveground bamboo grass (hereafter “regrowing culm” on the trail, Fig. 3 (A)) was harvested with pruning shears and measured in the summer of 2022. The culm height and diameter at the base were recorded after harvesting. In addition, the culm along the trailside leaning over the trail (hereafter “leaning culm”, Fig. 3 (A)) was counted at each plot because it also obstructed the trail. The density of the leaning culm was calculated as the number of culms divided by the longitudinal length of the trail (2 m for each plot), as they existed linearly along the trail, unrelated to the trail width.

Regarding the environmental factors that could affect the regrowth of the bamboo grass, we considered the geographical conditions and residual living bamboo grass. Concerning the geographical conditions, we recorded the elevation, slope direction, trail gradient, and slope gradient for each plot at the same time the plot was established.

Concerning the residual living bamboo grass, the height of the remaining stubble on the trail was measured at the time of harvesting. The height of the remaining stubble was measured by examination of the basal part of each harvested culm. This height was considered to provide an estimation of the cutting height in 2020. However, after inspecting the data, we reached a reasonable conclusion using the maximum value for each plot to avoid underestimation, as some of the stubble had been already dead and decayed before the survey. The reason we were unable to design the cutting height experimentally in 2020 was that the work of cutting the thick population of bamboo grass and recovering the trail was excessively difficult, and the future regrowth on the trail was unknown immediately after cutting.

Besides, both the culm height and density of the bamboo grass along the slope of the trailside were measured at the time of harvesting. The culm height and density along the trailside slope at each plot, which was left intact in 2020, considered to be associated with the storage mass to invest in the regrowth of bamboo grass on the trail after cutting.

The relationships between these environmental factors and the regrowth of bamboo grass on the trail were analyzed using Pearson’s correlation coefficient.

Fig. 3 States of the trail before and after the cutting work in 2022. A: Before cutting, B: After cutting (both at plot No. 2). Length of the red and white striped pole = 2 m.

RESULTS

Regrowth of Bamboo Grass

Among the 19 survey plots, bamboo grass appeared in 17. Two plots (Nos. 11 and 16) and their trailside slopes were devoid of bamboo grass. The

diameter at the base showed no significance among plots (analysis of variance, F-test), and the mean diameter ± standard deviation of all 17 plots was 3.73 ± 0.92 mm.

Table 3 shows the estimated cutting height and regrowth of the bamboo grass. The estimated cutting height was 0–56 cm. Regrowing culms were observed in all 17 plots, with a density of 1.3–7.1 culms/m^2 and a height of 24–147 cm. The density of the leaning culms, mostly from the uphill slope, was 0.0–18.5 culms/m.

Table 3 Regrowth of bamboo grass on Nagaone trail at 2 years after cutting for each survey plot

No.	Estimated cutting height (cm)	Regrowing culm on the trail		Learning culm
		Density per m^2	Height (cm)	Density per meter
1	13	4.0	88	5.5
2	44	7.1	147	18.5
3	21	2.5	50	4.0
4	38	4.6	65	3.5
5	44	4.6	76	3.0
6	21	4.2	84	1.5
7	29	5.8	97	4.0
8	25	3.2	122	2.0
9	29	3.0	126	7.0
10	56	5.0	65	6.5
11	-	-	-	-
12	29	2.7	35	1.0
13	0	3.2	98	2.0
14	6	2.9	25	2.0
15	20	3.0	34	0.0
16	-	-	-	-
17	29	4.4	48	0.5
18	32	6.0	67	3.0
19	0	1.3	24	2.0

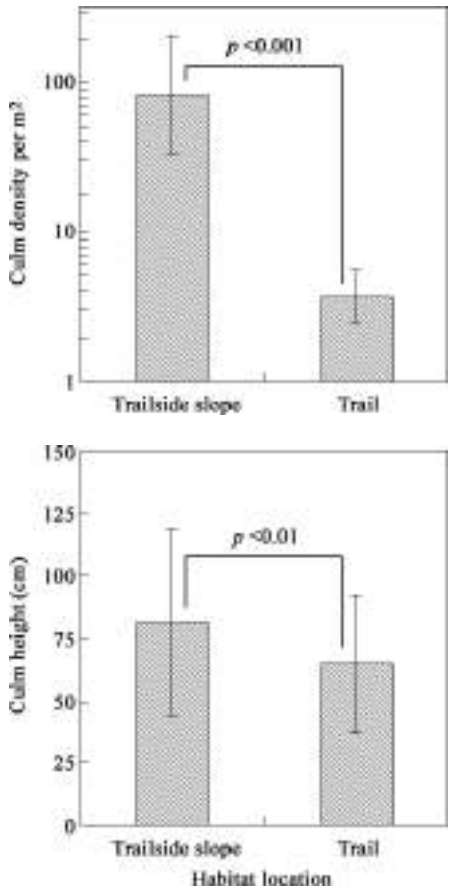

Fig. 4 Culm density and height of bamboo grass on the trailside slope (natural growth left intact) and Nagaone trail (regrowth at 2 years after cutting). The line on each bar indicates the range of ±1 standard deviation (n = 17).

All 17 plots and trailside slopes could be considered replications of the regrowth of bamboo grass on the trail after cutting and leaving natural growth intact, respectively. Fig. 4 shows the results of a comparison of culm density and height between the plots and trailside slopes. The culm density was significantly larger on the trailside slope than on the trail (84.0 vs. 3.9 culms/m^2 on average, respectively; Tukey's honestly significant difference (HSD) test, $p < 0.001$. The culm height was also significantly larger on the trailside slope than on the trail (81.0 vs. 64.8 cm, respectively; Tukey's HSD test, $p < 0.01$).

Relationships between Environmental Factors and the Regrowth of Bamboo Grass

Table 4 shows the relationships between environmental factors and the regrowth of bamboo grass. Regarding the factor of geographical conditions (Table 4 (A)), significant negative correlations were found between the trail gradient and regrowing culm density, between elevation and regrowing culm height, and between elevation and leaning culm density (around r = –0.5, $p < 0.05$, F-test). Although trail width was also planned to be an environmental factor, it was excluded from the analysis because it was considered an outlier (1.15 m at plot No. 9, Table 2) and therefore to disturb the correlation.

Regarding the factors related to the residual living bamboo grass (Table 4 (B)), the culm density in the trailside slope was significantly positively correlated with regrowing culm height and leaning culm density (around r = 0.7, $p < 0.01$, F-test), the culm height on the trailside slope was significantly positively correlated with regrowing culm height (r = 0.914, $p < 0.001$, F-test), and the estimated cutting height was significantly positively correlated with regrowing culm density (r = 0.689, $p < 0.01$, F-test).

Concerning the relationships between the regrowing culm density, height on the trail, and leaning culm density, significant positive correlations were observed (r = 0.5–0.6, $p < 0.05$, F-test).

Table 4 Relations between environmental factors and the regrowth of bamboo grass (Pearson's correlation coefficient, r; n = 17)

Factors	Regrowing culm on the trail		Learning culm
	Density per m^2	Height (cm)	Density per meter
(A) Geographical conditions			
Elevation	ns	-0.515*	-0.538*
Trail gradient	-0.487*	ns	ns
Slope gradient	ns	ns	ns
(B) Residual living bamboo grass			
Culm density	ns	0.648**	0.713**
Culm height	ns	0.914***	0.427
Cutting height	0.689**	ns	0.439

*Correlation coefficients less than $p < 0.1$ are shown. *, **, and *** denote significance at $p < 0.05$, 0.01, and 0.001, respectively. Culm density and height were measured on the trailside slope, and cutting height was estimated at 2 years after cutting.*

The factors related to the residual living bamboo grass were more important than those of the geographical conditions because the former can be controlled by cutting work, whereas the latter cannot. Table 5 shows the relationships with the factors related to the residual living bamboo grass. Regarding the factors of geographical conditions (Table 5 (A)), culm height was significantly negatively correlated with elevation ($r = –0.516$, $p < 0.05$, F-test), and trail gradient was significantly negatively correlated with estimated cutting height ($r = –0.571$, $p < 0.05$, F-test). The factors related to the residual living bamboo grass were not influenced by the slope gradient.

Regarding the relationships between the factors related to the residual living bamboo grass (Table 5 (B)), a significant correlation was detected only between the culm density and height on the trailside slope ($r = 0.567$, $p < 0.05$, F-test).

Table 5 Relations with the factors related to residual living bamboo grass (Pearson's correlation coefficient, r; n = 17).

Factors	D	H	C
(A) Geographical conditions			
Elevation	-0.414	-0.516*	ns
Trail gradient	ns	ns	-0.571*
Slope gradient	ns	ns	ns
(B) Residual living bamboo grass			
Culm density (D)	1		
Culm height (H)	0.567*	1	
Cutting height (C)	ns	ns	1

*Correlation coefficients less than $p < 0.1$ are shown. * denotes significance at $p < 0.05$.*
Culm density and height were measured on the trailside slope, and cutting height was estimated at 2 years after cutting.

DISCUSSION

Cutting Work

Concerning the cutting work, the culms and leaf blades of bamboo grass are recommended to be removed from the trail after cutting so as not to hide the trail [5]. Besides, the surface roughness of bamboo grass is considerably minute even 2 years after cutting (R_{max} around 0.01 mm, unpublished data by the authors). Surface roughness is reported to be related to the coefficient of friction between material and snow [13]; therefore, failing to remove scattered culms and leaf blades would increase the risk of a snowslide or falls by hikers.

On the other hand, the steep cutting sections of culms are also detrimental to the safety of hikers and cutting-work operators. It is recommended first to cut culms effectively using a long-handle sickle or billhook, and then to make the cutting section blunt with pruning shears and remove the harvested culms and leaf blades from the trail.

Regrowth of Bamboo Grass

Bamboo grass was observed to regrow on the trail at 2 years after cutting. However, the density of the bamboo grass on the trail was still far lower than that on the trailside slope. By contrast, the culm height on the trail appeared to have already become close to that on the trailside slope, even though there was a significant difference between them (Fig. 4). The bamboo grass population on the trail would scarcely be distinguishable from the population on the trailside slope if the culm density were left to increase in the near future. Because dwarfing of bamboo grass is one of the signs of animal damage, primarily by sika deer [11], the damage caused by cutting was considered to disappear after 2 years.

Among the geographical condition factors, elevation and trail gradient had a negative influence on the regrowth of bamboo grass (Table 4 (A)). However, because these factors are uncontrollable, this implies a favorable habitat for bamboo grass. Most bamboo species (subfamily Bambsoidae, containing bamboo grass) are distributed in tropical areas, and the species group of bamboo grass is distributed in northern areas [1]. High elevation, i.e., low temperatures, deep snow, and short growing periods, are considered to restrain the growth of bamboo grass. Trail gradients are not supposed to be related to temperature, but may be unfavorable for producing erect culms or rhizome growth.

The culm density and height on the trailside slope were positively correlated with not only the regrowth of bamboo grass on the trail, but also leaning culms (Table 4 (B)). Although we had considered that the gap on the trail after cutting would increase the growth of leaning culms from the

trailside, no negative correlation was observed between them, and both were encouraged by the trailside population. This suggests that bamboo grass can transport storage substances from adjacent trailside populations through rhizomes [9]. To date, most of the literature on controlling the growth of bamboo grass focuses on forestry on a large scale, not leaving bamboo grass intact in experimental plots. Therefore, considering the absence of residual living populations with abundant storage substances, reports that bamboo grass is suppressed for many years after large-scale cutting or the application of chemicals are reasonable [7,8,12]. On the other hand, the positive correlation observed between cutting height and regrowing culm density was considered to have been caused by the remaining lateral buds: shooting from lateral buds gives bamboo grass a broom-like branching form, which has been reported as a sign of animal damage, primarily by sika deer [11]. Cutting at a high position tends to leave many lateral buds intact, which can lead to rapid regrowth from the residual culm itself, photosynthesis, and increased storage substances, thereby encouraging the production of new culms on rhizomes, in addition to the support received from the trailside population.

Concerning the factors that affect the regrowth of bamboo grass on the trail, if we suppose that the population on the trail before cutting corresponded approximately to that of bamboo grass on the trailside slope, then it is important to consider that the cutting height was not influenced by the culm density or height, but rather, by the trail gradient (Table 5). The reason behind this relationship is unclear in the present study, but it seemed easier for the cutting-work operators to see and reach the base of the culms on a steep compared with a gentle slope. This finding suggests that attention should be paid to the slope gradient during cutting work, as opposed to cutting at a high position on a gentle slope and flat land.

On the other hand, the negative correlation with elevation (Table 5 (A)) showed similar relationships in Table 4 (A), implying a favorable habitat for bamboo grass: high elevation would decrease the growth of natural bamboo grass populations. The positive correlation observed between culm height and density (Table 5 (B)) is therefore reasonable because each indicates the growth of the population.

However, missing the important data, such as the height and density of bamboo grass before cutting in 2020 in each survey plot, would undermine the quality and reliability of the results in the present study. Hereafter, survey plots should be established before the population of bamboo grass on the mountain trail becomes too thick.

CONCLUSIONS

In the present study, we established a research area where bamboo grass had covered a mountain trail abandoned for decades. Two years after cutting, the regrowth of bamboo grass and environmental factors were investigated and their relationships were analyzed.

Concerning cutting work, it is recommended to cut effectively with a long-handle sickle or billhook at first, and then to make the cut sections blunt with pruning shears and remove the harvested culms and leaf blades from the trail for the safety of hikers and cutting-work operators themselves. Concerning the regrowth of bamboo grass on the trail after cutting, the results were as follows.

(1) The residual living population of bamboo grass on the trailside slope was significantly positively correlated with both the regrowth on the trail and the leaning culm density from the trailside after 2 years, probably because of the transportation of storage substances through rhizomes.

(2) The cutting height was significantly positively correlated with the regrowing culm density, probably because of the increase in storage substances caused by the rapid regrowth from lateral buds on residual culm.

(3) Concerning the factors related to the regrowth of bamboo grass, the growth of the population on the trailside slope was influenced by elevation, and the cutting height was influenced by the trail gradient, but not by the culm density or height.

In conclusion, monitoring the growth of bamboo grass on the trailside is important: low cutting or recutting at shorter intervals is needed if the growth of the trailside population is vigorous. In addition, monitoring the slope gradient is important to avoid cutting at a high position on gentle slopes and flat land.

REFERENCES

[1] Ishizuka, K. Mountain Vegetation, in Numata, M. ed., the Flora and Vegetation of Japan. Kodansha Ltd., 1974, pp.173-210

[2] Janzen, D.H., Why Bamboos Wait So Long to Flower, Annual Review of Ecological Systems, Vol. 7, 1976, pp. 347-391

[3] Kobayashi, M., The Illustrated Book of Plant Systematics in Color, Bambusoideae in Japan. The Hokuryukan Co., Ltd., 2017, 435 pp.

[4] Arase, T., Nishio, A., Okano, T. and Uchida, T., Effect of Suspending Traffic on a Highway in a Mountainous Region in Central Japan on the Succession of Slope Vegetation. International Journal of GEOMATE, Vol. 16; Issue 56, 2019, pp.85-91

[5] Akaho, Y., Inui, Y. and Shikida, A., Action Research of Management for herbaceous Mountain trail of Bamboo Grass in Piedmont and Forest Zone – a Case Study of Mowing in North Part of Hakusan National Park -. Technological Reports of Landscape Architecture, Vol. 2, 2023, pp.30-33

[6] Hikosaka, H., Kobayashi, T., Asano, Y. and Takahashi, T., The Analysis of the Factor of Trail Erosion with Special Reference to the Trail-side Vegetation in Tanzawa Mountains. Journal of the Japanese Society of Revegetation Technology, Vol. 25, Issue 3, 2000, pp.221-229

[7] Niiyama, K., Shibata, M., Saitoh, T. and Naoe, S., The 30 Years Dynamics of Three Dwarf Bamboo Species in Ogawa Research Site in Northern Ibaraki Prefecture, Japan. Bulletin of FFPRI, Vol. 20, Issue.4, 2021, pp.339-351

[8] Arase, T., Okano, T. and Shirota, T., Colonization and Morphological Changes of a Sedge Restricting Regeneration after Wind Damage in a Natural Forest, International Journal of GEOMATE, Vol. 12; Issue 31, 2017, pp.100-104

[9] Saitoh, T., Seiwa, K. and Nishiwaki, A., Effects of Resource Heterogeneity on Nitrogen Translocation within Clonal Fragments of *Sasa palmata*: an Isotopic (^{15}N) Assessment. Annals of Botany, Vol. 98, 2006, pp.657-663

[10] Sakai, R. and Yoshida, T., Effects of Man-powered Scarification and a Rhizome Cutting Treatment on Natural Regeneration of Tree Species in Dwarf-bamboo Grassland. Journal of the Japanese Forrest Society, Vol. 102, Issue 5, 2022, pp.300-305

[11] Yamane, M., Habuto, H., Iwaoka, T., Nagata, K. and Furubayashi, K., GIS Application to Monitoring the Range and Habitat Condition of Sika Deer (*Cervus Nippon*) in the Tanzawa Mountains, Japan. Japanese Journal of Forest Planning, Vol. 35, Issue 2, 2001, pp.63-74

[12] Saitoh, T., Sakai, T., Kabeya, D., Sugita, H., Kushima, H., Hoshino, D., Tate, N., Hayakawa, K., Kubo, T., Imamura, M. and Kuroda, M., Effect of Suppression Treatment on Dwarf Bamboo under the Canopy Using Weeding and Herbicide: Examination of Silvicultural Operation for the Purpose of Advanced Regeneration Practices in Natural Hinoki (*Chamaecyparis obtusa*) Forests. Journal of the Japanese Forestry Society, Vol. 103, Issue 3, 2021, pp.179-185

[13] Tomabechi, T., Takakura, M. and Ito, T., Influence of the Surface Roughness of Roofing Materials on Snow Sliding. Journal of Snow Engineering, Vol. 12, Issue 3, 1996, pp.3-9.

Copyright © Int. J. of GEOMATE All rights reserved, including making copies, unless permission is obtained from the copyright proprietors.

15th Int. Conf. on Geotechnique, Construction Materials & Environment,
Kyoto, Japan, 11-13 November 2025, ISBN 978-4-909106124 C3051

EFFECT OF DIFFERENT GRAYSCALE CONVERSION METHODS ON ROUGHNESS MEASUREMENT USING BINARIZATION

Nozomu Urahata[1], Kenji Okajima[1] and Seiya Nagaoka[1]

[1]Graduate school of Bioresources, Mie University, Japan

ABSTRACT

Currently, roughness deterioration of concrete is a problem in agricultural canals in Japan. Roughness is caused by abrasion from water and sand flowing through the canals. Rough concrete surfaces impede water flow, so it is necessary to measure roughness. Previously, we showed that it's possible to measure roughness using binarization and lighting, by analyzing the shadows on the concrete surface. In binarization, RGB images are converted to grayscale images and then to binary images. However, previous studies have only examined one conversion method for converting to grayscale images. The objective of this study was to clarify the impact of different grayscale conversion methods on measurements. The analysis revealed that there were large differences in the coefficient of determination between the previously used grayscale conversion method and the newly examined conversion method in some cases. Additionally, it was found that there exists a conversion method with a higher coefficient of determination than the previous one, suggesting the potential for improved measurement accuracy.

Keywords: Roughness of concrete, Binarization, Grayscale conversion, Collimated light

INTRODUCTION

Currently, concrete roughness deterioration is a problem in Japan's agricultural canals, which have a total length of 400,000 km. Roughness is caused by abrasion from water and sand flowing through the canals. A rough concrete surface impedes water flow, causing a decrease in flow velocity and a rise in water level. Furthermore, as abrasion progresses and the surface becomes rougher, the cross-sectional area of the concrete decreases, which affects the durability of the canal. Therefore, roughness is measured, and the canal is repaired accordingly. Several quantitative measurement methods for roughness have been established. The arithmetic mean roughness R_a is used as an evaluation index for the roughness of canal concrete. The following three measurement techniques for R_a have been established.

First, there is the laser distance meter [1]. This method reads the unevenness of the concrete in 0.1 mm increments and converts it into roughness. Roughness is obtained as line information and is highly accurate. However, since the obtained roughness is line information and the measurement is precise, it takes time, making it unsuitable for measuring extensive canals.

Second, there is the profile gauge [2]. This method involves pressing multiple connected needles against the concrete to read the unevenness and convert it into roughness. It is an inexpensive and simple measurement method. However, like the laser distance meter, the roughness is obtained as line information with a resolution of approximately 150 mm, and analysis currently takes time.

Third, there is aerial ultrasonic [3]. This method involves irradiating concrete with ultrasound and measuring roughness based on the strength of the reflected wave's voltage. Unlike laser distance meters and profile gauges, this method can measure the roughness of a 160 mm diameter area, making it more efficient than the two methods mentioned above. However, it is not widely used because of the large variation in sensors and the effort required for calibration.

While these measurement techniques have been established, the Ministry of Agriculture, Forestry and Fisheries guidelines [4] stipulate that the evaluation method for roughness is non-quantitative visual inspection.

Our research, therefore, aims to develop a quantitative and more efficient roughness measurement method than existing techniques. We have shown the possibility of quantitative and efficient roughness measurement by using binarization, one of the image processing, and collimated light [5]. The measurement method involves first irradiating light onto the concrete surface from the side in darkroom and then capturing the shadows created by the unevenness of the surface with a camera. Binarization is used to extract shadow area from the captured image. The measurement principle is that the larger the arithmetic mean roughness R_a, the larger shadow area (%) that appear on the concrete surface.

In binarization, an RGB image (24-bit) represented by three colors is converted into a grayscale image (8-bit) represented by a gradient from white to black, and finally converted into a binary image (1-bit) represented by only two colors, white and black. Previous studies [5] have used the

National Television Standards Committee (NTSC) method shown in equation (1) for grayscale conversion.

$$Y = 0.2989\,R + 0.5870\,G + 1.140\,B \quad (1)$$

Y: luminance value, *R*: red value, *G*: green value, *B*: blue value. The NTSC is included as a default in many image libraries and is commonly used.

On the other hand, this study has only used equation (1) so far. Since RGB images store three color values per pixel, there are many other methods for converting to the luminance value Y besides the above (1) equation. Therefore, the validity of the equation has not been examined, and there may be more accurate equations available. Thus, the objective of this study is to clarify the effects of different grayscale conversion methods on roughness measurement method using binarization.

RESEARCH SIGNIFICANCE

Since RGB images contain three colors, there are many methos for converting them to grayscale images. Previous studies have only examined one grayscale conversion method (NTSC). By clarifying the impact on measurements, it is possible to find a more accurate method. In addition, the validity of selecting a certain grayscale conversion method can be indicated in this measurement.

MATERIALS AND METHOD

Concrete

Thirteen types of concrete with different roughness levels were used. The measurement area was set at 100 × 300 mm, and R_a was measured using a profile gauge. R_a is calculated using equation (2).

$$R_a = \frac{1}{l}\int_0^l |f(x)| \quad (2)$$

l: length of the profile gauge (mm), *f*(*x*): difference between the roughness curve and the linear approximation of the roughness curve. R_a was measured at eight points within the measurement area, and the average of these measurements is used as the representative value. The R_a values of the concrete are, in order, 0.04, 0.19, 0.31, 0.32, 0.41, 0.49, 0.49, 0.50, 0.52, 0.65, 0.72, 1.04, 1.11mm. Among these, the concrete with R_a = 0.04 mm has a smooth surface with almost no unevenness, while the other concrete has exposed aggregates and unevenness on the surface.

Methods For Obtaining Images

To create shadows on the concrete, a HOLOLIGHT (Pi PHOTONICS Inc.) was used to emit collimated light (Figure 1). The light source dimension is 100 × 100 mm, and it is a white LED surface light source. Unlike general lighting, this lighting does not spread light and can reproduce collimated light similar to sunlight. The images were taken in a dark room to eliminate the effects of artificial lighting and natural light other than the lighting used. The lighting was applied from the side of the concrete measurement area with a short side of 100 mm, and RGB images of the resulting shadows were acquired. Then, the lighting was applied again from the opposite short side, and RGB images were acquired. A total of two images were acquired for each concrete sample. In addition, considering the property of collimated light that does not spread, the angle of lighting was set at 1.0 to 3.0° in 1.0° increments to compare the effects of the angle. A digital camera (RICOH WG-80, RICOH IMAGING COMPANY, LTD.) was used to capture the images. The camera has approximately 16 million effective pixels and is equipped with a 1/2.3-inch CMOS sensor. From the image, a 100 x 300 mm measurement area was cut out at 1200 x 3650 px (4.3 million pixels) and used for binarization. A schematic of the experiment is shown in Figure 2.

Calculation of Shadow Area Using A New Grayscale Conversion

In the binarization used to calculate the shadow area, the RGB image is first converted to a grayscale image and then to a binary image. Until now, NTSC in equation (1) has been used to convert RGB to

Fig.1 Collimated light

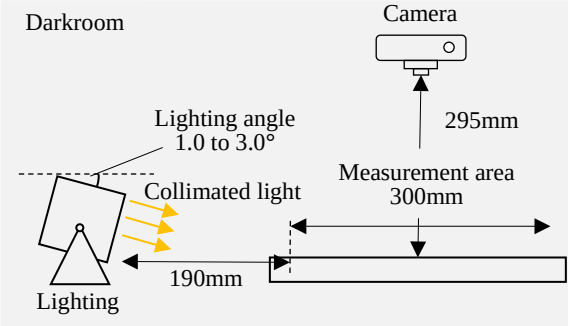

Fig.2 A schematic of the experiment
Note: Adapted from Urahata et al. [1]

grayscale images. In this study, we have used new methods: the average method, which simply Averages the RGB values; the Max method, which adopts the maximum value among RGB; the Min method, which adopts the minimum value among RGB; and the R method, G method, and B method, which adopt the RGB values as they are. The conversion equations for each method are shown in the following.

$$Y = \frac{R+G+B}{3} \quad (3)$$

$$Y = \max(R, G, B) \quad (4)$$

$$Y = \min(R, G, B) \quad (5)$$

$$Y = R \quad (6)$$

$$Y = G \quad (7)$$

$$Y = B \quad (8)$$

In the conversion from grayscale images to binary images, two types of thresholding methods were used: the Exhaustive method, which uses all thresholds from 0 to 255, and the Otsu method, which determines the optimal threshold for each image. Figure 3 shows the binarization used in this study. The grayscale conversions were compared and evaluated based on the shadow area values obtained.

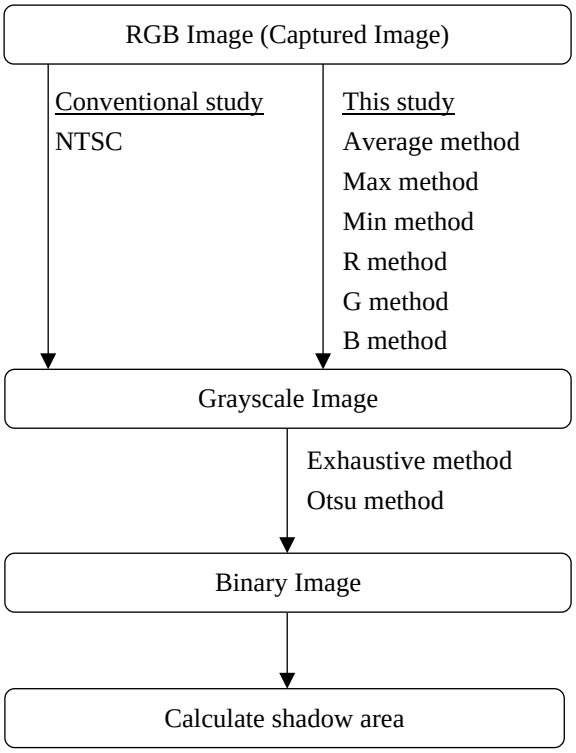

Fig.3 The binarization used in this study

RESULTS AND DISCUSSION

The relationship between the shadow area at a lighting angle of 2.0° and the arithmetic mean roughness R_a is shown in figures 4 to 9. In the Exhaustive method, analysis was performed for all thresholds from 0 to 255, and it was found that, regardless of the grayscale conversion method, a shadow area occurs even on smooth surfaces without unevenness at thresholds of approximately 50 to 100 or higher. In general, it is desired that the shadow area be 0% on smooth surfaces without unevenness. Therefore, in the Exhaustive method, comparisons were made between thresholds of 0 to 50.

The results of the Exhaustive method showing the highest coefficient of determination R^2 are shown in the figures 4 to 0. Additionally, the threshold for each methods are shown in Table 1 along with the NTSC results (from previous studies). Furthermore, the R^2 for each method are shown in Figure 10 and Table 2 for the Exhaustive method and Figure 11 and Table 3 for the Otsu method, along with the NTSC results. In addition, Figure 12 shows a captured image of concrete with R_a = 0.50 mm at a lighting angle of 2.0°, as well as grayscale and binary images obtained using the R method and B method.

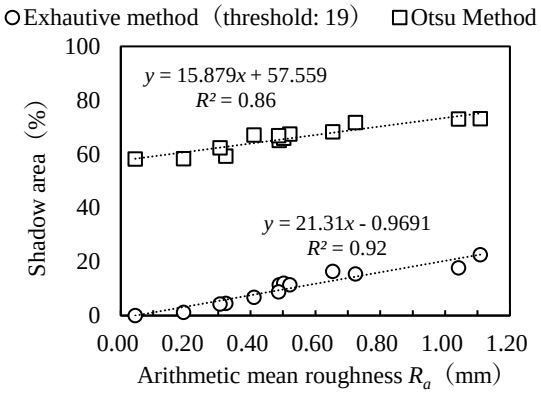

Fig.4 Result of the Average method at the angle 2.0°

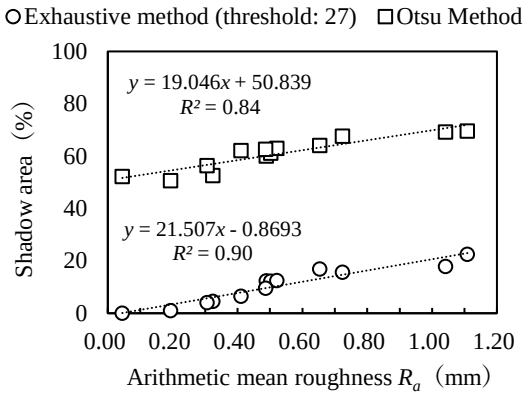

Fig.5 Result of the Max method at the angle 2.0°

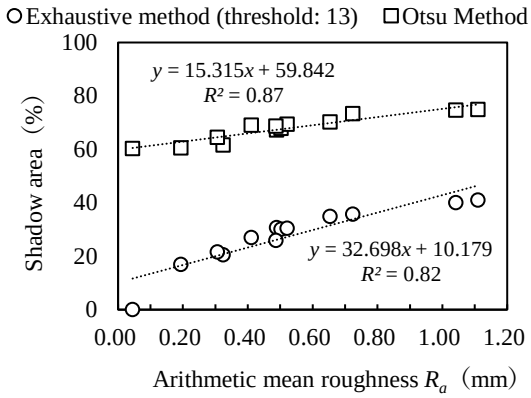

Fig.6 Result of the Min method at the angle 2.0°

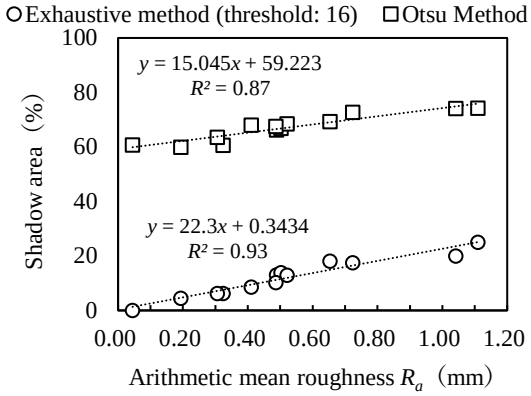

Fig.7 Result of the R method at the angle 2.0°

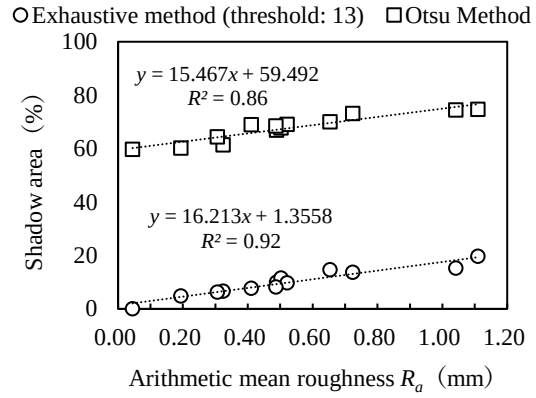

Fig.8 Result of the G method at the angle 2.0°

Table 1 Threshold for each method in the Exhaustive method

Angle (º)	NTSC	Ave rage	Max	Min	R	G	B
1.0	17	19	25	14	16	14	17
2.0	16	19	27	13	16	13	16
3.0	16	20	27	14	16	14	16

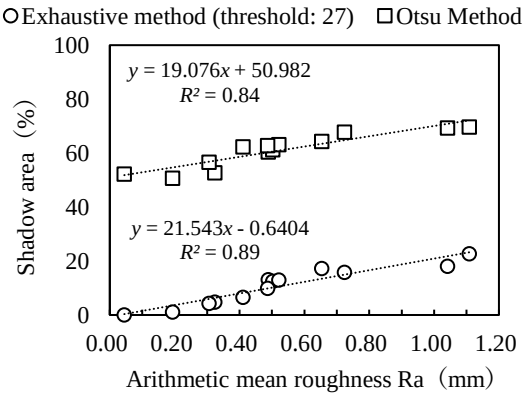

Fig.9 Result of the B method at the angle 2.0°

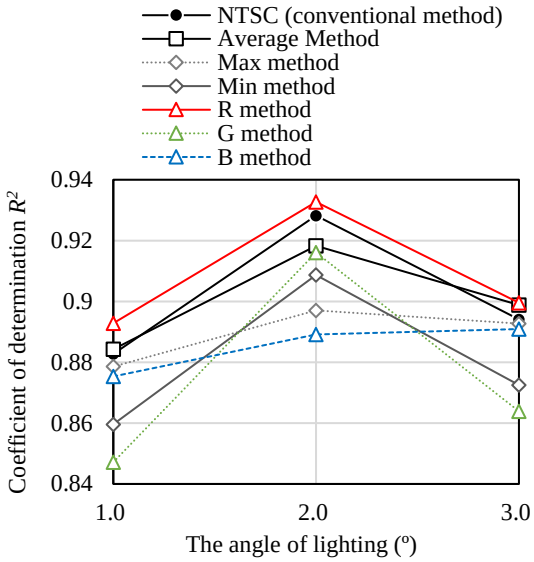

Fig.10 R^2 for each method in the Exhaustive method

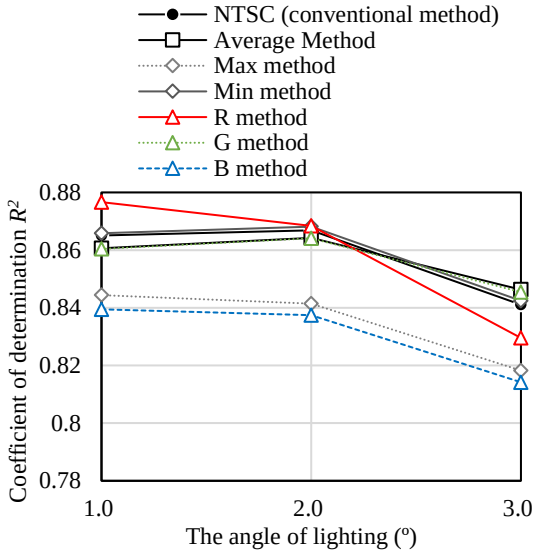

Fig.11 R^2 for each method in the Otsu method

Table 2 R^2 for each method in the Exhaustive method

Angle (º)	NTSC	Average	Max	Min	R	G	B
1.0	0.88	0.88	0.88	0.86	0.89	0.85	0.88
2.0	0.93	0.92	0.90	0.91	0.93	0.92	0.89
3.0	0.89	0.90	0.89	0.87	0.90	0.86	0.89

Table 3 R^2 for each method in the Otsu method

Angle (º)	NTSC	Average	Max	Min	R	G	B
1.0	0.87	0.86	0.84	0.87	0.88	0.86	0.84
2.0	0.87	0.86	0.84	0.87	0.87	0.86	0.84
3.0	0.84	0.85	0.82	0.84	0.83	0.85	0.81

Evaluation of The Coefficient Of Determination

Figures 10 and 11 show that all coefficient of determination R^2 were high, with values of 0.8 or higher. All conversion methods and threshold methods showed high R^2. In the exhaustive method shown in Figure 10, all conversion methods showed high R^2 values when the lighting angle was 2.0°. In addition, the R method showed higher R^2 values than the NTSC (conventional method) at all angles. Furthermore, the average method showed R^2 values similar to the conventional method. Other methods showed lower R^2 values than the NTSC.

In Figure 11, Otsu method showed almost the same R^2 for both 1.0° and 2.0°, with a tendency to decrease at 3.0°. The Min method and B method showed lower R^2 than NTSC at all angles.

In conclusion, the Exhaustive method showed higher R^2 in all cases and was found to be suitable for measurement. This trend was consistent with the results shown in previous studies [5].

About The Threshold of The Exhaustive Method

Table 1 shows that there was no difference in the threshold of the Exhaustive method depending on the angle, and the threshold values were almost constant for each conversion method. This trend is the same as the results shown in previous studies [5]. On the other hand, it became clear that the values tended to differ depending on the conversion method.

Differences Between Conventional Conversion Method (NTSC) And New Conversion Methods

We performed a paired t-test with a significance level of 5% for the R^2 values of NTSC in previous studies and the R^2 values of each conversion method used in this study. The results are shown in Table 4. As shown in Table 4, in the Exhaustive method, a

Table 4 Results of the paired t-test

		Exhaustive method			
Average	Max	Min	R	G	B
0.811	0.327	0.002*	0.061	0.067	0.282
		Otsu method			
Average	Max	Min	R	G	B
0.856	0.004*	0.024*	0.943	0.753	0.002*

*Note: * $p < 0.05$*

(a) Captured image

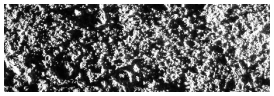

Grayscale image

Exhaustive method
Threshold: 16

Otsu method

Binary image

(b) R method

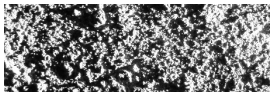

Grayscale image

Exhaustive method
Threshold: 27

Otsu method

Binary image

(c) B method

Fig.12 Captured grayscale and binary images of concrete with R_a = 0.50 mm at a lighting angle of 2.0° by R method and B method

significant difference was observed only in the Min method. No significant differences were observed in other conversion methods, such as the R method, which showed an R^2 greater than NTSC, and the Average method, which showed almost the same value as NTSC. Therefore, although no significant difference was observed, it became clear that there is

a grayscale conversion that shows a larger R^2 than the conventional method. At the very least, it was found that the R method has an R^2 equal to or greater than NTSC, suggesting the possibility of improved measurement accuracy. In addition, it became clear that the average method has an equivalent R^2, suggesting that there is no difference in measurement accuracy. On the other hand, the Min method, which showed a significant difference and had a lower R^2.

In the Otsu method, significant differences were observed between the Max method, Min method, and B method. Therefore, it was suggested that the Max method and B method had lower measurement accuracy than NTSC. Although there was almost no difference in the R^2 value of the Min method compared to NTSC, a significant difference was observed, so it could not be evaluated this study.

Furthermore, considering the above results, it was suggested that NTSC, which has been used in previous studies, is a valid measurement method. When considering future measurements, NTSC, Average method, and R method are likely to be suitable for the Exhaustive method, which is a threshold setting method with a high R^2 value.

On the other hand, since the sample size in this study is only 3, the statistical robustness is low. Therefore, the optimal conversion method cannot be determined for measurement. In the future, it will be necessary to verify by increasing the sample size, such as acquiring data at a larger lighting angle (4.0° or more).

CONCLUSION

This study aimed to clarify the effects of different grayscale conversion methods on roughness measurement method using binarization, and the effects were verified. The findings of this study are summarized in the following.

- It was found that grayscale conversion methods affect measurements.
- It was suggested that some conversion methods improve measurement accuracy, while others reduce it.
- The validity of the conventional NTSC method was also indicated.
- As in previous studies, it was found that the exhaustive method is more suitable than the Otsu method for setting thresholds.

As mentioned in the Results and Discussion section, the challenge for the future is the need to use a large amount of data due to the small sample size. In addition, to establish this research, it is necessary to investigate the effects of different types of lighting and cameras on measurements. In particular, the lighting used in this study is collimated light, which has characteristics different from general lighting, so investigation is essential. Furthermore, although the experiments are conducted in a darkroom environment, it is also necessary to develop a method for conducting experiments in actual canals.

REFERENCES

[1] Asano I., Tokashiki M., Mori M. and Nishihara M., Development of Erosion Monitoring System on Laser Displacement Meter for Cementitious Surface Coating Method, The Japanese Society of Irrigation, Drainage and Rural Engineering, Vol. 82, No. 5, 2014, pp. 285-296.

[2] Kawakami A., Asano I., Mori M., Kawabe S. and Tokashiki M., Abrasion Measurement Method Using a Profile Gauge, The Japanese Society of Irrigation, Drainage and Rural Engineering, vol. 85, No. 1, 2017, pp. 77-84.

[3] Okajima K., Nagaoka S., Ishiguro S., Ito R., Watanabe K. and Ito T., Measurement of the Roughness of the Concrete Surface by the Peak to Peak Value of the Aerial Ultrasonic Wave, The Japanese Society of Irrigation, Drainage and Rural Engineering, Vol. 84, No. 3, 2016, pp. 233-240.

[4] Ministry of Agriculture, Forestry and Fisheries, i n Japan, Guidance for Functional Diagnosis of A gricultural Water Utilization Facilities, 2023, pp. 34,35. [online] https://www.maff.go.jp/j/nousin/mizu/sutomane/attach/pdf/kinouhozen-201.pdf [Accessed 10 July 2025]

[5] Urahata N., Okajima K. and Nagaoka S., Possibility of Roughness Measurement of Concrete by Binarization, Water, Land and Environmental Engineering, Vol. 93, No.6, 2025, pp.7-10.

Copyright © Int. J. of GEOMATE All rights reserved, including making copies, unless permission is obtained from the copyright proprietors.

15th Int. Conf. on Geotechnique, Construction Materials & Environment,
Kyoto, Japan, 11-13 November 2025, ISBN 978-4-909106124 C3051

ANALYSIS AND INTERVENTION DESIGN FOR HIGH-RISK ROAD SEGMENTS IN BUENG KAN PROVINCE, THAILAND

Pattarawadee Prasomsab[1], Jintapha Besun[1], Chamroeun Se[2], Thanapong Champahom[3], Sajjakaj Jomnonkwao[1] and Vatanavongs Ratanavaraha[1]

[1]School of Transportation Engineering, Institute of Engineering, Suranaree University of Technology, Nakhon Ratchasima 30000, Thailand; [2]Institute of Research and Development, Suranaree University of Technology, Nakhon Ratchasima 30000, Thailand; [3]Department of Management, Faculty of Business Administration, Rajamangala University of Technology Isan Nakhon Ratchasima 30000, Thailand

ABSTRACT

Bueng Kan, Thailand's newest province located in the northeast region, has experienced increasing tourism alongside rising road safety concerns. The province faces challenges with crash-prone roadways and a shortage of road safety engineering specialists. This research aims to identify high-risk road segments in Bueng Kan and develop targeted safety interventions that local authorities can readily implement. The methodology employed a three-phase approach: (1) statistical analysis of historical crash data; (2) identification of high-risk areas through agency data integration and comprehensive field investigations; and (3) development of evidence-based countermeasures using engineering solutions, behavioral interventions and monitoring systems. All proposed interventions were evaluated according to International Road Assessment Programme (iRAP) standards. Results identified six critical road segments scoring 1 star or lower on the iRAP star rating system within Bueng Kan Province. These segments fall under the jurisdiction of local administrative organizations and Bueng Kan Municipality. Following the implementation of the proposed safety improvements—including warning signage installation, road surface reinforcement, enhanced lighting and pavement markings—safety ratings improved to 3 stars or higher across all segments, demonstrating significant safety enhancements. Overall, the interventions are projected to reduce crashes by 41.9%, with the Ban Burapha-Ban Khok Krachae route demonstrating the highest economic benefit-cost ratio. This research provides local authorities with data-driven solutions to effectively improve road safety and a framework for optimizing budget allocation for long-term road safety improvement planning, ultimately reducing injuries and fatalities among road users in Bueng Kan Province.

Keywords: Road Safety, iRAP, Integration, Bueng Kan, Thailand

INTRODUCTION

Road traffic crashes remain a major public health and safety concern in Thailand, especially in rural provinces where infrastructure and traffic management systems are still underdeveloped. Bueng Kan, located in the upper northeastern region of Thailand, became a separate province from Nong Khai in 2011 [1] and is currently undergoing development efforts to enhance its overall capacity. Despite having a relatively small population compared to other provinces, Bueng Kan continues to face significant road safety challenges, particularly during major holidays such as Songkran, when crashes noticeably increase. According to crash statistics from 2023–2024, most crash victims were aged between 36 and 60 years and motorcycle-related incidents accounted for as much as 89% of total crashes [2] Although the number of fatalities and injuries has decreased compared to the previous year, hazardous road segments remain prevalent across the province—especially on roads under the responsibility of local administrative organizations.

To support sustainable development and enhance road safety, this research focuses on analyzing high-risk areas in Bueng Kan Province using traffic engineering principles combined with statistical data and field surveys. It aims to identify dangerous road segments and develop practical intervention measures that can be readily implemented. The ultimate goal is to provide local authorities with actionable insights for effective spatial planning and risk mitigation at the local level.

RESEARCH SIGNIFICANCE

This research is significant in analyzing and addressing road safety issues in Bueng Kan Province, with a focus on identifying high-risk locations and proposing intervention strategies to improve hazardous areas. The aim is to help reduce road crashes and associated injuries. The research findings will support the development of appropriate solutions for local authorities and promote long-term road safety improvements.

LITERATURE REVIEW

Statistical Model for Analyzing Crash Severity

Logistic regression is the primary statistical method commonly used to model crash severity, as it effectively handles categorical dependent variables and provides clear interpretations through odds ratios. This method has been widely applied to identify and quantify factors influencing crash severity outcomes. For instance, Wei et al. [3] employed both a Multinomial Logistic Regression Model (MN-logit) and a Random Parameter Logit Model (RP-logit) to explore the factors affecting injury severity. Ye and Lord [4] compared logistic regression with other statistical techniques, focusing on sample size and the efficiency of each method. Meanwhile, Abay [5] used a bivariate logistic regression model to analyze injury severity for both drivers and pedestrians in vehicle-pedestrian crashes, helping to better understand the complex relationship between injury outcomes for both involved parties.

Kernel Density Estimation (KDE)

Kernel Density Estimation **(** KDE) is a widely used non-parametric spatial analysis technique that serves as an effective tool for analyzing road crash data, particularly when location-specific crash information is available. This method enables the visualization and analysis of areas with frequent crash occurrences. By estimating the density of events within a given area using crash data distributed across various points in a continuous space—such as roads or urban zones—KDE helps to identify crash hotspots. [6-8] Furthermore, KDE has been proven to be well-suited for application in rural road networks and areas where GPS data is unavailable, demonstrating its flexibility and effectiveness in various geographic contexts. [9**,** 10]

iRAP Star Ratings

The International Road Assessment Programme (iRAP) provides a globally recognized method for assessing road infrastructure safety. Its Star Rating system evaluates roads from 1-star (least safe) to 5-star (most safe). Globally, only a small portion of travel occurs on 3-star or better roads, particularly for vulnerable road users. iRAP promotes a global target: ensuring that most road travel occurs on 3-star [11]

The iRAP (International Road Assessment Programme) methodology has been adopted in many countries to identify and rank risks across road networks, especially in areas where crash data is incomplete or inaccurate. For example, Algeria has implemented iRAP in combination with GIS systems to assess the safety levels of different segments of its road network [12-14] Additionally, the Star Rating for Schools (SR4S) program, developed by iRAP, has been used to evaluate road safety around school zones, enabling the design of appropriate and targeted intervention measures. [15**,** 16]

RESEARCH METHODOLOGY

The conceptual framework of this study represents a systematic process for enhancing road safety in Bueng Kan Province. It begins with the collection of historical crash data to understand the causes of road crashes and the factors contributing to crash severity within the study area. This information is then used to develop models identifying crash severity and high-risk locations. Subsequently, the data is utilized to conduct road safety assessments based on established criteria and checklists through Road Safety Audits (RSAs) [17], in parallel with an iRAP analysis—an internationally recognized methodology for evaluating road safety. These assessments lead to the development of conceptual solutions and intervention strategies proposed to local authorities. The final stage involves evaluating both the direct and indirect economic feasibility of the proposed measures prior to actual implementation, as illustrated in Fig. 1.

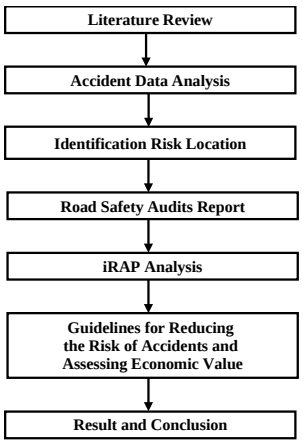

Fig.1 Research Framework

HISTORICAL CRASH DATA ANALYSIS

Historical crash data in Bueng Kan Province from 2019-2021 Data from the Bueng Kan Provincial Road Safety Operation Center, the Royal Thai Police and local hospitals will be used to create a Multinomial Logistic Regression model to analyze the factors affecting the severity of crashes. The dependent variable is the severity of the crash, which is divided into 3 levels: slightly injured, Serious injuries and deaths are caused by the model consisting of two models: a model that analyzes crashes where the victims are vulnerable road users and a model that analyzes crashes on roads that are intersections. The logit function of the covariates is defined as follows:

$$Y_k = \text{logit}(P_k) = \log\left(\frac{P_k}{1-P_k}\right) = \beta_0 + \beta_1 \cdot x_{i2} + \beta_2 \cdot x_{i2} + \ldots + \beta_i \cdot x_{in} \quad (1)$$

Hence, the probability of crash *i* resulting in injury severity *k* (k = 1 is a fatal crash and k = 0 is a non-fatal crash) can be written as:

$$P_k = \frac{EXP\left(\beta_0 + \beta_1 \cdot x_{i2} + \beta_2 \cdot x_{i2} + \ldots + \beta_i \cdot x_{in}\right)}{1 + EXP\left(\beta_0 + \beta_1 \cdot x_{i2} + \beta_2 \cdot x_{i2} + \ldots + \beta_i \cdot x_{in}\right)} \quad (2)$$

where β_i is a parameter estimate corresponding to the independent variable x_i. This paper uses *EXP(β)* (Odds Ratio) to interpret the influence of each independent variable.

Then, the Logistic Regression model was analyzed using the principle of selecting variables one at a time, based on the relationship between the independent and dependent variables. Out of a total of 16 variables, there was 1 dependent variable, FATALITY and 15 independent variables. Then, the Cox & Snell R Square and Nagelkerke R Square values were considered to indicate the efficiency of the model and its consistency with the empirical data.

The analysis of the accident model in the vulnerable group of accident victims found that driving faster than the legal limit is approximately 13.5 times more likely to cause death than other causes. The model that analyzes crashes at road intersections can be interpreted that if the victim wears a helmet at the time of the crash, the chance of death is only a 23.2 percent. Full regression tables and parameter values are provided in Tables 1-2.

Table 1 Results of the analysis of the severity of the crash involving vulnerable road users.

Variable	B	S.E.	Wald	df	Sig.	Exp(B)	95% C.I. for EXP(B)	
							Lower	Upper
GENDER	1.379	0.501	7.577	1	0.006	3.969	1.487	10.593
HELMET	-1.582	0.354	19.931	1	0	0.206	0.103	0.412
DRUNK	-1.197	0.565	4.485	1	0.034	0.302	0.1	0.915
EXCESS_SPEED_LIMIT	2.602	0.366	50.396	1	0	13.487	6.576	27.66
DARK	0.717	0.28	6.567	1	0.01	2.048	1.184	3.544
Constant	-3.646	0.562	42.127	1	0	0.026		

Table 2 Results of the analysis of the severity of the crash in the intersection area.

Variable	B	S.E.	Wald	df	Sig.	Exp(B)	95% C.I. for EXP(B)	
							Lower	Upper
HELMET	-1.462	0.479	9.324	1	.002	0.232	-1.462	0.479
EXCESS_SPEED_LIMIT	2.532	0.734	11.897	1	.001	12.582	2.532	0.734
Constant	-2.216	0.607	13.310	1	.000	0.109		

Fig.2 shows the high-risk or hazardous locations using Kernel Density Estimation (KDE) within a GIS environment (ArcGIS Pro) using historical event data, using the 85th percentile density threshold. The analysis results revealed 6 areas with frequent and clustered accidents in Bueng Kan Province.

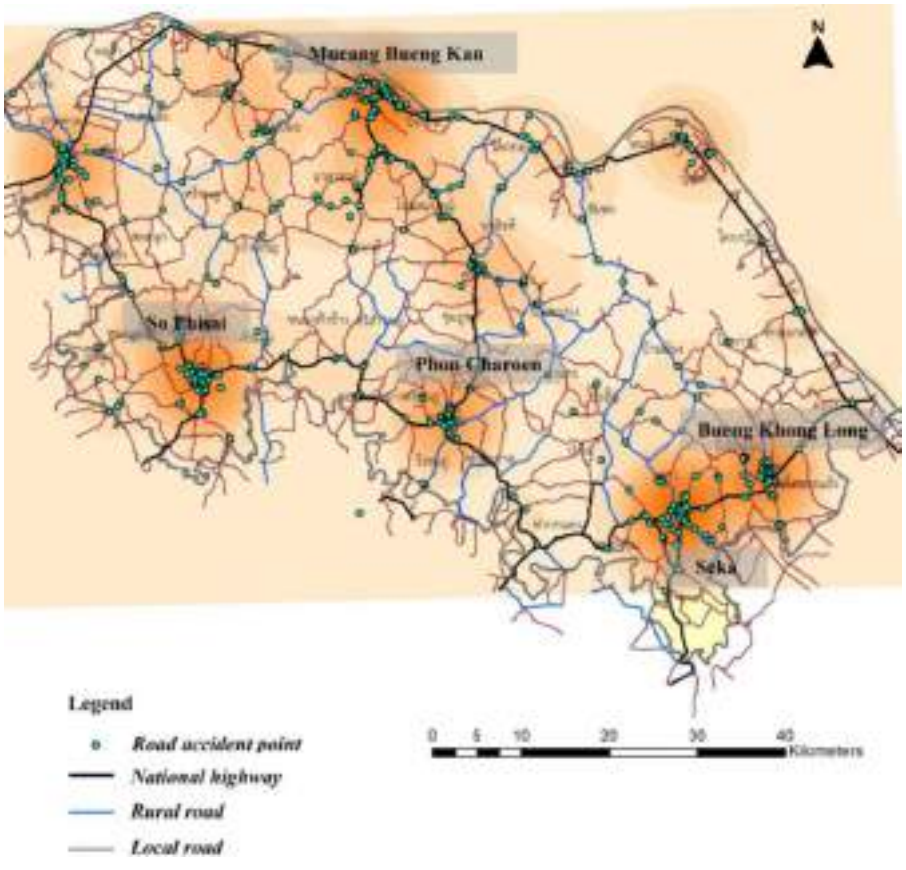

Fig.2 Results of crash cluster analysis in Bueng Kan province

ROAD SAFETY AUDIT (RSA) AND FIELD SURVEY

Selected high-risk locations undergo a thorough Road Safety Audit (RSA). The RSA process consists of:

1) Primary data collection: Collect existing road network maps, traffic volume data, historical crash details for specific areas and aerial photographs.

2) Preparing a checklist: Develop a standardized RSA checklist based on AUSTROADS, PIARC and Thai Highways Department guidelines, adapted to the local context.

3) Field inspection: Operated by a team of traffic engineering and road safety experts during different times (day/night, weekdays/weekends) and different weather conditions.

4) Data recording and analysis: Record observations, photographs and videos, as well as road user behavior.

Key issues examined include road courses and sections, intersection characteristics, drainage, road signs, traffic lights, road surface markings, roadside hazardous materials, road surface conditions and lighting.

From the KDE analysis, several crash clusters were identified. Based on crash frequency, severity, field surveys, RSA inspection results and consultation with local authorities, six high-risk road sections were prioritized for the design of remedial measures:

1) At the Bueng Kan Municipality roundabout: (3 points: roundabout, intersection of Bueng Kan Road and Phon Thuk Phai Road, intersection of Bueng Kan Road and Rak Song Road)

2) Roads under the responsibility of the Provincial Administrative Organization (PAO Roads): (3 points: Ban Saen Samran-Ban Huai Kong Road, Ban Burapha-Ban Khok Krachae Road, Ban Yang Rian Road)

IRAP STAR RATING ASSESSMENT

The International Road Assessment Programme (iRAP) methodology was used to assess the safety of selected road sections and the potential impacts of corrective measures. The assessment process and an example of software for iRAP assessment are shown in Fig.3-4 and is divided into three parts:

1) Road Coding: Road features were systematically encoded every 100 m using ViDA software. Over 50 roadway features related to design and traffic control features that influence crash probability and crash severity were recorded, using digital imagery and field data.

2) Star Rating Generation: From the encoded characteristics, a star rating (1 star to 5 stars) is generated for car users, motorcyclists, pedestrians and cyclists.

3) Selection of corrective measures and investment planning: Evidence-based corrective action measures, iRAP methodology, are proposed. It enables modeling of the impact of these measures on star ratings and assessment of reductions in fatalities and serious injuries (FSIs).

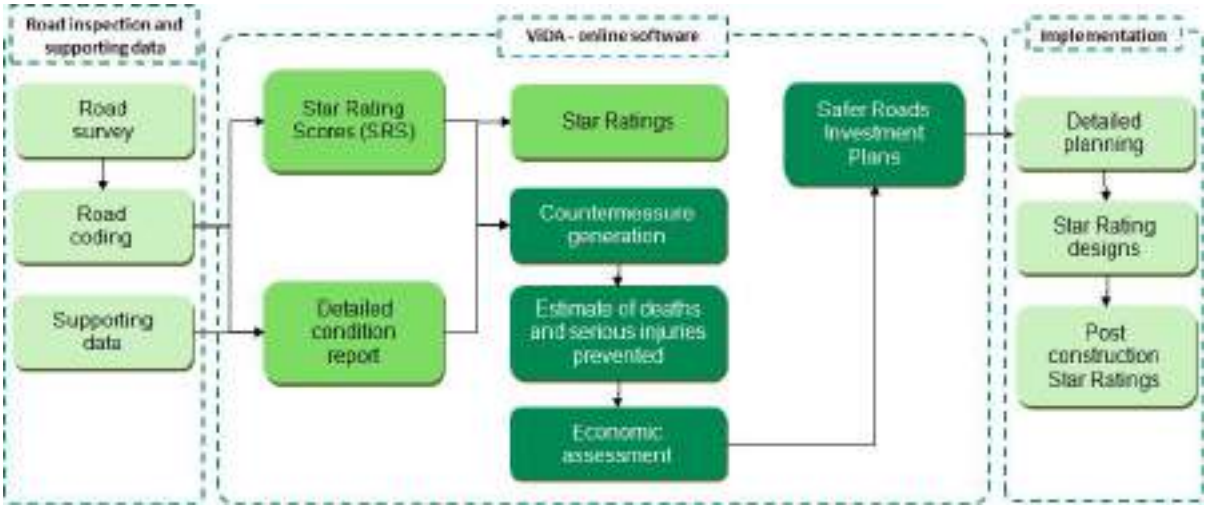

Fig.3 iRAP Assessment Process

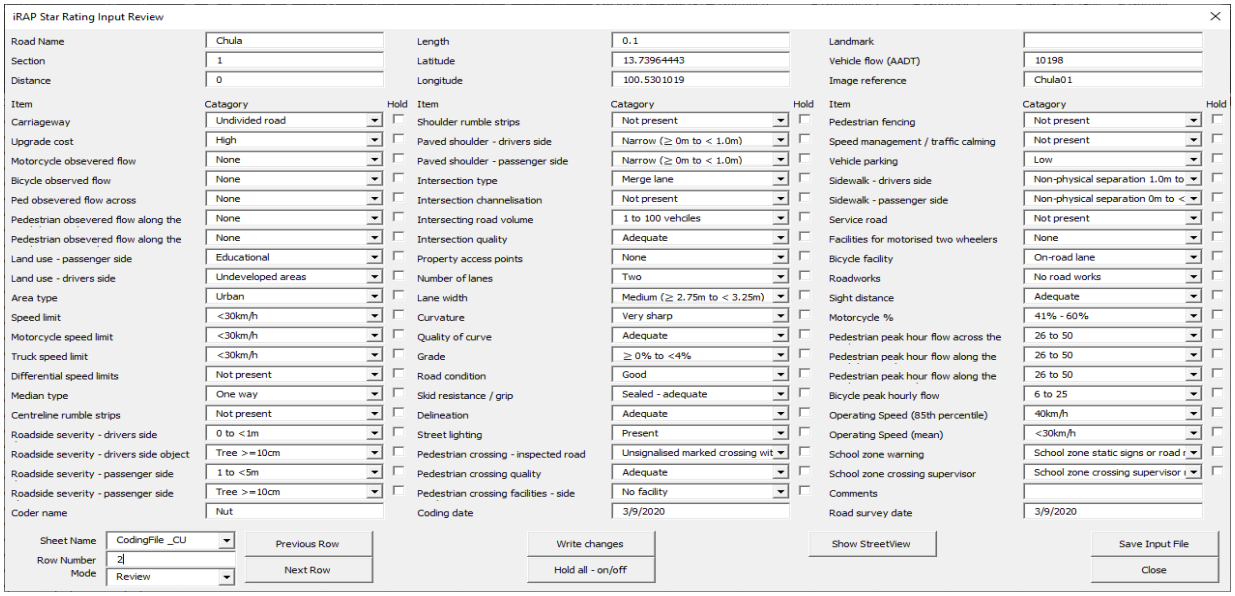

Fig.4 iRAP Assessment Process

The proposed remedial measures for the six high-risk road sections are expected to reduce crashes by an average of 41.9%, with all improved roads expected to receive an iRAP star rating. A rating of 3 stars or above for all road user groups, which is a significant safety improvement from the previous 1 or 2 stars, demonstrates that targeted, evidence-based engineering solutions can significantly improve road safety performance. The safety assessment results according to the iRAP criteria, conducted using the iRAP PreProcessor program, were based on analyzing images within a 100-meter radius and considering over 50 variables. The safety evaluation results according to the iRAP criteria after the improvement measures are shown in Table 3 and Fig. 5.

Table 3 The safety assessment results according to the iRAP criteria for the Ban Burapha - Ban Khok Krachae route Bok.3032 Road Mueang Bueng Kan District after the improvement measures.

Road User Group	Safety Rating (Stars)
Car Users	> 4 stars
Motorcycle Users	> 4 stars
Pedestrians	> 4 stars
Bicycle Users	> 4 stars
Car Users	> 4 stars
Motorcycle Users	> 4 stars

ECONOMIC COST ANALYSIS (CBA)

The economic value of the proposed remedial measures was assessed using (Cost-Benefit Analysis: CBA) using a project life expectancy of 10 years. Discount rate: 12% (based on the World Bank and National Economic and Social Development Board guidelines) Cost calculation includes initial construction and installation costs. Maintenance costs (regular and routine) and operating costs. Benefits will arise from reducing economic and social costs resulting from crashes, including reducing the cost of death.

Fig.5 Sample of iRAP's safety assessment results at the Ban Burapha - Ban Khok Krachae route Bok.3032 Road Mueang Bueng Kan District After the renovation

Estimated using the Value of Life Statistics (VSL) from the Office of Transport and Traffic Policy and Planning (OTP) (10.2 million baht per death, adjusted for 2021) Reducing the cost of injury: Serious injury (0.31 million baht/case), Minor injury (0.08 million baht/case) according to the NESDB and Reducing the cost of property damage: (0.05 million baht/case) in terms of indicators: Net Present Value (NPV), Benefit

Cost Ratio (BCR) and Internal Rate of Return (IRR).

Economic analysis showed different levels of cost-effectiveness. As seen in Table 4, while Bueng Kan Municipality Roundabout had the highest investment cost but a relatively low BCR (0.48), which may be due to the complexity of the area and the lower severity of previous crashes, Ban Burapha-Ban Khok Krachae Road showed the highest economic benefit-cost ratio (BCR = 1.55), indicating that investment in improving curves on high-crash rural roads could yield significant economic returns. Other areas showed BCR values between 0.69 and 0.91, even for areas with BCR < 1. Non-monetary benefits, such as improved quality of life, reduced suffering and improved community safety perception, were also significant and supported the implementation of these safety measures.

Table 4 Results of prioritization in resolving frequently problematic points/areas and economic analysis

Point/Area	Cost of troubleshooting (baht)	Reduced accident benefits (baht)	Benefit to Cost Ratio (B/C)	Ranking results
1. Bueng Kan Municipality roundabout area	2,266,532	331,977	0.48	6
2. Bueng Kan Road intersection, cutting across Phon Thuk Phai Road	1,563,762	342,331	0.71	4
3. Intersection of Bueng Kan Road and Raksong Road	1,319,999	331,977	0.82	3
4. Area along the route Baan Saen Samran - Baan Huai Kong, Road 3217, Mueang Bueng Kan District	850,735	238,575	0.91	2
5. Area along the Ban Burapha-Ban Khok	856,648	407,514	1.55	1
6. Area along the Ban Yang Rian route, Road 4015, Seka District	1,745,918	368,324	0.69	5

DISCUSSION

From the analysis of road crash data in Bueng Kan Province, it was found that crashes occurring on local roads are influenced by several factors that contribute to the severity of injuries and fatalities. In particular, vulnerable road users (VRUs) and crashes occurring at intersections are significant contributors. The findings are presented as follows:

Factors Affecting the Severity of Crashes

Using logistic regression to analyze the factors affecting the severity of crashes, several statistically significant factors were identified. These include exceeding the speed limit which increases the likelihood of death by up to 13.5 times, emphasizing the need for strict speed control. The gender of the driver shows that male drivers are 3.969 times more likely to die from a crash compared to female drivers. Crashes occurring at night without lighting increase the likelihood of death by 2.048 times. Wearing a helmet reduces the chance of death by 79.4% and driving under the influence may reduce the severity of the crash due to lower speed but it remains a significant risk factor.

Risk Areas and Solutions

Using Kernel Density Estimation (KDE) to analyze crash data, areas with high crash frequencies were identified. The areas with the highest crash density in Bueng Kan province include Muang Bueng Kan District (the municipal roundabout, which has traffic control and speed regulation issues), Bung Khong Long District (Highway 2026, a major road with high traffic volume), Se Ka District (Seka subdistrict, particularly at the intersection with the main highway) and Phon Charoen and So Phisai Districts (Highway 2095 and local roads).

Improvement Measures for Road Safety

The study suggests several measures to enhance road safety, including speed reduction measures (such as clear traffic signs, Optical Speed Bars and enforcement of speed limits), improvements in lighting systems (installing street lights at intersections and high-risk areas, especially rural roads), improving intersections (e.g., stop signs, yield signs, advance warning signs and considering roundabouts in high-traffic areas), road surface enhancements to increase friction (to reduce skidding, especially on wet roads, curves, intersections, or frequent braking zones), promoting helmet use (through law enforcement and public awareness campaigns) and upgrading road infrastructure (such as widening lanes, improving shoulders and drainage systems). The findings highlight factors affecting crash severity on local roads in Bueng Kan province, identifying six high-risk areas requiring infrastructure and policy improvements to enhance safety. Four main measures were emphasized: installing speed warning signs, reinforcing road surfaces, installing streetlights and placing road markings, which could reduce crashes by up to 41.9%. The cost-benefit analysis revealed that the Ban Burapa-Ban Khok Krachaeng route has the highest B/C ratio of 1.55, while the roundabout in the municipal area of Bueng Kan has the lowest B/C ratio of 0.48.

CONCLUSION

Crashes in Bueng Kan are chiefly linked to speeding, driver gender, night-time driving, helmet non-use, and drink-driving. Hot-spot districts—Muang Bueng Kan, Bung Khong Long, Se Ka, Phon Charoen, and So Phisai—need targeted upgrades: tighter speed control, better lighting, smoother intersections, stronger pavements, and campaigns to boost helmet use. Priority countermeasures—speed-warning signs, resurfacing, street lights, and clear road markings—could cut crashes by up to 42%. Cost-benefit analysis shows the Ban Burapa–Ban Khok Krachaeng corridor offers the best return (B/C = 1.55), while Bueng Kan's municipal roundabout

ranks lowest (B/C = 0.48).

ACKNOWLEDGMENTS

The authors gratefully acknowledge the financial support provided by the National Research Council of Thailand (NRCT) and the data support from relevant agencies in Bueng Kan Province.

REFERENCES

[1] Royal Thai Government Gazette, "Bueng Kan Province Establishment Act, B.E. 2554 (2011)," Royal Thai Government Gazette, 2011.

[2] Thai Road Safety Center. "Road Accident Statistics Report 2023–2024," April 8, 2025; https://www.thairsc.com.

[3] Fulu Wei, Yuxin Han and Yanyong Guo, “Analysis of Factors Affecting the Severity of Injuries in Electric Two-Wheeled Vehicle Crashes with or without Violation: A Random Parametric Logit Model considering Heterogeneity of Means and Variances,” Journal of Advanced Transportation, vol. 2024, no. 1, pp. 1-15, 2024.

[4] Fan Ye and Dominique Lord, “Comparing three commonly used crash severity models on sample size requirements: Multinomial logit, ordered probit and mixed logit models,” Analytic Methods in Accident Research, vol. 1, pp. 72-85, 2014.

[5] Kibrom A. Abay, “Examining pedestrian-injury severity using alternative disaggregate models,” Research in Transportation Economics, vol. 43, no. 1, 2013.

[6] T. K. Anderson, “Kernel density estimation and K-means clustering to profile road accident hotspots,” Accident Analysis & Prevention, vol. 41, no. 3, pp. 359-364, 2009.

[7] Zhixiao Xie and Jun Yan, “Kernel Density Estimation of traffic accidents in a network space,” Computers, Environment and Urban Systems, vol. 32, no. 5, pp. 396-406, 2008.

[8] B. W. Silverman, Density estimation for statistics and data analysis, London: Chapman & Hall, 1986.

[9] Homayoun Harirforoush and Lynda Bellalite, “A new integrated GIS-based analysis to detect hotspots: A case study of the city of Sherbrooke,” Accident Analysis & Prevention, vol. 130, pp. 62-74, 2019.

[10] Khanh Giang Le, Pei Liu and Liang-Tay Lin, “Traffic accident hotspot identification by integrating kernel density estimation and spatial autocorrelation analysis: a case study,” International Journal of Crashworthiness, vol. 27, no. 2, 2022.

[11] Sejal S.Bhagat, Masira Mo and Arif Nalbandh, “Road Safety Assessment and Star Rating Using iRAP Along NH-48 (Kadodara-Kosamba) in Surat City,” Journal of Emerging Technologies and Innovative Research (JETIR), vol. 10, no. 5, pp. 124-129, 2023.

[12] Abdelhak Derras, Khaled Amara and Ramdane Oulha, “Application of the IRAP Method Combined with GIS to Improve Road Safety on New Highway Projects in Algeria,” Periodica Polytechnica Transportation Engineering, vol. 50, no. 4, pp. 414-425, 2022.

[13] Armana Sabiha Huq, "An iRAP Based Risk Impact Analysis at National Highway-1 for a Proposed Route Connecting Coastal Areas of Bangladesh," Advances in Road Infrastructure and Mobility, Sustainable Civil Infrastructures Amin Akhnoukh, Kamil Kaloush, Magid Elabyad, Brendan Halleman, Nihal Erian, Samuel Enmon II and Cherylyn Henry, eds., Springer, Cham: 21 Apil 2022, 2022.

[14] Athiappan Kamalasekar, Karthik Chandran, Subrata Chowdry, J. A. Alzubi, R. M. , Christian Fernández-Campusano, Mehdi Gheisari, Hamidreza Rabiei-Dastjerdi and Abolfazl Mehbodniya, “Road crash analysis and countermeasures on hilly roads in a developing country using iRAP,” International Journal of Crashworthiness, 2025.

[15] Ali Zayerzadeh and Mohsen Fallah Zavareh, “School Zone Road Safety Assessment Using the iRAP Star Rating for Schools (SR4S) Methodology in Khorasan Razavi Province,” Journal of Injury & Violence Research, vol. 11, no. 4 Suppl 2, pp. 71, 2025.

[16] Estiara Ellizar, Sukma Larastiti, Titis Efrindu Bawono, Windu Mulyana and Cahyadi Kurniawan, “Youth Participation in School Safety Zones Assessment: A Case Study in Indonesia,” Journal of Road Safety, vol. 30, no. 2, pp. 1-9, 2023.

[17] Asian Development Bank, CAREC Road Safety Engineering Manual: Star Ratings. Manila: ADB, 2022. [Online]. Available: http://dx.doi.org/10.22617/TIM220272-2.

Copyright © Int. J. of GEOMATE All rights reserved, including making copies, unless permission is obtained from the copyright proprietors.

15th Int. Conf. on Geotechnique, Construction Materials & Environment,
Kyoto, Japan, 11-13 November 2025, ISBN 978-4-909106124 C3051

INFLUENCE OF PORE SPATIAL DISTRIBUTION ON THE RELATIONSHIP BETWEEN MINOR LOSS AND FORCHHEIMER COEFFICIENTS

Junichiro Takeuchi[1] and Masayuki Fujihara[1]

[1]Graduate School of Agriculture, Kyoto University, Japan

ABSTRACT

Darcy's law states that there is a linear relationship between the flow velocity and the gradient of the piezoelectric head when the flow velocity in the porous media is sufficiently small. When the flow velocity increases to some extent, Forchheimer's law is applied by adding a squared term of the flow velocity to Darcy's law. Various equations have been proposed to estimate the coefficient of the squared term (Forchheimer coefficient) from the grain size and porosity. On the other hand, the Forchheimer coefficient is known to depend on the heterogeneity of the spatial distribution of the pores. The above equations do not consider the heterogeneity of the pore distribution. In this study, we investigate the relationship between the shape loss coefficient in the pores and the Forchheimer coefficient under laminar flow conditions using a pore network modeled as a network of interconnected pores in a porous medium. Specifically, a series of numerical experiments are conducted by changing the spatial distribution of the pores as well as the mean and variance of the shape loss coefficients. As a result, it is shown that there is a proportional relationship between the average of the shape loss coefficient in each pore and the Forchheimer coefficient. Furthermore, it is shown that the proportionality coefficient strongly depends on heterogeneity of porous media.

Keywords: Forchheimer coefficient, Minor loss coefficient, Pore network model, Network flow

INTRODUCTION

Generally, flow in groundwater is modeled by Darcy's law. However, even in laminar flow, when the flow velocity becomes sufficiently high, the pressure head loss due to the inertial effect can no longer be ignored, rendering Darcy law inapplicable. In such cases, Forchheimer's law, which adds a squared term of the flow velocity is added to Darcy's law, is used to describe the relationship between flow velocity and head loss.

Forchheimer's equation includes two coefficients related to the properties of the porous medium. One is related to the friction loss and corresponds to the permeability in Darcy's law, while the other, called the Forchheimer coefficient, is related to the inertial effect and is characteristic of Forchheimer's law. Many empirical formulas, such as Ergun's formula, have been proposed for these coefficients. In many cases, they are expressed using parameters such as the porosity and particle size of the porous medium [1,2]. However, the Forchheimer coefficient depends on the spatial heterogeneity of pores [3], which cannot be represented by macroscopic parameters like porosity and particle size.

On the other hand, the squared term of velocity in the Forchheimer equation is thought to originate from minor losses due to pore expansion, contraction, and/or bending [4]. By calculating flow within pores using methods such as the lattice Boltzmann method and the finite element method, loss coefficients for expansion/contraction regions or bending regions can be determined [5]. The Forchheimer coefficient for porous media can be calculated by computing flow in pores of a whole porous medium [6]. Additionally, by using a pore network model to calculate flow in a pipe channel that considers shape loss due to pore expansion and/or contraction, it is possible to evaluate flow within a porous medium. El-Zehairy et al. (2019) estimated shape loss coefficients from pore sizes obtained through micro-X-ray CT data and investigated the effects of porosity heterogeneity on non-Darcy flow [4].

The relationship between the minor loss coefficient and the Forchheimer coefficient has not been investigated. In direct methods that directly calculate flow within pores using LBM or FEM, it is difficult to predefine the desired minor loss coefficients. Therefore, the pore network approach is employed to prescribe arbitrary shape loss coefficients. This study aims to clarify the relationship between the minor loss coefficient and the Forchheimer coefficient, as well as the influence of porous media heterogeneity on them, through numerical experiments.

RESEARCH SIGNIFICANCE

This study quantitatively clarifies the link between the Forchheimer and minor loss coefficients

in porous media, emphasizing the critical role of pore-scale heterogeneity. The findings enhance the predictive accuracy of non-Darcy flow models, contributing to improved designs in groundwater management, civil engineering, and environmental protection where accurate flow prediction through porous media is essential.

MODEL DESCRIPTION

In this study, we investigate the relationship between Forchheimer coefficients at the macro scale and shape loss coefficients at the pore scale.

Darcy-Forchheimer Equation

Flow in porous media with relatively high Reynolds numbers is described not by Darcy's law but by Forchheimer's law, which considers the influence of the inertial term. Here, the following Forchheimer equation is used as an empirical formula representing the flow rate per unit area and the hydraulic gradient in a porous medium with a constant cross-section [4].

$$\frac{\Delta h}{L} = \alpha_F q + \beta_F |q| q \tag{1}$$

$$h = \frac{p}{\rho g} + z \tag{2}$$

$$q = \frac{Q}{A} \tag{3}$$

where Δh is the difference of the hydraulic head between the inlet and outlet of an objective porous medium, L is the length of the objective porous medium, q is the flow rate per unit cross-sectional area, p is the pressure, ρ is the fluid density, g is the gravitational acceleration, z is the height from a reference plane, Q is the total flow rate through the porous medium, A is the cross-sectional area of the porous medium, and α_F and β_F are the coefficients. The coefficient α_F is the inverse of the hydraulic conductivity K and is represented as follows.

$$\alpha_F = \frac{1}{K} \tag{4}$$

The quadratic term in q is due to inertial effects caused by pore expansion and/or contraction, etc.

Flow in Pore Network

The pores in a porous medium can be modeled as a network of repeatedly dividing and merging pores. Here, we use the SNOW algorithm to extract the pore network from the porous medium [7]. The extracted pore network consists of PBs (pore bodies) and PTs (pore throats). PBs constitute the bifurcation nodes, and PTs constitute the pipes between the bifurcation nodes in a pipe network. For a pipe network flow, the flow rate within each pipe (PT) and the piezometric head at the bifurcation nodes (PBs) are unknown variables. The solution can be obtained by simultaneously solving the following equations: the equations for head loss in each PT, the continuity equation at the PBs, and the equations for the hydraulic head at the inflow and outflow PBs.

$$h_j - h_k = f_i \frac{l_i}{d_i} \frac{q_i |q_i|}{2 g a_i^2} + \sum_m b_{i,m} \frac{q_i |q_i|}{2 g a_i^2} \tag{5}$$

$$d_i = \frac{4 a_i}{P_i} \tag{6}$$

where index i denotes the i-th PT and i is included in the set Λ^{PT} of PT indices, h_j and h_k are the hydraulic head at the both ends of PT i, and indices j and k are included in the set Λ_i^{PB} of PB indices at both ends of PT i. l_i, d_i, q_i, a_i and P_i are the length, hydraulic diameter, flow rate, cross-sectional area, and perimeter of PT i, respectively. f_i is the friction factor, and $b_{i,m}$ is the minor loss coefficient (e.g., for expansion and contraction), where multiple factors are assumed to exist within a single PT. When the flow in a PT is laminar, the friction factor f_i is represented as follows.

$$f_i = \frac{\gamma}{Re_i} \tag{7}$$

$$Re_i = \frac{d_i |q_i|}{v a_i} \tag{8}$$

where γ is a constant that depends on the shape of the cross-section. Typical values are 64, 56.908, or 53.333 when the cross section is a circle, square, or equilateral triangle, respectively. Re_i is the Reynolds number of the reach i, v the dynamic viscosity coefficient of water. Substituting Eqs. (7) and (8) into Eq. (5) yields Eq. (9), which describes head loss including the minor loss in laminar flow.

$$\frac{h_j - h_k}{l_i} = \alpha_i q_i + \beta_i q_i |q_i| \tag{9}$$

$$\alpha_i = \frac{\gamma v}{2 g a_i d_i^2} \tag{10}$$

$$\beta_i = \frac{\sum_m b_{i,m}}{2 g l_i a_i^2} \tag{11}$$

In this study, the head loss coefficients α_i and β_i are referred to as the friction loss coefficient and the shape loss coefficient, respectively.

The mass balance equations at each PB are represented as follows.

$$\sum_{i \in \Lambda_j^{\mathrm{PT}}} q_i = 0 \tag{12}$$

where Λ_j^{PT} is the set of PT indices connected to junction $j \in \Lambda^{\mathrm{PB}}$.

In addition to these equations, specified water heads are given at the upstream and downstream ends of the network.

$$h_j = h_{\mathrm{IN}} \qquad (j \in \Lambda_{\mathrm{IN}}^{\mathrm{PB}}) \qquad (13)$$

$$h_j = h_{\mathrm{OUT}} \qquad (j \in \Lambda_{\mathrm{OUT}}^{\mathrm{PB}}) \qquad (14)$$

where $\Lambda_{\mathrm{IN}}^{\mathrm{PB}}$ and $\Lambda_{\mathrm{OUT}}^{\mathrm{PB}}$ are the sets of PB indices of inlets and outlets, respectively.

The nonlinear equations system of Eqs. (9) through (14) is solved by the Newton-Raphson method.

Estimation Of Forchheimer Coefficients From Network Flow

From the total flow Q, which is obtained by summing all inflow or outflow rates, the apparent hydraulic conductivity K_{app} is calculated as follows.

$$K_{\mathrm{app}} = \frac{L}{h_{\mathrm{IN}} - h_{\mathrm{OUT}}} \frac{Q}{A} \qquad (15)$$

$$Q = \sum_{i \in \Lambda_{\mathrm{IN}}^{\mathrm{PT}}} q_i \left(\text{or } = \sum_{i \in \Lambda_{\mathrm{OUT}}^{\mathrm{PT}}} q_i \right) \qquad (16)$$

where $\Lambda_{\mathrm{IN}}^{\mathrm{PT}}$ and $\Lambda_{\mathrm{OUT}}^{\mathrm{PT}}$ are the sets of indices of PTs connected to the inlet and outlet, respectively.

On the other hand, the apparent hydraulic conductivity is represented by the following equation derived from Eq. (1).

$$K_{\mathrm{app}} = \frac{1}{\alpha_{\mathrm{F}} + \beta_{\mathrm{F}} |q|} \qquad (17)$$

By changing the head at the upstream end h_{IN}, apparent hydraulic conductivities for various flow rates can be obtained. From the relationship between the apparent hydraulic conductivities and flow rate (*i.e.*, Darcy velocity), the Forchheimer coefficients α_{F} and β_{F} are estimated using the least squares method.

Comparison Of Forchheimer Coefficients and Head Loss Coefficients

In this study, we derive the Forchheimer coefficients, which are characteristic of porous media, from the prescribed shape loss coefficients in a pore network. When comparing these coefficients, the flow rate per unit area q in Eq. (1) is the Darcy velocity, whereas the flow rate q_i in Eq. (9) is the flow rate within the pores, *i.e.*, the actual velocity. Therefore, Eq. (9) is converted to a Darcy velocity equivalent using the relationship between the Darcy and actual velocities.

$$q_i = \frac{q_i^{\mathrm{D}}}{\phi} \qquad (18)$$

where ϕ is the porosity of the porous medium. Then the Darcy velocity version of Eq. (9) becomes:

$$\frac{h_j - h_k}{l_i} = \frac{\alpha_i}{\phi} q_i^{\mathrm{D}} + \frac{\beta_i}{\phi^2} q_i^{\mathrm{D}} \left| q_i^{\mathrm{D}} \right| . \qquad (19)$$

$$\bar{\beta} = \frac{1}{\left| \Lambda^{\mathrm{PT}} \right|} \sum_{i=1}^{\left| \Lambda^{\mathrm{PT}} \right|} \beta_i \qquad (20)$$

where $|\Lambda|$ is the number of elements in a set Λ.

In the numerical experiments conducted in this study, the relationship between β_{F} and β_i (specifically, the average of β_i, *i.e.*, $\bar{\beta}$) is investigated. This is done by arbitrarily varying α_i in each reach while maintaining the connectivity of the pore network and the spatial positions of the junctions. Varying α_i implies changing γ and/or d_i.

NUMERICAL EXPERIMENTS

Virtual Porous Medium and Pore Network

A virtual porous medium is created using the discrete element method by randomly packing spherical particles and a pore network is extracted using SNOW algorithm [7]. When extracting a pore network, several PT features can be obtained, such as inscribed radius, equivalent radius, perimeter, and cross-sectional area. As with PTs, the inscribed radius, volume, and surface area of PBs can be obtained. Here, PTs of the pore network are assumed to be circular tubes, and their radius is defined as that of the inscribed circle.

Figures 1 and 2 show the created porous medium and its extracted pore network. The porous medium was created by randomly packing 5,747 spherical particles with a diameter of 2 mm into a container with a 3.6 cm square base side length.

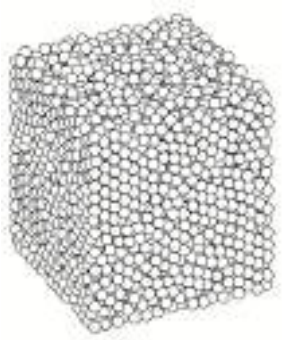

Fig.1 Virtual porous medium

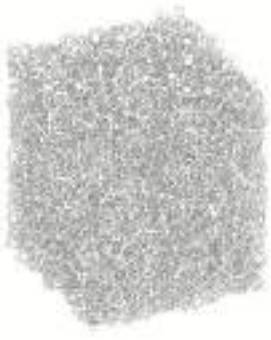

Fig.2 Extracted pore network

Head Loss Coefficients

To investigate the relationship between the shape loss and Forchheimer coefficients as the heterogeneity of the porous medium changes, four types of pore network are prepared here: Original, Homo, Hetero1, and Hetero2. Original refers to the original pore network extracted from the virtual porous medium. Homo refers to the one with all friction loss coefficients set to the average of Original's friction loss coefficients.

$$\alpha_i^{\mathrm{Homo}} = \bar{\alpha} \coloneqq \frac{1}{|\Lambda_{\mathrm{R}}|} \sum_{m \in \Lambda_{\mathrm{R}}} \alpha_m^{\mathrm{Original}} \tag{22}$$

where α_i^{Homo} and $\alpha_i^{\mathrm{Original}}$ are the friction loss coefficients for Homo and Original pore networks, respectively, and $\bar{\alpha}$ is the average of $\alpha_i^{\mathrm{Original}}$. Physically interpreted, this means that longer PTs are given a larger diameter.

Hetero1 and Hetero2 refer to the ones with friction loss coefficients following uniform random numbers as follows.

$$\alpha_i^{\mathrm{Hetero}} \sim U(\xi_\alpha, \eta_\alpha) \tag{23}$$

$$\frac{1}{2}(\xi_\alpha + \eta_\alpha) = \bar{\alpha} \tag{24}$$

$$r_\alpha \coloneqq \eta_\alpha - \xi_\alpha = \begin{cases} \bar{\alpha} & \text{for Hetero1} \\ 1.8\bar{\alpha} & \text{for Hetero2} \end{cases} \tag{25}$$

Where $U(\xi_\alpha, \eta_\alpha)$ is the random variable following a uniform distribution ranging from ξ_α to η_α. Here, ξ_α and η_α satisfy Eqs. (24) and (25). That is, the average of the random variable is $\bar{\alpha}$, and the width is $\bar{\alpha}$ for Hetero1 or $1.8\bar{\alpha}$ for Hetero2.

The shape loss coefficients are also given by a random variable following a uniform distribution ranging from ξ_b to η_b. Here, to clarify the physical meaning, the random number is assigned to the sum of $b_{i,m}$ instead of β_i.

$$\sum_m b_{i,m} \sim U(\xi_b, \eta_b) \tag{26}$$

Sixteen types of minor loss coefficients are generated by combinations of four types of averages and four types of widths.

$$\frac{1}{2}(\xi_b + \eta_b) = \bar{b} \in \{0.0, 0.1, 0.5, 1.0\} \tag{27}$$

$$r_b \coloneqq \eta_b - \xi_b \in \{0, 0.5\bar{b}, \bar{b}, 2\bar{b}\} \tag{28}$$

where $\bar{b}$ is the average minor loss coefficient in a single PT.

For numerical experiments, a total of 64 (=4×16) models with head loss coefficients are examined. Furthermore, to check the individual differences within each model, five samples were created using different random number seeds. The difference in piezometric heads between the inlet and outlet was set to 25 values ranging from 0.01 to 10 cm.

RESULTS

Typical flow distributions in the pore networks are shown in Figs. 3 to 5. Figure 3 shows the effect of the magnitude of $\bar{b}$, where the maximum flow velocity is suppressed as $\bar{b}$ increases. Figure 4 shows the flow velocity distribution for each model when the same spatial distribution of shape loss coefficients is applied. In the homogeneous medium Homo, the flow velocity distribution is nearly uniform in the vertical direction. In contrast, in the heterogeneous media Original and Hetero2, selective flow occurs. Hetero2, which is considered to have greater heterogeneity than Original, shows a stronger tendency. Figure 5 shows the effect of the variance of the shape loss coefficients in homogeneous media. It is shown that selective flow develops as the variance increases.

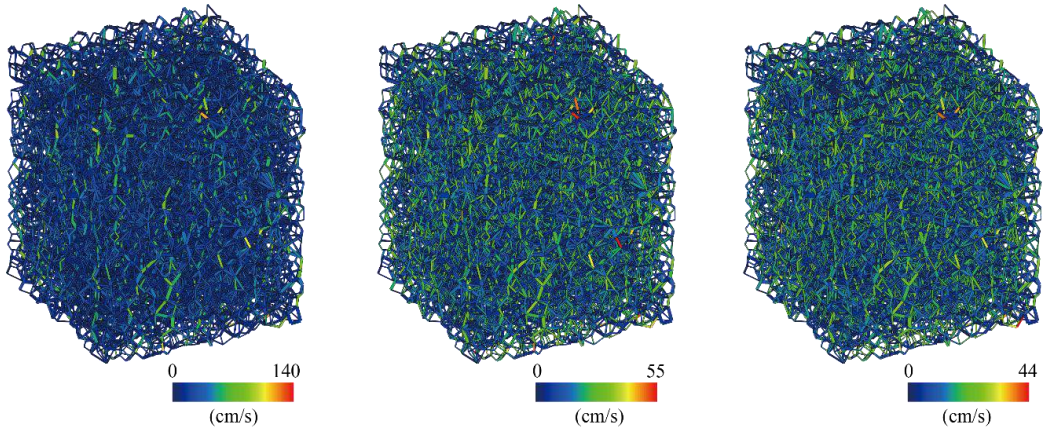

(a) Original (0, 0) (b) Original (0.5, 0.5$\bar{\boldsymbol{b}}$) (c) Original (1.0, 0.5$\bar{\boldsymbol{b}}$)

Fig. 3 Effect of shape loss coefficients on flow distribution in Original ($\bar{\boldsymbol{b}}, \boldsymbol{r_b}$) when $\boldsymbol{\Delta h}$ = 10 cm

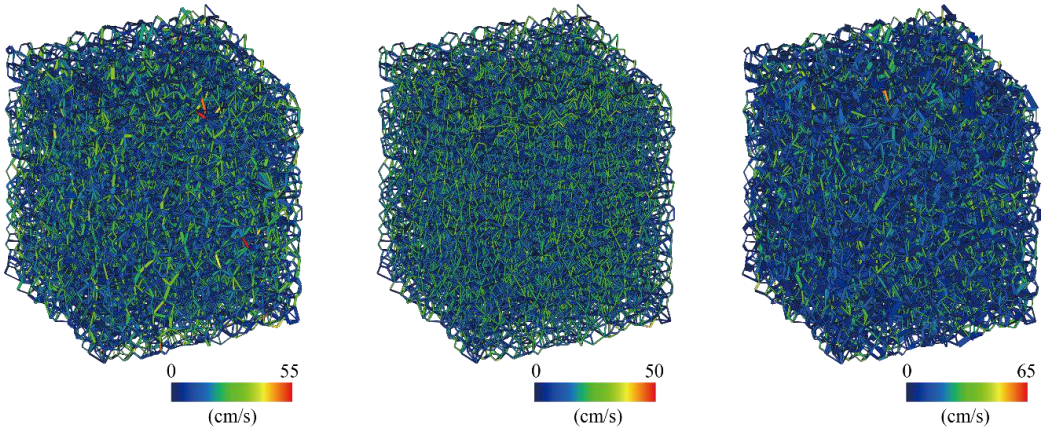

(a) Original (0.5, 0.5$\bar{b}$) (b) Homo (0.5, 0.5$\bar{b}$) (c) Hetero2 (0.5, 0.5$\bar{b}$)

Fig. 4 Effect of homogeneity on flow distribution in each model ($\bar{b}, r_b$) when Δh = 10 cm

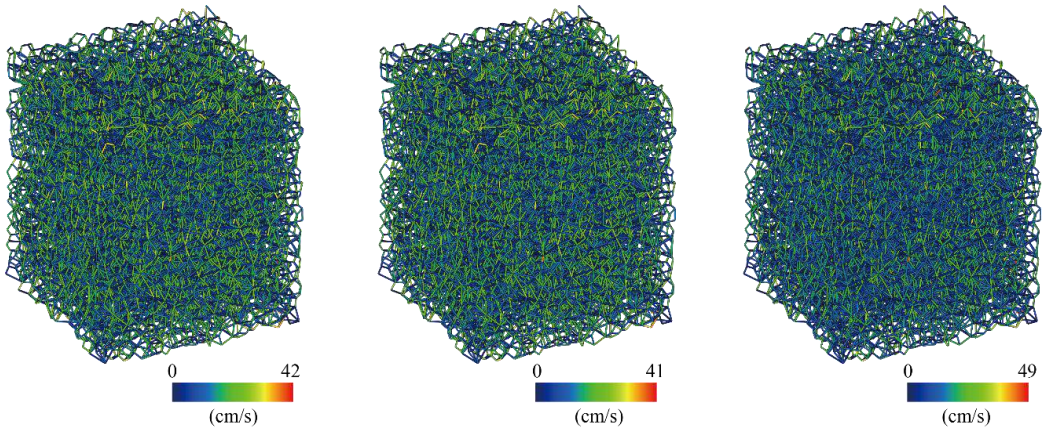

(a) Homo (0.5, 0.0) (b) Homo (0.5, 0.1$\bar{b}$) (c) Homo (0.5, 1.0$\bar{b}$)

Fig. 5 Effect of valiance of shape coefficients on flow velocity in Homo ($\bar{b}, r_b$) when Δh = 10 cm

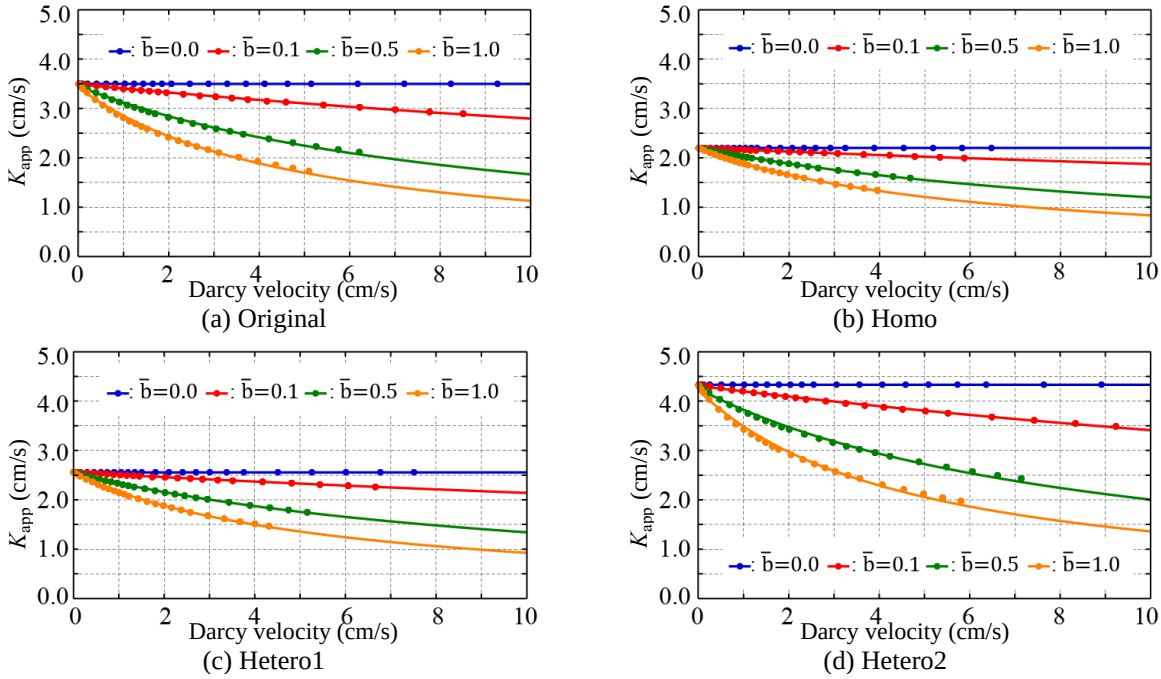

Fig. 6 Apparent hydraulic conductivity in each porous medium model ($r_b = 0.5\bar{b}$)

Table 1 Estimated Forchheimer coefficients ($r_b = 0.5\bar{b}$)

	Original		Homo		Hetero1		Hetero2	
$\bar{b}$	α_F	β_F	α_F	β_F	α_F	β_F	α_F	β_F
0.0	0.286	0.00	0.454	0.00	0.391	0.00	0.231	0.00
0.1	0.287	7.14×10^{-3}	0.454	7.97×10^{-3}	0.392	7.59×10^{-3}	0.232	6.11×10^{-3}
0.5	0.289	3.12×10^{-2}	0.455	3.79×10^{-2}	0.393	3.53×10^{-2}	0.235	2.64×10^{-2}
1.0	0.291	5.96×10^{-2}	0.456	7.43×10^{-2}	0.394	6.86×10^{-2}	0.237	4.99×10^{-2}

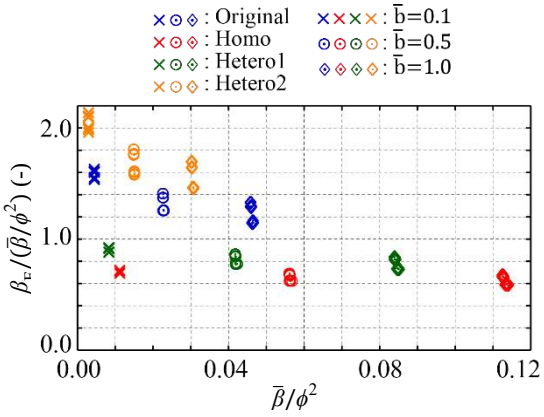

Fig. 7 Ratio of Forchheimer coef. to minor loss coef.

Figure 6 shows the changes in the computed apparent hydraulic conductivities and estimated regression curves for each porous medium model with $r_b = 0.5\bar{b}$. The horizontal axis shows the Darcy velocity (Q/A) when the difference in piezometric heads between the inlet and outlet varies from 0.01 to 10 cm, and the vertical axis shows the apparent hydraulic conductivity. These figures show that, even though the same spatial distribution of the minor loss coefficient is applied, the manner in which the apparent hydraulic conductivity emerges depends on the heterogeneity of the media. Table 1 shows the hydraulic conductivities and Forchheimer coefficients estimated from the computed results. The larger the degree of heterogeneity, the larger the Forchheimer coefficient.

Figure 7 shows the ratio of the Forchheimer coefficient to the corresponding minor loss coefficient. When the medium is homogeneous or has low heterogeneity, the ratio of the Forchheimer coefficient to the corresponding minor loss coefficient is less than 1, and the ratio increases as heterogeneity increases. These findings also demonstrate the dependence of the Forchheimer coefficient on the heterogeneity of porous media.

CONCLUSIONS

In this study, the relationship between the Forchheimer coefficient of a porous media and the shape loss coefficient in PTs was investigated through numerical experiments with pore network models. The results showed that the Forchheimer coefficient strongly depends on the heterogeneity of porous media. When a porous medium is homogeneous, the Forchheimer coefficient was slightly less than the average of corresponding minor loss coefficients. As the degree of heterogeneity became large, the ratio of the Forchhier coefficient to the corresponding minor loss coefficient also increased to about twice as much.

REFERENCES

[1] Ergun S., Fluid Flow through Packed Columns, Chemical Engineering Progress, Vol. 48, No. 2, 1952, pp.89–94.
[2] Kadlec H. R., Knight L. R., Treatment Wetlands. Lewis Publishers, 2009, pp.21–57.
[3] Muljadi B. P., Blunt M. J., Raeini A. Q., and Bijeljic B., The Impact of Porous Media Heterogeneity on Non-Darcy Flow Behaviour from Pore-scale Simulation, Advances in Water Resources, Vol.95, 2016, pp.329–340.
[4] El-Zehairy A. A., Nezhad M. M., Joekar-Niasar V., Guymer I., Kourra N., and Williams M. A., Pore-network Modelling of Non-Darcy Flow through Heterogeneous Porous Media, Advances in Water Resources, Vol. 131, 2019, 10.1016/j.advwatres.2019.103378.
[5] Sidiropoulou M. G., Moutsopoulos K. N., and Tsihrintzis V. A., Determination of Forchheimer equation coefficients a and b, Hydrological Processes, Vol.21, No.4, 2007, pp.534–554.
[6] Takeuchi Y., Takeuchi J., Izumi T., and Fujihara M., Two-Dimensional Numerical Analysis of Non-Darcy Flow Using the Lattice Boltzmann Method: Pore-Scale Heterogeneous Effects, Journal of Fluids Engineering, Vol.143. No.6, 2021, https://doi.org/10.1115/1.4049689.
[7] Gostick J. T., Versatile and Efficient Pore Network Extraction Method Using Marker-Based Watershed Segmentation, Physical Review. E, Vol. 96, Issue 2-1, 2017, 023307.

Copyright © Int. J. of GEOMATE All rights reserved, including making copies, unless permission is obtained from the copyright proprietors.

15th Int. Conf. on Geotechnique, Construction Materials & Environment,
Kyoto, Japan, 11-13 November 2025, ISBN 978-4-909106124 C3051

URBAN PUBLIC SPACE DESIGN AND UTILIZATION AS WELL AS THE DKI JAKARTA CITY GOVERNMENT'S EFFORTS TO EMPOWER STREET VENDORS

Elisabeth Ratu Rante Allo [1], Ruslan Prijadi [2] and Chotib [3]

[1,3] School of Strategic and Global Studies Universitas Indonesia; [2] Faculty of Economics and Business Universitas Indonesia

ABSTRACT

Problem Statement this research examines the utilization of public space by street vendors and its implications in Jakarta. The local government established a designated center for street vendors, known as the Binaan Location, equipped with essential facilities for electricity and water at reasonable costs. However, it has not attracted significant interest from street vendors, who tend to favor sporadic trading practices. Research Approach this research uses the Explanatory Sequential Mixed Method approach, where the quantitative phase is carried out first, and continued with the qualitative phase to enrich the quantitative findings. Field surveys and in-depth interviews were conducted utilizing a qualitative approach, complemented by ArcGIS mapping to analyze the spatial distribution of street vendor locations, the distance from the Binaan Location to these distributions, accessibility via public transportation networks, and spatial analysis through the overlay method of land use and resident density. Results the findings of this study are as follows: (1) The majority of Binaan locations experience low foot traffic and are distanced from populated areas; (2) Several structures within the Binaan location are inadequately maintained; (3) Street vendors are inclined to pay higher fees to thugs when operating outside the Binaan Location due to the influx of visitors.

Keywords: Urban Public Space Design, Street Vendors, Informal Economy, Spatial Analysis, Urban Planning

INTRODUCTION

Urban growth in developing countries like Indonesia has generated substantial informal sectors, with DKI Jakarta's informal economy employing over 193,000 individuals who make significant contributions to the local economy. Street vendors operating in public spaces such as sidewalks and parks create conflicts over urban space usage, reflecting the complex dynamics where informal economy needs clash with city modernization visions according to [1]. In a global context, similar issues are also experienced by various major cities in developing countries as noted [2].

Despite regulations like Governor Regulation No. 10/2015 intended to provide legal certainty and suitable locations for street vendors, implementation faces persistent challenges including vendor resistance and infrastructure limitations, leading to continued evictions that demonstrate policy-practice inconsistencies. The Jakarta government's Binaan Location program was designed as a win-win solution offering structured spaces with supporting facilities including drainage systems, waste management, public toilets, and electrical access, while maintaining urban order.

However, the program's underutilization reveals deeper structural issues in street vendor regulation approaches. The paradox remains that vendors continue to prefer sporadic selling using public facilities despite facing higher illegal levies, rather than utilizing well-organized designated locations with affordable cleanliness and security costs. This resistance indicates the need for comprehensive understanding of vendor preferences, consumer patterns, and informal economy dynamics to create effective and sustainable solutions that truly address the complex realities of urban informal commerce rather than imposing top-down spatial arrangements that fail to align with vendor economic logic..

RESEARCH SIGNIFICANCE

Street Vendor Concept In Jakarta

In Indonesia, street vendors are known as "kakilima" (five-foot), a term originating from the physical form of pushcart vendor [3]. The name represents five supporting points: two vendor legs, two cart wheels, and one additional cart support for balance when stationary.

According to DKI Jakarta Governor's Regulation No. 10/2015, street vendors are defined as "business actors who engage in trade using mobile or immobile business facilities, utilizing city infrastructure, social facilities, public facilities, land, and buildings owned by government and/or private entities on a temporary/non-permanent basis" (Peraturan Gubernur DKI Jakarta Nomor 10 Tahun 2015).

Figure 1. Illustration of a Street Vendor

Street Vendor as Urban Informal Sector

The term 'street vendor' generally refers to retail or wholesale trade of goods and services on the street and other related public thoroughfares such as alleys, roads, and boulevards. There are several other terms often used to describe 'street vendors,' such as Non-Permanent, street vendors, and small traders. The practice of street vendors can be observed in many countries; however, they are most prevalent in third-world countries, especially in urban areas as documented.

Street vendors are part of the informal sector. In fact, street vendors are the most visible manifestation of the informal economy. As an urban informal sector, street vendors have created job opportunities for the growing urban workforce, while also offering flexibility and innovation in the economy.

The term 'informal' indicates that street vendor activities are different from other 'formal' economic activities. The most important difference between the formal and informal sectors is the recognition by the relevant authorities. Street vendors have several weaknesses in terms of spatial planning provisions for their trading activities. The government's allocation of trade space is prioritized for formal economic activities, while the space available for street vendors is more limited as noted by [4].

Figure 2. Urban street vendors

Additionally, there is also a possibility of a connection between the formal and informal sectors. For example, street vendors might serve as an extension of formal economic activities, selling leftover goods or second-quality products from officially registered stores according to [5]. These examples show the unclear distinction between formal and informal activities as discussed [6].

Characteristics of Street Vendors in Jakarta City

Street vendors in Jakarta City vary greatly in scale, time, location, remuneration, labor, and the types of goods and services they offer, according to the opinions of [7] and [8]. One of the prominent characteristics of street vendors in Jakarta is their mobility and flexibility in daily operations.

Pachecho [9] describes two main types of street vendors based on their level of mobility, classifying them as permanent or non-permanent. Permanent types include vendors with kiosks or permanent stalls that remain in the same location all the time, even when there is no trading activity. Non-permanent types include vendors who are truly mobile or those who have structures that can be easily assembled and disassembled over time.

Also made another classification of street vendors, in terms of their operational methods. The first category is street vendors, who continuously move from one place to another to sell goods or offer their services. The second category is office supply traders who offer their goods and services at a fixed location. These traders are fixed in certain locations, and they can sell from permanent kiosks, trays, boxes and baskets, and carts. The nature of street vendors allows them to operate from one place to another. From here, they can establish markets that only operate on certain days, such as Sunday markets or during specific seasons according to [10].

Concept of Urban Public Space

This research argues for a fundamental shift in how urban planners approach street vendors - from viewing them as problems to recognizing them as valuable urban assets. The key findings emphasize that street vendors demonstrate remarkable resilience, can adapt to regulations, survive economic downturns, and potentially formalize their operations.

The study identifies critical flaws in current Binaan Location programs, particularly their failure to understand what vendors actually want, how consumers behave, and how informal economies function. Rather than simply allowing poor people to sell, policies should strategically integrate vendors into broader urban development frameworks.

The research outlines essential policy principles: adopting humane rather than punitive approaches, avoiding policies that inadvertently encourage rural-urban migration, rejecting one-size-fits-all solutions,

and accepting that integration will require substantial bureaucratic investment.

Success requires centralized, coherent policies that provide local governments with clear frameworks for community service. Most importantly, effective street vendor integration demands deep understanding of spatial relationships, vendor behaviors, and the complex dynamics between formal and informal urban economies. The emphasis is on strategic integration rather than elimination or mere tolerance.

RESEARCH METHODS

This study employs an Explanatory Sequential Mixed Method approach, combining quantitative and qualitative phases. The research utilized: (1) Field surveys and in-depth interviews; (2) ArcGIS mapping for spatial distribution analysis; (3) Statistical analysis of vendor willingness to relocate; and (4) Multistage random sampling with 1,400 respondents across Jakarta's administrative areas

Table 1. Number and Distribution of Samples Based on Location Typology

Criteria	Sample	Percentage	City	District	Village
Built Location	140	10%	28	14	7
Temporary Location	490	35%	98	49	35
Educated	70	5%	14	7	4
Not Set/Other	700	50%	140	70	35
Total	1400	100%	280	140	71

Source: DKI Government Database (2021)

RESULTS

Statistical Analysis Results

The statistical analysis examined the supporting factors for the willingness of street vendors to move to the selling locations provided by the DKI Jakarta Provincial Government. The data analysis was processed by the author in 2025 and reveals several significant patterns.

Table 2. Distribution willing to move by Location of Street Vendors

Location	Willing to Move			
	0. No	1. Yes	Total	
	Row N %	Row N %	Count	Row N %
0 = Others	84.40%	15.60%	758	100.00%
1=Built Location	70.60%	29.40%	153	100.00%
2=Temporary Location	89.20%	10.80%	498	100.00%
Total	84.60%	15.40%	1409	100.00%

Source: processed by the author (2025)

Out of a total of 1409 respondents, the majority of traders representing 84.60% stated that they are not willing to relocate, while only 15.40% are willing to move. When the data is broken down by location category, traders located elsewhere show the highest unwillingness rate at 84.40%, followed by traders at construction sites at 70.60%, and traders at temporary locations at 89.20%. Interestingly, although traders at temporary locations have the highest percentage of unavailability, they also show the greatest variation in location distribution with 496 respondents.

Table 3. Distribution willing to move by Education of Street Vendors

Education	Willing to Move			
	0. No	1. Yes	Total	
	Row N %	Row N %	Count	Row N %
0= <= Junior High School	84.50%	15.50%	717	100.00%
1= >= Senior High School	84.70%	15.30%	692	100.00%
Total	84.60%	15.40%	1409	100.00%

Source: processed by the author (2025)

The education level analysis presented in Table 3 shows the distribution based on the education level of the traders. The data shows a pattern consistent with the previous findings, where the majority of traders at all education levels are unwilling to relocate. Merchants with education up to high school show a reluctance rate of 84.50%, while those with education above high school have a slightly higher reluctance rate of 84.70%. The distribution of respondents based on education shows that 717 traders with education below high school and 692 traders with education above high school, indicating a relatively even distribution in both education categories.

Table 4. Distribution willing to move by Owner of Street Vendors

Owner	Willing to Move			
	0. No	1. Yes	Total	
	Row N %	Row N %	Count	Row N %
0 = Others	84.70%	15.30%	98	100.00%
1 = Own his/herself	84.60%	15.40%	1311	100.00%
Total	84.60%	15.40%	1409	100.00%

Source: processed by the author (2025)

Table 4 categorizes respondents based on their business ownership status. The results show that both traders who own their own businesses and those who work for others have almost identical levels of unwillingness, namely 84.70% and 84.60%, respectively. The distribution of ownership shows a significant dominance of traders who own their own businesses, with 1311 respondents, compared to only 98 traders who work for others. This illustrates the dominant entrepreneurial character among street vendors.

Table 5. Statistic Summary of turnover by Willing to Move

Willing to Move	Mean	Median	Mode	Std	Minimum	Maximum	Count
0. No	6833032	4500000	3000000	11907328	70000	250000000	1192
1. Yes	8275942	5000000	4000000	10575638	200000	90000000	217
Total	7054278	4500000	3000000	11778552	70000	250000000	1409

Source: processed by the author (2025)

The statistical summary of turnover by willingness to move is presented in Table 5, showing comprehensive numerical distribution. For the group that is not willing to move, the average mean value recorded is 6,833,032, with a median value of 4,500,000, and the most frequently occurring mode value is 3,000,000. The very high standard deviation of 11,907,328 indicates a significant variation in the data, with a value range from a minimum of 70,000 to a maximum of 250,000,000 from a total of 1,192 respondents.

Meanwhile, the group willing to relocate shows a different pattern with an average of 8,275,942, a median of 5,000,000, a mode of 4,000,000, and a standard deviation of 10,575,638, with a range of values from 200,000 to 90,000,000 from 217 respondents. Overall, the combination of the two groups resulted in a total average of 7,054,278 with a median of 4,500,000 and a standard deviation of 11,778,552 from a total of 1,409 respondents.

Business Type Analysis

Table 6. Distribution willing to move by Type of Business

Type of business	Willing to Move			
	0. No	1. Yes	Total	
	Row N %	Row N %	Count	Row N %
0 = Others	90.90%	9.10%	164	100.00%
1 = Culinary	83.80%	16.20%	1245	100.00%
Total	84.68%	15.40%	1409	100.00%

Source: processed by the author (2025)

Table 6 analyzes the distribution of willingness to relocate based on the type of business run by street vendors. The data shows that traders with culinary businesses have a lower unwillingness rate compared to other traders, at 83.80%, while 16.20% are willing to relocate. On the other hand, traders with other types of businesses show a higher level of unwillingness at 90.90%, with only 9.10% willing to move. The distribution of respondents shows a significant dominance of culinary traders with 1,245 respondents compared to 164 traders from other types of businesses. These findings indicate that the type of business influences the flexibility of traders in considering relocation, with culinary traders being more open to the possibility of moving locations.

Hypothesis Testing Results

Table 7. Odd Ratio by Independent Variables determining willingness to move

Independent Variables	OR	Sig.
Location		0
Location(1) = Built Location	2.673	0
Location(2) = Temporary location	0.747	0.148
Educ(1) = High School++	1.072	0.663
Owner(1) = Owned by Me	1.069	0.825
Revenue	1	0.069
Type(1) = Culinary	1.856	0.031
Allocation(1) = proper allocation	0.709	0.066
Constant	0.094	0

Source: processed by the author (2025)

This odds ratio analysis identifies key factors influencing street vendors' willingness to relocate to designated areas (Binaan Locations). The study confirms five hypotheses through statistical analysis:

1 **Location and Accessibility (Hypothesis 1 - Proven)**: Vendors at construction sites show 2.67 times higher odds of relocating, while those at temporary locations are 25% less likely to move, demonstrating that physical location significantly affects relocation willingness.
2 **Education Level (Hypothesis 2 - Proven):** Higher education slightly increases relocation willingness (odds ratio 1.072), though the effect isn't statistically significant.
3 **Income Level (Hypothesis 3 - Proven):** Income shows statistical significance at the threshold level (p=0.069), with minimal impact per income unit increase, confirming income affects relocation decisions.
4 **Business Type (Hypothesis 4 - Proven):** This is the most significant factor - culinary vendors have 1.856 times greater odds of relocating compared to other business types (p=0.031).
5 **Location Suitability (Hypothesis 5 - Proven):** Vendors satisfied with their current location allocation are 30% less likely to relocate (odds ratio 0.700, p=0.066).

The analysis reveals that business type (particularly culinary) is the strongest predictor of relocation willingness, while location satisfaction creates resistance to moving. These findings suggest successful relocation programs must consider business categories and ensure adequate location allocation to maximize vendor participation.

Spatial Analysis of Street Vendors in DKI Jakarta

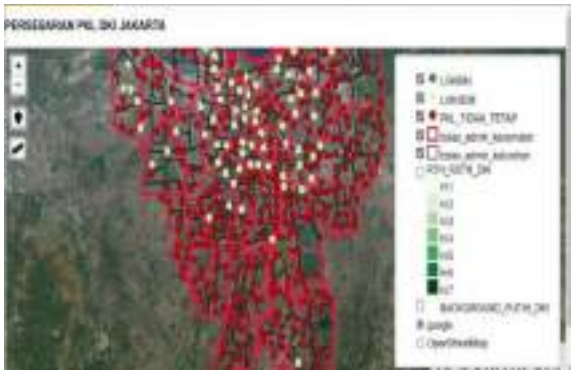

Figure 3. Distribution Map of Built Location, Temporary Location, and Non-Permanent Street Vendors in DKI Jakarta in 2021

The locations of non-permanent street vendors are evenly distributed throughout the DKI Jakarta area, while Built Locations are concentrated in the central and northern parts, and Temporary Locations are more sparsely distributed. The distribution of street vendor numbers in DKI Jakarta in 2021, based on the locations of Built Locations, Temporary Locations, and non-fixed street vendor locations, shows that the number of vendors at non-fixed street vendor locations is very high in all Administrative City areas.

The largest number is in the East Jakarta area with 6,777 traders, followed by North Jakarta, Central Jakarta, South Jakarta, and West Jakarta. The most Binaan traders are in West Jakarta, followed by East Jakarta and South Jakarta. Meanwhile, the largest number of traders in the Temporary Location is in South Jakarta, followed by West Jakarta and North Jakarta.

Figure 4 provides clearer visualization of the number of Built Location, Temporary Location, and Non-Permanent Street Vendors in DKI Jakarta in 2021.

Specifically, vendors at Non-Permanent street vendor locations are divided into three types: culinary vendors, non-culinary vendors, and service vendors. The locations of Non-Permanent street vendors in DKI Jakarta are dominated by culinary vendors, with the highest number in East Jakarta at 5,687 vendors, followed by North Jakarta and Central Jakarta. The highest number of non-food street vendors is also in East Jakarta, followed by North Jakarta and Central Jakarta.

The spatial analysis studies using Geographic Information System technology through several approaches including interpolation method with density estimation

method to analyze the spatial distribution of the locations of Built Location, Temporary Location, and Non-Permanent street vendors, range and road network analysis and its impact using buffer analysis, map overlay analysis between the locations of Built Location, Temporary Location, and Non-Permanent street vendors, land use, and population density, and spatial analysis for the capacity of temporary street vendor locations.

Coverage and Transportation Network Analysis

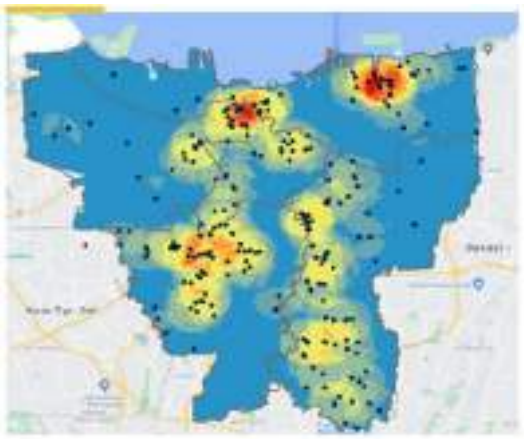

Figure 5. Map of Built Location and Temporary Location Distribution in DKI Jakarta in 2021.

The distribution of Built Location and Temporary Location points is concentrated around the areas of Kota Lama, Tanjung Priok, and Kebayoran Baru. They are also heavily distributed along Kampung Melayu-Dewi Sartika Main Road to Bogor Main Road. In other locations, they are still rare. The spatial distribution of street vendor locations is not evenly spread throughout the DKI Jakarta area along existing roads, except for the areas around Monas, TMII, and Halim PK Airport.

The analysis of the coverage and transportation network specifically MRT and Trans Jakarta with the locations of Built Location and Temporary Location points is shown in Figure 6. The concentration points of Built Location and Temporary Location locations appear to be quite appropriate, except in the Cilincing area, which is not accurate, as well as along the western and eastern routes. For the southern and southeastern routes, they are already appropriate.

Arguments For and Against Street Vendors

In the city of Jakarta, the presence of streetvendors can almost be seen in urban public places such as streets, parking lots, intersections, pedestrian sidewalks, parks, and other locations. In fact, it is impossible to avoid their presence in the cities as part of daily life, leading to both pros and cons regarding the existence of street vendors.

If linked to the consideration of both forms of arguments, it is possible to combine both arguments to a certain extent, raising the question of how far the presence of street vendors can be accepted in the city of Jakarta.

Further suggests that every argument, whether supporting or opposing street vendors, should consider

various aspects such as time, location, type of vendor activity, type and level of official control, as well as the background and aspirations of the individuals involved. This shows that the issue of street vendors in urban areas is fundamentally complex [11].

Spatial Justice and Right to the City

Emphasizing the political economy dimension of the right to the city, argues that the right to the city is not just about individual access to urban resources, but also about the collective right to change and control the process of urbanization. In the context of street vendors, this means not only providing physical space but also involving them in the planning and decision-making processes [12].

The concept of spatial justice becomes relevant in understanding why the Built Locations are often ineffective. Spatial justice is not only about equitable distribution but also about ensuring that all community groups have equal access to the economic and social opportunities provided by urban spaces. Provides a perspective on how informal cities contest public space. Donovan shows that street vendors not only use public space but are also active in creating new meanings and functions for that space. Donovan's approach emphasizes the importance of understanding street vendors as creative and adaptive urban agents [13[.

Sustainable Urban Planning Perspectives

Introduced the concept of ecocity, which emphasizes the importance of integrating ecological, economic, and social aspects in urban planning. Although the focus is on ecological sustainability, its principles can be applied in the context of street vendors where solutions must consider not only economic aspects but also social and environmental impacts.

In the context of Jakarta, the application of ecocity principles can mean creating Built Locations that are not only economically viable but also environmentally friendly and integrated with public transportation systems. This requires a holistic approach that considers various aspects of sustainability. Provides a perspective on how technology can be used to enhance the efficiency and effectiveness of urban services. In the context of street vendors, technology can be used to monitor the use of designated locations, analyze consumer movement patterns, and optimize the locations of supporting facilities [14].

DISCUSSION

This research reveals fundamental disconnects between urban planning policies and street vendor realities, where despite government provision of basic facilities and affordable fees at designated Binaan Locations, vendors overwhelmingly resist relocation, indicating deep policy-practice misalignments. The spatial analysis demonstrates a critical mismatch between successful vendor locations that feature high foot traffic, residential proximity, and commercial integration, versus many Binaan Locations that lack pedestrian flow and public transport connectivity, explaining why vendors pay premium informal fees for unauthorized but commercially viable spots.

Statistical analysis confirms that culinary vendors show greater relocation willingness than non-culinary vendors, suggesting policies need business-specific approaches rather than uniform solutions, while higher-income vendors

display slightly greater relocation willingness, indicating cost isn't the primary adoption barrier. The research fundamentally reframes street vendors from passive policy recipients to active economic agents making rational decisions based on sophisticated market knowledge and spatial understanding, where their preference for unauthorized locations reflects superior grasp of consumer patterns and urban economics rather than stubborn non-compliance.

The key implication is that vendors' resistance to relocation represents informed economic choice rather than obstacles to overcome, demonstrating that successful integration requires recognizing vendors as knowledgeable urban actors whose location expertise should inform policy design rather than viewing them as problems requiring correction.

CONCLUSION

The research demonstrates that the informal sector must be viewed as an asset for urban development rather than a problem to be eliminated. Street vendors can be regulated, can grow sustainably, withstand economic crises, and can potentially

transition to the formal sector. The failure of current Binaan Location programs stems from insufficient understanding of vendor preferences, consumer patterns, and informal economy dynamics.

The study reveals that street vendor policies should not only focus on allowing the poor to sell but also on integrating them strategically within urban development policies. This requires realizing policies that are humane and not repressive, ensuring that national development policies do not become a new magnet for rural-urban migration, recognizing that there is no single universal policy formula for street vendor arrangement, and understanding that the process of integrating the informal economy into urban development will incur significant bureaucratic costs.

The research emphasizes the need for reorganizing and providing orderly guidance and supervision to street vendors by creating centralized and clearly integrated policies that can serve as an umbrella for local government to perform its function of serving the community. The findings suggest that successful street vendor integration requires comprehensive understanding of spatial dynamics, vendor behavior patterns, and the complex interplay between formal and informal urban economies.

REFERENCES

[1] Nurbaiti, R., and Chotib. (2020). Urban informal sector and economic resilience: The case of Jakarta street vendors. Indonesian Journal of Geography, 52(1), pp 23-35.

[2] Mpanje, D., Gibbons, P., and Çela, E. (2018). Street vending in developing countries: A systematic review. World Development, 109, pp 121-137

[3] Ersahin, Z., and Neufel, L. (2018). Street vendors in developing countries: A case study of Indonesia. Urban Development Journal, 15(3), pp 45-62.

[4] Carteau, L. (1997). Urban informal sector and spatial planning. Development Studies Press.

[5] Ordonez, P. (2010). Formal-informal sector linkages in urban economies. Economic Development Quarterly, 24(2), pp. 156-169.

[6] Cross, J.C. (2000). Street vendors, modernity and postmodernity: Conflict and compromise in the global economy. International Journal of Sociology and Social Policy, 20(1/2), pp. 29-51.

[7] Bromley, R. (2000). Street vending and public policy: A global review. International Journal of Sociology and Social Policy, 20(1/2), pp 1-28.

[8] Bass, S. (2000). Street vendors and the urban informal sector. Urban Studies Journal.

[9] Pachecho, M. (2017). Classification and characteristics of street vendors: A comparative study. Urban Studies International, 42(4), pp 445-461.

[10] Paul, S. (2020). Mobile markets and seasonal trading patterns. Journal of Development Economics, 147, pp 102-118.

[11] Liu, Y. (2020). Street vendors in urban planning: Challenges and opportunities. Cities, 98, pp. 102-115.

[12] Lefebvre, H. (1991). The Production of Space. Blackwell Publishing.

[13] Donovan, M.G. (2008). Informal Cities and the Contestation of Public Space. Journal of Urban Affairs, 30(3), pp 293-308.

[14] Dameri, R. P. (2014). Smart City Implementation. Springer.

Copyright © Int. J. of GEOMATE All rights reserved, including making copies, unless permission is obtained from the copyright proprietors.

15th Int. Conf. on Geotechnique, Construction Materials & Environment,
Kyoto, Japan, 11-13 November 2025, ISBN 978-4-909106124 C3051

MODELING WELFARE-DRIVEN COMMUNITY TRANSFORMATION: AN INVESTIGATION IN REMOTE AREA, LABUAN BAJO, EAST NUSA TENGGARA, INDONESIA

Mohamad Axel Putra Hadiningrat [1], Beti Nurbaiti [2], and Chotib Hasan [3]

[1,3] Universitas Indonesia, Depok, Indonesia , [2] Universitas Bhayangkara Jakarta Raya, Jakarta, Indonesia

ABSTRACT

Problem Statement from this research is to analyze important factors in developing a welfare model that includes social capital, innovation, and motivation from the Labuan Bajo community, at East Nusa Tenggara, Indonesia. The research approach is a quantitative method where the existing findings are enriched with Focus Group Discussions (FGD), and in-depth interviews. This research uses field surveys by collecting data from 303 respondents with questionnaires, and 10 informants for FGD and in-depth interviews. The results of this research is that based on the Sobel Test, it is proven that the motivation variable is an intervening variable between the social capital and innovation variables on the welfare of the Labuan Bajo community. Additionally, social capital has been proven to have a direct positive impact on motivation and well-being, where the community helps each other materially and non-materially to meet daily needs. Moreover, community innovation is necessary because it has a direct positive impact on their motivation and well-being. The motivation of the local community has a direct positive impact on well-being. Another finding is that motivation has proven to be an intervening variable between social capital and innovation on welfare, as there is an indirect influence through the motivation variable. High-quality human resources can encourage the community to be absorbed into the labor market in the tourism industry sector as a super-priority destination area, which will impact their welfare. Traditional leaders, religious leaders, and local community leaders play a significant role in providing material and non-material assistance.

Keywords: Transformation; Welfare; Modeling; Social Capital; Innovation; Motivation

INTRODUCTION

Known for its stunning natural surroundings and rich cultural heritage, Labuan Bajo is situated in East Nusa Tenggara Province's West Manggarai Regency. The ethnic city of Labuan Bajo is encircled by hills and vast savannas, creating an extremely unusual sight, particularly after sunset. Labuan Bajo is also referred to as the city of a million sunsets because of its splendor (Hanita, 2023).

Although it already exists as community capital, this social capital has not been used to its full potential. In order to overcome obstacles in their daily lives, the Labuan Bajo population should make use of this capital.The community benefits from the presence of kinship, familial ties, and mutual trust through community approaches, particularly in trying times (Putnam and Robert, 2000). The Labuan Bajo community's social capital, which is bolstered by the environment and culture that now exist, inspires them to act to meet their everyday needs and innovate to produce innovations that result in economically useful services and goods. Social capital therefore helps them come up with new ideas to improve the welfare of the community, such as bringing people together for joint ventures, sharing ideas and talents, and cooperating to use solar power to create electricity, especially in rural locations.

The driving force behind the innovations that the Labuan Bajo community has been able to implement comes from social capital, driven by their motivation to complement each other's shortcomings. These innovations are still local in nature and have not yet been able to fully make the community prosperous; they require external support, particularly from regional and central governments. This inspiration serves as the catalyst for the community to turn its obstacles into opportunities for collective success (Hanita, 2023).

This study designed to address the following research questions :

1) Is there a direct effect of social capital on the welfare of the community in Labuan Bajo, East Nusa Tenggara?
2) Is there a direct effect of innovation on the welfare of the community in Labuan Bajo, East Nusa Tenggara?
3) Is there an indirect effect of social capital on the welfare of the community in Labuan Bajo, East Nusa Tenggara, through the intervening variable of motivation?
4) Is there an indirect effect of innovation on the welfare of the community in Labuan

Bajo, East Nusa Tenggara, through the intervening variable of motivation?
5) Is there a direct effect of social capital on the motivation of the community in Labuan Bajo, East Nusa Tenggara?
6) Is there a direct effect of innovation on the motivation of the community in Labuan Bajo, East Nusa Tenggara?
7) Is there a direct effect of motivation on the welfare of the community in Labuan Bajo, East Nusa Tenggara?

RESEARCH SIGNIFICANCE

Social Capital

Social capital can be explained by three different topologies: (1) bonding social capital; (2) bridging social capital; and (3) linking social capital. Social capital indicators, such as social cohesiveness and inclusion, are used to measure this. Social modalities help people in a community engage with one another and work together more successfully. For instance, the ability to link or promote interactions between individuals and groups with disparate identities is referred to as the usage of social modalities as social bridges (Narayan and Michael, 2016).
In Pierre Bourdieu's (1995) research, social capital is also incorporated into three key ideas: (1) Field, (2) Capital, and (3) Habitus. Finding important players with connections in the field is the following stage, which is based on these three ideas. According to Bourdieu, concentrating only on results is not enough; we also need to measure the variables that influence relationships, transactions, and important field occurrences. Powerful actors will control and possibly monopolize the industry. In the next phase, researchers examine the amount of money these individuals have contributed to the field in connection to their ties. Economic capital, social capital, cultural capital, and symbolic capital are all included in this capital.

Innovation

According to Nicholls et. al. (2019), innovation is defined as a novel concept that successfully solves issues by addressing unmet social demands. Rebalancing power disparities and economic disparities in society is a common emphasis of this innovation, which is related to shifts in social connections. This study makes use of social innovation, which is defined as the creation and implementation of novel concepts regarding how individuals ought to plan social interactions or interpersonal activities in order to accomplish one or more shared objectives.
According to Hussain et al. (2014), innovation is the capacity of commercial companies to comprehend, create, implement, and scale new goods, services, procedures, and business models for their clientele. In the meantime, innovation is a component that gives companies a competitive edge, claim Thiangtam et al. (2016). Company innovation can be divided into three categories: process, service, and product innovation.

Motivation

The Hygiene Factors hypothesis of Herzberg and Frederick (1968) and Adair (2006) is the motivation theory that is used. This theory emerged because, in work contexts, there are conditions that individuals within a community or organization perceive as "satisfying" and others as "dissatisfying." Findings related to individual achievement success are greatly influenced by their motivation, which is divided into two factors:
1) Extrinsic Motivation: encompasses material aspects such as salary, wages, incentives, bonuses, and allowances that can be measured in monetary terms.
2) Intrinsic Motivation: includes non-material aspects such as praise, recognition, career development opportunities, and self-actualization.

Therefore, to keep motivation burning within yourself, you must continuously seek the "fuel that ignites it." This type of motivation represents the strongest and most enduring form of motivation in humans. Intrinsic motivation is driven by personal interest or enjoyment in the activity, without external rewards or pressure. Intrinsic motivation drives individuals to share knowledge based on their own interest or pleasure in doing so, without expecting material rewards. Extrinsic motivation, on the other hand, is driven by action outcomes and focuses on goals such as monetary rewards or career advancement (Sudaryono et al., 2015).

Welfare

Alatartseva and Barysheva (2015) argue that welfare is measured from two perspectives: (1) the objective side, where welfare can be measured materially, and (2) the subjective side, where welfare represents each individual's inner experience rather than material possessions. Since both requirements must be met for someone to be deemed "wealthy," having a lot of material belongings does not ensure that someone will be deemed "wealthy" if they are unable to find inner peace, have little time for worship, feel inferior, oppressed, or repressed, or if they are denied the ability to express their thoughts, manifest themselves, and come together as social beings.

According to Abdullahi et al. (2021) and Ogwumike et al., (2018), welfare is a prerequisite for meeting citizens' material, spiritual, and social needs to live and develop adequately while fulfilling their social responsibilities. The objective aspect consists of wages/income, expenditure (consumption), wealth, living conditions, education, and health. The following are examples of objective aspects: (1) Having employment with sufficient income for basic needs including clothing, food, and housing;(2) The ability to meet nutritional needs such as healthy food; (3) Access to healthcare and education; and (4) Having a decent place to live.

The subjective aspect encompasses psychological, spiritual, and social welfare. This aspect typically refers to an individual's capacity regarding: (1) A lifestyle that maintains balance between work and family; (2) Interpersonal relationships, social networks, and community support; (3) A well-established relationship with the Creator through proper worship.

RESEARCH METHODS

The study employs a quantitative or deductive methodology, which is evaluated using observational data from surveys. Researchers use questionnaires as research tools, and collected data from 303 respondents. The researcher additionally does in-depth interviews to enhance and supplement the findings of the quantitative analysis (Creswell, 2016).

In Labuan Bajo, East Nusa Tenggara, 310 community members participated in a survey method used for primary data collecting. Of the 303 respondents' responses, 303 were deemed legitimate. The purposive sampling technique was used to determine the number. The Labuan Bajo area and its environs, which comprise other sub-districts in the West Manggarai Regency, served as the site for the data gathering.

There are 7 hypothesis in this research :

H1 : There is a direct effect of social capital on the welfare of the community in Labuan Bajo, East Nusa Tenggara.

H2 : There is a direct effect of innovation on the welfare of the community in Labuan Bajo, East Nusa Tenggara.

H3 : There is an indirect effect of social capital on the welfare of the community in Labuan Bajo, East Nusa Tenggara, through the intervening variable of motivation.

H4 : There is an indirect effect of innovation on the welfare of the community in Labuan Bajo, East Nusa Tenggara, through the intervening variable of motivation.

H5 : There is a direct effect of social capital on the motivation of the community in Labuan Bajo, East Nusa Tenggara.

H6 : There is a direct effect of innovation on the motivation of the community in Labuan Bajo, East Nusa Tenggara.

H7 : There is a direct effect of motivation on the welfare of the community in Labuan Bajo, East Nusa Tenggara.

RESULTS AND DISCUSSION

Descriptive Statistics Processing Results

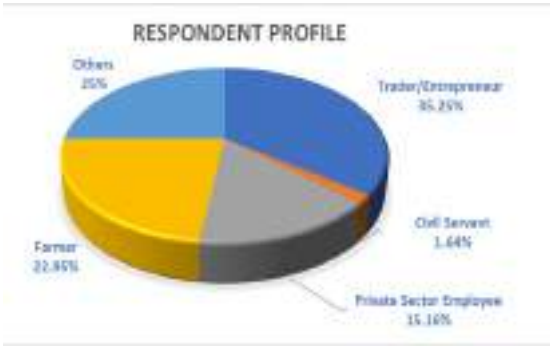

Figure 3. Respondent Profile

The majority of responders (35.25%) are traders or entrepreneurs, with other occupations, teachers, religious leaders, community leaders, and homemakers coming in second (25%). Next, the proportion of civil servants (1.64%), private workers (15.16%), and farmers (22.95%). The majority of survey participants were traders or entrepreneurs, including shop owners and MSME players, according to the profiles of the respondents.

This entrepreneurial career demonstrates that Labuan Bajo residents have a strong sense of entrepreneurship and are not dependent on office work. This further demonstrates the local community's strong desire to use its capital independently. Given the high cost of living, where the prices of daily essentials are high and not adequately offset by a Regional Minimum Wage (UMR), the local community must innovate to create new sources of revenue.

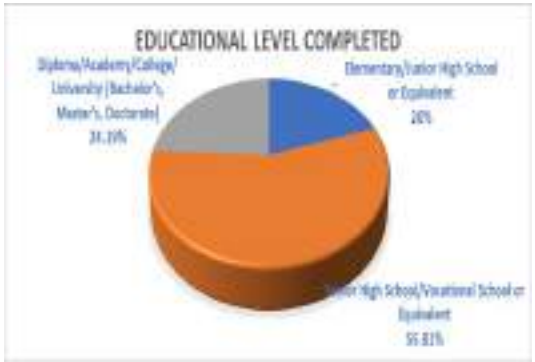

Figure 4. Education Level of Respondents Completed

High school/vocational school/equivalent accounts for 55.81 percent of respondents' education

levels, followed by diploma/academy/university (24.19%) and elementary/middle school/equivalent (20%). According to the aforementioned research findings, the majority of respondents have completed secondary education, such as high school, vocational school, or its equivalent, and the proportion of graduates with higher and lower education is about equal. This circumstance suggests that the local government must formally raise educational standards.

Programs for free school fees, building schools in outlying areas, enhancing the caliber of teaching staff's human resources (HR), donating school supplies like textbooks and stationery in accordance with the relevant curriculum, and supporting the infrastructure for road access from teachers' or students' homes to the school are all examples of how the government can help. Both the federal government and the municipal government, through the appropriate departments, are in charge of the educational component.

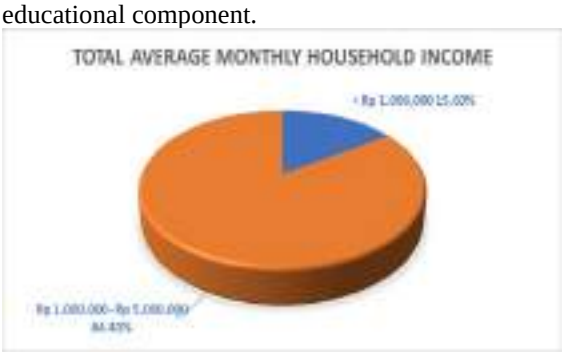

Figure 5. Average Monthly Household Income

Respondents' average monthly household income during the six months prior to the study was primarily between Rp 1 million and Rp 5 million. This scenario indicates that the growth in locals' income has not yet been affected by Labuan Bajo's designation as a Super Priority Destination (DSP). The cost of basic requirements is two to three times more than on the island of Java, so efforts to raise the community's income must be stepped up. Given that the majority of the community's resources are used to address comparatively high daily requirements, this conclusion is consistent with their capacity to seek higher education.

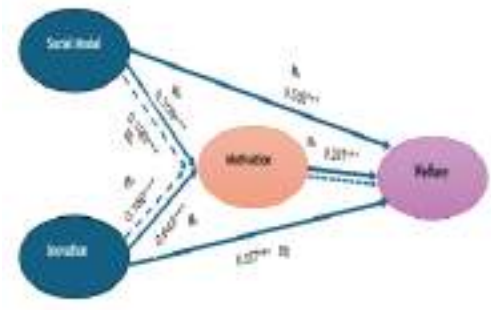

Figure 12. Conceptual Research Model

The respondents' average monthly household expenses for the previous six months were equal to their income, with the majority lying between Rp 1 million and Rp 5 million. Given that they are required to pay for high expenses, this scenario indicates that investments and savings are still not given priority. The community's income must at least double its expenses in order for them to have savings and investments.

Table 1. Estimation of Parameters for Path Analysis and Sobel Test

No	Route	Direct Effect Coeff. (Standardized)	Unstandardized Coeff.	Standard Error	Significance
1.	MB → WELF	0.528***	1.587	0.068	Sign. pada α=1%
2.	DADV → WELF	0.357***	2.284	0.042	Sign. pada α=1%
3.	MB → MOT	0.720***	0.840	0.086	Sign. pada α=1%
4.	DADV → MOT	0.665***	1.227	0.049	Sign. pada α=1%
5.	MOT → WELF	0.281***	2.388	0.049	Sign. pada α=1%
No	Route	Total Effect Coeff. (Standardized)	Sobel Test Statistics	2-tailed Prob.	Significance
6.	MB → MOT → WELF	0.720 x 0.281 = 0.190***	3.9327	0.000	Sign. pada α=1%
7.	DADV → MOT → WELF	0.665 x 0.281 = 0.130***	4.3955	0.000	Sign. pada α=1%

Source: Data processed by the author (2024)

Based on the Sobel test above, it can be seen that all hypotheses (H1, H2, H3, H4, H5, H6, H7) are accepted, both direct and indirect effects through the intervening variable of motivation.

The Sobel Test results were confirmed by field findings through FGD and in-depth interviews. As a Remote Area town, Labuan Bajo's residents have not had the same access to high-quality education as those on Java Island. The primary barrier preventing the population from traveling great distances from their homes is geography, particularly in coastal regions and in communities of fishermen's villages. Furthermore, a large number of interprovincial routes remain without illumination. As a DSP area, Labuan Bajo has not yet been affected by the trickle-down effect. Their household incomes have increased, but the effect of tourism has not yet been consistent. The "sweetness of the development cake" from the explosion of five-star hotels, cafes, restaurants, and entertainment venues frequented by both domestic and foreign tourists is only enjoyed by a small percentage of the community. The quality of local human resources, which has not yet been able to be substantially absorbed by the labor market in the tourism sector, is the traditional issue that provides the explanation.

The supply chain and distribution channels of primary production elements, including fuel oil (BBM), are the cause of high costs for the community

as consumers and for small and medium-sized enterprises (SMEs). The "eternal" reason for high fuel costs outside of Java is the high cost of fuel, which is still mostly supplied by oil refineries on Java Island.

Because it has to do with distribution and transportation, fuel affects the cost of essentials. Government initiatives and laws aimed at eliminating fuel distribution inefficiencies have a major effect on lowering gasoline prices, which in turn lowers the cost of consumer goods. Ceteris paribus, revenue will not decline if costs are reduced and the society may set aside money for investments and savings.

When one individual/group in the community has difficulty marketing their goods, another group within the same community will help provide market access, free of charge. This is one example of the application of social capital, as there is a sense of mutual trust and assistance. When one group needs business capital and their application to the bank is rejected, another group can provide a free loan because of the mutual trust and support within that community. Another finding in the field encountered during the survey was that many novice individuals in the food and beverage business, who lacked the necessary skills, were taught for free by other groups within the community.

According to Qian and Yin, 2019, social cohesiveness and inclusiveness are equally significant sub-dimensions of social capital. This sub-dimension is a component of social capital that shows how closely people are bonded to one another in a community or society. When mutually beneficial contacts take place, networks—intangible resources that aid in resolving issues within particular societies—are created, and this is referred to as social cohesiveness. Beliefs and values, community organizations, laws, social ties and interactions, and social patterns all have an impact on social cohesiveness. The quality of family-based relationships can be enhanced by social capital, regardless of theoretical differences, where this finding is inline with the research conducted by Nurbaiti and Chotib (2020).

The innovations carried out by the community are largely generated from existing networks and supported by local traditional and religious leaders. For example, in terms of marketing innovation, when a group involved in fish floss production intends to market their product, local leaders assist in selling the product through bazaars during traditional ceremonies. The intricate process of community innovation involves introducing new plans, processes, or outcomes that fundamentally alter the underlying resource flows, authority structures, and trust systems of the community in which the innovation takes place. According to Suryana (2013), innovation can be interpreted in a number of significant ways, including as novelty, change, and advantage. In essence, innovation as novelty is a new value that people can obtain. A type of additional value in goods, services, or procedures is the subject of innovation. More socially acceptable technical solutions are always used to illustrate innovation. Innovation produces benefits in the form of managerial products, technology, methods, and process innovation.

Motivation needs to be encouraged at the community level with support from local community leaders. Although the local government has provided assistance, the community is more motivated in their daily lives by local figures. Motivation that originates from outside sources is known as external motivation, and it runs out fast. Fundamentally, everyone's motivation originates from within themselves; motivation is like a stove that continuously burns and must be constantly fueled to keep burning—without fuel, motivation will gradually die until it is completely extinguished. According to Tamara et al. (2020) , Lapsomboonkamol et al. (2020), the act of motivating or persuading someone to accomplish their desires.

Although the people of Labuan Bajo are far from the national capital, with an average income below the national average, and the prices of goods being relatively high because they have to be brought in from outside the region, they are able to overcome these limitations by utilizing social capital, doing innovation and motivation in the spirit of community. Society assesses well-being not only by the material possessions one has but also by non-material aspects such as time spent with family members, the ability to worship peacefully, participating well in traditional events, thereby fostering good relationships and networks. This finding is in line with Alatartseva and Barysheva (2015) that well-being consists of two types, namely subjective (material) and objective (non-material).

CONCLUSION

The transformation has occurred in the community of Labuan Bajo City, Komodo District, West Manggarai Regency, both in terms of economic, social, and spatial transformation. Remote location of Labuan Bajo contributes to the high cost of living, which is not covered by local population income. Stated differently, Labuan Bajo's status as a DSP has not yet resulted in the trickle-down effect. With all the existing limitations, it turns out that social capital has a significant impact on the transformation of the Labuan Bajo community in achieving its prosperity, where the most influential aspects of social capital are Trust and Solidarity and Information and Communication.

The innovation of the Labuan Bajo community is currently not optimal in the process of transforming Labuan Bajo into a more prosperous society. The Labuan Bajo community still needs to be encouraged from outside the community, by the local government and related parties. The role of traditional leaders, religious figures, and the community is very important in motivating the society to reach welfare.

REFERENCES

[1] Abdullahi, A. A., Ntozini, A., & Oguntayo, R. (2021). Socio-Contextual Factors as Determinants of Psychological Wellbeing of Selected Aged in South Africa : A Moderating Approach. Social Sciences & Humanities, 29(1), 349–366.

[2] Adair, J. (2006). Leadership and Motivation : the fifty - fifty rule and the eight key principles of motivating others. London: Kogan Pae Ltd, 69–86.

[3] Alatartseva, E. & Barysheva, G. (2015). Well-being : Subjective and Objective Aspects. Procedia- Socia and Behavioral Sciences, 166, pp 36-42.

[4] Bourdieau, Pierre. 1995. Languange and Symbolic Power. Cambridge: Polity Press.

[5] Creswell, J. W. (2016). Research Design Pendekatan Metode Kualitatif, Kuantitatif, dan Campuran. (Terjemahan). Yogyakarta: Pustaka Pelajar.

[6] Hanita, M. (2023). Buku "Ketahanan Nasional

[7] Teori, Adaptasi dan Strategi". UI Publishing.

[8] Hezberg & Federick. (1968). one more time how do you motivate employees. Harvard Business Review.

[9] Hussain, W. M. H. W., Rahman, M. N. A., Zainol, Z. A., & InayahYaakub, N. (2014). Mechanism and Government Initiatives Promoting Innovation and Commercialization of University Invention. Social Sciences & Humanities, 22(December 1980), 131–148.

[10] Lapsomboonkamol, S., Wiriyapinit, M., Bhattarakosol, P., & Rajchamaha, K. (2020). Motivational Factors for Knowledge Sharing in Co-Working Spaces : Co-Working Spaces in Thailand from the Management Perspective. Social Sciences & Humanities, 28(3), 1835–1854.

[11] Narayan, D and Michael Woolcock. 2016. Measuring Social Capital : An Integrated Questionnaire. Washington DC: World Bank Working Paper No. 18.

[12] Nicholls, A., Simon, J., & Gabriel, M. (2019). New Frontiers in Social Innovation Research (Nesta 2015). Palgrave Macmillan.

[13] Nurbaiti, B., & Chotib. (2020). The Impact of Social Capital on Welfare : the Evidence from Urban Informal Sector in East Flood Canal (Bkt), Jakarta. IOP Conference Series: Earth and Environmental Science, 436(1), 1–9. https://doi.org/10.1088/1755-1315/436/1/012004.

[14] Qian, X, Y.Caia & C. Yin. 2019. Driving Force Grassoorts Self-Governance in Beijing's Neighborhoods Social Capital, Community Network and Community Service Motivation. Journal of Local Self Government 17(1):159-177.

[15] Sudaryono, Gede Lanang, Sri Handayani, (2015). Mindset Revolution to Becoming a Champion, Membuktikan 10 Rahasia Kekuatan Pribadi. Jakarta Pusat : Lentera Ilmu Cendikia.

[16] Suryana. (2013). Ekonomi Kreatif, Ekonomi Baru : Mengubah Ide dan Menciptakan Peluang. Jakarta Selatan : Salemba Empat.

[17] Tamara, D., Wulandari, R., & Veronica, S. (2020). Exploring Employee ' s Motivation and Performance Factors : Evidence in a 3 Star Hotel in Indonesia by Contrasting Maslow ' s and Cetin ' s Model. Social Sciences & Humanities, 28, 75–86.

[18] Thiangtam, S., Anuntavoranich, P., & Puriwat, W. (2016). Impact of Perceived Company ' s Innovativeness , Service Quality and Customer Satisfaction on Repurchase of Life Insurance. Social Sciences & Humanities, 24, 145–154.

Copyright © Int. J. of GEOMATE All rights reserved, including making copies, unless permission is obtained from the copyright proprietors.

15th Int. Conf. on Geotechnique, Construction Materials & Environment, Kyoto, Japan, 11-13 November 2025, ISBN 978-4-909106124 C3051

A PILE DOWNDRAG STUDY FOR LNG PROJECTS

Anil Bhandari [1], and Jianchun Cao [1]

[1] Bechtel Corporation, Houston, Texas, USA

ABSTRACT

With the projected increase in global energy demand from approximately 580 quadrillion Btu in 2024 to 650 quadrillion Btu in 2050, Liquefied Natural Gas (LNG) is poised to play a significant role in the transition towards a carbon-neutral energy landscape. In the United States, natural gas accounts for about one-third of primary energy consumption, primarily for heating and electricity generation. The LNG export capacity from North America is anticipated to more than double by 2027. Many LNG projects are situated in near-shore areas, where thick layers of very soft and highly compressible fine-grained soils are prevalent. These soils undergo substantial settlement under site-grading fill applied during site development, necessitating consideration of drag load in pile foundation design. Drag load imposes an additional compressive axial load on the pile, potentially altering geotechnical resistance during operational conditions. This paper presents a pile-soil interaction model developed using t-z and Q-W curves, calibrated with measured skin friction and end bearing resistances from a pile load test. The investigation into drag load on a pile designed for an LNG project revealed a decrease in drag load as the load applied to the pile head increased. The drag load determined with consideration of operational load on the pile head was employed for the final pile design. The paper discusses several pile design strategies to mitigate or accommodate drag load, including: Reducing soil settlement potential through pre-loading techniques to consolidate soils prior to construction. Controlling pile settlement by reducing the utilization factor of pile capacity, ensuring compliance with stringent settlement requirements for supported structures. Decreasing drag load by increasing the utilization factor of pile capacity, applying a lower factor of safety. Enhancing pile end bearing, such as using expanded bottom piles, to counteract the effects of drag load.

Keywords: Liquefied natural gas (LNG); dredged material; soil settlement; drilled soil displacement concrete pile (DD pile); drag load; neutral plane; pile capacity; pile skin friction; pile end bearing

INTRODUCTION

An LNG project typically comprises various structures such as process trains, flares, spill impoundment basins for process areas and transfer lines, heavy haul roads, piperacks, and associated structures. Most LNG projects are developed in near-shore areas characterized by the presence of very soft, fine-grained deposits, necessitating the use of deep foundations to support major structures. The phenomenon of drag load, caused by the long-term excessive settlement of these subsurface soils, particularly in thick and soft fine-grained deposits, is a significant concern in deep foundation design.

Various studies have explored the impact of downdrag and estimation of drag load (Fellenius, 1998; Lee and Ng, 2004). However, there is a lack of literature that specifically addresses LNG projects.

To investigate the impact of downdrag on pile design for LNG projects, a TZPILE model was developed utilizing a typical generalized soil profile and the estimated long-term soil settlement. Drilled soil displacement concrete piles (DD piles) were the focus of this study, although the findings are also applicable to other types of deep foundations used to support structures for LNG projects.

The drag load was calculated for the operational scenario, with an applied load of 778 kN on the pile head. The paper outlines several strategies to mitigate the impact of downdrag on pile design, including reducing potential soil settlement, optimizing the utilization factor of pile capacity, and enhancing the pile's end bearing capacity (e.g., using expanded bottom piles) to counteract the effects of drag load.

This study focuses on a single pile size (diameter and length) and one soil profile. Pile drag load is related not only to the total pile capacity, but also to the ratio of friction to end bearing (assuming the same soil settlement profile). Parametric studies—including various pile sizes and different soil profiles—can help deepen our understanding of this topic and extend the study results to different conditions. We plan to expand this research into a future journal paper, in which a parametric study will be included. When an LNG project presents a different soil profile or alternative pile sizes are selected, the pile drag load should be estimated using the methodology presented in this paper.

GENERALIZED SUBSURFACE PROFILE AND SOIL SETTLEMENT

Generalized Subsurface Profile

Geotechnical investigations for the case study LNG project have revealed that the dredged fill,

which comprises alternating layers of very loose to loose sands and very soft to firm clayey material, extended from the existing grade to depths ranging from 3 meters to 10 meters, with an average thickness of approximately 6 meters.

Underlying the dredged fill was bauxite residue, characterized by very loose to loose clayey sand and soft clay, with thickness varying from 2.5 meters to 7.5 meters and an average thickness of about 3.5 meters.

Beneath the bauxite residue, alternating layers of competent stiff to hard clays and medium dense to dense sands were typically encountered to the maximum explored depths of approximately 100 meters below the existing grade.

Based on the characteristics of these soil conditions, a generalized subsurface profile for this study consists of 10 sub-layers of soils from the grade to a depth of about 45m below. They are Fill/Stabilized Soil, Dredged Material (Clay), Very Soft Bauxite Residue, Stiff Clay, Medium Dense to Dense Silty Sand, Very Stiff Clay, Dense Silty Sand and Clayey Sand, Very Stiff to Hard Clay, Very Dense Silty Sand, and Hard Clay. The thickness of each sub-layer and the design soil parameters are presented in Table 1. Pre-loading technique (surcharge) was used to reduce the soils' settlement of the site.

Soil Preloading and Soil Stabilization

The substantial layer of very soft and highly compressible fine-grained soils encountered at the case study LNG project site necessitated a significant settlement mitigation. To address this issue, site development processes included the implementation of wick drains and preloading with a surcharge of 2-5 meters of fill. The upper 1.5 meters of existing soft clay was stabilized using a combination of lime and cement. This approach ensured a stable working platform, provided support for construction equipment, and enhanced the lateral capacity of pile foundations.

To monitor the soil settlement and ensure that 90% of the consolidation settlement was achieved before removing the surcharge fill, a field monitoring system, including settlement plates and vibration wire piezometers, was installed. Weekly settlement readings were taken during fill placement and for the first two months afterward, followed by bi-weekly readings. The measured settlement data was analyzed using Asaoka's (1978) observational procedure to estimate the final settlement. Approximately four months later, the measured settlement exceeded 90% of the estimated total settlement.

Table 1: Generalized Subsurface Profile and Design Soil Parameters

Layer No.	Soil Type	Layer Thickness (m)	Total Unit Weight (kN/m^3)	Su (kPa) or Friction Angle (°)
1	Fill/Stabilized Soil	1.8	17.0	85
2	Dredged Material (Clay)	1.8	16.0	5
3	Very Soft Bauxite Residue (Clay)	4.0	16.0	10
4	Stiff Clay	3.4	18.5	70
5	Medium Dense to Dense Silty Sand	3.1	19.5	40
6	Very Stiff Clay	5.5	19.0	165
7	Dense Silty Sand and Clayey Sand	3.1	20.0	38
8	Very Stiff to Hard Clay	3.6	20.5	200
9	Very Dense Silty Sand	8.7	20.5	40
10	Hard Clay	9.5	19.5	200

Long-term Settlement of Subsurface Soils

Although the primary consolidation of the subsurface soils was completed prior to the construction of the structures and buildings, the secondary consolidation settlement will take a considerable amount of time to achieve. Based on the field geotechnical investigations for the project, a perched water condition existed near the surface, with the groundwater table located approximately 1 to 2 meters below ground surface (BGS). It is anticipated that the groundwater level will drop by 3 meters over the long term, to approximately 4.5 meters BGS after 25 years of design life. This potential decline in the initial groundwater table will induce additional ground settlement. The long-term settlement of the subsurface soils, including both secondary consolidation settlement and settlement due to groundwater reduction, will create a drag load on the pile foundations. It should be noted that a small relative movement between pile and soil is sufficient to mobilize the shaft resistance, and the drag load can be induced by a small amount of secondary consolidation itself.

The estimated long-term settlement of the subsurface soils within the design pile penetration depth for this study is presented in Figure 1 and has been used to estimate the drag load.

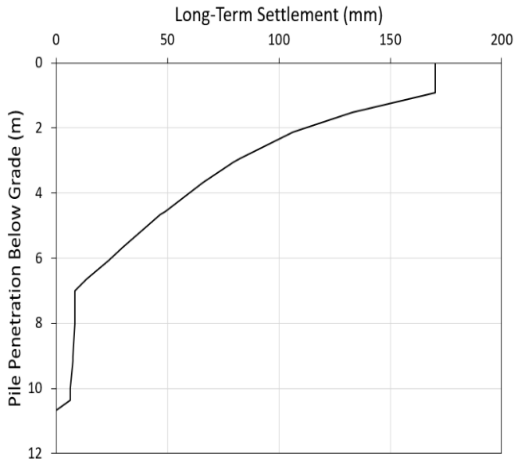

Figure 1: Estimated Long-term Settlement of Subsurface Soils

DESIGN PILE AND PILE LOAD TESTING

Based on the bearing pressures of the LNG facilities and the subsurface soil conditions outlined in Table 1, 0.46m-diameter DD piles were selected to support the buildings and structures. All piles were designed to a length of 12.2m, with the pile tips embedded approximately 0.6m into the Medium Dense to Dense Silty Sand layer.

The axial pile capacity was estimated using the API method and the soil design parameters provided in Table 1. Each 0.46m-diameter pile was calculated to have an ultimate capacity of approximately 1,606 kN, including a skin friction of 552 kN and an end bearing of 1,054 kN.

A static load testing program was conducted, which included tension load testing and compression load testing. Davisson's method (Davisson, 1972) was utilized to determine the pile's ultimate capacity for the static load tests. The measured total pile compression capacity was 2,140 kN, including skin friction of approximately 534 kN and end bearing of about 1,606 kN.

Comparing to the estimated pile capacity, the measured pile total capacity (i.e., 2,140 kN) is about 1.33 times the estimated total capacity (i.e., 1,606 kN). The measured pile skin friction (i.e., 534 kN) is close to the estimated (i.e., 552 kN). The measured pile end bearing (i.e., 1,606 kN) is about 1.52 times the estimate end bearing (i.e., 1,054 kN). A few factors may have contributed to the measured pile capacities being larger than the estimated values. Firstly, the actual diameter of the test pile was larger than the design pile diameter (i.e., 0.46 m). According to the Thermal Integrity Profiling (TIP) test results, the actual diameter of the test pile varied between 0.46 to 0.64 m along the depth, with an average value of 0.56 m. Secondly, the soil design parameters selected in Table 1 did not consider the densification of the sandy formation (Layer 5) on which the piles were terminated. Installation of the drilled displacement piles laterally pushed the soil and densified the sandy formation; thereby, increased the pile capacity (mostly end bearing component in this case).

The load testing results aligned closely with the API method, showing that a settlement of approximately 1%D (where D is the pile diameter) is required to fully mobilize the pile's ultimate friction, and a settlement of about 5–10%D is needed to mobilize the pile's end bearing capacity. These test results validated the applicability of the API method (t-z and Q-w curves) for pile drag load analysis. Furthermore, the load-settlement curve measured during pile load testing reflects the pile's short-term behavior, whereas pile drag load develops over the long term. Considering that only relative movement between the pile and soil can generate drag load, and that the development of drag load does not affect the performance of the pile foundation provided the maximum drag load is accounted for in the design, it is reasonable to use the pile load test results for calibrating the TZPILE model. This approach is both appropriate and reliable.

PILE DRAG LOAD ESTIMATION

Pile downdrag refers to the ground settlement or downward soil movements relative to a pile. Typically, downdrag results in two primary effects on piles: 1) an additional compressive axial load, known as drag load, and 2) a reduction in geotechnical resistance. Downdrag often occurs due to the placement of construction fill near the pile group and should be considered in the design of deep foundations across all limit states.

The Neutral Plane method is commonly utilized to calculate the pile's drag load, as illustrated in Figure 2. A central concept in the Neutral Plane method is the relative movement between the soil and the deep foundation after installation, indicating a dynamic system. The neutral plane is the depth along a deep foundation element where soil and pile settlements are equal, resulting in zero mobilized side resistance at that specific location. Below the neutral plane, the settlement of the pile, due to loading, exceeds the settlement of the adjacent soil, leading to load transfer from the pile to the soil through side shear and end bearing. Above the neutral plane, the surrounding soil settles more than the pile, causing negative side resistance and axial compression load transfer from the soil to the pile through side shear, also known as drag load. The maximum drag load is calculated based on the nominal geotechnical side resistances of the soil layers located above the neutral plane depth.

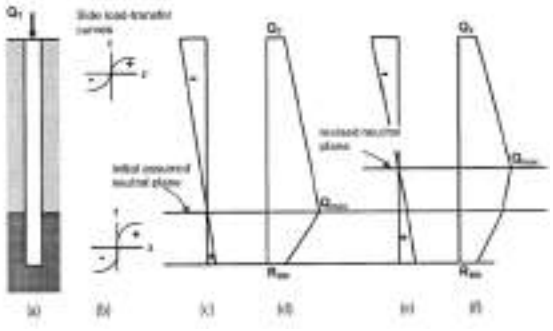

Figure 2: Mechanics of Downdrag Development and Possible Location of the Neutral Plane (Ensoft Inc., 2021)

Development of TZPILE Model

To estimate the drag load on a pile, the commercial software TZPILE was employed. TZPILE incorporates the well-established method of soil-structure interaction, commonly known as the t-z method, where t-z and Q-w curves are utilized respectively for load transfer in side resistance and end bearing. The t-z and Q-w curves can be internally generated for piles (or drilled shafts) with the provision of information regarding the supporting soil and the pile's geometry. This software is capable of calculating the drag load on a pile (Ensoft, 2021).

A TZPILE model was developed for a 0.46-meter diameter pile with a penetration depth of 12.2 meters, using the soil design parameters detailed in Table 1 and the API method. The model inputs included soil design parameters (i.e., undrained shear strength (s_u) and unit weight (γ) for clay, and internal friction angle (φ) and unit weight (γ) for sand), pile design parameters (i.e., ultimate unit skin friction and ultimate end bearing), and pile diameter and pile section modulus (i.e., AE - cross-sectional area multiplied by the pile's elastic modulus). The load versus deflection curves derived from the developed TZPILE model are presented in Figure 3.

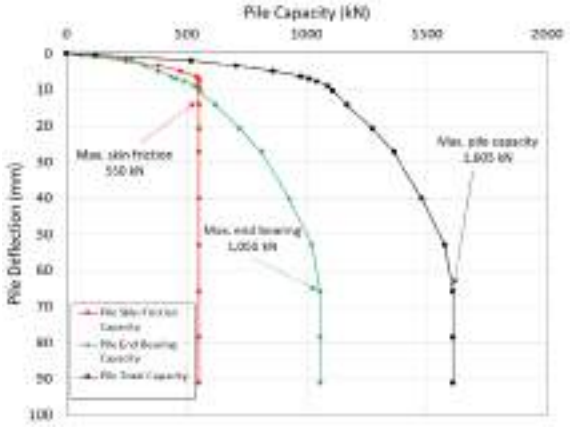

Figure 3: Load vs. Pile Deflection Curves – TZPILE Model

Figure 3 demonstrates that the pile's skin friction capacity, end bearing capacity, and total capacity obtained from the TZPILE model are 550 kN, 1,055 kN, and 1,605 kN, respectively. These figures closely correspond to those estimated using the API method, thereby validating the precision and reliability of the TZPILE model.

To align with the pile load test results, a load factor of 1.52 was applied to the end bearing in the developed TZPILE model. The load versus pile deflection curves from the matched TZPILE model are illustrated in Figure 4.

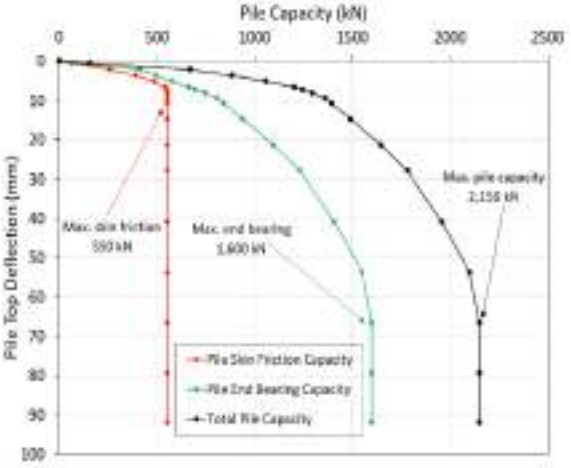

Figure 4: Load vs. Pile Deflection Curves – Matched TZPILE Model

Figure 4 illustrates that the matched TZPILE model exhibits a skin friction capacity of 550 kN, an end bearing capacity of approximately 1,600 kN, and a total pile capacity of about 2,150 kN. These values closely align with the results obtained from pile load tests, thus confirming the suitability of the matched TZPILE model for accurately estimating the drag load on the pile.

Estimated Drag Load

Utilizing the matched TZPILE model and considering the estimated long-term soil settlement presented in Figure 1, the downdrag analysis results are detailed in Table 2 and Figures 5 through 7. The axial load distributions versus pile head loads are illustrated in Figure 5, which also indicates the locations of the neutral plane. In each scenario, the drag load is determined by subtracting the pile head load from the load at the neutral plane depth. Figures 6 and 7 provide further insights, showing the neutral plane location versus pile head load and drag load versus pile head load, respectively.

Table 2: Downdrag Analysis Results vs. Pile Head Loads

Load on Pile Head (kN)	Total Capacity at Neutral Plane (kN)	Drag Load (kN)	Neutral Plane Location Below Pile Head (m)	Pile Top Movement (mm)
107	476	369	10.6	1.8
249	605	356	10.5	3.3
778	956	178	10.3	8.1
1,192	1,334	142	6.6	14.5
1,512	1,641	129	5.9	27.7
1,882	1,988	107	4.3	53.6
2,242	2,309	67	1.5	130.3

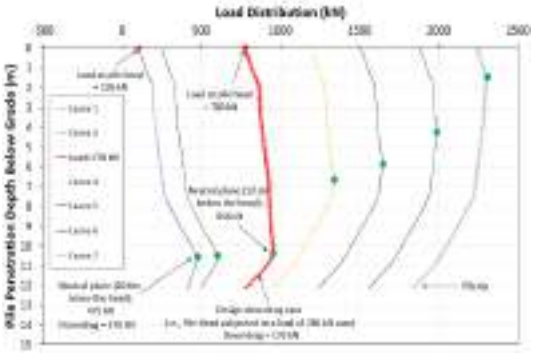

Figure 5: Load Distribution vs. Pile Head Load

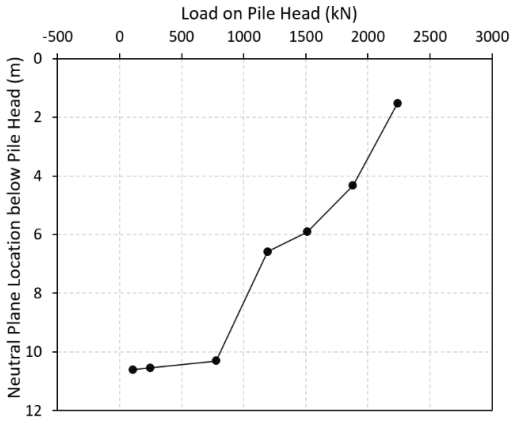

Figure 6: Neutral Plane Location vs. Pile Head Load

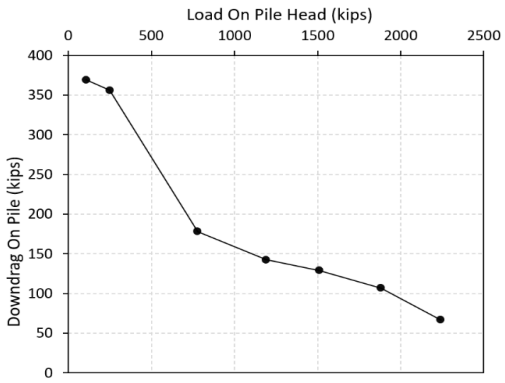

Figure 7: Drag Load vs. Pile Head Load

It can be observed from Table 2 and Figure 5 through Figure 7 that:

- Neutral plane moves upward with increase in pile head load (Table 2, Figure 5 and Figure 6). For example, if the pile head load increases from 249 to 1,192 or 249 to 1,882 kN, the neutral plane moves up to from 10.5 to 6.6 and 4.3m respectively (Curve 2, Curve 4 and Curve 6).
- Drag load decreases with increase in pile head load (Table 2 and Figure 7). For example, the drag load decreases from 369 kN to 178 kN with pile head load increasing from 107 kN (Curve 1) to 778 kN (Curve 3).
- Curve 1 presents the maximum drag load case (an extreme case). The maximum drag load is about 369 kN which corresponds to the case that the pile has negligible or no movement (i.e., the case with largest relative movement between pile and soil).
- The estimated drag load during operating (i.e., pile head is subjected to the design load of 778 kN) is about 178 kN.

STRATEGIES TO REDUCE THE INFLUENCE OF DOWNDRAG

Various pile design strategies can be employed to mitigate the effects of downdrag, including selecting an appropriate utilization factor for pile capacity, reducing long-term settlement of subsurface soils, and increasing pile end bearing capacity.

Utilization Factor of Pile Capacity

Increasing Utilization Factor of Pile Capacity: For a design pile (with a defined diameter and penetration) and a specified long-term soil settlement profile, the drag load decreases as the pile head load increases (Figure 7). Therefore, enhancing the utilization factor of pile capacity is an effective strategy to mitigate the impact of downdrag. This approach can be applied under the following conditions: 1) high confidence in the design loads and soil parameters, 2) tolerance for relatively large settlement and differential settlement in the structure/building, and 3) insignificant consequences in the event of structural failure. Using a lower factor of safety in these scenarios can result in a cost-effective design.

Decreasing Utilization Factor of Pile Capacity: While increasing pile head load can reduce drag load, it also leads to increased pile displacement, as illustrated in Figures 8 and 9. For instance, pile head displacement rises from 3.3 mm to 53.6 mm when the

pile head load increases from 249 kN to 1,882 kN. Therefore, for structures/buildings with stringent settlement requirements, decreasing the utilization factor of pile capacity (applying a higher factor of safety) can help to minimize the effects of downdrag. However, this strategy typically results in a more cost-intensive design.

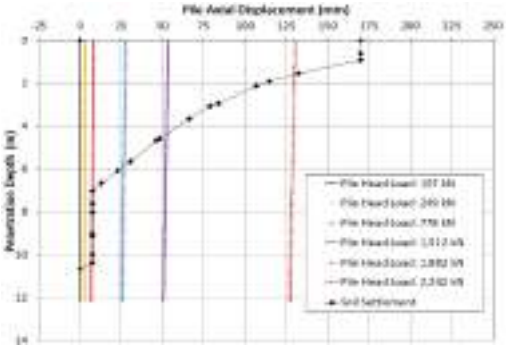

Figure 8: Pile Axial Displacement vs. Pile Head Load

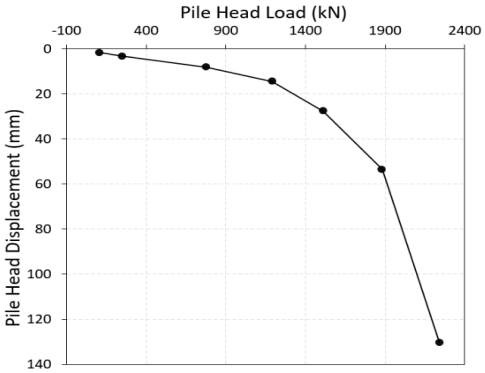

Figure 9: Pile Head Displacement vs. Pile Head Load

Reducing Settlement of Subsurface Soils

Theoretically, reducing the long-term settlement of subsurface soils can effectively decrease the drag load on the pile. Utilizing the matched TZPILE model, a series of analyses were conducted for various settlement scenarios while maintaining a constant pile head load of 780 kN. The findings of these analyses are presented in Table 3, Figure 10, and Figure 11.

Table 3: Downdrag Analysis Results Considering Reducing Settlement of Subsurface Soils

Settlement (mm)	Relative Settlement (%)	Load at Pile Head (kN)	N.P. Depth BGS (m)	Capacity at Neutral Plane Level (kN)	Drag Load (kN)	Relative Drag Load (%)
170.2	100	778	10.3	956	178	100
127.6	75	778	8.2	930	151	85
85.1	50	778	6.8	921	142	80
42.5	25	778	6.4	912	133	75
21.3	12.5	778	5.4	890	111	63

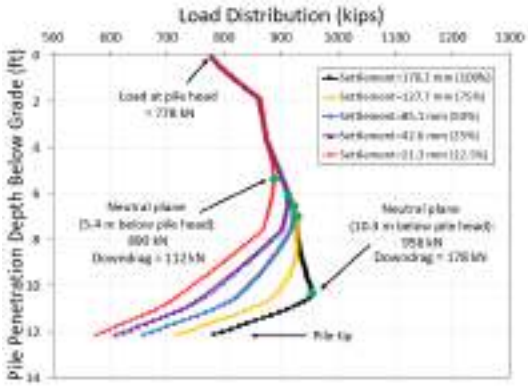

Figure 10: Load Distribution vs. Settlement

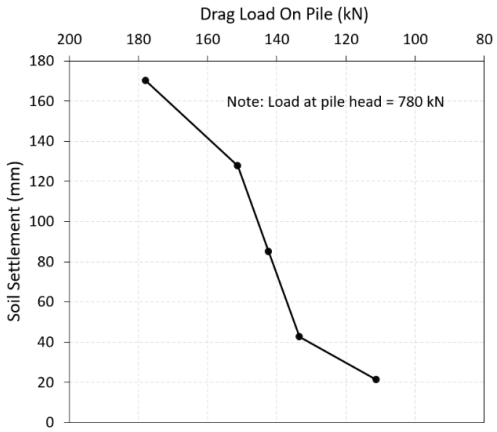

Figure 11: Soil Settlement vs. Drag Load

It can be seen from Table 3, Figure 10, and Figure 11 that for a given pile head load (i.e., 778 kN):

- The drag load decreased with the reduction in the settlement of soils. For example, the drag load decreases from 178 kN when soil settlement is 170.2 mm to 142 kN when soil settlement is reduced to 85.1 mm and further reduces to 111 kN when soil settlement is reduced to 21.3 mm.
- The rate of decrease in drag load is smaller than the rate of decrease in soil settlement. For example, when the soil settlement decreased from 170.2 mm to 85.1 mm (50%) or 170.2 mm to 21.3 mm (12.5%), the drag load decreases from 142 kN to 142 kN (80%) and 111 kN (63%) respectively.

The strategy of reducing long-term settlement of subsurface soils prior to pile installation has potential to mitigate the drag load (downdrag) on piles. However, the effectiveness of this method is often limited by significant settlement in thick layers of highly compressible, fine-grained soils. Additionally, secondary consolidation can further contribute to the drag load. From a practical perspective, this approach may be seen as laborious and time-intensive.

Increasing Pile End Bearing Using Expanded Bottom Pile

Another method to mitigate the effects of downdrag is by enhancing the pile's end bearing capacity using an expanded bottom pile. As illustrated in Figure 12, a conventional expanded bottom pile was employed in this study. To streamline the analysis, the physical expansion of the pile bottom was not simulated. Instead, the end bearing capacity in the TZPILE model was artificially augmented by applying a larger load factor. To assess the impact of the expanded bottom pile on downdrag, a series of TZPILE analyses were conducted considering various pile end bearings, while maintaining a constant pile head load of 778 kN. The findings are detailed in Table 4, Figure 13, and Figure 14.

Table 4: Downdrag Analysis Results Considering Increasing Pile End Bearing

Pile Dia. (m)	Relative Increase of Pile Dia. (%)	End Bearing (KN)	Total Capacity (kN)	Increase of Total Capacity (kN)	Load at Pile Head (kN)	Drag Load (kN)	Increase of Drag Load (kN)	Net Increase of Capacity (1) (kN)
0.46	0.0	1,600	2,139	0	778	178	0	0
0.51	11.8	2,000	2,540	400	778	258	80	320
0.56	22.5	2,400	2,940	801	778	298	120	681
0.60	32.3	2,800	3,340	1,201	778	329	151	1,050
0.65	41.4	3,200	3,741	1,601	778	347	169	1,432

Note: (1) Net Capacity = Total Capacity - Downdrag

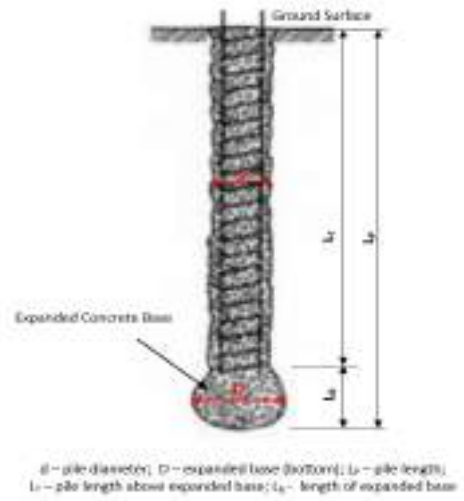

Figure 12: An example of Expanded Bottom Pile

It can be observed from Table 4 and Figure 13 that for a given pile head load of 778 kN, the drag load experiences an increase with an enhancement in the pile's end bearing. For instance, if the pile's end bearing augments from 1,600 kN to 2,400 kN or 1,600 kN to 3,200 kN, the drag load increases from 178 kN to 298 kN and 347 kN, respectively.

Additionally, as illustrated in Table 4 and Figure 14, both the drag load and pile capacity exhibit an

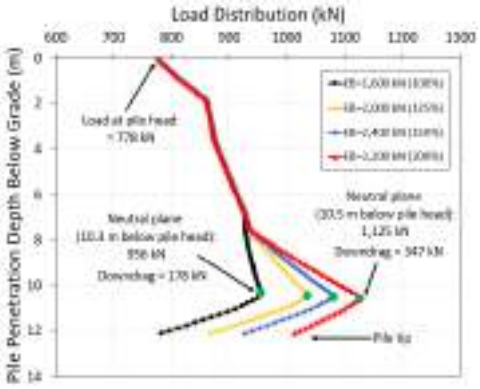

Figure 13: Load Distribution vs. End Bearing

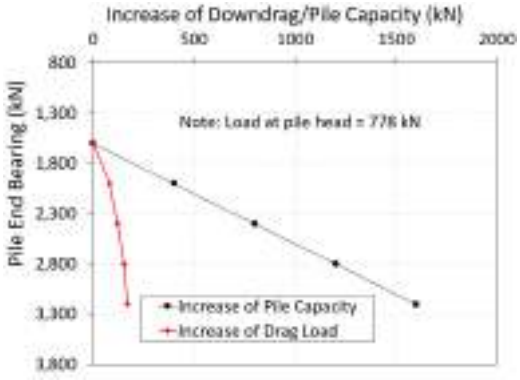

Figure 14: Increase of Drag Load/Pile Capacity vs. Pile End Bearing

upward trend with an increase in the pile's end bearing. Notably, the increment in the pile capacity surpasses the increment in the drag load, resulting in a higher net capacity of the pile. For example, when the pile's end bearing increases from 1,600 kN to 2,400 kN, the drag load increases by 120 kN (from 178 kN to 298 kN), while the pile's capacity increases by 801 kN (from 2,139 kN to 2,940 kN). Consequently, the net capacity of the pile increases by 681 kN (801 kN - 120 kN). This suggests that enhancing the pile's end bearing serves as an effective strategy to mitigate the impact of downdrag.

To increase the pile's end bearing, expanding the pile's bottom proves to be an efficient solution, particularly when the pile bottom is embedded in sandy soils. As depicted in Figure 15, when the pile's bottom diameter increases from 0.46 meters to 0.56 meters (a 22.5% increase) or from 0.46 meters to 0.65 meters (a 41.4% increase), the end bearing rises from 1,600 kN to 2,400 kN (a 50% increase) and to 3,200 kN (a 100% increase), respectively. It should be noted that the results above are based on a simplified model—specifically, the physical expansion of the pile bottom was not directly simulated. Modeling the actual pile geometry, soil–pile interaction, stress distribution, and soil failure mechanisms around the expanded base with the finite element method may yield more realistic and accurate results.

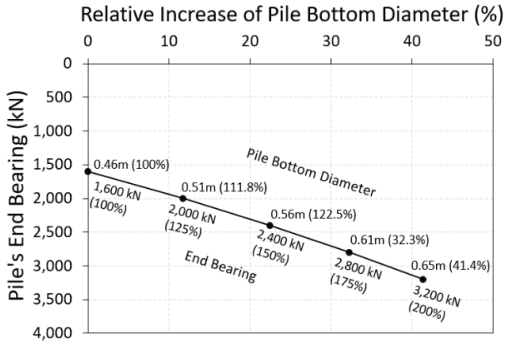

Figure 15: Pile Bottom Diameter Vs. Pile End Bearing

These aspects will be addressed in future extensions of this study for journal publication. Furthermore, additional research is needed on strategies for mitigating drag load, so that quantitative design guidance and cost–benefit analyses can be developed. This includes the creation of specific design charts or equations relating pile capacity utilization to expected settlements, cost comparisons among various mitigation methods, recommendations for when to consider each strategy, and construction feasibility and quality control requirements for each approach.

CONCLUSIONS

This paper has presented the development of the TZPILE model for a 0.46-meter diameter downdrag (DD) pile to investigate the impact of downdrag, using a generalized soil profile derived from LNG projects and accounting for excessive long-term settlement, primarily caused by a relatively thick layer of very soft and highly compressible fine-grained soils. The following conclusions can be drawn:

- For the design pile (i.e., 0.46-meter diameter pile with 12.2-meter penetration depth), the drag load decreases with the pile head load. A more realistic drag load would be achieved when the operating load is considered in the downdrag analysis.
- To mobilize the pile ultimate capacity, relatively large pile movement will occur to overcome the downdrag effect. For structures with stringent settlement requirements, reducing the utilization factor of pile capacity (i.e., using a larger factor of safety) is an effective approach to control the pile's settlement.
- For structures that represent a low hazard to human life in the event of failure, increasing the utilization factor of pile capacity (i.e., using a relatively smaller factor of safety) is an effective approach to reduce the impact of downdrag.
- Reducing long-term settlement before pile installation is another solution to mitigate the impact of downdrag. However, this is time-consuming and the effectiveness of this approach is limited.
- Increasing the pile's end bearing will increase the drag load; the impact of downdrag (drag load) can be effectively managed by increasing the pile's end bearing, as the pile's capacity increases more than the drag load.
- The pile's end bearing can be enhanced by expanding its bottom. Using an expanded bottom pile is an effective solution for projects with a sandy soil bearing stratum underlying a thick layer of very soft and highly compressible fine-grained soils.

ACKNOWLEDGMENT

The authors gratefully appreciate the support by the management of Bechtel Corporation in preparing and publishing this paper.

REFERENCES

[1] API RP 2A-WSD (R2020). “Planning, Designing, and Constructing Fixed Offshore Platforms—Working Stress Design,” Twenty-Second Edition.

[2] Asaoka (1978). “Observational procedure of settlement prediction,” Soils and Foundations, 18 (4) (1978), pp. 87-101.

[3] ASTM (1994). “Standard Test Method for Piles Under Static Axial Compressive Load,” ASTM D1143.

[4] ASTM (2022). “Standard Test Methods for Deep Foundation Elements Under Static Axial Tensile Load,” ASTM D3689.

[5] Davisson, M.T. (1972). “High Capacity Piles, Proceedings, Soil Mechanics Lecture Series on Innovations in Foundation Construction,” American Society of Civil Engineers, ASCE, Illinois Section, Chicago, 81-112.

[6] Ensoft Inc. (2021). “TZPILE 2021 User’s Manual, Analysis of Load versus Settlement for Axially-Loaded Deep Foundations,”

[7] Fellenius, B.H. (1998). “Recent Advances in the Design of Piles for Axial Loads, Dragloads, Downdrag, and Settlement,” ASCE and Port of NY &NJ Seminar, April 22 and 23.

[8] FHWA Resource Center (2019). “Geotechnical Solutions Notebook (GSN), ISSUE F-1 (2019) (rev. 0): Accurate valuation and Consideration of Downdrag Effect in the Design of Deep Foundations,”

Copyright © Int. J. of GEOMATE All rights reserved, including making copies, unless permission is obtained from the copyright proprietors.

15th Int. Conf. on Geotechnique, Construction Materials & Environment,
Kyoto, Japan, 11-13 November 2025, ISBN 978-4-909106124 C3051

DESERTIFICATION IN SAUDI ARABIA: IMPACTS OF EXCESSIVE IRRIGATION AND CLIMATE CHANGE ON VEGETATION LOSS THROUGH MATHEMATICAL MODELING

Dalal Adnan Maturi [1]

[1]Departement of Mathematics, Faculty of Science, King Abdulaziz University, Jeddah, Saudi Arabia

ABSTRACT

In Saudi Arabia, as defined by the United Nations Convention to Combat Desertification (UNCCD) as "land degradation in arid, semi-arid, and dry sub-humid areas resulting from various factors, including climatic variations and human activities" desertification is becoming a more serious environmental issue, particularly in regions like Al-Qassim While climate change makes water scarcity and vegetation degradation worse, over-irrigation speeds up soil degradation The purpose of this study is to determine how vegetation dynamics are impacted by dust pollution, over-irrigation, and climate change Three differential equations representing dust pollution (D), vegetation density (P), and climatic change intensity (G) were used to create a nonlinear mathematical model. The model captures essential environmental dynamics, emphasizing how vegetation helps mitigate climate change, the challenges posed by limited water availability, and the impact of dust on plant life. Using MATLAB, numerical simulations were performed to explore different environmental scenarios and evaluate their effects. Results showed that excessive irrigation and high dust pollution lead to soil salinization and weaken plant resilience, accelerating vegetation decline. In contrast, reforestation and sustainable irrigation play a crucial role in stabilizing plant ecosystems and slowing desertification. Maintaining ecological balance requires a well-planned combination of afforestation, dust control, and responsible water management. If left unchecked, uncontrolled irrigation and rising dust levels speed up land degradation, highlighting the urgent need for climate adaptation measures and sustainable water policies. By leveraging mathematical modeling and numerical simulations, engineers and ecologists can gain valuable insights into managing agriculture and environmental sustainability in arid regions like Saudi Arabia. These tools help develop data-driven strategies that improve long-term land use and conservation efforts.

Keywords: Desertification, Irrigation, Climate Change, Vegetation Loss, Mathematical Modeling.

INTRODUCTION

The Climate change scenarios predict shifts in aridity across the Middle East and North Africa (MENA) region, including Saudi Arabia. Under the Paris Agreement scenarios, Saudi Arabia is expected to experience increased rainfall, which may transition some areas from hyper-arid to arid conditions. However, the increase in potential evapotranspiration (PET) could offset these benefits, leading to a drier climate overall [1]. The increase in temperature and decrease in precipitation exacerbate water scarcity, impacting agricultural productivity and leading to desertification [2]. Excessive irrigation in Saudi Arabia has led to increased evaporation and altered local climates. The Saudi Green Initiative, which involves large-scale forestation, requires significant irrigation, further straining water resources and potentially increasing local temperatures due to lower albedo and higher evaporation rates [3]. The use of irrigation in agriculture has been shown to increase latent heat flux, which can affect local climate conditions and contribute to desertification if not managed sustainably [4]. Mathematical models, such as the FAO-CROPWAT and SALTMED, have been used to estimate crop water requirements and assess the impacts of climate change on irrigation needs. These models indicate that irrigation water requirements will increase significantly under high emission scenarios, leading to higher deficits in water availability for major crops [5]. Optimizing water use through improved irrigation planning and crop pattern selection can mitigate some adverse effects. For instance, reallocating water resources among competitive crops like date palms can enhance water use efficiency and reduce overall water demand [6]. Soil erosion, driven by high rainfall intensity and lack of vegetation cover, is a critical factor in land degradation and desertification. The Revised Universal Soil Loss Equation (RUSLE) model, coupled with GIS, has been used to assess soil erosion risk in Saudi Arabia, highlighting areas with high erosion potential due to steep slopes and sparse vegetation [7].The study investigates the regional climate impact of irrigated forested areas on temperature and precipitation in the Arabian Peninsula, particularly focusing on the effects of Saudi Arabia's "Saudi Green Initiative," which aims to plant ten billion trees despite challenges such as insufficient rainfall and the need for irrigation, which

increases evaporation and alters local climate conditions [8]. The study focuses on estimating crop water requirements (CWR) in Saudi Arabia, where agriculture heavily depends on limited water resources such as groundwater and desalinated water. It utilizes high-resolution satellite data and environmental variables to improve the accuracy of CWR estimations, addressing the challenges posed by a lack of micro-level data in agricultural systems [9]. The study investigates the impact of climate change on soil salinity and pomegranate productivity in the Al-Baha region of Saudi Arabia, where groundwater depletion, rising temperatures, and decreasing precipitation have led to deteriorating groundwater quality and reduced agricultural productivity. Over a 24-year period, average temperatures increased by 1.1 °C–1.6 °C, while rainfall decreased by 24–41%, prompting the use of the SALTMED model to analyze future scenarios [10]. The study estimates the greening effect over the desert in Saudi Arabia using a meteorological numerical model (MM5) combined with a sophisticated land surface model (LSM), revealing that greening by grassland vegetation can increase regional rainfall by +65% [11]. In recent years, mathematical modeling techniques have played a pivotal role in understanding environmental challenges such as desertification, particularly in arid regions like Saudi Arabia. The phenomenon of vegetation loss due to excessive irrigation and climate-induced heat stress requires robust models that simulate soil heat dynamics and water transfer processes. Finite Difference Methods (FDM), as demonstrated by Maturi and colleagues in modeling heat conduction in granite and brick materials [12-13], provide a foundational approach for approximating thermal changes in semi-arid soil environments.

Moreover, analytical and semi-analytical methods such as the Adomian Decomposition Method and Variational Iteration Method, used by Maturi in solving singular integral and Laplace equations related to heat and groundwater flow [14-15],[18] 2024), can be extended to simulate evapotranspiration, root-zone temperature profiles, and subsurface hydrologically critical to vegetation sustainability in desert-prone regions. Notably, recent work on heat transfer modeling in biological materials, such as apple refrigeration and heat flow in metallic electric cables [16-17], illustrates the potential to apply these methods to plant physiology under stress conditions caused by irrigation mismanagement or high ambient temperatures. These mathematical tools not only enhance our predictive understanding of desertification dynamics but also aid in designing mitigation strategies by quantifying soil-water-heat interactions in deteriorating ecosystems.

RESEARCH SIGNIFICANCE

This study addresses the escalating challenge of desertification in Saudi Arabia by quantitatively analyzing the synergistic impacts of excessive irrigation and climate change on vegetation loss. By integrating variables such as soil moisture, groundwater dynamics, and irrigation policies into a mathematical framework, the research offers a novel predictive tool to assess ecosystem vulnerability. The findings provide critical insights for sustainable water management, enabling policymakers to balance agricultural demands with groundwater preservation. This model not only deepens our theoretical understanding of how desertification happens in dry regions, but it also offers a practical framework that other countries facing water shortages can adapt. It contributes to global sustainability efforts, such as the United Nations' Sustainable Development Goals (SDGs), and fits perfectly within the framework of Saudi Arabia's Vision 2030.

GENERAL FORM OF THE DPG MODEL

The DPG system is given by:

$$\begin{cases} \frac{dD}{dt} = A - \mu_0 D - \alpha DP = F_1(D,P), \\ \frac{dP}{dt} = rP\left(1 - \frac{P}{K-cG}\right) - \beta DP = F_2(D,P,G), \\ \frac{dG}{dt} = Q - \gamma_1 DG - \gamma_2 PG - \mu_1 G = F_3(D,P,G). \end{cases} \quad (1)$$

The Jacobian matrix for the system is:

$$J = \begin{bmatrix} \frac{\partial F_1}{\partial D} & \frac{\partial F_1}{\partial P} & \frac{\partial F_1}{\partial G} \\ \frac{\partial F_2}{\partial D} & \frac{\partial F_2}{\partial P} & \frac{\partial F_2}{\partial G} \\ \frac{\partial F_3}{\partial D} & \frac{\partial F_3}{\partial P} & \frac{\partial F_3}{\partial G} \end{bmatrix} \quad (2)$$

Substituting the partial derivatives:

$$J = \begin{bmatrix} -\mu_0 - \alpha P & -\alpha D & 0 \\ -\beta P & r - \frac{2rP}{K-cG} - \beta D & -\frac{rcP^2}{(K-cG)^2} \\ -\gamma_1 G & -\gamma_2 G & -\gamma_1 D - \gamma_2 P - \mu_1 \end{bmatrix} \quad (3)$$

Local stability analysis of $Z_1 = (D_1, 0, G_1)$:

Equilibrium point :

$$D_1 = \frac{A}{\mu_0}, \quad P_1 = 0, \quad G_1 = \frac{Q\mu_0}{A\gamma_1 + \mu_0\mu_1} \quad (4)$$

Jacobian at point Z_1:

$$J(Z_1) = \begin{bmatrix} -\mu_0 & -\alpha D_1 & 0 \\ 0 & r - \beta D_1 & 0 \\ -\gamma_1 G_1 & -\gamma_2 G_1 & -\gamma_1 D_1 - \mu_1 \end{bmatrix} \quad (5)$$

Eigenvalues of $J(Z_1)$:The eigenvalues (λ) are obtained by solving:

$$\det(J(Z_1) - \lambda I) = 0 \quad (6)$$

This simplifies to:

$$\begin{vmatrix} -\mu_0 - \lambda & -\alpha D_1 & 0 \\ 0 & r - \beta D_1 - \lambda & 0 \\ -\gamma_1 G_1 & -\gamma_2 G_1 & -\gamma_1 D_1 - \mu_1 - \lambda \end{vmatrix} = 0 \quad (7)$$

Since the matrix is lower triangular, the eigenvalues are the diagonal elements:

$$\lambda_1 = -\mu_0, \quad \lambda_2 = r - \beta D_1, \quad \lambda_3 = -\gamma_1 D_1 - \mu_1 \quad (8)$$

Stability Conditions for Z_1:

- All eigenvalues must be negative for stability.
- $\lambda_1 = -\mu_0 < 0$ (always true since $\mu_0 > 0$).
- $\lambda_3 = -\gamma_1 D_1 - \mu_1 < 0$ (always true).
- $\lambda_2 = r - \beta D_1 = r - \frac{\beta A}{\mu_0}$.

Thus, Z_1 is locally stable if: $r < \frac{\beta A}{\mu_0}$

Bifurcation at Z_1:

- If $r = \frac{\beta A}{\mu_0}$, $\lambda_2 = 0 \rightarrow$ Transcritical bifurcation occurs.
- If $r > \frac{\beta A}{\mu_0}$, Z_1 becomes unstable, and Z_2 emerges as stable.

The SECOND- LOCAL STABILITY ANALYSIS OF Z_2

Equilibrium point $\boldsymbol{Z_2}$:

$$\boldsymbol{D_2 = \frac{A}{\mu_0 + \alpha P_2}}, \quad \boldsymbol{G_2 = \frac{Q(\mu_0 + \alpha P_2)}{\alpha\gamma_2 P_2^2 + (\mu_0\gamma_2 + \mu_1\alpha)P_2 + (A\gamma_1 + \mu_0\mu_1)}} \quad (9)$$

where $\boldsymbol{P_2}$ is a root of

$$f(P) = e_1 P^4 + e_2 P^3 + e_3 P^2 + e_4 P + e_5 = 0. \quad (10)$$

Jacobian at point $\boldsymbol{Z_2}$:

$$J(Z_2) = \begin{bmatrix} -(\mu_0 + \alpha P_2) & -\alpha D_2 & 0 \\ -\beta P_2 & r - \frac{2rP_2}{K - cG_2} - \beta D_2 & -\frac{rcP_2^2}{(K - cG_2)^2} \\ -\gamma_1 G_2 & -\gamma_2 G_2 & -(\gamma_1 D_2 + \gamma_2 P_2 + \mu_1) \end{bmatrix} \quad (11)$$

LOCAL STABILITY ANALYSIS OF

Characteristic Equation:

The eigenvalues are solutions of:

$$\lambda^3 + S_1\lambda^2 + S_2\lambda + S_3 = 0 \quad (12)$$

where:

$$\boldsymbol{S_1 = \mathrm{tr}(J) = -(J_{11} + J_{22} + J_{33})},$$
$$\boldsymbol{S_{12} = \text{sum of principal minors}}$$
$$\boldsymbol{S_3 = -\det(J)},$$

Routh-Hurwitz Stability Criterion. For stability, the following must hold:

1. $S_1 > 0$,
2. $S_3 > 0$,
3. $S_1 S_2 > S_3$.

If these conditions are met, Z_2 is locally asymptotically stable.

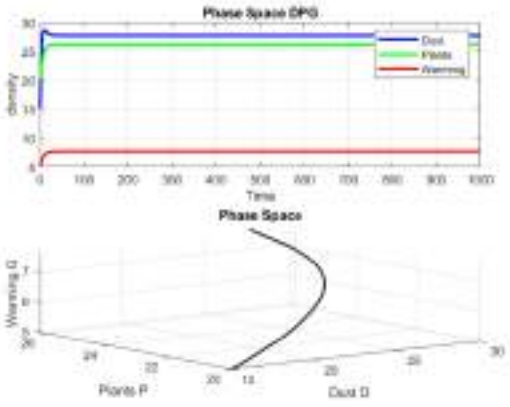

Fig.1 Dynamic simulation of DPG model for Scenario Value1, Dust concentration D(t) in mg/m³, vegetation biomass P(t) in kg/ha, and temperature anomaly G(t) in °C. This scenario represents moderate dust emissions and plant growth rates.

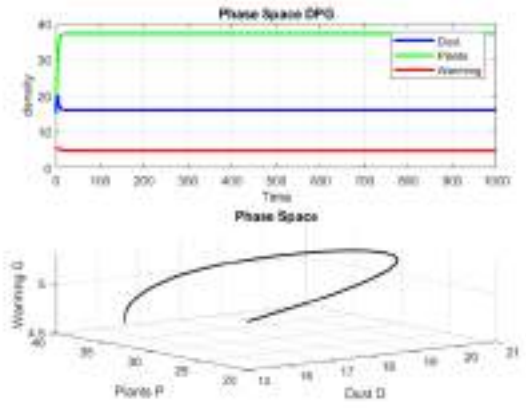

Fig.2 Dynamic simulation of DPG model for Scenario Value2 — Same variables and units as Fig. 1, but with higher dust emission and reduced plant growth resilience.

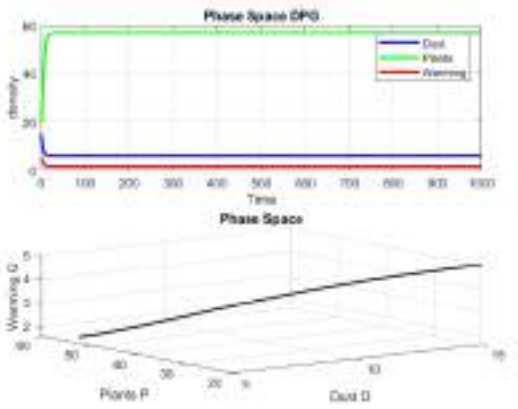

Fig.3 Dynamic simulation of DPG model for Scenario Value3. Represents high carrying capacity with moderate warming sensitivity.

Table 1 Description of DPG System Parameters with Value

Items	Description	Units	Value1	Value2	Value3
A	Dust emission rate	mg/m³/day	10	15	13
μ_0	Natural dust depletion rate	day⁻¹	0.1	0.2	0.5
α	Plant-induced dust removal coefficient	m³/(kg·day)	0.01	0.02	0.03
r	Plant intrinsic growth rate	day⁻¹	0.22	0.44	0.33
K	Plant carrying capacity	kg/ha	30	40	60
c	Warming-induced desertification coefficient	ha/(kg·°C·day)	0.01	0.02	0.03
β	Dust-induced plant degradation rate	m³/(mg·day)	0.001	0.002	0.003
Q	Global warming increase rate	C/year°	0.821	0.841	0.861
γ_1	Dust cooling effect on warming	C·m³/(mg·day)°	0.001	0.002	0.003
γ_2	Plant cooling effect on warming	C·ha/(kg·day)°	0.003	0.004	0.009
μ_1	Human mitigation of warming	year⁻¹	0.001	0.002	0.003

APPLICATIONS

We model the interaction between plant biomass and dust pollutants using two ODEs:

$$\begin{cases} \frac{dP}{dt} = rP\left(1-\frac{P}{K}\right) - aPD & \text{(Plant growth)} \\ \frac{dD}{dt} = Q - bD - cPD & \text{(Pollutant dynamics)} \end{cases}$$

$P(t)$: Plant biomass
$D(t)$: Dust pollutant concentration
r: Intrinsic growth rate of plants
K: Carrying capacity of plants
a: Pollution stress coefficient
Q: External pollutant input rate
b: Natural removal rate of pollutants
c: Interaction rate (plants removing pollutants)

At equilibrium, $\frac{dP}{dt} = \frac{dD}{dt} = 0$: Non-Desertification Equilibrium ($P^* > 0, D^* > 0$):

We solve: $\begin{cases} rP^*\left(1-\frac{P^*}{K}\right) = aP^*D^* \\ Q = bD^* + cP^*D^* \end{cases}$

1. From Plant Equilibrium:
$$r\left(1-\frac{P^*}{K}\right) = aD^* \Longrightarrow D^* = \frac{r}{a}\left(1-\frac{P^*}{K}\right)$$
2. From Pollutant Equilibrium:
$$Q = bD^* + cP^*D^* \Longrightarrow P^* = \frac{Q - bD^*}{cD^*}$$
3. Substitute D^* into P^*:
$$P^* = \frac{Q - b\left(\frac{r}{a}\left(1-\frac{P^*}{K}\right)\right)}{c\left(\frac{r}{a}\left(1-\frac{P^*}{K}\right)\right)}$$

This is a nonlinear equation in P^* and must be solved numerically.

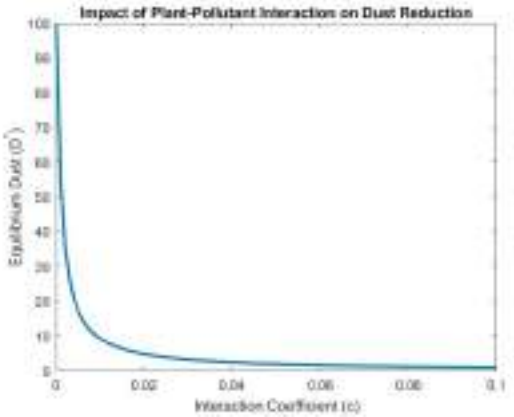

Fig.4 Impact of plant-pollutant interaction on dust reduction . D(t) in mg/m³ decreases as interaction rate c increases.

We study how D^* changes as c varies using implicit differentiation.

1. Differentiate Pollutant Equilibrium w.r.t. c:

$$0 = b\frac{dD^*}{dc} + P^*D^* + cD^*\frac{dP^*}{dc} + cP^*\frac{dD^*}{dc}$$

2. From Plant Equilibrium, express $\frac{dP^*}{dc}$ in terms of $\frac{dD^*}{dc}$:

$$\frac{dD^*}{dc} = -\frac{r}{aK}\frac{dP^*}{dc}$$

3. Substitute and solve for $\frac{dD^*}{dc}$:

$$\frac{dD^*}{dc} = \frac{-P^*D^*}{b + cP^* + \frac{aKcD^*}{r}}$$

Since all terms in the denominator are positive, $\frac{dD^*}{dc} < 0$, meaning increasing c decreases D^*.

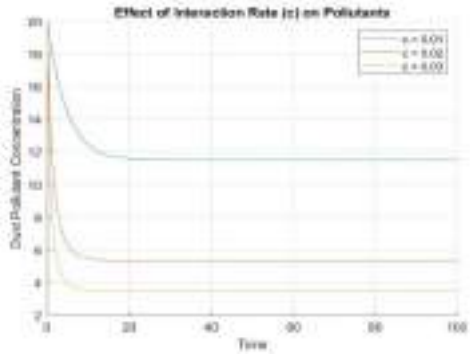

Fig.5 Effect of interaction rate c on pollutants. Detailed sensitivity curves showing negative slope, confirming that increased plant-dust interaction reduces dust concentration.

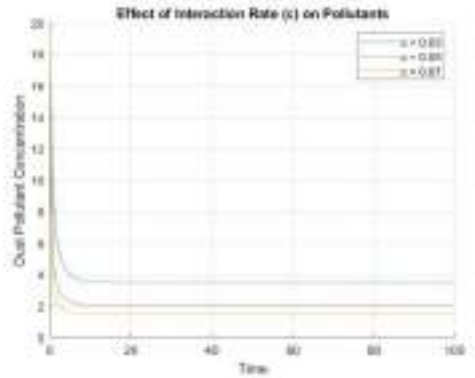

Fig.6 Effect of interaction rate c on pollutants . Detailed sensitivity curves showing negative slope, confirming that increased plant-dust interaction reduces dust concentration.

Equilibrium Analysis: If c increases → D^* decreases (more pollutant removal by plants).

If Q increases → D^* increases (more external pollution).

Sensitivity: $\frac{dD^*}{dc} < 0$ confirms that higher plant-pollutant interaction reduces dust concentration.

CONCLUSIONS

Dust pollutants, in conjunction with global warming, pose a significant threat to the ecological environment. This phenomenon may lead to the gradual conversion of verdant areas into ecologically unsustainable zones. The present study introduces and critically assesses a mathematical model designed to explore the effects of global warming and dust contaminants on the growth of plant biomass. The analytical framework employs the stability theory of differential equations to facilitate a comprehensive evaluation of the model. The analysis reveals that the system is characterized by two equilibrium states: the non-desertification equilibrium and the desertification equilibrium. The model analysis presents several compelling insights regarding the stability of these equilibrium states. Furthermore, the analysis uncovers noteworthy findings pertaining to various bifurcation types, including transcortical and Hopf bifurcations surrounding the equilibrium points. Additionally, the following results were discerned through numerical simulations. The atmospheric concentration of dust pollutants diminishes as the interaction rate between dust contaminants and plant biomass escalates. The plant biomass is threatened with the transition of green spaces into desertified areas if the intrinsic growth rate of plant biomass, the dust pollutants-induced depletion coefficient of plant biomass, and the natural depletion coefficient for dust pollutants remain uncontrolled. The potential for averting desertification exists if the conditions delineated in Theorem 1 ensure that plant biomass can persist alongside global warming and dust pollutants in a stable equilibrium. From the sensitivity analysis of the non-desertification equilibrium point, the findings indicate that the carrying capacity of plant biomass is a pivotal parameter that significantly mitigates the adverse effects of dust pollutants and global warming. Consequently, enhancing vegetation via reforestation initiatives is imperative for preventing desertification and fostering stability at the non-desertification equilibrium. In future research endeavors, we will explore the extension of the model to encompass interactions with additional ecological factors, such as animal populations, with a particular emphasis on herbivorous species.

ACKNOWLEDGMENTS

This paper was supported by the Deanship of Scientific Research (DSR), King Abdulaziz University, Jeddah.

REFERENCES

[1] Hamed, M. M., Sobh, M. T., Ali, Z., Nashwan, M. S., & Shahid, S. (2024). Aridity shifts in the MENA

region under the Paris Agreement climate change scenarios. Global and Planetary Change, 238, 104483. https://doi.org/10.1016/j.gloplacha.2024.104483

[2] Alghamdi, A. A., Aly, A. A., & Ibrahim, S. M. (2022). Effect of Climate Change on the Quality of Soil, Groundwater, and Pomegranate Fruit Production in Al-Baha Region, Saudi Arabia: A Modeling Study Using SALTMED. Sustainability, 14(20), 13275. https://doi.org/10.3390/su142013275

[3] Stenchikov, G. L., Lopez, O., Mostamandi, S., & Novikova, T. (2023). Impact of Forestation and Land-use Changes on Desert Climate. https://doi.org/10.5194/egusphere-egu23-1745

[4] Hozumi, Y., & Ueda, H. (2005). Numerical estimation for greening effect over the desert in Saudi Arabia. 48, 181–187.

[5] El-Rawy, M., Fathi, H., Zijl, W., Alshehri, F., Almadani, S., Zaidi, F. K., & Gabr, M. E. (2023). Potential Effects of Climate Change on Agricultural Water Resources in Riyadh Region, Saudi Arabia. Sustainability, 15(12), 9513. https://doi.org/10.3390/su15129513

[6] Al-Abdulkader, A. M., Al-Amoud, A. I., & Awad, F. S. (2016). Adaptation of the agricultural sector to the effects of climate change in arid regions: competitive advantage date palm cropping patterns under water scarcity conditions. *Journal of Water and Climate Change*, *7*(3), 514–525. https://doi.org/10.2166/WCC.2016.096.

[7] Saad, S. A. D. M., & Mallick, J. (2014). Risk assessment of soil erosion in semiarid mountainous watershed in SaudiArabia by RUSLE model coupled withremote sensing and GIS.

[8] Stenchikov, G. L., Lopez, O., Mostamandi, S., & Novikova, T. (2023). Impact of Forestation and Land-use Changes on Desert Climate. https://doi.org/10.5194/egusphere-egu23-1745

[9] Haq, M. A., & Khan, M. Y. A. (2022). Crop Water Requirements with Changing Climate in an Arid Region of Saudi Arabia. *Sustainability*, *14*(20), 13554. https://doi.org/10.3390/su142013554

[10] Alghamdi, A. A., Aly, A. A., & Ibrahim, S. M. (2022). Effect of Climate Change on the Quality of Soil, Groundwater, and Pomegranate Fruit Production in Al-Baha Region, Saudi Arabia: A Modeling Study Using SALTMED. *Sustainability*, *14*(20), 13275. https://doi.org/10.3390/su142013275.

[11] Hozumi, Y., & Ueda, H. (2005). *Numerical estimation for greening effect over the desert in Saudi Arabia*. *48*, 181–187.

[12] Maturi, D. A., & Aljedani, A. I., & Alaid100 × 100 grid arous, E. S. (2019). Finite Difference Method for Solving Heat Conduction Equation of the Granite. International Journal of GEOMATE, 17(61), 135–140. DOI: 10.21660/2019.61.135.

[13] Maturi, D. A. (2020). Finite Difference Approximation for Solving Transient Heat Conduction Equation of the Brick. International Journal of GEOMATE, 18(68), 114–119. DOI: 10.21660/2020.68.114

[14] Maturi, D. A., & Simbawa, E. A. (2020). The Modified Decomposition Method for Solving Volterra Fredholm Integro-Differential Equations Using Maple. International Journal of GEOMATE, 18(67), 84–89. DOI: 10.21660/2020.67.084.

[15] Maturi, D. A. (2022). The Adomian Decomposition Method for Solving Heat Transfer Lighthill Singular Integral Equation Using Maple. International Journal of GEOMATE, 22(89), 16–23. DOI: 10.21660/2022.89.016.

[16] Maturi, D. A. (2023). Numerical and Analytical Study for Solving Heat Equation of the Refrigeration of Apple. International Journal of GEOMATE, 24(103), 61–68. DOI: 10.21660/2023.103.061

[17] Maturi, D. A. (2023). Study of the Heat Equation and the Effect of Temperature Inside an Electric Cable Consisting of Aluminum and Copper Metals. International Journal of GEOMATE, 24(106), 61–68. DOI: 10.21660/2023.106.061.

[18] Maturi, D. A. (2024). Variational Iteration Method and Analytic Solution for Laplace Equation for Steady Groundwater Flow. International Journal of GEOMATE, 26(113), 90–97. DOI: 10.21660/2024.113.090.

Copyright © Int. J. of GEOMATE All rights reserved, including making copies, unless permission is obtained from the copyright proprietors.

15th Int. Conf. on Geotechnique, Construction Materials & Environment,
Kyoto, Japan, 11-13 November 2025, ISBN 978-4-909106124 C3051

AUTOMATION AND INNOVATION IN PRECAST CONCRETE MANUFACTURING: A STRATEGIC APPROACH

*Amalia Rizka Sugiarto[1,2], Yusuf Latief [1]

[1] Faculty of Engineering, University of Indonesia, Indonesia
[2] Faculty of Engineering, University of Singaperbangsa Karawang, Indonesia

ABSTRACT

The precast concrete manufacturing industry is undergoing a transformation toward digitalization and automation, driven by the need for improved efficiency, precision, and integration across production stages. However, the adoption of automation technologies remains fragmented, with most implementations focusing only on isolated processes. This study aims to develop a strategic framework that maps digital and automation technologies systematically across the full cycle of precast concrete production. Using a conceptual and literature-based approach, the research identifies key production stages—from design and material preparation to casting, curing, quality control, and on-site installation—and aligns them with relevant technologies such as Building Information Modeling (BIM), Enterprise Resource Planning (ERP), RFID, IoT, robotics, Digital Twin, and 3D printing. The study results in a comprehensive visual framework that integrates these technologies with stakeholder roles (designer, factory, contractor) and system layers (physical, control, data, decision). In addition to the framework, this paper presents a technology matrix, system architecture model, and stepwise adoption roadmap to guide gradual implementation. The framework offers strategic value by enabling closed-loop control, predictive monitoring, and real-time decision-making. It also addresses the research gap regarding holistic technology mapping in precast production and supports the construction industry's transition toward Industry 4.0. Future research is recommended to validate the proposed framework through industrial case studies and practical application.

Keywords: Precast concrete, Industry 4.0, Visual framework, Automation technologies

INTRODUCTION

The construction industry has undergone significant transformation along with advances in automation and digitalization technology in recent decades [1][2]. One construction sub-sector that has received special attention is precast concrete manufacturing [3]. Precast products have been proven to increase construction time efficiency, reduce waste at project sites, and provide more consistent quality [4][5]. However, the conventional precast production process still faces various challenges, such as dependence on manual labor, inefficiency of production flows, human error, and limitations in real-time quality control systems [6].

In the Industry 4.0 era, various technologies such as Building Information Modeling (BIM), Enterprise Resource Planning (ERP), robotics, intelligent sensors (IoT), and Digital Twin have developed rapidly and offer the potential to be integrated into the precast production process [7] [8]. The integration of these technologies allows companies to build smarter, more adaptive, and high-precision production systems [9][10][11]. For example, the use of automated cutting and curing robots can replace manual activities with higher accuracy; RFID and IoT sensors can improve supply chain visibility; and the application of Digital Twin allows digital product simulation and monitoring to improve quality [12][13].

Although various studies have discussed digital technology in construction, there is still a gap in the literature regarding a strategic approach that systematically maps the implementation of automation technology based on the entire precast production cycle. This study aims to develop a strategic framework that integrates automation technology into every stage of the precast concrete production process. By developing this framework, it is expected to contribute to more efficient, measurable, and high-quality construction manufacturing practices.

RESEARCH SIGNIFICANCE

This research has significance in supporting digital transformation in the precast concrete manufacturing sector through a strategic approach based on automation technology. By compiling a technological framework according to the stages of precast production, this research provides an application guide for the industry in integrating systems such as BIM, ERP, robotics, and smart sensors. The results of this research are expected to improve operational efficiency, product quality, and the readiness of the construction industry to face the

challenges of Industry 4.0.

MATERIAL AND METHODS

This study adopts a conceptual and descriptive approach to develop a strategic framework for automation integration in precast concrete manufacturing. The objective is to systematically map digital and automated technologies into each stage of the precast production cycle [14] [15].

Literature Review

A comprehensive review was conducted on current technologies in digital construction and industrial automation, including Building Information Modeling (BIM), Enterprise Resource Planning (ERP), Internet of Things (IoT), Digital Twin, and robotics in precast production systems [16][17].

Identification of Production Stages

The typical precast production cycle was analyzed and classified into key stages: design and modeling, material supply, mold setup, casting and curing, quality control, and distribution [18]. These stages formed the basis for mapping relevant technologies [19][20].

Technology Mapping

A dataset of technologies applicable to precast production was compiled from industrial sources and previous studies [21][22]. Each technology was matched to the most appropriate stage in the production cycle based on its function, capability, and integration potential [23][24][25].

Framework Construction

Using the mapped data, a visual framework was constructed to illustrate how automation systems interact with each phase of the precast process [26][27]. The diagram reflects data flows, system integration points, and the role of each actor involved (designer, factory, specialty contractor, and general contractor) [28][29][30].

No physical experiments were conducted; instead, this research is based on a conceptual system design using validated data and technologies already applied in real-world precast contexts.

RESULT AND DISCUSSION

General Stages of Precast Concrete Production

The production of precast concrete involves a series of structured and sequential stages that must be carefully managed to ensure quality, efficiency, and consistency. The process begins with the design and modeling phase, where structural and reinforcement drawings are prepared using digital tools to define the dimensions, geometry, and specifications of the precast components. This stage plays a crucial role in determining the accuracy of downstream activities and is often supported by Building Information Modeling (BIM) to enhance coordination across disciplines.

Following the design phase, the next stage is the preparation of materials and logistics, which includes procurement, inventory management, and the scheduling of deliveries. Efficient material handling is essential to avoid delays and reduce waste. The process continues with the setup of formwork and reinforcement, where molds are prepared and rebar or other reinforcement components are placed based on production drawings.

Once formwork is completed, the casting and curing stage begins. In this phase, concrete is poured into molds under controlled conditions, followed by curing to achieve the desired strength and durability. After the curing process, the elements undergo demoulding and finishing, where the products are removed from the molds, cleaned, and surface-treated as needed.

The final phases include quality control, which ensures the components meet design specifications and tolerances, and storage and delivery, where precast elements are organized, tracked, and prepared for transportation to the construction site. These stages are increasingly supported by digital and automated systems, enabling more precise, traceable, and scalable production workflows.

Integration of Automation Technology Based on Production Stages

Through literature studies and analysis of technology data available in the industry, this study develops a mapping of automation technology based on the stages of the precast concrete production process. This mapping includes not only the name of the technology, but also the main functions, types of systems used, and examples of commercially available applications. The results of the mapping are presented in Table 1.

Tabel 1. Automation and Digital Technologies in Precast Concrete Manufacturing

Business Process Stage	Technology	Software	Function
Design	Building Information Modeling (BIM)	Autodesk Revit, Tekla Structures, ArchiCAD	Creating 3D digital models of precast components; real-time multidisciplinary collaboration
Design & Simulation	Digital Twin	Siemens NX, ANSYS TwinBuilder, Dassault 3DEXPERIENCE	Digital representation of physical components for simulation and precision analysis
Production Planning	ERP System	SAP ERP, Oracle NetSuite, Microsoft Dynamics	Integration of planning, material management, and precast production scheduling
Supply Chain & Inventory	RFID (Radio Frequency ID)	RFID management software such as Zebra RFID Software	Real-time material tracking, loss prevention, inventory optimization
Production – Cutting	Cutting Robot	Robotic software (FANUC, ABB, KUKA Sim)	Cutting steel bars and molds with high accuracy based on BIM model
Production – Printing	3D Printing (non-mass production)	Rhino & Grasshopper, Autodesk Fusion, 3D Slice Software	Fabrication of unique/custom components such as architectural façades, non-standard panels
Production – Assembly	Robotic Assembly Line	PLC-based Control System, SCADA	Automated assembly of rebar, formwork, and material setup before curing
Production – Curing	Curing Robot	Automated temperature & humidity control (custom SCADA)	Precision control of curing environment to ensure optimal concrete quality
Production Monitoring	ERP (integrated with MES)	SAP Manufacturing Execution System, Oracle MES	Real-time monitoring of production status, daily output, and technical issues
Quality Control	Digital Twin & Computer Vision	AI QC software, Digital Twin Analyzer	Comparing physical results with digital models, defect detection, deviation tolerance
Internal Logistics	Autonomous Crane Navigation	Crane Pathing Software, AI	Automatically lifting and transferring precast elements to shipping area
Delivery to Site	RFID & ERP Integration	Fleet Tracking System, ERP Logistics Module	Ensuring real-time scheduling and logistics status, improving delivery efficiency
On-Site Installation	BIM & AR / MR Viewer	Trimble XR10, Microsoft HoloLens, Fuzor	Precise component positioning on-site using digital guidance
Feedback Loop	IoT Monitoring & AI Analytics	Power BI, Grafana, custom AI dashboard	Collecting post-installation performance data to improve future design and production

Strategic Discussion

The results of automation technology mapping in Table 1 show that a strategic approach to automation in the precast concrete industry cannot be done partially. An integrative framework is needed that unites the digitalization process from upstream to downstream. The use of BIM at the design stage, for example, not only functions as a visualization tool, but also as the main data source that flows into the ERP system and Digital Twin platform for product validation.

Tabel 2. Strategic Benefits of Key Technologies in Precast Concrete Manufacturing.

Technology	Primary Function	Strategic Benefit
Building Information Modeling (BIM)	Design coordination and data integration	Enhances design accuracy and reduces rework
ERP System	Production planning and resource control	Improves efficiency, material flow, and project cost control
RFID	Inventory and logistics tracking	Enables real-time visibility and minimizes material loss
Robotics	Automation of physical tasks (cutting, handling)	Increases precision, speed, and labor efficiency
Digital Twin	Simulation and virtual inspection	Enables predictive quality control and scenario planning
3D Printing	Customized element production	Allows design flexibility and fast prototyping
IoT Sensors	Monitoring temperature, humidity, or equipment	Supports real-time condition tracking and maintenance
Autonomous	Automatic lifting	Reduces manual labor

Technology	Primary Function	Strategic Benefit
Crane	and positioning	and improves safety in handling operations
AI Analytics	Post-process evaluation and optimization	Enables continuous improvement through performance insights

Table 2 summarizes key technologies and their corresponding benefits in improving operational and decision-making efficiency**.** Furthermore, the ERP system plays a role in integrating cross-functional data—from supply chain, production monitoring, to quality management. This system enables real-time data-based decision making, while minimizing process inefficiencies.

Robotic and sensory technologies such as robotic arms, curing robots, and autonomous cranes increase precision and speed in the physical production stage. Meanwhile, the use of Digital Twin and laser scanners in quality control allows early detection of product non-conformities before being sent to field projects.

The use of 3D concrete printing offers great opportunities in producing non-standard or complex components that are uneconomical when done conventionally. This opens up new potential in modular design, time efficiency, and reduction of production waste.

Fig. 1 Strategic Framework Precast Production

From a strategic perspective, the adoption of this technology still faces several challenges, starting from High initial investment, especially for robots and advanced ERP systems. Limited human resources who understand cross-digital system integration and Readiness of data and network infrastructure, especially in the application of sensors and real-time communication.

However, with gradual planning and a clear implementation roadmap, the transformation towards automation-based precast manufacturing can be a long-term solution in increasing the competitiveness of the construction industry, both in terms of cost efficiency, product quality, and operational sustainability.

Strategic Discussion and Research Gap

Although automation has been increasingly adopted in precast concrete manufacturing, its implementation remains largely fragmented. Many companies integrate specific technologies such as Building Information Modeling (BIM), Enterprise Resource Planning (ERP), or Internet of Things (IoT) in isolated processes, without a unified data architecture or workflow. This disconnection reduces the potential efficiency and visibility that a fully integrated automation system can offer.

One of the most significant innovation opportunities lies in establishing end-to-end digital connectivity across systems. The integration of BIM with ERP allows design data to be seamlessly linked to procurement and scheduling. When coupled with IoT-based monitoring and Digital Twin simulations, the entire production process—from design to quality control—can be tracked, validated, and optimized in real-time. This creates a closed-loop control environment, where feedback from the field or production floor informs upstream decisions on design and planning.

In contrast, traditional precast production workflows rely heavily on manual labor, paper-based documentation, and visual inspections, making them

vulnerable to human error, inefficiency, and lack of traceability. Without digital tools, design revisions are slow to propagate, inventory and logistics are difficult to monitor, and quality assurance often lacks objective verification.

Despite the growing body of research on digital construction technologies, there is a noticeable lack of studies that provide a comprehensive and structured framework mapping these technologies across the full precast production cycle. This gap highlights the need for strategic guidance to help stakeholders understand where and how automation technologies can be adopted incrementally. The framework developed in this study seeks to fill that void by offering a practical, stage-based roadmap for automation integration that aligns with both operational requirements and the broader goals of Industry 4.0 transformation in construction.

CONCLUSIONS

This research has produced a strategic framework for the integration of automation technology in the precast concrete production process. The framework systematically maps the stages of precast production from design to installation in the field, and links them to key technologies such as BIM, ERP, IoT, RFID, robotics, Digital Twin, and 3D Printing.

Through this approach, the precast production process can be transformed to be more efficient, precise, and digitally documented. This framework also shows the importance of connectivity between digital systems and integrated data management to support decision making based on real-time information.

The main contribution of this research lies in the preparation of a comprehensive precast production cycle-based technology mapping, which until now has rarely been discussed in full in the literature. This framework can be used as a basis for developing an automation roadmap by precast construction companies that are transforming towards industry 4.0.

Further research can be directed at validating this framework in a real industrial context, including case studies of the implementation of part or all of the system in a real precast production environment.

ACKNOWLEDGMENTS

The author would like to thank University of Indonesia and University of Singaperbangsa Karawang for providing support in the preparation of this article. This research was funded by the Agency for the Assessment and Application of Technology (BPPT) and the Indonesia Endowment Fund for Education (LPDP), Ministry of Finance of the Republic of Indonesia. Gratitude is also expressed to the parties who have provided input, data, and relevant references, so that this research can be completed properly.

REFERENCES

[1] N. Rane, S. Choudhary, and J. Rane, “A New Era of Automation in the Construction Industry: Implementing Leading-Edge Generative Artificial Intelligence, such as ChatGPT or Bard,” SSRN Electron. J., 2024, doi: 10.2139/ssrn.4681676.

[2] E. Crisan, “The digital transformation of the construction industry : a review,” no. November, 2024, doi: 10.1108/IRJMS-04-2024-0035.

[3] A. Al-Bazi and N. Dawood, “Simulation-based genetic algorithms for construction supply chain management: Off-site precast concrete production as a case study,” OR Insight, vol. 25, no. 3, pp. 165–184, 2012, doi: 10.1057/ori.2012.7.

[4] R. W. M. Wong and B. P. Y. Loo, “Sustainability implications of using precast concrete in construction: An in-depth project-level analysis spanning two decades,” J. Clean. Prod., vol. 378, no. May, 2022, doi: 10.1016/j.jclepro.2022.134486.

[5] Y. Shao et al., “Comprehensive Utilization of Industry By-Products in Precast Concrete: A Critical Review from the Perspective of Physicochemical Characteristics of Solid Waste and Steam Curing Conditions,” Materials (Basel)., vol. 17, no. 19, 2024, doi: 10.3390/ma17194702.

[6] G. Sua-Iam and N. Makul, “Potential Future Direction of The Sustainable Production of Precast Concrete with Recycled Concrete Aggregate: A Critical Review,” Eng. Sci., vol. 28, 2024, doi: 10.30919/es1075.

[7] C. Roumeliotis, M. Dasygenis, V. Lazaridis, and M. Dossis, “Blockchain and Digital Twins in Smart Industry 4.0: The Use Case of Supply Chain-A Review of Integration Techniques and Applications,” Designs, vol. 8, no. 6, pp. 1–30, 2024, doi: 10.3390/designs8060105.

[8] S. Chauhan, R. Singh, A. Gehlot, S. V. Akram, B. Twala, and N. Priyadarshi, “Enabling Technologies : A Sustainable Perspective,” 2023.

[9] S. Reichenbach and B. Kromoser, “State of practice of automation in precast concrete production,” J. Build. Eng., vol. 43, no. March, 2021, doi: 10.1016/j.jobe.2021.102527.

[10] M. I. Khan et al., “Integrating industry 4.0 for enhanced sustainability: Pathways and prospects,” Sustain. Prod. Consum., vol. 54, no. December 2024, pp. 149–189, 2025, doi: 10.1016/j.spc.2024.12.012.

[11] D. F. R. Parracho et al., “Modular Construction in the Digital Age: A Systematic Review on

Smart and Sustainable Innovations," Buildings, vol. 15, no. 5, 2025, doi: 10.3390/buildings15050765.
[12] S. Reichenbach and B. Kromoser, "State of practice of automation in precast concrete production," J. Build. Eng., vol. 43, no. November, p. 102527, 2021, doi: 10.1016/j.jobe.2021.102527.
[13] M. Soori, F. K. G. Jough, R. Dastres, and B. Arezoo, "Additive manufacturing modification by artificial intelligence, machine learning, and deep learning: A review," Addit. Manuf. Front., vol. 4, no. 2, 2025, doi: 10.1016/j.amf.2025.200198.
[14] L. Xu, Y. Zou, Y. Lu, and A. Chang-Richards, "Automation in manufacturing and assembly of industrialised construction," Autom. Constr., vol. 170, no. December 2024, 2025, doi: 10.1016/j.autcon.2024.105945.
[15] C. Chen, T. Phang, and L. K. Tiong, "Planning semi-automated precast production using GA," Int. J. Ind. Constr., vol. 1, no. 1, pp. 48–63, 2020, doi: 10.29173/ijic215.
[16] H. Omrany, K. M. Al-Obaidi, A. Husain, and A. Ghaffarianhoseini, "Digital Twins in the Construction Industry: A Comprehensive Review of Current Implementations, Enabling Technologies, and Future Directions," Sustain., vol. 15, no. 14, pp. 1–26, 2023, doi: 10.3390/su151410908.
[17] L. Ai and P. Ziehl, "Advances in digital twin technology in industry : A review of applications , Advances in digital twin technology in industry : A review of applications , challenges , and standardization," no. May, 2025.
[18] C. Chen and R. Tiong, "Solutions to Address the Low-Capacity Utilization Issue in Singapore's Precast Industry," Inf., vol. 15, no. 8, pp. 1–19, 2024, doi: 10.3390/info15080458.
[19] L. Wang, Y. Zhao, and X. Yin, "Precast production scheduling in off-site construction: Mainstream contents and optimization perspective," J. Clean. Prod., vol. 405, no. November 2022, 2023, doi: 10.1016/j.jclepro.2023.137054.
[20] J. H. Chen, M. C. Su, S. Lin, H. W. Tai, and S. C. Hsu, "Evaluating Complexity of Construction Precast Component: Empirical Study in Taiwan," J. Civ. Eng. Manag., vol. 31, no. 3, pp. 266–280, 2025, doi: 10.3846/jcem.2025.23323.
[21] X. Wang and Q. Tang, "Research on detailed design methods of precast components in prefabricated buildings based on BIM technology," Heliyon, vol. 10, no. 16, 2024, doi: 0.1016/j.heliyon.2024.e35922.
[22] J. Cai, X. Wang, J. Shi, X. Xie, Y. Feng, and Y. Wu, "Research on a Data-Driven Modeling Method for Precast Concrete Balcony Components," Buildings, vol. 14, no. 1, pp. 1–21, 2024, doi: 10.3390/buildings14010096.
[23] M. A. T. Dvaipayana, I. K. Sriwana, and Y. Prambudia, "Design of supply chain risk mitigation system using house of risk and Fuzzy AHP methods in precast concrete," Sinergi (Indonesia), vol. 28, no. 1, pp. 93–102, 2024, doi: 10.22441/sinergi.2024.1.010.
[24] Y. Zou, Q. Gao, and S. Wang, "Optimization of the Stacking Plans for Precast Concrete Slab Based on Assembly Sequence," Buildings, vol. 12, no. 10, 2022, doi: 10.3390/buildings12101538.
[25] C. Ciacci and F. Bazzocchi, "Retrofitting of the Italian precast industrial building stock. LCA analysis as decision-making tool," J. Clean. Prod., vol. 478, no. October, 2024, doi: 10.1016/j.jclepro.2024.143933.
[26] K. Li, V. J. L. Gan, M. Li, M. Y. Gao, R. L. K. Tiong, and Y. Yang, "Automated generative design and prefabrication of precast buildings using integrated BIM and graph convolutional neural network," Dev. Built Environ., vol. 18, no. December 2023, 2024, doi: 10.1016/j.dibe.2024.100418.
[27] C. Zhang, X. Zhou, C. Xu, Z. Wu, J. Liu, and H. Qi, "Automatic Generation of Precast Concrete Component Fabrication Drawings Based on BIM and Multi-Agent Reinforcement Learning," Buildings, vol. 15, no. 2, 2025, doi: 10.3390/buildings15020284.
[28] M. Senthilvel, K. Varghese, and N. Ramesh Babu, "Building Information Modeling for Precast Construction: A Review of Research and Practice," Constr. Res. Congr. 2016 Old New Constr. Technol. Converg. Hist. San Juan - Proc. 2016 Constr. Res. Congr. CRC 2016, no. May, pp. 2250–2259, 2016, doi: 10.1061/9780784479827.224.
[29] M. Sami, U. Rehman, and M. T. Shafiq, "Automated Computer Vision-Based Construction Progress Monitoring : A Systematic Review," Buildings, pp. 1–32, 2022.
[30] A. Pal, J. J. Lin, S. H. Hsieh, and M. Golparvar-Fard, "Automated vision-based construction progress monitoring in built environment through digital twin," Dev. Built Environ., vol. 16, no. June, 2023, doi: 10.1016/j.dibe.2023.100247.

Copyright © Int. J. of GEOMATE All rights reserved, including making copies, unless permission is obtained from the copyright proprietors.

15th Int. Conf. on Geotechnique, Construction Materials & Environment,
Kyoto, Japan, 11-13 November 2025, ISBN 978-4-909106124 C3051

CHARACTERIZING pH DEPENDENCE OF ARSENIC ADSORPTION AND DESORPTION FOR LATERITE GRAINS IN VIETNAM

Akihiro Matsuno[1], Tessin Fujisaki[2], Kengo Nakamura[2]and Ken Kawamoto[2]

[1] Faculty of Geo-Environmental Science, RISSHO University, Japan;
[2] Graduate School of Science and Engineering, Saitama University, Japan;

ABSTRACT

Arsenic contamination in groundwater has been reported in lowland areas such as Red River Delta and Mekong River Delta in Vietnam, and it is required to apply a low-cost and feasible arsenic-contaminated groundwater treatment technology by using local available materials. In this study, we focused on Vietnam laterite that is rich in metal oxides/hydroxides as an easy available adsorbent for developing the low-cost groundwater treatment system. The surface of metal oxides/hydroxides can be expected to form surface complexes with arsenic ion in water and to promote the arsenic removal from arsenic-contaminated groundwater. Several studies have examined the arsenic adsorption characteristics of Vietnam laterite, on the other hand, the combined studies of arsenic adsorption and desorption are limited. In this study, therefore, we evaluated the effect of pH on the arsenic adsorption and desorption characteristics for raw laterite grains (RL) and thermal-treated laterite grains (TTL) using a series of batch experiments in the laboratory. Results showed that the maximum arsenic adsorption capacities became 3.65 mg/g for RL and 6.28 mg/g for TTL at initial solution pH=2.0. The maximum desorption efficiencies became 16.4% for RL and 26.6% for TTL at pH=8.0. Based on the analysis of adsorption isotherms, it was implied that the adsorption process was mainly controlled by the multilayer adsorption for both RL and TTL. In addition, the adsorbed arsenic was hardly desorbed at low pH condition but was desorbed to a certain extent at high pH condition.

Keywords: Laterite, Arsenic, Adsorption, Desorption, Batch test, Vietnam

INTRODUCTION

Solid arsenic is widely distributed in nature and can leach into groundwater through natural processes and anthropogenic activities [1]. For example, the risk of drinking groundwater with arsenic concentrations of 10 μg/L is considerable, with approximately 45 million people in Bangladesh at high risk, with arsenic-related mortality reported to be 1 in 18 adult deaths [2].That is why achieving compliance with the maximum permissible limit of 10 μg/L requires implementing measures to limit the sources of arsenic contamination and utilizing highly efficient purification technologies.

There is a river called Red River from the fact that the water is red due to the iron oxide contained in it. In the Red River Delta, the presence of arsenic in groundwater was first discovered in Hanoi in 1998, with a maximum concentration of 3050 μg/L (average of 127 μg/L) [3]. Other locations in the Red River Delta provinces of Hanoi, Ha Nam, Ha Tay, and Hung Yen were observed as areas of high arsenic contamination, close to 890 μg/L [4]. The arsenic concentration in some areas of both deltas exceeds the permissible limit of 10 μg/L. In these areas, arsenic-contaminated groundwater is used as a freshwater source for domestic water and agricultural activities, so arsenic contamination in groundwater is a serious problem [5].

Currently, methods used to treat arsenic include ion exchange, adsorption, phytoremediation, chemical precipitation, electrokinetic, and electrocoagulation. Although these methods help remove arsenic from soil and water, each has drawbacks in terms of cost and efficiency. The selection of an appropriate arsenic treatment method is determined by various factors, including limitations on soil and water treatment technologies, requirements of local and national authorities, the country's stage of development, and regional strategies regarding arsenic levels in industrial and water systems [6].

Among the techniques for treating arsenic in water, adsorption is efficient and cost-effective, depending on the adsorbent used. It also does not require advanced technology or large amounts of electricity, making it suitable for practical use in developing countries. Adsorption has shown a high quantitative efficiency of over 95% in the removal of both As(III) and As(V) [7]. The effectiveness of this technique relies on a separation process based on van der Waals forces and electrostatic attraction between adsorbed molecules [8]. Adsorbents used for arsenic include kaolinite [9], zeolite [10], iron oxide [11], iron oxide-coated cement [12], activated carbon [13], lightweight cellular concrete [10]. The efficiency of arsenic adsorption is influenced by various factors, such as exposure period, pH conditions, presence of

other elements, adsorbent dosage, initial arsenic concentration, and temperature [14]. Among them, pH is considered a very influential parameter in the arsenic removal process since it determines the predominant chemical species in the water.

In this study, we focused on soil called laterite as an arsenic adsorbent. Soil composed of iron and aluminum oxides, kaolin, etc. is generally called laterite [15]. Laterite is also used in Southeast Asian architecture and is widely used as a building stone. Laterite is rich in active charge carriers on the surface, which are expected to promote anionic metal adsorption by forming surface complexes. Arsenic adsorption is a chemical and physical adsorption phenomenon that occurs on the hydroxyl and acid groups on the surface of iron and aluminum, the main components of laterite [16,17].

The treated laterite that had been chemically treated with hydrochloric acid and sodium hydroxide was used as an arsenic adsorbent [16]. The maximum Langmuir adsorption capacity of the treated laterite for As (V) and As (III) was 24.1±4.0 and 8.0±1.4 mg/g, respectively, which was approximately 30 − 40 times higher than the arsenic adsorption capacity of raw laterite. Other studies have also shown that the adsorption capacity of laterite increases when it is subjected to thermal or chemical treatment [18,19,20].

As mentioned in the previous section, numerous studies have focused on laterite and treated laterite as arsenic adsorbents, with many publications on the adsorption process. However, there are few studies on the adsorption and desorption processes of arsenic adsorbed on laterite, which is an essential characteristic of the water treatment process. Therefore, it is necessary to evaluate its characteristics. Since previous studies have found that the adsorption process is affected by pH, likely, the desorption process is also affected by pH at the same time.

MATERIALS AND METHODS

Granular laterite was used as the sample in this study. Laterite, an industrial by-product from Vietnam, was crushed and sieved to obtain samples with particle sizes of 0.25-0.60 mm. Previous study has shown that heat treatment of laterite increases its arsenic adsorption capacity (Sanou et al., 2020). Laterite was heated in a muffle furnace at 500°C for 1 hour to obtain thermal-treated laterite (TTL), which was used as the adsorbent. In this study, the laterite that was not thermal-treated is referred to as raw laterite (RL) to distinguish it from TTL.

Table 1 shows the measured values of each physical property. No significant difference was observed between RL and TTL in specific gravity and SSA. Table 2 shows the metal oxide ratios measured by wavelength dispersive XRF and the element ratio measured by SEM-EDS.

Arsenic solutions for adsorption tests were prepared by dissolving disodium hydrogen arsenate heptahydrate ($Na_2HAsO_4 \cdot 7H_2O$: Fujifilm Wako Pure Chemical Industries, Ltd.) in deionized water.

Table 1 Physical properties of RL and TTL

Items	Particle size (mm)	Specific Gravity (g/cm^3)	AD (%)	pH	SSA (m^2/g)
RL	0.25-0.6	2.90	2.0	4.3	53.2
TTL	0.25-0.6	2.96	2.6	5.4	52.1

Note: AD is water content of Air dry, SSA is Specific Surface Area.

Table 2 Chemical properties of RL and TTL

Items	Metal oxide (%)			Element ratio (%)		
	SiO_2	Fe_2O_3	Al_2O_3	Si	Fe	Al
RL	33.2	22.2	28.1	12.9	9.9	16.0
TTL	38.8	20.7	29.7	17.1	4.9	20.4

The mass of disodium hydrogen arsenate heptahydrate was adjusted so that the arsenic concentrations were 50, 100, 250, 500, 750, and 1000 mg/L. After that, the pH was adjusted by mixing the arsenic solution with nitric acid or sodium hydroxide solution, resulting in a pH of 2.0, 5.0, or 8.0 for each concentration. In addition, for the liquid to be used in the desorption test, deionized water containing no arsenic was mixed with nitric acid or sodium hydroxide solution to adjust the pH to 2.0, 5.0, or 8.0.

The adsorption test was carried out according to the standard batch method of the Organization for Economic Co-operation and Development [21]. In the adsorption test, 30 mL of arsenic solution and 3 g of adsorbent (liquid-solid ratio 10) were placed in the same centrifuge tube and shaken horizontally at 20°C and 100 rpm for 24 hours using a shaker (MMS-310 Multishaker, EYELA Tokyo Rikakikai Co., Ltd., Japan). Three centrifuge tubes were prepared for each condition. The solution was then centrifuged at 8000 rpm for 15 minutes (LCX-100, TOMY, Japan) and filtered through the 0.22 μm membrane filter to prepare the test solution. In the desorption test, the adsorbent from the adsorption test and deionized water with the same pH as the arsenic solution used in the adsorption test were placed in the same centrifuge tube and shaken horizontally at 20°C and 100 rpm for 24 hours, with a liquid-solid ratio of 10. The solution was then centrifuged and filtered to prepare the test solution. The pH and EC were measured before, after, and after the adsorption test. The test liquid was also analyzed with an atomic absorption spectrophotometer (AA-6200, Shimadzu Corporation, Japan) to measure the concentrations of iron, aluminum, and calcium along with arsenic. The atomic absorption spectrophotometer atomizes the

test liquid at high temperature, irradiates it with light, and measures the absorption spectrum to quantify the elements in the test liquid. The concentration range of the standard solution in the atomic absorption spectrophotometer is 0-20 mg/L.

RESULTS AND DISCUSSION

The Freundlich equation shown in Equation (1) and the Langmuir equation shown in Equation (2) were used to prepare the adsorption isotherm.

$$\text{Log } Q_e = \text{Log } K_f + (1/n)\text{Log } C_e \quad (1)$$

where Q_e is the amount of arsenic adsorbed per adsorbent at equilibrium (mg/g), K_f is the Freundlich adsorption capacity (L/g), $1/n$ is the adsorption strength and C_e is the equilibrium concentration of arsenic (mg/L).

$$C_e/Q_e = 1/bQ_m + C_e/Q_m \quad (2)$$

where C_e is the equilibrium concentration of arsenic (mg/L), Q_e is the amount of adsorption per adsorbent at equilibrium (mg/g), b is the Langmuir constant (g/L) representing the binding strength, and Q_m is the maximum adsorption capacity (mg/g).

These equations are initially suitable for adsorption by homogeneous chemicals. Since soils such as laterite exist in the natural environment and are not homogeneous, neither equation is entirely suitable. However, it is important to determine which adsorption isotherm is suitable for the adsorption in this study in order to clarify the adsorption mechanism. In addition, the adsorption isotherm enables a quantitative evaluation of the adsorption capacity, which facilitates comparison with adsorbents used in other studies. The adsorption isotherm curves for each adsorbent are shown in Figs. 1. The amount of adsorption was calculated using Eq. (3).

$$M_a = (C_i - C_e) \times (V/M) \quad (3)$$

where M_a is the amount of arsenic adsorption (mg/g), V is absorbent volume and M is Absorbent amount. Tables 3 and 4 show the parameters of the Freundlich and Langmuir equations obtained from each adsorption isotherm. From Fig. 1 and Tables 3 and 4, it can be seen that the arsenic adsorption capacity of heat-treated laterite was greater than that of natural laterite when compared under the same pH conditions. In Table 3, for example, the values of $1/n$ for RL was 0.296 at pH 2.0 and that was 0.485 for TTL, indicating the improvement of adsorption capacity by heat treatment. Comparing the determination coefficients of the Freundlich equation and the Langmuir equation (R^2 in Tables 3 and 4), it was found that the Freundlich equation was larger overall. Comparing the average value of the actual adsorption amount and its error bars plotted in Fig. 1, it can be seen that the Freundlich model fits better. From this, the Freundlich equation is more suitable for expressing adsorption in this study.

Table 3 Parameters of Freundlich equation

	RL			TTL		
pH	2.0	5.0	8.0	2.0	5.0	8.0
$1/n$	0.296	0.298	0.268	0.485	0.109	0.365
R^2	0.876	0.741	0.838	0.883	0.181	0.948

Table 4 Parameters of Langmuir equation

	RL			TTL		
pH	2.0	5.0	8.0	2.0	5.0	8.0
Q_m	3.65	3.61	2.31	6.28	4.14	2.34
R^2	0.834	0.808	0.450	0.975	0.380	0.837

On the other hand, the parameters of the Langmuir equation obtained in this study were compared with those of previous studies, and it was found that the Q_m of TTL at pH 2.0 is larger than those of other studies that used kaolinite [9], zeolite [10], activated carbon [13], and iron oxide-coated cement [12] to adsorb As, making it a superior adsorbent.

In this study, desorption tests were conducted three times in total, and the formulas [22] for calculating the arsenic desorption rate on a weight basis from the arsenic concentration after the desorption tests are given by Eqs. (4) and (5).

$$M_d = C_d \times (V/M) \quad (4)$$

where M_d is the amount of arsenic desorbed (mg), Arsenic equilibrium concentration C_d (mg/L) after desorption test.

$$R_d = M_d/M_a \times 100 \quad (5)$$

where R_d is the arsenic desorption rate (%). In this research, if arsenic is completely desorbed after three times desorption tests, the sum of the three R_d will be 100%.

Figures 2 (a) and (b) showed the stacked results of the three R_d for each sample. These results show that the arsenic concentration is highest after the first desorption test, and that, although there is some variation, the arsenic concentration was the highest at pH=8.0, followed by pH 5.0 and 2.0. The maximum desorption efficiencies became 16.4% for RL and 26.6% for TTL at pH 8.0. Also, looking at each sample, it can be seen that the R_d is high for the first time, and the R_d for the second and third times are much lower than that for the first time. This indicated that desorption caused by shaking is almost complete within the first 24 hours and that little desorption occurs with subsequent shaking.

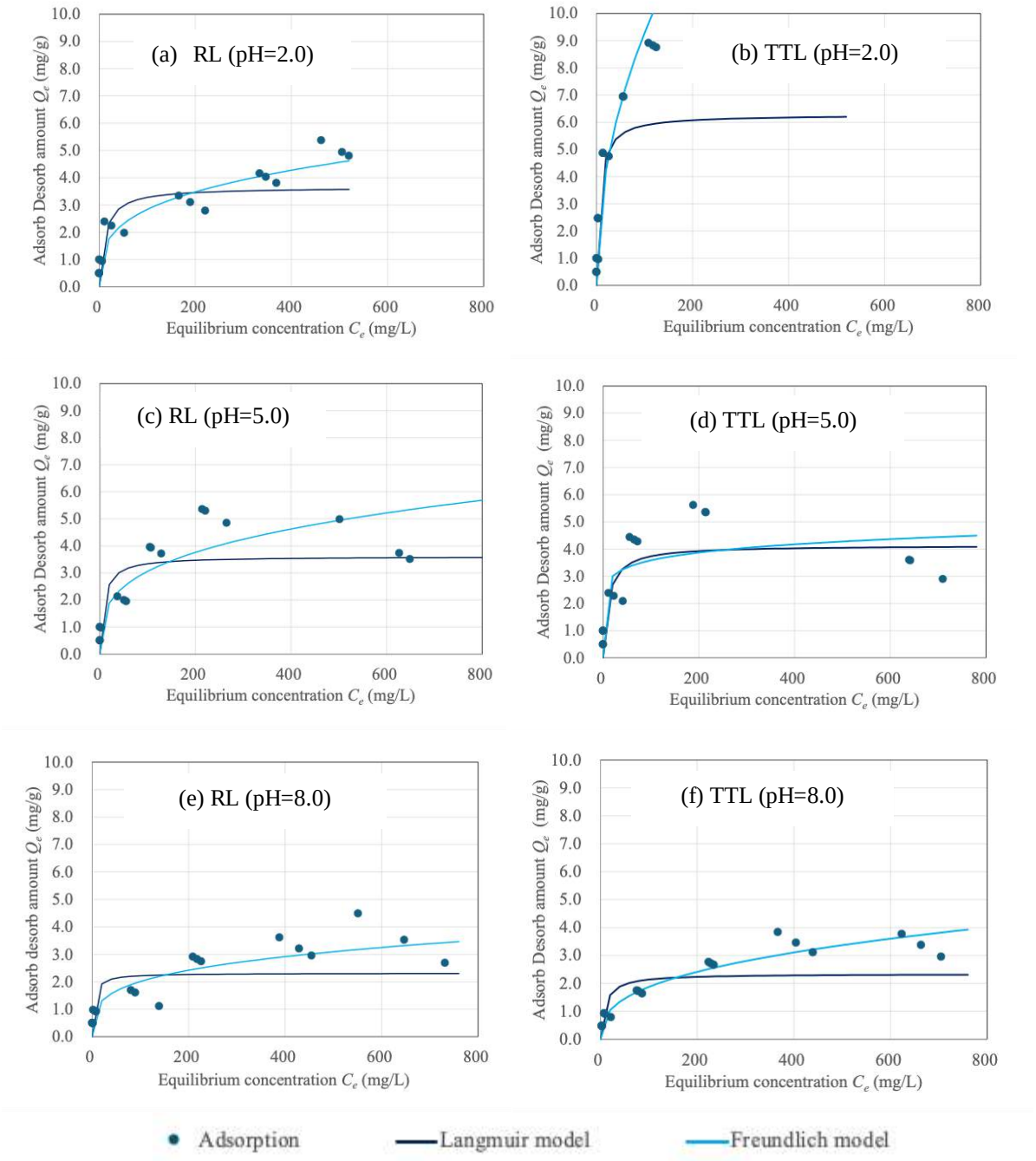

Fig.1 Adsorption isotherm curves for RL: (a) pH=2.0 (c) pH=5.0 (e) pH=8.0 and TTL: (b) pH=2.0 (d) pH=5.0 (f) pH=8.0).

In addition, when comparing the results for different initial pH values under the same initial arsenic concentration, the order of R_d was pH=8.0, pH=5.0, and pH=2.0. This is the opposite of the adsorption results (Fig.1). It was shown that adsorption on laterite occurs more easily in an acidic environment. While desorption occurred more easily in an alkaline environment, implying that more negatively charged surface areas appeared on the laterite at higher pH. The results of the desorption test also showed the larger variation in arsenic concentration at initial pH 5.0 than those at initial pH 2.0 or 8.0. This resulted in the maximum R_d was about 25% under the conditions of the desorption test in this study. Therefore, arsenic could not be completely desorbed. This shows that even when arsenic is used as an adsorbent, it can continue to be used as an adsorbent while retaining a certain amount of arsenic.

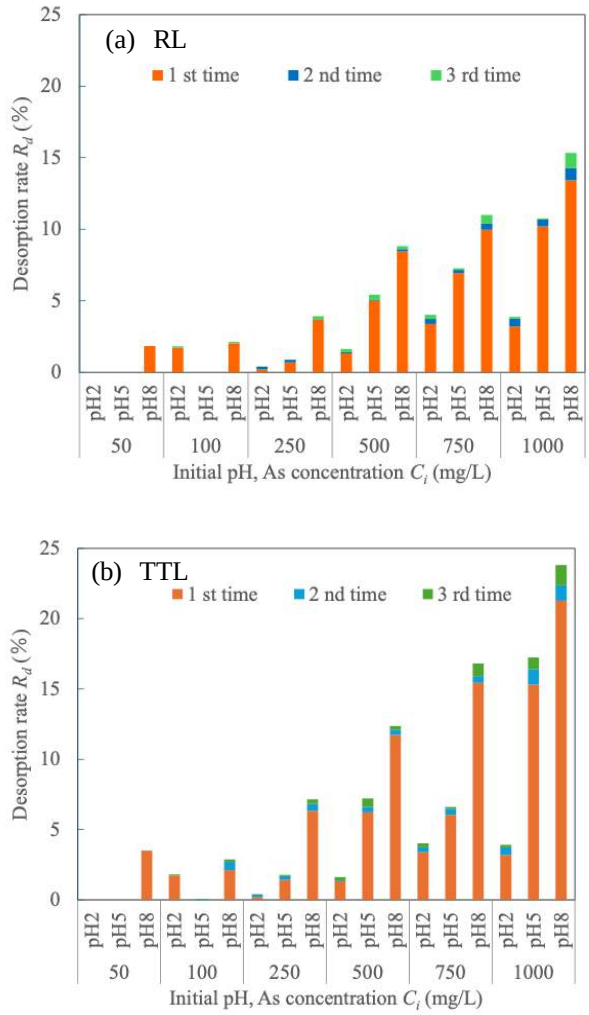

Fig.2 Adsorption isotherm curves for (a) RL and (b) TTL (pH=2.0, 5.0, 8.0)

CONCLUSIONS

In the batch test, the arsenic adsorption and desorption characteristics of RL and TTL were evaluated. The adsorption test showed that the laterite had more adsorption sites and stronger arsenic adsorption capacity due to heat treatment. RL and TTL are excellent arsenic adsorbents, and TTL in particular had a higher maximum adsorption amount than other adsorbents. The tested results showed that the maximum arsenic adsorption capacities became 3.65 mg/g for RL and 6.28 mg/g for TTL at initial solution of pH 2.0. The adsorption amount increased in the order of initial pH 2.0, 5.0, and 8.0. This is thought to be because laterite has a positive surface charge in an acidic environment, which attracts arsenic anions, but in an alkaline environment, a negative surface charge appears and repels arsenic anions. OH- in the solution may inhibit arsenic adsorption. The desorption test showed that the desorption rate was particularly low when the initial arsenic concentration was low, and that laterite had strong arsenic adsorption. The desorption amount increased in the order of initial pH 8.0, 5.0, and 2.0. This is thought to be because the negative surface charge of laterite in an alkaline environment repels the adsorbed arsenic.

ACKNOWLEDGMENTS

This research was supported by the project of Japan Science and Technology Agency (JST) – Japan International Cooperation Agency (JICA) on Science and Technology Research Partnership for Sustainable Development (SATREPS) (No. JPMJSA1701) and the research grant from Saitama University Strategic Research Center.

REFERENCES

[1] Smedley, P. L., and Kinniburgh, D. G. A review of the source, behaviour and distribution of arsenic in natural waters. Applied Geochemistry,Vol. 17, 5, 2002, pp.517-568.

[2] Zheng, Y. Global solutions to a silent poison. Science,Vol. 368, 6493, 2020, pp.818-819.

[3] Berg, M., Tran, H. C., Nguyen, T. C., Pham, H. V., Schertenleib, R., and Giger, W. Arsenic Contamination of Groundwater and Drinking Water in Vietnam: A Human Health Threat. Environmental Science & Technology,Vol. 35, 13, 2001, pp.2621-2626.

[4] Pham, L. H., Nguyen, H. T., Van Tran, C., Nguyen, H. M., Nguyen, T. H., and Tu, M. B. Arsenic and other trace elements in groundwater and human urine in Ha Nam province, the Northern Vietnam: contamination characteristics and risk assessment. Environ Geochem Health,Vol. 39, 3, 2017, pp.517-529.

[5] Nhu Nguyet, P., Luu, T. L., Ai Le, N., Thi Kim Ngan, N., and Thi Huyen Trang, N. Groundwater arsenic pollution in Vietnam: Current opinion on the mobilization and remediation. Current Opinion in Environmental Science & Health,Vol. 44, 2025.

[6] Alka, S., Shahir, S., Ibrahim, N., Ndejiko, M. J., Vo, D.-V. N., and Manan, F. A. Arsenic removal technologies and future trends: A mini review. Journal of Cleaner Production,Vol. 278, 2021.

[7] Kumar, R., Patel, M., Singh, P., Bundschuh, J., Pittman, C. U., Jr., Trakal, L., and Mohan, D. Emerging technologies for arsenic removal from drinking water in rural and peri-urban areas: Methods, experience from, and options for Latin America. Sci Total Environ,Vol. 694, 2019, pp.133427.

[8] Maitlo, H. A., Kim, J. H., Kim, K.-H., Park, J. Y., and Khan, A. Metal-air fuel cell electrocoagulation techniques for the treatment of arsenic in water. Journal of Cleaner Production,Vol. 207, 2019, pp.67-84.

[9] Mohapatra, D., Mishra, D., Chaudhury, G. R., and Das, R. P. Arsenic adsorption mechanism on clay minerals and its dependence on temperature. Korean Journal of Chemical Engineering,Vol. 24, 3, 2007, pp.426-430.

[10] Arachchillage Buddhika Priyadarshani, B., Gajanayaka Mudalige Pradeep, K., Akihiro, M., Takeshi, S., Tran Thi Viet, N., and Ken, K. Examination of crushed laterite brick for removal of chromium and arsenic from wastewater. GEOMATE Journal,Vol. 19, 74, 2020, pp.22-30.

[11] Zeng, H., Zhai, L., Qiao, T., Yu, Y., Zhang, J., and Li, D. Efficient removal of As(V) from aqueous media by magnetic nanoparticles prepared with Iron-containing water treatment residuals. Sci Rep,Vol. 10, 1, 2020, pp.9335.

[12] Kundu, S., and Gupta, A. Adsorptive removal of As(III) from aqueous solution using iron oxide coated cement (IOCC): Evaluation of kinetic, equilibrium and thermodynamic models. Separation and Purification Technology,Vol. 51, 2, 2006, pp.165-172.

[13] Dang, S. V., Kawasaki, J., Abella, L. C., Auresenia, J., Habaki, H., Gaspillo, P.-a. D., and Kosuge, H. Removal of arsenic from synthetic groundwater by adsorption using the combination of laterite and iron-modified activated carbon. Journal of Water and Environment Technology,Vol. 6, 1, 2008, pp.43-54.

[14] Sarkar, A., and Paul, B. The global menace of arsenic and its conventional remediation - A critical review. Chemosphere,Vol. 158, 2016, pp.37-49.

[15] Young, A. (1976). Tropical soils and soil survey.

[16] Maiti, A., Basu, J. K., and De, S. Development of a Treated Laterite for Arsenic Adsorption: Effects of Treatment Parameters. Industrial & Engineering Chemistry Research,Vol. 49, 10, 2010, pp.4873-4886.

[17] Phat, V. V., and Le Luu, T. Review on the removal of Arsenic in groundwater using laterite adsorbent. Current Opinion in Environmental Science & Health,Vol. 35, 2023.

[18] Sanou, Y., Balogoun, C. K., Tiendrebeogo, R., Kabore, R., Tchakala, I., and Pare, S. Physico-chemical and spectroscopic properties of two laterite soils for applications in arsenic water treatment. Inter. J. Multidisc. Res. Dev,Vol. 7, 5, 2020, pp.12-17.

[19] Sanou, Y., and Pare, S. Comparative study of adsorption capacity of two mixed materials for arsenic remediation. Journal of Environmental Treatment Techniques,Vol. 9, 3, 2021, pp.559-565.

[20] Nguyen, P. T. T., Yacouba, S., Pare, S., and Bui, H. M. Removal of Arsenic from Groundwater Using Lamdong Laterite as a Natural Adsorbent. Polish Journal of Environmental Studies,Vol. 29, 2, 2020, pp.1305-1314.

[21] Co-operation, O. f. E., and Development (2000). Test No. 106: Adsorption--Desorption Using a Batch Equilibrium Method, OECD publishing.

[22] Grigoras, C. G., Simion, A. I., and Favier, L. Exploration of Reactive Black 5 Dye Desorption from Composite Hydrogel Beads-Adsorbent Reusability, Kinetic and Equilibrium Isotherms. Gels,Vol. 9, 4, 2023.

Copyright © Int. J. of GEOMATE All rights reserved, including making copies, unless permission is obtained from the copyright proprietors.

GEOMATE 2026

Bangkok, Thailand

17-20 November 2026

- The "International Journal of GEOMATE" is a Scientific Journal of the GEOMATE International Society that encompasses a broad area in Geotechnique, Construction Materials, and Environment.
- The key objective of this Journal is to promote interdisciplinary research from various regions of the globe.
- The editorial board of the Journal is comprised of extensively qualified researchers, academicians, and scientists from Japan and other countries of the world.
- It is a peer-reviewed Journal that is published quarterly till 2015 and now monthly. All articles published in this Journal are available online.
- Contributors may download the manuscript preparation template for submitting the paper or contact the Editors-in-Chief. [editor@geomatejournal.com].